AD-A226 343

REPORT DOCUMENTATION PAGE

Form OMB No. .

Public reporting burden for this collection of information is estimated to average 1 hour per response, including the time for reviewing instructions, searching existing data sources, gathering and maintaining the data needed, and completing and reviewing the collection of information. Send comments regarding this burden estimate or any other aspect of this collection of information, including suggestions for reducing this burden to Washington Headquarters Services, Directorate for information Operations and Reports, 1215 Jefferson Davis Highway, Suite 1204, Arlington, VA 22202-4302, and to the Office of Management and Budget, Paperwork Reduction Project (0704-0188), Washington, DC 20503.

1. AGENCY USE ONLY (Leave blank)	2. REPORT DATE	3. REPORT TYPE AND DATES COVERED
	1990	Final 1 Oct 89 -30 Sep 90

4. TITLE AND SUBTITLE

Twelfth International Conference on Lasers and Applications

5. FUNDING NUMBERS

DAAL03-89-G-0124

6. AUTHOR(S)

Dennis G. Harris
T. M Shay

7. PERFORMING ORGANIZATION NAME(S) AND ADDRESS(ES)

Society for Optical and Quantum Electronics
P.O. Box 245
McLean, VA 22101

8. PERFORMING ORGANIZATION REPORT NUMBER

9. SPONSORING/MONITORING AGENCY NAME(S) AND ADDRESS(ES)

U. S. Army Research Office
P. O. Box 12211
Research Triangle Park, NC 27709-2211

10. SPONSORING/MONITORING AGENCY REPORT NUMBER

ARO 27385.1-PH-CF

11. SUPPLEMENTARY NOTES

The view, opinions and/or findings contained in this report are those of the author(s) and should not be construed as an official Department of the Army position, policy, or decision, unless so designated by other documentation.

12a. DISTRIBUTION/AVAILABILITY STATEMENT

Submitted for announcement only.

12b. DISTRIBUTION CODE

13. ABSTRACT (Maximum 200 words)

DTIC
ELECTE
AUG 30 1990
S B D

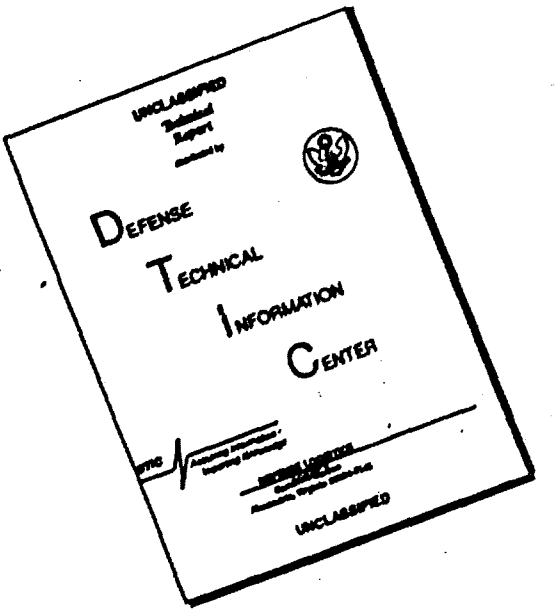
DISTRIBUTION STATEMENT A
Approved for public release;
Distribution Unlimited

14. SUBJECT TERMS	15. NUMBER OF PAGES
	16. PRICE CODE

17. SECURITY CLASSIFICATION OF REPORT	18. SECURITY CLASSIFICATION OF THIS PAGE	19. SECURITY CLASSIFICATION OF ABSTRACT	20. LIMITATION OF ABSTRACT
UNCLASSIFIED	UNCLASSIFIED	UNCLASSIFIED	UL

DTIC FILE COPY

DISCLAIMER NOTICE

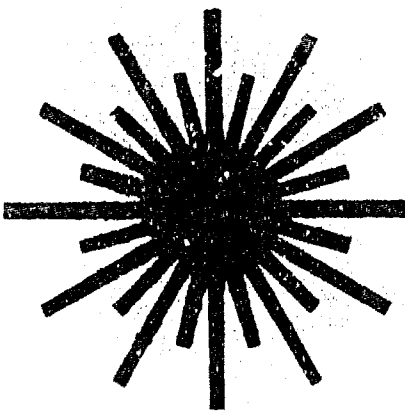


THIS DOCUMENT IS BEST QUALITY AVAILABLE. THE COPY FURNISHED TO DTIC CONTAINED A SIGNIFICANT NUMBER OF PAGES WHICH DO NOT REPRODUCE LEGIBLY.

ARO 21385.1-PH-

PROCEEDINGS

OF THE
INTERNATIONAL CONFERENCE
ON



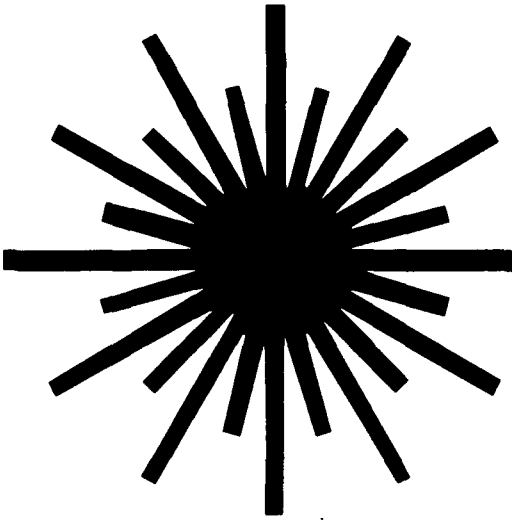
LASERS '89

BEST
AVAILABLE COPY

90 08 27 320

PROCEEDINGS

OF THE
INTERNATIONAL CONFERENCE
ON



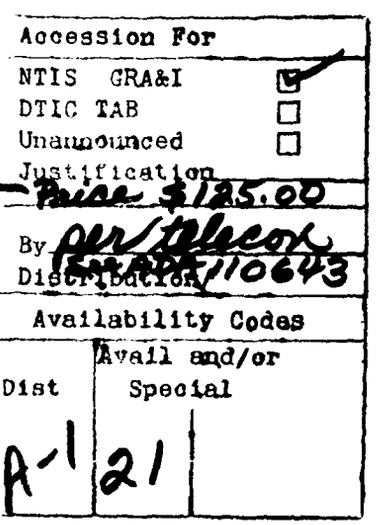
LASERS '89

NEW ORLEANS, LOUISIANA **DECEMBER 3-8, 1989**

D.G. Harris
and
T.M. Shay
Editors

CONFERENCE SPONSORED BY
THE SOCIETY FOR OPTICAL & QUANTUM ELECTRONICS

STS PRESS • McLEAN, VA • 1990



AVAILABLE FOR $125.00 from STS Press
P.O. Box 245, Mclean, VA 22101
TELECON 8/28/90 VG

Conference Organized By:
Society For Optical & Quantum Electronics
(A Non-Profit Organization)
P.O. Box 245
McLean, VA 22101
(703) 642-5835

First published in 1990 by STS Press, P.O. Box 177, McLean, VA 22101



© STS Press 1990

All rights reserved. No part of this publication may be reproduced, stored in a retrieval system or transmitted in any form or by any means, electronic, mechanical, photocopying, recording or otherwise, without the prior permission of STS Press.

ISSN 0190-4132

CONTENTS

FOREWORD XIV

CONFERENCE COMMITTEE XV

KEYNOTE ADDRESS

Plasma Lasers: Promises And Limitations 1
W. T. Silfvast (Invited)

XUV, X-RAY, AND GAMMA-RAY LASERS

Pulsed-Power Driven X-Ray Lasers: Fantasy Or Reality? 7
J. P. Apruzese and J. Davis (Plenary, Invited)

Lithium-Like Recombination Scheme For X-UV Lasers 13
P. Jaegle, G. Abdelatif, A. Carillon, P. Dhez, B. Gauthe, G. Jamelot, A. Klisnick, and J. P. Raucourt (Invited)

Sodium Z-Pinches For X-Ray Laser Research On The 6-TW Double-Eagle Generator 21
C. Deeney, T. Nash, R. R. Prasad, M. Krishnan, D. Hinshelwood and F. C. Young (Invited)

Small Scale Soft X-Ray Lasers; Applications To Microscopy 27
C. H. Skinner, D. S. DiCicco, D. Kim, D. Voorhees and S. Suckewer (Invited)

Analysis Of A Soft X-Ray Frequency Doubler 34
M. H. Muendel and Peter L. Hagelstein

Adiabatic Whisper-Gallery Mirrors For EUV And Soft X-Ray Laser Cavities 37
J. P. Braud

Basic Physics Studies For Novel X-Ray Laser Schemes Using Ultra-Short Laser Pulses 43
O. Willi, T. Afshar-rad, V. Barrow, J. Edwards and R. Smith (Invited)

The Mössbauer Effect In The 40-Sec First-Excited Nuclear Level Of ^{109}Ag 52
S. Rezaie-Serej, G. R. Hoy and R. D. Taylor

EXCIMER LASERS

Development Of KrF Lasers For Fusion 58
J. F. Figueira (Plenary, Invited)

Clinical Excimer Laser Angioplasty : The Italian Program 63
R. Pini, R. Salimbeni, M. Vannini and A. Guasti, V. Gallucci and R. Viligiardi (Invited)

Damping Of Acoustic Waves In A 1 kHz Repetition Rate XeCl Laser 69
M. L. Sentis, P. Canarelli, P. Delaporte, B. M. Forestier and B. L. Fontaine (Invited)

Compact Long-Pulse Excimer Lasers For Medical Applications 76
R. C. Sze

High Repetition Rate Excimer And CO_2 Tea Lasers 80
H. M. von Bergmann and P. H. Swart

Performance Of The Aurora KrF ICF Laser System 88
J. E. Jones, S. J. Czuchlewski, T. P. Turner, R. G. Watt, S. J. Thomas, D. A. Netz, C. R. Tallman, J. M. Mack and J. F. Figueira (Invited)

Energy Deposition Measurements For E-Beam Pumped Excimer Lasers 96
M. C. Gates, K. L. Robertson, P. C. Meixner, D. P. Greene and V. O. Romero

Absorption Experiments On Electron-Beam Pumped Rare Gases 102
A. W. McCown, E. A. Rose, B. J. Krohn, D. E. Hanson and S. J. Czuchlewski

Generation Of 400 FS Pulse In KRF Laser Amplifier With UV Saturable Absorber 110
H. Nishioka, H. Kuranishi, K. Ueda and H. Takuma

10 x 10 cm^2 Aperture 1 Hz Repetition Rate X-Ray Preionized-Discharge Pumped KrF Excimer Laser 116
H. Mizoguchi, A. Endoh, J. Jethwa and F. P. Schafer

Condensed Phase Rare Gas Halide Exciplex Lasers 121
V. A. Apkarian (Invited)

Wideband Tuning Experiments With An Injection-Controlled XEF (C→A) Laser 127
W. L. Wilson, C. B. Dane, S. Yamaguchi, T. Hofmann, R. Sauerbrey and F. K. Tittel (Invited)

A 20 J Flow Compatible XECL Laser 134
A. J. W. Brown, E. G. Sergoyan, F. E. White, M. vonDadelszen and C. H. Fisher

X-Ray Triggering Of A Ten-Liter Discharge Excimer System 139
S. Bollanti, P. Di Lazzaro, F. Flora, G. Giordano, T. Letardi, N. Lisi, G. Schina and C. E. Zheng

High Optical Quality Laser Beams With Negative Branch Unstable Resonators 145
J. W. Chen, V. Nassisi and M. R. Perrone (Invited)

VUV Emission From Electron Beam Excited CsF Vapor At High Pressures Of He Or Ne Buffer Gas 153
V. T. Gylys, R. D. Bower, D. G. Harris and T. T. Yang

Gain Measurements On The KrF (B-X), XeF (B-X), And XeF (C-A) Laser Transitions In A XeF (C-A) Laser Gas Mixture 164
A. Cheville, T. Zhang, R. Sauerbrey, W. L. Wilson and F. K. Tittel

FREE-ELECTRON LASERS

3-Dimensional FEL Theory 172
G. Dattoli, H. Fang, A. Torre and R. Caloi (Invited)

CHEMICAL LASERS

Space Based Lasers For Strategic Defense 180
N. Griff, D. Kline and S. Lissit (Invited)

Effect Of Velocity Cross-Relaxation And Mode Separation Upon The Power Spectrum Of A Chemical Oxygen-Iodine Laser 189
D. A. Copeland

Parametric Study Of Chemical Oxygen Iodine Laser 212
T. Sawano and S. Yoshida

High Power Chemical Oxygen-Iodine Laser Of Good Beam Quality 218
K. Shimizu and S. Yoshida

Q-switching Operation Of Chemical Oxygen Iodine Laser 223
F. Matsuzaka, T. Ohga, M. Imachi and T. Uchiyama

A Singlet Oxygen Monitor For Photodynamic Therapy 228
S. J. Davis and M. K. Willscher (Invited)

Visible Chemical Lasers 232
G. P. Perram (Invited)

Short-Wavelength Chemical Laser Development 241
J. M. Herbelin (Invited)

Progress Towards A Short Wavelength Chemical Laser 247
S. J. Davis (Invited)

NUCLEAR PUMPED LASERS

Modeling Of Nuclear Pumped Lasers On He-Mixtures With Cd,Zn,Hg,Mg,Sr,Ca And Ba Vapors 251
V. I. Derzhiev, A. V. Karelin and S. I. Yakovlenko (Invited)

Gasdynamic Phenomena In Nuclear-Reactor-Pumped Lasers 255
J. R. Torczynski (Invited)

Nuclear-Driven Solid-State Lasers 263
M. A. Prelas (Invited)

Nuclear-Induced UV Fluorescence For Stimulation Of The Atomic Iodine Laser 270
W. H. Williams, G. H. Miley and H. J. Chung

Beam Propagation In Direct Nuclear Pumped Laser Amplifiers 278
W. A. Neuman, J. R. Fincke, G. D. Lassahn and L. M. Montierth (Invited)

Lasers In Irradiation Field Of A Stationary Nuclear Reactor 289
G. A. Batyrbekov (Invited)

HIGH POWER GAS LASERS

Laser Generation Characteristics On Xe Infrared Atomic Transitions 301
V. I. Derzhiev, O. V. Sereda, S. I. Yakovlenko and A. G. Zhidkov

Amplified Spontaneous Emission Shaping In A Scattering Laser Plasma With Due Regard For Refraction 306
V. I. Derzhiev, A. V. Gulov, A. O. Terskih, S. I. Yakovlenko and A. G. Zhidkov

Kinetics Of Active Media In High-Pressure Metal Vapor Lasers 311
V. I. Derzhiev, A. V. Karelin, S. I. Yakovlenko and A. G. Zhidkov

Shortwavelength Gain Computer Calculations On Ion Transitions In Expanding Plasma 317
A. V. Borovskii, E. V. Chizhonkov, A. L. Galkin, I. V. Kardash and V. V. Korobkin

Excimer XeCl Laser With Narrowband Output Spectrum 325
V. B. Karpov, I. N. Knyazev, V. V. Korobkin and A. M. Prokhorov

Volume Self-Sustained Discharge Stability In Gas Lasers 330
V. V. Apollonov, G. G. Baitsur, A. V. Ermachenko, K. N. Firsov and S. K. Semenov

Shock-Wave-Initiated Stationary Discharge In Penning's Mixtures Of Inert Gases And Laser Generation On ArII And NeII Ions, Pumped By CO_2-Laser Optical Breakdown 338
V. V. Apollonov, S. I. Derzhavin, D. A. Noraev and A. A. Sirotkin

CO_2 LASERS

Pt/SnO_2-Based Co-Oxidation Catalysts For CO_2 Lasers 347
B. Upchurch, D. Schryer, R. Hess, K. Brown, J. Van Norman, D. Brown and B. Sidney (Invited)

VISIBLE GAS LASERS

Development Of A 100-W Copper Vapor Laser 354
H. Sugawara, M. Yamaguchi, A. Wada, T. Shirakura, N. Tokunaga and H. Yamamoto

Development Of High-Power Copper Vapor Lasers Driven By Solid-State Pulse Generator 359
A. Iwata, K. Hara, S. Ueguri and Y. Ueda

DYE LASERS

Development And Applications Of Dye Laser's 363
S. E. Neister (Invited)

Advances In Blue-Green, Flashlamp Pumped Dye Laser Development 371
R. K. Elkins

Higher Efficiency Excimer Laser Pumped Blue-Green Dye Laser 373
F. J. Duarte, D. R. Foster and C. H. Chen

A High-Average-Power Blue-Green Laser For Underwater Communications 376
D. P. Pacheco, H. R. Aldag, D. E. Klimek, P. S. Rostler, R. Scheps and J. F. Myers

Limits On Efficiency Of Optically Pumped Dye Lasers 383
P. N. Everett

Performance And Modeling Of A Flashlamp-pumped Dye Laser With Aqueous Acetamide As A Solvent 393
P. N. Everett

Tunable, Simultaneous Multi-Wavelength Dye Laser 403
W. E. Davenport, J. J. Ehrlich and T. S. Taylor

Characterization Of Pyrromethene-BF_2-Complexes As Laser Dyes 408
W. E. Davenport, J. J. Ehrlich and S. E. Neister

State Of The Art Laser Dye 415
S. E. Neister (Invited)

Developments In Bridged Oligophenylene Laser Dyes 420
J. Kauffman, C. Kelley, A. Ghiorghis, E. Neister, C. Seliskar and R. Steppel (Invited)

Novel Environments For Laser Dyes 426
G. Jones, II and M. A. Rahman (Invited)

Effects Of B-Cyclodextrin On Selected Xanthene Dyes, Coumarins And Pyrromethene-BF_2 Complexes In Aqueous Solutions 434
I. R. Politzer, K. T. Crago, S. Garner, J. Joseph, J. H. Boyer and M. Shah

HIGH POWER SOLID STATE LASERS

Chromium Doped Forsterite L ser 441
R. R. Alfano, V. Petricevic and A. Seas (Plenary, Invited)

Operational Characteristics Of An Imaging, Unstable Ring Resonator Using ND:YLF As Active Medium 449
D. Y. Park, W. Seka, Y. Lin and D. L. Brown

A Nd:Glass Slab Laser For X-Ray Lithography 457
M. Reed and R. L. Byer (Invited)

Wavefront And Depolarization Calculations For A GGG Slab Laser 458
J. A. Blink, J. L. Cook and L. E. Zapata

BLUE SOLID STATE LASERS

Alexandrite Blue Lasers 465
M. L. Shand (Invited)

Frequency Doubled Operation Of A Ground State Depleted Laser Using The Nd^{3+} $^4F_{3/2}$-$^4I_{9/2}$ Transition In Y_2SiO_5 469
R. Beach, G. Albrecht, S. Mitchell, B. Comaskey, R. Solarz, W. Krupke, C. Brandle and G. Berkstresser (Invited)

CW-Frequency-Doubled ND:YAG Laser With High Efficiency 482
W. Rupp and P. Greve

SOLID STATE LASERS FOR LIDAR AND LASER RADAR

5J Phase Conjugate Nd:Glass Slab Laser With Nearly Diffraction Limited Output 487
M. S. Mangir and D. A. Rockwell (Invited)

Depletion Mode Pumping Of Solid State Lasers 490
D. Mundinger, R. Solarz, R. Beach, G. Albrecht and W. Krupke (Invited)

Active Frequency Stabilization Of Monolithic, Diode Laser Pumped, Solid State Lasers 498
T. Day, E. K. Gustafson and R. L. Byer (Invited)

A Long Wavelength Nd:YAG Laser 501
S. Wong, P. Pace, P. Mathieu and J. Tulip

COHERENT SOURCES FOR LIDAR AND LASER RADAR

CO_2 Laser Oscillators For Laser Radar Applications 510
C. Freed (Invited)

Excimer Lasers And Lidar 526
R. C. Sze (Invited)

Alexandrite Laser Characterization And Engineering Evaluation 531
J. K. Dempsey, R. D. Barber, W. E. Davenport and W. D. Mullins (Invited)

Recent Developments In Ti:Sapphire For Remote Sensing Application 544
J. C. Barnes (Invited)

Assessment Of Dye Laser Sources For Lidar Applications 549
F. J. Duarte

Dispersive Alexandrite Lasers 552
F. J. Duarte and R. W. Conrad

LIDAR AND LASER RADAR

Recent Experiments With Laser Radar 555
F. K. Knight (Plenary, Invited)

Multiwavelength CO_2 Dial System Designed For Quantitative Concentration Measurement 567
J. Leonelli, J. van der Laan, P. Holland, L. Fletcher, R. Warren,and D. McPherrin and J. Comeford

Atmospheric Water Vapour Measurements From The ENEA Ground Based CO_2 Lidar Station 574
R. Barbini, F. Colao and A. Palucci

Techniques For Determination Of Cloud Particle Size From Laser Scattering And Lidar Measurements 579
R. Dubinsky

Convex Set Estimation From Support Line Measurements And Applications To Target Reconstruction From Laser Radar Data 587
S. R. Kulkarni, A. S. Willsky and A. S. Lele

Scalar Reflectance 611
R. Anderson

Fluorescence Remote Sensing Of Vegetation And Soils Of The Mountain Ecological Systems By A Laser Lidar Technique 618
T. A. Trifonova, A. N. Nazarian and V. G. Atanessian

Development Of A Low-Cost Differential-Absorption Remote Sensor For Hydrocarbons 624
J. E. van der Laan, C. B. Carlisle and J. Leonelli

Heterodyne Doppler Velocimetry Measurements At 353 nm 630
R. G. Morton, W. J. Connally, T. Olson, K. Avicola and C. Buczek (Invited)

A Novel SDI Shortwavelength Ladar Deployment Scheme And Its Critical Technologies 638
C. A. Bjork, Jr., R. Turansick, L. Marquet and J. Blodget

Acceleration And Deformation Measurements Using Coherent Laser Radar 644
M. G. Roe, A. L. Huston and B. L. Justus

LASER PROPAGATION

Propagation Of Intense Laser Radiation In Aerosol 651
O. A. Volkovitsky (Invited)

Cloud Hole Boring With Infrared Lasers-Theory And Experiment 659
E. Caramana, R. Morse, G. Quigley, J. Stephens, R. Webster and G. York (Invited)

Interactions Of High-Irradiance CO_2 Laser Beams With Individual Micron-Sized Water Droplets 664
R. L. Armstrong (Invited)

Experimental Study Of The Optical Properties Of Shear Layers 668
L. Chew and W. Christiansen

Experimental And Theoretical Investigation Of Small-Scale Blooming 675
S. M. Ebstein, C. Duzy, and R. Myers (Invited)

Natural Amelioration Of Beam Quality Degradations Caused By Atmospheric Propagation Of High Energy Laser Radiation 683
N. C. Mehta (Invited)

Measurement Of The Stimulated Thermal Rayleigh Scattering Instabiltiy 693
T. J. Karr, M. C. Rushford, J. R. Murray and J. R. Morris

Propagation Of High Energy Laser Beams Through "Clear" Air In The t^3 Regime 703
S. M. Chitanvis and E. T. Salesky (Invited)

Single And Multiaperture Zernike Correlations In The Atmospheric Turbulence Problem 709
J. Stone and P. H. Hu

SPECTROSCOPY OF ATMOSPHERIC MOLECULES AND AEROSOLS

Nonlinear Optical Effects In Laser Irradiated Micron-Sized Droplets 717
R. L. Armstrong (Invited)

Remote Measurements Of The Fluorescence Lifetime Of Aerosols 722
R. B. Loveland, R. Gonzalez and Y. P. Yee (Invited)

Advances in 1.06 um Atmospheric Propagation Modeling 725
R. L. Spellicy, W. O. Gallery, S. G. O'Brien and B. K. Matise (Invited)

Evidence Of Laser Induced Degradation And Graphitization Of Aromatic Pollutants 731
A. Giardini Guidoni, R. Teghil, A. Morone, M. Snels, A. Mele T. Letardi and P. Di Lazzaro

LASER SPECTROSCOPY

Picosecond Multiphoton Ionization Of Atomic And Molecular Clusters 737
D. B. Smith and J. C. Miller (Invited)

Thermal Lens Spectroscopy Under Conditions Of High Background Absorbance 743
D. R. Bobbitt (Invited)

Use Of Various Lasers For Sample Introduction In Atomic And Mass Spectroscopy 750
J. Sneddon (Invited)

Laser Optogalvanic Spectroscopy 753
S. P. McGlynn and D. Kumar (Invited)

Nature Of Laser Optogalvanic Signals 757
D. Kumar and S. P. McGlynn

Frequency-Modulation Spectroscopy With Multimode Lasers 761
J. M. Supplee and E. A. Whittaker

Kinetics And Spectroscopy Of KrF (B) And Kr_2F ($4^2\Gamma$) 767
A. W. McCown and D. P. Greene (Invited)

VUV And Laser Raman Study Of The Correlation Between Atomic And Molecular Polarizabilities And The Number Density Shifts 774
K. Rupnik

DYNAMIC GRATINGS AND WAVE MIXING

Phase Coherence, Diffusion And Recombination Of Excitons In II-VI Compounds 782
C. Dornfeld, R. Renner, H. Schwab, J. M. Hvam, G. Noll, E. O. Gobel and C. Klingshirn (Invited)

Application Of A Novel Picosecond Pulsed Laser Driven X-Ray Source In Time Resolved Diffraction Experiments 788
B. Van Wonterghem and P. M. Rentzepis (Invited)

Phase Conjugation By Degenerate Four-Wave Mixing In Saturable-Dye Doped Planar Waveguides 795
S. Miyanaga and H. Fujiwara (Invited)

NONLINEAR AND QUANTUM OPTICS

Nonlinear Magneto-Optics Of Vacuum 802
A. E. Kaplan and Y. J. Ding (Invited)

Quantum Limited Optical Parametric Image Amplification 808
D. Guthals and D. Sox (Invited)

A Perturbation Analysis Of Brillouin-Enhanced Four-Wave Mixing 816
R. B. Holmes

Coherent Two-Photon Excitation Of Alkali Metal Vapors 826
M. T. Jacoby, D. G. Harris, J. A. Goldstone, J. Stone and R. Whitley

Effect Of Atomic State Coherence On Three-Level Dynamics 832
D. A. Cardimona, M. P. Sharma and M. A. Ortega

Three-Photon Population Dynamics Of A Four-Level Atom Including A Loss Mechanism 838
D. A. Cardimona and M. P. Sharma

Direct Measurement Of Nonlinear Refractive Index Spectrum In ZnSe Using Self-Bending Of A Pulsed Laser Beam 843
Y. J. Ding, C. L. Guo, G. A. Swartzlander, Jr., J. B. Khurgin and A. E. Kaplan

Study Of Mid IR Fiber Transmission And Mode Patterns Under Laser Induced Stimulated Brillouin Scattering 849
C. Yu, Y. C. Chong and H. Zhou

Temperature Measurement With Hydrogen Pure Rotational Cars Spectrum 854
J. P. Singh and F. Y. Yueh

Effect Of Pumping Beam Quality On The Stimulated Raman Scattering And Raman Beam Clean Up 858
Q. H. Lou, Y. S. Huo, J. X. Dong, Y. R. Wei, H. Y. Gao

Competitive Wave Interactions And Instabilities In An Anisotropic Medium With Threshold High Nonlinearity; The Role Of Molecular Fluctuations 865
S. M. Arakelian, Y. S. Chilingarian, A. S. Karaian, R. B. Alaverdian and V. E. Drnoian

Experimental Demonstration Of Large Aperture Compression Of Short Laser Pulses In Bragg - Resonance Condition 873
R. B. Alaverdian, S. M. Arakelian, Y. S. Chilingarian, L. P. Gevorkian, B. A. Makarov and T. A. Papazian

SEMICONDUCTOR LASERS

Experimental Results Of Aging And Thermal Effects In High-Power Laser Diodes 882
J. W. Rupert, M. J. Landry, A. Mittas and T. L. Woolston

SPECTRAL CONTROL OF DIODE LASERS

Frequency-Locked 1.3 And 1.5-μm DFB Lasers For Lightwave Systems Applications 892
Y. C. Chung (Invited)

Dual Optically Stabilized Semiconductor Lasers For Coherent Optical Communications 899
W. R. Babbitt and R. G. Beausoleil (Invited)

Narrow Band, High Power Light From Diode Lasers 906
S. Q. Shang and H. Metcalf (Invited)

Comparison Of Coherent And Incoherent Laser Diode Frequency Sweeping Techniques For Fiber Optic Sensor Systems 914
P. L. Fuhr, D. N. Maynard and D. L. Kunkel

A Study Of The Chirping Of Gain-Modulated Mode-Locked Diode Lasers 920
O. P. McDuff and D. Thati

LASERS COMMUNICATIONS AND ATOMIC RESONANCE FILTERS

Sunlight Suppression By Fraunhofer-Wavelength Atomic Resonance Filters 928
J. A. Gelbwachs (Invited)

Image Preserving Atomic Line Filter 933
E. Korevaar, M. Rivers, K. Choi, S. Bloom, K. Slatnick and C. S. Liu (Invited)

A Fast Atomic Line Filter/Field Ionization Detector 941
S. H. Bloom, E. Korevaar, M. Rivers and C. S. Liu

ULTRAFAST PHENOMENA

Picosecond Laser-Induced Reorientation And Ultrasonics In The Liquid Crystal 5CB 949
H. J. Eichler and R. Macdonald

Effect Of An Intensity Dependent Response Time On The Phase-Conjugate Efficiency In Semiconductor Doped Glasses 953
B. Van Wonterghem, S. M. Saltiel and P. M. Renzepis

Direct Measurement Of Geminate Recombination And Vibrational Cooling In Iodine Using Picosecond Raman Spectroscopy 960
X. B. Xu, S. C. Yu, J. B. Hopkins and R. Lingle Jr.

Direct Observation Of Solvent Cage Dynamics Following Photodissociation Of Iodine Using Picosecond Raman Spectroscopy 964
R. Lingle Jr., X. B. Xu, S. C. Yu, Y. J. Chang and J. B. Hopkins

Observation Of Vibrational Energy Relaxation Following Photodissociation Of $Cr(CO)_6$ 968
S. C. Yu, X. B. Xu, R. Lingle Jr., and J. B. Hopkins

IMAGING

Contrast And Sensitivity Enhancement In Scanning Optical Systems 972
C. W. See, and M. Vaez Iravani (Invited)

Interferometric Evaluation Of Holographic Material 978
R. C. Sumner and P. Mouroulis

LASERS IN MEDICINE

The Effect Of Helium-Neon Laser And Osteopathic Manipulation On Soft Tissue Trigger Points 984
C. H. Greene, D. A. DeBias, D. Heilig, A. S. Nicholas, K. M. England, W. Ehrenfeuchter and W. L. Young (Invited)

OPTICAL INSTRUMENTATION METROLOGY

HOE Holographic Optical Elements 990
E. Stijns and S. Roose (Invited)

Initialization Of Dynamic Laser Networks 995
R. E. Newman-Wolfe, S. L. Davis and Y. C. Chow

Spectral Sampling Signal Recovery Technique For Wavelength Encoded Fiber Optic Sensors 1002
P. J. Kajenski, P. L. Fuhr and W. B. Spillman, Jr.

Multiple Strip Lines For Picosecond Optoelectronic Pulses 1008
J. Witters, P. Janssen, D. Schoemaker and E. Goovaerts

An Avalanche VMOS Driver For Pulsing Semiconductor Laser Diodes 1010
A. Kilpela, R. Ahola, J. Kostamovaara, and R. Myllyla

LASER MATERIALS PROCESSING

CO_2-Laser-Induced Homoepitaxy Of Amorphous Silicon Films 1016
R. B. James

Defect Formation in Fused Silicas Due To Photon Irradiation At 5 And 50 EV 1020
P. W. Wang, G. Escher, R. F. Haglund Jr., D. L. Kinser, N. H. Tolk and R. A. Weeks

Boiling Process In PMMA Irradiated By A CO_2 Laser Radiation 1025
R. Joeckle

IC Failure Analysis Using The Laser Scanning Microscope 1031
J. Fritz and R. Lackmann

POSTER SESSION

Coaxial Optical Fiber For Communication And Sensing Applications 1038
K. Y. Chen, J. S. Chen, S. L. Tzeng, C. Y. Leung, I. F. Chang and J. S. Wu

EPR Study Of Tea $(TCNQ)_2$ In The Far Infared 1042
P. Janssen, A. Mordijck, L. Kesters and K. U. Leuven

Analysis Of Unstable Resonators With Radially Variable Reflectivity Mirrors 1046
S. De Silvestri, V. Magni, O. Svelto, G. Valentini and P. Laporta

A New Technique For Measuring Mode Coupling, Pulse Length And Mode Size In Pico And Femto Second Laser Pulses 1054
A. Cutolo, L. Zeni and S. Solimeno

DC Glow Discharges For The Excitation Of CO Lasers 1061
H. v. Bulow and E. Zeyfang

Higher Order Nonlinear Optical Processes In Organic Crystal MBA-NP 1065
Q. Z. Wang, P. P. Ho, R. R. Alfano and R. Kashyap

Degenerate Cross-Phase-Modulation And Pulse Compression Of Ultrashort Laser Pulses 1068
Q. Z. Wang, P. P. Ho and R. R. Alfano

Optical Imaging Of Quasi Point Source Inside Semi-Opaque Media Using Ultrafast Laser Pulse Technology 1074
L. M. Wang, C. Liu, G. Zhang, P. P. Ho and R. R. Alfano

Investigation Of Third Order Effects In Acetone 1077
M. E. Bergeron, J. F. Harmon, P. A. Chernek and M. E. Rogers

Development Of A Solar-Powered Infrared Injection Laser Microminiature Transmitting System 1081
D. D. Falter, G. T. Alley, K. G. Falter, J. M. Rochelle, K. H. Valentine, R. D. Westbrook, G. E. Jellison Jr., and P. H. Fleming

High-Power Laser Action At λ = 222 nm Under Pumping By Self-Sustained Discharge 1088
A. N. Panchenko, V. F. Tarasenko and E. V. Bukatyi

The Laser Action On The Atomic Transitions Of Ne And Xe On Pumping With Electron Beam 1092
A. S. Bugaev, N. N. Koval, G. A. Mesyats, V. V. Ryzhov, V. S. Skakun, V. F. Tarasenko, I. Y. Turchanovsky, A. V. Fedenev and P. M. Shchanin

A Doppler Lidar With CO_2-Laser Intracavity Detection 1099
A. P. Godlevskii, E. P. Gordov, A. I. Zhiliba and P. P. Sharin

Laser-Induced Nonlinear Effects In Three-Photon Resonant Ionization And Above-Threshold Dissociation Of Diatomic Molecules 1103
A. I. Pegarkov, L. P. Rapoport and I. I. Tugov

Wall Interaction-Free Vapor Confinement By Light-Induced-Drift 1109
S. Gozzini, D. Zuppini, C. Gabbanini and L. Moi

Estimation Of Laser Welding Maximum Parameters 1116
S. G. Gorny, T. N. Karpov, V. A. Lopota, M. M. Malish, V. A. Saburov, I. G. Rudoy and A. M. Soroka

Nd-Glass Burst Laser 1122
H. M. Epstein, J. L. Dulaney, J. F. O'Loughlin, W. P. Altman and C. T. Walters

Measurement Of Laser Glass Energy Storage Efficiencies 1129
J. L. Dulaney and H. M. Epstein

PANEL DISCUSSION

Strategic Defense Initiative (SDI) 1135
F. J. Duarte, C. A. Brau, R. L. Gullickson, K. Johnson, T. Meyer, J. Miller, K. Patel, M. O. Scully, E. Teller and L. Wilson

AUTHOR INDEX 1156

FOREWARD

The Twelfth International Conference on Lasers and Applications was held in New Orleans, Louisiana, December 3rd through December 8, 1989. The meeting brought together participants from throughout the world, and provided a forum for both formal and informal discussions. This volume is a record of the exciting research papers presented at the Conference.

The Keynote Address was delivered by Professor William T. Silfvast of the Center for Research in Electro-Optics and Lasers at the University of Central Florida. In a paper entitled, "Plasma Lasers: Promises and Limitations", Professor Silfvast provided new perspectives and new insights into plasma lasers. He also suggested some research avenues which would lead to more efficient laser operation and to the development of new lasers at shorter wavelengths.

Dr. Frank J. Duarte organized a popular and well attended panel discussion on the Strategic Defense Initiative. Professor Charles Brau graciously served as Moderator for the spirited and thought-provoking remarks of the Panel Members and the audience. We thank these gentlemen, the Panel Members, and the audience for their participation.

The 1989 Einstein Prize for Laser Science was shared by two scientists: Professor H. Jeffrey Kimble of the California Institute of Technology and Dr. Richard E. Slusher of AT&T Bell Laboratories. Professor Kimble discussed his research in a paper entitled: "Squeezed States of Light" and Dr. Slusher elucidated his investigations in a paper entitled: "Squeezed Light Enhanced Microscopy".

The "Lasers '89 Award" for the best contributed paper, reflecting the most innovative and timely research, was also shared by two research groups. The first was "Application of a Novel Picosecond Pulsed Laser Driven X-Ray Source in Time Resolved Diffraction Experiments", by Dr. B. Van Wonterghem and Professor P. M. Rentzepis of the University of California at Irvine. The second paper honored was "Measurement of Absorption and Electrostriction in Gases Near 1.06 μm", by Drs. M. M. Tilleman and S. F. Fulghum of Science Research Laboratory Inc.

We wish to express our appreciation to the Program Committee for their valuable assistance and counsel. The Society for Optical and Quantum Electronics provided excellent management, organization and editorial support. In particular the efforts of Dr. Vincent J. Corcoran as Conference Chairman and Ms. Kathleen Duke as Conference Secretary/Treasurer are greatly appreciated. We gratefully acknowledge the generous financial support of the Society for Optical and Quantum Electronics, the U.S. Army Research Office, the U.S. Air Force Office of Scientific Research (EOARD), the Eastman Kodak Company (Photographic Products Group and MCED), EG&G Princeton Applied Research, New Mexico State University and the Rockwell International Corporation.

Dennis G. Harris
Canoga Park, CA

Thomas M. Shay
Las Cruces, NM

January 1990

Conference Committee

CONFERENCE CHAIRMAN
V.J. Corcoran, Potomac Synergetics, Inc.

PROGRAM CHAIRMAN
D.G. Harris, Rockwell International

PROGRAM CO-CHAIRMAN
T.M. Shay, New Mexico State University

ADVISORY COMMITTEE
F.J. Duarte, Eastman Kodak Company
A. Kantrowitz, Dartmouth College
J. Caulfield, University of Alabama
J. Gallagher, Georgia Institute of Technology

CHAIRMAN OF INTERNATIONAL ARRANGEMENTS
R.W. Conrad, U.S. Army, MICOM
W.B. Lacina, Hughes Aircraft Company

Program Committee

R.R. Alfano — City College of New York
J. Apruzese — Naval Research Laboratory
V.V. Apollonov — General Physics Institute
H.E. Bates — Towson University
M. Benedetto — Center of Ophthalmic Research
A. Budgor — Department of Navy
D. Castro — University of California, Los Angeles
W.B. Colson — Berkeley Research Associates
R.W. Conrad — U.S. Army, MICOM
V.A. Danilychev — Lebedev Physics Institute
D. DeBias — Philadelphia Col. of Osteopathic Medicine
D.K. Dew — Orlando Regional Medical Center
F.J. Duarte — Eastman Kodak Company
J.G. Eden — University of Illinois
J.J. Ehrlich — U.S. Army, MICOM
H.J. Eichler — Technische Universitat Berlin
R. Fields — Aerospace Corporation
J. Goldstone — Rockwell International
R.L. Gullickson — SDIO
R. Gupta — University of Arkansas
D.G. Harris — Rockwell International
P.P. Ho — City College of New York
P. Kepple — Naval Research Laboratory
D. Klick — MIT Lincoln Laboratory
W.B. Lacina — Hughes Aircraft Company
R. Lysiak — Texas Christian University
R.W. McMillan — Georgia Tech
H. Mirels — Aerospace Corporation
P. Mouroulis — Rochester Institute of Technology
T.G. Pavlopoulos — Naval Ocean Systems
G.P. Quigley — Los Alamos National Laboratory
S.K. Salib — Eastman Kodak Company
E.T. Scharlemann — L L N L

Program Committee *(continued)*

S. Scott — British Aerospace
M.O. Scully — University of New Mexico
T. Shay — New Mexico State University
J. Sneddon — Lowell University
D.J. Spencer — Aerospace Corporation
R.C. Sze — Los Alamos National Laboratory
R. Trebino — Sandia National Laboratories
C.E. Turner, Jr. — Rockwell International
J. Wallace — Far Field Incorporated
R.A. Walters — University of Central Florida
C.P. Wang — Optodyne Incorporated
R.W. Waynant — F & D A
T.T. Yang — Rockwell International
G. York — Los Alamos National Laboratory

International Conference Committee

Belgium
E. Styns — Vrige Universiteit Brussel
Germany
H.J Eichler — Technische Universitat Berlin
Great Britain
S. Scott — British Aerospace
V.M. Weerasinghe — Imperial Col. of Science & Tech.
Hungary
J.S. Bakos — Central Res. Inst. of Physics, Budapest
USSR
V.V. Apollonov — General Physics Institute, Moscow
A.B. Bakhtadze — Inst. of Stable Isotopes, Tbilisi
V. Yu Baranov — Kurchatov Inst. of Atomic Energy, Moscow
N.G. Basov — Lebedev Physics Institute, Moscow
V.A. Danilychev — Inst. for High Temperature, Moscow
G.A. Mesyats — Ural Science Ctr., Sverdlovsk
V. Ye. Zuev — Inst. of Atmospheric Optics, Tomsk

PLASMA LASERS: PROMISES AND LIMITATIONS

William T. Silfvast
Professor of Physics and Electrical Engineering
University of Central Florida
Center for Research in Electro-Optics and Lasers
12424 Research Parkway
Orlando, Florida 32826

Abstract

Most gaseous or plasma layers operate in a regime where the electron or plasma density is high enough to be a limiting factor in laser power output. Improvements can therefore only be achieved by increasing the ratio of upper-laser-level population to electron density. Two relatively unstudied types of lasers, recombination-pumped lasers and photoionization-pumped lasers, have the potential to improve this ratio and thus, yield higher efficiency.

Introduction

Since the demonstration of the first laser[1] in 1960, considerable effort has been expended in discovering and developing new lasers and improving older ones. Occasionally, calculations are made or parameters are further optimized on an existing laser to try to obtain more power output. The large field of gas or plasma lasers is no exception in this attempt towards optimization. Plasma lasers span a much larger wavelength range than any other class of lasers, from the far infrared to the soft-x-ray regions of the spectrum. But, for the most part, these lasers have evolved over the years from efforts of relatively separate groups of researchers who have expertise in specific types of discharges or plasmas.

It seems appropriate at this time to try to look at this class of lasers as a whole, rather than at specific parts, and try to come to some conclusions about plasma lasers in general. Another way of wording the title might be: "Plasma Lasers: How are we doing?"

Requirements For Making A Laser

There are two principal requirements for making a laser. The first is a population inversion. This requirement is a necessary but not a sufficient condition for laser action. The second requirement is having enough population in the upper-laser-level (or enough difference in population between the upper and lower laser levels) to produce enough gain for the laser intensity to reach the saturation level during the excitation or pumping cycle. This requirement is the "sufficient" requirement and is in fact the much more critical and difficult-to-achieve requirement.

Population Inversion

It can be shown by a simple analysis of an atomic or molecular species that if one excites such a system to produce a population of high-excited energy levels, a very large number of inversions will automatically occur amongst the various excited levels as the population relaxes back to the ground state during the pumping cycle. This is due to the fact that, as you go to the higher and higher energy levels and thus higher principal quantum numbers of the species, the radiative decay rate of those levels to all lower-lying levels continues to decrease. Thus, when the excited population reduces to the point where radiative decay dominates over all other decay processes, the lower levels will decay faster than the higher levels and inversions will be established throughout the spectrum of levels. Hence, population inversions are almost always inevitable.

Thus, it is not surprising that population inversions were observed at 182 Å in a decaying carbon plasma[2] as early as 1974, long before the first soft-x-ray laser was achieved[3] in 1985 in a selenium plasma. The report in 1974 generated a lot of interest at the time. It would have been much more surprising, however, if an inversion had not been seen! The observed gain was only .000003, far too small to make a laser. In fact, even with all of the more recent efforts to make a laser on the carbon transition[4], a large enough inversion has yet to be achieved that will allow the intensity to reach saturation, the test of a true laser.

Enough Upper-Laser-Level Population

The difficult process in producing a laser is in achieving enough population in the upper-laser-level (while still maintaining an inversion) to produce enough gain to allow the amplified beam to reach saturation and thus begin to efficiently extract energy from the amplifier. The reason this is difficult is that, as the medium is pumped harder (to produce more excited states), more detrimental species such as free electrons are produced which tend to reduce or destroy the population inversion. For example, electron collisions with atoms tend to be relatively unselective in exciting various energy levels. The net result is that higher pumping rates tend to drive populations more toward thermal equilibrium, a distribution that is not inverted and is consequently far from the large inversions that are necessary for laser action.

How much upper-laser-level population is enough? "Enough" can be quantified as a dimensionless number, equal to the product of the stimulated emission cross section times the population difference between the upper and lower laser level times the effective gain length, with a value approximately equal to 10. The stimulated emission cross section is proportional to wavelength and thus decreases linearly towards shorter wavelengths. The effective gain length is the length of the gain medium the beam can pass through, and extract energy from, before it exists the medium. For a gain medium with no mirrors this would be just the length of the amplifier. For a medium with one mirror, this would be twice the length of the medium. For a medium with mirrors at each end of the elongated amplifier, aligned parallel to each other and normal to the amplifier axis, the effective length can be up to 100 to 200 times the amplifier length depending upon the reflectivity of the mirrors.

Thus, while making lasers at any wavelength is not an easy task (until you know how, of course), making them at shorter wavelengths is much more difficult. Not only does the stimulated emission cross section get smaller, but mirror reflectivities become significantly lower, thereby producing a smaller effective amplifier length. Also, the lifetime of upper-laser-levels becomes shorter at shorter wavelengths, resulting in a shorter duration that the excited population remains, to benefit from the reflected beam from the mirrors, thereby shortening the effective gain length even more. It is thus not too surprising that the first lasers were developed in the infrared, then came visible lasers and then a few ultraviolet lasers. Vacuum ultraviolet lasers are very few and far between and XUV and soft-x-ray lasers (if defined as beams that reach saturation within the amplifier) are almost non-existent.

Improvement In Laser Output

From the simple analysis discussed above, the laser output can be improved by two possible techniques. Either the effective length can be increased or the population in the upper-laser-level can be increased.

Increased Gain Length

Increasing the gain length seems like an obvious and simple choice in improving laser output. It can, at the most, double the laser output for a doubling of the gain length if the original length is already long enough to bring the intensity above saturation. In fact, the output does not quite double since the geometry factors are such that as the mirrors get farther apart, the requirements for reaching saturation are actually increased somewhat and the efficiency decreases. As a practical matter, users prefer smaller lasers rather than larger ones and thus increasing the length is not necessarily effective. One of the principal drives towards semiconductor lasers, in addition to their efficiency, is their compact size. In many instances, doubling the size or length of a laser would make it unusable in a product.

Increased Power Input

Increasing the power input per unit gain volume, to provide a higher excitation rate to the upper laser level, seems like a more desirable choice than increasing the effective gain length. Not only could the size of the laser be kept down, but presumably the output would go up, thereby not only increasing the usefulness but perhaps decreasing the production cost by allowing a smaller laser to be made for the same power level. Why then is this not routinely done? What are the limitations in power input per unit volume?

By a simple energy analysis it can be shown that for a one-percent efficient laser with an effective gain length of 10 cm (including mirror considerations) the power output per unit volume can be written as:

$$\text{Power/volume} = 3.6\text{x}10^{-15}/L\text{x}\lambda^4 \qquad (\text{Watts/cm}^{-3})$$

where L is the gain length in centimeters and λ is the wavelength in centimeters. Longer effective gain lengths will reduce the coefficient by the appropriate length ratio.

Limitations

Power Input

A limitation that becomes apparent by looking at the above equation is that power input is a serious problem at shorter and shorter wavelengths. While there is no problem in operating a helium-neon laser at 6328 Å with a power input of 10-20 Watts/cm^3, it becomes extremely difficult to inject 10^{10} - 10^{11} Watts/cm^3 to attempt to make a 100 Å laser or even more improbable to try to deposit 10^{14} - 10^{15} Watts/cm^3 to make a 10 Å laser. A second limitation is that in injecting more power to make the upper-level-population higher, the gain can also become higher thus producing stimulating emission in unwanted directions thereby limiting the potential increase in output power.

Thermalization

While both of these conditions are restrictive, neither is a universal problem. There is, however, one universal problem: thermalization! Thermalization is nature's way of bringing things to a normalized condition. If species such as gaseous atoms interact by collisions at a high enough rate then they will reach a distribution in population and velocity that is related to a Boltzman temperature distribution (which does not allow the possibility of a population inversion). The only methods of dealing with this problem are to either put the energy into the gain medium and extract the beam before thermalization occurs (rapidly-pulsed lasers), or to operate under conditions where thermalizing effects don't occur so as to take advantage of radiative decay, which is a non-thermalizing process that can dominate at lower gas densities.

Thermalization almost always occurs in gas lasers via electrons (which are present in all gas lasers, some much more than others). Hence, the reference to plasma lasers in the title of the paper. The simplest way to estimate the deletirious effects of electrons is to calculate the electron density n_e, at which electron collisional decay from a given level equals or exceeds the radiative decay from that level[5]. This electron density, denoted as n_e^{max}, is equal to:

$$n_e^{max} = 0.13\text{x}T_e^{0.5}/\lambda^3$$

where T_e is the electron temperature in degrees Kelvin and λ is the wavelength in centimeters. It can be seen that this equation is strongly wavelength dependent. Any value of n_e above n_e^{max} for a given wavelength will preclude an inversion. Therefore, since this is an important parameter, Table I shows a listing of various plasma lasers, their respective wavelengths, the associated n_e^{max}, the experimental value of n_e reported for each laser, and the upper-laser-level density, N_{ULL}. It can be seen that the measured or estimated volume of n_e is at or near n_e^{max} for most plasma lasers. The only exceptions are the very low plasma density, low-input-power helium-neon and helium-cadmium lasers, which operate in a unique low-current regime as compared to most plasma lasers, and the carbon soft-x-ray laser which is produced in such a way that n_e^{max} cannot be reached.

TABLE I

Laser Type	Laser Wavelength (angstroms)	n_e^{max} (cm^{-3})	n_e (cm^{-3})	N_{ULL} (cm^{-3})	N_{ULL}/n_e^{max}
Pb	7229	$8x10^{13}$	$1x10^{14}$	$7x10^{12}$	0.09
He-Ne	6328	$9x10^{13}$	$1x10^{11}$	$8x10^{9}$	0.00009
Cu	5105	$1x10^{14}$	$1x10^{14}$	$9x10^{11}$	0.009
Ar^{+}	4880	$1x10^{14}$	$2x10^{14}$	$2x10^{9}$	0.00002
He-C	4416	$1.3x10^{14}$	$1x10^{12}$	$4x10^{11}$	0.003
Ar^{++}	3360	$2x10^{14}$	$1x10^{14}$	$2x10^{9}$	0.00005
KrF	2480	$1x10^{15}$	$8x10^{14}$	$1x10^{14}$	0.1
Xe	1089	$5x10^{16}$	$2x10^{16}$	$2x10^{13}$	0.0004
Se^{24++}	206	$9x10^{19}$	$2x10^{20}$	$7x10^{15}$	0.00008
C^{5+}	182	$1x10^{20}$	$5x10^{18}$	$3x10^{15}$	0.00003

Since most plasma lasers involve ionic laser levels, the maximum N_{ULL} would be equal to n_e^{max} divided by the charge state X of the laser species. Thus, the maximum possible ratio of N_{ULL}/n_e^{max} is of the order of unity or slightly less, depending upon the ionization stage Z of the laser state.

Since electron densities are at or near n_e^{max} for most well-known lasers, it can be expected that increasing the pumping power, which directly increases the electron density, will not produce an increase in the laser output. If n_e is increased above n_e^{max}, N_{ULL} will not increase because electron collisions will either maintain or reduce that density, thereby decreasing the efficiency of the laser.

Increased Efficiency

The only way to increase the efficiency of lasers is to increase the ratio of N_{ULL}/n_e^{max}. From Table I, it can be seen that lasers such as the Ar^{+}, the Ar^{++}, and the Se^{24+} lasers have the lowest ratios of N_{ULL}/n_e^{max}, whereas excimer lasers have one of the highest ratios. The low ratios result from the excitation mechanism of direct electron collisions. Because electron collisions are not particularly selective, they tend to excite a wide range of levels equally and thus dilute their effectiveness. A survey of electron collisionally-excited levels[6] has shown that N_{ULL}/n_e^{max} is typically 10^{-5} which is similar to the values for Ar^{+} and Se^{24+} shown in Table I. How can we be more selective?

An increase in N_{ULL}/n_e^{max} can be achieved by the following processes: (1) using ground state or metastable excited ions that are efficiently and selectively produced in large quantities during electron excitation (particularly as a result of their serving as a reservoir to collect all of the decaying excited states), or (2) by using photoionization processes that can more selectively excite a specific excited ion level than can electron excitation.

Recombination Lasers

Ground state ions have been used effectively to makes lasers by a number of processes including electron-ion recombination, molecular formation (such as excimers), and by charge transfer. In effect, these are all recombination processes since the donor ion reduces its charge state or recombines. Perhaps the best example of using ions in a recombination process is the class of lasers known as excimer lasers. The word excimer results from "excited state dimer" and the excitation process involves first the production of noble gas ions in the discharge and then their "recombination" with a halogen donor to produce an excited state dimer. The effectiveness of such a process can be seen in Table I where the KrF laser has the highest ratio of $N_{ULL}n_e^{max}$ (0.1). It should be recognized that these lasers are extremely effective in converting each ion created in the excitation process into a lasing species.

Atomic recombination lasers offer the same potential for efficiency that excimer "recombination" lasers offer in that the recombination process (known as collisional recombination) can "funnel" each recombining ion to a specific upper-laser-level by electron collisional de-excitation. Such a specific upper-laser-level is determined by its being one of the lowest lying levels above a large energy gap between levels. Bound electrons are thus moved to that level where they accumulate to a large enough population to produce laser action. Such lasers have the potential of having every recombining ion pass through the upper-laser-level and thereby contribute to the laser flux. Perhaps the best known short wavelength laser using this process is the 182 Å carbon soft-x-ray laser[4]. Other lasers at longer wavelengths using this process are described in references 7 and 8. None of these has yet achieved the potential high-efficiency that such lasers are, in principle, capable of.

There are also many lasers operating by charge exchange types of recombination processes. One example of this is the helium-selenium laser described in reference 9. Also lasers operating in the ultraviolet via this process are discussed in reference 10 but again, none of these has as yet achieved notable efficiencies.

Photoionization-Pumped Lasers

Electrons can also be used to generate efficient broad-band sources such as laser-produced plasmas. Such soft-x-ray sources can then be used to pump photoionization lasers. Photoionization lasers were first proposed[11] in 1967, but were not successfully demonstrated[12] until 1983, when two transitions in Cd vapor were excited in this fashion. A number of other lasers have since been demonstrated[13] including two short-wavelength transitions in Xe[14] and Cs vapor[15]. In the cadmium laser, the ration N_{ULL}/n_e^{max} is 0.6, one of the highest ever achieved for an ion laser, thus indicating the potential efficiency of this type of process.

Such lasers are the gaseous analogy of the flashlamp-pumped solid state lasers such as the neodymium and ruby lasers. Photoionization cross sections to specific levels have a very broad energy range and thus very broadband sources can be used for selective pumping to specific levels. The wavelength range for excitation is typically in the HUV or soft-x-ray spectrum, an area where there has been little effort in broadband source development.

Conclusions

Greater efforts should be made in the development of recombination-pumped lasers, including molecular ion recombination, atomic ion recombination and charge transfer processes. Also, further investigation of photoionization-pumped lasers are needed, with particular emphasis at the stage on the development of efficient broad-band soft-x-ray sources as pumping sources. If such efforts are made, we will achieve more efficient lasers with higher output energies over a broad spectral range from the infrared to the soft-x-ray region.

References

1. T.H. Maiman, Nature 1987, 493 (1960).

2. F.E. Irons and N.J. Peacock, J.Phys.B:Atom.Molec.Phys. 7, 1109 (1974).

3. D.L. Mathews, et. al., Phys.Rev.Lett. 54, 106 (1985).

4. C. H. Skinner, C. Keane, H. Milchberg, S. Suckewer and D. Voorhees, "Laser Techniques in the Extreme Ultraviolet," Eds. S.E. Harris and T.B. Lucatorto (AIP, N.Y. 1984) P. 372.

5. O.R. Wood II and W.T. Silfvast, Appl.Phys. Lett. 41, 121 (1982).

6. W.T. Silfvast and O.R. Wood II, Optics Lett. 8, 169 (1983).

7. W.T. Silfvast, L.H. Szeto, and O.R. Wood II, Appl.Phys.Lett. 36, 615 (1980).

8. O.R. Wood II, J.J. Macklin, and W.T. Silfvast, Appl.Phys. Lett. 44, 1123 (1984) and O.R. Wood II, J.J. Macklin, and W.T. Silfvast, IEEE J. Quantum Electron. QE-21 1714 (1985).

9. W.T. Silfvast and M.B. Klein, Appl.Phys.Lett. 17, 400 (1970).

10. J.R. McNeil, G.J. Collins, K.B. Persson, and D.L. Franzen, Appl.Phys.Lett. 27, 595 (1975), and J.R. McNeil, W.L. Johnson, G.J. Collins, and K.B. Persson, Appl.Phys.Lett. 29, 1972 (1976).

11. M.A. Duguay and P.M. Rentzepis, Appl.Phys. Lett. 10, 350 (1967).

12. W.T. Silfvast, J.J. Macklin and O.R. Wood II, Optics Lett. 8, 551 (1983).

13. W.T. Silfvast and O.R. Wood II, J. Opt.Soc.Am.B, 4, 609 (1987).

14. H.C. Kapteyn, R.W. Lee and R.W. Falcone, Phys.Rev.Lett. 57, 2939 (1986) and M.H. Sher, J.J. Macklin, J.F. Young, and S.E. Harris, Opt.Lett. 12, 891 (1987).

15. C.P.J. Barty, D.A. King, G.Y. Yin, K.H. Hahn, J.E. Field, J.F. Young, and S.E. Harris, Phys.Rev.Lett. 61, 2201 (1988).

PULSED-POWER DRIVEN X-RAY LASERS: FANTASY OR REALITY?

J.P. Apruzese and J. Davis

Naval Research Laboratory, Washington, D.C. 20375-5000

Abstract

All existing laboratory x-ray lasers utilize as a gain medium a linear plasma created by a line-focused high power Nd:glass or CO_2 laser. In this paper we assess the prospects of creating an x-ray laser by employing pulsed electrical discharges as the energy source for the plasma gain medium. Progress toward achieving a pulsed-power driven soft x-ray laser via electron pumping and/or photoexcitation is reviewed. Advantages and disadvantages of pulsed-power drivers compared to laser drivers are discussed. At present, resonant photoexcitation appears to be the most promising candidate for early success as a pulsed-power x-ray laser. Recent progress at the Naval Research Laboratory, Physics International Corporation, and Sandia National Laboratories (discussed in detail elsewhere in these proceedings) has brought the realization of such an x-ray laser within reach.

1. Introduction

During the 1980s x-ray lasers moved from the realm of theoretical calculations and proposed inversion schemes to reality in the laboratory. Present x-ray lasers consist in part of a plasma amplifying medium, created by a line-focused high power optical or infrared laser. Lasing occurs either via pure amplified spontaneous emission or, in some cases, with the assistance of amplification using multilayer mirrors. Population inversions in the plasma are set up by either electron collisional excitation or recombination, or a combination of the two, depending on the chosen element and ionization stage. Schemes thus far successfully demonstrated are: collisional excitation and/or recombination in neonlike[1-4] and nickel-like ions[5,6], and recombination in hydrogenic[7-10] and lithiumlike[11,12] ions. Wavelengths at which gain has been demonstrated in these devices range from about 45 to 300 Å, with the shortest wavelength now attributable to recent success with nickel-like tantalum at Lawrence Livermore National Laboratory[6]. Pulsewidths for the laser lines range from 170 ps for neonlike selenium[4] to 4 ns for recombining lithiumlike aluminum[11], to 10-30 ns for magnetically confined recombining hydrogenic carbon[8]. Total energies in the soft x-ray laser lines have been measured at 3 μJ for neonlike Ge[3], 0.5 mJ for neonlike Se[4], and 1-3 mJ for hydrogenic carbon[8].

For virtually any application envisioned for x-ray lasers, the more coherent x-ray photons available, the better. This is especially true for holography[13]. Also, it is easier to utilize a cavity if the x-ray laser pulse is at least several nanoseconds to allow photon transits between the mirror(s) and the gain medium. These considerations, as well as others discussed below, motivate a search for x-ray laser drivers other than high power optical or infrared lasers.

2. Potential Advantages of a Pulsed-Power Driver

Laser-driven x-ray laser research, as noted above, has met with considerable success in the 1980s. However, the potential advantages of a pulsed-power driver are considerable and strongly indicate that the goal of a pulsed-power driven x-ray laser is well worth pursuing. Many of these advantages are also relevant to the inertial confinement fusion (ICF) effort. An excellent source of comparative data for large lasers and pulsed-power devices is the 1986 ICF review conducted by the National Academy of Sciences (NAS) (Ref. 14). Pulsed-power is currently superior to large laser drivers in three significant areas: cost, available energy on target, and wall-plug efficiency.

In Ref. 14, the cost of drivers is expressed in dollars per joule of installed capacity. The largest ICF-class laser now in existence, the NOVA device at Lawrence Livermore National Laboratory, can deliver ~100 kJ on target with the 10 beam configuration at 1.06 μm. However, the 2-beam line focused x-ray laser target chamber, perhaps the finest such facility anywhere, can deliver 5.6 kJ to a linear target at 0.53 μm. According to Ref. 14, the cost of NOVA was $200 million or $2000/J. By contrast, the pulsed-power PBFA-II light-ion-fusion accelerator at Sandia National Laboratory can potentially deliver 1-2 MJ to target at an installed cost[14] of $30/J. The estimated wall-plug efficiency (20%) is typical of a modern pulsed-power generator. By contrast, the overall efficiencies of high power, short-pulsed laser drivers[15] range from around 1% for Nd:glass to 5% and 8% for CO_2 and KrF lasers, respectively. Therefore, in terms of cost, energy on target, and efficiency, pulsed-power currently possesses clear advantages over lasers.

If x-ray lasers are to come into common use in research and industry, it is clear that substantial reduction in their overall size must occur. Recent advances in inductive energy storage technology at the Naval Research Laboratory[16] provide a realistic basis for reduction in the physical volume of pulsed-power generators by as much as two orders of magnitude. In summary, a pulsed-power driven x-ray laser offers the potential for significant reductions in size as well as cost. Together with greater efficiency and deliverable energy, these advantages continue to provide motivation for maintaining a strong effort to achieve gain at soft x-ray wavelengths using a pulsed-power device.

3. Potential Disadvantages of a Pulsed-Power Driver

The fact that only high power lasers have succeeded to date in creating extractable gain in plasma may be partially indicative of the greater resources which have been devoted to such experiments. However, it is also clear that lasers are currently better suited to precisely tailor the desired characteristics of an amplifying plasma. Z pinch plasmas have long been plagued by kink and sausage instabilities which can prevent establishment of sufficient linear uniform gain length. Inhomogeneities may result in unacceptable refraction of the soft x-ray beam. In Z pinch plasmas created by supersonic nozzles which puff gas into the diode, residual cold gas may absorb the soft x-rays before they reach the diagnostic instruments. The above difficulties do not occur with laser-produced plasmas.

Another potentially troublesome aspect of the pulsed-power driver is that the characteristic time scale for rise and persistence of current is at least ten nanoseconds. This is reflected in similar plasma lifetimes. Therefore, recombination laser schemes which demand cooling on a subnanosecond time scale would be difficult to implement on pulsed-power machines. Since the current cannot be reduced so rapidly some other cooling technique, perhaps stagnation onto a capillary as investigated by Krishnan, Nash, and Lepell[17], might be required, complicating the experiment.

Photopumped x-ray lasers, which have not yet been realized either by laser drivers or pulsed-power generators, are discussed below as one of the most promising areas for pulsed-power research, However, to optimize the "flashlamp" pump power at the lasant, the pumped and pumping plasmas should be located in close proximity. The presence of large currents and fields, combined with the need for a return current configuration, leads to difficulties in such close placement of two different plasmas. However, significant progress has recently occurred in this regard as the Sandia group has succeeded in reducing the separation to 2 cm[18].

In summary several possible barriers to the achievement of a pulsed-power driven x-ray laser exist and must be overcome if such a device is to be realized. We now turn from these general considerations to a specific discussion of approaches to a pulsed-power x-ray laser and their current experimental status.

4. Approaches to a Pulsed-Power Driven X-Ray Laser

4.1 Neonlike Krypton Gas-Puff Z Pinch

Highly charged neonlike ions, where 3p-3s population inversions result naturally from the rapid decay of 3s levels to the $2p^6\ ^1S_0$ ground state and the population of 3p levels by collisional excitation and recombination, have proven to be very robust sources of soft x-ray amplification. At present, 11 neonlike ions ranging in atomic number from 28 to 47 have exhibited gain in the laboratory. The neonlike selenium (Z=34) laser was the first to be demonstrated[1,2] and is the most intensively investigated to date[4]. Krypton (Z=36) is an excellent source for gas-puff Z pinches and its neonlike stage could certainly produce 3p-3s population inversions with plasma conditions similar to that required for its neighbor in the periodic table, selenium. Electron densities of 3×10^{20} - 10^{21} cm^{-3} and temperatures of 0.6 - 1.2 keV in a uniform linear plasma would produce gain on 3p-3s lines in the 150 - 200 Å spectral region. Detailed one-dimensional radiation hydrodynamic modeling[19] of a krypton double-puff Z pinch suggests such gain would persist for a few ns.

A series of experiments was undertaken at Physics International Corporation by M. Krishnan and colleagues in an effort to demonstrate laser action in a neonlike krypton gas-puff Z pinch. The "Double-Eagle" generator, supplying currents of ~3 MA with a 90 ns risetime, was employed in a standard single-puff configuration as well as in a design using a double-puff -- an outer puff stagnating on an inner krypton jet in an effort to provide stability and improve the plasma's morphology. The outer-inner puff configuration did indeed result in a more suitable plasma. On one shot, the plasma remained quite linear for ~5 ns for a 1.5 cm length. X-ray spectra revealed the presence of both neonlike and fluorinelike Kr. However, pinhole images revealed some degree of nonuniformity within this linear plasma. On no shot could the expected 3p-3s laser lines be positively identified and demonstrated to be amplified. Krishnan and Deeney[20] have speculated that one or more of the following deleterious effects may account for this negative result. Cold gas from the puff may have absorbed a significant fraction of the gain lines' energy. On time-integrated axial spectra, continuum emission which persists for tens of nanoseconds may have swamped the laser lines which are expected to last a few nanoseconds. Remaining nonuniformities - especially in density - may have caused deleterious refraction of the soft x-rays. Since the x-ray spectra in the 1.5 - 2.0 keV range were very similar to spectra taken of Se at Livermore[21] during actual Se laser shots, it is likely that some gain was indeed achieved in these experiments, even though amplification could not be demonstrated. The negative result brings sharply into focus the difficulties which need to be surmounted in pulsed-power x-ray laser research. By no means can it be concluded that a pulsed-power neonlike x-ray laser is unattainable. For instance, a series of experiments using wires to form the plasma - perhaps copper or zinc (Z = 29, 30) would at least eliminate cold gas absorption and might produce a stable plasma. For the time being, however, most effort is directed toward other schemes as discussed below.

4.2 Photoionization and Recombination Schemes

Hussey and co-workers at Sandia National Laboratories have developed an interesting design[22] for a pulsed-power driven x-ray laser which features a hollow cylindrical target, to generate a neonlike recombination laser pumped by photoionization. The outer layer of the cylinder would contain a fairly low atomic number element such as Al, whose heliumlike resonance line

could photoionize the neonlike lasant (nickel, for example) but not the fluorinelike stage. Such targets can be optimized to produce modest gain for driving currents in the 3.5-5.5 MA range. As explained in Ref. 22 (which should be consulted for full details), the outlook for experimental achievement of gain is guarded because of expected implosion nonuniformities as well as uncertainties in the expansion hydrodynamics of the lasant inside the cylinder.

Krishnan and co-workers have presented some experimental evidence[17] suggestive of recombination-pumped gain in Ne X which was imploded onto an Al-coated on-axis parylene capillary. The capillary may act as a heat sink, promoting cooling and recombination. No conclusive evidence of lasing has since been observed, but the general design is promising and is worthy of continued effort. Ref. 17 should be consulted for details.

4.3 The Sodium-Neon Photoresonant Scheme

One of the most active areas currently under investigation in pulsed-power x-ray laser research is the line-coincidence sodium-neon flashlamp laser. In 1975 Vinogradov and co-workers[23] pointed out that the 11 Å Na X $1s^2$ - $1s2p\ ^1P_1$ transition coincides in wavelength with the Ne IX $1s^2$ - $1s4p\ ^1P_1$ line, within a thermal Doppler width. This scheme was later analyzed in detail[24-26]. Its essential features are presented in Fig. 1. The intense helium-alpha Na X line pumping a relatively cool (50 - 100 eV) neon plasma of ion density $7x10^{17}$ - $2x10^{19}$ cm^{-3} can greatly overload the heliumlike neon n=4 levels, resulting in population inversions in the 4-3, and possibly 4-2 and 3-2 singlet transitions of Ne IX located near 230 Å, 58 Å, and 82 Å, respectively. The 50-100 eV temperature range for neon promotes most ions into the desired heliumlike stage without collisionally exciting the n=2 and 3 lower laser levels which would spoil the inversions. The principal requirement for the sodium-bearing plasma is that it generate sufficient power in the pumping transition. In practice this means temperatures of 200-600 eV and electron densities at least 10^{20} cm^{-3}, preferably higher. Clearly the conditions for the sodium pump and neon lasant are sufficiently different as to require spatially separate plasmas. Before considering the present status of sodium-neon experiments it is appropriate to review its considerable advantages in a pulsed-power configuration.

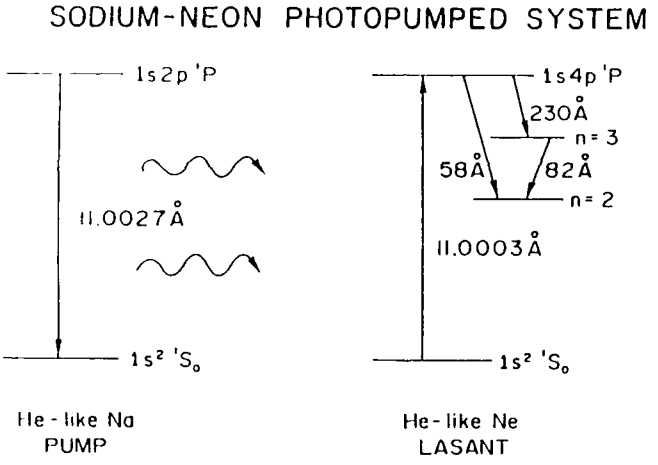


Fig. 1. Simplified energy level diagram showing the essential features of the Na/Ne photoresonant system.

One obvious attraction is that instabilities in the pumping sodium plasma are largely irrelevant. As long as sufficient pump power is attained, gain is achievable in the separate, presumably more stable neon lasant. At worst, non-uniform sodium emission would result in spatial variations in the neon gain coefficient -- probably very mild variations since the Na/Ne separation would greatly reduce the radiative flux variations at the neon lasant surface. An additional advantage is that the relatively cool, tenuous neon plasma can be created by much smaller driver currents, or purely by the x-rays emanating from the sodium plasma. As detailed elsewhere in this conference[18], the Sandia group has recently succeeded in photoionizing neon to the heliumlike stage using x-rays from a sodium-bearing plasma. It is conceivable that a relatively modest laser (10^{11} - 10^{12} W cm^{-2}) could successfully drive a cryogenic or gas-jet neon target to the appropriate lasant conditions for pumping by the sodium source.

There are additional advantages. Z pinch plasmas have long demonstrated their ability to produce tens of kilojoules of K shell x-rays[27] in the atomic number range in which sodium is located. The lasant may produce amplified soft x-rays for as long as the pump power is sufficient - that is at least 10 ns, which would facilitate cavity operation. Finally, gain length

studies may be accomplished in an efficient, clean, straightforward fashion by deploying lasant targets of various lengths around the pump plasma[18] or shadowing different sections of lasant plasma from the pump[20].

How much power is required of the Na X $1s^2$ - $1s2p\ ^1P_1$ pump transitions to create gain in the Ne IX 4f-3d singlet transition at 230 Å? (This is the most promising laser line.) Of course, the answer to this critical question depends upon the emitted spectral width of the pump line and the Na/Ne separation, as well as the assumed neon conditions. If it is assumed that opacity broadening widens the sodium line to 4.5 Doppler widths ($3x10^{14}$ Hz) and that the neon plasma can be created at nearly optimal conditions (ion density $3x10^{18}$ cm^{-3}, temperature 50 eV), Table 1 contains the required pump power as a function of Na/Ne separation for a 2-cm long Na pinch. Of course if the pump line is narrower, the numbers in the table are pessimistic since more of the Na line's energy would be concentrated in the highly absorbing neon line's core. For lower neon densities, the reduction in gain (or required increase in pump power) is nearly linear. For neon ion densities exceeding $2x10^{19}$ cm^{-3}, no gain is attainable due to collisional quenching of the population inversion(s).

Table 1. Power in the 11 Å sodium pump line required to produce a gain of 1 cm^{-1} in the 4f-3d singlet transition of Ne IX, as a function of Na/Ne separation, under plasma conditions described in the text.

Na/Ne SEPARATION (cm)	POWER (GW)
5.0	255
4.0	164
3.0	97
2.0	47
1.5	30

Table 1 is based upon the detailed calculations described in Ref. 26. For a gain of 1 cm^{-1}, a pump line power of 47 GW is needed at Na/Ne separation of 2 cm; for 5 cm this power increases dramatically to 255 GW.

Much of the recent progress in the Na/Ne scheme is the steady increase in the demonstrated pump line power to the point where currently available sources are sufficient for gain at separations ≤ 3 cm. The first step in developing a suitable sodium source for a Z pinch was taken by the Naval Research Laboratory experimental group which has demonstrated 25-30 GW of pump line power reproducibly at the relatively modest current of 1 MA available on NRL's Gamble-II generator. Note that this approach utilizes a NaF capillary discharge and that roughly half the energy is absorbed by the useless fluorine ions. Full details of this source development are contained in Refs. 28-32. Very recently (Fall 1989) this capillary source was successfully adapted to the Double-Eagle generator at Physics International Corporation, using 3 MA driving currents. Line pump powers of 100-130 GW were reproducibly demonstrated despite the presence of the fluorine. Details are given elsewhere in these proceedings[33].

Also very recently, Deeney and co-workers at Physics International have successfully extruded, mounted, and fired pure Na wires on the Double Eagle generator[33]. A record pump line power of 150 GW was demonstrated on a single shot, but only 90-100 GW could be consistently produced. Initial difficulties with the sodium wire technology resulted in non-uniformities in the wires which probably account for the large shot-to-shot variations. Future experiments are likely to result in significant improvements. Ref. 33 describes in detail these latest developments using the Double-Eagle generator.

Significant attention has been devoted to the neon lasant and Na/Ne photopumping experiments demonstrating fluorescence have been performed at the Naval Research Laboratory[30,31] and Sandia National Laboratories[18]. At NRL, one of the return current posts was replaced by the neon plasma pumped by the central sodium-fluorine plasma. Na/Ne separation in this geometry was 5 cm. Photopumping of the neon was confirmed by fluorescence indicated by the enhanced brightness of the pumped 4-1 neon line compared to the 3-1 line. This enhancement (Fig. 2) occurred only when the neon plasma assembled during the period of high power sodium emission, and was not seen when a NaF discharge was replaced with a MgF_2 discharge, nor when no pump plasma at all was present. It is encouraging that fluorescence is detectable in time-integrated x-ray spectra at relatively modest pump powers of 25-30 GW at a fairly large separation of 5 cm. The recent successful fluorescence experiments at Sandia National Laboratories are described elsewhere in these proceedings[18].

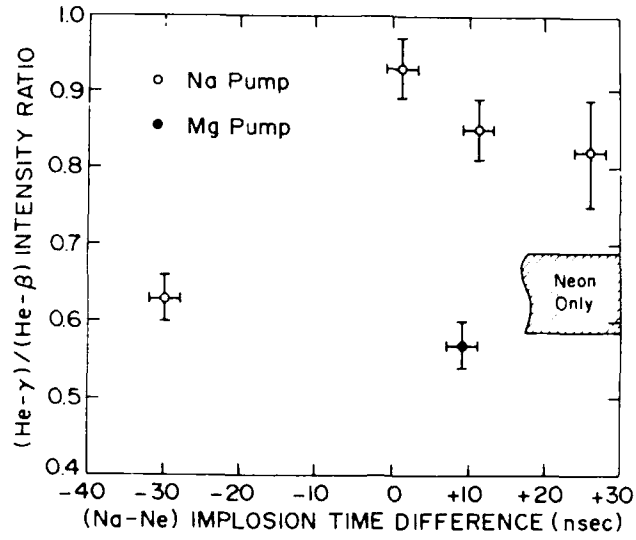


Fig. 2. Ne IX γ(1-4) to β(1-3) line ratio as a function of Na/Ne plasma implosion time difference. Also shown are shots with no pump plasma present and with MgF_2 replacing the NaF plasma. Figure courtesy of Dr. Frank Young of the Naval Research Laboratory.

5. Summary and Current Prospects

Even though all present x-ray amplifiers are driven by high-power optical or infrared lasers, the goal of a pulsed-power driven x-ray laser is well worth pursuing. Pulsed-power generators are advantageous compared to lasers with respect to cost, energy on target, and efficiency. The emergence of inductive storage technology promises significant reductions in physical size as well. Potential obstacles to attainment of a pulsed-power driven x-ray laser include Z pinch instabilities, inherent plasma time scales which are too long for some lasing schemes, possible absorption of the soft x-ray beam by cold matter, and difficulties in situating dual component pump-lasant plasmas in close proximity. Approaches to pulsed-power x-ray lasing which have been pursued include neonlike krypton via gas puff Z-pinches, recombination induced by neon puffs stagnating onto hollow on-axis cylinders, and photon pumping (either photoionization or resonant excitation). Currently, the sodium-neon resonant photoexcitation scheme is being vigorously pursued at the Naval Research Laboratory, Physics International Corporation, and Sandia National Laboratories. At Physics International's Double Eagle 3 MA generator, sodium pump powers have already been achieved (using two different sodium sources) which are adequate for pumping gain in neon at Na/Ne separations ≤ 3 cm. In the relatively near future, improvements to these sources will be implemented which have excellent prospects for increasing this power by a factor of two or more. Pulsed-power driven x-ray lasers, while not yet demonstrated, are now much closer to reality than fantasy.

6. Acknowledgments

It is a pleasure to acknowledge many stimulating discussions with our experimental colleagues at the Naval Research Laboratory, especially Frank Young, Dave Hishelwood, Steve Stephanakis, Carolyn Mehlman, and Phil Burkhalter. Equally valuable insights were obtained in extensive conversation with M. Krishnan and C. Deeney at Physics International Corporation. We are grateful to M. K. Matzen of Sandia National Laboratories for permission to mention some of Sandia's exciting recent results in this review.

X-ray laser research at the Naval Research Laboratory and Physics International Corporation has been supported by the SDIO Office of Innovative Science and Technology.

7. References

1. M. D. Rosen et al., Phys. Rev. Lett. 54, 106 (1985).
2. D. L. Matthews et al., Phys. Rev. Lett. 54, 110 (1985).
3. T. N. Lee, E. A. McLean, and R. C. Elton, Phys. Rev. Lett. 59, 1185 (1987).
4. C. Keane, N. M. Ceglio, B. J. MacGowan, D. L. Matthews, D. G. Nilson, J. E. Trebes, and D. A. Whelan, J. Phys. B 22, 3343 (1989).

5. B. J. MacGowan et al., Phys. Rev. Lett. 59, 2157 (1987).
6. S. Maxon et al., this conference.
7. D. Jacoby, G. J. Pert, L. D. Shorrock, and G. J. Tallents, J. Phys. B 15, 3557 (1982).
8. S. Suckewer, C. H. Skinner, D. Kim, E. Valeo, D. Voorhees, and A. Wouters, Phys. Rev. Lett. 57, 1004 (1986).
9. C. Chenais - Popovics et al., Phys. Rev. Lett. 59, 2161 (1987).
10. G. J Tallents et al., this conference.
11. G. Jamelot, A. Klisnick, A. Carillon, H. Guennou, A. Sureau, and P. Jaéglé, J. Phys. B 18, 4647 (1985).
12. P. Jaéglé, A. Carillon, P. Dhez, B. Gauthe, F. Gadi, G. Jamelot, and A. Klisnick, Europhys. Lett. 7, 337 (1988).
13. J. Trebes, J. Phys. (Paris) 47, C6-309 (1986).
14. Review of the Department of Energy's Inertial Confinement Fusion Program, National Academy of Sciences (National Academy Press, Washington, D.C., 1986)
15. J. F. Holzrichter, D. Eimerl, E. V. George, J. B. Trenholme, W. W. Simmons, and J. T. Hunt, J. Fusion Energy 2, 5 (1982).
16. R. J. Commisso, in Naval Research Laboratory 1987 Review, NRL Publication 112-2630, p. 69 (1988).
17. M. Krishnan, T. Nash, and P. D. Lepell, IEEE Trans. Plasma Sci. 16, 491 (1988).
18. M. K. Matzen et al., this conference.
19. J. Davis, R. Clark, J. P. Apruzese, and P. C. Kepple, IEEE Trans. Plasma Sci. 16, 482 (1988).
20. M. Krishnan and C. Deeney, private communication.
21. Selenium comparison spectra, courtesy of Dr. J. Scofield.
22. T. W. Hussey, M. K. Matzen, E. J. McGuire, and H. E. Dalhed, J. Appl. Phys. 66, 4112 (1989).
23. A. V. Vinogradov, I. I. Sobelman, and E. A. Yukov, Kvant. Elektron. (Moscow) 2, 105 (1975) [Sov. J. Quantum Electron. 5, 59 (1975)].
24. J. P. Apruzese, J. Davis, and K. G. Whitney, J. Appl. Phys. 53, 4020 (1982).
25. P. L. Hagelstein, University of California Report No. UCRL-53100, 1981 (unpublished).
26. J. P. Apruzese and J. Davis, Phys. Rev. A 31, 2976 (1985).
27. W. Clark et al., in Proceedings of the Fifth International Conference on High Power Particle Beams 1983, (University of California, San Francisco, California, 1983) pp. 236-241.
28. F. C. Young et al., Appl. Phys. Lett. 50, 1053 (1987).
29. J. P. Apruzese et al., Phys. Rev. A 35, 4896 (1987).
30. S. J. Stephanakis et al., IEEE Trans. Plasma Sci. 16, 472 (1988).
31. F. C. Young et al., Proceedings, International Conference on Lasers '88, R. C. Sze and F. J. Duarte, Eds. (STS Press, McLean, VA, 1989), pp. 98-105.
32. B. L. Welch, F. C. Young, R. J. Commisso, D. D. Hishelwood, D. Mosher, and B. V. Weber, J. Appl. Phys. 65, 2664 (1989).
33. C. Deeney et al., this conference.

LITHIUM-LIKE RECOMBINATION SCHEME FOR X-UV LASERS

P. Jaeglé, G. Abdelatif, A. Carillon, P. Dhez, B. Gauthé, G. Jamelot, A. Klisnick, J.P. Raucourt

LSAI, CNRS and Université Paris-Sud, Bât. 350, 91405 ORSAY CEDEX and
LULI, CNRS and Ecole Polytechnique, 91128 PALAISEAU CEDEX, France

Abstract: Recombination in lithiumlike ions in a rapidly cooling plasma is an attractive way towards X-ray lasers because, at a given lasing wavelength, it requires less pumping energy than most other pumping schemes. In this paper we describe the status of experiments relative to the Li-like scheme, and we discuss the problem of increasing the gain-length product necessary to achieve efficient X-ray lasers.

I - INTRODUCTION

The first proposal by Gudzenko and Shelepin of recombination pumping[1] considered the relaxation of an hydrogen plasma produced by a gas discharge. For lasing at short wavelengths, the recombination scheme in hydrogenlike ions has been extensively studied since 1974 with C^{5+} ions in laser-produced plasmas[2,3]. The first evidence of the exponential increasing of a aluminium lithium-like line has been presented in 1981 at the same conference[4]. In the case of Li-like ions, the plasma temperature must reach the point where the ionization is such as the plasma contains mainly helium-like ions. So, during expansion and cooling the free electrons recombine with ions leading to Li-like ions in highly excited states. This is the condition for the production of population inversions. The ionization energy of Li-like ions being much less than for H-like ions, the lithium-like scheme requires less laser energy than most other schemes.

Several elements from magnesium to chlorine have proved to give amplification for lines lying between 80 Å and 200 Å. Aluminium has been studied much more extensively than any other element and the results

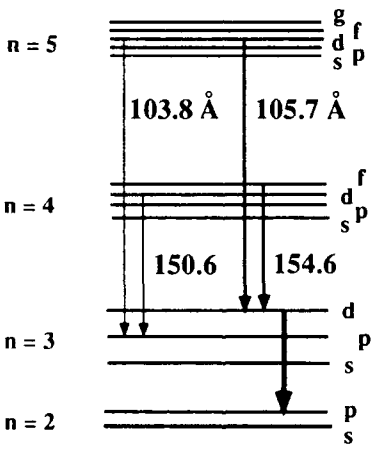


Figure 1: Simplified energy-level diagram of lithiumlike ions. The wavelengths correspond to aluminium.

obtained with Li-like aluminium allow to give a good account of what has been achieved till now regarding the lithium-like scheme and of the problems which remain to be solved.

Let us recall the diagram of levels of Li-like ions. Figure 1 shows transitions of interest for soft X-ray amplification. The wavelengths are given for aluminium. In a plasma of intermediate density (10^{17} to 10^{21} cm^{-3}) when the pumping laser turns off, the temperature fastly falls down and three-body recombination populates strongly the upper energy levels of the recombined Li-like ion. Recombination is followed by a radiative-collisional cascade to intermediate levels n = 4,5. At the same time, owing to the low electron temperature, electron-ion collisions from the ground state cannot balance the fast radiative decay of the lower excited levels (n = 3). These processes result in transient population inversions, especially between levels 3d on the one hand and 4f and 5f on the second hand.

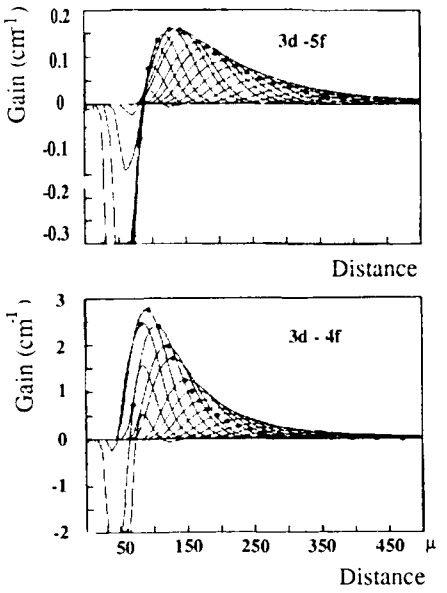


Figure 2: Gain calculated at various times as a function of the target distance for the 105.7 Å (above) and the 154.7 Å lines of Li-like aluminium. Two successive curves are separated by 50 ps.

Figure 2 gives examples of population inversions calculated in a recently improved plasma model[5]. Electron temperature and density are deduced from a one-dimensional lagrangian code. This last takes account of laser-radiation absorption in underdense plasma corona by inverse Bremsstrahlung, collisional ionization, radiative and collisional recombination, and thermal conduction[6] . Each curve on the figure displays the gain versus the distance to the target at given time. Time interval between the curves is 50 ps. The gain maximum occurs at 400 ps for the 4f line (470 ps for the 5f line) after the maximum of the laser pulse. It is noticeable the gain calculated at 154 Å is one order of magnitude larger than at 105 Å. This is a constant result of calculations which is not systematically verified in experiments. Plasma temperature at the gain maximum is of 45 - 50 ev. The value of gain is very sensitive to this parameter. Temperature reduction by means of an adjustable parameter results in a strong enhancement of the gain. Thus one can expect that increasing of plasma cooling, either by optimizing target shape or with using radiation loss from heavy element, will enhance amplification.

II - AMPLIFICATION IN SHORT PLASMA COLUMNS

Several experiments performed in different laboratories with different techniques have shown that aluminium plasma recombination actually provides gain at the wavelengths of the 5f or 4f lines. In this section we summarize a first set of experiments differing each other in many aspects but having in common the magnitude of the plasma column length used for measuring the gain. In these experiments the plasma length was 1 centimetre or less. We do so because - as we will see in the next section - new problems seem to be adressed from recent experiments when one attempts to increase the plasma length up to several centimetres. These experiments are described in section III.

The first measurements of amplification by Li-like ions have been performed by our group in the first eighties. The neodymium-glass laser (1.06 μ) of GILM at Palaiseau was used with a pulse duration comprised between 0.6 and 25 ns. The laser beam was focused on the target surface by combining either spherical and cylindrical lenses or two crossed cylindrical lenses. The focal-spot size was 0.1 mm x10 mm, later extended up to 20 mm with the use of two superimposed laser beams. The target used for producing the plasma was a plane sheet of spectroscopically pure metal. Emission from the plasma axis was analyzed using an X-UV spectrometer based on a 1 m radius concave grating of 3600 grooves per mm used at 6° angle of grazing incidence. Time integrated and time resolved spectra could be recorded owing to the use of either a scintillator coupled with an optical multichannel analyser (OMA) or an X-UV streak camera as detectors [7].

An extensive study of time-integrated emission of aluminium plasma has been made for laser irradiance comprised between 0.6×10^{11} and 3×10^{12} W/cm^2, [8]. A wavelength band wide of about 10 Å round the position of 3d - 5f transition was recorded by OMA. Strong absorption lines were observed, corresponding to transitions of lower charge ions. Regarding the 3d - 5f transition at 105.7 Å and, to a lower extent, the 3p - 5d one at 103.8 Å they give absorbing lines at very low irradiance, which turn progressively into negative peaks in the plasma absorption background when the irradiance rises above a threshold value of about 3×10^{11} W/cm^2. This behaviour is characteristic of the lithiumlike structure and not only of aluminium. Analogous negative peaks were observed in the absorption spectra of magnesium at 127.85 Å and sulphur at 65.2 Å the wavelengths of the 3d - 5f transition[9] .

Amplification time history has been studied in time-resolved experiments [10] . The X-UV streak camera provided a time resolution about 100 ps. It was connected either with photographic plate or with the OMA. A typical result corresponding to a laser irradiance of 3. 10^{12} W/cm2 and to a pulse duration of 2 ns is presented in figure 3. Time-resolved emission of two aluminium plasma columns, at the wavelength of 3d-5f transition, is shown on the upper part of the figure. The column lengths are respectively 7 and 3 mm. Let us notice that the time of maximum intensity is delayed with the column lengthening. The lower part of the figure shows the time evolution of gain, deduced at each time from the above intensities. The plasma is at first optically thick, and then it goes continuously from absorption to amplification; gain is decreasing again at the end of plasma recombination, when density has fallen. The maximum of gain is near 2 cm^{-1}. It occurs about 5 ns after the top of the laser pulse.

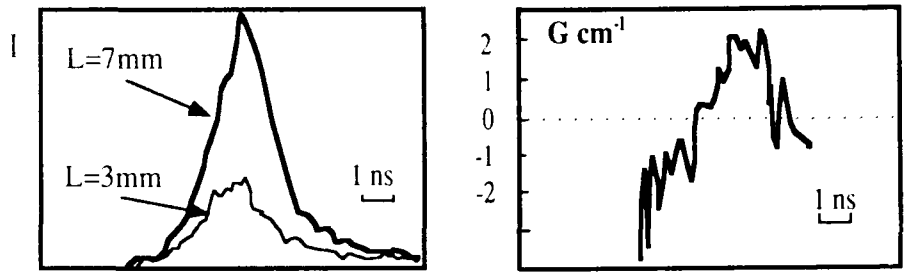


Figure 3: Time-resolved gain measurement at 105.7 A in Li-like aluminium . Onthe left: time variation of radiation emitted by plasma columns of lengths 3 mm and 7 mm. On the right: gain deduced from these intensities.Target: 0.2 μ of Al on a graphite plate. Laser wavelength 1.06 μ , pulse duration 2.0 ns, irradiance 3. 10^{12} W/cm^2.

The transition 3d - 4f is theoretically a better candidate than the 3d - 5f one for amplification: its radiative decay probability is about 3 times larger, and populations deduced from simulations are almost the same for both levels 4f and 5f. Evidence of amplification due to transition 3d - 4f has been found in time-resolved experiments but, in our experiments the gain value is not found significantly higher than for 3d-5f.

Since a few years, a number of X-ray laser experiments using the Li-like scheme have been carried out in various laboratories [11, 12, 13, 14] . Experimental parameters are very different from one experiment to another one, what does not permit close comparisons of gain values, but all experiments have shown evidence of gain involving one or both 3d - 4(5)f transitions.

The recombination scheme is studied at Princeton with particular characteristics of plasma column production including the possibility of magnetic confinement[15]. Heavy impurities may be introduced to radiatively increase the cooling. Owing to the use of a CO^2 pump laser, the plasma heating arises in a zone of electron density 10^{19} cm^{-3}, instead of 10^{21} cm^{-3} with a Nd-glass laser. Then, population inversions take place in a region of lower density they have a longer duration (owing to the magnetic confinement) than with other devices. The amplification in Li-like magnesium, aluminium and silicon has been studied in this confined plasma column [16]. Time-integrated plasma emission was recorded along both axial and transverse directions, the axial spectrometer being placed at two different transverse positions corresponding to gain and non-gain regions. GxL values about 1.5 at 187.2 Å in Mg X, at 129 Å in Si XII and 3 at 154.7 Å in Al XI have been reported. The 3d --5f transitions were not observed. That might be related to the low initial density of the plasma.

Amplification for 3d - 5f transitions has been observed in other experiments realized with frequency doubling and tripling of Nd-glass radiation. The Osaka group chose to study, in the same experiment, amplifications from H-like carbon and oxygen and Li-like aluminium by using targets made of 600 A-thick foils of formvar coated with 200 A of aluminium[17]. A 100 J-150 ps-laser beam at $\lambda = 0.53$ μ was focussed to a linear spot of 0.035 mm width and 15 mm length, which gives an irradiance of 1.3×10^{14} W/cm^2. Time integrated spectra covering the wavelength region of 100-300 Å exhibited amplification for the 3d - 5f and 3p - 5d transitions of Li-like aluminium, with gain coefficients of 1.5 cm^{-1} and 1 cm^{-1} respectively. Surprisingly, amplifications occurred only when the laser irradiated the formvar surface opposite to the aluminium, and not when the aluminium was directly irradiated. No amplification was detected at the wavelength of the 3d - 4f line.

In a similar experiment performed at Rochester by Moreno et al , amplifications were detected for 3 --4 as well as for 3 - 5 transitions [18]. The wavelength of the pump laser was shorter and the laser pulse has a longer duration (650 ps) than in the former experiment, but the irradiance on the target surface was analogous. Targets consisted of 5000 Å layer of aluminium and a 100 Å layer of gold on a 10 μ thick mylar backing. They were irradiated on both sides. Gold was included in targets in order to enhance the plasma cooling, but it did not have significant effect on aluminium-line intensities. Amplifications were deduced from time-integrated spectra with high-spectral resolution. Figure 4 shows a large increase of the amplifying lines from 3 mm- to 6 mm-long plasma columns. Gain values of 4.5 cm^{-1} and 3.5 cm^{-1} were found

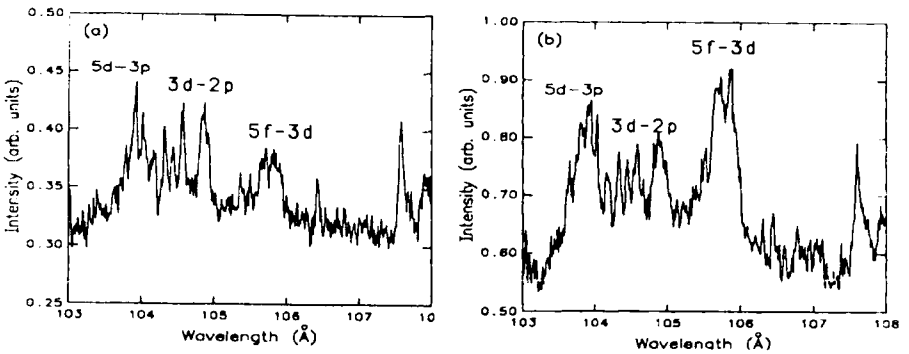


Figure 4: Time integrated spectra showing the 5f - 3d, 5d - 3p lines of Li-like aluminium to increase with the plasma column length. Gain coefficient: 3.5 cm^{-1}.Target: Al 0.5 μ on Au 0.01 μ and 10 μ mylar foil. Laser wavelength 0.35 μ, pulse duration 0.6 ns, irradiance 8. 10^{13} W/cm^2 (from ref. 18)

respectively for the 3d - 4f and 3d - 5f transitions. They are the largest experimental values measured up to now. However, the plasma-column length was short and the GxL values, 2.7 and 2.1, are of the same order as in other experiments.

Pumping by recombination in H-like systems, based on short-laser pulses and fibre targets is under investigation since years at Rutherford Appleton Laboratory [19]. A collaborative work has been undertaken between the British group and our own in order to test the Li-like scheme in the same experimental conditions [20]. Targets were 7 μ diameter and 7 to 12 mm-long carbon fibres coated by 3500 Å of aluminium. They were irradiated by two or four frequency-doubled beams of the VULCAN laser, which delivered 15 J per beam in 120 ps. The size of the focussing spot for each beam was 0.03 mm x 7 mm, which corresponds to an irradiance of 6. 10^{12} W/cm^2. The X-UV emission of the plasma was detected by two time-resolving spectrometers, one along column axis and the other one in the transverse direction. The transverse spectra exhibited intense resonance lines 2s - 3p and 2p - 3d, but 3d - 5f and 3p - 5d are barely discernible and their transverse intensities could not be measured. The exponential increase of 3d - 4f and 3d - 5f line intensities, given by the on-axis spectrometer at the time of peak gain for each transition, is shown in figure 5. It shows gain coefficients of 2.6 cm^{-1} and 1.6 cm^{-1}, respectively for the 3d - 4f and 3d - 5f transitions. The corresponding GxL values are 3.1 and 1.9.

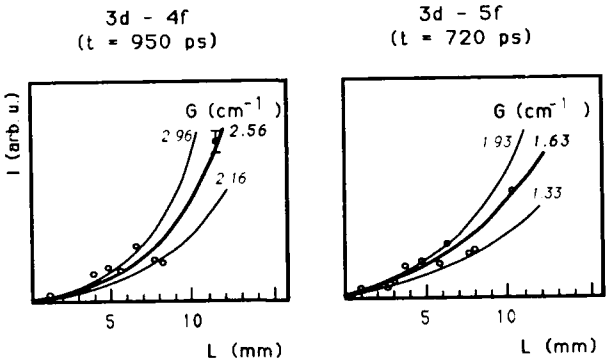


Figure 5: Exponential increase of 3d - 5f, 3p - 5d lines of Li-like aluminium as a function of plasma length. Target: Al-coated thin fibre. Laser wavelength 0.53 μ, pulse duration 0.12 ns, irradiance 5. 10^{13} W/cm^2 (from ref. 20)

Let us still point out the result recently reported by Zhizhan et al. noting gain of 3.1 cm^{-1} at 105.7 Å in aluminium[21]. In this work amplification is also observed at 88.9 Å in Li-like silicon.

A last experiment differs from the others by the very low target irradiance used for producing the plasma (2. 10^{11} W/cm^2) .from a Nd-glass laser (1.06 μ) with a long pulse (5 ns) [22]. A large increase of line intensities against the plasma column length is reported in this work. For the 3d - 4f and 3d - 5f transitions, this increase fits gain coefficients of 4.5 cm^{-1} and 3.4 cm^{-1} what corresponds to GxL products as high as 5.4 and 4.1. This result has given rise to some surprise. However, at the Conference Laser's 81 we reported the first evidence of non-linear intensity increasing at λ = 105.7 Å in aluminium, obtained for an irradiance of 3-5x10^{11} W/cm^2 and a 20 ns-laser pulse. A gain coefficient between 0.5 $cm^{-1}$and 2 cm^{-1} was deduced from line intensity measurements, this large uncertainty coming from the detector calibration [23]. In a further work (ref. 7 above) we studied the threshold of population inversion emergence in aluminium in using 3.5 ns-pulses[24]. We found it to be near 2x$10^{11}$$W/cm^2$, that is the value of Hara's experiment. But, near this threshold, the gain was very weak, (i.e. gain coefficient ≤0.01 cm^{-1}). On the other hand, computational

simulations never revealed us a possible large gain in similar conditions. Thus although our previous works are in agreement with the production of gain in the condition of Hara's experiment, the large values reported in this work remain to be explained. It seems us unlikely that a 2-D effect in plasma expansion will suffice to clear completely the point.

As a conclusion, disregarding now some differences between experiments - like the fact that gain is either for only one or for both 4f- and 5f- lines - one can deduce from the above results that, at laser irradiance from 10^{12} W/cm^2 to 10^{14} cm^2, plasma lines of length around 1 cm provide gain coefficients between 1 cm^{-1} and 4 cm^{-1}.

III - AMPLIFICATION IN LONG PLASMA COLUMNS

All the results summarized in the previous section make up a first stage of the research about the lithium-like scheme. It is obvious that they are not sufficient to carry out real X-ray lasers. The goal to be reached is to put the gain-length product at a value of 10 or 15, when it is only about 2 or 3 in the previous experiments. This requires new experiments in which the length of the plasma line is significantly increased, either directly or by using multipass devices made with multilayers mirrors.

We recently carried out preliminary experiments with a 6 cm-long plasma column [25]. Five of the six beams of the Nd-glass laser of LULI at Palaiseau were used to produce the plasma. They were located in a plane perpendicular to the column axis on one and the same side of the target. After focusing by cylindrical lenses of focal length 450 mm, the five beams were superposed on a rectangular spot of 0.2 mm x 64 mm. The target was 60 mm wide in order to avoid cold plasma at the ends of the column.The energy of each beam was about 100 J with a pulse duration of 2 ns. So the irradiance was of 2.x10^{12} W/cm^2 on the target surface.

The grazing incidence spectrometer used the Wadsworth circle (with radius equal to the fourth part of the radius of curvature of the concave grating) instead of the classical Rowland circle (half radius of curvature)[26]. This configuration has been chosen because it privileges the analysis of radiation having a strong directivity with respect to isotropic emission. An optical multichannel analyser was used as a detector. An analyser of beam divergence could be inserted between the plasma column and the spectrometer. It enabled to record, in a single shot, several spectra emitted along the column axis and along oblique directions. A multilayers tungsten/carbon mirror, with a 5 % synchrotron-radiation-controlled

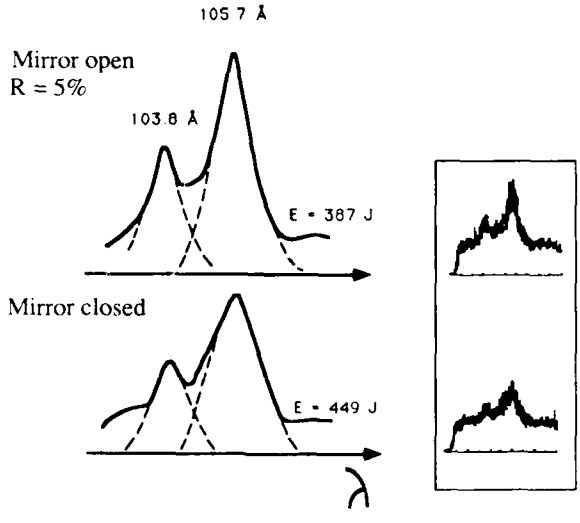


Figure 6: Effect of double-pass in a 6 cm-long plasma column on the intensities of 3p - 5d and 3d - 5f lines of Li-like aluminium. (Top) Mirror open (reflectivity 5 %). (Bottom) Mirror closed. Effective gain-length product: 4. Target: 0.1 μ of Al on a massive polymer slab. Laser wavelength 1.06 μ, pulse duration 2. ns, irradiance 2. 10^{12} W/cm^2 (from ref. 25)

reflectivity [27] in a narrow band around 105.7 Å, was set perpendicularly to the axis, at the end opposite to the detector. So 3d - 5f amplification was determined by comparison of single- and double-pass intensities.

To reduce the radiative trapping, the target was a 1000 Å layer of aluminium coating the surface of a massive plate made either of a polymer free of aluminium or of graphite. Experiments have shown amplification effectively to occur, the increasing of intensity from single- to double-pass case being of 1.7 (figure 6). This corresponds to a GxL value of 3, i.e. the gain coefficient was not larger than 0.5 cm^{-1}. As regards the "effective" GxL value, which takes the double-pass into account, it was of 4.

Although this value is large enough to conceive an X-ray laser using for instance a six-pass cavity, it is of importance to understand why the gain-coefficient comes to such small values in the case of long plasma columns, a fact that we have observed so far in all attempts we made to increase the plasma length. In the present case, radiation trapping must likely be ruled out because, with thin layer targets, the 2p-3d emission near the target surface cannot be strong. Moreover, the refraction of the amplified beam is negligible because the plasma density in the active region, as well as the density gradient in the direction perpendicular to the axis, are very small having regard to the value of the wavelength of the amplified line. Therefore we must turn to new considerations regarding the production of the plasma column.

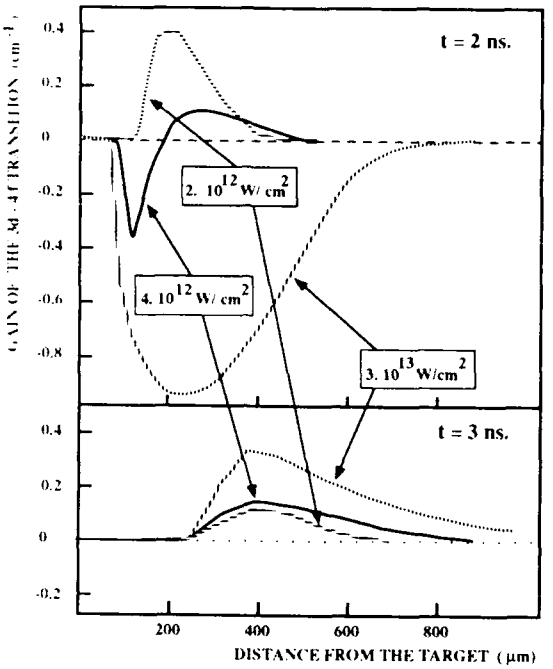


Figure 7: Calculation of gain versus target distance for the 154.7 Å line of Li-like aluminium. Laser wavelength: 1.06 μ, pulse duration: 0.6 ns, irradiance 2 , 4, and $20.x10^{12}$ W/cm^2. Curves are plotted at fixed time, i.e. 2. ns (upper curves) or 3.1 ns (lower curves) after laser pulse maximum.

We must keep in mind for instance that, in all gain measurement procedures, one assumes the plasma to be homogeneous in temperature and density along the column axis. Now the distribution of energy may be far to be constant from a point to another through the laser beam section and one is founded to wonder about the effects of inhomogeneities on the gain coefficient. Gain calculations in aluminium illustrated by figure 7 are intended to give a preliminary and yet suggestive response to this question. The figure displays the gain for the 3d - 4f transition as a function of target distance, in a plasma produced by a 600 ps laser pulse, for three different irradiances ($2x10^{12}$, $4.x10^{12}$, and $2x10^{13}$ W/cm^2). Results are given at two fixed times, i.e. 2 ns and 3.1 ns after laser pulse maximum. Let us consider now a plasma column produced by an inhomogeneous beam such as regions of low, middle and high irradiance are distributed along the focal spot. It appears from figure 7 the low irradiance region to give a large amplification at 2 ns, even when the high irradiance region, being still strongly absorbing, reduces or destroys the gain. This region becomes amplifying later and at larger distance from the target. From figure 7 we see this to occur at a time where the gain of the low irradiance region is already well reduced. The middle irradiance region has an intermediate behaviour. It is clear that the plasma column will provide much less amplification than if it was an homogeneous one. The point which is emphasized by this calculation is laser-beam inhomogenities to disynchronize the gain production along the plasma column and consequently to reduce the total gain. It has been often assumed that plasma inhomogeneities are quickly smoothed by electron-ion collisions. Nevertheless very few 2D-simulations are presently available to support this statement especially during plasma recombination.

Now it has been shown laser-beam inhomogeneity to actually produce long-scale plasma irregularities of such a type that they could result in a reduction of gain when plasma length increases [28]. In the case the LULI laser a complete mapping of the plasma is still missing but an image of a small part of the column has also revealed the presence of strong irregularities. This is shown in figure 8. Therefore the long-scale plasma inhomogeneity increasing is a good candidate for being the cause of the gain coefficient decreasing which is observed when the plasma column is lengthened above 1 or 2 cm..

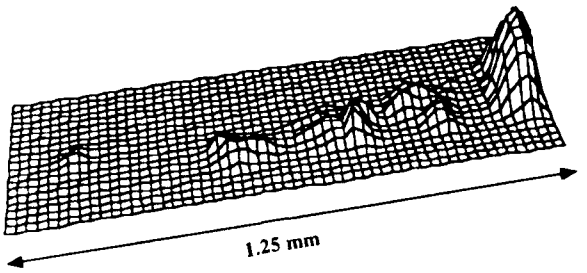


Figure 8: Pinhole image for 500 ev radiation of a small part (1.25 mm) of the plasma line produced in an experiment performed at LULI. Strong irregularities are visible.

IV - CONCLUSION

The recombination scheme in lithiumlike ions has proved to give gain at the wavelengths of 4f and 5f lines. It is an attractive way to an X-ray laser. Gain coefficients are very sensitive to details of experimental techniques which cannot be included in theoretical simulations. It is very likely that making the plasma cooling faster, either by adding heavy elements or by a suitable target design, will increase the gain. However large gain-length products are not yet achieved although attempts have been made with long plasma lines. Target parameters and target composition must be optimalized. A reasonable uniformity (20%-30%) of the plasma along its axis turns out to be a major requirement of future experiments.

This work has been supported by DRET under contract 88-236.

References:

[1] L.I. Gudzenko, L.A. Shelepin, Sov. Physics - Doklady **10** (1965) 147

[2] F.E. Irons and N.J. Peacock, J. Phys. B: Atom Molec Phys **7** (1974) 2084

[3] G.J. Pert, S.A. Ramsden, Optics Comm. **11** (1974) 270

[4] G. Jamelot ,P. Jaeglé, A. Carillon, A. Bideau, C. Möller, Proc. of the International Conference on Lasers'81 , C.B. Collins ed., STS Press 1982 p. 178

[5] A. Klisnick, A. Sureau, H. Gennou, C. Moller, J. Virmont, Applied Physics B, **50** (1990), in press

[6] J.C. Gauthier, J.P. Geindre, N. Grandjouan, and J. Virmont, J. Phys. D **16** (1983) 321

[7] A. Carillon, G. Jamelot, A. Klisnick, G. Tévanian, P. Jaeglé, and P. Dhez, Proceedings of the SPIE, Vol. 688, N.M. Ceglio and P Dhez, editors, (1987) p. 12

[8] G. Jamelot, A. Klisnick, A. Carillon, H. Guennou, A. Sureau, and P. Jaeglé, J. Phys. B: Atom. Molec. Physics, **18** (1985) 4647

[9] P. Jaeglé, A. Carillon, A. Klisnick, G. Jamelot, H. Guennou, and A. Sureau, Europhys. Lett. **1** (1986) 555 and P. Jaeglé, G. Jamelot, A. Carillon, A. Klisnick, J. de Physique **47** (1987) C6-31

[10] P. Jaeglé, A. Carillon, A. Klisnick, G. Jamelot, H. Guennou, and A. Sureau, Europhys. Lett. **1** (1986) 555 and P. Jaeglé, G. Jamelot, A. Carillon, A. Klisnick, J. de Physique **47** (1987) C6-31

[11] P. Jaeglé, in Physics of Highly-Ionized Ions, ed. by R. Marrus, NATO ASI Series, Series B: Physics vol. 201 p. 209, Plenum Press1988

[12] S. Suckewer, C.H. Skinner, H. Milchberg, C. Keane, and D. Voorhes, Phys. Rev. Lett. **55** (1985) 1753

[13] D. Kim , C.H. Skinner, A. Wouters, E. Valeo, D. Voorhees, and S Suckewer, OSA Proceedings on Short Wavelength Coherent Radiation: Generation and Applications, R.W. Falcone and J. Kirz eds. (Optical Society of America, Washington DC, 1988), Vol.2, p. 116

[14] Y. Kato, P.R. Herman, T. Tachi, K. Shihoyama, K. Kamei, and H. Shiraga, Springer Proceedings in Physics, Springer-Verlag, Vol. 30, C. Yamanaka editor, 1988, p. 57

[15] S. Suckewer, H. Fishman, J. Appl. Phys. **51** (1980) 1922

[16] see ref. 11

[17] Y. Kato, P.R. Herman, T. Tachi, K. Shihoyama, K. Kamei, and H. Shiraga, Springer Proceedings in Physics, Springer-Verlag, Vol. 30, C. Yamanaka editor, 1988, p. 57

[18] J.C. Moreno, H.R. Griem, S. Goldsmith, and J. Knauer, Phys. Rev. A **39** (1989) 6033

[19] C. Chenais-Popovics, R. Corbett, C.J. Hooker, M.H. Key, G.P. Kiehn, C.L.S. Lewis, G.J. Pert, C. Regan, S.J. Rose, S. Sadaat, R. Smith, T. Tomie, and O. Willi, Phys. Rev. Lett. **59** (1987) 2161

[20] C.L.S. Lewis, R. Corbett, D. O'Neill, C. Regan, S. Sadaat, C. Chenais-Popovics, T. Tomie, J. Edwards, G.P. Kiehn, R. Smith, O. Willi, A. Carillon, H. Guennou, P. Jaeglé, G. Jamelot, A. Klisnick, A. Sureau, M. Grande, C. Hooker, M.H. Key, S.J. Rose, I.N. Ross, P.T. Rumsby, G.J. Pert, and S.A. Ramsden, Plasma Phys. and Cont. Fus. **30** (1988) 35 and A. Carillon, J. Edwards, P. Jaeglé, G. Jamelot, M.H. Key, G.P. Kiehn, A. Klisnick, C.L.S. Lewis, D. O'Neill, G.J. Pert, S.A. Ramsden, C. Regan, S.J. Rose, and T.Tomie, J. Phys. B: Atom Molec Physics, 22 (1990) in press

[21] Zhizhan Xu, Zhenquan Zhang, Pinzhong Fan, Shisheng Chen, Lihuang Lin, Peixiang Lu, Xiangping Feng, Xiaofeng Wang, Jinzhi Zhou, Aidi Qian, A.P.S Conference 1989, Abstracts **34**, (1989) 2096

[22] T. Hara, K. Ando, N. Kusakabe, H. Yashiro, and Y. Aoyagi, Jap. J. of Appl. Physics **28** (1989) L 1010

[23] G. Jamelot, P. Jaeglé, A. Carillon, A. Bideau, C. Möller, H. Guennou, and A. Sureau, Proceedings of the International Conference on Laser'81, Carl B. Collins, editor, STS Press, p. 178, 1982

[24] see ref. 7.

[25] P. Jaeglé, A. Carillon, P. Dhez, B. Gauthé, F. Gadi, G. Jamelot, and A. Klisnick, Europhysics Letters, **7** (1988) 337

[26] A. Carillon, P. Dhez, B. Gauthé, P. Jaeglé, G. Jamelot, A. Klisnick, J. C. Lagron, X-Ray Instrumentation in Medecine and Biology, Plasma Physics, Astrophysics, ans Synchrotron Radiation, Proceedings of the SPIE, Vol. 1140, R. Benattar Editor (1989) , p.271

[27] M. Kühne , P. Müller, Proceedings of the SPIE, Vol. 1140, R. Benattar Editor (1989) , p.220

[28] J.C. Kieffer, M. Chaker, M. Hébert, H. Pépin D.M. Villeneuve, J.E. Bernard, H.A. Baldis, 19th Anomalous Absorption Conference, Fort Lewis College, Durango, Collorado, June 19-23, 1989.

SODIUM Z-PINCHES FOR X-RAY LASER RESEARCH ON THE 6-TW DOUBLE-EAGLE GENERATOR

C. Deeney, T. Nash, R. R. Prasad & M. Krishnan*

Physics International Company
2700 Merced Street
San Leandro, California 94577

D. Hinshelwood & F. C. Young

Naval Research Laboratory
4555 Overlook Ave, SW
Washington, DC 20375

Abstract

The sodium-neon photopumped X-ray laser scheme is under investigation at Physics International on the DNA/Double-EAGLE generator. A series of z-pinch implosion experiments, using a NaF capillary source as well as an extruded, pure Na wire, was performed to produce bright line emission from the $1s^2$ -1s2p resonance line of NaX. A peak power in this line of 150 GW and a peak total line yield of 8 kJ were measured.

Introduction

The sodium-neon photopumped[1] X-ray laser scheme uses the Na X $1s^2$-1s2p ^1P line(He-α) at 11.0027Å to resonantly photo-excite the Ne IX $1s^2$-1s4p ^1P line, at 11.0003Å. This excitation can result in inversions in the 4-3, 4-2 and 3-2 lines. Predictions of the gain[2,3] in the 4f-3d line, at 230 Å, give 2 cm^{-1} when the sodium and neon plasmas are 2 cm apart and the sodium plasma radiates 100 GW in the He-α pump line. These gain estimates assume an optimum neon ion density of $5x10^{18}$ cm^{-3} and electron temperature of 50-100 eV. At Physics International (PI), the sodium-neon scheme is investigated using pulsed power driven Z-pinches[4,5] to produce both the lasant and pump plasmas. A high power, 3-6-TW, high current, 2.5-4 MA waterline pulsed power generator is used to implode a sodium bearing load to produce the pump line, and a low-current, 100-400-kA capacitor bank is used to pinch a neon gas jet to produce the lasant plasma.

This approach of using two separate sources allows them to be independently optimized. In addition, in this geometry, length scaling studies to show exponential growth on-axis can be performed by shielding the neon lasant, effectively pumping different lengths of the lasant plasma. Ideally, for a successful experiment, the sodium pump plasma should radiate greater than 100 GW for longer than 10 ns. The long pulse length would allow for use of a multi-pass cavity. Moreover, the neon lasant plasma should be uniform over a 2 to 3-cm length, with the desired density and temperature for a time greater than the pump pulse width for maximum efficiency.

The sodium-neon X-ray laser scheme has been investigated on various pulsed power generators. A sodium-fluoride (NaF) capillary source[6] has been tested on the 1-TW, 1.2-MA Gamble II generator at Naval Research Laboratory, and these experiments gave 25 GW in the He-α line[7]. When one of the return rods in these experiments was replaced by a neon gas puff pinch, evidence of fluorescence was obtained[8]. Subsequent experiments[4,5] with a sodium-chloride (NaCl) discharge source on the 3-TW, 2.5-MA PITHON generator were aimed at increasing the sodium pump line power. In fact, the best pump power achieved was 65 GW, and it was concluded that to further improve the pump power would require (1) a better defined source than the NaCl discharge, (2) higher currents, and (3) the use of a pure sodium plasma. To achieve this, implosions have been performed on the 6-TW, 3-4-MA Double-EAGLE machine. Double-EAGLE produces higher radiation yields and powers. Indeed, recent radius scaling experiments[9] on Double-EAGLE achieved 40 kJ, 1 TW of 1 keV radiation from nickel wire array implosions. The results at the higher current levels, using a characterized NaF capillary source and sodium wire arrays, are presented in this paper.

The Sodium Fluoride Capillary Z-Pinch

The NaF capillary source fielded on Double-EAGLE is similiar to that described by Welch et al.[6], except that it is driven by a more energetic capacitor bank. The larger discharge current increases the mass flow from the capillary and thus enables efficient coupling to the higher current generator. The capillary was mounted on Double-EAGLE as depicted in Figure 1; it was fired from the anode (ground) into the transparent cathode. The cathode was a 4-cm-diameter, hollow stainless steel cylinder with a 25-μm tin-coated-copper-wire mesh wound on the open face. The mesh acted as the current path. In order to vary the parameters of the NaF-bearing plasma injected into the 3-cm anode-cathode gap, the delay between triggering the capillary and triggering Double-EAGLE could be adjusted, and the diameter of the graphite nozzle placed downstream of the capillary could be altered. During these experiments, the delay was scanned from 3 to 11 μs and 1.0-, 1.5- and 2.0-cm-diameter nozzles were tested.

Various spectroscopic X-ray diagnostics, described by Nash et al.[10], were mounted to study the radiation properties of the plasma and hence, determine the temperatures and densities. The sodium (and fluorine) K-shell X-ray emissions were measured with a 4-cm curved Mica crystal spectrometer with gated microchannel plates and a space-resolved 4-cm curved Mica crystal spectrometer. X-ray diodes and

* Present Address: Science Research Laboratory, Suite 100, 1150 Baliena Boulevard, Alameda, CA 94501.

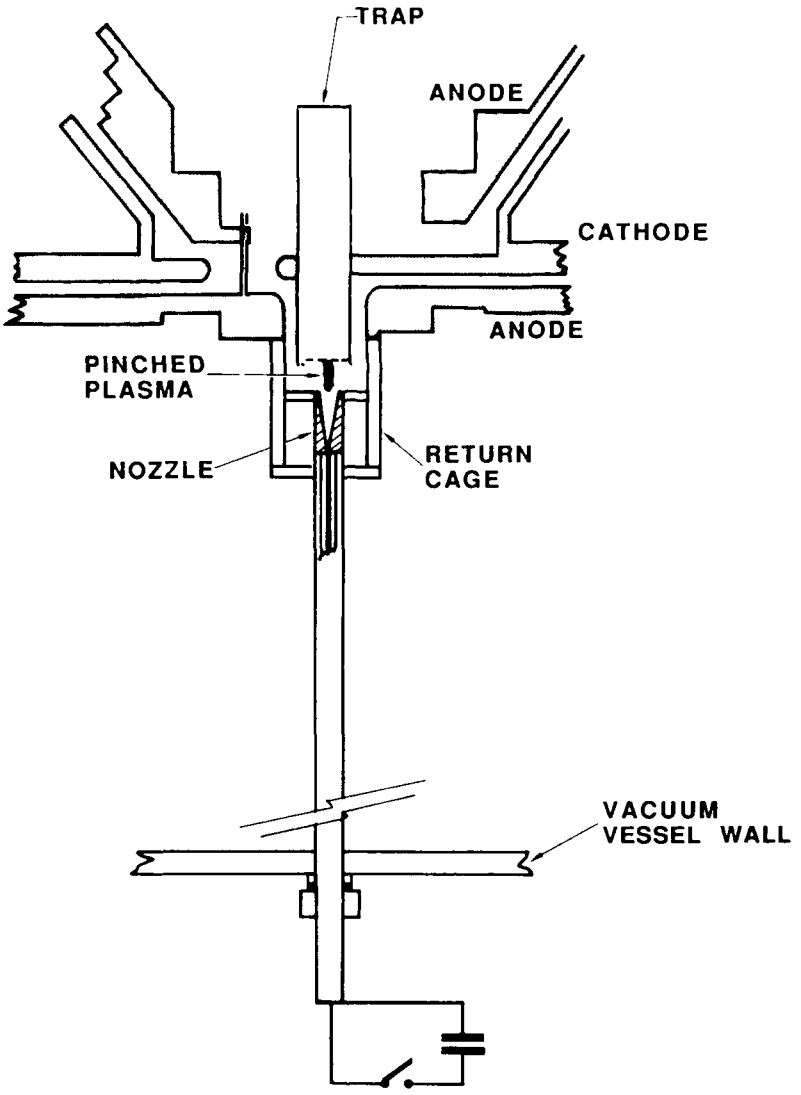


Figure 1. Sodium fluoride capillary mounted on Double-EAGLE.

calorimeters, filtered with 2-μm Kimfol plus 1.8-μm aluminum, gave measurements of the total K-shell yields and emission powers. Importantly, a copper cathode X-ray diode filtered by 2-μm germanium was used to measure the power emitted in the sodium He-α line, as proposed by F. C. Young et al.[11]. Finally, a time-resolved dual pinhole, dual filter X-ray camera was used to give information on the K-shell-emitting and L-shell-emitting X-ray regions. The filters were 2-μm aluminized Kimfol and 8-μm Kimfol plus 1.8-μm aluminum. The latter only transmits >1 keV X-rays.

Examples of the measured X-ray emissions and K-shell spectra are shown in Figures 2(a) and 2(b). The current from Double-EAGLE is shown, in Figure 2(a), along with the measured K-shell and He-α emission powers for Shot 2072. This shot was performed with a 1.5-cm diameter graphite nozzle, and Double-EAGLE was triggered 5.5 μs after the capillary driver bank. Shot 2072 was the highest power shot and 130 GW, 3.4 kJ was measured in the He-α line. The total K-shell yield was 14 kJ, and the peak K-shell emission power was 540 GW. The lower figure, 2(b), is a photograph of the space-resolved crystal spectra obtained on Shot 2072. The electrode orientation and axial scale are shown on the right hand side of the figure. In addition, below the photograph, the emission lines in the sodium and fluorine are indicated, as is the wavelength position of the L-edge of the germanium filter with transmits the Na He-α line but absorbs the Na Ly-α line. Notice that the spectrum is dominated by these two lines, with the Ly-α being the most intense. Taking a densitometer scan (not shown) of the spectrum and correcting for the filter transmissions, then the ratio of Ly-α to He-α is 2.45. Assuming that the measured 3.4 kJ is correct for the Na He-α line, this gives 8.4 kJ in the Na Ly-α line and a corresponding total radiated yield in these two lines of 11.8 kJ. This is consistent with the estimated total K-shell yield of 14 kJ.

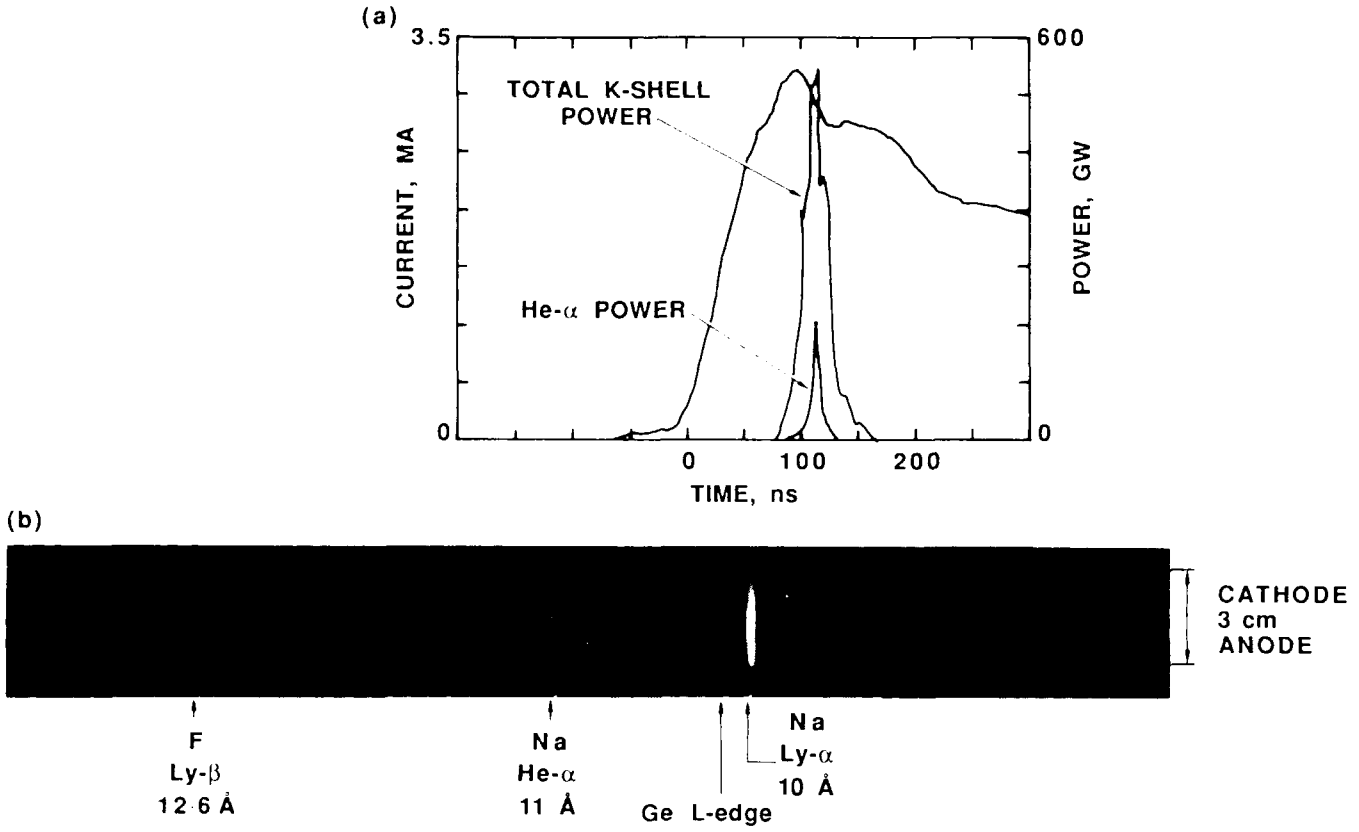


Figure 2. Double-EAGLE Current X-ray emission for a NaF capillary implosion.

Sodium Wire Array Experiments

Pure sodium wire array sources[12] have been developed at Physics International. These wire arrays are extruded in-situ while Double-EAGLE is at vacuum prior to a shot. The wire arrays were composed of 6 or 12 wires arranged equi-spaced on a diameter that varied from 9 to 12 mm. The thickness of the individual wires was adjusted by using different pinhole sizes on the extruder. Seventy-five to 150-μm-thick wires were tested.

Figure 3 shows the measured He-α power and K-shell power along with the Double-EAGLE current, for Shot 2098, which was a 12-mm diameter array having six, 150-μm diameter wires. The Na He-α power and yield were 153 GW and 8 kJ respectively. These were the highest power and yield with the sodium wires. The kimfol/aluminium filtered X-ray diode measured a K-shell yield of 31 kJ. A photograph of the space-resolved crystal spectrum for Shot 2098 is presented in Figure 4. Again, the axial scale and line indications are marked. Again, the spectrum is still dominated by the He-α and Ly-α lines, with the Ly-α line being the most intense.

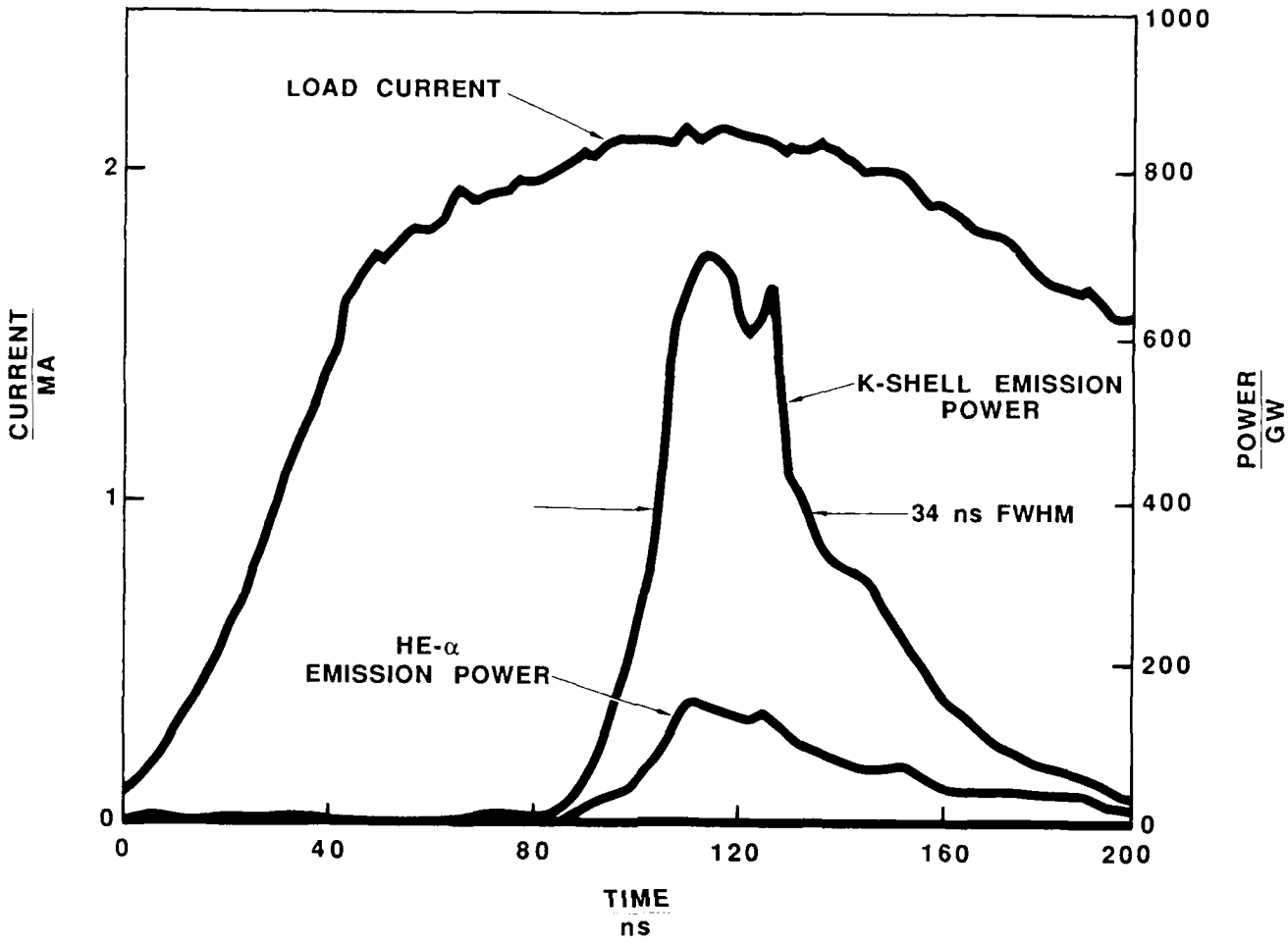


Figure 3. Double-EAGLE Current and X-ray emission for a 12 mm diameter Sodium wire Array.

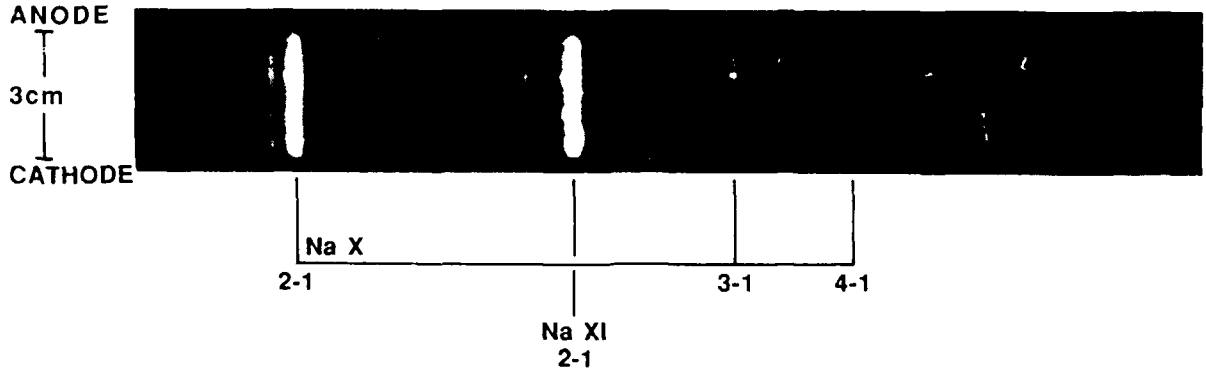


Figure 4. K-Shell Spectrum for a Sodium Wire Array Implosion.

Discussion of Sodium Source Experiments on Double-EAGLE

Previously, arguments have been made that the total K-shell emission power from a Z-pinch should scale as the current to the fourth power[13]. Moreover, Krishnan et al.[14] suggested that at some point, energetics would dictate that the K-shell emission power should roll-over to a current squared scaling, and theoretical modeling by K. G Whitney and J. W. Thornhill[15] has explored at what point this transition occurs for aluminum implosions. Now, from Figure 5, it seems that the Na He-α emission power is scaling proportional with the generator power. This translates into an effective current scaling of approximately I^2 from the Gamble II to Double-EAGLE results. However, this is an individual line, and the ratio of this pump line power to the total K-shell power would vary from experiment to experiment; therefore, further analysis is required to model this scaling. The scaling is exciting, though, because it suggests that an optimized sodium source on the 25-TW Saturn generator[16] at Sandia National Laboratories should give higher pump powers.

In summary, two different sodium sources have been successfully tested on the 6-TW Double-EAGLE generator, producing a maximum power of 150 GW and yield of 8 kJ in the Na X $1s^2$-1s2p ^1P line. This should be sufficient to produce fluorescence and gain in a properly prepared neon lasant plasma.

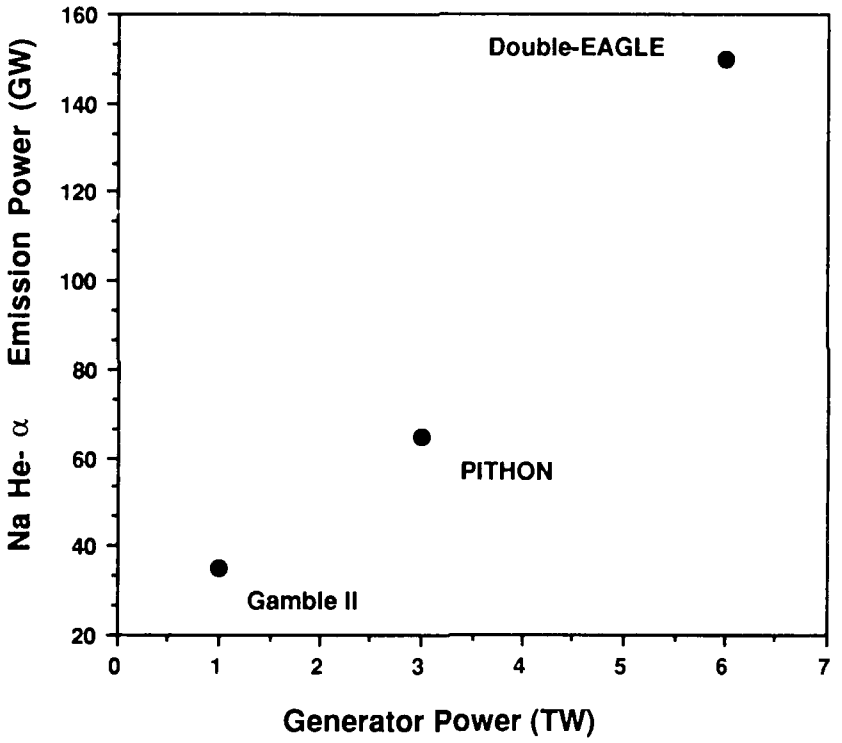


Figure 5. Experimentally observed He-α power scaling with generator power.

Acknowledgements

The assistance of N. Knobel, B. Kribs and the DNA/Double-EAGLE team is gratefully acknowledged. The authors would like to thank J. Apruzese, J. Giuilliani and J. Davis of NRL for their contributions to this work. K. Matzen and R. Spielman of SNL are also thanked for their interest in these experiments. This work was supported by SDIO/IST and directed by NRL. Additional support was given by the Defense Nuclear Agency, and the encouragement of Captain J. Fisher is appreciated.

References

1. J.P. Apruzese, J. Davis & K.G. Whitney, J. Appl. Phys., **53**(6), p4020, (1982).
2. M. Krishnan, SDIO USWL Review, Washington, December, (1989).
3. J.P. Apruzese & J. Davis, "Pulsed Power Driven X-ray Lasers: Fantasy or Reality?" Proceedings of the Intl. Conf. on Lasers 89, December, (1989).
4. C. Deeney, J. Levine, T. Nash, P.D. LePell & M. Krishnan, OSA Proc. on Short Wavelength Coherent Radiation: Generation and Applications, p157, (1988).
5. T. Nash, C. Deeney, J. Levine & M. Krishnan, Proceedings of the International Conference on Lasers '88, p82, (1988).
6. B. Welch, F.C. Young, R.J. Commisso, D.D. Hinshelwood, D. Mosher & B.V. Weber, J. Appl. Phys **65**(7), p2664, (1989).
7. F.C. Young, S.J Stephanakis, V.E. Scherrer, B.L. Welch, G. Mehlman, P.G. Burkhalter & J.P. Apruzese, Appl. Phys. Lett. **50**(16), p1053, (1987).
8. J.P. Apruzese et al., SPIE Proc. on Short and Ultrashort Wavelength Lasers, vol. 875, p2, (1988).
9. C. Deeney, T. Nash, P.D. LePell, M. Krishnan & K. Childers, AIP Conf. Proc. 195, p55, (1989).
10. T. Nash, C. Deeney & M. Krishnan, "Application of Time-Resolved Spectroscopy to Terawatt Z-pinches", Second Intl. Conf. on Dense Z-Pinches. Laguna Beach CA, (1989).
11. F.C. Young, S.J. Stephanakis and V.E. Scherrer, Rev.Sci. Instrm. **57**(8), p2174, (1986).
12. C. Deeney, R.R. Prasad, T. Nash & N. Knobel, "Extruded Sodium Wires for Z-Pinch Implosions.", To be published in Rev. Sci. Instrm., (1990).
13. J.P. Apruzese & J. Davis, NRL Memo Report 5406, (1984).
14. M. Krishnan, C. Deeney & T. Nash, AIP Conf. Proc. 195, p17, (1989).
15. K.G. Whitney & J. W. Thornhill, AIP Conf. Proc. 195, p143, (1989).
16. R.B. Spielman, R. Dukart, D.L. Hanson, B.A. Hammel, W.W. Hsing, M.K. Matzen & J.P. Porter, AIP Conf. Proc. 195, p3, (1989).

SMALL SCALE SOFT X-RAY LASERS; APPLICATIONS TO MICROSCOPY.

C.H. Skinner, D.S. DiCicco, D. Kim, D.Voorhees, and S. Suckewer

Princeton University Plasma Physics Laboratory,
Princeton, N.J. 08543

Abstract

The widespread application of soft x-ray laser technology is contingent on the development of small scale soft x-ray lasers that do not require large laser facilities. Progress in the development of soft x-ray lasers pumped by a Nd laser of energy 6-12J is reported below. Application of an existing soft x-ray laser to X-ray microscopy has begun. A soft X-ray laser of output energy 1-3 mJ at 18.2 nm has been used to record high resolution images of biological specimens. The contact images were recorded on photoresist which was later viewed in a scanning electron microscope. We also present a Composite Optical X-Ray Laser Microscope "COXRALM" of novel design.

1. Introduction

The field of x-ray laser technology has recently matured to the stage where the application of these devices to fields such as x-ray microscopy is underway[1] and commercial units are being planned with a view to industrial applications such as microlithography. A critical factor in such development is the scale and hence cost of these devices. The collisionally pumped soft x-ray laser in neon-like ions, developed at Livermore[2], requires a large scale laser facility such as Novette or Nova to create a plasma of appropriate conditions. A 3mJ, 182Å soft x-ray laser based on a recombining plasma was developed at Princeton[3] with an efficiency almost 2 orders of magnitude higher than the collisionally pumped case. However the pump laser required, a 300J CO_2 laser, was still large. In order to increase the output energy and efficiency of the 182Å soft x-ray laser we have been developing soft x-ray amplifiers. A gain of $8cm^{-1}$ has been measured in a 3mm long carbon plasma transversely pumped by a 3nsec Nd laser pulse of energy 25J, of which only 15J impinged on the target[4]. In this paper we will present initial gain measurements of 4.5 cm^{-1} at 182Å in a carbon plasma pumped by a 6J laser pulse[5]. Application of an existing soft x-ray laser to the field of x-ray microscopy will be described in section 3. An intensive effort to generate gain in

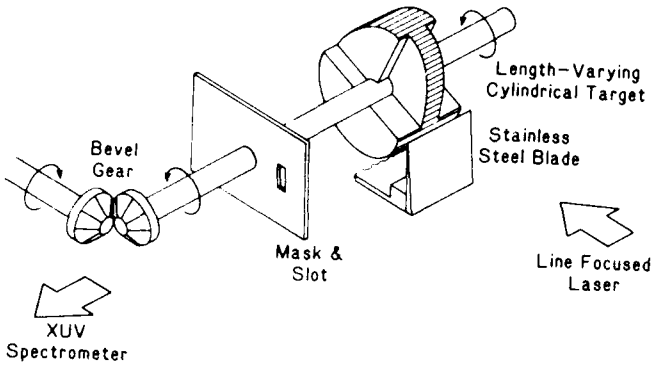


Fig. 1 The rotatable target system.

the region of 10 Å is also underway at Princeton and was described in the 1988 Proceedings of this conference[6]. The powerful sub-picosecond laser is now operating close to its full design goals of 150-250mJ in a 300fsec pulse[7] and work on the physics of laser-matter interactions at these ultra high intensities is underway. This article will concentrate on the development of small-scale soft x-ray lasers and their applications.

2. Amplification at 182Å with a 6J Pump Laser

In this section, we present gain measurements on the CVI 182Å transition in a carbon plasma produced with a 6J, 3 nsec Nd:glass laser pulse. The experimental set-up was the same as presented in an earlier paper[4]. Figure 1 shows the rotatable target system used . A 67-cm focal-length spherical lens and 450 cm focal length cylindrical lens were operated in a slightly defocussed arrangement to produce a ~200 μm x 5 mm line-focus on a length-varying cylindrical target. The target lengths used in this experiment were 1, 2.5, and 4.5 mm (limited by the diameter of the access ports in the target chamber). A 0.8 x 2 mm slot in a mask located 1.5 cm away from the target in the axial direction, selected a limited spatial region which was viewed by an axial soft x-ray spectrometer equipped with a multichannel detector. In the experiments the slot was placed in such a way that it selected a spatial region 0.0 - 0.8 mm from the target surface.

Figure 2 shows the intensity variation of the CV 135Å, OVI 173Å, CVI 182Å, and CV 186Å lines with respect to the plasma length using a 6J, 3 nsec. laser pulse. No stainless steel blade or magnetic field was used. The CVI 182Å line (3-2 transition) increased non-linearly while the CVI 135Å (4-2 transition) and some other lines increased linearly as expected from optically thin spontaneous emission from a homogeneous plasma of length equal to the length of the target. This was a clear indication of gain on the 182Å line. The difference in the length dependence of the 182Å and 135Å lines here is very important (the contribution of the 4th order of the CVI 33.74Å line to 135Å, even for the 1mm plasma, was negligible due to the large opacity of this line). The data were fitted by a nonlinear regression model which performed a least-square fit of the data to the relation:

$$I(L) = \frac{(\exp(GL) - 1)^{3/2}}{(GL \times \exp(GL))^{1/2}} \quad (1).$$

This describes the output intensity of a Doppler-broadened, homogeneous source of amplified spontaneous emission of gain-length product GL. The fit yielded a value of the gain of 4.5 / cm on the CVI 182Å line and of 0.5 / cm on the CVI 135 Å line (see Fig. 3). This result augers well for the commercial availability in the near

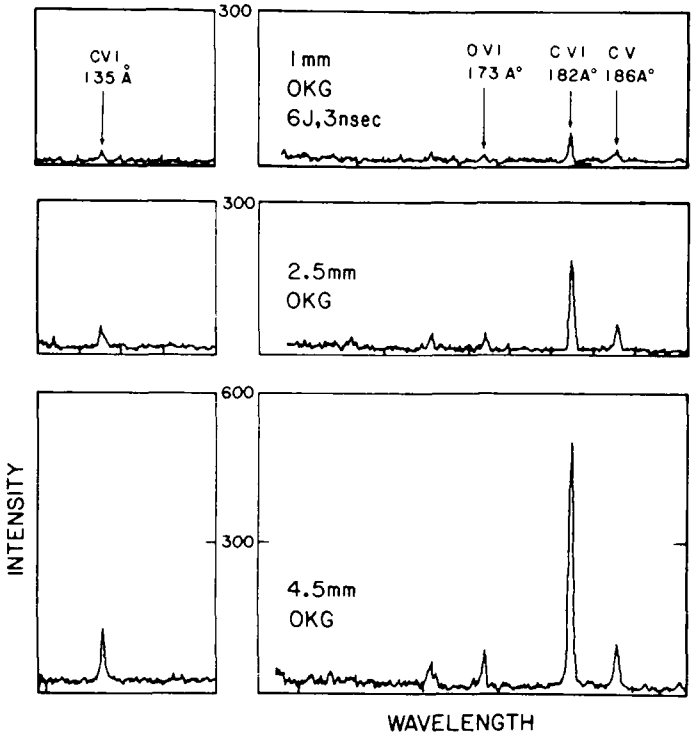


Fig. 2 Spectra obtained with 6J laser energy from carbon plasmas of length: (a) 1mm, (b) 2.5mm and (c) 4.5 mm.

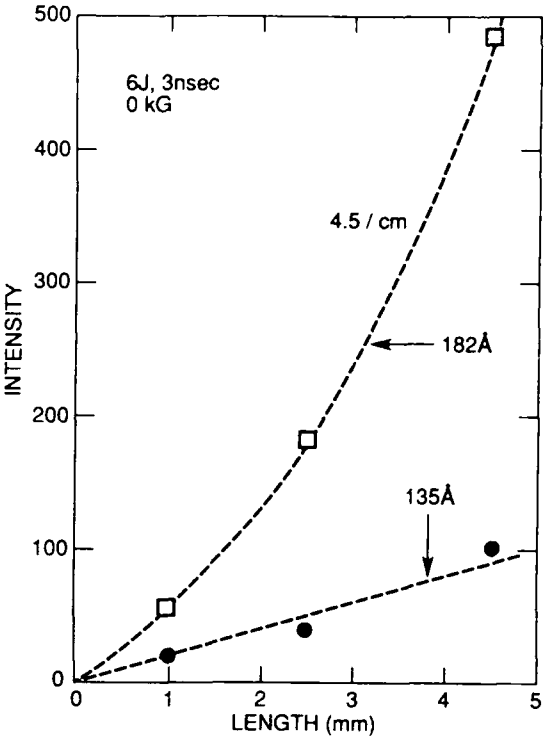


Fig. 3 Intensities of the CVI 182Å and CVI 135Å lines versus plasma length and (dashed line) a least squares fit to the gain equation (eqn. 1) with a gain of 4.5 cm^{-1} at 182Å.

future of relatively inexpensive soft x-ray lasers for a variety of novel applications.

Very recently there has been a report by Hara et. al.[8] of gain in the soft x-ray region produced by a small scale (6J) pump laser. The presence of gain was deduced from the non-linear rise in intensity with length of AlX and AlXI emission lines. However, in contrast to earlier work by Kim et al. [9] the non-linear rise of the "gain lines" with plasma length was not referenced to a linear rise of "no-gain lines" in AlXI such as the 14.1nm transition, leaving open the possible influence of other effects. A non-linear rise of intensity with length on the same transitions in a similar experiment[10] was shown to be due to non-uniformities in plasma conditions along the plasma region viewed by the detector and not due to stimulated emission.

3. Contact Microscopy using a Soft X-Ray Laser

Much progress has been made in Biology and Medicine due to the high resolution images obtained from electron microscopes. However, in order to be viewed by an electron microscope the specimen must undergo intensive specimen preparation techniques and it is clear that some information about the living cell is lost in the process. One can view a live cell with a light

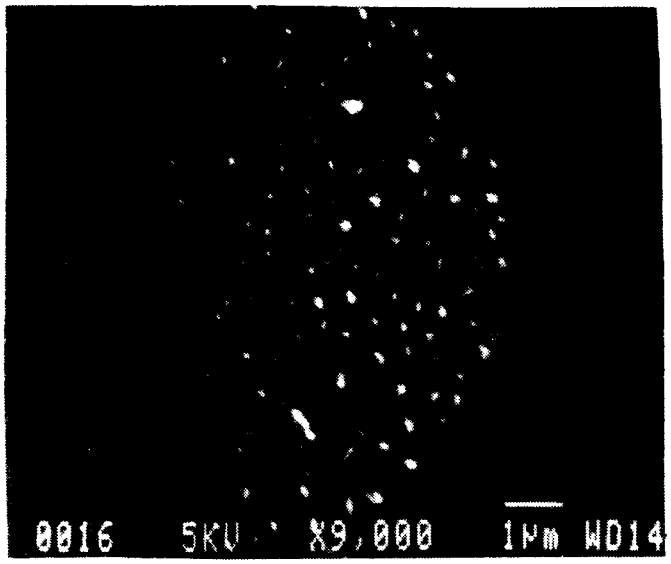


Fig 4: SEM image of replica of Granulocytes from *Limulus Polyphemus* (Horseshoe Crab).The replica was generated by contact microscopy using the 18.2 nm soft x-ray laser

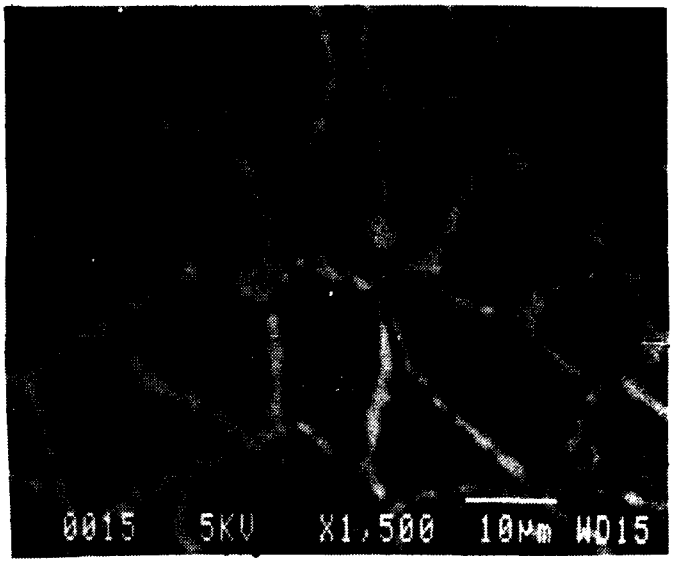


Fig.5: SEM image of replica of hela cells (Helen Lane cervical cancer cell) that was subject to an viral infection.

microscope with high fidelity but the resolution is, of course limited. Soft X-ray contact microscopy offers a new method to obtain high resolution images of live cells. The specimen is contained in an environmental cell isolated from the X-ray laser vacuum system by a 120 nm thick silicon nitride window. The image is recorded on photoresist which is later viewed by an electron microscope[11]. The highly collimated output beam of the soft X-ray laser, compared to a conventional plasma light source, has the advantage of less penumbral blurring of the image and more flexible microscope design. The soft X-ray laser also has the advantage of a 10-30 nsec exposure time enabling flash images of **live** cells to be recorded, unlike the several minutes needed for synchrotron sources which effectively prevents the imaging of live cells with synchrotrons.

One topic of considerable current interest in biology is immunology and since this involves the **dynamic** response of immune cells to foreign matter it is a natural subject for investigation by soft X-ray laser microscopy. One of the most primitive and hence simplest, immune systems is found in the horseshoe crab *(Limulus Polyphemus)* where there is only one type of immune cell to fulfill several functions. A sample of blood from the horseshoe crab was dehydrated in an ethanol series and critical point dried using the standard procedure but was not fixed or stained and an exposure was taken with the soft X-ray laser contact microscope. The resulting images viewed in an JEOL 840 scanning electron microscope are shown in Figure 4. The depressions apparent in the granulocyte are known to exhibit immune functions from work in conventional electron

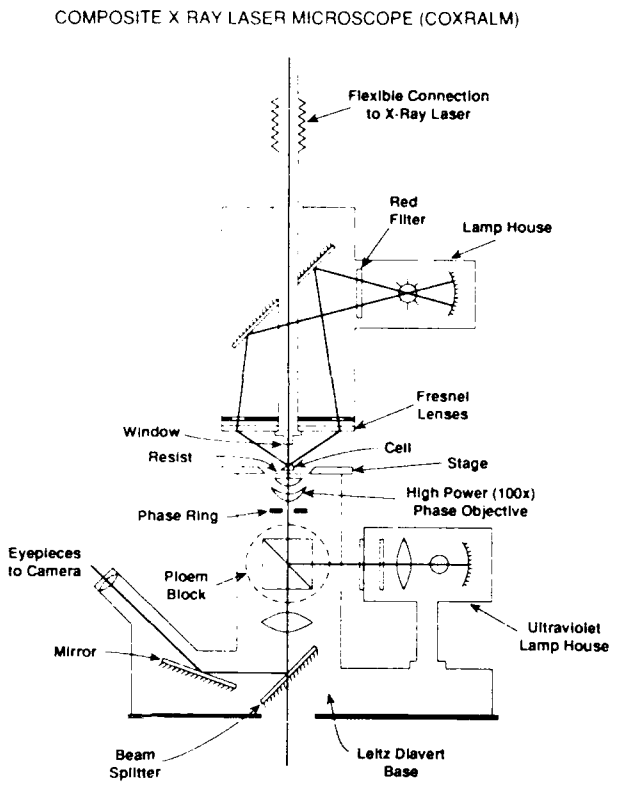


Fig.6: Schematic of Composite X-Ray Laser Microscope.

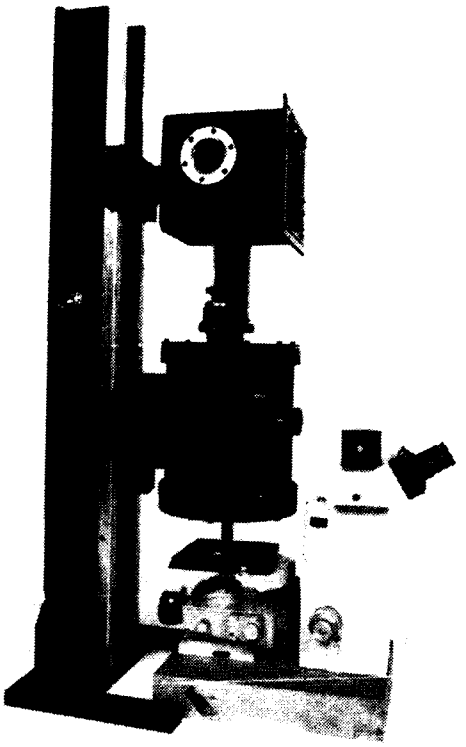


Fig.7: Composite X-Ray Laser Microscope: "COXRALM".

microscopy. The smaller white features covering the cell are new and were not apparent on images obtained in conventional electron microscopy. Their identity and function is presently unknown.

An improved technique using backscattered electrons for initial viewing of the specimen[1] was used to obtain the image shown in Fig. 5. This is a SEM image of a replica of hela cells (cultured human cervical cancer cells) . An embedment-free section of a monolayer of extracted hela cells that had been subject to an viral infection was prepared on a carbon/formvar base. The replica was generated by contact microscopy using the 18.2 nm soft x-ray laser.

4. Microscope Development

Perhaps the greatest potential for soft X-ray laser microscopy is in the study of dynamic processes in live cells. To maintain and manipulate cells in a living state is a considerable experimental challenge and for novel microscopic techniques to have a significant impact in biology they must be practical and convenient to use. To this end we have developed a Composite Optical Soft X-ray Laser Microscope, "COXRALM" (Figures 6,7). This is a new type of microscope combining an inverted phase contrast optical microscope with a soft X-ray laser contact microscope. The inverted optical microscope has already been used as a microspectrofluorometer for the study of

transient coenzyme fluorescence changes in living cells as a result of the intracellular microinjection of metabolites[12]. This research is aimed at understanding the pathology and physiology of cancer cells. However the inevitable limitations in resolution of the optical microscope meant that many features of the metabolic processes inside the cells remained obscure.

COXRALM offers the possibility of making an X-ray contact image of these cells while preserving the ability to select and observe through the optical microscope and perform microinjection of metabolites and/or inhibitors and xenobiotics just prior to X-ray exposure. The cells will be mounted on resist on a transparent substrate. When a contact X-ray image is desired the X-ray laser beam tube will be lowered until the silicon nitride vacuum window at the tip is in contact with the cell and then the X-ray laser is triggered. The system has been installed on the X-ray laser and was used in initial experiments without the optical microscope to generate the contact images shown in Figures 4 and 5.

Acknowledgements:

We gratefully acknowledge stimulating discussions with H. Furth, A. Gupta, J. Hirschberg, E. Kohen,R. Rosser and B. Williams. We thank E Valeo for assistance with the gain fitting computer program and J Schwarzmann for the target fabrication. We would also like to thank S.Orenberg and D. Ornelles for preparation of the biological specimens and E. Lenk for the Electron Microscopy, and acknowledge significant contributions from, L. Meixler, T. Bennett, and P.C. Cheng. The silicon nitride windows were provided by the IBM Watson Research Center and the P.B.S. resist by G. Taylor at A.T.&T Bell Labs. COXRALM was fabricated by Princeton X-ray Laser Inc. This work was supported by the U.S. Department of Energy, Advanced Energy Projects of Basic Energy Sciences.

References:

1 C.H. Skinner, D.S. DiCicco, D Kim, R.J. Rosser, S. Suckewer, A.P. Gupta, and J.G. Hirschberg *J. Micros.* (1990) in press.

2 D. L. Matthews et al. *Phys. Rev. Lett.* **54,** 110, (1985) and C.J.Keane,et al. *J. Phys B.* **22**, 3343, (1989).

3 S. Suckewer, C. H. Skinner, D. Kim, E. Valeo, D. Voorhees, and A. Wouters *Phys Rev. Lett.* **57**, 1004, (1986).

4 D.Kim, C.H. Skinner, G. Umesh, and S. Suckewer *Optics Letters*, **14**, 665-667, (1989).

5 S. Suckewer in *OSA Proceedings on Short Wavelength Coherent Radiation: Generation Applications* **2,** R.W. Falcone and J Kirz, eds. (Optical Society of America Washington DC (1988) pp 36-46, .

6 W. Tighe, L. Meixler, C. H. Nam, and S. Suckewer in Proceedings of the International Conference on Lasers '88

7 W.Tighe personal communication

8 T. Hara, K. Ando, N. Kusakabe, H. Yashiro, and Y. Aoyagi *Jpn. J. Appl. Phys.* **28**, 1010, (1989).

9 D. Kim, C.H. Skinner, A. Wouters, E. Valeo, D. Voorhees, S. Suckewer, in *OSA Proceedings on Short Wavelength Coherent Radiation: Generation and Applications* **2,** R.W. Falcone and J Kirz, eds. (Optical Society of America Washington DC 1988) pp.116-122, and S. Suckewer *Ibid* ,pp.36-46

10 C. H. Skinner, D. Kim, D. Voorhees, and S. Suckewer; Princeton University, Plasma Physics Laboratory Report # PPPL 2669 (January 1990) 24pp to be published.

11 P.C. Cheng, R. Feder, D.M.Shinozaki, K.H. Tan , R.W. Eason, A. Michette, R. J. Rosser, Soft X-ray Contact Microscopy. *Nucl. Instrum. Methods* **A246**, 668-674 (1986).

12 J.G.Hirschberg, A.W. Wouters, C. Kohn, B. Kohen, B. Thorell, B. Eisenberg, J.M. Salmon, H.S. Ploem; A High Resolution Grating Microspectrofluorometer with Topographic Option for Studies in Living Cells. in *ACS Symposium Series No 102* Y. Talmi ed. (American Chemical Society, 1979) pp 263-289.

ANALYSIS OF A SOFT X-RAY FREQUENCY DOUBLER

M. H. Muendel and Peter L. Hagelstein
Massachusetts Institute of Technology
Research Laboratory of Electronics
Cambridge, Massachusetts 02139

Abstract

A scheme to frequency-double (approximately) a soft x-ray laser using a four-wave mixing process in a plasma medium is proposed and investigated theoretically. The potential for considerable conversion is shown in a Na-like K plasma converting radiation at about 189 Å to radiation at about 95 Å .

I. Introduction

With the advent of laser sources in the EUV and soft x-ray regimes, it becomes of interest to consider the extension of optical laser techniques and applications to shorter wavelengths. Nonlinear optical phenomena in general have been of great interest and importance to laser physicists; the prospect of frequency mixing in the EUV is of special interest to our group, both for the eventual production of a bright tunable coherent source for applications, and for the prospect of achieving shorter wavelength radiation through doubling.

The mixing of x-ray radiation and optical radiation has been considered previously in Ref. 1 and Ref. 2. Our interest here is focused on mixing EUV radiation with EUV radiation for the purpose of developing a short wavlength laser source, since our group is working on a small scale (tabletop) EUV laser. In order to produce coherent radiation in the water window in a future generation laser system, we propose that it may more feasible technically to obtain short wavelength radiation through frequency mixing rather than to face the power requirements associated with obtaining substantial gain in the water window in a small scale system.

Unionized matter is highly absorbing in the EUV. Efficient frequency conversion in the EUV requires low loss, and we have concluded that a low density plasma will probably be most conducive to the mixing process This conclusion immediately rules out frequency doubling since parity selection rules cannot be satisfied in isolated ions which are found in such plasmas.

Our approach is therefore to study four-wave mixing, in which two EUV beams are combined with an intense third optical beam to generate harder EUV radiation at roughly double the frequency of the initial EUV beams. Since it is unlikely that ions can be found with two connected transitions at the same energy (to within a few linewidths), it may not be practical to carry out four-wave mixing experiments with only one EUV laser and one optical laser. Our choice of ion was initially motivated by the hope of developing a scheme in which only a single EUV laser frequency would be required.

The process which we have studied[3] is the four-wave mixing which produces ω_4 generated from

$$\omega_4 = \omega_1 + \omega_2 - \omega_3,$$

where ω_1 and ω_2 are x-ray laser photons with roughly equal energies, or possibly the same energy, and ω_3 is an optical laser photon.

This difference process is used rather than the straight sum process because in positively dispersive media such as plasmas, only difference processes can be noncollinearly phasematched. As we shall demonstrate, the conversion rates are sufficiently low to require phasematching, unless very high x-ray laser intensities are achieved; and of the various phasematching schemes only the noncollinear type appears feasible in a plasma medium. Like the sum process, tripling and higher-order harmonic processes also appear difficult to phasematch.

The low conversion rates also require us to use resonances on all three transitions; hence the desirability of different lasers for ω_1 and ω_2, chosen to match transitions. Of course, ω_3 must also be tuned to resonance.

II. Conversion Example: Na-Like K

As an example, we study conversion in a plasma of Na-like K, as shown in Figure 1.

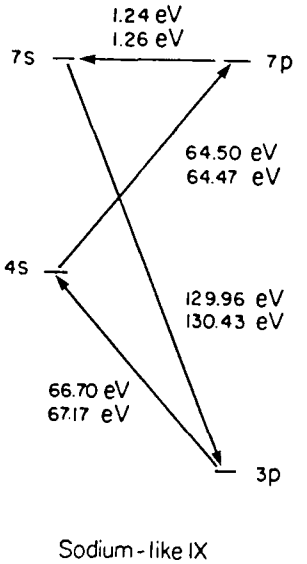


Figure 1: Schematic of K IX energy levels and the four-wave mixing scheme.

The initial state is the thermally populated $3p$, and each transition is LS-split. Note that either one x-ray laser at about 65.6 eV should be used, or, for better resonance, two different lasers, matching the transitions better.

The multiphoton transition rates can be calculated straightforwardly using Feynman diagrams, and the results are well known[4]. The nonlinear susceptibility is

$$\chi^{(3)}(-\omega_4 : \omega_1, \omega_2 - \omega_3) = \frac{1}{6\hbar^3}\Sigma\mu_{12}\mu_{23}\mu_{34}\mu_{41}\rho_{11} \times \left(\frac{1}{\omega_{21} - \omega_1 - i\Gamma_{21}} + \frac{1}{\omega_{21} - \omega_2 - i\Gamma_{21}}\right) \times \left(\frac{1}{\omega_{31} - (\omega_1 + \omega_2) - i\Gamma_{31}}\right) \times \left(\frac{1}{\omega_{41} - (\omega_1 + \omega_2 - \omega_3) - i\Gamma_{41}}\right) \quad (1)$$

where only the resonance denominators relevant for $\omega_1 \approx \omega_2 \gg \omega_3$ have been retained. Here ω_{ji} is the transition frequency from level i to level j. The results given in the figures of this work derive from numerical evaluation of this formula.

Expressing the converted intensity in dimensionless terms then gives us the scaling relation

$$I_4 \sim \frac{1}{\omega^8} I_1 I_2 I_3,$$

from which, in comparison with analogous schemes in the optical regime, the necessity of higher intensities, better resonance matching and phasematching is clear.

For the case of just one x-ray laser, with $\omega_1 = \omega_2$, the nonlinear susceptibility $\chi^{(3)}$ is shown in Figure 2.

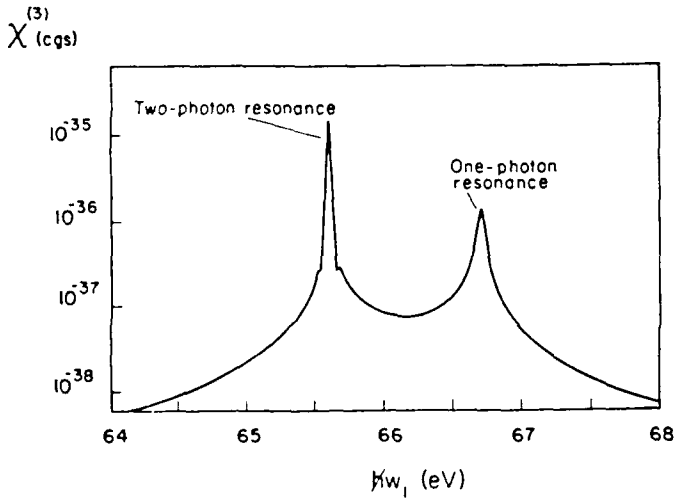


Figure 2: Nonlinear susceptibility for $w_4 = 2w_1 - w_3$ conversion as a function of $\hbar w_1$, assuming that $2\,\hbar w_1 - \hbar w_3 = 136.40$ eV. The ion temperature is taken to be $2 \times 10^5 K$ in this and in the following figures.

The single and two-photon peaks are visible. The linewidths, which are due primarily to Doppler broadening, are sufficiently wide to make the line-matching requirement not too demanding.

For the case of two separate x-ray lasers, we show in Figure 3 the dependence of $\chi^{(3)}$ upon $\hbar\omega_2$, assuming that $\hbar\omega_1$ has been fixed at 66.5 eV, fairly near the 66.7 eV resonance.

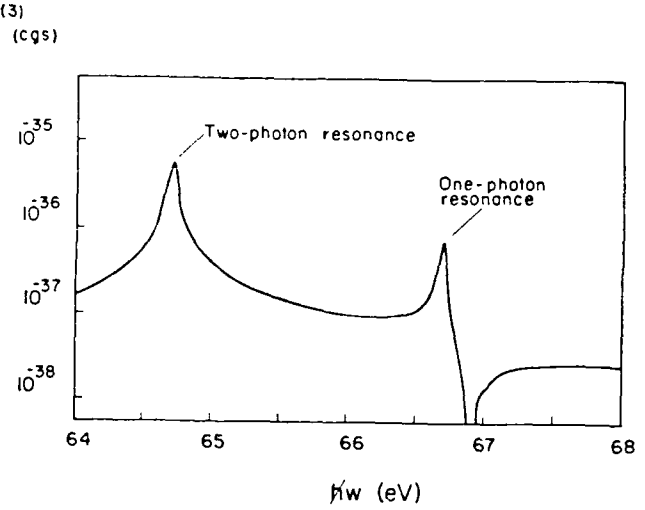


Figure 3: Nonlinear susceptibility for the $w_4 = w_1 + w_2 - w_3$ process as a function of $\hbar w_2$, assuming that $\hbar w_1 = 66.5$ eV and that $\hbar w_1 + \hbar w_2 - \hbar w_3 = \hbar w_4 = 136.40$ eV.

Some structure due to $7p$ fine structure splitting may be observed in the two-photon resonance. Also, a cancellation occurs at 66.9 eV.

Using input intensities of 10^{10} W/cm^2 for the x-ray lasers and 10^{12} W/cm^2 for the optical, we find the intensities shown in Figure 4 for the case corresponding to Figure 3.

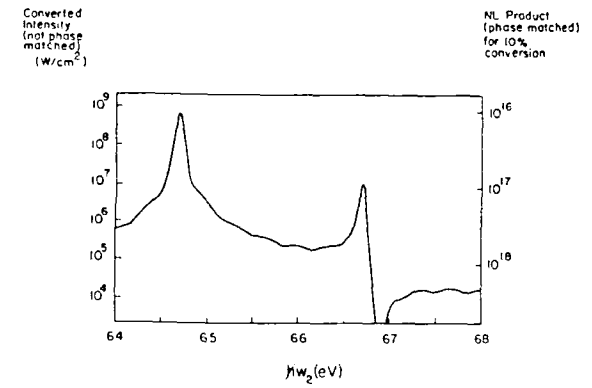


Figure 4: Nonlinear conversion for the $w_4 = w_1 + w_2 - w_3$ process as a function of $\hbar w_2$, assuming that $\hbar w_1 = 66.5$ eV and that $\hbar w_1 + \hbar w_2 - \hbar w_3 = 136.40$ eV. The intensities for this calculation are taken to be $I_1 = 10^{10} W/cm^2$, $I_2 = 10^{10} W/cm^2$, and $I_3 = 10^{12} W/cm^2$.

The scale on the left shows the maximum possible non-phasematched conversion before back-conversion begins. The right-hand scale shows, for phasematched operation, the value of NL required for 10% conversion, assuming that other processes do not limit the conversion.

As can be seen, the results are quite reasonable. In non-phasematched operation, the output should be sufficient to allow detection of signal and hence demonstration of the effect. Phasematching may allow efficient conversion of soft x-ray radiation.

We conclude from the promising results of this example calculation that nonlinear effects should be observable and useful in the soft x-ray regime, much as they are in the optical. The unfavorable scaling to this regime, however, will require both attention to phasematching and resonance matching, as well as high input intensities.

Acknowledgments

This work was supported by the U. S. Department of Energy, Division of Advanced Energy Projects, under contract DEFG02/89CR14012. One of us (MHM) acknowledges the support of an NSF graduate fellowship.

References

1. I. Freund and B. Levine, *Phys. Rev. Lett.* **23** 854 (1969).

2. P. M. Eisenberger and S. L. McCall, *Phys. Rev. A* **3** 1145 (1971).

3. M. H. Muendel and P. L. Hagelstein, submitted to *Phys. Rev. A*.

4. J. F. Reintjes, *Nonlinear Optical Parametric Processes in Liquids and Gases*, Academic Press, Orlando, 1984.

ADIABATIC WHISPER-GALLERY MIRRORS FOR EUV AND SOFT X-RAY LASER CAVITIES

John Paul Braud

Research Laboratory of Electronics
Massachusetts Institute of Technology
77 Massachusetts Avenue, Room 38-280
Cambridge, Massachusetts 02139

Whisper-gallery mirrors have been studied for use in laser cavities for the extreme ultraviolet and soft X-ray regimes. One cavity scheme proposed by Vinogradov would use a cylindrical whisper-gallery mirror and a pair of laser amplifiers. Unfortunately, the low-order modes of such a cavity are small in comparison with the amplifiers, and hence single-mode operation would be difficult to achieve. We examine a strategy for increasing the size of the cavity modes by using mirrors of an elongated shape. Based upon an analysis relating the mode structure of a mirror of arbitrary shape to that of a round mirror, we propose a particular family of curves as candidates for the form of the elongated mirrors.

1. Introduction

A whisper-gallery mirror (WGM) is an optical structure which, by means of a series of glancing-angle reflections, can deflect light through a large total angle. Such a mirror has been proposed for use in laser cavities for the extreme ultraviolet and soft X-ray regimes [1-6].

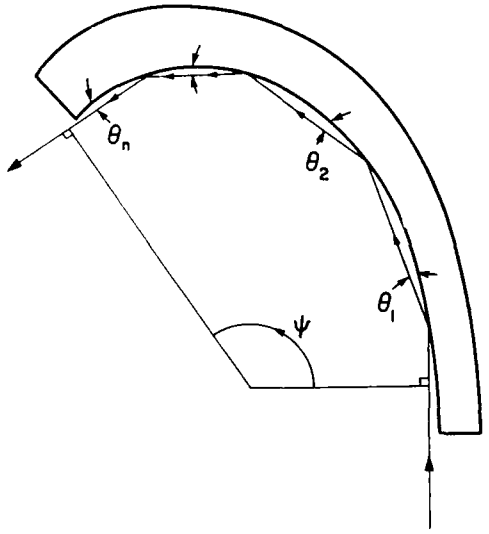


Fig. 1: Multiple reflections inside a whisper-gallery mirrror.

When analysing what happens to a beam as it passes through a WGM, it is useful to think in terms of a paraxial approximation [7]. Just as with the more familiar wave optics of Gaussian beams, the structure of the field is separated into its axial and transverse dependencies, corresponding respectively to variations in the one direction parallel and the two directions perpendicular to the beam axis. The transverse structure in turn separates into a "vertical" part for the direction perpendicular to the mirror surface and a "horizontal" part for the remaining direction tangential to the mirror surface (but orthogonal to the axial direction). The effect of a WGM upon a beam propagating along its surface is highly astigmatic: the vertical and horizontal structures evolve quite differently from each other.

The present paper concerns the mode structure in the vertical direction. We shall see below that for the wavelengths and mirror sizes likely to be of interest for an X-ray laser, the low-order modes of a circular WGM tend to be quite small in the vertical direction. As a consequence, it would be difficult to couple a laser amplifier into only one or just a few modes: the cavity Fresnel number would inevitably be large. Fortunately, it appears possible to increase the characteristic size of the low-order modes by employing elongated mirrors rather than round ones.

2. Modes of a cylindrical WGM

To get some feeling for the mode strucure of a WGM, it helps to consider the simplest scenario, that of a beam propagating azimuthally inside a cylindrical whisper-gallery mirror. In this case, the "horizontal" direction of the WGM lies parallel to the cylinder's axis, while the "vertical" direction extends radially inward from the mirror surface. The radial eigenmodes of a cylindrical WGM are presented by Vinogradov et. al. [4]. Their exact description involves Bessel functions of large, complex-valued order, but they may be well approximated in terms of Airy functions. In all of the low-order modes, the energy is localized close to the the mirror surface. The lowest order mode has one maximum, the second mode has two extrema separated by a node, and so forth for the modes of higher order. The characteristic height of the lowest-order mode is given roughly as

$$h \approx \frac{1}{2}(\lambda^2 R)^{1/3}, \qquad (1)$$

where λ denotes wavelength and R the mirror radius.

As an explicit example, consider the implications of this relation for the laser system recently described by Hagelstein [8]. That scheme would operate at 194 Å on the $4d \rightarrow 4p$ transition in Ni-like molybdenum; the amplifiers are to be repetitively pumped by a

Nd:glass slab laser at intervals of 3.5 ns. In order for the time between pump pulses to coincide with that required for X-rays to make one pass around the cavity, a mirror radius of 16.7 cm is required. This implies a mode height $h \approx 2$ μm, which is quite small in comparison with the 50 μm diameter typical of the laser amplifiers. In principle, it would be possible to increase the mode size by using a larger mirror, but the scaling is too weak to make this practical: raising h to 50 μm would require a mirror radius of 2.6 km.

3. Elongated mirrors and adiabaticity

The question thereby arises of how to obtain a greater mode size from a compact mirror. A proposed solution [7] is to use an elongated geometry in which the mirror's radius of curvature is large near the amplifiers, so as to give a useable mode height there, and smaller in between, so as to give a managable cavity size; see Fig. 2.

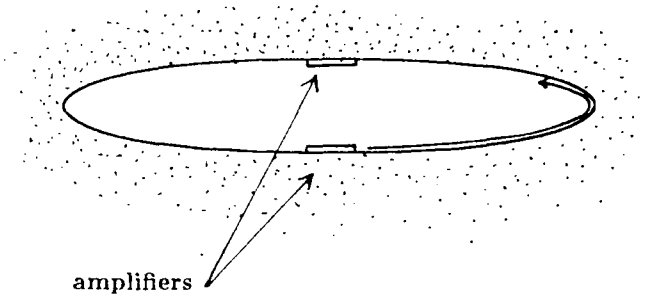


Fig. 2: Cavity having an elongated geometry in order to increase size of low-order modes.

This proposal tacitly assumes that the eigenmodes of a mirror of arbitrary shape should locally resemble the eigenmodes of a circular mirror. That is, within any section of the mirror small enough that the curvature is roughly constant, the n-th true eigenmode should be well approximated by the n-th Airy-function mode for a round mirror of equal curvature. This is in fact correct as long as the curvature changes very slowly along the mirror surface: radiation injected in one local Airy-type mode will remain in that form as it propagates, with the mode height varying appropriately in response to changes in the local radius of curvature. The argument here is analogous to that of the quantum adiabatic theorem, which describes the effects of a slowly time-varying potential upon a given initial wavefunction [9].

Within our constraints on perimeter and mode size, however, the curvature is forced to change so rapidly that truly adiabatic behavior is impossible. The locally Airy-like modes are still a legitimate and complete basis set for a description of the optical field, but they can no longer be considered eigenmodes. Any variation in curvature induces a certain coupling between these modes, and only in the adiabatic limit can the coupling be ignored.

4. Variational solution for minimal coupling

Although we cannot entirely avoid the mode coupling just described, we can attempt to reduce its effects. By choosing the mirror shape so as to minimize the net coupling, some kind of quasi-adiabatic behavior might be obtained. We conjecture that such a shape might be optimal in the sense of maximizing the mode height for a given overall mirror size.

Let $c(s)$ denote the curvature of the mirror as a function of arc-length along the surface. Any variations in $c(s)$ with respect to s will induce coupling between the locally Airy-like modes. (In the case of a circular mirror, the curvature $c(s) = 1/R$ is a constant, and the coupling vanishes.) The coupling between the lowest-order mode, $|1\rangle$, and the second mode, $|2\rangle$, is given by a matrix element of the form

$$M_{12} = \langle 2|\frac{d}{ds}|1\rangle, \tag{2}$$

dependent both upon the curvature and its rate of change. For the optimal mirror shape, we seek that $c(s)$ which minimizes the functional

$$I = \int ds\ |M_{12}|^2 = \int ds\ L(c(s), c'(s)). \tag{3}$$

The result is

$$c(s) = \frac{c_0}{(1-\beta s)^{3/2}}, \tag{4}$$

in which β and c_0 are arbitrary parameters. Different choices of these parameters correspond to various members of a family of spiral-shaped curves. The quantity $1/\beta$ sets the length scale, and any given curve terminates in an ever-tightening spiral as $s \to 1/\beta$. The dimensionless ratio $\alpha = 2c_0/\beta$ determines the curve's overall shape, with higher values of α corresponding to curves of larger initial curvature. Figure 3 depicts two curves having identical values of β but different values of α.

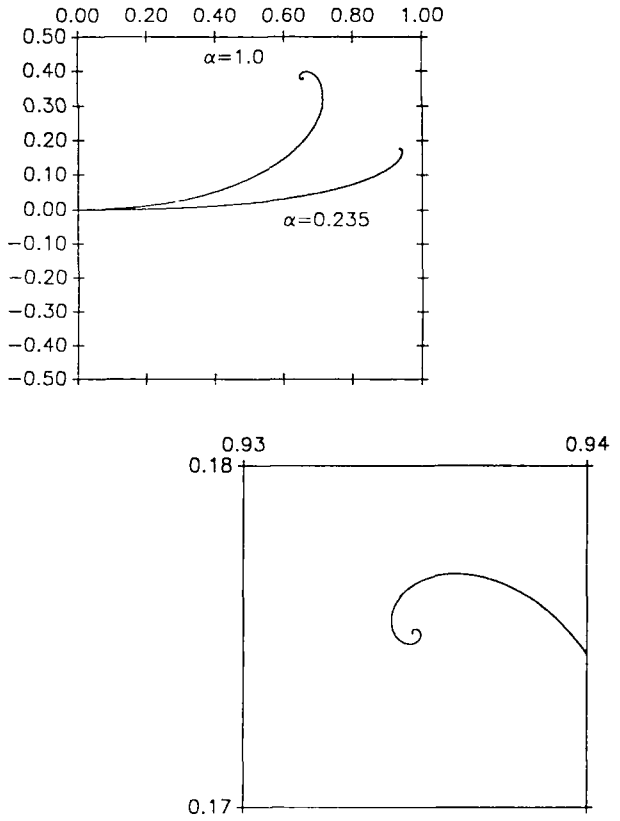


Fig. 3: Above, two examples from the curve family giving minimal coupling between modes. The axes represent Cartesian coordinates in units of $1/\beta$. Below, detailed view at the endpoint of the curve $\alpha = 0.235$.

Sections of these spiral curves can be pieced together to make a complete cavity. The cavity shown in Fig. 2 consists of four identical sections taken from the curve $\alpha = 0.235$.

5. Conclusion

In summary, the low-order modes of a round whisper-gallery are small in comparison with the sizes typical of an X-ray laser amplifier, and therefore a cavity incorporating such a mirror would have a large Fresnel number. A possible solution to this problem lies in using an elongated mirror. An approximate analysis of the eigenmodes of such a mirror can be constructed in terms of the eigenmodes of a circular mirror. When the condition of adiabaticity is not met, however, the analysis must be refined to include the effects of mode coupling. By choosing the mirror shape so as to minimize the net mode coupling, a special family of mirror shapes is obtained.

To what extent these elongated mirrors are an improvement over circular ones remains to be seen. It may be feasible to increase the mode height by a factor of ten or more in this fashion, but a better understanding is required of how the presence of coupling affects the mode height. We do not know, for example, just how large a coupling can be tolerated before the mode height predicted on the basis of truly adiabatic behavior becomes invalid; a more exact analysis is needed.

Acknowledgment

This work was supported by the United States Department of Energy, Division of Advanced Energy Projects, under contract DEFG02/89CR14012.

References

[1] J. Bremer and L. Kaihola, Appl. Phys. Lett. 37, 360 (1980)
[2] A. V. Vinogradov, N. A. Konoplev, and A. V. Popov, Sov. Phys. Dokl. 27, 741 (1982)
[3] A. V. Vinogradov, V. F. Kovalev, I. V. Kozhevnikov, and V. V. Pustovalov, Sov. Phys. Tech. Phys. 30, 145 (1985)
[4] A. V. Vinogradov, V. F. Kovalev, I. V. Kozhevnikov, and V. V. Pustovalov, Sov. Phys. Tech. Phys. 30, 335 (1985)
[5] A. V. Vinogradov, N. N. Zorev, I. V. Kozhevnikov, and I. G. Yakushkin, Sov. Phys. JETP 62, 1225 (1985)
[6] A. V. Vinogradov, V. M. Elinson, V. I. Zhilina, N. N. Zorev, G. F. Ivanovskii, I. V. Kozhevnikov, M. E. Plotkin, S. I. Sagitov, V. A. Slemzin, and V. V. Sleptsov, Sov. Phys. Dokl. 32, 64 (1987)
[7] P. Hagelstein and J. P. Braud, to be published.
[8] P. Hagelstein, in OSA Proceedings on Short Wavelength Coherent Radiation: Generation and Applications, R. W. Falcone and J. Kirz, Eds., (Optical Society of America, Washington D. C., 1988), pp. 28–35
[9] A. Messiah, Quantum Mechanics, Vol. 2 (North-Holland, Amsterdam 1962), pp. 739–759

BASIC PHYSICS STUDIES FOR NOVEL X-RAY LASER SCHEMES USING ULTRA-SHORT LASER PULSES

O. Willi, F. Afshar-rad, V. Barrow, J. Edwards and R. Smith

The Blackett Laboratory, Imperial College of Science, Technology and Medicine, London SW7 2BZ, UK.

ABSTRACT

The interaction of ultra-short high power laser pulses with matter offers great potential for the production of future X-ray laser media. To date, most X-ray and XUV laser experiments have required very large and expensive visible lasers to produce moderate gain and only very small conversion efficiencies from the optical to the XUV spectral region have been achieved. With the recent developments of sub- and picosecond optical tabletop lasers it has become possible to generate the required pump powers in moderate laser systems for the production of hot, high density plasmas as X-ray laser media.

This paper discusses some of the basic physics issues which are relevant to X-ray laser systems based on high temperature, high density plasmas produced by ultra-short laser pulses. In particular, the dominant laser absorption processes, energy transport and ionization mechanisms, at close to solid density, will be investigated and discussed in the context of experimental results recorded on solid targets irradiated with a 3.5 ps KrF laser pulse with an energy of up to a Joule. Finally, a novel and versatile diagnostic based on the Moire deflectometry technique is described which will allow the characterization of the spatial divergence and the transverse mode structure of an X-ray laser beam.

Introduction

Significant progress has been made in the development of soft x-ray lasers in recent years. XUV laser action has now been demonstrated on numerous transitions with wavelengths as short as 44 Å using collisional excitation[1-4] and recombination schemes.[5-9] All the present working XUV laser systems however are pumped by very large visible lasers. Consequently the research is very expensive and limited to a small number of laboratories. With the availability of multi-terawatt tabletop laser systems similar and novel x-ray laser schemes can now be investigated. The interaction of a single picosecond, high power KrF laser pulse with solid targets has recently been studied using time integrated and time resolved x-ray spectroscopy.[10-14] Fully ionised aluminium plasmas with temperatures of about 400 eV and densities well above 10^{23} cm^{-3} were observed.[10-12] It was inferred from titanium K_α emission measurements that about 20% of the incident laser energy was deposited in suprathermal electrons.[13] The level of ionization was investigated by observing K, L and M- shell emission on various targets.[14] The application of high density plasmas produced by picosecond laser pulses for recombination x-ray lasers has been discussed in a recent paper.[15]

This paper discusses some of the basic processes occurring during the interaction of ultra-short laser pulses with matter resulting in the production of hot, high density plasmas as pump media. In particular, the absorption of the laser energy, the transport of the absorbed energy into the solid material and the ionization of the solid are considered. A simple, novel technique based on Moire deflectometry is described which allows the spatial divergence and the transverse mode structure of an x-ray laser to be determined. If simultaneously the bandwidth of the lasing transition is measured then both the spatial and temporal coherence are known.

Basic Physical Processes

1. Absorption of the Laser Light Incident on Solid Targets

The absorption of laser pulses with a duration of tens of picoseconds to nanoseconds is now quite well understood.[16] An underdense plasma is formed rapidly resulting in the absorption of the laser energy close to or at the critical density surface via a combination of inverse bremsstrahlung and resonance absorption, depending on the laser conditions and target material. Resonance absorption becomes the dominant process for $I\lambda^2 > 2\times10^{14}$ $Wum^2\ cm^{-2}$.

In contrast when sub- or picosecond laser pulses are used the laser energy is absorbed close to or at the initial target surface since no significant hydrodynamic expansion can occur on these time scales. The laser energy may be absorbed through a variety of mechanisms including inverse bremsstrahlung, resonance absorption and others.[17-19] Inverse bremsstrahlung may not be very efficient because of the very steep density gradients produced under these ultra-short laser irradiance conditions. Absorption fractions of less than 10% are estimated for density scalelengths less than 5 μm using the absorption coefficient for inhomogeneous plasmas.[20] For solid densities higher absorption efficiencies are obtained when the evanescent part of the electromagnetic wave is taken into account.[21] However the efficiency falls very quickly when

the solid is heated to temperatures of a few tens of eV's. Consequently, if inverse bremsstrahlung were the only absorption mechanism operating, it might not prove possible to produce plasmas with temperatures of up to a keV which are required for x-ray laser pump media.

On the other hand resonance absorption may be quite an efficient process for energy deposition close to the target surface. According to linear resonance absorption theory,[22] the fractional absorption depends on $(k_0 L)^{2/3} \sin^{2}\vartheta$ and maximizes at approximately 50% for $(k_0 L)^{2/3} \sin^{2}\vartheta = 0.6$. The resonance absorption fraction can be estimated as a function of the plasma density scalelength. This is shown in figure 1 for two different angles. As can be seen, when an average value of $\sin^{2}\vartheta$ of 0.02, appropriate for f/2.5 optics, has been used, the predicted maximum absorption is obtained at a scalelength of about 3.5 μm.

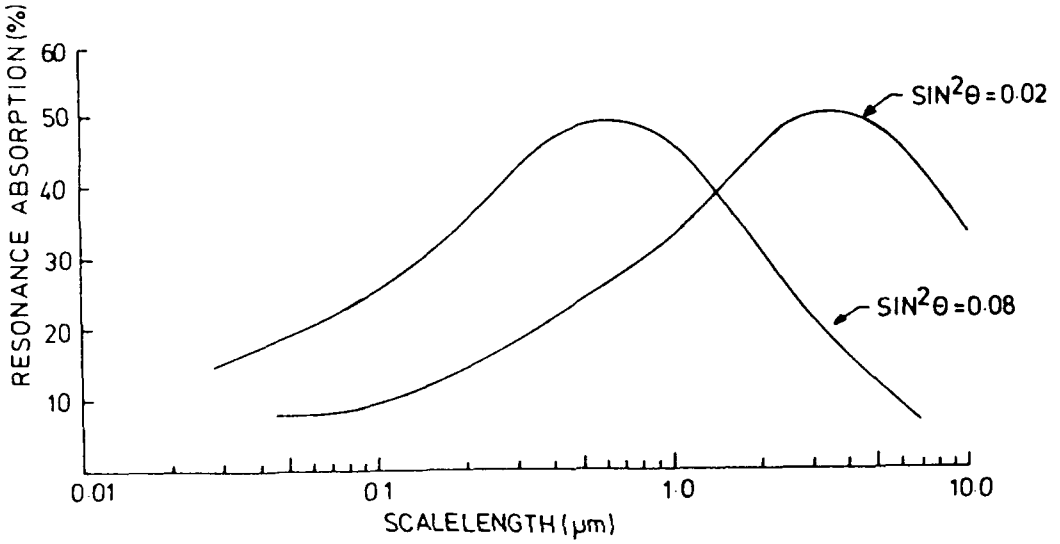


Figure 1. Predicted level of resonance absorption with an angle of incidence of $\sin^{2}\vartheta$ of 0.02 and 0.08 as a function of the density scalelength.

The efficiency of resonance absorption of short pulses has been investigated experimentally by observing the level of TiK_{α} radiation emitted from plastic overcoated titanium targets which were irradiated with a 3.5 ps p-polarised KrF laser pulse at an intensity of $3 \times 10^{16} Wcm^{-2}$.[13] Time integrated measurements of K_{α} emission have been used previously to determine the fraction of the incident laser energy that is deposited in the target by fast electrons generated by resonance absorption of long pulses.[23,24] Figure 2 shows the absolute levels of the TiK_{α} radiation as a function of the plastic layer thickness for a series of targets irradiated under similar laser conditions.

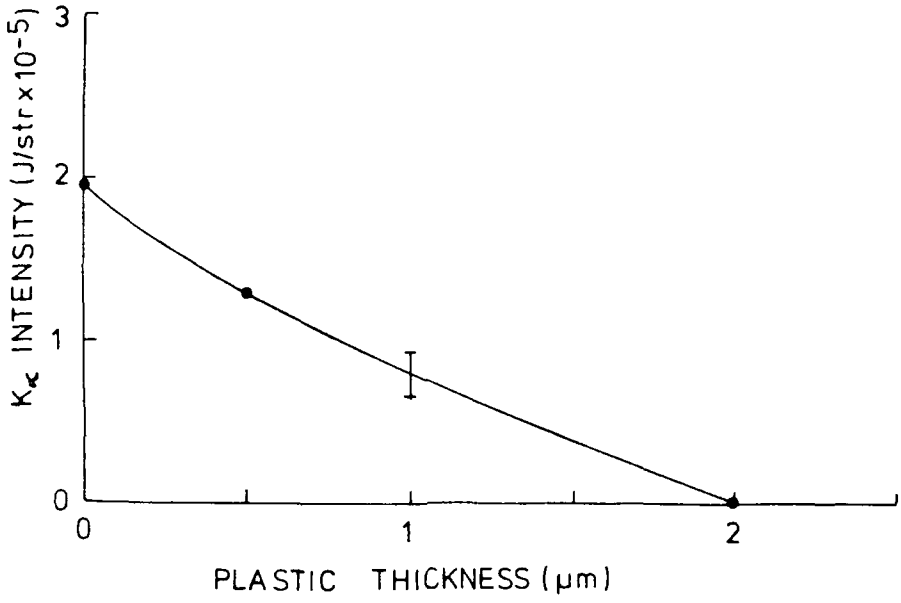


Figure 2. Absolute titanium K_α intensities as a function of layer thickness. The error bar is a result of uncertainties in the crystal reflectivity.

From the data presented in figure 2 a hot electron temperature can be inferred by assuming some distribution $f_0(E) = f_0 \exp(-E/kT_H)$. The best agreement is obtained for $kT_H = 9 \pm 1$ keV. This should be compared to the analytical expression of, for example, Estabrook and Kruer[25] $T_H/keV = (13 T_c/keV)^{0.25}[(I_L/10^{15})(\lambda/1.06)^2]^{0.39}$ where T_c is the thermal electron temperature. For the above laser conditions and $T_c = 400$ eV; T_H of 12.5 keV is obtained, in fair agreement with the measured value.

The energy deposited in the target by hot electrons can also be estimated using the data from an uncoated Ti target (plastic layer thickness = 0 μm in figure 2). The fast electron induced K_α radiation emitted from a fluorescent layer is not very sensitive to the fast electron velocity spectrum as long as the electron energy is significantly greater than the K shell ionization energy E_{KI}.[23,24] The energy deposited in the target whose fluorescence yield is ω, is then given by $I_{K\alpha}/(\omega x R x E_{KI})$ where $I_{K\alpha}$ is the energy emitted in K_α radiation and R is the total rate of energy loss into K shell ionisation to the total rate of energy loss by fast electrons. Applying this simplified expression to the measured TiK_α emission suggests that approximately 20% of the incident laser energy is deposited into hot electrons. According to figure 1 this would require a density scalelength of about 0.35 μm.

Detailed hydrodynamic simulations were carried out using the 1-D Lagrangian hydrodynamics code MEDUSA. All the simulations were performed with a laser wavelength of 248 nm and Al and plastic coated Ti targets. The laser energy was absorbed via inverse bremsstrahlung up to the critical density. Resonance absorption was simulated by dumping a fraction of the remaining energy, between 1 and 50%, at the critical density surface. The fraction of resonantly absorbed energy producing hot electrons was assumed to be 0.9. The hot electron temperature was calculated according to Giovanielli.[26]

The best agreement with the experimentally measured electron density and temperature was found for a resonance absorption fraction of 0.2 which is consistent with that obtained from the K_α measurements. A hot electron temperature of approximately 10 keV was obtained in the code. The simulations indicated that very little energy (less than 1%) was absorbed via inverse bremsstrahlung because of the steep density gradient. In addition, with an absorption of 20% a density wavelength of about 0.3 μm is predicted by the hydrodynamics simulations. This value is consistent with the density scalelength of 0.35 μm for 20% absorption obtained in figure 1. Close to maximum absorption should be achieved by irradiating the target at the optimum angle of incidence.

Alternative absorption processes have recently been studied theoretically.[18,19] However these models predict relative small absorption percentages.

2. Energy Transport

Several processes such as thermal conduction, radiation transport and hot electron transport may be responsible for the transport of the laser energy deposited close to the initial target surface into the solid material causing ionization close to solid density.

2.1 Thermal electron transport

The laser energy deposited by the short laser pulse is transported to higher densities and into the solid by heat conduction. The equation of heat conduction can be written as[27]

$$\frac{\delta T}{\delta t} = \nabla \cdot (\chi \nabla T) + q$$

where T is the temperature, χ is the electron thermal diffusivity ($aT^{5/2}$), q is $W/\rho c_p$, W is the energy input, ρ is the density and c_p is the specific heat. Solutions to this nonlinear equation generate sharply bounded heat waves travelling into the cold material.

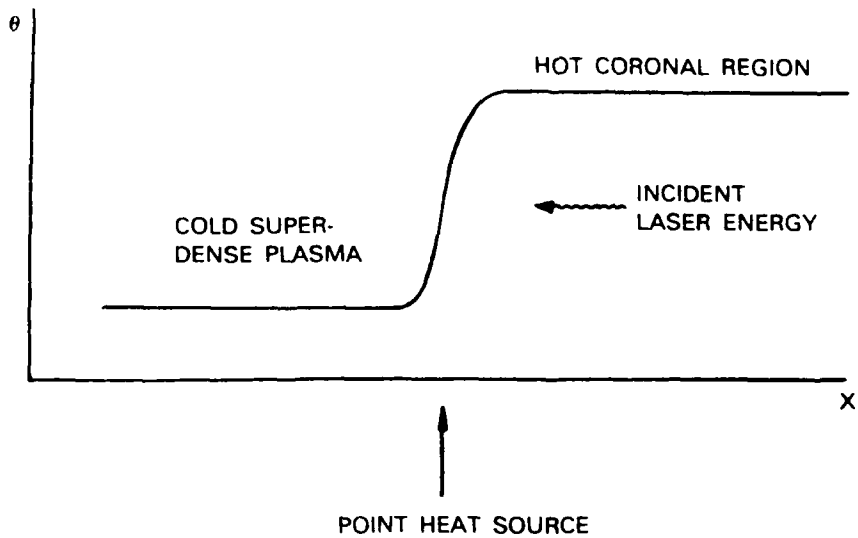


Figure 3. Thermal wave propagation

In order to study the heat propagation at solid densities, the laser absorption must occur close to solid density and in a pulselength short compared to the plasma hydrodynamic response time. The hot, dense plasma only persists until the rarefaction wave driven by the plasma expansion overtakes the thermal front. An upper limit can be placed on the laser pulse duration by estimating the lifetime of the solid state plasma through comparison of the heat wave velocity and the hydrodynamic expansion velocity. The lifetime of the solid state plasma can be written as[28]

$$t_0 = a \left[\frac{M}{2k} \right]^{3/2} \left[\frac{3}{2} k N \right]^{-2} I$$

I is the laser irradiance in Wcm^{-2}, M is the ion mass, k is Boltzmann's constant and N is the number density of the solid.

For typical laser and target conditions with $I = 5 \times 10^{16}$ Wcm^{-2} and aluminium as the target material, t_0 = 18 ps, in order that a heat wave can propagate into the solid, a laser pulse shorter than 18 ps must be used.

Computer simulations have been carried out to study the propagation of the heat wave into the solid density material. Figure 4 shows the result of a simulation for a 5 ps KrF laser pulse focussed to an irradiance of 4×10^{16} Wcm^{-2}. A large heat wave is clearly seen to exist beyond the position of the initial surface travelling into the solid.

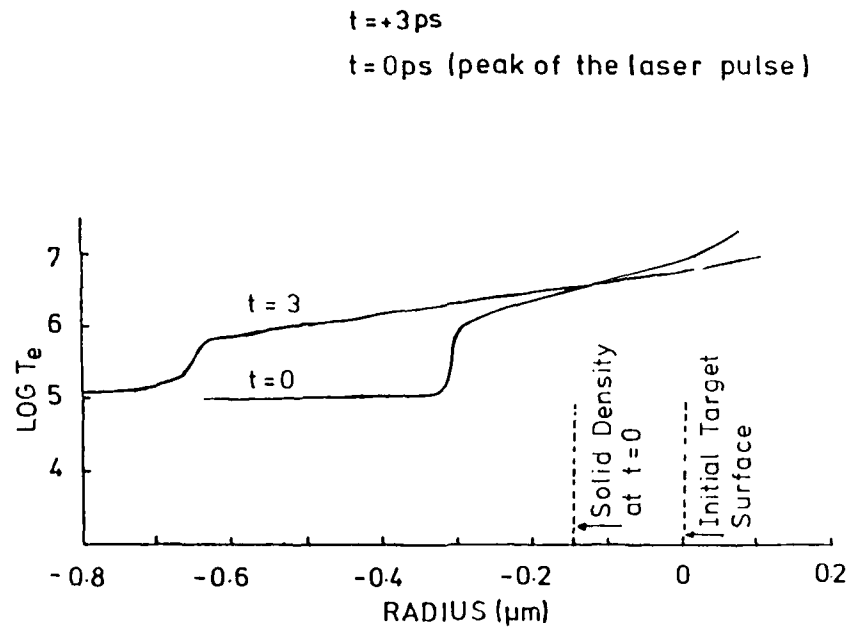


Figure 4. Computer simulation showing heat wave propagation into solid density material.

Thermal transport for ultra-short pulses was further studied with a 2-D Fokker-Planck code.[29] For short pulses the Fokker-Planck simulations showed that almost all of the absorbed energy is transported into the target ie. towards higher electron densities. A flux of 0.1 times the free streaming limit was found to be appropriate even for 10 μm diameter focal spots. This is in contrast to the longer pulse case in planar geometry where a large fraction of the absorbed energy is spread laterally across the target surface.

2.2 Radiation Transport

Since the laser energy is absorbed and the plasma formed close to solid densities a large fraction of the absorbed energy may be converted into soft x-ray radiation. Consequently radiation transport may be a dominant energy transfer mechanism in plasmas produced by ultra short laser pulses. Because of the high plasma density and transient nature of the system, detailed line shape and ionization/radiation packages will be required to investigate the problem fully.

2.3 Suprathermal electron transport

As discussed above a large fraction of the incident laser energy may be deposited in suprathermal electrons as a result of resonance absorption. The suprathermal electrons are emitted predominantly down the density gradient. However, the generation of space-charge electric fields draws them back into the target where their energy is deposited giving rise to heating of the solid. A detailed analytical model of energy deposition by suprathermal electrons has recently been derived and compared with experimental date.[31]

3. Ionization Physics

The production of hot plasmas via conventional laser absorption mechanisms relies upon the formation of an ionized medium. Central to the problem of creating hot, dense plasmas with ultra-short pulses are, therefore, plasma ionization times.

The ionization of plasmas resulting from absorption of 3.5 ps,KrF laser pulses with irradiances in excess of 10^{16} Wcm^{-2} at the target surface has been investigated using time resolved and time integrated x-ray spectroscopy. In particular, aluminium (Z=13), selenium (Z=34) and tantalum (Z=73) targets were used. Figures 5(a) and (b) show densitometer traces of spectra obtained for a laser irradiance close to $3x10^{16}$ Wcm^{-2} from Se and Ta targets in the region of the Se L-shell and Ta M-shell respectively. As can be seen, strong emission from several ionization stages is observed in each case. The alumimium K-shell spectrum is shown in figure 7a. Evidently, at least partial ionization of the K, L and M-shells of Al, Se and Ta respectively is possible over the laser pulse duration of several picoseconds.

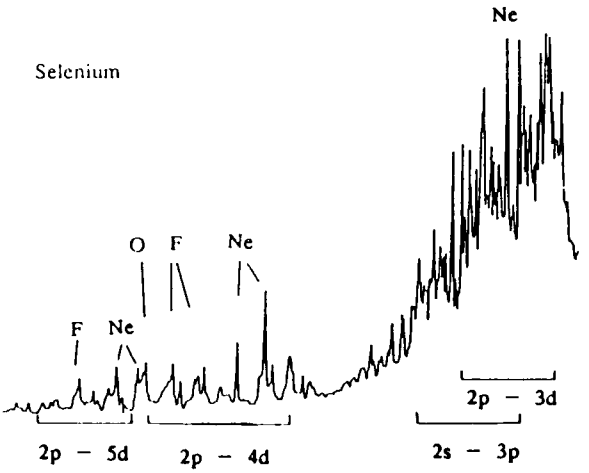


Figure 5a. Microdensitometer trace of selenium L-shell spectrum showing Ne-like ions.

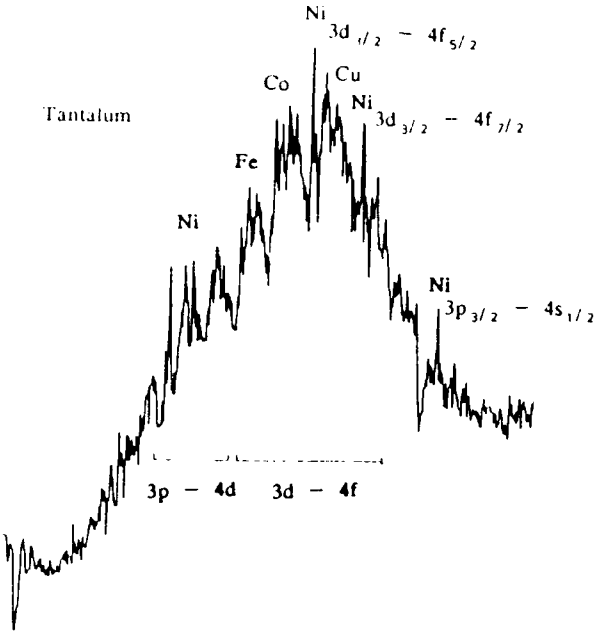


Figure 5b. Microdensitometer trace of tantalum M-shell spectrum showing Ni-like ions.

The experimental conditions have been simulated for a Se *target using* MEDUSA assuming conditions and parameters identical to those used above (see section 1). The average degree of ionization in the sample was followed with a time-dependent, zero-dimensional, average-atom, screened-hydrogenic atomic physics model. The collisional processes considered to contribute to the (de)population of an atomic level are collisional (de)excitation, ionization and three body recombination. Any suprathermal component to the electron distribution function is ignored although this will have some effect on the ionization balance. The plasma is considered completely optically thin and radiative coupling between levels is via spontaneous decay only. This assumption is probably not justified under these conditions. However, a preliminary investigation indicates that the inclusion of a radiation field in the hot plasma will be unlikely to alter significantly the main conclusion drawn here, although the ionization rate and average degree of ionization may be slightly increased. Multi-photon processes have not been included. The ionization calculation is initiated assuming all atoms are once ionized.

Figure 6(a) shows density and temperature profiles calculated by MEDUSA for the Se target near the peak of the laser pulse. Figure 6(b) shows the temporal evolution of the plasma conditions near the front of the target together with the time-dependent average degree of ionization. As can be seen the plasma is rapidly ionized during the laser pulse rise and significant L-shell emission should be evident before the end of the pulse.

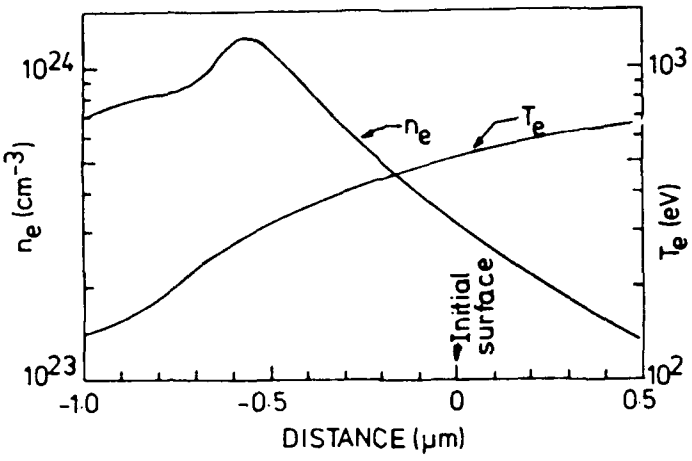


Figure 5a. Temperature and electron density profiles calculated by MEDUSA near to peak of the laser pulse for a selenium target.

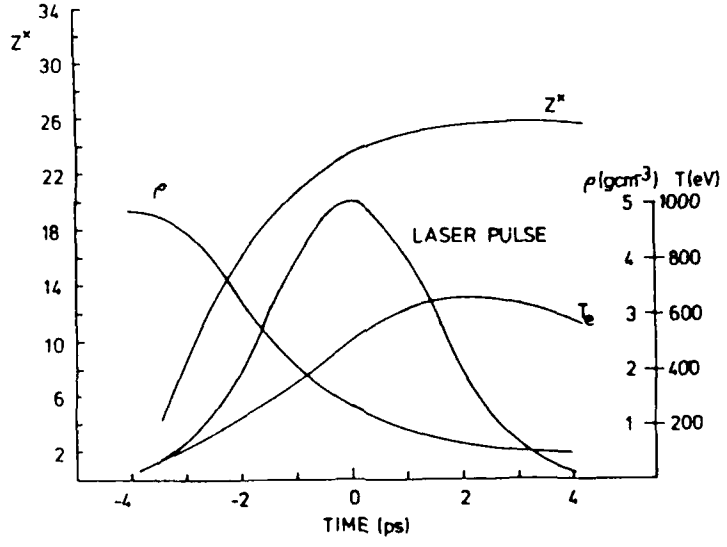


Figure 5b. Temporal evolution of plasma conditions and degree of ionization near the front of a selenium target.

The results are encouraging and at least qualitatively in agreement with the experimental data.

Density and temperature measurements

The plasma conditions such as the electron density and temperature have been obtained by recording time resolved X-ray spectra from aluminium targets which were irradiated by the 3.5 ps KrF laser pulse. Figure 7a shows a streaked spectrum taken on an aluminium target irradiated at an intensity of $3 \times 10^{16} Wcm^{-2}$. As can be seen, the Al Heß ($1s^2$-$1s3p$) transition is very wide and intense, and dominates the spectrum. The Heγ($1s^2$-$1s4p$) transition, which is far less intense, turns on approximately 15 ps after the Heß transition. In addition, the higher members of the H-like and He-like series are extremely faint.

This and other X-ray spectra were analyzed to determine the plasma electron temperature and electron density. The electron density is obtained by comparing the experimental Stark profile with those predicted by the atomic physics codes RATION and SPECTRA. Figure 7b compares a synthetic line profile with a microdensitometer trace of the Heß line profile shown in figure 7a. The trace was taken 15ps after the start of the emission. The best fit was found for an electron density of 1.4×10^{23} cm^{-3}. The calculations of the synthetic spectra assume small opacity corrections using a plasma of one micron in size and electron temperature of 400eV. The x-ray line emission continues after the end of the short laser pulse since the target is largely heated by suprathermal electrons and the resultant cooling time of the large hot plasma determines the x-ray emission lifetime.

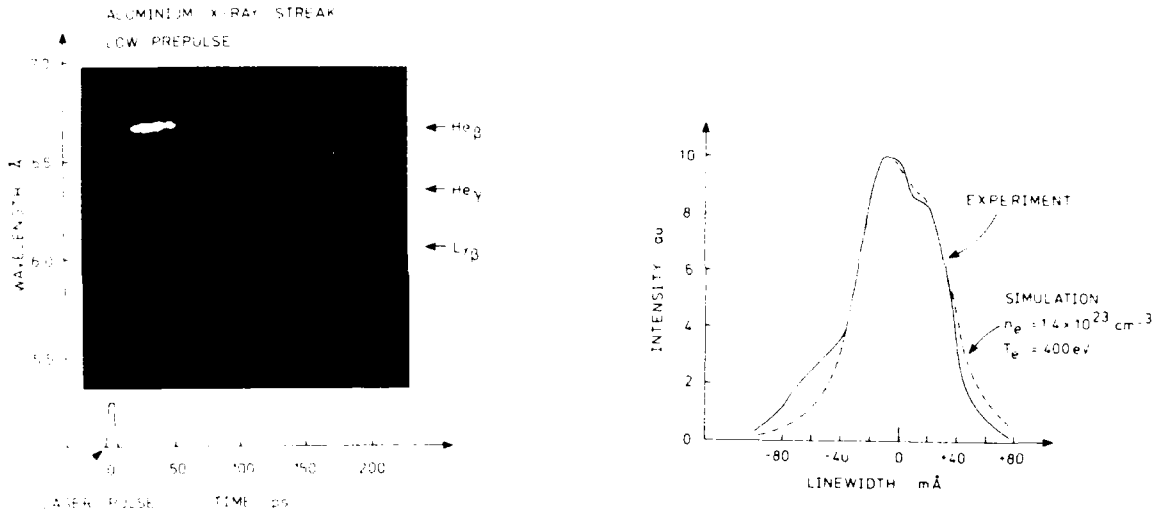


Figure 7a. Streak record of an aluminium target irradiated with a 3.5ps laser pulse.

Figure 7b. Comparison of the experimental line profile of Al Heß with a predicted profile calculated with T_e = 400eV and $n_e = 1.4 \times 10^{23}$ cm^{-3}.

The electron temperature is derived from the line ratio of Al Lyα:Al Heα recorded on time integrated spectra. An electron temperature of 400 ± 50eV is obtained by using estimates of self-absorption factors to correct for opacity effects. A reasonable electron temperature can be obtained from time integrated measurements since the bulk of the x-ray line emission occurs over a short period of time when the plasma is near its peak temperature, as observed in the time resolved spectra. The electron temperature is consistent with spectral observations recorded with KCl targets, where no hydrogenic line emission was seen. RATION/SPECTRA predictions show that the minimum electron temperature required for hydrogenic chlorine emission is approximately 700eV.

Characterization of X-ray Laser Beams

With the recent successful demonstration of XUV laser action, the development of fully quantitative diagnostics suitable for x-ray laser beam characterization has become important. In particular, measurements of the spatial and temporal coherence, beam divergence and wavefront distortions are vital for the development of coherent sources in the x-ray spectral wavelength region. A simple novel technique based on Moire deflectometry has recently been proposed[32] which allows the spatial divergence and the transverse mode structure to be determined. If simultaneously the bandwidth of the x-ray laser transition is measured then the spatial and temporal coherence are known.

Moire deflectometry in its usual configuration consits of two Ronchi type gratings G1 and G2 of equal pitch P. These are square wave linear transmission gratings with opaque and transparent stripes of equal width. For wavelengths in the x-ray region they are constructed of a mesh of free-standing copper stripes to form a grid of uniform pitch.

A spatial map of the inherent divergence of the beam can be plotted from the deflectogram together with any geometrical ray effects. The inherent divergence of the beam derives from two sources. The finite aperture of the beam, responsible for the diffraction-limited divergence and the quality of the radiation itself, is defined as the number of transverse modes. The divergence is determined from the degree of reduction in contrast of the local Moire fringe profile. From the relationship proven to exist between the inherent beam divergence and the number of transverse modes[33,34] the latter can be determined and is given by

$$N_T = \left[\frac{PA}{\lambda D} \quad \frac{1}{1 + C} \right]^2$$

N_T is the number of transverse modes, A is the width of the beam aperture and C is the local fringe contrast which is calculated by dividing the average intensity of the two dark fringes bordering the bright fringe by the intentisy of the latter at that location. The use of this technique for the much shorter soft x-ray wavelength region, together with the typical grating specifications of pitch P=40-100μm and separation between gratings D≤10mm, geometrical optics can be applied to the propagation of radiation between the gratings. Consequently, since the intensity profile of the Moire fringes resulting from a spatially coherent beam is a triangular function any smearing observed in the fringes will be the result of the inherent beam divergence.

The feasibility of Moire deflectometry in the x-ray region has been demonstrated recently. Figure 8 shows two Moire fringe pattern generated by a pair of Ronchi gratings with a pitch of 40 μm and separation of 30 mm using a laser produced point-source x-ray backlighter with a wavelength of about 10 A (Heα of magnesium). Fig 8b shows the effect of increasing the sensivity of the Moire deflectometer by reducing the angular mismatch θ between the two gratings. Also shown is a densitometer trace illustrating the characteristic triangular Moire fringe profile. The fringe profile can be used to determine the number of spatial modes which in this case is small as expected for a point-source.

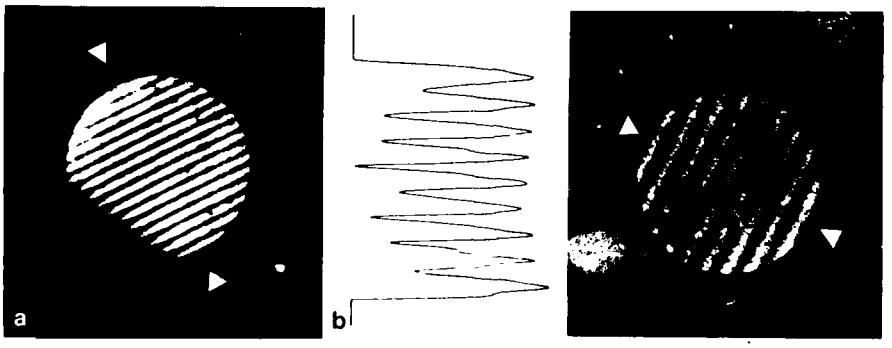
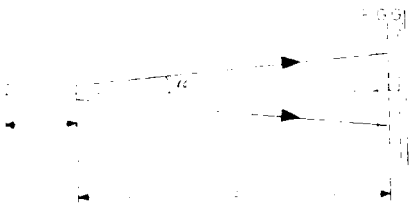


Figure 8a. An X-ray Moire fringe pattern generated using a point-source X-ray backlighter.

Figure 8b. An X-ray fringe pattern with increased sensivity due to a reduction in the gratings mismatch angle θ, and the corresponding densitometer trace showing the triangular fringe profile.

A schematic shown in Figure 9 presents a suitable configuration for characterizing the beam profile of a typical x-ray laser system. The sensitivity of the Moire deflectometer is set by the suitable choice of grating pitch P, which is fixed for a particular grating pair, and the grating separation D. This separation is variable and allows a continuous scan in sensitivity. The specific setting fpr the gratings is determined primarily by the inherent divergence of the beam.

Figure 9. Schematic of the experimental arrangement for x-ray laser beam profiling . The target to grid separation S is typically 50-100cm for an overall beam divergence of 10-20mrads, such that the beam diameter at the detector fills the gratings.
F is a filter.



Conclusions

In summary some of the physical processes occurring during the interaction of ultra-short laser pulses with matter have been discussed. Hot, high density plasmas are produced by ultra-short laser pulses which are suitable pump media for present and novel x-ray laser schemes. In addition, a novel diagnostic for the characterization of x-ray laser systems has been described.

Acknowledgements

The experimental work was carried out at the SERC Central Laser Facility. This work was partly supported by the SERC and by the Innovative Science and Technology Office directed by the Naval Research Laboratory.

References

1. D. Matthews, P. Hagelstein, M. Rosen, M. Eckart, N. Ceglio, A. Hazi, H. Medecki, B. MacGowan, J. Trebes, B. Whitten, M. Campbell, C.W. Hatcher, A.M. Hawryluk, R. Kauffman, L.D. Pleasance, G. Rambach, J.H. Scofield, G. Stone and T.A. Weaver, Phys. Rev. Lett. 54, 110 (1985).
2. B. MacGowan, S. Maxon, P. Hagelstein, C. Keane, R. London, D. Matthews, M. Rosen, J. Scofield and D. Whelan, Phys. Rev. Lett. 59, 2157 (1987).
3. B. MacGowan et al., J. Opt. Soc. Am. B5, 1858 (1988).

4) T.N. Lee, E.A. McLean and R.C. Elton, Phys. Rev. Lett 59, 1185 (1987).
5) C. Chenais-Popovics, R. Corbett, C. Hooker, M. Key, G. Kiehn, C. Lewis, D. Pepler, G. Pert, C. Regan, S. Rose, S. Saadat, R. Smith, T. Tomie and O. Willi, Phys. Rev. Lett. 59, 2161 (1987).
6) G. Jamelot, A. Klisnick, A. Carillon, H. Guennou, A. Sureau and P. Jaegle, J. Phys. B. 18, 4647 (1985).
7) S. Suckewer, C.H. Skinner, H. Milchberg, C. Keane and D. Voorhees, Phys. Rev. Lett. 55, 1753 (1985).
8) O. Willi, D. Bassett, C. Chenais-Popovics, R. Corbett, M. Grande, P. Hawkins, C. Hooker, M. Key, G. Kiehn, C. Lewis, G. Pert, S. Ramsden, C. Regan, S. Rose, R. Smith and T. Tomie, Proc. of the SPIE 688, 2 (1986).
9) A. Carillon, J. Edwards, M. Grande, M. Henshaw, P. Jaegle, G. Jamelot, M. Key, G. Kiehn, A. Klisnick, C. Lewis, D. O'Neill, G. Pert, S. Ramsden, C. Regan, S. Rose, R. Smith and O. Willi, accepted in J. Phys. B.
10) O. Willi, G. Kiehn, J. Edwards, V. Barrow, R. Smith, J. Wark and E. Turcu, Europhys. Lett. 10, 141 (1989).
11) O. Willi, G. Kiehn, J. Edwards, V. Barrow and R. Smith, OSA Proc. on Short Wavelength Coherent Radiation:Generation and Applications, edited by R. Falcone and J. Kirz, Vol. 2, 194 (1988).
12) O. Willi, G. Kiehn, J. Edwards, V. Barrow, R. Smith, J. Wark, G. Rickard, A. Bell, E. Turcu and E. Epperlein, Proc. of the 16th European Conference on Controlled Fusion and Plasma Physics, edited by S. Segre, H. Knoepfel and E. Sindoni, 849 (1989).
13) O. Willi, G. Kiehn, V. Barrow and J. Edwards, submitted to Appl. Phys. Lett.
14) J. Edwards et al., to be published.
15) R.A. Smith, V. Barrow, J. Edwards, G. Kiehn and O. Willi, Appl. Phys. B. 50, accepted.
16) Laser Plasma Interaction, Proc. of the 20th Scottish Universities Summer School in Physics, ed. by R.A. Cairns and J.J. Sanderson, 1980.
17) F. Brunel, Phys. Rev. Lett. 59, 53 (1987).
18) P. Mulser, S. Pfalzner and F. Cornolti, Proc. of ECLIM, in Laser Interaction with Matter, edited by G. Velarde, E. Minguez and M. Perlado, World Scientific, 142 (1989).
19) S.C. Rae and K. Burnett, OSA Proc. on High Energy Density Physics with Subpicosecond Laser Pulses, Vol. 17, 52 (1989).
20) J.M. Dawson, P. Kaw and B. Green, Phys. Fluids, 12, 875 (1968).
21) R.M. More, Z. Zinamon, K.H. Warren, R. Falcone and M. Murnane, J. de Phys., Colloque C7, Tome 49, C7-43 (1988).
22) D.W. Forslund, J.M. Kindel, K. Lee, E.L. Lindman and R.L. Morse, Phys. Rev. A 11, 679 (1975).
23) J.D. Hares, J.D. Kilkenny, M.H. Key and J. Lunney, Phys. Rev. Lett.45, 1216 (1979).
24) J.D. Hares and J.D. Kilkenny, J. Appl. Phys. 52, 6420 (1981).
25) K. Estabrook and W.L. Kruer, Phys. Rev. Lett. 44, 651 (1978).
26) D.N. Giovanelli, Bull Amer. Phys. Sec. II, 9, 1074 (1976).
27) P. Lee and O. Willi, Laser and Particle Beams, 3, 262 (1985) and references therein.
28) A. Caruso and R. Gratton, Plasma Phys., 11, 839 (1969).
29) G.J. Rickard, A. Bell and E.M. Epperlein, Phys. Rev. Lett. 62, 2687 (1989).
30) J. Edwards, V. Barrow, O. Willi and S. Rose, accepted in Europhys. Lett.
31) R.J. Harrach and R.E. Kidder, Phys. Rev. A, 23, 887 (1981).
32) T. Afshar-rad and O. Willi, Appl. Phys. B 50, accepted.
33) Z. Karny, S. Lavi and O. Kafri, Opt. Lett. 8, 409 (1983).
34) I. Glatt, A. Livnat and O. Kafri, J. Opt. 5.

THE MÖSSBAUER EFFECT IN THE 40-SEC FIRST-EXCITED NUCLEAR LEVEL OF ^{109}Ag*

Shokrollah Rezaie-Serej, Gilbert R. Hoy
Physics Department, Old Dominion University
Norfolk, VA 23529
and
R. Dean Taylor
Los Alamos National Laboratory
Los Alamos, NM 87545

Abstract

Narrow spectral lines associated with recoilless nuclear gamma-ray transitions (the Mössbauer effect) are prerequisites for the development of gamma-ray lasers. A successful observation of the Mössbauer effect in the 40-sec, first-excited state of ^{109}Ag will reveal valuable information on the practical limits of such narrow lines. We have used the temperature dependence of the self-absorption of 88-keV gamma rays in a ^{109}Cd-doped silver single crystal to observe the Mössbauer effect. Our results in the horizontal geometry, in agreement with our previous experiments in the vertical geometry, indicate a 0.2% Mössbauer effect at 4.9 K.

Introduction

Since narrow linewidths are a prerequisite for the operation of possible gamma-ray lasers, it is of interest to know how narrow the linewidth of a recoillessly emitted or absorbed gamma ray can actually be. There is a practical limit set by inhomogeneities that exist in real single crystals. The first-excited nuclear level of ^{109}Ag has a half-life of 40 sec and a corresponding natural linewidth of approximately 10^{-17} eV. This is obviously a difficult case for the observation of the Mössbauer effect considering the size of the often quoted[1] lower limit for inhomogeneous line-broadening effects in real crystals of 10^{-13} eV. Therefore, a successful observation of the Mössbauer effect in ^{109}Ag will provide valuable information on the practical limit of ultra-narrow lines and the size of the related line-broadening fields in real crystals.

Other researchers[2-4] have produced evidence for such an effect, but to substantiate this, more detailed corroborating results are needed. Wildner and Gonser[4] used the temperature dependence of the self-absorption of gamma rays in a ^{109}Cd-doped silver single crystal to detect the occurrence of the Mössbauer effect. Following their pioneering method, we have, in addition, monitored the self-absorption of the ^{109}Cd x rays to account for count-rate changes due to solid angle effects. In our method we obtain the ratio of x-ray to gamma-ray counts as a function of temperature. The primary advantages of using the ratio are that the time dependence due to the source decay, and the solid angle effects, to first order , cancel out.

The results of our experiments in the vertical geometry have previously been reported [5-7]. In continuation of our efforts to carry out a comprehensive study of the effect, here we report the results of our recent experiments in the horizontal geometry. These new results, in agreement with our previous results, indicate the occurrence of the Mössbauer effect.

Experimental Results and Analysis

The details of our experimental procedure to observe the Mössbauer effect have already been reported[5-7]. We observe the number of 88-keV gamma rays and 22-keV K_α x rays from a ^{109}Cd-doped silver single crystal using a solid-state germanium detector. The count rates as a function of time are recorded at different temperatures. In our previou experiments[5-7] which were done in the vertical geometry, the detected photons fell along the gravitational field. For this experiment, in the horizontal geometry, the detected photons travel a path roughly perpendicular to the gravitational field. Figure 1 shows a

*The research described in this article was supported by IST/SDIO and directed by NRL.

schematic representation of the sample holder, sample, and detector assembly. We have measured the count rates as a function of time for the gamma rays and the x-rays at four temperatures: 295 K, 190 K, 78 K, and 4.9 K. The results are shown in Fig. 2. These data were recorded over a five-week period with a 22-hour counting time for each run. As the temperature is lowered the count rate for the gamma rays decreases. From room temperature to the liquid nitrogen temperature, the drop in the counting rate is due to the increase in the electronic absorption and solid angle effects. Remember that the solid angle subtended by the detector at the sample is temperature dependent. For temperatures below 78 K the recoilless fraction of ^{109}Ag in silver becomes significant and a further count rate drop due to possible occurrence of the Mössbauer effect is anticipated. Assuming that the distribution of the source nuclei, as a function of distance into the sample, follows a gaussian shape, the intensity of the gamma radiation reaching the detector from the sample can be obtained from the following equation[7]:

$$I_\gamma = C_\gamma C_0 \lambda e^{-\mu_\gamma x_0 - \lambda t} \int_0^{x_0} G(x) e^{-\alpha x^2 + \mu_\gamma x} dx \left[(1-f) + f e^{-\mu_N x_N} \right] \qquad (1)$$

where: C_γ is a constant, C_o is the source density per unit length, λ is the source decay constant, x_o is the sample thickness, and α is the source distribution parameter. The electronic absorption is governed by μ_γ and the possible occurrence of nuclear resonance absorption by μ_N; x_N is the effective Mössbauer thickness parameter; f is the recoilles fraction. G is the solid angle geometrical factor which is a function of both $Z_o(T)$ and d which are shown in Fig. 1. There is a similar expression[7], Eq. (2), which expresses the result for the 22-keV, x-ray radiation. In this case there is, of course, no contribution due to nuclear resonance absorption.

$$I_{K\alpha} = C_{K\alpha} C_0 \lambda e^{-\mu_{K\alpha} x_0 - \lambda t} \int_0^{x_0} G(x) e^{-\alpha x^2 + \mu_{K\alpha} x} dx \qquad (2)$$

where $C_{K\alpha}$ is a constant. Since C_o, $\mu_{K\alpha}$, μ_γ, μ_N, f, x_o, and G(x) are all temperature dependent, both I_γ and $I_{K\alpha}$ are functions of time, t, and temperature.

We use Eqs. (1) and (2) to analyze our data. Wildner and Gonser[4] analyzed their data qualitatively by comparing the size of the count-rate drop when the temperature was lowered from 78 K to 4.2 K with the count-rate drop when the temperature was decreased from room temperature to 78 K. It is important to note that the temperature dependence of the solid angle can play a major role in these count-rate changes. Our data for the count rates of the x rays in Fig. 2 clearly show this. As is seen, the count rates at 4.9 K are higher than the count rates at 78 K, which is contrary to one's expectations. This behavior is explained by referring to the schematic of the experimental configuration in Fig. 1. Our sample at room temperature was misaligned with the detector and its center was below the center of the detector. As the temperature was lowered, the sample holder contracted and the sample moved up, giving rise to an increase in the solid angle. The change in the solid angle is largest when the temperature is lowered from 78 K to 4.9 K. This is due to further contractions of the liquid helium container.

These solid-angle effects must either be eliminated by experimental means or taken into consideration in the analysis of the data. Our x-ray data make it possible to determine these solid-angle effects. We fit our gamma-ray and x-ray data to Eqs. (1) and (2) by using a nonlinear, least-squares fitting routine. The solid lines in Fig. 2 are the results of this fitting procedure. A useful method to analyze the data is to obtain the ratio of x-ray to gamma-ray counts as a function of temperature. We obtain these ratio data from our count rate data in Fig. 2 using a least-squares analysis. The results are shown in Fig. 3. In this case the time dependence of the count rates cancel out, and since the solid-angle geometric factors are the same for both the x-ray and gamma-ray

data, the solid angle effects also cancel to first order. In fitting the ratio data ,i.e., the ratio of Eq. (2) to Eq. (1), we find a value of 4.5×10^{-4} cm for the effective Mössbauer thickness parameter x_N, and a value of 1200 cm^{-2} for the source distribution parameter α. In Fig. 3 we have also shown our results for the ratio of x-ray to gamma-ray counts in the vertical geometry. The value of the effective Mössbauer thickness parameter obtained from these data is 4.8×10^{-4} cm.

Conclusions and Future Work

Our results in the horizontal geometry indicate the occurrence of the Mössbauer effect in the first-excited nuclear level of ^{109}Ag. The size of the effect is 0.2% at 4.9 K. Comparing this with the size of the effect previously observed[7] in the vertical geometry which is also 0.2%, we see no effect due to the influence of the gravitational field within the limits of our experimental error. Further experiments are in progress. Particularly, we are investigating the possibility of minimizing the sources of inhomogeneities in our samples by using higher purity silver single crystals and various types of heat treatment. A more physical model is being developed to interpret the measured Mössbauer effect in terms of line broadening and inhomogeneous fields effects.

REFERENCES

1. R. Coussement, G. Scheveneels, F. Hardeman, and P. Boolchand, Hyperfine Interactions 42, 1169 (1988)

2. G.E. Bizina, A.G. Beda, N.A. Burgov, and A.V. Davydov, Soviet Phys. JETP 18, 973 (1964)

3. V.G. Apatov, A.G. Beda, G.E. Bizina, A.V. Davydov, and M.M. Korotokov, Proc. Int. Conf. on Mössbauer Spectroscopy, Bucharest, Romania (1977).

4. W. Wildner and U. Gonser, J. Phys. (Paris) 40, C2-47 (1979)

5. G.R. Hoy and R.D. Taylor, J. Quant. Spect. and Rad. Trans., 40, 763 (1988)

6. R.D. Taylor and G.R. Hoy, SPIE Short and Ultrashort Wavelength Lasers 875, 126 (1988)

7. G.R. Hoy, S. Rezaie-Serej, and R.D. Taylor, Proc. Int. Conf. on Applications of Mössbauer Effect, Budapest, Hungary (1989), paper 15.7.

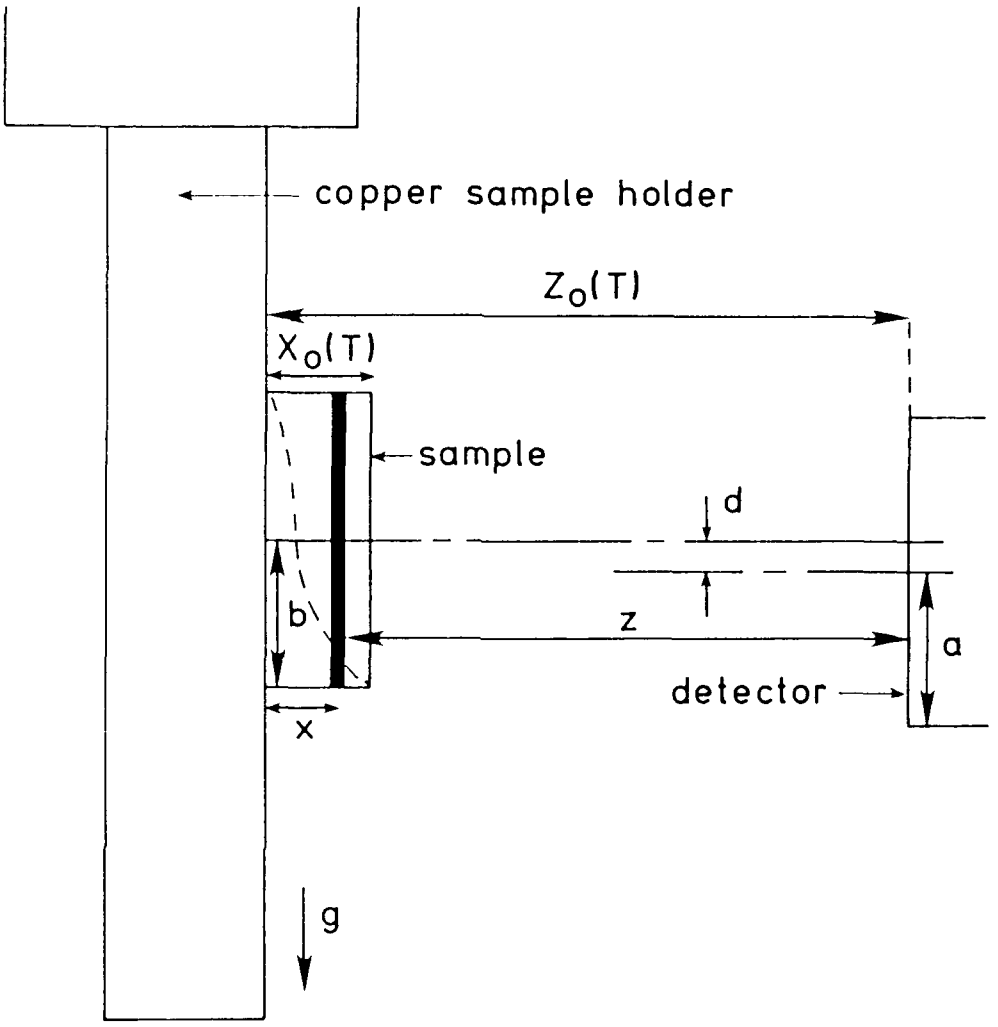


Fig. 1. A schematic representation of the experimental configuration in the horizontal geometry. Notice that the solid angle subtended by the detector is temperature dependent due to the contraction of the materials as the temperature is lowered. Particularly, note that the sample moves up as the temperature is lowered. The values of the parameters are as follows:

$x_o(295) = 5.21 \times 10^{-2}$ cm, $Z_o(295) = 6.45$ cm, a = 0.50 cm, and b =0.48 cm.

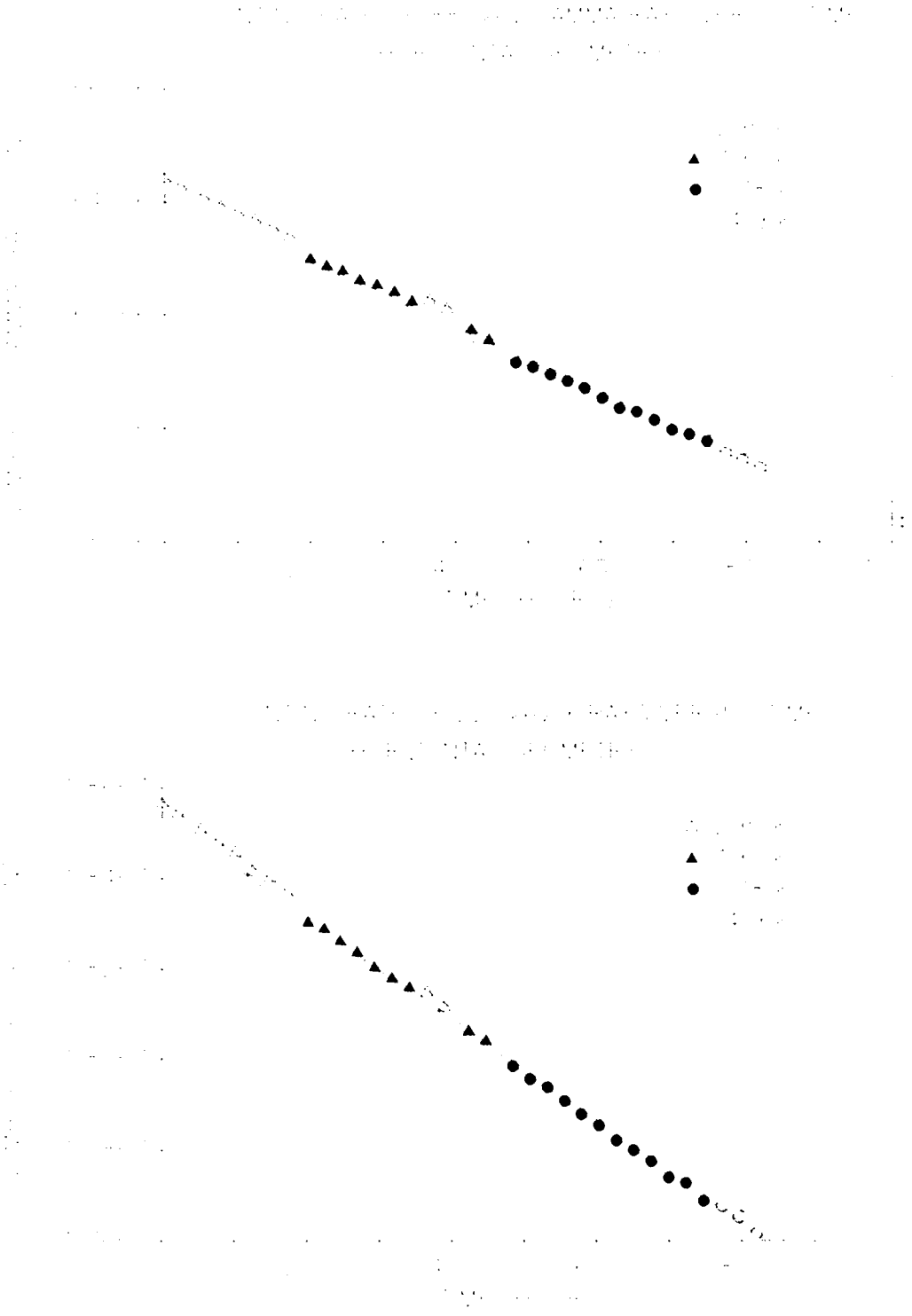
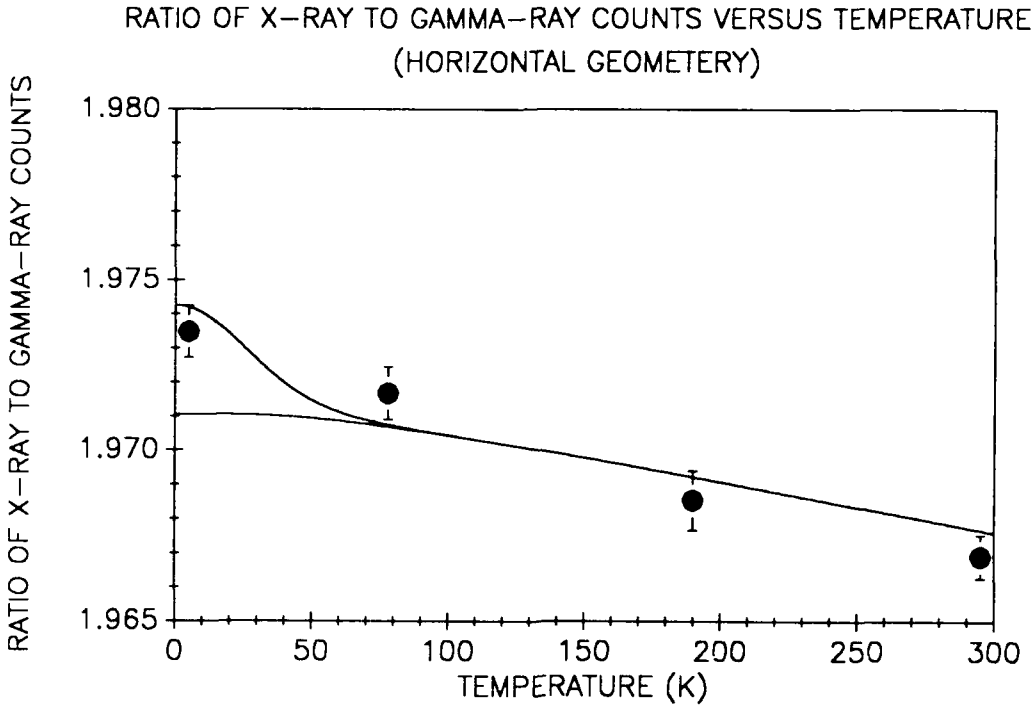


Fig. 2. The top half of the figure shows our experimental data for the counting rate of the 88-keV gamma rays as a function of time at four temperatures. The drop in the counting rate at lower temperatures is due to thermal contractions, geometrical solid angle effects, and possibly the Mössbauer effect. The solid lines are obtained by a least-squares fitting procedure in which the known decay constant for ^{109}Cd is used. The two arrows on the side of the figure show the count-rate drop that we have determined to be associated with the occurrence of the Mössbauer effect at 4.9 K. The lower half of the figure shows similar data for the 22-keV x rays that were used to determine the solid angle effects.



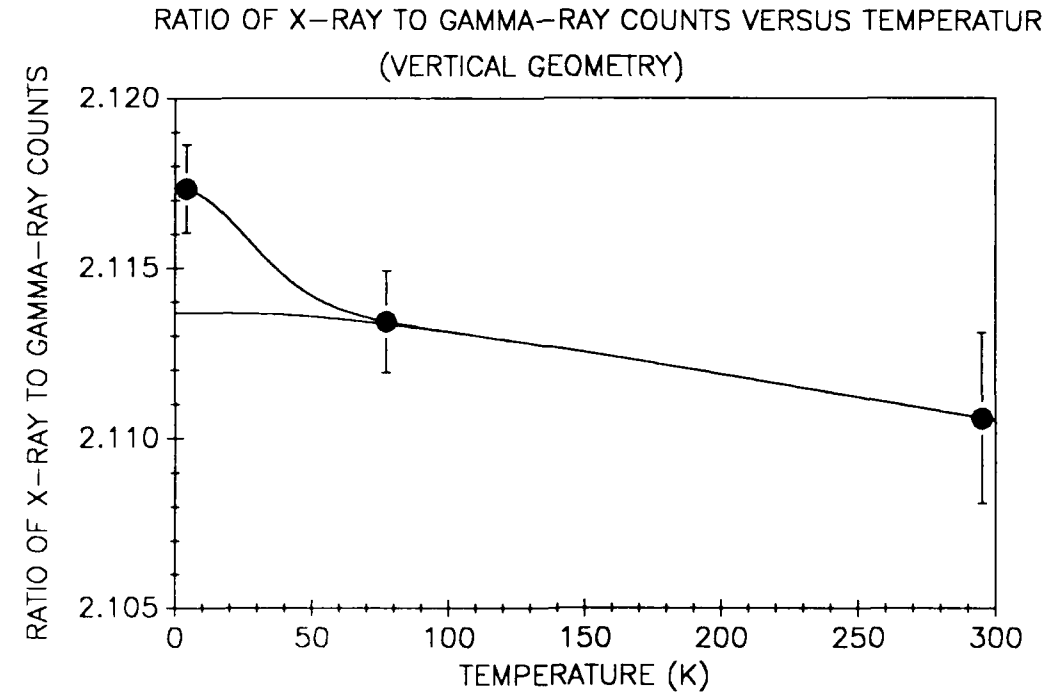


Fig. 3. The top half of the figure shows our experimental results for the ratio of 22-keV x-ray to 88-keV gamma-ray counts at four temperatures; namely 295 K, 190 K, 78 K, and 4.9 K for the horizontal geometry. In the lower half of the figure, similar data at three temperatures: 295 K, 78 K, and 4.8 K for the vertical geometry are shown. The two solid curves show the results of our theoretical analysis. The lower curve in each figure is obtained by putting the Mössbauer effect equal to zero. The higher one includes the presence of the Mössbauer effect.

DEVELOPMENT OF KrF LASERS FOR FUSION

Joseph F. Figueira
Chemical and Laser Sciences Division
Los Alamos National Laboratory
MS E548
Los Alamos, New Mexico 87545

ABSTRACT

Short-pulse, high-intensity excimer lasers are being developed for a variety of atomic physics and inertial confinement fusion applications. In this paper, we will discuss the status of KrF laser technology and its application to ICF. Current progress worldwide will be described with emphasis on the Los Alamos program.

Introduction

The Los Alamos National Laboratory has been actively engaged in the development of high-power gas lasers for inertial confinement fusion applications for twenty years beginning with the highly efficient long wavelength CO_2 laser. Based on results from the target experimental programs in the early 1980s, a national shift in the required laser wavelength occurred, and the Los Alamos ir laser program was terminated in favor of the short wavelength KrF gas laser.

The KrF laser is relatively new to the ICF community; it was demonstrated in 1975 (Brau and Ewing 1975), followed immediately by other confirmations of spectroscopy and lasing (Brau 1975; Ewing and Brau 1975; Ault et al. 1975; Mangano and Jacob 1975; Searles and Hart 1975; and Tisone et al. 1975). The development of high peak power KrF laser technology for Inertial Confinement Fusion (ICF) applications is actively in progress throughout the world with major facilities underway in Japan, Canada, England, the USSR, and the US. Because of the newness of the technology, most of these efforts are a strong mixture of facility engineering, advanced technology research and development, and advanced conceptual design studies. The Los Alamos National Laboratory KrF laser development program is probably the largest effort in the world. It addresses both near-term integrated laser demonstrations and longer-term advanced design concepts and technology advancements required for larger fusion laser systems. We will review the basic features of the KrF lasers, describe the status of the worldwide KrF technology program, provide an overview of the Los Alamos laser development program, describe current progress on the near-term technical activities, and discuss the future directions of the Los Alamos KrF laser development program.

Basic Features of the KrF Laser

KrF lasers operate by electrically pumping high-pressure gas mixtures of krypton (Kr), fluorine (F_2), and a ballast gas such as argon (Ar) with self-sustained electrical discharges or with high-energy electron-beams. The electrical excitation initiates a complex chain of reactions that results in the production of the krypton fluoride (KrF*) molecule and various absorbers. The KrF* molecule can then lase to the unbound lower level, emitting a photon at 248 nm. The upper state lifetime is very fast in the excited KrF molecule, and storage times are limited to approximately 5 ns by quenching and spontaneous emission. KrF is the second most efficient member of a class of excimer lasers that also include the well-studied XeCl (lasing at 308 nm), XeF (lasing at 351 nm), and ArF (lasing at 193 nm), which is the most efficient.

A unique combination of features appears to make the KrF laser well suited as a driver for inertial confinement fusion drivers. These features are summarized below.

- The laser directly operates at 248 nm, optimizing the ICF target efficiency without added wavelength conversion complexity.
- Unlike other ICF lasers, the KrF laser is basically not a storage laser; it prefers to operate in the continuous energy extraction mod Because of this feature, loaded KrF amplifiers tend to be very linear with little temporal pulse shape distortion. This allows for very robust pulse-shaping capability that may prove absolutely essential for efficient target performance.
- Electron-beam pumped KrF lasers are scalable to large energies in a single module. This feature has been clearly demonstrated by amplifier architectures now under development. The Aurora large aperture module has already demonstrated 10 kJ extracted from a 2000 l volume, and advanced Los Alamos designs will explore amplifiers in the 50-kJ to 250-kJ region.
- The laser operates with a broad lasing bandwidth in excess of 200 cm^{-1} that allows the use of spatial and temporal smoothing techniques for both direct and indirect target drive applications.
- Although all of the current ICF related KrF laser technology development programs are emphasizing single-shot facilities, the basic design features of the KrF gas laser will permit extensions to repetitively pulsed devices in the future, if commercial energy applications are pursued.
- The laser medium is a non-damaging gas, eliminating the need for extensive protection systems to insure the survivability of the laser medium. This feature also allows KrF to readily adapt to multiple-pulse operation for commercial applications.

Worldwide Progress

Since their invention in 1975 by Brau and Ewing, excimer lasers have been the subject of steady and increasing interest. Major progress has been made in the commercial development of high average power devices, with 1-kW devices being actively developed on several continents through individual companies or industrial consortia. More recent interest has centered on the development of high peak power devices as potential replacements for harmonically converted glass lasers in inertial confinement fusion and extremely high intensity atomic physics applications. Active research and technology programs are in progress in the United States and competitive programs are being pursued in Japan, Canada, Germany, the United Kingdom, and the Soviet Union. These programs have led to a series of first-generation, integrated laser-target systems that are in design, construction, or testing. Table 1 shows a current compilation of these laser systems. The Lawrence Livermore National Laboratory (LLNL) RAPIER system was operated briefly in the early 1980s and then decommissioned. The SPRITE laser, built at the Rutherford-Appelton Laboratories in the United Kingdom, was the first truly high-power KrF facility in operation. The UK government is considering an upgrade of this facility to the 3-kJ level and designs are currently in progress for a 100-kJ Euro-laser option based on KrF. The Naval Research Laboratory (NRL) is the other Department of Energy (DOE) US participant in the KrF laser development program. NRL has started construction of the NIKE laser that will produce 2 to 4 kJ. The University of Alberta at Edmonton is proposing to build a 1-kJ facility, utilizing some of the components from the LLNL RAPIER laser that have been provided by the DOE through a joint US/Canada protocol. Several Japanese universities are actively involved in the pursuit of KrF lasers; the major operating facility in operation is the ASHURA laser at the Electro-Technical Laboratory of the University of Tokyo. In addition, the Kurchatov Institute of the USSR is constructing a kJ-class KrF facility in collaboration with Evremov Electro-Technical Institute and is pursuing conceptual designs for a 10-kJ class device. All of these facilities are based on electron-beam pumped KrF laser technology; they employ several different optical architectures and different design philosophies. This broad array of activities will continue to enrich the technology available to KrF lasers and to improve the performance and reduce the cost of many system components.

TABLE 1. KrF Laser Technology Is Being Pursued Internationally for ICF Applications

Laser System	Status	Energy	Power
Rapier (LLNL)	1982	800J	1×10^{10}W
SPRITE (Rutherford)	1983	200J	3×10^{9}W
Euro-Laser (Rutherford)	~1996	100kJ	variable
AURORA	1985	10kJ	2×10^{10}W
(Los Alamos)	1988	1kJ	2×10^{11}W
	1989	4kJ	10^{12}W
Nike	1989	10J	------
(NRL)	~1993	2kJ	------
Rapier B	1988	100J	-------
(U of Alberta)	(proposed)	1kJ	-------
Ashura (Electro-Technical	1988	500J	5×10^{9}W
Lab, Japan)	(future)	1kJ	2×10^{11}W

Overview of KrF Laser Development Program

In the preceding we have discussed both the potential advantages of KrF lasers and the international effort now underway in KrF laser technology. The potential advantages of the laser are well recognized, but they must be demonstrated at current scale size in integrated laser-target systems. More importantly, these advantages must be shown to scale economically to the 100-kJ to 10-MJ sizes required for future progress in the ICF program. The Los Alamos laser development program is composed of three major elements that are intended both to aggressively address near-term feasibility of the KrF laser concept and to show the way to the cost and performance improvements required for future laser facilities.

- The Aurora Laser Facility is a 1-TW KrF laser designed as an integrated performance demonstration of a target-qualified excimer laser system.
- An advanced design effort evaluates the concepts that offer the improved performance and lower cost that will be essential for the construction of future lasers in the 0.1- to 10-MJ class.
- A laser technology program addresses both performance and cost issues that will be important in advanced laser system designs.

Each of these programs is briefly described below.

Aurora

The near-term goal for Los Alamos is the successful integration and operation of the of the Aurora Laser Facility at the multi-kilojoule level with powers approaching 1 TW. Aurora is a short-pulse, high-power, krypton-fluoride laser system. It serves as an end-to-end technology demonstration prototype for large-scale excimer laser systems of interest to short wavelength ICF investigations. The system employs optical angular multiplexing and serial amplification by electron-beam driven KrF laser amplifiers to deliver multi-kilojoule laser pulses of 248 nm and 5-ns duration to ICF relevant targets. The design goal for the complete system is 5 kJ in 48 laser beams. Figure 1 shows a conceptual schematic diagram of an angularly multiplexed laser system showing a single front end pulse being split into three replicas, delayed, angularly encoded and then feed to a power amplifier for efficient, quasi-cw energy extraction. Figure 2 shows the floor plan of the Aurora Facility with the laser bay to the right, target chamber to the left and the optical beam transport system in the long tunnel connecting the two subsystems.

Substantial progress has been made on the facility in the last several years including the following highlights:

- Demonstration of 96-beam multiplexing and amplified energy extraction, as evidenced by the integrated operation of the front end, the multiplexer (12-fold and 8-fold encoders), the optical relay train, and three electron-beam driven amplifiers;
- Assembly and installation of the demultiplexer optical hardware, which consists of over 300 optical components ranging in size from several centimeters square to over a meter square;
- Completion of pulsed-power and electron-beam pumping upgrades on the LAM (Large Aperture Module), PA (Pre-Amplifier), and Small Aperture Module (SAM). The SAM shows a 40% increase in deposited electron beam energy, and the PA deposited energy has been increased by a factor of two; and
- Integration of the entire laser system; the extraction of 4 kJ from the laser in 96 beams; and the delivery of 1.3-kJ to the target chamber in 36 beams with intensities in excess of 100 TW/cm^2 in pulse durations adjustable between 3 and 7 ns.

Advanced Laser System Design

In the longer term, the national ICF program will continue to plan for the construction and operation of the next generation driver for ICF physics experiments. To determine the applicability of KrF laser technology to future generations of fusion drivers, Los Alamos has begun a design effort to explore systems in the 100kJ to 10MJ range. This Advanced KrF Laser Design effort provides information to the KrF program on the design and cost of future KrF laser-fusion systems and provides directions and goals to the KrF technology development effort. Because no current ICF driver has demonstrated both the required cost and the performance scaling, and because uncertainties exist in laser-matter interactions and target physics, Los Alamos is currently pursuing a range of advanced KrF laser design activities: work is currently in progress to scope a 10-MJ Laboratory Microfusion Facility (LMF), a 750-kJ LMF Prototype Beam Line, a 250-kJ Amplifier Module (AM), and a 100-kJ Laser Target Test Facility.

The purpose of the Department of Energy sponsored scoping study for a Laboratory Microfusion Facility is to examine a facility with a capability of producing a target yield of 1000 MJ in a single-pulse mode. An example of a KrF design for an LMF beam line that requires only minor extrapolations in pulsed-power technology is shown in Fig. 3. This system uses angularly multiplexed amplifier modules 1.3 x 3.9 x 3.8 m^3, each of which produces 250 J of 248-nm radiation. These units are then arranged in a tri-fold cluster, to form an LMF beam line that produces 750 kJ. These beam lines can then be arranged to produce the total required energy ranging from 750 kJ to 10 MJ.

KrF Technology

The current costs of all laser drivers are unacceptable for an LMF scale system. To reduce these costs to an acceptable level, advanced technology programs are being designed to address the major cost drivers identified by the LMF studies. Optics and pulse power account for 60% of the total cost for the Aurora design; this produces an unacceptably high laser system cost when scaled to larger facilities. Advanced design concepts have identified technology areas that can be improved to reduce the overall system costs. The optics and pulse power costs have been reduced to 19% of the total system cost, and the total subsystem cost is reduced by a factor of 5. The KrF laser technology development program addresses performance improvements and cost reductions for the LMF designs in the areas of optics, pulse power, and laser performance, as well as those technical issues effecting system reliability and modeling accuracy. These improvements include increases in the optical damage fluences for uv radiation from the current value of 12 J/cm^2 to 20 J/cm^2 (20-ns pulses @ 248 nm); increases in power amplifier size from the current 10-kJ modules used in Aurora to units in the 50- to 250-kJ class; and electron beam pumping densities in the 125 to 175 J/l range with intrinsic efficiencies in excess of 10%. These technology and cost reduction programs will utilize a mixture of industrial, university, and government laboratory involvement and could lead to the required subscale technology demonstrations in the next three- to five-year period.

Conclusion

High-energy, high-peak power KrF lasers represent a promising new technology for inertial confinement fusion applications. To evaluate this technology, Los Alamos is conducting a series of integrated system demonstrations with the Aurora Laser Fusion facility. Future ICF applications of the KrF laser are being evaluated by a coordinated program of advanced designs and technology development. If these evaluations are successful, KrF lasers will provide the national ICF program with an attractive future driver candidate for the Laboratory Microfusion Facility in the late 1990s.

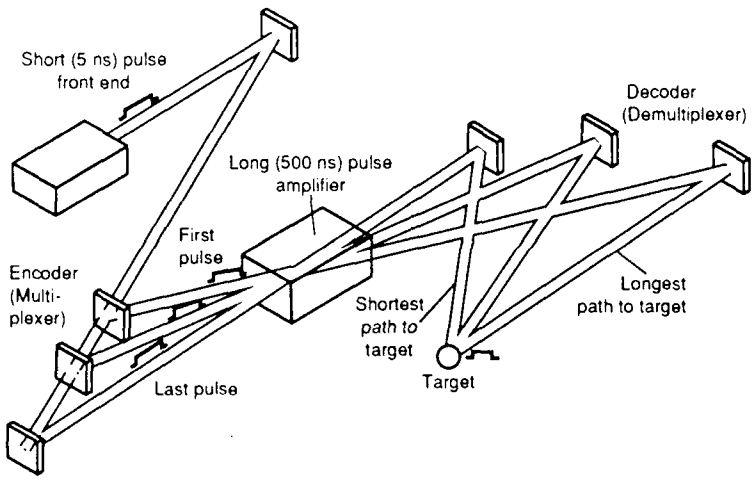


Fig. 1. Angular optical multiplexing allows for efficient energy extraction of long pulse amplifiers. A single 5-ns pulse is split and delayed and feed through the 500-ns amplifier. After amplification the angle encoded time channels are recombined in synchronism at the target. In the schematic shown, this technique allows a power multiplication of x 100 when 100 optical channels are used.

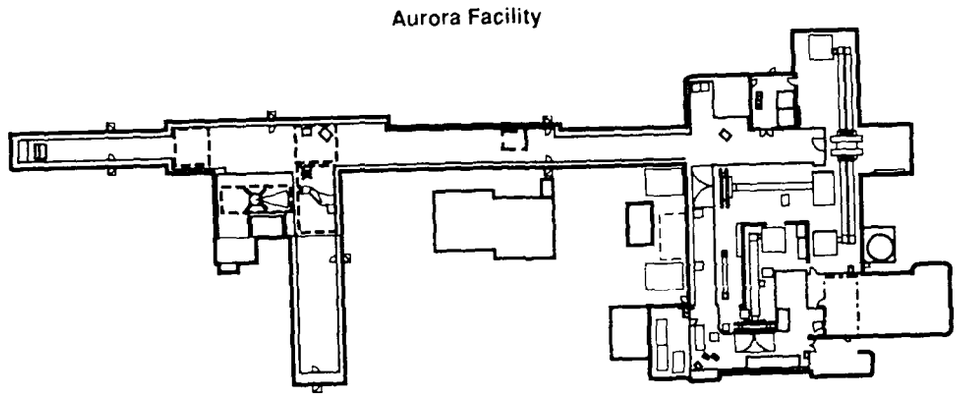


Fig. 2. Schematic of the three major Aurora subsystems: target chamber, beam transport and decoder, and power amplifiers and front end (left to right).

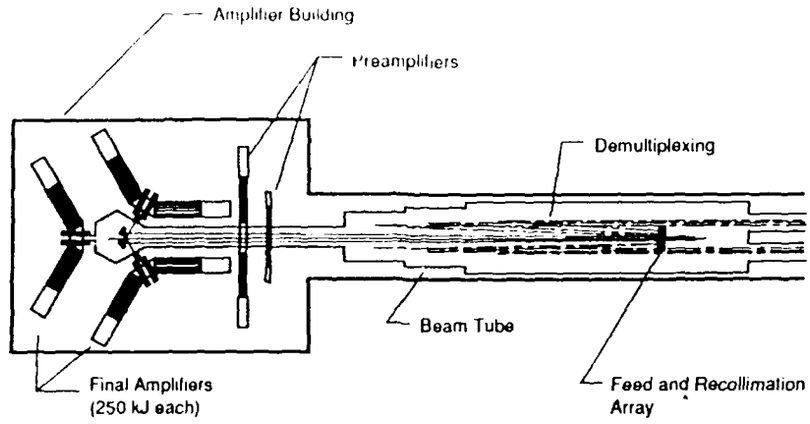


Fig. 3. LMF beam line showing a tri-fold array of 250-kJ modules.

References

1. E. R. Ault, R. S. Bradford, Jr., and M. L. Bhaumik, Appl. Phys. Lett. 27, 413 (1975).

2. C. A. Brau and J. J. Ewing, Appl. Phys. Lett. 27, 435 (1975).

3. J. J. Ewing and Brau, C. A., Appl. Phys. Lett. 27, 350 (1975).

4. J. A. Mangano and J. H. Jacob, Appl, Phys. Lett 27 495 (1975).

5. S. K. Searles and G. A. Hart, Appl. Phys. Lett. 27, 243 (1975).

6. G. C. Tisone, A. K. Hays, and J. M. Hoffman, Opt. Commun. 15, 188 (1975).

CLINICAL EXCIMER LASER ANGIOPLASTY : THE ITALIAN PROGRAM

R.Pini, R.Salimbeni, M.Vannini, A.Guasti

Istituto di Elettronica Quantistica del CNR,
Via Panciatichi 56/30, 50127 Florence, Italy

V.Gallucci, R.Viligiardi

Istituto di Chirurgia Cardiovascolare, University of Padua, Italy.

Abstract

Because of the great promise of using excimer lasers for medical applications, a research program was started in 1986, supported by the Italian National Research Council (CNR). The object of the project is to develop reliable medical laser systems devoted mainly to the clinical application of laser angioplasty techniques.

In the preliminary phase, using a standard short pulse excimer laser, problems related to high power coupling into optical fibers were addressed. These ones concerned the clarification of which type of fibers are optimum and which optical catheter configurations are the most proper.

In vitro ablation experiments on human aorta samples showed that a multifiber catheter geometry is the most practical solution to obtain large emitting areas able to produce ablation channels of 2-2.5 mm in diameter. This size has been considered the lower limit for satisfactory coronary neo-lumina.

At first the research program was limited to intraoperative laser angioplasty in coronary vessels. The first clinical coronary recanalization was successfully performed in June 1989 using a properly designed surgery room excimer laser system.

Introduction

Following the early works of Srinivasan on excimer laser etching of organic compounds[1], Laudenslager and Grundfest [2] proposed in 1985 the use of excimer lasers for the angioplasty techniques. In effects the peculiar ablation process was extremely promising also in this biomedical field, overcoming the thermal problems showed in the attempts to use other types of lasers [3]. Furthermore high power transmission through optical fiber was previously demonstrated at the IEQ-CNR [4]. With these premises it was possible since 1986 to start in Italy a research program devoted to develop a clinical excimer laser angioplasty technique. The program was part of the finalized Project TBMS (BioMedical and Sanitary Techniques) of the CNR. Later it has also received valuable contributions from CESVIT (Organization for the advanced technology of the Florence Province) and from private industries.

The aim of the program was bound to several targets:

1) to devise a laser angioplasty method which has to be simple and repeatable because the pathology is chronic and evolutive,
2) to design an excimer laser system in all the most important components, namely the laser itself with the most proper characteristics, and a class of optical catheters suitably developed to meet many different angioplasty demands,
3) clinical application of the system to validate the technique and to point out and possibly address all the different types of problems tightly related to the surgeon handling experience.

For these reasons the program has been organized in three phases which have been necessarily started in sequence, but then can proceed together in a mutual coordination and interaction. They are :1) Pre-clinic experimentation, 2) Surgical excimer laser system design and construction, 3) Clinical experiences.

Pre-clinic experimentation

In this phase, carried out mostly at the IEQ-CNR, we have included all the activities related to the preliminary investigations on fiber coupling of high power excimer laser radiation, ablation tests on biological samples and hystological evaluation of the obtained channels.

As previously mentioned an accurate knowledge of the peculiar fiber coupling limitations was available[4]. These experiments were carried out using a standard short pulse (25 ns) laser. It was clear that with such a short duration the fiber damage threshold was dangerously near to the operating energy density required for the plaque ablation; nevertheless experiments devoted to the basic catheters features could start, delaying the reliability achievement to a future work on the laser pulse duration.

So in the experiments it was used an excimer laser of our own design available at the moment in which the pulse shape was sligthly smoothed to 30-40 ns and the output energy was in the order of 100 mJ. Pertinent biological samples were provided by the "Istituto di Anatomia Patologica" of the Padua University which could also take care of the histological evaluation. The samples consisted of human aorta samples, human hearts quickly carried at the IEQ-CNR in Florence after transplants performed at the "Istituto di Chirurgia Cardiovascolare" in Padua, and some autoptic hearts too.

The investigation on a selected choice of commercially available fibers made clear soon that, with a propagating energy density only a factor 3 to 5 lower than the damage limit, almost every reshaping of the fiber end could produce internal focussing with a consequent damage. So the only practical finishing of the fiber output face is a bare flat one. This fact is important in the sense connected to the width of the ablated channel. In facts for the catheter progression two independent conditions have to be fulfilled: 1) energy density at the irradiation site larger than the ablation threshold, 2) ablation channel diameter larger than the overall catheter size. The second one can be called a progression condition[5]. To be achieved with multifiber catheters it can require some attention. These effects are shown in figs.1a and 1b for the case of a catheter composed of 3x600 μm. In fig. 1a the irradiation was performed almost in contact with a sample of aorta, while in fig. 1b a gap allowed the single lobes expansion to overimpose their contribution in order to avoid the formation of flaps which could slower or stop the catheter progression. This observation does not take in consideration the averaging effect provided by the natural wandering of the catheter tip, but suggests to optimize the geometry of multifiber catheters in maximizing the overall emitting area in respect to the total one.

Another important validation was related to the overall flexibility of the catheter. During this phase it was possible to test in quite fresh human hearts, explanted a few hours before, how well relatively long tracts of coronary arteries could be passed through by different catheters geometries. The approximation of the experimental conditions was considered close enough to an intraoperative situation, and relying on the natural elasticity it was possible to pass through the anterior descendant almost down to the heart apex also with the previously described 3x600 μm. Long tracts of the right and left descendant were also recanalized.

These results confirmed the possibility of performing recanalization diameters of 2 mm at least in the pseudo-straight tracts of the coronary vessels.

Surgical excimer laser system

The first phase made possible to clarify the design parameters of a prototype consisting of a laser, a fiber coupler and a set of catheters, suitable for starting a clinical validation. The system is shown in fig.2. It has been constructed by EL.EN. of Florence in cooperation with the IEQ-CNR. Main design criteria are the following:

1) demonstrated e.m. noise compatibility in the surgery room environment (pace-maker, monitors could be severely affected by high power discharges unless double shielding is not provided)
2) no connection is needed except the power cord (a closed loop stabilizes the gas temperature, avoiding the need of tap water connections)
3) all the gas handling components are included in the cabinet, and the eventual refill can be accomplished automatically with one push button operation,
4) ready in five minutes, unless the refill is needed,

5) from ready the laser operates only by pedal switch controlled by the surgeon,
6) no catheter alignment is needed (it would require trained personnel and is time spending, passive stabilization of the alignment ensures the operating conditions)
7) fast catheters interchange (due to point 6 a change is accomplished in seconds without loosing alignment)

The laser emission specifications are listed in Table 1. The choice of the XeCl wavelength is due to several indipendent features:

1) 308 nm represents the best compromise between 351 nm and 249 nm in terms of fiber transmission reasonably high (90% out of 2 m fiber length) and ablation threshold reasonably low (1-1.5 J/cm^2 for lipid rich plaque); KrF has, in facts, higher losses, and XeF has a 3 times higher ablation threshold,
2) XeCl operates with Cl donors and requires simpler technological solutions to achieve long refill lifetime,
3) Chlorine has a lower electron attachment than fluorine and provides less source of discharge instabilities which ultimately can limit the pulse duration; this feature is very important in order to relax the fiber damage hazard propagating the required pulse energy in a long pulse with a low peak power. Stabilization of the discharge over hundreds of nanoseconds would be rather difficult with a fluorinated excimer, while several electrical schemes are available for XeCl[6,7,8] . Pulse lengths up to 1 μs have been reported by Taylor[9]. In our design the pulse width has been inductively stretched according to the scheme proposed by Sugii[10] . Fig.3 shows the pulse shape in which no spike is present relatively satisfying the desired "top hat" energy distribution. Further pulse lengthening is anyway in program.

Clinical experiences

The performance of the surgical system has been evaluated again in the following preliminary tests :

a) recanalizations in vitro of coronary arteries in human explanted hearts,
b) recanalizations in vitro of segments of human femoral arteries,
c) recanalizations in vivo of rabbit femoral arteries in which post-traumatic stenoses were previously induced.

These tests confirmed the recanalization possibilities of the system and a limited tissue reaction, as observed in vivo.

The clinical activity began in May 1989 at the "Istituto di Chirurgia Cardiovascolare" in Padua with the selection of a group of coronaropathic patients. For them it was supposed to associate at the standard A.C. by-pass procedure a laser angioplasty technique to the purpose of:

1) to reduce the number of by-passes
2) to improve their distal flux in order to locate as proximal as possible the distal anastomosis and to obtain a better overall vascularization.

In the period June-December a total number of 5 patients have been treated. For all cases the introductory site of the catheter was the distal anastomosis of the by-pass. Then the catheter was advanced up to the obstruction site and the laser was turned on (usually in a pulse burst of 10 to 30 sec, at 3 J/cm^2 and 30 to 50 Hz rep. rate). During the irradiation the catheter was gently pushed until a complete recanalization was accomplished. After this angioplasty the by-pass was applied.

With this method 7 stenoses have been treated (4 anterior descendant, 1 rigth, 1 circumflex, 1 diagonal). Coronarographic control at 7 days has shown a good result in 2 cases (fig. 4a and 4b show a rigth coronary before and after the laser treatment, demonstrating a significant improvement of the neolumen diameter), 2 dissections and 3 thrombotic occlusions .

Since September 1989 a clinical activity has been started in Florence at the "Sezione Laser Angioplastica, USL10/D", for a validation in the peripheral districts. Up to December 8 patients have been treated by means of a percutaneous femoral technique with 12 positive results (fig.5 show a femoral segment previously completely occluded with the neolumen obtained only by laser treatment) 1 popliteal perforation, 1 III distal perforation and 1 untreatable patient.

Conclusions

Despite organization difficulties which have hindered for a long time the desired advancement of the program, now it is developed in all the planned phases. Improvements are expected from the device performance in terms of a higher energy density available at the fiber end, and also to provide a homogeneous pumping of larger size catheters (>3 mm2). A complete set of high flexibility catheters is also beeing prepared, for a full coverage of the required recanalization diameters. Diagnostic aid is definitely needed. In the intraoperatory approach ultrasonic imaging is on schedule soon, while in the percutaneous one auto-fluorescence spectroscopy could be the closest technique to be effectively included in the angioplasty system everyday operation.

References

1) Srinivasan R. et al., J.Polym.Sci. 22, 2610 (1984)
2) Grundfest W. et al., Amer.J.Surg. 150, 220 (1985)
3) Abela G.S. et al., Amer. J. Cardiol. 5, 1199 (1982)
4) Pini R. et al., Appl. Optics 26, 4185 (1987)
5) R.Viligiardi et al., 2nd Int.Symp.on Lasers in Cardiovascular Diseases, Vienna (1988)
6) Sze R.C., J Appl. Phys. 54, 1227 (1983)
7) Long W.H. et al., Appl. Phys. Lett. 43, 735 (1983)
8) Pacala J.T. et al., Appl. Phys. Lett. 44, 658 (1984)
9) Taylor R.S. et al., J. Appl. Phys. 65, 22 (1989)
10) Sugii M. et al., IEEE JQE, QE-23, 1458 (1987)

Table 1
Surgical excimer laser emission specifications.

Excimer	XeCl
Pulse Energy	100 mJ
Pulse Width	70 ns FWHM
Repetition Rate	10-100 Hz
Attenuations levels	75%, 50%, 25%

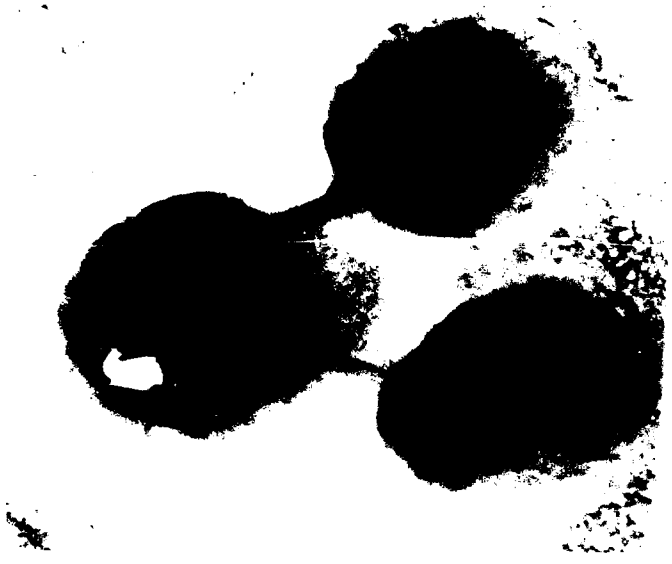


Fig.1a



Fig.1b

Fig.1 - SEM images of ablated areas obtained in aortic walls by means of a 3 fibers catheter: 1a) in contact, 1b) about 1 mm gap.

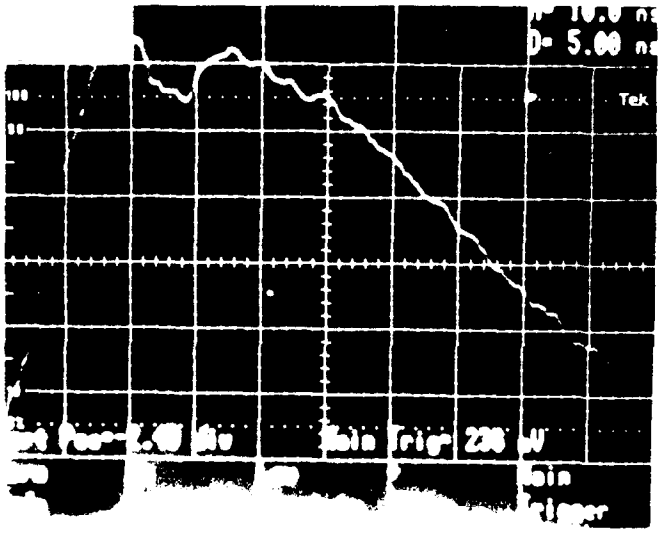


Fig.2 - Surgical excimer laser.

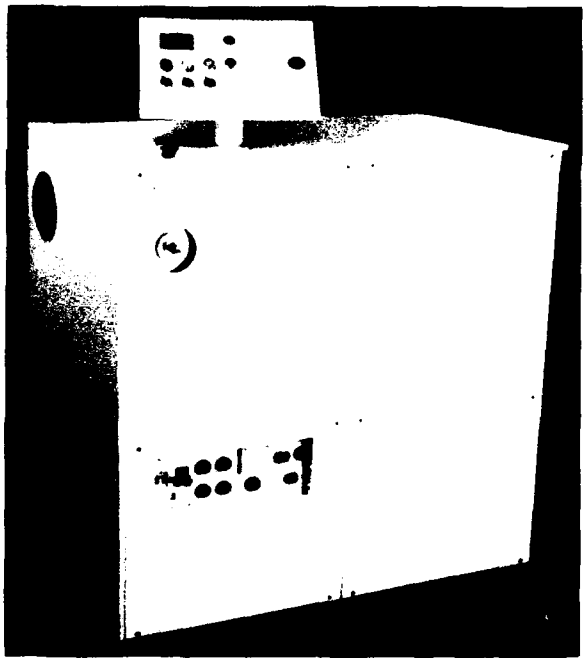


Fig.3 - Pulse shape. 10 ns/div.



Fig.4a



Fig.4b

Fig.4 - Coronarographies of the same right coronary before (4a) and after (4b) the laser treatment.

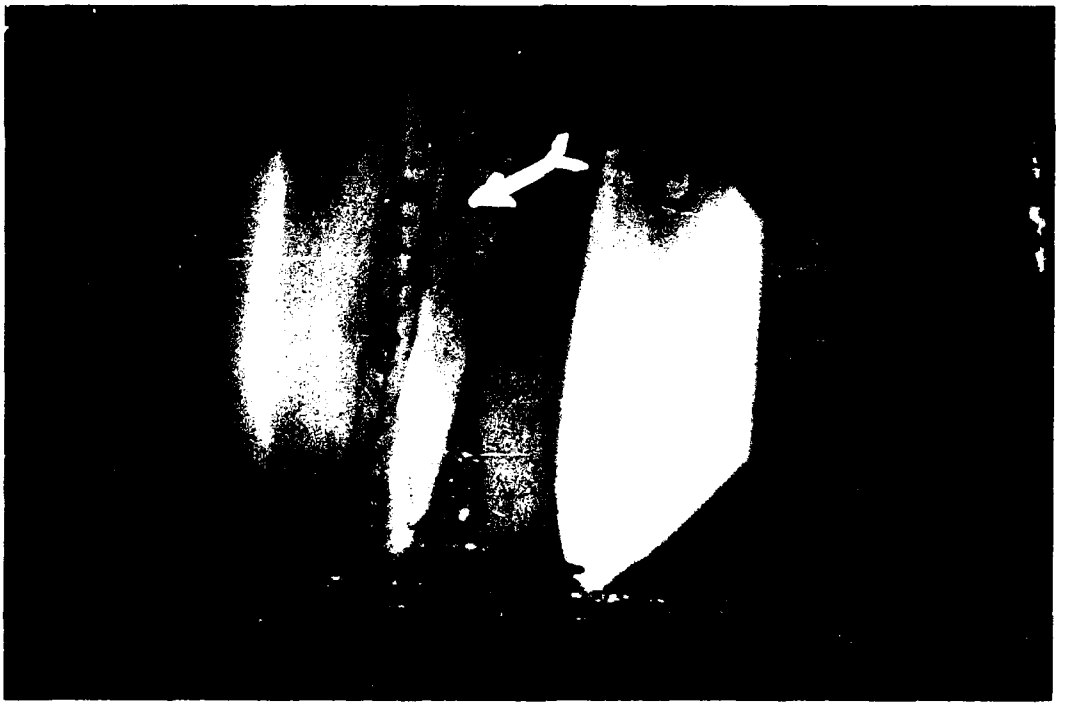


Fig.5 - Angiography of a femoral segment treated for a total occlusion located at the arrow site.

DAMPING OF ACOUSTIC WAVES IN A 1 kHz REPETITION RATE XeCl LASER.

M.L. Sentis, P. Canarelli, Ph. Delaporte, B.M. Forestier, B.L. Fontaine.

Institut de Mécanique des Fluides, Aix-Marseille University, UM 34 CNRS, Marseille 13003, France.

ABSTRACT

To increase the pulse repetition frequency, the average power, and the beam quality of excimer laser systems, damping of the strong acoustic waves induced by the active medium excitation must be solve. In order to achieve this goal different electrodes and acoustic damping configuration have been studied.

Excitation of active medium (energy deposition : 50 to 150 J/l) at high repetition rate (up to 1000 Hz) in a subsonic loop (flow velocity : up to 65 m/s) is achieved by means of a classical discharge, through transfers capacitors. The discharge is preionized by X-Ray generated by a wire ion plasma gun.

Previous studies on acoustic wave propagation done at I.M.F.M.[1] have shown that transversal acoustic waves and small changes in channel geometry and electric field distribution play a leading role on the power deposition and the stability of the discharge at high repetition rate frequency. Here we will present and discuss use of different kinds of electrodes (solid, screen, nickel felt) and transversal acoustic dampers on stability of discharge and on pulse to pulse output energy.

The effect of the acoustic waves on the pulse to pulse output energy evolution has been separated from the thermic effect.

1. INTRODUCTION

The output laser characteristics (pulse energy, pulse duration, beam profile) of gas discharge lasers are very sensitive to discharge stability and discharge quality. The non uniform energy deposition generates waves and density perturbations. Especially, due to the short wavelength of an ultraviolet laser, the density fluctuations level has to be very low ($dr/r < 10^{-3}$) to obtain stable discharges in electronegative excimer active medium mixtures.

Two main problems have to be solved to achieve a high average output power at high repetition rates : a) the heated gas has to be swept out of the laser cavity between two successive excitations (1 ms at 1 kHz PRF), b) the density fluctuations induced by shock waves inside the laser cavity have to be damped in the same time scale.

In the frame of the European program on Research and Development EUREKA, a multinational program called "Eurolaser-Excimer" has been started in Europe in 1986 in order to develop an industrial excimer laser of 1 to 3 KW average power. The planned basic technology is as follow : XeCl laser transition λ = 308 nm, fast flow closed loop, X-ray preionization, discharge excitation, 500 - 1000 Hz PRF, 1 to 5 joules per pulse.

A program to investigate extensively the XeCl laser system (308 nm) for conditions of relatively long pulse (50 to 100 ns), high PRF (1 KHz) and high average power (100 to 500 watts) has been undertaken at I.M..F.M. A laser test-bed called LUX for "Laser Ultraviolet préionisé par rayons X", already described in previous papers [2][3], has been developed. It permits to achieve an average power of 200 watts in a 250 shot burst. The laser head has been recently upgraded to allow the studies of wave behavior and wave damping.

Experimental results of use of different kinds of electrodes (solid, screen, nickel felt) and transversal acoustic dampers on stability of discharge and on pulse to pulse output energy are presented and discussed.

2. EXPERIMENT

The LUX test-bed is mainly composed by a fast flow subsonic closed wind tunnel and a high average power electrical excitation system. Gas mixture is Ne/Xe/HCl 5300/50/10 flowing up to 80 m/s in the laser discharge head (2.5 x 30 cm2 cross section). The maximum working pressure is 2.5 atmospheres. The electrical excitation system consists essentially of a X-ray preionizer and a main discharge circuit.

A new laser head, whose total volume has been strongly increreased to manage the possibility to set acoustic dampers in the immediate vicinity of excitation zone, has been built (figure 1). This increase of total volume does not facilitate the electrical circuit optimization and limits the power density injected in active volume. Such a design will allows however a more precise analysis of acoustic dampers. The design chosen for the discharge geometry use a shaped solid cathode and a plain flat plate or grid as anode. It will be possible to put in this backing volume absorbing materials or wave deflectors.

Specific diagnostics allow to study quantitatively key parameters of LUX. They have been described elsewhere [4]. Lux test bed allows pressure time history recordings at different locations of flow channel. The results given hereafter have been achieved with fast pressure transducers (PCB 112A22) whose rise time is equal to 2us and cut off frequency equal to 140 kHz .Two locations have been used (figure 1).

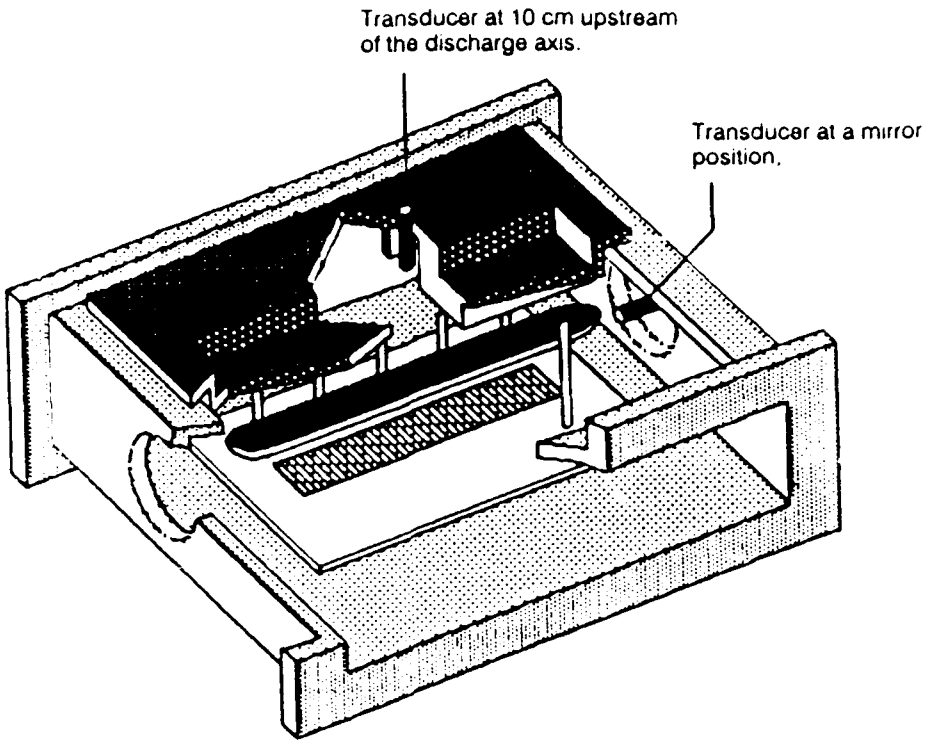


Fig. 1 : Shematic view of the laser head and transducer locations.

3. RESULTS AND DISCUSSION.

3.1. Shock wave characterization:

Interferometric study of the flow field have been undertaken with a classical Michelson streak interferometer. The optical source is a cw argon ion laser associated to an electro-mechanical shutter. The fringe pattern is recorded by means of a drum camera which permits to follow fringe shift as a function of time during 4 ms with a resolution on the film of 5.4 µs/mm. The observation zone is defined by a slit optically conjugated with the film and the laser head.

The results presented hereafter have been obtained with an horizontal or vertical slit. The analysis of interferograms leads to the evolution of flow density as a function of time along X or Y axis. The vertical slit use permits a much more precise study of the transversal waves propagating between the electrodes. The influence of these waves on laser characteristics have been already underlined in a previous paper [5].

The interferogram of Fig. 2 shows up the fringe pattern recorded with a horizontal slit with two shots at 1 kHz PRF. It permits to follow the evolution of density fluctuations over the total width of the laser cavity for a time greater than 1.3 ms. The fringe pattern before the time of electrical excitation may be considered as a tare. In this interferogram two sets of induced shock waves flowing upstream and downstream are clearly visible. The columns of heated gas, swept out of excitation zone by the flow, are also visible as well as the effects of thermal diffusion between heated slugs and cold gas. The reflection of induced shock waves by the previous thermal slug is relatively weak. The main disturbances yet visible 1ms after a shot are due to the propagation of transversal acoustic waves in a orthogonal direction to the flow and laser beam axis.

Fig. 3 shows a first shot (Y,t) interferogram when the observation zone is located just upstream of the excitation zone (1mm). The straight fringes at the bottom correspond to the flow density field in the laser head just before the first energy deposition. The first inge displacement (toward the left) is induced by the density increase due to the arrival of the compression wave in the observation zone. During a short time (dt = 3 µs), according to classical theory, the density field is relatively stationary before the passage of expansion waves which lead to a fringe shift toward the right. Following these three classical zones, the fringe shift permits to deduce the density flow field at the entrance of the laser head ; the reflections of transversal waves by the electrodes are clearly visible. These waves carry most of density perturbations even 1 ms after the first energy deposit.

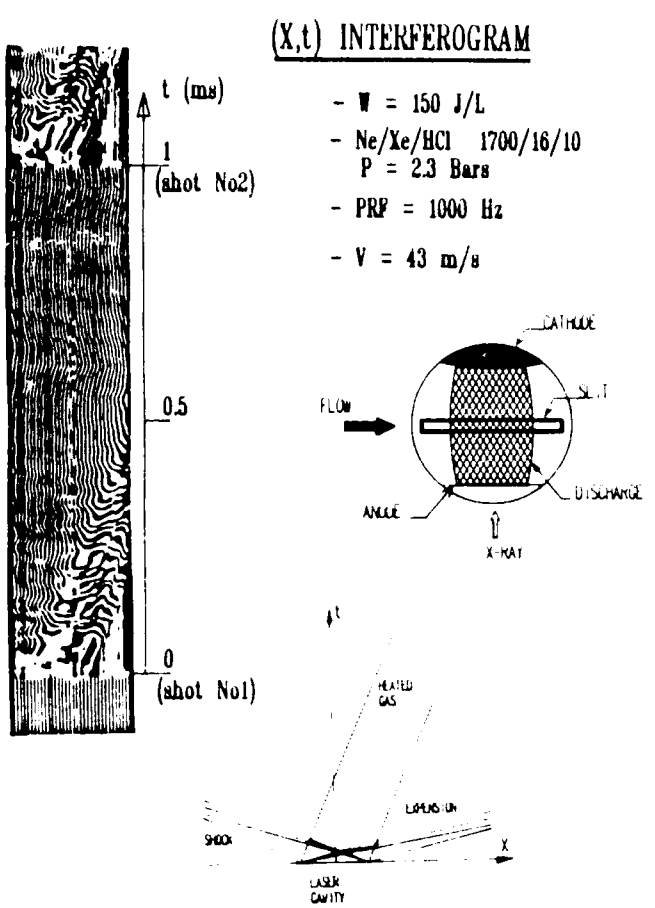


Fig. 2. : (X,t) Interferogram of two energy depositions at 1000 Hz.

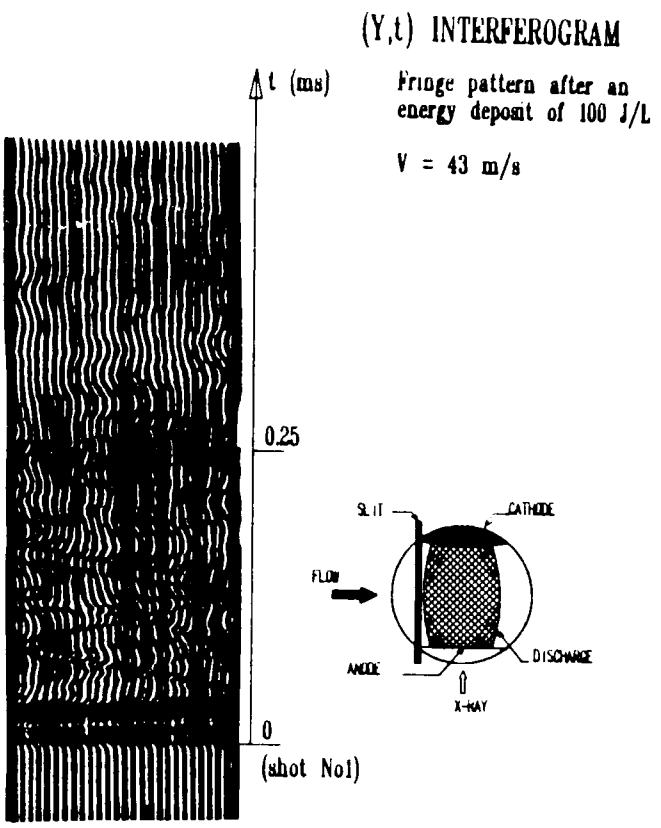


Fig. 3: (Y,t) Interferogram of one energy deposition.

3.2. Shock wave damping :

Here after are presented some experimental results on shock wave damping for different laser head configurations.

Figure 4 shows a comparison of pressure variation recordings of two different anode configurations : (a) a thin (0.5mm) aluminum plain flat foil and (b) a thin (0.5mm) perforated aluminum flat foil which the transparency is equal to 20 % (hole diamemeter 1mm). The comparison of first pressure jumps of traces (a) and (b) underlines the decreasing (b) of initial shock wave induced by the useful energy deposition. This decreasing is caused by the expansion of the heated gas in the backing volume through the perforated anode foil. Unfortunately the ratio of useful energy (first jump) to wasted energy (other jumps) is lowered when perforated plate is used. The pressure jump, visible on the waveform (b) about 1ms after the first one, appears at a time corresponding to the reflection of initial shock wave by the ends of the backing volume which does not yet contain absorbing materials. The acoustic energy which has not been transported away of discharge zone is so redistributed later in the laser head.

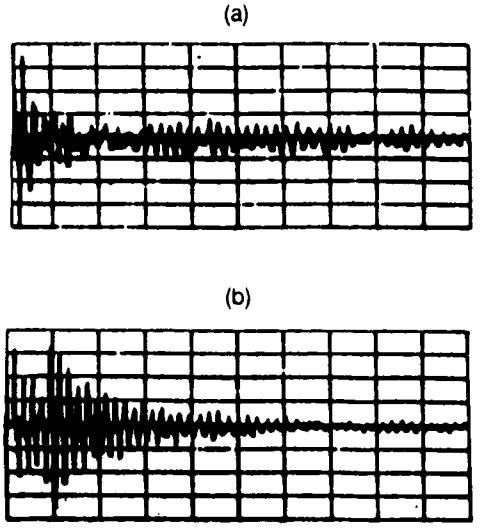


Fig. 4 : Comparison of pressure time variations recorded with : (a) a solid thin aluminum foil as anode and (b) a thin perforated aluminum foil as anode.

Figure 5 presents the evolution of residual pressure variations of one shot for (a) a solid cathode with a small radius (r = 16 cm) and (b) a porous cathode (nickel foam) with the same radius as a function of time and Log(ΔP/P) as a function of the acoustic transit number (c.t/h) for the two different configurations (a) and (b). The behavior and the damping of the acoustic waves are similar to those described in the previous figure. Here, the shape of the electrode for the solid cathode is predominant to push the shock waves out of the discharge zone , but with the porous cathode and from 0 to about 0.6 ms the acoustic energy is trapped between the two electrodes because the porous electrode back face is flat and so forms with the flat anode like a acoustic resonator. The use of a porous cathode could be an appropriate solution to operate up to a PRF of approximately 500 Hz but the life time of the material (nickel foam) could be a limitation. The use of a solid cathode with a very small radius is a possible solution to work at high PRF but has a strong limitation to develop a laser with a laser beam larger than about 5 mm.

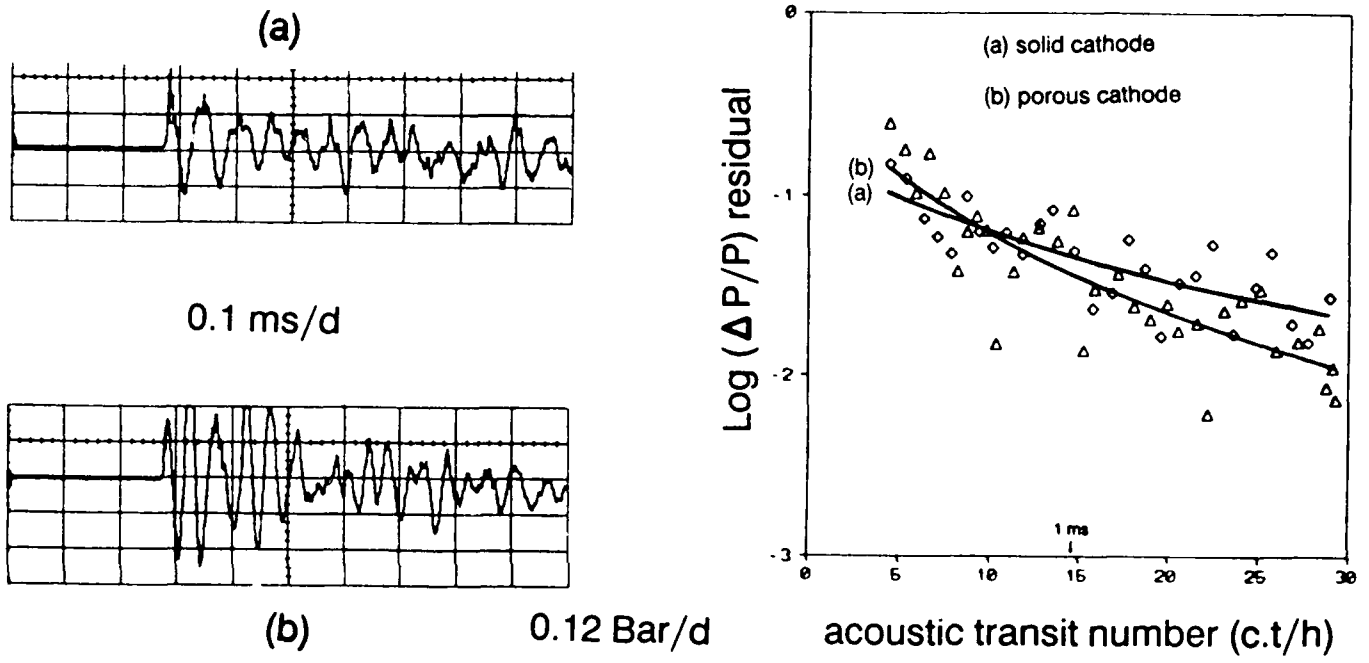
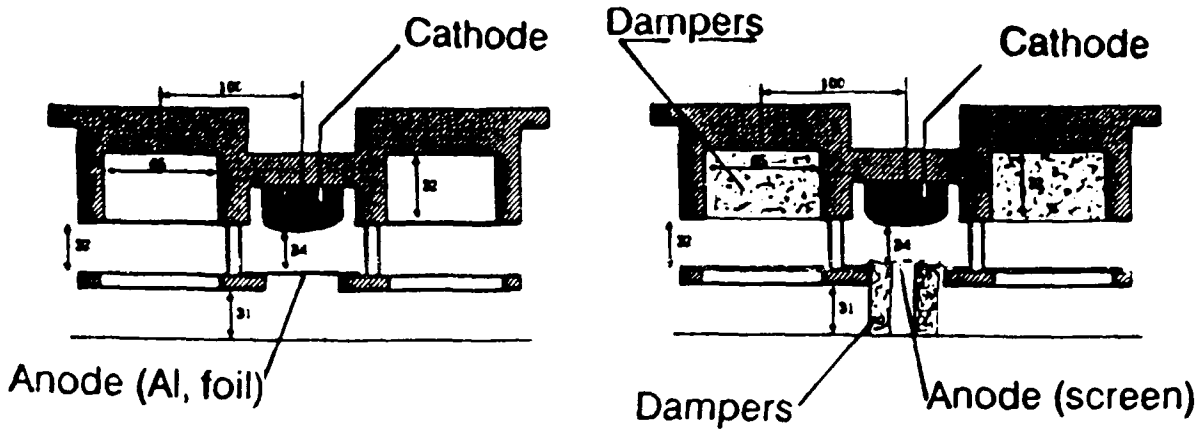
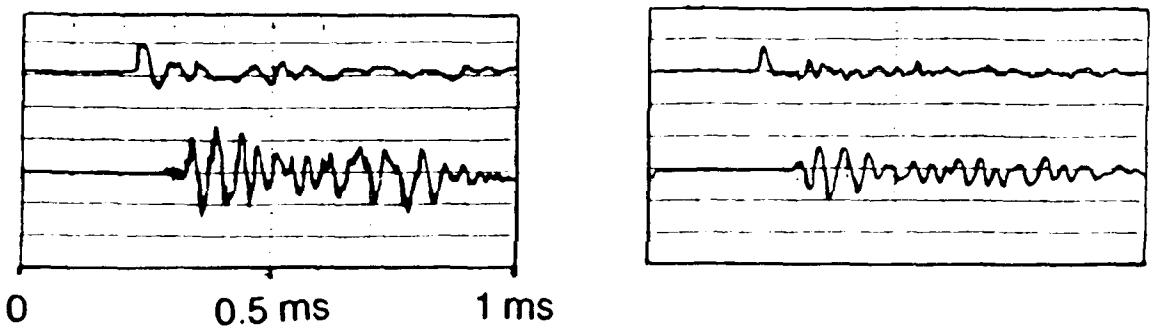


Figure 5 : Evolution of residual pressure variations of one shot for:
- a) a solid cathode with a small radius (r = 16 cm),
- b) a porous cathode with the same radius.

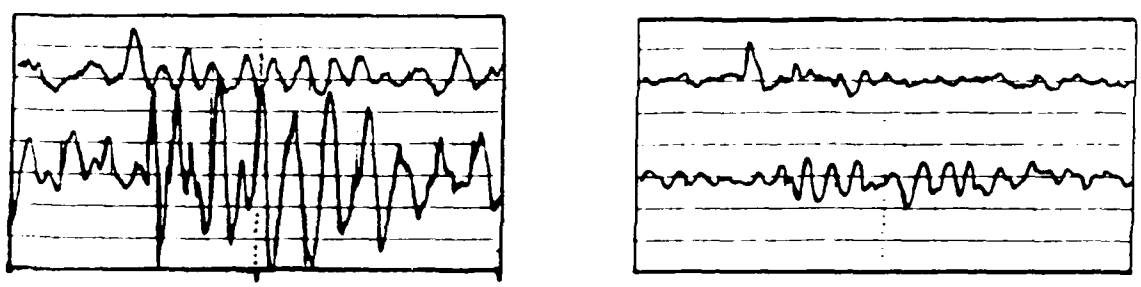
Figure 6 shows a comparison of pressure wave recordings of two different laser head configurations. The first one is without any acoustic dampers, a flat thin solid aluminum foil as anode and a solid cathode with a radius of 16 cm. The second one is with acoustic dampers, a flat perforated aluminum foil as anode with acoustic dampers in the back volume and the same cathode as in the first configuration. The acoustic damper material is nickel foam with a pore diameter of 0.05 mm, a specific surface of 24 000 m^2/m^3, and a density of 0.25 g/cm. This material is compatible with the presence of HCL. For each recording the upper trace corresponds to measurements of a transducer positioned at 10 cm upstream of the discharge axis and flush-mounted in the middle of horizontal channel wall, and the lower trace to measurements of a transducer at a mirror position 13 cm away of the discharge volume end. The experimental conditions were an electrical energy deposition of 100 J/L.bar, a total pressure of 2.3 bars, a flow speed of 43 m/s, and a repetition rate of 1000 Hz. The comparison shows a very effective acoustic wave damping and the level of the residual pressure perturbations at the next energy deposition time (shot n°3) is much lower with acoustic dampers.



Shot n°1



Shot n°3



10 Shots

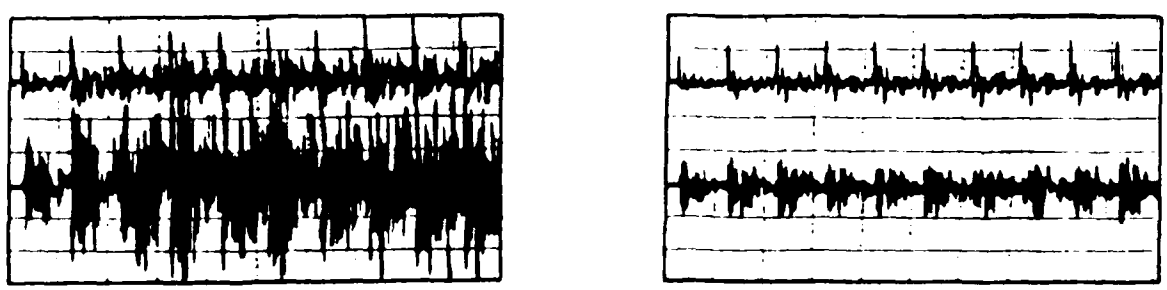


Figure 6 :comparison of residual pressure variations without damper and with dampers.

In the figure 7 the residual pressure perturbations and laser average power of a 10 shot burst are displayed as a function of the repetition rate up to 1000 Hz for the same experimental conditions and laser head configurations. The acoustic damper effects on the laser average power are very beneficial indeed with acoustic dampers the laser average power increases linearly as a function of the PRF which is not the case without acoustic dampers. Otherwise these diagrams allow the possibility to establish a direct correlation between the residual pressure perturbation (the pressure amplitude at the energy deposition time) and the laser average power. Indeed it seams the threshold value of $\Delta P/P$ residual have to be less than 5% to achieve a stable discharge.

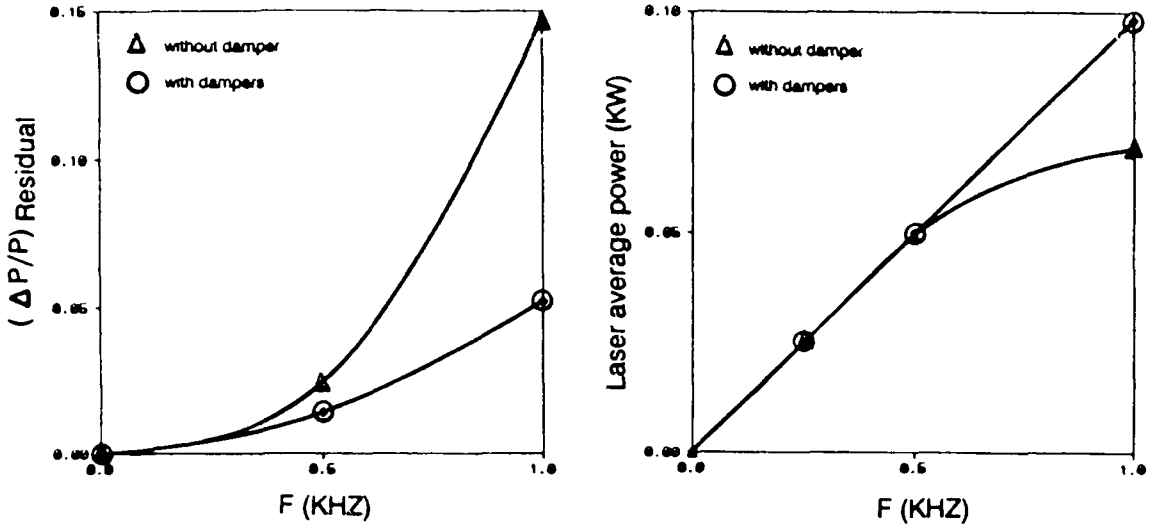


Figure 7 : Residual prssure perturbations and laser average power as a function of P.R.F.. comparison of 10 shot bursts without damper and with dampers.

The figures 8 (a) and 8 (c) show a series of 250 laser output pulses at a repetition frequency of 1000 Hz. These figures have been obtained for the same experimental conditions and the both laser head configurations as those for figures 6 and 7. Without acoustic damper (fig. 8a) the drop in energy as a function of the pulse number already occurs very strongly for the first shots. With dampers (fig. 8b), the first 20 shots have approximately the same output power as shown in the figure 7, but after these first shots the output power approximately decrease linearly like the configuration without acoustic damper (fig. 8a). However a study of the residual pressure variations with acoustic dampers has shown a same residual perturbation level for the 250 first shots. So the discharge stability degradation seams to be for these conditions independent of the pressure perturbations and could be attributed to the increase of the thermal boundary layers and the increase of the thermal fluctuations inside the discharge volume.

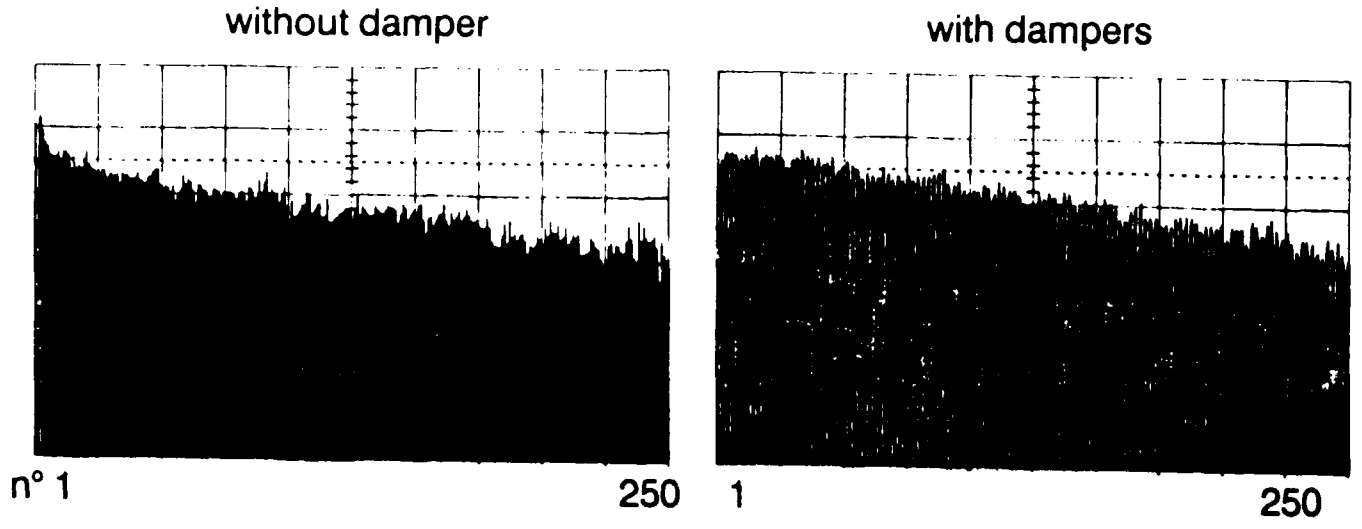


Figure 8 : Pulse to pulse time resolved power histogram at 1000 Hz. (a) without damper, (b) with dampers.

3. CONCLUSION

Characterization and damping of acoustic waves in a high repetition rate (up to 1000 Hz) XeCl laser are in progress at I.M.F.M.. The acoustic wave characterization by mean of Michelson interferometer or pressure transducers has allowed to clearly identified three acoustic wave families. The waves propagating between the electrodes and generated by the non-uniformity energy deposition at the vicinity of the electrodes beat very strongly and during long time inside the discharge zone. They lower discharge stability and so have to be damped. The use of appropriate geometrical laser head configurations with acoustic dampers in the right positions has shown the possibility to increase very efficiently the average power. This study allows to establish a direct correlation between the residual pressure perturbations and the discharge stability. The required level of residual perturbations to obtain the same laser energy for each energy deposition seams to be to have less than 5%. According to the output laser, or the laser beam size, or the repetition rate required, different adapted solutions like perforated anode, porous cathode, small cathode radius, acoustic dampers very close to the discharge zone can be used. But this study has shown the energy per pulse decreases on a longer time scale for all the laser head configurations. This energy drop could be related to increase of thermal inhomogeneities and of thermal boundary layers. A solution of this problem may be to increase the flow velocity between the electrodes. The next step at I.M.F.M. will be to study this phenomena and operate for longer time scales.

ACKNOWLEDGMENTS

The research work leading to this paper was performed under M.R.E.S., C.N.R.S., C.G.E., and P.A.C.A. through EUREKA program.

REFERENCES

1. M.L. Sentis, P. Canarelli, Ph. Delaporte, B.M. Forestier, B.L. Fontaine : Proceedings of the international conference on LASERS' 88, paper No HI.11, p. 147, Lake Tahoe, Dec. 4-9, 1988).5. M.L.
2. M.L Sentis : Revue Entropie No 115, (1984).
3. M.L. Sentis, P. Delaporte, B.M. Forestier,B.L. Fontaine : J. App. Phys. **66**, 1925 (1989).
4. Ph. Delaporte and al. : Proceedings of the 4th Int. Symp. on Optical and Optoelectronic applied Science and Engineering (High Power Lasers), SPIE Vol 801, (1987), p 86.
6. M. Bessafi and al. : Proceedings of the 17th Symp. on Shock Tube and Shock Wave Research, Bethlehem, U.S.A., (July 1989).

Compact Long-Pulse Excimer Lasers for Medical Applications

Robert C. Sze
Stablelase Inc.
1042 Stagecoach Road
Santa Fe, New Mexico 87501

Abstract

A compact, long-pulse, excimer laser with full width half maximum (FWHM) pulse length of 180 ns is developed producing an energy of 140 mJ per pulse in XeCl. Previous studies using inductive stabilization show the technique capable of long-pulse operation in KrF and XeF as well. We present parametric studies of a long-pulse laser device, and show the uniformity of the laser beam and compactness of the design.

Introduction

The technique of using a segmented electrode structure with each discharge segment stabilized by an inductance was shown capable of sustaining long lasing pulses (90 ns FWHM) in excimer gas mixtures[1,2] of XeCl, XeF, and KrF. Additional benefits noted in these studies were order of magnitude increased pulse repetition frequency[3] for a given gas flow and improved pulse to pulse energy variations[4] when compared with unstabilized electrodes. One of the most important aspects of this technology is that it allows for very simple pulse power circuits that tend to result in compactness in design and cost effectiveness in construction. Here, we show the technique capable of generating much longer pulse lengths than previously obtained. The 180 ns FWHM and 250 ns total lasing times obtained in these studies are simply the result of longer power deposition times. The maximum pulse length capability using this technique is not known at this time.

Circuit Description

The general circuit configuration is shown in the schematic in Fig.1. The energy stored in capacitor C_s is deposited into the discharge gap when the switch S is closed. Because the preionization is through a corona discharge achieved via the dV/dt of the rising voltage pulse, preionization only exists before the breakdown of the discharge. Since the main part of the circuit that deposits power to the discharge volume is slow, a peaking capacitor array C_p is needed to provide an initial current in the discharge after gas breakdown. The value of the peaking capacitor is only 1/10th to 1/20th the value of the storage capacitance and the energy stored in the peaking capacitors represents a very small part of the energy deposited into the gas. However, even this small capacitance is enough to result in

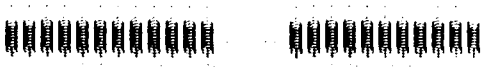


Figure 1. Schematic of inductively stabilized excimer laser discharge circuit. C_s = storage capacitance, C_p = peaking capacitance, and S = switch.

a modulation of the power deposition as shown in the output lasing waveform given in Fig.2. The main part of the circuit can be relatively slow so that the power deposition is spread over 250 ns. The discharge remains stable over this period because of the presence of the segmented electrode structure with an inductor stabilizing each segment against arcs. Experiments show that for stable discharges in the hundreds of nanosecond timescales an inductance value that gives an impedance corresponding to a 5 percent change in voltage across the inductor compared to the voltage drop across the discharge gap is sufficient

to suppress arcing. In Fig. 3 we show the uniformity of the laser output with a 1.4 cm X 1.4 cm square discharge cross-section operating in XeCl at 140 mJ per pulse.

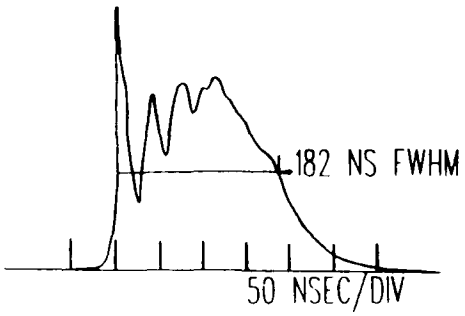


Figure 2. Temporal waveform of the XeCl laser.

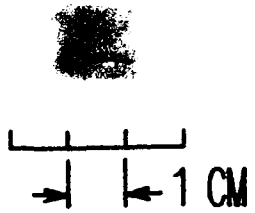


Figure 3. XeCl laser burn spot on Krylox paper.

The laser can be modeled fairly accurately by simply assuming the discharge to be a switch and a constant voltage source. In Fig.4 we use an instantaneous switch and a zener diode to approximate the discharge in a simple electronic circuit program. The 140 nH inductance in the main discharge loop is due primarily to the inductance of the thyratron.

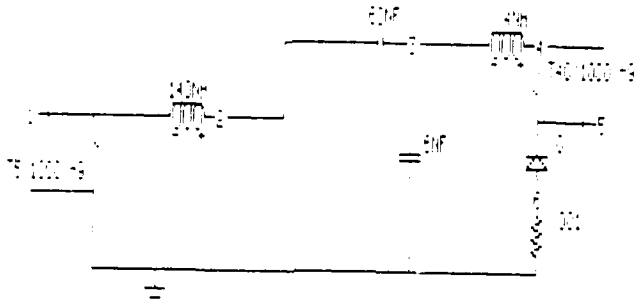


Figure 4. Circuit of discharge on computer simulation.

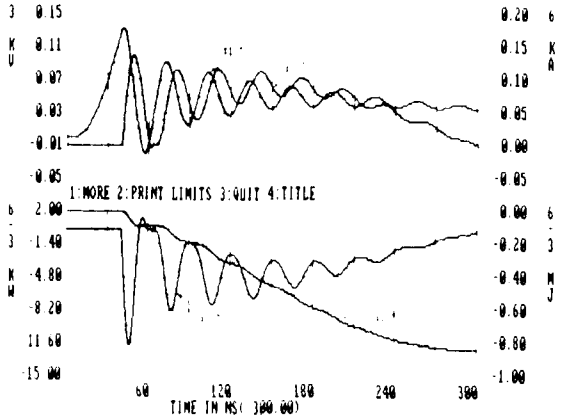


Figure 5. The voltage, current, power and energy temporal waveforms from computer simulation.

The 60 nF capacitance is the storage capacitance. The 6 nF capacitance is the peaking capacitance and the 4 nH inductance is the combination of the head inductance and the sum of the stabilization inductances connected in parallel. The thyratron switch is set to

close 5 ns into the program and the discharge gap switch is set to close 35 ns after the closing of the switch when the voltage across the gap has reached four times the steady state discharge voltage. The voltage risetime in this circuit is fast because the LC time constant is determined by the 140 nH inductance and the combination of the storage capacitance and the peaking capacitance in series (which is approximately the peaking capacitance). The voltage, current, power and energy waveforms are given in Fig. 5. The scaling is such that the real voltage and current have values 100 times that given in the vertical captions and the power and energy have values 10^4 times that given in the vertical captions. We see the modulation and the total power deposition times agree well with the lasing waveform given in Fig. 3. The charging voltage is 20 kV and the steady state voltage of the discharge is set at 3 kV. The breakdown voltage of the discharge gap is at 13 kV. The initial current peak due to capacitor C_p gives 14 kA with the later current peaks slightly lower. The energy stored at 20 kV is 12 J and the energy deposited is 8.4 J. The efficiency of energy deposited to energy stored is therefore 70 % according to the circuit analysis. The laser is of very compact design. Figure 6 shows the overall pulse power packaging and dimensions of the laser.

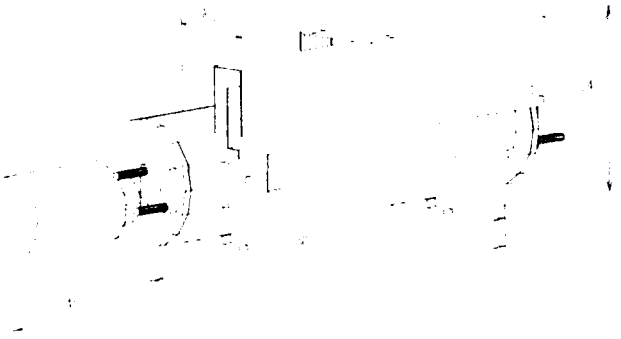


Figure 6. Drawing of laser system.

Parametric Behavior of the XeCl Laser

Figure 7 gives the variations of output energy and FWHM pulse length as a function of charging voltage at the optimum gas mixture for the best energy output. Note that the energy per pulse increases linearly with increasing voltage. The FWHM pulse length, however, is decreasing. We believe this is due to impedance mismatch between the energy storing part of the circuit and the discharge. Since the discharge behaves roughly as a constant voltage source, the higher charging voltages give higher currents through the discharge and, thus, a lower dynamic impedance. Figure 8 gives variations of the energy and wall-plug efficiency as a function of charging voltage. The laser operates in XeCl

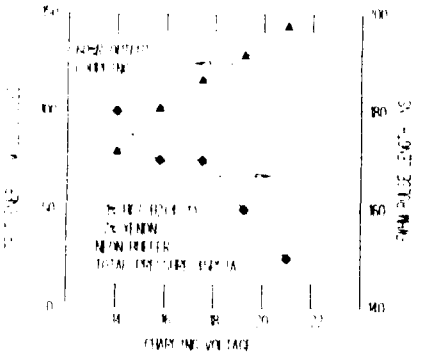


Figure 7. Plot of output energy and FWHM pulse length versus charging voltage in XeCl.

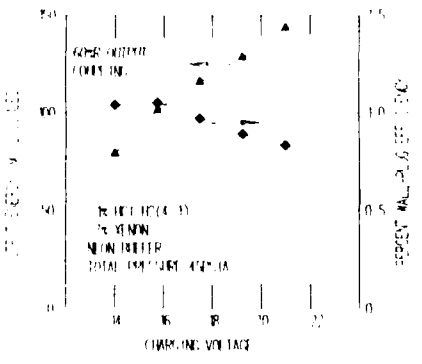


Figure 8. Plot of output energy and wall-plug efficiency versus charging voltage in XeCl.

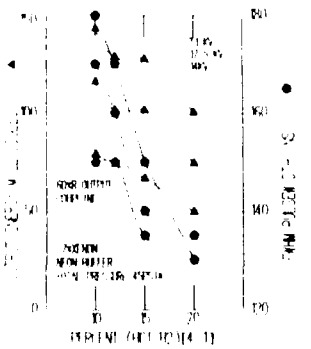


Figure 9. Output energy and FWHM pulse length versus $HCL-H_2$ partial pressure.

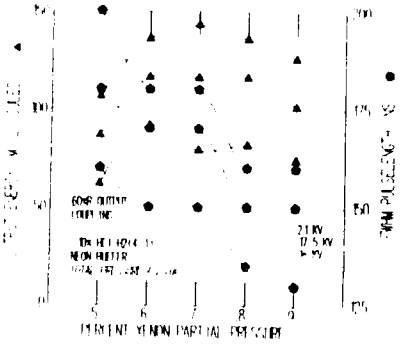


Figure 10. Output energy and FWHM pulse length versus Xe partial pressure.

with one percent efficiency at the 100 mJ energy level. Output energy and FWHM pulse length data in Figs. 9 and 10 for variations in $HCl-H_2$ concentration and Xe concentration respectively show the possibility of tailoring FWHM pulse lengths by changing the impedance of the discharge through different gas mixtures. Note that 200 ns FWHM pulse lengths is possible with 80 mJ per pulse output energy in an .1% $HCl-H_2$ gas mixture.

Discussion

We have shown the operation of a compact, long-pulse, excimer laser with one to one aspect ratio that is excellent for high energy transmission through thin optical fibers for medical applications. The laser operates with a FWHM pulse length that is parametrically adjustable between 150 to 200 ns. The laser is designed for a pulse repetition rate of 100 Hz although presently we have only operated the device up to 40 Hz due to power supply limitations. The technique is especially powerful as it allows long pulse operation in XeCl, KrF and XeF wavelengths.

References

1. R.C. Sze, "Inductively stabilized rare-gas halide minilaser for long-pulsed operation," J. Appl. Phys., 54, 3, pp. 1224-1227 (March 1983)

2. R.C. Sze, "Review of long-pulse laser development," Proceedings of Conference on Metal Vapor, Deep Blue, and Ultraviolet Lasers, SPIE Vol. 1041, Ed. J.J. Kim, R. Kimball, and P.J. Wisoff, pp. 176-185 (1989)

3. R.C. Sze, "A high repetition rate inductively stabilized long pulse excimer laser," Proceedings of the Fifth International Symposium on Gas Flow and Chemical Lasers (Aug. 1984), Inst. Phys. Conf. Series, No. 72, pp. 227-232, Adam Hilger Ltd., England (1985)

4. M. Sentis, R.C. Sze, F. Hommeau, B. Forrestier, B. Fontaine, "High repetition rate studies of the XeCl laser comparing inductively stabilized and normal shaped electrodes," American Institute of Physics Conference Proceedings, No. 172, Optical Science and Engineering Series, Ed. Rita Lerner, pp. 59-61 (New York 1988)

HIGH REPETITION RATE EXCIMER AND CO_2 TEA LASERS

H. M. von Bergmann and P. H. Swart
Rand Afrikaans University
P.O.Box 524
Johannesburg, 2000, South Africa

Abstract

High average power industrial excimer and CO_2 TEA laser systems, capable of being operated at repetition rates of several kHz, with multi kilowatt outputs, have been developed through an R&D program by the Group for Pulse and Laser Technology (PULSTEK) at the Rand Afrikaans University. The subject of this paper is a laser system utilizing a magnetically coupled, large diameter, axial flow fan in a recirculating gas system which provides gas flow velocities of up to 90 m/s. It employs a spark-preionized discharge unit with an electrode length of 800 mm and a discharge volume of 0.25 l. The laser has been operated as a KrF excimer laser, as well as a CO_2 TEA laser and average output powers of respectively 500 W and 2.5 kW have been achieved at pulse repetition rates of up to 2 kHz. The pulsed power conditioning system used for the excitation of the laser consists of an LC-inversion circuit aided by double-stage magnetic pulse compression and is switched by a single 5" thyratron.

Introduction

High repetition rate excimer and CO_2 TEA lasers, with output powers extending into the kilowatt range, are becoming important in a large number of industrial applications. Maximum outputs of 500 W have been reported for excimer lasers[1] and 10 kW for CO_2 TEA lasers[2] at repetition rates of 500 Hz and 1 kHz respectively. These lasers are, however, not commercially available and the Group for Pulse and Laser Technology (PULSTEK) of the Rand Afrikaans University has therefor initiated an extensive R&D program aimed at the development of high-repetition-rate, high-average-power industrial excimer and CO_2 TEA laser systems with projected repetition rates of several kiloherz and multi kilowatt outputs.

As part of the program, we have investigated several lasers utilizing various types of gas recirculation systems, including compact cross-flow fan driven systems[3] with flow velocities of up to 40 m/s as well as large, fast-flow systems driven by axial and centrifugal fans with flow velocities in excess of 100 m/s. These lasers utilize a number of alternative pulser configurations[4], including single and multiple thyratron switched LC-inversion circuits, assisted by single and double stage magnetic pulse compression and multistage pulse compressors, switched by low voltage thyristors through step-up pulse transformers.

This publication reports on a KrF excimer and CO_2 TEA laser system, designed for repetition rates of 2 kHz and average electrical input powers of up to 50 kW. Projected optical output powers are 1 kW for excimer and more than 3 kW for CO_2 laser operation. A photograph of the laser system is shown in Figure 1. Developments have reached the prototype stage for an industrial laser system and therefor aspects such as system reliability, component lifetime and operating costs are currently of overriding importance. As a consequence, the present design prefers simple and proven technology, being cautious of possibly more efficient, but more complex and therefor higher risk approaches such as x-ray preionization and prepulse double discharge excitation.

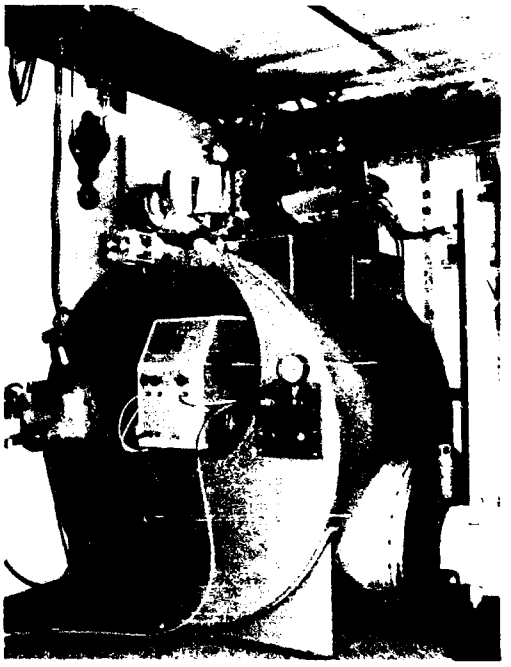


Figure 1. High repetition rate, high power laser system

Description of Laser System

Discharge Electrode Assembly

A large number of electrode geometries and preionization arrangements have in the past been applied for the excitation of excimer and CO_2 TEA lasers. The

choice is, however, limited to only a few geometries for industrial laser systems operating at kiloherz repetition rates and output power levels in the kilowatt range. Screen type electrodes in conjunction with behind-the-screen spark or corona preionization, widely employed for low and medium repetition rate applications, are not suitable at the required power levels because they are intrinsically fragile and can easily be destroyed by discharge arcing at high repetition rates. Solid electrodes, which for excimer laser applications have to be nickel plated or fabricated from solid nickel, have been chosen. Preionization can be effected by uv radiation from sparks or corona discharges and by x-rays. Whilst x-ray preionization is known to provide improved discharge uniformity and superior laser performance, there are no high repetition rate x-ray generators with proven long term reliability available. In addition the high x-ray fluxes required at high repetition rates, necessitate elaborate x-ray shielding and are therefor generally not desirable in systems for industrial use. Corona preionization is difficult to implement in high repetition rate systems employing solid electrodes, where side lighting is required, since the extended sources will hinder gas circulation. Conventional spark preionization is best suited for high repetition rate high power applications and is utilized in our design.

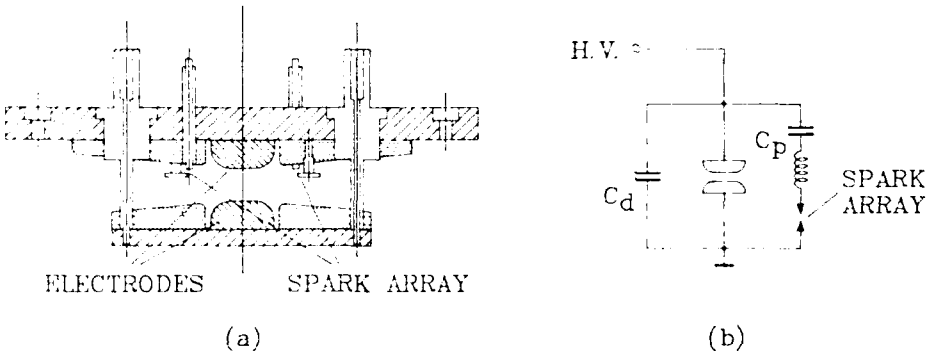


Figure 2. Electrode structure and preionization arrangement. (a) Cross-sectional view, (b) Circuit diagram.

The mechanical design and a schematic circuit diagram of the electrode structure are shown in Fig.2. The electrode structure employs a grounded electrode mounting plate supporting a pair of nickel plated discharge electrodes. Preionization is carried out by two spark arrays mounted adjacent to the electrodes. The discharge electrodes have been machined to a uniform field profile, using the design procedure according to Staepparts'. The electrode length is 800 mm with a separation of 20 mm. The electrode system provides a discharge volume of 740x20x15 mm^3 (0.22 l) for excimer laser and 740x20x20 mm^3 (0.3 l) for CO_2 laser operation. The two spark arrays, which consist of 36 sparks each, are connected in parallel with the discharge electrodes and peaking capacitors. This arrangement effects automatically timed preionization early during the rise of the discharge voltage. The sparks are individually inductively balasted and their energy is limited by the preionization capacitor C_p. Fine-tuning of the amount of energy channelled into the preionization is accomplished by adjusting C_p. This energy has to be minimized in order to avoid excessive spark electrode erosion at high repetition rates. Typically less than 10 % of the stored energy is used for the preionization. The upper electrode mounting plate, which is an integral part of the pressure vessel containing the laser gas, has been manufactured from stainless steel to reduce distortion of the electrode structure at the high operating pressures required for excimer laser operation. The peaking capacitors are mounted externally to avoid contact with the laser gas and are connected to the high voltage electrode (cathode) by current feedthroughs. The latter are furnished with electrostatic shields to prevent surface tracking. The electrode assembly incorporates flow profiles which are part of the gas flow nozzle design. The spark gap geometry has been selected to minimize interference with the gas flow.

Optical Resonator

The optical resonator employed for excimer laser operation consists of a flat, dielectrically coated total reflector and a flat uncoated MgF_2 output coupler. For CO_2 laser operation a 20 m radius copper total reflector and a flat 60 % reflectivity ZnSe output coupler are used. Higher laser outputs can be extracted from the CO_2 laser using output couplers of higher reflectivities, however, at an increased risk of optics damage. The mirror mounts are furnished with facilities for water cooling of the optics and for purging of the laser windows with clean gas.

Gas Flow System

High repetition rate operation of the laser requires replacement of the gas in the discharge volume between successive laser shots. At a repetition rate of 2 kHz and a clearing ratio of approximately 2, flow velocities of more than 80 m/s are required. Furthermore, operating pressures of up to 4 bar, needed for efficient excimer laser operation, necessitate low distortion mechanical design. Several flow system geometries and fan arrangements have been investigated and finite element structural analysis has been utilized to design low distortion pressure vessel geometries.

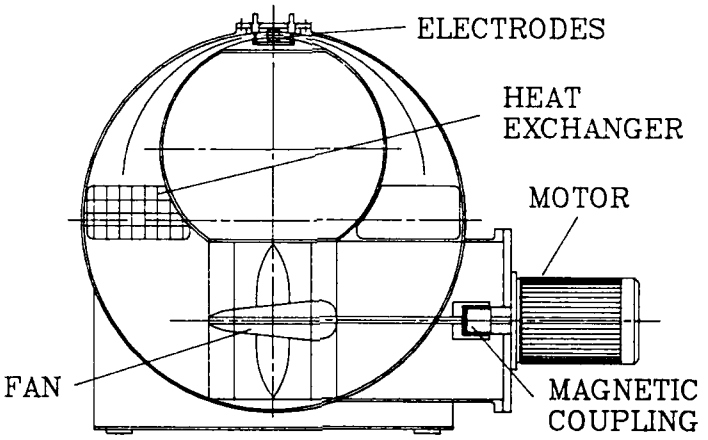


Figure 3. Cross-sectional view of gas flow system.

A cylindrical flow system, as shown in Fig.3, was found to yield the optimum design. The pressure vessel has an outer diameter of 1850 mm, a length of 1050 mm and a total gas volume of approximately 1300 l. It employs a magnetically coupled, two stage axial fan, driven by a 15 kW variable speed induction motor. A finned tube heat exchanger with a capacity of 60 kW is placed upstream from the discharge channel. The system has been manufactured from mild steel and has been nickel plated to make it compatible with excimer laser gasses. All insulators in contact with the gas are manufactured from either alumina ceramic or PTFE. Distortion of less than 50 μm has been measured at the electrode plate flange at the full operating pressure of 3.5 bar.

High Voltage Pulser

Excitation of the laser requires electrical input pulse energies ranging from 15 to 25 J at repetition rates of up to 2 kHz. Under these conditions average electrical input powers in excess of 50 kW have to be furnished. Peak voltages of 40 kV and voltage rise times of 120 ns (10-90%) are necessary for efficient laser operation. Thyratrons are still employed as switching elements in low and medium power industrial excimer and CO_2 TEA lasers, since they are the only switches that can operate reliably and with acceptable service lifetimes at the required high voltages and repetition rates. For high power laser systems, however, direct switching necessitates switch requirements far in excess of the capabilities of even state of the art thyratrons and their lifetimes are reduced to unacceptably low values as a consequence. Direct switching, employing multiple paralleling of thyratrons, although feasible for laboratory systems[6], is impractical for industrial lasers. This is so because of the need for complex synchronization electronics and the high investment and replacement cost for large size thyratrons.

An alternative to this costly and complex direct switching technique is the use of magnetic pulse compression[7], which effectively reduces the switching adversities in high power lasers. The switching voltage can be reduced to levels compatible with single gap thyratrons by LC-inversion type pulsers. These techniques have been successfully employed to raise thyratron lifetimes to close to their design value of 5000 hours.

Various pulsing circuits suitable for excitation of the laser have been evaluated theoretically[8] and experimentally[4]. We have used a number of thyratron switched pulsers based on the LC-inversion principle with single and double stage pulse compression, as well as an experimental thyristor switched multistage pulse compressor. These pulsers are shown schematically in Fig.4 and are listed together with their relevant operating parameters in Table 1.

The LC-inversion pulser with single stage pulse compression as shown in Fig.4(a) has been switched by two thyratrons connected in parallel. Synchronization of the thyratrons is not critical at the comparatively slow switching times and current sharing is enforced by partial uncoupling through split storage capacitors. Thyratrons employed were large diameter, hollow anode metal envelope types. The pulser can operate at repetition rates of more than 2 kHz, corresponding to average input powers of 50 kW. Operation at 2 kHz, employing a single thyratron, had to be limited to time durations of a few minutes or to burst mode operation at low duty cycles to avoid overheating of the thyratron. This pulser performs satisfactorily but it has the disadvantage that it requires state of the art thyratrons, which are costly and not readily available.

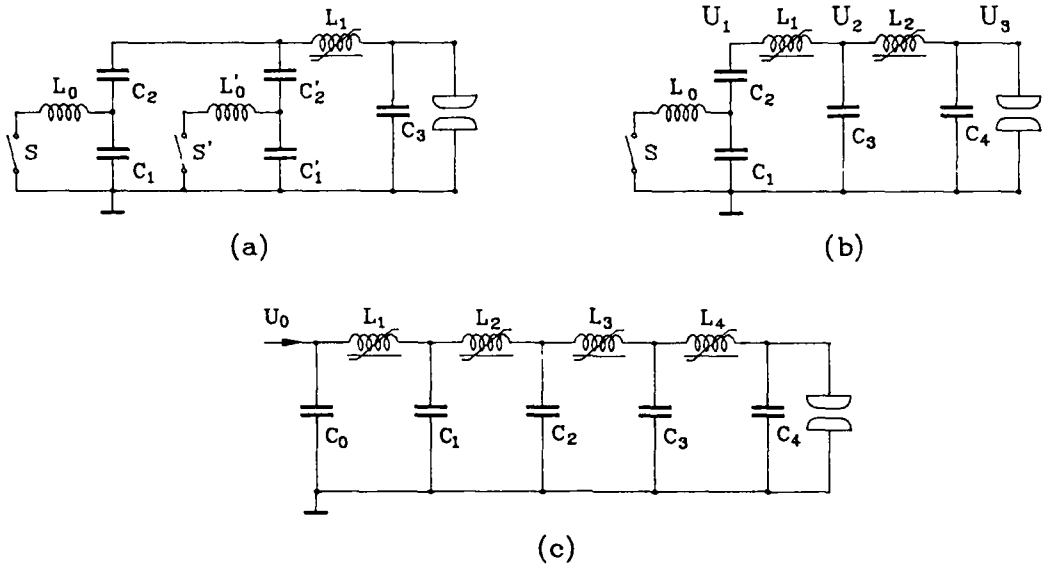


Figure 4. Pulser configurations. (a) LC-inversion with single stage pulse compression, (b) LC-inversion with double stage pulse compression, (c) multistage pulse compressor.

By equipping the LC-inversion pulser with double stage pulse compression, as shown in Fig.4(b), it is possible to relax the switching requirements to such an extent that the laser can be operated continuously at repetition rates of up to 2 kHz using a single, low cost 5" thyratron. This pulser is currently being employed because of its relative economy and its technical superiority over the single stage thyratron pulser.

Saturable inductors have been constructed from amorphous, Z-type toroidal core material. In the final stages, strip line windings are used to reduce conduction loss, while for the initial stages, where the number of turns is higher, multiple parallel windings are used, each wound with a number of enamel insulated wires in parallel. The cores and windings are directly cooled by circulating low viscosity insulating oil through the inductor enclosures.

Table 1: SWITCHING PARAMETERS OF EMPLOYED PULSERS

TYPE OF PULSER	CHARGING VOLTAGE [kV]	SWITCH CURRENT Peak [A]	RMS [A]	Ave. [A]	Duration [ns]	di/dt [kA/µs]	COMPRES. FACTOR δ	STORED ENERGY [J]	OVERALL EFFICIENCY [%]
LC-Inversion, Single-Stage Single Switch	21.9	10100	189	4.5	370	95.0	2.3	25	79
LC-Inversion, Single-Stage Double Switch	21.9	5050	94.5	2.25	370	47.5	2.3	25	81
LC-Inversion, Double-Stage Single Switch	23.0	2020	84.0	4.30	1650	4.0	12.7	25	77
All-Solid-State, Multistage (High Voltage Side)	43.2	45	4.5	0.57	68000	0.004	264	22	77

The oscillogram in Fig.5 depicts the voltage waveforms and the thyratron current for the LC-inversion pulser with double stage pulse compression. The traces were recorded at a charging voltage of 23 kV and during high repetition rate operation. Maximum thyratron current is 2.0 kA with an overall pulse compression ratio of 13.

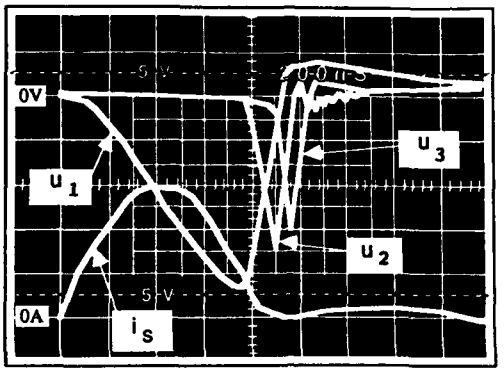


Figure 5. Oscillogram of thyratron current i_S (uncalibrated) and voltages U_1, U_2 and U_3 for the LC-inversion, double stage pulser. 400 ns, 5 kV/full div.

While the LC-inversion pulser with double stage pulse compression constitutes a major advancement in thyratron life and replacement costs, thyratron life is still limited and replacements of about twice a year will be required. It is therefor desirable to replace thyratrons by solid state switching elements which can have a practically unlimited lifetime. This requirement can be realized by the experimental thyristor switched compressor shown schematically in Fig.4(c). This circuit employs four stages of magnetic pulse compression to bring switching times into the regime of commercially available thyristors. The experimental multistage compressor has been constructed with inductors wound on toroidal magnetic cores and insulated against high voltage breakdown by applying a coating of silicon based high voltage insulating compound. The dielectric insulation obtained by this simple procedure has enabled operation at input voltages of up to 42 kV and repetition rates of up to 650 Hz. Operation had to be restricted to low duty cycles, in order to prevent overheating of the cores. A prototype compressor, using oil for cooling and insulation is presently under construction and will operate continuously at repetition rates of up to 2 kHz.

Power Supply

Power is supplied to the laser by a regulated, thyristor switched, resonant pulsed power supply[9] which charges the laser with pulses of 50 µs pulse width. These power supply units are used to supply thyratron switched pulsers in the command charge mode, but are also adequate for pulsing the multistage pulse compressor. Voltage regulation of the power supply is better than 0.1 % furnishing acceptable levels of output pulse jitter in multistage pulse compressor operation. The power supply is of modular design and a single module can deliver output powers of up to 12.5 kW and is capable of driving the laser at a repetition rate of 500 Hz. Four modules are multiplexed in an alternate mode for 2 kHz operation.

EXPERIMENTAL RESULTS

GAS FLOW STUDIES

Gas flow velocity measurements have been conducted for a variety of gas mixtures and pressures using a calibrated, small diameter pitot tube. The results are plotted as a function of rotational fan speed in Fig.6. The flow velocity increases linearly with fan speed and reaches maximum values of 90 m/s at fan speeds of 3900 r.p.m. The flow velocity profile along the laser axis has essentially a flat distribution with only a slight fall towards the electrode ends. It was found, however, that the current feedthroughs obstruct the flow resulting in a velocity drop of approximately 10 % behind the feedthroughs. This effectively reduces the flow velocity as indicated by the error bars in Fig.6.

A simple optical Schlieren technique[10] employing an expanded HeNe laser beam has been used to study the recovery time for optical density perturbations in the laser medium following the electrical discharge. The technique has a deflection angle threshold of approximately 0.2 mrad. Fig.7 shows the density perturbation recovery at a laser repetition rate of 2 kHz and gas flow velocity of 90 m/s for a CO_2 laser mixture of CO_2:N_2:He - 1:1:8 at a total gas pressure of 1000 mbar. These results indicate that the gas density fluctua-

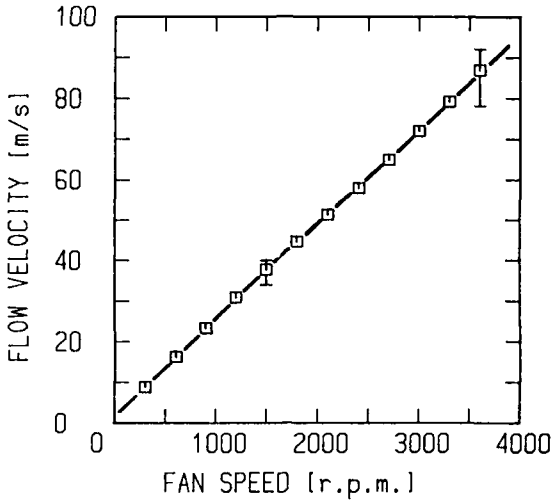


Figure 6. Gas flow velocity versus fan speed.

tions are reduced to their initial value after approximately 250 µs which is considerably shorter than the inter pulse time at a repetition rate of 2 kHz. The recovery time increases almost linearly with decreasing flow velocity. At this stage no active means for damping of shock waves caused by the electrical discharge have been incorporated in the flow system. However, the flow channel has been designed to reflect longitudinal shock waves downstream, out of the discharge region.

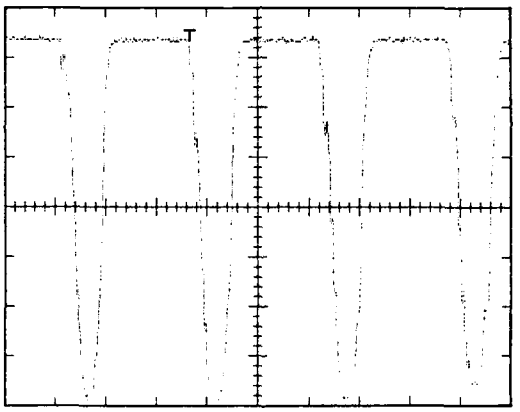


Figure 7. Optical density perturbation of discharge volume versus time. 200 µs/div.

The maximum repetition rate of the laser at which arc-free glow discharges can be obtained has been measured for KrF excimer and CO_2 laser gas mixtures at input pulse energy levels of 24 J. The results of these measurements are shown against gas flow velocity in Fig.8. With CO_2 laser gas mixtures (CO_2:N_2:He - 1:1:8, p = 1000 mbar) the maximum arc-free repetition rate increases almost linearly with flow velocity and a maximum value of 2 kHz is reached at a flow velocity of 85 m/s. With KrF laser mixture (F_2:Kr:He - 1:20:680, p = 3500 mbar) the maximum repetition rate is 1.6 kHz. These values are limited at higher repetition rates by down-stream arcing between the bottom discharge electrode (cathode) and the preionization electrodes and over the insulator surfaces. Higher repetition rates will be obtained by increasing the distance between the bottom electrode to the preionization electrodes and by increasing the tracking path length.

Laser Output Measurements

Preliminary, not fully optimized laser output measurements have been undertaken for operation of the laser as a KrF excimer and CO_2 TEA laser. The average output power of the laser is shown versus repetition rate in Fig.9.

KrF excimer laser. The KrF laser experiments were conducted using helium based gas mixtures of F_2:Kr:He - 1:20:680 at a total pressure of 3500 mbar. As shown in Fig.9(a) the average output power increases approximately linearly with repetition rate and reaches a maximum of 500 W at 1.6 kHz. Single-shot and low repetition rate pulse energies of 350 mJ have been measured, corresponding to an overall efficiency of 1.45 %. These values decrease slightly to 315 mJ and 1.3 % at a repetition rate of 1.6 kHz. At higher repetition rates the output reduces sharply as a result of degrading discharge conditions. Significantly higher output energies can be obtained with neon based gas mixtures and single shot energies of 450 mJ have been measured. Unfortunately the limited magnetic coupling torque did not allow operation at high repetition rates with these gas mixtures.

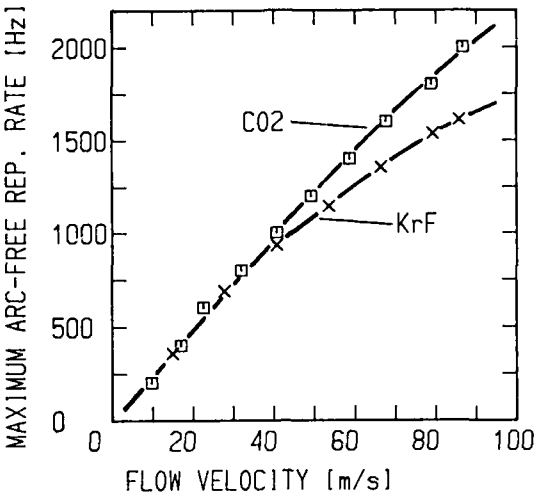


Figure 8. Maximum arc-free repetition rate versus gas flow velocity for KrF and CO_2 laser mixtures versus gas flow velocity.

CO_2 laser. The laser has been operated as a CO_2 TEA laser with a standard gas mixture of CO_2:N_2:He - 1:1:8 at a total pressure of 1000 mbar. The average output power versus repetition rate is plotted in Fig.9(b). The output power increases linearly with repetition rate and reaches a maximum of 2.5 kW at a repetition rate of 2 kHz. This corresponds to single-shot pulse energies of 1.25 - 1.20 J and an overall efficiency of 5 %.

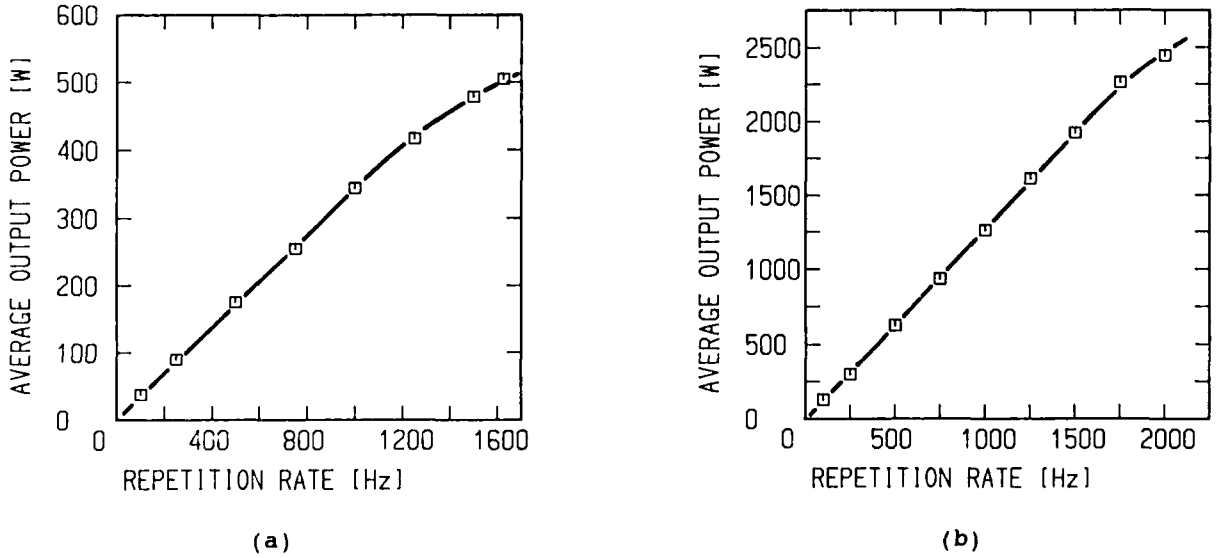


Figure 9. Average laser output power versus repetition rate.
(a) Krf laser, (b) CO_2 TEA laser.

Conclusions

The high repetition rate, high average power industrial laser system which has been described delivers average output powers of 500 W at a repetition rate of 1.6 kHz as a KrF laser and 2.5 kW at 2 kHz as CO_2 laser. Laser performance is limited by the design of the electrode structure and insufficient uniformity of the gas flow leading to down-stream arcing at high repetition rates. The laser system is being upgraded at the moment by redesigning the electrode structure and improvements made to the flow system. These changes will enable operation of the laser at repetition rates beyond 2 kHz and, together with optimization of the laser gas mixtures, it is expected that maximum average outputs of more than 3 kW for the CO_2 laser and 1 kW for the KrF laser will be obtained.

REFERENCES

1. P Oesterlin and W. Mueckenheim, SPIE, 1023, 51-54 (1989)
2. V. Yu. Baranov, IEEE J. Quantum Electron., QE-19, 1577 (1983)
3. H. M. von Bergmann, G. L. Bredenkamp and P. H. Swart, SPIE, 1023, 20 (1989)
4. P. H. Swart and H. M. von Bergmann, Presented at the 7th IEEE Pulsed Power Conference, Monterey (1989), paper 11-4
5. E. A. Staepparts, Appl. Phys. Lett., 40, 1018 (1982)
6. A. J. W. Brown and P. W. Smith, Proceedings, 17th IEEE Power Modulator Symposium, Seattle, (1986), pp. 191-195
7. D. Basting, K. Hohla, E. Albers and H. M. von Bergmann, Optoelektronik, 16, 128-136 (1984)
8. P. H. Swart, G. L. Bredenkamp and H. M. von Bergmann, Proceedings, 6th IEEE Pulsed Power Conference, Arlington, (1987), pp. 680-683
9. G. L. Bredenkamp, P. H. Swart and H. M. von Bergmann, Proceedings, 6th IEEE Pulsed Power Conference, Arlington, (1987), pp. 723-726
10. M. Matera, R. Buffa, L. Fini and R. Salimbeni, Proceedings OPTO 84, (1984), pp. 182-184

PERFORMANCE OF THE AURORA KrF ICF LASER SYSTEM

J. E. Jones, S. J. Czuchlewski, T. P. Turner, R. G. Watt, S. J. Thomas,
D. A. Netz, C. R. Tallman, J. M. Mack, and J. F. Figueira

University of California, Los Alamos National Laboratory
P. O. Box 1663, MS E548, Los Alamos, NM 87545
(505)667-6900

Abstract

Because short wavelength lasers are attractive for inertial confinement fusion (ICF), the Department of Energy is sponsoring work at Los Alamos National Laboratory in krypton-fluoride (KrF) laser technology. Aurora is a short-pulse, high-power, KrF laser system. It serves as an end-to-end technology demonstration prototype for large-scale ultraviolet laser systems for short wavelength ICF research. The system employs optical angular multiplexing and serial amplification by electron-beam-driven KrF laser amplifiers. The 1 to 5 ns pulse of the Aurora front end is split into 96 beams which are angularly and temporally multiplexed to produce a 480 ns pulse train for amplification by four KrF laser amplifiers. In the present system configuration half (48) of the amplified pulses are demultiplexed using different optical path lengths and delivered simultaneously to target.

During the last year integration of the Aurora laser system has been completed, and the system and has entered the initial operational phase by delivering pulse energies of greater than one kilojoule to target. During the initial target shot series, 36 beams were aligned to target, and the remaining 12 beams were intercepted by calorimeters at the target chamber lens plate. The system achieved a maximum output energy of approximately 4500 J in 96 beams. A maximum of 1300 J was delivered to target in 36 beams with pulse durations in the range of 3 to 7 ns and focal spot diameters of 450 to 600 μm. The maximum target irradiance was in excess of 200 TW/cm^2. A maximum system shot rate of four shots per day was achieved. The system has not been optimized, and several near-term improvements are expected to result in significant increases in both delivered energy and target irradiance.

Introduction

The potential advantages of KrF lasers for inertial confinement fusion have been recognized for several years and have been discussed in detail in earlier publications [1-3]. The objectives of the Aurora KrF/ICF laser facility are twofold: to conduct laser physics and technology experiments important for future laser system development and to conduct target physics experiments relevant to weapons and ICF applications. Aurora is a prototype system built initially to study and resolve key technology issues for scaling large KrF lasers for ICF research. These issues include:

- Uniform e-beam pumping of large laser volumes
- Optical angular multiplexing and demultiplexing
- Control of amplified spontaneous emission and parasitics
- Large amplifier staging
- Alignment of multibeam KrF systems
- UV pulse propagation over long paths
- Novel approaches to less expensive optics

All of these issues have been successfully addressed by the Aurora system, and while additional progress is anticipated in several areas, initial system performance has indicated that no serious unsolved technical problems remain. The system is now operational with major activities supporting both investigations of the laser physics of large KrF amplifiers and laser-target interaction experiments.

System Description

ICF applications require pulse durations on the order of 5 ns, whereas efficient extraction of high energy from KrF amplifiers requires amplifier pulse durations of hundreds of nanoseconds. Optical angular multiplexing matches the pulse duration requirements of target physics and the amplifiers by encoding 5 ns pulses for serial amplification and then decoding the amplified pulses for simultaneous delivery to target. This concept is at the heart of the design of the Aurora laser system. The system has been described in detail in several earlier publications [4-9]. Only an overview will be presented here.

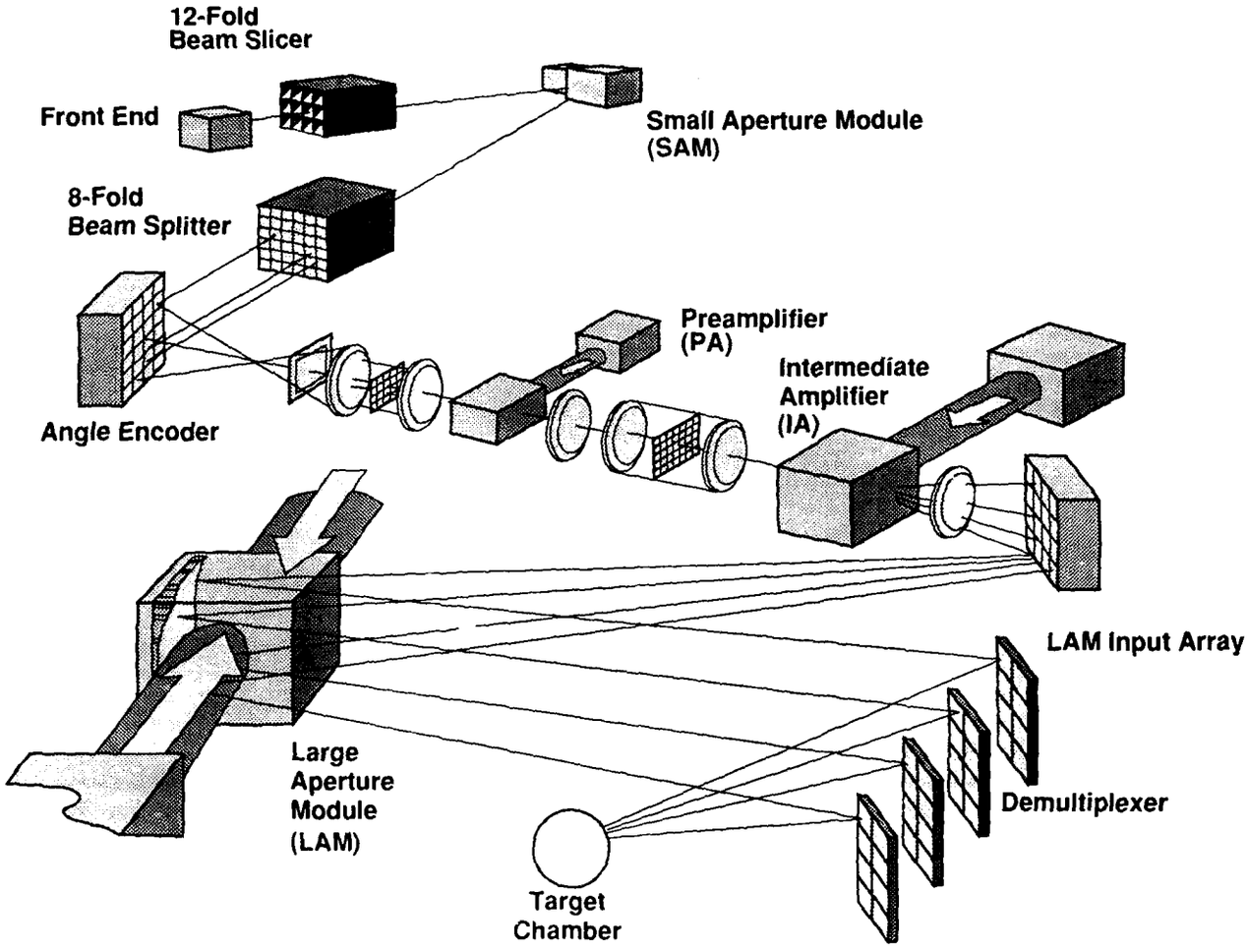


Figure 1: A conceptual layout of the Aurora laser system. All of the main optical and laser elements from the front end, through the final amplifier and on the target are shown.

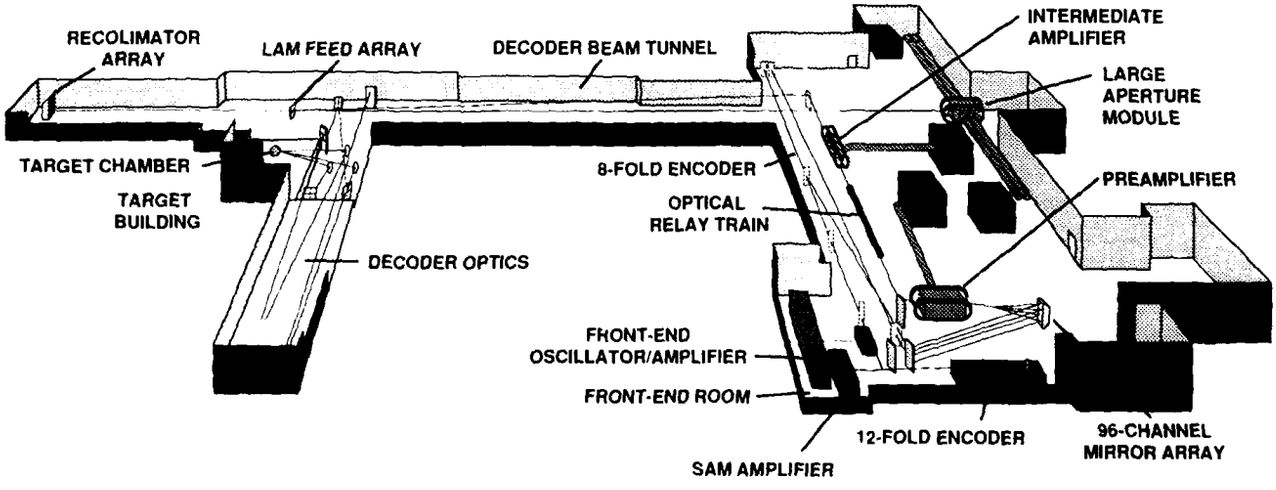


Figure 2: A physical layout of the Aurora laser system. The part of the building on the right contains the front end, the optical multiplexer (encoder), most of the optical relay train, and the laser amplifiers. The structures on the left house the optical demultiplexer (decoder), the final aiming mirrors, and the target facility. To determine the scale, it should be noted that the distance from the Large Aperture Module (LAM) to the recollimator array is approximately 100 m.

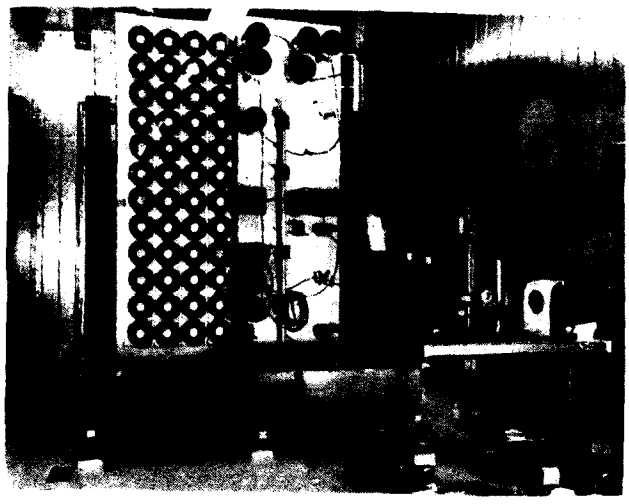


Figure 3: The recollimator array. The first 48 beams from the LAM are recollimated and sent on to the decoder and then to the target. The second 48 beams are intercepted at this point (and others) by calorimeters, fast photodiodes, and beam footprint paper.



Figure 4: Final aiming mirrors and target chamber lens plate. The computer-controlled mirrors aim each individual beam through its lens and to the target. Calorimeters are mounted on 12 of the lens holders in this photo.

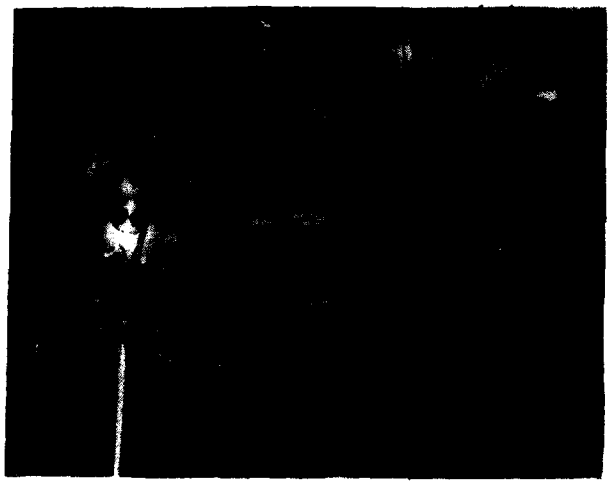


Figure 5: The Aurora target chamber with some early diagnostics in place. The lens plate is located on the end of the beam cone (at right). Fine focusing on target is accomplished by translating the entire beamcone.

Amplifier	g_0 (%/cm)	E_{in} (J)	E_{out} (J)	Stage Gain
SAM	3.0	0.2	3.0	15
PA	2.2	0.3	50	165
IA	1.0	40	300	7.5
LAM	2.3	250	4500	18

Table 1: Typical Performance of Aurora Amplifiers

Figure 1 is a conceptual layout of the Aurora system showing all the main elements. Figure 2 shows the physical location of all elements within the Aurora building. The front end produces pulses for multiplexing and amplification by the Aurora amplifiers. For target physics work the pulse duration is typically between 1 and 5 ns; pulses with durations up to 20 ns are used for laser physics investigations [10]. The front end output is divided into 12 channels by aperture division with each channel delayed from the previous channel by 5 ns. The 60-ns pulse train is then amplified by a double pass through the Small Aperture Module (SAM) amplifier. The output of the SAM goes to an 8-fold beam splitter array where each group of 12 beams is delayed from the previous group by 60 ns, resulting in a 480 ns pulse train. Each of the 96 beams strikes a mirror on the computer-controlled angle encoder and is directed into the input pupil of the Preamplifier (PA). A lens system images the PA input pupil through the PA and the Intermediate Amplifier (IA) and onto the Large Aperture Module (LAM) input array (feed array). From here beams are double passed through the LAM for final amplification and travel to the recollimator array, shown in Figure 3 (but not shown in Figure 1). In the current configuration half of the beams are terminated at the recollimator array. The other half (48) are recollimated and sent on to the decoder for demultiplexing and final delivery to target. The final aiming mirrors and the target chamber lens plate are shown in Figure 4. Figure 5 shows the Aurora target chamber.

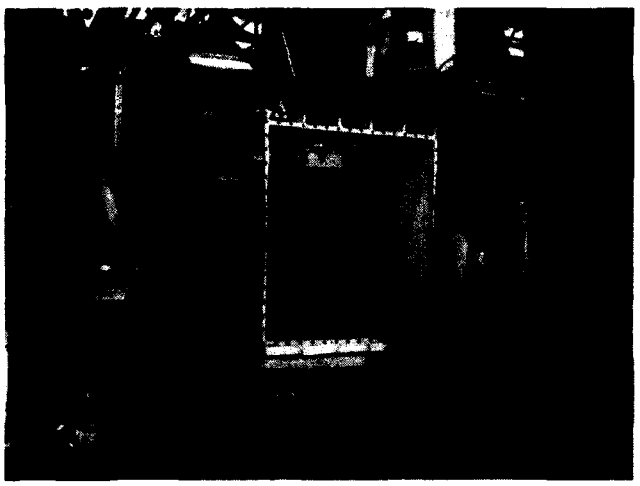


Figure 6: The Large Aperture Module (LAM) awaiting installation of the LAM mirror. The LAM laser volume is pumped from both sides by 1 m x 2 m electron beams. The large guide field magnets are clearly visible.

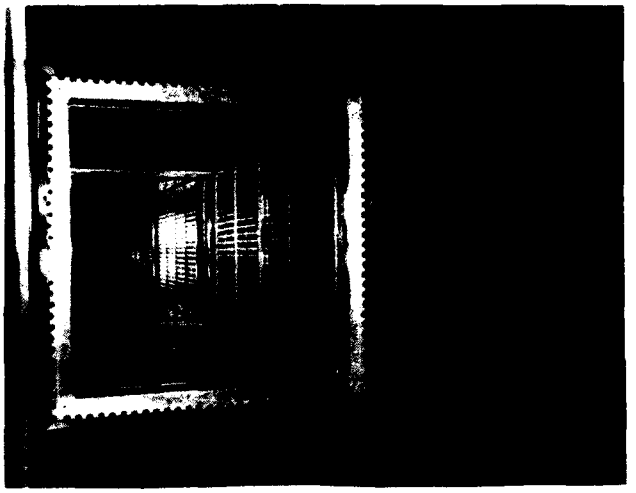


Figure 7: The Large Aperture Module (LAM) 1 m x 1 m aperture with the window and mirror in place. The electron beams enter through the 2-mil titanium foils on the side of the cavity.

The SAM has an active volume of 10 cm x 12 cm x 1 m. The PA has an active volume of 20 cm x 20 cm x 2.8 m. The IA has an active volume of 40 cm x 40 cm x 2.8 m. The SAM, PA, and IA all employ single-sided e-beam pumping. The LAM, shown in Figures 6 and 7, has an active volume of 1 m x 1 m x 2 m and employs double-sided e-beam pumping. Typical performance data for the individual amplifiers is given in Table I. More detailed descriptions of the Aurora amplifiers and their performance may be found in earlier publications [4, 7, 8, 11, 12].

Laser Physics

The laser physics program has three goals: to characterize, analyze, and optimize Aurora laser performance; to generate an extensive data base in order to refine the KrF kinetics code and support the design of larger KrF systems; and to investigate fundamental laser physics, such as pulse shape and bandwidth effects.

At present laser diagnostics consists mainly of calorimeters and, for temporal information, fast photodiodes. Data is digitized and stored on computer for further analysis. Typical experiments have included temporal pulse shaping, amplifier bandwidth, absorption, and ASE measurements. For the SAM, PA, and LAM amplifiers, small-signal gain (SSG) measurements have been made as a function of vertical position, distance from the foil, F_2 concentration, total gas pressure, and Marx charge voltage. Measurement of the spatial uniformity of the PA small-signal gain along the vertical dimension has also been conducted. Detailed reports of the results of laser physics experiments may be found elsewhere [13-17].

The size of the final Large Aperture Module was chosen to address issues associated with the scaling of these devices to higher energy and lower cost. Due to its large physical size, energy deposition uniformity and ASE could affect energy extraction. ASE modeling codes for the LAM (with small-signal gain g_0, absorption α, and wall reflectivity as parameters) predict that ASE lowers the measured SSG and reduces energy extraction by 20%. Preliminary measured gains are in agreement with model predictions [13, 14].

Spectral bandwidth is recorded at the decoder on each shot with a 1 m spectrometer. With a conventional front end, typical bandwidths at the target are about 20 cm^{-1}. Work is in progress to increase this with the installation of a broadband (200 cm^{-1}) front end.

Target Physics

Aurora is in the early stages of use as a target-physics facility, and reliable operation of target instrumentation has recently been verified. To date, target diagnostics have been used primarily to characterize the plasma formed by the focused, overlapped beams on target foils. The diagnostic capabilities include filtered x-ray pinhole cameras which record an image of the plasma as a function of x-ray energy. A transmission grating spectrometer records an x-ray energy spectrum. The appearance of certain atomic bands provides confirmation of the target irradiance. Filtered x-ray diodes provide temporal information on the x-ray emission at a variety

of x-ray energies. Streak and framing cameras yield additional temporal information. More complete details of Aurora target diagnostic capabilities are available in Ref. 18.

Final System Integration

The goals for the Aurora KrF/ICF laser facility during FY89 were:

- Complete system integration and deliver kilojoule-level energy to target.
- Demonstrate reliable system operation.
- Deliver greater than 25 TW/cm^2 to target.

Laser system integration was completed in December 1988 with the extraction of 2500 J from the LAM and the delivery of 780 J to the target-chamber lens plate in 48 beams. For this shot the full size LAM mirror was not available. A down-sized mirror with an area of 20% of the full LAM aperture was used, resulting in lowered LAM output energy and stage gain. Only 48 of the 96 amplified beams are taken to the target area by the present Aurora optics system. The energy delivered to the lens plate on this shot was further reduced by losses on optical surfaces between the LAM and the lens plate (estimated at 15%) and additional loss due to absorption by impurities in the air in the beam tunnels (estimated at 27% based on absorption measurements).

The full-sized LAM mirror arrived and was installed in May 1989. Tunnel air absorption was reduced to about 10% by the addition of an air-handling system and filter bank. Damage to the optics in the centered optical system occurred during the previous shot series that included final integration and the delivery of kilojoule-level light to the lens plate. These damage problems were substantially reduced in following months, but because a full set of spare optics was not available, the gain of the PA was reduced (by reducing laser gas pressure) to preserve the damaged optical elements for as long as possible.

System integration was completed in June 1989 with the first full system shot to target. 770 J was delivered to target in 36 beams in a 7 ns pulse (FWHM) with 80% of the energy in a spot 600 μm in diameter, producing a target irradiance in excess of 30 TW/cm^2.

System Performance During Initial Target-Physics Experiments

The first series of target-physics experiments using the Aurora KrF/ICF laser facility was conducted during August 1989. The goals of this target shot series, called the "High Intensity Campaign," were to increase the irradiance on target, to check out target physics diagnostics, and to demonstrate the repeatability and reliability of the Aurora laser system. Alignment of the laser system was accomplished using the automatic input-pupil alignment system and the automated LAM alignment system. Final beam alignment to target was accomplished manually since the final target alignment system was not operational at that time. During this shot series 36 beams were aligned to target, and the remaining 12 beams were intercepted by calorimeters at the lens plate for diagnostic purposes. The second 48 beams were used for calorimetry and burn patterns at other points in the system.

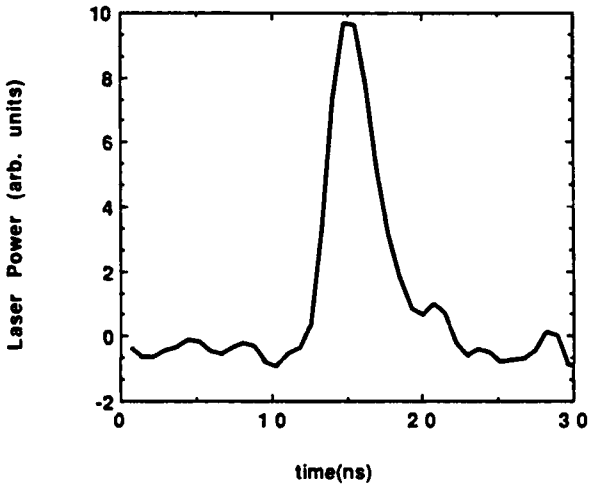


Figure 8: The ultimate pulse shape used during the final stages of the High Intensity Campaign. The low level structure on this trace is instrumental in the digital data store and is not a part of the actual laser pulse.

The temporal pulse shape was measured throughout the system using photodiodes with a risetime of 270 ps and 1.35-GSample/s digitizers (742 ps/sample) with typical system risetime resolution limited by analog bandwidth effects to approximately 435 MHz (590-ps risetime resolution). During the High Intensity Campaign the pulse duration from the front end was varied to study system performance with different pulse widths and to verify the fidelity of the Aurora amplifiers. Figure 8 shows the pulse shape used in the latter stages of the campaign. This pulse shape was measured in the decoder and is very similar to the pulse produced by the front end. This and other pulse-shape data indicates that the entire amplifier chain has good fidelity and that the shape of the output pulse can be controlled by controlling the front end pulse shape.

The focal spot size of the 36 overlapped beams on target was measured by visible fluorescence from a UV sensitive fluor at target center and was confirmed using x-ray images taken with filtered pinhole cameras. Optical images from visible fluorescence using the front end only indicated a minimum focal spot diameter of about 350 μm for 36 overlapped beams. Since this technique could not be used for full energy shots,

x-ray pinhole images were used to estimate the focused spot size. Such images provide an upper limit of the spot size since the plasma producing the x-rays expands to a larger size than the actual focused laser spot. Figure 9 shows a pinhole camera image of x-ray emission from a typical target shot. This image was taken with a 1.9 mil Be filter in front of a 25-μm pinhole at 8x, with a resolution of approximately 26 μm. The x-ray cutoff of this filter occurs at approximately 1.7 keV, so only the central hot plasma regions are shown in this image. Five other filter thicknesses were also present on this camera, and smaller pinholes and other filters were used on other shots. In all cases lowering the energy cutoff of the filter resulted in larger images, but the effect was not pronounced until the filter cutoff was reduced to the several hundred eV range. The FWHM width of the focused spot on this shot was <450 μm. Based on similar data from all target shots, the spot size has varied from 450 to 600 μm depending on the accuracy of manual alignment and the beam quality of individual beams for a given shot, which is dependent on environmental variables in the beam transport path.

Table II lists the energies, pulse durations, and calculated peak target irradiances for 12 successful target shots performed during the August campaign. Energies were measured using 12 calorimeters on the lens plate and extrapolated to the 36-beam energy. Pulse durations were measured in the decoder. Focal spot sizes were measured using x-ray pinhole camera images for the individual shots. The peak irradiance achieved is over 200 TW/cm^2.

For the first three shots of the series, the front end was operated in its normal configuration with two Lumonics post amplifiers producing a total output energy of 400 to 500 mJ. The amplifier ASE contributed to the total pulse width on target resulting in a significant tail and increased pulse width. For the remainder of the shots the Lumonics amplifiers were removed. This reduced the front end output energy to 20 mJ or less, but caused only a slight reduction in energy on target. This allowed better control of pulse duration and shorter pulses on target.

The maximum 36-beam energy delivered to target was 1300 J. This represents a 96-beam energy of 3470 J. Assuming transmission losses of 15% on optical surfaces and 10% to air absorption yields a total LAM output energy of approximately 4500 J.

A high shot rate and good system reliability were successfully demonstrated during the High Intensity Campaign. A total of 12 successful target shots were fired in 12 working days. The first shot attempted on August 31 was unsuccessful because of a minor problem with a LAM output switch. Following that attempt the switch was repaired and three successful target shots were fired that day.

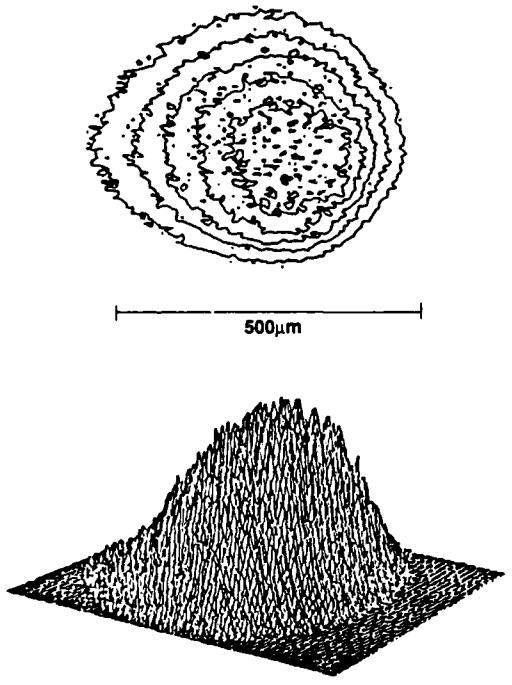


Figure 9: Typical x-ray pinhole camera image of focused spot (36 beams) on target. This image was taken at 45 degrees with a 1.9 mil Be filter in front of a 25 m pinhole at 8x, with a resolution of approximately 26 m. Computer processing has been applied to remove the effects of film tilt.

Shot Date	36 Beam Energy (J)	Pulse Length (ns)	Peak Irradiance (10^{14} W/cm^2)
8/15	1290	7.0	>1.0
8/16	1300	6.0	2.2 ± 0.9
8/16	1130	7.0	>1.9
8/17	960	4.5	>1.1
8/22	850	5.0	>0.7
8/22	730	3.5	1.5 ± 0.4
8/23	910	3.5	1.2 ± 0.4
8/23	580	4.0	
8/30	250	3.5	1.1 ± 0.4
8/31	940	3.5	1.1 ± 0.4
8/31	840	3.0	1.3 ± 0.5
8/31	900	3.5	1.1 ± 0.3

Table II: High Intensity Target Shot Series (August 15 - 31, 1989)

Anticipated Future System Performance

The system has not yet been optimized, and several near term improvements are expected to result in significant increases in both delivered energy and target irradiance. The most obvious of these is to remove the 12 calorimeters from the lens plate allowing 48 beams to go to target and increasing delivered energy by 33% over the present value. Relatively minor modifications to the front end should result in a 30% increase in output energy. Replacement of damaged relay optics will increase transmission into the PA by at least 25%. New optics and the further reduction of retropulses and parasitics will allow the PA stage gain to be increased by up to 50% (by operating the PA at the upgrade design levels). Thus far the LAM has been operated at a conservative Marx charge voltage of 50 kV for all system shots. In the past it has been successfully operated at 60 kV during pulsed power tests. Figure 10 shows the present and anticipated performance of the LAM amplifier. Thus far target alignment has been accomplished manually, but the final automatic target alignment system is nearing operation. It should result in both faster alignment and better beam overlap for a smaller spot. These improvements should allow maximum target irradiance to approach 500 TW/cm^2 in the near term.

The near term plans for Aurora include:

- Full characterization of the laser performance of the LAM and other e-beam pumped amplifiers.
- Investigations of target prepulse from crosstalk and ASE.
- Measurements of energy absorbed by the target and x-ray conversion efficiency.
- Studies of the temporal pulse shaping capabilities of KrF systems.
- Demonstration of broad bandwidth capability of KrF amplifiers.

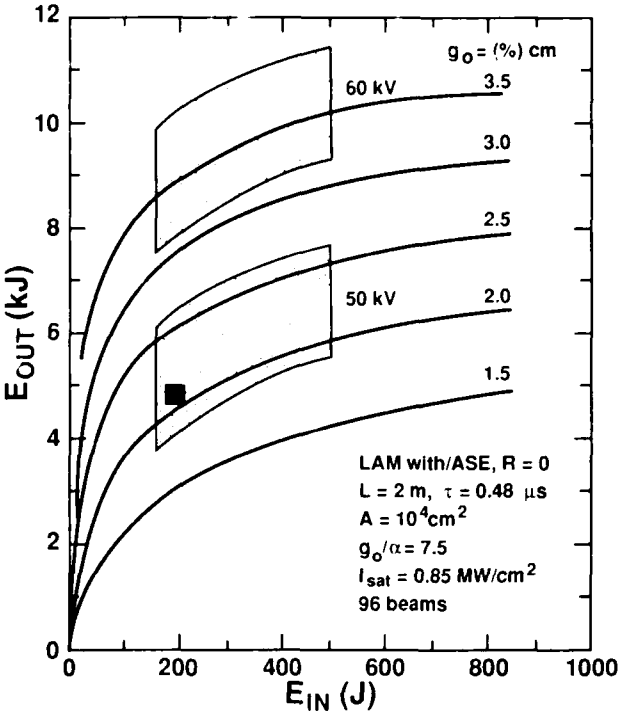


Figure 10: Plot of LAM output enegy versus input energy showing the operating regions for 50 kV and 60 kV Marx charge voltages. The square indicates the present operating point. Improvements in the optical system and the performance of the PA and IA amplifiers will result in increased LAM input (and output) energy.

Additional performance improvements are planned during the next two years. The installation of IA and LAM upgrades will result in output energies in the 15-20 kJ range. Improvements in the optical system and the environmental control of the beam path will allow focal spot diameters of less than 350 μm with an ultimate goal of 200 μm. Ultimately, target irradiance in excess of 10^{15} W/cm^2 is expected.

Summary

The development of the Aurora KrF/ICF laser facility shows continual progress in establishing that KrF laser technology is the leading candidate for future ICF drivers. Final integration of the system is complete, and Aurora has begun initial operations as a target physics facility. Recent accomplishments include demonstration of:

- high energy, with multi-kilojoule output and the delivery of kilojoule-level pulses to target in 36 beams;
- high intensity, with maximum target irradiance in excess of 200 TW/cm^2; and
- system reliability, with a sustained average shot rate of one shot per day and a maximum demonstrated shot rate of four per day.

Continued improvements in system performance are anticipated in both the near and far terms, with the goal of achieving routine operation with target irradiance in excess of 10^{15} W/cm^2.

References

1. Gibson, A. F., "Lasers for Compression and Fusion," *Contemp. Phys.* 23, 285 (1982).

2. Holzrichter, J. F., D. Eimerl, E. V. George, J. B. Trenholme, W. W. Simmons, and J. T. Hunt, "High Power Pulsed Lasers," *J. Fusion Energy*, 2, 5 (1982).
3. Jensen, R. J., "KrF for Fusion: An Overview of Laser Issues," *Fusion Technol.* 11, 481 (1987).
4. Rosocha, L. A., J. A. Hanlon, J. McLeod, M. Kang, B. L. Kortegaard, M. D. Burrows, and P. S. Bowling, "Aurora Multikilojoule KrFLaser System Prototype for Inertial Confinement Fusion," *Fusion Technol.* 11, 497 (1987).
5. Hanlon, J. A. and J. McLeod, "The Aurora Laser Optical System," *Fusion Technol.* 11, 635 (1987).
6. McLeod, J., "Output Optics for Aurora: Beam Separation, Pulse Stacking, and Target Focusing," *Fusion Technol.* 11, 564 (1987).
7. Rosocha, L. A. and L. S. Blair, "Recent Progress on the Los Alamos Aurora ICF Laser System," Proceedings of the Int. Conf. on Lasers '87, pp. 164-174 (1988).
8. Rosocha, L. A., R. G. Anderson, S. J. Czuchlewski, J. A. Hanlon, R. G. Jones, M. Kang, C. R. Mansfiled, S. J. Thomas, R. G. Watt, and J. F. Figueira, "Progress Toward the Delivery of High Energy Pulses with the Aurora KrF Laser System," Proceedings of the Int. Conf. on Lasers '88, pp. 154-160 (1989).
9. Rosocha, L. A., "The Aurora Laser Facility," Section V-B in "Inertial Confinement Fusion at Los Alamos, Progress Since 1985," Los Alamos National Laboratory Report LA-UR-89-2675, D. C. Cartwright, Ed., Los Alamos National Laboratory, Los Alamos, NM (1989).
10. Thomas, S. J., K. W. Hosack, L. J. Lopez, I. J. Bigio, and N. A. Kurnit, "Improved Performance of the Aurora Front End with the Use of a Phase-Conjugate Mirror," Digest of Technical Papers, CLEO '88, p. 82 (1988).
11. Rosocha, L. A. and K. B. Riepe. "Electron-Beam Sources for Pumping Large Aperture KrF Lasers," *Fusion Technol.* 11, 576 (1987).
12. Kang, M., "Aurora Ampliier Upgrades and Performance" in "Developments of KrF Lasers for Inertial Confinment Fusion," CLS-Division Annual Report LA-11600-PR, p. 3, Los Alamos National Laboratory, Los Alamos, NM (1989).
13. Czuchlewski, S. J., W. T. Leland, M. J. Kircher, D. P. Greene, J. A. Oertel, V. O. Romero, and H. S. Steele, "Effect of Volumetric ASE on the Performance of Large KrF Amplifiers," presented at CLEO '89, Baltimore, MD, (1989), paper ThP2.
14. Greene, D. P. and S. J. Czuchlewski, "LAM Small Signal Gain and ASE Measurements," in "Developments of KrF Lasers for Inertial Confinment Fusion," CLS-Division Annual Report LA-11600-PR, p. 3, Los Alamos National Laboratory, Los Alamos, NM (1989).
15. Czuchlewski, S. J., D. E. Hanson, B. J. Krohn, A. R. Larson, and E. T. Salesky, "KrF Laser Optimization," *Fusion Technol.* 11, 560 (1987).
16. McCown, A. W., T. P. Turner, B. J. Krohn, S. J. Czuchlewski, R. G. Watt, V. O. Romero, and H. S. Steele, "Performance of the Small Aperture Module Electron-Beam Pumped Amplifier on the Aurora KrF Laser Facility," presented at CLEO '89, Baltimore, MD, (1989), poster TuJ40.
17. McCown, A. W., T. P. Turner, R. A. Tennant, and B. J. Krohn, "Determination of Fluorescence Energy Loss from an Electron-Beam Pumped KrF Laser," presented at CLEO '89, Baltimore, MD, (1989), paper ThP1.
18. Kristal, R., "Target Irradiation" Section V-D in "Inertial Confinement Fusion at Los Alamos, Progress Since 1985," Los Alamos National Laboratory Report LA-UR-89-2675, D. C. Cartwright, Ed., Los Alamos National Laboratory, Los Alamos, NM (1989).

ENERGY DEPOSITION MEASUREMENTS FOR E-BEAM PUMPED EXCIMER LASERS

M. C. Cates, K. L. Robertson and P. C. Melcher
Maxwell Laboratories, Inc.
8888 Balboa Avenue
San Diego, California 92123

D. P. Greene and V. O. Romero
Los Alamos National Laboratories
Los Alamos, New Mexico 87545

Abstract

The energy deposition of the e-beam pumped MLI Two-Meter Laser was measured and compared using dosimetry films, electron calorimetry, current measurements, and pressure rise measurements. The measurements agreed within their uncertainties.

Introduction

In order to design a large e-beam pumped excimer laser system for Inertial Confinement Fusion, the laser efficiency must be accurately known, as small changes in efficiency lead to large variations in the ICF laser system cost. In order to determine efficiencies, the energy deposition of the e-beam pump must be known. The methods of determining energy deposition vary, and each laboratory has their favorite technique. With this in mind, the purpose of this work was to survey and compare various commonly used energy deposition measurement techniques, with the ultimate goal of increasing confidence in the laser efficiencies reported by this and other laboratories.

Two-Meter Laser

The e-beam device utilized in this study was the MLI Two-Meter Laser. This device is powered by a seven stage marx bank capable of storing 151 kJ, and has a maximum erected voltage of 840 kV. The diode voltage was 350 kV for this study. A self breaking peaking switch sharpens the rising edge of the pulse, while a diverter switch terminates the pulse. The resulting e-beam pulse is 1 μs long, and has a near top hat intensity profile. The carbon felt cathode used for this study was 10 x 200 cm^2. A guide field of 600 gauss was used to assist in the transport and deposition of the e-beam. The pumped volume in the laser chamber was approximately 15 x 20 x 185 cm^3; the total volume was 355 l. No baffles were used to confine the e-beam to a specific volume. The gas mix utilized for most of the deposition measurements was 90% Ar and 10% Kr at a total pressure of 800 Torr.

Dosimetry Films

Two types of dosimetry films[1] were used to measure the deposited energy: a nylon film using triphenylacetonitrile dye, and a chlorostyrene film using malachite green methoxide dye. The films are in the form of thin (2 mil) sheets, which are hung in the laser chamber and turn blue upon exposure to ionizing radiation. The optical density at 632 nm was measured with a HeNe Laser densitometer, and the deposited energy determined using a calibration graph, which gives the deposited energy in units of $Mrad_{H20}$. The dose into water must be converted to dose into the Ar/Kr mix by using the ratio of the stopping powers of Ar/Kr (mole fraction weighted) and H_20. Stopping powers may be found in the ICRU tables[2]. The advantage of the film technique is the ease and simplicity of its use and the spatially resolved nature of the measurement; the deposition can be determined at any point in the laser chamber. There are, however, cautions for the technique. Acidic gasses such as NO_2, SO_2, HCl (and probably F_2) attack the dye and color the film in seconds[3], thus the deposition cannot be determined in a laser mix. Gasses such as CO_2, CO, H_20, H_2, and hydrocarbons have no effect on the film.

The film is sensitive to UV light, so that exposure to sunlight or fluorescent room lights darken the film in several minutes. The film therefore cannot be used inside a laser resonator where a high flux is present. The UV fluorescence normally found in an e-beam excited Ar/Kr mixture, however, is not sufficient to color the film; the threshold is roughly 100 mJ/cm^2. In addition, although the film darkens immediately upon exposure, the maximum optical density is reached several days after irradiation. Upon readout, the film may produce interference fringes at low optical densities, so that readout wavelength and film thickness variations could lead to spurious results.

The optical absorption of the Chlorostyrene film peaks at 630 nm, so that the film saturates at an optical density of 4 for a 2 mil thick film. The range of the film can be increased by measuring the optical density off the peak at 430 nm. The nylon film has an absorption maximum at 610 nm, and saturates at an optical density of 2 at 632 nm. The deposited energy range covered by these two films is similar.

The measured optical density is dependent on film thickness. It was found that the film thickness can vary by 15% from the nominal 2 mil for different batches, although within a batch the thickness is constant. The optical densities were normalized to reflect a 2 mil film thickness for use with the calibration curves.

The calibration curve for the Chlorostyrene film was supplied by Far West Technology and based on measurements using a calibrated ^{60}CO source. Optical densities at 630 and 430 were provided. The calibration

curve for the nylon film was supplied by Far West Technology at a wavelength of 600 nm. This was converted to a curve at 632 nm by measuring the absorption spectra of the exposed film at various doses, and determining the OD at 600 and 632 nm. A new calibration curve at 632 was constructed using the pair of OD's (at 600 and 632 nm) at the same dose and the 600 nm calibration curve. The measurements using the nylon film are therefore regarded as having less accuracy. The calibration curves are shown in Figure 1.

The measured pump power in the center of the e-beam is shown in Figure 2 as a function of distance from the foil for both types of dosimetry film. The solid and open data points represent measurements using nylon and Chlorostyrene films; several batches of film were used, and are represented by different symbols. Excellent agreement is found when using a single type of film; measurements made a year apart agreed within 5%. The nylon and Chlorostyrene films agree within 15%.

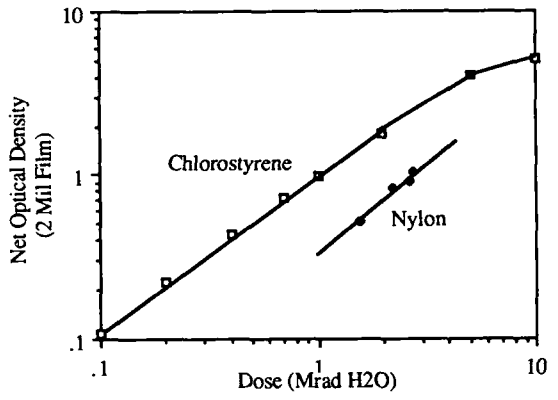


Figure 1. Calibration Curves for Dosimetry Films.

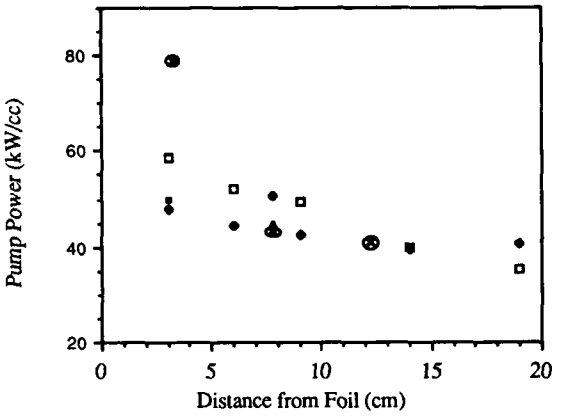


Figure 2. Pump Power Versus Distance from the Foil. The Open Data Points are Chlorostyrene Film, the Solid Points are Nylon Film, and the Circled Crosses are Calorimetry Results.

Calorimetry

The energy deposition was measured using total stopping e-beam calorimetry. The e-beam energy was measured at various distances from the foil; a subtraction yields the amount of energy deposited into the gas.

The calorimeter design is illustrated in Figure 3. The electrons are absorbed by a 0.3 cm thick piece of POCO AXF 5Q graphite[4], which has a fine grain structure with reproducible characteristics and whose thermophysical properties are well known[5]. The 0.3 cm thickness was chosen to be three times the CSDA range[1] of 350 KeV electrons; subsequent calorimeter designs would utilize a thinner graphite slab for increased temperature rise and sensitivity. The graphite slab is supported on a NEMA 310 cylinder, and the temperature rise determined using a chromel-constantan thermocouple, which is non magnetic. An insulated aluminum shield protects the calorimeter from scattered electrons.

The results of the measurements are shown in Figure 2. Because the calorimeters were separated by 4.5 cm, the energy deposition is averaged over this distance. There was a ± 7% standard deviation in the absorbed energy of each calorimeter; when calorimeter energies are subtracted to obtain the energy deposited in the interval between them, the result is a ± 50% error in pump power. Nevertheless, the agreement with the dosimetry film results is excellent.

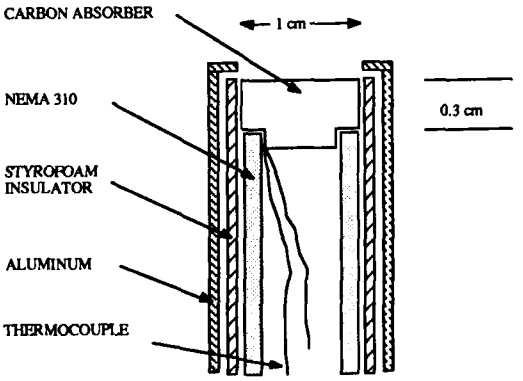


Figure 3. Calorimeter Design. The Carbon Absorbs Electron Beam While Insulated Aluminum Shield Protects Against Scattered Electrons.

Current Measurements

The e-beam current in the laser chamber is an excellent measure of device performance, however, a Monte Carlo electron transport and deposition code is necessary to determine the energy loss of the electron beam. The energy loss (kV/cm) multiplied by the e-beam current (A/cm^2) yields the pump power (kW/cm^3). The value of 7.5 kV/cm for 350 keV electrons at a distance of 3 cm from the foil and a pressure of 800 torr of Ar/Kr mix was obtained using the BETA-II Monte Carlo code. The current was measured with several Faraday cup designs; the agreement with the film and calorimeter results is shown in Figure 4.

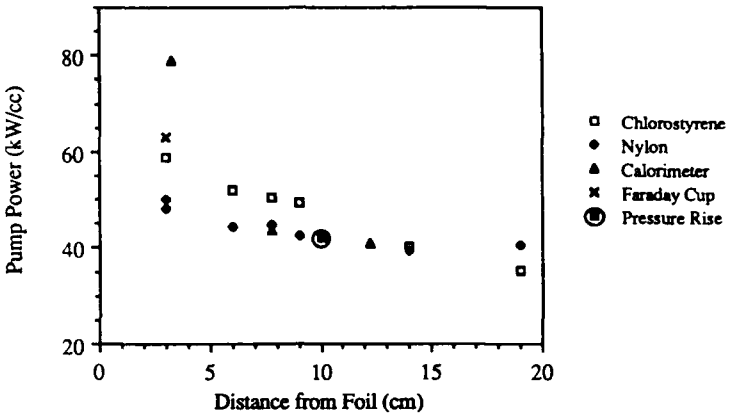


Figure 4. Pump Power Results for all Methods.

The transmitted e-beam current was measured using three Faraday cup designs. The first design, shown in Figure 5, has been used extensively at MLI; it is simple, inexpensive, and reliable. A carbon block (POCO AXF 5Q), 2.5 cm in diameter and 1.2 cm thick, collects the electron flux. A connector is affixed to the rear of the block with conductive epoxy; the signal lead is taken outside the laser chamber, run through a Pearson Probe[6] (Model 110A) and grounded on the laser chamber. The collected electron current induces a voltage in the Pearson Probe, which is measured with an oscilloscope; a calibration factor yields the current. A shield (aluminum or lucite) was necessary to restrict the electron flux to the front surface of the carbon block. A thin (0.5 mil) Kapton film was required to improve the rise and fall times of the current signal under certain conditions. This Faraday cup design was insensitive to the position of the signal lead ground, however, the small collection area resulted in some noise on the current trace.

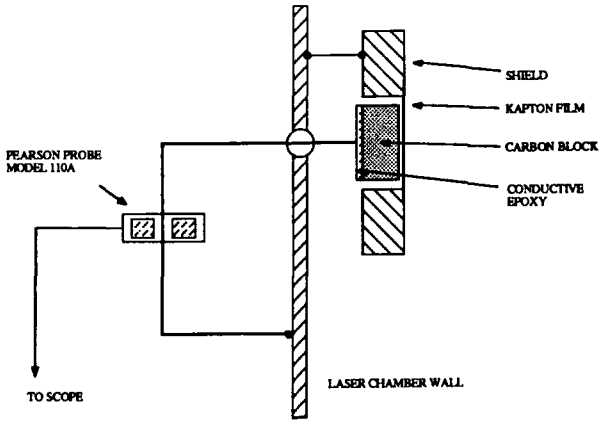


Figure 5. MLI Faraday Cup Design.

The second Faraday cup was designed and constructed by Spectra Technology[7], and is shown in Figure 6. The cup is enclosed in a grounded box, and has a thin Kapton window. The carbon block collector is serrated, although this does not result in increased collection efficiency. A calibrated resistor bank is enclosed between two metal plates; the voltage drop of the collected current is measured with an oscilloscope. The ground connection was carefully made with a wide strap of copper foil. The large (7 x 7 cm^2) collection area resulted in good signal-to-noise ratios.

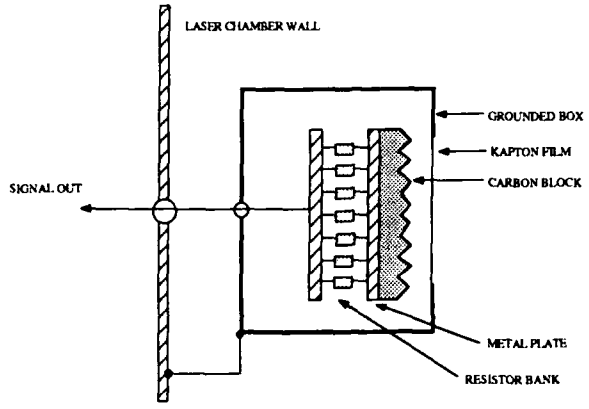


Figure 6. Spectra Technology Faraday Cup Design.

The third Faraday cup, dubbed the LANL design, combines the best features of the MLI and STI cups, and is shown in Figure 7. The cup is enclosed in a grounded box with a 0.5 mil Kapton window, and has a 10 x 10 cm^2 collection area. A carbon plate is clamped to a metal pedestal, which is attached to the box and ground. The collected electron current flows through pedestal, and induces a voltage in the Pearson Probe, which surrounds the pedestal. The signal is taken out and fed into an oscilloscope. Grounding is accomplished via a wide copper strap. The signal-to-noise was excellent, due to the large collection area.

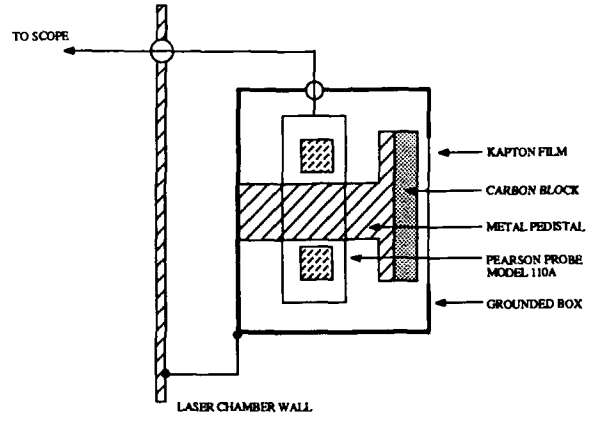


Figure 7. LANL Faraday Cup Design.

The Faraday cup performance is compared in Figures 8, 9, and 10 for Air, 1 atm of Argon, and vacuum (~1 torr). The MLI cup is shown with and without the Kapton film. The current measured using the MLI cup (with the Kapton) and the STI cup were taken on the same shot; the MLI (w/o Kapton) and LANL cup traces were taken on different shots. The Two-Meter Laser is extremely reproducible, so these comparisons are valid. The value of the current for all three cup designs agreed within 10%; part of this was due to the fact that the e-beam uniformity was 7% over a 7 cm height at the Faraday cup position; the various size cups averaged over different parts of the e-beam.

All of the Faraday cups performed well in Argon, Air and Vacuum, with the exception of the MLI cup without the Kapton Film. The STI cup does not return to the baseline after the shot, while the MLI (w/Kapton) design rings. These effects were ignored, as all the traces were found to overlap and give the same shape during the pulse.

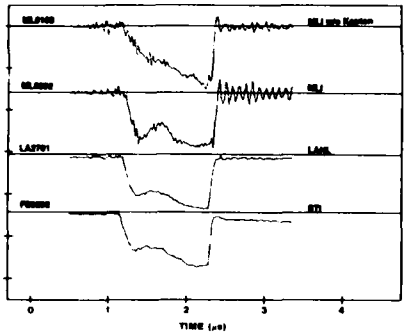


Figure 8. Faraday Cup Performance in 1 Atm of Air.

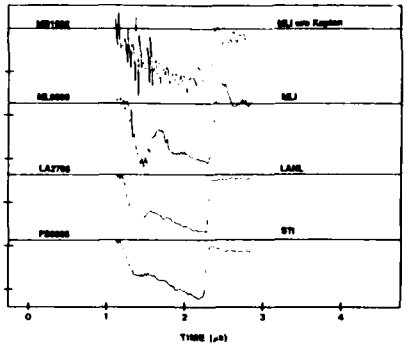


Figure 9. Faraday Cup Performance in 1 Atm of Argon.

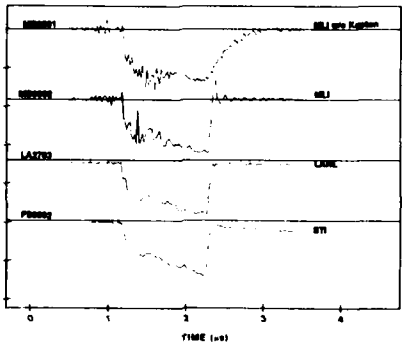


Figure 10. Faraday Cup Performance in Vacuum (~1 Torr).

Pressure Rise

The deposited e-beam energy is ultimately converted into light and heat, so that in a measurement of pump power using the pressure rise method, the fluorescence efficiency and pumped volume must be known accurately. The fluorescence efficiency was determined using a CO_2 poisoning method: CO_2 was added to a Ar/Kr mix while the pressure rise and sidelight fluorescence were monitored. The sidelight intensity was reduced by 100 with the addition of 30 torr of CO_2; at this point the net pressure rise was approaching and asymptotic value. The fluorescence efficiency, after correcting the pressure rise for the addition of CO_2, was found to be 18.7%.

The e-beam was not confined to a specific volume with baffles, however,a magnetic guide field and low gas pressure resulted in an e-beam with fairly sharp boundaries, which were determined using dosimetry film. The energy deposition was determined using the following formula:

$$\frac{E}{V} = 0.20\Delta P \frac{J}{l}$$

where the pressure rise ΔP is in Torr, and the energy density E/V is in J/l. The energy density in the pumped region was determined by multiplying by the ratio of unpumped to pumped volumes, and correcting for the fluorescence loss. This formula was derived from the equipartition of energy for an ideal gas, and hence does not account for work done by the pumped gas on the unpumped regions. For these reasons, the accuracy of the pressure rise measurement is estimated as ±25%.

The pressure rise was measured using two MKS Baratrons (models 317HA and 122AA), which have response times of approximately 1.0 ms and 20 ms, and recorded using a Linsis L2005 chart recorder with 1 m/s writing speed. The pressure rise was also recorded on an oscilloscope, which indicated the recorder was fast enough. No significant difference was observed with the two Baratron models. The pressure rise result, which is averaged over the pumped region, is plotted in Figure 4.

Conclusions

The energy deposition for an e-beam pumped laser was measured using four techniques; dosimetry film, calorimetry, Faraday cup, and pressure rise measurements. Within the uncertainty of each technique, all the methods agree.

Table 1 summarizes the strengths and weaknesses of each technique. It is apparent that no method yields a complete knowledge of the deposition in time and space; in fact, a combination of methods must be used. For example, a Faraday Cup measurement depends on the accuracy of a Monte Carlo electron transport code, which may be validated with a pressure rise or calorimeter measurement. The selection of a particular deposition technique depends on the depth of the knowledge and accuracy required for the problem at hand, as well as the time available to perform the measurement.

Table 1.

METHOD	STRENGTH	WEAKNESS
Dosimetry Film	- Spatially resolved - Independent of fluorescence yield	- Integrates over time - Saturates - Calibration curve needed
Calorimetry	- Independent of fluorescence yield	- Integrates over time and space - Relatively inaccurate
Faraday Cup	- Independent of fluorescence yield - Time and spatially resolved	- Need code to determine energy loss (kV/cm) - Many measurements needed to get spatial resolution
Pressure Rise	- Ease of use	- Not spatially or temporally resolved - Dependent on fluorescence yield - Must know pumped volume accurately

Acknowledgements

This work was supported by the Department of Energy under the Inertial Confinement Fusion Program.

References

1. Far West Technology, Goleta, CA.
2. H. O. Wyckoff, et. al., Stopping Powers for Electrons and Positrons, ICRU Report 37, ICRU, Bethesda, MD.
3. William P. Bishop, Kent C. Humpherys, and Peter T. Randtke, Rev. Sci. Instrum. 44, p. 443 (1973)
4. Poco Graphite Inc. Decatur, Texas.
5. R. E. Taylor and H. Groot, High Temperatures - High Pressures 12, p. 147 (1980)
6. Pearson Electronics, Inc., Palo Alto, CA.
7. J. F. Seamans and W. D. Kimura, Presented at the Conference on Lasers and Electro-Optics, Baltimore, MD (1989), paper WF16.

Absorption Experiments on Electron-Beam Pumped Rare Gases

A. W. McCown, E. A. Rose, B. J. Krohn, D. E. Hanson and S. J. Czuchlewski
Mail Stop E543
Los Alamos National Laboratory
Los Alamos, NM 87545

Absorption experiments have been performed on electron-beam pumped rare gases (argon and krypton) as a function of pump power at 248.4 nm and 257.3 nm. Energy deposition into the gas was varied by attenuating the electron beam with one or two stainless steel screens and by varying the gas density. The results from two separate energy deposition diagnostics agreed to within 20%. The Los Alamos National Laboratory KrF kinetics code calculations came into agreement with experimental results after the Ar_2^* absorption cross section was lowered to 1.8×10^{-18} cm^2 and the Ar_2^* radiative decay rate was increased to 4.4×10^6 s^{-1}.

Introduction

Because they impose a fundamental limit on the extraction efficiency of rare gas halide excimer lasers, absorption processes in the laser medium are an important area of both experimental and theoretical study. Recently, measurements in electron-beam-pumped F_2/Kr/Ar mixtures have yielded absorption coefficients that are as much as a factor of two greater than predictions of kinetics models.[1-4] To better understand these absorption processes, experiments have been performed on e-beam-pumped rare gases in the *absence* of fluorine, affording a much simpler kinetics picture that allows for a more precise benchmark of the kinetics model than is usually obtained in laser experiments involving a gas mix of Ar, Kr, and F_2.

Absorption measurements were performed at 248.4 nm and 257.3 nm over a wide range of pressures and pump powers. Results from these experiments have provided input to the KrF kinetics code that is currently in use at the Los Alamos National Laboratory. In addition, two different techniques for measuring the energy deposited into the gas have been employed and their results compared to determine the most accurate manner of measuring the energy deposition.

Experimental Apparatus

The experimental apparatus used in these experiments is illustrated in Fig. 1. A Lambda Physik EMG-101 excimer laser (run on XeCl: 308 nm) pumped a dye laser whose output was frequency doubled in a beta-barium borate crystal to 248.4 nm or 257.3 nm. Half of the ~5-ns full width at half maximum (FWHM) beam was reflected by a 50% beamsplitter and directed through the absorption cell in a three-pass configuration while the other half (reference) bypassed the cell. The two beams were then reflected onto the same photodiode, whose output was displayed on a Tektronix 7104 oscilloscope. The difference in path length of the beams resulted in a ~23-ns separation of their leading edges, with the reference beam arriving at the photodiode first. Neutral density filters reduced

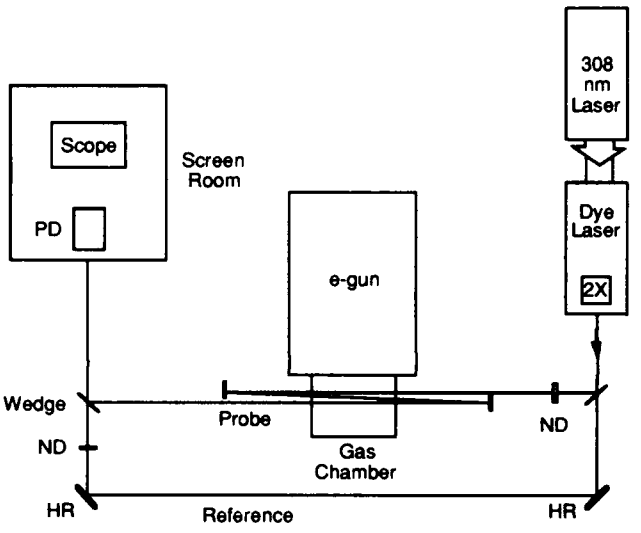


FIG. 1. Diagram of the experimental apparatus. A 248.4-nm beam from a frequency doubled dye laser probed the e-beam-pumped argon or krypton gas three times before being detected by a photodiode. A reference beam bypassed the cell and was reflected into the same photodiode, arriving 23 ns earlier than the probe.

the intensity of the probe beam to ~50 kW/cm^2 as it entered the gas cell on its first pass.

The electron gun[5] produced a 200-ns FWHM voltage pulse with a peak current density of 50 A/cm^2. The 400-kV electrons which were emitted from the hemispherically shaped cathode were constrained by a 1.5-kG magnetic guide field. After traversing the wire anode / hibachi / foil structure (1.5 mil titanium), they entered the gas chamber (see Fig. 2 for a detailed diagram of the gas chamber) and deposited energy into the gas. A stainless steel plate having a 3.5 x 8.0-cm^2 aperture was located 5.1 cm from the foil and served to define a uniformly pumped region of gas. The current density that was transmitted through the aperture could be measured with a Faraday cup when the gas cell was pumped to a vacuum. It was also possible to reduce the current density by a factor of 2 or 4 by mounting 1 or 2 stainless steel screens between the foil

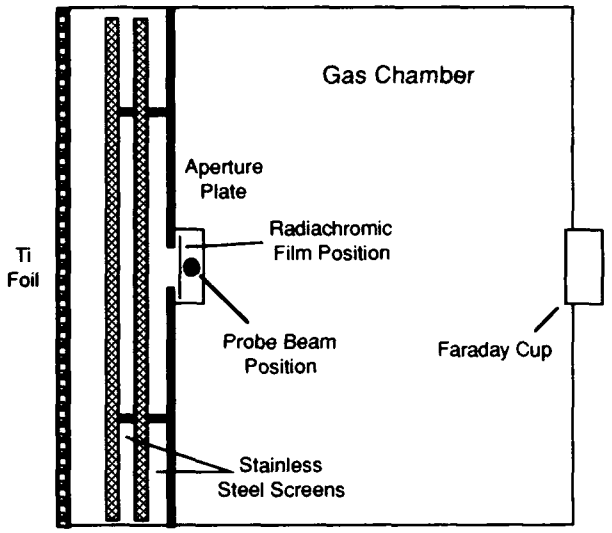


FIG. 2. Side view of the gas chamber showing the positions of the screens, aperture plate, radiachromic film, probe beam and Faraday cup.

and the aperture plate. The probe laser beam was aligned slightly past the aperture plate, at a distance of 5.8 cm from the foil, and ran transverse to the electron-beam, furnishing a single-pass absorption length of 8 cm. The temporal delay between the firing of the e-beam and the probe laser was controlled with a digital delay generator. The gas chamber was filled with either 2, 1 or 1/2 amagat of argon or krypton. The pressure rise in the gas for each shot was determined using a capacitance manometer. Data were taken under the experimental conditions given in Table I. Typical electron-gun waveforms are displayed in Fig. 3.

Absorption Measurement

The absorption measurement consisted of first filling the gas cell with the appropriate density of argon or krypton and taking a number of reference waveforms. The reference beam intensity was varied until the intensities of the beams were nearly equal. The e-beam and laser were then fired, and a picture of the reference and probe waveforms was taken and compared to the reference waveform. This was repeated for a total of three shots on a gas fill. Several reference waveforms were then taken and the average

TABLE I. Experimental conditions

Gas	Gas Density	Current Density
Argon	2 amagats	50, 25 and 12 A/cm^2
	1 amagat	50 and 25 A/cm^2
	0.5 amagat	50 A/cm^2
Krypton	2 amagats	50 and 25 A/cm^2
	1 amagat	50 A/cm^2

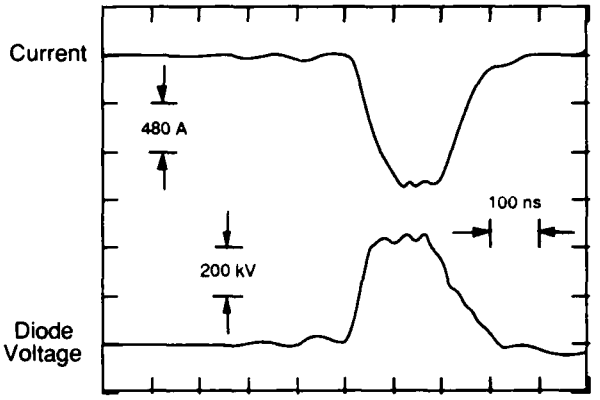


FIG. 3. Waveforms of the diode voltage and current produced by the electron gun. The voltage waveform has a 200-ns FWHM while the current waveform has a 180-ns FWHM.

reference beam to probe beam peak intensity ratio was calculated. The transmission of the probe beam through the e-beam-pumped gas was calculated by dividing the probe beam to reference beam intensity ratio obtained during the shot by the average reference to probe beam intensity ratio in the absence of the e-beam. The absorption was calculated by taking the natural log of the transmission and dividing by 24 cm, the three pass absorption length.

Since the same photodiode detected both the reference and probe beams, the uncertainty in the reference to probe beam intensity ratio was small, typically ± 3%, which translated into an uncertainty in the transmission of ± 5%, giving a one standard deviation uncertainty in the absorption coefficient of ± 0.2 %/cm. However, shot-to-shot variations in the e-beam increase the uncertainty to ± ~0.3 %/cm. Typical photodiode waveforms of the reference and probe beams with and without the firing of the e-beam are given in Fig. 4.

Determination of Deposited Energy

Knowledge of both the temporal shape and the peak value of the pump power is necessary to make code calculations of the absorption. The temporal behavior can be deduced from the current and voltage waveforms while the peak pump power is determined from the total energy deposited in the gas. The pressure rise technique[6] was not used to determine deposited energy, since a large volume of the gas was unpumped.

Two techniques were employed in these experiments to measure the peak pump power. A strip of radiachromic (RK) film was placed at the position shown in Fig. 2 (just in front of the path of the probe laser beam) and was exposed to the e-beam. The amount of energy deposited in the film was determined from the change in transmission of 600-nm light through the film.[7] The second technique involved calculating the energy deposition-per-electron-per-cm using a Monte Carlo, electron-beam energy deposition code[8] (EBDC) and multiplying by the peak current density to determine the peak pump power.

Exposures of RK film were taken under the experimental conditions given in Table I, and analyzed

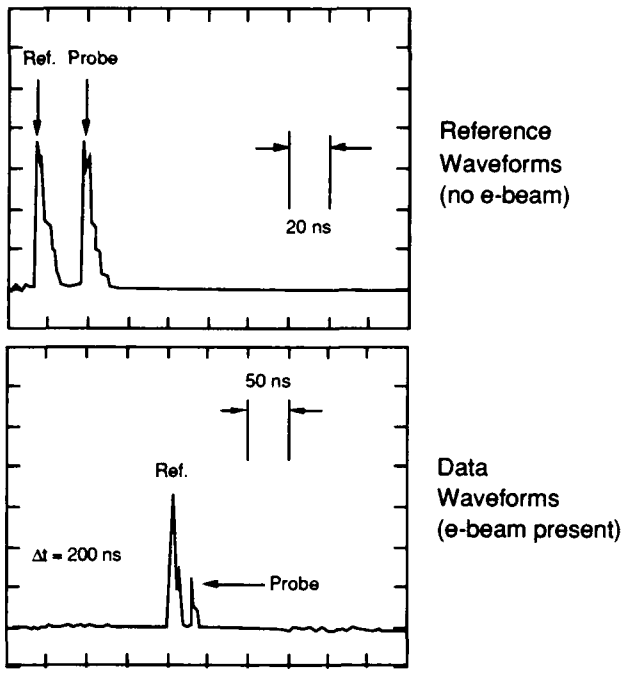


FIG. 4. Photodiode waveforms in the absence and presence of the e-beam. The top waveform displays the reference and probe beams when the e-beam is not fired, while the lower trace demonstrates the effect on the probe beam when absorption takes place. The upper trace is expanded compared to the lower by a factor of 2.5, and the time delay between the arrival of the e-beam at the gas cell and the probe beam on its second pass (lower trace) is 200 ns.

to give the energy deposited. An example of the electron energy deposition into 2 amagats of argon along the absorption line is displayed in Fig. 5. The vertical axis is the change in optical density of the film that has resulted from the exposure to the e-beam. This is proportional to the energy that was deposited in the film. There is some spreading of the e-beam past the aperture, but most of the electrons are confined within the 8 cm. From the figure, however, it is clear that the pump power, the current density and the absorption are not constant along the optical axis, and determining the absorption is not as simple as dividing the natural logarithm of the probe beam transmission by the path length (24 cm).

For an argon density of 2 amagats at a maximum current density of 50 A/cm^2, peak pump powers of 600 kW/cm^3 were determined from the RK technique at the position that the absorption was measured. Table II displays the peak pump powers for the different experimental conditions, and as can be seen, the pump power in argon is roughly proportional to both gas density and current density.

Calculations of deposited energy density were made using the EBDC for electrons of energy 400-keV scattering into the various densities of argon and krypton. Although the electron-gun cathode was round, implying a cylindrical geometry, the EBDC assumed cartesian coordinates. However, since the e-beam was apertured to less than half the cathode diameter, this approximation did not represent a serious compromise to the modelling. The electrons

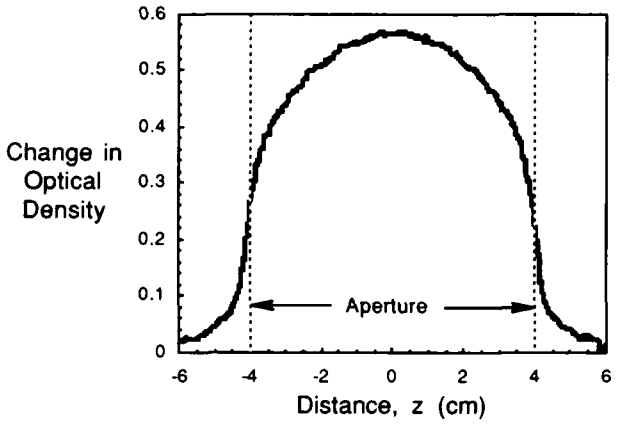


FIG. 5. Scan of radiachromic film giving the change in optical density in the probe beam direction at a distance of 5.8 cm from the foil compared to an unexposed sample. Optical density is converted to energy deposited in the nylon film, and a conversion is made to deposited energy in the gas. The dashed lines mark the boundaries of the e-beam aperture along the optical axis.

were taken to be incident on a square foil with 15-cm sides.

A plot of energy deposited-per-electron-per-cm in 2, 1 and 0.5 amagats of argon vs distance from the foil in the electron-beam direction (x) is shown in Fig. 6. Each curve represents an average of the depositions in the y-(vertical) and z-(optical axis) directions. The dashed line shows the probe beam position. A similar curve for deposition in the vertical direction is presented in Fig. 7. The dashed lines mark the edges of the foil, and the absorption measurement is taken at y = 0. From symmetry considerations, the deposition in the z-direction is identical to that in the y-direction.

From Figs. 6 and 7, the deposited energy density at the probe position for the 2-amagat argon run is 70 J/cm^3/coulomb, giving a peak pump power of 780 kW/cm^3 for a current density of 50 A/cm^2 incident

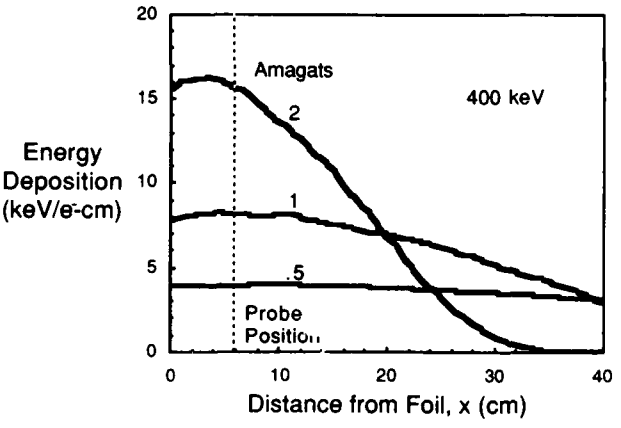


FIG. 6. EBDC calculation of electron energy deposition in argon in the electron-beam direction (transverse to the optical axis). The dashed line marks the probe beam position, and depositions are given for 2-, 1- and 0.5-amagat runs. In the calculation for 2 amagats, each electron, on the average, gives up an energy of 295.2 keV to the gas (area under the curve). An initial electron energy of 400 keV was used in the calculations.

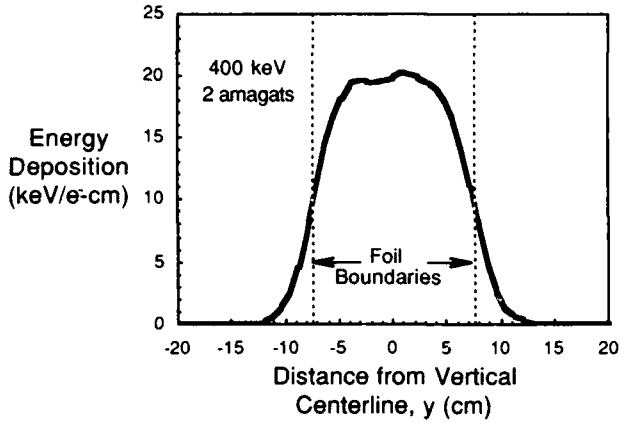


FIG. 7. EBDC calculation of electron energy deposition into 2 amagats of argon transverse to the electron beam. The dashed lines mark the foil edges. The calculation for deposition in the z-direction is identical to this due to symmetry . An initial electron energy of 400 keV was used in the calculations.

on a 225 cm^2 section of foil. This value is somewhat larger than the 600 kW/cm^3 value derived from the RK film data, and may be partially due to not having an accurate knowledge of the electron energy. A similar calculation of energy deposition into 2 amagats of krypton, displayed in Fig. 8, yields a deposited energy density of 106 J/cm^3/coulomb, or a peak pump power of 1.2 MW/cm^3.

Results

The temporal dependence of the absorption was measured for the cases of pumping 2 and 1 amagat of argon at the peak current density of 50 A/cm^2. Since the probe beam passes through the gas three times, it is actually absorbed over a time period of ~27 ns. It is therefore necessary to define a time delay, Δt, which corresponds to the separation in time between the arrival of the e-beam and the probe beam at the gas cell. By definition, $\Delta t = 0$ is the simultaneous arrival of the electron-beam with the probe beam at the beginning of its *second* pass through the gas cell.

A plot of absorption coefficient versus Δt for an argon density of 2 amagats is disclosed in Fig. 9. Note that the absorption peaks at the end of the pump pulse and decays exponentially. A linear least squares fit of data points with $\Delta t \geq 225$ ns to a decaying exponential is seen as a dashed curve in the figure, and yields a decay time of 230 ns. This corresponds to the effective lifetime of the absorber, and is much larger than the 50-ns decay of the current pulse. A similar plot for data taken at 1 amagat of argon yielded a decay time of ~500 ns, but there is some uncertainty in this value since the absorption values were lower and more uncertain.

Also shown in Fig. 9 is the kinetics code calculation (smooth curve) of the temporal dependence of the absorption. This was obtained by increasing the Ar_2^* decay rate in the present version of the kinetics code from 3.3×10^5 s^{-1} to 4.4×10^6 s^{-1} and decreasing the Ar_2^* absorption cross section from 1.0×10^{-17} cm^2 to 1.8×10^{-18} cm^2. This brings the calculation into good agreement with the peak experimental absorption coefficient, and it has little effect on the predicted absorption of an e-beam pumped KrF mix, since the argon dimers and dimer ions do not form appreciably in the presence of krypton and fluorine.

An important test of the kinetics code was to accurately predict the effect of varying the pump power on the absorption in two different regimes: by changing the current density, which should have little effect on the formation and decay rates, but may affect the Ar_2^* $^1\Sigma_u \leftrightarrow {}^3\Sigma_u$ mixing rate, and by changing the argon pressure, which affects the mixing rate and the three-body formation rates. In addition, because of the simplicity gained by having only a single rare gas constituent in the code, there are fewer constants to vary in bringing code results into agreement with the experimental data.

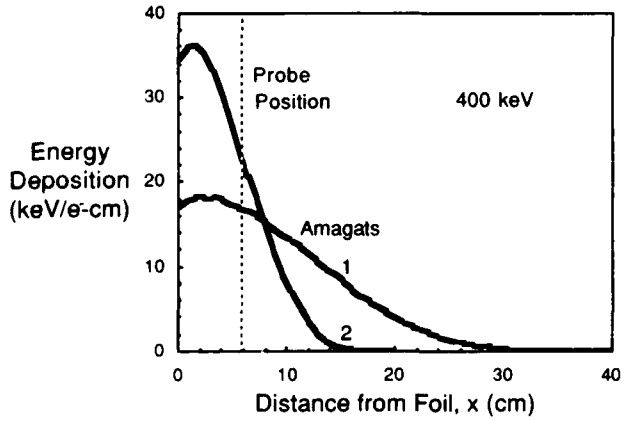


FIG. 8. EBDC calculation of electron energy deposition in krypton in the electron-beam direction. The dashed line marks the probe beam position, and depositions are given for 2- and 1-amagat runs. In the calculation for 2 amagats, each electron, on the average, gives up an energy of 267.2 keV to the gas (area under the curve). An initial electron energy of 400 keV was used in the calculations.

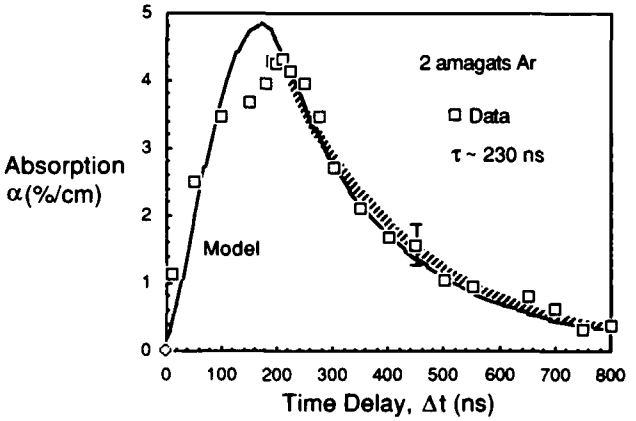


FIG. 9. Temporal dependence of the absorption at 248 nm of 2 amagat of Ar excited by a 50-A/cm^2 e-beam. The boxes are the experimental data points, and the smooth curve is a calculation by the kinetics code. The dashed line represents a linear least squares fit of the $\Delta t \geq 225$ ns data to a decaying exponential, and the decay constant is 4.4×10^6 s^{-1}. The uncertainty in the data is as shown.

The effect of varying the argon density on the absorption coefficient for a current density of 50 A/cm^2 is depicted in Fig. 10. Experimental results are denoted by squares, and the code predictions are represented by triangles. In each case, the code over-predicts the absorption coefficient, although the agreement is quite good. The calculated functional dependence of the data is different from the measured dependence, however, and this may be partially due to the uncertainty in the data. The effect of reducing the current density on the absorption coefficient at an argon density of 2 amagats is demonstrated in Fig. 11. In this case, the code over-predicts the 50 A/cm^2 data point, but under-predicts the other data. Overall, the agreement is reasonable.

All of the absorption data, including both the krypton and the argon results, are given in Table II. One series of data points was taken at a wavelength of 257.3 nm in 2 amagats of krypton, and the resulting absorption coefficient was a factor of 2 larger than the 248.4-nm absorption coefficient. This agrees with the predicted wavelength dependence of the Kr_2^+ (and by analogy, Kr_2^*) absorption cross section made by Wadt.[9] At the present time, the modelling results for the krypton data are preliminary, but indicate a larger predicted absorption than what has been seen, implying the need to reduce the Kr_2^* absorption cross section.

Discussion

Exposures of radiachromic film have demonstrated the radial dependence of both the current density and the pump power, as seen in Fig. 5. Along the absorption line, a peak pump power of 600 kW/cm^3 has been determined from energy deposition measurements in 2 amagats of argon. This occurs on the e-beam axis, at the point (5.8,0,0). Since the pump power, and hence the absorption, is not constant along the absorption length, but has a z dependence, it is inexact to calculate the absorption coefficient by simply dividing the natural logarithm of the transmission by 24 cm. Instead,

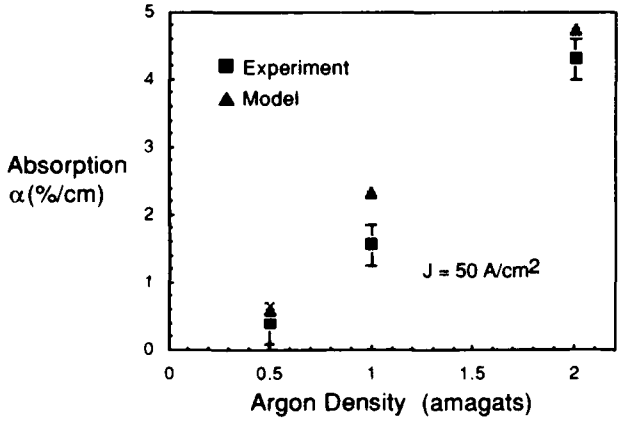


FIG. 10. Variation of the absorption coefficient with argon density. The experimental data (■) were taken under conditions of maximum e-beam pumping. Also shown are the kinetics code predictions (▲). The pump power is proportional to gas density.

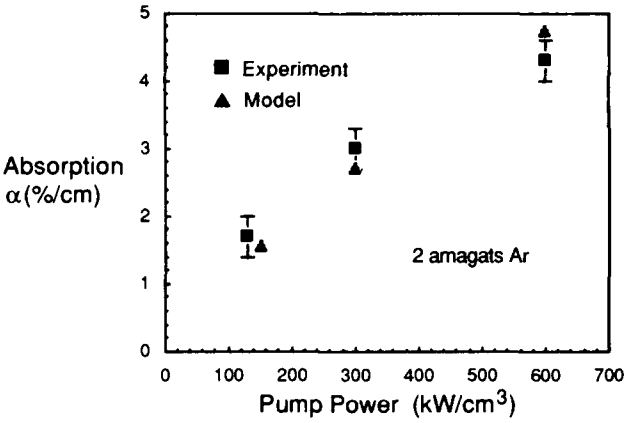


FIG. 11. Absorption coefficient as a function of pump power. Stainless steel screens reduced the current density by a factor of 2 (1 screen) and 4 (2 screens). The argon density was held constant at 2 amagats. Experimental data (■) and calculated data (▲) are shown. Pump powers were calculated from the radiachromic film technique.

$$-3\int^{z}\alpha(z)\,dz = \ln(T), \qquad (1)$$

where the path length is over the 8-cm aperture, and in order to calculate the absorption coefficient, the functional dependence of α must be known. From Fig. 11, at 2 amagats, the absorption has roughly a $P^{0.8}$ dependence, where P is pump power, and the z dependence of the pump power is obtained from Fig. 5. Although this is only an approximation, the resulting z dependence of the absorption coefficient is illustrated in Fig. 12. The functional form can be expressed as

$$\alpha(z) = \alpha_0\, f(z) \qquad (2)$$

where α_0 is the absorption coefficient at y = z = 0 and $f(z)$ is the absorption distribution function, which has a maximum value of 1 at z = 0. Eqn. (1) can then be rewritten

$$-3\,\alpha_0\int^{z} f(z)\,dz = \ln(T) \qquad (3)$$

and the integral of $f(z)$ dz can be determined by finding the area under the curve in Fig. 12. In so doing, one obtains the result

$$\int^{z} f(z)\,dz = 7.8 \text{ cm},$$

which implies that assuming a constant pump power along the 8-cm absorption length results in a determination of the peak (at (5.8,0,0)) absorption coefficient that is accurate to within 2.5%. If the absorption is assumed to be linear with pump power, then $f(z)$ is identical to the curve in Fig. 5, and

$$\int^{z} f(z)\,dz = 7.3 \text{ cm}.$$

TABLE II. Peak pump powers (kW/cm^3) and peak absorption coefficients (α, %/cm.) at 248 nm for the different experimental conditions. Pump power values were determined from both the EBDC and radiachromic film techniques. In the case of krypton, a second series of measurements was also made at 257.3 nm (shown in parentheses). The screens reduced the current density by a factor of 2 (1 screen) and 4 (2 screens).

Gas	Density (amagats)	Current (A/cm^2) (# Screens)	Pump Power (kW/cm^3) EBDC	RK film	α (%/cm)
Argon	2	50 (0)	780	600	4.3
	2	25 (1)	390	300	3.0
	1	50 (0)	400	340	1.6
	2	12 (2)	180	130	1.7
	1	25 (1)	200	160	0.9
	0.5	50 (0)	200	170	0.4
Krypton	2	50 (0)	1190	-	1.3 (2.6[a])
	1	50 (0)	870	-	0.8
	2	25 (1)	600	-	0.5

[a] Measured at 257.3 nm

Therefore, the absorption coefficient calculated in the simple way given in the experimental set-up section is nearly equal to the value of the absorption coefficient at (5.8,0,0), at least to within 10%.

A similar analysis can be carried out for the the Faraday cup measurement. The current density peaks in the center and has a radial dependence up to the aperture, which can be approximated by separate y- and z-dependences. The z-dependence is seen in Fig. 5, and the current density is relatively constant in the y-direction over the 3.5-cm aperture. By expressing the current density, J(y,z), in the form

$$J(y,z) = J_o\, f_y(y)\, f_z(z) \qquad (4)$$

where $f_y(y)$ and $f_z(z)$ describe the distribution of the current density in the y- and z-directions and J_o is the current density at y = z = 0, the total current measured by the Faraday cup (I) is

$$I = J_o \int^{y}\int^{z} f_y(y)\, f_z(z)\, dy\, dz. \qquad (5)$$

Performing the integrals by determining the areas under the curves yields a value for J_o of 50 A/cm^2 for a measured current of 1.3 kA. Coupled with the Monte Carlo calculation for energy deposited into 2 amagats of argon, this leads to the value of 780 kW/cm^3 as the peak pump power at (5.8,0,0). This is somewhat larger than the value obtained from the RK measurement, and it is clear that more effort must be expended into determining the accuracy of the techniques on a better calibrated instrument.

Pumping 2 amagats of argon with a 50 A/cm^2 e-beam produced a peak absorption of 4.3 %/cm. Prior to these measurements, the value of the absorption cross section at 248 nm for Ar_2^* given in the KrF kinetics code[9] was 1 x 10^{-17} cm^2 and the radiative lifetime was given as 3.0 μs (triplet state).[10] However, the code over-predicted the absorption by a factor of 5, and it was clear that the absorption cross section needed to be reduced and that electron and possibly rare gas mixing of the dimer singlet and triplet states (the triplet state is lower in energy than the singlet, and the singlet state has a radiative lifetime[11] of 4 ns) was reducing the effective lifetime of the dimer absorber. A measurement of the decay time of the absorption (τ_d = 230 ns) provided an effective Ar_2^* decay rate of 4.4 x 10^6 s^{-1} to be used in the code . In order to bring code calculations into agreement with the data, the Ar_2^* absorption cross section was reduced to 1.8 x 10^{-18} cm^2. These changes did not have any significant effect on the predicted absorption of an e-beam pumped KrF mix.

Incorporating these changes into the code resulted in the temporal dependence of the absorption given in Fig. 9. Figure 13 depicts a breakdown of the absorption into contributions by the major absorbers.

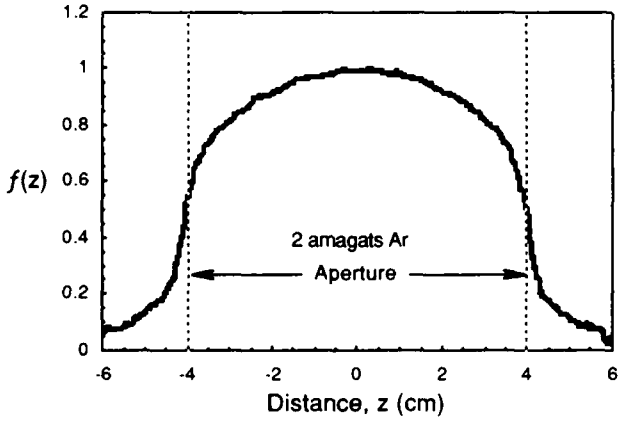


FIG. 12. Absorption coefficient distribution function versus position along the probe beam direction, assuming that α varies as the pump power to the 0.8 power, and taking Fig. 5 as the z dependence of the pump power. The absorption coefficient is equal to α_o times $f(z)$, where α_o is the value of the absorption coefficient at z = 0.

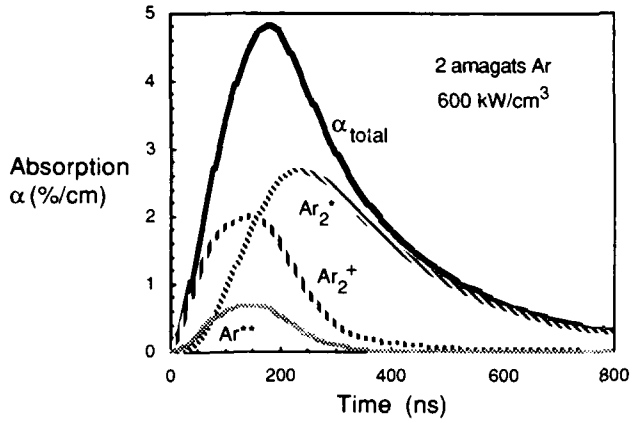


FIG. 13. Kinetics code calculation of the temporal dependence of the absorption at 248 nm of 2 amagats of Ar pumped with a 600 kW/cm^3 e-beam. The solid curve is the total absorption, and the dashed curves are the contributions by the major absorbers. At late times, Ar_2^* is the main absorber, and the decay rate of the total absorption matches that of Ar_2^*.

The early time behavior is attributed to dimer ion (Ar_2^+) and excited atom (Ar**) absorption, while at late times, Ar_2^* is the main absorber. Since Ar_2^+ and Ar_2^* are expected to have similar absorption spectral shapes and peak cross sections, an alternative to bringing calculations into agreement with the data by reducing the Ar_2^* absorption cross section alone is to reduce both the Ar_2^* and the Ar_2^+ cross sections proportionately.

The dependence of the absorption coefficient on pump power is understood by considering the kinetics of the system. The electron beam produces both excited argon atoms and argon ions. The excitation rate is proportional to the argon ground state density and the current density. The ions form dimer ions in three-body collisions with neutrals, and the dimer ions dissociatively recombine with electrons to form Ar**. Electron and neutral mixing de-excite the Ar** atoms to the metastable level (Ar*), and three-body collisions lead to the formation of the excited dimers, Ar_2^*. These processes can be simply described by the following rate equations:

$$\frac{d[Ar^+]}{dt} = \beta J [Ar] - k_{3i} [Ar]^2 [Ar^+] \qquad (6)$$

$$\frac{d[Ar_2^+]}{dt} = k_{3i} [Ar]^2 [Ar^+] - \alpha_{dr} n_e [Ar_2^+] \qquad (7)$$

$$\frac{d[Ar^{**}]}{dt} = \alpha_{dr} n_e [Ar_2^+] - \frac{[Ar^{**}]}{\tau_a'} \qquad (8)$$

$$\frac{d[Ar^*]}{dt} = \gamma J [Ar] + \frac{[Ar^{**}]}{\tau_a'} - k_{3n} [Ar]^2 [Ar^*] \qquad (9)$$

$$\frac{d[Ar_2^*]}{dt} = k_{3n} [Ar]^2 [Ar^*] - \frac{[Ar_2^*]}{\tau_d'} \qquad (10)$$

where brackets denote particle densities, β and γ are excitation rate coefficients of the ion and metastable atom, respectively, in units of cm^2/A-s, J is the current density, k_{3i} and k_{3n} are three-body formation rate constants for the dimer ion and the excited dimer, α_{dr} is the dissociative recombination rate coefficient, n_e is the electron density and τ_a' and τ_d' are the effective lifetimes of the excited atom and molecule, including the effects of quenching.

Admittedly, this is not an exact treatment of the kinetics, but it does allow us to gain insights into the dependence of the absorption on pump power. Since the absorption at the end of the e-beam pulse is mostly the result of argon dimer absorption, we will consider the effect of argon density on the dimer population.

At large argon densities, where the three-body formation rates are large compared to the inverse of the e-beam pulse length, ions which are formed in Eqn. (6) will quickly form dimer ions, which will in turn rapidly form excited atoms. These will quickly populate the metastable level, so that Eqn. (9) can effectively be rewritten

$$\frac{d[Ar^*]}{dt} \approx (\gamma+\beta) J [Ar] - k_{3n} [Ar]^2 [Ar^*] \qquad (9')$$

and, assuming a square pump pulse of duration T_L (200 ns), the Ar* and Ar_2^* densities can be solved for exactly.

$$[Ar^*] \approx \frac{(\gamma+\beta) J}{k_{3n} [Ar]} [1 - \exp(-k_{3n} [Ar]^2 t)] \qquad (11)$$

and

$$[Ar_2^*] \approx (\gamma+\beta) J [Ar] \tau_d' \left\{ \frac{k_{3n} [Ar]^2 [1 - \exp(-\frac{t}{\tau_d'})] - \frac{1}{\tau_d'} [1 - \exp(-k_{3n} [Ar]^2 t)]}{k_{3n} [Ar]^2 - \frac{1}{\tau_d'}} \right\} \qquad (12)$$

If $k_{3n}[Ar]^2 >> 1/T_L$ and $1/\tau_d'$ (that is, if the formation rate of the dimer is much larger than either its loss rate or the inverse of the laser pulse width) then at the end of the e-beam pulse, the Ar_2^* density can be approximated by the following expression.

$$[Ar_2^*] \approx (\gamma+\beta)\, J\, [Ar] \left\{ \tau_{d'} \left[1 - \exp\left(-\frac{T_L}{\tau_{d'}}\right)\right] - \frac{1}{k_{3n}[Ar]^2} \right\} \quad (13)$$

Expanding the exponential in Eqn. (13) out to two terms results in the following:

$$[Ar_2^*] \approx (\gamma+\beta)\, J\, [Ar]\, T_L \,. \quad (14)$$

Thus, the dimer population, and hence the absorption, at the end of the pulse is linear with argon and current density. At 1 amagat, $k_{3n}[Ar]^2 = 1.4 \times 10^7\ s^{-1}$ for $k_{3n} = 2 \times 10^{-32}\ cm^6/s$, $1/T_L = 5 \times 10^6\ s^{-1}$ and $1/\tau_{d'} \approx 2 \times 10^6\ s^{-1}$. As the argon density increases, the effective lifetime of the dimer decreases, so that $\tau_{d'} < T_L$, and the dependence of dimer density on pump power will be less than linear.

At pressures lower than an amagat, the three-body rate is slow, and if one neglects contributions to the metastable level from the ion, Eqn. (9) can be solved to give

$$[Ar^*] \approx \frac{\gamma J}{k_{3n}[Ar]} \left[1 - \exp\left(-k_{3n}[Ar]^2\, t\right)\right] . \quad (15)$$

At the end of the pulse, if $k_{3n}[Ar]^2\, T_L << 1$ and $\tau_{d'} >> T_L$,

$$[Ar^*] \approx \gamma\, J\, [Ar]\, T_L \quad (16)$$

and the solution for the dimer density is

$$[Ar_2^*] \approx \frac{\gamma\, J\, k_{3n}\, [Ar]^3\, T_L^2}{2} \,. \quad (17)$$

Therefore, at low pressures and at the end of the e-beam pulse, the dimer population, and hence the absorption, is expected to have a pressure cubed dependence. Since the peak in the dimer density occurs after the e-beam has terminated, the peak dimer density will actually vary as pressure squared.

At all pressures, this simple analysis predicts a linear dependence of dimer concentration on current density. This is not observed to be the case, and is probably due to the fact that a higher current density will produce more secondary electrons, and electron mixing will be faster. In addition, the dissociative recombination rate is a function of the electron density. This analysis does not attempt to consider the effects of electrons.

Conclusions

Absorption measurements have been performed on e-beam pumped argon and krypton under a variety of pumping conditions. The pump power was varied by changing the gas density and the current density entering the gas. Good agreement has been obtained between experimental results and code calculations after reducing the Ar_2^* absorption cross section and increasing the Ar_2^* radiative decay rate in the kinetics code. Following these changes, no effect was seen in the predicted absorption of a KrF mix. This implies that Ar_2^* absorption does not contribute significantly to the total absorption in a KrF mix. Two methods of measuring the energy deposited in the gas by the electron beam were compared, and agreed to within 20%.

Acknowledgements

The authors appreciate the technical assistance of Jody Godard, Stewart Halbig and Thom Bell as well as helpful discussions with Dennis Greene. This work was supported by the Department of Energy under the Inertial Confinement Fusion program.

References

[1]F. Kannari, M. Obara, and T. Fujioka, J. Appl. Phys. **57**, 4309 (1985).
[2]S.J. Czuchlewski, D.E. Hanson, B.J. Krohn, A.R. Larson, and E.T. Salesky, Fusion Tech. 11, 560 (1987).
[3]D.C. Thompson, R. Fedosejevs, A.A. Offenberger, J. Santiago, and H.R. Manjunath, IEEE J. Quantum Electron. **QE-25**, 2161 (1989).
[4]J.F. Seamans, W.D. Kimura, and D.E. Hanson, in Proceedings, International Conference on Lasers '88, R.C. Sze and F.J. Duarte, Eds. (STS Press, McLean, VA, 1989), pp. 167-170; and W.D. Kimura and J.F. Seamans, Final Report to Los Alamos National Laboratory (Contract # 9-X65-W1478-1) Spectra Technology, Inc. (1989).
[5]Final Technical Report to Los Alamos National Laboratory (Report # SRL-07-F-1987) Science Research Laboratory, Inc. (1987).
[6]A.W. McCown, T.P. Turner, R.A. Tennant, and B.J. Krohn, presented at the Conference on Lasers and Electro-Optics, Baltimore (1989), paper ThP1.
[7]W.P. Bishop, K.C. Humphreys, and P.T. Randtke, Rev. Sci. Instru. **44**, 443 (1973).
[8]J.C. Comly, W.T. Leland, C.J. Elliott, A.M. Hunter, and M.J. Kircher, IEEE J. Quantum Electron. **QE-17**, 1786 (1981).
[9]W.R. Wadt, J. Chem. Phys. **73**, 3915 (1980).
[10]C.H. Chen, M.G. Payne, and J.P. Pudish, J. Chem. Phys. **69**, 1626 (1978).
[11]J.W. Keto, R.E. Gleason, and G.K. Walters, Phys. Rev. Lett. **33**, 1375 (1974).

GENERATION OF 400 FS PULSE IN KRF LASER AMPLIFIER WITH UV SATURABLE ABSORBER

H.Nishioka, H.Kuranishi, K.Ueda, and H.Takuma
Institute for Laser Science, University of Electro-communications
1-5-1 Choufugaoka, Chofushi, Tokyo 182 JAPAN

Abstract

Optical pulse compression and ASE free amplification in UV saturable absorber(acridine) and KrF amplifier arrangements have been demonstrated. The DOUBLE SATURABLE ABSORBER was used to obtain fast and stable pulse shaping. We have obtained a 400fs pulse from a 10ps pulse with the output energy of 20mJ including less than 0.1% ASE fraction. The frequency chirping due to self phase modulation can not be observed.

1. Introduction

Generation of a high power and ultra-short pulse with an excimer laser system have been intensively pursued by many groups. In recent work, S.Szatmari et al. have obtained a 45fs[1] laser pulse after the prism pulse compressor using with an advanced DFDL. S.Watanabe et al. have generated a multi-terawatt uv pulse with a large aperture electron beam pumped amplifier[2].

In such multi-staged systems, an ultra-short optical pulse generated in former stages is degraded during amplification by the ASE (Amplified Spontaneous Emission)[3]. The ASE generated in the front-end part shows small beam divergence which is much the same as that of a laser beam so that the ASE can not be rejected with a spatial filter. Furthermore saturation energy for ASE Es(ASE) is much higher than that for laser pulse Es(laser) because ASE should be amplified in steady state condition. When input pulse width much shorter than effective lifetime of gain medium the ratio of saturation energy Es(ASE)/Es(laser) corresponds to the ratio of (pump time)/(effective gain lifetime). In a typical discharge type laser (assuming the pump pulse width of 30ns, the effective lifetime of 1.5ns and the small signal gain length product $g_oL=8$), saturation energy for ASE of 40mJ/cm^2 is 20 times higher than that for gain. So ASE energy will easily excess laser energy when we have double pass amplification even if the initial laser to ASE contrast ratio is 10^8.

In addition to ASE problem, non-linear optical phenomena (the multi-photon absorption and optical Kerr effect) and optical dispersion which can not be rejected as long as the transparent optics are used broaden laser pulse width and spectrum. These phenomena is considered to be a function of inverse square of pulse width or more sensitive, as a result, an high power and ultra-short pulse having less than 1ps width is drastically modulated and is broadened in the optical system.

The real problems we have identified here are due to basic physics and not to practical limitation, therefor it is certain that these problems will be critical as the increase of total gain and/or number of optical component to increase output power.

The conventional and inessential methods[3] widely used to address these problems are the operation in the small signal gain region or the weak saturated region and the use of large aperture optics to decrease intensity to optical components. These methods can not only solve the problems but also they make system complex and are inefficient for the energy extraction.

The absorber-amplifier arrangement is a convenient method for ASE free amplification. A saturable absorber having short recovery time compared with the effective gain lifetime shows unequal saturation property between laser and ASE as the similar manner for gain saturation mentioned above. Therefor the absorber can select only a laser pulse due to high saturation energy for ASE. If the saturable absorber has small signal absorption which is equal to small signal gain of a following amplifier, the total gain of the absorber amplifier arrangement for ASE is kept unity so ideal ASE free amplification will easily be realized. Moreover, a laser pulse after passing through a saturable absorber changes its shape and has a fast rise time. This change of pulse shape is suitable for pulse compression in a saturated amplifier. This effect permits that a input pulse has moderate long duration compared with the desired output pulse width as a result the optical broadening can be relaxed. In dye laser systems, Y.Taira et al. have demonstrated pulse compression from 15ps to 0.8ps with two stage arrangement of DODCI/Rh6G[4], however the pulse shortening in the KrF amplifier has never been demonstrated for the lack of an

effective saturable absorber.

In this paper, we have demonstrated the pulse compression and the ASE free amplification in a simple KrF system using with the DOUBLE absorber-amplifier arrangement. After two stage of absorber-amplifier arrangement, the pulse width of 400fs have been obtained with good stability.

2.Pulse shaping with DOUBLE saturable absorbers

It is well known that when input pulse width is much less than the effective lifetime of gain medium, namely storage type amplification, temporal and dynamic gain saturation cause pulse distortion. The pulse deformation in the saturated amplifier strongly depends on slope of leading part of input pulse. In order to obtain strong pulse sharpening the leading edge of the input pulse must have a rise time substantially shorter than the desired output pulse length. Using with saturable absorber one can reduce rise time on the leading edge, however, the conventional "SINGLE" absorber-amplifier arrangement has practical trade off between the pulse shortening and the stability as the follows. The change of absorption-length product of saturable absorber $\Delta \alpha L$ is a function of absorbed energy Eabs normalized with absorption saturation energy Es as,

$$\Delta \alpha L = \sigma \Delta (nL)$$
$$= \sigma \cdot Eabs/h\nu$$
$$= Eabs/Es \qquad (1).$$

Where σ and nL are absorption cross-section and total number of molecule along optical axis, respectively. If we assume that absorber is optically thick and its transmittance T1 is much less than unity during bleaching i.e. $T1(t) << 1$ then the absorption saturation rate $d\alpha L/dt$ can be denoted with input intensity I(t) instead of absorption energy Eabs,

$$\frac{d\alpha L}{dt} = I(t)/Es \qquad (2).$$

In a theoretical point of view, the desired rise time can be obtained by increase of the input intensity for a saturable absorber. In practice, however, since input pulse has finite rise time the increase of input intensity (or the decrease of saturation energy) only hasten a breaching point far from the peak of a input pulse as shown in Fig.1 (a). In this situation, the bleaching will be caused by the optical noise (very small pre-pulses, ASE or ringing) on the former part. As it is, bleaching speed and timing are determined independently of a input pulse and have fatal instability. Consequently, the compression ratio of a SINGLE absorber-amplifier arrangement is practically limited within a few times and strongly depends on the signal to noise ratio.

The main issue that we have identified is how to get high speed bleaching by the peak of a pulse. In order to address this issue we have used a stacked saturable absorber which was made of two absorbers having different saturation energy as shown in Fig.1(b). The pre-absorber which has high saturation energy absorbs the first half and the following main

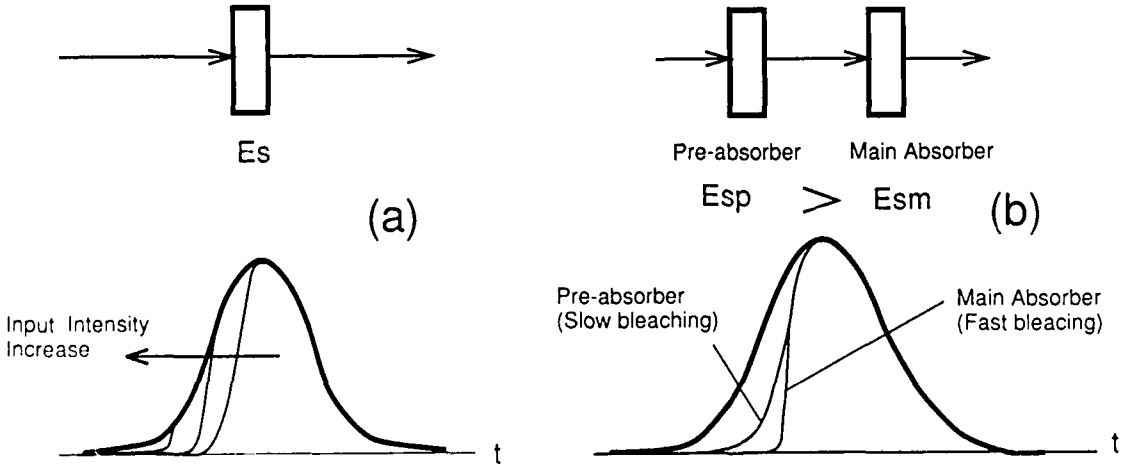


Fig.1 Pulse shaping with (a)SINGLE and (b) DOUBLE saturable absorbers.

absorber sharp cuts the leading edge with low saturation energy. The pre-absorber and the main absorber determine TRIGGER LEVEL and TRIGGER SPEED respectively and the former is insensitive to the optical noise so that system is kept stable.

3.Experimental setup and result

The experimental setup is shown in Fig.2. We have employed a short cavity dye laser (Lambda physik FL-4000T type modified) as a seed pulse generator at 497nm. C102 and C307 laser dyes were alternatively arranged in the amplifier chain in order to prevent ASE growth at peak gain wavelength for each dye. Also we have applied the double absorber and amplifier technique to this dye laser. A pair of Schott glass filter OG-530 2mm thickness and lenses were inserted between 2nd and 3rd amplifier stages. The output pulse width of 10ps was quarter of typical value without absorbers as shown in Fig.3 (a) and (b). The spectrum width of 0.05nm is twice of the transform limit if we assume that the pulse shape was hyperbolic secant squared.

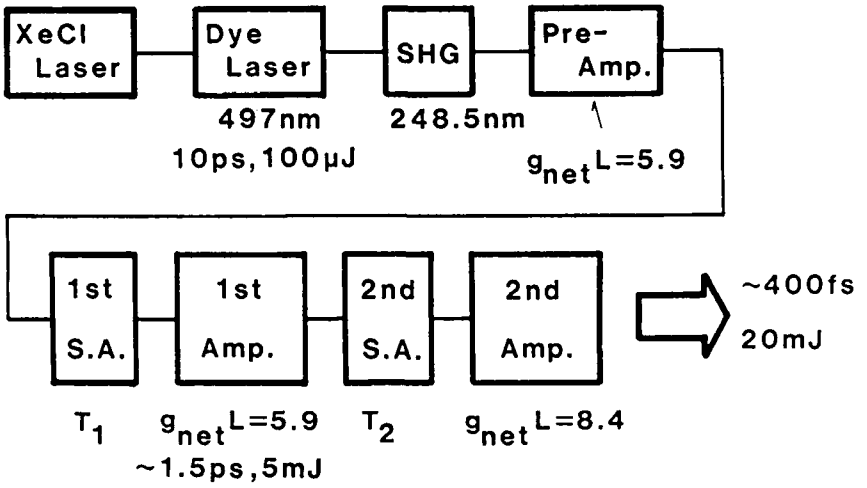


Fig.2 Schematic diagram of femtosecond generator.

An output pulse from the dye laser was frequency doubled with a β -BaB_2O_4 crystal and was amplified by a discharge laser (Lambda physik EMG-150) providing two discharge modules as shown in Fig.4. The pressure and the mixture ratio of gain medium in these chambers were set to obtain the maximum gain and the optimum timing which is suitable for effective pulse shortening and highest output energy without the consideration for the ASE suppression ($He/Kr/F_2$=2374/120/6 mbar). The smaller chamber was used as a double pass amplifier making a pre-amplifier and 1st stage amplifier. The measured small signal net gain was $g_{net}L=5.9$ per pass. The large amplifier ($g_{net}L=8.1$) was used as a final amplifier to obtain high output energy. Methanol solution of acridine showing the saturation energy of 1.2mJ/cm² and the ratio of primary/excited absorption cross-section of 6.3:1 was used as uv saturable absorber. Its recovery time of 0.4 ns is sufficient for the effective ASE filtering. The detail of saturation characteristics of acridine,

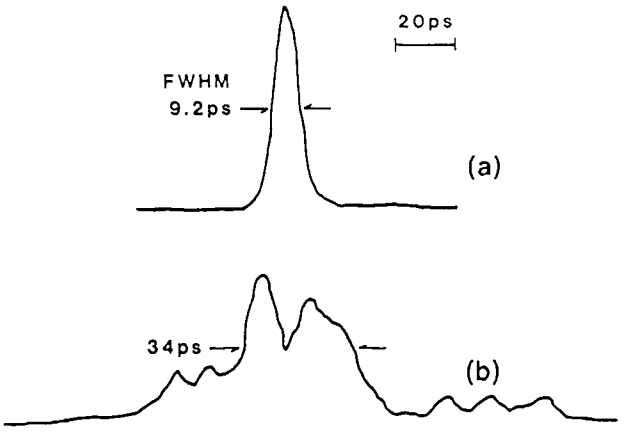


Fig.3 Dye laser output (a) with double absorbers and (b) without absorbers.

the solvent effects and its ASE suppression have been reported elsewhere[5,6]. The thickness of solution was set at 0.5mm in order to prevent multi-photon absorption and the optical Kerr effect. An evacuated spatial filter located before final amplifier was used to reject backward ASE irradiation to the 2nd absorber and was unnecessary when the absorber and the amplifier was spaced a few meter away.

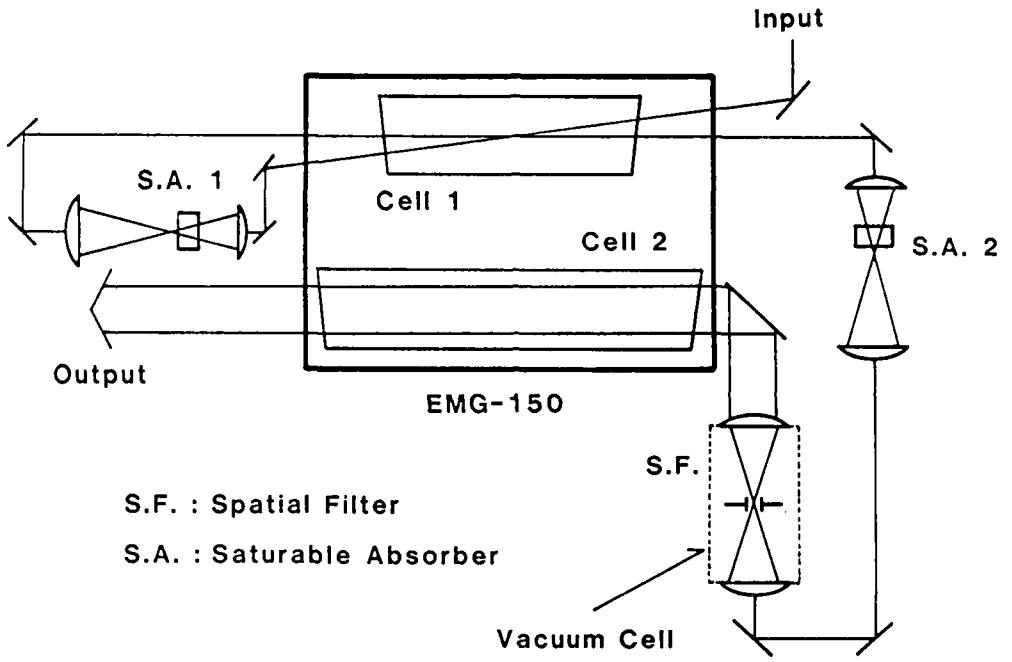


Fig.4 Absorber and amplifier arrangement.

The output pulse width was measured with the auto-correlation method by the means of three photon fluorescence of XeF C-A transition[7]. The output pulse from final amplifier was separated into two beams and was focused with a f=500mm CaF_2 lens into a small chamber filled with $Ar/Xe/F_2$=2.15/1.00/0.85 atm. The two pulses were collided precisely at focal point. An image of fluorescence was magnified by a reversely mounted camera lens (Nikon NIKKOR f=35mm F/2.8) and was monitored with a silicon intensified target camera with a multi-channel analyzer. The laser spectrum was measured in 5th order diffraction of a monochromator (NIKON G-500Ⅲ) with a linear-image sensor (HAMAMATU S2304-256Q).

We have measured output pulse width as a function of small signal transmittance T_1 and T_2 for the first (between 1st and 2nd path) and the second (between 2nd and 3rd path) absorbers. The laser fluence on each saturable absorber was approximately 100mJ/cm² which corresponds to 50 times higher than its threshold. This intensity was determined by the threshold of the self beam trapping due to the optical Kerr effect in the solution. The result when the SINGLE absorber-amplifier arrangement was used and T_2=1, is shown in Fig.5. Output pulse width decreased with T_1 up to 10^{-4} and the shortest achievable pulse width was 1.5ps.

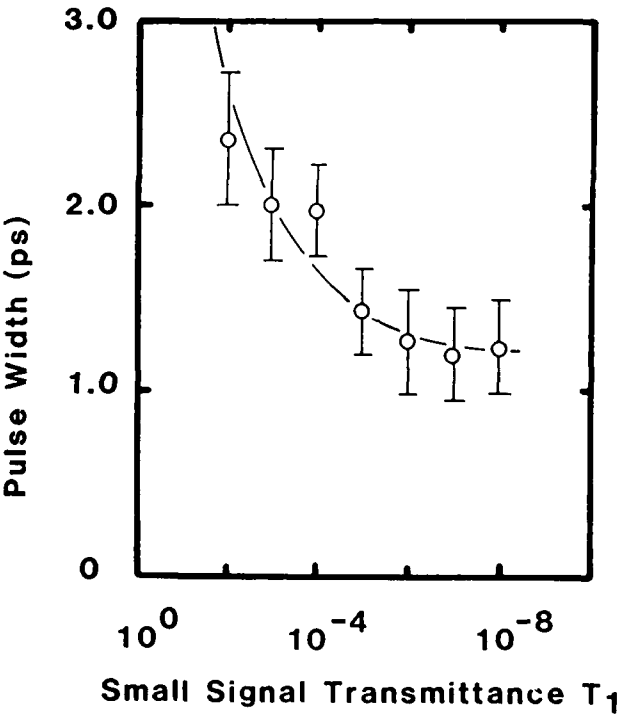


Fig.5 Pulse shortening with 1st stage pulse compressor.

Double saturable absorbers were realized by a two absorbers under different input intensity each other. In the following measurements, a pair of fused silica cells filled with acridine solution located before focal point of telescope were used as the double absorbers as shown in Fig.6 instead of the single absorber. The pre-absorber and the main absorber are employed around 5 times and 50 times above their threshold, respectively.

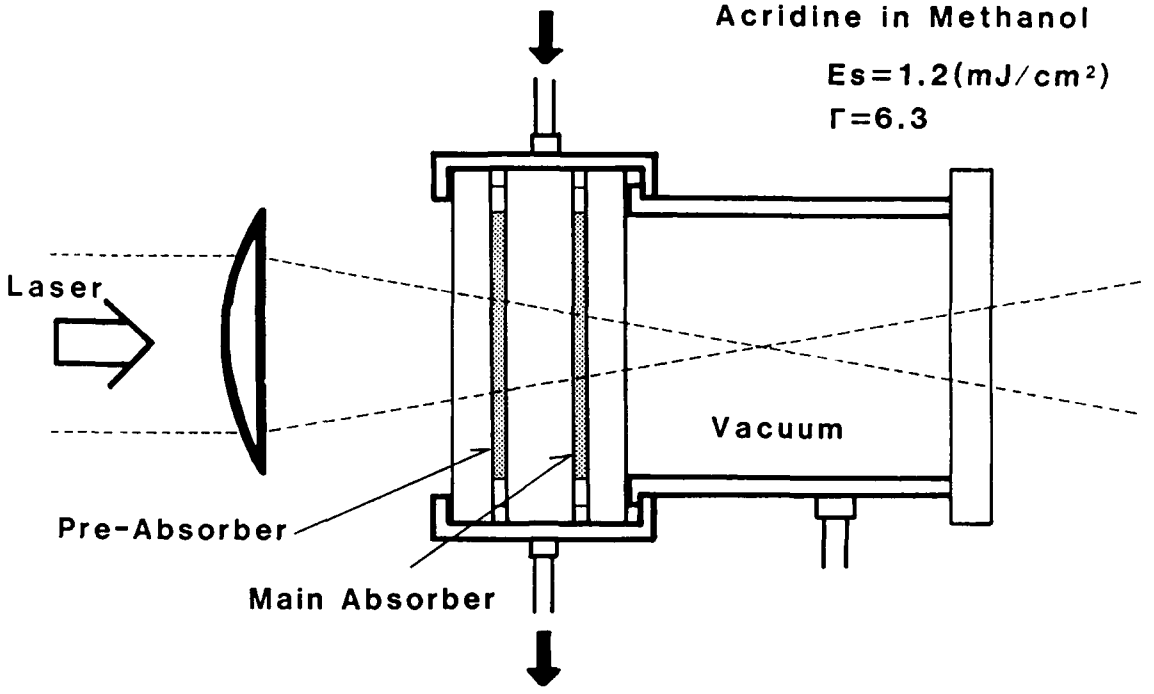


Fig.6 Double saturable absorber for KrF band.

The comparison of the single and the double absorber is shown in Fig.7. With single absorber, the pulse width around 750fs was obtained at $T_2=10^{-4}$ however fluctuation due to the hasty bleaching was the range of more than factor of 2. In contrast, when double saturable absorber was used with the condition $T_1=T_2=10^{-4}$, the pulse width of 400fs was achieved with good stability. Figure 8 shows auto-correlation trace of an output pulse with this condition. The correlation with 450fs corresponds to pulse width of 350 fs if we assume pulse shape of hyperbolic secant squared. In the region of $T_2<10^{-5}$ in Fig. 7, absorption from the excited state of acridine caused insufficient saturation of the final amplifier as a result pulse width became longer. The output energy was 20mJ including less than 0.1% ASE energy which was measured at a distance of 3m from the final amplifier. The residual ASE was the contribution from only a final amplifier. The pulse width and frequency band product of a output pulse was 0.44. This value is near transform limited product if we assume that the output pulse shape is hyperbolic secant squared and indicates that significant frequency chirping did not occur.

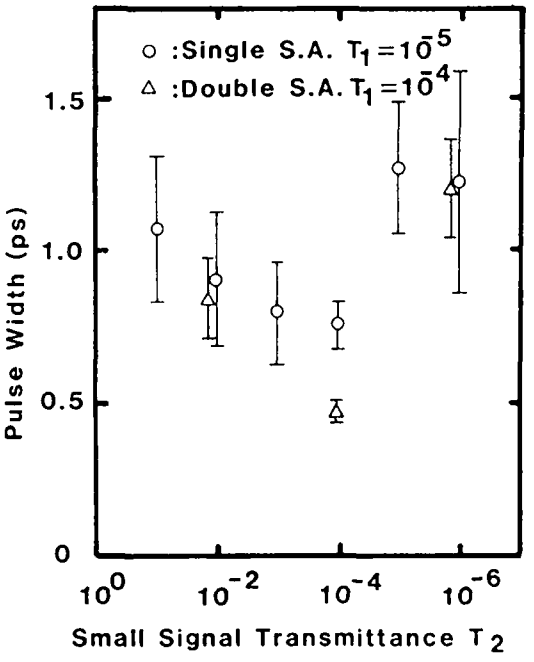


Fig.7 Comparison of SINGLE and DOUBLE saturable absorber in output pulse width.

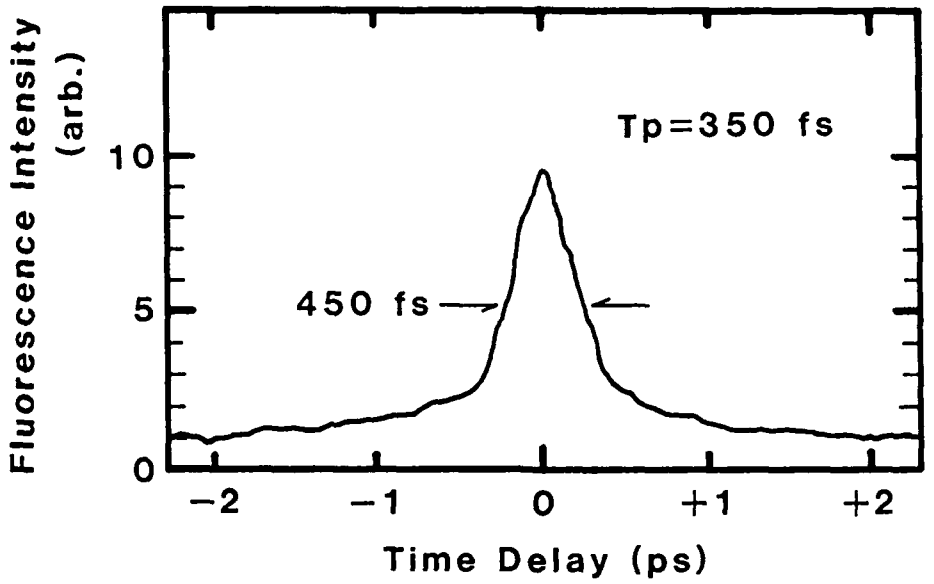


Fig.8 Auto correlation trace of an output pulse.

4.Conclusion

We have demonstrated generation of sub-picosecond pulses and ASE free amplification in strongly saturated amplifiers. Double saturable absorber was used to obtain stable and fast pulse shaping. A pulse was compressed by the factor of 25 with two stage of absorber-amplifier arrangements. The output energy of 20mJ having less than 0.1% of ASE fraction was obtained. The significant frequency chirping by the self phase modulation can not be observed in a output pulse. This effective and useful pulse compression scheme can be applied to other short pulse systems.

The authors would like to thank Y.Mizoguchi for his help in making pulse width measurements.

REFERENCES

1.S.Szatmari and F.P.Schafer,"Generation of High Power UV Femtosecond Pulses", Ultrafast PhenomenaVI , Springer-Verlag,1988.
2.A.Endoh, M.Watanabe, N.Sarukura, and S.Watanabe, "Multiterawatt Subpicosecond KrF Laser",Opt.Lett.,Vol.14,pp.353-355,1989.
3.A.Endoh, M.Watanabe, and S.Watanabe, "Picosecond Amplification in Wide-aperture KrF Lasers",Opt.Lett.,Vol.12,pp.906-908,1987.
4.Y.Taira and T.Yajima, "High Power Subpicosecond Pulse Generation from a Synchronously Pumped Dye Laser Combined with an External Compressor", Optics Comm., Vol.29,pp.115-118,1989.
5.H.Nishioka, H.Kuranishi, K.Ueda, and H.Takuma, "UV Saturable Absorber for Short Pulse KrF Laser Systems", Opt.Lett.,Vol.14, pp.692-694,1989.
6.H.Nishioka, H.Kuranishi, K.Ueda, and H.Takuma, "Development of UV Saturable Absorber Acridine and Its Application for a Short Pulse KrF Laser", The Review of Laser Engineering, Vol.17,pp.652-661,1989.
7.N.Sarukura, M.Watanabe, A.Endoh, and S.Watanabe, "Single-shot Measurement of Subpicosecond KrF Pulse Width by Three-photon Fluorescence of the XeF Visible Transition", Opt.Lett.,Vol.13, pp.996-998,1988.

10 × 10 cm² APERTURE 1 Hz REPETITION RATE X-RAY PREIONIZED-DISCHARGE PUMPED KrF EXCIMER LASER

H. Mizoguchi[+], A. Endoh, J. Jethwa, and F. P. Schäfer

Max-Planck-Institut für biophysikalische Chemie, Abteilung Laserphysik,
Postfach 28 41, D-3400 Göttingen, Fed. Rep. Germany

Abstract

A 10 × 10 cm² aperture X-ray preionized discharge-pumped KrF excimer amplifier for subpicosecond pulse amplification is demonstrated experimentally in the oscillator mode operation. A fast pulse-forming line (36 nF, 340 kV) together with a peaking capacitor (6 nF) switched with a rail-gap switch, and collimated X-ray preionization is employed to obtain a wide and uniform discharge. The active cross section of the laser beam is about 10 × 8 cm² and the intense plateau region is about 10 × 5.5 cm². The laser pulse energy exceeds 4.7 J in a 28 ns pulse (FWHM).

1. Introduction

Recently wide aperture excimer lasers have been used as amplifiers in several high power short pulse generation systems.[1,2] It is also known that the properties of KrF amplifiers are remarkably better than that of XeCl amplifiers in the short pulse (subpicosecond) region.[3] From the point of primary requirements for a subpicosecond amplifier, uniform gain, wide aperture, medium gain (~5 % · cm^{-1}), medium gain window (~30 ns), medium repetition rate (~1 Hz) with KrF excimer is desirable.

Up to now most of the wide aperture (more than 10 × 10 cm²) KrF excimer lasers have used E-beam excitation instead of discharge excitation because of scalability and high homogeneity. However, discharge excitation has some significant advantages, namely high repetition rate, compactness, easy maintenance and ease of operation. The discharge pumping power is limited by the laser head inductance, therefore the scalability of discharge-pumped excimer lasers is limited. Especially in the case of discharge-pumped KrF excimer lasers, the requirement of pumping power for operation is higher than that of XeCl excimer lasers. Hence the discharge-pumped wide aperture KrF excimer laser is more difficult to realize than the XeCl excimer laser. As far as we know a 10 × 10 cm² full aperture discharge-excited KrF excimer laser has not been achieved as yet.

Our group has already developed a 6 × 5 cm² discharge-excited excimer laser.[4] We have now realized a 10 × 8 cm² active aperture discharge-pumped KrF excimer laser for a subpicosecond pulse amplifier. We employed a fast pulse-forming line together with a peaking capacitor switched with a rail-gap switch and used collimated X-ray preionization to realize the wide aperture discharge. We report here the experimental results of this device in the oscillator mode operation.

Present Address :
[+] Komatsu Ltd., Manda 1200, Hiratsuka-shi, Kanagawa 254, Japan

2. Experimental System

This wide aperture KrF amplifier system is shown in Fig. 1. The laser head is mounted on the top of a deionized water tank. Rod-edge rail-gap switch, pulse-forming line and peaking water capacitor are situated inside the tank. The compact X-ray preionizer is mounted on the top of the laser head. The total height is about 250 cm and the foot-print is 140 cm × 80 cm. The device is supported by a water and gas management system and a Marx-bank to enable 1 Hz operation.

Figure 2 is a block diagram of the subpicosecond wide aperture amplification system and each of these elements will be described in the following sections in detail. In these experiments we have used only the parts sketched by solid lines. We will use parts shown by dashed lines for amplification experiments to realize precise synchronization together with other systems.

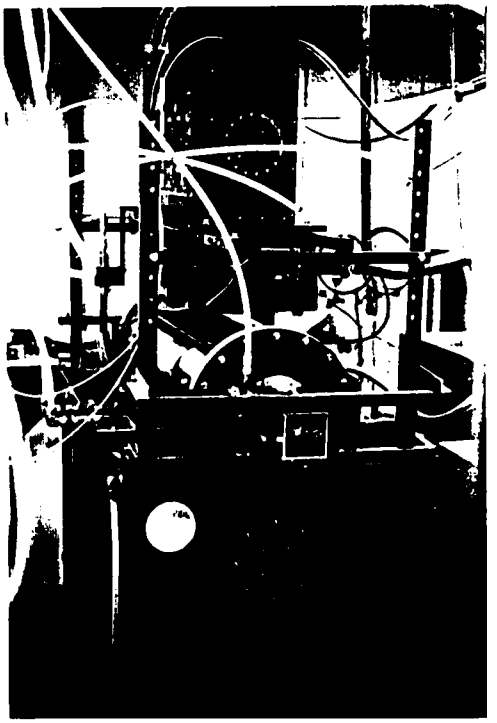


Fig. 1 X-ray preionized KrF laser

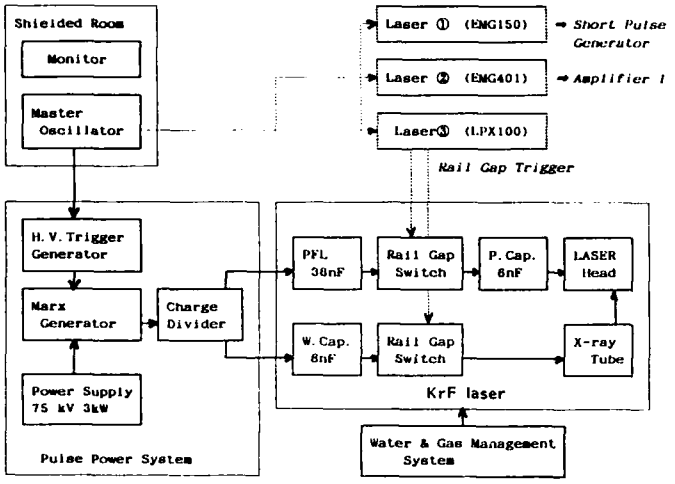


Fig. 2 System block diagram of laser device.
Solid line: Oscillator mode experiments
Dashed line: Amplifier mode experiments (scheduled)

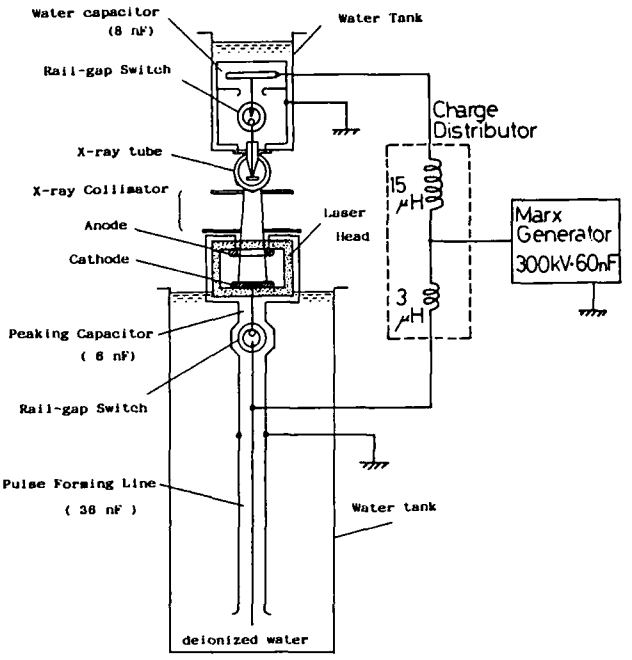


Fig. 3 Schematic of laser, pulsed power, and X-ray preionizer

3. Pulsed Power

The laser schematic is shown in Fig. 3. The double parallel-plate PFL for the main discharge (0.4 Ω, 36 nF) and water-capacitor for the X-ray gun (8 nF) are negatively pulse-charged simultaneously by a Marx generator through an inductive charge distributor. With this single primary energy storage design, we realize a very simple and compact laser system.

The primary energy storage source is a 5-stage Marx generator with a maximum repetition rate of 1 Hz with SF_6 gas isolation. It consists of five 300 nF capacitors and each capacitor can be dc-charged up to 75 kV. After charging, the X-ray gun is triggered by a multichannel rail-gap switch[5] and the discharge region in the laser head is thus preionized by the collimated X-ray emission. After approximately 100 ns from firing the X-ray gun, a second rail-gap switch for the main discharge is triggered. The charge stored in the PFL is transferred to a peaking water capacitor (6 nF). The main laser discharge now starts in the preionized region. The timing between the two rail-gap switches can be changed with the operational pressure of the switches and inductance ratio of the inductive charge distributor.

In the oscillator mode experiments, precise synchronization is not necessary, so we operate the rail-gap switches in the self-breakdown mode using edge-rod geometry electrodes. For 340 kV PFL switching, we use 3.7 bar N_2 gas. The number of spark channels is 4 ~ 5, the distance between edge and rod is 30 mm and the jitter of the rail-gap switch is less than 20 ns. Laser trigger[6] is preferred to reduce the jitter for amplification experiments as shown in Fig. 2 with dashed line.

4. X-Ray Preionizer

The X-ray preionizer schematic is also shown in Fig. 3. The basic design of this tube originated from reference.[7] The X-ray tube is made from 5 mm thick aluminum tube of 150 mm diameter. It uses a transmission geometry with a Ta foil anode and 2 × 40 cm carbon-felt cold-cathode. The cathode is held by three parallel high voltage feed-throughs and the distance between the cathode and the anode is 15 mm. The tube is connected to the secondary energy storage water capacitor (8 nF) which is charged by the Marx generator through the inductive voltage distributor described in section 3 and switched by a rail-gap switch. For 300 kV water-capacitor switching, we use 4.0 bar N_2 gas, the number of channels is again 4 ~ 5, distance between edge and rod is 23 mm and the jitter of the rail-gap switch is less than 20 ns. The typical X-ray dose with the water capacitor charged to 300 kV is about 1 R at the top of the laser head which is situated 16 cm away from the X-ray gun anode.

5. Laser Head

The cross section of the laser head is shown in Fig. 4. The housing is made of 5 mm thick PVDF and an outer layer of 30 mm thick glass-fiber-enforced epoxy. The anode is a 1 mm thick aluminum plate spot-welded onto a frame to avoid X-ray absorption in the anode. The cathode is made of solid brass with nickel coating. Both electrodes have the modified Chang profile. The effective length of the electrodes is 50 cm and the central distance between them is 10 cm. The active region width is determined by collimating the X-ray emission with two lead apertures.

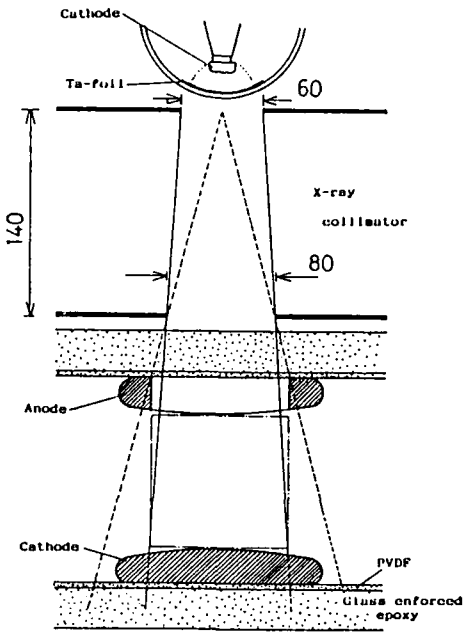


Fig. 4 Cross section of laser head and collimated X-ray preionization

The windows are made of CaF_2 with a diameter of 14 cm and 15 mm thickness. The rear mirror is a dielectric total reflection mirror. For the front mirror we use the reflection from the front window and the additional reflection from one uncoated suprasil plate.

The laser gas and the rail-gap gas are circulated through heat exchangers and filters by the water and gas management system to facilitate 1 Hz repetition rate operation.

6. Results and Discussion

The laser was operated with a gas mixture of 4 mbar F_2, 160 mbar Kr, and 4000-4500 mbar Ne. The output voltage of the Marx-bank is between 150 and 300 kV. In case of 275 kV Marx output, the stored energy in the PFL is about 2.0 kJ at 337 kV and in the X-ray storage capacitor it is about 0.36 kJ at 300 kV, repectively. Typical charging time of the PFL is about 800 ns.

The output energy was measured by a pyroelectric detector (Gentec ED-500). The maximum obtained laser energy was 4.7 J/pulse at a total pressure of 4500 mbar and 275 kV Marx output.

The photographs shown in Fig. 5a,b are the fluorescence image on a scaled white paper. These two pictures were taken with open shutter and different F-number aperture. The scaled paper was kept 40 cm away from the output window. Figure 5a shows that the cross section of laser output is about 10 cm × 8 cm. Figure 5b with less exposure shows that the intense plateau region is about 10 cm × 5.5 cm. The beam profile shown in Fig. 5c was taken by using thermo-sensitive paper. There the image shows a beam cross section of about 10 cm × 6.5 cm and an intense plateau of about 10 cm × 5.5 cm. The difference between these two methods arises from the different threshold behavior of the two methods.

The temporal profiles of (a) the X-ray preionization, (b) the laser head voltage, (c) the discharge current, and (d) the laser emission are shown in Fig. 6 at 250 kV Marx output. The X-ray emission was measured by a PIN diode (UDT pin 10) protected with a thin aluminum foil from visible light. The voltage was measured by combination of a $CuSO_4$-solution voltage divider and a resistor voltage divider.[8] The current wave form was measured by a current-viewing resistor of 0.0025 Ω (T&M Research Products Model No. W2K4-6.5S-0025). The optical output was measured by a vacuum photodiode (Hamamatsu R1193U-01). All signals were recorded on a 6 GHz digitizing oscilloscope (Tektronix 7250) in a shielded cabin.

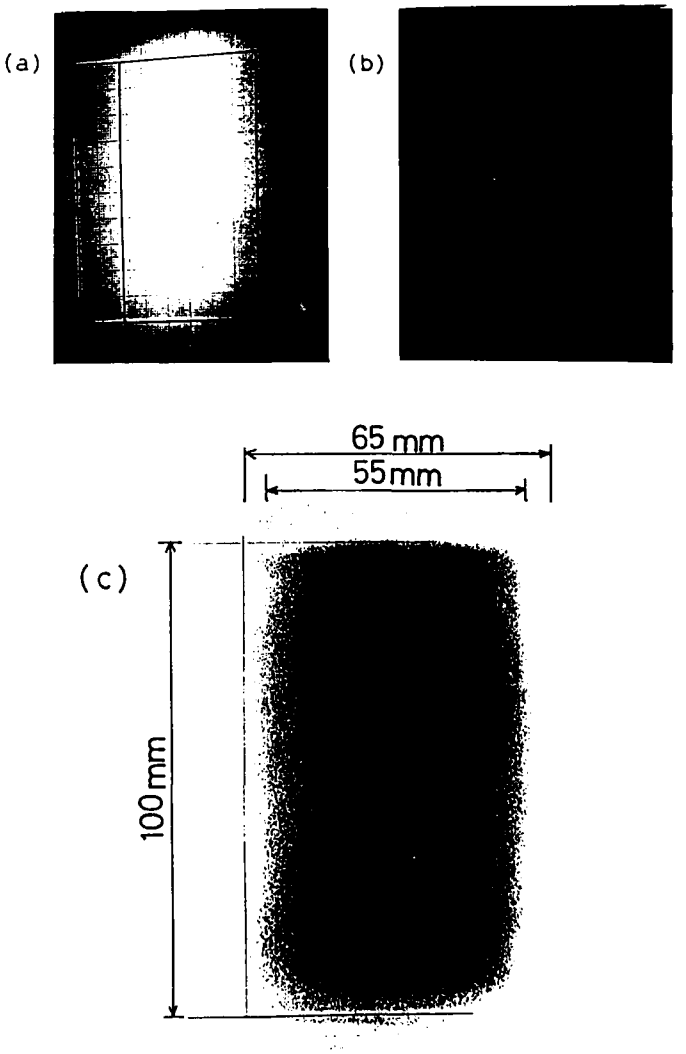


Fig. 5 Observations of laser beam (a) photograph of fluorescence image on scaled white paper, (b) smaller aperture of photo lens than (a), (c) beam image on thermo-sensitive paper. In case of laser gas total pressure 4 bar, N_2 gas pressure in main rail-gap-switch 3 bar and in X-ray rail-gap-switch 3.5 bar, and output voltage of Marx-bank 250 kV.

The temporal profile of the X-ray emission measured by a PIN diode covered with an aluminum foil is shown in Fig. 6a. The pulse width is 80 ns (FWHM) with rise time about 20 ns (10-90 %). The X-ray preionization starts about 120 ns earlier than the main discharge. The voltage waveform in Fig. 6b shows a fast ringing caused by the peaking capacitor and the inductance of the laser head. The inductance of the laser head calculated from the ringing period of 86 ns and peaking capacitance (6 nF) is about 33 nH including the laser head and peaking capacitor itself. The breakdown voltage on the laser head is 175 kV. The current waveform (c) shows three peaks. However, the discharge voltage is terminated after the second peak. So the effective pumping is obtained only at the first current peak (~100 kA) transiently. The electrical pumping power at the first current peak is about 6.3 GW (1.6 MW/cm^3). The current rise time (10-90 %) is 18 ns. The laser output (d) shows a simple single peak waveform. The pulse width of the laser is 28 ns (FWHM). The measured discharge with high spatial uniformity and wide aperture is partially due to fast current rise time. The discharge width was observed to decrease with reduced current risetime.

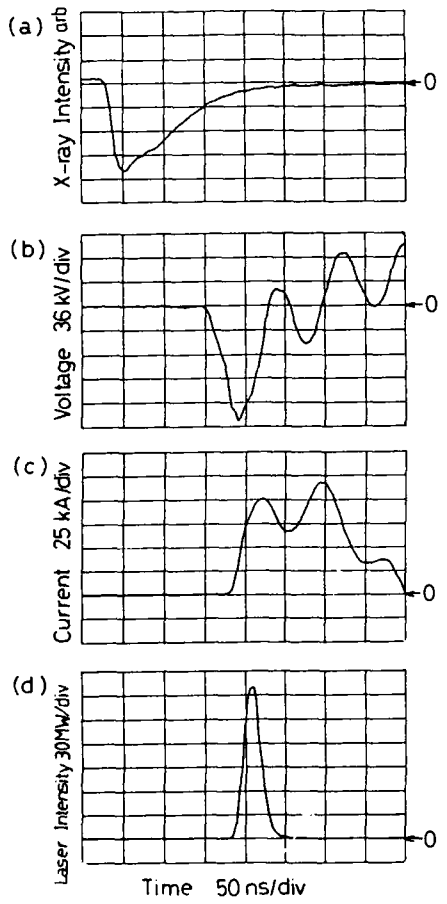


Fig. 6 Typical pulse shapes (a) X-ray preionizer intensity, (b) the electrode voltage, (c) discharge current, and (d) laser light intensity in case of laser gas total pressure 4 bar, N_2 gas pressure in main rail-gap-switch 3 bar and in X-ray rail-gap-switch 3.5 bar, and output voltage of Marx-bank 250 kV

7. Conclusion

In conclusion, we have demonstrated a reasonable uniformity of intensity over the cross section of a discharge-pumped KrF laser using a fast pulse-forming line together with a peaking capacitor switched with a rail-gap switch and collimated X-ray preionization. The active cross section of the laser beam is about 10 × 8 cm^2 and the intense plateau region is about 10 × 5.5 cm^2. The laser pulse energy exceeds 4.7 J in a 28 ns pulse (FWHM). Finally we show the overview of the data of this system in Table 1.

We are preparing 1 Hz operation experiments and soon we shall use this laser device as an amplifier for subpicosecond pulse amplification experiments.

8. Acknowledgements

The authors are indebted to Dr. B. Rácz for his help and advice in the early stage of the construction and also to Dr. M. Steyer for his suggestions for the basic design of the X-ray preionizer. One of us (H. Mizoguchi) acknowledges a research scholarship from Komatsu Ltd. This work has been supported by the "Bundesministerium für Forschung und Technologie" and by the "Deutsche Forschungsgemeinschaft" through its Leibniz program.

9. References

1. A. Endo, M. Watanabe, N. Sarukura, and S. Watanabe, Opt. Lett. 14, 353 (1989)
2. C. R. Tallman, A. J. Taylor, J. P. Roberts, C. S. Lester, and T. R. Gosnell, *TUJ46, CLEO '89* (1989)
3. S. Szatmári and F. P. Schäfer, J. Opt. Soc. Am. B 4, 12 (1987)
4. B. Rácz, M. Steyer, H. Mizoguchi, and F. P. Schäfer, Opt. Quant. Electronics (to be submitted)
5. A. Endo, S. Watanabe, and M. Watanabe, J. Appl. Phys. 55, 1322 (1984)
6. R. S. Taylor and K. E. Leopold, Rev. Sci. Instrum. 55, 52 (1984)
7. M. Steyer, J. Phys. D (in press)
8. W. J. Sarjeant and A. J. Alcock, Rev. Sci. Instrum. 47, 1283 (1976)

Geometrical cross section	10 × 10 cm^2
Repetition rate	1 pps*
Laser energy	4.7 J (PFL 340 kV charging)
Pumping power	2 MW/cc (PFL 340 kV charging)
Small signal gain	3 %/cm**
Laser pulse width	28 ns (FWHM)
Laser Head	
Active length	50 cm
Active cross section	10 × 8 cm^2 (plateau 10 × 5.5 cm^2)
Active volume	4 liters
Gas pressure	4 bar (F_2 4 mbar, Kr 160 mbar, Ne rest)
Head inductance	33 nH
Breakdown voltage	175 kV
Sustaining voltage	50 kV
Sustaining current/impedance	150 kA/0.4 Ω (PFL 340 kV)
Rail Gap Switch (main)	
Switch voltage	170 - 340 kV
Working gas	N_2/1 - 5 bar (abs.)
Repetition rate	1 pps*
Trigger	ArF laser (>10 mJ)*
Jitter tolerance	<5 ns (self-breakdown mode ≤20 ns)
Water Capacitor (main)	Pulse forming line/peaking capacitor
Capacitance	36 nF/6 nF
Transit time	48 ns/5 ns
Impedance	0.4 Ω/0.4 Ω
Preionization	X-ray (cold cathode type)
Repetition rate	1 pps*
Operation voltage	≤300 kV
Storage capacitor	Water capacitor/8 nF
Switch	Rail gap switch
Primary Energy Storage	5 stage Marx generator
Charging voltage	75 kV/stage
Stored energy	4.2 kJ/60 nF
Insulation	SF_6 gas
Repetition rate	1 pps

Table 1. Overview of KrF Amplifier

* scheduled ** estimated value

CONDENSED PHASE RARE GAS HALIDE EXCIPLEX LASERS

V. Ara Apkarian
Professor of Chemistry
Department of Chemistry
University of California
Irvine, California 92717

Abstract

XeF doped solid argon constitutes the first solid state exciplex laser in which lasing action over the B→X, C→A, and D→X bands have been demonstrated. The results of these studies are summarized. Generalization of principles to other members of the large family of condensed phase exciplexes is considered. Ternary X:Rg:Rg' solids in which the diatomic exciplexes can be isolated, should all behave as ideal four level lasers. The same is also expected for X:Rg binary solids in which the $Rg_2^+ X^-$ exciplexes form. However, experimental studies detailed for the case of Kr_2F, indicate that transient adsorption losses may prevent lasing. The prospects of high temperature, supercritical fluids or ultra high pressure solids, as broadly tunable sources is discussed.

I. Introduction

Research in the field of condensed phase excimer and exciplex lasers has a long history. The first successful excimer laser, Xe_2^*, was demonstrated by Basov and coworkers by electron beam pumping of liquid Xe.[1] This led to a frenzy of activity in excimer laser development, which resulted in the well established science and technology of gas phase rare gas halide exciplex lasers.[2] Research in the development of electron beam pumped liquid phase lasers continues, and in addition to Xe_2^* and Kr_2^*, XeO dissolved in liquid Ar has been reported by Loree and coworkers.[3] The prospects, and promises of solid state excimer lasers had been realized early on.[4] However, while tremendous insight has been obtained in the excitonic dynamics of rare gas crystals, and very large excited state number densities have been achieved, the development of electron beam pumped solid state rare gas lasers have not lived up to their promise.[5] Optical pumping schemes of condensed phase systems have only recently been considered. In the liquid phase, efficient lasing was demonstrated on the XeF (B→X) band by optical pumping of solutions of F_2 and Xe dissolved in liquid Ar.[6] The first solid state, optically pumped exciplex lasers, were most recently demonstrated at Irvine in the same system.[7,8] In addition to the XeF (B→X) transition, laser action was demonstrated on both the XeF (C→A)[7] and XeF (D→X)[8] transitions in free standing crystals of argon. In this paper I will first summarize the results of those demonstrations, and consider the prospects and possible problems associated with the generalization of principles to the entire family of rare gas halide exciplexes.

II. Solid State XeF Laser

The pair interactions between halogen atoms, X, and rare gas atoms, Rg, are well understood in isolation, in the gas phase.[2] The ground state potentials between $X(^2P_{3/2}, ^2P_{1/2})$ and an $Rg(^1S_0)$ atoms lead to the three surfaces, X ($\Sigma_{1/2}$) and A ($\Pi_{3/2}$, $\Pi_{1/2}$), which are dominated by dispersive interactions. Deep, Coulombically bound potentials arise from the interactions between Rg^+ ($^2P_{3/2}$, $^2P_{1/2}$) and X^- (^1So) ions, namely the B ($\Sigma_{1/2}$), C ($\Pi_{3/2}$) and D ($\Pi_{1/2}$) surfaces. This general scheme, which is strictly valid for diatomic interactions, is illustrated in figure 1, and an experimental emission spectrum is shown for XeF doped crystal argon. In the spectrum, the D→X, D→A, B→X, and

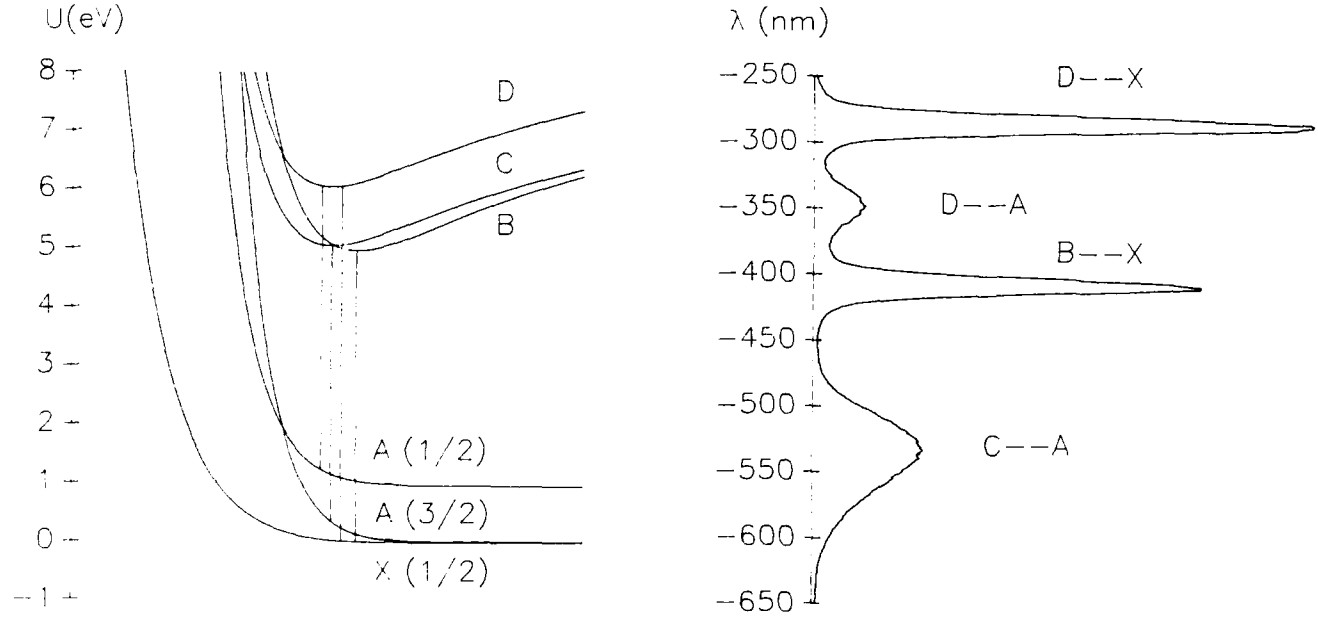


Figure 1: The lowest energy pair potentials for diatomic RgX are shown in the left panel (parameters for XeI are chosen since all six potentials are visible on the same energy scale). The vertical tie lines indicate the strongest transitions between the ionic and covalent manifolds. All of these transitions can be seen in XeF doped solid argon, as shown in the right hand panel.

C→A bands of XeF, at 286, 360, 411 and 540 nm are clearly identified. With gated, delayed detection, the C→X emission at 408nm, can also be seen (not shown). Beside some minor matrix perturbations, the most obvious and general of which is a large spectral red shift, the gas phase pair potentials are quite adequate for the interpretation of these spectra. The parentage of this solid state spectrum cannot be mistaken, in the case of XeF the argon host acts as an inert dielectric medium. As such, all of the characteristics that make XeF an ideal gas phase laser are to be expected to be preserved. Moreover, there are now several new attributes gained, that make the solid state exciplexes particularly attractive for laser applications. Chief among these are the much higher number densities attainable in solids without introducing any nonradiative decay channels for the exciplexic state. The packing density of solid argon is 3×10^{22} cm^{-3}. Therefore even at a dilution of 1:1000, which is sufficient for isolation of dopands, exciplex number densities nearly three orders of magnitude higher than those obtained in standard gas phase lasers are possible. We have also verified, that at these number densities the B, C and D states relax strictly by radiation. Moreover, when the D state is accessed directly, negligible population flows to the lower states by intersystem crossing.

XeF doped Ar crystals are grown in an insulating mold in contact with the cryotip, by deposition of an Xe:F_2:Ar premixed gas sample at a backing pressure of ~200 Torr. Molecular fluorine is subsequently photodissociated in situ, and the F atoms are allowed to migrate and trap at Xe sites. The details of this process are the subject of both theoretical and experimental investigations, and are only now becoming understood.[9,10] For the present, suffice to note that F atoms are quite photomobile in the bulk of Ar, however, they trap at Xe sites due to the XeF(X) potential which is much deeper than ArF(X). As a result, stoichiometric samples of XeF/Ar are possible to prepare, in the form of optically clear free standing polycrystals.

The first laser demonstrations were performed by longitudinal pumping of such a crystal, along its 6mm thickness, through the dichroic cavity mirrors. The flat cavity mirrors, were mounted inside the vacuum shroud of the cryostat. Laser action on both the B→X and C→A transitions were obtained when the crystal was pumped at 351 nm. Spectral collapse, temporal collapse, small signal amplification and gain saturation measurements were conducted to characterize the medium. Characterization of the D→X transition was conducted in a similar geometry, however in the absence of cavity mirrors. This system was therefore characterized by its superradiant spectral collapse. The following conclusions were derived in those first demonstration studies:

- Ideal four level laser behavior.
- High gain: Gain, in excess of 100 cm^{-1}, could be demonstrated on the B→X and C→A bands, and 7 cm^{-1} demonstrated on the D→X band.
- Broad tunability: the C→A band was shown to be broadly tunable by observing small signal amplification of greater than 100% over a 70nm bandwidth in the green.
- High efficiency: optical quantum conversion efficiencies greater than 30% were realized.
- High energy density: extractable energies in excess of 50 KJ/L were established.
- High damage thresholds: optical pumping damage thresholds near 300 MW cm^{-2} were established.

None of these parameters should be regarded as optimized, in fact many of them have recently been surpassed in recent transverse pumping geometries. As an example, a gain coefficient of ≥ 40 cm^{-1} has been reached for XeF (D→X).[11] These demonstrations serve the purpose of illustrating the potential of solid state exciplex lasers. Given the fact that XeF/Ar is but one of the large family of rare gas halides, the generalization of principles becomes a very important issue.

In what follows, the known photodynamics of condensed phase rare gas halides, as they relate to laser applications, will be discussed. An emphasis is placed on the possible sources of deviation from the ideal behavior exemplified above.

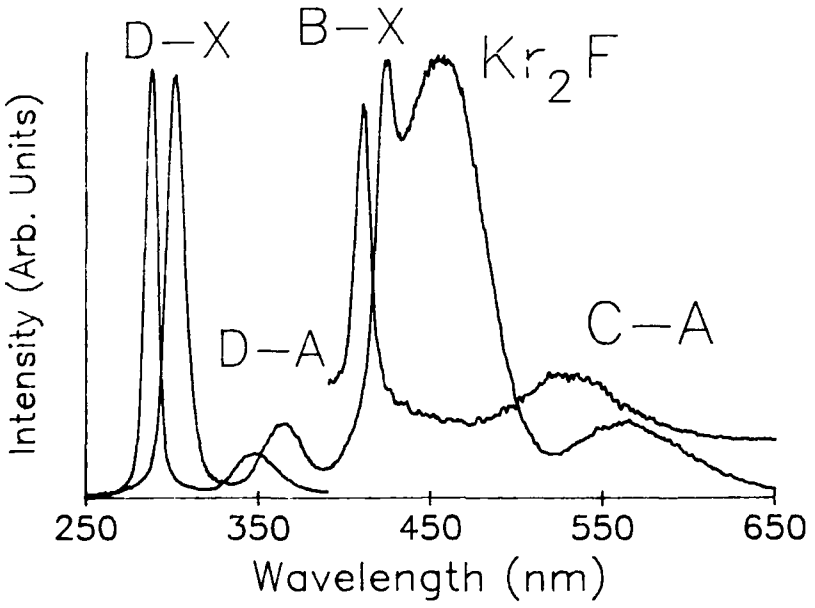


Figure 2: Emission spectra of XeF trapped in solid Ar and Kr are shown superposed. All of the diatomic emissions are present in both with nearly identical profiles, however, in all cases the bands in Kr are red shifted relative to the bands in Ar. The broad peak at 452 nm is assigned to Kr_2F. The latter is the only emission in binary F/Kr solids.

a) Ternary Solids

The most direct extrapolation of the XeF/Ar results, is the consideration of other X:Rg:Rg' ternary mixtures, in which the diatomic exciplexes can be isolated. In fact by simply changing the host from Ar to Kr, the solid state XeF emission bands can be significantly shifted. This is shown in figure 2, in which all of the diatomic emission bands can be seen to shift to longer wavelengths (by as much as ~30 nm for the C→A band). The photodynamics of XeF/Kr is nearly identical to XeF/Ar and expected to be as ideal a laser candidate.

A rather different situation prevails in the case of F:Kr:Ar solids. As shown in figure 3, in such a solid the KrF (B←X) vibronic progression is observed with a vibrational frequency and anharmonicity, within experimental error, identical to that of the gas phase KrF(B). However, in the emission spectrum, a single broad band is observed, which can be identified as the $(ArKr)^+F^-$ mixed triatomic exciplex. The relaxation from KrF(B) to $(ArKr)^+F^-$ has been determined to occur on a timescale of 20 fs $< \tau <$ 500 fs. The latter relaxes radiatively with a lifetime of 60 ns. This example clearly establishes the fact that not all diatomics can be isolated in condensed media, and the energetics of mixed triatomics are not well enough established to predict with certainty which exciplexes can be isolated. The diatomic KrF can for example be isolated in solid Ne. We note however, that the condensed phase triatomic exciplexes are themselves, at least in principle, ideal laser candidates. The photodynamics of these species are best studied in binary solids.

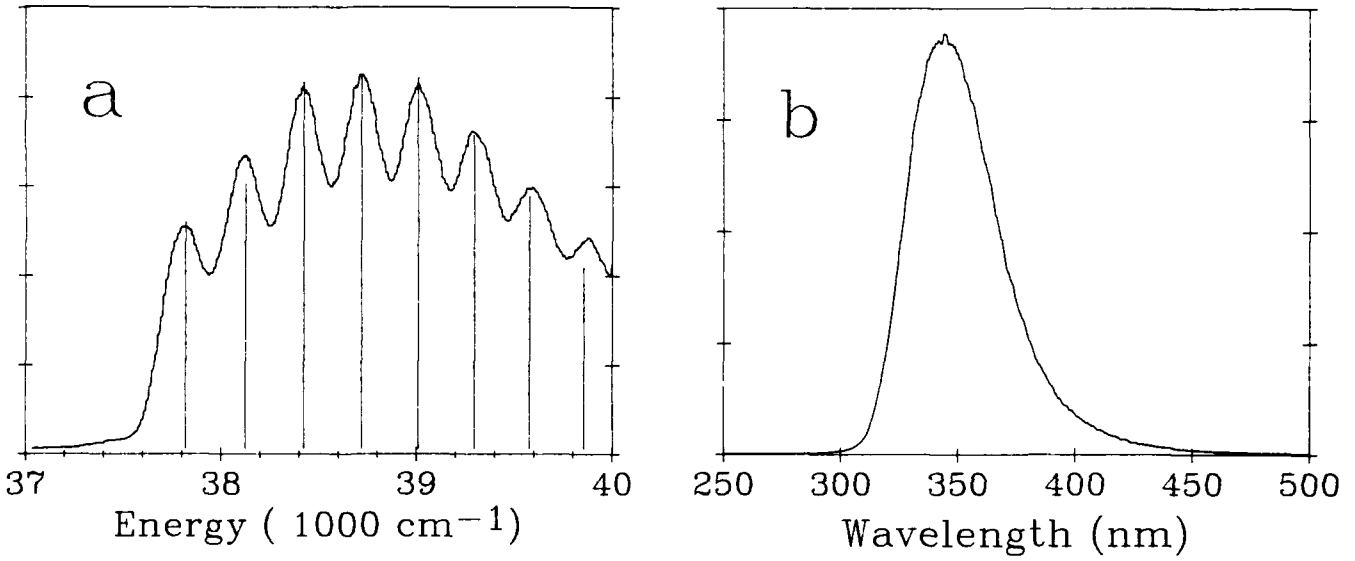


Figure 3: Excitation (a) and emission (b) spectra from an F:Kr:Ar solid. The excitation spectrum shows the KrF (B ← X) vibronic resonance with $\omega_{e'} = 309 \pm 10$ cm^{-1} and $\omega_e\chi_{e'} = 2.28 \pm 0.8$ cm^{-1}, which, within experimental error, are identical to those of KrF (B) in the gas phase. The emission spectrum shows a single broad band assigned to $(ArKr)^+F^-$ (see ref. 10).

b) Binary Solids

The charge transfer photodynamics of halogen atom doped solid xenon has been extensively studied in the past.[12] We have also investigated the spectroscopy of solid Kr doped with all atomic halogens, and F doped solid Ar. In all cases, optical excitation near the diatomic B←X origin leads to a single broad band emission, which can be ascribed to the $Rg_2^+X^-(4^2\Gamma)$ state. Spectra of the solid state Kr_2X (X = F, Cl, Br, I) are shown in figure 4. The gas phase diatomic terminology, is inadequate for the description of the vertically accessed charge transfer states in such solids. The molecular states should now be expanded in the symmetry group of the trap site (O_h for most systems) and charge delocalization effects should be taken into consideration. It has for example been shown that the vertically accessed charge transfer states in Xe correspond to a Rydberg progression of hole states,[13] while in Kr, the hole state are delocalized among nearest neighbors only.[10] In all cases, however, these optically accessed states relax on a subpicosecond timescale to the most stable charge transfer configuration, namely the localized molecular triatomic exciplex, $Rg_2^+X^-(4^2\Gamma)$, and the latter relaxes radiatively over a bound to strictly repulsive transition. Thus, a four level laser description well represents the photodynamics of these lower states, see figure 5.

Among the many attractive features of these systems as laser media, are a) the broad emission bands over which continuous tunability would be expected, b) the wide spectral coverage attained by the different X:Rg combinations. Tunability of a given Rg_2X emission band by density (or equivalently, pressure) is another attractive feature. Due to the large dipole of the exciplexic state, polarization of the dielectric medium lowers the upper state. Another important consideration, is that under relatively moderate pressure, all rare gases become solids at room temperature. These two considerations are summarized by the density dependent lineshift of Xe_2Cl shown in figure 6. The data span gas, fluid, liquid and solid phases, and the pressure ranges from 0.01 bar to 100 Kbar. The highest density results are for room temperature solid xenon. It is impressive to note that in the range studied, the band maximum shifts by more than 1eV, while the band profile remains nearly constant (fwhm = 2200 cm^{-1}).

Despite these rather exciting possibilities, there has not yet been a successful demonstration of a condensed phase triatomic rare gas halide laser. In our own attempts on several systems, both liquid and solid, we have identified possible sources of deviation from the ideal behavior described above. These are discussed next.

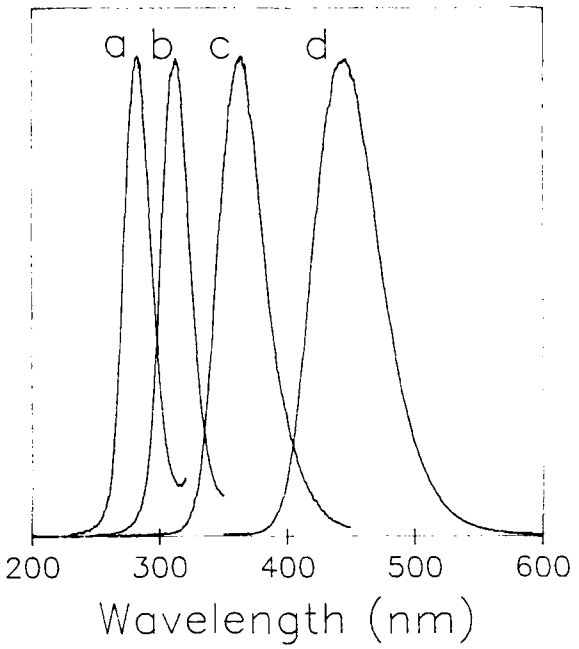


Figure 4: Emission spectra of triatomic exciplexes in solid krypton, a)Kr_2I, b) Kr_2Br, c) Kr_2Cl, d) Kr_2F.

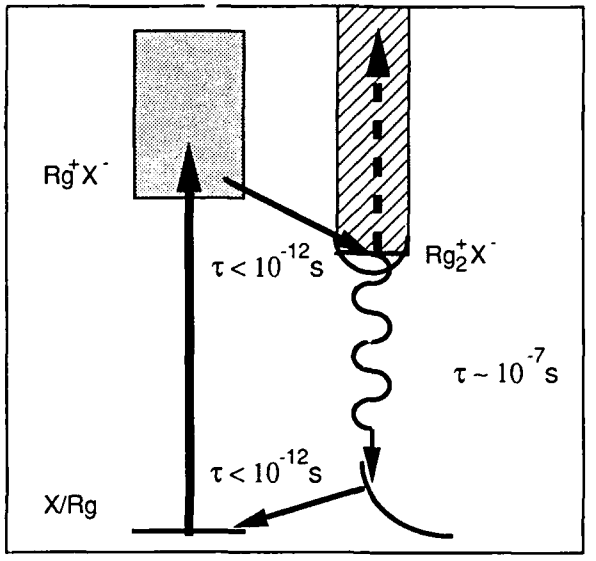


Figure 5: Four level laser scheme, applicable to binary X/Rg solids. The pump transition is the Rg-X charge transfer absorption. The interconversion from the Franck-Condon accessed vertical states to the triatomic configuration proceeds on a timescale shorter than 10^{-12}s. The triatomic exciplex relaxes radiatively to the repulsive wall of the ground state. The dashed arrow represents a possible reabsorption loss channel. The gray and hatched blocks represent the diatomic and triatomic ionic manifolds.

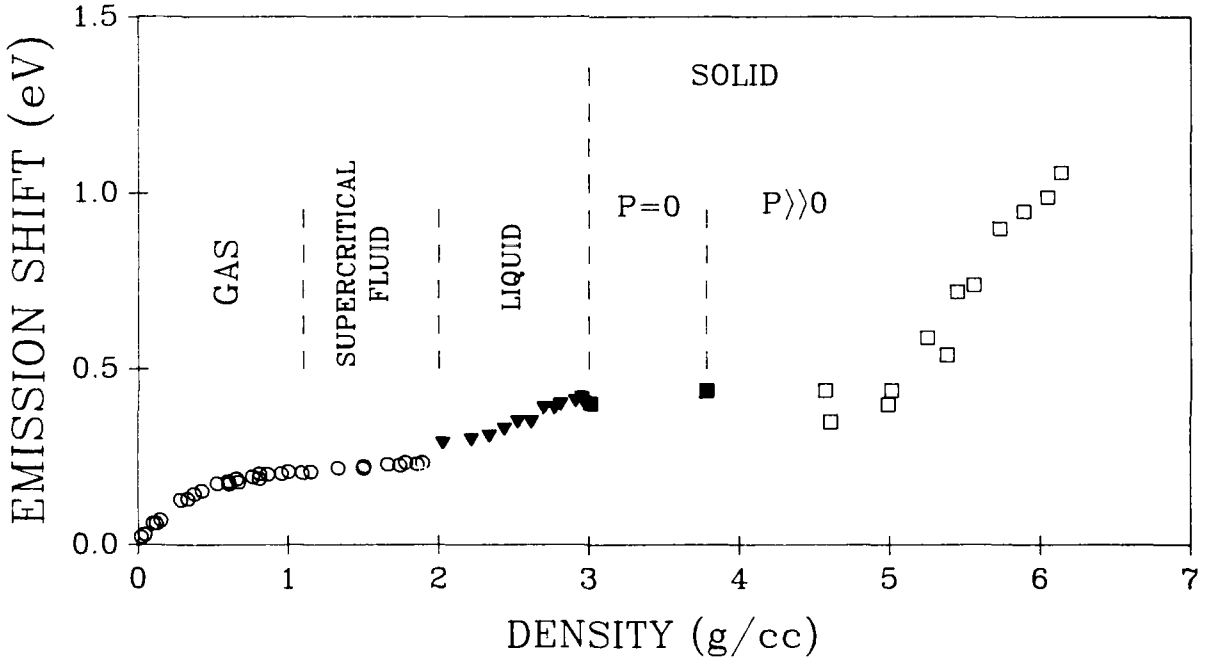


Figure 6: Spectral shift of Xe_2Cl emission as a function of Xe density. On the ordinate, the shift of the emission band maximum relative to its zero pressure value of 479nm is plotted. Open circles = room temperature gas/fluid phase data spanning a pressure range of 50 Torr-150 atm, (see reference 14). Filled triangles = liquid phase data spanning a temperature range from 220K to 160K, (see ref. 15). Filled squares = cryogenic solid spanning a temperature range of 160K - 12K. Open squares = room temperature ultra high pressure solid, P = 10 - 100 Kbar, (see reference 16).

c) Liquid/Fluid Phase Dynamics

The photodynamics of rare gas halide exciplexes in liquid, or supercritical fluid rare gases, is not substantially altered from that of the solid state behavior described above. The main difference is now the existence of translation degrees of freedom. In all studied cases to date, the exciplexes are observed to relax by radiation in dilute solutions. The new non-radiative relaxation channel that is introduced in such systems, is diffusion controlled collisions with the molecular halogen donors (e.g. molecular halogens). At high enough densities, and dilutions, diffusion controlled encounter rates can be reduced such that within the radiative lifetime of the exciplexes this channel of relaxation becomes insignificant. This has been demonstrated in several cases in our laboratory, XeF in liquid Ar, Xe_2Cl[15] and Xe_2Br[17] in liquid Xe, and XeCl in supercritical Xe up to 150 atm,[14] are examples. In essence, in such systems the exciplexes can be isolated from each other, and from the halogen donor within their radiative lifetime. Therefore, given laerge enough exciplex densities, these high temperature media also qualify as efficient laser media. This point has already been well illustrated by the demonstration of the XeF laser in liquid Ar.[6] The key issue now is the devise of efficient methods for the photogeneration of high densities of exciplexes, and two-photon pumping schemes are the most profitable. A particularly efficient exciplex photogeneration scheme is that provided by coherent two-photon induced intermolecular charge transfer transitions, which has been shown to lead to the efficient photogeneration of exciplexes in condensed phases. This mechanism, which has been referred to as photo-induced harpooning, can be summarized as:[18]

$$Rg + X_2 + 2h\nu \rightarrow [Rg^+X_2^-] \rightarrow Rg^+X^- + X.$$

As in all two-photon transitions, the cross section of this intermolecular absorption can also be enhanced by intermediate state resonances. Moreover, the intermolecular charge transfer is usually followed by an efficient ejection of a neutral halogen out of the solvent cage, and at least in Xe, the resulting exciplex is shielded from back reactions by clustering with the polarizable solvent.[19] In binary solutions, as in binary solids, the diatomic exciplex interconverts to the lowest energy triatomic exciplex. Emission spectra of all the liquid phase xenon halides has previously been published.[20] Efforts in our laboratory in observing laser action in both liquid phase and supercritical xenon have benn unsuccessful. Instead of gain, transient loss is observed when the solutions are pumped by gas phase excimer lasers. The exact origin of the transient loss channel is subject to speculation at present.

d) Pump Probe Studies

Several possible sources of deviation from ideality exist in the photodynamics of condensed phase exciplexes. Of these, the two most important are: transient absorption and scattering losses due to shock waves created by the release of kinetic energy upon radiative dissociation of exciplexes. Both of these phenomena have been recently characterized in F doped solid Kr. The experimental geometry used in those experiments is illustrated in figure 7. The pump beam, coincident with F/Kr charge transfer absorption at 275 nm, is overlapped in the crystal with a probe beam coincident with the Kr_2F emission at 453 nm. The transmission of the probe is then monitored as a function of delay, and as a function of spatial displacement between the two beams. An example of such a measurement is provided in figure 7. Several types of scattering processes are observed as illustrated in figure 8. The generation of acoustic waves is one that is most easily verified by measuring the group velocity of the wave as a function of lateral displacement between pump and probe. Both ballistic and dispersive phonon propagation is observed. Under pump powers exceeding 300 MW cm^{-2}, permanent damage of the solid is also observed. While these phenomena may limit the extractable power from such lasers; they are not critical to its operation, since acoustic waves are temporally delayed from the time origin of the pump pulse. A prompt loss of probe transmission, the loss peak at t = o in figure 8, is more serious.

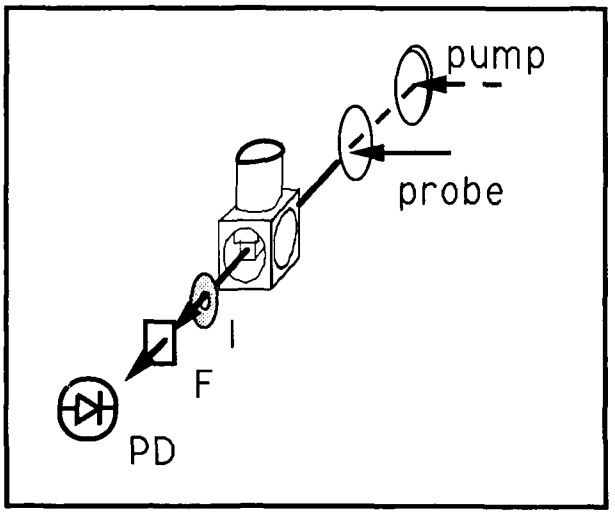


Figure 7: Experimental setup used in pump/probe studies. The probe transmission is measured with a fast photodiode (PD), after passing through an iris (I) and a filter (F) used to block the pump beam. Transmission as a function of temporal and spatial overlap between the two beams is measured.

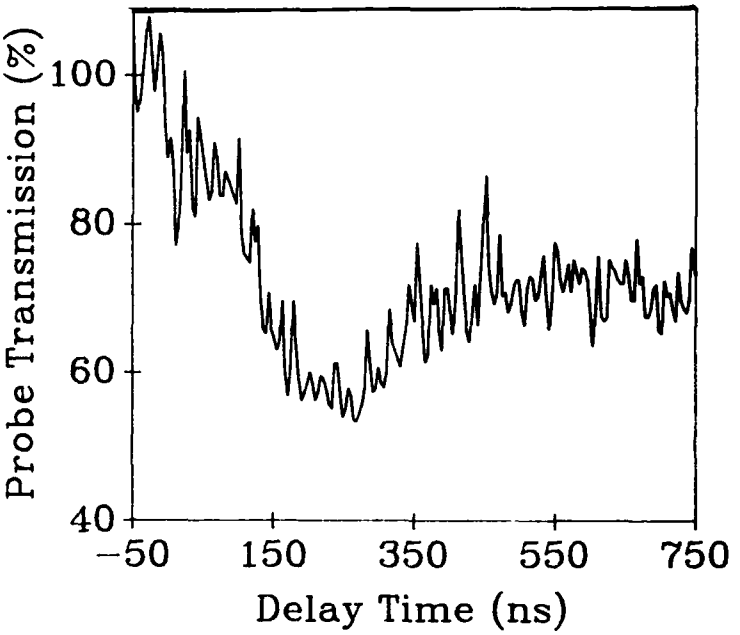


Figure 8: Transmission of the probe beam as a function of delay between pump and probe for an F/Kr free standing crystal. Negative time corresponds to probe preceding the pump. At t = 0, ~15% attenuation is observed and attributed to optical reabsorption by the exciplex (Kr_2F). The main loss at ~200ns, is due to scattering by acoustic waves. The relaxation of this wave is diffusive, and does not reach the baseline even after 750ns. A long longer lived relaxation (~2μs) is attributed to annealing of defects.

The latter is taken to be due to an optical process, namely a transient absorption by the exciplex itself. This same system has also been studied in the gas phase, and the transient absorption there is attributed to the $9\,^2\Gamma \leftarrow 4\,^2\Gamma$ transition of the triatomic.[21] The same absorption could also be operative in condensed media. Despite transient absorptions, several triatomic exciplexes have been made to lase in the gas phase.[2] However, we have failed to observe any stimulated emission in this system. In principle, the ionic manifold of the rare gas halide exciplexes could coalese in the dense media, such that the entire emission band is strongly reabsorbed. Whether this happens, and the generality of such absorptions in the different rare gas halides is not yet established. Our failure to observe spectral narrowing in several investigated systems -- Xe_2Cl, Xe_2Br, Kr_2F, Ar_2F -- would indicate that such an optical loss channel may be at work. An understanding of the spectroscopy of the upper ionic states of rare gas halides, seems crucial to the effective development of this large family of lasers.

IV. Future Outlook

While difficult to predict all of the exciting directions that research in condensed phase exciplex lasers may assume, it is possible to enumerate some of the most obvious, worthwhile directions of pursuit. Whether in diatomics, or triatomics, resorting to the lighter rare gases and heavier halogens, could lead to the development of broadly tunable VUV-UV lasers. Resorting to high pressures, could lead to the development of high temperature condensed phase exciplexes, either in the form of supercritical fluids, or as high pressure, high temperature solids. Such systems e.g. room temperature solids would be truly, broadly tunable. Given the absence of pumping thresholds in these cryogenic bound-free lasers, the broad band of emission, and the low group velocity dispersion of rare gas solids, applications in ultrafast domains, either as lasers or amplifiers is an obvious target. For such developments to occur, a deeper understanding of both energetics and dynamics in these systems has to evolve.

V. Acknowledgements

I would like to acknowledge my coworkers in this rather exciting field of research. Prof. N. Schwentner, who spent a summer at Irvine, was the key contributor in the development of the first solid state exciplex laser. Several of my students, and postdoctoral coworkers have contributed to the understanding of photodynamics in condensed phase rare gas halides, among whom M.E. Fajardo, L. Wiedeman, F. Okada, J. Feld, H. Kunttu and Dr. A.I. Katz, have played a major role. The major support for this work has been provided by the U.S. Air Force Astronautics Laboratory, under contract F04611-87-K-024.

References

1. N.G. Basov, E.M. Balshov, O.V. Bogdankevitch, V.A. Danilychev, G.N. Kashinokov, N.P. Lantzor, and D.D. Khodankevitch, J. Lumin. 1,2, 834 (1970).
2. C.K. Rhodes, "Excimer Lasers", Topics in Applied Physics, vol. 30 (Springer-Verlag, Berlin, 1979).
3. T.R. Loree, R.R. Showalter, T.M. Johnson, B.S. Birmingham, and W.M Hughes, Opt. Lett. 11, 510 (1986).
4. J. Jortner, L. Meyer, S.A. Rice, and E.G. Wilson, J. Chem. Phys. 42, 4250 (1965).
5. H. Nahme, T. Kessler, R. Markus, M. Chergui, and N. Schwentner, J. Lumin. 40/41, 21 (1988).
6. M. Shahidi, H. Jara, H. Pummer, H. Egger, and C.K. Rhodes, Opt. Lett. 10, 448 (1985).
7. N. Schwentner and V.A. Apkarian, Chem. Phys. Lett. 154, 413 (1989).
8. A.I. Katz, J. Feld, and V.A. Apkarian, Opt. Lett. 14, 441 (1989).
9. R. Alimi, R.B. Gerber, and V.A. Apkarian, J. Chem. Phys., in press.
10. H. Kunttu, J. Feld and V.A. Apkarian, J. Chem. Phys., in press.
11. N. Schwentner, private communications.
12. M.E. Fajardo and V.A. Apkarian, J. Chem. Phys. 89, 4102, 4124 (1988).
13. N. Schwentner, M.E. Fajardo, and V.A. Apkarian, Chem. Phys. Lett. 154, 237 (1989).
14. F. Okada and V.A. Apkarian, J. Chem. Phys. (in press).
15. L. Wiedeman, M.E. Fajardo, and V. A. Apkarian, J. Phys. Chem. 92, 342 (1988).
16. A.I.Katz and V.A. Apkarian, (manuscript in preparation).
17. W. G. Lawrence and V. A. Apkarian, Israel J. Chem., (in press, 1990).
18. M. E. Fajardo, R. Whithnall, J. Feld, F. Okada, W. Lawrence, L. Weideman, and V. A. Apkarian, Laser Chem. 9 ,1 (1988).
19. F. Okada and V. A. Apkarian, J. Phys. Chem. 93, 1267 (1989).
20. L. Wiedeman, M.E. Fajardo, and V. A. Apkarian, in *Digest of International Quantum Electronics Conference* (Optical Society of America, Washington D.C., 1987), paper PD-16.
21. D.B. Geohegan and J.G. Eden, J. Chem. Phys. 89, 3410 (1988).

WIDEBAND TUNING EXPERIMENTS WITH AN INJECTION-CONTROLLED XEF (C→A) LASER

W.L. Wilson, C.B. Dane, S. Yamaguchi
Th. Hofmann, R. Sauerbrey and F.K. Tittel

Department of Electrical and Computer Engineering
Rice Quantum Institute
William Marsh Rice University
Houston, TX 77251-1892

Abstract

This paper reports on scaling experiments on an electron beam pumped XeF (C→ A) laser. Scaling from an active mode volume of 0.02 liters to 0.5 liters resulted in an increase in output energy from ~30 mJ to ~ 1J. Intrinsic efficiency was 1.5% with an output energy density of ~ 2 J/liter. Details of the tuning characteristics and spectral purity of the laser are reported.

Introduction

The XeF (C→ A) laser is an efficient, tunable source of radiation in the blue-green region of the spectrum (See **Figure 1**). Efficient operation of this laser system has been demonstrated over a wide range of electron beam excitation energy densities ranging from 250 kW/cm^3 to 12 MW/cm^3 [1-4]. When short pulse, high current density electron beam excitation is used, peak values of the small signal gain exceeds 3%/cm, which permits efficient operation under injection control. This leads to very narrow band, wavelength agile operation across the entire 450 nm to 530 nm band of operation for this device. Over the range from 470 nm to 510 nm, an output energy exceeding 1 J/ℓ has been achieved.

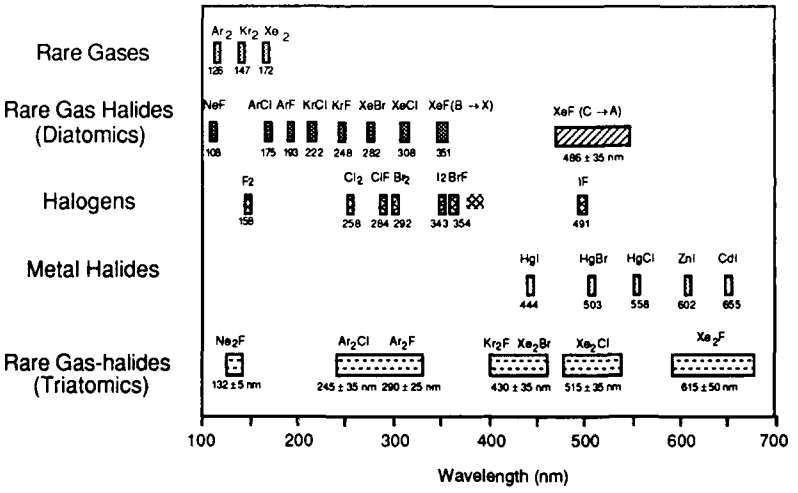


Figure 1. Spectral Characteristics of Excimer Transitions

Because the XeF (C→ A) laser operates in a gaseous medium, it is readily scalable to the high power and energies which would be required for remote sensing, materials processing, optical communications and the amplification of ultrashort pulses. This paper describes recent experiments on scaling of the XeF (C→ A) laser from a relatively small active volume of ~0.02 ℓ [5] to one of ~ 0.5 ℓ. A unique numerical model developed to aid in the design of the optical cavity for the scaled-up configuration is described, as well as re-optimization procedures for the five component gas mixture for operation under much longer gain lengths than were used in the small volume experiments.

Experimental Apparatus

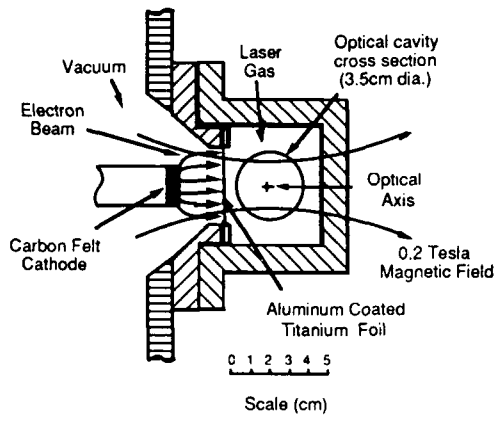


Figure 2. Cross Section of e-Beam Pumped Laser Cell

The XeF (C→ A) excimer laser was transversely pumped with a short (10 ns FWHM) high energy (650 keV) electron beam with a current density of about 150 A/cm^2. The electrons were emitted from a 50 cm × 2 cm carbon felt cathode, and entered the laser cell through a 25 μm thick titanium foil as shown in **Figure 2.** The peak current emitted from the cathode was about 80 kA. This electron beam generator was specifically designed for this application, and is capable of repetitive operation at up to 1 Hz. [6].

A 0.2 Tesla guiding magnetic field was used, and resulted in a three-fold increase in the electron beam current delivered at the optical axis. The spatial distribution of the energy deposited into the gas was measured with a radiachromic chlorostyrene film [7]. An average of about 150 J/ℓ was deposited along the 50 cm long optical axis, with ± 15 % variations. In the transverse direction, the energy varied with distance from the foil as would be expected from scattering and energy absorption by the 6.5 atmosphere argon gas mixture in the cell.

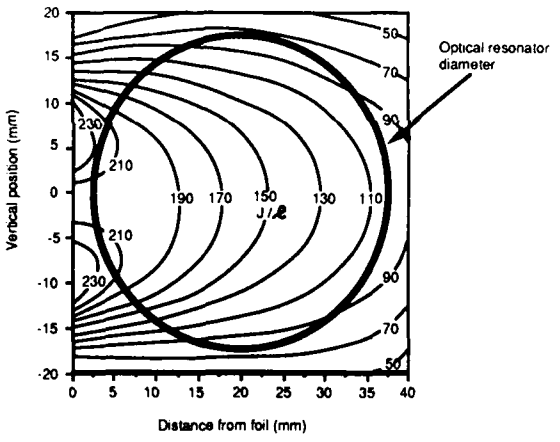


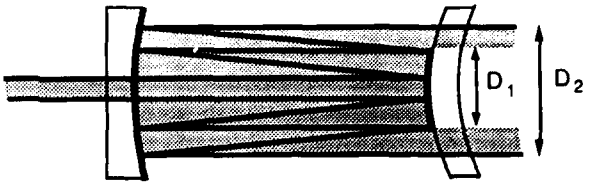
Figure 3 Contours of Energy Deposition Density within the e-Beam Pumped Cell

A contour plot of the spatial variation of the energy deposition through a cross-section of the cell is shown in **Figure 3.** The deposition energy ranged from over 200 J/ℓ near the foil to less than 100 J/ℓ at the back wall of the cell. Over the 3.5 cm diameter region which was defined by the active laser cross-section, the energy deposition averaged over the active volume was about 120 J/ℓ. Measurements of the transient pressure rise which followed an electron beam pulse were consistent with the integrated radiachromic film measurements.

The laser cell was constructed entirely of stainless steel, with Viton and Teflon vacuum seals used throughout. After exposure to air, the cell and all of its associated gas handling system were passivated by filling the system with 3 atmospheres of a 10% F_2 in Argon gas mixture for a period of at least 24 hours.

In order to prevent interaction between the fluorine in the gas mixture and the titanium pressure foil through which the electrons entered the laser cell, the inside surface of the foil was coated with a 5 μm thick layer of ion vapor deposited aluminum. This resulted in significantly increased gas lifetimes, and prevented the formation of TiF_4 powder which would otherwise deposit on the laser optics. The laser gas components were delivered through an all stainless steel manifold to the laser cell were they were mixed by circulating through an external loop at a rate of about 1 ℓ/min. An optimized five component gas mixture comprised of 12 Torr NF_3, 1 Torr F_2, 12 Torr Xe and 750 Torr Kr, in sufficient Ar buffer gas to make a total pressure of 6.5 atmospheres was used throughout these experiments.

In the experiments reported here, the optical cavity consisted of of a positive branch confocal unstable resonator, as shown in **Figure 4.** The input mirror was a plano-concave lens, with the concave surface (radius of curvature = R_1) coated for maximum reflectivity form 465 to 505 nm, and for greater than 80% transmission near the 350 nm wavelength of the competing XeF (B→ X) transition. A small 1.5 mm injection hole was centered on the mirror by masking during the coating process.



Magnification $M = \frac{D_2}{D_1}$

Figure 4. Ustable Resonator Configuration

The output coupler was a double meniscus lens (with radii of curvature = R_2, and $-R_2$) with a large round maximum reflectivity spot placed on the center of the convex surface. The distance between the two mirrors was adjusted to the confocal spacing of $L = \frac{R_1 - R_2}{2}$. The magnification of the cavity M is given by $M = \frac{R_1}{R_2} = \frac{D_2}{D_1}$ the ratio of the outer diameter of the near-field output beam to the "hole" in its center.

A detailed numerical model was developed in order to provide guidance for the choice of the optical cavity parameters [8]. Due to the nature of the XeF (C→ A) e-beam pumped laser (2-3 %/cm gain, gain lifetime comparable to cavity photon lifetime, saturable absorbers) the analyses had to proceed in a somewhat unique way. After properly unfolding the unstable resonator cavity, the model numerically integrates the growth of the photon flux as it passes through the cavity.

The gain and/or absorption are computed using experimentally derived values for the production of both excited state XeF molecules, as well as broad-band absorbers obtained from small signal gain and fluorescence data. In this way, optimum cavity magnification values could be obtained for both internal as well as external cavity optics.(**See Figure 5.**) Placing the cavity optics outside the laser cell removes the mirrors from exposure to the corrosive effects of the fluorine atmosphere within the cell, but results in slightly less output energies as a result of losses associated with the cell windows, as well as the added amount of unpumped volume within the resonator.

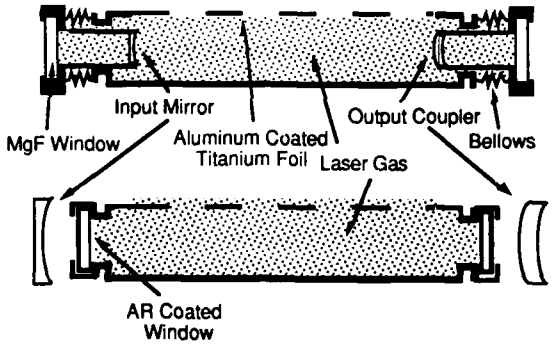


Figure 5. Comparison of Internal and External Resonator Schemes

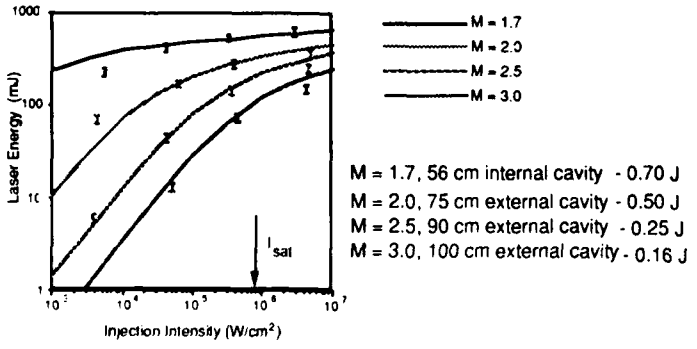


Figure 6. Model Results Compared with Experimental Data

Results of the model calculations, as well as experimental data obtained from the XeF (C→ A)l laser itself are presented in **Figure 6.** With sufficient injection intensity (corresponding to 1-2 mJ of total injected energy) the laser under external cavity operation approaches that using internal optics.

For the internal optics, the resonator had a magnification of 1.7 and an output spot diameter of 21 mm. The mirror spacing was 56 cm. The optics were overcoated with aluminum oxide for protection from the fluorine environment.

Several different magnification values were used with the external cavity, as shown in **Figure 6**. The cell windows for the external configuration were AR-coated fused silica, tilted by 3° to prevent any unwanted cavity effects resulting from them.

In most of the experiments reported here, the injection source was a dye laser pumped with a 60 ns FWHM XeCl excimer laser, resulting in a 40 ns FWHM injection pulse. The linewidth of the output from the dye laser was ~ 0.005 nm, except when a special intercavity etalon was used, in which case the linewidth was reduced to < 0.001 nm. The relatively long injection pulse allowed complete filling of the unstable resonator cavity before the e-beam was fired, which resulted in quasi-CW injection. The injection intensity could be varied using neutral density filters. The maximum energy which could be delivered to the unstable resonator injection aperture was about 2 mJ (after taking into account losses due to turning mirrors, telescope and the delay line which is used to prevent damage to the dye laser resulting from energy reflected from the injection aperture).

A computer controlled diagnostic system was developed to extensively characterize the performance of the XeF (C→ A) laser on each shot. As shown in **Figure 7** the output beam from the laser is directed to several sensors. A pyroelectric energy meter was used as a primary measurement of the total output from the device. A vacuum photodiode (with < 1 ns resolution) was used to obtain the temporal profile of the output pulse, while an optical multichannel analyzer (OMA) monitored the spectral characteristics. The performance of the electron beam generator was monitored with current and voltage monitors, while a pressure transducer monitored the shot-to-shot energy deposition within the cell.

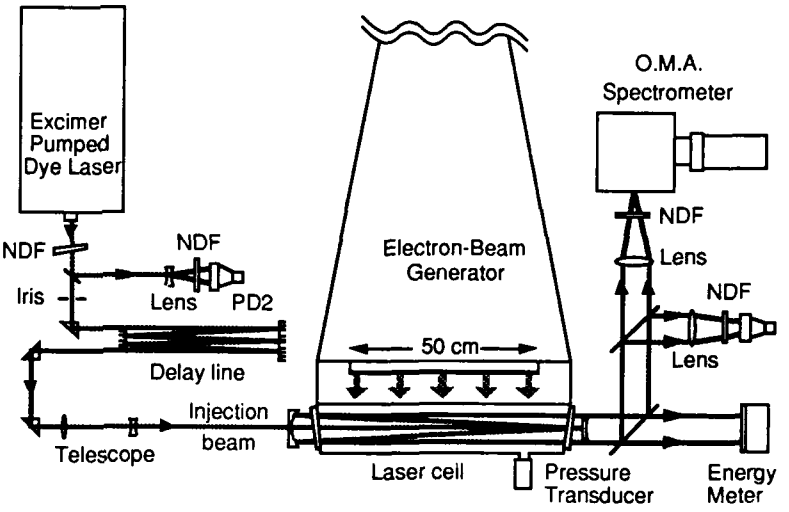


Figure 7. Diagram of the Experimental Layout

Experimental Results

As shown in Figure 3, the energy deposition within the laser cell varied significantly from front to back. Because of this, it was possible to measure the variation of XeF (C→ A) small signal gain as a function of energy deposition by changing the position of the gain probe beam as it passed through the cell.

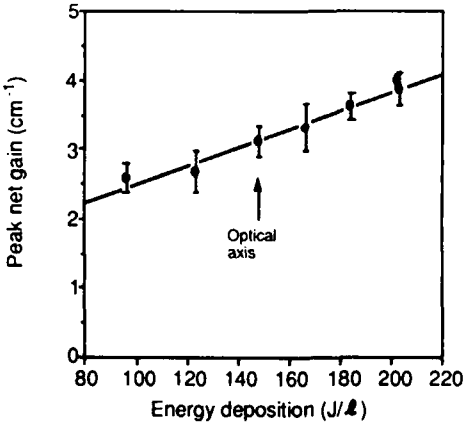


Figure 8. Gain as a Function of Energy Deposition

Figure 8 shows the results of this study. As can be seen, the gain increases almost linearly with deposition energy density up to 200 J/ℓ . Previous measurements on the small scale laser indicated the onset of gain saturation for a deposition energy density of about 80 J /ℓ with a peak in the intrinsic efficiency occuring at about 90 J /ℓ [5]. The interpretation of the earlier results however was complicated by very non-uniform electron beam pumping (no magnetic guide field was being used then) For the results obtained here, under much better controlled conditions, it appears that further increases in gain (and hence laser output energy) could be achieved with even greater pumping intensities.

Figure 9 shows the variation of the output energy from the XeF (C→ A) laser as a function of *average* energy deposited in the laser cell. The deposition energy was varied by adjusting the charging voltage of the Marx bank in the e-beam generator between 65 kV and 95 kV. Again, a nearly linear dependence is observed with no apparent indication of saturation up to the maximum average deposition of 125 J/ℓ. Using an internal resonator with a magnification of 1.7 and an optimized five-component gas mixture [9], and an injection intensity of about 3 MW/cm^2 (~ 2 mJ), laser output energies as high as 0.92 J have been achieved at 490 nm, near the peak of the XeF (C→ A) gain spectrum. This corresponds to an energy density of about 1.85 J /ℓ and an intrinsic efficiency of 1.5%.

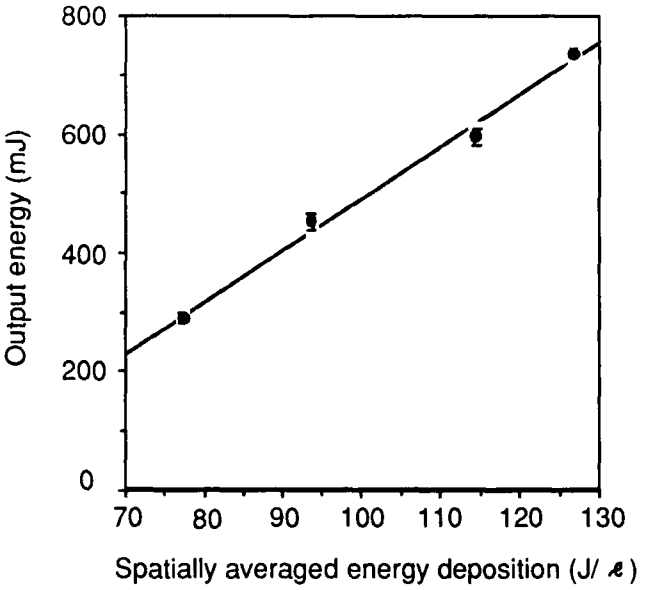


Figure 9. Output Energy as a Function of Spatially Averaged Energy Deposition

In order to investigate the spectral characteristics of the XeF (C→ A) laser, a set of wavelength tuning experiments was performed. An unstable resonator with a magnification of 1.34 was chosen in order to obtain good performance in the wings of the XeF (C→ A) laser spectrum. The somewhat reduced output coupling (as compared with the M=2 optics) significantly enhanced the performance of the laser in the low-gain wings, while not lowering the output in the central region too much. Three different sets of optics, with coating reflectivities optimized for specific regions of the spectrum were used for these measurements. Four different Coumarin dyes (460, 480, 503 and 521) were necessary in order to completely scan the tuning range of the XeF (C→ A) laser. The intensity injected into the unstable resonator cavity was adjusted to 2 MW/cm^2, corresponding to about 1.5 mJ injected energy, so that the performance at different wavelengths for the XeF (C→ A) laser could be compared at the same injection intensity.

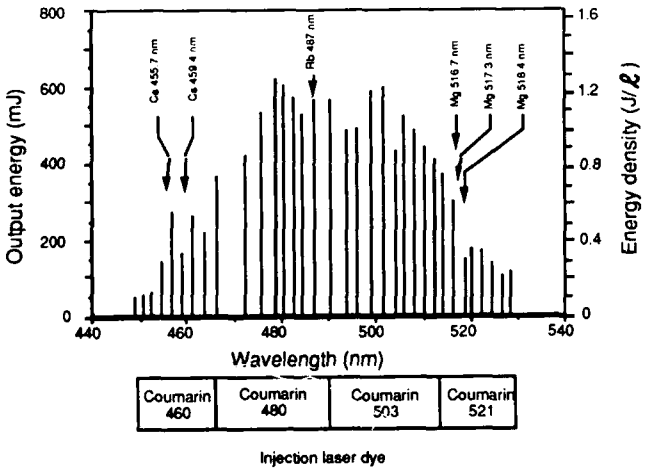


Figure 10. Spectral Characteristic of the Injection Controlled XeF (C→ A) Laser

Figure 10 shows the output energy of the XeF (C→ A) injection controlled laser as a function of wavelength from 450 to 530 nm, at wavelengths chosen not to coincide with known narrowband atomic absorptions. The injected signal had a linewidth of 0.005 nm and was held at a constant intensity of 2 MW/cm^2. Also shown in Figure 9 are some of the atomic resonance filter lines which might be employed for optical communications purposes in the blue-green region of the spectrum.

When the XeF (C→ A) laser is operated in a "free running" mode - that is with no injection and the signal allowed to build up from spontaneous emission, it is found that a number of narrow-band absorption lines appear in the spectrum, resulting from excited atomic absorbers created by the electron beam excitation. The effect of these absorbers can be significantly reduced by injection control of the XeF (C→ A) laser. Because the stimulated cross-section for the (C→ A) transition is relatively small, it is possible to build up sufficient intensity within the cavity to bleach or saturate these absorptions before the laser transition itself saturates. This effect is evident in **Figure 11,** which depicts the output energy as a function of injection intensity both on and off one of these narrow band absorptions. As can be seen, when the injection intensity is sufficiently large, the ratio between the output on an absorption and off is significantly reduced, showing saturation of the absorbing species.

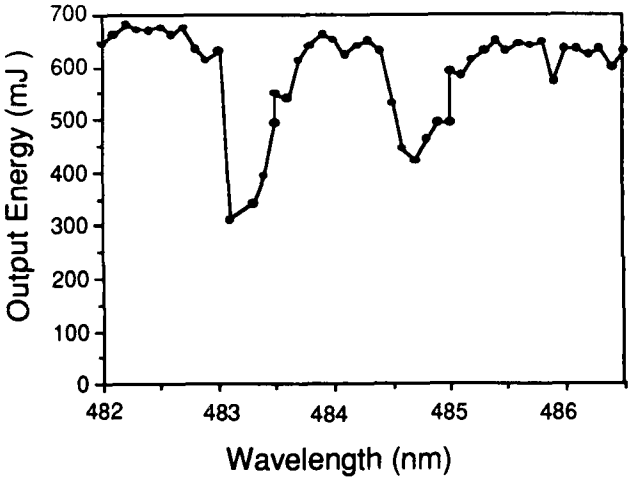


Figure 12. Detailed Wavelength Scan Using Agile Injection Source

In order to measure the spectral bandwidth of the injection controlled XeF (C→ A) laser, an intercavity etalon was installed in the dye laser which narrowed its output to ~0.001 nm FWHM. The output from the XeF (C→ A) laser was focused onto an opal glass diffuser with a 50 cm focal length plano-convex lens placed in front of an air-spaced plane-plane etalon with a finesse of 30 and a free spectral range of 9 GHz. The resulting circular interference pattern was then imaged onto a CCD array, and the variation in fringe intensity along one axis analyzed by computer software. **Figure 13** shows the analysis of both the injection signal itself, as well as the output from the XeF (C→ A) laser. As can be seen the spectral purity of the amplified signal very closely matches that of the input.

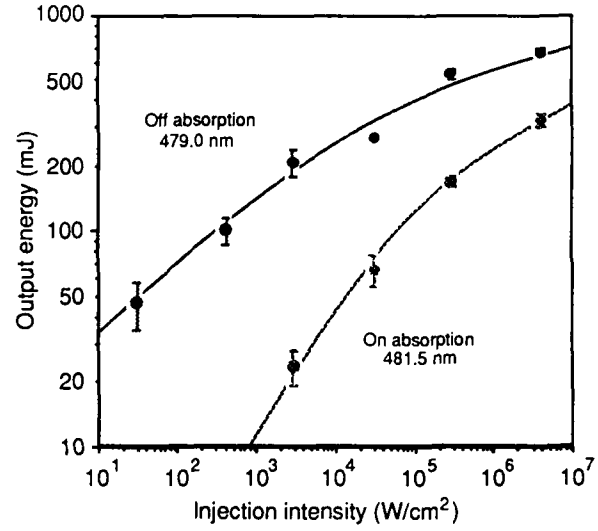


Figure 11. Output Energy as a function of Injection Intensity both On and Off a Narrow Band Absorption

To more fully take advantage of the ease of tuning via injection control, a novel wavelength agile injection source was developed by the United Technologies Research Center for use with this laser [10]. By selecting the desired wavelength of interest by computer control of a dye laser cavity and galvometric mirror wavelength adjustment, exact wavelength control (to ~0.01 nm) for a *random* sequence of wavelengths is possible. In order to demonstrate this, a spectral region from 482 to 486.5 nm was scanned using 0.1 nm steps. The results of this detailed investigation of the output spectral characteristics of the injection controlled XeF (C→ A) laser are shown in **Figure 12.**

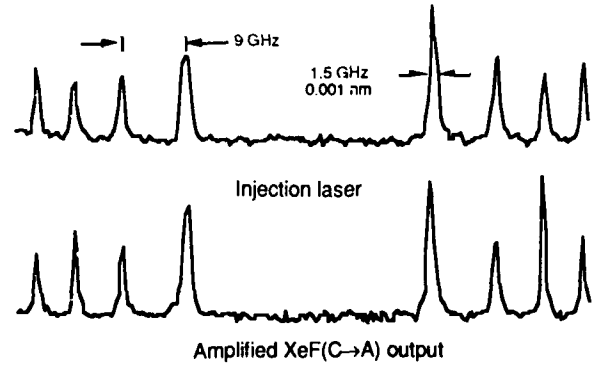


Figure 13. Comparison of the linewidth of the Injection Spectrum and that of the Amplified XeF (C→ A) Output

Conclusions

The XeF (C→ A) laser has been successfully scaled from a 0.02 liter to a 0.5 liter active volume. A peak output energy of 920 mJ, corresponding to an energy denisty of 1.85 J/ℓ at 1.5 % intrinsic efficiency has been observed near the gain maximum. The laser has been tuned, using injection control, over a bandwidth extending from 450 nm to 530 nm with several hundred mJ of output energy in a bandwidth of less than 0.001 nm. Using a unique wavelength agile injection source, rapid tuning, under automated control has been demonstrated. Careful measurements of both the small signal gain as well as output energy with e-beam deposition indicate that improved performance can be expected from more intense excitation of the laser active medium.

References

1. W.L. Nighan, R. Sauerbrey, Y. Zhu, F.K. Tittel and W.L. Wilson, IEEE J. Quantum Electronics, 23, 253 (1987)
2. G.J. Hirst, C.B. Dane, W.L. Wilson, R. Sauerbrey, F.K. Tittel and W.L. Nighan, Appl. Phys. Lett, 54, 1851 (1989)
3. P.J.M. Peters, H.M.J. Bastiaens, W.J. Witteman, R. Sauerbrey, C.B. Dane and F.K. Tittel, IEEE J. Quantum Electronics (submitted)
4. A. Mandl and L.H. Litzenberger, Appl. Phys. Lett., 53, 1690 (1989)
5. N. Hamada, R. Sauerbrey, W.L. Wilson, F.K. Tittel and W.L. Nighan, IEEE J. Quantum Electronics, 24, 1571 (1988).
6. S. Lloyd, Y.G. Chen, G. McAllister, M. Montgomery, T. Olson, J. Shannon, B. Dane, G. Hirst, R. Sauerbrey, F. Tittel and W. Wilson, in Proceedings of the Seventh IEEE Pulsed Power Conference, Monterey CA.
7. W.P. Bishop, K.C. Humphreys and P.T. Randike, Rev. Sci. Instrum., 44, 443, (1973)
8. C.B. Dane, Th. Hofmann, G.J. Hirst, S. Yamaguchi, R. Sauerbrey and F.K. Tittel (to be published in Appl. Phys. Lett.)
9. C.B. Dane, G.J. Hirst, Y. Yamaguchi, Th. Hofmann, W.L. Wilson,. Jr., R. Sauerbrey, F.K. Tittel, W.L. Nighan and M.C. Fowler IEEE J. Quantum Electronics (to be published)
10. R.A. Rubino, W.L.Nighan, W.H. Glenn, A.J. Cantor and M.J. Roman in Proceedings of the 1989 LEOS Annual Meeting, 160, Orlando, FL (1989).

A 20 J FLOW COMPATIBLE XECL LASER

Andrew J.W. Brown, Edward G. Sergoyan, Fred E. White,
Mike vonDadelszen, and Charles H. Fisher

Spectra Technology, Inc.
2755 Northup Way
Bellevue, Washington 98004

Abstract

We have fabricated and tested single shot the laser head and fast pulser for a high energy, flow compatible, x-ray preionized XeCl laser. The pulsed power used to drive the 12x9x120 cm discharge utilizes a high efficiency spiker sustainer circuit with a magnetic isolation switch. A single pulse output energy of 19 J at 2.2% efficiency and pulse length of 230 ns has been demonstrated, corresponding to an extracted energy density of 1.5 J/L.

INTRODUCTION

Following their conception there has been a continuing effort to improve the extracted energy and efficiency of excimer lasers. Of the various excimers, XeCl has demonstrated the best performance and has been the focus of extensive research. In particular preionized discharge excitation schemes have received much attention because of their simplicity and potential high efficiency. The aperture over which a uniform discharge can be generated has increased dramatically since the introduction of x-ray preionization, enabling large scale devices to be built. Preionized discharge XeCl lasers have achieved energies of 66 J per pulse at efficiencies approaching 1%[1] and typically operate at efficiencies of approximately 2% at substantially lower energy.

Novel discharge excitation schemes using spiker sustainer circuitry have improved the efficiency of these lasers to approximately 4% at the 3-4 J level.[2,3] In this technique a fast rising, high voltage pulse from the spiker circuit is used to break the gas down and the separate, low impedance, Pulse Forming Network (PFN) supplies the majority of the pump energy. This allows optimization of the PFN charge voltage to ideally twice the discharge self sustaining voltage for maximum efficiency. Isolation between the spiker and sustainer circuits can be achieved using a rail gap switch,[2] two gap laser head[4] or a saturable magnetic switch.[3,5] The simplicity and high reliability of the magnetic isolator made it the preferred choice for the system described here.

Recent development of these lasers has been directed towards achieving output power at the kilowatt level. At this high average power close attention must be given to the pulse power design to achieve efficient electrical pumping combined with long lifetime. Flow considerations are also important to ensure the hot gases are removed from the discharge region prior to the next pulse. This paper describes the proof-of-principal, single-shot experiments for a flow-compatible, XeCl laser head and pulser designed for 20 J per pulse at 50 Hz repetition rate.

Figure 1 shows a cross section of the flow compatible laser head and discharge region. The design of such a head must satisfy the conflicting requirements of minimizing flow disturbance while maintaining a low inductance geometry to achieve the required high pump power and fast electrical discharge characteristics. In addition, the large apertures required for high energy lasers lead to inductive laser head geometries to prevent tracking at the high voltages necessary for gas breakdown. The laser head was designed to satisfy these conflicting demands using modeling tools developed for excimer and other gas discharge lasers.

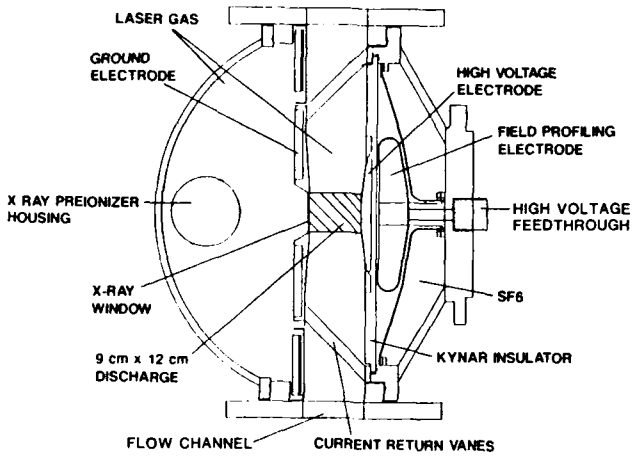


Figure 1. Cross Section of Flow Compatible XeCl Laser Head.

The laser head is divided into two volumes, one housing the high voltage feedthrough and the other containing the discharge and flow region. A pressure balanced SF_6 insulator system eliminates mechanical stresses on the Kynar dielectric which separates the feedthrough region from the high pressure laser gas. This configuration facilitates a low inductance design for the electrical feeds. The materials used in the laser head that are in contact with the gas mixture are limited to Kynar for the high voltage insulator and aluminum for the electrodes, shell, and current returns to minimize any compatibility problems.

The discharge electrode profiles were designed following electric field analysis of the discharge region using a finite element code TOPAZ, to minimize field enhancements while maintaining the flow compatibility of the device. The high voltage electrode is recessed into the dielectric to both more effectively shield the electrode - dielectric - gas interface and to provide a smooth flow channel to minimize disturbances. A field shaping electrode was positioned behind the high voltage electrode in the SF_6 region to minimize the field enhancement associated with the triple point and to distribute the equipotentials uniformly across the dielectric.

The ground electrode was similarly profiled for field uniformity and flow compatibility. Current return vanes hold this electrode in position 12 cm from the high voltage electrode, while minimizing the head inductance and flow interference. A 9 x 120 cm portion of this electrode was machined to a thickness of 4 mm to maximize transmission of x-rays from the preionizer into the discharge region. The x-ray preionizer was housed in the dome behind the low voltage electrode but isolated from the laser gas by a 3 mm thick aluminum tube, allowing access for maintenance without disturbing the gas.

The preionizer used was a commercially available x-ray generator capable of operation up to 50 Hz (Beta model #150-065). This unit has various operating modes which determine the initial stored energy and the resulting x-ray pulse length, selected by changing the capacitance of the unit. All of the experimental results presented in the next section were taken with the preionizer operating at its longest pulse length (~500 ns) and maximum voltage (~125 kV).

Figure 2 shows a schematic of the discharge pulser. Spark gap switches were used for the proof-of-principal single shot experiments reported here. However, a pulsed power system for a 1 kW XeCl laser has been designed which utilizes the major fast portions of the present pulser, but substitutes thyratron switches for the spark gaps and includes magnetic pulse compression in the spiker circuit.[6] The PFN is a tri-plate structure fabricated from ceramic capacitors (TDK) and designed to have an impedance of 0.25 Ω and a pulse length of 250 ns.

Fourteen rows of eighteen capacitors wide, stacked two in series were used for each side of the double sided PFN. The pulse duration was extendable by simply adding more rows of capacitors to the structure at the end opposite the laser. The individual capacitors were recessed into an aluminum flux excluder plate to reduce the series inductance. The PFN was pulse charged from a storage capacitor in approximately 3 μs.

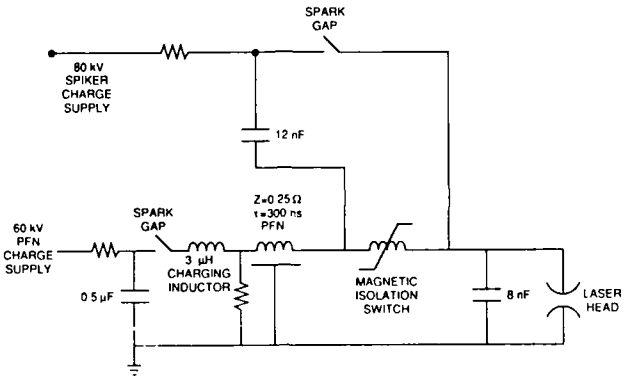


Figure 2. Schematic Diagram of Spiker/Sustainer Pulser with Magnetic Isolation Switch Used for Single Pulse Tests.

The spiker circuit was made from ceramic capacitors arranged in a coaxial configuration around a midplane spark gap switch to minimize its inductance. Eight 23 Ω cables (RG-17/14) were used to provide a low inductance connection to the laser to ensure a fast spiker risetime. The spiker unit was "floated" to the PFN charge voltage to minimize the spiker charging voltage.

When the spiker circuit is triggered it delivers a fast rising voltage spike with respect to the PFN charge voltage which, when timed appropriately with the preionization pulse, breaks the gas down uniformly. A saturable magnetic switch isolates the spiker circuit from the low impedance pulse forming network until the gas breaks down. Following breakdown the switch saturates in the forward direction allowing current to flow from the PFN to the discharge.

The saturable switch was made from a race track ferrite approximately one meter wide. It was fabricated from microwave ferrite material with a magnetic core area of ~42 cm^2. The voltage-time hold off for the switch was estimated at 4 x 10^{-3} V-sec. To minimize the spiker charge voltage and the quantity of magnetic material required in the isolation switch, the spiker pulse had the same polarity as the PFN charge voltage. Previous experience with a lower energy, high efficiency XeCl laser at STI indicated no significant difference in device performance when the same and opposite polarity spike voltages were used.[3]

The timing sequence for laser operation was as follows. The PFN was pulse charged in 3 μs from the storage capacitor and at the peak of its charge cycle the x-ray preionizer was triggered to establish an initial, uniform electron density in the gas. Using a charge collection technique this density was estimated to be on the order of 10^8 electrons cm^{-3}. At a pre-determined time after the x-ray pulse, the spiker circuit was fired, rapidly increasing the voltage across the laser head to rapidly avalanche the electron density to its final value.

Timing between the x-ray and spiker pulses was found to be critical for optimum laser performance. The timing had to be set within a window approximately 40 ns wide; outside this window the laser performance rapidly degraded. Under optimum conditions the spiker was initiated approximately 300 ns after the beginning of the x-ray preionization pulse, which had a temporal profile 500 ns wide (FWHM) and risetime approaching 250 ns. The optimum timing corresponded to the spiker pulse occurring close to the peak in x-ray emission, and thus

discharge formation corresponds to the point of maximum preionization. Firing the spiker too early resulted in non-uniform discharge formation and reduced output as a consequence of the low level of preionization when the discharge was initiated. Firing the spiker too late or not at all resulted in an x-ray switched discharge and poor laser performance.

During the initial experiments with the device the output energy was observed to peak at a lower charge voltage than anticipated from scaling predictions. The maximum charge voltage was limited by streamer formation in the gas, resulting in reduced output energy. This lower charge voltage limited the stored energy on the PFN, necessitating the addition of more capacitance to achieve the design energy. An extra four rows of capacitors were added to the back of the tri-plate structure, increasing the nominal length of the PFN from 250 ns to 300 ns. Figure 3 shows the device waveforms for the laser driven by the 300 ns PFN for optimum operating conditions. The output energy in this case was 19 J at an efficiency of 2.2% in a 230 ns (FWHM) pulse. The open shutter photo in the figure shows the discharge to be uniform and arc free. Burn marks on Dupont Dylux paper and carbon paper were also very uniform measuring 12 cm x 9 cm. The optical cavity which gave optimum performance consisted of a 100% reflector with a 10 m radius of curvature and a flat 30% reflectivity output coupler.

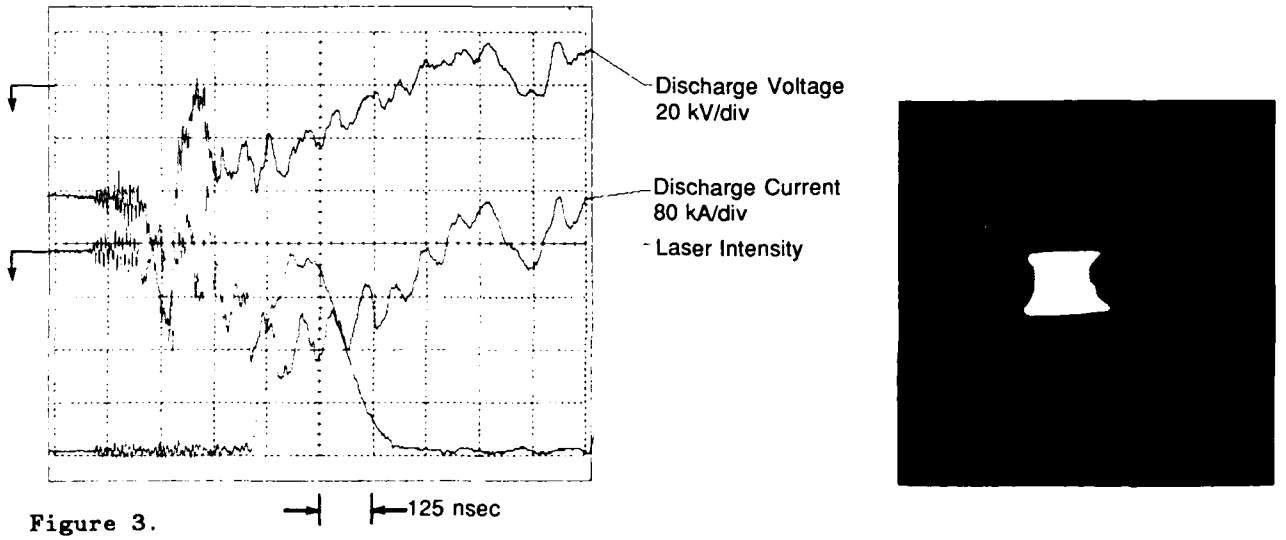


Figure 3.

a) Temporal Shape of Voltage, Current and Laser Pulses

b) Open Shutter Photograph of Arc Free Discharge for 19 J Laser Pulse

Table 1 shows a summary of the laser performance as a function of gas mix. In general, higher HCl concentration produced higher peak power but with shorter pulse duration; lower HCl concentration resulted in lower peak power but longer pulses which terminated with the discharge power pulse. The optimum HCl concentration was 0.02%. Laser performance increased with Neon buffer gas pressure up to the design limit of 5 atm. Varying Xe concentration showed little effect on laser performance over the range of mixes used. Replacing the fused silica laser windows, which had accumulated a deposit on the surface in contact with the laser gas, made a substantial increase of 40% in laser output energy emphasizing the importance of minimizing optical losses in these short wavelength lasers.

In conclusion, under signle shot conditions we have demonstrated uniform, arc free discharges resulting in a laser energy of 19 J at greater than 2% efficiency with a XeCl laser head designed for gas flow adequate for 50 Hz operation. Coupling this laser head and fast PFN with the appropriate flow loop and power conditioning system should allow average XeCl laser powers of 1 kW to be achieved.

Table 1

SUMMARY OF XeCl LASER PERFORMANCE FOR SEVERAL DIFFERENT PUMPING CONDITIONS

%Xe	%HCl	V_{charge} (kV)	τ Pulse (ns)	E_{out} (J)	η (%)	COMMENTS
5 atm Neon Buffer Gas						
0.625	0.045	55	95	10	1	250 ns PFN
0.5	0.03	49	155	12	1.4	250 ns PFN
0.35	0.02	50	105	12.5	1.4	250 ns PFN
0.2	0.02	48	210	13.5	1.7	250 ns PFN
0.3	0.02	45	210	13.5	1.4	300 ns PFN
0.22	0.015	44	220	12	1.4	300 ns PFN
New Windows						
0.3	0.02	46	200	15	2.1	250 ns PFN
0.2	0.02	44	230	19	2.2	300 ns PFN

The work presented here is the culmination of a large team effort at Spectra Technology, Inc. We would especially like to thank Chris Young and Ken McDonald for their help in the design of the device and also Marc Norsen and Dave Boss for their assistance in the experiments.

This work was supported by Naval Research Laboratory contract number N00014-87-C-2110.

REFERENCES

1. L.F. Champagne, A.J. Dudas, and N.W. Harris, J. Appl. Phys. 62, 1576 (1987).

2. W.H. Long, Jr., M.J. Plummer, and E.A. Stappaerts, Appl. Phys. Lett. 43, 735 (1983).

3. C.H. Fisher, M.J. Kushner, T.E. DeHart, J.P. McDaniel R.A. Petr and J.J. Ewing, Appl. Phys. Lett. 48, 1574 (1986).

4. W.H. Long Jr. and M.J. Plummer "Tandem Discharge Pumped Excimer Laser," presented at the Conference on Lasers and Electro-Optics, Baltimore (1985), paper THZZ8.

5. R.S. Taylor and K.E. Leopold, Appl. Phys. Lett. 46, 335 (1985).

6. K. McDonald, P. Ingwerson, E. White, C. Young, E. Sergoyan, and C. Fisher, "Design of a Magnetically-Isolated Pulsed Power System for a 1 kW XeCl Excimer Laser," Eighteenth Power Modulator Symposium, Hilton Head, South Carolina, 1988, paper 10.6.

X-RAY TRIGGERING OF A TEN-LITER DISCHARGE EXCIMER SYSTEM

S. Bollanti, P. Di Lazzaro, F. Flora, G. Giordano, T. Letardi, N. Lisi*,
G. Schina, C.E. Zheng**

ENEA, Dip. TIB, U.S., Fisica Applicata, C.R.E. Frascati,
C.P. 65 - 00044 Frascati, Rome (Italy)

ABSTRACT

The switchless discharge technique has been successfully applied to a 10 liter active volume XeCl laser system by using X-rays as a photoionization source. A 8 J per pulse output energy at λ = 308 nm, uniformly distributed over a (7×10) cm^2 near-field laser spot size was achieved. The average output power was 45 W at 6 Hz repetition rate, actually power-supply limited.

INTRODUCTION

Discharge excited gas lasers are usually operated through a gas preionization followed by a fast, high voltage main discharge. Such a scheme implies the use of a low inductance, fast switch between the energy storage system and the laser discharge electrodes.

The commonly used switch element is the hydrogen thyratron. Unfortunately, efficient operation of high power gas lasers, e.g. excimers, require values of both rate of current rise (~ 10^{12} A/s) and transferred charge (~ 10 mC) which limit the commercial thyratron lifetime to ≤ 10^8 discharges. The overpowered working conditions are even more heavy for large volume (> 5 liters) systems. Magnetic switches[1] and prepulse techniques[2] have been proposed as possible solutions. However, their somehow stiff properties, the noticeable circuital complexity and the further cost of manufacturing and maintenance added make these techniques far from the ideal solution.

A new operation mode was recently proposed[3] to overcome this problem. In these experiments, the laser head is directly connected to the storage capacitor and slowly loaded up to the maximum voltage value V_B allowed by the electrodes profile and by the gas pressure and composition. A pulse of ionizing radiation is then injected into the gas mixture, quickly creating the required electron-ion pair density to trigger a uniform avalanche discharge.

Up to date, however, the use of the outlined "switchless" technique has been limited to specially designed excimer lasers with a maximum active volume of about one liter.[4] In this paper we report the results of a large active volume X-ray triggered XeCl discharge with a conventional laser head design.

EXPERIMENTAL

Figure 1 shows the cross section of the XeCl excimer laser we used in this experiment. A detailed description of the system is reported in Refs. 5-7 and only a brief account is given here.

A double reflection diode is located in a vacuum chamber (on the left of Fig. 1). The electron clouds generated by the plasma cathodes[5,8] are accelerated toward the high voltage pulsed target anodes, wrapped with a high atomic number material (e.g. Pb, Ta). When the electrons impinge the anodes, brehmsstrahlung X-ray emission occurs, in the direction of the laser chamber. After passing through the 0.5 mm thick Al vacuum window (see Fig. 1), the x-rays cross the 0.5 mm thick Al electrode, enter the laser discharge region and preionize the laser gas mixture.

The performances of the preionizer system have been carefully measured using the techniques reported in Refs. 5,7,8,9. The results are summarized in Table I.

The discharge electrodes are shaped with a Stappaerts profile[10] and no attempts were made to improve the electric field uniformity and the static self-breakdown level of a given mixture. As a matter of fact, this laser head bas been designed (and the laser system operated as well) to work in the conventional preionization followed by a spark-gap switched discharge mode.[6,7]

---

* ENEA Student

** ENEA Guest. Permanent address: Institute of Optics and Fine Mechanics, Shanghai, China

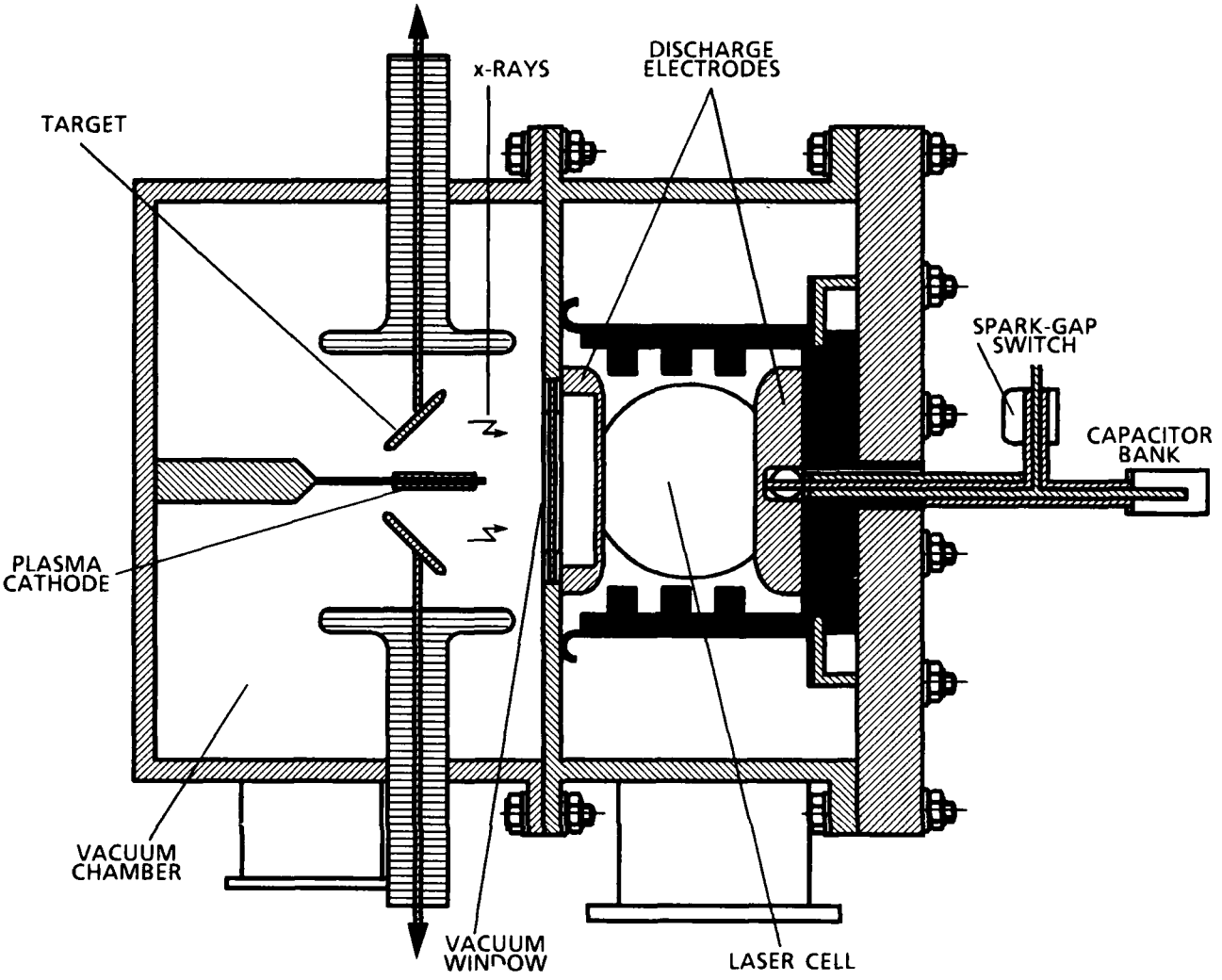


Fig. 1 - Vertical section of the X. discharge laser system used in the experiment. The active medium dimensions are (10×10×100) cm^3. (From Ref. 7)

TABLE I - X-Ray preionizer source

Operation mode	Double diode, pulsed, reflection geometry
Cathode type	Surface plasma
Input energy	(6÷60) J
Max anode voltage	V - L(dI/dt) = 70 kV
Repetition rate	10 Hz
X-ray pulse duration	300 ns FWHM
Dosage in the laser cell	(30÷34) mR/shot
Dosage uniformity	70%
Dosage drop anode-cathode	35%
Preionization electron density	up to 6×10^8 cm^{-3} in 1 atm Ne

The discharge energy was fed by a resonant charge, transfer type excitation circuit with a primary and a secondary Maxwell capacitor bank of 1.2 μF and 0.64 μF capacitance value, respectively.

RESULTS

A slowly raising voltage is applied to the discharge anode. After less than 1 μs, the voltage approaches the V_B value, and a pulse of X-rays from the preionizer is injected into the gas mixture, as shown in Fig. 2. Here is actually reported the X-ray diode current waveform. However, the risetime of the X-ray optical pulse and that of the corresponding current are almost the same, as shown in Fig. 3, so they can be easily compared.

The timing of the X-ray pulse injection is critical to achieve the optimum electron avalanche development. For example, if T_B is the time necessary to reach V_B, the ionizing radiation pulse has to be injected before the time $t=(T_B-T_S)$, where T_S is the streamer forming time. Anyway, when the X-ray pulse timing is appropriate, efficient energy transfer occurs, thus leading to the laser pulse emission, in the time scale shown in Fig. 4.

An interesting measurement is the laser output energy as a function of the X-ray photon energy. The results, summarized in Fig. 5, show a clear threshold effect around 25 keV. The corresponding electron number density measured in 1 atm Ne by electric charge collection[8,9]

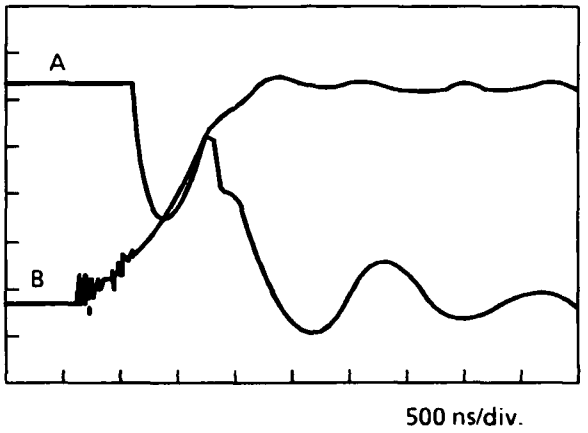


Fig. 2 - Time evolution of the typical discharge voltage (B) and of the X-ray diode current (A)in the switchless operation mode. Horizontal: 500 ns/div. Voltage: 10 kV/div. Current: 580 A/div

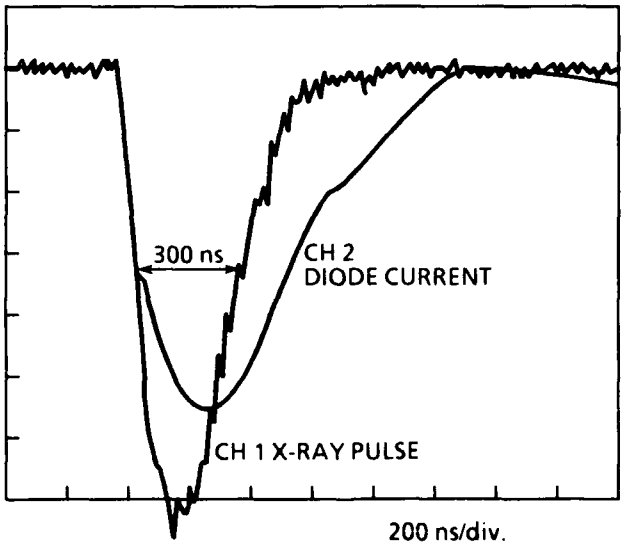


Fig. 3 - X-ray diode current and X-ray photon signal detected by a plastic scintillator and a photomultiplier. Time scale: 200 ns/div

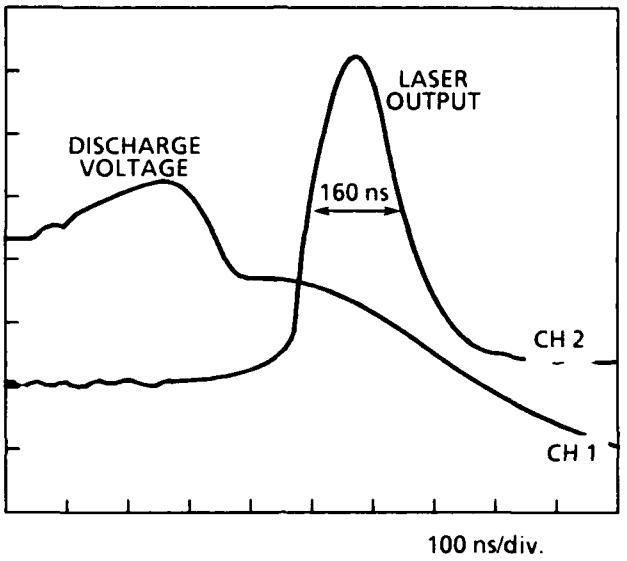


Fig. 4 - Discharge voltage and output laser intensity time evolutions. Horizontal: 100 ns/div. The laser output FWHM is 160 ns. The wavelength is λ = 308 nm

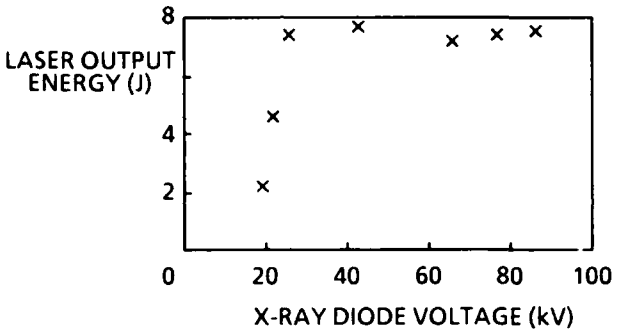


Fig. 5 - Laser output energy vs X-ray diode voltage. Discharge voltage: 34 kV. Gas mixture: 1.5 Torr HCl, 10 Torr Xe, Ne balanced up to 3 atm

is $n \sim 10^6$ cm^{-3}. In this case, however, only a fraction of the X-ray photons are useful to the avalanche triggering, because of the short e-folding time. We can define the useful preionization duration T_e as the time during which the electron generation rate from direct preionization is larger than the electron avalanche contribution. Both T_s and T_e are sharply decreasing with the total gas pressure P and the reduced field E/P, as discussed in Ref. 11. For the same working point, $T_e \ll T_s$, and we can speculate T_e is the essential parameter of the phototriggered discharge as it tells us how long is the effective working time of the preionizing pulse to drive the electron avalanche development. Taking T_e into account, from Fig. 5 we have a threshold electron number density $n_t \sim 2.6 \times 10^4$ cm^{-3}.

Both the laser output energy $\mathcal{E}$ and the FWHM laser pulsewidth increase almost linearly with the discharge voltage V. In particular, the $\mathcal{E}$ growth is twofold (from 4 J to 8 J) increasing V from 28 kV to 35 kV.

The laser pulsewidth is strongly dependent on the HCl partial pressure, as it increases up to the 60% of its value reducing the HCl pressure from 3 Torr to 0.4 Torr, as shown in Fig. 6. At the same time, $\mathcal{E}$ has a rather broad maximum around 1 Torr HCl. From Fig. 6, the output peak power increases with [HCl] up to 1 Torr of partial pressure, remaining almost constant at ~ 47 MW level for larger HCl concentrations.

The quite long 210 ns FWHM laser pulsewidth achieved at 0.4 Torr, P = 3 atm (see Fig. 6) was not the longest one we got in this experiment. A 270 ns FWHM pulsewidth was obtained at P = 1.5 atm, as shown in Fig. 7. Here appears also a slight saturation of $\mathcal{E}$ with P, probably due to the E/P decrement from 1.5 kV/(cm·atm) at P = 1.5 atm, to 1 kV/(cm·atm) at P = 3.5 atm.

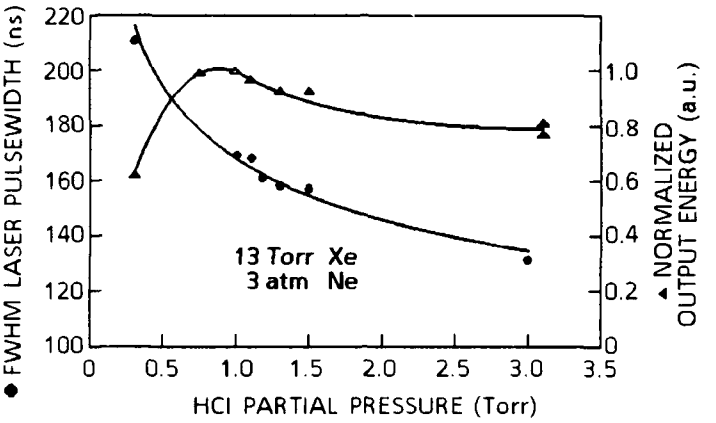


Fig. 6 - Normalized output energy (triangle) and FWHM laser pulsewidth (full dot) vs the HCl partial pressure. Xe partial pressure 13 Torr, balanced Ne up to 3 atm

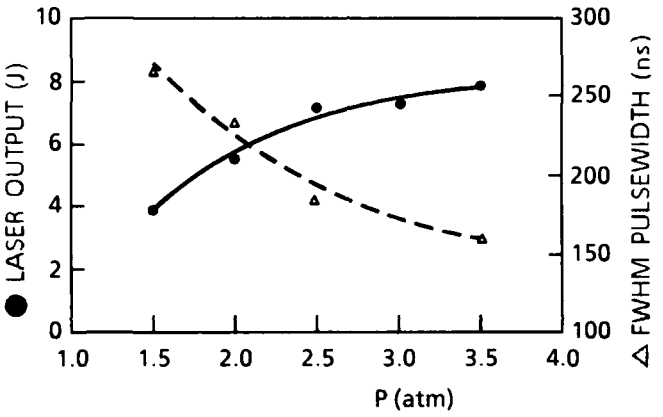


Fig. 7 - Laser output (full dot) and FWHM pulsewidth (triangle) vs total gas pressure. Gas mixture composition HCl:Xe:Ne = (1:9:2062)

In all the reported experiments, the spatial laser energy distribution (monitored using a Dylux sensitive paper) was very uniform over the (7×10) cm^2 near-field spot area. The reduction of the laser spot area from the designed (10×10) cm^2 to the measured (7×10) cm^2 is mainly due to the X-rays distribution, as shown in Fig. 8, where a 7 cm spatial width of the X-ray dosage along the direction perpendicular to the discharge electric field E is reported.

Finally, the discharge performances have been investigated in the repetitive operation mode using a longitudinal flowing loop with a maximum gas speed of 12 m/s through the (10×10) cm^2 discharge cross section. The minimum clearing factor to obtain stable laser output intensity was 1.1. The maximum 45 W average output power achieved at 6 Hz repetition rate is actually power-supply limited, being the measured charging time of the primary capacitor as long as 180 ms.

CONCLUSIONS

The switchless technique has beeen successfully applied to a 10 liter discharge XeCl laser. Both the 8 J output energy and the 0.74% plug efficiency obtained compare very well with the performances achieved in the conventional operation mode.[7] Most important, this technique allow us to operate for the first time our large system in the repetitive mode. This goal could not be easily attained using a single thyratron or a spark-gap as electrical switch.

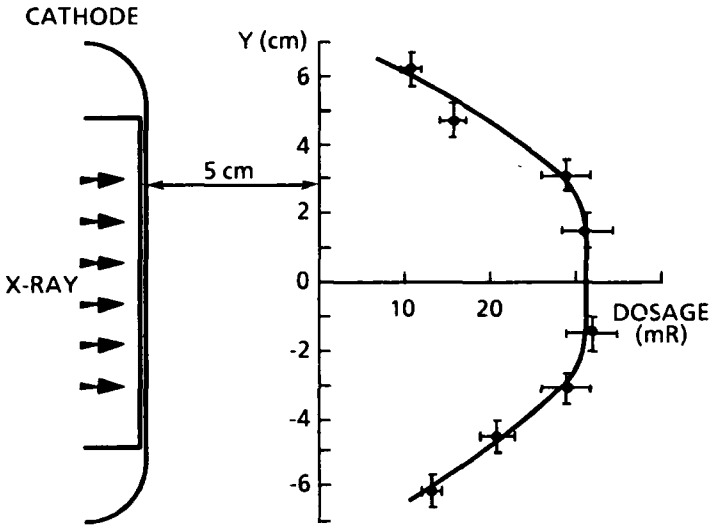


Fig. 8 - X-ray dosage distribution on the middle of the discharge region, in a direction Y perpendicular to the electric field E

REFERENCES

1. D. Basting, K. Hohla, E. Albers, H.V. Bergmann, Laser & Optoelektronik, 2, 128 (1984)
2. W.H. Long, M.J. Plummer, E.A. Stappaerts, Appl. Phys. Lett., 43, 735 (1983)
3. B. Lacour, C. Vannier, J. Appl. Phys. 62, 754 (1987)
4. D. Beaupere, C. Gagnol, M. Gaillard, M. Huguet, B. Lacour, A. Lavenant, P. Pinson, in Proc. ECO 1 Conf. on Excimer Lasers and Applications, SPIE Vol. 1023, D. Basting Ed. (1988) pp. 25-29
5. T. Letardi, P. Di Lazzaro, G. Giordano, C.E. Zheng, Appl. Phys. B48, 55 (1989)
6. T. Letardi, S. Bollanti, P. Di Lazzaro, F. Flora, G. Giordano, T Hermsen, C.E. Zheng, in Proc. ECO 1 Conf. on Excimer Lasers and Applications, SPIE Vol. 1023, D. Basting Ed. (1988) pp. 30-37
7. S. Bollanti, P. Di Lazzaro, F. Flora, G. Giordano, T. Hermsen, T. Letardi, C.E. Zheng, "Performance of a Ten-Liter Electron Avalanche Discharge XeCl Laser Device" Appl. Phys. B, to be published
8. S. Bollanti, P. Di Lazzaro, F. Flora, G. Giordano, T. Letardi, C.E. Zheng, in Proc. Int. Conf. on Lasers 88, R.C.Sze and F.J. Duarte Ed. (STS Press, McLean, VA 1989) pp. 141-146
9. G. Giordano, T. Letardi, C.E. Zheng, Il Nuovo Cimento, 101B, 569 (1988)
10. E.A. Stappaerts, Appl. Phys. Lett., 40, 1018 (1982)
11. T. Letardi, S. Bollanti, C.E. Zheng: Internal Report ENEA RT/TIB/1989

HIGH OPTICAL QUALITY LASER BEAMS WITH NEGATIVE BRANCH UNSTABLE RESONATORS

J.W. Chen, V. Nassisi and M.R. Perrone

Centro Interuniversitario di Elettronica Quantistica e Plasmi
Dipartimento di Fisica dell'Universita'
Via Arnesano 73100 LECCE, Italy

Abstract

Confocal and non-confocal negative branch unstable resonators with an intracavity spatial filter have been applied to a high-gain short-pulse UV preionized XeCl laser. The near- and far-field radiation characteristics have been investigated in both configurations for different spatial filter diameter values. Laser beams of quite high brightness and with a regular intensity spatial profile have been obtained, in particular laser beams of larger brightness have been obtained with non confocal schemes. A maximum beam brightness of $1.3 \times 10^{14} Wcm^{-2}Sr^{-1}$ has been achieved. A low sensitivity to mirror misalignments has also been observed.

Introduction

Laser beams of high brightness are required to improve and widen the scientific and industrial applications of such devices. Any effort in such direction must try to satisfy the following requirements. Firstly, the laser field mode volume must be made as large as possible in order to fill all the active volume and get high energy, high power laser beams. Secondly, laser beams spatially coherent across the entire beam cross section and with a smooth and regular intensity spatial profile must be generated to obtain an efficient laser energy transport and tight focalization spots. Finally, the laser beam parameters should not be very sensitive to mirror misalignments.

To satisfactory fulfil the previous requirements an extensive work has been devoted to the development and study of optical resonators, since the first appearance of laser devices. The laser beam optical quality is mainly determined by the cavity transverse mode structure.

It has been reported by Siegman [1] that, high mode volumes and high quality laser beams can mainly be obtained by applying to laser devices unstable cavity configurations. The unstable resonator studies for lasers under quasi-continuous conditions are not very useful when such cavities are applied to high-gain short-pulse excimer lasers. In such lasers the upper level population lifetime is comparable with the time taken by a photon to travel along the resonator and the time for the development of a photon avalanche. An extensive analysis of the build up of modes in unstable resonators for high-gain short-pulse lasers has been presented in a series of papers by Anan'ev[2], by Zemskov et al.[3] and by Isaev et al.[4].

The key concepts that emerge from their analysis are that the unstable cavity magnification must be sufficiently large, to enable a diffraction-limited mode to become the dominant mode in the resonator, in a time less than the time during which the laser exhibits gain. Moreover, the laser medium gain coefficient must be sufficiently small so that the lasing threshold is not reached before such a mode have had time to build up.

Positive branch unstable resonators have been generally applied to high power excimer oscillators to generate good-optical-quality and high-energy laser beams[5]. Up to now, the negative branch unstable resonators have not received much attention, since the presence inside the cavity of a focal point makes them unattractive for high power systems. However, a negative branch cavity called "Self-Filtering Unstable Resonator " (SFUR) has been proposed few years ago[6] and such resonator seems particularly suited to the high-gain, short-pulse excimer lasers, to obtain diffraction limited laser beams with a regular intensity spatial profile[7,8,9].

To get higher mode volumes and shorter resonator lengths with respect to the SFUR scheme a non confocal SFUR called "Generalized Self Filtering Unstable Resonator" (G-SFUR) has been furtherly proposed[10,11,12]. The SFUR and G-SFUR working principles and main features will be presented in the next section.

It is purpose of this paper to investigate and compare the performance of confocal and non-confocal SFUR schemes having the same cavity length and applied to a high-gain short-pulse UV preionized XeCl laser. The effect of the spatial filter size on the laser beam energy and brightness has been investigated in both configurations. The sensitivity to mirror misalignments of both schemes has also been tested.

II. Theory

The SFUR is a confocal cavity with a filtering aperture FA at the confocal plane (Fig. 1). The main SFUR idea is to choose the filtering aperture radius a in order that a plane

wave striking FA is focused by the shorter radius concave mirror M_2 to an Airy disk of radius a. This means[6]:

$$a = (0.61\lambda f_2)^{1/2} \qquad (1)$$

where λ is the laser wavelength and f_2 is the focal length of M_2. In such conditions, only the Airy disk propagates further beyond the aperture, is magnified and collimated by the mirror M_1. An exact Fourier transform relation connects the field distribution at FA and the new field distribution at the same plane after the field has been reflected by one of the mirrors (self imaging condition).

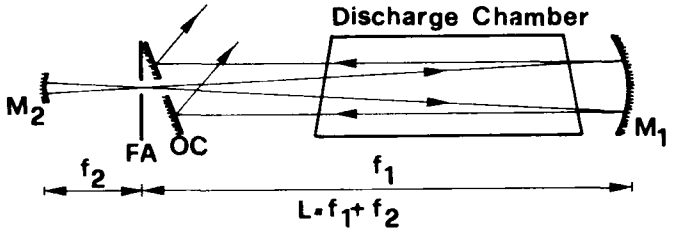


Fig. 1 Experimental set up of the confocal scheme; M_1 and M_2 concave mirrors; FA spatial filtering aperture of diameter $2a$; OC - output coupler

It comes out that the Airy disk choice removes the hot focal point, since the diffraction from the filtering aperture contrasts the focusing action of the M_2 mirror. Such a choice allows also, a fast establishment of the steady state laser field, since minimizes the number of round trips needed to establish a laser mode starting from incoherent fluorescence. Moreover, a smooth field profile, completely free of modulations, can be obtained with such resonator scheme[7,8]. However, the main drawback of this configuration is due to the dependence of the laser beam mode volume on the magnification value M and on the radiation wavelength. In fact, the output beam reaches zero amplitude at a radius $R \cong 1.5\ |M|\ (0.61\ f_2\ \lambda)^{1/2}$ and, when the SFUR is applied to short-pulse excimer lasers quite small mode volumes can be achieved. This arises firstly from the explicit dependence of the R value on laser wavelength. Secondly, the excimer laser pulse duration limits resonator length, maximum magnification value and then laser beam cross section. To partially overcome this problem it has been proposed[10] a Generalized Self Filtering Unstable Resonator (G-SFUR). The G-SFUR is a non-confocal resonator made up by a plane mirror, a concave mirror and an intracavity field limiting aperture (Fig. 2). In such scheme the filtering aperture size and its location with respect to both mirrors, are chosen in order to get a configuration having the same features of SFUR.

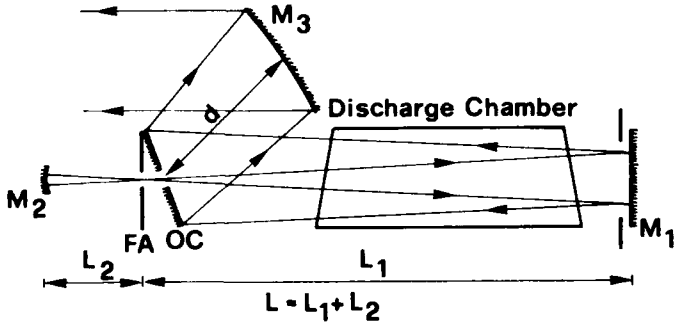


Fig. 2 Experimental set up of the non confocal scheme; M_1 plane mirror; M_2 concave mirror; FA spatial filtering aperture of diameter $2a$; OC output coupler; M_3 collimating mirror

In particular, the FA location and therefore its distance L_1 from M_1 and its distance L_2 from M_2, must be determined by requiring that the image plane of the pinhole, after one round trip, corresponds to the pinhole plane itself (self-imaging condition)

$$L_2 = f_2(1+f_2/2\ L_1) \qquad (2)$$

Secondly, the FA radius must be chosen in order to cut off the oscillations of the eigenmode TEM_{00} in the short part of the cavity, so:

$$a = [L_2\ \lambda\ (1-L_2/2f_2)]^{1/2} \qquad (3)$$

The magnification is then:

$$M = -\frac{L_1}{L_2}\,\frac{1}{1-L_2/(2f_2)} \qquad (4)$$

From the previous relations it comes out that the G-SFUR magnification can be simply varied by varying the L_1 flat mirror distance from FA. Moreover, from equations (2) and (4) it comes out that for $L_1 \gg f_2$, the G-SFUR scheme allows to get M values about twice larger than the M values obtained with a SFUR scheme having the same less curved mirror and resonator length.

Since in the G-SFUR cavity the wave fronts of the modes are curved, the output beam extracted near the pinhole screen can be collimated by a mirror M_3 having focal length[10]

$$f_3 = d - \frac{2L_2(1-L_2/2f_2)}{1-L_2/f_2} \qquad (5)$$

were d is the distance between FA and M_3.

III Experimental Apparatus

The UV-preionized discharge excited XeCl laser used in this experiment has been realized locally. The discharge is of the capacitor charge transfer type, with a primary and secondary capacitance of 150 nF and 25 nF, respectively. The laser chamber is made from a 68 cm long, commercially available PVC tube which contains the electrode structure. The discharge electrodes 50 cm long, 5 cm wide are set at a distance of 2 cm. The UV preionization is provided by a spark array rod located on one side of the electrode structure. The preionization rod is driven by a capacitor C_P=10nF which is switched simultaneously with the primary capacitor, by a spark gap made locally. The electrode assembly cross section and the schematic electrical diagram of the laser system are shown on Fig. 3. The laser chamber sealed with Brewster angle windows is about 80 cm long. A standard gas mixture (.1% HCl, 2.1% He, 1.3% Xe, 96.5% Ne) at a total pressure of 400 kPa has been used.

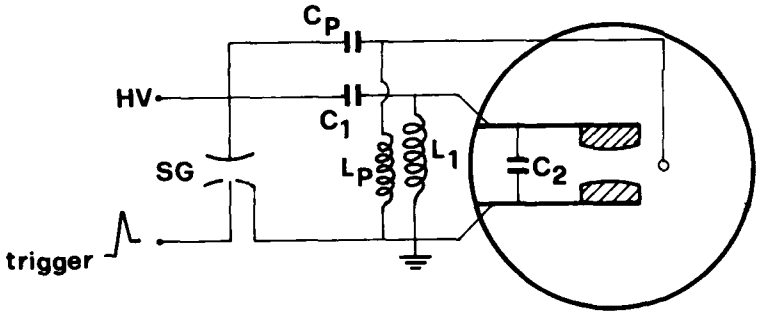


Fig.3 Electrode assembly cross section and schematic electrical diagram of the laser system

With a plane parallel optical resonator, made up of an aluminized silica reflector and an UV grade silica output coupler, an output beam (1.1x2) cm^2 of 250 mJ and 32 ns duration, full width at half maximum (FWHM), has been obtained at the highest value of the breakdown voltage of the internal capacitors (Vb=43kV). A laser extraction energy density of 2.3 mJ/cm^3 has been then achieved.

A schematic set up of the negative-branch confocal unstable configuration, is shown on Fig. 1. M_1 and M_2 are concave mirrors of focal length f_1 =100 cm and f_2 =10 cm respectively, then, the cavity magnification is $|M|$ =10. FA is the filtering aperture, made of a 25μm thick stainless steel disc with a drilled hole of radius *a* located at the confocal plane. A plane mirror OC set near FA has been used as laser beam output coupler. To fulfil the "SFUR self-filtering condition" the spatial filter diameter must be set at $2a$=0.27 mm under our experimental conditions.

In order to realize a G-SFUR having the same cavity length and the same M_2 mirror as in the SFUR scheme previously described, the values of L_1 and L_2 have been set at 99.5 cm and at 10.5 cm respectively, in accordance with Eq. (2). Moreover, a filtering aperture of diameter $2a$ =0.25 mm has been used, as required by Eq. (3). A cavity with a magnification $|M|$ = 19.9 has been then realized. This value is about twice larger than the M value of the corresponding confocal scheme. To collimate the laser output beam, a concave mirror M_3 of 239 cm focal length, placed at about 39.5 cm from OC has been used, as it comes out from Eq. (5). A schematic set up is shown on Fig. 2.

IV Experimental Results and Discussion

By applying the SFUR scheme to our XeCl laser, a laser beam of 11.5 mJ and of 22 ns duration (FWHM) has been obtained at the highest value of the breakdown voltage (Vb=43 kV). A laser extraction energy density of 1.8 mJ/cm^2 has been then achieved.

The high quality of the laser beam can be easily inferred from the burn spots on a sensitive paper at different distances from the output coupler (Fig. 4). Near OC ($\simeq$ 0.1 m) the burn spot has a central hole due to the output coupler aperture. At 1.5 m from OC, the beam spot shows a ringed pattern due to the diffraction effect of the hole. A uniform spot is then obtained at longer distances.

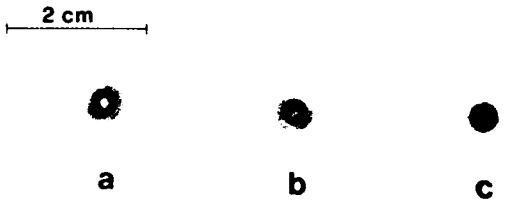


Fig. 4 Burn spots of the SFUR laser output beam at (a) 0.1 m, (b) 1.5 m, (c) 5m from the output coupler.

The far field beam divergence was determined by measuring the laser beam diameter at the focal plane of a 5 m lens. From the experimental results it has been found that more than 85% of the far field beam energy is comprised in a spot corresponding to a full angle beam divergence ϑ=0.28 mrad. Therefore, a nearly diffraction limited laser beam has been obtained with the SFUR scheme. In fact, ϑ is only 1.5 times larger than the diffraction limited value $\vartheta d=2.44\ \lambda/3a\ |M|$. Thus a beam brightness of about 7×10^{13} Wcm^{-2} Sr^{-1} has been achieved.

With the G-SFUR scheme applied to the same XeCl laser, a beam of 21 mJ and of 18 ns duration (FWHM) has been obtained at Vb=43 kV. The high optical quality of the output beam can be inferred from Fig. 5 which shows the laser beam burn spots recorded on sensitive paper at a) 0.1 m, b) 1.7 and c) 5 m from the collimating mirror M_3.

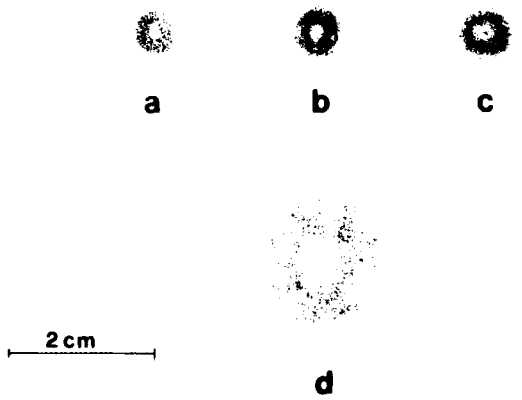


Fig. 5 Burn spots of the G-SFUR laser output beam at (a) 0.1 m, (b) 1.7 m and (c) 5 m from the collimating mirror M_3, (d) laser spot at 5 m from OC without the collimating mirror

By measuring the collimated laser beam diameter at the focal plane of a 5m lens, a full angle beam divergence of 0.16 mrad has been obtained. Since a laser beam diameter of 7.3 mm has been measured on M_3, the divergence is 1.6 times larger than the diffraction limited value which is 0.1 mrad. The just given divergence value depends on the collimating mirror position. It is convenient to find out the G-SFUR divergence value corresponding to the beam diameter on the output coupler mirror OC, to better compare the SFUR and G-SFUR performance parameters. A beam diameter of 6.3mm has been measured on the OC mirror, then a beam divergence and brightness of 0.19 mrad and 1.3×10^{14}Wcm^{-2}Sr^{-1} respectively, have been achieved with the G-SFUR configuration. Moreover, a laser extraction energy density of about 2.2 mJ/cm^3 has been achieved. Such extraction energy density value is very close to value obtained with a plane-parallel cavity scheme.

From the experimental results just reported, we observe a shorter pulse duration of the laser beam obtained with the G-SFUR configuration, with respect to the SFUR laser beam time length. This can be due to the nigher magnification value of the G-SFUR scheme and so to the higher mode losses of such cavity, which are determined by $(1-1/M^2)$. Therefore, the

gain factor of the active medium is greater than the threshold gain value for a shorter time in this last configuration[7].

We observe that a higher energy density has been extracted and a beam brightness 50% larger has been achieved with the G-SFUR scheme.

The laser energy E_o and pulse width Δt as a function of the breakdown voltage have also been measured in both resonators. The experimental results plotted on Fig. 6 and Fig. 7 show a nearly equal behaviour of E_o and Δt versus Vb in both cavities.

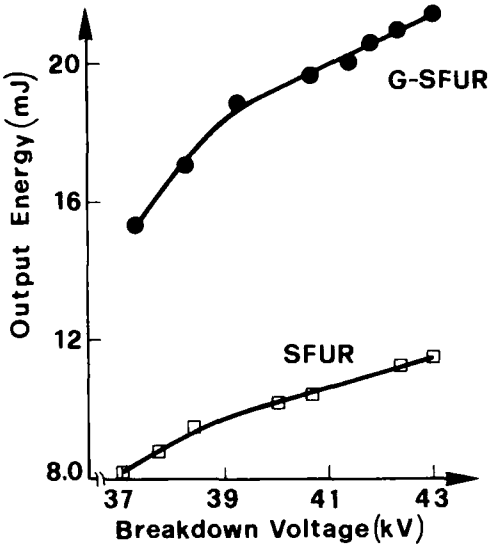


Fig.6 Output energy as a function of the breakdown voltage for the SFUR (□) and for the G-SFUR (●) scheme

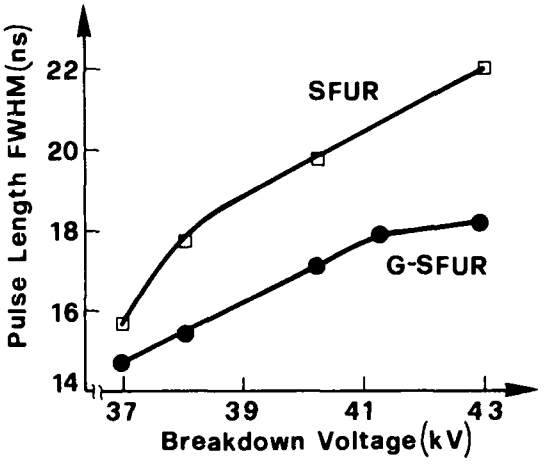


Fig. 7 Pulse width (FWHM) as a function of the breakdown voltage for the SFUR (□) and for the G-SFUR (●) scheme

It has also been observed that the sensitivity to mirror misalignments is nearly the same in both configurations. The experimental measurements of the normalized output energy as a function of the mirror tilting angle are shown on Fig. 8. It turns out that the value of the tilting angle which halves the normalized output energy is is about 1.5 mrad for both cavities.

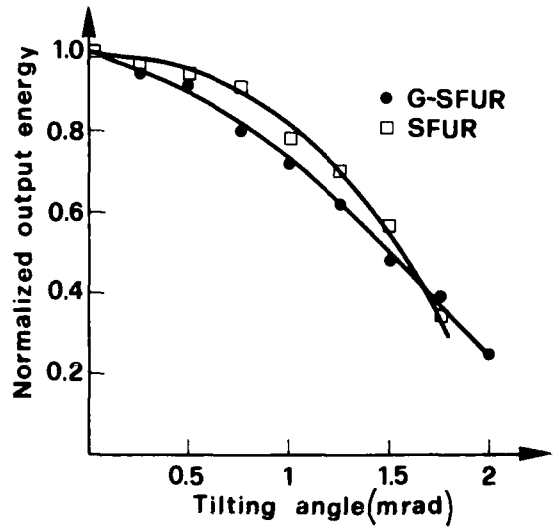


Fig. 8 Normalized output energy as a function of the tilting angle for the SFUR (□) and for the G-SFUR (●) scheme

Therefore, it has been found that in accordance with theory, the G-SFUR maintains the excellent properties of SFUR, like high transverse mode discrimination, fast establishment of nearly diffraction limited output beams, low sensitivity to mirror misalignments, but allows to have larger mode volumes with shorter resonator lengths, with respect to the SFUR scheme.

It is important to observe that with such resonator configurations, larger mode

volumes can also be obtained by increasing the filtering aperture radius beyond the value required by the "self-filtering condition". Therefore, the FA radius, a, has been varied and its effect on the output beam energy and divergence has been investigated in the confocal and in the non-confocal configuration.

Three filtering apertures with a diameter of 0.5, 0.7 and 0.9 mm respectively have been tested in the confocal scheme. Fig. 9 shows the burn spots of the output beam recorded on a sensitive paper at about 10 cm from the output coupler. The burn spot of the output beam obtained with $2a$=0.27 mm (SFUR self-filtering condition) is shown on Fig. 9a. It is important to point out that only in this last condition the output beam diameter gets zero amplitude at a value $D \cong 1.5|M|2a$. By increasing the filtering aperture radius beyond the value required by the "SFUR self-filtering condition", the output beams get zero amplitude at $D \cong |M|2a$.

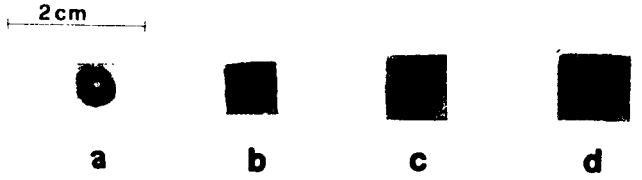


Fig. 9 Burn spots of the confocal scheme laser beam, at about 10 cm from OC for a) $2a$ =0.27 mm, b) $2a$=0.5 mm, c) $2a$=0.7 mm, d) $2a$=0.9 mm.

Fig.10 shows the burn spots of the output beam obtained by varying the FA diameter in the non-confocal scheme. Three filtering apertures with a diameter of 0.3, 0.4 and 0.5 mm respectively have been tested and laser beams with a diameter of 7.5, 9 and 11 mm respectively, have been measured on the OC mirror. The beam burn spots have been recorded on a sentitive paper at about 10 cm from OC.

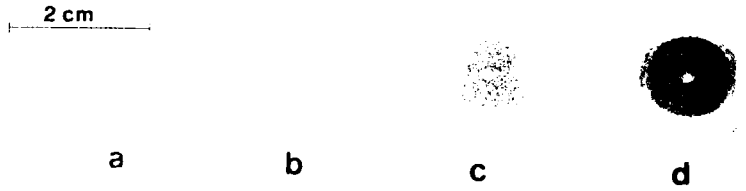


Fig.10 Burn spots at the non-confocal scheme output beam at about 10 cm from OC for a) $2a$ =0.25 mm, b) $2a$ =0.3 mm, c) $2a$=0.4mm, d) $2a$ =0.5 mm.

From Figs. 9 and 10 it turns out that, in both configurations, the laser output beams show a regular intensity spatial profile even at a values larger than those required by the "self-filtering condition". This is a peculiar property of such negative branch unstable resonators. It is well known that with positive branch unstable cavities, the intensity radial variation of the output beam shows, instead, a characteristic ring pattern which arises from diffraction effects.

The effect of the filtering aperture size on the output laser beam energy and divergence, is shown on Figs. 11 and 12 for the confocal and non-confocal configuration, respectively. The experimental results plotted as a function of $2|M|a$ show in both schemes a linear growth of the output energy as the laser beam cross section increases (Fig.11). But, laser beams of higher energy are obtained with the confocal scheme at a given $2|M|a$ value. This can be due to the lower mode losses and to the higher feedback signal (i.e. higher a value) of this last configuration.

The laser beam divergence does also grow as the a value and then the beam diameter are increased. A faster rise of the laser beam divergence versus $2|M|a$ is observed in the confocal scheme. Since the filtering aperture size affects strongly the mode selection in both schemes, we observe that laser beams of higher energy, but of lower optical quality, are obtained at larger a values. It is important to point out that, the number of round trips to get a diffraction-limited beam starting from spontaneous emissions, gets larger by increasing the a value, beyond the value required by the "self-filtering condition", as it comes out from simple geometrical optics considerations[3-7]. Fig.13 gives the beam brightness versus $2|M|a$. In both configurations the beam brightness slows down by increasing the a values. Neverthless, with the non confocal scheme a beam of quite high brightness has been obtained at the largest $2|M|a$ value investigated.

It is important to point out that, in both schemes, not hot spots have been observed at the resonator focal plane, at the highest excitation rates and up to a repetition rate of 1 Hz. Moreover, the radius a of FA after more than 1000 shots was unchanged in both cavities respectively.

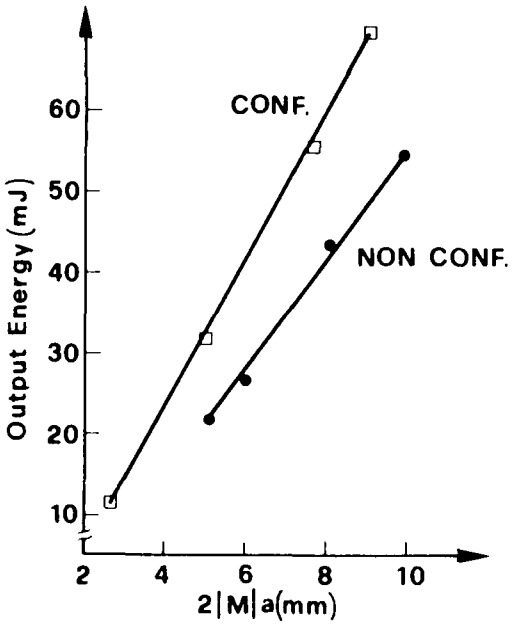


Fig. 11 Output laser beam energy versus $2|M|a$ for the confocal (□) and non-confocal (●) scheme.

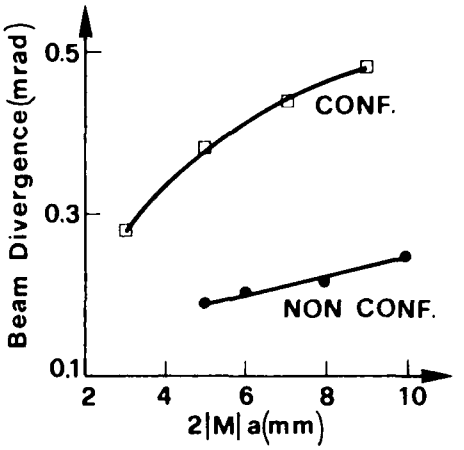


Fig. 12 Laser beam divergence versus $2|M|a$ for the confocal (□) and non-confocal (●) scheme

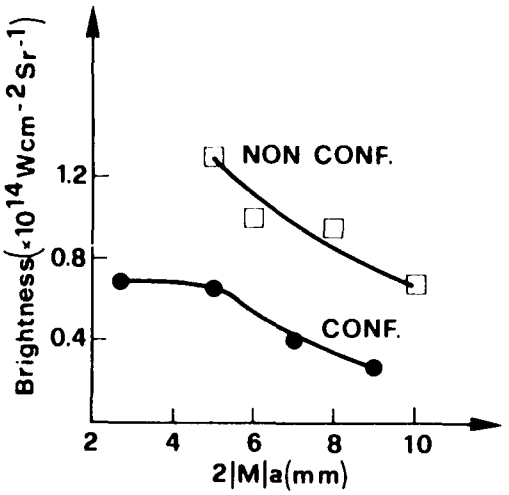


Fig. 13 Laser beam brightness versus $2|M|a$ for the confocal (●) and non-confocal (□) scheme

Conclusions

Confocal and non-confocal negative branch unstable resonators with an intracavity spatial filter have been applied to a high-gain short-pulse UV-preionized XeCl laser. By setting the spatial filter diameter equal to the value required by the SFUR and the G-SFUR "self filtering condition" respectively, nearly diffraction limited beams have been obtained with both schemes. But, a laser beam with a brightness 50% higher has been achieved with the G-SFUR configuration. In fact, in accordance with theory, the G-SFUR maintains the excellent properties of SFUR, but allows to have larger mode volumes with shorter resonator lengths with respect to SFUR.

By increasing in both configurations the spatial filter diameter beyond the value required by the "self-filtering condition" respectively, laser beams of higher energy, but of relatively lower optical quality, have been obtained. In fact, the spatial filter size affects strongly the mode selection in both schemes.

Neverthless, it is important to point out that laser beams of quite high brightness and with a regular intensity spatial profile can be obtained by applying such resonators to high gain short pulse excimer lasers.

Acknowledgements

Dr Chen Jianwen (on leave from Shanghai Institute of Optics and Fine Mechanics, Academia Sinica, Shanghai, China) has carried out this work with the support of the "ICTP Program for Training and Research in Italian Laboratories, Trieste, Italy".

Work partially supported by Consiglio Nazionale delle Ricerche.

References

1. A.E. Siegman: Appl. Optics 13, 353 (1974)
2. Yu. A. Anan'ev: Sov. J. Quant. Electron. 5, 615 (1975).
3. K.I. Zemskov, A.A. Isaev, M.A. Kazaryan, G.G. Petrash and S.G. Rautian: Sov. J. Quant. Electron. 4, 474 (1974).
4. A.A. Isaev, M.A. Kazaryan, G.G. Petrash, S.G. Rautian and A.M. Shalagin: Sov. J. Quant. Electron. 7, 746 (1977).
5. E. Armandillo, A. Luches, V. Nassisi and M.R. Perrone: Optics Comm. 56, 225 (1985)
6. P.C. Gobbi, S. Morosi, G.C. Reali and A.S. Zarkasi: Appl. Optics 24, 26 (1985).
7. A. Luches, V. Nassisi and M.R. Perrone: Appl. Optics 28, 2047 (1989).
8. J.W. Chen, A. Luches, V. Nassisi and M.R. Perrone: Optics Comm. 72, 225 (1989).
9. J.W. Chen, A. Luches, V. Nassisi and M.R. Perrone: J. Modern Optics 37, 75 (1990).
10. P. Di Lazzaro, T. Hermsen and C.E. Zheng: IEEE J. Quantum Electron. QE-24, 1543 (1988)
11. P. Di Lazzaro, V. Nassisi and M.R. Perrone: IEEE J. Quantum Electron. QE-24, 2284 (1988).
12. A. Luches, V. Nassisi, M.R. Perrone and E. Radiotis: Optics Com. 71, 97 (1989).

VUV EMISSION FROM ELECTRON BEAM EXCITED CsF VAPOR AT HIGH PRESSURES OF He OR Ne BUFFER GAS

V. T. Gylys, R. D. Bower, D. G. Harris and T. T. Yang

Abstract

CsF vapor in a buffer gas of He or Ne was excited by an electron beam. In a charge transfer reaction from He ions to CsF, emission at 185 nm has been observed. It has been tentatively assigned to the (B→X) transition of $Cs^{2+}F^-$.

Introduction

Excimer lasers have proven their capability to produce high power coherent radiation from the visible to the UV with high efficiency. Recently, Sauerbrey and Langhoff[1] suggested an approach for generation of stimulated emission in the 80-200 nm region by making use of ionic molecules that are isoelectronic with rare-gas halide excimers. In particular, a scheme based on excited ionic states of alkali halides was proposed.

The estimated spectroscopic properties of ionic alkali halide systems are summarized in Table 1.[1] The estimated radiative lifetimes are typically near 1 nsec or about an order of magnitude shorter than those for rare gas halide systems. Experience with the XeF laser has shown that with lifetimes this short, the development of gain will be dominated by radiative process [2,3] and require high pump rates.

Table 1.

Molecule	Wavelength(nm)	Radiative Lifetime(ns)	Stimulated Emission ($10^{-16}cm^2$)
$K^{2+}F^-$	86-110	0.54	0.72
$Rb^{2+}F^-$	115-130	0.67	0.95
$Cs^{2+}F^-$	154-195	1.47	1.50
$Cs^{2+}Cl$	131-205	1.80	1.10
$Cs^{2+}Br$	117-190	1.92	0.77
$Rb^{2+}Br^-$	80-100	0.91	0.50

In this work, a concept has been developed for the extension of rare-gas halide laser technology to shorter wavelength by means of isoelectronic ionic excimer transitions. The similarity of the ionic excimer molecules with the rare gas halide excimer molecules should by very helpful in the study of these systems.

By using a Rittner potential [4] for the upper state and a Born-Mayer potential [5] for the repulsive interaction, the range of the emitted wavelengths has been predicted [1,7,8]. The potential energy diagrams for these systems are shown in Figure 1. The emission should exhibit structure similar to that observed for rare gas halide excimers. The main intensities are due to the B→X and C→A transitions.

Since for the rare gas halides no stable ground state molecules exist, only a reactive formation of the upper lasing state is possible. Contrary to rare-gas halides, due to the existence of stable alkali halide molecules, a variety of excitation methods for the ionic alkali halide excimer states are possible. These include direct excitation of the alkali halides by charge transfer using atomic or molecular ions, optical pumping such as soft x-ray excitation, collisional excitation transfer using metastable rare gas states, and the reactive formation after excitation of the molecular constituents.

Figure 1 shows the relative energy levels between ionic CsF and various atomic and molecular metastables and ions of He. For CsF, collisional transfer using metastable helium and charge transfer using atomic and molecular He ions appears to be the logical scheme for direct excitation.

Experimental

Two approaches were chosen to investigate the spectroscopic properties of the molecules. In the first approach, soft x-ray excitation of the molecules was chosen because of its simplicity and ease of use. Radiation from a high power laser is focussed onto a target. The resulting soft x-rays emitted from the laser produced plasma photoionize an inner shell electron from the candidate molecules. The molecule subsequently fluorescences. This fluorescence is detected and identifies the promising transitions in the molecules.[9]

The second approach addresses the feasibility of electron beam excitation of the candidate molecules. As e-beam experiments are more difficult and time consuming, the initial laser produced plasma survey provided a spectroscopic guide which saved time and effort. The candidate molecules were added to a buffer gas (He or Ne) in a heatpipe. The e-beam excited the buffer gas which transferred its excitation to the ionic alkali halide. Spectroscopic measurements were subsequently carried out.

A versatile facility, as shown in Figure 2 was assembled to investigate the feasibility of electron beam pumping of the ionic excimers. Two electron beam sources were procured with the specifications listed in Table 2.

Table 2.

	FEBETRON 706	HP-45710-A
Avg. Energy	0.6 MeV	1.0 MeV
Peak Current	7000 A	2000 A
Pulse LEngth	3 nsec	30 nsec

Two heatpipe cells were fabricated. The electron beam generator and heatpipe were enclosed in a lead shielded room to contain the x-ray emission. The electron beam passed through a 0.001" foil and into the heatpipe cell where it excited the gas. Two solenoid magnets confined the beam to the cell. Fluorescence emission from the gas in the heatpipe was again detected with a monochromator and photomultiplier (PMT) or VUV Optical Multichannel Analyzer. The data acquisition electronics were contained in an EMI shielded room to reduce the electromagnetic noise produced by the e-beam.

Two high pressure heatpipes (HPH-1) and HPH-2) were designed and fabricated. HPH-1 is a concentric design (Figure 3) with an outer pipe which has Cs as a working fluid. This heatpipe was constructed of inconel to allow operation over 1000°C and up to 40 atm of pressure. Two ports allowed the monochromators to view the plasma both longitudinally and transversely to the e-beam. A photograph of HPH-1 is shown in Figure 4. The second heatpipe (HPH-2) was of a more conventional linear design and could operate up to 10 atms of pressure.

Either of two VUV monochromators were used to collect and disperse the fluorescence. A 1.0 meter monochromator was equipped with a 1200 groove/mm and a 300 groove/mm grating. Both gratings were Al with a MgF coating for protection, and could be used efficiently above 100 nm. For operation below 200 nm, an iridium coated 2400 groove/mm grating was installed. The second monochromator was a 0.25 meter VUV monochromator with an Al-MgF coated, 1200 groove/mm grating.

The fluorescence was detected with either of two detector systems. Initially a photomultiplier (PMT) with a sodium salicylate scintillator was used. Time-resolved measurements were made by connecting the PMT to a high-speed oscilloscope equipped with a digitizing camera. The camera was interfaced to a computer to allow data acquisition and processing to be carried out. The rise-time of this acquisition system was 5 nsec.

A second detector was designed and fabricated. This was a VUV Optical Multichannel Analyzer (OMA) with nearly single photon detection between 30 and 250 nm. This detector consisted of a microchannel plate detector interfaced to a reticon array. The VUV photons strike a CsI scintillator, which emits photoelectrons. The photoelectrons are amplified in the microchannel plate, and then converted to visible radiation by a phosphor, which is interfaced through a fiber optic bundle to a reticon array. The array was read out to a computer which allowed signal processing. The resulting instrument, a very sensitive and versatile VUV detector, permits a spectrum to be acquired on a single excitation pulse. It also allows averaging and subtraction of spectra as well as other data processing to be carried out.

Results

The emission spectrum of e-beam pumped $Cs^{2+}F^-$ was recorded for various concentrations of CsF and buffer gases, He and Ne. The effect of H concentration on the $Cs^{2+}F^-$ emission is shown in Figure 5. Both spectra have 2 torr or CsF but the He pressure is 3.28 atm in upper spectrum and 9.21 atm in the lower spectrum. The $Cs^{2+}F^-$ is most likely formed by the bimolecular and termolecular charge transfer and Penning ionization reactions.

$$He_2^+ + CsF \rightarrow Cs^{2+}F^- + 2\ He$$

$$He_2^+ + CsF + He \rightarrow Cs^{2+}F^- = 3\ He$$

$$He^*(2^3S) + CsF \rightarrow Cs^{2+}F^- + He + e^-$$

$$He^*(2^3S) + CsF + He \rightarrow Cs^{2+}F^- + 2\ He + e^-$$

Excitation transfer by He^+ is not expected to be significant at the high pressures studied in the e-beam experiments due to the termoclecular association process

$$He^+ + 2\ He \rightarrow He_2^+ + He$$

which has a rate coefficient of $1.4 \times 10^{-31}\ cm^6 sec^{-1}$.

The spectrum with 3.28 atm of He is the sum of six e-beam pulses whereas the spectrum at 9.21 atm of He is a single e-beam pulse. Thus, increasing the He pressure a factor of three caused approximately a factor of 15 increase in the $Cs^{2+}F^-$ emission intensity. This increase in intensity is the result of several effects. First, increasing the He pressure increases ion-pair production rate.[3,4] Secondly, increasing the He pressure raises the importance of three body processes. The increase in ion-pair production rate would account for approximately a factor of three increase in signal. This leaves a factor of 5 to be accounted for by the kinetics. The kinetics of this system are quite complicated, however the rate of a three body process involving two He atoms would increase nine fold for an increase of 3 in He pressure. Thus it is not unreasonable that the $Cs^{2+}F^-$ emission intensity could increase by a factor of 5 due to kinetic considerations.

The $Cs^{2+}F^-$ radiative lifetime is reported to be approximately 1 nsec.[1] Thus the $Cs^{2+}F^-$ emission intensity should reach steady state in approximately 1 nsec. The time response the detection system was estimated to be approximately 20 nsec. The observed risetime of the $Cs^{2+}F^-$ emission is the response time of the detection electronics. The decay should be due to a decline in $Cs^{2+}F^-$ production rate. Both He_2^+ and $He^*(2^3S)$ have sufficient energy to excite CsF to $Cs^{2+}F^-$. The $Cs^{2+}F^-$ emission decay rate is then due to the disappearance of these energetic species. As the pressure is increased the species disappear faster.

The deactivation of $Cs^{2+}F^-$ can occur by recombination with electrons and negative ions, by collisions with electrons and molecules or by radiation. Examples are

$$Cs^{2+}F^- + e^- \rightarrow CsF^*$$
$$\rightarrow Cs^* + F$$
$$\rightarrow Cs + F^*$$
$$\rightarrow Cs^+F + e^-$$
$$\rightarrow \text{other}$$

$$Cs^{2+}F^- + F^- \rightarrow CsF^* + F$$
$$\rightarrow CsF + F^*$$
$$\rightarrow Cs + F_2$$
$$\rightarrow \text{other}$$

$$Cs^{2+}F^- + M \rightarrow Cs^+F + M$$
$$\rightarrow CsF + M^+$$
$$\rightarrow \text{other}$$

$$Cs^{2+}F^- \rightarrow Cs^+F + h\nu$$

Assuming rate constants for the recombination and collisions with electrons of $10^{-7}cm^3s^{-1}$, recombination with negative ions of $3 \times 10^{-6}cm^3s^{-1}$, collisions with molecules of $10^{-10}cm^3s^{-1}$, a radiative rate of 10^8s^{-1} and particle densities of $5 \times 10^{15}cm^{-3}$ for electrons, $3 \times 10^{14}cm^{-3}$ for negative ions and $10^{17}cm^{-3}$ for gas kinetic molecular quenchers, then the deactivation rates are $5 \times 10^8s^{-1}$ for recombination with negative ions, 10^7s^{-1} for collisions with molecules and $5 \times 10^8s^{-1}$ for collision with electrons. The total deactivation rate is approximately $3 \times 10^9s^{-1}$. Therefore about one-third of the $Cs^{2+}F^-$ formed should radiate.

Figure 6 shows the $Cs^{2+}F^-$ emission spectrum for 2 Torr of CsF and 2.3 atm of Ne. The spectrum is the sum of six e-beam shots. Since the stopping power of the gas is approximately proportional to its atomic number, 2.3 atm of Ne should have the same stopping power as 11.5 atm of He. Therefore, the decrease in $Cs^{2+}F^-$ emission intensity relative to the 9.21 atm He spectrum is due to the relative kinetics and energetics of the two systems. In the case of helium, He^+, He_2^+ and $He^*(2^3S)$ are all sufficiently energetic to produce $Cs^{2+}F^-$ either by charge transfer or Penning ionization. However, with Ne buffer gas, only Ne^+ and Ne_2^+ have sufficient energy. This suggests that $He^*(2^3S)$ plays a major role in the excitation of $Cs^{2+}F^-$ in the He buffer system.

The $Cs^{2+}F^-$ emission spectrum dependence on the CsF concentration is shown in Figure 7. The emission intensity is observed to decrease dramatically with increasing CsF concentration. This could be due to ground state CsF absorption of the 185nm light emitted by $Cs^{2+}F^-$.

The time-resolved fluorescence intensity of the $Cs^{2+}F^-$ was determined with the electron beam excitation. A Febetron 706 was used as the e-beam source. It has a 3 nsec pulse width and a peak current of 7000A. The fluorescence was detected with a 1-meter VUV monochromator and solar blind photomultiplier tube. The ouput of the photomultiplier tube was recorded with a digital storage oscilloscope. Several e-beam shots could be averaged together on the oscilloscope.

Time decays were recorded at various CsF and He buffer gas concentrations. Figures 8, 9, 10 and 11 show the time decay at the $Cs^{2+}F^-$ emission for 2 Torr of CsF at He buffer gas pressure at 813, 2580, 4088 and 6795 T respectively. Note the different time bases on the decays. The initital decay rate increases with increasing He pressure. Figure 12 shows the time dependence for 10 T CsF and 8113 T He. Comparing Figures 11 and 12 shows that increasing (CsF) has little effect on the initial decay but decreases the long time component of the flurescence. The time evolution of the $Cs^{2+}F^-$ emission in a neon buffer is shown in Figure 13. The (CsF) was 2 T and (He) was 2595 T. The initial species are believed to be the $Cs^{2+}F^-$ emission and the long decay may be fluorescence from the window. $Ne^*(3^3P_2)$ is the only long lived spcies which should be present. Since $Ne(3^3P_2)$ does not have sufficient energy to excite CsF to $Cs^{2+}F^-$, there should be no long term production of $Cs^{2+}F^-$.

Summary

Ionic excimer emission has been observed 184.5 nm from electron beam excited CsF. We have tentatively assigned this emission to the (B→X) transition in $Cs^{2+}F^-$. The pressure dependence of this emission has been investigated.

Acknowledgements

The authors gratefully acknowledge the excellent technical assistance of E. Rinehart and L. Martin. This effort was supported by the Department of Energy.

References

1. R. Sauerbrey and H. Langhoff, IEEE J. Quantum Electron. QE-21, 178 (1985).

2. T. T. Yang, J. A. Blauer, C. E. Turner, Jr., and D. A. Copeland, Proceedings of Lasers in Fluid Mechanics and Plasma Dynamics AIAA Journal, 23, No. 5, 741-748 (1985).

3. J. A. Blauer, T. T. Yang, C. E. Turner, Jr., and D. A. Copeland, Appl. Optics 23, 4352 (1984).

4. E. S. Rittner, J. Chem. Phys., 19, 1030 (1930).

5. A. A. Abrahamson, Phys. Rev. 178, 76 (1969).

6. F. Steigerwald, F. Emmert, H. Langhoff, W. Hammer, and T. Griegel, Opt. Commun. 56, 240 (1985).

7. F. Steigerwald and H. Langhoff, Chem. Phys. 88, 7376 (1989).

8. T. T. Yang, V. T. Gylys and D. G. Harris, J. Opt. Soc. Am. B6, 1536 (1989).

9. V. T. Gylys, D. G. Harris, T. T. Yang and J. A. Blauer, Proceedings International Conference on Lasers '89 (STS Press, McLean, VA 1990).

10. J. M. Pouvesle, Thesis, Université d' Orleans, France (1981) [unpublished]

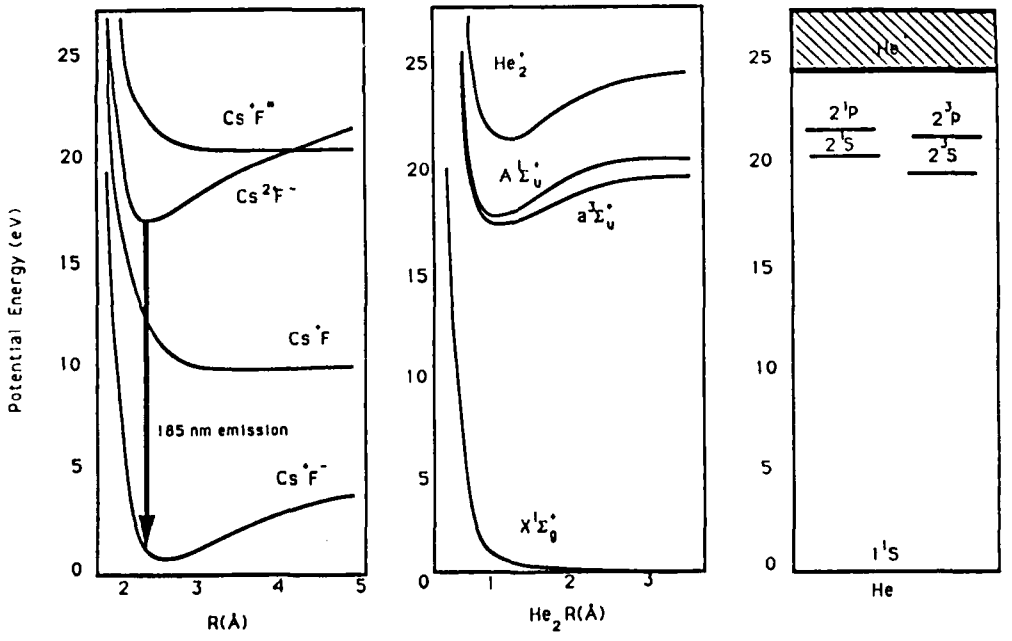


Figure 1. Potential Energy Curves for CsF, He_2 and He.

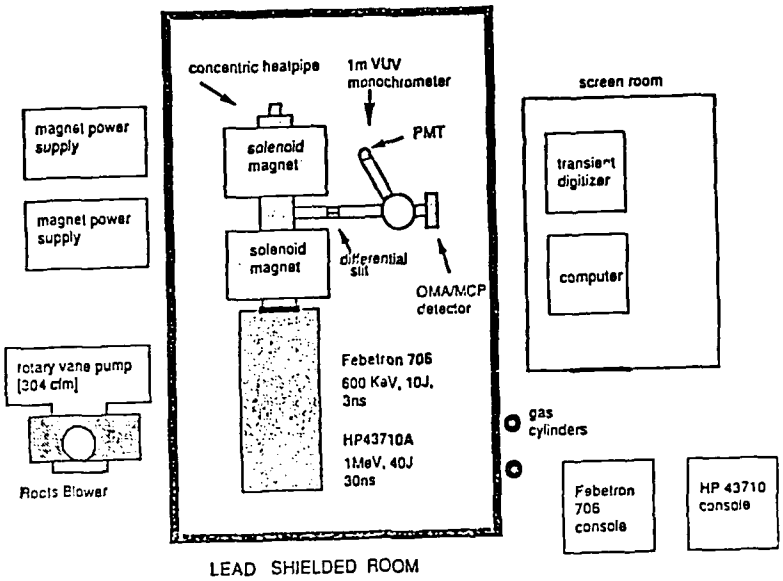


Figure 2. Schematic of the electron beam facility. The facility was equipped with both Febetron 706 and Hp-43710A electron beam pulsers. The HPH-1 had a transverse arm permitting both longitudual and transvers viewing of the excited gas.

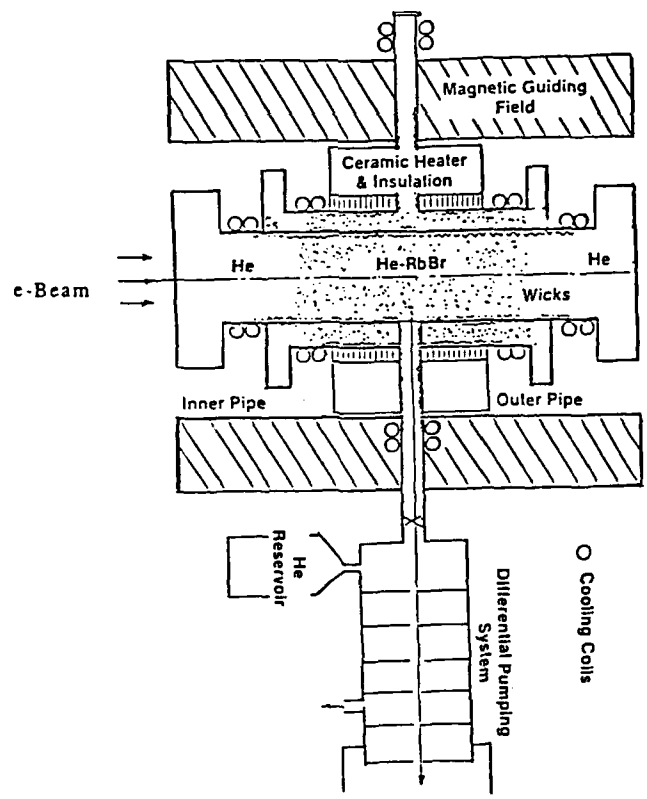


Figure 3. Schematic diagram of concentric heatpipe used in electron beam excitation experiments. The outer heatpipe used Cs as a working fluid. The alkali halide and buffer gas are in the inner heatpipe.

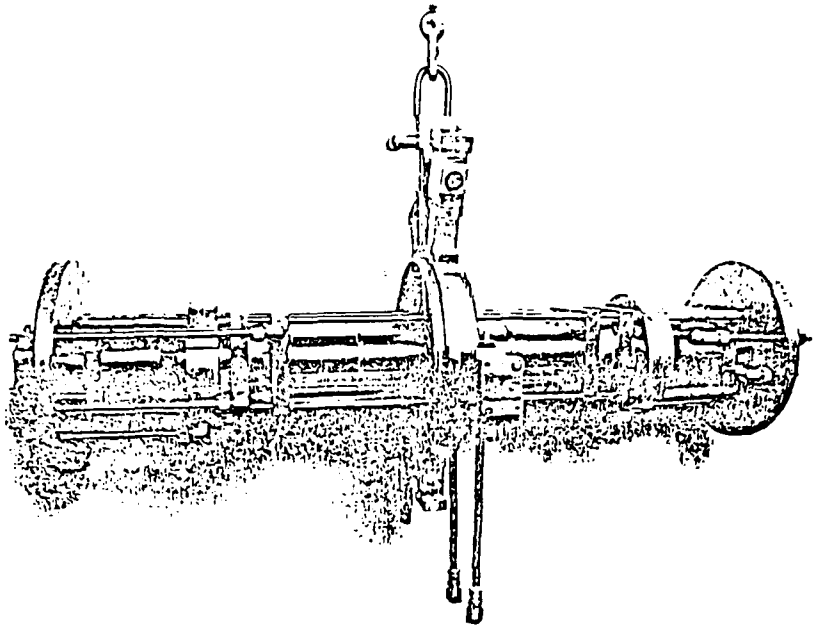
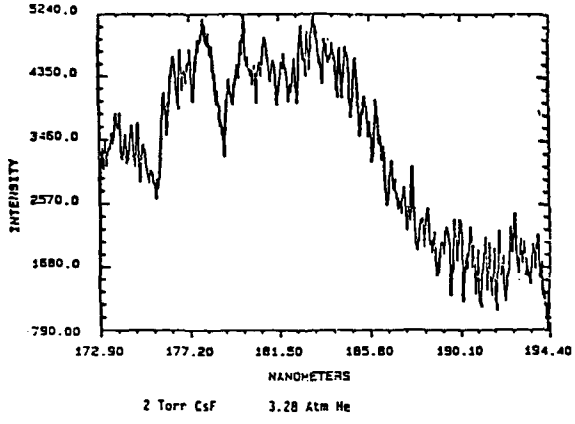


Figure 4. Photograph of concentric heatpipe used in high temperature (1000°C), high pressure (40 atm), electron beam excitation studies.



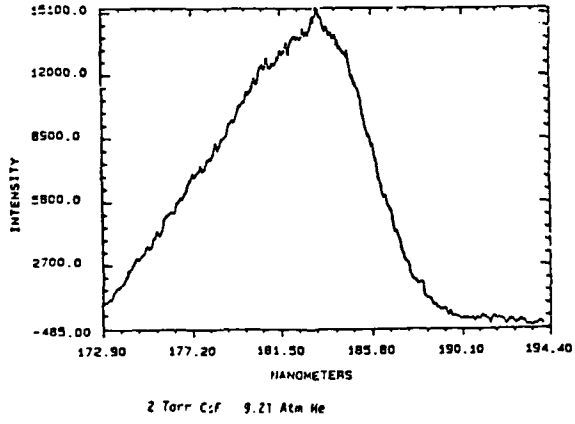


Figure 5. $Cs^{2+}F^-$ fluorescence from an e-beam pumped gas mixture of 2 Torr CsF and He pressures of 3.3 and 9.2 atm.

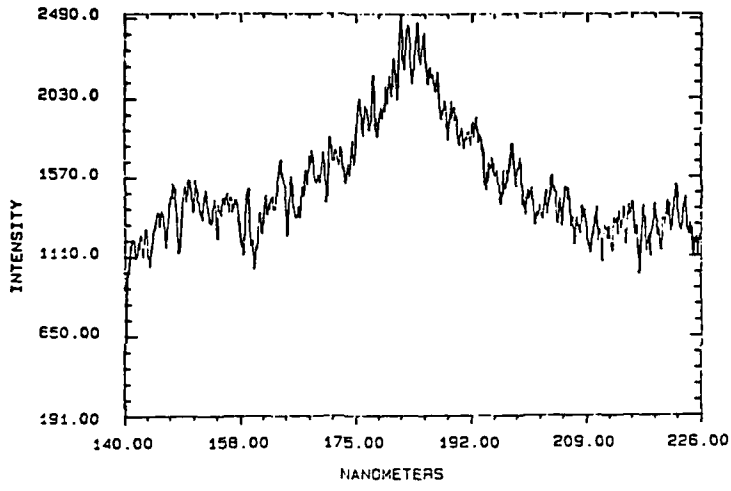
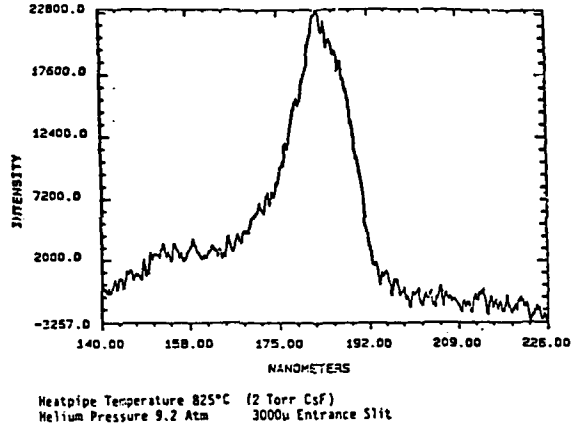


Figure 6. $Cs^{2+}F^-$ fluorescence from an e-beam pumped gas mixture of 2 Torr CsF and 2.3 atom Ne.



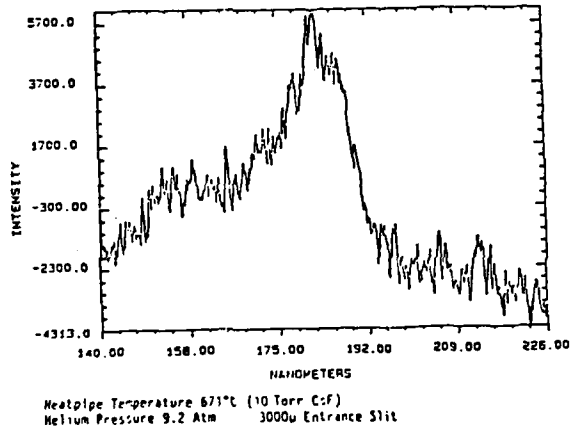


Figure 7. $Cs^{2+}F^-$ fluorescence from an e-beam pumped gas mixture of 9.2 atm He and CsF pressures of 2 and 10 Torr.

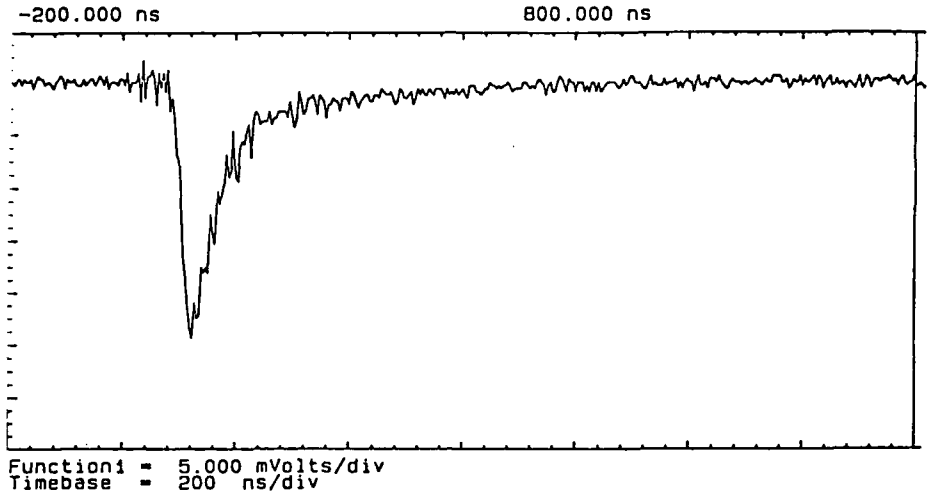


Figure 8. Temporally resolved $Cs^{2+}F^-$ fluorescence at 189.5 nm from an e-beam pumped gas mixture of 2 Torr CsF and 813 Torr of He.

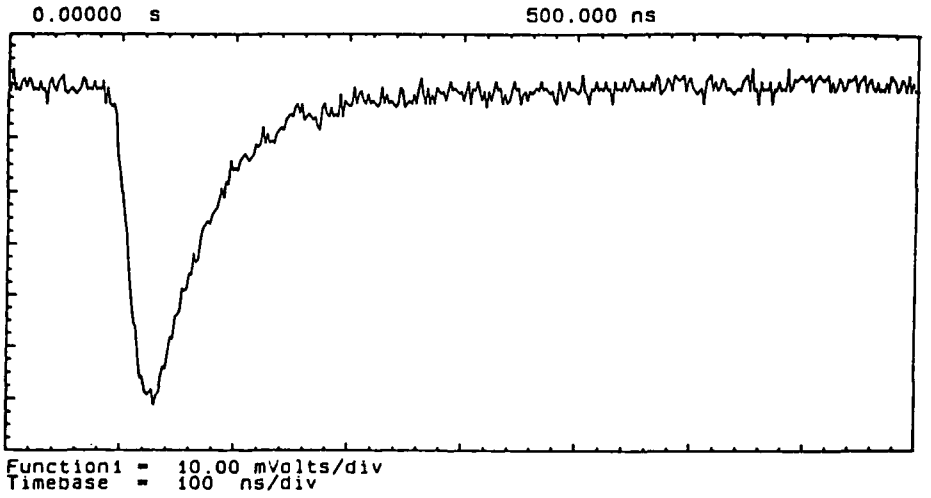


Figure 9. Temporally resolved $Cs^{2+}F^-$ fluorescence at 184.5 nm from an e-beam pumped gas mixture of 2 Torr CsF, and 2580 Torr of He.

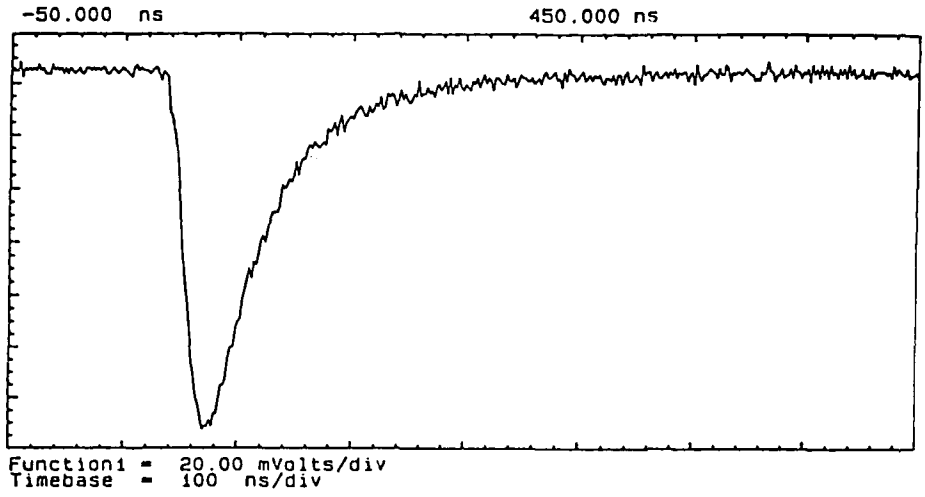


Figure 10. Temporally resolved $Cs^{2+}F^-$ fluorescence at 184.5 nm from an e-beam pumped gas mixture at 2 Torr CsF, and 4088 Torr of He.

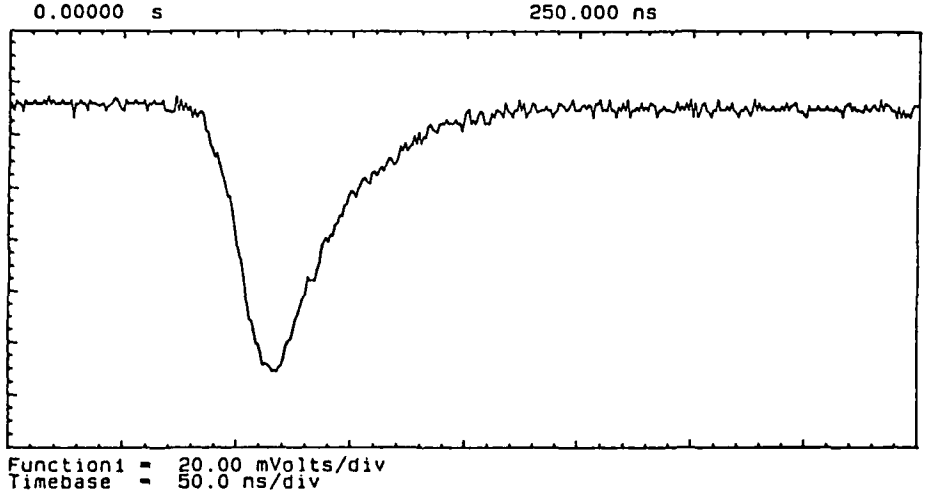


Figure 11. Temporally resolved $Cs^{2+}F^-$ fluorescence at 189.5 nm from an e-beam pumped gas mixture of 2 Torr CsF, and 6795 Torr of He.

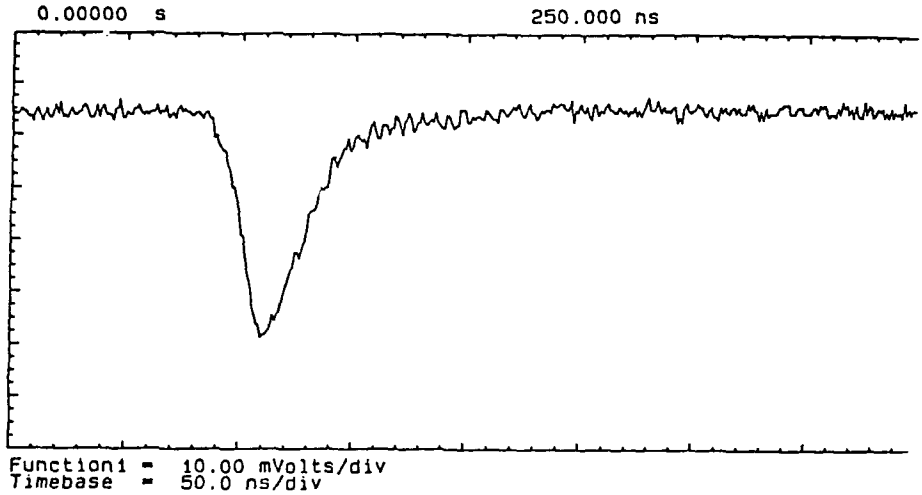


Figure 12. Temporally resolved $Cs^{2+}F^{-}$ fluorescence at 189.5 nm from an e-beam pumped gas mixture of 10 Torr CsF and 8113 Torr of He.

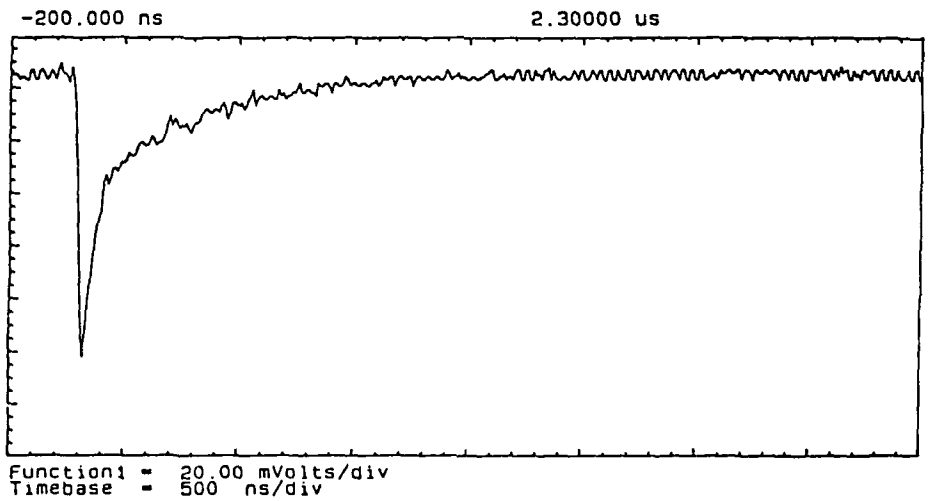


Figure 13. Temporally resolved $Cs^{2+}F^{-}$ fluorescence at 189.5 nm from an e-beam pumped gas mixture of 2 Torr CsF and 2595 T rr of Ne.

Gain Measurements on the KrF (B-X), XeF (B-X), and XeF (C-A) Laser Transitions in a XeF (C-A) Laser Gas Mixture

A. Cheville, T. Zhang, R. Sauerbrey, W.L. Wilson, and F.K. Tittel
Electrical and Computer Engineering Dept.
Rice University
Houston, TX. 77251-1892

ABSTRACT

Gain and absorption were measured on three excimer transitions in an optimized electron beam pumped XeF (C-A) gas mixture. The high net gains on the KrF (B-X), XeF (B-X), and XeF (C-A) transitions demonstrate the feasibility of developing a UV/visible multicolor excimer laser.

I INTRODUCTION

In recent years the XeF (C-A) laser has shown considerable promise as a broadly tunable, high power laser in the blue-green region of the spectrum [1]. The XeF (C-A) laser exhibits many desirable characteristics for use as a source in optical communications, laser spectroscopy, remote detection, and ultra-short pulse amplification. The spectral tuning range of the laser is greater than 90 nm and efficient laser operation has been demonstrated from 440 to 530 nm with up to 1.5 % conversion efficiency. Using injection tuning, narrow bandwidth (< .001 nm) tunable high intensity output has been demonstrated [2]. Initial work carried out at Rice used a 20 cm^3 volume and achieved output energy densities on the order of 1.5 J/l [1]. More recent work with a scaled up electron beam source exciting a 500 cm^3 volume has shown the same extraction level [3].

The performance characteristics and wavelength tuning of the XeF (C-A) laser are influenced by the presence of both broadband and narrow-line absorbers in the active medium. The identification of these absorbing species and subsequent gas tailoring [2], [4], [5] have permitted continuous tuning with increased extraction efficiency.

The temporally short, intense electron beam pumping scheme used in this device combined with the high pressure multicomponent gas mixtures found optimum for the XeF (C-A) laser also supports two other diatomic excimer transitions; both of which are in the UV spectral region and have significantly larger stimulated emission cross-sections than that of the XeF (C-A) transition. Figure 1 shows spectral characteristics of the ultraviolet emissions at 351 nm [XeF (B-X)] and 248 nm [KrF (B-X)], and the blue-green XeF (C-A) spectrum. The XeF (C-A) laser is affected by distinct valleys in the free running spectral profile due to transient, narrow-band atomic absorption lines from the rare gases used as well as broadband atomic and molecular absorptions. Shown at the top of figure 1 are absorption bands of several of the broadband transient absorber species formed by the electron beam excitation of the laser gas mixture [5].

Because of their high net gain coefficients, both the XeF (B-X) and KrF (B-X) laser transitions have a considerable impact on design considerations for a XeF (C-A) laser. The presence of these transitions indicates the potential for developing a multicolor excimer laser operating simultaneously in the blue-green spectral region on the XeF (C-A) transition as well as in the UV on the XeF (B-X) and/or the KrF (B-X) transition.

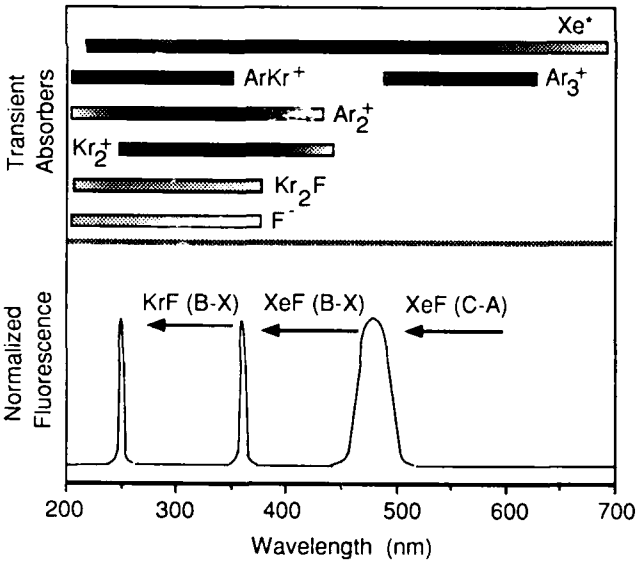


Fig. 1. The spectrum of an optimized XeF (C-A) electron beam pumped laser gas mixture shows three characteristic excimer laser transitions: the KrF (B-X) transition at 248.5 nm, XeF (B-X) transition at 351.1 nm, and the broadband free-running XeF (C-A) transition centered at 80 nm. The shaded bars on the top part of the figure indicate the main broadband absorbers present in the XeF (C-A) laser medium as a result of intense electron beam pumping. Darker shading indicates larger photoabsorption cross-sections.

The KrF laser transition demonstrates a higher gain coefficient than the XeF (B-X) transition making it a better candidate for simultaneous oscillation with XeF(C-A). A long gain length XeF (C-A) laser has demonstrated greater than 100 mJ of KrF output for about 500 mJ of total output when injection tuned in the blue-green spectral region [6]. Judicious selection of the proper five component gas mixture can significantly reduce competing gains, however.

This paper describes gain measurements at the KrF (B-X) (248 nm) and XeF (B-X) (351 nm) regions of the spectrum made in an optimized XeF (C-A) laser gas mixture. Gain and absorption were measured as a function of gas partial pressures, and energy deposition. A brief discussion of how these results pertain to XeF (C-A) kinetics is presented, as well as a discussion concerning the feasibility of a novel single excimer laser operating simultaneously on the XeF (C-A) and KrF (B-X) lines.

II EXPERIMENTS

The experimental setup used in this study is shown in Fig. 2. A Physics International 110 electron beam generator was used to transversely excite a high pressure gas mixture contained in a cell with 20 cm^3 active volume. The generator produces a 10 ns (FWHM) pulse of 1 MeV electrons with a total current of 24 kA. Electrons produced by field emission from a carbon felt cathode traveled through a wire mesh false anode, a short (3 cm) evacuated drift region, and through a 50 μm thick titanium foil into the gas cell. A hibachi structure provided mechanical support for the foil. The electron beam is confined in the drift region by an external magnetic field. The strength of the field, measured in the drift region, could be adjusted from 0 to 2200 gauss on a shot to shot basis. In the current experimental configuration the spatial variation of the energy deposition is less than ± 10% over the entire gain length. The spatially averaged energy density in 6.5 bar of Ar on the optic axis varied from approximately 100 J/l with no magnetic field, to 225 J/l with the full magnetic field.

The laser gas mixtures were contained in a nickel plated stainless steel reaction cell. Gases were added to the cell one component at a time with good gas mixing assured by rapid turbulent flow. Previous work with the XeF (C-A) laser system has shown that the optimum gas mixture utilized for a short gain length laser is 8 torr Xe, 1 torr F_2, 8 torr NF_3 , and 300 torr Kr in a buffer of 6.5 atm. of Ar [1], [4], [5] . In the experiments reported here all measurements utilized this optimum multi-component mixture. While studying the effect of gas composition on the gain coefficients, only one component of the mixture was varied while the ratio of the other gasses remained fixed. The gas was replaced at least every 10 shots to avoid inconsistent data resulting from gas degradation.

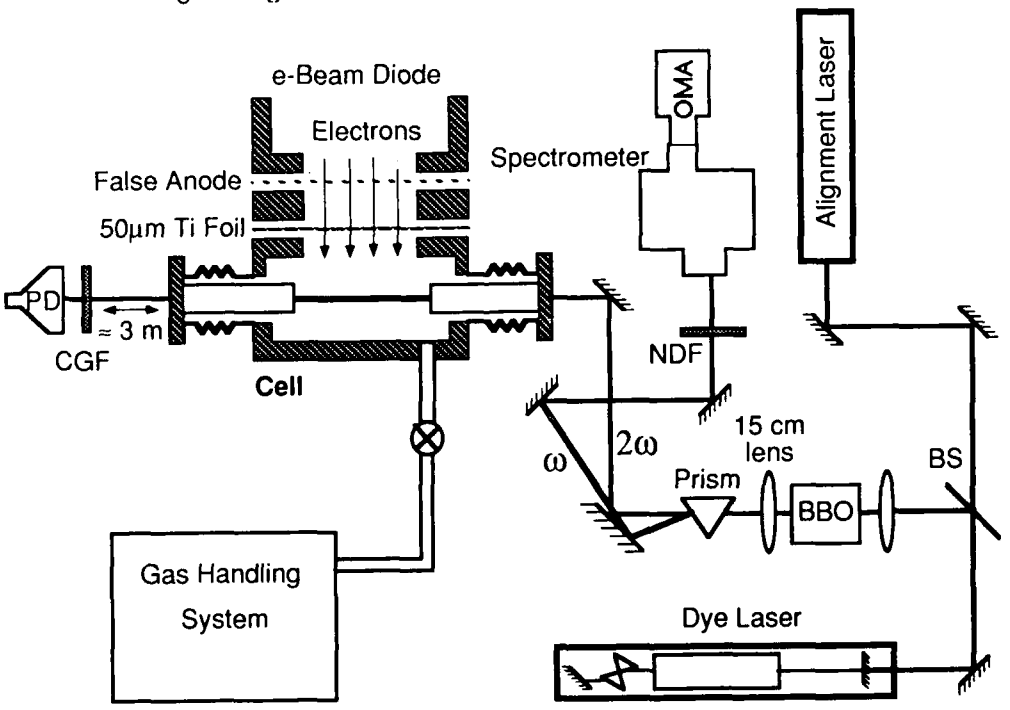


Fig. 2. The schematic diagram of the experimental set-up for the measurement of gain and absorption in an electron beam pumped laser medium. PD: photodiode, W: MgF_2 window, M: mirror, OMA: Optical Multichannel analyzer, BBO: ß- Barim Borate SHG crystal, BS: beam splitter, NDF: neutral density filter, CGF: color glass filter.

The direct output from a flashlamp pumped dye laser (Phase-R Corp. FL2000) was used as the probe beam for measurements in the blue-green spectral region. In the UV region two ß-barium borate (BBO) crystals were used to produce the ultraviolet probe beam at either 248 nm or 351 nm by second harmonic generation of the visible dye laser. The crystals were mounted in sealed cells with AR coated windows located between two 15 cm focal length fused silica lenses in a confocal arrangement. Tuning was accomplished by changing the fundamental wavelength of the dye laser and adjusting the phase matching angle of the BBO crystal. The fundamental pump beam consisted of 10 mJ, 250 ns FWHM pulses.

The pump and second harmonic beams were spatially separated by a prism and two iris diaphragms. The frequency doubled probe beam was attenuated to < 50 kW by the use of neutral density filters before it passed through the cell. The probe signal was detected using a fast vacuum

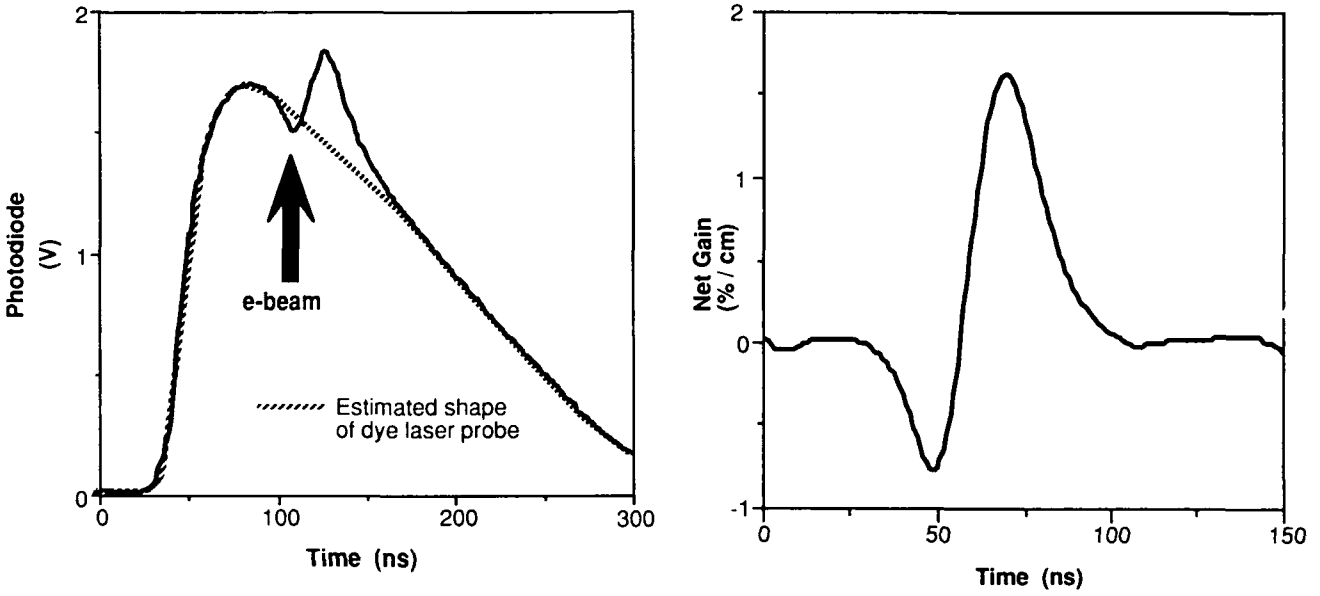


Fig. 3. The solid line shown in (a) is a typical photodiode signal showing the gain and absorption superimposed on a flashlamp pumped dye laser probe beam. The arrow represents the 10 ns wide electron beam pulse. The estimated shape of the probe beam is represented by the dashed line. Part (b) of the figure depicts the net gain and absorption signal separated the probe beam.

photodiode (ITT F4000). Narrow band interference filters and color glass filters were used to define a spectral range of observation. The output of the photodiode was monitored using a transient digitizer (Tektronix 7912AD) with a 500 MHz bandwidth. The wavelength characteristics of the fundamental dye laser pulse was monitored by using an optical multichannel analyzer (EG&G PARC OMA III) connected to a 0.25 m spectrometer. Both the transient digitizer and OMA were controlled by an IBM AT type computer. The timing of the probe beam and e-beam excitation pulse were monitored using a fast storage scope (Tektronix 7834).

The signal from the photodiode was a superposition of the temporal shape of the probe beam and the gain and absorption signals. The gain/absorption signal were separated from the probe beam in order to determine the gain/absorption ratio as a function of time. This was accomplished by dividing the actual signal (gain and probe) by the signal measured without firing the electron beam. The solid line in Fig. 3 (a) shows a typical gain measurement made on the XeF (C-A) transition. The initial absorption is followed by gain in the after-glow regime. This behavior has been discussed elsewhere [1], [4], [5]. The dashed line in this figure represents a spline-fit estimate of the dye laser probe signal. Figure 3 (b) shows the temporal evolution of the gain and absorption after being separated from the probe beam signal.

Accurate measurements depend on correct timing between the dye probe beam and firing of the electron beam. The gain measurements are estimated to be accurate to 0.2 % cm^{-1} for the XeF (C-A) measurements, and $\leq$ 1 % cm^{-1} for the UV measurements due to shot to shot uncertainties of fitting the actual shape of the probe beam to the measured probe pulse with gain superimposed.

III EXPERIMENTAL RESULTS

The experimental method described in the preceeding section allows an accurate measurement of the temporal evolution of gain and absorption. Gain values given in the following sections are peak *net* gain values (gain - absorption). While it is rather difficult to measure absorption at the laser transition, a good estimate for the absorption coefficients can be achieved by tuning the probe off the gain peak. Hence absorption coefficients are defined as *absolute* values.

A] XeF (C-A) Gain Measurements

Net gain coefficient measurements were performed near the center of the XeF (C-A) gain profile at 486.8 nm. These measurements agreed well with previous work [1] and served as a useful calibration for the measurements in the UV spectral region. A measurement of absolute per pass absorption by tuning off the gain peak was not possible because of the broad spectral width of the XeF (C-A) transition which would have forced an absorption measurement too far away from the gain maximum for meaningful data.

The small signal gain coefficient was measured as a function of the Xe and Kr concentration in the gas mixture. The result is shown in Fig. 4. The per pass gain rises rapidly as the Xe concentration is increased. Maximum gain occurs with a Xe concentration of .15%- corresponding to 8 torr in 5300 torr total pressure. As the Xe partial pressure is further increased the net gain declines; most likely as a result of broad band absorption by excited xenon states [5], [7] and two and three-body quenching of the XeF (C) state [5], [8], [9]. Previous work [1], [4], [5] has shown that a small amount of Kr, on the order of 6% of the total concentration, greatly increases extraction efficiency- primarily by reducing transient absorption. This work observes similar behavior; adding 300 torr of Kr increases the small signal gain coefficient by about 0.5 % cm^{-1}. The addition of more Kr has a negative effect, however, decreasing the net gain coefficient. A large concentration of Kr increases the energy deposition in the gas; and it is believed [5] that this leads to greater transient absorption by Kr^{**} and Xe^{**} thus reducing the net gain.

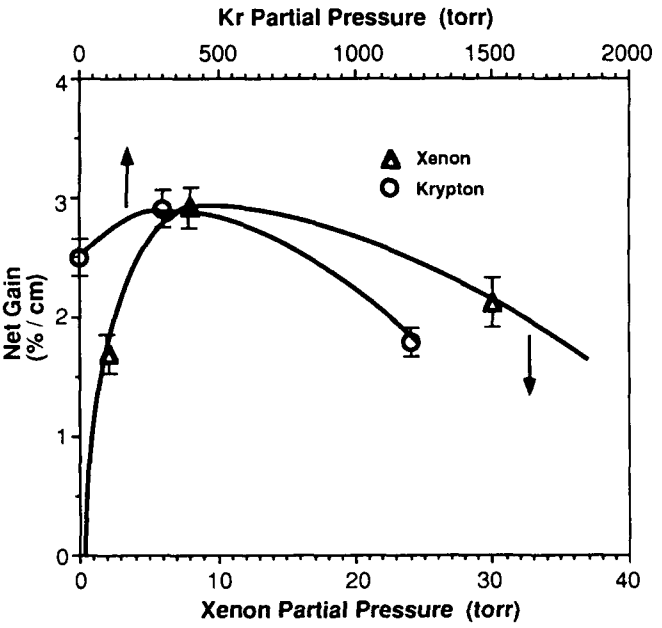


Fig. 4. Dependence of small signal XeF (C-A) gain coefficient at 486.8 nmon variations of Kr and Xe partial pressure. The gas mixture used was (8 torr Xe, 1 torr F_2, 8 torr NF_3, 300 torr Kr, and 6.5 bar Ar) was identical to that previously found optimum for a short gain length XeF (C-A) laser. The Xe and Kr gas component scans were done independently. The variations in the net gain coefficient from shot to shot are attributable to variations in the electron beam pumping source.

B] KrF (B-X) Gain and Absorption Measurements

The dye laser probe beam used for the XeF (C-A) gain measurements was frequency doubled to 248.5 nm for net gain measurements, and to 244 nm (about 5 nm off the KrF laser transition) for absorption measurements. The low damage threshold of ß-BBO at 248 nm limited the maximum permissible intensity of the dye laser probe beam. As a result, these net gain and absorption measurements have a somewhat larger uncertainty for any given gas fill. The maximum error is approximately ±1 % cm^{-1}.

Gain measurements on the KrF transition in an electron beam excited mixture have been reported previously. However none of these studies examined a mixture optimized for XeF (C-A) laser operation. The major difference between the XeF (C-A) laser gas mixture and those commonly used for KrF lasers is the addition of small amounts of xenon, and the high pressures (6.5 bar) required for good collisional mixing between the XeF (B) and (C) states in the XeF (C-A) laser.

Figure 5 shows the effect of varying Kr and Xe partial pressure on the net gain and absorption coefficients. In Figure 5(a) the KrF gain coefficient rises rapidly to about 8 % cm^{-1} as the concentration of Kr in the mixture approaches 6 %. As Kr concentration is increased to 27 % the gain coefficient slowly falls to 5 % cm^{-1}. Xenon on the other hand, is found to strongly quench the KrF (B-X) gain coefficient.

This decrease in the net gain coefficient with increasing Xe partial pressure can be explained by a corresponding rise in absorption coefficient seen in Fig. 5 (b)- from 2.7 % cm^{-1} with no Xe in the mixture, to 8 % cm^{-1} at Xe partial pressures of 30 torr. Part of this absorption is thought to be from excited Xe states [5], [7], however the absorption cross-section of Xe** at 248 nm cannot fully explain the observed trends. We also find that the absorption coefficient demonstrates somewhat unexpected behavior as the Kr concentration is varied. Although various krypton species are predicted to be among the dominant absorbers at 248 nm [5], the absorption per pass falls as Kr partial pressure is increased to around 300 torr, then rises again as Kr partial pressure is increased beyond this point. The changing contributions of the absorbers Ar_2^+, $ArKr^+$, and Kr_2^+ as Kr concentration is varied are predicted to be responsible for this behavior.

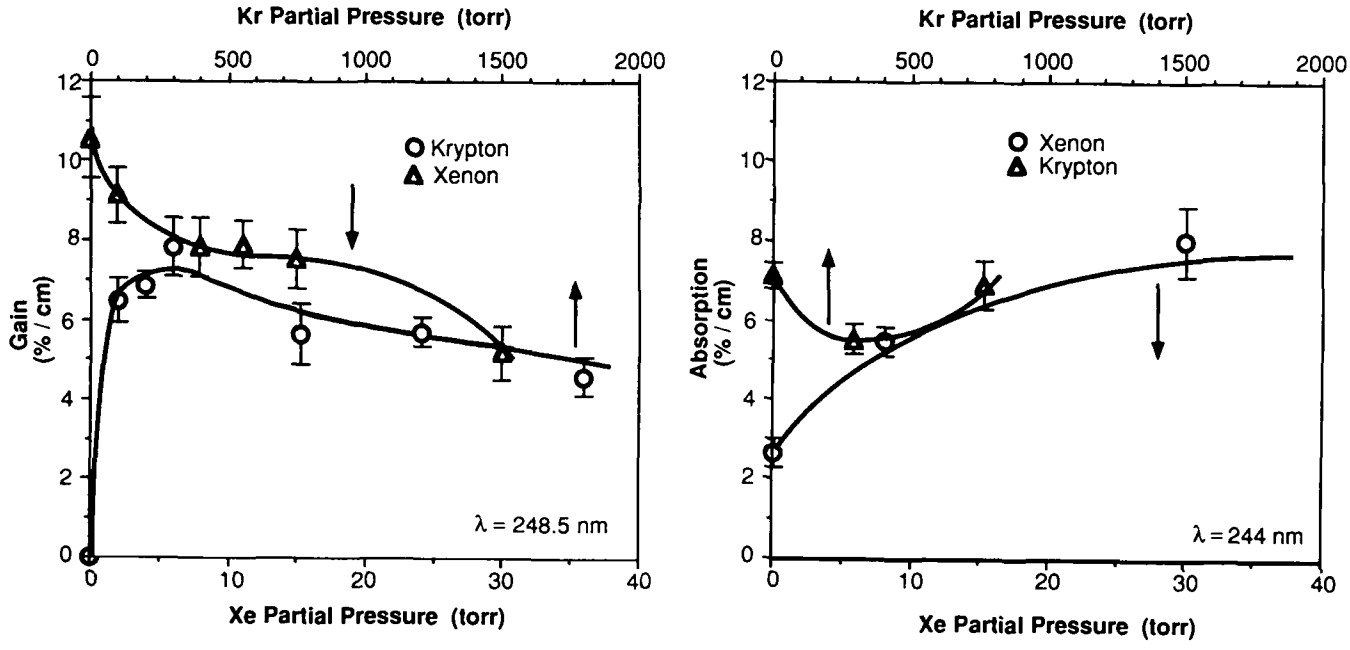


Fig. 5. Dependence of the KrF (B-X) gain coefficient (a) and absorption coefficient (b) on variations in Kr and Xe concentration of the excited gas mixture. The intensity of the probe beam was limited to 50 kW/cm^2 to avoid gain saturation.

C] XeF (B-X) Gain and Absorption

A fundamental dye laser wavelength of 702.2 nm was frequency doubled using a ß-BBO crystal to produce a probe beam of 351.1 nm for gain coefficient measurements and 346 nm for absorption coefficient measurements. For the XeF (B-X) gain and absorption coefficient measurements intracavity aperatures were used. The error is estimated to be .5 % cm^{-1}.

Figure 6(a) shows the small signal gain coefficient as a function of Kr and Xe partial pressures in the gas mixture. The decrease in gain in figure 6(a) with increasing Kr partial pressure corresponds roughly to the increase in absorption shown in Fig. 6 (b). Any differences are probably due to inaccuracies of the measurement method for low absorption coefficients. The effect that varying the Xe concentration has on the small signal gain and absorption coefficients can also be seen in Fig. 6(a). The net gain coefficient rises as the Xe partial pressure increases, peaking at a Xe concentration of 1.9%, corresponding to ≈ 100 torr of Xe in the gas mixture. Beyond 100 torr partial pressure of Xe the net gain coefficient decreases slowly, falling to 5 % cm^{-1} at 4.5% Xe concentration (240 torr, the largest point measured). Two-body and three-body quenching of XeF (B) by Xe are the likely explanations for the decline of the net gain coefficient at higher Xe partial pressures [8].

Figure 6 (b) illustrates the effect changing Kr and Xe partial pressures have on the absorption coefficient. As the Kr partial pressure was increased, the absorption coefficient increased rapidly, probably as a result of the increased production of Kr species with large absorption cross-sections near 351 nm [5]. It can also be seen from Fig. 6(b) that the absorption coefficient decreases rapidly as the xenon partial pressure is increased. We attribute this behavior to very rapid charge transfer reactions

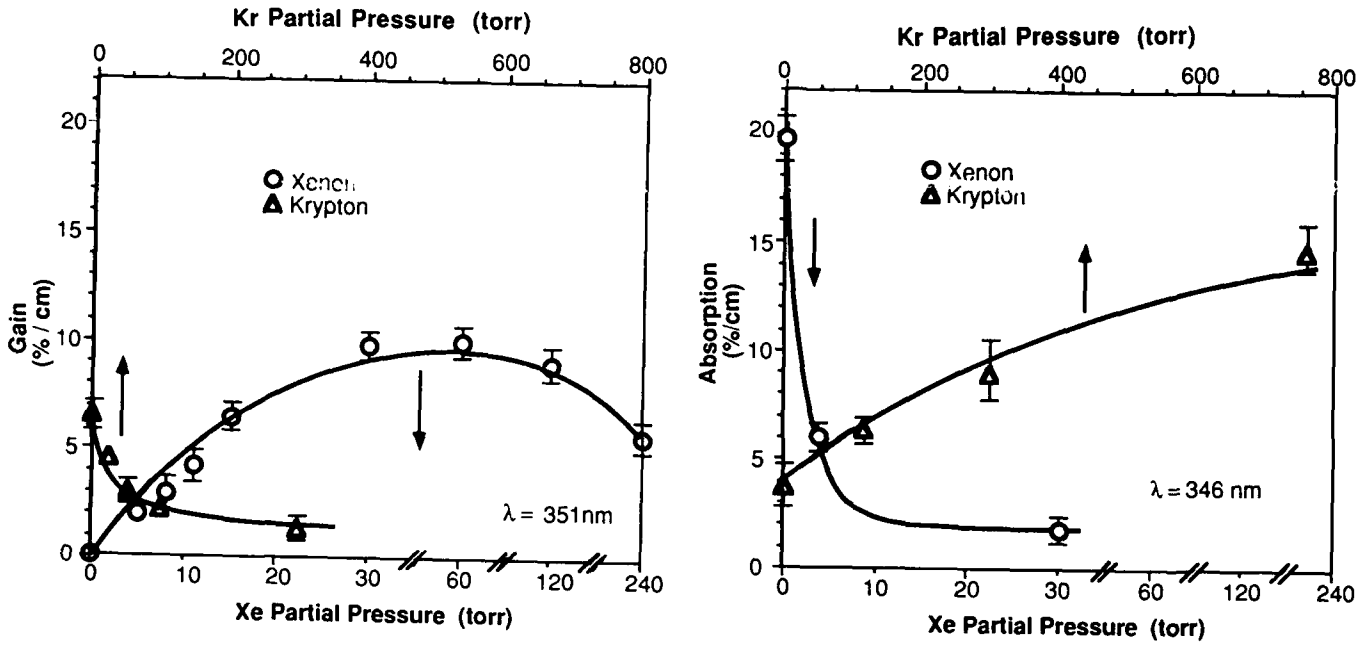


Fig. 6. The variation of the net gain coefficient (a) and absorption coefficient (b) are shown in this figure as a function of the Xe and Kr partial pressures of the gain medium. The intensity of the probe beam was limited to 50 kw/cm2 to limit saturation of the excited gas mixture. The improved accuracy of these measurements over those on the KrF (B-X) transition is attributable to less depdence of the gain coefficient on shot to shot variations in e-beam pumping.

from strongly absorbing ionic Ar and Kr dimers as well as displacement reactions between the absorber Kr_2F and Xe.

D] Effect of Energy Deposition on Net Gain

The net gain coefficients for all three transitions were also measured as a function of energy deposition in the laser gas mixture. These results are shown in Fig. 7. The standard, optimized gas mixture of 8 torr Xe, 1 torr F_2, 8 torr NF_3, and 300 torr Kr in a 6.5 bar Ar buffer was used for all measurements while the energy deposition in the gas mixture was varied by adjusting the magnetic field.

KrF gain showed the greatest sensitivity to variations in energy deposition. A factor of ≈ 2 increase in the energy deposition from 80 to 150 J/l resulted in an increase of the gain coefficient from 6 % cm^{-1} to 11% cm^{-1}. Although the XeF (C-A) and (B-X) gain coefficients also rise with increasing energy deposition, the change is much less dramatic. An increase of energy deposition by a factor of 2 results in an increase in the gain coefficient of about 1 % cm^{-1} for the XeF (B-X) and (C-A) transitions. The dependence of the gain on energy depositions for these two transitions follow each other closely as is expected since the (B) and (C) states are closely coupled.

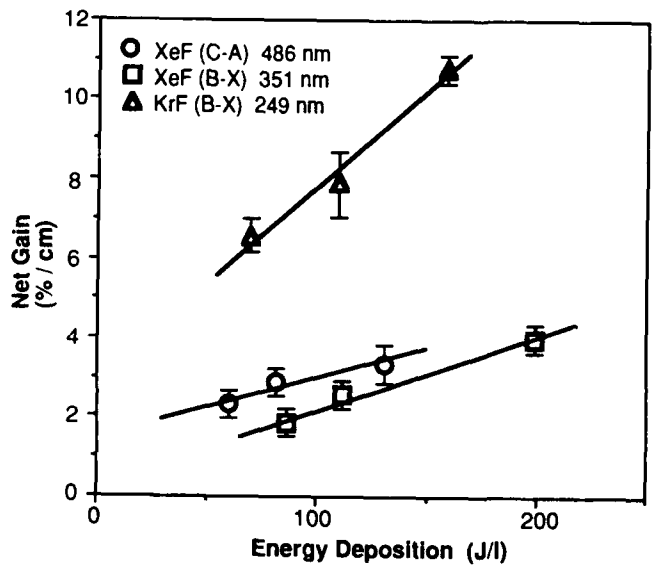


Fig. 7. Optical net gain of the KrF (B-X), XeF (C-A), and XeF (B-X) laser transitions as a function of energy deposition.

IV DISCUSSION AND FUTURE DIRECTIONS

Proper gas tailoring of the XeF (C-A) laser medium allows the adjustment of the small signal gain of the three laser transitions in this medium. Reducing gain coefficients in the UV region of the spectrum should provide better extraction efficiency in the XeF (C-A) regime. This study has shown that a reduction in KrF gain can be achieved by increasing the Xe concentration- at a cost of slightly reducing the small signal gain of the XeF (C-A) laser.

The optimized XeF (C-A) laser medium exhibits a high small signal gain coefficient in the ultraviolet region of the spectrum on the KrF (B-X) transition at 248.5. This high UV gain should allow the reduction in KrF gain can be achieved by increasing the Xe concentration- at a cost of slightly reducing the small signal gain of the XeF (C-A) laser.

The optimized XeF (C-A) laser medium exhibits a high small signal gain coefficient in the ultraviolet region of the spectrum on the KrF (B-X) transition at 248.5. This high UV gain should allow the construction of a two, or even three, color excimer laser system. Such a multicolor UV-visible excimer laser operating at optimum XeF (C-A) laser parameters has direct impact on the development of a practical, tunable XeF (C-A) laser system.

Current methods of wavelength tuning the XeF (C-A) laser require a second laser to act as an injection source. There are drawbacks of cost, complexity, and timing inherent in such a scheme. Some of these difficulties can be avoided in a self pumped injection scheme in which the electron beam could be used to simultaneously excite a second, UV laser (such as KrF) which acts as the pump for a dye laser or optical parametric oscillator which can then be used as the XeF (C-A) injection source.

Such a dual wavelength laser is desirable to investigate since the population of the KrF (B) and XeF (B) states are predicted to peak before that of the XeF (C) state [5]. Fluorescence measurements of the XeF (B) and (C) states have shown this to be true [8] for the XeF (B) state. In fact, a two color excimer laser developed previously at Rice demonstrated such behavior [10].

A discharge pumped XeF (C-A) laser has used a technique similar to the one proposed here to boost the XeF (C-A) output by more than an order of magnitude [11]. However the dischage pumped device did not demonstrate high output energies in the blue-green spectral region nor broadband, narrow linewidth tunability. Preliminary work to investigate the feasibility of a self injection scheme using the KrF (B-X) transition to excite a small dye laser is currently being conducted at Rice.

V CONCLUSION

Gain measurements using a frequency doubled dye laser probe beam were conducted on three laser transitions in an electron beam pumped XeF (C-A) excimer laser mixture. An optimal five component gas mixture demonstrates relatively high (≥ 3 % cm^{-1}) gains on the KrF (B-X), XeF (B-X), and XeF (C-A) transitions. These high gains raise the possibility of constructing a high power two or three color UV-visible excimer laser. Furthermore, the temporal variation between the onset of KrF (B-X) and XeF (C-A) laser action suggests a simple and novel self injection scheme for the XeF (C-A) laser.

ACKNOWLEGEMENTS

The authors would like to thank Jim Hooten and Chris Kringle for invaluable assistance during this research. We would also like to thank Dr. Brent Dane and W.L. Nighan of United Technologies Research Center, East Hartford for their many insightful comments. Funding for this research was provided by the Robert Welch Foundation, the Office of Naval Research, and the National Science Foundation

REFERENCES

1] N. Hamada, R. Sauerbrey, W.L. Wilson Jr., F. Tittel, and W.L. Nighan, IEEE JQE, QE24, 1571, 1988.

2] G. Marowsky, N. Nishida, H. Stiegler, F.K. Tittel, W.L. Wilson, Y. Zhu, and W.L. Nighan, Appl. Phys. Lett., vol. 47, 657, 1985.

3] G. Hirst, C.B. Dane, W.L. Wilson, R. Sauerbrey, F. K. Tittel, W.L. Nighan, Appl. Phys. Lett., vol. 54, 1851, 1989.

4] W.L. Nighan, R. Sauerbrey, Y. Zhu, F.K. Tittel, W.L. Wilson Jr., IEEE JQE, QE23, 253, 1987.

5] W. L. Nighan and M.C. Fowler, IEEE JQE, QE26, 791, 1989

6] B. Dane, Private Communication.

7] C. Duzy and H.A. Hyman, Phys. Rev. A, vol. 22, 1878, 1980

8] R. Sauerbrey, W. Walter, F.K. Tittel, W.L. Wilson, J. Chem. Phys., vol. 78, 735, 1983.

9] H.C. Brashears and D.W. Setser, J. Chem. Phys., vol. 26, 4932, 1982.

10] R. Sauerbrey, Y. Zhu, F.K. Tittel, W.L. Wilson Jr., N. Nishida, F. Emmert, W.L. Nighan, IEEE JQE, QE21, 418, 1985

11] R.C. Hollins, D.L. Jordan, A. Feltman, Opt. Comm., vol. 63, 61, 1987.

3-DIMENSIONAL FEL THEORY

G. Dattoli, H. Fang* and A. Torre, R. Caloi**

ENEA, Dip. TIB, U.S. Fisica Applicata, CRE Frascati,
C.P. 65 - 00044 - Frascati, Rome, Italy

ABSTRACT

In this paper we discuss a three-dimensional theory of an FEL operating with a continuous e-beam. The theory is base on a generalized method of solution of the FEL Helmholtz equation in the high gain small signal regime.

1. INTRODUCTION

The complete analysis of the FEL dynamics is hardly actuable with purely numerical or analytical methods. As a consequence, it has been approached partly with analytical and partly with numerical techniques. A general code, indeed, describing the FEL physics should take into account the undulator inhomogeneities, the effect of the finite emittance and energy spread of the e-beam, the transverse mode evolution, and the longitudinal mode dynamics due to the finite length of the electron pulse. It is therefore evident that such a code requires a noticeable numerical effort with a consequent enormous expense of computer time. Consequently, the codes so far developed account for only some of the above-quoted effects as it is for the 1-D code FELP[1] and for the 3-D code FELEX,[2] both of them developed at Los Alamos.

A numerical code including both the longitudinal and transverse dynamics would be therefore highly useful from a theoretical and practical point of view.

However, although analytical methods can be applied only under simplifying hypotheses, they stand out as useful tools to get a physical insight into the problem under study and to provide a check with the results of more sophisticated numerical computations. The integro-differential equation describing the FEL pulse propagation in the low-gain and small-signal regime, for instance, has been reduced into an evolution-type equation in the long-bunch approximation,[3] this allowing to infer interesting and useful informations about the gain dependence on parameters, as the cavity detuning and the coupling parameter.[4] Similarly, in Ref. (5) an approximate analysis of the Colson wave-equation[6] governing the transverse mode dynamics for an FEL operating with a continuous e-beam in the small signal regime has been carried out. In the low-gain regime, indeed, and in the hypothesis of a parabolically-shaped transverse distribution of the e-beam, the evolution equation can be reduced to a form, basically equivalent to that of the parabolic equation describing the paraxial propagation of an e.m. wave through a non-homogeneous medium with a parabolic dependence of the dielectric constant on the transverse coordinates. Consequently, it is possible to account for the FEL transverse mode evolution within the context of the well-established methods of optics.

Furthermore, in Ref. (7) a more general analysis has been presented, approaching the problem with operational techniques developed both in classical and quantum optics.[8] The use of operational methods allow to treat the transverse and longitudinal mode dynamics within the context of a unifying formalism. In the present paper, we reconsider the FEL wave-equation firstly in the simplest case (no transverse and longitudinal mode structures) and, then, including the effect of the transverse structure. Sec. 2 is indeed devoted to illustrate an alternative approach to the one-dimensional Colson wave-equation. In Sec. 3 we generalize the methods to describe the dynamics of the transverse modes, thus providing a scheme for a numerical computation. Section 4 is finally devoted to concluding remarks.

---

* ENEA Guest. Permanent address: Institute of Fine Mechanics and Optics, Shanghai, China
** Dipartimento di Fisica, 1^ Università di Roma "La Sapienza", P.le Aldo Moro, 5
00100 - Rome, Italy

2. SINGLE-MODE DYNAMICS

The one-dimensional Colson wave-equation[9]

$$\frac{d}{d\tau} a(\tau) = -i\mu g_0 \int_0^\tau \tau' e^{i\nu\tau'} a(\tau-\tau') d\tau' \tag{2.1}$$

rules the evolution of the complex amplitude $a(\tau)$ of the optical field for a continuous e-beam in the slowly varying amplitude approximation and small signal regime. In the above equation the dimensionless variable τ measures the time in unity of the interaction interval; g_0 and ν are the gain coefficient and the resonance parameter respectively.

Introducing the shift operator $e^{-\tau'\partial/\partial\tau}$, we can recast Eq. (2.1) as

$$\frac{d}{d\tau} a(\tau) = -i\mu g_0 \int_0^\tau d\tau' \, \tau' \, e^{\tau'\hat{T}} a(\tau) \tag{2.2}$$

the operator $\hat{T}$ being given by

$$\hat{T} = -i\nu + \frac{d}{d\tau} \tag{2.3}$$

The eigenstates $\phi_{\delta\nu}$ of $\hat{T}$ can be specialized as

$$\phi_{\delta\nu}(\tau) = \phi_0 \exp\{i(\nu+\delta\nu)\tau\} \tag{2.4}$$

with the real and imaginary parts of the eigenvalue $\delta\nu$ specifying the shift of the frequency with respect to ν and the rate of variation of the amplitude respectively.

Let's express the optical field $a(\tau)$ as a superposition of the $\phi_{\delta\nu}$'s, namely

$$a(\tau) = \sum_{\delta\nu} a_{\delta\nu} \exp\{i(\nu+\delta\nu)\tau\} \tag{2.5}$$

with unspecified coefficients $a_{\delta\nu}$.

Inserting (2.5) into Eq. (2.2) yields the equations

$$\delta\nu^2(\nu+\delta\nu) - \mu g_0 = 0 \tag{2.6}$$

$$\sum_{\delta\nu} \frac{a_{\delta\nu}}{\delta\nu^2} = 0 \,, \qquad \sum_{\delta\nu} \frac{a_{\delta\nu}}{\delta\nu} = 0 \tag{2.7}$$

Consequently, the eigenvalue $\delta\nu$ specializes as a solution of the cubic equation (29). On the other hand, combining (2.6) and (2.7) with the initial conditions provides a set of three algebraic equation for the coefficients $a_{\delta\nu}$ as

$$\sum_{j=1}^{3} a_j = a_0 \qquad \sum_{j=1}^{3} \delta\nu_j a_j = -a_0\nu \qquad \sum_{j=1}^{3} \delta\nu_j^2 a_j = -a_0\nu^2 \tag{2.8}$$

with a_0 denoting the initial value of the field complex amplitude. In the above equations we have denoted with $\delta\nu_j$ a solution to (2.6) and with a_j the corresponding coefficient in the superposition (2.5). In conclusion, the optical field specializes as

$$a(\tau) = \sum_{j=1}^{3} a_j \, e^{i(\nu+\delta\nu_j)\tau} \tag{2.9}$$

It is worth stressing that the explicit knowledge of $\delta\nu_j$ and a_j is unnecessary. Expanding the exponential in (2.9), indeed, we can rewrite $a(\tau)$ as

$$a(\tau) = e^{i\nu\tau} \sum_{k=0}^{\infty} \frac{(i\tau)^k}{k!} a^{(k)} \tag{2.10}$$

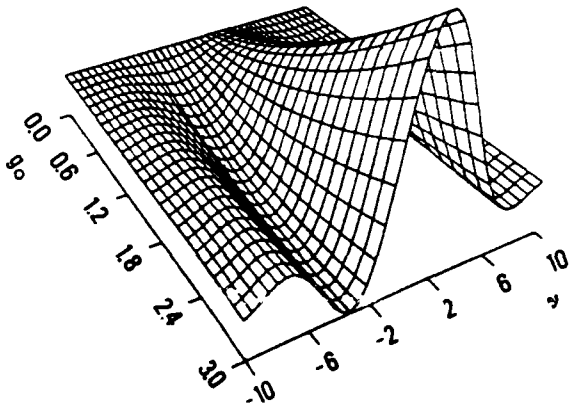


Fig. 1 - Three-dimensional plot of gain vs resonance parameter and gain coefficient

which clearly displays that $a(\tau)$ is determined by sums of the type

$$a^{(k)} \equiv \sum_{j=1}^{3} (\delta\nu_j)^k a_j \tag{2.11}$$

Equation (2.8) specify the value of $a^{(k)}$ for k=0,1,2 as

$$a^{(0)} = 1 \qquad a^{(1)} = -\nu \qquad a^{(2)} = \nu^2 \tag{2.12}$$

where for sake of simplicity it has been assumed a_0=1. The other $a^{(k)}$ for k>2 can be obtained from Eq. (2.6), which provides, indeed, the following recursive relation

$$a^{(k)} + \nu a^{(k-1)} - ig_0 a^{(k-3)} = 0 \tag{2.13}$$

with the condition $a^{(o)}$=1 for k=0 and $a^{(-k)}$=0 for k>0.

The FEL gain is obviously given by the relative energy variation after one undulator passage, that is

$$G = |a(1)|^2 - 1 \tag{2.14}$$

An idea of the gain dependence on ν and g_0 is offered by Fig.1,[12] where a three-dimensional plot of G vs ν and g_0 is reported. For small values of g_0, that is for g_0 less than unity, the gain curve exhibits the well-known antisymmetric shape, while for increasing g_0 a significantly modified profile appears, as a consequence of the interplay between the interferential and exponential effects contributing to the gain process. For a more detailed analysis of the gain deviations from the linear regime, the reader is referred to Ref. (12), where a perturbative approach, the perturbation parameter being the gain coefficient g_0, to Eq. (2.1) has been carried out, thus providing an explicit expression of the gain as a third-order polynomial in g_0 with coefficients depending on the resonance parameter ν. The effect of the beam quality on the gain curve has been also analyzed in the quoted reference.

3. TRANSVERSE-MODE DYNAMICS

The equation governing the transverse mode dynamics for a FEL operating with a continuous e-beam in the small signal regime and slowly varying amplitude approximation has been derived in Ref. (6) in the paraxial approximation as

$$\left(\frac{i}{4}\nabla_\perp^2 + \frac{\partial}{\partial\tau}\right) a(x_\perp,\tau) = -ig_0 j(x_\perp) \int_0^\tau d\tau' \tau' e^{i\nu\tau'} a(x_\perp, \tau-\tau') \tag{3.1}$$

where $\nabla_\perp^2$ represents the two-dimensional Laplacian

$$\nabla_\perp^2 = \frac{\partial^2}{\partial\xi^2} + \frac{\partial^2}{\partial\eta^2} \tag{3.2}$$

with ξ and η denoting the transverse coordinates x and y normalized to $\sqrt{\lambda L/\pi}$, that is

$$\xi = \left(\frac{\pi}{\lambda L}\right)^{1/2} x \qquad\qquad \eta = \left(\frac{\pi}{\lambda L}\right)^{1/2} y \tag{3.3}$$

L ≡ undulator length

Finally $j(\mathbf{x}_\perp)$ is the transverse current, whose shape is determined by the transverse distribution of the e-beam.

Let us introduce the field $\tilde{a}(\mathbf{x}_\perp,\tau)$ defined as

$$a(\mathbf{x}_\perp,\tau) = e^{-i(\tau/4)\nabla_\perp^2}\,\tilde{a}(\mathbf{x}_\perp,\tau) \tag{3.4}$$

and satisfying the equation

$$\frac{\partial}{\partial\tau}\tilde{a}(\mathbf{x}_\perp,\tau) = -ing_0\,\hat{J}(\mathbf{x}_\perp,\tau)\int_0^\tau d\tau'\tau' \exp\left\{i\tau'\left(\nu + \frac{1}{4}\nabla_\perp^2\right)\right\}\tilde{a}(\mathbf{x}_\perp,\tau-\tau') \tag{3.5}$$

where $\hat{J}(\mathbf{x}_\perp,\tau)$ denotes the operator

$$\hat{J}(\mathbf{x}_\perp,\tau) = e^{i(\tau/4)\nabla_\perp^2}\,j(\mathbf{x}_\perp)\,e^{-i(\tau/4)\nabla_\perp^2} \tag{3.6}$$

Introducing as before the shift operator $e^{-\tau'(\partial/\partial\tau)}$, Eq. (3.5) turns into

$$\frac{\partial}{\partial\tau}\tilde{a}(\mathbf{x}_\perp,\tau) = -ing_0\,\hat{J}(\mathbf{x}_\perp,\tau)\int_0^\tau d\tau'\tau' e^{-\tau'\hat{T}}\,\tilde{a}(\mathbf{x}_\perp,\tau-\tau') \tag{3.7}$$

with $\hat{T}$ being a generalation of the operator (2.3), that is

$$\hat{T} = -i\nu - \frac{i}{4}\nabla_\perp^2 + \frac{\partial}{\partial\tau} \tag{3.8}$$

The eigenstates of $\hat{T}$ are easily inferred in the form

$$\Phi_{\delta\nu nm} = \phi_{nm}(\mathbf{x}_\perp,\tau)\,e^{i(\nu+\delta\nu)\tau} \tag{3.9}$$

with $\Phi_{nm}(\mathbf{x}_\perp,\tau)$ being the Hermite-Gaussian modes, explicitly given by

$$\phi_{nm}(\xi,\eta,\tau) = \frac{1}{(n!m!2^{n+m}\pi)^{1/2}\,\omega(\tau)}\,H_m\left(\frac{\xi}{w(\tau)}\right)H_m\left(\frac{\eta}{w(\tau)}\right)\cdot\exp\left\{i\,\frac{(\xi^2+\eta^2)}{(\tau/2)-i}\right\}\exp\left\{i(n+m+1)\arctan\frac{\tau}{2}\right\} \tag{3.10}$$

where

$$w(\tau) = \sqrt{1+\tau^2/4} \tag{3.11}$$

denotes the spot size at τ normalized to the beam waist $w_0=(\lambda L/\pi)^{1/2}$. Expanding $\tilde{a}(\mathbf{x}_\perp,\tau)$ in terms of the $\Phi_{\delta\nu nm}$'s as

$$\tilde{a}(\mathbf{x}_\perp,\tau) = \sum_{\delta\nu n'm'} a_{\delta\nu n'm'}\,\Phi_{n'm'}(\mathbf{x}_\perp,\tau)\,e^{i(\nu+\delta\nu)\tau} \tag{3.12}$$

Equation (3.5) turns into

$$\sum_{\delta v n' m'}' (v+\delta v)\, a_{\delta v n' m'} \phi_{n' m'}(\mathbf{x}_\perp,0)\, e^{i\delta v \tau} + \sum_{\delta v n' m'}' (v+\delta v)\, a_{\delta v n' m'} \left| \frac{1}{4} \nabla_\perp^2 \phi_{n' m'}(\mathbf{x}_\perp,0) \right| e^{i\delta v \tau} + \tag{3.13}$$

$$+ \pi g_0 j(\mathbf{x}_\perp) \sum_{\delta v n' m'}' g_1(\delta v,\tau)\, a_{\delta v n' m'} \phi_{n' m'}(\mathbf{x}_\perp,0)\, e^{i\delta v \tau} = 0$$

where $g_1(\delta v,\tau)$ denotes the function

$$g_1(\delta v,\tau) \equiv \int_0^\tau d\tau' \tau' e^{-i\delta v \tau'} = \frac{1}{\delta v^2} \left| (e^{-i\delta v \tau} - 1) + \frac{i\tau}{\delta v} e^{-i\delta v \tau} \right| \tag{3.14}$$

Multiplying Eq. (3.13) on the left by $\phi^*_{nm}(\mathbf{x}_\perp,0)$ and exploiting the orthogonality relation satisfied by the Hermite-Gaussian modes we end up with the equations

$$(v+\delta v)\, a_{\delta v n m} + \sum_{n' m'}' d_{\substack{nm \\ n' m'}} a_{\delta v n' m'} - \frac{\pi g_0}{\delta v^2} \sum_{n' m'}' j_{\substack{nm \\ n' m'}} a_{\delta v n' m'} = 0 \tag{3.15}$$

$$\sum_{\delta v n' m'}' \frac{1}{\delta v} j_{\substack{nm \\ n' m'}} a_{\delta v n' m'} = 0 \qquad \sum_{\delta v n' m'}' \frac{1}{\delta v^2} j_{\substack{nm \\ n' m'}} a_{\delta v n' m'} = 0 \tag{3.16}$$

where $d_{\substack{nm \\ n' m'}}$ and $j_{\substack{nm \\ n' m'}}$ denote the matrix elements

$$d_{\substack{nm \\ n' m'}} = \int_{-\infty}^{+\infty} d\mathbf{x}_\perp \phi^*_{nm}(\mathbf{x}_\perp,0) \frac{1}{4} \nabla_\perp^2 \phi_{n' m'}(\mathbf{x}_\perp,0) \tag{3.17a}$$

$$j_{\substack{nm \\ n' m'}} = \int_{-\infty}^{+\infty} d\mathbf{x}_\perp \phi^*_{nm}(\mathbf{x}_\perp,0)\, j(\mathbf{x}_\perp)\, \phi_{n' m'}(\mathbf{x}_\perp,0) \tag{3.17b}$$

Equations (3.15, 3.16) can be appropriately utilized to infer a set of recursive relations, aimed at specifying the evolution of the field $a(\mathbf{x}_\perp,\tau)$, which, according to Eqs. (3.4) and (3.12), can be written as

$$a(\mathbf{x}_\perp,\tau) = e^{i\nu\tau} \sum_{n,m}' \left(\sum_{j=0}^{\infty} \frac{(i\tau)^j}{j!} a^{(j)}_{nm} \right) \phi_{nm}(\mathbf{x}_\perp,0) \tag{3.18}$$

where the quantities

$$a^{(j)}_{nm} = \sum_{\delta v}' \delta v^j a_{\delta v n m} \tag{3.19}$$

can be determined iteratively. Let us notice, indeed, that $a_{nm}^{(0)}$'s represent the coefficients of the expansion of the field $a(\mathbf{x}_\perp,\tau)$ at the initial time in terms of the Hermite-Gaussina modes, namely

$$a^{(0)}_{nm} = \int d\mathbf{x}_\perp \phi^*_{nm}(\mathbf{x}_\perp,0)\, a(\mathbf{x}_\perp,0) \tag{3.20}$$

Correspondently multiplying (3.15) by δv^j and summing over δv; one gets the recursive relation

$$a^{(j)}_{nm} + \nu\, a^{(j-1)}_{nm} + \sum_{n' m'}' d_{\substack{nm \\ n' m'}} a^{(j-1)}_{n' m'} - \pi g_0 \sum_{n' m'}' j_{\substack{nm \\ n' m'}} a^{(j-3)}_{n' m'} = 0 \qquad a^{(-j)}_{nm} = 0 \tag{3.21}$$

with $a_{nm}^{(0)}$ specified by (3.20).

The relation (3.21) correspond to the recursive equations (2.13), relevant to the single-mode Eq. (2.1). They exhibit however a more intrigued structure, as a consequence

of that they account for the dynamics of the transverse modes, as it is displayed by the sums over the coupled modes, the strength of the coupling being determined by the matrix elements (3.17).

In particular, by taking the explicit expression of the matrix elements, $d_{nm}^{n'm'}$ Eq. (3.21) specializes as

$$a_{nm}^{(j)} + \left| v - \frac{1}{4}(n+m+1) \right| a_{nm}^{(j-1)} + \frac{1}{8}\sqrt{n(n-1)}\; a_{n-2,m}^{(j-1)} + \frac{1}{8}\sqrt{(n+1)(n+2)}\; a_{n+2,m}^{(j-1)} + \frac{1}{8}\sqrt{m(m-1)}\; a_{n,m-2}^{(j-1)} \tag{3.22}$$

$$+ \frac{1}{8}\sqrt{(m+1)(m+2)}\; a_{n,m+2}^{(j-1)} - ng_0 \sum_{n'm'} j_{nm}^{n'm'}\, a_{n'm'}^{(j-3)} = 0$$

It is particularly interesting to notice a kind of shift into the resonance parameter v, which can be taken into account defining a v-parameter depending on the mode-indices as

$$v_{nm} \equiv v - \frac{1}{4}(n+m+1) \tag{3.23}$$

For a deeper discussion, the reader is addressed to Ref. (7), where the resonance parameter has been replaced by an appropriate operator, accounting for the shift of the frequency as a consequence of the transverse mode dynamics. It is evident that the recursive relations (3.23) must be handled with a computer. However, analytical results can be obtained for specific shapes of the transverse current.

A uniform transverse current, for instance, leads to the simplified form of (3.22)

$$a_{nm}^{(j)} + v_{nm}\, a_{nm}^{(j-1)} + \frac{1}{8}\sqrt{n(n-1)}\; a_{n-2,m}^{(j-1)} + \frac{1}{8}\sqrt{(n+1)(n+2)}\; a_{n+2,m}^{(j-1)} + \frac{1}{8}\sqrt{m(m-1)}\; a_{n,m-2}^{(j-1)} \tag{3.24}$$

$$+ \frac{1}{8}\sqrt{(m+1)(m+2)}\; a_{n,m+2}^{(j)} - ng_0\, a_{nm}^{(j-3)} = 0$$

Let us suppose that at the initial time the field is given by the fundamental eigenmode, i.e.

$$a(\mathbf{x}_\perp, 0) = \phi_{00}(\mathbf{x}_\perp, 0) \tag{3.25}$$

Consequently, the coefficients $a_{nm}^{(0)}$ specialize as

$$a_{nm}^{(0)} = \delta_{n0}\delta_{m0} \tag{3.26}$$

which is the starting point for inferring iteratively the $a_{nm}^{(j)}$'s for $j>0$. Evaluating the $a_{nm}^{(j)}$'s up to $j=3$, we get the following approximate expression of the field after one passage through the undulator (that is for $\tau=1$)

$$a(\mathbf{x}_\perp, 1) \approx \frac{e^{iv} e^{-\rho^2/2}}{\sqrt{\pi}} \left\{ a_0(v) - \frac{i}{6} ng_0 + a_1(v)\rho^2 + a_2(v)\rho^4 + a_3(v)\rho^6 \right\} \tag{3.27}$$

where $\rho^2 \equiv \xi^2+\eta^2$ and the explicit dependence of the coefficients a_k, $k = 0,1,2,3$ on the resonance parameter v is not reported here for sake of brevity. For a more detailed discussion , the reader is addressed to Ref. (14), where a parabolically shaped current has been considered as well, along with a numerical analysis of arbitrarily shaped currents.

4. CONCLUSION

In the present note, we have illustrated a possible method for analyzing the transverse mode dynamics in a FEL operating with an electron beam longitudinally continuous but transversally shaped. The method consists basically in expanding the optical field in terms of Hermite-Gaussian modes, taken at the entrance to the undulator. The coefficients of that expansion are expressed in form of a superposition of plane-waves with complex-frequencies. As a result, we get a set of recursive relations, partly

reproducing those obtained within the context of the single-mode evolution and partly displaying the effect (revealed by a coupling among the modes) of both the diffraction and the interaction with the e-beam.

The results presented here might be the starting point to analyze the effects of the transverse structure on the FEL optical field evolution.

Just to illustrate some of these effects, let us consider the variaiton of the beam-waist of the fundamental Hermite-Gaussian mode along the undulator. In Fig.2, we have reported a three-dimensional plot of the beam waist vs g_o and τ. These results have been obtained by exploiting the matrix methods of ray optics, applied according to Ref. (5) to the FEL interaction in the low-gain regime. A focusing effect of the interaction is evident and is further displayed in Fig. 3, where the beam waist at the output from the undulator is plotted as a function of g_o.

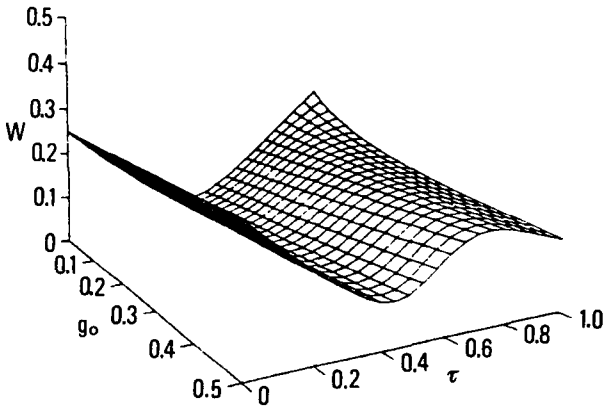


Fig. 2 - Three-dimensional plot of the beam waist vs g_o and τ

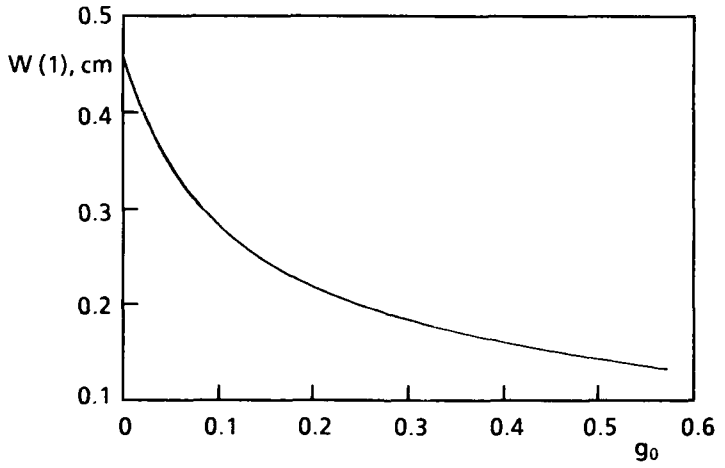


Fig. 3 - Beam waist at the output from the undulator as a function of g_o

REFERENCES

1. W.B. Colson and S.K. Ride in Phys. of Quantum Electr., vol. VII, Eds. S.F. Jacobs, H.S. Piloff, M. Sorgent III, M.O. Scully and R. Spitzen (Addison-Wesley, Reading MA, 1980) p. 337

J.C. Goldstein et al., "Simulation Codes for Modelling Free-Electron Laser Oscillators", Proc. SPIE 1045 Conference on Modelling and Simulation of Laser Systems, Los Angeles CA, January 1989

2. J.C. Goldstein et al., "Three-Dimensional Simulation of an XUV Free Electron Laser" in International Conference on Insertion Devices for Synchrotron Sources, Eds. R. Tatchyn and J. Lindan, Proc. SPIE **582**, 350 (1986)

3. G. Dattoli, T. Hermsen, L. Mezi, A. Torre and J.C. Gallardo, Nucl. Instrum. Methods **A272**, 350 (1988) and references therein

4. G. Dattoli, L. Giannessi, T. Hermsen, A. Renieri, M. Richetta and A. Torre, "FEL Gain in the Pulsed Regime: A Comparison between Numerical and Analytical Results" to appear in Nuovo Cimento D

5. G. Dattoli, A. Torre, H. Fang, J.C. Gallardo and M. Richetta "The 3-D FEL Pulse Propagation Equation: an Analytical Treatment in the Low Gain and Small Signal Regime" submitted for publication on Phys. Rev. A

6. W.B. Colson and J.L. Richardson, Phys. Rev. Lett. **50**, 1050 (1983)

7. G. Dattoli, H. Fang, J.C. Gallardo, M. Richetta and A. Torre, to appear in the Proceedings of 11th Int. Conference on Free Electron Lasers '89 Naples, Florida (1989)

8. G. Dattoli, J.C. Gallardo and A. Torre, La Rivista del Nuovo Cimento, **11** (1989)

9. W.B. Colson in "FEL Handbook" 1, eds. W.B. Colson, C. Pellegrini and A. Renieri (North-Holland Amsterdam)

10. I. Bernstein and J.L. Hirshfield, Phys. Rev. **A20**, 1661 (1970)

11. P. Sprangle, Cha Mei Tang and W.M. Manheimer, Phys. Rev. **A21**, 302 (1980)

12. C. Centioli, G. Dattoli, M. Richetta and A. Torre, Nucl. Instrum. & Methods in Phys. Res. **A285**, 108-114 (1989)

13. A. Yariv, "Quantum Electronics", John Wiley & Sons (N.Y. 1975)

SPACE BASED LASERS FOR STRATEGIC DEFENSE

by
Neil Griff, Deputy Director
Strategic Defense Initiative Office
Directed Energy Office
The Pentagon
Washington, D.C. 20301-7100
and
Douglas Kline, Director of Operations,
Scott Lissit, Member Technical Staff
W. J. Schafer Associates, Inc
1901 N. Fort Myer Drive
Arlington, VA 22209

ABSTRACT

In this review of Space Based Chemical Laser (SBCL) progress, critical technology programs are updated. This is followed by a program motivation discussion. Next, major accomplishments in each of the SBCL technology areas (Device, Beam Control, Large Optics, Acquisition, Tracking and Pointing (ATP), and Integration) are reviewed. A more detailed description of all programs that support each technology area is presented, followed by a short discussion of advanced technology programs that support the SBCL. The paper closes with several review comments that put the status of the SBCL program in context.

Introduction

Since its inception, the SDIO Strategic Defense System (SDS) concept has included high power laser weapons, primarily because directed energy weapons are especially effective in exploiting the leverage of boost phase defense, i.e., negating hostile ICBMs in boost phase, before reentry vehicles are released. The high energy laser that is furthest along in its development process is the SBCL, which has been studied for nearly two decades, and is well understood. The SBCL is especially versatile, and has significant strategic defense capabilities beyond the basic boost-phase intercept mission. These include bus intercept, mid-course interactive discrimination, self defense and defense of other SDS assets, and sensor augmentation.

This paper will review the SBCL technology development programs, focusing on the progress of individual technologies, and measure that progress against what has yet to be attained in order to reach the capabilities required for an entry-level SBCL system.

SBL Technology Update - 1989

This year has seen significant progress in development and demonstration of key SBL technologies. The most important, and most visible, is the Alpha laser program. This is the first program to build and test a laser device designed specifically for use in a space-based system. In its initial ground tests, short duration lasing was successfully demonstrated, and power and beam quality were measured.

In another key program, the LAMP (Large Advanced Mirror Program) mirror has completed government acceptance testing. This is a large, seven-segment mirror constructed specifically to demonstrate design features required by the pointing mirror of a space-based laser. LAMP has met all major performance objectives and has demonstrated the required state-of-the-art for large optics for near-term SBLs.

The LODE (Large Optics Demonstration Experiment) brassboard experiment demonstrated and validated beam control concepts for large space-based lasers. Advanced concepts for highly accurate beam control were used in these experiments, including holographic optical elements (HOEs) and outgoing wavefront sensing (OWS). The results have verified SBL and Zenith Star beam control schemes.

In the acquisition, tracking and pointing (ATP) area, progress continues at a good pace. The major program here, Starlab, now has the majority of its hardware completed.

The Zenith Star program is assigned the task of integrating all the above technologies into a space-based laser demonstration experiment. Zenith Star successfully completed a systems requirements review (SRR) in 1989. During the past year, the SBCL program has added the Alpha/LAMP Integration (ALI) experiment to assemble an end-to-end SBL optical beam train on the ground,

propagate a high energy laser beam through it, and demonstrate most beam control concepts as an intermediate step towards a major space experiment.

SBL Program Motivation

Numerous studies and analyses have been performed over the past few years that show DEWs can add significant capability to SDS Phase I architectures. Boost-phase intercept of ICBMs is made possible by the speed-of-light travel times of a high-power laser beam, which augments the capabilities of kinetic energy weapons. Extensive cost and producibility analyses have been performed for SBCL subsystems and components that convince us that SBCLs remain promising candidates for augmenting a deployed Phase I system based on kinetic kill vehicles.

Space-based chemical laser technology has successfully demonstrated many of the technologies necessary to make a confident decision on further development. Chemical lasers were under development by the Department of Defense long before the concept of SDI was officially put forth in 1983. Since then, under the guidance of the SDIO, chemical lasers and related technologies have continued to mature to their present level. Integrating the individual technologies into a single system is the principal remaining challenge for the SBCL program.

SBL Accomplishments Over The Past Fifteen Years

Significant progress has been made in all technical areas over the last fifteen years. The highlights and major accomplishments are shown in Table 1. These test programs have clearly demonstrated that lasers can produce high-power beams which can be propagated reliably towards fast-moving targets. They show that lasers can function on the ground, in an airplane, or in space; that a laser beam can be accurately controlled and aimed; and that irradiation of targets causes considerable damage. Each major accomplishment was the result of exhaustive analysis and design, construction, test and evaluation, and involved a large number of activities both government and civilian. Fundamental physics problems were addressed and solved, many requiring complex computer models to predict performance. The result is that today we have in place the expertise, and much of the hardware, to proceed with integration and test of the weapon subsystem.

TABLE 1 - Accomplishments over the Past Fifteen Years

Laser Device	Acquisition, Tracking and Pointing
BDL (1973)	ABTS Satellite Track (1982)
NACL (1976)	Airborne Laser Lab (1983)
MADS (1980)	R2P2 (1986)
MIRACL (1980)	Sealite Beam Director (1987)
Sigma Tau (1983)	
Alpha Verification Module (1985)	Large Optics
Alpha (1989)	Army Pointer Tracker (1975 - 1983)
	Navy Pointer Tracker (1976 - 1978)
Beam Control	Sealite Beam Director Mirror (1984)
Airborne Laser Lab (1983)	LAMP (1989)
LODE (1983 - 1989)	
	Integration
	Airborne Laser Lab (1983)
	High Power Tests at WSMR (1987)

Near-term SBL Program Description

The SBL program can be divided into five major developmental areas: laser device, beam control, large optics, ATP, and integration. Technology programs have been sponsored by SDIO to advance the state-of-the-art in all five areas, and significant progress has occurred in each area. The following sections list major program elements in each area, review the progress in terms of historical milestones, and project the progress that still must occur to meet SBL program goals.

Device

The major element of this area is the Alpha laser. Alpha is a high power hydrogen fluoride chemical laser, cylindrical in shape and designed specifically for use as an SBL. Its wavelength is 2.7 micrometers, which is in the mid-infrared and is well suited for propagation in space, but not

in the low atmosphere. Although its power level is below that required for an entry-level weapon, its design allows easy increase to the required power by adding additional rings to the Gain Generator Assembly, shown in Figure 1. The beam quality of Alpha is designed to meet strategic defense requirements. The Alpha laser is currently being tested in the Space Test Chamber in San Juan Capistrano, California, shown in Figure 2. Figure 3 depicts the past history and projected milestones of the Alpha program.

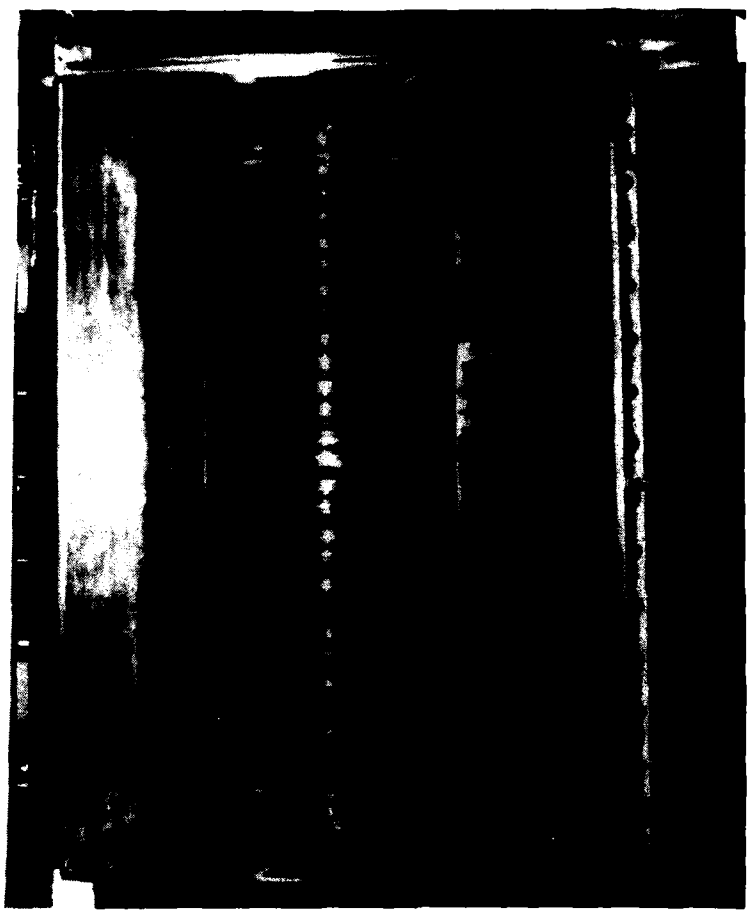


FIGURE 1 Alpha Gain Generator Assembly

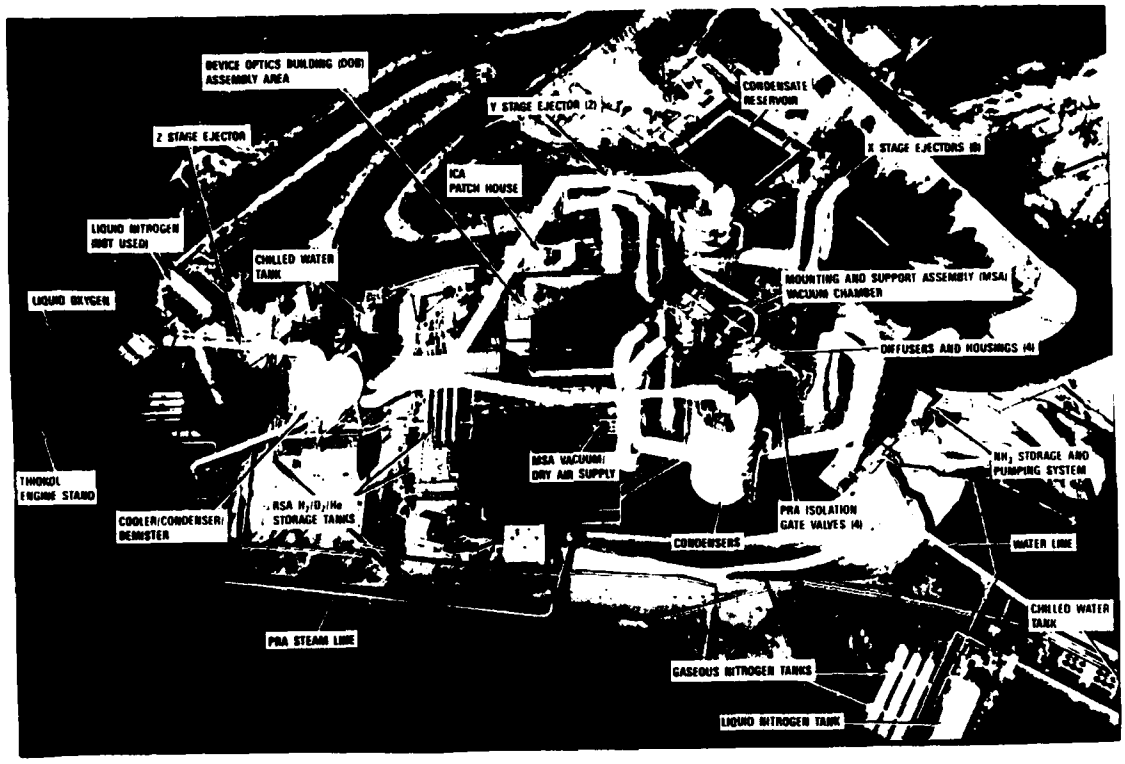


FIGURE 2 Space Test Chamber That Houses the Alpha Laser

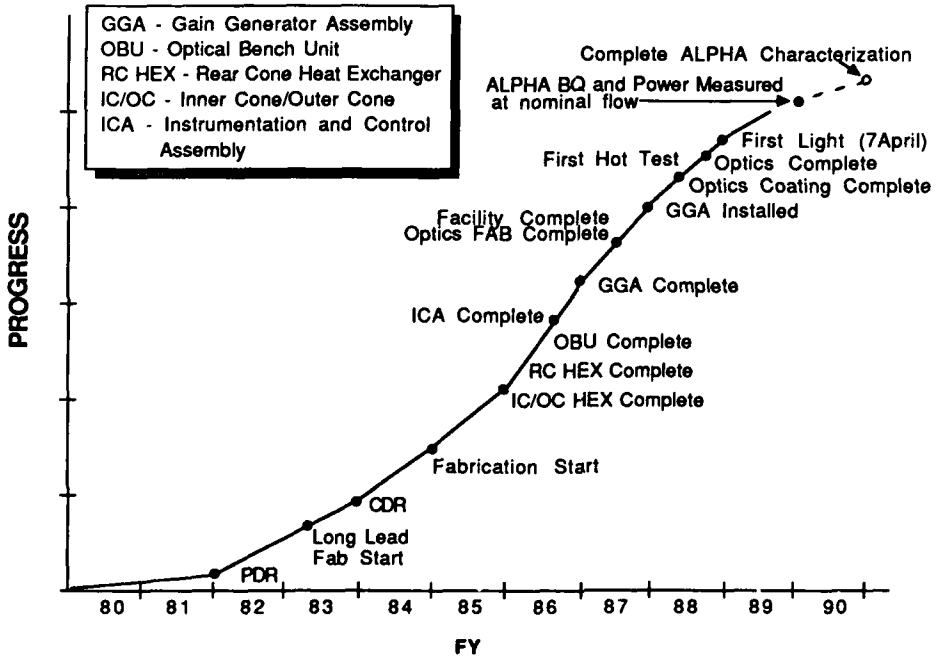


FIGURE 3 Alpha Program History

Beam Control

The major elements of this area are the LODE and ABCS (Advanced Beam Control System) programs. Beam control techniques are used to direct the high energy laser beam from the laser device to the large pointing telescope optics, and to ensure that the beam has the required characteristics to maximize brightness on target. To accomplish this the beam must be maintained to within fractions of a millimeter for accurate beam pointing. Also, the beam phase profile must be "cleaned-up" to produce a flat, uniform phase front, which is accomplished by using a wavefront sensor and deformable mirrors to sense the aberrations and then correct them. A uniform phase front, quantified by the "beam quality" parameter, is important for obtaining a very small spot when the beam is focussed on a target. Jitter, tilt and defocus, each of which can diminish the laser platform brightness at a target, are controlled to tight tolerances. The beam spatial profile is shaped to match the optical beam train by clipping and dumping excess power over small portions of the beam so that instruments and hardware in certain locations in the beam train will not be damaged. The multiple segments on the large pointing optic are kept in precise alignment by using holographic optical elements (HOEs) and Outgoing Wavefront Sensors (OWS) to control actuators behind the surface of the mirror segments. Figures 4 shows the past history and projected milestones of the LODE program.

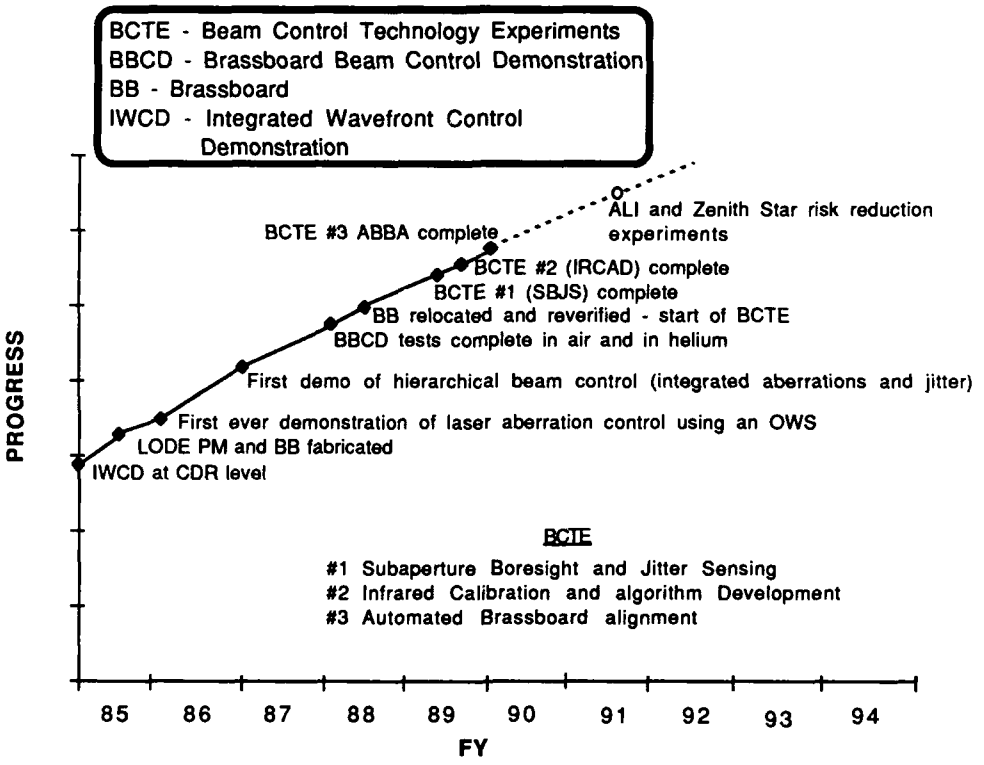


FIGURE 4 Wavefront Control (LODE) Program History

Large Optics

The major elements of this area are the LAMP and Large Optical Segment (LOS) programs. The LAMP mirror, shown in Figure 5, is a large, seven-segment, actively controlled mirror that demonstrates the manufacturing capability and sensor/control technology necessary to build a space-based laser pointing mirror. It represents a breakthrough in large optics technology. The LAMP mirror has gone through an extensive test series on the ground, satisfying all requirements, and now will be used in the Alpha/LAMP Integration experiment. Lightweight and flight-qualifiable, a modified LAMP is included in the Zenith Star space experiment.

The Large Optical Segment program involves the design and eventual manufacture of the larger mirror segments required for a weapon system. The basic technologies needed to support this program have already been developed and demonstrated in such programs as LAMP, HoGPOWS, and others, and the scale-up of facilities necessary to produce this mirror will significantly improve the state-of-the-art of mirror manufacturing so that it is fully able to meet near-term SBL needs. Figure 6 shows the progress of these programs over the last five years and projected progress over the next five years.

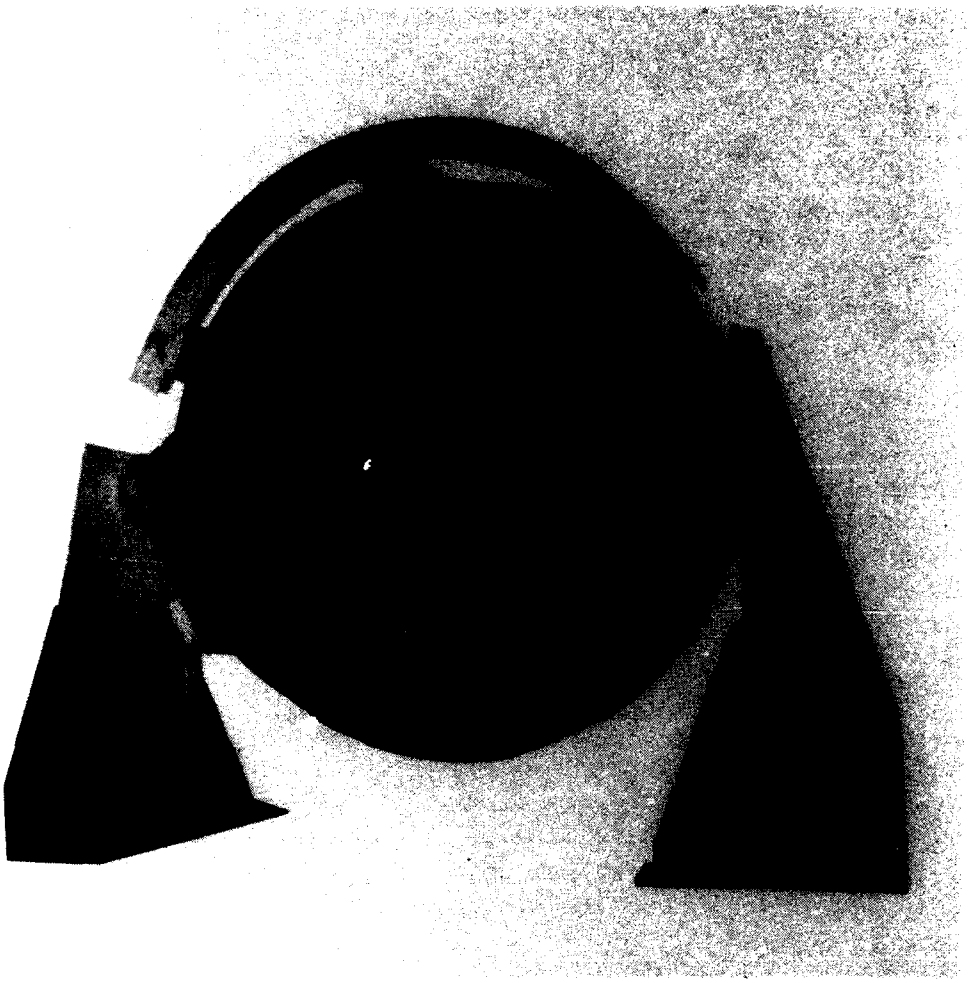


FIGURE 5 The LAMP Mirror

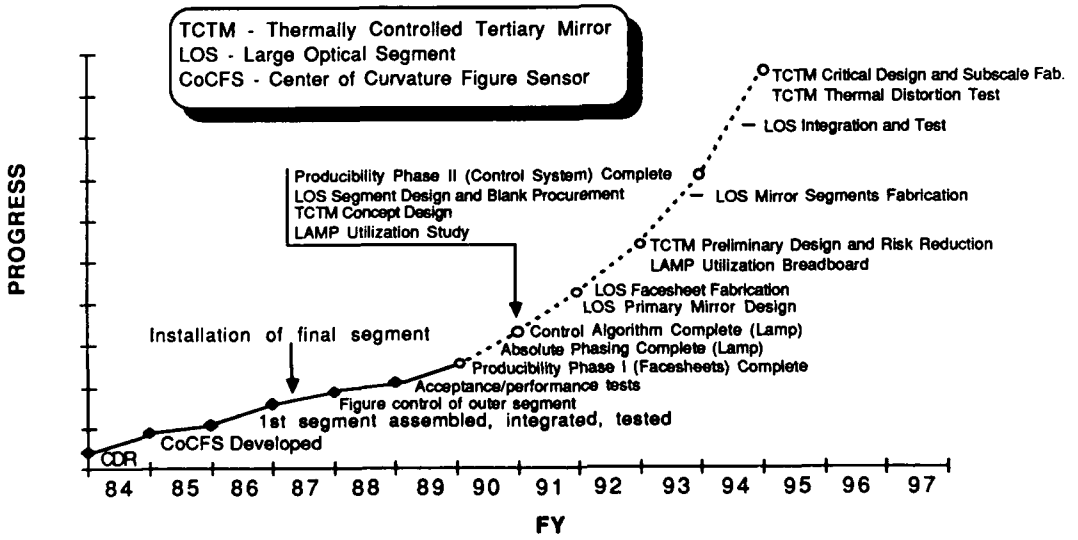


FIGURE 6 Large Optics Program History

ATP

Major elements of this area supporting the SBCL concept are Starlab and the Common Module Tracker program. Starlab is an ATP testbed that has a hardware legacy dating back to the Talon Gold program. It provides a flexible modular approach towards gathering data for ATP systems, with a range of sensors from the UV to the IR. The optical tracking configuration is applicable to all DEW platforms. Starlab is designed to be lofted into orbit in the cargo bay of the Space Shuttle, and is used in conjunction with the Spacelab which houses payload specialists who perform manual target acquisition during a seven day mission. The primary objective is acquisition and active tracking of a thrusting booster. A by-product of the experiment is data collection of plumes and mid-course object phenomenology.

The Common Module Tracker program is a study to design, fabricate and test a single tracker for all DE weapon candidates, including SBLs, GBL fighting mirrors, and NPB platforms. Many facets of the acquisition, tracking, and pointing process are similar for each of these DEWs. For example all must acquire and track booster plumes, and locate the booster hardbody. All must locate midcourse objects for discrimination missions. All must compute point-ahead angles and direct the outgoing beam at the target. If a single tracker unit can be built for all DE applications, with only minor software modifications required for each specific application, then costly overlaps can be avoided. Figure 7 shows past progress and anticipated milestones of all major acquisition, tracking and pointing programs for SBLs.

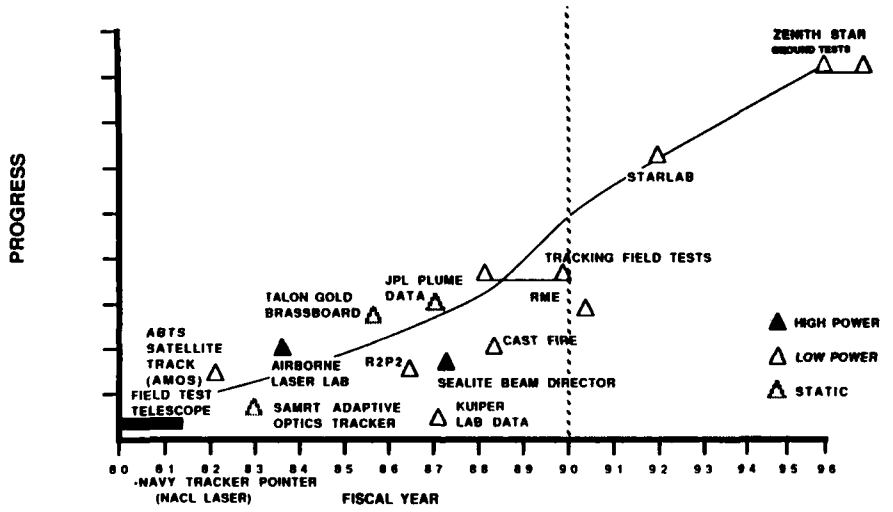


FIGURE 7 Acquisition, Tracking and Pointing Program History

Technology Integration

Two major elements of the technology integration activity for near-term SBLs are the Zenith Star program and the Alpha/LAMP Integration (ALI) experiment. The Zenith Star program will design build and test subscale space-based lasers, resolving issues that can only be tested in an actual space environment. Figure 8 is an artist's depiction of the Zenith Star laser in orbit. The objectives of the Zenith Star program are to resolve key technical issues in sufficient detail to support a confident decision on developing space-based chemical lasers for strategic defense, and to resolve key acquisition, tracking and pointing issues for boost and post-boost objects. Recently the Alpha/LAMP Integration (ALI) experiment was added to the program. The ALI experiment will assemble an end-to-end SBL optical beam train on the ground, propagate a high energy laser beam through it, and demonstrate most beam control concepts as an intermediate step towards a space experiment. Figure 9 shows the program history for SBL integration program activities.

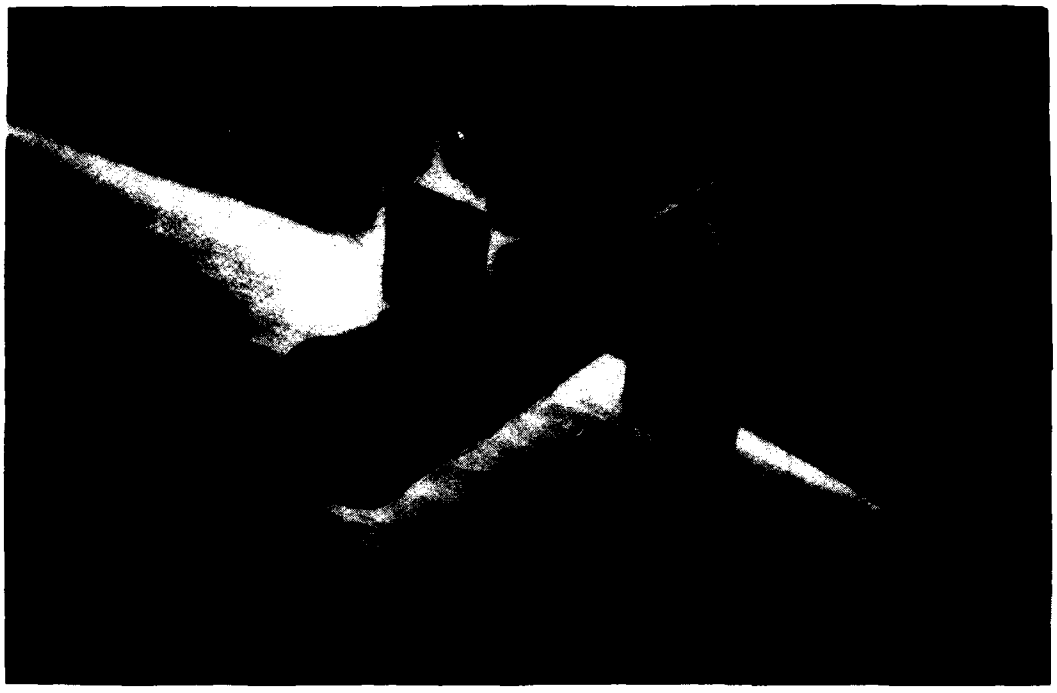


FIGURE 8 Zenith Star Space-Based Laser Experiment

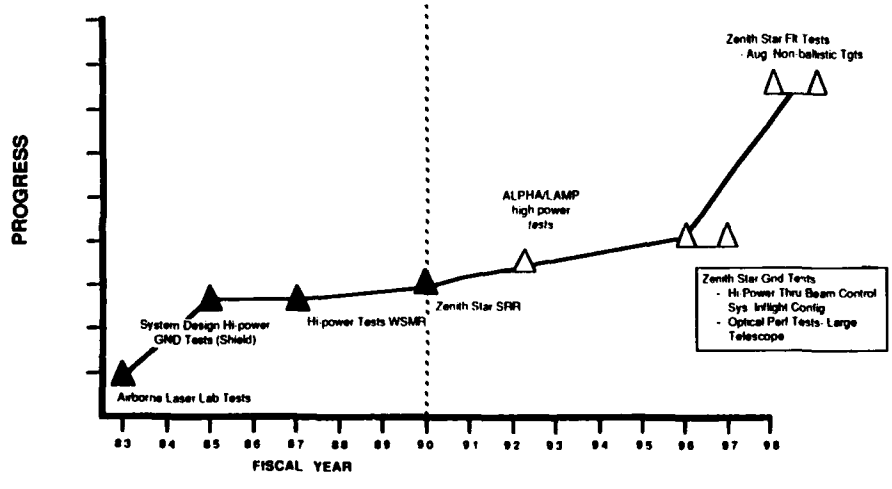


FIGURE 9 SBL Integration Program History

SBL Advanced Technologies

Advanced technologies are being developed to facilitate the requirement to produce high-brightness laser systems for the far-term SDS. These technologies promise to make the laser platforms smaller, lighter, less complex, and easier to manufacture. A constellation of individual laser modules is effective against the near term threat, however as the threat evolves, modules are combined coherently to create very-high-brightness systems. This is accomplished using nonlinear optical phenomena (Stimulated Brillouin Scattering) or conventional amplifier coupling and array phasing technologies. APACHE and APEX programs are developing nonlinear optical phenomena, and their progress is shown in Figure 10. Additionally, development of short-wavelength chemical lasers (overtone) also provides potential for higher brightness systems. Aggressive pursuit of APACHE/APEX technology and efficient overtone operation may improve prospects for near- and far-term space laser applications by providing real-time phase cleanup for reduced optical figure requirements and short wavelength operation for smaller optics.

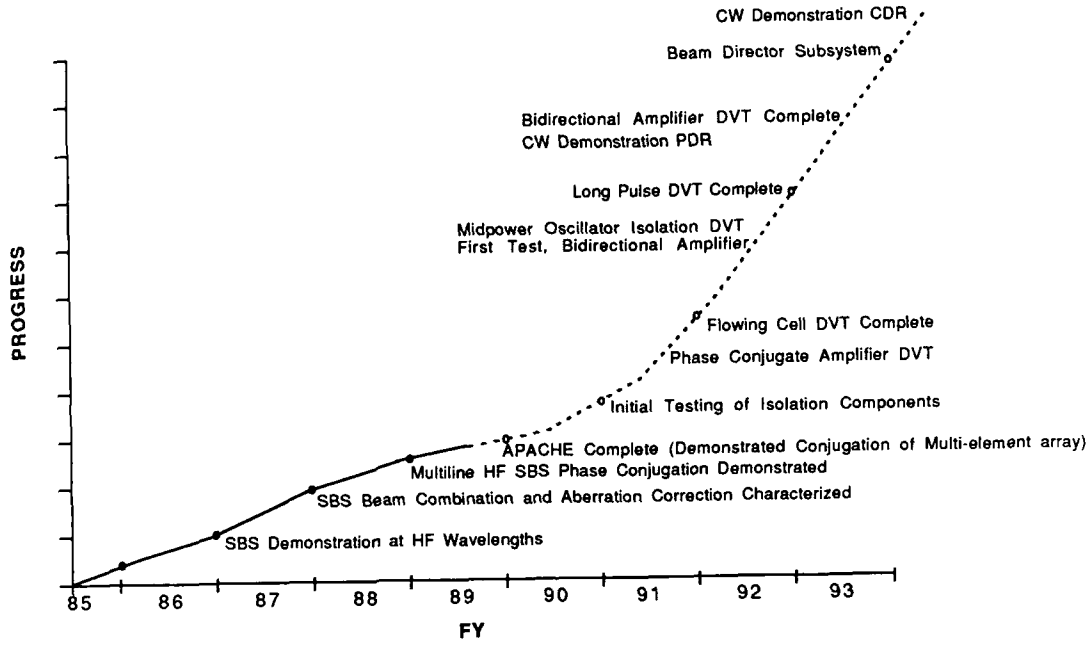


FIGURE 10 APACHE/APEX Program History

Closing Comments

Significant progress has been made in developing technologies essential for space-based lasers. This progress has been across-the-board, covering all key technology development areas. The technologies are feasible - no "show-stoppers" have been identified to date. Integration of the individual technologies into a total system is the largest remaining issue for space-based laser development. The current plan is to address this in subscale space experiments, which will demonstrate that SBLs do indeed have a role in a missile defense system.

The SBCL program is well balanced with both near term and longer term concepts being pursued in parallel. This will result in near-term system options, and also permit planned growth as the threat evolves over time.

EFFECT OF VELOCITY CROSS-RELAXATION AND MODE SEPARATION UPON THE POWER SPECTRUM OF A CHEMICAL OXYGEN-IODINE LASER

DREW A. COPELAND
ROCKETDYNE DIVISION/ROCKWELL INTERNATIONAL
6633 CANOGA AVENUE, CANOGA PARK, CA 91303

ABSTRACT

A gain model for the CW oxygen-iodine laser medium is described. The model uses a simplified, temperature-dependent, chemical kinetics package which consists of several reactions among the $^3\Sigma$, $^1\Delta$, and $^1\Sigma$ states of oxygen, atomic and molecular iodine, water, and helium. The Heidner I_2 dissociation mechanism is included to allow for incomplete dissociation. Gas flow is treated using a pre-mixed, one-dimensional streamtube model which accounts for gas expansion and heat release in the cavity. Elastic collisional cross-relaxation effects upon the Doppler-broadened line are treated using a Fokker-Planck diffusion model of the velocity distribution of the upper and lower laser levels. This gain model, in conjunction with a geometric optics, multi-mode model of an unstable standing-wave confocal resonator, is used to examine the influence of velocity cross-relaxation and mode separation upon the laser output power and mode spectrum. It is shown that lasing will occur on all available modes even when the mode separation is less than the collision linewidth.

I. INTRODUCTION

Recently there has been considerable interest in both subsonic and supersonic CW chemical oxygen-iodine lasers (COIL) because of their short-wavelength, single-line operation, and their potential for scaling to high power, high optical quality operation. For those applications requiring scaling to high power and optical quality a detailed understanding of optical extraction from the oxygen-iodine medium is required if large scale devices employing unstable resonators are to be successfully designed and built.

The primary physical mechanisms affecting the gain and saturation character, and hence, the laser output power and spectrum, of the oxygen-iodine medium are the $O_2(^1\Delta)$ pump reaction, hyperfine relaxation, Doppler and collisional line-broadening of the transition, and collisional cross-relaxation. Because the pumping mechanism is a transfer reaction, the small signal gain (SSG) and saturation parameter of the medium are strong functions of the local $O_2(^1\Delta)$ density (Ref. 33). In addition, although the nascent velocity distribution produced by the pumping reaction is not known, reasonable assumptions about it imply that the pump reaction quickly re-equilibrates the loaded iodine velocity distributions, at least for the conditions considered here, in which the stimulated emission rate is less that the total $O_2(^1\Delta)$ pump rate. Finite-rate hyperfine relaxation does not, to first order, decrease the SSG, but does reduce the saturation parameter since the effective lifetime of the upper laser level is increased (Ref. 15). As is well-known a realistic gas laser model must account for the thermal motion of the lasing atoms as well as their collisions to properly treat the medium's saturation behavior. The thermal motion of the atoms along the optical propagation direction causes their center frequency to be Doppler-shifted so that each velocity group of atoms has a different probability for interacting with the radiation within the cavity, as is indicated schematically in Figure 1A. In the absence of collisions the medium is said to be inhomogeneously broadened. Elastic collisions between atoms of the medium continuously redistribute the thermal velocity population and so tend to restore homogeneity to an otherwise inhomogeneous Doppler-broadened line, as shown in Figure 1B. If the collision rate is sufficiently fast in comparison to the pumping rate and the stimulated emission rate then only one longitudinal mode will have sufficient gain to lase and the laser is said to be homogeneous. The rate of velocity cross-relaxation determines the specific spectral character of the laser output spectrum, either homogeneous, inhomogeneous, or 'mixed' (Ref. 14).

The purpose of the present work was to examine the effects of velocity cross-relaxation upon power extraction from the oxygen-iodine medium in an unstable resonator. To this end a gain model of the oxygen-iodine medium was developed which uses a simplified, temperature-dependent, chemical reaction rate package consisting of several reactions among the $^3\Sigma$, $^1\Delta$, and $^1\Sigma$ states of oxygen, atomic and molecular iodine, water, and helium. The Heidner I_2 dissociation mechanism is included to allow for incomplete dissociation (Ref. 9). For simplicity, hyperfine relaxation is assumed to be fast enough that the levels in question were populated statistically, and consequently, only lasing on the $3 \rightarrow 4$ transition is considered. Gas flow is treated using a pre-mixed, one-dimensional streamtube model which accounts for

gas expansion and heat release in the cavity (Ref. 1). Elastic collisional cross-relaxation effects upon the Doppler-broadened line shape are treated using a Fokker-Planck diffusion model of the velocity distribution within the upper and lower laser levels of iodine (Ref. 19). This gain model was then used in a three-dimensional, geometric optics, multi-mode model of an unstable confocal resonator (Ref. 30) to determine the laser output.

This paper is organized as follows. In Section II the gas flow model is reviewed. In Section III a simplified oxygen-iodine kinetics model, which is suitable for modeling optical extraction from the COIL medium, is described and discussed. Section IV discusses the velocity cross-relaxation model. In Section IV-A the general Boltzmann formalism together with the Keilson and Storer collision kernal is used to derive both the strong collision or relaxation model and the integral and differential forms of the weak collision or diffusion model. The boundary conditions appropriate for the differential form of the weak collision model are described. In section IV-B the approach used to estimate the required velocity diffusion coefficients is described while in Section IV-C an estimate of their magnitude is made. In Section V the pumping, quenching, and stimulated emission terms required by the diffusion model and the expressions used to compute the loaded gain are described. Section VI briefly describes the approximations and numerical algorithm used to solve the coupled partial and ordinary differential equations comprising the model. In Section VII the model is exercised for conditions typical of a supersonic oxygen-iodine laser and the effects of velocity relaxation and resonator mode separation upon the laser output power and spectrum are examined.

II. GAS FLOW MODEL

A one-dimensional, premixed model of steady, inviscid, reacting, ideal-gas flow in an expanding cavity, similar to that discussed by Emanual (Ref. 1), is used to describe the gas flow in the laser cavity. In order that the flow can be approximated as one-dimensional it is required that the fractional rate of change of the area of the cavity with distance downstream be small (Ref. 2). While it is, in general, desirable to introduce area relief into the cavity to reduce heating of the gas, too rapid expansion of the gas could cause extreme thermal gradients and/or shocks which would disturb and diminish the optical beam quality. Thus, this requirement is not only mathematically necessary but desirable from a practical point of view as well. That a premixed description of the reacting gas in the laser cavity be a reasonable approximation it is necessary that the reacting gas streams, here O_2 and I_2, be well-mixed prior to entering the cavity. In practice, this is insured by careful design of the nozzle and injection geometry as well as the choice of secondary buffer gas flows to optimize the penetration of the secondary I_2 stream into the primary O_2 stream. Further discussion of the conditions under which the flow can be approximated by a one-dimensional, premixed model is given in Refs. 1 and 2. Here it will be assumed that such a description is adequate.

The fundamental equations describing inviscid, non-reacting flow of an ideal gas are derived and discussed by many authors including Knudsen and Katz (Ref. 3) and Bird, Stewart, and Lightfoot (Ref. 4). The equations appropriate for a steady, one-dimensional, inviscid, non-reacting flow of an ideal gas in a cavity with variable area are discussed by Shapiro (Ref. 2). In general, the state of a steadily flowing, non-reacting gas is determined by its mass density, temperature, pressure, velocity, and the cross-sectional area of the cavity through which it is moving. These five macroscopic variables are related to each other and constrained by the requirements of mass conservation, Newton's second law for momentum change, energy conservation, and the thermodynamic equation of state. However, for a one-dimensional flow, that is, one for which these variables depend only upon the distance downstream these four requirements are insufficient to determine the state of the flowing gas and an ancillary constraint between these variables is required to uniquely determine the state of the gas. An example of such a constraint is that the area of the cavity be specified as a function of the distance downstream.

In the following it is assumed that the flow is along the x-direction and that the cross-sectional area of the cavity, A, and its rate of change, dA/dx, are specified functions of x. The gas mixture will be taken to consist of N_R components some of which may react while the remainder of which will be assumed to act as a diluent, contributing only to the deactivation of the reacting components and to the molecular weight and heat capacity of the gas mixture. Furthermore, it is assumed that the cavity walls are thermally non-conducting and frictionless, assumptions which are easily relaxed, if necessary, as discussed by Shapiro (Ref. 2). The steady-state flow equations, generalized to describe reacting flow (Ref. 5), can be written as

$$\rho' + u' + A' = 0 \tag{1a}$$

$$u' = - P'/(\gamma M^2) \tag{1b}$$

$$C_pT' = C_pQ' + RP'/W \tag{1c}$$

$$P' = \rho' + T' - W' \tag{1d}$$

$$\rho u\, dn_i/dx = r_i \qquad i = 1...N_R \tag{1e}$$

$$W = (\Sigma n_i)^{-1} \tag{1f}$$

$$W' = - W \Sigma r_i/\rho u \tag{1g}$$

$$\rho u\, dQ/dx = - \Sigma h_i r_i \tag{1h}$$

where a prime denotes the logarithmic derivative of a variable, e.g. $T' = d(\ell nT)/dx$ with the exception that by definition $Q' \equiv dQ/dx/(C_pT)$. Here P, T, ρ, W, u, M, and R denote the gas pressure, temperature, mass density, molecular weight, speed, Mach number, and universal gas constant, respectively. Q denotes the heat energy per unit mass added to the gas by chemical reactions. n_i denotes the mole-mass ratio of species i which is the moles of species i per unit mass of gas. The more familiar molar concentration, c_i, and the particle number density, N_i, are expressed in terms of the mole-mass ratio as $c_i = \rho n_i$, and $N_i = N_A \rho n_i$, respectively, where N_A denotes Avogadro's number. h_i and r_i denote the enthalpy per mole and the net molar production rate per unit volume of species i, respectively. γ denotes the ratio of the heat capacity per unit mass at constant pressure, C_p, to that at constant volume, C_V, i.e. $\gamma = C_p/C_V$. In terms of the heat capacity per mole at constant pressure of species i, denoted C_{pi}, and the mole-mass ratio of species i, $C_p = \Sigma C_{pi} n_i$ and analogously for C_V. It follows from these definitions and the thermodynamic identity $C_{pi} = C_{Vi} + R$ that $C_p = C_V + R/W$ and $C_p = (\gamma/(\gamma - 1))R/W$. The Mach number is the ratio of the speed of the gas to that of sound at temperature T i.e. $M = u/c$ where for an ideal gas $c = (\gamma RT/W)^{1/2}$.

Equations (1a), (1b), and (1c) follow from the requirements of mass continuity, Newton's second law, and energy conservation, respectively. Equation (1d) follows from differentiating the equation of state for an ideal gas, $P = \rho RT/W$. Equation (1e) is the species continuity equation describing the molar rate of change of species i due to chemical reactions. It is best expressed in terms of the species mole-mass ratios rather than molar concentrations or particle densities since it is the mass of a flowing, expanding gas that is conserved, not the volume. Equation (1f) follows from the definition of the mole-mass ratio. Equation (1g) can be derived from Equations (1e) and (1f). Equation (1h) defines dQ/dx. The sums appearing in Equations (1f), (1g), and (1h) are over all components of the gas mixture including those which do not react since for the latter $r_i \equiv 0$ and n_i is constant. Note that Equations (1) depend only upon the logarithmic derivative of A and not A or dA/dx separately; dependence upon A enters through the boundary conditions.

Since the molecular weight and its logarithmic rate of change, the specific heat of the gas, and the rate of heat addition to the gas can be computed if the mole-mass ratios are known, and the gas pressure can be obtained from the thermodynamic equation of state if the gas density, temperature, and molecular weight are known, the state of the gas can be completely specified by the thermodynamic variables ρ, u, T, A, and the mole-mass ratios, n_i, $i = 1...N_R$. In other words, the vector $y = (\rho, u, T, A, n_1, n_2, ...)$ forms a 'basis' with which to represent the state of the flowing, reacting gas. Since the flow is one-dimensional y is only a function of distance along the duct, i.e. $y \equiv y(x)$.

The boundary condition required to complete the specification of the problem is now briefly discussed. Here it is assumed that the gas flowing into the laser cavity is spatially uniform across the extent of the cavity inlet plane and that its density, velocity, temperature, area, and species mole-mass ratios are known. Taking the cavity inlet plane to be located at $x = 0$ and, denoting the value of y at this point by y_0, the boundary condition is simply

$$y(x) = y_0 \quad \text{at} \quad x = 0 \tag{2}$$

To recast Equations (1), subject to the boundary condition (2), into a form to which standard numerical solution techniques and software for ordinary differential equations [ODE] can be applied, it is necessary that the spatial derivatives of ρ, u, T, A, and n_i, $i = 1...N_R$ appear only on the right hand side. Since the logarithmic derivative of the area is specified and dW/dx and dQ/dx can be computed from the state of the gas using Equations (1g) and (1h), Equations (1a-d) are four equations for the logarithmic derivatives of ρ, u, T, and A which can be solved to obtain

$$\rho' = [Q' - W' - M^2A']/[M^2 - 1] \tag{3a}$$

$$u' = - \rho' - A' \tag{3b}$$

$$T' = [(\gamma M^2 - 1)Q' - (\gamma - 1)M^2(A' + W')]/[M^2 - 1] \quad (3c)$$

$$A' = \text{specified} \quad (3d)$$

Equations (3) together with the N_R species continuity equations, (1e), can be integrated numerically subject to the boundary condition (2) to obtain the state of the gas as a function of distance downstream from the cavity inlet.

III. OXYGEN-IODINE KINETICS MODEL

In this section a brief review of the oxygen-iodine kinetics pertinent to optical extraction is presented. A more general and critical review of the kinetics of the oxygen-iodine medium is given by Plummer et al. (Ref. 6) while a more complete overview of CW COIL operation is given by Avizonis and Nuemann (Ref. 7). Although no specific recommendation regarding a kinetics model for optical extraction was made by Plummer et al. (Ref. 6), from their general recommendations a rate package for optical extraction, similar to that recommended by Shea (Ref. 8), has been established. The model is summarized in Table 1, in which I and I^* denote $I(^2P_{3/2})$ and $I(^2P_{1/2})$ states of atomic iodine, respectively.

TABLE 1. CAVITY KINETICS MODEL FOR OPTICAL EXTRACTION MODELING

No.	REACTION	RATE [cm^3/s-particle]
1.	$I + O_2(^1\Delta) \rightarrow I^* + O_2(^3\Sigma)$	$2.33\times10^{-8}/T$
2.	$I^* + O_2(^3\Sigma) \rightarrow I + O_2(^1\Delta)$	reverse of (1), $K=0.75e^{(401.42/T)}$
3.	$I^* + H_2O \rightarrow I + H_2O$	2.0×10^{-12}
4.	$I^* + O_2(^1\Delta) \rightarrow I + O_2(^1\Sigma)$	$4.0\times10^{-24}T^{3.8}e^{(700/T)}$
5.	$I^* + O_2(^1\Delta) \rightarrow I + O_2(^1\Delta)$	1.1×10^{-13}
6.	$I^* + O_2(^1\Delta) \rightarrow I + O_2(^3\Sigma)$	0.0
7.	$I^* + I_2 \rightarrow I + I_2^*$	$1.6\times10^{-11}e^{(272/T)}$
8.	$I_2^* + O_2(^1\Delta) \rightarrow 2I + O_2(^3\Sigma)$	3.0×10^{-10}
9.	$I_2^* + O_2(^3\Sigma) \rightarrow I_2 + O_2(^3\Sigma)$	5.0×10^{-11}
10.	$I_2^* + He \rightarrow I_2 + He$	4.0×10^{-12}
11.	$I_2^* + H_2O \rightarrow I_2 + H_2O$	3.0×10^{-10}
12.	$O_2(^1\Sigma) + H_2O \rightarrow O_2(^1\Delta) + H_2O$	6.7×10^{-12}

Atomic iodine lases at 1.315 μm on the magnetic dipole transition between the F'=3 and F=4 hyperfine levels of the $^2P_{1/2}$ and $^2P_{3/2}$ iodine electronic levels, respectively. A population inversion can be produced between these levels by collisional energy transfer from metastable excited $O_2(^1\Delta)$ to I via Reaction (1) which is exothermic. At room temperature the forward rate is about 7.6×10^{-11} cm^3/s-particle while the equilibrium constant is about 2.9. The energy defect of the pump reaction is about 279 cm^{-1}.

In a flowing oxygen-iodine laser $O_2(^1\Delta)$ is produced by reacting an alkali hydroxide, eg. NaOH or KOH, with hydrogen peroxide and flowing molecular chlorine in a separate rotating disk, aerosol spray, or sparger generator. Molecular iodine is injected into the flowing stream of oxygen and is subsequently dissociated by the excited $O_2(^1\Delta)$ and $O_2(^1\Sigma)$ through a sequence of still incompletely understood reactions (Ref. 6). In order that the majority of the $O_2(^1\Delta)$ is not spent dissociating the molecular iodine, the injected iodine densities are a small fraction, typically 1 to 2 percent, of the total oxygen density. With careful design of the injection and nozzle geometry, and low water content in the flow, the iodine is very nearly fully dissociated by the time it reaches the optical cavity.

In these devices water, a by-product of $O_2(^1\Delta)$ generation, is the primary species responsible for deactivation of the excited iodine by Reaction (3) of Table 1. While much of the water is usually removed from the primary oxygen stream by a cold trap prior to injecting the molecular iodine, its deactivation rate is large enough that even small amounts can potentially shut off the laser. High water content in the flow is deleterious in several ways: 1) it causes the

molecular iodine to be incompletely dissociated in the nozzle thereby necessitating loss of excited iodine and oxygen to dissociate it in the cavity, 2) water deactivates both excited atomic and molecular iodine adding heat to the gas which slows the pump reaction, and 3) water deactivates I^* which reduces the amount of excited iodine from which energy can be extracted.

The energy pooling processes, Reactions (4), (5), and (6) of Table 1, also quench I^* and are included in the present model. Note that Plummer et al. (Ref. 6) have recommended a temperature-dependent rate for channel (4) but not for (5). The recommended rate for channel (6) is zero. At the temperatures of present interest, ~ 150 K, the rate for (4) is ~ 7.9×10^{-14} cm^3/s-particle making it somewhat less important than channel (5) as a quenching mechanism. Under conditions of interest here and for the rates summarized in Table 1 the rate of quenching due to each of reactions (4) and (5) is about 1/20 that due to water. However, because the concentration of $O_2(^1\Delta)$ is several times that of H_2O these energy pooling reactions are comparable in importance to (3) and are believed to be the major contributors to the heat added to the gas. Note that while the quenching of I^* by channel (5) does not destroy an $O_2(^1\Delta)$, quenching by channel (4) does. However since the rate of quenching of $O_2(^1\Sigma)$ by water is very rapid, ~ 6.7×10^{-12} cm^3/s-particle, the $O_2(^1\Delta)$ is rapidly recovered, at least for high water content.

The Heidner dissociation model (Ref. 9) is used to describe the dissociation of the molecular iodine by the $O_2(^1\Delta)$. This mechanism consists of the energy transfer reaction from excited iodine to form an intermediate excited iodine molecule, Reaction (7), followed by the dissociation of the excited molecular iodine through energy transfer with an $O_2(^1\Delta)$ molecule, Reaction (8). The rate for (7) recommended by Plummer et al. (Ref. 6) has not been used in the present work since at low temperatures it extrapolates to a value which is unrealistically large, i.e. ~ 10^2 times the gas kinetic rate (Ref. 10), and because with the recommended value the model produced unrealistically large SSGs. The present value was derived by comparing the predicted gain with previously obtained experimental SSG data (Ref. 11). Quenching of the excited iodine molecules by ground state oxygen, the helium buffer gas, and water, which interrupts the dissociation process, is also accounted for by including Reactions (9), (10), and (11) in the model.

Because Reaction (4) produces $O_2(^1\Sigma)$ the first three electronic states of oxygen are retained in the model. Consequently, the quenching of $O_2(^1\Sigma)$ by water to form $O_2(^1\Delta)$, Reaction (12), is also included in the model.

Although incomplete chlorine utilization is to be expected in practical $O_2(^1\Delta)$ generator systems so that chlorine could be present in the laser cavity, the chlorine-iodine catalytic chemistry (Ref. 6) has been neglected in the present model. This is because under optimal generator operating conditions the chlorine utilization is very nearly complete, ≥ 90%, and because preliminary modeling has shown that, although some I^* deactivation by chlorine occurs, it has a small effect on the gain and power extraction. Also, although the rate of deactivation of I^* by hydrogen peroxide is about ten times that of water, it is expected that the amount of hydrogen peroxide present in the cavity is less than 1/50 the amount of water so that deactivation by hydrogen peroxide can be neglected. Finally, iodine recombination chemistry has been neglected since recombination is negligible for the flow lengths of interest here.

With these assumptions the equations describing the steady-state rate of change of the iodine and oxygen species are

$$\rho u\, d[I^*]/dx = + (k_F{}^1\Delta I - k_R{}^3\Sigma I^*) - I^*/\tau - S \quad (1a)$$

$$\rho u\, d[I]/dx = - (k_F{}^1\Delta I - k_R{}^3\Sigma I^*) + I^*/\tau + 2k_8{}^1\Delta I_2^* + S \quad (1b)$$

$$\rho u\, d[{}^1\Delta]/dx = - (k_F{}^1\Delta I - k_R{}^3\Sigma I^*) - (k_4 + k_6)^1\Delta I^* - k_8{}^1\Delta I_2^* + k_{12}{}^1\Sigma H_2O \quad (1c)$$

$$\rho u\, d[{}^3\Sigma]/dx = + (k_F{}^1\Delta I - k_R{}^3\Sigma I^*) + k_6{}^1\Delta I^* + k_8{}^1\Delta I_2^* \quad (1d)$$

$$\rho u\, d[{}^1\Sigma]/dx = + k_4{}^1\Delta I^* - k_{12}{}^1\Sigma H_2O \quad (1e)$$

$$\rho u\, d[I_2]/dx = + (k_9{}^3\Sigma + k_{10}He + k_{11}H_2O)I_2^* - k_7 I^* I_2 \quad (1f)$$

$$\rho u\, d[I_2^*]/dx = + k_7 I^* I_2 - (k_8{}^1\Delta + k_9{}^3\Sigma + k_{10}He + k_{11}H_2O)I_2^* \quad (1g)$$

$$1/\tau = k_3H_2O + (k_4 + k_5 + k_6)^1\Delta + k_7 I_2 \quad (1h)$$

and [i] and i denote the mole-mass ratio and molar concentration of species i, respectively, k_F, K, and $k_R \equiv k_F/K$ denote the forward reaction, equilibrium, and reverse reaction rates of (1) in molar units, k_i denotes the rate of reac-

tion i as listed in Table 1 in molar units, $1/\tau$ denotes the total quenching rate of I^*, and S denotes the molar stimulated emission rate per unit volume, the specific form of which will be discussed in Section V. As expected Equations (1) imply that both the total mole-mass ratio of iodine atoms and oxygen molecules are conserved. Also, as a consequence of incomplete iodine dissociation, the sum of the net molar production rates per unit volume of the reacting species is non-zero, i.e. $\Sigma r_i = k_8 \Delta I_2^* \neq 0$ and, as a result, the molecular weight of the gas mixture is not constant.

In the present model the temperature dependence of the specific heat and enthalpy for each species present in the gas was taken into account. For atomic iodine and helium as well as the residual water and chlorine in the mix the specific heats are assumed constant and the enthalpy computed using standard thermochemical theory (Ref. 12). For oxygen and molecular iodine it is necessary to account for the temperature dependence of the specific heat due to its vibrational and rotational modes. This was done using the standard representation of the specific heat and enthalpy in terms of the spectroscopic constants of a diatomic molecule (Ref. 13).

IV. VELOCITY CROSS-RELAXATION MODEL

A. BOLTZMANN FORMALISM

The Kan and Wolga collisional relaxation model for CO_2 lasers (Ref. 14), in which the lasing atom velocity distribution is described by a simple relaxation equation, is appropriate for a lasing species of low molecular weight in a heavier diluent gas since the momentum transfer to the lasing species is large. The relaxation or strong collision model was used by Zagidullin et al. (Ref. 15) to describe collisional relaxation effects in the oxygen-iodine medium. However, the strong collision model is not well-suited for this medium, since iodine is a heavy species in comparison with the usual reacting and buffer gases, e.g. O_2 and He (Ref. 19). In this case momentum transfer to iodine by collisions with O_2 and He is small and the effect of collisions upon the distribution of lasing molecules should be described by a diffusion equation (Refs. 16, 17, and 18). Paxton (Ref. 19) recently used such a diffusion or weak collision model to describe velocity cross-relaxation effects in oxygen-iodine lasers. As shown here both models can be derived from the Boltzmann equation.

Letting v denote that component of the gas velocity in the z-direction along which the radiation in the cavity is assumed to be propagating then the population distribution of molecules in either the upper or lower laser level can be described, in general, by the following Boltzmann equation (Ref. 14)

$$\rho D[n(v)]/Dt = P - Q \pm S - \{\int dv' s(v,v')n(v) - \int dv' s(v',v)n(v')\} \tag{1}$$

where $[n(v)]$ and $n(v)$ denote the mole-mass ratio per unit velocity and molar concentration per unit velocity, respectively, of molecules whose velocity lies between v and v+dv; P, Q, and S denote the pumping, quenching, and stimulated emission terms appropriate to the laser chemistry under consideration; $s(v',v)$ denotes the probability per unit time per unit velocity that a particle with velocity v' will scatter into dv about v; ρ denotes the mass density; and D/Dt denotes the convective derivative $\partial/\partial t + u\partial/\partial x$. The first argument of s denotes the initial velocity while the second denotes the final velocity. The first term in brackets describes collisions which cause molecules to scatter molecules out of v while the second term describes those that scatter into v. Note that P, Q, and S depend on the velocity, v, as discussed in Section V.

To describe collisional cross-relaxation phenomena Keilson and Storer (Ref. 16) proposed using the approximate Kernal

$$s(v,v') = \tau^{-1} (\beta/\pi)^{1/2} \exp(-\beta(v'-\gamma v)^2) \tag{2a}$$

$$\beta = [(1 - \gamma^2)w^2]^{-1} \tag{2b}$$

Here τ denotes the mean free time between collisions, γ denotes ratio of the average velocity after collision to that before collision which is given approximately by the ratio M/(M+m), M denotes the molecular mass of the lasing species, m denotes the molecular mass of the buffer gas, and w denotes the average thermal velocity of the lasing gas which is $(2kT/M)^{1/2}$ where k denotes the Boltzmann constant. As discussed by Keilson and Storer (Ref. 16) and Rautian (Ref. 18) the kernal S satisfies certain general constraints and is appropriate to treat either strong or weak collisions.

Consider the strong collision limit of a light-weight lasing species in a heavy-weight diluent gas. In this case each collision of the lasing species with the buffer gas entails a large momentum transfer, $\gamma \simeq 0$, and the distribution of

lasing molecules after a collision is nearly independent of their initial velocity v. In the limit $\gamma = 0$, the kernal (2) becomes

$$s(v,v') = \tau^{-1} f(v') \tag{3a}$$

$$f(v') = (1/w\pi^{1/2}) \exp(-(v'/w)^2) \tag{3b}$$

and equation (1) for the population distribution becomes

$$\rho D[n(v)]/Dt = P - Q \pm S - \tau^{-1} (n(v) - f(v)\int dv' n(v')) \tag{4}$$

which has the form of a relaxation equation, in which the population n(v) relaxes to a Boltzmann distribution, f(v), at a rate $1/\tau$.

Now consider the weak collision limit of a heavy-weight lasing species in a light-weight diluent, as is the case for the oxygen-iodine laser. In this case, each collision results in a relatively small velocity change of the lasing species, $1 - \gamma << 1$, and the velocity of the lasing species after a collision is very nearly what it was before the collision. Substituting the kernal (2) into (1) we find

$$\rho D[n(v)]/Dt = P - Q \pm S - \tau^{-1}(n(v) - (\beta/\pi)^{1/2}\int dv' \exp(-\beta(v-\gamma v')^2) n(v')) \tag{5}$$

Notice that in the limit $\gamma \to 1$, $s(v,v') \to (1/\tau)\ \delta(v'-v)$, and the bracketed term of (1) is absent, i.e. there is no change in the velocity after the collision and hence no change in the distribution of molecules. Equation (5) is an integral form of the weak collision model.

A differential form of the weak collision model can be derived by using the Fokker-Planck approximation to evaluate the integrals in (1). Following the procedure, as outlined in Ref. 16, we find

$$\rho D[n(v)]/Dt = P - Q \pm S + \partial/\partial v(D_1(v)n(v) + \partial/\partial v(D_2(v)n(v))) \tag{6a}$$

$$D_1(v) = \int dv'(v - v')s(v,v') \tag{6b}$$

$$D_2(v) = \tfrac{1}{2}\int dv'(v - v')^2 s(v,v') \tag{6c}$$

are the first and second diffusion coefficients which are expressed in terms of the moments of the kernal S. Since the Fokker-Planck expansion of the integral equation has been truncated at two terms, self-consistency of the resulting diffusion equation requires that, at equilibrium, the particle flux density in velocity space be zero (Ref. 17) or that

$$(D_1(v)n_B(v) + \partial/\partial v(D_2(v)n_B(v))) = 0 \tag{7a}$$

where $n_B(v) = n_0 f(v)$ denotes the Boltzmann equilibrium distribution function and n_0 denotes the total particle concentration. Substituting $n_B(v)$ into (7), differentiating, and solving for D_1 yields

$$D_1 = (2v/w^2)D_2 \tag{7b}$$

so that Eqn. (6) may be written as

$$\rho D[n(v)]/Dt = P - Q \pm S + D\partial/\partial v(\partial n(v)/\partial v + (2v/w^2)n(v)) \tag{8}$$

where $D \equiv D_2$ is the velocity space diffusion coefficient which has been taken to be independent of the particle velocity. Equation (8) is the appropriate differential form of the weak collision model.

A relationship between the integral and differential forms of the weak collision model can be obtained by evaluating the D coefficients in Eqn. (6) using the approximate Keilson-Storer kernal (2) for S. Evaluating the required integrals yields

$$D_1(v) = (1 - \gamma)v/\tau \tag{9a}$$

$$D_2(v) = (1 - \gamma^2)w^2/(4\tau) + (1 - \gamma)^2 v^2/(2\tau) \tag{9b}$$

so that to lowest order in $(1 - \gamma) << 1$

$$(2v/w^2)D_2 = (1 - \gamma)v/\tau \equiv D_1 \tag{10}$$

as required by (7b).

Since Equation (8) is a second-order partial differential equation in t, x, and v, boundary conditions in x and v and an initial condition are required. The boundary conditions in v are obtained by demanding that the total number of particles, $n \equiv \int n(v)dv$, be conserved. Integrating Equation (8) over velocity and imposing this requirement requires that the particle flux in velocity space vanish as $v \to \pm \infty$ or

$$\partial n(v)/\partial v + (2v/w^2)n(v) = 0 \qquad \text{as } v \to \pm \infty \tag{11}$$

As a practical matter when implementing the weak model it is preferable to use the differential form, Equation (8), rather than the integral form, Equation (5), since the differential form avoids any assumptions about the exact form of the kernal s. Furthermore, numerical evaluation of the derivatives in (8) leads to a sparse matrix whereas numerical evaluation of the integrals in (5) leads to a non-sparse matrix. Finally, as discussed below, the required velocity diffusion coefficients can be directly related to the spatial diffusion coefficient whereas the constants $1/\tau$ and γ, required by the integral form, depend upon the assumptions about the kernal and are less directly derivable from the available experimental database.

It should be emphasized that while the weak model is theoretically more correct for treating the oxygen-iodine laser it may be difficult to distinguish between the strong and weak models since the competition between pumping, quenching, stimulated emission, and velocity cross relaxation may mask any such differences. In other words because of the fast pump rate of iodine by $O_2(^1\Delta)$ and the assumptions about the nascent distribution of I^* and I atoms produced [for which there is little experimental data] these effects may overwhelm and hide the differences between the two relaxation models. Furthermore, the experimental database which is available to compare the two models may not allow an unambiguous distinction between the models to be made.

B. FORMULAS FOR ESTIMATING THE VELOCITY DIFFUSION COEFFICIENT

In this section the approach used to estimate the required velocity diffusion coefficients is discussed. As shown by Landau and Lifshitz (Ref. 17a) the spatial diffusion coefficient, D_S, for a small concentration of heavy particles in a light diluent is

$$D_S = 3(kT/m)^2/(N\langle\sigma_T v^3\rangle) \tag{12}$$

where N denotes the total number density of gas, σ_T denotes the momentum transfer cross section, v denotes the speed of a particle of reduced mass mM/(m+M), m denotes the mass of the light diluent gas, M denotes the mass of the heavy species, and the brackets denote an average over a Boltzmann distribution. Equation (12) applies to a binary mixtures of the particles; mixtures will be discussed below. Landau and Lifshitz (Ref. 17b) also discuss the momentum space diffusion equation for a heavy particle in a light diluent and derive the momentum diffusion coefficient, D_M, which is related to its velocity space counterpart, D_V, by $D_V = D_M/M^2$. The velocity diffusion coefficient for a small concentration of heavy particles in a light diluent is (Ref. 17c)

$$D_V = N\langle\sigma_T v^3\rangle(m/M)^2/3 \tag{13}$$

It follows from (12) and (13) that D_V can be expressed in terms of D_S as

$$D_V = (kT/M)^2/D_S \tag{14}$$

so that given D_S at a particular temperature and pressure D_V can easily be computed.

Since mixtures of interest to the oxygen-iodine laser contain, in addition to iodine, a substantial amount of both oxygen and a helium buffer gas, the velocity diffusion coefficient of iodine in a mixture of He and O_2 is required. This can be determined with the aid of the Stefan-Maxwell relation (Ref. 4) which states that the effective binary spatial diffusion coefficient for a species I, D_{SI}, in an n component mixture is

$$1/D_{SI} = [\Sigma_J(1/D_{SIJ})(x_J N_I - x_I N_J)]/[N_I - x_I \Sigma_K N_K] \tag{15}$$

where D_{SIJ} denotes the binary spatial diffusion coefficient of species I in species J, x_I denotes the mole fraction of species I, N_I denotes the molar flux of species I which is given by $c_I v_I$, where c_I and v_I denote the concentration and velocity of species I, respectively, and Σ denotes the sum over the components of the mixture. In the present case (15) can be simplified considerably by taking the index I to denote iodine, and recognizing that since $v_I < v_{O2} < v_{HE}$ and $c_I << c_{O2}, c_{HE}$ it follows that $N_I << N_{O2}, N_{HE}$. Using this, the definition N_J, the fact that $v_J \propto (M_J)^{-1/2}$, and relation (14), the velocity diffusion coefficient of iodine in mixtures of oxygen and helium is approximately given by

$$D_V = xD_{VO2} + (1 - x)D_{VHE} \tag{16a}$$

$$x = (1 + (c_{HE}/c_{O2})(M_{O2}/M_{HE})^{1/2})^{-1} \tag{16b}$$

Observe that if there is no helium in the mix $x = 1$ and $D_V = D_{VO2}$ whereas if there is no oxygen in the mix $x = 0$ and $D_V = D_{VHE}$, as expected.

C. VELOCITY DIFFUSION COEFFICIENTS FOR I IN He AND O_2 MIXTURES

For the ground state of iodine experimental values of the spatial binary diffusion coefficient of iodine in O_2 and He are not available. However, the spatial diffusion coefficient for binary mixtures of non-polar gases, whose interaction potential can be represented by a Lennard-Jones potential, can be estimated using the Chapman-Enskog kinetic theory (Ref. 4). To obtain the velocity diffusion coefficient of iodine in a particular species the spatial diffusion coefficient for iodine in the species was computed at one atmosphere for temperatures ranging from 100 K to 300 K and then least-squares fit to the following temperature- and pressure-dependent form

$$D_S = A(T/300)^n(760/P) \tag{17}$$

Once the fit parameters A and n for the spatial diffusion coefficient of a species have been determined the corresponding velocity diffusion coefficient is computed from (14). The total velocity diffusion coefficient for iodine in mixtures of oxygen and helium is then computed using (16). In the present work the Lennard-Jones parameters for the gases of interest, except atomic iodine, were obtained from the experimental data correlation of Svehla (Ref. 20). For iodine, rather than use the theoretical estimates provided by Svehla, the experimentally inferred parameters of Hayhurst and Springett (Ref. 21) were used. The Lennard-Jones parameters σ and ϵ for He, O_2, and I were taken to be 2.551 A and 10.22 K, 3.467 A and 106.70 K, and 4.360 A and 300.0 K, respectively.

The computed fit parameters A and n for the spatial diffusion coefficient of iodine in He and O_2 at one atmosphere are summarized in Table 2. The maximum error in the fits was $\leq$ 7% over the temperature range 100 to 300 K. For O_2, since the temperature dependence of D_S is very nearly quadratic over the range 100 to 300 K, the velocity diffusion coefficient is nearly independent of temperature, and the value of D_V reported in Table 2 is that computed at 200 K. Over the temperature range of interest here this value suffices to estimate D_V. For He the temperature-dependent form is obtained by substituting (17) with the appropriate fit parameters into (14).

For the first excited state of iodine a different approach was used to estimate the required diffusion coefficients since experimental data, summarized in Table 3, for the spatial diffusion of I^* atoms in the rare gases at 300 K and 1 atmosphere pressure is available (Refs. 15 and 22). Observing that $D_S \propto W^{-1/2}$, where W denotes the reduced molecular weight of the collision partners [see Ref. 4], a semi-empirical correlation of iodine's diffusion coefficient at 300 K and 1 atmosphere pressure was used to obtain the corresponding diffusion coefficient in O_2. A least squares fit of the data of Abrahamson together with the value for Xenon reported by Zagidullin, and the value zero when $W^{-1/2} = 0$ yields

$$D_S = 1.9073/W^{1/2} - 0.0346 \tag{18}$$

with a regression coefficient of 0.98 indicating a very good correlation. For O_2 the value of D_S at 300 K and one atmosphere obtained from (18) is 0.3427 cm^2/s and, observing that the temperature dependence for the ground state D_S is almost exactly quadratic, the temperature dependence for the excited state D_S is taken to be quadratic. For He, D_S is assumed to vary as $T^{3/2}$, as follows for a rigid sphere interaction potential (Ref. 4). The fit parameters A and n for the temperature- and pressure-dependent form (17) of the spatial diffusion coefficient and the corresponding values of the velocity diffusion coefficient, as computed from (14) and (17), are summarized in Table 2.

Now the magnitude of the velocity diffusion coefficients is estimated for gas mixtures of interest here. Since $\gamma_{HE} \simeq 0.969$ while $\gamma_{O2} \simeq 0.799$, during collisions of iodine with oxygen more momentum is transferred from oxygen to iodine

than in a collision of helium with iodine. In this case one would expect D_V for oxygen to be larger than for helium. Since $D \propto (1 - \gamma)$ [see Eqn. (10)], all other things being equal, one has $D_{O2}/D_{HE} = (1 - \gamma_{O2})/(1 - \gamma_{HE}) \simeq 6.5$. Using the values derived in Table 2 it follows that at 2.2 Torr and 135 K D_{O2}/D_{HE} is ~ 4 to 5 which is roughly consistent with this estimate.

TABLE 2. THE DIFFUSION COEFFICIENT FIT PARAMETERS AND THE VELOCITY DIFFUSION COEFFICIENT FOR I AND I^* IN He AND O_2

SPECIE	$D_S = A(T/300)^n 760/P$		D_V at 1 atm	D_S	D_V [at 2.2 Torr and 135 K]	Total D_V
	A (cm^2/s)	n	$(cm/s)^2/s$	(cm^2/s)	$(cm/s)^2/s$	$(cm/s)^2/s$
I-He	0.497058	1.73767	$1.75 \times 10^{16} T^{0.262}$	43.3	1.8×10^{14}	2.5×10^{14}
$I-O_2$	0.109400	1.95501	3.50×10^{17}	7.7	1.0×10^{15}	
I^*-He	0.95	1.5	$2.35 \times 10^{15} T^{0.5}$	100.1	7.8×10^{13}	9.9×10^{13}
I^*-O_2	0.3427	2.0	1.10×10^{17}	24.0	3.3×10^{14}	

TABLE 3. EXPERIMENTAL DATA OF ABRAHAMSON (REF. 22) AND ZAGIDULLIN (REF. 15) FOR THE SPATIAL DIFFUSION COEFFICIENT OF I^* IN THE RARE GASES.

SPECIE	MOLECULAR WEIGHT (gm/mol)	$w^\dagger$	$w^{-1/2}$	D_S at 300 K AND 1 ATM ZAGIDULLIN (cm^2/s)	ABRAHAMSON (cm^2/s)
He	4.00	3.8778	0.5078	1.02	0.95 ± 0.09
Ne	20.179	17.4105	0.2397	0.40	0.40 ± 0.03
Ar	39.994	30.4100	0.1813	0.41	0.36 ± 0.06
Kr	83.8	50.4709	0.1408	0.11	0.11 ± 0.02
Xe	131.3	64.5313	0.1245	0.25	-

†Reduced Molecular Weight

Next consider the magnitude of D_V of the upper state relative to the lower state. From the values in Table 2 we find at 2.2 Torr and 135 K that $D_U/D_L \simeq 0.33$ for oxygen and $D_U/D_L \simeq 0.43$ for helium where D_U and D_L denote the species upper and lower velocity diffusion coefficient, respectively. This is consistent with the fact that the spatial diffusion coefficient for the excited state is two to three times that of the ground state. Under these conditions $D_I/D_{I^*} \sim 2.5$, where D_i denotes the total velocity diffusion coefficient for the species i, and thus, since the lower level re-equilibrates somewhat faster than the upper level, one would expect on the basis of these estimates that the reduction of the inversion due to a build-up of molecules in the lower level, sometimes referred to as 'bottlenecking', would not be too significant.

However, there is no apriori reason to expect the spatial diffusion coefficient of excited iodine [for which there is experimental data] to differ very much from that of ground state iodine [for which there is no direct experimental data] since the long-range interaction potentials should not be too different (Ref. 23). In this case one would expect $D_U \simeq D_L$. Considering the method by which the Lennard-Jones potential parameters are inferred from the transport data and the fact the spatial diffusion coefficient for the excited state is two to three times the computed value for the ground state, one would have to conclude that the present estimates, while reasonable, may be in error. These uncertainties motivated, in part, the need to examine the influence of these rates upon laser output.

V. GAIN AND STIMULATED EMISSION

In this section the pump, quenching, and stimulated emission terms in the diffusion Equation (IV-8) appropriate for the oxygen-iodine laser are discussed and the expressions used to compute the gain are summarized. The pump rate distribution, P(v), is determined by the distribution of I^* atoms between the translational degrees of freedom and the hyperfine levels whenever an iodine atom is produced. Following Zagidullin (Ref. 15) it is assumed that the iodine atoms are produced with a Maxwellian velocity distribution. Here relaxation among the hyperfine sublevels is assumed to be sufficiently fast that the levels remain in statistical equilibrium regardless of the imposed flux. As a consequence only lasing on the 3 → 4 transition needs to be considered. It is not difficult to generalize the model to account for a finite hyperfine relaxation rate (Ref. 24).

Let $[I^*(v)]$ and $I^*(v)$ denote the total mole-mass ratio and molar concentration per unit velocity, respectively, of the excited iodine atoms and similarly for the ground state iodine atoms. Since the hyperfine levels are populated statistically the population of a particular hyperfine level, f, of I^* for example, is given by $(g_f/g^*)I^*$, where g_f and g^* denote the degeneracy of sublevel f and the total degeneracy of the I^* level, respectively. Let D^* and D denote the I^* and I level velocity diffusion coefficients. With this notation, and the above assumptions regarding hyperfine relaxation and the pump rate, the equations describing the steady-state rate of change of the upper and lower laser level population distributions are

$$\rho u\, d[I^*(v)]/dx = + k_F{}^1\Delta I f(v) - (k_R{}^3\Sigma + 1/\tau)I^*(v) - S(v) + D^*\delta I^*(v)/\delta v \tag{1a}$$

$$\rho u\, d[I(v)]/dx = - k_F{}^1\Delta I(v) + ((k_R{}^3\Sigma + 1/\tau)I^* + 2k_8{}^1\Delta I_2{}^*)f(v) + S(v) + D\delta I(v)/\delta v \tag{1b}$$

where by definition $\delta I(v)/\delta v \equiv \partial/\partial v(\partial I(v)/\partial v + (2v/w^2)I(v))$ and $I^* = \int dv I^*(v)$ and $I = \int dv I(v)$ denote the total excited and ground state iodine populations, respectively, and the remainder of the notation is as in Sections III and IV.

Prior to describing the molar stimulated emission rate per unit volume per unit velocity, S(v), it is necessary to describe the field which stimulates the medium. Since the present objective is to develop a kinetics model which can be used as part of an optical model to determine the fields within an oscillator or amplifier the total magnetic field is the sum of several travelling waves which may have different frequencies and/or directions. With this in mind consider the stimulated emission rate appearing in Equation (1). The molar stimulated emission rate per unit volume per unit velocity can be derived using the well-known density matrix formalism, modified to include the motion of the atoms, and making the usual rate equation approximation (Ref. 25); the result for S(v) is

$$S(v) = (\sigma_0/h\nu_0)\Sigma(F_{m+}\mathcal{L}_{m+}(v) + F_{m-}\mathcal{L}_{m-}(v))(I^*(v) - \tfrac{1}{2}I(v)) \equiv R(v)(I^*(v) - \tfrac{1}{2}I(v)) \tag{2a}$$

$$\mathcal{L}_{m\pm}(v) = (\tfrac{1}{2}\Delta\nu_C)^2/[(\nu_{m\pm} - \nu_0(1 \pm v/c))^2 + (\tfrac{1}{2}\Delta\nu_C)^2] \tag{2b}$$

$$\sigma_0 = (7/12)(\lambda_0{}^2/8\pi)\, A\, (\pi\tfrac{1}{2}\Delta\nu_C)^{-1} \tag{2c}$$

where $h\nu_0$, $\nu_0 \equiv c/\lambda_0$, and σ_0 denote the photon energy, frequency, and effective stimulated emission cross section of the 3 → 4 transition at line center, respectively, A denotes the Einstein A-coefficient of the 3 → 4 transition which was taken to be 5.0 s^{-1} (Ref. 26), $\mathcal{L}_{m\pm}(v)$ denotes the dimensionless Doppler-shifted Lorentzian at frequency ω_m and velocity v, $\Delta\nu_C$ denotes the collision linewidth (FWHM), $F_{m\pm}$ denotes the time-averaged intensity of the m^{th} field travelling in the ±z direction, and ν_m denotes the frequency of the m^{th} stimulating field. The factor of 7/12 appearing in σ_0 accounts for the degeneracy of the hyperfine levels. Equation (4a) serves to define R(v), the total stimulated emission rate at v. Here the line shifts and asymmetries in the field-atom interaction caused by collisions have been neglected since the resulting line shifts, $\Delta\nu_S$, satisfy $\Delta\nu_S/\Delta\nu_C \leq 0.1$ (Refs. 26 and 27).

The collision linewidth may be expressed as (Ref. 1)

$$\Delta\nu_C = (T_0/T)^{1/2} P_W \Sigma n_i \Gamma_i \tag{3}$$

where Γ_i denotes the line-broadening strength of species i per unit pressure (FWHM) at a reference temperature T_0 and the remaining notation is as in Section II. For He the experimental value of Γ obtained by Padrick and Palmer (Ref. 27) was used. For water Γ was estimated semi-empirically from the data of Padrick and Palmer by linear interpolating a plot of Γ versus molecular weight in accord with the theoretical dependence of Γ upon molecular weight (Ref. 1). For

iodine and oxygen the values recommended by Shea (Ref. 8) were used. At a reference temperature of 298 K the values of Γ for He, H_2O, I, and O_2 were taken to be 3.6, 5.5, 16.2, and 7.5 MHz/Torr, respectively.

Observe that the equations describing the steady-state rate of change of I^* and I, Equations (III-1a) and (III-1b), respectively, are obtained by integrating Equations (V-1) over velocity. Thus, the total molar stimulated emission rate per unit volume, S, appearing in Equations (III-1) is

$$S \equiv \int dv S(v) = \Sigma(g_{m+}F_{m+} + g_{m-}F_{m-})/N_A h\nu_0 \tag{4a}$$

$$g_{m\pm} = \sigma_0 N_A \int dv (I^*(v) - \tfrac{1}{2}I(v))\mathcal{L}_{m\pm}(v) \tag{4b}$$

$g_{m\pm}$ denotes the gain at $\nu_{m\pm}$, in units of cm^{-1}, corresponding to the $m^{\pm}$ field.

VI. SOLUTION ALGORITHM

The above gain model was used in conjunction with a three-dimensional geometric optics model of a confocal unstable, standing-wave resonator (Ref. 30) to parametrically explore the effects of velocity cross-relaxation and mode separation upon laser output. This optical extraction model treats the variation of the gain along the optical direction using the well-known gain sheet method (Ref. 31) and determines the lowest-loss modal distribution iteratively in a manner similar to that employed by Fox and Li (Ref. 32). Beginning with an estimate of the optical beam at the feedback mirror the beam is geometrically propagated to the location of the first gain sheet where the loaded gain is computed by integrating the medium equations [see below]. This gain is applied to the field and the field propagated to the next gain sheet where the process is repeated. The calculation continues by geometrically propagating the beam through the remainder of the resonator, computing the gain as necessary, until a roundtrip has been completed and a new estimate of the output field and feedback beams are obtained. This procedure is repeated iteratively until the output power converges to a specified tolerance. The extraction model does not include frequency shifts due to the medium's anomalous dispersion. Because the medium in a standing-wave resonator may locally experience fields traveling in both directions, and because the gain model explicitly accounts for inhomogeneity of the transition due to Doppler broadening, fluxes of the same frequency which travel in opposite directions acquire different gains since they interact with different velocity groups of molecules.

Given an estimate of the resonator flux distribution, when the loaded gain is required, it is necessary to integrate the coupled medium equations consisting of the flow Equations, (II-3), the species continuity Equations, (III-1), and the laser level velocity distribution Equations, (V-1), subject to the boundary conditions (II-2) and (IV-11). To integrate these partial differential equations (PDE) the approximation that

$$|\rho u\, \partial[n(v)]/\partial x| \ll |r(v)| \tag{1}$$

where here r(v) denotes the right hand side of Equation (V-1), has been made. This implies that at each point along the flow the iodine velocity population distributions remain in quasi-equilibrium. With this approximation, the coupled PDE's devolve into a set of ODE's in x for the flow and species variables and, at each x, a set of ODE's in v for the laser level velocity distributions. Equations (V-1) become

$$D^*\partial/\partial v(\partial I^*(v)/\partial v + (2v/w^2)I^*(v)) + P^* f(v) - Q^*(v)I^*(v) + \tfrac{1}{2}R(v)I(v) = 0 \tag{2a}$$

$$D\,\partial/\partial v(\partial I(v)/\partial v + (2v/w^2)I(v)) + Pf(v) - Q(v)I(v) + R(v)I^*(v) = 0 \tag{2b}$$

$$P^* = k_F{}^1\Delta I \tag{2c}$$

$$P = k_R{}^3\Sigma I^* + I^*/\tau + 2k_8{}^1\Delta I_2{}^* \tag{2d}$$

$$Q^*(v) = k_R{}^3\Sigma + 1/\tau + R(v) \tag{2e}$$

$$Q(v) = k_F{}^1\Delta + \tfrac{1}{2}R(v) \tag{2f}$$

and the remaining notation has been previously defined. P^* and $Q^*(v)$ denote the total pump rate and quenching rate at v of I^* atoms, respectively, and similarly for P and Q(v). Notice that Equations (2) depend only parametrically upon the gas temperature, pressure, and total species densities, etc. Thus, at each point along the flow, given the total populations of the various species and the gas temperature, pressure, etc. Equations (2) are the coupled ODE's to be solved, subject to the boundary conditions, Equations (IV-11), for the velocity distribution of the lasing

populations. The total populations, gas temperature, etc. are determined by integrating the coupled ODE's, Equations (II-3) and (III-1), describing the chemically reacting flow subject to the boundary condition (II-2). When integrating the later equations Hindmarsh's implementation of Gear's method for stiff ODE's is used (Ref. 35) and the total stimulated emission rate, S, appearing in Equation (III-1) is determined at each point along the flow by solving Equations (2) for $I^*(v)$ and I(v) and then integrating S(v) over velocity. The method of solving (2) is discussed in the Appendix.

VII. RESULTS AND DISCUSSION

To apply the model it is necessary to specify the $O_2(^1\Delta)$ number density, gas temperature, Mach number, etc. which can be done in a variety of ways provided the required parameters are self-consistent. Table 4 summarizes the nominal operating conditions used in the present study from which the model parameters are derived as discussed in Ref. 33. Here, for simplicity, the gain height and width were each taken to be 10 cm. For these conditions the power available per unit nozzle area is ~ 175 W/cm^2, assuming the cost to dissociate the I_2 in units of $O_2(^1\Delta)$ molecules is 5. The resonator configuration was identical to that used by Bullock and Yun (Ref. 34) in their study of adjoint-coupled iodine lasers except that its length was taken to be 10 m so that the mode separation, ~ 15 MHz, was comparable to the collision linewidth, ~ 14.4 MHz (FWHM), for the present medium conditions. The Doppler linewidth in MHz is given approximately by $14.49T^{1/2}$ which is ~ 168 MHz (FWHM) at 135 K.

Figure 2 shows the extraction efficiency defined as the ratio of the laser output power to the power available as a function of the degree of gain saturation when the velocity diffusion coefficients are infinitely fast. Here the degree of gain saturation is characterized by the ratio of the SSG averaged over the spatial extent of the mode along the flow direction, $\langle g_0 \rangle$, to the resonator threshold gain, g_{THR}. For these calculations, performed by keeping the resonator feedback ratio constant and varying the medium gain length, the spatially-averaged SSG was 0.825 %/cm. As shown in the figure when the ratio $\langle g_0 \rangle / g_{THR}$ exceeds 1.5 the extraction efficiency is in excess of 60%. Also, as expected, when the average spatial gain equals the threshold gain the resonator fails to lase.

The effect of finite velocity cross-relaxation upon laser power is shown in Figure 3 in which the output power for finite velocity diffusion relative to the output power for infinitely fast velocity diffusion is shown as a function of the relative velocity diffusion rate for differing degrees of gain saturation. In Figure 3 a relative rate of one corresponds to the total velocity diffusion values (D_V) summarized in Table 2 and both the upper and lower level velocity diffusion coefficients were reduced by the same relative factor. While the effect of finite velocity cross-relaxation is, in general, to reduce the power which can extracted from the medium, notice

TABLE 4. NOMINAL OPERATING CONDITIONS

PARAMETER	VALUE	PARAMETER	VALUE
Chlorine Flow Rate	5.0 Mol/s	I_2 Dissociation Fraction	95 %
Chlorine Utilization $[O_2/Cl_2]$	95 %	Water Mole Fraction	1 %
Primary Diluent Ratio $[He/Cl_2]$	3/1	Cavity Mach Number	2
$O_2(^1\Delta)$ Yield at the Nozzle Exit	50 %	Cavity Temperature	135 K
Secondary Helium Flow $[He/I_2]$	40/1	Cavity Pressure	2.2 Torr
Fuel Ratio $[I_2/Cl_2]$	1.5 %		

that the relative degradation is considerably less if the medium is well-saturated, when $\langle g_0 \rangle / g_{THR} = 1.927$, and much more pronounced near the lasing threshold, when $\langle g_0 \rangle / g_{THR} = 1.156$. As will be seen below, when the medium is better saturated more modes can lase and thus, more of the available laser energy under the Doppler linewidth is extracted.

The number of modes which lase is also dependent on the rate of velocity cross-relaxation. Figure 4 shows the spatially-averaged SSG as a function of frequency, relative to atomic line center. For a given mode separation the maximum number of modes is simply the number of modes for which the average SSG lies above the threshold gain, which is indicated by a horizontal line. With a 15 MHz mode separation a maximum of 5, 7, or 11 modes can lase at the

indicated degree of gain saturation. The actual number that lase is dependent upon the degree of medium inhomogeneity which is determined by the velocity cross-relaxation rate. Figure 5 shows the number of lasing modes as a function of the relative velocity diffusion rate for a given degree of gain saturation. In all three cases, for the present medium conditions, when the relative velocity diffusion rate is 1/1000 of the nominally estimated value, the medium is behaving 'fully' inhomogeneously, i.e. the maximum number of modes is observed. Notice that when the medium is well-saturated all the modes under the Doppler profile lase, which is why the reduction in power relative to the infinite rate is less than if the medium is poorly saturated. At the other extreme, when the velocity diffusion rate is sufficiently fast, only one mode lases and the medium behaves homogeneously. Because the estimates of the velocity diffusion coefficients made in Section IV-C may be in error by a factor of as much as ~ 10 it is expected that the oxygen-iodine laser behaves as neither purely homogeneous or inhomogeneous but instead exhibits a 'mixed' broadening behavior.

The relative power in each mode as a function of the relative velocity diffusion coefficient for $\langle g_0 \rangle / g_{THR}$ ratios of 1.927 and 1.345 is shown in Figures 6 and 7, respectively. As mentioned above, for a given rate more modes lase if the medium is more saturated since then more of the gain profile is above threshold. Also, as the relative diffusion rate decreases more modes lase, as expected, since the medium is then more inhomogeneous. Notice that for intermediate diffusion rates the distribution of modes is not a simple 'bell' distribution. For example, when the medium is well-saturated and the relative rate is 1/10 its nominal value there is slightly more power in the modes at 30 MHZ than the remaining modes, even those at line center or ± 15 MHz. A bell distribution only results if the velocity diffusion rate is sufficiently slow or the strong relaxation model were appropriate and all the molecules, regardless of velocity, relax toward a Boltzmann distribution at the same rate. The relative peaking of these modes near the outer edge of the spectrum is because, in the weak collision model, molecules with different velocities relax to equilibrium with a rate that depends upon the local distribution. In addition, molecules in the 'tails' of the distribution, where the gain is below threshold, can diffuse 'inward' where the gain is sufficient that they are extracted.

Finally the effect of mode separation upon the spectral distribution of the laser was briefly examined. Figures 8 and 9 show the output power in each mode normalized to the peak mode power as a function of the mode separation of the resonator for relative velocity diffusion rates of 1/3 and 1/10, respectively. For a given diffusion rate the total power was nearly constant, independent of the number of modes that lased. Notice that lasing occurred on all of the available modes when the resonator length was doubled so as to decrease the mode separation from 15.0 MHz to 7.5 MHz. All the available modes lase even though the mode separation is less than the collision linewidth. More importantly, as can be seen from the figures, the spectral shape or profile is very nearly independent of the number of lasing modes.

A model of the flowing oxygen-iodine gain medium has been developed and used with a multi-mode geometrical optical extraction model to explore the effect of incomplete velocity relaxation and mode separation upon optical extraction. Although not a comprehensice review of the the effect of all of the variables affecting optical extraction from the oxygen-iodine medium under low-pressure CW conditions these examples indicate the character of that extraction and show some of its important dependencies.

APPENDIX

To solve Equations (VI-2) in the finite region $[-v_{MAX}, v_{MAX}]$ a standard finite difference technique (Ref. 29) is employed. Since the boundary condition in v contains both the unknown function and its derivative at the boundary a grid with its first and last sample points outside the finite region $[-v_{MAX}, v_{MAX}]$ is used. Denoting the total number of sample points <u>within</u> the region $[-v_{MAX}, v_{MAX}]$ by K the sample points are taken to be located at

$$v_k = - v_{MAX} + (k - \tfrac{1}{2})\Delta v \quad k = 0,1...K,K+1 \tag{A-1}$$

where $\Delta v = 2v_{MAX}/K$. The points v_k, k = 1...K, lie within the region $[-v_{MAX}, v_{MAX}]$. The "virtual" points v_0 and v_{K+1} are shifted by $\frac{1}{2}\Delta v$ from the boundaries at $-v_{MAX}$ and v_{MAX}, respectively. With K chosen odd there is a sample point at v = 0. Typically, to adequately span the velocity distribution of the lasing atoms, v_{MAX}, fixed throughout the computation, is taken to be several times the average thermal velocity of the atoms at x = 0, i.e. $v_{MAX} = sw_0$, where s ≈ 3 to 4 and $w_0 = (2RT/W)^{1/2}$.

In discretizing the ODE's (VI-2) only the values of $I^*(v)$ and $I(v)$ at v_k for $k = 1...K$ are computed since the boundary conditions at $\pm v_{MAX}$ are used to eliminate the values of $I^*(v)$ and $I(v)$ at v_0 and v_{K+1}. This is done as follows. At $-v_{MAX}$, n and $\partial n/\partial v$ are approximated by the first-order correct finite differences (Ref. 29)

$$n = \tfrac{1}{2}(n_1 + n_0) \tag{A-2a}$$

$$\partial n/\partial v = (n_1 - n_0)/\Delta v \tag{A-2b}$$

while at v_{MAX} the corresponding approximations

$$n = \tfrac{1}{2}(n_{K+1} + n_K) \tag{A-2c}$$

$$\partial n/\partial v = (n_{K+1} - n_K)/\Delta v \tag{A-2d}$$

are used. Substituting the finite difference approximations (A-2) into the boundary conditions (IV-11) and solving for the values of the unknown, n, at the points v_0 and v_{K+1} we find

$$n_0 = \alpha n_1 \tag{A-3a}$$

$$n_{K+1} = \alpha n_K \tag{A-3b}$$

$$\alpha = [1 - (2/K)(v_{MAX}/w)^2]/[1 + (2/K)(v_{MAX}/w)^2] \tag{A-3c}$$

Notice that $0 < \alpha < 1$ so that as $K \to \infty$, $\alpha \to 1$ and that, although v_{MAX} is fixed, the average thermal velocity, w, depends on the gas temperature, so that α depends on the distance downstream.

Next consider the differential equations (VI-2). The finite difference approximations for the first and second derivatives of $n(v)$, correct to second-order, are (Ref. 29)

$$\partial n/\partial v = (n_{k+1} - n_{k-1})/(2\Delta v) \tag{A-4a}$$

$$\partial^2 n/\partial v^2 = (n_{k+1} - 2n_k + n_{k-1})/(2\Delta v) \tag{A-4b}$$

Substituting these approximations into (VI-2) and rearranging, the following coupled, finite difference equations are obtained for $k = 1...K$

$$A^*_k I^*_{k-1} + B^*_k I^*_k + C^*_k I^*_{k+1} + D_k I_k = S^*_k \tag{A-5a}$$

$$D^*_k I^*_k + A_k I_{k-1} + B_k I_k + C_k I_{k+1} = S_k \tag{A-5b}$$

where for $k = 1...K$

$$A_k = d\xi_{k-} \tag{A-5c}$$

$$B_k = -2d\xi - Q_k \tag{A-5d}$$

$$C_k = d\xi_{k+} \tag{A-5e}$$

$$D_k = R_k \tag{A-5f}$$

$$S_k = -Pf_k \tag{A-5g}$$

with the exceptions that

$$A_1 = C_K = 0 \tag{A-5h}$$

$$B_1 = -2d\xi - Q_1 + \alpha d\xi_{1-} \tag{A-5i}$$

$$B_K = -2d\xi - Q_K + \alpha d\xi_{K+} \tag{A-5j}$$

where the definitions

$$d = D/(\Delta v)^2 \tag{A-5k}$$

$$\xi = 1 - (\Delta v/w)^2 \tag{A-5l}$$

$$\xi_{k\pm} = 1 \pm (\Delta v/w)^2 (v_k/\Delta v) \tag{A-5m}$$

have been introduced and here $I^*_k = I^*(v_k)$, $I_k = I(v_k)$, $f_k = f(v_k)$, $Q_k = Q(v_k)$, and $R_k = R(v_k)$. A^*, B^*, C^* and S^* are defined analogously to A, B, C, and S except that d^* replaces d, Q^* replaces Q, P^* replaces P, and $D^*_k = \frac{1}{2}R_k$. The linear algebraic equations (A-5) are a special case of the more general bi-tridiagonal form and can be solved using the bi-tridiagonal solution algorithm (Ref. 29). Specializing this procedure to the present problem the algorithm for solving Equations (A-5) is

(A) Initialize the scalars $\beta_1, \beta_2, \beta_3, \beta_4, \delta_1, \delta_2, \mu$:

$$\beta_1 = B^*_1$$
$$\beta_2 = D_1$$
$$\beta_3 = D^*_1$$
$$\beta_4 = B_1$$
$$\delta_1 = S^*_1$$
$$\delta_2 = S_1$$
$$\mu = (\beta_1\beta_4 - \beta_2\beta_3)^{-1}$$

(B) Initialize the arrays $\lambda_1, \lambda_2, \lambda_3, \lambda_4, I^*$, and I:

$$\lambda_{1,1} = \mu\beta_4 C^*_1$$
$$\lambda_{2,1} = -\mu\beta_2 C_1$$
$$\lambda_{3,1} = -\mu\beta_3 C^*_1$$
$$\lambda_{4,1} = \mu\beta_1 C_1$$
$$I^*_1 = \mu(\beta_4\delta_1 - \beta_2\delta_2)$$
$$I_1 = \mu(\beta_1\delta_2 - \beta_3\delta_1)$$

(C) FOR k = 2...K DO

$$\beta_1 = B^*_k - A^*_k\lambda_{1,k-1}$$
$$\beta_2 = D_k - A^*_k\lambda_{2,k-1}$$
$$\beta_3 = D^*_k - A_k\lambda_{3,k-1}$$
$$\beta_4 = B_k - A_k\lambda_{4,k-1}$$
$$\delta_1 = S^*_k - A^*_k I^*_{k-1}$$
$$\delta_2 = S_k - A_k I_{k-1}$$
$$\mu = (\beta_1\beta_4 - \beta_2\beta_3)^{-1}$$
$$\lambda_{1,k} = \mu\beta_4 C^*_k$$
$$\lambda_{2,k} = -\mu\beta_2 C_k$$
$$\lambda_{3,k} = -\mu\beta_3 C^*_k$$
$$\lambda_{4,k} = \mu\beta_1 C_k$$
$$I^*_k = \mu(\beta_4\delta_1 - \beta_2\delta_2)$$
$$I_k = \mu(b_1\delta_2 - \beta_3\delta_1)$$

ENDDO

(D) Backsolve to find I^* and I:

FOR k = K-1...1 DO

$$I^*_k = I^*_k - \lambda_{1,k}I^*_{k+1} - \lambda_{2,k}I_{k+1}$$
$$I_k = I_k - \lambda_{3,k}I^*_{k+1} - \lambda_{4,k}I_{k+1}$$

ENDDO

An efficient algorithm to evaluate the Boltzmann distribution, f(v), on the symmetric sample grid (A-1) for odd K is now described. The advantage of the method is that requires the evaluation of a single exponential rather than K exponentials as the straight-forward but naive evaluation of f(v) would require. Since the Boltzmann distribution is symmetric in v, i.e. f(-v) = f(v), it suffices to evaluate f(v) on the 'half-grid' extending from v = 0 to v = v_{MAX} and use symmetry to obtain the values of f(v) for negative values of v. Let U_j denote the points on the half-grid extending from v = 0 to v = v_{MAX} so that

$$U_j = v_{j+N} = (j - 1)\Delta v \quad j = 1 \ldots N+1 \tag{A-6}$$

where K = 2N + 1 defines N. It follows from the definition of f(v) and (A-6) that

$$f(U_1) = 1/w\pi^{\frac{1}{2}} \equiv \alpha$$
$$f(U_2) = (1/w\pi^{\frac{1}{2}})\exp(-(\Delta v/w)^2) \equiv \alpha\beta$$
$$\ldots$$
$$f(U_j) = \alpha\beta^{(j-1)^2}$$
$$\ldots$$
$$f(U_{N+1}) = \alpha\beta^{N^2}$$

where $\beta \equiv \exp(-(\Delta v/w)^2)$. Since

$$f(v_j) = f(v_{K+1-j}) = f(v_{2K+2-j}) = f(U_{K+2-j}) \tag{A-7}$$

by the symmetry property of f(v) and the definitions of the v and U grids an efficient algorithm to evaluate f(v) on the original v grid is

$$\beta = \exp(-(\Delta v/w)^2)$$
$$\gamma = \beta^*\beta$$
$$f_{N+1} = 1/w\pi^{\frac{1}{2}}$$

```
FOR J = 2,N+1 DO
    f_{J+N} = β f_{J+N-1}
    f_{N+2-J} = f_{J+N}
    β = β*γ
ENDDO
```

where the dimension of the vector f is K and, as above, $f_k \equiv f(v_k)$.

To compute the required integrals, (V-4), the trapezoidal rule can be used. With the present choice for the location of the sample points the trapezoidal rule is

$$S = \Delta v \Sigma S_k - (1 - \alpha)(S_1 + S_K)/8 \approx \Delta v \Sigma S_k \qquad \text{(A-8)}$$

where S_k denotes the value of the integrand and the last approximation is valid for sufficiently large K since $\alpha \to 1$. In choosing K, the total number of points spanning the region $[-v_{MAX}, v_{MAX}]$, to accurately compute the integrals it is necessary that several points lie under each collision linewidth. If M such points are to lie under a collision linewidth it is straightforward to show that

$$K \geq (2/(\ell n 2)^{1/2})\ sM\ \Delta\nu_D/\Delta\nu_C \qquad \text{(A-9)}$$

Thus, for example, if M = 5, s = 3, $\Delta\nu_D$ = 180 MHz, and $\Delta\nu_C$ = 20 MHz, K ≈ 325. Typically, for the conditions considered here, taking K = 401 is adequate.

ACKNOWLEDGEMENTS

The author would especially like to thank A. H. Bauer, J. A. Blauer, J. H. Errikla, D. A. Holmes, W. P. Latham, A. H. Paxton, R. F. Shea, and T. T. Yang for many helpful discussions during the course of this work. He also thanks K. Jones for his assistance with the computer program.

REFERENCES

1. G. Emanual, "Numerical Modeling of Chemical Lasers," in Handbook of Chemical Lasers, ed. by R. W. F. Gross and J. F. Bott, (Wiley, New York, 1976), pgs. 469-549.
2. A. H. Shapiro, The Dynamics and Thermodynamics of Compressible Fluid Flow, Vols. I and II, (The Ronald Press, New York, 1954).
3. J. G. Knudsen and D. L. Katz, Fluid Dynamics and Heat Transfer, (McGraw Hill, New York, 1958).
4. R. B. Bird, W. E. Stewart, and E. N. Lightfoot, Transport Phenomena, (Wiley, New York, 1960).
5. S. S. Penner, Introduction to the Study of Chemical Reactions in Flow Systems, (Butterworth, London, 1955).
6. "The Proceedings from the 1987 Air Force Weapons Laboratory Conference on Chemical Oxygen-Iodine Laser (COIL) Kinetics," edited by D. N. Plummer, R. F. Heidner, III, and G. Perram, RDA Logicon, R&D Associates, System Engineering Division, P.O. Box 9377, Albuquerque, New Mexico, 87119.
7. P. V. Avizonas and D. K. Nuemann, "The Chemical Oxygen-Iodine Laser," (Unpublished).
8. R. F. Shea (private communication).
9. R. F. Heidner, III, C. E. Gardner, G. I. Segal, and T. M. El-Sayed, "Chain Reaction Mechanism for I_2 Dissociation in the $O_2(^1\Delta)$ - I Atom Laser," J. Chem. Phys. 78, 2348 (1983).
10. T. T. Yang (private communication).
11. S. Hurlock, D. Schwamb, and J. Davis, "Oxygen-Iodine Supersonic Technology Program", AFWL-TR-84-37, Vol. I, Parts 1 to 4 (March, 1985).
12. J. E. Mayer and M. G. Mayer, Statistical Mechanics, (Wiley, New York, 1940).
13. D. R. Stull and H. Prophet, JANAF Thermochemical Tables, 2nd Edition, NBS 37, Office of Standard Reference Data, National Bureau of Standards, Washington, D. C., 20234, June 1971.
14. T. Kan and G. J. Wolga, "Influence of Collisions on Radiative Saturation and Lamb Dip Formation in CO_2 Molecular Lasers," IEEE J. Quan. Elect. QE-7, No. 4, April 1971, pgs 141-150.

15. M. V. Zagidullin, V. I. Igoshin, and N. L. Kupriyanov, "Kinetics of Saturation of the active medium of an Oxygen-Iodine Laser," Sov. J. Quant. Elect. 14 (7), July 1984, pgs. 930-936.

16. J. Keilson and J. E. Storer, "On Brownian Motion, Boltzmann's Equation, and the Fokker-Planck Approximation," Quart. Appl. Math. 10 (1952), pgs. 243-253.

17. E. M. Lifshitz and L. P. Pitaevskii, Physical Kinetics, Landau and Lifshitz Course of Theoretical Physics, Vol. 10, Pergamon Press, Oxford, 1981.a) Pg. 42, Eqn. (12.4); b) Chapter II, Section 21, pg. 89; c) Pg. 92, Problem 1; d) Section 11, Pg. 39, Eqn. (11.10).

18. S. G. Rautian, "The Effect of Collisions on Spectral Characteristics of Gas Lasers," Sov. Phys. JETP 24, 788-796, (1967).

19. a) A. H. Paxton, "Theory of Oxygen-Iodine Lasers with Multiple Longitudinal Modes: Final Report," MRC/ABQ-R-1097, Mission Research Corporation, 1720 Randolph Road SE, Albuquerque, NM 87106-4245. b) A. H. Paxton and W. P. Latham, Jr., "Low-pressure iodine laser: effect of collisional relaxation of velocity distribution on efficiency and longitudinal mode spectrum," in the Proceedings of the SPIE OE/LASE Conference, Vol. 1045, Jan. 1989.

20. R. A. Svehla, "Estimated Viscosities and Thermal Conductivities of gases at High Temperature, " NASA Technical Report R-132 (1962).

21. A. N. Hayhurst and M. J. Springett, "Flame Photometric Determination of Diffusion Coefficients, Part 6. Results for Carbon Monoxide and free atoms of Bromine, Iodine, and Thalium," J. Chem. Soc., Faraday Transactions I, Vol. 74, No. 3, pgs. 715-719 (1978).

22. E. W. Abrahamson, L. J. Andrews, D. Husain, and J. R. Wiesenfeld, "Electronically Excited Iodine Atoms, I($5^2P_{1/2}$), Diffusion in Noble Gases, the Mean Radiative Lifetime and Atomic Recombination," J. Chem. Soc., Faraday Transactions II, Vol. 68, No. 1, pgs 48-54 (1972).

23. J. A. Blauer (private communication).

24. S. Churassy, R. Bacis, A. J. Bouvier, C. P. dit Mery, and B. Erba, "The chemical oxygen-iodine laser: Comparison of a theoretical model with experimental results," J. Appl. Phys. 62 (1), July 1, 1987, pgs. 31-35.

25. M. Sargent, III, M. O. Scully, and W. E. Lamb, Jr., Laser Physics, (Addison-Wesley, Reading, Massachusetts, 1974).

26. V. S. Zuev, V. A. Katulin, V. Yu. Nosach, and O. Yu. Nosach, "Investigation of the Luminescence Spectrum of Atomic Iodine ($^2P_{1/2}$ - $^2P_{3/2}$ Laser Transition)," Soviet Physics JETP, Vol. 35, No. 5, Nov. 1972, pgs. 870-873.

27. T. D. Padrick and R. E. Palmer, "Pressure Broadening of the Atomic Iodine $5^2P_{1/2}$ - $5^2P_{3/2}$ Transition," J. Chem. Phys., Vol. 62, No. 8 (1975), pgs. 3350-3352.

28. G. Brederlow, E. Fill, and K. J. Witte, The High Power Iodine Laser, Springer Series in Optical Sciecnes, Vol. 34 (1983), Section 2.1.

29. D. U. von Rosenberg, Methods for the Numerical Solution of Partial Differential Equations, (American Elsevier, New York, 1969).

30. D. A. Copeland, "Geometric Multi-Mode Confocal Resonator and Amplifier (MCFOCAL) Model," Rocketdyne Internal Letter 88-102/AB-055, June 3, 1988 (Unpublished).

31. P. W. Milonni, "Critera for the Thin-Gain Sheet Approximation," Applied Optics, Vol. 16, No. 11, Nov. 1977, pgs. 2794-2795.

32. A. G. Fox and T. Li, "Resonant Modes in a Maser Interferometer," Bell Syst. Tech. J., Vol. 40, March 1961, Pgs 453-488.

33. D. A. Copeland, C. Warner, and A. H. Bauer, "Simple Model for Optical Extraction from a Flowing Oxygen-Iodine Medium using a Fabry-Perot Resonator," Paper No. 1224-43 in the Proceedings of the Conference on High Power Gas Lasers, SPIE's Symposium on High Power Lasers and Optical Computing, OE LASE '90, Los Angeles, CA.

34. D. L. Bullock and J. S. Yun, "Fundamental Beam Quality Considerations for Modes of Adjoint-Coupled Lasers," Paper No. 1045-10 in the Proceedings of SPIE's Symposium on Lasers and Optics, OE LASE '89, Los Angeles, CA.

35. A. C. Hindmarsh, "ODEPACK, A Systemized Collection of ODE Solvers," in Scientific Computing, ed. by R. S. Stepleman et al., (North-Holland, Amstersdam, 1983, Vol. 1 of IMACS Transactions on Scientific Computation), pgs. 55-64.

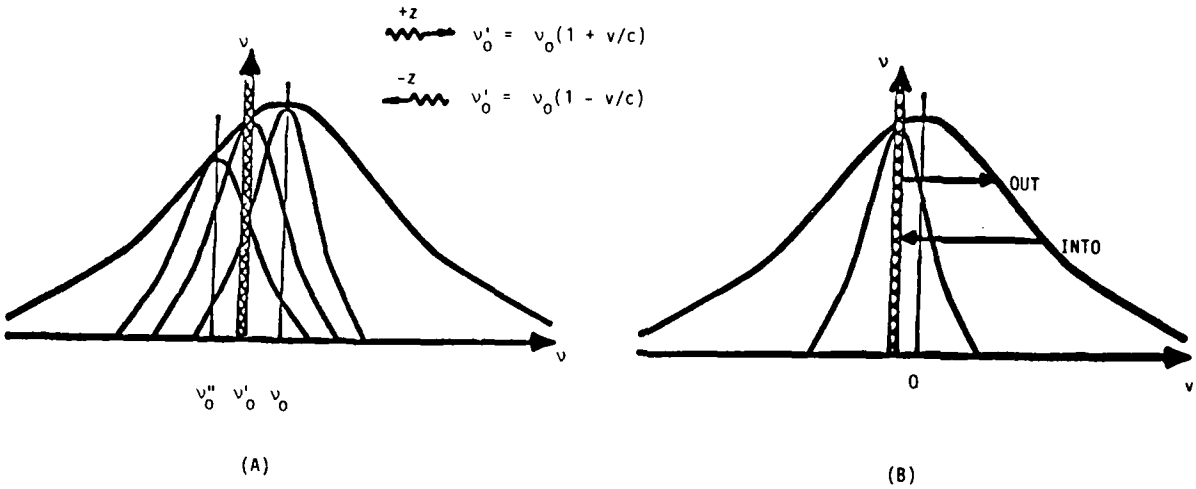


FIGURE 1. SCHEMATIC SHOWING (A) THE INTERACTION OF LIGHT OF FREQUENCY ν WITH GROUPS OF ATOMS WHOSE CENTER FREQUENCIES ARE AT ν_0, ν_0', AND ν_0'' AND (B) HOW COLLISIONS CAUSE ATOMS TO MOVE OUT OF AND INTO THE INTERACTION REGION WITH LIGHT OF FREQUENCY ν

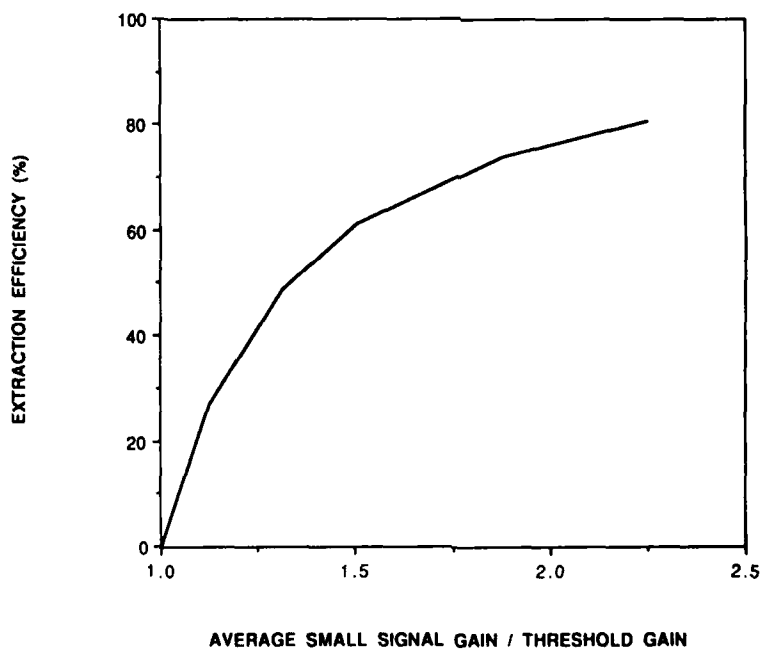


FIGURE 2. EXTRACTION EFFICIENCY AS A FUNCTION OF GAIN FOR INFINITELY FAST VELOCITY CROSS-RELAXATION WHEN $\langle g_o \rangle$ = 0.825%/CM.

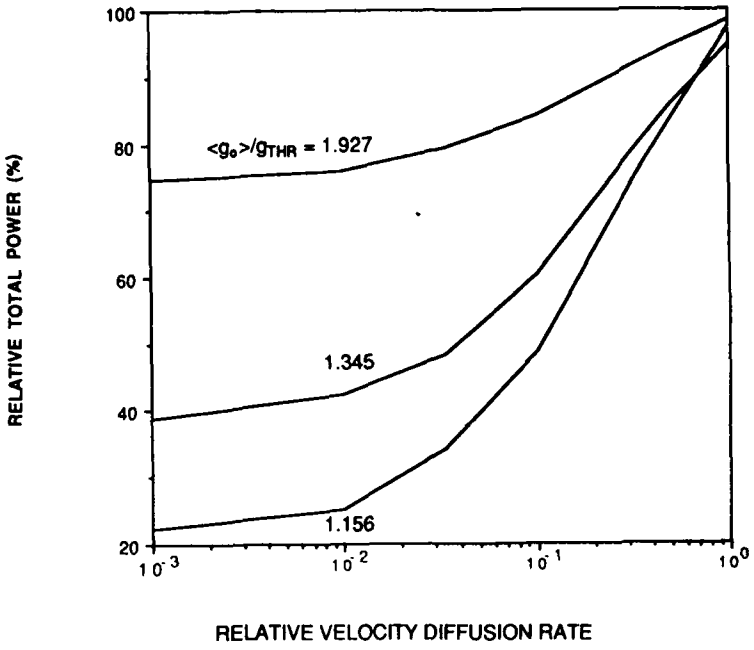


FIGURE 3. RELATIVE POWER DEGRADATION AS A FUNCTION OF THE RELATIVE VELOCITY DIFFUSION RATE AND THE DEGREE OF GAIN SATURATION, $\langle g_o \rangle / g_{THR}$.

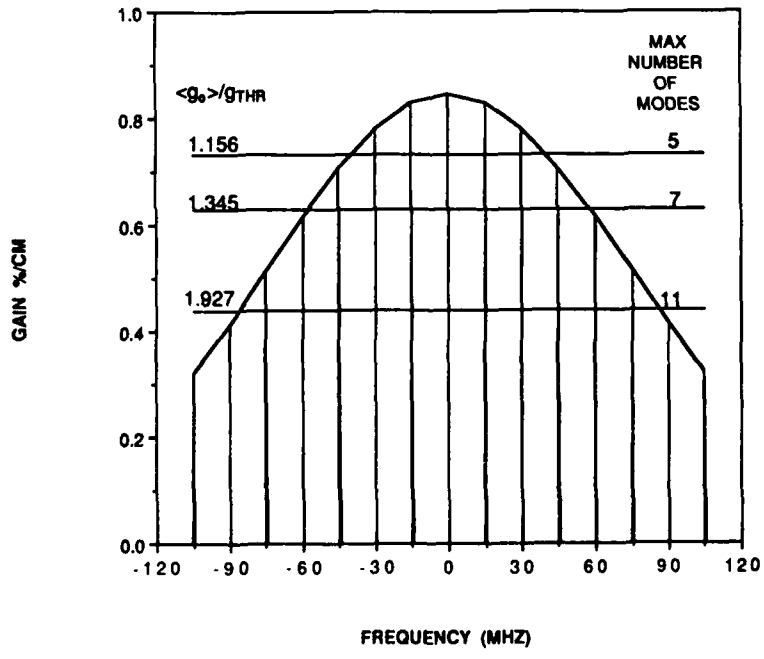


FIGURE 4. THE SPATIALLY AVERAGED SMALL SIGNAL GAIN, $\langle g_o \rangle$, AS A FUNCTION OF FREQUENCY.

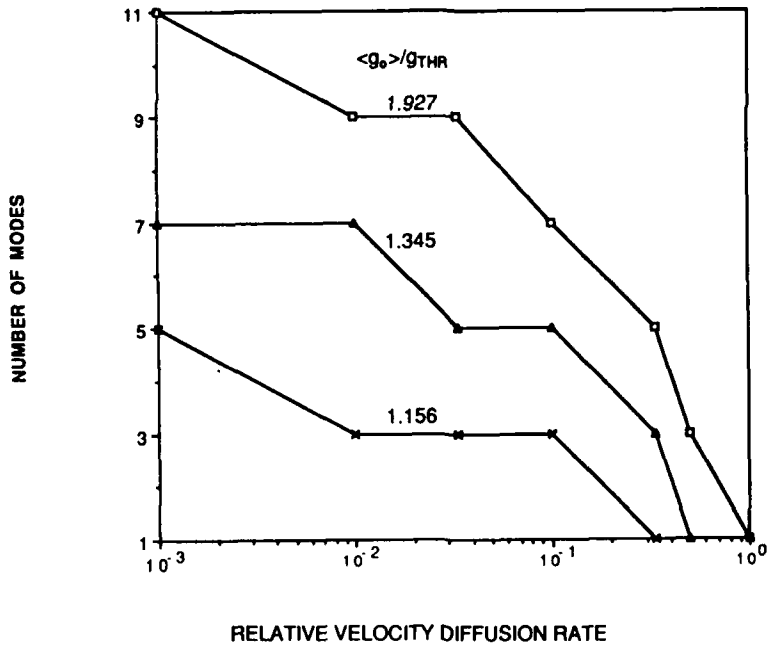


FIGURE 5. THE NUMBER OF LASING MODES AS A FUNCTION OF THE RELATIVE VELOCITY DIFFUSION RATE AND THE DEGREE OF GAIN SATURATION, $<g_o>/g_{THR}$.

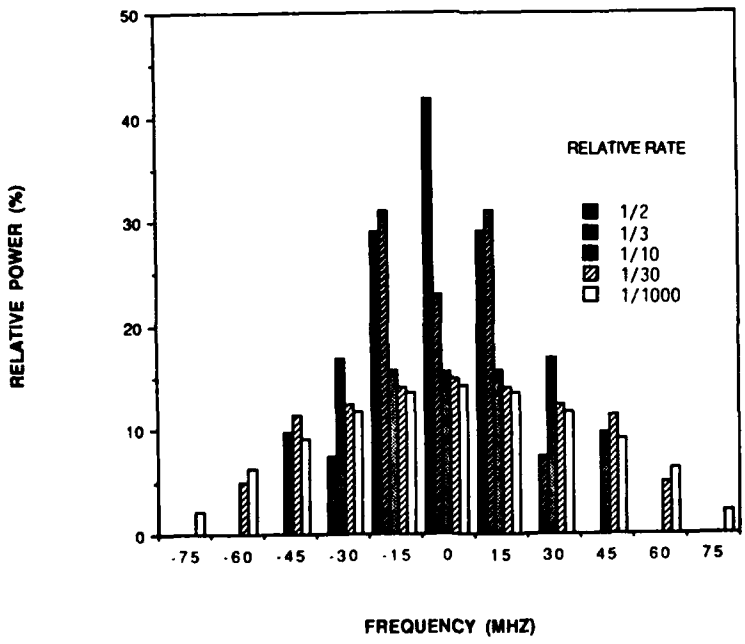


FIGURE 6. THE RELATIVE POWER IN EACH MODE AS A FUNCTION OF THE RELATIVE VELOCITY DIFFUSION RATE WHEN $<g_o>/g_{THR} = 1.927$.

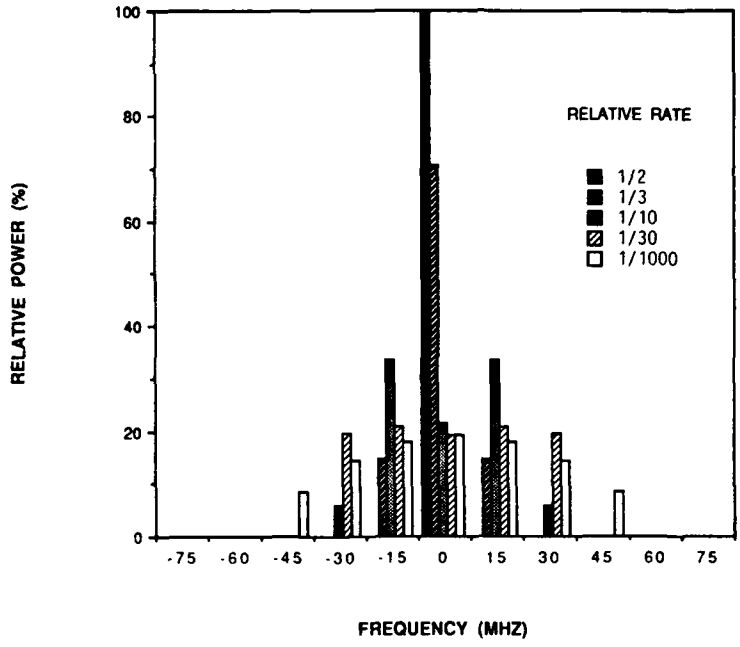


FIGURE 7. THE RELATIVE POWER IN EACH MODE AS A FUNCTION OF THE RELATIVE VELOCITY DIFFUSION RATE WHEN $\langle g_o \rangle / g_{THR} = 1.345$.

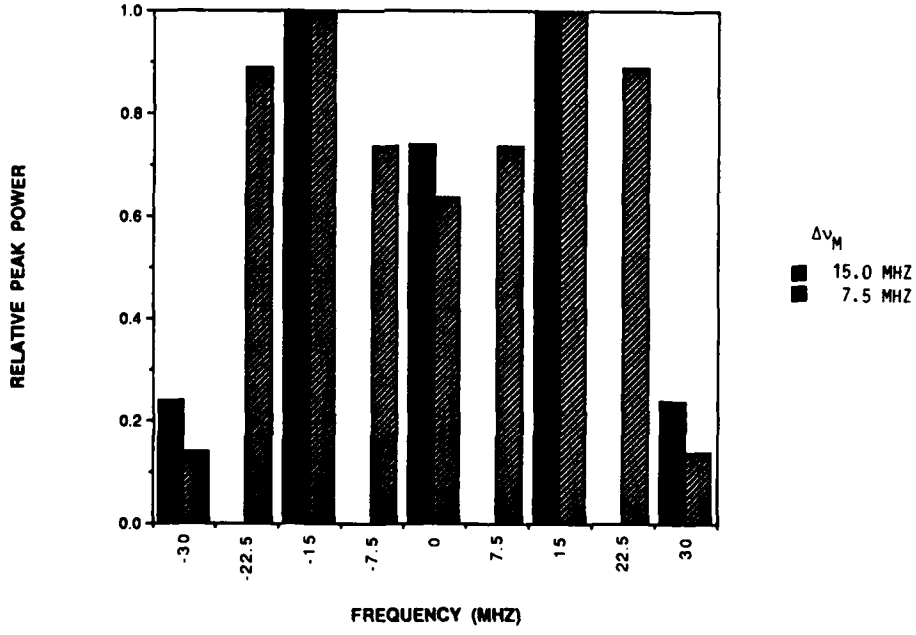


FIGURE 8. THE RELATIVE PEAK POWER IN EACH MODE AS A FUNCTION OF MODE SEPARATION FOR A RELATIVE VELOCITY DIFFUSION RATE OF 1/3.

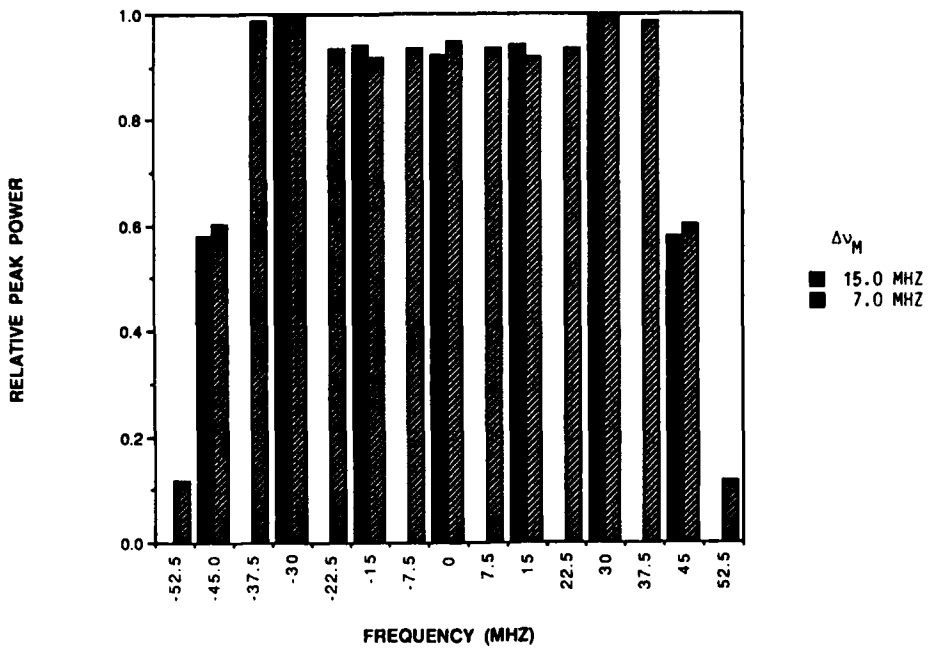


FIGURE 9. THE RELATIVE PEAK POWER IN EACH MODE AS A FUNCTION OF MODE SEPARATION FOR A RELATIVE VELOCITY DIFFUSION RATE OF 1/10.

Parametric study of chemical oxygen iodine laser

T.sawano and S.Yoshida

Laser Laboratory, Institute of Research and Innovation
Kashiwa, Chiba 277, Japan

Abstract

We have developed a high power, efficient chemical oxygen iodine laser system with industrial applications in mind. Employing dilute hydrogen peroxide the present system can operate stably at 1kW for 10 minutes, and 500 W for over 30 minutes. We are now interested in understanding correlations between laser power and other operating parameters such as mirror transmission. Recent results of parametric experiments are discussed. Besides the high power and long stable operation under the optimized condition we found by the parametric study, we have demonstrated power delivery through a silica fiber with 70% transmission efficiency at 250 W input power. We also performed operation with high water-vapor-trap temperature and obtained 800 W output power at -40 °C water-vapor-trap temperature. These demonstrations will be useful for commercial uses.

Introduction

The chemical oxygen iodine laser (COIL) is an energy transfer chemical laser operating at 1.315 m. The lasing action is summarized by the following four processes;

$$H_2O_2 + 2NaOH + Cl_2 \rightarrow O_2(^1\Delta) + 2NaOH + 2NaCl + 2H_2O \quad (1)$$

$$I_2 \rightarrow 2I \quad (2)$$

$$O_2(^1\Delta) + I \rightarrow O_2(^3\Sigma) + I^* \quad (3)$$

$$I^* \rightarrow I + h\upsilon \quad (4)$$

Our COIL system is schematically illustrated in Figure 1. This system is composed of a singlet oxygen generator, a water vapor trap, a cavity, and an exhaust pump system. First, according to reaction (1) excited state oxygen, $O_2(^1\Delta)$, is generated by chlorination of an alkaline solution of H_2O_2 in the singlet oxygen generator (SOG). Cl_2 gas is introduced into the alkaline hydrogen peroxide solution through a bubbler made of teflon tubes. Next, water vapor is removed in the water vapor trap (WVT) because H_2O molecule deactivates the excited state oxygen and iodine. WVT is a straight glass tubes immersed in ethanol which is normally cooled to dry ice temperature (-70°C). At the laser cavity, iodine vapor spouts out into the active region from an iodine injector. Energy is transferred from singlet oxygen to iodine molecules, and immediately, iodine molecules are dissociated into iodine atoms according to reaction (2). Then the singlet oxygen energy is transferred to atomic iodine atom according to reaction (3). Finally, the laser operates at a wavelength of 1.315 m as shown by reaction (4).

As compared with CO_2 and yttrium aluminum garnet (YAG) lasers. COIL seems to be suitable for industrial uses because of the following advantages;
(A) The oscillation wavelength, 1.315 m, is good for low loss power transmission through a silica fiber. This offers flexible maneuver of the beam.
(B) Because of good scalability, a very high power system can be constructed with the same design concept for smaller-scale systems.
(C) Since the COIL is a pure chemical laser, no electrical energy is required for lasing. This enables applications of a COIL in a remote place such as in the space or mountains.

In spite of these attractive features, nobody has tried to apply a COIL to industrial applications. This situation motivated us to develop a high power and efficient COIL system with its industrial applications in mind. Thus we started a long term project a few years ago.

Parametric study

In the course of the present project we have already demonstrated a maximum cw power of 1kW[1] and a maximum chemical efficiency of 40%[2], respectively. We are presently interested in understanding of correlations between laser power and other operating parameters. The COIL system has been operated with various operational conditions. Controlled parameters include the exhausting speed, oxygen and iodine carrier gas flow rates, gas flow velocity in the active region, reflectivity of the mirrors, distance between the iodine injector and optical axis , etc. Here we discuss results of our parametric study in which we varied optical parameters such as mirror transmission dependence or dependence on distance between the iodine injector and optical axis.

Following the results obtained in the parametric study, we have demonstrated high power and long stable operation as typical performance under an optimized condition. In addition, power delivery through a silica fiber and high trap temperature operation have been performed. These experiments are also shown in this paper. We have employed 35% hydrogen peroxide in these experiments because highly concentrated H_2O_2 is more dangerous to handle and is less cost effective than low concentration H_2O_2. Thus dilute H_2O_2 is preferable for practical devices such as an industrial apparatus. The only problem associated with utilizing such a low concentration hydrogen peroxide is that it generates more water vapor which deactivates the excited state oxygen and iodine. We have solved this problem by designing SOG and WVT properly. Singlet oxygen excitation ratio as high as 80% has been achieved.

Experimental results and discussion

Dependence of laser output power on mirror transmission is plotted in Fig.2. From this figure, 96% output mirror seems better for obtaining high output power. And Fig.3 is a diagram of iodine injector-optical axis distance dependence. In Fig.3, the peak of power appears at a distance of 30-40mm. The optimal injector-optical axis distance seems to be determined by the trade off between $O_2(^1\Delta)/I_2$ mixing and quenching; if the optical axis is too closed the injector, the degree of population inversion is insufficient because of poor $O_2(^1\Delta)/I_2$ mixing, while if the optical axis is too downstream, excited oxygen and iodine are quenched more. These two figures gave us the optimum mirror condition of our COIL system.

Then we operated the COIL system under the optimized optical condition of 96% output mirror and 35mm distance between the injector and optical axis. Figure 4 shows a typical performance of such operation. In Fig.4, calculated chemical efficiency is defined as the ratio of output power to consumed H_2O_2 energy per second. We obtained 1kW at about over 60mmol/sec Cl_2 flow rate with a chemical efficiency between 20% and 30%. Our power meter did not cover over the 1kW range, we could not measure output power of over kW precisely. Next, typical long stable operation is shown in Figure 5. In this case the COIL was operated at a lower Cl_2 flow rate, 20mmol/sec. We have could maintain oscillation for over 40 minutes with a power of about 450 W.

In Figure 6, dependence of power on WVT temperature is plotted. From Fig.6, -40°C WVT coolant temperature seems to be practically sufficient for a high power system. For example, as high as 800 W can be achieved at this higher WVT temperature. If the WVT can be operated at this relatively high temperature, a COIL system will run more economically. But in order to obtain high efficiency, lower temperature, closely to -70°C (=dry ice temperature), seems more advantageous.

Finally, in Fig.7 we show a preliminary result of our experiments on power delivery through a silica fiber. Laser beam could be delivered with high transmission efficiency of 70% at 250 W input power. Futher details about fiber transmission experiments will be given by another paper[3].

Summary

We would like to summarize this work;
(A) COIL has been studied parametrically.
(B) Based on the parametric study, we obtained over 1kW and 23.6% chemical efficiency and achieved long stable operation over 30 minutes at about 500 W under the optimized condition.
(C) The practicability of high trap temperature operation at -40°C has been certified. This is quite favorable from the industrial point of view because we can select a coolant source for WVT widely and can operate a system more economically.
(D) Laser power was deliverd through a silica fiber with good transmission efficiency.

These results encourage us to develop a COIL system for new application fields in industry such as the material processing for which currently available industrial lasers are not useful.

Acknowledgment

The present work was supported by Kawasaki Heavy Industries.

Reference

1. S.Yoshida, T.Sawano, T.Tokuda, K.Shimizu, H.Fujii, and T.Fujioka, T.digest of CLEO '89, ThA6, p.252 (1989).
2. S.Yoshida, M.Endo, T.Sawano, S.Amano, H.Fujii, and T.Fujiioka, J.Appl.phys., 65, p.870, (1989).
3. K.Simizu and S.Yoshida, To be published in this proceedings.

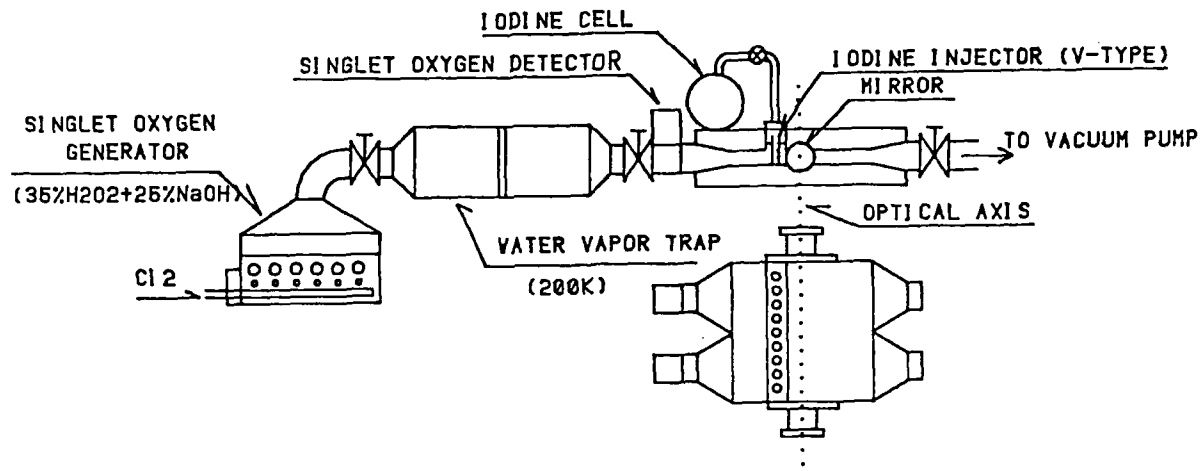


Fig.1 COIL system

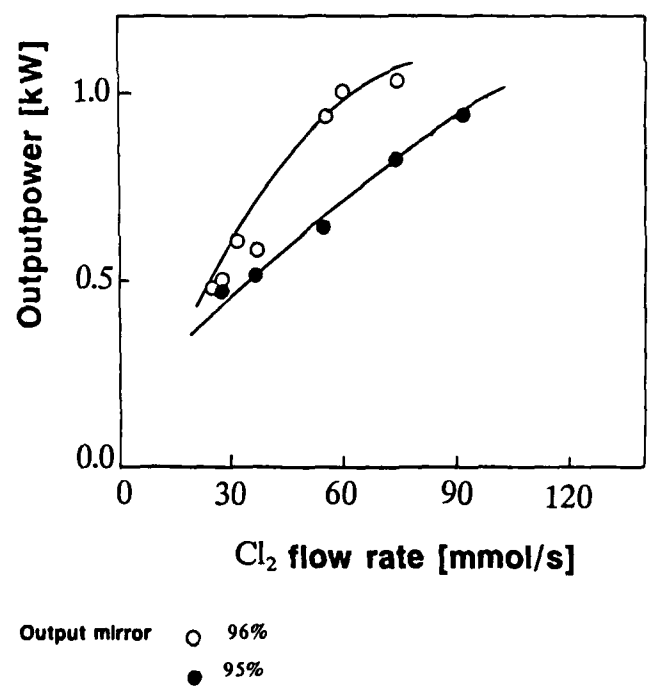


Fig.2 Mirror transmission dependance

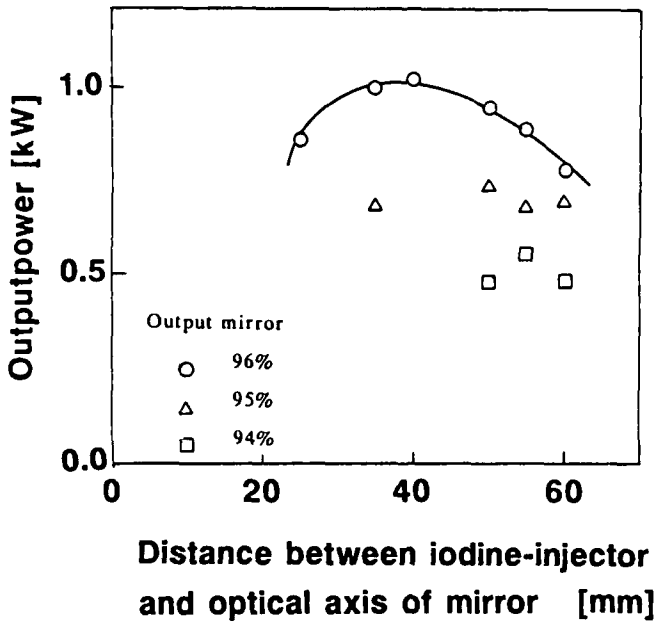
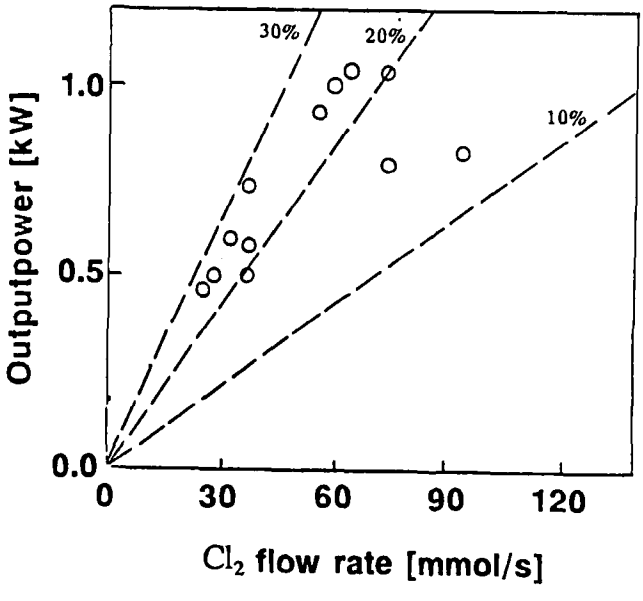


Fig.3 Injector-Optical axis distance dependance



Output mirror : 96%

Reflection mirror : 100%

Broken line : Calculated chemical efficiency

Fig.4 Output power vs Cl_2 flow rate

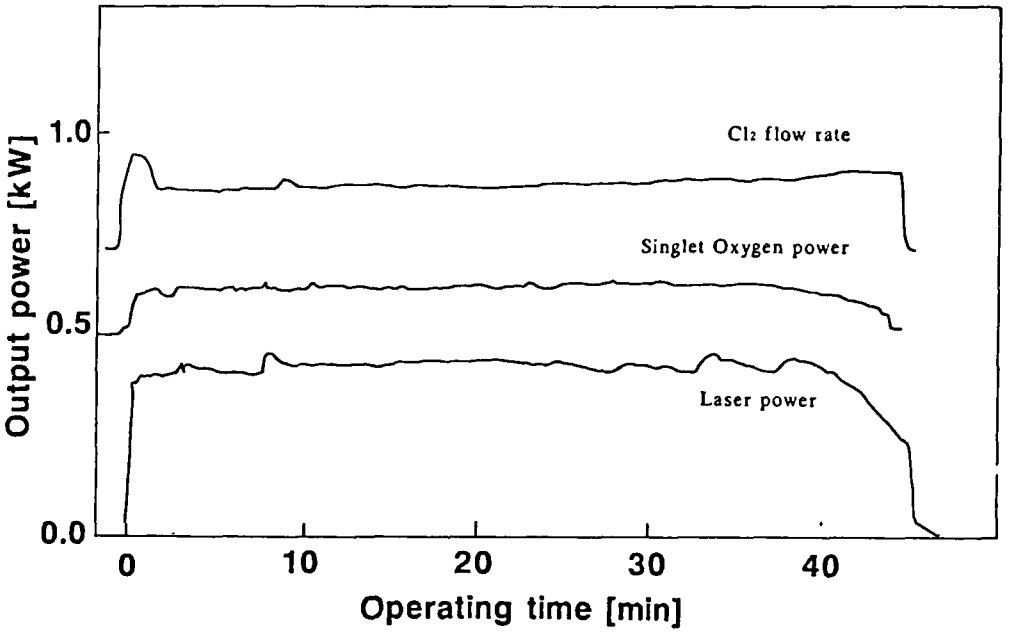


Fig.5 Long stable operation

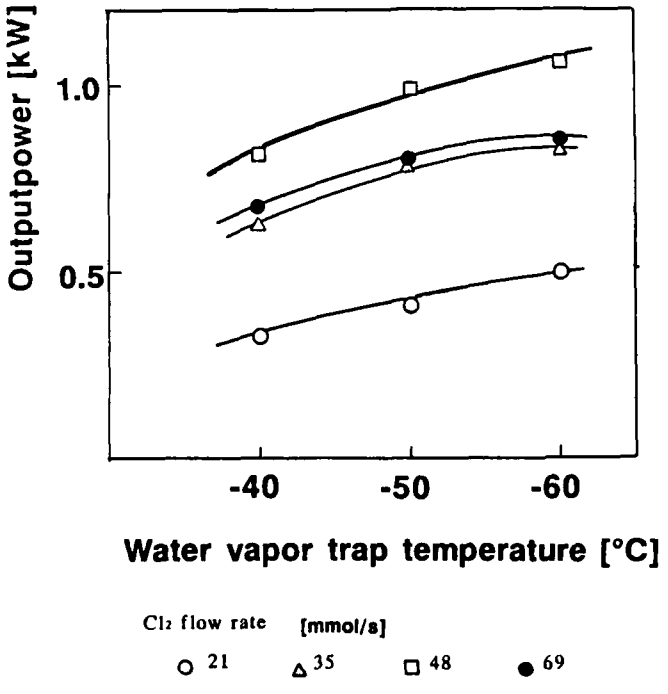


Fig.6 Trap temperature dependance

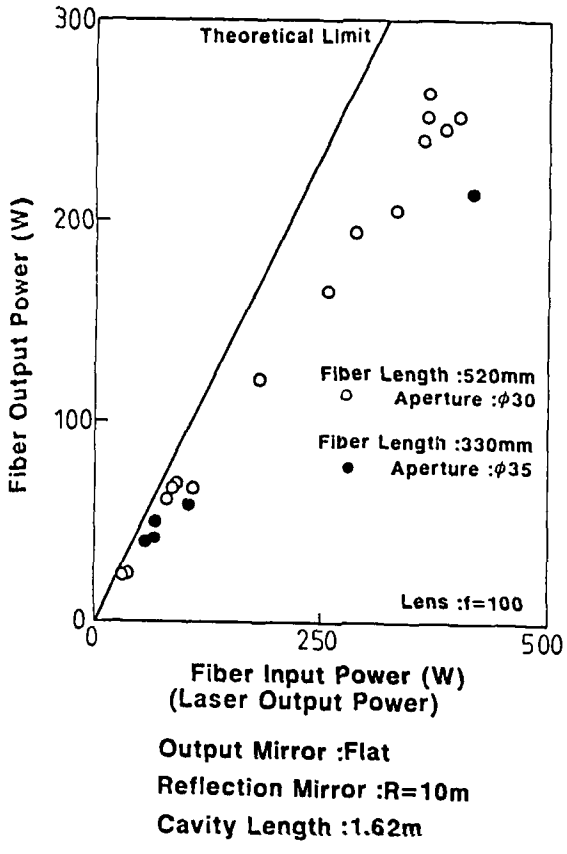


Fig.7 Fiber output power vs fiber input power

High power chemical oxygen-iodine laser of good beam quality

K.Shimizu, S.Yoshida

Laser Laboratory, Institute of Research and Innovation
1201 Takada, Kashiwa, Chiba 277, Japan

Abstract

The chemical oxygen-iodine laser is a pure chemical laser with high-efficiency, high-power capability. It has good beam quality at a wavelength favorable for low-loss transmission through silica fibers, making it attractive for industrial applications. Recently we developed a high power COIL system with its industrial uses in mind. We already reported on its performance. The aim of the present work is to improve the beam quality of this system. Currently we set our target at beam divergence angle of 6 mrad with laser power over 500 W. This divergence allows efficient focusing of laser beam into a commercially available optical fiber using a lens of practical focal length; eg. 600 m core-diameter with a lens focus f=100 mm. Since the COIL has a small gain coefficient, we employed a stable resonator geometry. Varying optical parameters, such as mirror curvature or resonator length, we attempted to achieve low divergence at high power. The best performances, for the time being, include 7.7 mrad at 1 kW and 5 mrad at 300 W. We present details about the experiment as well as theoretical analyses. We also carried out fiber transmission experiments using the present system to demonstrate efficient delivery of 247 W through a 18.5 m long, 600 m core-diameter fiber.

Introduction

Because of the capabilities of good beam quality, good scalability and efficient interaction with most materials including common metals, the chemical oxygen iodine laser (COIL) is a candidate for the next generation high power industrial lasers. In those capabilities, the COIL can, in principle, be superior to currently available industrial lasers such as the carbon dioxide or yttrium aluminum garnet lasers.

The COIL can be characterized by three major features. Firstly, since all the energy required for the lasing action is produced by chemical reactions, it does not need electricity to lase. Since the chemical energy is generally more efficient to be produced and larger in volumetric density than the electrical energy, this feature enables to construct a very high power, efficient system of reasonable size. Secondly, as a gas laser operating at a low pressure, the COIL should offer good beam quality. Thirdly, since the oscillation wavelength, 1.3 m, lies in a minimum of the transmission loss characteristics of silica, the COIL offers the capability of highly efficient power transmission through a silica fiber. These features, together with the high efficiency in material interactions due to the shortness in wavelength, make the COIL attractive for industrial uses.

Taking those advantages, we started developing an efficient, high power COIL system. In the course of this development we demonstrated a maximum chemical efficiency of 40% and stable operation at laser output over 1 kW. We reported on the performance elsewhere[1]. The aim of the present work is to improve the beam quality of this system. As the first step, we set our target at beam divergence angle of 6 mrad with laser power over 500 W. This divergence allows efficient focusing of the laser beam into a commercially available optical fiber using a lens of practical focal length; eg. 600 m core-diameter with f=100 mm. In this paper, we report on the relation between beam quality and laser output power when the stable resonator is used and fiber transmission using a silica fiber.

Experiments and results for beam quality

Our kW class COIL system is illustrated in Fig.1. This system is similar to one described in Ref.1. Briefly it consists of three sections and a vacuum system; a singlet oxygen generator (SOG), a water vapor trap (WVT) and a laser cavity. The SOG employed is a conventional bubbler reactor. The WVT is a shell and tube type heat exchanger using methanol cooled down to dry ice temperature as the coolant. The laser cavity consists of an iodine injection system and a laser resonator. Iodine vapor spouts out into the oxygen flow from vertical tubes with several holes. The laser head is a 6 cm x 100 cm rectangular duct. Since the COIL has a small gain coefficient [2], we employed a stable resonator geometry. For studying the relation between the beam quality and laser output power, we carried out oscillation experiments varying the resonator length and the curvature radius of the total reflector with the other parameters unchanged. The divergence angles were determined by dividing the spot diameter measured at the focus of a f=300 mm lens.

Fig.2 shows measured divergence angle as a function of resonator structure. The horizontal axis is the cavity length. The solid lines show the corresponding theoretical values based on high order Gaussian modes. From this figure, it is found that output from our COIL can be treated as a high order gaussian beam, and that we obtained 3.7 mad as the minimum divergence angle. The minimum divergence angle was obtained with the resonator structure of 3.2 m resonator length and 20 m curvature radius. The maximum output power obtained in each resonator structure are shown in Table 1. In the cases of curvature radii of 5 and 10 m, output power in the range of 770 W - 1 kW was obtained at 74.4 mmol/s Cl_2 flow rate. In the case of 20 m curvature radius, about 300 W output power was obtained at 37.2 mmol/s Cl_2 flow rate. In this case, the laser output higher than 300 W was not stable, because the mirror holders were heated by the laser beam resulting in misalignment. Therefore in the case of curvature radius of 20 m, if a more powerful cooling system is used, higher output power will be obtained.

Fig.3 shows the power density at the lens focus as a function of resonator structure. We obtained in the order of 10^5 W/cm^2 power density. Since commercial lasers generally offer power density in the range of 10^3 - 10^7 W/cm^2, our COIL system may be classified in the middle class in power density.

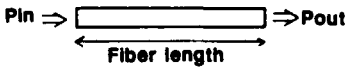
Fiber transmission

i)Arrangement

We carried out power transmission experiments using a silica fiber. The experimental arrangement is shown in Fig.4. The used silica fiber was a Quasi Step Index type with 600 m core-diameter. The divergence angle of the laser beam was 6.7 mrad, but the spot diameter at the focus of a f=100 mm silica lens (see Fig.4) was not smaller than 1 mm because of aberration. Hence, some part of laser power was lost at the entrance of the fiber. We performed the fiber transmission experiment as follows. First, we operated the COIL and measured the output laser power by the first power meter placed between the laser and the focal lens (Fig.4). After measuring the laser power, we removed the first power meter so that the laser beam might be focused into the fiber core, and measured the transmitted power by the second power meter. At this time, we fine-tuned the position of fiber relative to the lens, monitoring the second power meter reading. We repeated the same procedure for various incident laser powers, fiber lengths and bending radii.

ii)Theoretical limit

Prior to the fiber transmission experiments, we calculated the theoretical transmission limit. Assuming that the refractive index of the fiber was 1.46 and the absorption in the fiber was 4 dB/km (from the catalog), we estimated the transmission limit as about 92.7% for the used fiber length.



$$\frac{P_{out}}{P_{in}} = 92.7 \pm 0.5\%$$

refractance = 1.46
absorption = 4 dB/km
fiber length < 18.5m

As the beam diameter at focus was larger than the fiber core in the experiments, we estimated what percent of the laser beam was coupled into the fiber by assuming the intensity profile by means of a simple ray matrix calculation. Consequently, it turned out that about 87% of the power entered into the core.(Fig.5) Therefore, the overall theoretical limit for the present experiment became as follows:

$$\frac{P_{out}}{P_t} = (92.7 \pm 0.5\%) \times (87\%) = 80.5 \pm 0.5\%$$

iii)Results

Fig.6 shows relation between the output power and input power as a function of fiber length. Solid and broken lines are theoretical values. The solid line is the case that the beam spot diameter is smaller than the core diameter; i.e. 92.7%. The broken line is the realistic limit for the present experiment where the spot diameter is 1 mm; i.e. 80.5%. For any length, the output power increases in proportion to the input power.

Fig.7 shows relation between the transmissivity and input power as a function of fiber length. The solid and broken lines are theoretical values as Fig.6. From this figure, it is found that for the fiber length shorter than 18.5 m, the average transmissivity is 72% regardless of the fiber length. We consider that in the loss of 28%, 7% is the unavoidable

loss due to reflections and absorption, 13% is due to the focal spot diameter larger than the core diameter, and the rest 8% is due to roughness on the end surface.

Fig.8 shows relation between the output power and input power as a function of the bending radius of the fiber. As experimental conditions, we selected three different curvature radii of 5 cm, 9 cm and straight. The fiber length was constant at 1.14 m. From this figure, it is found that the fiber bending does not do any harm.

Conclusion

Employing a stable resonator geometry, we demonstrated high power COIL beams with practically low divergence. Comparison with theory indicated that the obtained laser beams were high order gaussian. We focused the laser beam into a commercially available silica fiber. The experiment showed fairly high transmission efficiency regardless of the fiber length as long as 18.5 m. Theoretical analysis indicated that the transmission efficiency should be further improved by making the beam spot diameter smaller than the fiber core diameter.

Acknowledgment

The present work was supported by Kawasaki Heavy Industries.

Reference

1) S.Yoshida,T.Sawano,T.Tokuda,K.Shimizu,H.Fujii and T.Fujioka, in CLEO'89 Conference on Lasers and Electro-optics, p.252, 1989.
2) K.Watanabe,S.Kashiwabara,K.Sawai,S.Tosh and R.Fujimoto, IEEE J. of Quantum Electronics, Vol.QE-19, No.11, Nov. 1983.

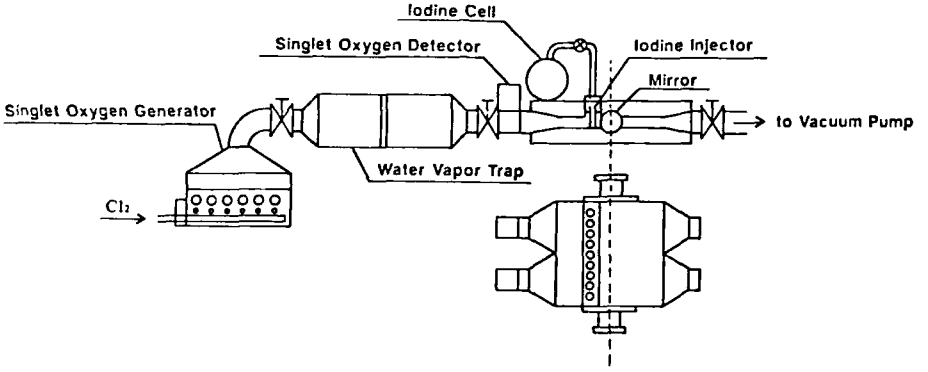


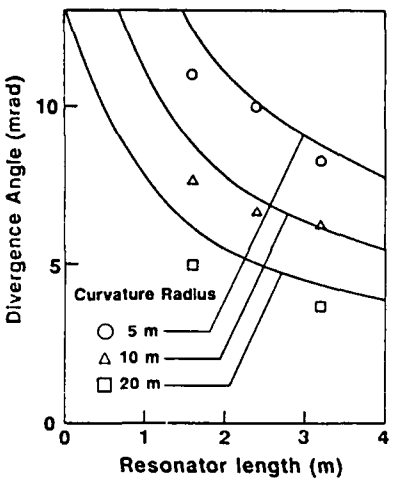
Fig.1 Schematic View of the Apparatus

R \ L	1.6 m	2.4 m	3.2 m	Cl_2 flow rate
5 m	890 W	770 W	780 W	74.4 mmol/s
10 m	1000 W	780 W	800 W	74.4 mmol/s
20 m	300 W	——	260 W	37.2 mmol/s

L: Resonator length

R: Curvature radius of total reflector

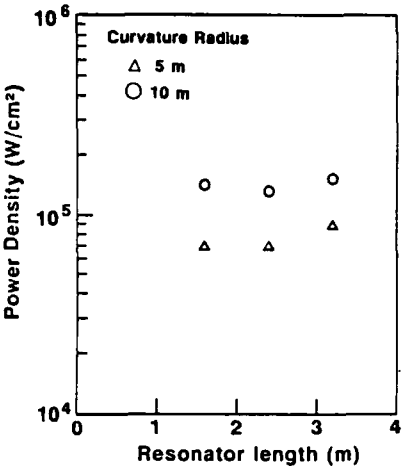
Table 1. Maximum Output Power in Each Resonator Geometry



Output Mirror: Flat, 96%

Aperture: ϕ35

Fig.2 Divergence angle
for various resonator structures



Output Mirror : Flat, 96%

Aperture : ϕ35

Cl_2 : 74.4 mmol/s

f=100

Fig.3 Power density for
various resonator structures

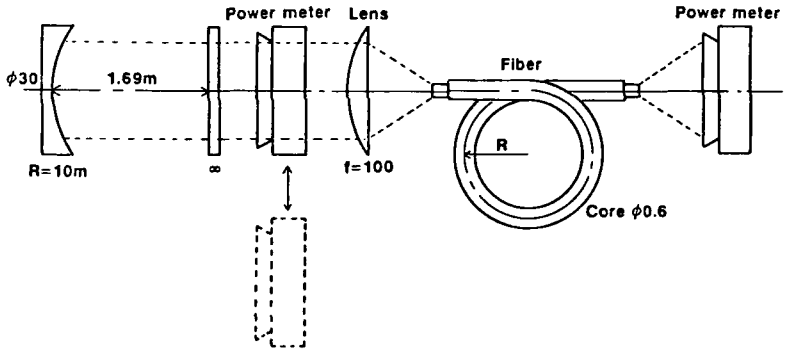


Fig.4 Arrangement for fiber transmission experiment

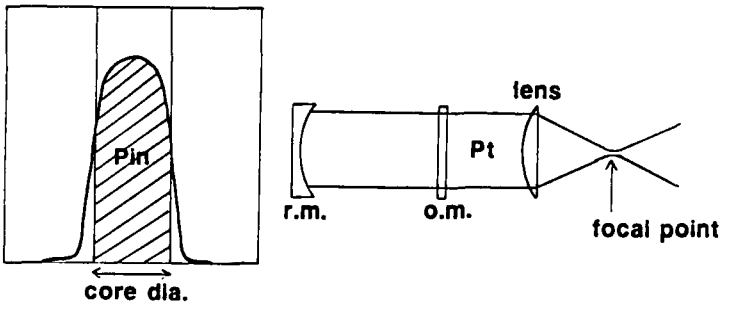
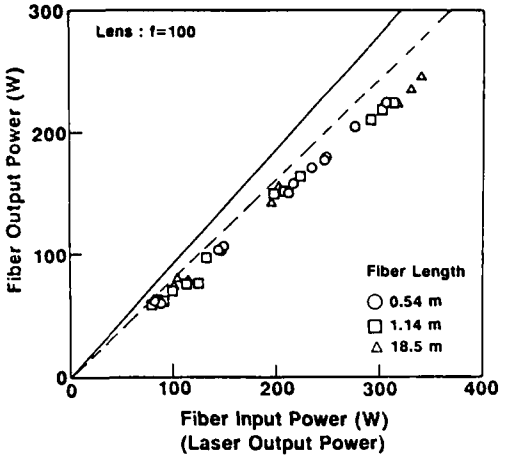
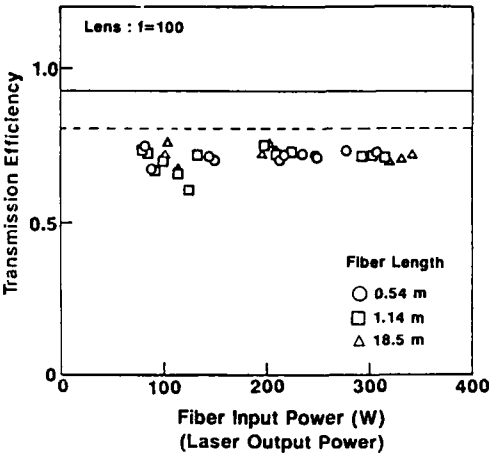


Fig.5 Beam profile at focal point



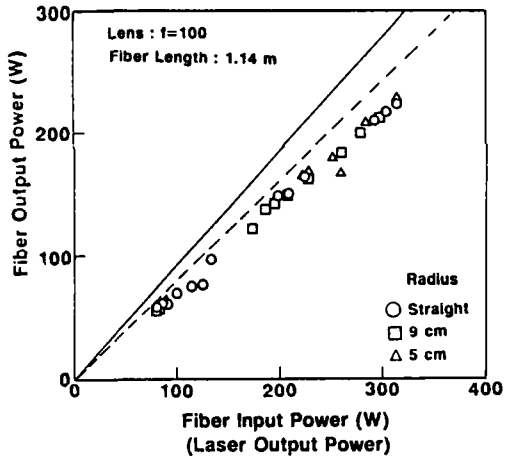
Output mirror : flat
Reflection mirror : R=10m
Cavity length : 1.69m
Aperture : ϕ30

Fig.6 Fiber output power for various fiber lengths



Output mirror : flat
Reflection mirror : R=10m
Cavity length : 1.69m
Aperture : ϕ30

Fig.7 Transmission efficiency for various fiber lengths



Output mirror : flat
Reflection mirror : R=10m
Cavity length : 1.69m
Aperture : ϕ30

Fig.8 Fiber output power for
various bending radii of fiber

Q-switching Operation of Chemical Oxygen Iodine Laser

Fumio Matsuzaka, Tomoji Ohga, Masahiro Imachi, and Taro Uchiyama
Dept. of Elect. Engineering, Faculty of Science and Technology, Keio University
3-14-1, Hiyoshi, Kohoku-ku, Yokohama, Kanagawa, Japan, 223

Abstract

Q-switching operation of chemical oxygen iodine laser was studied. Peak power, pulse shape, and Q-switch frequency was investigated. A rotating chopper was used for Q-switching device. The pulse shape has several enhancement peak and large time constant. The ratio of peak power to CW power is the largest of 11 and typical of 5 to 6. Q-switching frequency depends on velocity of the laser medium. In this case, blanks between pulses need 150μsec.

Introduction

Chemical Oxygen Iodine Laser (COIL,wave length =1.315μm) is attractive for laser material processing. A KW class CW system is exist[1], and a continuous operation over 2 hours was reported[2]. COIL has capacity to obtain effective laser processing, because its wave length is on the least loss range of the quartz fiber and is shorter than of CO_2 laser. On the other hand, it is known that a rapid repetitive pulse laser is more effective in laser processing and higher in quality than a CW laser. So Q-switching operation of COIL, which is a CW laser usually, is desired to realize the rapid repetitive pulse operation. The properties of Q-switching operation of COIL is expected as follows. (1) Large store energy in the laser medium and high peak pulse are not expect, because inversion population is determined by energy equilibrium constant between oxygen molecule and iodine atom. Stored energy of the laser medium in Q-switching off, is limited by oxygen pumping ratio and iodine content ratio. (2) The effective operation isn't obtained when the period of the frequency of Q-switching is more rapid than the clearance time, because energy isn't supplied. Energy is supplied by energy transfer from singlet oxygen to laser medium. In this study, we made some experiments and calculations as follows for basic study of the effective Q-switching operation of COIL. (1) Observations and calculations of the pulse. (2) Calculations of the relation between iodine content ratio and peak power. (3) Observations and calculations of the relation between the mirror transmittance and peak power. (4) Determination of the Q-switching frequency. Sequence of theory, experiment, result, and summary are described.

Theory

From the calculation, the behavior of the Q-switching operation was obtained with two parameters, the mirror transmittance and iodine content ratio. The rate equations of COIL were numerically calculated. A lot of chemical reactions are shown in Ref.3 etc., but here, for easily, follows three main equations are calculated

$$\partial[I^*]/\partial t + v\,\partial[I^*]/\partial x = K_1[I^*][O] - K_2[I][O^*] - K_3[I^*][H2O] - K_4 np\Delta N \qquad (1)$$

$$\partial[O^*]/\partial t + v\,\partial[O^*]/\partial x = -K_1[I^*][O] + K_2[I][O^*] \qquad (2)$$

$$\int(dnp/dt)dx = \int(K_4 np\Delta N - \gamma np)dx \quad . \qquad (3)$$

And follows are assumed. (1) Partial oxygen pressure and partial iodine pressure are constant. (2) Iodine molecules are mixed uniformly and dissociated perfectly as soon as mixing. The resolution of one iodine molecule needs four excited oxygen molecules (Eq.(4))

$$I_2 + 4O_2^* \rightarrow 2I + 4O_2 \quad , \qquad (4)$$

and iodine atoms are pumped initially written as next

$$[I^*]_0 = \frac{K_1[O_2^*]_0([I] + [I^*])}{(K_1 - K_2)[O_2^*]_0 + K_2([O_2] + [O_2^*]) + K_3[H_2O]} \quad . \qquad (5)$$

(3) The shape of cross section of laser beam is rectangle, and width and height are 10mm, and photon density is uniform. (4) Velocity of the laser medium is constant. Then some parameters are fixed for agreement with condition of the experiment. Velocity is 40m/sec, chlorine flow rate is 250mmol/min, initial oxygen pumping ratio is 60%, water vapor pressure is 0.1Torr, the cavity length is 148cm, the mirror curvature is 76cm, the gain length

is 36cm, and one-pass loss is 0.4% (except the mirror transmittance). In the calculation, loss is varied as step function. Initial photon density is calculated by using Eq.(6), spontaneous emission is assumed for photon generation.

$$np_0 = t_r \cdot 2L / C \cdot [I^*]_0 \cdot t_s^{-1} \cdot (D_s / (L / 2))^2 \cdot (4\pi)^{-1} \qquad (6)$$

Experimental apparatus

The experimental apparatus is shown in Fig.1. The solution tank is 200mm across in diameter and 1m high. In this tank hydrogen peroxide solution is cooled and is mixed with alkaline solution. Concentration of hydrogen peroxide solution is 35%, and alkaline solution is 10N potassium hydroxide solution. The mixed solution is fed to Singlet Oxygen Generator (SOG) by a pump. SOG is a porous pipe type, composed of a ceramic pipe with a lot of pores, which diameter is 10μm, and a shower, which can pour the solution on the surface of the porous pipe uniformly. Chlorine gas is fed to inside of the pipes, and, film of the solution is made on surface of the pipes. Then chlorine gas blows up through the pores in the pipe, and the gas and the solution react, and excited oxygen is generated. The generated oxygen flow through the 196K cold trap which length is 1.1m, in which most of water vapor is trapped. Temperature of the iodine cell is hold a constant level (30°C-100°C), the cell is connected with the iodine injector. The iodine injector is 36cm long stainless steel with holes, which diameter is 0.5mm and stand in line along the tube with 5mm space. Carrier gas of iodine is argon. The laser cavity is made by lucite, and has two laser arms at both side of it. On one side, an internal mirror is mounted, on the other side a brewster window is mounted. Outside of it, a switching device and an outside mirror are mounted. The cavity length is 148cm, the mirror curvature is 76cm. By them, the resonator is composed nearly concentric, so laser beam is focused at center of the resonator. A rotating chopper is used as a switching device, because it has low loss and Q-switching frequency don't need very high speed. Rotating rate is 13500 rpm. The chopper is mounted at center of the resonator. At the downstream of the cavity, a 88K cold trap is placed, and iodine and chlorine is trapped.

Experiment

The experimental method is as follows. At first, COIL is to be oscillated with CW operation, then the power is measured. Next, after making system stable the chopper is rotated, and the average power at the output mirror is measured (by OPHIR OPTICS; Model L-1504). From the total reflectance mirror the pulse is measured by a Ge detector and is observed by an oscilloscope (YOKOGAWA ELECT.; DL-2100).

Result

1, Q-switching pulse shape

Q-switching pulse were obtained from the experiments and the calculations. A pulse obtained from the calculation is shown in Fig.2. A rise time was within 5μsec, a time constant of decay was approximate 30μsec, then the power level balanced at CW power level at 150μsec. On the other hand, a shape from the experiment is shown in Fig.3. Basic of the shape was the same as one from the calculation, but rise was slower and decay was faster. And some shapes were observed as relaxation shown in Fig.4. In this case, peak didn't become high. The reason that the rise time from the experiment was slower than from the calculation is slow chopping speed of the chopper and higher loss in the experimental apparatus more than the calculation. As rotating speed of the chopper is 1413rad/sec, crossing speed at the place of laser mode is 56.5m/sec, then if diameter of the beam at nearly focus is 0.5mm, the cross time becomes 8.8μsec. This is larger than the rise time from the calculation, so this becomes a rise loss, then becomes a reason of increase of rise time and of decrease of peak power. The time constant of decay is very large than one of Q-switching operation of another lasers. The time constant of COIL depends on decrease rate of excited oxygen compared with coefficient of induced emission of iodine atom, because iodine is supplied energy from excited oxygen by energy transfer reaction simultaneous with induced emission. Q-switching operation of COIL belongs to an operation that keep high level power for long time, but cannot get very high peak power.

2, Peak power

Peak power is expressed by the ratio to power of CW operation. It has an advantage to show an effect of Q-switch operation. The peak power was examined with parameters as the mirror transmittance and iodine content ratio. (On the experiment, only the mirror transmittance) From the calculation, the ratio of peak power to CW power is obtained as shown in Fig.5. When the mirror transmittance was 1.5% and iodine content to oxygen content was 2.5%, the ratio of peak power to CW power became the largest one. From the experiment, when the transmittance was 0.85%, the ratio was the largest of 11, typical of 5 to 6. With 0.1%

transmittance peak wasn't seen, with 1.5% transmittance the ratio was approximate 3, and with 2.7% transmittance the laser did not oscillate. (Fig.6)

From them, followings are thought. Peak power was obtained at most the ratio of 11, this shows large population inversion isn't obtained on COIL as expected at first. It is determined by the pumping ratio of oxygen, iodine content, and balance of them. Pumping ratio of oxygen is limited by ability of SOG (pumping ratio becomes over 90% in SOG, but it is quenched to approximate 60% by a collision with a wall, water vapor, and oxygen molecules each other[4]), so population inversion is determined by iodine content mainly. But if iodine content increases so much, a lot of excited oxygen is used to dissociate iodine molecule (four to six excited oxygen molecule is need to dissociate an iodine molecule), so large population inversion cannot be obtained after all. In practice, it isn't obtained, since not uniformity of iodine content or imperfect of resolution of iodine molecule. The mirror transmittance with which the largest peak was obtained on the experiment is lower than by the calculation. Particularly, in case that the mirror transmittance is 2.7%, with which a large gain is obtained by the calculation, the laser didn't oscillate on the experiment.

3,Determination of Q-switching frequency

As described in introduction, it is thought that Q-switching frequency is limited by velocity of the laser medium. To know this relation, efficiency is measured, varying closed time of the chopper and fixing open time. As open time is fixed, it is expected that energy per pulse is constant if there is no effect before pulse. And if closed time is short, there is effect before pulse, and energy per pulse should been decreased. The result of measurement for this is shown in Fig.7. The horizontal axis shows closed time of the chopper and the vertical axis shows energy per pulse expressed by the ratio of average power of Q-switching to power of CW operation normalized by duty cycle. This graph shows that energy per pulse decreases in case that closed time is under 150μsec. As velocity of the laser medium on the experiment was 40m/sec, it agrees with the time that needs the laser medium crosses the average beam width if the beam width is 6mm. This beam width is reasonable. So it is known that for enough energy per pulse the laser medium has to be exchanged completely every pulse. Then this shows that Q-switching frequency depends on velocity of the laser medium. And on an experiment, the efficiency, which is the ratio of average power of Q-switching to power of CW operation, was able to be increased to 75% when closed time was 150μsec and duty cycle was 50%.

Summary

In this the fundamental study of Q-switching operation of COIL was described. The pulse shape, peak power, and Q-switch frequency was studied from the theory and the experiment. The pulse was a wide pulse compared with another laser. The ratio of peak power to CW power was the largest of 11, typical of 5 to 6 when mirror transmittance was 0.85% and chlorine flow rate was 250mmol/min. Q-switching frequency depends on velocity of the laser medium. When rotating chopper with which optimum Q-switch frequency obtained from this result is accomplished is used, the efficiency is increased. The problem after this is the acquisition of more effective and more stable operation and larger peak power.

References

1) W. E. Mcdermott, "The chemical oxygen-iodine laser", Invited paper, presented at 4th International Symposium on Gas-flow and Chemical Laser, 1982.
2) H. Fujii, M.Iizuka, T. Atsuta, S. Yoshida,
"Chemical Oxygen Iodine Laser capable of stable and long duration operation", presented at the 49th autumn meeting of the Japan society of applied physics, 1988.
3) G. A. Fisk and G. N. Hays,
"Kinetic rates in the oxygen-iodine system", J. Chem, Phys. Vol.77(10), 1982.
4) K. Takehisa, N. Shimizu, and T. Uchiyama,
"Singlet oxygen generator using a porous pipe", J. Appl. Phys., Vol.61(1), pp.68, 1987.

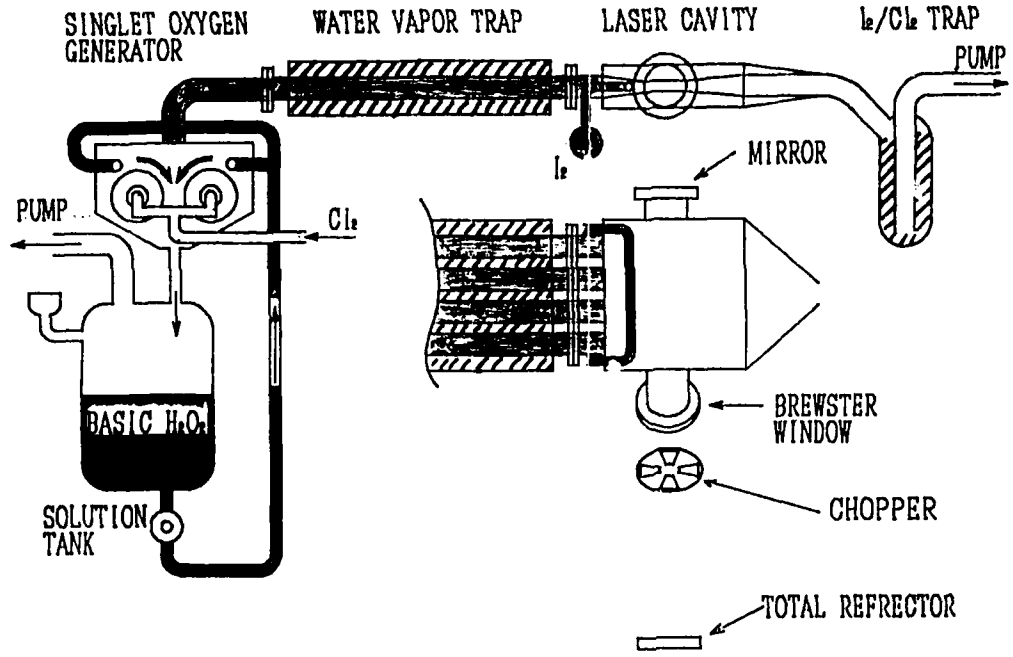


Fig.1 Schematic of the Experimental Apparatus

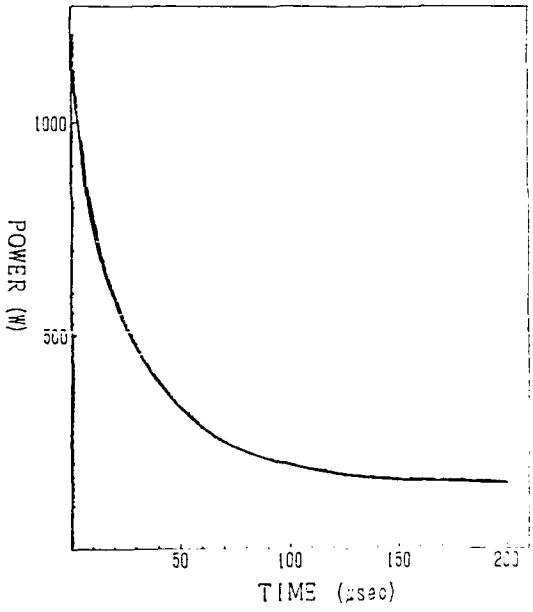


Fig.2 The pulse shape from the calculation. One-pass loss is 0.4%, the mirror transmittance is 0.85%, chlorine flow rate is 400mmol/min.

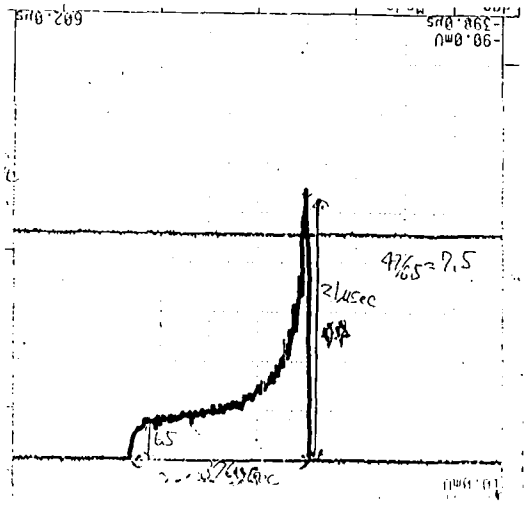


Fig.3 The pulse shape from the experiment. The mirror transmittance is 0.85%, chlorine flow rate is 250mmol/min.

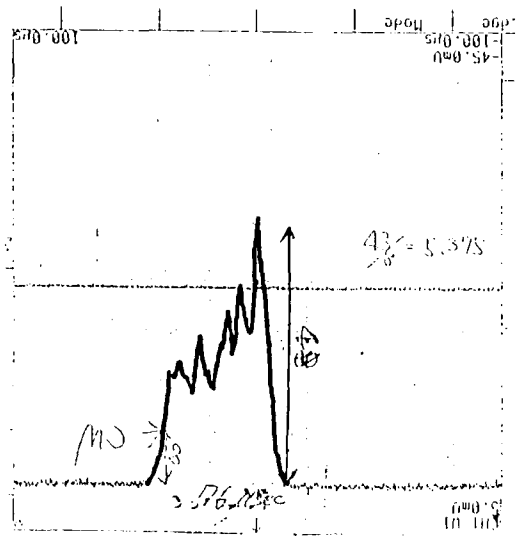


Fig.4 The pulse shape from the experiment. Relaxation is shown.

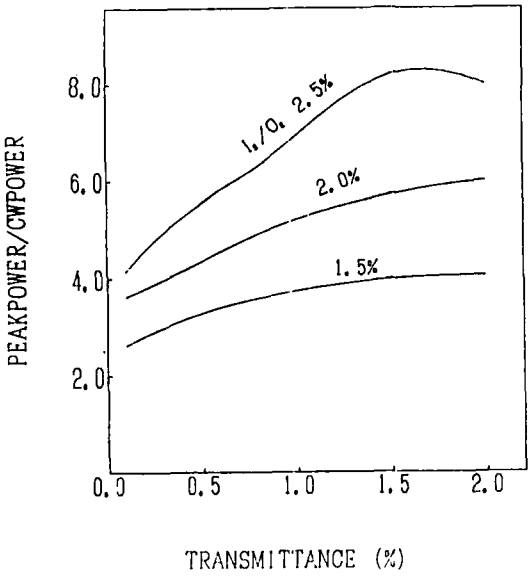


Fig.5 Relation between peak power and mirror transmittance from the calculation.

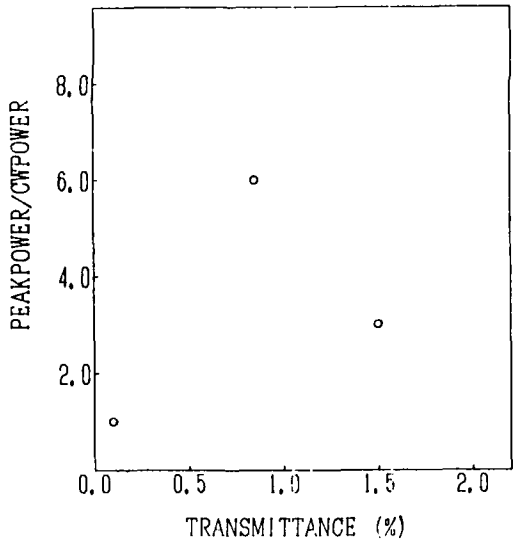


Fig.6 Relation between peak power and mirror transmittance from the experiment.

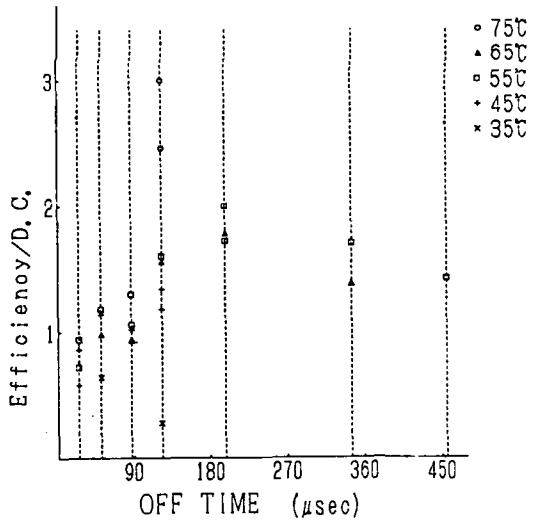


Fig.7 Relation between closed time of the chopper and energy per pulse.

A SINGLET OXYGEN MONITOR FOR PHOTODYNAMIC THERAPY

Steven J. Davis
Physical Sciences Inc.
20 New England Business Center
Andover, MA 01810

and

M.K. Willscher
Davison Laser Center
Elliot Hospital
Manchester, NH 03104

Abstract

Photodynamic Cancer Therapy (PDT) is potentially one of the most important medical applications of visible wavelength lasers. The PDT process involves the preferential retention of photosensitive dye molecules, e.g., hematoporphyrin, by tumors followed by visible laser irradiation of the tumor. The laser radiation causes a photochemical reaction to occur that leads to cell necrosis for those cells containing the dye molecules. The PDT treatment is becoming one of the important new weapons against cancer and is beginning to be incorporated throughout the world. Since the process requires visible radiation (500 to 700 nm), tunable, visible wavelength lasers are being considered for this application.

Although PDT is beginning to find widespread application in oncology, e.g., bladder, lung, and skin cancers, the mechanism of cell destruction is not thoroughly understood. Metastable singlet delta oxygen $O_2(^1\Delta)$ is suspected of being the agent responsible for malignant cell destruction.

In this paper we present preliminary data of real time detection of $O_2(^1\Delta)$ evolution from laser irradiated solutions containing hematoporphyrin derivative (HPD). Data are presented that show a linear dependence of $O_2(^1\Delta)$ upon the laser excitation energy.

1. Introduction

Singlet O_2 is strongly suspected of being the active species in cancer cell destruction when tumors containing hematoporphyrin derivative (HPD) or other porphyrin compounds are irradiated with visible light.[1-10] The accumulation of singlet O_2 following irradiation has been detected previously by indirect analytical techniques that require several hours to complete. It would be of great benefit to be able to monitor singlet O_2 in real-time, simultaneously with the irradiation treatment.[11] The ability to correlate the amount of singlet O_2 produced to the percentage of cancer cell destruction could lead to much more efficient treatments.

The photodynamic therapy process is based upon the observation that dyes such as hematoporphyrin derivative (HPD) are preferentially retained in cancerous cells following intravenous injection. Upon exposure to red light (usually from a laser) the photosensitive HPD type compound causes a chemical reaction to occur that causes cancer cell necrosis. Although the detailed mechanisms for the process are not known, it is generally believed that subsequent to the absorption of the laser radiation, the HPD undergoes an intersystem transfer to a triplet state.[12,13] This triplet state then excites the highly metastable $O_2(^1\Delta)$ level via an energy transfer collision. This process is shown in Figure 1. Thus, the HPD acts as a catalyst that facilitates the excitation of $O_2(^1\Delta)$, the species that appears to cause all destruction. Although the mechanism is not known, the energetic $O_2(^1\Delta)$ may simply rupture the cell wall or mutate cell mitochondria.

Regardless of the actual cell destruction mode, a real time monitor of $O_2(^1\Delta)$ produced via the photoactivation process would be an extremely valuable tool. For example, treatment efficacy could be correlated with the concentration of $O_2(^1\Delta)$. In addition, some detailed studies to illuminate the kinetic mechanisms would be possible.

2. Experiment

Our technique is based upon the well known, near-infrared $O_2(^1\Delta \rightarrow {}^3\Sigma)$ emission bands near 1.27 μm. Surprisingly, one can detect this emission even through the $O_2(^1\Delta \rightarrow {}^3\Sigma)$ radiative rate is only 3600 s^{-1}. Parker[14] has proposed monitoring this emission and has reported some preliminary data.

To-date, we have performed most of our work on liquid samples containing HPD. A schematic of the experimental arrangement is presented in Figure 2. The laser source was a CW ring dye laser (Coherent Radiation 699-05) pumped by a Coherent Radiation Innova 100-20 Ar^+ laser. The laser beam was delivered to the curvette that contained the HPD via a bifurcated optical fiber. The output from the second leg of the optical fiber was focused onto a 0.2m monochromator. Optical detection was accomplished by mounting an intrinsic germanium detector at the output of the monochromator. Lock-in detection techniques were also employed as indicated in Figure 2.

3. Results

In Figure 3 we show a resolved fluorescence spectrum from HPD in methanol obtained by scanning the monochromator while holding the dye laser wavelength at 583 nm. The spectrum is clearly that of the $O_2(^1\Delta \rightarrow {}^3\Sigma)$ system, and the bandwidth is predominately instrumental. While the spectrum shown in Figure 3 was obtained for a 1×10^{-3} molar solution in methanol we have obtained satisfactory signals for 1×10^{-5} molar solutions. Strong signals were also observed in ethanol solutions. The observed $O_2(^1\Delta)$ signals in HPD/H_2O solutions were much weaker.

In Figure 4 we present data indicating that the $O_2(^1\Delta)$ concentration varied linearly with dye laser power in agreement with the model depicted in Figure 1. Finally, in Figure 5 we show that there was an apparent dependence of the $O_2(^1\Delta)$ concentration upon the excitation wavelength. Note that the ordinate in Figure 5 has been normalized by the laser power.

The preliminary data presented here are encouraging and demonstrate the viability of the optical detection technique. We are, at present, performing studies on tissue samples from laboratory rats. These results will be reported at a later date.

Acknowledgment

This work was supported in part by the Davidson Laser Center and in part by PSI IRAD funds.

References

1. L. Tomio, F., Calzavora, and G. Jori, Laser Photobiology and Photomedicine, Ed. (S. Martellucci and A.N. Chester, Plenum Press, New York, 1985) p. 117.

2. D.P. Valenzano, IEEE Journal of Quantum Electronics, QE12, 1439 (1984).

3. K.R. Weishaupt, C.J. Gomer, and T.J. Dogherty, Cancer Research, 36, 2326 (1976).

4. C.J. Gomer and T.J. Dougherty, Cancer Research, 39, 146 (1979).

5. T.J. Dougherty, R.E. Thoma, D.G. Boyle, and K.R. Weishaupt, Cancer Research, 41, 401 (1981).

6. R.L. Lipson, E.J. Balder, and A.M. Olsen, J. National Cancer Inst. 26, 1 (1961).

7. D. Kessel and T. Chow, Cancer Research, 43, 1994 (1983).

8. J. Ye, Y. Yeng, Y. Li, and F. Li, Proceedings of 1985 Conference on Lasers and Electro Optics, 84 (1985).

9. A.E. Profio, IEEE Journal of Quantum Electronics, QE20, 1502 (1984).

10. F. Docchio, R. Ramponi, C.A. Sacchi, G. Boltiroli, and I. Freitas, Laser Photobiology and Photomedicine, Ed. (S. Mertellucci and A.N. Chester, Plenum Press, New York, 1985) p. 83.

11. A.E. Profio and D.R. Doiran, Lasers in Surgery and Medicine 7, 1 (1987).

12. H. Kautsky and H. DeBruyen, Naturwissenschaften 19, 1043 (1931).

13. H. Kautsky, Trans. Faraday Soc. 35, 216 (1939).

14. J. Parker, American Society for Laser Medicine and Surgery Meeting, Boston, MA (May 1986).

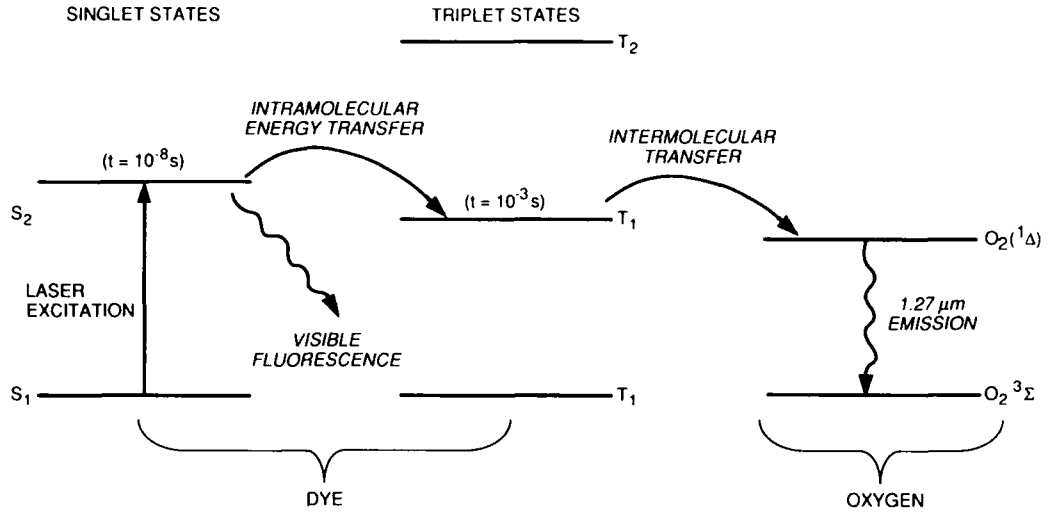


Figure 1. Excitation of $O_2(^1\Delta)$ via Photo-initiated Energy Transfer

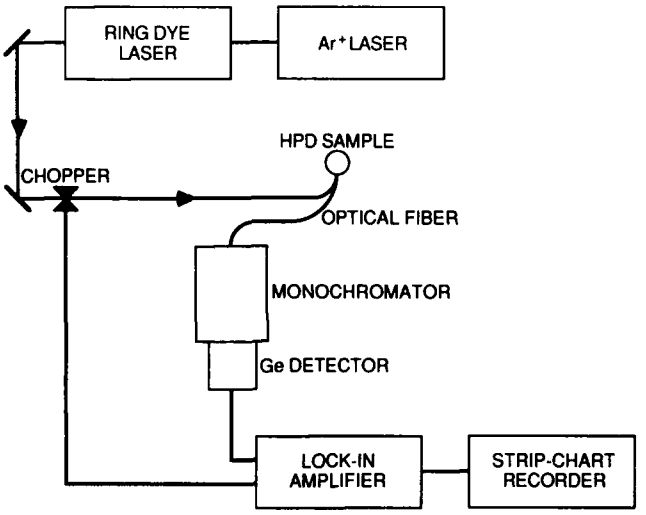


Figure 2. CW Excitation Apparatus

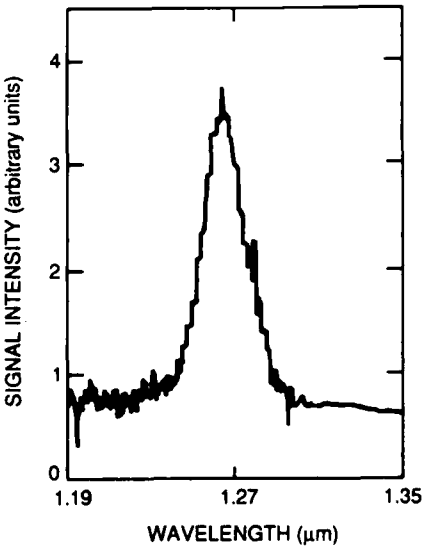


Figure 3. Resolved Fluorescence from Laser Excited HPD/MeOH Solution

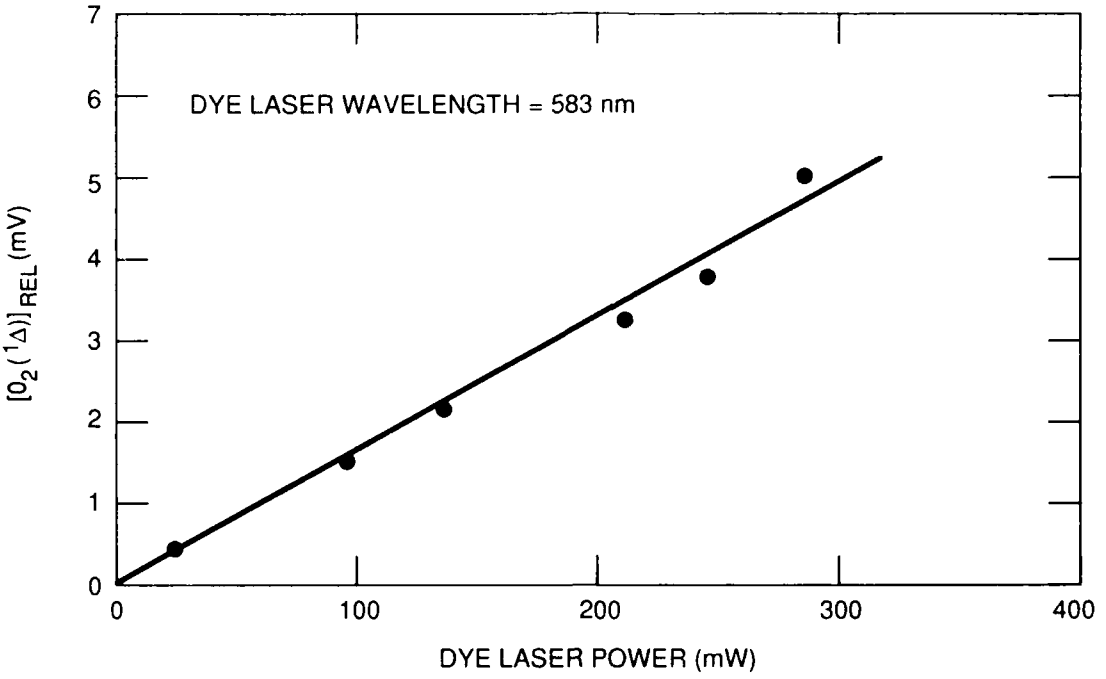


Figure 4. Dependence of $[O_2(^1\Delta)]$ Upon Laser Intensity

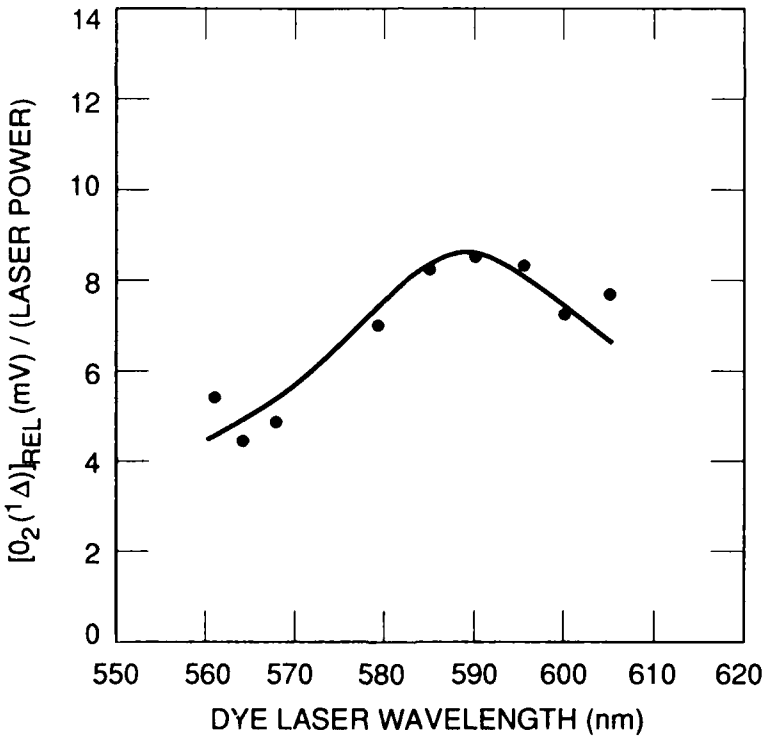


Figure 5. Dependence of $[O_2(^1\Delta)]$ Upon Excitation Wavelength

VISIBLE CHEMICAL LASERS

by

Glen P. Perram
Department of Engineering Physics
Air Force Institute of Technology
Wright-Patterson Air Force Base, Ohio 45433

Abstract

Visible chemical lasers have great potential as highly efficient, wavelength agile, deployable, high brightness laser systems. Applications for such devices include directed energy weapons for both tactical and strategic military missions, imaging and diagnostic missions, and scientific laboratory instruments. A laser demonstration is challenging and requires the integration of chemical kinetics, reactive mixing technology, and optical physics. Most current research is focused on demonstrating such a laser based on the metastable energy transfer concept. An extensive data base has been developed over the past decade to evaluate candidate visible chemical laser systems. Recent accomplishments in the development of an energy transfer visible chemical laser firmly establish the opportunity for a near term lasing demonstration.

I. Introduction

Many of the earliest chemical lasers[1-5] were based on the establishment of an inversion between vibrational states as proposed by J.C. Polanyi in 1965.[6] Exothermic reactions, liberating their energy into the stretching of newly formed chemical bonds can provide both complete and partial vibrational inversions. After Cool and Stevens[5] demonstrated an HF laser requiring no electrical input, high power, highly efficient chemical lasers were envisioned.[7] HF lasers with powers exceeding 1 MW have been demonstrated and are in an advanced state of development.[8] These devices are inherently high gain lasers with significant diffraction limited beam divergence.

To achieve lasing in the visible portion of the spectrum, the higher energies of excited electronic states are required. The early photolytic iodine laser[9] led to a search for a chemical means of exciting atomic iodine. The shortest wavelength chemical laser in existence today is the Chemical Oxygen-Iodine Laser (COIL) which operates on the $5^2P_{1/2} - 5^2P_{3/2}$ transition in atomic iodine at 1.315 μm.[10] These lasers are driven by resonant energy transfer from the metastable singlet oxygen. While chemical oxygen-iodine lasers are in the early stages of large scale development, a 25 kW device is being tested at the Air Force's Weapons Laboratory and scaling to high output power devices with excellent beam quality is under active investigation.[8]

Early attempts to demonstrate a visible chemical laser were based on analogy to HF/DF lasers where a chemical reaction is used directly to excite an upper laser level. Research during the 1970's on candidate systems such as BaO have been reviewed elsewhere.[11-12] These early efforts failed in large part because the reaction chemistry was not constrained to efficiently produce a single electronically excited state. The current Air Force Short Wavelength Laser program addresses this issue by investigating highly energetic chemical reactions which are constrained by spin conservation rules to efficiently generate excited metastable species. These metastable species then act as a large reservoir of chemical energy which may be efficiently transferred to a suitable lasant molecule.

II. Why Visible Chemical Lasers?

In light of the availability of several high power chemical lasers, why should we invest in the development of a visible chemical laser? There are several compelling answers to this question which depend on the anticipated application. Both directed energy weapons and imaging missions will be discussed.

A. Directed Energy Weapons

The ability of a laser to damage a distant target is often characterized by the source brightness which depends on the laser output power, beam divergence, beam jitter, optical quality of the beam and other parameters. Device powers of multi-megawatts and brightnesses of $10^{20} - 10^{23}$ W/sr are required for some military missions.[8] The intensity delivered to the target is reduced by beam divergence during propagation. This beam divergence is controlled by diffraction at the limiting aperture and thus, the delivered beam intensity depends inversely on the square of the laser wavelength. For example, a

NF/BiF(A-X) laser operating in the blue would provide a factor of 30-40 increase in intensity over an equivalent power HF laser. This strong advantage for shorter wavelengths can be realized if the pointing and tracking optics establish a low value for beam jitter on the target. Atmospheric turbulence can significantly increase beam divergence above the diffraction limit, but may be compensated by adaptive optics.[8] It is clear that short wavelength lasers could provide a strong enhancement in brightness.

The highest payoff for visible chemical lasers are for space based applications. Chemical laser systems contain their own energy source and thus, are lightweight and have great flexibility in deployment. The electronic state transitions of visible chemical lasers promise greater mass efficiency, σ, and nozzle power flux, δ, than the current generation of chemical lasers. The higher energy stored per molecule in electronic states provides for laser output energies per mass of input reactants on the order of σ=1 MJ/kg. These efficiencies are important for space based missions to the extent that the required payload mass is driven by chemical reagents. The required fuel payload is usually measured in tons per second of laser run time. Theoretical values of mass efficiency can easily be calculated from the energy content per molecule, but are often substantially reduced by the diluent gas flows required to control the thermal conditions of the laser. Mass efficiency is also driven by reagent stoichiometry and key reaction branching ratios.

Continuous-wave visible chemical lasers offer a high duty cycle, good thermal kill characetristics, low peak powers, and high atmospheric transmission.

B. Imaging and Diagnostic Missions

Laser sources provide a high degree of control over the wavelength, bandwidth, directionality, polarization, and temporal characteristics of radiation for diagnostic purposes. Indeed, the field of diagnostic spectroscopy has been revolutionized by tunable laser sources.[13] The opportunities for applying these advances to military imaging missions are diverse. Laser based illuminators, beacons, compensators, designators, radars, and communications are a few such applications.

Visible laser sources are desired for imaging missions due to the availability of highly sensitive detectors, namely photo-multiplier tubes. The visible chemical laser offers quasi-continuous wavelength tunability and potential pulsed or CW operation. Wavelength agility is achieved from the many rotational-vibrational transitions characteristic of diatomic lasants. Pulsed operation might be achieved with approaches similar to the Zeeman gain-switching recently demonstrated for COIL devices.[14]

C. Spin-Off Technologies

The extensive data base developed in support of visible chemical lasers has already found use in several related Air Force programs, including: (1) atmospheric kinetics, (2) rocket fuels, and (3) electrical lasers. In particular, the development of advanced rocket fuels with significant increases in specific impulse possesses many similarities with the visible chemical laser program. The investigation of chemically-bound excited states, or CBES materials, is particularly promising for both lasers and rocket fuels. Visible chemical lasers have also been suggested for fusion drivers and laboratory lasers.[11]

III. Concepts, Requirements and Approaches

The above characteristics of visible chemical lasers provide high payoff for the development of this class of laser device. They also impose great constraints to potential systems. To develop an efficient, scalable, high brightness laser system operating in the visible under chemical excitation is indeed a difficult problem.

A. Visible Chemical Laser Concepts

Proposals for chemically driven visible lasers may be divided into several classes according to the excitation mechanism. Several concepts currently or previously under consideration are: (1) direct chemical lasers based on analogy to HF, (2) energy transfer chemical lasers based on analogy to COIL, (3) pulsed, detonation driven chemical lasers, (4) optically driven lasers where a very intense, explosively driven light source is used for excitation, (5) hybrid electro-chemical lasers where electrical power is used to initiate highly exothermic reactions, (6) frequency doubled COIL, (7) the vibrational overtone HF laser, and (8) miscellaneous initiation techniques.

Considerable emphasis is currently given to the metastable energy transfer concept. The advantages of this approach will be discussed below and the remainder of this paper will address this concept.

A generic reaction mechanism for the energy transfer concept is shown in Figure 1. The production of the metastable energy reservoir is usually achieved through an exchange reaction (A + BC --> AB + C) involving ground state atomic species such as hydrogen, nitrogen, or oxygen. Electron spin correlation arguments can lead to selective excitation of electronic states if the reagents are low mass and the product ground state possesses an electron spin different than the excited state. Spin correlation arguments also depend on the spin of the reaction intermediate.[31] The spin selectivity during reaction also implies the product is radiatively metastable and thus a poor lasant. Several reactions that efficiently produce usable metastable species are provided in Table I. The branching ratio, ϕ, is defined as the ratio of rate coefficients for the production of a specified excited state with respect the total rate for all products.[11]

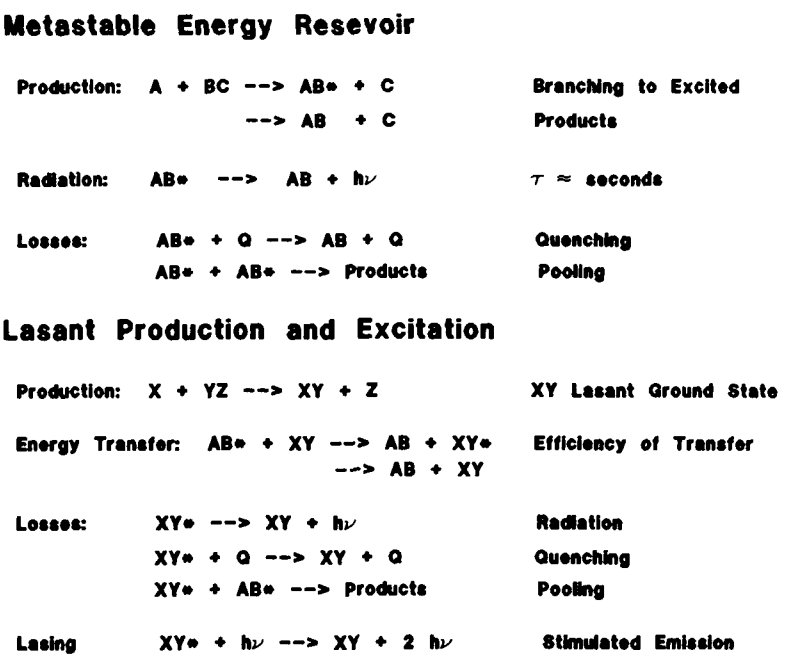


Figure 1. Metastable Energy Transfer Concept.

Energy may be lost from the reservoir due to quenching and pooling reactions. Typically, the metastables are transported from a chemical generator to a nozzle assembly where they are mixed with the lasant molecules. Excited-state to excited-state interactions (energy pooling) must be minimal to prevent significant losses upon pressure scaling. Singlet states are desirable in this regard, since their paired electrons tend to be less reactive. Several important metastable pooling reactions are given in Table II.

Unfortunately, most lasant candidates are thermodynamically or kinetically unstable and must be produced in the laser flow. Rapid and efficient transfer of energy from the reservoir to the upper lasant level is required. Several candidate systems, most notably the NF(b)-IF(B-X) laser,[23] have faltered on the efficiency of the energy transfer step. Required chemical pumping rates are discussed below. Losses to the upper laser level include radiation, quenching and pooling. Pooling of the upper laser level with the metastable is often a dominate loss mechanism.

Table I
Excitation Selectivity and Spin Correlation

Reaction	Yield	Radiative Lifetime (seconds)	Reference
$H(^2S) + NF_2(^2B_1) \rightarrow HF(^1\Sigma) + NF(^1\Delta)$	$\phi > 90\%$	$\tau(NF^1\Delta)=5.6$	15-16
$N_2(^4S) + N_3(^2\Pi_g) \rightarrow N_2(^3\Pi_g, ^3\Delta_u) + N_2(^1\Sigma_g)$	$\phi \sim 50\%$	$\tau(N_2{}^3\Pi)=2.0$	17
$F(^2P) + N_3(^2P) \rightarrow N_2(^1\Sigma_g{}^+) + NF(^1\Delta)$	$\phi \sim 80\%$	$\tau(NF^1\Delta)=5.6$	18

Table II
Excited State Interactions (Energy Pooling)

Reaction	Rate Coefficient (cm^3/molecule-s)	Reference
$O_2(a^1\Delta) + O_2(a^1\Delta)$ --> Products	6×10^{-17}	19
$NF(a^1\Delta) + NF(a^1\Delta)$ --> Products	2×10^{-12}	20
	$< 1 \times 10^{-13}$	21
$N_2(A^3\Sigma) + N_2(A^3\Sigma)$ --> Products	3×10^{-10}	22

B. Kinetic and Mixing Requirements

The kinetic excitation requirements for a visible chemical laser were described in 1980 by T.A. Cool.[24] Laser gain can be described by the equation[25]

$$\gamma(\nu) = (\lambda^2/8\pi)\ \Delta\ g(\nu)\ /\ \tau_r \qquad (1)$$

where

$\Delta = N_2 - (g_2/g_1)\ N_1$ = population inversion

τ_r = radiative lifetime

$g(\nu)$ = lineshape factor

The gain, $\gamma(\nu)$, must exceed the cavity losses, which can be characterized as a cavity lifetime, τ_c.[25] Thus, for a Doppler broadened line, the required population inversion is:

$$\Delta > (4\pi^2/\lambda^3)\ (8kT/\pi mc^2)^{1/2}\ \tau_r/\tau_c \qquad (2)$$

The required inversion increases quite rapidly as we move from the infrared to visible portion of the electromagnetic spectrum. Evaluating this inversion requirement in the visible (λ=500 nm) for a minimum gain of 10^{-3} cm^{-1} provides a critical fluorescence rate of $\Delta/\tau_r > 10^{16}$ molecules/cm^3-second.

Consider the chemical pumping rate required to achieve this critical fluorescence rate. Figure 2 illustrates a generic excitation process. For simplicity a direct excitation mechanism is shown. The reagents must cross a small activation barrier with a nearly gas kinetic rate. Even if the branching of products is near unity for a selected electronic state, the population in a single rotational-vibrational state will be diluted by at least a factor of 10^3 for most diatomic lasants. If the lower laser level is assumed to be unpopulated and the only loss process for the upper laser level is radiation, then the steady-state population inversion would be

$$\Delta_{ss} = k_p\ \phi\ [A]\ [BC]\ \tau_r \qquad (3)$$

where

k_p = kinetic pumping rate coefficient ~ 10^{-10} cm^3/molecules-second

ϕ = branching ratio to upper laser level ~ 10^{-3}

Applying this result to the critical fluorescence rate provides required reagent concentrations of [A] [BC] > 10^{29} $molecules^2/cm^6$ or an excitation rate of 10^{19} molecules/cm^3-second. A few candidate systems have demonstrated a potential to scale to this rate of excitation and will be discussed below.

These rapid kinetic excitation rates are often limited by diffusion of reagents in a supersonic mixing nozzle. If the time scale for mixing is long compared to the radiative lifetime, then the effective excitation rate is substantially reduced and the required reagent concentrations correspondingly increased. Current nozzle technology limits the mixing time to values greater than 1-10 μs. On the other hand, long radiative lifetimes imply large population inversions for a given critical fluorescence rate. Thus, lasants with radiative lifetimes of about 10 μs are highly desirable.

The complete collisional dynamics of the excited and ground electronic states of the lasant must be favorable as well. In the above analysis we assumed that all the excitation could be channeled to a single vibrational state without kinetic loss. To achieve this condition, the vibrational thermalization processes must be rapid with respect to quenching, dissociation, pooling and other kinetic losses. The above analysis also assumed the lower laser level was unpopulated. Bottle-necking in the ground electronic state can be a severe problem. Systems with displaced potential curves (large

difference in equilibrium internuclear separation), repulsive ground states, or reactive ground states can help considerably in this regard.

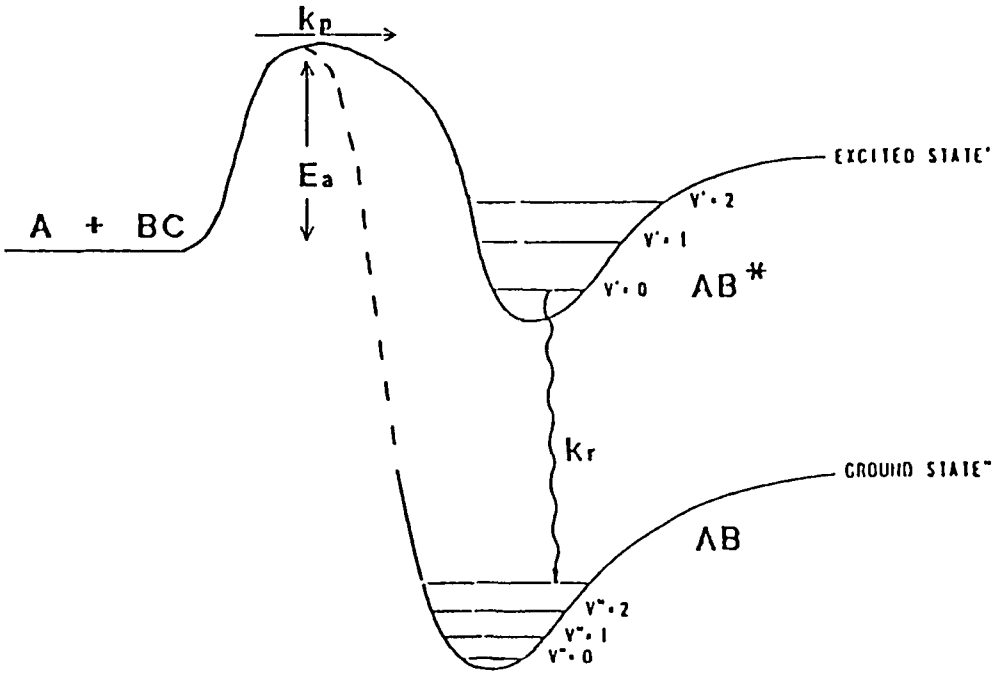


Figure 2. Chemical Laser Kinetics.

Finally, several miscellaneous requirements and issues should be considered. There exist many chemical engineering issues involved with preparing the high flow rates of toxic, highly energetic, unstable, low vapor pressure, and reactive species necessary for both metastable and lasant production. Low temperatures are desirable to maintain a low rotational dilution and suggest supersonic expansion after combustion or high heat release processes. Once stimulated emission is achieved, the kinetics may be dramatically altered by this very rapid optical process. The assessment of scalability and efficiency must include the effects of stimulated emission. The inherent low gains achievable in these systems suggest potential problems with high intracavity flux and long photon build-up times. Pulsed initiation or excitation may relax some of the above kinetic requirements.

Based on the system performance criteria discussed above, the requirements for a visible chemical laser system are rigorous. A highly exothermic reaction involving lightweight molecules with near unit branching of products to a single, excited electronic state is required to chemically drive the laser. The reaction barrier should be low as the rate for product formation must be nearly gas kinetic, yet reagents must be acceptably stable. The energy transfer chemical laser must also identify a suitable lasant molecule which efficiently and rapidly receives energy from the metastable reservoir. The rate of chemically pumping the lasant must be of the order 10^{19} molecules/cm^3-sec and critical inversion densities are typically 10^{13} molecules/cm^3. Near unit efficiency in the energy transfer is required for efficient operation and all energy loss mechanisms ultimately result in thermal control problems.

While the requirements for a visible chemical laser are rigorous, a few candidate systems remain promising and are discussed below. First, let us examine the approach to laser development.

C. Approach to Laser Development

A three-fold approach to developing a visible chemical laser based on the energy transfer concept is being pursued: (1) development of highly efficient chemical generators of energetic metastable species, (2) identification of potential laser species with the required spectroscopic and kinetic properties, and (3) coupling of a suitable metastable generator to a lasant and the demonstration of a scalable visible chemical laser. Figure 3 presents a flow chart embodying this approach.

Identification and characterization of potential lasant species usually involves several different studies including spectroscopy, lasant production kinetics, radiative

and collisional dynamics of excited and ground electronic states, and optically pumped laser demonstrations. Optically pumped lasers are particularly useful in studying the kinetics under approximated chemical laser conditions.[11] Producing a metastable energy reservoir involves basic kinetic studies of highly energetic reactions and scaling of reagents to engineer a small scale metastable generator. These activities must be coordinated to insure the development of a complete system with efficient coupling of the metastable and lasant. Energy transfer excitation studies, examination of pressure scaling laws, and chemical compatibility studies are included in this phase. Several candidate systems that have passed the tests of these steps are provided in Figure 4.

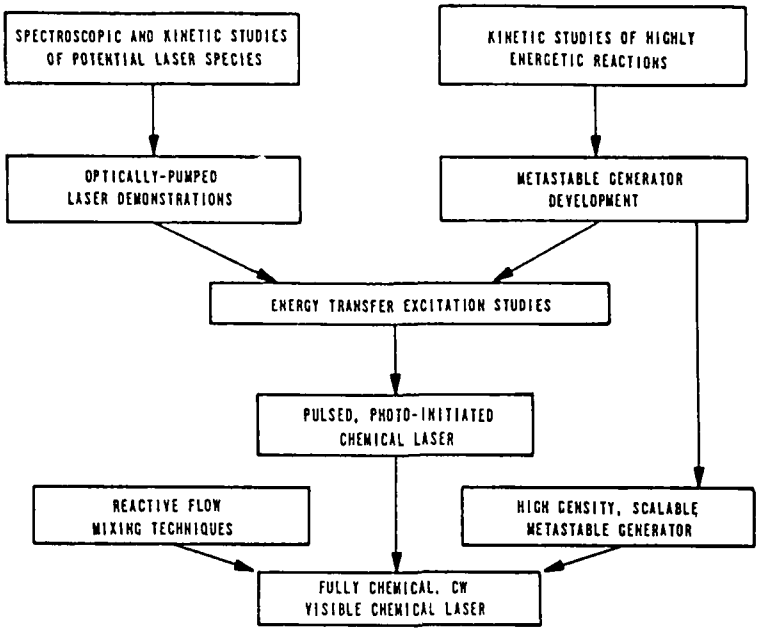


Figure 3. Approach to Developing a VCL Based on Energy Transfer Concept.

Currently, research efforts are focused on demonstrating a visible chemical laser with pulsed, photo-initiated techniques. Such efforts can be undertaken at modest cost, circumvent reactive mixing requirements and relax several kinetic requirements. Once a laser is demonstrated, an intensive effort to develop a fully chemical, continuous-wave laser will follow.

IV. Survey of Candidate Energy Transfer Systems

Several candidate visible chemical laser systems are presented in Figure 4. The technology status including currently achievable energy densities and efficient means for extracting this energy in the form of lasing photons is summarized. The metastable energy carriers are ranked according to experimentally obtained energy densities. Prime opportunities for a laser demonstration are suggested below. The promising singlet oxygen driven iodine monofluoride laser has been reviewed previously[11] and will not be discussed.

A. Excited NF Driven Lasers

The first excited electronic state of nitrogen fluoride, $NF(a^1\Delta)$, is a premier candidate for a metastable energy carrier to drive a visible laser. Energy densities of greater than 6.7 Joules/liter have been demonstrated.[26] $NF(a^1\Delta)$ can be chemically generated with near unit efficiency from several reaction mechanisms,[15-16,18,26] is highly immune to pooling and quenching energy loss mechanisms,[20,27-30] and possesses a reactive ground state.[15,30-32] The production chemistry is potentially compatible with existing HF laser hardware and lasing could be achieved in the blue near 450 nm.

NF is iso-electronic with molecular oxygen and has an analogous electronic structure with only three electronic states at energies less than 5 eV: $NF(X^3\Sigma^-)$, $NF(a^1\Delta)$ and $NF(b^1\Sigma)$. This feature significantly reduces the pathways for energy partitioning during production and subsequent transport of NF(a). NF(a) has an energy content per molecule of 1.4 eV and a radiative lifetime of 5.6 seconds.[15]

Metastable Energy Carrier	Energy (eV)	Obtained Energy Density	Lasant Transition	Lasant Lifetime (μs)	Wavelength (nm)
O2(a1Δ)	0.98	16 kJ/m3	IF(B-X)	7.0	625
NF(a1Δ)	1.4	6.7 kJ/m3	BiF(A-X)	1.4	450
			NF(b-X)	2.3E+4	530
			Bi(4P-2P)	~ 15	915
N2(A3Σ)	6.2	0.1 J/m3	IF(B-X)	7.0	625
			SO(A-X)	35	299
			NO(A-X)	0.2	248
N2(x,v"$\geq$5)	1.5	24 J/m3	IF(B-X)	7.0	625

Figure 4. Candidate Visible Chemical Laser Systems.

Efficient, chemical production of $NF(a^1\Delta)$ has been demonstrated using several different chemistries. Clyne and White[33] were the first to observe a chemiluminescent reaction between H and NF_2 that produced both NF(a-X) and NF(b-X) emissions. Herbelin and Cohen[34] proposed an addition-elimination reaction that directly produces singlet NF:

$$H + NF_2 \rightarrow HNF_2^* \rightarrow HF + NF(a^1\Delta) \qquad (4)$$

Malins and Setser[15] and more recently, Koffend et al[16], have demonstrated that spin is conserved in the reaction and the branching to the NF(a) product is greater than 91%. The reaction is rapid with a room temperature rate coefficient of $k_3 = 1.5 \pm 0.2 \times 10^{-11}$ cm^3/molecule-sec.[32] The partitioning to HF(v) and NF products is well characterized.[15] In the presence of excess hydrogen atoms, the singlet NF reacts slowly with H to produce excited nitrogen atoms, $N(^2D)$, and an NF(a) and $N(^2D)$ interaction produces electronically excited nitrogen.[35] Thus, the stoichiometry is usually chosen to be lean in hydrogen atoms when excited NF is the desired product. Supersonic flows with NF(a) concentrations as high as 6×10^{15} molecules/cm^3 have been achieved using this chemistry.[36]

The $a^1\Delta$ state of NF can also be efficiently generated by the reactions of fluorine atoms with hydrogen azide, followed by a second reaction of a fluorine atom with the resulting azide radical:

$$F + HN_3 \rightarrow HF + N_3 \qquad (5)$$

$$F + N_3 \rightarrow NF(a^1\Delta) + N_2 \qquad (6)$$

The rate of NF(a) production is limited by reaction (6) with a moderately fast rate coefficient of $4\pm2 \times 10^{-11}$ cm^3/molecule-sec.[17] The yield of NF(a) is high, about 85%. However, this production chemistry does not scale well, as $N_3 + N_3$ interactions significantly reduce the efficiency of NF(a) production. Indeed, this azide chemistry has been shown to be an efficient source of electronically excited nitrogen.[22]

Recently, Benard and coworkers[26] recognized that this scaling limitation might be removed if fluorine azide, FN_3, could be used directly. Reaction (6) must proceed through an FN_3 intermediate and thus one might expect fluorine azide to dissociate to singlet NF products under the proper conditions. Fluorine azide is the most energetic of the halogen azides and is a model for a chemically bound excited state (CBES) material. This energetic compound may be viewed as an $NF(a^1\Delta)$ molecule weakly bound (0.6 eV) to a ground state nitrogen molecule, $N_2(X^1\Sigma)$. In a pulsed thermolysis experiment where a premixed SF_6/FN_3 gas is rapidly heated by CO_2 laser pumping, $NF(a^1\Delta)$ concentrations of greater than

3×10^{16} molecules/cm^3 have been achieved with yields of 70 ± 25 %.[26]

Methods for extracting the energy stored in singlet NF in the form of coherent photons, or lasing, are currently under active investigation. Most excited NF driven laser systems invoke an energy pooling mechanism to establish lasing in the green or blue portion of the visible spectrum.

Initial work by Capelle et al[37] led to the investigation of bismuth atoms as a receptor of NF(a) energy. The energy transfer is near resonant, proceeds at a gas kinetic rate, and would lead to a laser completely analogous to $O_2(a)$ pumped I^*. In 1983, Herbelin et al[39] attempted to scale the production of $Bi(^2D)$ in this system. Upon scaling, the $Bi(^2D)$ was efficiently converted to electronically excited bismuth fluoride emitting at λ=420-480 nm. While the excitation chemistry is complex, considerable data is available on the scaling of BiF(A) with NF(a) and clearly indicates a quadratic dependence. Near threshold BiF(A) concentrations of about 10^{13} molecules/cm^3 have been achieved.[39]

A second approach to using energy stored in NF(a) to achieve lasing in the visible is based on energy pooling with a second energy carrier such as HF(v), $O_2(a^1\Delta)$, or I^* to produce NF(b). NF(b) can then be used to transfer energy to a suitable lasant molecule or lased directly. One particularly promising concept is the NF(b-X) green laser outlined by J. Herbelin in 1986.[40]

B. Excited Nitrogen Driven Lasers

The excited nitrogen laser is based on the generation of either electronically or vibrationally excited nitrogen metastables and subsequent energy transfer to a suitable lasant such as IF, NO or SO. While several schemes for efficiently producing excited nitrogen have been identified and characterized,[17,22,41] chemical generators capable of delivering excited nitrogen at concentrations sufficient to drive a visible laser have not been developed. However, these systems provide high payoff in that the energy stored in $N_2(A^3\Sigma)$ is sufficient for lasing at wavelengths as short as 200 nm without energy pooling.

The three lasant candidates, IF, NO and SO, are efficiently excited by energy transfer from $N_2(A)$ with nearly gas kinetic excitation rates and branching ratios of 0.4-1.0.[42-44] Iodine monofluoride is a particularly good visible lasant that has been well characterized both spectroscopically and kinetically.[45] The short radiative lifetime of NO(A) would introduce difficult mixing problems for any CW laser driven by $N_2(A)$. Features of SO(A) as a lasant are discussed in a following paper from this conference.

A primary difficulty for the excited nitrogen laser is the very rapid energy pooling reaction noted in Table II. Several approaches have been taken recently to overcome this problem. A pulsed $N_2(A)$ driven laser might succeed if the metastable and lasant are premixed and the rate of $N_2(A)$ production is exceptionally fast. S. Rosenwaks is currently investigating an explosively driven lead azide laser concept that uses this approach.[46] Alternatively, one might allow the energy pooling to proceed to completion with final products including large concentrations of highly vibrationally excited ground state nitrogen. Vibrational to electronic energy exchange with a lasant such as IF might then be used as the laser excitation mechanism.[47]

V. Conclusions

Visible chemical lasers provide important and unique opportunities for both directed energy weapons and diagnostic applications. The long term, low level investment in this technology area during the past decade firmly establishes the opportunity for a lasing demonstration in the near term. It is time to capitalize on this mature scientific data base and apply sufficient resources to engineer the facilities for a significant laser demonstration.

Acknowledgment

The author gratefully acknowledges the many insights on chemical lasers provided to him by the numerous, dedicated researchers and supporters of visible chemical lasers. This review article is in large part a synthesis of their ideas, results, and understandings.

References

1. J.V.V. Kasper and G.C. Pimentel, Phys. Rev. Lett. 14, 352 (1965).
2. K.L. Kompa and G.C. Pimentel, J. Chem. Phys. 47, 857 (1967).
3. J.R. Airey and S.F. McKay, Appl. Phys. Lett. 15, 401 (1969).
4. D.J. Spencer, T.A. Jacobs, H. Mirels, and R.W.F. Gross, Int. J. Chem. Kinet. 1, 493

(1969).
5. T.A. Cool and R.R. Stephens, Appl. Phys. Lett. 16, 55 (1970).
6. J.C. Polanyi, J. Chem. Phys. 34, 347 (1961).
7. A.N. Chester, Proc. IEEE 61, 414 (1973).
8. N. Bloembergen and C.K.N. Patel (Co-chairs), Rev Mod Phys, 59(3), Part II (1987).
9. J.V.V. Kasper and G.C. Pimentel, Appl. Phys. Lett. 5, 231 (1964).
10. W.E. McDermott et al, Appl. Phys. Lett. 32, 469 (1978).
11. S.J. Davis in Gas Flow and Chemical Lasers, S. Rosenwaks Ed. (Springer-Vrelag, Berlin, 1987), pp 522-534.
12. L.E. Wilson, S.N. Suchard, and J.I Steinfeld, Electronic Transition Lasers (MIT Press, Cambridge, MA, 1977).
13. B.P. Stoicheff, in Laser Spectroscopy III, J.L Hall and J.L. Carlsten Eds. (Springer-Verlag, Berlin, 1977), pp. 1-8.
14. R. Highland, E. Dunkle, L. Hanko, and G.D.Hager, to be published in J. Appl. Phys. (1989).
15. R.J. Malins and D.W. Setser, J Phys Chem, 85, 1342, 1981.
16. R. F. Heidner III, H. Helvajian, J.S. Holloway, and J.B. Koffend, J. Phys. Chem. 93, 7813 (1989).
17. R.D. Coombe et al, AFWL-TR-87-112, Kirtland AFB, NM (1988).
18. R.D. Coombe et al, AFWL-TR-81-211, Kirtland AFB, NM (1982).
19. G.P. Perram and G.D. Hager, AFWL-TR-88-50, Kirtland AFB, NM (1988).
20. J. Habdas, E Quinones, and D.W. Setser, J. Phys. Chem. 91, 5155 (1987).
21. J.B. Koffend, C.E. Gardner, and R.F. Heidner, III, J. Chem. Phys. 83, 2904 (1985).
22. L.G. Piper et al, AFWL-TR-86-95, Kirtland AFB, NM (1988).
23. H. Cha and D.W. Setser, J. Phys. Chem. 91, 3758 (1987).
24. T.A. Cool in Physical Chemistry of Fast Reactions Vol 2, Ed I. Smith (Plenum Press, New York, 1980), pp 215-272.
25. A. Yariv, Introduction to Optical Electronics (Holt, Rinehart and Winston, New York, 1976).
26. D.J. Benard, B.K. Winker, T.A. Seder, and R.H. Cohn, J. Phys. Chem. 93, 4790 (1989).
27. J. Habdas, S. Wategaonkar, and D.W. Setser, J. Phys. Chem. 91, 451 (1987).
28. J. Habdas and D.W. Setser, J. Phys. Chem. 93, 229 (1989).
29. H. Cha and D.W. Setser, J. Phys. Chem. 93, 235 (1988).
30. D.J. Benard, M.A. Chowdhury, A.T. Pritt, J. Appl. Phys. 60, 4051 (1986).
31. J.M. Herbelin, Chem. Phys. Lett. 42, 367 (1976).
32. C.T. Cheah, M.A.A. Clyne, and P.D. Whitefield, J.C.S. Faraday Trans II, 76, 711 (1980).
33. M.A.A. Clyne and I.F. White, Chem. Phys. Lett. 6, 465 (1970).
34. J.M. Herbelin and N. Cohen, Chem. Phys. Lett. 20, 605 (1973).
35. C.T. Cheah and M.A.A. Clyne, J. Photochem. 15, 21 (1981).
36. M.A. Kowk, J.M. Herbelin, R.R. Geidt, and W.R. Warren, AIAA/SDIO High Power Laser Device Conference, 2-4 March 1987.
37. G.A. Capelle, D.G. Sutton, and J.I. Steinfeld, J. Chem. Phys. 69, 5140 (1978).
38. J.M. Herbelin, R.R. Geidt, and H.A. Bixler, J. Appl. Phys. 54, 28 (1983).
39. J.M. Herbelin, presented at International Conference on Lasers '89, New Orleans, LA (1989), paper TE.3.
40. J.M. Herbelin, Appl Optics, 25(13), 2138, 1986.
41. G. Black, L.E. Jusinski, M.-R. Taherian, T.G. Slanger, and D.L. Huestis, J. Phys. Chem. 90, 6842 (1986).
42. L.G. Piper, W.J. Marinelli, W.T. Rawlins, and B.D. Green, J.Chem. Phys. 83, 5602 (1985).
43. L.G. Piper, L.M. Cowles, and W.T. Rawlins, J. Chem. Phys. 85, 3369 (1986).
44. De-Shao Cao and D.W. Setser, Chem. Phys. Lett. 116, 363 (1985).
45. S.J. Davis, L.Hanko, and R.F. Shea, J. Chem. Phys. 78, 172 (1983).
46. I. Bar, D. Heflinger, Y. Kaufman, G. Miron, M. Sapir, Y. Tzok, and S. Rosenwaks in Gas Flow and Chemical Lasers (SPIE 1031, 1988), pp 340-352.
47. L.G. Piper et al, AFWL-TR-84-156, Kirtland AFB, NM (1985).

SHORT-WAVELENGTH CHEMICAL LASER DEVELOPMENT

J. M. Herbelin
Aerophysics Laboratory, Laboratory Operations
The Aerospace Corporation, El Segundo, CA 90245

Abstract

The results of a series of subsonic and supersonic continuous-wave (cw) flow studies directed toward the development of a cw supersonic laser device that operates in the visible (blue-green) region of the spectrum are summarized. They clearly support the theoretically predicted quadratic dependence of excited-state BiF* on NF*. Based on this observed scaling dependence, a supersonic flow system is described and related operating conditions are identified. The performance of this supersonic visible chemical laser system is then predicted.

Introduction

Since its discovery in 1984, the nitrogen fluoride/bismuth monofluoride, NF(a)/BiF, reaction system has been under constant investigation as an efficient energy source to power a supersonic blue-green continuous-wave (cw) laser system.[1-6] During that time a series of subsonic and supersonic flow studies were conducted. The results, when taken collectively, support the scalability of this reaction system to the BiF* density levels required to demonstrate lasing. This paper reports on the results of the work, which focused on correlation and interpretation of past kinetics and radiation experiments, and the modeling of logical steps toward the development of a supersonic laser system.

Scaling Law

In Figure 1, the scaling results are summarized as a log-log plot of the density of electronically excited BiF(A), the lasing species, versus the density of NF(a), the energy source. BiF* is generated by the following sequence of reactions:[2,3]

for NF* generation,

$$F + H_2 \longrightarrow HF + H \quad (1)$$

$$H + NF_2 \longrightarrow HF + NF^*; \quad (2)$$

for BiF* generation,

$$Bi + NF^* \longrightarrow Bi^* + NF, \quad (3)$$

$$Bi^* + NF^* \longrightarrow BiF^* + N, \quad (4)$$

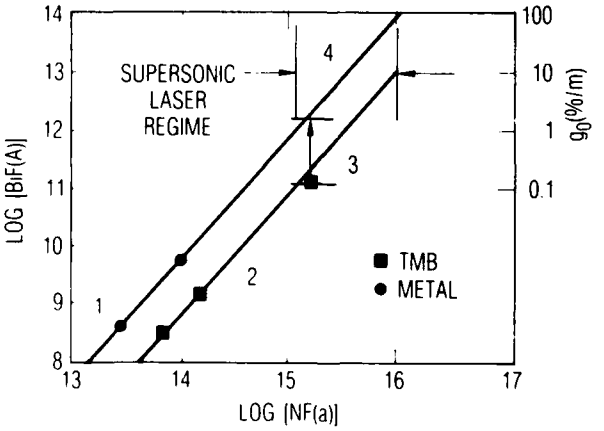


Figure 1. Summary of the BiF(A) scaling results for pure metal (●) and TMB (■) as bismuth sources in the (1) low-density subsonic, (2) intermediate-density subsonic, and (3) high-density supersonic flow experiments. The projected system performance is indicated by (4).

and

$$BiF^* \longrightarrow BiF + h\nu; \tag{5}$$

and for bismuth atomic regeneration,

$$H + BiF \longrightarrow HF + Bi. \tag{6}$$

NF*, Bi*, and BiF* refer to the excited states of $NF(a^1\Delta)$, $Bi(^2D_{3/2})$, and $BiF(AO^+)$, whereas NF, Bi, and BiF are the respective ground states.

With reactions (1) and (2), we have been able to scale up the NF* density to the order of approximately 10^{16} molecules/cm^3 in a thermally controlled (T = 300°C) supersonic flow. The vertical lines in Figure 1 indicate the demonstrated operating regime[4,5] of such a supersonic NF* flow. From reactions (3) and (4), we see that two NF* are required to produce one BiF*, resulting in the quadratic dependence

$$BiF^* \propto [NF^*]^2, \tag{7}$$

indicated by the two linear curves with slopes of 2. These lines are distinguished by whether the pure metal or the compound trimethylbismuthine (TMB) was used to introduce the bismuth into the NF* flow stream. The pure-metal performance (●) appears to be an order of magnitude better than that of the TMB (■) because of the absence of undesirable side reactions involving the TMB and its reaction products. Nevertheless, it is quite clear that the same quadratic dependence holds for both bismuth sources.

The results from the original low-density flow tube study[1] are indicated by the numeral 1 in the lower left-hand corner of Figure 1. Because of the low densities and slow velocities involved in that study, we could treat the system as premixed, and the value of each of the two data points for the pure-metal and TMB cases was accepted without adjustment.

As one scales to higher densities, however, the large physical sizes and masses of Bi and TMB result in the relatively slow diffusion of these species, and mixing becomes the limiting process. Consequently, mixing considerations become important, and the mixing flamesheets must be analyzed carefully to determine the correct scaling properties. In the next set of experiments (numeral 2 in Figure 1), well-defined side-by-side laminar flows of NF* and either Bi metal or TMB were developed.[6] Since these experiments have been described in detail elsewhere,[7] here we present the major findings that relate to the scaling issue. Figure 2 shows a typical cross section of the flamesheet that is produced in a subsonic facility. The bismuth flow is on the left side of the figure and joins the NF* on the right side. This contact between the two streams first produces the Bi* on the left, which is subsequently converted into BiF* in the center.

In the previous experiments, it was not possible to measure the Bi* and NF* distributions directly; they had to be deduced from blue BiF* and other visible emissions. In later experiments, we focused on a direct measurement of each of these species, which confirmed the correctness of deduced distributions. Consequently, the peak BiF* density has a well-defined value that can be computed from the Bi* and NF* densities measured in the same volume. The value is given by the theoretically derivable relationship

$$[BiF^*] = k_4 [NF^*][Bi^*]/A, \tag{8}$$

where k_4 is the rate coefficient of reaction (4) and A is the Einstein coefficient for the spontaneous emission of reaction (5). This computation enabled us to pinpoint the concentrations for the metal and TMB subsonic flow tests shown in Figure 1.

For the supersonic flow results (numeral 3 in Figure 1), the analysis was complicated by a rather poorly defined flame zone, owing directly to the type of mixing scheme used to introduce the bismuth: side-wall injection. In this scheme, tetrafluorohydrazine (N_2F_4) and a mixture of TMB and He were injected into a supersonic stream of fluorine atoms in helium through an array of small holes on the sides. Farther downstream, H_2 was injected and then the resulting NF*, Bi*, and BiF* signals were measured.

In this type of side-wall injection, the flow streams are not distinct as in the subsonic flow. Therefore, the "average" value of the BiF* density (■ in Figure 1) is a lower bound to the peak density, defined above. From simple diffusion arguments, the BiF* flamesheet is expected to occupy a minimum 15 to 20% of the flow volume, so an upper bound to the peak value would be a factor of 5 to 7 times this average value, as indicated by the arrow in Figure 1. Since these two bounds bracket the quadratic scaling curve for TMB, our confidence in the scaling laws is increased.

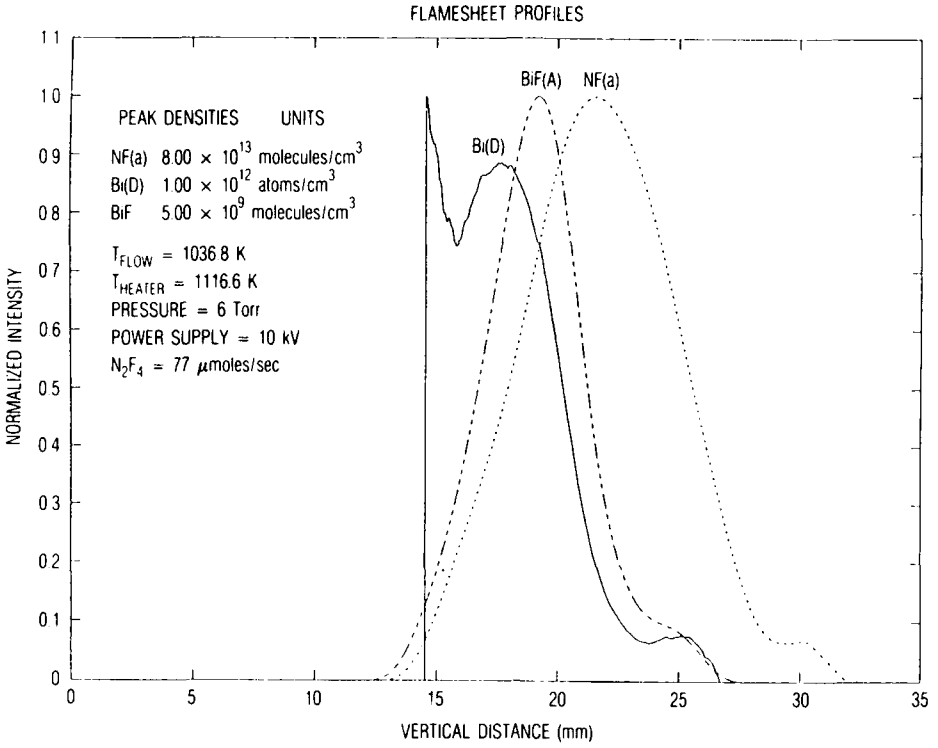


Figure 2. Transverse flamesheet profiles measured in the intermediate-density subsonic flow facility.

BiF* Demonstrator

The next step in the development of a blue-green laser would be to scale the system to a lasable density. This could be accomplished by introducing a supersonic stream of bismuth metal in helium into the supersonic NF* flow operating in the above-mentioned regime (numeral 4 in Figure 1). A cross-sectional view of a device capable of achieving this condition is shown in Figure 3.

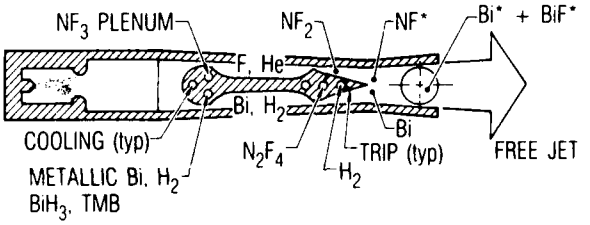


Figure 3. Cross-sectional view of a prototype BiF laser demonstrator using a dual-plenum/ nozzle concept to generate both the oxidizer, NF*, and receptor, Bi, supersonic streams.

This particular design employs an arc-driven plenum to produce a flow of hot (T = 1800 K) helium that is then split into two subplenums. A fluorine source is introduced into the upper subplenum and a bismuth-atom source is introduced into the lower one. These flows are expanded supersonically as N_2F_4 is injected into the upper stream. The injection of H_2 follows, as shown, using trip-nozzle technology to enhance the mixing in the resulting reaction zone. This approach is expected to produce a reasonably well-defined BiF* flamesheet at a density in excess of 10^{13} molecules/cm^3, as indicated by the numeral 4 in Figure 1.

An efficient, low-risk way to implement this demonstration would be subdivided into three subtasks:

- The development of a supersonic flow of bismuth atoms using pure-metal or bismuth compounds or both. The bismuth density would be measured using dye laser probes.

- "Marriage" of NF* and bismuth supersonic flows using conventional and trip-flow technologies to achieve excited-state scaling in a well-defined laminar flow field.
- Measurement of gain and demonstration of laser action.

Following an initial demonstration, many design variations could be explored for short-wavelength chemical lasers:

- The use of a combustor instead of an arc.
- The use of bismuth compounds such as TMB or BiH_3 instead of pure metallic bismuth.
- Investigation of alternative sources for generating NF_2 in place of N_2F_4.

These different approaches offer important trade-offs that need to be considered for the more advanced designs of this potential space-based laser system.

BiF Laser System Design

In order to establish the feasibility of a larger system, and to anticipate major problems, a preliminary system design was performed. One of several concepts for a BiF supersonic laser is shown in Figure 4. The design is similar to existing cw HF laser devices based on the cold F + H_2 reaction system. This particular concept uses a linear array of vertical slit nozzles in a bank 1 m long and 10 cm high. The key difference between this BiF system and existing HF machines is the somewhat more sophisticated nozzle required to introduce the additional ingredients NF_2 and Bi.

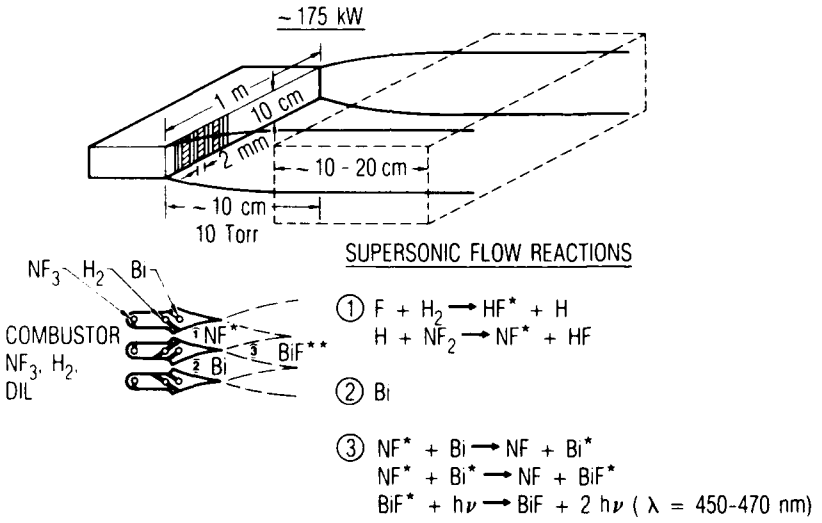


Figure 4. Conceptual design of a cw supersonic BiF* laser based on established HF laser device technology.

The NF* and Bi supersonic streams are prepared using a common plenum. In one throat, excess NF_3 is used to produce the fluorine atoms that are converted into NF* with the subsequent introduction of NF_2 followed by injection of H_2, as was done in previous flow experiments. (It is conceivable that the NF_2 radical, as well as the fluorine atoms, can be generated from NF_3 by proper design of the plenum and throat, since experiments have confirmed that reasonable yields of NF_2 can be produced from wall-catalyzed reactions. However, more research is needed before this added simplification can be relied upon.) In the other throat, excess H_2 together with a bismuth source such as BiH_3 or TMB is added to generate the bismuth atoms. By injecting the compound into the plenum, complete dissociation will occur and performance equivalent to pure-metal injection should be obtained.

A second concept has been developed that could greatly simplify the nozzle design. This approach relies on the introduction of BiH_3 directly into the reaction stream together with the hydrogen. The BiH_3 is stable at low temperatures,[8] but should dissociate rapidly in the presence of electronically excited NF*:

$$BiH_n + NF^* \longrightarrow BiH_n^* + NF \qquad (9)$$

and

$$BiH_n^* \longrightarrow BiH_{(n-1)} + H \qquad (10)$$

for n = 3,2,1. Hydrogen atoms, which are produced in large quantities by means of reaction (1), are also available to contribute to this dissociation process by the reactions

$$H + BiH_n \longrightarrow H_2 + BiH_{(n-1)} \longrightarrow Bi^* + \left(\frac{n+1}{2}\right) H_2. \qquad (11)$$

These latter reactions are particularly interesting, since theory suggests that the bismuth should be produced in the excited state, which enhances the system efficiency. However, the kinetics of the BiH_3 dissociation need to be studied before this approach can be adopted with confidence.

The predicted performance of this conceptual laser device is shown in Figure 5. The calculations were performed using the simple kinetic scheme [reactions (1)-(6)] combined with a laminar flamesheet mixing model. This approach is similar to the one used to develop the analytical diffusion model (ADM), which was successful in describing the general performance of cw HF/DF lasers to an accuracy of approximately 10%.[9]

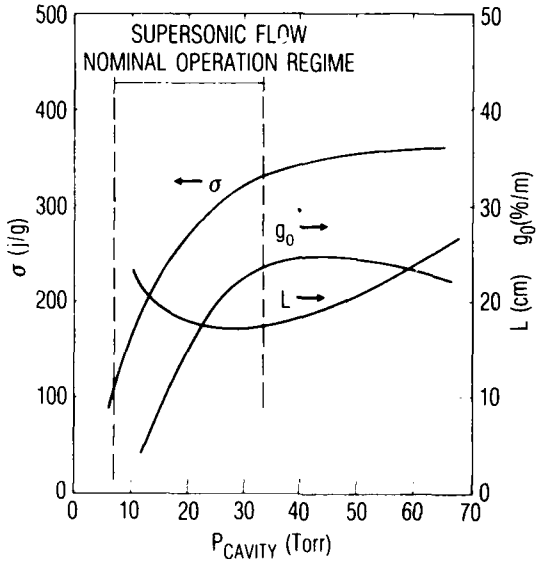


Figure 5. Predicted performance of a cw supersonic BiF laser.

The optical resonator used in these calculations is a version of the reverse-wave-suppressed unstable ring cavity used to demonstrate excellent beam quality from a 2-kW HF laser system.[10,11] The resonator in these experiments was operating at an equivalent gain per unit length well below that expected to be generated in the BiF* device. To be specific, when scaled from the 2.7-μm HF wavelength to the 0.45-μm BiF wavelength, the equivalent gain requirement for this cavity is 3.8%/m. It is well below the 20%/m gain predicted for the BiF* system.

In order to take advantage of the long cavity length of the ring, we will employ a folded path over an extended gain zone. The gain zone for the BiF is predicted to range from 18 to 25 cm in length, allowing ample space for a multiple-pass geometry (see Fig. 5). This stems from the fact that the mixing and deactivation processes are slower in the BiF laser than in the HF laser--it takes approximately 10 times longer to consume the NF*.

Because we are dealing with visible light, mirror loading problems are greatly reduced. The output beam of the resonator is approximately 1.3 cm in diameter for an equivalent 100 kW/cm^2 flux. However, since good optical coatings in the visible exhibit <10 ppm absorption, the worst-case heat loading would be 2 W/cm^2 at this mirror. If this resonator is designed to couple out 25% of the power, the maximum internal loading is 8 W/cm^2, which is well within the capabilities of current technology.

Conclusions

The results from a series of subsonic and supersonic flow experiments clearly support the theoretically predicted quadratic scaling law for excited-state BiF* as a function of NF*. On the basis of these results, the described small-scale supersonic flow device achieves laser action and provides a test-bed for future studies.

References

1. J. M. Herbelin, "Efficient Production of Electronically Excited BiF(AO^+) via Collisions with NF(a)," Int. J. Chem. Kinet. 16, 849 (1984); also ATR-85(8315)-2, The Aerospace Corp. (22 June 1987).

2. J. M. Herbelin, "Electronic Energy Transfer Between NF(a) and BiF(X)," Proceedings of the International Conference on Lasers '86, STS Press (1986).

3. R. F. Heidner et al., "BiF(AO^+,v') Radiative Lifetime and Rate Coefficients for V-T Transfer and Electronic Quenching," J. Chem Phys. 84, 2137 (1986).

4. J. M. Herbelin and R. R. Giedt, "Production of Electronically Excited Bismuth in a Supersonic Flow," J. Appl. Phys. 54, 28 (1982).

5. M. A. Kwok et al., Proceedings of the AIAA/SDIO High Power Laser Device Conference, Boulder, Colorado, 2-5 March 1987.

6. J. M. Herbelin, "Short-Wavelength Laser Development," Proceedings of the International Conference on Lasers '87, STS Press (1987), p. 218.

7. J. M. Herbelin, "Short-Wavelength Laser Development," Aerospace Sponsored Research Summary Report, Exploratory Technology, ATR-86A(8498)-2, The Aerospace Corp. (1 December 1987), p. 58.

8. I. A. Brovko, A. Davirov, and G. M. Tolmacheva, "Kinetics of Thermal Decomposition of Bismuthine on a Graphite Tube," Uzb. Khim. Zh. (1), 25 (1986).

9. J. M. Herbelin, "Continuous-Wave ($F+H_2$) Chemical Lasers: A Temperature-Dependent Analytical Diffusion Model," Appl. Opt. 15 (1), 223 (1976).

10. J. M. Bernard, R. A. Chodzko, and H. Mirels, "Reverse-Wave Suppressor Mirror Effects on CW HF Unstable Ring Laser Performance," Appl. Opt. 25 (5), 666 (1986).

11. R. A. Chodzko et al., "Zero-Power-Gain Measurements in CW HF(DF) Laser by Means of a Fast Scan Technique," J. Quantum Electron. 12 (11), 660 (1976).

PROGRESS TOWARDS A SHORT WAVELENGTH CHEMICAL LASER

Steven J. Davis
Physical Sciences Inc.
20 New England Business Center
Andover, MA 01810

Abstract

Research efforts to develop a short wavelength chemical laser have continued to show progress during the last few years. In this paper we present a brief history of these efforts and we discuss some recent results that involve energy transfer from metastable species to potential laser molecules.

1. Introduction

Short wavelength lasers that derive their energy from chemical pumping have been of interest to the laser community since the early 1970's. To date, however, the frequency doubled (λ = 657.6 nm) chemical oxygen iodine laser[1,2] is the only system that has produced visible wavelength output. Indeed, the COIL[1] device operating at 1315 nm is the only other chemically pumped laser that produces an output at a wavelength shorter than the HF vibrational laser (λ ~2.7 μm). Several potential applications have motivated the research to develop a short wavelength chemical laser (SWCL). There are a variety of defense related applications such as strategic defense and secure communications. These devices might also find uses in the medical community.

2. Early Efforts

The search for a SWCL began soon after the advent of vibrational chemical lasers such as the HF(Δv=1) system that provides output near 2.7 μm. Since HF has the largest vibrational spacing of any heteronuclear diatomic molecule one must invoke excited electronic states to obtain short wavelength lasing on a diatomic molecule. For atomic lasers one might be able to lase between two terms of a ground state configuration. The COIL device is an example of this; lasing occurs on the $^2P_{1/2} \rightarrow {}^2P_{3/2}$ transition which is in actually two spin orbit terms of the ground state atomic configuration. However, COIL and other potential analogous atomic systems are considered to be electronic transition lasers.

There were numerous attempts to develop SWCL's in the 1970's based upon metal oxide type molecules, and BaO was an archetypical example. Using the HF laser pumping reaction as a model:

$$H_2 + F \rightarrow HF(v) + H \quad , \tag{1}$$

reactions such as

$$Ba + N_2O \rightarrow BaO^* + N_2 \tag{2}$$

were investigated. While it initially appeared that large populations of electronically excited molecules could be produced,[3] later work demonstrated that reaction (2) produced, almost exclusively, vibrationally excited ground electronic state BaO.[4] Excitation of BaO excited states was by intersystem energy transfer. It is now generally believed that this process was operative in many of the metal oxide candidate systems.

One very important result of all the early work in this field was the recognition that reactions that efficiently partition energy into excited electronic states are rare. Indeed, there are at this writing only two documented cases of efficient production of excited species at densities high enough to be relevant to SWCL production. These are $O_2(a^1\Delta)$[1] and its isoelectronic cousin $NF(a^1\Delta)$.[5,6] The ground states of each of these is $X^3\Sigma$. Thus, the a$\rightarrow$X systems are spin forbidden, and the species are very metastable. Correlation rules[7] for spin and orbital angular momentum predict that most efficient production of excited electronic states will occur if: a) there is an excited product state of the same symmetry as that for the reactants, and b) a similar correlation does not exist for the ground state product. Usually electronic spin is the more rigorous constraint. These correlations are readily calculated using standard direct product tables.

We note that $O_2(a^1\Delta)$ is the species that excites the COIL device via the rapid and efficient energy transfer reaction

$$O_2\left(a^1\Delta\right) + I\left(^2P_{3/2}\right) \rightleftarrows O_2\left(X^3\Sigma\right) + I\left(^2P_{1/2}\right) \qquad (3)$$

Lasing occurs on the atomic iodine ($^2P_{1/2} \rightarrow {}^2P_{3/2}$) transition at 1.315 μm. This transfer laser involving a metastable energy reservoir and a laser specie can serve as a model for other potential systems.

If we examine $O_2(a)$ and NF(a) as potential reservoirs for SWCL applications we must question the ability of these two metastables to pump transfer partners that could lase at visible wavelengths. Although the respective electronic term values, T_e, for $O_2(^1\Delta)$ and $NF(^1\Delta)$ (7918 cm^{-1} and 12,003 cm^{-1}) would appear to be insufficient to produce visible lasing, there have been numerous observations of visible chemiluminescence produced via energy transfer from these species. For example $I_2(B)$,[8] IF(B),[9-11] BrF(B)[9] can be excited by $O_2(^1\Delta)$ and BiF(B) is produced via energy transfer from $NF(^1\Delta)$.[12-14] The details of the excitation mechanisms are not understood, but it is clear that at least two metastable singlet delta molecules are required for each excitation. A clear example of this was demonstrated in a recently in our laboratories when we showed that the IF(B) concentration scaled as the square of the $O_2(^1\Delta)$ concentration.[11] The important point is that there are examples of energy transfer from metastables that have mature chemical generation technologies to species that are exceedingly promising laser candidates.

Of these laser candidates, the IF(B→X) and BiF(B→X) systems are relatively advanced with respect to chemical laser development. The NF/BiF system is at present being investigated by several groups[12-14] and scaling to laser densities is being performed. Both pulsed and CW, tunable IF lasers (550 to 750 nm) using laser excitation[15,16] have been reported. The IF(B) state is immune to numerous quenchers[17-19] and has large stimulated emission cross sections, e.g., $\sigma_{SE} \approx 7 \times 10^{-17}$ cm^2 for the R(21) branch of the (0,4) band. The radiative properties of BrF(B)[20] are similar to those of IF(B) and we expect similar laser potential.

3. Recent Results

In some recent work examining energy transfer from $O_2(a^1\Delta)$ to IF(B) we have observed some interesting and significant results. While it has been shown previously that ground state IF can be excited to IF(B) using metastable O_2, we recently observed dramatic enhancements (nearly three orders of magnitude) in the IF(B) production efficiency when the IF(X) was vibrationally excited prior to reacting with the $O_2(^1\Delta)$.[21] The experiments were performed in a fast flow reactor. The degree of vibrational excitation was monitored using standard laser induced fluorescence techniques. The experiments were done by reacting both vibrationally cold IF(X,v=0) and vibrationally hot IF(X,v>>0) with $O_2(^1\Delta)$. From here on we call IF(X,v>>0) $IF^\dagger$. The cold IF(X) was formed by the CF_3I+F reaction[22] and $IF^\dagger$ was produced using I_2+F.[23,24] A comparison of the IF(B→X) chemiluminescence intensities produced using both CF_3I and I_2 as iodine donors is shown in Figure 1. Although each iodine donor produced equal total [IF(X)], the temporal profiles and the intensities of IF(B→X) emissions are strikingly different for the two cases. The [IF(B)] temporal profile originating from $CF_3I + F + O_2^*$ has a much longer decay time and is at least two orders of magnitude smaller in amplitude than the profile obtained from the $I_2 + F + O_2^*$ reaction. (The signal growth at short reaction times (~0.5 ms) is ascribed to mixing.) Although it is not immediately obvious from the plots shown in Figure 1, the chemiluminescence intensitys from the $I_2 + F + O_2^*$ reaction was only a factor of 2 greater than that from the $CF_3I + F + O_2^*$ reaction at long times (>5 ms). Thus, at long reaction times, the two reaction schemes appear to give comparable IF(B) excitation rates. These observations are consistent with vibrationally hot IF(X) being involved in the excitation process when F + I_2 is used to form IF(X). As described previously, nascent vibrational distribution produced from F + I_2 is very non-Boltzmann[23,24] while CF_3I + F produces a much more thermal distribution.[22] Our interpretation of the data shown in Figure 1 is that vibrationally hot $IF^\dagger$ produced by reaction (3) is pumped by O_2^* to IF(B) much more efficiently than is the cold IF(X) produced from reaction (2). At longer reaction times, $IF^\dagger$ is relaxed by V-T transfer with the Ar bath gas, and the excitation of IF(B) becomes much less efficient. When $IF^\dagger$ is totally relaxed one would expect the excitation process to be identical to that using CF_3I, and indeed the [IF(B)] produced become comparable at reaction times exceeding 5 ms. We performed some preliminary mechanistic studies that showed that the following sequential pumping model was probably operative.

$$I_2 + F \rightarrow IF^{\dagger} + I \quad (4)$$

$$IF^{\dagger} + O_2(^1\Delta) \rightarrow IF(A') + O_2 \quad (5)$$

$$IF(A') + O_2(^1\Delta) \rightarrow IF(B) + O_2 \quad (6)$$

where $IF^{\dagger}$ is vibrationally excited ground state IF. We found that IF(X,v≥9) were the active species. This can be explained by the energy levels shown in Figure 2. Examination of Figure 2 shows that the two step process (reactions 5 and 6) requires considerable internal energy in IF(X). We found that as IF(X,v≥9) was removed the production efficiency fell concomitantly as shown in Figure 1. The $IF^{\dagger}$ is quite immune to quenching and it could be transported tens of cm in a supersonic flow laser.

There are other reported observations that highly vibrationally excited ground state molecules can excite electronic energy levels that subsequently chemiluminesce. For example, the $A^1\Sigma$ and $A'^1\Sigma$ states of BaO are populated by intramolecular energy transfer from BaO(X,v) through collisions with argon.[3] In addition, BaO(X,v) also appears to excite electronic energy levels in atomic Ba when Barium atoms are mixed with BaO(X,v).[25] Note that BaO(X,v) is the primary product of the Ba + N_2O reaction.[4] The salient point is that this chemically produced vibrational energy appears to open pathways to electronic excitation. We hope to pursue this approach to determine whether vibrationally assisted electronic energy transfer is a general phenomenon that can be utilized for SWCL applications.

References

1. W.E. McDermott, N.R. Pchelkin, D.J. Benard, and R.R. Bousek, Appl. Phys. Lett. 32, 469 (1978).

2. D.E. Johnson, R.H., Humphreys, Jr., P. Keating, and G.D. Hager, AIAA Thermophysics, Plasmadynamics and Lasers Conference, San Antonio, TX (June 1988) Paper No. AIAA-88-2749.

3. C.R. Jones and H.P. Broida, J. Chem. Phys. 60, 4369 (1974).

4. Y.C. Hsu and J.G. Pruitt, J. Chem. Phys. 76, 5849 (1982).

5. J.M. Herbelin and N. Cohen, Chem. Phys. 20, 605 (1973).

6. C.T. Cheah and M.A.A. Clyne, J. Photo. Chem. 15, 21 (1981).

7. K.E. Shuler, J. Chem. Phys. 21, 624 (1953).

8. R.G. Derwent and B.A. Thrush, Faraday Soc. 67, 2036 (1971).

9. M.A.A. Clyne, J.A. Coxon, and L.W. Townsend, JCS Faraday Trans. II 68, 2134 (1972).

10. P.D. Whitefield, R.F. Shea, and S.J. Davis, J. Chem. Phys. 78, 6793 (1983).

11. S.J. Davis, A.M. Woodward, L.G. Piper, and W.G. Marinelli, Physical Sciences Inc. Final Report, Contract No. F29601-86-C-0017, Report No. AFWL-TR-87-92 (1987).

12. R.F. Heidner, III, H. Helvajian, J.S. Holloway, and J.B. Koffend, The Aerospace Corporation, Report No. SD-TR-87-19 (1987).

13. J.M. Herbelin and R.A. Klingberg, Int. J. Chem. Kinet. 16, 849 (1984).

14. D.J. Benard, B.K. Winker, T.A. Seder, and R.H. Cohn, J. Phys. Chem. 93, 4790 (1989).

15. S.J. Davis, L. Hanko, and R.F. Shea, J. Chem. Phys. 78, 172 (1983).

16. S.J. Davis, L. Hanko, and P.J. Wolf, J. Chem. Phys. 82, 4831 (1985).

17. P.J. Wolf, J.H. Glover, L. Hanko, R.F. Shea, and S.J. Davis, J. Chem. Phys. 82, 2321 (1985).

18. P.J. Wolf and S.J. Davis, J. Chem. Phys. 83, 91 (1985).

19. P.J. Wolf and S.J. Davis, J. Chem. Phys. 87, 3492 (1987).

20. M.A.A. Clyne, and J.S. McDermid, JCS Faraday II 74, 1376 (1978).

21. S.J. Davis and A.M. Woodward, Selectivity in Chemical Reactions, NATO, ASE Series, Kluver Academic Publishers, Ed. (J.C. Whitehead, 1988).

22. L. Stein and J. Wanner, J. Chem. Phys. 72, 1128 (1980).

23. T. Trickl and J. Wanner, J. Chem. Phys. 78, 6091 (1983).

24. B. Girard, N. Billy, Gouédard, and J. Vigué, J. Chem. Phys. 88, 2342 (1988).

25. N. Djeu, in "Electronic Transition Lasers," Ed. (J.I. Steinfeld, MIT Press, 1975).

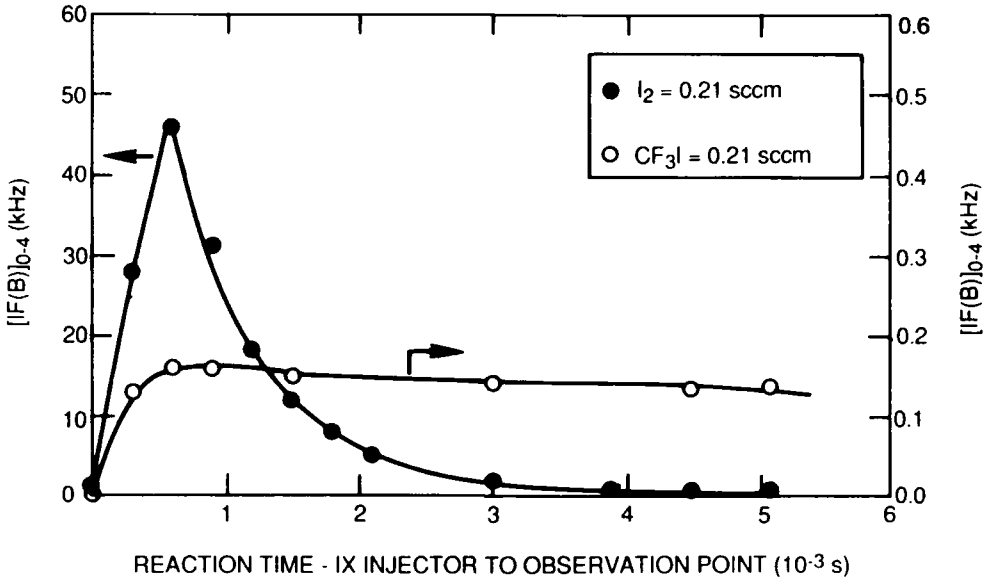


Figure 1. Chemiluminescence Intensity of IF(B→X) Following Excitation by $O_2(^1\Delta)$: ● - vibrationally hot IF(X,v) produced by I_2 + F, o - vibrationally cold IF(X,v) produced by CF_3I + F. Note the large scale difference in the two ordinates. Data obtained in 0.8 Torr Ar bath gas.

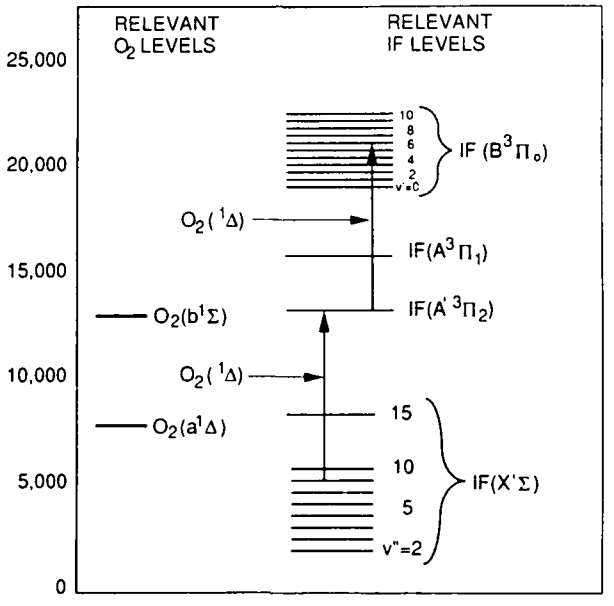


Figure 2. Energy Levels for O_2 and IF Showing Role of IF(X,v) in the Excitation Process. Pumping by $O_2(^1\Delta)$ indicated by vertical arrows

Acknowledgment

Work supported in part by the Air Force Office of Scientific Research.

MODELING OF NUCLEAR PUMPED LASERS ON HE-MIXTURES WITH Cd,Zn,Hg,Mg,Sr,Ca AND Ba VAPORS

V.I. DERZHIEV, A.V. KARELIN, S.I. YAKOVLENKO

General Physics Institute, Academy of Sciences of the USSR
Vavilov Str. 38, Moscow, 117942, USSR

Abstract

Detailed nonstationary kinetic models of nuclear pumped high-pressure II group metal vapors lasers have been constructed and analyzed. Theoretical results are in a good agreement with available experimental data.

Introduction

Progress in realization of plasma lasers (i.e. lasers, in which active medium is a nonequilibrium recombination plasma) allows to hope for a wide use of charged products of nuclear reactions for direct conversion of nuclear energy into coherent light radiation. A possibility of direct nuclear pumping is discussed in literature for a long time (see reviews [1,2]). For the present time lasing have been attained in more than 10 laser media in IR and visible region of spectrum on the transitions of CO, ArI, NeI, KrI, XeI, CI, NI, CdI, CdII, HgII, ZnII.

Active media excitation was realized by the charged products of $^{3}He(n,p)^{3}T$, $^{10}B(n,\alpha)^{7}Li$ and $^{235}U(n,f)f$ nuclear reactions.

The maximal active medium efficiency as high as 2 % and lowest lasing threshold were attained for the laser on XeI transitions.

For the efficiency rise it is necessary to search active media radiating in the visible and UV spectrum regions. For this purpose it was interesting to investigate rare gas mixtures with metal vapors, in which favourable conditions develop for originating population inversion in nonequilibrium recombination plasma. Moreover, the usage of metal vapors sufficiently increases the number of possible laser transitions suitable for lasing in nuclear pumping conditions.

Lasers on II group metal vapors have been investigated for a long time. They were started with different types of discharges under low and middle pressures. The plasma laser principle was realized for the first time by Latush and Sem in 1973 on these mixtures (He-Sr laser) [3]. In 1978 the He-Cd nuclear pumped laser under atmospheric pressure was produced, this laser is presently the most shortwave nuclear pumped laser[4]. Later on this laser was started with e-beam pumping [5-7].

The major advantages of the II group metal vapor lasers are as follows : 1) relatively low thresholds of excitation; 2) visible and UV region of radiation, which may be convenient for different applications. So it was necessary to develop detailed kinetic models of the corresponding high-pressure active media, which capable of describing adequately a relatively weak stationary nuclear reaction products pumping, as well as powerful pulsed e-beam or i-beam pumping. Development of such models is necessary both for optimization of working lasers and for a search of new perspective active media.

We have constructed and analyzed detailed nonstationary kinetic models of 11 high-pressure active media: He-Cd, He-Zn, He-Hg, He-Mg, He-Be, He-Ca, He-Sr, Ne-Sr, He-Xe-Sr and He-Ba, in which 14 most perspective (from our point of view) transitions were considered.

The PLASER-1 program package developed at the General Physics Institute was used for the calculations of active media local kinetics. Radiaton was calculated to zero-dimensional approximation (i.e. volume averaged). There are special modules in PLASER-1 package suitable for 2- and 3-dimentional calculations of radiation. But it is necessary only for calculating wide apperture systems. In the case of investigating active media, zero-dimensional approximation is quite sufficient and requires appreciably less computer time.

Results

In the plasma created by hard ionizer, the calculations were carried out of nonstationary relaxation kinetics of ions, electrons and active media excited components' concentrations, electron and ion temperatures, and time-dependent functions of gain koefficient, output lasing power and energy. The number of equations in different models was varied from 25 to 30. From 9 to 13 excited states were taken into account in kinetic schemes of active ions. Thus, altogether from 100 to 160 plasmochemical reactions were considered in models (including excited states kinetics).

Here we shall point out only the main processes responsible for the upper working levels pumping.

For the He-Cd (λ = 441.6 nm and 325.0 nm) and He-Zn (λ = 747.9 nm) there will be the following reactions :

$$He_2^+ + Me = 2He + Me^{+*} \quad , \quad (1)$$

$$He^* + Me = He + Me^{+*} + e \quad , \quad (2)$$

for the He-Cd (λ = 533.7 and 537.8 nm), He-Zn (λ = 758.8 nm), He-Hg (λ = 615.0 nm) and He-Be :

$$He^+ + Me = He + Me^{+*} \quad , \quad (3)$$

$$Me^{+**} + e = Me^{+*} + e \quad , \quad (4)$$

$$Me^{+**} = Me^{+*} + h\nu \quad , \quad (5)$$

for the He-Mg, He-Ca, He-Sr and He-Ba :

$$He_2^+ + Me = 2He + Me^{++*} \quad , \quad (6)$$

$$He^+ + Me = He + Me^{++} + 2e \quad , \quad (7)$$

$$Me^{++} + 2e = Me^{+*} + e \quad , \quad (8)$$

$$HeMe^{++} + e = Me^{+*} + He \quad , \quad (9)$$

for the He-Xe-Sr :

$$Xe^+ + Sr = Xe + Sr^{+*} \quad . \quad (10)$$

Naturally, this separation of processes is quite conventional, it emphasizes only some differences of the active media.

The other most significant criterion of separation is the mechanism of creation of population inversion, i.e. the mechanism of the lower working level clearing.

By the criterion the lasers under consideration are classified into two groups:

1. Lasers with radiational clearing of the lower working level (reaction (5)), such as: He-Cd,Zn,Hg,Mg and He-Be (λ = 467 nm);
2. Lasers with electron-collisional clearing of the lower working level (reaction (4)), they are: He-Sr,Ca,Ba,Ne-Sr, He-Xe-Sr and He-Be (λ = 177.6 nm).

Lasers with radiational clearing of the lower working level have the lowest pumping thresholds, because there is no necessity for producing high quantity of plasma electrons. Consequently, among them one should search possible candidates for usage at weak nuclear pumping.

He-Cd and He-Zn lasers are best explored both experimentally and theoretically. So we shall consider them in more detail.

In the fig.1 there are dependences of output lasing energy (fig.1.a, solid lines - experiment, dashed lines - calculations) for the He-Cd (λ = 441.6; 533.7 and 537.8 nm) and He-Zn (λ = 747.9 nm) lasers and relations of plasma parameter N_e and components of He-Cd plasma with respect to active medium temperature. The presence of optima is shown, which are caused by the formation of the Me_2^+ - type molecular ion (see fig.1.b) in the case of He-Cd (λ = 441.6 and 325.0 nm) and He-Zn (λ = 747.9 nm) lasers,and by deexcitation of the upper working level in Penning reaction with its own atom in the case of He-Cd (λ = 533.7 and 537.8 nm) lasers. The calculation results are in satisfactory agreement with experimental data.

The fig.2a presents the dependences of laser radiation output energy(λ = 441.6 nm) upon buffer gas pressure (solid lines - experiment, dashed lines - calculations). Upper and lower dashed lines differ from each other by the spurious absorbtion coefficient $k^- = 1.E-4$ and 5.E-4 1/cm, respectively. The presence of optimum is caused by the broadening of the working transition line.

In the fig.2b are calculated dependences of output lasing power (solid lines) and laser efficiency (dashed lines) for the He-Cd and He-Zn lasers depending on the neutron flux. The presence of laser efficiency optimum is caused by the electron deexcitation of the upper working level.

Conclution

The summary calculated results are presented at the table 1. There are optimal active media parameters, energy deposition, maximal laser efficiency and threshold characteristics of the II group metal vapor nuclear pumped lasers. As it follows from the calculation results, He-Cd laser with λ = 441.6 nm is the most suitable for the purposes of direct nuclear pumping. It has one of the lowest generation thresholds, highest laser efficiency, relatively low working temperatures, quite short wavelength and the possibility of working at relatively high pressures, that allows, on principle, to realize optimal energy deposition at the presently working or technically available reactors. An optimal diameter of lasing tube for this laser in case of pumping from uranium foils is about 3 cm. This circumstance plays an important role for the design of reactor-laser systems.

The numerical analysis anabled to draw the following conclusions :

1. In high-pressure He-Cd (λ = 325.0 and 441.6 nm) and He-Zn (λ = 747.9 nm) lasers optimum values of temperature and pressure are due to competition between the relaxation flux pumping the upper level and deexcitation of this level through the formation of a Me_2^+ -type molecular ion.
2. In high-pressure lasers on the metal ion single-electron transitions with radiational clearing of the lower working state the presence of temperature optimum can be attributed to competition of the pump fluxes to the upper working level and its deexcitation due to Penning reaction with its own atom.
3. In high-pressure lasers on metal ions with electron-collisional clearing of the lower working level the presence of optima depending on the active media temperature is due to competition of a rising relaxation flux to the upper le-

vel and deterioration of the lower level clearing owing to the drop of plasma electron concentration. An important role plays intensive deexcitation of high-lying levels in Penning reactions with its own atoms.

4. In the active media of high-pressure metal vapor lasers with the temperature elevation above an optimum value depending on buffer gas pressure, the plasma electron concentration falls down due to dissociative recombination of the Me_2^+ -type molecular ions. This deteriorates generation characteristics of the lasers with electron-collisional clearing of the lower working level.

References

1. K. Thom and R.T. Schneider, AIAA Journal, 10, 400 (1972).
2. R.T. Schneider, in Advances in Nuclear Science and Technology (Plenum Press, N.Y., 1984), pp. 123-287.
3. E.L. Latush and M.F. Sem, Sov. J. Quantum Electron., 3(15), 66 (1973).
4. A.B. Dmitriev, V.S. Ilyashenko, A.I. Mis'kevich and B.S. Salamakha, Soviet Phys. - Tech. Phys. Lett., 6, 352 (1980).
5. J.J. Rocca, H.L. Mancini, B. Wernsman, IEEE J. Quantum Electron. QE-22, 509 (1986).
6. V.I. Derzhiev, A.G. Zhidkov, A.V. Karelin, D.Yu. Nagornyi, V.S. Skakun, V.F. Tarasenko, A.V. Fedenev, S.I. Yakovlenko, Soviet Phys. - Tech. Phys. Letters, 14(1), 18 (1988).
7. F.G. Goryunov, V.I. Derzhiev, A.G. Zhidkov, A.V. Karelin, D.Yu. Nagornyi, V.S. Skakun, V.F. Tarasenko, A.V. Fedenev, S.I. Yakovlenko, Sov. J. Quantum Electron., 16(10), 2039 (1989).

Table 1. Optimal parameters of nuclear pumped metal vapor lasers.

mixture	wavelength, nm	T,deg C	p,atm	P, kW/cm**3	F, n/cm**2·s	η, %	q,thresh. W/sm**3
He-Cd	441.6	360-390	3-5	2	5.e14	0.7	15
	325.0	360-400	2-3	2	2.e16	0.2	300
	533.7	450-500	1-1.5	2.5	1.e15	0.13	7
	537.8						
He-Zn	747.9	450-490	3-5	2	1.e15	0.08	25
	758.8	600	~2	1	1.e15	0.1	10
He-Hg	615.0	200-250	1-2	2	7.e15	0.02	100
He-Mg	448.1	700-720	2-3	1	1.e15	0.2	13
	921.8	700	1-2	0.3	0.3-2.e15	0.03	10
He-Sr	430.5	650	3-4	2.5	4.e16	0.2	800
He-Ca	373.7	650	2-4	10	2.e16	0.11	400
He-Ba	490.1	850-900	2-4	5	5.e16	0.02	1000

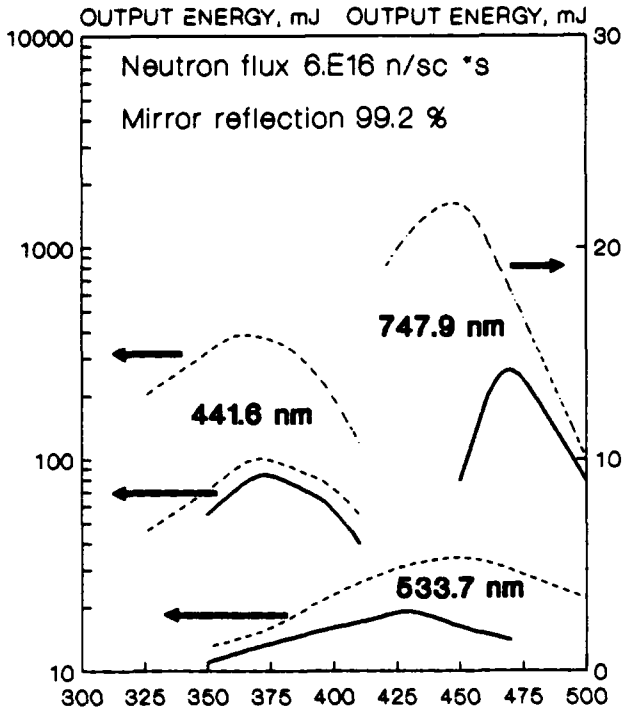


Fig.1a. Temperature dependence(reactor pump)

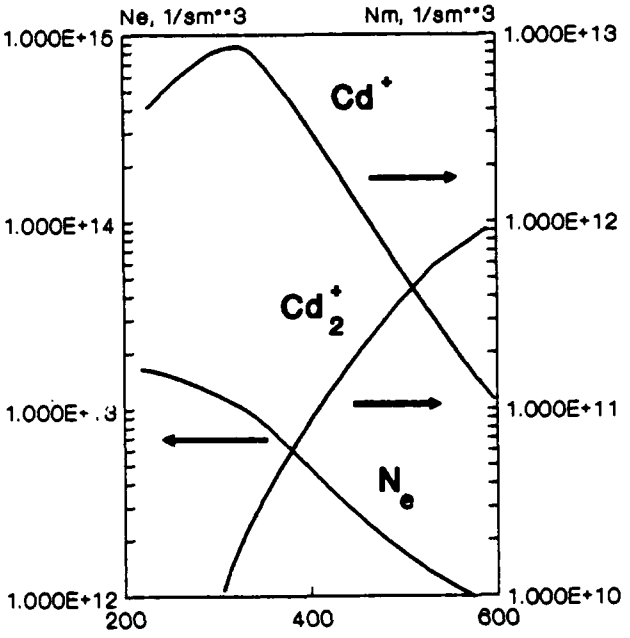


Fig.1b. Temperature dependences of electrons and some charged components of He-Cd plasma

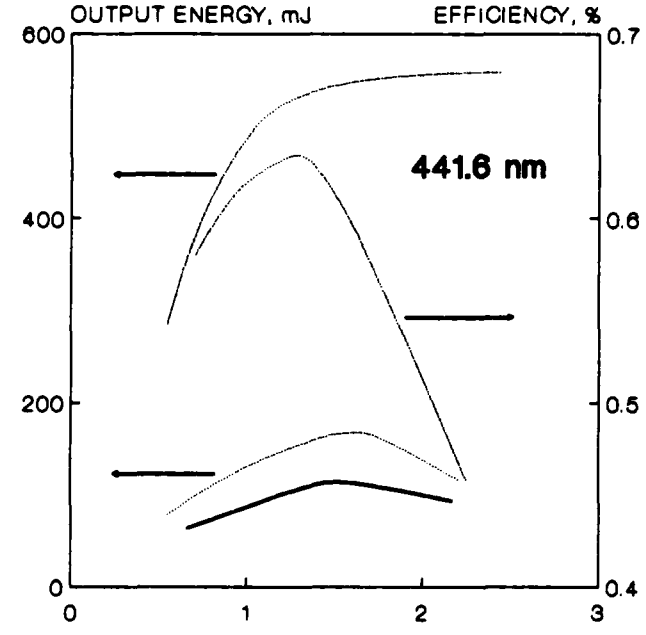


Fig.2a. Generation characteristics of the nuclear pumped He-Cd laser

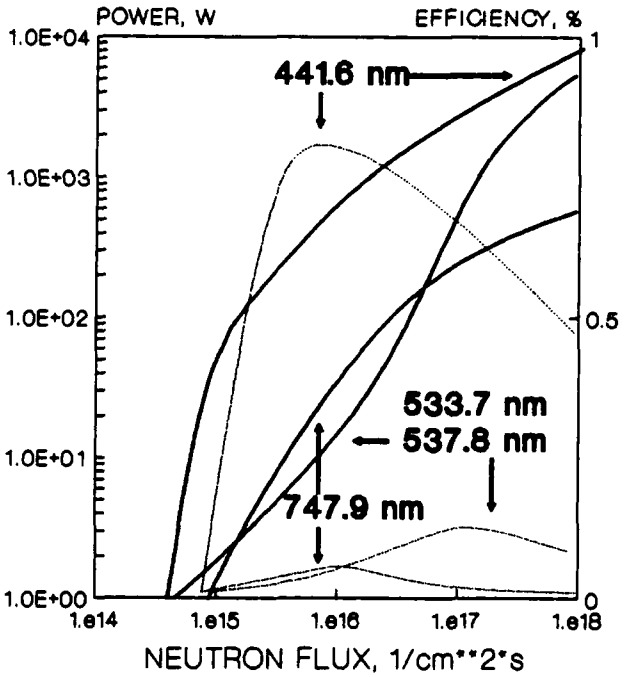


Fig.2b. Output power and efficiency of He-Cd and He-Zn lasers versus neutron flux (solid - power, dashed - efficiency).

Gasdynamic Phenomena in Nuclear-Reactor-Pumped Lasers

J. R. Torczynski
Sandia National Laboratories
Albuquerque, NM 87185-5800

Abstract

In nuclear-reactor-pumped lasers, the fission-fragment heating is spatially nonuniform and as such induces gas motion. The competing effects of heating nonuniformity and thermal conduction on overall gas motion and laser optical behavior are examined, and a parameter is developed which categorizes the induced gas flow into three regimes. The effect of fission-fragment heating on perturbations in the gas density field is also examined, and a scaling relation describing the reduction of the rms density perturbation is developed in terms of the pressure rise produced by the heating.

1. Introduction

Fragments from fission reactions induced by a pulse of neutrons from a nuclear reactor have been used to pump a variety of gas lasers.[1-10] These "nuclear-reactor-pumped" lasers offer several advantages over more conventional pumping schemes. First, the fission-fragment energy is used to excite atomic or molecular lasing states directly, rather than first being converted to heat, electricity, and possibly light with the attendant efficiency losses.[11] Second, the large power density associated with nuclear power implies a compact power source.[11]

Figure 1 shows a schematic diagram of one possible arrangement. The reactor serves as the source of fast neutrons, which are moderated by polyethylene. The resulting slow neutrons are incident on thin layers of fissionable material (coating the inner surfaces of the laser gas cell), which emit fission fragments into the adjacent gas. These fission fragments pump the lasing states and heat the gas. One difficulty in this approach is evident from Figure 1. The fission fragments enter the gas from the side walls in this arrangement and heat the gas in these regions more strongly than they heat the gas near the optical axis. This heating nonuniformity induces an inward flow and establishes density gradients perpendicular to the optical axis. Since gradients of the gas density are proportional to gradients of the refractive index, the laser gas acts as a temporally varying gradient-index lens. This gasdynamic lensing can be of strength sufficient to induce transitions in laser resonator stability (see Figure 2).[12-14]

In this paper, the effects of fission-fragment heating on the gas density field are examined. First, the overall gas motion resulting from the spatial nonuniformity of fission-fragment heating is studied, and the resulting flows are characterized in terms of the ratio of the duration of the heating to the thermal-conduction timescale. Second, the effect of fission-fragment heating on small perturbations in the gas density field is analyzed. The density-dependence of fission-fragment heating is shown to result in a damping of density perturbations. This damping is seen to be relatively broadband, and a scaling relation is developed for the reduction of the rms density perturbation level.

2. The Model Problem

A diagram of a typical laser cell is shown in Figure 3. The geometry here is rectangular, rather than cylindrical as in Figure 1. Since the fissionable material is located on the two side walls normal to the x-axis, the heating nonuniformity induces flow in the x-direction. Although there are heating nonuniformities in the y- and z-directions that also induce gas motion, these nonuniformities are usually minor compared to the nonuniformity in the x-direction and are neglected in this study.

The gas in the laser cell is taken to be a mixture of perfect gases with nonzero shear and bulk viscosities and thermal conductivity. Its motion is governed by the conservation equations for mass, momentum, and energy, in which variations are permitted only in time and in the x-direction (see the appendix). At the side walls, the gas velocity is assumed to vanish, and the gas temperature is taken to be the wall temperature (presumed to be the initial gas temperature). Fission-fragment heating appears in the energy equation as a large, transient, volumetric energy source term. This source term has the form $Q = Q_0 f[x;\rho] h(t)$, where Q_0 is the amplitude of the pumping, $h(t)$ is the time variation of the neutron flux and hence the heating, and $f[x;\rho]$ is the spatial variation of the heating. Figure 4 indicates the general forms of the functions f and h. The precise shape of the function f depends on the density field ρ since the gas molecules are essentially absorbers.[15-18] If the density field is made to vary in the laser cell, this variation in the distribution of absorbers produces a corresponding change in the function f: where the number of absorbers is increased, f is increased, and where the number of absorbers is decreased, f is decreased. Thus, gas motion and fission-fragment heating are coupled.[18]

The combination of fission-fragment heating and thermal-conduction loss induces a flow that moves gas toward the "coldest" spots and away from the "hottest" spots.[19] Here, the term "coldest" indicates the regions where the sum of the fission-fragment heating and thermal-conduction loss is smallest (most negative), and similarly the term "hottest" indicates the regions where the sum of fission-fragment heating and thermal-conduction loss is largest (most positive). This points out an interesting aspect of the induced flow. Fission-fragment heating is largest near the side walls and smallest at the center (see Figure 4); therefore, fission-fragment heating acts to induce flow inward toward the center. Thermal-conduction effects are most negative near the cold side walls and vanish near the center; therefore, thermal-conduction effects act to induce flow outward away from the center. Thus, the effects of heating nonuniformity and thermal conduction are oppositely directed, so the type of flow that results is determined by whichever effect is stronger.[19]

3. Gas-Flow Regimes

There are four timescales involved in describing the induced gas motion: t_A, the time required for an acoustic wave to travel from the center to the side walls; t_C, the time required for heat to be conducted from the center to the side walls; t_D, the duration of the heating (see Figure 4); and t_Q, the time required for the fission-fragment heating to raise the pressure by an amount comparable to the initial gas pressure. For conditions of interest, the acoustic timescale t_A is much smaller than the other three timescales. Because of this, the equations of motion can be acoustically filtered,[18-22] and the timescale t_A does not enter the resulting equations (the acoustically filtered equations are contained in the appendix).

Of the remaining three timescales, two dimensionless ratios may be formed. The ratio t_D/t_Q sets the scale, relative to the initial gas pressure, for the pressure rise induced by fission-fragment heating. The ratio t_D/t_C determines the flow type and is given by the relation

$$\frac{t_D}{t_C} \approx \frac{16(\gamma-1)k_0T_0t_D}{p_0L^2}, \tag{1}$$

where γ is the specific heat ratio of the gas, k_0 the initial thermal conductivity of the gas, T_0 the initial gas temperature, p_0 the initial gas pressure, and L the distance between the side walls. As such, t_D/t_C can be interpreted as a normalized thermal conductivity, so the magnitude of t_D/t_C determines the importance of thermal conduction over the duration of the pulse. Three distinct regimes of flow behavior are possible depending on the magnitude of t_D/t_C. In the negligible-conduction regime ($t_D/t_C \ll 1$), the flow is dominated by the spatial variation of the fission-fragment heating. In the dominant-conduction regime ($t_D/t_C \gg 1$), the flow is dominated by thermal-conduction effects. In the mixed regime ($t_D/t_C \sim 1$), fission-fragment heating and thermal-conduction effects are of comparable importance.

3.1 Negligible-Conduction Regime

The negligible-conduction regime corresponds to conditions for which $t_D/t_C \ll 1$. An analytical solution exists in the limit that this ratio becomes vanishingly small.[18-19] From this solution, it is seen that gas moves inward from the side walls toward the center of the laser cell. This is as expected since the center is the "coldest" region in the absence of thermal-conduction effects. This inward gas flow creates a central maximum in the density field, so the laser cell is optically focusing. The uniformity of the fission-fragment heating is improved by this flow since gas molecules (absorbers) are transported out of regions of large heating near the side walls into regions of small heating near the center. Another fact that emerges from the analytical solution is that the added *energy*, not the applied heating *power*, determines the shape of the density profile. Consider two experiments identical in all particulars except that in one case the heating is applied at half the power but for twice the duration of the other case. Since the same amount of energy is added in both cases, the same density profile is produced in both cases.

As an example, consider helium, initially at 300 K and 200 kPa, confined between side walls separated by a 1-cm gap and coated with 1-μm UO_2 layers. A constant power density of 3550 W/cm^3 is used to heat the gas for 0.1 ms. These conditions correspond to a value of 0.0095 for t_D/t_C. Figure 5 shows results from a simulation of the acoustically filtered equations (not the limiting analytical solution). The central density maximum is clearly seen and continues to grow with increasing energy addition. Note the appearance of thin thermal boundary layers adjacent to the side walls. These result from the nonzero value of t_D/t_C; nevertheless, the flow in the central region is relatively unaffected by thermal-conduction effects.

3.2 Dominant-Conduction Regime

The dominant-conduction regime corresponds to conditions for which $t_D/t_C \gg 1$. An analytical solution exists in the limit that this ratio becomes infinitely large.[19] From this solution, it is seen that gas moves outward from the center of the laser cell toward the side walls. This is as expected since the side walls are the "coldest" regions when thermal-conduction effects are very large. This outward gas flow creates a central minimum in the density field, so the laser cell is optically defocusing. The uniformity of the fission-fragment heating is degraded by this flow since gas molecules (absorbers) are transported out of regions of small heating near the center into regions of large heating near the side walls. Another fact that emerges from the analytical solution is that the applied heating *power*, not the added *energy*, determines the shape of the density profile. If the applied heating power is held constant, the density profile does not change even though energy is continually added.

As an example, consider helium, initially at 300 K and 200 kPa, confined between side walls separated by a 1-cm gap and coated with 1-μm UO_2 layers. A constant power density of 2.22 W/cm^3 is used to heat the gas for 160 ms (these values differ by a factor of 1600 from the values used in the previous example but maintain the same energy addition). These conditions correspond to a value of 15 for t_D/t_C. Figure 6 shows results from a simulation of the acoustically filtered equations (not the limiting analytical solution). The central density minimum is clearly seen and does not change much with increasing energy addition. The slight changes in the density field with increasing energy addition is indicative of the finite value of t_D/t_C.

3.3 Mixed Regime

The mixed regime corresponds to conditions for which $t_D/t_C \sim 1$. Unfortunately no analytical solution is known for this regime, so insight must be gleaned from numerical solutions for many different sets of conditions. The following observations can be made.[19] At early times in the pulse and for gas near the center, the motion resembles the negligible-conduction regime. However, at later times and for gas near the side walls, the motion resembles the dominant-conduction regime. Thus, the gas near the center moves toward the center, and the gas near the side walls moves toward the side walls. This complex gas motion creates a central density maximum and density minima propagating inward from the side walls toward the center, so both focusing and defocusing regions are present. Both the added energy and the applied heating power affect the gas motion in the mixed regime, and the uniformity of the fission-fragment heating is improved near the center but degraded near the walls.

As an example, consider helium, initially at 300 K and 200 kPa, confined between side walls separated by a 1-cm gap and coated with 1-μm UO_2 layers. A constant power density of 89 W/cm^3 is used to heat the gas for 4.0 ms (these values are the geometric means of the values used in the two previous examples and as such maintain the same energy addition). These conditions correspond to a value of 0.38 for t_D/t_C. Figure 7 shows results from a simulation of the acoustically filtered equations. The central density maximum and the density minima near the side walls are clearly seen. These minima travel noticeably inward during the pulse. Note that the curvature of the central density maximum remains relatively constant as the overall density falls in the central region. This phenomenon is often observed although it is not currently explained.

4. Density Perturbations

In the previous section, the effect of the combination of fission-fragment heating and thermal-conduction loss on the overall gas motion was considered. In this section, the effect of fission-fragment heating on small density perturbations is examined. Since density perturbations are hard to avoid and their presence generally exerts a detrimental effect on laser optical behavior, it is of

interest to examine the interaction of fission-fragment heating with density perturbations, particularly regarding growth, damping, or lengthscale change.

The basic effect of fission-fragment heating on density perturbations is illustrated in Figure 8. This figure shows an expanded view of a small portion of the density profile which contains two density perturbations. The positive perturbation contains more gas molecules (absorbers) and is heated more strongly than surrounding regions of gas. This excess heating creates a slightly larger pressure in the perturbation than in neighboring regions, and this pressure difference acts to transport gas away from the perturbation, reducing its height. Similarly, the negative perturbation contains less gas molecules (absorbers) and is heated less strongly than surrounding regions of gas. This shortfall of heating creates a slightly lower pressure in the perturbation than in neighboring regions, and this pressure difference acts to transport gas toward the perturbation, reducing its depth. Thus, fission-fragment heating smooths out density perturbations.

As an example, consider argon, initially at 300 K and 68.9 kPa, confined between side walls separated by a 1-cm gap and coated with 1-μm UO_2 layers. Figure 9 shows the evolution with increasing energy addition of two different initial density fields, one with perturbations and one without. To illustrate the role of fission-fragment heating in damping density perturbations, thermal-conduction effects have been suppressed, and artificially large density perturbations have been used for initial conditions (it is shown below that the perturbation amplitude does not matter). The inward flow of gas toward the center is evident for both the perturbed and unperturbed density fields. Moreover, the amplitude of the density perturbations is reduced with increasing energy addition. This fact is highlighted by Figure 10, which displays the difference between the perturbed and the unperturbed density fields for successive amounts of energy addition.

Careful scrutiny of Figure 10 reveals another aspect of the damping process. Both broad and narrow features exhibit the same amount of damping (for example, compare the broad feature near 0.42 cm to the narrow features near 0.38 cm). Figure 11 shows the evolution of two density profiles having perturbations with the same amplitudes but with wavelengths differing by a factor of 10. Note that both perturbations are contained within the same envelope at successive values of energy addition. The damping is thus seen to be broadband and relatively insensitive to wavelength.

The broadband nature of the damping process suggests that it can be characterized in terms of the rms density perturbation,

$$\Delta\rho_{\text{rms}} = \left[\frac{1}{L}\int_0^L (\rho - \rho_U)^2\, dx\right]^{1/2}, \tag{2}$$

where ρ is the perturbed density field and ρ_U is the unperturbed density field. The reduction in perturbation amplitude is given by $\Delta\rho_{\text{rms}}/\Delta\rho_{\text{rms},0}$, where $\Delta\rho_{\text{rms},0}$ is the initial rms density perturbation. Simulations of different cases can be used to determine the manner in which this reduction varies with increasing energy addition. Table 1 shows the conditions of four such cases, and Figure 12 shows the reduction in terms of the quantity $(\bar{p}/p_0)^{1/\gamma}$. In this representation, the results all collapse onto one line with a slope of -1, so the following scaling relation is determined:

$$\frac{\Delta\rho_{\text{rms}}}{\Delta\rho_{\text{rms},0}} \approx \left(\frac{\bar{p}}{p_0}\right)^{-1/\gamma} \tag{3}$$

If the perturbation amplitude is small compared with the initial gas density, the analytical solution for the negligible-conduction regime can be used to derive this result.[23] Note that this damping is algebraic in the pressure rise and thus requires large pressure rises to produce significant damping.

Table 1. Conditions for cases shown in Figure 12.

Symbol	p_{He} (kPa)	p_{Ar} (kPa)	T (K)	Gap L (cm)	UO_2 Thickness (μm)
△	0.0	68.9	300	1.0	1.0
▽	0.0	68.9	300	1.5	1.0
□	68.9	68.9	300	1.0	1.0
○	68.9	68.9	300	1.5	1.0

5. Conclusions

The gas motion in nuclear-reactor-pumped lasers induced by fission-fragment heating has been examined. The spatial nonuniformity of fission-fragment heating induces a flow of gas toward the center of the laser cell, whereas thermal-conduction effects induce flow toward the side walls. Since these effects are oppositely directed, the type of flow that results is determined by whichever effect is stronger. The ratio of the heating duration to the thermal-conduction timescale, t_D/t_C, characterizes the importance of thermal-conduction effects, and the flow can be categorized into three regimes depending on the value of this ratio. If t_D/t_C is much less than unity, then the flow is in the negligible-conduction regime, in which a central density maximum is produced and the added energy determines the height of the maximum. If t_D/t_C is much greater than unity, then the flow is in the dominant-conduction regime, in which a central density minumum is produced and the applied heating power determines the depth of the minimum. If t_D/t_C is comparable to unity, then the flow is in the mixed regime, in which both a central density maximum and density minima traveling inward from the side walls are produced and both the energy and the power influence the motion.

The density-dependence of fission-fragment heating is seen to result in damping of density perturbations. A scaling relation has been developed describing the reduction of the rms density perturbation in terms of the pressure rise produced by fission-fragment heating. This damping is broadband in the sense of being insensitive to the wavelength of the density perturbation. However, the algebraic nature of the scaling relation indicates that large pressure rises are required to produce significant damping.

Acknowledgments

The author gratefully acknowledges many discussions with Dan Neal, Joe Alford, Dave McArthur, Bill Sweatt, Bob Gross, Jim Rice, Paul Pickard, and Gerry Hays. This work was performed at Sandia National Laboratories, supported by the U. S. Department of Energy under contract number DE–AC04–76DP00789.

References

1. K. Thom and R. T. Schneider, *AIAA J.* **10**, 400–406 (1972).
2. D. A. McArthur and P. B. Tollefsrud, *Appl. Phys. Lett.* **26**, 187–190 (1975).
3. H. H. Helmick, J. L. Fuller, and R. T. Schneider, *Appl. Phys. Lett.* **26**, 327–328 (1975).
4. G. H. Miley, in *Laser Interaction and Related Plasma Phenomena* **4**, edited by H. Hora and G. Miley (Plenum, New York, 1976), pp. 181–228.
5. M. A. Prelas, M. A. Akerman, F. P. Boody, and G. H. Miley, *Appl. Phys. Lett.* **31**, 428–430 (1977).
6. R. J. De Young, Y. J. Shiu, and M. D. Williams, *Appl. Phys. Lett.* **37**, 679–6681 (1980).
7. A. M. Voinov, L. E. Dovbysh, V. N. Krivonosov, S. P. Mel'nikov, I. V. Podmoshenskii, and A. A. Sinyanskii, *Sov. Tech. Phys. Lett.* **7**, 437 (1981).
8. G. N. Hays, D. A. McArthur, D. R. Neal, and J. K. Rice, *Appl. Phys. Lett.* **49**, 363–365 (1986).
9. J. K. Rice, G. N. Hays, D. R. Neal, D. A. McArthur, and W. J. Alford, in *Proceedings of the International Conference on Lasers '86*, edited by R. W. McMillan (STS Press, McLean, VA, 1987), pp. 571–578.
10. D. A. McArthur, G. N. Hays, W. J. Alford, D. R. Neal, D. E. Bodette, and J. K. Rice, in *Laser Interaction and Related Plasma Phenomena* **8**, edited by H. Hora and G. Miley (Plenum, New York, 1988).
11. G. H. Miley, *Direct Conversion of Nuclear Radiation Energy* (American Nuclear Society, LaGrange, IL, 1970), Chaps. 3–4.
12. J. R. Torczynski and D. R. Neal, Sandia Report SAND88-1318, Sandia National Laboratories (1988).
13. D. R. Neal, J. R. Torczynski, and W. C. Sweatt, in *Proceedings of the International Conference Lasers '88*, edited by R. C. Sze and F. J. Duarte (STS Press, McLean VA, 1989), pp. 245–252.
14. D. R. Neal, W. C. Sweatt, and J. R. Torczynski, in *Current Developments in Optical Engineering III*, edited by R. E. Fischer and W. J. Smith, *SPIE Proceedings* **965**, 130–141 (1989).
15. G. H. Miley and P. E. Thiess, *Nucl. Appl.* **6**, 434–451 (1969).
16. J. C. Guyot, G. H. Miley, and J. T. Verdeyen, *Nucl. Sci. Eng.* **48**, 373–386 (1972).
17. A. K. Chung and M. A. Prelas, *Nucl. Sci. Eng.* **86**, 267–274 (1984).
18. J. R. Torczynski, *J. Fluid Mech.* **201**, 167–188 (1989).
19. J. R. Torczynski, in *Proceedings of the 5th AIAA/ASME Thermophysics and Heat Transfer Conference*, submitted (1990).
20. R. G. Rehm and H. R. Baum, *J. Res. Nat. Bur. Stand.* **83** (3), 297–308 (1978).
21. S. Paolucci, Sandia Report SAND82–8257, Sandia National Laboratories (1982).
22. J. R. Torczynski, in *Proceedings of the International Symposium on Nonsteady Fluid Dynamics*, submitted (1990).
23. J. R. Torczynski, *Nucl. Sci. Eng.*, submitted (1990).
24. R. C. Reid, J. M. Prausnitz, and B. C. Poling, *The Properties of Gases and Liquids* (McGraw-Hill, New York, 1986), pp. 514–518, 530–531.

Appendix

The equations describing the one-dimensional motion of a perfect gas can be acoustically filtered if the acoustic timescale is much smaller than other relevant timescales so that the Mach number of the induced flow is small.[18–22] Let the gas have a density field ρ, a pressure field p, a temperature field T, an energy field (per unit mass) e, a velocity field u, a specific heat ratio γ, temperature-dependent[24] shear and bulk viscosities μ and μ_v, and temperature-dependent[24] thermal conductivity k. Confine the gas between two side walls separated by a distance L, and heat the gas with the power density field Q. The gas motion is described by the perfect-gas equation of state and the conservation equations for mass, momentum, and energy:

$$p = R\rho T = (\gamma - 1)\rho e \ , \tag{A1}$$

$$\frac{\partial \rho}{\partial t} + \frac{\partial}{\partial x}\rho u = 0 \ , \tag{A2}$$

$$\frac{\partial}{\partial t}\rho u + \frac{\partial}{\partial x}\rho u^2 + \frac{\partial p}{\partial x} = \frac{\partial}{\partial x}\left[\left(\tfrac{4}{3}\mu + \mu_v\right)\frac{\partial u}{\partial x}\right] , \tag{A3}$$

$$\frac{\partial}{\partial t}\rho\left(e + \tfrac{1}{2}u^2\right) + \frac{\partial}{\partial x}\rho u\left(e + p/\rho + \tfrac{1}{2}u^2\right) = Q + \frac{\partial}{\partial x}\left(k\frac{\partial T}{\partial x}\right) + \frac{\partial}{\partial x}\left[u\left(\tfrac{4}{3}\mu + \mu_v\right)\frac{\partial u}{\partial x}\right] . \tag{A4}$$

Acoustic filtering is accomplished in the following manner. The gas pressure p is partitioned into two terms: $\bar{p}$, the average pressure in the x-direction; and $\hat{p} = p - \bar{p}$, the deviation from the average. Since the acoustic timescale is very small, it is not possible to build up large pressure gradients, so $\hat{p}$ is always very small compared to $\bar{p}$. Inserting the expansion $p = \bar{p} + \hat{p}$ into the equations of motion, neglecting small terms, and performing averaging yields the following set of equations:[18-21]

$$\frac{\partial \rho}{\partial t} + \frac{\partial}{\partial x}\rho u = 0 , \tag{A5}$$

$$\frac{\partial}{\partial t}\rho u + \frac{\partial}{\partial x}\rho u^2 + \frac{\partial \hat{p}}{\partial x} = \frac{\partial}{\partial x}\left[\left(\tfrac{4}{3}\mu + \mu_v\right)\frac{\partial u}{\partial x}\right] , \tag{A6}$$

$$\frac{d\bar{p}}{dt} = (\gamma - 1)\left[\bar{Q} + \overline{\frac{\partial}{\partial x}\left(k\frac{\partial T}{\partial x}\right)}\right] , \tag{A7}$$

$$\gamma\bar{p}\frac{\partial u}{\partial x} = (\gamma - 1)\left[\hat{Q} + \widehat{\frac{\partial}{\partial x}\left(k\frac{\partial T}{\partial x}\right)}\right] , \tag{A8}$$

$$\overline{(\cdot)} = L^{-1}\int_0^L (\cdot)\,dx , \qquad \widehat{(\cdot)} = (\cdot) - \overline{(\cdot)} . \tag{A9}$$

Equations (A5) and (A6) are the conservation equations for mass and momentum, respectively. The pressure term in the momentum equation incorporates $\hat{p}$ since $\bar{p}$ is a function of time alone by virtue of averaging. Note that $\hat{p}$ appears only in Equation (A6), so this equation needs to be solved only for times at which knowledge of $\hat{p}$ is desired. Equation (A7) shows that the mean pressure rise is determined by the total average heat addition (fission-fragment heating and thermal-conduction loss) and as such is the ideal gas law in an unusual form. Equation (A8) determines the gas velocity in terms of the excess heating. If the sum of the excess fission-fragment heating and the excess thermal-conduction loss is positive, then $\partial u/\partial x$ is positive and the flow is locally expansive: gas is transported away from points with heating that is larger than average. If the sum of the excess fission-fragment heating and the excess thermal-conduction loss is negative, then $\partial u/\partial x$ is negative and the flow is locally compressive: gas is transported toward points with heating that is smaller than average.

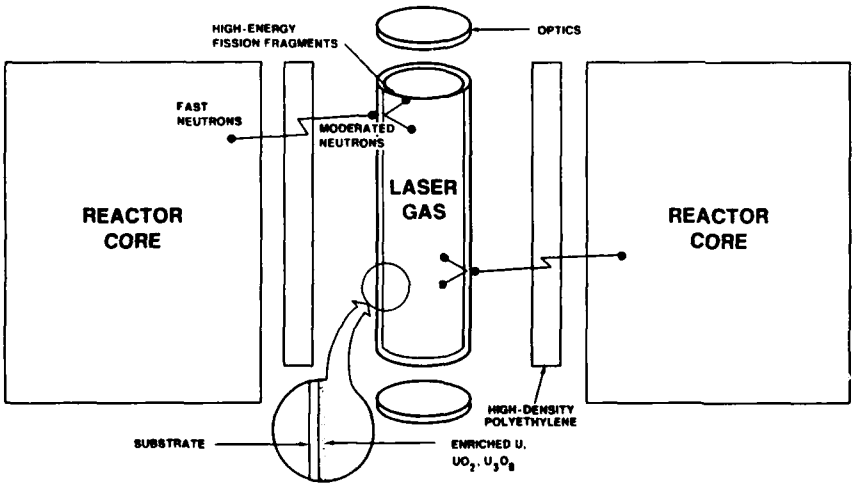


Figure 1. Schematic diagram of a nuclear-reactor-pumped laser experiment.

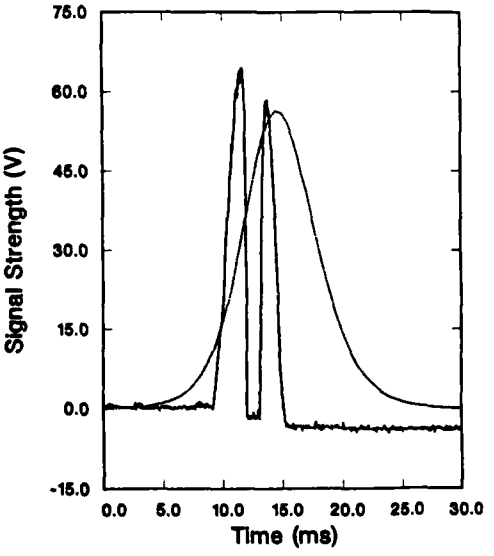


Figure 2. Lasing intensity (solid curve) and pumping pulse (dotted curve). Resonator stability transitions induced by gas-dynamic lensing result in the lasing termination and reinitiation seen at 12 ms and 13 ms, respectively (peak pumping is at 15 ms).

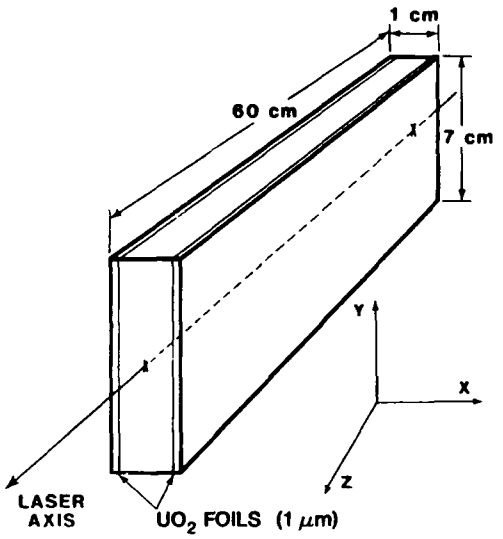


Figure 3. Diagram of a rectangular nuclear-reactor-pumped laser cell.

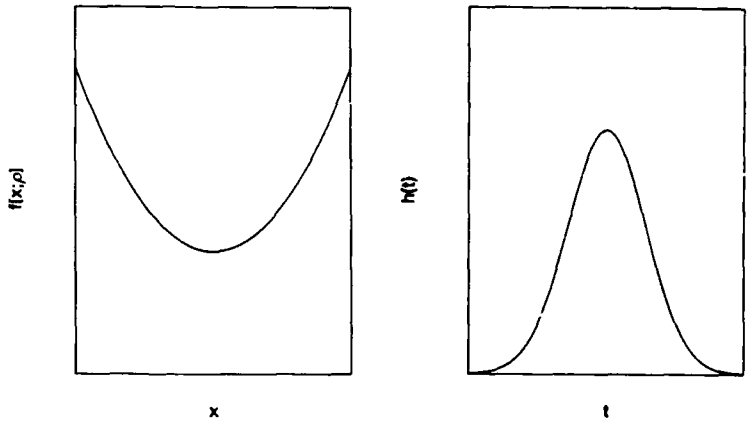


Figure 4. The spatial variation of fission-fragment heating is shown on the left. It is largest near the side walls and smallest near the center. The temporal variation of fission-fragment heating is shown on the right.

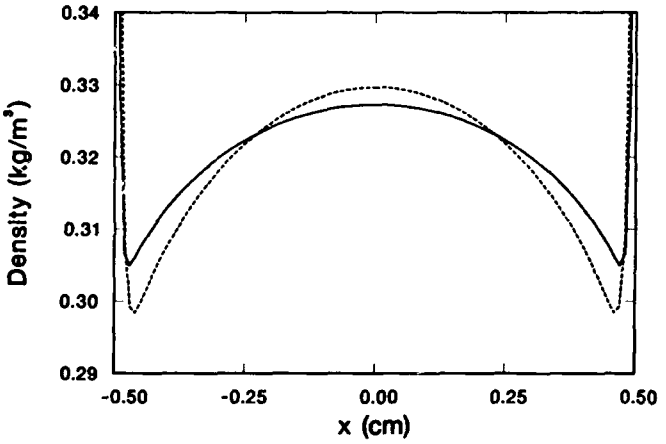


Figure 5. Density profile for a case in the negligible-conduction regime: solid curve, midway through the pulse; dashed curve, end of the pulse.

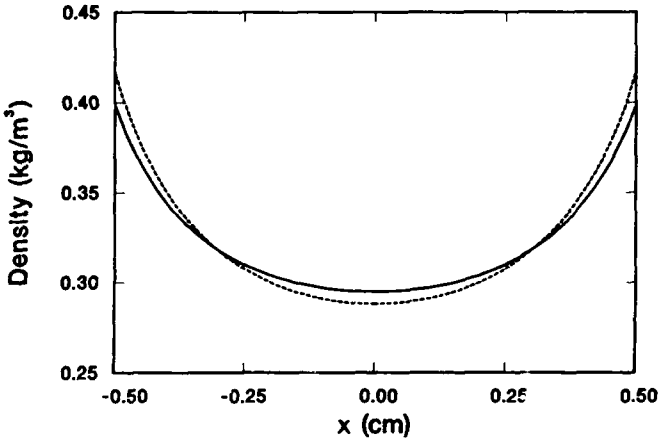


Figure 6. Density profile for a case in the dominant-conduction regime: solid curve, midway through the pulse; dashed curve, end of the pulse.

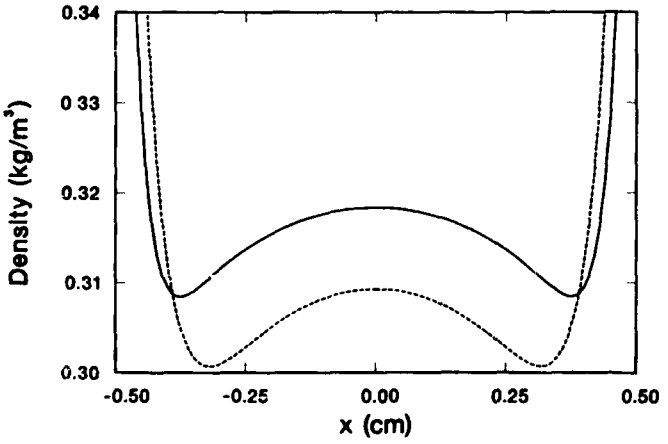


Figure 7. Density profile for a case in the mixed-conduction regime: solid curve, midway through the pulse; dashed curve, end of the pulse.

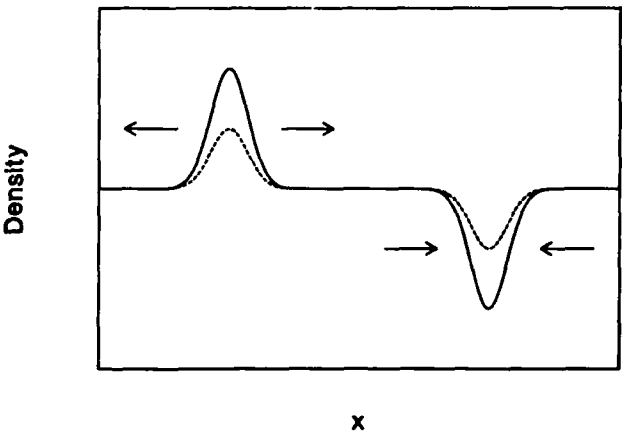
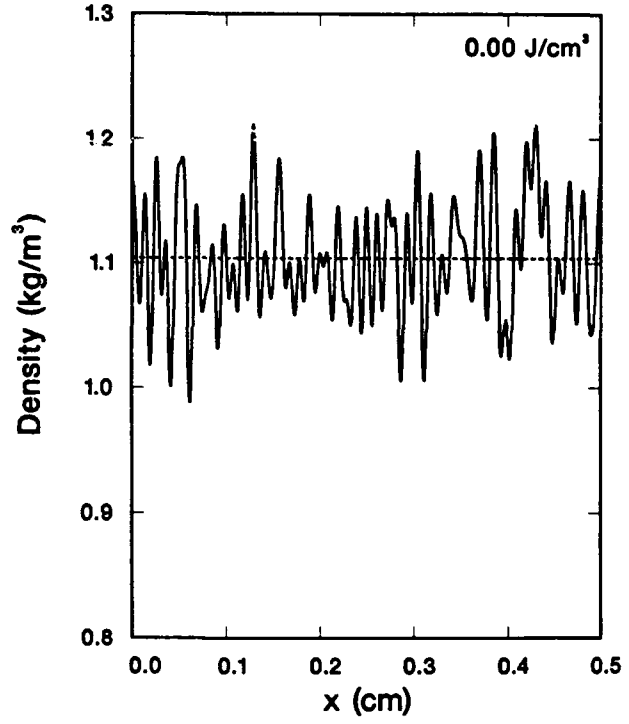
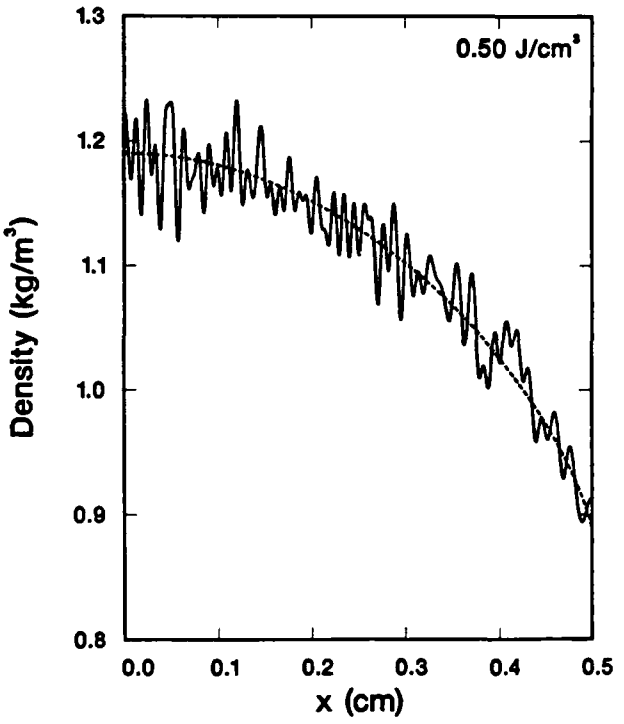
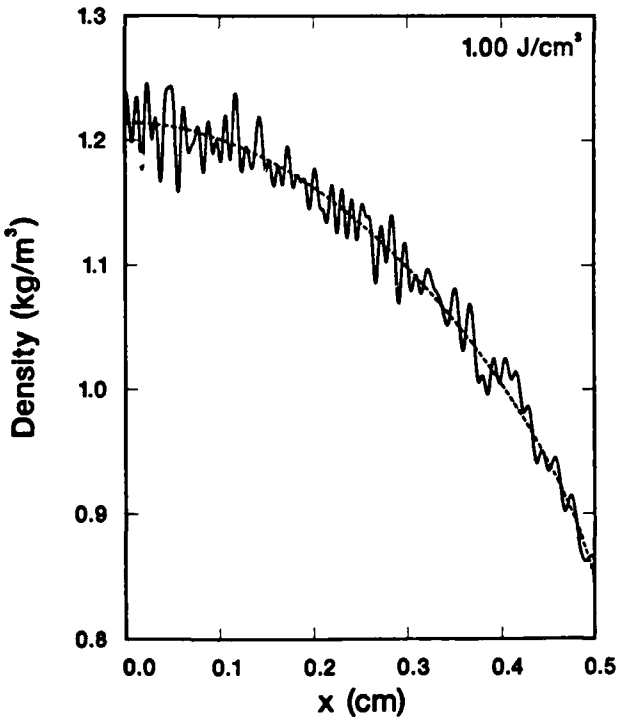


Figure 8. Expanded view of a small portion of the density profile (solid curve) with two density perturbations. These perturbations are smoothed (dashed curve) by fission-fragment heating. Arrows indicate the induced flow.







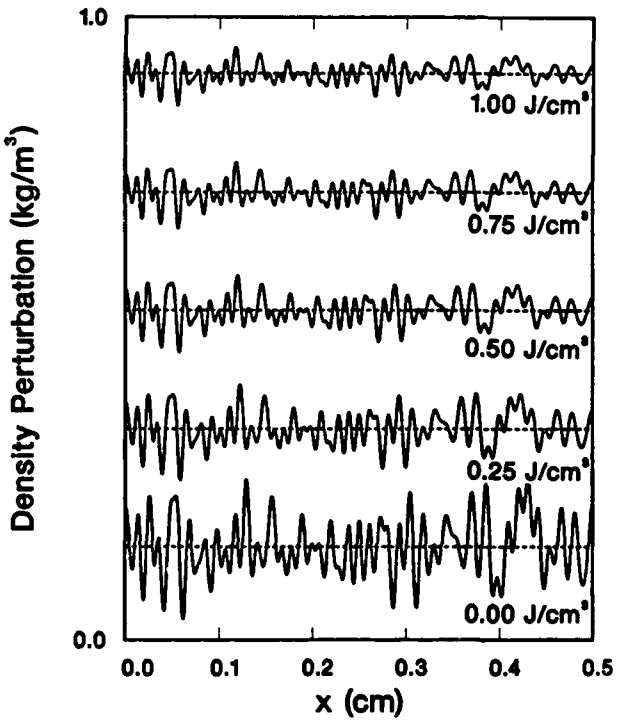


Figure 9. Density profiles at successive amounts of energy addition: solid curves, perturbed density field; dashed curves, unperturbed density field. Profiles are symmetric and thus are shown from center to wall, rather than from wall to wall.

Figure 10. The density perturbation profiles (the difference between the perturbed and the unperturbed profiles) are shown as a function of energy addition.

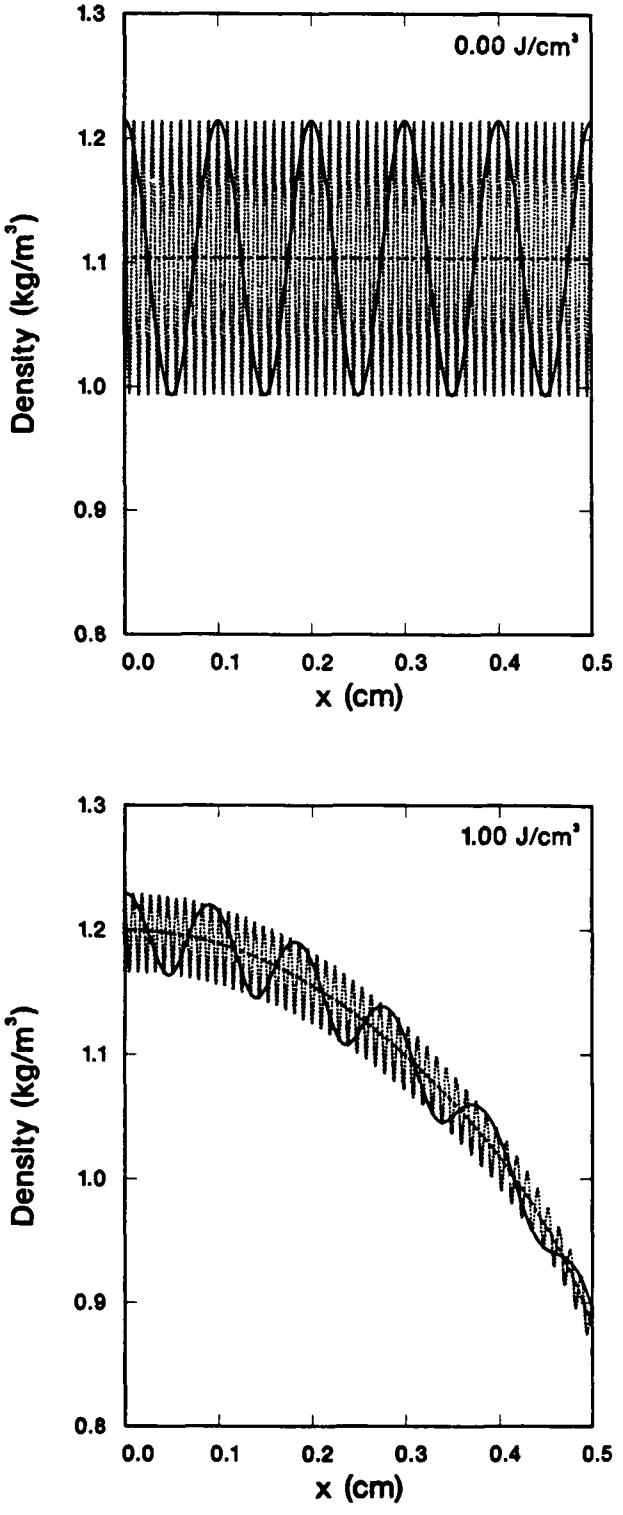


Figure 11. Two density profiles having perturbations with greatly differing wavelengths evolve in a similar fashion.

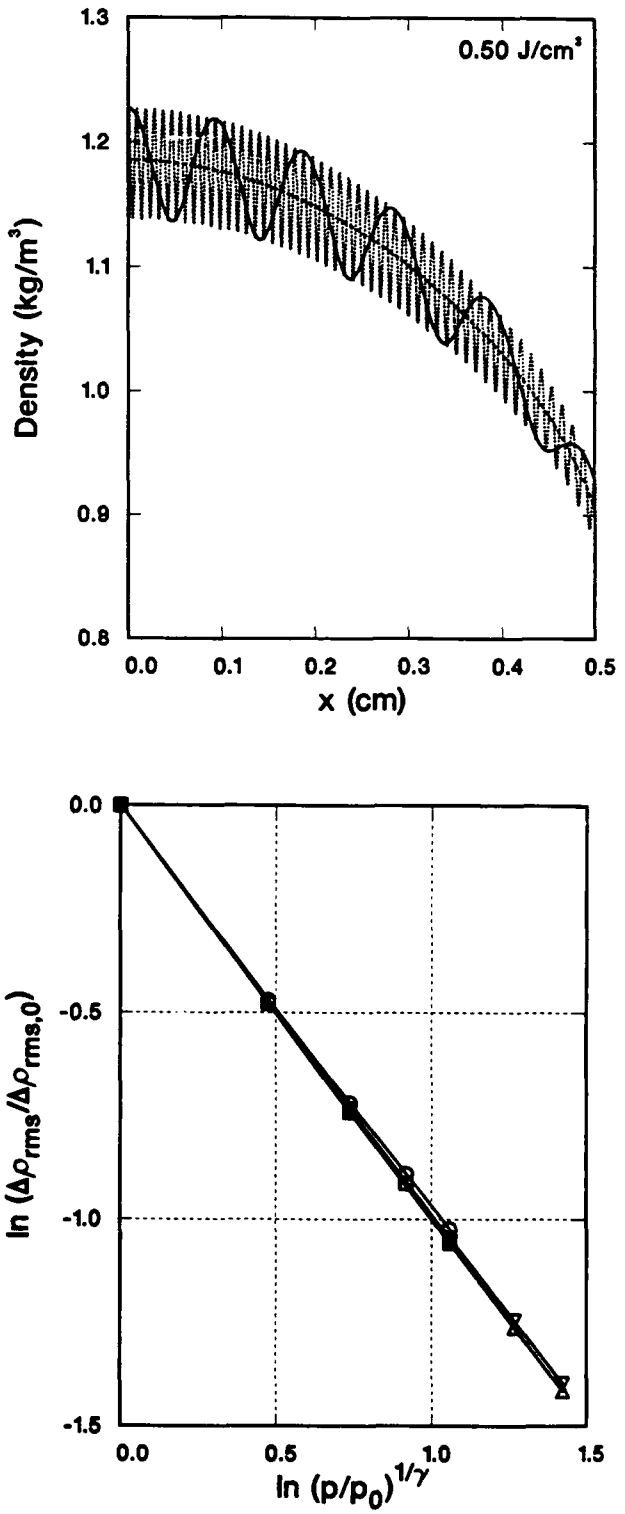


Figure 12. The quantity $\ln(\Delta\rho_{rms}/\rho_{rms,0})$ is plotted against $\ln(\bar{p}/p_0)^{1/\gamma}$ for a variety of different cases (see Table 1). The data exhibit a scaling relation.

NUCLEAR-DRIVEN SOLID-STATE LASERS

by Mark A. Prelas

Fusion Research Laboratory, Nuclear Engineering Program, University of Missouri-Columbia, Columbia, MO 65211

Abstract

A total system efficiency of 3% is calculated for very high average power active mirror solid-state laser amplifiers of co-doped material, such as Nd:Cr: GSGG, pumped by visible nuclear-driven alkali metal excimer fluorescence. The fluorescence is transported around a radiation shield, separating the fluorescer and the laser, by a large diameter-to-length ratio hollow lightpipe. Parameters for a system with peak power of 6 MW for 1 ms pulses at 1 Hz for an average power output of 6 kW are presented. This type of system would require the development of a small 200 kW thermal nuclear reactor (similar in size to small University research reactors). A much larger system can be developed as well.

Introduction

This paper describes a method of remotely driving solid-state lasers with nuclear-generated fluorescence sources. In the first part of this paper, the method and scaling will be described. The second part of this paper will discuss experimental results of small scale experiments used to verify the remote pumping technique.

The keys to achieving solid-state lasers with very high average power output are the pumping geometry and the pumping source. To ensure beam quality, the pumping geometry must be one that produces thermal gradients only in the direction of propagation, i.e. a large diameter thin disk, insulated on the edge and uniformly illuminated and cooled on the face. The then unavoidable axial gradient can be minimized by keeping the disk thin and using the STON effect [1]. The effects of the minimized axial gradient are themselves minimized by double passing through the laser medium.

Geometry has been a problem because large diameter disks have been available only in Nd:glass, which has a high saturation intensity, narrow absorption bands, and poor thermal conductivity. Nd:YAG has much better laser and thermal properties, but even narrower absorption bands and can not be grown in large diameters. Pump sources able to meet the demands of large saturation intensity and narrow absorption bands have been inefficient, expensive, and of limited area, making uniform illumination difficult.

New Nd^{+3},Cr^{+3} co-doped solid-state laser materials that can be grown in large diameters [2], and which boast both relatively low saturation intensities and broad absorption spectra, which make them easier to pump, and which have the high thermal conductivity of crystals (relative to glasses), such as GSGG [3], promise to change this by making possible the use of pump sources that were not previously feasible. One of those pump sources may be nuclear-driven fluorescers.

Nuclear-driven fluorescers (NDFs) utilize charged particles from nuclear reactions, such as fission, to excite fluorescer gases. While limited to charged particle power densities of <10 kW/cm^3, nuclear excitation can efficiently and uniformly excite large volumes without additional power conversion hardware [4]. NDFs are inherently high average power quasi steady-state devices, but the deleterious effects of nuclear radiation, as well as low peak fluorescence intensities, have made NDFs impractical for pumping solid-state lasers. We have developed a new geometry for NDFs that solves the radiation problem by shielding the laser from radiation and using a lightpipe to transport the fluorescence around the shield. This geometry also substantially concentrates the fluorescence which, combined with the lower saturation intensity requirements, brings the required pumping power density into the range of NDFs.

The remotely-located nuclear-driven fluorescer concept is illustrated in Figure 1. Key features are: 1) the use of a visible nuclear-driven excimer fluorescer that will efficiently produce photons that can be absorbed by solid-state laser media and 2) a large diameter to length ratio hollow "lightpipe" that efficiently transports the fluorescence around the radiation shield to the laser medium. While similar in concept, this approach varies significantly in detail from one we proposed previously for pumping photodissociation excimer gas lasers [5], in which the fluorescer and laser media were separated by only a thin window. That geometry was dictated by the facts that the fluorescence was VUV and could not be transported long distances (one or two reflections), that the gas laser medium was not damaged by radiation, and that the larger saturation intensity of the gaseous medium required higher power densities. Even though the laser medium was not subject to radiation damage, optics -- even thin windows -- have proved to be quite sensitive to radiation-induced absorption, particularly in the UV. Radiation-induced absorption is much less of a problem for visible fluorescence. The desire to remove the optics from the radiation field and to switch to the visible, combined with the recent advances in solid-state laser materials, led us to solid-state lasers.

Visible Nuclear-Driven Fluorescers

The requirements for an NDF laser pump are 1) efficient conversion of fission fragment energy to light, 2) wavelength of the fluorescence within the laser medium's absorption band and long enough to be efficiently reflected by the walls of the fluorescence cell and lightpipe, and 3) transparency to its own output. At the pressures of hundreds of torr needed to stop fission fragments before they hit the wall, resonance line radiators are highly self-absorbed so that, for the long path lengths in the fluorescer inherent with NDFs, excimer fluorescers are preferred. With

excimers the ground state of the molecule is unstable so that the molecule dissociates almost immediately after radiation and only a small amount of the radiation gets reabsorbed. Yet, because they radiate to the ground state from the first excited level or higher, and because there is usually only one radiation channel, their fluorescence efficiency is high, as high as 50% for rare-gas excimers. Most excimers, however, tend to be efficient fluorescers only at short wavelengths because the initial excited state is formed in rare-gas buffers which have large W* values. Thus only a few of the well known rare-gas, rare-gas halide, and metal halide excimers fall within the visible, mostly in the metal halides, and the efficiencies tend to be in the 10-15% range.

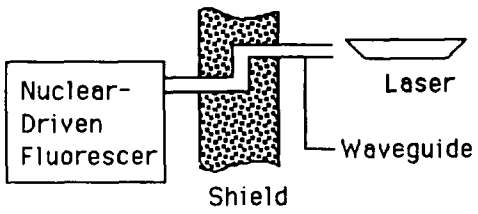


Figure 1. Nuclear-pumping using a remotely located nuclear-driven fluorescer. Isolation of the laser from radiation enables the use of a solid-state laser medium

Since the photon energies of low saturation intensity solid-state lasers are 1-2 eV, to achieve a reasonable laser system efficiency, the energy cost or W* value of the fluorescence photon precursor must be minimized. This means the use of an atom with low excited state energies and first ionization energy but, to avoid wasteful higher ionizations, a high second ionization energy. The materials that best fulfill these criteria are the alkali-metals. Table 1 lists first and second ionization potentials, I_1 and I_2, estimated W* value, excimer radiation wavelength, λ_{ex} [6], and the temperature required to provide a vapor pressure of 100 torr, T_{100} [7], for each of the alkali-metals. Since published W* values, $W^*=W/(1+N_{ex}/N_i)$, for alkali-metals do not exist, they are estimated as 1.2 times I_1, in analogy to the W^*/I_1 values we calculate from published [8] W and N_{ex}/N_i values for rare and molecular gases. Additionally, the D-line radiation efficiency of low pressure sodium lamps is about 34% of the power deposited in the vapor, which translates to an effective energy absorbed per photon emitted of $1.2 \cdot I_1$ in agreement with the W* estimates.

TABLE 1. Alkali Metal Properties

Alkali Metal	λ_{ex} (nm)	I_1 (eV)	I_2 (eV)	W^*_{est} $=1.2\ I_1$	$\frac{h\nu_{ex}}{W^*_{est}}$	T_{100} (C)
Li	459	5.36	75.3	6.4	0.42	1097
Na	437	5.12	47.1	6.1	0.46	701
K	575	4.32	31.7	5.2	0.42	586
Rb	605	4.16	27.4	5.0	0.41	514
Cs	713	3.87	23.4	4.6	0.37	509

Dimers exist at significant densities in electrically excited alkali-metals, but only in the bound singlet ground state. However they are formed in both singlet and triplet excited states. At the high power densities of lamp and most other electrically pumped systems, the triplet states are rapidly converted to singlet states by collisions with electrons. The singlet radiation is then absorbed by the high density of ground states. While the excimer radiation from sodium lamps, either at low or high pressure, is normally quite small, the excitation conditions typical of lamps — high power and electron density — are the opposite of those required for producing excimer radiation. The excimer bands were first clearly observed in potassium by Rebbeck and Vaughn [9], in an unusual discharge with very low power and electron density, similar to that produced by nuclear excitation. The strongest radiation under these conditions was the excimer band.

Coupling

Figure 2 traces a visible fluorescence photon from its emission in the NDF to its absorption in the solid-state laser medium. In the fluorescence cell, fission fragments from reflectively coated fissioning source material, with dimensions of a few μm,, present as an aerosol [4,5] or loaded in a "glass wool" [10], excite an alkali-metal excimer fluorescer to emit visible photons which reflect off the source material and the cell walls and are transmitted through the fluorescer/fuel mixture and the cell window to the hollow lightpipe. Tapering the walls of the fluorescer cell reduces the angular spread of the fluorescence, improving both extraction efficiency and transmission by the lightpipe, which, due to this and its high diameter-to-length ratio, transmits >90% of the fluorescence to an active mirror laser amplifier, similar to one developed at the U. of Rochester [11]. Since the fluorescence profile in the lightpipe is uniform, so is the absorbed power in the active mirror, minimizing radial temperature gradients. Both pump and laser are double passed, minimizing the effects of the unavoidable axial temperature gradients.

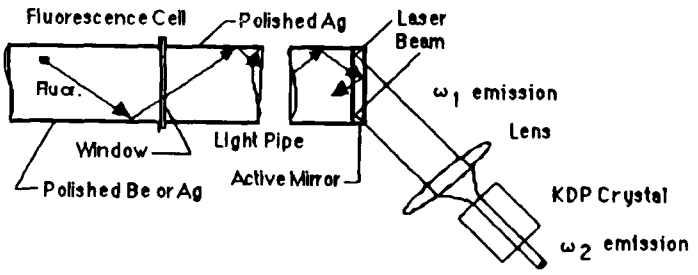


Figure 2. Coupling of visible nuclear-driven fluorescence to an active mirror solid-state laser amplifier.

A number of loss mechanisms make the coupling of the fluorescence to the laser less than perfect. They include 1) absorption of the fluorescence within the fluorescence cell by either the fluorescer or by the fuel, with which is mixed; 2) absorption by the reflecting surfaces of the fluorescence cell due to an absorbing film, which may be present, and to less than perfect reflectivity; 3) absorption in the output window due to radiation-induced absorption or the deposition of a film of fuel or fluorescer; 4) absorption due to the less than perfect reflectivity of the lightpipe walls,

especially at angles neat the principle angle for the π-polarized component of the fluorescence; 5) gaps in the lightpipe waveguide or the fluorescence cell wall to allow for cooling; and 6) imperfect absorption in the laser medium.

Reabsorption in the fluorescer is minimized by using an excimer. By design the reactor core fuel loadings do not exceed a few mg/cm^3 so that absorption by the fuel is small [4]. Film formation on cell walls is minimized by maintaining them at elevated temperatures. In the visible, radiation-induced absorption in the thin output window is drastically reduced by thermal annealing [12], at the high temperatures characteristic of both alkali-metal vapors and NDFs, and by photobleaching [12-13].

Although the total internal reflection of solid lightpipes is attractive, they have problems with radiation-induced absorption, acceptance angle, and excessive mass. Hollow lightpipes minimize radiation-induced absorption, can be quite light and their acceptance angle is essentially ±90°. However, they do not reflect perfectly and, at large angles with respect to the direction of propagation, a large number of reflections is required even for propagating short distances. Thus the number of reflections must be kept to a minimum by using a large diameter to length ratio. This ratio is maximized by combining the fluorescence, from as many cells as are required to produce a critical reactor, to feed only one large diameter lightpipe at each end of the core as shown in Figure 3. At the active mirror end, the lightpipe would split to match the transverse dimensions of the active mirrors. The reflecting material will probably be silver because it has the highest reflectivity with the least angle dependence at the wavelengths of interest. We calculate a transmission of 0.9, at 550 nm, for a 5-m long silver coated hollow lightpipe with a diameter of 1.2-m and two 90° bends, such as is shown in Figure 3.

Due to the large angular spread of the fluorescence, the laser disk must be located very close to the end of the waveguide to minimize losses. This probably precludes the use of brewster angle arrangements and pumping from both both faces, but is compatible with an active mirror configuration as is shown in Figs. 2 and 3. A small cooling gap for cooling between the end of the lightpipe and the disk will not increase losses greatly because most of the fluorescence at angles near 90° is highly attenuated by the large number of reflections.

Performance Estimate

We have estimated the performance of a large-scale remote NDF pumped solid-state laser such as shown in Figure 3., with a core made up of 24 fluorescence cells with a length of 1.2 m and an inside diameter of 0.20 m for a total active core volume of 1 m^3. The cells have a Be wall, coated with silver and 1/4 λ of diamond or sapphire, and sapphire output windows. The reactor produces 1 ms pulses at 1 Hz. Peak power is 510 MW and average power is 510 kw. The peak charged particle power density in the fluorescer is 100 W/cm^3. The efficiency of each of the conversion steps is listed in Table 2. For a fluorescence efficiency of 40% (Table 1), the peak fluorescence power is 40 MW.

The laser performance is based on the alexandrite peak absorption coefficient of 3 cm^{-1} at 600 nm. An alexandrite crystal with a 0.77 cm thickness will absorb 99% of the input intensity. The power density in the 0.77 cm thick crystal will be 3735 W cm^{-3} which is well above the predicted threshold value show in Table 3. The fluorescence intensity at the surface of the alexandrite active mirror is 3 kW/cm^2. With a spectral matching efficiency of 50%, an active mirror thickness of 0.5 cm, a Cr doping such that the absorbed power fraction is 80%, and assuming a fluorescence lifetime of 260 μs [3], the average upper state density is 2.6x10^{18}cm^{-3} and the stored energy is 0.5 J/cm^3. Using an effective σ_e for alexandrite of 0.2x10^{-19} cm^2 [2], the small signal gain is 0.13 cm^{-1} and, assuming an extraction efficiency of 80%, the extracted laser power is 6 MW. The total system efficiency, nuclear power to light power, is 3%. If higher fluorescence or spectral matching efficiencies had been assumed, the total system efficiency would be even higher, as shown in Table 2.

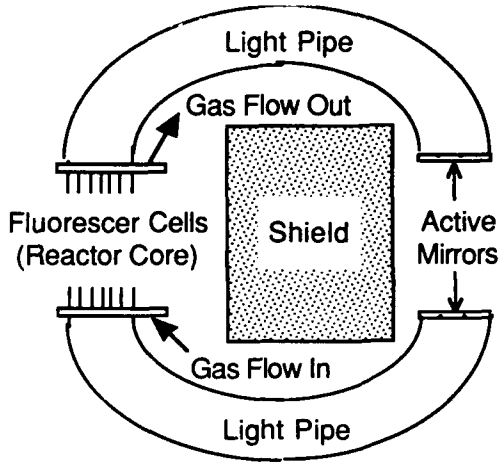


Figure 3. Layout of Remote Nuclear-Driven Fluorescer Pumped Solid-State Laser showing locations of the fluorescence cells (which together comprise the reactor core), radiation shield, lightpipes, and active mirrors.

Conclusion of Simplified Feasibility Study

We have presented a promising new concept, the remote nuclear-driven fluorescer, for pumping very high average power solid-state lasers. We have presented an example system with peak power of 6 MW, average power of 6 kW, and total system efficiency of 3% We have presented a promising new concept, the remote nuclear-driven fluorescer, for pumping very high average power solid-state lasers. We have presented an a tuneable, frequency tripled alexandrite laser as an example system. Nuclear-driven alkali metal excimers are used as the pump photon source. The pump photon source is excited by 1 ms nuclear reactor pulses, at a 1 Hz frequency. (Through the use of mode locking techniques this 1 ms output can be modified to produce five 10-20 ns pulses in a 1 ms burst.) Tuneable laser output at ω_1 emission between 700 to 818 nm, ω_2 emission between 350 to 409 nm, and ω_3 emission between 233 to 273 nm with a peak power of 6 MW at a 1

Hz frequency, an average power of 6,000 W, and a total system efficiency of 3% is predicted by our initial modeling.

TABLE 2. Potential Efficiency of Solid-State Laser Pumped by Remotely Located Nuclear-Driven Fluorescer.

Type of Efficiency	Efficiency
Nuclear-Pumping Efficiency	0.6
Alkali Fluorescence Efficiency	0.2 to 0.4
Cell Extraction Efficiency	0.7
Lightpipe Transmission Efficiency	0.96
Spectral Matching Efficiency	0.5 to 0.9
Active Mirror Absorption Efficiency	0.8
$\lambda_{pump}/\lambda_{laser}$ (605 nm /1.05 μm)	0.6
Laser Extraction Efficiency	0.9
Frequency Tripling Efficiency	0.5 to 0.7
Mode Locking Efficiency	0.9
Total Efficiency	**0.0078 to 0.04**

Other Potential Laser Media

Even though an alexandrite system was presented other potential laser media may be used as well. In addition to alexandrite ($Cr:BeAl_2O_4$), co-doped GSGG (Nd:Cr:GdScGa-Garnet), chromium-doped GSGG (Cr:GdScGa-Garnet), emerald ($Cr:Be_3Al_2Si_6O_{18}$), and titanium:sapphire ($Ti:Al_2O_3$) are candidate materials [5].

Table 3. Properties of laser media.

Medium	ω_1 (μm)	σ_{se} (10^{-19} cm^2)	τ_{ul} (μs)	k $(\frac{W}{m\text{-}K})$	Threshold Power Density* (Wcm^{-3})	Size** (cm)
Nd Cr GSGG	1 06	1 3 at 300K	222	6	115	9 6x19x0 5
Cr:GSGG	0 75 to 1 0	0.1 at 300K	120	6	1149	9 6x19x0 5
Alexandrite	0 7 to 0 82	0 2 at 450K	260	23	636	r=1, l=10
Ti Al_2O_3	0 72 to 0 92	4 1 at 300K	3.2	??	3024	r=3, l=15
Emerald	0 73 to 0 81	0.2 at 300K	200	??	827	??

*Estimated threshold power density, and ** size presently achievable with modern growing techniques.

Nd:Cr:GdScGa-Garnet has excellent properties in that the product of the stimulated emission cross section and upper laser level lifetime is greater than that of alexandrite (by approximately a factor of 2) thereby being easier to pump, but has a non-tuneable ω_1 emission of 1060 nm. Additionally, Nd:Cr:GdScGa-Garnet is a much easier crystal to grow than alexandrite. This material has a high probability of working in the proposed concept (see Table 3). As shown in Figures 4 and 5, Cr co-doped crystals have broader absorption bands than do Nd doped crystals.

Conversely, $Ti:Al_2O_3$ has a much lower stimulated emission cross section and upper laser level lifetime product (by approximately a factor of 100), has a ω_1 emission between 720 to 920 nm, and is a much easier crystal to grow then alexandrite. It may be possible to use multiple fluorescence cells to produce enough pump intensity from visible excimer photon sources to drive a $Ti:Al_2O_3$ laser.

Of the materials listed in Table 3, emerald is the most difficult to grow. However, emerald has the lowest power density threshold next to Nd:Cr:GSGG and alexandrite.

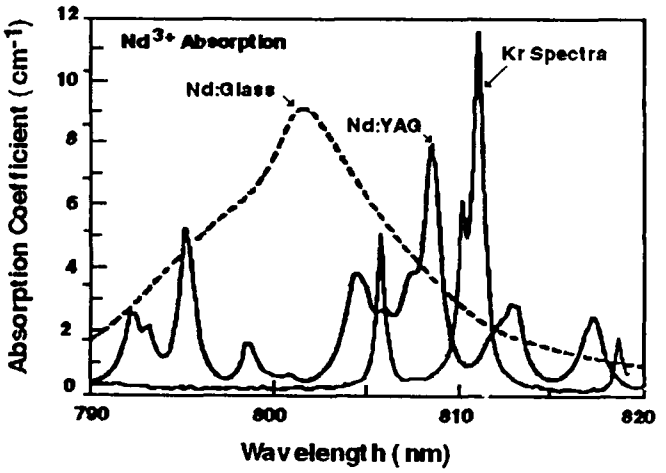


Figure 4. Nd:YAG and Nd: Glass Absorption Bands. Fluorescence Spectra from nuclear-driven Kr is superimposed.

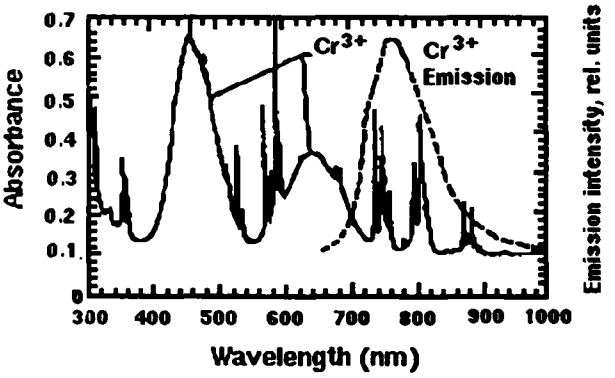


Figure 5. Absorption bands for the Nd,Cr:GSGG crystal.

Experimental Results

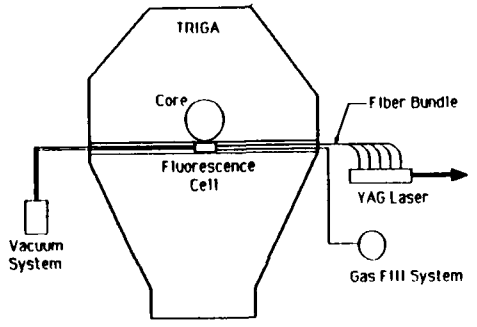
The remotely driven solid-state laser concept study was initiated by through the development of a ray tracing computer code called "Concentrator" [14]. This code was designed to examine the propagation of photons in a cylindrical cavity with reflective walls, windows, and various fill media. Using the code "Concentrator", an small scale experiment was designed to demonstrate the nuclear remotely-driven solid-state laser concept.

Since the cost of building an alkali excimer fluorescence cell was beyond the budget of this experiment, a much less expensive rare gas fluorescence cell was designed. The

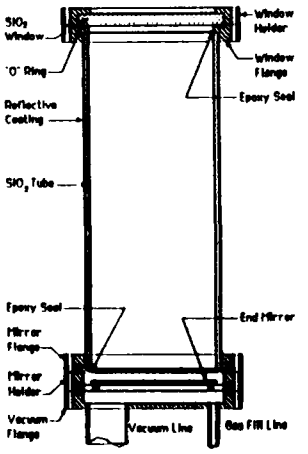
cell used the $^3He(n_{thermal},p)T$ reaction to produce the energetic ions to excite the rare gas. In addition, a 1 cm^2 fiberoptic bundle was used for the waveguide, rather than a hollow waveguide, due to expense. The individual fibers at the output were coupled to a Nd:YAG laser rod.

The crucial elements to the experiment were to 1) generate nuclear-driven fluorescence, 2) absolutely calibrate the optical system in a high radiation environment, 3) absolutely calibrate the nuclear-driven fluorescence source, 4) demonstrate absorption of the nuclear-driven fluorescence by the Nd:YAG laser rod, and 5) demonstrate the concept of remotely pumping a solid-state laser media. All of these goals were experimentally achieved.

The experimental set is shown in Figure 6. Here, the reaction cell is placed next to the reactor and a fiberoptic waveguide (using 225 μm fused silica fibers with a plastic clad) is used to transport nuclear-generated fluorescence to the Nd:YAG laser rod. The optical system and the nuclear fluorescence source were calibrated with the set up shown in Figure 7. This calibration set up utilized a NBS traceable calibrated tungsten-halogen lamp for the light source. The fiberoptic bundle was placed in the reactor and the optical system detectors were absolutely calibrated.



Schematic Drawing of
Nuclear Fluorescence Pumped Nd:YAG Laser Experiment.



Fluorescence Cell for
Nuclear Fluorescence Pumped
Nd:YAG Laser Experiment

Figure 6. Set up of the Nd:YAG experiment using the University of Illinois's TRIGA reactor and the reaction cell.

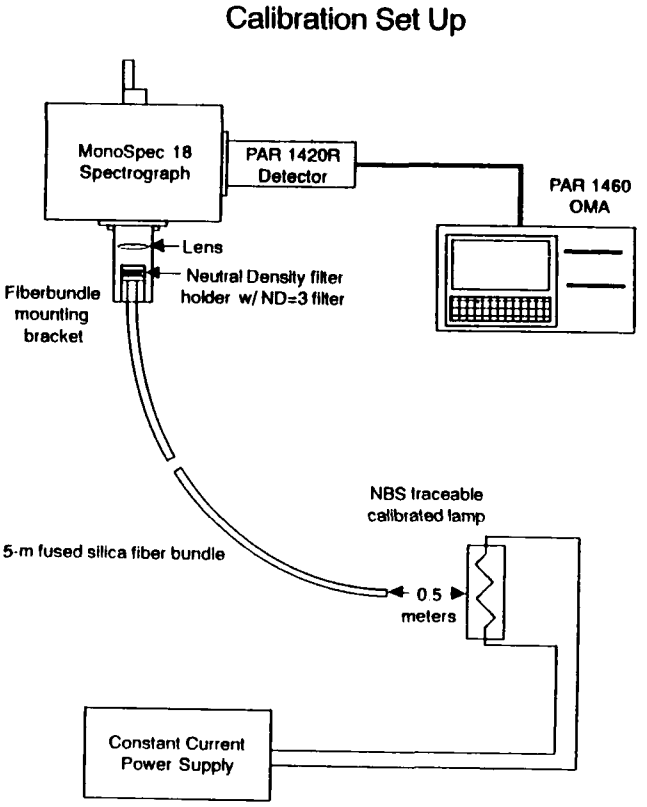


Figure 7. Set up of the optical calibration technique.

Results

Using the calibration set up shown in Figure 7, the optical transmission of the fiber optics was measured. Shown in Figure 8 are the results from the optical system calibration. Two curves are shown, one with a TRIGA reactor power of 50 kW and the other for a TRIGA reactor power of 1500 MW. As can be seen, the change in the optical transmission is not linear with power. This indicates that the color center formation and damage site production is not linear with power.

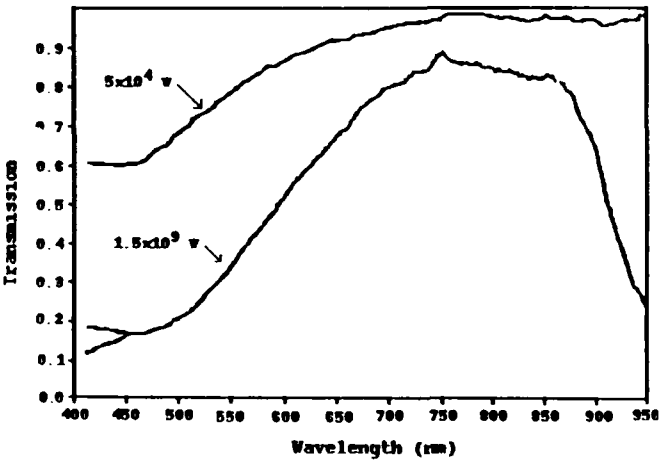


Figure 8. Calibration of the optical fiber bundle at different reactor power levels (the fibers are 225 μm plastic clad fused silica).

The reaction cell was then placed into the TRIGA reactor and filled with a combination of ^3He and other rare gases (e.g., Xe, Kr, Ar, Ne) in various pressure ratios. An absolutely calibrated spectra was obtained for the fluorescence. For example a calibrated Kr spectra is shown in Figure 9. As seen in Figure 4, the Kr spectra has a line which somewhat matches an absorption band in Nd:YAG. It is interesting to note that there are differences between electrical discharge-pumped Kr spectra and nuclear-pumped Kr spectra (See Table 4).

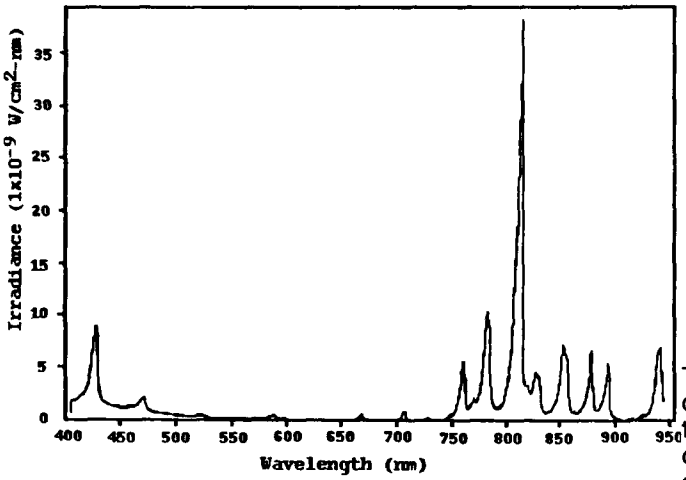


Figure 9. Nuclear-pumped Kr fluorescence at a power density of 0.9 mW cm^{-3}

Table 4. Comparison of Relative Nuclear-Driven and Electrically Excited Line Intensities for Visible Kr Lines.

λ (nm)	A ($10^8 s^{-1}$)	I_{elec}	I_{nuc}
768.52	0.49	1000	1440
---	---	---	---
826.32	0.35	3000	6032
---	---	---	---
828.10	0.19	1500	2333
785.48	0.23	800	2304
850.89	0.24	3000	3590
805.95	0.19	1500	5866
758.74	0.51	1000	2899
---	---	---	---
819.01	0.11	3000	1881
760.15	0.31	2000	2899
829.81	0.32	5000	4372
769.45	0.056	1200	1440
877.67	0.27	6000	8160
810.40	0.13	4000	4980
---	---	---	---
811.29	0.36	6000	13170
---	---	---	---
892.87	0.37	2000	10704

With the data from Figures 4, 8, and 9, the performance of the remotely pumped Nd:YAG rod can be estimated with the code "Concentrator". Calculations were made for an experiment to measure spontaneous emission from a Nd:YAG rod remotely driven by a nuclear-pumped Kr fluorescence source (as shown in Figure 10). This experiment uses the set up shown in Figure 6. The theoretical prediction for pulsed TRIGA reactor with a peak power level of 1500 MW, indicated that the intensity of the 1.06 μm line would be 0.1 mW. Experimental results for a Kr nuclear-driven lamp pumped by a pulsed TRIGA reactor with a peak power level of 1500 MW demonstrated that the 1.06 μm emission from the Nd:YAG rod was 0.12 mW.

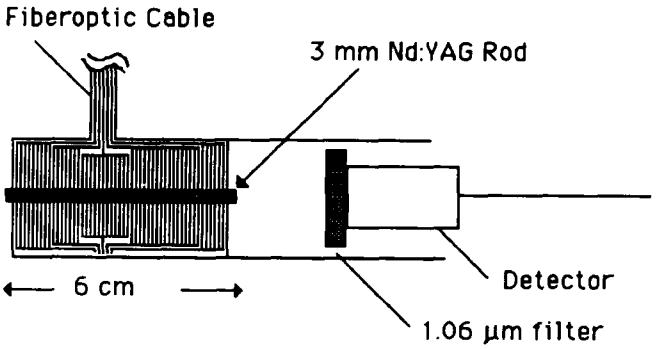


Figure 10. Experimental set up to measure 1.06 μm radiation from a Nd:YAG rod pumped remotely with nuclear-driven fluorescence.

Conclusions From Experimental Study

The results from the 1.06 μm emission experiment demonstrates that the code "Concentrator" is able to predict the behavior of a remotely driven Nd:YAG rod under some conditions. As part of the ongoing effort in the study of solid-state lasers remotely pumped by nuclear-driven fluorescence sources, the predictions of the code "Concentrator" will be tested over a broad range of conditions. In the future, using alkali metal excimer sources, a demonstration laser experiment will be carried out.

Overall Conclusions

Preliminary design studies of solid-state lasers remotely pumped by nuclear-driven excimer fluorescence sources have indicated that it is possible to build very efficient (≈ 3%) large scale laser systems. It is possible to use this method to drive solid-state lasers with a single frequency emission $\omega_1 \approx 1.06$ μm, a frequency doubled emission $\omega_2 \approx 530$ nm, and a frequency tripled emission of $\omega_3 \approx 353.33$ nm.

By using vibronic laser technology, large scale tuneable solid-state laser systems are possible with emission $\omega_1 \approx 720$ to 920 nm, a frequency doubled emission $\omega_2 \approx 360$ to 460 nm, and a frequency tripled emission of $\omega_3 \approx 240$ to 306.67 nm.

In addition, technology for efficient (≥96%), light weight waveguides was developed using the computer code "Concentrator". This technology uses thin wall, hollow core waveguide. The inner wall is coated with a reflective metallic coating (e.g., silver for visible wavelengths), and a protective layer of dielectric material such as diamond or sapphire.

Through the use of the solid-state laser remotely pumped by nuclear-driven fluorescence sources and the light weight waveguide technologies, it is possible to develop light weight, high average power, and high efficiency lasers.

Many types of solid-state laser materials can be driven by this method including the vibronic materials. Therefore, it would be feasible to add tunability to the potential features of lasers using the concepts developed by the author.

Small scale experiments were performed to demonstrate the remote pumping concept and to test the predictions of the code "Concentrator" over some conditions. Results from these experiment were successful.

Acknowledgements

The author wishes to acknowledge the support of the Lasers and Particle Beam Group within the Physics Division of Idaho National Engineering Laboratory, and the TRIGA research reactor and the Nuclear Engineering Department at the University of Illinois. Additionally, the author wishes to thank Dr. F. P. Boody, Dr. Tom Speziale, Dr. D. M. Woodall, and Dr. G. H. Miley for many fruitful discussions.

References

1. I.A. Shcherbakov, IEEE J. Quant. Electron. **24**, 979 (1988).

2. Laser Focus World, p. 24, March 1989.

3. see for example, W.F. Krupke, M.D. Shinn, J.E. Marion, et al., J. Opt. Soc. Am. B **3**, 102 (1986).

4. M.A. Prelas, F.P. Boody, J.F. Kunze, and G.H. Miley, Lasers and Particle Beams **6**, 25,(1988).

5. F.P.Boody and M.A. Prelas, *Excimer Lasers-83*, C.H. Rhodes, H. Egger, & H. Pummer, eds., (AIP,1983), 349.

6. Wei-Tzou Luh, John T. Bahns, A. Marjatta Lyyra, et al., J. Chem. Phys. **88**, 2235 (1988).

7. *Handbook of Chemistry and Physics* 45th Ed., p. D-95, (Chemical Rubber, 1964).

8. R.L. Platzman, Int. J. Appl. Radiat. Isotopes **10**, 116 (1961).

9. M.M. Rebbeck and J.M. Vaughn, J. Phys. B: Atom. Molec Phys. **4**, 258 (1971).

10. P. Harteck and S. Dondes, Nucleonics **15**, 94 (1957).

11. J.H. Kelly, D.L. Smith, J.C. Lee, et al., Opt. Lett. **12**, 996 (1987).

12. Peter B. Lyons, SPIE Vol. 541, 89 (1985).

13. W. Schneider, U. Babst, H. Henschel, et al., SPIE Vol. 721, (1986).

14. M. A. Prelas, F.P. Boody, D. M. Woodall, T. Speziale, and G. H. Miley, "Solid-State Lasers Driven by Remotely Generated Nuclear Fluorescence", Proceedings Laser Interactions and Related Plasma Phenomena, Naval Post Graduate School, Monterey, CA (Oct. 1987).

NUCLEAR-INDUCED UV FLUORESCENCE FOR STIMULATION OF THE ATOMIC IODINE LASER

W.H. Williams, G.H. Miley, H.J. Chung
Univ. of Illinois
Fusion Studies Laboratory
100 Nuclear Engineering Lab
103 S. Goodwin Ave.
Urbana, IL 61801

Abstract

A study is in progress to investigate the nuclear-induced fluorescence of the eximer XeBr for application in the atomic iodine laser. Measurements of fluorescence induced by the $^{10}B(n,^{4}He)^{7}Li$ reaction in varying gas mixtures with Br_2 and $CHBr_3$ as bromine donors are presented. A conceptual design of the photolytic laser planned to utilize this fluorescence is also discussed.

Introduction

The potential of using nuclear reaction energy to drive a laser has been studied for many years in a variety of laser systems. Ref. 1 gives some of the highlights of this research. Studies have shown that Nuclear Pumped Lasers (NPL's) have the potential of being scaled to very high powers[2,3,4], due to the ability to pump large laser volumes (good penetration of neutrons through materials) and potential for high efficiencies (no Carnot cycle limitations). As a result, NPL's also have a significant advantage in high power space-based applications where the nuclear fuel represents a much smaller, lighter energy storage system than is required for large electrically pumped lasers.

One specific type of NPL utilizes nuclear reactions to cause fluorescence in a gas mixture. The fluorescence is then coupled into a separate laser cell, acting as the light source for photolytic lasing. The component of this system which uses nuclear reaction energy to initiate fluorescence of a gas mixture is termed a Nuclear Driven Flashlamp (NDF).

The three principle reactions considered for NDF testing, as well as most NPL work, are:

$$n + {}^{10}B \rightarrow {}^{4}He + {}^{7}Li + 2.3\ MeV;$$
$$n + {}^{3}He \rightarrow T + p + 0.8\ MeV;\ and$$
$$n + {}^{235}U \rightarrow ff + 200\ MeV.$$

The cross section for the last reaction is smaller than the other two, but when its much larger energy release is factored in, the ^{235}U reaction is able to provide the largest power density per unit neutron flux. Because of special use restrictions with enriched uranium, and contamination problems of the gas by fission fragments, the first two reactions are used, or planned for use in the present work. ^{10}B is used as a thin wall coating on the inside of the test cell, and ^{3}He as a fluorescent gas diluent.

This experimental effort is supported by a kinetics study done by Wilson[5] showing that nuclear excitation of the eximer XeBr should provide an excellent UV light source for the atomic iodine photodissociation laser. The atomic iodine laser involves photodissociation of an iodine containing gas molecule, e.g. C_3F_7I or CF_3I, giving I* lasing at 1.31 micron, and has been used as a high power laser system.

This work attempts to substitute the traditional electrically-driven UV source with an NDF. Use of an eximer in a UV NDF has been suggested by Miley and Prelas, et al[6,7]. Eximers, in general, are a good choice for UV fluorescence generation because of the high conversion efficiencies with which eximer mixtures convert deposited energy to ultra-violet light (up to 50%). The eximer XeBr* is chosen for this application because it emits at 282 nm, which is near the peak of the absorption cross-sections for two common atomic iodine lasants, C_3F_7I and CF_3I.

In these experiments the eximer is used as an NDF gas to power a photolytic laser. An attempt to stimulate lasing of the eximer itself is discouraged for two reasons: 1) Test facilities for this work cannot induce the high power densities needed for a UV laser; and 2) The reactor radiation environment causes transient and permanent transmission losses in optical materials. This induced loss is higher at shorter wavelengths. Previous work by our group[8] has shown the radiation-induced loss in fused silica in the UV to be sufficiently small that a single light pass is not significantly attenuated through a

window. The multiple passes through laser cavity end windows, however, would represent a large loss for the system, and would need a very high gain medium to mitigate. The losses are much smaller in the IR, so lasing at 1.31 micron should be easier.

Figure 1 shows a schematic of the planned laser cell. The cell utilizes two concentric tubes, the inner containing the lasant gas, and the outer containing the fluorescing eximer with ^{3}He. The diameter of the outer cell is approximately 5 cm, and the length 1 meter. The cell is placed in a thermal neutron field from a reactor. UV light generated by the XeBr is coupled into the lasant in the inner cell. To maximize this coupling efficiency the inner wall of the outer cell is to have a high reflectivity coating to allow UV photons to be reflected into the inner cell. This design necessitates the use of ^{3}He, which is transparent to UV photons, as the reactant, since ^{10}B or ^{235}U are useable only as poorly reflective wall coatings.

The Univ. of Illinois TRIGA reactor produces a peak thermal flux of 3×10^{15} n/cm^2-sec. in a 12 msec. pulse. Extrapolation of the kinetic analysis of Wilson[5] predicts a XeBr fluorescence yield of 5 Watt/cm^3 using ^{3}He in the TRIGA. After coupling of this radiation to the atomic iodine lasant in a high Q cavity a laser power of 1 to 10 Watts is anticipated.

Testing to date has been to determine XeBr* fluorescence efficiencies of varying mix ratios of fluorescing gas constituents, using two different bromine donors under nuclear excitation.

Experimental Set-Up

All testing for this work is being done in the Univ. of Illinois TRIGA reactor. The TRIGA is a light water reactor capable of running in steady state or pulsed mode. Pulsed operation used for this work provides a transient thermal neutron flux 1000 times that of steady state operation. The characteristics of a pulse are shown in Table 1.

Table 1. TRIGA Pulsing Characteristics

- 12 msec fwhm
- 3×10^{15} n/cm^2-sec peak thermal flux
- 4 pulses/hour

Figure 2 shows a schematic of the reactor test set-up. This shows the special suitability of this facility for doing NDF testing, in that a six inch diameter "throughport" runs through the reactor shielding, adjacent to the core. Test cells can be placed in this port, and emitted light directed into detection equipment with the use of mirrors. The core is large enough that a test cell 1 meter in length can receive a reasonably uniform irradiation.

Figure 3 shows the test cell constructed for the present phase of fluorescence tests. It consists of a 1 inch diameter aluminum tube, coated on the interior with a thin ^{10}B coating. The cell ends are closed with fused silica windows. A ^{10}B coated cell was used for this phase because it allows flexibility to test a large number of gas mixes. ^{3}He, which has a significant cost, will be used in later testing with a new test cell after an optimum gas mixture has been selected.

Since it is desirable to change gas fills remotely (i.e., with the cell in the throughport) due to neutron-induced activation of the cell structural materials, a series of pneumatic valves and vacuum/gas fill lines are attached to the cell. In addition, in order to measure the energy deposited in the cell gas for fluorescence efficiency calculations, a piezoresistive pressure transducer (Kulite IPT1100-250A) was attached to the cell, a technique used by other investigators[9]. This technique yields the average thermal energy deposited in the gas as this energy heats the gas and raises the pressure in the closed cell volume. This transducer proved to be sufficiently resistant to radiation to allow a large number of shots before replacement.

Two types of fluorescence analysis are conducted on each test: a time-integrated spectrum of the light is obtained with an Optical Multi-channel Analyzer (OMA), and a time-dependant trace of one spectral line is obtained with a monochromator and photomultiplier tube. The OMA is used for fluorescence efficiency determinations. The test set-up was designed and aligned to allow absolute determination of the light generated in the cell. The time-dependent photomultiplier measurement is used to look for dose rate or total dose dependence in the fluorescence during the pulse.

Test Results

A typical trace of the pressure rise during a pulse is shown in Figure 4. The peak pressure occurs near the end of the pulse, with pressure decreasing quickly thereafter as

the heated gas (approx. 300 deg. C.) cools against the cell wall. This pressure peak corresponds to an energy deposition of 0.13 J/cm^3, which correlates well with other experimental and theoretical determinations of dose for this cell geometry and neutron flux[10,11].

Figure 5 shows a typical fluorescence spectrum as recorded by the OMA, for 1 torr Br_2, 250 torr Xe, and 550 torr Ar. The coarseness of the spectrum is due to low sensitivity of the detector, but the XeBr* peak at 282 nm can be plainly seen, as well as the broad Xe_2Br* peak at 425 nm.

The 282 nm fluorescence production efficiency (light produced/energy deposited in the gas) with varying gas mixes is shown in Figure 6. This was for a fixed Br_2 pressure of 1 torr, and a total pressure of 800 torr. It is seen that a maximum in the fluorescence occurs near 100 torr Xe. Two or three consecutive pulses were also performed on each fill, these indicated by the letters A, B, and C; and two separate fills done at 250 torr Xe. It is seen that the fluorescence intensity appears to decrease with continued pulsing. The cause for this has not been fully determined. It is speculated that impurities adsorbed on the cell wall may be driven off during a pulse to contaminate subsequent pulses. An alternate possibility is depletion of the bromine concentration. Bromine radicals formed during the pulse may react with boron on the wall to form stable BBr_3. Future testing with ^{3}He fill and no wall coating should distinguish between these two possible causes for the decrease in intensity.

Figure 7 shows results with two different bromine donors, Br_2 and $CHBr_3$. It is observed that $CHBr_3$ is the better fluorescer of the two, and peaks at a lower concentration than does Br_2. These dependencies on gas composition agree well with that found in e-beam pumping[12]. The peak efficiency (4-5%) is somewhat less than the 13-15% predicted in ref. 5, and the 11% measured in e-beam pumping by ref. 13. This discrepancy is likely due to a difficulty in performing absolute calibration of the light detection set-up, as well as gaseous impurities from the vacuum/gas handling system. The long vacuum and fill lines required for remote evacuation and filling of the cell have made attainment of a clean system difficult. These causes are being investigated for future testing through changes in system design and impurity doping of the gases.

It was found that the fluorescence output measured on the monochromator was generally synchronous with the temporal shape of the reactor pulse, indicating minimal dose rate or dose effects for the gas mixes tested.

The suitability of this fluorescence to the atomic iodine laser is shown in Figure 8 where it is seen that the major XeBr* line corresponds very well with the peak of the photodissociation cross-sections of two of the common lasants.

Conclusions

The fluorescence of the exímer XeBr under nuclear reaction-induced excitation is being studied. The $^{10}B(n,^4He)^7Li$ reaction has been used to date. Parametric testing has been done to give optimum mix ratios of Br_2/Xe/Ar and $CHBr_3$/Xe/Ar systems, and has shown $CHBr_3$ to be a better bromine donor. Future testing will be done with at least one additional bromine donor, and then with ^{3}He as the reactant. Following this, a laser will be tested utilizing this fluorescence to pump the photolytic atomic iodine laser.

Acknowledgement

This material was prepared with the support of the U.S. Dept. of Energy (DOE) , Agreement No. DOE DEFG07-88ER12821. However, any opinions, findings, conclusions, or recommendations expressed herein are those of the authors and do not necesarily reflect the views of DOE.

References

1. G.H. Miley, et al., 50 Years with Nuclear Fission, 1 (American Nuclear Society, La Grange Park, IL, 1989), pg. 333.

2. S. Balog, et al., Fusion Technology, 15, 383 (1989).

3. D.E. Wessol, et al., Laser Interaction and Related Plasma Phenomena, 8 (Plenum Publishing, 1988), pg. 27.

4. G.H. Miley, Atomkernenergie/Kerntechnik, 45, 14 (1984).

5. J.W. Wilson, Appl. Phys. Lett. 37(8), 695 (1980).

6. G.H. Miley, et al., Bult. APS, 24, 117 (1978).

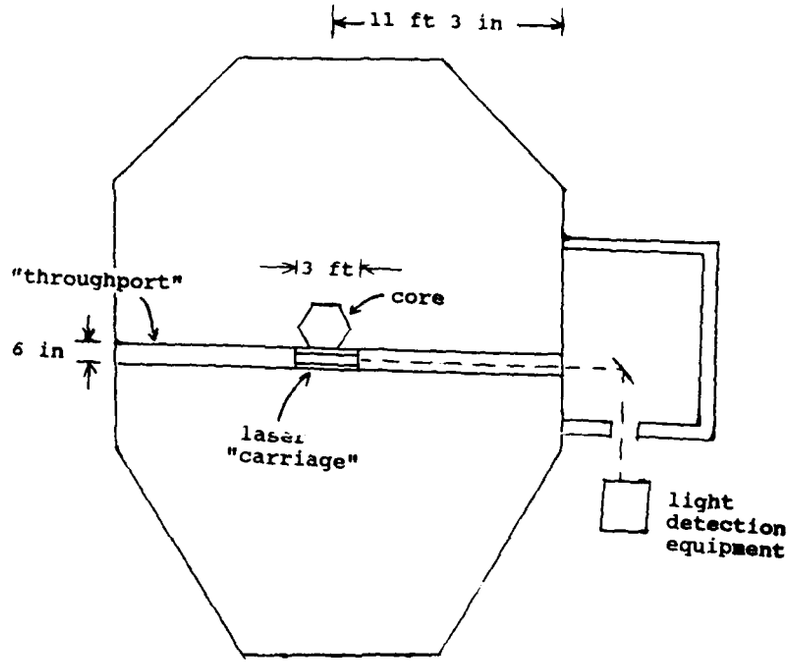


Figure 2. TRIGA reactor and test set-up at the Univ of Illinois.

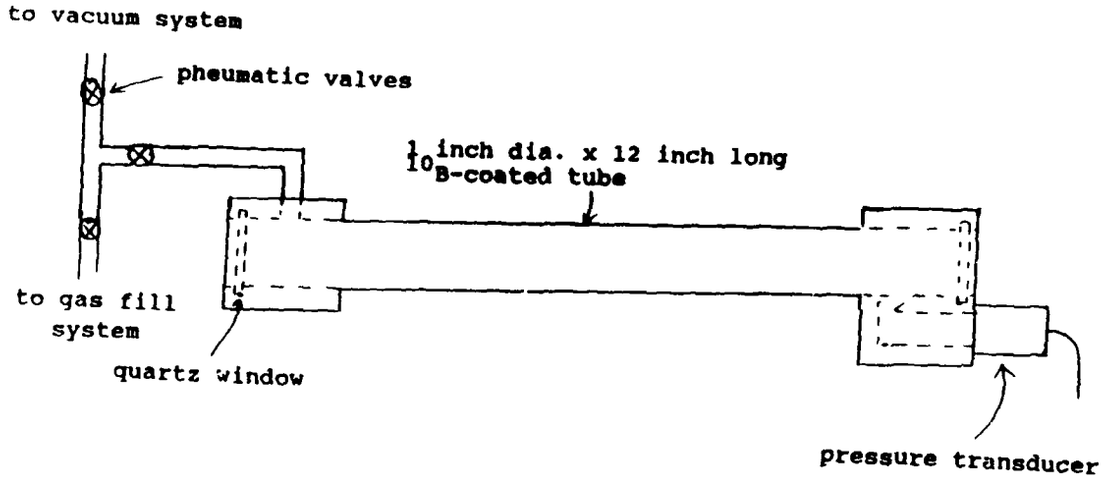


Figure 3. Test cell for ^{10}B testing.

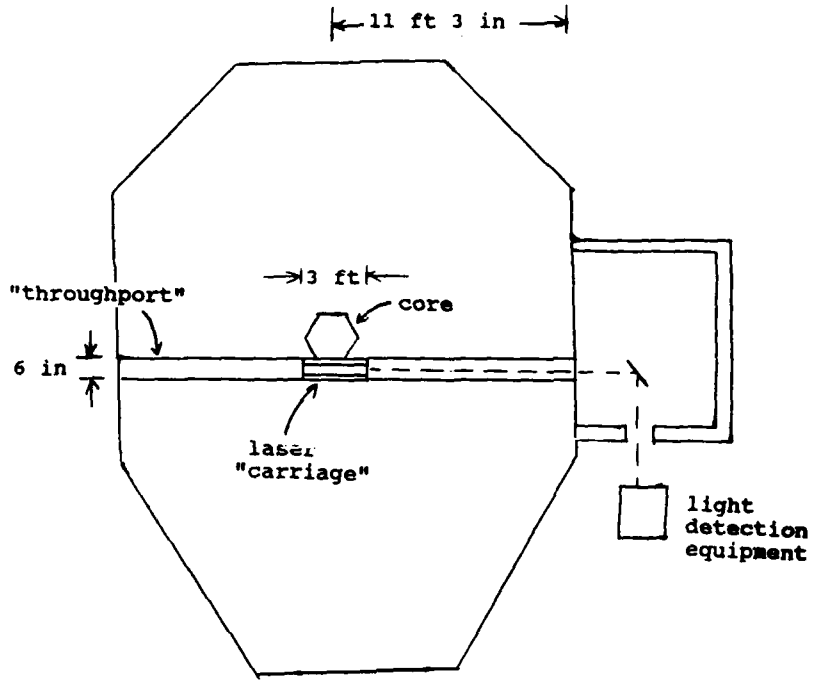


Figure 2. TRIGA reactor and test set-up at the Univ of Illinois.

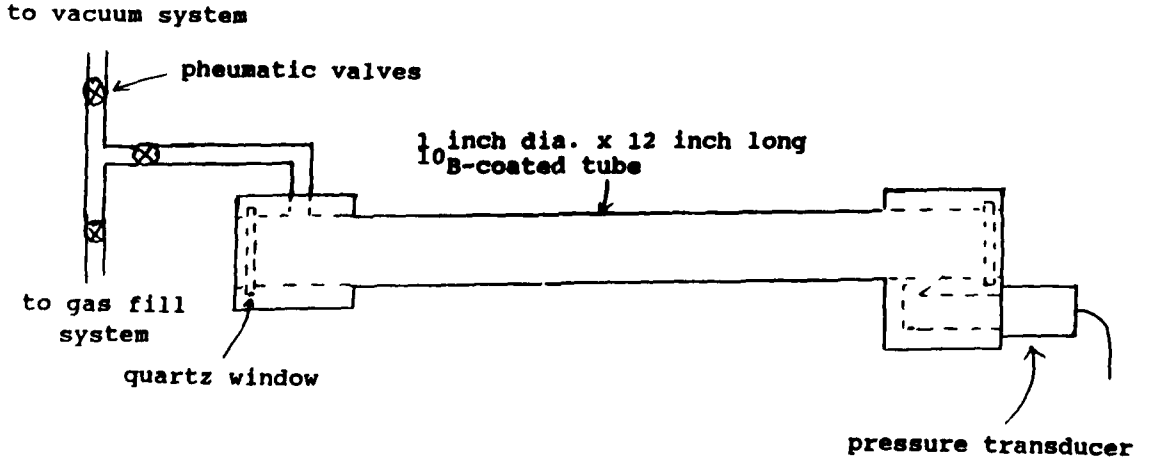


Figure 3. Test cell for ^{10}B testing.

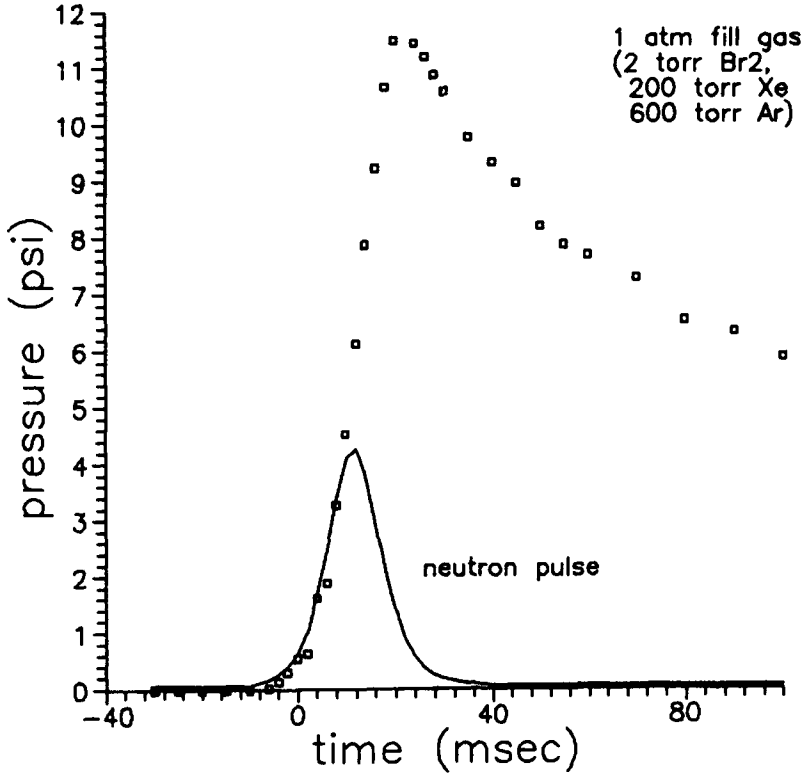


Figure 4. Typical pressure transducer results.

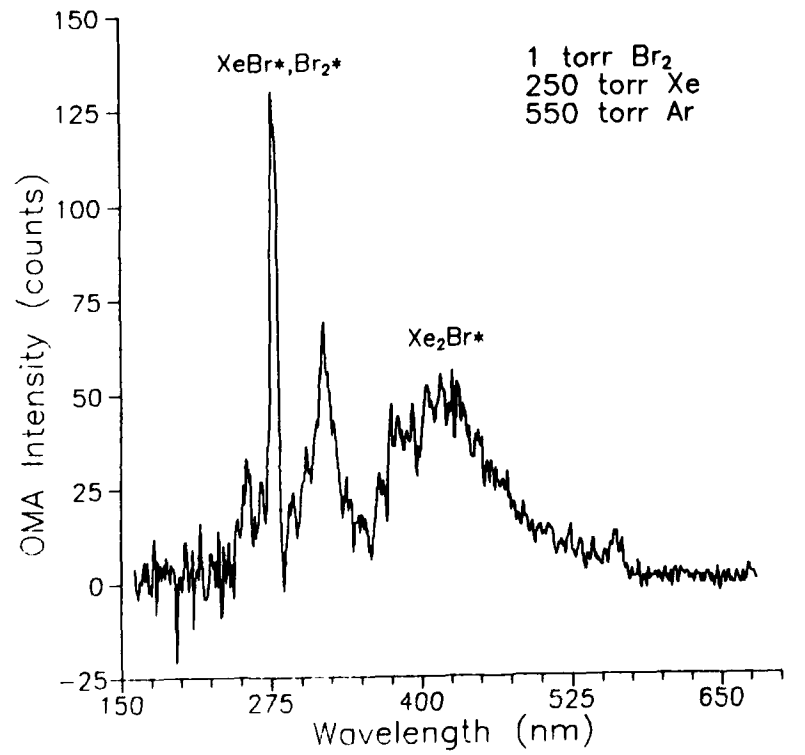


Figure 5. Typical fluorescence spectrum

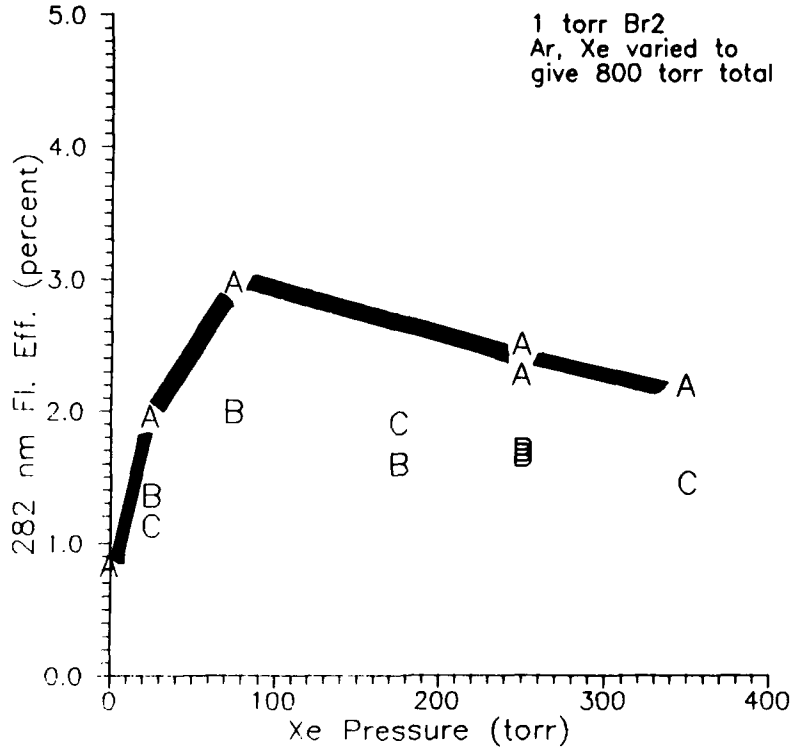


Figure 6. Peak fluorescence at 282 nm. The letters A, B, C represent sequential pulses on one fill. Fluorescence efficiency is the ratio of the fluorescence to the energy deposited in the gas.

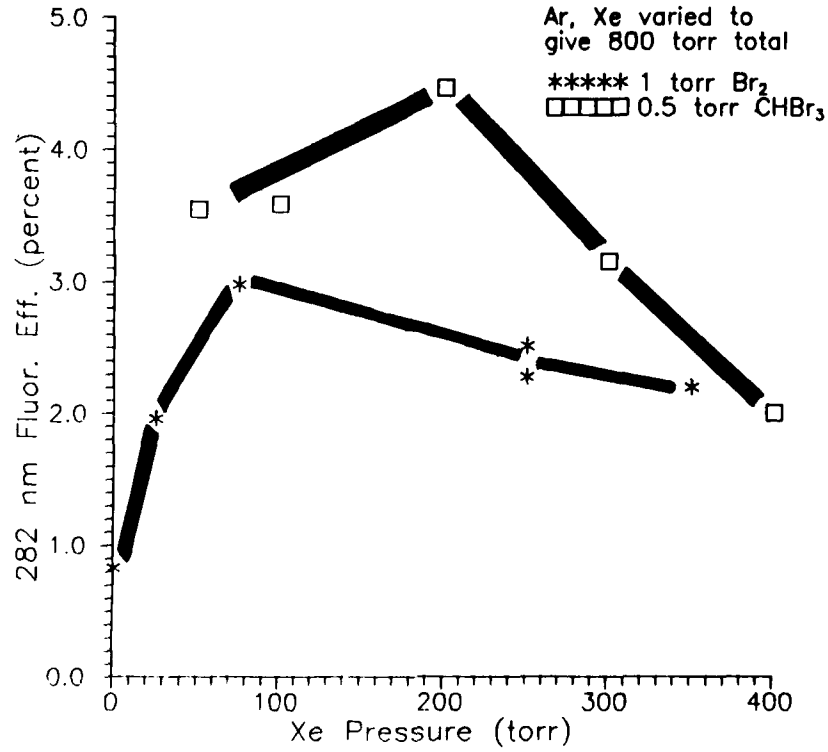


Figure 7. Peak fluorescence at 282 nm for two different bromine donors.

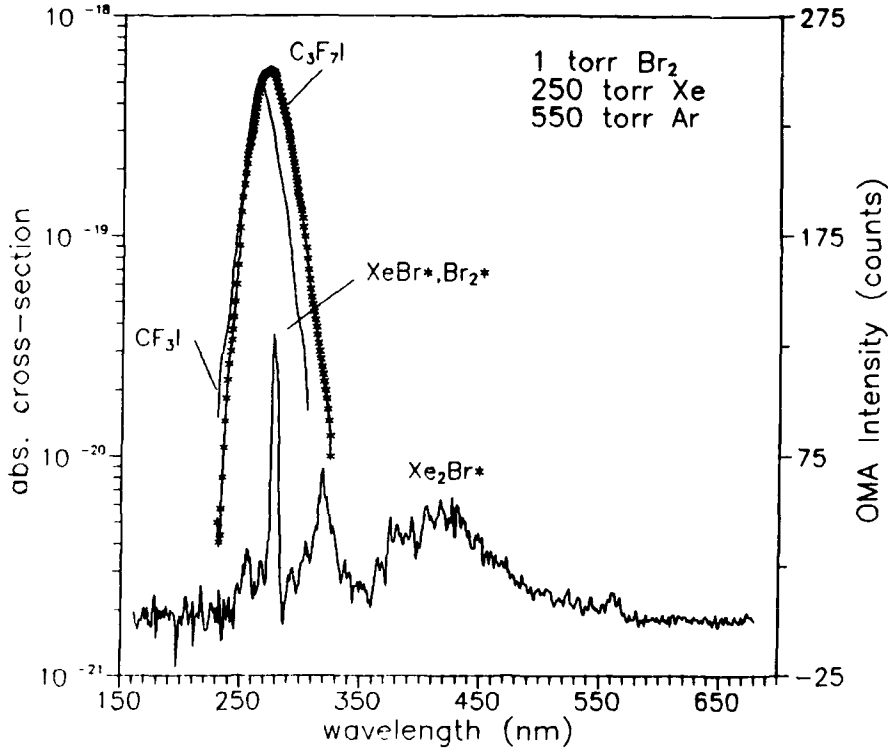


Figure 8. Comparison of nuclear induced XeBr* fluorescence with the photoabsorption cross sections of two atomic iodine lasants.

BEAM PROPAGATION IN DIRECT NUCLEAR PUMPED LASER AMPLIFIERS

W. A. Neuman, J. R. Fincke, G. D. Lassahn and L. M. Montierth

Idaho National Engineering Laboratory
EG&G Idaho, Inc.
P.O. Box 1625
Idaho Falls, Idaho 83415-3515

Abstract

Thermal distortions in transverse flow, direct nuclear pumped laser amplifiers and the resulting effect on beam propagation is investigated. Nuclear pumping occurs from surfaces, either from plates parallel to the flow direction, from screens or porous material perpendicular to the flow direction, or from the combination of the two. The analysis presented is topically divided into the analysis of the energy deposition of the energetic charged particles in the amplifying media and the analysis of the beam propagation in the amplifier and to the far field. The spatially varying energy deposition produces large index of refraction variations in the nuclear pumped amplifier. These variations are modeled by a Zernike polynomial expansion and their effect on the propagation of a uniform intensity plane wave is discussed. For purposes of illustration, an amplifier with a 1 m gain length and 1 atm (101 kPa) argon gas flowing at 100 m/s is presented. With approximately 150 W/cm^3 average charged particle pumping in the amplifier the beam qualities range from 7 to 27 times diffraction limited when the primary (tilt and focus) aberrations in the amplifier are corrected.

Introduction

Over the past few years nuclear pumped lasers have been investigated primarily to determine their feasibility[1] and the gain or efficiency of various lasents.[2] In this paper the quality of the resulting laser beam is discussed, specifically, the effect that nuclear pumping has on a beam propagating through an amplifier. Direct nuclear pumping geometries are described, i.e. the energetic charged particles produced in a nuclear reaction deposit their energy directly into the lasent gas. Passive cavities are studied, therefore the effect of gain variations on the beam are not considered.

The analysis of nuclear pumped lasers is complicated by geometry restrictions dictated by reactor configurations, charged particle transport and energy deposition of the nuclear pump source, and most importantly for steady state operation, lasent gas flow. A flowing gas system enables large energy depositions to be achieved in reactor pumped lasers without the excessive temperature increases present in static concepts. The geometry examined in this work is shown in Figure 1. The optical cavity is essentially a section of a rectangular duct which transports the lasent into and out of the reactor. The pump energy source can be a variety of thin ($\sim$ few microns) films coated on plates, screens, or other structural materials. This fuel coating serves to absorb neutrons generated by the reactor and produce energetic charged particles. The coating must be sufficiently thin to allow a significant fraction of the charged particles to escape into the lasent gas. Some typical fuel coatings are boron, which produces energetic alpha and lithium particles by the ^{10}B(n,α)^{7}Li reaction, and fissile materials, such as ^{235}U, ^{233}U, ^{239}Pu, and ^{241}Am, which generate very energetic fission fragments when fissioned by neutrons.

The phenomena to be addressed deal primarily with the internal cavity aberrations which result from non-uniform energy deposition. The charge particle energy is inherently non-uniform because the range of the particles is typically on the order of the cavity cross-sectional dimension in order to best utilize the pump source. This is true even with a uniform neutron flux, which produces a uniform charged particle source exiting the thin films (for uniform film thickness). For uniform neutron flux conditions and the geometry shown in Figure 1 the energy deposition is very two dimensional (2-d) in the plane perpendicular to the optical axis (x-y). In order to determine this complicated energy deposition profile and resulting index of refraction profiles a 2-d, time-dependent coupled fluid dynamics and charged particle transport computer code has been developed. The resulting index of refraction aberrations generated by these calculations are then fit with a series of Zernike polynomials. The effects of the internal cavity aberrations on an optical beam can then be investigated with a standard Fourier propagation code.[3] This procedure and the results from several pump source geometries will be discussed in the remainder of the paper.

Energy Deposition Analysis

The analysis of the charged particle generation, transport, and energy deposition coupled with the fluid dynamics yields a description of the index of refraction variations in the optical cavity. These index of refraction aberrations can severely deteriorate the beam quality of the amplifier output. The following sections discuss the modeling of this coupled transport and fluid dynamics problem and the resulting aberrations for several amplifier pump geometries.

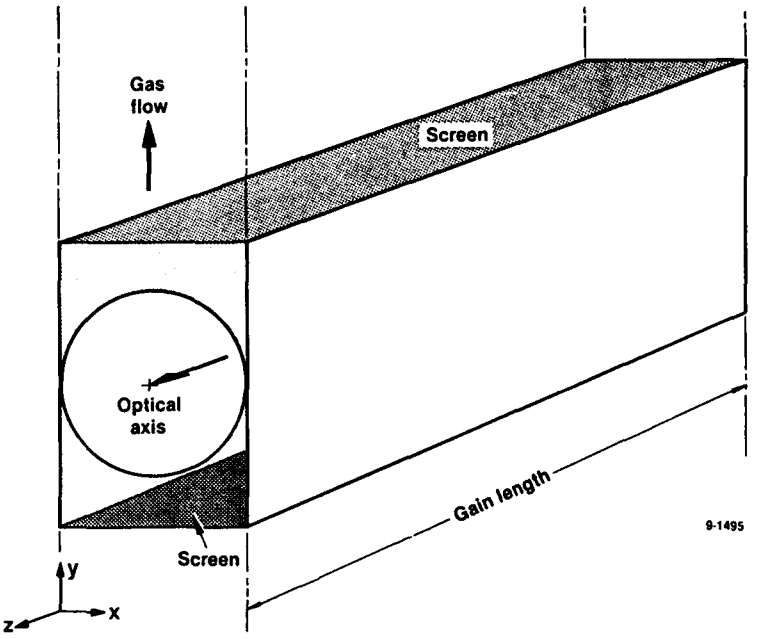


Figure 1. Direct nuclear pumped amplifier geometry.

Modeling

The modeling of the pump energy deposition in the optical cavity includes many phenomena which are interdependent. These include: generation of charged particles resulting from a neutron flux; the transport of the charged particles in the thin fuel film and into the gas; the energy loss of the charged particles along their path in the gas; the perturbations of the local gas density as a result of the energy deposition and subsequent heating; and the coupling of the fluid flow in the channel with this non-uniform energy source term. A general discussion of these phenomena and how they are interrelated follows rather than a detailed description of the various differencing schemes and coding algorithms used.

The model geometry is 2-d in the plane perpendicular to the optical axis (the x-y plane in Figure 1). Gas flow is from bottom to top in the figure, i.e. in the direction of increasing y. Input fluid conditions (temperature, pressure, and flow velocity) are specified along the x dimension at the inlet, $y = 0$. The fuel can be coated on the walls (plates) parallel to the flow direction or on screens or other porous material perpendicular to the flow direction. The thickness and location of the fuel coating must be specified along with the neutron absorption cross section and mass and energy of the charged particles generated by the neutron absorption. Multiple charged particle species are permitted to correctly model the transport of product species with different mass and energy. For fuel coatings in the flow path (i.e. screens at fixed y positions) the open flow area fraction and geometric shadowing factors must also be specified.

The temporal behavior of the neutron flux is an input to the calculation and the flux is assumed uniform in space. This imposed neutron flux along with the cross section for charged particle generation determines the charged particle source throughout the fuel films during the calculation. The various charged particle species are then transported through the fuel films and lasent gas with a method based on characteristics. The particles obey a standard range-energy relationship

$$E = E_0 \left(1 - \frac{S}{R}\right)^r \tag{1}$$

where S is the path length, E is the particles energy, E_0 is the particles initial energy, R is the particles range in the media given by

$$R = R_0 \left(\frac{E}{E_0}\right)^{1/r} \tag{2}$$

and R_0 is the range at E_0. The exponent r varies depending on the type of charged particle. For heavy particles typical of those generated during fissioning events the exponent is $r = 2$. For the light particles generated in the $^{10}B(n,\alpha)^7Li$ reaction the exponent is $r = 1.25$. When the charged particles are transported in the lasent gas the current local gas conditions are used to determine the range, coupling the transport and fluid dynamics calculations. As the gas heats and becomes less dense the range will increase. This decreases the source term to the energy equation in the regions where the gas has been heated, i.e. adjacent to the fuel films.

The fluid dynamics model is a finite difference representation and permits multiple component gases. Ideal gas behavior is assumed which is quite reasonable in the temperature and pressure ranges and low ionization fractions typical for reactor pumped lasers. The model allows both compressible laminar or turbulent fluid flow and viscosity effects are included. Thermal conduction in the gas is included as well as energy transfer between the heated surfaces (fuel films) and the gas. The fluid boundary conditions also can be time varying. In equation form the fluid model is:

$$\frac{\partial \rho}{\partial t} + \nabla \cdot \rho \vec{v} = 0 \tag{3}$$

$$\rho \frac{\mathrm{D}\vec{v}}{\mathrm{D}t} = -\nabla P - \nabla \cdot \overleftrightarrow{\tau} \tag{4}$$

$$\rho C_v \frac{\mathrm{D}T}{\mathrm{D}t} = \nabla \cdot \kappa \nabla T - P \nabla \cdot \vec{v} - \overleftrightarrow{\tau} : \nabla \vec{v} + \varepsilon_{cp} \tag{5}$$

where ρ is the mass density, t is the time, $\vec{v}$ is the velocity, P is the pressure, $\overleftrightarrow{\tau}$ is the viscosity, C_v is the specific heat at constant volume, κ is the thermal conductivity, T is the temperature, ε_{cp} is the charged particle energy source term, and D/Dt is the total derivative. The charged particle energy source term is given simply by

$$\varepsilon_{cp} = -\nabla \cdot \vec{F}_{cp} \quad , \tag{6}$$

where $\vec{F}_{cp}$ is the charged particle energy flux. Equations (3-5) are the standard continuity, momentum and energy equations, respectively.

Solving the coupled set of fluid and transport equations in the 2-d geometry generates a description of the large scale density perturbations in the optical cavity. These density variations and the index of refraction variations which result are discussed in the following section.

Results

The results presented are for a steady state laser amplifier. The gas conditions at the inlet are 1 atm (101 kPa) of Argon with a uniform inlet flow velocity of 100 m/s. Argon was chosen as an illustrative example because of its wide use as a buffer gas. Helium is also a typical buffer gas and has a much smaller index of refraction. Therefore with similar energy deposition gradients the deleterious effects on the optical beam will be substantially larger with argon. The channel width is chosen as 2.5 cm. The charged particles mass and energy are arbitrarily chosen to yield ranges approximately the channel width at the gas inlet conditions.

Several pump configurations were studied. They include fuel material coated on plates parallel to the flow direction, fuel material on screens in the flow path, and a combination of fuel material on plates and screens as shown in Figure 2. In all cases the inlet fluid boundary conditions were imposed a few centimeters upstream of the fueled surfaces. The screens have a projected area fraction of 0.37, a total hemispherical surface area of 1.57 times the projected area and a geometric shadowing factor of 0.85. Thus with equivalent thicknesses of fuel coating the net charged particle escape flux is 0.37 × 1.57 × 0.85 ~50% that of the plate fuel. The charged particle source is a function of the product of the absorption cross section in the film and the neutron flux. This product was chosen arbitrarily to yield similar energy depositions (~100 W/cm^3) in the center of each channel studied. This enables the differences in beam quality between the different amplifier to be investigated under similar pumping conditions (and presumably similar amplifier gains).

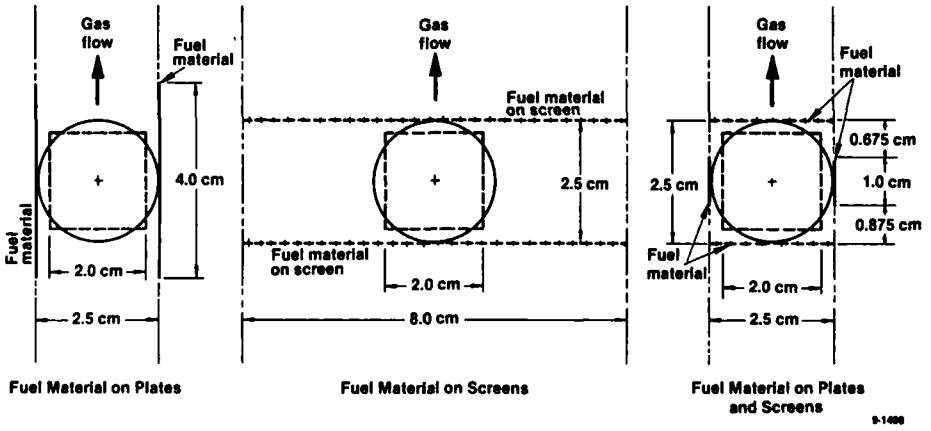


Figure 2. Fuel configurations used in the nuclear pumped amplifier analysis.

The charged particle energy deposition for the three pump geometries discussed is shown in Figure 3. The energy deposition for all cases is ~100 W/cm^3 in the center of the channel and the peak deposition adjacent to the fueled surfaces is on the order of 400 W/cm^3. Note that only the central 4.0 cm of the screen amplifier case is shown. The screen pumped amplifier has essentially one dimensional gradients in all but the outer few centimeters next to the channel walls. A summary of the energy deposition and temperature rise in the three channels can be found in Table I. In the screen fueled cases only the surface facing the amplifier aperture is coated with fuel. The screen fueled amplifiers produce a larger bulk temperature rise in the gas because all the energy generated in producing the charged particles is deposited in the gas, not just the energy of the escaping particles. In steady state the energy of the particles which do not escape the screens results in sensible heat being transferred directly to the gas. For the plates the heat is conducted to the surrounding walls which can be cooled from outside the optical cavity. The temperature rise is of interest because of material considerations and because of possible effects on the kinetics of various laser systems.

The index of refraction, n, resulting from the pump conditions for the three amplifier geometries is shown in Figure 4 (The refractive index variations are presented as $(n-1)$). The largest refractive index variations occur with the plate fueled amplifier. For this amplifier the difference between the maximum and minimum refractive index values in the central region of the cavity are about 2-3 times as large as the variations of the other two amplifier geometries. The index of refraction variations are summarized in Table I. Note the large drop in the index of refraction that occurs when the gas flows past a screen location, corresponding to a large temperature rise and density reduction. The effect of these index of refraction variations on an optical beam is discussed in the following sections.

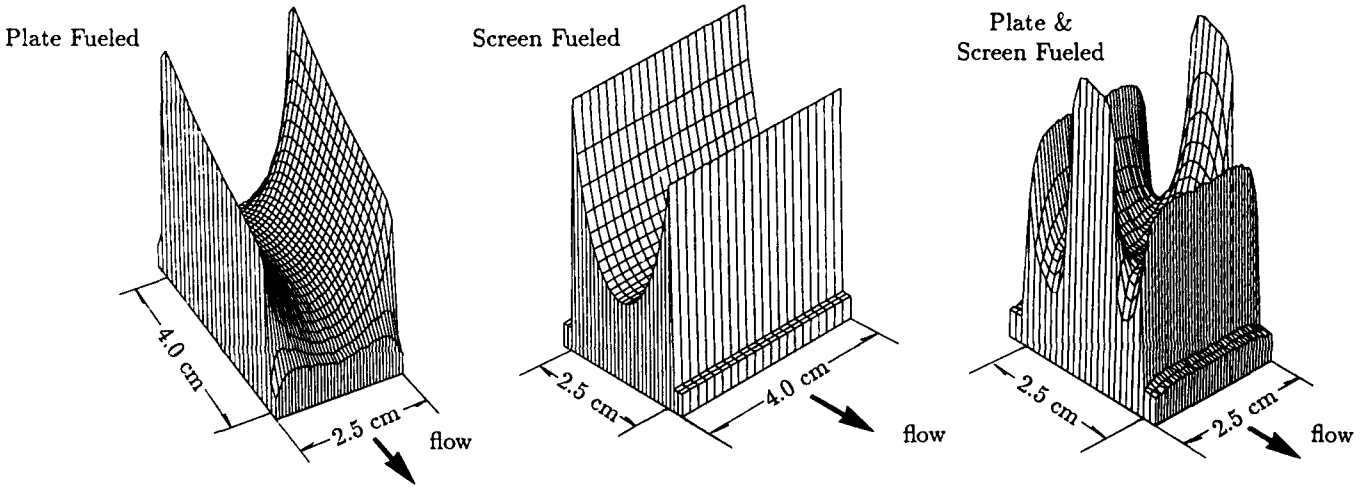


Figure 3. Charged particle energy deposition for the amplifier pump geometries.

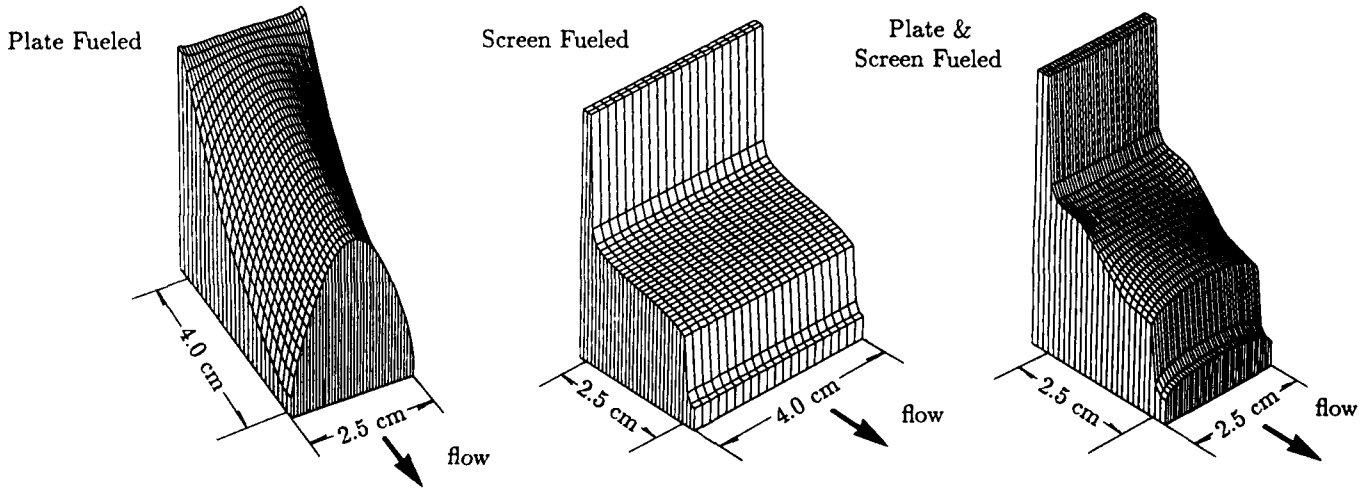


Figure 4. Resulting index of refraction variations in the nuclear pumped amplifiers.

Table I. Comparison of different pump geometries for direct nuclear pumped amplifiers.

	Fuel Form		
	Plates	Screens	Plates & Screens
Deposition in Center of Channel (W/cm^3)	100	100	100
Average Deposition over 2.5 cm Circular Aperture (W/cm^3)	160	161	156
Average Deposition over 2.0 cm Square Aperture (W/cm^3)	148	148	141
Index of Refraction Variation over 2.5 cm Circular Aperture $((n-1)\times 10^6)^a$	87	36	35
Index of Refraction Variation over 2.0 cm Square Aperture $((n-1)\times 10^6)^a$	67	20	24
Bulk Temperature Rise (K)	76	192	145

[a] Difference between the maximum and minimum index of refraction values

Beam Propagation Analysis

The quality of the optical beam produced by direct nuclear pumped lasers is a question of practical importance in the development of the technology. Because physical access to nuclear reactors is generally difficult, implementation of elaborate beam clean up schemes may be difficult. With this in mind the following sections will discuss the resulting beam quality for the amplifier geometries presented in Figure 2. Corrections which can be accomplished with simple deformable mirrors, i.e. tilt and focus, will be considered.

Modeling

A uniform intensity plane wave is launched into a 1 m long single pass amplifier, which has apertures at both ends. The wavelength, λ, used in the beam propagation is 1 μ. Two apertures are investigated: a 2.5 cm diameter circular aperture which is the largest circular aperture possible for the channels considered; and a 2.0 cm square aperture which avoids the most severe refractive index gradients adjacent to the cavity surfaces.

The index of refraction gradients are modeled as a series of Zernike polynomials. Zernike polynomials are convenient because the lower order terms in the expansion have physical interpretations. The Zernike terms included in the analysis are listed in Table II. The plate fueled amplifier presented in the previous sections has the largest index of refraction gradients and the dominant aberration is a focus across the channel in the x direction. It is therefore useful to directly combine the Zernike defocus, U_{20}, and third order 0° astigmatism, U_{22}, terms to represent x and y focus. This representation of the focus is:

$$\begin{aligned} A_f &= C_{20}U_{20} + C_{22}U_{22} \\ &= (C_{20x} + C_{20y})U_{20} + (C_{22x} + C_{22y})U_{22} \\ &= [C_{20x}U_{20} + C_{22x}U_{22}] + [C_{20y}U_{20} + C_{22y}U_{22}] \end{aligned} \tag{7}$$

where

$$\begin{aligned} C_{20x} &= \frac{1}{2}C_{20} + \frac{1}{4}C_{22} \qquad & C_{22x} &= C_{20} + \frac{1}{2}C_{22} \\ C_{20y} &= \frac{1}{2}C_{20} - \frac{1}{4}C_{22} \qquad & C_{22y} &= -C_{20} + \frac{1}{2}C_{22} \end{aligned} \tag{8}$$

are the modified coefficients for the Zernike terms. The first quantity in brackets in Eq. (7) is the x focus and the second in the y focus.

The effects of the aberrations in the cavity are determined by propagating the plane wave through the amplifier and to the far field with the GLAD[3] (Generalized Laser Analysis and Design) Fourier propagation code. The information derived from this analysis includes the intensity, I, and phase, ϕ, of the beam at the exit aperture (near field) and in the far field from which a measure of the beam quality can be obtained.

Table II. Zernike polynomials used in modeling the index of refraction variations in the amplifiers.

Aberration Type	Zernike Polynomial	Comment
x Tilt	$\rho\cos\theta$	zero by symmetry
y Tilt	$\rho\sin\theta$	
Defocus	$2\rho^2-1$	
Third Order 0° astigmatism	$\rho^2\cos 2\theta$	
Third Order 45° astigmatism	$\rho^2\sin 2\theta$	zero by symmetry
Third Order x Coma	$(3\rho^3-2\rho)\cos\theta$	zero by symmetry
Third Order y Coma	$(3\rho^3-2\rho)\sin\theta$	
Third Order x Clover	$\rho^3\cos 3\theta$	zero by symmetry
Third Order y Clover	$\rho^3\sin 3\theta$	
Third Order Spherical	$6\rho^4-6\rho^2+1$	

Results

In order to evaluate the effects of the index of refraction aberrations a plane wave was propagated through an amplifier with no aberrations as a base case. The intensity profiles at the exit aperture (near field) near and in far field for the 2.0 cm square aperture amplifier are shown in Figure 5 (note there is a scale change between the near and far field plots). The central lobe half width in the far field is $L\lambda/D$, where L is the distance propagated into the far field, and D is the width of the aperture. For the unaberrated case the energy inside the central lobe is ~84% of the exit aperture energy. A measure of the quality of the aberrated beam is the size of the spot which contains the equivalent energy as the central lobe of a diffraction limited beam. The spot size is commonly normalized to the diffraction spot size, $L\lambda/D$ for a square aperture, and referred to as the number of times diffraction limited (TDL). For circular apertures the central lobe size is $1.22 \cdot L\lambda/D$, where D is the diameter of the beam. The central lobe of the circular beam contains a slightly larger fraction of the exit aperture energy than the square beam (~86%).

Two different sets of aberrated beam results will be presented for each amplifier pump geometry. The average tilt of the wave front can be simply compensated for, therefore all results have this component of the aberrations eliminated. The different cases presented are then: 1) all second and third order aberrations included; and 2) only third order aberrations included in the beam propagation. The second order aberrations, which are the focusing terms, can be corrected by deformable mirrors without great difficulty. The results for the plate, screen, and plate and screen fueled amplifiers are shown in Figures 6-8, respectively. The much larger aberrations introduced in the plate fueled amplifier than in the screen fueled amplifier results in a significantly more divergent beam in the far field. The required tilt correction for the plate fueled amplifier was also larger than the screen fueled cases, ~18 waves versus ~12 waves aperture center to edge.

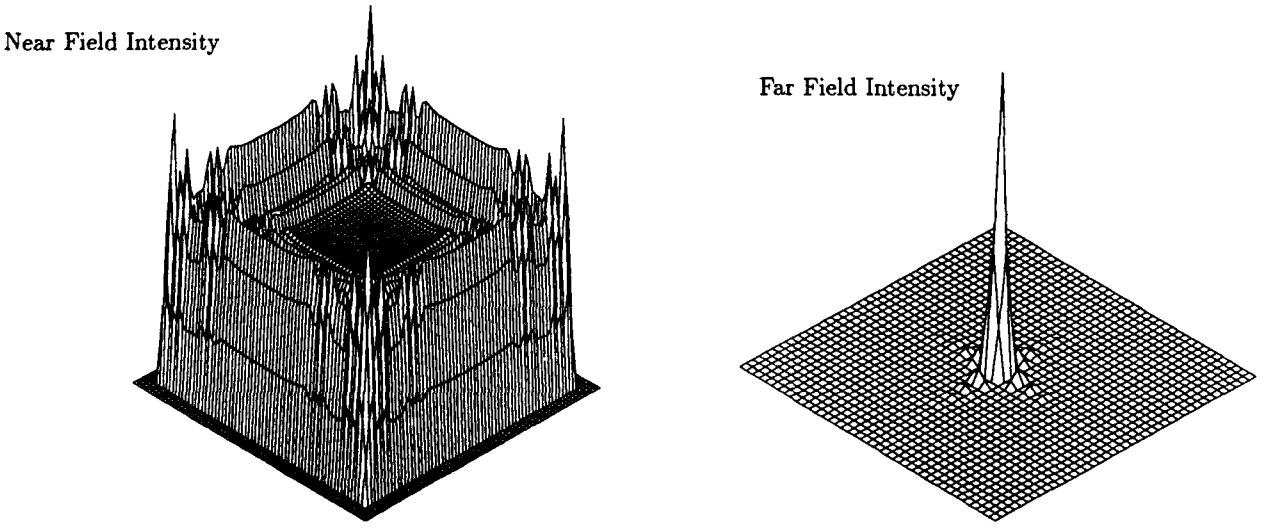


Figure 5. Intensity of an un-aberrated beam at the exit aperture (near field) and in the far field for the 2.0 cm square aperture amplifier, arbitrary scaling.

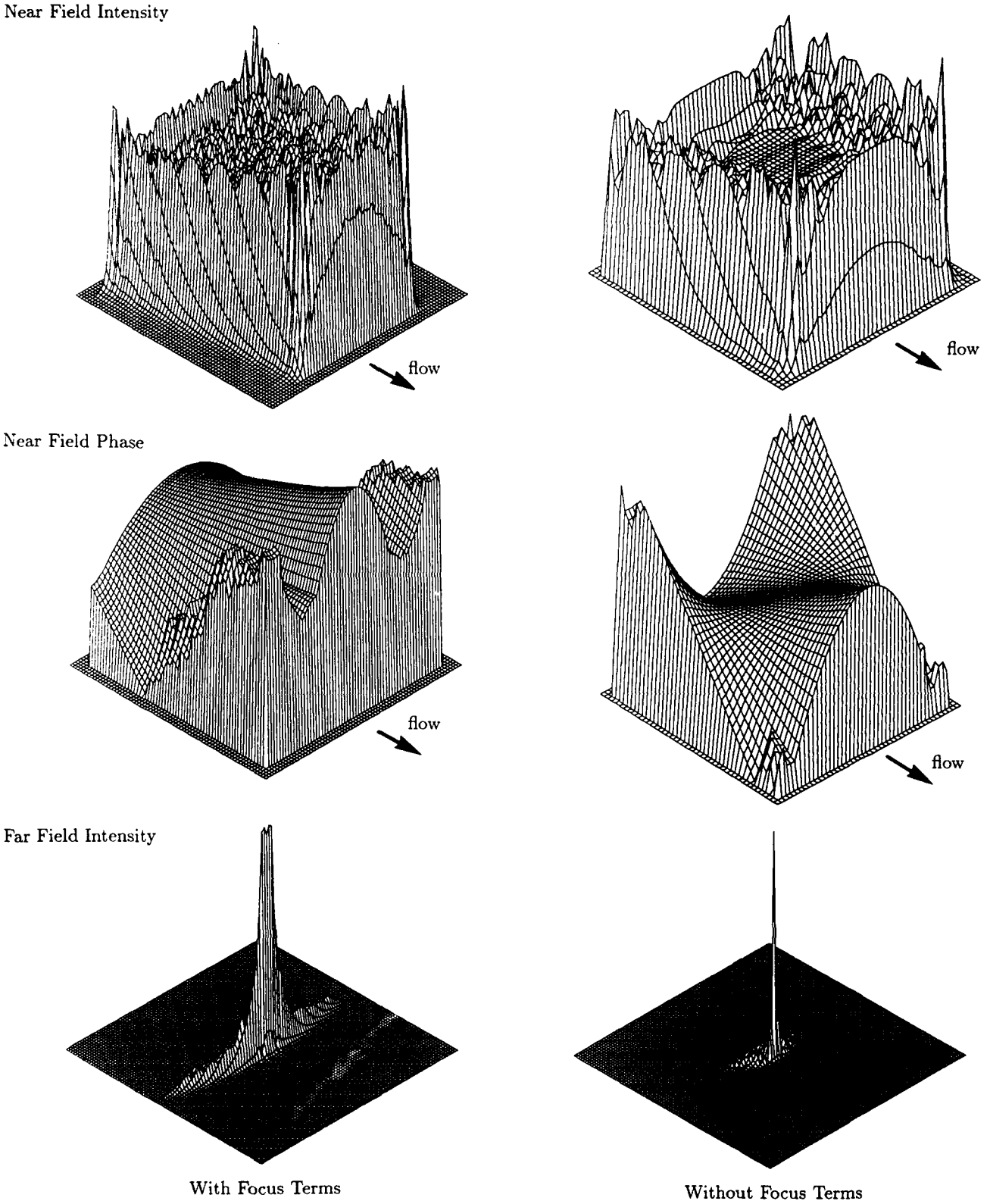


Figure 6. Beam propagation results for the plate fueled amplifier, arbitrary scaling.

(Individual plots have different scales and therefore present qualitative features, not quantitative differences. The plots on the left have the Zernike focus terms included, those on the right have the focus terms removed. Not all of the calculation points are included in the plots.)

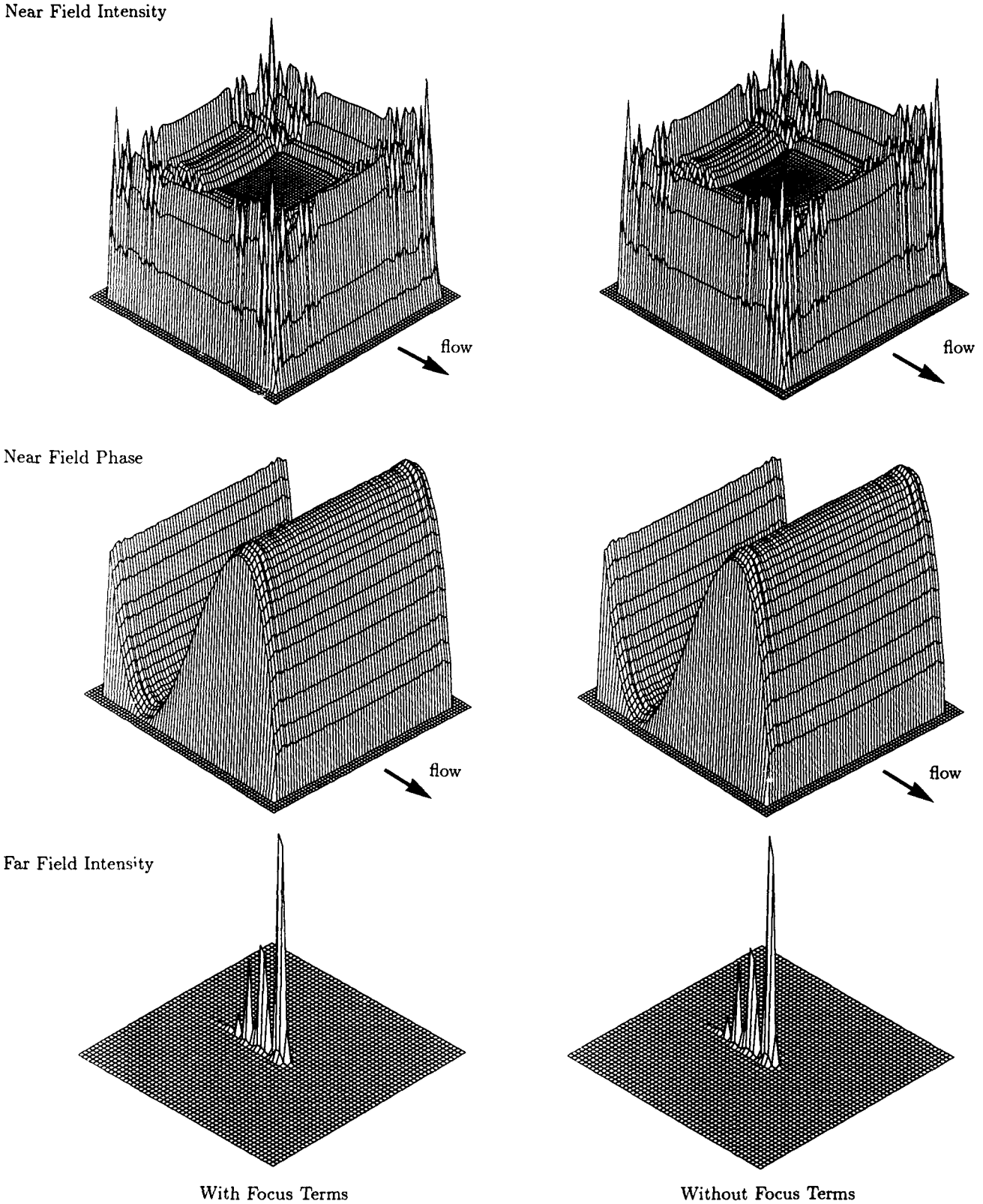


Figure 7. Beam propagation results for the screen fueled amplifier, arbitrary scaling.

(Individual plots have different scales and therefore present qualitative features, not quantitative differences. The plots on the left have the Zernike focus terms included, those on the right have the focus terms removed. Not all of the calculation points are included in the plots.)

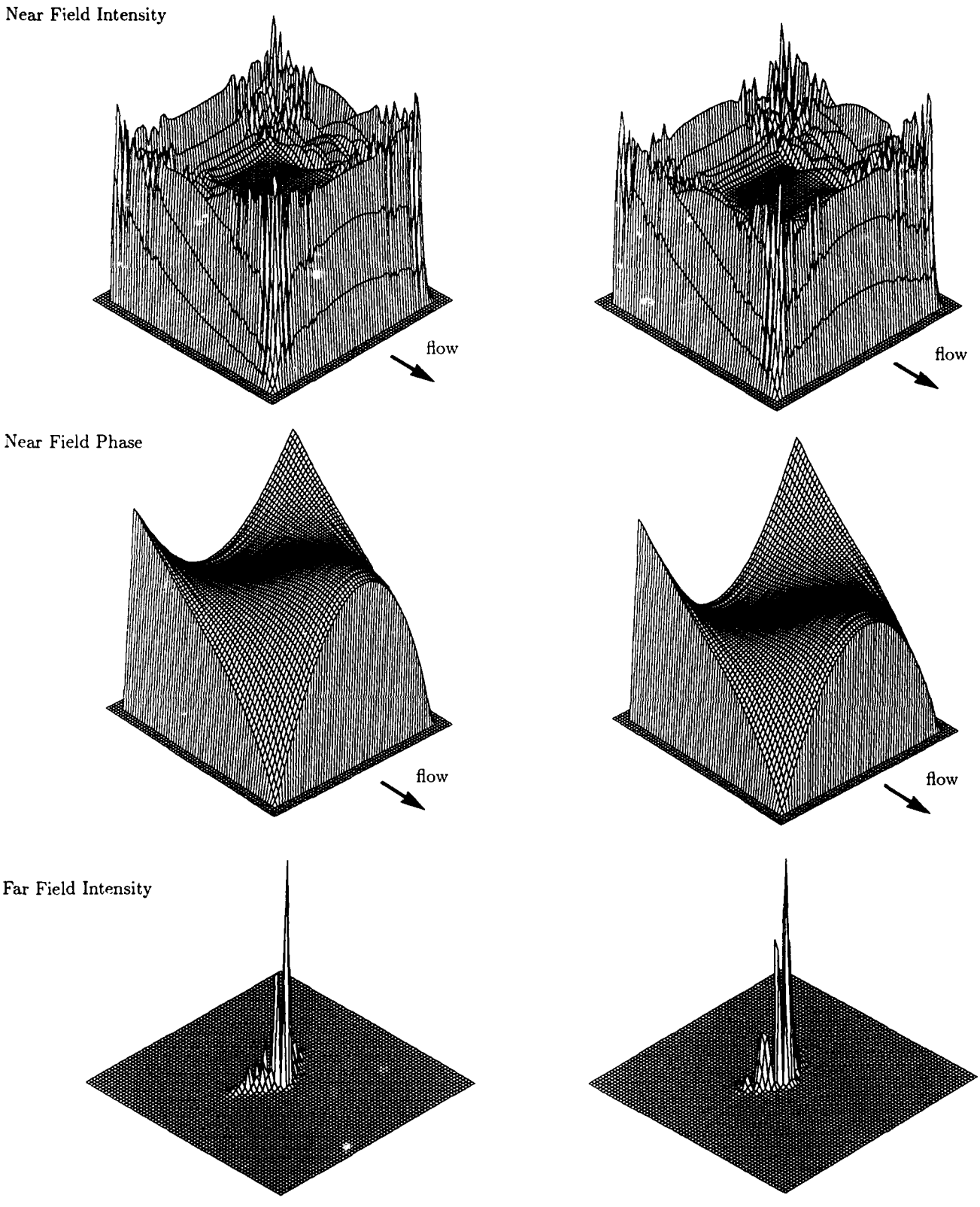


Figure 8. Beam propagation results for the plate and screen fueled amplifier, arbitrary scaling.

(Individual plots have different scales and therefore present qualitative features, not quantitative differences. The plots on the left have the Zernike focus terms included, those on the right have the focus terms removed. Not all of the calculation points are included in the plots.)

The removal of the focus aberrations from the plate fueled amplifier has a significant effect on the resulting beam quality. The TDL of the beam improved from 100 to 23 for the square aperture amplifier by removing the focus terms. Removing the focus in the plate fueled amplifier also increased the utilized mode volume as is apparent from Figure 6. The near field intensity plot (at the amplifier exit aperture) with the Zernike focus terms included is has narrowed significantly in the direction of the strong x focus. In contrast, the screen fueled amplifier's beam quality improved little with the removal of the focus aberrations because they are much smaller than the third order aberrations. The plate and screen fueled amplifier's beam quality improved modestly with the removal of the focus terms which are of comparable magnitude to the third order aberrations in that amplifier. Notice that even with the focus aberrations removed in the plate fueled amplifier the beam quality is still poorer than for the other two geometries. The beam propagation results for the square aperture amplifiers are summarized in Table III.

The results for the circular aperture amplifiers follow the same tendencies as the square aperture cases. In all cases the beam quality is poorer for the circular aperture than the square aperture. The 2.5 cm circular aperture includes the large index of refraction gradients adjacent to the fueled surfaces where the 2.0 cm square aperture avoids the worst aberrations. The square aperture does have less cross-sectional area than the circular aperture thus if the energy extraction is uniform across the amplifier a smaller output energy would result. The details of the energy extracted would require specific knowledge of the gain characteristics of the amplifier which is beyond the scope of this paper. The beam propagation results for the circular aperture amplifiers are summarized in Table IV.

Table III. Summary of the beam propagation results for the amplifiers with 2.0 cm square apertures.

	TDL[a]	Residual Waves Distortion[b]	Dominant Aberration
Plate Amplifier			
With Focus	100	25	x Focus
No Focus	23	6	y Clover
Screen Amplifier			
With Focus	7	1	y Coma and y Clover
No Focus	7	1	y Coma and y Clover
Plate & Screen Amplifier			
With Focus	9	2	x Focus y Coma
No Focus	8	2	y Coma

[a]Times Diffraction Limited spot size, see text.
[b]Maximum phase variation from aperture center to edge.

Table IV. Summary of the beam propagation results for the amplifiers with 2.5 cm circular apertures.

	TDL[a]	Residual Waves Distortion[b]	Dominant Aberration
Plate Amplifier			
With Focus	160	30	x Focus
No Focus	27	7	y Clover
Screen Amplifier			
With Focus	18	4	y Coma and y Clover
No Focus	18	4	y Coma and y Clover
Plate & Screen Amplifier			
With Focus	18	4	x Focus y Coma
No Focus	17	3	y Coma

[a]Times Diffraction Limited spot size, see text.
[b]Maximum phase variation from aperture center to edge.

Summary and Conclusions

The effects of direct nuclear pumping in optical amplifiers on beam quality are analyzed. The amplifiers considered are rectangular with transverse flowing gaseous laser media and surface pumping from the walls and from screens in the flow path. A gain length of 1 m and gas pressure of 1 atm are used for illustration. The analysis includes a multi-dimensional coupled charged particle transport and fluid dynamics calculation to determine the aberrations resulting from index of refraction variations. The aberrations are fit with Zernike polynomials and used with a Fourier propagation calculation of the beam propagation. The beam quality is derived from the far field spot sizes of the various amplifier configurations.

The results of the analysis show that the amplifiers without second or third order aberration removal have beam qualities between 7 and 160 TDL with average pump power depositions of $\sim$150 W/cm^3. The best beam quality results from pumping with screens in the flow path, the worst is from amplifiers pumped by plates parallel to the flow direction. The disadvantage of screen pumping is an increased energy load to the gas compared with plate pumping. Additionally, only large scale density perturbations are considered here. Small scale turbulence related density fluctuations may be more important in the screen pumped geometry than in the plate pumped geometry, making the resulting beam less desirable. The plate fueled amplifier beam quality is improved substantially (to 23 TDL with the 2.0 cm square aperture) by correcting for the strong x focus, but still has poorer beam quality than the other pump geometries analyzed.

A comparison of two different apertures shows an improvement in the beam quality can be obtained by a smaller aperture to avoid the strong index of refraction gradients adjacent to the fueled surfaces. The price paid is a reduction in gain volume of the amplifier. In order to determine the optimal aperture size and shape a detailed study is necessary with the specific information on gain variations in the amplifier included.

Acknowledgment

This work was performed under the auspices of the U. S. Department of Energy under contract number DE-AC07-761D01570.

References

1. N. W. Jalufka, "Direct Nuclear-Pumped Lasers," *NASA Technical Paper*, no. 2091 (1983).
2. W. J. Alford and G. N. Hays, "Measured Laser Parameters for Reactor-Pumped He/Ar/Xe and Ar/Xe Lasers," *J. Appl. Phys.*, **65**, 3760 (1989).
3. The computer program GLAD has been developed by Applied Optics Research, the Air Force Weapons Laboratory, and the Los Alamos National Laboratory. See C. E. Knapp, V. K. Viswanathan, Q. D. Appert, S. C. Bender, and B. D. McVey, "Optical Analysis of High Powered Free Electron Laser Resonators," *AIAA 19th Fluid Dynamics, Plasma Dynamics and Lasers Conference*, Hawaii, June 8-10, 1987.

LASERS IN IRRADIATION FIELD OF A STATIONARY NUCLEAR REACTOR

G.A.Batyrbekov

Institute of Nuclear Physics, Academy of Sciences of KazSSR
480082 Alma-Ata, USSR

Nowdays two conceptions of the nuclear reactors usages for lasers excitation are developed. The first one is the more wide spread according to which excitation of lasers is carried out by the direct nuclear pumping in the impulse nuclear reactors[1,2,3]. The second conception suggested and investigated by us is excitation of lasers by the non-self maintained discharge in a radiation field of the stationary nuclear reactors[4,5,6] or by the low-threshold direct nuclear pumping. The stationary nuclear reactors allow to create uniformly ionized large volumes of lasers at high pressure generating continuous wave or high frequency wave rays. This is important for some practical applications. Moreover, non-self maintained discharge usage in the stationary nuclear reactor allows to create many visible and UV-regions lasers, for example excimer XeF* laser[7]. This is impossible in case of the direct nuclear pumping in any impulse nuclear reactor. Practical significance of those lasers increases when electrical energy required for its pumping is generated by the same reactor itself [5]. In this case the possibility to create autonomy nuclear energetic plant generating electrical energy and laser rays' energy.

I would like to report on researches carried out in the stationary nuclear reactor (power 10 Mwatts) at the Institute of Nuclear Physics, Academy of Sciences of the Kazakh SSR.

We have fulfilled complex researches of plasma of different gas mixtures, created by products of the nuclear reaction $^3He(n,p)^3H$ in the stationary nuclear reactor core to create lasers or source of nuclear pumped optical irradiations. With this purpose different diagnostic methods for investigation of charge plasma densities and spectra of plasma irradiation in the reactor have been used.

$CO_2 + N_2 + {}^3He$ and $CO + N_2 + {}^3He$ were first gas mixtures whose plasma was investigated [8,9,10,11,12]. As a result the possibility of creation of CO_2- and CO lasers was shown. Then these lasers were created [4,5,6,12].

(Slide 1). On the first slide experimental and calculation electron densities are presented. Experimental data have been obtained by the probe method versus neutron flux density for different gas density. Points and lines indicate experimental and calculation results, respectively, for gas mixture with ratio $CO : N_2 : {}^3He = 1 : 6 : 7$. Electron density is equal to 10^{10}-10^{11} cm^{-3}, when neutron flux density increases 10^{12} n/cm^2s. In this case the space charge does not limit the discharge current.

The impulse and continuous wave generations of CO_2- and CO-lasers have been reached in the stationary nuclear reactor core.

(Slide 2). Parameters of CO-impulse laser are presented on this slide. The maximum reached values of the specific output energy and efficiency are equal to (18 ± 5) j/l·amagat and (12 ± 4)%, respectively, for temperature ~150K, $\varphi_T \approx 10^{13}$ n/cm^2s.

Continuous wave generation of CO-laser was got for gas mixture with ratio $CO : N_2 : {}^3He = 1 : 6 : 7$ with density 0.15 amagat, rate of gas pump flow 15 g/s, gas temperature 150K, thermal neutron flux density $\varphi_T \approx 10^{13}$ n/cm^2s. Irradiation power of CW CO-laser was equal to (32 ± 10) watt, the efficiency ~0.7%.

Then the possibility and condition of generation receipt excimer lasers excited by the non-self maintained discharge in stationary nuclear reactor have been considered. Hence plasma of gas mixture for excimer lasers $^3He + Xe + NF_3$ and $^3He + Xe + CCl_4$ excited by the products of the nuclear reaction $^3He(n,p)^3H$ has been investigated [13].

(Slide 3). On this slide the kinetic processes in plasma of gas mixture $^3He : Xe : NF_3 = 350 : 1.5 : 1$ for one atmosphere are indicated. Moreover, velocities of processes and components' densities are also shown here.

(Slide 4). On this slide experimental and calculation densities of the ions and electrons versus the thermal neutron flux density are shown. As it is seen the calculation data are in agreement with the experimental results. Ion density values are greater than electron ones by a factor of 10 to 100. They have different dependence on neutron flux density. The ion density growth is approximately proportional to the square root of neutron flux density whereas the electron density is directly proportional to it.

Due to the published data the minimum ion and electron densities must be $Ni \sim 10^{10}$ cm^{-3} and $Ne \sim 10^8$ cm^{-3}, respectively, to provide the generation of XeF* excimer discharge laser, controlled by an electron beam . According to these data we can conclude that XeF* excimer discharge laser with the nuclear preionization will be generated in the nuclear reactor for the thermal neutron flux density increase $\gtrsim 10^{12}$ n/cm^2s.

To create the excimer laser operating in the stationary nuclear reactor core we investigate the property change of capacitors and optical materials (LiF, NaCl, sapphire windows) depending on the reactor radiation dose [15]. It was shown that sapphire does not change transparent property for UV-rays until neutron fluent 10^{18} n/cm^2. In the case of infrared rays its stability is preserved for greater values of neutron flux density.

(Slide 5). On this slide the experimental excimer laser arrangement is shown [7]. There are two pairs of electrodes and two resonators in the laser chamber. Electrode length is 50 cm; the distance between them is 9 mm; the width of discharge region is 6mm. UV laser irradiation from the first resonator passes over the polished tube on the upper reactor cover, where it is registered by PEM (photoelectric multiplier). Laser radiation from the second resonator registered the calibrated thermoelement probe. Each laser resonator was formed by an aluminium spherical mirror (radius 5 m) and a sapphire plate.

To get a short discharge impulse the electric power supply system including two capacity contours has been used. The accumulating capacitors bank (40 nanofarad) was placed one metre from the reactor core. It was charged from the high voltage rectifier. The voltage from the accumulating capacitors bank was transferred over controlled discharge gap, waveguide, high-voltage hermetical electrical input to the capacitors which shorten impulse (5 nanofarad) placed in a laser chamber and then to the electrodes. Gas mixtures $^3He : Xe : NF_3 = 350 : 1.5 : 1$ and $^4He : ^3He : Xe : NF_3 = 250 : 100 : 1.5 : 1$ at pressures 1 and 3.5 atm., respectively, were ionized by the products of $^3He(n,p)^3H$ nuclear reaction. On the given laser arrangement XeF* excimer laser generated UV radiation in the stationary nuclear reactor core [7]. The maximum specific discharge energy was equal to $\sim$ 50 j/l. The specific radiation energy was $\sim 10^{-2}$ j/l, the efficiency was $\sim$ 0.02%. The minimum threshold of the thermal neutron flux density for generation of the excimer laser was $\sim 10^{12}$ n/cm^{2}s. It is in a good agreement with data, obtained from experimental plasma research.

In addition, radiation heat of capacities, which short impulse, limited the maximum neutron flux density by $\varphi_T \sim 10^{13}$ cm^{-2}s^{-1} value. These capacities were broken at greater values of the neutron flux density.

Moreover, this laser arrangement was not optimum. In future when we create more optimum resonator, shorter impulses, more thermally stable capacities the output parameters of excimer laser will increase.

The discharge xenon laser with nuclear preionization in the stationary nuclear reactor core has been investigated on three arrangements [14]. Arrangement N1 was similar to that on which excimer laser investigation was carried out. Arrangements N2 and N3 had one capacity contour only, shortening capacities and waveguide were absent. It allows to operate at prolonged impulses, at greater neutron flux density and higher temperature. On arrangements N1 and N3 gas mixture was ionized by the products of $^3He(n,p)^3H$ nuclear reaction. Arrangement N2 had no helium. It was ionized by the fission fragments of ^{235}U which covered the electrodes' surface. The thickness of ^{235}U layer was $\sim$10 mg/cm^{-2}.

Laser arrangement N3 allowed wide regulation of temperature. For this purpose the laser chamber had a double casing, whose external side was cooled by reactor water. There was helium with variable pressure between casings. It allowed to vary temperature of the internal casing and gas mixture.

The experiments carried out indicate that the minimum neutron flux density providing work of discharge xenon laser with nuclear preionization is equal to $\varphi_T \sim 10^{11}$ cm^{-2}s^{-1}. It corresponds to the electron concentration Ne $\sim 2 \cdot 10^{10}$ cm^{-3}.

(Slide 6). On this slide the output energy of radiation on the wavelength $\lambda \approx 1.73$ mkm versus voltage of accumulating capacities for different neutron flux densities equal to $3 \cdot 10^{13}$ cm^{-2}s^{-1} is shown. As it is seen generation saturation for $\varphi_T \sim 10^{14}$ cm^{-2}s^{-1} and voltage $\sim$ 20 kV is not reached. That indicated the possibility of the laser parameters' improvement with the charge voltage growth. The maximum specific output energy and the radiation efficiency for neutron flux density $\varphi_T \sim 10^{14}$ cm^{-2}s^{-1} and for charge voltage $\sim$20 kV are equal to $\sim$ 0.1 j/l and 0.1$\div$0.2%, respectively. Thus, exclusion of helium from the gas mixture and prolongation of discharge impulse allow to increase laser energy parameters 50 times.

The possibility of lasers to work at high temperatures is important for its usage in the nuclear reactor. For this purpose laser generation investigations from 50°C to 600°C were carried out.

(Slide 7). On this slide the results for gas mixture $^4He : ^3He : Ar : Xe = 50 : 50 : 50 : 1$ at pressure 1.5 atm and at the charge voltage $\sim$20 kV are represented. Note that temperature change in the interval from 0°C to 600°C does not affect the laser work. It is explained by the fact that generation occurs on the transition of xenon atoms located in the high-energy region.

Moreover, generation of discharge xenon laser with ionization by α-particles of radioisotope source Po^{210} is obtained and investigated [16]. Electrodes and α-particles sources are positioned in a dielectric laser chamber. Transverse excitation with discharge of low inductivity capacity (10-30 nF) through ionized gas is used in the laser. Twenty capacitors $220\pi\Phi$ uniformly distributed along electrodes were used for intensity discharge current impulse. The volume of active region is equal to 50 x 1 x 0.3 cm. Twenty α-particles sources Po^{210} are arranged along discharge space. Radioactivity of one source was $1.5 \cdot 10^{19}$ Bk., diameter on radiation layer was 7 mm. Ionization rate was $2 \cdot 10^{12}$ cm^{-3}s^{-1}, electron concentration was $2 \cdot 10^9$ cm^{-3} for mixture He(1.5 atm) + Ar(0.5 atm). Laser resonator includes a spherical mirror with silver coating and sapphire plate. The laser generation was obtained on the mixture He-Ar-Xe.

(Slide 8). On that slide optimization results of the mixture composition are shown. Spectral measurements have not been made but it is shown that 40 per cents of laser energy are radiated on the transition with wavelength 1.73 mkm. It was determined by means of

filter kit. Mechanical strength does not allow to work at pressure more than 2 atm. (Slide 9). Nevertheless, the achieved value of specific laser radiation energy was $2 \cdot 10^{-2}$ j/l that is demonstrated on this slide.

Investigation to prove possibility to create quasi continuous operation laser on the triplet 7^3S_1-6^3P_2.$6^3P_1$$6^3P_0$ (λ = 546.1; 435.8 and 404.7 nm) transitions of the mercury atoms by nuclear pumping was carried out [17]. Mechanisms of 7^3S_1 level population by ionization pumping and possibility of fast selective quenching low 6p-levels of mercury atoms was investigated. For this purpose emission spectrum measurement for mixtures of mercury vapor and rare gases with molecular gas additions was carried out. These mixtures were excited by products of nuclear reaction $^3He(n,p)^3H$ in nuclear reactor and α-particles of radioisotopes sources ^{210}Po and ^{239}Pu.

Gas mixtures were in soldered glass ampoules $\phi 30 \times 60$ mm^2 with a radiation-resistant cerium glass window in the reactor experiment. Ampoules were positioned in the central channel of the WWR-K nuclear reactor active zone. The lower part of the experimental channel (length - 700 mm) consisted of concentric tubes made from stainless steel. The gap between them was equal to 2 mm. It was possible to change temperature in an ampoule varying ^4He pressure in a gap. Light emission passed through the stainless steel tube with 6 m length. It was registered by means of monochromator with a quartz prizm and photomultiplier tube working in the regime of photons account.

The set with α-particle excitation allowed to carry out measurement for low temperature and for wide variety of mixture and pressure in more wide spectral region $\lambda \sim 200$-830 nm. It is shown on Slide 10.

In paper by Miskevich et al. the pumping possibility of mercury 7^3S_1 state by a step exciting over a resonance level has been indicated. Particle concentration can be rapidly decreased on the resonance level by adding hydrogen (or deuterium) as the corresponding quenching rate constant ($\sim 4 \cdot 10^{-10}$ cm$^3 \cdot$s^{-1}) is essentially high.

The dependence of radiation intensity of resonance (λ = 253.7 nm) and trippled (λ = 435.8 nm) mercury lines on hydrogen pressure for mixture exciting He-Xe-Hg-H_2 is shown on Slide 11.

As it is seen the trippled line intensity does not depend practically on resonance level population. Therefore, 7^3S_1 level population is not realized by a step exciting. Luminescence intensity dependence of the triplet line on hydrogen pressure allows to evaluate rate constant of quenching by hydrogen of 7^3S_1 state: $K_{quench.} \approx 4 \cdot 10^{-11}$ cm^{3}s^{-1} (evaluation for deuterium leads to the same value). Thus, hydrogen rapidly and selectively quenches the low 6p levels; due to evaluations hydrogen concentrations on level 20-30 torr are necessary for generation. Nitrogen addition into the mixture caused intensity increase of mercury resonance line because of population of 6^3P levels for interaction of $N_2(A^3\Sigma_u^+)$ molecules with mercury atoms.

Slide 12 shows that intensity of lines does not practically depend on mercury vapor pressure in region (10^{-3}-0.3) torr at radioisotope and reactor sets, respectively. It excludes possibility of the direct excitation of 7^3S_1 level from the ground state by the electron impact.

We suppose that the more probable channel of 7^3S_1 level population is a dissociative recombination of Hg_2^+ mercury molecular ions. The more essential processes in Xe + Hg plasma are shown on Slide 13. Intensity of triplet line falls down quickly if mercury vapor pressure is less than 10^{-6} torr. It is conditioned by decrease of the dissociative recombination of the mercury molecular ions Hg_2^+ because of competing process. In that case luminescence decrease of the triplet lines at Hg pressure increasing up to 100-300 torr is determined by quenching itself of the excited states. Evaluation of 7^3S_1 quenching rate constant gives $K_{quench.} \approx 10^{-11}$ cm^{3}s^{-1}.

As 7^3S_1 level pumping is carried out by dissociative recombination channel, xenon can serve as a buffer gas because charge exchange between xenon and hydrogen is realized slowly [20]. Kripton usage is worse because of small rate constant of charge exchange Kr^+ on mercury atoms ($< 10^{-12}$ cm^{-3}s^{-1} [21]).

Efficiency of 7^3S_1 level population was determined by comparison of line intensity of mercury triplet and the second positive nitrogen system in mixture Ar + N_2. Luminescence efficiency of Ar + N_2 was determined by calculation. Population efficiency for mixture 760 torr Xe + 1.5 torr Hg was ~ 0.8.

Therefore, gas mixture (He)-Xe-Hg-H_2 is a perspective active medium for generation in blue-green spectrum region at the pumping by reactor ionizing radiation. Efficiency can get 7-8% on λ = 546 nm and 10% on λ = 405 nm with the account of pumping efficiency.

Calculated generation threshold values are $W_{thresh.} \sim 1.6$ W/cm^3 (λ = 546 nm) and $W_{thresh.} \sim 3.5$ W/cm^{-3} (λ = 436 nm) (without account of loss at absorption in an active medium for $\alpha_{thresh.} \sim 2 \cdot 10^{-4}$ cm^{-1}). These values are close to maximum specific powers deposited in a gas medium for stationary nuclear reactor. However, the experiments carried out with laser on the triplet transitions of mercury atoms with the direct nuclear pumping in our reactor do not allow to obtain generation.

REFERENCES:

1. G.H.Miley. Direct Nuclear Pumped Laser-Status and Potential Applications 4th Workshop

on Laser Interaction and Related Plasma Phenomena, November, 1976, Tray, New-York, V.4A, p.181-224.
2. A.M.Voinov, L.E.Dovbysh, V.N.Krivonosov, S.P.Melnikov, A.T.Kazakevich, I.V.Podmoshensky, A.A.Sinansky. Nuclear Pumped Infrared Lasers on ArI, KrI and XeI Transitions. Pisma v JTF, V.15, No.7, 12, 1979.
3. H.S.Rhoads and R.T.Schneider. Nuclear Enhancement of CO_2 Laser Output. Trans.Am.Nucl. Soc. 14. 429 (1971).
4. G.A.Batyrbekov, V.A.Danilychev, I.B.Kovsh, M.P.Mardenov, M.U.Khasenov. Electroionized CO_2-Laser Generating in the Active Zone of the Stationary Nuclear Reactor. Quantum Electronics, v.4, No.5, p.1166, 1977.
5. G.A.Batyrbekov, V.A.Danilychev, A.A.Ionin, I.B.Kovsh, S.K.Kunakov, M.P.Mardenov, M.U.Khasenov. Excitation of Laser Mixtures CO + N_2 + ^{3}He by Non-selfmaintained Discharge in the Active Zone of Nuclear Reactor. Izvestiya AN SSSR, ser.fiz. v.42, No.12, p.2484, 1978.
6. G.A.Batyrbekov, V.A.Danilychev, A.A.Ionin, M.U.Khasenov. Electroionized CO-Laser, Cooled in the Active Zone of the Stationary Nuclear Reactor. Pisma v JTF, v.5, No.19, p.837-840, 1979.
7. N.G.Basov, G.A.Batyrbekov, V.A.Danilychev, O.I.Kerimov, Yu.E.Kuzmin, A.B.Tleuzhanov, M.U.Khasenov. Excimer Laser Ionized by the Nuclear Reactor Radiation. Pisma v JTF, v.5, No.11, p.1044-1047, 1985.
8. G.A.Batyrbekov, V.A.Danilychev, I.B.Kovsh, M.P.Mardenov, M.U.Khasenov. Non-self-maintained Discharge in CO_2:N_2:^{3}He Plasma, Generated in the Radiation Field of the Stationary Nuclear Reactor. Kratkiye soobshcheniya po fizike, P.I AS SSSR, No.3, 1977.
9. G.A.Batyrbekov, V.A.Danilychev, I.B.Kovsh, M.P.Mardenov, M.U.Khasenov. The Investigation of CO_2:N_2:^{3}He Plasma Parameters, Generated in the Active Zone of the Stationary Nuclear Reactor. JTF, v.48, No.1, p.39, 1978.
10. G.A.Batyrbekov, V.A.Danilychev, A.A.Ionin, S.K.Kunakov, M.P.Mardenov, M.U.Khasenov. The Investigations of Plasma Parameters and Non-self-maintained Discharge of the Gas Mixture CO:N_2:^{3}He, Installed in the Active Zone of the Nuclear Reactor. JTF, v.49, No.1, p.55, 1979.
11. G.A.Batyrbekov, S.A.Kostritsa, M.U.Khasenov. Chemical Processes in the CO:N_2:^{3}He Plasma, Generated in the Active Zone of the Nuclear Reactor. C.H.E., v.17, No.3, p.266, 1983.
12. G.A.Batyrbekov, V.A.Danilychev, A.A.Ionin, I.B.Kovsh, M.P.Mardenov, M.U.Khasenov. Investigations of the CO and CO_2 Electroionized Lasers, Operating in the Active Zone of the Stationary Nuclear Reactor. Q.E., v.9, No.7, p.1493-1496, 1982.
13. G.A.Batyrbekov, V.A.Danilychev, S.A.Kostritsa, Yu.E.Kuzmin, A.B.Tleuzhanov, M.U.Khasenov. On the Possibility of the Excimer Laser Action in Nuclear Reactor Irradiation. Pisma v JTF, v.8, No.13, p.719, 1982.
14. G.A.Batyrbekov, E.G.Batyrbekov, V.A.Danilychev, A.B.Tleuzhanov, M.U.Khasenov. Xenon Electroionized Laser Activated by the Weak Source of Ionization. Q.E., v.16, No.8,1989.
15. G.A.Batyrbekov, O.N.Kerimov, A.B.Tleuzhanov, M.U.Khasenov. Radiative Stability of Some Elements of the Nuclear Laser Set. Izvestiya AS KazSSR, ser.fizmat., v.6, p.23, 1986.
16. G.A.Batyrbekov, E.G.Batyrbekov, V.A.Danilychev, A.B.Tleuzhanov, M.U.Khasenov. Electroionized Laser Activated by the Radioisotope Ionization. JTF, v.57, No.4, 1987.
17. G.A.Batyrbekov, E.G.Batyrbekov, V.A.Danilychev, A.A.Soroka, M.U.Khasenov. On the Possibility of Laser Action of the 7^3S-6^3P Transitions of Mercury Pumped by Ionizing Radiation. Q.E., v.14, No.6, p.1216, 1986.
18. G.A.Batyrbekov, E.G.Batyrbekov, M.U.Khasenov. Measurement of the Light-Nuclear Energy Transformation Coefficients in Xe + Hg, Kr + Hg Mixtures. J.A.S., 47, No.4, p.652, 1987.

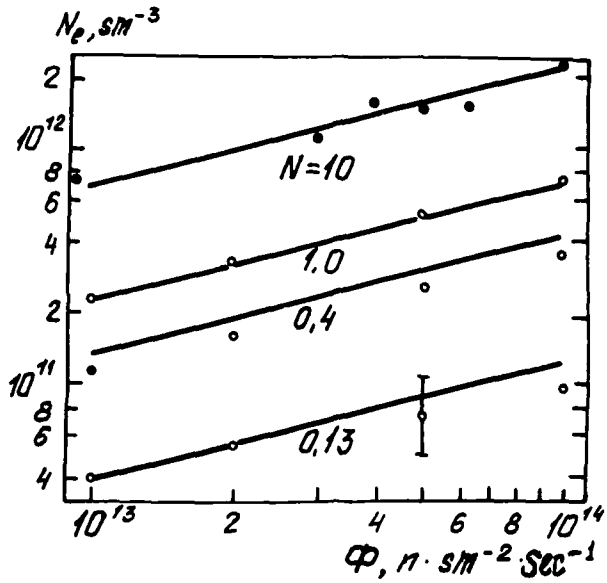


Fig.1. Electron density versus neutral flux density and total gas pressure in $CO_2 : N_2 : {}^3He$ (1 : 4 : 5) and $CO : N_2 : {}^3He$ (1 : 6 : 7) gas mixtures.

$\Phi \cdot 10^{13}$ n/sm-Sec	T, K	U/Nh KV/sm-amagat	$\frac{Qe}{e}$ J amagat	τ ms	$Q^{Sp.amp}_{rad.}$, J/cat	Efficiency (%)
1,5	150	1,8	27	1,1	182	12
3,5	205	2,3	43	0,7		
8	240	3,3	100	0,4		
10	~300	~4	~120	0,4	~0,2	0,3

Fig.2. Threshold output energy CO-lasers characteristics.

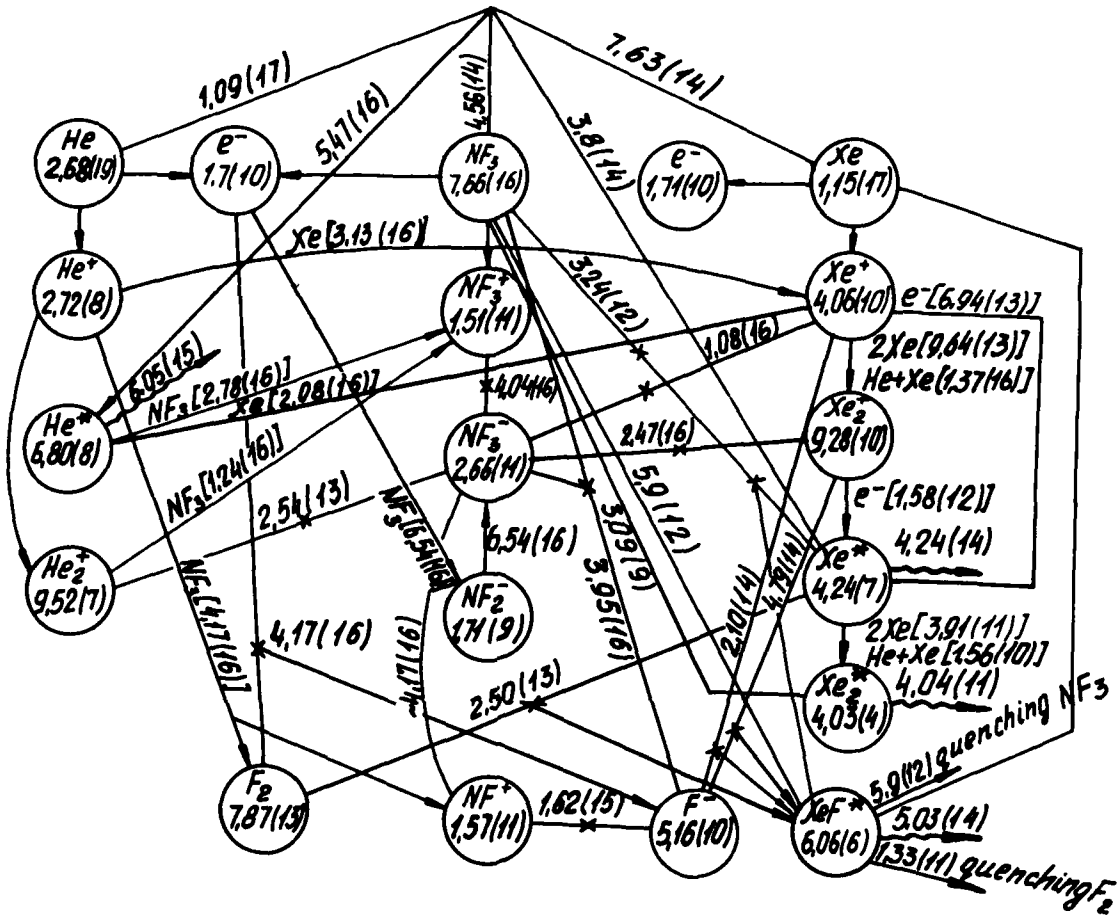


Fig.3. The kinetic model of the elementary processes in He : Xe : NF_3 plasma, generated by the $^3He(n,p)T$ in the neutral flux $\varphi = 2 \cdot 10^{13}\ sm^{-2}\ sec^{-1}$.

A is the concentration of A type particles (sm^{-3}),
is denoting order of (He 2.43 9 = 2.43 .109 value

$A \xrightarrow{R} B$ is rate of R process causing transformation of A to B

$A \dashrightarrow B$ is recombination A to B.

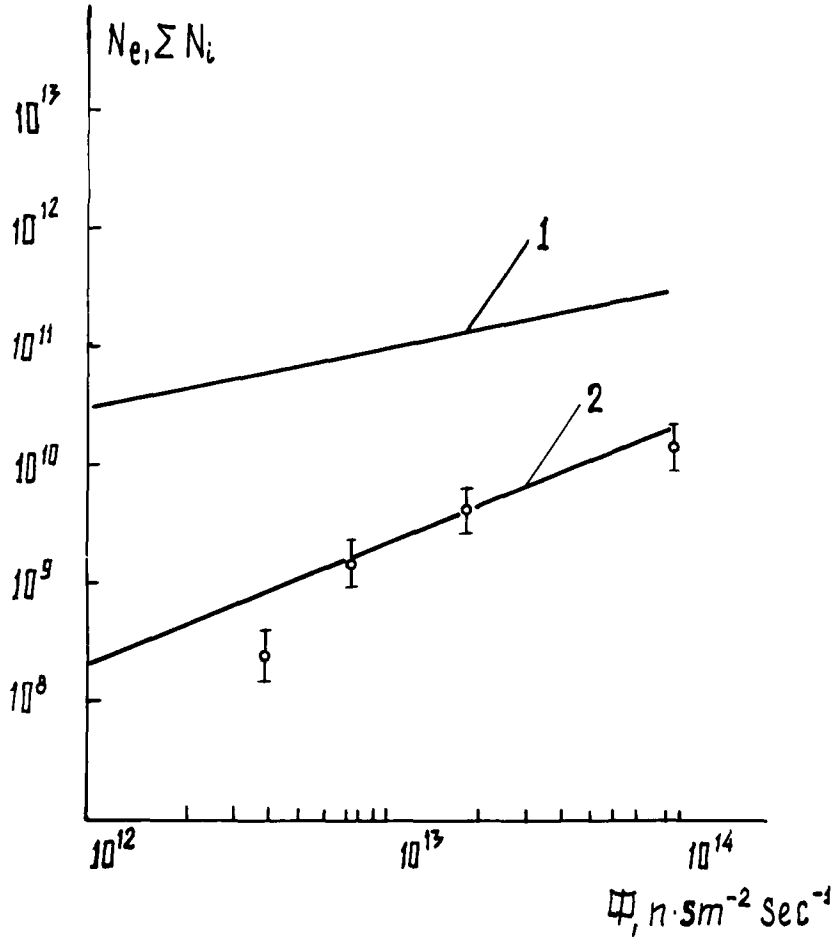


Fig.4.
Density of electrons and negative ions in plasma of gas mixture ^3He : Xe : NF_3 = 760 : 3 : 2 versus the flux of neutrons.
0 - experiment
1 - negative ions
2 - electrons

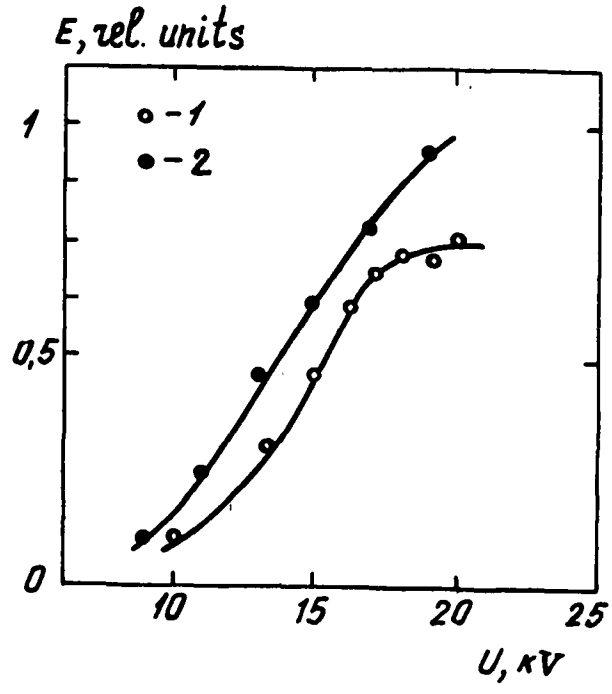


Fig.6.
Generation energy dependence on the charge voltage of the accumulating capacitances. Mixture Ar : Xe = 100:1, P = 2 atm. Φ = 3.10^{13}(o), 10^{14} (●) n/sm^2s.

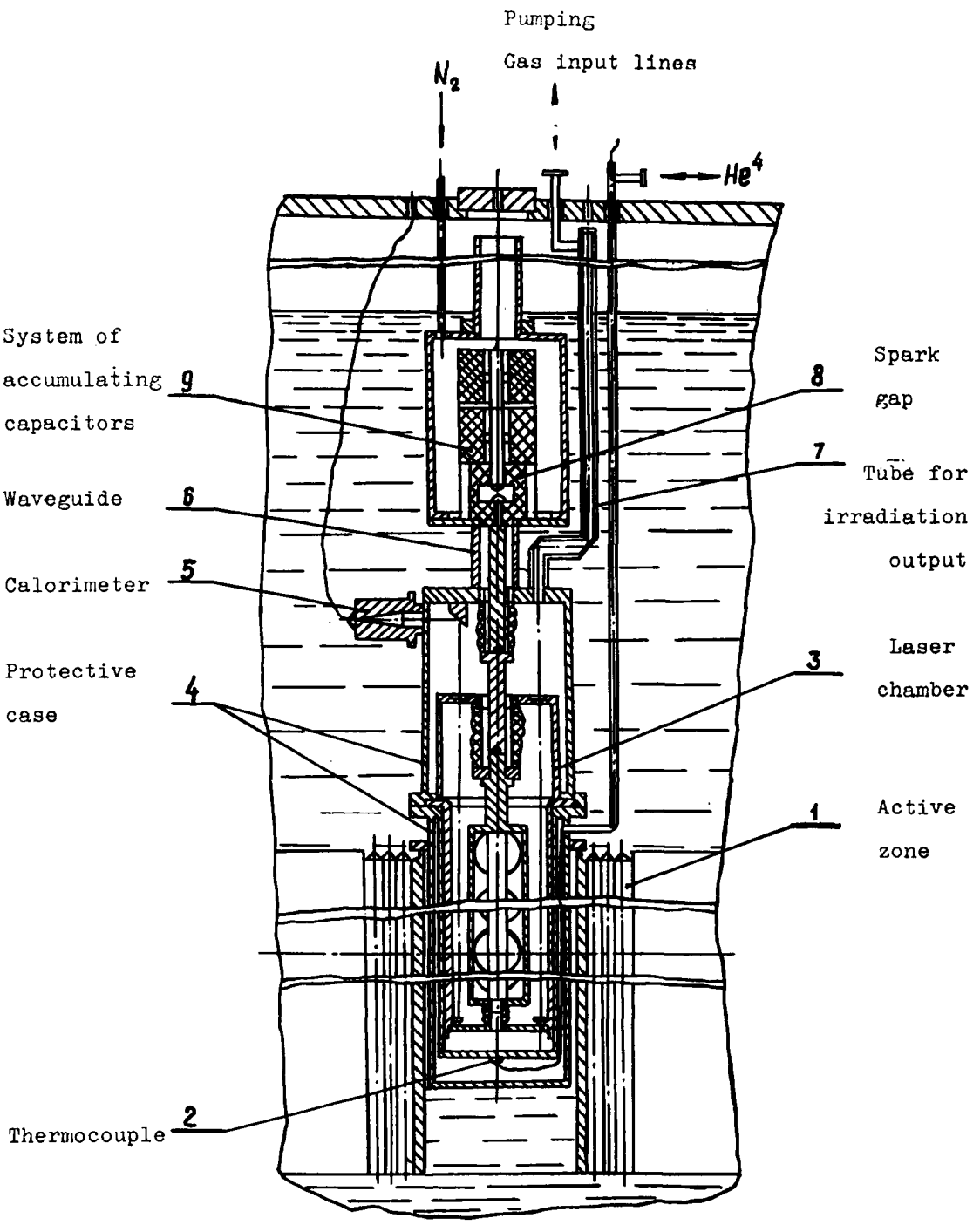


Fig.5. Experimental excimer laser arrangement.

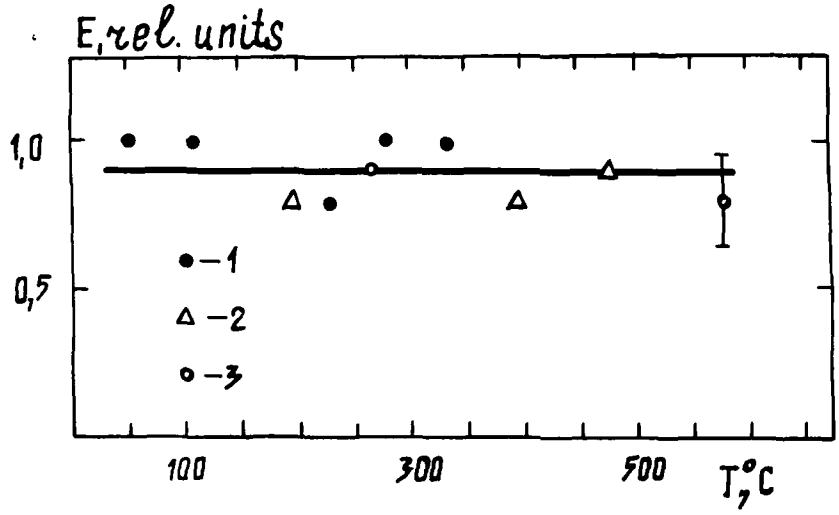


Fig.7. Temperature effect on the laser output energy characteristics. Mixture ^4He : ^3He : Ar : Xe= 50 : 50 : 50 : 1, for P = 1.5 atm, and U=20 kV. $\Phi = 10^{13}$(●), 2.10^{13}(△), 3.10^{13}(○) n/sm^{2}s.

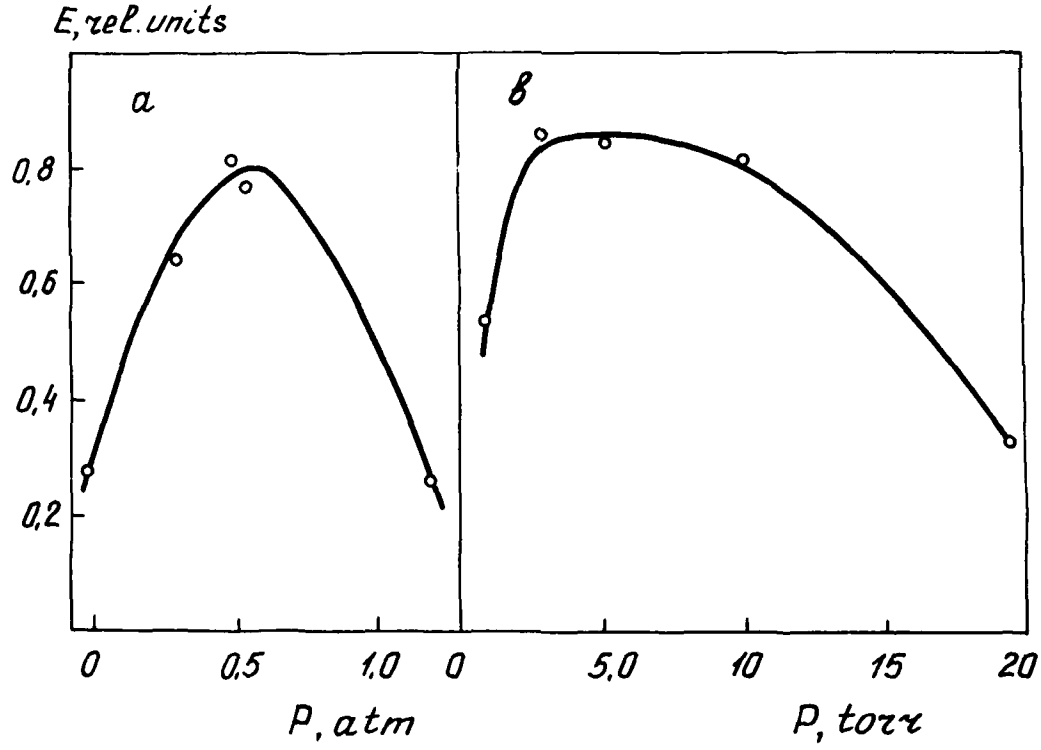


Fig.8. Xe-laser output energy versus
(a) partial pressure of Argon in the mixture He+Ar+Xe(5 torr); total pressure is 1.8 atm. (b) partial pressure of Xenon in mixture ^3He(1.3atm)+Ar(0.5atm)+Xe.

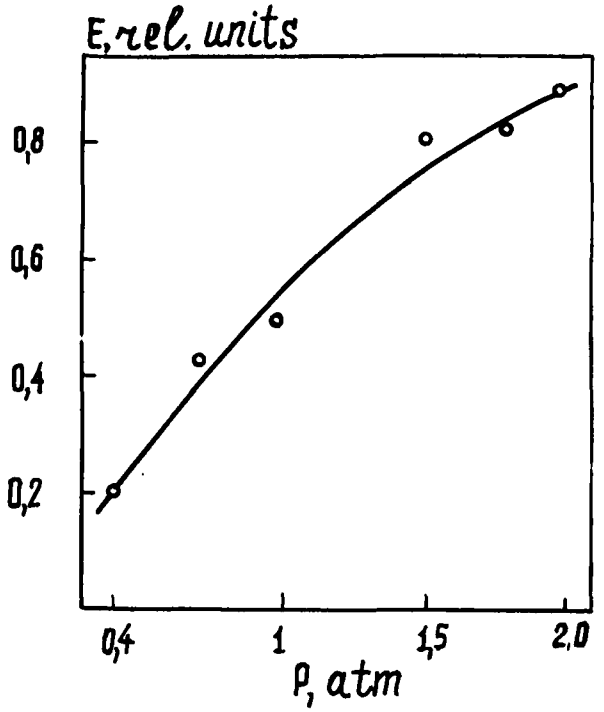


Fig.9. Laser output energy versus the pressure of the gas mixture He : Ar : Xe = 175 : 75 :1.

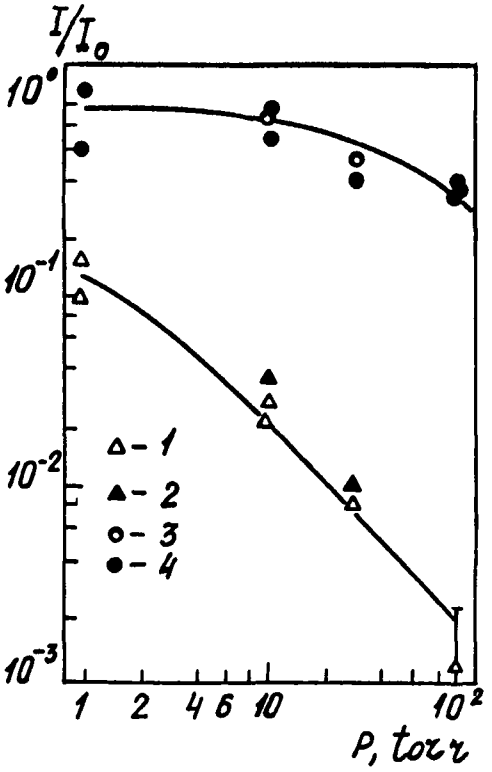


Fig.11. The mercury resonance (1,2) and triplet (3,4) intensity lines versus hydrogen (2,3) and deuterium (1,4) pressure in He(1 atm) + Xe(1 atm) + Hg(1.5 mtorr) + $H_2(D_2)$ mixture. I_0 is an intensity line in the pure mixture excluding H_2 or D_2

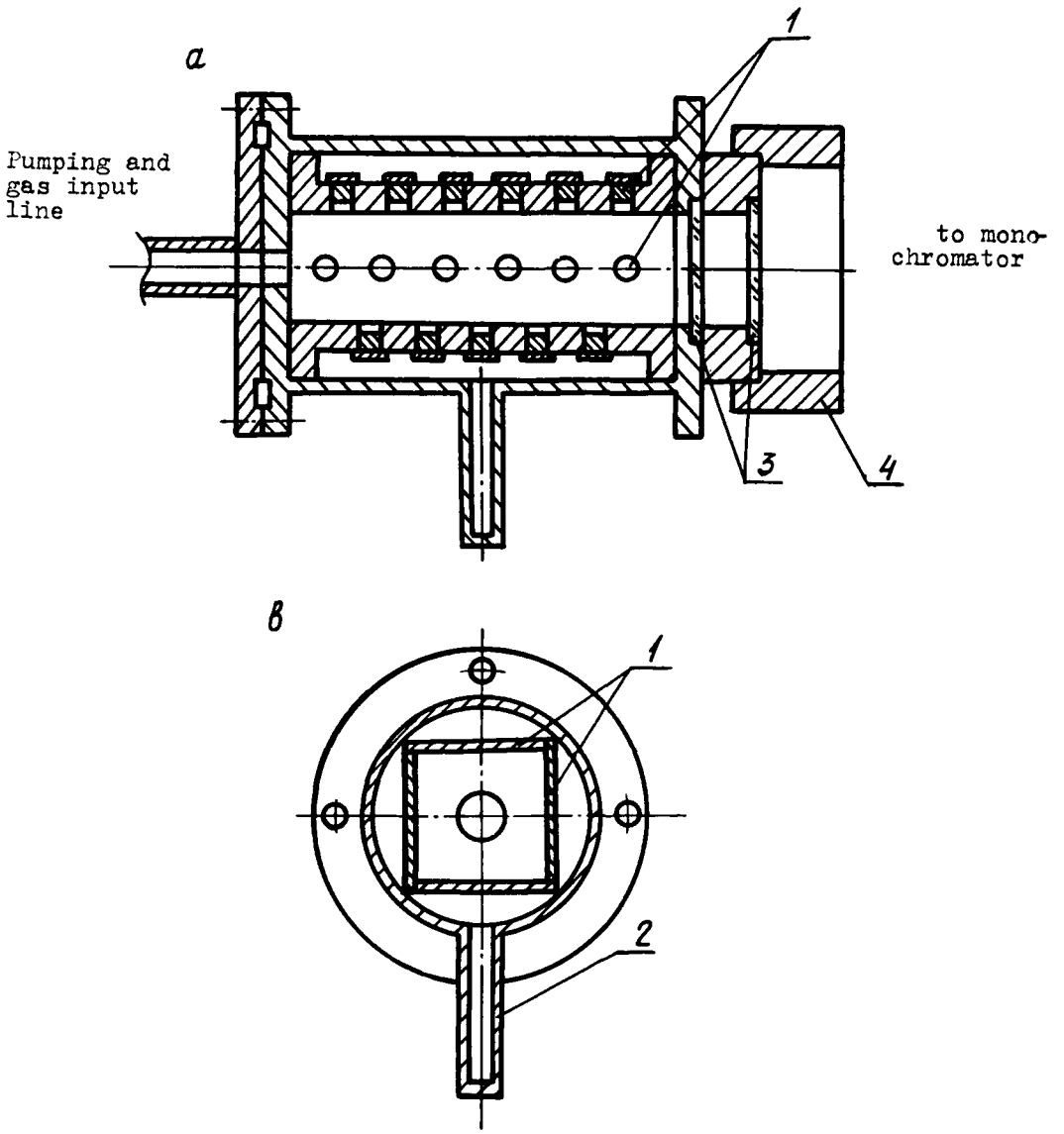


Fig.10. Isotope chambers.
1. Po^{210} (a) and Pu^{239} (b) sources.
2. Mercury transport line.
3. Sapphire plates.
4. Ebonite tube.

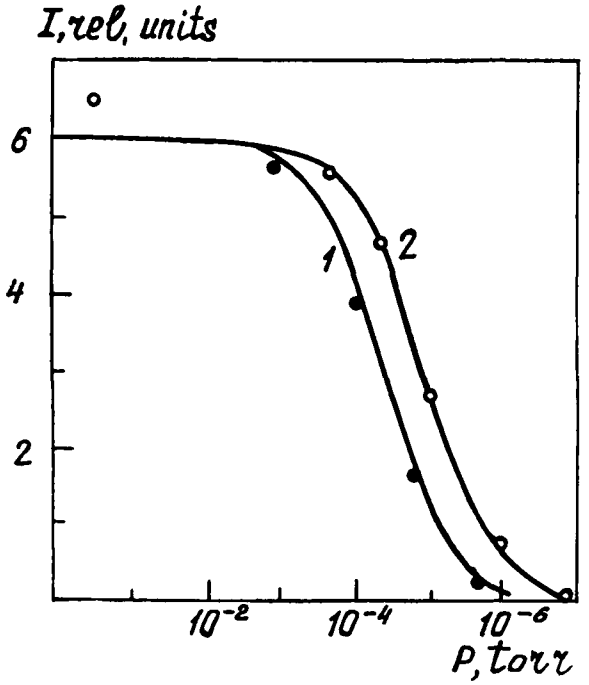


Fig.12.
Luminescence intensities (line λ = 435.8 nm) versus mercury pressure in the mixtures ^{3}He - Xe - Hg (1) and ^{3}He - Kr - Hg (2).

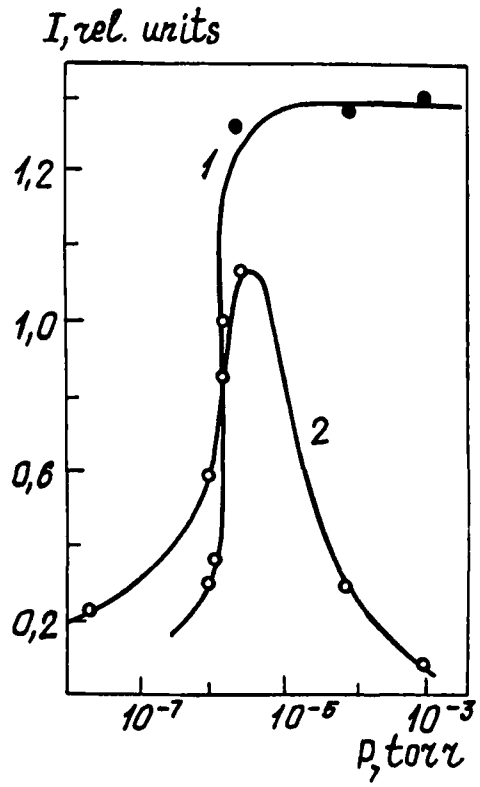


Fig.13.
Intensity lines 435.8 nm (1) and 365.0 nm (2) versus mercury vapour pressure in ^{3}He (2 Amagat) + Hg.

LASER GENERATION CHARACTERISTICS ON Xe INFRARED ATOMIC TRANSITIONS

V.I.Derzhiev, O.V.Sereda, S.I.Yakovlenko and A.G.Zhidkov

General Physics Institute, Academy of Sciences of the USSR
Vavilov Str. 38, Moscow, 117942, USSR

Abstract

Laser temporary and spectral characteristics on Xe IR atomic transition, in a mixture with Ar-Xe, at λ=1.73,2.03,2.63,2.65,3.37 μm are analyzed on the basis of numerical computations. Pumping by a hard ionizer and by discharge sustained by an electron beam is discussed. Results of computations are in adequate agreement with the experiment.

Introduction

Laser behavior on XeI IR atomic transitions from the moment of triggering [1] evokes keen interest of investigators last time [2-5]. Efficiency of 2-3 % at low-threshold nuclear pumping has already been reached [2,6].Generation energy of 80 J has been attained by combined pumping [5].

Despite these considerable achievement, opinions differ as to mechanism of producing population for laser IR transitions of XeI by inversion.

This paper presents, on the strength of a specially developed kinetic model, results of theoretical investigation of Ar-Xe laser generation at the wavelength of λ=1.73,2.03, 2.63,2.65,3.37 μm. Mechanisms of bringing about inversion for these transitions are discussed. Results of computations adequately agree with the data obtained by different experimental groups.

Kinetic Model

Computations in this paper are based on a kinetic model [7] which takes care of the ions of Ar^+ , Ar_2^+ ,$ArXe^+$,Xe^+ ,Xe_2^+ , excited atomic and molecular states of Ar^* ,Ar^{**} , $ArXe^*$,Ar_2^* ,Xe_2^* as well as 12 states of the atom Xe($2s_i$,$2p_i$,$3d_i$). The mixing of excited atoms of Xe with atoms Ar,Xe and electrons was also taken into account.

We shall point briefly some special features characteristic of pumping by an electron beam. The beam's electrons deposit their energy for buffer gas ionization and excitation. In dense mixes, the ions of Xe_2^+ and $ArXe^+$ are generated effectively and are subsequently undergo dissociative recombination into various states of XeI atoms. Computations indicate that in the case of a beam pumping of a dense mixes over 70 % of the relaxation flux are subjected to dissociative recombination of the ions of Xe_2^+ and $ArXe^+$. These processes constitute a major contribution to populating the states of Xe5d[3/2]1, which in itself is a upper level for transitions at λ=1.73,2.03,2.65μm(Fig.1)

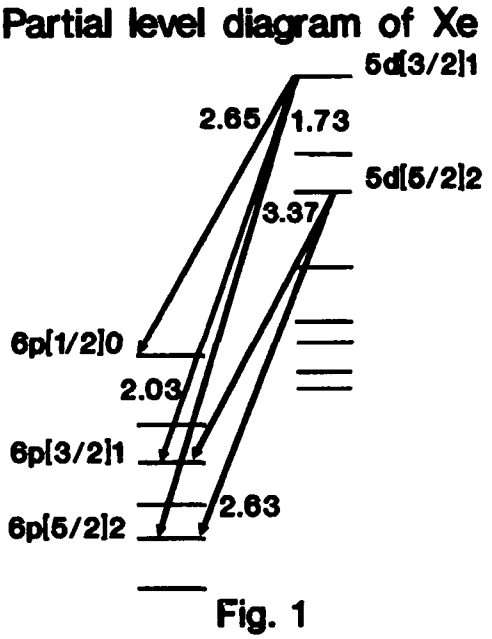


Fig. 1

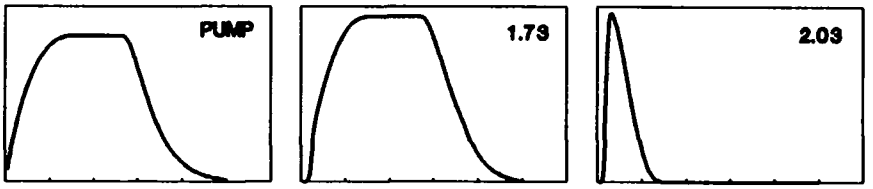
At low pump power, there is definitely a predominance of a flux preconditioned by dissociative recombination of the ion of Xe_2^+ ;as pumping increase, dissociative recombination of the ion of $ArXe^+$ proves to be efficient pumping channel. As we consider only one of the mechanisms of populating the 5d[3/2]1 level, it appears virtually impossible to provide a satisfactory description of the available experimental data within a wide range of environmental and pumping para meters. Transfer of excitation from one atom of argon is only tangible at low pump power.

The level 5d[5/2]2 of Xe atom, which is a upper working level for transitions at λ=2.63,3.37 μm, may be populated with both a dissociative recombination of the ions of $ArXe^+$,Xe_2^+ and in the course of the 5d[3/2]1 level quenching, in reactions of the type:

$$Xe(5d[3/2]1) + Rg = Xe(5d[5/2]2) + Rg, \quad Rg=Ar,Xe \qquad (1)$$

Generation at λ=1.73 μm

This transition (5d[3/2]1-6p[5/2]2) as is clear from the experimental data [8] and



one division - 1μs

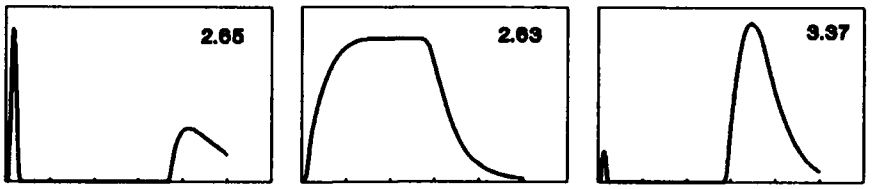
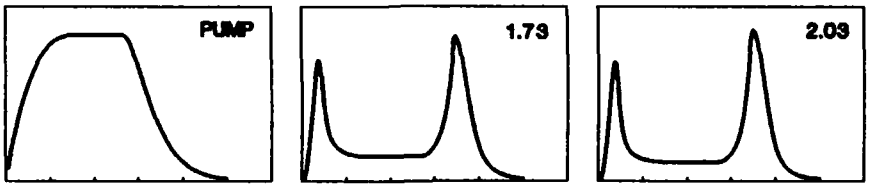


Fig.2 Generation dynamics in Ar:Xe=100:1 at 3.5 atm



one division - 1μs

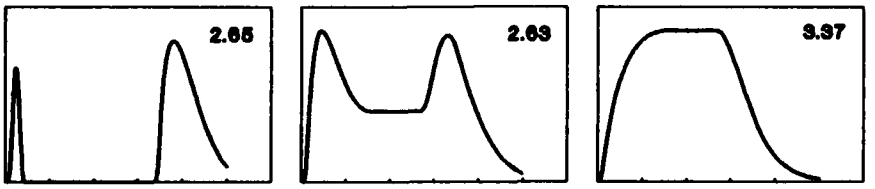


Fig. 3 Dynamics generation in Ar:Xe=4:1 at 3.5 atm

from our calculation [7], is most effective within a wide range of pumping power.Maximum efficiency >2 % has been attained both with pumping by product of nuclear reaction [6] and with pumping by an electron beam [9]. Under the conditions of a low pump power [6], an optimum pressure is equal to 0.5 atm. An increase in pressure leads to faster quenching of the upper working level in the processes (1), and, consequently, to a drop of efficiency. In the case of pumping by an electron beam [10], the 5d[3/2]1 level is quenched in reactions of the type:

$$Xe(5d[3/2]1) + e = Xe(5d;6p;6s) + e \qquad (2)$$

Therefore, an optimum pressure in this case is 3 to 4 atm. Any further growth of pumping capacity will result in a greater speed of the reaction (2) and, conversely, in a drop of laser efficiency. Thus, an increase of the electron beam flux density from 1.7 A/sm**2 to 5 A/sm**2 leads to a decrease of efficiency from ~2%[9] to 1%[10]. Should the electron beam density grow any further, generation is likely to decline or to be suppressed altogether as long as the beam is effective. The drops radiating power at the time of pumping, induced by growth of electron beam current ("double-humped" pulses), that were observed earlier [11], were also obtained in our computations. It must be noted, too, that with generation at λ=1.73 μm the lower laser level XeI is cleared by the atoms of Ar:

$$Xe(6p[5/2]2) + Ar = Xe(6s) + Ar.$$

Generation at λ=2.03,2.63,2.65,3.37 μm.

Alongside the most intensive line in the generation spectrum, four other lines can be observed, whose intensity may increase both in proportion to the growth of Xe content [12] and to increased pump power [13]. In the work [12], they measured both the time dependencies of lines intensity at λ=1.73, 2.03,2.63,2.65,3.37 μm and the radiation energies in these spectral line in relation to Xe content. We calculated spectral composition of radiation on the basis of the relationship δ=[Xe]/[Ar] under the condition similar to,those [12] (Fig. 2-4).

Let us discuss the nature of obtained relationship for the cases of δ=0.01 and δ=0.25. With [Xe]/[Ar]=0.01 (Fig.2), the next most intensive line after 1.73 m is that of λ=2.63 μm (transition 5d[5/2]2-6p[5/2]2), at which quasi-stationary generation is obtained. The 5d[5/2]2 level is populated in the course of processes (1) and, in smaller measure, when the dissociative recombination of Xe_2^+ ,$ArXe^+$ ions is in progress. For this reason, as the content of Xe increases, the quantity of radiation energy in this line also grows (Fig. 4).

The transition that occur at λ=2.03 μm (5d[3/2]1-6p[3/2]1) and at λ=2.65 μm (5d[3/2]1-6p[1/2]0) are characterized by the same upper work level as the transition at λ=1.73 μm. As the mechanism of populating the excited states of the XeI atom is

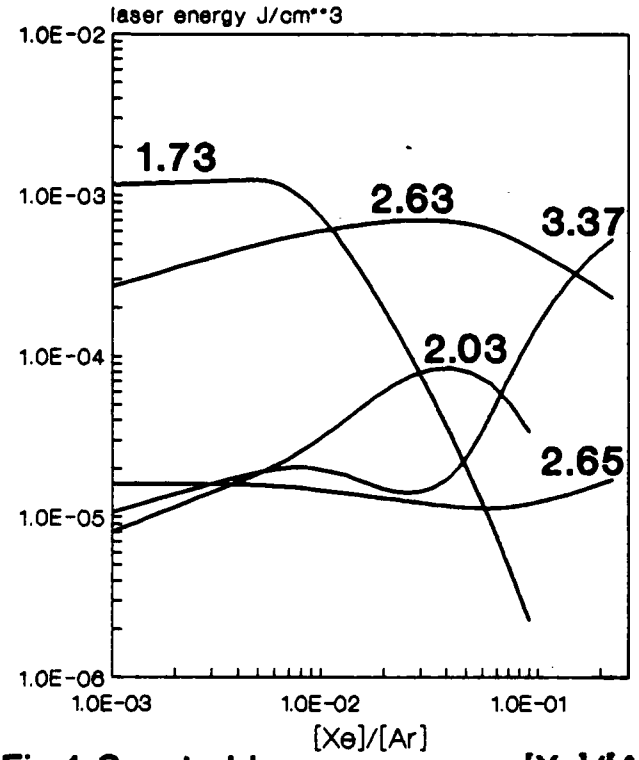


Fig.4 Spectral laser energy vs [Xe]/[Ar]

essentially that of recombination, the front edge of the pumping pulse, when the states of Xe(6p) are still at an early stage of being populated, features proper conditions for generation essentially in transitions at λ= 2.03, 2.65 μm that have greater cross sections of induced transitions than λ=1.73 μm. As the pumping power increases, population of the lower working level grows, which results in virtual suppression of generation at λ=2.65,2.03 μm. For the same reason, generation at λ = 3.37 μm (5d[5/2]1 - 6p[3/2]1) is also suppressed at the front edge of the pumping pulse. Conditions at the trailing edge of the pumping pulse, when populations of the Xe(6p) decline, again become favorable for generation at λ =2.65 and 3.37 μm.

At Xe:Ar=1:4, the generation spect - rum undergoes a substantial change. In this case, maximum of the generation energy occurs at λ= 3.37 and 2.63 μm. This is due to the fact that in a situation like this the quenching of the upper and lower working levels for generation transitions takes place in collisions with the atoms of Xe. A faster rate of clearing the 6p[3/2]1 level in collisions with Xe results in that maximum energy is now concentrated at λ=3,37 μm. It should be noted that according to our computations, there is no generation in pure Xe at the five lines being investigated.

An increased flux of the electron beam leads to a change of the radiation spectral composition [13]. Thus, at j=36 A/cm**2, the lines at λ=2.65 and 2.63μm are most intensive. An increase of generating power at λ=2.63μm is associated with a faster rate of populating the level 5d[5/2]2 in the course of step-by-step excitation of Xe atoms. A higher generation power at λ= 2.65μm is due to an improved clearing of the 6p[1/2]0 level by electrons.

A Discharge Sustained by the Electron Beam

Superposition of the electric field at the time when the electron beam is effective leads to a considerable increase of the laser energy and efficiency [5,9,14,15].

To model a non-self-sustained dis - charge, a system of balance equations for populations was resolved jointly with the Boltzman equation and the equations of the electric circuit, where discharge gap resistance calculated on the basis of the energy electron distribution function obtained.

Generation curves of the Xe laser were calculated for the experiment [14] , which did not investigate the radiation spectral composition. It was only because generation at three lines was taken into account, that it became possible to attain good adequacy with the experimental data (fig.5). Under these conditions, most energy is concentrated at λ= 2.63μm. Calculated energy of the pulse is 1.3 J, the value obtained as a result of the experiment is 0.9 J.

Calculations were also made for the specific conditions of the experiment [5], in which a generation energy of 80 J was achieved. These calculations were made for λ=1.73μm. Fig.6 shows good adequacy of the calculations and the experiment.

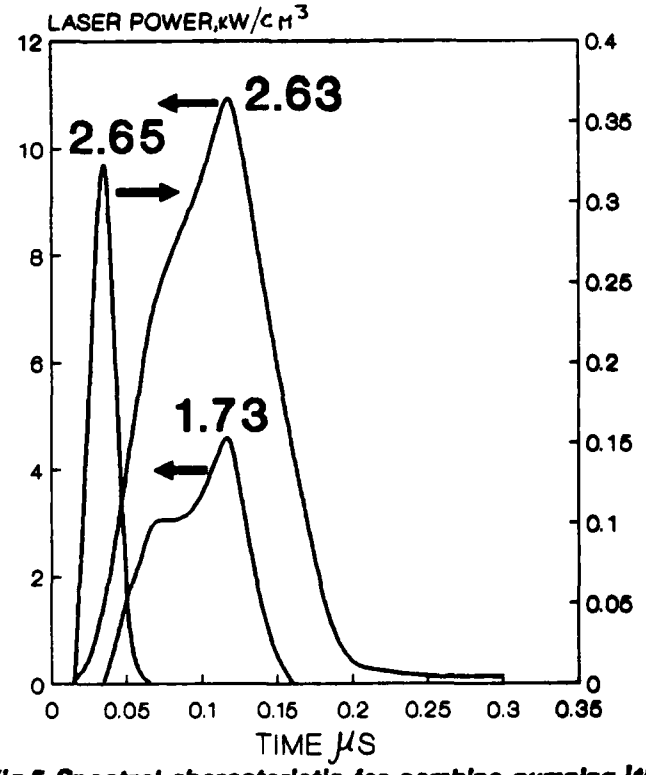


Fig.5 Spectral characteristic for combine pumping [15]

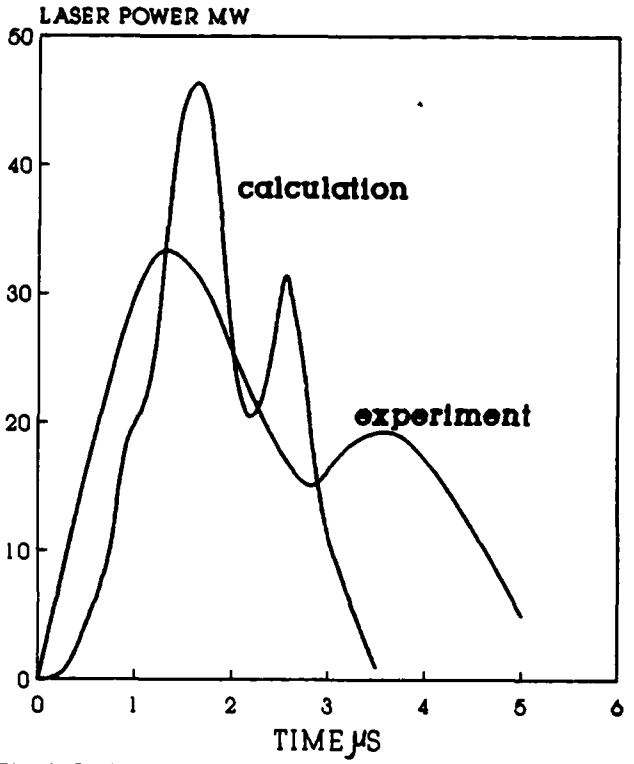


Fig.6 Output at 1.73 m for combine pumping (6)

The calculations prove there is a mechanism responsible for the storage of energy in metastable atoms [15], which substantially increases laser energy and efficiency in the case of electric field superposition. In our calculations,the efficiency defined as the ratio of the generation energy to the put into the active medium by a discharge and the electron beam, reaches 4 - 5 % and more. However, an increase of electric field beyond a certain value (which depends on specific conditions) results in greater populations of Xe atoms, metastable atoms and, as a consequence, in a stepped ionization instability, which was observed in our calculations, too.

REFERENCES

1. P. O. Clark, IEEE J.QE-1, 109, (1965)
2. W. J. Alford & G. N. Hays, J. Appl. Phys. 65, 3760 (1989)
3. P. J. M. Peters, Mei Qi-Chu & W. J. Witteman, Appl. Phys. B. 47, 187 (1988)
4. P. J. M. Peters, Mei Qi-Chu & W. J. Witteman, Appl. Phys. Lett. 54, 193 (1988)
5. V. V. Baranov, V. A. Danilychev, A. Yu. Dudin, D. A. Zayarniy, A. V. Romanov, N. N. Ustinovsky, I. V. Kholin & A. Yu. Chugunov, Sov. Phys. JTP 58, 2187 (1988)
6. A. M. Voinov, L. E. Dovbysh, V. N. Krivonosov, S. P. Mel'nikov, I. V. Podmoshensky & A.A. Sinyansky, Sov. Phys.- Tech. Phys. Lett. 5, 422 (1979)
7. V. I. Derzhiev, A. G. Zhidkov, O. V. Sereda & S. I. Yakovlenko, Sov. Phys. Lebedevs Institute Reports, 4, 34 (1989)
8. L. G. Visitenko, V. I. Gushenetc, N. N. Koval', G. I. Mesyatc, V. S. Skakun, V. F.Tarasenko, A. V. Fedenev & P. M. Schanin, Sov. Phys. - Doklady, 288, 609 (1986)
9. N. G. Basov, V. V. Baranov, V. A. Danilychev, A. Yu. Dudin, D. A. Zayarniy, A. V. Rzhevskiy, N. N. Ustinovsky, I. V. Kholin & A. Yu. Chugunov, Sov. J. Quant. Electr. 13, 1543 (1986)
10. Yu. I. Bichkov, V. F. Losev, V. F. Tarasenko & E. N. Tel'minov, Sov. Phys. JTP Lett. 8, 837 (1982)
11. V. Yu. Baranov, I. M. Isakov, A. G. Leonov, D. D. Maluta, I. V. Novobrantcev, Yu. B. Smakovsky & A. P. Strel'tzhov, Sov. Phys. JTP Lett., 9, 1124 (1983)
12. A. Yu. Dudin & I. V. Kholin, PREPRINT FIAN, 193, 1989, Moscow
13. V. I. Derzhiev, A. G. Zhidkov, O. V. Sereda, V. S. Skakun, V. F. Tarasenko, A. F. Fedenev & S. I. Yakovlenko, Sov. J. Quant. Electron (to be published)
14. V. F. Losev & V. F. Tarasenko, Sov. J. Quant. Electron., 7, 664 (1980)
15. S. A. Lawton, J. B. Newman, L. Specht & T. A. DeTemple, J. Appl. Phys., 50, 3888 (1978)

AMPLIFIED SPONTANEOUS EMISSION SHAPING IN A SCATTERING LASER PLASMA WITH DUE REGARD FOR REFRACTION

V.I.Derzhiev, A.V.Gulov, A.O.Terskih, S.I.Yakovlenko, A.G.Zhidkov
General Physics Institute, Academy of Sciences of the USSR
Vavilov Str. 38, Moscow, 117942, USSR

ABSTRACT

The divergence of an amplified spontaneous emission in laser plasma is computed wiht due regard for refraction of free electrons. Analysis of the radiation divergence on the 3p-3s transition of the Ne-like ions is performed.

An interest to the analysis of angular distribution of the amplified spontaneous emission (ASE) was stimulated by the research aimed at generation of emission at the transitions of multi charged ions in the plasma formed by a hide-power laser impulse. Starting from the works in 1985, Matthews, et al., a considerable number of publications have appeared reporting attainment of amplification at the transitions of the Ne- and H-like ions.In all the works the growth of the enhanced radiation intensity in the region far from saturation was observed to depart from exponential low.

The phenomenon was accounted for by the influence of refraction due to inhomogeneous distribution of the electron density (Matthews et al.,1986). In this connection, we consider it actual to develop programs for computation of the amplification coefficients in the expanding plasma (Derzhiev et al.,1987) and for determining the ASE angular distribution with the refraction taken into account. For this purpose Zhidkov et al. (1988) generalize the method of the "particles in the cell", suggested for calculation of the emission generation characteristics by Molodych et al., (1984) . The method employs a three-dimensional equation of radiation transport.The active medium is divided into N cells which are randomly filled with the particles moving by the trajectories described by :

$$\frac{d(n\vec{l})}{dS} = \operatorname{grad}(n); \quad \frac{d\vec{S}}{dt} = c\vec{l} \qquad (1)$$

where $n=n(\vec{r})$ is the refraction index, c is light velocity, $\vec{l}$ is the vector tangent to the particle trajectory S. Equation (1) is numerically solved. The weight of the k-th particle, n_k , is determined from the equation :

$$\frac{dn_k}{dt} = (\varkappa^+ - \varkappa^-) c n_k + Q_k$$

Q_k is the power of spontaneous radiation, $\varkappa^-$ is the coefficient of nonresonant absorbtion, the saturated amplification coefficient is determined from the nonstationarity balance equation for the populations, which takes into account the simultaneous contribution of all the particles in a cell (approximation of the average field). After reflection from the boundary the particle weight is assumed to be equal to zero. The total weight of the particles reaching for the time interval Δt the boundary at an angle is averaged and the brightness in the angle $\theta \div \theta+\Delta\theta$ is determined in terms of Wt/cm**2*strad. Note that the boundary may adiabatically change in time. Without refraction, the results are controlled by the computations using the method of "saturation functional" (Zhidkov et al ,1987), having a controllable accuracy. The gist of this method is in a numerical solution of the integral equation for the value:

$$\Phi(\vec{r}) = \int d\omega \frac{S_\omega}{S_0} \int d\Omega_{\vec{n}} \frac{I_\omega(\vec{n})}{I_{SAt}}$$

determining the degree of saturation of the working transition with radiation; S_ω is the spectral function of the transition, $I_\omega(\vec{n})$ is the ASE frequency intensity ω in the direction $\vec{n}$, I_{SAt} is the saturating flux.

Fig.1a illustrates the ASE angular distribution at the 4-3 transition of the CaXX ion in the strong saturation mode ($\varkappa^+=18.5$ cm^{-1}, $\varkappa^-=1$ cm^{-1}, active medium is a parallelepiped, $\Delta L*L$ = 0.1 cm * 4 cm) for various dependencies of the reflective index n upon the coordinate (Fig. 1b).Without refraction (curve 1) the radiation divergence is close to being geometric.For the refraction index dependencies (2) and (4), ASE constitutes a ring with a maximum brightness at the angle $\theta_m = \sqrt{\Delta n}$, where Δn is the refraction index variation (for version 2: $\Delta n=3*10$, $\theta_m=0.055$ rad ; for version 4: $\Delta n=10$, $\theta_m=0.1$ rad). The situation changes radically if n(x) varies weakly in the center (curve 3), which is typical of the laser plasma.In this case the intensity distribution has two maximums. Though the area of the region n(x)=const makes up only 6% of total area, the radiation brightness at $\theta=0$ exceeds by an order of magnitude that at $\theta=\theta_m$.

The impact of refraction upon the ASE divergence was probably for the first time observed for the 3p-3s transition of the Ne-like Se ion (Mattews et al,1986).Therefore we have used the same conditions to compute the ASE characteristics for 3p-3s transition of the Ne-like Se ion in dependence of line length. The kinetic matrix required to determine the saturating power was taken from work by Matthews et al (1985) .

Fig.2a presents the computation results for the ASE angular distribution performed for a homogeneous unsaturated amplification coefficient $\mathcal{K}^{+}=4cm^{-1}$, $\mathcal{K}^{-}=10^{-2}$ cm^{-1}, $\Delta L=10^{-2}cm$. The electron density distribution in these computations was assumed to be parabolic with a maximum equal to $10^{21}cm^{-3}$. With increasing length of the active medium the ratio of the brightness at the refraction angle to that at $\theta=0$ aharply drops.For instance,at $\mathcal{K}^{+}L=16$ the ratio is close to 1/10 and at $\mathcal{K}^{+}L=32$ we have already $\lesssim 10^{-2}$.

The radiation power at $\theta=1$ mrad vs the active medium length is presented in Fig.2b. As it is evidently, the influence of the refraction is noticeable already at $L=4$ cm, and actual variation in the power at this angle is small and may differ only some times.

We have made calculation of the plasma gain properties on the 3-2 transition of $C\overline{VI}$ ion for the condition of experiments of Chenais-Popovics (1987). These calculations have been stimulated by a strong discrepancy between the value of the experimentally observed amplification time and our theoretical results.

We have consider the cylinder geometry plasma bunch expansion having at the end of the heating laser pulse (70 ps) homogeneous distribution of plasma density, temperature of ions and electrons, charge distribution, and a linear distribution of velosity along radius. The ablation mass was estimated through the experimental value of the energy absorbed in the target, E = 2.6±0.6 J/cm (Chenais-Popovics et al,1987),assuming Saha distribution over the charge states .This value was varied in calculations.Because of low electron thermal conductivity,the temperature of the solid-state part of the fiber is cold.That enables to consider the expansion of the plasma bunch having cylinder layer geometry with inner radius R_1 (varied in calculations in accordance with the target mass evaporated). Energy contribution per 1 particle is determined from the relationship:

$$E_p = E/\pi(R_0^2 - R_1^2)N_{i0}$$

where R_0= 3.5 μm, N_{i0} is ion solid density. In the energy distribution an account was taken of the contribution to the thermal energy E_t, energy of macroscopic motion E_m and ionization energy,it was assumed that $E_m \approx E_t$ and this relationship was varied.

For calculation we have used 1D hydrodynamics code (initial equations are in many aspects analogous to those used in Derzhiev et al,1987). The $H_\alpha C\overline{VI}$ line wight (18.2 nm) was calculated with an account of Doppler, Holtsmark and electron broaderning. The level kinetics of the H-like ion was calculated with due regard for reabsorption of the Lyman series in the escape factor approximation.

Numerical modeling showed that an evaporation of 0.1 μm thick layer from the surface of carbon fiber at a heating laser pulse energy of ~2.6 ± 0.6 J/cm , a peak gain coefficient of 3 cm^{-1}(18.2 nm) is attained for ≈ 0.2 ns . One of the versions of our calculations is presented in the Fig.3. Fig.3 illustrates also the experimental data of Chenais-Popovics et al, 1987 and results of specified measurements of gain in RAL(Rose 1988) based on comparison axial and transverse intensities. Our results are in agreement with the latest experimental data. It should be noted that such an exact coincidence is random. However, temporal characteristics of the amplification properties are in good agreement with the available theoretical concepts.

We have calculated the evolution of both Formvar plasma ($O\overline{VIII}$ ion, 4-3 transition, Derzhiev et al, 1987) and ASE characteristics for line with L = 8 cm. For this purpose we calculated the parameters of the Formvar plasma, N_e, T_e,and of its ionizational content by ID equations of gas dynamics taking into account the nonequilibrium energy release to the electron gas (see Derzhiev et al, 1987) .

In computation the boundary velocity was taken to be equal to that of the plasma expanding velocity $U_0(t)$. The calculation results of the ASE angular distribution are presented in Figs.4,5. Fig.4b illustrates the calculations performed regardless of refractions. As it is seen, the results in Figs.4a and 4b differ rather noticeably, and in the region of $t \lesssim 0.2$ ns there is even qualitative difference.The refraction makes the radiation brightness at $\theta=0$ by an order of magnitude less due to broaderning of angular distribution. More over, its influence leads to a radical change of the temporal dependence $I(\theta=0,t)$ (Fig.5). With decreasing electron density N_e, refraction looses its influence. At t=1 ns and $\theta = 0$ the brightness differs ~5 and markedly decreases already for t > 1.5 ns , for t= 1.5÷2 ns it equals half the maximum.Thus, for the 4-3 transition (and logerwave transitions) of the ions with small $Z \lesssim 10$ the impact of refraction is rather weak, facilitating the observation of enhanced spontaneous radiation in the superradiation regime. However, with increasing charge Z of the H-like ion, the optimum value of the electron density, N_{opt} at which the amplification coefficient is maximum,increases as $Z^7$and the transition frequency - as Z^2, then the refraction index would increase as Z^3 (the refraction angle increases in this case as $Z^{3/2}$) and, correspondingly, the refraction influence becomes stronger. This is especially important when proceeding to short laser pulses and highly charged ions.

REFERENCES

1. J.P. Apruzese et al,1985,Phys. Rev.,55,1877;
2. C. Chenais-Popovics et al,1987 Phys. Rev. Lett. 59 2161;
3. V.I. Derzhiev et al,1987,J.Pfys.B.,20,6765;
4. Lee et al, 1988, Plasma Phys. and Contr. Nucl. Fus. Res.;
5. D.L. Matthews et al, 1984, Appl.Phys.Lett.,45,226;
6. D.L. Matthews et al, 1985, Phys.Rev.Lett.,54,110;
7. D.L. Matthews et al, 1986, J. de Physique,47,C6-1;
8. S.I. Rose, 1988, private communication;
9. M.D. Rosen et al, 1985, Phys.Rev.Lett.,54,106;
10. M.D. Rosen et al, 1986, LLL Rep.VCRL,2-26;
11. J.F. Seely et al, 1985, Opt. Com.,54,289;
12. S. Suckewer et al, 1985, Phys.Rev.Lett,55,1753;
13. A.G. Zhidkov et al, 1987, Preprint of General Phys. Inst.;
14. A.G. Zhidkov et al, 1988, Lebedev Phys. Institute Reports, 9, 27 ;
15. A.G. Molodych et al, 1983, Sov. J. Quant. Electronics,10,8.

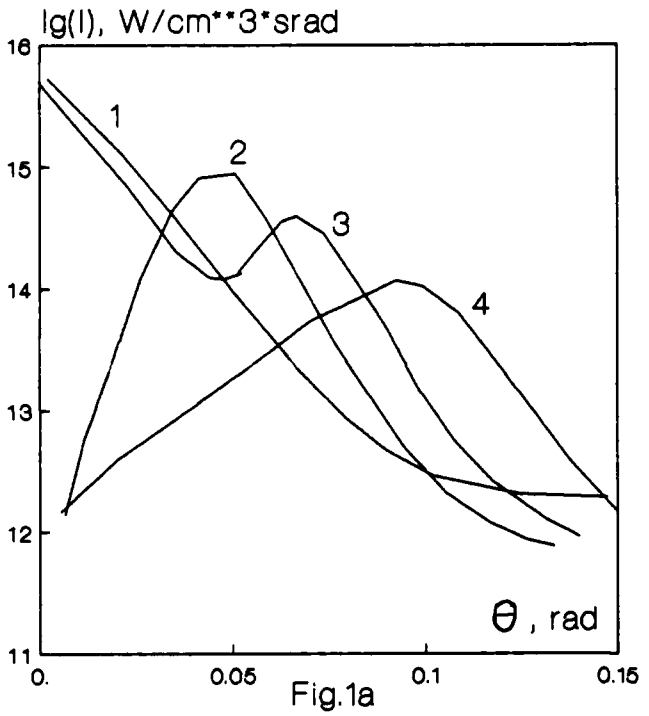


Fig.1a

Model computation of the ASE angular distribution with due regard for refraction.

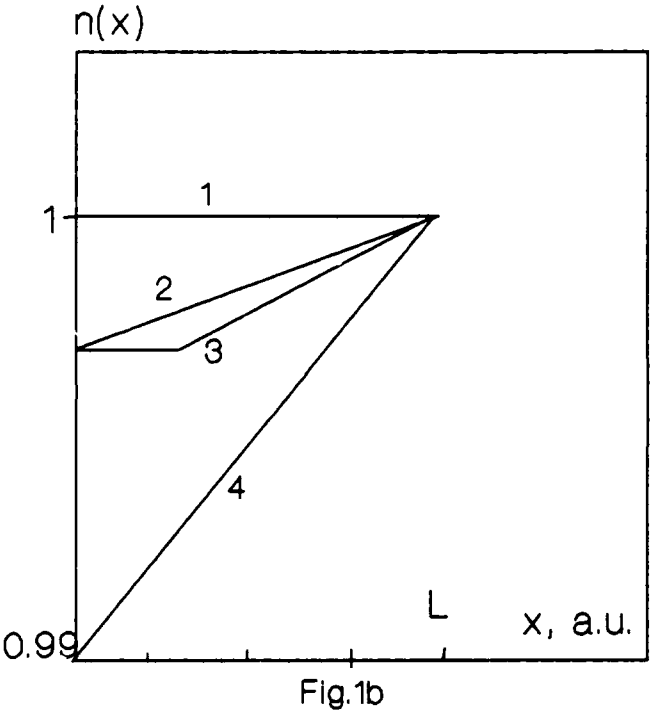


Fig.1b

Different dependencies of refraction index for model computation.

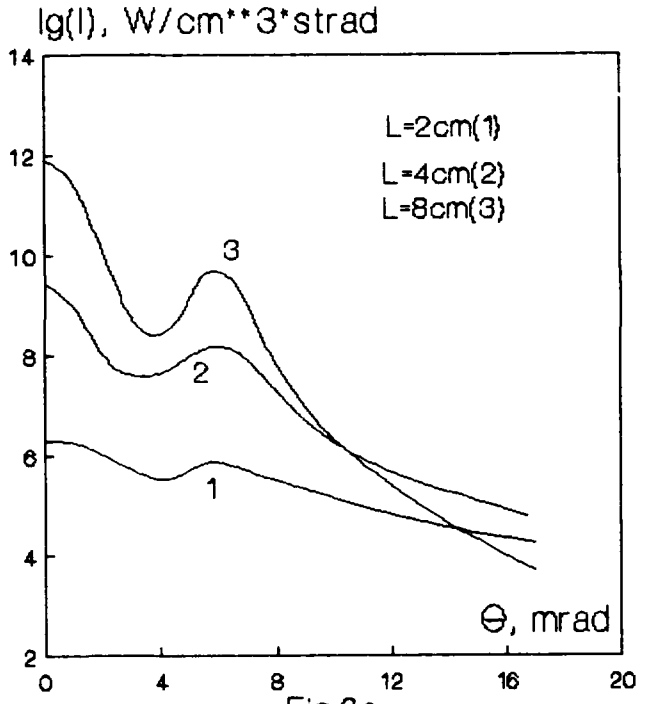


Fig.2a

ASE divergence at the 3p-3s transition $Se\overline{XXV}$ ion for different lengths of active medium.

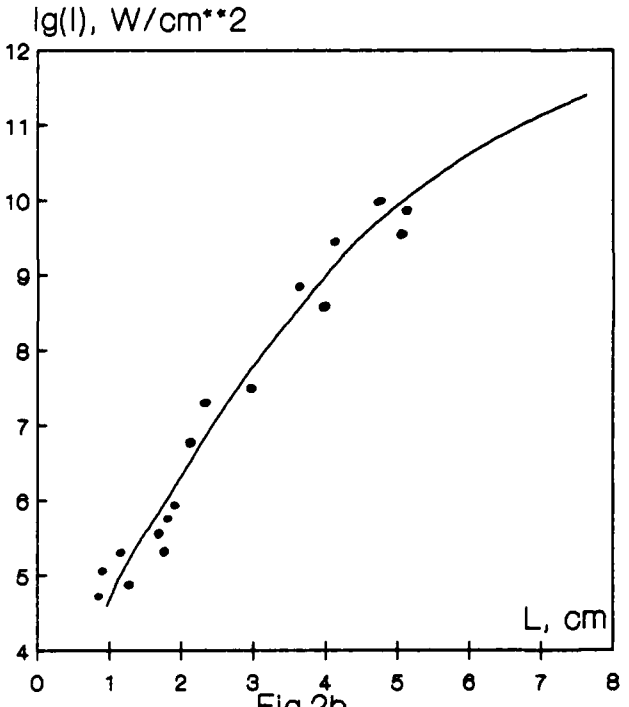


Fig.2b

Dependence of radiation energy at Θ=1mrad vs the active medium length and comparison with experiment (see 6).

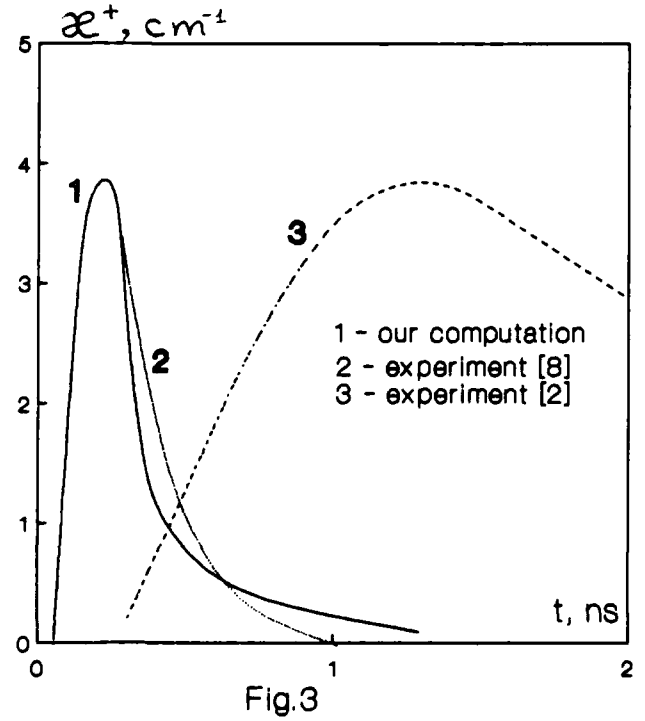


Fig.3

Temporal dependence of the gain coefficient of H_α $C\overline{VI}$ line and comparison with experiments.

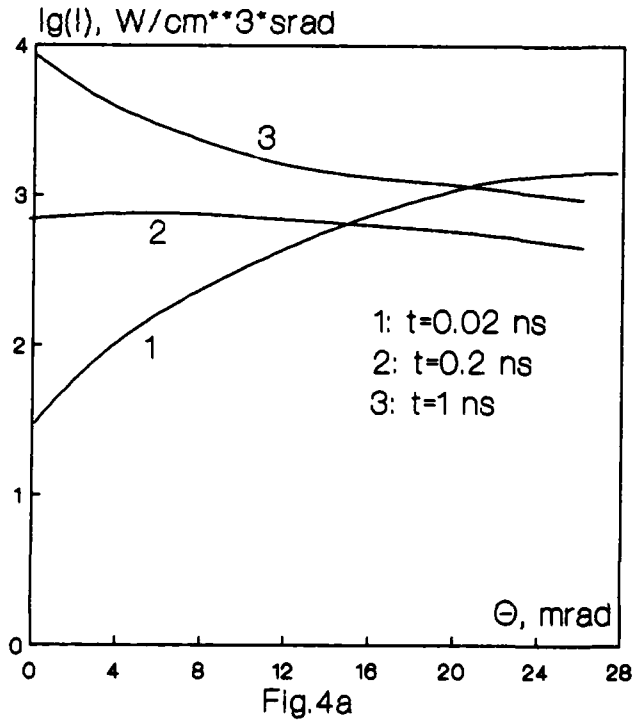


Fig.4a

Evolution of the ASE divergence at the 4-3 transition of the $O\overline{VIII}$ ion in time with due regard for refraction.

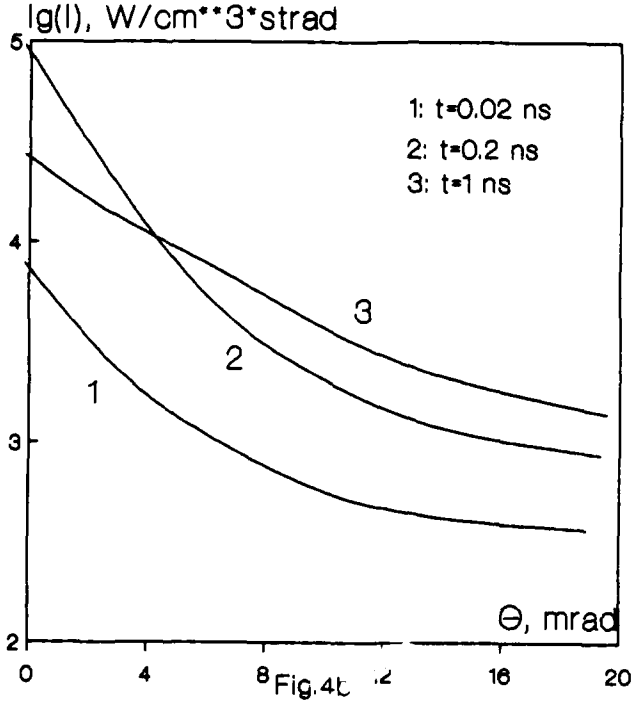


Fig.4b

Evolution of the ASE divergence at the 4-3 transition of the OVIII ion in time regardless of refraction.

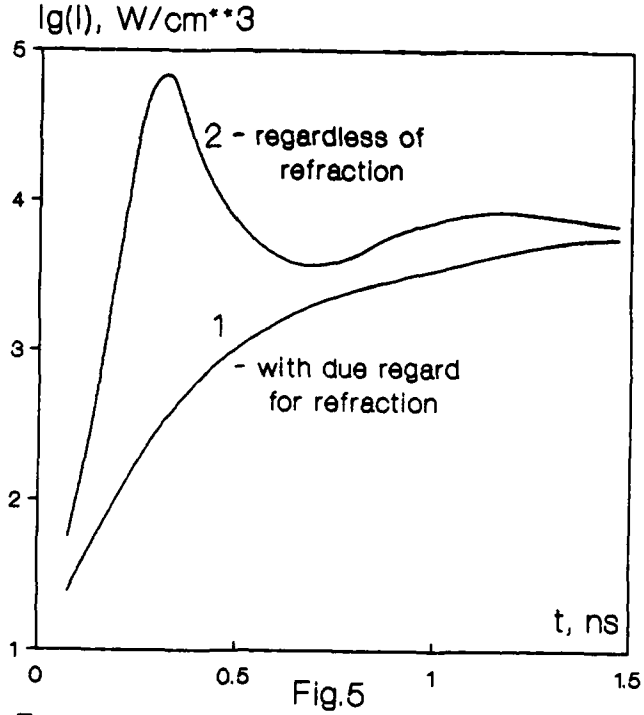


Fig.5

Temporal variation of the ASE brightness along the line (Θ=0) in the near zone at the 4-3 transition of the OVIII ion .

KINETICS OF ACTIVE MEDIA IN HIGH-PRESSURE METAL VAPOR LASERS

V.I.Derzhiev, A.V.Karelin, S.I.Yakovlenko and A.G.Zhidkov

General Physics Institute, Academy of Sciences of the USSR
Vavilov Str. 38, Moscow, 117942, USSR

Abstract

Detailed nonstationary kinetic models of high-pressure He-Cd, He-Zn, He-Hg, He-Mg, He-Ca, He-Sr, Ne-Sr, He-Xe-Sr, He-Ba and He-Be lasers pumped by e - and i - beams have been constructed and analyzed at the General Physics Institute (Moscow). The lasing characteristics were optimized depending on the active media parameters and energy deposition.

Results

The PLASER-1 program package developed at the General Physics Institute was used for calculations of local kinetics. Radiation was calculated to a zero-dimensional approximation (i.e. volume averaged). The calculation method and brief description of some models are presented in [1].

More detailed calculations were made for pumping by a compact RADAN-150 type accelerator with the parameters: beam current density j = 100 A/sc, pump pulse duration over the base t = 10 ns, electron energy E = 100 keV.

Fig.1 presents a comparison of numerical modeling results for the He-Cd laser (λ = 325,0; 441,6; 533,7 and 537,8 nm) (dashed curves) and the experimental medium temperature dependent data obtained at the Institute of High-Current Electronics of the Siberian Department of the Academy of Sciences of the USSR (solid curves)[1 - 3].

Numerical modeling enabled to establish for high pressure hard ionizer pumped He-Cd (λ = 325,0 and 441,6 nm) and He-Zn (λ = 747,9 and 589,4 nm) lasers temperature-dependent optima for output lasing power and laser efficiency are due, on the one hand, to increasing of pumping to the upper level with growing metal vapor concentration and, on the other hand, to deexcitation of this level in the conversion reaction of the Cd and Zn atomic ions into Me - type ions with subsequent dissociative recombination of molecular ions, for example :

$$He_2^+ + Cd = 2 * He + Cd(5s^2\,{}^2D_{5/2}) , \qquad (1)$$

$$He(2\,{}^3S) + Cd = He + Cd(5s^2\,{}^2D_{5/2}) + e , \qquad (2)$$

$$Cd(5s^2\,{}^2D_{5/2}) + Cd + He = Cd_2^+ + He , \qquad (3)$$

$$Cd_2^+ + e = Cd^* + Cd . \qquad (4)$$

In high-pressure He-Cd (λ = 533,7 and 537,8 nm), He-Zn (λ = 758,8 nm), He-Mg (λ = 448,1 and 921,8 nm) and He-Hg (λ = 615,0 nm) lasers, the temperature optima are caused by deexcitation of the upper active level in the Penning reaction with its own atom (fig.1,b), for example :

$$He^+ + Cd = He + Cd^{+*} , \qquad (5)$$

$$Cd^{+*} + Cd = Cd^+ + Cd^+ + e . \qquad (6)$$

Fig.2 presents output power of He-Cd laser (relative units) versus helium pressure (2,a) and versus resonator mirrors reflection (2,b). Solid lines - experiment, dashed lines - calculations. The helium pressure optimum for the green lines is caused by the competition between the growth of upper working level pumping in the reaction (5), on the one hand, and by the conversion of He^+ ions with a formation of He_2^+ ions, on the other hand. The same situation takes place for He-Zn (λ = 758,8 nm), He-Hg (λ = 615,0 nm) and He-Mg lasers.

The buffer gas optima for He-Cd (λ = 325,0 and 441,6 nm) and He-Zn (λ = 747,9 nm) lasers are reached 3 - 5 atm. depending on the resonator reflection. The presence of optima is attributed to the growth of the upper working level pumping in Penning and charge transfer reactions (1),(2) - type as well as to collisional broadening of the working transition line. Moreover, at high concentrations of buffer gas the three-body reaction of (3) - type gives a negative contribution either.

It is general for the lasers discussed above that the clearing of lower working level is a result of radiation decay. This leads to the fact, that such lasers have quite low thresholds, however this circumstance leads to some limit on maximal energy deposition to an active medium.

Further on we shall consider lasers with another mechanism of population inversion creation which involves collisional clearing of a lower working level. High-pressure He-Sr, Ne-Sr, He-Xe-Sr (λ = 430,5 nm), He-Ca (λ = 373,7 nm) and He-Ba (λ = 490,1 nm) lasers are related to this type of lasers.

In the fig.3 there are calculated dependences of lasing efficiency the active media considered upon buffer gas pressure. Numerical simulation has proved that not only recombination of doubly ionized Me^{++}-type atomic ions , but also dissociative recombination of doubly ionized heteronuclear HeMe - type ions can be the dominant channel of the upper working level pumping.

The fig.4 illustrates the dependences of output lasing power and active media efficiency of the lasers upon active medium temperature and e-beam current density.

Optima occur due to formation of Me - type molecular ions and their susequent dissociative recombination, which leads to the drop of electron density and, as a cosequence , to decline of lower working state clearing. Other important processes leading to the drop of output lasing power with temperature growth, are deexcitation of high-lying states of metal vapor single ions in Penning reaction with its own atoms and, in the case of low buffer gas concentration and high temperature, charge transfer reaction of double Me ions with its own atoms as well.

The presence of optima with respect to the e-beam current density is explained by the effective electron deexcitation of the upper working levels.

It should be noted that according to calculations a small adding of Xe to He-Sr mixture leads to exclusion of the spurious channel of lower working level population around upper working level and, thereby, to a laser efficiency rise (at sufficiently high temperature).

It was interesting to investigate a possibility of lasing on 4 --> 3 (λ = 467.3 nm) and 3 --> 2 (λ = 177.6 nm) transitions of a single BeII ion mixture with He and without it.

It our calculations we proposed that the mixture is pumped by a proton beam with parameters: The pumping duration over the base t=100 ns, proton enrgy E=1 MeV,current density was varied in the range j = 100 - 1000 A/sc.

In the fig.5 it is shown that the inversion on the 4 --> 3 and 3 --> 2 transitions in high-pressure He-Be laser takes place at substantially different Be concentrations. At relatively low Be concentration (~1.E15-1.E17 1/cc) there is inversion on 3 --> 2 transition due to the intensive clearing of the lower working state. Inversion on the 4 --> 3 transition is absent because the electrons clear the upper level better than the lower one. When the Be concentration rise, an intensive generation of the Be molecular ions with subsequent dissociative recombination leads to the electron density drop and inversion quenching on the 3p-->2s transition. On the other hand, domination of radiational decay over electron-collisional transitions leads to inversion emergence on the 4-->3 transition.

In conclution, in the table 1 there is a summary of the theoretical results including optimal active media parameters, optimal energy (for nonstationary pumping) and power (for quasi-stationary pumping) deposition and maximal theoretical laser efficiency.

REFERENCES

1. A.M. Boichenko, V.I. Derzhiev, A.G. Zhidkov, A.V. Karelin, A.V. Koval', O.V. Sereda and S.I. Yakovlenko, in Plasma Lasers of Visible and UV Regions, A.M. Prokhorov, Ed. (General Physics Institute Reports, v.21, M., Nauka, 1989), p.p. 44-115.
2. V.I. Derzhiev, A.G. Zhidkov, A.V. Karelin, D.Yu. Nagornyi, V.S. Skakun, V.F. Tarasenko, A.V. Fedenev and S.I. Yakovlenko, Soviet Phys. - Tech. Phys. Letters, 14(1), 18 (1988).
3. F.G. Gorunov, V.I. Derzhiev, A.G. Zhidkov, A.V. Karelin, D.Yu. Nagornyi, V.S. Skakun, V.F.Tarasenko, A.V. Fedenev and S.I. Yakovlenko, Sov. J. Quantum Electron., 16(10), 2039 (1989).

Table 1. Optimal parameters of high-pressure metal vapors lasers

mixture	wavelength, nm	T,deg C	p,atm	q, mJ/cm**3	P, kW/cm**3	η, %
He-Cd	441.6	360-390	3-5	~1	2	0.9
	325.0	360-400	2-3	~1	2	0.25
	533.7	450-500	1-1.5	~1	2.5	0.15
	537.8					
He-Zn	747.9	450-490	2-3	~1	2	<0.1
	758.8	>500	~1	~0.2	1	~0.1
He-Hg	615.0	200-240	2-3	2	2	0.04
He-Mg	448.1	700	2-3	0.5	1	0.3
	921.8	620-650	~1	0.1	0.3	~0.01
He-Sr	430.5	800-850	4-6	6	2.5	<1
Ne-Sr		720-850	>1	6		0.7
He-Xe-Sr		>850	3			>1
He-Ca	373.7	750-800	2-5	50	10	0.7
He-Ba	490.1	950-1100	2-5	30	5	0.15
He-Be	177.6	5.E16 *	1-1.5	350		0.9
	467.3	1.E19 *	2	350		0.7

* dimension 1/cm**3

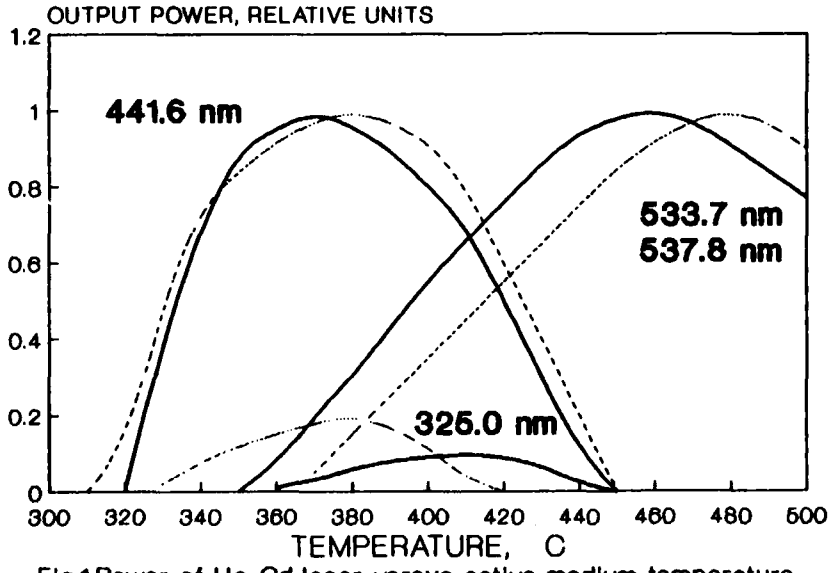


Fig.1.Power of He-Cd laser versus active medium temperature

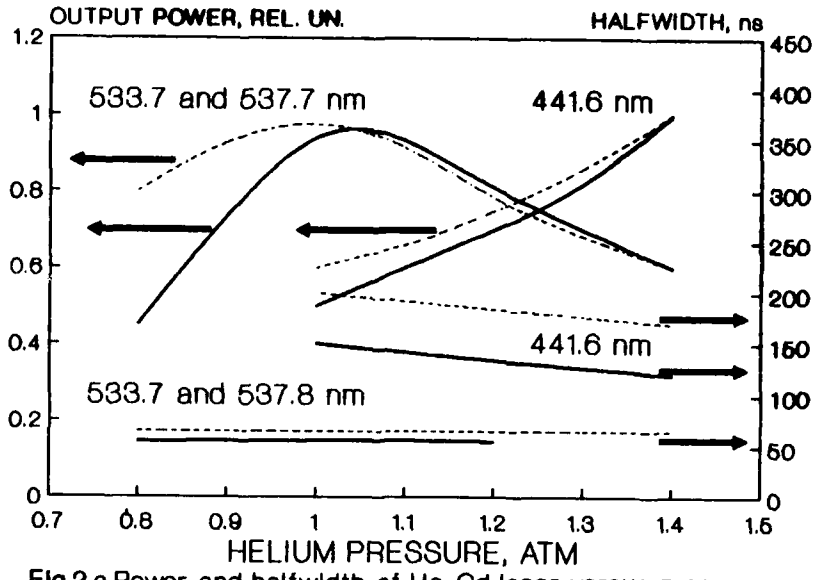


Fig.2.a.Power and halfwidth of He-Cd laser versus pressure

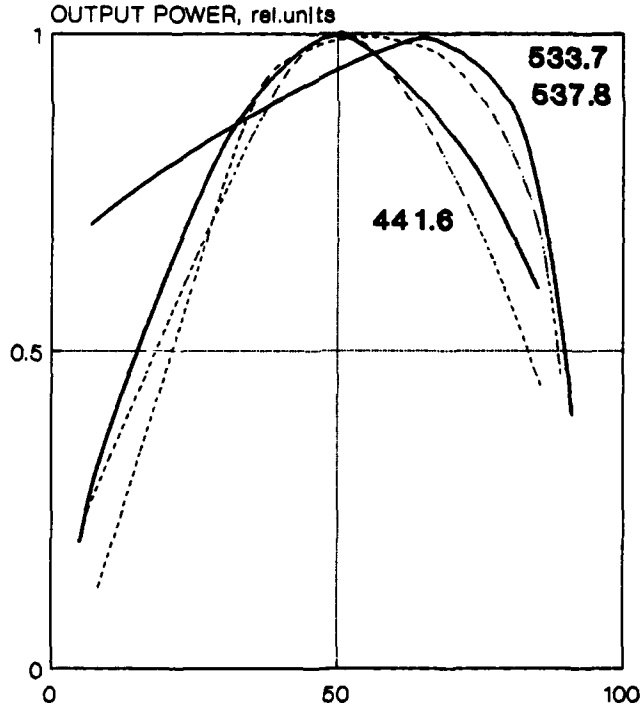


Fig.2b. He-Cd laser power vs mirrors reflection

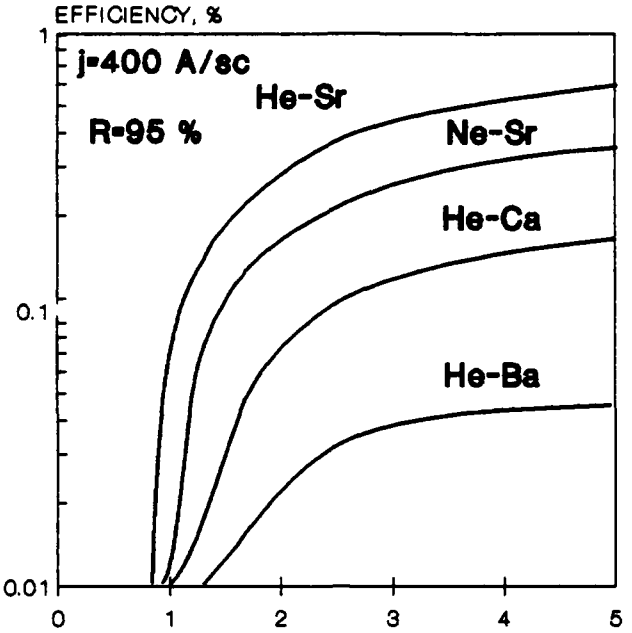


Fig.3.Efficiency of electron-collisional purificated lasers versus buffer gas pressure

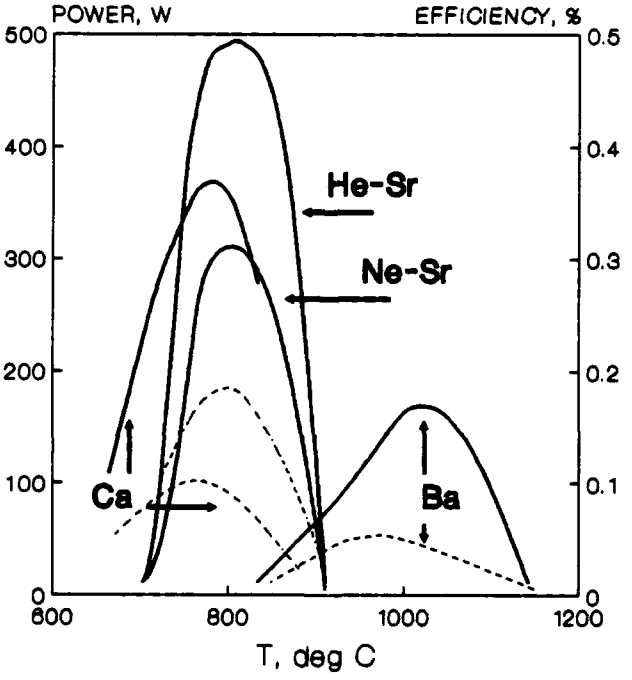


Fig.4a.Temperature dependences of the lasers with electron-collisional purification (solid - power, dashed - efficiency).

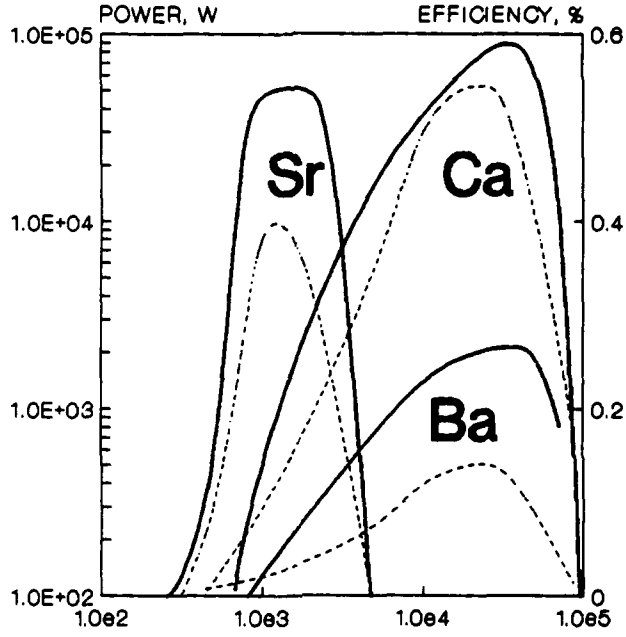


Fig.4b.E-beam current density dependences for lasers with electron-collisional purification (solid - power, dashed - efficiensy).

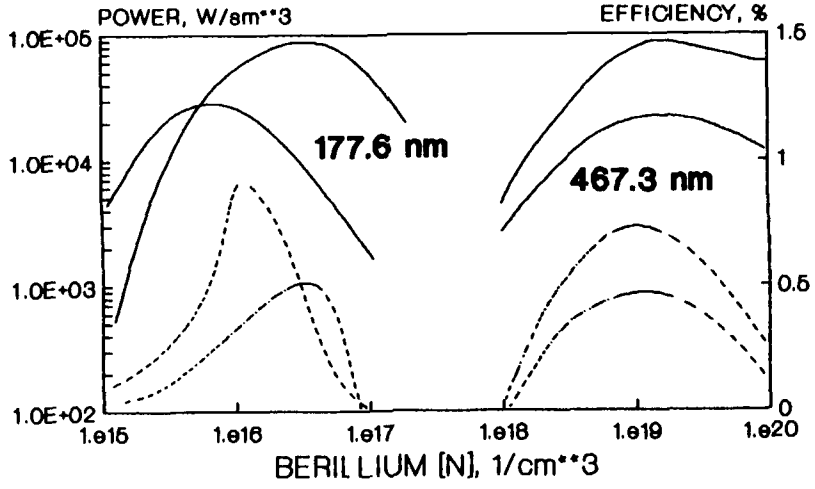


Fig.5.Power and efficiency dependences for the I-beam pumped He-Be laser (solid - power, dashed - efficiency).

SHORTWAVELENGTH GAIN COMPUTER CALCULATIONS ON ION TRANSITIONS IN EXPANDING PLASMA

A.V.Borovskii, E.V.Chizhonkov, A.L.Galkin, I.V.Kardash, V.V.Korobkin

ABSTRACT

The theoretical models and main numerical results concerned the pumping of multiply charged ions in expanding plasma are represented.

Last years the intensive progress of experimental and theoretical works was observed in obtaining of the stimulated shortwavelength ($\lambda<50$ nm) emission on the external electron shell transitions of multiply charged ions in plasma. Being interested in recombination scheme, we shell analyse several types of recombination pumping of multiply charged ions. We not pretend on exhaustive review of all works dealing with this question. We should emphasize that authors of papers [1-5] have been made the great contribution in the solution of this problem.

The theory of this question includes simultaneous solution of following problems: hydrodynamics of multicharged plasma in accordance with the evolution of ion composition, kinetics of excited levels for active ion, dynamics of stimulated and spontaneous radiation in plasma volume.

Hydrodynamics of multicharged nonequilibrium ionization state plasma. A set of following equations are solved for some chemical element plasma (further - for carbon plasma):

$$\frac{\partial r}{\partial t} = u, \quad \frac{\partial}{\partial t}(1/\rho) = \frac{\partial}{\partial s}(r^{\nu}u), \quad \frac{\partial u}{\partial t} = -r^{\nu}\frac{\partial p}{\partial s}, \tag{1}$$

$$\frac{\partial}{\partial t}(\varepsilon_e + \varepsilon_i + \varepsilon_{ion} + \frac{u^2}{2}) + \frac{\partial}{\partial s}(r^{\nu}up + w_e) = -j + \varphi, \tag{2}$$

$$\frac{\partial}{\partial t}\varepsilon_i + p_i\frac{\partial}{\partial s}(r^{\nu}u) - q_{ei} = 0, \tag{3}$$

$$\frac{\partial}{\partial t}\vec{\alpha} = \hat{B}^T\vec{\alpha}, \quad \vec{\alpha} = (\alpha_k,\ k=1,2,\ldots K), \quad \sum_{k=1}^{K}\alpha_k = 1, \tag{4}$$

Here t - time, $s=\int_0^r \rho(r')r'^{\nu}dr'$ - mass variable, ρ - mass density, ν - geometry factor ($\nu=0,1,2$ for plane, axial and spherical geometries accordingly), r - Eiler coordinate, u - plasma velosity, p - total pressure, wich is sum of the electron p_e and ion p_i plasma component pressures, ε_e and ε_i - internal thermal per mass energies for electron and ion plasma components, ε_{ion} - per mass ionization energy, w_e - is propotional to electron heat flow, q_{ei} - collisional electron-ion energy-exchange rate, j - radiative losses, φ = external energy source, $\vec{\alpha}$ - "vector" of ion fractions in ion composition (we account for different orders of ionization and ion excitation) , K - a number of energy states, wich are taken into account, $\hat{B}$ - relaxation matrix, wich nondiagonal elements represent the transition rates between corresponding energy states, and diagonal ones - the total decay rates of states ($B_{ii} = -\sum_{j\neq i} B_{ij}$).

Idial gas relations between pressures, mass thermal energies, temperatures of plasma components and its density used in this model are

$$p = p_e + p_i, \quad p_{e,i} = \frac{2}{3}\rho\varepsilon_{e,i}, \quad \varepsilon_e = \frac{3k}{2m}\langle Z\rangle T_e, \quad \varepsilon_i = \frac{3k}{2m}T_i. \tag{5}$$

k - Boltzmanns constant, m - ion mass.

Let us put the elements of $\vec{\alpha}$-vector as follows: $\vec{\alpha}=\{\alpha_k,\ k=1,2,\ldots k_1; k_1+1, k_1+2,\ldots k_2; \ldots; k_{z-1}+1, k_{z-1}+2,\ldots k_z; K\}$. The group of elements $k=1,2,\ldots k_1$ denotes the relative populations of ground and excited atomic states, $k=k_1+1, k_1+2,\ldots k_2$ - of ground and excited states for the first order of ionization ions and so on, last element denotes fraction of the completely stripped nucleus. Here Z - nucleus charge of chemical element. In such

denotements the average charge and average plasma charge square equal

$$\langle Z\rangle=\sum_{l=1}^{Z}\sum_{k=k_{l+1}}^{k_{l+1}}\alpha_k l,\quad \langle Z^2\rangle=\sum_{l=1}^{Z}\sum_{k=k_{l+1}}^{k_{l+1}}\alpha_k l^2. \tag{6}$$

The mass ionization energy is given by expression

$$\varepsilon_{ion}=\frac{k}{m}\sum_{k=1}^{K}E_k\alpha_k, \tag{7}$$

where E_k - total energy, which should to spend in order to get energy state k from unexcited atom (do not confuse with ionization potential).

Electron heat conductivity and Coulomb energy-exchange are discribed approximately basing on the results [6]

$$w_e=-r^{2\nu}\rho\varkappa_e(T_e,\langle Z\rangle,\langle Z^2\rangle)\frac{\partial}{\partial s}T_e,$$

$$\varkappa_e(T_e,\langle Z\rangle,\langle Z^2\rangle)=\frac{1.9\text{x}10^9}{\Lambda}\frac{\langle Z\rangle}{\langle Z^2\rangle}T_e^{5/2}. \tag{8}$$

$$q_{ei}=\frac{2.73\text{x}10^{27}}{a^3}\langle Z\rangle\langle Z^2\rangle\rho\Lambda\frac{T_e-T_i}{T^{3/2}}. \tag{9}$$

Λ - Coulomb logarithm, a - medium atomic wheight. Physical values are given in the CGS system of units, but temperature in eV.

Radiation losses are consisted of bremstrallung [7], photorecombination and line emissions

$$j=j_b+j_p+j_l,\quad j_b=\frac{5.54\text{x}10^{22}}{a^2}\langle Z\rangle\langle Z^2\rangle\rho T_e^{1/2}, \tag{10}$$

Expressions for j_p and j_l we'l give in process of further development of model.

Expression for external mass energy source (laser puls with power per fiber length unit $F_o(t)$ and wavelength λ_l) is the solution of laser puls transfer problem. In underdense plasma we have

$$\varphi(s,t)=\frac{1}{c(\nu)}\frac{\mu(s,t)}{\rho(s,t)r^{\nu}(s,t)}F_o(t)\left\{\exp\left[\int_{s_b}^{s}\frac{\mu(s_1,t)ds_1}{\rho(s_1,t)r^{\nu}(s_1,t)}\right]+\right.$$

$$\left.+\exp\left[-\int_{o}^{s}\frac{\mu(s_1,t)ds_1}{\rho(s_1,t)r^{\nu}(s_1,t)}-\int_{o}^{s_b}\frac{\mu(s_1,t)ds_1}{\rho(s_1,t)r^{\nu}(s_1,t)}\right]\right\}. \tag{11}$$

In opposit case energy source takes the form

$$\varphi(s,t)=\begin{cases}\dfrac{F_o(t)}{c(\nu)}\left[\dfrac{\mu(s,t)}{\rho(s,t)r^{\nu}(s,t)}+\delta(s-s_{cr})\right]\exp\left[\displaystyle\int_{s_b}^{s}\frac{\mu(s_1,t)ds_1}{\rho(s_1,t)r^{\nu}(s_1,t)}\right], & s>s_{cr}\\ 0, & s<s_{cr}\end{cases} \tag{12}$$

Numerical factor $c(\nu)=[1,\nu=0;\ 2\pi,\nu=1;\ 4\pi,\nu=2]$. In considering problem only the bremstrallung losses for heating laser puls are taken into account. The attenuation factor μ is defined by expression [8]

$$\mu=6\text{x}10^{-39}g(T_e)\frac{\lambda^2/\text{мкм}/}{T_e^{3/2}}\frac{N_eN\langle Z^2\rangle}{\sqrt{1-(\omega_p/\omega_l)^2}},\quad \omega_p^2=\frac{4\pi e^2}{m_e}N_e,\quad \omega_l=\frac{2\pi c}{\lambda_l},$$

$$N_e=\langle Z\rangle N,\quad N=\rho/m \tag{13}$$

Function $g(T_e)$ is given in [8].

In practic calculations a number of kinetics equations (4) may be not too large K<20-30. In the same time a number of energy states existing in plasma is very large K>>20-30. Therefore let us consider some simplifications.

1) *The steady state flow approach for excited ion levels* has been

introduced into hydrodynamic calculations in [5,10,16]. This approach uses the difference in decay times of ground and excited ion states, wich allows to retain in (4) time derivatives $\frac{\partial}{\partial t}\alpha_k$ only for ground states. The derivatives for all excited states should be equal to zero. In this case $\vec{\alpha}$-vector contains fractions of ions with different ionization order (ion composition of plasma). $\hat{B}$ matrix has three diagonals. The ionization γ and recombination β rates are the nondiagonals elements of $\hat{B}$. They are expressed by the rates of elementary processes and populations of ions' excited states. In the case of partially reabsorped plasma the laters are the solutions of nonlinear algebraic equation systems.

Often additional simplification is used. Plasma is assumed to be optically thin for spectral lines. This allows to get rid of nonlinearity factor in equation systems for the excited level populations, caused by spectral line reabsorption. As a result populations satisfy the linear equation systems, and the values γ, β and δ (δ - energetic coeffitients) may be tabulated as the functions of N_e and T_e. (If we take into account the lines' reabsorption, such tabulation is not possible, as the result depends on the velosity field $u(r,t)$.) Photorecombination and spectral line losses take the following form

$$J_{\Phi}+J_{\Pi}=\frac{k}{\bar{m}}\sum_{l=1}^{Z}(\alpha_{l+1}\beta_l\delta_l^{\beta}I_l+\alpha_l\gamma_l\delta_l^{\gamma}I_l). \qquad (14)$$

The numerical values of β,γ,δ in practic calculations are put in hydrogenlike form [11], see also [12-14]. I_l- ionization potential for ion of order "l". Namelly such approach is used in first step of our simulations.

The obtained radial profils of hydrodynamic variables and of ion composition are used to determine populations of excited levels of H-like ion taking into account the reabsorption of spectral lines. Problem is nonlinear and is solved by itterative method. Some results of such calculations for the case of initially fully stripped carbon fiber expanded into vacuum without external energy souce (φ=0) are represented in [15].

The whole, discribed approximation is inconsistent in three points: at-first, hydrodynamics is considered for optically thin plasma, but selective calculations of the populations and gain take into account lines' reabsorpsion; at-second, it is not clear the error value for populations of the excited levels of ions entered by steady state flow approach; at-third, H-like approach is not quite correct to discribe He-, Li- like and others ions. Let us note, that enumerated circumstancies are essential only for calculation of the ion composition and excited level populations and in practice they are not influence on the calculation results of the crude hydrodynamic variables u,ρ,r,T_e,T_i.

2) *Hydrodynamics with nonstationary kinetics of the excited levels of H-like ion.* The structure of $\vec{\alpha}$-vector and $\hat{B}$-matrix used in second set of calculations include the ground states of Li- and He-like ions k=1,2, ground and eight excited states of H-like ion k=3,4...11, and fully stripped nuclei k=12. Li- and He-like ions and the radiation losses on them are discribed as in the previous item. The H-like ion discription changes cardinally.

The relaxation matrix for CVI-ion takes the form

$$K_{ij}=A_{ij}+N_eV_{ij},\ i,j=1,2...,9,\ i\neq j. \qquad (15)$$

The meaning of the subscripts i,j is the main quantum numbers of H-like ion states. Levels, wich are above i=9, make up quasicontinuum. A_{ij}- radiative matrix, V_{ij} - collisional one. Ionization rates for discrete levels and recombination ones on they take the form

$$J_i = (V_{ie} + V_{ic})N_e, \quad R_i = (V_{ei} + V_{ci} + B_{ei})N_e, \quad i=1,..9. \qquad (16)$$

V_{ie}- ionization rate to continuum, V_{ic} - to quasicontinuum, B_{ei} - photorecombination rate on level i. The connection with quasicontinuum is taken into account only for levels i=8,9. Details concerned with matrix **K** are represented in appendix 1.

Energy photorecombination losses [7] and line emission losses on H-like ion are given as follows

$$J_{\Pi}^{H} = \frac{k}{m_t} \sum_{i=4}^{11} \sum_{j=3}^{i-1} \alpha_i A_{n_i m_j} (E_i - E_j), \quad n_i = i-2, \quad m_j = j-2, \qquad (17)$$

$$J_{\Phi}^{H} = \frac{1.793 \times 10^{24}}{a^2} Z^4 \frac{\rho}{T_e^{1/2}} \langle Z \rangle \alpha_{12} . \qquad (18)$$

The system of equations (1)-(4) is solved at following initial and bounde conditions

$$\rho(s,0)=\rho_0, \quad T_e(s,0)=T_t(s,0)=T_0, \quad u(s,0)=0, \quad r(s_\Gamma,0)=R_0, \quad u(0,t)=0,$$

$$\frac{\partial T_e}{\partial s}(0,t)=0, \quad \rho(s_\Gamma,t)=0, \quad T_e(s_\Gamma,t)=0, \quad \hat{B}^T(s,0) \times \vec{\alpha}(s,0)=0. \qquad (19)$$

To solve the problem (1)-(19) numerical method, wich has been worked out in [16], is used. Method is based on fully conservative slihgtly dissipative numerical scheme [17].

The aim of investigation is the gain calculation on laser transitions for example on 3-2 transition of hydrogenlike carbon CVI (λ=18.2nm)

$$\varkappa_{32}^{+} = \frac{\pi^2 c^2}{\omega_{32}^2} A_{32}^{H} Z^4 \frac{(N_3 - N_2 g_3/g_2)}{\Delta\omega_{32}}, \quad \Delta\omega_{32} = \sqrt{\pi}\, \omega_{32} \frac{v_t}{c},$$

$$v_t = \sqrt{2kT_t/m_t}, \quad N_3 = \alpha_5 \rho/m_t, \quad N_2 = \alpha_4 \rho/m_t. \qquad (20)$$

The results obtained in concerned above model give a qualitative accordance with [1], see fig.1.

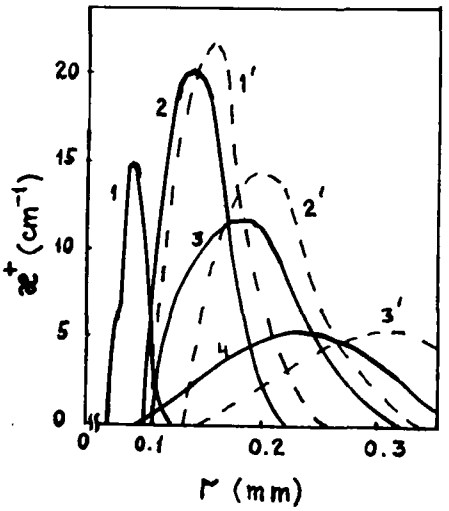


Fig.1. The free expansion into vacuum of the initially fully stripped homogeneous carbon fiber with initial density $\rho_0=6\cdot10^{-3}$ g/cm^3, temperature $T_{i0}=T_{e0}=T_0=600$ eV and radius $R_0=1.7\cdot10^{-3}$ cm. The calculation in frame of the second hydrodynamic model, described in the text. (The gain $\varkappa_{32}^{+}(r)$ radial profils for CVI ion: (——) - from [1] at time instants 300(1),500(2),700(3),900(4) ps; (-----) - profils calculated in this work at time instants 340(1'),450(2'),810(3') ps. $\varkappa_{32}^{+}\cdot6$ values are given.)

The comparison of calculations of ionic plasma composition using both models is presented in [23]. This comparison shows that quasistationary approach for CVI ion levels kinetics overestimates ion recombination rates and that reabsorption considerably affects evolution of ion plasma

composition.

Cylindrical layer plasma expansion with unevaporated solid kern of carbon fiber has been observed in [1]. In our work the comparison was made for the gain in a freely expanding plasma fiber with and without solid kern. We used the second more complex model and put the second type of the bound conditions for heat flow on interior unmoving bound. The results for the both cases were approximately the similar.

The simulation of fiber expansion heated by laser radiation was carryed out for underdense plasma. This case is not satisfactory for recombination pumping mechanism due to plasma overheat and the gain value is decreased.

Dynamics of stimulated emission. Particularly The gain is the main quantitative characteristics of shortwavelength stimulated emission on multicharged ion transitions. But to fully estimate this effect it is worth while to consider the problem of light amplification in plasma with parameters perspective for this purpose. Such consideration leads to the third problem on the way of the full modelling, namelly - to the problem of space radiation transferr.

The two-dimensional space dynamics of the stimulated radiation (with friquence ω) through axial-symmetric transvers-inhomogeneous plasma fiber (with radius R) is described by eikonal method. In the frame of such approach intensity $J(y,r)$ of stimulated emission is given by equation

$$\frac{\partial J}{\partial y} = -\frac{1}{r}\frac{\partial}{\partial r}\left[r\frac{\partial \varphi}{\partial r}J\right] + \left[\frac{\varkappa^{+}(r)}{1+J/J^{s}(r)} - \varkappa^{-}(r)\right]J, \qquad (21)$$

$\varphi(y,r)$ - eikonal, $\varkappa^{+}$- gain, $\varkappa^{-}$- nonresonant absorpsion coeffissient, $J^{s}(r)$ - saturation intensity for lasing transition. The first term in right side (21) describes the light refraction (defocusing). The second term - amplification and attenuation of light. Initial condition for equation (21) is $J(0,r)=j(r)$. Eikonal $\varphi(y,r)$ satisfies equation, wich is derived from radiation transfer equation for complex electro-magnetic wave amplitude. As the surface of constant phase propagates along the fiber its form reaches to the cone. In this case eikonal is given by

$$\frac{\partial \varphi}{\partial r} = \left[\frac{\omega_p^2(0) - \omega_p^2(r)}{\omega^2}\right]^{1/2}, \quad \omega_p^2(r) = \frac{4\pi e^2}{m_e} N_e(r). \qquad (22)$$

Equations (21),(22) may be used for description of stimulated radiation transfer along the transvers inhomogeneous plasma fiber. In frame of proposed method it can be taken into account resonant line reabsorpsion, several lasing transitions, saturation of inversly populated transitions by spontaneous radiation and some others effects [18,15]. The results of such simulation for 3d5/2-2p3/2 transition of CVI ion is shown on fig.2.

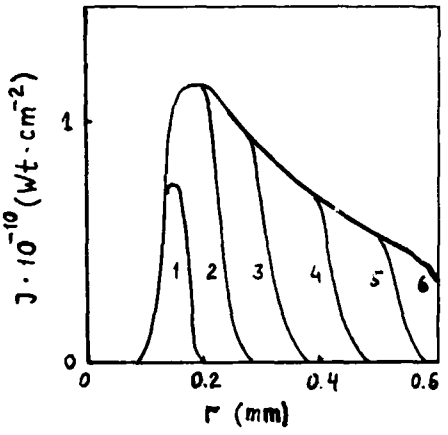


Fig.2. The 0.75 ns time instant of the free expansion into vacuum of the initially fully stripped homogeneous carbon fiber with initial density $\rho_0=2\cdot10^{-3}$ g/cm^3, temperature $T_{i0}=T_{e0}=T_0=200$ eV and radius $R_0=2\cdot10^{-3}$ cm. The calculation in frame of the first simplified hydrodynamic model, described in the text. (The radial behaviour of the CVI-ion spectral line $3d_{5/2}-2p_{3/2}$ intensity calculated by eikonal method for 1(1),5(2),10(3),15(4),20(5),25(6) cm y-distancies along the fiber axis.)

Conclusions. In this paper the theory of recombination X-lasers is developed. The theory consists of hydrodynamics with nonstationary kinetics of ion composition including the consideration of the excited levels for lasing ion in stationary and nonstationary maner, dynamics of the stimulated radiation in active medium.

The several pumping schemes are discussed. Some interesting numerical results are represented. They allow to make conclusions about the values of the shortwavelength gain, refraction losses, light intensity and also about the time-space evolution of this characteristics in expanding plasma.

The Dopplers gain in the expanding plasma fiber on 3-2 CVI-ion transition has the value $\varkappa^{+}$ =1-5 cm^{-1} in all variants of our exect calculations. The radial profil of the gain has circular form. The 3d5/2-2p3/2 spectral component is lasing. The complex hydrodynamics, nonstationary behaviour of level populations during plasma expansion, reabsorpsion of resonant spectral lines in plasma volume, strong saturation of working transition by spontaneous radiation, thin splitting of H-ion levels, refractive losses of the stimulated radiation are the most essential phenomena affected physics of recombination X-laser.

APPENDIX 1

To fill in matrix **K** the folloing formulas are used:

$$A_{ij}=\begin{cases} Z^4 A^H_{ij}\theta_{ij}, & i>j, \\ 0, & i\leqslant j. \end{cases} \qquad (23)$$

Radiative matrix for hydrogen atom is [7] -

$$A^H_{ij} = 8.05\ 10^9\left(\frac{1}{j^2}-\frac{1}{i^2}\right)^2 f_{ij}, \quad i>j. \qquad (24)$$

Loss oscilator strength is [19] -

$$f_{ij}=\frac{32}{3\sqrt{3}\pi}\frac{1}{j^3}\frac{g(i,x)}{x^3},\ x=1-\frac{i^2}{j^2},\quad i<j,$$

$$g(i,x)=\sum_{l=0}^{2}\frac{g_l(i)}{x^l}. \qquad (25)$$

i	1	2	⩾ 3
g_0	1.1330	1.0785	$0.9935+0.2328/i-0.130/i^2$
g_1	-0.4059	-0.2319	$-0.6282/i+0.5598/i^2-0.530/i^3$
g_2	0.0701	0.0295	$0.3887/i^2-1.181/i^3+1.470/i^4$

Reabsorpsion factor [20] is introduced for three bases Lyman-lines

$$\theta_{ij}=\begin{cases} 1; & j\neq 1;\ i>4,\ j=1; \\ \dfrac{1-\exp(-\chi_i)}{\chi_i}\ \dfrac{\chi_i+1/2}{3/2\chi_i+1/2}; & j=1,\ i=2,3,4. \end{cases} \qquad (26)$$

$$\chi_i=\frac{\pi^2 c^3 i^2 Z^4 A^H_{i1}}{\omega^3_{i1}|\vec{\nabla}u|}(\alpha_3\rho/m_i),\quad \omega_{ij}=2.068\text{x}10^{16}\left[\frac{1}{j^2}-\frac{1}{i^2}\right]Z^2.$$

Collisional matrix is [21] -

$$V_{ij}=\begin{cases} 3.2\text{x}10^{-7} f_{ij}\left(\dfrac{Ry}{|\Delta\varepsilon_{ij}|}\right)^{3/2}\dfrac{\beta_{ij}^{1/2}P(\beta_{ij})}{\exp(\beta_{ij})}, & i<j, \\ 0, & i=j, \\ 3.2\text{x}10^{-7}\dfrac{j^2}{i^2}f_{ji}\left(\dfrac{Ry}{|\Delta\varepsilon_{ij}|}\right)^{3/2}\beta_{ij}^{1/2}P(\beta_{ij}), & i>j, \end{cases} \qquad (27)$$

$$\beta_{ij}=\frac{|\Delta\varepsilon_{ij}|}{T_e},\quad \Delta\varepsilon_{ij}=RyZ^2\left[\frac{1}{j^2}-\frac{1}{i^2}\right]=6.579\text{x}10^{-16}\,\omega_{ij}\ /eV/.$$

β	0.01	0.02	0.04	0.1	0.2	0.4	1	⩾ 2
P	1.160	0.977	0.788	0.554	0.403	0.290	0.214	0.200

$P(\beta) = -0.288(0.577+\ln\beta)$, $\beta \leq 0.01$.

Ionization rate into continuum is [21] -

$$V_{ie} = 6\times10^{-8}\left(\frac{Ry}{|\varepsilon_i|}\right)^{3/2}\beta_i^{1/2}E_1(\beta_i), \quad \beta_i = \frac{|\varepsilon_i|}{T_e}, \quad \varepsilon_i = -RyZ^2/i^2,$$

$$V_{ei} = 2i^2V_{ie}(3.3\times10^{-24}\exp(\beta_i)\left(\frac{Ry}{T_e}\right)^{3/2}N_e). \qquad (28)$$

Ionization rate into cvasycontinuum is [22] -

$$V_{ic} = \frac{3.2\times10^{-7}}{Z^3}\, i^3\exp(-\beta_i)S_i,$$

$$V_{ci} = \frac{3.2\times10^{-7}}{Z^3}\, i^5(3.31\times10^{-22}N_e/T_e^{3/2})S_i,$$

$$S_i = \sum_{j=i0}^{\infty} f_{ij}\frac{j^3}{(j^2-i^2)^{3/2}}\beta_{ij}^{1/2}\exp(\beta_{ij})P(\beta_{ij}). \qquad (29)$$

Photoionization rate is [21] -

$$B_{ei} = 5.2\times10^{-14}Z\beta_i^{3/2}\exp(\beta_i)E_1(\beta_i). \qquad (30)$$

1. G.J.Pert. Phil.Trans.R.Soc.London, A300,631(1981); J.Opt.Soc.Am. B4, 602(1987).
2. F.V.Bunkin, V.I.Derzhiev, S.I.Yakovlenko. Sov.J.Quantum Electron., 11,981(1981).
3. V.A.Boiko, F.V.Bunkin, V.I.Derzhiev, S.I.Yakovlenko. Izv. Akad.Nauk SSSR, Ser.Fiz., 47,1880(1983).
4. F.V.Bunkin, V.P.Bikov. Kvantovaya Elektron.(Moskow). 13,869(1986).
5. V.I.Derzhiev, S.A.Maiorov, S.I.Yakovlenko, A.G.Zhidkov. Kvantovaya Electron.(Moskow), 15,412(1988);
6. V.P.Silin. Introduction to Kinetic Theory of Gases [in Russian], Nauka, Moskow, 1971.
7. I.I.Sobelman. Introduction to the Theory of Atomic Spectra. Pergamon Press, Oxford (1973).
8. K.A.Brueckner, S.Jorna. Laser Driven Fusion. USA, 1973.
9. A.V.Borovskii, V.V.Korobkin, Ch.K.Muchtarov, et al. Kvantovaya Electron.(Moskow), 12,289(1985); 12,2456(1985); 14,968(1987); 14,2269(1987); Izv. Akad. Nauk SSSR, Ser.Fiz., 50,1158(1986).
10. A.V.Borovskii, A.L.Galkin, V.V.Korobkin, V.G.Priimak. Preprint No.89, [in Russian], M.V.Keldish Institute of Applied Mathematics, Academy of Science of the USSR, Moskow, 1988.
11. A.V.Borovskii, V.V.Korobkin, L.Ya.Polonskii, L.N.Pyatnitskii, M.I.Uvaliev. Kvantovaya Electron., 16,538(1989).
12. R.W.McWhirter, A.G.Hearn. Proc.Phys.Soc., 82,641(1963).
13. H.W.Drawin, F.Emard. Physica, C85,333(1977).
14. V.I.Derzhiev, S.I.Yakovlenko, A.G.Zhidkov. Radiation of ions in nonecvilibrium high density plasma. Moskow, Energoatomizdat, 1986 (in Russion).
15. A.V.Borovskii, A.L.Galkin, V.V.Korobkin, V.B.Mokrov. Preprint No.183 [in Russian]. Institute of General Physics, Academy of Science USSR, Moskow, 1987.
16. N.S.Bahvalov, A.V.Borovskii, E.V.Chizhonkov, M.E.Eglit, V.V.Korobkin, E.A.Yakubenko. Preprint No.187 [in Russian]. Institute of General Physics, Academy of Science USSR, Moskow, 1985.
17. V.Ph.Kuropatenko. Jurnal Vichislitelnoy Matematici i Matematicheskoy Physici [in Russian], 25,№8(1985).
18. A.V.Borovskii, A.L.Galkin, V.V.Korobkin. Kvantovaya Electron. 15,1457(1988).
19. L.C.Johnson. Astrophys.J., 174,227(1972).
20. A.V.Borovskii, A.L.Galkin, V.V.Korobkin, V.B.Mokrov. Kratkie Soobscheniy po Physice, №9, p.35-36(1986); №12, p.9-11(1987); №3, p.35-37(1988) [in Russian]. P.N.Lebedev Physical Institute, Academy of Science USSR, Moskow.

21. L.A.Vainshtein, I.I.Sobelman, E.A.Yukov. Excitation of Atoms and Broadening of Spectral Lines [in Russian], Nauka, Moskow, 1978.
22. A.V.Borovskii, V.V.Korobkin, L.Ya.Polonskii, L.N.Pyatnitskii, M.I.Uvaliev. Preprint No.5-186 [in Russian]. Institute of High Temperatures, Academy of Science USSR, Moskow, 1986.
23. A.V.Borovskii, V.M.Staroverov, E.V.Chizhonkov. Preprint No.32 [in Rassian]. General Physics Institute, Academy of Science USSR, Moscow, 1989.

EXCIMER XeCl LASER WITH NARROWBAND OUTPUT SPECTRUM

V.B.Karpov, I.N.Knyazev, V.V.Korobkin, A.M.Prokhorov
Institute of General Physics, USSR Academy of Sciences
Vavilov st 38 Moscow USSR 117942

Summary

Simple interferometric resonator is used in XeCl excimer laser in order to achieve a narrowband lasing with $\Delta\nu \simeq 0.003$ cm^{-1} at pulse energy 50 μJ and pulse duration (FWHM) 10 ns. Two stage XeCl amplifier with SBS heptane phase conjugation mirror was used. Output energy of 15 mJ was obtained in narrowband diffraction limited laser beam.

To achieve narrowband excimer laser output the grazing incidence diffraction gratings are ordinarily used[1]. Comparatively low laser pulse energy 5-10 μJ are usually obtained at laser spectrum width $\Delta\nu \simeq 0.15$ cm^{-1} due to high optical losses of the gratings in resonator. In the present work a low-loss interferometric spectral selective resonator provides XeCl (λ = 308 nm) lasing linewidth $\Delta\nu \simeq 0.003$ cm^{-1} at pulse energy 50 μJ. This narrowband system was employed as a master oscillator for two-stage XeCl amplifier with Stimulated Brillouin Scattering (SBS) phase conjugation mirror[2-8].

Experimental set up is shown at Fig.1. Interferometric quartz selector with four plane parallel uncoated surfaces serves as an output spectral selective mirror[9]. Additional laser spectrum narrowing is created by tilted intracavity Fabry-Perot etalon.

Fabry-Perot interferometers with various free spectral intervals (FSI) and finesses (F) were used for linewidth measurements. A broadband lasing of nonselective regime was analyzed with the 0.3 mm air-spaced FP-interferometer (17 cm^{-1} FSI, F = 10). A fine spectral measurements were carried out with the 1.0 cm quartz etalon (0.33 cm^{-1} FSI, F = 10, instrumental function FWHM 0.03 cm^{-1}). Laser pulse shape was registered by the fast photodiode with risetime 0.3 ns and 5 GHz oscilloscope. This corresponds to the maximum optical spectral interval 0.03 cm^{-1} in the Fourier transform spectrum.

By choosing the proper tilt angle of the intracavity etalon the narrowband one-component spectrum laser output was observed (Fig.2c). The total registered spectral width does not exceed essentially the instrumental one of the FP-etalon. As it followed from the Fourier transform of laser pulse oscillogram (Fig.3) there are no components with comparable intensity in the spectral interval 0.003 cm^{-1} ÷ 0.03 cm^{-1} of the laser spectrum. Thus the laser linewidth observed is about $\nu \simeq 0.003$ cm^{-1}. Oscillator pulse energy measured by joulemeter was about 50 μJ. Oscillator beam divergence derived from the far field intensity profile at L = 12 m (see Fig.4) was $\theta \leqslant 2XDL$.

Note for comparison laser parameters for two other experimental schemes. For nonselective resonator (AL-coated rear mirror and R ≃ 8 % quartz window) the used ELI-91 model excimer laser produced optical pulse energy 50 mJ at spectral linewidth 15 cm^{-1} (Fig.2a) and divergency 5 ÷ 10 mrad. For coatingless selective resonator (Fig.1, upper dotted part) optical pulse energy 60 μJ was obtained at spectral linewidth 0.8 cm^{-1} (Fig.2b). Laser parameters of selective (with tilted etalon) and nonselective (Fig.2a) regimes are shown in Table 1.

SBS phase conjugation was investigated by using optical scheme Fig.5. The oscillator laser beam was directed through the 6.5$^{\times}$ telescope at small angle into the same gas discharge volume of the ELI-91 XeCl-laser. The output radiation had pulse energy 0.3 mJ at divergence $1.5 \cdot 10^{-4}$ rad (FWHM) and aperture 7 x 10 mm^2. This radiation was directed to the second stage four-pass amplifier. After second pass laser radiation was focused into the cell with liquid heptane and strong stimulated Brillouin scattering was obtained. Reflection coefficient of the SBS phase conjugate mirror was about 20% at laser power density ≃ 100 GW/cm^2. Reflected phase conjugated radiation after amplification on the back way in the second stage amplifier had pulse energy 15 mJ and divergence $4 \cdot 10^{-4}$ rad (FWHM). In some experiments with our optical scheme we observed specific distortion of the output laser beam, which we attribute to the self influence of crossed laser beams in the active medium of excimer laser.

Authors are expressed gratitude to A.K.Naboichenko for assistance in assembling the experimental set up.

TABLE 1

regime	nonselective	selective
pump	UV-preionised self-sustained discharge	
active volume	0.8 x 2 x 40 cm^3	
wavelength	308 nm	
gas mixture	HCl (4 torr): Xe (40 torr): He(2.5 atm)	
spectral linewidth	15 cm^{-1}	$3 \cdot 10^{-3}$ cm^{-1}
laser beam divergence	$(5 \div 10) \cdot 10^{-3}$ rad	$6 \cdot 10^{-4}$ rad
laser pulse duration (FWHM)	20 ns	10 ns
laser pulse energy	50 mJ	50 μJ
laser beam cross section	10 x 20 mm^2	ϕ 1.6 mm

References

1. E.Armandillo, D.Proch. Optics letters, 8, 523, (1983).
2. B.Zeldovitch, N.Pilipezkii, V.Shkunov. Wave reversal, Moscow, Nauka, 1985.
3. M.C.Gower, R.G.Cavo. Optics Letters, 7, 162, (1982).
4. M.C.Gower. Optics Letters, 7, 423, (1982).
5. M.C.Gower. Optics Letters, 8, 70, (1983).
6. M.Slatkine, I.J.Bigio, B.J.Feldman, R.A.Fisher. Optics Letters, 7, 108, (1982).
7. M.Sugii. IEEE J. of Quantum Electronics, 24, 2264, (1988).
8. N.A.Kurnit, S.J.Thomas. IEEE J. of Quantum Electronics, QE-25, 421, (1989).
9. А.Б.Егоров, В.В.Коробкин, Р.В.Серов. Квантовая электроника, 2, N 3, 513,1975. (A.B.Egorov, V.V.Korobkin, R.V.Serov.Quantum Electronics (USSR)2,№ 3,513,1975).

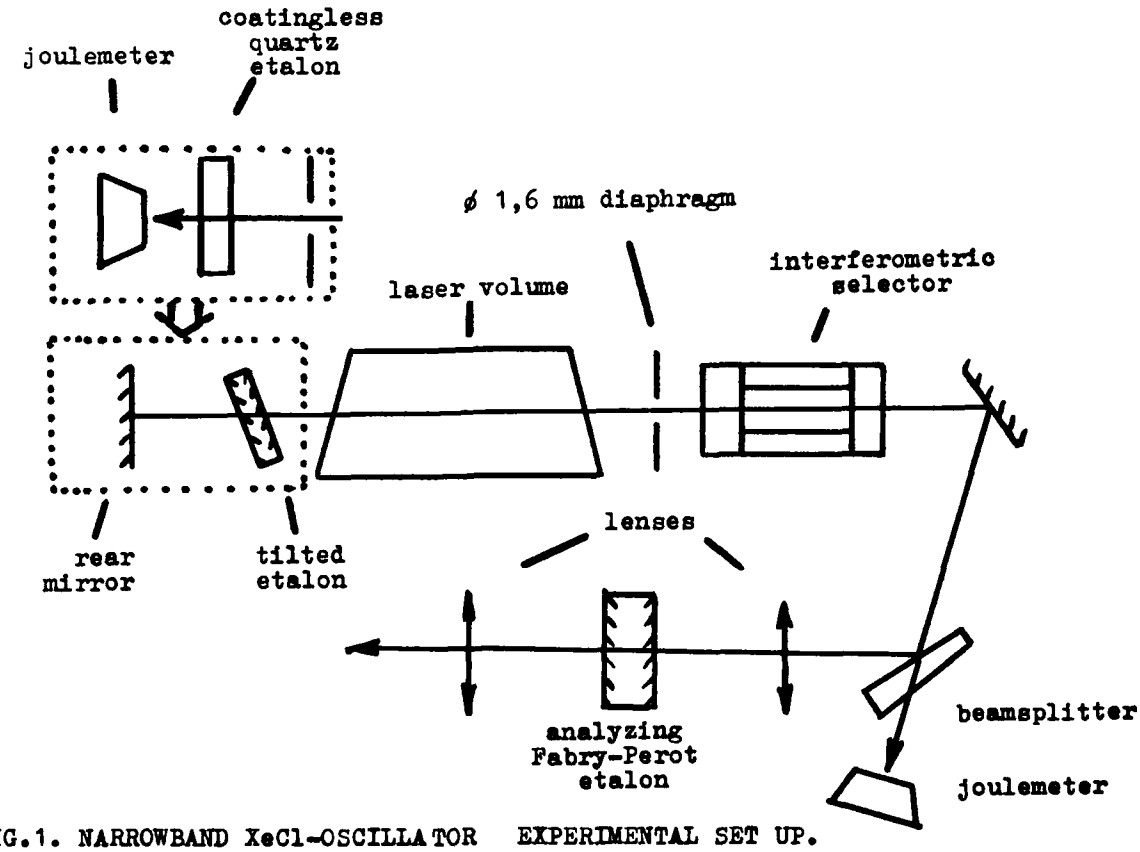


FIG.1. NARROWBAND XeCl-OSCILLATOR EXPERIMENTAL SET UP.

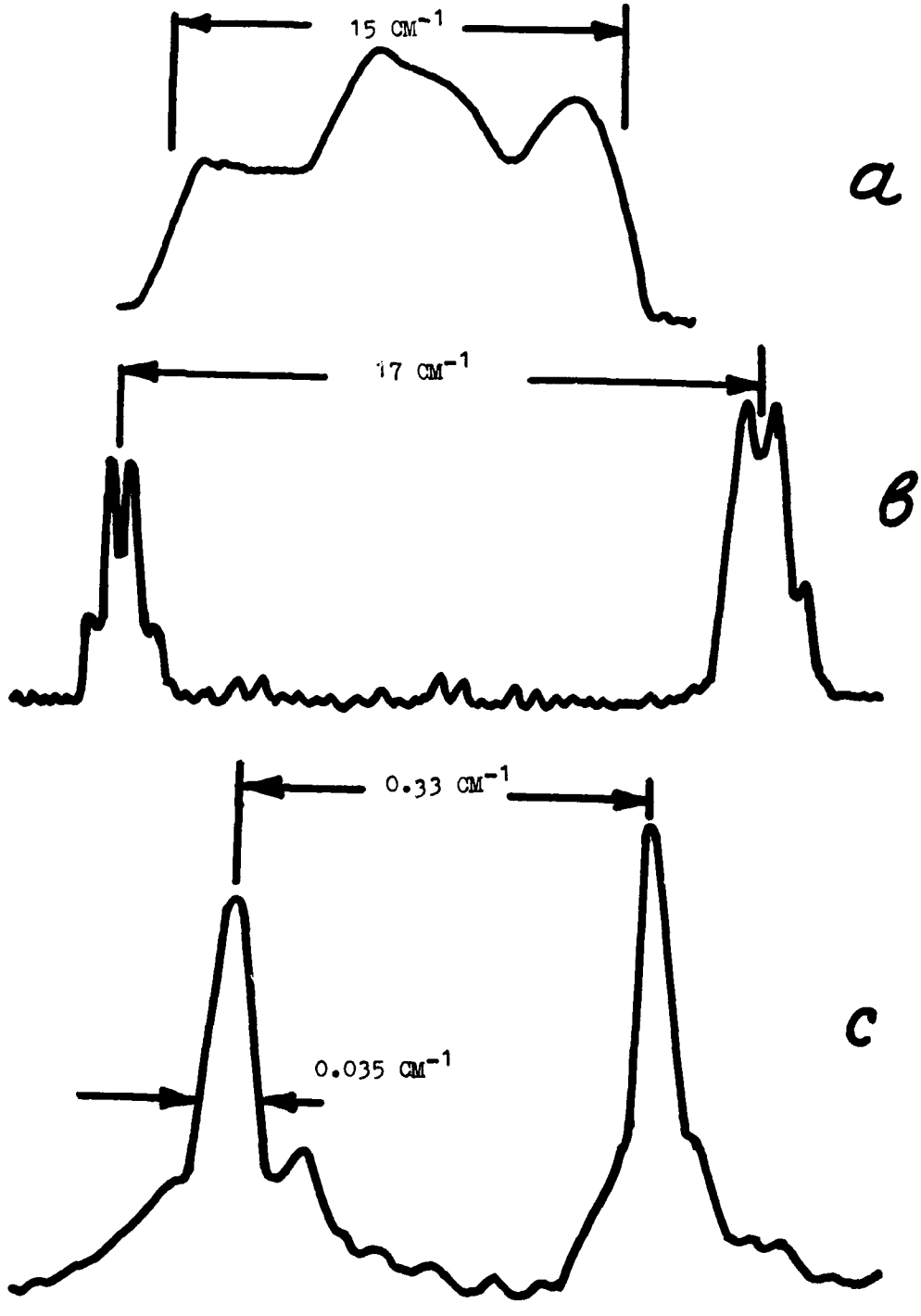


FIG.2. LASER SPECTRA INTERFEROGRAMS. (INTENSITY VS WAVENUMBER)
A - NONSELECTIVE RESONATOR, B - COATINGLESS SELECTIVE
RESONATOR, C - INTERFEROMETRIC SELECTIVE RESONATOR

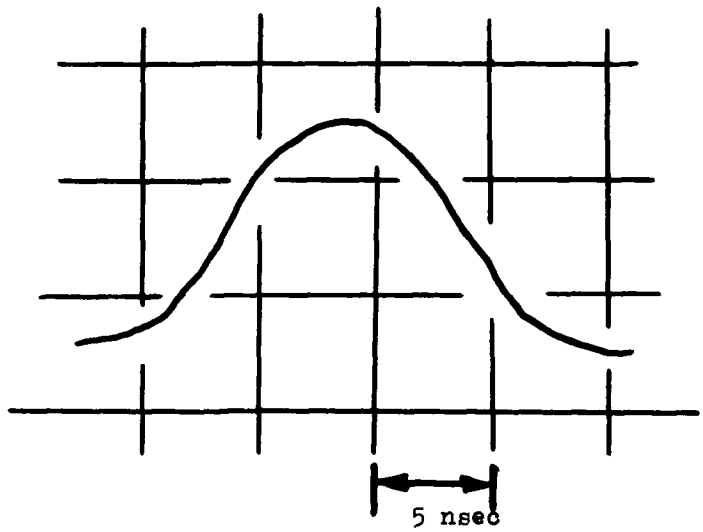


FIG.3. LASER PULSE OSCILLOGRAM

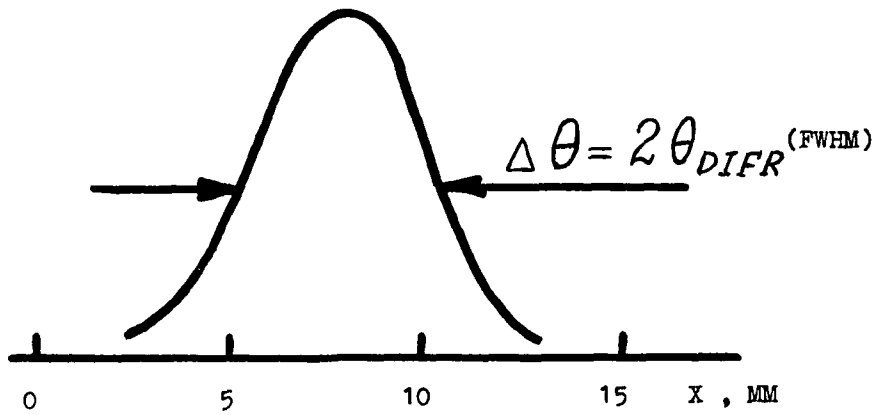


FIG.4. FAR FIELD LASER INTENSITY PROFILE L = 12 M.

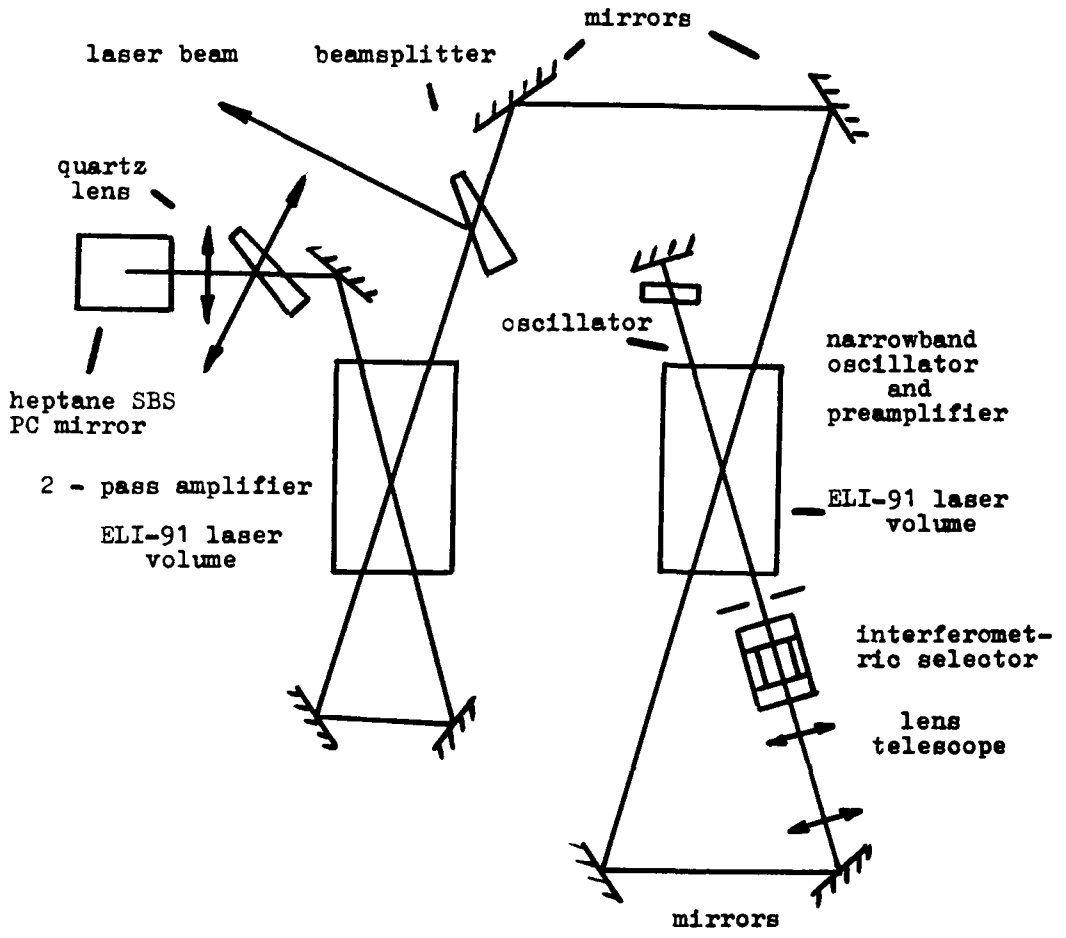


FIG.5. TWO-STAGE XeCl AMPLIFIER WITH NARROWBAND OSCILLATOR AND SBS PHASE CONJUGATION MIRROR.

VOLUME SELF-SUSTAINED DISCHARGE STABILITY IN GAS LASERS.

V.V.Apollonov, G.G.Baitsur, A.V.Ermachenko, K.N.Firsov, S.K.Semenov

General Physics Institute Academy of Sciences , Moscow , USSR

Abstract

Pulsed CO_2 and N_2O lasers are the most powerful infrared source of coherent radiation. Volume self sustained discharge (VSD) is the simplestand conventient method of their pumping. But the main problem of such lasers construction is just the VSD obtaining. The results of experimental investigation of the VSD contraction basic mechanisms in CO_2 and N_2O gas mixtures and of the low ionized additives influence on the VSD stability are presented in their paper.

Experimental arrangement

The spark channel growth dynamics and metastable $A^3\Sigma_u^+$ N_2 population dynamics were controlled in the experiment. Multiframe photoregistration of VSD plasma and inter resonator laser spectroscopy in the range of $A^3\Sigma_u - B^3\Pi_g$ N_2 transitions were carried out. The electrical scheme of discharge arrangement is presented in Fig. 1. VSD was formed by our method of preliminary discharge gap filling by electrons from the cathode source (low current discharge). The electric scheme allowed us to form current pulses with approximately constant power. The typical oscillograms of voltage (V)and current (I) for all gas mixtures and the dependence of the spark channel length (H) versus the time are presented in Fig.2. The time T between the current appearing and the beginning of current and Voltage deviation from their stationary values is the time of glow discharge firing. After this period of time the length of the spark channel approaches to 1/3 of the discharge gap. Photoregistration shows, that for the typical conditions of laser systems with high active medium volume (nonpolished electrodes with the rough surface) cathode spots appear on the early stage of discharge, when the electron concentration in the columne is about 10^{10} cm^{-3}. This isthe reason for the stability of T value (~10%) from shot to shot, so value T my be used as the measure of the discharge stability.

CO_2 -laser

Many authors have noted that in UV pre-ionization systems the discharge becomes more stable if readily ionizable substances are introduced into a mixture. This fact was attributed to the increase of an initial electron concentration due to the photoionization of additives, i.e. it was related to a particular mechanism of discharge initiation. We have shown that readily ionizable substance are a contributing factor in maintaining a stable discharge for much longer time,irrespective of the way in which it is initiated, including the conditions where photoionization is not predominant in the production of initial electrons. This conclusion draws on the earlier surmise that stability of a self-sustained discharge in CO_2-lasers is limited, to a large extend, by the instability related to stepwise ionisation of nitrogen and it is increased by introducing readily ionizable additives, which is due to the slower rate of supply of electron states in view of the reduced percentage of high-energy electrons in the gas-discharged plasma and, hence,of the corresponding slowing-down of stepwise ionization.The mechanism of instability related to stepwise ionization was proposed by Rakhimov et al of the Moscow University to account for the nonself-sustained discharge contraction in nitrogen.

To verify this presumption and substantiate the maintainability of a stable discharge in mixtures containing readily ionizable agents for a time sufficient to excite large volumes of an active medium, irrespective of the discharge initiation technique we have undertaken complex investigations of the mechanisms through which readily ionizable substances affect stability of a self-sustained discharge, with an initial electron concentration hardly dependent upon the gas mixture composition.

To establish the discharge stability limits in large-aperture systems, we were the first to examine contraction of a self-sustained discharge for electrode separation in excess of 20 cm [1]. Since the rate of growth of the spark channel is nonlinear dependent on its length, discharge stability does not increase any longer with an electrode separation and spark channel length versus time. We have also found out a maximum time of stable discharge to be 10 mksec for a 20-cm electrode separation in atmospheric -pressure mixtures

typical of CO_2 lasers, containing 50% molecular gases and readily ionizable additives with an input energy of 200 J per liter. It follows from this figure that this value is maximal for systems with apertures larger than 20 cm, too. Straight forward estimates indicate that 10 μs is sufficient to pump a single discharge unit of 1 m^3.

The authors were also the first to study a self-sustained discharge in mixtures of carbon dioxide and nitrogen with argon and water as buffer gases in the presence of readily ionizable agents. These mixtures are applicable for CO_2 lasers without imparing their characteristics, as compared to conventional CO_2:N_2:He systems.

The suggested mechanisms of self-sustained discharge instability in CO_2 laser active media and of stability impact by readily ionizable substances have been confirmed by the findings on the spark channel dynamics and by spectroscopically measured populations of nitrogen electron states in a discharge plasma /2-4/.

Instability induced by stepwise ionization is mainly noted for the rapidly increasing spark channel in gases, where this effect is pronounced and expected to show up in the discharge integral characteristics and in the correlation between a stable discharge time and the electronic level population on addition of readily ionizable agents and other admixtures to nitrogen These features are actually observed in experiment. Figure 5 shows oscillograms of the discharge voltage and current in pure nitrogen and CO_2 and in their mixtures with a readily ionizable substance- triethylamine. Addition of triethylamine increases markedly the time of stable discharge, including the CO_2 medium, which has nothing to do with variations in the initial electron concentration under the specified experimental conditions. In pure nitrogen, the discharge contracts much faster
than it does in pure CO_2, but the opposite is true when triethylamine is introduced. This indicates that the channel growth in N_2 and CO_2 is determined by different ionization processes and that in a nitrogen -triethylamine mixture the ionization is of different nature. Figure 6 plots the time dependence of the channel length for pure N_2 and N_2 containing triethylamine. The slowing-down of the spark-channel growth on incorporation of an additive supports our hypothesis that discharge stability is related to the effect of readily ionizable substances on the kinetics of gas-discharge plasmas, rather than to the variations in the initial conditions of its initiation.

Figure 7 gives time dependencies of the population of one of the vibrational levels of the $A^3\Sigma_u^+$ metastable state of N_2 in plasmas of N_2 and its mixtures. As a matter of fact, the metastable state population is correlated with the time of a stable discharge. The population in a nitrogen-triethylamine mixture proved to be lower than the recording threshold of intracavity spectroscopy. Thus, the above results are not in conflict with the claim that the most probable mechanism of discharge contraction in nitrogen and in high-nitrogen mixtures is instability related to stepwise ionization.

The cause of reduced electronic level population in a gas containing readily ionizable additives is clearly seen in figure 8. This figure shows part of the absorption spectrum for pure and triethylamine-containing nitrogen in the band $A^3\Sigma_u^+ - B^3\Pi_g$ recorded for a 100-nsec discharge current pulse. The sharp drop of absorption corresponding to reduction of level population by a factor of twenty or more within 100 nsec cannot be attributed to collisional deexcitation, even under the assumption of the highest values of the known rate constants of this process. Consequently, the basic mechanism responsible for the reduced population of the electron state in a gas containing readily ionizable agents is depletion of the energy of electrons as a result of their changed energy distribution function. Accordingly, the observed prolongation of a stable discharge in CO_2 with added readily ionizable agents is consistently accounted for by the electron energy loss and by the resultant slowing down of the rate of dissociative electron attachment to CO_2.

Thus, readily ionizable substances help to obtain a stable discharge capable of exciting large volumes of CO_2:N_2:He gas mixtures, whatever a discharge initiation technique may be.

The electron concentration in our experimental conditions was n_e 10^{11}-10^{12} cm^{-3}. The total population of N_2 $A^3\Sigma_u^+$ state in this conditions was two orders of magnitude greater then the value n_e, but according to simple evaluations, the part of ionization stream due to stepwise ionisation was less than 10%. That is why the influence of stepwise ionisation on the instability development can be attributed only to the increase of channel growth rate due to large values of n_e in channels head compared with discharge plasma column.

The results of measurements of temporal evolution of population $N_{v''=3}$ of $v''=3$ vibrational level N_2 $A^3\Sigma_u$ metastable state are presented in fig.9 : curve 1- for the measurements at fixed point for the whole time of channel development, curve 2- for the measurements of $N_{v''=3}$ in the channel head (moving point). The points on curve 1 are correspond to the area over the head of the channel (1), in the head (2) and in channels body (3). According to the curves presented, the value of $N_{v''=3}$ in the head of channel is growing faster than its body, which can be accounted for the electric field distortion near the head as the contraction process develops. When channel come to its critical length, the evaluated N_2 $A^3\Sigma_u$ metastable state total population is 10^{16} cm^{-3} with the value $n_* \sim 3 \cdot 10^{14}$ in the channel. According to qualitative evaluation, at these conditions the stepwise ionisation can significantly influence the channel growth rate in the glow discharge contraction process.

N_2O - laser

N_2O systems are the highest-power devices after CO and CO_2 lasers. This invoked our interest in them and encouraged investigations. However, the maximum output energies per unit volume and the efficiency of the electroionization N_2O laser recently constructed at the Lebedev Physical Institute turn to be much higher than those of previously created lasers pumped by a self-sustained discharge. The authors of the Lebedev Institute system related this fact to nonoptimal excitation of N_2O molecules due to the high value of the E/P parameters in a self-sustained discharge plasma. At the same time, we have shown that once the discharge is initiated by techniques ensuring a hugh homogeneity of an active medium in CO_2 lasers, their output characteristics do not virtually differ from those of electroionization CO_2 lasers. Employing the above discharge initiation techniques we expected to improve markedly the efficiency and output energy of lasers pumped by a self-sustained discharge.

Just an in the case of CO_2 lasers, we have optimized the gas mixture composition in order to achieve a maximum homogeneity and duration of a stable discharge, thereby substantiating feasibility of N_2O lasers with a large active medium volume. Optimization was carried out in accordance with the procedure that we had developed for CO_2 lasers /5/.

To compensate the dissociative electron attachment, we added CO into the laser active medium. Fig.10 plots time of a stable discharge T versus rations of CO and N_2O partial pressures, K. For $K<6$, the time of discharge T increases with K, provided the pumping power is the same. For $K>6$, this time is hardly dependent on K and E/P at the discharge stationar stage goes down to its minimum value, i.e. the loss of electron via attachment is nearly completely compensated. For specific pumping powers $Q=70 mW/l \cdot atm$ the time of stable discharge in a mixture $N_2O:CO:He$ is close to the value T for a $CO_2:N_2:He$ mixture without addition of readily ionizable substances of the same composition. This offers an opportunity for creating lasers with active volumes as large as tens of liters. When the discharge was initiated by pre-filling the gap with electrons in a 10-l volume ($10x10x100$ cm^3) or by a weak-current electron beam in a volume of 60-l (an aperture of 20 cm), it was stable at tabulated gas mixture compositions and maximum input energies. Limitations on the operating pressure and contents of molecular components were imposed by maximum voltages of the pumping sources (144 and 275 kV, respectively). The oscillograms of the pumping current and emitted laser pulse are typical of pulsed CO_2 and N_2O lasers. It must be noted, That addition of low ionized substances to the mixture in the case of N_2O laser practically doesn't increase the discharge stability because the electron levels of N_2 are depopulated by N_2O.

Lasing in an N_2O device took place simultaneously on four lines P(19), P(20), P(21) and P(22) of the $(00^0 1 - 10^0 0)$ transition of the N_2O molecule with a maximum on the P(21) line. Simulations laser action was also observed on the transitions of the CO_2 and N_2O molecules in a four-component mixture.

Fig.11 compares the relationships of the efficiency (in relative units) to the pumping energy for N_2O and CO_2 lasers. One can see that the efficiency drops suddenly with increasing pumping energy in a mixture.

Addition of helium to the mixture contributes to the laser output energy and efficiency. The results indicate more stringent requirements imposed on the population of the low-lying laser level in active media of an N_2O laser, compared to CO_2 lasers.

Table compiles efficiencies, output energies per unit volume, and total laser output energies for the most effective mixtures in N_2O lasers with active volumes of 10 and 60 l. The observed efficiencies and output energies per unit volume exceed all the previously known values for N_2O lasers pumped

by a self sustained discharge, while the extracted laser output energy is higher than any yet reported for N₂O lasers.

Thus, we can assert that the modest efficiency of N₂O laser pumped by a self sustained discharge observed earlier, as compared to electroionization systems, is the result of an insufficiently uniform excitation of an active medium, rather than of the high E/P values in a discharge plasma.

In concluding, we wish to note that the suggested principle of obtained a discharge for pumping gas lasers make it possible to create high-power, compact, and simple-design pulsed CO_2 and N_2O lasers wits large apertures. Our experiments have revealed that the suggested approach is applicable to discharge initiation in any molecular gas without marked loss of electrons due to attachment or admitting, just as in the case of N_2O lasers, the use of effective detachers.

LITERATURE

1. V. V. Apollonov, G. G. Baitsur, K. N. Firsov, S. K. Semenov, B. G. Shubin, E. E. Trefilov, Lett. to Sov. J. of Techn. Phys., v. 14, , p. 1662, 1988
2. V. V. Apollonov, G. G. Baitsur, K. N. Firsov, A. M. Prokhorov, S. K. Semenov, Sov. J. Quantum Electron., v. 15, p. 553-557, 1988
3. V. V. Apollonov, G. G. Baitsur, A. V. Ermachenko, K. N. Firsov, N. A. Raspopov, E. A. Sviridenkov, S. K. Semenov, Sov. J. Quantum Electron., v. 16, p. 269-271, 1989
4. A. V. Ermachenko, K. N. Firsov, V. I. Lozovoi, N. A. Raspopov, S. K. Semenov, Lett. to Sov. J. of Techn. Phys., v. 15, N6, p. 7-11, 1989
5. V. V. Apollonov, G. G. Baitsur, K. N. Firsov, I. G. Kononov, S. K. Semenov, V. A. Yamschikov, Sov. J. Quantum Electron., v16, p. 1303-1305, 1989.

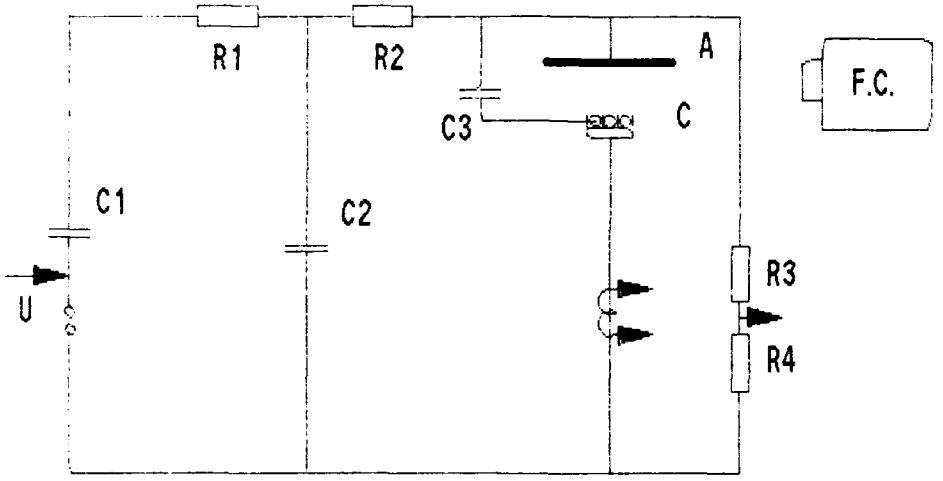


Fig. 1 Setup scheme

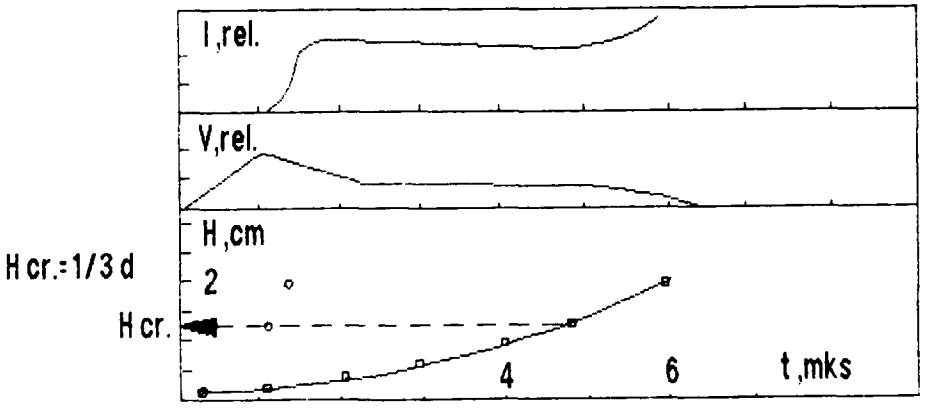


Fig. 2

DISCHARGE STABILITY IN LARGE GAPS

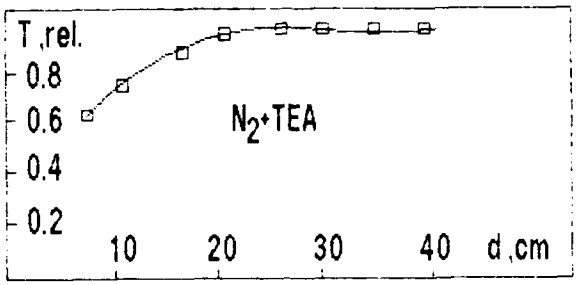


Fig.3 The dependence of VSD stable burning time T on gap length d

SPARK CHANNEL GROWTH

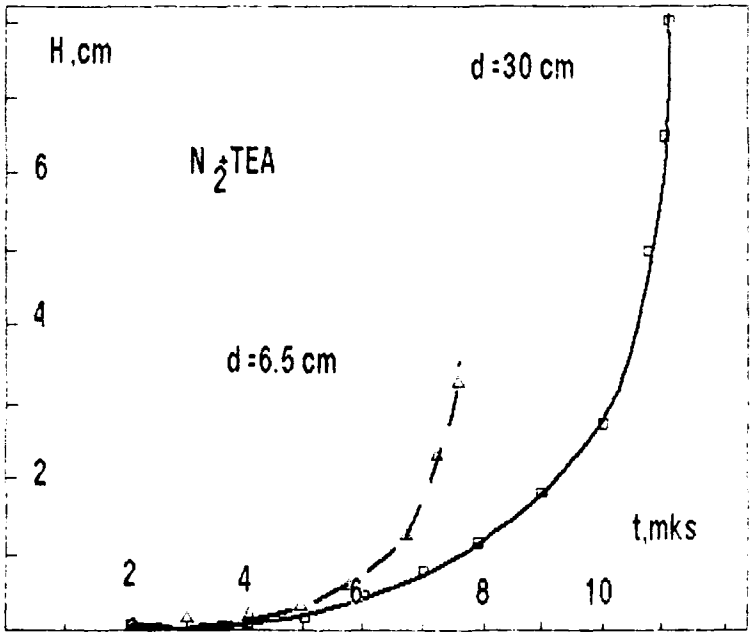


Fig.4

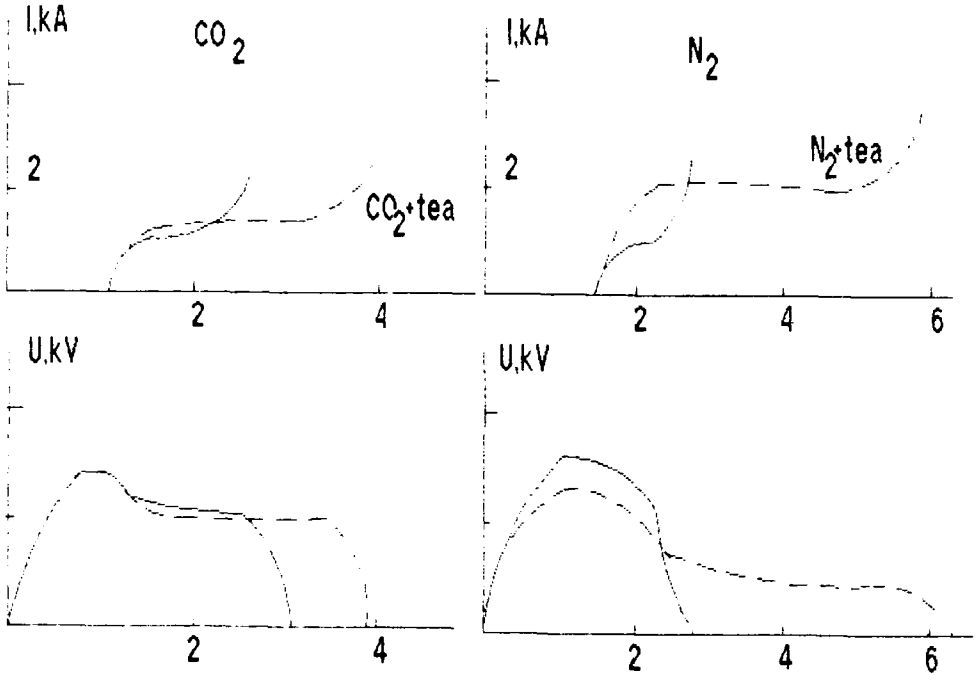


Fig.5 V and I waveforms in CO_2 and N_2

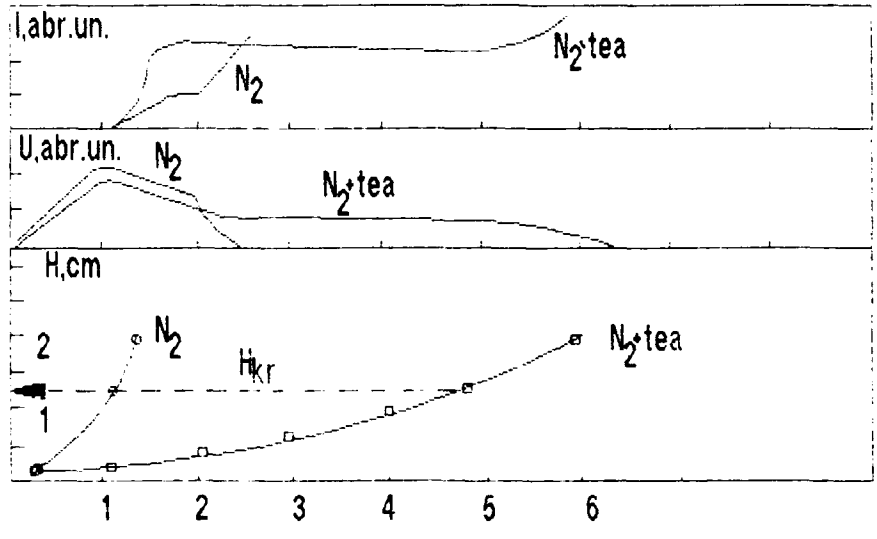
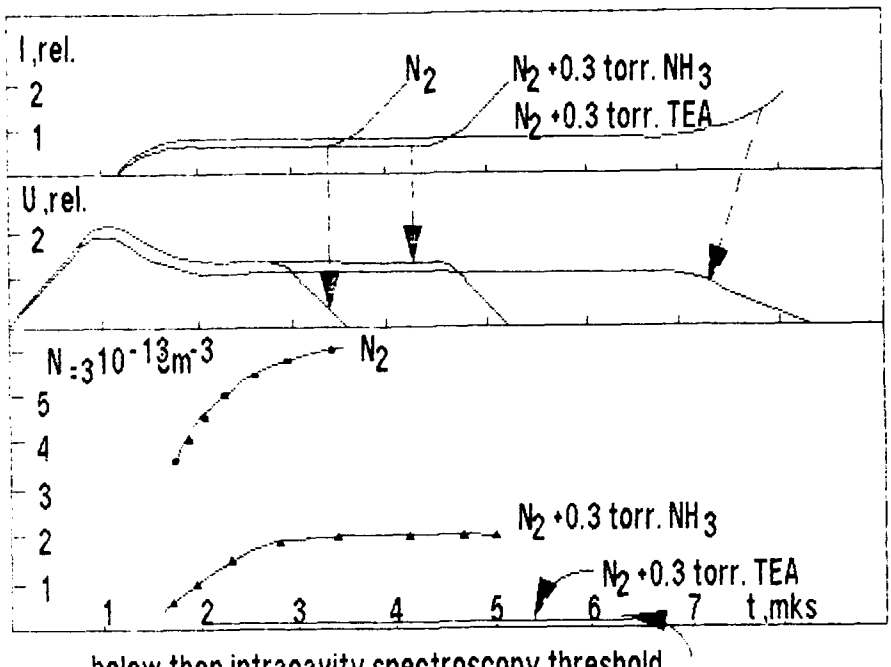


Fig.6 a) I and V waveforms in N_2 with low ionized additive tea

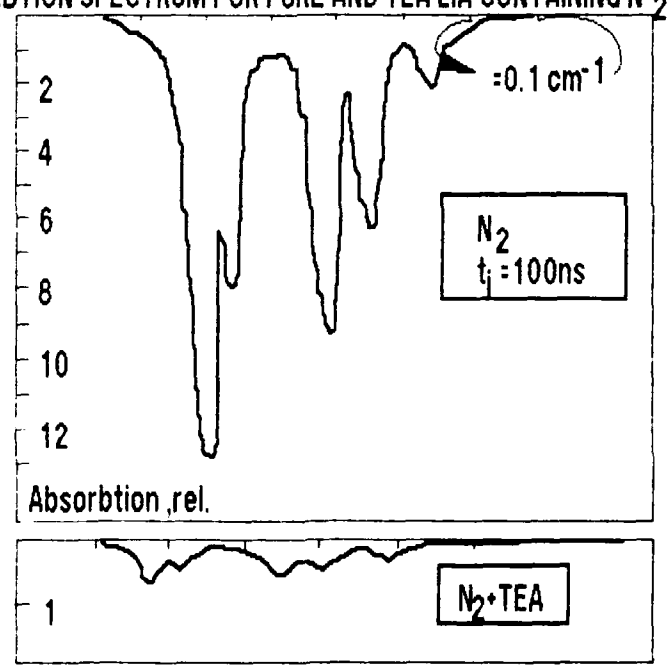
b) The dependence of channel length H on time in N_2 and in N_2 with tea



below then intracavity spectroscopy threshold

Fig.7 I(a) and V(a) waveforms and dependence of level v=3 population $A^3\Sigma_u^+$ on time(c). Total gas pressure p=0,3atm.

ABSORBTION SPECTRUM FOR PURE AND TEA LIA CONTAINING N_2



LIA CHANGE ELECTRONS DISTRIBUTION FUNCTION
(even for very short discharges)

Fig.8

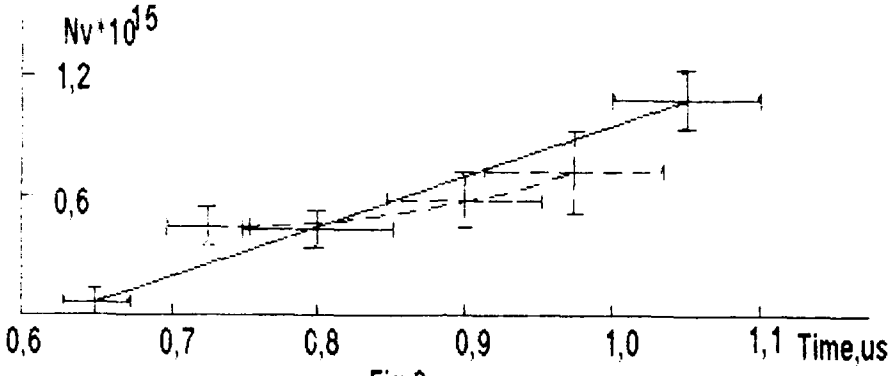


Fig.9

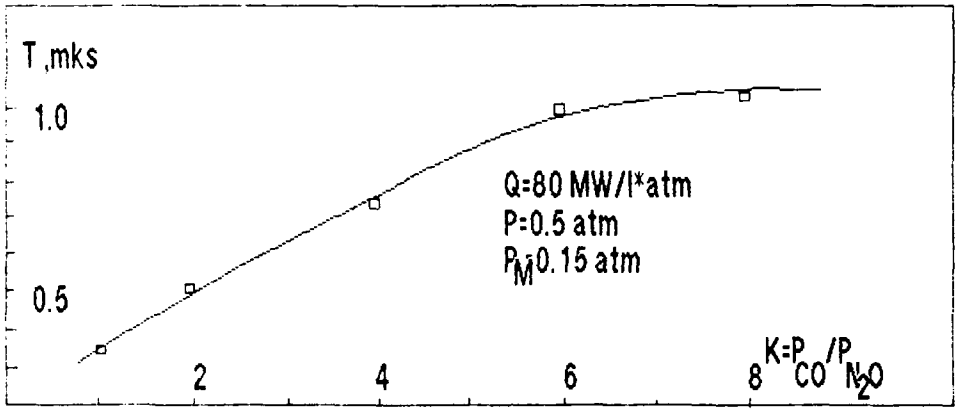


Fig.10 The dependene of discharge stable burning time T on $K=P_{CO}/P_{N_2O}$; P_m=0,15atm, P=0,5atm, Q=80 megavatt/l*atm

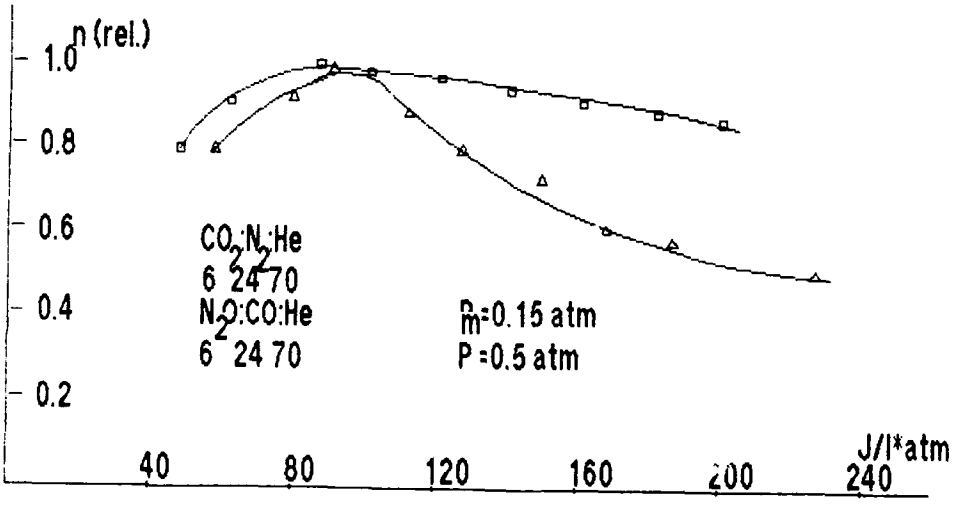


Fig.11

SHOCK-WAVE-INITIATED STATIONARY DISCHARGE IN PENNING'S MIXTURES OF INERT GASES AND LASER GENERATION ON ArII AND NeII IONS, PUMPED BY CO_2-LASER OPTICAL BREAKDOWN.

V. V. Apollonov, S. I. Derzhavin, D. A. Noraev, and A. A. Sirotkin
General Physics Institute,
USSR Academy of Sciences
38 Vavilov Street, 117942 Moscow, USSR

PART 1. Shock-wave-initiated stationary optical discharge in penning mixtures (He:Xe, He:Ar) formed by CO_2-laser radiation electromagnetic field.

Laser oscillation excited by a CO_2-laser-produced optical breakdown has been first achieved on transitions of the Ar, Kr and Xe inert gas atoms/1,2/. The authors have claimed that active media for mixed-inert-gas lasers form in the course of expansion of hot plasmas originating from targets under a focused CO_2-laser radiation. In this case plasmas cool fast as a result of adiabatic expansion and collisions with the buffer (He) gas. Inversions are created due to recombination of single-charged ions of an active gas medium (Ar, Kr, Xe). The authors of /3/ also adhered to a similar interpretation. No comprehensive investigations, however, have been carried out to verify the suggested mechanism of active media formation.

It is common knowledge that an optical breakdown in gas in accompanied by the production of dense plasmas, strong shock waves, ultraviolet and X-rays, effect of the electromagnetic radiation from the laser.

The role and contribution of each of the above mechanisms can be estimated only on the basis of systematic and multiple studies of the active media of these lasers, including a broad range of activities on plasma diagnostics and laser action. This approach is particularly important for laser systems where pumping is accomplished with the active medium exposed to the simultaneous effect of several physical factors.

In this work we have taken a multiple approach to the parameters of the active media of lasers pumped by an optical breakdown in inert gas mixtures, an approach permitting clarification of the mechanisms of their formation. Interferometric and spectroscopic investigations have been made over wide ranges of pump energy E_p, pump pulse duration τ_p, gas pressure P, mixture proportion of inert gases.

The experimental arrangement is shown in Fig. 1. The radiation from a pumping CO_2-laser (λ=10.6 μm) with a linear density of energy E=1÷2 J/cm was focused by a cylindrical lens L into a 0.8 mm * 60 mm long strip on an aluminum target T. The intensity of radiation was around 10^7-10^8 W/cm^2. The target was mounted in a vacuum chamber and filled either with pure helium or with mixtures of inert gases He:Ar or He:Xe in the 1000:1 proportion at a pressure ranging from 0.2 to 1 atm.

The same figure also gives the pulses from the pumping CO_2-laser and from a 2.03-μm He:Xe laser. It is evident that there are detected two generated

pulses : one is related to the leading edge of the pump pulse ,while the other is observed in the afterglow. the inversion developed in the former case cannot be attributed to the recombination of an expanding plasma.

In our interferometric investigations of active media of mixed-inert-gas lasers pumped by an optical breakdown we employed three methods:

-double-exposure holografic interferometry;

-nonlinear dispersive interferometry;

-Schlieren method,

It is shown /4/ that optical-breakdown-produced plasmas cannot directly participate in the formation of active media in the afterglow either,since they are not able to reach the caustic region of a He:Xe laser by the instant at which oscillations commence. It is seen in the interferograms /4/ that the onset of oscillations in the afterglow coincides with the arrival time of the shock wave.

Using the resonance absorption technique,we have examined the space-time distributions of excited atoms of the active and buffer gases. It is established /5/ that ahead of the expanding plasma and the shock wave front the density of excited atoms N_a is around $10^{12} \div 10^{13}$ cm^{-3}. The arrival of a shock wave reduces the density of metastable atoms of the buffer gas,on the one hand,and increases that of the active gas behind the shock wave front.

As is known,in discharge-excited mixed-inert-gas lasers,population of the upper laser levels takes place by transmission of excitation from the buffer gas to the active atoms in the course of plasmochemical reactions. Precisely these processes determine formation of active media excited by an optical breakdown in a pre-excited mixture compressed in a shock wave. The high compression($N_a/N_e \sim 3$) as well as the heating of the gas in a shock wave will accelerate plasmochemical reactions of the Penning and associative ionization types. Then,the electron-ion or dissociative recombination leads to population of the laser levels of active atoms.

Let us consider more closely the mechanisms of exciting atoms ahead of the shock wave front and effecting population inversion at the leading edge of the pump pulse from a CO_2-laser .

Formation of the laser active media under a cylindrical plasma expansion assumes nearly cylindrical spatial distributions of the parameters like density of excited atoms N_a,electron density N_e,and electron temperature T_e.

Figure 2 represents interferograms obtained by double-exposure holografic interferometry for two times relative to the onset of an optical breakdown. In Fig.2a corresponding to Δt around 100 nsec we see an expanding plasma. The other interferogram (Δt about 1 μsec) reproduces an optical-breakdown-produced plasma and a shock wave. In the two cases,the geometry is close to a cylindrical one.

Yet,during the CO_2-laser pulse,the interferograms display some departure from cylindrical symmetry. There is a major increase in the refraction within the pump CO_2-laser caustic in the optical-breakdown-produced plasma,in the shock wave,and ahead of the shock wave front. It is noteworthy that refraction increases both at early stages ofan optical breakdown prior to the formation

of a shock wave (see Fig.2a) and during the tail of the CO_2-laser pulse in times exceeding 1.5-2 μsec (see Fig.2b).

Of special concern is the refraction increase ahead of the shock wave front,since this feature has not been reported in previous publications.

Interferometric studies have revealed that the above-mentioned increase in refraction ahead of the expanding plasma and shock wave front is primarily due to the electron component rather than to the redistribution of heavy species,and is directly related to the CO_2-laser beam caustic.The electron density in this region is $N_e \sim 10^{15} \div 10^{16}$ cm^{-3}(see Fig.3).

It is also important that increased refraction before the shock wave front has been observed only in He:Xe mixtures but not recorded in pure helium.This is evident from the comparison of the interferograms of Fig.4 obtained in the same pumping conditions. In other words,the ionization process must proceed in the presence of admixed substances (in our case Xe or Ar) having a low ionization potential but not affecting the gas-dynamic processes in optical-breakdown-produced plasmas.

We have examined the space-time distributions of excited He ($2\ ^3P_2$), resonance-excited He ($2\ ^1P_2$),and metastable He ($2\ ^1S_0$) and Xe (6S (3/$'$)$_2$) atoms.The spatial distributions of excited atoms indicate that excited atoms of He ($2\ ^3P_2$) are detected only in the caustic region of the CO_2-laser beam (see Fig.5).

On the pump laser beam axis,the density of He ($2\ ^3P_2$) atoms is around $9*10^{11}$ cm^{-3},while at its fringe it is nearly an order of magnitude lower.The metastable atoms of He and Xe were initially detected in the caustic region of the pump laser beam but later on also outside this region (see Fig.5).

Thus,we have experimentally verified the existence of a conspicuous excitation region ahead of the expanding plasma and shock wave front in the caustic of the pumping CO_2-laser beam.

Moreover,the density of excited atoms is shown to depend upon the duration of a CO_2-laser pulse.For short pumping times (τ_p about 150 nsec),the density of excited atoms increases during the CO_2-laser action ,followed by rapid relaxation when this action is terminated.For τ_p around 1.5 μsec,excited atoms build up under the effect of a low-intensity tail of the CO_2-laser radiation until the arrival of a shock wave (see Fig.6).

Numerical estimates suggest that neither the high density of excited atoms (N about 10^{12}-10^{13} cm^{-3}) measured in this work nor the nature of the time dependence $N_a(t)$ in our experiments can be explained by the excitation through photoionization of a medium or diffusion of resonance emission from optical-breakdown-produced plasmas.

The observed ionization region seems to be related to the absorption of the CO_2-laser radiation in a pre-ionized gas.As will be recalled, electrons found in the electromagnetic wave field gradually acquire energy ε through their collisions with atoms,which amounts to values sufficient for atom excitation and ionization.

Once electron multiplication under an intense light radiation proceeds at a much faster rate than their loss,the result is cumulative ionization.If the

numbers of produced and lost electrons due to elastic and inelastic collisions,diffusion,
attachment,recombination,etc.are comparable,we deal with the so called "stationary" breakdown.This case includes breakdown in gases initiated by a DC field,microwave fields as well as by 10.6 m CO_2-laser pulses,i.e. the exposure to the field exceeds 10^{-7}-10^{-6} sec.It must be mentioned that there exists a mechanism by which inelastic-collision losses lead to electron multiplication.We mean the Penning effect.

The processes involved in the development of a stationary discharge are sketched in Fig.7.The initial peak of the pulse of the CO_2-laser radiation focused into a strip on a target in a mixture of inert gases produces a dense plasma (region I in Fig.7a).As the medium is affected by ultraviolet rays and fast electrons from the optical-breakdown-produced plasma,it becomes surrounded by a photoionization region (region II in Fig.7a) and an initial distribution of the electron density establishes itself.The energy of these electrons increases in the CO_2-laser radiation field,thereby causing excitation and ionization of atoms.But the laser radiation intensity is not sufficient to give rise to cumulative ionization.The ionization maximizes near the plasma and decays with increasing distance therefrom (Fig.7a).This is due to the fact that the initial electron distribution is dependent on absorption of ultraviolet rays in a gas.So,in front of a plasma,along the CO_2-laser beam caustic,there must be a conspicuous region containing excited atoms of an active and buffer gases.

Subsequent to the formation and separation of the shock wave,the pattern is changed and the gas goes from the region of the optical-breakdown-produced plasma over to the shock wave front (see Fig.3).When the pre-excited mixture of inert gases is compressed,the electron density behind the shock wave front jumps through Penning-type plasmochemical reactions.The fairly high (N_e around $5*10^{16}$ cm^{-3}) electron density maintains the discharge that develops both ahead (region III in Fig.7b) and behind (region II in Fig.7b) the shock wave front.This latter circumstance is related to the CO_2-laser radiation traversing the shock wave.It is remarkable in this case that an optical -breakdown-produced plasma is no longer able to initiate a discharge ahead of itself as it did in the initial stage (Fig.2a).This happens because the gas is forced out from the region concerned,its density falls,collisions become less frequent and,hence,electrons acquire their energy at a slower rate.Precisely this situation shows up in the examination of the interferograms.

We should like to note that in our experimental conditions the ionization events are comparable with the electron losses.That is why the ionization region was observed only in He:Xe mixtures,where inelastic collisions invite electron multiplication via the Penning process rather than electron losses.This mechanism must work both in the initial period of a discharge and after a shock wave has been formed and separated.

An examination of the experimental data has led us to conclude that active media of lasers pumped by an optical breakdown in inert-gas mixtures form under the combined effect of the CO_2-laser radiation electromagnetic

field,shock wave,and ultraviolet rays from optical-breakdown-produced plasmas.

Inversions at the leading edge of the pump pulse are obtained by electron-collision excitation. Initial electrons are produced by photoionization a medium with the ultraviolet ray from an optical-breakdown plasma. Then they acquire energy in the electromagnetic field of the CO_2-laser radiation. It is evident from Fig.8 that the ionization and excitation region coincides with the lasing region and is directly related to the caustic of the pumping CO_2-laser beam.

According to estimates,at a radiation density of about 10^8 W/cm^2 within 20 nsec (the start oscillation time) an electron may acquire an energy up to 100 eV.

As the pumping time is increased by including the tail of a CO_2-laser pulse,excited atoms build up ahead of the shock wave front. Subsequent compression in the shock wave accelerates plasmochemical reactions and creates conditions for the formation of an active medium for the second pulse of generation.

The suggested mechanism of formation of active media in lasers pumped by an optical breakdown in a mixture of inert gases accounts for the experimental results obtained in this work as well as for the findings of other research groups.

PART 2. Laser generation on ArII NeII ions,pumped by CO_2-laser optical breakdown.

One of the most promising directions in the development of short wavelength lasers is connected with using optical breakdown (OB) and laser produced plasmas (LPP). Hot plasmas formation is accompanied by a power pulse of UV and soft-x-ray radiation,which is applicable for laser active medium (AM) photopumping. The generation,pumped by soft-x-ray radiation from LPP was investigated on a wide scale by W.T.Silfvast,S.E .Harris and other scientists. This method permits to obtain generation in visible,UV and VUV spectral regions. For example,on transition of ArII ion ($4p\ ^2P_{3/2}$--$4s\ ^2P_{1/2}$) the generation with wavelength λ=4765 A was obtained /6/. The Nd-laser with 25 mJ pulse energy and 70 psec pulse duration was used for OB plasmas formation. The comparison of efficiency of CO_2-laser and Nd-laser in the reception of soft-X-ray radiation from LPP was made by Silfvast and his collaborators /7/. The spectrum of OB plasmas radiation was approximated by black body one. It was shown that for the laser intensities up to 10^{12} W/cm^2 the temperature of this black body (T) depended on the intensity (I) and laser wavelength (λ) as follows: $T \sim (I\lambda^2)^{4/9}$ The conclusion was drawn that in this intensity region long wavelength lasers are more effective for soft-X-ray flux production.

The aim of present work is the reception of the generation on transitions in noble gas ions with photopumping by soft-X-ray radiation from laser plasmas,which is produced by focusing the radiation of powerful CO_2-laser at the surface of a target.

The experimental scheme is shown in Fig.9. The radiation of CO_2-laser with 10 J pulse energy (Fig.10a) was directed in the camera filled with some torrs of Ar or Ne. It was focused by a system of lenses on a target. The spots at the target were adjusted in line with a distance of 15 mm to one another. It is known that OB plasmas radiation depends on the target material and shifts to short wavelengths with increasing the atomic number of it /8/. Tantalum strip was used as a target. The luminescence of ArII and NeII spectral lines was observed along the plasma torches.

Using adequate mirrors at the gas pressure p~5 torr and distance between the target and active region L ~ 5 mm, the generation was obtained on the transitions in ArII : $4p\ ^2P_{3/2}$--$4s\ ^2P_{1/2}$ with wavelength λ=4765 Å; $4p\ ^2P_{3/2}$--$4s\ ^2P_{3/2}$ λ= 4545 Å; $4p'\ ^2P_{3/2}$--$4s'\ ^2D_{5/2}$ λ= 4278 Å. The laser generation was obtained also on the transitions in NeII between the levels with the same electron configurations : $3p'\ ^2P_{3/2}$--$3s'\ ^2D_{5/2}$ with λ= 3345 Å and $3p\ ^2P_{3/2}$--$3s\ ^2P_{3/2}$ with λ=3324 Å. The generation pulses of ArII or NeII lasers are shown in Fig.10b. The generation pulse arises in 10-20 nsec after OB formation at the front of CO_2-laser radiation. Without mirrors the typical shape of oscillogramms of ArII lines luminescence are shown in Fig.10c. One can see two strongly pronounced peaks. The first coincides in time with the generation pulse (Fig.10b). The dependence of the time delay between second luminescence peak and the front of CO_2-laser pulse *vs* working gas pressure is presented in Fig.11. The increase of the delay when the pressure decreases allows to say that the second peak arises due to electron relaxation on the level $4p\ ^2P_{3/2}$ ($3p\ ^2P_{3/2}$) from upper levels. Therefore the first luminescence peak is connected with a direct excitation of this level. The dependence of luminescence of ArII ions lines on pressure is shown in Fig.12. The maximum luminescence was found to place at 3 torr. Analogous dependence was received for the intensity of ArII and NeII laser generation.

Besides the proposed in /6/ the photopumping mechanism of working levels, the AM excitation can be caused by the electrons accelerated in the electromagnetic field of CO_2-laser radiation /9/ as well as by fast electrons from LPP. The electrons due to medium ionization by soft-X-ray flux swing in the E-M field of CO_2-laser radiation and can acquire the energy sufficient for the AM atoms and ions excitation. According to estimations in this case the concentration of exited ions ArII in the caustic of incident radiation mast be larger than outside one. The spatial distribution of the intensity of luminescence lines vs H (H-the distance in the direction perpendicular to the propagation of CO_2-laser radiation, Fig.9) is shown in Fig.13. Smooth course of the slope (Fig.13) and the absence of intensity splash for H=0 mm excludes the possibility of ionization and excitation of ArII (NeII) ions due to electrons swinging in CO_2-laser radiation field.

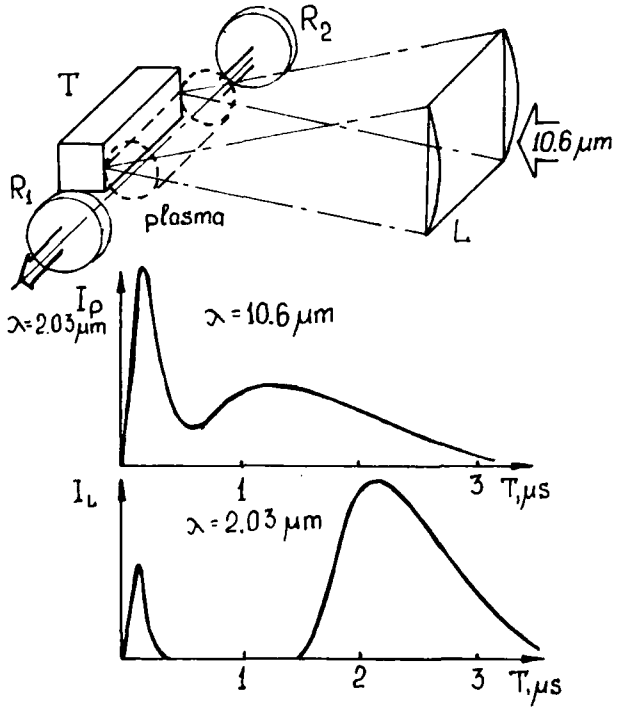
To investigate the role of the rapid electrons from laser plasmas the experiments, in which the detaining electrical field was applied, were carried out. The excitation energy of upper laser levels of ArII and NeII are in the region of 40-50 eV. The potential different between the target and screen (Fig.9) has been variable in the region 0-400 eV, that has permitted to stop

the electrons that could make the mainly contribution in the excitation of investigated levels. The experiments shown that even on the generation threshold the applied field has no influence on the generation value. At the same time the assumption that the ionization and excitation of Ar (Ne) is accomplished due to soft-X-ray flux from LPP is in a good agreement with Fig. 14. The distribution of intensity of NeII (ArII) lasers generation vs angle α with respect to the target's normal (Fig. 14) is also in a good agreement with the fact that soft-X-ray flux from LPP expands in a 90° angle cone /10/.

For the first time by means of pumping mode the generation on the transitions in ArII in visible λ=4545 A ; 4278 A and NeII in UV λ=3345 A; 3324 A. The obtained results creates the experimental base to the expansion in the more short wavelength spectral region.

REFERENCES:

1. W. T. Silfvast, L. H. Szeto, O. R. Wood II, Appl. Phys. Lett., v. 31, p. 334 (1977).
2. W. T. Silfvast, L. H. Szeto, O. R. Wood II, Appl. Phys. Lett., v. 34, p. 213 (1979).
3. V. A. Danilychev, V. D. Zvorykin, I. V. Holin, A. Yu. Chugunov, Sov. Jorn. of Quantum Electronic, v. 9, p. 22 (1982).
4. V. V. Apollonov, S. I. Derzhavin, A. M. Prokhorov, A. A. Sirotkin, Sov. Jorn. of Quantum Electronic, v. 12, p. 2389 (1985).
5. V. V. Apollonov, S. I. Derzhavin, A. M. Prokhorov, A. A. Sirotkin, SPIE High Intensity Laser Processes, v. 664, p. 291 (1986).
6. W. T. Silfvast, O. R. Wood II, JOSA, B. v. 4, 609 (1987).
7. O. R. Wood II, W. T. Silfvast, J. J. Macklin and P. J. Maloney, Opt. Lett., 11, 198 (1986).
8. J. M. Bridges, G. L. Cromer and T. J. McIlrath, Appl. Opt., 25, 2208 (1986).
9. V. V. Apollonov, S. I. Derzhavin, D. A. Noraev, A. A. Sirotkin, Lett. to Sov. Jorn. of Tech. Phys., v. 15, № 21, p. 12 (1989).
10. M. D. Rosen, Phys. Fluids, 22, 2020 (1979).



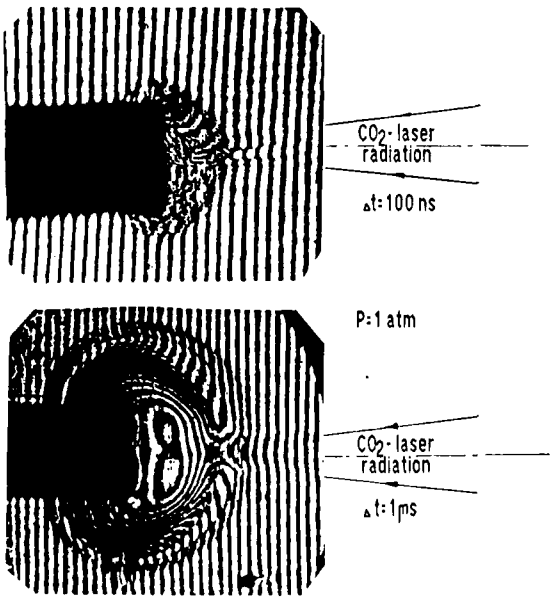


Fig. 1 Schematic diagram of the experiment

Fig. 2 Interferograms of active media

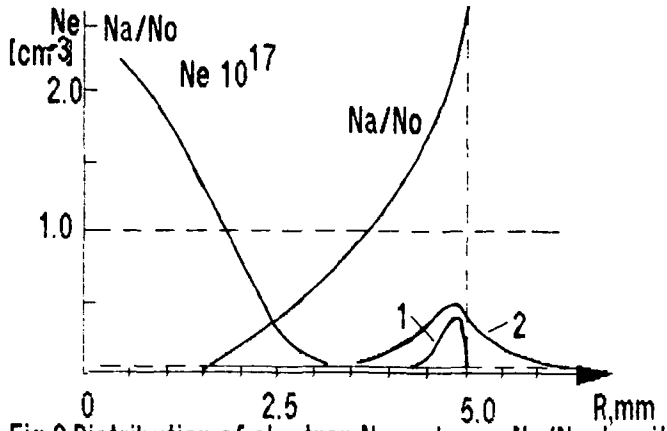


Fig.3 Distribution of electron Ne and gase Na/No density
1-off the caustic, 2-in the caustic

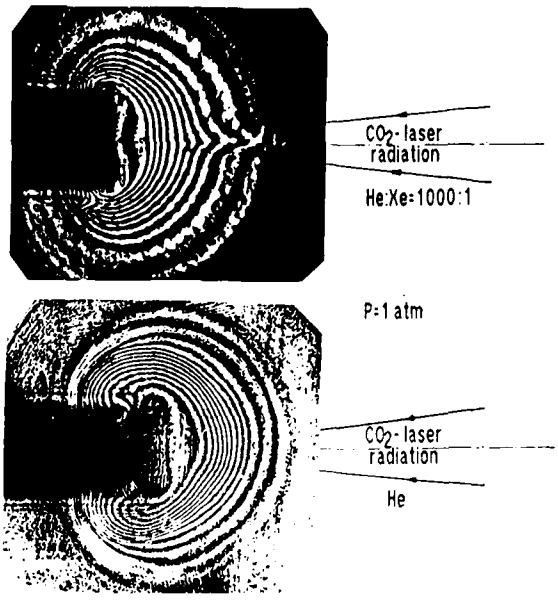


Fig.4 Interferograms of active media

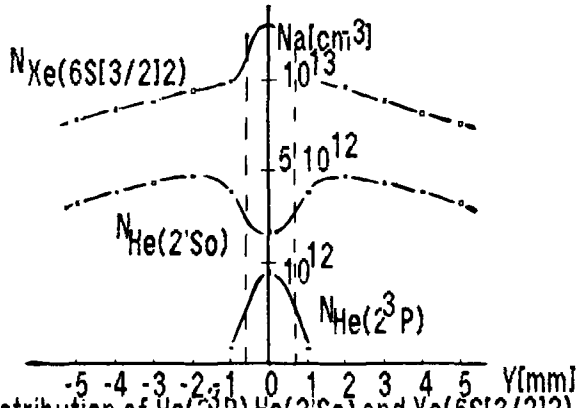


Fig.5 Distribution of $He(2^3P)$, He(2'So) and Xe(6S[3/2]2) excited atoms

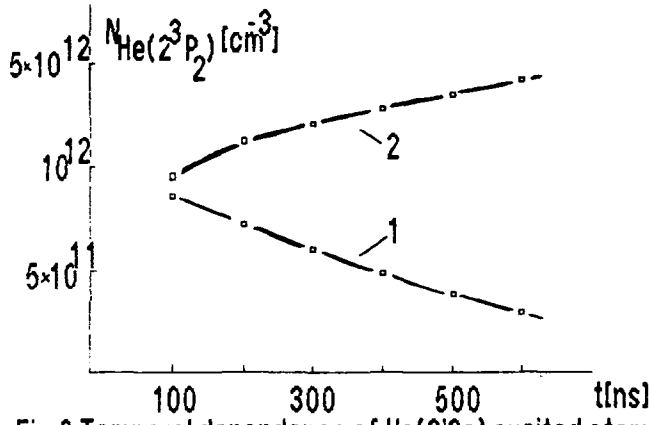


Fig.6 Temporal dependence of He(2'So) excited atoms
1-τ_p=150ns; 2-τ_p=1us

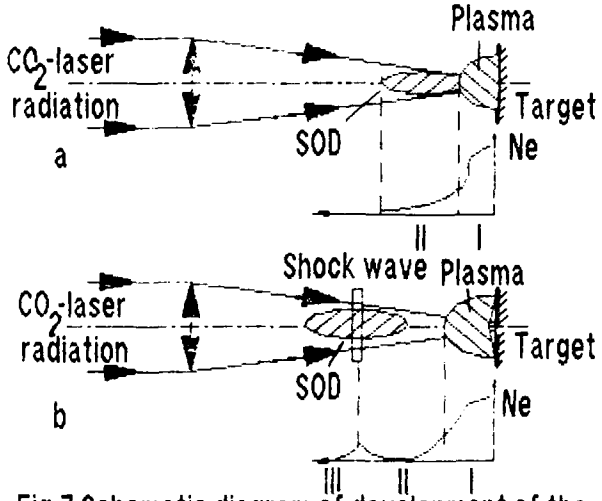


Fig.7 Schematic diagram of development of the stationary optical discharge(SOD)

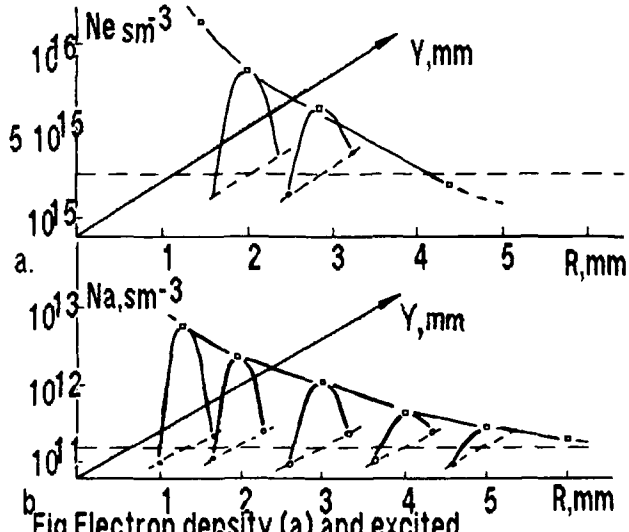


Fig.Electron density (a) and excited atoms $He(2^3P)$ (b) distribution; Δ t=100 ns

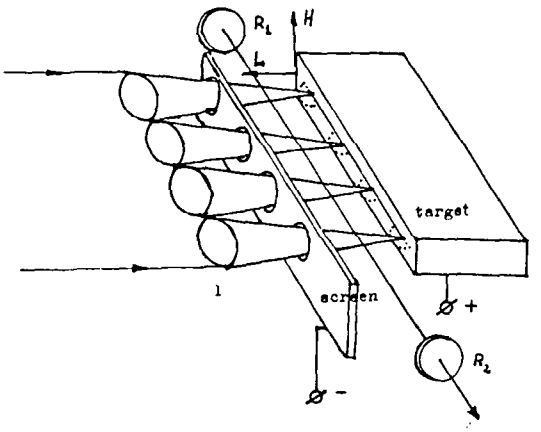


Fig.9 The experimental scheme.

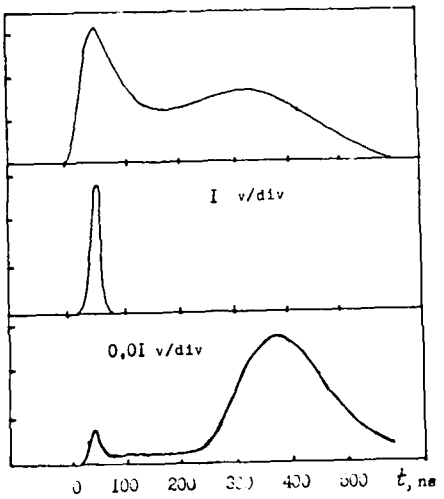


Fig.10
Oscillograms of :
a)the pulse of CO_2-laser;
b)the pulse of NeII-laser generation
c)the typical form of the luminescence pulse

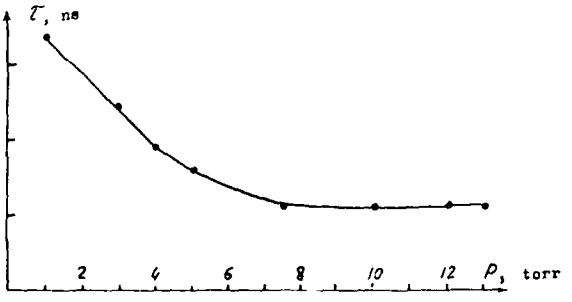


Fig.11
Dependence of the time delay vs pressure.

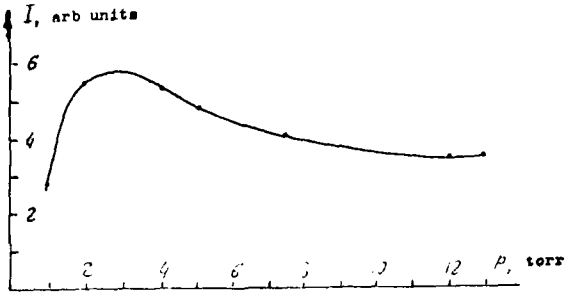


Fig.12
Dependence of the luminescence intensity vs pressure.

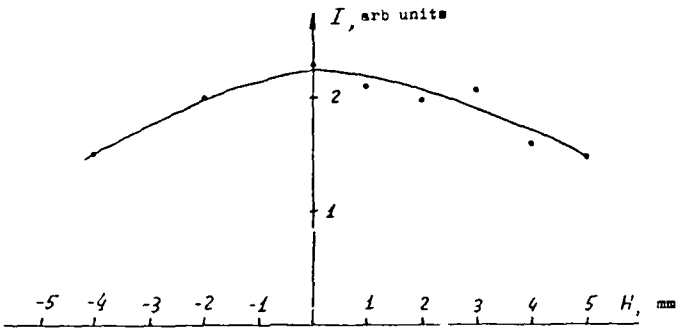


Fig.13
Dependence of the luminescence intensity vs distance H.

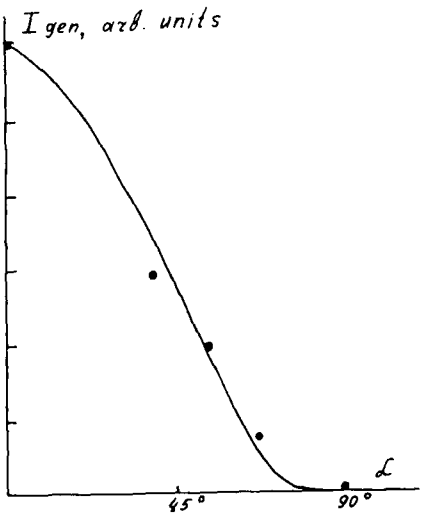


Fig.14
Dependence of the intensity of NeII-laser generation vs angle

Pt/SnO_2-BASED CO-OXIDATION CATALYSTS FOR CO_2 LASERS

Billy T. Upchurch, David R. Schryer, and Robert V. Hess
NASA Langley Research Center
Hampton, VA 23665

Kenneth G. Brown, John D. Van Norman, and David R. Brown
Old Dominion University
Norfolk, VA 23508

Barry D. Sidney
Science and Technology Corporation
Hampton, VA 23666

Abstract

The activity of Pt/SnO_2-based CO-oxidation catalysts has been maximized by optimizing pretreatment conditions and catalyst formulation. The role of H_2O in activating these catalysts and of CO_2 retention is deactivating them has been determined as has the interaction of these catalysts with rare-isotope $C^{18}O$ and $^{18}O_2$.

Introduction

Pulsed CO_2 lasers have several potential remote-sensing applications, both military and non-military, which require long-life operation with high conversion-efficiency and good power-stability. Two problems are potentially associated with such applications.

One problem is that the electrical discharge normally used to excite pulsed CO_2 lasers generally decomposes some of the CO_2:

$$CO_2 \xrightarrow[\text{Disch.}]{\text{Elec.}} CO + 1/2\ O_2$$

This decomposition is harmful to long-life laser operation both because of the loss of CO_2 and because of the buildup of O_2. The loss of CO_2 results in a corresponding gradual loss of laser power. The buildup of even relatively small concentrations of O_2 molecules can cause rapid power loss and even complete laser failure. Although CO_2 lasers differ somewhat in their tolerance of O_2, it is generally desirable to keep the O_2 concentration below a few tenths of 1 mole-percent. CO has no significant deleterious affect on laser performance at moderate concentrations.

The second problem is the fact that the atmosphere contains a significant concentration, about 300 ppm, of common-isotope CO_2 ($^{12}C^{16}O_2$). If common-isotope CO_2 is used in a CO_2 laser intended for atmospheric transmission, the emission frequencies available to the laser will correspond to the absorption frequencies of the atmospheric CO_2 and poor transmission will result.

The solutions to these two problems are: (1) continuously remove O_2 as it is formed and replenish CO_2 and (2) use some form of rare-isotope CO_2 (such as $^{12}C^{18}O_2$, $^{13}C^{16}O_2$, or $^{13}C^{18}O_2$) in lasers intended for applications involving atmospheric transmission so that the emission frequencies of such lasers will differ from the absorption frequencies of atmospheric $^{12}C^{16}O_2$.

Removal of O_2 and replenishment of CO_2 can be achieved in certain applications simply by operating the laser open-cycle with a continuous flow-through of fresh laser-gas and the consequent removal of dissociation products. However, for space-based applications or other applications involving weight and/or volume constraints, the amount of gas required for open-cycle operation would be unacceptable and, instead, closed-cycle laser operation with recycling of the laser gases would be imperative. Closed-cycle operation would also be highly desirable for any applications where rare-isotope CO_2 is used for enhanced atmospheric transmission because of the expense of the large volumes of rare-isotope gas which would be required for flow-through operation.

Achievement of closed-cycle operation of pulsed CO_2 lasers requires catalytic recombination of the decomposition products, CO and O_2, to regenerate CO_2.

$$CO + 1/2\ O_2 \xrightarrow{\text{Cat.}} CO_2$$

Candidate catalysts must have high efficiency at steady-state laser conditions which are, generally, 25°C to 100°C and about one atmosphere of total pressure with low partial-pressures of CO and O_2. Some excess CO may be added to the laser-gas mixture but generally it is not. It is desirable that little or no heating of the catalyst be required in order to minimize power consumption.

The catalytic oxidation of CO to CO_2 has been extensively studied at various conditions for a number of catalysts. These include the noble metals and various metal oxides[1,2] and the commercial catalyst, Hopcalite[3], which is a mixture of CuO and MnO_2 plus small quantities of other oxides. However, few catalysts have sufficiently high activity to allow operation at the low steady-state temperatures and low oxygen partial pressures characteristic of typical pulsed CO_2 lasers.

The most promising catalysts studied to date, whose performance has been verified by actual closed-cycle laser operation, consist of Pt and/or Pd on tin (IV) oxide[4,5]. A systemmatic study of (Pt, Pd)/SnO_2 catalysts for use with closed-cycle pulsed CO_2 lasers, including the preparation and testing of improved catalyst formations, has been in progress at the Langley Research Center of NASA (LaRC) for the past several years[5-16]. This study has been expanded by joint research with investigators at Old Dominion University, the University of Florida, the University of California, San Diego, and Science and Technology Corporation[1, 5-11, 13, 15-21].

Test Facilities

Catalyst research at LaRC is carried out both in laboratory reactors and in a commercial CO_2 TEA laser.

Laboratory Reactors

Laboratory reactors are used for catalyst study under controlled conditions. Several laboratory reactors are presently operational, most of which are flow-through (plug-flow) reactors. In these reactors a test-gas mixture flows through a reactor tube containing a catalyst sample which is situated in a temperature-controlled oven. The gas which enters and exits the reactor tube is quantitatively analyzed with either a gas chromatograph (GC) or mass spectrometer (MS) and from this analysis the amount of CO and O_2 converted to CO_2 by the catalyst sample is determined. For many tests the test-gas mixtures used are purchased premixed in a high-purity He carrier, typically 1.00 percent CO and 0.50 percent O_2 plus 2.00 percent Ne (as an internal calibration standard for gas analysis). For some tests the gas mixtures are blended in the laboratory using high-purity component gases and calibrated flow controllers.

All except one of the reactors are used with common-isotope gases and use GC's for gas analysis. These GC's are fully automated so that tests with common-isotope gases can be conducted in the flow-through reactors continuously around-the-clock. One flow-through reactor is used with rare-isotope gases and uses an MS for gas analysis.

Studies performed in the flow-through reactors are (1) parametric studies to determine the effect of such parameters as catalyst mass, temperature, reactor residence-time, pretreatment conditions, etc., on the performance of a given catalyst material, (2) comparison of different catalyst compositions (such as Pt/SnO_2, Pd/SnO_2, and Pt + Pd/SnO_2) and concentrations to determine the optimum catalyst formulation, (3) long-term performance tests (using an automated-GC reactor) to determine how a catalyst performs with long-term exposure to the test gases, and (4) isotopic studies (using the MS reactor) to determine the interaction of a given catalyst with rare-isotope gases.

A recirculating and a pulsed reactor are also available. In the recirculating reactor a gas mixture is continuously recirculated through a temperature-controlled reactor tube containing a sample of catalyst, and the conversion of CO and O_2 to CO_2 is monitored as a function of time. Gas analysis is performed with a GC. This reactor is used to study the kinetics and mechanism of catalysis for selected catalyst compositions.

With the pulsed reactor, the single-gas or gas-mixture to be studied (in a He carrier) is exposed to the catalyst sample in a series of discrete pulses. The pulses are spaced in time such that the gas exiting the reactor after each pulse can be analyzed by GC. The cumulative gain or loss of each species as a function of time can thus be more finely resolved than with the continuous flow-through and recirculating reactors. The pulsed reactor is used for both reaction and chemisorption studies.

Laser Reactor

A Lumonics model TEA-820 pulsed CO_2 laser (7 Watt, 1-50 pulses/second) is available for catalyst testing under actual laser operating conditions. The laser is operated closed-cycle with an external catalyst bed (in a temperature-controlled oven) and the results are compared with the open-cycle performance of the laser at the same flow rate. It is intended that ultimately the laser will be operated with no heating of the catalyst other than by the laser gas. Gas analysis is performed with a GC in current common-isotope tests. An MS will be used when the laser is operated with rare-isotope CO_2.

Results

The following results have been obtained in studies performed to date.

Common-Isotope Laboratory Studies

(1) Pt on SnO_2 (Pt/SnO_2) has significantly higher catalytic activity for CO oxidation than either Pt or SnO_2 alone[5]. The effect is clearly synergistic and apparently involves separate but complementary roles for the Pt and SnO_2 phases.

(2) The efficiency of Pt/SnO_2-catalyzed oxidation of CO to CO_2 is approximately proportional to catalyst mass until complete conversion is achieved[5].

(3) The catalyst mass required to achieve complete oxidation of a given concentration of CO is roughly proportional to the flow rate of the gas through the catalyst[7]. This makes possible the extrapolation of results obtained with laboratory reactors to CO_2 lasers.

(4) A technique for achieving much higher Pt loadings than are commercially available has been developed at NASA-LaRC[16]. Platinum loadings as high as 46 percent have been achieved.

(5) The activity for CO oxidation of Pt/SnO_2 catalysts increases with Pt loading until a maximum activity is reached at about 17 percent Pt[14]. Since Pt loadings between 11 percent and 17 percent and between 17 percent and 24 percent were not tested, the precise optimum loading is somewhat uncertain but it is believed to lie in the range of 15 to 20 percent.

(6) Bimetalic catalysts consisting of Pt and Pd on SnO_2 have a higher activity than catalysts with the same total loading of either metal alone. The optimum Pd loading for maximum catalyst activity is about 5 percent[22].

(7) A reductive pretreatment enhances the activity of Pt/SnO_2 catalyts relative to no pretreatment or to pretreatment with O_2 or an inert gas[15]. Pretreatment consists of a flow of the pretreatment gas (in a helium carrier, for safety and convenience) over the catalyst sample at an elevated temperature prior to exposure of the catalyst to the reaction gas mixture at the selected reaction temperature. Both CO and H_2 are suitable gases for reductive pretreatment[15]; in this study they were used at a concentration of 5 percent in He.

(8) The temperature at which a Pt/SnO_2 catalyst is pretreated can affect its subsequent activity[15]. Pretreatment temperatures of 125°C, 175°C, and 225°C resulted in equal catalytic activity, for the catalyst tested, but pretreatment at 100°C yielded somewhat lower activity.

(9) Duration of the pretreatment also affects subsequent catalyst activity[15]. Catalyst activity after a 20-hour CO pretreatment was found to be lower than after a 1-hour pretreatment. Too short a pretreatment also diminishes catalyst activity. For optimum results the effluent gases from the pretreatment should be analyzed and the pretreatment terminated when no significant yield of oxidation product (CO_2 or H_2O) is detected.

(10) Pretreatment of a Pt/SnO_2 catalyst sample at elevated temperatures--above about 125°C--results in an initial dip in catalyst activity before the steady-state activity is achieved for studies in the flow-through reactors[15]. No dip occurs if the catalyst is pretreated at lower temperatures. If the catalyst is exposed to moisture following pretreatment but prior to exposure to the reaction gas mixture, or if the reaction gas mixture is humidified, no dip occurs[15].

(11) In many cases moisture not only eliminates the initial dip in catalyst activity, it also enhances the activity of the catalyst[15].

(12) A Pt/SnO_2 catalyst supported on silica gel has been developed at NASA LaRC[16]. The hydrous silica gel supplies H_2O to the catalyst with minimal humidification of the laser gas.

(13) No initial dip in catalyst activity has been observed in flow-through reactor studies when the Pt loading exceeded 24 percent even at pretreatment temperatures of 225°C. No dip has been observed in studies in the recirculating reactor at any Pt loading or pretreatment temperature.

(14) The activities of Pt/SnO_2 catalysts exhibit some decay with time. Initial activity can be readily restored by outgassing the catalyst either by heating it or by exposing it to an inert gas for about 2 hours. In either case, restoration of activity has been found to be associated with outgassing of CO_2 from the catalyst but decay in activity occurs again when CO oxidation is resumed.

(15) The yield of CO_2 for a given catalyst sample and set of reaction conditions is increased by addition of O_2 to a stoichiometric mixture of CO and O_2 and decreased by addition of CO to such a mixture[22]. The reaction has been found to be first order with respect to O_2 concentration. Determination of the reaction order with respect to CO concentration is currently in progress. The true rate equation appears to be somewhat complex.

Rare-Isotope Catalyst Studies

(1) Reaction of $C^{18}O$ and $^{18}O_2$ on a common-isotope $Pt/Sn^{16}O_2$ catalyst yields about 85 percent $C^{18}O_2$ and 15 percent $C^{18}O^{16}O^{10}$. This concentration of the mixed-isotope species $C^{18}O^{16}O$ is unacceptable.

(2) A technique has been developed for modifying the surface of common-isotope Pt/SnO_2 so that all reactive surface oxygens are $^{18}O^{10}$. Reaction of $C^{18}O$ and $^{18}O_2$ over this modified catalyst yielded only $C^{18}O_2$, within experimental error, in a test of 17 days[23].

(3) Rare-isotope studies have indicated that some sort of carbonate or biocarbonate species is formed when CO is oxidized on Pt/SnO_2 catalysts[10].

Laser Studies

(1) The Lumonics Model TEA-820 laser has been operated closed-cycle with a catalyst bed of 150 g of 2 percent Pt/SnO_2 at 100°C[5,8]. The laser achieved 96.5 percent (± 3.5 percent) of steady-state open-cycle power for 28 hours (1×10^6 pulses at 10 pulses/second). Both the laser and catalyst were fully operational at the conclusion of the test. Additional laser tests are in progress.

(2) Herz and coworkers at the University of California, San Diego,[21] have developed a computer program which can be used to design catalyst monoliths for specific laser applications. The critical information a user needs to supply is the first-order-overall rate constant and activation energy for the catalyst formulation of interest. After the user supplies other information such as gas composition, gas flow rate and monolith dimensions, the program computes the conversion of oxygen and pressure drop as a function of monolith length. By varying input parameters, the user can investigate various design alternatives. One conclusion of a design study performed with the program is that standard off-the-shelf monoliths are not optimal for use in CO_2 laser applications. This is because standard monoliths have been designed for combustion or emission control applications where reactions occur very fast at high temperature and high gas flow-rates. Gas flow-rates in lasers are relatively low and reactions occur at low temperatures and thus, are relatively slow. Monoliths optimized for laser applications to provide for minimum monolith size will have thicker layers of active catalyst material than monoliths used for combustion and emission control. The computer program is available through NASA's COSMIC office.

Surface Characterization Studies

Extensive surface characterization studies have been performed by Hoflund and coworkers at the University of Florida. These studies utilized an ultrahigh vacuum system containing multiple surface techniques including ion scattering spectroscopy (ISS), electron spectroscopy for chemical analysis (ESCA), Auger electron spectroscopy (AES), and electron stimulated desorption (ESD) with pretreatment capabilities at elevated pressures and temperatures. Results have been presented in references 17-20.

Especially noteworthy is the observation that a Pt/Sn alloy with surface hydroxyl groups is formed when Pt/SnO_2 is reductively pretreated at conditions discussed herein. Both the alloy and the surface hydroxyls are believed to contribute to the observed catalytic activity.

Concluding Remarks

Noble-metal/tin-oxide based catalysts such as Pt/SnO_2 have been shown to be good catalysts for the efficient oxidation of CO at or near room temperature. They are the most promising catalysts for use in closed-cycle pulsed CO_2 lasers whose performance has actually been verified by tests in such lasers. The catalysts require a reductive pretreatment and traces of hydrogen or water to exhibit their full activity. Addition of palladium enhances the activity of these catalysts with about 15 to 20 percent Pt, 5 percent Pd, and the balance SnO_2 being an optimum composition. Unfortunately, these catalysts presently exhibit significant decay due in part to CO_2 retention, possibly as a carbonate or bicarbonate. Research on minimizing the decay in activity of these catalysts is currently in progress. Also in progress is research on other noble-metal/reducible-oxide (NMRO) catalysts.

References

1. Herz, Richard D.: Chemical Engineering Design for CO Oxidation Catalysts. Closed-Cycle Frequency-Stable CO_2 Laser Technology, Carmen E. Batten, Irvin M. Miller, George M. Wood, Jr., and David V. Willetts, Eds., NASA CP-2456, pp. 103-112, 1987.

2. Engel, T., and Ertl, G.: Oxidation of Carbon Monoxide. The Chemical Physics of Solid Surfaces and Heterogeneous Catalysis, P. A. King and D. P. Woodruff, Eds., pp. 73-93, Elsevier, New York, 1982.

3. Kiang, San: Transient Isotopic Tracing Technique for the Resolution of the Room Temperature Oxidation of Carbon Monoxide Catalyzed by Commercial Hopcalite Catalyst. Pd.D. Thesis, Columbia Univeristy, 1978.

4. Stark, D. S.; Crocker, A.; and Steward, G. J.: A Sealed 100 Hz CO_2 TEA Laser Using High CO_2 Concentrations and Ambient-Temperature Catalysts. J. Phys. E. Sci. Instrum., vol. 16, pp. 158-161, 1983.

5. Brown, Kenneth G.; Sidney, B. D.; Schryer, D. R.; Upchurch, B. T.; Miller, I. M.; Wood, G. M.; Hess, R. V.; Batten, C.; Burney, L. G.; Paulin, P. A.; Hoyt, R.; and Schryer, J.: Catalytic Recombination of Dissociation Products with Pt/SnO_2 for Rare and Common Isotope Long-Life, Closed-Cycle CO_2 Lasers. SPIE Proc., vol. 663, pp. 136-144, 1986.

6. Rogowski, R. S.,; Miller, I. M..; Wood, G. M.; Schryer, D. R.; Hess, R. V.; and Upchurch, B.T.: Evaluation of Catalyst for Closed-Cycle Operation of High Energy Pulsed CO_2 Lasers. SPIE Proc., vol. 415, pp. 112-117, 1983.

7. Miller, I. M.; Wood, G. M. Jr.; Schryer, D. R.; Hess, R. V.; Upchurch, B. T., and Brown, K. G.: Optimization of the Catalytic Oxidation of CO for Closed-Cycle CO_2 Laser Applications. NASA TM-86421, 1985.

8. Sidney, Barry D.; Schryer, David R.; Upchurch, Billy T.; Hess, Robert V.; Wood, George M.; Miller, Irvin M.; Burney, L. Garland; Brown, Kenneth G.; Van Norman, John D.; and Schryer, Jacqueline: Research on Catalysts for Long-Life Closed-Cycle CO_2 Laser Operation. SPIE Proc., vol. 783, pp. 162-168, 1987.

9. Schryer, David R.; Sidney, Barry D.; Miller, Irwin M.; Hess, Robert V.; Wood, George M.; Batten, Carmen E.; Burney, L. Garland; Hoyt, Ronald F.; Paulin, Patricia A.; Brown, Kenneth G.; Schryer, Jacqueline; and Upchurch, Billy T.: NASA-LaRC Research on Catalysts for Long-Life Closed-Cycle CO_2 Lasers. Closed-Cycle Frequency-Stable CO_2 Laser Technology, Carmen E. Batten, Irvin M. Miller, George M. Wood, Jr., and David V. Willetts, Eds., NASA CP-2456, pp. 113-120, 1987.

10. Upchurch, Billy T.; Wood, George M. Jr.; Hess, Robert V.; and Hoyt, Ronald F.: Rare Isotope Studies Involving Catalytic Oxidation of CO Over Platinum-Tin Oxide. Closed-Cycle, Frequency-Stable CO_2 Laser Technology, Carmen E. Batten, Irvin M. Miller, George M. Wood, Jr., and David V. Willetts, Eds., NASA CP-2456, pp. 193-198, 1987.

11. Batten, Carmen E.; Miller, Irvin M.; Paulin, Patricia A.; and Schryer, Jacqueline: Studies of CO Oxidation on Pt/SnO_2 Catalyst in Surrogate CO_2 Laser Facility. Closed-Cycle, Frequency-Stable CO_2 Laser Technology, Carmen E. Batten, Irvin M. Miller, George M. Wood, Jr., and David V. Willetts, Eds, NASA CP-2456, pp. 193-198, 1987.

12. Sidney, Barry D.: Studies of Long-Life Pulsed CO_2 Laser with Pt/SnO_2 Catalyst. Closed-Cycle, Frequency-Stable CO_2 Laser Technology, Carmen E. Batten, Irvin M. Miller, George M. Wood, Jr., and David V. Willetts, Eds., NASA CP-2456, pp. 211-218, 1987.

13. Brown, K. G.; Schryer, J.; Schryer, D. R.; Upchurch, B. T.; Wood, G. M.; Miller, I. M.; Sidney, B. D.; Batten, C. E.; and Paulin, P. A.: Characterization of Pt/SnO_2 Catalysts for CO Oxidation. Closed-Cycle, Frequency-Stable CO_2 Laser Technology, Carmen E. Batten, Irvin M. Miller, George M. Wood, Jr., and David V. Willetts, Eds., NASA CP-2456, pp. 219-226, 1987.

14. Hess, R. V.; Buoncristiani, A. M.; Brockman, P.; Bair, C. H.; Schryer, D. R.; Upchurch, B. T.; and Wood, G. M.: Recent Advances in Efficient Long-Life, Eye-Safe Solid-State and CO_2 Lasers for Laser Radar Applications. SPIE Proc., vol. 999, pp. 2-18, 1989.

15. Schryer, David R.; Upchurch, Billy T.; Van Norman, John D.; Brown, Kenneth G.; Schryer, Jacqueline; and Sidney, Barry D.: Enhancement of the Activity of Pt/SnO_2 Catalysts for CO_2 Lasers by Optimizing Their Pretreatment. Low-Temperature CO-Oxidation Catalysts for Long-Life CO_2 Lasers, NASA Conference Publication, 1990.

16. Upchurch, Billy T.; Schryer, David R.; Wood, George M.; and Hess, Robert V.: Development of CO Oxidation Catalysts for the Laser Atmospheric Wind Sounder (LAWS). SPIE Proc., Vol. 1062, 1989.

17. Hoflund, Gar B.; Grogan, Austin L., Jr.; Asbury, Douglas A.; and Schryer, David R.: A Characterization Study of a Hydroxylated Polycrystalline Tin Oxide Surface. Thin Solid Films, vol. 169, pp. 69-77, 1989.

18. Gardner, Steven D.; Hoflund Gar B.; Davidson, Mark R.; and Schryer, David R.: Evidence of Alloy Formation During Reduction of Platinized Tin Oxide Surfaces. J. Catalysis, vol. 115, pp. 132-137, 1989.

19. Gardner, Steven D.; Hoflund, Gar B.; and Schryer, David R.: Surface Characterization Study of the Reduction of an Air-Exposed Pt_3Sn Alloy: Part IV. J. Catalysis (in press).

20. Gardner, Steven D.; Hoflund, Gar B.; Schryer, David R.; and Upchurch, Billy T.: Platinized Tin Oxide Catalysts for CO_2 Lasers: Effects of Pretreatment. SPIE Proc., vol. 1062, pp. 21-28, 1989.

21. Herz, R. K.; Guinn, K.; Goldblum, S.; and Noskowski, E.: Design of Catalytic Monoliths for Closed-Cycle Carbon Dioxide Lasers. Final Report for NASA Contract NAG-1-823, Univ. of Califiornia, San Diego, 1989.

22. Upchurch, Billy T.; Brown, David R.; Miller, Irvin M., and Schryer, David R.: LaRC-Developed Catalysts for CO_2 Lasers. Low-Temperature CO-Oxidation Catalysts for Long-Life CO_2 Lasers, David R. Schryer and Gar B. Hoflund, Eds., NASA Conference Publication, 1990.

23. Upchurch, Billy T.; Miller, Irvin M.; Brown, David R.; Wood, George M., Jr.; Schryer, David R.; and Hess, Robert V.: Rare-Isotope and Kinetic Studies of Pt/SnO_2 Catalysts. Low-Temperature CO-Oxidation Catalysts for Long-Life CO_2 Lasers. David R. Schryer and Gar B. Hoflund, Eds., NASA Conference Publication, 1990.

DEVELOPMENT OF A 100-W COPPER VAPOR LASER

H. Sugawara,* M. Yamaguchi,** A. Wada,** T. Shirakura,** N. Tokunaga,** H. Yamamoto***

* Hitachi Works, Hitachi, Ltd., 1-1-1 Saiwai-cho, Hitachi-shi, Ibaragi-ken, 317, Japan
** Hitachi Research Laboratory, Hitachi, Ltd., 4026 Kuji-machi, Hitachi-shi, 319-12, Japan
*** Nuclear Power Generation Division, Hitachi, Ltd., 4-6, Kanda-Surugadai, Chiyodaku, Tokyo, 101, Japan

Abstract

This paper describes a development of a large bore copper vapor laser, with the bore diameter of 80 mm and the electric discharge length of 1570 mm, and its features. It is said that in general, some limitation exists in enlarging the bore of a copper vapor laser to increase output power, because of causing relatively low power density in the central zone. However, the large bore copper vapor laser of 80 mm in diameter described in this paper does not show such a power depression in the central zone, though the laser light emission is delayed in the central zone. The calculational results on the current distributon in the discharge tube indicate that the impedance mismatching adversely affected the skin effect causing the discharge current to flow only in the peripheral zone of the plasma.

Introduction

The copper vaper laser (CVLs) emmit two visible lights, green(510nm) and yellow(578nm). They are more than ten times as efficient as the ion lasers which are typical ones with the transitions in the visible spectrum region. Therefore, the CVLs have been scaled to high average power around 100 watts[1], order of magnitude larger than that of the ion lasers. Since the CVLs yield short pulses at high repetition rate of a few kilohertzs in the visible apectrum regior, they are adequate to pumping the dye lasers, and are expected to be suited for future photochemical applications, especially the research and development of isotope separation technology utilizing the CVLs.

It is estimated that a total laser output power of a CVL system of a few tens of kilo-watts will be required in energy applications.[2] Consequently, improvement in the efficiency, accordingly in the laser output power of a single CVL, is one of the major factors to determine whether the laser isotope separation system can have an economic advantage over the other separation schemes.

Volumetric power scaling of a single CVL has been accomplished by both lengthening the discharge and increasing its diameter. Availability in long-length ceramic tubes have made it possible to experiment with the tube up to 3-m long, and an output power of 150 W has been obtained with a 60-mm-diameter tubes by length scaling.[3]

A 100-W CVL is being developed with a-1570-mm-length discharge by increasing the discharge -tube diameter up to 80 mm. In an author's trial manufacture of a CVL with a 1570-mm-length and 100-mm-diameter discharge tube, the laser output power was limited to a few watts. The volumetric power scaling by increasing the discharge diameter was unable to be applied, since the laser beam formed an annular profile without any beam intensity in the central part, which failed in making the most of the whole discharge volume.

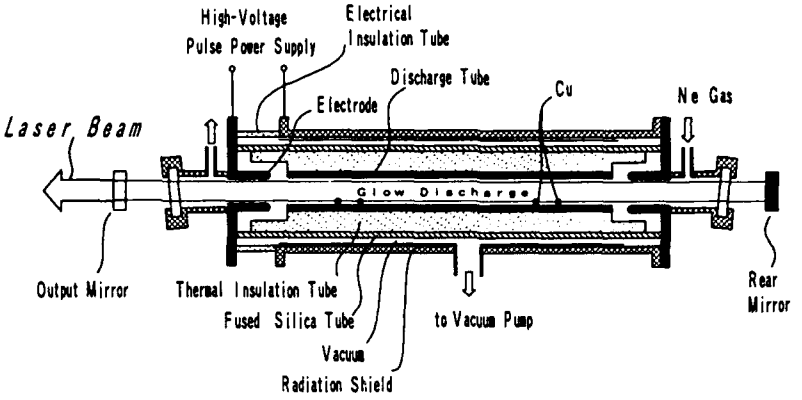
Some investigations showed that the increase in the diameter leaded to the decrease in the discharge resistance resulting in the impedance mismatching between the electrical circuit and the discharge tube. They also showed that the impedance mismatching adversely affected the skin effect causing the discharge current to flow only in the peripheral zone of the plasma. Eventually, the authers have been successful in obtaining an laser output power of 100 watts with a reduced-diameter tube of 80 mm by accomplishing the impedance matching.

The laser output characteristics and the impedance-matching results for the 100-W CVL will be described here.

Outline of 100-W CVL

A configuration of the 100-W CVL is depicted in Fig. 1. An alumina ceramic discharge tube is

surrounded by an alumina-fibrous thermal shield and a silica glass tube. Ne buffur gas is filled inside the glass tube, and a vacuum thermal isolation layer exists outside the glass tube. A radiation shield plate is placed inside an outer metal jacket which serves both as a curreut return and structural member. A left part of the vacuum vessel consists of an electrical-insulation ceramic tube. Electrodes are placed at both ends of the discharge tube. When a high-voltage pulse is applied between two flanges at both ends of the insulation tube, the discharge is established between the electrodes. The current flows from the electrode to the discharge, and returns to the opposite terminal through the outer metal jacket. The coaxial configuration reduces the discharge -tube inductance.

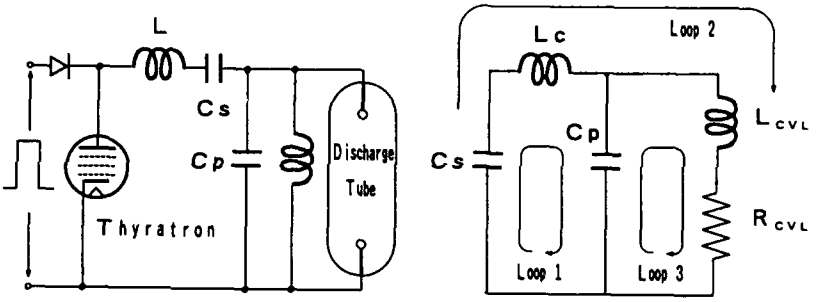


Fig, 1 Configuration of the Copper Vapor Laser (CVL)

Since the discherge tube is thermally insulated by the alumina-fibrous layer and the vacuum layer, the tube temperature increases to about 1500°C by the discharge, and the copper is vaporized. The copper vapor excited by the discharge emitts the laser beam. The discharge tube is 80 mm in inner diameter, and 1570mm long.

Electrical circuit

Fig. 2 (a) shows an electrical circiut of the CVL. The pulse power supply charges the storage capacitor Cs through the inductor, and is electrically insulated after the completion of charging. Then, the thyratron is closed by a controlled trigger signal, the charge in the Cs is transfered to the peaking capacitor Cp through the thyratron, and the terminal voltage of the discharge tube increases. When the discharge takes place, the current flows in the discharge tube from both Cs and Cp. As a result, the copper vapor is excited and the laser oscillation occurs. The current ceases to flow after the energy supplied from the pulse power supply is completely dissipated in the discharge and other electrical elements. Then, the thyratron recovers its insulation, the circuit restores the initial condition, and the power supply begins to charge Cs.



(a) Electrical Circuit of the CVL (b) Equivalent Circuit

Fig, 2 Electrical Circuit of the CVL and Equivalent Circuit

Impedance matching

Fig. 2 (b) shows an equivalent circuit where the discharge tube is represented by an inductance and a time-dependent variable registance. The circuit forms a loop 1 from Cs to Cp, a loop 2 from Cp to the discharge tube, and a loop 3 from Cs directly to th tube. Since the lifetime of the excited atoms is short in the CVLs, it is necessary to deposit the high - power energy into the discharge within a very short period of ~100ns, in order to obtain the efficient oscillation. Therefore, it is important to match the circuit impedance $\sqrt{(L/C)}$ with the discharge registance.

Fig. 3 shows the CVL current profile and the integrated energy deposited in the discharge for three equal circuit impedances of 6Ω and the discharge registance of 6Ω. The integrated energy is represented by the rate to the energy initially stored in Cs. When the discharge registance is equal to the circuit impedances, 82.5% of the energy is deposited in the

discharge during the first wave of the current.

Since the laser oscillation takes place around the peak of the first wave of the current, it is necessarey for the energy to be deposited in the discharge during the first wave in order to make the most of the stored energy.

Fig. 4 shows a variation of the energy deposited during the first wave as a furction ofthe discharge registance. The circuit condition is the same as that in Fig. 3 where the first wave period of 160ns is indicated by the dashed line.

The abscissa corresponds to the discharge registance, and the ordinate corresponds to the energy deposited within 160ns. The figure shows that the energy deposited is reduced to 70% for the registance of 2.5Ω or 12Ω. The impedances can be matched by the additional inductance to the external circuit in case of a relatively large discharge registance. When the registance is small enough, however, there is a limit in reducing theinductances in the tube and the external circuit.

Even if the input power is increased at the cost of the efficiency, the discharge registance becomes smaller, which leads to the further mismatching.

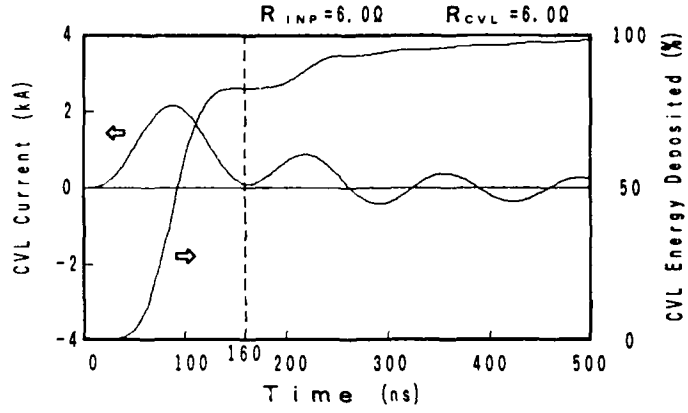


Fig. 3 CVL Current Profile and the Integrated Energy Deposited

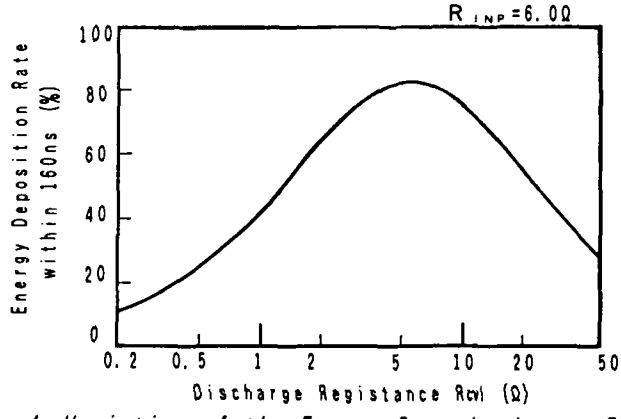


Fig. 4 Variation of the Energy Deposited as a Function of the Discharge Registance

Table 1 shows a comparison of the discharge tube registance with the circuit impedanceas a function of the discharge tube diameter for a constant dischage length or 1500mm.

The discharge registance is calculated from a conductivity of 1.5 $\Omega^{-1}cm^{-1}$.[1] The inductance is computed as the coaxial round-trip circuit with a constant insulation thickness of 40mm and the electrode length twice as large as the diameter. The capacitance is determined on condition that the stored energy is proportionai to the cross section of the discharge tube for a constant voltage of 20kV and a constant pulse repetition rate of 5kHz.

The disharge registance for a 35-mm diameter is 2.1 times larger than the circuit impedance, and becomes 4.7 times larger then that for a 100-mm diameter. It is clear from the table that the impedance matching is not obtained at all for larger discharge diameters. There seems to be a fundamental problem in the volumetric power scaling by increasing the diameter.

Table 1 Impedance Matching and Discharge-Tube Diameter

Discharge Tube Diameter(mm)	Circuit Inductance L (nH)	Capacitance C (nF)	Circuit Impedance(Ω)	Discharge Resistance(Ω)
35	472	2.0	21.7	10.4
60	382	6.0	11.3	3.5
80	343	10.6	8.0	2.0
100	318	16.7	6.2	1.3

Skin effect and impedance matching

The impedance mismatching adversely affects the plasma skin effect, consequeiently thelaser beam

profile dose not exhibit a uniform distrifution but an annular one.

Fig. 5 shows an equivalent circuit for a calculation of the radial discharge current. The discharge plasma is divided so that the cross section of each element becomes equal each other. The inductance is calculated by both self and mutual inductance.

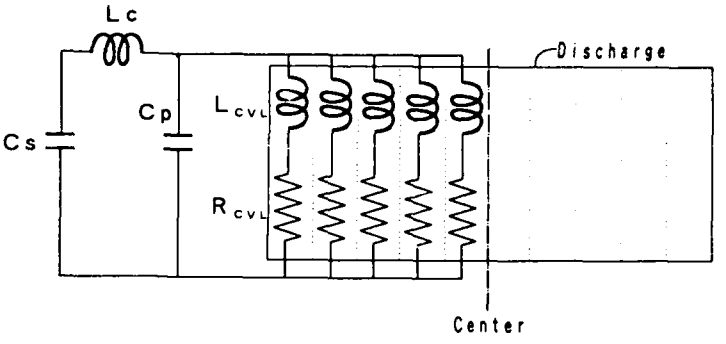


Fig. 5 Equivalent Circuit for a Calculation of the Radial Discharge-Current Distribution

Fig. 6 shows computed results of the current and the integrated energy deposited in the discharge for a well - matched case with a 7.5 Ω circuit impedance and a 7.5Ω discharge registance. The discharge region is divided into 5 elements. The current in the central zone is approximately equal to that in the peripheral zone, though a slight time delay is obserbed. And it is true of the energy deposited. It takes about 20-ns time delay for the energy deposited in the central zone to become equal to that in the peripheral zone. The difference of the energy deposited between the peripheral zone and the central zone is only 8%.

Fig. 7 shows similar computed results for a mismatched case with the 7.5-Ω circuit impedance and a reduced discharge registance of 1.5Ω. The current peak value in the central zone is 60% of that in the peripheral zone, and the amount of the energy deposited is reduced to less than half that for the well -matched case. The impedance mismatching in the CVLs causes the energy deposition only in the peripheral zone of the plasma, resulting in the annular beam profile.

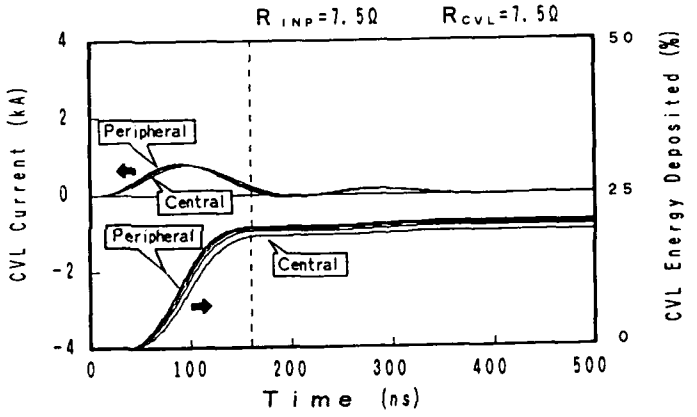


Fig. 6 Axial Differences of the Current and the Energy Deposited (Rinp≒Rcvl)

Fig. 8 shows laser output characteristics and a photograph of th 80-mm-diameter CVL in operation, which has been developed by the authors. A maximum output power of 100 watts is obtained with an operating temperature of 1450°C.

Fig. 9 shows a radial laser beam intensity distribution. The power density becomes maximum in the central portion of the intensity distribution.

Fig. 10 shows temporal laser power profiles in various positions in the beam. A peak value of the laser power profile in the center in larger than that in the peripheral position, though the oscillation in the peripheral position starts 20ns earlier.

It is considered that the impedance matching is sufficiently accomplished in the 80-mm- diameter CVL.

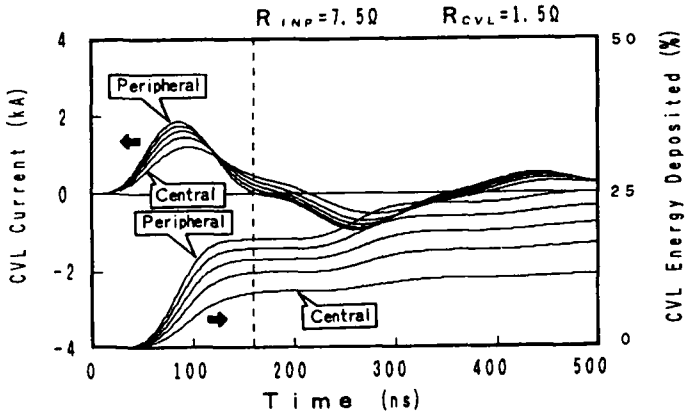
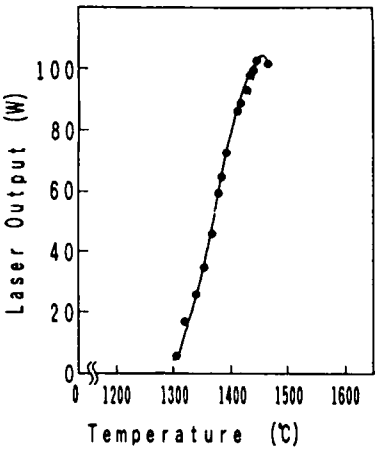


Fig. 7 Axial Differences of the Current and the Energy Deposited (Rinp≪Rcvl)



(a) Laser Output vs. Temperature Characteristics



(b) the CVL Emitting the Laser Beam

Fig. 8 Laser Output Characteristics and Photograph of the CVL in Operation

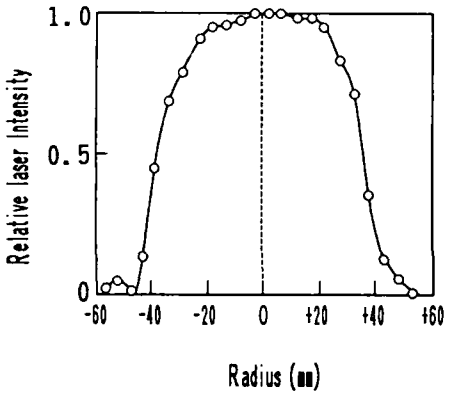


Fig. 9 Radial Laser Intensity Distribution Obtaied with the CVL of 80-mm Bore Diameter

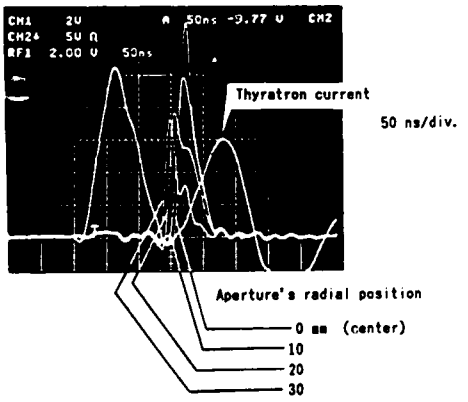


Fig. 10 Laser Power Pulses Measured in Various Positions through an Aperture of 12-mm Diameter

Concluding remarks

A 100-W copper vapor laser with the discharge tube of 80 mm inner diameter and the electric discharge length of 1570 mm, was developed. The large bore copper vapor laser did not show the power depression in the central zone. It shows the possibility of increasing the total power by enlarging the bore diameter and accomplishing the impedance matching between the electrical circuit and the discharge resistance.

References

1. M. J. Kushner and B. E. Warner, J. Appl. Phys. 54, 2970 (1983)

2. J. L. Emmett, W. F. Krupke, and J. I. Davis, IEEE J. Quantum Electron. QE20, 591 (1984)

3. N. Arai, Reports on Topical Meeting of the Laser Society of Japan, No. RTM-89-17, (1989)

DEVELOPMENT OF HIGH-POWER COPPER VAPOR LASERS DRIVEN BY SOLID-STATE PULSE GENERATOR

Akihiko Iwata, Kazuhiko Hara, Shigeo Ueguri, and Yoshihiro Ueda

Central Research Laboratory
Mitsubishi Electric Corporation

8-1-1, Tsukaguchi Honmachi
Amagasaki, Hyogo, 661
JAPAN

Abstract

A solid-state pulse generator which consists of only fast semiconductors without a saturable reactor has been developed. With this pulse generator, a laser power of 112 W has been obtained with a high-power 80 mm bore copper vapor laser. The switching time is 38 ns, the rate of rise of the pulse current is 20 A/ns, and the switched pulse energy is about 2 J with the high repetition rate of 6 kHz and the voltage of 17 kV. These values are comparable to those obtained with a modern thyratron.

1. Introduction

The technology of controlling the high-power nanosecond pulse current is necessary to obtain high-power pulse lasers.

At present, the high-power nanosecond pulse current is obtained by discharging the condenser instantly by a switching device. A thyratron tube is mainly used for this switching device. But it has some problems of short lifetime and unstable quality For that reason, many studies on a solid-state switching device for replacing a thyratron have been carried out. Many papers [1,2,3,4] with a magnetic pulse compression curcuit(MPC) applied to pulse lasers were published. But there are problems that the MPC has jitters in the switching owing to the fluctuation of the cuicuit conditions such as charging voltage. Because of the jitters, laser amplifiers can't be excited synchronously in a time order of nanosecond in a master oscillator and power amplifier (MOPA) laser system, resulting a low efficiency of amplification of laser power.

To solve these problems, we have developed a solid-state pulse generator which consists of only semiconductors without a saturable reactor. In this report, we describe the chracteristics of the solid-state pulse generator and the application to a high-power 80mm bore copper vapor laser (CVL).

2. The chracteristics of a solid-state pulse generator

A schematic diagram of a electric circuit used in CVL is shown in Fig. 1. A discharge capacitor(Cd) is charged by DC high voltage power supply. When this voltage is switched by a solid-state switching device, a pulse current flows into a discharge tube. This pulse current excites a laser medium and a laser oscillation is generated. A solid-state pulse generator is composed of a solid-state switching device, a gate circuit and a tigger oscillator. The solid-state switching device is activated by the signal of the trigger oscillator with a high repetition rate.

A schematic diagram of the solid-state pulse generator is shown in Fig. 2. The switching device consists of only semiconductors, MOSFET's(Metal Oxide Semiconductor Field Effect Transistor), in which a multistage of several parallel FET's are installed to switch the high voltage and high current. Each stage is connected to each insulated gate curcuit. The switching signal of the trigger oscillator is inputed to the gate curcuits through the optical fibers to switch all FET'S at the same time in nanosecond order. Because of the fast switching operation of the FET's, no saturable reactor for sharpening the current pulse waveform is used in this solid-state pulse generator.

It is necessary to make equal the current and the voltage at each FET in a solid-state switching device which consists of series and parallel connectoin of FET's so that the large switched power can be obtained. First, the current distribution in each FET connected in series and parallel at the rise of a nanosecond pulse current depends on the reverse induced electromotive force by inductance in a switching device rather than a on-stage voltage of each FET. The equalization of the current at each pararllel FET is obtained by installing all FET's and a plate for a returning current parallel, making equal a value of inductance in each loop which is made up of each FET and the plate. As a result, the value of the current of each FET deviates within 13 % from a value, which is defined as I/N (I is the total current, N is the total number of the paralell FET's). Secondly, we must make equal the voltage per stage at the multistage because the excessive voltage over the rating of the FET would cause to destory the FET. The equalization of the voltage is obtained by ajusting the installation of the FET's. The result is shown in Fig. 3. The horizontal line is the stage number and 100% is the total number of the multistage. In this case, the fluctuation of the voltage per stage is obtained within 15 %.

Figure 4 shows the waveforms of the FET current and FET voltage when the solid-state pulse generator is switched. In this case, the peak current and the charging voltage are 1.7 kA, 17 kV and the repetition rate is 6 kHz. a pulse energy of 1.93 J has been stably switched. The switching time is 38ns and the rate of rise of the current pulse is 20A/ns. These values are comparable to those obtanied with a modern thyratron.

The switching loss in the solid-state pulse generator contains both the loss in the transient switching and in the steady state switching. In Fig. 4, the sum of the on-stage voltage of the FET's in multistage is about 1 KV. The loss in the trnasient switching is about 0.05 J and the loss in the steady state switching is about 0.16 J, which is three times than the loss in the transient switching. The total loss is 1.26 KW, which means that the conversion efficiency from the switching electrical power to the input power into a load is about 90 %.

3. An application of the solid-state pulse generator to a 80 mm bore CVL

A shcematic diagram of a caharge tube in a 80 mm bore CVL is shown in Fig. 5, which is a vonvetional l ngitudinal one. There is a alumina tube in the center and each electrode in the both side of the alumina tube. The pulse discharge occurs between the electrode. The length of the dischage tube is about 2 m.

The solid-state pulse generator has been applied to the 80 mm bore CVL. Figure 6 shows the waveforms of the FET current and the discharge current and the laser power. In this case, the laser power 112 W has been obtained when the switched pulse energy is 2 J with the repetition rate 5 kHz. The maximum of the discharge current is 1500 A. The high efficiency more than 1 % is obtained with the electrical input power of 10 KW ($1/2CdV^2f$, Cd: discharge capacitance, V: charging voltage, f: repetition rate).

4. Conclusions

We have developed the solid-state pulse generator which consists of only semiconductors, FET's, which is activated with the high repetition rate.

(1) The laser power 112 W has been obtained with the 80 mm bore CVL.

(2) The swicthing time is 38ns and the rate of rise of the pulse current is 20 A/ns. The convertion efficiency of the swicthing power of 10KW is about 90 % in the swicthed pulse energy of 2 J with the repetition rate of 6 KHz.

Reference

1. Shmadsa, Obara, Rev. Sci. instrum. 56(11), 2018-2020 (1985)
2. S. P. Dashuk, Insturm exp Tech. 26, 1, 188-189 (1983)
3. M. L. Muchnik, Insturm exp Tech, 26, 3, 592-593 (1983)
4. A. N. Meshkov, Insturm Exp Tech. 27, 2, 362-364 (1984)

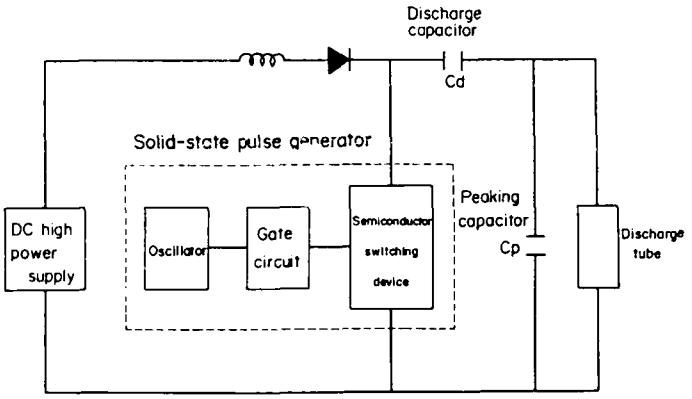


Fig. 1 A schematic diagram of a electric circuit in CVL

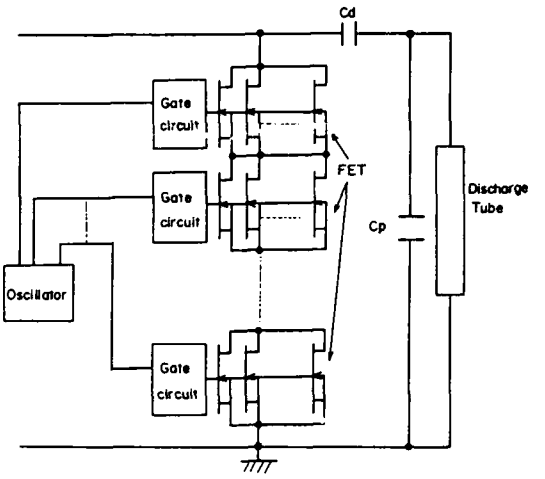
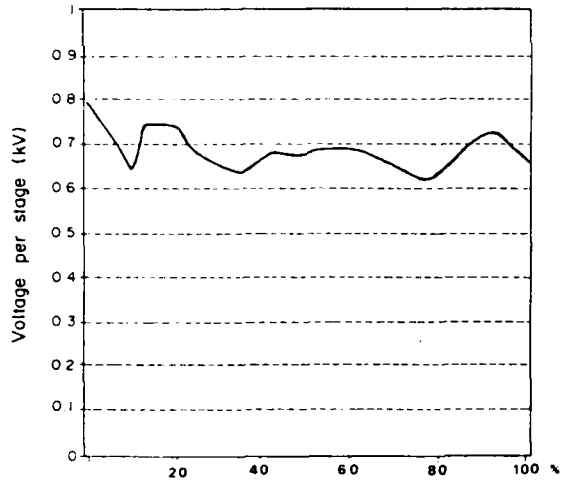


Fig. 2 A schematic diagram of a solid-state pulse generator



stage number in the multistage.

Fig. 3 The voltage per stage at the multistage of the solid-state pulse generator

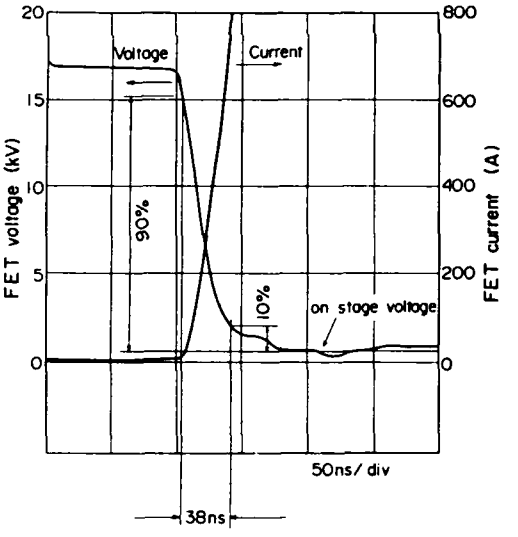


Fig. 4 The waveforms of the FET current and FET voltage

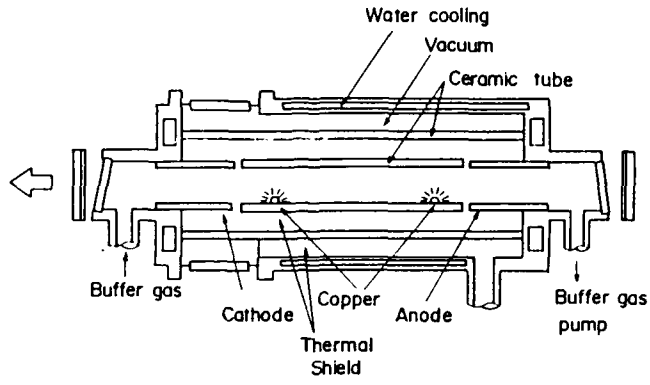


Fig. 5 A shematic diagram of a discharge tube in a 80 mm bore CVL

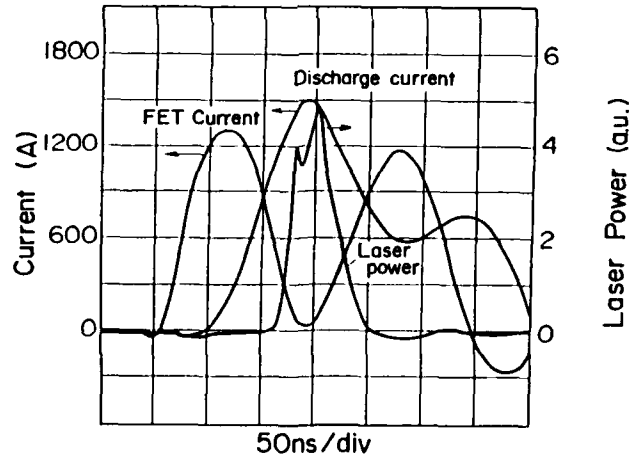


Fig. 6 The waveforms of the FET current and the discharge current and the laser power

DEVELOPMENT AND APPLICATIONS OF DYE LASER'S

S. Edward Neister
Vice President/Research & Development
Phase-R Corporation
54 Old Bay Road
New Durham, NH 03855

Abstract

This is a general review article for people who are entering the dye laser field for the first time. Quickly I will review the different types of dye lasers, and their difference in beam characteristics. Next will be discussed the development of dye and where it is today, the development of optical systems on the various dye lasers and the applications relating to dye lasers.

Types of Dye Lasers

There are two basic types of dye lasers. There are laser pumped dye lasers which use another laser type to pump a dye cell. These types of lasers consist of using a Nd:YAG, frequency doubling it's output to obtain 530nm light which is used for pumping a dye cell that contains dyes that absorb 530nm. Excimer lasers are used to pump dye cells and their UV excitation at 308nm is particularly useful for exciting many of the different dyes. Nitrogen lasers can be used to pump a dye cell and it's UV output at 331nm is also absorbed by many different dyes. In both the Excimer and Nitrogen laser, however, the more red the dye, less absorption of the UV occurs. The relative efficiency of dyes in the red and the near infrared region becomes less for Excimer and Nitrogen pumped dye lasers. Copper vapor has a yellow excitation of 577nm and is very useful for pumping dyes that have absorptions at 577 or above. The Argon Ion laser is a continuous (CW) laser. It has a blue green excitation region of 488nm or 514nm and pumps dyes that are flowing through the focal point of the beam to produce a continuous dye laser. Krypton Ion can also be used in place of Argon.

The flashlamp pumped dye lasers use a flashlamp to excite a dye cell. There are two basic types of flashlamps, the coaxial flashlamp where the dye flows through the center of the flashlamp, and the linear flashlamp which uses an outside reflector to direct its light into an adjacent dye cell.

The top of Figure 1 shows a ruby laser used to excite a dye cell. The lower two diagrams show the configuration of an argon laser used to pump the flowing cell.

Figure 2a is a layout of what a linear flashlamp system would look like with its adjacent dye cell. Also shown, is the energy level diagram for dyes.

Figure 2b shows how the dyes self absorption forces the lasing spectra to be red shifted from the fluorescent peak.

A dispersive element in the resonator cavity will make the lasing output tunable. It will also increase the spectral intensity of dye laser. The greater the dispersion, the more narrow is the linewidth of the output. Dye lasers are tunable and this is their primary advantage.

Figure 3 shows the coaxial flashlamp. The dye flows through the center of the flashlamp. The coaxial flashlamp is unique in that it can pump the dyes much more efficiently than the linear flashlamp. The coaxial flashlamp has extremely low inductance. Consequently its rise time is very fast and can match the fast fluorescent time constant of the dye which is in the order of 3-4ns.

In Figure 4 an example of a pulse produced by a coaxial flashlamp pumped dye laser is shown. Notice how quickly the laser pulse rises to about 50% of it's amplitude and then after the peak, has a gradual rollover that is a nice, smooth, laser pulse.

Beam Characteristics

The beam characteristics of the different dye lasers are important to understand. Generally speaking, if a laser is used to pump a dye cell, then the temporal behavior of a dye cell will closely follow that of the pumping source. For example, 20ns Nd:YAG will produce 20ns dye laser pulses. The Copper Vapor and Excimer pulses are in the order of 6-

10ns. The Nitrogen laser is around the 1-2ns, whereas the Argon Ion or Krypton lasers are continuous wave. Dye lasers made by excitation from these lasers will have the same temporal characteristics.

Flashlamp pumped dye lasers are quite different. Flashlamp pumped dye lasers can be made at different pulse widths and consequently the dye laser will generally follow the flashlamp excitation time. We have been able to produce flashlamp dye lasers that produce coherent light pulses from about 20ns all the way up to in excess of 1ms.

The linewidths of the lasing output from either a flashlamp pumped or laser pumped dye laser, are all controlled by the amount of the dispersion introduced into the dye cavity. Typical linewidths are in the order of 0.1A° to 40A°. 3-5 MHz linewidths can be attained in pulsed and in CW systems. Generally, as the linewidth is reduced, the amount of energy or pulse intensity from the dye laser is also reduced.

The divergence of the dye laser beam is typically in the order of 1-5mr. Near diffraction limited quality can be obtained similar to other laser types.

The output energy or power of dye lasers can run the full range available from any other type of laser. In the continuous mode using the Argon or Krypton systems, milliwatts to 3 or 4 watts is available. In the pulsed mode, energies from microjoules to as much as 150 joules or powers from kilowatts to 5 GW have been obtained.

Development of Laser Types

The development of dye lasers really started back in 1968 when Peter Sorokin at IBM was doing some florescent measurements with a very simple type of coaxial flashlamp. From his work the first commercial dye laser evolved at a company called General Laser Corporation using a coaxial flashlamp. The first flashlamp pumped dye laser was made available in early 1969. Avco and Exxon formed a team later in the 1970's to develop a high average power linear flashlamp system for isotope separation. Many of the high average power designs and concepts and the problems associated with running flashlamp pumped dye lasers at high rep rates came from the studies done at Avco and Exxon by this team. There are two principle flashlamp dye laser houses in the United States. One is Candela that primarily works with the linear flashlamp systems and Phase-R Corporation which has developed the coax to where they have an all metal to quartz seal, making that flashlamp a very reliable flashlamp when compared to the linear.

CW dye lasers began when Ben Snavely at Kodak fathered the concept of using an Argon Laser to pump a fast flowing dye. Initially, this began with the dye flowing between two windows but as Coherent and Spectra Physics began using higher and higher powered Argon lasers, they found that the dye was actually being plated onto the windows. Consequently, the dye jet using glycol evolved with a nozzle approach so that the high intensity would not cause the thermal effect associated with the boundary layer between the dye and the glass.

Laser pumped dyes began at Avco because Avco was an early manufacturer of a Nitrogen Laser. One of the first experiments that someone did at Avco was to make jello with dye and actually make it lase. Other cells were developed, and laser pumped dye lasers began to evolve. Other manufacturers that produced Excimer or Nd:YAG or Ruby lasers began to see that there was a market for their lasers and all developed various dye cells that would fit to their lasers.

By and large all dye lasers would not be used if the dye is not efficient, if it is short lived, and it must be used in toxic solvents. Consequently, the dye and its associated characteristics are extremely important to the usefulness of the dye laser.

Development of Dyes

The development of dyes began back in 1968-1970. Several books were written on it, but the synthetic development of the dye and the actual studies really didn't start to move until the Air Force in 1975 started to spend some money on the development of red dyes. The Navy started to see that blue/green dye lasers could have a beneficial effect to some applications in the Navy. In 1977 they pioneered development programs to develop blue green dyes. In 1986 the Army got the concept and idea and wanted to understand how much power a dye laser could produce. Consequently, high power dyes were considered an important part of the dye program study. In 1985 the Navy began to fund an acrylic rod concept where the dye would be mixed into an acrylic rod so that the dye laser could possibly evolve into a tunable "solid state" type of laser which could in the worst case, be a throwaway type of system.

Future development on dyes is going to be required on dyes for many years until we have long lived, very stable, high efficient dyes at every part of the near UV to near IR spectrum. In the 20 years since 1970, some striking examples of good dyes have evolved. However, there are many holes in the spectrum that do not have good dyes at all. What is needed is development on long life dyes that produce high energy and are capable of being water soluble or at least operating in a solvent that is non-flammable over any part of the visible and near UV, IR spectrum. Another development will be using dyes mixed in PMMA or Acrylic type rod systems. Dyes are beginning to have medical applications where photodynamic therapy and its effect on cancer produce striking results. There could very well be concepts that have been learned in making synthetic laser dyes used to help develop associated dye materials that would be very beneficial for the PDT type of application.

In figure 5 is an example of the various dyes that exist today. Please note that the same dye will lase at a different wavelength depending on how it is pumped. Notice how the red mark of Rhodamine 590 for a Krypton system lases at a different wavelength compared to a flashlamp system.

Figure 6 is an example of the pulse response of various dyes with flashlamp excitation. It is interesting to note that the chemistry of the dye and its effect with the solvent can produce very efficient or very bad performance. Notice that some dyes have a scalloping effect as the intensity decreases. This indicates that triplet-triplet absorption is starting to become a substantial part of the excitation mechanism.

Development of Optical Systems

As the dye laser began to evolve, initially it was used as a tunable source for very basic research and very basic applications. Then as it became more accepted, the development of optical systems for liquid type lasers, namely dye lasers, began to evolve. The fundamental difference with liquid dye lasers and the optical systems they use is that the liquid lasing media is moving, it can have thermal gradients that exist not only longitudinally but transversely. The gain of the dye can be changed for a given diameter and length ratio, which has an effect in the design of optical resonator systems.

Something that had never been used before in other types of lasers were dispersive elements. In the dye laser, the dispersive element is a very important concept because the dye is so tunable. Introducing dispersive elements into the dye laser produced the ability to tune from one wavelength to the other using the same dye lasing material. Various dispersive elements have been studied from prisms, to gratings, to birefringent filters, to etalons, to a combination of all of these. Every laser pumped dye cell and every flashlamp pump type of dye laser have all had studies done with all of these various devices.

The ideal use is for a laser to produce coherent light that is diffraction limited. The focus ability of the laser light is important for many applications. Consequently diffraction limited resonators were studied with dyes. The concept of the unstable resonator became very important not only for the CO_2 laser, but for large diameter flashlamp pumped dye lasers. Other studies involved resonators that produced extremely narrow linewidths. A unique type of resonator was developed with a dye laser. It was the cavity dumper, as opposed to a Q Switch. A Q Switch laser uses lasing materials where the energy is maintained in the upper
excited state until the optical resonator is quickly aligned. A cavity dumper is used with lasing materials that have very short florescent time constants. Consequently, the energy in the beam has to be stored as photon flux and then it is literally dumped from the cavity. The cavity dumper was studied and developed by a group at Avco who did the initial pioneering work and was also studied and further refined and developed at Phase-R Corporation.

The dye laser appeared to be able to scale towards larger sizes. Development began on very high average power type laser systems. In the CW systems, they evolved from the cell to the glycol fluid window. For the laser pumped systems, flowing cells became necessary as the repetition rates of the laser pump systems increased. For the coaxial flashlamp, a triax or trivac tube was necessary to isolate the dye cell from the flashlamp. For linear flashlamps, transverse pumping became an ideal means where the dye did not have to be passed down the entire length of the flashlamp before the next pulse. It could just be passed transverse or through the distance of the diameter of the flashlamp instead.

One of the outgrowths of solid state lasers that became directly applicable for dye lasers was frequency doubling. Frequency doubling of the Nd:YAG was very predominant in being able to produce green light from infrared. The dye laser, because it was tunable, gave the operator the ability to tune ultra violet light. There were many studies done on crystals, tunability, and crystal damage and the relative efficiencies of frequency doubling crystals.

The figures that follow are examples of some simple setups and simple optical systems used with the flashlamp pumped dye lasers. Simple frequency doubling or second harmonic generation is shown in figure 7. A coaxial flashlamp has the ability to pump two dyes simultaneously and is shown in figure 8. Two separate cells could be tuned and used with the dispersive prism.

Figure 9 shows the difference between an optical chopper setup and a cavity dumper. An optical chopper means just literally, chopping out part of the laser pulse; whereas the cavity dumper compresses the energy and stores it so that a single giant pulse is obtained from the laser.

Applications

Parameters which dictate the use of a dye laser are the required wavelength and linewidths of the laser beam. Generally it's necessary to have the tunability or the ability to reach a particular wavelength that is not accessible by other laser types. The pulsewidth or continuous operation is a necessary criteria for choosing the type of dye laser. And then the power/energy will dictate the type of model of laser used. Of course, the underlying parameter will be the cost, utility and maintenance of a dye laser and in most cases a flashlamp pumped dye laser are much less expensive than a laser pumped dye laser simply because two lasers do not have to be purchased.

By and large, dye lasers are used for the interaction of matter in the research field. One can be classified as spectroscopy and the other could be classified as an excitation or destruction mechanism.

The other major application for dye lasers has turned out to be the medical area. Photodynamic therapy, is being used to kill cancers. Dye lasers are being used to break up kidney stones and gallstones. In dermatology they are being used to remove skin defects and surface veins. They are currently being used in ophthalmic research and there is a possibility that dye lasers can be used to break up plaque in blood vessels.

Figure 10 shows a coaxial flashlamp pumped dye laser that was used with an optical chopper. It was put in a 16 inch diameter cylinder and was used as an undersea illuminator for the US Navy back in the late 1970's. It had the nickname "Nessy".

Another unique application had the dye laser was put into a van and computer controlled. It was used to monitor the smoke exhaust from the Columbia Shuttle.

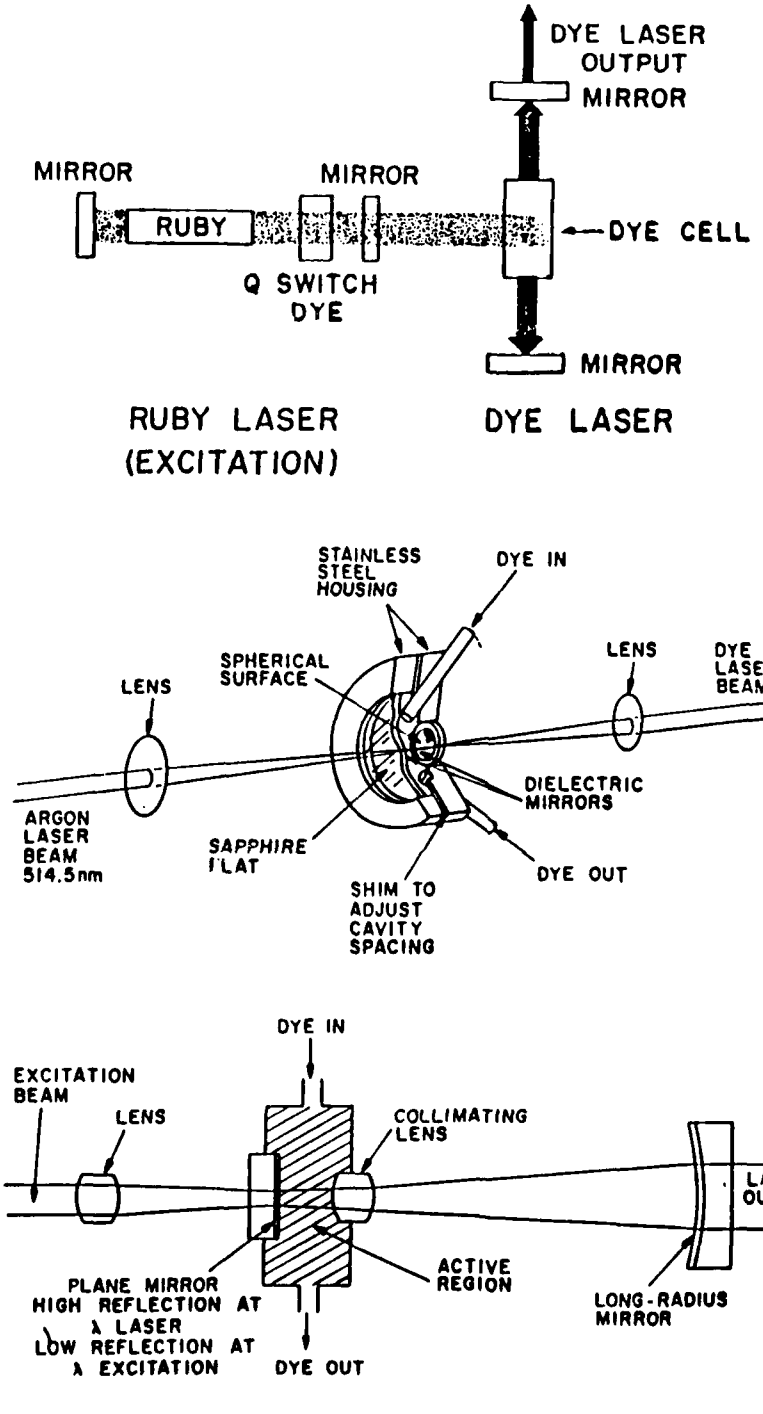

DYE LASER
OUTPUT
MIRROR
MIRROR
MIRROR
RUBY
DYE CELL
Q SWITCH
DYE
MIRROR
RUBY LASER
(EXCITATION)
DYE LASER
STAINLESS
STEEL
HOUSING
DYE IN
SPHERICAL
SURFACE
LENS
LENS
DYE
LASER
BEAM
DIELECTRIC
MIRRORS
ARGON
LASER
BEAM
514.5nm
SAPPHIRE
FLAT
DYE OUT
SHIM TO
ADJUST
CAVITY
SPACING
DYE IN
EXCITATION
BEAM
LENS
COLLIMATING
LENS
LASER
OUTPUT
ACTIVE
REGION
PLANE MIRROR
HIGH REFLECTION AT
λ LASER
LOW REFLECTION AT
λ EXCITATION
DYE OUT
LONG-RADIUS
MIRROR

FIGURE 1

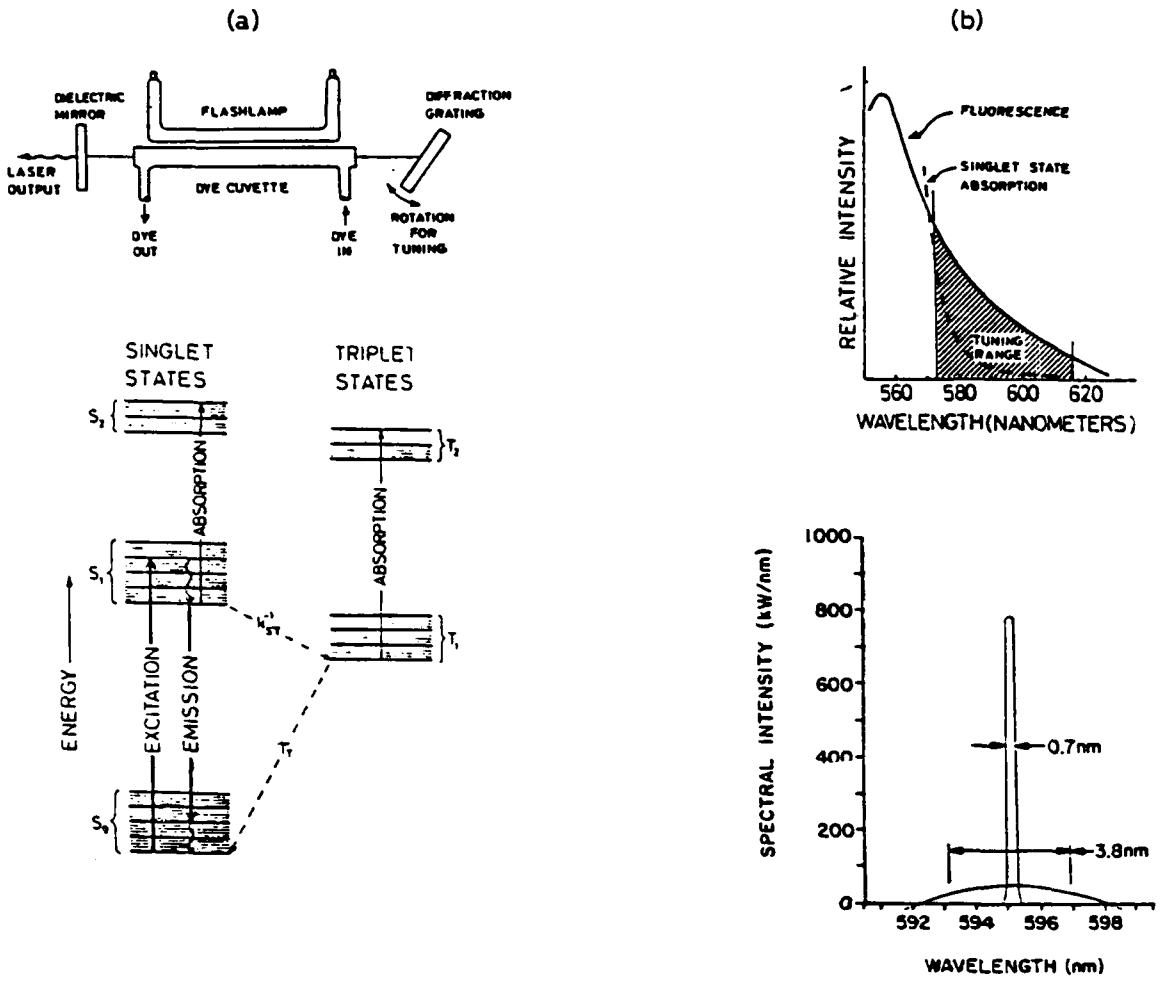


FIGURE: 2

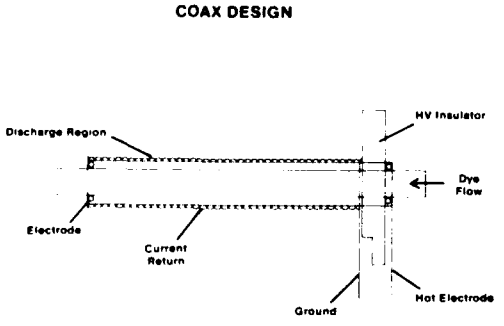


Figure 3

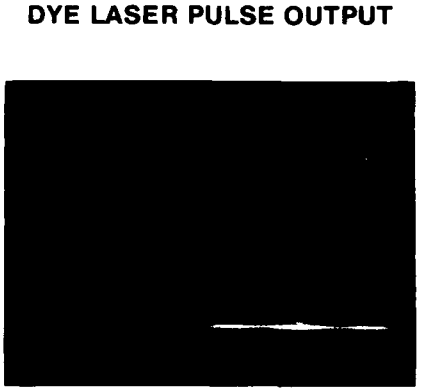
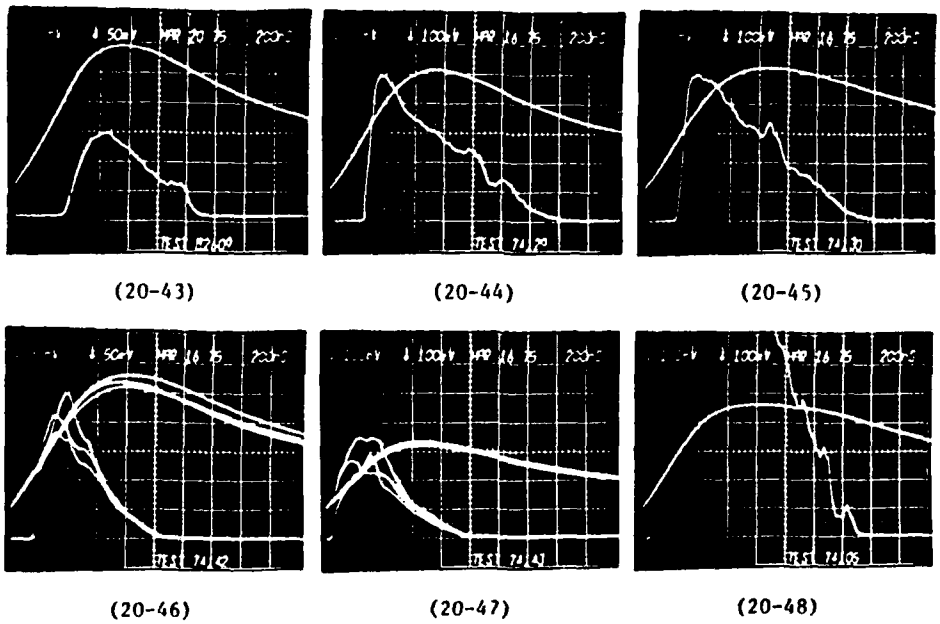


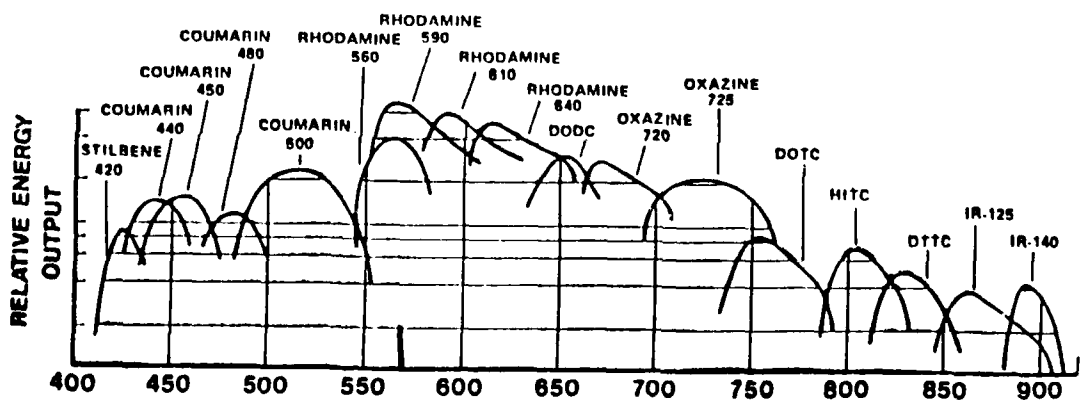
Figure 4



(20-43) (20-44) (20-45)

(20-46) (20-47) (20-48)

FIGURE: 5



COAXIAL FLASHLAMP PUMPED DYES (Phase-R)

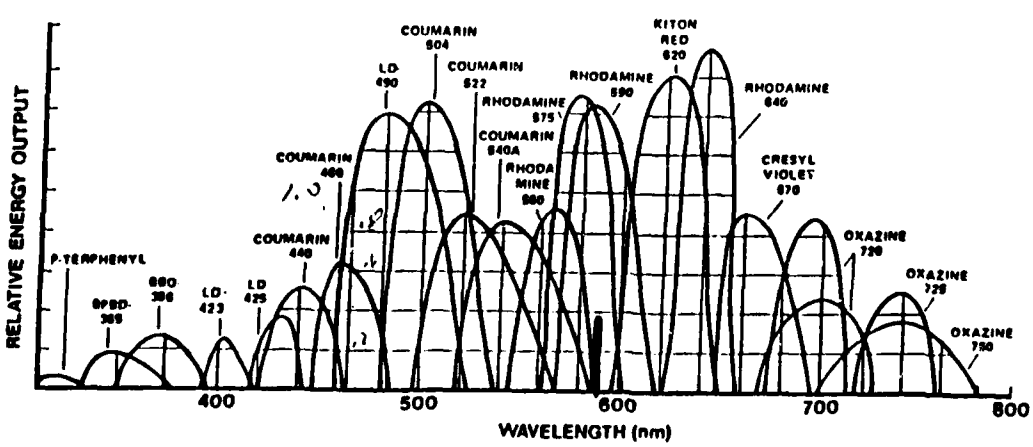


FIGURE: 6

SIMPLE SHG SET UP



Figure 7

TWO COLOR DYE LASER



Figure 8

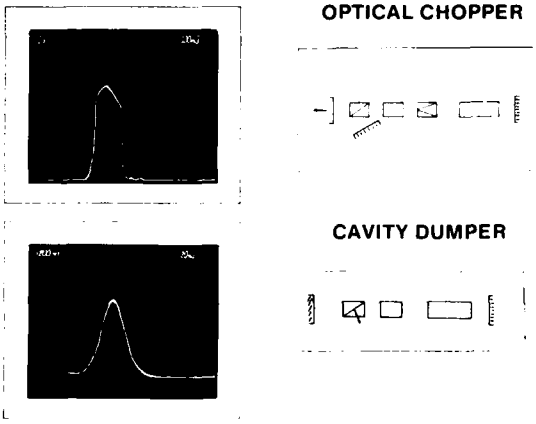


Figure 9

"NESSY"

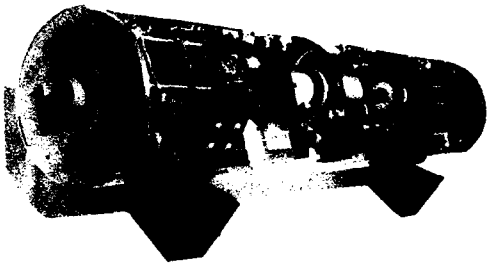


Figure 10

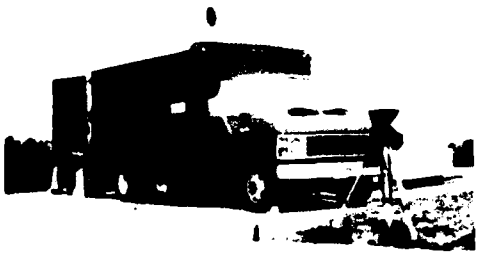


Figure 11

TRIAX CONFIGURATION

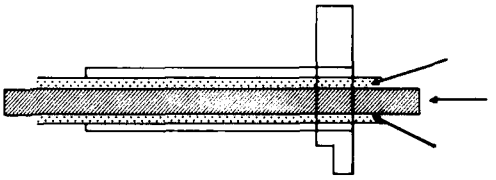


Figure 12

ADVANCES IN BLUE-GREEN, FLASHLAMP PUMPED DYE LASER DEVELOPMENT

Robin Keith Elkins, President
R-K Manufacturing Company
4018 North 30th Avenue
Hollywood, Florida 33020

Abstract

A significant improvement in the performance characteristics of flashlamp pumped dye lasers in the blue-green spectrum is due to the introduction of Kodak Coumarin 314T dye. Numerous experiments are conducted to illustrate this advancement.

Introduction

The object of our research work was to obtain useful data about the performance of a flashlamp pumped dye laser using the new Kodak dye Coumarin 314T. Then, to compare this performance with other well known laser dyes using the same laser.

R-K Manufacturing has been sucessfully building flashlamp pumped dye liquid lasers since 1981. The majority of our work relied on the well known dye Rhodamine 6 G or "R6G". Additional studies were conducted with other dyes. One such dye is Kiton Red 620. It's red colored output beams were a good match for optics made for helium-neon lasers. The Kiton Red dye could be used with either methanol or ethanol as the solvent, and produced laser beams with significant output radiant flux.

Meanwhile, there was for some time, a major thrust of research activity in the United States towards the development of high-power, blue-green lasers. We conducted experiments with several dyes known to lase in the blue-green such as 7 Diethelamino - 4 Methelcoumarin, Sodium Flourescein, and Coumarin 504. The results of our experiments were not encouraging, so we all but forgot about the idea of having an efficient, high-powered, blue-green laser. Another dye laser worth mentioning is one where we used Oxazine 720 as a laser dye, with ruby laser optics to closely match the wavelength of our ruby lasers.

Earlier this year we received a sample of a new laser dye from Kodak. The dye is called Kodak Coumarin 314T. This laser dye falls under the claims of a U.S. Patent # 4,736,032, issued in 1988 to Eastman Kodak Company. The peak lasing wavelength of this dye is in the blue-green at 490 nm. The results of our first tests with this new dye provided us with evidence that a flashlamp pumped high power dye laser in the blue-green spectrum could be developed.

Description of the Laser

The laser is an R-K Manufacturing Model 6000 Dye laser working with a series 9000 power supply.

The laser Head consists of a dual, linear flashlamp pumped cavity (a close-coupled configuration). The flashlamps are EG&G FX47-3 lamps. The dye cell is our standard small dye cell of 112mm (length) x 5mm (bore) and having a 1mm wall thickness. Certified fused quartz is the material of the dye cell. For laser mirrors used on the tests with Coumarin 314T and Coumarin 504, an NRC high reflector (R = Max. @ 520nm coating) type high power laser mirror on a 1" substrate was used. The radius of curvature of the high reflector is 28 centimeters. The output coupler is a CVI high power laser output coupler, on a 1" diameter, plano-plano substrate. The high power dielectric mirror coating is of 80% reflectivity maximized about 532 nm, and second surface AR coated. The resonant cavity length is 242 mm. No tuner was used. Note that the optics were selected (on purpose) to be a close match to the C504 dye lasing maximum. This was to further evidence the superiority of C314T over C504.

For operation with R6G, the high power dielectric reflector is a CVI high reflector coated for R = Max. @ 590 nm, and has a radius of curvature of 0.3 meters. The output coupler is a CVI high powered dielectric mirror of 80% reflectivity for 590 nm, with an AR coated second surface. The output coupler has a 1" diameter, plano-plano substrate.

The power supply has an output voltage of 3,000 volts D.C., with a capacitance of 20 microfarads (90 joules). Pulse widths of the discharges measured 10 microseconds. Discharge peak currents measured 10 kiloamperes. An external high voltage trigger pulse of 15 kV was applied to the pump chamber to initiate the laser discharge.

The dye circulator pump is a peristaltic, traveling wave type with a flow rate of 1 litre per minute. A 1 litre capacity Nalgene mason jar contained the small volume test solutions. These measured from 200 to 500 mililitres each.

Test Instrumentation

A Scientech Model 365 power/energy meter was used as the primary energy measurement instrument. Additional energy measurement devices included the R-K Manufacturing Model 10 laser power/energy detector with a Tektronics T-922 Oscilloscope with calibration traceable to the NTIS, and a Molectron Detector Model J3-09.

Test Results

Output Energy per Pulse With C314T:

267 mj, 255 mj, 258 mj, 255 mj, 251 mj, 242 mj, 244 mj, 239 mj, 249 mj, 238 mj

Output Energy per Pulse With C504:

207 mj, 205 mj, 231 mj, 208 mj, 200 mj, 191 mj, 201 mj, 204 mj, 220 mj, 201 mj

Output Energy per Pulse With R6G:

245 mj, 380 mj, 300 mj, 300 mj, 280 mj, 375 mj, 225 mj, 367 mj, 270 mj, 325 mj

Tests were conducted to check for laser outputs emitted from the high reflector end of the laser. Such an output is due to the minute deviation from a 100% reflective high reflector (typically some 0.2%), the narrow spectral response of the high reflector in relation to the wavelength of the dye lasing (maximum), and any possible mismatch. Tests showed that with the green optics in the laser, the output pulse energies with C314T from the HR end of the laser were greater than 3.6 millijoules. With the same optics, and C504 dye, the output energies of pulses from the HR end were less than 1 millijoule. With the Rhodamine 6G optics (R6G dye), the output from the HR end was again less than 1 millijoule per pulse. The values listed for laser output energies were not adjusted to account for these outputs. Only the laser outputs through the output couplers were listed.

Numeric Relations

Electrical Input to Optical Output:
(from pulse energy maxima)

C314T - $\frac{267\text{mj (output)}}{90\text{j (input)}} = 2.966 \times 10^{-3} = 0.3\%$ (1)

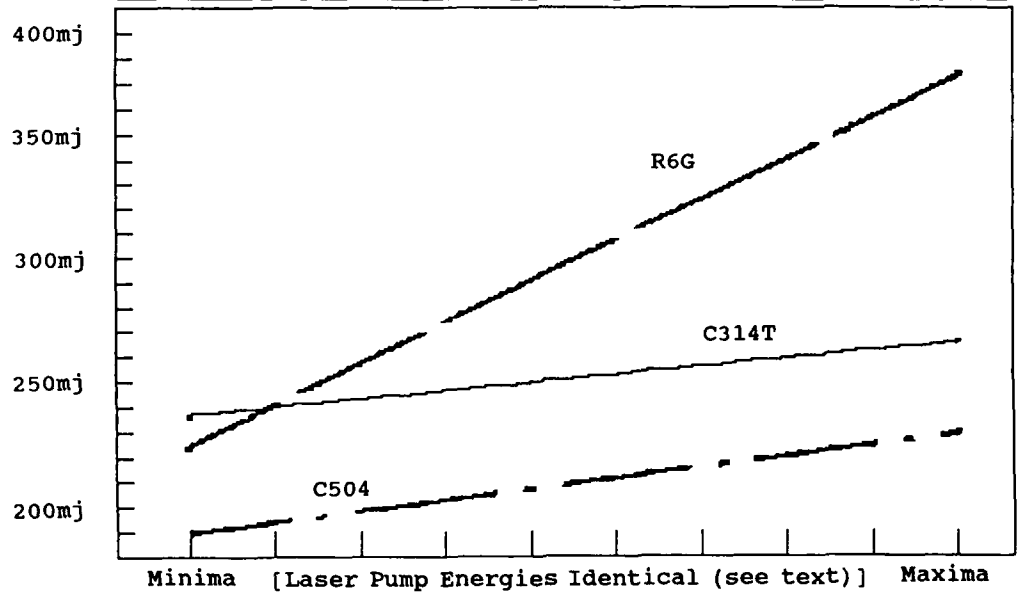
C504 - $\frac{231\text{mj}}{90\text{j}} = 2.566 \times 10^{-3} = 0.026\%$ (2)

R6G - $\frac{380\text{mj}}{90\text{j}} = 4.22 \times 10^{-3} = 0.42\%$ (3)

Average Output Energy:

C314T = 249.8mj (17% over C504) (4)
C504 = 206.8mj (32.5% less than R6G) (5)
R6G = 306.7mj (18.5% over C314T) (6)

Relative Range of Outputs for the Dyes Tested; Output Energies



Conclusion

Use of the new Kodak laser dye, Coumarin 314T, significantly improves the performance of flashlamp pumped dye liquid lasers operating in the blue-green spectrum. Output pulse energies from blue-green flashlamp pumped dye laser can now approach or exceed output pulse energies from similar flashlamp pumped lasers in the yellow, orange, and red. This improvement has immediate application to studies that require the greater energy per photon that the shorter wavelengths (blue-green) provide. Because of this, experiments reliant upon excitation from a blue-green laser pulse can meet their needs for energy more efficiently.

HIGHER EFFICIENCY EXCIMER LASER PUMPED BLUE-GREEN DYE LASER

F. J. Duarte
Photographic Research Laboratories - Photographic Products Group
Eastman Kodak Company, Rochester, NY 14650-1744

D. R. Foster
Analytical Technology Division - Electronic Spectroscopy Group
Eastman Kodak Company, Rochester, NY 14650-1731

C. H. Chen
Corporate Research Laboratories - Molecular Design and Dynamics Group
Eastman Kodak Company, Rochester, NY 14650-2115

Abstract

Efficiency experiments using coumarin 314-T laser dye, manufactured by Eastman Kodak Company, are reported. Measurements in a simple excimer-laser pumped dye laser show that C 314-T provides twice the efficiency of either C 314 or C 504. The tetramethyl coumarin dye has been found to lase in the $1 \times 10^{-3} - 1 \times 10^{-1}$ M range.

I. Introduction

In this short communication we report on recent efficiency experiments involving the new Kodak coumarin 314-T laser dye. In an earlier publication[1] lasing in a whole new family of coumarin dyes based on 1,1,7,7-tetramethyl-8-hydroxyjulolidine was described using the $B^2\Sigma^+_{1/2} - X^2\Sigma^+_{1/2}$ transition of the XeCl laser at 308 nm. The dyes investigated in those experiments were the C 102-T, C 338-T, C 314-T, C 334-T, and C 153-T. Characteristic of those measurements was an improvement in efficiency performance (of up to 24%) of the new compounds and a significant increase in solubility. In those experiments C 314-T was found to lase in the 478-525 nm spectral range with $\lambda_{max} \sim 506$ nm (at 5×10^{-3} M in ethanol).

II. Experimental

In the present experiments C 314-T (molecular structure shown in Fig. 1) was utilized in ethanol solutions varying from 1×10^{-3} to 1×10^{-1} M in a simple broadband mirror-mirror cavity excited transversely by a 22-33 mJ per pulse excimer laser. Details of the experimental procedure have been given previously.[1,2] The most important point here is that extreme care is observed to provide identical excitation conditions for each dye solution tested. For each set of measurements we monitored the excitation energy and the dye laser emission energy. Results presented here correspond to averages taken for a set of measurements. A typical standard of deviation for a set of laser pulse energy measurements is < 5%.

III. Results

Results of these experiments are summarized in Fig. 2. Here we plot laser efficiency for C 314-T, C 504, and rhodamine 590, as a function of dye molecular concentration. The basic feature of these results is that C 314-T

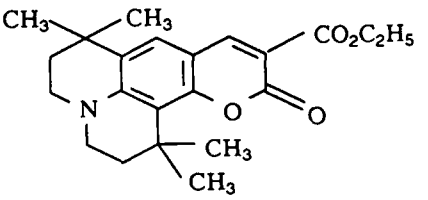


Fig. 1. Molecular structure of C 314-T (MW = 369.35).

offers a significant improvement in laser efficiency relative to C 504 (or C 314). These dyes in conjunction with rhodamine 590 demonstrate a severe decline in efficiencies at concentrations approaching 1×10^{-2} M. By contrast the *response* observed in C 314-T is quite different. Here, lasing is observed, at reasonable efficiencies, up to concentrations approaching 1×10^{-1} M. It should be noted that C 314-T was observed to be freely soluble in ethanol at these high concentrations. The wider response observed in C 314-T was obtained by optimizing the excimer laser pump geometry to eliminate regions of unexcited dye at the extremes of the active dye region. The efficiency obtained at a concentration of 5×10^{-3} M of rhodamine 590 with an identical excitation geometry was 17.5%.

In addition to the laser experiments we carried out a series of absorption measurements utilizing conventional spectrometry at various dye concentrations. These spectra are shown in Fig. 3.

IV. Discussion

The results shown in Fig. 2 demonstrate that C 314-T offers significant advantages for ultraviolet laser excitation. First, the dye is highly soluble in solvents such as methanol and ethanol. In addition, lasing is observed for a wide range of dye concentrations including number densities as high as 2.22×10^{22} molecules cm^{-3}. This phenomenon is in clear contrast with the usual behavior observed in traditional dye compounds such as C 504 (or C 314) and rhodamine 590. As such, this appears to be a fundamental advantage offered by these new tetramethyl compounds. The increased efficiency is attributed both to the increased solubility, that provides larger populations of useful dye molecules per unit volume, and to more fundamental differences in the molecular structure.[1]

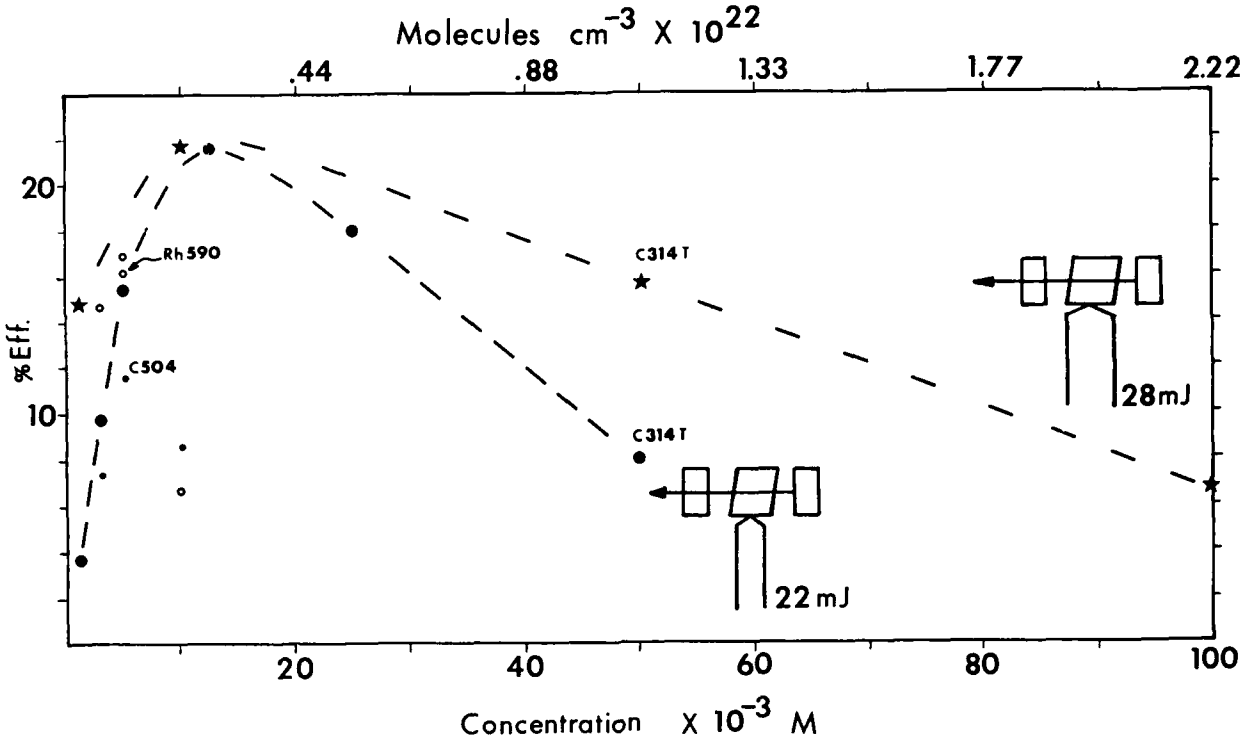


Fig. 2. Dye laser efficiency as a function of dye concentration.

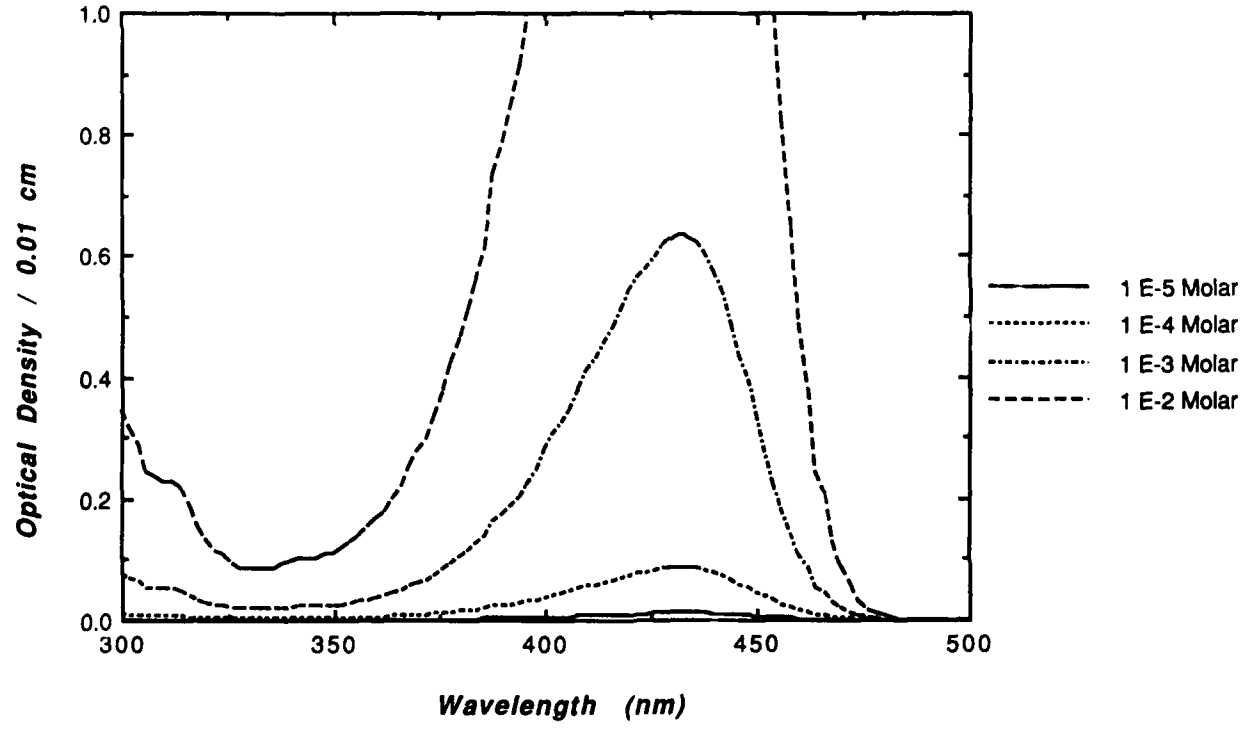


Fig. 3. Absorption spectra for C 314-T as a function of concentration.

As explained earlier, the enhanced performance observed with C 314-T was obtained by illuminating the whole dye molecular active length that eliminates unexcited dye regions, which can contribute to dye laser emission reabsorption. This type of excitation geometry has been previously discussed by Duarte and Piper.[3,4]

For comparison purposes, it should be indicated that C 102 (or C 480) provides some of the best conversion efficiencies, for conventional dyes, under excimer laser excitation at 308 nm. This is well known. In our previous study[1] we reported 18.4% conversion efficiency for C 102 and 20.8% conversion efficiency for C 102-T (λ_{max} ~ 475 nm). These measurements were done under identical experimental conditions. In those experiments[1] the measured efficiency for C 314-T was 18.1%. Experiments are in progress to provide further characterization of C 102 -T.

An important observation illustrated in Fig. 3 is that we have not seen the formation of dimer dye molecular species even at very high concentrations in the tetramethyl compounds. This is an encouraging development, which indicates that further improvements in efficiency are possible by increasing the pump laser energy and optimizing the excitation geometry to improve the coupling of the pump photon flux to the active region. In this area the use of thin dye regions with double colinear transverse excitation may prove useful.

References

1. C. H. Chen, J. L. Fox, F. J. Duarte, and J. J. Ehrlich, Appl. Opt. **27**, 443 (1988).
2. F. J. Duarte, in *Proceedings of the International Conference on Lasers '86*, R. W. McMillan, Ed. (STS Press, McLean, VA, 1987), pp. 416-419.
3. F. J. Duarte and J. A. Piper, Opt. Commun. **35**, 100 (1980).
4. F. J. Duarte and J. A. Piper, Appl. Opt. **23**, 1391 (1984).

A HIGH-AVERAGE-POWER BLUE-GREEN LASER FOR UNDERWATER COMMUNICATIONS

D. P. Pacheco, H. R. Aldag, D. E. Klimek and P. S. Rostler
Avco Research Laboratory/Textron
2385 Revere Beach Parkway
Everett, MA 02149

and

R. Scheps and J. F. Myers
Naval Ocean Systems Center
271 Catalina Boulevard
San Diego, CA 92152-5000

Abstract

In this paper, we describe the design and initial operating characteristics of a high-average-power, flashlamp-pumped dye laser built for underwater communications. Tests have been conducted at 458 nm, which is close to the operating wavelengths of the narrow-bandpass, wide-field-of-view Cs atomic resonance filter (455/459 nm). With minor modifications, the laser can operate anywhere from the near UV to the near IR.

The paper is divided into two parts. In the first part, we discuss the engineering aspects of the laser. Major features of the design include: 1.) a multiple-lamp laser head which incorporates flow channels for a spectral-converter dye solution; 2.) wavelength stabilization using a feedback loop which contains a Cs cell as an absolute reference; and 3.) a dye replenishment system for long service life of the dye solution (> 3 x 10^6 shots). The laser head is modular for ease of assembly and maintenance.

In the second part, we present preliminary data on laser performance. To date we have demonstrated > 4 J/pulse broadband, and > 1.5 J/pulse at 30 mÅ bandwidth with the laser tuned to 458 nm. Additional experiments have shown that the tuned output can be increased further by reducing the feedback of the resonator.

Introduction

Flashlamp-pumped dye lasers are an attractive option for applications requiring high average power in the visible. Kilowatt devices employing a single laser head were built at Avco Research Laboratory (ARL) as early as 1976. Lasers operating at the several hundred watt level and tuned to atomic resonance lines were developed for laser isotope separation. These performance levels are possible because of the high gain of laser dyes and the excellent thermal control achievable with a flowing medium. Since these earlier days, a number of technical advances have been made to further improve efficiency and spectral control. In this paper, we will discuss the present state of the art in the context of the design and preliminary testing of a high-average-power device for underwater communications. The transmission of sea water strongly favors a blue transmitter. The laser described here was designed to operate at the Cs atomic resonance filter wavelengths near 460 nm.

In Table 1, we summarize the major specifications addressed in this work. The device is designed to provide > 100 W of optical power with the capability of going to > 200 W for brief periods by providing a higher rep rate. The service life requirement is > 3 x 10^6 shots; this requires careful design, since the short pulse duration and high energy loading stresses the flashlamps, and the high optical pump power places heavy demands on the dye solution. Ultimately, the laser is to operate unattended in the field, so we have designed a closed-loop feedback system to stabilize the output wavelength. At this point, we have designed, built, and initiated testing of a compact laser capable of meeting all these requirements.

Table 1 Transmitter Specifications

ENERGY/PULSE	3 J
PRF	40 Hz (Average)
LIFE	3 x 10^6 Shots
PULSE WIDTH	< 2 μsec
WAVELENGTH	455/459 nm
BANDWIDTH	10 mÅ (1.4 GHz)

There are several distinct advantages of flashlamp-pumped dye lasers for this application. First, this type of device has already achieved each specification in the table; the purpose of the present work is to put it all together in a single laser device. The high average power required has been routinely demonstrated in a single head, which makes the laser relatively compact. Secondly, the desired output wavelength is achieved directly. That is, no frequency doubling, Raman shifting, or sum-frequency processes are required. This considerably simplifies the design. Furthermore, the above nonlinear processes require careful control over beam quality for efficient wavelength conversion. This is not an issue for the present device. Third, the requisite thermal control is easily achieved by flowing the dye solution. The dye laser is not limited by thermal conductivity of the gain medium; a fresh volume of dye solution is available for each pulse. In addition, we have developed strategies to minimize waste heat deposited in the laser solution. Finally, changes in detector wavelength are readily accommodated. A great deal of work is ongoing to develop wide-angle, narrow-bandwidth detectors operating at other visible wavelengths (e.g., Fraunhofer lines). If a superior detector is identified at a later time, we simply need to change the dye solution (and possibly the optical coatings).

Features of the Design

The end use of this laser requires that it be relatively compact and run unattended for long periods of time "on color". As a result, a premium was placed on system efficiency, simplicity of design, and long service life.

For the past few years, ARL has made considerable progress in improving the design of the laser head itself. This has culminated in a compact, modular structure which efficiently uses the flashlamp pump light both spatially and spectrally. The most significant features are a nonimaging flashlamp reflector and spectral conversion of the pump light. The reflector has a special shape which allows uniform pumping of large active volumes, resulting in high output energies. Beam quality measurements on a device with this reflector design have shown excellent spatial properties of the output,[1] which confirms the pump uniformity.

Significant increases in energy output have been demonstrated by using a second dye solution to convert some of the broad (nearly blackbody) pump flux into the absorption band of the laser dye.[2] Although the percentage improvement depends on the dye concentrations, we have demonstrated increases of a factor of two for conditions of interest.[3]

Laser Head

For purposes of discussion, we have included a photograph of the laser head designed for this work (Figure 1). The head contains a three-channel dye cell in the form of a planar sandwich.[3] The laser dye flows through the center channel, while the converter solution uses the outer ones. This geometry provides excellent optical coupling of the converted photons, since > 80% make at least one pass through the laser dye and about two-thirds are trapped in the sandwich by total internal reflection. The latter therefore have many opportunities to be absorbed in the lasing solution. There are two additional advantages of this approach. First, the converter solution absorbs much of the waste heat and conducts it away. In fact, the converter channel significantly reduces both the absolute value of the waste heat and the differential heat deposition across the gain medium (important for good beam quality).[3] Secondly, the UV light from the lamp, which accelerates the degradation of the laser dye, is filtered out. The life of the converter dye is much less critical, since its function is simply to fluoresce through a relatively short path length (on the order of millimeters).

The inlet flow hardware, which is the result of much development, includes a specially contoured flow nozzle and flow-straightener screens. The latter are needed to break up any large-scale turbulence in the flow, which would degrade optical quality. We have monitored the flow quality in such devices using a HeNe in double pass and projecting the beam into the farfield. Comparison of the resultant spatial profile with that of a perfect (1 x DL) beam has shown Strehl ratios on the order of 0.8.

The head contains a total of six flashlamps, three per side. This number is chosen to achieve the desired output consistent with the life requirements given earlier. An advantage of multiple lamps is the graceful degradation of performance in the event of a lamp failure. In one- or two-lamp systems, failure of a single lamp disables the device. It is worth noting that with the nonimaging reflector, loss of a lamp does not leave a hole in the pump profile because each lamp illuminates an extended region of the gain medium.

Resonator

The requirement is for a design which can achieve the desired spectral properties and is conducive to a feedback-control loop to correct for wavelength drift. The design we have chosen, which is similar to the Hansch resonator,[4] is depicted in Figure 2.

The only tuning element is a large grating operated in Littrow. A cylindrical, Galilean telescope expands the 3-mm width of the beam to fill the grating. This not only utilizes the full resolving power, but also reduces the fluence levels and provides a nearly square output beam. The grating has a resolving power of about 4.9×10^5, which corresponds to a single-pass bandwidth < 10 mÅ at 460 nm. The observed bandwidth of tuned dye lasers is often less than would be expected based on the single-pass calculation because of gain narrowing.[4,5]

The grating is mounted on a PZT-driven rotary stage for fine adjustment. A feedback loop based on a Cs fluorescence cell monitors drifts in output wavelength and corrects the grating angle to achieve the desired stability. Control software developed in this work is capable of effecting corrections at the peak rep rate of the laser. Correction at this rate, however, is probably not needed. Our past experience with a flashlamp-pumped dye laser operating at an atomic resonance line has shown that the dominant wavelength shift is a slow thermal drift, which can be corrected on a time scale on the order of seconds.

Flashlamp Driving Circuitry

The flashlamp modulator is based on conventional technology, and utilizes flowing-gas spark gaps to switch the voltage. Spark gaps were chosen over thyratrons because of the RMS and peak current requirements together with the need for compactness. A one-lamp driving circuit configured as shown has been operated at 40 Hz for extended periods and at 80 Hz in bursts with a jitter < 200 ns.

Dye Replenishment

With dyes that are presently available, the service life of three million shots requires a subsystem to replenish the dye solution. To this end, ARL has developed a patented scheme for cleaning a portion of the dye solution without interrupting the operation of the laser.[6] This approach can be seen in the flow diagram of Figure 3. The replenishment system consists of the elements in the right-hand side of the figure, namely the charcoal filter, concentration monitor, metering pump, and dye concentrate reservoir. A small fraction of the dye flow from the main reservoir is diverted through an activated charcoal filter. The filter removes virtually all the dye and degradation products in one pass. Before the clean solvent is reintroduced into the main reservoir, a small amount of dye concentrate is metered in to establish the desired concentration. The concentration is checked with an on-line monitor, which switches the metering pump on or off, as needed. The resulting fluid volume of the laser system is much smaller than it would be if the main reservoir was simply enlarged to provide the desired number of shots.

In the above approach, a certain level of photoproducts is tolerated in the dye solution, and therefore the laser is not operating at full output. (Steady state is reached when the rates of generation and removal of degradation products are equal.) The overall size of the dye replenishment system depends on the service life, dye life, operating point, and dye removal capabilities of the carbon. Data taken in our laboratory show that a suitable replenishment system will not significantly add to the volume and weight of the overall system. Furthermore, the dye and carbon cartridges can be replaced easily in the field.

System Components Limiting Service Life

The major life-limiting components are the spark gaps, flashlamps, and dye solution. The dye solution was discussed immediately above, so we will focus on the first two.

The life of spark gaps is usually quoted in terms of coulombs tranferred or "switched". For commercial flowing-gas gaps, the life is > 35,000 coulombs. Under the present design conditions of 8.5 mC/shot/gap, the useful life exceeds 4×10^6 shots. Still longer life is achievable through improved materials of construction, e.g., tungsten instead of molybdenum for the electrodes, and pyrex in place of polycarbonate for the main body.

The life of flashlamps is typically given as the number of shots required for the light output to drop to a certain specified level. This depends of course on the lamp size and loading. There is an empirical model well-known in the industry[7] and verified at Avco. Using this model, the lamp life may be written:

$$N_{90} = 0.2\left(\frac{K\,A\,\sqrt{t}}{E}\right)^{8.5} .$$

N_{90} is the number of shots for the light output to decline to the 90% level, "A" is the bore surface area (in cm^2), "t" the pulse duration (in sec), and "E" the energy (in J) delivered to the lamp. K is an empirically determined constant; measurements in our laboratory yield a typical value of 8500 $J/cm^2/sec^{0.5}$. The present design has 5-mm bore x 18" long lamps, a 2-μs electrical pulse, and 120 J/pulse/lamp. This yields $N_{90} > 3.8 \times 10^6$ shots.

Preliminary Results of Laser Performance

The results to date were taken either single-shot or at low rep rate (0.5 Hz) for purposes of initial characterization and system checkout. The first measurements were made with a short, broadband resonator and 50% feedback. An unoptimized output of 4.4 J was achieved in a 2.5 μs pulse (Figure 4) with Coumarin 450 (1.2×10^{-4} M/l) in $MeOH/H_2O$ as the laser dye solution. The laser free-ran near 460 nm.

Tuned measurements were made with the resonator shown in Figure 2. The cavity was aligned with an Ar-ion laser tuned to 458 nm, which is quite close to the target wavelengths of 455 and 459 nm. Because of the longer resonator and consequently higher threshold, the pulse duration is shorter than in the broadband case. A representative trace of the output is shown in Figure 5, together with the major experimental parameters. The output energy of 1.6 J/pulse is not optimized, as will be discussed later. Simultaneous bandwidth measurements were made as depicted in Figure 6. A small fraction of the output was incident on a diffuser plate and analyzed by a Fabry-Perot. A lens brought the transmitted light to focus, and the ring structure was displayed on a reticon area camera. A framegrabber board in a PC acquired the spatial profile; special software analyzed the results. A monitor was available for viewing the profile in real time. Figure 6 also contains a portion of the fringe pattern seen on the monitor. The measured bandwidth (FWHM) is 4 GHz (30 mÅ). This is rather close to the goal of 10 mÅ and was achieved without significant adjustment of the telescope elements. Careful adjustment during repped operation is required for minimum bandwidth, and should result in improved values. The resonator is designed to allow the addition of a single etalon, if needed, to reduce the laser bandwidth. Our preliminary results, however, show that this will probably not be needed. We also see no effect of rep rate on bandwidth in these early measurements. Data taken single-shot and at 0.5 Hz were essentially identical.

It was mentioned above that the output energies achieved to date are not optimized. Since the maximum output depends on the two dye concentrations as well as resonator feedback, the correct procedure would be to obtain data on energy as a function of output coupling for a number of different dye concentrations. There is evidence that generating this matrix will lead to increased outputs. An experiment was performed in which the grating was replaced by a series of conventional partial reflectors. For the same dye concentrations that yielded 1.6 Joules, the energy output was found to be 20% higher for R = 0.25 than for R = 0.65 (the grating feedback). The output can also be improved by reducing the water content of the solvent mix.

Summary

In this paper, we have described a flashlamp-pumped dye laser designed for high average power at an atomic resonance line and long service life. Initial characterization has yielded promising results: broadband output in excess of 4 J/pulse, and tuned output greater than 1.5 J/pulse at 458 nm and 30 mÅ bandwidth. System optimization is in progress and should result in improvements in all these numbers.

Acknowledgements

This work was funded by DARPA through the Naval Ocean Systems Center, San Diego, CA, under Contract No. N66001-89-C-6007.

The authors would like to acknowledge the able technical assistance of Louis Ruotolo, Gloria Londono, Michael Reilly and Fred Bourgelais in the performance of this work.

References

1) H.R. Aldag, "The Development of a High Average Power Dye Laser," presented at the International Conference on Lasers '89, New Orleans (1989), paper HG.1.

2) Patrick N. Everett, Henry R. Aldag, John J. Ehrlich, G. Sargent Janes, Daniel E. Klimek, Franklin M. Landers and Dennis P. Pacheco, "Efficient 7-J Flashlamp-Pumped Dye Laser at 500-nm Wavelength," Appl. Opt. 25, 2142 (1986).

3) D.P. Pacheco, H.R. Aldag, and P.S. Rostler, "The Use of Spectral Conversion to Increase the Efficiency of Flashlamp-pumped Dye Lasers," in Proceedings of the International Conference on Lasers '88 (STS Press, McLean, VA, 1989), pp. 410-419.

4) T.W. Hansch, "Repetitively Pulsed Tunable Dye Laser for High-Resolution Spectroscopy," Appl. Opt. 11, 895 (1972).

5) F.P. Schafer, "Principles of Dye Laser Operation," in Dye Lasers, Second Revised Edition, Springer-Verlag, New York, 1977, p. 68.

6) Patent Number 4,364,015: "A Compact Reservoir System for Dye Lasers," Assigned to Jersey Nuclear-Avco Isotopes, Inc. Issued December 14, 1982.

7) See, for example, Flashlamp Applications Manual, (EG&G Electro-Optics, March 1983), pp. 31 and 32.

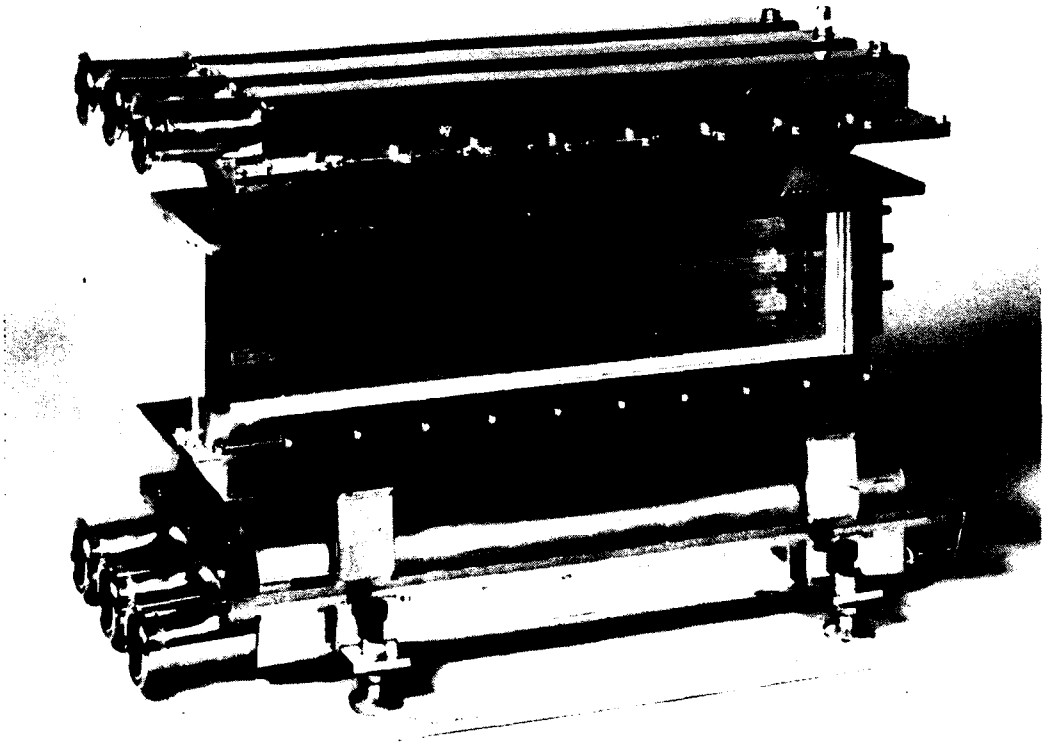


Figure 1 Side View of Laser Head Built for This Work. One reflector has been removed to show the three-channel dye cell.

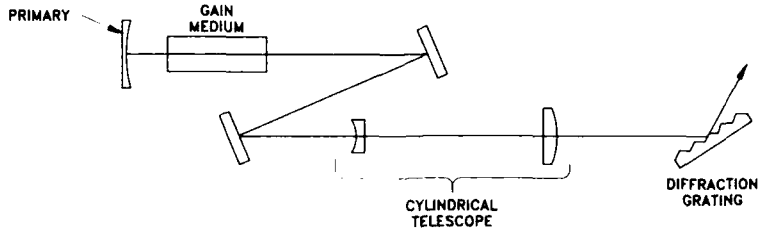


Figure 2 Resonator Used for Narrow-Band Operation in the Blue. A feedback loop has been designed to stabilize the output wavelength.

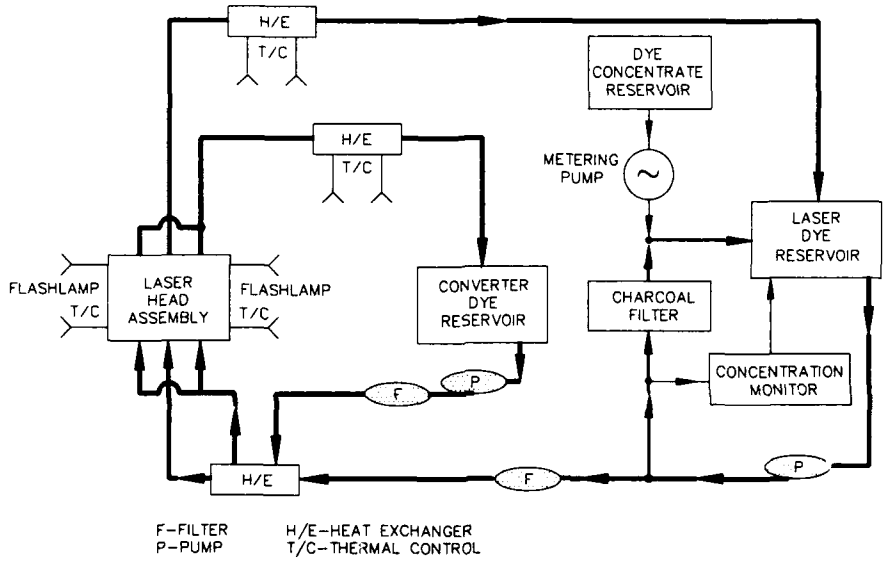
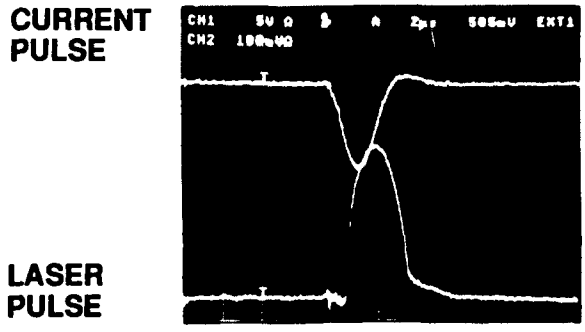


Figure 3 Dye Flow Functional Diagram Showing the Dye Replenishment Subsystem



ENERGY: 4.4 J/PULSE

PULSE DURATION: 2.5 μs

WAVELENGTH: 460 nm

LASER DYE SOLUTION:

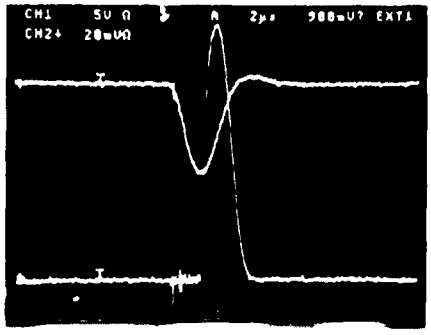
C450 (1.2×10^{-4} M/ℓ) IN MeOH/H_2O

RESONATOR FEEDBACK: 50%

Figure 4 Laser Performance with a Broad-Band Resonator

CURRENT PULSE

LASER PULSE



ENERGY: 1.6 J/PULSE

PULSE DURATION: 1.5 μs

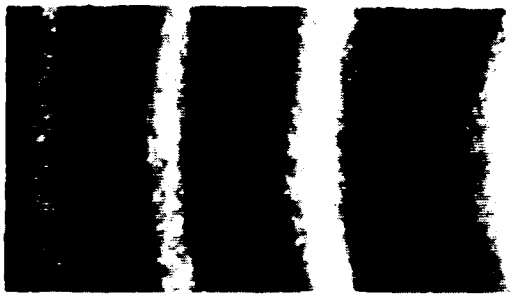
WAVELENGTH: 458 nm

LASER DYE SOLUTION:

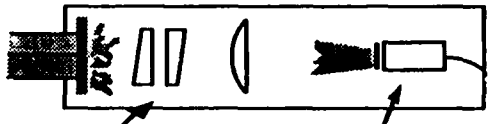
C450 (1.5×10^{-4} M/ℓ) IN $MeOH/H_2O$

BANDWIDTH: 4 GHz (30 mA)

Figure 5 Laser Performance with the Tuned Resonator of Figure 2



$\Delta\upsilon$ = 4 GHz (30 mÅ)



FABRY-PEROT

RETICON AREA CAMERA

CCD CAMERA RECORDS FRINGE PATTERN IN FOCAL PLANE OF LENS

FSR = 15 GHz (≃ 110 mÅ)

Figure 6 Bandwidth Measurement of the Tuned Output

Limits on Efficiency of Optically Pumped Dye Lasers*

Patrick N. Everett
Lincoln Laboratory, Massachusetts Institute of Technology
Lexington, MA 02173-9108

Abstract

The efficiency of transferring energy from the pumping flux to the lasing flux in a dye laser is investigated. Useful relations are developed for quantum efficiency and loss from dye degradation, with nine key dimensionless parameters introduced to express the competing loss mechanisms. The modeling adds insight and helps optimize performance.

Introduction

It has been shown (see Siegman, p. 293)[1], from a first-order steady-state rate analysis of the most significant transitions, that the exponential gain g_L is related to the small signal value g_{L0} by the relation

$$g_L = g_{L0}/(1 + I_L/I_{SAT}) , \qquad (1)$$

where I_L is the lasing photon intensity, and I_{SAT} is the saturation value of the lasing intensity, at which g_L has dropped to half of g_{L0}. Also, the ratio R of induced to spontaneous transitions is given by

$$R = I_L\tau_{eff}\sigma_{LE} = I_L/I_{SAT} , \qquad (2)$$

where τ_{eff} is the natural lifetime of the excited state, and σ_{LE} is the cross-section for stimulated emission. It follows immediately that the quantum efficiency η_L of converting absorbed pump photons into lasing photons has an upper bound given by

$$\eta_L \le 1/(1 + I_{SAT}/I_L) . \qquad (3)$$

Thus the lasing process can only be reasonably efficient if it is running in a saturated mode, with its lasing intensity exceeding I_{SAT}, under which conditions the induced transitions dominate over the spontaneous ones. Efficiency requires that most of the excited molecules be stimulated down by lasing photons before they decay spontaneously. On the other hand, high gain can only be achieved by maintaining high population in the excited state, which is inherently inefficient because of the consequently high spontaneous emission. This is particularly significant for dye lasers because I_{SAT} is generally high. The values of σ_{LE} and τ_{eff} for Rhodamine 6G, at 600 nm, are about 1.3×10^{-16} cm^2 and 3×10^{-9} s, leading to I_{SAT} equivalent to 0.9 MW/cm^2. These results are obtained from a first order quasi-steady-state analysis, ignoring loss mechanisms other than the inherent spontaneous emission. Note that, since σ_{LE} is wavelength dependent, I_{SAT} will vary with the lasing wavelength. If a laser is tuned away from the peak of the emission curve, then I_{SAT} will increase. In the following we will develop an approach for handling other loss mechanisms in the dye, and discover the importance of nine dimensionless parameters. This extends an earlier publication.[2]

We will examine an element of dye immersed in fluxes of pumping and lasing photons, and develop conditions for efficient conversion of pump photons into lasing ones in terms of the dimensionless parameters p_{ij}. This conversion ratio will be called the lasing quantum efficiency η_L. Useful insight will be gained from an approximation, valid when all the p_{ij} values are small, of the form $\eta_L \approx 1 - \Sigma(p_{ij})$.

Each of these parameters p_{ij} is associated with a particular loss mechanism. Nine will be identified, and a framework will be set up for introducing others if judged to be significant. Most of these parameters will contain the lasing intensity, the pumping intensity, or a ratio of them, as well as a ratio between two dye parameters. Hence, the quantum efficiency can be optimized by appropriate choice of the intensities taking the dye parameters into account. This will be discussed after we develop the general relation. Before developing the analysis we will briefly summarize the essential dye spectroscopy.

Essential Dye Spectroscopy

Each electronic state of a dye molecule has an associated vibronic complex. The non-radiative thermalizing transitions are so rapid (about 10^{12}/s) that they maintain a population distribution within

*This work was sponsored by the Defense Advanced Research Projects Agency and the Department of the Air Force.

each vibronic complex determined by the Boltzmann ratio (ref. 1, pp 27 and 202) and Schafer (p. 19)[3]. At room temperature the population in any occupied complex will have an energy spread of about 4×10^{-21} J; whereas, the typical visible photon has energy of about 4×10^{-19} J. Consequently we expect a minimum smearing of about 1% in any observed spectrum of absorption or emission (about 5 nm in the visible). Additional smearing occurs because absorption and emission can result from transitions into any available vibronic levels of the electronic states.

The typical dye laser is a four-level one since the exciting photon lifts the molecule to an upper level of the excited vibronic complex, from which it then decays by a radiationless process to a thermally populated level. This is the upper lasing level, from which it lases or spontaneously decays to an upper level of the ground vibrational complex, and then goes through a further radiationless decay to a thermally populated level.

The upward transitions go through a larger energy difference than the downward ones. This causes an offset between the typical spectral distributions of absorption and emission. Typically the broadening of each is about 50 nm, and the offset is about 30 nm. The broadenings are generally asymmetric, with the absorption approximately a mirror-image of the spontaneous emission. In a lasing situation the gain will tend to be higher for transitions into unoccupied levels, giving a further offset dependent on the levels available. Typically this lasing shift is about 50 nm from the absorption peak, unless purposely tuned by a frequency dependent element.

The spectra are normally "homogeneous" because of the rapid thermalization. Hence the population rapidly redistributes in any vibrational complex to fill any "holes" in population left by an outgoing transition. Thus, "hole-burning" in the linewidth, from intense narrow band radiation, will not be observed unless the resultant transition rate exceeds the thermalization rate (a rare occurrence).

Significant Transitions

The significant spectroscopic processes for the dye laser are shown in the eigenstate diagram of Figure 1, modeled after Schafer (ref. 3, p. 28) and Snavely[4]. The five electronic states of interest are the ground, the first and second singlet, and the first and second triplet, with population densities N_0, N_1, N_2, N_T and N_{T2}, respectively. Each of these states has its vibronic complex which rapidly thermalizes. The pumping and lasing intensities I_P and I_L are involved in radiative transitions between the ground and singlet states and can also be absorbed while causing excitation of higher singlet and triplet states. The transitions are divided into three groups; arising from the pump, from the lasing flux, and from spontaneous transitions. The spontaneous rates from the singlet γ_{10} and γ_{1T} are generally of the order of 10^8/s, but the triplet emptying rate γ_{T0} tends to be much slower, about 5×10^5/s for Rhodamine 6G if there is no triplet quenching (ref. 3, p. 59). This allows population to build up in the triplet state. The resulting absorption of light by the triplet state generally becomes a serious loss for laser pulses lasting more than a few hundred nanoseconds, unless an effective triplet quencher is included. Fortunately oxygen, which is present anyway when the dye is equilibrated with air, is a triplet quencher for at least some dyes (ref. 3, p. 59). Excitations into higher singlet and triplet states generally return non-radiatively to their respective singly excited levels with high transition rates of the order of 10^{12}/s. For our analysis we will assume the relaxation is immediate.

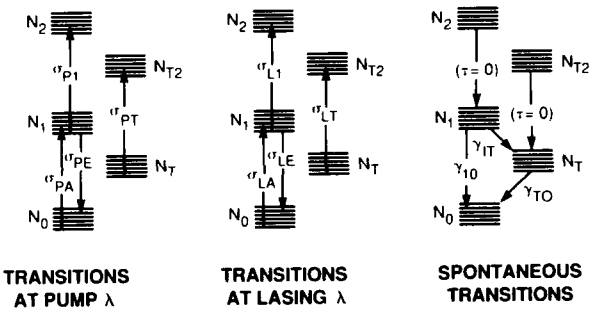


Fig. 1. Transition diagram

Cross Sections and Frequency Dependence

If $\sigma_{ij}(\lambda)$ were the radiative cross-section for transition at wavelength λ between individual electronic-vibrational states i and j then we would expect $\sigma_{ij}(\lambda) = \sigma_{ji}(\lambda)$. However, we would need to keep track of the populations in all the vibrational levels of all the significant electronic states to use this reciprocal relationship. Our analysis will keep track only of the population in the various electronic states, N_i being the population density in electronic state i, and $\sigma_{ij}(\lambda)$ being the radiative cross-section between electronic states E_i and E_j. We will thus lose the direct reciprocal relationship. But it will generally be observed that the value $\int\sigma_{ij}(\lambda)d\lambda$ over each line is at least close to the value of $\int\sigma_{ji}(\lambda)d\lambda$ over the same line, albeit displaced by maybe 30 nm (ref. 3, p. 20). As temperature changes, the thermalized distribution in the vibronic complexes will vary somewhat and affect the measured values of $\sigma_{ij}(\lambda)$. However, this is normally a small effect.

We must allow for the wavelength dependence of each of the cross sections. For our initial analysis we will assume that the pumping and lasing fluxes are each at a discrete wavelength. Each cross section will then take the value for the relevant wavelength, and hence have different values for the pumping and lasing wavelengths. The spontaneous transitions radiate into a wavelength distribution, but we will be concerned only with the total probability.

Labeling

In the following analysis we will adopt a labeling scheme in which the first subscript will be P if caused by the pumping flux, and L if caused by the lasing flux. The second subscript will be A or E to denote an absorbing or emitting transition between the ground and singlet states, and 1 or T if an absorption from the singlet or triplet to the next higher state.

Quantum Efficiencies

The fluorescent quantum efficiency η_F is the ratio between the number of photons emitted by transitions from singlet to ground level to the number of pump photons absorbed under conditions of negligible stimulated emissions. It is given by $\eta_F = \gamma_{10}/(\gamma_{10} + \gamma_{1T})$. In the case of Rhodamine 6G, the values of γ_{10} and γ_{1T} are about 2.9×10^8/s and 2.0×10^7/s, respectively. Hence $\eta_F \approx 0.93$, which is very close to the value 0.92 cited by Snavely (ref. 3, p. 90) as having been measured by F. Grum at Kodak Research Laboratories. When a laser is working optimally, the number of stimulated transitions from the singlet to the ground state exceeds the spontaneous ones. Hence it is theoretically possible for the lasing quantum efficiency to be much greater than the fluorescent quantum efficiency. Therefore, a dye candidate should not be dismissed solely on grounds of low fluorescent quantum efficiency.

Rate Equation Analysis

Application of rate-equation analysis, based upon knowledge of cross sections and transition-probabilities, allows good understanding of the processes involved (ref. 1, p. 25). To keep the equations uncluttered with hν we will generally use photon intensities (i.e photons cm^{-2} s^{-1}) rather than power densities. However, we will switch to power densities when more convenient.

The rate equation approximation applies whenever the rate of change of population is slow compared with the natural linewidth. This condition is generally met since dye natural line widths tend to be about 2×10^{13} Hz, and typical pumping cycles are longer than 1 ns. A fuller discussion of the limits of rate analysis will be found in Siegman's book (ref. 1, p. 223).

The transitions essential to the operation of the laser involve the pumping cross section σ_{PA} and the lasing cross section σ_{LE}. The spontaneous transition rate γ_{10} to the ground state is a major interfering factor, and is inherently associated with the other two. We will call these transitions the "basic" ones. All the other transitions illustrated in Figure 1 are detrimental to the process. We want to minimize their effect by choice of dye and operating conditions.

We will consider an element of dye exposed to pumping and lasing fluxes, as illustrated in Figure 2. A simple picture will first be obtained by including only the basic transitions just discussed,

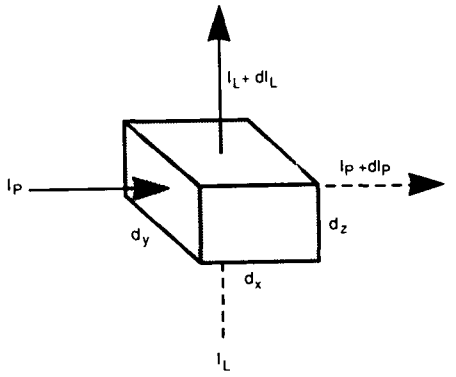


Fig. 2. Dye element

assuming discrete frequencies of pumping and lasing. These basic transitions involve σ_{PA}, σ_{LE}, and γ_{10}. We will then develop the analysis to include all of the transitions shown in Figure 1; and then further develop it for handling pump power with a distributed spectrum, as occurs in flashlamp-pumped lasers. We will develop relations for gain, saturation, and lasing quantum efficiency. The same framework will allow adding further loss mechanisms if thought significant. We will use conventional rate analysis, and follow the approach of Hargrove and Kan[5], and assume quasi steady state to make it more tractable. This is valid because the transition rates will be much faster than the rate at which the pumping flux will change, with the possible exception of the triplet-emptying rate γ_{T0}. However, there will normally be a quenching agent (such as oxygen) present in a practical laser, which will make the effective value of γ_{T0} sufficiently high that the assumption will be satisfactory. Homogeneous broadening will be assumed.

Gain and Saturation - Basic Transitions

In quasi steady-state, the population densities will remain almost constant on the time-scale of the various transition rates, so conventional rate analysis yields the following as a good approximation.

$$N_1/N_0 = I_P\sigma_{PA}/(I_L\sigma_{LE} + \gamma_{10}) \ , \qquad (4)$$

where I_P and I_L are the pumping and lasing photon intensities respectively (photons $cm^{-2}\ s^{-1}$). The lasing exponential gain coefficient is

$$g_L = N_1\sigma_{LE} \ . \qquad (5)$$

Hence, in terms of N_0 it is

$$g_L = N_0\sigma_{LE}I_P\sigma_{PA}/(I_L\sigma_{LE} + \gamma_{10}) \qquad (6)$$

and "small signal" gain g_{L0} (putting $I_L = 0$) is

$$g_{L0} = N_0\sigma_{LE}I_P\sigma_{PA}/\gamma_{10} \ . \qquad (7)$$

Therefore, the saturation behavior is described by

$$g_L/g_{L0} = 1/(1 + 1/p_{S1}) \ , \qquad (8)$$

introducing the dimensionless parameter p_{S1}

$$p_{S1} = \gamma_{10}/(I_L\sigma_{LE}) \ . \qquad (9)$$

It has value unity when the exponential gain has dropped to half the small signal value. It is the ratio between spontaneous and stimulated transitions to the ground state. Since I_{SAT} is the lasing intensity that causes the exponential gain to drop to half of its small signal value, then

$$I_{SAT} = \gamma_{10}/\sigma_{LE} \text{ photons } cm^{-2}\ s^{-1}. \qquad (10)$$

This is consistent with Eq. (1), since from the above two relations

$$p_{S1} = I_{SAT}/I_L. \qquad (11)$$

Since $\tau_{eff} = 1/\Sigma\gamma_{1j}$ and γ_{10} dominates, then

$$\tau_{eff} \approx 1/\gamma_{10} \ . \qquad (12)$$

Hence

$$I_{SAT} \approx 1/(\tau_{eff}\sigma_{LE}) \text{ photons } cm^{-2}\ s^{-1}, \qquad (13)$$

which is in agreement with Siegman (ref. 1, p. 293).

The exponential gain seen by the pumping photons, ignoring bulk absorption because of the typically short pumping path, is

$$g_P = - N_0\sigma_{PA} \ . \qquad (14)$$

We expect this to be negative, since pumping photons are absorbed.

Quantum Efficiency - Basic Transitions

Suppose the lasing intensity I_L is flowing in direction z, and the pumping intensity I_P is flowing in direction x, as shown in Figure 2. Then the photons dN_L added to the lasing flux, and the photons dN_P removed from the pumping flux, in the element of dye, are respectively

$$dN_L = dI_L(dxdy) = g_LI_Ldz(dxdy) \ , \qquad (15)$$

and

$$dN_P = -dI_P(dydz) = - g_PI_Pdx(dydz) \ . \qquad (16)$$

Hence, the lasing quantum efficiency is

$$\eta_L = dN_L/dN_P = - g_LI_L/(g_PI_P) \ . \qquad (17)$$

So from relations Eqs (6) and (14)

$$\eta_L = I_L\sigma_{LE}/(I_L\sigma_{LE}+\gamma_{10}) \ . \qquad (18)$$

Eq. (9) then gives

$$\eta_L = 1/(1+p_{S1}) \ . \qquad (19)$$

From Eq. (11), $p_{S1} = I_{SAT}/I_L$, so the above is consistent with the earlier Eq. (3). If the flow directions are chosen differently, the same relations will always be obtained.

Gain and Saturation - Including other Losses

We will now revisit the relations for gain and efficiency just developed, adding the effects of all the other transitions shown in Figure 1. As the analysis progresses we will keep finding the dimensionless relationships appearing that are listed in Table 1.

TABLE 1
List of Dimensionless Parameters

Symbol	Description	Parameter
p_{S1}	Spontaneous singlet	$\gamma_{10}/(I_L\sigma_{LE})$
p_{ST}	Spontaneous triple	$\gamma_{1T}/(I_L\sigma_{LE})$
p_{L1}	Lasing absorption singlet	σ_{L1}/σ_{LE}
p_{LT}	Lasing absorpt. triplet	$(\sigma_{LT}\gamma_{1T})/(\sigma_{LE}\gamma_{T0})$
p_{L0}	Lasing absorpt. ground	$(I_L\sigma_{LA})/(I_P\sigma_{PA})$
p_{LB}	Lasing absorption bulk	$(kI_L)/(N_0I_P\sigma_{PA})$
p_{P1}	Pump absorption singlet	$(I_P\sigma_{P1})/(I_L\sigma_{LE})$
p_{PT}	Pump absorpt. triplet	$(I_P\sigma_{PT}\gamma_{1T})/(I_L\sigma_{LE}\gamma_{T0})$
p_{PX}	Pump stimulated singlet	$I_P\sigma_{PE})/(I_L\sigma_{LE})$

The rate equations now give, for quasi steady-state equilibrium of the first singlet population

$$\frac{N_1}{N_0}=\frac{\left(I_p\sigma_{PA}+I_L\sigma_{LA}\right)}{\left(I_L\sigma_{LE}+I_p\sigma_{PE}+\gamma_{10}+\gamma_{1T}\right)}. \qquad (20)$$

i.e.,

$$\frac{N_1}{N_0}=\frac{I_P\sigma_{PA}\left(1+p_{L0}\right)}{I_L\sigma_{LE}\left(1+p_{S1}+p_{ST}+p_{PX}\right)}. \qquad (21)$$

where the terms p_{ij} are defined in Table 1. In quasi steady-state for the triplet population N_T (no longer zero) we have

$$\frac{N_T}{N_0}=\left(\frac{N_1}{N_0}\right)\left(\frac{\gamma_{1T}}{\gamma_{T0}}\right). \qquad (22)$$

The exponential gain, for the lasing light, taking all the transitions into account is

$$g_L = N_1(\sigma_{LE} - \sigma_{L1}) - N_T\sigma_{LT} - N_0\sigma_{LA} - k\,. \qquad (23)$$

Using Eqs. (21) and (22) to eliminate N_1 and N_T, and making p_{ij} substitutions from Table 1 gives

$$g_L=\frac{N_0I_P\sigma_{PA}\left(1+p_{L0}\right)\left(1-p_{L1}-p_{LT}\right)}{I_L\left\{\left(1+p_{S1}+p_{ST}+p_{PX}\right)-p_{L0}-p_{LB}\right\}}. \qquad (24)$$

Equation (24) is more complex than the earlier Eq. (6) obtained when only the "basic" transitions were considered. But it becomes identical if all the p_{ij} terms except p_{S1} are equated to zero.

Pumping - Including other Losses

The gain seen by the pumping photons, ignoring bulk absorption because of the typically short pumping path, is

$$g_P = N_1(\sigma_{PE} - \sigma_{P1}) - N_T\sigma_{PT} - N_0\sigma_{PA}\,. \qquad (25)$$

We expect this to be negative, since pumping photons are absorbed. Again using Eqs. (21) and (22) to eliminate N_1 and N_T, and making p_{ij} substitutions from Table 1, we obtain

$$g_P=-N_0\sigma_{PA}\left\{1-\frac{\left(1+p_{L0}\right)\left(p_{PX}-p_{P1}-p_{PT}\right)}{\left(1+p_{S1}+p_{ST}+p_{PX}\right)}\right\}. \qquad (26)$$

This is again more complex than Eq. (14), but becomes the same if the p_{ij} terms other than p_{S1} go to zero.

Quantum Efficiency - with Other Losses

The ratio of lasing photons gained to pumping photons lost in the cell, from Eq. (17) is still

$$\eta_L = -\,g_LI_L/(g_PI_P)\,. \qquad (27)$$

Hence, from Eqs. (24) and (26), making the p_{ij} substitutions,

$$\eta_L = (A - B)/(C - D)$$

where

$$\begin{aligned} A &= (1 + p_{L0})(1 - p_{L1} - p_{LT}) \\ B &= (p_{L0} + p_{LB})(1 + p_{S1} + p_{ST} + p_{PX}) \\ C &= (1 + p_{S1} + p_{ST} + p_{PX}) \\ D &= (1 + p_{L0})(p_{PX} - p_{P1} - p_{PT})\,. \end{aligned} \qquad (28)$$

This is the rate equation result with no additional approximations. If we now assume that all $p_{ij} << 1$ we obtain the first order solution

$$\eta_L \approx 1 - p_{S1} - p_{ST} - p_{P1} - p_{PT} - p_{L1} - p_{LT} - p_{LB}\,. \qquad (29)$$

This is useful for assessing whether any individual loss is significant. Later we will find that, even with a good dye such as Rhodamine 6G, it is hard to ensure that p_{S1} and p_{LT} satisfy the smallness criterion. Also, we will want to investigate the impact of p_{LB} rather closely. If we restrict

ourselves to assuming all the others are small, then we obtain the intermediate approximation

$$\eta_L \approx \frac{1 - p_{L1} - p_{LT} - p_{LB} - p_{S1}(p_{L0} + p_{LB}) - p_{LT}p_{L0} - p_{LB}p_{PX}}{1 + p_{S1} + p_{ST} + p_{P1} + p_{PT}}. \quad (30)$$

It is still somewhat easier to assess the impact of the individual components in this relation than in the accurate form of Eq. (28).

Note that each of the loss parameters is made up of *ratios* between pairs of cross sections and transition rates, usually modified by the ratio I_L/I_P, I_P/I_L, or by I_L alone. *Never does a single dye property appear on its own.* Also, different dyes may perform best with different values of I_L and I_P. Consequently, we should beware of "comparisons" between dyes which do not include re-optimization of both I_L and I_P.

Effect of Dye Concentration

The only loss parameter containing a population density is the bulk loss p_{LB}. Even that one may wash out if the contamination arises from the dye molecules, since k may then be proportional to N_0. The dye concentration may be kept as an open parameter for optimizing the pump absorption profile. If too concentrated, the inner dye molecules will see low I_L, causing inefficiency. If too dilute, the pump energy will pass right through. Clearly the optimum concentration will be inversely proportional to the pumping depth. The insensitivity to dye concentration justifies approximating the total population as N_0 rather than as the sum of N_0, N_1 and N_T.

Generalize for Spectrally Broad Pump

So far, discrete optical frequencies have been assumed for all the fluxes. This will be sufficiently accurate for the lasing intensity I_L, but not for I_P if pumping with a conventional source. However, all the relations and coefficients can be generalized by substituting $\int I_P(\lambda)\sigma_{ij}(\lambda)d\lambda$ in Table 1 wherever the product $I_P\sigma_{ij}$ appears. The spectral dependence of any cross section $\sigma_{ij}(\lambda)$ will generally vary more rapidly than that of the lamp's spectral photon intensity $I_P(\lambda)$, so an approximation for the integral may be made as follows. Equate the integral to $I'_{P\lambda}(\lambda).\sigma'_{ij}(\lambda).\Delta\lambda$ with the components as follows. $I'_{P\lambda}(\lambda)$ is the local value of the spectral pumping intensity in the regime of the spectral feature, $\sigma'_{ij}(\lambda)$ is the peak of the spectral feature, and $\Delta\lambda$ is its bandwidth (fwhm).

In some cases, where beam quality is not of great importance, the dye concentration may be increased to a point where much of the pump light in the tails of the dye pump band is absorbed. In such a case the pump intensity, and its spectral distribution, will vary rapidly with depth into the dye. The appropriate approximation will then be more complicated. The uneven heat deposition in such a situation degrades the beam quality and so is not usually an attractive way to run the laser.

Dye Degradation

As the dye solution ages in the intense illumination, there is a tendency to form products which absorb at the lasing wavelength and so diminish the output. This loss is described by P_{LB}. Let us differentiate Eq (30), which is the approximation allowing for significant values of P_{LB}, to obtain

$$\frac{d\eta_L}{dp_{LB}} = -\frac{(1 + p_{S1} + p_{PX})}{(1 + p_{S1} + p_{ST} + p_{P1} + p_{PT})}. \quad (31)$$

In terms of the loss coefficient k this becomes

$$\frac{d\eta_L}{dk} = -\frac{I_L(1 + p_{S1} + p_{PX})}{N_0 I_P \sigma_{PA}(1 + p_{S1} + p_{ST} + p_{P1} + p_{PT})}. \quad (32)$$

The degradation proceeds more rapidly as the ratio I_L/I_P is increased. With flashlamp pumping, this ratio is inevitably high, since it is hard to exceed I_P =30 kW/cm^2 and efficiency requires $I_L > I_{SAT}$ (about 1 MW/cm^2 for Rhodamine 6G). However with laser pumping, I_L/I_P can be much closer to unity, so the degradation can be orders of magnitude slower. The N_0 factor also will usually favor the laser pumping situation because of the typically higher concentration used.

For the reasons just discussed, we expect the output loss as the dye ages to depend upon the operating conditions. This may explain the varying conclusions on the life of individual dyes obtained by different experimenters. Note that loss of dye is generally a small factor in the degradation since N_0 appears only in the P_{LB} loss parameter.

Discussion

In an "ideal" dye we would be able to find working ranges of I_L and I_P which would result in all the values of all $p_{ij} << 1$. The designer's task would then be to ensure that all elements of dye are exposed to lasing to obtain a quantum lasing efficiency close to unity. The penalty of small departures from those conditions would be

apparent from Eq. (29). In practice, all known dyes depart from the "ideal", and lasing quantum efficiency is generally less than 70%. Then, while Eq. (29) becomes an inadequate approximation, it will still allow qualitative insight into which loss mechanisms are significant. If all the significant dye parameters are known, then the better approximation of Eq. (30) should allow a quite accurate forecast of the lasing quantum efficiency. For the most precise optimization the accurate form of Eq. (28) is needed. All of these relations lend themselves to easy manipulation in a personal computer.

The high brightness from laser pumping allows almost almost unlimited choice of I_P. Selection of feedback in an oscillator, or input signal in an amplifier, also allows almost unlimited choice of I_L. The real limitation will generally come from damage or non-linear effects.

Pumping with a flashlamp, however, usually limits I_P to a less than optimum range. The irradiance entering the dye is always less than the irradiance surrounding the lamp (sometimes referred to as the Brightness Theorem). It is still possible to obtain high values of I_L, but the resulting high ratio I_L/I_P may increase the values of P_{L0} and P_{LB} (lasing losses from ground state and bulk absorption) to a point where they adversely affect the efficiency and the degradation rate.

It has been shown that a high level of I_P throughout the dye is needed to obtain reasonable efficiency. This is hard to achieve if pumping from only one side, or from one end, unless a large portion exits unused. If pumping is from both sides or ends, the uniformly high pump flux can be obtained with little loss at the exit, since the fluxes flowing in opposite directions add. However, if laser pumping, care has to be taken to avoid standing waves, and consequent nulls, as a result of the coherence.

At present this modeling has limited value, because a large portion of the parameters are known for only a few of the commonly used dyes. Hopefully, in the future this situation will improve so that dye comparison and laser optimization will become less empirical.

The author acknowledges with gratitude the information from D. E. Klimek of Avco Textron Research Laboratory, which was used in the preparation of the following list of resources for dye information: Papers by A. N. Fletcher[6,7], P. R. Hammond[8], F. P. Schafer (ref. 3), and the current Exciton Corporation Catalog give locations of fluorescence and absorption maxima. For complications of entire spectra that are harder to find, see also R. E. Schlier[9] and T. H. Koch[10]. Further information on cross sections for various dyes is given by T. G. Pavlopoulos and P. R. Hammond[11] and S. T. Gaffney and D. Magde[12]. P. R. Hammond[13,14,15] discusses detailed spectrum of Rhodamine 6B and Rhodamine B. A list of quantum yields of many dyes is given by A. N. Fletcher (ref. 7). Quantum yields, lifetimes, and dependence on solvents is given by G. Jones II, et al.[16]. Absorption in the solution from reaction with O_2 is discussed by R. E. Schwerzel and N. A. Edie[17]. Triplet quenching, with examples, is discussed by J. B. Marling, et al.[18,19]. Triplet coefficients, and their measurement, are discussed by Schafer (ref. 3, p. 155). Formation of absorbers is discussed by P. R. Hammond[20a] and by B. H. Winters, et al.[20b] Photophysics and photochemistry of a number of coumarin dyes have been analyzed by G. Jones II, et al.[21-26]. For selection of a dye for a particular lasing frequency and mode of operation, see papers by A. N. Fletcher (refs. 6 and 7) and by P. R. Hammond, et al.[8,27,28]. Effects of solvent polarity, viscosity and surfactants, have been investigated by G. Jones II, et al. (refs. 24 and 25). The listed authors have also published other useful papers. Further information on many aspects of dyes is in the *Proceedings of the Dye Laser/Laser Dye Technical Exchange Meeting, 1987.*[29]

Example Analysis for Rhodamine 6G

Rhodamine 6G is the most completely documented laser dye, so we will use it as an example. Its parameters are listed in Table 2. The cross sections for the pumping are given at the wavelength corresponding to the peak value of σ_{PA} at 530 nm, and the lasing cross sections at an assumed lasing wavelength of 600 nm. If pumping with a laser (such as frequency-doubled Nd:YAG), then we can consider discrete frequencies for the lasing and pumping fluxes. If pumping with a flashlamp then it is appropriate to use the approximation for I_P discussed above. The pumping bandwidth is taken as 50 nm (fwhm), and the useful pump power is that within this bandwidth. This assumes use of a pyrex water jacket preventing pumping to the higher excited states.

The value for γ_{T0} in Table 2 assumes the presence of oxygen for triplet quenching, as a result of equilibration with air. Without such quenching its value would be orders of magnitude lower, resulting in a value of p_{LT} so large as to prevent sustained lasing.

Using the dye parameters from Table 2, the values of the various p_{ij}, the population ratio

between the excited singlet and ground state, and the estimated quantum efficiency, for various combinations of I_L and I_P are shown in Table 3. For convenience, the values of I_L and I_P are presented as power densities instead of photon intensities. The same central wavelength and bandwidth are used for all the pump loss mechanisms. All photons outside that band will be considered lost anyway. It is hard to obtain even 30 kW/cm^2 into the 50 nm pump bandwidth, hence the 1 MW pump intensity of Table 3 corresponds to laser pumping.

TABLE 2
Dye Parameters for Rhodamine 6G

Param.	Description	Value.*	Ref.
σ_{PA}	Pump absorption	4.5×10^{-16}cm^2.	13
σ_{LA}	Lasing absorption	1×10^{-19} cm^2	13
σ_{PE}	Pump emission	2×10^{-17}cm^2	13
σ_{LE}	Lasing emission	1.3×10^{-16}cm^2	13
σ_{P1}	Pump singlet absorption	4×10^{-17}cm^2	13
σ_{L1}	Lasing singlet absorption	1×10^{-17}cm^2	13
σ_{PT}	Pump triplet absorption	1×10^{-17}cm^2	30
σ_{LT}	Lasing triplet absorption	4×10^{-17}cm^2	30
γ_{10}	Singlet-ground spontaneous	2.9×10^{8}/s	13
γ_{1T}	Singlet-triplet spontaneous	2.0×10^{7}/s	30
γ_{T0}	Triplet-ground spontaneous	2.0×10^{7}/s**	30
k	Bulk absorption	0.002/cm	a
N_0	Population density	1×10^{16}/cm^3	b

* Pump at 530 nm, lase at 600 nm.
** Value estimated for equilibration with air
a This corresponds to 0.2% loss per cm.
b Based on 2×10^{-5} molar.

The lasing quantum efficiency is plotted as a function of I_L and I_P in Figure 3, using the accurate relation of Eq. (28). These curves help establish the trade-offs, but the impact of the individual loss mechanisms is now less transparent. From the curves, the importance of having $I_L > I_{SAT}$ is clear. A parameter space can be selected on the plot in which one can operate to maximize efficiency. It can be seen that increasing I_P can always produce higher efficiency provided an associated optimum I_L can be generated. In an amplifier, I_L can be controlled by optically expanding or contracting the beam to be amplified, and in an oscillator by controlling the feedback. The general limits will come from how high a pump power density can be obtained, and how high a lasing power density can be withstood by the optical elements. Both of these limits become lower with longer pulses.

TABLE 3
Values of p_{ij} and η_L for Rhodamine 6G Example
(Using dye values from Table 2)

I_P	10 kW/cm^2			30 kW/cm^2			1 MW/cm^2		
I_L MW/cm^2	1.5	4	10	1.5	4	10	1.5	4	10
p_{S1}	.49	.18	.07	.49	.18	.07	.49	.18	.07
p_{ST}	.03	.01	.01	.03	.01	.01	.03	.01	.01
p_{L1}	.08	.08	.08	.08	.08	.08	.08	.08	.08
p_{LT}	.31	.31	.31	.31	.31	.31	.31	.31	.31
p_{L0}	.04	.10	.26	.01	.03	.09	.00	.00	.00
p_{LB}	.08	.20	.51	.03	.07	.17	.00	.00	.00
p_{P1}	.00	.00	.00	.01	.00	.00	.18	.07	.03
p_{PT}	.00	.00	.00	.00	.00	.00	.05	.02	.01
p_{PX}	.00	.00	.00	.00	.00	.00	.09	.03	.01
N_1/N_0	.014	.007	.003	.04	.02	.01	1.2	.61	.28
η_L eq (28)	.30	.26	.005	.37	.43	.36	.35	.48	.55

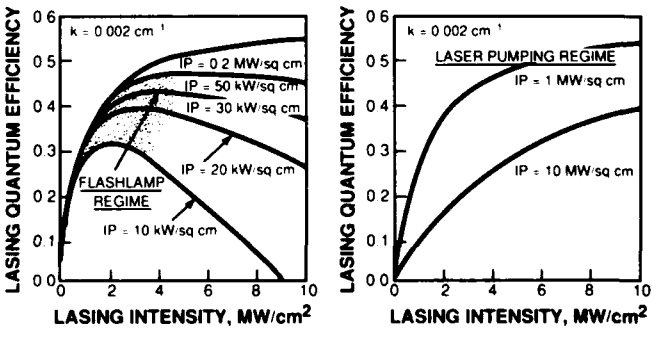


Fig. 3. Efficiency depends on conditions (Rhodamine 6G example)

The cross-sections are wavelength dependent, so if the laser is tuned to a different wavelength the curves will change. In particular I_{SAT} will increase as a laser is tuned from the wavelength of peak spontaneous emission.

Population Distribution and Effect on Lasing Wavelength

When pumping with a flashlamp, the attainable value of I_P is orders of magnitude less than the value of I_L needed to ensure $I_L > I_{SAT}$. Since σ_{PA} and σ_{LE} have approximately the same value, it follows from Eq. (21) that most of the population will remain in the ground state. This means that absorption by the ground state is then a significant factor, which tends to push the lasing to longer wavelengths. With laser pumping, I_P can be much higher, leading to a higher ratio N_1/N_0 as seen in Table 3. Consequently, ground state absorption will be less significant and the lasing will not move so far to the longer wavelength.

Dye Degradation

It will be seen from Table 3 that at the lower values of I_P associated with flashlamp pumping the impact of the bulk absorption term p_{LB} is much more significant than it is at the higher values of I_P that would be used with laser pumping. It also depends considerably on the precise details of the power levels in the lamp pumping regime. Hence, not only will the performance be affected much more by a given amount of dye degradation with a flashlamp pumped dye laser, but the effect will be very dependent upon the details. Unfortunately the trade-off that increases I_L to reduce p_{S1} also increases p_{LB}; i.e., reducing the spontaneous losses can increase the degradation problem. This situation is illustrated in the curves of Figure 4, in which the photon efficiency is plotted against the bulk absorption coefficient for various values of lasing intensity. The curves on the left correspond to pumping with a flashlamp, assuming $I_P = 20$ kW/cm^2. The curves on the right correspond to laser pumping, with $I_P = 1$ MW/cm^2. With flashlamp pumping, the higher values of lasing intensity give relatively high efficiency when the bulk absorption is very small. However, as the value of k becomes higher, as we expect when the dye degrades, then the efficiency drops off much more rapidly than when the lasing intensity is smaller. The optimum value of I_L is quite different for the badly degraded dye. The slopes show a 10-fold variation in degradation rate. Care should be taken to optimize the feedback of a flashlamp pumped dye laser only when the dye is fresh. The curves for the laser pumped case yield much slower deterioration in output as the dye solution becomes more absorbing. The deterioration in output will also be faster if a dye is tuned away from the peak emission, because of the wavelength dependency of the cross sections and hence of the p parameters.

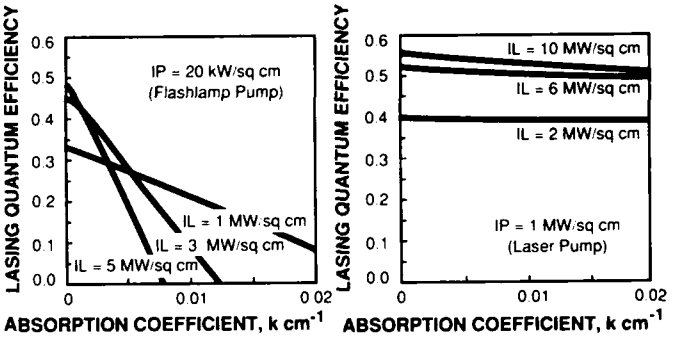


Fig. 4. Dye degradation also depends on conditions (Rhodamine 6G example)

Conclusion

Dye lasing efficiency has been modeled in the presence of the many competing transitions, and useful conclusions drawn. Nine dimensionless parameters have been introduced to reduce the complexity. The approach will allow other suspected loss mechanisms to be introduced into the framework. It is shown how performance, including degradation, is affected by the operating conditions. Useful insight is obtained from the relations, and optimization will be aided. Care is needed when comparing laser dyes, since they may optimize under different operating conditions.

Acknowledgment

The author wishes to acknowledge particularly helpful discussions with D. E. Klimek, D. P. Pacheco, and R. E. Schlier, as well as S. J. Richardson for preparing the manuscript.

References

1. A. E. Siegman, "Lasers" (University Science Books, CA, 1986).

2. P. N. Everett, in Proceedings, Dye Laser/Laser Dye Technical Exchange Meeting '87, J. H. Bentley, Ed. (Special Report RD-DE-87-1, AMSMI-RD-DE, U.S. Army Missile Command, Redstone Arsenal, AL, 1987) pp 506-524.

3. F. P. Schafer, Ed.: "Dye Lasers," 2nd rev. ed., Topics Appl. Phys. 1 (Springer, Berlin, Heidelberg, 1977).

4. B. B. Snaveley, Proc. IEEE **57**, 1374 (1969) .

5. R. S. Hargrove and T. Kan, IEEE J. QE **16**, 1108 (1980).

6. A. N. Fletcher, Appl. Phys. **14**, 295 (1977).

7. A. N. Fletcher, Appl. Phys. **16**, 93 (1978).

8. P. R. Hammond, A. N. Fletcher, R. A. Henrey, R. L. Atkins and D. W. Moore, "Near-ultraviolet Lasing Dyes. Part I. Search for New Dyes and Summation of Results," Naval Weapons Center, NWC TP 5768 (Sept 1975).

9. R. E. Schlier, in Proceedings, Dye Laser/Laser Dye Technical Exchange Meeting, 1987, J. H. Bentley, Ed. (Special Report RD-DE-87-1, AMSMI-RD-DE, U.S. Army Missile Command, Redstone Arsenal, AL, 1987) pp 69-107.

10. T. H. Koch, in Proceedings, Dye Laser/Laser Dye Technical Exchange Meeting, 1987, J. H. Bentley, Ed. (Special Report RD-DE-87-1, AMSMI-RD-DE, U.S. Army Missile Command, Redstone Arsenal, AL, 1987) pp 399-429.

11. T. G. Pavlopoulos and P. R. Hammond, J. of Am. Chem. Soc. **96:21**, 6568 (1974)

12. S. T. Gaffney and D. Magde, "Excited Singlet Absorption in Blue Laser Dyes: Measurement by Picosecond Flash Photolysis," ThB9-1, Univ. of California at San Diego, Dept. of Chemistry.

13. P. R. Hammond, IEEE J QE **16**, 1157 (1980).

14. P. R. Hammond, J. Chem. Phys. **70**, 3884 (1979).

15. P. R. Hammond, IEEE J. QE **15**, 624 (1979).

16. G. Jones II, W. R. Jackson and A. M. Halpern, Chem. Phys. Lett. **72**, 391 (1980).

17. R. E. Schwerzel and N. A. Edie, "Mechanisms of Photochemical Degradation in Xanthene Laser Dyes," Final Technical Report, Battelle Columbus Laboratories, (February 1981).

18. J. B. Marling, D. W. Gregg and L. Wood, Appl. Phys. Lett. **17**, 527 (1970).

19. J. B. Marling, "Dye Laser Performance Enhancement by Chemical Quenching of the Triplet State," Lawrence Radiation Laboratory, Univ. of California, TID-4500, UC-34 (July 1971).

20a. P. R. Hammond, Appl. Phys. **14**, 199 (1977).

20b. B. H. Winters, Mandelberg and W. B. Mohr, App. Phys. Lett. **25**, 723 (1974).

21. G. Jones II, "Photochemistry and Photophysics of Laser Dyes," Office of Naval Research, Technical Report No. 8 (October 31, 1983).

22. G. Jones II, S. F. Griffin, C. Choi and W. R. Bergmark, "Electron Donor-acceptor Quenching and Photo-induced Electron Transfer for Courmarin Dyes," Office of Naval Research, Technical Report No. 3 (October 31, 1983).

23. G. Jones II and W. R. Bergmark, "Photodegradation of Courmarin Laser Dyes. An Unexpected Singlet Self-Quenching Mechanism," Office of Naval Research, Technical Report No. 4 (October 31, 1983).

24. G. Jones II, W. R. Jackson and C. Choi, "Solvent Effects on Emission Yield and Lifetime for Courmarin Laser Dyes. Requirements for a Rotatory Decay Mechanism," Office of Naval Research, Technical Report No. 5 (October 31, 1983).

25. G. Jones II, W. R. Jackson, S. Kanoktanoporn and W. R. Bergmark, "Photophysical and Photochemical Properties of Courmarin Laser Dyes in Amphiphilic Media," Office of Naval Research, Technical Report No. 6 (October 31, 1983).

26. G. Jones II, W. R. Jackson, S. Kanoktanoporn and W. R. Bergmark, "Products of Photodegradation for Coumarin Laser Dyes," Office of Naval Research, Technical Report No. 7 (October 31, 1983).

27. P. R. Hammond, R. L. Atkins, A. Henry and A. N. Fletcher, "Azacoumarin Dye Lasers," United States Patent No. 4, 103, 257 (July 25, 1978).

28. P. R. Hammond, R. L. Atkins and A. Henry, "Azaquinolone Dye Lasers," United States Patent No. 4, 103, 257 (July 25, 1978).

29. Proceedings: Dye Laser/Laser Dye Technical Exchange Meeting '87, J. H. Bentley, Ed. (Special Report RD-DE-87-1, AMSMI-RD-DE, U.S. Army Missile Command, Redstone Arsenal, AL, 1987).

30. D. E. Klimek, private communication.

Performance and Modeling of a Flashlamp-pumped Dye Laser with Aqueous Acetamide as a Solvent*

Patrick N. Everett
Lincoln Laboratory, Massachusetts Institute of Technology
Lexington, MA 02173-9108

Abstract

Further information is presented on performance of a 300 Watt, 6-beam, dye laser reported at last year's conference. The use of Acetamide as a dye solvent is discussed. The lasing results are coupled with modeling of flashlamps and dye, to demonstrate a useful approach to design of dye lasers. Lamps may be driven harder than traditionally accepted.

Introduction

Last year, the engineering and performance of the initial beam of a laser system being built at an experimental field site were reported.[1,2] The laser heads were developed by Candela Corporation, and the laser power supplies by A.L.E. Systems Inc. The laser uses Coumarin 504 dye dissolved in aqueous acetamide solution and is flashlamp pumped. Each beam, 14 mm diameter, is generated in a confocal resonator of optical length 2.5 m, and magnification 2.7. The resonator contains two laser heads, each powered by a pair of 2-foot lamps of 7 mm bore. The dye flows longitudinally. The full system will have six independent beams, each running at 10 pps, 5 to 10 J/pulse, tunable around 508 nm wavelength, in 2-μs pulses. Further results will now be reported. Emphasis will be on the use of acetamide, understanding the resonator, and modeling the performance of the dye and lamps. It will be shown that acceptable models are available for designing such lasers, and that lamps can be driven harder than some of the existing literature indicates.

Acetamide and Aqueous Solutions

Water has many desirable properties as a solvent. It has excellent thermal properties, is non-flammable, inexpensive, and easy to dispose of. But many laser dyes have low solubility in water and tend to dimerize. The dimers often absorb at the lasing wavelength of the monomer and don't lase well themselves. Crozet and Meyer[3] have discussed the addition of certain organic compounds to suppress dimerization. They, as well as Megie and de Witte[4], de Witte[5], and Dezauzier et al[6] demonstrated improved performance of Rhodamine 6G in aqueous acetamide solution. Some activity as a triplet quencher was suggested by de Witte. Detergents also reduce dimerization and may act as triplet quenchers.[7] But the sudsing action can be detrimental.

This system initially used a 50% methanol/water mix as the dye solvent. But the perceived danger of storing 1200 gallons of flammable liquid, pumping it at 360 gpm through 12 dye laser heads, and exciting it with 24 flashlamps at 40 kV, began to dominate the project. At the suggestion of B. Kirstein, of SAIC Inc., aqueous acetamide (acetic acid amide) solution was tested as an alternative, although not previously demonstrated with Coumarin 504. It gave equivalent output performance but with shorter dye life. The shorter life was not a problem since ample dye cleaning capability was being installed. However, the limited solubility made it difficult to prepare a concentrate for dye replenishment. This problem was solved, at the suggestion of J. L. Dwyer of Ventec Corp., by milling dye powder in cleaned aqueous acetamide solvent for several hours to obtain a finely divided slurry. This dissolves within seconds when squirted into a slip-stream of the working fluid.

The cleaning system, using carbon filters, has worked well with the acetamide solution. There have been hundreds of hours of operation with the initial fill. This is important because the acetamide costs $15,000 for one fill and disposal is a problem. Hundreds of gms of dye have been used and cleaned out.

Performance

The good effect of oxygen reported last year, and shown in Figure 1, has been confirmed in operation. The curves of Figure 2 show energy measured in the far-field through various diameter apertures with the oxygen at 72% of the sea level content. At twice the sea level value the single laser beam has generated over 6 J total energy, with more than 2.5 J through a 17 fλ/D aperture (f is the focal length of an analyzing lens, λ

*Sponsored by the Defense Advanced Research Projects Agency and the U. S. Air Force.

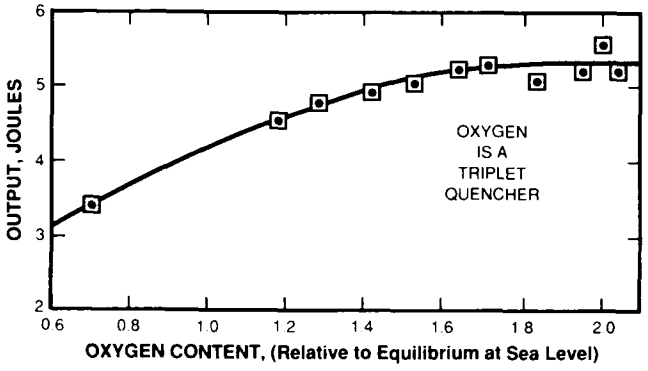


Fig. 1. Improvement with Oxygen

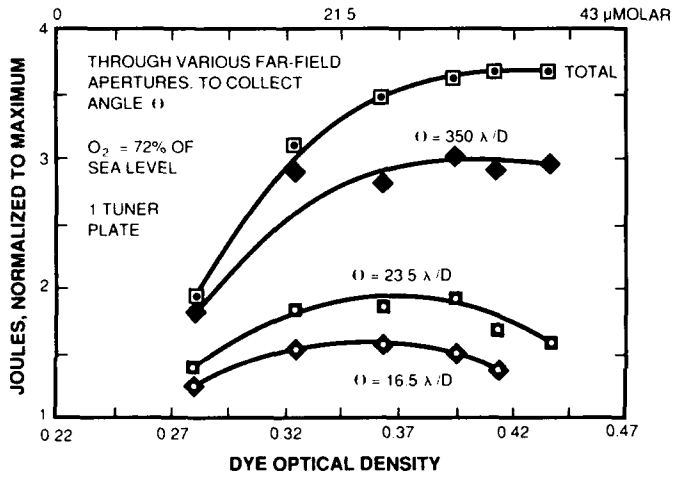


Fig. 2. Performance vs. Dye Concentration

the wavelength, and D the beam diameter). It has run consistently with more than 5.5 J total output and 2J measured through the 17fλ/D aperture. Lensing must occur in the medium during the pulse. It could be at least partially compensated by adjusting the length of the resonator, and thus improve performance. But pressure of supporting experiments has prevented such development. The optimal dye concentration for energy in the center of the far field is lower than that for total energy, as seen in Figure 2 and Table 1. The dye concentrations are deduced from optical density comparison at 450 nm with a known solution.

All pulse lengths are "full width half maximum" (fwhm) unless otherwise stated. The current pulse is 2.6 µs long (slightly underdamped), and energy through far-field aperture of 17fλ/D is 2.0 µs (slightly longer outside the aperture). Figure 3 shows the relationship between output and pumping energies.

TABLE 1
Optimal Concentration of Dye and Impact on Laser

How Parameter Optimized	Energy measured (Joules)	Estimate Conc.* (molar)	Estim. transv. transm.	Center/ Edge Ip
E in 17λ/D	2 to 2.5J	2.2×10^{-5}	43%	92%
Total En.	5 to 6J	$>3.0 \times 10^{-5}$	<31%	<85%

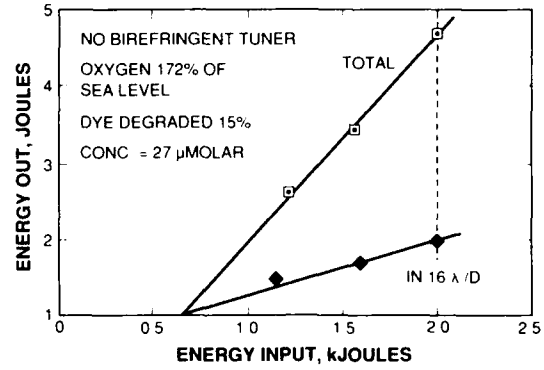


Fig. 3. Output vs. Input

Dye Degradation

The optical density of the dye measured at 550 nm wavelength, in a 1-meter long in-line cell, increases linearly with cumulative exposure to the flashlamps, as shown in Figure 4. The loss in

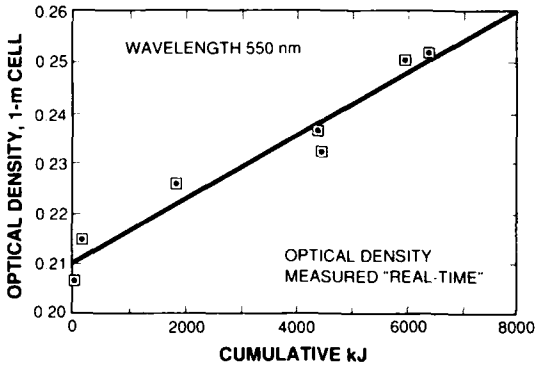


Fig. 4. Dye Absorption vs. Exposure to Lamps

laser output closely follows the same pattern. The energy drops by 10% for each 900 J of flash lamp energy per liter of dye solution, while the optical density of the 1-meter cell increases by 0.02. No change was observed in the dye concentration, monitored at 450 nm in a 5-mm in-line cell. During a single pulse, 94 ml of dye solution in each laser head is exposed to 1,000 J of flashlamp energy. This results in expected loss

of 71% of output energy, which is not observed in the pulse shape. This has two implications. Firstly, most of the degradation must occur after the pulse is over (probably from nascent oxygen produced by the excitation). Second, when the system runs at full power, taking into account the three interchanges of dye between pulses, the dye solution will emerge degraded to an average loss of 28% in output. Thus, a large proportion of the degradation product needs to be removed before re-entering the lasers. Since the removal process also takes out the dye, then the dye must be replaced.

Resonator Control

The alignment method reported in the earlier paper (ref. 1) has continued to be successful. A full sized collimated cw-laser beam is introduced into the resonator off a beam splitter, shrinks, and then expands on successive passes, emerging as a simulation of the pulsed laser beam. Some lensing must occur in the dye solution during the pulse, but the simulated laser beam is still useful in tracing the path and beam performance of the pulsed laser. This success is attributed, at least partially, to the spatial filtering through which they both must pass on the way to the experiment.

Birefringent filters are used to polarize the output and to give tuning capability when needed. Tuning has not yet been needed from the 508 nm wavelength at which it naturally runs. The birefringent plates have been used with their ordinary axes either in the plane of inclination, or perpendicular, to give full polarizing effect but zero tuning. For maximum tuning effect the plates would be rotated together through about 45°, and then fine-tuned in angle to obtain the required wavelength. Initial operation with only one birefringent inclined at 45° to the laser axis (with small reflection used as a diagnostic) resulted in 3:1 polarization ratio. Addition of a second at Brewster's angle gave a ratio of better than 10:1. The polarization measurements, taking into account the corrective action of the birefringent plates, is consistent with depolarization occurring at about 2% per foot on passing through the dye solution.

Modeling

Key aspects of the laser operation will now be modeled, starting with sensitivity to imperfections in the resonator. Then the lamp performance will be modeled, followed by the coupling to the dye and the performance of the dye itself, using material from the preceding paper. This will lead to an estimate for the overall efficiency of the laser, and then the loss in output as the dye degrades. Finally, lamp life will be discussed and conclusions summarized.

Resonator Sensitivity to Imperfections

The sensitivities have been analyzed, using the Kogelnik and Li formulation for Gaussian propagation.[8] The design values give a solution resulting in a collimated zero-order Gaussian output. The amount of change in each parameter needed to change from collimation to an included angle equivalent to $10\ \lambda/D$ was found and is shown in Table 2. This angle corresponds to about ten times the diffraction angle. A geometric approach based on virtual source analysis[9] gave the same results. The mirror angle errors were obtained from simple geometric analysis.

TABLE 2
Sensitivity to Imperfections in the Resonator

Parameter	Design Value	Error to cause 10 λ/D effect*	Comments
Reson. length	2.5 m	-35 cm	incr→ converg
Back mirror rad.	+8.0 m	+70 cm	incr→ diverg
Front mirror rad.	-3.0 m	+70 cm	incr→ diverg
Lensing	0 dioptre	-0.01 dioptre	in each head
Back mirror θ	0.0 mrad	0.11 mrad	in same sense
Output mirror θ	0.0 mrad	0.30 mrad	in opp. sense

*To cause full angle divergence, or angular deviation, equivalent to 10 λ/D.

Flashlamps

In the following paragraphs, the operation of the flashlamps will be modeled. It will be shown that, for our regime, they can be approximated as black body radiators. This allows quantitative estimates of performance, as well as insight. The lamp modeling will then be combined with the modeling of the dye performance, from the preceding paper, to analyze the overall performance. Finally, the life expectation of the lamps will be discussed. It will be concluded that the lamps can safely be driven harder than would be expected from previously published literature.

Markiewicz and Emmett[10] investigated the non-linear oscillatory equations describing the discharge into the varying resistance of the flashlamp through the inherent inductance in the circuit. They plotted computer solutions of the current and power input (I^2R) vs time for different values of a "damping term" α determined by the electrical parameters. They normalized time to the electrical time-constant

$\tau = \sqrt{(LC)}$, where L and C are inductance and capacitance of the circuit and storage capacitors. They found critical damping highest peak power input is obtained when $\alpha = 0.8$. This is generally considered optimum, with sometimes a little overshoot to help quench the switching device after the pulse is over. Their data are used to plot the curves of Figure 5. They show normalized time development of current and power input for damping of $\alpha = 0.8$. Note that the power curve is significantly shorter than the current curve. A curve of the normalized temperature is added, based on the lamp emitting as a black body in quasi-equilibrium following the Stefan Boltzmann law (to be discussed later). Table 3 shows the characteristic pulse durations and rise times defined in a variety of ways, expressed in terms of the electrical time constant τ.

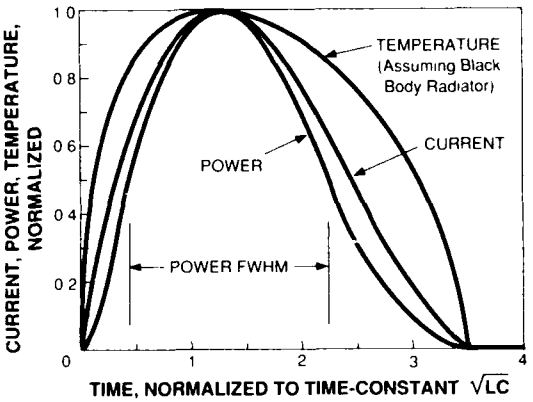


Fig. 5. Pulse Current, Power and Temperature

TABLE 3
Pulse Durations by Various Definitions for Critically Damped Current and Power in Terms of Time Constant $\tau = \sqrt{(LC)}$

	Rise 10-90%	Width fwhm.	Between 1/3 pts	Initial to 20%	Between 10% pts	Base Line
Current	0.77τ	2.1τ	2.5τ	3.0τ	3.1τ	3.5τ
Power	0.76τ	1.8τ	2.1τ	2.7τ	2.75τ	3.5τ
Temp.	0.61τ	2.95τ	3.20τ	3.4τ	3.4τ	3.5τ

Emission Characteristics

At temperatures below about 10,000 K the discharge plasma is partially transmitting, and line emission, characteristic of the fill gases, tends to predominate.[11] At higher temperatures the plasma becomes more opaque, and the output becomes dominated by the black-body curve corresponding to the electron temperature in the plasma.[12,13] For example Goncz and Newell reported (ref. 11) that the spectrum of an EG&G FX-47A flashlamp between 0.3 and 1.1 μm closely approximated a black body at 9400 K when excited with 5300 amps/cm^2. When excited with only 1700 amps/cm^2 it approximated a black body at 7000 K (but not so closely). The measured proportions of the excitation energy radiated into various spectral intervals are shown in Table 4. At the higher excitation temperature nearly 100% of the electrical energy must have been radiated by the plasma, with a considerable portion outside the spectral interval that was measured, much of it absorbed by the quartz.

TABLE 4
Emission from EG&G Lamp FX-47A, Pulse Length T = 750 μs (ref. 11)

En. (kJ)	Current Density (A/cm^2)	Equiv Temp	Efficiency % in μm range 0.35 - 0.5	0.5 - 0.7	0.7 - 0.9	0.9 - 1.1	Total 0.35 -1.1
1	1700	7000 K	18	18	16	11	63
5	5300	9400 K	27	20	11	6	64

Other investigators who have contributed to the understanding of the emission characteristics of lamps at different excitation levels include Perlman[14,15], Sorokin et al[16], Oliver and Barnes[17], Holzrichter and Emmett[18], Furumoto and Ceccon[19], Ferrar[20], Holzrichter and Schawlow[21], Oliver and Barnes[22], Mavroyannakis[23], Gibson[24], Ewanizky and Wright[25], Gunther[26], Morrow and Price[27], Baker and King[28], Gusinow[29-32], Dishington et al[33], Efthymiopoulos and Garside[34], and Gavrilov[35]. An excellent review of practical lamp considerations is given by Furomoto.[36] Pacheco et al[37] recently reported quantitative spectral measurements very relevant to our study. Simmer was maintained between pulses. The measured emissions closely matched that of a black body at 20,000 K and 15,000 K, respectively over the range 0.45 to 0.8 μm, with the departures greater for the lower excitation. We will return to these results after discussion of black body emitters.

Black Body Model

Our model will assume that the lamps behave as black body emitters, with the instantaneous radiation balancing the electrical input power, based upon the results cited above. The results of the modeling will agree with observation sufficiently well that we will conclude the modeling is justified, and is a helpful approach for the laser designer.

The quantitative emission characteristic of a black body surface is completely determined by its temperature, which is in turn proportional to the fourth root of the total power density radiated from the surface by the Stefan Boltzmann law. The blackbody characteristics are well known and tabulated[38]. Useful curves for our discussion are in Figure 6, based on relations from the Infrared Handbook[39]. We should however note that the flashlamp envelope is generally of fused silica which absorbs radiation at wavelengths shorter than about 180 nm, depending on its grade.

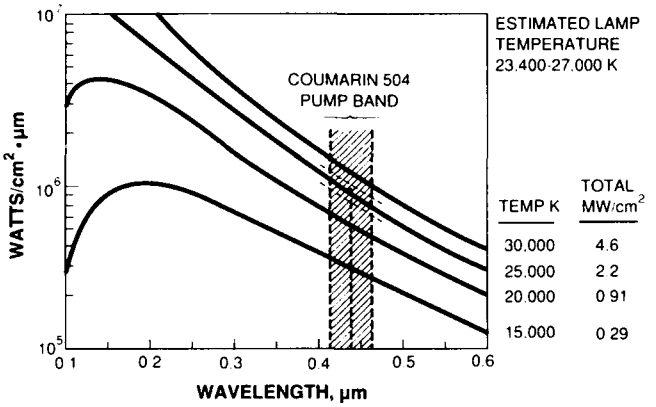


Fig. 6. Black Body Emission Curves

If a lamp is radiating as a black body with the radiating power balancing the input power, then the instantaneous temperature will be determined by the instantaneous electrical power per unit area of bore surface. It is reasonable to define a "representative" temperature that will be determined by a "representative" value of the power per unit area of bore surface. Reference to the power curve of Figure 5 confirms that a rectangular pulse with the same peak power and full width at half maximum (fwhm) duration would contain the same energy as the actual pulse, to quite a close approximation. Since the power duration is 1.8τ fwhm (see Table 3), a good choice of "representative" power density P_R is given by

$$P_R = E/(1.8\tau A) , \qquad (1)$$

where A is the bore surface area. Hence the representative temperature T_R is given by

$$T_R = \left(E/(k_S 1.8\tau A)\right)^{1/4} , \qquad (2)$$

where k_S is the Stefan Boltzmann constant. In as much as a lamp is a black body in quasi-equilibrium, then its "representative" emission characteristics will be governed by the ratio $E:1.8\tau A$; and its "representative" plasma temperature and spectral distribution can be at least approximately obtained from the black body curves represented by those in Figure 6. We can expect the "representative" characteristics to be a close approximation to the measured integrated ones. Reference to the curves of Figure 6 will confirm that errors expected in prediction of temperature (and hence spectral distribution) are likely to be smaller than the errors in the prediction of power radiated, because of the 4th power relationship.

Lamp Temperature

Pacheco et al (ref. 37) excited a lamp of 7 mm bore diameter and 18" arc length with 8 μs (fwhm) pulses of 440 and 140 J, and made quantitative spectral measurements over the range 0.24 to 0.8 μm. Simmer was maintained between pulses. From Table 3 we infer that, for their pulse, $\tau = 3.8$ μs, and hence the fwhm of the electrical power input pulse was 6.8 μs. The lamp internal bore surface area A was 100 cm². Thus in their 440 and 140 J cases, we infer values for representative total power P_R from eq (1), of 650 and 210 kW/cm², respectively, corresponding temperatures of 18,400 K and 13,900 K. However the measured emissions closely matched that of a black body at higher temperatures of 20,000 K and 15,000 K over the range 0.45 to 0.8 μm (the departures were greater for the lower excitation). The results indicate that the lamp was emitting more efficiently into the wavelengths of interest than would a black body . Pacheco has suggested[40] that this may have resulted from the deep UV being absorbed by the envelope with resulting reradiation back into the plasma. This would give an apparent emissivity, in the UV, of less than unity . In addition, some of the radiated light must return to the lamp, either from imperfections in coupling to the dye cell, or after being transmitted by the dye cell. Since the plasma is opaque, this light must be reabsorbed and contribute to a higher effective efficiency. This is the first intimation the author is aware of that intensely driven lamps may actually be more efficient than black bodies for achieving power at the required wavelengths. Estimates made by this approach should become more accurate as the lamp is driven harder. Simmering, or prepulsing, allows such harder driving, and also increases the output in this regime. Hence it contributes toward the black body behavior.

Lamp Performance in this Laser

In the laser being reported, each lamp has bore diameter 7 mm and length 2'. Thus A = 134 cm². The excitation is 500 J per pulse (into each of the four lamps associated with a beam), with discharge duration of 2.6 μs fwhm. From Table 4 we estimate τ as 1.24 μs and the power pulse length as 2.2 μs fwhm. Hence the P_R value from eq (1) is 1.7 MW/cm². This gives a temperature estimate of 23,400 K. It is recognized

that the pulses are shorter than those of Pacheco et al, but the observed laser pulse lengths of about 2 μs in the center of the far-field, and a little longer outside, are consistent with the quasi steady state model.

The Coumarin 504 pump band is centered at 440 nm. The effective pump bandwidth is about 50 nm (fwhm of absorption band). At 440 nm, from Figure 6, the spectral intensity from a black body at 23,400 K is 750 kW/cm^2 μm, yielding 38 kW/cm^2 leaving the surface of each flashlamp in the effective bandwidth. Since the representative electrical input power is 1.7 MW/cm^2 of flashlamp bore surface, then effective efficiency of the lamps is 2.2%.

The curves of Figure 6 show the lamps running at a higher temperature than would give optimum efficiency into the pump band. But, running the lamps at the optimal matching temperature would reduce the useful output more than tenfold. The performance of the laser would drop even more dramatically because the lower pumping intensity would reduce the efficiency of the dye.

Coupling to the Dye Cell and Dye

The pump-cavity reflectors have diffuse white surfaces with high reflectance. The lamps and the dye cell are the major absorbers and have equal surface area. We thus assume that 50% of the useful radiated lamp energy is coupled into the dye cell (and the other half back into the lamp). From Table 1, about 57% of the useful light entering the dye cell will be absorbed.

We could at least double the coupling efficiency by eliminating the pyrex water tubes (so that the UV pump band would also be used) and by increasing the dye concentration. But these steps would give poorer beam quality from extra heat distributed non-uniformly in the medium. A better way to increase the efficiency would be spectral enhancement by using one or more intervening dyes Levin and Cherkasov[41], Everett et al[42] and Pacheco et al (ref. 37). The potential can be seen in the curves of Figure 6, showing higher intensity at the wavelengths shorter than those tapped by the Coumarin 504. This would also reduce undesirable heat deposition in the solution. Another promising approach is that of Baranov et al.[43] They demonstrated that the efficiency of a lamp could be increased by depositing an interference dielectric coating on the envelope to reflect light with wavelengths that were not useful in the application. This light was reabsorbed by the plasma. Their application was in the pumping of Nd YAG lasers, but the principle also applies to the shorter wavelengths more often used for dye lasers. P. Lacovara of MIT Lincoln Laboratory has suggested incorporating a spectral transfer agent such as salicylic acid in the reflective coating of the pump cavity. These approaches were not followed because of time constraints.

The Dye and the Overall Efficiency

The modeling from the preceding paper will be used. We do not have the coefficients for Coumarin 504 dye, so will assume it is sufficiently like Rhodamine 6G that we can use the same parameters, as listed in Table 2 of the preceding paper.

We need to estimate the intensities I_P and I_L in the lasing medium. Since 38 kW/cm^2 will leave the lamps within the pump band, and the expected transfer efficiency to the dye cell surface is 50%, then about 19 kW/cm^2 will arrive at the dye surface. From Table 1, about 43% of the pump energy is transmitted when the laser is optimized for energy within 17λ/D. Hence the total at the surface (coming and going) will be 27 kW/cm^2. Based on a simplified 1-dimensional model, with the light entering from two sides, the pump intensities in the middle will be 92% of that, i.e., 25 kW/cm^2. Hence, we will assume a representative I_P = 26 kW/cm^2. The lasing intensity I_L is estimated at between 1 and 2 MW/cm^2 in different parts of the medium. Using these values, and clean dye, the modeling from the preceding paper yields quantum efficiencies of 30% and 40% for the two lasing intensities. The midpoint, 35%, when modified by the photon energy ratio, yields 30% as the representative energy efficiency in the dye.

The individual efficiencies thus obtained are listed in Table 5. The expected overall efficiency is seen to be 0.19% when the dye is clean. But, the observed efficiency is considerably higher, at 0.25%. This is based on total of 2,000 J lamp input yielding about 5 J output.

The reasons for the discrepancy may include lack of accuracy in our measurements (believed to be ± 10%), our using the Rhodamine 6G parameters, the triplet quenching being better than assumed, and reabsorption of enegy making the lamps hotter than estimated. Coumarin 504 is generally considered less efficient than Rhodamine 6G, so use of the 6G parameters is more likely to give a discrepancy in the other direction. The reabsorption is probably a factor, since we have estimated that half the potentially useful light returns to the lamps and must be reabsorbed in the black body model. We already have evidence indicating that the lamps in the earlier experiments by Pacheco et al ran hotter than

our black body modeling would indicate, probably because of reabsorption.

TABLE 5
Modeled Efficiency Balance for the Laser System

Step	Modeled Efficiency
Electric Power to Flashlamp output within pumping band	2.2%
Coupling to pass into dye	50%
Absorbed by dye	57%
Converted by dye into lasing output	30%
Hence expected overall Efficiency	
a) with fresh dye	0.19%
b) when degraded by 10%	0.17%

The discrepancy would be satisfied if the lamps emitted an extra 30% into the pump band, which would require them to be at at 27,000 K (at this level the total radiated power would be increased by a factor of 1.8 from the original 23,400 K modeled temperature). The conclusion is that the lamps are probably running at a higher temperature than 23,400 K but no higher than 27,000 K, with representative pump density I_p of between 26 and 34 kW/cm^2. The average is chosen to obtain the first modeling plot in Figure 7. The curves show that in the applicable lasing intensity regime of 1 to 2 Mw/cm^2, with clean dye, the quantum efficiency is expected to average about 35%, giving energy efficiency of about 30%. They also indicate that, when the dye is clean, higher lasing intensity would increase the efficiency. Thus the feedback is less than optimal for clean dye.

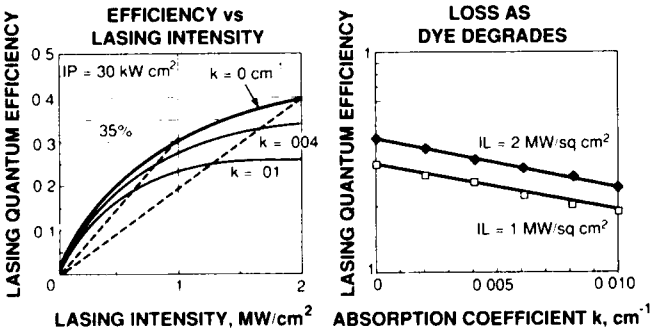


Fig. 7. Dye Efficiency and Degradation Modeling

Dye Degradation

As the lasers operate, the output gradually drops because the value of k increases due to dye degradation. Taking into account the reduction in I_L as k increases, the performance will slide down lines such as the dashed ones in Figure 7. The dashed lines are drawn for initial I_L values of 1 and 2 MW/cm^2, which is the estimated range in the medium. The resulting drop of lasing quantum efficiency is shown in the second plot of Figure 7 for the two starting points. An exponential decay is predicted with a 10% loss in output when k reaches 0.0026, which would result in a 1-m path of dye having its transmission drop to 77% of the clean value. We monitor the degradation by measuring the transmission of a 1-m path, at 550 nm wavelength, and observe the transmission drop to 95% of the initial value when the output has dropped 10%. This suggests that the absorption coefficient of the degradation product is about fivefold higher at the lasing wavelength of 508 nm. Alternatively we may really be monitoring the presence of a product that has a stronger excited level absorption.

Lamp Life Expectation

Lamp life is a strong function of energy applied, and length of the excitation pulse. Goncz[44] reported the following empirical expression for energy that will just explode the lamp. It was derived from testing lamps with pulse time constants varying from 5 μs to 3 ms, bore diameters varying from 4 mm to 28 mm, and various lengths.

$$E_x/L = 90D\sqrt{T} \quad \text{Joules/inch,} \qquad (3)$$

when the bore diameter D is in mm and the duration of the discharge pulse between 1/3 maximum current points is T ms. This can be rearranged to give

$$E_x/A = 3570\sqrt{T} \ \text{J/cm}^2 \qquad (4)$$

where A is the bore surface area in cm^2 and T is the pulse length between 1/3 maximum current points in seconds. Thus the sustainable energy density on the bore of the lamp is proportional to the square root of the pulse duration.

Goncz also reported that life testing with varied lamps gave the results shown in Table 6, relating life to flash energy normalized to the explosion energy. He noted that helical lamps and ones in enclosed cavities should be derated since some of the energy reflects back to the lamp.

The above data has been amplified in EG&G data sheets.[45] These are in general agreement with eq. (3) and Table 6. They provide a guide to ultimate energies and life expectations for a wide range of lamp sizes and pulse lengths, with wall thickness of 1 mm. N_L is the number of pulses before the output drops by 50%. The data covers

the pulse lengths of 10 μs to 10 ms, so does not quite extend to our regime, but we have no other.

TABLE 6
Expected Flashlamp Life (ref. 44)

Flash energy (percent of E_x)	Flashlamp life (number of flashes)
100%	0-10
70%	10-100
50%	100-1000
40%	1000-10,000
30%	10,000-100,000

The minimum and maximum life limits from the EG&G data sheets approximately follow the relation

$$(E_0/E_x)^{-5.5} < N_L < (E_0/E_x)^{-11} . \quad (5)$$

ILC report[46] that N_L can be obtained from the relation

$$N_L = (E_0/E_x)^{-8.5} . \quad (6)$$

This curve runs right down the center of the EG&G life data. ILC does restrict the relation to lamps with bore of less than 15 mm bore (they report an inverse 14th power for larger diameters). There is a slight difference in that ILC define N_L as the number of pulses at which the energy is down to 70% of its initial value. ILC also reports (ref. 46) that the explosion energy is given by

$$E_x/L = 0.577\ f(D)D\sqrt{T'}\ \text{Joules} , \quad (7)$$

where f(D) = 24,600 for D < 8 mm and 17,000 for D ≥ 19 mm, L is arc length in cm, D = bore diam in cm, T' is the pulse duration in seconds by the ILC definition, but they do not say how much spread to expect in the results. When expressed in the same units as eq. (4) this becomes

$$E_x = k'A\sqrt{T'}\ \text{Joules} , \quad (8)$$

where k' = 4518 for D < 8 mm and 3122 for D ≥ 19 mm.

It is difficult to completely correlate the EG&G and ILC data because of some uncertainty in the pulse length definition of the latter. In an ILC technical bulletin (ref. 46, p. 8) it is implied that pulse duration is normally defined as time between current initiation and when it has fallen back to 20% of peak, which would yield 3.0τ in the critically damped case (see Table 4). In an ILC brochure entitled "Linear Flashlamps," the definition between 10% current levels is used, yielding 3.1τ in the critically damped case. EG&G uses the time between the 1/3 levels of current, corresponding to 2.5τ. If eq. (8) has T modified by the ratio 2.5/3.0 to bring it into line with the EG&G definition of pulse duration, it becomes

$$E_x = kA\sqrt{T}\ \text{Joules} , \quad (9)$$

where k = 3760 for D < 8 mm and 2600 for D ≥ 19 mm. This agrees with (eq.) 4 within the precision of the data.

All the above data has been developed for operation of the lamps with no significant return of the emitted radiation. If the pumping cavity allows such return of radiation (which it usually does), then the lamps should be derated (ref. 44).

Apply to Present Laser

The lasers now being reported upon have current pulses of 2.6 μs fwhm, which from Table 4 corresponds to 3.1 μs between 1/3 peak power points. The lamp bore surface area is 134 cm^2. Hence from either eq. (4), the value of E_x is 842 J. At the 500 J input we are thus operating at 59% of the E_x value. From the EG&G data we would expect life to be no more than 300 pulses. In practice we have many thousands of pulses with insignificant loss. When reabsorption of radiation is taken into account, we are driving the lamps even hotter.

Other Evidence on Lamp Life

Earlier experiments by Everett et al (ref. 37) demonstrated life exceeding 300,000 pulses using lamps of length 18" and 7 mm bore diameter, excited with 410 J in current pulses of 3.2 μs fwhm. From Table 3 this yields 3.8 μs between 1/3 points. From eq. (3) we obtain 699 J for Ex. Hence the lamp was running at 59% of the traditional explosion level, and from the EG&G data the expected life would lie between only 30 and 300 pulses to the 50% level, orders of magnitude less than demonstrated.

In the experiments of Pacheco et al (ref 37), discussed earlier, lamps of length 18" and bore diameter 7 mm were excited with as much as 440 J in current pulses of 8 μs fwhm duration, i.e., 9.5 μs between 1/3 points. From eq. (3) we obtain 1105 J for E_x, and hence the lamps were being run at 40% of the traditional explosion level. Thus, from the EG&G data, the expected life would lie between 1,000 and 20,000 pulses. By comparison with the above results, it seems that the lamps were being run quite conservatively.

Discussion of Lamp Life Expectation

These reports, comments by ILC (ref. 46, p. 38), and by Furomoto (ref. 36), indicate that flashlamps in this pulse regime may be driven much harder than would be forecast from extrapolating the manufacturers' published data, provided that simmering or prepulsing is used (ref. 46, p. 26). Unfortunately, life-testing data on flashlamps is very expensive to generate and consequently published reports from which generalized conclusions can be drawn are rare.

It must be emphasized that such good life can only be expected when the lamps are produced under excellent quality control, to the best available design, and then are used under ideal conditions. Premature failure can be caused by contamination of fill, electrodes, or envelope; by incorrect handling, mounting or cooling; or by non-optimum excitation or simmering. If there is anything wrong, the laser tends to die not gracefully! Without more information it is probably safe to assume that, in the regime of interest, a conservative estimate of simmered lamp performance can be obtained from the EG&G and ILC data (extrapolated to shorter pulses if necessary), and then in practice it will probably be safe to drive the lamps up to twice as hard, but the performance would need to be verified in the application.

Since dye lasers have a substantial threshold in their operation, the output energy tends to increase at a much higher rate than the pumping energy. So there is strong incentive to drive the lamps as hard as is compatible with acceptable life. When lamps are driven at these high temperatures, a large portion of the energy is at wavelengths between the cutoff of the silica envelope and the onset of the pump band, for a large range of commonly used dyes. This gives a strong incentive to develop spectral conversion by intermediary dyes (refs. 37 and 42).

It should be noted that the lamp-manufacturers' definitions are in terms of life to the 50% or 70% output level. In general the output of a laser degrades much faster than that from the lamps, particularly if working close to lasing threshold. The difficulty of defining the end of life is discussed by ILC (ref. 46, p 34 and 38).

Conclusion

Results have been reported for a flashlamp pumped dye laser, using Coumarin 504 dye dissolved in aqueous acetamide. The performance has been compared with expectations from modeling of the lamps and the dye solution, and new insight has been developed. Some practical aspects of the design and operation of the laser have been presented.

The author is indebted to a large number of individuals and organizations who contributed to these results. The laser heads were developed and the flashlamps supplied by Candela Corporation. Power supplies were by A.L.E. Systems Inc. Fluid handling systems were engineered by Stone and Webster Inc, and fabricated by the FELS Company. B. Kirstein of SAIC, Inc. consulted on the dye handling aspects and engineered experimental equipment. R. Kaiser of Argos Associates and J. L. Dwyer of Ventec Corp. also contributed useful suggestions on the dye handling. B. G. Zollars, R. E. Hatch, J. L. Swedberg, J. M. Mahan, R. A. Brousseau, and E. D. Ariel helped bring the system to fruition by many hours of dedicated work, and S. Richardson prepared the manuscript.

References

1. P. N. Everett, in Proceedings, International Conference on Lasers '88, F. J. Duarte, Ed. (STS Press, McLean, VA, 1989), pp 404-409..

2. B. G. Zollars, R. H. Rediker, J. L. Swedberg, J. M. Mahan and R. E. Hatch, in Proceedings, International Conference on Lasers '88, F. J. Duarte, Ed. (STS Press, McLean, VA, 1989), pp 425-432.

3. P. Crozet and Y. Meyer, Quantum Electronics, C. R. Acad. Sc., Paris, France, t. 271, Serie B, 718 (Oct. 1970).

4. G. Megie and O. De Witte, Revue de Physique Appliquee, **6**, 341 (1971).

5. O. de Witte, IEEE J. QE-**8**, 530 (1972).

6. P. Dezauzier, A. Eranian and O. de Witte, Appl. Phys. Lett. **22**, 664 (1973).

7. F. P. Schafer, Ed.: "Dye Lasers," 2nd rev. ed., Topics Appl. Phys. 1 (Springer, Berlin, Heidelberg, 1977), pp 4 and 24.

8. H. Kogelnik and T. Li, Appl. Opt. **5**, 1550 (1966).

9. A. E. Siegman, "Lasers" (University Science Books, CA, 1986).

10. J. P. Markiewicz and J. L. Emmett, IEEE J. QE **2**, 707 (1966).

11. J. H. Goncz and P. B. Newell, J. Opt. Soc. Am **56**, 87 (1966).

12. "An Overview of Flashlamps and CW ARC Lamps," ILC Technical Bulletin 3, Sunnyvale, CA, p. 23 (1986).

13. J. L. Emmett, A. L. Schawlow and E. H. Wienberg, J. Appl. Phys. **35**, 2601 (1964).

14. D. E. Perlman, Rev. Sci. Instr. **37**, 340 (1966).

15. D. E. Perlman, Rev. Sci. Instr. **38**, 68 (1967).

16. P. P. Sorokin, J. R. Lankard, V. L. Moruzzi and E. C. Hammond, J. Chem. Phys. **48**, 4726 (1968).

17. J. R. Oliver and F. S. Barnes, IEEE J. QE-**5**, 232 (1969).

18. J. F. Holzrichter and J. L. Emmett, Appl. Opt. **8**, 1459 (1969).

19. H. W. Furumoto and H. L. Ceccon, Appl. Opt. **8**, 1613 (1969).

20. C. M. Ferrar, Rev. Sci. Inst. **40**, 1436 (1969).

21. J. F. Holzrichter and A. L. Schawlow, Ann N.Y. Acad. Sci. **168**, 703 (1970).

22. J. R. Oliver and F. S. Barnes, Proc. IEEE **59**, 638 (1971).

23. E. G. Mavroyannakis, IEEE Trans. Elect. Dev. ED-**18**, 115 (1971).

24. A. J. Gibson, J. Phys. E. Sci. Inst. **5**, 971 (1972).

25. T. F. Ewanizky and R. H. Wright, Jr., Appl. Opt. **12**, 120 (1973).

26. K. Gunther, Opt. Spectrosc. **34**, 620 (1973).

27. T. Morrow and H. T. W. Price, Opt. Commun. **10**, 133 (1973).

28. H. J. Baker and T. A. King, J. Phys. E. **8**, 219 (1975).

29. M. A. Gusinow, J. Appl. Phys. **44**, 4567 (1973).

30. M. A. Gusinow, Appl. Opt. **15**, 190 (1975).

31. M. A. Gusinow, J. Appl. Phys. **46**, 4847 (1975).

32. M. A. Gusinow, IEEE J. QE-**11**, 929 (1975).

33. R. H. Dishington, W. R. Hook and R. P. Hilberg, Appl. Opt. **13**, 2300 (1974).

34. T. Efthymiopoulos and B. K. Garside, Appl. Opt. **16**, 70 (1977).

35. V. E. Gavrilov, O. B. Danilov, A. P. Zhevlakov and S. A. Tul'skil, Sov. J. Opt. Technol. **49**, 403 (1982).

36. H. Furumoto, SPIE **609**, 111 (1986).

37. D. P. Pacheco, H. R. Aldag and P. S. Rostler, in Proceedings, International Conference on Lasers '88, F. J. Duarte, Ed. (STS Press, McLean, VA, 1989), pp 410-419.

38. M. Pivovonsky, M. Nagel, "Tables of Blackbody Radiation Functions," MacMillan, New York (1961).

39. W. L. Wolfe, G. J. Zissis, Eds., *The Infrared Handbook*, IRIA, ERIM (1978).

40. D. P. Pacheco, private communication.

41. M. B. Levin and A. S. Cherkasov, Sov. J. Quantum Electron. **19**(2), 157 (1989).

42. P. N. Everett, H. R. Aldag, J. J. Ehrlich, G. S. Janes, D. E. Klimek, F. M. Landers and D. P. Pacheco, Appl. Opt. **25**, 2142 (1986).

43. S. A. Baranov, I. V. Kolpakavo, M. Yu. Konova, A. A. Mak and O. A. Motovilov, Sov. J. Quantum Electron. **8** (1), 102 (1978).

44. J. H. Goncz, ISA Transactions **5**, 28 (1966).

45. EG&G data sheet F1002D4 (March 1988)

46. "An Overview of Flashlamps and CW ARC Lamps," ILC Technical Bulletin 3, Sunnyvale, CA (1986).

TUNABLE, SIMULTANEOUS MULTI-WAVELENGTH DYE LASER

Wayne E. Davenport, John J. Ehrlich, Travis S. Taylor
U. S. Army Missile Command
Redstone Arsenal, AL 35898-5245

ABSTRACT

A dye laser operating at simultaneous multiple-wavelengths in the 540 to 590 nm region was demonstrated utilizing prisms and a new laser dye chosen for its broad tuning curve (539-620 nm) and high gain.

INTRODUCTION

A dye laser operating at simultaneous multiple-wavelengths in the 540 to 590 nm region was demonstrated utilizing a new laser dye along with prisms as dispersive elements. Typically, a dye laser tends to lase at the peak of its gain curve. For example, Rhodamine-6G (R-6G), when flashlamp pumped, tends to lase near 590 nm which is close to the peak of its gain curve. Previous experiments have utilized intra-cavity holographic gratings as tuning and dispersive elements in order to force the dye laser to operate at wavelengths other than the peak of the gain curve. By utilizing intra-cavity gratings, it has been reported[1,3] that R-6G would lase two simultaneous lines 40 nm apart with output energies of 6 mJ per line. The objective of our experiment was to increase these output energies, and the line separation.

EXPERIMENT

In order to increase the output energies, dispersive elements other than holographic gratings had to be utilized since these gratings are fragile and cannot withstand very high energy densities. Hence, prisms were used as the dispersive elements since they are able to withstand much higher energy densities than gratings. Utilizing a multiple prism, multiple 100% reflector cavity, and R-6G, much higher energies (in the range of 50 mJ) were produced. However, the line separation did not improve. Previous work with a new dye, Disodium salt of 2,6 - disulfonato - 1,3,5,7,8, - pentamethylpyrromethene - BF2 - complex, revealed that this new dye has a broad gain curve.[2] Therefore, it was suspected to be a good candidate for simultaneous multi-line laser operation. With a multiple prism, multiple 100% reflector cavity (see Figure 1) and this new dye, we were able to increase output energies to 50 mJ per line, and also demonstrate line separation of 51 nm.

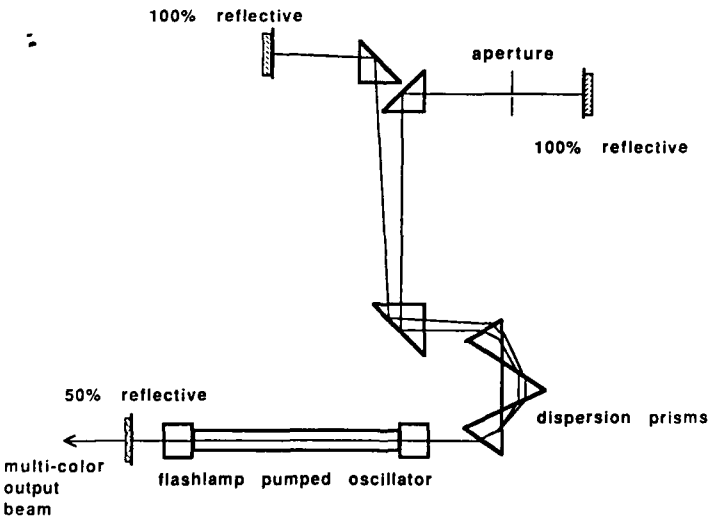


Figure 1. Schematic of Simultaneous Multi-Line Cavity

In order to force the dye laser to lase two lines simultaneously, essentially two different laser cavities must exist. Our optical arrangement utilized three equilateral dispersion prisms (see fig. 1) in order to spread the laser beams of different wavelengths as far apart from each other as possible. In addition, to keep the cavity as short as possible, three turning prisms were utilized to turn the shorter wavelengths to one particular 100% reflector and the longer wavelengths to a different 100% reflector. A two line cavity of this type can be constructed without the turning prisms, however, the separate cavities must be much longer to allow for the physical size of the reflectors and their optical mounts. In fact, two lines were observed simultaneously without the turning prisms. However, the cavities were nearly three meters long, so the energies per line were rather low - only a few millijoules per line. With the turning prisms the cavities were reduced to about one meter and the energy was greatly improved - to about 50 millijoules per line. As it turned out, the new dye that we were using had a much higher gain at the shorter wavelength (green) than it did at the longer wavelength (orange) and would not lase unless the green beam was suppressed in some way. Therefore, an aperture was inserted into the green line's cavity and was reduced in diameter until the orange line lased at an energy near that of the green line. It should also be mentioned that the output energy of each line was lower by slightly more than a factor of two when one 100% reflector and two output couplers were used rather than when only one broadband output coupler and two 100% reflectors were used. The reason being that with two total reflectors, more of the photons make a return pass through the active media of the laser stimulating more molecules, thus causing more output photons to be produced.

RESULTS

Once the multi-line cavity was fully optimized for the Phase-R DL-2100, with a stored energy of 26 Joules, output energies of 50 mJ per line were measured with a line separation of 51 nm. The lines were observed to be 590 nm and 539 nm. The separation between lines could be increased, but the energies began to drop dramatically. The line separation and linewidths were measured via an Tracor-Northern Optical Multi-channel Analyzer (OMA). Figure 2 is an OMA trace of simultaneous multi-wavelength lasing. Note that the two lines are 544.3 nm and 571.4 nm not 590 and 539. This is because at 590 and 539 the lines are separated too far apart to both fit on the OMA display at the same time. However, at 571.4 nm and 544.3 nm both lines will fit on the same screen and this data is representative of the multi-line lasing at other wavelengths. Note that the shorter wavelength line seems to have a broader linewidth than does the longer line. This was not observed to always be true. The linewidth of each line seemed to vary from shot to shot. However, 1.2 nm to 2.5 nm are typically the smallest and largest linewidths that were observed.

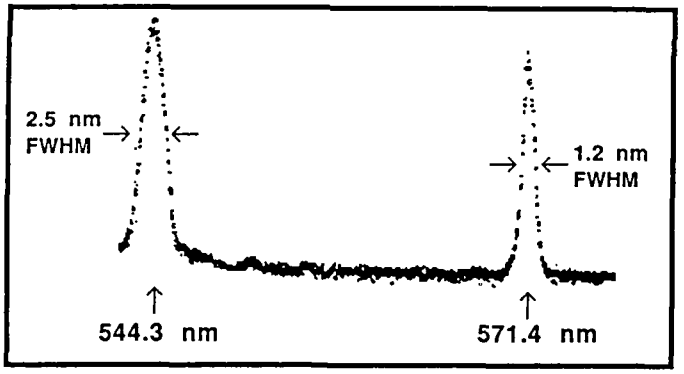


Figure 2. OMA Trace of Simultaneous Multi-Line Lasing

Figure 3 is the temporal profile of the simultaneous 539 nm and 590 nm lines. The total pulsewidth of the combined lines at FWHM is about 350 nsec. The pulse appears as the superposition of the two lines and looks as if it is single mode. Looking at the temporal profiles of the simultaneous multi-line lasing when separated by prisms (see Fig. 4) reveals that the green line begins lasing nearly 175 nsec before the orange; this hints that the gain for the green is higher than the gain for the orange. From the profile it appears that when the orange line begins to lase the green line is robbed of its peak energy. Apparently the two lines are in direct competition with each other in the gain media. Furthermore, the orange line is most definitely parasitic to the green line once it begins to lase. This can be seen by physically blocking the path of the orange line and observing the temporal profile of the green line (see Fig. 5). This measurement revealed that the green line did not drop off abruptly as it did when both lines were lasing. Although FWHM was still about 300 nsec the shape of the pulse was more rounded at the peak. Figure 6 reveals that the temporal profile of the orange pulse changes very little when the green line is blocked.

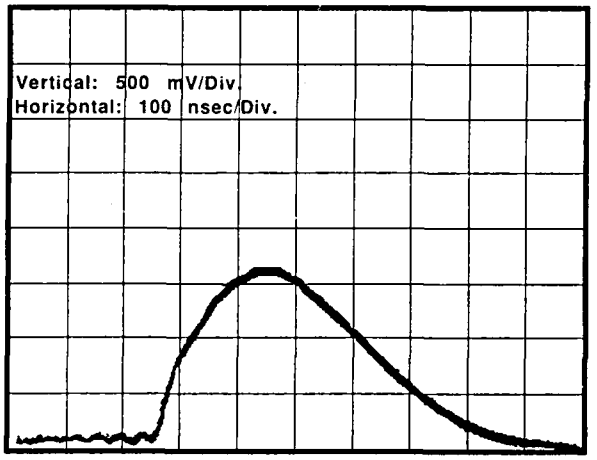


Figure 3. Temporal Profile of Simultaneous 539 nm and 590 nm Lines

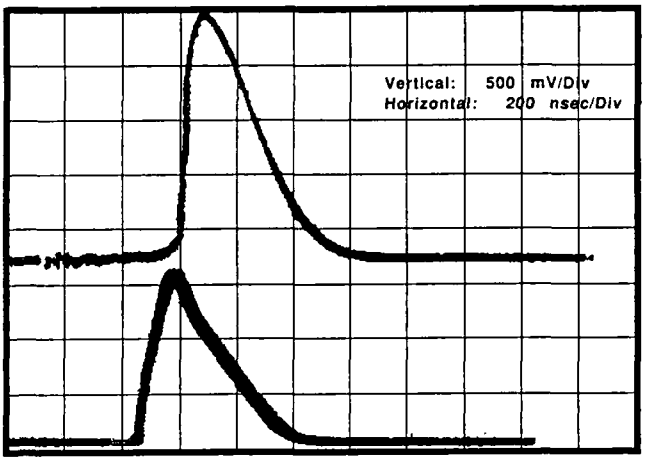


Figure 4. Temporal Profile of Simultaneous Multi-Line Lasing
Upper Trace: 590 nm line 300 nsec FWHM
Lower Trace: 539 nm line 300 nsec FWHM

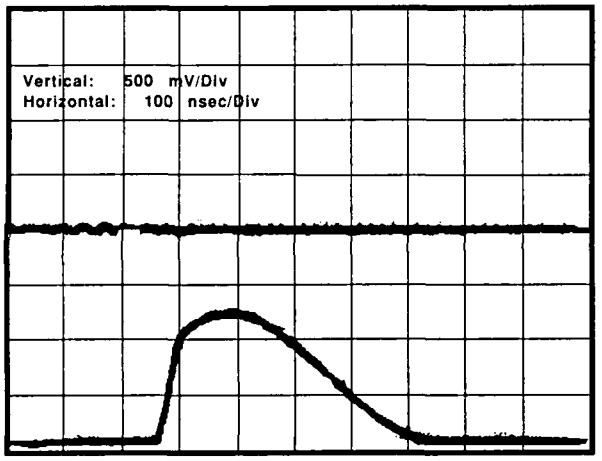


Figure 5. Temporal Profile of 539 nm Line
Upper Trace: 590 line blocked
Lower Trace: 539 line 300 nsec FWHM

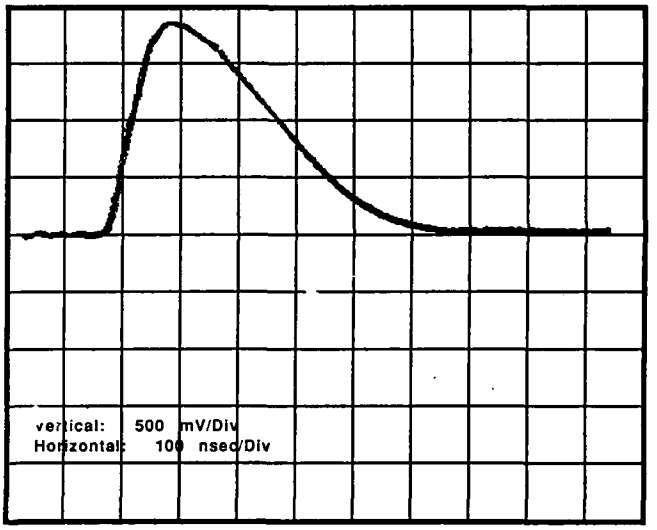


Figure 6. Temporal Profile of 590 nm Line
Upper Trace: 590 line 275 nsec FWHM
Lower Trace: 539 line blocked

Utilizing framegrabber hardware and beam analysis software, the spatial profiles of the multi-line lasing were observed and analyzed. Figure 7 is the spatial profile of the orange beam and as can be seen is the fairly representative of a Gaussian profile. Figure 8 is the spatial profile of the green beam. From this figure it can be seen that the profile of the green beam is not quite as Gaussian as that of the orange beam. However, it does not show the structure typical of multi-mode operation. Also notice that the green beam is smaller in diameter than the orange beam. This is because of the aperture that was placed in the green cavity to reduce the gain of the green, so that the orange would lase. Figure 9 shows the spatial profile of both lines operating simultaneously and is basically a superposition of Figures 7 and 8. Again, this profile represents a fairly Gaussian output beam. This data, when presented in a contour fashion, (Fig. 10) again suggests that the simultaneous multi-wavelength output beam is a superposition of the green and orange beams.

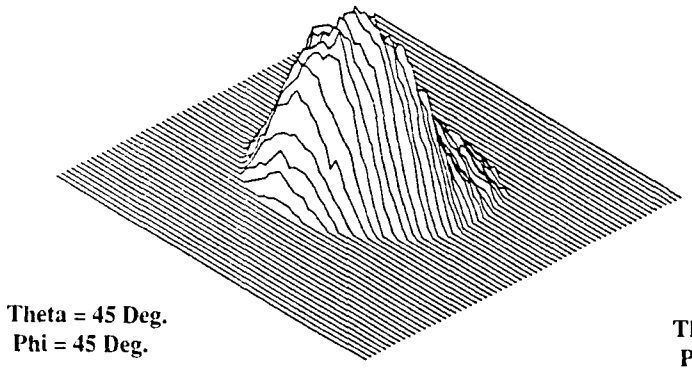


Figure 7. Spatial Profile of Orange Beam

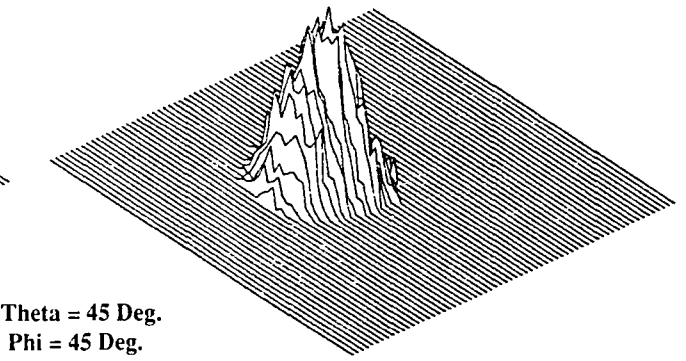


Figure 8. Spatial Profile of Green Beam

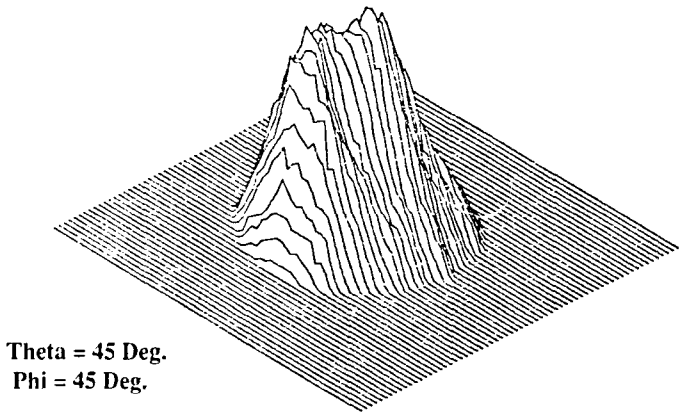


Figure 9. Spatial Profile of Simultaneous Mult-Line Laser Beam

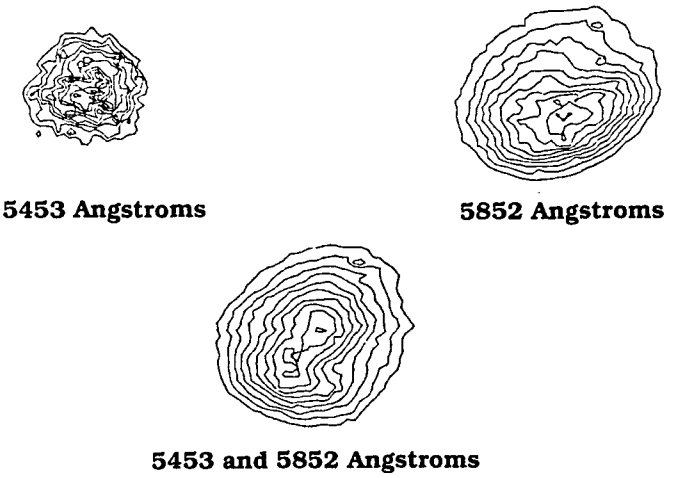


Figure 10. Contours of Green, Orange and of the Simultaneous Multi-Line Beams

Once the simultaneous two-line cavity was completely characterized, an effort was made to force the laser to lase in more than two lines simultaneously. Figure 11 is the schematic of the optical set-up that lased three lines simultaneously. This cavity is basically the same as that for the two-lines with the addition of one more 100% reflector and one more aperture. To add the optics required for the third line, the cavity length or the amount of dispersion had to be increased. The dimensions of our optical bench limited us to an increased cavity length of approximately 3 meters. Obviously, the output energy achieved was not as high as that of the shorter two-line cavity. Like the cavity for the two-line system, the gain of the shorter wavelength lines had to be reduced by apertures so that the longer wavelength line would lase. Each line produce only a few millijoules per pulse and had spatial and temporal profiles similar to that of the two-line system. The three lines observed to lase simultaneously were 539, 567, and 590 nm. It is possible that more than three lines could be made to lase simultaneously, however our research suggests that more intra-cavity dispersion than was achieved by the three dispersion prisms would be required. It might also be possible to increase the gain of the media in some way (a larger laser) and lengthen the cavity more.

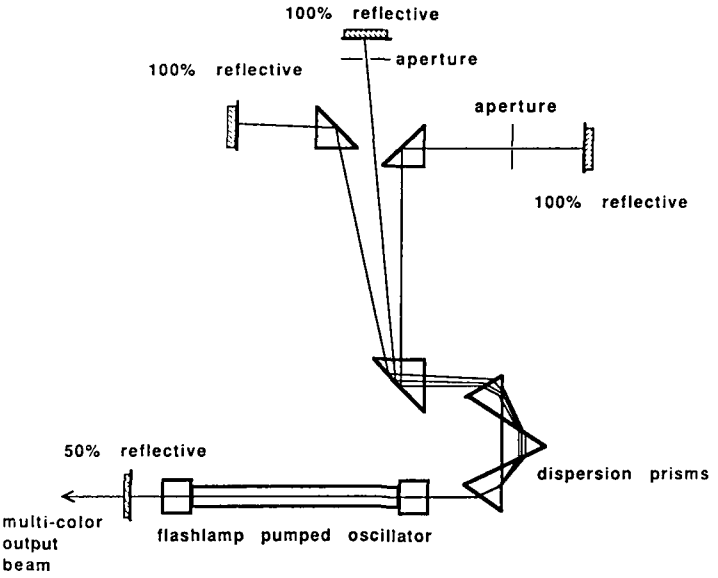


Figure 11. Schematic of Simultaneous Multi-Line Cavity

CONCLUSION

With further advances, it may turn out that simultaneous multi-line lasers will be more convenient for particular applications than are other laser systems. At present, in applications where multi-color radiation is needed, either more than one laser, or more than one dye flow channel is used. For simultaneous multi-wavelength operation only one dye laser is needed; obviously, this is much less expensive than buying multiple lasers for the application. Simultaneous multi-line systems are also favorable over multi-channel systems, because multi-channel flow systems are very complex and also more expensive than the flow system of a single dye laser. Since these multi-line systems lase simultaneously there is no need for complicated synchronization circuitry as is needed to with multiple single laser systems. The only real trouble with these systems is that the multi-line range is limited to the tuning curve of the dye and most dyes are only tunable through small portions of the spectrum. Also, there is the parasitic type competition that goes on between the simultaneous laser lines as is shown in Figures 4-6. Although extreme optical "finesse" is a necessity of these systems, our research suggests that simultaneous multi-wavelength lasers are demonstrate-able and, with some effort, can have high enough energies and large enough separation between laser lines to make them a worthy candidate for applications where multi-color sources are needed.

REFERENCES

1. C. Kittrell and R. A. Bernheim, Opt. Commun. 19, 5 (1976)
2. W. E. Davenport, J. J. Ehrlich, and S. E. Neister, presented at the International Conference on Lasers '89, New Orleans (1989) paper HN.6.
3. L. G. Nair and K. Dasgupta, IEEE J. Quantum Electron. QE-16, 111 (1980)

CHARACTERIZATION OF PYRROMETHENE-BF_2-COMPLEXES AS LASER DYES

Wayne E. Davenport, John J. Ehrlich
U.S. Army Missile Command
Redstone Arsenal, AL 35898-5245

S. Edward Neister
President
Phase-R Corporation
Old Bay Road
New Durham, New Hampshire 03855

Abstract

This paper compares the dye service lifetimes, slope efficiencies, tuning curves, and output energies of two Pyrromethene-BF_2-Complexes to that of Rhodamine 590 Chloride. Service lifetimes were tested with and without the addition of caffeine as a UV filter. Due to the reported low triplet state absorption, the flashlamp pulse-widths were varied from two microseconds to ten microseconds in an effort to detect its presence.

Introduction

A new family of laser dyes, Pyrromethene-BF_2-complexes, were introduced this year by Dr. Joseph Boyer of the University of New Orleans. The two laser dyes tested in our lab were 1,3,5,7,8-Pentamethylpyrromethene-BF_2-complex (JB1), and the Disodium salt of 2,6-disulfonato-1,3,5,7,8-pentamethylpyrromethene-BF_2-complex (JB2). The molecular structures of JB1 and JB2 are shown in Figure 1 and Figure 2 respectively. Their performance as laser dyes in general are discussed elsewhere in these proceedings[1].

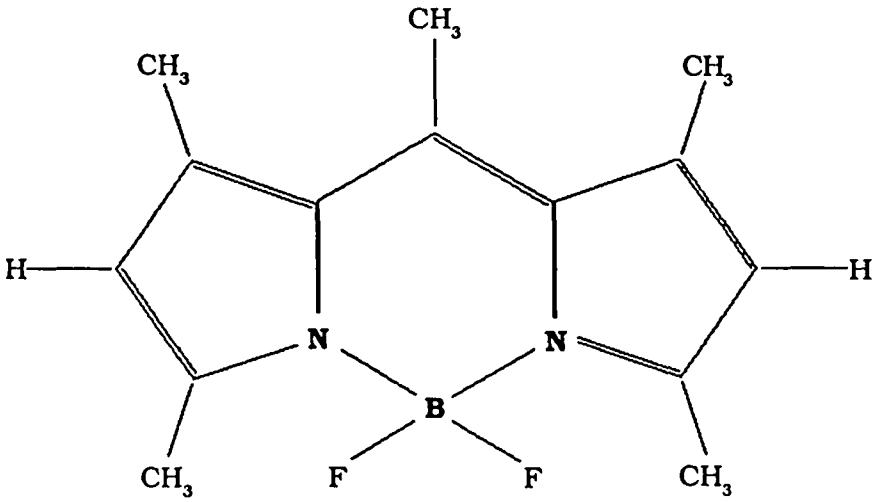


Figure 1. Molecular structure of 1,3,5,7,8-Pentamethylpyrromethene-BF_2-complex.

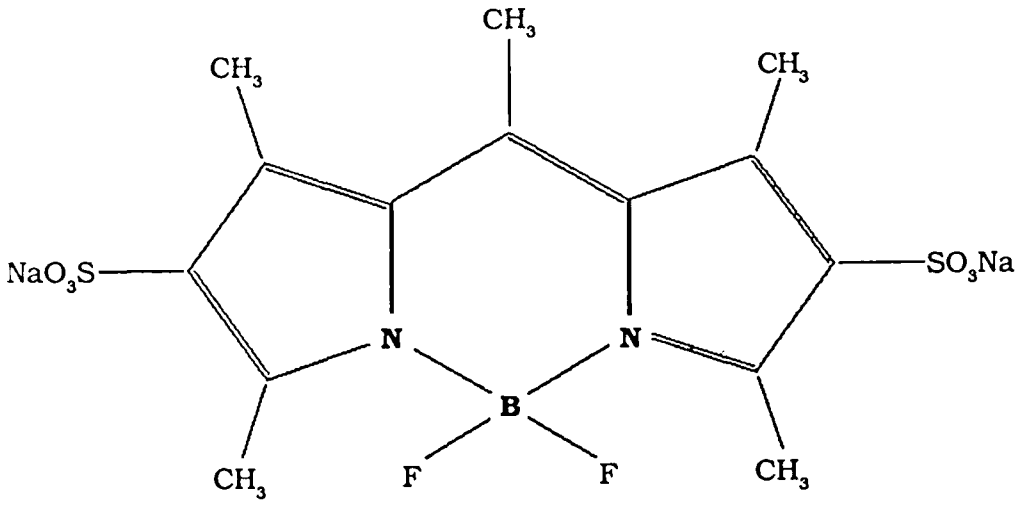


Figure 2. Molecular structure of the Disodium salt of 2,6-disulfonato-1,3,5,7-8 pentamethylpyrromethene-BF_2-complex.

Experimental

Each dye was tested in a Phase-R 1200 coaxial flashlamp pumped dye laser. A triax tube was inserted which allowed UV filtration by adding caffeine to the cooling water. The triax configuration was maintained throughout these experiments whether UV filtration was used or not. This configuration brings the bore size down to approximately 2.5mm in diameter by 193.0mm in length. The input voltage was maintained at a constant 18KV, (which corresponds to an energy of 25.9J in the .16 microfarad capacitor) for all tests, except for the slope efficiency measurements, during which it was varied from 14KV-20KV (15.7J-32J). Concentrations for JB2 and Rhodamine 590 Chloride were optimized by slowly increasing the dye concentration until the output energy reached a maximum. In our test laser these concentrations were 2.5×10^{-4} Molar and 2.0×10^{-4} Molar respectively. Since the availability of JB1 was limited, the optimum concentration of this dye was chosen to be equal to that of JB2, i.e. 2.5×10^{-4} Molar. Burn patterns of the laser output with JB1 did not show the typical annular structure associated with too high a concentration of dye. Since all of the dyes investigated were soluble, and performed well in methanol, it was chosen as the primary solvent. We also tested the dyes in a 50/50 mixture of ethanol/water (EtOH/H_2O). JB1's solubility in the EtOH/H_2O mixture was very poor and therefore we were unable to obtain any results with this solvent/dye combination. The optimum output couplers were 20% reflective for both the Pyrromethenes as well as the Rhodamine. Slightly lower or higher reflectivities may give increased performance of these dyes, however they are not in our current inventory. Due to the large losses associated with the cavity configuration used in the determination of the tuning curves, a 50% reflective broadband output coupler was used in place of the 20% reflector.

Results

First, the fluorescence and absorption spectra for each dye were examined. A Perkin-Elmer model MPF-66 spectrophotometer was used to detect the fluorescence emissions and a Shimadzu UV-VIS model UV-260 was used to scan the absorption bands. From these curves, absorption maxima. fluorescence maxima, stokes shift, and molar extinction coefficients can be calculated. These results are shown in Figures 3-7. Due to the insolubility of JB1 in EtOH/H_2O, we were unable to obtain fluorescence and absorption data for this combination.

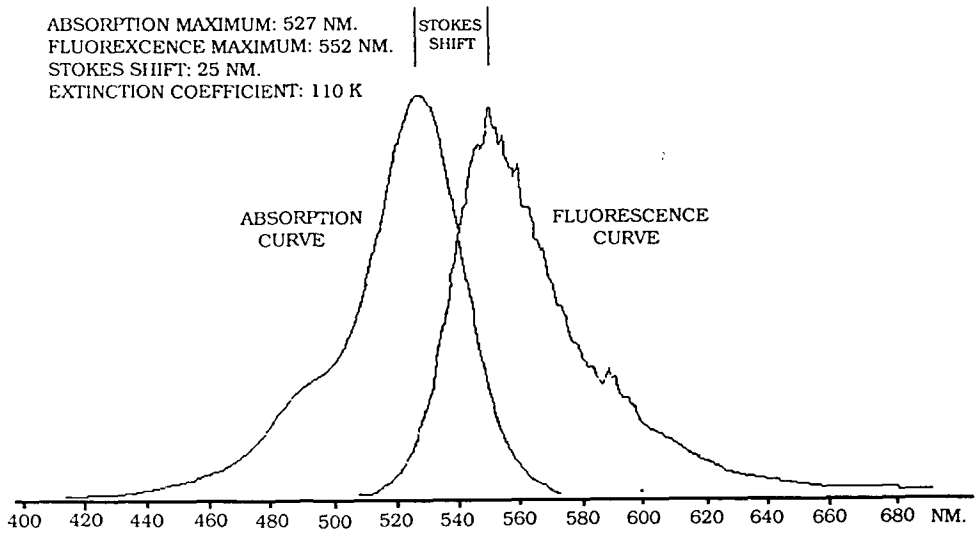


Figure 3. Fluorescence and absorption data of Rh590 Chloride in MeOH.

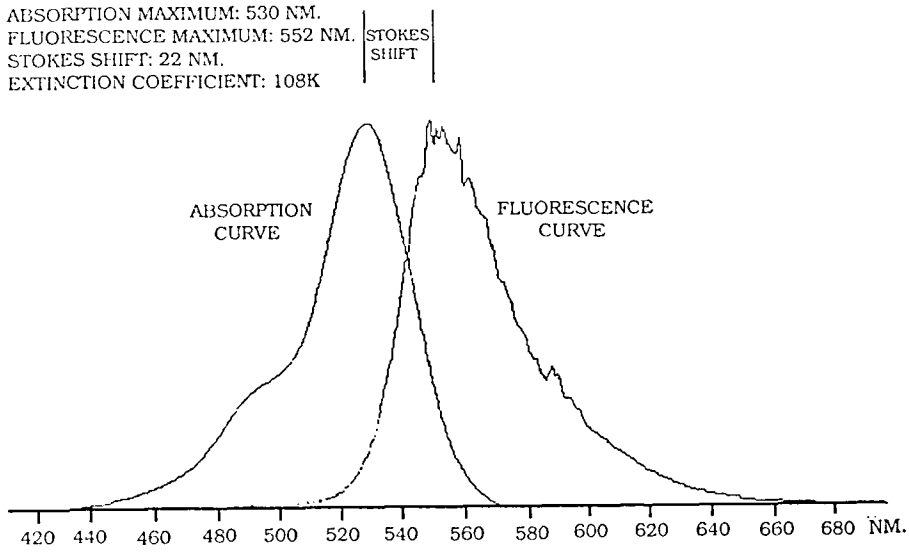


Figure 4. Fluorescence and absorption data of Rh590 Chloride in EtOH/H_2O.

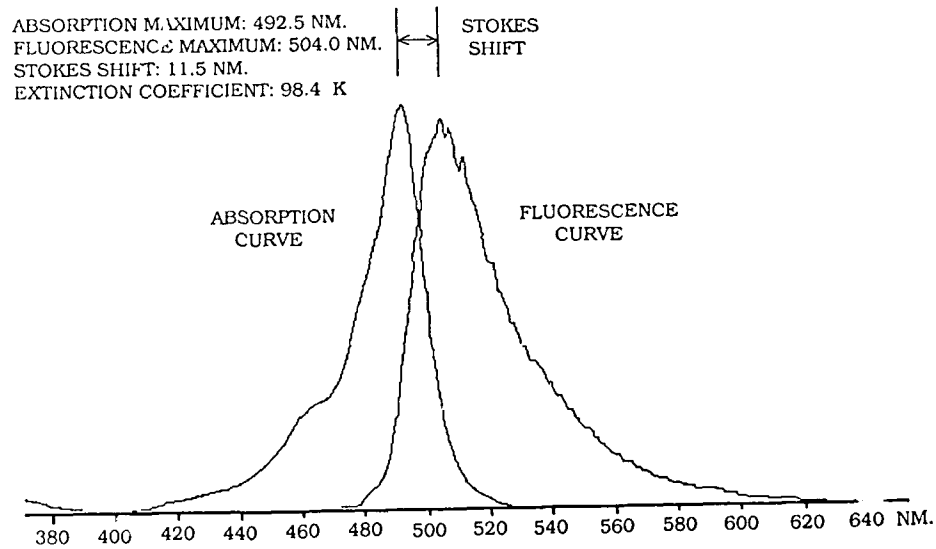


Figure 5. Fluorescence and absorption data of JB1 in MeOH.

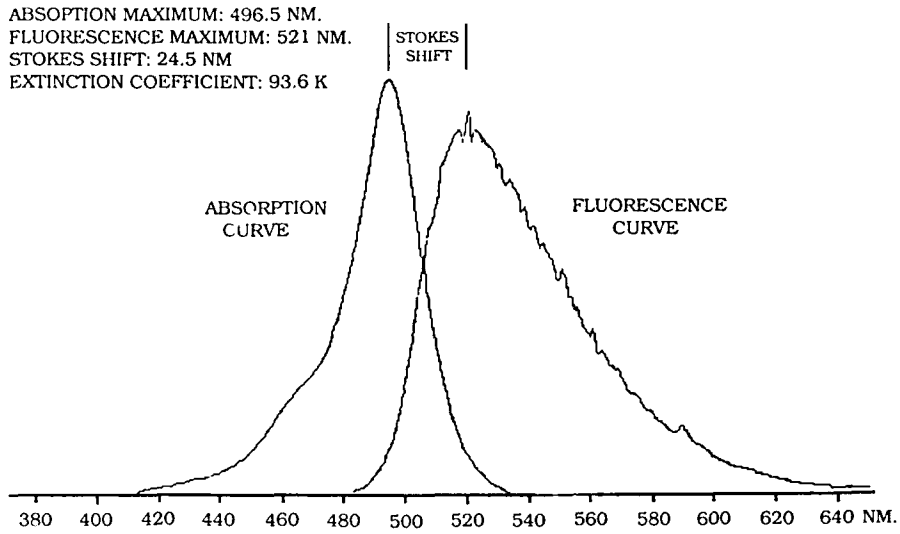


Figure 6. Fluorescence and absorption data of JB2 in MeOH.

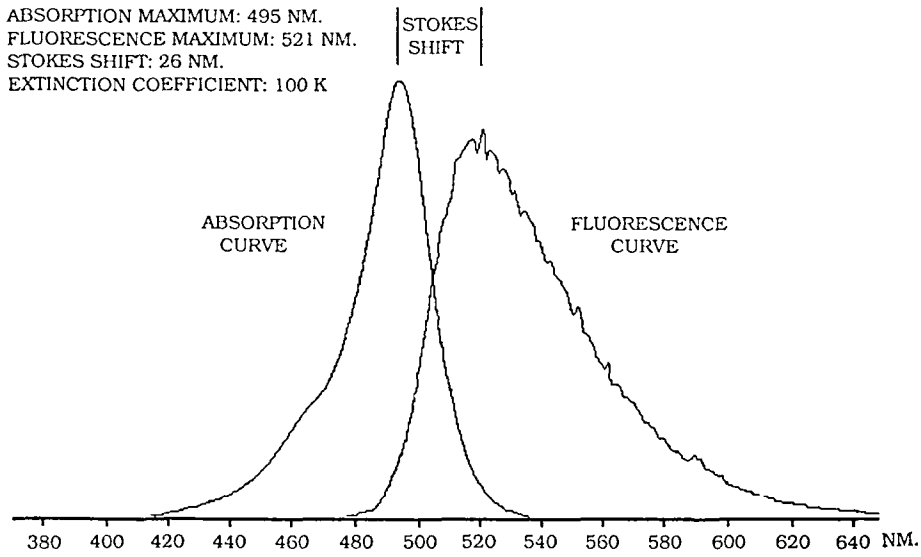


Figure 7. Fluorescence and absorption data of JB2 in EtOH/H_2O.

Lasing tunability of the dyes were determined using the Phase-R 1200 dye laser, multi-prism expander, broadband 50% reflective output coupler, and a 2400 line/mm holographic grating. The experimental setup is shown in Figure 8. Tunability of JB1, JB2, and Rh590 in MeOH are shown in Figures 9-11. The "useful tunability" for each dye is also indicated in these figures, and is defined as the tuning range over which the output energy is at least 50% of the peak energy of the curve.

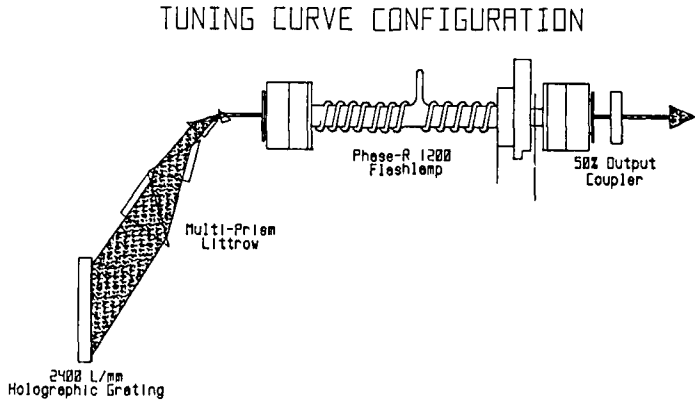


Figure 8. Setup used to determine the lasing tunability of selected dyes.

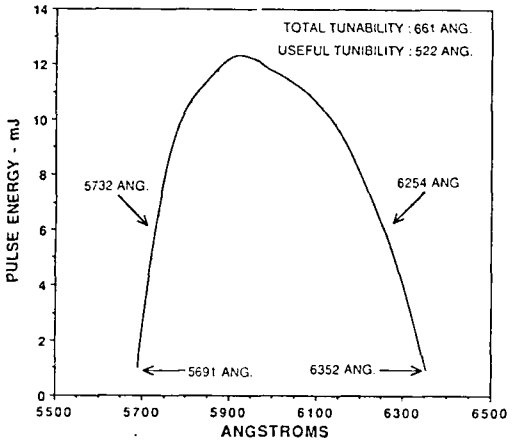


Figure 9. Lasing tunability of Rh590 in MeOH.

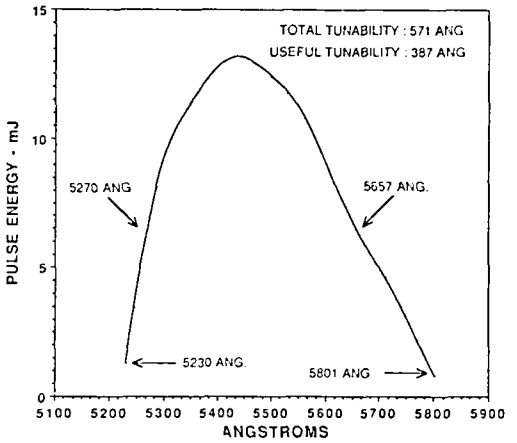


Figure 10. Lasing tunability of JB1 in MeOH.

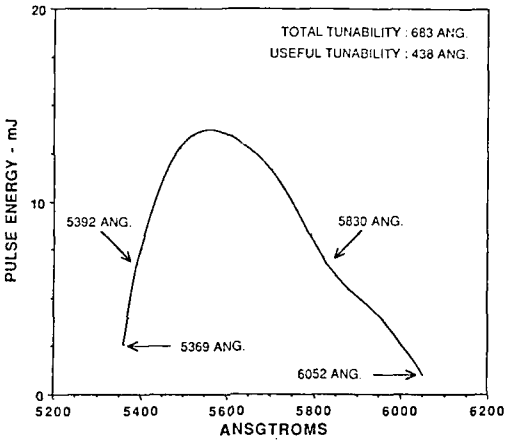


Figure 11. Lasing tunability of JB2 in MeOH.

Slope efficiencies of the selected laser dyes were determined by increasing the input voltage from 14KV (15.7J) to 20KV (32J) while monitoring the corresponding increase in output energy. Both of the pyrromethenes output performed Rh590 chloride in MeOH by approximately 29%. Slope efficiences for JB1, JB2, and Rh590 in MeOH were 0.287%, 0.289%, and 0.228% respectively. The slope efficiencies are graphed in Figure 12.

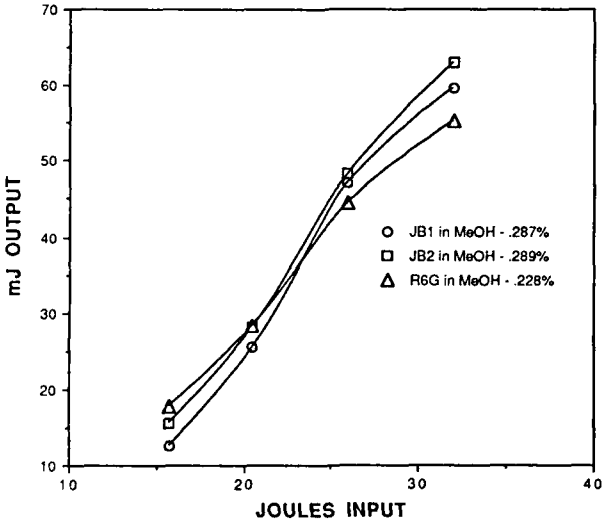


Figure 12. Slope efficiencies of JB1, JB2, and Rh590 in MeOH.

Flashlamp pulsewidths were lengthened as a test for triplet absorption. At a flashlamp pulsewidth of 2 microseconds, lasing efficiency of JB2 increased 28% with UV filtering. All other dyes we have tested to date have shown a decrease in lasing efficiency due to the loss of pumping energy in the UV absorption bands. When the flashlamp pulsewidths were increased to 3.5 and 7.0 microseconds, the lasing efficiency again increased to 33% and 66% respectively. Lasing ceased for JB2 when flashlamp pulsewidths were increased beyond 40 microseconds.

Dye service lifetimes were measured using a computer controlled Phase-R 1200 dye laser. The user can control the dye laser repetition rate, the number of laser pulses between data points, and total number of data points to be taken via the data acquisition software. The computer controls a servo driven beam dump that opens only after a pre-determined number of pulses have occurred. When the beam dump is open, a Scientec model 365 digital energy meter records the energy of one laser pulse and sends that information to the computer for storage. Also recorded during this event is information on flashlamp peak intensity, flashlamp pulse integrated intensity, and capacitor voltage.

Reporting dye service lifetimes in Kilojoules/liter appears to be standard procedure. In this instance, and undoubtedly many others, two different concentrations of laser dyes were used in determining the service lifetimes. Since one solution of dye contains more molecules than the other, it may stand to reason that the service lifetime may be distorted in favor of the higher concentrated solution. Unfortunately, "Kilojoules/liter" contains no information on dye concentration which may help in interpreting the differences in service lifetimes. In an effort to make service lifetimes meaningful, we are factoring out the different concentrations and reporting them in "Megajoules/gram of dye." Service lifetimes of JB2, and Rh590 are shown in Figures 13-15. Again, due to the limited availability of JB1, the service lifetime was unable to be attained.

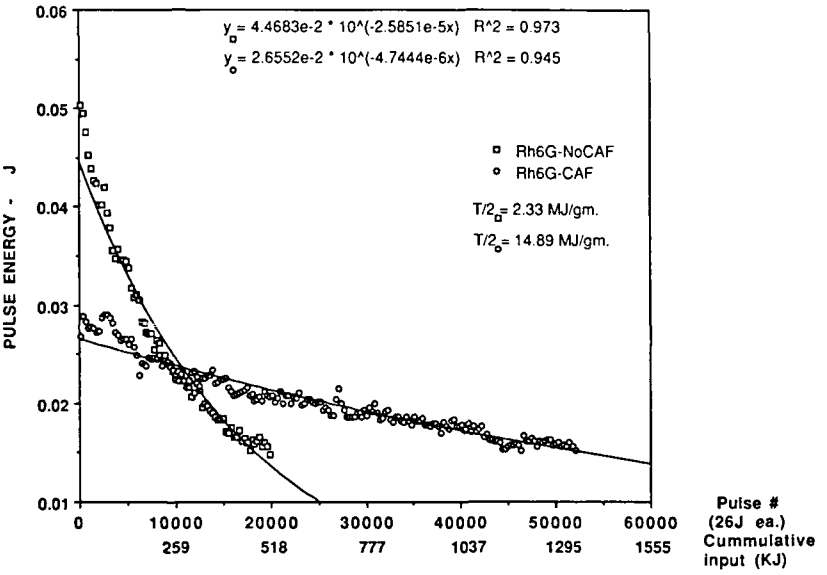


Figure 13. Service lifetimes of Rh590 Chloride in MeOH with and without caffeine added in the cooling water as a UV filter.

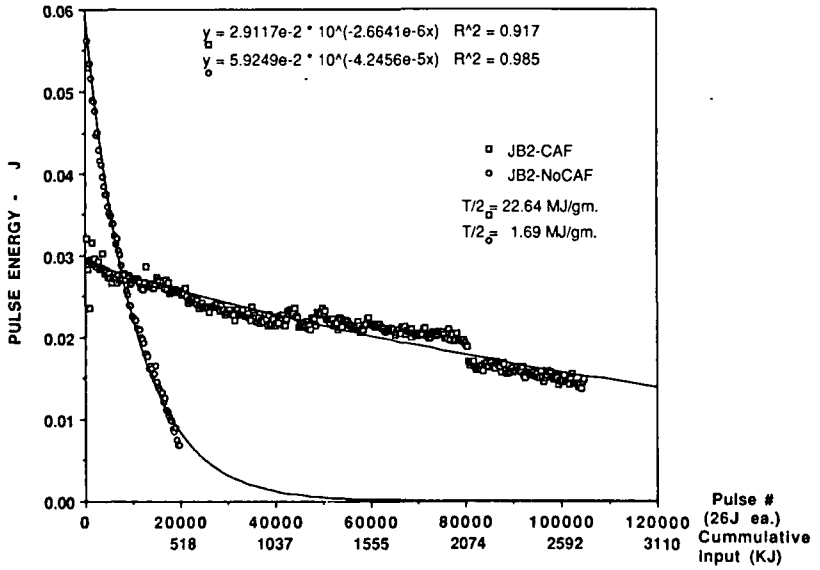


Figure 14. Service lifetimes of JB2 in MeOH with and without caffeine added in the cooling water as a UV filter.

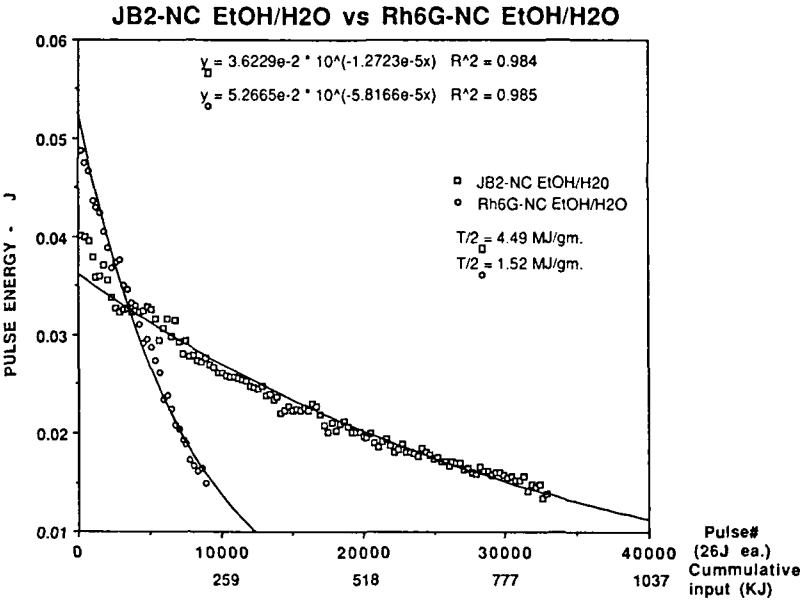


Figure 15. Service lifetimes of Rh590 Chloride and JB2 without UV filtering and EtOH/H_2O as the solvent.

Conclusions

The pyrromethene-BF_2-complexes appear to be an excellent family of laser dyes. The two dyes that we tested in MeOH, JB1, and JB2, were found to be superior to Rh590 chloride in slope efficiency and output energy. Our results indicate JB2 has a 27% shorter service lifetime in MeOH and without UV filtering than Rh590 under the same conditions. However, with UV filtering and MeOH as the solvent, JB2 has a 52% longer service lifetime than Rh590 under the same conditions. Pump energy in the UV appears to be very destructive to JB2 in MeOH. When comparing service lifetimes of JB2 with and without UV filtering, we can see that by filtering the UV we can extend the service lifetime on the order of 1200%. This is quite a dramatic increase when compared to Rh590 which has about a 500% extended service lifetime under the same conditions.

References

1. J. H. Boyer, M. Shah, K. Thangaraj, L. T. Wolford, T. G. Pavolpoulos, J. Hsia, presented at the International Conference on Lasers '89, New Orleans (1989), paper HN.11.

STATE OF THE ART LASER DYE

S. Edward Neister
Vice President/Research & Development
Phase-R Corporation
54 Old Bay Road
New Durham, NH 03855

Abstract

The development and synthesis of the ideal laser dyes has been under development since 1970. The paper begins with what constitutes an ideal laser dye. It then discusses factors affecting laser performance, dye testing criteria, chemical structures of new dyes, and presents a table of some new synthetic dyes. Standardization is called for in forming the name of new dyes and a guideline is presented.

Ideal Laser Dyes

With the beginning of the dye laser, Chemists and Laser Physicists have been working towards having a longer life and "better" lasing dye material. Since 1970 many different synthetic dyes have been developed and we can now classify and project what an ideal laser dye can be.

A laser dye can be characterized by its chemical as well as its lasing properties. From the chemical aspect, there are four basic criteria that must be satisfied if the dye is to be considered ideal or the "best" to date. The florescent quantum efficiency (FQE) must be greater than 0.8. The limit for flashlamp pump dyes is as low as 0.75 and for laser pumped dyes, as low as 0.5. Generally speaking, if the FQE is greater than 0.8 the dye should be very good.

The dye must have a high extinction coefficient greater than 50,000. This criteria is only broken by some of the coumarin's that have extinction coefficients of only 27,000.

The solubility of the dye must be greater than 10^{-3} Molar in non- caustic solvents to be useful. The ideal dye will be one that lases very well in a non-flammable, non-caustic material like water.

There are three basic lasing criteria for the ideal dye. It's D number must be greater than 1. This is a relative comparison of it's lasing output compared to Rhodamine 590. The ideal laser dye has to be more efficient than Rhodamine 590.

The lifetime of the dye should be something in the order of 10^7 joules per liter or 2 times 10^8 joules per gram. This is the excitation energy that is put into a volume of dye from the pumping source.

The dye must also have broad tunability to be useful and be characterized as an ideal lasing dye. Typical tunabilities today are 400 to 500 angstroms. Some new ones are tunable over 1000 angstroms.

Factors Affecting Lasing Performance

There are three factors which affect lasing performance. Solvent and its relationship to the dye is one. Contamination of the solvent-dye solution is another. And finally certain basic laser criteria must be met.

There is a big difference in the polar or non-polarity of the solvents and their effect on lasing performance. Some dyes will perform very well in polar solvents and very poorly in non-polar. Other dyes are just the opposite. The viscosity of the solvent is important and depends on what the pumping source of the dye is.
Viscosity of the lasing solvent and any apparent optical distortion caused by the solvent will effect the lasing performance of the dye.

UV absorption of the solvent or the dye-solvent solution is of paramount importance because it is the UV photons that cause the solvents and the dyes to break up much more quickly than they should. This leads to the photo-degradation byproducts of the solvent and dye. It has been shown that some solvents produce byproducts that act as catalysts in

the process of breaking the dye molecule down. If a long life dye is to be developed, it must be able to work in a solvent that doesn't produce byproducts that can be detrimental to the dye molecules existence.

Contamination of the solvent and the dye is very critical. The manufacturing process of the dye must be clean and pure. If there is cross contamination with other materials during the manufacture of the dye, then its lasing performance can be severely affected. I think that within the next few years the dye manufacturers should start putting lot numbers or batch numbers on the dye materials as a cross check for potential contamination in the manufacturing process.

In the lasing system it is very easy to get cross contamination between one lasing material with one that is previously used in the laser. Impurities in the solvents will also have a big effect on dye lasing efficiency. Acetone and benzene are two notable materials that effect lasing performance in most dyes to the point where many materials will not lase if either are present.

In general, good dye lasing performance depends on three criteria that all must be optimized; dye concentration, the resonator reflectors reflectivity, and the attainment of the proper pumping density over lasing threshold. All three are interrelated. Changing any one will effect the lasing performance. Once the concentration is chosen for a given reflectivity, introducing more losses to the reflective cavity will necessitate a change in concentration or a change in pumping density in order to maintain a given output performance.

Dye Testing Criteria

Because of the large number of dyes being developed, testing procedures and many basic measurements made must become standardized. All dye test should be done on a standardized setup so that comparisons can be made. Different lasers will produce different results. Different flashlamp pumped dye lasers will produce different results. The excitation intensity, how the dye cell is excited by either a flashlamp or laser, the excitation spectrum of the flashlamp, will all have an effect on the performance of every dye.

Standardization is going to have to come to how the test data is presented and recorded. The dye naming procedure must be standardized. There are many dyes that are named for where they lase. But there are also many dye names that have no bearing on where they lase. This does and will cause a lot of confusion. As more dyes become available, it becomes more important that the name bears some resemblance to its lasing performance.

Florescent Quantum Efficiency measurements are very difficult to make with any degree of accuracy. This procedure must be standardized and it was suggested in the question and answer period that the standard FQE measurement criteria be used as outlined by the Journal of Chemistry and Physics.

Triplet state absorption measurements should be made if they can be made meaningful. The triplet-triplet absorption appears to have a dramatic effect on the lasing performance. The method on how data is taken and how it is reported is important if it is going to be meaningful. It must be standardized.

The required data is generally broken down into six areas. The D number or relative efficiency of a new dye to rhodamine 590 is important to get an idea of what its capability is. The lasing wavelength, and it's tunability or band width should be measured at an energy density that is twice what the lasing threshold is for any given laser. The output energy of that dye compared to other dyes in the system should be made at two times and/or three times above lasing threshold and they should be written as $E_{2\times}$ and $E_{3\times}$. The pumping density should be listed at lasing threshold in joules per cubic centimeter. This will give people with different systems the ability to relate how each dye compares to a different lasing system. The lifetime of the dye must be measured and reported as either joules per liter or joules per gram. This is the total energy deposited into the particular volume of dye or into a particular quantity of dye, when the lasing output has been reduced to half of its original value.

It is extremely important to mention whether the dye test included a UV filter between the flashlamp and the dye lasing material or not.

Chemical Structures

As a means of understanding what an ideal laser dye is, I'd like to briefly talk about the chemical structures of the dye and point out what historically has been bad dyes and some general rules that good dyes seem to behave to. Historically the worst laser dye for flashlamp excitation has been the fluorescein disodium salt. This was one of the first

dyes used in the green region. After 25 shots, the dye ceased to lase. Acridine red seems to have a very large triplet absorption and for this reason it is very difficult to get any amount of energy out of the dye when flashlamp excited. Brilliant Sulfoflavin is affected dramatically by the amount of oxygen or nitrogen saturation effect of the solvent.

Characteristically most red dyes have very good performance.Rhodamine B which is Rhodamine 610 has a low output for a red dye. Good laser dyes should not have large detrimental effects when run in air equilibrated solutions. Rhodamine 640 for example has an extremely high output and very long lived for one of the early laser dyes. New UV dyes that are called oligophenylenes are the best UV synthetic dyes made to date. There are some new dyes called oxazoles that have extremely long life. Their lasing efficiency is not as good as say the Rhodamine 590. There are some new pyromethane BF2 complexes which again have extremely long life and have surprisingly good efficiency.

It is only through repeated testing that a chemist can develop models that work for each type of molecule. As an example, we have found that bridged quarterphenyls are much better than unbridged. We have found that rigidized amino group structures prevent collisional deactivation of the dye. We have seen reduced output if all the aromatic rings are not planar. There is an indication that a good dye should have a large change in its first excited state dipole, something in the order of 20 debye. In general, the chemist must follow the ideal dye laser properties and devise his own set of rules of the chemistry makeup through testing.

Table 1 is a list of some of these dyes with some of the data that should be presented if a good comparison of dyes and how they relate to one another is possible. The table lists 6 different dyes of which Rhodamine 640 and Rhodamine 590 are of the older type used since the early 1970's. The oxizols and the BF2 complexes, the oligo's and the coumarin 314T all relatively new synthetic materials. To repeat, an ideal laser dye should have a D number of 1 or better, the energy efficiency at 2 times lasing threshold should be close to 1, and the lifetime of the dye should be high. Notice that the BF2 complex dye has over 1,000,000 joules per liter.

As a result of the past 20 years work in developing new laser dyes, the time has come where the dye name and the way the dye is assigned it's name is standardized. Table 2 is a presentation of a suggestion for standardization. We have at the beginning of the name up to 5 letters which designate the dye type. They can be abbreviations or they can be the full word. I suggest we keep these no longer than 5 and preferably 2 or 3. The wavelength of the expected lasing is the next three numbers and this should be with a particular testing method. Generally speaking a flashlamp system is used, because it is the less expensive laser and there are more flashlamp systems. The letter after the expected wavelength of lasing is a batch designator or compound variation. That designator would become useful if the dye becomes commercially available. The next 4 numbers are strictly for the experimental people in the laboratory to be able to associate their numbers with the eventual commercial name. These numbers could be associated to the various chemistry of the compound for easy designation. Generic names or the letters representing the first letter of the various names of the chemistry can be used, but in any case, it should be a very simple designator so that the whole structure ties together. An example of the old and new nomenclature is shown. The chemistry designator could also be tied to a universal chemistry compound number as listed in the library of congress.

I think that as part of this standardization it is important that we recognize that the dyes that exist today with different names than associated with their lasing wavelength area should not be changed. People understand those names and know those names. However, as the chemists develop new dyes, it is important to formulate and standardize in a method of naming dyes instead of taking the next consecutive number for a new dye that is tested. As dyes become more and more plentiful, it is going to be very difficult for new people entering the field to realize that Coumarin 314 actually lases at around 480nm whereas, Rhodamine 560 lases at about 560nm.

In the next 20 years, it will become very difficult to sort out 500 or so different dye types unless the dye name, and the entire testing and reporting procedure is standardized. New materials will become less likely to be used because the laser user will not simply have the time to try in his laser many different materials which exist at different parts of the spectra.

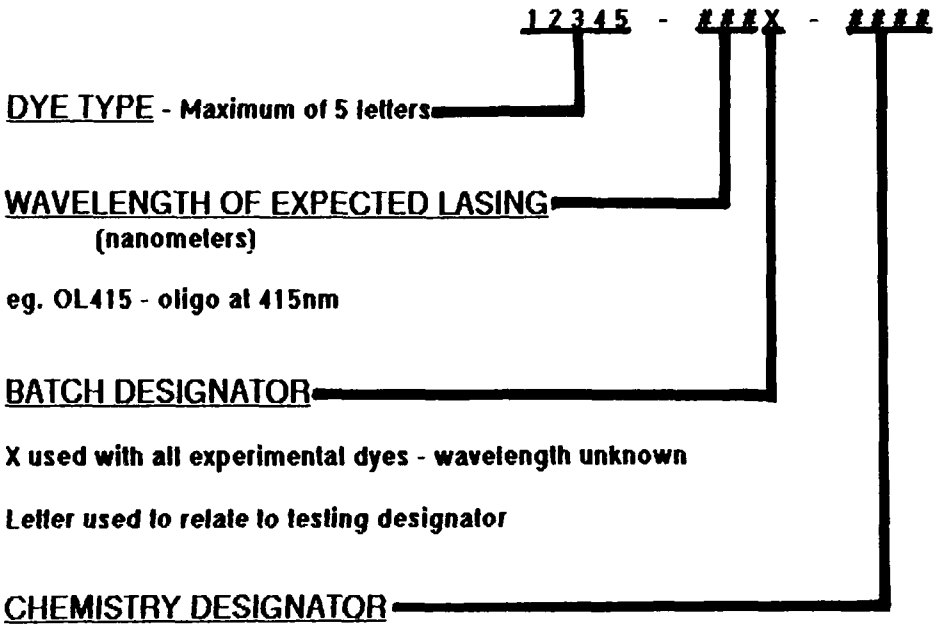
DYE NUMBERS

DYE	TYPE	WAVELENGTH	D*	E2X	E	T 1/2
OX2Z3	OXAZOL	580	0.3	0.3	3 J/CM3	50 KJ/L
JB2	BF2	555	0.8	0.55	3.7	1400
OL415	OLIGO	415	0.4	0.71	4.5	70
COU314T	COUMARIN	500	0.6	0.9	3.0	163
R640	RHODAMINE	640	1.4	1.2	3.0	500
R590	RHODAMINE	590	1.0	1.0	3.0	50

DYE	T 1/2	E	FQE	UV FILTER	SOLVENT	T-T
OX2Z3		50,000	0.92	N	ETOH/H2O	?
JB2	255 MJ/gm	77,000	0.98	Y	MEOH	2,000
OL415		90,000	>.9	N	ETOH	?
COU314T		?	0.9	N	MEOH	?
R640		95,000		N	MEOH	7,400
R590				Y	MEOH	9,000

TABLE: 1

STANDARDIZATION OF DYE NAMES



Used only to correlate different versions of series with chemistry Batch designator letter - is assigned if dye is considered useful

eg.	OLD NOMENCLATURE	NEW NOMENCLATURE
	OX2	0XZOL - 555A - MeMs
	OX2Z3	OXZOL - 555B - SPRZ
	JB1	pyroM - 542A - BF2
	JB2	pyroM - 555B - DSBF2
	JB3	pyroM - 537C - TMBF2
	JB4	pyroM - 568D - DEBF2
	JB5	pyroM - 380X - BF3

As dye becomes useful; common name drops the chemistry designator

OL415
OXZOL 555B
pyroM 555B

TABLE: 2

DEVELOPMENTS IN BRIDGED OLIGOPHENYLENE LASER DYES

Joel M. Kauffman
Associate Professor of Chemistry
Chemistry Department, Philadelphia College of Pharmacy & Science,
43rd St. & Kingsessing Mall, Phila., PA 19104, USA;

Charles J.Kelley
Associate Professor of Chemistry

Alem Ghiorghis
Doctoral Student
Chemistry Department, Massachusetts College of Pharmacy & A.H.S.,
179 Longwood Ave., Boston, MA 02115, USA;

Edward Neister
President
Phase-R Corp., Old Bay Rd., New Durham, NH 03855, USA;

Carl J. Seliskar
Professor of Chemistry
Chemistry Department, University of Cincinnati, OH 45221

Richard N. Steppel
President
Exciton, Inc., P.O. Box 31126, Overlook Station, Dayton, OH 45431, USA

Abstract

We reported at LASERS '87 that dipropylmethylene-bridged quaterphenyls make better laser dyes in all respects than their unbridged counterparts when flashlamp-pumped. We now describe the effects of various molecular substituents in increasing solubility,broadening the range of wavelengths obtainable, and improving dye lifetime, especially with xenon chloride excimer (XeCl*) laser pumping. To improve the solubility of these dyes in polar solvents, 2-methoxyethyl groups were substituted for propyl groups. This new side chain also increased the lifetime by 40% with XeCl* pumping. To obtain dyes with other wavelengths, the terminal hydrogens of oligophenylenes were substituted with ether or tertiary (t-) alkyl groups. Substitution of two methoxy groups on a quaterphenyl gave a 12nm red-shift in the untuned lasing peak to 386nm. Cyclic 6-membered ether auxofluors gave a further 5nm shift to 391nm. Cyclic 5-membered ether groups gave an additional 4nm shift to 395nm, with a 50% increase in lifetime, all when flashlamp-pumped. We found that t-alkyl groups as auxofluors gave excellent lifetimes with either type of pumping. A bridged terphenyl with t-alkyl auxofluors peaking at 358nm had outstanding lifetime when XeCl* laser pumped. A doubly-bridged sexiphenyl with methoxy auxofluors made an outstanding laser dye when flashlamp pumped, peaking at 415nm. A related sexiphenyl was equally good when XeCl* laser pumped, despite the presence of ether auxofluors.

Introduction

While 2-phenylbenzoxazole dissolved in cyclohexane was reported to lase at 330nm with a 20% conversion efficiency when pumped with the 4th harmonic of a Nd-glass laser[1], and a series of benzoxazoles in cyclohexane lased when XeCl* laser pumped[2], and a pair of 2,6-diphenylbenzobisoxazoles in dioxane lased at @390nm with 12-14% conversion efficiency and good lifetime when XeCl* laser pumped[3]; oxazoles in general do not lase well when flashlamp pumped[4]. Oligophenylenes such as terphenyl (14 in Fig.8) and quaterphenyls have been among the most sucessful laser dyes in the ultraviolet region of the spectrum[4,5]. However, their lack of solubility, especially in polar, non-toxic, non-flammable solvents, has severely limited their use.

Attempts to place substituents on the internal ortho positions of the aromatic rings improved the solubility, but reduced both the fluorescence quantum yield (FQE) and the conversion efficiency. Still, with XeCl* laser pumping, this type of dye has given the shortest tunable lasing wavelengths ever reported without frequency doubling[6], and some dyes with exceptional lifetimes[7]. Sulfonation of quaterphenyl produced a dye, "polyphenyl 1", which was soluble only in viscous solvents, and apparently suitable only for low power outputs[8]. Placement of other solubility-promoting groups on the meta and para positions of the outer phenyl rings had little effect on solubility unless the groups were large[9], and even 12-carbon substituents did not provide satisfactory solubility in the desirable laser dye solvents methanol, ethanol, DMA, or DMF[10]. Thus all types of simple substitutions were shown to have their limitations.

In bridged oligophenylenes such as fluorene (Fig.1) the ortho (o) carbon atoms of adjacent benzene rings are connected, holding both rings in a plane, raising FQE and reducing Stokes' loss[11]. Barnett et al.[11] showed that the o,o′ methylene-bridged quaterphenyls 2,2′-bifluorene and 2,7-diphenylfluorene (dye 1 in Fig.2 where R=H) gave superior pulse heights to that of quaterphenyl in liquid scintillation counting, a process related to lasing at least in that the $S_1 \rightarrow S_0$ transition of the fluor or dye occurs mainly by fluorescence. Pavlopoulos and Hammond suggested that methylene-bridged quaterphenyls might prove

to be superior laser dyes[13].

This was partly borne out when Rinke et al.[14] reported very high conversion efficiency (but short lifetime) for 2,2'-bifluorene when pumped with a XeCl* laser. Other bridged quaterphenyls, with oxygen and with ethylene bridges, lased with lower conversion efficiency and greater lifetime. Kauffman et al.[10] found that 2,2'-bifluorene lased with high energy output when flashlamp-pumped, and then focused on dyes such as 1 (Fig.2) in which any benzylic hydrogen atoms on the bridge were replaced with propyl groups to obtain better solubility and lifetime. It was found that these dialkylated carbon bridges were superior to oxygen, nitrogen, or silicon bridges, and also that in quaterphenyls a central single bridge was as effective as two bridges, giving ultraviolet-emitting (@380nm) dyes with greatly improved lifetime (@30 KJ/l) as well as high energy output. Use of ether groups as auxofluors improved all properties, and provided dyes with lasing peaks at 386, 391, and 395nm[15]. The present investigation sought to provide laser dyes which would (1) be soluble in the water-miscible solvents mentioned above, (2) show both high energy output and extended lifetime with either flashlamp or XeCl* pumping, and (3) span a much greater range of wavelengths.

Experimental

The general methods of synthesis of the dyes, sources of solvents, determinations of solubilities and measurement of spectral data including FQEs, and the triaxial flashlamp system (DL-1200, Phase-R, New Durham, NH, USA) have been described[10,15]. The flashlamp data were taken over a period of 5 years. The data in each Figure accurately represent the relative merit of the dyes in that Figure, since each group was tested on the same day, and values for energy output and lifetime of Rhodamine 6G were obtained each time. Under conditions where Rhodamine 6G in ethanol showed a lifetime (to 50% of initial laser pulse energy) of 30KJ/l, the adjusted initial energy outputs and lifetimes for some of the dyes were:

Dye No.	Energy	Lifetime
1	2mJ	30KJ/1
2	2	30
6	<1	30
7	2	30
8	<1	3
10	4	30
11	4	30
12	4	45
13	6	60
18	8	90

The XeCl* system (201 MSC, Lambda Physik, Göttingen, FRG) pumped a dye laser (3002E, Lambda Physik) equipped with high-speed flow cells. Both the oscillator/preamplifier and amplifier dye reservoirs consisted of the small (@100ml) system of Lambda Physik. The procedures used were similar to those of previous workers[5]. The excimer laser output was 130-190 mJ per pulse, and half of the excimer output was used to pump the dye laser. A repetition rate of 3 Hz was used to determine the optimum dye concentration, at which maximum lasing wavelength and conversion efficiency were measured. Photochemical stability ("lifetimes") of the dyes were determined at a repetition rate of 60Hz. The lifetimes are expressed as the total absorbed excimer pump energy required to reduce the dye laser pulse energy to 50% of its initial optimum value. Correction was made for degradation of the excimer laser output when needed.

Results and Discussion

Improved Side Chains

Dye 1 (Fig.2), a hydrocarbon, was compared with Dye 2, which bears 2-methoxyethyl groups instead of propyl groups. This was intended to provide sites for hydrogen bonding with protic solvents such as alcohols. Not much difference in solubility was observed in ethanol. A 66% increase was obtained in methanol, and a 3-fold increase in N,N-dimethylformamide (DMF), a polar, non-toxic, water-miscible solvent which is non-protic.

There was little difference between these dyes when they were flashlamp pumped in a mixture of ethanol and N,N-dimethylacetamide (DMA). DMA was found more stable than DMF with flashlamp pumping.

With XeCl* laser pumping the conversion efficiencies were about the same, but the lifetime of Dye 2 was 27% greater.

The new 2-methoxyethyl side chains were superior to propyl side chains in solubility and lifetime in the fluorophor tested.

Improved Auxofluors

4-Alkoxyterphenyls (Fig.3). Terphenyls with a single ether auxofluor, acyclic in dye 3, cyclic in dyes 4 and 5 had been reported not to lase when flashlamp pumped[15]. In this series both extinction coefficients and quantum yields dropped, unexpectedly,

With XeCl* laser pumping dyes 3 and 4 lased with typical conversion efficiencies (10%) at this wavelength, but short lifetimes. Dye 5 was not tested.

4,4''-Dialkoxyterphenyls (Fig.4). With flashlamp pumping dye 7 with its cyclic auxofluors had the same lasing peak and lifetime as dye 6 but had @5X the energy output and better solubility. Dye 7 lases at the shortest wavelength of any flashlamp-pumpable dye considered "good".

With XeCl* laser pumping these dyes had a typical conversion efficiency, but short lifetimes.

4,4''-Dialkoxyquaterphenyls (Fig.5). With flashlamp pumping these dyes have poor energy output and lifetime. This behavior seems due to poor coupling between the ends of these longer unabridged molecules in the excited state[15].

4,4''''-Dialkoxy-3',2'-dipropylmethylenequaterphenyls (Fig.6). When dyes 8 and 9 were bridged, the corresponding dyes 10 and 11 had much higher energy outputs and good lifetimes when flashlamp pumped. Dye 12 was constructed with 5-membered cyclic ethers bearing the 4 additional propyl groups to aid oxidative stability, lifetime, and solubility[15]. A 50% improvement in lifetime over the other 2 dyes in this group was also obtained. The expected red-shifts were obtained: 386→391→395 nm, thus each dye is individually useful.

With XeCl* laser pumping these dyes had 13-20% conversion efficiency, but moderate lifetimes. This behavior observed with so many dyes bearing ether auxofluors may be related to an absorption of the S_1 state at 308nm[16]. Better auxofluors were sought.

Tertiary-Alkyl Groups on a Bridged Quaterphenyl (Fig.7). The low FQE attributed to the "loose bolt" effect of the tertiary-butyl group on benzene[17] does not seem to apply in larger molecules. Substitution of t-butyl groups for hydrogen in the bisoxazoles mentioned above raised the FQE in both cases[3]. We found no difference in FQE between dyes 2 and the t-butyl version 13; moreover dye 13 had a significantly higher extinction coefficient. When flashlamp pumped dye 13 had 3x the energy output and 2x the lifetime of dye 2. A bathochromic shift in lasing peak of 7nm was observed. Dye 13 was also much more soluble.

With XeCl* laser pumping these dyes had 12-13% conversion efficiency, but dye 13 had a lifetime of 430KJ/1, about 2x that of dye 2. This was the first evidence of the value of t-butyl groups and auxofluors in the terminal para positions of oligophenylenes. The value of t-butyl groups in the terminal meta positions of oligophenylenes in promoting solubility and lifetime has been demonstrated[7].

Extension to Dyes with Other Useful Wavelengths

Tertiary-Alkyl Groups on Terphenyls (Fig.8). In a series of simple terphenyls, including dyes 14 and 15, and quaterphenyls pumped by a XeCl* laser, we observed that dye 15 had the best lifetime, and that it was 2X that of dye 14. Where dye 14 has 3 sets of four equivalent hydrogens, only the terminal hydrogens are present as a pair. It seemed obvious that replacement of the other terminal hydrogen in dye 15 would give a dye with very long lifetime. However, it was recognized that the t-butyl group does not project beyond the "cylinder" of benzene rings, and that the symmetrical di-t-butyl compound would have been too insoluble; so the di-t-amyl compound 16 was prepared instead. It was soluble enough, and doubled the lifetime of dye 15. A bridged version with the better side chains was prepared, dye 17, which showed typical conversion efficiency and a big improvement in solubility.

Doubly-Bridged Sexiphenyls (Fig.9). The "stretched" version of dye 12, the sexiphenyl 18, was found to be an excellent dye when flashlamp pumped in DMA/ethanol, peaking at 415nm with a lifetime of 90KJ/1. Unbridged oligophenylenes up to octiphenyls show a convergence in absorption maxima[18], extinction coefficient, and fluorescence maxima[11] which limits their utility. Dyes 18 and 19 exhibit uniquely high values for all 3 properties.

Dye 19, despite the presence of ether auxofluors, had excellent properties when XeCl* laser pumped in dioxane, including a lifetime of 97KJ/1.

Future develop ment will seek to combine all the desirable substitutions in the same molecule, as in sexiphenyl 20 and octiphenyl 21 (Fig.10).

Acknowledgments

Partial financial support from the Philadelphia College of Pharmacy & Science's Summer Faculty Research Fund is gratefully acknowledged. This work was supported in part (C.J.S.) by State of Ohio Academic Challenge and Research Challenge Grants, and by a Thomas Edison Fund Grant. Stimulating discussion was provided by Theodore G. Pavlopoulos, Aaron N.Fletcher, Jeffrey A. Lindsay, James H. Bentley, Walter Boyko, and others. Technical Assistance was provided by Nancy B. Rainey, Steven J. Imbesi, Paul Erndwein, Lisa Ruby Jeffrey K. Adams, Ali Khalaj, Kimberly Galinsky, Damien T. Cole, Paul A. Fleitz, David Schneider, Dave Landis, and Walter Boyko.

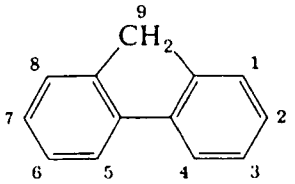
References

1. C. Rullière and J. Joussot-Dubien, Opt. Commun. 24, 38(1978).
2. V.V.Gruzinskii, V.T.Kopylova, P.I.Petrovich, and E.Yu.Shishkina, Sov.J.Quantum Electron. 10,678(1980).
3. H.Güsten, M.Rinke, C.Kao, Y.Zhou, M.Wang, and J.Pan, Opt. Commun. 59,379(1986).
4. H.W.Furumoto and H.L.Ceccon, IEEE J.Quantum Elect. Qe-6, 262(1970).
5. M.Rinke, H.Güsten, and H.J.Ache, J.Phys. Chem. 90, 2661(1986).

6. W.Zapka and U.Brackmann, Appl. Phys. 20, 283(1979).
7. H.Güsten, M.Rinke, and H.O.Wirth, Appl. Phys.B 45, 279(1988).
8. W.Hüffer, R.Schieder, H.Telle, R.Raue, and W.Brinkwirth, Opt. Commun. 33, 85(1980).
9. H.O.Wirth, K.H.Gonner, R.Stück, and W.Kern, Makromol. Chem. 68, 53(1963).
10. J.M.Kauffman, C.J.Kelley, A.Ghiorghis, E.Neister, L.Armstrong, and P.R.Prause, Laser Chem. 7, 343(1987).
11. I.B.Berlman, H.O.Wirth, and O.J.Steingraber, J. Phys. Chem. 75, 318(1971).
12. M.D.Barnett, G.H.Daub, F.N.Hayes, and D.G.Ott, J. Am. Chem. Soc. 81, 4583(1959).
13. T.G.Pavlopoulos and P.R.Hammond, J. Am. Chem. Soc. 96, 6568(1974).
14. M.Rinke, H.Güsten, and H.J.Ache, J. Phys. Chem. 90, 2666(1986).
15. J.M.Kauffman, C.J.Kelley, A.Ghiorghis, E.Neister, and L.Armstrong, Laser Chem. 8, 335(1988).
16. R.S.Taylor and S.Mihailov, Appl. Phys. B.38, 131(1985).
17. N.Turro, Modern Molecular Photochemistry (Benjamin/Cummings, Menlo Park, CA, 1978), pp.113, 172.
18. H.O.Wirth, J.Mol. Cryst. 4, 321(1968).

Fig. 1: A Simple Bridged Oligophenylene

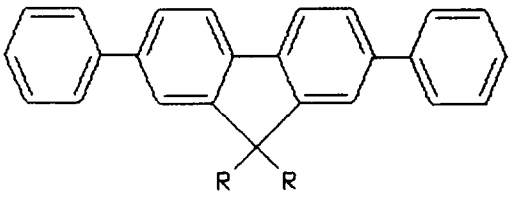
Fluorene is a biphenyl in which two *ortho* positions are linked by a methylene group. It is obtained commercially from coal tar.



fluorene

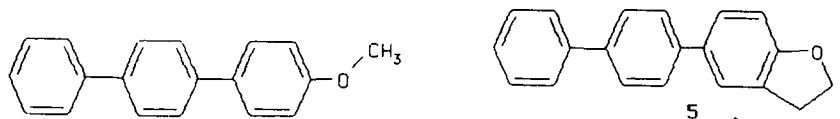
The 2- and 7-positions correspond to the *para* positions of biphenyl and are, accordingly, the most reactive positions in electrophilic aromatic substitution reactions.

Fig 2: Improved Side Chains on Bridged Oligophenylene Laser Dyes



Property of Dye No. →	**1** R = $-CH_2CH_2CH_3$	**2** R = $-CH_2CH_2OCH_3$
Ultraviolet Spectrum	λ_{max} = 322 nm e = 48,000	λ_{max} = 329 nm e = 47,000
Solubility		
DMF	1.1×10^{-2}M	3.3×10^{-2}M
ethanol	1.3×10^{-3}	1.0×10^{-3}
methanol	5.8×10^{-4}	9.6×10^{-4}
Lasing		
Flashlamp P in DMA:ethanol 1:19	374 nm 10 mJ at 20 KeV 30 kJ/l	373 nm 10 mJ at 22 KeV 30 kJ/l
XeCl* P in dioxane	376 nm 12 % eff 13 kJ/l	376 nm 13 % eff 16.5 kJ/l

Fig. 3 Improved Auxofluors: 4-Alkoxyterphenyls

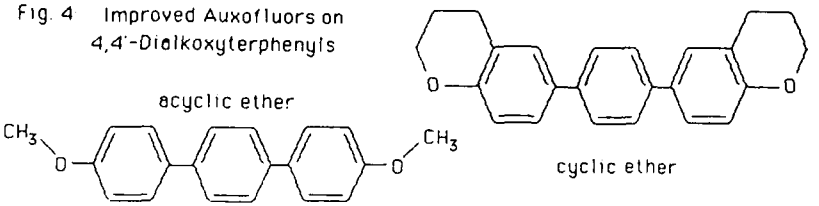


acyclic ether 3 — 5 — cyclic ethers — 4

Property of Dye No →	3	4	5
Ultraviolet λ_{max} in DMF	286 nm, e = 39,000	284 nm, e = 27,000	289 nm, e = 32,000
Fluorescence λ^{em}_{max} in DMF, FQE	360 nm, 70%[a]	372 nm, 44%	372 nm, 51%
Lasing			
Flashlamp P	nil	nil	nil
XeCl* P in dioxane	355 nm, 9% eff, 15 kJ/l	361 nm, 9% eff, 22 kJ/l	—

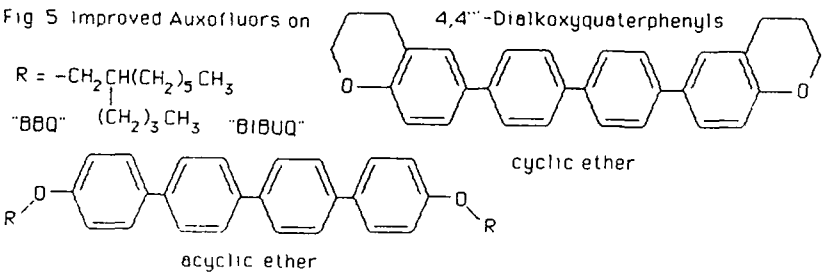
[a] Fluorescence quantum efficiency vs terphenyl at 77%. Reported for dye 3 74%

Fig. 4 Improved Auxofluors on 4,4''-Dialkoxyterphenyls



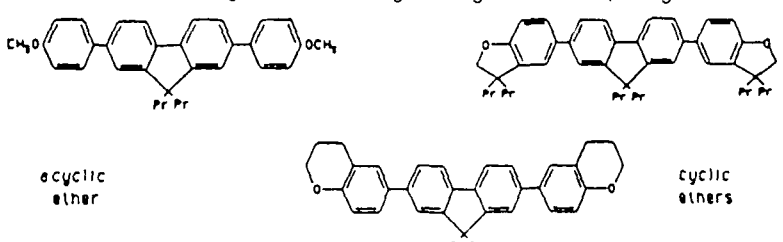
Property of Dye No →	6	7
Ultraviolet λ_{max} in DMF	288 nm, e = 39,000	289 nm, e = 39,000
Lasing		
Flashlamp P in DMA	20 KeV thr, <1 mJ, 371 nm, ≈30 kJ/l	16 KeV thr, 2 mJ, 371 nm, ≈30 kJ/l
XeCl* P in dioxane	360 nm at 10% eff, 8 kJ/l	365 nm at 11% eff, 12.5 kJ/l

Fig. 5 Improved Auxofluors on 4,4'''-Dialkoxyquaterphenyls



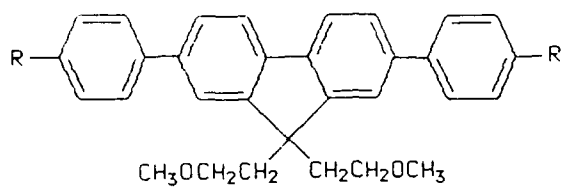
Property of Dye No →	8	9
Ultraviolet λ_{max} in C	305 nm, e = 54,000	310 nm, e = 54,000
Lasing		
Flashlamp P in DMA or DMF	18 KeV thr, ≈0.5 mJ, 389 nm, 3 kJ/l	17 KeV thr, ≈0.5 mJ, 389 nm, —

Fig. 6: Improved Auxofluors on 4,4'''-Dialkoxy-3',2''-dipropylmethylenequaterphenyls



Property of Dye No →	10	11	12
Ultraviolet λ_{max} in DMF	331 nm, e = 55,000	334 nm, e = 52,500	335 nm, e = 52,300
Lasing			
Flashlamp P in 1,4 DMA ethanol	15 KeV thr, 12 mJ, 386 nm, 30 kJ/l	15 KeV thr, 12 mJ, 391 nm, 30 kJ/l	14 KeV thr, 12 mJ, 395 nm, 45 kJ/l

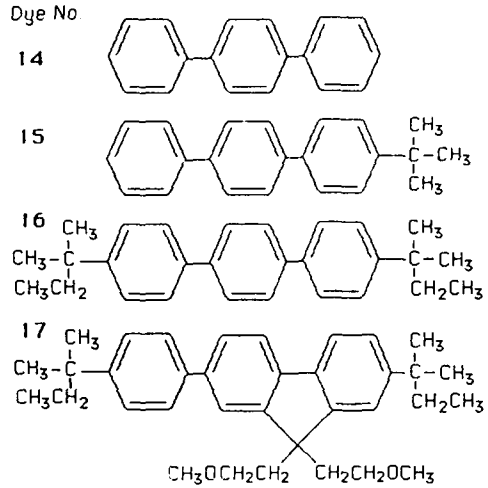
Fig. 7: Improved Auxofluors – *tertiary* -Alkyl Groups on Bridged Quaterphenyl



Property	2 R = –H	13 R = –C(CH3)2–CH3
Ultraviolet Spectrum	λ_{max} = 329 nm ε = 47,000 in DMF	λ_{max} = 332 nm ε = 62,000 in DMA
Lasing Flashlamp P. in DMA or DMA ethanol 1:19	373 nm 2 mJ at 22 KeV 30 kJ/l	380 nm 6 mJ at 20 KeV 60 kJ/l

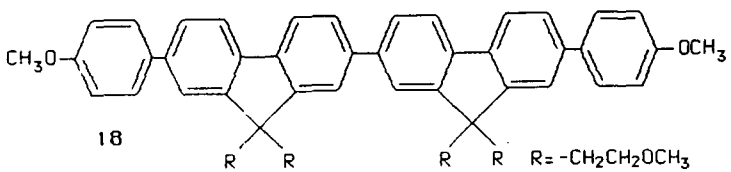
Fig. 8: Improved Auxofluors on *tertiary*-Alkyl Groups on Terphenyls

Dye No.	Lasing: XeCl* P. in dioxane		
14	340 nm; 12% eff.; 130 kJ/l		
15	346	12	240
16	350	11	480
17	358	11	126

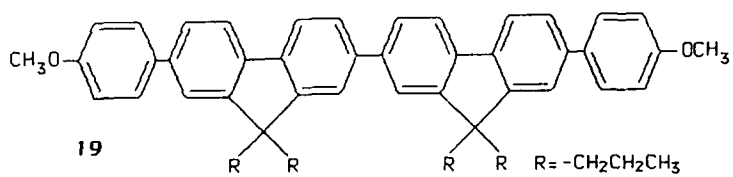


λ_{max} = 318 nm
ε = 34,000 in dioxane
ε = 33,600 at 308 nm

Fig. 9: Doubly-Bridged Sexiphenyls with Auxofluors as Laser Dyes

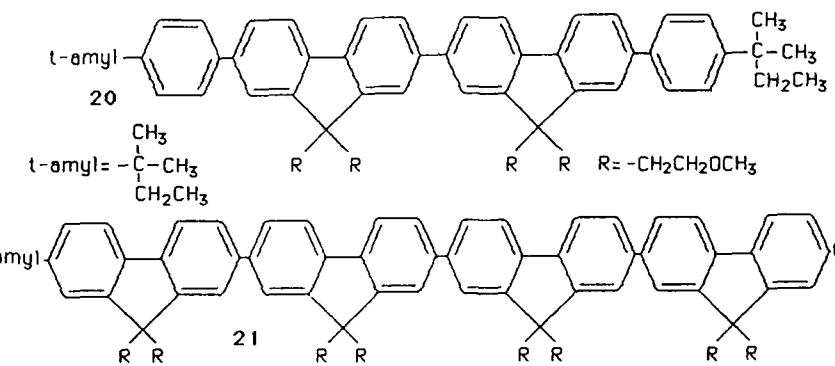


360 nm; ε = 90,000
Lasing, flashlamp p. in DMA/ethanol: 8 mJ at 415 nm; 90 kJ/l



Ultraviolet spectrum in dioxane: λ_{max} = 352 nm; ε = 84,000
Lasing, XeCl* p. in dioxane: 15% eff. at 415 nm; 97 kJ/l

Fig. 10: Other Bridged Sexi- and Octiphenyls Proposed as Laser Dyes



NOVEL ENVIRONMENTS FOR LASER DYES

Guilford Jones, II* and Mohammad A. Rahman
Department of Chemistry, Boston University, Boston, MA 02215

Summary

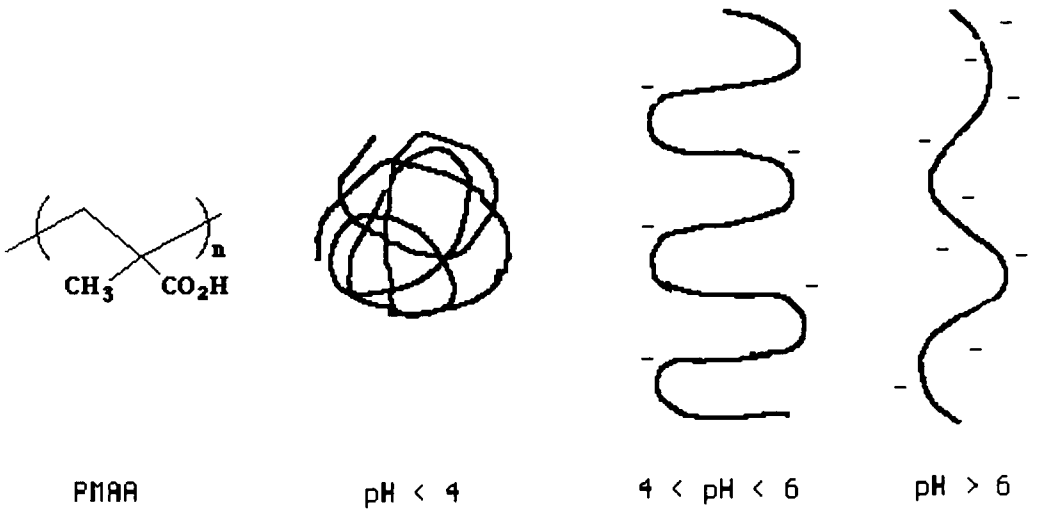
Photophysical properties of coumarin dyes solubilized in aqueous poly(methacrylic acid) (PMAA) solutions were investigated including measurement of absorption and emission maxima, and fluorescence quantum yield and polarization. Significant enhancement of solubility of the dyes in water was observed in the presence of high concentrations of PMAA ($P/D > 500$) at low pH (<5). Subsequent to solubilization in the globular PMAA hypercoil, interesting alterations of the photophysical parameters of the dyes were observed. For some dyes a significant blue-shift of the emission maximum and enhancement of fluorescence quantum yield were observed. Highly polarized fluorescence ($P \sim 0.3$) of the PMAA solubilized dyes indicated the presence of dye molecules in the hydrophobic microdomain of the PMAA hypercoil. The extent of solubilization and alteration of photophysical parameters were found to be dependent on dye structure (e.g., rigidity of the 7-amino-nitrogen, presence of trifluoromethyl group at position 4). The study was also extended to some rhodamine dyes and interesting alterations of photophysical parameters were observed upon binding of dye molecules to globular PMAA. Aggregation of these cationic dyes in moderately concentrated aqueous solution was found to be retarded by addition of the polymer.

Introduction

Solvents play very important roles in the performance of dye lasers.[1,2] Of the different effects of solvents, worth-mentioning are controls on rates of photodegradation, aggregation of the dyes at moderately high concentrations and optical inhomogeneity due to thermally induced gradients of refractive index, developed during pumping. The solvent ethanol has been the medium of choice for most dyes due to the reduced tendency for dye aggregation and good photochemical stability associated with this medium. But for ethanol, optical inhomogeneity remains a persistent problem which is particularly important for the development of high power lasers and for continuous-wave dye lasers. On inspection of the optical properties of solutions, water emerges as an ideal solvent for laser dyes. Specifically, the variation of refractive index of water with temperature is much smaller than that for ethanol.[3] However, many laser dyes, particularly those that do not carry formal charges, have very poor water solubility. Again, for most water-soluble laser dyes, aggregation at moderately high concentration of dye in pure water remains a problem.[1] Such aggregates quench internally the dye fluorescence and prevent effective lasing.

Different approaches have been taken to increase the water solubility of laser dyes and to create suitable aqueous media which can prevent aggregation and provide substantial photostability. An interesting approach that addresses both the strategy of solubilization of dyes in water and, in principle, provides "protective" media of high photostability involves microencapsulation of dye in small colloid-like structures. Detergents or cyclodextrins can provide such microenvironments which can solubilize the relatively water insoluble dyes in the hydrophobic microdomains. Solubilities for coumarin dyes in water are increased over fiftyfold (up to 1×10^{-3} M) by adding cetyltrimethylammonium bromide (CTAB) or sodium dodecyl sulfate (SDS) at 10-40 mM concentration.[4] Addition of 1% by weight (10^{-2}M) β-cyclodextrin to 5×10^{-3}M aqueous solution of rhodamine B retards dimerization of the dye.[5] Moreover such solutions are found to exhibit strong lasing, whereas pure aqueous solutions of similar concentration do not lase.[5]

Polyelectrolytes with ionizable side chain substituents linked to a hydrocarbon backbone provide an opportunity for formation of hydrophobic microdomains in aqueous solution. Depending on the degree of ionization, some polyelectrolytes attain different conformational forms. Poly(methacrylic acid) (PMAA) is known to exist in three distinct conformational forms at different pH regimes[6] (Scheme 1). At pH lower than 4, the unionized PMAA attains a globular form with the methyl groups projecting toward the interior of the globule due to hydrophobic interaction. The carboxylic acid groups project outward and interact with the water phase. The interior of the PMAA globule has been found to be rather non-polar as measured using a pyrene emission probe.[7] Unionized PMAA ($mm \sim 10^5$) aqueous solutions are capable of solubilizing some polycyclic aromatic hydrocarbons such as phenanthrene, anthracene, and pyrene derivatives.[8] On the other hand, at higher pH(>7), the carboxylic groups are almost completely ionized, and the PMAA chain is stretched out due to repulsion of the anionic groups. The hydrocarbon solubilizing power of the polymer is abruptly lost under such condition.[8] In the intermediate pH range of 4 to 6 the partially ionized and partially open polymer attains a coiled conformation.[9]



Scheme 1. Different conformational forms of poly(methacrylic acid) in aqueous solution.

In the present study solubilization and subsequent photophysical behavior of several representative aminocoumarin dyes in water with added low molecular weight poly(methacrylic acid) has been examined. The study has also been extended to several rhodamine dyes in which case deaggregation of the dyes in moderately concentrated solutions ($\sim 10^{-4}$M) and subsequent restoration of luminescent properties result on addition of polymer.

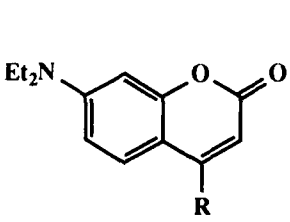
Materials and methods

The structures of the coumarin and rhodamine dyes employed in the present study are shown in Scheme 2. C1 was obtained from Aldrich and purified by recrystallization from methanol/water. C35 was prepared and purified as previously reported.[10] C102, C153, C120 and C339 and all the rhodamine dyes were laser grade dyes obtained from Eastman Kodak and were used as received after checking the purity by thin layer chromatography. Poly(methacrylic acid) used in the present study was synthesized by radical polymerization using potassium persulfate as initiator. The polymer was purified by repeated precipitation from methanolic solution by adding ethyl ether. Molecular weight of the polymer was found to be ~ 15,000 by viscometry.

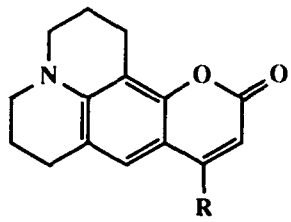
Dyes were employed at a concentration of 10^{-5}M for the measurement of absorption and emmision spectra. For the determination of solubility of the dyes in aqueous polymeric solution, 10^{-3} M stock solution in ethanol was diluted to make 10^{-5} M solution (filtered where necessary), optical density of the resulting solution was measured and compared with that of ethanolic solution. Absorption spectra were recorded on a Perkin-Elmer 552 spectrophotometer. Emission spectra were recorded on a Perkin-Elmer MPF-44A fluorescence spectrophotometer. Fluorescence quantum yields were measured using the cut and weigh method by taking the previously known value of each dye in ethanol as standard.[11,12] Fluorescence polarization values (P) were measured by placing polarizers on the paths of the excitation and emission beams and measuring the emission intensities with different combinations of the plane of the excitation and emission polarizers.

Results and discussion

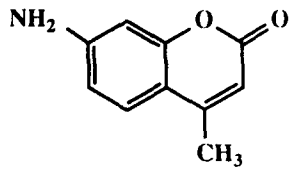
In the case of the study with coumarin dyes the most interesting alterations of the photophysical properties of the dyes are observed upon solubilization in aqueous PMAA, apparently in the globular PMAA supercoil (low pH, ~ 3). The extent of solubilization and alteration of photophysical parameters are found to be dependent on dye structure (e.g., rigidity of the 7-amino-nitrogen, presence of trifluoromethyl group at position 4). Table 1 summarizes different observable parameters of C 153 in water including absorption and emission maxima ($\lambda a, \lambda f$) in presence of PMAA under different conditions of pH and P/D, where P is the concentration of polymer monomer unit and D is dye concentration.



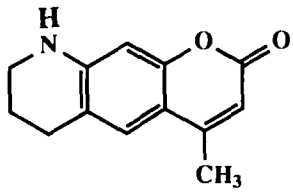
R = CH_3, C1(460)
R = CF_3, C35



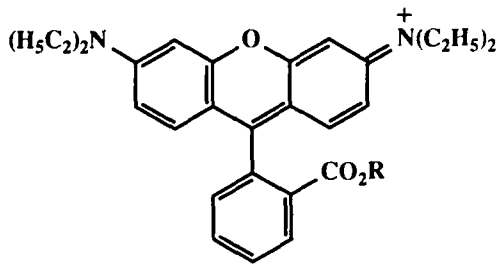
R = CH_3, C102(480)
R = CF_3, C153(540A)



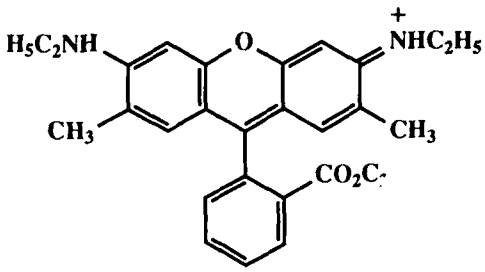
C120(440)



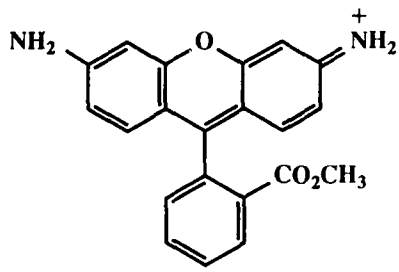
C339



R = H, RB
R = C_2H_5, R3B



R6G



R123

Scheme 2. Structure of coumarin and rhodamine dyes.

C153 is practically insoluble in water. The data in table 1 indicate that water solubility is considerably enhanced by adding PMAA at pH's 3 and 5. Under these conditions the dye is solubilized in the hydrophobic non-polar domain of the polymer. At pH 8 the polymer has no effect on solubilizing the dye in water, because the ionized rod-like polymer does not maintain any hydrophobic pocket. PMAA solubilization highly enhances the fluorescence quantum yield of the dye in water. At P/D higher than 200 Φf is even higher than the value in ethanol. Actually, the enhancement of Φf can be taken as a measure of the extent of the solubilizing effect of PMAA and Figure 1 shows a plot of Φf for C153 vs. P/D under two different conditions, pH 3 and pH 5.

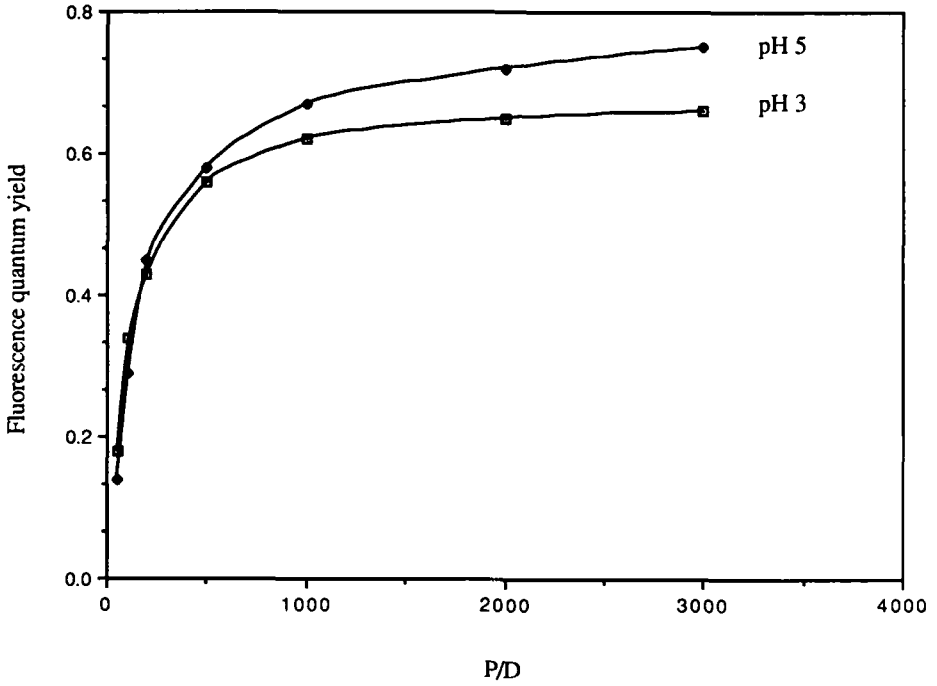


Figure 1. Fluorescence qunatum yield of C153 vs. P/D at pH 3 and pH 5

It is clear from figure 1 that though there remains a tendency for further enhancement of Φf beyond P/D 1000, especially for pH 5; P/D 1000 can be taken to meet the optimum condition for PMAA solubilization of C153.

Another important observation is that PMAA solubilization induces a solvatochromic blue-shift of the emission maximum of the dye. The blue-shift reflects migration of dye molecules from a polar aqueous environment to non-polar hydrophobic domain of the polymer. The extent of this solvatochromic shift is found to be dependent on the pH of the medium. Figure 2 shows the variation of λf of C153 in aqueous PMAA at P/D 1000 with respect to pH of the medium.

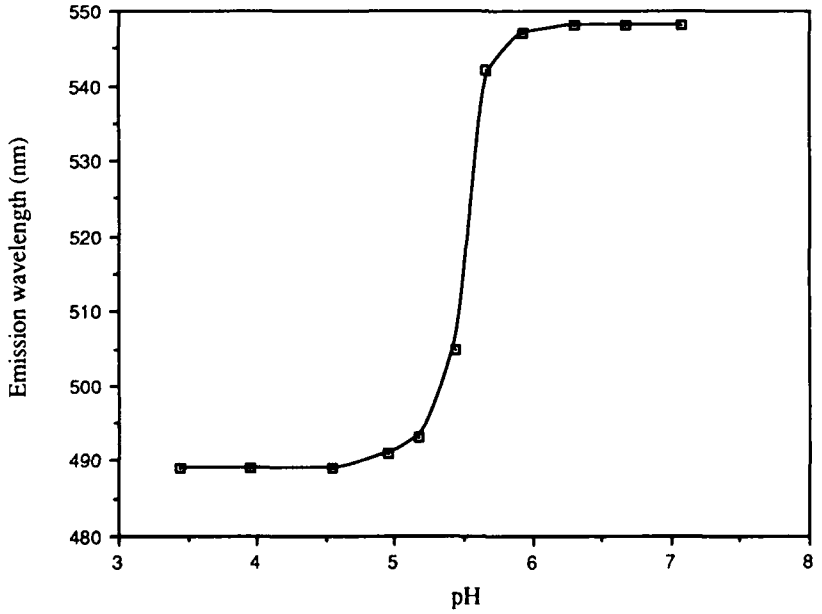


Figure 2. Emission maximum (λf) of C153 in aqueous PMAA at P/D 1000 vs. pH of the medium.

Figure 2 shows a very interesting feature. At high pH (above 6), where the ionized PMAA attains an elongated rod-like conformation, the dye appears to reside in water without experiencing the polymer environment. When the pH of the medium decreases, the polymer starts to attain the coiled conformation entrapping the dye molecule in the hydrophobic non-polar environment. This phenomenon is reflected by the gradual blue-shift of λf. The blue-shift of λf attains a maximum at pH lower than 4 where the dye resides in the globular PMAA practically free from water

Such solvatochromic shift of emission maximum for coumarin dyes is a well documented phenomenon. The position of emission maximum of a solvatochromic coumarin dye in a particular solvent gives a measure of the polarity of the solvent.[13] Figure 3 shows the emission spectra of C153 in different media, e.g.; water, ethanol, aqueous PMAA and cyclohexane.

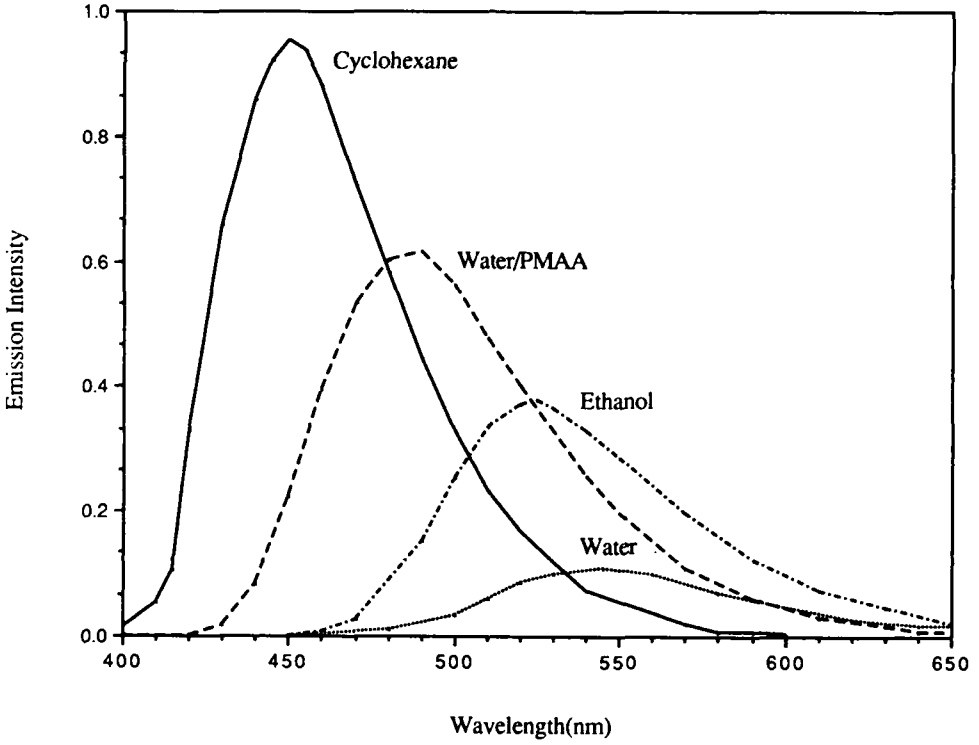


Figure 3. Emission Intensity of C153 in different media.

It is seen from Fig. 3 that the emission maximum of the dye attains a gradual blue-shift with a decrease in polarity of the medium. It also shows that the polarity of PMAA microdomain is very nonpolar (i.e., intermediate between that of ethanol and cyclohexane). Quenching of the dye emission in aqueous solution and enhancement of the emission intensity in the aqueous polymeric solution (P/D 1000, pH 3) is vividly evident in Fig. 3.

The study is extended to other coumarin dyes and the results are presented in Table 2. Throughout the study the concentration of PMAA is kept as P/D 1000 as it has been found to be the optimal.

The data included in table 2 show some quite interesting features.

a) Aqueous PMAA at low pH (< 5) solubilizes C1, C35, C102 and C153 in the hydrophobic polymer domain, which is indicated by the high value of fluorescence polarization, P(~ 0.3). Dyes having H atom substitution on the 7-amino nitrogen, namely, C120 and C339 do not enter the polymer domain due to stronger H-bonding interaction with water.

b) PMAA solubilized dyes, namely, C1, C35, C102 and C153 show a strong solvatochromic blue-shift of fluorescence maxima.

c) For several dyes, namely, coumarin 1, coumarin 35 and coumarin 153 PMAA solubilization highly enhances the fluorescence quantum yield compared to the values in water. For the fluorinated dyes C35 and C153, Φf values in aqueous PMAA globule are several times higher than even the values in ethanol.

The study was extended to a series of rhodamine dyes. In aqueous PMAA solution at high P/D and low pH rhodamine dyes show red-shift of absorption and emission maxima, high values for fluorescence polarization (P) and enhancement of fluorescence quantum yield in some cases. Table 3 summarizes the photophysical parameters for different rhodamine dyes under conditions of binding with PMAA at high P/D and low pH as compared to the behavior in pure water.

The data in the Table 3 indicate that dye molecules are bound to the PMAA globule as monomers. Enhancements of fluorescence quantum yield for PMAA bound rhodamine B and rhodamine 3B are quite significant. High values for fluorescence polarization (P) indicate the presence of dye molecules in the interior of the PMAA globule. Such solubilization of dye molecules in the polymer globule could prevent aggregation of dyes at higher concentration. Figure 4 shows absorption spectra of 10^{-4}M rhodamine 6G in water and in aqueous PMAA at P/D 500 and pH 3.

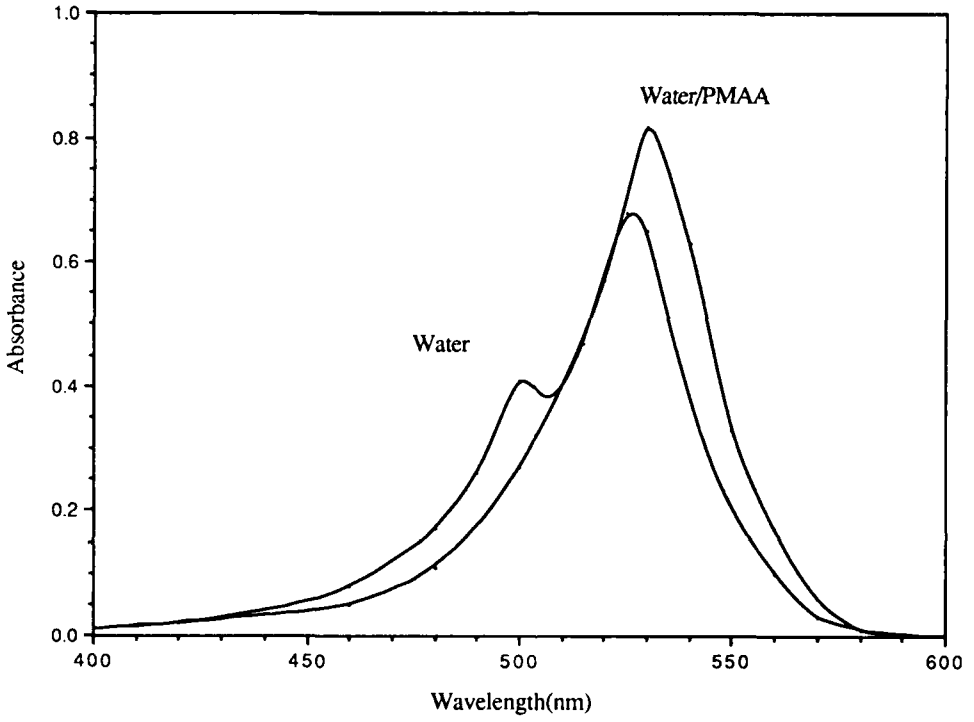


Figure 4. Absorption spectra of 10^{-4}M rhodamine 6G in water and aqueous PMAA at P/D 1000 and pH 3.

It is clear from figure 4 that even at 10^{-4}M concentration rhodamine 6G forms appreciable amounts of aggregate in water and this aggregation can be removed by adding poly(methacrylic acid) to the aqueous solution of the dye and adjusting P/D and pH.

Conclusion

Aqueous poly(methacrylic acid) appears to be an interesting medium for laser dyes of the coumarin and rhodamine families. Enhancement of fluorescence quantum yield for some coumarins in such medium is significant. For rhodamine dyes retardation of dye aggregation in water solution by the addition of the polymer suggest further utility for polyelectrolyte solutions.

Acknowledgements

The authors wish to thank the Office of Naval Research and the Army Research Office for support of this research.

References

1. K. H. Drexhage, in Topics in Applied Physics Vol.1: Dye lasers, F. P. Schaefer, Ed. (Springer-Verlag, New York, 1973), pp. 144-193.

2. G. Jones II, in Dye Laser Principles: With Applications, F. Duarte, Ed. (Academic Press, 1990), pp 287-343.

3. K. H. Drexhage, G. R. Erickson, G. H. Hawks, and G. A. Reynolds, Optics Commun 15, 339 (1975).

4. G. Jones II, W. R. Jackson, S. Kanoktanaporn, and W. R. Bergmark, Photochem. and Photobiol. 42, 477 (1985).

5. Y. Degani, I. Willner, and Y. Haas, Chem. Phys. Lett. 104, 477 (1984).

6. A. Katchalsky, and H. Eisenberg, J. Polym. Sci. 6, 145 (1951).

7. T. Chen, and J. K. Thomas, J. Polym. Sci. Part A-1, 17, 1103 (1979).

8. G. Barone, V. Crescenzi, A. M. Liquori, and F. Quadrifoglio, J. Phys. Chem. 71, 2341 (1967).

9. A. F. Olea, and J. K. Thomas, Macromolecules 22, 1165 (1989).

10. E. J. Schimitschek, J. A. Trias, M. Taylor, and J. E. Celtio, IEEE J. Quantum Electron. QE 9, 781 (1973).

11. G. Jones II, W. R. Jackson, C. Choi, and W. R. Bergmark, J. Phys. Chem. 89, 294 (1985).

12. R. F. Kubin, and A. N. Fletcher, J. Lumin. 27, 455 (1982).

13. G. Jones II, W. R. Jackson, S. Kanoktanaporn, and A. M. Halpern, Optics Comm. 33, 315 (1980).

Table 1. Absorption and emission parameters of C153 in aqueous PMAA at different pH's.

medium	λ_a(nm)	O.D.	λ_f(nm)	Φ_f
Ethanol	422	0.215	525	0.38
Water	435	0.165	548	0.10
		pH=3		
P/D=50	427	0.065	492	0.18
P/D=100	427	0.126	491	0.34
P/D=200	427	0.155	490	0.43
P/D=500	427	0.178	488	0.56
P/D=1000	424	0.191	487	0.62
		pH=5		
P/D=50	426	0.058	492	0.14
P/D=100	426	0.107	491	0.29
P/D=200	426	0.140	490	0.45
P/D=500	426	0.171	489	0.58
P/D=1000	426	0.191	488	0.67
		pH=8		
P/D=50	430	0.045	548	0.09
P/D=100	430	0.077	548	0.10
P/D=200	430	0.091	548	0.11
P/D=500	430	0.102	548	0.09
P/D=1000	430	0.102	548	0.08

Table 2. Absorption and emission parameters of different coumarin dyes.

medium	$\lambda_{a(nm)}$	O.D.	$\lambda_{f(nm)}$	Φ_f	P
			C1		
Ethanol	373	0.248	443	0.73	0.004
Water	385	0.225	467	0.09	0.067
P/D=1000, pH=8	385	0.215	467	0.06	0.069
P/D=1000, pH=5	385	0.215	433	0.43	0.304
P/D=1000, pH=3	385	0.103	432	0.64	0.320
			C35		
Ethanol	402	0.234	500	0.09	0.045
Water	414	0.209	534	0.03	0.116
P/D=1000, pH=8	412	0.183	530	0.03	0.079
p/D=1000, pH=5	405	0.205	470	0.41	0.30
P/D=1000, pH=3	403	0.194	468	0.49	0.31
			C102		
Ethanol	389	0.227	462	0.95	0.011
Water	397	0.183	483	0.96	0.001
P/D=1000, pH=8	393	0.173	483	0.87	0.004
P/D=1000, pH=5	400	0.209	448	1.05	0.30
P/D=1000, pH=3	399	0.208	447	1.08	0.29
			C339		
Ethanol	378	0.298	442	0.85	0.014
Water	374	0.209	457	1.00	0.004
P/D=1000, pH=8	371	0.204	458	0.93	0.014
P/D=1000, pH=5	373	0.215	456	0.85	0.060
P/D=1000, pH=3	372	0.194	456	0.82	0.063

Table 3. Photophysical parameters of rhodamine dyes in water and in aqueous PMAA at P/D 1000 and pH 3.

System	$\lambda_{a(nm)}$	$\lambda_{f(nm)}$	ϕ_f	P
R6G /H_2O	527	554	0.88	0.02
R6G/PMAA/H_2O	537	562	0.85	0.31
R3B/H_2O	559	585	0.25	0.02
R3B/PMAA/H_2O	569	590	0.65	0.30
RB/H_2O	553	579	0.33	0.02
RB/PMAA/H_2O	564	586	0.65	0.28
R123 /H_2O	501	526	0.90	0.02
R123/PMAA/H_2O	510	531	0.89	0.26

EFFECTS OF β-CYCLODEXTRIN ON SELECTED XANTHENE DYES, COUMARINS AND PYRROMETHENE-BF_2 COMPLEXES IN AQUEOUS SOLUTIONS

Ieva R. Politzer,[a*] Kathleen T. Crago,[a] Shunda Garner,[a] Jocelyn Joseph,[a] Joseph H. Boyer,[b] and Mayur Shah[b]

[a]Department of Chemistry, Xavier University, New Orleans, LA 70125
[b]Department of Chemistry, University of New Orleans, New Orleans, LA 70148

Abstract

The effects of β-cyclodextrin were explored on the lasing, fluorescence and UV absorption of selected laser dyes in aqueous solution. Three xanthene dyes; rhodamine 6G, rhodamine B and the disodium salt of fluorescein were used with and without added β-cyclodextrin. β-Cyclodextrin enhances both fluorescence and lasing for all three dyes in concentrated dye solutions. In dilute solutions, β-cyclodextrin can induce either enhancement or quenching of fluorescence and absorption depending on the nature and concentration of dye.

The fluorescence, absorption and lasing of the 1, 3, 5, 7, 8-pentamethylpyrromethene-BF_2 complex and its 2,6-disulfonate disodium salt were examined in aqueous solutions for any effects from added β-cyclodextrin. No major, consistent effects were noted. The fluorescence of the pyrromethene salt was, however, markedly affected by dilution. The coumarin laser dyes 7-hydroxycoumarin, Na and K salts of 7-hydroxy-4-methylcoumarin, coumarin 102 and coumarin 153 were studied with and without β-cyclodextrin. β-Cyclodextrin quenches the absorption of the first two dyes and does not affect coumarin 102. It enhances the fluorescence of 7-hydroxycoumarin and coumarins 102 and 153 but quenches the fluorescence of freshly prepared solutions of the 7-hydroxy-4-methylcoumarin salts. Aging can affect these observations. The lasing of the hydroxycoumarins is not affected by β-cyclodextrin; however, lasing efficiency is very base sensitive.

Introduction

The effects of β-cyclodextrin (B-CD) were examined on the fluorescence, UV absorption and lasing of aqueous solutions of selected laser dyes. Cyclodextrins have received attention in recent years because of their ability to modify fluorescence, phosphorescence, and UV absorption as well as to increase solubility and lasing.[1-5] Examples of the well-established xanthene and coumarin laser dyes were chosen as well as the recently synthesized pyrromethene-BF_2 complexes. Among the factors which were considered were the concentration of the dye as well as the age and pH of the dye solutions.

Experimental

The laser dyes and B-CD were obtained from the following sources and were used as received: Rhodamines B, 6G, the disodium salt of fluorescein and coumarins 102 and 153 (Eastman Kodak Company), 7-hydroxycoumarin, 7-hydroxy-4-methylcoumarin and B-CD (Aldrich Chemical Company), sodium salt of 7-hydroxy-4-methylcoumarin (Sigma Chemical Company), 1, 3, 5, 7, 8-pentamethylpyrromethene-BF_2 complex and its 2,6-disulfonate disodium salt (Dr. J.H. Boyer).

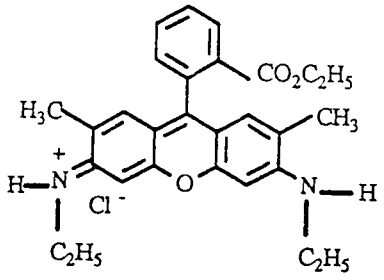
Fluorescence and absorption spectra were recorded on a Kontron SFM 25 spectrofluorometer and a Perkin-Elmer Lambda 3B spectrophotometer, respectively. Spectra were determined at ambient room temperature without thermostatting the cells. A Phase-R Corporation DL1100 flash-lamp-pumped dye laser was used for lasing determinations.

Aqueous solutions of the laser dyes were prepared in deionized water as follows. Initially, a stock solution was prepared of each dye. All subsequent dilutions were made from these stock solutions. For studies with B-CD, an aliquot of each solution at the desired molarity was removed and dry B-CD was added to make the aliquot 10^{-2}M in B-CD. This procedure ensured that the concentration of the analyte remained constant both in the presence and absence of B-CD.

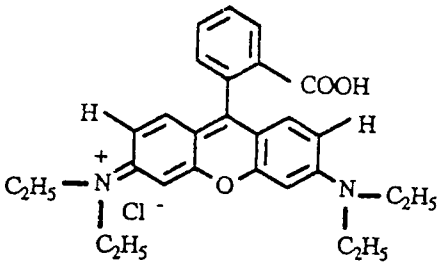
Results and Discussion

Xanthene dyes in aqueous solutions

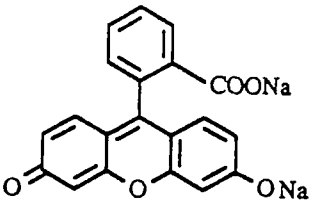
We examined the laser dyes rhodamine 6G and B and the disodium salt of fluorescein in aqueous solutions in the presence and absence of B-CD.[6] The structure and dimensions of B-CD as well as the structures of these dyes are shown in Figure 1.



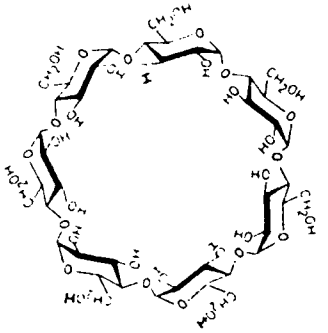
Rhodamine 6G



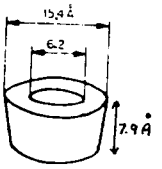
Rhodamine B



Fluorescein disodium salt



β-Cyclodextrin



Molecular dimensions of β-cyclodextrin

Figure 1. Structures of rhodamine 6G, rhodamine B, fluorescein disodium salt, β-cyclodextrin and the dimensions of β-cyclodextrin.

The effects of dilution and B-CD on the fluorescence of these xanthene dyes are summarized in Table 1. There is a blue shift in the fluorescence emission upon dilution of the dyes. In concentrated (10^{-3}M) solutions, addition of B-CD induces fluorescence enhancement. In more dilute solutions (10^{-4} to 10^{-8}M), however, variable B-CD effects are observed.

TABLE 1

EFFECT OF β-CYCLODEXTRIN (10^{-2}M) ON THE FLUORESCENCE EMISSION OF RHODAMINE 6G, THE DISODIUM SALT OF FLUORESCEIN AND RHODAMINE B IN AQUEOUS SOLUTIONS

Dye conc. (M)	RHODAMINE B		RHODAMINE 6G		FLUORESCEIN DISODIUM SALT	
	λem (nm) (λex =500 nm)	effect of B-CD	λem (nm) (λex =475 nm)	effect of B-CD	λem (nm) (λex =450 nm)	effect of B-CD
10^{-3}	613-624	enhance	593-604	enhance	535	enhance
10^{-4}	587	quench	566-568	enhance	520	enhance
10^{-5}	580	quench	553	quench	506	quench
10^{-6}	574	quench	548	quench	503	quench
10^{-7}	575	quench	547	enhance	504	quench
10^{-8}	570	quench	547	enhance	500	quench

The addition of B-CD results in a strong quench of the UV absorption of the disodium salt of fluorescein, Table 2. In contrast, B-CD induces an absorption enhancement and a slight red shift for rhodamine 6G. Variable effects from B-CD are observed for rhodamine B, depending upon the dye concentration.

TABLE 2

EFFECTS OF B-CYCLODEXTRIN (10^{-2}M) ON THE UV ABSORPTION OF RHODAMINE 6G, RHODAMINE B AND THE DISODIUM SALT OF FLUORESCEIN IN AQUEOUS SOLUTIONS.

DYE:	RHODAMINE 6G		RHODAMINE B		FLUORESCEIN DISODIUM SALT	
CONC. (M)	λmax nm	effect of B-CD	λmax nm	effect of B-CD	λmax nm	effect of B-CD
10^{-3}					487	strong quench
10^{-4}	520	enhance shift to 527 nm	552	no effect	435,475	strong quench shift to 450 nm
10^{-5}	525	enhance shift to 530 nm	557	quench shift to 553 nm	435,475	strong quench shift to 450 nm
10^{-6}	525	enhance shift to 530 nm	557	quench shift to 553 nm	480 sh 460	strong quench
10^{-7}	520	enhance shift to 526 nm	557	enhance		

Rather dramatic effects of B-CD on lasing are found with rhodamine B. Lasing in aqueous solutions of this compound occurs only in the presence of B-CD. B-CD greatly enhances the lasing of rhodamine 6G but only slightly enhances the lasing of the disodium salt of fluorescein. These results are summarized in Table 3.

TABLE 3

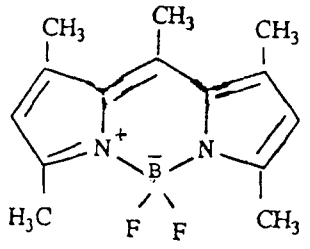
THE LASING OF 10^{-3}M AQUEOUS SOLUTIONS OF RHODAMINE B, RHODAMINE 6G AND THE DISODIUM SALT OF FLUORESCEIN IN THE PRESENCE AND ABSENCE OF 10^{-2}M β-CYCLODEXTRIN

DYE SOLUTION	RHODAMINE B lasing (kV)		RHODAMINE 6G lasing (kV)		FLUORESCEIN DISODIUM SALT lasing (kV)	
	THRESHOLD	INTENSE	THRESHOLD	INTENSE	THRESHOLD	INTENSE
WITHOUT B-CD	no lasing		15	18	12	14
WITH B-CD	11	14	8	12	11	13

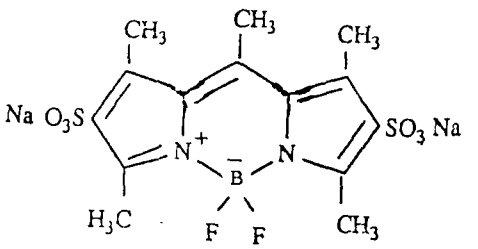
We suggest that dispersion of xanthene dye aggregates by B-CD in concentrated solutions and inclusion complexation of dye monomers in dilute solutions may explain some of these results.

Pyrromethene-BF_2 complexes in aqueous solutions

The structures of the recently synthesized (Dr. J.H. Boyer's laboratories) 1, 3, 5, 7, 8-pentamethylpyrromethene-BF_2 complex and its 2,6-disulfonate disodium salt are shown in Figure 2.



1,3,5,7,8-pentamethylpyrromethene-BF_2 complex



disodium 1,3,5,7,8-pentamethylpyrromethene-2,6-disulfonate-BF_2 complex

Figure 2. Structures of 1,3,5,7,8-pentamethylpyrromethene-BF_2 complex and its disodium 2,6-disulfonate salt.

The fluorescence, UV absorption and lasing of these complexes as well as the effects of B-CD are described in Tables 4 and 5. Overall, B-CD has no significant effect on the fluorescence, UV or lasing of these complexes. It is noted that there is a considerable change in the position of fluorescence emission and excitation maxima as the disodium salt of this dye is diluted from 10^{-3}M to 10^{-8}M. This suggests that there may be aggregation of the dye in concentrated aqueous solutions and dissociation to monomers in dilute solutions.

TABLE 4

FLUORESCENCE AND UV CHARACTERISTICS OF 1, 3, 5, 7, 8-PENTAMETHYLPYRROMETHENE-BF_2 COMPLEX AND DISODIUM 1, 3, 5, 7, 8-PENTAMETHYLPYRROMETHENE-2,6-DISULFONATE-BF_2 COMPLEX

1, 3, 5, 7, 8-pentamethylpyrromethene-BF_2 complex:
very water insoluble. Em 496 nm (λex = 460 nm) Ex 484 nm (λem = 530 nm)
effects of B-CD on fluorescence: slight quench of Em, when λex below 450 nm. slight enhancement of Em, when λex above 450 nm.

disodium 1, 3, 5, 7, 8-pentamethylpyrromethene-2, 6-disulfonate-BF_2 complex:

Fluorescence in aqueous solutions

Molarity	10^{-3}	10^{-4}	10^{-5}	10^{-6}	10^{-7}	10^{-8}
Em λ max, nm λex=404 nm	534	524	517	513	509	509
Ex λ max, nm λex=534 nm	404	444	484	486	486	486

effects of B-CD: very small enhancement (1-2%) of fluorescence emission

UV aqueous solutions: λmax 490 nm. Not affected by B-CD

TABLE 5

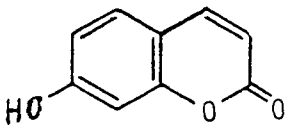
THE LASING OF AQUEOUS SOLUTIONS OF DISODIUM 1, 3, 5, 7, 8-PENTAMETHYLPYRROMETHENE-2,6-DISULFONATE-BF_2 COMPLEX IN THE PRESENCE AND ABSENCE OF 10^{-2}M B-CYCLODEXTRIN

LASING RANGE: 530 - 555 nm

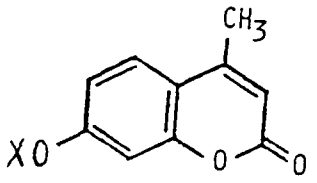
Molarity of dye solution	10^{-3}		10^{-4}	
	lasing (kV)		lasing (kV)	
	threshold	intense	threshold	intense
without B-CD	9	9	12	13
with B-CD	9	10	13	15

Coumarin dyes in aqueous solutions

The coumarin dyes 7-hydroxycoumarin, Na and K salts of 7-hydroxy-4-methylcoumarin, coumarin 102 and coumarin 153 were investigated. Their structures are shown in Figure 3.

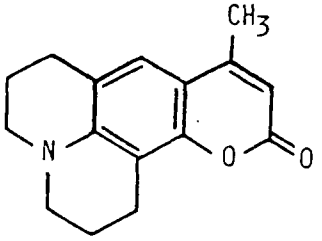


7-hydroxycoumarin

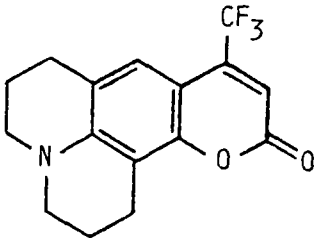


X =Na, K

salts of 7-hydroxy-4-methylcoumarin



coumarin 102



coumarin 153

Figure 3. Structures of 7-hydroxycoumarin, Na and K salts of 7-hydroxy-4-methylcoumarin, coumarin 102 and coumarin 153.

The effects of B-CD on the fluorescence and UV absorption of these compounds are summarized in Table 6. B-CD induces a UV absorption quench for 7-hydroxycoumarin and a quench and red shift for the salts of 7-hydroxy-4-methylcoumarin. There is no effect on the absorption of coumarin 102 and solutions of coumarin 153 were too dilute for meaningful UV analysis with our instrumentation. Fluorescence is enhanced in the presence of B-CD for 7-hydroxycoumarin as well as coumarins 102 and 153. The latter two dyes also show a small blue shift. The K and Na salts of 7-hydroxy-4-methylcoumarin, both show a quench of fluorescence with B-CD in fresh solutions. The K salt was produced in situ using KOH and 7-hydroxy-4-methylcoumarin in solution with a final pH 11.6. The Na salt was used as received and gave a solution with pH 9.0. It is noted that with age, both of the solutions of K salt and Na salt undergo shifts of fluorescence excitation λ_{max} to shorter wavelengths. Also with age, solutions containing B-CD retain their fluorescence intensity longer than solutions without B-CD. The protective effect of B-CD against photodecomposition has been reported.[7]

TABLE 6

FLUORESCENCE AND UV CHARACTERISTICS OF SELECTED COUMARINS IN AQUEOUS SOLUTIONS IN THE PRESENCE AND ABSENCE OF 10^{-2}M B-CYCLODEXTRIN

	7-hydroxycoumarin 10^{-3}	Na or K Salts of 7-hydroxy-4-methylcoumarin, 10^{-3}M in basic solutions	Coumarin 102 10^{-5}M	Coumarin 153 ~10^{-7}M
fluorescence, λmax, nm	Em 451 (ex 358)	Em 445 (ex 402)	Em 485 (ex 403)	Em 536 (ex 423)
	Ex 358 (Em 451)	Ex 402 (Em 444)	Ex 403,378 (Em 485)	Ex 424,430 (Em 536)
effect of B-CD	small enhancement	quench	enhancement blue shift to 476 nm	enhancement blue shift to 531 nm
UV, λmax, nm	324	362	392	
effect of B-CD	quench	quench red shift to 366 nm	no effect	

B-CD has no major effect on the lasing of 7-hydroxycoumarin or the Na and K salts of 7-hydroxy-4-methylcoumarin. Our lasing results are shown in Tables 7-9. We found no previous reports of 7-hydroxycoumarin lasing in aqueous solution. Its lasing range in aqueous solution is 450-473 nm. The lasing of the K and Na salts of 7-hydroxy-4-methylcoumarin is very base sensitive. Lasing for the K salt is obtained over the dilution range $4x10^{-3}$M to $5x10^{-4}$M (similar to earlier results[8]) and a pH range of 11.6 to 11.1. However, at pH 12, only the concentrated, $4x10^{-3}$M, solution gave very weak lasing. Thus, aqueous basic solutions do not appear to be good lasing media for these coumarins.

TABLE 7

LASING OF K SALT OF 7-HYDROXY-4-METHYLCOUMARIN IN BASIC AQUEOUS SOLUTION WITH AND WITHOUT B-CYCLODEXTRIN. LASING RANGE 445-460 nm.

dye solution, molarity	B-CD molarity	pH	lasing threshold without B-CD,kV	lasing threshold with B-CD, kV
4×10^{-3}	1×10^{-2}	11.6	10.5	10.5
2×10^{-3}	5×10^{-3}	11.3	10.5	10.5
1×10^{-3}	2.5×10^{-3}	11.2	10.5	12
5×10^{-4}	1.3×10^{-3}	11.1	11	12.5

TABLE 8

LASING OF Na SALT OF 7-HYDROXY-4-METHYLCOUMARIN IN AQUEOUS SOLUTION (pH=9) WITH AND WITHOUT 10^{-2}M B-CYCLODEXTRIN

	pump input energy, kV	average laser output, mj soln. without B-CD	average laser output, mj soln. with B-CD
lasing of 1×10^{-3}M dye solution	12	1.27	1.97
	14	4.97	3.93
lasing of 5×10^{-4}M dye solution	12	----	----
	14	1.4	0.9

TABLE 9

LASING OF 10^{-3}M AQUEOUS SOLUTIONS OF 7-HYDROXYCOUMARIN (pH=5) IN THE PRESENCE AND ABSENCE OF 10^{-2}M B-CYCLODEXTRIN LASING RANGE: 450-473 nm

	pump input energy, kV	average laser output, mj soln. without B-CD	average laser output, mj soln. with B-CD
lasing of 1×10^{-3}M dye solution	12	.97	1.09
	14	3.34	3.30

Acknowledgement

Support of this research by the US Army Research Office is gratefully acknowledged. We thank S. Lewis for typing the manuscript.

References

1. W. Saenger, Angew. Chem. Intern. Ed. Engl. 19, 344 (1980).
2. S. Scypinski and L.J.C. Love, Anal. Chem. 56, 322 (1984).
3. A. Orstan and J.B.A. Ross, J. Phys. Chem. 91, 2739 (1987).
4. J. Szejtli, in: Inclusion compounds, Vol. 3, eds. J.L. Atwood, J.E.D. Davies and D.D. MacNicol (Academic Press, New York, 1984) p. 331.
5. Y. Degani, I. Willner and Y. Haas, Chem. Phys. Letters 104, 496 (1984).
6. I.R. Politzer, K.T. Crago, T. Hampton, J. Joseph, J.H. Boyer and M. Shah, Chem. Phys. Lett. 159, 258 (1989).
7. J. Szejtli, Cyclodextrin Technology (Kluwer Academic Publishers, Dordrecht, 1988) p.262.
8. B.B. Snavely, O.G. Petersen, and R.F. Reithel, Appl. Phys. Lett., 11, 275 (1967).

CHROMIUM DOPED FORSTERITE LASER

R. R. Alfano*, V. Petričević, and A. Seas
Institute for Ultrafast Spectroscopy and Lasers
The City College of New York
138th Street & Convent Avenue
New York, NY10031

Abstract

Spectroscopic, quantum electronic, and laser properties of chromium-doped forsterite ($Cr:Mg_2SiO_4$) are reviewed. Spectroscopic data suggest that the lasing center in chromium-doped forsterite is tetravalent chromium ion (Cr^{4+}), not the common trivalent chromium (Cr^{3+}). Pulsed, continuous-wave, and tunable operation in the 1167-1345nm region are presented.

Introduction

During the last 10 years tunable solid state lasers have emerged as an alternative to dye lasers. Dye lasers have the advantage of high gain, low cost, and there are many dyes spanning the visible and near infrared region. Many disadvantages of dye lasers such as toxicity, poor long term reliability, narrow wavelength range, make dye lasers unsuitable for hospital, airborn, mobile, or spaceborn use. Tunable solid state lasers are expensive to build and have lower gain coefficient. On the other hand, tunable solid state lasers offer broad tunability range, higher reliability, compactness and long term stability.

Chromium-doped forsterite ($Cr:Mg_2SiO_4$) laser is an important member of the ever growing family of tunable solid state lasers based on chromium ion as the lasing center.[1-3] Pulsed[1] and continuous-wave[4] laser operation have been achieved for 532-nm and 1064-nm.The tuning range now covers the 1167 - 1345 nm range.[5] The most interesting and distinguishing feature of laser action in $Cr:Mg_2SiO_4$ is that the lasing ion is not trivalent chromium (Cr^{3+}), as is the case with the rest of the chromium-based lasers, the active ion is tetravalent chromium (Cr^{4+}).

In this presentation, we review the spectroscopic and laser properties of chromium doped forsterite

Spectroscopic Properties

The spectroscopic properties of forsterite distinctly depend on the growth atmosphere since the relative concentration of Cr^{3+} and Cr^{4+} ions in Mg_2SiO_4 depends on the growth atmosphere. Growing the crystal in a reducing atmosphere the relative concentration of Cr^{4+} ions can be reduced and that of Cr^{3+} increased. We will compare measurements on crystals grown by Czochralski[6] method under standard conditions with those grown in reducing atmosphere, and attempt to identify the contributions from different centers.

Earlier spectroscopic work[8] on chromium-doped forsterite was based on the assumption that only trivalent chromium (Cr^{3+}) substitutes for the octahedrally coordinated Mg^{2+} ions in Mg_2SiO_4 host. There are two inequivalent Mg^{2+} sites in forsterite, one with mirror symmetry (C_s) and the other with inversion symmetry (C_i). Trivalent chromium ion enters the inversion and the mirror site in a ratio of 3:2. The existence of Cr^{3+} ions in the two sites in the ratio given above has been verified by EPR and ENDOR measurements.[9,10] Our recent spectroscopic measurements indicate that, in addition to Cr^{3+} ions in those sites, tetrahedrally coordinated Cr^{4+} ions are also present in the Czochralski-grown forsterite. Similar conclusions have been reached for crystals grown by LHPG method as well.[7]

The absorption spectrum of $Cr:Mg_2SiO_4$ grown under standard conditions (referred to as sample 1, henceforth), for different orientation of the crystal are shown in Fig. 1. The spectra are characterized by three broad absorption bands spanning the near ultraviolet to near infrared spectral regions. The absorption spectra depend strongly on the polarization of the incident radiation with respect to the crystallographic axes of the host. In particular, the peak position of the strongest band in the red-green spectral region shifts considerably with the polarization. Smaller shift has been observed in the near infrared region as well. The polarization dependence of the absorption spectra may be explained in terms of lower site symmetry of chromium ions invoking the polarization selection rules.

To distinguish between the contributions from Cr^{3+} and Cr^{4+} ions to the absorption spectra, we have complemented the absorption spectrum in Fig. 1 by the spectrum of sample 2 which was grown in a reducing atmosphere, shown in Fig. 2. Sample 2 contains mostly Cr^{3+} ions as compared to sample 1 which has both the Cr^{3+} and Cr^{4+} centers. The near infrared absorption band is almost missing in the spectrum of sample 2, which implies that the band is due to transitions within the states of Cr^{4+} ion.

For the visible and the near ultraviolet absorption regions the contributions from the two valence states cannot be distinguished so easily since the absorptions due to Cr^{3+} and Cr^{4+} ions overlap in these spectral regions. To gain further insight, we have analyzed both the spectra in terms of Tanabe-Sugano formalism.[11]

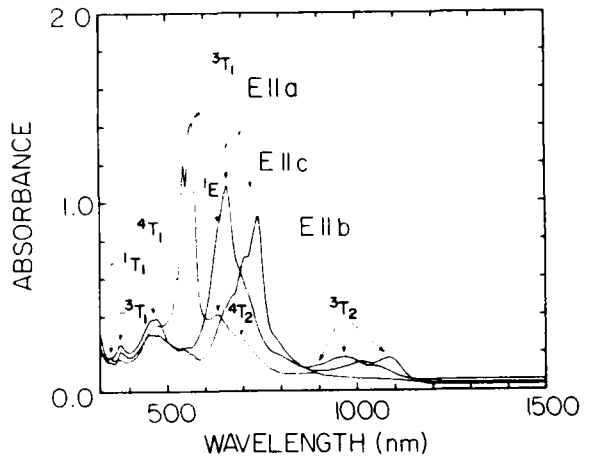


Fig. 1 Room temperature absorption spectrum of $Cr:Mg_2SiO_4$ grown under standard conditions for all three crystal orientations

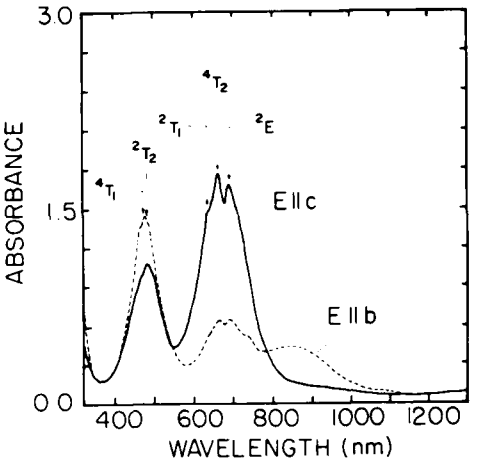


Fig. 2 Room temperature absorption spectrum of $Cr:Mg_2SiO_4$ grown in a reducing atmosphere for two different crystal orientations.

We have taken Cr^{3+} to be in octahedrally coordinated sites and Cr^{4+} to be in tetrahedrally coordinated sites. Comparison of the predicted values of tetrahedral Cr^{4+} and octahedral Cr^{3+} in forsterite with the measured values are presented in Tables 1 and 2, respectively. The transition assignments in Figs. 1 and 2 follow from this analysis.

TABLE 1: Energy Levels of $Cr^{4+}:Mg_2SiO_4$

Transition	Energy (cm^{-1}) Measured	Predicted
$^3A_2 \rightarrow {}^3T_2$	9,150	(9,150)
$^3A_2 \rightarrow {}^3T_1$	15,430	15,150
$^3A_2 \rightarrow {}^1E$	15,875	16,245
$^3A_2 \rightarrow {}^3T_1$	26,810	26,800
$^3A_2 \rightarrow {}^1T_1$	28,735	28,700
$^3T_2 \rightarrow {}^3A_2$	8,750	(8,750)

TABLE 2: Energy Levels of $Cr^{3+}:Mg_2SiO_4$

Transition	Energy (cm^{-1}) Measured	Predicted
$^4A_2 \rightarrow {}^4T_2$	15,100	(15,100)
$^4A_2 \rightarrow {}^2E$	14,450	14,600
$^4A_2 \rightarrow {}^2T_1$	15,380	15,300
$^4A_2 \rightarrow {}^2T_2$	21,050	21,300
$^4A_2 \rightarrow {}^4T_{1a}$	21,500	21,780
$^4A_2 \rightarrow {}^4T_{1b}$	33,780	33,940
$^4T_2 \rightarrow {}^4A_2$	11,100	(11,100)
$^2E \rightarrow {}^4A_2$	14,450	14,600

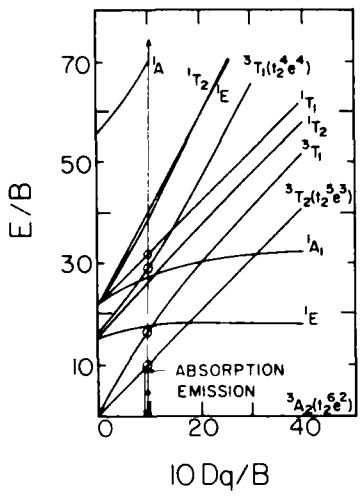


Fig. 3 Tanabe-Sugano diagram for Cr^{4+} in tetrahedral coordination.

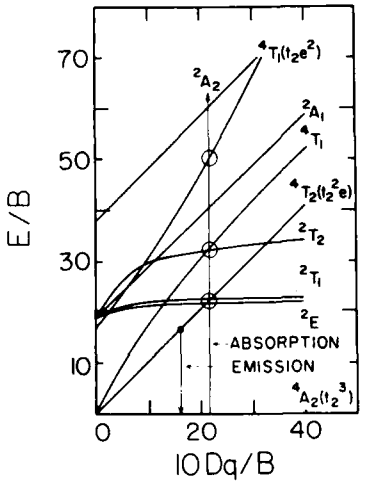


Fig. 4 Tanabe-Sugano diagram for Cr^{3+} in octahedral coordination.

Predicted values given in Table 1 are based on Tanabe-Sugano diagram for tetrahedral Cr^{4+} with parameters: B=970 cm^{-1}, C=3,980 cm^{-1}, and Dq=915 cm^{-1}. For bands whose position vary with the polarization of the incident light, average position (the centroid of three bands marked $^3T_1$ in Fig. 1, for example) is taken for this analysis. Predicted values shown in Table 2 are based on the Tanabe-Sugano diagram for octahedral Cr^{3+} with parameters: B=695 cm^{-1}, C=3,130 cm^{-1}, and Dq=1,510 cm^{-1}. The Tanabe-Sugano diagrams, with transitions indicated, are presented in Figs. 3 and 4.

The fluorescence spectra of Cr:forsterite taken for the Cr^{4+}-rich sample (sample 1) are shown in Figs. 5 and 6. The spectra for sample 2 (containing mostly Cr^{3+}) are shown in Fig. 7. The room temperature spectrum taken with sample 1, excited by the 488-nm line of Ar^+ laser, is a broad band spanning 680 - 1400 nm range. At liquid nitrogen temperature the spectrum breaks up into three structured bands. The fluorescence covering the 1100 - 1400 nm range is the Stokes-shifted counterpart of the near infrared absorption, and is attributed to $^3T_2 \rightarrow {}^3A_2$ transitions in Cr^{4+} ion. The sharp zero-phonon line corresponds to purely electronic transition between the $^3T_2$ and $^3A_2$ states and appears as a prominent feature in both absorption and emission spectra. Near infrared room temperature and liquid nitrogen temperature absorption and fluorescence spectra (fluorescence excited by 1064-nm radiation) for E||b axis are shown in Fig. 6. Features displayed in Fig. 6 are completely absent from the near infrared spectra of sample 2.

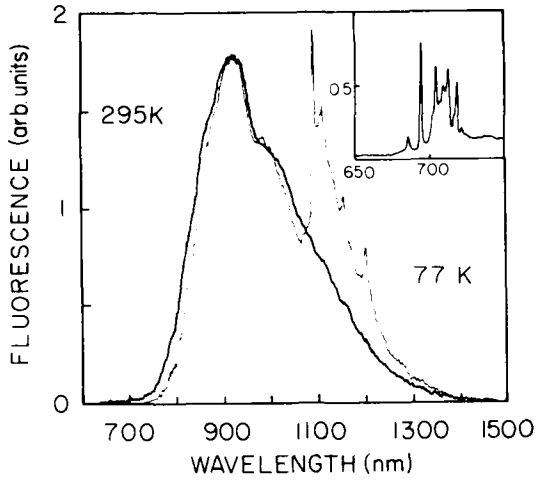


Fig. 5 Room temperature (thicker line) and liquid nitrogen temperature (thin line) fluorescence spectrum of Cr:Mg_2SiO_4 grown under standard conditions for 488-nm excitation parallel to b axis.

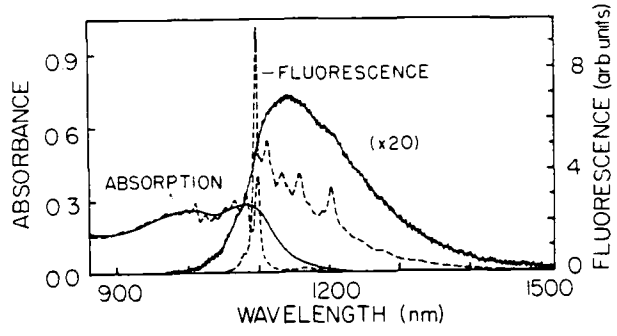


Fig. 6 Room temperature (solid line) and liquid nitrogen temperature (broken line) absorption and fluorescence spectra (fluorescence excited by 488 nm radiation) of Cr:Mg_2SiO_4 grown under standard conditions for E || b axis.

The sharp line at 692 nm observed at liquid nitrogen temperature is attributed to $^2E \rightarrow {}^4A_2$ transition (R-line) in Cr^{3+} ions. This line, followed by a structured sideband that extends to 750 nm is also present in the fluorescence spectrum of sample 2. These features are shown as insets in Figs. 5 and 7.

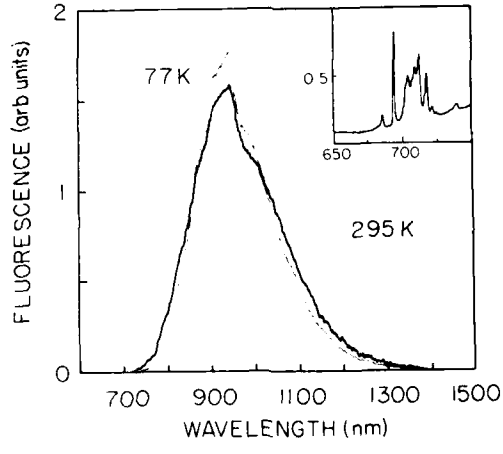


Fig. 7 Room temperature (thicker line) and liquid nitrogen temperature (thin line) fluorescence spectrum of Cr:Mg_2SiO_4 grown in a reducing atmosphere for 488-nm excitation and E || b axis. The spectra were taken with PbS detector which was not sensitive enough to detect the 692-nm zero-phonon line and its sideband shown in the inset. These features were resolved with a photomultiplier tube with S-20 response.

The room temperature spectrum of simple 2 extends only to 1200 nm, and shows contribution from Cr^{3+} ions predominantly. The emission transitions for both Cr^{3+} and Cr^{4+} ions are indicated in the Tanabe-Sugano diagrams.

We have measured fluorescence lifetime as a function of wavelength both at room and liquid nitrogen temperatures using streak camera coupled to a spectrometer. The fluorescence lifetime for Cr^{4+} emission in 1100-1400 nm range is 2.7 μs at room temperature, and 25 μs at liquid nitrogen temperature. The 15 μs lifetime measured at shorter wavelengths, characteristics of Cr^{3+} fluorescence, did not change significantly at liquid nitrogen temperature. Temperature dependence of the fluorescence lifetime indicates presence of strong nonradiative relaxation for Cr^{4+} ions, which is not so prominent for Cr^{3+} ions in this temperature range.

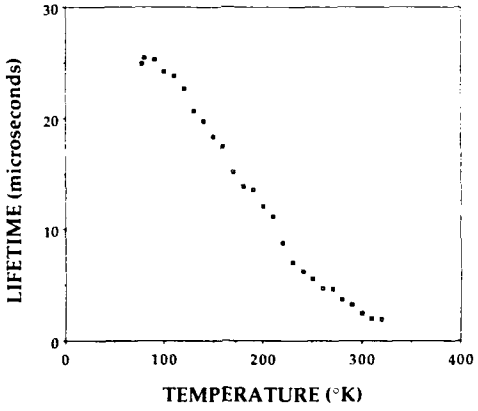


Fig. 8 Temperature dependence of the fluorescence lifetime of chromium-doped forsterite for 1064-nm excitation.

Laser Operation

I. Pulsed Laser Action

Laser experiments were conducted with samples rich in Cr^{4+} in a stable cavity. Details of the cavity arrangement is shown in figure 9 and have been described elsewhere.[1,5]

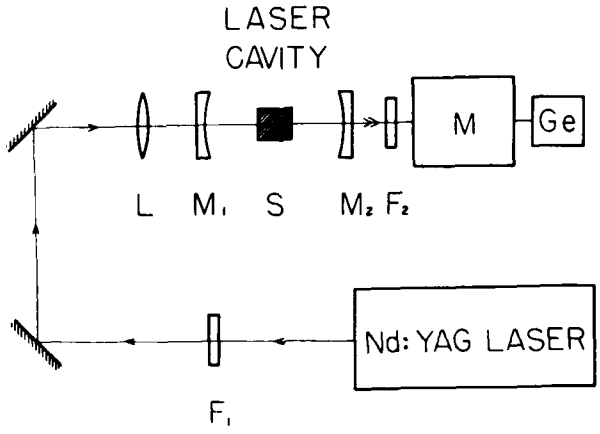


Fig. 9. Cavity arrangement for the forsterite laser

The fundamental and the second harmonic beams from a Q-switched Nd:YAG laser operating at 10-Hz repetition rate were used for excitation of the near infrared and the visible bands. Pulsed laser action was observed for both the 1064-nm and 532-nm pumping.[1] The amplitude and duration of the $Cr:Mg_2SiO_4$ laser pulse, as well as its delay with respect to the pump pulse, varied with the pump pulse energy fluctuation. For similar level of excitation and within the time resolution of the experiment, no difference in the delay between the pump pulse and the output laser pulse for the two pump wavelengths was observed. The spectra of the free-running laser radiation for both the 1064-nm and 532-nm pumping peaked at 1235 nm and had linewidth of 30 nm and 27 nm, respectively. These facts clearly indicate that the same center is responsible for laser action for both the 1064-nm and 532-nm excitations. In case of 1064-nm pumping the lasing level is directly populated. Similar results were obtained for pumping with the 629-nm radiation obtained by stimulated Raman scattering of the 532-nm radiation in ethanol.

To improve the laser performance, sample 1 was anti-reflection coated such that reflectivity over the 1050-1250 nm range was less than 0.5 %. Attempts were made to overlap the pump beam and the cavity mode more accurately. The sample was longitudinally pumped by 1064-nm, 10-ns pulses from a Q-Switched Nd:YAG laser in a cavity similar to that used earlier. Different sets of laser mirrors were used. Summary of the laser performance for three different laser cavities is presented in Table 3.

TABLE 3: Summary of Laser Parameters for Pulsed Laser Operation (1064-nm pumping)

Parameter	Output Coupling 13%	2%	6%
Lasing Wavelength	1200 nm	1235 nm	1250 nm
Free-running Bandwidth	-	30 nm	-
Threshold Abs. Energy	0.38 mJ	0.20 mJ	0.27 mJ
Slope Efficiency	22.8%	5.1%	12.1%
Gain Cross Section (10^{-19} cm^2)	1.40	1.44	1.40

Surface damage of the Cr:forsterite laser crystal was observed for pumping energies greater than 4mJ, for 5ns pulses, at 10Hz repetition rate, focused to 250μm radius spot.This corresponds to damage threshold energy density greater than 6J/cm^2, for 5ns pulses. Therefore, a 1cm diameter laser pumped forsterite rod can be used to generate high energy pulses in the joule range.

Output energy of the forsterite laser as a function of absorbed pump energy for three different output couplers is shown in Fig. 10.

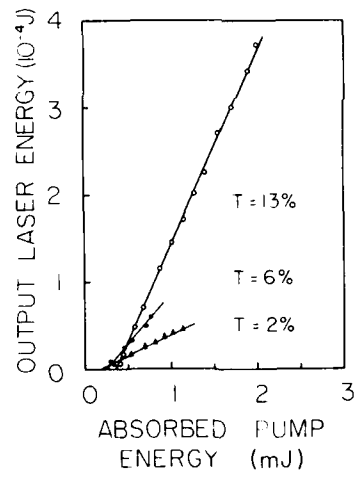


Fig. 10 Output energy of Cr:Mg_2SiO_4 laser as a function of absorbed pump energy for 1064-nm pumping and E ∥ b axis for three different output couplers.

Using data from Table 4 we have estimated the passive loss L of the forsterite laser to be 11%, and calculated the laser gain cross section.

Laser gain cross section shown in Table 4 for three different output mirrors was calculated using the expression[13]

$$\sigma = \frac{\pi \tau_P h\nu_P \omega_L^2 (L+T)(a^2+1)}{4\tau\left[1-\exp(-\alpha l)\right]\left|1-\exp(-\tau_P/\tau)\right| E_{Pth}}$$

where τ_P is the pump pulsewidth, $h\nu_P$ is the pump photon energy, ω_L is the cavity mode spot size, L is laser internal loss, T is the output mirror transmission, $a=\omega_P/\omega_L$, where ω_P is the pump beam spot size, τ is the upper lasing level radiative lifetime taken to be ~25 μs, α is the absorption coefficient for the pump radiation, l is the length of the crystal, and E_{Pth} is the threshold pump energy incident on the crystal.

II. Continuous-Wave Laser Operation

To obtain cw laser action a sample of chromium-doped forsterite (sample 1) was placed at the center of a nearly concentric cavity formed by two 5-cm radius-of-curvature mirrors such that a cavity mode waist was 75 μm. The output mirror was dielectric coated to have ~1% transmission for the 1175 - 1250 nm range, and to transmit most of the 1064-nm pump beam. The pump radiation from a cw Nd:YAG laser was focused by a 75-mm focal length lens to pump the sample longitudinally along the 30 mm path length. The pump beam was linearly polarized along the b axis and propagated along the a axis of the crystal . The beam was chopped at a duty factor of 9:1 to reduce heating effects. The waist of the pump beam at the center of the sample was measured to be 70 μm.

Quasi-cw laser operation was obtained for pumping above the lasing threshold of 1.25 W of absorbed power. The measured slope efficiency was 6.8%. The cw output power of the Cr:forsterite laser as a function of absorbed pump power is displayed in Fig. 11. Laser operation was possible even when the pump beam was not chopped, but at 40% reduced output indicating losses induced by local heating.

The spectrum of the free-running laser output peaks at 1244 nm and has a bandwidth of 12 nm.

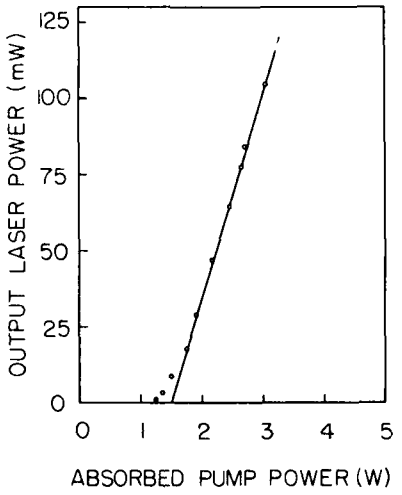


Fig. 11 Output power of the cw $Cr:Mg_2SiO_4$ laser as a function of absorbed pump power.

Using results obtained from CW lasing experiment, a value of 12.7% for L the internal loss has been estimated[12]. This value is in reasonable agreement with the value of 11% obtained from pulsed measurements. The gain cross section was estimated to be $1.47 \times 10^{-19} cm^2$, in excellent agreement with the value obtained from pulsed laser experiments. Threshold population inversion density was estimated to be $1.6 \times 10^{17} cm^{-3}$. The key continuous-wave laser parameters are summarized in Table 4.

TABLE 4: Properties of cw Laser Operation of $Cr:Mg_2SiO_4$ laser

Property	Value
Lasing Wavelength	1244 nm
Spectral Bandwidth (FWHM)	12 nm
Lasing Threshold (Absorbed Power)	1.25 W
Slope Efficiency	6.8%
Threshold Inversion Density	1.6×10^{17} cm^{-3}
Gain Cross Section	1.47×10^{-19} cm^2

III. Tunable Operation of Forsterite Laser

Tunable operation of Cr:forsterite laser has been obtained over the 1167 - 1345 nm spectral range,[5] using single crystal quartz birefringent plate, extending the tuning range of chromium-doped laser crystals further into near infrared. The ratio of the Cr:forsterite laser output to the absorbed pump energy as a function of wavelength is shown in Fig.12

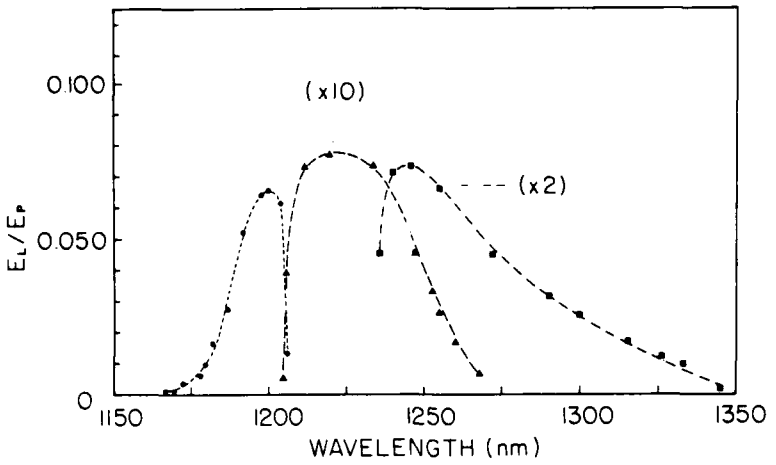


Fig. 12 The ratio of the Cr:forsterite laser output (E_L) to the absorbed pump energy (E_P) as a function of wavelength. The three curves correspond to the three output couplers used in tuning measurements.

Conclusion

Measurements of absorption and emission spectra , as well as the wavelength dependence of fluorescence lifetime indicate that chromium ion may enter forsterite (Mg_2SiO_4) host in more than one valence states. Trivalent chromium (Cr^{3+}) enters substitutionally for divalent magnesium (Mg^{2+}) in two inequivalent octahedrally-coordinated sites, while tetravalent chromium (Cr^{4+}) substitutes presumably for Si^{4+} at tetrahedrally coordinated sites. Of the two Cr^{3+} centers, the one with mirror symmetry (C_s) is optically active and accounts for a number of features in absorption and emission spectra. The absorption and emission due to transitions within the states of Cr^{4+} ion overlap with those within the states of Cr^{3+} ion. The absorption and emission in the near infrared spectral region between 850 and 1150 nm is primarily due to transitions between the $^3A_2$ ground state and the first excited state $^3T_2$, of the Cr^{4+} ion. The four-level, vibronic mode of laser operation in Cr-doped forsterite feeds on $^3T_2 \rightarrow {}^3A_2$ transition.

Chromium-doped forsterite is an important laser in the near-infrared spectral region. Table 5 lists the thermal and optical properties of forsterite and YAG crystals, which suggests that forsterite may be developed in a reliable tunable source of radiation for the near infrared region. Forsterite can be operated both in the pulsed and cw mode of operation and is tunable over 1167 - 1345 nm range. The large fluorescence bandwidth promises ultrashort pulse generation through mode-locked operation. Since large single crystals can be easily grown, the crystal has potential for being used as an amplifier medium in the near infrared spectral region and to produce joule energy pulses .

Table 5: Physical, Thermal and Optical Properties of Forsterite and YAG Crystals

	Forsterite	YAG
Chemical Formula	$Cr:Mg_2SiO_4$	$Nd:Y_3Al_5O_{12}$
Concentration (cm^{-3})	~3-6x 10^{18}	1.38 x 10^{20}
Melting Point (°C)	1890	1970
Density (g/cm^3)	3.22	4.56
Moh's Hardness	7	8.5
Thermal Expansion Coeff.	9.5 x 10^{-6}	8.0 x 10^{-6}
Thermal Conductivity (W/cm°K)	0.08 (@ 300°K)	0.13 (@ 300°K)
$\partial n/\partial T$ ($°K^{-1}$)	Not Measured	7.3 x 10^{-6}
Emission Bandwidth	1350 cm^{-1}	6 cm^{-1}
Stimulated emission Cross Section (cm^{-2})	1.44 x 10^{-19}	6.5 x 10^{-19}
Relaxation time of Terminal Lasing Level	<10ps (Estimated)	30ns
Radiative Lifetime	25µs	550µs
Spontaneous Fluorescence	2.7µs	230µs
Loss Coefficient	0.02 cm^{-1}	0.002 cm^{-1}
Index of Refraction	1.635	1.82 (@1.0µm)

* Presented the plenary talk

References

1. V. Petričević, S. K. Gayen, R. R. Alfano, K. Yamagishi, H. Anzai, and Y. Yamaguchi, Appl. Phys. Lett. **52**, 1040 (1988); V. Petričević, S. K. Gayen, and R. R. Alfano, Appl. Phys. Lett. **53**, 2590 (1988).
2. For a list of Cr-based tunable solid state lasers see J. A. Caird, S. A. Payne, P. R. Staver, A. J. Ramponi, L. L. Chase, and W. F. Krupke, IEEE J. Quantum Electron. **24**, 1077 (1988), and references therein.
3. A. A. Kaminskii et. al., Inorg. Mater., **24**, 579 (1988).
4. V. Petričević, S. K. Gayen, and R. R. Alfano, Opt. Lett. **14**, 612 (1989).
5. V. Petričević, S. K. Gayen, and R. R. Alfano, Appl. Opt. **28**, 1609 (1989).
6. N. Nishide, Y. Segawa, P. H. Kim, S. Namba, and A. Masuyama, Reza Kagaku Kenkyu **7**, 89 (1985).
7. H. R. Verdun, L. M. Thomas, D. M. Andrauskas, T. McCollum, and A. Pinto, Appl. Phys. Lett. **53**, 2593 (1988).
8. H. Rager and G. Weiser, Bull. Mineral. **104**, 603 (1981).
9. H. Rager, Phys. Chem. Minerals **1**, 371 (1977).
10. L. V. Bershov, J. M. Gaite, S. S. Hafner, and H. Rager, Phys. Chem. Minerals **9**, 95 (1983).
11. S. Sugano, Y. Tanabe, and H. Kamimura, *Multiplets of Transition-Metal Ions in Crystals*, Academic, New York, 1970.
12. V. Petričević, S.K. Gayen, and R.R. Alfano, in *Tunable Solid-State Lasers*, Vol.5 of the OSA Proceeding Series, M.L. Shand and H.P. Jenssen, eds. (Optical Society of America, Washington, D.C., 1989), pp. 77-84.
13. P. F. Moulton, IEEE J. Quantum Electron. **QE-21**, 1582 (1985).

OPERATIONAL CHARACTERISTICS OF AN IMAGING, UNSTABLE RING RESONATOR USING ND:YLF AS ACTIVE MEDIUM

D. Y. Park[a]

W. Seka

Y. Lin

and D. L. Brown

Laboratory for Laser Energetics
University of Rochester
Rochester, NY 14623-1299

Abstract

We have constructed and tested an imaging unstable resonator using Nd:YLF as the active medium. Incorporated in this oscillator are a small angle Faraday rotator and a pair of etalons (10 mm, R = 60%, and 2 mm, R = 25%) that guarantee unidirectional, single-axial-mode operation of the oscillator. Q-switched monomode operation is obtained through self-injection seeding. The oscillator has been characterized in the time, frequency, phase, and spatial domain using fast diodes, high-resolution interferometry and near-field photography.

[a] Permanent address: Physics Department, INHA University, Inchon, Korea.

1. Introduction

Unstable resonators are an attractive solution for high-gain laser systems. They are widely used commercially in Nd:YAG, CO_2, KrF, and other laser systems. They have been shown to be well suited for injection-seeded mono-mode lasers[1,2,3] operating in the Q-switched mode, particularly with Nd:YAG as active medium lasing at $\lambda = 1.064$ μm. In addition, the central hole usually associated with unstable resonator outputs, as well as the strong diffraction patterns associated with the limiting apertures in these laser systems, have been eliminated or largely mitigated through the use of appropriately graded reflectors.[4] However, no detailed phase maps have been obtained for the output beams of these lasers and one should expect significant phase distortions associated with these graded mirrors.

On the other hand, Nd:YLF, which lases at $\lambda = 1.054$ μm (or 1.047 μm), has not seen as much development as Nd:YAG, in part, because of its uniaxial crystal structure that exhibits gain only for linearly polarized light in its commonly available form. This precludes the use of circularly polarized light inside the active medium to avoid spatial hole-burning effects in linear resonators, making monomode operation much more difficult. For the same reasons it is much harder to design powerful monomode injection laser sources analogous to those developed for Nd:YAG.[5]

Nd:YLF is a very attractive laser medium due to its thermo-optic properties and its low index of refraction, which lead to very low depolarization and thermal lensing problems.[6] In addition, Nd:YLF can be operated at very high gain, particularly at $\lambda = 1.047$ μm where a gain over 1000 is achievable.[7] Therefore, this active medium is of considerable interest for applications in unstable resonators for small, but powerful lasers.

2. Experimental Layout

Experimental and theoretical work on unstable laser resonators has been discussed in the literature extensively.[8] Negative-branch, imaging unstable resonators, on the other hand, have only been discussed theoretically.[9,10]

A negative-branch, imaging unstable ring resonator may be thought of as a Newtonian telescope wrapped around in a ring such that the magnified image of the scraper mirror is projected onto itself after one round trip (see Fig. 1). The two confocal lenses making up the telescope (focal lengths f_1 = 25 cm and f_2 = 50 cm) have the scraper mirror in one of their two common focal planes and a pinhole of variable aperture in the other. In the collimated section and just ahead of the scraper mirror is the active medium, which separates the cavity into a high- and a low-intensity section. Damage-prone elements, such as intracavity etalons, are preferably placed in the low-intensity region between the long-focal-length lens and the active medium.

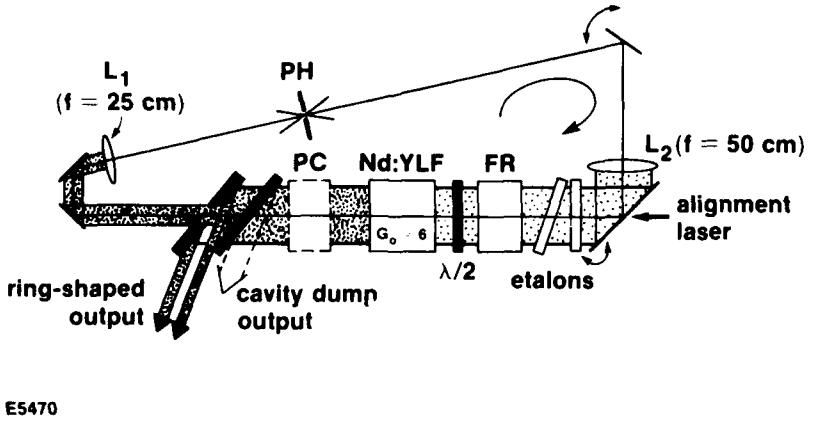


Fig. 1. Optimized setup for imaging, negative branch, unstable resonator. The length of the cavity is $L \approx 2f_1 + 2f_2$. The collimated section of the resonator can be separated into high-intensity and low-intensity regions as indicated by the dot density in the beam cross section.

Our study of this oscillator was directed toward evaluating its capability to operate as a monomode (single-axial-mode) oscillator. To this end we have placed a Faraday rotator with a $\lambda/2$ wave plate into the low-intensity section of the ring to achieve unidirectional operation. (The rotator was a readily available 22° permanent magnet rotator, although, a much smaller rotator capable of a few degrees of rotation should be sufficient.) Reliable monomode operation was observed with a pair of solid glass etalons, a 10-mm and a 2-mm thick with 65% and 25% reflective coatings, respectively.

The experimental layout for the imaging unstable resonator is shown in Fig. 1 in a configuration in which we avoid placement of any optical components in regions where the intracavity intensity exceeds the intensity at the output of the active medium. Also shown in this figure is a Q-switch Pockels cell and a polarizer. The latter is necessary if the Q-switch is combined with a cavity dump arrangement in order to extract a pulse without a central hole. However, this arrangement is energetically interesting only if the laser-pulse duration and the high-voltage switching times are of the order of the cavity round trip time (5 ns in our case).

The scraper mirror used in these experiments was a mirror at Brewster's angle that was coated for high reflectivity for "p" polarization everywhere except in the central, elliptical hole, which was left uncoated. Thus, the central, circular (2.5-mm) beam suffered minimal losses at this mirror while the outer ring was ejected from the cavity. The mirror was fabricated in-house using lithographic techniques.

The placement of optical components inside the collimated section of the cavity required a small adjustment of the cavity length to preserve proper imaging. We determined this adjustment, as well as the exact focal lengths of the lenses, experimentally using an upcollimated diode-pumped Nd:YLF alignment laser operating at 1.053 μm whose state of collimation was verified with a lateral shearing interferometer.

The same diode-pumped laser, shown in Fig. 1, was used to align the cavity. The laser was injected into the cavity through one of the high reflectance mirrors and collimated at ≈2-mm FWHM at the scraper mirror. Proper alignment of the cavity requires pointing and centering of the beam inside the cavity after one round trip, where the scraper mirror is the centering reference. Proper pointing is achieved by viewing the reflection from the polarizer. High-contrast interferograms can be obtained by appropriately rotating the $\lambda/2$ plate of the Faraday rotator. The interferogram is produced by successive reflections from the polarizer after the first, second, etc., passes through the cavity. The cavity is properly pointed if an infinite fringe interferogram is obtained. Correct centering is verified in the reflection from the scraper mirror where one can easily distinguish the first reflection from that after one round trip. It also allows for easy centering of the active medium and the Faraday rotator, both of which were 1/4-in. rods and produced sufficient diffraction of the alignment laser to allow accurate alignment. This alignment procedure leads to excellent alignment within 2 to 3 iterations. Positioning of the variable aperture pinhole (≥700-μm diameter) is easily and accurately done with the alignment laser after the final alignment iteration. Apart from final adjustments to the Fabry-Perot intracavity etalon this alignment procedure requires no further active corrections to reduce the lasing threshold or improve the beam quality. In fact, attempts to make further improvements during actual laser operation have not been very successful. The interferograms, etc., were viewed with a CID camera and stored on a computer using a video frame grabber.

3. Results

In these experiments the laser was operated as a pulsed monomode laser in both the free-running (relaxation oscillation) and Q-switched mode. We have analyzed the output intensity and phase-front distribution as well as monomode behavior of the output. All time-integrated, spatially resolved data were digitized for numerical processing at a later time. All time-resolved data were taken using either a photodiode and a 500-MHz scope with ≥1-ns time resolution or a fast diode and a 6-GHz scope with an experimentally determined, 150-ps combined time resolution.

In Fig. 2 we show near-field images of both the scraper mirror and polarizer output. The polarizer output simulates the output in the cavity dump mode. This image was taken in the image plane of the scraper mirror and is essentially free of diffraction rings [Fig. 2(a)] while the scraper ring output [Fig. 2(b)] was taken at ≈5 cm from the mirror and showed noticeable diffraction rings due to the inner edge of the scraper mirror. The influence of the variable pinhole in the spatial filter section (≥0.7-mm diameter) was minimal; at its minimum diameter it softened the outer edges of the output beam without introducing noticeable diffraction rings on the beam.

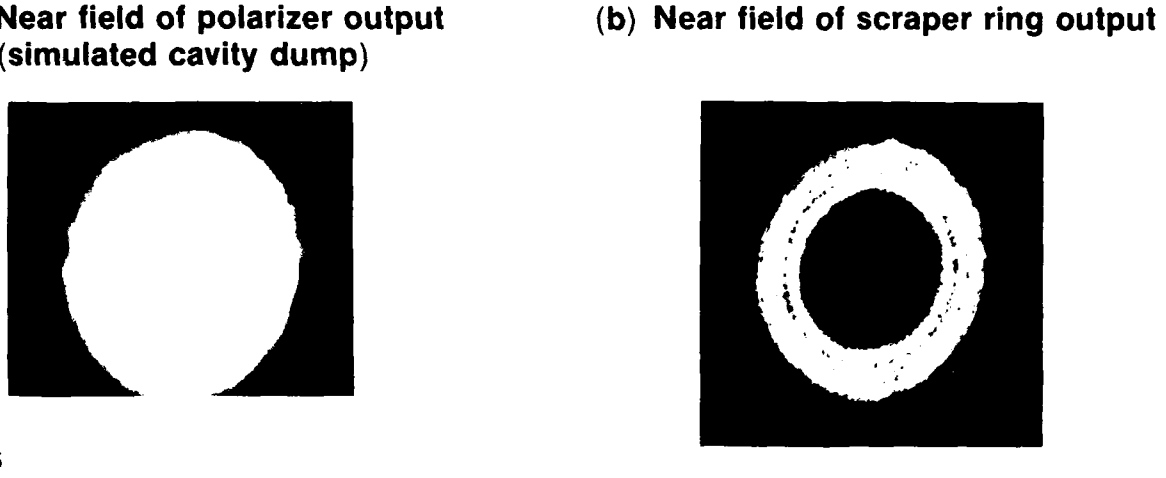


Fig. 2. Output-beam patterns from the polarizer (a) and the scraper mirror (b). The polarizer output is taken in the image plane of the scraper mirror, whereas (b) is taken 5 cm beyond the image point; hence, the diffraction-ring structure due to inner edges of the scraper mirror.

The brightness of the oscillator output is sensitively influenced by its phase-front distribution. We have therefore constructed a "self-referencing Mach-Zehnder interferometer" or "radial shear interferometer"[11] as shown in Fig. 3. In order to obtain the phase information over the whole-beam

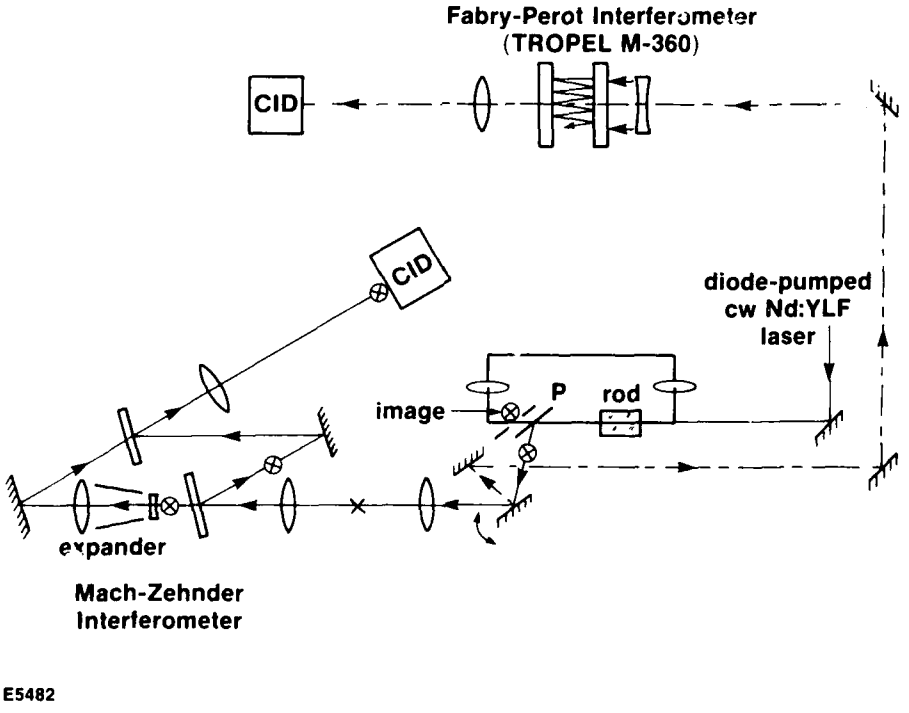


Fig. 3. Schematic setup of the Mach-Zehnder and Fabry-Perot interferometers.

cross section inside the oscillator we have used and enhanced the output from the polarizer (see Fig. 1) by rotating the wave plate in the Faraday rotator by a small amount. The reference beam is derived from the same output beam through (10X) upcollimation inside one of the arms of the interferometer. A high-resolution phase map is then obtained applying the technique of spatial synchronous phase detection.[12] The high-contrast Mach-Zehnder interferogram is first Fourier transformed numerically [(Fig. 4(b)]; we then select one of the two main side lobes, which are associated with the high-frequency background fringes. This side lobe contains all the phase information imprinted on the beam while all the intensity information is contained in the well-separated, central zero-order maximum. Shifting the selected side lobe to the center and inverse Fourier transforming it results in a phase map of high quality, as shown in Fig. 4(c).

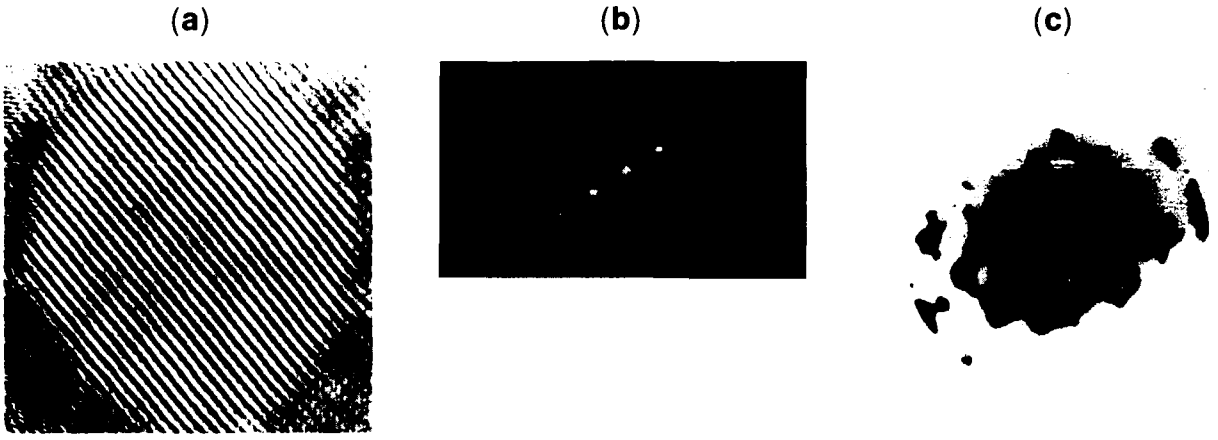


Fig. 4. Phase maps of unstable resonator output using spatially synchronous phase detection. (a) High background fringe Mach-Zehnder interferogram, (b) image of the numerically generated Fourier transform, one of the main side-lobs is used for the inverse Fourier transform to generate the output phase map (c).

The phase map shown in Fig. 4(c) was obtained for an oscillator using a 6.35-mm-diam x 40-mm-long Nd:YLF rod of excellent quality. The contour lines in Fig. 4(c) are spaced $\lambda/25$ apart; the overall rms phase-front error is ≈ 0.05 waves with a peak-to-valley error of 0.12 waves. Matching Zernicke polynomials to the two-dimensional phase front, we have identified 0.1 waves of astigmatism and 0.06 waves of spherical wave-front error. This analysis does not include the outer-most regions of the output beam where the intensity has dropped to less than 10% of the average center intensity. In those regions the phase front clearly shows the influence of the reflective coating on the scraper mirror, which causes the phase to be retarded (curled up) by ≈ 0.2 waves (see Fig. 5). Using different laser rods of varying optical quality we have found that the output phase map primarily reflects the phase errors present in the unpumped laser rod. This implies that most of the output phase-front errors in this laser are caused by the final round trip of the laser beam inside the resonator.

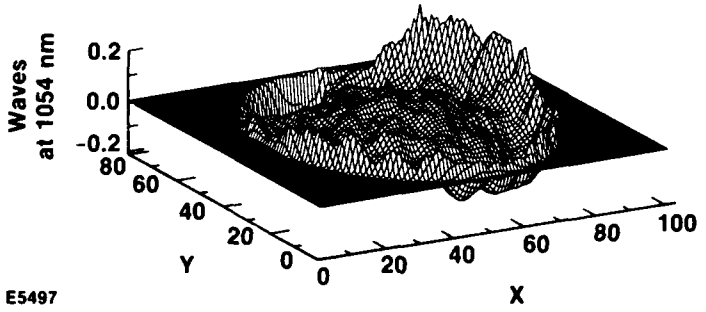


Fig. 5. Phase map of the output beam including the outer-most regions where the phase exhibits the retardance caused by the dielectric scraper mirror after the final round trip inside the cavity. The intensity in this region is typically less than 10% of the center-beam intensity.

Monomode (single-axial-mode) output was easily obtained with this oscillator and has been verified by a number of techniques. When operating high above threshold, the regular decay of the relaxation oscillations is a reliable indication of monomode operation [Fig. 6(a)]. In addition, time-resolved data show no mode beating [Fig. 6(b)]. Finally, we have taken Fabry-Perot interferograms with $\Delta\lambda_{FSR} \approx 0.14$ Å, and $\Delta\lambda_{res} \approx 1.6 \times 10^{-3}$ Å, which easily resolved individual axial modes ($\Delta\lambda_{mod} \approx 7.5 \times 10^{-3}$ Å) of the 5-ns round trip cavity. Figure 7 shows two such interferograms, one for the typical monomode output and one for a purposely detuned cavity lasing on two neighboring modes. The line-outs shown in this figure have been corrected for the variable dispersion of the plane parallel plate Fabry-Perot near the zero'th order. The interferograms verified the monomode nature of the output. It should be noted that we have never observed modes separated by any intracavity etalon mode spacings when both intracavity etalons were in place.

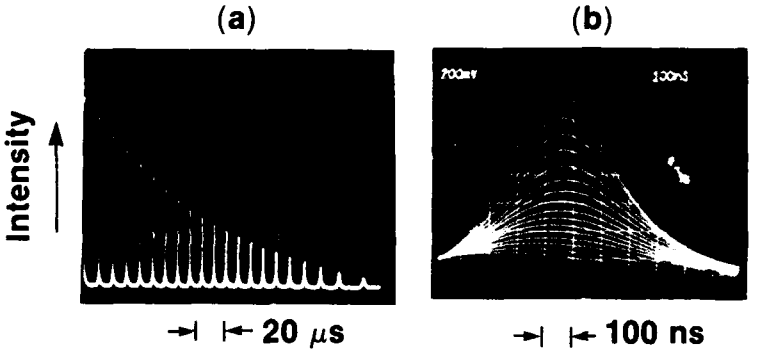


Fig. 6. Output from unstable ring resonator. Regular decay of relaxation oscillations (a) and absence of mode-beating in each of the relaxation spikes (b) indicate single-axial mode (monomode) output.

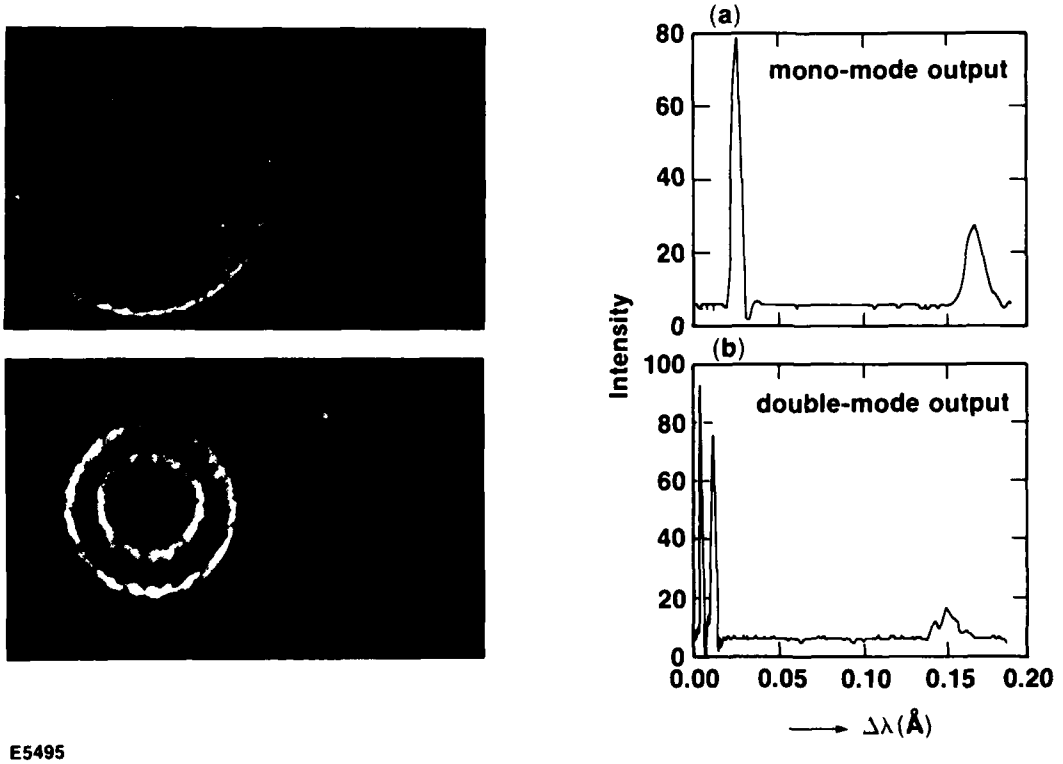


Fig. 7. Fabry-Perot interferograms of monomode output (a), and double-mode operation of a purposely detuned cavity (b). The line-outs of the Fabry-Perot interferograms have been corrected for the variable dispersion near the zero'th order.

Single-axial-mode Q-switched operation was obtained using self-injection seeding.[13] Here we apply a voltage to the Q-switch just below the lasing threshold voltage, allowing for the slow buildup of one or two relaxation oscillations in the absence of Q-switching. A photodiode detects the buildup of the first relaxation oscillation and triggers the Q-switch. Experimental data showing the prelase and subsequent Q-switch build-up are shown in Fig. 8. Q-switched pulse durations were limited to ≥80 ns in these experiments due to limited pumping capability.

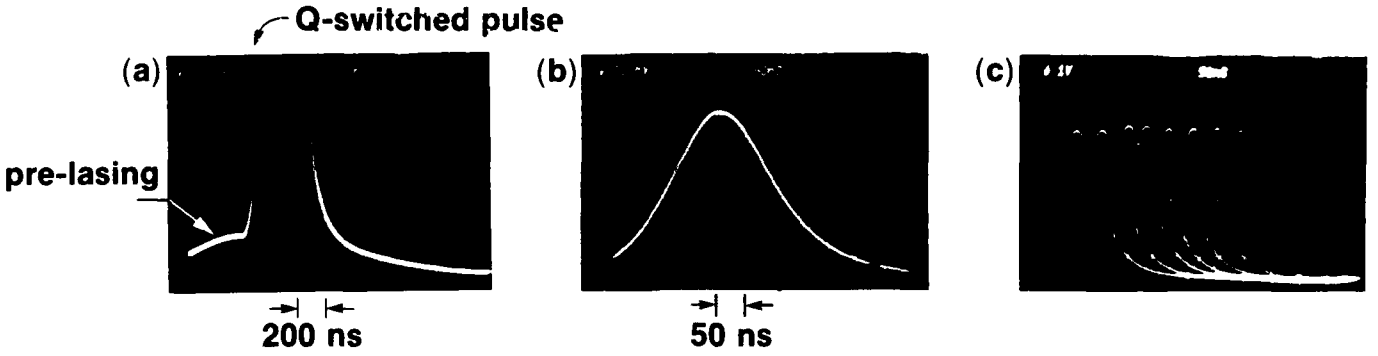


Fig. 8. Self-injection-seeded, monomode Q-switched output. Photodiode trace in (a) shows prelase (first relaxation oscillation) with subsequent Q-switch pulse off-scale. A single Q-switched pulse in a 1-GHz scope demonstrating absence of mode-beating due to neighboring modes (b). Ten successive output pulses indicate the high degree of output reproducibility (c).

The reproducibility of the output is shown in Fig. 8, which displays photodiode signals of several Q-switched pulses where the origin of the trace was manually moved between pulses. Excellent reproducibility is evident and a statistical analysis of data taken with the 6-GHz oscilloscope over a large number of shots shows that the output energy is 55 mJ ±1%, the pulse duration 80 ns ±1%, and the Q-switch pulse buildup time is ≈100 ns ±1~2 ns. These data demonstrate that this type of oscillator is well suited for synchronization to external events. Such synchronization has already been demonstrated in similar systems[14] where an electronic feed-back to the Q-switch voltage clamps the prelase intensity near the cw laser intensity (well below the intensity of the first relaxation oscillation).

4. Conclusions

We have constructed and tested an imaging unstable resonator, which is eminently well suited for monomode operation in the free-running and self-injection-seeded, Q-switched mode. We have further examined the phase front of the output beam and found that it reflects primarily the final pass through the outer zones of the active medium. Thus, a predictable output-beam phase front is obtainable from a knowledge of the phase-front errors due to the active medium and any other optical elements inside the resonator that may have poor optical quality. However, at present the optical quality of commercially available Nd:YLF rods with >5-mm clear apertures is usually the optical element in the cavity that sets the output phase-front errors. The self-injection-seeded, Q-switched laser output is also well suited for synchronization to external events and the excellent reproducibility of pulse durations, pulse energies, and buildup time make this laser interesting for many applications in nonlinear optics.

Acknowledgments

The authors would like to thank Douglas Smith of the Optical Coating Shop of LLE for the lithographically fabricated scraper mirrors used in these experiments. They would also like to thank Steven Swales and Terry Kessler for reducing the interferograms using the spatial synchronous detection method.

This work was supported by the U.S. Department of Energy Division of Inertial Fusion under agreement No. DE-FC03-85DP40200 and also by the Laser Fusion Feasibility Project at the Laboratory for Laser Energetics which has the following sponsors: Empire State Electric Energy Research Corporation, New York State Energy Research and Development Authority, Ontario Hydro, and the University of Rochester. Additional support was provided by the United States Air Force Office of Scientific Research under contract F49620-87-C-0016 to the Ultrafast Optical Electronics Center at the Laboratory for Laser Energetics of the University of Rochester.

References

1 Y. K. Park, G. Giuliani and R. L. Byer, Opt. Lett. 5, 96 (1980); P. Esherick and A. Owyoung, J. Opt. Soc. Am. B 4, 41 (1987).

2. R. Barbini, A. Ghigo, M. Giorgi, K. N. Iyer, A. Palucci, and S. Ribezzo, Opt. Commun. 60, 239 (1986).

3. J.-M. Chiquier, R. Buffa, L. Fini and F. Pradère, Opt. Commun. 56, 267 (1985).

4. A. Parent and P. Lavigne, Opt. Lett. 14, 399 (1989).

5. T. J. Kane and R. L. Byer, Opt. Lett. 10, 65 (1985).

6. J. E. Murray, IEEE J. Quantum Electron. QE-19, 488 (1983); H. Vanherzeele, Opt. Lett. 13, 369 (1988), and Appl. Opt. 27, 3608 (1988).

7. M. G. Knights, M. D. Thomas, E. P. Chicklis, G. A. Rines, and W. Seka, IEEE J. Quantum Electron. QE-24, 712 (1988).

8. see, for instance, A. E. Siegman, LASERS, Chap. 22 and 23 (University Science Books, Mill Valley, CA, 1986).

9. K. E. Oughstun, P. A. Slaymaker and K. A. Bush, IEEE J. Quantum Electron. 19, 1558 (1983).

10. A. H. Paxton and T. C. Salvi, Opt. Commun. 26, 305 (1978).

11. OPTICAL SHOP TESTING, edited by D. Malacara, (John Wiley and Sons, New York, 1978), p. 156.

12. M. Takeda, H. Ina, and S. Kobayashi, J. Opt. Soc. Amer. 72, 156 (1982); University of Rochester, Laboratory for Laser Energetics, LLE Review 31, 114 (1987).

13. I. D. Carr, D. C. Hanna, and K.-H. Wong, Opt. Commun. 55, 179 (1985); A. J. Berry, D. C. Hanna and C. G. Sawyers, Opt. Commun. 40, 54 (1981); D.C. Hanna et al., Electron. Lett. 8, 369 (1972); G. B. Michelangeli, A. Landoni, M. Neri, G. Giuliani, E. Palange, and G. Salvetti, Opt. Commun. 65, 283 (1988).

14. I. N. Ross et al., IEEE J. Quantum Electron. QE-17, 1653 (1981).

A Nd:GLASS SLAB LASER FOR X-RAY LITHOGRAPHY

Murray Reed and Robert L. Byer
Stanford University
Edward L. Ginzton Laboratory, Stanford University, Stanford, CA. 94305

Abstract A Nd:Glass slab laser has been used to generate laser produced plasmas (LLP). The plasma emission in the keV range useful for x-ray lithography has been measured. Lithography with sub-micron linewidths has been demonstrated with a thin absorbing mask.

The Nd:Glass slab laser is operated in a Q-switched one-dimensional unstable resonator [1]. The resulting beam quality is a few times diffraction limited and is focused to an area less than the 10^{-5} cm^2 in our vacuum chamber. We have operated at 5 J up to 4 Hz repetition rate without any degradation of the laser output. Injection mode locking of the Nd:Glass laser [1] with 0.7 ns pulses increases the intensity of the Q-switched laser output by about a factor of 10 and allows us to achieve a total integrated pulse length of less than 10 ns. Optical damage limits the laser intensity. The damage threshold for injection mode-locked pulses focused into a Nd:Glass slab outside the laser cavity is about 20 J/cm^2. However, we have observed another damage mechanism at lower intensities in Nd:Glass slabs in use in the laser head. Brown discoloration occurs in filaments along the laser beam path and we believe polarization with the help of self-focusing and the ultraviolet flashlamp radiation may be occuring. We are still investigating this phenomenon but at present it is limiting the laser output to only 2 J per pulse.

The focused laser intensity is 2.10^{13} W/cm^2 on a solid copper target in our vacuum chamber. The plasma emission in the keV x-ray range has been measured through a variety of thin film x-ray filters with a Hamamatsu micro-channel plate detector. Using the published values for the detector quantum efficiency, the micro-channel plate gain, and the filter's transmission spectra, we estimate that the conversion efficiency in the plasma from laser radiation to soft x-rays of energy greater than 0.5 keV is around 1%. We have performed single-level demonstration exposures of PMMA resist through a 12 μm thick aluminised Kapton debris shield and a 4 μm thick Boron Nitride x-ray mask supplied by Piero Pianetta at the Stanford Synchroton Research Laboratory. The 1.0 μm linewidth gold absorber patterns on the mask are accurately reproduced in the resist. The PMMA resist exposure rate at a 5 cm working distance from the plasma has been measured as 0.2 micron per 10^4 of total laser energy so we obtain a single layer exposure in about 30 minutes.

The potential for improvement is enormous. The x-ray signal measured through the mask increases exponentially with the laser energy on target so increasing the focused intensity will reduce exposure rates dramatically. Available improvements in higher average power lasers and sensitised resists both offer an order of magnitude improvement over this system. These results indicate excellent potential for commercial LPP x-ray lithography.

1. M.K. Reed and R.L. Byer, submitted to IEEE Journal of Quantum Electronics.

WAVEFRONT AND DEPOLARIZATION CALCULATIONS FOR A GGG SLAB LASER*

James A. Blink, James L. Cook, and Luis E. Zapata
Lawrence Livermore National Laboratory
L-487, P.O. Box 5508, Livermore, CA 94550

Abstract

For a vortex-stabilized-lamp pumped, zigzag GGG slab amplifier with diffuse and specular reflectors, the transient-3D Tecate codes calculated the temperature, deformation, stress, wavefront, and depolarization for several estimated and measured source distributions.

Introduction

To develop technology for the DoD Free Electron Laser Program, LLNL has built a GGG zigzag slab amplifier. The 5 x 70 x 184 mm slab is pumped by two pulsed Vortek™ lamps which have a spiraling water coolant between the plasma and the envelope; these lamps are capable of operating at a total power of 260 kWe. Both specular and diffuse reflector cavities have been used. The hardware and experimental data obtained with this system are described in more detail in a companion paper[1]. Here, the computational modeling used both for hardware design and for data interpretation are described.

Computer Codes

The transient-3D family of TECATE codes[2,3] was used to calculate the time dependent temperature, deformation, stress, wavefront, and depolarization of the amplifier as a function of Vortek lamp power. The computations were accomplished in a series of steps. First, the distribution of the heat source was calculated using either analytic models or ray trace codes to model the pump cavity. Two ray trace codes were used. For the specular reflector (second surface thin glass plates backed by heat sinks), a 3-D Monte Carlo ray trace code[4] (MIR3D) was used. For the diffuse reflector (curved Spectralon[5] shell in a heat sink), a 2-D code was used[6]. The results of these codes were used to construct two sets of reflector hardware.

The optical performance of a slab laser is very sensitive to the heat source distribution. Calculation of that distribution can be very time consuming, and significant uncertainties remain, for example, the effect of fluorescence redistribution of energy within the slab. Therefore, we used analytic models to approximate a series of source distributions in order to determine the optimum distribution. These models include the capability to modulate the source in accordance with experimentally determined data. Once the optimum distribution is determined, the reflector design codes may be used iteratively to determine the appropriate reflector design.

The energy equation can be solved when one specifies the slab geometry, material properties, heat source distribution, thermal boundary conditions, and initial temperature. We used HT3D, a transient version of the TECATE HEAT code[2,3] to solve the energy equation. This code uses the Dynamic Alternating Directions Implicit (DADI) method to efficiently solve the finite difference representation of the energy equation. The finite differencing scheme pays particular attention to the discretization accuracy at surfaces, edges, and corners since these regions strongly influence the optical performance of a zig-zag slab laser. The HT3D code provides the time dependent temperature of each of the 31,775 nodal points of the slab. A preliminary calculation showed that pulsing the lamp (and thus the heat source) did not significantly affect the temperature solution. Therefore, the transient source was treated as a step function, turning on at time zero and continuing to the specified time of 40 s. In most cases, the slab temperature distribution reached steady state after only 10 s of operation. In a few cases, the slab end temperatures were still evolving after 40 s.

The balance of force equations can be solved for material stresses, strains, and deformations at any point in time when one specifies the slab geometry, material properties, temperature distribution (from the HT3D code), mechanical boundary conditions, and initial strain (zero). All of our calculations were at 40 s after the start of heating. We used ST3D which was derived from the TECATE TORA code[2,3]. This code also uses the DADI method with carefully discretized equations at the slab surfaces.

The geometric optics equations can be solved at any point in time when one specifies the slab geometry, material properties, temperature distribution (from HT3D), stress, strain, and deformation distributions (from ST3D), and a propagation direction. The phase and depolarization fronts are calculated at a reference surface after the beam exits following one or more passes through the slab. We used OP3D which was derived from the BREW code[3].

Several pre- and post-processors were used in conjunction with these codes. Because the slab performance is dominated by the surfaces and transition regions between heated and

---

* Work performed under the auspices of the U.S. Department of Energy by the Lawrence Livermore National Laboratory under contract number W-7405-ENG and for the Department of Defense under SDIO/SDC/ATC MIPR No. W3-RPD-53-A127.

non-heated portions of the slab, the codes were set up to accommodate variable zoning. The ZONER program written in the QuickBASIC language[7] was used to view the zoning for user-selected input parameters. The TECATE package includes a graphics postprocessor[3] to produce cross-sectional views of the source, temperatures, strains, stresses, and residual computational errors. This postprocessor, GF3D, was adapted to also provide lineouts of these quantities and time evolution graphs for temperature at selected nodes.

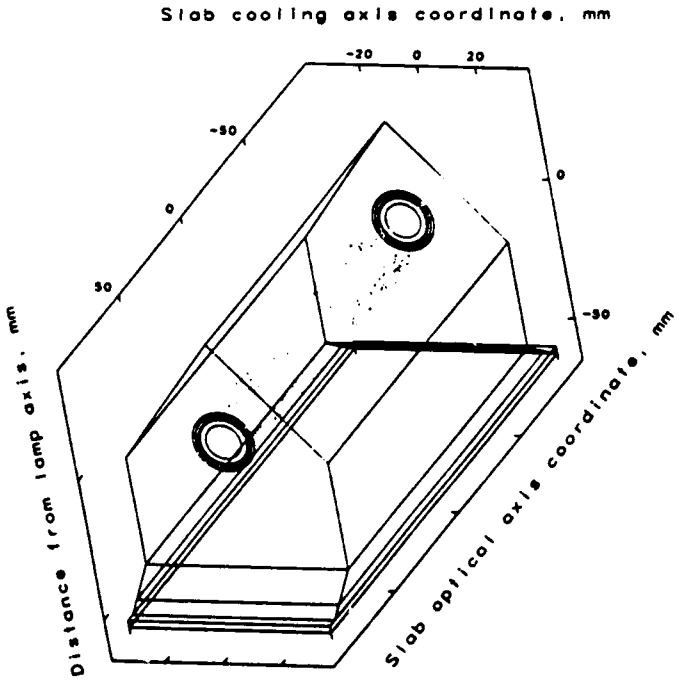
The MathGraf language[8] was used in three postprocessors. For MIR3D, the MIRMATH macro produces 3-D views of the reflector, lamp, and slab geometry, the energy flow from the electrical circuit to the inversion, and the 3-D distribution of energy in the slab. In addition, the energy distribution can be manipulated to increase the Monte Carlo statistics in symmetry situations, to simulate fluorescence redistribution, and to sum the distribution over one or two of the dimensions (producing summed lineout plots).

The MGST macro produces 3-D views of the slab surface grids with user-selected magnifications of the mechanical distortions. These views can be output with colors indicating the degree of distortion for each node. This diagnostic output is extremely useful in evaluating a design's performance.

Finally, the MGOP macro produces 3-D views, 2-D contours, and lineouts of the phase front and depolarization. The phase components due to dn/dT, slab distortion, and stress-optic effects are also shown separately for rays traveling paths determined by the sum of these effects. (The material constants - dn/dT, coefficient of thermal expansion, and stress-optic coefficients - can also be changed in the OP3D code input to fully isolate the separate effects.) In the area of slab distortion, either the slab TIR surfaces or the wedge surfaces can be artificially flattened to determine the separate influence of each surface's distortion. The MGOP macro also curve fits the phase with either second degree or sixth degree polynomial functions in each aperture dimension. Second degree fits can be used to evaluate the improvements available by using tilted or cylindrically focussing optics in the laser train. Sixth degree fits are accurate enough to use interpolation to find the phase at any given point, allowing estimation of multipass phase distortion using sub-apertured beams that are optionally expanded, inverted, or translated between passes. (A proper calculation of multipass phase distortion also requires consideration of both diffraction and the propagation between each pass.)

Reflector Design

The 2-D reflector design code was used to specify the curved surface of the Spectralon[5] reflector. The reflector shape did not vary along its length (parallel to the lamp), and the ends were specular (second surface glass). The design code predicted some small variations in uniformity, and the reflector was built oversized to reduce the source droop near the slab edges.

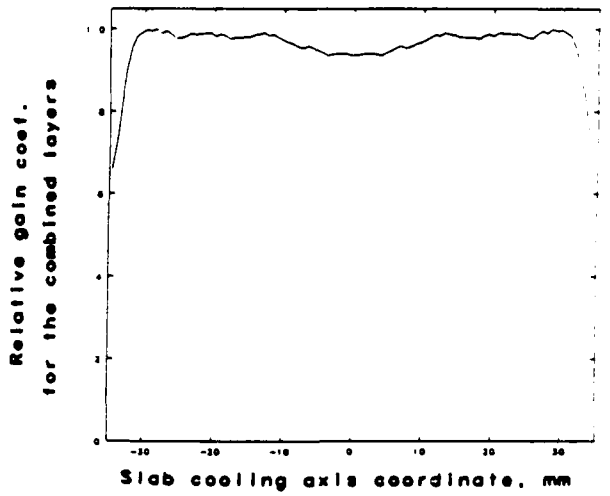


The specular reflector was designed using the MIR3D code, and it was fielded before the diffuse reflector. The specular reflector was not oversized; that feature is recommended for future designs since uniformity improvements appear to outweigh the efficiency penalty. The design, which was done very quickly to allow construction of the experiment, is shown in Fig. 1. The anticipated performance of the reflector is shown in Fig. 2 which shows the energy deposited in the slab as a function of the short dimension of the TIR surface. In this figure, the results have been summed along the slab length and through the slab thickness. The droop near the edges and the slight depression in the center are marks of a less-than-optimum design, and they carry through to the overall system performance. Experimental interferograms for the specular reflector case show "eyes" along the long axis of the aperture; these eyes correspond to the regions of higher pumping in Fig. 2.

Figure 1. Three-dimensional view of the specular reflector design. One-half the slab thickness is shown, and the wedged ends are not modelled since very little pump light reaches those ends. Note the large standoff of the reflector from the slab due to the thicknesses of the window and coolant channels.

Source Functions Used to Calculate the Wavefront

For the wavefront calculations, we used an idealized source function to facilitate zoning, use of a new diffuse reflector material, and adjustment of the source function using experimentally determined results. The idealized source is a "cone model" with a cone originating at each element's centroid. The cone angle is determined by Snell's law (based on the slab index of 1.939 and the evanescent coating index of 1.445), and the cone's intersection with the surface specifies the surface region contributing to the local interior source function. The surface source was a universally distributed Lambertian, and it was truncated at specified locations.



For the wavefront calculations using the diffuse reflector, we used the cone model with the surface source truncated at the slab edge. In the experiments, the diffuse reflector was oversized, providing additional source near the edge to reduce the source droop. The specular reflector was not oversized in either the calculation or the experiments, and its surface source uniformity was modulated along the TIR surface's short dimension to approximate the 1-D experimental distribution of fluorescence.

Figure 2. Predicted performance of the specular reflector. The profile is quite flat except for a dip in the center and droop near the edges. The dip could be removed by adjusting the design, and the droops could be countered by designing an oversized reflector.

For both reflectors, the source function contours are shown in Fig. 3 for a cut midway between the two entrance faces. For the specular reflector, the small central dip and the large edge droop shown in the reflector design code output (Fig. 2) are both evident in the source function contours. The resulting wavefront also has these features. Figure 4 shows lineouts of the phase along the long dimension of the aperture, at mid-thickness, for both reflectors. The diffuse reflector has a constant phase except near the edges. (For the oversize diffuse reflector fielded in the experiments, the edge phase aberrations should be even smaller.) The specular reflector has about five times more phase distortion, and both the edge droop and the central dip are clearly visible. The overall phase distortion is 2.0 waves in the thin dimension and 5.9 waves in the long dimension for the diffuse and specular reflectors, respectively. The depolarization is negligible. For the diffuse reflector run, it is about 0.1% at the worst location (0.5% if the full slab is used for extraction), and about 0.04% when averaged over the aperture.

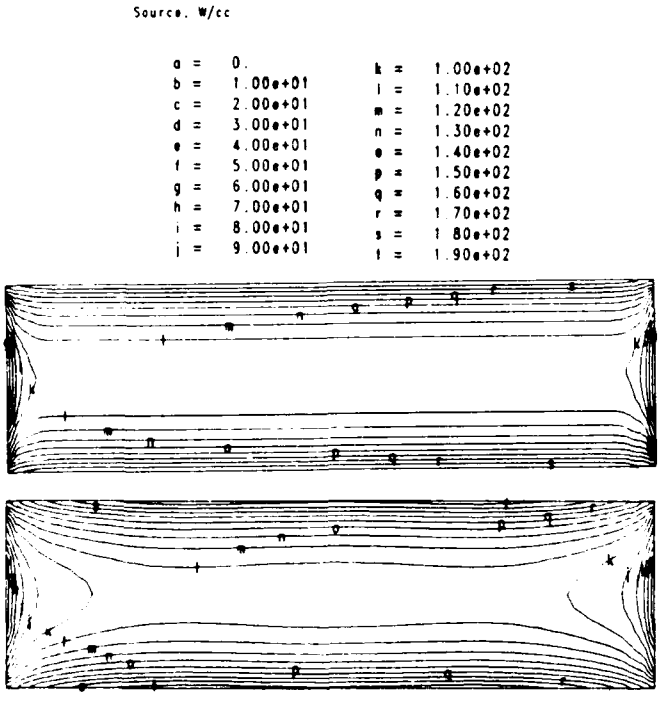


Figure 3. Source function contours in a plane midway between the entrance and exit faces. The horizontal dimension corresponds to the long dimension of the aperture, and the thin dimension is the thickness. The thin dimension is expanded by about a factor of four to enhance visualization of the distribution. The upper plot is for the diffuse reflector, and the lower plot is for the specular reflector.

Effects of Uncooled Ends

For both reflectors, the cooling length was set equal to the reflector cavity length, and the ends of the TIR surfaces were cooled only incidentally by the ambient air. However, the standoff of the reflector from the slab, due to the window and coolant thicknesses, causes the heat source to extend into the uncooled ends. Thermal conduction extends the hot region into the slab ends. Figure 5 shows the heat source, cooling extent, and resulting temperature distribution for the diffuse reflector slab. It is clear that the slant propagation of pump light in the slab produces a heat source in the uncooled region even when the standoff of the reflector from the slab is ignored. The tip temperature reaches 50°C after 40 s, and further increases would occur for longer calculation times. In addition, at the cooling termination location, the TIR surface temperature climbs abruptly from 30°C to 55°C.

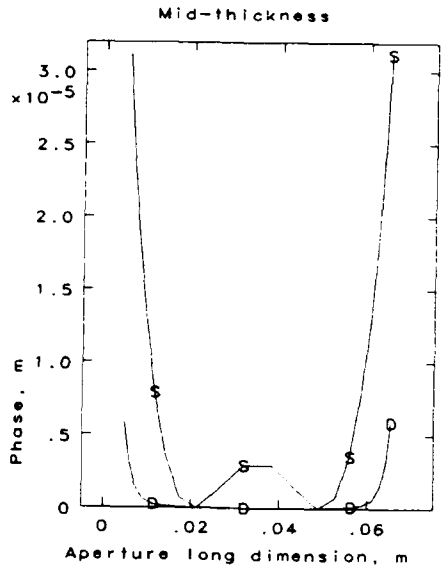


Figure 4. Lineouts of the phase along the long dimension of the aperture, at mid-thickness. In each case, one slab-thickness was removed from the beam at each end of the aperture.

These effects result in distortions of the slab surfaces, as shown in Fig. 6. The arrow in the figure indicates a bulge in the cooling transition region near the beveled end of the TIR surface. The figure also shows that the slab ends shrink with respect to the central regions of the slab. The temperature of the slab ends was less than the average temperature in the central region that was both strongly heated and vigorously cooled.

The calculated wavefront for the slab with diffuse reflectors and uncooled ends is shown in Fig. 7. The contours are at half-wave intervals. There are about two waves of distortion across the thin dimension of the beam, and this distortion is due to the temperature variation and mechanical deformation in the slab ends. When the beam path is determined by all three effects, the thin dimension distortion is 1.5 waves due to dn/dT, 0.6 waves due to deformation, and 10^{-2} wave due to stress-optics effects.

The lineout across the slab thickness shows that the phase is distorted in the center, mostly due to one pair of the four cooling transitions. There are two transitions on each TIR surface, and the footprints of the beam on the TIR surfaces roughly align the beam center with the transition in two cases and the beam edges in the other two cases. The phase distortion near the beam centerline was experimentally confirmed

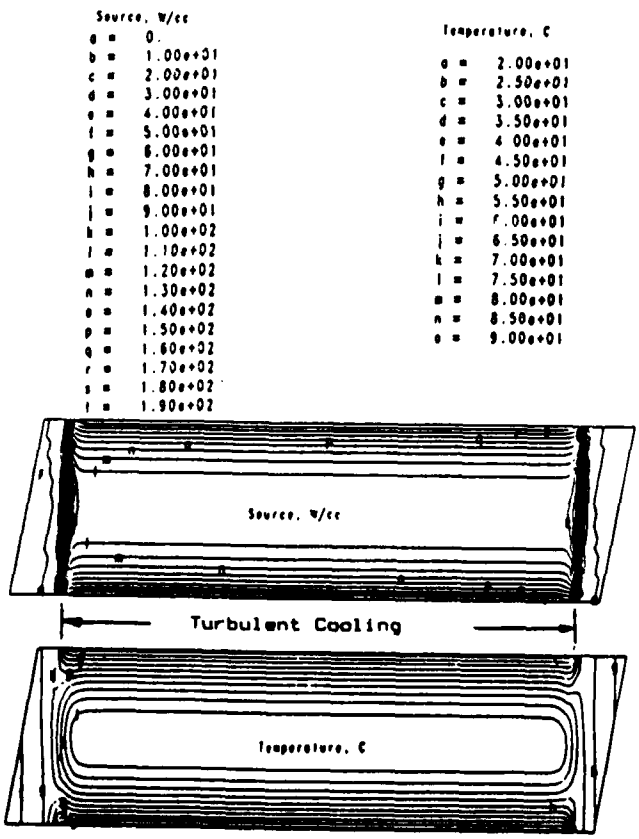


Figure 5. Contours of the source and the temperature in center cut of the slab with uncooled ends. The limits of turbulent water cooling are also shown. The long dimension is the slab optical axis while the thin dimension is the slab thickness, which is expanded by a factor of about ten for clarity.

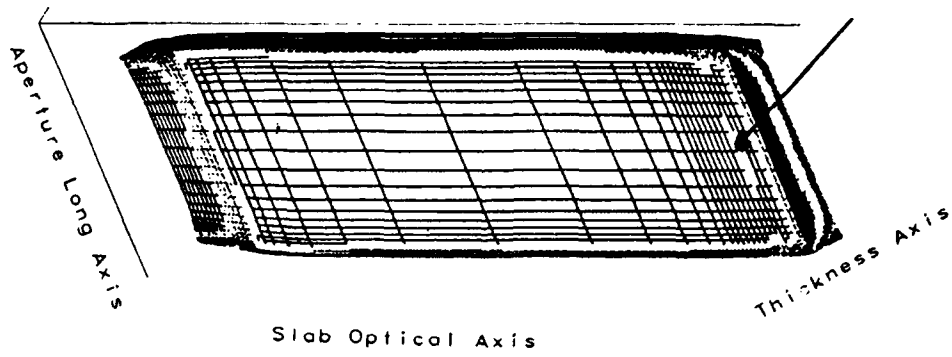


Figure 6. The displaced grid of three surfaces of the slab with uncooled ends and a diffuse reflector. The finer zoning in the transition and edge regions is evident. The shades of gray (which can also be displayed as colors) represent the normal displacement of the surface. These displacements have been magnified by a factor of 3000 for clarity. The arrow indicates a bulge in the TIR surface. Also note the contraction of the ends of the slab.

by the lack of extracted beam in this region when the diffuse reflector experiment was operated as an oscillator. The distortion at the edges of the thin dimension is partially due to shrinking of the slab ends, but mostly due to the other pair of cooling transitions. About 2/3 of the thin edge distortion is due to dn/dT, and there are no radical temperature fluctuations at the intersections of the TIR and entrance surfaces. Further, artificially flattening the entrance surfaces and the TIR faces (in separate calculations) shows that the deformation contribution is purely from the TIR surfaces. Finally, examination of a run with expanded (rather than contracted) slab ends shows the same thin dimension lineout shape as this run.

The logical improvement is to extend cooling over a larger region of the TIR surface. The hardware was modified to cool the end TIR surfaces with turbulent water, but experiments have not yet been run with this hardware. For an end coolant temperature of 20°C, the calculated wavefront improves for both reflectors, to 1.0 waves in the thin dimension and to 4.3 and 27 waves in the long dimension for the diffuse and specular reflectors, respectively. In the long dimension, elimination of two (rather than one) slab thicknesses at each end would remove most of the aberration. Alternatively, the source function must be prevented from drooping at the slab edges.

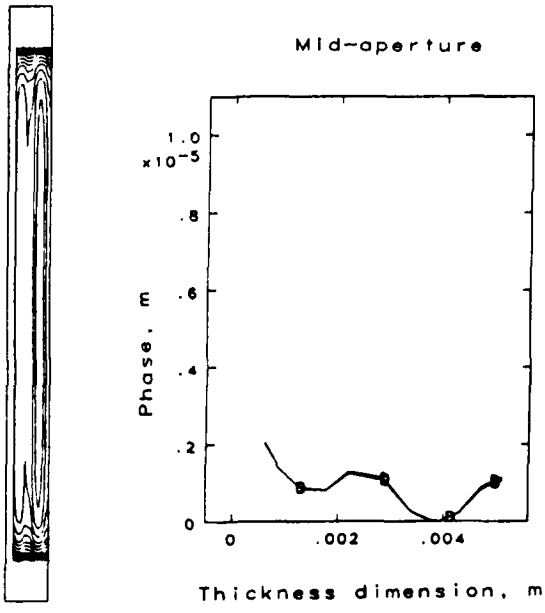
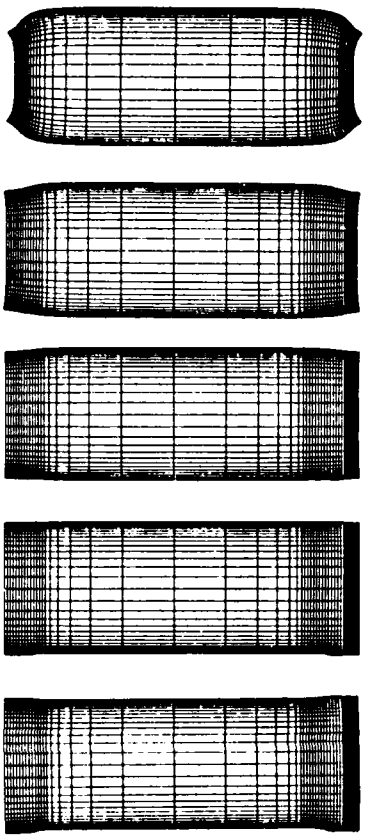


Figure 7. Phase for the slab with uncooled ends and diffuse reflectors. The left graph is a simulated interferogram with half-wave contours. The right graph is a lineout of the phase across the thin dimension (for both specular and diffuse reflectors).

Effects of End Coolant Temperature

Although the fully cooled results are a distinct improvement, it is clear that much of the remaining distortion is due to the overcooled ends. A series of runs for the diffuse reflector used a heated water coolant on the ends of the TIR surfaces; temperatures of 20, 48, 55, 62, and 66.7°C were used. In each case, the slab ends quickly approach the end coolant temperature (and with less than 0.1°C variation within the region). The resulting deformed grids are shown in Fig. 8 for the five runs. The ends undergo transition from contraction to expansion at about 60°C. Since 62°C is the thickness-averaged temperature of the pumped region of the slab, the end expansion or contraction is also influenced by other factors, such as the contraction of the mounting edges caused by the source function droop at those locations.



The thin-dimension wavefronts for the five cases are 1.0, 0.6, 0.8, 1.2 and 1.4 waves in order of increasing end coolant temperature. The wavefront for the 48°C end coolant case is shown in Figs. 9 and 10. This run has a smoother wavefront than either the run with less mechanical distortion of the ends or the run with less temperature variation between the core and the ends. There is a competing effect, the localization of the temperature transition. As the end coolant temperature increases, the temperature transition on the TIR surface between the two cooled regions becomes more abrupt. Since dn/dT is the prime driver of the wavefront, a more localized temperature transition concentrates the dn/dT effect in a smaller region of the beam, resulting in a larger phase distortion.

Figure 8. Deformed grids for the five runs with heated end coolants. From top to bottom, the end coolant temperatures are 20, 48, 55, 62, and 66.7°C, respectively. The central coolant temperature is 20°C in each case. The view is along a normal to a TIR surface; one mounting surface and one entrance surface are visible at the top and right of each grid. The grid deformations have been exaggerated by a factor of 3000 for clarity.



Figure 9. Interferogram for the diffuse reflector with 48°C end coolant temperature. One slab thickness has been removed from each end. The contour interval is 1/2 wave.

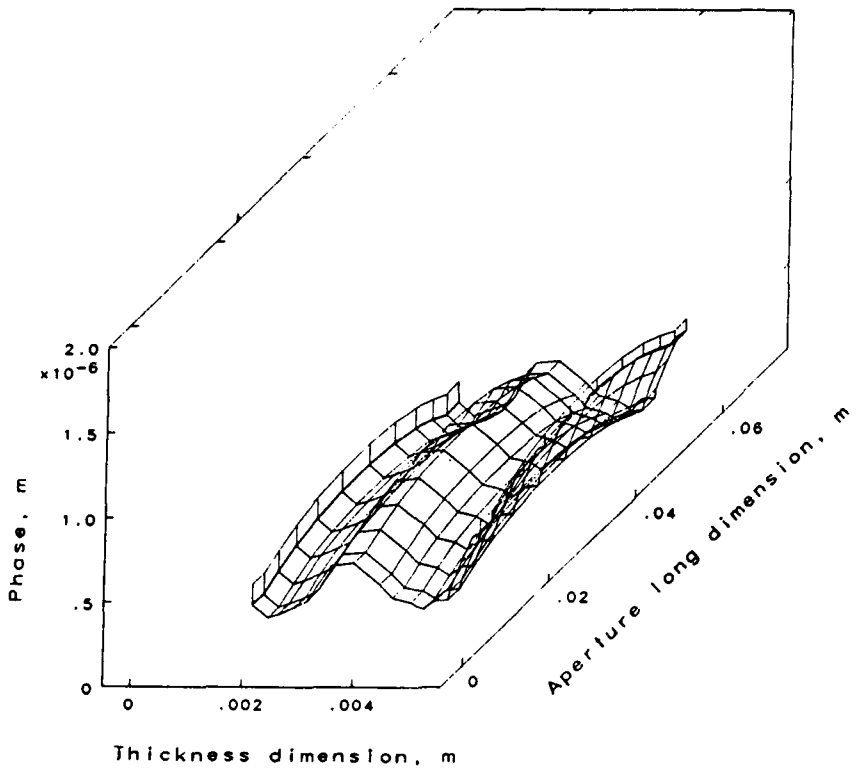


Figure 10. Phase for the diffuse reflector with 48°C end coolant temperature. Two slab thicknesses have been removed from each end.

Summary

The suite of computer codes needed to model zig-zag laser performance is in place. These codes are being used to design high-average power lasers and to interpret their experimental performance. The calculations indicate that with only minor modifications, the Vortek pumped Nd:GGG slab laser is capable of producing in excess of 1 kW of high quality output.

References

1. L. Zapata, K. Manes, D. Christie, J. Davin and J. Blink, "Characteristics of a 500 Watt Nd:GGG Zigzag Slab Oscillator" (This proceedings)
2. S. Doss, R. Gelinas and N. Carlson, "Finite Difference Solutions of Thermoelasticity in Anisotropic Crystals. An application of the Dynamic ADI Method" (Lawrence Livermore National Laboratory Report UCRL-92134, Feb 15, 1985)
3. R. Gelinas and S. Doss, "LASRPAK: A Set of 3-D Thermal, Stress, and Optical Ray Trace Codes for Modelling High Average Power Slab Lasers" (Lawrence Livermore National Laboratory Report, to be published)
4. E. Goodwin, "Flashlamp Pump Cavity Design Code - MIR3D," Lawrence Livermore National Laboratory Report (To be published)
5. Labsphere, "Spectralon Data Sheet," (North Sutton, NH, 1988)
6. L. Zapata, private communication (Lawrence Livermore National Laboratory, Jun 1989)
7. Microsoft Corp., "QuickBASIC 4.0" (Redmond, WA, 1987)
8. Caren Co., "MathGraf" (Tracy, CA, 1988)

Disclaimer

This document was prepared as an account of work sponsored by an agency of the United States Government. Neither the United States Government nor the University of California nor any of their employees, makes any warranty, express or implied, or assumes any legal liability or responsibility for the accuracy, completeness, or usefulness of any information, apparatus, product, or process disclosed, or represents that its use would not infringe privately owned rights. Reference herein to any specific commercial products, process, or service by trade name, trademark, manufacturer, or otherwise, does not necessarily constitute or imply its endorsement, recommendation, or favoring by the United States Government or the University of California. The views and opinions of authors expressed herein do not necessarily state or reflect those of the United States Government thereof, and shall not be used for advertising or product endorsement purposes.

ALEXANDRITE BLUE LASERS

Michael L. Shand
Allied-Signal Inc.
Columbia Road & Park Ave.
Morristown, NJ 07962

Abstract

The tunability, energy per pulse, and average power of alexandrite lasers, together with nonlinear wavelength conversion techniques are used to produce a compact and efficient blue laser source.

Introduction

A number of groups are addressing blue lasers for laser communications from a satellite to submarines (satellite laser communications or SLC). SLC requires the light to be transmitted through seawater so a source in the approximately 420 nm to 550 nm region is required. Furthermore, the signal must be separated from sunlight which is done with an atomic resonance filter (ARF) receiver. The atomic resonance has a narrow bandwidth (~several picometers) and, of course, requires a transmitter operating at the wavelength of the atomic resonance. The most developed ARF receiver uses cesium (Cs) which has absorption bands near 455 nm and 459 nm. Each band is about 4 pm wide. This paper summarizes the approach Allied-Signal has taken to produce a transmitter for the Cs ARF, an approach based on the alexandrite ($BeAl_2O_4$:Cr) laser[1].

The work which has resulted in this summary has been carried out mainly at two departments: Electro Optical Products, Allied-Signal Guidance Systems Division, Westlake Village, California, and Laser R&D, Allied-Signal Research and Technology, Morristown, New Jersey. A number of individuals have contributed to this project including, in alphabetical order, Yehuda Band, Da Wun Chen, Tim Chin, John Fleming, Don Heller, Jerzy Krasinski, Jerry Kuper, Ken Leslie, Lisa Fernandez, Kevin Masters, Bob Morris, Paul Papanestor, Ross Rapoport, Richard Sam, Mike Shand, Don Siebert, and Jen Jye Yeh.

Alexandrite Lasers

Alexandrite ($BeAl_2O_4:Cr^{3+}$) lasers have high energy, high peak power and tunability from 720 nm to over 850 nm. Figure 1 shows early alexandrite laser data which demonstrates many of the properties of alexandrite. First, although this data is over ten years old, the energy output is measured in Joules, not milliJoules which is typical of many new laser materials. The high energy output is a result of the very high storage energy of alexandrite. Second, the output is continuously tunable from 730 nm to past 790 nm. In more recent experiments, the alexandrite laser has been shown to be tunable past 850 nm when heated sufficiently. A large (400 mJ, 250 Hz) laser has been built for LANL which operates from 790 nm to 793 nm demonstrating high energy output away from the peak output. Third, alexandrite laser output increases with increasing temperature. This feature has allowed development of a conductively cooled pump chamber made of sapphire, shown in Fig. 2. The long pulse output of a laser using this pump chamber is shown in Fig. 3. Output energy over 3 J was demonstrated with an overall efficiency of over 3%.

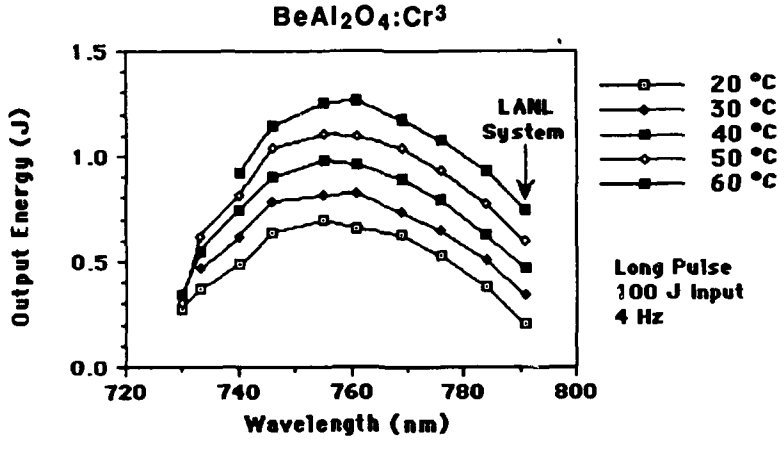


Figure 1: Alexandrite Laser Performance

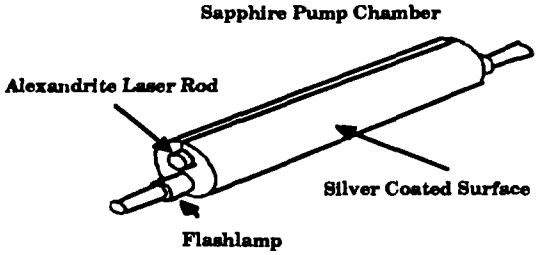


Figure 2: Sapphire Pump Chamber

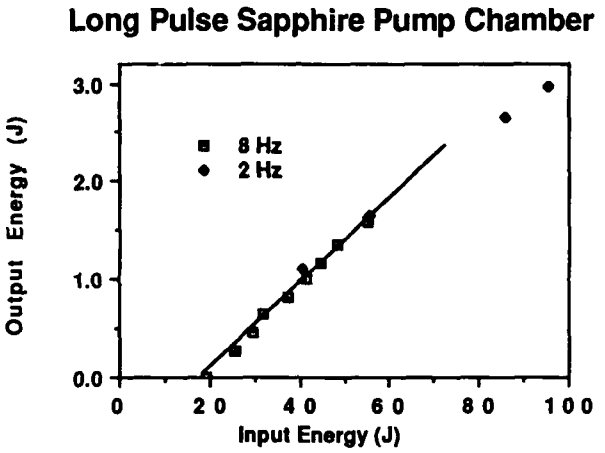


Figure 3: Sapphire Pump Chamber Laser Output

Wavelength Conversion Approaches

Generating blue light at 455 nm starting with alexandrite requires nonlinear frequency conversion techniques. Three have been considered: (1) alexandrite output (red) followed by second harmonic generation (SHG) (UV) followed by Stokes Raman conversion (blue), (2) alexandrite (red) followed by Stokes Raman conversion (IR) followed by SHG (blue), and (3) alexandrite and Nd output mixed by sum frequency generation. The third choice could be very efficient, but would require more extensive development. The first two differ in the choice of which nonlinear process must handle the highest optical power. The rest of this paper discusses the first approach, which has received the most development.

The block diagram of the process is shown in Fig. 4. This approach has the advantage that a number of parameters are isolated, rather than dependent on a single laser subsystem. The source is an external cavity diode which controls the system wavelength and bandwidth. The oscillator controls the spatial and temporal profiles of the red laser. The amplifiers give the required red energy output.



Figure 4: Block Diagram of Blue Laser System

Alexandrite Laser Subsystems

The source is an external cavity diode laser with output of ~10 mW cw. The cw output allows wavelength measurement with a wavemeter with 1 pm accuracy. A simple feedback control can maintain the diode laser wavelength. The diode laser bandwidth is much less than 1 pm.

The output of the diode laser injection seeds an alexandrite oscillator. Under contracts with LANL and NASA, Allied-Signal has investigated injection seeding and shown that only 10 μW is needed intracavity to control an alexandrite oscillator[2]. Generally, two longitudinal modes are excited in the oscillator with a narrowband source; two modes are sufficiently narrow for producing blue light within the CsARF. Injection seeding power gains of 10^{12} have been demonstrated with the alexandrite laser output matching the diode laser input.

The design of the amplifier depends on a tradeoff between the energy out of the oscillator and the gain required in the amplifier. The better the beam quality in the oscillator, the less energy is available from the oscillator and the more gain is required in the amplifier. In one configuration, a TEM_{00} oscillator is used with a tandem double pass amplifier (tandem meaning two alexandrite laser rods in series, double pass meaning a mirror to reflect the beam back through the two rods) and a phase conjugate mirror (stimulated Brillium scattering in nitrogen gas) to produce 1.5 J in a near diffraction limited beam at 10 Hz[3].

Blue Laser Schematic

The nonlinear conversion schematic is shown in Fig. 5 with estimates of the energy at several stages which will result in 500 mJ blue light. Two SHG stages are planned to convert more of the red to UV than if only one stage is available. Both KDP and BBO have been tested for SHG materials. We have found KDP can handle more optical power so the first crystal is KDP. The second crystal can be KDP or BBO. SHG results have been 35% conversion with KDP at 300 mJ UV output and 33% conversion with BBO at 105 mJ UV output.

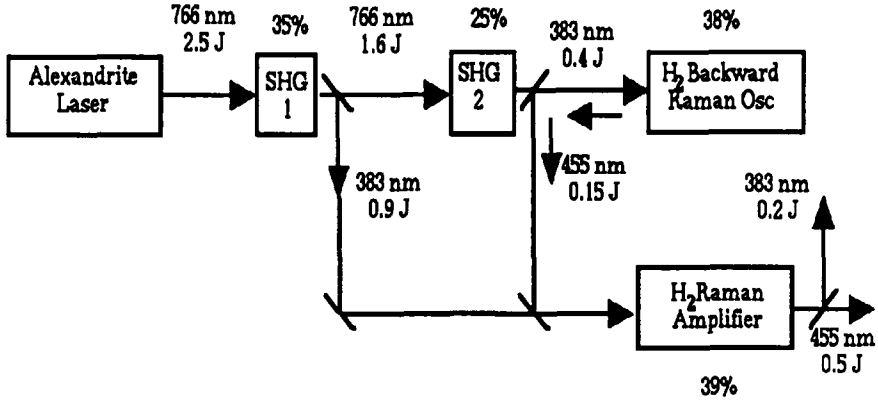


Figure 5: Nonlinear Conversion Schematic

The Raman conversion process uses a backward Raman oscillator and a forward Raman amplifier. The backward oscillator is selected because it maintains a narrow bandwidth, is efficient, and produces a good blue beam quality. In Raman conversion experiments using an oscillator, hydrogen gas, and UV input, we have demonstrated 100 mJ in the first Stokes wavelength at 33% efficiency. In the same experiment 85 mJ was generated in the second Stokes. The stored energy is providing the output energy for both beams. In an amplifier the total output is available yielding over 50% conversion.

Considerations of packaging requirements and energy required have led to a design point for the system with 1% efficiency from capacitor bank energy to blue output.

Future Considerations

The work described here is based on flashlamp excitation of alexandrite. For satellite applications, efficiency and lifetime issues are critical and diodes are the most likely excitation source for the laser transmitter. Diode pumping of alexandrite is shown schematically in Fig. 6 with a comparison to a Ti:Sapphire diode pumped laser. The alexandrite laser requires diodes at 650 nm or 680 nm. The 680 nm diodes pump the R-line of alexandrite and require a narrow diode output, similar to that of the 808 nm diodes for Nd pumping. The 650 nm diodes pump a broad absorption band in alexandrite and can have more than several nanometers bandwidth. The high energy storage of alexandrite compared to YAG:Nd means an oscillator can be used rather than an oscillator-amplifier configuration. Allied-Signal has a team in place including Sarnoff Research Center, Cornell University, and Laser Technology Associates to fabricate diode laser arrays at 650 - 680 nm and design, optimize, and produce diode pumped alexandrite lasers in the range of 1 J/pulse.

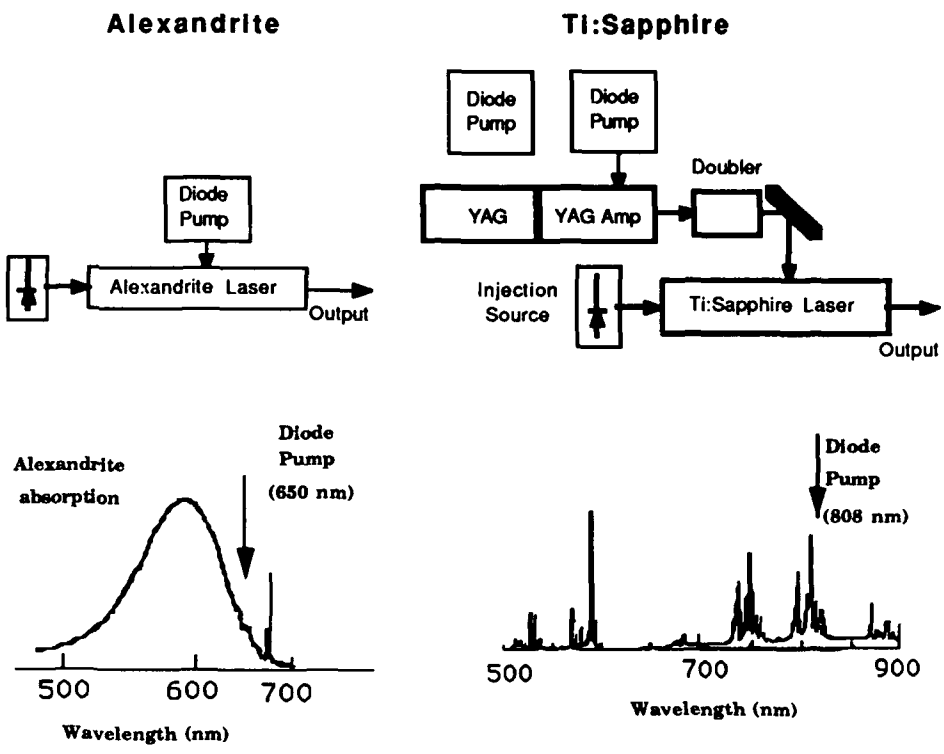


Figure 6: Diode Pumped Tunable Lasers

Very recently, Scheps et al. have demonstrated a diode pumped alexandrite laser with pumping on the R line[4].

Conclusion

The maturity and opto-mechanical properties of alexandrite lasers has led to a straight forward design of a 500 mJ output blue laser using a diode laser injection source, an alexandrite oscillator-amplifier, SHG, and Raman conversion.

References

1. J.C. Walling, O.G. Peterson, H.P. Jenssen, R.C. Morris, and E.W. O'Dell, "Tunable Alexandrite Lasers," IEEE JQE Vol. QE-16, 1980, p. 1302.

2. J. Krasinski, P. Papanestor, J.A. Pete, and D.F. Heller, Tunable Solid State Laser II, A.B. Budgor, L. Esterowitz, and L.D. DeShazer, Ed., Springer-Verlag, 1986, p. 191; NASA Goddard Space Flight Center, Final Report, Contract NAS5-30102, 1988.

3. W.R. Rapoport, J.W. Kuper, J.S. Krasinski, T. Chin, "High Brightness Alexandrite Laser," OSA Topical Meeting on Advanced Solid State Lasers, March, 1990, Salt Lake City.

4. R. Scheps, B.M. Gately, J.F. Myers, D.F. Heller, and J.S. Krasinski, "Laser Diode Pumped Tunable Solid State Laser," OE LASE '90, Los Angeles, January, 1990.

FREQUENCY DOUBLED OPERATION OF A GROUND STATE DEPLETED LASER USING THE Nd^{3+} $^4F_{3/2}$ - $^4I_{9/2}$ TRANSITION IN Y_2SiO_5

R. Beach, G. Albrecht, S. Mitchell, B. Comaskey, R. Solarz, and W. Krupke
Lawrence Livermore National Laboratory
P.O. Box 5508, L-495
Livermore, California 94550

C. Brandle and G. Berkstresser
AT&T Bell Laboratories
600 Mountain Avenue
Murray Hill, NJ 07974

Abstract

A ground state depleted (GSD) laser has been demonstrated at 912 nm in the form of a Q-switched oscillator operating on the Nd^{3+} $^4F_{3/2}$ - $^4I_{9/2}$ transition in Y_2SiO_5. Samarium scandium gallium garnet has been demonstrated effective at selectively suppressing the competing and much stronger $^4F_{3/2}$ - $^4I_{11/2}$ lasing transition. Efficient harmonic generation has been demonstrated using non-critically phase matched $KNbO_3$.

Introduction

Ground state depleted (GSD) lasers[1,2] are characterized by a low laser ion doping density (5-10 x 10^{18} cm^{-3}) and a large fractional excited state population inversion density (4-8 x 10^{18} cm^{-3}). For efficiency, these lasers must be pumped by narrow band (< few nm), intense (>50-100 kW/cm^2) sources. The large fractional excited state population inversion allows efficient quasi-four level laser operation to a high lying Stark level in the ground state electronic manifold. In this manuscript we report on progress made in the experimental demonstration of a GSD laser using the Nd^{3+} $^4F_{3/2}$ - $^4I_{9/2}$ transition. This transition is of interest because it offers the possibility of constructing a laser operating at the wavelengths of 911 or 919 nm giving access to Cs atomic resonance filters[3] through simple and efficient harmonic doubling.

In an effort to identify suitable hosts for a GSD laser, spectroscopic measurements have been performed in various Nd doped crystalline materials to extract parameters (Stark resolved emission spectra, branching ratios, fluorescence lifetimes, and stimulated emission cross sections) important to the laser design. Desirable features of Nd-hosts for depletion pumped lasers used for our particular application are:

1. A $^4F_{3/2}$ - $^4I_{9/2}$ fluorescence band dominated by a transition peaking at approximately 911 or 919 nm, ensuring adequate emission at one of the desired operating wavelengths.

2. A terminal Stark level with an energy 300-400 cm^{-1} above the lowest lying Stark level, ensuring a small fractional thermal population in the terminal laser level at room temperature.

3. A branching ratio for the $^4F_{3/2}$ - $^4I_{9/2}$ transition >0.3 and a $^4F_{3/2}$ radiative lifetime of 100-300 μsec, which together with condition 1 ensure a stimulated emission cross section of 2-5 x 10^{-20} cm^2 on the desired laser transition.

4. A crystal host that can be grown to sizes of approximately 1 cm x 1 cm x 10-20 cm.

5. A $^4F_{3/2}$ - $^4I_{11/2}$ fluorescence band not dominated by a single transition line limiting the peak emission cross section for this emission band and minimizing ASE and 1060 nm hold off problems.

Host Crystal and Nd^{3+} Spectroscopy

Table 1 lists Nd doped crystals that have been fabricated and evaluated at Lawrence Livermore National Laboratory (LLNL) for suitability as GSD lasers operating at 911 or 919 nm. The detailed Stark spectroscopy of the $^4F_{3/2}$ and $^4I_{9/2}$ manifolds for Nd^{3+} in one of these crystals, yttrium orthosilicate (Y_2SiO_5), is shown in Fig. 1 for both types of optical sites that Nd^{3+} is reported to occupy.[4] This host material is attractive because of the possible 911 nm laser transition from the lowest lying Stark level of the $^4F_{3/2}$ manifold to the Stark level 355 cm^{-1} above the lowest lying one of the $^4I_{9/2}$ manifold. It becomes even more attractive on examination of an emission spectrum because the transition between the Stark levels of interest dominates the $^4F_{3/2}$ - $^4I_{9/2}$ emission as shown in Fig. 2.

Crystal	Z_1 (cm^{-1})	λ (nm)	τ, μsec
* $Bi_4Si_3O_{12}$	450	918.6	230
* $Bi_4Ge_3O_{12}$	423	918.9	220
* $Ca(NbO_3)_2$	522	~921	125
$LaNbO_4$	506	918.9	120
* $Na_{15}La(BO_3)_7$	570	920.8 (77 K)	80
$YAlO_3$	670	919.8	180
$LuAlO_3$	662	919.8	160
$Y_2Si_2O_7$	—	919	310
* $LuPO_4$	423	911	120
$LaAlO_3$	604	910.8	460
$NaLa(WO_4)_2$	424	910.8	180
* $LiYO_2$	445	911.6	150
* $Ba_2LaNb_5O_{15}$	428	910.6	230
$Ba_2LaTa_5O_{15}$	417	910.8	212
Y_2SiO_5	—	912	240
Gd_2SiO_5	—	~911	—
0.7 Ga 0.27 La 0.03 Nd sulfide glass	—	911	—

Table 1. Nd doped crystals that have been fabricated and evaluated at LLNL for suitability as GSD lasers operating at 911 or 919 nm.

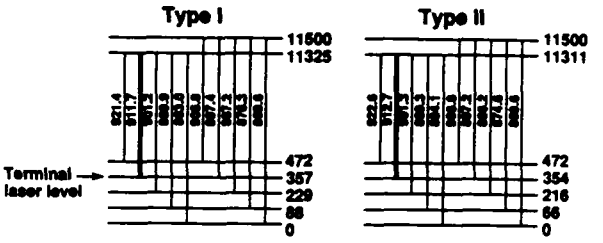


Figure 1. Detailed Stark spectroscopy of the $^4F_{3/2}$ and $^4I_{9/2}$ states in Nd^{3+}:Y_2SiO_5 for both types of optical sites Nd^{3+} is reported to occupy.[4]

Because of development work done on the growth of this material for applications other than lasers,[5] substantial size boules were immediately available. An example of an undoped boule of Y_2SiO_5 is shown in Fig. 3. As a result of the large laser quality crystals that were growable and the encouraging results of our own initial unoriented spectroscopic evaluation, a more complete spectroscopic study was undertaken. Because Y_2SiO_5 is a monoclinic crystal of class 2/m (space group c2/c) it is biaxial. This introduces a directional anisotropy in the optical properties of the crystal that necessitated the acquisition of both orientationally and spectrally resolved emission and absorption spectra. The acquired absorption spectra were then analyzed using a Judd-Ofelt type analysis for radiative transition rates between the levels of interest for the operation of our laser.

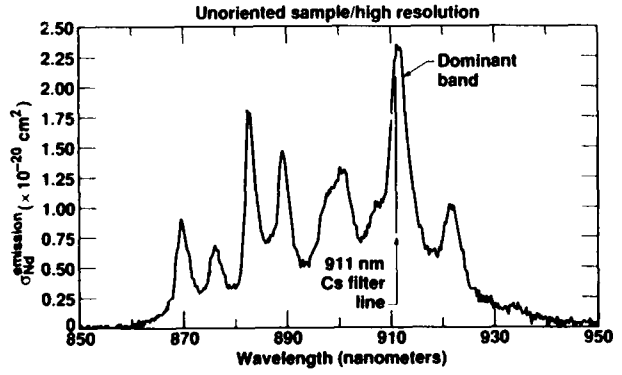


Figure 2. $^4F_{3/2}$ - $^4I_{9/2}$ emission spectrum from an unoriented sample of Nd^{3+}:Y_2SiO_5. The arrow indicates twice one of the Cs-ARFs acceptance wavelengths.

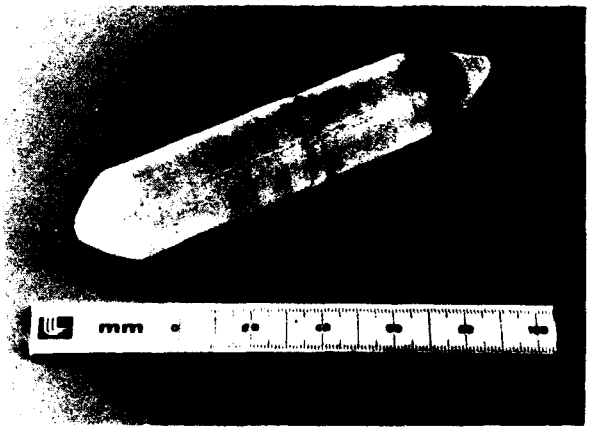


Figure 3. Photograph of a Y_2SiO_5 boule grown by Dave Brandle of AT&T Bell Laboratories using a Czochralski technique.

The Judd-Ofelt[6,7] model has become a standard tool for calculating the parity-forbidden electric-dipole radiative transition rates between the various levels of rare earth ions in both glass and crystalline hosts. This technique is based on an analysis of measured optical absorption line strengths[8,9] and is easily applied to isotropic host materials. The same analysis can be applied to anisotropic crystals if proper account is taken of the fact that measured absorptions can vary with directions in these crystals. Such an analysis was first performed by Lomheim and DeShazer[10] in their investigation of Nd^{3+} in the uniaxial crystal YVO_4. The central point made in their analysis was that because the Judd-Ofelt theory uses line strengths summed over all directions and polarizations some suitable type of averaging would have to be performed on the measured line strengths to properly apply the Judd-Ofelt theory to anisotropic crystals.

As a reasonable approximation to actually measuring absorption line strengths over all possible directions and polarizations, a rectangular sample was fabricated with each of its sides oriented perpendicular to one of the principal axes of the optical indicatrix. We denote these principal axes by X, Y, and Z for the fast, intermediate, and slow vibration directions, respectively. Using this sample then allowed the measurement of absorption spectra along the three mutually perpendicular principal axes of the indicatrix. The orientation of the cube was accomplished by first identifying the ⟨010⟩ direction which is a two-fold symmetry axis of the crystal using an X-ray back reflection Laue camera. Symmetry requires that a principal axis of the optical indicatrix be parallel to the ⟨010⟩ direction.[11] Fabricating a sample with faces normal to the ⟨010⟩ direction then allowed the remaining two principal axes to be found by identifying extinction directions with the sample viewed between crossed polarizers.

Figure 4 shows measured absorption cross sections for the three different orientations studied in the spectral regions that are of interest for laser exciting this material with either an alexandrite or an AlGaAs semiconductor laser. Measured and orientationally averaged line strengths for the absorption bands presented in Fig. 4 as well as six others between 400 and 900 nm are detailed in Table 2. Using these measured line strengths, the three Judd-Ofelt intensity parameters, $\Omega_{(t)}$, can be found by solving the overdetermined set of equations[12]

$$S_{meas}(J \rightarrow J') = \sum_{t=2,4,6} \Omega_t \left| \langle \psi J \right| \left| U^{(t)} \right| \left| \psi' J' \rangle \right|^2 \qquad (1)$$

where the matrix elements $\langle \psi J \| U^{(t)} \| \psi' J' \rangle$ are the doubly reduced unit-tensor operators of rank t calculated in the intermediate-coupling approximation. Values of these reduced matrix elements for the spectroscopic band assignments detailed in Table 2 were compiled using values calculated by W. T. Carnall et al.[13] Solving the set of equations in (1) for the Judd-Ofelt parameters that give the best least-square fit to the measured line strengths gives[8,12]

$$\Omega_2 = 3.34 \times 10^{-20}\ \text{cm}^2$$

$$\Omega_4 = 4.35 \times 10^{-20}\ \text{cm}^2 \qquad (2)$$

$$\Omega_6 = 5.60 \times 10^{-20}\ \text{cm}^2$$

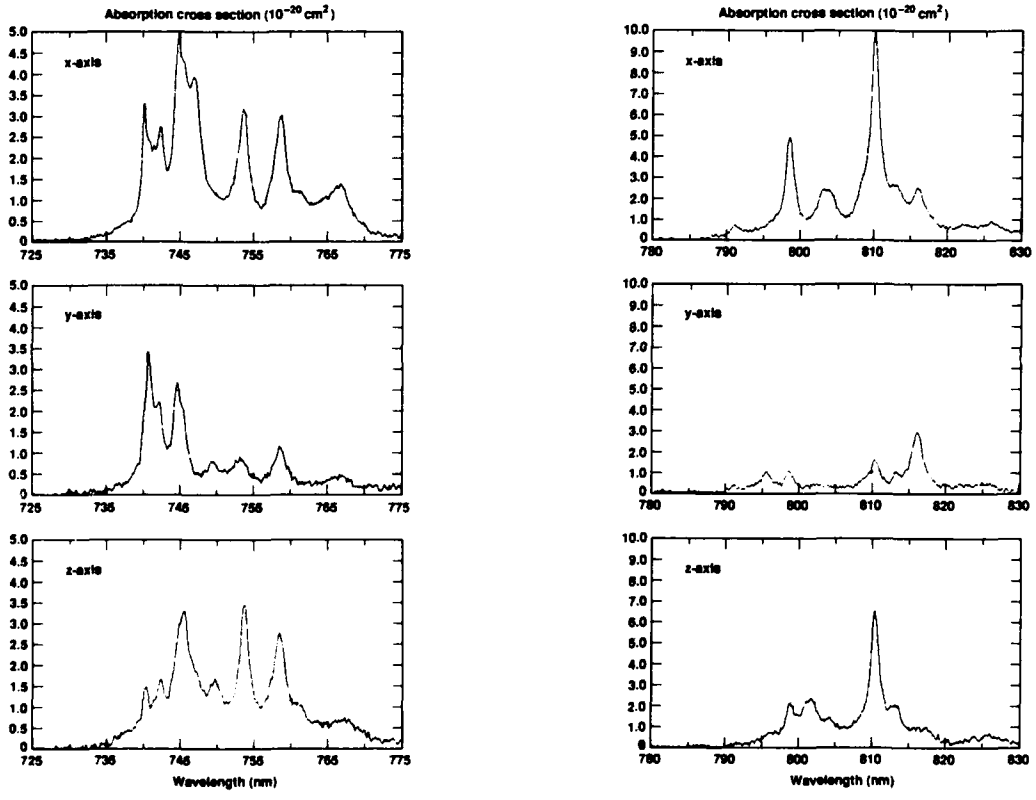


Figure 4. Orientationally resolved absorption spectra in the spectral regions used for alexandrite and AlGaAs semiconductor laser excitation.

These values of the Judd-Ofelt parameters and Eq. (1) can now be used to calculate the transition line strengths between any two levels of Nd^{3+} in Y_2SiO_5. In particular, if we use these Judd-Ofelt parameters to go back and calculate the line strengths of the eight absorption bands used in our analysis, we can get an idea of the validity of our polarization averaging approximation. The theory predicted or calculated line strengths are displayed along with the measured line strengths in Table 2. Defining ΔS to be the difference between the measured and calculated line strength values and defining RMS ΔS by

$$\text{RMS } \Delta S = \sqrt{\frac{\Sigma(\Delta S)^2}{(\text{number of transitions}) - 3}} \tag{3}$$

the RMS ΔS value for the line strength set listed in Table 2 is 0.146×10^{-20} cm^2. A measure of the relative error of the fit is given by (RMS ΔS)/(RMS S) = 0.048, giving one a high degree of confidence in the validity of our original polarization averaging approximation. Although the self consistency of the Judd-Ofelt parameter values is very good, our absolute values are limited to ±10%, the accuracy to which we know the Nd concentration of the crystal.

				Polarization Averaged		
Transition ($^4I_{9/2}$)	$\lvert\langle U^2\rangle\rvert^2$	$\lvert\langle U^4\rangle\rvert^2$	$\lvert\langle U^6\rangle\rvert^2$	$\bar{\lambda}$(nm)	S_{meas}(10^{-20} cm^2)	S_{calc}(10^{-20} cm^2)
$^2P_{1/2} + {}^2D_{5/2}$	0	0.0398	0.0017	433.6	0.118	0.183
$^4G_{11/2} + {}^4G_{9/2} + {}^2D_{3/2} + {}^2K_{15/7}$	0	0.0306	0.0229	470.8	0.437	0.261
$^4G_{7/2} + {}^2G_{9/2} + {}^2K_{13/2}$	0.0711	0.2295	0.1279	526.0	1.965	1.953
$^4G_{3/2} + {}^2G_{7/2} + {}^2H_{11/2}$	0.9682	0.5873	0.0724	587.0	6.195	6.197
$^4F_{9/2}$	0.0009	0.0092	0.0406	686.0	0.251	0.270
$^4F_{7/2} + {}^4S_{3/2}$	0.0011	0.0431	0.6619	751.6	3.774	3.896
$^4F_{5/2} + {}^2H_{9/2}$	0.0101	0.2419	0.5178	809.3	4.151	3.985
$^4F_{3/2}$	0	0.2283	0.0554	887.2	1.134	1.304

Table 2. Polarization averaged absorption transition intensities in Nd^{3+}:Y_2SiO_5.

Using the determined Judd-Ofelt parameters, line strengths corresponding to transitions from the $^4F_{3/2}$ to the $^4I_{11/2}$, $^4I_{13/2}$, and $^4I_{15/2}$ manifolds can now be calculated. The calculated line strengths for these transitions as well as the measured $^4F_{3/2}$ to $^4I_{9/2}$ line strength are listed in Table 3. From these line strengths radiative transition rates can be calculated using the relation

$$A(J \rightarrow J') = \frac{64\pi^4 e^2}{3h(2J+1)\bar{\lambda}^3} \frac{n(n^2+2)^2}{9} S(J \rightarrow J') \tag{4}$$

These rates recorded in Table 3 predict a total radiative rate out of the $^4F_{3/2}$ level equal to 4438 s^{-1} or a radiative lifetime for the meta-stable $^4F_{3/2}$ state of 225 μsec. Comparing this calculated value for the Nd^{3+} $^4F_{3/2}$ radiative lifetime with our measured value of 214 μsec for the $^4F_{3/2}$ fluorescence lifetime implies a quantum efficiency of 0.95.

Knowing the radiative transition rates of the $^4F_{3/2}$ level down to the various ^4I levels, it is possible to calculate absolute emission cross sections from calibrated emission spectra using the relation,

$$\sigma_{J \rightarrow J'}(\lambda) = A(J \rightarrow J') \frac{\lambda^4}{8\pi c n^2} g(\lambda) \tag{5}$$

where $g(\lambda)$ is the normalized line shape function. Figure 5 details the orientationally resolved emission cross sections for both the $^4F_{3/2}$ - $^4I_{9/2}$ and $^4F_{3/2}$ - $^4I_{11/2}$ transitions.

Transition	$\bar{\lambda}$(nm)	Polarization Averaged	
		S_{calc} (10^{-20} cm²)	A(s^{-1})
$^4F_{3/2}$ - $^4I_{15/2}$	1830	0.157	24.4
$^4F_{3/2}$ - $^4I_{13/2}$	1330	1.17	474
$^4F_{3/2}$ - $^4I_{11/2}$	1050	2.90	2390
$^4F_{3/2}$ - $^4I_{9/2}$ *	894	1.13	1550

*Measured not calculated

Table 3. Calculated transition rates in Nd^{3+}:Y_2SiO_5

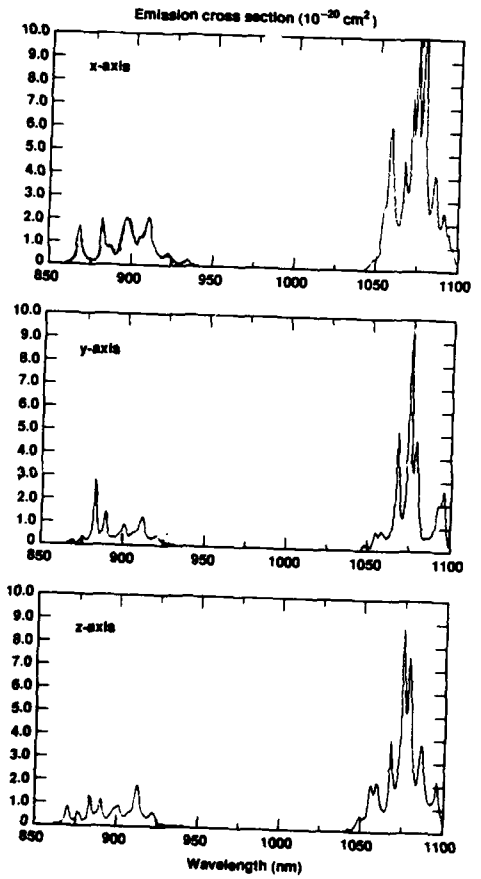


Figure 5(a). Stimulated emission cross sections of the $^4F_{3/2}$ - $^4I_{9/2}$ and $^4F_{3/2}$ - $^4I_{11/2}$ transitions of Nd^{3+}:Y_2SiO_5 along the three principal axis of the optical indicatrix.

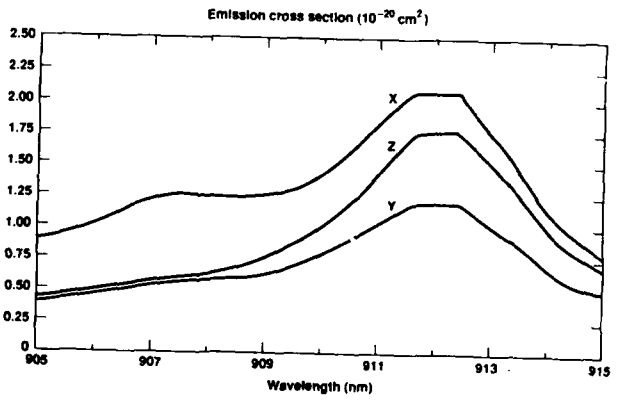


Figure 5(b). Emission cross sections of the $^4F_{3/2}$ - $^4I_{9/2}$ transition in the region of interest for transmitters capable of accessing Cs ARFs. Here the three orientations are overlaid on each other. The wavelength of twice one of the Cs ARF's acceptance wavelengths occurs at 85% of the gain peak.

Nd^{3+} $^4F_{3/2}$ - $^4I_{11/2}$ Gain Suppression

An important design consideration in Nd^{3+} based GSD lasers and one pointed out by the data of Fig. 5 is standing off the competing $^4F_{3/2}$ - $^4I_{11/2}$ transition. In the case of Nd^{3+}:Y_2SiO_5, the peak $^4F_{3/2}$ - $^4I_{11/2}$ cross section is 5 times larger than the cross section of the desired $^4F_{3/2}$ - $^4I_{9/2}$ lasing transition. The response we have used to address this issue is to introduce a material in the laser cavity that selectively absorbs at 1.07 μm but is transparent at 912 nm. Our current laser design uses samarium scandium gallium garnet (SSGG) as the selective absorber. Figure 6 presents an absorption spectrum of this stoichiometric crystal which exhibits strong features near 1074 nm but is completely transparent at 912 nm.

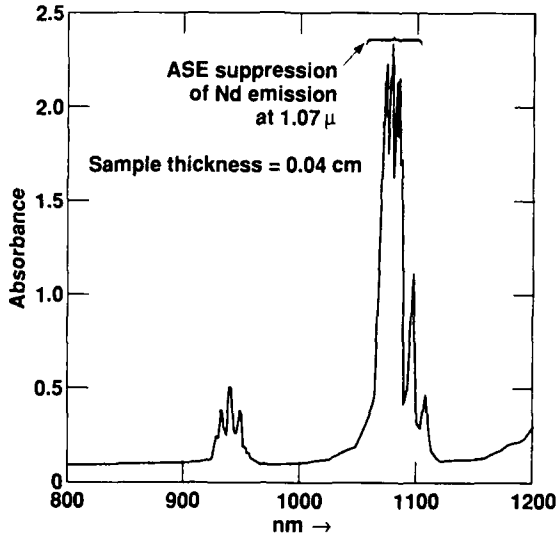


Figure 6. Samarium scandium gallium garnet (SSGG) absorption spectrum.

912 nm Laser Demonstration and Modeling

Q-switched oscillator experiments have been performed to demonstrate the principles of GSD laser operation. In particular, these experiments were designed to demonstrate 912 nm extraction efficiency, the feasibility of using SSGG in the laser cavity to suppress the undesired gain of the Nd^{3+} $^4F_{3/2}$ - $^4I_{11/2}$ transition, and finally to demonstrate closure with our laser performance computer modeling codes.

A schematic drawing of our Q-switched oscillator is shown in Fig. 7. The oscillator cavity was 100 cm long. the Nd^{3+}:Y_2SiO_5 laser sample was 7.1 cm long and doped with Nd^{3+} at 0.9×10^{19} cm^{-3}. The SSGG sample was 0.5 mm thick and had an insertion loss of approximately 4% at the 912 nm laser wavelength. The SSGG sample served the dual purpose of providing a polarization selective loss in the cavity for Q-switching and also suppressing the Nd^{3+} $^4F_{3/2}$ - $^4I_{11/2}$ gain. The flat high reflector had a greater than 99% reflectance at 912 nm and a transmission of ~70% at 745 nm to allow the 745 nm pump beam to enter the cavity and longitudinally pump the laser sample. Two different output couplers were available with reflectances at 912 nm of either 70 or 80%.

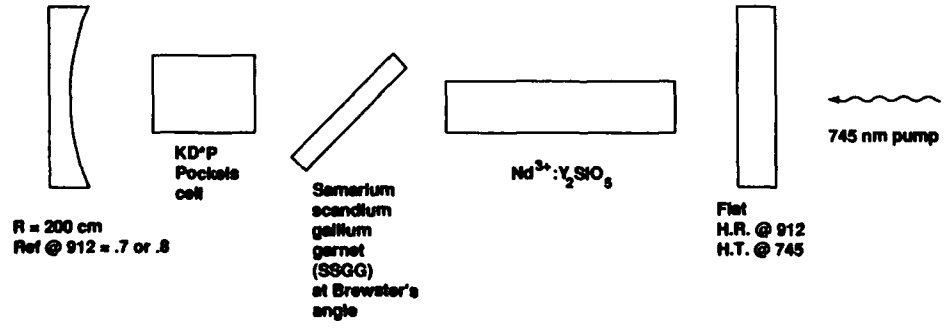


Figure 7. Schematic drawing of the Q-switched oscillator used in our laser demonstration experiments.

The boules from which our laser samples of Nd^{3+}:Y_2SiO_5 were cut were grown with their boule axis 20° off the ⟨010⟩ direction, as shown in Fig. 8. Laser samples were then cut with their faces normal to the boule axis. In terms of the optical indicatrix, this means the axis of the laser samples used in our experiments were 20° away from the X-axis and tipped toward the Y-axis. With no polarization selective components in the cavity, 912 nm free lasing was always observed to occur with the electric field parallel to the Z-axis. For our particular orientation of the crystal, this is what one would expect based on the oriented emission cross section data of Fig. 5.

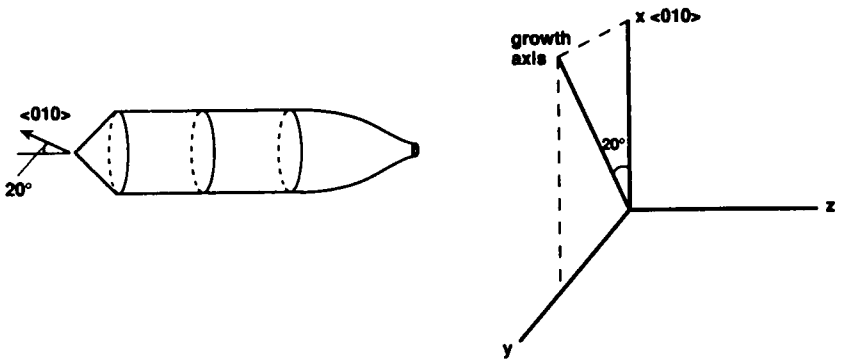


Figure 8. This sketch shows the orientation of our laser samples relative to the optical indicatrix of Y_2SiO_5. Laser samples were cut with their faces normal to the boule growth axis.

To model the excitation of the laser sample during the application of the bleach wave pump pulse, the following equations were used in generating our bleach-wave pump-pulse propagation code,

$$\frac{\partial n_{^4F_{3/2}}(x,t)}{\partial t} = \frac{\sigma_P}{h\nu_P} I_P(x,t)\left[n_{Nd} - n_{^4F_{3/2}}(x,t)\right] - \frac{1}{\tau_F} n_{^4F_{3/2}}(x,t) - \Gamma_{Auger}\, n^2_{^4F_{3/2}}(x,t)$$

$$\frac{1}{c}\frac{\partial I_P(x,t)}{\partial t} + \frac{\partial I_P(x,t)}{\partial x} = -\sigma_P I_P(x,t)\left[n_{Nd} - n_{^4F_{3/2}}(x,t)\right] \qquad (6)$$

where:

n_{Nd} is the Nd^{3+} number density

$n_{^4F_{3/2}}(x, t)$ is the local Nd^{3+} excited state number density

σ_P is the absorption cross section seen by the pump wave

$h\nu_P$ is the energy of a pump photon

$I_P(x, t)$ is the local pump wave intensity

τ_F is the Nd^{3+} $^4F_{3/2}$ fluoresence lifetime

Γ_{Auger} is the Auger decay rate and included because of the high excitation levels required for laser operation

Figure 9 shows predictions made by our pump pulse propagation code along with the results of experimental measurements. Figure 9a shows the time resolved excited state fraction that our code predicts will result from the application of the displayed 745 nm excitation pulse. Overlaid with this prediction is the experimentally measured $^4F_{3/2}$ fluorescence decay signature that was measured by monitoring $^4F_{3/2}$ - $^4I_{11/2}$ fluorescence at 1074 nm during and after a shot of the exciting alexandrite laser. The excellent agreement between the shapes of the predicted excited state fraction and the measured $^4F_{3/2}$ fluorescence signature which should follow the excited state fraction are a strong indication that our code is correctly modeling the physics of the excitation process. As a further check of the code's validity, Fig. 9b displays the predicted time resolved excited state fraction and a plot of the natural log of the

experimentally measured small signal gain at 912 nm. The small signal 912 nm gain was measured during and after an alexandrite shot using a 912 nm probe beam generated by a Ti-sapphire laser. The natural log of this small signal gain should follow the transient excited state fraction. Again, the excellent agreement between measurement and code prediction gives us confidence in the code's validity.

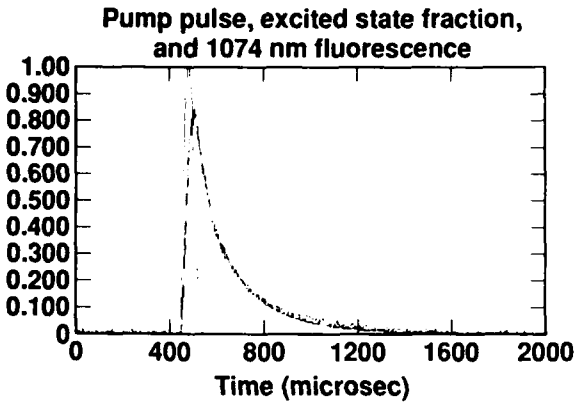


Figure 9(a). Computer predicted excited state fraction is overlaid with the measured Nd^{3+} $^4F_{3/2}$ time resolved fluorescence signature.

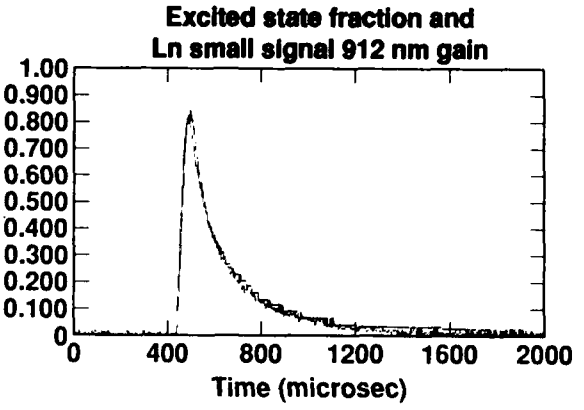


Figure 9(b). Computer predicted excited state fraction is overlaid with the natural log of the measured 912 nm small signal gain.

A series of computer codes have also been written to model the 912 nm energy extraction of the laser. The starting point for generating these laser performance codes is the laser rate equations. In this analysis we assume that intra-manifold relaxation occurs on a time scale much shorter than any inter-manifold processes. This means the various manifolds involved in the lasing process will remain in thermal equilibrium throughout the generation of an output pulse. Of particular importance to our rate equation analysis will be the fractional thermal population of the $^4F_{3/2}$ and $I_{9/2}$ manifolds that lie in the laser initial and final crystal field states. Figure 1 shows detailed Stark splittings of the Nd^{3+}:Y_2SiO_5 $^4F_{3/2}$ and $^4I_{9/2}$ manifolds for both types of cationic sites that Nd can occupy as reported by Tkachuk, et al.[4] The fractional thermal population of the $^4F_{3/2}$ manifold located in crystal field level that serves as our initial laser level is given by the Boltzmann occupation factor as

$$f_b = \frac{e^{-E_b/kT}}{\sum_i e^{-E_i/kT}} \qquad (7)$$

(All crystal levels in the $^4F_{3/2}$ manifold)

where we have neglected the degeneracies of the various crystal field states as they are all doubly degenerate. Using the splittings in Fig. 1, the value of f_b is calculated to be 0.70. A similar calculation for f_a, the Boltzmann occupation factor of the terminal laser level, gives 0.078. The rate equations appropriate for our laser now take the form

$$\frac{d\phi}{dt} = \phi\left[c\sigma\frac{\ell}{\ell'}(n_b - n_a) - \frac{\delta}{t_n}\right]$$

$$\frac{dn_b}{dt} = -f_b(n_b - n_a)c\sigma\phi \qquad (8)$$

$$\frac{dn_a}{dt} = f_a(n_b - n_a)c\sigma\phi$$

where ϕ is the cavity photon density, n_a and n_b are the final and initial crystal field level population densities, respectively, ℓ is the sample length, ℓ' is the cavity length, δ is the fractional round trip cavity loss given by $-Ln(T^2R_{OC})$, t_r is the round trip cavity time and given by $2\ell'/c$, and σ is the actual spectroscopic cross section of the laser transition. This last distinction is an important one as the emission cross sections derived from our previous Judd-Ofelt analysis were effective cross sections and $\sigma_{eff} = f_b\sigma$.

As a check on the validity of the performance codes we have written, a comparison of code predictions and experimentally measured laser performance has been made. The laser cavity shown in Fig. 7 was pumped by an alexandrite laser at 745 nm. The effective absorption cross section seen by the pump laser was 3.2×10^{-20} cm^2 (see Fig. 4). To optimize the 912 nm performance of the laser, an analysis was made to determine what spot size the pump should have at the sample for a given fixed amount of pump energy to maximize the 912 nm Q-switched output energy. The tradeoff here is between the pump induced excited state fraction in the sample at the time the Q-switch is opened and the total volume of sample excited by the pump. The results of this analysis are shown in the map of Fig. 10 where the sample length and the diameter of the pump excited region at the sample are varied and for each possible combination the output 912 nm energy of the laser is calculated. For the particular map shown in Fig. 10, the output coupler was assumed to be 70% reflective at 912 nm, the one-way cavity transmission was fixed at 0.9, and the pump was assumed to be capable of delivering 4.5 Joules at the input side of the laser sample. The output energy represented by the contours increases going toward the top center of the plot, and for our particular sample length of 7.1 cm the optimum pump geometry occurs when the pump fluence is adjusted to be 25 J/cm^2 and is not very sensitive in the range between 20 and 30 J/cm^2. Taking the pump sat fluences as $h\nu_P/\sigma_P$ = 8.4 J/cm^2 means the optimum pump configuration corresponds to pumping between 2.5 and 3.5 sat fluences.

Laser performance measurements were made using a pump fluence of 21.2 J/cm^2. Figure 11 shows the measured temporal profile of the alexandrite laser used in our experiments together with the calculated excited state fraction induced by the pump excitation pulse. The Q-switch was opened at the time the excited state fraction was at its maximum value – the time of peak inversion. As a measure of the efficiency with which energy was extracted from the sample during the Q-switched pulse, the population in the $^4F_{3/2}$ level was tracked by monitoring the $^4F_{3/2}$ - $^4I_{11/2}$ fluorescence at 1074 nm. A scope trace of this fluorescence signal is shown in Fig. 12a and demonstrates the operation of the laser at an internal extraction efficiency of 70%. For this particular measurement, the output coupler reflectivity was 0.8 at 912 nm and the cavity transmission was estimated at 0.86 using a 912 nm probe beam. Figure 12b shows the internal extraction efficiency predicted by our laser modeling code as a function of cavity transmission and parameterized by the excited state fraction just prior to opening the Q-switch. At our estimated cavity transmission of 0.86 and excited state fraction of 0.63 (see Fig. 11), the projected internal extraction efficiency of the laser is 0.7, in excellent agreement with the results of our measurements.

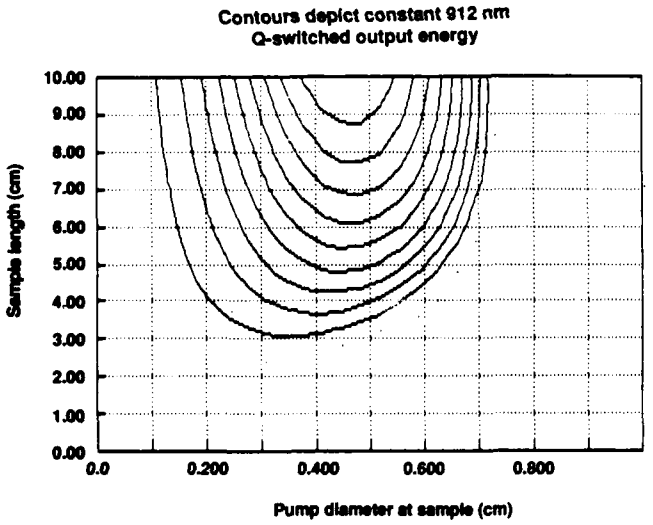


Figure 10. Optimization map in which contours of constant 912 nm Q-switched output energy are plotted against sample length and the diameter of the pump excited region at the sample. For this particular map, it was assumed the output coupler was 70% reflective, the one-way cavity transmission was .9, and the pump laser was capable of delivering 4.5 J of 745 nm energy to the input side of the sample.

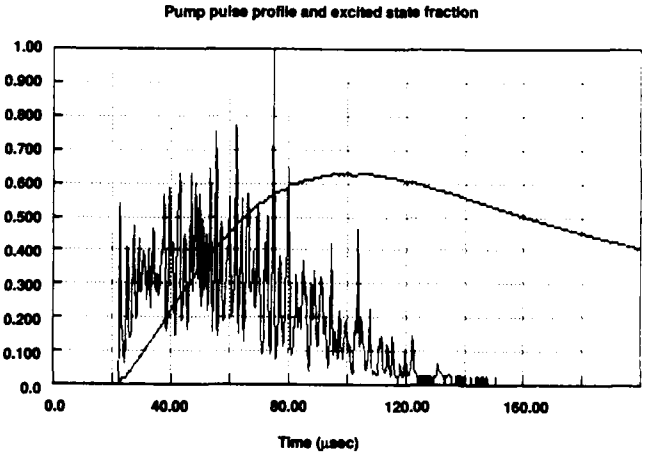


Figure 11. Temporal profile of the 745 nm alexandrite laser excitation pulse used in our experiments. The solid line shows the calculated excited state fraction induced by the excitation pulse in the laser sample for an assumed input pump fluence of 21.2 J/cm^2 (2.5 x Γ_{sat}).

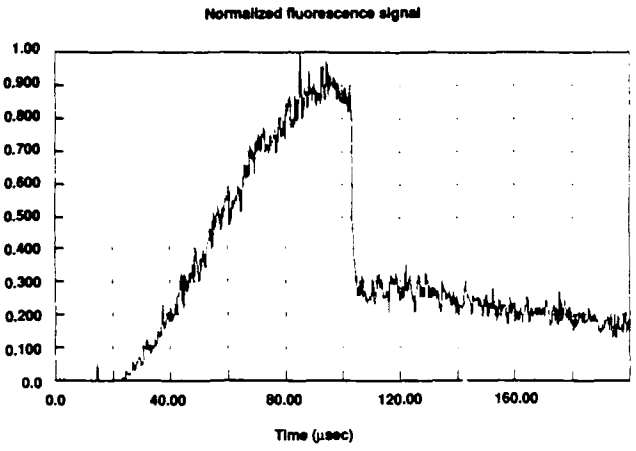


Figure 12(a). 1074 nm fluorescence trace showing the operation of the GSD laser at an internal extraction efficiency of 70%.

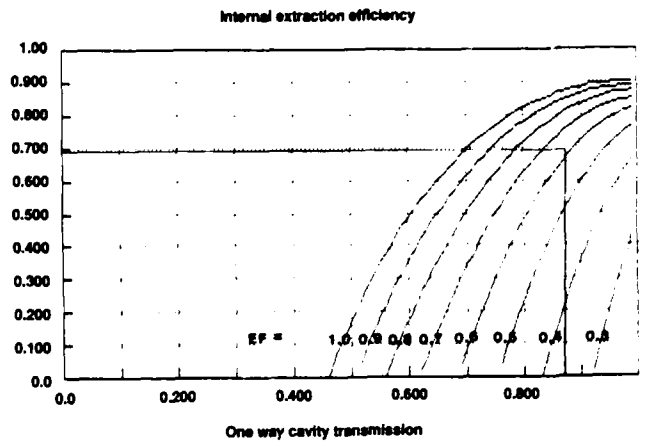


Figure 12(b). The predictions of our laser performance code for the internal extraction efficiency of the GSD laser as a function of the one-way cavity transmission and parameterized by the excited state fraction just prior to the opening of the Q-switch. The operation point of the laser for the measurement in (a) is as indicated. The contours of constant excited state fraction start at 1.0 on the left and decrement by 0.1 going to the right.

In addition to validating the operating principles of the GSD laser and demonstrating the effectiveness of using SSGG in the cavity to standoff the 1074 nm gain, the foregoing measurements demonstrate the efficiencies that can be reasonably obtained with such lasers. The limiting factor in the operation of our present laser is scatter losses at the sample interface due to a degradation in the AR coatings on the $Nd^{3+}:Y_2SiO_5$ sample with laser operation. This problem has been successfully addressed at the crystal growth stage using the REPTILE laser damage facility at LLNL to assess crystal quality. At present, selected samples of $Nd^{3+}:Y_2SiO_5$ have bulk and AR sol-gel (AlOOH) coated surface damage thresholds of 40 J/cm^2 for 10 nsec, 10 Hz, 1.06 μm test pulses. This damage threshold is adequate for the foreseen operational envelope of the present GSD laser as the sat fluence at 912 nm is ~9 J/cm^2.

Because of the modest values of cavity transmission achieved in our present laser, we have found we can increase the output energy per pulse by using a higher transmission output coupler. Figure 13a shows the time resolved Q-switched output pulse as measured by a fast photodetector for an output coupler reflectivity of 0.7 at 912 nm. At this operating point, the output energy per pulse was measured to be 375 mJ and the sample was lased over an area having a diameter of 0.42 cm (area = .14 cm^2). The sample was being excited by the same 21.2 J/cm^2 alexandrite pulse depicted in Fig. 11 and so the excited state fraction as predicted by the pump pulse propagation code is 0.63. Knowing the laser cavity transmission is 0.86, a self-consistent check of the laser operation was made to experimentally determine the excited state fraction present in the sample just prior to the opening of the Q-switch. By measuring the initial risetime of the laser pulse when plotted on a semi-log scale, the initial excited state fraction can be determined. This is easiest to see by making a slight rearrangement in Eq. (8a)

$$\text{slope} = \frac{\frac{d\phi}{dt}}{\phi} = c\sigma\frac{\ell}{\ell'}(n_b - n_a) - \frac{\delta}{t_n} \quad . \tag{9}$$

This method relies on measuring the slope before the building laser pulse has had a chance to significantly deplete the $^4F_{3/2}$ excited state. Figure 13b takes the same pulse displayed in Fig. 13a and plots it in a semi-log scale. Fitting a line to the initial rising part of the pulse gives a slope of 0.049/nsec, which together with Eq. (9) leads to an excited state fraction of 0.60. Again this value is in good agreement with the pump pulse propagation code prediction of 0.63.

Figure 14 plots our laser performance code prediction for the external extraction efficiency as a function of output coupler reflectivity and parameterized by the excited state fraction just prior to Q-switching. The cavity transmission was set at 0.86 in this calculation, leading to a predicted external extraction efficiency of 0.30 for a 70% reflective output coupler and an initial excited state fraction of 0.60. For our 7.1 cm long sample doped with Nd^{3+} at 0.9 x 10^{19} cm^{-3} and

lased over an area of .14 cm^2, the stored 912 energy in the active laser volume just prior to Q-switching is 1.18 Joules. The performance code prediction of 0.3 for the external extraction efficiency then implies the output energy should be 353 mJ, which is in good agreement with our measured value of 375 mJ.

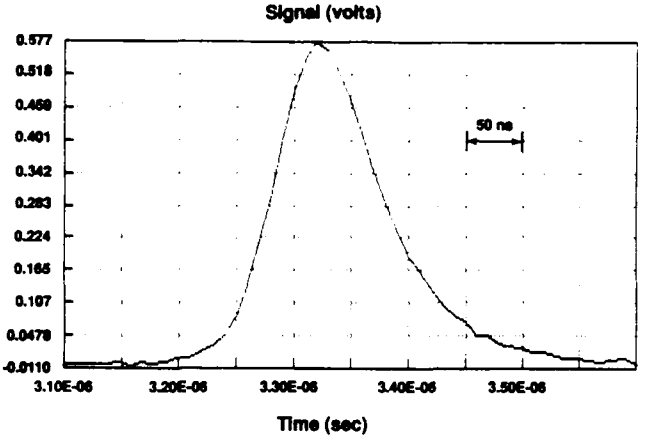


Figure 13(a). Time resolved 912 nm Q-switched output pulse from the GSD laser. The output coupler used had a 912 nm reflectivity of 0.7 and the measured output energy was 375 mJ/pulse.

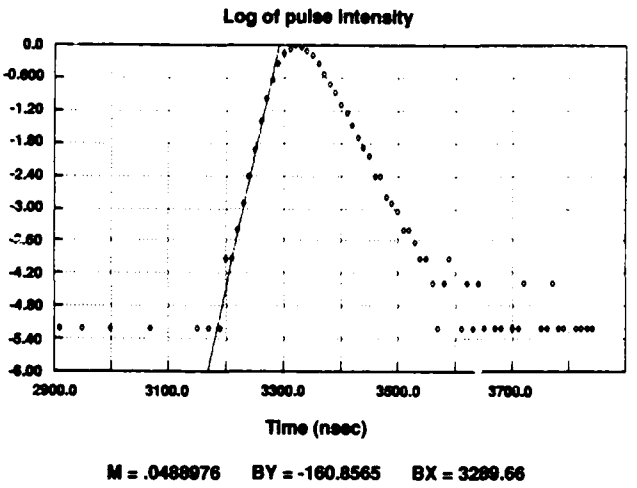


Figure 13(b). The same experimentally measured pulse of (a) but plotted on a semi-log scale. Fitting a straight line to the initial rise of the pulse leads to a slope of 0.049/nsec.

Harmonic Generation

Doubling of the 912 nm output of the laser has been accomplished using an A-cut crystal of $KNbO_3$. For this orientation of crystal, efficient non-critically phase matched harmonic generation can be accomplished using fundamental light polarized parallel to the $KNbO_3$ B-axis and propagating along the A-axis with the crystal held at approximately 135°C. Figure 15 shows a map of doubling efficiency (taken from Ref. 14) as a function of the input beams dephasing parameter and drive,

$$\eta_0 = C^2 I L^2 \text{ (drive)}$$
$$\delta = \frac{1}{2} \Delta k l \text{ (dephasing)} \qquad (10)$$

where

$$C = 5.46\, d_{eff} \left(\frac{pm}{v}\right) \frac{1}{\lambda_1 (n_1\, n_2\, n_3)^{\frac{1}{2}}} \qquad (11)$$

Because of the large nonlinear optical coefficient of $KNbO_3$ used for this doubling geometry [d_{32} = 19.7 (pm/v)],[15] modest values of input laser intensity give sufficiently large drives to achieve good doubling efficiencies even with high order multi-transverse mode beams. To date the best doubling efficiencies we have observed has been in a $KNbO_3$ crystal supplied by Virgo Optics and having an input aperture of 5 mm x 5 mm and a length of 15 mm. Using an input 912 nm pulse with an average intensity of 7 MW/cm^2 and a beam divergence of 9 mrad (FW), making it 5 times diffraction limited, we have achieved conversion efficiencies of 25%. We estimate the drive of this beam to be 18 and the dephasing parameter to be approximately 0.9, putting us in the fringe area of the secondary lobe on the doubling efficiency map of Fig. 15. From the map it is clear that we can increase our doubling efficiency to values of 50-60% without any improvement in beam quality by either increasing the drive from its present value of 18 to 24 or by decreasing it to 3. This work is currently in progress.

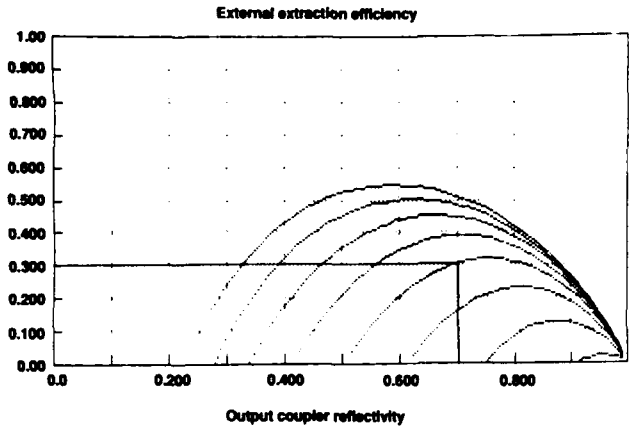


Figure 14. Our laser performance code prediction for the external extraction efficiency of the GSD laser as a function of the output reflectivity and parameterized by the excited state fraction just prior to the opening of the Q-switch. The operating point of the laser for the operating point depicted in Figure 13 is as indicated. The contours of constant excited state fraction start at 1.0 on the left and decrement by 0.1 going right.

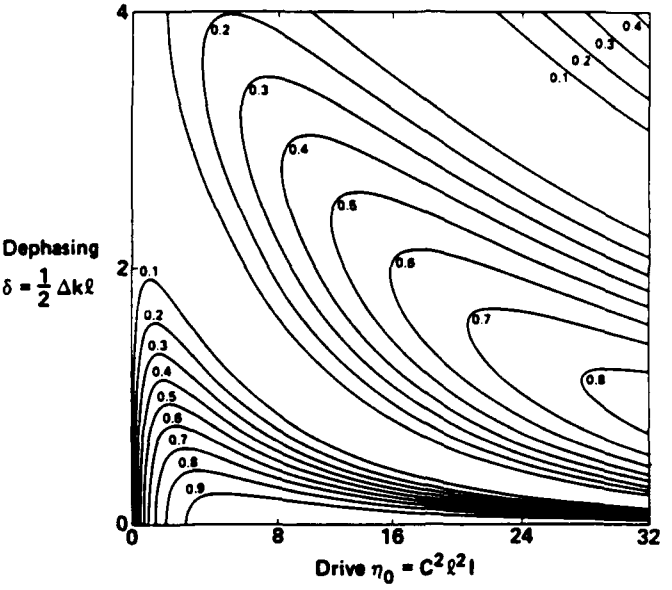


Figure 15. Contour plot of the conversion efficiency η as a function of the (dimensionless) drive C^2l^2I and the dephasing (1/2) Δkl. The line of zeros between the first and second lobes follows the approximate curve $\delta = 8\eta_0^{1/2} \exp(-\eta_0^{1/2})$. Conversion using the first lobe becomes increasingly sensitive to detuning at higher drive. Taken from Reference 14.

Conclusion

A spectroscopic evaluation of Nd^{3+} in the biaxial crystal yttrium orthosilicate has been performed. Using the Judd-Ofelt theory to analyze optical line strengths measured in absorption, we have extracted radiative rates for transitions from the Nd^{3+} $^4F_{3/2}$ manifold to the various ^4I manifolds and emission cross sections for the $^4F_{3/2}$ - $^4I_{9/2}$ and $^4F_{3/2}$ - $^4I_{11/2}$ transitions. The $^4F_{3/2}$ - $^4I_{9/2}$ transition is of particular interest to laser communication programs using receivers based on the Cs atomic resonance filter because of the fortuitous Stark structure of Nd^{3+} in Y_2SiO_5 giving rise to a peak in the emission spectrum near twice one of the filter's acceptance wavelengths. In connection with this we have also measured optical absorption spectra that will be of interest to experimenters wanting to laser pump this material. We have demonstrated for Nd^{3+}:Y_2SiO_5 that instead of the polarization and direction averaging strictly required for the application of the Judd-Ofelt technique, it suffices to average over the three principal directions of the optical indicatrix as evidenced by the good agreement (4.8%) between measured and calculated line strengths used in the fitting procedure. The advantage of being able to do this lies largely in the experimental simplicity that ensues from being able to use a single oriented rectangular sample for all measurements.

GSD laser operation has been demonstrated on the Nd^{3+} $^4F_{3/2}$ - $^4I_{9/2}$ transition at the lasing wavelength of 912 nm. The physics of the bleach wave excitation process and the 912 nm Q-switched energy extraction process have been modeled in a series of computer codes that accurately predict the performance of the actual laser. SSGG has been demonstrated as an effective gain suppressor of the unwanted and competing Nd^{3+} $^4F_{3/2}$ - $^4I_{11/2}$ transition at 1074 nm which has a cross section 5 times larger than the lased 912 nm transition. Additionally, the level of efficiency that one can reasonably expect from GSD lasers has been demonstrated in our energy extraction measurements that have documented internal extraction efficiencies as high as 70%. Finally, doubling efficiencies of 25% have been demonstrated using $KNbO_3$ in a non-critically phase matched geometry. Because of the large nonlinear optical coefficient of $KNbO_3$ and the non-critical phase matched geometry used, the doubling is forgiving of beam quality and allows efficiencies of 50-60% for our present 5 times diffraction limited laser at modest laser intensity levels.

Acknowledgments

This research was performed under the auspices of the U.S. Department of Energy by the Lawrence Livermore National Laboratory under contract W-7405-Eng-48.

References

1. W. F. Krupke and L. L. Chase, "Ground state depleted solid state lasers: principles, characteristics, and scaling," SPIE Proceedings Vol. 1040, ed. G. Dubé.

2. R. J. Beach, R. W. Solarz, S. C. Mitchell, L. R. Brewer, S. K. Weinzapfel, "Ground State Depleted Laser Experiments," SPIE Proceedings Vol. 1040, ed. G. Dubé.

3. J. B. Marling, J. Nilsen, L. C. West, and L. L. Wood, "An Ultrahigh Q Isotropically Sensitive Optical Filter Employing Atomic Resonance Transitions," J. Appl. Phys., 50, 610, (1979).

4. A. M. Tkachuk, A. K. Przhevusskii, L. G. Morozova, A. V. Poletimova, M. V. Petrov, and A. M. Korovkin, "Nd^{3+} optical centers in lutecium, yttrium, and scandium silicate crystals and their spontaneous and stimulated emission," Opt. Spektrosk. 60, 288-296 (1986).

5. C. D. Brandle, A. J. Valentino, and G. W.Berkstresser, "Czochralski Growth Of Rare-Earth Orthosilicates (Ln_2SiO_5)," J. of Crys. Growth 79, 308-315 (1986).

6. B. R. Judd, "Optical Absorption Intensities of Rare-Earth Ions," Phys. Rev. 127, 750 (1962).

7. G. S. Ofelt, "Intensities of Crystal Spectra of Rare-Earth Ions," J. Chem. Phys., 37, 511 (1962).

8. W. F. Krupke, "Radiative Transition Probabilities Within the $4f^3$ Ground Configuration of Nd:YAG," IEEE J. Quan. Elec., vol. QE-7, 153 (1971).

9. W. F. Krupke, "Induced-Emission Cross Sections in Neodymium Laser Glass," IEEE J. Quan. Elec., vol. QE-10, 450 (1974).

10. T. S. Lomheim and L. G. DeShazer, "Optical-absorption intensities of trivalent neodymium in the uniaxial crystal yttrium orthovanadate," J. Appl. Phys. 49, 5517 (1978).

11. E. A. Woods, "Crystals and Light, An Introduction to Optical Crystallography," Second Revised Edition (1977) 123-132 Dover Publications, Inc. New York.

12. A. A. Kaminski, "Laser Crystals," Springer Series in Optical Sciences, D.L.MacAdam Ed., (1981) 149-160 Springer-Verlag Berlin.

13. W. T. Carnall, H. Crosswhite, and H. M. Crosswhite, "Energy Level Structure and Transition Probabilities of Trivalent Lanthanides in LaF_3," Published by the Department of Physics, The Johns Hopkins University.

14. D. Eimerl, "High Average Power Harmonic Generation," IEEE J. Quan. Elec., Vol. QE-23, 575 (1987).

15. J. C. Baumert, J. Hoffnagle, and P. Gunther, "Nonlinear optical effects in $KNbO_3$ crystals at $Al_x Ga_{1-x}$ As, dye, ruby, and Nd:YAG laser wavelengths," SPIE Vol. 492 ECOOSA '84, 374 (Amsterdam, 1984).

DISCLAIMER

This document was prepared as an account of work sponsored by an agency of the United States Government. Neither the United States Government nor the University of California nor any of their employees, makes any warranty, express or implied, or assumes any legal liability or responsibility for the accuracy, completeness, or usefulness of any information, apparatus, product, or process disclosed, or represents that its use would not infringe privately owned rights. Reference herein to any specific commercial products, process, or service by trade name, trademark, manufacturer, or otherwise, does not necessarily constitute or imply its endorsement, recommendation, or favoring by the United States Government or the University of California. The views and opinions of authors expressed herein do not necessarily state or reflect those of the United States Government or the University of California, and shall not be used for advertising or product endorsement purposes.

CW-FREQUENCY-DOUBLED ND:YAG LASER WITH HIGH EFFICIENCY

W. Rupp, P. Greve
Carl Zeiss, Laser-Flab
P.O. Box 1369,/1380, D-7082 Oberkochen, West Germany

Abstract

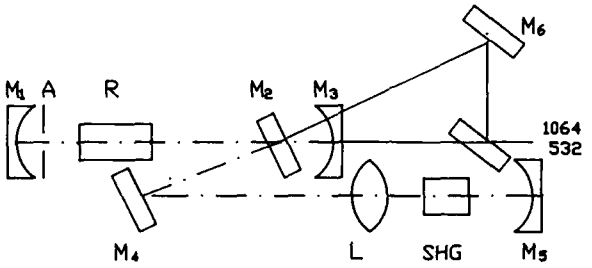
A cw intracavity frequency-doubled Nd:YAG laser has reached an overall efficiency of about 3 ‰ : nearly 15 W multimode output at 532 nm was achieved. KTP was used within a folded cavity.

1. Introduction

For many applications, especially in the medical field it is most desirable to have a high power cw green laser with good conversion efficiency. Argon lasers in this respect are limited to approximately 1 % , that means one can achieve about 4-5 W output power at a wavelength of 514 nm from 4-5 kW electrical plug-in power. We therefore evaluated the possibilities of frequency doubled Nd:YAG lasers in pure continous wave operation.

2. Experimental setup

The experiments are done with a twice folded resonator and an intracavity second harmonic generator. The principle setup is shown in Fig. 1.



M1 . . . M6 dielectric mirrors
R laser rod ; L focusing lens
SHG second harmonic generator (KTP)

Fig. 1: Folded resonator for intracavity SHG

The pump cavity (R) includes a Nd:YAG laser rod (4 x 83 mm) and 2 arc lamps with 2500 W electrical input power each. The resonator is closed up by the mirrors M_1 and M_5 for the fundamental and the second harmonic radiation. The two folding mirrors M_2 and M_4 are highly reflective for the fundamental wave. The mirror M_2 is dichroitic and transmits the second harmonic radiation, which couples out here. Moving out this mirror a separate resonator between morrors M_1 and M_3 is built up, so that the fundamental wave is coupled out through the partial reflective mirror M_2. Mirror M_6 and the following beam splitter allow for adjustment and coaxiality of fundamental and second harmonic radiation.

The nonlinear crystal is placed within the cavity and the radiation is focused into this crystal by means of an optical system with focal length f and the rear resonator mirror M_5. For our experiments we used different nonlinear crystals (KTP, BBO and $LiJO_3$). As described elsewhere[1], only the results with KTP have been promising so far for Nd:YAG lasers. The parameters of the KTP crystal are given in Table 1. It has the highest nonlinear coefficient and the greatest acceptance angle. The walk off angle is very small. Therefore a good focusing with high apertures and small focus diameter within the resonator is possible.

Table 1: Properties of potassium titanyl phosphate (KTP)

Phase matching angle (Type II)	:	25°
Walk-off angle	:	0.06°
Effective nonlinear coefficient d_{eff}	:	6×10^{-23} As/V^2

The dimensions of the crystal are 3 x 3 x 5 mm^3, the focus diameter within the crystal is about 30 µm. The main design features of the resonator have been to avoid internal resonator losses as far as possible by developing good coatings for the optical surfaces and to achieve a high quality focus within the nonlinear crystal for high field intensities. The last feature was accomplished by resonator calculations including thermal effects in the laser rod.

An example for the coatings is given in Fig. 2. Both sides of the KTP crystal are coated with a two wavelength AR-coating. For both wavelengths and both sides the rest reflectivity is below 0.05 %.

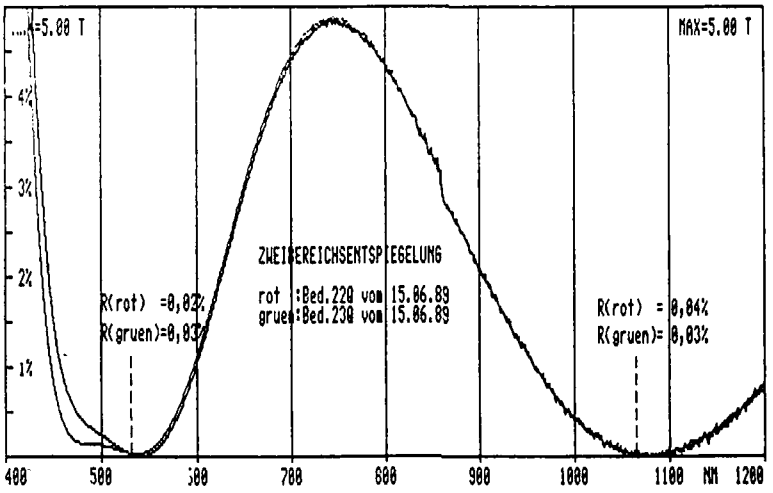


Fig. 2: Anti-reflection coatings on KTP

3. Experimental results

The output power at 533 nm as a function of the electrical input power is given in Fig. 3.

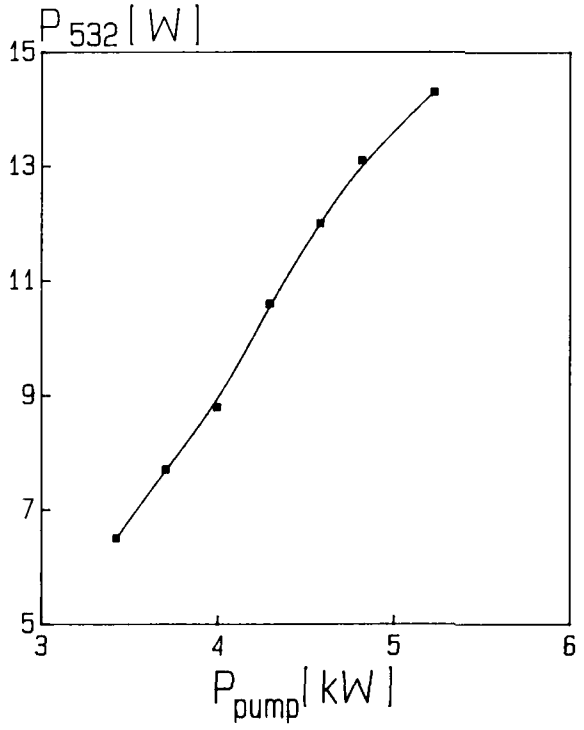


Fig. 3: Output power with KTP

One can reach about 14 W green power at 5 KW electrical plug-in power. This gives an efficiency of 2.8 % . The output power is adjustable by means of the input power in some range. Full adjustment cannot be made because of the thermal lensing of the laser rod which differs for different input powers. Therefore the resonator is not optimized for all pumping conditions.

The beam radius (532 nm) as a function of the distance from the outcoupling mirror is shown in Fig. 4.

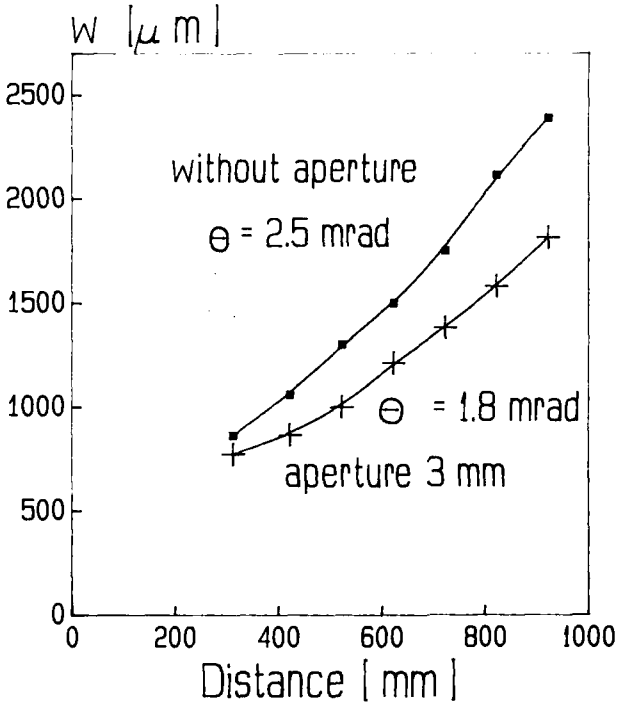


Fig. 4: Beamradius of the SHG-beam

Without an aperture within the resonator the diameter ($1/e^2$ - points) at the outcoupling mirror is about 1.8 mm, the half angle divergence in this case 2.5 mrad. Using a 3 mm aperture within the resonator the beam diameter at the outcoupling mirror is only slightly smaller but the beam divergence reduces to 1.8 mrad. These values have been measured with an electrical pump power of 3.9 KW.

The nonlinear process within the KTP crystal exhibits some temperature dependence. Theoretically it can be calculated by the following equation[1]:

$$\Delta T = \frac{0.44 \cdot \lambda}{l \cdot dn/dT} \quad \text{with} \quad \frac{dn}{dT} = 1.9 \times 10^{-9} \ 1/°C \qquad (1)$$

For our conditions the so-called full width half maximum temperature (FWHM)ΔT, that means the temperature for which the output power has dropped to 50 % can be calculated to 50 degrees. Experimental verification can be done by mounting the nonlinear crystal into a copper block which can be temperature stabilized by means of an external cooler/heater system.

Fig. 5 shows the experimental results for different temperatures. The experimental FWHM-temperature is measured to 52° C in good accordance with the theoretical value.

The green radiation (532 nm) has some overlay by the fundamental wave. This is measured using dichroitic filters and the result is given in Fig. 6. For green output powers from 1 to 10 W the fundamental wave power is in the range of 0.2 %, that means maximum 20 mW at 10 W green.

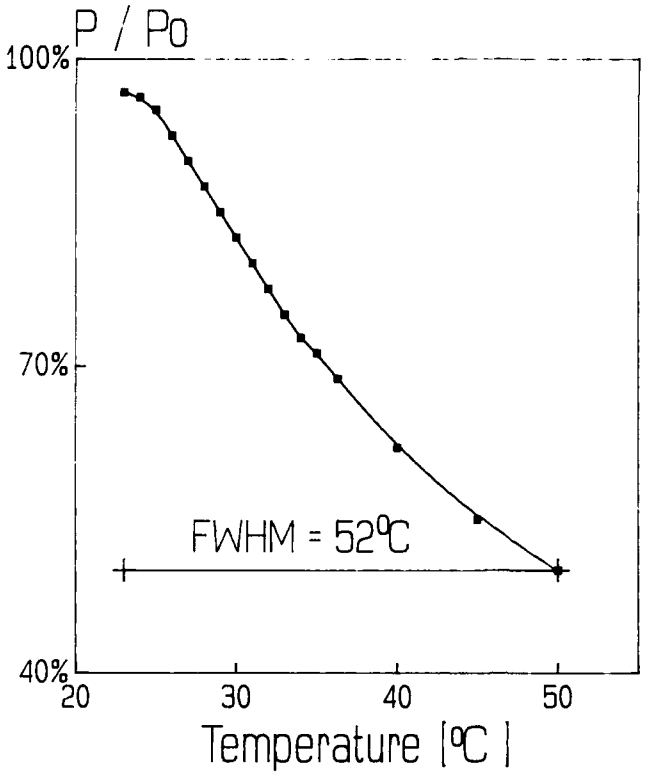


Fig. 5: Temperature dependence of the output power

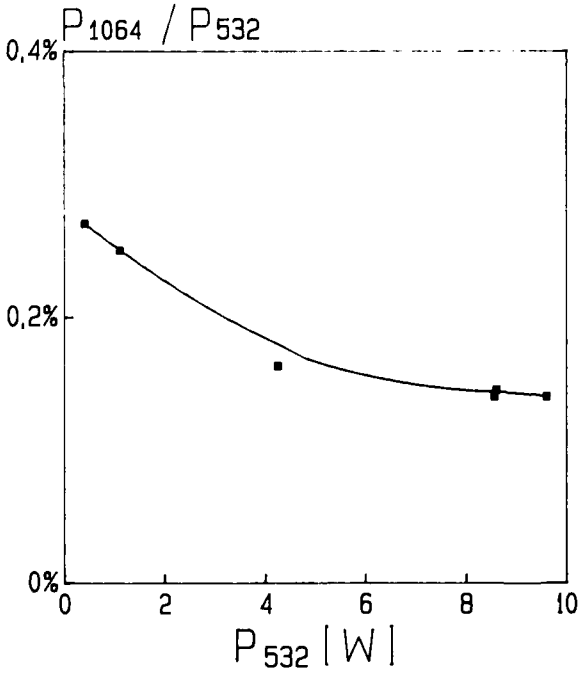


Fig. 6: Portion of 1064 nm in the SHG-wave

Due to the nonlinear process the polarization of the second hammonic wave is quite high. Fig. 7 gives the degree of polarization as a function of the output power: from 2 to) W (532 nm) it is greater than 95 %.

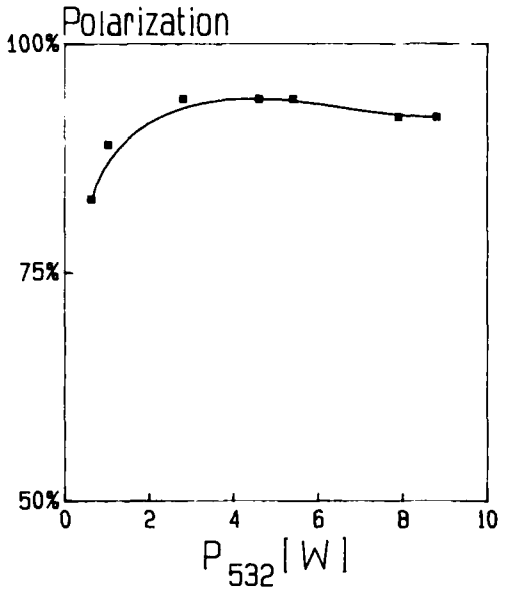


Fig. 7: Degree of polarization

4. Summary

In summary we have developed a laser system which can produce up to 14 W cw green power at 532 nm in multimode operation. Preliminary specifications are given in Table 2. The electrical input power for the system is between 3 and 5 kW. Therefore the system exhibits an overall efficiency close to 3 ‰ which is almost a factor of 3 higher than for conventional argon laser systems.

Table 2: Preliminary specifications

		1064 nm	532 nm
max. cw power	W	40	13
beam diameter	mm	3	3
beam divergence ($1/e^2$ half angle)	mrad	4.5	3.5
polarization (linear)		unpolarized	95%
portion of 1064 in 532-radiation			0.2%
laser head weight	kg	10	
laser head size	cm	13 × 13 × 92	
typical electrical input power	kW	3 . . . 5	

5. References

1. W. Koechner, Solid-State Laser Engineering (Springer-Verlag, New York, 1988)

5J PHASE CONJUGATE Nd:GLASS SLAB LASER WITH NEARLY DIFFRACTION LIMITED OUTPUT

Metin S. Mangir and David A. Rockwell
Optical Physics Department
Hughes Research Laboratories
Malibu, California 90265

ABSTRACT

We built a Q-switched Nd:YLF/Nd:Glass phase-conjugate laser producing 5J/pulse at 1μm and 2.5J/pulse at 0.5μm with 1.5 times diffraction limited beam quality at 1Hz. We use slabs with a straight-through beam path and correct thermally induced aberrations with SBS phase conjugation.

We describe a phase-conjugate Nd:glass laser we designed and built which reliably produces ~5 J at 1.053 μm, and 2.5 J at 526.5 nm operating either continuously at 1 Hz, or at 5Hz with 20 % duty cycle. Based on the location of the first nulls in the far-field energy distribution shown in Figure 1, we estimate the green beam to be ~1.5 times diffraction limited. While a slab geometry is being utilized to minimize the thermally induced medium distortions and the possible fracture of the laser medium, many features of the design, notably the use of phase conjugation[1] with a straight-through beam path parallel to the slab axis, represent significant departures from designs incorporating zig-zag beam paths.

We have chosen this unconventional slab path to avoid many engineering challenges encountered in practical zig-zag slabs. Although the zig-zag path in an ideal slab cleverly solves the thermally induced focussing, its practical realization has proven to be difficult. The requirements for very high quality optical finishes over large surface areas and tight dimensional tolerances make it expensive to produce. It is highly susceptible to parasitic oscillations. Efficient utilization of the pumped volume is not always possible due to the internal reflection angle dictated by the index difference between the laser and coolant media. Due to non ideality of the slab there are additional problems, such as surface degradation due to coolant corrosion, residual aberrations due to slab end effects, mechanical difficulty in holding the slab and sealing the coolant without interfering with the beam path, and susceptibility to beam wander due to slab bending. In the past dozen years, these problems have been addressed and ways to minimize them have been found, albeit difficult to implement. The disadvantage of our design is that the strong thermal focussing in Nd:glass has to be dealt with. As will explained later, with the optimum choice of glass host, focussing can be minimized, and even more complicated distortions can be mostly corrected with phase conjugation.

The phase-conjugate Nd:glass MOPA configuration is shown schematically in Figure 2. The output of dye Q-switched, 40 ns long single longitudinal mode (SLM), TEM_{oo} Nd:YLF oscillator double passes a Nd:YLF preamplifier, and produces a 15 mJ pulse. After a Faraday rotator, the beam passes through a combination of spherical and cylinderical lenses to produce a beam with an elliptical cross-section that fits better the rectangular aperture of the slab amplifiers. Then the s-polarized beam is reflected from a Brewster plate to drive the neodymium-doped phosphate glass amplifiers. The 2 cm wide beam path is folded in the 5 cm wide slabs, permitting two gain passes through the amplifiers before reaching the SBS phase conjugate mirror (PCM). The phase conjugate beam undergoes two more gain passes on the way out. A 90° phase matched, temperature-tuned (82.3 C) CD*A frequency doubling crystal (0.8x3x2.5 cm^3) placed on the output beam just before the Brewster plate converts about 50% of the 1.053 μm output to 526.5 nm, which is polarized perpendicular to the 1 μm light so that it passes through the Brewster plate with no loss. Most (>50 %) of the residual 1.05 μm radiation also passes through the Brewster plate; approximately 20% is reflected back toward the preamp, but it is stopped by the optically-induced gas breakdown plasma shutter and Faraday isolator.

The 0.5x5x22 cm^3 slabs are pumped on each side by two 0.8 cm dia., 15 cm long xenon flashlamps, in a diffuse cavity coated with barium sulfate. They are held in place by simple o-ring seals. The slabs are water cooled on their large surfaces. We use LG-760 glass with $2.8x10^{20}$ ions/cm^3 neodymium doping from Schott, which has far less thermal focusing in a straight-through slab geometry compared to LHG-5 glass from Hoya, although

its thermo-mechanical properties are not as good. For an uniformly pumped LG-760 slab with straight-through beam path, the thermal focussing coefficient[2], α_y, is zero, because stress-optical and thermo-optical (dn/dT) effects cancel each other. But due to slab end effects[3], there is some thermally induced focussing in the slabs. The thermal lensing is managed by placing the two slabs two thermal focal lengths apart. This was one reason we chose an amplifier design with two slabs in series. In fact, this focusing automatically incorporates imaging of slabs onto each other (in one plane), thus lessening the diffractive propagation losses in the amplifier. Phase conjugation corrects for residual aberrations.

With 250 J input, the energy storage efficiency η_{st} was 3.9%. At 500 J input (our operating point), η_{st} was reduced to 3.3% (ϵ_{st} = 0.42 J/cm^3) mostly due to increased amplified spontaneous emission (ASE) inside each slab. We ascertained that if the two slabs are kept more than 80 cm apart, as we are doing, there is no increased ASE from coupling of the two glass slab amplifiers despite the large (≈200) single-pass small-signal gain in the amplifier chain. Due to the low optical density along the 0.5 cm thickness of each slab, the measured gain has only 20% difference between the center and the pumped surfaces. Along the 5cm width of the slabs, the gain is uniform in the central 4 cm section. The gain nonuniformity of ~20% in the 0.5 cm zone near the edges on either side is not important, since we do not use these portions of the slabs. Because of the edge effects, these portions would cause strong depolarization and impose complicated aberrations on the beam, even with a zig-zag design[3].

One advantage of the straight-through pass of the slabs is that the large side surfaces need not be polished; thus parasitic oscillations are minimized, and surface degradation due to water exposure is not a problem.

We have pumped the slabs at full input power at 10 Hz, without lasing, indicating that stress-induced fracture damage would not prevent 10 Hz operation. This fact is consistent with our calculations of heat and stress generated in the slabs. The heat generated per unit volume, P_H, is given by $\epsilon_{st}\chi f$, where ϵ_{st} is the energy storage density, χ is the normalized heating parameter, and f is the repetition rate. Earlier we had measured χ to be about 2 for flashlamp pumped Nd:phosphate glasses[4]. Thus, for ϵ_{st}=0.45 J/cm^3 and f=10 Hz, P_H is ~9W/cm^3. Then the calculated thermally induced stresses, σ_m, at the slab surfaces are about 28 MPa, for the 0.5 cm thick LG-760 glass slab[5]. Given this value of σ_m, we estimate the fracture probability of our 0.5x5x22 cm^3 slabs to be much less than 1%, using the typical fracture parameters available for LHG-5 glass samples[5].

It is possible to obtain up to 10 J from this laser, since more than 30 J is stored in the slab amplifiers. At the moment, the output energy of the laser is limited to 5 J at 1 μm by the available oscillator energy.

REFERENCES

1. D. A. Rockwell, IEEE J. Quantum Electron., **24**, 1132-1140,(1988)

2. J.M. Eggleston, T.J. Kane, K. Kuhn, J. Unternahrer, and R.L. Byer, IEEE J. Quantum Electron., **20**, 289-300, (1984)

3. J.M. Eggleston, T.J. Kane, J. Unternahrer, and R.L. Byer, Opt. Lett., **7**, 405-407, (1982)

4. M.S. Mangir and D.A. Rockwell, IEEE J. Quantum Electron. **22**, 574-580, (1986)

5. J. E. Marion, J. Appl. Phys., **60**, 69, (1986)



FIGURE 1. Contour plot of the far-field energy distribution at 0.5μm. Tha appearent asymmetry between the vertical and horizontal directions are due to the program that prints the TV image. The corresponding width of an ideal diffraction limited beam is also shown for comparison.

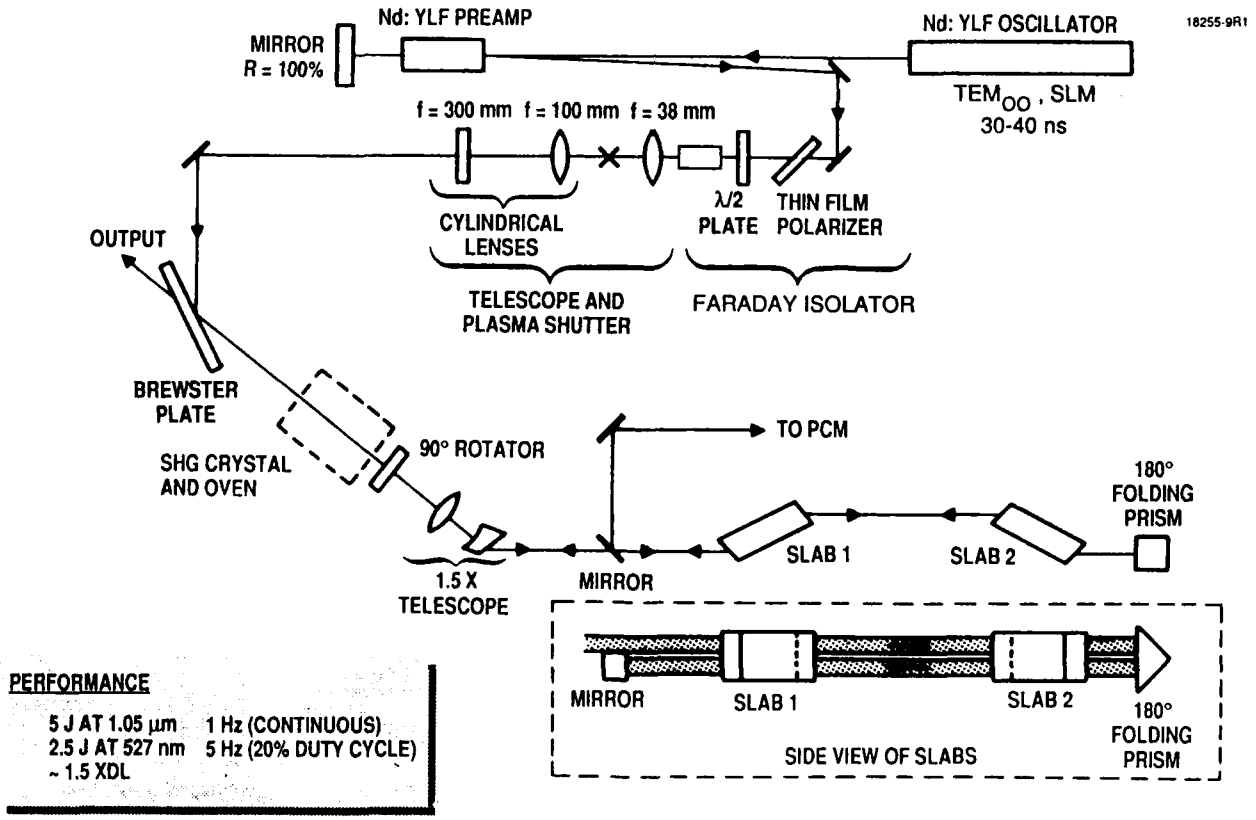


FIGURE 2. Nd:glass pump laser schematic, Inset shows side view of slabs and scheme for folding beam path through slabs before proceeding to phase-conjugate mirror (PCM).

DEPLETION MODE PUMPING OF SOLID STATE LASERS

D. Mundinger, R. Solarz, R. Beach, G. Albrecht, W. Krupke
Lawrence Livermore National Laboratory, Livermore CA 94550

Abstract

Depletion mode pumping of solid state lasers is a new concept which offers features that are of interest for many practical applications. In this paper we will discuss the physical properties and mechanisms that set the design requirements, present model calculations for a practical laser design, and discuss the results of recent experiments.

1. Introduction

The development of highly efficient lasers such as Chromium doped materials and semiconductor lasers makes it practical to consider lasers which are pumped by other lasers. Flashlamp pumped Alexandrite or LiCAF can be 5% to 10% efficient which is interesting for many applications, while semiconductor lasers can be greater than 40% efficient.

Both the Chromium doped lasers as well as the semiconductor lasers can be configured so as to produce pump sources with intensities greater than 10^5 watts / cm^2 which is sufficient to saturate pump transitions in Nd and other rare earth ions, thereby inverting a large fraction of the population. This opens up possibilities for new wavelengths, and increased performance levels in terms of efficiency, beam quality, and average power performance.

For example, one wavelength of particular interest is 911 nm or 919 nm which could be frequency doubled to match up with the cessium atomic resonance for undersea communications applications. The .9 um regime is also interesting for active sensor applications since it is compatible with high gain, low noise, negative electron affinity photocathode detectors.

Apart from the new wavelengths that are enabled there are other performance advantages to lasing back to the ground state. It lowers the amount of heat deposited in the host during operation for lower thermal distortion. Also, by bleaching the medium, the gain is uniform and therefore the thermal source distribution is uniform, both of which are desirable for maintaining good wavefront control at high average power and high peak power.

Depletion mode pumping also provides architectural options to the more conventional transverse pumping which is popular for high average power lasers but which puts constraints on slab thickness and doping densities which are awkward to handle in the presence of other design considerations. For example, depletion mode pumping allows the use of thinner slabs for better thermal control without causing undesirable thermal gradients, as in the case of conventional end pumping, which limit the average power capability of the laser.

In what follows we will first go thru the basic principles of depletion mode pumping, and outline the general design considerations. Then several models will be described which have been developed for projecting performance of depletion mode pumped, ground state lasers. We have also made several experiments to validate performance models and examine the design space

Primarily, the work we have done has been with Nd doped into various oxides and fluorides, however, the principles and scaling apply as well to other rare earth ions such as Tm, Ho, Er, Yt and these systems are also interesting for many practical applications.

2. Basic principles, characteristics, and scaling laws

The basic principles of operation, characteristics, and scaling laws have been worked out by Bill Krupke and Lloyd Chase and in ref. 1 they discussed the relationships between cross sections, storage lifetimes, pumping intensities, and how efficiency, and inversion uniformity are related to spectroscopic and configurational parameters.

In summary, if the figures of merit for the system are high efficiency and good beam quality, then the laser design is pushed into the regime where the optical thickness at the pump wavelength is as large as possible, limited by only by parasitics, amplified spontaneous emission, or damage. This provides the best utilization of the pump energy, the highest inversion fractions for good extraction efficiency, and the highest gain uniformity for good beam quality. Typically optimized designs are characterized by low doping density, usually around 10^{19} /cm^3 which means that the stored energy density and the specific gain are very similar to conventional rare earth doped solid state lasers. Also, since the level of gain depends on the level of inversion to varying degrees depending on the spectroscopic details, they operate at high inversion fractions, typically greater than 50%, and pump intensities typically 5 or 10 times saturation intensity.

$$\Phi_{pump} = (5 - 10)*(h\nu_p/\sigma_a\tau_f) \quad (W/cm^2)$$

where $h\nu_p$ = energy of pump photon (Joules)
σ_a = absorption cross section (cm^2)
and τ_f = fluorescence lifetime (sec)

Fig. 1 shows a sequence of times during the pump pulse which illustrates how the optical field, and inversion fraction evolve and form a bleach wave that propagates thru the medium. At early times when the integrated flux is well below the saturation fluence, the intensity falls off exponentially as a function of distance and the excited state density also falls off exponentially. At this stage the situation is similar to flash lamp pumping

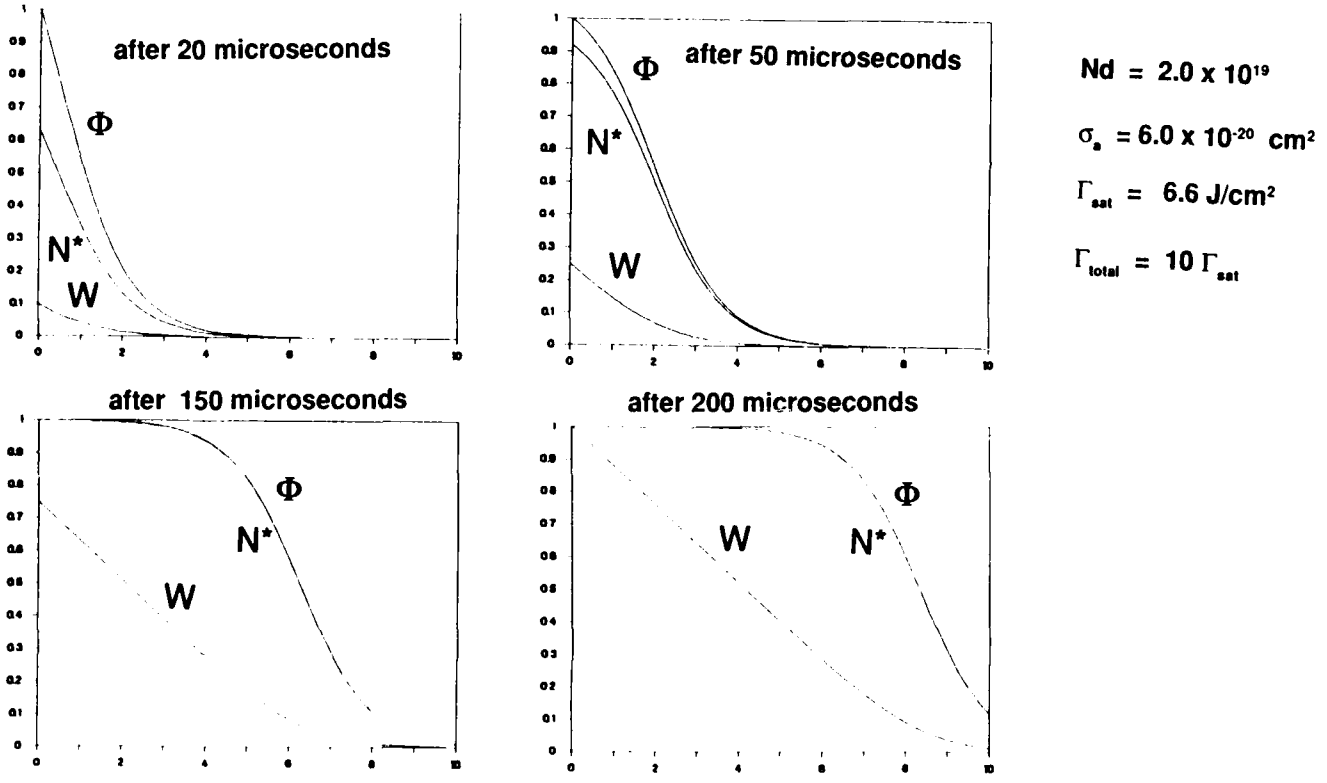


Fig. 1 Sequence of snapshots showing the time evolution of the pump intensity, and the inversion fraction under depletion mode pumping conditions.

At later times a wavefront is forming, leaving behind a bleached medium. The excited state density tracks the pump intensity very closely. The velocity of the wavefront is:

$$V = (\Phi/h\nu_p)^*N_o$$

where N_o = doping density

The pump intensity has to be sufficient to bleach thru the material in a time less than the fluorescent lifetime. The transition region is inversely proportional to the optical thickness, and generally the smaller this transition region is compared to the total length, the more efficient the laser will be.

There are also spectroscopic properties that are important to note in selecting a host for optimum performance. First of all there has to be sufficient stimulated emission cross section, as in any solid state laser, so that energy can be extracted without damaging the material. Typically, the intercavity fluence will be several times the saturation fluence of the laser transition:

$$\Gamma = (1 - 2)^*(h\nu_\ell/\sigma_e) \qquad (J/cm^2)$$

where $h\nu_\ell$ = energy of a laser photon
and σ_e = stimulated emission cross

If there is more than one mode lasing, there can be local intensity peaks several times larger than the average, so, for typical strong materials the cross section for emission should be greater than 2×10^{-20} cm^2.

Another important consideration is competing gain on other transitions. This is particularly a concern in Nd because the gain at 1.06 um is typically many times larger than it is at .9 um, so a desirable host would have less competition on other lines. There are ways of dealing with gain competition, one can either selectively absorb at the wavelength of the competing line, and that is a technique that we have used successfully, alternatively, dichroic coatings can be used to put a high loss in the cavity for competing lines.

Finally, because the lower level does fill back up during lasing, it's important for efficient, room temperature operation, that the lower laser level be several kT above the ground state.

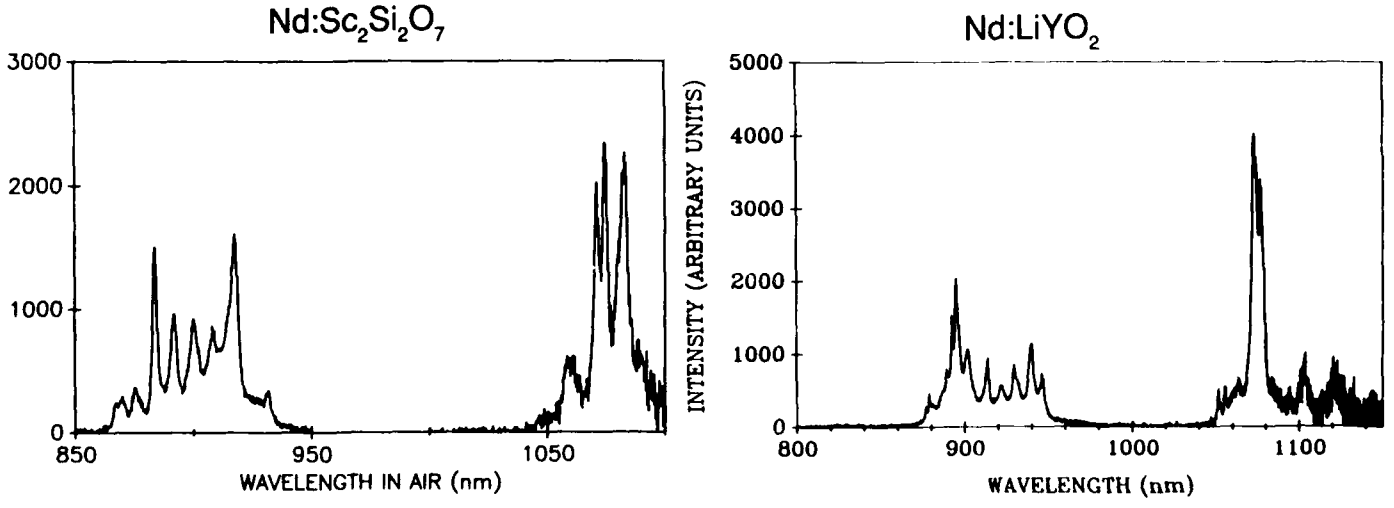


Fig. 2 Fluorescence spectra of two Nd doped oxides which illustrate the desirable and undesirable characteristics for depletion mode pumped ground state lasers.

To illustrate these two points fig. 2 shows two emission spectra which illustrate a good candidate, and a poor candidate. In the scandium orthosilicate the gain to the $4I_{11/2}$ manifold is spread out over several lines while the 9/2 manifold shows a fairly strong feature at about 500 cm^{-1} above the ground state. On this basis, $Sc_2Si_2O_7$ is an interesting candidate. On the other hand, the $LiYO_2$ has a single dominate feature in the 11/2 manifold while the strongest feature in the 9/2 manifold is only about 200 cm^{-1} above the ground state and so it's thermal population at room temperature is fairly high. Because of this $LiYO_2$ is not a desirable candidate.

3. Depletion mode pumping: Modeling and Experiments

Next we will describe the modeling and experiments that we have done to characterize the pump dynamics and to demonstrate the utility of this kind of laser and to validate performance against model calculations. The equations that describe the excited state population and the pump intensity are as follows:

$$\frac{\partial}{\partial t} N^*(x,t) = \frac{\Phi(x,t)}{\Phi_{sat}\tau_f}[N_o - N^*(x,t)] - \frac{1}{\tau_f} N^*(x,t) - \Gamma_{Auger} N^{*2}(x,t)$$

$$\left(\frac{1}{c}\frac{\partial}{\partial t} + \frac{\partial}{\partial x}\right)\Phi(x,t) = \sigma_a \Phi(x,t)[N_o - N^*(x,t)] - \Sigma\Phi N^*(x,t)$$

where $\Phi(x,t)$ = pump intensity
$N^*(x,t)$ = population in upper manifold
N_o = doping density
τ_f = fluorescent lifetime
σ_a = absorption cross section
Φ_{sat} = saturation intensity $h\nu/\sigma_a\tau_f$
Σ = cross section for excited state absorption

The pump beam propagates thru the material, energy is lost by absorption out of the ground state manifold and thru excited state absorption. The population in the excited state manifold changes at a rate depending on the pump intensity, the fluorescent lifetime, and quenching. At high excitation levels there is the possibility of Auger recombination and so we have included in the model a term proportional to the excited state density squared.

Implicitly in this model we assume that the inter-Stark relaxation rates are very fast, on the time scale of the pump pulse. That is, everything decays instantly from the pump level down to the metastable level. Also, we assume that the populations in the various Stark levels in the ground state manifold are always in thermal equilibrium. Finally, we assumed that if there is any ESA or concentration quenching, that would populate other levels, that everything decays rapidly either to the upper metastable level or the ground state manifold.

Several experiments were made to verify that depletion mode pumping is indeed possible and that the population dynamics can be reasonably described by this set of equations. Basically, these experiments were designed to look for any mechanism that would reduce the storage efficiency.

Fig. 3 shows a schematic illustration of the experiment to measure gain and to observe the population dynamics during the pump excitation pulse.

An Alexandrite laser was used as the excitation source. In these experiments approximately 1J pulse energy was used. The pulse length was 80 usec, and the spot size was about 1.5 mm in diameter. Density filters of various attenuations were inserted between the pump and the sample so that the total fluence could be adjusted. The samples of yttrium orthosilicate that were pumped ranged in length from less than 1 cm up to several cm and the doping density varied from less than 1.0e10 up to almost 5 x 10^{19}. The doping density was known to about 10% and the fluorescent lifetime at low doping was know quite accurately. The gain was sampled using a Ti:saphire probe laser tuned to 912 nm. The power in the probe laser was 10 mw cw, well below saturation fluence, and the beam was detected after passing thru the pumped region, on a photodiode. We did have a reasonable

estimate of the stimulated emission cross section from a Judd Ofelt analysis of the absorption lineshapes and this was used, along with the doping density to derive the excited state fraction. There was also a diagnostic looking at the fluorescence at 1074 as well as the fluorescent in the blue which we thought might show up if there were ESA. The fluorescent at 1074 gives a good measure of the instantaneous excited state population and should be sensitive to Auger quenching and what excited state density that would become important. In general we were concerned about any non radiative mechanisms coming into significance and at what levels of excitation. Measurements were made over a variety of doping densities and excited state densities and then compared with model calculations to validate our understanding of the pump dynamics.

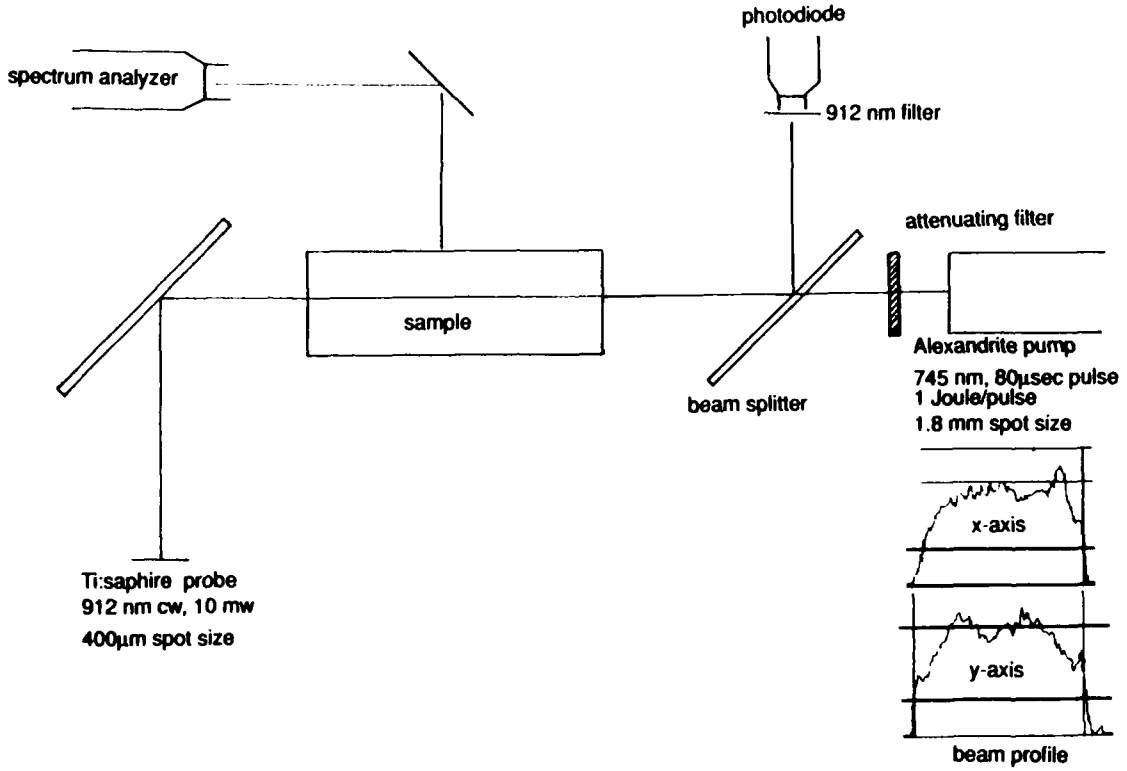


Fig. 3 Schematic illustration of the experiment for measuring excited state fractions during depletion mode pumping.

Based on the measured beam profile, the doping density, and sample length, and how much energy went into the sample we can simulate the fluorescent signal and compare that to what was measured. Data was taken over a range of doping densities and pump fluences and good agreement was obtained with the data assuming an Auger parameter of 1.3×10^{-22}. Fig. 4 shows a comparison of the excited state fraction based on the fluorescent signal compared to the model calculation of the fluorescent signal. Fig. 5 shows the excited state fraction derived from the small signal gain. The only scale factor here is the emission cross section. The emission cross section that seems to give the best fit in both the gain measurements and the energy extraction experiments was about 2.1×10^{-19} which is about 15% smaller than the cross section derived from the Judd Ofelt analysis. Fig. 6 shows the excited state fraction as a function of pump fluence. The circles on this plot are backed out from the gain measurements again using a cross section of 2.1×10^{-20} and the triangles are calculated from the pump model using a quenching rate of 1.3×10^{-22}

In summary, over the range of excited state densities, and pump fluences of interest, the time dependence of the excited state density predicted by the model and the excited state fraction derived from the gain measurements are in good agreement. The uncertainty in the analysis is 15%.

4. Extraction Dynamics: Models and Experiments

Additional models were developed to describe the photon field and population dynamics during the extraction process. During extraction everything takes place on a much faster

time scale and we were looking for any mechanisms that would limit extraction efficiency.

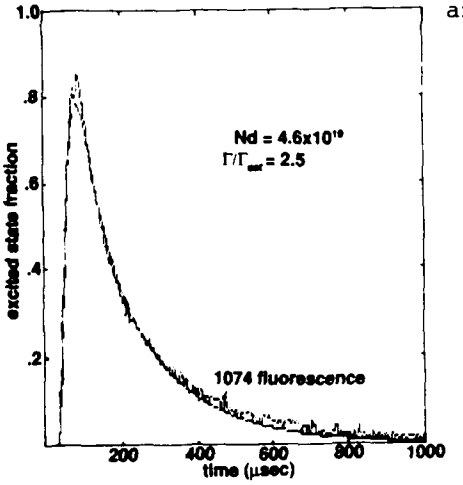
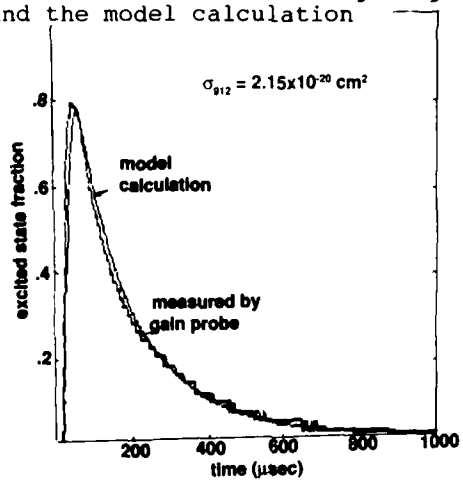


Fig. 4 Excited state fraction vs. time as derived from the model and from the 1074 nm fluorescence signal

Fig. 5 Excited state fraction vs. time derived from the small signal gain and the model calculation



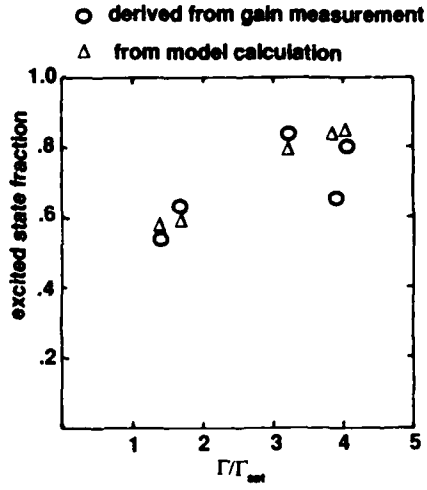


Fig. 6 Excited state fraction vs. pump fluence from gain measurements and model calculations

The equations for the photon field, the upper state population, and the lower level populations are:

$$\frac{d\Psi}{dt} = \Psi\left[c\sigma\frac{L}{L'}(n_b - n_a) - \frac{\delta}{t_r}\right]$$

$$\frac{dn_a}{dt} = f_a(n_b - n_a)c\sigma\Psi$$

$$\frac{dn_b}{dt} = -f_b(n_b - n_a)c\sigma\Psi$$

$$f_b = \frac{\exp\{-\varepsilon_b/kT\}}{\Sigma_j \exp\{-\varepsilon_j/kT\}} \qquad f_a = \frac{\exp\{-\varepsilon_a/kT\}}{\Sigma_j \exp\{-\varepsilon_j/kT\}}$$

where Ψ = laser field
n_a = population in terminal laser level
n_b = population in upper laser level
L = optical length of sample
L' = optical length of cavity
σ = spectroscopic cross section of laser transition
t_r = cavity round trip transit time
δ = fractional round trip cavity loss

Again, we assumed that the inter-Stark relaxation times are short compared with the length of the extraction pulse which was about 100 ns. In these experiments, the Q-switch was opened near the peak of the stored energy and so the population levels are tracked during the pump pulse using the pump dynamics model and after that the populations are driven by the laser field.

Fig. 7 shows a schematic illustration of the experiment used to characterize the extraction dynamics and to measure the pulse shape and the fraction extracted for comparison with model calculations.

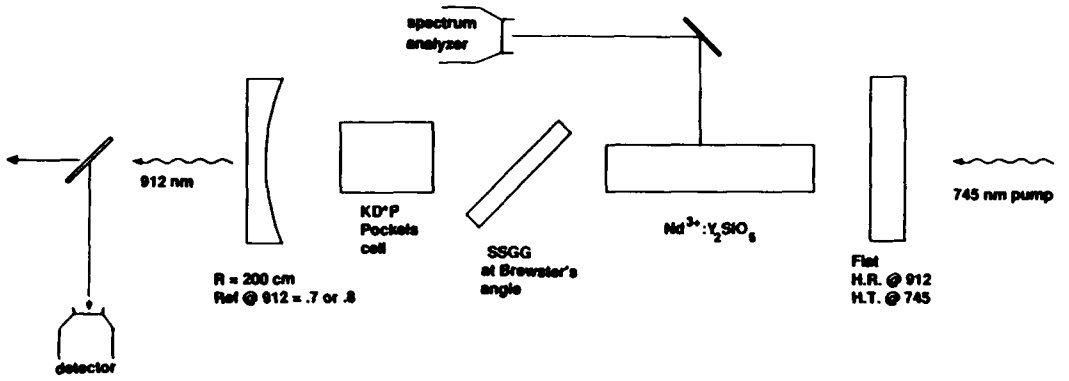


Fig. 7 Schematic illustration of the experiment for validating extraction dynamics.

In addition to measuring energy in, energy out, and pulse shape, the gain was independently monitored by looking at the 1074 fluorescence which we knew from earlier experiments tracked the gain very closely.

The internal extraction efficiency, that is how much of the stored energy was actually removed by stimulated emission, was measured as well as the external extraction efficiency. This experiment was repeated at two different output couplers, one with a reflectivity of .7 and the other with a reflectivity of .8. Fig. 8 shows two traces of the 1074 fluorescent signal showing the drop in excited state density as the Q switch is opened for the two different output couplers.

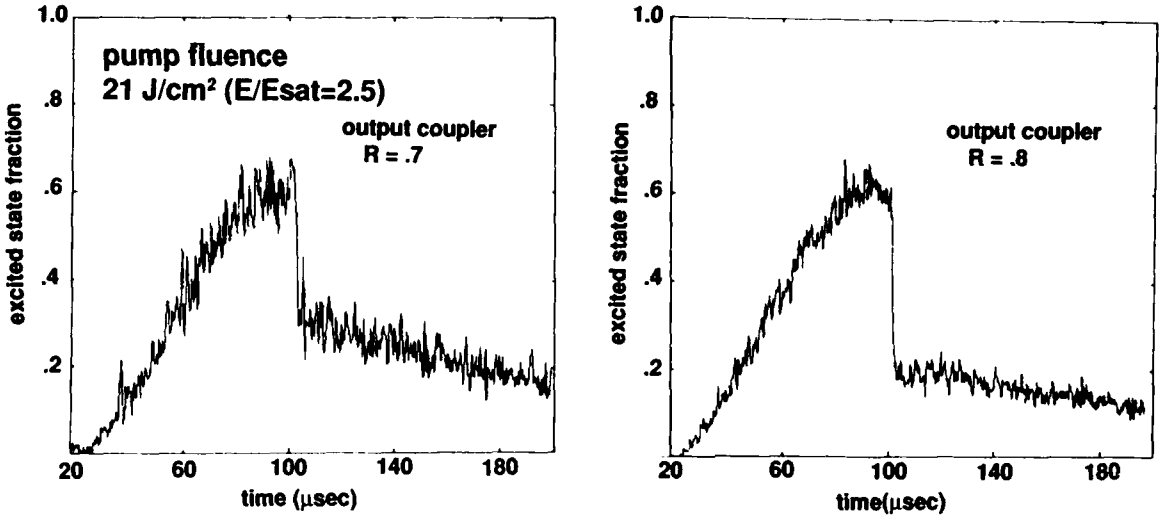


Fig. 8 Excited state fraction vs. time during the Q-switch pulse for two different output coupler reflectivities.

Knowing the energy in the pump beam, the cross sections, lifetime, and thermal populations of all the sublevels the equations for the pump pulse and the extraction process were solved numerically for the internal extraction efficiency. Fig. 9 shows the model calculations for the extraction efficiency as a function of excited state fraction and output coupler reflectivity, using the measured absorption cross section and the emission cross section derived from Judd-Ofelt analysis. Superimposed on these calculations are the measured values of both the internal and external extraction efficiency.

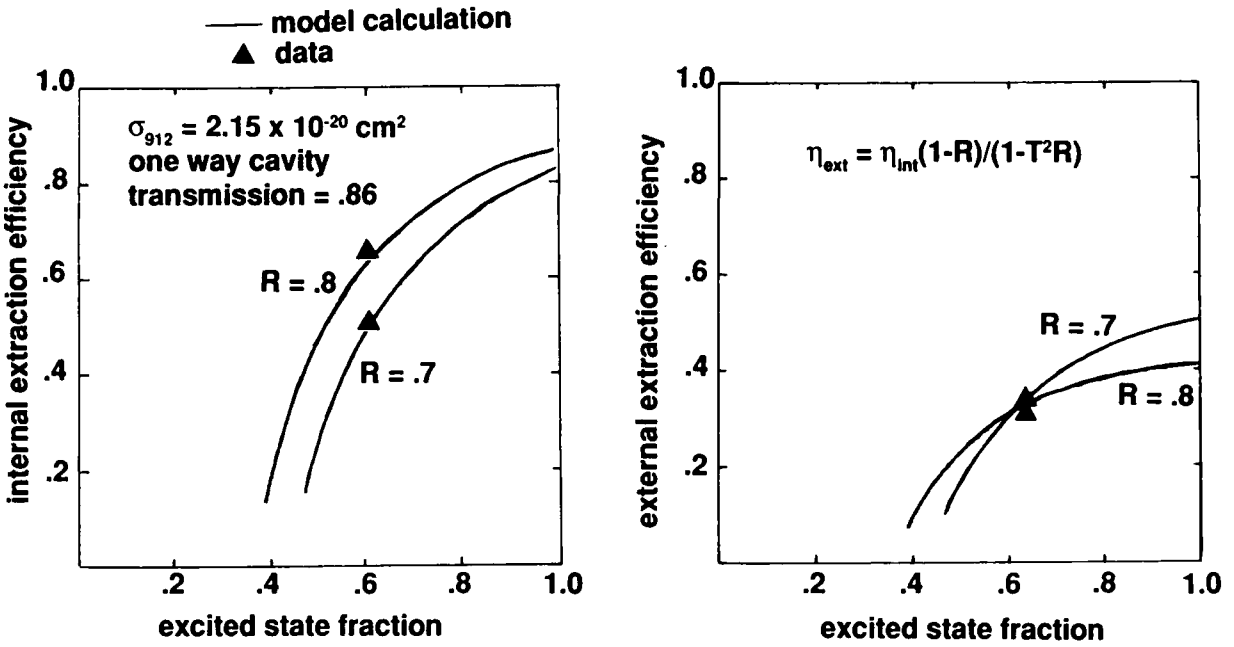


Fig. 9 Internal extraction efficiency and external extraction efficiency as a function of excited state fraction. Solid lines are based on model calculations and the triangles are data points from the extraction experiments.

5. Summary/Conclusions

Lasing has been demonstrated on a ground state transition and extraction efficiency and pulse shape are in good agreement with modeling. Bleach mode pumping to high inversion levels (>50%) has been demonstrated and agrees well with simple model calculations. Based on these experiments and model projections we believe that ground state depletion mode pumped solid state lasers are practical, and can achieve high efficiency and high peak and average power performance.

Currently activities are underway to develop diode pump sources that can deliver sufficient intensity to saturate pump transitions. In addition, other active ions such as Tm, Ho, Er, Yt are being evaluated as well as other hosts for a variety of applications

Acknowledgment

This work was performed under the auspices of the U.S. Department of Energy by the Lawrence Livermore National Laboratory under contract W-7405-Eng-48.

References

1. W.F. Krupke, L.L. Chase, SPIE vol. 1040, High Power and Solid State Lasers II (1989)

DISCLAIMER

This document was prepared as an account of work sponsored by an agency of the United States Government. Neither the United States Government nor the University of California nor any of their employees, makes any warranty, express or implied, or assumes any legal liability or responsibility for the accuracy, completeness, or usefulness of any information, apparatus, product, or process disclosed, or represents that its use would not infringe privately owned rights. Reference herein to any specific commercial products, process, or service by trade name, trademark, manufacturer, or otherwise, does not necessarily constitute or imply its endorsement, recommendation, or favoring by the United States Government or the University of California. The views and opinions of authors expressed herein do not necessarily state or reflect those of the United States Government or the University of California, and shall not be used for advertising or product endorsement purposes.

ACTIVE FREQUENCY STABILIZATION OF MONOLITHIC, DIODE LASER PUMPED, SOLID STATE LASERS

T. Day, E.K. Gustafson and R.L. Byer
Edward L. Ginzton Laboratories
Stanford University
Stanford, CA. 94305
(415) 723-0226

Abstract

Laser frequency stabilization is briefly reviewed with an emphasis on the requirements in monolithic, diode laser pumped, solid state lasers. Recent work on the active stabilization of a diode laser pumped, non-planar ring oscillator to less than 3 Hz of relative linewidth is included and improvements necessary to reach the quantum limit are discussed. Results using these sources in a coherent communication link and to injection lock a 13 W laser are also presented.

Frequency stable lasers are required as master oscillators in many applications, including coherent communication, high resolution spectroscopy and gravity wave detection. Helium-neon, dye and argon-ion lasers have been successfully stabilized for potential use in these fields[1,2,3]. These lasers are typically made from discrete elements and have wideband frequency noise requiring complex locking servos. Diode laser pumped Nd:YAG rod lasers have also been stabilized to reference interferometers[4]. However, without a reference oscillator the frequency stability of these lasers is commonly analyzed using the closed loop error signal which can only provide a lower bound on performance. These lasers also require additional elements to force single axial mode operation as well as provide isolation against optical feedback.

The diode-laser pumped nonplanar ring oscillator (NPRO), invented in 1985 by Kane and Byer[5], overcomes many of the difficulties associated with discrete element systems. Short term free running linewidths of 3-10 kHz have been reported for diode laser pumped Nd:YAG NPRO's[6,7] and spectral densities of frequency noise have been measured to be approximately 100 Hz/$\sqrt{\text{Hz}}$ at 100 Hz and 16 Hz/$\sqrt{\text{Hz}}$ at 1 kHz[8]. These impressive frequency properties are attributed to the low noise diode laser pumping together with the monolithic nonplanar ring geometry. Diode laser pumping avoids frequency noise associated with flashlamps and the unidirectional oscillation made possible by the nonplanar ring geometry eliminates spatial hole burning forcing single mode operation and provides feedback isolation. Furthermore, the monolithic construction requires no external elements and is, therefore, less sensitive to ambient acoustics.

The lasers we used in our stabilization studies were modified Lightwave Electronics model 120 NPRO's with 2 mW of typical output power[9]. The Nd:YAG laser crystals were replaced with Nd:GGG crystals optimized for improved resistance to optical feedback[10] and PZT actuators were bonded directly to the gain medium to provide fast frequency tuning. The PZT tuning coefficient was 450 kHz/V with a tuning bandwidth of 500 kHz and a dynamic range of greater than 20 MHz. In addition, these lasers could be temperature tuned at 3 GHz/°C with a modulation bandwidth of approximately 1 Hz.

Our locking scheme[11], shown in Fig. 1, used a frequency discriminant technique known as FM or Pound-Drever locking[12].

Laser 1 was phase modulated at a frequency of 10.9 MHz and laser 2 was modulated at 20.3 MHz. The two laser beams were mode matched into a high finesse interferometer (Newport Research Corporation model SR-150 Super Cavity). The interferometer had a free spectral range of 6.327 GHz and a finese of greater than 22,000. The interferometer transmission bandwidth was, therefore, less than 288 kHz. Typically no more than two higher order transverse modes were measurably excited. The amplitudes of these modes were more than 14 dB below the fundamental and their frequencies were offset from the axial mode by 0.811 and 1.62 GHz. The phase modulation sidebands of each laser lie well outside the interferometer passband and were, therefore, completely reflected with essentially no relatively phase shift. The polarizing beam splitter and quarter-wave plate served to isolate the reflected and incident beams as well as provide additional resistance to optical feedback.

On resonance approximately 60% of each carrier is reflected from the cavity. However, near resonance the carrier experiences a strongly dispersive phase shift[13]. The phase shifted carriers beat with their respective sidebands at detector D2 and the components at frequencies f_1 and f_2 are detected at the output of the two mixers. The amplitude of these signals is proportional to the frequency offset relative to the cavity resonance and serves as an error signal used in the locking loop The error signals were amplified by high gain servos and fed back to the PZT actuators bonded to the laser crystals. The controller had a DC loop gain of 125 dB with a unity gain point of 100 kHz.

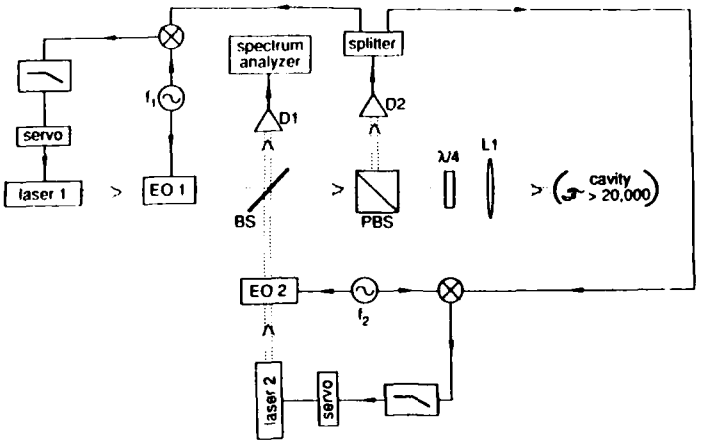


Figure 1: FM locking of two diode laser pumped nonplanar ring oscillators to adjacent axial modes of a high finesse interferometer

The two lasers were independently locked to adjacent axial modes of the interferometer and due to the large interferometer free spectral range could not phase lock. Locking the two lasers to the same interferometer also provides limited common mode rejection against cavity fluctuations. Detector D1 served as a diagnostic port, outside the control loop, enabling direct measurements of the lasers relative stability via the heterodyne beam note.

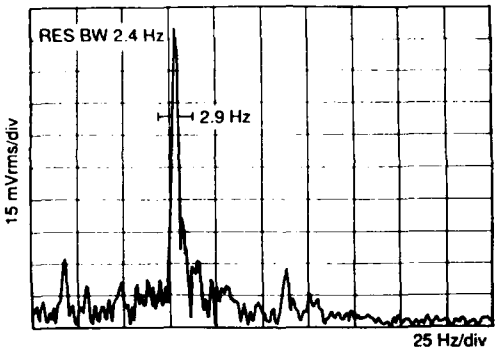


Figure 2: The heterodyne beatnote between two lasers independently locked to adjacent axial modes of a high finesse interferometer

Figure 2 shows a spectrum analyzer trace of the heterodyne beat note signal detected at this port. The 6.327 GHz signal was mixed down to 20 kHz with a precision RF oscillator and analyzed with an audio spectrum analyzer (Hewlett Packard model 3561A). We measured a 2.9 Hz heterodyne beat note linewidth. Figure 2 shows sideband structure on the signal. This sideband structure is due to the short length of the reference interferometer as well as to electrical pickup (note the 60 Hz sidebands). This arises because the amount of common mode rejection that can be achieved is proportional to the length of the reference interferometer. With our cavity a 0.1 nm length fluctuation corresponds to a 24.9 Hz shift in the free spectral range.

The beat note linewidth is determined by system noise[3]. Shot noise on the laser beam together with amplifier noise are interpreted by the servos as frequency fluctuations and are, therefore, imposed directly upon the lasers output frequency. This spectral density of voltage fluctuations is converted into frequency fluctuations with a conversion factor given by the inverse slope of the frequency discriminant[3]. We measured this to be 2.5 MHz/V. On the resonance the optical power at detector D2 was approximately 77 μW. This corresponded to a photo current of 38.4 μA and, therefore, a shot noise current density of 3.5 pA/$\sqrt{\text{Hz}}$. The amplifier noise current was 14.5 pA/$\sqrt{\text{Hz}}$. The voltage gain of the discriminant was 15,810 V/A and, therefore, the system noise was determined to be 0.33 μV/$\sqrt{\text{Hz}}$. This corresponds to an imposed spectral density of frequency fluctuations of 0.834 Hz/$\sqrt{\text{Hz}}$. In the regime where the size of the frequency fluctuations is small compared to their bandwidth the resultant linewidth of an oscillator is related to its spectral density (Δ) by[14] $\Delta\nu_{laser} = \pi\Delta^2$. Thus each laser had a theoretical, noise limited linewidty, of approximately

2.2 Hz; in good agreement with the experiment.

To reduce the relative linewidths to a shot noise limited level the discriminant slope must be increased. The discriminant slope increases proportionally with the optical power while the shot noise is proportional only to the square root of power. With only 77 μW of optical power at the detector the amplifier noise dominates the system performance and prevents shot noise limited linewidths. In the absence of amplifier noise the shot noise limited linewidth is approximately 150 mHz.

These low power lasers have been used to injection lock a higher power oscillator[15]. In this technique a low power (30 mW) NPRO was used as a master laser and injected into and amplified by a high power, CW, lamp pumped slave laser. The slave laser in free running operation was capable of up to 20 W of multimode output power. When the slave laser was locked to the master, in the same manner that the low power NPRO was locked to a Fabry-Perot cavity, single mode frequency stable operation was achieved. Output powers as high as 13 W have been achieved with no significant degradation in the phase noise.

The low phase noise of diode laser pumped NPRO's and their demonstrated ability to be easily stabilizedas well as used to injection lock high power oscillators make them ideal candidates for use in coherent communication applications. To demonstrate this potential we developed an optical phase locked loop (OPLL) for use in a coherent homodyne receiver utilizing nonplanar ring oscillators for both the transmitter and receiver. The local oscillator and transmitter were the same Lightwave Electronics model 120 nonplanar ring oscillators described above.

Our locking circuitry can be described as a type II third order PLL, which offers the advantages of very high gain at low frequencies together with a small equivalent noise bandwidth. The OPLL achieved tight locking for several hours with transmitter powers of less than -34 dBm on the phase detector. The spectral density of closed loop phase noise was measured by spectrally analyzing the voltage fluctuations at the phase detector output on a Hewlett Packard model 3561A dynamic signal analyzer. The measured noise spectral density corresponded to an rms phase error of 11.6 mrad (0.69°.

The minimum phase error in an optical phase lock-loop was derived by Kazovsky in 1986[16]. In his analysis, he assumed that $\Delta\nu$, the lasers Lorentzian linewidth, is the dominant term in the laser's spectral density of frequency noise. While this is true for diode lasers, it is not the case for many diode-laser-pumped solid state lasers which have very small Lorentzian linewidths and are primarily flicker noise dominated. In order to compare our experimentally achieved phase error to that predicted by Kazovsky's theory, we measured the equivalent noise bandwidth of our loop filter and the free-running noise spectral density of our lasers. We found a value of 31.5 kHz for the equivalent noise bandwidth of the loop filter. Previous measurements had determined that the spectral density of noise was flicker noise dominated with (in Kazovsky's notation) k_a of 6.5×10^3 Hz^2 and an equivalent $\Delta\nu$ of 0.33 Hz. At the power levels of these experiments, shot noise is negligible and the theoretically predicted minimum phase error is 9.0 mrad. This agrees well with our experimentally observed phase error of 11.6 mrad.

Diode laser pumped solid state lasers have now been able to achieve less than 3 Hz of relative linewidth in active stabilization experiments, less than 1° of closed loop rms phase noise in an optical phase locked loop, and up to 13 W of CW, frequency stable output in an injection locked system. Additionally, their monolithic structure makes them extremely rugged and diode laser pumping results in high efficiency. These results demonstrate that solid state lasers can be built to have extremely low levels of frequency noise and should provide an attractive alternative for applications ranging from coherent communications to gravity wave detection.

References

1. J. Hough, D. Hils, M.D. Rayman, Ma L.S; L. Hollberg, and J.L. Hall, Appl. Phys. B 33, 197 (1984).
2. C.N. Man, and A. Brillet, Opt. Lett. 9, 333 (1984).
3. C. Salomon, D. Hils, and J.L. Hall, J. Opt. Soc. Am. 5, 1576 (1988).
4. D. Shoemaker, A. Brillet, C.N. Man and O. Cregut, Opt. Lett. 14, 609 (1989).
5. T.J. Kane and R.L. Byer, OPt. Lett. 10, 65 (1985).
6. T.J. Kane, A.C. Nilsson, and R.L. Byer, Opt. Lett. 12, 175 (1987).
7. S.P. Bush, A. Gungor, and C.C. Davis, Appl. Phys. Lett. 53, 646 (1988).
8. K.J. Williams, A. Dandridge, A.D. Kersey, J.F. Weller, A.M. Yurek, and A.B. Tveten, Electron. Lett. 25, 774 (1989).
9. Lightwave Electronics, 1161 San Antonio Rd, Mountain View, California 94043.
10. A.C. Nilsson, E.K. Gustafson, and R.L. Byer, J. Quant. Electron. 25, 767 (1989).
11. T. Day, E.K. Gustafson, and R.L. Byer, to be published in Opt. Lett. 15, (1990).
12. R.W.P. Drever, J.L.Hall , F.V. Kowalski, J. Hough, G.M. Ford, A.J. Munley and H. Ward, Appl. Phys. B 31, 97 (1983).
13. A.E. Sigeman, Lasers, (Mill Valley:University Science Books, 1986), ch.11.
14. D.S. Elliot, R. Roy and S.J. Smith, Phys. Rev. A 26, 12 (1982).
15. C.D. Nabors, A.D. Farinas, T. Day, S.T. Yang, E.K .Gustafson, and R.L. Byer, Opt. Lett. 14, 1189 (1989).
16. L.G. Kazovsky, J. Lightwave Technology, LT-4, 182 (1986).

A Long Wavelength Nd:YAG Laser

S. Wong P. Pace P. Mathieu J. Tulip

Defence Research Establishment Valcartier
P.O. Box 8800, Courcelette, P.Q.
Canada

Abstract

An experimental and theoretical study of the characteristics of a long-wavelength Nd:YAG laser have been performed. The calculations indicate that operation at $1.06\,\mu m$ and at $1.44\,\mu m$ is possible. The results have been verified experimentally both under Q-switched and non Q-switched conditions.

1 INTRODUCTION

The armed forces presently have a large number of devices that are based on the technology of Nd^{3+}:YAG lasers. These systems range from small hand-held devices to larger rangefinders/designators that are utilized as part of complete weapons systems. With the proliferation of these lasers, the technology has now been developed to a high degree of sophistication. It is nowadays widely recognized that the Nd^{3+}:YAG laser is a very convenient and relatively high-performance source of near infrared radiation at $1.06\,\mu m$. The spectroscopy of Nd^{3+}:YAG indicates that there are several transitions in the ${}^4F_{3/2} \rightarrow {}^4I_{9/2}, {}^4I_{11/2}$, and ${}^4I_{13/2}$ manifolds [1]. It has been suggested that laser emission is possible on most of these transitions [2]. Previous work [3] has indicated that long-wavelength pulsed operation of the Nd:YAG laser is possible at $1.44\,\mu m$ using a transition in the ${}^4F_{3/2}$ to ${}^4I_{13/2}$ band. Light at this wavelength is eyesafe and it is feasible that a standard laser can be modified to operate at the longer wavelength. There is also the possibility of switching the output between $1.06\,\mu m$ and $1.44\,\mu m$ depending upon the desired application.

This report summarizes a theoretical investigation into long wavelength Nd^{3+}:YAG laser operation and it presents the results of an experimental study into both the Q-switched and non Q-switched lasing characteristics at $1.44\,\mu m$. The results indicate that dual wavelength operation is possible and that the device has potential as a source for several applications including medical and military systems.

2 THEORY

The operation of the laser is simulated using a 4-level model of the Nd^{3+} ions. A generalized 4-level model is shown in Figure 1. This model includes fourteen laser transitions ranging from $0.9\,\mu m$ to $1.44\,\mu m$. The large number of transitions utilized is intended to provide a realistic representation of the competing characteristics of the various transitions when a set of restrictions are imposed by the design of the laser cavity. The goal of the simulation is to determine the conditions that would favour the transition at $1.44\,\mu m$ over all the other ones possible.

The wavelengths of the transitions employed in the model along with the laser parameters are listed in Table 1 and a more detailed identification of these transitions is shown in Figure 2. A set of temporal rate equations describing the evolution of the population densities in the 4-level model are presented below,

$$\frac{dn_1}{dt} = -P - n_1\omega_{12} + n_2\omega_{21} + n_3A_3\beta_{31} + n_4A_4\beta_{41} + N_1\delta_1 I_1 c\frac{l}{L}$$

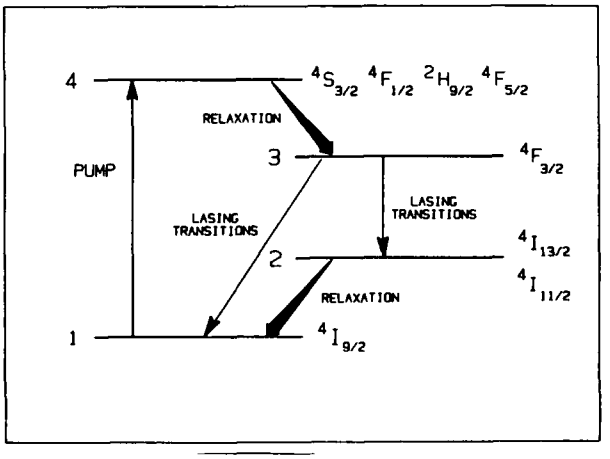


Figure 1: A generalized 4-level model of the Nd^{3+} ions

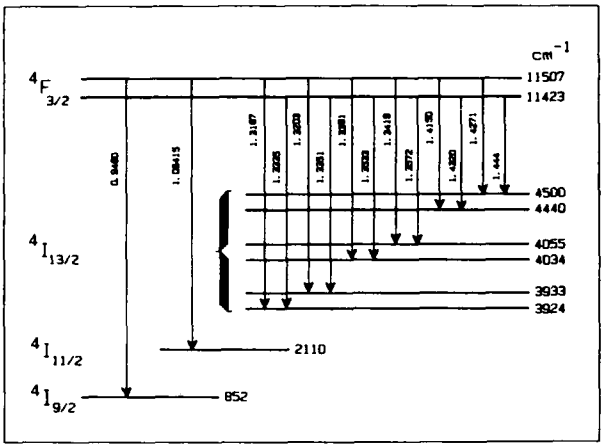


Figure 2: Lasing transitions used in the model

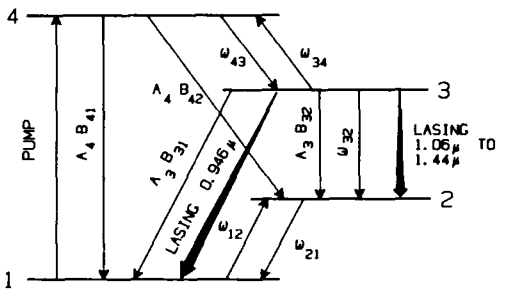


Figure 3: The 4-level model of the Nd^{3+} ions

Table 1: Model Parameters

ν	$\lambda(\mu m)$	peak δ (cm^2)
1	0.946	5.80×10^{-20}
2	1.064	3.00×10^{-19}
3	1.3187	0.95×10^{-19}
4	1.3203	0.23×10^{-19}
5	1.3335	0.44×10^{-19}
6	1.3351	0.54×10^{-19}
7	1.3381	1.00×10^{-19}
8	1.3419	0.36×10^{-19}
9	1.3533	0.28×10^{-19}
10	1.3572	0.73×10^{-19}
11	1.4150	0.20×10^{-19}
12	1.4271	0.08×10^{-19}
13	1.4320	0.13×10^{-19}
14	1.4444	0.28×10^{-19}

A_3	=	$3.93 \times 10^3 sec^{-1}$
A_4	=	$2.00 \times 10^4 sec^{-1}$
β_{31}	=	0.3
β_{32}	=	0.7
β_{41}		.35
β_{42}	=	0.65
ω_{21}	-	$1.00 \times 1.09 sec^{-1}$
ω_{12}	$\ll$	$\omega_{21}\omega_{12} = 0$
ω_{32}	=	$1.82 \times 10^3 sec^{-1}$
ω_{43}	=	$1 \times 10^9 sec^{-1}$
ω_{34}	$\ll$	$\omega_{43}\omega_{34} = 0$
l	=	$10cm$
L	=	$15cm$

$$\frac{dn_2}{dt} = \sum_{\nu=2}^{14}\left(N_\nu \delta_\nu I_\nu c \frac{l}{L}\right) + n_1\omega_{12} - n_2\omega_{21} + n_3(A_3\beta_{32} + \omega_{32}) + n_4 A_4 \beta_{42}$$

$$\frac{dn_3}{dt} = -\sum_{\nu=1}^{14}\left(N_\nu \delta_\nu I_\nu c \frac{l}{L}\right) - n_3(\omega_{34} + \omega_{32} + A_3) + n_4\omega_{43}$$

$$\frac{dn_4}{dt} = P + n_3\omega_{34} - n_4(\omega_{43} + A_4) \qquad (1)$$

n_i	is the population density (cm^{-3}) in level i
ω_{ij}'s	are the nonradiative transistion rates (s^{-1})
i, j	are the upper and lower levels respectively, *i.e.* $i \geq j$
A_i's	are the spontaneous emission rates (s^{-1})
β_{ij}'s	are the spontaneous emission branching probabilities
p	is the excitation pumping rate $(cm^{-3}s^{-1})$
N_ν	is the effective population inversion at frequency $\nu(cm^{-3})$
δ_ν	is the stimulated emission cross section at $\nu(cm^2)$
I_ν	is the laser photon density at frequency $\nu\,(cm^{-3})$
c	is the speed of light (cms^{-1})
l	is the length of the Nd:YAG rod (cm)
L	is the length of the cavity (cm)

Figure 3 is a schematic diagram illustrating the various radiative and nonradiative transitions in the 4-level model described by the above rate equations. The subscript ν in equation [1] indexes the lasing transitions.

In addition, a set of rate equations are also used to describe the growth of the photon density at each frequency ν. The gains and losses in the laser caused by the various mechanisms are modeled for a cavity configuration shown in Figure 4. The corresponding set of rate equations for the photon density are given by,

$$\frac{dI_\nu}{dt} = \left[\frac{\delta_\nu N_\nu 2l}{2L/c} - \frac{ln\left(\frac{1}{R_{1_\nu}R_{2_\nu}Q(t)}\right)}{2L/c} - \frac{ln\left(\frac{1}{T_\nu^2}\right)}{2L/c} - \frac{\xi_{\nu 2l}}{2L/c}\right] I - \nu + \frac{n_3}{A_3} \qquad (2)$$

where $\nu = 1, 2, 3, \ldots, 14$

R_{1_ν}, R_{2_ν}	are the front and back mirror reflectivities at frequency ν respectively
$Q(t)$	is the Q-switch function that controls the oscillation of the cavity
T_ν	is the spectral transmissivity of the filter F at frequency ν
ξ_ν	is the absorption loss of the Nd:YAG rod at frequency ν (cm^{-1})
$2L/c$	is the double-pass transit time of the cavity
A_3	is the spontaneous emission decay time of level 3

The last term in equation [2] corresponds to the noise photon density generated by spontaneous emission.

It is well known that each of the states ($^4F_{3/2}$, $^4I_{3/2}$, $^4I_{9/2}$) of the Nd^{3+} ions is comprised of many Stark components resulting from the removal of the arbitrary degeneracy by the crystal field [4]. Therefore, the lasing transitions can originate from one of the Stark components in the upper level and terminate on one of the Stark components on the lower level. To take this into account, the effective population inversion at lasing frequency ν is modified as follows,

$$N_\nu = \frac{e^{\frac{-\Delta E_{ui}}{kT}}}{\sum_i e^{\frac{-\Delta E_{ui}}{kT}}} n_u - \frac{e^{\frac{-\Delta E_{lj}}{kT}}}{\sum_j e^{\frac{-\Delta E_{lj}}{kT}}} n_l \qquad (3)$$

where $e^{\frac{-\Delta E_{ij}}{kT}}$ is the Boltzmann factor of the i^{th} Stark component, n_u is the upper lasing state population density, n_l is the terminating state population density, k is the Boltzmann constant and T is the temperature (set to 300° K). For the conditions $\nu = 1, u = 3$ the parameter l is set equal to unity while for $\nu = 2$ to $14, l$ is set equal to 2. The subscripts i and j are indexes for the Stark multiplets of the states corresponding to the lasing transition at frequency ν.

It should be noted that the stimulated emission cross section δ_ν, strickly speaking, is given by,

$$\delta_\nu = \delta_0 L(\nu) \tag{4}$$

where δ_0 is the peak value of the cross section at line centre and $L(\nu)$ is the normalized line profile function with line centre frequency ν. As a first approximation we assume that the value of the cross section is roughly constant over the line profile. *i.e.* $\delta_\nu = \delta_0$.

3 COMPUTATIONAL RESULTS

The objective of this study was to determine the conditions that would allow $1.44-\mu m$ lasing action from the Nd:YAG crystal while suppressing all the other transitions. It is well known that Nd:YAG lases readily at $1.06\,\mu m$. Therefore, we must find a scheme to discriminate against the $1.06\,\mu m$ transition and to favour that at $1.44\,\mu m$. There are a number of methods that can be used to achieve this objective. The reflectivity of the cavity mirrors could be controlled to favour lasing at $1.44\,\mu m$. Alternatively, the propagation of the $1.06\,\mu m$ radiation could be attenuated along with that from all the unwanted transitions by inserting a filter into the laser cavity.

In the model, we impose the condition that both the mirrors have the spectral reflectivity profiles shown in Figure 5. A special filtering element could also inserted to attenuate all the undesirable wavelengths; however, it should allow maximum transmission at $1.44\,\mu m$.

Because of the relatively low gain of the $1.44\,\mu m$ transition, strong optical pumping is required However, under these conditions, the much higher gain of the $1.06-\mu m$ transition will deplete the inverted population through amplified spontaneous emission. As a result, a large fraction of the pump energy will be wasted. For an input electrical pumping energy of 267 J, our model indicates that the reflectivity of the two end faces of the Nd:YAG rod must be smaller than 0.25%. If this condition is not met, the rod will act as its own resonator at $1.06\,\mu m$. Therefore, proper anti-reflection coatings are required if the laser is to operate satisfactorily at $1.44\,\mu m$. An alternate solution is to cut the ends of the rod at Brewster's angle.

Finally, we have taken into account the spectral absorption of the Nd:YAG rod. This absorption is assumed to be 0.4% cm^{-1} from 1.3 to $1.44\ \mu m$ and 0.22% cm^{-1} at 0.946 and $1.06\mu m$. The pumping of the Nd:YAG rod has been simulated by one or more flash lamps. To predict the amount of output laser energy that can be obtained at $1.44\,\mu m$ for a given electrical input energy, the performance specifications of commercially available flash lamps were used in selecting the values of the pumping parameters used in the model. We took into account prac-

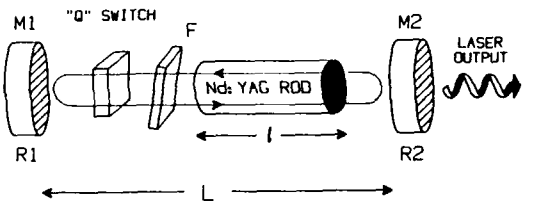


Figure 4: A schematic diagram of the laser cavity

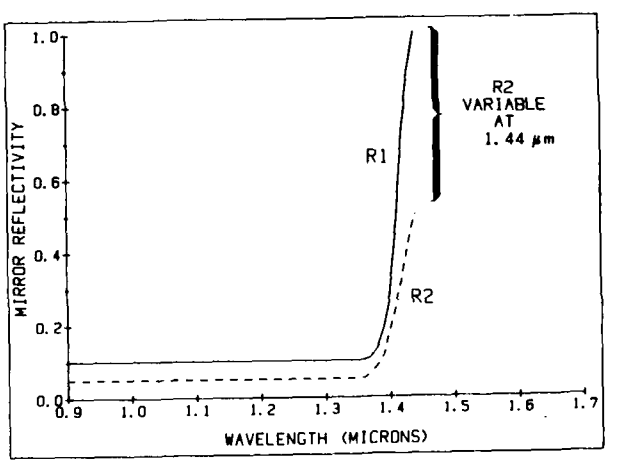


Figure 5: Reflectivity of the front (R_2) and rear (R_1) mirrors

tical considerations such as the flash lamp lifetime and pulse duration requirements in choosing the values of the pumping parameters.

For efficient Q-switched operation of the laser, a flash lamp that has a lifetime of 10^6 pulses with a pulse duration as short as $50\,\mu s$ is desirable. To meet these requirements, the maximum electrical energy that can be supplied to the lamp is approximately 13 J/cm. If we assume a typical standard Nd:YAG rod dimension of 0.6-cm diameter by 10 cm in length, the maximum electrical energy input into a linear flash lamp would be 133 J. We further assume that only 1% of the electrical input energy is converted into useful optical energy in pumping the Nd^{3+} ions from level 1 into level 4. Moreover, it is specified that the flash lamp pump pulse has a temporal profile of the form,

$$P(t) = P_0 t e^{\frac{-t}{5\tau_p}} \tag{5}$$

where P_0 is the peak pump value (J $cm^{-3}s^{-1}$) and τ_p is the pump-pulse duration. Furthermore, we assume that the pump-pulse amplitude falls off to $\frac{1}{10}^{th}$ of the maximum amplitude at time $t = \tau_p$ and that all the electrical energy required is delivered within the pulse duration τ_p; *i.e.*,

$$\int_0^{\tau_p} P_0 t e^{\frac{-t}{5\tau_p}} dt = \frac{E_f}{V} \tag{6}$$

where E_f is the energy delivered by the flash lamp and V is the physical volume of the Nd:YAG rod. Note that the factor 5 in the exponential gives the correct "fall-off" of the pump amplitude to 0.1 of the maximum value at time $t = \tau_p$.

The switching function $Q(t)$ in equation [2] provides the model with the capability to simulate a Q-switched laser pulse. A Q-switched giant laser pulse with high peak power at $1.44\,\mu m$ is desirable in some of the potential applications. The Q-switch is assumed to open completely within 100 ns. It is set to open at time $t = \tau_p$; that is, immediately after the required optical energy has been deposited into the laser medium.

Equations [1] and [2], which describe the lasing characteristics of the Nd:YAG laser, were solved numerically using standard numerical-integration techniques. A flash lamp input energy of 267 J has been used (two lamps) and pump-pulse durations of $50\,\mu s$ and $100\,\mu s$ were investigated. The laser output energy and peak power at $1.44\,\mu m$ were computed as a function of the output mirror reflectivity. The laser energy was computed using,

$$E_l = \int_0^{\infty} I(t)_{\nu=1.44} \frac{h\nu_{1.44}}{\tau_{1.44}} V dt \tag{7}$$

where $I(t)_{\nu=1.44}$ is the instantaneous laser photon density (cm^{-3} at $1.44\,\mu m$), $\tau_{1.44} = \ln\left(\frac{1}{R_1 R_2}\right)_{\nu=1.44}/(2L/c)$ is the cavity decay time, $h\nu_{1.44}$ is the energy per photon at $1.44\,\mu m$ and V is the volume of the Nd:YAG rod. The peak output power is given by [5],

$$P_{max}(1.44\mu m) = \frac{I_{max}(1.44\mu m)}{\tau_{1.44}} \tag{8}$$

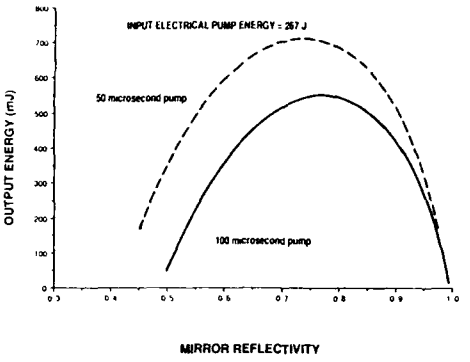


Figure 6: Laser output energy as a function of mirror reflectivity

The computed results for the laser energy are shown in Figure 6 and the results for the peak power are shown in Figure 7. A maximum laser energy of 720 mJ and a maximum peak power of 26 MW are predicted by the simulations. It is also noted that there exists an optimum value for the output mirror reflectivity that gives a maximum in both the output energy and the power. This will be discussed below. It can be seen that the overall energy and peak power are smaller when the flash lamp duration is lengthened from $50\,\mu s$ to $100\,\mu s$. This is because the excited populations in both levels 3 and 4 have more time to decay through spontaneous emission, resulting in a smaller inversion [6].

The simulations indicate that the amount of laser energy extracted is highly dependent on the mirror reflectivity. A low reflectivity implies a high cavity loss term in the laser photon-density rate equations. In this case the oscillation condition is only slightly above threshold and, therefore, only a small fraction of the inversion is converted into

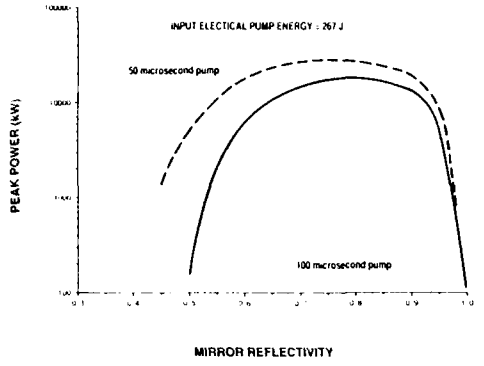


Figure 7: Laser power as a function of mirror reflectivity

laser photons. As the mirror reflectivity is increased, the cavity loss is reduced and the oscillation condition inside the cavity becomes more favourable. Therefore, more of the inversion can be converted into laser photons. The optimum coupling for extracting the laser energy is determined by a balance between the laser photon density attained inside the cavity and the coupling of the output mirror.

The temporal profiles of the calculated laser pulses are shown in Figure 8. They are plotted from the time the Q-switch starts to open. The results indicate that under the proper conditions, oscillation at $1.44\,\mu m$ is possible with laser energies in the hundred millijoule range and laser peak powers in the megawatt range. This operation can be achieved using standard commercially available laser technology.

4 EXPERIMENTAL RESULTS

4.1 Linear Configuration

It was found that controlling the reflectivity of the mirrors was adequate to suppress the strong transitions and allow the oscillation of the $1.44\,\mu m$ transition. This was demonstrated by setting up the laser in a simple linear configuration as shown in Figure 9. The alignment of the mirrors was very critical and small misalignments would cause the laser to oscillate on the $1.06\,\mu m$ transition.

Under the proper conditions, more than 1 J of energy was extracted at $1.44\,\mu m$. The laser energy as a function of the input electrical energy for two different output coupler reflectivities (90% and 80%) is shown in Figures 10 and 11 repectively. Laser efficiency, the ratio of the laser output energy to the input electrical energy, is approximately 0.5%.

As can be seen from Figures 10 and 11 as the pump energy in-

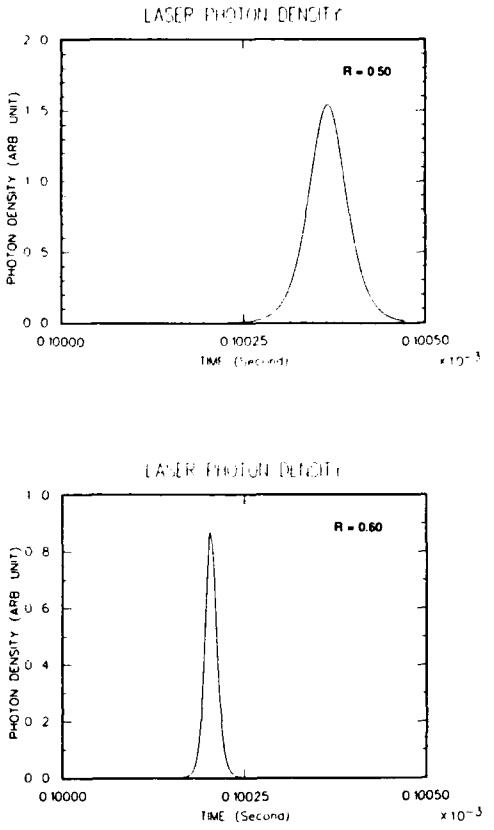


Figure 8: Computed temporal characteristics of the output laser pulse

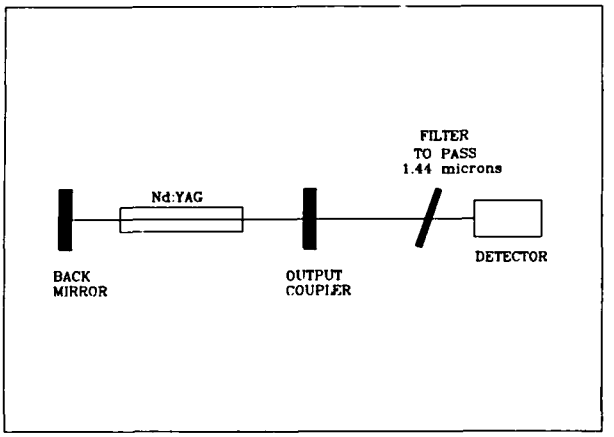


Figure 9: Linear laser configuration

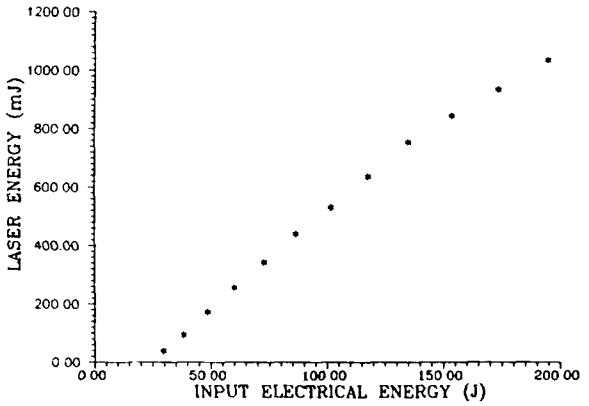


Figure 10: Output energy, linear configuration (90% coupler)

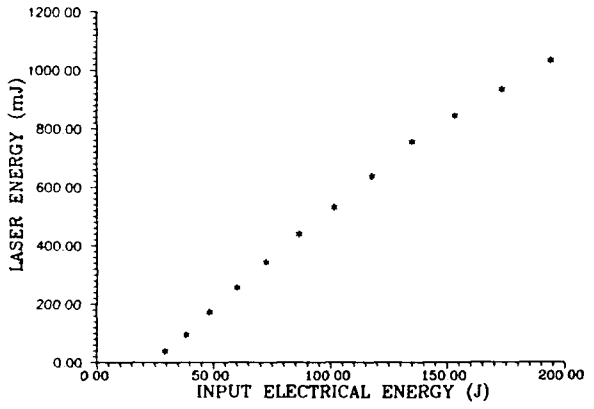


Figure 11: Output energy, linear configuration (80% coupler)

creases, there appears to be a saturation effect in the output laser energy at $1.44\,\mu m$. Further investigation has revealed that lasing of the $1.06\,\mu m$ transition is partly responsible for the apparent saturation. It is observed that as the input energy is increased beyond 90J, lasing at $1.06\,\mu m$ begins to occur.

Note that in figure 9, there is a 100% reflectance mirror at $1.06\,\mu m$ in front of the energy detector. It serves as a blocking filter at $1.06\,\mu m$. Thus the energy detector registers essentially only the radiation at $1.44\,\mu m$. The lasing of the $1.06\,\mu m$ transition was observed qualitatively be monitoring the temporal signals of the $1.06\,\mu m$ and the $1.44\,\mu m$ lines. The experimental arrangement is shown in Figure 12.

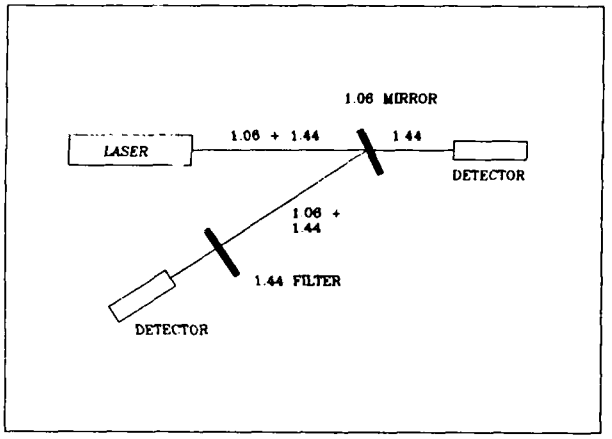


Figure 12: Pulsed output monitoring arrangement

A series of oscilloscope traces of the results are shown in Figure 13. It can be seen that the $1.06\,\mu m$ transition is just on the threshold of lasing at 86 J of input pump energy. As the pump energy is increased, the $1.06\,\mu m$ signal increases. Thus, qualitatively, it is evident that the $1.06\,\mu m$ transition is lasing at the expense of the $1.44\,\mu m$ transition since the two transitions are competing for the same energy stored in the population inversion.

A quantitative measurement has also been carried out. This was done by measuring the energy at $1.44\,\mu m$ passing through the $1.06\,\mu m$ mirror and the $1.06\,\mu m$ energy reflected from the mirror. The correlation between the two has been examined. Firstly, the total laser energy

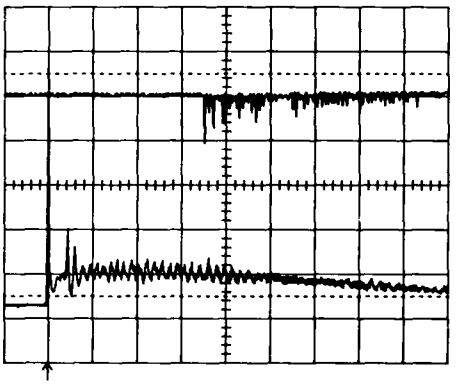


Figure 13: Non Q-switched temporal laser pulses 20 μs/div, $1.06\,\mu m$ upper, $1.44\,\mu m$ lower

is measured as a function of the input pump energy. The results are shown in Figure 14. Note that there is a slight saturation in the laser output at higher values of the pump energy. The laser output energy at $1.44\,\mu m$ is also shown in Figure 14 after having been corrected for the mirror transmission losses. It can be seen that at low input pump energies, the total laser output detected and the output at $1.44\,\mu m$ are essentially the same (within 10 mJ). This indicates that there is virtually no energy output at $1.06\,\mu m$. As the pump energy is increased a noticeable difference occurs between the two energies. The increase in the $1.44\,\mu m$ output decreases as the competition from the transitions at $1.06\,\mu m$ becomes stronger.

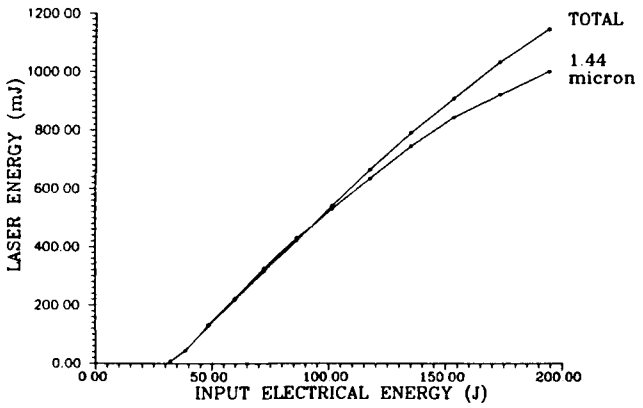


Figure 14: Laser output energy (total and at $1.44\,\mu m$)

Measurements were also taken for the total laser energy (both $1.06\,\mu m$ and $1.44\,\mu m$) as a function of the input electrical energy. The results of these measurements are shown in Figure 15. It can be seen that there is an initial linear increase in the output energy, but as the input energy is increased above 86 J there is an increase in the rate of output energy growth. The initial slope at lower pump energies is a result of energy at $1.44\,\mu m$ only. At increased pumping energies, both the $1.44\,\mu m$ and the $1,06\,\mu m$ lines lase. This accounts for the change in the slope of the output curve.

4.2 Q-Switching Configuration

To obtain Q-switching of the laser pulse, a prism was inserted into the laser cavity to act as a polarizing element. Moreover, it also served to discriminate against the unwanted lasing transitions. A schematic

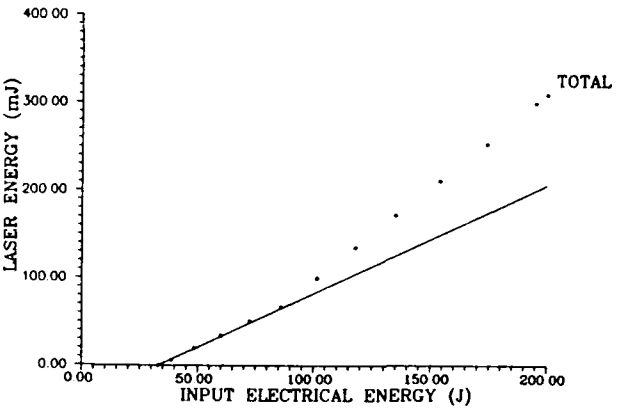


Figure 15: Laser energy at $1.06\,\mu m$ and $1.44\,\mu m$

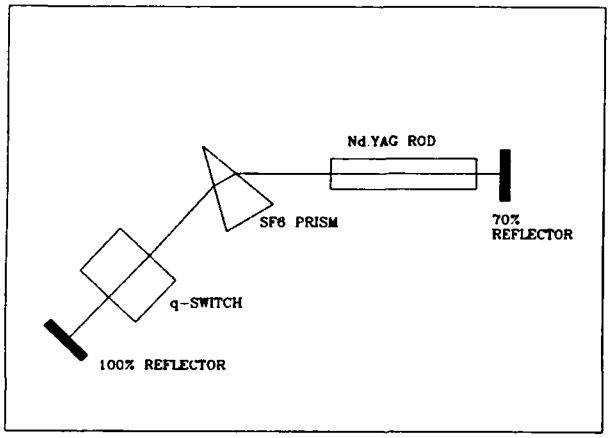


Figure 16: Q-switched experimental configuration

diagram of this configuration is shown in Figure 16. The prism was cut at Brewster's angle with respect to the $1.44\,\mu m$ beam propagation direction inside the laser cavity to minimize the reflection losses. A lithium niobate crystal was used as the Q-switching material. Since this material is very susceptible to optical damage, care was taken to restrict the energy density within the laser cavity.

Output couplers of three different reflectivities have been tested ($R = 70\%, 75\%$ and 80%). The output with the 70% coupler was considerably less than that from the two others of higher reflectivity. This means that the intensity inside the laser cavity would be less prone to cause optical damage in the Q-switched mode. In particular, consideration must be given to the occurrence of "hot spots" in the laser beam that could cause damage in the litium niobate material. It is obvious that even a lower reflectivity output coupler would be desirable;

however, a trade-off must be made between the laser efficiency and the optical damage considerations.

With the insertion of a prism into the laser cavity, the laser becomes tunable. The dispersion of the prism enables the laser to tune to

Table 2: Observed lasing transitions

$\lambda(\mu)$	Relative Intensity
1.06415	600
1.3187	150
1.3381	-
1.3572	213
1.4150	374
1.4444	325

various lasing transitions of the Nd:YAG by the rotation of the rear mirror of the cavity. Six different lasing transitions have been observed; they are tabulated in table II.

It is interesting to note that the $1.415\,\mu m$ transition lases as strongly as the one at $1.444\,\mu m$ (in the non Q-switched mode). It is also to be noted that when the laser is tuned to the $1.44\,\mu m$ transition, the $1.06\,\mu m$ output reaches threshold when the input pump energy is about 100 J. This is not significantly different than in the linear case described above. It is not presently understood why the prism does not offer a better discrimination against the $1.06\,\mu m$ radiation.

To obtain Q-switching of the laser, the lithium niobate crystal was inserted into the cavity and aligned along the direction of the $1.44\,\mu m$ beam. With the proper alignment, the insertion loss was minimal. We noticed only about a 10-15 mJ reduction in the output energy with the crystal in place. A $\frac{\lambda}{4}$ voltage was applied to the Q-switch to achieve a 90° rotation of the polarization. The output pulses were obtained by momentarily turning off the $\frac{\lambda}{4}$ voltage with a krytron. When the Q-switch is aligned and the laser energy is maximized in the long-pulse mode, the Q-switched pulse energy is about 65-70% of that of the non Q-switched energy at all pump energies investigated. The pulse width of the output is relatively wide as can be seen in Figure 17. Q-switched laser energies around 100 mJ and pulse widths of 85 ns have been obtained with an input pump energy of 80 J. This corresponds to greater than 1 MW of peak power. We have operated the laser at repetition rates to 10 Hz at the 100 mJ output energy level with no noticeable degradation on the characteristics of the output Q-switched laser pulse. There is no doubt that higher Q-switched laser energies

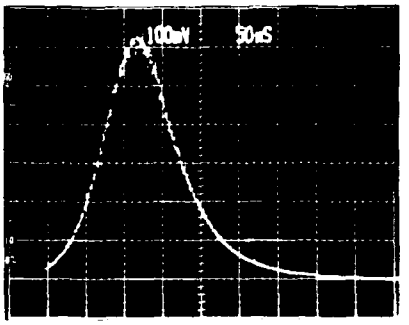


Figure 17: Temporal Q-switched laser output

and shorter pulse durations can be obtained. Because of the concern of optical damage to the lithium niobate material, we did not operate the laser in the Q-switched mode with input pump energies greater than 80 J. Studies are now in progress to determine the optical damage threshold of the lithium niobate crystal at $1.444\,\mu m$.

5 CONCLUSION

It has been demonstrated that Q-switched and non Q-switched operation of an Nd:YAG laser is feasible at an output wavelength of $1.444\,\mu m$. The stimulated emission cross section at $1.44\,\mu m$ is not unduly small and a relatively high laser energy can be extracted. The eyesafe nature of the $1.444\,\mu m$ radiation offers many potential applications both in the military and in the civilian sectors; such applications include rangefinding, surveying, telecommunications, laser radar and medical applications. It could also be a potential source for locating faults in sections of optical fibres that are tens of kilometers in length. It could also be used for Raman amplification in fibre wavequides employed in communication systems. There is also a potential application in interferometric fibre-optic gyroscopes where the shot noise limited random drift can be further reduced using a $1.444\,\mu m$ source.

With the accelerating pace in the development of diode pumped Nd:YAG technology, the $1.444\,\mu m$ source stands a good chance of being miniaturized. This would open up applications in space, such as a direct laser communication system, where eyesafety could be a major concern. The use of nonlinear frequency shifting techniques, such as

frequency mixing and stimulated Raman scattering, would allow the laser to be shifted to the $4\,\mu m$ region where there is presently a shortage of laser sources operating in the $3-5\,\mu m$ atmospheric window.

References

[1] Singh, S., Smith, R.G. and Van Uitert, L.G., Phys. Rev. B, Vol 10, pp. 2566-2572, 1974

[2] Marling, O., "1.05-1.44 μm Tunability and Performance of the CW Nd^{3+}:YAG Laser", IEEE J.Q.E., QB-A, pp. 56-62, 1978.

[3] Wong, S., Pace, P. and Tulip, J., "A Long-Wavelength Nd:YAG Laser", DREV Report 4492/88, March 1988

[4] Kaminskii, A.A., "Laser Crystals", Springer-Verlag, New York, 1981, p. 336.

[5] Lengyel, B.A., "Introduction to Laser Physics", John Wiley and Sons Inc., New York, 1966, p. 241.

[6] Siegman, A.E., "Lasers", University Science Books, Mill Valley California, 1985, p. 1010.

CO_2 LASER OSCILLATORS FOR LASER RADAR APPLICATIONS*

C. Freed
Massachusetts Institute of Technology
Lincoln Laboratory
244 Wood Street
Lexington, Massachusetts 02173

Abstract

This paper reviews the spectral purity, frequency stability and long-term stabilization of $C0_2$ isotope lasers developed at MIT Lincoln Laboratory. Extremely high spectral purity, and short-term stability of less than 1.5×10^{-13} have been achieved and will be discussed. A brief description on using CO_2 isotope lasers as secondary frequency standards and in optical radar is given. The design and output characteristics of a single frequency, TEM_{00q} mode, variable pulse width, hybrid TE CO_2 laser system is also described. The frequency chirp in the output has been measured and almost completely eliminated by means of a novel technique.

Introduction

This paper will be given in two parts. The first and major portion of the paper will review the spectral purity and frequency stability of a family of ultrastable CO_2 lasers that were developed and have been in use at MIT Lincoln Laboratory for well over 20 years by now. These lasers have an easily demountable and convertible modular design with cw output powers ranging between 1 and 50 watts.

The second part of the paper will describe the design and output characteristics of a single frequency, TEM_{00q} mode pulsed TE hybrid CO_2 laser system which does not have a gain switched spike and whose output pulse-width is variable from about 5 to 70 μs with a peak power output of about 5KW.

First and foremost, however, I want to express my deepest gratitude for the collaboration and encouragement received from several colleagues and co-authors of mine in the MIT/Lincoln Laboratory community who are listed in alphabetical order in the acknowledgement. The results to be presented in this paper must be credited to a very large extent to the active participation of these colleagues.

*This work was sponsored by the Defense Advanced Research Projects Agency of the Department of Defense, the Department of Energy, the NASA Langley Research Center, and the Department of the Navy under contract F19628-85-C-0002.

Spectral Purity and Short-Term Stability

The theoretical linewidth of a laser above threshold was first derived by Schawlow and Townes[1] as:

$$\Delta f = \frac{\alpha \pi h f_o}{P_o}\left(\frac{f_o}{Q_c}\right)^2 \qquad (1)$$

where Δf is the full width between half-power points of the laser output (FWHM) which should have a Lorentzian lineshape if limited by quantum phase noise; α, h, f_O, P_O, and Q_C denote the population inversion parameter, Planck's constant, the center frequency, power output and "cold" cavity Q of the laser, resepectively.

In a well designed small CO_2 laser the "cold" cavity Q is given by:

$$Q_c \sim \frac{2\pi L f_o}{c T_r} \qquad (2)$$

where L, c, T_r denote the cavity length, velocity of light and mirror transmission, respectively (diffraction losses are usually negligible compared to output coupling loss). In a small CO_2 laser with L = 50 cm, T_r = 5%, Q_C is of the order of 10^7; thus for a typical power output of 1 to 10 Watts (which is easily obtainable with a small TEM_{ooq} mode CO_2 laser) the quantum phase noise limited linewidth is less than 10^{-6} Hz.

In actual practice, however, so-called "technical" noise sources dominate[2,3] over the quantum phase noise limited Schawlow-Townes linewidth. Examples of technical noise sources are acoustic and structure-born vibrations, power supply ripple and noise, etc. These can cause frequency instabilities by perturbing the effective cavity resonance frequency via the sum of fractional changes in the refractive index n and the cavity length L.

$$\Delta f = f\left(\frac{\Delta n}{n} + \frac{\Delta L}{L}\right) \qquad (3)$$

As an example, a change of only 10^{-3} Angstrom, about 1/1000 of the hydrogen atomic diameter, in a 50cm long CO_2 laser cavity will cause a frequency shift of approximately 6 Hz. A 6 Hz variation in the approximately 3 x 10^{13}Hz frequency of CO_2 lasers corresponds to a fractional instability of 2 x 10^{-13}. A frequency stability at least as good as 2 x 10^{-13} is implied in Fig. 1, which shows the real time power spectrum of the beat signal between two free running lasers, designed and built at MIT Lincoln Laboratory. The frequency scale in Fig. 1 is 500 Hz/cm, indicating that the optical frequencies of the two lasers producing the beat note were offset by less than 3 x 10^3Hz. The discrete modulation side-bands were primarily due to line frequency harmonics, fan noise and slow drift; however, each spectral line was generally within the 10 Hz resolution bandwidth of the spectrum analyzer. The measurement of the spectral width was limited to 10Hz resolution by the 0.1s observation time set by instrumentation and not by the laser stability itself.

Figure 2 shows another beat note of the same two lasers as in Figure 1 before, but with increased acoustical background noise coupling to the lasers. The increased level of the resulting spurious noise modulation sidebands is self-evident in Figure 2. The logarithmic display portion of Figure 2 also shows a gaussian line shape envelope with σ = 209Hz fitted to the beat note spectrum. Also note, that the levels of the spurious modulation spectral lines fall more than 35db below the carrier for frequencies more than about 1.2kHz removed from the beat frequency carrier.

The spectra shown in Figures 1 and 2 clearly imply that the masking effects of the spurious modulation sidebands can be overcome by frequency and/or phase locking two stable CO_2 lasers with feedback loop bandwiths of only a few kHz.

Figure 3 shows the real time power spectrum of the beat note of two ultrastable CO_2 lasers which were phase-locked with a fixed 10 MHz frequency offset between the two lasers and with the unity-gain bandwidth of the servoamplifier set to about 1.2kHz. Note, that in Figure 3 the horizontal scale is only 2 x 10^{-2}Hz/division and the vertical scale is logarithmic, with 12.5 db/division. Figure 3 implies that the FWHM spectral width of the beat note was only about 9 x 10^{-6}Hz. It took 26.67 minutes of measurement time to obtain just a single scan with the frequency resolution of Figure 3. Since tracking even by a very good servo system would still be limited by quantum phase noise, the narrow linewidth in Figure 3 is an indirect, but clear confirmation of the high spectral purity of CO_2 lasers, as was predicted by the Schawlow-Townes formula.

Laser stabilities are most conveniently measured by heterodyning two lasers, as shown in Figures 1, 2, and 3. However, the results are not altogether foolproof because the disturbances causing frequency jitter of the lasers may be at least partially correlated. In an optical radar one may compare the laser with its own output delayed by the round trip time to and from the target. Hence, effects due to disturbances with correlation times less than the round trip time of the transmitted signal will be included in the measured beat note spectrum.

Figure 4 shows a greatly simplified block diagram of a 10.6μm laser radar at the MIT Lincoln Laboratory Firepond Facility[4,5] in Westford, Massachusetts. In Figure 4 wavy and solid lines denote optical and electrical signal paths, respectively. The 0.5 meter local and the 1.5 meter power oscillators were designed and constructed at Lincoln Laboratory[2,6]. The higher power oscillator was phase-locked to the local oscillator with a fixed 10MHz frequency offset between the two lasers.

The frequency stability of the CO_2 laser radar facility at Firepond was verified from observations on GEOS-III, a NASA geodetic satellite equipped with an IRTRAN II solid cube corner retro-reflector. Radar returns from GEOS-III have been used to determine the radial velocity of the satellite using Doppler measurements, and to set an upper bound to the laser oscillator instability[7]. During these measurements the satellite range was 1063km, which corresponds to a round-trip signal travel time of 7.09 milliseconds (ms). During these measurements the constant frequency, amplified CO_2 laser output signal was chopped by means of a duplexer so that a 25% duty cycle pulse train consisting of 4ms duration pulses 16ms apart was transmitted to the orbiting satellite.

The spectra that result from a radio frequency (R.F.) test signal of 4 ms duration processed in the same manner as the optical radar data are shown in Figure 5. In Figure 5, the horizontal rows simulate logarithmic displays of the power spectra of a consecutive sequence of radar return signals; this type of display is the Doppler-time-intensity (DTI) plot in radar terminology. The $sinc^2$ function shape of the spectra due to the 4 ms pulse duration is quite evident. The average spectral width 10db below the peak is 383Hz, and the standard deviation of the spectral width is 5Hz.

Figure 6 shows the DTI plot of the actual CO_2 radar signal return from GEOS-III at a 1063km range. Notice the striking similarity to the simulated DTI plot in Figure 5, which was obtained from a high quality frequency synthesizer (that was also part of the radar receiver). A comparison of Figures 5 and 6 shows that the -10 db average spectral width of the radar return signal broadened from 383 to 399Hz and the standard deviation of this spectral width increased from 5 to 18.5Hz. These figures thus indicate that the short-term stability of the entire CO_2 radar system, including round trip propagation effects caused by fluctuations in the atmosphere, was better than 1.5×10^{-13} for the 7.09ms roundtrip duration.

Figure 6 also shows that he standard deviation of pulse-to-pulse centroid jitter of the spectra was 117Hz during the test run. No effort was made to line-center stabilize either one of the lasers since the longterm stability of the free-running laser was more than adequate for typical optical radar applications.

Laser Design

Figure 7 illustrates the most basic CO_2 laser structure developed at MIT Lincoln Laboratory[2,6] more than twenty years ago. In order to achieve maximum open loop stability, a very rigid optical cavity design was chosen, which utilized stable materials. Four thermally, magnetically, and acoustically shielded low expansion superinvar rods define the mirror spacing of the optical cavity. The mirrors are internal to the vacuum envelope, and are rigidly attached to the composite granite and stainless steel mirror holders bolted to the four invar rods. In spite of the rigid structure, the laser design is entirely modular, and can be rapidly disassembled and reassembled; mirrors may be interchanged, and mirror holders can be replaced by piezoelectric and grating controlled tuners. It should be noted that the philosophy and many other aspects of the stable CO_2 laser design may be easily traced back to the original He-Ne laser design of A. Javan.

Figure 8 shows a 1.5 m piezoelectrically tunable laser which is phase-locked with a 10 MHz frequency offset to a 0.5 m local oscillator reference in the coherent CO_2 radar at the Firepond facility of Lincoln Laboratory.

Figure 9 illustrates a grating controlled, stable, TEM_{00q} mode laser. Many variants of these basic designs exist both at Lincoln Laboratory and elsewhere. This particular unit was built for high power applications, such as optical pumping and frequency shifting. The first order reflection of the grating was coupled through a partially reflecting output mirror. For heterodyne spectroscopy, zero-order output coupling is preferable. Some of the lasers also have short internal

absorption cells, which may be utilized either for frequency stabilization or for very stable high repetition rate passive Q-switching.

Long-Term, Line-Center Stabilization of CO_2 Lasers

The width of the Doppler broadened gain profile of a CO_2 laser is about 53MHz. Thus the CO_2 lasers may operate anywhere up to at least tens of MHz away from the center frequency of the oscillating transition. In many applications it is therefore desirable to find a narrow reference line within the operating frequency range of the laser and lock to this reference. In 1970 we have demonstrated[8,9] at MIT Lincoln Laboratory that, by using a small low pressure room temperature CO_2 reference stabilizing cell, the standing wave saturation effect in the CO_2 reference cell can be detected by observing the change in the intensity of the 4.3μm spontaneous fluorescence emission over the entire (001) - (000) transition band as the laser frequency is tuned across the Doppler profile of the corresponding 10μm absorption line. The change in the spontaneous fluorescence emanating from the entire band is due to the fact that radiation-induced change in the population of an individual rotational level is accompanied by a change in the populations of all rotational levels of the same vibrational state; this is caused by the coupling among the rotational levels, which tends to maintain a thermal population distribution. Figure 10 graphically illustrates[11,12] the experimental arrangement in which low pressure, room temperature CO_2 , serving as the saturable absorber, is subjected to the standing wave laser field generated in a stabilizing cell placed either internal or external to the laser cavity, with the laser oscillating in any preselected (00°1) regular or ($01^{1}1$) hot band transition. In the vicinity of the absorption line center a resonant change in the 4.3μm fluorescence signal appears which is analogous to a Lamb-dip.

Figure 11 shows the block-diagram of a two-channel heterodyne calibration system[10,11,12] in which two low pressure, room temperature CO_2 gas cells external to the lasers were used to line-center stabilize two grating controlled stable lasers filled sequentially with 9 different CO_2 isotopic species.

Figure 12 illustrates the time domain frequency stability that has been routinely achieved with the two-channel heterodyne calibration system using the 4.3μm fluorescence stabilization technique.[12] The open and filled circles represent two separate measurement sequences for the Allan Variance of the frequency stability.

$$\sigma_y(\tau) = \frac{1}{2M} \sum_{j=1}^{M} (y_{j+1} - y_j)^2 \qquad (4)$$

Each measurement consisted of M=50 consecutive samples for a sample time duration (observation time) of τ seconds. Figure 15 shows that $\sigma_y < 2 \times 10^{-12}$ has been achieved for $\tau \equiv 10$s, which means that a frequency measurement precision of about 50Hz may be readily achieved within a few minutes.

The triangular symbols in Figure 12 represent the frequency stability of a Hewlett-Packard (HP) model 5061 cesium atomic frequency standard as specified in the 1987 HP catalogue. Clearly, the frequency stabilities of the CO_2 and the cesium stabilized systems shown in Figure 12 are about the same.

The upper bound short-term stabilities, as measured in the laboratory (see Fig. 1) and determined from CO_2 radar returns at the MIT Lincoln Laboratory Firepond facility (see Fig. 6) are also indicated by the two crossed circle symbols in the lower left corner of Figure 12. It is quite obvious that a least two to three orders of magnitude better short-term stabilities have been achieved in the CO_2 radar compared to Microwave Systems.

CO_2 Isotope Lasers

In CO_2 molecular lasers transitions occur between two vibrational states. Since each vibrational state has a whole set of rotational levels, a very large number of laser lines, each with a different frequency (wavelength) can be generated. Moreover, isotopic substitution of the oxygen and /or carbon atoms make 18 different isotopic combinations possible for the CO_2 molecule. Approximately 80 to 150 regular band lasing transitions may be generated for each of the CO_2 isotopic species. By using optical heterodyne techniques, the beat frequencies between laser transitions of individually line-center stabilized isotopic CO_2 laser pairs were accurately measured. As a result, the absolute frequencies, vacuum wavenumbers, band centers, and ro-vibrational constants for $^{12}C^{16}O_2$, $^{13}C^{16}O_2$, $^{13}C^{18}O_2$, $^{12}C^{18}O_2$, $^{12}O^{17}O_2$, $^{16}O^{12}C^{18}O$, $^{16}O^{13}C^{18}O$, $^{14}C^{16}O_2$, and $^{14}C^{18}O_2$, have been simultaneously calculated from well over 900 beat frequency measurements.[13] The accuracies of these frequency determinations are, for the majority of the transitions, within about 5 kHz relative to the primary Cs frequency standard. Consequently, in the 8.9-12.3 μm wavelength region line-center stabilized CO_2 isotope lasers can be conveniently used as secondary frequency standards. One can also utilize difference frequencies and harmonics of CO_2 lasing transitions to synthesize precisely known reference lines well beyond the 8.9-12.3 μm range. Figure 13 graphically illustrates the frequency and wavelength domain of the nine CO_2 isotopic species which were measured to date. $^{14}C^{16}O_2$ extends the wavelength range to well beyond 12μm, while $^{12}C^{18}O_2$ transitions reach below 9μm.

In CO_2 radar applications the existence in the ambient atmosphere of approximately .03% (by volume) of the most abundant $^{12}C^{16}O_2$ isotope will cause severe absorption in long range narrowband CO_2 radar. In wideband CO_2 radar the problem is made even worse because of frequency dispersion by the absorption line shape.[14] The use of rare CO_2 isotopic species can virtually eliminate both problems. Both NASA and ESA (European Space Agency) are also planning on the use of $^{12}C^{18}O_2$ in wind velocity mapping CO_2 radars because of the higher backscatter at the shorter wavelengths where $^{12}C^{18}O_2$ lasers are more powerful compared to $^{12}C^{16}O_2$, in addition to having smaller absorption under normal atmospheric conditions.

Design and Output Characterization of a Pulsed CO_2 Hybrid TE Laser System

The CO_2 MOPA laser radar at the Firepond facility of MIT/Lincoln Laboratory has achieved unsurpassed spectral purity and short-term stability, as described before; however, it is a very large installation. There are many applications where a more compact system is needed and the utmost spectral purity is not really necessary, such as in pulsed radars for instance. This paper will next discuss a technique of obtaining a long-pulse, moderately high power laser transmitter with a potentially high temporal coherence. The principle of operation is based on the chirp cancelling capability of an acousto-optic modulator placed external to a TE hybrid laser oscillator.

The new CO_2 laser is basically a small MOPA system.[15] It is capable of delivering smooth, TEM_{qoo} mode pulses of variable widths from about 5μs to about 70μs duration. The available output energy is about 230mJ in a 35μs nearly flat-top pulse.

The optical layout of the system is shown schematically in Figure 14. The hybrid TE CO_2 laser consists of an intracavity cw discharge gain cell in series with a pulsed discharge low pressure gain cell. Beam forming optics are used to change the beam spot size to various diameters along the optical path, 3mm $1/e^2$ diameter at the A-O cells and to about 2 cm $1/e^2$ diameter at the pulsed laser amplifier. For heterodyne measurements, the beams are combined in front of a 10MHz bandwidth detector near the laser local oscillator. Figure 15 is a photograph of the optical layout showing various optical components just as they are positioned in Figure 14.

Figure 16 shows a close-up view of the hybrid TE CO_2 laser oscillator itself. The optical resonator and cw discharge tube structures are based on the stable cw laser design shown previously in Figures 7, 8 and 9. The pulsed gain cell within the stable laser cavity and the pulsed amplifier following the beam expander are variants of the dual LP-30 and LP-140 lasers respectively which are commercially available from Pulse Systems, Inc. in Los Alamos, N.M.

The main components of the CO_2 laser MOPA and chirp measurement system are shown in block diagram form in Figure 17. The low-pressure hybrid TE CO_2 laser produces a smooth single TEM_{qoo} mode, 80mJ pulsed output with a pulse width of about 70μs (FWHM). The output beam temporal profile is shaped by passing the beam through two acousto-optic (A-0) cells operating in series in a frequency up-shift and down-shift mode. The pulse slicing is produced in the first A-O cell by applying a 35μs 40MHz 30W peak power RF pulse to the A-O cell about 17.5μs before the peak of the 70μs optical output pulse of the hybrid TE laser oscillator. The input to the RF amplifier driving the second A-O cell may be connected to either a 40MHz cw oscillator or to a HP8770A RF waveform generator. With the fixed frequency 40MHz input, the second A-O cell will simply shift the CO_2 laser output frequency back to the CO_2 line center and enable us to measure the laser frequency chirp generated during the pulsed excitation. This frequency chirp may be almost completely cancelled by applying an appropriate chirped RF waveform to the second A-O cell using the HP8770A waveform generator in the switch position as shown in the upper right hand corner of Figure 17. A low-pressure pulsed CO_2 laser amplifier, a modified version of the standard Model LP-140 made by Pulse Systems Inc., is used to amplify the pulse energy to about 0.25J. The system has operated at a pulse repetition frequency of 5Hz for millions of shots without any problem.

Figure 18 shows the superimposed pulse energy outputs of 50 consecutive laser pulses. The pulse energy repeatability is estimated to be about ±5%. Figure 19 shows the pulse output after the hybrid TE laser pulse is chopped by the first A-O cell and is amplified by the pulsed laser amplifier. The pulse is nearly rectangular in shape with very short rise and fall times, determined by the acoustic transit time in the A-O cell for the 3mm diameter optical beam. A more rectangular shape could be obtained by optimizing the pulse shape of the RF drive to the first A-O cell relative to the rectangular shape used for obtaining the pulse shape shown in Figure 19. By varying the pulse width of the 40MHz RF drive applied to the first A-O cell, the output laser pulse width can be varied easily from a few microseconds to about 70μs. This is very useful in some applications and is a unique feature of the present laser system.

The spatial profile of the optical beam at the laser amplifier output was recorded by a 32 x 32 pyroelectric detector array. The output beam profiles are shown in Figures 20 and 21 in isometric view and in a plane containing the optical axis of the Gaussian beam respectively; it can be seen that the beam profile is essentially Gaussian in shape. The small irregularities are caused by noise pickup and some minor beam distortion in going through the amplifier.

Chirp Measurements

The chirp in the output of the hybrid laser and the overall chirp in the output of the laser amplifier were measured by using a heterodyne method. The heterodyne measurement setup was previously shown schematically in the lower half of Figure 17. For the 10MHz HgCdTe photoconductive detector, about 3-4mW of LO power was used. The pulsed laser peak power was attenuated sufficiently using several plates of CaF_2 until the beat frequency display on the oscilloscope appeared like a burst of a sinusoidal wave.

Figure 22 shows the beat frequency between the laser local oscillator (LO) and the pulsed laser as a function of time over a 35μs interval. The zero beat was adjusted to occur at the beginning of the pulse. The chirp shown in Figure 22 is an upchirp, approximately linear over the 35μs interval. The frequency deviation of the chirp is about 2MHz. The 35μs pulse width is a part of the FWHM 70μs laser pulse of the laser oscillator. We have also recorded the output of the pulsed laser alone without the beam slicer operating. Figure 23 is a scan of the chirp frequency vs. time for an unsliced pulse. The cw LO laser frequency was deliberately set far below the pulsed laser frequency so that there is no foldover of the beat frequency. Note that at the beginning of the pulse, there is a short downchirp. The chirp frequency first decreases and then reverses upward. It moves up exponentially at first and then becomes nearly linear out to more than 80μs, where it finally flattens out. The overall chirp range is about 4.5MHz. Qualitatively, this kind of chirp variation is typical of previous observations on TEA CO_2 lasers.[16] The chirp has been found to be caused by the combined effects of the laser induced medium perturbation or LIMP for short,[16] and heating of the pulse-excited gas mixture.

Chirp Cancellation Scheme and Measurement Results

Intrapulse chirps such as those shown in Figures 22 and 23 are undesirable in many laser radar applications. A number of techniques have been utilized to design laser cavities with much lower energy per unit volume in order to minimize the effect of LIMP. Cavity cross sections have been enlarged by using an intracavity telescopic lens[17] or a special Gaussian-profiled output coupler configuration.[18] The use of active techniques for correcting or cancelling the chirp have also been suggested[19,20] and attempted.[19,20]

The chirp cancellation method described in this paper is based on the fact that an appropriate compensating chirp can be subtracted from the existing chirp in the laser beam by means of either an electro-optic or an acousto-optic cell placed into the beam path following the laser output. Maximum cancellation is achieved if the magnitude and phase are equal and opposite to those of the laser beam chirp, respectively. The chirp cancellation method can be understood by referring to the schematic diagram of Figure 17. A waveform generator is used, instead of the 40MHz fixed frequency cw oscillator, to produce a linear upchirp of 30μs duration with a frequency excursion from 39 to 41MHz. This waveform is applied to the input of a 25W RF amplifier which in turn drives the second A-O cell. The chirp in the laser output is measured by sending the heterodyne signal from the detector to the time and frequency analyzer which is capable of measuring the instantaneous frequency from dc to 500MHz. With just a cw RF input to the A-O cell, we obtained the chirp of the laser itself, shown by the upper trace (solid line) in Figure 24, which has a total frequency excursion of about 2.2MHz for the 30μs pulse duration (in this measurement, we only used the output of the hybrid TE laser, since we found that the low pressure laser power amplifier introduced only a very small chirp). By switching to the chirp correcting waveform shown by the dashed-line lower trace in Figure 24, we obtained the residual chirp shown in Figure 25 which has a frequency excursion of 320kHz, which corresponds to only about ±7% of the original chirp in the laser. We believe that this is the first time that this kind of chirp cancellation has been successfully demonstrated.

A similar type of chirp cancellation was first attempted with reasonable success by Willetts and Harris, who utilized an intracavity E-O modulator using peak dc voltages as high as 5 kV.[19] The correction scheme described in this paper was performed with an A-O modulator that is external to the laser cavity; we believe that this kind of compensation may have a higher degree of thermal and mechanical stability. Furthermore, the pulse durations were much longer than those previously attempted and the use of acousto-optic devices require only low voltages for operation. In an acousto-optic modulator, the output beam direction changes as the input drive frequency is varied. However, the angular deviation turns out to be negligibly small for the present case (~ ±0.5mrad).

Summary and Conclusions

A chirp cancellation scheme has been carried out using an acousto-optic modulator. Preliminary results demonstrated a chirp reduction of about 90%. Higher degree of cancellation would have been possible had we tailored the chirp of the correcting waveform somewhat closer to the chirp generated in the laser. We believe that this type of chirp cancellation could be further

improved by improving the laser design and through rapid sampling of and correcting for the residual laser chirp itself.

CO_2 lasers have demonstrated greater spectral purity and better short term stability than any other oscillator at any frequency. These results were confirmed by laboratory measurements and also deduced from analysis of CO_2 radar returns from orbiting satellites. A long-term stabilization technique, using low pressure room temperature CO_2 gas as a reference, was also developed so that long-term CO_2 laser stabilities at least comparable to commercial grade atomic clocks have been achieved. By using a line-center stabilized, two-channel CO_2 laser heterodyne system, the absolute frequencies of lasing transitions and the ro-vibrational constants of nine CO_2 isotopic species were determined to within about 5kHz relative to the primary cesium frequency standard. These results allow the CO_2 system to be used as a secondary frequency standard in the infrared spectrum. Furthermore, the results described in this paper were achieved with laser designs and components which were, for the most part, developed more than 20 years ago. Extensive experience gained by working with these lasers clearly indicates that at least one to two orders of magnitude improvements of both short-term and long-term stabilities should be readily achievable with improved designs.

Acknowledgement

The work reported here represents the cumulative efforts of many individuals at the MIT/Lincoln Laboratory Community. The author wishes to particularly thank the contributions of the following individuals (listed in alphabetical order): L. C. Bradley, R. S. Eng, J. A. Daley, J. G. Grimm, T. R. Gurski, H. A. Haus, A. Javan, R. H. Kingston, W. E. Keicher, D. G. Kocher, R. G. O'Donnell, K. L. SooHoo, D. L. Spears, L. J. Sullivan.

References

1. Schawlow, A. L. and Townes, C. H., Phys. Rev. 112, 1940 (1958)

2. C. Freed, IEEE J. Quantum Electron. QE-4, 404 (1968)

3. C. Freed, Proceedings of the 31st Annual Symposium on Frequency Control held in Atlantic City, N.J. 1-3 June (1977)

4. R. H. Kingston, SPIE, Vol. 227, CO_2 Laser Devices and Applications, 148, (1980)

5. L. J. Sullivan, SPIE, Vol. 227, CO_2 Laser Devices and Applications, pp.148-161, (1980)

6. C. Freed, pp. 226-261, Proceedings of the Frequency Standards and Metrology Seminar, Sponsored by the National Research Council of Canada and Universite Laval, Quebec, Canada, August 30, 31 - September 1, (1971)

7. T. R. Gurski, J. Opt. Soc. Am. 66, 1133A (1976)

8. C. Freed and A. Javan, Applied Phys. Letters 17, 53 (1970)

9. A. Javan and C. Freed, U.S. Patent No. 3686585 issued August 22, (1972)

10. C. Freed, SPIE Proceedings, 894, 86 (1988)

11. C. Freed and R. G. O'Donnell, Metrologia 13, 151 (1977)

12. K. L. SooHoo, C. Freed, J. E. Thomas and H. A. Haus, IEEE J. Quantum Electron. QE-21, 1159 (1985)

13. L. C. Bradley, K. L. SooHoo and C. Freed, IEEE J. Quantum Electron, QE-22, 234 (1986)

14. A. L. Kachelmyer, R. E. Knowlden, W. E. Keicher, SPIE Proceedings, 783, 101, (1987)

15. R. S. Eng, J. G. Grimm and C. Freed, SPIE Proceedings, 1103, 32, (1989), gives a more detailed description of the Hybrid TE CO_2 System design and operating characteristics.

16. D. V. Willetts and M. R. Harris, J. Phys. D: Appl. Phys. 15, 51-67(1982)

17. D. V. Willetts and M. R. Harris, IEEE J. Quant. Electron. QE-21, 188-191(1985)

18. P. Lavigne, A. Parent, D. Pascale, and N. McCarthy, IEEE J. Quant. Electron. QE-22, 220-2203(1986)

19. D. V. Willetts and M. R. Harris, J. Phys. D: Appl. Phys., 18, 185-189(1985)

20. Ali Javan, private communications.

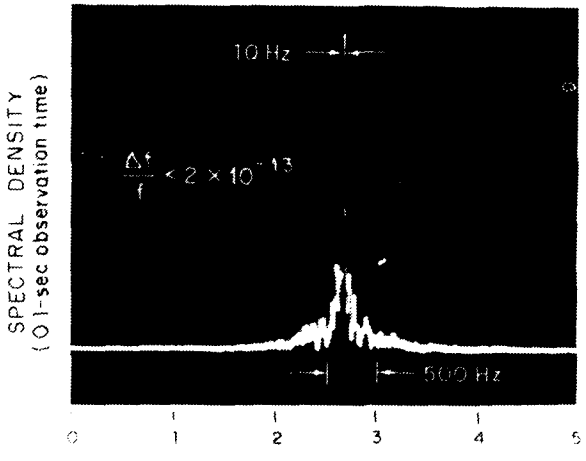


Fig. 1. Real time power spectrum of the beat signal between two free running CO_2 Lasers.

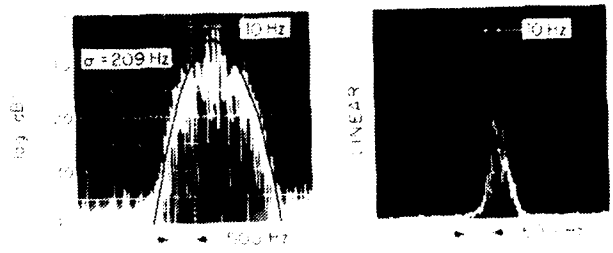


Fig. 2. A beat note similar to Figure 1, but measured under somewhat noisier environmental conditions.

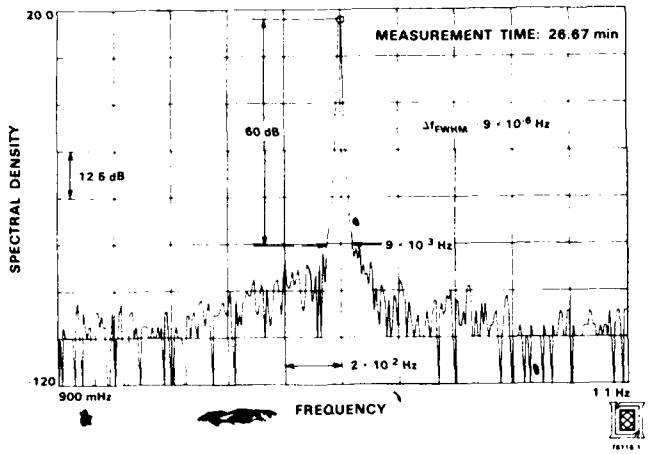


Fig. 3. Spectral purity of beatnote between two phase-locked lasers.

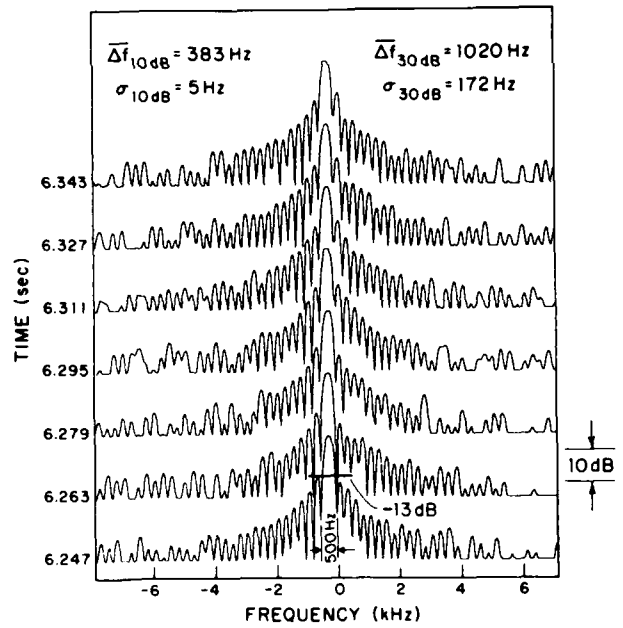


Fig. 5. Doppler-Time-Intensity plot for a 4-ms duration R.F. Test Signal.

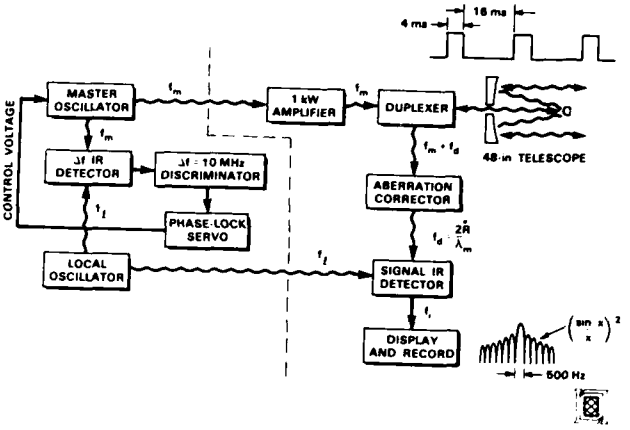


Fig. 4. Infrared radar system block diagram.

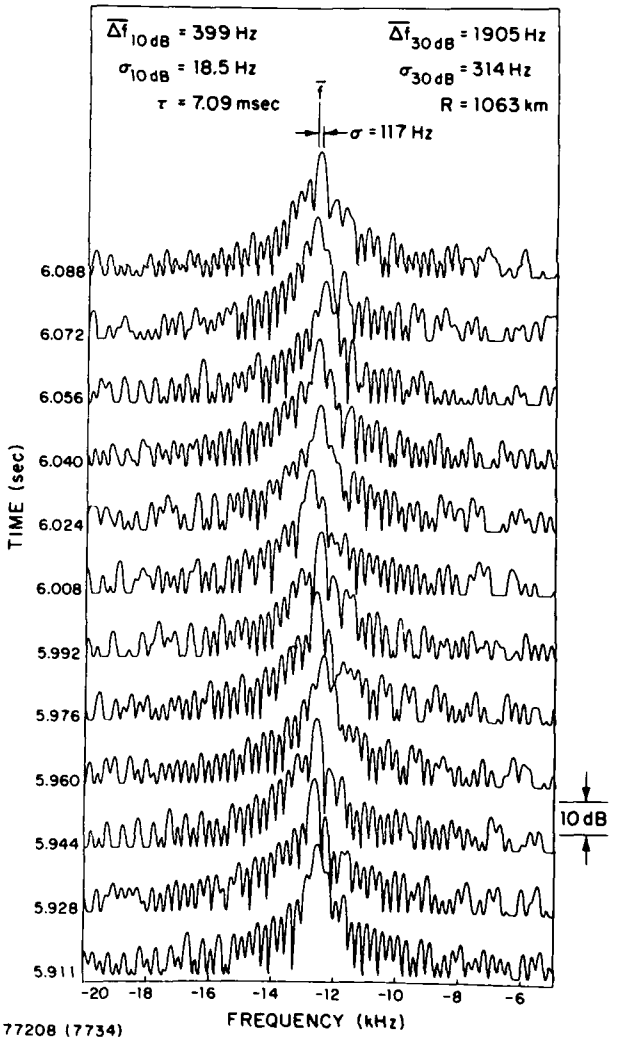


Fig. 6. Doppler-Time-Intensity plot for the GEOS-III return signal.

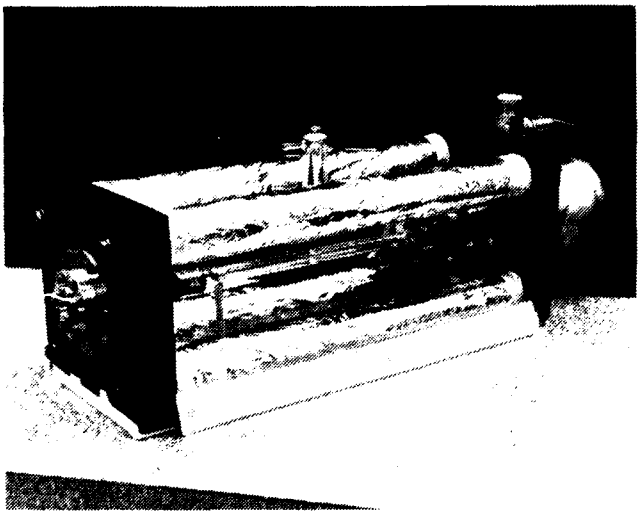


Fig. 7. Basic stable laser structure developed at MIT/Lincoln Laboratory.



Fig. 8. Offset-locked lasers in the coherent CO_2 radar at the Firepond Facility.

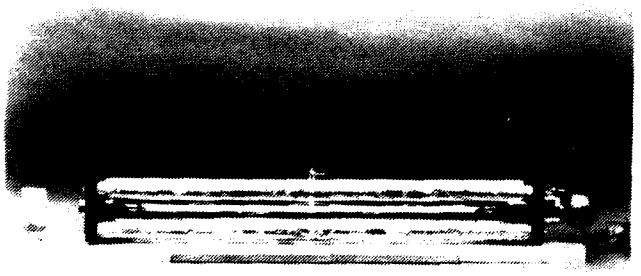


Fig. 9. Basic grating-controlled stable TEM_{00Q} Mode CO_2 Laser.

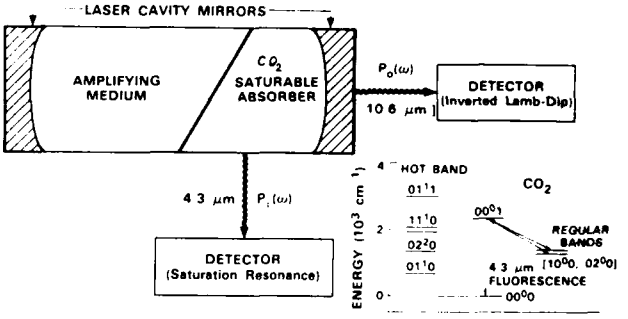


Fig. 10. Graphic illustration of the saturation resonance observed in CO_2 fluorescence at 4.3μm. The figure shows an internal absorption cell within the laser cavity. External cells may also be used.

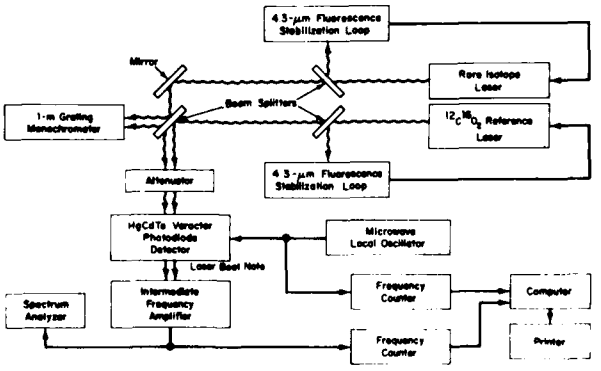


Fig. 11. Block diagram of the two-channel line-center stabilized CO_2 isotope calibration system.

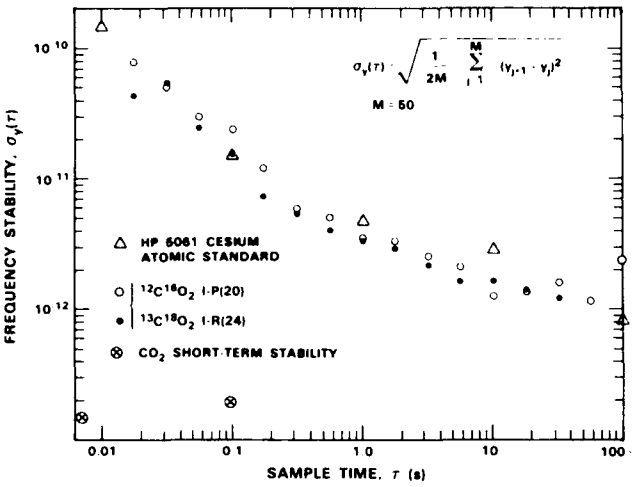


Fig. 12. Time domain frequency stability of the two-channel heterodyne calibration system using the 4.3μm fluorescence stabilization technique

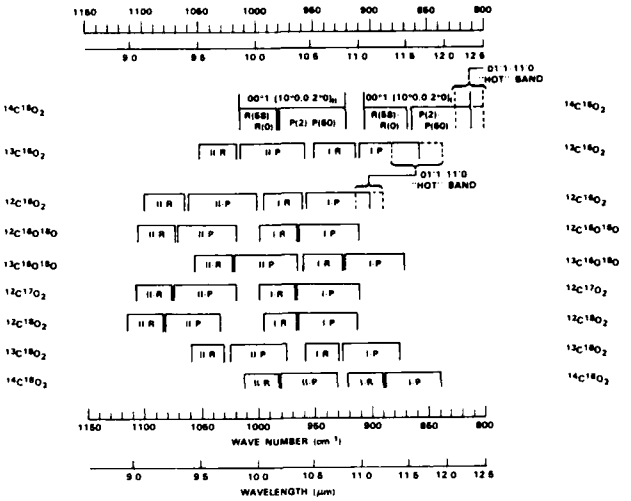


Fig. 13. Frequency and wavelength domain of nine CO_2 isotopic species

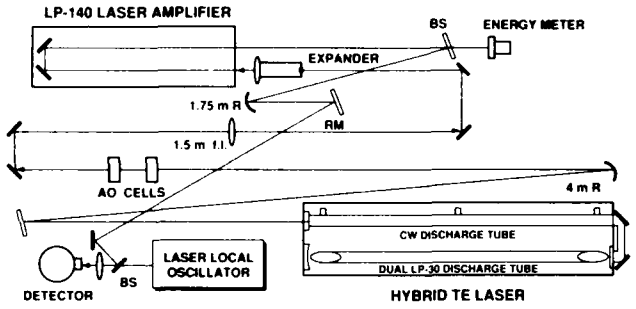


Fig. 14. Optical layout of CO_2 laser system.

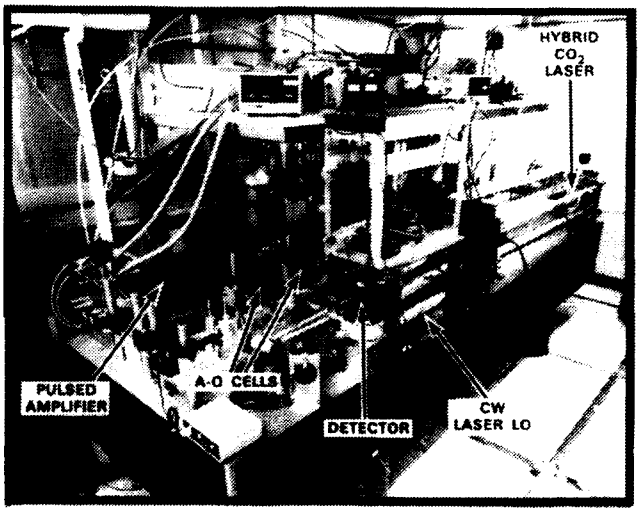


Fig. 15. Photograph of optical layout.

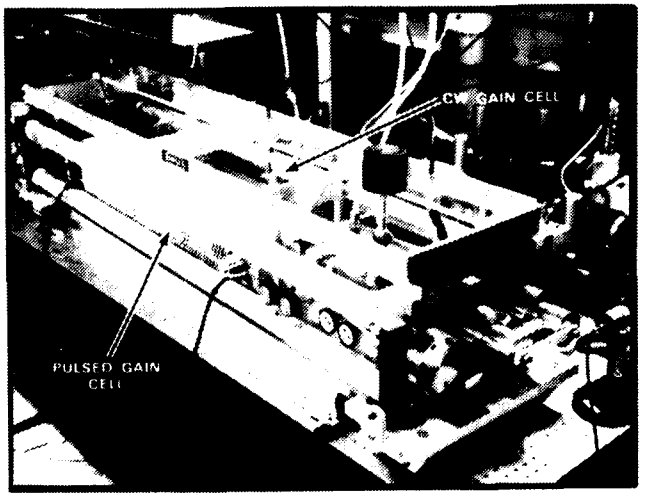


Fig. 16. Photograph of hybrid CO_2 laser (isometric view).

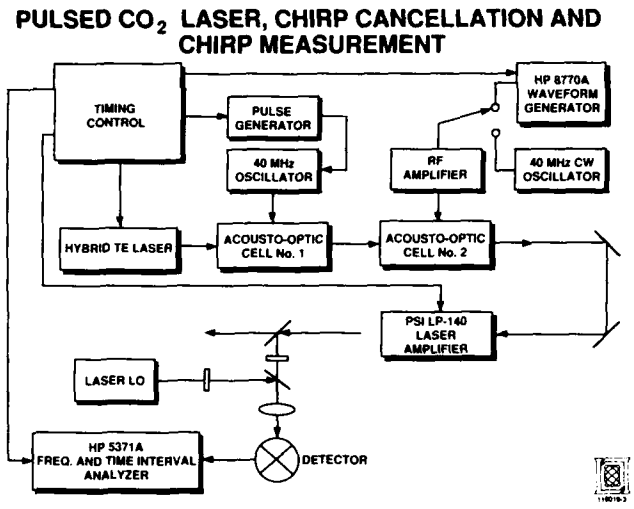


Fig. 17. Pulsed CO_2 laser, chirp cancellation and chirp measurement setup.

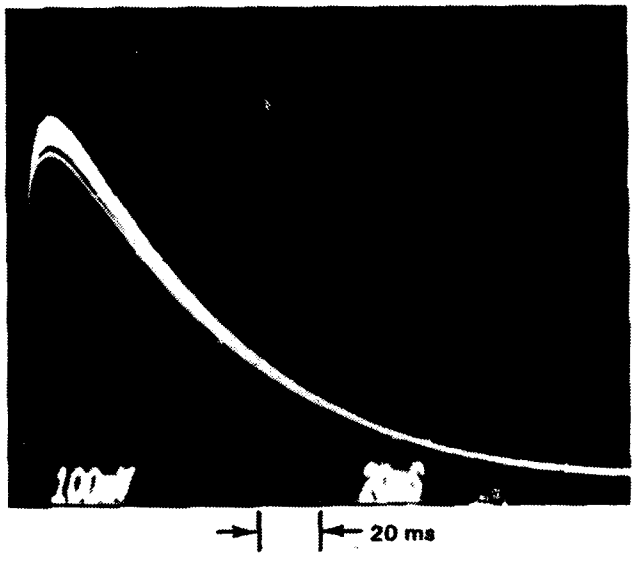


Fig. 18. Superimposed pulsed energy readouts of 50 consecutive laser pulses at output of hybrid TE laser.

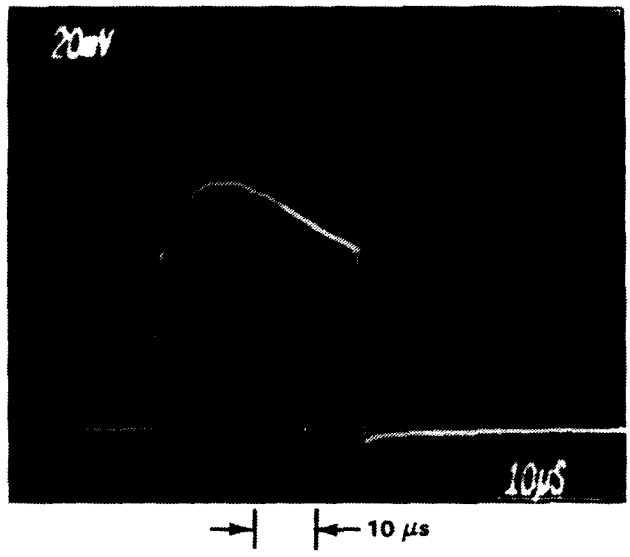


Fig. 19. Temporal profile of laser pulse after amplification by pulsed laser amplifier.

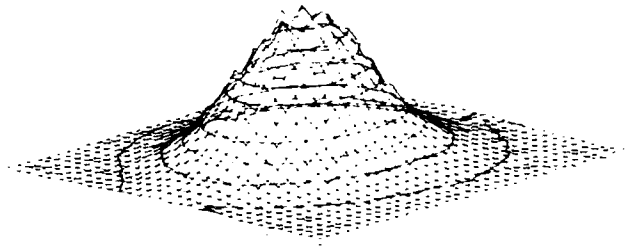


Fig. 20. Isometric view of spatial profile of laser pulse at the output of the pulsed laser amplifier.

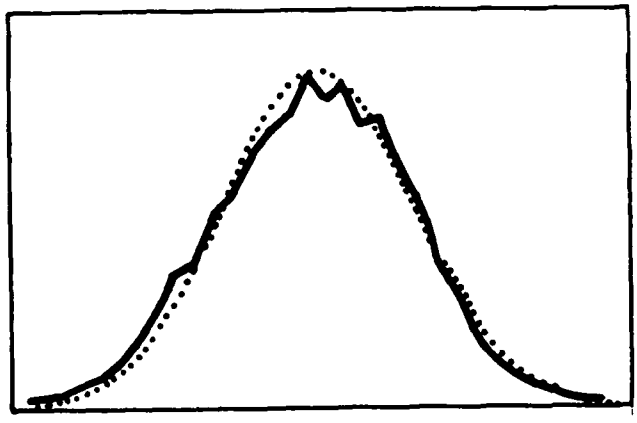


Fig. 21. One-dimensional beam profile obtained by a plane cut through the optical axis of the beam (solid curve); dotted curve is a fit using a Gaussian intensity distribution.

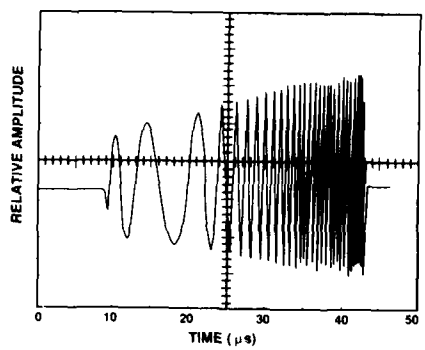


Fig. 22. Beat frequency chirp between a 35μs duration hybrid CO_2 laser pulse and the cw local oscillator.

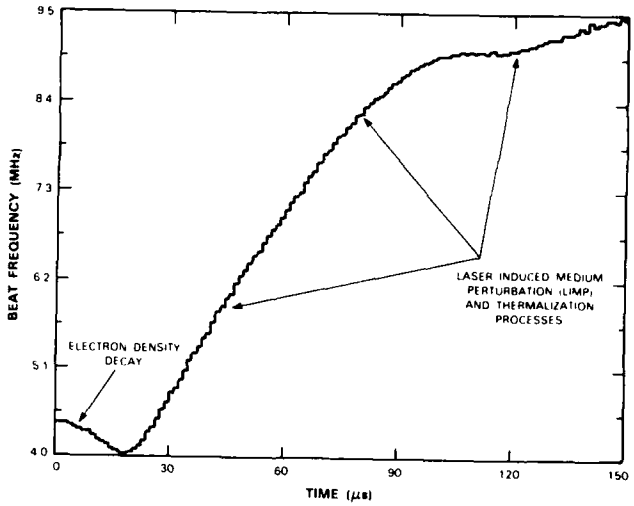


Fig. 23. Time variation of the beat frequency between the pulsed hybrid CO_2 laser and the cw local oscillator, showing both down-chirp and up-chirp.

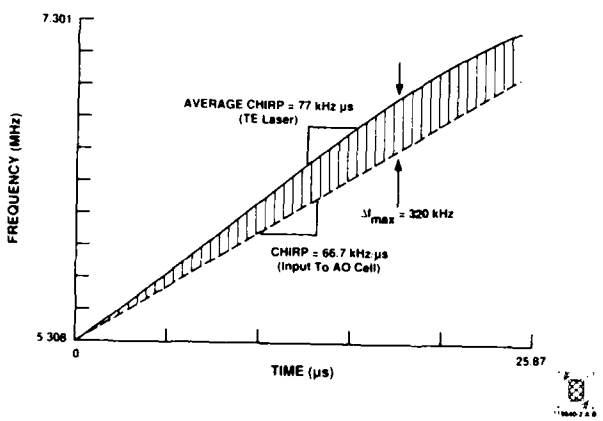


Fig. 24. Pulsed hybrid TE CO_2 laser frequency chirp showing that the chirp is about 77kHz/μs.

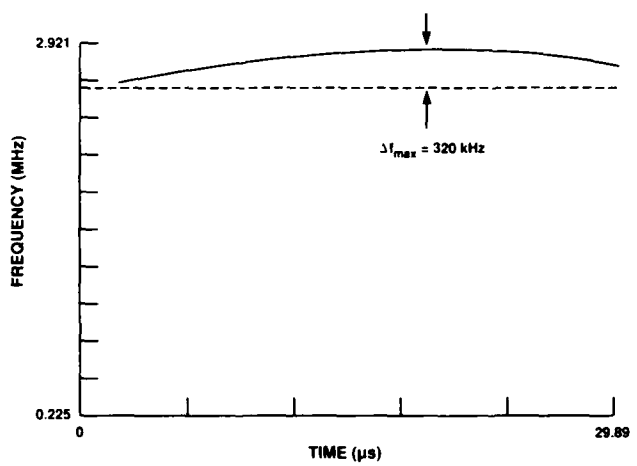


Fig. 25. Residual chirp at A-O modulator output.

Excimer Lasers and LIDAR

Robert C. Sze
Los Alamos National Laboratory
M.S. E543, Group CLS-5
Los Alamos, New Mexico 87501

Abstract

Excimer lasers used in LIDAR applications have a number of benefits over lasers at other wavelengths. Among these is that the signal wavelengths can be in the solar blind region permitting comparable signal to noise ratios for both day and night time detection. We give a specific example for the most common use of an excimer laser in LIDAR, that of inducing fluorescence or Raman scattering in species of interest. We will then discuss some recent laser developments including multi-wavelength, long-pulse, and ultra short-pulse lasing, and show how they maybe used for atmospheric and hydrographic LIDAR applications.

Introduction

The availability of powerful ultraviolet sources using excimer lasers introduces unique possibilities for LIDAR because the photons are energetic enough to induce fluorescence or Raman scattering in nearly all materials and because these induced signals from materials of interest may lie deep enough in the ultraviolet to be in the solar blind region of the spectrum (230-300 nm). With the LIDAR return signal in the solar blind region we can do both day and night time detection with equivalent signal to noise ratios. Thus, it appears possible to use a single laser source to interrogate many different species. Such a system is, however, limited by the induced fluorescence and Raman scattering cross-sections which can be many orders of magnitude less than resonance scattering processes that require wavelength specific sources. Table 1 gives the cross-section ranges of a number of LIDAR processes. We see that laser induced fluorescence usually has fairly large cross-sections, but non-resonant Raman scattering is over seven

Table 1. LIDAR techniques and their appropriate cross-sections ($d\sigma/d\Omega$)

Process	$(d\sigma/d\Omega)[cm^2.sr]$
Mie Scattering	10^{-8}-10^{-9}
Atomic Fluorescence	10^{-14}-10^{-15}
Differential Absorption and Scattering (DAS)	10^{-18}-10^{-24}
Molecular Fluorescence	10^{-20}-10^{-21}
Rayleigh Scattering	10^{-25}-10^{-26}
Raman Scattering	10^{-28}-10^{-30}

orders of magnitude lower. These techniques, nonetheless, can compare favorably with resonance processes such as resonance-induced atomic fluorescence and differential absorption and scattering LIDAR techniques. This is because signal-to-noise ratios can be improved by frequency filtering for laser-induced fluorescence or Raman scattering return LIDAR signals whose wavelengths are far away from the laser wavelength but is not possible for resonance LIDAR processes whose wavelengths are at the same wavelength as the laser wavelength. The unwanted scattering noise at the laser wavelengths can be very large due to signals coming from elastic scattering of other atmospheric constituents (Mies and Rayleigh scattering).

In this presentation we will give an example of a LIDAR application using Raman backscattering. We will then present some recent laser developments at Los Alamos which may be helpful in certain atmospheric and hydrographic LIDAR applications.

Example of Raman Scattering LIDAR

Due to the small cross-section for Raman Scattering, LIDAR using this technique is limited to the detection of molecular species of interest at a few parts per million. Thus, Raman scattering has limited utility in pollution monitoring when detectivity of parts per billion are required.

Evapotransiration plays an important role in global climate change. We give an example here of the measurement of water vapor content over vegetation canopy to illustrate the technique involved. These data are presented here courtesy of Robert Karl at the Los Alamos National Laboratory. The details of this work are presented in Ref.[1]. A broad-band one joule per pulse KrF laser at 248 nm wavelength is used as the exciting source. The backscattered Raman signals from H_2O at 273 nm and N_2 at 263 nm are measured and the H_2O concentrattion is calculated according to the formula,

$$[H_2O]_R = [N_2]_R \times (\Omega_{H2O}/\Omega_{N2}) \times (P(\lambda_{H2O},R)/P(\lambda_{N2},R) \times K$$

where $[N_2]_R$ = nitrogen number density for all R determined by a single measurement of atmospheric pressure and temperature assuming standard nitrogen atmospheric abundance, R = range along the laser, Ω_x = the Raman backscatter cross-sections, $P(\lambda_x,R)$ = optical power received, λ_x = Raman scattered wavelength with x = H_2O and N_2, and K = the product of telescope transmission, reflectance and detector sensitivity factors. The normalization with respect to nitrogen should be done whenever possible to eliminate corrections in signal fluctuations caused by laser power variations, atmospheric transmission changes as a function of range, and the change in telescope-to-laser-beam overlap along the sampled

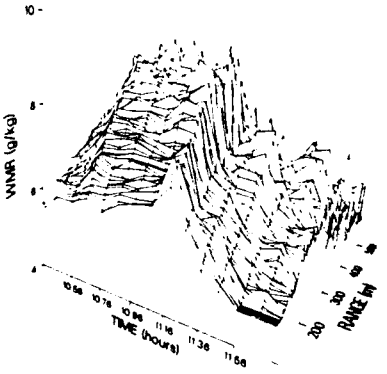


Figure 1. WMR plotted as a function of time and range over cotton canopy.

path length. In Fig. 1 water concentration is converted to a water mixing ratio (WMR) defined as the grams of water vapor in kilograms of air and plotted as a function of time and range down field over an area covered by cotton plants. These LIDAR data agree very well with data obtained from point source measurements at Bowen Ratio Energy Balance stations (BREB). Note that one can monitor the evapotranspiration over large areas. One can see that after twelve hours the water vapor over the cotton field has decreased to very low levels and the plants are becoming dangerously stressed due to lack of watering.

Two Wavelength Excimer Laser Operation

Recent work at Los Alamos dealing with two wavelength lasers serving as a seed input into the Aurora Fusion Laser system to generate broadband lasing at the target[2] may find useful applications in LIDAR. Figure 2 shows laser output from the oscillator (a) and through an amplifier (b) and at ten times the signal scale (c) of (b) to show the beginning of contributions at line center from amplified spontaneous emission (ASE). The etalon has 90 % reflectivity mirrors with 203 cm^{-1} separation. After one pass through an amplifier the energy level in the two lasing lines are at 55 mJ per pulse. This is at an energy level that should be useful for LIDAR. We believe with some care, such as proper beam expansion, a few hundred millijoules per pulse can be easily achieved in an amplifier that nominally delivers one joule per pulse as an oscillator.

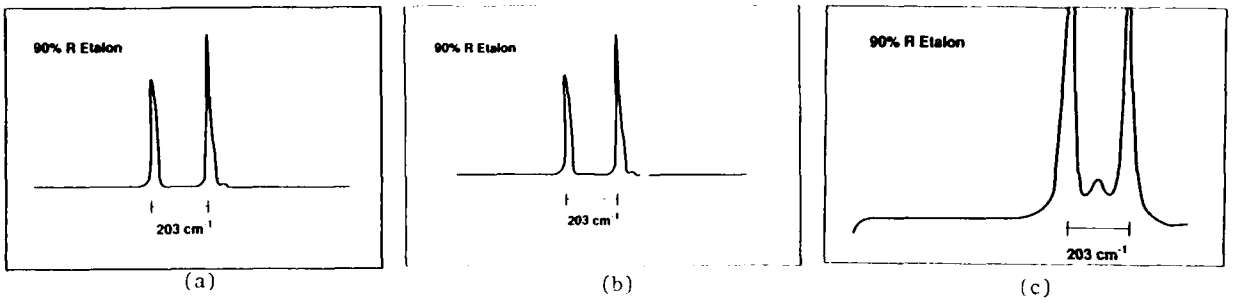


Figure 2. Two frequency lasing with 90%R etalon in KrF at 248 nm (a) oscillator output, (b) through amplifier, and (c) amplifier signal magnified by factor of 10.

The ability to tune the two modes about line center is minimal because as soon as one mode sees a much higher gain it has a tendency to dominate. This effect is much more severe when the separation between the two lasing modes is small. Thus, in order to place one of the modes on an absorption feature for resonance fluorescence or differential absorption LIDAR it is best to tune by changing the etalon spacing. If the absorption should be near line center this two wavelength approach would not work. When the lasing wavelength separation is greater than 100 cm^{-1}, the two wavelengths are easily separated by a 1/2-meter spectrometer. A specific possibility of using this technique is the detection of [OH] radical using absorptions at the XeCl (308 nm region) or XeBr (282 nm region) excimer laser transitions. Of course, in the case of XeCl where the gain bandwidth is not completely homogeneously broadened, more than two lasing lines may appear and one must take proper precautions.

Compact long-pulse and ultra-short pulse excimer lasers.

Long-pulse excimer lasers can be useful when narrow-band lasers are required with very little laser superfluorescence background. The depth resolution is, of course, limited by the pulse length. A possible application is in atmospheric temperature measurements where one remotely sense the induced rotational Raman back-scattering lines from nitrogen. Compact lasers of this type are now available using the inductive stabilization technique and operating in the 100 mJ energy region for XeCl, KrF and XeF. Figure 3 gives the temporal pulse shape of such a device in XeCl[3] and Fig. 4 is a laser burn spot on Krylox paper showing the lasing cross-section and lasing uniformity. Note that with the inductive stabilization technique any aspect ratio is possible. Fig. 4 gives a laser where the aspect ratio is approximately one to one.

There are many LIDAR applications where depth resolution is unimportant and long pulse lasers of any duration can be used. A particular example is in the hydrographic area where excimer lasers are used to identify the type and thickness of oil spills. The technique uses an excimer laser to excite fluorescence from the oil film. The fluorescence spectrum for many of the different fuels have different identifiable spectra peaking at different wavelengths[4]. For some crude oil spills that have similar spectra the differences in their fluorescence lifetimes are measured[4] in order to properly identify the species. The lifetimes range from 1 to 10 ns and are presently deconvoluted from the 15-20 ns exciting excimer laser pulse. At Los Alamos we have generated very short pulses through acousto-optic mode locking of a small long-pulse laser oscillator. The technique only adds a few centimeters to the oscillator cavity length and will greatly facilitate these lifetimes measurements. The mode-locked pulse train is sent through a Pockels cell to select out one pulse which is subsequently sent through an amplifier (which nominally gives one joule per pulse as an oscillator). Figure 5 gives the mode-locked pulse train from the oscillator. The pulse becomes increasingly narrower as a function of the increasing number of round-trips in the cavity, and reaches a minimum some 40 ns into the long-pulsed discharge excitation as shown in Fig. 6[5]. In work done by Shay, Sze and Maloney[6] one pulse is picked off and amplified. The picked-off pulse is shown in Fig. 7 and the total output pulse energy obtained as a function of the input pulse energy is shown in Fig. 8. We see that over 37 mJ/cm^2 is obtained after amplification of a 120 ps FWHM input pulse. The thickness of the oil film is calculated by comparing the water Raman signal with and without the oil film and by knowing the oil attenuation coefficient.

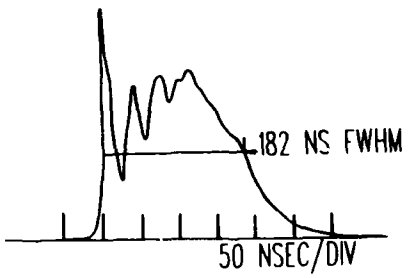


Figure 3. Temporal pulse shape of XeCl lasing using inductive Stabilization electrodes.

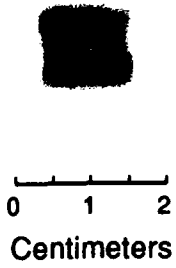


Figure 4. Uniformity and dimensions of XeCl using burn pattern on Krylox paper.

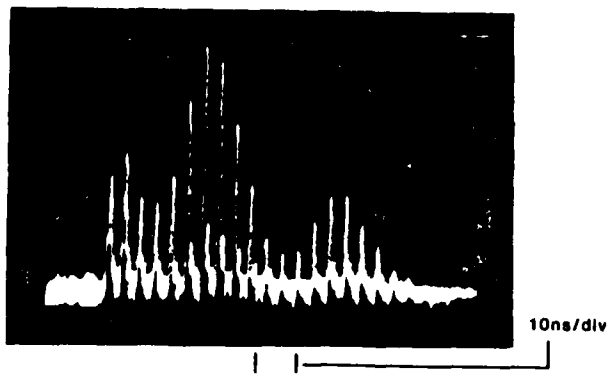


Figure 5. Actively mode-locked pulse train from inductively stabilized XeCl mini-laser.

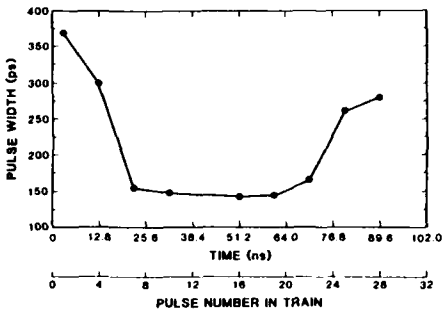


Figure 6. Time evolution of the pulse width in the mode-locked pulse train.

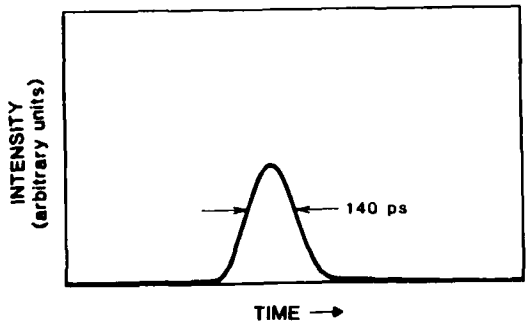


Figure 7. A picked-off single mode-locked pulse.

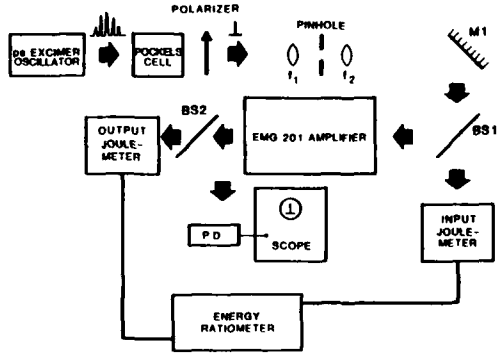


Figure 8. Experimental set-up for the short pulse amplification experiment.

Thus, a long-pulse excimer laser system with the short-pulse gererating scheme described above would be an ideal compact system to do all the measurements for this hydrographic application.

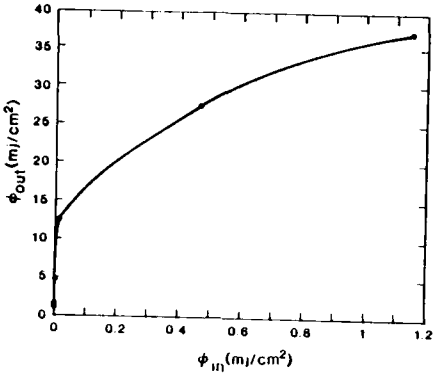


Figure 9. Energy density out for a given energy density in for 120 ps pulse amplification in XeCl.

Discussion

We have tried to show in this discussion the wide applicability of excimer lasers to LIDAR and have presented certain specific new features of compact excimer laser systems that may be specially relevant to specific applications. As the problems of the environment become evermore important in the consciousness of the public at large, the remote sensing of the quality of our atmosphere and our waters, as well as the monitoring of important parameters which affect global climate change will become evermore needed. We believe excimer laser systems will have an important role to play in this effort.

References

1. F.J. Barnes, R.R. Karl, G.L. Stone, K.E. Kunkel, "LIDAR determination of horizontal and vertical variability in water vapor over cotton," to be published in Remote Sensing of the Environment, a special issue dedicated to the MACIII experiments, June 1988

2. R.C. Sze, S.J. Thomas, N.A. Kurnit and C.W. Patterson, "Wide bandwidth control studies for the advanced Aurora KrF fusion front end," to be presented at the Conference on Lasers and Electro-Optics, Anaheim, CA. (May 1990)

3. Courtesy of Stablelase, Inc., 1042 Stagecoach Rd., Santa Fe, New Mexico 87501

4. R.M. Measures, Laser Remote Sensing: Fundamentals and Applications, pp. 427-438, John Wiley & Sons 1984

5. T. Shay, R.C. Sze, M. Maloney and J.F. Figueira, "120 ps duration pulses by direct mode locking of an XeCl laser," J. Appl. Phys., 64, pp. 3758-3760 (1988)

6. T. Shay, R.C. Sze and M. Maloney, (unpublished)

ALEXANDRITE LASER CHARACTERIZATION AND ENGINEERING EVALUATION

John K. Dempsey, Robert D. Barber, Wayne E. Davenport,
and William D. Mullins
U.S. Army Missile Command
Redstone Arsenal, Alabama

Abstract

A recent development in solid state pulsed lasers is the alexandrite laser, built by the Allied - Signal Corporation of Westlake Village, California. The laser uses a flashlamp pumped alexandrite crystal for the lasing medium and produces radiation between 0.750 and 0.760 micron wavelengths. The U.S. Army Missile Command (MICOM) recently acquired two of these lasers and conducted characterization and operational performance evaluations. Included in the characterization/evaluation are such parameters as output energy, efficiency, beam profile, temporal pulse shape, pulse width, divergence, linewidth, ASE/laser intensity ratios, and lasing wavelength and stability. Statistical methods were used as a basic analysis approach for some of the data. System performance and reliability were also observed. This paper presents the results of that evaluation.

Introduction

The Alexandrite laser is a flashlamp pumped, solid state laser which uses an alexandrite crystal rod as the lasing medium and produces energy at 750-760 nanometer (nominally) wavelength. This wavelength is just on the fringe of the visible spectrum extending into the near infrared. When viewed as a diffuse reflection the radiation appears as a deep red color. The Alexandrite material is chromium doped $BeAl_2O_4$ (Chrysoberyl) and is manufactured by the Allied/Signal Corporation of Westlake Village, California. The active lasing medium in the Alexandrite material is the Chromium Ion (Cr^{+++}).

The Alexandrite laser is a more recent development than other solid state lasers such as Ruby or Neodymium Yag and thus the open literature is much more limited. The U.S. Army Missile Command, Research, Development, and Engineering Center (RD&EC), Directed Energy Directorate (DED), recently acquired two repetitively pulsed Alexandrite lasers, both built by Allied/Signal, for use in in-house test activities. The two lasers are referred to as the Mallet and the Compact lasers. This paper describes the characterization and engineering evaluation of these two lasers. Included in the characterization/evaluation are such parameters as energy output, efficiency, beam profile, temporal pulse shape, pulse width, divergence, linewidth, ASE/laser intensity ratios, lasing wavelength and stability, and other observations made during the course of this effort.

Laser Description

The Mallet laser is a repetitively pulsed alexandrite device designed to operate in a long pulse mode with an approximately 80 microsecond (μsec) pulse length (350 μsec with additional capacitor bank) at different pulse repetition frequencies (PRF). Emitted energy levels per pulse were up to 6 Joules (350 μsec) at 1 Hz and 1 Joule at 6 Hz. The laser also has an optional Q-switch capability.

The Mallet alexandrite rod is 0.7 cm x 10 cm. An aperture of approximately 0.65 cm included in the cavity serves as the limiting aperture. In some of these tests a beam expander/collimator was used to expand the laser aperture by a factor of approximately 12 to 1.

The resonator consists of two elliptically coupled flashlamps, the laser rod, a porro prism for 100% reflection, and a slightly concave output coupler of approximately 50% transmission (Fig. 1a). The porro prism, a single axis corner cube, is used for ease of alignment and physical stability of the resonator. However, it introduces unusual mode patterns onto the beam. The near field is essentially top hat in a horizontal direction and has two modes in the vertical direction (Fig. 1b). The line of zero intensity that divides them corresponds to the vertex of the porro prism. This pattern can be explained by realizing that the resonator is optically equivalent to one consisting of two half cylindrical rods with an output coupler on each end, and correspondingly two output beams propagating in opposite directions (Fig. 1c). The porro prism folds the resonator back on itself and places the two beams adjacent and parallel to each other (Fig. 1d). They are, however, two separate and distinct beams and are not coherent with respect to each other. In the far field, the two beams overlap and give rise to an intensity profile which is Gaussian-like in form but several times wider than the diffraction-limited beam from an equivalent aperture.

The laser was operated with two different partial reflectors as the output coupler. The earlier testing utilized a 50% reflector which was later changed to an 80% reflector. The only data taken with the higher reflectance mirror were the spectral and efficiency determinations.

The natural birefringence of the alexandrite crystal forces a horizontal linear polarization state on the beam. The output window of the laser head is at Brewster's angle and thus introduces no losses.

The laser control contains a vertical light emitting diode (LED) display indicating output energy based on energy samples taken by a photodiode located near the laser exit aperture. The amount of emitted laser energy is controlled by varying the voltage to the flashlamps. The manufacturer states that in the long pulse configuration mode, operating at 1 Hz, an emitted energy of approximately 1 Joule corresponded to a 60 reading on the LED meter. This was the recommended operating configuration for extended runs.

The laser rod is heated to and maintained at approximately 78 degrees centigrade for optimum lasing efficiency. The flashlamp fluid cooling system is maintained at approximately 45 degrees centigrade.

The Compact laser has a flashlamp pumped alexandrite laser rod of virtually identical dimensions to the Mallet (0.635 cm x 10 cm). A maximum reflectance mirror, the rod, and the output coupler form the laser resonator. The flashlamp energy is coupled to the rod in a single ellipse reflector. The laser differs in that it has no liquid cooling of the flashlamps but rather is conductively cooled. The laser as originally delivered did not include an external (to the pump chamber) fan but was added shortly thereafter along with a change in the maximum reflector to a shorter radius of curvature. Additionally, there is no stabilization of the rod temperature as in the Mallet. It operates essentially as a single pulse device in the long pulse mode although it has some capacity for repetitive pulses. An 8x beam expander/collimator is installed on the laser.

These lasers were both acquired as broadband lasers under a set of specifications emphasizing energy output and beam quality.

Experimental Details

All energy output measurements were taken with a Scientech model 38-0101 volume absorbing disc calorimeter and a digital readout unit. The only exception being the rep rate measurements (1 Hz) taken with the Mallet laser. The time constant for the calorimeter was too long to allow measurements at this rep rate. These measurements were taken with a Laser Precision RjP-745 pyroelectric radiometer which was calibrated against the calorimeter.

Temporal pulse forms were taken with a Hammamatzu vacuum photodiode. The signal from the photodiode was fed to an oscilloscope or to a Tektronix 7912 programmable digitizer. The digitizer provides a video output which was recorded on a VCR and reduced post-test. Photographs presented in this paper were taken from the oscilloscope with a standard scope camera.

Intensity profiles for the Mallet were acquired through the use of a standard vidicon camera in conjunction with a Teledyne Brown Profilometer model VCP 1. The camera was used to observe the laser spot on a white target board and was stopped down so as to produce a good (unsaturated) signal. The video signal was then interfaced to the Profilometer which scans it in three dimensions and produces an X, Y, and Z output to an oscilloscope. Photographs were again taken with a scope camera.

The beam spatial fluence profile for the Compact laser was measured with a beam profiler developed by MICOM DED. The device consists of a 10 x 10 array of 1-inch square black anodized aluminum tiles with a small thermistor attached to the back of each. These independently detect energy by measuring temperature changes. Output from each tile in the array is multiplexed five times per second and recorded by a computer. The device provides 100 array data points of the beam fluence distribution for graphic display.

Linewidth measurements and ASE/Laser intensity ratios were taken using a Spex spectrometer and a Photo Multiplier Tube (PMT) or a Jarrel Ash spectrometer in conjunction with a Tracor Northern 1710 Optical Multichannel Analyzer (OMA) or some combination thereof. A split off portion of the beam was directed into the Jarrell Ash spectrometer and the OMA while the remainder entered the Spex and PMT. The entire spectral distribution of the lasers could thus be monitored on each pulse (OMA) while the spectrum was methodically scanned for intensity variations as a function of wavelength (PMT). This set-up became necessary because of the pulse-to-pulse variation in spectral content which could significantly effect the intensity readings. The wavelength and output energy dependence of the

Alexandrite medium on temperature is well documented.[1-3] The rod temperature is dependent on the time between pulses (for a fixed flow rate) particularly in the conductively cooled Compact. Thus, it became critical to pulse the lasers when the rods were at the same temperature to improve success at determining an ASE/Laser intensity ratio. Under this criterion, the lasers were pulsed and data taken only after the rods had sufficient time to return to a stabilized temperature. This amounted to room temperature for the Compact laser and 78 degrees centigrade for the Mallet. The OMA was monitored to verify that lasing was indeed occurring at approximately the same wavelength before using the intensity data from the PMT. Linewidth could be taken directly from the OMA or determined from the intensity plots produced by the SPEX/PMT.

Test Results And Discussion

Output Energy

The results of the output energy for both lasers are presented in Table 1. The output energy for the Compact laser was measured in a smaller sample size. This was primarily due to the fact that by being conductively cooled, the laser was restricted in the number of continuous pulses that could be fired due to heat build-up in the pump chamber. The Compact data represents a combination of two runs of about 105 shots each at approximately 1/4 Hz with a cool down period between them. The Compact data was taken after the aforementioned fan and mirror modification.

Table 1. Output Energy Data

Emitted Energy (J)

	Mallet		Compact
	Long Pulse	Q Switch	
MEAN	0.9096	0.4604	3.9070
MAX	1.0167	0.5045	4.2514
MIN	0.8266	0.4407	1.1793
STD	0.0015	0.0088	0.2956
COV	2.89%	1.90%	7.57%
#SHOTS	1001	1000	210

The Coefficient of Variance (COV) is determined by dividing the standard deviation by the mean and is presented as a percent. It is the percent of the first standard deviation of the mean value and allows a comparison of variance between different types of data or data where the mean values are different.

Figures 2a, 2b, and 2c represent the frequency distribution curves of this data for the Mallet long pulse and Q-switch and the Compact, respectively. The frequency distribution curves present essentially the same curve profile of data distribution around the respective mean for all three cases. These data indicate a consistent pulse-to-pulse emitted energy. This is evidenced by the low COV's of 1.9% for the Mallet Q-switch and 2.89% for the Mallet long pulse. The Compact data was a little more inconsistent with a COV of 7.57%. This is an expected result due to the temperature stabilization and rod cooling in the Mallet versus the conductive cooling of the Compact.

Temporal Data

The measured pulse width data, summarized in Table 2, indicates that the Mallet pulse is approximately 81 µsec and 57 nsecs (FWHM) in the long pulse and Q-switch modes, respectively. Figures 3 and 4 present examples of the temporal pulse forms from which these pulse widths were determined.

Table 2. Mallet Pulse Width Summary

	Pulse Width	
	Long Pulse (µsec)	Q-switch (nsec)
AVG	81	57
MAX	96	96
MIN	64	48
STD	5.897	3.363
COV	7.29%	5.94%
#SHOTS	297	301

The data for pulse width on the Compact laser was a much smaller sample than for the Mallet. The data averaged approximately 150 μsec. Statistical parameters (other than the mean) were not employed because of the small sample size. Figure 5 shows an oscilloscope trace of a typical temporal pulse form for the Compact laser.

The temporal pulse forms for the Mallet were expanded to observe the individual spikes that make up the long pulse. The spikes ranged from 45 to 200 nsec in duration measured at the FWHM. The lower end of this range corresponds to measurements taken after the aforementioned output coupler modification and the higher end to those before. These were measured both with the normal cavity configuration and with a 1.5 mm diameter aperture placed between the rod and the output coupler. The effect of the aperture was to produce spike pulse forms that were more gaussian in nature by reducing the number of transverse modes. A typical spike is shown in Figure 6. Figure 7 shows a spike further expanded in the horizontal to reveal a condition of longitudinal multiple-moding. This varied from pulse to pulse with some single mode forms as well as some exhibiting three or more modes.

The effect of the aperture in the Mallet cavity on the temporal pulse is shown in Figures 8 and 9. Figure 8 shows a typical pulse with a 1.5 mm diameter aperture and Figure 9 without. The aperture allowed for only 2 to 3 spikes within the flashlamp pulse. A 10 shot average of output energy during this testing both with and without the aperture in place was 10 mJ and 1.2 J, respectively.

ASE/Laser Intensity Ratios

ASE/Laser intensity ratio results are summarized in Table 3.

Table 3. ASE/Laser Intensity Ratio Data

Method/Configuration	Ratio
Avg all data/Mallet w/o aperture	2.5 x 10-4
Avg all data/Mallet w/aperture	1.4 x 10-4
Select data/Mallet w/o aperture	3.7 x 10-4
Select data/Mallet w/aperture	2.4 x 10-5
Select data/Compact	1.6 x 10-5

There are four different determinations of intensity ratio for the Mallet and one for the Compact. Each of these was taken from an intensity versus wavelength plot. Figure 10 is the intensity plot from which the smallest Mallet ratio was taken and Figure 11 represents the Compact data. The plots were made on both 5 cycle log and linear scales. The first two table entries were arrived at with the sole use of the Spex/PMT for the Mallet laser as indicated under "method" in the table. Acquisition of data for the first table entry involved large pulse-to-pulse variations in intensity at a given wavelength. A digital scope with averaging capability was used to average sixteen data points at each wavelength with the laser in a 1 Hz continuous run mode. The OMA was then employed to observe the spectral content on a pulse to pulse basis. It was found that the spectral content (the OMA trace) was varying in width, shape, and magnitude, from pulse to pulse in the 1 Hz continuous run mode. A 1.5 mm intercavity aperture was employed which produced a much more consistent spectral output. The improvement was theorized to be due to a decrease in the number of modes running and to a reduction in lasing medium over which a temperature gradient could develop. Mann and Weber[4] did an indepth study of various factors affecting rod temperature gradient and its stabilization. They described some rather large gradients between rod center and surface (120 degrees centigrade) and spoke of how this gradient could be held constant if the surface heat transfer coefficient (SHTC) was adapted to the pumping power. It is possible that a mismatch of these parameters was present in the Mallet at the 1 Hz rep rate causing this spectral inconsistency. Intensity data was repeated with the aperture in place and the results shown as the second table entry. The third entry is a result of using both the OMA and the Spex/PMT as described earlier in the experimental details section of this paper to select for "typical" spectral data, i.e., an OMA trace centering on approximately the same wavelength and having the same general shape. It was found that by waiting for temperature stabilization between laser pulses, this "typical" data could be produced on a fairly consistent basis. Entry four of Table 3 involves the advantages of the aperture again in addition to the selection technique and by comparison yields the lowest ASE/Laser ratio for the Mallet. The final entry is for the Compact laser which was inherently more stable from a spectral standpoint. The only deterrent to determining the intensity ratio was the centerline wavelength variation as a function of rod temperature. Selection for typical data with the OMA was incorporated and lasing occurred dependably at the same centerline when the rod was allowed to

stabilize at room temperature between pulses. The time interval for "stabilization" of the rods was longer for the Compact because it is forced air cooled rather than fluid temperature stabilized as with the Mallet. The intensity ratios varied from 2.4×10^{-5} to 3.7×10^{-4} for the Mallet with the Compact yielding a slightly lower ratio (1.6×10^{-5}) than the lowest Mallet ratio. These numbers are consistent with calculated estimates for these lasers.

Linewidth

Linewidth results are presented in Table 4. A linewidth was determined from each of the intensity plots (see examples in Figures 10 and 11) discussed above. Linewidth was also measured directly from the OMA and a comparison can be made from the table. An example of an OMA trace for the Compact laser is given in Figure 12.

Table 4. Linewidth Data (Angstroms)

Laser/Configuration	Method		
	Intensity Plots		OMA
	Avg All Data At 1 Hz	Select Typical Stabilized	
Mallet w/aperture	32.5	21.5	27.6
Mallet w/o aperture	27.5	40.0	31.4
Compact	--	18.0	20.0

The numbers are comparable between the different methods and configurations but more confidence is placed in the OMA data because it is a much more direct method. Linewidth determinations from the intensity plots were more a check on the Spex/PMT data (for intensity ratio purposes) than for their own merit.

Spectral Observations

The Mallet produced a fairly consistent spectral distribution when the intercavity aperture was in place and/or the laser rod temperature was allowed to stabilize between pulses. Rep rate runs (1 Hz), particularly without the aperture, produced highly irregular and inconsistent spectral traces but did remain at about the same general wavelength. The Compact, however, while being much more consistent in the shape of the spectral trace and linewidth at 1 Hz, did have a centerline change proportional to the length of run time (number of pulses) as can be seen in Figure 13. This plot is for a 30 shot run which the manufacturer states in the operator's manual to create about a 25 degree centigrade rise in the pump chamber. The change in wavelength over this range is 6.8 nanometers. Guch and Jones[3] described a change of 38 nanometers over a delta of 276 degrees centigrade with their laser. This slope is about half that of our finding with the Compact. Additionally, the linewidth remained fairly constant out to about pulse number 15 where a definite broadening began to take place as shown in Figure 14. It was desired to investigate this effect out to higher temperatures but the danger of overheating certain pump chamber components precluded further investigation. The Compact laser's centerline wavelength changes with rod temperature while the Mallet's fluid temperature control system maintains a more consistent rod temperature.

The alexandrite lasers are known to produce higher energies at higher temperatures and is the reason for rod heating in the Mallet to maintain a temperature of 78 degrees centigrade. Also, the absence of cooling other than forced air in the Compact allows an increase in rod heating and thus output energy as more pulses are put on it. This is exhibited in Figure 15 which shows the output energy as a function of the pulse number at approximately 1/4 Hz in two extended runs for the Compact. The output for these extended Compact runs peaked at about 80 pulses which should correspond to a stabilization of the rod temperature at an equilibrium between the conductive cooling capacity and the thermal input at the 1/4 Hz rep rate. Guch and Jones[3] demonstrated an increase in output energy out to 225 degrees centigrade with controlled heating of the rod.

The tradeoff for more energy appears to be a deterioration of spectral quality. Some applications, however, might favor or be indifferent to a wavelength drift, broadband spectral character, and/or inconsistent spectral distributions.

Beam Divergence

Beam divergence for the Mallet was not determined in the laboratory but rather estimated by observing the beam spot size at 1200 meters under low scintillation-high visibility conditions and dividing the spot diameter by the range. This work was accomplished earlier

by Barber et. al.[5] in a set of propagation experiments performed at DED MICOM. The beam divergence for the Compact was determined by the United States Army Environmental Hygiene Agency at the MICOM test site. These data were taken in the single shot mode and the results are summarized in Table 5.

Table 5. Divergence Data

Laser	Divergence With Beam Expander	Base System
Mallet	0.191 mrad	2.3 mrad
Compact	0.44 mrad	3.5 mrad

Beam Spot Analysis

Beam profiles for the Mallet were obtained as described in the experimental details section and are presented in Figures 16 and 17. They represent the Mallet profiles as viewed from the vertical and the horizontal for the long pulse and Q-switch modes, respectively. The profiles are basically Gaussian.

The Profilometer was not used with the Compact but rather the 10 x 10 array thermal beam profiler discussed in the experimental details section. The beam fluence contour plot shown in Figure 18 was taken with the array at 400 meters under low scintillation, high visibility conditions.[5] The table insert gives the relative intensities for each tile. The near uniform energy distribution is apparent.

Efficiency

The efficiency for the two lasers was calculated as the average energy out of the laser per pulse divided by the total energy on the storage capacitors supplying the flashlamps. The calculated efficiencies were approximately 1.3% and 1.8% for the Mallet (long pulse) and Compact lasers, respectively.

Reliability

A word about observed reliability is included here although a formal reliability study was not performed. The number of shots on each laser could only be estimated as they were used in many different tests with no actual count made. The Mallet head was estimated to have been fired in excess of 50,000 shots and the Compact in excess of 20,000.

The Mallet had some power supply problems when first received and then again at the end of this testing. A short to the casing in the control electronics which destroyed several circuit boards also occurred early on. The only failure in the head was a breakdown of the reflective coating in the pump chamber housing which was primarily due to improper maintenance of the deionized coolant water.

The pump chamber reflective coating in the Compact laser was burned off over a period of time due to excessive heating. This occurred prior to installation of the fan and has not been a problem since. The only other failure was damage to the small lens in the beam expander which occurred on two occasions.

Conclusions

The results of our findings for the characterization of these two Alexandrite lasers are summarized in Table 6.

Table 6. Summary of the Mallet and Compact Characterization

Parameter	Mallet		Compact
	Lone Pulse	Q-Switch	
Output Energy (J)	0.91	0.46	3.91
Pulse Width	81 µsec	57 nsec	150 µsec
ASE/Laser Intensity Ratio	2.4×10^{-5}*	-----	1.6×10^{-5}
Linewidth from OMA (Angstroms)	27.6 w/aperture 31.4 w/o aperture	-----	20.0
Divergence (mrad)	2.3	-----	3.5
Efficiency	1.3%	-----	1.8%

*Represents lowest ratio for Mallet

In addition to these parameters spectral conclusions are in agreement with prior findings for Alexandrite lasers. The lasing wavelength is dependent on rod temperature and will change from pulse to pulse unless the temperature is stabilized as was seen with the Compact. The linewidth for the Compact laser was observed to broaden with increased temperature out to the recommended limits of operation. Inconsistencies in the Mallet were seen as far as linewidth and spectral content when operated at rep rate (1 Hz). This was probably related to variations in rod temperature gradient from pulse to pulse caused by a mismatch between the Surface Heat Transfer Coefficient and the pumping power as discussed earlier.

Energy output was also observed to increase with an increase in rod temperature and was more consistent from pulse to pulse in the temperature stabilized Mallet than in the conductively cooled Compact.

References

1. J. W. Kuper, W. E. Langert, et. al., "Compact Integrated, High Efficiency Alexandrite Lasers," November 1986, Proceedings of the Nineth International Conference on Lasers and Applications, 1987.

2. S. T. Lai and M. L. Shand, "Temperature Dependence of Gain in CW Alexandrite Laser," December 83, Proceedings of the International Conference on Lasers and Applications, 1985.

3. S. Guch, Jr., and C. E. Jones, "Alexandrite-Laser Performance at High Temperature," Optics Letters, Vol. 7, December 1982, pp. 608-610.

4. K. Mann and H. Weber, "Surface Heat Transfer Coefficient, Heat Efficiency, and Temperature of Pulsed Solid-State Lasers," Journal of Applied Physics (ISSN 0021-8979), Vol. 64, August 1, 1988, pp. 1015-1021.

5. R. D. Barber, J. K. Dempsey, et. al., "Alexandrite Laser Propagation Experiments," March 1989, Proceedings of the SPIE 1989 Symposia on Aerospace Sensing Conference, 1989.

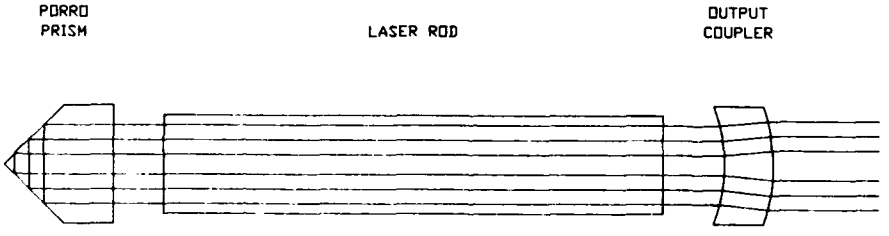


Fig. 1a. Mallet Laser Resonator.

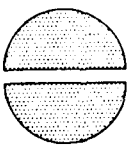


Fig. 1b. Mallet Laser Near Field Intensity Pattern.

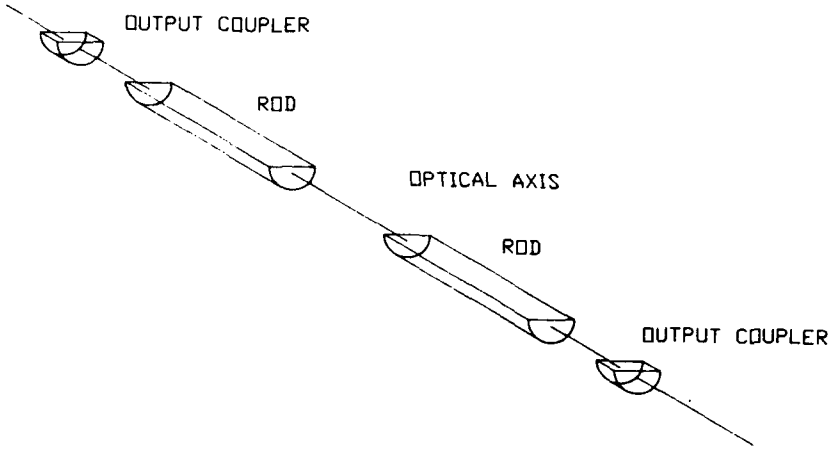


Fig. 1c. Mallet Laser Optical Equivalent of Resonator.

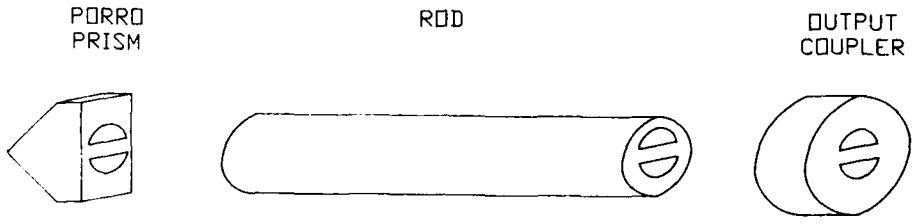


Fig. 1d. Mallet Laser Beam Footprint in Resonator.

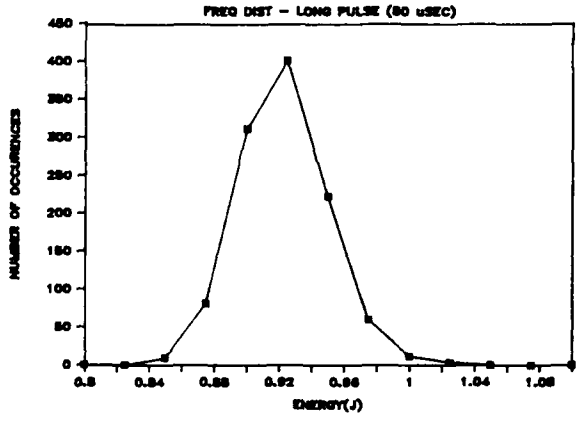


Fig. 2a. Mallet Laser Output Energy Distribution - Long Pulse.

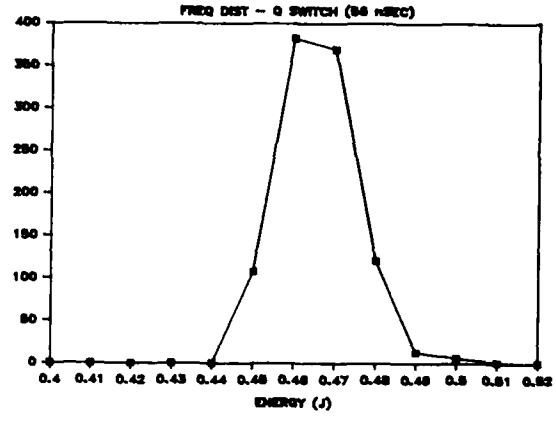


Fig. 2b. Mallet Laser Output Energy Distribution - Q-Switch.

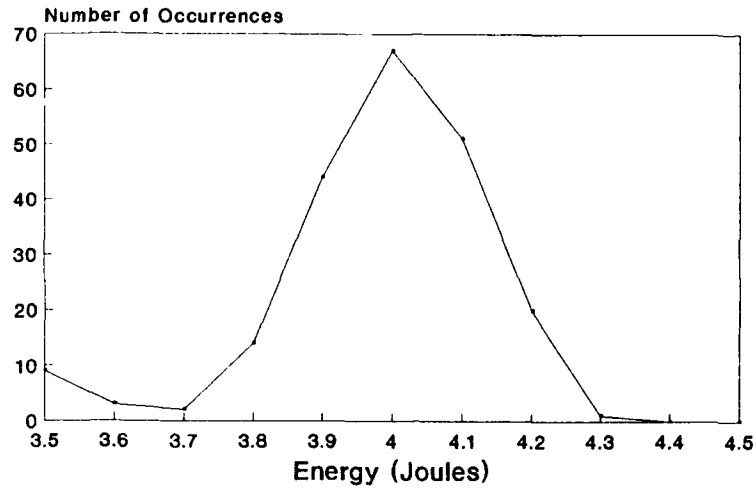


Fig. 2c. Compact Laser Output Energy Distribution.

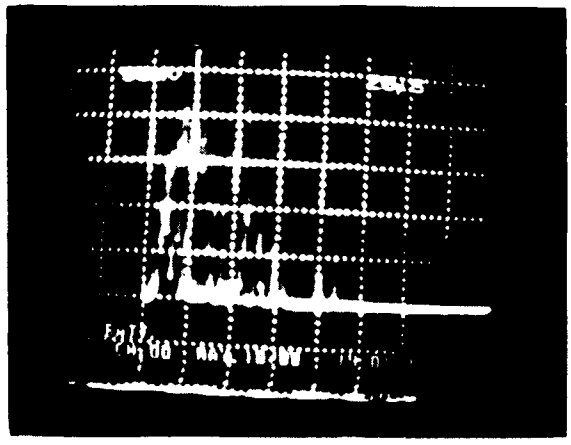


Fig. 3. Mallet Laser Temporal Long Pulse (~ 80 μsec).

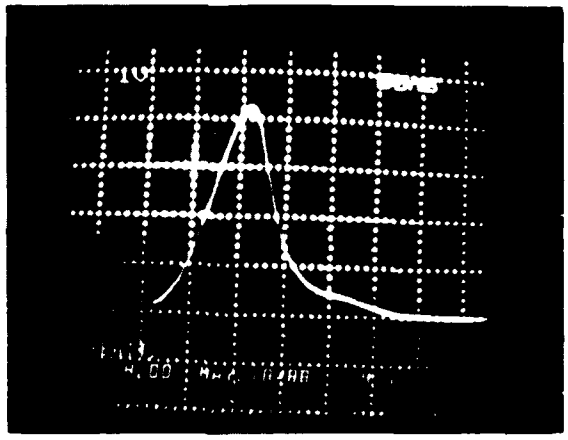


Fig. 4. Mallet Laser Temporal Q-Switch Pulse (~ 50 nsec).

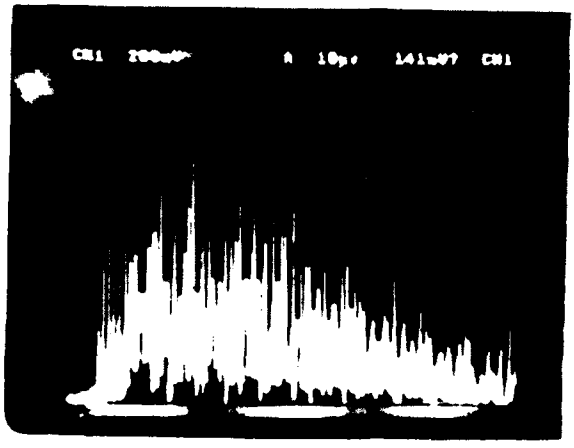


Fig. 5. Compact Laser Temporal Pulse Form.

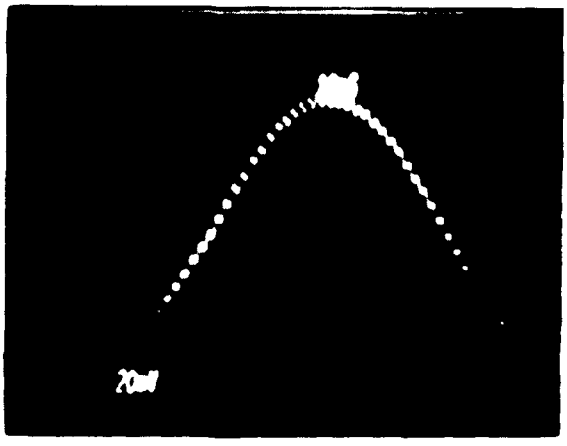


Fig. 6. Mallet Laser Long Pulse Spike Form (~ 60 nsec at FWHM).

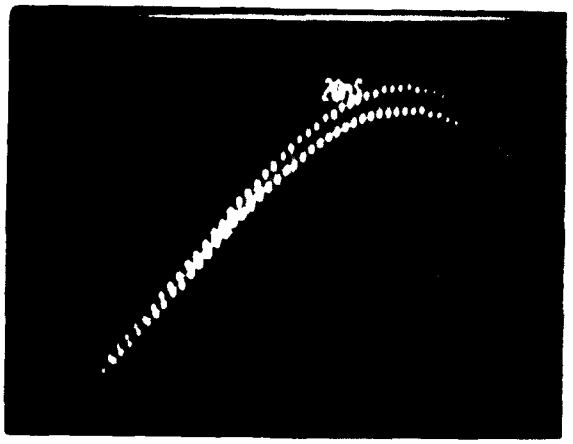


Fig. 7. Mallet Laser Long Pulse Spike Expanded to Show Multi-Moding.

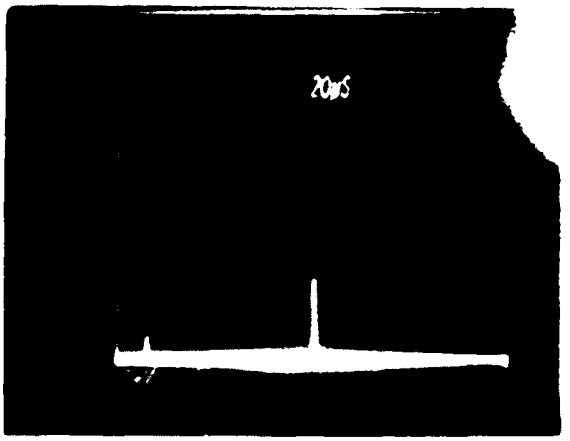


Fig. 8. Mallet Laser Temporal Long Pulse With 1.5 mm Intercavity Aperture.

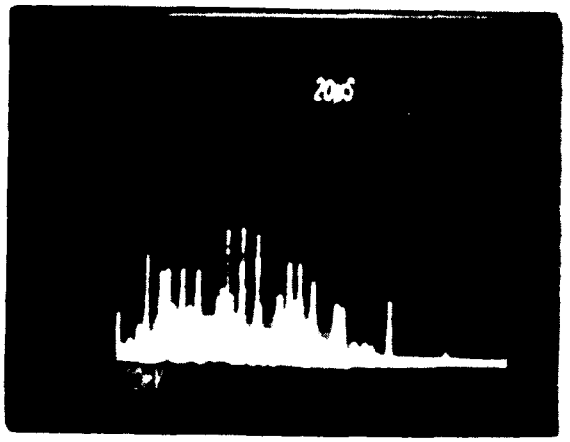


Fig. 9. Mallet Laser Temporal Long Pulse Without Aperture (~100 μsec).

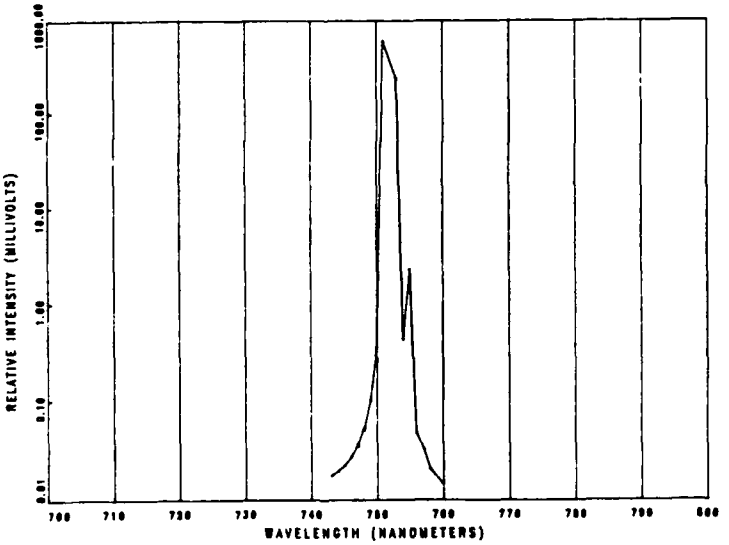


Fig. 10a. Intensity vs Wavelength Plot for Mallet Laser with 1.5 mm Intercavity Aperture and Data Selection for "Typical" Data on 5 Cycle Log Scaling.

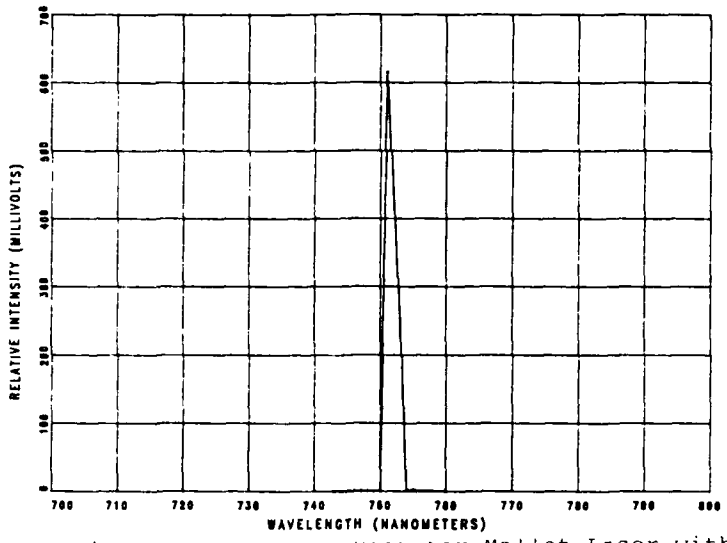


Fig. 10b. Intensity vs Wavelength Plot for Mallet Laser with 1.5 mm Intercavity Aperture and Data Selection for "Typical" Data on Linear Scaling.

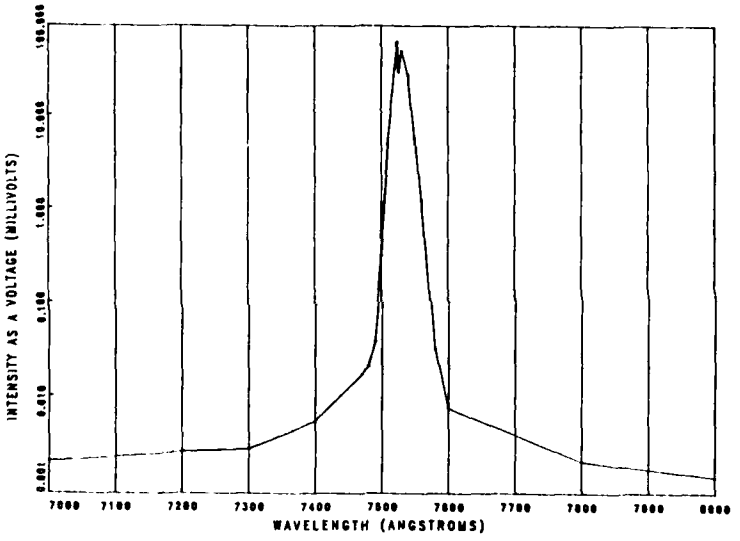


Fig. 11a. Intensity vs Wavelength Plot for Compact Laser Using Data Selection for "Typical" Data on 5 Cycle Log Scaling.

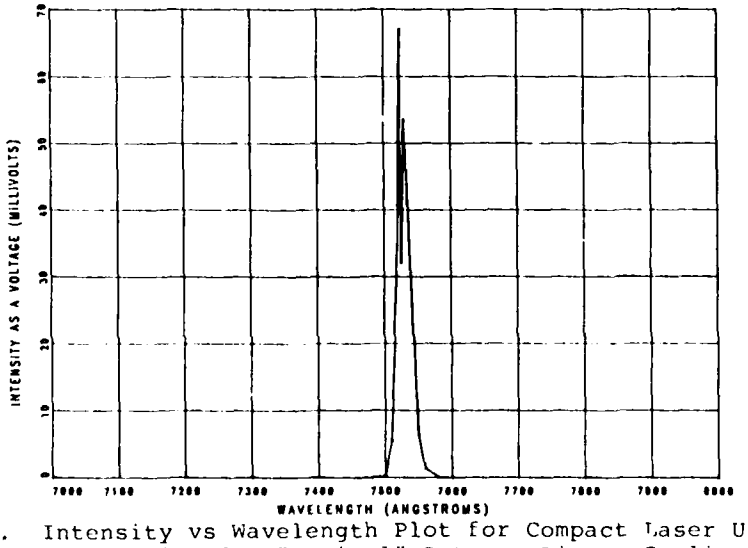


Fig. 11b. Intensity vs Wavelength Plot for Compact Laser Using Data Selection for "Typical" Data on Linear Scaling.

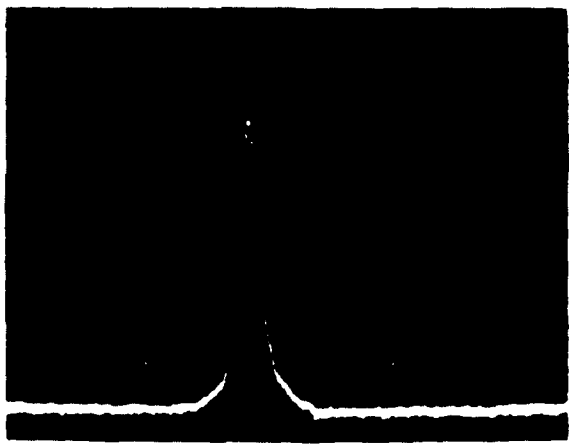


Fig. 12. Optical Multichannel Analyzer Plot for the Compact Laser - Linewidth ~20 Angstroms.

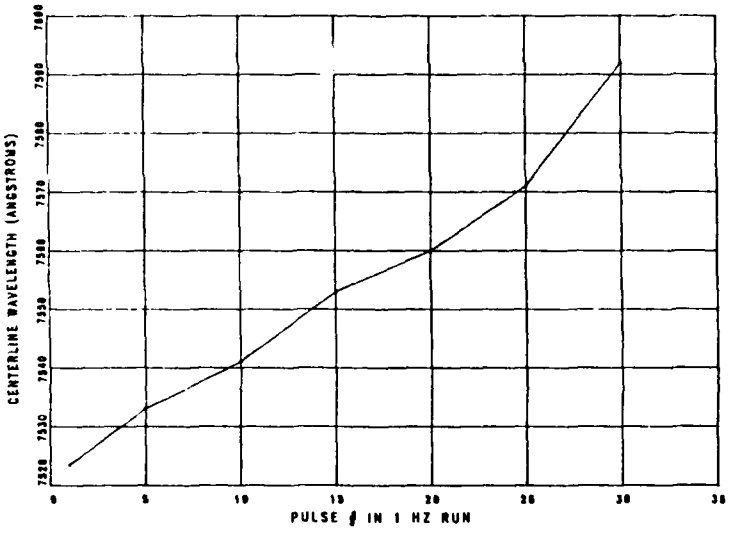


Fig. 13. Centerline Wavelength vs Pulse Number at 1 Hz for the Compact Laser.

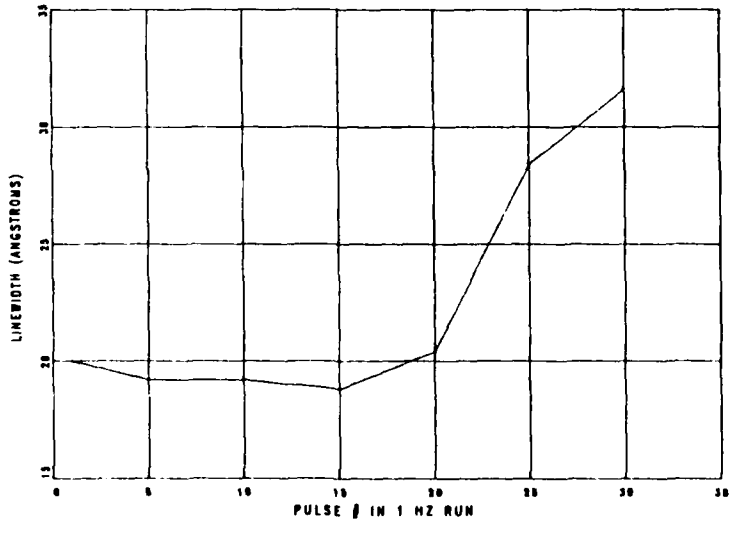


Fig. 14. Linewidth vs Pulse Number at 1 Hz for the Compact Laser.

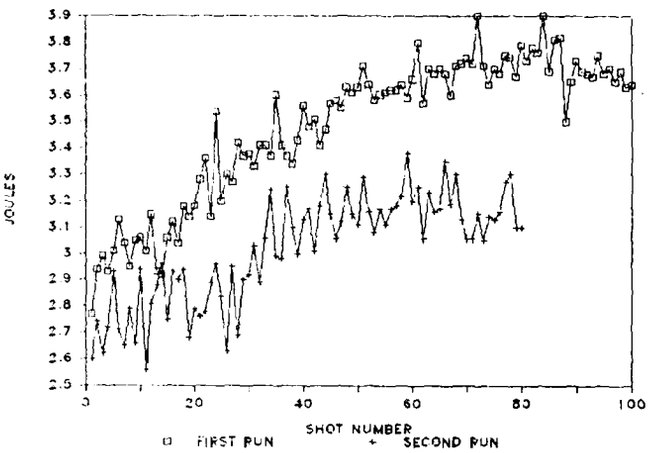


Fig. 15. Output Energy vs Pulse Number at 1/4 Hz for the Compact Laser.



Fig. 16a. Mallet Laser Beam Profile in the Horizontal Axis - Long Pulse.

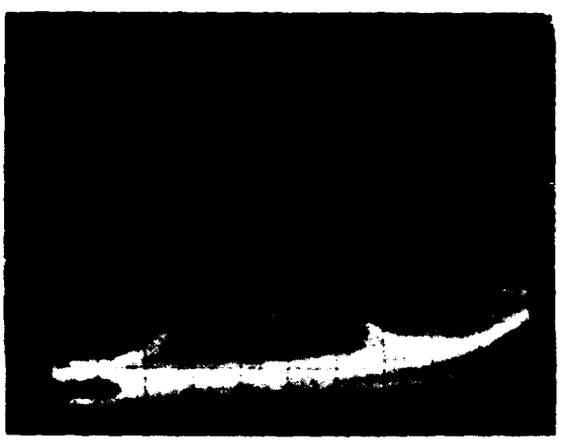


Fig. 16b. Mallet Laser Beam Profile in the Vertical Axis - Long Pulse.



Fig. 17a. Mallet Laser Beam Profile in the Horizontal Axis - Q-Switch.

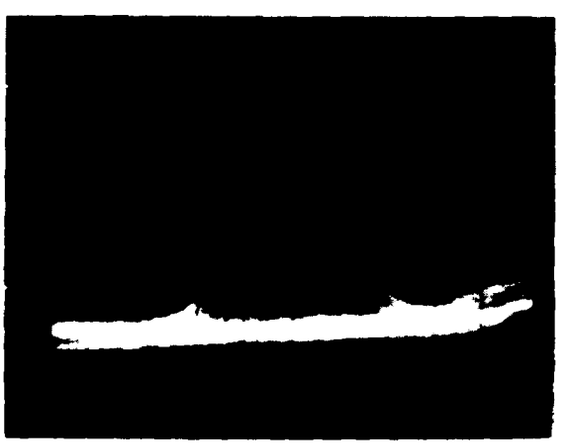
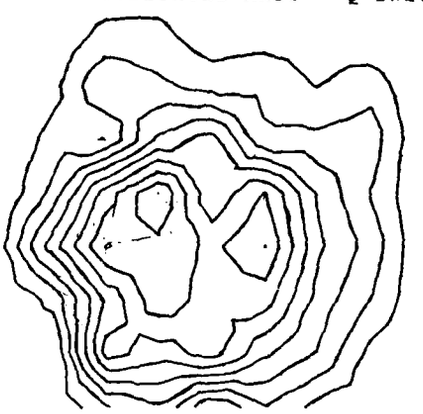


Fig. 17b. Mallet Laser Beam Profile in the Vertical Axis - Q-Switch.



DATA SET# 34 OF FILE

0	0	0	0	0	0	0	0	0	0
0	0	0	2	0	0	0	0	0	0
0	0	4	14	7	4	2	0	0	0
6	20	16	25	20	3	9	4	0	1
9	17	24	24	28	13	7	4	1	0
0	20	20	21	16	17	5	1	0	0
6	13	20	25	22	7	5	2	0	0
2	9	11	13	12	7	3	1	0	0
1	2	6	8	6	8	5	0	0	0
0	0	0	0	0	0	0	0	0	0

Fig. 18. Contour Plot and Data Set for Compact Laser Energy Distribution.

RECENT DEVELOPMENTS IN TI:SAPPHIRE FOR REMOTE SENSING APPLICATION

James C. Barnes
Senior Research Physicist
NASA Langley Research Center
Hampton, Virginia 23665-5225

Abstract

A historical overview of titanium-doped sapphire (Ti:Al_2O_3) material and of NASA lidar systems, leading to Ti:Al_2O_3 as a candidate lidar transmitter, is presented. Progress on the design and development of a Ti:Al_2O_3 laser for NASA lidar applications is reported. Also reported are advances by NASA and others demonstrating the versatility of the laser material for remote sensing applications.

Introduction

Ti:Al_2O_3 was first lased by Dr. Peter Moulton in 1982 at MIT Lincoln Laboratory.[1] Although it was a promising laser material, Dr. Moulton and others observed and measured anomalous absorption losses at laser wavelengths.[2,3] The losses limited the efficiency of the material and contributed to lowering the damage threshold. In 1985, NASA contracted Union Carbide Corporation for materials development in an attempt to reduce the absortion at the laser wavelengths. A total of four Ti:Al_2O_3 boules were grown with NASA Langley researchers performing spectroscopic and laser characterization of material from each boule before the growth of the next boule began. The initial boule was measured to have losses at 780 nm of 0.20 cm^{-1} and the final boule, with refined growth and processing techniques employed, exhibited losses less than 0.02 cm^{-1}.[4] Commercial suppliers now consistently produce material with losses less than 0.01 cm^{-1}.[5]

NASA Langley's interest in Ti:Al_2O_3 can be attributed to the advantages presented by its laser characteristics over other tunable materials such as alexandrite and dyes. The wide tuning range of Ti:Al_2O_3, from 660 nm to 1100 nm, coupled with nonlinear devices extending the range into the UV allows the laser to address many atmospheric molecular species including OH_x, O_x, NO_x, and SO_x via lidar remote sensing. The high damage threshold, greater than 12J per cm^2 when pumped with 15 ns pulses of reasonable beam quality 532 nm light, lends well to long duration space deployment of Ti:Al_2O_3. As does the fact that it can be pumped by all solid state, frequency-doubled Nd laser systems. In addition, the high efficiencies of the laser, at high energy outputs, make it a "good neighbor" on space platforms that support more than one experiment.

Langley began its' lidar remote sensing in 1970 using a Ruby laser at 347 nm and 694 nm to measure aerosols and N_2 from a ground based system with a 48 inch telescope. In 1978, the first airborne missions were flown on an Electra aircraft. From that time to the present, the Electra has flown Ruby, YAG, YAG pumped dye, and alexandrite lasers to measure aerosols, water vapor, and ozone. The progeny of the Electra flights will be the LASE (Laser Atmospheric Sensing Experiment) mission scheduled to fly in 1990 aboard an ER-2 aircraft, capable of altitudes up to 60,000 feet. The LASE transmitters are a pair of alexandrite lasers tuned to 725 nm to perform differential absorption lidar (DIAL) measurements of H_2O on the initial flights, and tuned to 760 nm in later flights to address O_2 for temperature-pressure profile determination. The LASE instrument technology development will provide a precursor to NASA Langley's first spaceborne lidar mission, LITE (Laser In-space Technology Experiment). Scheduled to fly as a shuttle payload in 1993, LITE will measure aerosol backscatter as a demonstration of laser capability for spaceborne lidar applications. The laser transmitter will be a high power Nd:YAG laser with 0.5 J in the fundamental, 0.5 J of the second, and 0.2 J of the third harmonic providing simulateneous probe wavelengths.[6,7] Beyond LASE and LITE, NASA has not approved any major laser remote sensing programs. Langley strongly feels that, given the development efforts required, Ti:Al_2O_3 is a natural for follow up programs to both LITE and LASE. To support this contention Langley has embarked upon an aggressive effort to develop and demonstrate the capabilities of Ti:Al_2O_3 as a transmitter for remote sensing applications.

NASA Ti:Al_2O_3 DIAL Transmitter

As one might expect, spaceborne laser transmitter requirements are more stringent than aircraft transmitter requirements. Langley has directed its' efforts towards developing Ti:Al_2O_3 for spaceborne remote sensing applications, taking the position that converting a space system for aircraft applications would be more easily realized than the converse. NASA atmospheric scientist have provided the major laser requirements for making DIAL measurements of H_2O column content and profile, and O_2 for temperature-pressure determination, two enabling measurements for understanding the chemistry and dynamics of the atmosphere.[8] The transmitter must deliver at least one joule per pulse operating at a 10 Hz rep-rate. This insures that the return signal to the lidar telescope receiver is sufficient to perform viable data analysis with good resolution. The laser should be tunable to 725 nm and 940 nm to address H_2O in the lower and upper atmosphere respectively and should be tunable to

760 nm to address O_2. The laser linewidths are 1 pm for H_2O and 0.5 pm for O_2 with a spectral purity requirement of better than 99.9%. Reliability, defined as autonomous operation at linewidth and wavelength with energy degradations of no more than 25%, requires 10^6 shots for shuttle missions and 10^9 shots for polar platform deployments.

Figure 1 is a block diagram which illustrates NASA Langley's concept of an all-solid-state Ti:Al_2O_3 transmitter for spaceborne atmospheric sounding and altimetry. The transmitter selectively operates in one of two available modes; the backscatter mode for measuring aerosols or the DIAL mode for H_2O and O_2 measurements. The transmitter package incorporates diode array pumping of Nd systems. In the backscatter mode, two of the Nd:YAG lasers' fundamental outputs serve to generate the second and third harmonics which are transmitted along with the residual fundamental to probe aerosols. In the DIAL mode, all of the Nd:YAG lasers are optimized for second harmonic energy which is used to pump the Ti:Al_2O_3 oscillators and amplifiers. Tuning and linewidth control of the Ti:Al_2O_3 transmitter are achieved in the Nd:YLF pumped master oscillator modules. The modules provide two beam-lines tuned onto a molecular absorption line and one beam-line just off of the absorption line. Timing controls and other electronics are not shown but are being addressed by Langley, as are the array pump and receiver technologies.

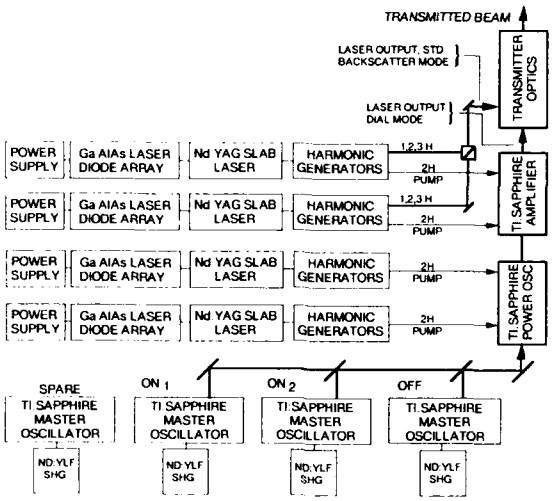


Figure 1 Block diagram illustrating NASA engineer's concept of an all solid state transmitter for spaceborne lidar.

NASA and Contractor Efforts

NASA Langley has demonstrated the capability of Ti:Al_2O_3 lasers to meet many of the space transmitter requirements. Langley has demonstrated less than 1 pm linewidths with tunability from 700 to 960 nm. Injection locking of power oscillators have been demonstrated using narrow linewidth injection sources, including dye lasers, single diode lasers, Ti:Al_2O_3 lasers, and self-injection locked Q-switched Ti:Al_2O_3 lasers.[9,10,11] In addition, the spectral purity of a Ti:Al_2O_3 amplifier system was measured.[12] This experiment encompasses the achievements listed above and will be used to illustrate Langley's development efforts. Spectral purity requires that 99.9% of the total transmitter pulse energy reside within a spectral band less than or equal to 5 pm as viewed through a spectral window of 200 pm. The primary source for out of band energy is amplified spontaneous emission, ASE, which is a result of high-gain amplification of spontaneous emission internal to the laser medium. Because the gain of Ti:Al_2O_3 is between that of relatively low-gain alexandrite which displays essentially no ASE and high-gain dyes which exhibit unacceptable levels of ASE, there was concern as to which of these media Ti:Al_2O_3 would most closely resemble. The measurement of ASE generated by a Ti:Al_2O_3 amplifier system was performed using the narrowband absorption features of rubidium gas at 780 nm which is near the gain maximum of Ti:Al_2O_3. Figure 2 is a schematic representation of the experimental arrangement. The laser system consists of an oscillator, a regenerative amplifier, and a 49 mm long, BBAR coated Ti:Al_2O_3 amplifier. The oscillator is narrowed to the pm linewidth range and tuned by a system of etalons, filters, and prism which are described more completley in reference 12. The line-narrowed oscillator is used to injection-lock the regenerative amplifier which outputs serve as the extraction beam to the amplifier. The laser is tuned to an absorption line of the rubidium gas. Transmission of amplifier pulses through a Rb absorption cell are measured at various temperatures, thus allowing the measurement of the weak ASE in the vicinity of strong laser pulses. A model for the transmission of Rb as a function of temperature and as a function of wavelength was used to validate the ASE measurements, again a more complete description of the model can be found in reference 12. Figure 3 graphically illustrates the close agreement between model predictions and experimental measurement of transmission as a function of temperature for a given wavelength. The amplifier energy transversing the cell is collected by a calibrated lens and focused onto a large area silicon detector. For each set of data taken, the transmitted signal is first incident without insertion of a bandpass filter (full spectrum transmission) and then sequentially with 8.7 nm and 3.2 nm bandpass filters centered and calibrated at 780 nm inserted in front of the detector. The fraction of the amplifier pulse transmitted by the Rb cell, when zero trannsmission is predicted by the Rb absorption model, is the on-axis ASE. One of the several sets of measured transmission as a function of gain and pump energy,

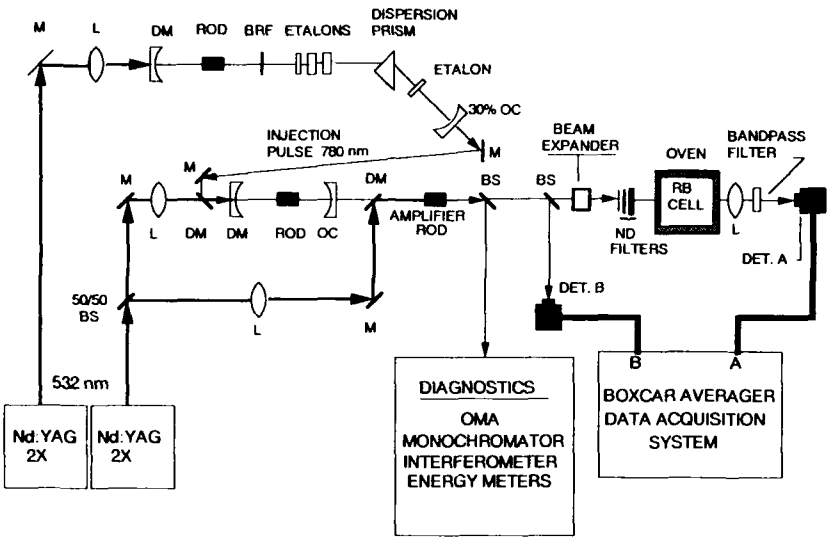


Figure 2. Schematic of the experimental arrangement used to measure amplified spontaneous emission.

at a temperature for which the model predicts zero transmission, is given in Table 1. These measurements indicate that the ASE generation property of Ti:Al_2O_3 more closely resembles that of alexandrite than dye. Further, when the on-axis ASE of less than 2×10^{-4} measured in a 32 angstrom window is scaled to the specified 2 angstrom window, less than 10^{-5} ASE is expected for pump fluences up to 600 MW/cm^2 much less than the 10^{-3} ASE allowed.

Table 1. Measured transmission as a function of gain and pump energy

PUMP ENERGY (mJ)	AMPLIFIER GAIN	FULL SPECTRUM TRANSMISSION AVERAGE	8.7 nm BANDPASS FILTER TRANSMISSION	3.2 nm BANDPASS FILTER TRANSMISSION
50	4.3	.0007	0	0
60	4.6	.0009	0	0
70	5.0	.0009	0	0
80	5.5	.0015	.00023	.00017

Rb Cell Temperature = 150°C
Laser Linewidth = 1pm
Laser Wavelength = .7805972 microns
Max. Pump Density = 2J/sq. cm

To address the one joule per pulse output energy requirement, Langley is working in conjunction with Schwartz Electro-Optics Research Division (SEORD) to demonstrate 1 J output at a 10 Hz pulse repetition rate. Using a graded reflectivity mirror (GRM) unstable resonator configuration, SEORD obtained in excess of 400 mJ of energy output at 10 Hz which is the highest energy output at 10 Hz reported to date.[13] The Nd:YLF pump laser used for this demonstration provided two 527 nm pump beam lines of up to 0.55 J each. Figure 4 is the energy input-output curve for the GRM resonator taken from reference 13. At a little more than 5 times threshold, the resonator is approaching the theoretical efficiency limit of ~50%. The complete Ti:Al_2O_3 laser system has been delivered to NASA Langley where efforts to achieve pm linewidth, Ti:Al_2O_3 laser outputs of one joule per pulse will be continued by Langley researchers with the consultation of SEORD.

Other Ti:Al_2O_3 Development Efforts

The highest Ti:Al_2O_3 energy output reported to date, 3 J per pulse at 2 Hz, was obtained from a flashlamp pumped laser using a fluorescent dye converter. An elliptical pump cavity with a 7.5 inches long, 8 mm diameter rod with matching short pulse flashlamp were used for this demonstration. A little less than 0.02 conversion efficiency was realized.[14] With the use of longer rods and flashlamps it is predicted that up to 4.5 J can be obtained from a single cavity with a factor of 2 improvement in efficiency. Using a similar cavity but with a shorter rod and different dye converter, output energy greater than 1.1 J was achieved at a 5 Hz rep-rate.[15] The conversion efficiency of this system was also slightly less than 0.02.

In a dye laser pumped Ti:Al_2O_3 demonstration researchers were able to achieve 2 J output for 10 J of microsecond pump pulses at low rep-rates. With 40 to 50 J per cm^2 pump density, there were no parasitic oscillations observed.[16] The same researchers

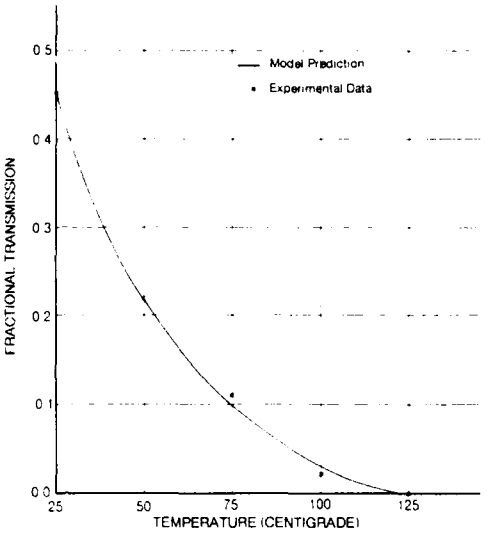


Figure 3 Transmission of Rb gas as a function of temperature.

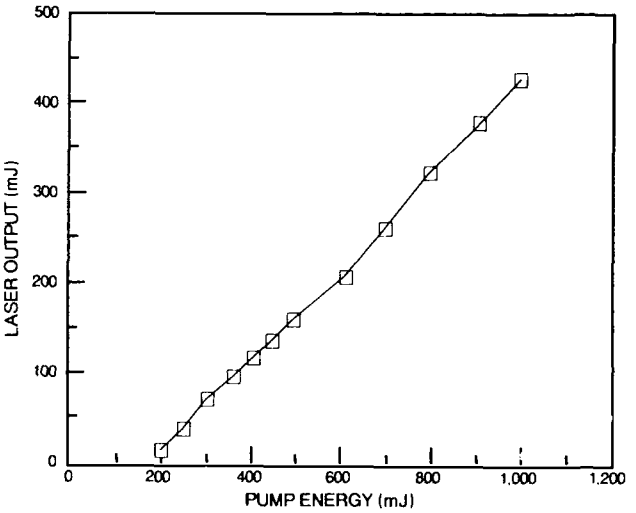


Figure 4. GRM unstable resonator output as a function of pump energy, taken from reference 13.

were able to double 1 mJ of single longitudinal mode, 911 nm Ti:Al_2O_3 to 455 nm with 0.30 efficiency using KD*P. Higher doubling efficiencies are expected with higher fundamental energies and use of frequency mixing techniques.[17]

Summary

The outlook for Ti:Al_2O_3 being used for remote sensing applications is excellent. Large diameter, long length, quality material can be readily obtained from commercial vendors. The material's damage threshold is more than sufficient to reliably produce the high energies required of lidar transmitters and the efficiency of the material lends well to high energy output. The material can be pumped by solid state and flashlamp based lasers including Nd, dyes, and gas, and can also be pumped directly in dye filled flashlamp cavities. This offers several scenarios for converting existing remote sensing systems to Ti:Al_2O_3 eg. NASA's LASE and LITE Systems. Energy output up to 3 J have been demonstrated at low repetition rates, a 1 J per pulse 10 Hz system is being developed by NASA and SEORD. Diode array pumped Nd technology is being addressed with the goal of a 1 J system expected to be realized by the end of 1990. NASA Langley Research Center has demonstrated many of the required laser characteristics for a spaceborne Ti:Al_2O_3 lidar transmitter and is actively pursuing a project using Ti:Al_2O_3 technology for DIAL applications.

Acknowlegements

The author acknowledges the technical contributions of Langley Personnel to work discussed in this paper. Some of the more notable contributors were N. Barnes, G. Lockard, P. Cross, J. Byrd, C. Bair, P. Brockman, and E. Browell. The author also acknowledges the discussions and information provided by P. Moulton, G. Rines, E. Erickson, Y. Carts, M. Kokta, D. Lowenthall, and J. Chang.

References

1. Operation of the Ti:Al_2O_3 laser was first reported by Dr. Moulton at the Twelfth International Quantum Electronics Conference in Munich in June, 1982. A brief article appeared in "Physics News in 1982," P. F. Schewe, ed.

2. G. F. Albrecht, J. M. Eggleston, and J. J. Ewing, "Measurements of Ti:Al_2O_3 As A Lasing Material," Opt. Comm., Vol. 52, No. 6, 401-404, 1985.

3. P. F. Moulton, "Spectroscopic and Laser Characteristics of Ti:Al_2O_3," J. Opt. Soc. of Am. B, Vol. 3, 125-133, 1986.

4. M. Kokta, "Titanium-Doped Sapphire Crystal Growth," NASA Contract No. NAS1-18095 Final Report, 1986.

5. Y. A. Carts, "Titanium Sapphire's Star Rise," Laser Focus World, 73-88, September, 1989.

6. J. H. Chang and M. D. Thomason, "Laser Transmitter Module for the Space Transportation System," CLEO Technical Digest, Vol. 7, April, 1988.

7. Personal Participation in Energy Measurements of the Prototype Laser at Spectron Development Laboratory, September, 1989.

8. R. J. Curran, "Satellite-Borne Lidar Observations of the Earth: Requirements and Anticipated Capabilities," Proc. of the IEEE, Vol. 77, No. 3, 478-490, March, 1989.

9. P. Brockman, C. H. Bair, J. C. Barnes, R. V. Hess, and E. V. Browell, "Pulsed Injection Control of a Titanium-Doped Sapphire Laser," Opt. Lett., Vol. 11, No. 11, November, 712-714, 1986.

10. N. P. Barnes, J. A. Williams, J. C. Barnes, and G. E. Lockard, "A Self-Injection Locked, Q-Switched, Line-Narrowed Ti:Al_2O_3 Laser," IEEE J. of Quant. Electronics, Vol. 24, No. 6, 1021-1028, June, 1988.

11. J. C. Barnes, N. P. Barnes, and G. E. Miller, "Master Oscillator Power Amplifier Performance of Ti:Al_2O_3," IEEE J. of Quant. Electronics, Vol. 24, No. 6, 1029-1037, June 1988.

12. J. C. Barnes, N. P. Barnes, G. E. Lockard, and P. L. Cross, "Amplified Spontaneous Emission Measurement of a Line-Narrowed, Tunable, Ti:Al_2O_3 Amplifier Using Rubidium Absorption," Tunable Solid State Lasers, M. Shand and H. Jenssen, eds., Vol. 7, 9-15, May, 1989.

13. G. A. Rines and P. F. Moulton, "Performance of Gain-switched Ti:Al_2O_3 Unstable-Reasonator Lasers," Submitted for Publication, Optics Lett., October, 1989.

14. E. G. Erickson, "The Flashlamp Pumped Titanium Sapphire Laser," Technical Digest of the Tunable Solid State Laser Conference, May, 1989.

15. B. Treacy, Candela Laser, personal communications.

16. C. H. Mueller III, D. D. Lowenthall, and K. W. Kangas, "2.0 J Ti:Sapphire Laser Oscillator," Optics Lett., Vol. 13, No. 5, 380-382, May 1988.

17. D. D. Lowenthall, "Narrow-Band Blue, Ti:Sapphire Sources," Presented at Lasers '89, December, 1989.

ASSESSMENT OF DYE LASER SOURCES FOR LIDAR APPLICATIONS

F. J. Duarte
Photographic Research Laboratories - Photographic Products Group
Eastman Kodak Company, Rochester, NY 14650-1744

Abstract

Pulsed narrow-linewidth dye lasers are characterized in terms of laser linewidth, wavelength stability, and amplified spontaneous emission. A literature survey of relevant dye laser configurations is given and several approaches to optimize performance are discussed.

Introduction

In this short and preliminary review, we examine some of the emission characteristics of pulsed dye lasers for applications to lidar. The parameters to be incorporated in the discussion include laser linewidth, wavelength stability, and amplified spontaneous emission (ASE). The assessment provided is focused on the value of these fundamental parameters and in approaches known to yield improvements in the value of these variables.

First, we note that a brief literature search indicates that the linewidth values of dye lasers utilized in lidar applications vary from a few GHz to a few hundred MHz.[1-9] Secondly, reported wavelength stability figures vary from a few parts in 10^{-6} to a few parts in 10^{-7} (see Refs. 2 and 8). ASE levels tend to vary from 0.1% to 1% (see Refs. 3, 6 and 7). The literature on remote sensing applications of dye lasers to monitor industrial pollution is reviewed by Klick.[10]

Recently, several authors[6,7,11] have expressed concerns related to ASE levels in available narrow-linewidth dye lasers since even a 1% ASE content can introduce considerable uncertainty in lidar measurements.[6] Other authors have commented in the difficulty encountered in maintaining appropriate low levels of ASE.[7]

In this communication, we discuss the properties of existing narrow-linewidth pulsed dye lasers with an emphasis in emission linewidth characteristics and ASE figures. We also describe methods to reduce the ASE to very low levels.

First, we provide a brief description of an appropriate ASE measurement definition.[12,13] A widely used figure is the ASE percentage defined as the total spectrally integrated broadband ASE energy over the energy contained in the laser narrow linewidth emission. A problem with this definition is that no information on the linewidth or brightness of the laser is provided. A definition that does provide information on these important parameters and that is easily applicable to spectrometric measurements of ASE is the spectral density approach described by Duarte.[12,14] In this definition we take the ratio of the ASE spectral density (ρ_{ASE}) over the laser emission spectral density (ρ_ℓ):[14]

$$\{\rho_{ASE}/\rho_\ell\} = \left\{ (\Delta\Lambda)^{-1} \int_{\Lambda_1}^{\Lambda_2} W(\Lambda)\ d\Lambda \ /\ (\Delta\lambda)^{-1} \int_{\lambda_1}^{\lambda_2} E(\lambda)\ d\lambda \right\}$$

for very small $\Delta\Lambda_n$ segments. In this definition $\Delta\Lambda$ is the full width of the broadband emission and $\Delta\lambda$ is full-width dye laser linewidth. Measurement techniques are discussed in Refs. 12 and 14. It should be noted that for identical energy distribution functions the $\{\rho_{ASE}/\rho_\ell\}$ ratio reduces to a simple ratio of the maximum ASE intensity over maximum laser intensity (I_{ASE}/I_ℓ).

In Table I we list the emission characteristics of several dye laser systems with potential applicability to lidar measurements. Parameters considered are laser linewidth ($\Delta\nu$), wavelength stability ($\delta\lambda/\lambda$), and (I_{ASE}/I_ℓ) ratio.

The laser reported by Bos[15] was an oscillator amplifier system yielding 165 mJ per pulse at a 55% overall conversion efficiency. The efficiency of the telescopic oscillator was 6%. The high pulse repetition frequency (prf) laser reported in Ref. 17 was a hybrid multiple-prism grazing-incidence (HMPGI) dye laser oscillator excited by a copper vapor laser (CVL) operating at a prf in excess of 10 kHz. The linewidth reported here was a long term value that integrated frequency jitter for more than two million laser pulses. The conversion efficiency of the HMPGI oscillator was in the 4-5% range. The use of an intracavity etalon in a multiple-prism Littrow (MPL) oscillator can yield linewidths as low as 60 MHz at a conversion efficiency of 5% for a prf of 6 kHz (see Ref. 16). Flamant et al.[18] reported up to 0.3 J per pulse in a master-oscillator forced-oscillator configuration.

In the experiments reported by Duarte and Conrad[19] the flashlamp-excited MPL and HMPGI oscillators yielded single- and double-longitudinal-mode oscillation at $\Delta\nu \leq 375$ MHz. The oscillators provided 5-10 mJ, and this energy was increased to 600 mJ in a master-oscillator forced-oscillator configuration. The ASE figure quoted here is an upper limit and the ($\delta\lambda/\lambda$) value is a short term figure.[20] The ASE level quoted in Table I corresponds to $<< 0.1\%$ and was measured at the oscillator stage.[20]

Table I. Emission Characteristics of Narrow-Linewidth Dye Lasers

Excitation Source	Oscillator Configuration	Δν (MHz)*	(δλ/λ)	(I_{ASE}/I_ℓ)	Ref. No.
Nd:YAG (2nd H)	Telescopic plus etalon	320	$< 6 \times 10^{-7}$		15
CVL	MPL plus etalon	60		2×10^{-7}	16
CVL	HMPGI	~ 400	$< 7 \times 10^{-7}$	5×10^{-7}	17
Flashlamp	Multiple etalons	345			18
Flashlamp	MPL and HMPGI	< 375	$\sim 10^{-6}$	$<< 10^{-7}$	19

* 1000 MHz = 0.033 cm^{-1}

At this stage a number of strategies to reduce ASE levels at the oscillator stage should be considered.[14] First, all broadband parasitic reflections in the cavity should be eliminated. Thus, one should use dye cells of a trapezoidal or parallelogrammatic geometry. In the case of intracavity telescopes and multiple-prism beam expanders, antireflection coatings should be utilized. The efficient design of intracavity multiple-prism beam expanders in orthogonal configurations is discussed by Duarte[21] and Trebino.[22] Transmission efficiency in nonorthogonal multiple-prism configurations is discussed by Duarte.[23] Also, dye concentrations should be optimized for an optimum $\{\rho_{ASE}/\rho_\ell\}$ ratio. Careful observation of the design constraints listed above have produced $\{\rho_{ASE}/\rho_\ell\} \sim 8 \times 10^{-8}$ for an excimer laser-pumped MPL oscillator yielding $\Delta\nu \approx 714$ MHz. The dye utilized was rhodamine 590 at 5×10^{-4} M (see Ref. 14).

At the amplification stages one should also take advantage of the broadband, high divergence features of ASE. Thus, careful use of spatial and spectral filters[24] can help considerably. Also, since most ASE in oscillators occurs prior to the narrow-linewidth emission, then the use of an appropriate delay in the excitation of the amplifier can contribute to minimize the overall ASE content. Reported delay factors vary from a few to ~ 9 ns.[25,26]

At this stage it has been demonstrated that laser-excited narrow-linewidth dye lasers are capable of delivering single-longitudinal-mode oscillation ,which is extremely stable.[16,17] Also, the ASE levels observed in these oscillators, originally developed for laser isotope separation (LIS), are quite low and should easily meet the requirement for lidar. In the area of flashlamp-pumped narrow-linewidth dye laser oscillators, we have recently demonstrated single- and double-longitudinal-mode oscillation at beam divergences close to the diffraction limit.[19] Also, the ASE levels have been found to be extremely favorable.[20] One question that needs further investigation is the wavelength stability, which has only been measured in the short-term regime.

Given the complex nature of the flashlamp-pumped dye lasers involving flow, mechanical, and thermal variables, this may present some difficulties which may require active stabilization.

Finally, an issue relevant for field deployment is dye lifetime. In this area the development of new, more stable, and highly soluble dyes[27,28] provides good reason for optimism. In addition, the use of effective carbon filter systems demonstrated by Everett and Zollars[29] indicates that the issue of dye lifetime can be neutralized.

The author is grateful to Dr. W. B. Grant (NASA) for useful discussions.

References

1. E. V. Browell, T. D. Wilkerson, and T. J. McIlrath, Appl. Opt. **18**, 3474 (1979).
2. E. V. Browell, A. F. Carter, S. T. Shipley, R J. Allen, C. F. Butler, M. N. Mayo, J. H. Siviter, and W. M. Hall, Appl. Opt. **22**, 522 (1983).
3. M. N. Menchev, M. N. Martin, and Y. H. Meyer, Appl. Opt. **24**, 1957 (1985).
4. B. E. Grossmann, U. N. Singh, N. S. Higdon, L. J. Cotnoir, T. D. Wilkerson, and E. V. Browell, Appl. Opt. **26**, 1617 (1987).
5. A. L. Butakov, V. I. Voronov, G. S. Evtushenko, V. V. Zuev, V. E. Zuev, A. E. Kirilov, A. N. Maltsev, S. Y. Mirza, Y. P. Polunin, V. B. Sukhanov, and V. O. Troitskii, in *Proceedings of the International Conference on Lasers '87*, F. J. Duarte, Ed. (STS Press, McLean, VA, 1988), pp. 729-732.
6. J. Bosenberg, in *Technical Digest, Topical Meeting on Laser and Optical Remote Sensing: Instrumentation and Techniques* (Optical Society of America, Washington, DC, 1987), pp. 22-25.
7. U. N. Singh, R. Mahon, and T. D. Wilkerson, in *Technical Digest, Topical Meeting on Laser and Optical Remote Sensing: Instrumentation and Techniques* (Optical Society of America, Washington, DC, 1987), pp. 258-261.
8. H. Edner, G. W. Faris, A. Sunesson, and S. Svanberg, Appl. Opt. **28**, 921 (1989).
9. H. J. Kolsch, P. Rairoux, J. P. Wolf, and L. Woste, Appl. Opt. **28**, 2052 (1989).
10. D. Klick, in *Dye Laser Principles*, F. J. Duarte and L. W. Hillman, Eds. (Academic Press, New York, 1990), in press.
11. W. B. Grant, Opt. Eng., in press.

12. F. J. Duarte and J. A. Piper, Opt. Commun. **35**, 100 (1980).
13. F. J. Duarte and J. A. Piper, Appl. Opt. **20**, 2113 (1981).
14. F. J. Duarte, in *Proceedings of the International Conference on Lasers '86*, R. W. McMillan, Ed. (STS Press, McLean, VA, 1987), pp. 416-419.
15. F. Bos, Appl. Opt. **20**, 1886 (1981).
16. A. F. Bernhardt and P. Rasmussen, Appl. Phys. B **26**, 141 (1981).
17. F. J. Duarte and J. A. Piper, Appl. Opt. **23**, 1391 (1984).
18. F. H. Flamant, D. Josse, and M. Maillard, Opt. Quantum Electron. **16**, 179 (1984).
19. F. J. Duarte and R. W. Conrad, Appl. Opt. **26**, 2567 (1987).
20. F. J. Duarte, J. J. Ehrlich, W. E. Davenport, and T. D. Taylor, submitted for publication.
21. F. J. Duarte, Opt. Commun. **53**, 259 (1985).
22. R. Trebino, Appl. Opt. **24**, 1130 (1985).
23. F. J. Duarte, Opt. Commun. **71**, 1 (1989).
24. R. Wallenstein and T. W. Hansch, Opt. Commun. **14**, 353 (1975).
25. T. J. McKee, J. L. Lobin, and W. A. Young, Appl. Opt. **21**, 725 (1982).
26. P. Dupre, Appl. Opt. **26**, 860 (1987).
27. T. G. Pavlopoulos, M. Shah, and J. H. Boyer, Opt. Commun. **70**, 425 (1989).
28. C. H. Chen, J. L. Fox, F. J. Duarte, and J. J. Ehrlich, Appl. Opt. **27**, 443 (1988).
29. P. N. Everett and B. G. Zollars, in *Proceedings of the International Conference on Lasers '87*, F. J. Duarte, Ed. (STS Press, McLean, VA, 1988), pp. 291-296.

DISPERSIVE ALEXANDRITE LASERS*

F. J. Duarte
Center for Advanced Studies, The University of New Mexico, Albuquerque, NM 87131

R. W. Conrad
U.S. Army MICOM, AMSMI-RD-DE-UB, Redstone Arsenal, AL 35898-5245

Abstract

In this paper we provide a theoretical evaluation of multiple-prism Littrow (MPL) and hybrid multiple-prism grazing-incidence (HMPGI) alexandrite oscillators. It is found that for long-pulse lasing (~ 400 ns at FWHM) this type of oscillator should easily provide single- and double-longitudinal-mode oscillation at energy levels approaching 10 mJ per pulse. A comparison with MPL and HMPGI narrow-linewidth flashlamp-pumped dye laser oscillators is also provided.

I. Introduction

In this communication, we report on recent developments in our program on tunable narrow-linewidth pulsed lasers. This program is an extension of earlier work on compact narrow-linewidth laser-pumped pulsed dye lasers[1-3] and its main focus has been on long-cavity flashlamp-excited pulsed dye lasers.[4,5] The dispersive approach to be discussed here has also been applied to gas lasers.[6,7]

As result of this long-term study we have built and characterized a number of narrow-linewidth flashlamp-excited pulsed dye lasers. These oscillators have been demonstrated to yield efficient single- and double-longitudinal-mode ($\Delta\nu \leq 375$ MHz) oscillation in a nearly diffraction limited beam[4] and very low amplified spontaneous emission (ASE) levels ($< 10^{-7}$). Recent advances on new more soluble[8] and more stable dyes[9] in the blue-green spectral region provide further reason for optimism for enhancing the applicability of these lasers.

Our interest in narrow-linewidth alexandrite lasers originates in the apparent difficulty to obtain stable dye species in the near infrared. Hence this paper deals with a theoretical evaluation of multiple-prism Littrow (MPL) and hybrid multiple-prism grazing-incidence (HMPGI) oscillators utilizing an alexandrite crystal (Cr^{3+} doped $BeAl_2O_4$) as active medium. A comparison with known output characteristics of narrow-linewidth flashlamp-pumped dye laser oscillators is also provided. As discussed in previous publications,[7] interest in multiple-prism grating arrangements originates in the inherent ease of tuning, relatively high efficiency, the absence of intracavity etalons, and the significant reduction in the intracavity energy flux incident on the grating.

II. Long-Pulse Alexandrite Laser Characteristics

In order to design the narrow-linewidth oscillator it is necessary to measure the basic emission characteristics of the alexandrite laser. The measurements considered here relate to the long-pulse mode since conditions for narrow-linewidth oscillation are more favorable in the long-pulse regime. The alexandrite crystal rod was 115 mm long with a 7 mm diameter. Utilizing a simple resonator with 55% output coupler provides ~ 750 mJ per pulse. The pulse energy output is reduced to ~20 mJ when an intracavity aperture with a ~1 mm diameter is employed. Under these conditions the laser provided a single-transverse- mode (TM_{00}) in a near-Gaussian pulse with 400 ns duration (FWHM).

III. Dispersive Resonators

In order to assess the likely narrow-linewidth characteristics of a dispersive alexandrite laser we assume a 1 mm diameter TM_{00} intracavity beam. The resonators to be considered are those of a MPL and HMPGI configuration.[3] The principal wavelength of design is 760 nm (see Ref. 10).

In addition to the 1 mm intracavity beam the total expansion needed is determined by a 150 mm wide 2400 lines/mm holographic grating utilized in its first order for Littrow operation. For operation in HMPGI configuration the grating is assumed to be given an incidence angle of ~85°.

Previous designs of multiple-prism expanders indicate that the most effective and efficient configuration involves about four stages of magnification. Following Duarte[11,12] we choose a (+, +, +, -) configuration for the MPL oscillator and a (+, +, -) configuration for the HMPGI oscillator. For optimized transmission characteristics the reader should also refer to Trebino.[13] These prismatic expanders are designed to provide zero dispersion at 760 nm.

The dispersive characteristics and the design of the multiple-prism expander is accomplished using the dispersive equation given by[14]

$$\frac{d\phi_{2,r}}{d\lambda} = \left[\prod_{j=1}^{r} k_{1,j} \prod_{j=1}^{r} k_{2,j}\right]^{-1} \sum_{m=1}^{r} (\pm 1)\, \frac{\tan\phi_{2,m}}{n_m}\, \frac{dn_m}{d\lambda} \left[\prod_{j=1}^{m} k_{1,j} \prod_{j=1}^{m} k_{2,j}\right] + \sum_{m=1}^{r} (\pm 1)\, \frac{\tan\phi_{1,m}}{n_m}\, \frac{dn_m}{d\lambda} \left[\prod_{j=m}^{r} k_{1,j} \prod_{j=m}^{r} k_{2,j}\right]^{-1} \qquad (1)$$

where the beam expansion factors are given by $k_{1,m} = (\cos\psi_{1,m}/\cos\phi_{1,m})$ and $k_{2,m} = (\cos\phi_{2,m}/\cos\psi_{2,m})$. Here $\phi_{1,m}$ is the angle of incidence at the mth prism and $\phi_{2,m}$ is the corresponding angle of emergence (see Ref. 11 for further details). The overall beam magnification factor for r prisms is given by

$$M = \prod_{j=1}^{r} k_{1,j} \prod_{j=1}^{r} k_{2,j} \qquad (2)$$

The double-pass prismatic dispersion is given by

$$\left(\frac{d\Phi}{d\lambda}\right)_R = 2\left[\prod_{j=1}^{r} k_{1,j} \prod_{j=1}^{r} k_{2,j}\right]\left(\frac{d\phi_{2,r}}{d\lambda}\right) \qquad (3)$$

and the overall return-pass cavity dispersion including the grating can be expressed as

$$\left(\frac{d\Theta}{d\lambda}\right)_C = M\left(\frac{\partial\theta}{\partial\lambda}\right)_G \pm \left(\frac{d\Phi}{d\lambda}\right)_R \qquad (4)$$

At the central wavelength of design $\phi_{2,1} = \phi_{2,2} = ... = \phi_{2,m} = 0$ and $\psi_{2,1} = \psi_{2,2} = ... = \psi_{2,m} = 0$ so that $k_{2,1} = k_{2,2} = ... = k_{2,j} = 1$ and Eq. (1) reduces to[12]

$$\frac{d\phi_{2,r}}{d\lambda} = \left[\prod_{j=1}^{r} k_{1,j}\right]^{-1} \sum_{m=1}^{r} (\pm 1)\left[\prod_{j=1}^{m} k_{1,j}\right] \tan\psi_{1,m} \frac{dn_m}{d\lambda} \qquad (5)$$

The grating efficiency is either measured directly[2] or is determined using the electromagnetic theory of gratings.[15] Since the prisms provide strong anisotropy which yields p-polarized beams[3] we utilize the usual Fresnel equation to determine losses at the incidence surface at each prism. The reflection losses at the orthogonal exit surface are determined by the characteristics of the antireflection coatings (~ 0.3% reflective). The cumulative single-pass reflection losses at the mth prism are determined using[7]

$$L_m = L_{(m-1)} + (1 - L_{(m-1)})\, l_m \qquad (6)$$

where $L_{(m-1)}$ provides the cumulative losses up to the previous prism and l_m represents the individual losses at the mth prism.

For the MPL oscillator utilizing (+, +, +, -) configuration the additive stage is composed of three identical prisms (made of fused silica with the following incidence angles $\phi_{1,1} = \phi_{1,2} = \phi_{1,3} = 77.1395^o$ and $\psi_{1,1} = \psi_{1,2} = \psi_{1,3} = 42.1045°$ (which is also the common apex angle). This provides $k_{1,1} = k_{1,2} = k_{1,3} = 3.3333$ for fused silica at 760 nm. For the fourth prism $\phi_{1,4} = 61.2996°$ and $\psi_{1,4} = 37.1026°$ so that $k_{1,4} = 1.6607$ and $M \cong 61.51$.

For the HMPGI oscillator employing a prismatic arrangement in the (+, +, -) configuration we have $\phi_{1,1} = \phi_{1,2} = 75.6048^o$ and $\psi_{1,1} = \psi_{1,2} = 41.7702°$ thus providing $k_{1,1} = k_{1,2} = 3$. For m = 3 we have $\phi_{1,3} = 59.9936°$ and $\psi_{1,3} = 36.5525°$ so that $k_{1,3} = 1.6063$ and $M \cong 14.46$.

These expanders at $\lambda = 760$ nm provide zero dispersion, that is $(d\phi_{2,r}/d\lambda) = 0$, so that at this wavelength the spectral characteristics of the cavity are determined by the grating exclusively. For operation away from the design wavelength small beam deviations from prism to prism occur so that the incidence angle at the mth prism is modified by

$$\phi'_{1,m} = \phi_{1,m} \pm \phi_{2,(m-1)} \qquad (7)$$

where $\phi_{1,m}$ is the incidence angle at $(d\phi_{2,r}/d\lambda) = 0$ and $\phi_{2,(m-1)}$ is the deviation from orthogonality at the (m - 1)th prism and the sign (+ or -) depends on the configuration employed. For oscillation away from the design wavelength $(d\phi_{2,r}/d\lambda) \neq 0$ and the prismatic expander now contributes to the overall dispersion of the cavity.

In the case that the last prism is configured in the additive mode then the whole arrangement is additive (that is, +, +, +, +) and the prismatic dispersion is now quite large. In Table I we list the calculated prismatic dispersions for the configurations of interest.

The return-pass grating dispersion is estimated to be 3.5989×10^8 m^{-1} for the Littrow configuration at 760 nm and 7.9619×10^8 m^{-1} for the near-grazing incidence geometry. Assuming a diffraction limited beam ($\Delta\theta \cong 0.48$ m rad. at 760 nm) the calculated dispersive linewidths are also given in Table I .

A further illustration that differentiates the additive from the compensating expanders can be given in terms of the angular deviation experienced a 740 nm. For instance $\phi_{2,4} \cong 0.0000054°$ for the (+, +, +, -) configuration while $\phi_{2,4} \cong 0.034°$ for the (+, +, +, +) configuration. Similar differences are evident for the three prism expander.

IV. Discussion

In this theoretical evaluation we have found that for MPL alexandrite oscillators the estimated double-pass dispersive linewidth is in the 686-804 MHz range. An important assumption in these calculations is that we would obtain a near-diffraction limited beam. Experience with flashlamp-pumped and laser-excited MPL and HMPGI dye laser oscillators[4, 16] lead us to be fairly confident about this assumption.

The estimated length of these resonators is about 30 cm, which yields a cavity mode spacing of about 499 MHz. Given the long- pulse characteristics of the alexandrite laser (400 ns at FWHM) it should be relatively easy to reach double- and single- longitudinal-mode lasing with the MPL oscillator, which provides better efficiencies than the HMPGI alternative. These emission characteristics should be possible at an energy output level of a few mJ per pulse.

At this stage it appears that narrow-linewidth MPL and HMPGI alexandrite oscillators should perform as well as equivalent dye laser oscillators in the visible. The question to be resolved now is related to the overall system attractiveness for operation both in the visible and in the near infrared.

In the visible we know that MPL and HMPGI flashlamp-pumped oscillators can provide efficient double and single-longitudinal-mode oscillation at $\Delta\nu \leq 375$ MHz in a near-diffraction-limited beam at very low ASE levels. We also know that a master-oscillator forced- oscillator configuration can provide high fidelity amplification.[4] Ultimately, a system could be built to provide a few hundred Joules per

Table I. Dispersive and Linewidth Characteristics of MPL and HMPGI Oscillators

Configuration	λ (nm)	~M	$\lvert(d\Phi/d\lambda)_R\rvert$ (m^{-1})	~ Δν (MHz)	T(%)
MPL					
(+, +, +, -)	760	61.51	0.0000	697	53.34
(+, +, +, +)	760	61.51	5.6927×10^6	686	
(+, +, +, -)	740	61.39	1.8026×10^3	804	
(+, +, +, +)	740	61.39	5.6803×10^6	790	
HMPGI					
(+, +, -)	760	14.46	0.0000	315	70.42
(+, +, +)	760	14.46	1.3114×10^6	314	
(+, +, -)	740	14.45	5.3017×10^2	324	
(+, +, +)	740	14.45	1.3113×10^6	323	

pulse in the visible.[17] Extension into the near infrared could be best provided using first-Stokes emission from H_2. Hanna et al.[18] have demonstrated that this process can be quite efficient.

On the other hand there should be no problem in providing a few Joules of narrow-linewidth operation with a single stage of amplification with an alexandrite system. At present, operation of alexandrite lasers at a few hundred Joules per pulse remains to be demonstrated. Frequency up-conversion into the visible can be achieved utilizing Raman-shifting via anti-Stokes radiation.

A present, it appears that dye lasers provide a formidable alternative for the generation of narrow-linewidth tunable radiation in the visible. This is particularly true with the introduction of new long-lived dye molecules.[9] Alexandrite lasers provide a very attractive alternative in the near infrared where dyes tend to suffer efficiency and lifetime limitations. Reaching the near infrared with visible dye lasers in conjunction with Raman conversion is perhaps a more attractive avenue but involves further complexity. A similar disadvantage is experienced in reaching the visible using Raman conversion of the alexandrite laser. Thus, at this stage we consider the alexandrite and the dye laser not as competitive systems but rather as complementary tools.

The authors acknowledge the cooperation and assistance of J. J. Ehrlich, W. D. Mullins, and J. K. Dempsey.

*V *International Tunable Laser Conference*, Lake Baikal, USSR, 1989, Invited Paper.

References

1. F. J. Duarte and J. A. Piper, Opt. Commun. **35**, 100 (1980).
2. F. J. Duarte and J. A. Piper, Appl. Opt. **20**, 2113 (1981).
3. F. J. Duarte and J. A. Piper, Appl. Opt. **23**, 1391 (1984).
4. F. J. Duarte and R. W. Conrad, Appl. Opt. **26**, 2567 (1987).
5. F. J. Duarte, J. J. Ehrlich, S. P. Patterson, S. D. Russell, and J. E. Adams, Appl. Opt. **27**, 843 (1988).
6. F. J. Duarte, Appl. Opt. **24**, 1244 (1985).
7. F. J. Duarte and R. W. Conrad, in *Proceedings of the International Conference on Lasers '85*, C. P. Wang, Ed. (STS Press, McLean, VA, 1986), pp. 145-152.
8. C. H. Chen, J. L. Fox, F. J. Duarte, and J. J. Ehrlich, Appl. Opt. **27**, 443 (1988).
9. T. G. Pavlopoulos, M. Shah, and J. H. Boyer, Opt. Commun. **70**, 425 (1989).
10. J. C. Walling, Laser Focus, **18** (2), 45 (1982).
11. F. J. Duarte and J. A. Piper, Opt. Commun. **43**, 303 (1982).
12. F. J. Duarte, Opt. Commun. **53**, 259 (1985).
13. R. Trebino, Appl. Opt. **24**, 1130 (1985).
14. F. J. Duarte, Opt. Commun. **71**, 1 (1989).
15. D. Maystre, in *Electromagnetic Theory of Gratings*, R. Petit, Ed. (Springer-Verlag, Berlin, 1980) pp. 63-100.
16. F. J. Duarte, Opt. Quantum Electron. **21**, 47 (1989).
17. F. N. Baltakov, B. A. Barikhin, and L. V. Sukhanov, JETP Lett. **19**, 174 (1974).
18. D. C. Hanna, M. T. T. Pacheco, and K. H. Wong, Opt. Commun. **55**, 188 (1985).

RECENT EXPERIMENTS WITH LASER RADAR *

Frederick K. Knight
Lincoln Laboratory
Massachusetts Institute of Technology
244 Wood St.
Lexington, MA 02173

Abstract

This paper introduces the field of laser radar, describes current capabilities of two laser radar systems, and describes two recent experiments using visible laser radar. While current laser radars provide range and velocity resolution comparable to microwave radar, the main advantages of laser radar are better resolution in angle and the promise of range and velocity resolution that exceeds that possible with microwave radar. However, all-weather operation remains an important advantage of microwave radar. The two laser radar systems are a transportable, scanning CO_2 system and a visible, diode-pumped, Nd:YAG system. The two recent experiments are reflective tomography and 3-D imaging using a single laser pulse.

1. Introduction

I will speak today about recent experiments with laser radar. This is not a review talk, but I will say some general things about the field of laser radar. I'll begin by introducing the field of laser radar, comparing it to microwave radar and dividing the field by wavelength: infrared and visible. I will briefly describe the current capabilities of laser radars and then discuss recent experiments with visible laser radars in detail. Finally, I'll make some concluding remarks.

Figure 1 compares the capabilities of long-range microwave and laser radars. The main differences are wavelength and power. First, the wavelength of an infrared or visible laser radar is a factor of 10^3 to 10^5 times shorter than that of microwave radars, theoretically yielding an increase in angular resolution by the same factors for a fixed aperture diameter. However, retaining the same aperture diameter is not generally achievable, so the increase in resolution may be 10^2 to 10^3, resulting in beam widths of 10 to 100 μrad for laser radar. The shorter wavelength also allows more rapid Doppler measurement, as described below. Second, laser radars are generally less powerful than microwave radars, and hence have shorter ranges. However, the smaller beamwidth does produce high target irradiance, so a weaker transmitter is more effective. In addition, the atmosphere absorbs 10 to 20 times more energy in the visible than at 10 GHz. In fact, weather is the most important factor. Rainfall increases the atmospheric loss for laser radars dramatically, and clouds, shall we say, compromise operation effectively. All-weather operation remains an important advantage of microwave radar. The main advantage of the laser radar is resolution in angle—the ability to resolve a target into cells—while extracting range and velocity information comparable to microwave radar.

Table 1 compares various resolution parameters: angle, range and velocity. Microwave radar cannot resolve most targets in angle. This limits the tangential velocity estimate as well. For laser radar, the combination of good range and angular resolution allows a good estimate of tangential velocity. Coupled with good Doppler resolution, the laser radar can obtain a good estimate of the state vector of the target. However, poor weather can ruin this good performance. Since range resolution is proportional to bandwidth and bandwidth is limited to be less than half the carrier frequency, the range resolution for laser radar can theoretically be very high. In practice, optical bandwidth is limited by receiver technology, but 12 GHz has been demonstrated. This and higher bandwidths cannot be achieved

*This work is sponsored by the Department of the Navy.

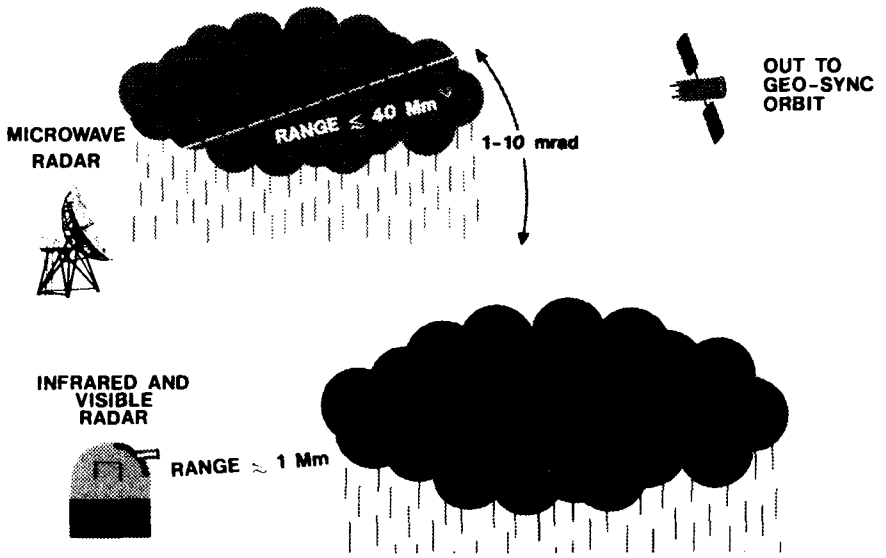


Figure 1: Laser radar provides finer angular resolution than microwave radar but will not penetrate clouds. Microwave radar has longer range.

	Resolution Parameter			
	Position		Velocity	
	Angular	Range	Tangential	Radial
Microwave Radar	Inadequate	Good	Inferior to Ladar	Good
Laser Radar (Ladar)	Good	Good	Good	Good

Table 1: Resolution for two active measurement techniques, adapted from Bachman[1].

with a microwave radar operating below K band (24 GHz). Ultimately, the range resolution of the laser radar could surpass the range resolution possible with a microwave radar. Since velocity resolution is inversely proportional to wavelength and measurement time, a laser radar can achieve a given Doppler resolution more rapidly than a microwave radar. Thus, changes in velocity can be detected more accurately using a laser radar. However, Doppler shifts for rapidly-moving targets can exceed detector bandwidths, so tracking of the center Doppler frequency is often implemented to reduce demands on the detector. Other topics of interest that may be of interest for various applications are:

- *Acquisition of a target in range, angle, and velocity*— For example, the narrow FOV of a laser radar may require a wide-FOV acquisition sensor.
- *Resistance to jamming*—If a sensor has intrinsically narrow beamwidth, it is less sensitive to jamming. The jammer must lie within the narrow FOV.
- *Noise*—The limits of range and velocity resolution may be imposed by transmitter and receiver characteristics, especially if high power is necessary for long-range operation. Jon Grossman will discuss these issues in a talk to be given tomorrow morning in the laser radar session.
- *Safety*—Precautions must be taken to prevent eye exposure, both in the infrared and in the visible.

Laser radar can be applied effectively where the short wavelength and a narrow beam width have an advantage. Specific applications include[2]:

- *Tactical Imaging Systems*
- *Missile Guidance*
- *Aircraft Guidance*
- *Sensors for Clear Air Turbulence and Severe Storms*

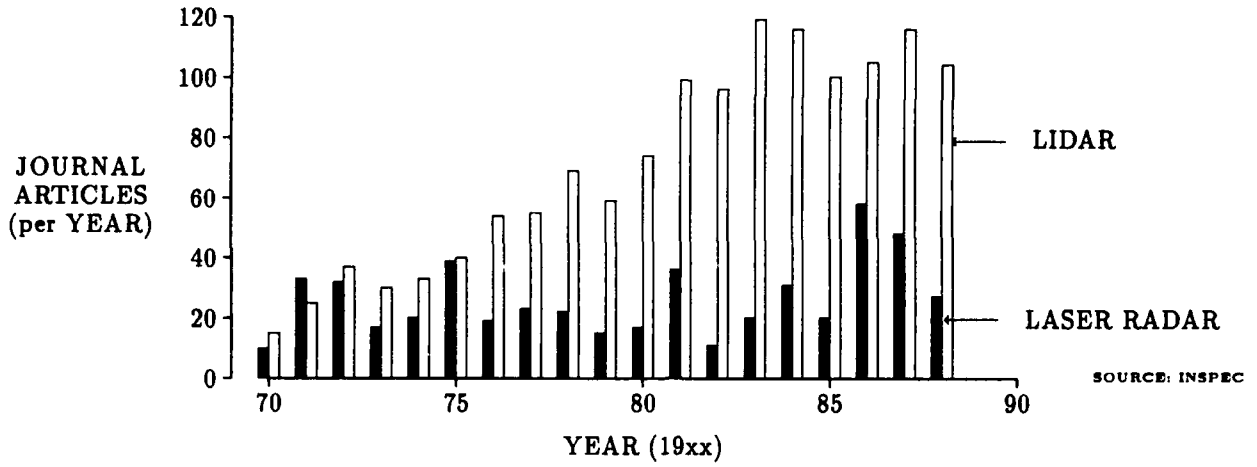


Figure 2: A comparison of open-literature journal articles published in two fields, laser radar and Lidar, that overlap slightly. For comparison, in 1988, there were 787 articles published in the field of robotics.

- *Fire Control and Line-of-Sight Command Systems*
- *Satellite Tracking*
- *Strategic Defense Systems*
- *Remote Sensing of Atmospheric Constituents*

Remote sensing of the atmosphere has been traditionally called LIDAR, for LIght Detection And Ranging, originating from the use of Xenon flash lamps instead of lasers. The distinction between laser radar and LIDAR continues today.

Figure 2 looks at one measure of activity in the fields of laser radar and LIDAR: journal articles published versus time. Note that research in LIDAR produces more articles, and presumably more knowledge, and the advent of high-power laser sources has enabled more research to be conducted, indicated by the significant increase in the late 1970's and 1980's. By contrast, the number of open-literature publications in laser radar has showed little sustained growth with spurts possibly due to increases in government funding. Comparisons using the number of government reports or the number of patents issued versus year show the same trends. I want to make two points. First, researchers still separate the fields: only 5-15 articles per year are grouped in both categories. Second, for comparison, there were 787 journal articles on robotics in 1988, approximately eight times the number of LIDAR articles.

2. Current Laser Radar Capabilities

Now I'll discuss two examples of current laser radars. The first is a multi-dimensional CO_2 laser radar developed by the Opto-Radar Group at Lincoln Laboratory. The second is a visible laser radar using a diode-pumped, frequency-doubled Nd:YAG laser developed by the Quantum Electronics Group at Lincoln Laboratory. I note also that other approaches to visible laser radar, namely heterodyne detection using Nd and dye lasers, are discussed in other papers on Laser Radar at this meeting.

2.1. Infrared: CO_2 Laser Radar

The CO_2 laser radar can operate in a number of modes: a continuous-wave, Doppler-intensity mode, a pulsed, range-intensity mode or a combination ("pulse-tone"). The radar is a scanning system with a continuous-wave power of 10W, output through a 13 cm aperture, which defines the 0.2 mrad instantaneous FOV. The scanned field measures $0.7° \times 0.7°$ or 128×128 resolution elements. The radar's frame rate is 1 Hz. Since the early 1980's, the system has been housed indoors on a test-bed, as shown in the picture, in a truck, and in an airplane. Here I show three examples of the Doppler-intensity mode taken from the test-bed. These figures show how a CO_2 laser radar can be used to obtain simultaneous Doppler and intensity information with high angular resolution. A pulsed CO_2 laser radar can yield simultaneous range and intensity information. A frequency-modulated CO_2 laser radar can yield simultaneous range, Doppler, and intensity information.

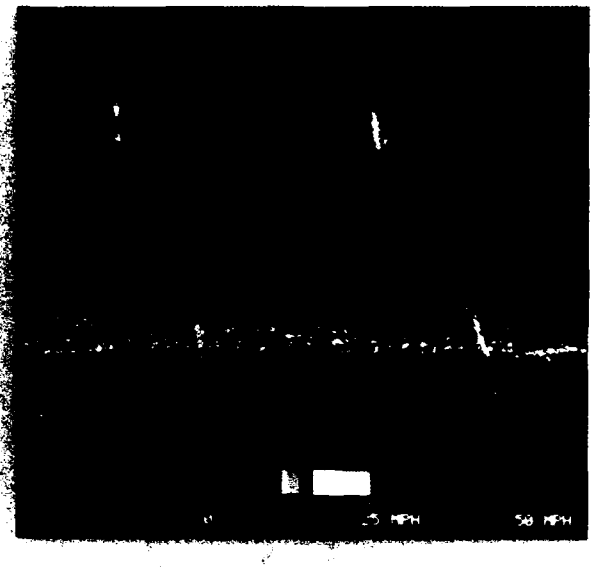


Figure 3 shows a four-frame sequence of a car overtaking a bicyclist. Each frame is scanned in one second. The gray-scale encoding represents velocity relative to the radar. The Doppler resolution is ≈ 0.6 mph, but the gray scale spans larger intervals. The cyclist's legs show up in different shades because their relative velocity differs by a few mph. The car is moving faster. Each gray level is modulated in intensity based on the strength of the signal in the corresponding angular pixel. As the cyclist approaches, there is a slight tilt due to the scanning rate, that is, the cyclist moves sufficiently far in angle during the frame that later scan lines show a shift in angular position.

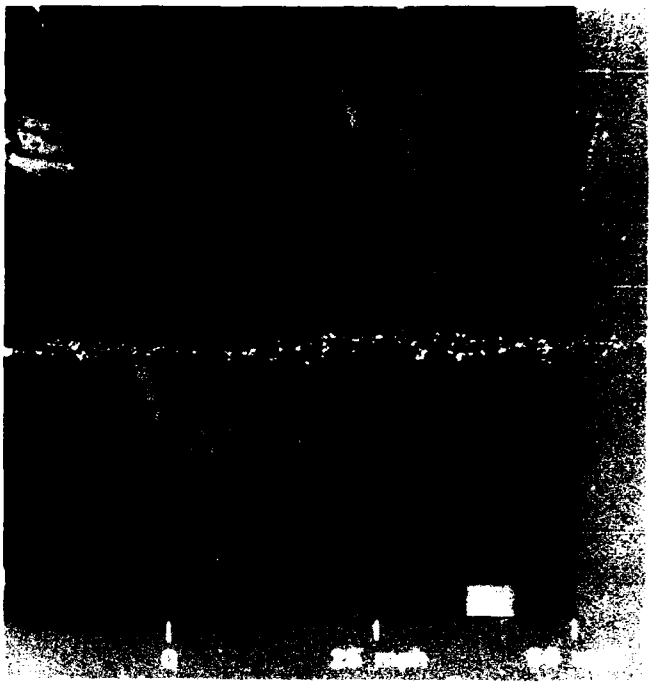


Figure 4 shows a similar four-frame sequence of a car overtaking a truck. The gray-scale encoding is different but again represents velocity. Notice the front surfaces of the two right front tires of the truck are moving faster than the truck. The range to the vehicles is about 0.5 km. The imagery demonstrates operation in poor weather. Do you see why? The truck's windshield wiper is moving and shows up in two Doppler bins. Since the aspect angle is about 20° away from head-on, the wiper's velocity has a component along the line-of-sight.



Figure 5 shows another object, this time at a range of 2 km. The blimp happened to be moving slightly toward the receiver, but its entire front surface fell into one Doppler bin. Hence, the gray-scale encoding shows variation in infrared reflectance over the surface. This is a composite of multiple angular fields-of-view.

2.2. Visible: Nd:YAG Laser Radar

The second example of a laser radar is a visible laser radar utilizing a Nd slab laser pumped by an array of diode lasers. A laser radar based on a solid state laser, like Nd:YAG, can be versatile because of the variety of operating modes and radar waveforms that can be used. The shorter the pulse length the better the range resolution; the higher the pulse repetition frequency the shorter the unambiquous range interval. For wide application, a laser radar should have a wide range of pulse lengths and prf's. A solid state oscillator can be operated from cw to pulsed with pulses as short as 10 ps. Pulse trains are also available inside a longer coherent envelope. In a master oscillator/amplifier configuration, input pulses can be temporally tailored for specific applications. The alternative to short pulses to obtain high range resolution is frequency modulation, either using an external modulator or an intracavity modulator to utilise the large gain bandwidth.

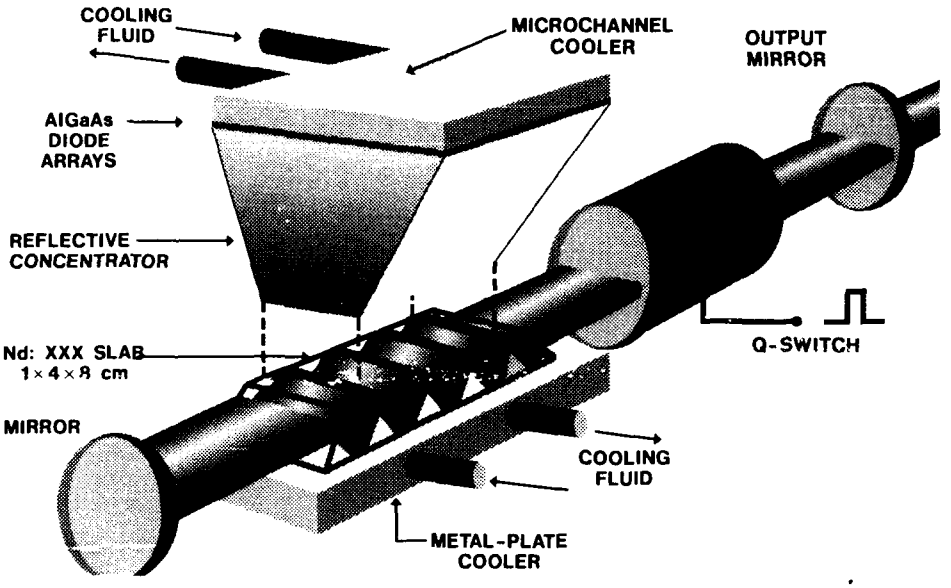


Figure 6: A diagram of a Nd laser transmitter operating at 1.06 μm and 532 nm. The laser is pumped with an array of diode lasers. The output is Q-switched to obtain fast pulses. A version with 10 W output power at 1.06 μm has been built and is operated at 532 nm to allow direct detection with a photomultiplier tube.

Because of a number of properties, the solid state laser of choice is a Nd laser with transition-metal dopants (*e.g.* YAG) suited for the particular application. These properties are:

- *high electrical efficiency*—Pumping with diode lasers, whose output wavelength is optimized for absorption by the solid state laser and whose optical output is coupled efficiently to the solid state laser, can produce efficiencies of 10-20 %. This high efficiency of converting electrical energy into laser light is particularly helpful in spacecraft applications where decreased power and reduced thermal load are important.
- *solid state design*—In contrast to gas lasers, solid state lasers offer increased reliability, low-voltage drivers, and lower volume and weight.
- *operation in the visible and uv*—Using crystals that can be tuned to convert a large fraction of the lasing wavelength into visible or uv light, a system can attain high angular resolution with modest optics and utilize direct-detection receivers, which have high sensitivity (single-photon detection) and high temporal resolution (< 1 ns).

Figure 6 shows a transmitter utilizing diode pumping for high electrical efficiency and a slab laser for high power. AlGaAs diode arrays are fabricated to emit in the region of 800 nm. The light is concentrated to illuminate the Nd:xxx slab, which is operated in a Q-switched mode to obtain short pulses for good range resolution. The output can be doubled to 532 nm to allow direct detection. A 10-W version of this system utilizes a slab laser, which is pumped by five modules, each containing two 1-cm^2 diode arrays.

3. Two Examples in Detail

I'll turn now to two examples discussed in detail. Both use a visible laser: a mode-locked, Nd:YAG laser doubled to 532 nm. The first is reflective tomography. The second is 3-D imaging using a single laser pulse.

3.1. Visible: Reflective Tomography

The well-defined techniques of transmission tomography can be applied to data obtained using a non-penetrating radiation. We call this reflective tomography. In transmission tomography, a penetrating radiation, like X-rays, γ-rays, or positrons, is used to resolve the interior mass of an object. In reflective tomography, a non-penetrating radiation, like microwaves, infrared light, or visible light, is used to resolve the surface features of an object, *i.e.*, to describe its shape. As shown in Fig. 7, both types use a collection of 1-D projections, taken from different aspect

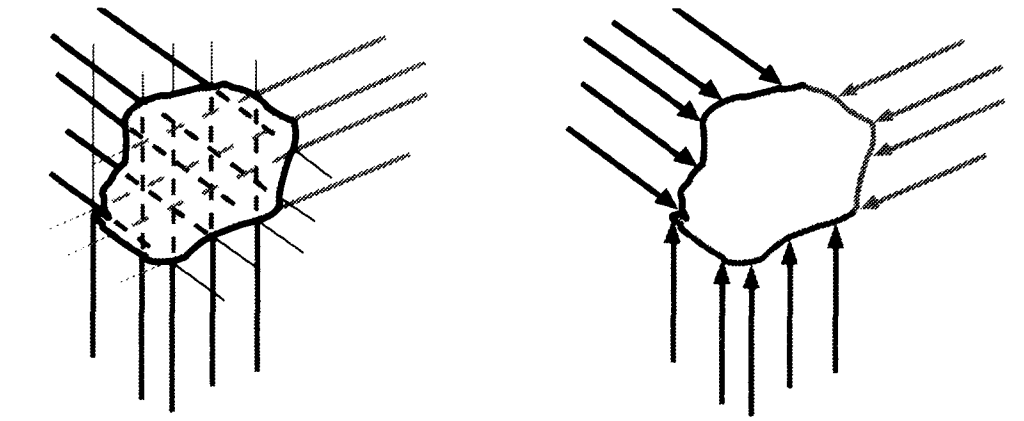


Figure 7: Types of tomography

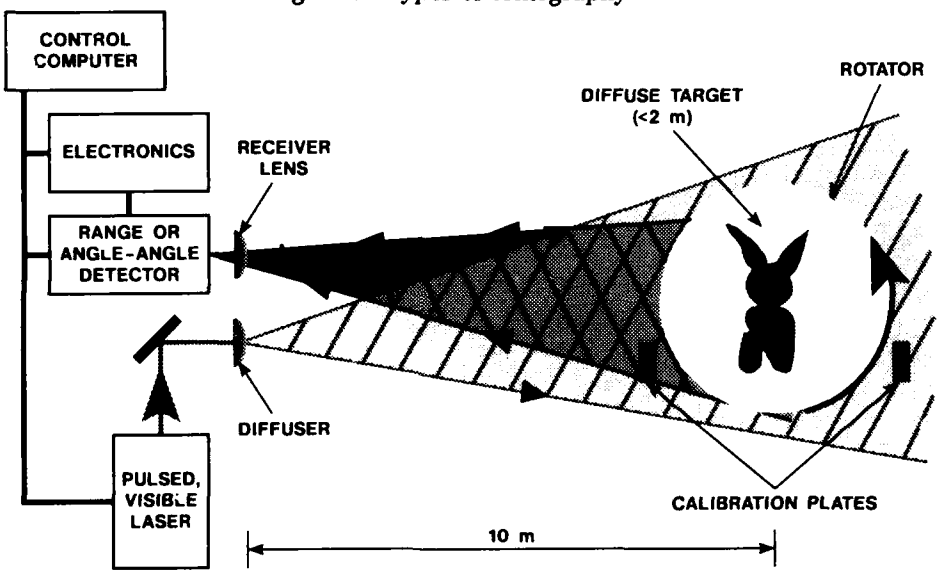


Figure 8: Laboratory for visible laser radar measurements.

angles, and combine them to form a 2-D image or slice of the 3-D object.

Our experiments[3-7] in reflective tomography have been conducted using an indoor range and meter-size targets, as shown in Fig. 8. The short-pulse laser illuminates the target, and the signal is received by a time-resolving detector. The pulse must be short enough to resolve the target into many range cells, and the receiver must be faster than the laser pulse width. The target is on a rotator, allowing data to be acquired at any aspect angle. Taking data at many aspect angles around 360° provides the data for tomography. The end result is a silhouette of the target in the plane of rotation. The target is positioned so that the plane of rotation cuts the target in an interesting way. In other words, the target is cooperative, and we know its placement and orientation, just as in transmission tomography.

The necessary feature of the laser radar is that it resolves the target in range, as shown schematically in Fig. 9. The range resolution must be smaller than the target depth, which means that the laser pulse must be short. A pulse of 250 ps duration yields range resolution of a 4 cm. The received signal is spread in time by the target and depends on the target area, orientation, and reflectance as a function of depth along the line-of-sight.

The signal will vary with the orientation of the target in a predictable way, as shown in Fig. 10. Here a diffuse cone is illuminated with the range-resolving laser radar from many aspect angles. The signals from three angles are

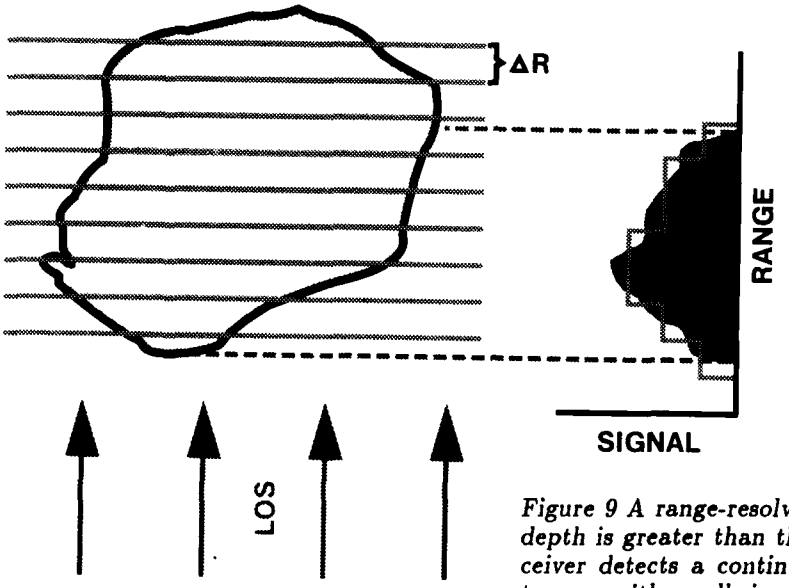


Figure 9 A range-resolving radar views an object whose depth is greater than the range resolution ΔR. The receiver detects a continuous signal and produces a histogram with a cell size ΔR.

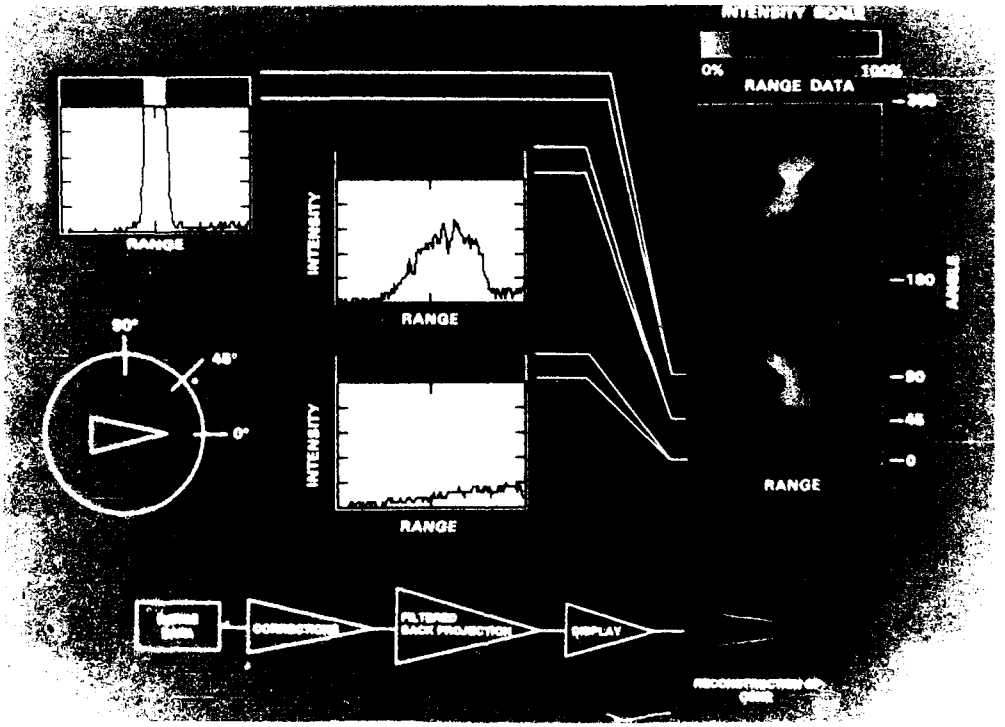


Figure 10: Range tomography of a diffuse cone.

graphed as intensity versus range. At 0° or head-on, the signal increases with depth along the cone axis. At 45° the signal is stronger over a shorter projected depth. At 90° the signal is intense for a short range because the pulse is incident nearly normal to the side of the cone. A convenient way to represent all the data taken over 360° is by gray-scale encoding the intensity into a display whose dimensions are range and angle. These data are the inputs to tomography. We use the standard method of filtered back projection to produce a 2-D projection image of the cone, shown at the lower right.

Figure 11 shows similar data for another target of interest. This shiny toy rabbit, loaned to us by a young scientist, was rotated in the plane of the viewgraph to produce that data in the center panel. From the display one

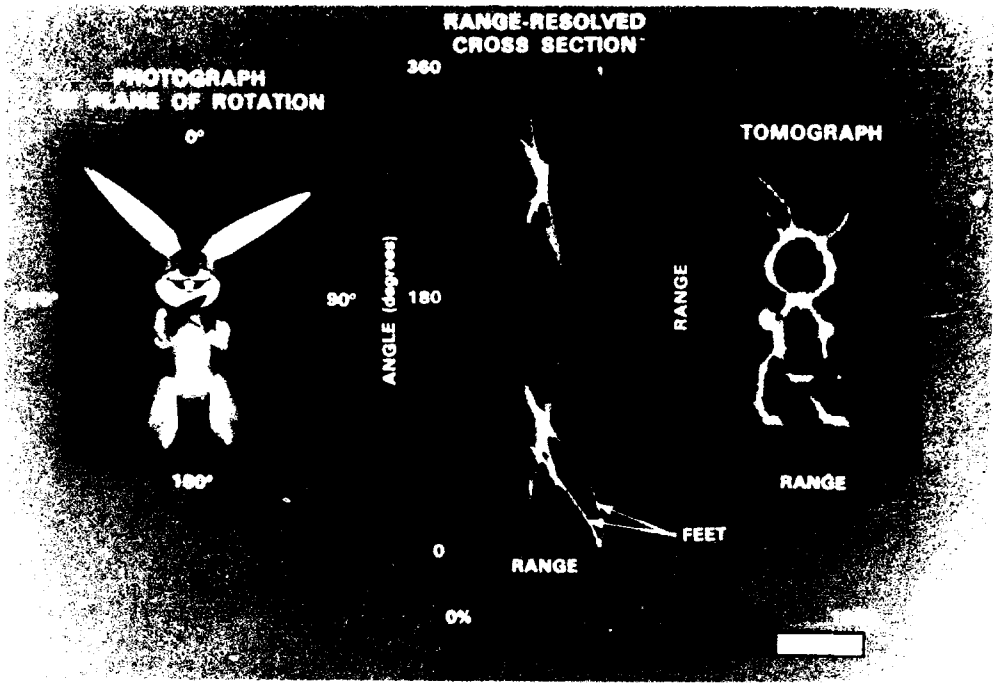


Figure 11: Range tomography of a toy rabbit.

can follow discrete reflectors as their projected range varies sinusoidally with angle. The amplitude of the sine wave is the distance of the reflector from the center of rotation, while the phase represents its polar angle measured with respect to 0°. Notice that a discrete point reflects over a wide range of aspect angles and fades either because the reflected intensity decreases or because it is shadowed by another part of the object. The fact that light is reflected over a wide range of angles makes the tomographic technique produce a realistic image, as shown at the right. The 2-D image has high contrast.

Figure 12 shows 2-D images of three satellite models measured in the laboratory. Each image has high dynamic range because there are large, flat surfaces with bright specular reflections as well as many small, diffuse surfaces. The slide illustrates the use of simple data scaling to enhance portions of the wide dynamic range. The linear scale emphasizes the specular reflections off solar panels. The log scale enhances the diffuse components more than the linear scale did. The sum of linear and log combined with the use of thresholding produce the highest contrast.

In summary, reflective tomography using a range-resolving laser radar produces realistic images. Diffuse reflectance of most targets at visible wavelengths makes this possible. Although I have discussed only tomography using range-resolving laser radar, tomography using angle-angle and Doppler-resolving laser radars has been demonstrated.

3.2. Visible: 3-D Imaging

The final topic is 3-D imaging using the same pulsed, mode-locked Nd:YAG laser but a different receiver[8].

Figure 13 shows the concept. A short laser pulse illuminates a target, the red cone, and a 3-D detector records the signal. At the center we see the short light pulse passing the target. At the bottom we see the images formed in rapid succession by the detector. The two main attributes of the detector are the ability to image and to separate images in time, which corresponds to range.

Figure 14 shows what the detector must do and the important components. The image formed on a focal plane must be sampled, and the signal from each sample must be recorded rapidly. The logical candidate for sampling is fiber optics. The detector with the highest time resolution is a streak camera. The important concept is one of recording lots of information, namely the intensity on the focal plane, rapidly in parallel channels, and then holding it for readout and processing. Let's look at the streak camera first. A single input to the streak camera's photocathode produces an electron beam, which is accelerated and streaked to produce a column of output on a phosphor. The

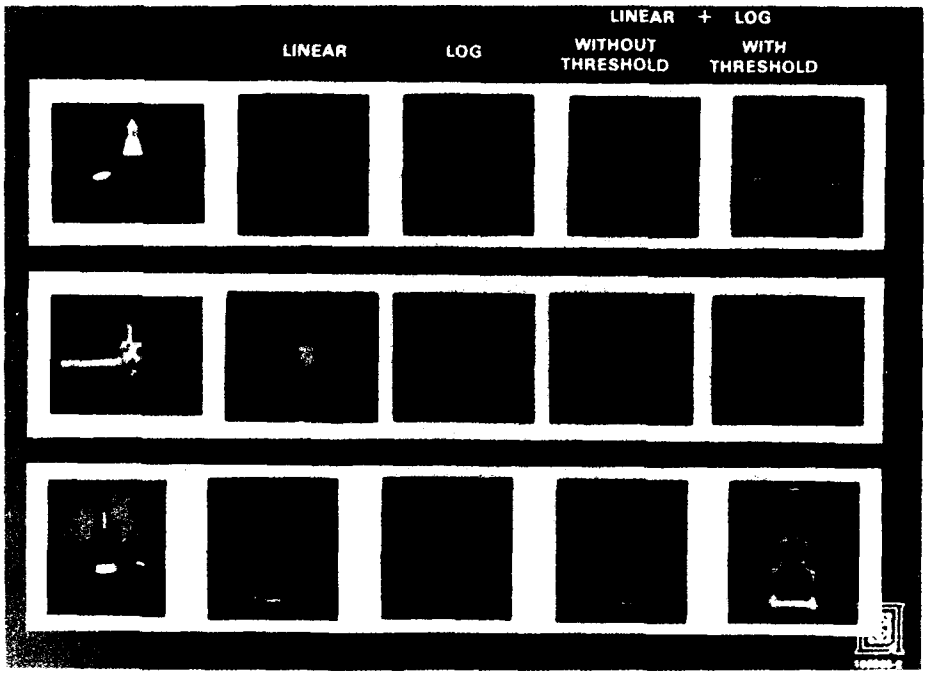


Figure 12: Range tomography of satellite models.

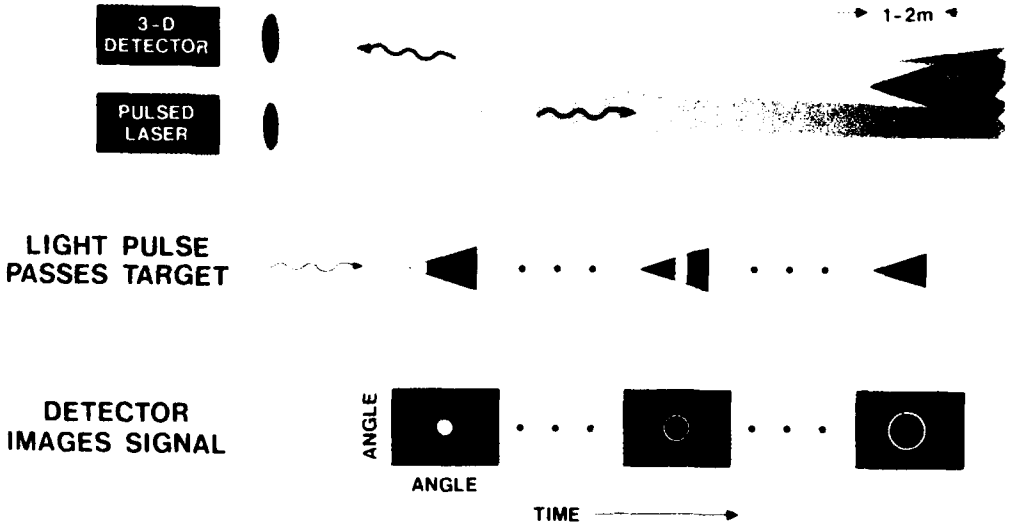


Figure 13: 3-D imaging using a single laser pulse

intensity along the streak is proportional to the intensity in time at the input. Fortunately, streak cameras can record many signals simultaneously, so the input can be a line of inputs. The output is a 2-D array with one dimension time and the other, input position or fiber number.

The only problem is that we want to time-resolve the pixels on a focal plane, so we use a fiber optic image converter to map the square focal plane into a line of fibers, which forms the input to the streak camera. The array is 16 × 16, and, with the addition of some calibration fibers, the line array is 273 fibers long.

Figure 15 shows the 3-D receiver. A lens to control the field-of-view images the signal onto the fiber optic image converter. A relay lens images the line of fibers onto the streak camera photocathode. The streak camera provides the time resolution and holds the data long enough for a readout system to record the signals in digital form. Finally,

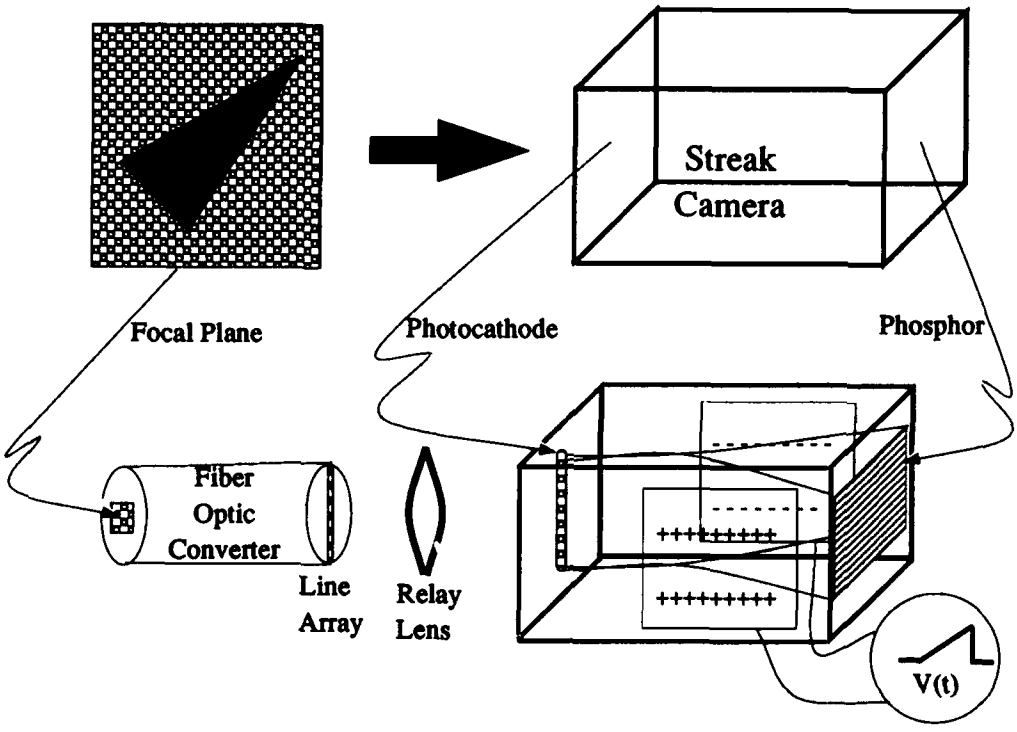


Figure 14: The 3-D imaging components showing the concept (top) and the details (bottom).

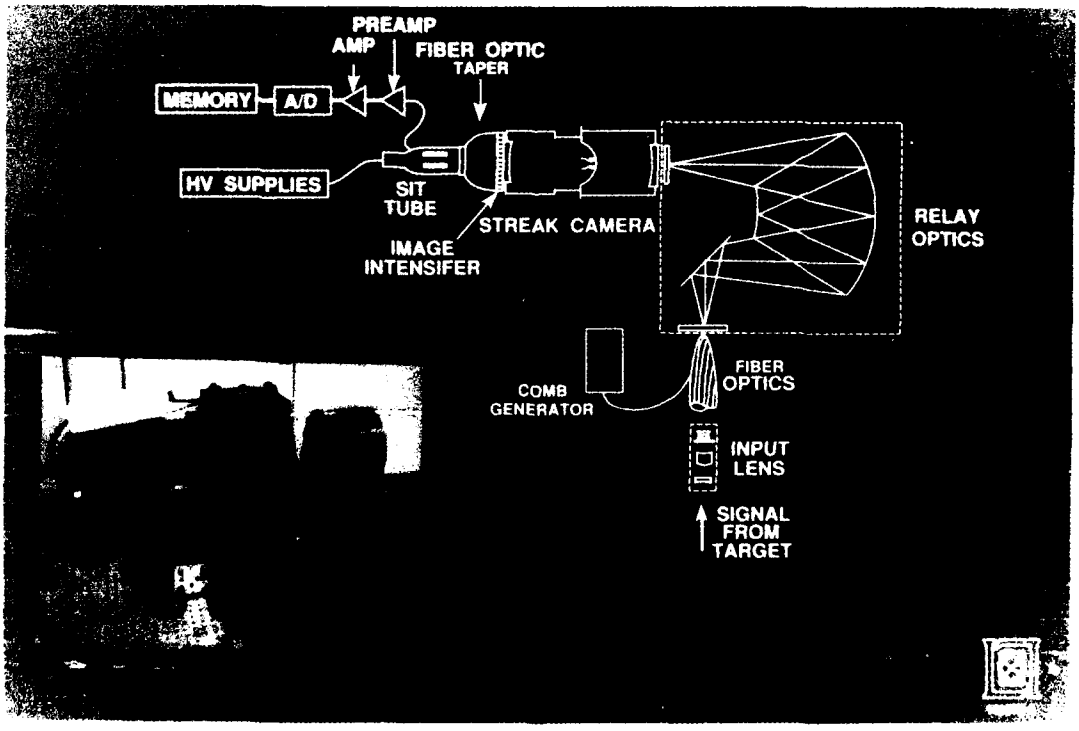


Figure 15: The 3-D imaging system.

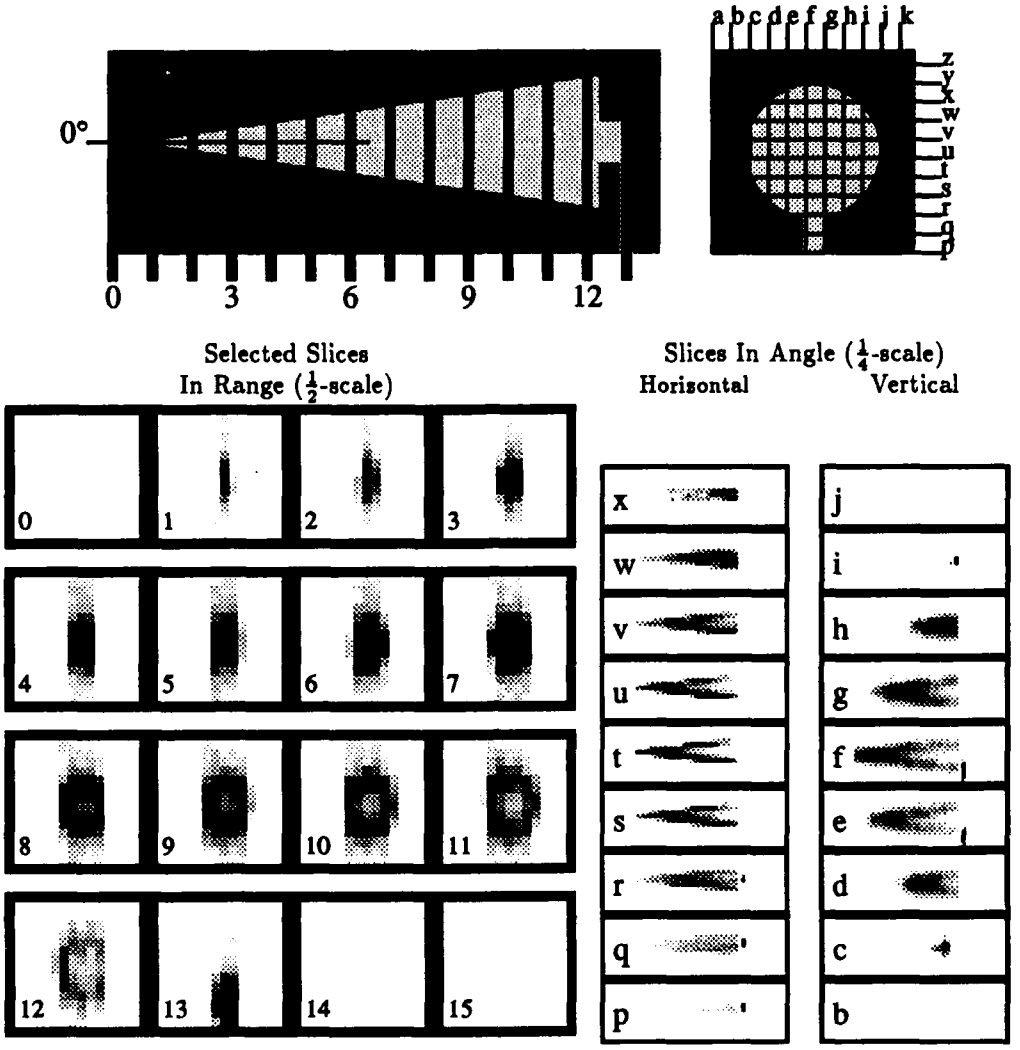


Figure 16: 3-D image of a diffuse cone.

a computer converts the signal back into a 3-D image of the target.

Figure 16 shows the 3-D image of the diffuse cone used in the tomography experiment. The aspect angle is 0° or head-on. It is difficult to project the 3-D image, so the displays are 2-D cuts along three orthogonal axes: the range axis and two angular directions. The side and front views of the cone appear at the top and are overlayed with lines marking the positions of the images shown below. The slices in range are shown at half scale; the others at quarter scale. The target is mounted on a stand at the rear. Look at image 10; it shows the annular image of the surface of the cone sliced in range. Look at image s; it shows a parabola, the result of cutting the cone horizontally. Look at image f; it shows a parabola, the result of cutting the cone vertically, and also the target holder. These 2-D cuts indicate the 3-D nature of the data and show how realistic the data are. The finite resolution in angle limits the detail available from the images. However, the structure of the cone is apparent in the slices—indicating that this laser radar can characterize the shape and orientation of a simple target instantaneously in three dimensions. This laser radar could be used to characterize complex motions of a target by taking a series of 3-D images. It could provide a 3-D image for machine vision. It could remotely sense an object in a lethal environment or at long range.

4. Summary

Laser radars provide good resolution in angle, range, and velocity. Bad weather impares their performance more than in the microwave case, so uses of laser radar exploit the increased angular resolution and higher bandwidths available at infrared and optical frequencies. Infrared and visible lasers, notably CO_2 and Nd:YAG lasers, are good

illuminators, offering varied capabilities. Current systems include tactical and strategic CO_2 systems and short-pulse Nd systems.

5. Acknowledgements

Brian Edwards, Robert Hull, and Antonio Sanchez-Rubio provided figures on current laser radars. I thank William Keicher and David Klick for helpful discussions.

6. References

1. C. G. Bachman, *Laser Radar Systems and Techniques* (Artech House, Dedham, MA, 1979)

2. A. V. Jelalian, W. H. Keene, E. F. Pearson, "Tactical and Atmospheric Coherent Laser Radar Technology," in *Optical and Laser Remote Sensing*, D. H. Killinger and A. Mooradian, eds. (Springer-Verlag, New York, 1983) pp. 341-349

3. J. K. Parker, E. B. Craig, D. I. Klick, F. K. Knight, S. R. Kulkarni, R. M. Marino, J. R. Senning, and B. K. Tussey, "Reflective Tomography: Images from Range-resolved Laser Radar Measurements," *Applied Optics*, **27**, 2642-2643 (1988)

4. F. K. Knight, A. M. Beckman, D. I. Klick, D. P. Ryan-Howard, K. I. Schultz, J. R. Theriault, Jr., B. K. Tussey, "Two-dimensional tomographs using range measurements," *SPIE*, **999**, 269-280 (1988)

5. F. K. Knight, D. I. Klick, D. P. Ryan-Howard, J. R. Theriault, Jr., B. K. Tussey, A. M. Beckman, "Laser radar reflective tomography utilizing a streak camera for precise range resolution," *Applied Optics*, **28**, 2196-2198 (1989)

6. R. M. Marino, R. N. Capes, W. E. Keicher, S. R. Kulkarni, J. K. Parker, L. W. Swezey, J. R. Senning, M. F. Reiley, and E. B. Craig, "Tomographic image reconstruction from laser radar projections," *SPIE*, **999**, 248-268 (1988)

7. F. K. Knight, S. R. Kulkarni, R. M. Marino, and J. K. Parker, "Tomographic Techniques Applied to Laser Radar Reflective Measurements," *Lincoln Laboratory Journal*, **2**, 143-160 (1989)

8. F. K. Knight, D. I. Klick, D. P. Ryan-Howard, J. R. Theriault, Jr., B. K. Tussey, A. M. Beckman, "Three-dimensional Imaging Using a Single Laser Pulse," *SPIE*, **1103**, 174-189 (1989)

MULTIWAVELENGTH CO_2 DIAL SYSTEM DESIGNED FOR QUANTITATIVE CONCENTRATION MEASUREMENT

Joseph Leonelli, Jan van der Laan, Peter Holland, Leland Fletcher,
Russell Warren, and David McPherrin
SRI International, Electro-Optics Systems Laboratory
333 Ravenswood Avenue, Menlo Park, California 94025
and
Jack Comeford
U. S. Army Dugway Proving Ground, Chemical Laboratory Division/MT-C
Dugway, Utah 84022-5000

Abstract

The real-time, quantitative measurement of specific chemical vapor concentrations in the atmosphere is an essential capability for any test and evaluation program designed to study and monitor the propagation and dispersion characteristics of environmentally safe simulants of toxic and potentially hazardous chemical vapor clouds. SRI International has designed and developed a multi-wavelength CO_2 direct-detection differential absorption lidar (DIAL) system capable of providing range-resolved vapor concentration contour plots of a $1000m^2$ grid at 20-m spatial resolution in 10-s intervals. The self-contained, mobile system is modular in design and capable of detection, identification, quantification, and mapping of chemical vapor clouds having significant spectral structure in the 9- to 11-μm region.

The DIAL system will be able to collect and process data in both the column-content and range-resolved modes. The maximum effective range is 5km in the range-resolved mode and 20 km in the column-content mode. The system sensitivity to SF_6 at 1 km is $0.02mg/m^3$.

Background

Quantitative measurements of vapor and aerosol clouds in the atmosphere are essential in any test program that evaluates detection equipment. Current vapor-sampling systems employ several hundreds or thousands of sequentially aspirated bubblers for sample collection over a test grid. The bubbler system yields an integrated (averaged) vapor concentration value or dosage over the sampling interval, but does not permit real-time measurement. The bubbler vapor-sampling system, in addition, is labor-intensive; each bubbler must be (1) filled with a fluid capable of absorbing the vapors, (2) placed at the field sampling station, and (3) retrieved after the test. The contents of each returned sampler must then be analyzed in the chemical laboratory. This system permits neither rapid point coverage of expanding plumes nor immediate test results. Other problems with collected samples include sampling reliability (e.g., slip and desorption of collected material through or from the bubbler) and storage stability of the bubbler contents.

The objective of the differential-absorption lidar (DIAL) program is to develop and implement a real-time quantitative measurement system, using CO_2 laser lidar technology, for Dugway Proving Ground (DPG) field-test sites.[1,2,3]

Dial System Design

Design Goals

The design goals of the direct-detection DIAL system are:[4]

- Self-contained, mobile operation
- Column-content and range-resolved concentration measurement capability
- Detection of any chemical vapor having significant spectral structure in the 9- to 11-μm region
- 0.02 mg/m^3 sensitivity to SF_6 at 1 km
- 360° scan capability
- Near-real-time concentration map of a 1 km x 1 km grid at 10-s intervals, with 20-m resolution.

System Specifications

A partial list of the DIAL transmitter and receiver specifications is given in Table 1.

Table 1

DIAL System Specifications

Subsystem	Specification
Laser Transmitter	
Lasers	Four tunable, pulsed, TEA CO_2 lasers (Questek Model 7240)
Pulsewidth	Clipped with plasma shutters 130 to 160 ns (full-width, half maximum)
Energy	1.2 J in gain-switched spike on 10P(20)
Repetition rate	20 Hz
Wavelength	76 lines in spectral region 9.2 to 10.8 μm
Beam divergence	4 mrad
Tuning	Automatic tuning of one laser, manual tuning of three lasers
Receiver	
Telescope	16-inch Dall-Kirkham, f2.5
Field of view	5 mrad
Detector	HgCdTe photovoltaic, liquid-nitrogen-cooled

Dial System Description

Vehicle and Associated Equipment

The DIAL system is housed in a 31-ft Front Runner van manufactured by Wolverine Western (Figures 1 and 2). A 30 kW Kohler generator mounted in the rear of the van provides electrical power for self-sufficient operation. Hydraulic jacks at each corner of the vehicle provide for leveling and stability. The vehicle includes a custom climate control system capable of temperature control to with 1°C. This dual-purpose system also supplies cooling water for the lidar package. Additional features include a built-in operator workstation and equipment racks, maintenance workspace, and storage. An electrical load center allows the operator to monitor electrical power and to switch easily from commercial to generator power.

Lidar Package

The lidar package includes:

- Four tunable 4-J, 20Hz, TEA CO_2 lasers with power supplies
- Plasma shutter pulse clippers to eliminate the nitrogen tail of the laser pulses and limit the pulse duration to 130 to 160 ns
- Transmit and receive optics
  - 16-inch f2.5 receiver telescope
  - 2-mm, liquid-nitrogen-cooled, HgCdTe photovoltaic detector with an external lens system that results in an effective field of view (FOV) of approximately 5 mrad
- Built-in diagnostics
- Data-acquisition and data-processing subsystems.

A full-hemispherical scanner containing two 24-inch turning mirrors and a bore-sighted video camera are mounted directly to the lidar package. The only components not included as integral parts of the lidar package are the laser cooler, the operator terminal, the display monitors, and the tape drive.

Figure 3 shows the laser access end of the lidar package. All subsystem controls, status indicators, and the data subsystems are located for easy operation and access. The laser grating tuners are accessed through the laser access doors below. Each laser can be removed through these doors for maintenance. The laser electronic control systems are accessible through these doors without removing the lasers. Laser pulse shape, energy, and wavelength are displayed with digital readouts and a digital oscilloscope. The detector is readily accessible from the side of the lidar package.

Figure 4 shows the transmit and receive optics end of the lidar package. The output beams of the four lasers are directed through four plasma shutter pulse clippers and are combined by four beam-stacking mirrors. Most of the beam energy is directed upward to the scanner, but a small fraction is directed to the beam diagnostic and monitoring system. This consists of a spectrum analyzer for measuring the laser wavelength, an X-Y error monitor for monitoring beam pointing, and the transmit power monitor. The received backscatter signal is reflected from a large turning mirror into the telescope, which focuses it onto the liquid-nitrogen-cooled detector. The transmit and receive optics ar protected by airtight enclosures, but are easily accessible for alignment and maintenance.

Data System

Except for the operator terminal, displays, and tape drive, the data-acquisition and data-processsing subsystems are housed within the lidar package. The data-acquisition subsystem receives and records DIAL data during each scan. At the end of each scan, it sends the data to the data-processing subsystem for processing and display. The two subsystems work in parallel for the greatest data throughput. While the data-processing subsystem is processing data from one scan and producing an output plot, the data-acquisition subsystem is recording data from the next scan

The data-acquisition subsystem consists of:

- Computer-automated measurement and control (CAMAC) crate controller
- 40-MHz coherent clock
- Two-channel programmable gain amplifier
- Three 40-MHz, eight-bit digitizers.

One digitizer records the output energy and the waveform of the laser pulse for use in diagnostics and concentration-estimation algorithms. The other two digitizers record the lidar returns from the high-gain and low-gain channels of the programmable amplifier. Using the two eight-bit digitizers with different gains achieves an effective digitization capability of greater than 8 bits of 40 MHz. The digitizers have the capacity to store all the data from one complete scan of the test grid (125 lines of sight with a range of 1,920 m).

The heart of the data-processing subsystem is a Digital Equipment Corporation (DEC) MicroVAX-3200 computer. The DEC MicroVAX computer used for data processing also controls the operation of the entire DIAL system. Near-real-time data are displayed on a 15-inch color graphics monitor and a graphics printer. All data are written to a tape drive for posttest analysis and along-term storage. Detailed posttest analysis can also be performed by the MicroVAX computer.

The DIAL system is able to collect and process data in both the column-content and range-resolved modes. The maximum effective range (5 km is the range-resolved mode and 20 km in the column-content mode for SF_6) depends on the absorbtivity of the simulant and atmospheric conditions. System sensitivity to SF_6 at 1 km is 0.02 mg/m^3.

Pulse Clipper Development

The pulse clippers are used to eliminate the nitrogen tail of the CO_2 laser pulse to (1) produce pulse durations of 130 to 160 ns, and (2) yield range resolution of 20 m. Figure 5a shows a typical TEA CO_2 laser output pulse. Approximately 30% of the energy is contained in the gain-switched spike; the remaining 70% is in the nitrogen tail. The presence of the nitrogen tail degrades the range resolution of the DIAL system to a minimum range-cell size of approximately 100 m. Range resolution can be improved to a range cell size of 20 m by clipping the pulse at the end of the gain-switched spike and thus eliminating the nitrogen tail. A clipped pulse with the required duration of 130 ns is shown in Figure 5b.

Several kinds of pulse clippers were proposed, including saturable absorbers, electro-optical devices, acousto-optical devices, high-speed rotating mirrors inside the laser cavity, and plasma shutters. Each technique was evaluated for use in the DIAL system. All have been used to control the pulse duration of low-energy CO_2 lasers, but only the plasma shutter offers reliable and economic application for the higher-energy laser used in the DIAL system.

The final design of the pulse clippers (Figure 6) incorporates flowing gas, water cooling, adjustable triggering, and a lens adjustment to maintain low-beam divergence when the laser wavelength is changed.

Summary

An infrared differential-absorption lidar (DIAL) system has been developed for use on the Dugway Proving Ground test grids and is currently undergoing final tests and evaluation. The multiwavelength CO_2 direct-detection DIAL system produces range-resolved vapor concentration contour plots of a 1 km x 1 km grid at 20-m spatial resolution in 10-s intervals. The DIAL system can detect, identify, quantify, and map chemical vapor clouds having significant spectral structure in the 9- to 11-μm region.

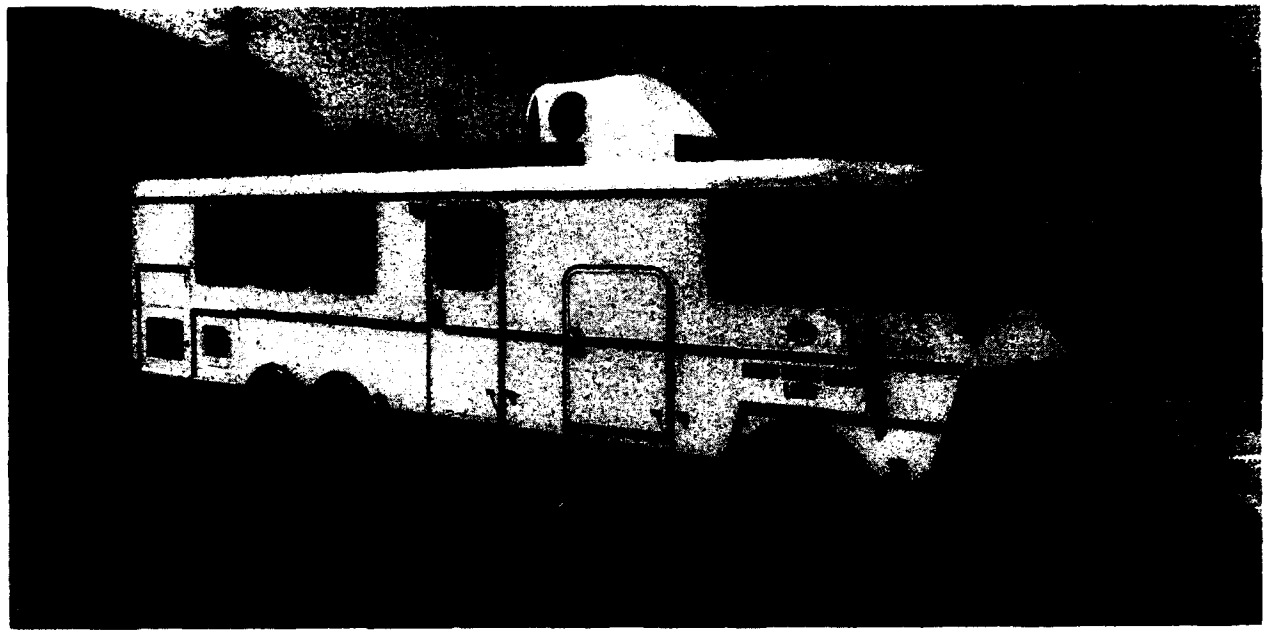
References

[1] D. A. Leonard, T. D. Wilkerson, and R. L. Taylor, "Evaluation of Real-Time Monitoring Systems for Quantitative Measurement of Chemical Agents and Simulants Over a Field Test Grid," DPG Report TR-83-902, University Research Foundation, Greenbelt, Maryland, July 1983.

[2] D. W. Johnson, J. C. Barnard, C. R. Batishko, B. W. Brenden, B. A. Cooke, K. C. Davis, and K. A. Stahl, "Design Review Summary and Technical Response for the PNL Dugway Differential-Absorption Lidar System," DPG Report TR-86-094, Battelle Pacific Northwest Laboratories, Richland, Washington, April 1986.

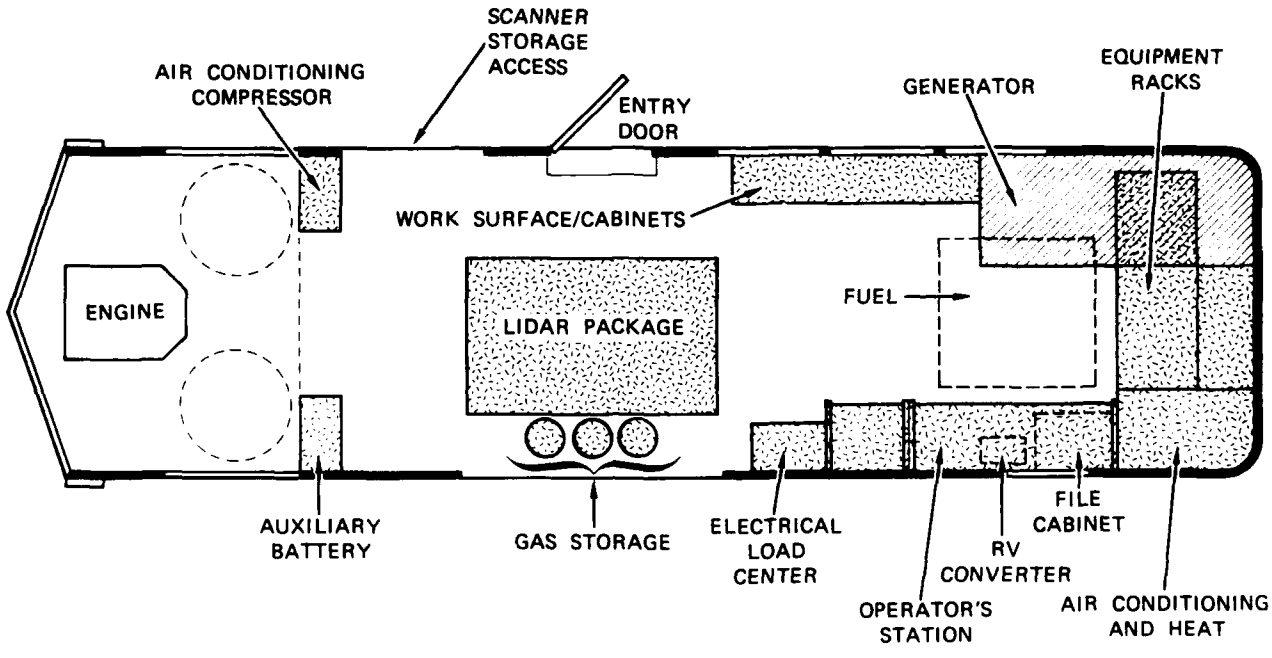
[3] D. W. Johnson, E. W. Kleckner, C. R. Batishko, and G. M. Stokes, "Real-Time Sampler for Chemical Agents: Annual Report for August 1984," Battelle Pacific Northwest Laboratories, Richland, Washington, August 1985.

[4] J. E. Jones, J. E. van der Laan, P. L. Holland, and L. D. Fletcher, "Dugway Proving Ground Lidar System Final Design," Technical Report, Contract DAAD11-82-C-0158, SRI Project 4900, SRI International, Menlo Park, California, February 1987.



p89-016/f1

Figure 1 DIAL SYSTEM VEHICLE



p89-016/f2

Figure 2 FLOOR PLAN OF DIAL SYSTEM VEHICLE

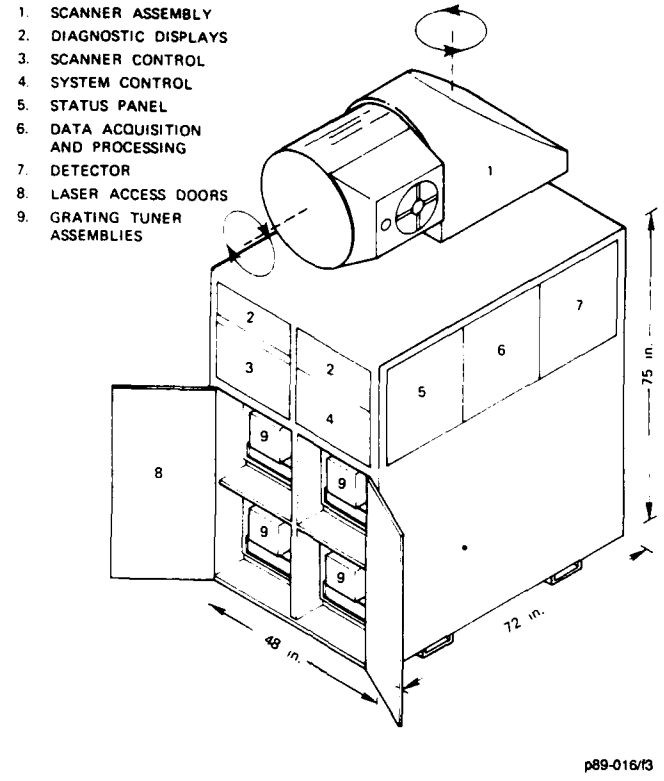


Figure 3 LASER ACCESS END OF LIDAR PACKAGE

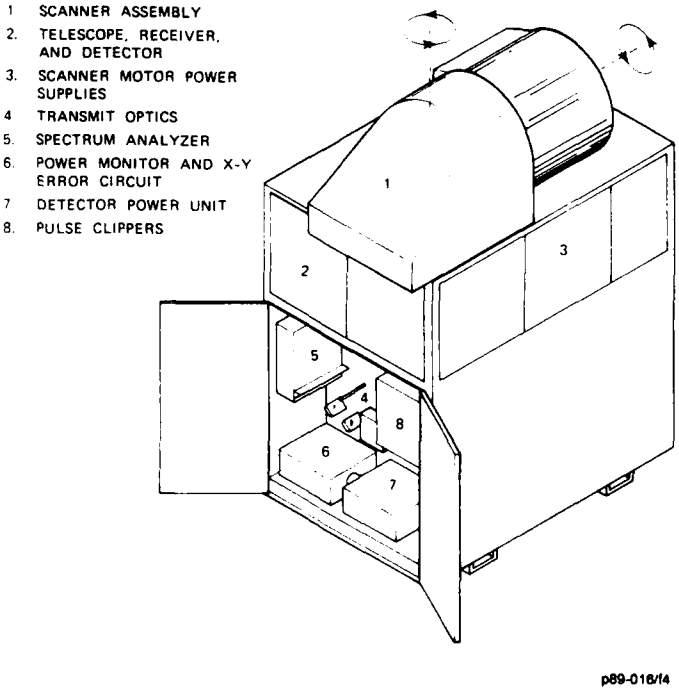


Figure 4 TRANSMIT OPTICS END OF LIDAR PACKAGE

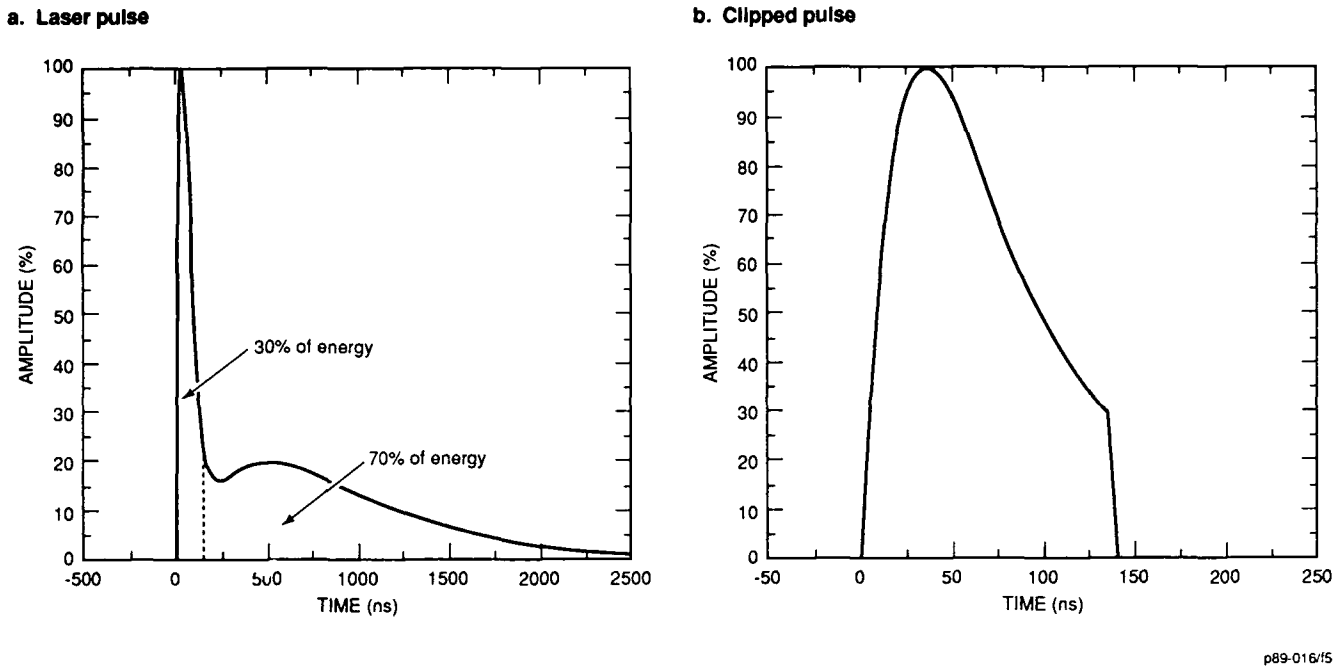


Figure 5 TYPICAL LASER PULSES BEFORE AND AFTER CLIPPING

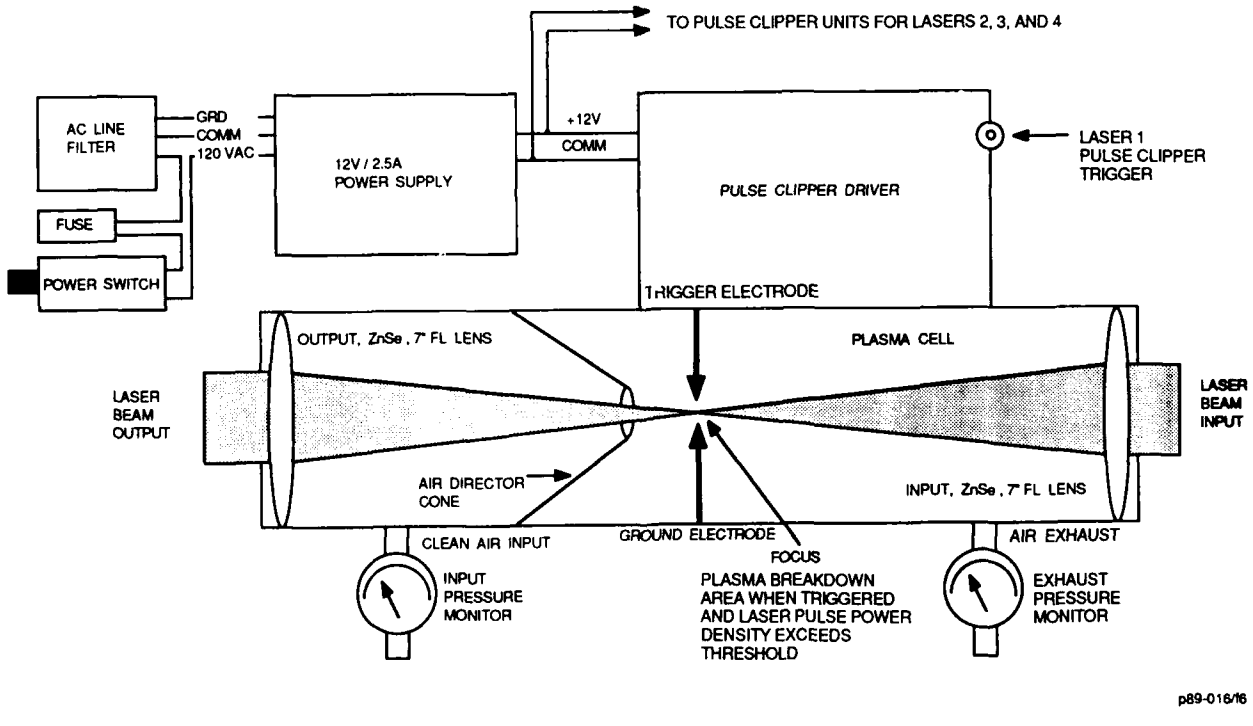


Figure 6 PULSE CLIPPER FUNCTION

ATMOSPHERIC WATER VAPOUR MEASUREMENTS FROM THE ENEA GROUND BASED CO_2 LIDAR STATION

R.Barbini, F.Colao, A.Palucci

ENEA, Dip. TIB, U.S., Fisica Applicata, C.R.E. Frascati,
C.P. 65 - 00044 Frascati, Rome (Italy)

ABSTRACT

Ground based differential absorption measurements of water vapour concentration were obtained with our CO_2 Lidar DIAL apparatus. We describe our initial field measurements as well as examples of range resolved profiles.

INTRODUCTION

Since fall 1988 the first Italian CO_2 Lidar facility has been installed at the ENEA Centre in Frascati, for studies upon the atmospheric dynamics (wind, temperature, pressure) as well as for remote sounding the concentration of atmospheric minor components (ozone, water vapour) or gaseous pollutants. The preliminary activity of the station has been mainly devoted to system alignment and calibration, and for this pourpose DIAL measurements have been performed using atmospheric water vapour as a diffusive target gas.

THE CO_2 LIDAR STATION

The station is based upon a large container and a dome covered tower, supporting the send-receive telescope.[1] The site has been chosen so as to have a view over the south-eastern metropolitan area of Rome.

The LIDAR/DIAL apparatus (Fig. 1) has been installed inside the container and its characteristics are summarized in Table I. The two TEA CO_2 laser transmitters have been

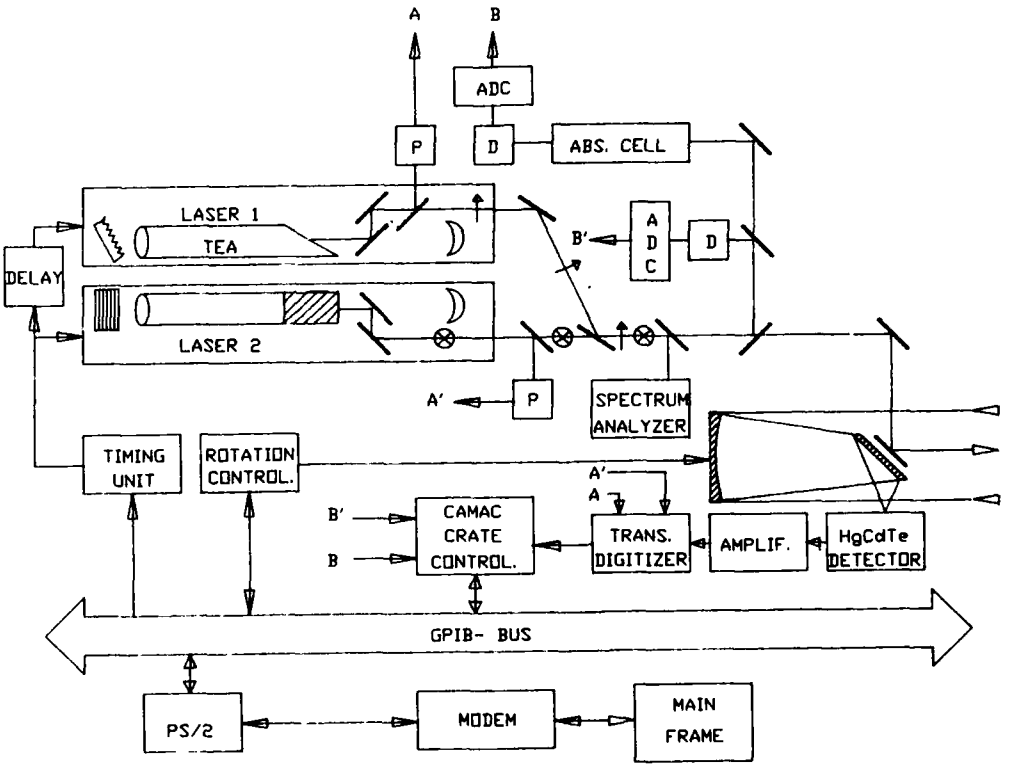


Fig. 1 - Layout of the experimental apparatus

Table I - The LIDAR/DIAL apparatus

TRANSMITTER TWO TEA CO_2 LASER		RECEIVER TELESCOPE	
Emission	λ = 9-12 μm	Type	Newtonian
Pulse energy	E = 1-4 J TEM_{oo}	Mirror diameter	D = 38 cm
Pulse length	t = 80 ns	F-number	F ≠ 3
Beam divergence	θ = 1 mrad (f.a.)	Field of view	FOV = 1 mrad
DETECTOR HgCdTe @ 77 K		TRANSIENT DIGITIZER	
Type	SBRC/PC	DSP Transiac	Mod 2012
Area	A = 1×1 mm^2	Sampling	10 Msamples/s
Detectivity	D* = 2×10^{10} cm $\sqrt{Hz}/W$	Resolution	12 bits
NEP (video)	NEP = 1×10^{-8} W		

designed and assembled in our laboratory using a SFUR (Self Filtering Unstable Resonator) cavity, a configuration which allows for high energy extraction and line by line wavelength selection over a broadband infrared region.[2] System controls and instrument settings are done by a dedicated personal computer, through the general purpose CAMAC interface link. The acquired atmospheric backscattering data are transmitted via modem to a PDP 11/24 micro-computer together with ancillary environmental data for a more detailed analysis.

SIGNAL ANALYSIS AND WATER VAPOUR PROFILES

As a necessary backup to field measurements, absorption coefficients of various pollutant and minor atmospheric gaseous components are being measured in the lab with our lasers, as sketched in Table II.[3] The actual field activity has been started by first testing the apparatus subassemblies and by collecting then atmospheric echoes with direct

Table II - ABSORPTION MEASUREMENTS $(atm\ cm)^{-1}$[300K]

CO_2 laser 001-020 band							CO_2 laser 001-100 band					
line	NH_3	C_2H_4	O_3	line	NH_3	C_2H_4	line	NH_3	C_2H_4	line	NH_3	C_2H_4
P36	0.55		8.3	R06	0.17		P36	8.98		R06	19.41	2.45
P34	4.60		5.6	R08	1.58	0.32	P34	11.36	1.58	R08	13.35	1.09
P32	0.32	0.63	6.8	R10	0.25	0.67	P32	10.05	1.13	R10	0.61	1.55
P30	0.12	0.98	7.4	R12	0.42	0.10	P30	1.27	1.54	R12	0.32	1.74
P28	0.10	0.21	9.3	R14	0.73	0.33	P28	0.50	1.39	R14	4.46	1.47
P26	0.16	0.24	7.0	R16	8.55	0.31	P26	0.53	1.93	R16	0.17	1.09
P24	0.32	0.34	3.9	R18	0.20	0.46	P24	0.24	2.82	R18	0.08	0.72
P22	0.37	0.74	4.5	R20	0.13	0.15	P22	0.16	1.60	R20	0.12	1.20
P20	2.72	0.44	6.4	R22	0.18	0.22	P20	0.22	2.08	R22	0.06	2.53
P18	0.30	0.65	7.9	R24	0.12	0.08	P18	0.31	3.17	R24	0.02	3.78
P16	0.25	0.21	9.3	R26	0.24	0.20	P16	0.64	4.44	R26	0.09	1.99
P14	0.40	0.09	11.9	R28	0.49	0.13	P14	0.93		R28	0.14	2.05
P12	1.04	0.14	11.4	R30	81.00	0.12	P12	0.77	4.50	R30	0.13	0.67
P10	0.50	0.40	7.3	R32	0.86	0.08	P10	0.30	3.24	R32	0.14	1.23
P08	0.11	0.72	11.2	R34	0.32		P08	0.41	1.84	R34	0.25	
P06							P06		2.49			

detection (video). Examples of signals received (actual and range normalized) are displayed in Fig. 2.

An initial analysis shows that data are strongly affected by alignment procedures (superposition of the two laser beams and their overlap with the telescope field of view), as well as by the detector fine positioning in the telescope focal plane. Saturated signals have been collected at transmitted energies in excess of 2 J, showing the need of increasing the available dynamic range of the detector electronic, by compressing signals with logarithmic amplifiers, as shown in Fig. 3.

First field sounding were concerning water vapour whose absolute range resolved concentration has been obtained by the DIAL technique. The laser transmitters have been tuned at the 10R20 (a_{on}=8.8×10^{-4} cm^{-1} atm^{-1}) and 10R18 (a_{off}=1.1×10^{-4} cm^{-1} atm^{-1}) lines, respec-tively. At the end of each sounding cycle, the signals are energy normalized and averaged. Typical resulting waveforms are shown in Fig. 4. The range resolved concentration is extracted by ratioing the Mie backscattered on and off laser returns according to the well known formula:

$$N(R) = \frac{1}{2\,\delta R\,\delta a}\,\ell n\,\frac{P_{off}(R)\,P_{on}(R+\delta R)}{P_{on}(R)\,P_{off}(R+\delta R)}$$

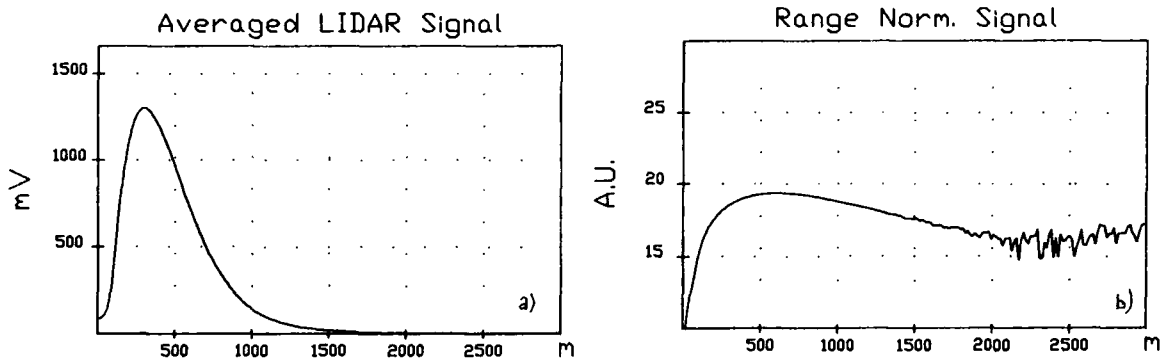


Fig. 2 - Typical LIDAR echo: a) backscattered signal; b) range normalized signal

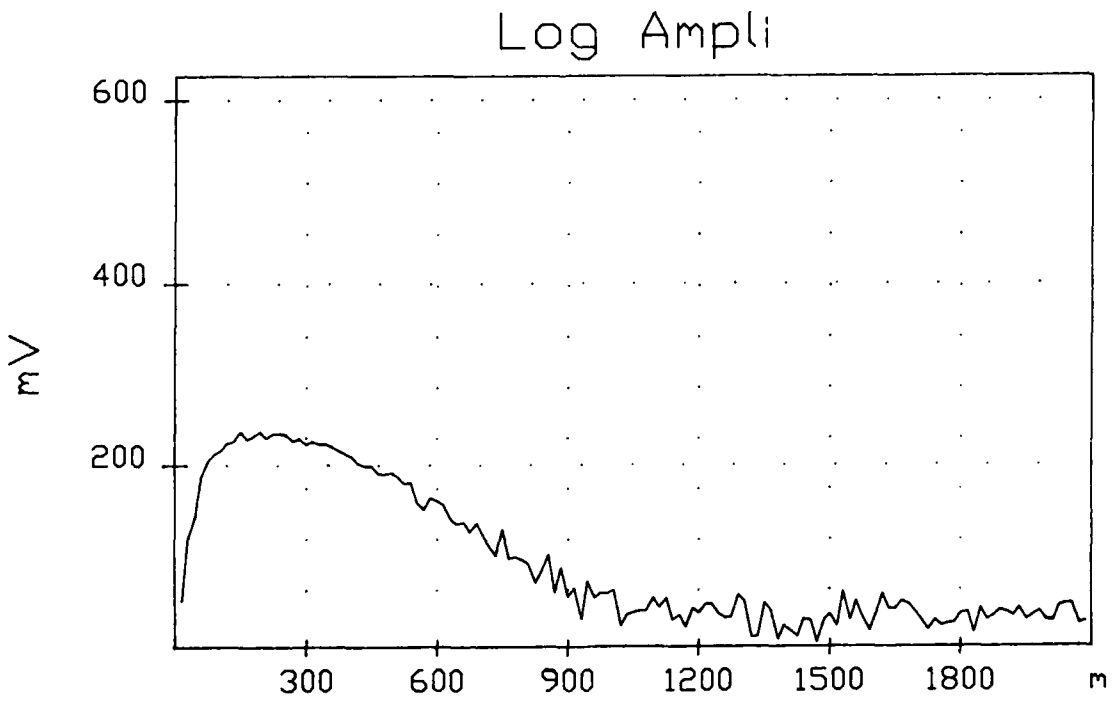


Fig. 3 - LIDAR signal compression obtained with a logarithmic amplifier

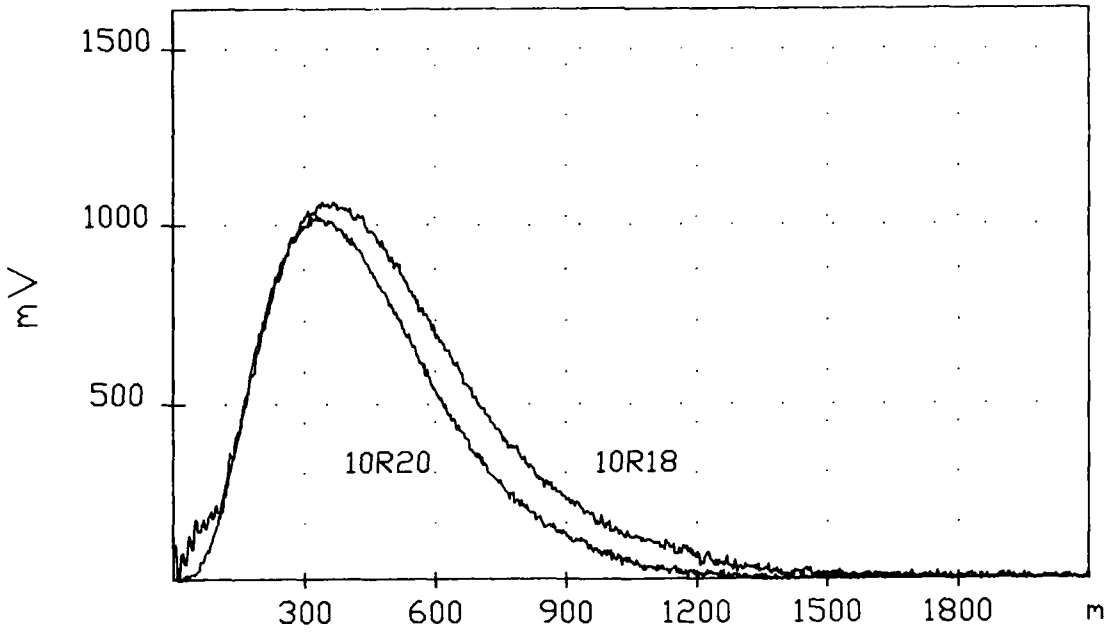


Fig. 4 - Lidar signals for lines 10R20 and 10R18. Time 10:00 am. Oct.20,1989, 0 deg elevation, T= 18 °C; RH= 72%

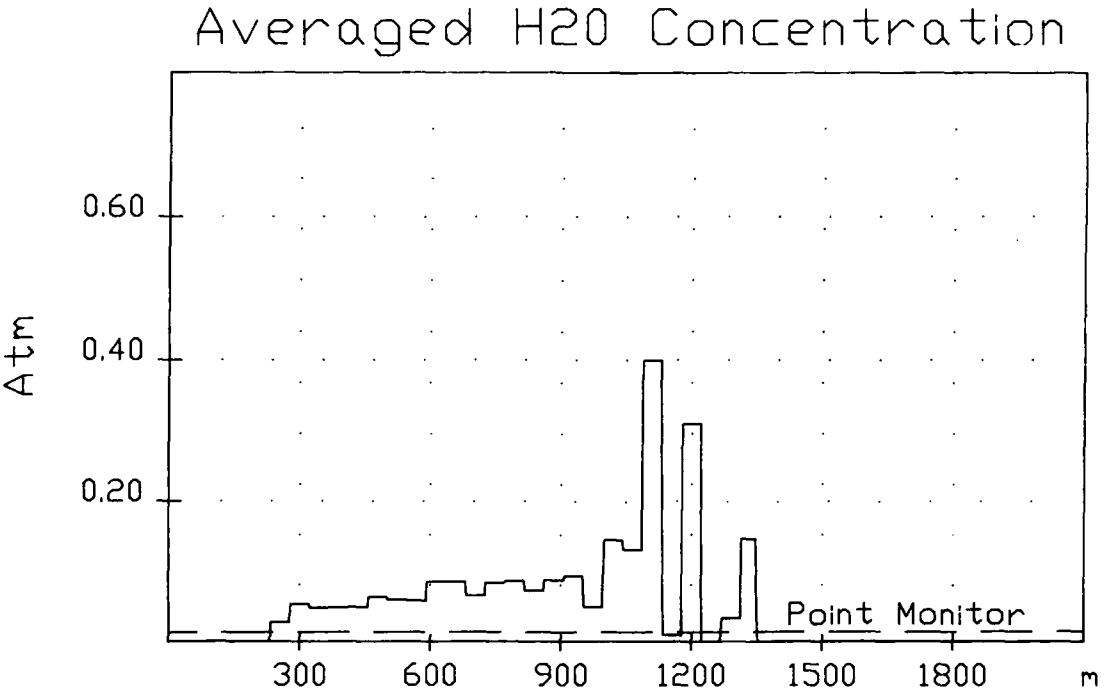


Fig. 5 - Averaged signals and water vapour concentration (atm) for the 10R18 and 10R20 line pair. Time 10:00 am, Oct.24,1989

where $\delta\alpha = \alpha_{on} - \alpha_{off}$ is the differential absorption coefficient ($\delta\alpha = 7.7\times10^{-4}$ cm^{-1} atm^{-1}), δR is the path length cell and P(R) is the power collected by the detector from a range R.

Horizontal water vapour profiles have been obtained under different meteorological conditions (Figs. 5,6). DIAL results are consistent with values measured with a hygrothermograph placed near to the lidar station.

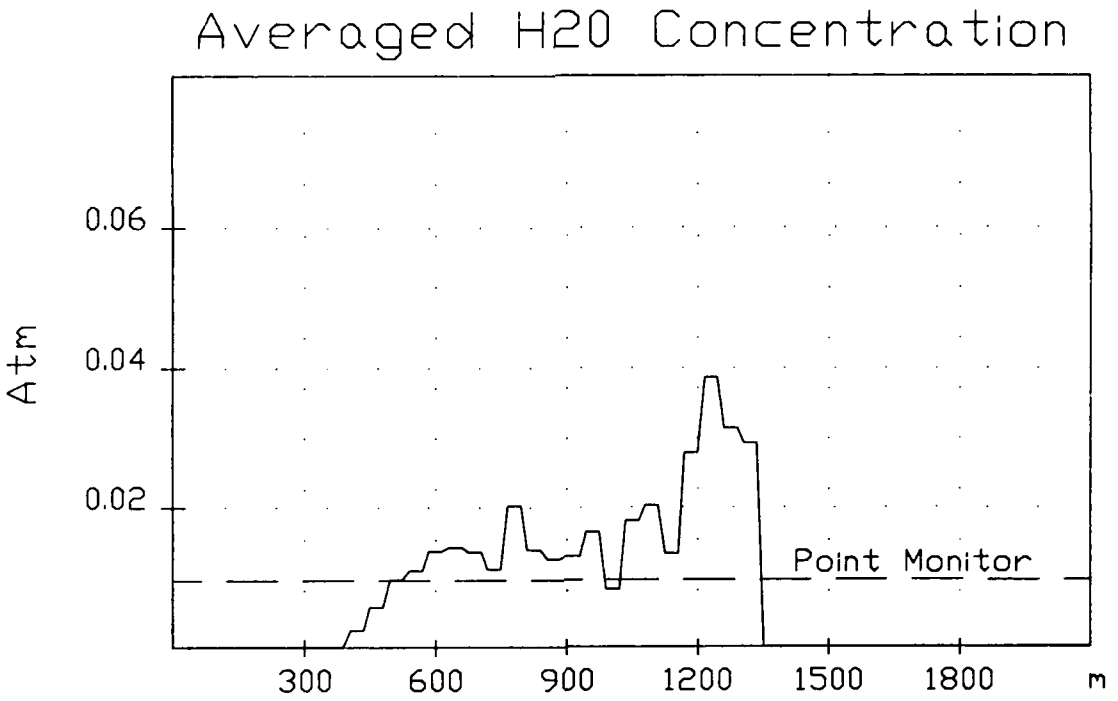


Fig. 6 - Averaged water vapour concentration (atm). Time 11:00 am. Oct.24, 1989, 0 deg elevation, T= 24 °C; RH= 52%

CONCLUSIONS

Preliminary atmospheric echoes have been collected with direct detection (video) at the ENEA ground based station. Atmospheric humidity profiles within a useful range of up to 2 Km have been obtained.

Further improvements in operation and measurements are expected when a VAX main-frame computer will be added, with a graphic station. Thereafter, a systematic measurements campaign on atmospheric constituents, comprising tropospheric ozone profiles will be started.

REFERENCES

1. R.Barbini, F.Colao, A.Palucci, A.Petri, in Proceedings of Int. Laser Radar Conf. (Innichen-San Candido, June 1988), pagg. 228-232

2. R.Barbini, A.Ghigo, M.Giorgi, K.N.Iyer, A.Palucci, S.Ribezzo, Opt. Commun. 60, 239, (1986). Opt. Commun. 68, 41, (1988).

3. R.Barbini et al., "Absorption Coefficient Measurements of Pollutant Gases for CO_2 Lidar Apparatus", ENEA Internal Report RT/TIB/89/33.

R.Barbini et alt.,"Gaseous Absorption measurements with the ENEA CO_2 LIDAR source", Submitted Appl. Opt.

4. R.Barbini, F.Colao, A.Palucci, "Atmospheric Backscattering Measurements from the Ground Based CO_2 Lidar Station", Int. Conf. on Laser and Electo-Optics, April (1989), Baltimora USA.

TECHNIQUES FOR DETERMINATION OF CLOUD PARTICLE SIZE FROM LASER SCATTERING AND LIDAR MEASUREMENTS

Richard Dubinsky

Sky Council
689 Indian Road, 3rd Floor
Toronto, Ontario
Canada M6P 2E1

Telephone: (416) 767-5156

Abstract

Data based on laboratory measurements, theoretical analysis and experimental field results from laser remote sensing using the lidar technique are used to infer a relationship between the optical properties and particle size of clouds. Ice particles are distinguished from water droplets and solid aerosols using lidar depolarization signatures. Each category is identified with a modal diameter representing the suspended particle size distribution. The extinction coefficients (σ) are plotted against the backscatter coefficients (β) for the different types of clouds studied, i.e. composed of ice particles, water droplets and stratospheric aerosols. Linear relationships were found for σ vs β and the ratio [β/σ] or k* (i.e. k* = β/σ corrected for 4π sr) are used to correlate particle size from the results based on theoretical and laboratory studies. This technique is examined for its usefulness in estimating relative modal diameters of cloud particle size distributions for the purpose of monitoring cloud evolution, classifying clouds and to obtain additional information from simple elastic backscattering measurements.

Introduction

Remote sensing of atmospheric properties using lidar techniques such as elastic (Mie) backscattering and DIAL (differential absorption) are now well established and reliable[1-5] . The lidar monitoring of fogs, aerosols, industrial plumes and clouds in the troposphere and stratosphere is becoming routine. Macro - physical properties such as cloud base, height, width, thickness and velocity can be easily and accurately monitored whereas lidar monitoring of microphysical properties including cloud liquid water content, particle size and composition represents a greater challenge. An increase in applications and interest is expected with the introduction of compact and relatively inexpensive lidar designs. Most of these studies generate large data bases and a definite need exists for a means of categorizing the cloud data according to a common parameter such as particle size. There is extensive theoretical information available concerning the optical scattering properties of particulates[6,7] . An important requirement is to simplify the interpretation of light scattering from aerosol particles to obtain an estimate of their size.

The objective of this presentation is to examine the relationship of aerosol particle size and laser scattering at the visible wavelengths near 0.5 um (micrometers) using laboratory and lidar measurements. Relatively few studies have been done in obtaining microphysical properties such as particle size from Mie lidar field measurements of clouds. Theoretical analysis and experimental results have shown that linear and relatively simple relationships exist between laser scattering measurements and microphysical parameters[8-11].

In this study samples of cloud data obtained from consistent lidar operating conditions were catagorized according to cloud height and depolarization characteristics to differentiate between ice and water particles. The data base for this study consisted of continuous lidar cloud measurements made during the third Italian Antarctic expedition by the IROE/CNR (Istituto di Ricerca sulle Onde Elettromagnetiche / Consiglio Nazionale della Ricerche) Lidar group as part of PNRA (Italian National Program for Antarctic Research).

Direct measurements from laboratory data and inversion techniques from the lidar field data were used to obtain cloud optical parameters including extinction coefficients (σ) ; the backscatter coefficient (β) was calculated in terms of the lidar equation. The extinction coefficients were plotted against backscatter for a range of cloud types and an estimation of modal particle size was done by comparison with previous laboratory data for water droplet fogs[8] . In the laboratory studies the laser wavelength of 514 nm is assumed to have approximately similar scattering properties as the IROE/CNR lidar wavelength of 532 nm. The laboratory studies[8] indicated linear relationships between σ and β which can be represented by an effective radius, r_e . Comparison with the field measurements indicated the usefulness of this technique for classifing clouds and monitoring cloud evolution.

Theory

The basis for the lidar elastic backscatter analysis is the lidar equation which applies to a monostatic single wavelength pulsed lidar used in these experiments: i.e.

$$P(R) = P_o (ct/2)K(A/R^2)\beta \exp\int\{-2\sigma(R')dR'\} \qquad (1)$$

where P(R) is the backscattered intensity received at the detector, P_o is the intensity of the laser pulse, of duration t , c is the speed of light, K is a constant, A is the receiver area, R is the range, β is the backscatter coefficient and σ is the extinction coefficient. In actuality, the signal received at the detector, usually a photomultiplier, is the principal source of information. There exists a number of variations for equation (1) which may be derived from first principles[4] .

The inversion technique used in the lidar analysis to obtain the extinction coefficients consisted of an iterative approach developed by the IROE lidar group whereas in the laboratory experiments, the σ and β were directly evaluated. For a single particle the σ/β ratio is dependent on the particle size. However, for a wide size distribution of particles the variations tend to be averaged out and the distribution can be approximated by a simple relationship between σ and β. For the case of non-absorbing clouds, the relationship can be used to obtain an estimate of the size distribution in terms of a modal particle diameter.

The laboratory studies[8] have shown that the relationships between σ and C, the water droplet concentration, are linear and related to the modal or "effective" radius, r_e , representing the droplet size distribution; i.e. $\sigma = 3C/2r_e$. The range of fog size distributions studied in the laboratory indicated a systematic trend where the backscatter to extinction ratio was found to be linear and proportional to the size distribution.

Experimental

Laboratory Measurements

The laboratory measurements were designed to simulate the lidar configuration with simultaneous measurement of extinction and backscattering using well characterized clouds. The experimental design is shown in Figure 1. The arrangement permits numerous concurrent investigations into the optical and microphysical properties of the generated clouds. The laser source was a chopped cw Argon ion laser (514 nm) and photo detectors were located in both the forward and backward directions measuring the scattering intensity. Stable and reproducible clouds covering a range of concentrations and particle sizes were generated. Three different size distributions were generated and characterized by their modal diameters, d_m , representing a wide size range of interest found in atmospheric situations. The three distributions are referred to as S, M and L, related to small, medium and large droplets, respectively. Figure 2 shows the M size distribution generated using an ultrasonic nebulizer (d_m = 5 um), as an example. The L size distribution was generated using liquid shear techniques creating droplet diameters from 1 to 50 um (d_m = 12 um) and the small size distribution was generated using a thermal condensation technique of a water - ethane diol solution (d_m = 0.02 um). Particle sizing was done manually.

Lidar Field Measurements

An extensive series of cloud field measurement data collected using the IROE/CNR Mie scattering lidar located in the Italian base at Terra Nova Bay in Antarctica at (74° 41' 42" S) latitude and (164° 07' 23" E) longitude was made available for this study. The lidar installation is part of the Italian National Program for Antarctic Research (PNRA). The lidar operated daily from December 30, 1987 to February 10, 1988. Measurements consisted of cloud base and cloud height, cloud velocity, video imaging and depolarization.

The lidar system incorporated a NdYAG laser transmitter operating at 532 nm. having an output energy of 350 mJ at a repetition rate of 4 Hz. The laser beam divergence of 0.25 mrd was monitored by a 14 inch Newtonian telescope with a 0.3 mrd field of view. The detector system consisted of two photomultipliers and a CAMAC data acquisition system. The lidar system maintained its alignment throughout the entire mission and all parameters were unchanged during cloud monitoring experiments. Parallel and cross polarization back - scatter return signals were separated with a polarizing cube into two channels. Multiple scattering was considered unimportant and single scattering approximation was assumed due to the use of a very narrow (0.3 mrd.) field of view. Continuous measurement sequences were displayed as averages over one minute intervals. Additional details concerning the IROE/CNR lidar system and data acquisition procedures are described elsewhere[12] .

Results and Discussion

The purpose of this study is to observe trends for the variations of cloud particle sizes from lidar measurements and to establish a straightforward method to monitor changes in cloud particle sizes in order to classify different cloud types for catagorization and simplification of large data bases.

Examples of stable homogeneous cloud types for this investigation were obtained from the IROE/CNR

Antarctic lidar data base. The following catagories of stable cloud types were examined: a high level ice cloud (cirrus), a low level water droplet cloud (stratus) and stratospheric aerosol. The cirrus ice crystal and stratus type clouds were identified from relative depolarization, D, measurements. The relative depolarization is defined as ($D = S_r / S_p$) where S_r is the cross (perpendicular) component of the return signal and S_p is the parallel component. Clouds having a high depolarization ($D > 0.1$) were considered to be composed of ice crystals having relatively large diameters. Low depolarization values ($D < 0.1$) indicate the presence of water droplets. The particle size distributions of the water droplet clouds generally have modal diameters of approximately 10 microns. The final catagory is background stratospheric aerosol where scattering occurs from aerosols and condensation nucleii having sub-micron modal diameters.

Since a wide size distribution has the tendency to average out the scattering properties of single particles, the distribution can be represented by a modal particle diameter (d_m). The relationship between the three different water droplet size distributions with σ and β from laboratory studies[8] is shown in Figures 3 a, b, c. These results were used in the present study as an approximation for estimating the particle size and correlating this to the trends observed.

In the Antarctic lidar experiments, linear relationships were observed for plots of extinction coefficient vs backscatter coefficient for the stable clouds studied. The slopes of the plots will be indicative of differing scattering efficiencies of the particles if all lidar parameters are held constant. Figures 4 and 5 are a comparison between two sets of lidar data observed during the Antarctic mission. Figure 4 corresponds to a low level water droplet cloud (stratus) at a height of approximately 1 km. on January 13, 1988 observed for one hour from 11:56 local time and averaged over one minute intervals. Figure 5 represents a high ice crystal cloud (cirrus) at approximately 7 km. recorded on January 8, 1988 from 9:40 to 10:40 local time and averaged over 1 minute intervals similar to Figure 4. Parts (a), (b), and (c) of Figures 4 and 5 respectively represent the, (a) range corrected signal vs height vs time, (b) the depolarization with time and (c) the extinction vs backscatter coefficients.

Part (a) of Figures 4 and 5 show three dimensional representations of the range corrected signal vs height (Range) in kilometers for a period of one hour. The range corrected signals in the two figures are on different scales as indicated on the z-axis. Figure 4 represents a dense cloud characteristic of stratus whereas Figure 5 corresponds to a more tenuous cloud at about 7 km. indicative of cirrus. The stratus and cirrus nature of these two clouds are further supported in Figure 4(b) and 5(b) which shows the depolarization observed. Figure 4(b) indicates very low deploarization (less than 4%) indicating that this cloud is composed of mainly water droplets typical of stratus. Figure 5(b) shows much larger depolarization values from approximately 5% to 50% indicating the presence of ice crystals typically found in cirrus clouds.

The extinction to backscatter ratio is plotted in Figure 4(c) and 5(c). Both of these cases exhibit a linear behaviour extending from low to high relative cloud densities. In Figure 4(c) a straight line with a slope $\sigma/\beta = 23$ demonstrates a consistent relationship between extinction and backscatter representing a stable size distribution of particulates. Comparing the slope with the results of reference 8, a modal droplet diameter of approximately 5 microns can be inferred. Figure 5(c) shows a greater scatter observed in the σ vs β plot with a smaller value for the slope ($\sigma/\beta = 18$) in agreement with the trend observed in Ref. 8, i.e. larger particles show a diminished scattering efficiency and a reduced slope. For the case of Figure 5(c) the modal diameter of the scattering ice particles can approximately be estimated to be larger than 12 microns. Additional experimental data, particularly using ice crystals, would be helpful in obtaining a better estimate of the modal diameter for the cirrus type cloud. Actual insitu samples from the clouds would also be useful in this respect.

The main point of this comparison is to indicate that an estimate of the modal particle size can be obtained from the lidar measurements. The same trend is observed in the lidar data as in the laboratory experiments where smaller particles showed higher σ/β ratios than the larger particles. For this case, the high cloud in Figure 5, composed of ice crystals is expected to have a larger modal diameter than the lower water droplet cloud shown in Figure 4; this was the case observed. With additional experimentation and cloud sampling for the determination for the precise relationship between modal particle size and of extinction to backscatter ratio, this technique could be used on a routine basis.

For the case of stratospheric aerosol measurements, the signal levels were very low and convergence of the inversion iteration was not attained. Subsequent correspondence with the IROE group indicated a σ/β ratio of approximately 38 to 45 which supports the trends observed. An improvement in the correlation was definitely observed with increasing σ/β ratios indicating increased scattering efficiency resulting from the presence of very small (sub-micron) particles.

It would be valuable to obtain data from laboratory experimental conditions using different known size distributions at the usual lidar wavelengths for the confirmation of theoretical calculations and for comparison to field lidar data.

Conclusion

This paper demonstrates a straightforward technique using lidar data to estimate the relative particle size distribution in clouds by the examination of the corresponding extinction (σ) and backscatter (β) coefficient values for different cloud types. A summary of the results is shown in Table 1.

Table 1 Summary of Results

σ/β (sr)	β/σ (sr^{-1})	k* (β/σ corrrected for 4π sr)	Relative Size (microns)	
50	.020	.25	.02	Small drops
38 - 45	.026 - .022	.327 - .276	.10	Stratospheric Aerosol
23.3	.043	.54	5	Medium IROE Stratus @ 1km
20	.050	.63	12	Large drops
17.8	.056	.70	> 12	IROE Cirrus at 7 km.

For cases where insitu cloud particle size measurements are made or additional laboratory results are available, this technique can be used to establish a calibration for cloud particle size with respect to the lidar signals observed when all lidar parameters are held constant. As seen from these results a linear relationship exists between σ and β for the atmospheric clouds observed. Comparison of these results with actual insitu cloud particle measurements will provide information about cloud dynamics and evolution. This technique does not take into consideration, multi modal size distributions, very dense clouds or variable conditions. The single scatter approximation is assumed since beam replenishment from multiple scattering in laboratory studies did not occur even at high densities of up to 3 gm/m^3 . The effects of ice crystals were not studied in the laboratory.

Since the slope is related to particle size, additional information can be easily obtained for cloud growth and evolution by observing the change in σ/β with time. Further work with insitu measurements is required to establish this procedure for the characterization of cloud types. The relationship between σ and β can be used for very large data bases to help in the organization and characterization of aerosols. Once this technique is established, a specific lidar system can be used to obtain additional and more precise information for the remotely sensed cloud.

Acknowledgements

Sincere appreciation is extended to A. Carswell and S. Pal at York University for valuable discussions and advice concerning the laboratory measurements and to the National Sciences and Engineering Research Council of Canada for financial support. Special thanks to L. Stefanutti and the IROE lidar group for access to their data and support as a visiting scientist in Florence. Appreciation is also extended for the expert data analysis and lidar engineering to M. Morandi, M. DelGuasta, V.M. Sacco, F. Castagnoli, V. Venturi, L. Zuccagnoli and E. Palchetti of the IROE/CNR lidar group. Additional acknowledgement to PNRA (Italian National Program for Antarctic Research) for financial support of the IROE/CNR lidar program.

References

1. A. I. Carswell, Can. J. Phys. 61, 378 (1983)
2. T. Kobayashi, Rem.Sens.Rev. 3,1 (1987)
3. V. Zuev, Laser Beams in the Atmosphere (Plenum, New York, 1982)
4. R.M. Measures, Laser Remote Sensing, Fundamentals and Applications (John Wiley & Sons, Toronto, 1984)
5. R. Dubinsky, Lasers & Optronics 7, 92 (1988) and 8, 45 (1989)
6. D. Deirmendjian, Electromagnetic Scattering on Spherical Polydispersions (Amer. Elsevier, New York 1969)
7. C. Bohren and D. Huffman, Absorption and Scattering of Light by Small Particles (Wiley Intersc. N.Y.'83)
8. R. Dubinsky, A.I. Carswell and S.R. Pal, App. Opt. 24,1614 (1985)
9. E.E. Uthe, App. Opt. 21, 454 (1982)
10. C.M.R. Platt, N.L.Abshire and G.T.McNice, J. App. Met. 17, 1220 (1978)
11. R.G. Pinnick, S.G.Jennings, P.Chylek & H.J.Auvermann, J.Atmos.Sci. 36,1577 (1979)
12. L. Stefanutti, M. Morandi, F. Castagnoli, V.M. Sacco, V. Venturi, L. Zuccagnoli and M. Del Guasta, presented at the 14th International Laser Radar Conference at Innichen - San Candido, Italy (1988), papers in Conference Abstracts, pp.32,296,318,429

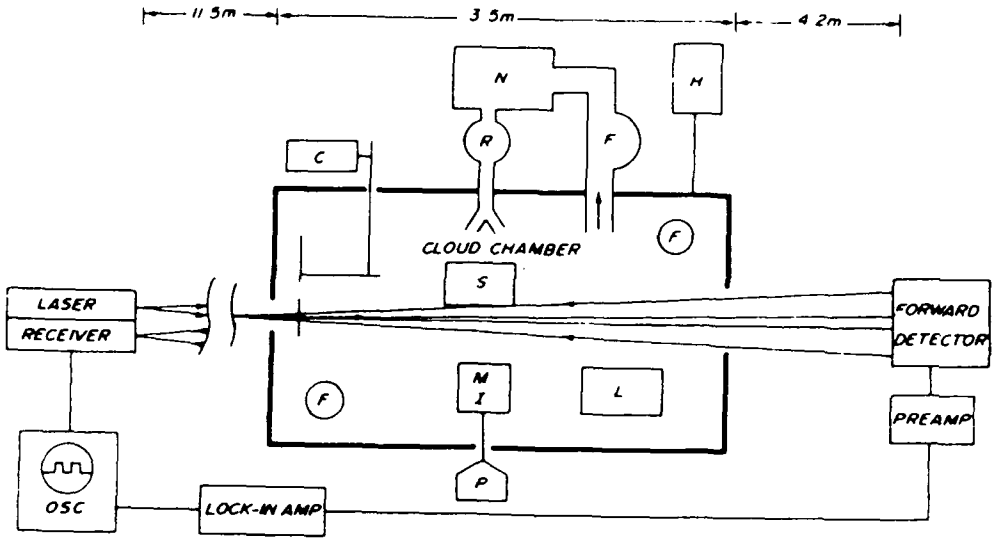


Figure 1. Schematic diagram of the experimental system: C, laser beam chopper; F, mixing fans; H, humidity sensor; I, cascade impactor; M, mass sampling system; L, large particle generator; N, ultrasonic nebulizer; R, flow regulator; S, submicron particle generator.

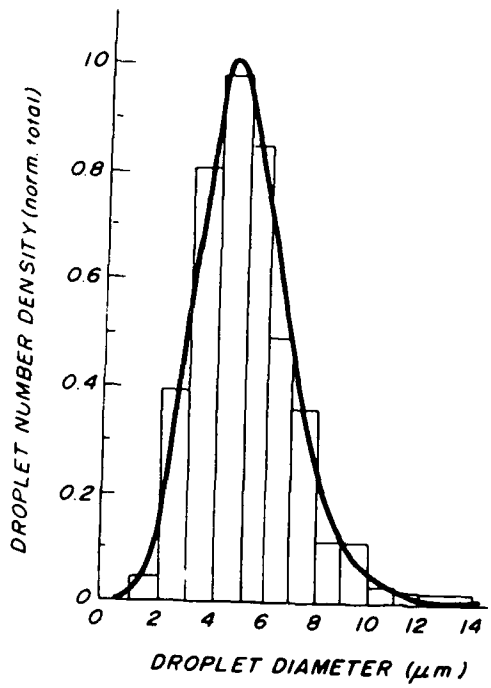


Figure 2. M size distribution.
(d_m = 5 um)

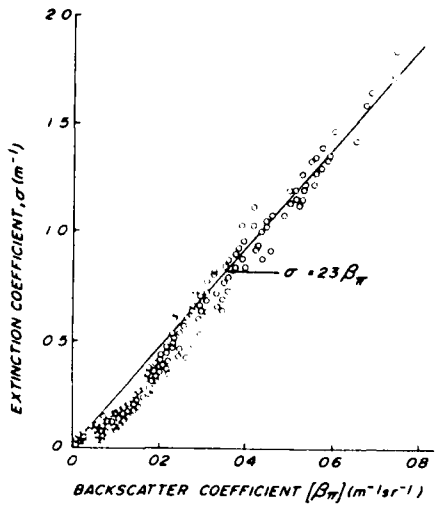


Figure 3 (a)

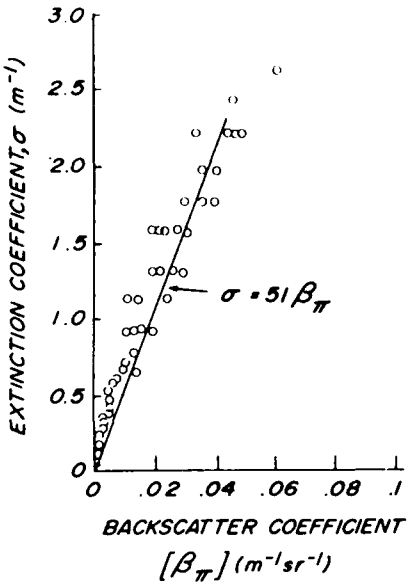


Figure 3 (b)

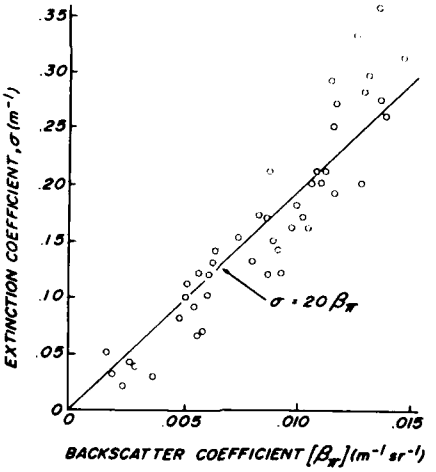


Figure 3 (c)

Figure 3. Relationship between the extinction and backscatter coefficient showing a linear fit to the data.
(a) for M size distribution
(b) for S size distribution and
(c) for L size distribution

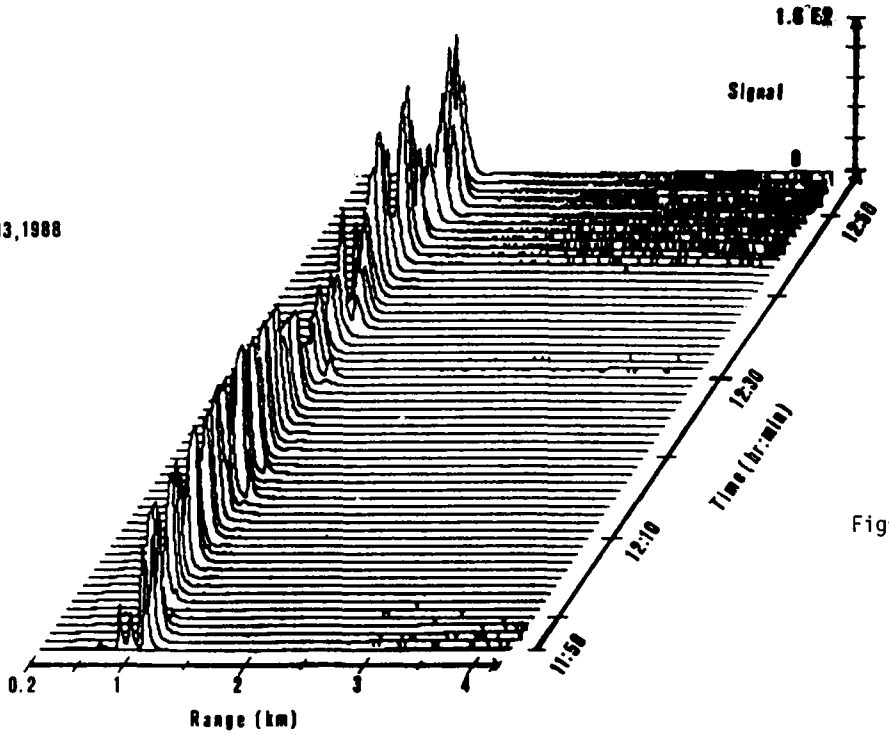


Figure 4 (a)

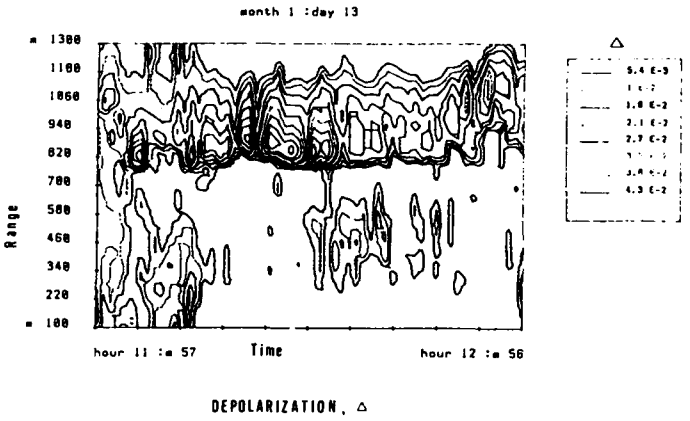


Figure 4 (b)

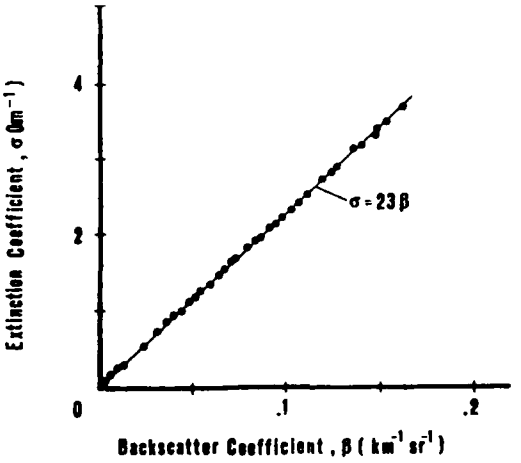


Figure 4 (c)

Figure 4(a) Three dimensional representation of lidar return signals for a low (approximately 1 km.) water droplet (stratus type) cloud on January 13, 1989 from 11:56 to 12:55 local time, averaged at one minute intervals along the y axis. The height of the range corrected return signal (peaks) correspond to the scale on the z axis indicating a maximum value of 160. The lidar signal is shown from 0.2 to 4.2 km as the x axis.

Figure 4(b) Depolarization return signals (.005 - .04) for low stratus type cloud shown in Figure 4(a).

Figure 4(c). Plot of σ and β values for low stratus type cloud shown in Figure 4(a) indicating a modal diameter of approximately 5 microns when compared to results from Reference 8.

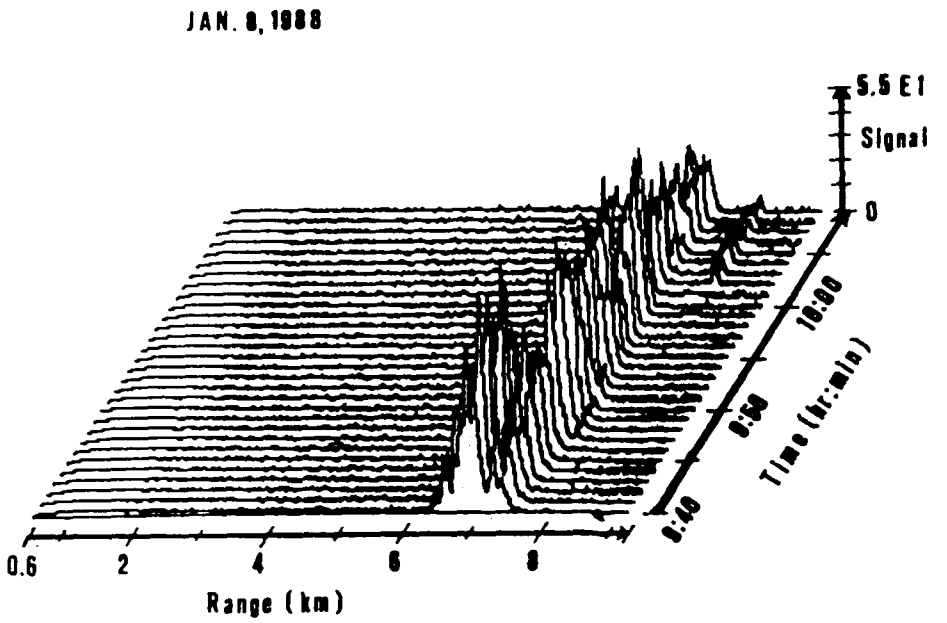


Figure 5 (a)

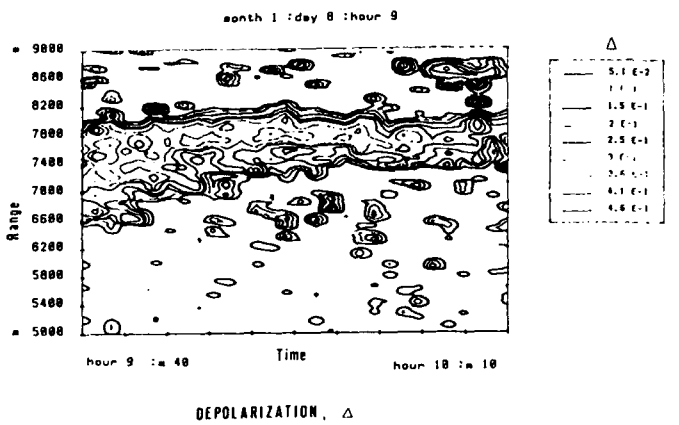


Figure 5 (b)

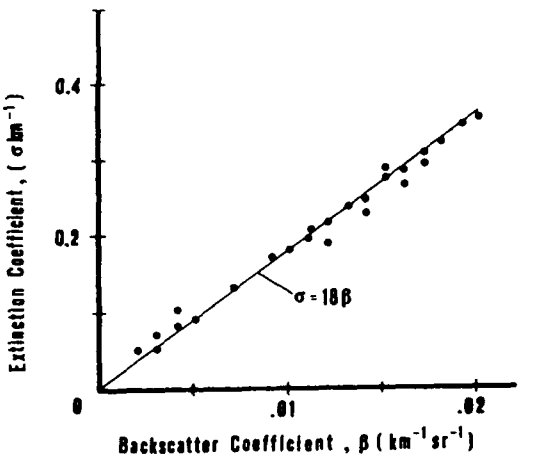


Figure 5 (c)

Figure 5(a) Three dimensional representation of lidar return signal for a high (approx. 7 km) ice particle (cirrus type) cloud on January 8,1988 from 09:40 to 10:10 local time averaged at one minute intervals shown on the y axis. The height of the range corrected signal (peaks) correspond to the scale on the z-axis having a maximum value of 55. The lidar signal is shown from 0.6 to 9.6 km as the x-axis.

Figure 5(b) Depolarization return signals (.05 - .46) for high ice particle cirrus type cloud shown in Figure 5(a).

Figure 5(c) Plot of a vs. B values for cirrus type cloud shown in Figure 5(a). The a/B slope of 18 indicates larger particle sizes (d_e > 15 microns) than that shown in Figure 4(c) when compared with laboratory data using water droplets.

CONVEX SET ESTIMATION FROM SUPPORT LINE MEASUREMENTS AND APPLICATIONS TO TARGET RECONSTRUCTION FROM LASER RADAR DATA*

S.R. Kulkarni[1,2] A.S. Willsky[2] A.S. Lele[1,2]

[1]Massachusetts Institute of Technology
Lincoln Laboratory
244 Wood Street
Lexington, Massachusetts 02173

[2]Massachusetts Institute of Technology
Center for Intelligent Control Systems and
Laboratory for Information and Decision Systems
77 Massachusetts Avenue
Cambridge, MA 02139

Abstract

In this paper, we extend techniques of convex set reconstruction from support line measurements and apply these to laser radar data. Specifically, the techniques are applied to both range-resolved and Doppler-resolved data, which provide one and two support line measurements respectively. The resulting reconstructions provide size and shape estimates of the targets under observation. While such information can be obtained by other means (e.g. from reconstructed images using tomography), the present methods yield this information more directly. Furthermore, estimates obtained using these methods are more robust to noisy and/or sparse measurement data or data suffering from registration errors. Finally, the present methods are used to improve tomographic images in the presence of registration errors.

1. Introduction

In this paper we present algorithms that provide direct size and shape estimates of targets from laser radar data. Resolved laser radar measurements of a target provide information as to the extent of the target in space. For example, a range-resolved measurement indicates where the target begins in range along the radar line of sight. If a line is drawn at this range perpendicular to the line of sight, the target lies completely to one side of this line and in fact is just grazed by this line. A line that grazes the target in this manner is referred to as a *support line*, and range-resolved measurements from a number of aspects all lying in a plane yield a set of support lines. Furthermore, Doppler-resolved measurements of a spinning target contain support line information. Given the support lines of a target at all aspects in a plane, the convex hull of the projection of the target onto this plane may be determined by intersecting halfplanes corresponding to the support lines.

In practice, however, the support line measurements are noisy, due to errors in determining the nonzero extent of a resolved measurement suffering from, say, speckle effects, as well as in incorrectly registering the support lines taken at a set of aspects to a common point. In this case, the measured support lines may be inconsistent with one another, so that taken together there is *no* target having all of the measured lines as support lines. Our objective is to estimate the target which gave rise to the measured laser radar data in some optimal fashion.

*This research was conducted at M.I.T. Lincoln Laboratory, sponsored by the Department of the Navy, and at M.I.T. under U.S. Army Research Office contract DAAL03-86-K-0171 and National Science Foundation contract ECS-8700903.

The basic estimation procedure presented in this paper may be decomposed in the manner indicated by Figure 1. Given laser radar data at a number of aspects in a plane, we first extract support line information using an estimation procedure known as *knot location.* We then produce an optimal estimate of the target that gave rise to the laser radar data given the support line measurements, consistency constraints on the support lines, and any prior knowledge as to target shape. In terms of algorithm development, the focus of the present work is on the second module. In particular, we introduce three algorithms that utilize varying degrees of prior information. We use an algorithm developed by others[12, 13] for the first module.

The estimation procedure of Figure 1 (for each of the three algorithms of the second module) is applied to range-resolved measurements and Doppler-resolved measurements obtained through a simulation model and through field measurements. Furthermore, we compare the reconstructions obtained by using the present methods with the reconstructed images produced by standard tomographic methods. On inducing registration errors, we find that the present methods are far more robust, due to the fact that they are based on consistency constraints that tend to reduce such errors. Finally, we introduce and demonstrate a method by which the tomographic reconstructions from unregistered data may be greatly improved using our estimation procedure as a preprocessor of the data.

2. Laser Radar Data and Support Line Measurements

In this section, we describe the laser radar data to be used as input to the reconstruction algorithms (namely, range-resolved and Doppler-resolved data). We then discuss the notion of a support line measurement, and show that the laser radar data contain support line information. We conclude the section by describing a technique to extract support line information from the laser radar data.

2.1. Laser radar data and problem scenario

By illuminating a target and receiving the reflected signal, laser radars provide information about the surface characteristics of the target. Laser radars can be designed to resolve the return from the target with respect to various quantities[1, 20]. In this paper, we restrict attention to range-resolved and Doppler-resolved laser radar data. Furthermore, we consider only the case of a monostatic radar, in which the transmitter and receiver are at the same location.

A *range-resolved* measurement (also called a range spectrum) is one in which the return is distributed in range along the line of sight (LOS) of the laser radar. That is, only those parts of the target that are a distance r_0 away from the laser radar (with distance measured along the LOS) may contribute to the value of the range spectrum at range r_0. Although a range-resolved measurement is ideally a continuous function of range, in practice it takes the form of a histogram with bins of finite range extent, where each bin is referred to as a range bin.

Alternatively, for a target undergoing motion, different parts of the target may have different components of velocity along the LOS. A *Doppler-resolved* measurement (also called a Doppler spectrum) is one in which the return is distributed with respect to these variations in velocity. As with a range spectrum, the Doppler spectrum takes the form of a histogram. The value associated with a particular Doppler bin arises from the return of all illuminated parts of the target with the corresponding component of velocity along the LOS.

The received intensity from a surface illuminated by a laser radar is dependent on the geometry and reflectance properties of the surface. The reflectance properties are usually characterized by a function known as the bidirectional reflectance distribution function (BRDF) [14]. For the case of a monostatic radar and a surface with isotropic reflectance properties, the BRDF is given by $\rho(\psi)$ where ψ is the angle between the LOS and the local surface normal. In the case where the wavelength of the illumination is large compared to surface aberrations of the target, the received intensity is proportional to

$$\sigma = 2\pi \iint_S \rho(\psi) \cos^2 \psi \, dA, \tag{1}$$

where the integration is performed over the visible (illuminated) part of the surface, denoted by S. The quantity σ is referred to as the *laser radar cross section* (LRCS) of the target. Hence, for resolved data, the intensity value associated with a particular bin is proportional to the LRCS arising from those portions of the target that contribute to that bin.

In this paper, we investigate some methods to reconstruct a target from a series of range-resolved or Doppler-resolved measurements. Throughout, we consider only the case in which the data is taken at aspects around a

great circle, so that the lines of sight all lie in a plane. With this restriction, the entire scenario is reduced to a two dimensional problem in the plane containing the lines of sight. For range-resolved measurements, we can consider the data as being obtained either with a single sensor revolving around a stationary target, or with the sensor fixed and the target rotating, with known rotation rate, about an axis perpendicular to the plane in which the measurements are taken. For Doppler-resolved measurements, target motion is required to resolve the target, and so in this case we assume that the target is rotating as above with a fixed sensor.

Alternatively, we may think of the data as being obtained simultaneously by a number of sensors distributed about the target. As we shall see, the relative positions of the sensors are needed to reconstruct targets from both range-resolved and Doppler-resolved measurements. In addition, for Doppler-resolved measurements, we assume that the target is rotating about an axis perpendicular to the plane of aspects, with known rotation rate. Moreover, if the target is translating, the Doppler velocity of the target's center of gravity relative to each sensor must be known. Since each sensor is presumably tracking the target, we assume knowledge of the necessary quantities. In what follows, we view the problem from this multi-sensor perspective.

2.2. Support line measurements from laser radar data

Given a range-resolved measurement, the minimum range $r_{\min}$ with nonzero return intensity indicates that the distance from the sensor to *any* part of the target is at least $r_{\min}$. Under far-field assumptions, the above indicates that the target lies completely on one side of the line perpendicular to the LOS at range $r_{\min}$. Moreover, since some part of the target is at range $r_{\min}$, this line actually grazes the target.*

A Doppler-resolved measurement contains similar information. For a target undergoing simple rotation with known rate ω, the Doppler frequency due to a point on the target is proportional to the distance from the point to the rotation axis in a direction perpendicular to the LOS (also called the cross-range distance of the point). The minimum and maximum Doppler frequencies, $D_{\min}$ and $D_{\max}$, with nonzero return intensity correspond to the minimum and maximum cross-range of any part of the target. Thus, from a Doppler-resolved measurement we can extract two lines parallel to the LOS that graze the target which lies between them.

In the mathematical literature [8, 21, 23], lines that just graze a two-dimensional object, or set, are referred to as *support lines*. Specifically, using a coordinate frame fixed with respect to a set S, the support line of S at angle θ_0 (denoted by $L_S(\theta_0)$) is defined to be the line orthogonal to the unit vector $\omega(\theta_0) = [\cos\theta_0 \ \sin\theta_0]^T$ that just grazes the set (see Figure 2). The *support value* $h_S(\theta_0)$ is defined as the maximum projection onto $\omega(\theta_0)$ of all points in S:

$$h_S(\theta_0) = \sup_{s \in S} s^T \omega(\theta_0). \tag{2}$$

The magnitude of $h_S(\theta_0)$ is the minimum distance from $L_S(\theta_0)$ to the origin. From all of this, it follows that the set S lies in a particular one of the two halfplanes defined by $L_S(\theta_0)$.

As θ_0 varies from 0 to 2π, the *support function* $h_S(\theta)$ of the set S is defined. This function is continuous and periodic with period 2π. We will also refer to the set of values of $h_S(\theta)$ sampled at a finite number of angles $\theta_1, \theta_2, \ldots, \theta_M$ as a *support vector* $h_S = [h_S(\theta_1) \ \ h_S(\theta_2) \ \ \cdots \ \ h_S(\theta_M)]^T$.

The algorithms of Section 3 provide polygonal estimates of the *convex hull* of the target's projection in the plane of the aspect angles, given noisy support value measurements. The convex hull of a set S, denoted by $\mathrm{conv}(S)$, is defined to be the smallest set satisfying $S \subseteq \mathrm{conv}(S)$ and $\overline{xy} \subseteq \mathrm{conv}(S)$, $\forall x, y \in \mathrm{conv}(S)$. Since the convex hull of a set and its support function satisfy a one-to-one relationship (i.e., one uniquely determines the other), and since the support function of a polygon $h_P(\theta)$ is completely determined by the support vector h_P having support values at the polygonal face angles, estimating h_P is equivalent to estimating a convex polygon P, i.e., one for which $P = \mathrm{conv}(P)$.

To identify the support value(s) associated with the support line(s) provided by a range or Doppler spectrum, a coordinate frame such as that in Figure 2 is needed. This frame must serve as a common reference for all of the aspects, so that the sets of data may be spatially aligned, or *registered*.

*Note that the maximum range $r_{\max}$ with nonzero return intensity *does not necessarily* provide another grazing line. This is because parts of the target at ranges greater than $r_{\max}$ may be blocked by parts of the target at lower range. Consequently, they will not be visible to the radar and will not contribute to the target's range spectrum.

For range-resolved measurements, the assumption that the positions of the laser radars are known relative to one another allows us to establish such a frame, say, with origin at the average of the laser radar position coordinates and 0° aspect defined by the LOS of the first laser radar. The resulting position and orientation of this coordinate frame is, of course, arbitrary; an alternate choice of frame would yield support values of a shifted and/or rotated target. Given such a coordinate frame, the support value corresponding to the i^{th} laser radar's range spectrum is equal to the minimum nonzero range $r_{\min}$ subtracted from the distance from the laser radar to the origin along the i^{th} LOS. The set of support values obtained in this manner for the set of laser radars forms a support vector y.

A coordinate frame for Doppler-resolved measurements is established in the same way as for range-resolved measurements. From above, the i^{th} sensor (at aspect θ_i) gives rise to support values at $\theta_i \pm 90°$. Since target cross-range is proportional to Doppler frequency after shifting the Doppler spectrum by the Doppler frequency shift D_i produced by the target's translational velocity relative to the sensor, the support values are given by $\frac{\lambda}{2\omega}|D_{\min} - D_i|$ and $\frac{\lambda}{2\omega}|D_{\max} - D_i|$, where λ is the wavelength of the laser illumination. Hence, the support values arising from the Doppler spectra of the set of laser radars form a support vector y.

Since a Doppler spectrum at aspect θ_i provides two support values, at $\theta_i \pm 90°$, the aspects θ_i and $\theta_i + 180°$ yield duplicate support values, if the support values are free of noise. For noisy data (discussed below), the duplicate values may be averaged, thereby reducing the noise in the support measurements.

In general, this support vector y arising from range or Doppler data is noisy and may be invalid, due to two types of measurement errors. One type of error arises in incorrectly estimating the values of $r_{\min}$ or $D_{\min}$ and $D_{\max}$ amid noise in the range or Doppler spectra. Secondly, incorrect knowledge of the relative laser radar positions (and for Doppler data, incorrect knowledge of the Doppler velocity of the target's center of gravity relative to each sensor) leads to registration errors.[†] The reconstruction algorithms in Section 3 produce shape estimates of targets given support vectors having these measurement errors.

2.3. Knot location

Although determining $r_{\min}$ or $D_{\min}$ and $D_{\max}$ is simple if the data is noise-free, doing so for noisy data is a quite difficult problem in general. The most obvious method—thresholding the data—suffers greatly from its nonrobustness to noise 'spikes' in the data. As a result, we turn to a method based on a technique developed by Willsky and Jones [24] for detecting abrupt changes in dynamic systems, and later applied by Mier-Muth and Willsky [13] to spline estimation. To cast our problem in the framework of [13], we model the range or Doppler spectrum as a linear *spline*, or piecewise linear function. The points of discontinuity in derivative are referred to as *knots*. Our goal is to determine the first knot in a range spectrum and the first and last knots in a Doppler spectrum.

The basic approach consists of using a Kalman filter based on a linear ramp model for the range or Doppler spectrum. Initializing the filter with zero slope, we run the filter along the spectrum. At each bin, we use the innovations sequence to determine a set of maximum-likelihood (ML) estimates of the slope of the ramp at the current bin assuming that a knot was located at each of the previous bins in some finite window. Using the ML estimates for each bin in the window, we perform a generalized likelihood ratio (GLR) test for the two hypotheses 'knot present' and 'knot absent' in order to determine whether a knot actually exists at the locations of any of the ML estimates. The first bin for which the GLR exceeds a prespecified threshold corresponds to the first knot in the spectrum. For a Doppler spectrum, to locate the last knot, we repeat the above process running the Kalman filter backwards along the spectrum. Details concerning the performance of this algorithm may be found in [24], [13], and [12].

In concluding this section, we note that it is in general more difficult to locate knots in a Doppler spectrum than in a range spectrum. This difference is due to the properties of typical target materials combined with the viewing geometries associated with the two data types [5]. In particular, the values of the laser radar return at ranges just higher than $r_{\min}$ are determined by parts of the target whose surface normals roughly coincide with the LOS. As a result, $\psi \approx 0°$, maximizing $\cos\psi$ in Equation 1. Furthermore, since materials typically give high intensity return at near-normal incidence and low intensity return at near-grazing incidence, the BRDF $\rho(\psi)$ is near maximum. Hence, range spectra generally exhibit an abrupt increase in intensity at the knot having range $r_{\min}$.

In contrast, the values of the laser radar return at Doppler velocities just greater than $D_{\min}$ and just less than $D_{\max}$ are determined by parts of the target having surface normals that are nearly perpendicular to the LOS. Consequently, $\psi \approx 90°$ giving rise to values of $\cos\psi$ and $\rho(\psi)$ that are nearly zero. Hence Doppler spectra generally

[†]Errors in knowing the laser radar positions may also cause angular errors (i.e., errors in knowing the aspects). However, in this paper we ignore angular errors and assume throughout that the aspects of the measurements are known perfectly.

vary slowly in intensity near the two knots.

3. Reconstruction from Support Line Measurements

In the previous section, we saw that range-resolved or Doppler-resolved measurements of a target give rise to support measurements. We also noted that exact support values at all angles characterize the convex hull of the target. However, in general only a finite number of noisy measurements are available. In this section, we discuss some algorithms for obtaining estimates of the target from such measurements. It appears that the problem of shape estimation from noisy support line measurements was first studied by Prince [16, 17, 18]. (Greschak [3], Stark and Peng[22], and others have done related work.) The algorithms below represent various extensions of Prince's work [16].

3.1. Formulation

We model our support value measurements $y_1, y_2, \ldots, y_M$ as consisting of the true support values of the target $h_i = h(\theta_i)$ corrupted by noise. That is, $y_i = h_i + n_i$ for $i = 1, 2, \ldots, M$ where the $\{n_i\}$ are i.i.d. samples from a Gaussian distribution. As previously mentioned, we emphasize that by noisy measurements we mean uncertainty in the support values and not in the measurement angles.

The noisy measurements $\{y_i\}$ may not correspond to the set which gave rise to them and, in fact, may not correspond to *any* set. For example, there is *no* object having $y = [1\ 2\ 1\ 2\ 1\ 2\ 1\ 2]^T$ as its support vector at uniformly spaced angles. In such a case, the support values are said to be *inconsistent* (or, equivalently, the support vector is said to be *invalid*). Our objective is to estimate the *valid* support vector $\hat{h}$ that is closest to y in Euclidean distance. The target shape estimate consists of the polygon bounded by the support lines corresponding to $\hat{h}$.

We choose to minimize Euclidean distance in support vector space despite the fact that we are more directly interested in minimizing some measure of distance in object space; computational considerations motivate this choice. However, we do *evaluate* the quality of our reconstructions in object space, by using a quantitative measure of the error between the true object S and its reconstruction $\hat{S}$. This measure of error is the area of their symmetric difference $S \Delta \hat{S} = (S \cup \hat{S}) \setminus (S \cap \hat{S})$, and is chosen for its geometric appeal.

The estimation algorithms that we present in the following three sections arise from increasingly general formulations of the problem of obtaining polygonal shape estimates from noisy support measurements. The most specific case was considered by Prince, in which a polygon with faces at a fixed number of uniformly-spaced measurement angles is estimated. A generalization of this algorithm results in relaxing the assumption of uniform spacing. A third formulation consists of estimating a polygon with faces at a set of prespecified reconstruction angles that are independent of the measurement angles. Both sets of angles are nonuniformly-spaced, in general. Fourth, we might allow rotations of the prespecified constellation of reconstruction angles in order to obtain joint orientation and shape estimates of objects. The fifth level of generality results in specifying only the number but not the values of the reconstruction angles. The most general formulation is one in which neither the number nor the values of the reconstruction angles is specified. Such an estimator would be essentially the same as the one just discussed, with the exception that larger numbers of reconstruction angles would be penalized. In what follows, we consider the second, third, and fourth formulations.

3.2. Reconstruction with sides at the measurement angles

In this problem, we have a finite set of noisy support measurements $\{y_1, y_2, \ldots, y_M\}$ at angles $\theta_1 < \theta_2 < \cdots < \theta_M$. We seek the following solution:

$$\hat{h} = \arg\min_{h\ valid} \sum_{i=1}^{M} (y_i - h_i)^2. \tag{3}$$

The only problem in solving Equation 3 lies in deriving a necessary and sufficient consistency condition on h for angles that are in general nonuniformly-spaced. Geometrically, we see in Figure 3 that given support lines L_{i-1} and L_{i+1} at θ_{i-1} and θ_{i+1}, a third support line at θ_i is consistent only if it lies to the left of the intersection point of L_{i-1}

and L_{i+1}. Together with sufficiency as shown in [16], this leads to the consistency condition for a triplet of support values adjacent and in general nonuniformly-spaced in angle, given by [10].

$$h_{i-1}\sin(\theta_{i+1}-\theta_i) - h_i\sin(\theta_{i+1}-\theta_{i-1}) + h_{i+1}\sin(\theta_i-\theta_{i-1}) \geq 0. \tag{4}$$

Enforcing this condition for all adjacent triplets yields a necessary and sufficient condition for a vector to be a valid support vector. With such a consistency condition, we can formulate the estimation algorithm which we refer to as NUA[‡]:

$$\hat{h} = \arg\min_{Ch\geq 0} \sum_{i=1}^{M} (y_i - h_i)^2 \tag{5}$$

where

$$C = \begin{pmatrix} -\sin(\theta_2-\theta_M) & \sin(\theta_1-\theta_M) & 0 & 0 & \sin(\theta_2-\theta_1) \\ \sin(\theta_3-\theta_2) & -\sin(\theta_3-\theta_1) & \sin(\theta_2-\theta_1) & 0 & 0 \\ 0 & \sin(\theta_4-\theta_3) & -\sin(\theta_4-\theta_2) & \sin(\theta_3-\theta_2) & 0 \\ 0 & \ddots & \ddots & \ddots & \ddots \\ \sin(\theta_M-\theta_{M-1}) & 0 & 0 & \sin(\theta_1-\theta_M) & -\sin(\theta_1-\theta_{M-1}) \end{pmatrix} \tag{6}$$

The matrix condition $Ch \geq 0$ enforces the consistency condition for all adjacent triplets of support values, so that the estimated support vector $\hat{h}$ is valid. Since the cost function is quadratic and the constraints are linear, the solution to this problem can be obtained using standard quadratic programming techniques [7, 11]. Incidentally, the space of valid support vectors forms a *cone* in $\mathbb{R}^M$. Following [16], we refer to this cone as the *support cone* $\mathcal{C}$. We may then offer the following geometrical interpretation of Equation 5: if $y \in \mathcal{C}$, then $\hat{h} = y$, and if $y \notin \mathcal{C}$, then $\hat{h}$ is obtained by projecting y onto $\mathcal{C}$ (see Figure 3).

To illustrate the behavior of NUA, we consider the following example. The (two-dimensional) target used in this example is an isosceles triangle with vertices at $(2,0)$, $(-0.25,0)$, and $(0.25,0)$. We use this triangle throughout the paper and refer to it as the 'standard triangle.' The data consist of $M = 24$ uniformly-spaced noisy measurements ($\sigma = 0.25$). Figures 4a,b depict the results in both object space and support function space using the estimator NUA. Figure 4a shows the bold outline of the true object (the standard triangle), the noisy support lines, and the shaded polygonal reconstruction produced by NUA. Correspondingly, Figure 4b shows the support function $h(\theta)$ of the true object, the noisy support values $\{y_i\}$, and the support function $\hat{h}(\theta)$ of the estimated object. The display conventions in Figure 4b are also used throughout the paper. The quantitative measure of reconstruction error that we use throughout the paper consists of the area of the symmetric difference between the reconstructed object and the true object, normalized by the area of the true object. This error is denoted by E, and for the present example has the value $E = 1.56$.

3.3. Best N-gon fitting M measurements with fixed reconstruction angles

Prior information as to target shape is often available in the analysis of laser radar data. In this section, we exploit prior information as to the angles of the target's sides, in order to obtain reconstructions of higher quality than those we expect to obtain using NUA, which utilizes no prior information. Specifically, we consider the problem of determining the best N-sided polygon with prespecified face angles that fits a set of noisy support values at M measurement angles. For example, one might wish to reconstruct the best equilateral triangle given a set of, say, twenty noisy measurements of an object known *a priori* to be triangular.

In formulating this problem, we let $\{\theta_1, \theta_2, \ldots, \theta_M\}$, $\{y_1, y_2, \ldots, y_M\}$, and $\{\phi_1, \phi_2, \ldots, \phi_N\}$ denote the M measurement angles, the measured support values at these angles, and the N reconstruction angles, respectively. Given these

[‡]NUA is an acronym for NonUniform Angles. The present algorithm is referred to as NUA because it is an extension of one developed by Prince for uniformly-spaced angles.

quantities, we wish to estimate an N-gon specified by the consistent set of support values $\{h_\phi(\phi_1), h_\phi(\phi_2), \ldots, h_\phi(\phi_N)\}$ which minimizes

$$J(h_\phi(\phi_1), h_\phi(\phi_2), \ldots, h_\phi(\phi_N)) = \sum_{i=1}^{M} (h_\phi(\theta_i) - y_i)^2, \tag{7}$$

where $h_\phi(\theta_i)$ denotes the value at θ_i of the support function $h_\phi(\cdot)$ of our estimated N-gon. Equation 7 corresponds to finding a set of support values at the reconstruction angles that minimizes the sum of the squared deviations between the measured support values and the piecewise sinusoidal support function of the reconstructed polygon (where this support function has the value $h_\phi(\phi_i)$ at ϕ_i).

Letting ϕ_{L_i} and ϕ_{R_i} denote the reconstruction angles immediately to the left and right of the i^{th} measurement angle θ_i, and letting h_{L_i} and h_{R_i} denote the corresponding reconstructed support values, we have that the support function of the reconstructed object evaluated at θ_i is given by

$$h_\phi(\theta_i) = \frac{\sin(\phi_{R_i} - \theta_i)}{\sin(\phi_{R_i} - \phi_{L_i})} h_{L_i} + \frac{\sin(\theta_i - \phi_{L_i})}{\sin(\phi_{R_i} - \phi_{L_i})} h_{R_i}. \tag{8}$$

From Equations 7 and 8, our problem is formulated as

$$\hat{h}_\phi = \begin{bmatrix} \hat{h}_\phi(\phi_1) \\ \hat{h}_\phi(\phi_2) \\ \vdots \\ \hat{h}_\phi(\phi_N) \end{bmatrix} = \underset{Ch_\phi \geq 0}{\arg\min} (Ah_\phi - y)^T A h_\phi, \tag{9}$$

where $y = [\ y_1 \quad y_2 \quad \cdots \quad y_M\ ]^T$ is the measurement vector, C is the consistency matrix used in **NUA**, and A is an $M \times N$ matrix mapping the M support values at the $\{\theta_i\}$ to induced support values at the $\{\phi_i\}$. The i^{th} row of the matrix A, corresponding to the i^{th} measurement, has two adjacent (modulo N) non-zero entries, $\frac{\sin(\phi_{R_i} - \theta_i)}{\sin(\phi_{R_i} - \phi_{L_i})}$ and $\frac{\sin(\theta_i - \phi_{L_i})}{\sin(\phi_{R_i} - \phi_{L_i})}$, corresponding to the reconstruction angles ϕ_{L_i} and ϕ_{R_i} on either side of θ_i.

We refer to the estimator of Equation 9 as **BNGON**. Since the cost function in Equation 9 is quadratic in the reconstructed support values and the consistency constraint is linear, the problem can be solved by QP techniques. Incidentally, under certain conditions there may be nonunique solutions[10]. However, this is not the generic case, and we will not concern ourselves with this here.

An example of **BNGON**, similar to that discussed in Section 3.2, is shown in Figure 4c,d. The example consists of reconstructing the best triangle with reconstruction angles at $7.125°, 82.875°$, and $270°$ equal to those of the standard triangle, given $M = 24$ uniformly-spaced noisy ($\sigma = 0.25$) support measurements. The pictures in both object space and support function space are shown, with the reconstructed object incurring an error $E = 0.17$ with respect to the true object.

The **BNGON** reconstruction in the figure originates from the same set of measurements as the **NUA** reconstruction in the same figure (i.e., the same noise realization was used), allowing us to compare the two. From a visual comparison, it is clear that the prior information that the true object is a triangle with known face angles allows **BNGON** to outperform **NUA**. This is also seen quantitatively by noting that $E_{\mathbf{BNGON}} = 0.17$ while $E_{\mathbf{NUA}} = 1.56$.

3.4. Best N-gon with fixed relative spacing of reconstruction angles

Although prior knowledge of the angles of the target's sides clearly improves reconstruction quality, the availability of such knowledge cannot be expected in general. Here, we assume somewhat less prior information by formulating a problem in which the *relative* (rather than the absolute) angles of the target's sides are known. Hence, the resulting problem is just as before with the exception that here the *orientation* of the target is not known.

Let $\{\theta_1, \theta_2, \ldots, \theta_M\}$ and $\{y(\theta_1), y(\theta_2), \ldots, y(\theta_M)\}$ denote the M measurement angles and the measured support values at these angles, as before. However, unlike before, the reconstruction angles are given by $\{\phi_1 + \alpha, \phi_2 + \alpha, \ldots, \phi_N + \alpha\}$, where $\{\phi_1, \phi_2, \ldots, \phi_N\}$ are known and $\alpha \in [0, 2\pi)$ serves as an unknown offset parameter fixing the absolute locations of the reconstruction angles. Essentially, we wish to minimize the cost function in Equation 9, with the exception that the estimator here is free to rotate the constellation of reconstruction angles in order to achieve minimum cost in the estimate. That is, we wish to jointly estimate values of α and $\{h_\phi(\phi_1 + \alpha), h_\phi(\phi_2 + \alpha), \ldots, h_\phi(\phi_N + \alpha)\}$ that minimize

$$J(\alpha, h_\phi(\phi_1 + \alpha), h_\phi(\phi_2 + \alpha), \ldots, h_\phi(\phi_N + \alpha)) = \sum_{i=1}^{M} (h_\phi(\theta_i) - y(\theta_i))^2 \tag{10}$$

where $h_\phi(\theta_i)$ is given by Equation 9 and is repeated here for convenience:

$$h_\phi(\theta_i) = \frac{\sin(\phi_{R_i} + \alpha - \theta_i)}{\sin(\phi_{R_i} - \phi_{L_i})} h_{L_i} + \frac{\sin(\theta_i - \phi_{L_i} - \alpha)}{\sin(\phi_{R_i} - \phi_{L_i})} h_{R_i} \tag{11}$$

and the $\{h_\phi(\phi_i + \alpha)\}$ are constrained to be a set of consistent support values. Unfortunately, the cost in Equation 10 is nonlinear in α and QP techniques cannot directly be used.

A 'brute-force' approach to minimize J is the following. We simply choose many values of α, solve the QP problem of Equation 9 for each, and then choose that value of α which yields minimum cost. The major drawback of this approach is a desired-accuracy versus computational-requirement tradeoff. Since J is sampled at finitely many values of α (say p values), our estimate $\hat{\alpha}$ will be somewhat inaccurate, being on average $(360/(4p))^\circ$ away from the true minimum α_{true}. So to achieve a reasonably accurate estimate, a prohibitively large number of QP problems would have to be solved. For these reasons, we consider a different algorithm.

First, we define the cost function $J_{h_\phi}(\alpha)$ by

$$J_{h_\phi}(\alpha) = \min_{\{h_\phi(\phi_i + \alpha)\}} J(\alpha, h_\phi(\phi_1 + \alpha), h_\phi(\phi_2 + \alpha), \ldots, h_\phi(\phi_N + \alpha)) \tag{12}$$

so that the solution to Equation 10 is given by $\min_\alpha J_{h_\phi}(\alpha)$. Our algorithm, to be referred to as **BNGONROT**, essentially consists of performing interleaved gradient ascent/descent steps and QP steps on $J_{h_\phi}(\alpha)$ from $\alpha = 0^\circ$ to $\alpha = 360^\circ$ to locate all local extrema. The solution is obtained by choosing that local minimum that yields minimum cost. Standard gradient ascent/descent requires knowledge of the gradient $\frac{dJ_{h_\phi}(\alpha)}{d\alpha}$. Since we do not have access to this quantity, we use $\frac{\partial J_{h_\phi}(\alpha)}{\partial \alpha}$ as an approximation.

Specifically, we begin at $\alpha = 0^\circ$ and solve the QP problem of Equation 9. Using the estimated support values, we compute $\frac{\partial J_{h_\phi}(\alpha)}{\partial \alpha}$ and perform a gradient ascent or descent step depending on whether its sign is positive or negative, to obtain a new value of α. We are then committed to performing gradient ascent until we reach the first maximum or gradient descent until we reach the first minimum. We then perform the following steps repeatedly: (1) solve Equation 9, (2) compute the gradient, and (3) perform a gradient step. Once an appropriate convergence criterion has been met (as discussed below), indicating that a local minimum or maximum has been found, we store this value of α. We then advance by some small amount in α, and by solving Equation 9 and computing the the gradient, determine whether our next series of interleaved steps will consist of gradient ascent or descent steps. Performing steps (1)–(3) repeatedly, we reach our next maximum or minimum. We continue this traversal of the interval $[0^\circ, 360^\circ)$ until we have located all maxima and minima, and then choose the global minimum $\hat{\alpha}$. Solving Equation 9 with $\alpha = \hat{\alpha}$ yields the solution to our problem.

The criterion for convergence is met when either of two conditions is satisfied. The first condition is the usual termination rule for standard gradient ascent/descent. The need for a second convergence condition is due to the inability of standard gradient ascent/descent algorithms (and their convergence criteria) to deal with cusps (discontinuities in slope) that can occur in the cost function $J_{h_\phi}(\alpha)$. To deal with this, we halve the step size λ of the gradient ascent/descent every time the sign of the derivative changes (indicating that a maximum or minimum

has been crossed) provided that the magnitude of the derivative is sufficiently large (assuring that we are near a discontinuity in slope rather than a smooth maximum or minimum). The second convergence condition is met when λ falls below some specified value.

Because the algorithm is based on standard gradient ascent/descent methods, modified to obtain precise solutions near cusps, we expect that its limitations are similar to those associated with the standard methods. Most important is the tradeoff of speed versus accuracy as determined primarily by the choice of λ and the convergence criterion. For a given desired accuracy this algorithm is generally much more efficient than the 'brute-force' approach of solving a QP problem at each of many independently chosen values of α and choosing that value having lowest cost.

An example of a reconstruction produced by **BNGONROT** is shown in Figure 4e,f. The true object and measurements are the same as before. The reconstruction forms an angle of $\alpha = 86.58°$ with the positive x-axis. The error E equals 0.42. Not surprisingly, the reconstruction is qualitatively and quantitatively far better than that corresponding to **NUA** (see Figure 4a,b). Moreover, it is not much worse than the **BNGON** reconstruction (see Figure 4c,d), indicating that not much is sacrificed in settling for a weaker prior, i.e., knowing relative rather than absolute reconstruction angles.

4. Target Reconstructions from Simulated and Field Laser Radar Data

In this section, we apply the target reconstruction algorithms described in the previous section to laser radar measurements of several targets, in order to obtain shape estimates of the targets. The examples presented are those of reconstructions from sets of range and Doppler spectra obtained either through a simulation computer program[9, 6] or laboratory or field measurements.

The data for the first two examples are simulated range-resolved and Doppler-resolved measurements of a cone of height 200 cm and radius 25 cm with Lambertian reflectance characteristics. The cone is positioned with the center of its base at the origin of a coordinate frame and oriented with its axis of symmetry lying in the xy-plane. In order to be resolved in Doppler, the cone rotates in the xy-plane about the z-axis at one revolution per second, in a manner resembling end-over-end tumble. Measurements are taken at an instant in time when the cone's axis is aligned with the frame's x-axis, at 72 aspects uniformly-spaced around the great circle of radius 10,000 m in the xy-plane, and with a resolution of 2 cm for the range data and a resolution of 3.750 KHz for the Doppler data.

To reconstruct the targets, we first locate the knots by the Kalman filtering technique described in Section 2.3 and convert them to support values. Modelling knot location errors and registration errors for each aspect by statistically-independent samples from Gaussian distributions[§] with variances σ_{kl}^2 and σ_{reg}^2, the effective measurement error is Gaussian, with variance $\sigma_{\text{eff}}^2 = \sigma_{\text{kl}}^2 + \sigma_{\text{reg}}^2$ for range-resolved data. However, for Doppler-resolved data at an even number of uniformly-spaced aspects, (1) registration errors for aspects 180° apart are negatives of each other, and (2) the duplicate support value measurements provided by aspects 180° apart are averaged together. As a result, the knot location error may be modelled by drawing samples from a Gaussian distribution with variance $\sigma_{\text{kl}}^2/2$ for each aspect. The registration error may be obtained by drawing samples from a Gaussian distribution with variance $\sigma_{\text{reg}}^2/2$ for aspects $\theta_1, \theta_2, \ldots, \theta_{M/2}$, and using the negatives of these samples for the aspects $\theta_{M/2+1}, \theta_{M/2+2}, \ldots, \theta_M$. The effective measurement error is given by the sum of these two errors, for each aspect.

The support lines resulting from locating knots and corrupting the support values by measurement noise are shown in Figure 5a for range-resolved data, with noise level $\sigma_{\text{eff}} = 0.50$. The reconstructions produced by **NUA**, **BNGON**, and **BNGONROT** from this set of noisy support line measurements are shown in Figures 5b–d. The display conventions of this figure will be used throughout this section. The reconstructions exhibit behavior similar to that seen for the standard triangle reconstructions of Sections 3.2–3.4. In particular, the prior knowledge of relative reconstruction angles allows **BNGONROT** to dramatically outperform **NUA**, but does not cause it to significantly underperform **BNGON**, which uses absolute angle information. Also, the quality of the reconstructions is rather impressive in light of the fact that the noise level is so high, having a standard deviation equal to the full width of the target. The corresponding results for the Doppler-resolved measurements arising from knot location error ($\sigma_{\text{kl}} = 0.25$) and registration error ($\sigma_{\text{reg}} = 0.25$) are shown in Figure 6.

The third example is one of reconstructing a triconic target of height 203 cm and base radius 39.5 cm (shown outlined in Figure 7a) given laboratory range-resolved measurements. The laboratory measurements were taken on a ten-meter indoor range at 72 uniformly-spaced aspects in the horizontal plane containing the target's axis

[§]In this section and the next, all Gaussian distributions are assumed to have zero mean.

of symmetry, with a range resolution of 1 cm. See [4] for details of the experimental set-up. Support lines and reconstructions using the three algorithms are shown in Figure 7 for the uncorrupted laboratory data and in Figure 8 for the laboratory data corrupted with measurement noise ($\sigma_{\text{eff}} = 0.25$).

Finally, we present reconstructions from Doppler-resolved field measurements. The target, a scaled aluminum model of the Thor-Delta rocket body (shown outlined in Figure 9a), was rotated at approximately 1 rpm about an axis normal to its axis of symmetry. The measurements, taken at 72 aspects in a plane normal to the rotation axis, were made using a 10.6μm CO_2 narrowband laser radar on a 5.4 km ground range, and had a Doppler resolution of approximately 200 Hz. Details of the experiment may be found in [4]. Support lines and reconstructions produced by the three algorithms are shown in Figure 9 for the uncorrupted field data and in Figure 10 for the field data corrupted with measurement noise ($\sigma_{\text{kl}} = 0.10$ and $\sigma_{\text{reg}} = 0.10$).

5. Comparisons With and Improvements to Tomographic Imaging Methods

In previous work, standard methods of tomographic image reconstruction [2] were applied to range-resolved and Doppler-resolved laser radar data[4, 15]. In this section, we compare the convex set reconstructions of the previous section with reconstructions produced using the tomographic methods. We then examine the effect of registration errors on both methods. As we shall see, the present algorithms are quite robust to registration errors, in contrast to tomographic reconstructions, which are rather sensitive to these errors. Finally, we show that the robustness of the present algorithms can be used to dramatically improve tomographic reconstructions from data with registration errors.

All of the tomographic reconstructions in this section were obtained using the standard method of filtered backprojection. (See [2] for methods of transmission tomography, and [4, 15] and references contained therein for the application of these methods to laser radar reflective data.) Parts (a) of Figures 6–14 show filtered backprojection reconstructions from the four data sets (free of registration errors) used in Section 4. It should be noted that the Doppler data sets were thresholded prior to being backprojected in order to improve the tomographic reconstructions. This is necessary since the high intensities that are typically near the center of a Doppler spectrum tend to give rise to a dominant high intensity region in the center of the reconstruction. Incidentally, we threshold the data sets prior to backprojecting rather than thresholding the reconstructed images themselves, since the former approach appears to yield better results.

Unlike the convex set reconstructions (shown in parts (b)–(d) of Figures 5–10), the tomographic reconstructions contain intensity information within the outline of the target. However, exactly what information the intensity values convey about the target's surface is not well understood. Furthermore, the tomographic images differ from their convex set counterparts in that they do not provide direct size or shape estimates of the target. While in principle techniques to extract edge and shape information could be used, the usual difficulties associated with image processing would be faced. This is especially true of reconstructions arising from Doppler data, where for reasons suggested in Section 2.3 and described and demonstrated in [5], reconstructed edges are not highlighted but are instead overwhelmed by the high intensities that are reconstructed in the interior of the target.

Like the convex set algorithms, tomographic techniques require knowledge of a common reference point, without which registration errors occur. The introduction of registration errors in the data has disastrous effects on the tomographic reconstructions that result. Parts (b) of Figures 6–14 show the tomographic reconstructions resulting from shifting the data in each spectrum by an amount given by a zero-mean Gaussian random variable with standard deviation $\sigma_{\text{reg}} = 0.50, 0.25, 0.25$, and 0.10 (with the shifts for the spectra being independent of one another, except for the Doppler data sets, where shifts for aspects 180° apart are negatives), and then using filtered backprojection. Clearly, one cannot expect any image processing algorithm to successfully extract shape information from the tomographic images in these figures.

In contrast, the convex set algorithms are rather robust to registration errors. This is seen by the reconstructions shown in parts (b)–(d) of Figures 5,6,8, and 10, obtained from data suffering from the *identical* registration errors as those used for the tomographic reconstructions (i.e., the same noise realizations were used), as well as knot location errors with the same standard deviations as above.

The difference in the robustness of tomographic and convex set methods to registration errors is due to the fact that the convex set algorithms attempt to register the data in the reconstruction process using implicit information as to the consistency of the measurements. That is, in adjusting the support values to achieve consistency, the algorithms are essentially shifting each range or Doppler spectrum such that the sum of the squares of the shifts is

minimal and such that the set of shifted laser radar data is *registered* data for *some* target.

In fact, we may exploit this registering property of the convex set algorithms as an aid to tomography, for data sets with registration errors. Specifically, we start with a possibly inconsistent set of measured support values $\{y_i\}$, which are estimated from the laser radar data by knot location. If we have no prior information as to the target's shape, we use **NUA** to obtain a consistent set of support values $\{\hat{h}_i\}$. If we have prior shape information, we use **BNGON** or **BNGONROT** to estimate a consistent set of support values at the reconstruction angles, and then sample the (piecewise-sinusoidal support function of the reconstructed polygon at the measurement angles to yield a consistent set of support values $\{\hat{h}_i\}$. Then, given the $\{\hat{h}_i\}$ and $\{y_i\}$, we shift the i^{th} range or Doppler spectrum by an amount $\hat{h}_i - y_i$, for all values of i. The resulting registered data set is then processed tomographically by filtered backprojection.

Parts (c) and (d) of Figures 6 and 12, parts (c)-(e) of Figure 13, and part (c) of Figure 14 show the tomographic reconstructions that result using this process. Quite clearly, the improvement in the tomographic images is dramatic. The tomographic reconstructions resulting from preprocessing by each of the three convex set algorithms are not included in some of the figures. In the cases that the reconstruction corresponding to **BNGON** was omitted, it could not be distinguished from that corresponding to **BNGONROT**. In the last figure where reconstructions for both **BNGON** and **BNGONROT** were omitted, they were indistinguishable from that corresponding to **NUA**.

6. Summary and Suggestions for Further Work

In this paper, we have introduced a method by which target shape estimates may be directly obtained from resolved laser radar data. The reconstruction process consists of first extracting what are known as support line measurements from the data, and then producing a shape estimate using the support line measurements, employing a consistency condition on the set of these measurements, and prior information, if available. We have presented three algorithms utilizing varying degrees of prior information, that serve as the second stage in the reconstruction process just outlined. Their application to laser radar data obtained through simulation and through field measurements has been demonstrated.

The reconstructions obtained through use of the present algorithms were compared to those produced by tomographic imaging methods. First, shape estimates are explicitly provided by our algorithms, as opposed to tomographic images, which can provide target shape information only after image processing techniques have been used. Second, we investigated the effects of registration error on both methods and found that the tomographic methods experience substantial degradation, unlike the present methods which are rather robust. These observations motivated us to exploit the tendency of our algorithms to correct unregistered data, in an effort to improve the quality of tomographic images.

Our work may be extended in a number of ways. Upon relaxing the restriction that aspects lie in a plane and allowing general aspects in three dimensions, shape estimates of a target (rather than those of its projection onto a plane) would be obtained. In addition, the application of our methods to two-dimensional laser radar data resolved in both range and Doppler may provide three-dimensional target shape estimates. Extending the viewing geometry to allow bistatic observations would prove useful as well. Finally, Prince obtained improved tomographic images by utilizing convex set reconstructions as prior information available to the tomographic algorithms. By coupling the data registration technique of the previous section with Prince's methods, we could expect further improvements to the tomographic images.

A variety of extensions to our reconstruction algorithms might be made. One such extension may consist of developing more general formulations of the best N-gon algorithm as discussed in Section 3.1, so that the use of less stringent prior shape information could be made. Another example might be the development of algorithms that provide smooth shape estimates of targets, as opposed to the polygonal estimates that are provided at present. Perhaps an estimation procedure using a polynomial or a bandlimited Fourier series representation of the support function could be used for this purpose.

7. References

1. C.G. Backman, *Laser Radar Systems and Techniques*, Artech House, Inc. (1979).

2. R.A. Brooks and G. DiChiro, "Principles of Computer Assisted Tomography in Radiographic and Radioisotopic

Imaging." *Phys. Med. Biol.* **21**, pp. 689-732 (1976).

3. J.P. Greschak, *Reconstructing Convex Sets.* Ph.D. thesis, Massachusetts Institute of Technology, Department of Electrical Engineering and Computer Science (1985).

4. F.K. Knight, *et. al.*. "Tomographic Techniques Applied to Laser Radar Reflective Measurements," *The Lincoln Laboratory Journal,* **2**, pp.143-160 (1989).

5. S.R. Kulkarni, A.S. Lele, M.F. Reiley, "On the Qualitative Differences Between Tomographic Reconstructions from Range-resolved Versus Doppler-resolved Data," Lincoln Laboratory Project Memorandum 52PM-ODT-0042 (August 1989).

6. S.R. Kulkarni and A.S. Lele, "TARMAN: A Model for the Prediction of Laser Radar Signatures of Multiple Complex Dynamic Targets," Lincoln Laboratory Project Report ODT-7 (November 1987).

7. A.H. Land and S. Powell, *Fortran Codes for Mathematical Programming.* Wiley-Interscience, London, (1973).

8. S.R. Lay, *Convex Sets and their Applications.* Wiley-Interscience, New York (1982).

9. A.S. Lele, *TARMAN: A Computer Model for Dynamic Target Simulation.* S.B. thesis, Massachusetts Institute of Technology, Department of Electrical Engineering and Computer Science (1987).

10. A.S. Lele, *Convex Set Reconstruction from Support Line Measurements and its Application to Laser Radar Data.* S.M. thesis, Massachusetts Institute of Technology, Department of Electrical Engineering and Computer Science (1990).

11. D.G. Luenberger, *Linear and Nonlinear Programming.* Addison-Wesley, Reading, MA, second edition (1984).

12. A.M. Mier-Muth, *Adaptive Knot Location for Spline Approximation.* S.M. Thesis, Massachusetts Institute of Technology, Dept. of Elec. Eng. (1976).

13. A.M. Mier-Muth and A.S. Willsky. *A Sequential Method for Spline Approximation with Variable Knots.* Technical Report ESL-P-759, M.I.T. Electronic Systems Laboratory (1977).

14. F.E. Nicodemus, *et. al.*, "Geometrical Considerations and Nomenclature for Reflectance," NBS Monograph 160, National Bureau of Standards, U.S. Department of Commerce, Washington, DC (October 1977).

15. J.K. Parker, *et al.*, "Reflective Tomography: Images from Range-resolved Laser Radar Measurements," *Applied Optics*, **27**, 2642 (1988).

16. J.L. Prince, *Geometric Model-Based Estimation from Projections.* Ph.D. thesis, Massachusetts Institute of Technology, Department of Electrical Engineering and Computer Science (1988).

17. J.L. Prince and A.S. Willsky, *Estimation Algorithms for Reconstructing a Convex Set Given Noisy Measurements of its Support Lines.* Technical Report LIDS-P-1638, M.I.T. Laboratory for Information and Decision Systems (January 1987).

18. J.L. Prince and A.S. Willsky, *Estimating Convex Shapes from Support Line Measurements Using Prior Geometric Information.* Technical Report LIDS-P-1823, M.I.T. Laboratory for Information and Decision Systems (October 1988).

19. J.L. Prince and A.S. Willsky, *A Hierarchical Algorithm for Limited-Angle Reconstruction.* Technical Report LIDS-P-1843, M.I.T. Laboratory for Information and Decision Systems (January 1989).

20. A.W. Rihaczek, *Principles of High-resolution Radar*, Mark Resources, Inc. (1977).

21. L.A. Santalo, *Integral Geometry and Geometric Probability.* Volume 1 of *Encyclopedia of Mathematics and its Applications,* Addison-Wesley, Reading, MA (1976).

22. H. Stark and H. Peng, "Shape Estimation in Computer Tomography from Minimal Data," in *Pattern Recognition and Artificial Intelligence,* E.S. Gelsema and L.N. Kanal, ed. Elsevier Science Publishers B.V., North Holland (1988).

23. F.A. Valentine, *Convex Sets.* McGraw-Hill, New York (1964).

24. A.S. Willsky and H.L. Jones, "A Generalized Likelihood Ratio Approach to the Detection and Estimation of Jumps in Linear Systems." *IEEE Trans. Auto. Control,* Vol. AC-21, pp. 108-112, (February 1976).

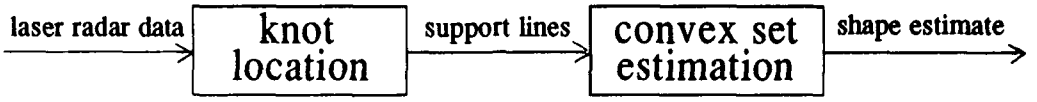


Figure 1: Block diagram of reconstruction procedure.

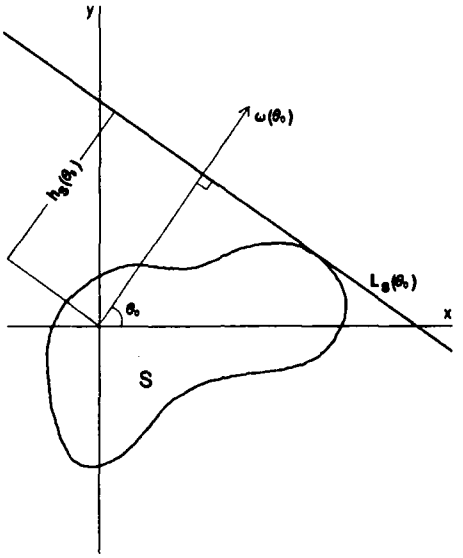


Figure 2: Support line of a set.

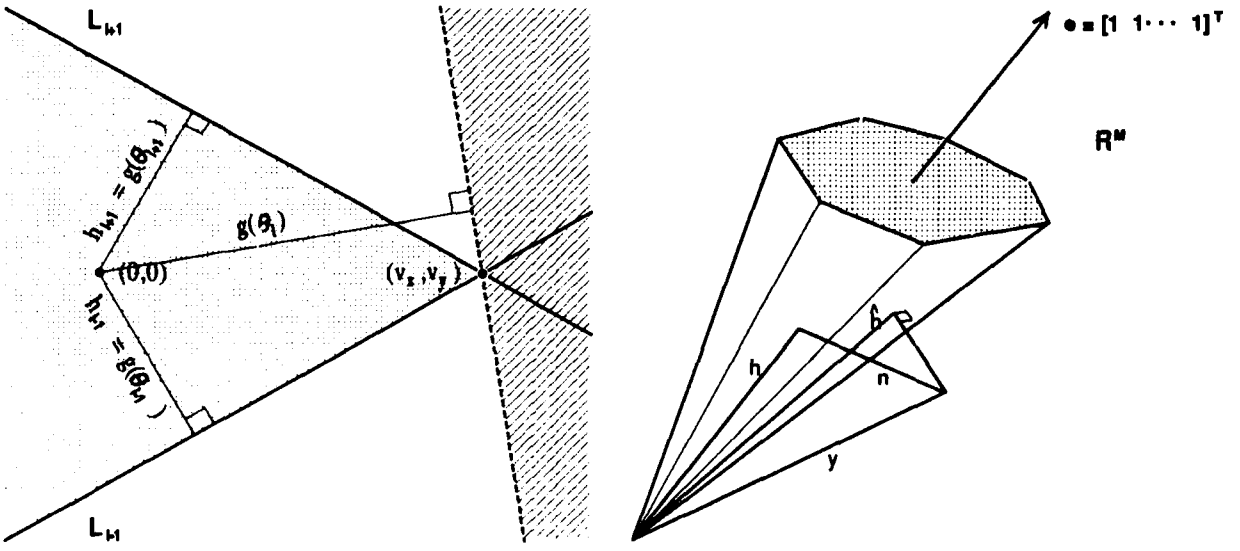


Figure 3: (a) Support line consistency is achieved only if L_i does not lie in the invalid region, shown hatched and to the right of the dashed line at angle θ_i. (b) Geometry illustrating the projection of the invalid support vector y onto the support cone C.

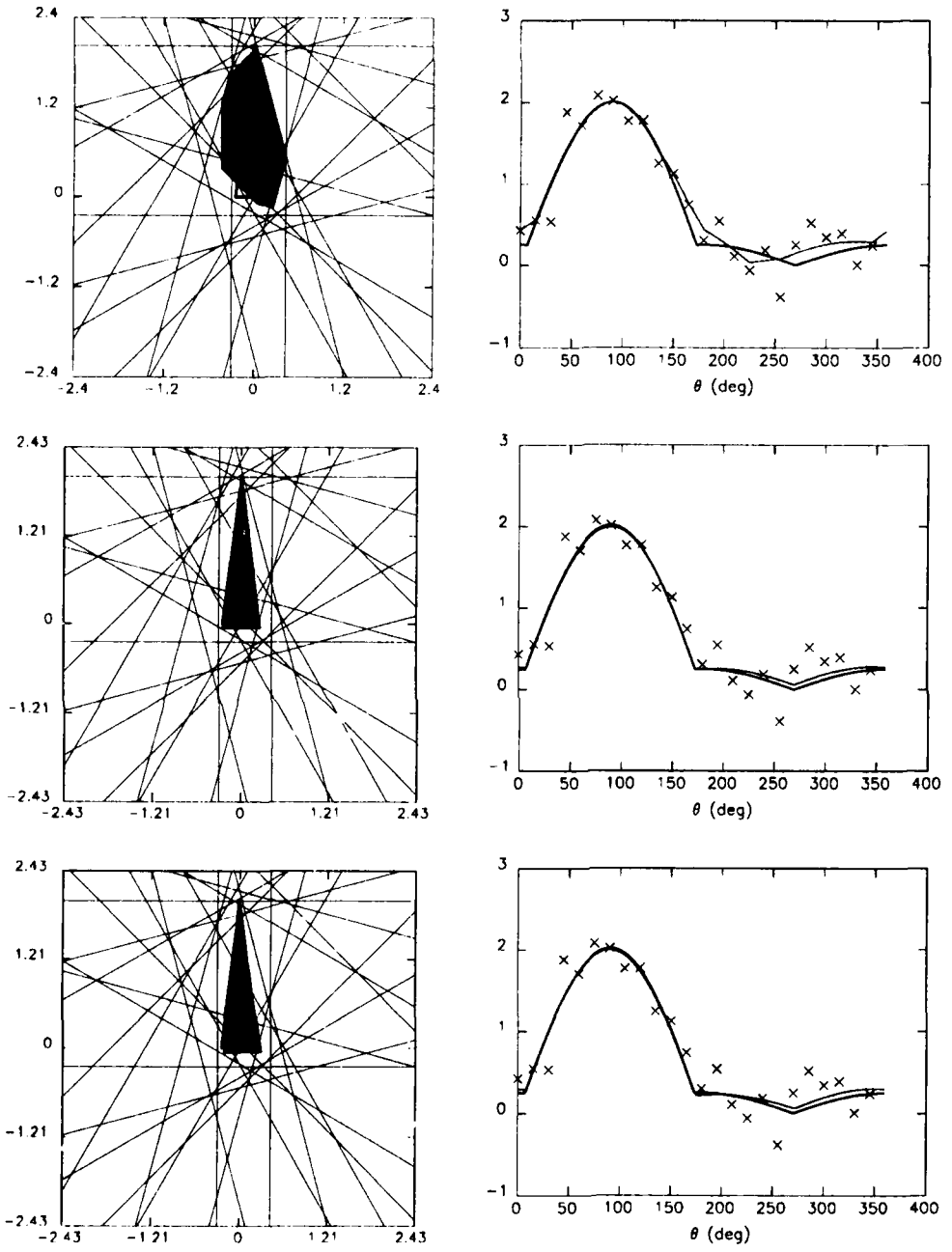


Figure 4: Examples of (a,b) **NUA**, *(c,d)* **BNGON**, *and (e,f)* **BNGONROT** *for the standard triangle in object space and support function space, for $M = 24$ uniformly-spaced noisy ($\sigma = 0.25$) measurements. In (b,d, and f), the support function of the standard triangle is plotted with a thick curve, the noisy support values $\{y_i\}$ are marked by $\times$'s, and the support function $\hat{h}(\theta)$ of the estimated object is plotted with a thin curve.*

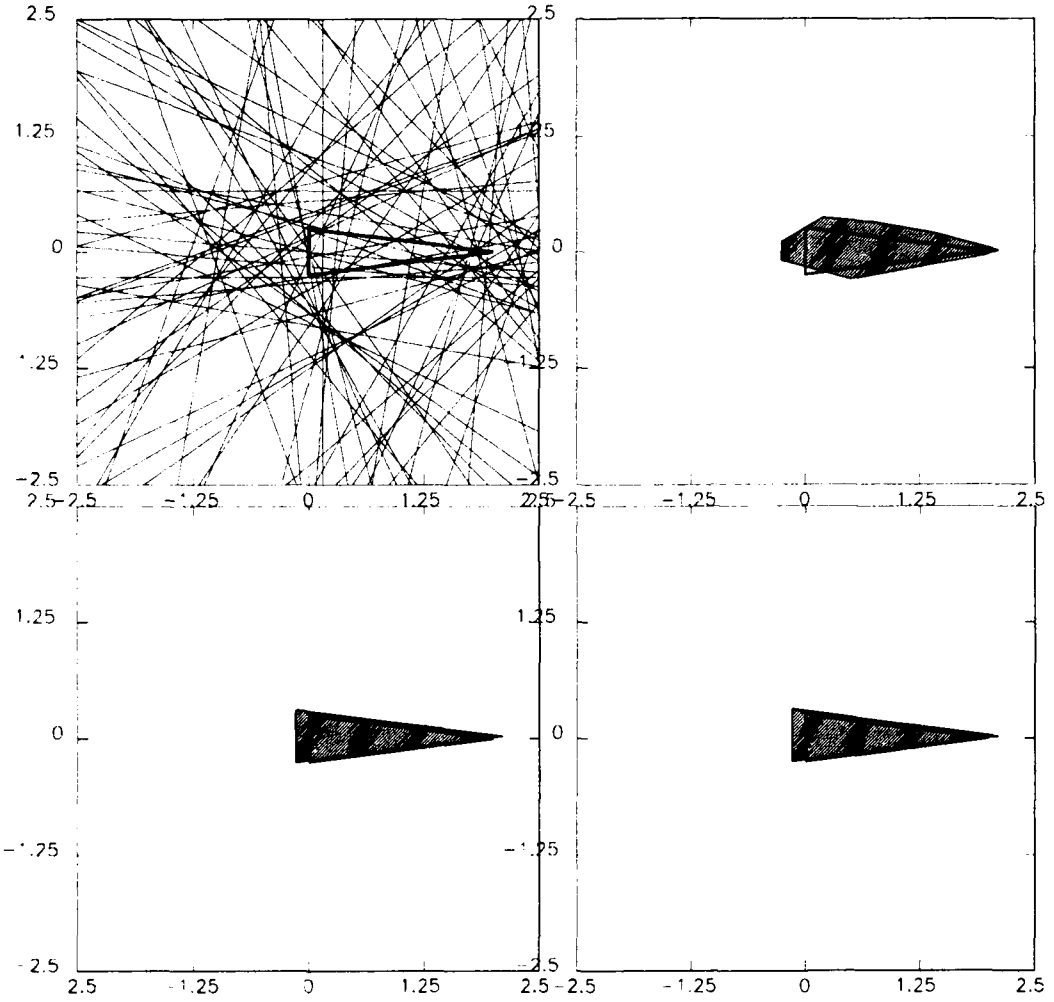


Figure 5: Support lines and convex set reconstructions for simulated range-resolved measurements of a cone. $\sigma_{\text{eff}} = 0.50$.

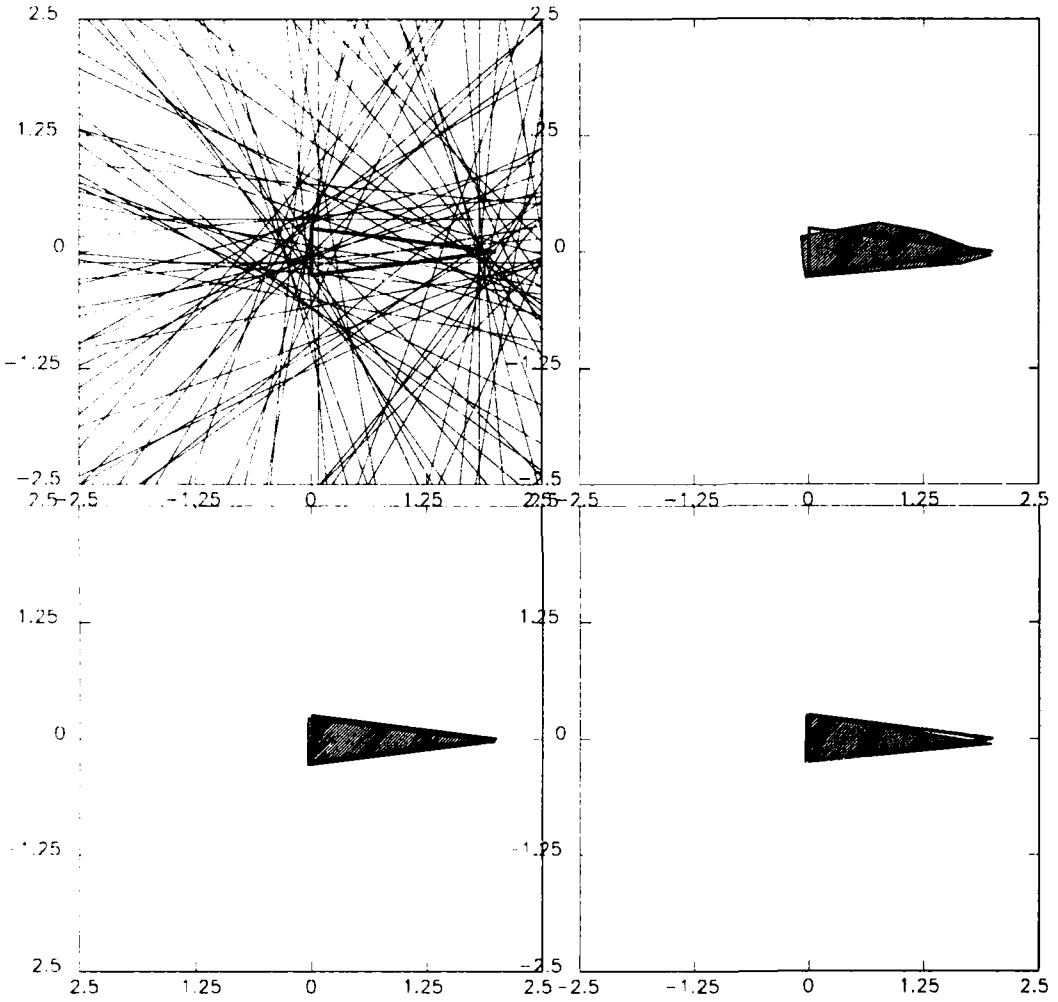


Figure 6: Support lines and convex set reconstructions for simulated Doppler-resolved measurements of a cone. $\sigma_{\mathbf{kl}} = \sigma_{\mathbf{reg}} = 0.25$.

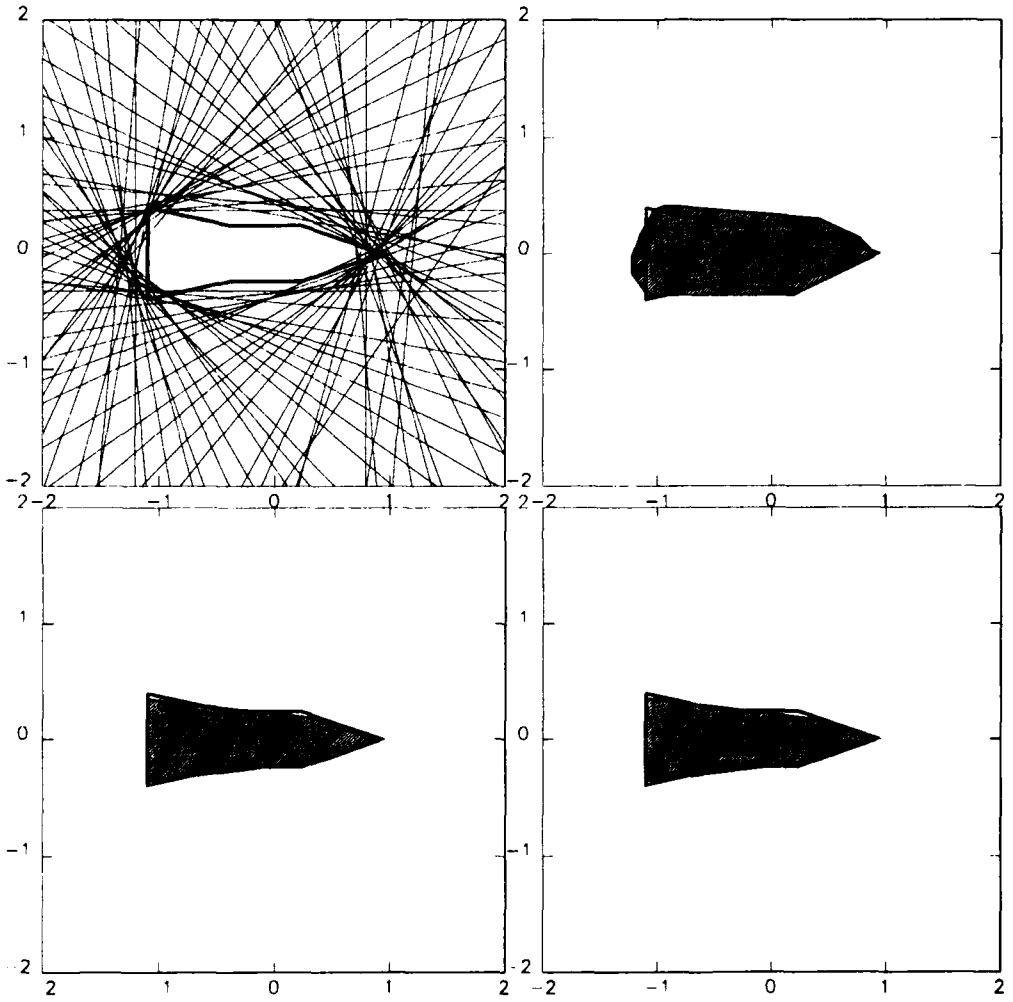


Figure 7: Support lines and convex set reconstructions for laboratory range-resolved measurements of the triconic. $\sigma_{\text{eff}} = 0$.

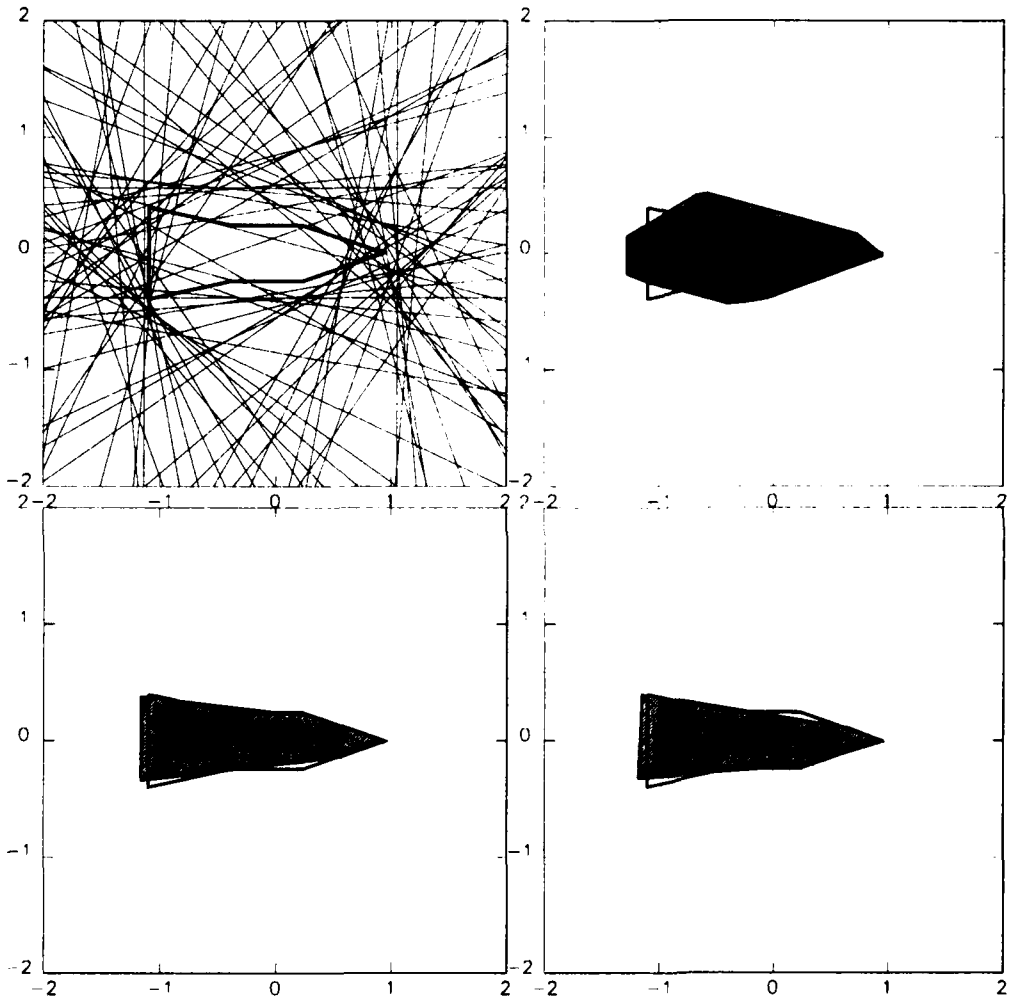


Figure 8: Support lines and convex set reconstructions for laboratory range-resolved measurements of the triconic. $\sigma_{\text{eff}} = 0.25$.

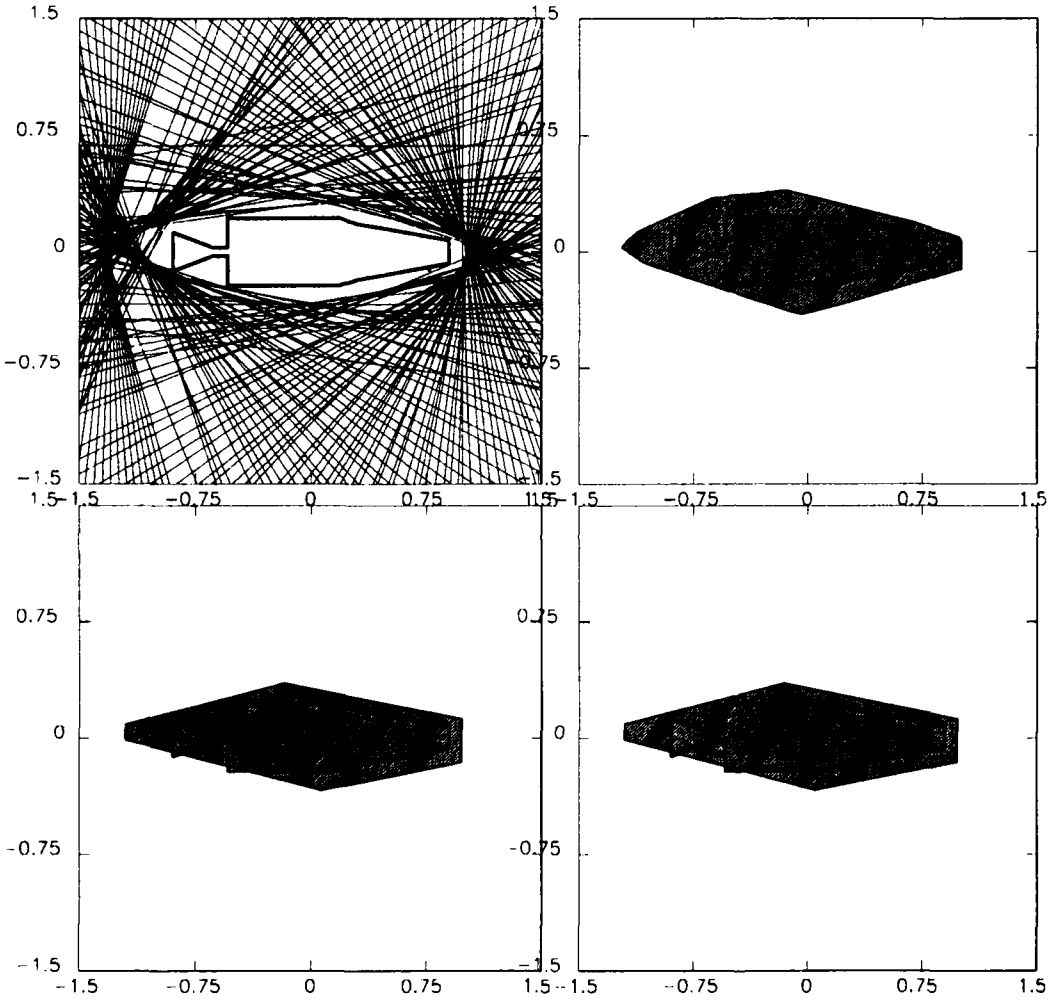


Figure 9: Support lines and convex set reconstructions for field Doppler-resolved measurements of the Thor Delta rocket body. $\sigma_{\mathbf{kl}} = \sigma_{\mathbf{reg}} = 0$.

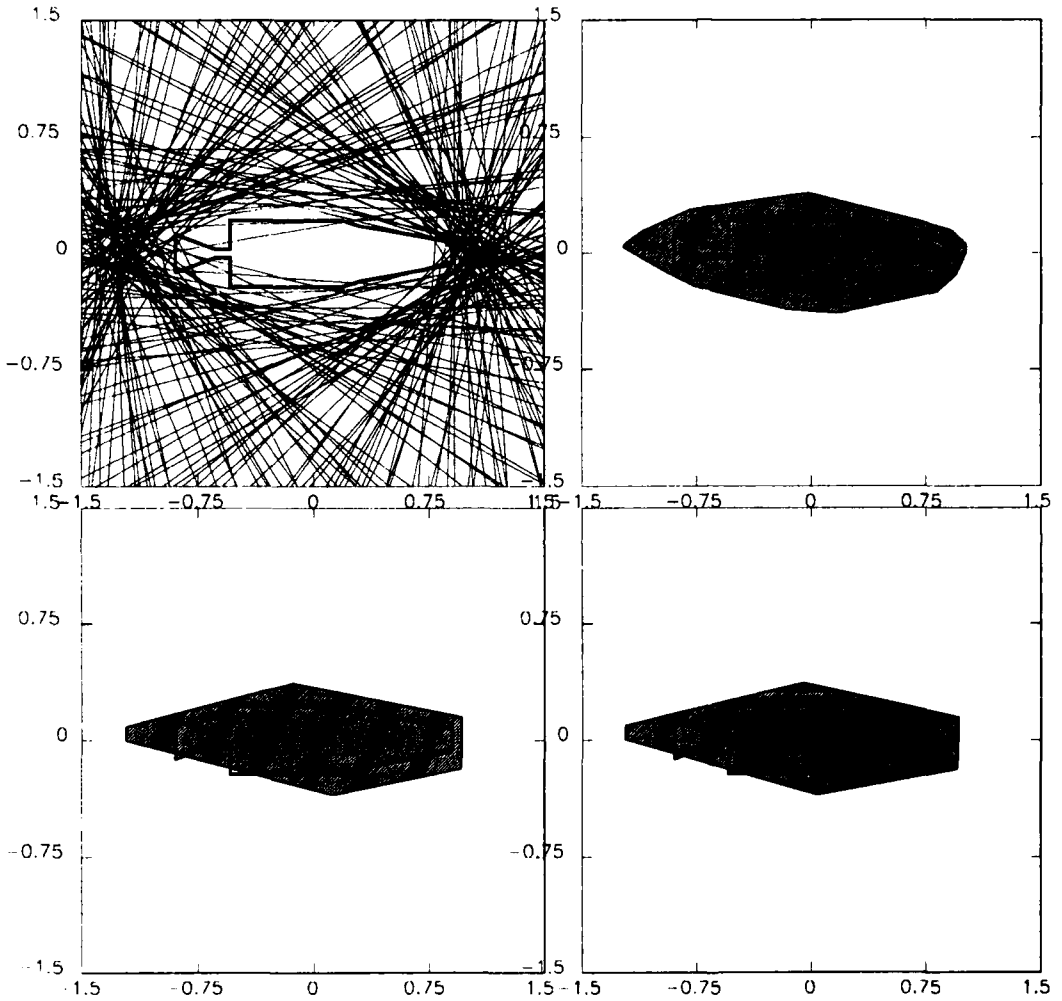


Figure 10: Support lines and convex set reconstructions for field Doppler-resolved measurements of the Thor Delta rocket body. $\sigma_{\mathbf{kl}} = \sigma_{\mathbf{reg}} = 0.10$.

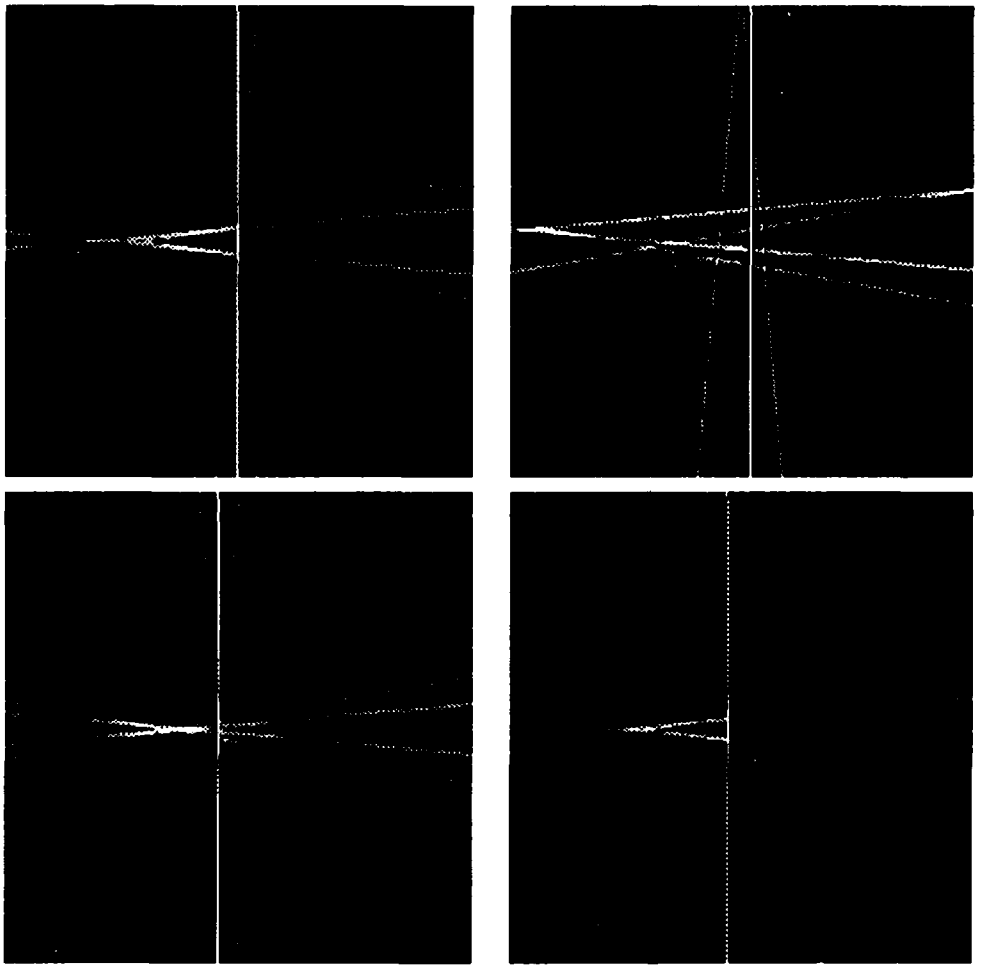


Figure 11: Tomographic reconstructions from simulated range-resolved measurements of a cone. $\sigma_{\text{eff}} = 0.5$.

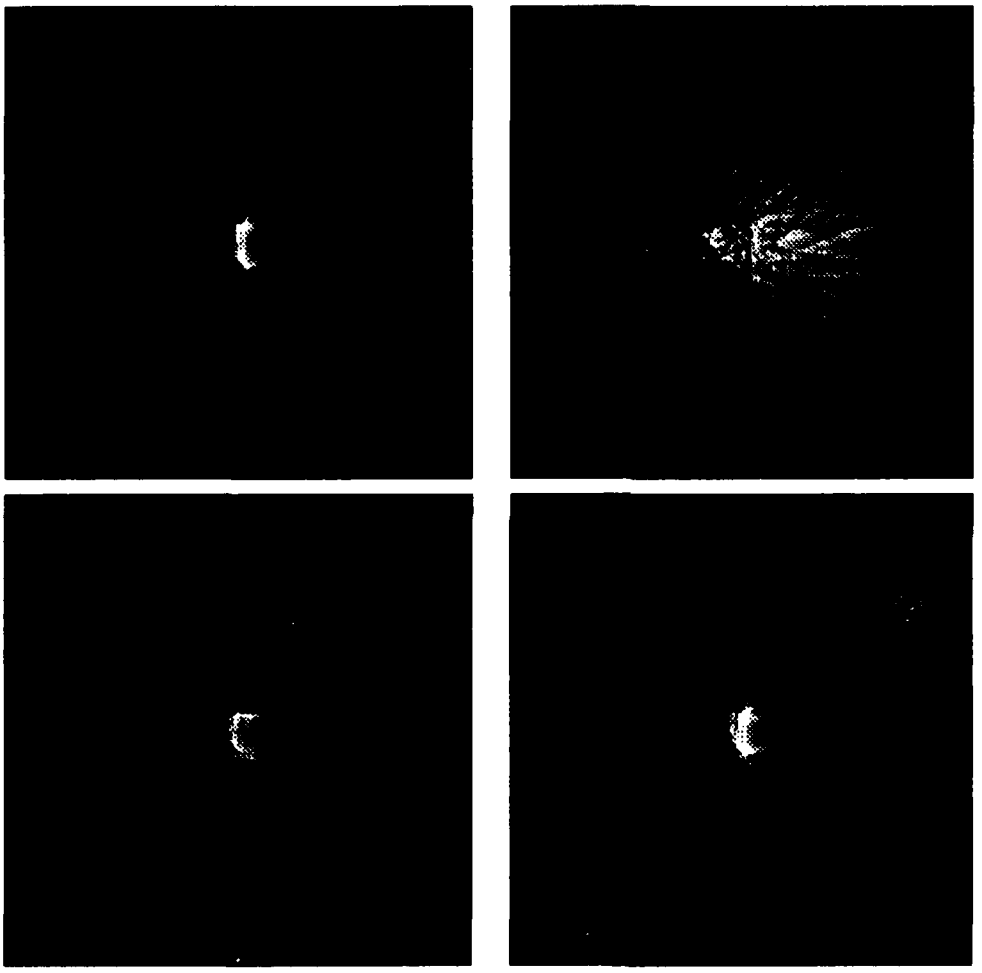


Figure 12: Tomographic reconstructions from simulated Doppler-resolved measurements of a cone. $\sigma_{\mathbf{kl}} = \sigma_{\mathbf{reg}} = 0.25$.

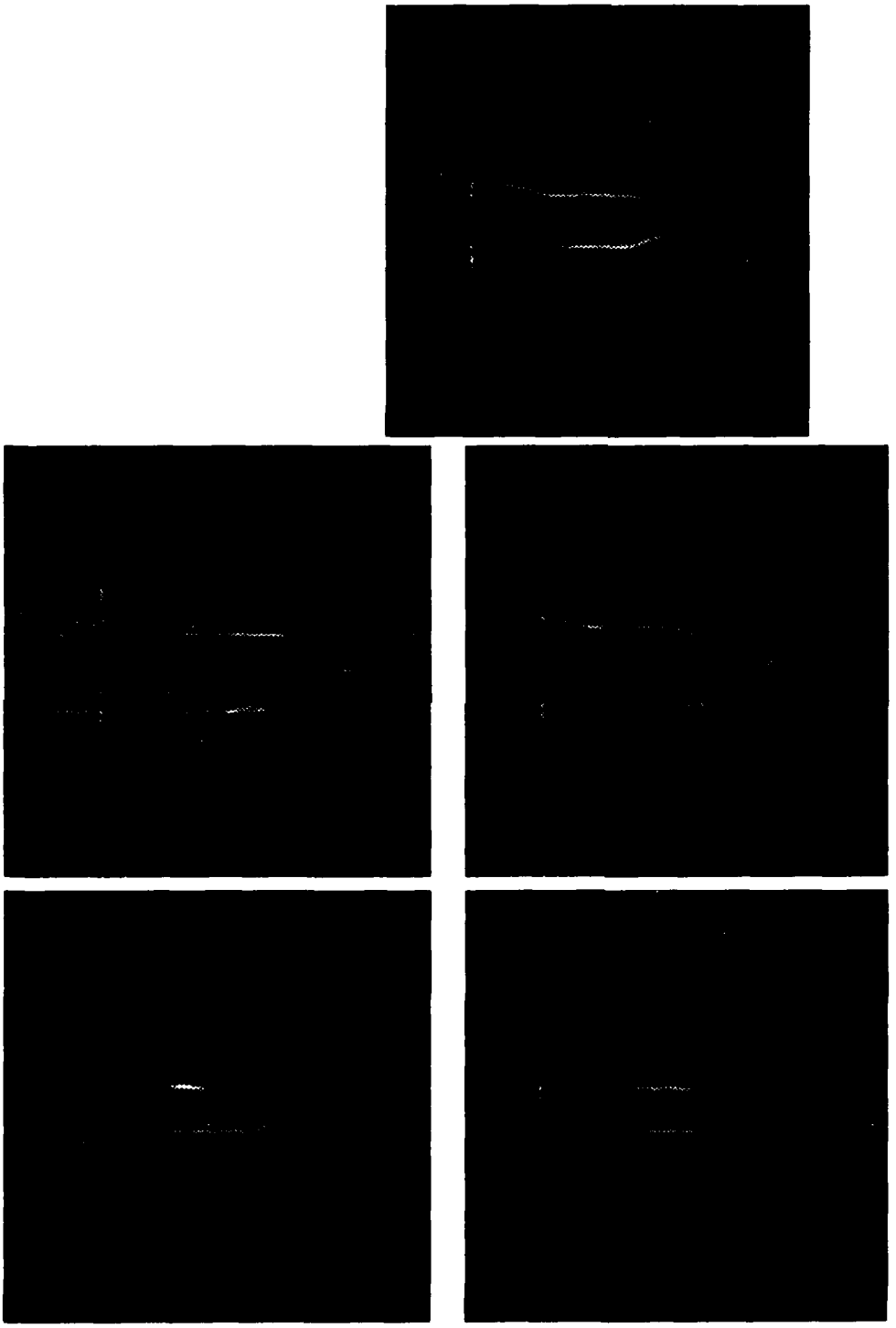


Figure 13: Tomographic reconstructions from laboratory range-resolved measurements of the triconic. $\sigma_{\text{eff}} = 0.25$.

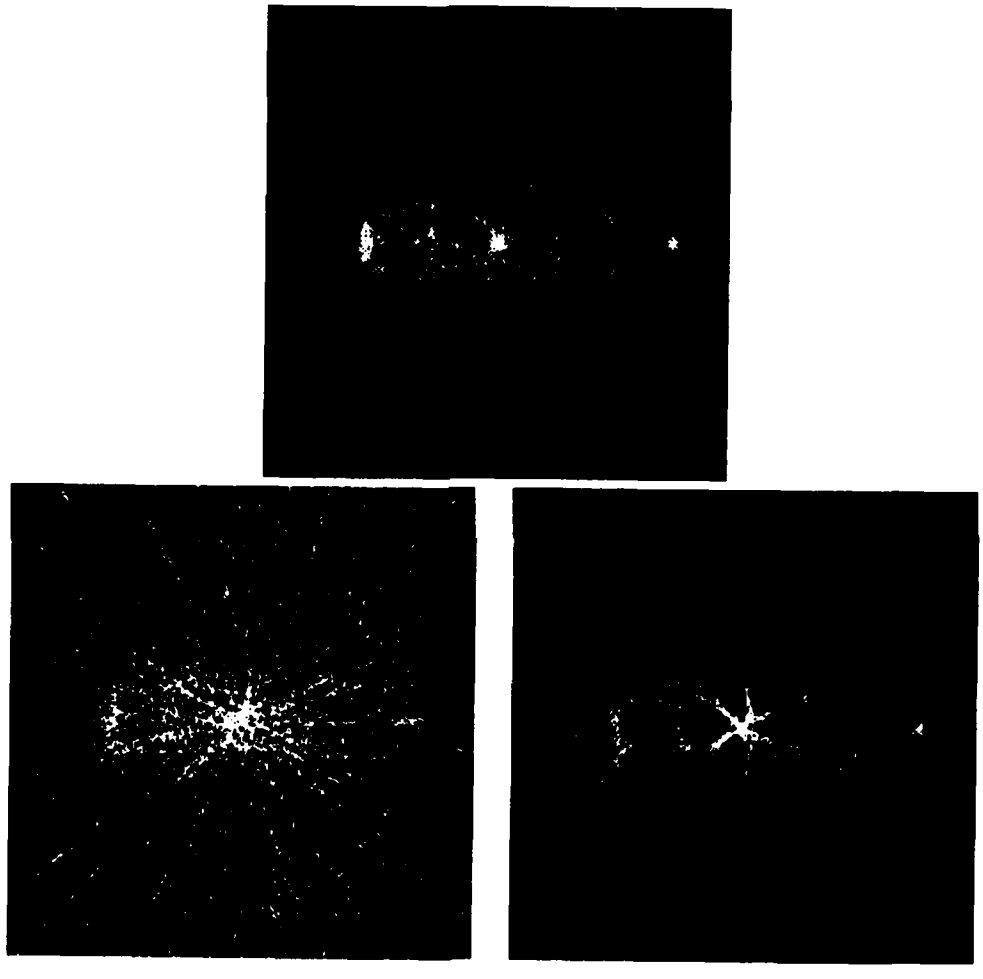


Figure 14: Tomographic reconstructions from field Doppler-resolved measurements of the Thor Delta rocket body. $\sigma_{\mathrm{kl}} = \sigma_{\mathrm{reg}} = 0.10$.

SCALAR REFLECTANCE

Richard Anderson
Professor of Physics
University of Missouri-Rolla
Rolla, MO 65401

Abstract

This paper indicates that the reflectance of a non-ideal statistical target is a (4x4) Mueller matrix. The usual reflectance measured is the bidirectional or biconical reflectance and is a function of the incident and the emergent angles $(\theta_i,\phi_i;\theta_r,\phi_r)$ and the polarization of the incident light beam and the state of polarization passed by the analyzer placed before the detector. In most scattering experiments the reflectance is treated as a scalar number and this paper will attempt to relate this scalar number to a certain combination of reflectance matrix components depending upon the polarization states of the polarizer and analyzer. In many backscatter experiments the reflectance and BRDF are measured, but it could also include the measurement of the atmospheric aerosol volume backscatter coefficient.

Introduction

The classical definition of the reflectance is the ratio of the reflected to the incident flux and is a scalar quantity. This definition is incorrect for unpolarized light reflected from a surface becomes partially polarized. Polarized, coherent laser source are used in most experiments and the incident light is represented by a definite (4x1) Stokes vector. This light is scattered by the target and the light intensity and polarization are changed, so the emergent flux is represented by a new Stokes vector. The interaction with the statistical surface is represented by an average interaction (4x4) Mueller matrix. Depending upon the experiment being performed this definition can define a definite type of reflectance, BRDF, or aerosol backscatter coefficient. When coherent sources are used the emergent signal contains two polarized components, the incoherent signal scattered from each independent surface scatterer and a polarized interference term which is gives rise to the speckle pattern observed at the detector plane. In order to reduce this speckle component the target is transversely translated, rotated, or tilted in a continuous manner to decorrelate the phase and reduce the speckle.

Light scattered from the diffuse statistical target may exhibit diffuse, retroreflected, off-specular, and specular reflected light[1]. Retroreflected and specular reflected light show strong polarization correlation with the polarized incident source and the off-specular light exhibits a weaker correlation. As a result, when polarized light is scattered from a diffuse statistical surface or is transmitted through a statistical phase screen, a vector-matrix theory must be used to analyze the data and the classical scalar theory is inappropriate.

Vector-matrix Theory

The scalar theory of radiometry was described by Nicodemus, et al.[2] for nine different irradiation geometries. This theory will be extended to the vector-matrix form. In radiometry the bidirectional reflectance and BRDF matrices are of most interest. The emergent polarized flux and the incident flux on the target can be equivalently described in terms of the reflectance and the BRDF matrices. Only the bidirectional and biconical irradiation geometries are considered.

Figure 1 shows the irradiation geometry used to measure the bidirectional and BRDF matrices. The target is assumed to be translated, rotated, or tilted to decorrelate speckle. An incident polarized flux represented by the Stokes vector $d\bar{\Phi}(\theta_i,\phi_i)$ is incident within a solid angle $d\omega_i$ at angles (θ_i,ϕ_i) upon an area dA_i of the target. The emergent flux Stokes vector $d\bar{\Phi}_r(\theta_r,\phi_r)$ is measured within a solid angle $d\omega_r$ at angles (θ_r,ϕ_r). The vector-matrix equation for the polarized emergent flux is

$$d\bar{\Phi}_r(\theta_r,\phi_r)=\hat{\rho}(\theta_i,\phi_i;\theta_r,\phi_r)d\bar{\Phi}_i(\theta_i,\phi_i) \qquad (1)$$

where $\hat{\rho}(\theta_i,\phi_i;\theta_r,\phi_r)$ is the bidirectional reflectance matrix which changes the magnitude and polarization of the emergent flux. In Nicodemus'[2] theory ρ is a doubly differential quantity and is designated $d\rho$, but this is a clumsy form in the vector-matrix theory. Equivalently the emergent flux is expressed in terms of the incident radiance as

$$d\bar{\Phi}_r(\theta_r,\phi_r)=\hat{\rho}(\theta_i,\phi_i;\theta_r,\phi_r)\bar{L}_i(\theta_i,\phi_i)\mathrm{Cos}(\theta_i,\phi_i)d\omega_i dA_i \qquad (2)$$

where L_i is the incident radiance and $d\Omega_i=\mathrm{Cos}(\theta_i)d\omega_i$ is the projected solid angle. The emergent polarized flux can be equivalently be expressed in terms of the BRDF matrix and the vector-matrix equation is

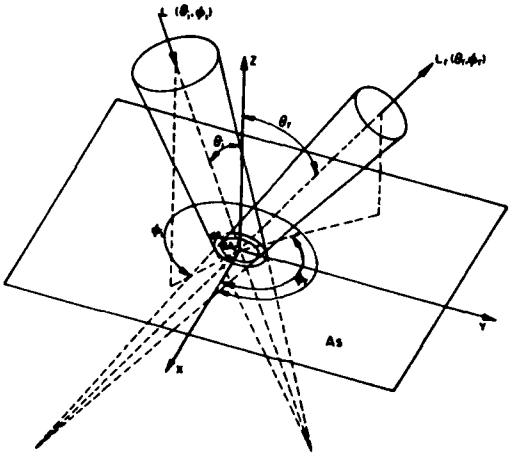


Figure 1. Irradiation Geometry.

$$d\bar{\Phi}_r(\theta_r,\phi_r)=\hat{f}(\theta_i,\phi_i;\theta_r,\phi_r)\bar{L}_i(\theta_i,\phi_i)\mathrm{Cos}\theta_i\mathrm{Cos}\theta_r d\omega_i d\omega_r dA_r \qquad (3)$$

In backscatter $\theta_r=\theta_i-\pi$ and $\phi_r=\phi_i$ and the corresponding emergent backscatter flux expressed in terms of the bidirectional reflectance and the BRDF matrices and the incident polarized flux is

$$d\bar{\Phi}_r(\theta_i-\pi,\phi_i)=\hat{\rho}(\theta_i,\phi_i;\theta_i-\pi,\phi_i)\bar{L}_i(\theta_i,\phi_i)\mathrm{Cos}\theta_i d\omega_i dA_i \qquad (4)$$

or

$$d\bar{\Phi}_r(\theta_i-\pi,\phi_i)=([\hat{f}(\theta_i,\phi_i;\theta_i-\pi,\phi_i)\bar{L}_i(\theta_i,\phi_i)\cos\theta_i d\omega_i]\mathrm{Cos}\theta_r d\omega_r dA_r) \qquad (5)$$

In most experiments finite irradiation and observation solid angles are used because of the source and detector size so the biconical reflectance is measured. In this case an incident polarized flux $\bar{\Phi}_i(\omega_i)$ is incident within a solid angle ω_i about angles (θ_i,ϕ_i) on an area A_i of the target. The emergent polarized flux $\bar{\Phi}_r(\omega_r)$ is emitted within a solid angle ω_r about angles (θ_r,ϕ_r) on an area A_r. Then

$$\bar{\Phi}_r(\omega_r)=\hat{\rho}(\omega_i;\omega_r)\bar{\Phi}_i(\omega_i) \qquad (6)$$

and in terms of the bidirectional reflectance matrix the last equation is

$$\bar{\Phi}_r(\omega_r)=\int_{\omega_r}\int_{\omega_i}\hat{\rho}(\theta_i,\phi_i;\theta_r,\phi_r)\bar{L}_i(\theta_i,\phi_i)\mathrm{Cos}\theta_i\mathrm{Cos}\theta_r d\omega_i d\omega_r A_i \qquad (7)$$

and in terms of the BRDF matrix it is

$$\bar{\Phi}_r(\omega_r)=\int_{\omega_r}\int_{\omega_i}\hat{f}(\theta_i,\phi_i;\theta_r,\phi_r)\bar{L}_i(\theta_i,\phi_i)\cos\theta_i\cos\theta_r d\omega_i d\omega_r A_r \qquad (8)$$

In the backscatter case these equations become

$$\bar{\Phi}_r(\omega_r)=\{\int_{\omega_r}[\int_{\omega_i}\hat{\rho}(\theta_i,\phi_i;\theta_i-\pi,\phi_i)\bar{L}_i(\theta_i,\phi_i)\cos\theta_i d\omega_i]\cos\theta_r d\omega_r A_i\} \qquad (9)$$

or

$$\bar{\Phi}_r(\omega_r)=\{\int_{\omega_r}[\int_{\omega_i}\hat{f}(\theta_i,\phi_i;\theta_i-\pi,\phi_i)\bar{L}_i(\theta_i,\phi_i)\cos\theta_i d\omega_i]\cos\theta_r d\omega_r A_r\} \qquad (10)$$

where the solid angle is $d\omega_r \neq d\omega_i$ because of difference in detection geometry.

Reflectance Backscatter Measurements

Most investigators desire only a number for the bidirectional reflectance or BRDF to completely characterize the target. In reality the number is a (4x4) matrix which depends upon the polarization of the incident light and the polarization state of the analyzer placed before the detector and upon the angles of irradiation $(\theta_i, \phi_i)$and the angles of observation (θ_r,ϕ_r). The relative bidirectional reflectance matrix components can be measured by a variety of techniques[3-10] involving a polarizer, analyzer, and two or more modulated compensators (Pockel cell, photoelastic modulator, or rotating compensator). These modulation techniques allow the first component of the Stokes vector to be determined and by Fourier analyzation the relative matrix components are evaluated. The technique of Thompson, et.al.[10] is shown in figure 2(a). The target is transversely translated, rotated, or tilted to decorrelate speckle. In order to obtain the matrix components of the target transmission and reverse transversal reflection matrix components of the beamsplitter must be determined and the experimental arrangements shown in figures 2(b) and 2(c). The vector-matrix equation for the systems shown in figure 2 is

$$d\bar{\Phi}_r(\theta_r,\phi_r)=\hat{M}_A \underset{\gamma=0^o}{} \hat{M}_4 \underset{\gamma=45^o}{} \hat{M}_3 \underset{\gamma=0^o}{} \hat{M}_X \hat{M}_2 \underset{\gamma=45^o}{} \hat{M}_1 \underset{\gamma=0^o}{} \hat{M}_P \underset{\gamma=90^o}{} d\bar{\Phi}_i(\theta_i,\phi_i) \qquad (11)$$
$$\omega_4 \quad \omega_3 \quad \omega_2 \quad \omega_1$$

where $M_{1,2,3,4}$ are the modulator matrices, $\omega_{1,2,3,4}$ are the modulation frequencies, γ is the angle the transmission and fast axis makes with the horizontal, and MX is either the beamsplitter transmission matrix M_T, the beamsplitter reflection matrix M_R, or the total target matrix M_S. M_S is

$$\hat{M}_S=\hat{M}_R\hat{\rho}(\theta_i,\phi_i;\theta_r,\phi_r)\hat{M}_T \qquad (12)$$

so

$$\hat{\rho}(\theta_i,\phi_i;\theta_r,\phi_r)=\hat{M}_R^{-1}\hat{M}_S\hat{M}_T^{-1} \qquad (13)$$

This last equation indicates the necessity of measuring the beamsplitter matrices M_T and M_R. The Fourier frequencies and the various matrix components measured at these frequencies are given in table 1.

Reflectance As A Scalar Number

In this section it will be shown that the polarization of the incident light and the detected light determine the value of the detected Stokes vector's first component. In this discussion the beamsplitter on transmission and reverse reflection will only attenuate the beam and can be represented by the matrices $M_T=k_TI$ and $M_R=k_RI$. The detector will be assumed polarization insensitive. The detected backscatter flux is

$$d\bar{\Phi}_r(\theta_i-\pi,\phi_i)=k_Tk_R\hat{M}_A\hat{I}\hat{\rho}(\theta_i,\phi_i;\theta_i-\pi,\phi_i)\hat{I}d\bar{\Phi}_i(\theta_i,\phi_i) \qquad (14)$$

where M_A is the Mueller matrix of the analyzer and $d\bar{\Phi}_i(\theta_i, \phi_i)$ is the incident polarized flux on the target. Only some of the possible incident and emergent states of

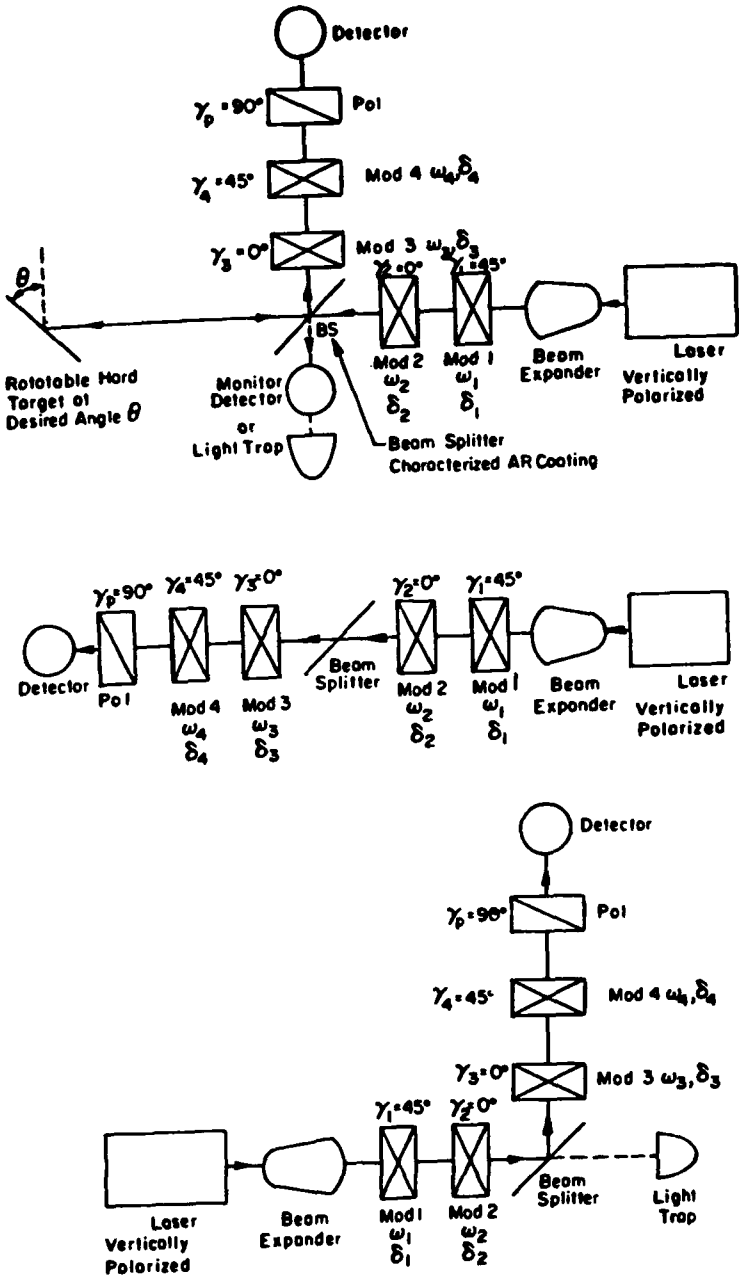


Figure 2. (a) Apparatus to measure scattering matrix $\hat{M}_S$ by Thompson et al.[10] (b) Arrangement of components to measure M_T. (c) Arrangement of components to measure M_R.

Table 1. Typical Fourier Frequencies and the Corresponding Amplitudes from the Signal Ratio $4d\Phi_{r1}/d\Phi_i$

Frequency	Amplitude
d.c.	M_{X11}
$2\omega_1$	$2M_{X12}J_2(\delta_0)$
$\omega_1+\omega_2$	$2M_{X13}J_1(\delta_0)^2$
$\omega_1+2\omega_2$	$2M_{X14}J_1(\delta_0)J_2(\delta_0)$
$2\omega_4$	$2M_{X21}J_2(\delta_0)$
$2(\omega_1+\omega_2)$	$2M_{X22}J_2(\delta_0)^2$
$\omega_1+\omega_2+2\omega_4$	$2M_{X23}J_1(\delta_0)^2J_2(\delta_0)$
$\omega_1+2\omega_2+2\omega_4$	$2M_{X24}J_1(\delta_0)J_2(\delta_0)^2$
$\omega_3+\omega_4$	$2M_{X31}J_1(\delta_0)^2$
$2\omega_1+\omega_3+\omega_4$	$2M_{X32}J_1(\delta_0)^2J_2(\delta_0)$
$\omega_1+\omega_2+\omega_3+\omega_4$	$2M_{X33}J_1(\delta_0)^4$
$\omega_1+2\omega_2+\omega_3+\omega_4$	$2M_{X34}J_1(\delta_0)^3J_2(\delta_0)$
$2\omega_3+\omega_4$	$2M_{X41}J_1(\delta_0)J_2(\delta_0)$
$2\omega_2+2\omega_3+\omega_4$	$2M_{X42}J_1(\delta_0)J_2(\delta_0)^2$
$\omega_1+\omega_2+2\omega_3+\omega_4$	$2M_{X43}J_1(\delta_0)^3J_2(\delta_0)$
$\omega_1+2\omega_2+2\omega_3+\omega_4$	$2M_{X44}J_1(\delta_0)^2J_2(\delta_0)^2$

where $\hat{M}_X$ is $\hat{M}_T$, $\hat{M}_R$, or $\hat{M}_S$

and

$\hat{M}_S=\hat{M}_R\hat{\rho}(\theta_i,\phi_i;\theta_r,\phi_r)\hat{M}_T$

Also

$\delta_0=2.404$ so $J_0(\delta_0)=0$

Table 2. The Emergent Flux and the Matrix Components of the Reflectance Involved in the Classical Scalar Reflectance, Classical Reflectance Defined as $\rho = d\Phi_r / k_T k_R d\Phi_i$

Horizontal-Horizontal	-45^o--45^o
$\rho = \rho_{11} + \rho_{12} + \rho_{21} + \rho_{22}$	$\rho = \rho_{11} - \rho_{13} - \rho_{31} + \rho_{33}$
Horizontal-Vertical	-45^o-+$45o$
$\rho = \rho_{11} + \rho_{12} - \rho_{21} - \rho_{22}$	$\rho = \rho_{11} - \rho_{13} + \rho_{31} - \rho_{33}$
Vertical-Vertical	$+45^o$-Aperture
$\rho = \rho_{11} - \rho_{12} - \rho_{21} + \rho_{22}$	$\rho = \rho_{11} + \rho_{13}$
Vertical-Horizontal	-45^o-Aperture
$\rho = \rho_{11} - \rho_{12} + \rho_{21} - \rho_{22}$	$\rho = \rho_{11} - \rho_{13}$
Horizontal-Aperture	Right Hand-Right Hand
$\rho = \rho_{11} + \rho_{12}$	$\rho = \rho_{11} + \rho_{14} + \rho_{41} + \rho_{44}$
Vertical-Aperture	Right Hand-Left Hand
$\rho = \rho_{11} - \rho_{12}$	$\rho = \rho_{11} + \rho_{14} - \rho_{41} - \rho_{44}$
$+45^o$--45^o	Left Hand-Left Hand
$\rho = \rho_{11} + \rho_{13} + \rho_{31} + \rho_{33}$	$\rho = \rho_{11} - \rho_{14} - \rho_{41} + \rho_{44}$
$+45^o$--45^o	Left Hand-Right Hand
$\rho = \rho_{11} + \rho_{13} - \rho_{31} - \rho_{33}$	$\rho = \rho_{11} - \rho_{14} + \rho_{41} - \rho_{44}$
Right Hand-Aperture	Left Hand-Aperture
$\rho = \rho_{11} + \rho_{14}$	$\rho = \rho_{11} - \rho_{14}$

Each ρ is a function of the input and emergent angles or solid angles depending upon whether the bidirectional or biconical reflectance is measured.

polarization are considered and the states are horizontal, vertical, $+45^0$ to the horizontal, -45^0 to the horizontal, right hand circular, and left hand circular polarized light and the simple aperture of the detector. In the table the first term in the title corresponds to the polarization of the incident light and the second to the state of polarization of the analyzer before the detector. The aperture corresponds to the unit matrix.

Depending upon the exact nature of the experiment it must be remembered that the matrix to be determined may be the reflectance, BRDF, or in an atmospheric backscatter experiments the volume backscatter coefficient of the aerosol.

Summary

A vector-matrix theory has been presented and should be used in scattering experiments to determine the reflectance, BRDF, etc. matrices. One experimental technique is reviewed which could be used to determine the matrix components. It is shown that the scalar reflectance measured by many investigators depends on the polarization of the incident light and the state of polarization of the detected light and it is a different linear combination of the matrix components depending upon the polarization states of the incident and detected beams. Also the reflectance, BRDF, etc. are functions of the angles of incidence and the angles of observation.

References

1. D. A. Haner and R. T. Menzies, Reflectance Characteristics of Reference Materials Used in Lidar Hard Target Calibration, Appl. Opt. 209, 857 (1989).

2. F. E. Nicodemus, J. C. Richmond, J. J. Hsia, I. W. Ginsberg and T. Limperis, Geometrical Considerations and Nomenclature for Reflectance, Self Study Manual on Optical Radiation Radiation Measurements: Part 1 Chapter 6, NBS Monograph 160 (1977).

3. W. Budde, Photoelastic Analysis of Polarized Light, Appl. Opt. 1, 201 (1967).

4. D. E. Aspnes and A. A. Studna, High Precision Scanning Ellipsometer, Appl. Opt. 14, 220 (1975).

5. D. E. Aspnes, Optimizing Precision of Rotating Analyzer Ellipsometer, J.O.S.A. 64, 639 (1974).

6. P. S. Hauge and F. H. Dill, A Rotating Compensator Fourier Ellipsometer, Opt. Comm. 14, 431 (1975).

7. P. S. Hauge, Automated Mueller Matrix Ellipsometer, Opt. Comm. 17, 74 (1976).

8. R. M. A. Azzam, Photopolarimetric Measurement of the Mueller Matrix by Fourier Analysis of a Single Detector Signal, Opt. Lett. 2, 148 (1978).

9. R. M. A. Azzam, Measurement of the Stokes Parameters of Light, A Unified Analysis of Fourier Photopolarimeter, Optik 52, 253 (1979).

10. R. C. Thompson, J. R. Bottinger, and E. S. Fry, Measurement of Polarized Light Interaction Via the Mueller Matrix, Appl. Opt. 19, 1323 (1980).

FLUORESCENCE REMOTE SENSING OF VEGETATION AND SOILS OF THE MOUNTAIN ECOLOGICAL SYSTEMS BY A LASER LIDAR TECHNIQUE

T. A. Trifonova, A. N. Nazarian*, and V. G. Atanessian

Division of Geography
Institute of Geological Sciences
Armenian Academy of Sciences
Yerevan, Armenia 375019 USSR

Abstract

The helicopter-boarded original pulsed laser-spectrometer with automatic PC-monitoring has been used for a fluorescence remote sensing of the open soils and of the natural as well as argricultural vegetation in the conditions of a mountain country. The specific spectra of fluorescence from different objects have been obtained and identified.

The fluorescence remote sensing of the vegetation and soils is very informative method for a study both of the physiological processes in the plants on the cell level and of the organic minerological composition of the soils [1]. In contrast with measurements of the reflecting parameters of the natural objects when the geometric factors play a significant role, this technique has a direct connection with internal physical processes being studied in the objects, in particular with the mechanism of the light-induced excitation of the organic mineral substances in the molecules. The measurement parameters for the fluorescence technique are the spectra of photoluminescence as well as the characteristic decay times of the excitation of the molecules. These two independent parameters which can be measured simultaneously, allow to carry out the detailed analysis (including the quantitative measurements) of the different types of the vegetation and soils for their classification and identification.

In the presented paper we perform the first aspect only of this study, i.e. the photoluminescence (fluorescence) spectra of the vegetation and soils of the mountain ecological systems by a laser lidar technique.

The helicopter-boarded original laser-spectrometer with automatic PC-monitoring [2] has been used for a fluorescence remote sensing both of the open soils (nearby the lake Sevan) and of the soils under natural as well as agricultural vegetation in the conditions of such mountain country as Armenia. The optical scheme of the system consists of the irradiating (laser) and detecting (telescope and polychromator) parts being disposed along the same axis (collinear scheme of excitation and detection). The linear aperture of the telescope was 260 mm (spot size of the sensing beam). The wavelengths of the pump intensity were the second, third and fourth harmonics of the pulsed YAG: Nd^{3+} laser (the wavelength λ = 1.06 nm), namely 532, 355, and 266 nm with pulse energy 26, 6, and 1mJ, accordingly. The pulse duration was ~15 nsec; the repetition frequency was up to 25 Hz. The spectral range of the sensing determined by the polychromator, is composed of the bandwidth 350 - 800 nm with 12.5 nm resolution. Any 22 discrete portion (with the same bandwidth 12.5 nm) of the whole spectrum have been brought out on photomultipliers by fiber branches. Thus, we had a multichannel detection system of optical spectrum with 22 channels. The signals from the photomultipliers were transformed by the analog-code transformer and inserted in the memory of the PC computer. Thus, the spectra of back-scattering radiation excited by a single laser pulse could be written in our case. The possibility of summation of the fluorescence spectra from the different laser pulses over the fixed program was used (important for the homogeneous irradiated surfaces).

The special standard light source of nanosecond pulses placed before the entrance of the telescope and representing a model source like the back-emitted radiation was used as a calibrator; by the variation of the amplification coefficients for each opto-electronic channel, the correspondence of the spectrum on the exit of the system to the real known spectrum of calibrator has been obtained. Both fluorescence intensity spectra from the studied objects and the spectra of natural reflected noise are detected simultaneously during the measurements.

* Division of Laser Technique, Yerevan State University.

The study of temporal characteristics (the decay times of fluorescence over the depth) demands the detection of the pulse shape during the radiation. The special electronic system has been used for that and the spatial resolution of 1m was obtained [2].

The average altitude of the helicopter flight was 70 - 200 m over the surface; the velocity was about 30 m/sec. Apart from the fact that the maximal intensity fluorescence corresponds to the flights at early morning [1], we have realized the flights at the hours of the day because of the technical reasons. The measurements have been carried out in October 1988.

A preliminary express visual analysis of obtained spectra reduce to the following*. Four characterisitic cases are verified: (1) the open [ploughed up or not] soils; (2) the soils being under natural (dry or juicy)vegetation; (3) the soils with the continuous layer of the cultural (or natural) plants, and finally, (4) the forest areas.

The specificities of fluorescence spectra for these cases are determined, on the one hand, by the fact that for the open soils with small quantity of the organic substances the mineral compositions play a principal role. But even for this case the existence of organic materials in the soil, e.g., of the humus in dark-brown or in black earth, is manifested exactly in obtained spectra. On the other hand, for soils with vegetation the spectrum parameters are determined by the total quantity of the green biomass, biochemical and physiological compositions and processes in the plants, quantity of water etc., but also by the layer soil surface. So, the detailed interpretation of the fluorescence spectra is a very complicated problem and we can speak about the specific tendencies and general behavior only. Typical series of obtained fluorescent spectra for mentioned above cases are shown in Figure 1 - 4.

The series in Figure 1 correspond to open soils, 1a is the brown semi-desert earth; 1b is the same but for ploughed up soil; 1c is also ploughed up soil but dark-brown (black) meadow earth.

The series in Figure 2 correspond to the soil with natural vegetation: 2a is the mountain subalpine soils under the faded vegetation; 2b is the green juicy plants (meadow-marchy vegetation).

The series in Figure 4 correspond to the forest area; 4a is the green leafy woods (100%); 4b is the same but when the area was irradiated by a pump of second harmonic (λ = 532 nm) of the fundamental laser radiation.

All the spectra types exhibit fluorescent emission in the blue range around the wave length 450nm. This characteristic band (440 - 480 nm) of fluorescence has been observed in many earlier studies (see e.g. [1]). The identity of the pigments responsible for the fluorescent maximum at 450 nm remains to be definitely established [1]. The fundamental substances being responsible for fluorescence in that range are probably the reduced piridinnucleotides and oxidated flavor proteins. These substances are in all cells of the plants and determine energetic processes in the cell.

Another characterisitic band of them is a green range at 525 nm (510 - 540 nm) but our measurements do not show exactly such line on the spectra. The small local maximum in this range is manifested in Figure 3a (and maybe in Figures 2a and 2b) only.

This fact probably supports the proposition existing in literature that the maximum at 525 nm can be connected with vegetation of wood and faded vegetation [3]. The definite role have to belong to mineral substances of the soil. In fact, the measurements on the isolated plants in laboratory conditions do not manifest this band of fluorescence [4]. On the other hand, the existence of mineral (and other) additions can result in absorption of fluorescence radiation.

The universal meaning for obtained spectra has a maximum in yellow range at 552 nm (especially this line is allotted in Figures 1a, 3b, and cd). Analysis shows that the maximum concerns just the properties of the soil and characterizes the mineral substances in it. In fact, figures 1a, 3b, 3c and 3d describe the open soils in the significant parts with a small magnitude of concentration of organic materials. In contrast, the soils with great ratio of the organic substances (see e.g. Figure 1c) or with a continuous layer of vegetation (figure 2b and 4a) have no such peaks in fluorescence.

---

*We discuss here the reults when we used as a pump the third harmonic (λ = 355 nm) only of the fundamental laser radiation.

The maxima in red range of spectrum around the lines 691 and 717 nm are easily identified practically in all spectra (the best case is in Figure 3b). This result is very well known and shows the fluorescence of chlorophyll in the plant cells (both for open vegetation and for organic materials in the soil). The observable fluorescence in this range is a universal evidence of the vegetative biomass because the chlorophyll is a fundamental pigment of photosynthesis [5]. The variation of the fluorescence intensity in this range is effective method of controlling the different mechanisms of the light energy migration in pigment systems and gives a good technique for study of them [6, 7]. E.g., the visible suppression of this spectrum in Figure 3a can be explained by high effective migration of the light energy over the chains of photosynthetic apparatus in winter-wheat.* (so, the energy dissipation in the form of fluorescence is small enough for this case)[3]. In contrast, the want of the water decreases the efficiency of photosynthesis and so, the fluorescence of chlorophyll is increased sharply (cf. Figure 2b) [8].

We can declare that our results show a specific difference between two lines at 691 and 717 nm. In fact, a simultaneous arising of these two peaks are more characteristic for open green vegetation (see Figures 2b, 3a, 3b, 3c, and 3d); as to open soils (visible green vegetation-less earth) the second peak (at 717 nm) only is manifested (Figures 1a, 1c, and 2a). Note, that the scattering of the data and deviation of characteristic lines of the spectra could be due to the type variety of the plants for each group [1](see e.g. Figures 2b, 3c, 3e). As to a local maximum at 541 nm (see Figures 1b, 1c; 3c, 4b) it can be introduced as corresponding to integral fluorescence from both organic and mineral parts of the vegetativeless soils and to more fine reasons [4,9,10]**.

It is interesting to compare two fluorescence spectra from different pump radiations (355nm - Figure 4a, 532nm - Figure 4b) for the forest area. Because of the energy conservation law the range of fluorescence meets a dramatic change: it shifts to the side of high magnitude of the wavelength***. The Specific chlorophyll lines are manifested very well in Figure 4b. The range about 650 nm can be also explained by the Raman scattering intensity in water [2] (cf. Figures 2b and 4b).

The analysis of obtained data has been carried out at the qualitative level and allowed us to identify the states both of soils and types of vegetation. This is a general but initial step of study of these problems and we discussed the preliminary results only. But even the problem of early prognosis of the stress states of the plants as well as of the detection of biomass and the plants phase development demands more detailed and consequential (with continuous variation of the investigated sign) measurements****. Such complete study is not developed yet[1]. Universal method of identification of the vegetation types by the laser fluorescence remote sensing technique does not even exist for the present time.

The identification of vegetation is based on the large enough and fundamental classes of the objects, i. e., vegetation of grass (monocots and dicots), of wood (leafy and pine), of water [3]. Out data concern in general to the former class only and the specification of the different structures in a frame of this class has been done. We showed that the approach useful for preliminary visual classification.

The next step is to find the quantitative parameters of this classification by means of mathematical data processing. Good results could be obtained by the correlation technique and by the image decoding (c.f. [11, 12]).

The relatively brief and simple analysis for identification of objects can be done using the mutual correlative (linear) coefficient K which shows the degree of the coupling of two stochastic values [12]. The decoding of the measured spectra is produced by a comparison of them with standard known (or initial) spectra (over discrete couple points of two spectra in the same range) being in the memory of the PC and composing the alphabet of the distinguished classes. If "K"=1 the shochastic values are completely correlated, if "K"=0 they are not.

---

*That also can lead to the shift of the fluorescence maximum (e.g., in Figure 3a the line at 666 nm arises instead at 691 nm).

**The line 641 nm is manifested for open soils; the existence of vegetation on soil suppresses this peak.

***The following condition $\lambda_{fluorescence} > \lambda_{pump}$ should be satisfied.

****For the soils the investigations are practically absent.

Here, we cite one example of the analysis made by us for demonstration only (cf. [2]. Our measurements of the spectra of two forests lead to the magnitude of K≈1*. As to comparison of the spectra of the forest and e.g., seaweed of Sevan lake (cf. Figures 4a and 2b) we obtained K≈ 0.39 - 0.61. So, in fact, this approach is informative enough and can be used for numerical identification. The most interesting application of it is to study the variations of the objects in dynamics, e.g., over the different seasons or due to ecological pollutions.

In conclusion, the helicopter-boarded original laser-spectrometer with automatic PC-monitoring has been used for a fluoresecence remote sensing both of the open soils and soils with vegetation (natural, agricultural and forest). The classification of the types of vegetation soils may be done by this technique including the quantitative parameters.

References

1. Laser remote sensing of vegetation, Ed. V. A. Roumyantsev, Academy of Science of USSR, Leningrad, 1987, p 168.
   Measures R. M. Laser Remote Sensing, Wiley, NY 1984 p 550.

2. Avetissian V. M., Atanessian V. G., Melik-Sarkissian A. A. et al., J. The Earth Study from Space (in Russian), 1988, N-3, p 81-85.

3. Chapelle E. W., Frank, M. W., Newcomb, J. W., Applied Optics 1985, 24, N-1 p74-80.

4. Chapelle E. W., McMirtrey J. E., Frank M. W., Applied Optics 1984, 24, N-1 p 139-142.

5. Kanevskii V. A., Riazantsev V. F., Perekrest O. N. et al., ibid [2], 1985, N-6, p37-39.

6. Rubin b. A., Gavrilenko V. F., Biochemistry and Physiology of the Photosynthesys, Moscow State University, Moscow, 1977, p 286.

7. Plant Biochemistry, J. Bonner and J. Karner, Eds., Academy Press, NY 1976, p854.

8. Primary Photoprocesses in Biology, Wiley, NY 1965, p 113.

9. McForlane J. C., Watson R. D., Tteisen A. F., Applied Optics 1980,19, 3287-3289.

10. Chapelle E. W., Wood F. M., Games Gr., Applied Optics 1984, 23, p 134-142.

11. O'Nwil, R. A., Buja-Bijunas L., Rayner D. M., Applied Optics 1980, 19, p 863-870

12. Bevington P. R. Data Reduction and Error ANalysis for the Physical Sciences, McGraw-Hill, NY 1969.

*The comparison has been done over the 12 couple points in the range of fluorescence 580 - 720 nm.

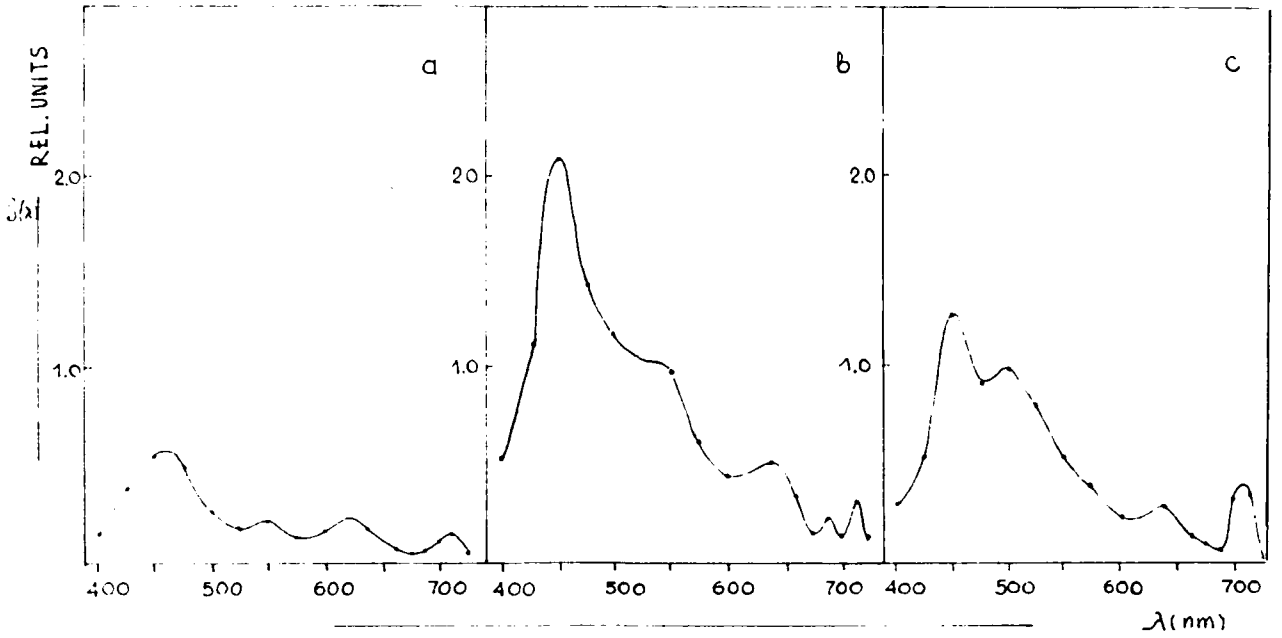


Figure 1. Fluorescence intensity spectra S(λ) for open soils:
a) Brown semi-desert earth b) The same as "a" but for ploughed up soil
c) Dark-brown (black), meadow ploughed up soils

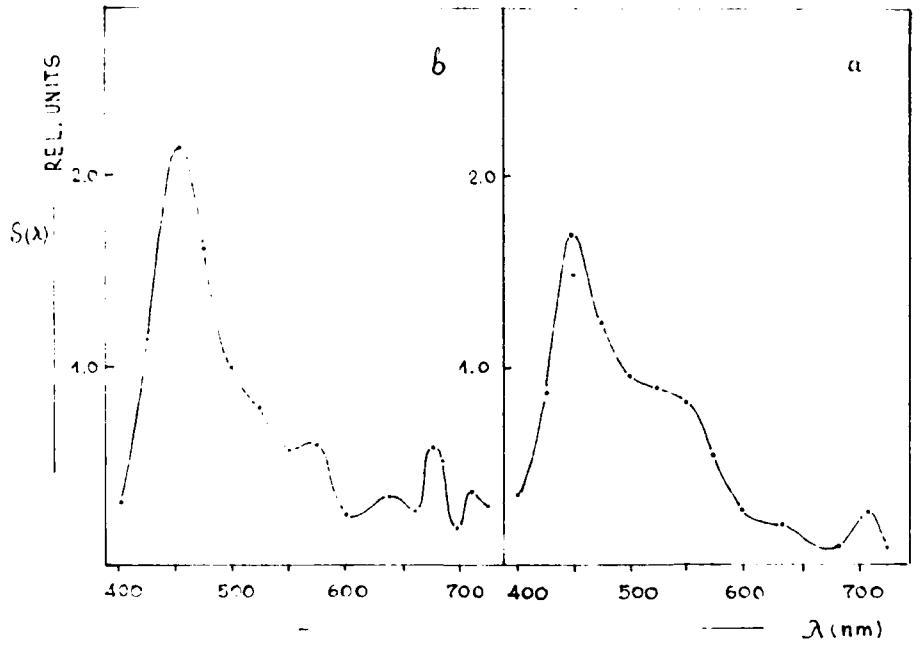


Figure 2. S(λ) for the soil with natural vegetation:
a) Mountain subalpine soil under faded vegetation
b) Green juicy plants (meadow-marchy vegetation)

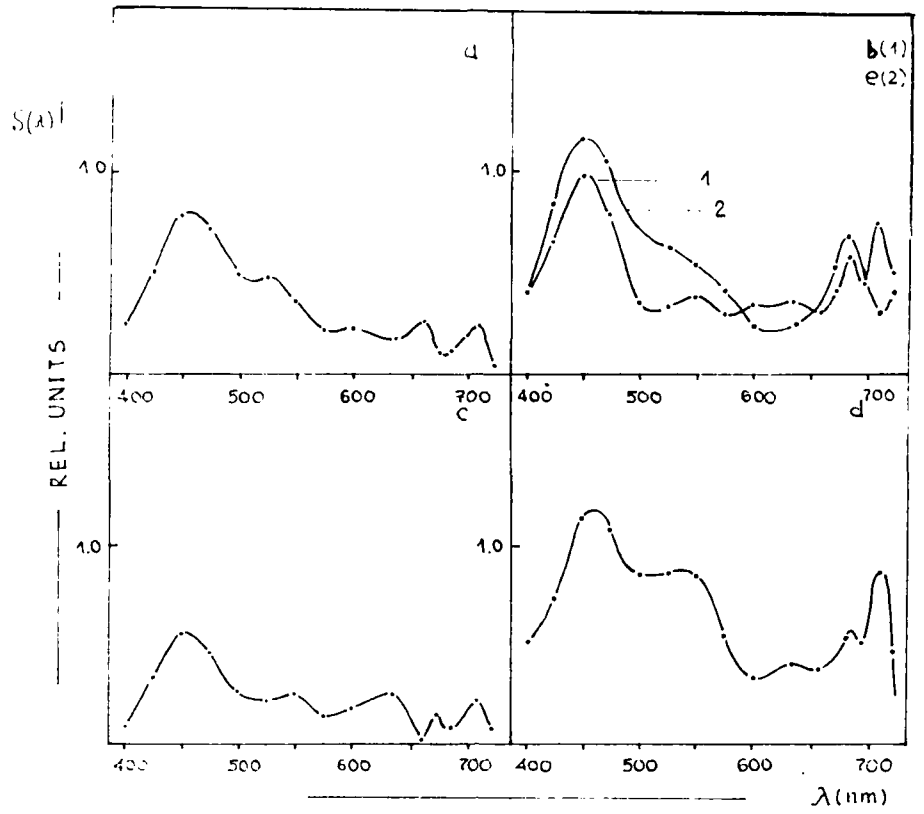


Figure 3. S (λ) for the cultural plants:
a) Green field of winter-wheat risings (60-70%) on the black earth
b) Cabbage-garden (80%) (30%) on the black earth
c) Mowed (light green) field (30%) on the brown soil
d) Vineyard
e) Feeding vegetables

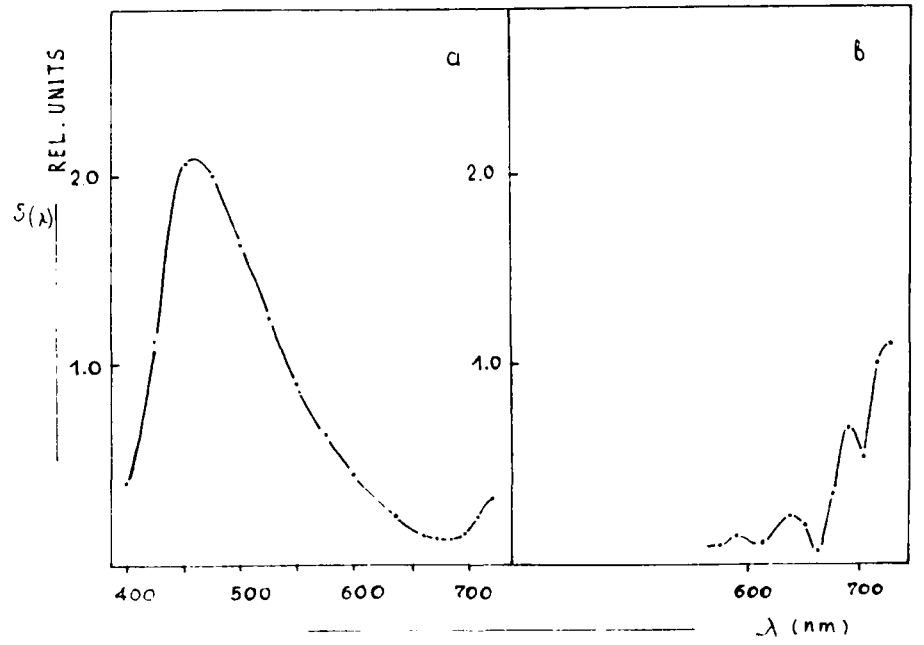


Figure 4. S (λ) for the forest area:
a) Green-leafy woods (100%)
b) The same as "a" but for the pump wavelength λ = 532nm

DEVELOPMENT OF A LOW-COST DIFFERENTIAL-ABSORPTION REMOTE SENSOR FOR HYDROCARBONS

Jan E. van der Laan, Clinton B. Carlisle, and Joseph Leonelli
SRI International
333 Ravenswood Avenue, Menlo Park, California 94025

Abstract

A remote sensor system for hydrocarbon detection applications has been developed by SRI International. The HeNe laser based system operates at 2.39 and 3.39 μm wavelengths. The 3.39 μm wavelength is highly absorbed by hydrocarbons (such as methane, propane, butane,and ether) while the 2.39 μm wavelength is nonabsorbed. The 1 μm spacing between laser lines, a rather large separation for differential measurements, is not a significant problem, since natural atmospheric constituances effect both wavelengths nearly equally. Systematic and minor atmospheric anomalies are cancelled out prior to operation by a simple balance adjustment.

Evaluations are being conducted over a 300 m test range at SRI, and longer-range tests are planned. The system uses retroreflectors placed at the far end of the test range and interrogates the path between the system and target. A sample chamber with quartz windows is placed in the laser beam anywhere along the path for calibration of sensitivity. Free releases of gas are also used for demonstration purposes. The system has a scanning mount and can be programmed to scan between a number of targets to provide area coverage. It is envisioned, because of the low cost per system, to use several units in a tomography configuration to provide grid area coverage.

Background

Since the early 1970s, SRI International has pioneered the development of ultraviolet (UV) and infrared (IR) differential absorption light detection and ranging (DIAL) remote sensing systems (Ref. 1 through 7). For the most part, the systems developed are range-resolved DIAL systems, which provide plots of concentration versus range. These systems employ relatively high-energy lasers and sophisticated data-acquisition systems that require highly trained personnel to operate them. SRI has developed a remote sensor system that is relatively simple to operate and is low cost when compared with alternate approaches to achieving the same area coverage. The hydrocarbon sensor system can be used to measure changes in the ambient levels of hydrocarbons (such as natural gas, methane, propane, butane, and ether) out to ranges of 1 km. The system operates in the column content mode and requires a retrorefelector target at the far end of the path of interest. Plume location and direction information can be obtained for a tomographic grid area.through measurements along multiple paths by two or more sensor units. The system provides real time information and a data storage capability for evaluation and documentation.

System Description

The Hydrocarbon Sensor System (Figure 1) consists of three units:

- Sensor Subsystem
- Scanner Platform and Interface Unit
- Control- Processing and Monitor Subsystem unit

A photograph of the system is shown in Figure 2.

Sensor Subsystem

A functional description of the sensor subsystem is shown in Figure 3. The two Continuous Wave (CW) IR HeNe laser outputs (2.39 and 3.39 μm) are alternately transmitted by a chopper that operates at 200 Hz. The two beams are directed parallel to each other through an AR-coated germanium (Ge) beamsplitter to the center of the output transmit mirror. Parallel beams are used rather than coaligned beams so that the maximum power can be transmitted. The transmit mirror directs the beams through the atmosphere to a retroreflector target that has been prealigned with the receiver telescope and detector. To aid in aligning the IR HeNe lasers with the retroreflector, a visible HeNe laser is used. The visible-HeNe laser is combined with the two IR laser beams on the Ge beamsplitter output surface, which is aligned to reflect the HeNe beam along the IR HeNe lasers transmit axis. The Ge beamsplitter will transmit 90% of the IR-HeNe laser power and reflect about 10% to the power monitor detector. A quartz lens is used to focus the laser beams on the thermoelectrically (TE) cooled, 3 mm diameter lead sulfide (PbS) power monitor detector. The detected power monitor signals are amplified and sent to an FET switch circuit (located in the interface unit) that separates the two wavelengths into two independent signals. The IR laser signals reflected by the retroreflector are collected by the 8 inch f10 telescope, which focuses the signals on to a TE-cooled quadrant PbS detector. A quadrant detector is used to generate error signals for the automatic positioning system. The outputs from each quadrant are amplified and sent to the FET switch circuits that separate the two wavelengths.

The sensor subsystem is mounted on a scanner platform that is controlled by the control-processing and monitor subsystem from a remote location. As configured, the operations can be located up to 100 ft from the sensor. Scanner operation is automatic in the normal operational mode or by joystick control when setting up operations. When multiple lines-of-sight (LOS) are being used, the operator will point the sensor at each retroreflector target and program its location into the scan routine software for use during automatic operation. The operator is aided in this operation by a video camera that is coaligned with the sensor receiver. When the

sensor is properly aligned on a retroreflector, the sensor's visible HeNe laser will be reflected back to the receiver and should be clearly visible on the video monitor screen. Although this initial alignment is sufficient to position the sensor to the desired LOS, it is not accurate enough for repetitive scan operations. This is because the laser beams are not spatially uniform in intensity, and they grossly overfill the small retroreflectors used. Because it would be cost-prohibitive to use a positioning system with precision enough pointing accuracy for this type of operation, our scan routine uses a closed-loop positioning circuit that is activated after the preprogrammed scan position is reached and prior to collecting data. This closed-loop circuit uses the receiver quadrant detector signals on the reference line (2.39 μm) to generate position-correcting control signals for the scanner.

Sensor Platform and Interface Unit

Figure 4 shows the components housed in the sensor platform and interface unit. The chopper control unit (top right) provides the drive signal for the chopper used to alternately transmit the two IR laser signals. This unit also provides the synchronization signal that controls the FET switch that separates the two wavelengths contained in the power monitor and received signals. This same synchronization signal is used as the lock-in reference signal for phase sensitive amplifiers used to reject noise and provide dc levels proportional to the signal intensities. The chopper synchronization signal is also used in the processor to identify wavelength. The FET switch circuits are located in the interface unit rather than in the sensor subsystem to minimize the number of signal leads coupling the two units. The power monitor and received quadrant signals (five signals) at the input to the FET switches exit the switches as ten independent signals (Figure 4). The two signals out of each FET switch are 180° out of phase, with one phase representing Laser 1 and the other Laser 2. For each signal output, one-half of the cycle will be at zero or ground potential and the other half cycle at some positive potential representative of the signal intensity detected. The two power monitor signals representing the reference 2.39 μm laser (1) and 3.39 μm laser (2) outputs are directed to two lock-ins that have a bandpass of a few Hz centered on the reference frequency (ie. 200Hz). These power monitor signals are sent to the processor unit for digital conversion and processing. The lock-in outputs are also used in the normalization process of analog data. The outputs from the FET switches associated with the quadrant signals are sent to two summing amplifiers before they are sent to their respective lock-in circuits. The two lock-in outputs representing the received intensities at the reference and sample wavelengths are sent to the processor and analog processing circuits as discussed above for the power monitor signals. The analog data output signal is a positive dc signal proportional to the concentration length product (CL) along the LOS path to the retroreflector. This analog data signal is used for real time system performance evaluations and does not involve computer processing. The outputs from the FET switch associated with the reference signal quadrant returns (1) are also sent directly to four lock-in circuits to derive dc signals for each quadrant. These signals are used in the error detection circuit to control pointing error for the automatic positioning, closed-loop software. The reference sum signal is also used in the error detection circuit for normalization.

Control-Processing and Display Subsystem

The control/processing and display subsystem (Figure 5) is a PC/AT-based processing system that uses one or more data acquisition cards to convert the sensor analog signals to digital format for processing. The number of acquisition cards required depends on the number of sensors used. In addition to the acquisition card, a scan control card is required and some type of graphics display card that can drive a video monitor (RS170 & RGB). We are currently using video processor cards for this purpose. A video recorder is used to store the data displayed on the video monitor, and a floppy disc is used to record the raw digitized data for postevaluation. The data-acquisition and processing software is basically the same for all data collected, regardless of the number of LOSs to be interrogated. For each data sample, the power monitor and receiver data are processed to provide the CL for that LOS and time. The number of data samples collected for each LOS depends on the application and type of display option selected. For example, if a single LOS is to be monitored, the stripchart/LOS display option may be used (Figure 5). In this case, data samples are collected continually and may be displayed as individual samples or as averaged samples. If multiple LOSs are to be observed, then the scan /bar graph option may be selected. In this example, the bar graph represents the average CL over the period of time the sensor samples each LOS. The last display option shown represents a grid area coverage which is similar to the multiple LOS processing; that is, each LOS data is averaged over a sample time interval. However, to provide the grid display, more than one sensor must be used in a tomography mode (Figure 6). The data from Unit 1 represents horizontal line data (X) and the data from Unit 2 represents the vertical line data (Y) in a two-dimensional array. A grey-scale intensity or multiple-color display is used to depict changes in concentration and only at beam crossover locations. To improve the grid resolution, more LOSs are required which means more retroreflectors and/or more sensors. Careful evaluations of the resolution requirements for this type of application are necessary when considering an area coverage system.

Only two operator controls need to be set once normal operation begins:

- The offset adjustment which is used to balance out any systematic errors and to compensate for ambient levels of hydrocarbons
- The threshold level that sets the alarm threshold to the desired sensitivity. When the threshold is exceeded, an audio alarm is sounded to alert the operator. These adjustments can also be set from a terminal, if used. The other operator controls are for the video camera and the scanner joystick operations which are utilized in setting up system operations.

References

[1] E. R. Murray et al., "Atmospheric Water Vapor Measurements with an Infrared (10μm) Differential Absorption Lidar System," Applied Physics Letters, Vol. 28, pp. 542-43 (1 May 1976).

[2] E. R. Murray, J. E. van der Laan, and J. G. Hawley, "Remote Measurement of HCL, CH, and N_2O Using a Single-Ended Chemical-Laser Lidar System," Applied Optics, Vol. 15, pp. 3140-47 (December 1976).

[3] R. A. Baumgartner et al., "Characterization of the EPRI Differential-Absorption Lidar (DIAL) System," Project 862-14, EPRIEA-1267, EPRI Final Report, Electric Power Research Institute, Palo Alto, California (December 1979).

[4] J. G. Hawley, L. D. Fletcher, and G. F. Wallace, "Ground-Based Ultraviolet Differential-Absorption Lidar (DIAL) System and Measurements," Workshop on Optical and Laser Remote Sensing, Monterey, California (9-11 February 1982).

[5] P. L. Holland, J. E. van der Laan, K. Phelps, and S. Gotoff, "A Four-Wavelength Infrared Differential-Absorption Lidar (DIAL) System," Proceedings of the International Conference on Lasers 87, pp. 694-95 (7-11 December 1987).

[6] J. Jones, J. E. van der Laan, P. L. Holland, L. D. Fletcher, and J. Comeford, "Design of a Mobile Differential-Absorption CO_2 Direct Detection Lidar System," Proceedings of the International Conference on Lasers 87 (7-11 December, 1987)

[7] J. E. van der Laan, W. Evans, J. Leonelli, and L. L. Altpeter, "DIAL-Lidar System for Remote and Selective Detection of Natural Gas Leaks Using a Frequency-Mixed CO_2 Laser,"Proceedings of the International Conference on Lasers 87, pp. 707-713 (7-11 December, 1987).

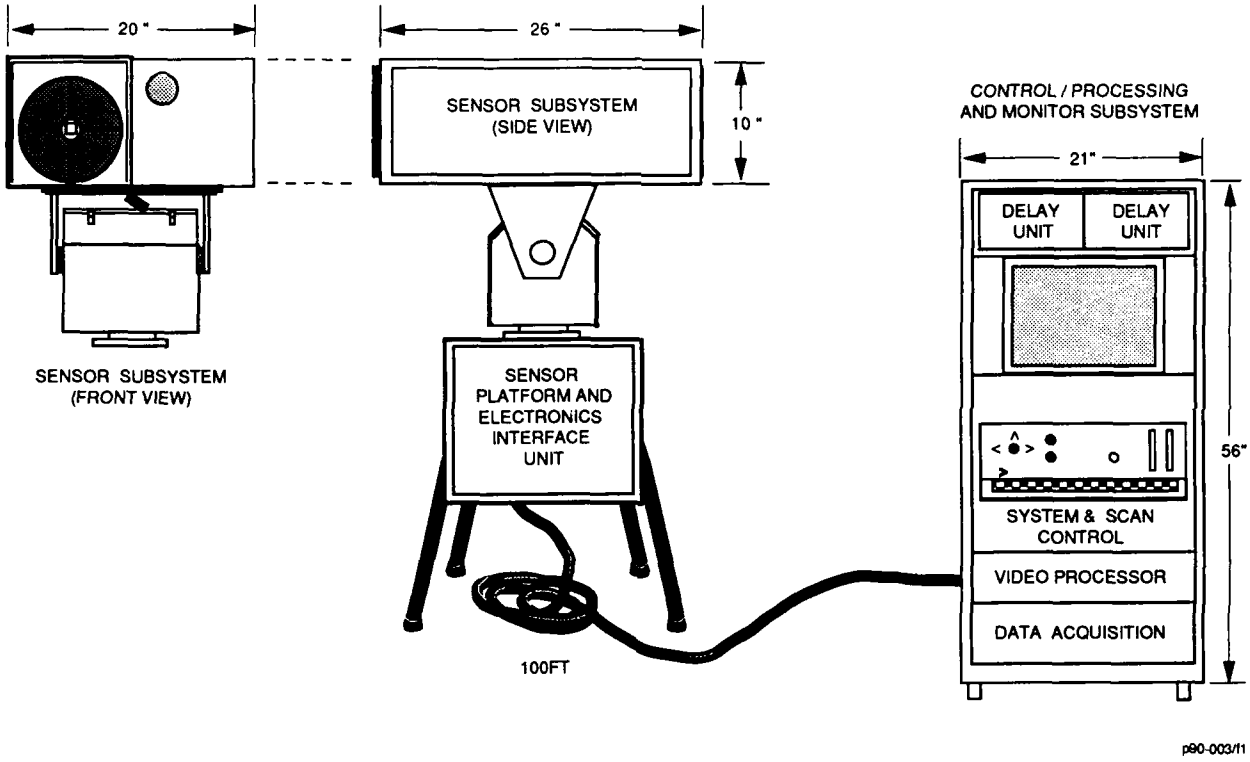


Figure 1 HYDROCARBON SENSOR SYSTEM ELEMENTS



Figure 2 HYDROCARBON SENSOR SYSTEM

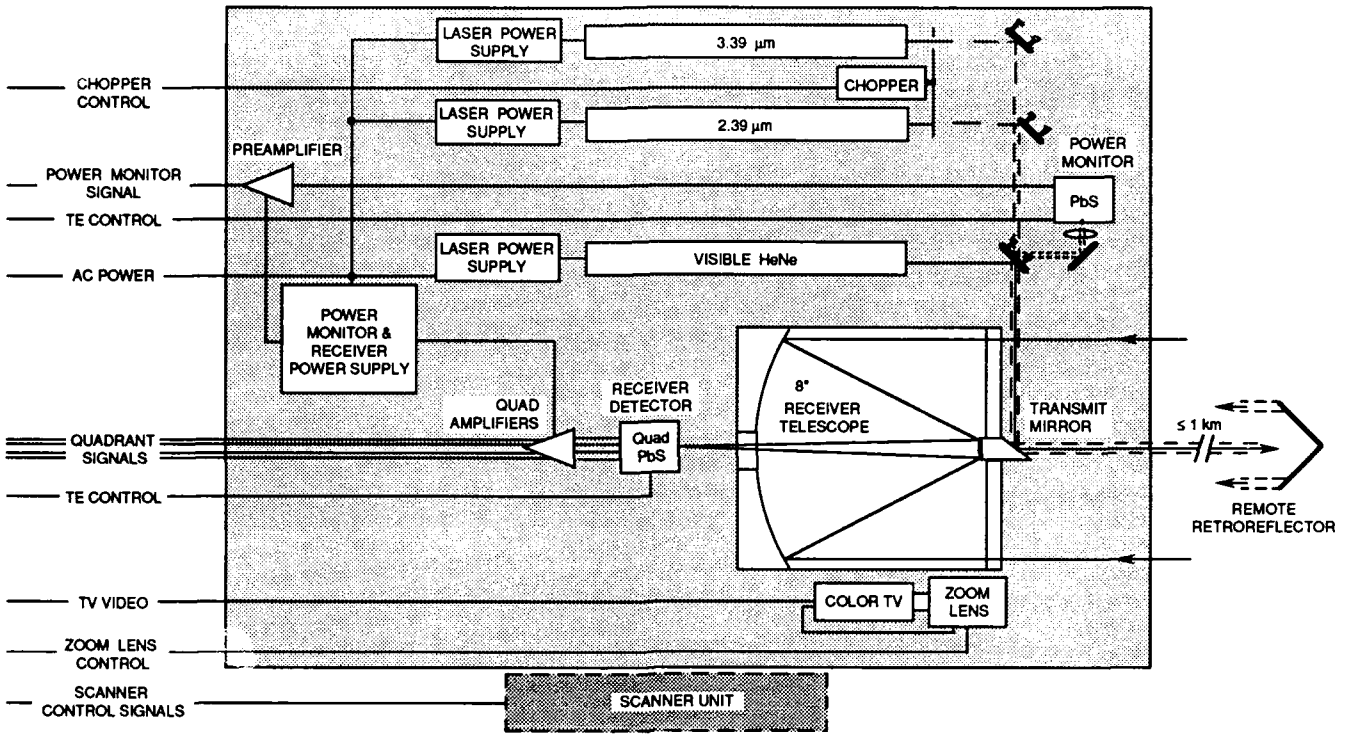
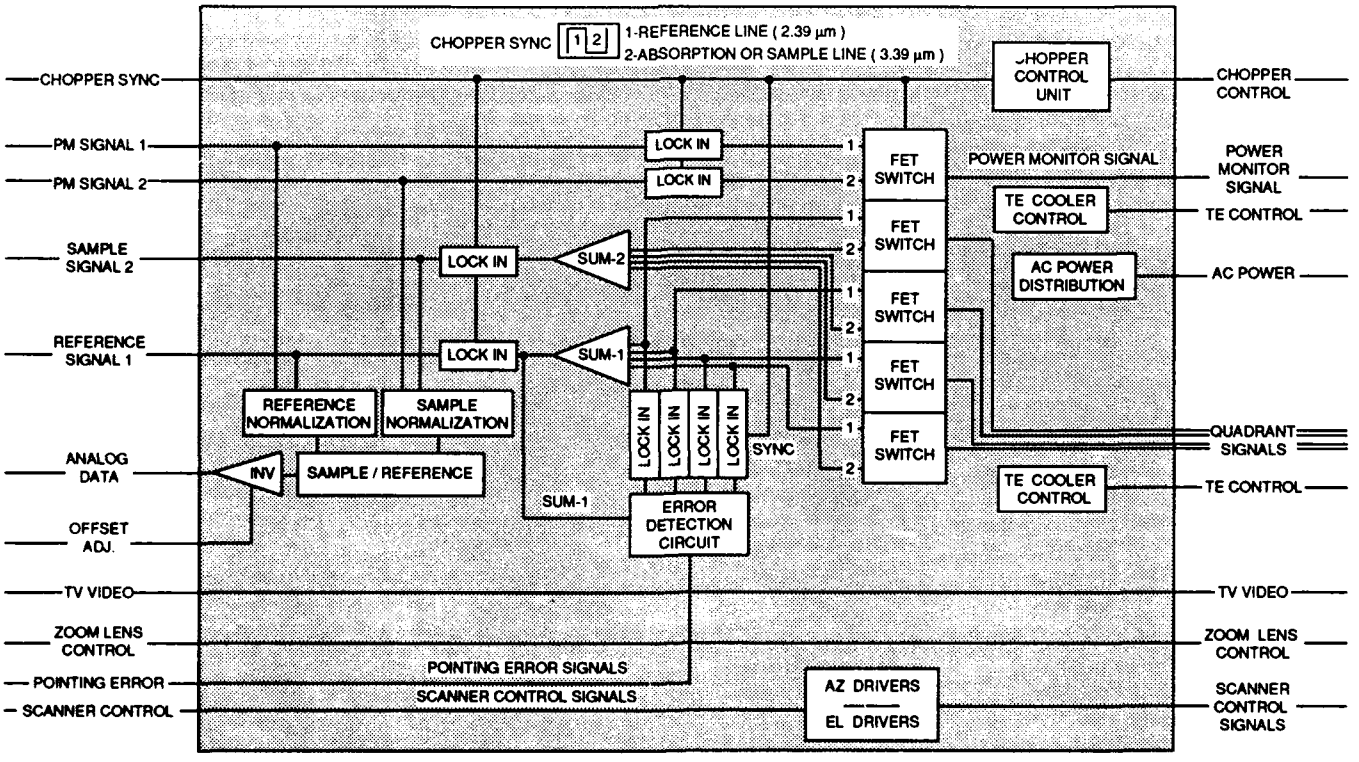


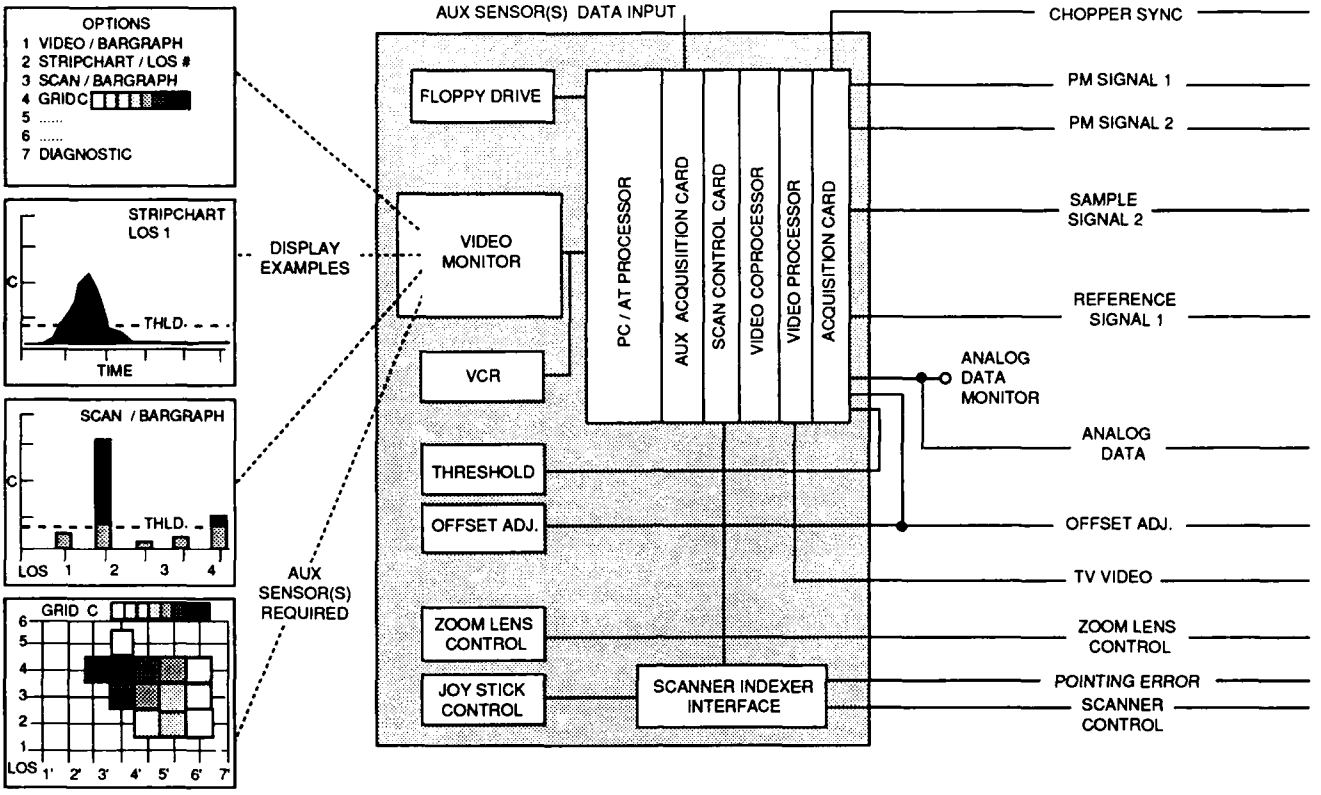
Figure 3 SENSOR SUBSYSTEM

p90-003/f2



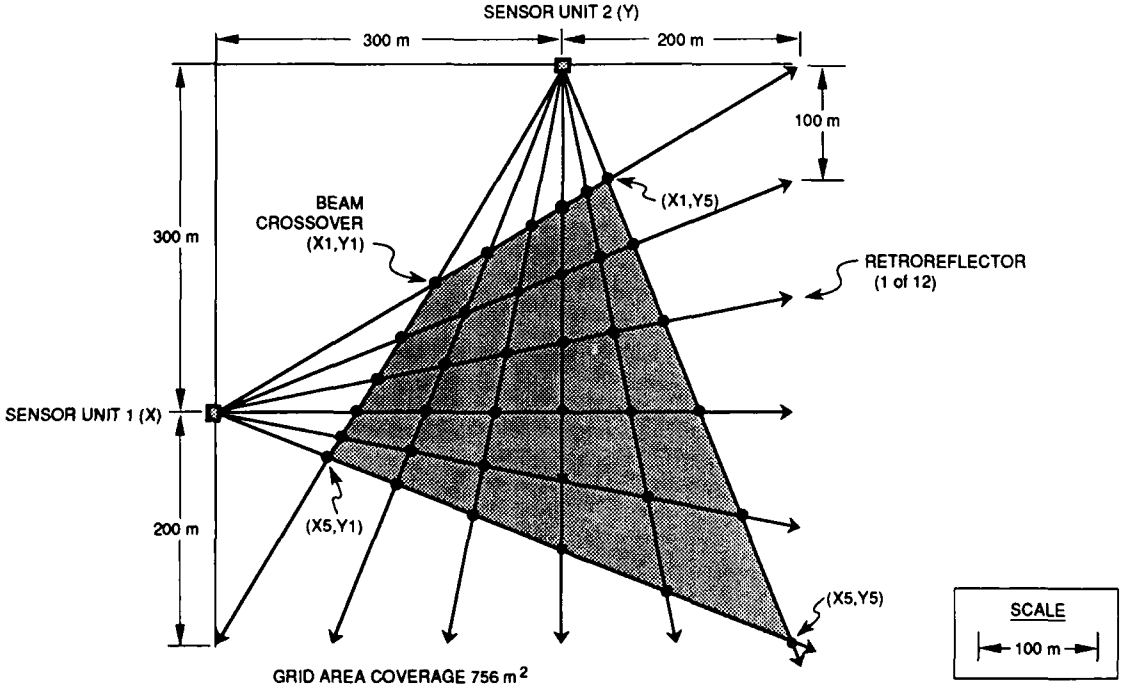
p90-003/f4

Figure 4 SENSOR PLATFORM AND ELECTRONIC INTERFACE



p90-003/f5

Figure 5 CONTROL / PROCESSING AND MONITOR SUBSYSTEM



p90-003/f7

Figure 6 GRID AREA COVERAGE EXAMPLE (2 SENSORS, 6 x 2 LOS)

HETERODYNE DOPPLER VELOCIMETRY MEASUREMENTS AT 353 nm

R.G. Morton, W.J. Connally, T. Olson, K. Avicola
Maxwell Laboratories, Inc.
8888 Balboa Avenue
San Diego, California 92123

and

C. Buczek
Laser Systems and Research, Inc.
1914 W. Mission Rd. #K,
Escondido, California 92025

Abstract

Heterodyne detection of light scattered from diffuse targets has been used to measure translational and rotational target velocities. Coherent ultraviolet light was derived from frequency doubled dye lasers and detection was accomplished with a photomultiplier.

Summary

Target velocity measurements have been made with coherent ultraviolet light at 353 nm using a photomultiplier detector in a heterodyne configuration. The target illumination beam was produced by a frequency-doubled dye laser system in the form of 1 μs pulses at a pulse repetition rate of 2 Hz, although all measurements were made on a single shot basis. The local oscillator signal was produced by Bragg cell shifting of a portion of the main beam by 13 MHz, a convenient intermediate frequency (IF) for heterodyne detection.

Targets were fabricated from a diffuse white ceramic and had a characteristic dimension of 1 mm. The targets were mounted on a mechanical turntable which was designed to produce both translational and rotational velocities relative to the detector, distant 6 m from the target.

Local oscillator and signal fields were mixed on the face of a 1 mm diameter quartz fiber which coupled the resultant modulation to a photomultiplier. Measurements were made at received energy levels of approximately 10^{-14} J.

Data were collected and analyzed for targets at a variety of translational and rotational velocities. The Doppler shift away from 13 MHz and line broadening were used to calculate the target translational and rotational velocities, respectively.

Introduction

Maxwell Laboratories, Inc. has been working on coherent ultraviolet laser radar for several years. Previous publications have dealt with the use of excimer lasers for image range and Doppler measurements,[1] Doppler velocimetry using coherent mode-locked pulse trains[2] and coherent sub-aperture ultraviolet imagery.[3] As titled, this paper discusses heterodyne Doppler velocimetry measurements at 353 nm, a wavelength suitable for amplification in e-beam pumped XeF lasers.

Experiment

The overall scheme for the heterodyne velocity measurements is shown in Figure 1. A pair of beams at 353 nm are generated with a difference frequency of 13 MHz; one serves as local oscillator, the other to illuminate targets. Scattered light from the target is beat against the local oscillator field at the heterodyne detector whose output is digitized and stored for processing at a later time.

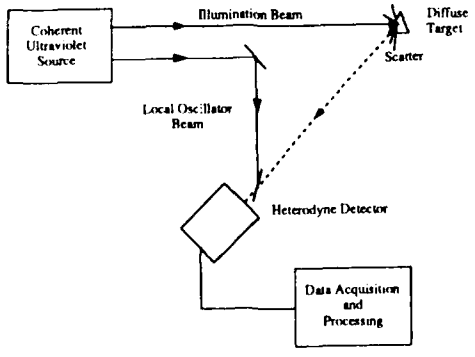
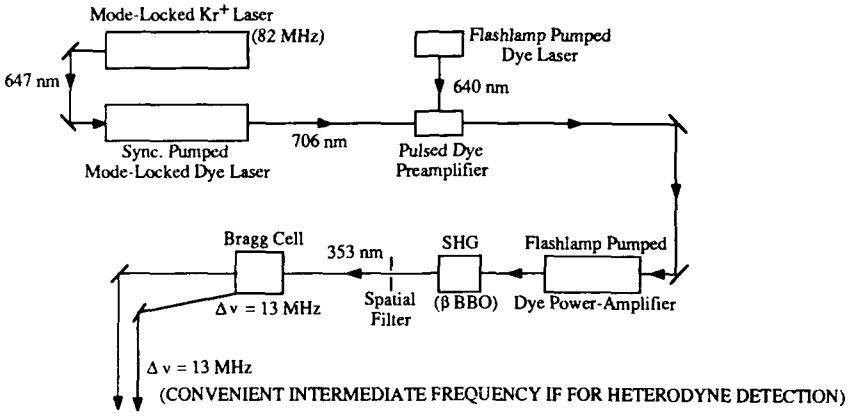


Fig. 1 Overall Scheme for Heterodyne Velocity Measurements

The details of the coherent ultraviolet pulse generator can be seen in Figure 2. Since there are no convenient sources emitting directly at 353 nm, the waveform is generated and amplified in the visible and then frequency doubled in a non-linear optical crystal. In this scheme an acousto-optically mode-locked krypton-ion laser emitting at 647 nm is used to synchronously pump a mode-locked CW dye laser which produces light at 706 nm. The output consists of a CW string of mode-locked pulses of nominal nanosecond duration at a rate of 82 MHz. This output is then pulse pre-amplified in a dye cell driven by a flashlamp pumped dye laser with about 2 μs pulse length. Overall gain in the preamplifier is about 300, single pass.



- ONE BEAM SERVES AS LOCAL OSCILLATOR
- OTHER BEAM SERVES AS TARGET ILLUMINATOR

Fig. 2 Coherent Ultraviolet Pulse Generator

In order to reach wavelength conversion efficiencies of about 30% it is necessary to further amplify the pulse in a flashlamp pumped dye laser to an energy level of 10 mJ. For the experiments reported in this paper this was done with a double pass through the power-amplifier, with no optical isolation. Net gain in the power amplifier was about 100, yielding a typical energy of 10 mJ contained in some eighty mode-locked pulses spanning a total pulse envelope of 1 μs.

The 10 mJ pulse at 706 μm was then frequency doubled to produce 3 mJ at 353 nm, using beta-barium borate cut for phase matching at small angles of incidence at these wavelengths. Spatial filtering was accomplished using a sapphire watch jewel bearing with a 100 μm diameter through-hole. This material withstood the peak power density of ~10^9 w/cm^2 impinging upon it with no resulting damage. This 10^9 w/cm^2 figure refers to the individual mode-locked spikes contained in the 1 μs string comprising the full macro-pulse. No previous material tried for spatial filtering at this 353 nm wavelength survived without vaporizing.

Following spatial filtering and recollimation, the ultraviolet beam was passed through a pair of Bragg cells (shown as a single unit in the figure for simplicity) to generate a second beam with a frequency offset of 13 MHz. In fact, one Bragg cell was used to upshift by 73 MHz and a second, in series, to downshift by 60 MHz. This arrangement was necessary due to the physical difficulty in constructing an efficient 13 MHz Bragg cell. The piezo electric transducers used do not operate well below a few tens of megahertz.

The final output of the coherent ultraviolet pulse generator (CUPG) consists of two beams differing in absolute frequency by 13 MHz, a convenient intermediate frequency (IF) for our heterodyne measurements. The two beams were then propagated to a separate laboratory for the velocimetry measurements.

Beams arriving from the CUPG are directed onto the receiver table which is shown in Figure 3. The local oscillator beam, labeled LO, was spatially filtered and conveyed via mirrors and a beamsplitter to the receiver. The main beam, labeled MO, was used alternately to illuminate a target and to back-light a beacon pinhole to aid in proper alignment for efficient heterodyne. The target was placed with its center at the previous beacon pinhole position during measurements, following proper spatial overlap of the local oscillator and received signals.

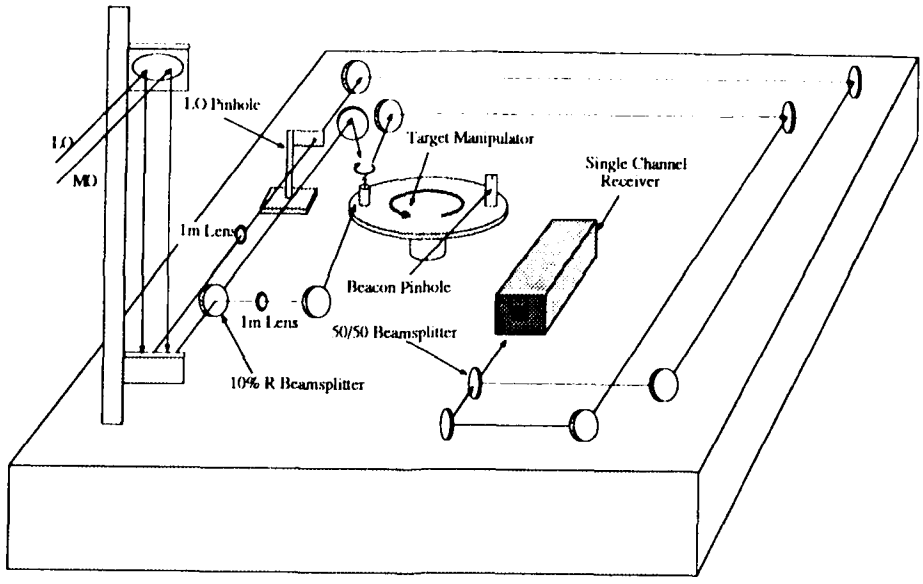


Fig. 3 Receiver Table Detail

The target was mounted on the shaft of a small motor for spin and the small motor in turn mounted on a relatively large diameter turntable for translational motion, as shown in Figure 4. An optical slot switch on the turntable was used to fire the laser when the target center was precisely placed at the previous location of the beacon pinhole. In this arrangement it was possible to record data from stationary, spinning, or translating targets, or from targets with combined spin and translation.

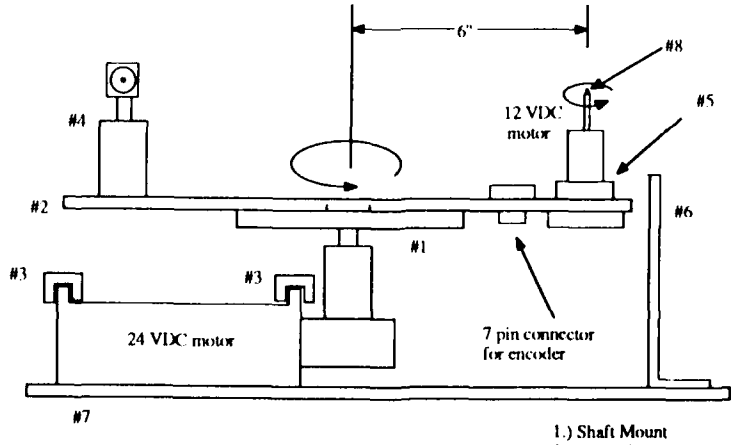


Fig. 4 Target Manipulator

The receiver, shown in Figure 5, consisted of a Hamamatsu #R647-01 photomultiplier with a 1 mm circular aperture and a 353 nm bandpass filter. Inserted between the PM tube and the output connectors from the receiver housing was a solid state buffer amplifier (Comlinear #CLC401). The purpose of this amplifier was to convert the high current gain inherent in photomultipliers to the high voltage signals typically required by digitizers. The receiver was housed in an EMI shielded case to eliminate noise originating from the pulsed laser system.

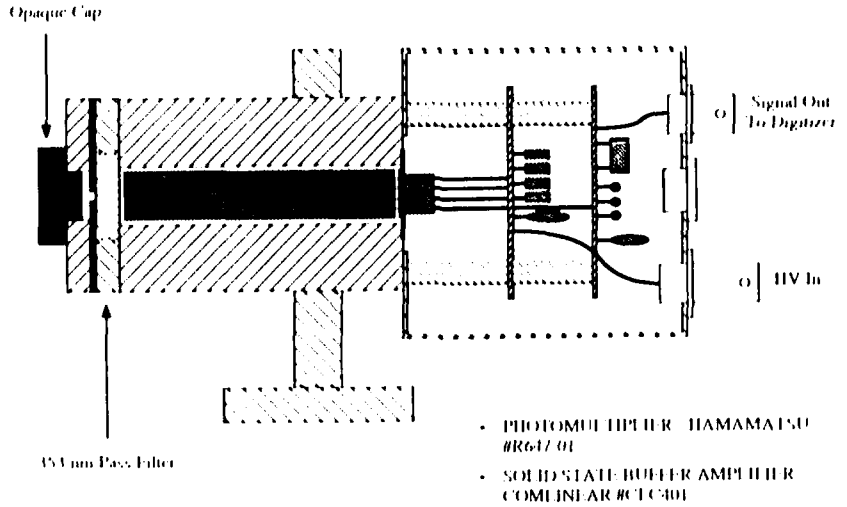


Fig. 5 Single Channel Detector Photomultiplier

As a check on the calculated heterodyne signal levels to be expected a white diffuse ceramic target was set up and illuminated with 3 μJ pulses from the CUPG, as in Figure 6. An oscilloscope recorded the signals from the diffusely scattering target, which were typically 200 mV into 50 Ω. Since this was within 20% of the expected value we proceeded to align the system for heterodyne detection.

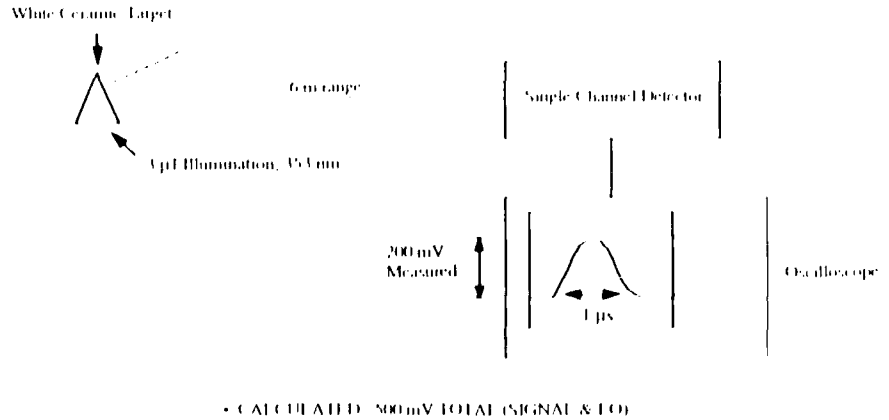


Fig. 6 Signal Level Check

Figure 7 displays a typical heterodyne signal, at 13 MHz, when the beacon pinhole is used to align the mirrors and beamsplitter which convey light to the receiver. The pinholes for both the LO and beacon were 50 μm diameter and the receiver was at a range of 6 m. The total number of collected photons from the beacon pinhole used to generate the signal was about 20,000, corresponding to a received energy of 10^{-14} J.

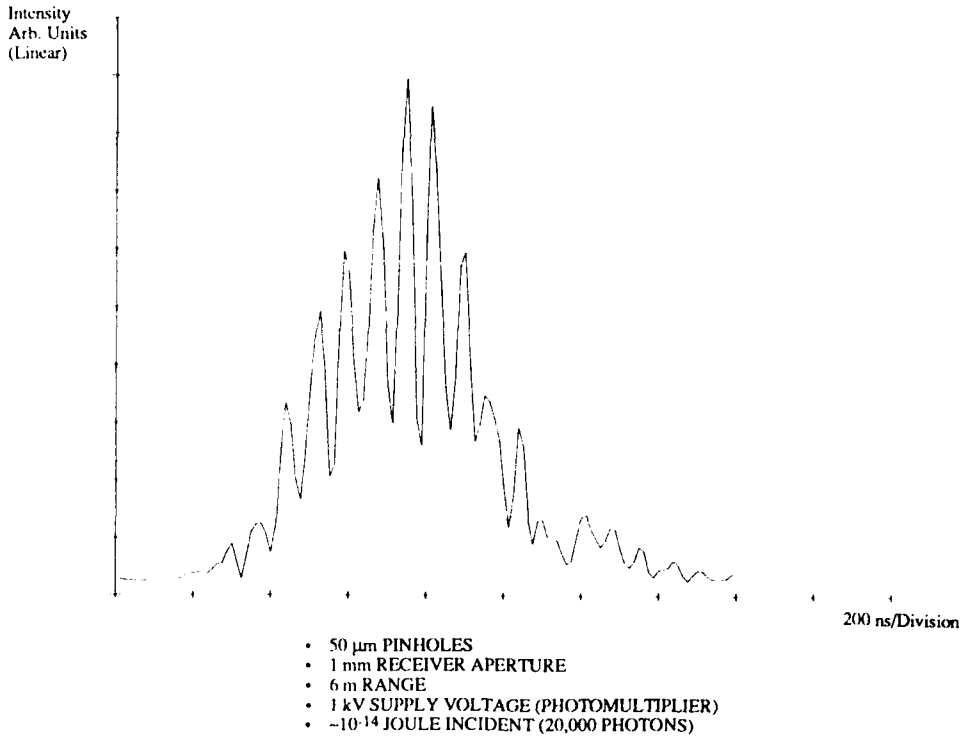


Fig. 7 Photomultiplier Single Channel Heterodyne Data

Data were acquired and analyzed by the system diagramed in Figure 8; consisting of a LeCroy #2262 digitizer and WYSE PC/AT 386 Computer. Incoming signals were sampled and digitized at an 80 Ms/s rate, more than sufficient for the 13 MHz IF frequency used in heterodyne detection. Processing consisted of removal of the laser pulse-shape carrier from the raw heterodyne data, followed by a Fourier transform into the frequency domain, as seen in Figure 9.

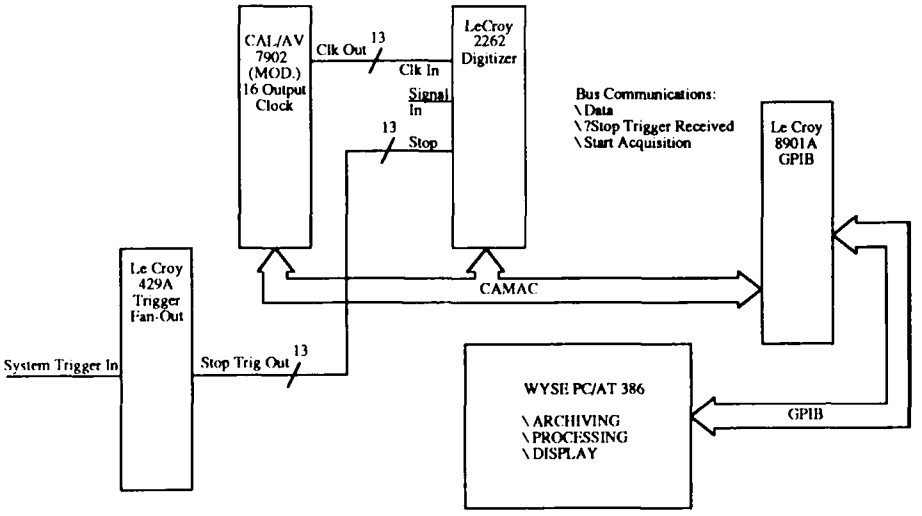


Fig. 8 Data Acquisition System Hardware Architecture

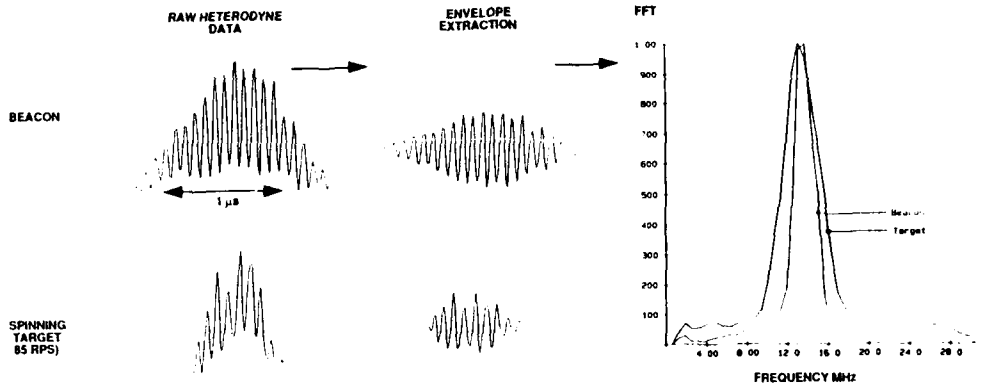


Fig. 9 Processing of Heterodyne Signals

In order to extract information about the frequency spread due to target spin-motion it was necessary to perform deconvolution of the experimental data with respect to the beacon signal in which no motion was present. This was most easily done by fitting a Lorentzian curve to the data in each case and then performing a relatively simple mathematical algorithm to deconvolute the target data. Figure 10 shows the Lorentzian fit and Figure 11 the results for targets spinning at 33, 76 and 85 RPS.

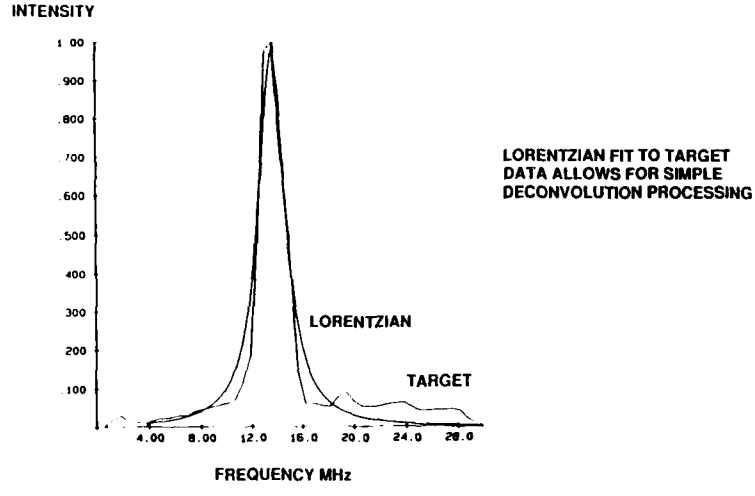


Fig. 10 Lorentzian Fit to Experimental Data

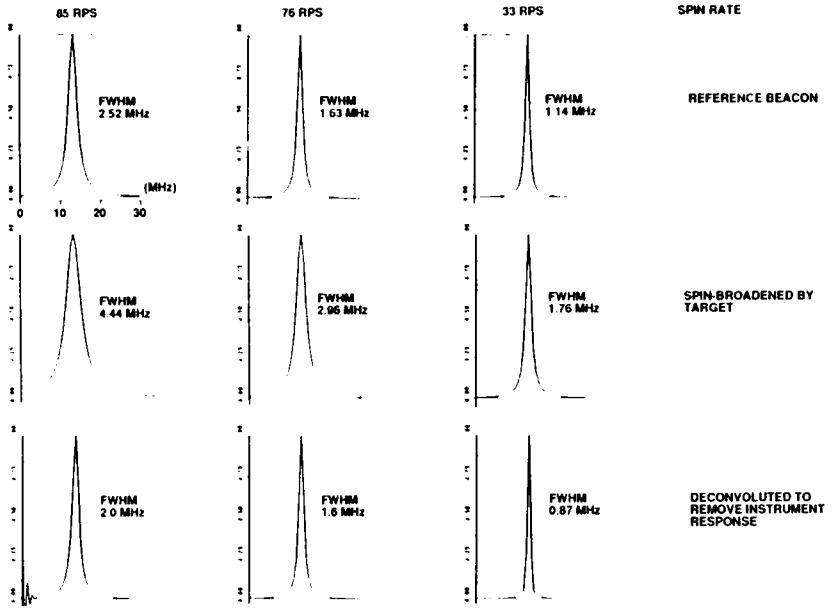
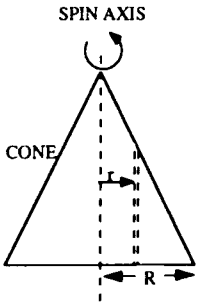


Fig. 11 Processed Spin Data

The simple approximation used to calculate the expected spin broadening from conical targets at known rotation rates is illustrated in Figure 12. This model takes account of the dropping projected area in each velocity bin as the edge of the cone is approached and the Lambertian scatter roll-off in one plane. As such, the model slightly over estimates the observed spin broadening. A comparison of the calculated and observed Doppler spreads is presented in Table 1.



LIGHT SCATTERED FROM SLICE OF SURFACE AT RADIUS "r" HAS INTENSITY:

$$I_r \cong \frac{k(R-r)\sqrt{R^2-r^2}}{R}, \quad k = \text{constant}$$

TO DETERMINE VALUE OF "r" FOR WHICH $I_r = \frac{I_o}{2}$, WHERE I_o = CENTRAL SLICE INTENSITY:

$$\frac{(R-r)\sqrt{R^2-r^2}}{R} = 0.5$$

WHICH YIELDS:

$$r = 0.443\,R$$

Fig. 12 Approximate Calculation of Expected Spin-Broadening

Table 1. Experimental Results

VELOCITY OF SURFACE AT RADIAL POSITION 0.443 R	SPIN RATE (RPS)	CALCULATED DOPPLER SPREAD (FWHM)	OBSERVED DOPPLER SPREAD
19.5 cm/s	85	2.22 MHz	2.0
17.5 cm/s	76	1.98 MHz	1.6
7.6 cm/s	33	0.86 MHz	0.87

VELOCITY RESOLUTION ~5 cm/s

The spin rates were measured directly from the shaft encoder on the motor. Observed Doppler spreads at the various spin rates spanned an amount corresponding to an absolute velocity resolution of 5 cm/s. The highest velocity at the edge of a 1 mm radius cone spinning about its axis of symmetry at 85 RPS is 53.4 cm/s.

Finally, an experiment was performed in which the conical target was both spinning and translating with respect to the receiver. The direct Doppler shift of -5 MHz indicated that the target was receding at a velocity of 88 cm/s and the frequency spread about the shifted peak indicated a spin rate of 82 RPS. This is shown in Figure 13. It was not possible to use the shaft encoder to measure the actual spin rate because the main turn table was rotating in this experiment. However, the motor which was spinning the target had previously been shown to turn at a steady rate within about 2% for extended periods of time. Absolute translational velocity resolution for our receiver was about 2 cm/s and rotational velocity measurement at a given point on target about 5 cm/s.

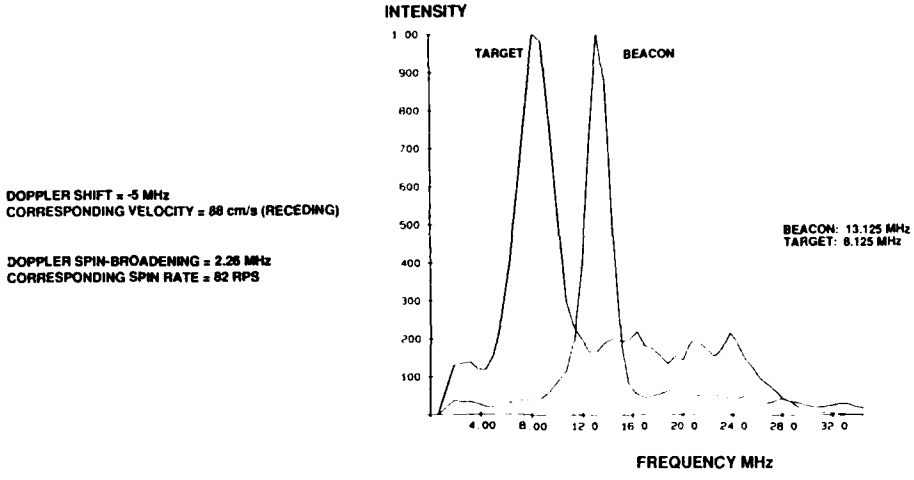


Fig. 13 Data from Target with Simultaneous Spin and Translation

References

1. "Excimer UV laser radar for image, range and Doppler measurements," G. McAllister, R. Morton, T. Olson, Maxwell Labs., Inc.; C. Buczek, Laser Systems and Research Inc., SPIE Vol. 783, Laser Radar II (1987).

2. "Ultraviolet Doppler velocimetry measurements using coherent, mode-locked pulse trains," R.G. Morton, W. J. Connally, Maxwell Labs., Inc., SPIE Vol. 999, Laser Radar III (1988).

3. "Coherent subaperture ultraviolet imagery," R. G. Morton, W. J. Connally, K. Avicola, D. Monjo, T. Olson, Maxwell Labs., Inc.; C. J. Buczek, Laser Systems & Research, Inc., SPIE Vol. 1103, Laser Radar IV (1989).

A NOVEL SDI SHORTWAVELENGTH LADAR DEPLOYMENT SCHEME AND ITS CRITICAL TECHNOLOGIES

Mr. Charles A. Bjork, Jr., Nichols Research Corp. (NRC),
P.O. Box 400002-1502 • Huntsville, AL 35815 USA • Ph.(205) 883-1140

Mr. Robert Turansick, (NRC)
1901 Dove St. • Newport Bch., CA 92660 USA • Ph.(714) 476-0800

Dr. Lou Marquet, (NRC)
8618 Westwood Ctr Dr • Vienna, VA 22182-2222 • Ph.(703) 893-9720

And

Dr. Jerry Blodget, Code 6530, U. S. Naval Research Laboratory
4555 Overlook Dr • Washington, DC USA 20375 • Ph. (202) 767-3674

Abstract

A novel ladar deployment scheme is described which makes feasible a near-term laser radar for long-range defense, remote sensing, and other long-range applications. The concept uses a ground-based laser transmitter linked to an orbital constellation of surveillance platforms by means of a rocket probe-borne relay mirror; other possible derivative forms of the concept are implied. Some of the required critical technologies and performances, which make such a system feasible in the near term, are identified. Atmospheric turbulence compensation is emphasized, and an innovative approach to ease the solution, called an "isoplanatic probe", is introduced. The measurement advantages of heterodyne detection receivers, currently being researched, are mentioned.

1. Introduction

This ladar deployment concept utilizes a powerful ground-based transmitter to project a beam to an orbital platform, called a "mission system", by way of a rocket-borne relay mirror, as shown in Figure 1. The orbital platform receives the beam with a large collecting mirror, and refocuses it through a separate aperture, as if the transmitter was on-board the platform, to whatever targets would be desired. Tracking, discrimination, designation, and many other measurement functions are possible. Targets could include those as diverse as missiles and their payloads or other military weapons being launched against the United States or other country, or regions of the atmosphere or "near space" for which remote sensing data are desired.

The use of a ground based transmitter in this way, obviates the need for a transmitter on board each of the space platforms. This is desirable because of the large weight required for a transmitter of sufficient capability. The additional optics required on the space platform, weigh far less than a space-based transmitter with sufficient capability, largely because the ladar operates at short wavelengths, e.g. in the visible or UV portion of the electromagnetic spectrum. In addition, the orbital platforms are relatively few in number, e.g. less than 20, making the ranges to possible targets up to 5000 km. An equation bounding the average target range, r, may be derived by assuming the constellation of orbital platforms lie in a spherical shell at altitude, H. Averaging-out the "phase noise" resulting from arbitrary engagement start times and constellation initial state yields

$$r = 2\sqrt{\frac{1}{N} + \frac{H^2}{4(R_e + H)^2}}\,(R_e + H) \qquad (1)$$

where R_e is the radius of a spherical earth, e.g. 6378 km. Equation (1) is plotted in Figure 2 for two (2) constellation altitudes, 1500 and 2000 km.

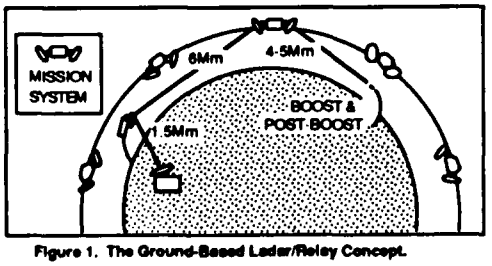


Figure 1. The Ground-Based Ladar/Relay Concept.

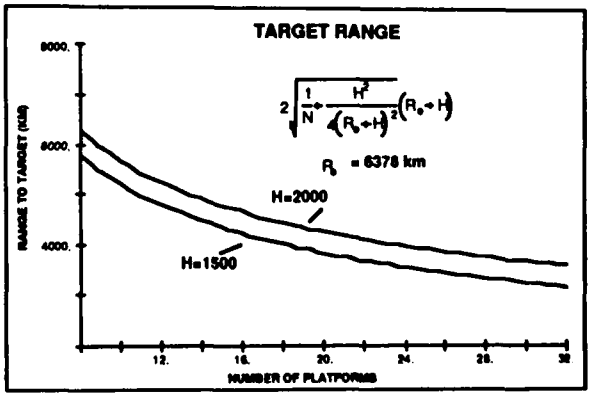


Figure 2. Target Range Bound as a Function of Constellation Size

Such target ranges stress the capabilities of ladars because of the diffraction spread which dilutes the power density of the beam; this generates the requirement for short wavelengths. However, the choice of short wavelengths makes the light optics possible, yielding the interesting weight trade and feasibility of using a ground based transmitter.

However, the choice of shortwave, ground-based ladars complicates the transmission link to the mission system through the relay. The turbulence of the atmosphere must be compensated for in order to maximize the beam quality and preserve the measurement capability. In addition, additional power must be available in the transmitter to overcome large scattering/attenuation losses from the atmosphere. In non-wartime, remote sensing and other applications would have to consider the safety implications of the power and short wavelength of the beam, if it is to be used in this capacity.

This concept is made feasible by the progress made in at least three critical technology areas: 1) powerful short wavelength transmitters, 2) atmospheric compensation, and 3) pointing stabilization.

2. The Ground-Based Transmitter

Powerful short wavelength transmitters capable of operating as ladars are being pursued by several organizations. Many of these have in common the general configuration of a precision waveform generator driving or operating as a master oscillator, which in turn drives a power amplifier in a master oscillator/ power amplifier (MOPA) configuration, like the one shown schematically in Figure 3. One desirable option being sought by several developers, is a heterodyne capability achieved by mixing the return signal with an offset reference oscillator. There are many measurement advantages to this form of detection, and many transmitters of interest have demonstrated sufficient stability to make this possible; however, it is not a hard and fast requirement.

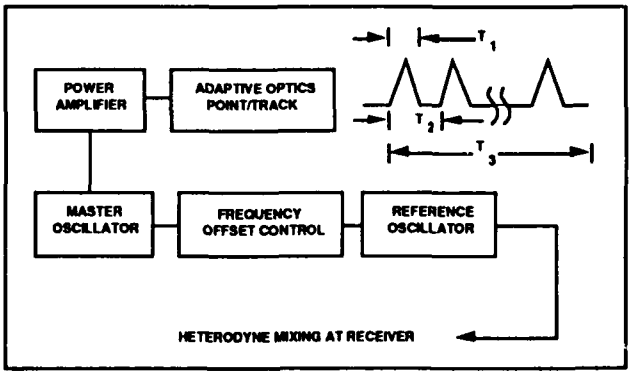


Figure 3. Ladar Transmitter Block Diagram

Ladar transmitter candidates and examples of interested developers include: near UV and lower visible excimers being developed by Maxwell Laboratories and Avco-Everett/Textron, visible and UV derivatives of solid state lasers being developed by MIT/Lincoln Labs and Hughes Aircraft Corp., and Free Electron Lasers (FELs), suitable for ladar applications, being pursued by Rocketdyne and Spectra Technologies, Inc.

3. Representative Atmospheric Effects and Compensation

One of the prices paid for selecting short wavelength ladars is in the propagation performance, which generally degrades as the wavelength falls through the visible into the UV. Although actual transmission is highly structured, the example in Figure 4 shows the behavior of the envelopes for different components of the attenuation as a function of wavelength. Not counting turbulence effects, the gain from diffraction improvement overcomes propagation losses until the strong ozone absorption sets in at about 0.32 μm. However, turbulence effects must be counted, which is why turbulence compensation is necessary.

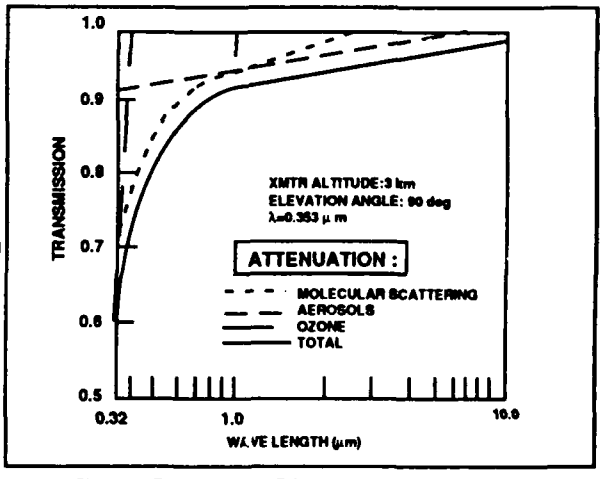


Figure 4. Representative Effects on Transmission

Strehl Ratio Improvements Using Adaptive Optics

The progress in adaptive optics has made useful ground-based ladar performance possible, even at visible wavelengths. This capability is being extended to shorter wavelengths, but with some difficulty. Predictions of strehl ratios after correction are not being met in practice, indicating at least a minor failing of our complete understanding of the wavefront compensation process. The example in Figure 5 shows two curves of "residual" strehl[1] ratios, **S**, that is strehl after correction, as a function of the actuator density, **p**. These have been generated using the exponential fit

$$S = e^{-\alpha\left(\frac{\left(\frac{1}{p}\right)}{r_0}\right)^{5/6}} \qquad (2)$$

where α is a fitting parameter from modulation transfer function (MTF) analysis. The exponential modulation transfer function coefficient for this fit was expected to be 1.0 or less; instead, in some cases, it is larger than 1.0. The cases shown are for the value of 1.0. It is hoped that this problem will be properly understood in less than a year. The parameter, r_0, is the coherence diameter[2], given as a function of wavelength, λ, by

$$r_0 = 0.185\left(\frac{\lambda^2}{\int_0^\infty C_n^2(z)dL}\right)^{\frac{3}{5}} \qquad (3)$$

In this equation, the integral is a path integral over line-of-sight, L, where the function C_n^2 is the square of the refractive index structure function[3]. Representative variations of this function over time and altitude, z, are shown in Figure 6. For this computation, the median value of the C_n^2 envelope shown in Figure 7 was used. This envelope was generated by averaging the models and measurement data[4] appearing in Figure 8.

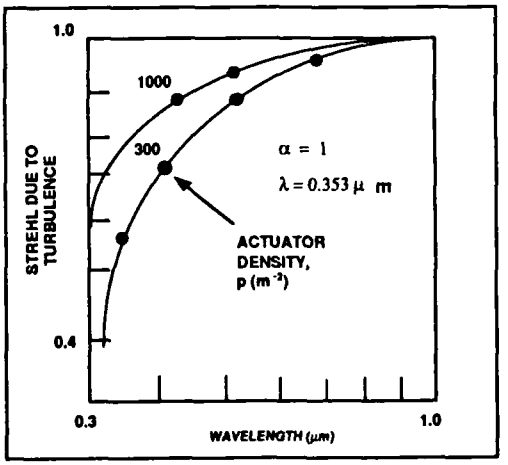


Figure 5. Strehl Improvements by Adaptive Optics

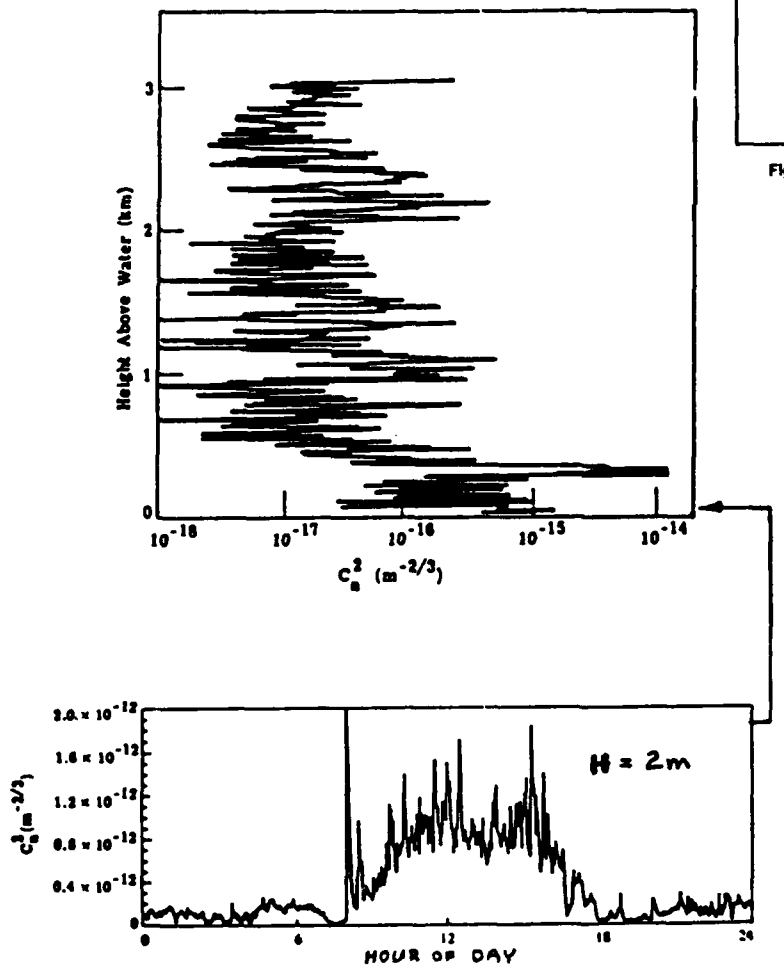


Figure 6. Typical Time and Altitude Dependence of the Refractive Index Structure Constant, C_n^2

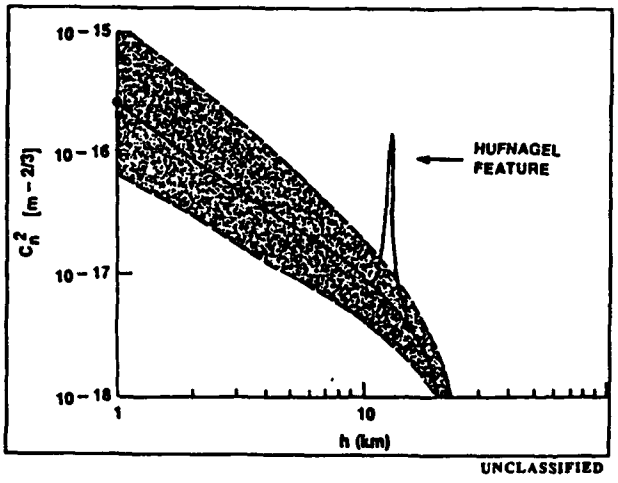


Figure 7. Envelope of the Refractive Index Structure Constant Developed from Model and Measurement Data

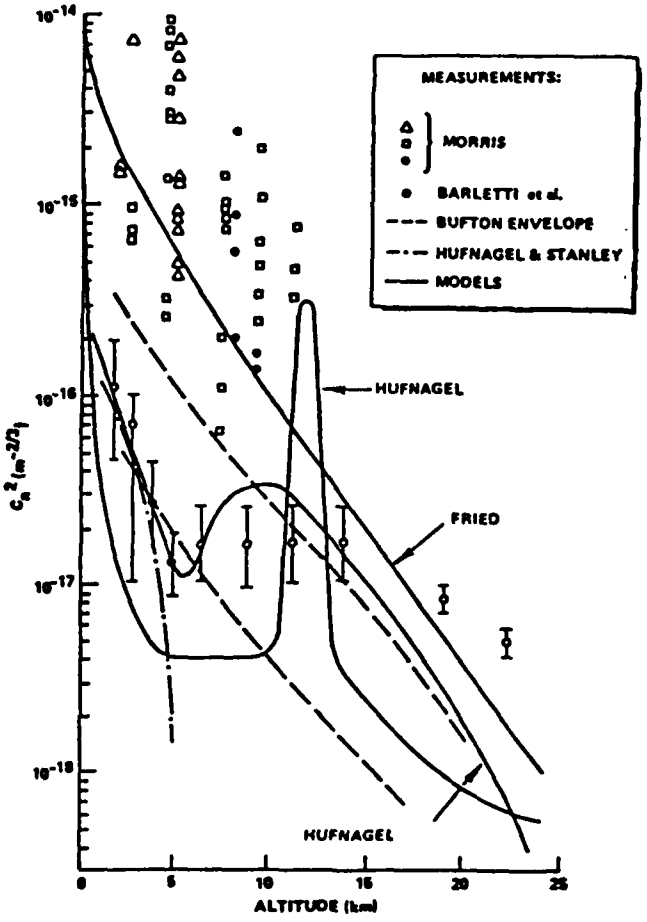


Figure 8. Representative Average Values of C_n^2, Measured and Computed from Models

Easing the Compensation Problem: The "Isoplanatic" Probe

A further complication in the atmospheric turbulence compensation problem, is the need for the anticipated turbulent atmosphere to be sampled to obtain correction data. Because the propagation medium may change during the time of the beam propagation--because of the platform motion, some means of sampling the "future" transmission path must be devised. For relay concepts, this is normally done by extending a beacon, or a corner reflector (which will become a beacon when illuminated from the ground), ahead of the relay motion, either on a long boom, or on a fly-along platform. This becomes even more complicated when the relay is a rocket-borne probe, rather than an orbital platform with a stable orbit.

To solve this problem, we take advantage of our ability to control the rocket trajectory, so that the relay is always within the "isoplanatic patch". This is the region around the line-of-sight (LOS) to the moving object, for which the medium is stable within the beam transit time. As indicated in Figure 9, the rocket trajectory is arranged to remain inside this "isoplanatic patch" during the measurement time. The angular size of the patch, $\Delta\theta$, can be estimated by the equation[5]

$$\Delta\theta = \left(\frac{0.058\lambda^2}{\int_0^{\infty} C_n^2(z) z^{5/3}\, dz} \right)^{3/5} \qquad (4)$$

Thus, by using a carefully planned trajectory, the compensation problem is greatly simplified.

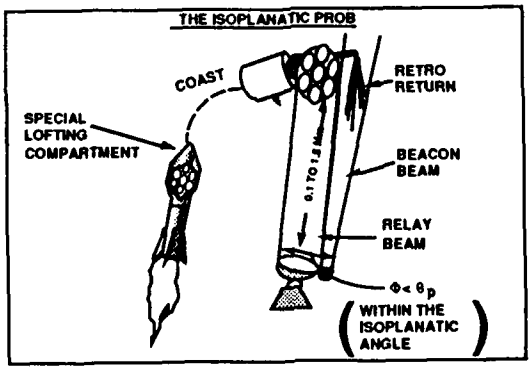


Figure 9. The Isoplanatic Probe

4. The Heterodyne Detection Receiver Option

The utilization of stabilized, short wavelength ladars yields some interesting possibilities[6] for measurement systems. The short wavelength makes feasible an optical receiver array, like the one illustrated schematically in Figure 10. This array could be of relatively small size, because of the wavelength-sensitive diffraction effects on the speckle pattern. A segmented array has certain weight advantages, and some imaging schemes are being explored in which segment phasing is done electronically rather than mechanically. Angle-Angle and Range-Doppler imaging, in various combinations, are possible, and the doppler shifts due to the short wavelength are large, yielding extraordinary measurement precisions. Laboratory experiments have yielded many interesting confirmations of the potential and near-term nature of these technologies.

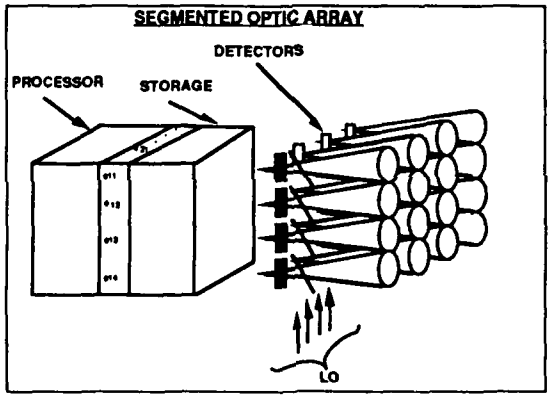


Figure 10. Schematic of Heterodyne Detection Receiver

5. Conclusion

A relatively near-term ladar concept has been defined which has the potential of yielding a remarkable measurement capability for defense and other applications. Demonstrated progress in three critical technologies make the concept truly feasible in the near term. However, there are some potential trouble spots, mostly in the atmospheric compensation area; they are expected to be resolved soon. A key area requiring continued attention is the rapidly developing isolation/stabilization technology--truly the key technology to the relay concept. The combination of short wavelength and stabilized performance, yields not only a remarkable measurement capability, but a robust growth path for future systems.

6. References

1. R. E. Hufnagel, in The Infrared Handbook, W. L. Wolfe & G. J. Zissis, Eds. (ERIM, Ann Arbor, MI, 1978), pp. 6_28 6_40.

2. Goodman, J. W., Statistical Optics, (Wiley, New York, 1985)

3. R. E. Hufnagel, op. cit., pp .6_9-6_14

4. T. W. Tuer, J. Mudar, J. R. Freeling, G. H. Lindquist, Atmospheric Effects on Low-Power Laser Beam Propagation, SAM-TR-80-51, (USAF School of Aerospace Medicine, Brooks AFB, TX), p 101.

5. D. L. Fried, J. Opt. Soc. Am., 72, 56 (1982)

6. R. Morton, W. Connally, SPIE Laser Radar III, 999, 226 (1988)

ACCELERATION AND DEFORMATION MEASUREMENTS USING COHERENT LASER RADAR

M. G. Roe, A. L. Huston, and B. L. Justus
Naval Research Laboratory
Optical Sciences Division
Code 6535
Washington D.C. 20375-5000

Abstract

A solid state coherent laser radar system was employed to measure accelerations and/or deformations of metal foils. The foils were ablatively accelerated by a short laser pulse to velocities of approximately 1 km/s. Velocity profiles were determined by digitizing the chirped waveform produced by the target as its velocity changes. This waveform was analyzed to determine the Doppler shift as a function of time. Measured velocity profiles were found to be in good agreement with a simple model of ablative acceleration. Vibrations of the target foils due to the accelerating pulse were also observed.

Introduction

The measurement of the velocity profiles of rapidly accelerating objects has traditionally been performed using velocity interferometers. Experimental techniques, such as ORVIS[1] and VISAR[2], compare the frequency of light scattered by a moving object at different times through use of a fixed time delay. Both of these techniques require complicated data interpretation and neither can monitor an object moving at constant velocity unless the complete velocity history of the object is known.

Coherent laser radar can directly monitor the velocity of an object as a function of time. Acceleration of the target leads to a chirped waveform that can be easily analyzed to obtain the velocity profile. The use of an offset local oscillator allows the object to be monitored even when it is not moving and also extends the bandwidth of the system since Doppler shifts can be measured both above and below the local oscillator frequency.

Laser Radar Apparatus

A diagram of the equipment comprising the coherent laser radar system is shown in Fig. 1. The local and master oscillators are single mode, diode-pumped, cw Nd:YAG ring lasers operating at 1064 nm. These lasers have narrow linewidths and can be tuned in frequency over 15 GHz without mode hops.[3,4] This permits the offsetting of large Doppler shifts.

The master oscillator is amplified by a flashlamp-pumped rod amplifier operating at 10 Hz and having a gain of 1000 when double passed. Return light from the target is separated using a combination of a thin film polarizer and a quarter wave plate. The return signal and the local oscillator are both coupled into single mode, polarization-preserving fibers and combined in a variable-ratio fiber mixer. The heterodyne signal is detected with a 1 GHz bandwidth silicon avalanche photodiode, and the output of the photodiode is digitized using a fast oscilloscope in conjunction with a CCD camera.

Laser Ablative Acceleration

Rapidly accelerating targets were produced using laser ablation of thin metal foils.[5,6] Foils were attached to the inside of a window on a vacuum chamber. The output of a 2 J Q-switched ruby laser was focussed to a 1.5 mm diameter spot on the foils resulting in peak power densities of up to 7 GW/cm^2. Between 10 and 15% of the drive pulse energy is converted into the kinetic energy of a foil flyer by the ablation process. Terminal velocities in excess of 2 km/s have previously been obtained using 1.5 mm diameter by 12 micron thick aluminum flyers.[7] The acceleration produced by laser ablation has been modeled by treating the plasma that is formed as an ideal gas that is trapped between an immovable wall and the flyer that is to be accelerated.[8,9] As the gas expands, its thermal energy is converted to the kinetic energy of the flyer. In the simplest model, the gas can be constrained to expand only in the di-

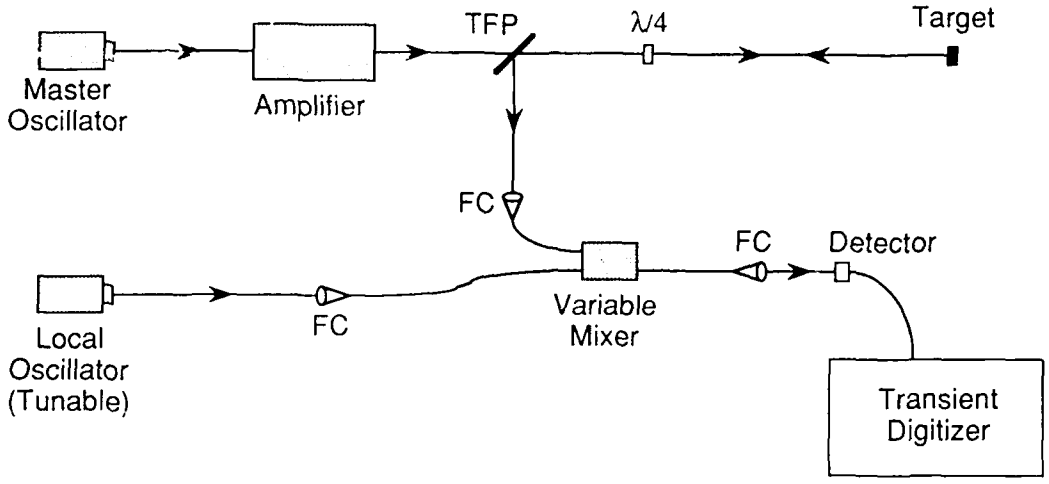


FIG. 1. Diagram of the coherent laser radar apparatus. Return light from the target and local oscillator are coupled into single mode polarization-preserving fibers and mixed. FC: Fiber Coupler. TFP: Thin Film Polarizer.

rection of motion of the accelerating flyer. With this assumption, the flyer will obey the equation of motion,

$$6z\frac{d^2z}{dt^2} + \left(\frac{dz}{dt}\right)^2 = \frac{2E}{m} \tag{1}$$

where z is the flyers displacement from the launch window, E is the energy contained in the gas, and m is the mass of the flyer. This equation can be solved numerically, with the only free parameter being the initial value of z. This simple model could be improved by considering the actual time profile of the drive laser pulse, treating the plasma expansion more realistically, taking into account the fact that part of the flyer is ablated away, and by allowing the flyer to be heated by the plasma.

Data and Discussion

A typical frequency-chirped waveform, produced by the acceleration of a 1.5 mm diameter by 25 micron thick aluminum flyer is shown in Fig. 2. The drive energy was 1.03 J and the local oscillator frequency was set 810 MHz above the master oscillator frequency. As the flyer accelerates, the beat frequency decreases, passing through zero in the vicinity of 25 ns and then increases. The measured frequencies span 1.5 GHz, well beyond the 1 GHz bandwidth of the detection electronics. This illustrates the extended measurement bandwidth possible with this technique.

The velocity profile derived from the waveform of Fig. 2 is shown in Fig. 3. After 50 ns, the flyer is moving at 800 m/s and is clearly still accelerating. Based on the drive energy used, the terminal velocity should be about 1500 m/s. The smooth line in Fig. 3, is a fit obtained from equation (1). The agreement with the data is quite good for such a simple model. Note, however, that there is an oscillation of the velocity on top of the overall shape.

The velocity profile can be integrated to determine the distance profile and differentiated to determine the acceleration profile. Fig. 4 shows the distance profile derived from the data of Fig. 3. The smooth line is again obtained from equation (1). The flyer moves only about 22 microns during the 50 ns measurement period. Thus, the assumption that the plasma only expands in the direction of motion is still valid, and the agreement with the prediction of the

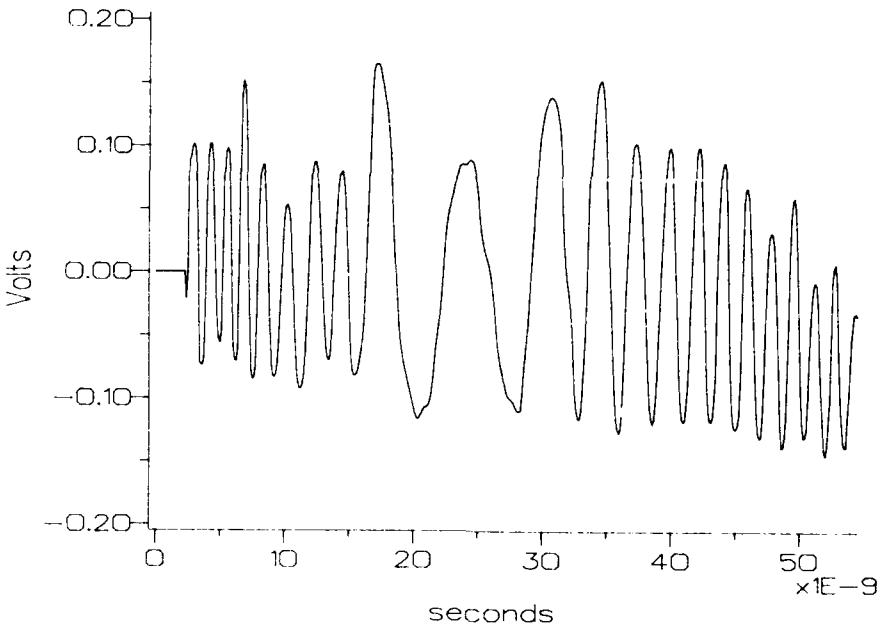


FIG. 2. Frequency-chirped waveform resulting from Doppler measurement of the acceleration of a 25 micron thick aluminum flyer. The local oscillator was offset by 810 MHz.

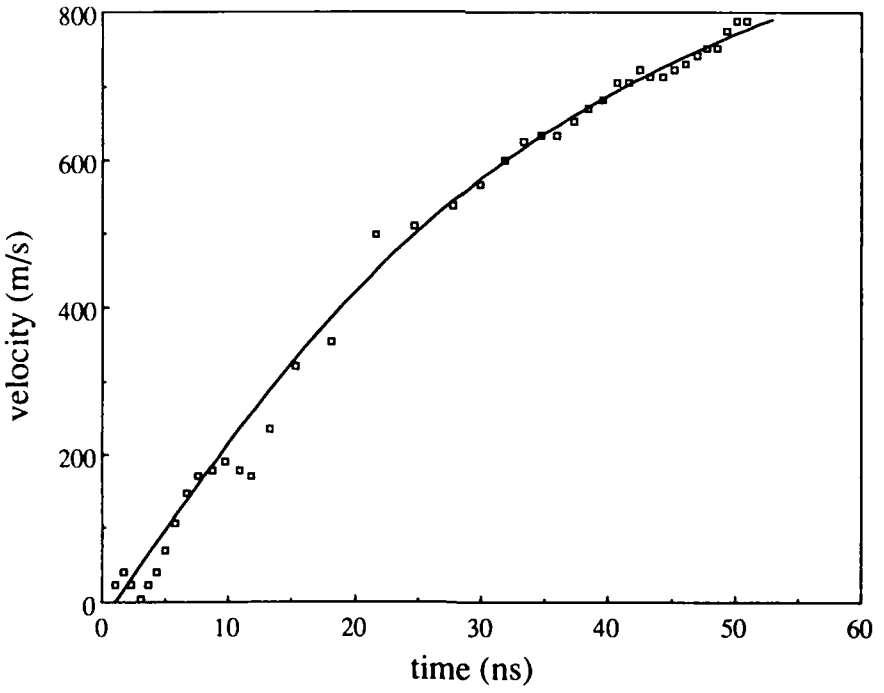


FIG. 3. Velocity profile obtained from the waveform of Fig. 2. Smooth line is a fit to a model of ablative acceleration.

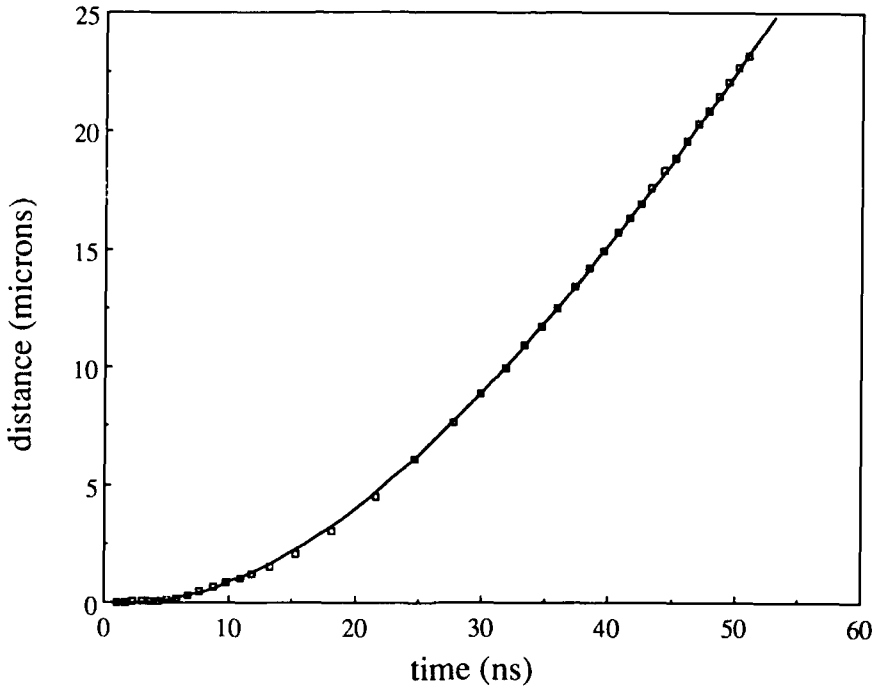


FIG. 4. Distance profile obtained by integrating the data of Fig. 3. Smooth line is a fit to a model of ablative acceleration.

simple model discussed earlier is not surprising.

The acceleration profile derived from the data of Fig. 3 is shown in Fig. 5. The data shows a large spread, and actually indicates negative accelerations at some times. The smooth line is derived from equation (1) and fits the general trend of the data points. The data show fairly regular oscillations with a period of about 8 ns. This is due to the fact that what is actually being measured is the velocity of the front surface of the flyer. The initial impact of the laser drive pulse generates a shock wave that reverberates within the flyer. The speed of sound in aluminum is 6420 m/s, indicating that the round trip travel time for a 25 micron thick flyer is 7.8 ns. This agrees well with the observed oscillation period.

The waveform produced by the acceleration of a 50 micron thick aluminum flyer is shown in Fig. 6. The drive energy was 1.23 J and the local oscillator offset was 750 MHz. The frequency crossover occurs at about 30 ns. The velocity profile obtained from this waveform is shown in Fig. 7. This data also shows oscillations, but with a period of about 16 ns and with smaller amplitude, which is what would be expected for a flyer that is 50 microns thick.

As a further experiment, a large 25 micron thick aluminum foil was glued onto the launch window in an effort to enhance the vibrations in the foil. The measured velocity profile is shown in Fig. 8. The foil only attains a velocity of about 100 m/s after 100 ns. Oscillations of the velocity are now clearly visible and negative velocities are even observed.

Conclusions

Coherent laser radar provides an alternative to traditional methods of measuring velocity profiles of rapidly accelerating objects. Because heterodyne detection is employed, local oscillator power can compensate for targets that have poor reflectivities, allowing a wider variety of targets to be measured. The use of a tunable local oscillator effectively doubles the bandwidth of the detection electronics and also permits the measurement of zero velocities. Data analysis is also much more straightforward than with other techniques.

Measurements of the velocity profiles of metal foils launched by laser ablation were found to be in good agreement with a simple model of ablative acceleration. Vibrations of the accelerated foils were observed, consistent with shock wave reverberations through the foils, indicating that the technique is quite sensitive.

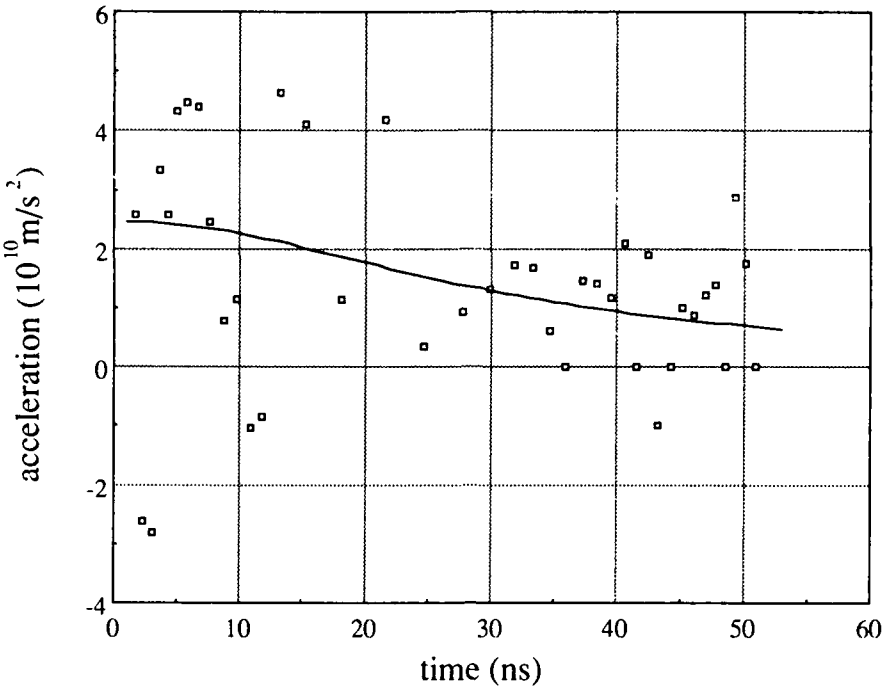


FIG. 5. Acceleration profile obtained by differentiating the data of Fig. 3. Smooth line is a fit to a model of ablative acceleration. Large oscillations are due to a shock wave reverberating in the foil flyer.

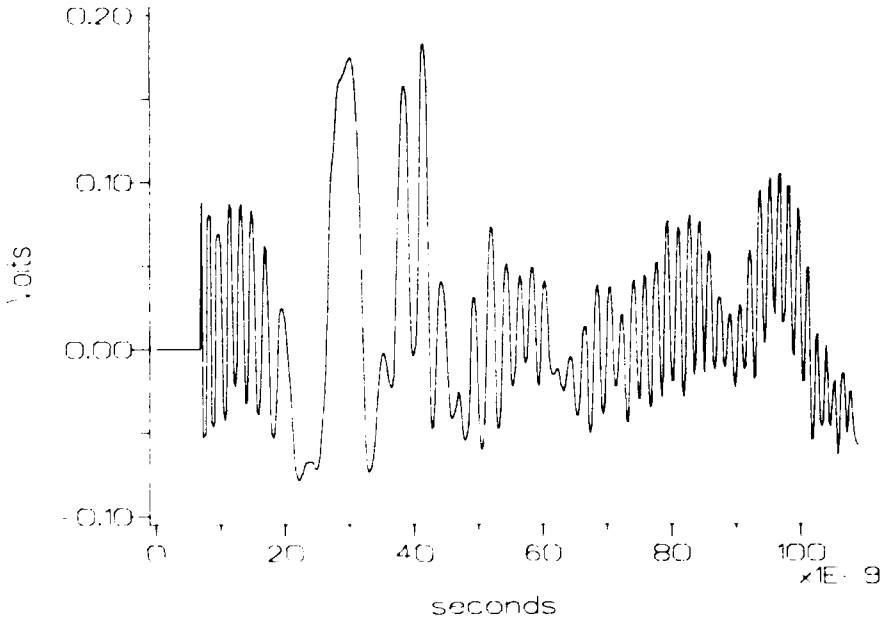


FIG. 6. Frequency-chirped waveform showing the acceleration of a 50 micron thick aluminum flyer. Local oscillator was offset by 750 MHz.

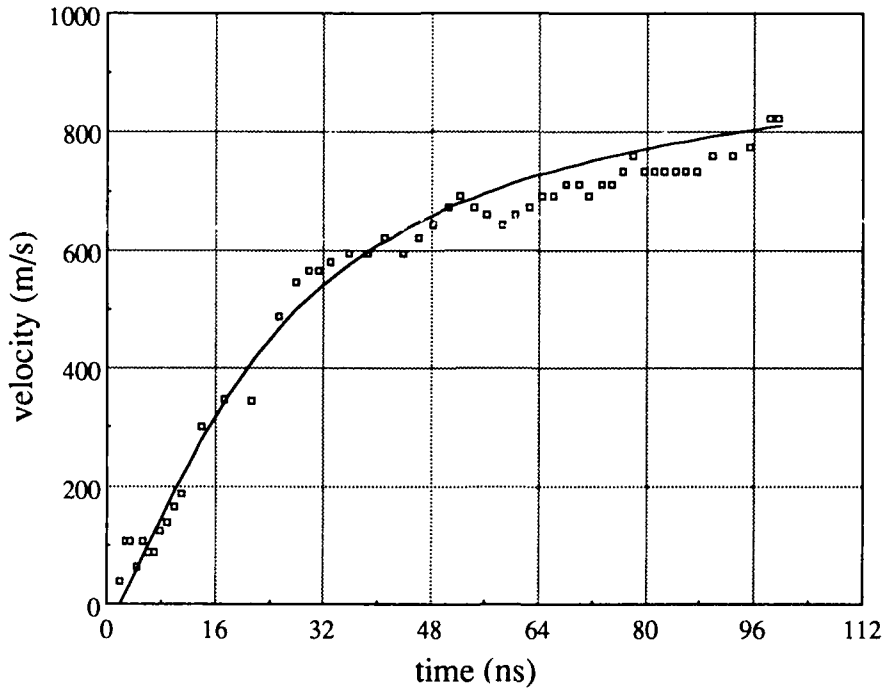


FIG. 7. Velocity profile obtained from the waveform of Fig. 6. Smooth line is a fit to an ablative acceleration model.

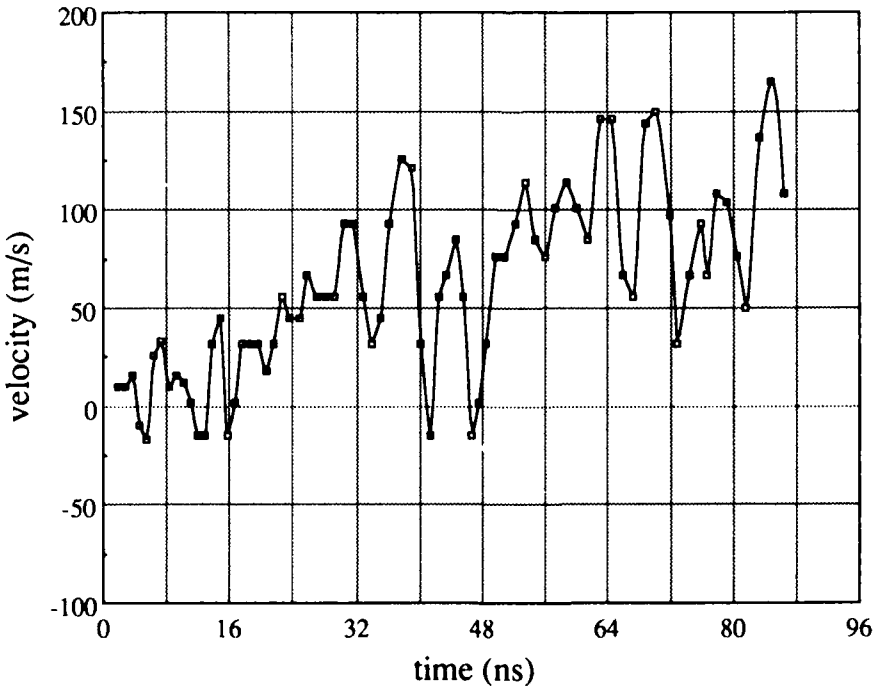


FIG. 8. Velocity profile of a large 25 micron thick foil that was glued to the launch window. Note large oscillations due to shock wave reverberation.

Acknowledgement

This work was supported by the Strategic Defense Initiative Organization.

References

1. D. D. Bloomquist and S. A. Sheffield, J. Appl. Phys. 54, 1717 (1983)

2. L. M. Barker, Soc. Photo. Opt. Instrum. Eng. 427, 116 (1983)

3. T. J. Kane, A. C. Nilsson and R. L. Byer, Opt. Lett. 12, 175 (1987)

4. S. P. Bush, A. Gungor and C. C. Davis, Appl. Phys. Lett. 53, 646 (1988)

5. B. H. Ripin, R. Decoste, S. P. Obenschain, S. E. Bodner, E. A. McLean, F. C. Young, R. R. Whitlock, C. M. Armstrong, J. Grun, J. A. Stamper, S. H. Gold, D. J. Nagel, R. H. Lehmberg and J. M. McMahon, Phys. Fluids. 23, 1012 (1980)

6. B. L. Justus, C. D. Merritt and A. J. Campillo, Chem. Phys. Lett. 156, 64 (1989)

7. A. L. Huston and M. G. Roe, to be published.

8. L. C. Yang, J. Appl. Phys. 45, 2601 (1974)

9. R. D. Griffin, B. L. Justus, A. J. Campillo and L. S. Goldberg, J. Appl. Phys. 59 (1986)

PROPAGATION OF INTENSE LASER RADIATION IN AEROSOL

O. A. Volkovitsky
Institute of Experimental Meteorology
249020 Obninsk, USSR

Theoretical and experimental studies on interaction of intense laser beams and aerosol are reviewed. Considered are physical effects arising from radiation interaction with solid and liquid particles (particle evaporation and destruction, overcondensation, optical breakdown and others) which result in spatial-temporal change of optical properties of the medium. The role of these effects in propagation of continuous and pulsed laser radiation in the atmosphere is discussed.

1. Introduction.

The research on spatial-temporal changes of optical cross-section of atmospheric components under radiation and their effect on radiation propagation has recently developed into a special area of atmospheric optics - non-linear atmospheric optics. This presentation seeks to cover only part of the phenomena arising from interaction of intense laser radiation with atmospheric aerosol particles and to show their role in propagation of laser radiation. Focus will be placed on particular problems of non-linear optics of aerosol. Hundreds of studies on the subject have been done since the late 1960's and therefore it seems unrealizable to give a comprehensive review within one communication. The task of reviewing is, to a certain extent, made easier by the fact that the books [51, 61, 62] have recently been published. These books address various aspects of interaction between intense laser radiation and cloud drops, crystals and atmospheric aerosol. The effects to be discussed in the paper and corresponding changes in optical properties of the medium are given in Table 1.

Table 1

Effects arising from interaction of intense laser radiation and aerosol particles

Effects	Radiation intensity W cm^{-2}	Type of particle			Variation of optical cross-section		Accompanying effects	
		0.1-5μm aerosol particle	1-10μm droplet	5-200μm crystal	Decrease	Increase	change in permittivity	induced turbulence
Diffusive evaporation	$I<10^3$	-	+	+	+	-	+	small
Convection evaporation	$10^3<I<10^4$	-	+	+	+	-	+	+
Overcondensation	$I>5\cdot10^3$	-	+	+	-	+	+	+
Explosion	$I>5\cdot10^4$	-	+	+	λ=10.6μm + λ=0.63μm -	- +	+	-
Breakdown	$I>10^6-10^8$	+	+	+	-	+	+	-

2. Propagation of intense laser radiation in clouds (the clearing effect).

The studies on interaction of continuons intense laser radiation with droplet aerosol were initiated in the late 1960's. It was noticed that radiation in the mid-IR spectrum region had a distinctive feature of being well absorbed by water and weakly absorbed by atmospheric gases and water vapor. Radiation in this spectrum region at the wavelength λ=10,6 μm was generated with the use of CO_2 lasers. In those years first theoretical works made their appearance which looked into droplet evaporation given internal sources of heat release [41, 49] and mist evaporation under radiation [26, 28, 54]. These studies have laid the foundation for a new direction in non-linear optics of clouds. The experimental work [32] was first to demonstrate that due to evaporation of fog droplets in a continuous CO_2 laser radiation beam the HeNe-laser radiation transmission was substantially improved. At that time, a hope emerged as to the prospects of CO_2 laser applicability for cloud dissipation. Indeed, no more than a cup of water was found to be in the way of a laser beam in a relatively thick cloud. The impression was that in order for droplets in a stationary cloud to evaporate, radiation of comparatively low power would be required.

In the 1970's, problem statement in non-linear optics of clouds became more complete. In

order that the problems of propagation of intense laser radiation in a droplet and a crystal cloud medium be solved with allowance made for medium motion, losses of radiation energy for medium heating and droplet scattering, as well as induced beam divergence and induced turbulence, equations were formulated for the electromagnetic field in aerosol. I shall not dwell on the mathematical side of the problem but let me point out that when the propagation of a laser beam in a cloud was evaluated, given fairly complete problem statement, it took several hours to solve the system of equations with computers. Today the time of computation has been sharply reduced, nevertheless the rate of computation is still much less that the velocity of the transparency front in a cloud, to say nothing of light velocity. Let us briefly overview the research efforts of those years. The studies [22, 39, 54, 60] contained diagrams for vaporization and explosion of cloud elements under radiation as a function of particle size, radiation intensity and medium temperature. The plots were constructed on the basis of theoretical considerations and experimental results for radiation interaction with cloud particles.

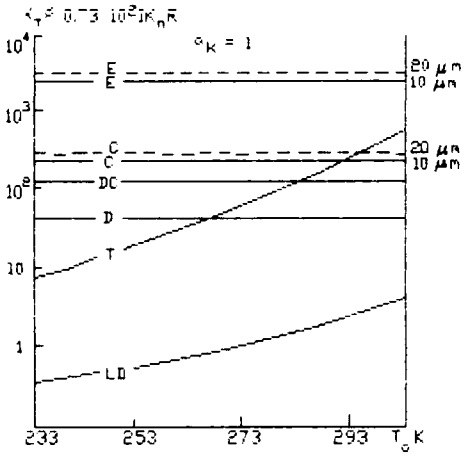


Fig.1. Evaporation, turbidification and explosive destruction modes [22, 40, 51]
LD - linear diffusive ($0.36 < \chi_T < 3.05$)
D - diffusive ($39.5 > \chi_T > 28$)
DC - diffusive-convective ($\chi_T > 110$)
C - convective ($\chi_T > 159$)
E - explosive-destruction ($\chi_T > 2400$)
T - turbidification ($540 > \chi_T > 8$).

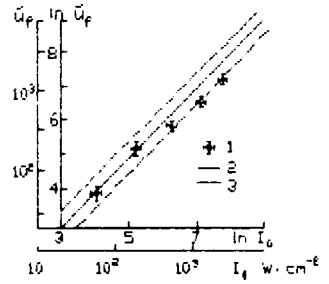


Fig.2. Normalized clearing front velocity $\bar{u}_f = \frac{u_f\, \alpha_0}{c}$ as function of intensity I_0 [51].
1 - experimental $\bar{u}_f$ for I_0 = 36, 180, 500, 1300, 2500 W cm^{-2},
2 - dependency $\bar{u}_f \sim I_0$,
3 - errors in determining $\bar{u}_f$.

With a number of simplifying assumptions, Glickler S.L. (1971) obtained formulas for the intensity field in the zone of radiation interaction with cloud. The problem was solved for a stationary cloud without regard to radiation losses in the so-called "water content" approximation. The authors of [44] proposed the solution of an analogous problem for a moving cloud in the so-called fine droplet approximation ($R < 3$ μm). The analysis of more exact numerical solutions and experimental results has allowed the extension of the above analytical solutions to propagation in a cloud of diverging beams, consideration for energy losses and writing formulas for optical thickness at the visible wavelength. The results of continuous radiation research in Institute of Experimental Meteorology in the 1970's are summarized in the book [51] mentioned above.

The formula for calculating spatial-temporal variations of CO_2 laser thermal effect function field in a homogeneous moving cloud under diffision-convection regime of evaporation for droplets with $R_w < 10$ μm has eventually taken the simple form

$$q(x, y, z, t) = \ln [1 + (\exp(q_0) - 1) \exp(-\tau)] , \qquad (1)$$

where

$$q(y, z, t) = \frac{3\Lambda\beta_T\beta_\rho}{4\rho H} \int_0^t I_0(y, z - v\eta, \eta)\, d\eta , \qquad (2)$$

β_T and β_ρ are the coefficients accounting for energy losses for medium heating and energy scattered by droplets, ρ and H are the water density and the evaporation heat, Λ is the constant, v-wind velocity.

The velocity of clearing wave propagation in cloud (the velocity of a clearing front) can be calculated with the formula

$$u_f(x, y, z) = \frac{CI_0(y, z)}{\alpha_0} = \frac{\beta_T\beta_\rho I_0(y, z)}{HW_0} , \qquad (3)$$

where α_0 and W_0 are coefficients of extinction and cloud water content. This furmula has been validated in experiments (Fig. 2).

The transparency of steady-state clearing zone of a moving cloud at $t > d/v$ is determined by the relation

where

$$\Pi(x, y, z) = I(x, y, z)/I_0(y, z) = [1 + Q(x, y, z)]^{-1} , \qquad (4)$$

$$Q(x, y, z) = (\exp(\tau) - 1) \exp[-q_0(y, z)] . \qquad (5)$$

Numereous experiments have confirmed the validity of this formula (Fig. 3).

Thus it may be asserted that for assessment of cloud clearing ("hole - boring") under diffusion-convection regimes of cloud element evaporation a robust theory has been developed and validated.

3. The effect of overcondensation on radiation propogation in cloud (the turbidification effect).

When droplets are evaporated in the laser radiation field, under certain conditions substantial supersaturation may occur which is able of promoting the formation of secondary droplets. The possibility of supersaturation occurrence was first noted by Sutton G.W. [45] The works [20, 27] included theoretical assessment of the supersaturation effect on restructuring of droplet spectrum. Since the latter authors did not consider a possibility of emergence of new droplets, the conclusion was made that increase of optical cross-section in the supersaturatin field was ruled out.

The experiments conducted by the author and his colleagues [23, 50] have shown that under certain conditions the supersaturation which occurs in the laser radiation field in the vicinity of evaporating droplets gives rise to the formation of a host of small droplets; this is the turbidification effect. Theoretical estimation we did in 1976 [51] have indicated that in the radiation field in the vicinity of droplets, supersaturation may occur sufficient for homogeneous vapor condensation.

The analysis of abundant experimental evidence of the turbidification effect occurring under radiation exposure of droplets and crystals with widely changing medium temperature has allowed the determination of a homogeneous condensation boundary. The results are shown in Fig. 1.

It is of interest to note that while the discovery of the clearing effect has led to an increased optimism as to generation of clearing zones in clouds, the discovery of the turbidification effect has given rise to a lot of scepticism coming from the view that the problem is unsolvable. And I believe, it is dedication of researchers which is to counterbalance the emotions on both sides.

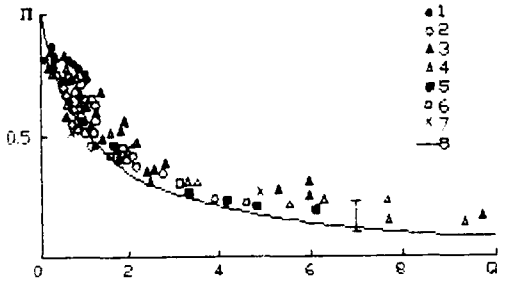


Fig.3 Transmission $\Pi = I(0)/I_0(0)$ at CO_2 laser beam axis (Z=0) for steady-clearing-state of droplet cloud medium as function of dimensionless parameter Q with changing thermal-action function due to variations in P_0, d_0, ... [51] 1-7 - experiments, 8 - calculation.

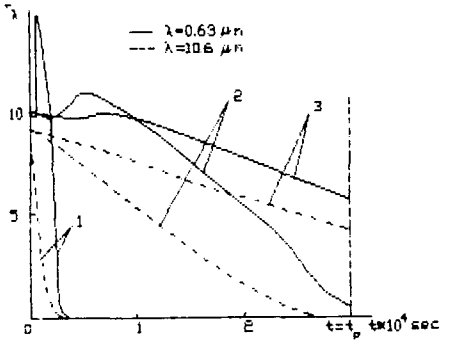


Fig.4 Optic thickness of cloud medium as function of time during its perturbation by radiation pulses with various intensity [5] 1,2,3 - I_0 = 1, 0.1, 0.01 MW cm^{-2} respectively

4. Propagation in cloud of radiation pulses. The role of explosive droplet destruction.

Increase in the velocity of clearing wave propagation in cloud is associated with increase in radiation intensity. An appreciable increase in radiation intensity is obtained in pulsed lasers. The feature of interaction between a series of radiation pulses and a moving cloud medium is that clearing during the pulse t_M alternates with the blurring of the cleared zone by wind in between pulses t_n and the mode of explosive droplet destruction is realized at radiation intensities $I > I_k$.

Propagation of pulsed radiation in clouds is the subject of research in [21, 38, 46, 55] where analytical and numerical methods are used to solve the problem of collimated radiation interaction with cloud medium under diffusive-convective mode of droplet destruction.

The works [53, 6] focus on peculiarities of propagation in cloud of pulsed diverging radiation at $I < I_k$ and collimated pulsed radiation at $I > I_k$. For a diverging beam, the problem was approximately solved in [53] and in the simpliest case with $q_{\theta j} >> 1$, $\Pi_\theta = 0,5$ the formula for $q_{\theta j}$ - thermal effect function of j-th pulse can be written as

$$q_{\theta j} = \tau_j = 1/\psi\left(\sqrt[3]{1 + 3\psi q_{j-1}} - 1\right), \qquad (6)$$

where $q_{j-1} = q_0\left(1 + \psi \sum_{k=1}^{j-1} \tau_k\right)^{-2}$, q_0 is the thermal effect function at the beginning of the path ($q_0 = CI_0 t_M$), $\psi = \theta/d_0\alpha_0$.

As has been pointed out, at $I > I_k$ explosive droplet destruction occurs and a jumpwise

change in optical properties of the clearing zone can be expected. Under certain conditions the formation of a host of fragments may give rise to considerable increase in the optical cross-section of a clearing zone, especially at the visible wavelength (Fig. 4) [5]. The turbidification of a cloud medium can also be brought about by phenomena of other nature than the overcondensation considered above.

5. Thermal distortion of laser beams in aerosols.

The character of propagation of intense laser beam in aerosols is affected not only by non-linear aerosol extinction, but also by non-linear refraction, whose effect is particularly pronounced on long paths. The physical cause of non-linear thermal refraction in aerosols, and in gases too, lies in spatial-temporal change of permittivity of the medium due to local temperature change. Local temperature changes under propagation of intense laser radiation in aerosol are far in excess of those in gas, and consequently, beam distortions in aerosol will be more conspicuous.

The authors of [34, 51] solved theoretically the problem of laser beam deflection in a moving cloud due to formation of asymmetric profile of dielectric constant under diffusion-convection conditions of droplet evaporation. The studies [4, 48] have shown that under certain conditions (cold fogs), self-focusing of the near-axis part of the Gaussian beam may occur. Calculations of laser beam thermal distortions in droplet aerosol were made in [56] with the use of numerical solution of parabolic equation and in [17] with the use a geometric approach.

Thermal distortions of laser beams in aerosol were investigated in great detail in [13, 14, 24] which contain experimental evidence on deflection of probing radiation in a cloud medium under wind for a wide range of temperature and other parameters and on beam blooming in a stationary cloud medium. Thermal distortions of a laser beam when it propagates in a solid aerosol was investigated in [3]. Theoretical research and experiments have exposed the following principal features of thermal distortions of laser beams:

- as the temperature of a cloud medium falls, with all other things being equal, beam deflection upwind becomes greater due to the increased thermal losses (smaller values of β_T) (Fig. 5);

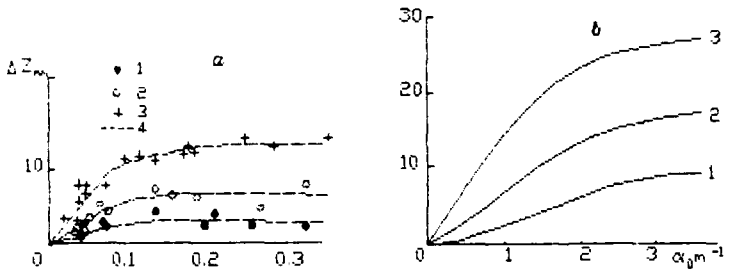


Fig.5 Deflection of central section of laser beam as function of attenuation coefficient at various temperatures of medium [14]. P_0 = 400 W, d_0 = 0.8 cm, v = 25 cm sec^{-1}. a - experiments; 1, 2, 3 - T_0 = 283, 260, 243 K, respectively. 4 - approximation; b - calculations.

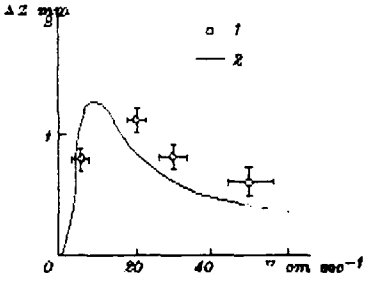


Fig.6 Deflection of central section of laser beam as function of wind velocity [14]. P_0 = 800 W, α_0 = 0.3 m^{-1}, d_0 = 4.6 cm, T_0 = 293 K, L = 4 m. 1 - experiments; 2 - calculations. Vertical and horizontal cuts - experimental errors.

- the dependence of beam deflection on wind velocity is of nonmonotonic character which is due to nonmonotonic dependence of permittivity asymmetry on wind velocity (Fig. 6);
- as particle size of solid aerosol grows, thermal blooming of the beam enlarges which is due to greater overheating of the meadium (Fig. 7).

Wind deflections of beams in aerosol on long paths are not expected to be appreciable, whereas symmetric blooming of unimodal beams and distortions of multimodal beams may be significant.

6. The role of induced turbulence in laser beam distortions.

Two sides can be indicated in the problem of non-linear radiation propagation with pulsating parameters in a turbulent aerodisperse medium:

- interaction between radiation with predetermined parameters and turbulent medium;
- interaction between radiation with fluctuating parameters and the medium with predetermined characteristics.

We now briefly consider the results of research related to the first problem. The principal mechanism giving rise to induced radiation fluctuations in this case is "mixing" of spatially inhomogeneous field of complex permittivity $\varepsilon(T, W_0)$ by the turbulent wind field. The variances σ_T^2 and σ_W^2 of temperature and liquid water content fluctuations in the cleared cloud medium were theoretically investigated in [1, 2] and relations for σ_T^2, σ_W^2 and related fluctuations of ϵ were obtained.

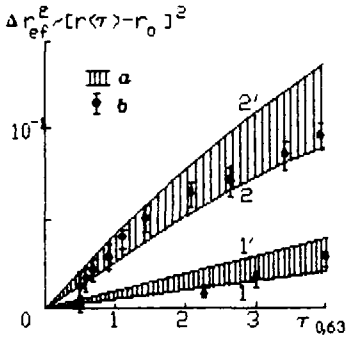


Fig.7. Relationship between radiation beam broadening and optic thickness of medium with path length fixed [3].
1, 1' - average particle radius 0.1-1μm;
2,2' - average particle radius 5-10 μm.
1', 2' - $I=10^3 W\cdot cm^{-2}$
1, 2 - $I=(1.5-2)10^3 W\cdot cm^{-2}$
a - calculations,
b - experiments.

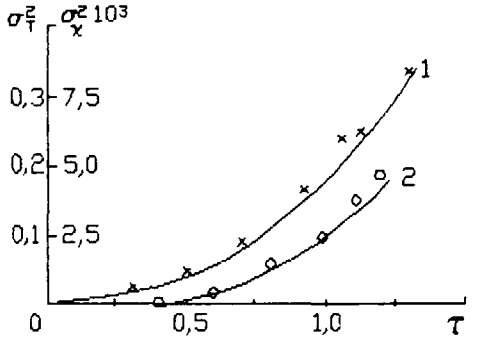


Fig.8. Dependencies of temperature fluctuation dispersion σ_T^2 and intensity level fluctuations σ_χ^2 on optic thickness of cloud medium τ [2].
1, 2 - calculations,
× - experiments for σ_T^2,
o - experiments for σ_χ^2.

Using the fields $\epsilon(T, W_0)$ obtained, one can calculate fluctuations of the intensity level for perturbing (σ_χ^2) and probing $(\sigma_{\chi\lambda}^2)$ beams in the approximation of the smooth perturbation method. The agreement between experimental and theoretical dependencies of σ_T^2 and σ_χ^2 on τ_0 is illustrated in Fig. 8. The second problem associated with the mechanism of perturbing additional fluctuations due to transformation in pulsations of initial amplitude-phase distribution of radiation field in a cloud medium was tackled in [1]. Typical curves showing the development of random inhomogeneities of liquid water content and aerosol temperature induced by fluctuating beam are given in Fig. 9 [7].

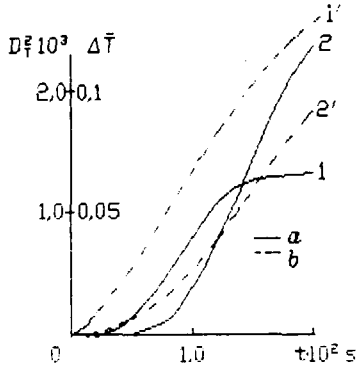


Fig.9. Time behavior of mean value $\Delta\bar{T}$ and fluctuation dispersion D_T^2 of temperature [7].
1, 2 - $\tau_0 = 3, 5$
a - D_T^2, b - $\Delta\bar{T}$, $I_0 = 10^3 W\cdot cm^{-2}$

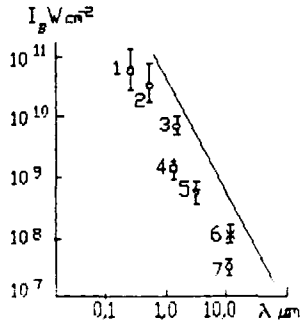


Fig.10. Threshold of aerosol optic breakdown as a function of wavelength.
1, 2, 3 - λ = 0.351, 0.537, 1.054 μm respectively, R_0 = 1-5 μm [25];
4 - λ = 1.06 μm; R_0 = 1-8 μm [58, 59];
5 - λ = 3.58-4.78 μm [8];
6 - λ = 10.6 μm; R_0 = 1-4 μm [9];
7 - λ = 10.6 μm; R_0 = 1-10 μm [61].
Solid line - pure gas breakdown (Ryzer Yu.P. (1974)).

7. Optical breakdown under propagation of laser radiation in aerosols.

The breakdown which occurs under propagation of high intensity laser radiation ($I_{th} > 10^{10} - 10^{11}$ W · cm^{-2} for λ = 10,6 - 0,5 μm) gives rise to formation of plasma and appreciable radiation extinction. Given liquid and solid aerosol particles in gases, the threshold of breakdown is significantly reduced (at λ = 10,6 μm $I_{th} < 10^8$ W·cm^{-2}). This may result in considerable deterioration of propagation conditions of intense laser radiation in the atmosphere at intensities of $I > I_{th}$.

Experimental investigations of optical breakdown in aerosols are extensively reported in literature [8, 9, 10, 29, 30, 31, 36, 37, 43, 58]. The theory of laser radiation propagation in aerosols above the breakdown plasma formation has not been developed to the extent to which was the theory of intense radiation propagation in droplet aerosol at $I < I_{th}$.

Let us briefly consider the major results of investigating optical breakdown in aerosols.

The threshold of optical breakdown is little dependent on the composition of aerosol particles and strongly dependent on radiation wavelength and pulse duration. Fig. 10 summarizes the results obtained by different researchers for a breakdown threshold I_{th} in the wavelength range λ = 0,35 - 10,6 μm. In the wavelength range under consideration the dependence $I_{th}(\lambda)$ is satisfactorily approximated by the relationship $I_{th} \sim \lambda^{-2}$ which is experimentally supported in [15, 29]. One can identify several types of optical breakdown on individual aerosol particles (solid and liquid) and on ensembles of them. Several types of optical breakdown at the wavelength λ = 1,06 μm are illustrated by the Table 2.

Tabl. 2

Types of optical breakdown

Effect	I, W·cm^{-2}	Type of particles	Author
Local optical discharge	$4 \cdot 10^{9}$-$2 \cdot 10^{11}$	Solid particles d = 0,2 - 40 μm	Lencioni D.C. (1974)
Local optical discharge	10^{9}-10^{10}	Water droplets d = 30 - 100 μm	Mamonov V.K. (1978)
Extended optical discharge (LLS)	10^{8}-10^{10}	Solid particles d = 2 - 16 μm	Basov N. et al. (1978) Parfenov V. et al. (1976) Zakharchenko S. et al. (1989)
Low-threshold collective optical discharge (LCOD)	$2 \cdot 10^{6}$-$2 \cdot 10^{7}$	Ensemble of solid particles N > 10^{3} cm^{-3} d > 2 μm	Zakharchenko S. et al. (1978)

The first studies on air breakdown on water droplets were carried out in [36, 37] with the use of ruby laser. It was established in [30] where the interaction of Nd^{3+}: YAG laser radiation (I_o = 10^{9} - 10^{10} W·cm^{-2}) with water droplets of 10 - 70 μm diameter was investigated that air breakdown was initiated only when primary sites of breakdown emerged in droplets. Two modes in evolving breakdown sites with spherically symmetric and asymmetric shock waves were identified.

The studies [30, 31, 36, 37] have shown that the reduction of air breakdown threshold which is observed in the presence of droplets is caused by the emergence of optical breakdown sites in them. These sites may be initiated by interaction of radiation with droplet microimpurities and the existense of diffraction maxima of intensity.

On extended atmospheric paths, optical breakdown is realized in the form of a long laser spark (LLS) which was observed on 2 - 60 m paths in [9, 11, 35, 58 and others]. Different hypotheses were put forward as to the mechanism of LLS formation. The aerosol nature of LLS at λ = 1,06 μm was substantiated in [59]. When LLS is formed the breakdown threshold falls as compared to breakdown threshold in the focal space of the beam.

In the dust-laden air (0,1 - 10 g·m^{-3}) the conditions emerge under which the threshold of optical breakdown is reduced to 10^{6} - 10^{7} W·cm^{-2} [57]. What we observe is the so-called low-threshold collective optical discharge (LCOD) under which breakdown sites near individual aerosol particles influence each other and develop collectively.

Physical understanding of spatial-temporal variations in optical cross-section of breakdown plasma and experimentally obtained dependencies of breakdown threshold on particle size as well as other findings allowed a member of authors to propose semi-empirical models which make it possible to assess aerosol transparency $T_\lambda = E/E_o$ under laser radiation pulse propagation [15, 59 and others]. The examples of calculating the dependencies of $T_{1.06}$ and $T_{10.6}$ on energy density of laser radiation E are given in Fig. 11 [15].

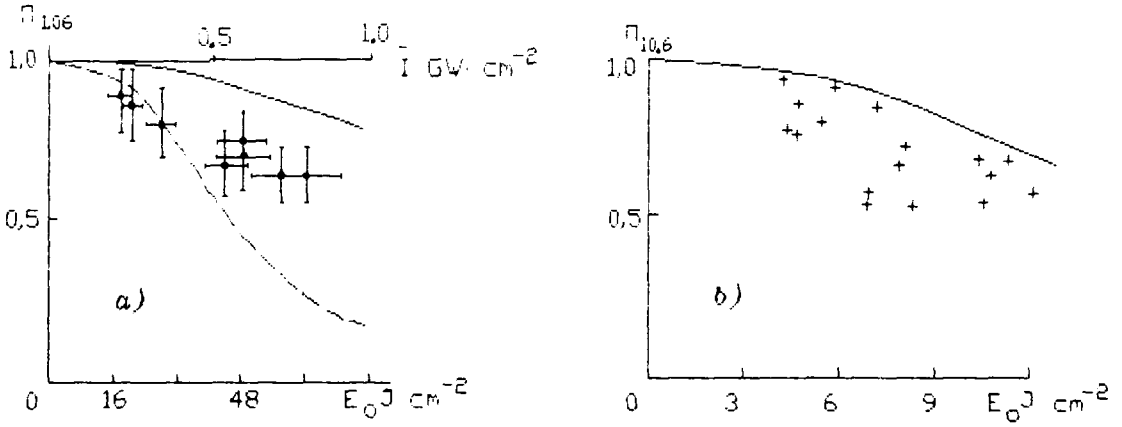


Fig.11. 1.06 μm (*a*) and 10.6 μm (*b*) radiation transmission as function of average energy density [15].

These models qualitatively describe dependencies of T_λ on E_o which were obtained in experiments.

An interesting feature of aerosol transparency variations under the effect of coupled CO_2 laser pulses was noted by Autric M. et al. [10]. It has been found that as the first pulse passes, a sort of cleaning of radiation propagation zone occurs due to evaporation of particles and their removal. Thus the zone becomes more "transparent" for passing the next pulse. The effect is the strongest and transparency may increase threefold when the time interval between pulses is about 100 μ sec.

8. Potential applications of effects of interaction between intense laser radiation and aerosol.

The potentialities in using some effects of interaction of intense laser radiation with liquid and solid aerosol particles were discussed in literature in the context of handling the following practical tasks:

- fog clearing over airport runways [33, 51];
- hole-boring in fogs and clouds [21];
- improvement of viewing range of laser beacon in fog [51, 52];
- improvement of picture transmission conditions in fog [24];
- remote identification of chemical composition of air pollutants with the use of LLS [12, 19].

Improvement of visibility range of laser beacons in fog seems a more realistic task. As was found in [51] the increase of several fold in detection range for visible laser light scattered in a clearing zone of 10 cm diameter (from 300 m to 1,5 km) will take CO_2 laser power less than 10^5 W. The efficacy of the method is reduced with a diverging CO_2 laser beam and improved with a converging one [52].

In conclusion let me apologize to those colleagues whose works were not mentioned in my review. I want to thank most warmly Dr. M. Autric, Dr. Sh. M. Chitanvis and Dr. G. W. Sutton that they have found it possible to send me the results of their recent studies. I also appreciate the assisstance I have received in preparing the review from my colleagues Drs R. Almaev, E. Ivanov, V. Mamonov, L. Semenov, A. Skripkin, A. Slesarev and S. Zakharchenko.

References.

1. R. Kh. Almaev and P. N. Svirkunov, JTPh Lett., 12, 719 (1978).
2. R. Kh. Almaev, S. D. Pinchuk, L. P. Semenov and O. A. Volkovitsky, J. Phys., suppl. No. 11, C9-107 (1980).
3. R. Kh. Almaev and A. M. Skripkin, Trudyi IEM, 26(99), 92(1981).
4. R. Kh. Almaev P. N. Svirkunov and A. G. Slesarev, in Proceedings, International Conference on Lasers'81, C. B. Collins, Ed. (STS Press, McLean, VA, 1981), pp. 928-932.
5. R. Kh. Almaev, O. A. Volkovitsky, Y. S. Sedunov and L. P. Semenov, Infrared Phys., 1/2, 475 (1985).
6. R. Kh. Almaev, L. P. Semenov, A. G. Slesarev and O. A. Volkovitsky, in Advances in Laser Science-III, A. C. Tam et al. Eds. (AIPh., New York, 1988) pp. 555-556.
7. R. Kh. Almaev, L. P. Semenov and A. G. Slesarev, Trudyi IEM, 49 (139), 3 (1989).
8. S. T. Amimoto, J. S. Whittier, F. G. Ronkowski et al., AIAA Journ., 8, 1108 (1984).
9. M. Autric, J. P. Carressa, Ph. Bournot et al., AIAA Journ., 11, 1415(1981).
10. M. Autric, P. Vigliano, D. Dufresne et al., AIAA Journ., 1, 65 (1988).
11. N. G. Basov, V. A. Boyiko, O. N. Krokhin and G. V. Sklizkov, DAN USSR, 3, 538 (1967).
12. E. B. Belyaev, A. P. Godlevsky and Yu. D. Kopyitin, Kvantovaya Elektronika, 11, 131 (1976).
13. V. A. Belt's, B. S. Vinevitch, O. M. Matveev et al., Trudyi IEM, 5(43), 104(1974).
14. V. A. Belt's, O. A. Volkovitsky, A. F. Nerushev and V. P. Nikolayev, Trudyi IEM, 18(71), 67(1978).
15. A. P. Budnik, L. P. Semenov, A. M. Skripkin and O. A. Volkovisky, in Proceedings, International GCL- 7 Symposium, Vien (1988) to be published.
16. Sh. M. Chitanvis, Appl Opt., 11, 1837 (1986).
17. Sh. M. Chitanvis, in Advances in Laser Science-III, A. C. Tam et al., Eds. (AIPh., New York, 1988), pp. 490-492.
18. Sh. M. Chitanvis and A. Zardecki, Appl. Opt., 12, 2495 (1988).
19. V. M. Gavrilov, S. L. Golub and A. M. Skripkin, in Proceedings, II Meeting on Laser Propagation in Aerosol, part 2 (Obninsk, 1982), pp. 130-133.
20. M. P. Gordin and G. M. Strelkov, Kvantovaya Elektronika, 3, 559 (1975).
21. R. C. Harney, Appl. Opt. 11, 2974 (1977).
22. E. V. Ivanov and V. Ya. Korovin, IPhJ, 5, 807 (1978).
23. E. V. Ivanov, V. Ya. Korovin, Yu. V. Tolstikov and O. A. Volkovitsky, J. Phys., suppl. No. 11, C9-293 (1980).
24. C. M. Kolomiets and V. V. Smirnov, Kvantovaya Elektronika, 12, 2594 (1976).
25. V. I. Kondrashov, Yu. P. Rudnitsky, S. F. Sitnikov and V. I. Sokolov, in Proceedings, III Meeting on Laser propagation in aerosol, part 4 Y. S. Sedunov et al. Ed. (Obninsk, 1985), pp. 78-79.
26. A. V Kizikovsky and S. S. Khmelevtsov, Izv. AN USSR, FAO, 3, 363 (1968).

27. A. V. Kizikovsky and S. S. Khmelevtsov, Izv. AN USSR, FAO, 4, 362 (1975).
28. G. L. lamb and R. B. Kinney, J. Appl. Phys. 1, 416 (1969).
29. D. C. Lencioni, Appl. Phys. Lett., 1, 12 (1973).
30. V. K. Mamonov, JTPh, 12, 2333(1985).
31. V. K. Mamonov, JTPh, 12, 2410(1986).
32. G. J. Mullaney, W. H. Christiansen and D. A. Russel, Appl. Phys. Lett., v. 13, 4, 145, (1968).
33. G. J. Mullaney, W. H. Christiansen and D. A. Russel, J. Aircraft, 2, 108(1971).
34. A. F. Nerushev, Trudyi IEM, 11(54), 41(1975).
35. V. A. Parfenov, L. N. Pakhomov, V. Yu. Petrunkin and V. A. Podlovsky, JTPh Lett., 16, 731(1976).
36. V. A. Pogodaev and A. Ye. Rojdestvensky, JTPh Lett., 5, 157(1979).
37. V. A. Pogodaev and A. Ye. Rojdestvensky, JTPh Lett., 8, 1541 (1983).
38. V. K. Pustovalov and I. A. Khorunjiy, JPS, 3, 377(1985).
39. J. Reilly, P. Singh and Sh. Glickler, AIAA pap. 659, 1(1977).
40. L. P. Semenov, Trudyi IEM, 18(71), 3(1978).
41. K. S. Shifrin and J. K. Zolotova, Izv. AN USSR FAO, 12, 1311(1966).
42. A. M. Skripkin, JTPh, 3, 554(1987).
43. D. C. Smith, J. Appl. Phys. 6, 2217(1971).
44. A. P. Sukhorukov, R. V. Khokhlov and E. N. Shumilov, JTPh, Lett., 14, 245(1971).
45. G. W. Sutton, AIAA Journ., 10, 1907(1970).
46. G. W. Sutton, Appl. Opt., 21, 3424(1978).
47. G. W. Sutton, Appl. Opt., 24, 4994(1988).
48. P. N. Svirkunov, Kvantovaya Elektronika, 4, 892(1978).
49. F. G. Volkov and A. M. Golovin, JPMTPh, 4, 83(1968).
50. O. A. Volkovitsky, E. V. Ivanov, M. P. Kolomeyev, N. K. Kraskovsky and L. P. Semenov, Izv. AN USSR, FAO, 8, 861(1975).
51. O. A. Volkovitsky, L. P. Semenov and Yu. S. Sedunov, Propagation of Intensive Laser Radiation in Clouds (Gidrometeoizdat, Leningrad, 1982).
52. O. A. Volkovitsky, Appl. Opt., 24, 5307 (1987).
53. O. A. Volkovitsky, in Advances in Laser Science-III, A. C. Tam et al., Eds. (AIPh., New York, 1988), pp. 557-560.
54. F. A. Williams, Int. J. HMT, 4, 575(1965).
55. K. D. Yegorov and V. D. Kandidov, in Proceedings, 5 Symposium on Laser propagation, part 3, V. E. Zuev, Ed. (Tomsk, 1979), pp. 65-68.
56. K. D. Yegorov, V. D. Kandidov and M. S. Prakhov, Kvantovaya Elektronika, 12, 2562(1979).
57. S. V. Zakharchenko, S. M. Kolomiets and A. M. Skripkin, JTPh Lett. 24, 1339(1977).
58. S. V. Zakharchenko, G. A. Sintyurin and A. M. Skripkin, JTPh 6, 1095(1984).
59. S. V. Zakharchenko, L. P. Semenov and A. M. Skripkin, Kvantovaya Elektronika, 12, 2487(1984).
60. V. E. Zuev, Propagation of the visible and infrared waves in the atmosphere (Sovetskoye Radio, Moskva, 1970).
61. V. E. Zuev, A. A. Zemlyanov, Yu. D. Kopyitin and A. V. Kuzikovsky, High Power Laser Radiation in the Atmospheric Aerosol (Nauka, Novosibirsk, 1984).
62. V. E. Zuev, A. A. Zemlyanov and Yu. D. Kopyitin, Nonlinear Optics of the Atmosphere (Gidrometeoizdat, Leningrad, 1989).

CLOUD HOLE BORING WITH INFRARED LASERS-THEORY AND EXPERIMENT

E. J. Caramana, R. L. Morse, G. P. Quigley
J. R. Stephens, R. B. Webster, G. W. York

MS E531 Los Alamos National Laboratory
Los Alamos, NM 85745

Results of experimental attempts to produce an optically clear channel in a water cloud by evaporating the cloud droplets with a CO_2 laser are presented. Using scattered light it is possible to visualize the clear channel produced. Measurements of the fraction of power transmitted through the channel at visible wavelengths give insight into the clearing mechanisms. The present data suggest that the water droplets explode in the process of clearing. A theoretical explanation of why this should occur is presented and predictions of the onset of droplet explosions are made.

Introduction

The ability to clear an optical channel in a cloud has applications ranging from defense to ground based meteorological observation. The interior of many natural clouds cannot be probed by conventional optical means due to the large optical depths often encountered. By evaporating the liquid water in a cloud, it is possible to temporarily create an optically clear channel. This paper presents results of laboratory experiments performed with the objectives of determining the conditions under which a high power pulsed CO_2 laser can produce an optically clear channel and identifying the physical mechanisms responsible for the clearing and closure of such a channel. In the present experiments, it appears that the droplets first explode resulting in an initial increase in turbidity. The smaller droplets formed by the explosion then evaporate leaving a partially cleared channel. This channel remains clear for a time period on the order of a second, finally closing by advection due to turbulence in the cloud. These findings are consistent with previous work using shorter and longer pulse lengths[1][2].

Experiment

The experiment consists of boring a hole in a cloud while monitoring the scattering and transmission of visible probe beams that are propagated through the hole. A schematic of the experimental arrangement is shown in Fig. 1. The cloud is produced in a recirculating wind tunnel built by Boeing Aerospace Corporation. Droplets are formed by high pressure impaction in the fog chamber and then carried by the flowing air into the cloud chamber. The cloud chamber is a tube 80cm in diameter and 5 m long. The clearing laser beam cuts across the cloud transverse to the direction of flow. Flow speed can be varied from 5 cm/sec to over 100cm/sec. Throughout this range the flow is turbulent. Measurements of the background cloud temperature, droplet size distribution and liquid water content are made to characterize the clouds with which the laser interacts. Typically these clouds have temperatures of 27°C . The liquid water content is measured with a probe manufactured by Gerber Scientific. Liquid water contents range from 0.6 gm/cm^3 to 2.4 gm/cm^3 . For the data presented in this paper the liquid water content is about 0.8 gm/cm^3 . The droplet distribution is measured using the Forward Scattering Spectrometer Probe manufactured by Particle Measuring Systems Inc.. The droplet size distribution is shown in Fig. 2. This distribution is insensitive to liquid water content and flow speed over the aforementioned ranges.

The hole is bored by illuminating the cloud of water droplets with the radiation from a CO_2 laser at 10.6μm . This wavelength is an efficient choice for cloud clearing because it is strongly absorbed by liquid water and weakly absorbed by water vapor; thus, most of the laser energy is used to evaporate water instead of heating the air. The laser used is the Meteor II laser at Los Alamos National Laboratory, which is an e-beam initiated DF$\rightarrow CO_2$ chemical laser. This laser produces pulsed outputs of up to 360 Joules with typical pulse lengths of 25 μsec . The laser output is a circular beam, 10cm in diameter with a nearly uniform flux distribution. The output beam is focussed to a 5cm diameter spot in the center of the cloud chamber. This yields fluences of up to 12 J/cm^2 at the focus, with 10 percent variations across the chamber. Plots of laser power as a function of time are shown by the solid curves in Fig. 3 (The scale for these curves is to the left of the plot). The gain switched spike at early times contains a few percent of the total energy of the pulse.

The simpler of the diagnostics used is the "sheet of light" in which a video camera records the slow time dependence of the forward scattering of a plane of 0.633μm light. The light sheet is produced by spreading the beam from a HeNe laser with a cylindrical lens just before the beam passes through the sapphire beam stop (see Fig. 1). The video camera is located on the other side of the cloud chamber several degrees off the axis of the clearing beam. In the schematic, the light sheet would be perpendicular to the page. Three photographs obtained with this method are shown in Fig. 4. The channel appears distorted by foreshortening due to the small angle and close proximity from which it is observed. In reality the sides of the channel are nearly parallel. By examining these photos, one sees that immediately following the clearing beam an optically clear channel, characterized by low scattering of visible light, has been produced. At later times ($\simeq$0.5 sec) the edges of this channel are beginning to break up due to fluid motion present in the cloud. It is not presently possible to form clouds without fluid turbulence in the cloud chamber.

While the hole is being bored, and for 2 msec afterwards, the fraction of power transmitted through the hole at 0.488μm is monitored. Fig. 3 presents data obtained when varying the clearing beam flux. The flux was varied by placing various plastic attenuator sheets in the beam path. The initial increase in turbidity (decrease in transmission) is characteristic of all of the data taken in which a rapid change in transmission is observed. It is clear from curve a) that this increase in turbidity does not preclude the possibility of clearing a channel. Although not apparent from the graphs, the final transmission levels were maintained for at least a 2 msec at which time the sampling of the signals was stopped. A possible explanation for the increase in turbidity is presented in the next section.

Theory

Because of the long duration of the increase in turbidity evident in Fig. 3 c), d) and e), it is unlikely that this increase is due to scattering caused by acoustic waves or vapor halos surrounding the evaporating droplets. Instead, it appears likely that the droplets are exploding, forming a new distribution of smaller droplets. When sufficient energy is present in the portion of the clearing pulse that comes after the explosions, as in Fig. 3a, the smaller droplets are evaporated and a clear channel is produced. If the remaining energy is insufficient to evaporate the small droplets, a partially cleared channel is produced (Fig. 3b) and in some cases the channel actually becomes more turbid as a result of the laser interaction (Fig. 3c-e).

The reason for this explosion is that heat deposited near the center of a droplet cannot diffuse to the droplet surface on the time-scale of the present laser-cloud interactions. Thus, the temperature at the center of the droplet can reach very high levels. The droplet explodes when the central temperature reaches the temperature of the spinodal curve for water at atmospheric pressure (approximately 305°C)[3]. Above the spinodal temperature, water is thermodynamically unstable to a continuous phase transformation. For temperatures near but below the spinodal temperature, the water is in a metastable state and can undergo a phase transition only by nucleation of a vapor bubble. In either event, pressures near 200atm are expected near the center of the droplet when the phase change occurs. These pressures will then rapidly disassemble the droplet. The details of disassembly are not discussed in this paper, rather a prediction is made of when such disassembly is to be expected.

We now develop a simple model for predicting the onset of droplet explosions. A similar model has been developed previously to explain the observation of explosions in single droplet experiments[4]. That model was necessarily more complicated because the droplets considered were large compared to the wavelength of radiation. Thus, focusing and attenuation of the radiation caused nonuniform heating. Because the droplets in the present experiment are small compared to the 10.6μm wavelength of the clearing beam, it is possible to assume that the rate of heating is uniform throughout. This reduces the problem to that of one-dimensional energy conservation in the radial direction. The relevant equations are conservation of energy at the surface,

$$L\frac{dM}{dt} - 4\pi\kappa_a R(T_s - T_a) = 4\pi\kappa_w R^2 \frac{\partial T}{\partial r}|_R, \tag{1}$$

and the heat conduction equation,

$$\rho C_V \frac{\partial T}{\partial t} = Q + \kappa_w(\frac{1}{r^2}\frac{\partial}{\partial r}r^2\frac{\partial T}{\partial r})|_R. \tag{2}$$

Here, R is the radius of the droplet, ρ is the density of liquid water and L is the latent heat of vaporization of water. $M \equiv 4\pi\rho R^3/3$ is the mass of the droplet. C_V is the specific heat for liquid water and κ_a and κ_w are the thermal conductivities of air and water. T is the droplet temperature with $T_s \equiv T(R)$. T_a is the ambient air temperature. Q is the volumetric heating rate. We take $Q = \frac{3\sigma_a I}{4\pi R^3}$, where I is the incident laser flux and σ_a is the absorption cross-section determined from Mie theory. For 10.6μm light interacting with water droplets less than about 5μm in radius, $Q \simeq 10^3 cm^{-1} I$. These equations, together with an equation specifying T_s, have been solved computationally for a variety of methods of determining T_s ranging from simply taking $T_s = 100°C$ to determining T_s from detailed particle balance with water vapor diffusing away from the droplet surface.

For the pulsed experiments considered here, the conditions under which a droplet will explode are not very sensitive to the method of specifying the surface temperature. The reason for this can be understood by comparing the time-scale for thermal diffusion in the droplet with the time needed to heat a droplet to 305°C . The time-scale for thermal diffusion is $\tau_D \simeq \rho C_V R^2/\kappa_w$ and for the 2.5μm droplets typical of the present experiments this is about 25μsec . For the 200kW and greater fluxes typical in the present experiments the time to reach 305°C is about 5μsec . Thus information regarding the boundary does not have time to diffuse in to the center of the droplet. Examination of Eq. 2 shows that if thermal diffusion is unimportant, the difference between the final central temperature T_f and the initial temperature T_i is related to the flux F measured in J/cm^2 by:

$$T_f - T_i = \frac{10^3}{\rho C_V}\int I dt = 240\ F. \tag{3}$$

If the threshold for droplet explosion is taken to be when the droplet's central temperature reaches 305°C having started at 27°C this implies a threshold flux of $1.2 J/cm^2$.

The above situation, in which diffusion can be neglected, constitutes one of two limits that can be easily analyzed. In the other limit, one can determine the incident laser flux I, that would lead to a steady-state central temperature of 305°C . It turns out that such a steady-state does not exist because the droplet is continually shrinking due to evaporation. Thus, estimating the threshold flux in this way leads to a lower bound. This estimate is close to the estimate provided by more detailed calculations because the droplet radius is changing slowly. The steady-state difference between the central temperature T_c and the edge temperature T_e in a volumetrically heated droplet is,

$$T_c - T_e = \frac{10^3}{6\kappa_w} I R^2, \tag{4}$$

where the approximate formula for Q has been used. For even modest I the edge of the droplet quickly reaches boiling, thus $T_e = 100°C$. This implies a threshold flux of

$$I = 7.2 \times 10^4 R^2. \tag{5}$$

For 2.5μm droplets this gives a flux of $115 kW/cm^2$.

Fig. 5 presents the results of more detailed computations of the explosion threshold for a 2.5μm droplet irradiated with a constant flux source, together with the experimental threshold values deduced from the data shown in Fig. 3. The solid curve is the theoretical threshold curve. The dashed curve is the simple power threshold estimate given by Eq. 5. The data points correspond to the values of fluence and average flux at a point in time denoted by the squares in figures 3a-f. Note that shattering was not observed in 3f, and for that case the average power was used for plotting. The error bars are an estimate of the error in the fluence based on an uncertainty of one time sample in the digitization of the power.

Conclusions

The good agreement between our simple model of droplet explosion thresholds and the experimental data make it likely that the droplets are exploding under the conditions of our experiments. As can be seen from photographs and transmission data, this does not preclude the possibility of producing an optically clear channel in a cloud. In fact such channels can be produced. Continuing effort is needed to determine the optical quality of such channels (phase distortion) and this work is presently under way at Los Alamos.

Acknowledgements

The authors wish to acknowledge useful discussions with Robert Armstrong and Bae-Sig Park. This work was supported by SDIO and the U. S. Department of Energy.

References

1. V. A. Belts, O. A. Volkovitsky, A. F. Dobrovolsky, E. V. Ivanov, Y. V. Nasedkin and L. N. Pavlova, 5th GCL Symp., Oxford (1984)
2. A. V. Kuzikovskii, L. K. Chistyakova and V. I. Kokhanov, Sov. J. Quantum Electron. 11, 1277 (1981)
3. J. G. Eberhart, J. Coll. and Int. Sci. 56, 262 (1976)
4. B. Park and R. L. Armstrong, Appl. Opt. 28, 3671 (1989)

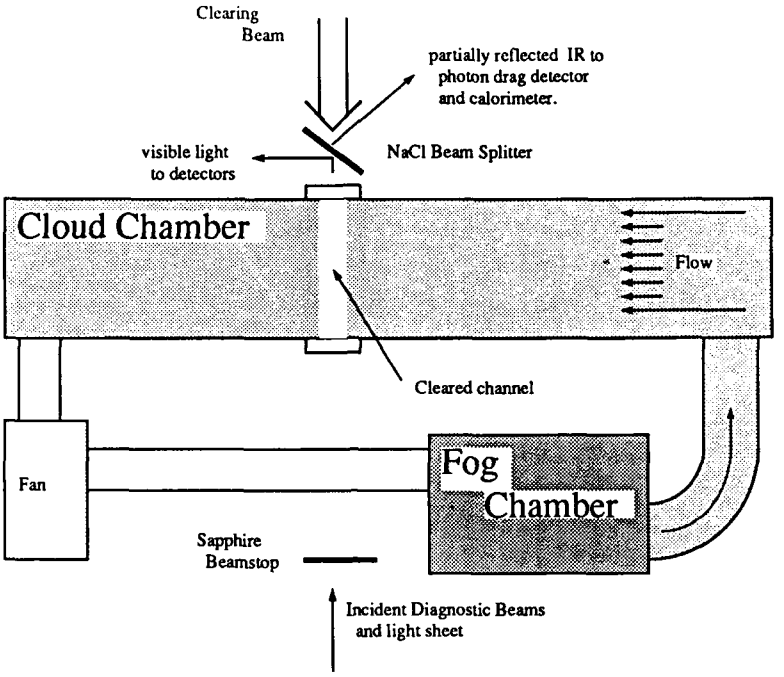


Fig. 1 Schematic Diagram of the Cloud Clearing Experiment

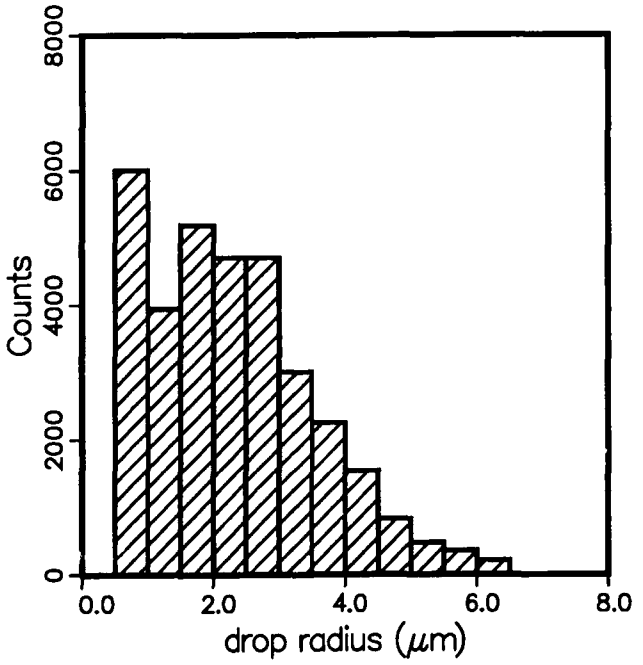


Fig. 2 Droplet Distribution

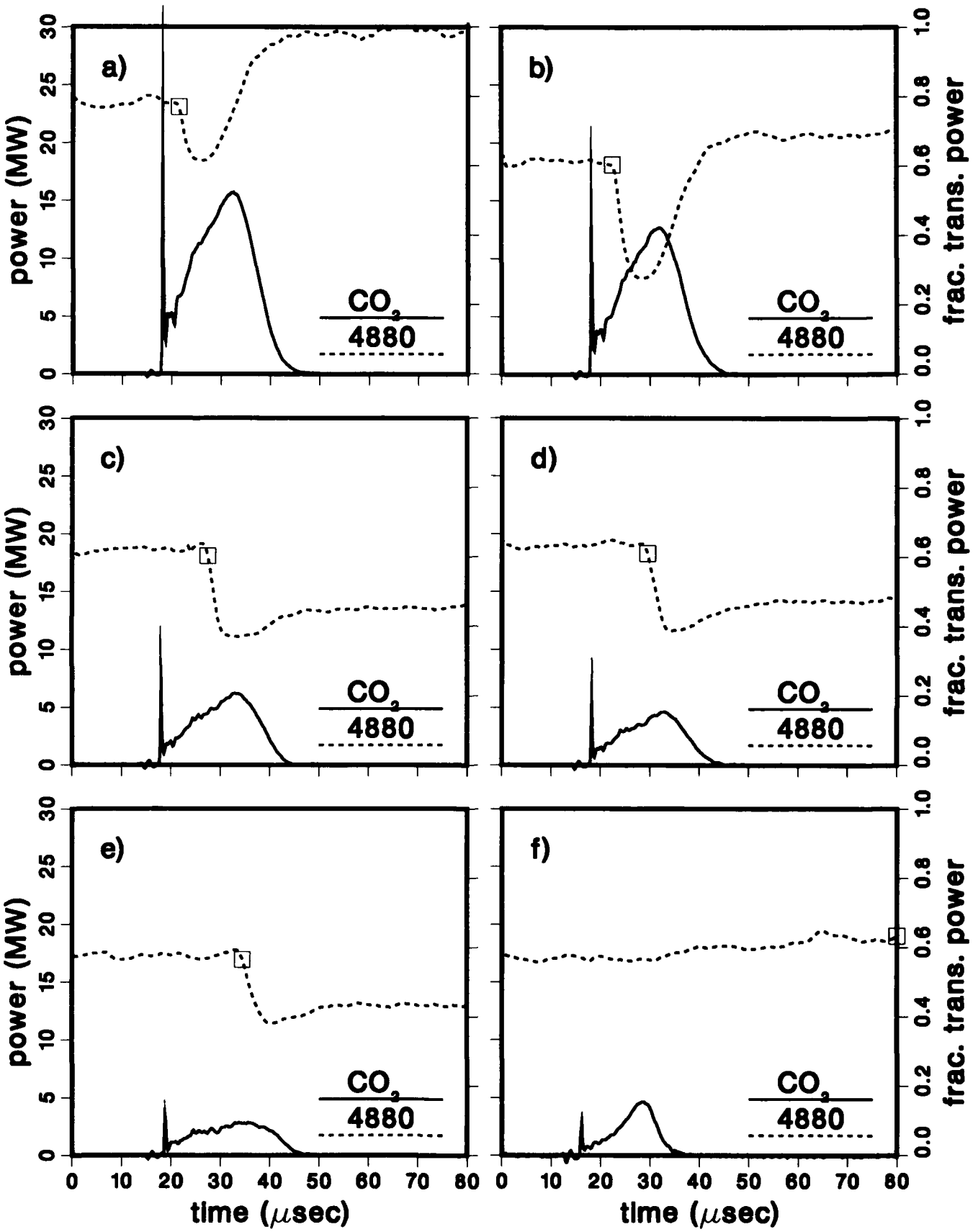


Fig.3 Visible probe transmission fraction and laser power

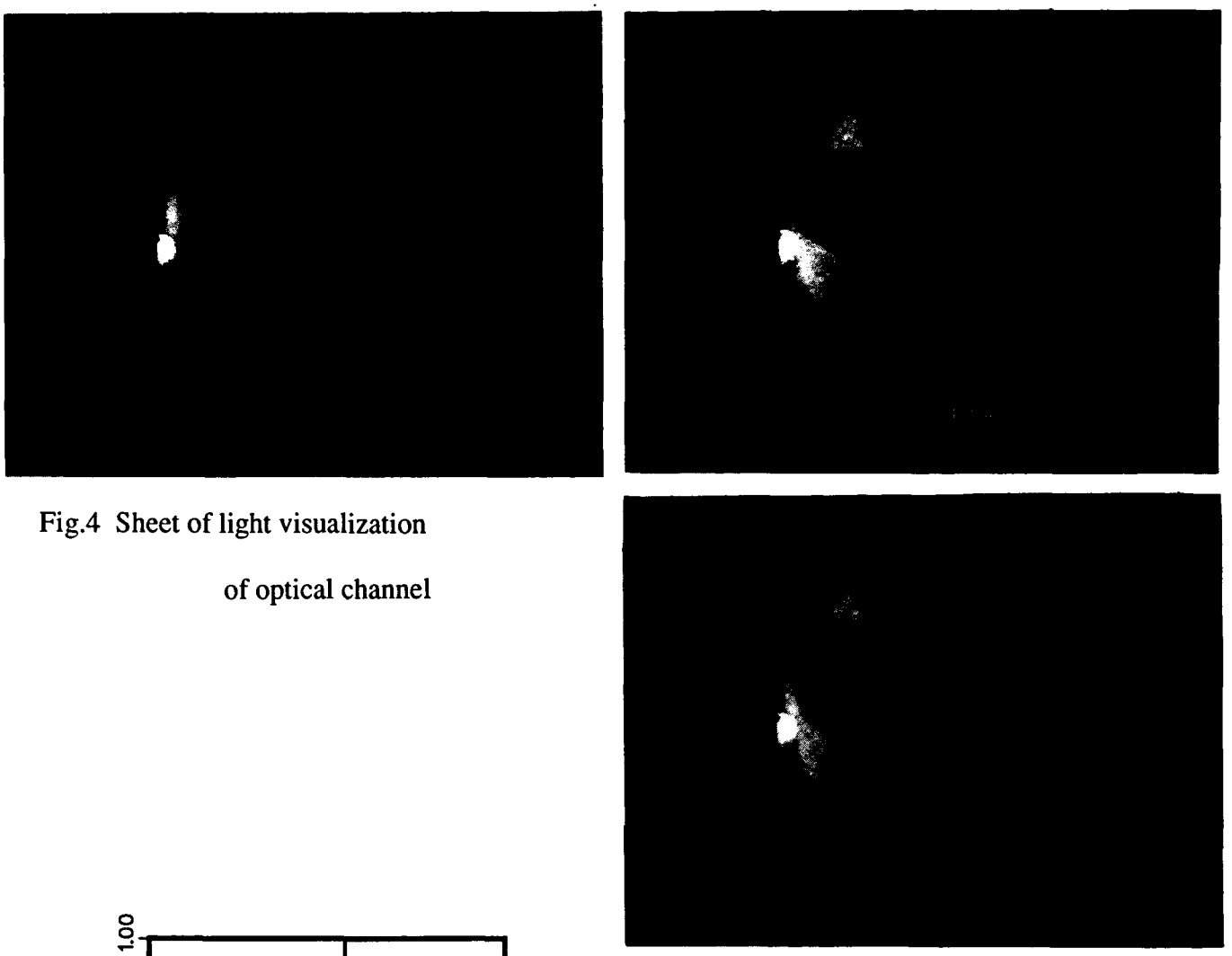


Fig.4 Sheet of light visualization of optical channel

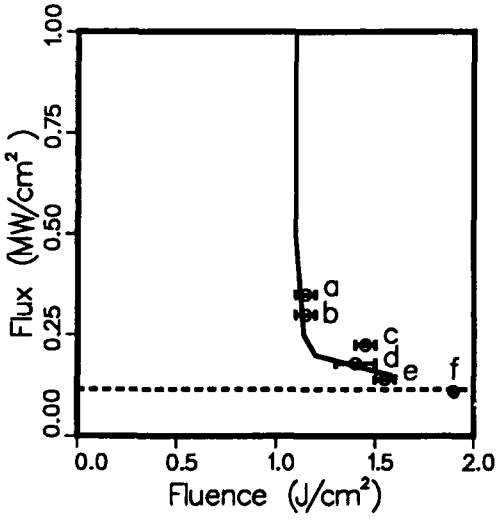


Fig.5 Comparison of theoretical estimate of droplet explosion conditions with experimental deductions

INTERACTIONS OF HIGH-IRRADIANCE CO_2 LASER BEAMS WITH INDIVIDUAL MICRON-SIZED WATER DROPLETS

R. L. Armstrong
(Physics Department, New Mexico State University, Las Cruces, NM 88003)

Abstract

Irradiation of absorbing aerosols with intense laser beams initiates many strong interactions, including droplet superheating and plasma formation. In this talk, we summarize recent experiments on the dynamics of laser beam single aerosol droplet interactions.

Introduction

The interaction of a high-irradiance laser beam with an absorbing, micron-sized liquid droplet has been the subject of numerous recent investigations.[1] Mie scattering theory[2] predicts the existence of high-intensity regions (hot spots) within the droplet that depend on droplet radius and complex refractive index. Inhomogeneous evolution of heat distribution in the droplet may result in the temperature within a hot spot reaching the superheat limit.[3] At this temperature, spontaneous homogeneous nucleation of vapor occurs followed by explosion of the droplet.[4] At still higher irradiance, the plasma breakdown threshold is reached and the primary cause of droplet destruction is the generation of an intense plasma near the irradiated droplet. In this paper, we review recent experimental work on the destruction of water droplets by intense laser beams.

Superheating and Plasma Thresholds

The role of superheating in droplet destruction has been recognized by several workers. Prishivalko[5] and his colleagues developed an approximate model of conductive energy transport in order to estimate droplet superheating behavior. Pendleton[6] neglected thermal conductive and transport processes to obtain estimates of superheated regions within irradiated water droplets, and suggested that the observed droplet explosion patterns[7] could be explained by prediction of what portion of the droplet reached superheat temperature during the CO_2 laser pulse. The previously cited work of Park and Armstrong[3] developed an improved thermal conductive heat and mass transport numerical algorithm to investigate droplet superheating. Two temporal regimes were delineated; a "fast-heating" regime, where superheat temperatures are reached within a thermal conductive time and a "slow-heating" regime, where longer times are required in order to reach superheat temperature. In the fast-heating regime of interest in this talk, thermal conduction and mass transport play a minor role in droplet superheating dynamics.

The experimental arrangement is shown in Fig. 1. We used a droplet generator in our experiments capable of producing a stream of nearly uniform droplets so that repetitive measurements could be made. To get sufficient laser fluence required for our experiment we operated the laser in a multiline mode (but with more than 90% energy output at the 10.591 μm wavelength) and focused the beam to an approximate 325 μm by 220 μm spot. A stream of droplets was then directed through the focal volume where disintegration of droplets, and at higher fluence levels, droplet-induced laser breakdown, occurred.

Time-resolved photographs of disintegrating droplets were made through a microscope by back-illuminating the droplets with an air-plasma generated by a pulsed Nd:YAG laser synchronized with both the generator and the CO_2 laser. Thus the Nd:YAG-produced plasma served as a fast (~100ns duration) strobe light allowing "snapshots" of exploding droplets to be taken with a conventional 35 mm camera as a function of time after initiation of the CO_2 pulse. A calorimeter permitted measurement of pulse energy; uniform plastic sheets provided for attenuation of laser energy.

As the CO_2 laser fluence incident on a droplet is increased, there exists a definite threshold above which explosion or disintegration occurs; below this threshold no observable change in the drop takes place. A representative time-resolved photograph of a disintegrating water droplet at fluence level near threshold is shown in Fig. 2. Water droplets with a radius somewhat larger than the wavelength explode on the illuminated side. The reason is that the high absorption of water causes the peak heating to be on that side. Also shown, for comparison, in Fig. 2 is a photograph of an exploding ethanol droplet which has less absorption and explodes on the shadow side. Water droplets have an extremely well-defined threshold for disintegration. In fact, at laser fluence levels slightly above threshold water droplets catastrophically explode. Disintegration threshold fluences range from about 2 to 5 J cm^{-2} and reveal negligible size dependence over the range of droplet sizes measured (radii ranging from ~ 10 - 50 μm).

The measurements are compared to predictions of the superheat fluence, the fluence required to heat any portion of the irradiated droplet to superheat temperature, which for water is approximately 305°C. In the fast heating regime, the super-heat

fluence given by

$$F = \frac{\rho\, c_p\, \Delta T\, \lambda}{4\pi\, n\, K\, S_{max}} \qquad (1)$$

where ρ and c_p are water density and specific heat at constant pressure, ΔT is the temperature difference between superheat and ambient temperatures, n and k are the real and imaginary parts of the complex refractive index of water at the wavelength λ, and S_{max} is the maximum value of the normalized source function within the water droplet.[4,6] The theoretically predicted fluence values are shown in Fig. 3 together with experimental thresholds; curve (a) denotes the fluence prediction taking into account the temperature dependence of material properties, and curve (b) the prediction neglecting temperature dependence. It is noteworthy that the former is in better agreement with our measurements of explosion thresholds. Considering that our absolute uncertainty in measurement of explosion thresholds is ~ 2.5, we suggest that agreement between our measured thresholds and superheat fluence predictions is good. We conclude that for highly absorbing water droplets heated by submicrosecond pulsed infrared lasers, the criterion for laser-induced explosion of droplets is that of superheat fluence.

Thresholds for droplet-induced breakdown were measured by increasing the laser energy (and fluence) until a visible spark was observed on about 50% of the laser shots. At threshold these sparks are much larger than those for similar measurements at visible and ultraviolet wavelengths.[9] A candidate explanation for this finding is the presence of laser supported detonation waves[8] which have more time to expand during the ~ 200 ns CO_2 laser pulse than during the much shorter 10ns Nd:YAG pulse in the cited experiment.[9] Breakdown threshold values cluster around laser intensities of 10^9 W/cm^{-2}, a factor of 4 below the clean-air breakdown threshold, but a factor of 50 above drop explosion thresholds. A trend of slightly higher thresholds for smaller droplets is evident.

Delays in Superheat Explosions

Homogeneous nucleation of vapor in super-heating is a statistical process described by a nucleation rate which is a nonlinear function of temperature and the thermophysical properties of the liquid-vapor systems.[10] Near the superheat threshold, only a small micro-volume of the droplet within the hot spot reaches the superheat limit temperature. For a finite nucleation rate, a time delay is anticipated between the deposition of heat by the laser pulse and the generation of a sufficient number of nucleated vapor bubbles to cause destruction of the droplet. This delay may, in principle, extend to times where thermal conduction cause a reduction in the hot spot temperature.

Using the experimental arrangement of Fig. 1, the earliest time for visual disruption of the droplet at each energy is recorded while varying the CO_2 laser energy. A minimum laser energy value is reached below which no droplet disruption occurs; this defines the threshold fluence F_{th}. Figure 4 shows τ versus R for several materials where τ is the delay in initiation of explosion and R is defined as $(F - F_{th})F_{th}$, F being the measured fluence. It is noteworthy that explosion of water droplets initiates long after passage of the CO_2 laser pulse, but within the thermal relaxation time for water assuming reasonable values for the hot spot dimensions. The data suggest that log τ is linearly proportional to R. Using homogeneous nucleation theory, near the explosive threshold only a small volume, V_h, of the order of the hot spot region, will be heated to a temperature equal to or exceeding the superheat limit, T_{sh}. With a finite nucleation rate J, a number $N = JV_h t$ nucleated bubbles of critical size will form in a finite time t. We assume the droplet will explode when a critical number N_c of such bubbles if formed. The expected delay in this case is

$$\tau = N_c / JV_h \qquad (2)$$

For a temperature $T \geq T_{sh}$, the nucleation rate is given by[10]

$$J = J_o \exp(-W/kT) \qquad (3)$$

where k is Boltzmann's constant and W is the work required to nucleate a bubble of critical size. Equation 2 may be approximately written in the form

$$\log \tau = a + b\, R \qquad (4)$$

where a and b are functions of the thermophysical constants.[10] Using published values of these constants, we estimate b = -1.04 which is in fortuitously good agreement with the experimental value, -1.02 (see Fig. 4). Two facts should be emphasized in qualifying this agreement; firstly high temperature thermophysical properties used in estimating b were determined by extrapolation of low temperature data and secondly the experimental errors do not permit a precise determination of slope. Hydrodynamic effects have justifiably been neglected in our model. The acoustic transit time for a 30μm droplet is about 20nsec and no distortion has been observed at this time scale. We do not attempt theoretical estimate of the intercept a, since it requires knowledge of the critical number N_c, as well as the volume of the heated region V_h. However the results do suggest that the dynamics of droplet heating

near the explosive vaporization threshold is adequately explained by classical nucleation theory and that thermal transport processes and the effect of bubble growth can be neglected.[10]

In conclusion, we have shown that observed delays in laser induced explosion of water droplets is explained by homogeneous nucleation of vapor caused by superheating and that energy and mass transport processes may be neglected.

Acknowledgements

The author acknowledges his colleagues, A. Biswas, B. -S Park, D. Pendleton, and R. G. Pinnick for collaborating on this project.

References

1. R. L. Armstrong in Optical Effects Associated with Small Particles, P. W. Barber, and R. K. Chang, ed. (World Scientific, 1988), and references therein.
2. C. F. Bohren, and D. R. Huffman, Absorption and Scattering of Light by Small Particles (Wiley, New York, 1983).
3. B. -S. Park, and R. L. Armstrong, Appl. Opt. 28, 3671 (1988).
4. R. G. Pinnick, A. Biswas, R. L. Armstrong, S. G. Jennings, J. D. Pendleton, and G. Fernandez, Applied Optics (in press).
5. A. P. Prishivalko, Sov. Phys. J. 26, 142 (1983).
6. J. D. Pendleton, Appl. Opt. 24, 1631 (1985).
7. P. Kafalas, and A. P. Ferdinand, Appl. Opt. 12, 29 (1973).
8. Y. P. Raizer, Sov. Phys. J.E.T.P.21, 1009 (1965).
9. R. G. Pinnick, P. Chylek, M. Jarzembski, E. Creegan, V. Srivastava, G. Fernandez, J. D. Pendleton, and A. Biswas, Appl. Opt. 27, 987 (1988).
10. B. -S. Park, A. Biswas, R. L. Armstrong, and R. G. Pinnick, Optics Letters (in press).

Figure Captions

Fig. 1. Experimental arrangement for measurement of laser fluence required fro droplet explosion and breakdown. Infrared radiation from a pulsed CO_2 laser is focused by a 38mm focal length germanium lens onto single droplets emanating from a vibrating orifice generator (generator not shown). Explosion of the droplets is viewed or photographed through the microscope by using back illumination from an air-plasma generated by a pulsed Nd:YAG laser operating synchronously with the CO_2 laser and droplet generator. This synchronization allows time-resolved photographs of exploding droplets to be made at selectable times after initiation of the CO_2 laser pulse.

Fig. 2. Photographs of 35 μm radius water and ethanol droplets showing the criterion used to define initiation of droplet disruption. Note that water explosion initiates on the illuminated side whereas ethanol explosion initiates on the shadow side.[8]

Fig. 3. Measures of CO_2 laser fluence required to explode water droplets compared to predictions of superheat fluence. Superheat fluence predictions (from Ref. 6) that account for temperature dependence of specific heat, density, and refractive index (curve a) are in better agreement with measurement than the prediction that neglects temperature dependence of material properties (curve b).

Fig. 4. Time delay for initiation of explosion, τ versus $R = (F - F_{th})/F_{th}$ for several liquid droplets. The least square fit lines for water and ethanol droplets are shown.

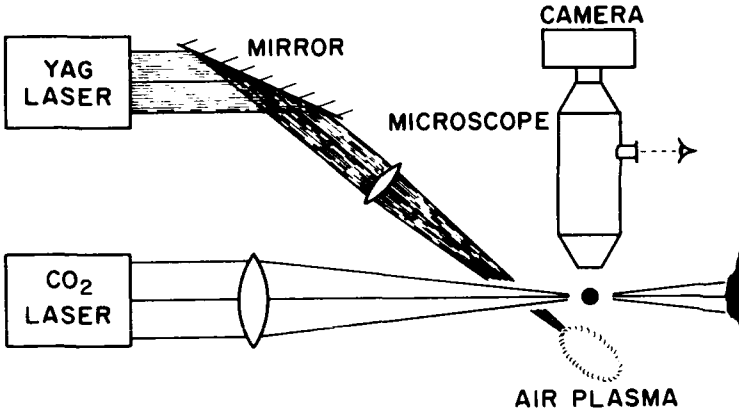


Fig. 1

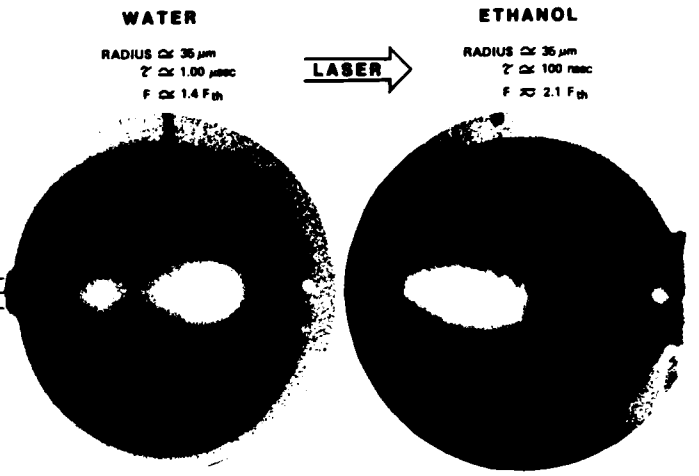


Fig. 2

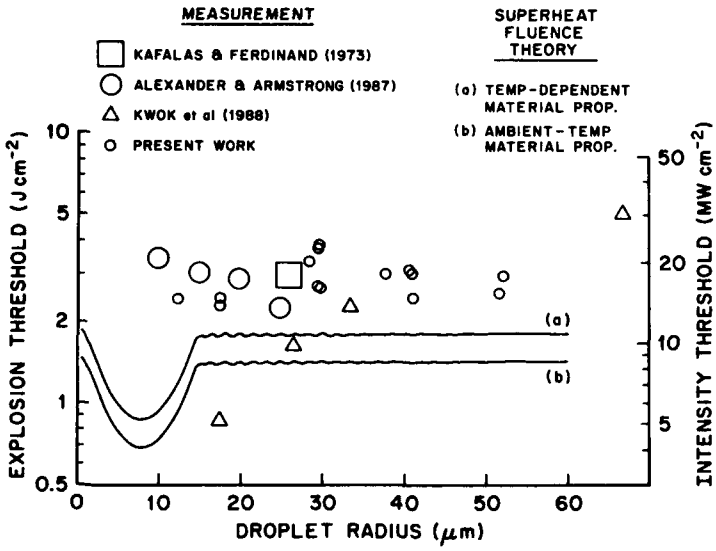


Fig. 3

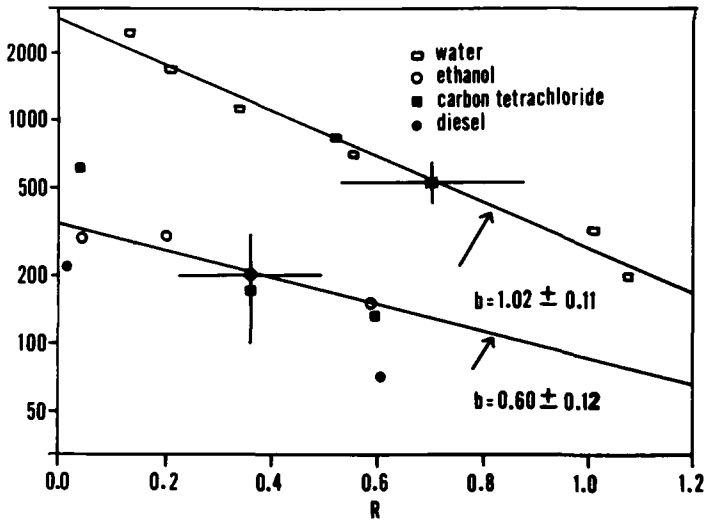


Fig. 4

EXPERIMENTAL STUDY OF THE OPTICAL PROPERTIES OF SHEAR LAYERS

Larry Chew* and Walter Christiansen**
Department of Aeronautics and Astronautics
University of Washington
Seattle, Washington

Abstract

This research investigated the effects of coherent structures and external perturbation on the optical quality of a laser beam propagating transversely through a shear layer. A low speed shear layer was generated using two parallel streams of gases (air and helium/argon mixture). A 6.5 cm diameter beam was passed through the shear layer and the far-field intensity profile was obtained to calculate its Strehl ratio. High speed intensity profiles showing multiple peaks instead of a singular Gaussian-like peak suggest that coherent structures influence the shape of far-field intensity profiles. Time averaged pictures showed that external harmonic perturbation of a shear layer can improve its Strehl ratio. In addition, fluid mechanical phenomena such as transition may decrease the Strehl ratio. These results demonstrate that the optical properties of shear layers may be controlled via fluid mechanical means.

Nomenclature

α	Experimental constant
β	Gladstone-Dale constant
δ	Shear layer thickness
Φ	Phase of wave
σ^2	Mean square of phase deformation
$<(\Delta n)^2>$	Mean square average of index difference
$< >$	Spatial average
$(\bar{\cdot})$	Time average
ρ_1	Fluid density of upper stream
ρ_2	Fluid density of lower stream
l	Integral length scale
n_1	Refractive index of upper stream
n_2	Refractive index of lower stream
SR	Strehl ratio
U_1	Fluid velocity of upper stream
U_2	Fluid velocity of lower stream

* Graduate student, Aerospace and Energetics Research Program, University of Washington. Student Member AIAA.
** Professor, Department of Aeronautics and Astronautics, University of Washington. Associate Fellow AIAA.

1. Introduction

Recent applications of high powered lasers and imaging systems have renewed interest in the study of laser propagation through turbulent mediums.[1] If these turbulent mediums consist of fluids with different refractive indexes, then random phase errors in the beam can be produced. Phase errors will cause substantial reduction in beam intensity and therefore loss in beam power transfer through the turbulent medium.[2] Gradients in refractive indexes are typically caused by temperature or density differences. Interaction between laser beam and turbulent flows are common occurrences in many engineering applications and two examples are the aerodynamics windows and ground based laser systems.[3]

One of the most common turbulent flow is the shear layer. It forms when two streams of fluid with different velocities meet to share a common interface. The shear stresses resulting from the different velocities initiates an instability called the Kelvin-Helmholtz instability to grow causing the flow to become turbulent.[4] The two streams may have different densities and refractive indexes.

Until recently, fluctuation in refractive index due to shear layer turbulence had been assumed to be homogeneous and isotropic. Using this assumption, Vu and Sutton modeled the optical performance of a homogeneous shear layer in terms of the Strehl ratio (defined as the ratio of the peak intensity of a beam with phase aberrations to the peak intensity of an ideal diffraction-limited beam).[5] For lack of a better model, this work was accepted by many researchers as a means of predicting the Strehl ratio, although the model has not been adequately tested experimentally to date. In addition, the assumptions on which this model was based has restricted its application to limited situations (for example, the assumption that shear layer turbulence is strictly homogeneous).

In 1971 however, Brown and Roshko observed large scale coherent structures during experimental flow visualization of a shear layer.[6] These large structures are vortices (also called eddies) which spin around and cause mass and momentum transfer across the shear layer. The spinning structures are convected downstream at the mean freestream velocity of the shear layer. The existence of coherent structures negates the assumption that shear layer are homogeneous and raises the question as to how coherent structures affect beam propagation characteristics. In addition, Oster and Wygnanski in 1982 showed that external perturbations affect the growth rate of these coherent structures.[7] If indeed coherent structures influences beam propagation and these structures can be controlled by external perturbation then that leads to an interesting possibility of controlling beam propagation through shear layers by using external perturbations.

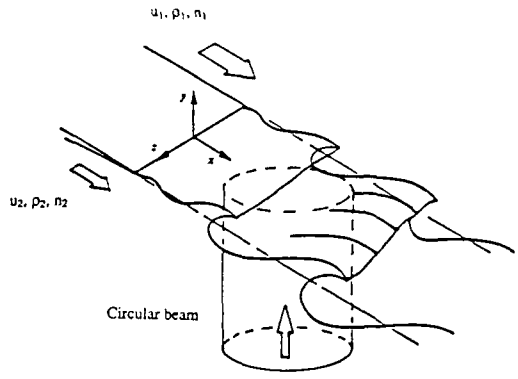


Fig. 1: Laser Beam Passing Through a Shear Layer Subscript 1 represent high speed fluid; subscript 2 represent low speed fluid. X is streamwise direction

This research investigated the effects of coherent structures on the optical quality of a beam propagating through a mixing layer and the possibility of perturbing a shear layer to control optical transmission. A shear layer was generated in a wind tunnel and a laser beam passed normal to the shear layer (see figure 1). The peak intensity of the laser beam was measured to obtain the Strehl ratio. The Strehl ratio was derived from far-field measurements of beam intensity, so that near-field aberrations were allowed to die out. The beam was directed through different sections of the coherent structures to demonstrate the effects of these structures upon beam propagation characteristics. Time averaged Strehl ratios were also obtained for unperturbed and perturbed shear layers to show the effects of controlling shear layer fluid mechanics on the Strehl ratio. Finally, the beam was passed through varying downstream positions of the shear layer to observe fluid mechanical influences on beam propagation.

2. Theoretical Background

In a mixing layer, turbulence creates random spatial and temporal fluctuations of gas density. These correspond to fluctuations in gas refractive index given by the Lorentz-Lorenz formula:

$$n = 1 + K\rho$$

where $K = \beta / \rho_{ref}$ and β is the Gladstone-Dale constant.[8]

Wave diffraction theory shows that beam degradation is primarily caused by phase distortion.[8] The Strehl ratio (SR) may then be given by the following expression:

$$SR = 1 - \sigma^2$$

where $\sigma^2 = \Phi^2 - (\Phi)^2$ is the spatial mean square deformation of the wave phase front, Φ. For accurate results, the phase distortion should be small. If the phase aberration is not small, a better approximation is given by the empirical formula: [9]

$$SR = 1 - \exp(-\sigma^2)$$

The mean square phase aberration was modeled by Sutton as:

$$\sigma^2 = 2 k^2 < (\Delta n)^2 > \lambda \delta$$

where k is the wave number, Δn is the index fluctuation, λ is the integral length scale and δ is the shear layer thickness.[5] In 1980, Vu, et al., using volume fraction arguments suggested that the index fluctuation may be written as $\alpha^2 (n_1-n_2)^2$.[5] Experimental results by Batt provided the values of alpha of 0.15 and $\lambda = \delta/4$ based on heat diffusion measurements.[10]

The final form of the Strehl ratio for a low speed homogeneous shear layer between two optically dissimilar gases was shown by Sutton to be

$$SR = \exp\{-2 k^2 \alpha^2 (n_1-n_2)^2 \delta^2 / 4\}$$

However, the Strehl ratio of a laser beam passing through a shear layer has not been well predicted using this equation, primarily because of the weakness in the assumptions used.

2.1 Fluid Mechanics Background

It was originally thought that a shear layer was homogeneously turbulent. However, in 1971 Brown and Roshko saw large coherent structures during their flow visualization of a shear layer. In 1973 Rebollo measured growth rate of the layer thickness, δ, defined as the vertical distance between positions in the flow where velocities have dropped to 99% of their respective freestream speeds.[11] He found that thickness, δ, grew linearly with downstream distance as long as there was no pressure gradient in the flow. Based on work done at the California Institute of Technology, Dimotakis modeled growth rate and showed that it was a function of velocity ratio and a weak function of density ratio.[4]

Winant and Browand showed that freestream fluid was entrained by these large vortices as they were convected downstream causing a growth in size.[12] In addition, the spinning vortices were seen to pair or amalgamate and therefore enhance the growth process. While studying chemical reaction and turbulent mixing in a shear layer, Breidenthal (1981) saw a region of marked increase in molecular scale mixing.[13] This transition region was characterized by a sudden increase in the number of three-dimensional vortices responsible for increased mixing. The pre-transition region was two-dimensional while the flow in the post-transition region was fully developed and self-similar.[13]

In 1982 Oster and Wygnaski perturbed a shear layer and observed a region of no growth.[7] At the resonant frequency, large vortices appeared axially aligned with uniform spacing. Each vortex cancelled the induced effects of the next, resulting in no net force and therefore constant layer thickness. These changes in shear layer fluid mechanics due to external perturbation suggested that the optical propagation characteristics of the shear layer may be controlled.

3. Experimental Apparatus and Experimental Procedures

The experimental apparatus consisted of the following:

1) Wind tunnel
2) Forcing mechanism
3) Optical set up
4) Data acquisition system

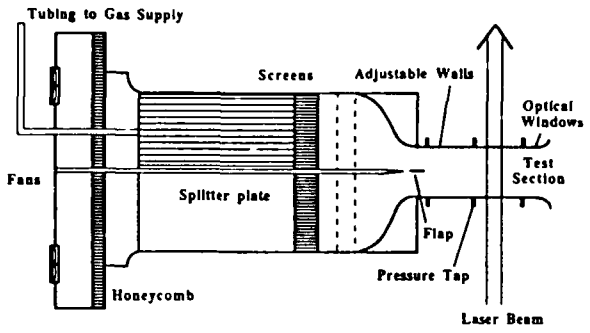


Fig. 2: Schematic Diagram of the Wind Tunnel

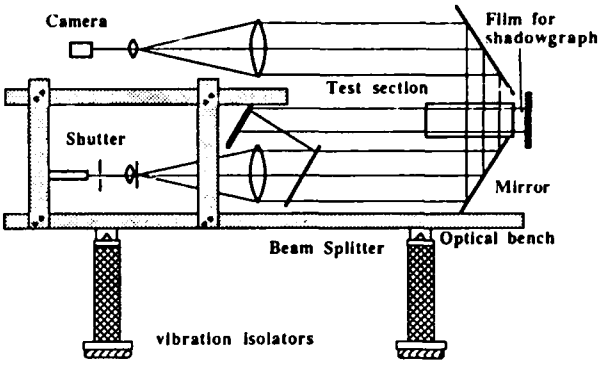


Fig. 3: Optical Setup

3.1 Wind Tunnel

The wind tunnel as shown in figure 2 consisted of two tunnels, one on top of the other, discharging two separate, optically dissimilar fluid streams into a common test section. Variable speed fans on the lower tunnel enabled the air velocity to be controlled. The upper chamber was separately fed with various gases from pressured bottles. The above configuration enabled the velocity ratio and density ratio of the shear layer to be independently varied. Honeycomb in both tunnels was used to straighten the flow, while the turbulence level was reduced by three screens. Hot wire measurements in the test section revealed a turbulence intensity of less than 0.5% at a mean velocity of 2.4 m/s. A 4-to-1 contraction ratio of the exit nozzles also helped to reduce the turbulence due to the favorable pressure gradient. The splitter plate extended throughout the entire length of the wind tunnel ending just at the exit of the nozzles. The test section measured twelve inches by four inches by two inches and was constructed out of plexiglass. The section contained four optical windows to allow passage of the laser beam. The top and bottom walls were mounted on steel plates enabling adjustment of their position so as to remove the streamwise pressure gradient in the flow. The two free streams, with velocities U_1, U_2 and densities ρ_1, ρ_2, initially mixed on contact in the test section to form the shear layer. Finally, the entire wind tunnel was positioned on a cart enabling the test section to be translated in the streamwise direction with respect to the optical system.

3.2 Forcing Mechanism

The source of external perturbation to the shear layer was a 10 mm wide, thin oscillating plate attached to the trailing edge of the splitter plate. The flap was connected by tensioned piano wires to two acoustic speakers which were driven at frequencies ranging from 0 to 350 Hz. In these experiments, the forcing frequency was 280 Hz and the flap peak to peak amplitude was 0.7 mm.

3.3 Optical Set Up

The optical apparatus, shown in figure 3, consisted of a spatial filter, collimating lens and receiving telescope mounted on an optical rail. The collimated, filtered beam was directed through a variable aperture which enabled the diameter of the beam to be adjusted between 0.5 cm to 6.5 cm. Two beam paths were formed by a beam splitter; the first beam was directed through the shear layer via three-axis mirrors and then intercepted by the receiving telescope. The far-field intensity pattern was focused onto the image plane through the receiving telescope. The second beam was passed, at right angles to the first beam, through the layer onto a photographic plate to obtain side view pictures of the shear layer at the same instant as the plan view intensity profile.

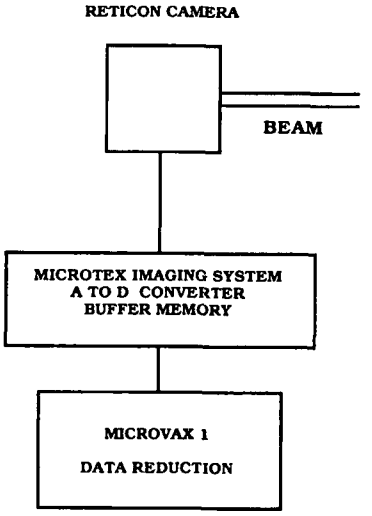
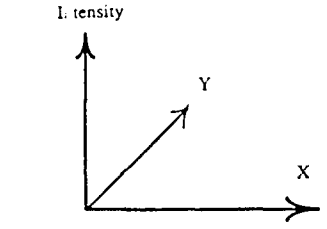


Fig. 4: Imaging and Processing



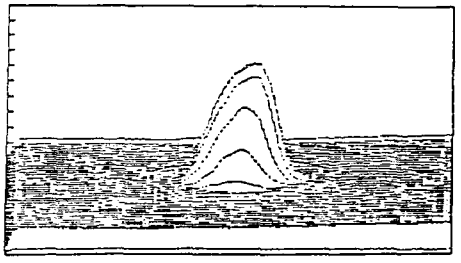


Fig. 5: Intensity Profile of Airy Pattern obtained by Image Processor

3.4 Data Acquisition System

An EG&G Reticon camera with 128 x 128 pixel array was used to integrate the image at the camera image plane over a period of either 2 seconds or 100 microseconds. The intensity image was digitized by a Microtex imaging computer system with 12 bit resolution and the image stored on a computer (see figure 4). The Strehl ratio of two digitized pictures was calculated by dividing the peak pixel amplitude of the distorted beam by that of the reference beam. Figure 5 is an example of the pictures obtained by the Microtex imaging system. The x and y coordinate of the figure correspond to the spatial coordinate of the image plane while the z axis indicates the digitized intensity. The picture shown in figure 5 is a pseudo 3-D intensity profile of an Airy pattern (the far field diffraction pattern of a circular, uniform phase laser beam). The central peak is the 3-D image of the Airy disk. The first ring of the Airy pattern can barely be seen in figure 5 because its peak intensity is about 1% of the central peak intensity.[8]

4. Experimental Procedures

In this investigation, the top and bottom streams of the shear layer consisted of a helium/argon mixture (1.8 m/sec) and air (3.0 m/sec). The velocity ratio of the two streams was therefore 0.6. Helium (30.6%) and argon (60.9%) were mixed to provide a density ratio of 1.0 with respect to air and also to provide a refractive index difference ($\Delta n = 6.4 \times 10^{-5}$) between the two streams. At such low speeds, density fluctuations were negligible. The growth rate ($d\delta/dx$) was 0.1, which agrees with that obtained by Brown and Roshko.[6] Spectral analysis of hot wire measurements established that the natural or resonant frequency of the flow for the above parameters was 280 Hz.

The experiment consisted of two parts: the first was to obtain instantaneous intensity profiles of a laser beam passing through different parts of a vortex within a shear layer to show the effect of coherent structures on laser beam quality. The second part of the experiment was to obtain time averaged Strehl ratios of a laser beam first passing through an unperturbed shear layer and then through a shear layer perturbed at 280 Hz.

5. Results

The experimental results are presented in two parts: the first are short duration (100 microsecond exposures) images of a laser beam propagating through a shear layer, and the second are time averaged images (2 second exposures) of the same laser beam.

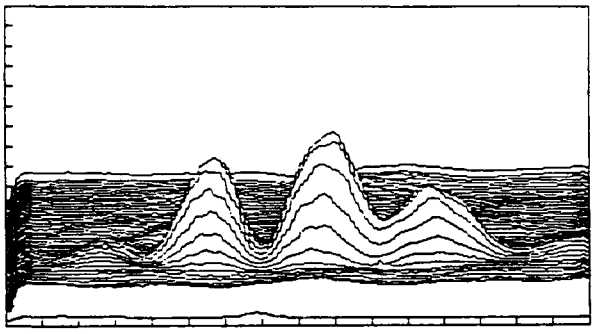
5.1 Short Exposure Result

Figure 6 shows the effect of coherent structures on a 6.5 cm diameter laser beam centered 5.0 cm downstream from the splitter plate. The upper picture is a 100 microsecond exposure side view shadowgraph of a mixing layer with visual growth rate ($d\delta/dx$) of 0.1, showing the vortices that affect the laser beam. The lower picture is an intensity profile revealing a main peak with smaller satellite peaks on both sides, indicating the effects of coherent structures on beam propagation. The shape differs from that expected for a homogeneous shear layer which has a wide spectrum of turbulent sizes. The far field intensity profile for a homogeneous layer would normally be a single, bell-shape peak with small amplitude fluctuations in the profile. Although not confirmed at this point, appearance of multiple peaks in the intensity profile might be due to the differences in optical pathlength across a shear layer. For example, a ray of light passing through a vortex would experience a very different optical path than a ray passing through a braid, the region between two vortices. These differences cause phase aberrations to the beam wave front resulting in a complicated far field diffraction pattern.

To further test the observation that coherent structures affect beam intensity profiles, a 6.5 cm diameter beam was passed through a series of pairing vortices caused by perturbing the flow at 140 Hz. Figure 7 was taken at 100 microsecond exposure and the beam centered 5 cm downstream from the splitter plate. The initial vortices amalgamated to form even larger vortices whose optical effects on the laser beam were apparent in the intensity profile shown in the figure.[12] Phase distortion of the laser beam by these large vortices along with complicated far-field diffraction resulted in multiple peak intensity profiles. A sequence of pictures also revealed that as these large vortices convected downstream, their corresponding intensity peaks also translated in the camera image - both temporally and spatially. This observation further demonstrated that it was the large vortices which caused multiple peaks to form in the intensity profiles. From these last two figures, there seems little doubt that coherent structures affect shear layer optical propagation characteristics.



(a) Instantaneous shadowgraph of the flow perturbed at the subharmonic frequency (140Hz)

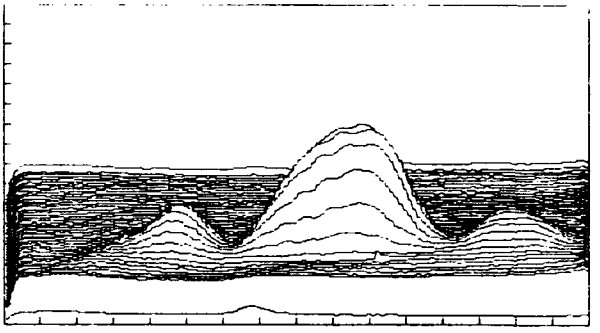


(b) Far-field intensity profile showing multiple peaks

Fig. 6: Effects of Unperturbed Coherent Structures (The 6.5 cm diameter laser beam is centered at 5 cm from the splitter plate. The exposure time is 100 microsecond.)



(a) Instantaneous shadowgraph of the unperturbed shear layer



(b) Far-field intensity profile showing a main peak with smaller satellite peaks

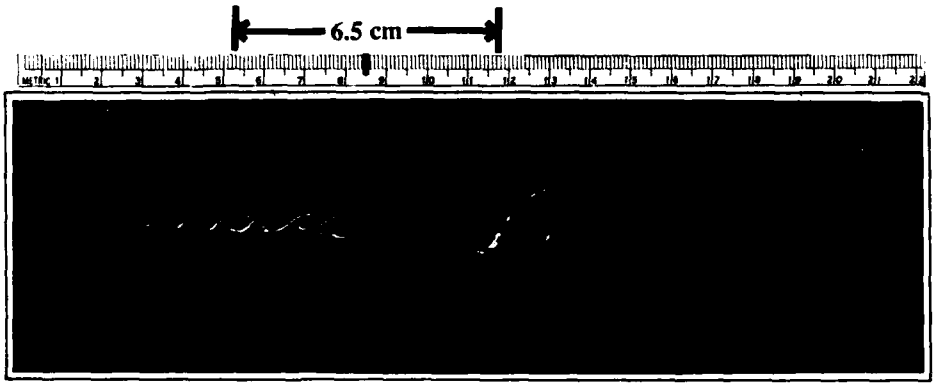
Fig. 7: Effects of Perturbed Coherent Structures (The 6.5 cm diameter laser beam is centered at 5 cm from the splitter plate. The exposure time is 100 microsecond.)

5.2 Long Exposure Results

Time averaged pictures (2 second exposures) integrated the optical effects of approximately 80-200 vortices passing through the beam. The time averaged Strehl ratio measured the quality of the beam after it passed through the vortex structures in the shear layer.

Shadowgraphs of an unperturbed and perturbed shear layer are given in figure 8 which demonstrates the effects of perturbation on shear layer growth. The natural shear layer grew linearly at a growth rate of 0.1. For this shear layer, the natural Kelvin-Helmholtz frequency (most amplified frequency according to linear instability analysis) was determined to be 280 Hz using a hot wire anemometer and spectrum analyzer. When the flap was oscillated at 280 Hz, the layer stopped growing as shown in the figure 8b. The resulting vortices were constantly spaced and marched downstream uniformly. About 11.5 cm from the splitter plate, the original growth rate was resumed.

To show the effects of perturbing a shear layer on the optical quality of the laser beam, a series of long exposures images were obtained. A 6.5 cm diameter laser beam was centered 8.5 cm from the splitter plate. The size of the beam and the position of the beam are marked on figure 8 to show the position of the beam relative to the shear layer. A two second time averaged picture of the ideal diffraction limited beam is shown in figure 9a. The beam is now Gaussian in shape (because of the time averaging) agreeing well with statistical bell-shaped distributions. The smaller peak on the left front corner is a reference peak used to normalize the peak intensity to remove the effects of laser power fluctuation. When the beam was passed through the linearly growing, unperturbed shear layer, the intensity profile in figure 9b flattened and the peak intensity dropped. The time averaged Strehl ratio was measured at 0.66. This loss of intensity was caused by phase distortions produced by the turbulent shear layer. However, when the same flow was perturbed at the natural or resonant frequency of 280 Hz, the intensity profile narrowed and the Strehl ratio increased to 0.91 (see figure 9c). In fifty sequential trials, the Strehl ratio improvement averaged 38% with a mean value of 0.90 ± 0.07. This remarkable result demonstrated that the optical propagation characteristics of a shear layer may be controlled by controlling its fluid mechanics; this opens new and interesting avenues of research for controlling optical behavior of shear flows.



(a)Unperturbed shear layer showing a linear growth rate: $\delta/x = 0.1$



(b) Shear layer perturbed at its fundamental frequency (280 Hz)

showing no growth from the splitter plate to X = 11.5 cm

Fig. 8: Example Shadowgraphs of Unperturbed and Perturbed Shear Layers (Note: The arrow represents the location of a 6.5 cm diameter beam used to obtain figure 6.)

Finally, figure 10 shows Strehl ratio plotted versus downstream distance from the splitter plate for an unperturbed and perturbed shear layer. The beam was passed through the shear layer starting at 4 cm from the splitter in increment of 1 cm. The Strehl ratio for the unperturbed shear layer clearly shows fluid mechanical influences on optics. The Strehl ratio is first constant at 0.9 from X= 4 cm to 8 cm. The SR then decreases rapidly and asymptotes to a value of about 0.35 at X= 18 cm. Notice that the region of rapid decrease corresponds well to the region of transition in the shear layer. The transition region is where there is a sudden and definite increase in molecular scale mixing. It is also the region where there is a sudden increase in three dimensional structures. This suggests that smaller scale three dimensional turbulence causes larger phase distortion to a beam than the larger scale two-dimensional vortices. The second line in the graph shows the Strehl ratio at different downstream locations for a perturbed shear layer. The noticeable difference here is that when a shear layer is forced it stops growing for a certain spatial distance (from X= 8cm to 10 cm) and during this time the Strehl ratio remains at a high value of 0.9. This suggests that no growth in shear layer thickness allows for better beam propagation. When the flow begins to grow linearly again the Strehl ratio decreases.

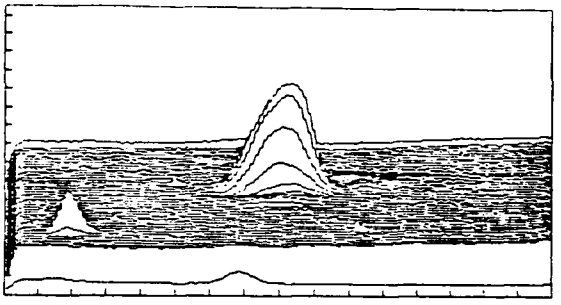
The most obvious difference between an unperturbed and perturbed shear layer is in growth rate. Whether the improvement in Strehl ratio is due wholly or in part, to the halt in layer growth is still not clear at this moment. Further experiments are needed to fully understand the fluid mechanical affects on beam quality. These resulis promise innovative methods of controlling the optical propagation characteristics of turbulent media, and perhaps methods of improving the transmission of lasers and the reception quality of imaging systems.

6. Summary

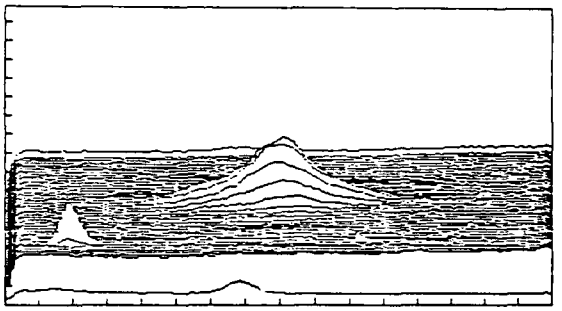
A wind tunnel was used to generate a low speed shear layer between two optically dissimilar gases. A 6.5 cm diameter laser beam was passed through the shear layer and the Strehl ratio was measured. Multiple peaks in the instantaneous intensity profile, instead of the usual singular Gaussian-like peak, clearly showed that coherent structures in shear layers affect beam propagation. Externally perturbing the shear layer altered its growth rate, indicating the possibility of controlling the optical propagation characteristics via changes in fluid mechanics of the flow. In particular, perturbing the shear layer at its resonant frequency altered the fluid mechanics of the flow in a manner which improved the Strehl ratio. This research showed that laser transmission through turbulent media may be improved via external control of shear layer fluid mechanics.

7. Acknowledgements

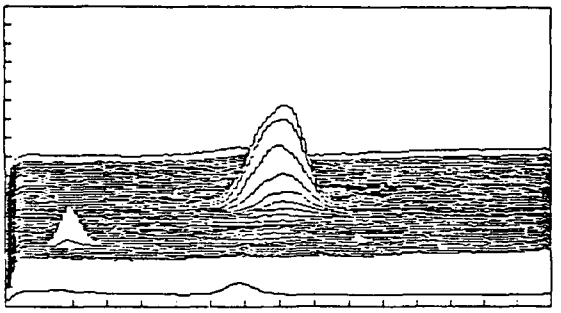
This work was sponsored by a grant from the Air Force Office of Scientific Research Contract No. AFOSR-87-0258, whose support is gratefully acknowledged.



(a) Far-field reference laser beam with no shear layer present: $\overline{SR}$ = 1.0



(b) Far-field laser beam after passing through a shear layer: $\overline{SR}$ = 0.66



(c) Far-field laser beam after passing through a shear layer forced at 280 Hz: $\overline{SR}$ = 0.91

Fig. 9: Effects of Shear Layer Perturbation on Strehl Ratio
(The 6.5 cm diameter laser beam is centered at 8 cm from the splitter plate.
The exposure time is 2 seconds.)

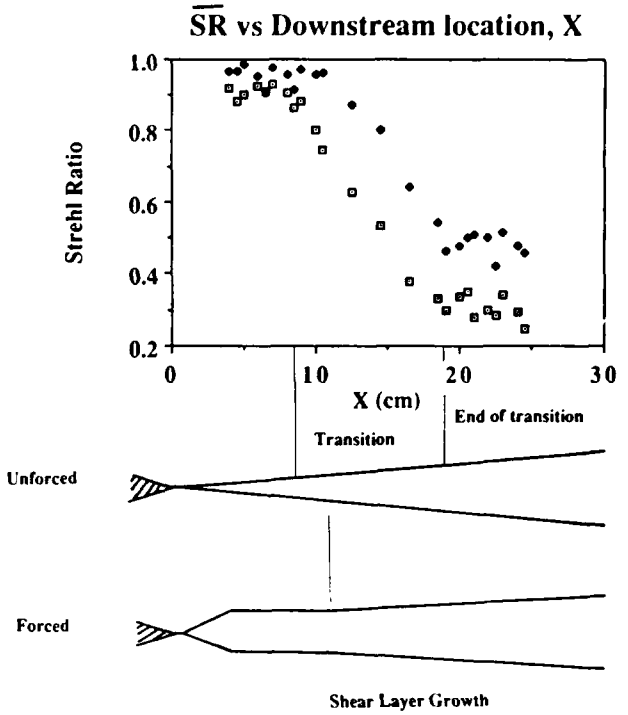


Fig. 10: Strehl Ratio Versus Downstream Distance

8. References

1) Booker, H.G. and Gordon, W.E., Proceedings of the IRE, Vol. 38, 1950, pp. 401-412.

2) Sutton, G.W., AIAA Journal, Vol. 23, No. 10, Oct. 1985, pp. 1525-1537.

3) Avidor, J.M., AIAA Journal, Vol. 17, No. 11, Nov. 1979, pp. 1267-1268.

4) Dimotakis, P.E., AIAA Paper 89-0262, 1989.

5) Vu, B.T., Sutton, G.W., Theophanis, G., and Limpaecher, R., AIAA Paper 80-1414, July, 1980.

6) Brown, G.L. and Roshko, A., Journal of Fluid Mechanics, Vol. 64, 1974, pp. 775-816.

7) Oster, D. and Wygnanski, I, Journal of Fluid Mechanics, Vol. 123, 1982, pp. 91-130.

8) Born, M and Wolf, E., Principles of Optics (Pergamon, New York, 1975).

9) Mahajan, V.N., J. Opt. Soc. Am., Vol. 73, No. 6, June 1983, pp. 860-861.

10) Batt, R.G., Journal of Fluid Mechanics, Vol. 82, 1977, pp. 53-95.

11) Rebollo, M.R., Ph.D. thesis, 1973, California Institute of Technology.

12) Winant, C.D. and Browand, F.k., Journal of Fluid Mechanics, Vol. 63, 1974, pp. 237-255.

13) Breidenthal, R.E., Journal of Fluid Mechanics, Vol. 109, 1981, pp. 1-24.

EXPERIMENTAL AND THEORETICAL INVESTIGATION OF SMALL-SCALE BLOOMING

Steven M. Ebstein
Carolyn Duzy
Robert Myers

North East Research Associates, Inc.
800 West Cummings Park, Suite 4500
Woburn, MA 01801-6338
617-935-5615

presented to:

Lasers '89

December 1989

ABSTRACT

Small-scale thermal blooming is investigated with a linear theory, a fully non-linear wave optics propagation code, and a laboratory experiment. The linear theory and the wave optics code show excellent agreement. The laboratory experiment shows excellent agreement with the modelling for the high spatial frequency modes.

STATEMENT OF THE PROBLEM

- Recently, attention has been directed to the effects of small-scale structure growth due to thermal blooming, which appears to limit laser propagation through the atmosphere for short wavelength, large diameter systems.
- Growth of small scale disturbances due to fixed irradiance fluctuations contains most of the essential physics of small scale thermal blooming.
- Considerable modelling with wave optics propagation codes and analysis has occurred.
- NERA has achieved agreement of codes and analysis for the initial value problem with a turbulence seed (Hatfield, Myers).
- This effort is our first attempt at anchoring the codes and analysis with experiment.

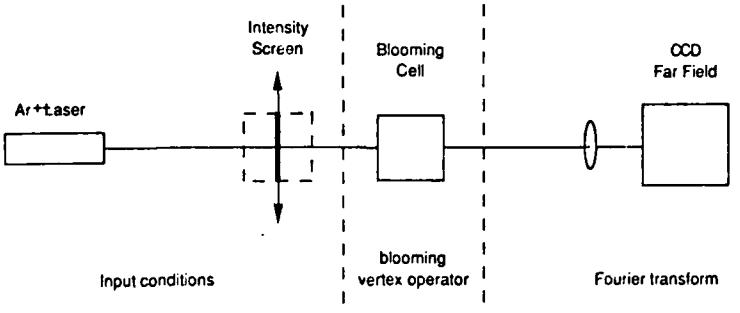
METHODS OF INVESTIGATION

- CODE
  - PHOTON, wave optics propagation code
  - turbulence, thermal blooming, NLO (Raman)
  - four dimensional: (x,y), z, t
- ANALYSIS
  - Neumann expansion of the linearized blooming equations for infinite beams (developed by Hatfield)
  - extension to finite beams
- LAB EXPERIMENT
  - seeded-growth in a liquid blooming cell

GOALS OF EXPERIMENT ANALYSIS

- Provide traceability from analytic theory of thermal blooming to laboratory data
  - Obtain agreement between analytic theory and PHOTON simulations
  - Obtain agreement between PHOTON simulations and laboratory data (Phase aberrations are present in laboratory experiment that are currently not accounted for in analytic theory.)
- Use time evolution of farfield spot of laser as a diagnostic for small scale thermal blooming
  - Growth of high frequency components corresponds to growth of small scale thermal blooming
- Finite beam effects must be included
  - Gaussian laser profile ⇒ non-uniform intensity
  - $1/e^2$ beam diameter ~15 times scintillation scale ⇒ whole beam effects on scales not too far removed from scintillation scale.

APPROACH FOR MODELLING LAB EXPERIMENT



- Treat laser intensity after intensity screen as input condition
  - Assume independent of time
- Assume blooming cell is a slab absorber ⇒ diffraction negligible in cell
- Propagation of beam to farfield can be performed using Fourier transform

LINEAR THEORY

- Complex amplitude of electric field can be written in terms of intensity and phase
  $u = \sqrt{I}\, e^{iS/2}$
- Contributions to complex amplitude from unperturbed laser and intensity screen
  - Screen treated as a perturbation to obtain a linear theory
    $I = I_0 (1 + I_1)$
    $S = S_0 + S_1$
- Whole beam parameters must be retained
- For modelling lab experiment

  I_0 - Gaussian intensity profile
  $S_0 = 0$ (uniform phase)
  I_1 - Gaussian random variable
  $S_1 = 0$
  Assume all input parameters are independent of time
- Predict growth of phase aberrations without further assumptions.

ANALYTIC THEORY: FARFIELD CALCULATION

- Farfield intensity:

$$\langle u(\kappa,t)\, u^*(\kappa,t)\rangle = \frac{1}{(2\pi)^2} \int dr \int dr'\, e^{-i\kappa\cdot(r-r')} \langle u(r,t) u^*(r',t)\rangle$$

where

$\langle\ \rangle$ denotes an ensemble average

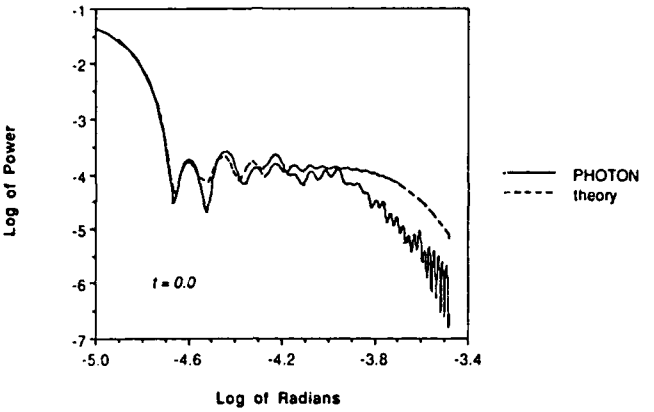
$$\langle u(r,t)\, u^*(r',t)\rangle = \sqrt{I_0(r)\, I_0(r')}\, e^{i/2[S_0(r)-S_0(r')]} \left\langle e^{1/2[I_1(r)+I_1(r')+i\, S_1(r)-i\, S_1(r')]} \right\rangle$$

- This quantity is the mutual coherence function, which allows one to predict the Strehl.
- Use properties of Gaussian random variables to evaluate ensemble average
- Perform angular integration of $\langle u(\kappa,t)\, u^*(\kappa,t)\rangle$ to produce farfield spectrum

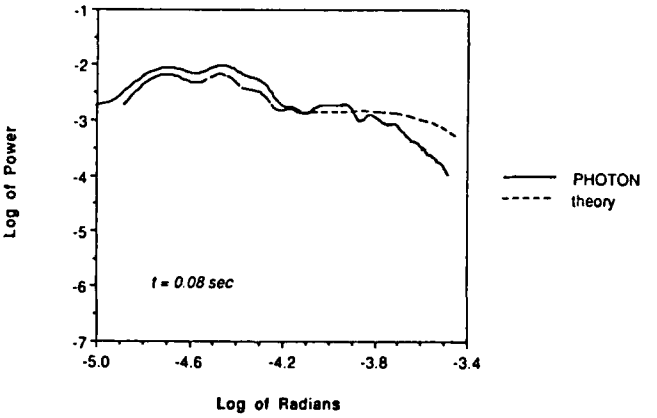
COMPARISON OF ANALYTIC THEORY/CODE SIMULATION

- Performed PHOTON run using following conditions:
  - Truncated Gaussian laser profile : $1/e^2$ diameter = 2.0 cm
  - Heating rate 32.7 radians/sec
  - Pulse length 0.02 sec
- Intensity screen
  - Generated using Gaussian random variable
  - Variance = 0.068
  - "Scintillation" scale ~ 0.15 cm

EVOLUTION OF FARFIELD INTENSITY



EVOLUTION OF FARFIELD INTENSITY (cont'd)



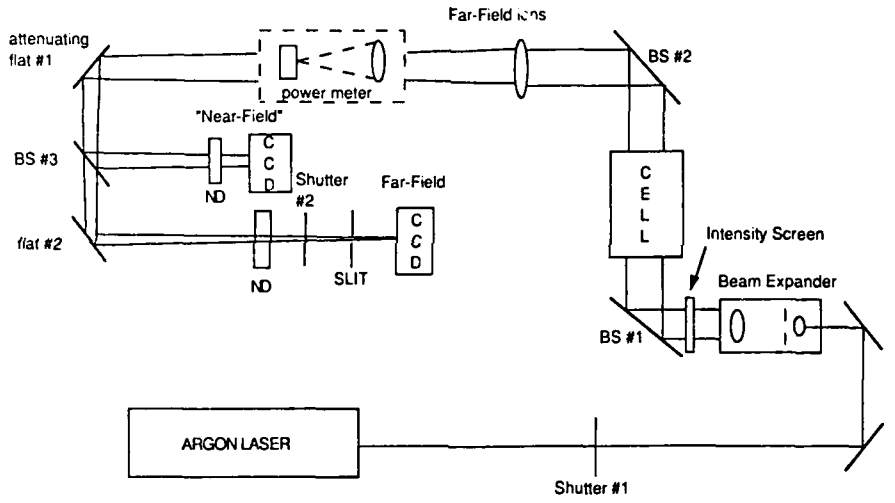
EXPERIMENT RESULTS

- Amount of energy scattered into large angles higher than computer simulation predicted.
- Assume additional wide angle scattering due to phase aberrations in the system (non-uniform laser phase, optics aberrations, thermal fluctuations in cell).
- Use lab data to determine point spread function due to phase aberrations in blooming all.
- Assume point spread function invariant over time of thermal blooming run ($\lesssim$ 1 sec) and convolve with code output at times greater than zero to predict time evolution of laboratory farfield spectrum.

EXPERIMENT FEATURES

- Uncompensated growth is diagnosed via the time evolution of the far-field intensity pattern.
- A realistic, multi-mode seed is employed, not a single sinusoidal mode. This allows one, in principle, to calculate and measure the reduction of the Strehl, not simply the growth of a single mode.
- The seed is a pseudo-random, fixed intensity screen.

CURRENT OPTICAL LAYOUT



HARDWARE SPECIFICATIONS

- 2w (514nm) Argon-ion laser
- 25cm long, 6cm diameter I_2:CCl_4 blooming cell manufactured by Adaptive Optics Associates.
- Cooled CCD with 12 bit readout
- Optics all $\lambda/20$ or $\lambda/10$; far field lens is a plano-convex, 2m f.l. lens.
- Cell was temperature regulated, ~.01°C/hr, to stabilize behavior but liquid still adds significant phase.

HARDWARE SPECIFICATIONS (cont'd)

- Intensity screen
  - 256x256 Gaussian white noise, Gaussian correlation function.
  - 2048x2048 binary pattern (opaque/clear) with each 8x8 region having average transmittance of a 256x256 pixel
  - contact printed in chromium onto λ/20 optical flat

"NEAR FIELD" INTENSITY THROUGH SCREEN



A THERMAL BLOOMING RUN

- Optics and filters are positioned, aligned, laser on.

EXPOSURES

- Oper shutter 1 to bloom the cell
- Expose and read out the far-field CCD 17 times:
  - open shutter #2 for 5ms
  - shift and read out a 32 pixel wide strip
- Close shutter 1

BACKGROUND MEASUREMENT

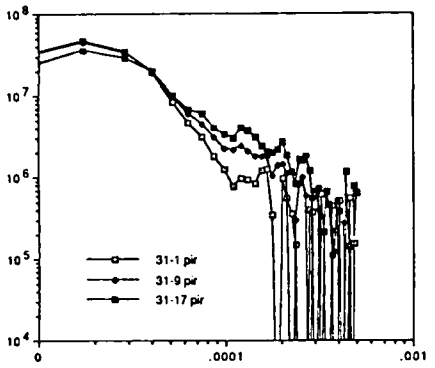
- Open shutter 1
- Read out the far-field CCD 17 times
  - shift and read out a 32 pixel wide strip with shutter #2 closed
- Close shutter 1

EXPERIMENT PARAMETERS

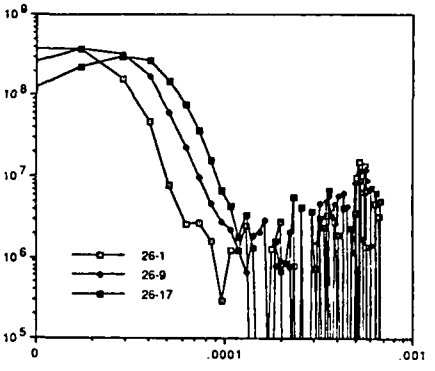
- 1.5 w through beam expander
- 33% average screen transmittance
- 33% absorption in cell
- 1s run time, 17 frames
- 5ms exposures, spaced ~ 60ms apart

EXPERIMENT WITH AND WITHOUT INTENSITY SCREEN

WITH SCREEN

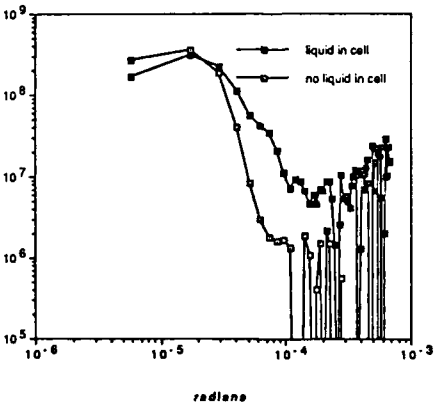


NO SCREEN



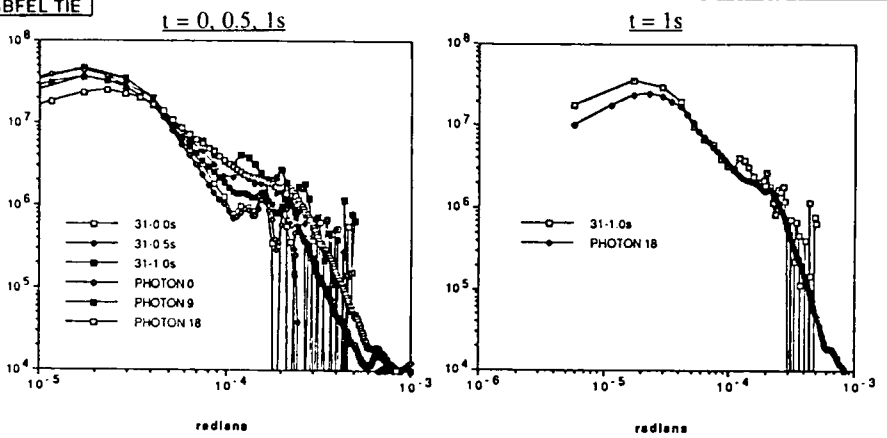
- High frequencies show relative growth with the intensity screen seed. With no screen, the high-frequency tail does not change shape – it just moves out.

UNBLOOMED LIQUID ADDS PHASE



- The t=0 spectra are quite different when the cell is empty or filled with CCl_4.
- These data, normalized for constant total power, show that the thermally stabilized liquid adds significant phase to the beam.

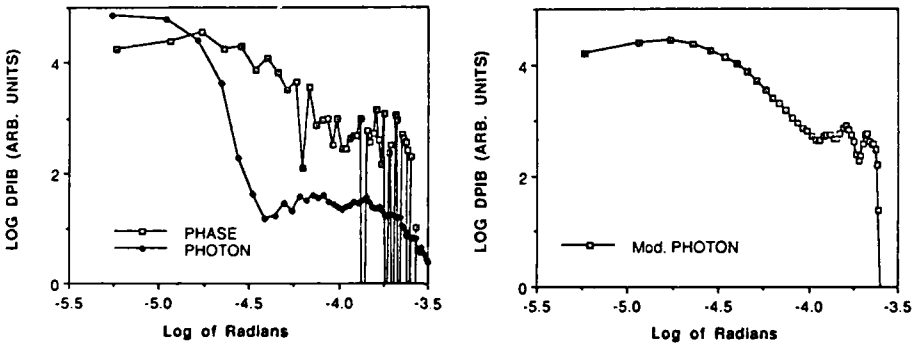
QUANTITATIVE AGREEMENT



- The high frequency growth is quantitatively the same for the lab experiment and the model corrected for the initial conditions and using the measured "near field".
- The high frequency growth agrees over the region of adequate SNR (down to <1 A/D unit measured intensity).
- The low frequencies disagree and the data also show bumps which are presumably non-stationary diffraction rings.

CONVOLVING PHOTON OUTPUT

- Phase aberrations in system significantly alter farfield intensity



CONCLUSIONS

- Linear theory and code simulation show excellent agreement.
- The experimental results verify the modelling predictions for the growth of the seeded, high frequency modes when the model is corrected for non-ideal initial conditions.
- Low-frequency/whole beam behavior currently disagrees. Possible explanations include details of the experiment protocol and are currently under examination.
- We have a triad of tools – linear theory, code simulation, and laboratory experiment – which agree on the effects of small-scale structure growth due to thermal blooming.

NATURAL AMELIORATION OF BEAM QUALITY DEGRADATIONS CAUSED BY ATMOSPHERIC PROPAGATION OF HIGH ENERGY LASER RADIATION*

Naresh C. Mehta
Optical Wave Propagation Group
Lockheed Palo Alto Research Laboratory
3251 Hanover Street
Palo Alto, CA 94304

ABSTRACT

Non-linear interactions of a high energy laser beam with the atmosphere lead to severe wavefront distortions and reduced performance of ground-based laser systems. We discuss the role of natural atmospheric dynamics in ameliorating these wavefront degradations and in improving system performance. Atmospheric wind fluctuations, both vector wind gradients and random variations, play a role in reducing the effects of thermal blooming. Computer simulations are used to calculate system performance in the presence of idealized linear wind shear and random mini-shear. Substantial seasonal performance improvement can be realized when natural ameliorating atmospheric effects are present. We also find that significant amounts of high energy laser power can be transmitted from a ground-based laser site in the southwestern United States.

INTRODUCTION

When a high energy laser (HEL) beam propagates through the atmosphere, it suffers wavefront degradations due to its interactions with the atmosphere. Two of the major physical effects responsible for these wavefront distortions are optical turbulence, thermal blooming and their mutual non-linear interactions. These HEL-atmosphere interactions lead to reduced energy deposition on a distant target. In order to improve the far-field performance of a ground-based-laser (GBL) system, one must find ways to ameliorate the wavefront distortions caused by HEL-atmosphere interactions.

One way of compensating the atmospheric effects on the HEL wavefront is to pre-distort the outgoing HEL beam with an adaptive optics (AO) system so that one can obtain an undistorted wavefront upon propagation through the atmosphere. But, if a phase-only AO system is used to correct the outgoing HEL wavefront, small scale structure on the HEL beam can grow unstable, leading to a catastrophic breakup of the HEL beam. This positive feedback mechanism between a phase-only AO system and the HEL beam has been named the phase compensation instability (PCI) [1]. PCI is characterized by an exponential growth in time of small-scale filamentary structure on the HEL beam as laser pulses propagate through the bloomed atmosphere.

It has recently been recognized that there exist natural processes in the atmosphere which also ameliorate the wavefront distortions caused by turbulence-blooming interactions, resulting in improved GBL system performance. In this paper, we investigate the role of such natural atmospheric effects in providing amelioration of HEL distortions and the ability to transmit HEL power through the atmosphere from a GBL site.

Significant progress has been made over the past few years in understanding the basic turbulence-blooming interactions which cause wavefront aberrations of an HEL beam propagating through the atmosphere. Analytical models and sophisticated computer simulation codes have been

developed to study the complex HEL-atmosphere interactions and have led to predictions of the performance of candidate GBL systems. Simple analytical models with uniform atmosphere have been developed to look at the role of wind fluctuations in damping PCI growth [2]; but, in this report, we present the results of a qualitative analysis using computer simulations. We have used a 4-D propagation code, GRAND, developed at the Lockheed Palo Alto Research Laboratory, which performs detailed wave optics calculations of the effects of turbulence and thermal blooming on an HEL wavefront, and includes models of a phase-only AO system and of time-dependent atmospheric kinematics.

After a brief description of amelioration provided by natural atmospheric processes, we discuss the role of idealized linear wind shear and of random wind fluctuations in ameliorating wavefront degradations and in improving GBL system performance. We then utilize atmospheric characterization from a GBL site, at the White Sands Missile Range (WSMR), New Mexico, to study the effects of real atmospheric dynamics on HEL propagation and the transmission of HEL power as a function of season. We conclude with a few cautionary remarks about predicting performance of larger GBL systems based on results discussed here.

AMELIORATION BY ATMOSPHERIC DYNAMICS

When an HEL beam propagates through the neutral atmosphere, some of its energy is absorbed to heat the atmospheric constituents. Although the temperature rise is minute compared to the ambient temperature, the resulting refractive index variations are large at optical wavelengths and can severely distort the propagating HEL beam. This non-linear process is called thermal blooming. Interactions of atmospheric turbulence and thermal blooming can lead to an enhancement of small scale structure on the HEL beam, resulting in a beam breakup and reduced far-field performance.

Any process which reduces the effects of thermal blooming on HEL wavefront helps in improving system performance. When there is no wind component transverse to the HEL beam path, heat accumulates in a column of air defined by the propagating beam and results in beam distortions due to severe thermal blooming. A uniform, unidirectional wind can transport some of the heat out of the beam path between HEL pulses, but cannot prevent the growth of PCI from small-scale structure on the wavefront. For damping PCI growth, one must somehow dealign or scramble the 3-D filamentary structure on the HEL wavefront and prevent it from being reinforced. A non-uniform atmospheric wind profile will cause such dealignment or scrambling of PCI structure to improve the overall system performance.

Although there is only one fundamental mechanism for suppressing PCI growth, we differentiate between the amelioration provided by a linear wind shear and by random wind fluctuations for the purposes of this paper. If there exists a change in wind speed with altitude, it dealigns the PCI modes along the downwind direction to stem their growth. In the case of a wind spiral, where the wind direction changes in height, a similar dealignment process is applicable, perhaps less efficiently. We call the amelioration by linear wind shear the linear dealignment. The second kind of wind amelioration is due to mini-shear where there are random fluctuations of transverse wind components with altitude. In this case, PCI modes are prevented from being reinforced by random fluctuations of vector wind as the HEL propagates through the atmosphere. We term the amelioration by random wind fluctuations the mini-shear scrambling. We will discuss the comparative roles of both linear dealignment and mini-shear scrambling in improving the performance of GBL systems.

The other major physical process which under certain circumstances can provide the required amelioration is turbulent mixing. Turbulent mixing is characterized by a time-dependent velocity field at a given height which induces local mixing of deposited heat; in comparison, mini-shear assumes uniform wind velocity at a given altitude. The physical processes of turbulent mixing relevant to HEL propagation are not yet fully understood and are an active area of investigation. Some researchers [3] in the propagation community have suggested that wind mini-shear will provide larger amelioration of HEL wavefront degradations than turbulent mixing in all relevant GBL scenarios, but the agreement is far from unanimous [4]. The relative importance of turbulent mixing vis-a-vis mini-shear in HEL amelioration remains unclear at this time. For these reasons, the ameliorating role of turbulent mixing will not be further pursued here.

GBL BASELINE PERFORMANCE

To assess the role of natural amelioration on HEL wavefront degradations, we must define a reference (baseline) GBL scenario, against which the effects of atmospheric dynamics can be judged. Table 1 lists a set of HEL, AO and atmospheric parameters that characterize the baseline GBL scenario. We have chosen the propagation medium to be a 5 km high uniform atmosphere. Optical turbulence is characterized by a 11.7 cm Fried r_o value. The total heating in the atmosphere is represented by an integrated absorption of 0.75%. We have assumed a unidirectional constant wind of 3 m/s. There is no beam slewing in the baseline scenario.

TABLE 1

GBL BASELINE SCENARIO

Uniform 5 km atmosphere
Turbulence r_o = 11.7 cm
Integrated absorption = 0.75%
Distortion number, N_D = 125
Unidirectional wind = 3 m/s
No beam slew
HEL wavelength = 1.06 μm
HEL rep. rate = 100 Hz
AO actuator spacing = 8 cm

We assume the HEL wavelength to be 1.06 μm and the HEL pulse repetition rate to be 100 Hz. The level of thermal blooming can be specified by the Bradley-Hermann distortion number N_D which is proportional to the HEL intensity (power/aperture) and the effective integrated heating (integrated absorption/wind speed) and is given by $N_D = C\,(P/D) \int (\alpha/v)\, dz$, where P and D are the HEL transmitted power and aperture, α and v are height-dependent absorption and wind speed, and C is a constant.

The power and aperture (diameter) of the GBL system were chosen to give an N_D of 125. This is a fairly stressing GBL scenario. It should be noted that the value of N_D decreases as wind speed v increases, but that a wind spiral alone does not change N_D. In cases where wind speed increases with altitude, as discussed in the next section, the value of cumulative N_D will be lower than the baseline value of 125. Since we are interested in the performance of a given GBL system, we do not change system parameters such as HEL power and aperture, and atmospheric parameters such as absorption profile to adjust the value of N_D in the parametric studies.

A simple low-pass filter model is used for the AO system in the GRAND simulations reported here, although a detailed AO model with multiple adaptive mirrors, wavefront sensors and wavefront reconstructor is available. The effects of such a low-pass filter correction on GBL system performance (including the effects of PCI onset and growth) can be represented by the effective actuator spacing on the deformable mirror (DM) in the AO system. We have used an 8 cm effective actuator spacing (projected on the primary mirror) for the current simulations.

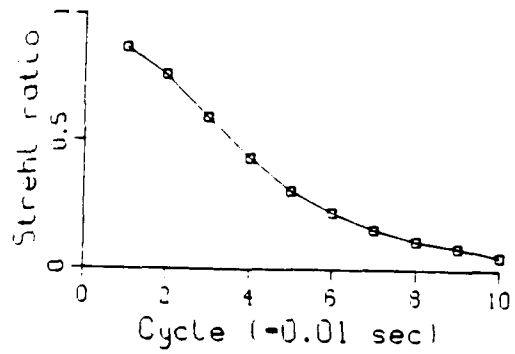


Figure 1. Performance (Strehl ratio vs. time) of baseline GBL system.

The GBL system performance is customarily represented by a Strehl ratio, defined as the ratio of peak intensity in the far-field normalized by that for the diffraction-limited case. (One can use other figures of merit such as encircled energy to measure system performance). The baseline GBL system performance is shown in Figure 1 as a plot of Strehl ratio vs time. Time is shown in terms of number of cycles or number of HEL pulses transmitted at the repetition rate of 100 Hz. We can see that the Strehl ratio degrades very quickly from an initial turbulence-limited value of about 0.87 to less than 0.1 in less than 10 cycles (0.1 sec). In the remainder of this paper, we discuss ways to improve the GBL system performance shown in Figure 1.

ROLE OF LINEAR WIND SHEAR

In the atmosphere, wind velocity changes (either in speed or direction or both) as a function of altitude above ground. In this section, we are more interested in systematic changes in wind velocity with height (linear shear) rather than random wind fluctuations that are characteristic of mini-shear. We discuss two types of linear wind shear: change in wind speed (speed shear) and in wind direction (direction shear).

The effect of linear wind speed shear on GBL system performance is shown in Figure 2a. The background wind profile is constant (3 m/s) and unidirectional, same as the wind profile used in the baseline scenario. We define a wind speed shear with $v(h) = v_0 + \alpha h$, where α is given in m/s/km and $0 < h < 5$ km. Strehl ratio vs. time curves for three values of α are shown in Figure 2a (GRAND runs were continued up to 25 cycles or 0.25 sec). Note that the distortion number N_D varies with the magnitude of speed shear and reduces from 125 for $\alpha = 0$ to about 76 for $\alpha = 4$ m/s/km.

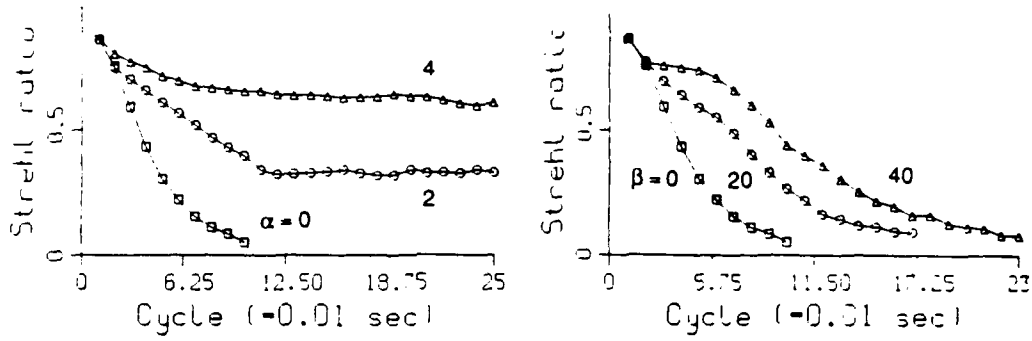


Figure 2. System performance with (a) wind speed shear and (b) wind direction shear.

It can be easily seen that substantial performance improvement can occur in the presence of linear wind speed shear. In the absence of speed shear ($\alpha = 0$), the Strehl ratio drops below 0.1 in less than 0.1 sec, whereas for $\alpha = 4$ m/s/km, which corresponds to wind speed increasing from 3 m/s at ground to 23 m/s at 5 km, the GBL performance achieves a quasi-steady state around a Strehl ratio of about 0.6. This is an example of amelioration by the linear dealignment process, where a strong transverse wind gradient can prevent the growth of PCI structure and improve the overall system performance. Note that a slewing beam following a moving target can also provide the large wind speed shear, even in the absence of ambient speed shear, and thus improve system performance.

Figures 2b demonstrates the effects of wind direction shear or wind spiral. As before, we have a background constant wind speed of 3 m/s ($N_D = 125$), but the wind direction changes with height and is given by $\theta(h) = \beta h$, where β is given in degrees/km and $0 < h < 5$ km. Three GRAND runs with $\beta = 0$, 20 and 40 degrees/km are shown in Figure 2b. Note that the case with $\beta = 40$ degrees/km corresponds to a total wind spiral of 200 degrees in an altitude of 5 km. A wind spiral also provides the linear dealignment of the small-scale filamentary structure on the HEL wavefront, but perhaps less efficiently; this leads to a weaker system performance improvement.

The combined effects of wind speed and direction shears, representative of the atmosphere, are shown in Figure 3. We have chosen a wind spiral of 100 degrees ($\beta = 40$ degrees/km) and a set of α values of 0, 1, 2 and 4 m/s/km. Here, both wind speed shear and wind spiral lead to a stronger dealignment of PCI modes and thus to a better system performance. We can expect a somewhat better performance enhancement for a 200 degree wind spiral.

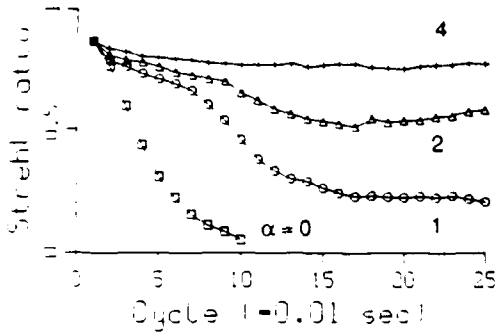


Figure 3. Combined effects of wind speed shear and wind spiral.

One concludes that in the presence of a moderate wind spiral, large wind speed shear provides strong amelioration of HEL wavefront degradations; a stronger spiral would provide further amelioration. Are these strong wind speed and direction shears realistic? As will be discussed in a later section, wind measurements at WSMR indicate that during some months of the year, wind profiles at WSMR do indeed include such large gradients in vector wind. Thus the performance improvement due to linear wind shear seen in GRAND simulations using ideal wind profiles could be reasonably expected at WSMR.

EFFECT OF RANDOM WIND FLUCTUATIONS

It is well established that the changes in vector wind with altitude do not occur monotonically or smoothly, but there is a significant random component in the overall wind profile. Unfortunately, the characteristics of these random variations are not well-known, at least at the spatial and temporal resolutions relevant to HEL propagation. The relevant vertical resolution is on the order of a few meters or less and the appropriate time scale is on the order of a fraction of a second.

In the absence of detailed knowledge of small-scale wind fluctuations, HEL propagation modelers use a model for the process of mini-shear. A mini-shear model included in the GRAND propagation code has been described by Herman and Westerman [5]. This model allows the correlation length to be height-dependent, although we assumed the correlation length to be constant in GRAND simulations used in this paper, primarily for computational economy. We now discuss the impact of random wind variations on HEL propagation.

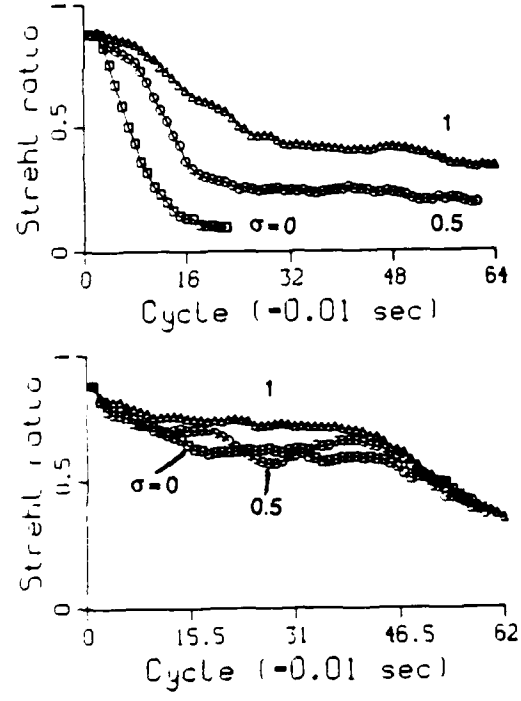


Figure 4. Effects of mini-shear (a) without linear shear and (b) in the presence of linear shear.

The mini-shear model is characterized by a constant correlation length of 100 m throughout the atmosphere. To obtain adequate correlation between neighboring heights and to limit the computational load in GRAND runs, a constant layer separation of 50 m was selected through a 2 km atmosphere. The strength (range) of wind fluctuations was specified by the rms (σ) values between 0 and 1 m/s. Note that since the cumulative contribution of mini-shear (random wind fluctuations) to the background heating is negligible, the N_D for each run in this section depends only on the background profile.

Figure 4a shows GRAND performance predictions in the presence of three levels of mini-shear when the background wind profile was constant and unidirectional (no linear shear).

Both levels of mini-shear provide some improvement in system performance over the case with no mini-shear, but the improvement is smaller than that with wind speed shear. The impact of mini-shear in the presence of linear wind shear is shown in Figure 4b. There is no significant additional amelioration due to mini-shear when there is a strong wind speed shear (4 m/s/km) and moderate wind spiral (100 degrees).

As discussed earlier, wind variations provide two mechanisms for ameliorating HEL wavefront degradations: linear dealignment by a large transverse wind gradient and scrambling of PCI growth by random wind fluctuations (mini-shear). From Figure 4a, we observe that in the absence of linear dealignment, mini-shear does provide moderate level of amelioration and improve system performance in PCI-dominated scenarios under consideration here. However, when a strong transverse wind component is present (Figure 4b), additional amelioration due to PCI scrambling by mini-shear seems insignificant.

GBL SEASONAL PERFORMANCE AT WSMR

Site Characterization

We have seen the potential impact of atmospheric wind variations, both linear shear and mini-shear, on the performance of GBL system performance. Are these variations present in the wind environment at WSMR? Unfortunately, this question cannot be answered accurately or confidently. The reason for this is the paucity of high-resolution measurements of wind, and other atmospheric parameters, at WSMR. The problem of atmospheric characterization has been looked at in some detail recently [6, 7]. It suffices to say here that appropriate wind measurements at WSMR are simply not available to adequately address the question of amelioration by wind fluctuations.

The only atmospheric measurements easily available from WSMR are so-called 1988 monthly mean profiles [8]. For each month of 1988, a selected set of atmospheric parameters are listed with altitude with a vertical resolution of about 1 km; only the turbulence (C_n^2) profile has higher resolution near ground and is also separated for day and night. These monthly mean profiles are obtained by combining all measurements in a given month regardless of atmospheric conditions during individual measurement campaigns. In spite of their shortcomings, we have used these 1988 monthly mean profiles to obtain a preliminary estimate of the seasonal effects on HEL propagation.

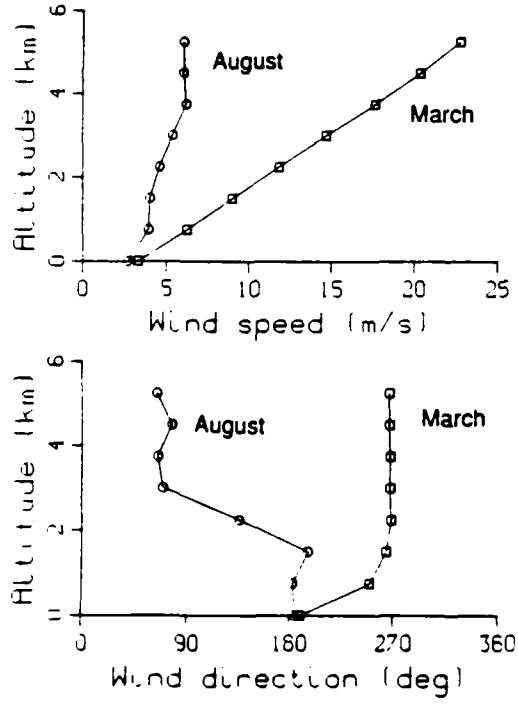


Figure 5. Seasonal wind speed and direction at WSMR for (a) March and (b) August.

Figures 5a and 5b show two examples of seasonal winds at WSMR. There is a large wind speed shear (about 4 m/s/km) in March, but that in August is much smaller. Conversely, there is much larger effective wind spiral in August than in March. Here, as a first approximation, we define an effective wind spiral as the sum of magnitudes of direction change between adjacent heights from ground to a certain height (5 km), rather than calculating the difference in wind directions at ground and 5 km. The rationale for doing this is that PCI smearing is provided whether wind changes direction clockwise or counterclockwise and that this smearing effect is cumulative.

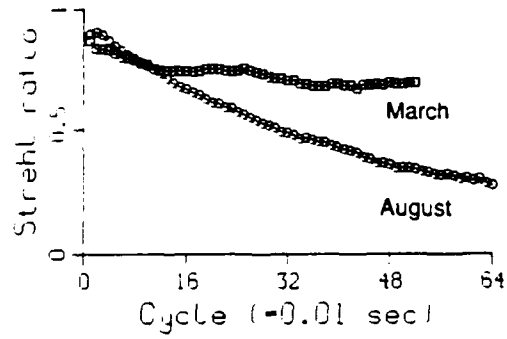


Figure 6. Baseline GBL system performance for (a) March and (b) August atmospheres.

GBL System Performance

The performance for a given GBL system at WSMR for the months of March and August is shown in Figure 6. Random wind fluctuations (mini-shear) have not been added to background wind in these calculations. The results demonstrate that the month of March provides the "best" conditions for power transmission at WSMR, where the Strehl ratio stays above 0.75 throughout a wind clearing time because of the strong wind speed shear. On the other hand, GBL system performance in the August WSMR environment drops below 0.3 at one wind clearing time. In August, a lack of wind speed shear, even in the presence of a strong wind spiral, leads to a degraded system performance. The GBL system performance in all other months is bounded by these two extrema.

TABLE 2

GBL SEASONAL PERFORMANCE

Month	r_o (cm)	α (%)	v_o (m/s)	Δv (m/s)	Spiral (deg)	N_D	SR
1	11.2	0.54	2.83	17.9	97	49	0.57
2	11.5	0.6	2.86	18	17	54	0.53
3	11.6	0.57	3.42	19.6	80	41	0.69
4	12.2	0.63	3.4	17.3	46	45	0.68
5	12.6	0.64	3.49	11	59	53	0.51
6	14.2	0.65	3.47	7.9	69	58	0.47
7	14.1	0.59	3.05	3.8	151	71	0.33
8	13.5	0.59	2.74	3.6	172	75	0.28
9	13	0.74	2.76	7	85	83	0.37
10	12.4	0.63	3.07	13.4	73	58	0.65
11	11.9	0.58	2.84	17.1	188	55	0.55
12	11.1	0.52	2.57	19.7	166	49	0.68

Nighttime turbulence profiles
Δv = cumulative wind speed shear between ground and 5 km
Spiral = cumulative effective direction shear to 5 km
SR = Strehl ratio as a performance indicator

Table 2 summarizes the seasonal performance of a GBL system at WSMR. For all twelve months, we have listed nighttime optical turbulence (r_0), total heating (integrated α), ground wind speed, cumulative wind speed shear (Δv) and effective wind spiral. The cumulative distortion number, N_D, for a particular GBL system and its performance (Strehl ratio, SR) at the end of one wind clearing time are also tabulated. One can see that the nighttime turbulence during summer is weaker (larger r_0) than that in winter, while

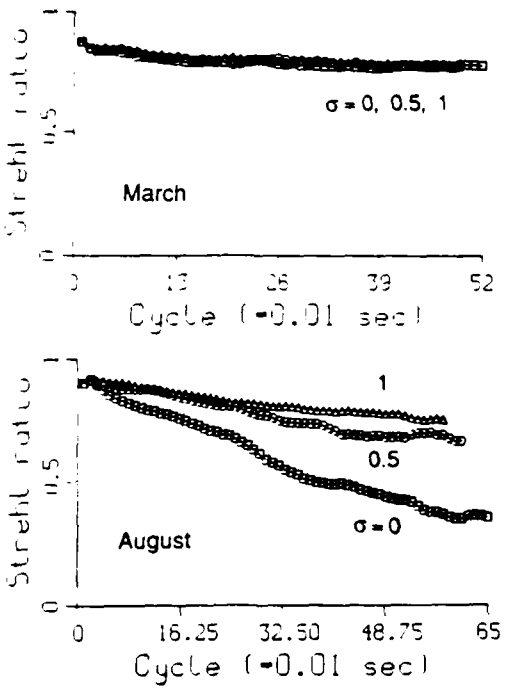


Figure 7. Effects of mini-shear on seasonal GBL performance for (a) March and (b) August.

the integrated absorption is a little stronger. The ground-level wind speed is fairly uniform throughout the year. There is a wide variation in vector wind gradient during the year. The wind speed shear between ground and 5 km is much larger in winter and spring (about 17-20 m/s) than in summer and fall (3-13 m/s). The wind spiral behaves somewhat differently, with relatively smaller values during winter and spring compared to other times of the year.

The seasonal trend in the Strehl ratio, given in the last column in Table 2, reflect the wind environment at WSMR. The best Strehl ratio of 0.69 in March is mainly due to the strong wind speed shear which reduces the cumulative distortion number (to 41) giving improved performance. The worst performance (Strehl ratio of 0.28) is seen in August, again primarily due to a weak speed shear. Strong wind spirals during late summer and fall do not help system performance if there is no speed shear.

Effect of Mini-Shear

What role can mini-shear play in improving the seasonal performance of a GBL system? We added the random correlated wind fluctuations to the background wind profiles for the months of March and August. The mini-shear parameters, as before, were constant 100 m correlation length, 50 m layer separation in a 2 km atmosphere and rms values of 0, 0.5 and 1 m/s. Figures 7a and 7b show GRAND predictions of system performance for the months of March and August. There is no noticeable improvement in system performance by adding mini-shear to the background wind profile in March, whereas there is substantial performance improvement for the month of August. When there is strong amelioration due to linear wind shear, particularly speed shear (e.g. in March), mini-shear provides little additional amelioration. On the other hand, when amelioration due to linear wind shear is weak (as in August), *mini-shear can provide significant additional amelioration for improved performance.* Note that the August GBL system performance with mini-shear almost approaches that in March. It is reasonable that stronger mini-shear (larger σ) should give better performance improvement.

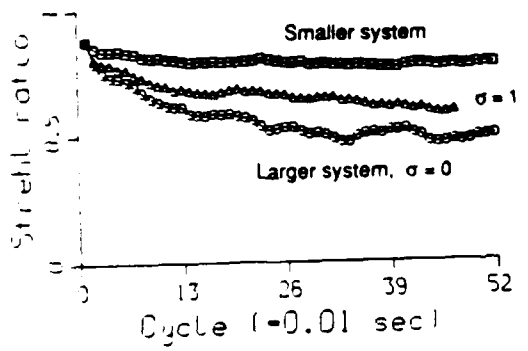


Figure 8. Performance of larger GBL system with and without mini-shear.

Performance of Larger GBL System

We have seen that a GBL system characterized by an N_D of 125 can successfully transmit HEL power through the WSMR atmosphere in the month of March with the Strehl ratio staying above 0.75 at one wind clearing time. How would a bigger GBL system perform under the same atmospheric conditions? Figure 8 presents the system performance of a GBL system at WSMR with N_D of 250 in comparison with a smaller system. The

performance of the larger GBL system degrades to a Strehl ratio of about 0.5, compared to 0.77 for the smaller system. If we add a mini-shear of 1 m/s to the larger system, the system improves somewhat, giving a Strehl ratio of 0.6 at one wind clearing time; stronger mini-shear would lead to better performance improvement. With a larger system (stronger thermal blooming), the PCI growth rates tend to be bigger leading to a worse performance, even in the presence of strong linear wind shear as we have in March. Additional amelioration is provided by the mini-shear scrambling. Note that the performance of a fairly large system (N_D of 250) stays above 0.5 in one wind clearing time even without the benefit of random wind fluctuations and almost approaches that of a smaller system with fairly strong mini-shear.

CONCLUDING REMARKS

We have investigated the role of natural atmospheric dynamics in ameliorating HEL wavefront degradations induced by turbulence-thermal blooming interactions. Computer simulations were performed with Lockheed 4-D wave optics propagation code, GRAND, using both ideal atmospheric conditions and using representative atmospheric conditions at WSMR. A secondary goal of this work was to demonstrate the power transmission capability from a GBL site in WSMR as a function of season.

A fairly stressing GBL scenario (N_D of 125), which led to poor system performance without wind fluctuations, was selected to illustrate the beneficial effects of atmospheric kinematics; the performance (Strehl ratio) of the baseline system fell below 0.1 in less than 0.1 second. A wind speed shear (defined as an increase in wind speed with height) provides substantial performance improvement by preventing the reinforcement of small-scale filamentary structure on the propagating HEL wavefront by a linear dealignment process. A wind spiral (change in wind direction with altitude) leads to a smaller performance improvement due to a less efficient linear dealignment.

Random wind fluctuations in height can provide system performance improvement by smearing or scrambling PCI growth which can otherwise lead to a catastrophic breakup of the HEL beam. The precise role of mini-shear in ameliorating HEL wavefront degradations depends on a particular GBL scenario. In the presence of a strong linear wind shear (speed shear or spiral or both), the additional amelioration provided by mini-shear can be small. The mini-shear amelioration can be substantial if there is no linear wind shear. Also, mini-shear can lead to Strehl ratio improvement for larger GBL systems where linear shear alone cannot provide adequate amelioration.

We also looked at the ability to transmit HEL power at WSMR during different times of the year. Large wind speed shear in March leads to a strong ameliorating effect and excellent system performance. The GBL performance in August is poor due to small speed shear, despite a strong spiral in the lower atmosphere. Mini-shear provides the additional amelioration to make system performance in August almost as good as that in March. One can conclude from these trends that the "best" GBL system performance occurs in winter and spring. Based on these limited computer simulations with GRAND propagation code, it seems significant amounts of HEL power can be transmitted through the atmosphere at WSMR. Finally, a few words of caution are in order.

There are two major handicaps of the results and conclusions presented here. The first pertains to the limited atmospheric characterization at WSMR. The atmospheric characterization used in GRAND simulations were monthly mean atmospheric profiles, where measurements from different atmospheric conditions were combined. Furthermore, even "individual" measurements involve poor vertical resolution (1 km) and up to 30 minutes of temporal averaging. High-resolution wind measurements are not available at all to characterize mini-shear. Some features of the wind profiles, such as large wind speed shear in winter and spring, are present in some "individual" WSMR wind profiles we examined. It is not known at present how representative this WSMR atmospheric characterization is if one were to obtain a consistent set of all atmospheric parameters at high spatial and temporal resolutions.

The second difficulty is with the scaling laws for HEL propagation. Due to computational complexity of GRAND code, the simulations were performed with small-aperture GBL systems. There is some

disagreement within the propagation community as to how these predictions can be scaled to apply to larger GBL systems under different operational scenarios. Till a robust scaling strategy can be developed, one must be careful in scaling performance predictions for small-aperture systems to operational GBL systems.

REFERENCES

1. T. J. Karr, J. Opt. Soc. Am., A-6, 1038, 1989.

2. M. N. Rosenbluth, JASON Report JSR-89-901, The Mitre Corp., June, 1989.

3. D. H. Chambers, J. A. Viecelli and T. J. Karr, presented at the SPIE conference on Propagation of High Energy Laser Beams Through the Earth's Atmosphere, Los Angeles. SPIE Proceedings, 1221-20, 1990.

4. C. L. Yee, presented at the SPIE Conference on Propagation of High Energy Laser Beams Through the Earth's Atmosphere, Los Angeles. SPIE Proceedings, 1221-22, 1990.

5. B. J. Herman and S. D. Westerman, LMSC Technical Report, May, 1989.

6. T. H. Pries, Ed., Interim Report of the Atmospheric Measurements Group, U. S. Army Strategic Defense Command, Ground Based Laser Project Office, November, 1989.

7. S. D. Westerman and N. C. Mehta, presented at the SPIE Conference on Propagation of High Energy Laser Beams Through the Earth's Atmosphere, Los Angeles. SPIE Proceedings, 1221-25, 1990.

8. D. Cousins, Technical Report K6DM-12188, U. S. Army Strategic Defense Command, Ground Based Laser Project Office, January, 1989.

MEASUREMENT OF THE STIMULATED THERMAL RAYLEIGH SCATTERING INSTABILITY

T.J. Karr, M.C. Rushford, J.R. Murray, and J.R. Morris

Lawrence Livermore National Laboratory
P.O. Box 808 L-495
Livermore, CA 94550

ABSTRACT

We report the first clear experimental demonstration of large amplification of small-scale spatial perturbations by stimulated thermal Rayleigh scattering (STRS) of a CW laser beam propagating through an absorbing medium in a context normally associated with thermal blooming. A single-mode argon-ion laser beam with $\lambda = 488$ nm was propagated vertically downward through a 1.2 m cell filled with CCl_4 that was doped with an absorber to have optical depths in the range 0.5-2.3 . A shear-plate interferometer near the cell input generated the perturbation. Fringe growth was rapid and visually obvious, as was competing growth from dust specks, etc. The measured growth rate is in good agreement with the asymptotic rate from analytic STRS theory.

1. INTRODUCTION

At transverse spatial scales that are much smaller than the beam diameter uncompensated thermal blooming of a collimated high-power laser beam is more aptly described as stimulated thermal Rayleigh scattering (STRS) than as thermal blooming. While both descriptions are physically correct when properly employed, the STRS description focuses attention on the growth of small-scale irregularities while the thermal blooming description tends to ignore them. Whole-beam blooming studies prior to 1986 and scaling laws developed from them lead one to believe that irregularities erase themselves because for the beam as a whole the thermal lens written into the propagation medium defocuses the beam where it is brightest. When the intuition based on such results is tested using three-space-dimension plus time wave-optics thermal blooming codes with initial conditions that include small-scale phase or intensity perturbations or include realistic refractive index turbulence, it is found to be incorrect if the thermal blooming optical path change is large and accumulates at a rapid rate. Rather than erasing themselves, the small scale irregularities grow rapidly by a successive overshoot process. The process is often called the open-loop (uncompensated) thermal-blooming instability, but is physically identical to STRS in the near-forward direction.

Using an STRS description of uncompensated small-scale thermal blooming is a major advance. It allows separation of the small-scale behavior from the very different whole-beam behavior. It also leads to a linear set of differential equations and to analytic solutions in simple, but interesting, cases.

STRS was actively studied[1-16] between 1968 and 1975, and a number of review and tutorial articles are available.[10,12,15,17,18] Most of the experiments of the 1968-75 period used Q-switched ruby laser pulses of about 20 ns duration and a 180° back-scatter geometry. However, the experiments of Rother, et al.[8] examined forward scattering at angles down to 7°. Mack[6] and Scarlet[11] studied scattering at angles down to 5 mrad with mode-locked ruby[6] or Nd-glass lasers.[11] Scarlet used about a 30 pulse train of 5-8 ps pulses spaced about 4 ns apart and superimposed two equal intensity beams with a 5 mrad angle between them in a liquid sample cell. However, none of these experiments clearly demonstrated large amplification of a weak probe beam in a context normally associated with isobaric thermal blooming, i.e., at near-forward propagation angles small enough that the pump and probe beams physically remain superimposed over the entire propagation path and on time scales much longer than the sound transit time across the interference fringe period. Furthermore, large amplification is counter-intuitive for anyone familiar with the self-defocusing associated with whole-beam thermal blooming. *The experiments we present here[26] directly observe large amplification of fringe contrast under isobaric thermal blooming conditions.*

Although the STRS research of 1967-75 emphasized 180° back-scattering of ≈ 20 ns pulses, for the Rayleigh component the scattering mechanism is the same for quasi-CW beams at the 1 mrad (or less) near-forward scattering angles of our laboratory experiment as long as the fringe spacing of the interference between the scattered and high-power beams remains small compared to the high-power beam diameter. In both cases the interference pattern creates an isobaric density inhomogeneity via absorption followed by thermal expansion, and the high-power beam scatters off the refractive index inhomogeneity associated with the density. In both cases transient STRS was observed since the diffusion time for back scattering in CCl_4 is 18 ns and for our near-forward scattering experiments it was 40-500 ms. One significant difference between our experiment and the near-forward STRS experiments of

Rother, et al.[8] is that in addition to amplification of the injected perturbation our experiment generated and amplified the mirror-image order (with respect to the high-power beam) with equal efficiency by direct scattering of the high-power beam. The reason is the difference in the phase-mismatch in the two experiments; in ours it is $\mathcal{O}(1\ m^{-1})$ while in Rother's it is $\mathcal{O}(10^4\ m^{-1})$ at 7°. In the linearized blooming theory[19-22] the small phase-mismatch is neglected and the two mirror image orders are combined into independent intensity and phase perturbation variables.

2. LINEARIZED THEORY WITH DIFFUSION

In the open-loop case linearized thermal-blooming instability theory closely parallels STRS theory as given in Rother[9] or Batra, Enns, and Pohl,[10] as it must since the physical scattering process is the same. However, there are some differences in notation and in the approximations employed. The earlier STRS studies retain the Brillouin scattering line throughout most of their analyses and identify the Rayleigh and Brillouin scattering as separate terms in the final result; the recent linearized thermal-blooming instability theory studies[19-22] neglect the Brillouin scattering from the beginning by using isobaric hydrodynamics. Because he is interested in substantial off-axis scattering angles, Rother[9] retains the exact spatial orientation of interference fringes between the pump and scattered waves; linearized thermal-blooming instability theory is only concerned with near-forward scattering angles of a few mrad or less so it treats the fringes as planes parallel to the propagation direction and uses two dimensional hydrodynamics with the propagation direction coordinate (z) as a parameter. Finally, because of the very small scattering angles, for each wavevector linearized thermal-blooming instability theory treats two mirror-image scattering directions on either side of the pump beam propagation direction simultaneously as tightly coupled waves, whereas Rother for the most part treats only a single scattered wave and only briefly discusses the other scattered waves using an uncoupled-wave treatment.

The simultaneous treatment of two mirror-image diffraction orders is hidden in Karr's[20] notation in his paper on the closed-loop instability. To explicitly identify the two orders and their relation to Karr's notation, we start with Fresnel wave equations for the scattered waves neglecting pump depletion:

$$-2ik\frac{\partial E_m}{\partial z} - \kappa^2 E_m + \frac{\omega^2}{c^2}\frac{d\varepsilon}{d\rho}\rho_m = 0, \qquad (m = \pm 1), \tag{1}$$

where E_m, $m = \pm 1$, are the ratios of the slowly varying envelopes of the two scattered waves to that of the pump wave, E_0, and $k = n\omega/c$ for index of refraction n. (For simplicity we have neglected transmission losses.) The plane wave fields corresponding to the envelopes in Eq. (1) have associated carrier waves of the form $\exp[i(\omega t - kz - m\boldsymbol{\kappa}\cdot\mathbf{x}_\perp)]$, $m = 0,\pm 1$. The remaining equation is the standard isobaric hydrodynamics equation augmented by a diffusion term:

$$\left(\frac{\partial}{\partial t} - i\boldsymbol{\kappa}\cdot\mathbf{v} + \mathcal{D}\kappa^2\right)\rho_m = \frac{-2n\Gamma}{\dfrac{d\varepsilon}{d\rho}}\left(E_m + E_{-m}^*\right) \tag{2}$$

(Note that $\rho_{-1} = \rho_1^*$ because ρ is real, so only the $m = 1$ case of Eq. (2) is retained). Karr's Eq. (10a) is Eq. (2) with the following variable changes:

$$\mu = \frac{1}{2n}\frac{d\varepsilon}{d\rho}\rho_1 \tag{3a}$$

$$F_\kappa = (E_1 + E_{-1}^*), \tag{3b}$$

and the variable which Karr eliminates to obtain his Eq. (10b) is

$$\Phi_\kappa = \frac{-1}{2i}\left(E_1 - E_{-1}^*\right). \tag{3c}$$

Karr's formalism replaces the two complex fields of the scattered plane waves with a net intensity perturbation, F_κ, and a net phase perturbation, Φ_κ, on the high-power field, E_0, and solves for a single transverse Fourier component of these fields instead of the coupled pair, κ and $-\kappa$, required in the complex-field STRS formalism.

Karr[20] gives the Green's function solution of the STRS equations as a function of z, the propagation distance, and v, the Laplace transform of the time variable t, for the case of a uniform medium with negligible extinction of the unperturbed beam. Karr also gives an explicit series expansion in z and t of the propagation kernel for blooming of frozen-flow turbulence for the extreme transient case where thermal diffusion damping can be neglected; this kernel is the time integral of the Green's function, again without diffusion. By using these facts and Karr's prescription for incorporating thermal diffusion, we derive an explicit series solution for STRS in a uniform medium with thermal diffusion.

From Karr's Eqs. (19) and (24) we obtain the following expression for the evolution of the irradiance part of the scattered field due to an impulse perturbation [$\delta(\tau)$] for which F(0) is the intensity impulse and $\Phi(0)$ is the phase impulse:

$$F_\delta(z,t) = \exp(-\mathcal{D}\kappa^2 t)\left(\delta(t) + \frac{\partial}{\partial t}\right)\xi_\kappa(z,t) \tag{4a}$$

with

$$\xi_\kappa(z,t) = \left[F(0)\frac{\partial}{\partial z} + 2a_\kappa\Phi(0)\right]K_\kappa(z,t) \tag{4b}$$

and

$$K_\kappa(z,t) = \sum_{n=0}^{\infty}\frac{(-\Gamma kzt)^n}{(n!)^2}z j_n(a_\kappa z)\,. \tag{4c}$$

Eq. (4c) is Karr's Eq. (24), $a_\kappa = \kappa^2/2k$, $\kappa = 2\pi/\Lambda$ for perturbation period Λ, and $k\Gamma z$ is the rate of change of the optical path length due to thermal blooming or the blooming rate in radians/sec. For a heavyside (step) function perturbation switched on at $t=0$ the irradiance at (z, t) is:

$$F_H(z,t) = \int_0^t dt' F_\delta(z,t') = \exp(-\mathcal{D}\kappa^2 t)\,\xi_\kappa(z,t) + \mathcal{D}\kappa^2\int_0^t dt' \exp\left(-\mathcal{D}\kappa^2 t'\right)\xi_\kappa(z,t') \tag{5}$$

The first term on the right-hand side of Eq. (5) is a purely transient term, the second yields the steady-state result as $t \to \infty$. Term-by term integration in time in Eq. (5) and explicit evaluation of the z-derivative in Eq. (4b) using the recursion relations for the spherical Bessel functions of the first kind,[23] $j_n(u)$, gives:,

$$F_H(z,t) = \sum_{n=0}^{\infty}\frac{(-k\Gamma zt)^n}{n!}\dot{\gamma}(n,\mathcal{D}\kappa^2 t)a_\kappa z\left[F(0)j_{n-1}(a_\kappa z) + 2\Phi(0)j_n(a_\kappa z)\right] \tag{6}$$

where

$$\dot{\gamma}(a,u) \equiv \frac{u^{-a}}{\Gamma(a)}\gamma(a,u)\,,$$

and $\gamma(a,u) \equiv \int_0^u dv\, v^{a-1}\exp(-v)$ is the normalized incomplete Gamma function.[24]

A shear-plate interferometer generates a perturbation by a double reflection, one off each of its nearly parallel plates. For a plane-wave unperturbed beam the perturbation is also a plane wave propagating at a small angle, κ/k, to the unperturbed beam. Being a plane wave, the perturbation has real and imaginary parts with equal amplitude and 90° out of phase. The mathematical embodiment of this is

$$\Phi(0) = i\,F(0)/2\,, \tag{7}$$

so for a sheared-beam perturbation the irradiance fringe amplitude is

$$F_s(z,t) = F(0)\sum_{n=0}^{\infty}\frac{(-k\Gamma zt)^n}{n!}\dot{\gamma}(n,\mathcal{D}\kappa^2 t)a_\kappa z\left[j_{n-1}(a_\kappa z) + i j_n(a_\kappa z)\right] \tag{8}$$

The shear-plate interferometer generates a field perturbation that is accurately sinusoidal, a distinct advantage for comparison with the theory embodied in Eq. (8). In addition, when $\mathcal{D}\kappa^2 t << 1$, where the $\mathcal{D} = 0$ result accurately approximates Eq. (8), the reader can verify from Eqs. (4b), (5) and (7) that

$$F_s(z, t) \propto \frac{\partial K_\kappa}{\partial z}(z, t) + i K_\kappa(z, t) \tag{9}$$

Thus, the square of the modulus of the *irradiance*, $|F_s(z,t)|^2$, is directly proportional to the same combination of Green's functions as is the *electric field spectrum at wavevector* κ *due to turbulence* concentrated near the beginning of the propagation path, $z = 0$. (see Chambers, et al.[19]) This combination of Green's functions, so important for the prediction of high-power propagation through atmospheric turbulence, is directly measured by the amplification of shear-plate fringes in a nonturbulent blooming cell.

For the case $k\Gamma zt << 32(a_\kappa z)^2/\pi^3$ with $k\Gamma zt > 2\pi$, Chambers, et al.,[19] have given an asymptotic formula for $K_\kappa(z, t)$ from which we obtain the following asymptotic formula for $\xi_\kappa(z, t)$ in the sheared-beam perturbation case:

$$\xi_\kappa(z,t) \sim F(0) \frac{1}{2\sqrt{\pi}} \frac{1}{\sqrt[4]{k\Gamma tz}} \exp\left[(1 + i)\sqrt{2k\Gamma zt} + i(a_k z - \pi/8)\right] \tag{10}$$

Substituting Eq. (10) in Eq. (5) gives an approximate time dependence. When several waves of thermal blooming optical path change accumulate in a diffusion time ($k\Gamma z >> 2\pi \mathcal{D}\kappa^2$) the integrand on the right-hand side of Eq. (5) oscillates rapidly and this term can be neglected for a few diffusion times to obtain an approximate functional form for fringe growth

$$|F_s(z,t)| \sim |F(0)| \frac{1}{2\sqrt{\pi}} \frac{1}{\sqrt[4]{k\Gamma tz}} \exp\left(\sqrt{2k\Gamma zt} - \mathcal{D}\kappa^2 t\right) \tag{11}$$

In the appropriate limit Eq. (8) agrees with Rother's results. From Eq. (7) and the relationship

$$\Phi_\kappa = \frac{1}{2a_\kappa} \frac{\partial F_\kappa}{\partial z} \tag{12}$$

we can derive an equation from $E_1(z, t)$ for a sheared beam perturbation. Rother's[9] Eq. (41) is obtained as the $a_\kappa z \to \infty$ limit (appropriate for the scattering angles Rother is considering) of the resulting expression by replacing all the spherical Bessel functions with their asymptotic form for large arguments.

3. EXPERIMENTAL LAYOUT

The experimental layout is shown in Fig. 1. An argon ion laser was spatially filtered and expanded to make a near-Gaussian collimated beam of the desired size. A shear–plate interferometer, similar to that used by Bliss, et al.,[25] in their small-scale self-focusing experiment, generated a weak reflected beam that served as the perturbation source. The angle between the transmitted and reflected beam determines the interference fringe spacing, which was varied from run to run. The reflectivity determines the perturbation amplitude which was typically a few percent. The combined beams were propagated down through a 1.2 m vertical thermal blooming cell filled with CCl_4 doped with an absorbing contaminant. The shear–plate interferometer was as close as possible (a few cm) to the input window of the cell, and the beam was propagated from the top to the bottom of the cell to keep the liquid stable against thermal buoyancy. The total extinction of the cell was 50-90% and was monitored daily by drawing a small sample of of CCl_4 from the cell and measuring its absorption with a calorimeter. The output window of the cell was imaged onto a CCD camera. The camera recorded the intensity time-averaged over 33 ms, the television frame scan time; it had an interlaced scan, and the even and odd lines were alternately transferred to a digital frame buffer every 16.7 ms.

A He-Ne diagnostic laser propagated back through the cell and was observed by an interferometer. This provided continuous monitoring of the optical quality of the CCl_4 column. An experiment run began when the He-Ne fringes indicated the cell was free of optical distortion due to turbulence or residual heat from an earlier run. (Typically it took 2-5 min for the distortion caused by a previous run to become undetectable.) Then the shutter was opened, and the argon-ion beam propagated through the blooming cell for about half a second. During this time rapid, visually-obvious perturbation growth on a background of somewhat slower whole beam thermal blooming was observed. Growth from dust specks, Fresnel rings from edge clipping, etc. was also obvious. Such competing uncontrolled perturbations had to be carefully minimized to obtain quantitative results from these experiments.

4. RESULTS AND COMPARISON WITH THEORY

Table 1 describes the experimental conditions for two runs. Due to the high thermal blooming rate, rapid amplification of the perturbation fringes was predicted and observed. Very rapid thermal blooming rates were used so that several waves of thermal blooming optical path difference would accumulate in a diffusion time, as would be the case for a high-power laser beam in the atmosphere. The whole-beam Fresnel number was large enough that in the absence of thermal blooming the laser beam would remain collimated throughout the blooming cell. About 90% of the light was absorbed in the perturbation Fresnel number $N_p = 0.45$ case, 60% in the $N_p = 1$ case.

As part of our comparison with theory we simulated these experiments using the ORACLE wave-optics propagation code developed at LLNL. ORACLE solves the following coupled nonlinear time-dependent set of equations in three space dimensions: the Fresnel wave equation for the optical beam and isobaric hydrodynamics including diffusion for the fluid density. In the simulations presented here the unperturbed laser irradiance profile at the entrance to the blooming cell was assumed to be a perfect Gaussian beam.

Figure 2 shows a comparison of the observed irradiance at the cell exit with an ORACLE calculation for the 2.3 optical depth, $N_p = 0.45$ experiment. The left column is the CCD camera output, the right column is the ORACLE result, both of which are displayed on the video monitor of the experimental laboratory. (The apparent ellipticity of the ORACLE and experimental results is an artifice of this video display. The CCD camera detector elements are rectangular, and the video display partially corrects for this, while the "pixels" in the ORACLE calculation are square.) In the first frame after the shutter opens the experimental fringes are hardly detectable, while in the ORACLE calculation they are visible due to the perfect, no noise beam profile in the ORACLE calculation. After 33 ms fringes are clearly visible in the experimental irradiance profile and the fringe contrast increase is obvious in both the experimental measurement and the ORACLE calculation. At 67 ms the modulation depth has reached a significant fraction of the unperturbed peak irradiance. Between 67 and 100 ms the fringe contrast doesn't change much, but a bright ring begins to form at the edge of the beam and the beam is noticeably expanding; the latter are whole beam blooming effects. Figure 2 qualitatively demonstrates that the calculated and experimental irradiance profiles agree even though the experimental data are 33 ms time averages while the ORACLE results are instantaneous irradiance profiles.

To obtain a more quantitative comparison for each measurement time we Fourier analyzed both the experimental and calculated irradiance profiles at the end of the cell. In both cases we selected the central 128 by 128 pixels by masking. Then for each horizontal line (across the fringes) we computed the modulus of its complex finite Fourier transform (FFT), and averaged over all the lines. Finally we extracted the modulus and spatial frequency of the highest perturbation peak and plotted them as functions of time. The modulus results are shown in Figs. 3 and 4. In both, the curve with the solid boxes is the experimental measurement, the curve with X's is the ORACLE calculation.

For the case in Fig. 3, which had 7 fringes across the full width at half maximum (FWHM) of the unperturbed beam, the agreement is excellent. The dashed curve in Figs. 3 is a four-bin weighted average of the results of linearized perturbation theory (STRS theory). The positive coordinate half of a one-dimensional Gaussian was divided into 5 equal-area (power) bins and the median intensity of each of the 4 center-most bins was used in four perturbation calculations using Eq. (8) truncated at 50 terms; the modulus of the complex results were added, time averaged with a 33 ms rectangular averaging window, and scaled to match the experimental results at the earliest sample times. Again, the agreement is remarkable; even some of the fine structure matches, although this is probably beyond the accuracy of our analysis of the experimental data.

For the case in Fig. 4, which had 4.4 fringes across a FWHM, the experimental data and the ORACLE calculation agree at times up to about 200 ms. However, thereafter the experimental data has a significant decrease, while the ORACLE calculation shows an increase in fringe contrast. The dashed curve in Fig. 4 is a linearized perturbation

analysis as described above for Fig. 3. It agrees adequately with the experimental results up to the center of the first main peak; thereafter, it behaves more like the ORACLE calculation than the experimental data.

Because of the smaller number of fringes across the beam FWHM, the exact intensity profile is expected to be more important for the case of Fig. 4 than for the case of Fig. 3. Also, beginning at about the time of the first peak, pronounced growth of diffraction rings due to two dust particles becomes clearly visible in the experimental intensity profiles; growth of these rings clearly competes with that of our initial perturbation, but the dust specks were not included in the ORACLE simulation. Additional ORACLE simulations and parameter studies with Eq. (8) indicate that after the first peak the results are sensitive to details of the irradiance profile and that a flatter irradiance profile with lower peak irradiance can produce a dip at about the time observed in our experiment.

We fit the experimental perturbation amplitude data points to the functional form $Ct^{-1/4}\exp(At^{1/2} - Bt)$ and compared the coefficient A to the predicted asymptotic growth rate, $\sqrt{2k\Gamma z}$. (The functional form is the envelope of the asymptotic result for diffusion-free STRS theory plus a phenomenological exp(-Bt) correction for diffusion.) To avoid significant bias due to whole-beam blooming effects we restricted our fit to the first 15 data samples (0.25 sec). We used half the peak irradiance of a Gaussian beam of the experimentally measured power and FWHM in the computation of Γ. The results tabulated in Table 2 show excellent agreement.

5. SUMMARY

Stimulated thermal Rayleigh scattering does indeed cause growth of high spatial frequency perturbations on a laser beam propagating in an absorbing fluid. The amplification can be large and is easily observed.

The observed growth rate agrees with analytic theory, at least at times before the defocusing due to whole beam-blooming is significant. The prediction of rapid growth after a few waves of blooming is convincingly demonstrated to the naked eye and is quantitatively confirmed.

Detailed wave-optics computer simulations reproduce the experimental phenomena. The differences are attributable to experimental uncertainties.

6. ACKNOWLEDGEMENTS

This experiment was made possible by the continuing support and encouragement of J. I. Davis and J. Z. Holtz. The work was performed under the auspices of the U.S. Department of Energy by Lawrence Livermore National Laboratory under contract W-7405-ENG-48.

7. REFERENCES

1. R. M. Herman and M. A. Gray, "Theoretical prediction of the stimulated thermal Rayleigh scattering in liquids," Phys. Rev. Lett. 19, 824-828 (1967).
2. K. A. Brueckner and S. Jorna, "Linearized theory of laser-induced instabilities in liquids and gases," Phys. Rev. 164, 182-193 (1967).
3. D. H. Rank, C. W. Cho, N. D. Foltz, and T. A. Wiggins, "Stimulated thermal Rayleigh scattering," Phys. Rev. Lett. 19, 828-830 (1967).
4. G. I. Zaitsev, Y. I. Kyzylasov, V. S. Starunov, and I. L. Fabelinskii, "Stimulated temperature scattering of light in liquids," JETP Lett. 6,255-257 (1967).
5. I. L. Fabilinskii, D. I. Mash, V. V. Morozov, and V. S. Starunov, "Stimulated scattering of light in hydrogen-gas at low pressures," Phys. Lett. 27A, 253-254 (1968).
6. M. E. Mack, "Stimulated thermal light scattering in the picosecond regime," Phys. Rev. Lett. 22, 13-15 (1969).
7. V. S. Starunov and I. L. Fabelinskii, "Stimulated Mandel'shtam-Brillouin scattering and stimulated entropy (temperature) scattering of light," Sov. Phys. Usp. 12, 463-489 (1970).
8. W. Rother, H. Meyer, and W. Kaiser, "Amplification of light in absorbing media: stimulated thermal Rayleigh scattering," Z. Naturforsch. 25a, 1136-1143 (1970); W. Rother, H. Meyer, and W. Kaiser, "Angular dependence of stimulated thermal Rayleigh scattering," Phys. Lett. 31A, 245-246 (1970).
9. W. Rother, "Theorie der lichtverstärkung in absorbierenden medien," Z. Naturforsch. 25a, 1120-1135 (1970).
10. I. P. Batra, R. H. Enns, and D. Pohl, "Stimulated thermal scattering of light," Phys. Stat. Sol. (b) 48, 11-63 (1971).
11. R. I. Scarlet, "Diffractive scattering of picosecond light pulses in absorbing liquids," Phys. Rev. Lett. 26, 364-366 (1971).
12. W. Kaiser and M. Maier, "Stimulated Rayleigh, Brillouin, and Raman spectroscopy," in Laser Handbook, vol. 2, F. T. Arrecchi and E. O. Schulz-DuBois, eds., (North Holland, Amsterdam, 1972), pp 1077-1150.

13. L. M. Peterson and T. A. Wiggins, "Forward stimulated thermal Rayleigh scattering," J. Opt. Soc. Am. 63, 13-16 (1973).
14. C. S. Hsu, N. D. Foltz, and C. W. Cho, "Stimulated thermal Rayleigh scattering in argon," Phys. Rev. A 9, 2365-2370 (1974).
15. A. Bambini, R. Vallauri, and M. Zoppi, "Nonlinear spectroscopy in the Rayleigh-Brillouin region of the spectrum of light scattered by fluids," in Proceedings of the International School of Physics "Enrico Fermi", Course LXIV, Nonlinear Spectroscopy, N. Bloembergen, ed., pp. 442-455, (North-Holland, Amsterdam, 1977).
16. N. M. Kroll and P. L. Kelley, "Temporal and spatial gain in stimulated light scattering," Phys. Rev. A 4, 763-776 (1971).
17. V. S. Averbakh, A. A. Betin, V. A. Gaponov, A. I. Makerov, G. S. Pasmanik, and V. I. Talanov, "Induced scattering and self-action in gases and their effect on propagation of optical radiation (survey)," Radiophys. and Quantum Electron. 21, 755-774 (1978).
18. H. J. Hoffman, "Thermally induced phase conjugation by transient real-time holography: a review," J. Opt. Soc. Am. B 3, 253-273 (1986).
19. D. H. Chambers, T. J. Karr, J. R. Morris, P. G. Cramer, J. A. Viecelli, and A. K. Gautesen, "Linear theory of uncompensated thermal blooming in turbulence," Lawrence Livermore National Laboratory Report UCID-21696 (February 7, 1989).
20. T. J. Karr, "Thermal blooming compensation instabilities," J. Opt. Soc. Am. A 6, 1038-1048 (1989).
21. J. R. Morris, "Scalar Green's function derivation of the thermal blooming compensation instability equations," J. Opt. Soc. Am. A 6 , 1859-1862 (1989).
22. T. J. Karr, J. R. Morris, D. H. Chambers, J. A. Viecelli, and P. G. Cramer, "Perturbation growth by thermal blooming in turbulence," to be published in J. Opt. Soc. Am. B (May, 1990).
23. M. Abramowitz and I. Stegun, eds., Handbook of Mathematical Functions (Dover, New York, 1972), p. 435.
24. Ibid., p. 260.
25. E. S. Bliss, D. R. Speck, J. F. Holzrichter, J. H. Erkkila, and A. J. Glass, "Propagation of a high-intensity laser pulse with small-scale intensity modulation," Appl. Phys. Lett. 25, 448-450 (1974).
26. T. J. Karr, M. C. Rushford, J. R. Murray and J. R. Morris, "Measurement of the Stimulated Thermal Rayleigh Scattering Instability", LLNL Technical Report UCRL-99967, 24 April 1989; paper WJ-3, Summaries of Papers Presented at the Conference on Lasers and Electro-Optics, Baltimore MD, 24-28 April 1989 (Optical Society of American 1989 Technical Digest Series, Vol. 11, p. 230)

Table 1. Experimental parameters of selected STRS experiments that were compared with ORACLE computations

Experiment ID:	121888.72c	12989j.488
Blooming rate	87	64 waves/sec
time for 1 wave	12	16 ms
Whole-beam Fresnel number	64	57
Perturbation Fresnel number	0.45	1.0
Diffusion time ($\mathcal{D}\kappa^2$)	48	246 ms
Diffusion Fresnel number at 10 waves	2.7×10^{-2}	1.6×10^{-2}
Absorption optical depths	2.3	0.51

Initial perturbation amplitude	3% (simulation 2%)
Sample rate	60 Hz
CCD integration time	33 ms

Table 2. Comparison of experimental and asymptotic growth rates

Experiment ID	$k\Gamma z/2\pi$ (waves/sec)	N_P	N_A	Growth "rates" (Nepers/sec $^{1/2}$) Experiment fit	Asymptotic prediction (for 1/2 I_{max})
121888.72c	87	0.45	2.3	22	23
121888.62c	83	0.45	2.3	25	23
121888.52c	75	0.45	2.3	22	22
121888.42c	55	0.45	2.3	32	19
12989k.488	62	1.9	0.40	22	20
12989j.488	64	1.0	0.51	19	20
12989i.488	57	0.70	0.40	17	19
12989g.488	64	0.46	0.51	17	20
12989f.488	61	0.23	0.51	19	20
12989e.488	63	0.16	0.51	20	20

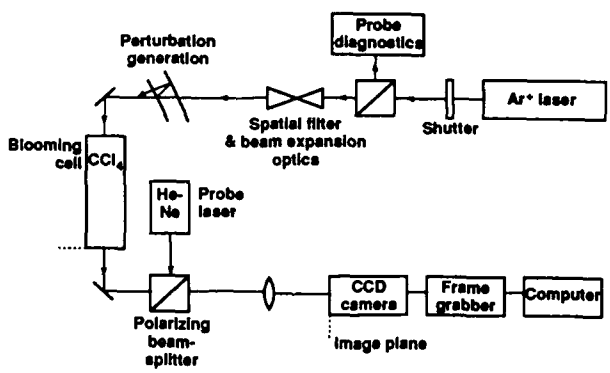


Fig. 1. Layout of the STRS experiment. The laser beam propagated from the top down to the bottom of the vertical CCl4 cell to keep the liquid stable against thermal buoyancy.

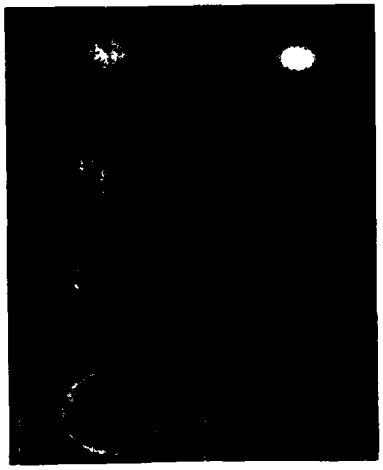


Fig. 2. Comparison of the experimentally measured and digitally computed irradiance profiles at the thermal-blooming cell exit window. The apparent ellipticity of the ORACLE irradiance profiles is an artifice of displaying square computational "pixels" on a video display designed for rectangular CCD camera pixels. The noise on the experimental irradiance profiles is primarily due to dirt which settled on the output window of the thermal blooming cell.

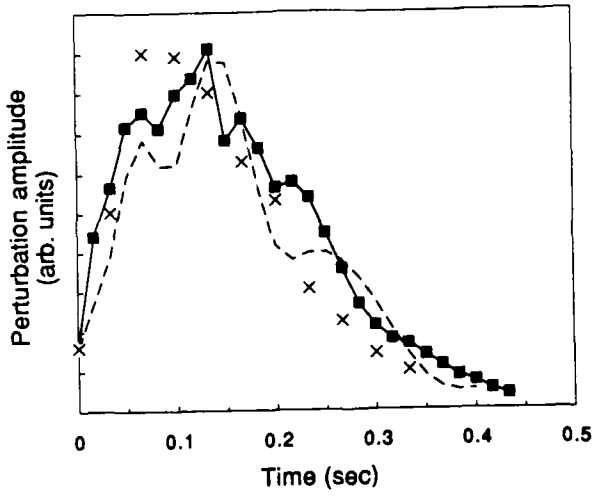


Fig. 3. Comparison of measured and calculated modulus of the intensity perturbation at the thermal-blooming cell exit window for the experiment with perturbation Fresnel number $N_P = 1.0$, absorption optical depth $N_A = 2.3$, and blooming rate 87 waves/sec. The experimental beam was 0.77W at the cell entrance, had a 2.7 mm FWHM, and had 2.6 fringes/mm. The curve with solid rectangles is the experimental data. The X's are the results of a calculation performed with the ORACLE time-dependent, three-space-dimensional wave-optics propagation code. The dashed curve is an analytic STRS theory calculation.

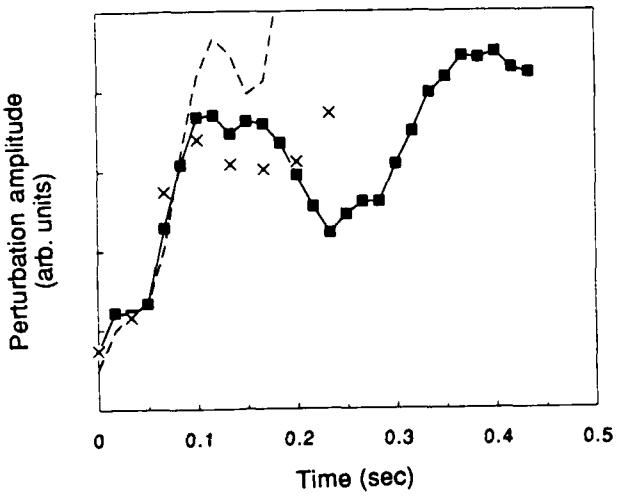


Fig. 4. Comparison of measured and calculated modulus of the intensity perturbation at the thermal-blooming cell exit window for the experiment with perturbation Fresnel number $N_P = 0.45$, absorption optical depth $N_A = 0.51$, and blooming rate 64 waves/sec. The experimental beam was 2.6 W at the cell entrance, had a 3.9 mm FWHM, and had 1.15 fringes/mm. The curve with solid rectangles is the experimental data. The X's are the results of a calculation performed with the ORACLE time-dependent, three-space-dimensional wave-optics propagation code. The dashed curve is an analytic STRS theory calculation.

PROPAGATION OF HIGH ENERGY LASER BEAMS THROUGH "CLEAR" AIR IN THE t^3 REGIME.

Shirish M. Chitanvis , Theoretical Division, T-12, *and*

Edward T. Salesky, CLS Division, CLS-5,

Los Alamos National Laboratory, Los Alamos, NM 87545.

ABSTRACT.

Large aperture, high energy gas lasers are expected to propagate in the t^3 thermal blooming regime through the atmosphere. Turbulence also has to be accounted for. We study the effect of atmospheric propagation on the beam using two models. The first model is a semi-analytic approach, in which we solve the differential equation for the mutual coherence function, which accounts for *both* thermal blooming and turbulence, using a generalization of the so-called aberrationless approximation. The resulting coupled ordinary differential equations were solved numerically. Secondly, we investigated the deterioration of the laser beam using an FFT (Fast Fourier Transform)-based code. The Strehl ratios obtained by both methods were compared, and we achieved good agreement, with errors of only a few percent.

Based on our analysis, we point out that shortening the pulse length and increasing the flux, while keeping the the fluence of the laser fixed, results in an increased Strehl ratio in the t^3 thermal blooming regime.

I. Introduction.

The effect of thermal blooming and turbulence on a high energy laser (HEL) beam propagating through a "clear" atmosphere has been studied for quite some time now. One of the first calculations was that of Wallace and Camac.[1] But in those days, only relatively low-power, CW lasers with a small diameter were available, so that it was the isobaric regime of thermal blooming that was investigated in great detail. But, for high-powered, pulsed lasers which have a wide diameter, the pulse length is much shorter than the acoustic transit time across the beam. Thus we are primarily in the t^3 blooming regime, where the the hydrodynamic effects do not have time to be established. The basic physics of the t^3 regime has been worked out by Wallace and Camac.[1]

For the purpose of obtaining general insight into the propagation problem, we developed a semi-analytic model, in which we derived an approximate differential equation for the mutual coherence function (MCF), which includes the effects of *both* blooming, as well as turbulence. An ansatz, which generalizes the aberrationless approximation,[2] is shown to solve the differential equation, provided a set of coupled ordinary differential equations (for the parameters used in the ansatz) is satisfied. This solution yields the Strehl ratio, which was compared successfully with the numerical simulations done with a propagation code, which we have named **MAXWELL**. This code propagates the beam using an FFT (Fast Fourier Transform) algorithm. It uses phase sheets to describe the effects of turbulence and blooming.

II. t^3 Thermal Blooming.

This term applies to the case when the acoustic transit time across the diameter of the beam is much longer than the pulse length. In other words, there is insufficient time for the acoustic effects to propagate and establish themselves during the pulse.

The linearized hydrodynamic equations, in the presence of electrostrictive effects (they are important for times less than a microsecond) are:

$$\frac{\partial \rho}{\partial t} \approx - \rho_0 \nabla \cdot \mathbf{v} \tag{2.1}$$

$$\rho_0 \frac{\partial \mathbf{v}}{\partial t} \approx - \frac{R}{\mu} \left(\rho_0 \nabla T \right) - T_0 \nabla \rho + \chi_0 \nabla \mathbf{E}^2 \tag{2.2}$$

$$\rho_0 C_v \frac{\partial T}{\partial t} \approx \alpha F \tag{2.3}$$

The third term on the right side of Eqn.(2.2) is the electrostrictive term. If we now drop all the spatial derivatives but those of the electric field and the temperature, we shall be in the short time, or, t^3 regime. The reason we retain the spatial derivative of the temperature is that the temperature rise is governed by the shape of the pulse (see Eqn. (2.2)) and this form is impressed upon the temperature profile instantaneously. We then obtain for the density:

$$\ddot{\rho} = \left[(\gamma - 1) \alpha t - \frac{4\pi \chi_0}{c} \right] \nabla^2 F \tag{2.4}$$

Here, we clearly see that the electrostrictive part is trying to focus the beam, while the other term is trying to defocus the beam. This blooming term is proportional to the time t, and at a certain moment t_{crit}, this term starts to dominate the focusing part of the beam:

$$t_{crit} = \frac{4\pi\chi_0}{c \alpha (\gamma - 1)} \tag{2.5}$$

Upon using $\chi_0 \sim 10^{-5}$, $\alpha \sim 3 \times 10^{-4}$ m^{-1}, $c = 3 \times 10^8$ m/s, $\gamma = 7/5$, we get $t_{crit} \sim 10$ ns. At this point, it might be tempting to say that if we could extract all the energy of the laser on this time scale, there would be no thermal blooming. But this would imply pushing up the laser flux very high, when air breakdown will be imminent. Henceforth, we shall not consider the electrostrictive term anymore.

If we have a laser pulse that is uniform in time, Eqn. (2.4) can be integrated trivially to obtain:

$$\rho(\mathbf{r},t) = \left[\frac{(\gamma - 1) \alpha t^3}{3!} \right] \nabla^2 F(\mathbf{r},t) \tag{2.6}$$

A derivation similar to ours may be found in the paper by Walsh and Ulrich.[3]

Using the Lorentz-Lorenz relation between the dielectric constant and the density, we obtain the change in the dielectric constant as:

$$\delta\varepsilon(\mathbf{r},z,t) = (\varepsilon_0 - 1) \frac{\rho(\mathbf{r},z,t)}{\rho_0} \tag{2.7}$$

where ρ_0 is the unperturbed density of air and where $\mathbf{r}$ refers to the x-y co-ordinates.

It must be noted that the distortion of the beam in the t^3 blooming regime is much less than occurs in the isobaric regime,[1] when the pulse length is much longer than the acoustic transit time across the beam. Eqn.(2.7) was inserted into the propagation code **MAXWELL**, which uses a phase-screen approach to model blooming. The transverse

Laplacian that occurs in the expression for the density change (Eqn.(2.6)) was represented by the usual five-point finite difference formula.

III. The Mutual Coherence Function.

In the absence of thermal blooming, the theory of calculating the mutual coherence function $\Gamma(z,\mathbf{r},\mathbf{r}') = \langle E(z,\mathbf{r}) E^*(z,\mathbf{r}') \rangle$ (where $\mathbf{r}$ refers to the x-y co-ordinates) is quite well-developed.[4] Here we shall sketch how to extend this formalism to the case when we have both turbulence and blooming. Furthermore, we shall give an approximate solution to the differential equation governing the mutual coherence function. This solution can be thought of as a generalization of the aberrationless solution to the paraxial equation.[2] The parameters of the ansatz are governed by a set of coupled ordinary differential equations. It displays at a glance the basic physics behind the interaction of thermal blooming and turbulence. We believe this is a new approach to a well-established problem.

The paraxial approximation to the scalar electromagnetic wave equation in a uniform medium is:

$$2ik \frac{\partial E(\mathbf{r},z)}{\partial z} + \nabla_r^2 E(\mathbf{r},z) = 0 \tag{3.1}$$

where $k = k_0 \varepsilon_0$. In the event that there are deviations $\delta\varepsilon(\mathbf{r},z)$ in the dielectric constant ε_0, the paraxial equation is "modified" thus:

$$2ik \frac{\partial E(\mathbf{r},z)}{\partial z} + \nabla_r^2 E(\mathbf{r},z) + k_0^2 \delta\varepsilon(\mathbf{r},z)\, E(\mathbf{r},z) \approx 0 \tag{3.2}$$

Now $\delta\varepsilon(\mathbf{r},z)$ in general could be due to both thermal blooming as well as turbulence:

$$\delta\varepsilon(\mathbf{r},z,t) = \delta\varepsilon_B(\mathbf{r},z,t) + \delta\varepsilon_T(\mathbf{r},z,t) \tag{3.3}$$

where the first term on the right hand side of Eqn.(3.3) refers to the change due to blooming, and the second term refers to to the change due to turbulence. $\delta\varepsilon_B$ is given by Eqn.(2.7), while $\delta\varepsilon_T$ is defined in terms of a correlation function:

$$\langle \delta\varepsilon_T(\mathbf{r},z,t)\ \delta\varepsilon_T(\mathbf{r}',z,t) \rangle = C_n^2(z,t)\, f(|\mathbf{r}-\mathbf{r}'|) \tag{3.4}$$

where various explicit forms for the right hand side of Eqn.(3.4) are given by Kolmogorov's theory.[7]

One can write down the complex conjugate form of Eqn.(3.2), and use it with Eqn.(3.2) to obtain an equation for the mutual coherence function $\Gamma(z,\mathbf{r},\mathbf{r}')$ defined above. Then, following the method outlined by Ishimaru, a few simple assumptions lead to the following approximate equation for $\Gamma(z,\mathbf{r},\mathbf{r}')$:

$$\begin{aligned} &ik \frac{\partial \Gamma(z,\mathbf{R},\bar{\mathbf{R}},t)}{\partial z} + \nabla_{\bar{R}} \cdot \nabla_R \Gamma(z,\mathbf{R},\bar{\mathbf{R}},t) + i\alpha\, \Gamma(z,\mathbf{R},\bar{\mathbf{R}},t) \\ &+ b(z,t) \left(\mathbf{R} \cdot \bar{\mathbf{R}}\right) \Gamma(z,\mathbf{R},\bar{\mathbf{R}},t) + ic\, \bar{\mathbf{R}}^2\, \Gamma(z,\mathbf{R},\bar{\mathbf{R}},t) = 0 \end{aligned} \tag{3.5}$$

where R and R bar represent central and difference co-ordinates respectively, and where:

$$b(z,t) = k^2 \left[\frac{(\varepsilon_0 - 1)(\gamma - 1)\alpha t^3}{3!\, \rho_0} \right] F_0 \exp(-\alpha z)\, \frac{32}{w^4(z)} \tag{3.6}$$

$$c(z) = \frac{3.28\, k^3\, C_n^2}{\xi^{1/3}} \tag{3.7}$$

where w(z,t) is the waist of the beam, and ξ is a typical length scale. In obtaining Eqns.(3.5)-(3.7), we have approximated F, which appears in Eqn.(2.6) by a Gaussian beam, expanded the Laplacian in powers of r, and retained only the lowest order terms in r. This is done keeping the aberrationless approximation in mind.[2] The second approximation made was in representing the turbulence term as a quadratic in the transverse difference co-ordinates. As Ishimaru points out, this is valid for propagation distances of the order of 10-100km.[7] However, we feel it is the *magnitude* of the turbulence rather than particular form ($r^{2/3}$ or r^2) that is crucial to the beam quality. At any rate, this approximation was made in the semi-analytic model to gain an insight into the problem. The numerical code does not appeal to such approximations.

The ansatz used for the solution is as follows:

$$\Gamma(z,\overline{\mathbf{R}}, \mathbf{R},t) = \Gamma_0 \exp(-s(z,t)\, R^2)\, \exp(-p(z,t)\, \overline{R}^2)\, \exp(\beta(z,t) \exp(-i\, q(z,t)\mathbf{R}\cdot\overline{\mathbf{R}}) \quad (3.8)$$

This ansatz has a very nice physical interpretation. s(z,t) describes the way in which the beam spreads, while p(z,t) describes the coherence of the beam, or, in other words, it yields the average size of the speckle spot created by turbulence. The third term describes the decay of the beam as it is absorbed and spreads. The fourth term is a phase factor.

This "Gaussian" ansatz clearly breaks down when the beam develops a doughnut shape, as the blooming sets in. But surprisingly, we have found that the Strehl ratio computed from this ansatz agrees quite well with that obtained from the numerical code even after the beam gets distorted into a non-Gaussian shape.

When this ansatz is substituted into Eqn.(3.5), we obtain a set of coupled ordinary differential equations that the parameters have to satisfy in order for the ansatz to be successful.[5] These equations are obtained by setting the coefficients of R^2, etc., equal to zero separately. Since the governing equations are coupled, this solution enables us to study the interaction of blooming and turbulence.

$$\frac{ds(z,t)}{dz} = \frac{2}{k}\, q(z,t)\, s(z,t) \quad (3.9)$$

$$\frac{dp(z,t)}{dz} = \frac{2}{k}\, (c + q(z,t)\, p(z,t)) \quad (3.10)$$

$$\frac{dq(z,t)}{dz} = \frac{1}{k}\, (-b - 4\, s(z,t)\, p(z,t) + q^2(z,t)) \quad (3.11)$$

$$\frac{d\beta(z,t)}{dz} = -\alpha + \frac{2\, q(z,t)}{k} \quad (3.12)$$

If we consider the case of propagation in vacuum, when there is no thermal blooming or turbulence, and the absorption coefficient α is zero, we notice that the differential equations are symmetric in s and p, which agrees with intuition.

Next, if we increase c, which is equivalent to increasing the turbulent structure constant C_n^2, we see from Eqn.(3.10) that p increases (thereby decreasing the transverse correlation length/ average speckle spot).

if we increase b (thermal blooming), q decreases, causing both s and p to be smaller, thereby implying that the beam spreads more (intuitively clear), but the average speckle size also grows, improving the correlation in the beam.

Thus we see that a certain amount of physics can be gleaned from Eqns.(3.9)-(3.12). In general, these equations describe an intimate interplay between turbulence and blooming.

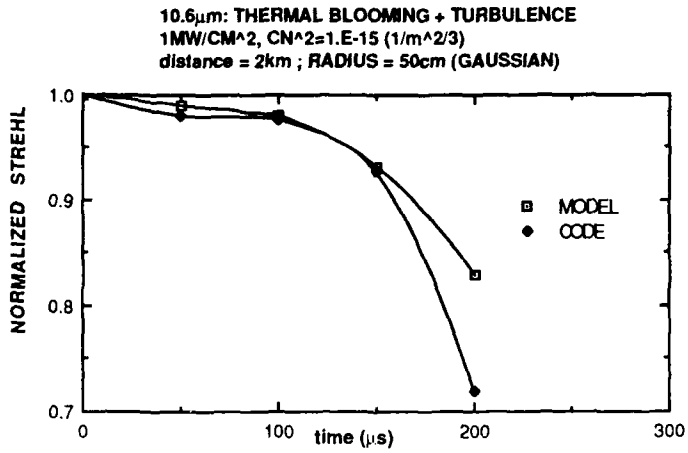
These equations were solved numerically, using an adaptive z-step to avoid problems with stiffness.

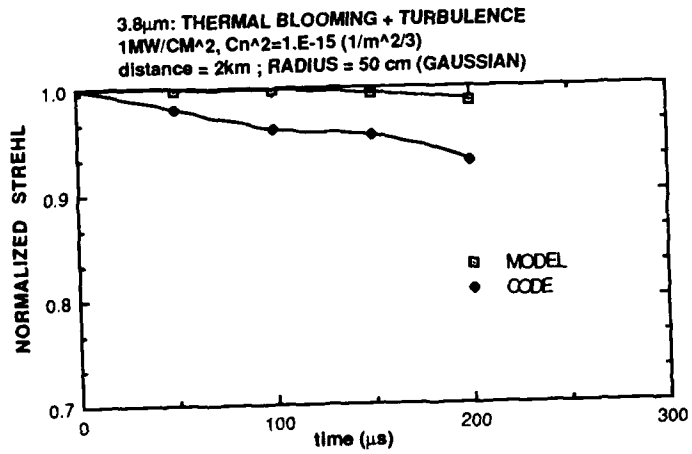
IV. Comparisons.

We compared the Strehl ratio S_{trehl} (from our model) defined to be:

$$S_{trehl} \equiv \frac{I_{distorted}(peak)}{I_{perfect}(peak)} \tag{4.1}$$

with the results from **MAXWELL**, with the turbulence and the (new) t^3 blooming modules turned on at 10.6μm and at 3.8μm. In these runs, we took a uniform atmospheric profile (purely for testing purposes), α = 0.3 km^{-1} at 10.6μm, and α = 0.02 km^{-1} at 3.8μm, an initial beam waist-size of 50cm, a flux level of 1.0 MW/cm^2, a pulse length of 200μs, and a propagation distance of 2km.





The average error is clearly < 10%.

It is interesting to note that the agreement at 10.6 microns is much better (on the average) with the semi-analytic model than at 3.8 microns. We believe that the reason for this is the sensitivity of the transverse coherence length to the wavelength.

Since there is a t^3 dependence, but only a linear dependence on the flux of the density perturbation due to blooming, there is a heightened dependence on the pulse lengths. Therefore, it is recommended that the lasers be operated at shorter pulse lengths and higher fluxes, while keeping the fluence fixed.

At this point we would like to note an idiosyncrasy of modeling blooming using a numerical scheme based on FFTs. If we want to propagate a "narrow" Gaussian beam, it is clear that we need many Fourier modes to represent this shape. Consequently, we need a large number of grid points in order to perform the propagation calculation correctly. This requirement is independent of the constraints on the number of points required to do the FFT to a given accuracy.[2]

V. Conclusions.

We developed a semi-analytic model to study the combined effect of thermal blooming and turbulence on the mutual coherence function. We compared Strehl ratios from our model with an FFT-based propagation code. We recommend that our semi-analytic model be used initially to get a quick feel for the deterioration of the Strehl ratio.

In fact, based on our calculations, we point out that in the t^3 regime, it is desirable to operate a high energy laser at shorter pulse lengths and higher fluxes (while keeping the fluence fixed), which helps maintain a higher Strehl ratio.

---

[1] J. Wallace and M. Camac, *J. Opt. Soc. Am.*, **60**, 1652 (1971).

[2] P.W. Milonni and J.H. Eberly, *Lasers*, (J. Wiley & Sons, N.Y. 1988).

[3] J.L. Walsh and P.B. Ulrich, *Laser beam propagation in the atmosphere*, J.W. Strohben, Ed., (Springer-Verlag, Berlin, 1978) pp. 133-144.

[4] A. Ishimaru, *Wave propagation and scattering in Random Media*, Vol. II, (Academic Press, N.Y. 1978).

[5] J. R. Ackerhalt, D.O. Ham, A.V. Nowak, C.R. Phipps and S.J. Thomas, IEEE J. Quant. Elec., **QE-19**, 1120, (1983).

SINGLE AND MULTIAPERTURE ZERNIKE CORRELATIONS IN THE ATMOSPHERIC TURBULENCE PROBLEM

J.Stone and P.H.Hu
Advanced Programs/Rocketdyne Division
Rockwell International Corporation
6633 Canoga Ave. FA04
Canoga Park, CA 91304

Abstract

We present a unified method of calculating covariances in atmospheric statistics. All quantities are expressed in the spatial wavevector representation. This allows correlation functions to be written down even for singular Kolmogorov statistics thereby avoiding the algebraic complexities of dealing with structure functions. A pseudo-three dimensional correlation function for the refractive index is defined which forms the basis for the wavevector approach. This function is used, together with a displacement relation for Fourier transforms to extend the Zernike covariances derived by Noll [R.J. Noll, J. Opt. Soc. Am. **66**, 207 (1976)] to the multiaperture case. Integrations required are compared with the direct coordinate space method.

I.Introduction

The extensive body of work of Tatarski[1] and the many who followed has made it possible to envision wavefront correction to compensate for atmospheric turbulence even when measurements are applied in some direction or configuration different from that which must be corrected. This is true because of statistical correlations which relate turbulence at different spatial locations. The analysis of Kolmogorov[2] showed that for a range of spatial separations bounded by inner and outer scales, the refractive index variance due to turbulence at two points is proportional to the 2/3 power of the separation, with the proportionality constant being determined by a strength parameter called the structure constant.

Because of variations in the atmosphere with altitude, the structure constant C_n^2 is a function of height, but otherwise the atmosphere can be assumed to be locally homogeneous and isotropic, allowing us to define a structure function D_n relating the refractive index $n(\vec{r})$ at different spatial points $\vec{r}_1$ and $\vec{r}_2$,

$$D_n(r_1 - r_2) \equiv 2 < (n(r_1)^2 - n(r_1)n(r_2)) > \tag{1}$$

which, in the Kolmogorov statistics is the quantity having the 2/3 power dependence.

One might expect, using Eq (1), to be able to define also the correlation function or covariance of the refractive index. However, using the physically reasonable assumption that the correlation should vanish for infinite separation, the covariance at any finite separation would have to be infinite. Therefore, although it can be seen that this situation in really an artifact of failing to account for the outer scale properly, as a practical matter, we cannot use covariances directly when applying pure Kolmogorov statistics.

The *spectral density function* for Kolmogorov statistics is nonetheless quite well defined, being, as is well known, proportional to the spatial wavevector κ raised to the -11/3 power. The singularity at the origin becomes an *integrable* singularity for most quantities of interest for applications and the potential advantage of working in the spatial wavevector space (κ space) can be significant.

In this paper we review the relationship between the structure function and spectral density formalisms and show, using some simple examples, how the latter formalism can be used to greatest advantage. We begin in Sec. II by considering the defining integrals relating the coordinate space and κ space quantities for both the refractive index and its integral along an optical path (the geometric optics phase.) We show that an approximate "pseudo-three dimensional" spectral density function[3] can be used for the refractive index to calculate all quantities depending on the cumulative refractive index. This function is derived from the exact full three dimensional spectral density function and allows us to incorporate (and give additional justification for) the usual assumption that refractive index correlations along the optical path can be neglected.

Then, as an example, we consider the Zernike coefficients of one or more wavefronts as statistical quantities whose covariance is to be calculated. Noll[4] calculated the covariances of the same or different Zernike modes for a plane wave propagating through a single aperture using simple expressions for the transforms of the Zernike polynomials involving Bessel functions. We are able to apply a κ space analysis which generalizes his development and leads to results for multiple apertures and for anisoplanatism of the various modes (Sec.III). Finally, we use the κ space analysis to find coordinate space (piston removed) correlation functions for partly corrected wavefronts (Sec.IV). Removal

of piston of the wavefront over a defined aperture makes the correlation function, which would otherwise be singular for Kolmogorov statistics, well-behaved.[5] With the analysis given here, any number of Zernike modes can be removed.

II. Spectral Densities and Structure Functions

The statistics of refractive index variations are important in optics problems because of the aberrations induced on a beam propagating through a turbulent medium. Structure functions and spectral densities for both the refractive index and the phase are considered below. The "pseudo-three dimensional" refractive index correlation function[3] is derived, a quantity which proves to be extremely advantageous in the phase aberration problem, compared with approaches based on a phase structure function obeying a 5/3 power law.

The refractive index in two different spatial points can be related, in an "ensemble" of similar atmospheres (with $\langle \cdots \rangle$ denoting the ensemble average), by the structure function

$$D_n(\vec{r}_1,\vec{r}_2) = \langle [n(\vec{r}_1) - n(\vec{r}_2)]^2 \rangle \tag{2}$$

If we assume that the atmosphere is homogeneous and isotropic, this can be written in the equivalent form

$$D_n(|\vec{r}_1 - \vec{r}_2|) = 2[C_r(0) - C_r(|\vec{r}_1 - \vec{r}_2|)] \tag{3}$$

where

$$C_r(|\vec{r}_1 - \vec{r}_2|) = \langle n(\vec{r}_1) n(\vec{r}_2) \rangle \tag{4}$$

or in terms of a spectral density function $\Phi_n(\vec{\kappa})$, dependent only on the magnitude of κ, as

$$D_n(\vec{r}) = 2\int d^3\kappa \quad \Phi_n(\vec{\kappa})[1 - \exp(2\pi i \vec{\kappa}\cdot\vec{r})] \tag{5}$$

The fundamental defining quantity for atmospheric turbulence is the structure constant $C_n^2(h)$, which defines the strength of turbulence as a function of altitude under a given set of conditions[1]. It provides the proportionality constant for the $r^{2/3}$ dependence predicted for Eq (1) by Kolmogorov statistics, which together with Eq (5), leads to

$$C_n^2(h) r^{2/3} = 2\int d^3\kappa \quad \Phi_n(\vec{\kappa})[1 - \exp(2\pi i \vec{\kappa}\cdot\vec{r})] \tag{6}$$

We can now solve Eq (6) to show that a spectral density function Φ_n proportional to $\kappa^{-11/3}$ gives the proper $r^{2/3}$ dependence for D_n. We note that if the correlation function itself existed, it would be given by just the second term of Eq (6). However, the integrand is proportional to $\kappa^{-5/3}$ and therefore has a non-integrable singularity at the origin. This confirms the impossibility, already noted, of defining the correlation function for the Kolmogorov distribution. With an appropriate low frequency cutoff function $g(\kappa)$, we can, however, write

$$\langle n(\vec{r}_1) n(\vec{r}_2) \rangle = \int d^3\kappa \quad C_n^2(h) C_A g(\kappa) \kappa^{-11/3} \exp(2\pi i \vec{\kappa}\cdot[\vec{r}_1 - \vec{r}_2]) \tag{7}$$

In the limit $g(\kappa) = 1$, evaluating the proportionality constant in Φ_n itself requires, after we do the angular integrations in Eq (6), evaluation of an integral

$$I_{II} = \int_0^\infty y^{-5/3}\left(1 - \frac{\sin y}{y}\right) dy = \frac{9}{20}\Gamma\left(\frac{1}{3}\right) \tag{8}$$

whose individual terms are divergent. Here $y = 2\pi\kappa r$. The result shown in Eq (8) is derived by first considering the following integral

$$I'_{II} \equiv \int_0^\infty y^{-\lambda}\left(e^{-\mu y} - \frac{\sin y}{y}\right) dy \tag{9}$$

The two terms can, for suitable values of λ and μ, be evaluated using the respective relationships[6]

$$\int_0^\infty x^\nu e^{-\mu x} dx = \mu^{-(\nu+1)}\Gamma(\nu+1) \text{ and } \int_0^\infty x^{\nu-1}\sin x\,dx = \Gamma(\nu)\sin(\pi\nu/2) \tag{10}$$

where for the first integral $Re\quad \mu > 0$, $Re\quad \nu > -1$ whereas, for the second, $Re\quad \nu < 1$

The restrictive conditions guarantee convergence of the two integrals at 0 and at ∞ and there is a common region of convergence for $-1 < Re\quad \nu < 1$. This allows us to use analytic continuation to obtain results when $\nu = -\lambda = -5/3$, outside the region of convergence for the separate terms. Therefore the integral in Eq (9) is given by

$$I'_{II} = \mu^{2/3}\Gamma(-2/3) - \Gamma(-5/3)\sin(5\pi/6) \tag{11}$$

The first term simply vanishes in the limit $\mu = 0$, leading to the result shown in Eq(8). So the spectral density for the refractive index is given by

$$\Phi_n(\vec{\kappa}) = C_A C_n^2(h)\kappa^{-11/3} \tag{12}$$

where we can denote C_A, which has the value

$$C_A = [8\pi I_{II}(2\pi)^{2/3}]^{-1} = \frac{5}{36}2^{1/3}\frac{1}{\pi^{5/3}\Gamma(1/3)} = .0096932$$

the atmospheric spectral constant, since it converts the structure constant into an appropriate constant for the spectral density. C_A is found to be identical to the combination of constants $C_1C_3/(2C_2)$ used in Ref [3].

In geometric optics, a phase can be determined from the refractive index variations from the relationship

$$\phi(\vec{r}, H) = k\int_0^H n(\vec{r}, z)dz \tag{13}$$

where k is the wavevector of the light. We have assumed that z is the propagation direction and let $\vec{r}$ represent the two remaining (transverse) coordinates. A phase correlation can be written in the form

$$< \phi(\vec{r}_1, H)\phi(\vec{r}_2, H) >= k^2\int_0^H\int_0^H < n(\vec{r}_1, z)n(\vec{r}_2, z') > dz\,dz' \tag{14}$$

Because we are typically interested in very large propagation distances, the range of integration for Δz (assuming we go to sum and difference coordinates in the two propagation distances) is effectively infinite and hence refractive index components with wavevectors significantly different from $\kappa_z = 0$ will give a very small net contribution. We therefore replace $|\kappa|$ by $[\kappa_x^2 + \kappa_y^2]^{1/2}$. Hence κ_z now appears only in the complex exponent and we identify this remaining expression involving κ_z as

$$\int_{-\infty}^{\infty} d\kappa_z \exp(-i2\pi\kappa_z(h_1 - h_2)) = \delta(h_1 - h_2) \tag{15}$$

with the result that the refractive index correlation can, for purposes of calculating the phases for this propagation geometry, be replaced by

$$< n(\vec{r}_1, h_1)n(\vec{r}_2, h_2) >= C_A\delta(h_1 - h_2)C_n^2(h_1)\int d^2\kappa \quad g(\kappa)\kappa^{-11/3}\exp(i2\pi\vec{\kappa}\cdot(\vec{r}_1 - \vec{r}_2)) \tag{16}$$

The vectors appearing here are now all transverse quantities. The use of Eq (16) to calculate phases will prove very much easier than the use of structure functions which require us to put everything into the form of *differences* of phase covariances such as those in Eq (14). With Eq(16) we can directly evaluate whatever covariances are naturally generated in the problem. Two such problems are considered in the following to sections. Nevertheless, the approach is completely *equivalent* to the usual approach using structure functions. We show this in the Appendix and demonstrate that Eq(16) is also *derivable* by standard approaches using structure functions.

III. Zernike Correlations for Multiple Apertures

Zernike modes constitute an orthogonal set on the unit circle. Therefore we can expand an arbitrary wavefront in a series of these functions

$$\phi(r_i + R\rho) = \sum_q a_q^i Z_q(\rho) \tag{17}$$

where the expansion coefficients are given by[4]

$$a_q^i = \int d^2\rho_i W(\rho_i)\phi(\vec{r}_i + R\vec{\rho}_i)Z_q(\vec{\rho}_i) \tag{18}$$

where $W(\rho) = 1/\pi$ for $\rho \le 1$

$$W(\rho) = 0 \text{ for } \rho > 1$$

This represents a 3-d integral, when the phase accumulation integral (Eq (13)) is included. With no further analysis, the covariance $< a_q^i a_{q'}^j >$, including *two* coefficients and an accounting for the proper phase correlations, would therefore be an integral of even higher dimension.

Analysis of this problem in κ space leads to a substantial reduction in the problem. The covariance, expressed in terms of direct space integrals is

$$< a_q^i a_{q'}^j >= \int d^2\rho_i \int d^2\rho_j W(\rho_i)Z_q(\rho_i)W(\rho_j)Z_{q'}(\rho_j) < \Phi(r_i + R\rho_i)\Phi(r_j + R\rho_j) > \tag{19}$$

where

$$< \Phi(\vec{r}_i + R\vec{\rho}_i)\Phi(\vec{r}_j + R\vec{\rho}_j) >= k^2 \int_0^H \int_0^H dh_1 dh_2 < n_1(\vec{r}_i + R\vec{\rho}_i, h_1)n_1(\vec{r}_j + R\vec{\rho}_j, h_2) > \tag{20}$$

and, using Eq (16),

$$< \Phi(\vec{r}_i + R\vec{\rho}_i)\Phi(\vec{r}_j + R\vec{\rho}_j) >= C_A k^2 \int_0^H dh_1 C_n^2(h_1)$$

$$\times \int d^2\kappa \quad g(\kappa)\kappa^{-11/3} \exp(i2\pi\vec{\kappa}\cdot(r_i - r_j)) \exp(i2\pi\vec{\kappa}\cdot R\vec{\rho}_i) \exp(-i2\pi\vec{\kappa}\cdot R\vec{\rho}_j) \tag{21}$$

We can also express the Zernike pieces in κ (κ_i and κ_j) space as

$$W(\rho_i)Z_q(\rho_i) = \int d^2\kappa_i \exp(-i2\pi\vec{\kappa}_i\cdot\vec{\rho}_i)Q_q(|\kappa_i|, \phi_i)$$

$$W(\rho_j)Z_{q'}(\rho_j) = \int d^2\kappa_j \exp(+i2\pi\vec{\kappa}_j\cdot\vec{\rho}_j)Q_{q'}^*(|\kappa_j|, \phi_j) \tag{22}$$

Here the Q functions are[4]

$$Q_{n,m,t}(\kappa, \phi) = K_{n,m}\frac{J_{n+1}(2\pi\kappa)}{\pi\kappa} i^m 2^{1/2}\{\delta_{t,1}\cos m\phi + \delta_{t,-1}\sin m\phi\} \tag{23}$$

where $J_{n+1}(x)$ is Bessel function of first kind and

$$K_{n,m} = (n+1)^{1/2}(-1)^{(n-m)/2} \quad \text{for } m \neq 0$$

$$K_{n,0} = (n+1)^{1/2}(-1)^{n/2}2^{-1/2}$$

All dependence on ρ_i or ρ_j is isolated in the complex exponentials so that the $d^2\rho_i$ and $d^2\rho_j$ integrals just give (2d) delta functions $\delta(\vec{\kappa}_i - \vec{\kappa}R)$ and $\delta(\vec{\kappa}_j - \vec{\kappa}R)$, respectively.

Applying these δ function relations leads to

$$< a_q^i a_{q'}^j >= C_A k^2 \int_0^H dh C_n^2(h) \int d^2\kappa \quad \exp(i2\pi\vec{\kappa}\cdot(\vec{r}_i - \vec{r}_j)) g(\kappa)\kappa^{-11/3} Q_q(\kappa R, \phi) Q_{q'}^*(\kappa R, \phi) \tag{24}$$

The final double κ – space integral can be simplified to a single a space integral involving a (third) Bessel function by carrying out the *angular* integration. The dot product in the exponential is expressed explicitly in terms of angles $\vec{\kappa}\cdot(\vec{r}_i - \vec{r}_j) = |\kappa|\,|(r_i - r_j)|\cos(\theta - \phi)$ where θ is the angle in the direct space. The dependence of Q_q and $Q_{q'}$ on $e^{\pm im\phi}$ and $e^{\pm im'\phi}$ is also introduced, allowing us to use the integral formula

$$J_p(z) = \frac{1}{2\pi}\int_0^{2\pi} \exp(-ip\phi + iz\sin\phi)d\phi \tag{25}$$

to replace the angular integral. The covariances can now be expressed in terms of integrals of the form[3]

$$\int_0^\infty \kappa^{-14/3} J_{n+1}(\kappa R) J_{n'+1}(\kappa R) J_{m+m'}(\kappa|r_i - r_j|)d\kappa \quad \text{or} \quad \int_0^\infty \kappa^{-14/3} J_{n+1}(\kappa R) J_{n'+1}(\kappa R) J_{|m-m'|}(\kappa|r_i - r_j|)d\kappa \tag{26}$$

combined with various angular factors[3], which are sines or cosines of $(m \pm m')\theta$. The use of the κ space analysis has reduced the result to the evaluation of a single height integral and a single κ space integral. The expressions in Eq(26) can also be written in terms of HJ3 functions defined in Ref[3], where

$$HJn(\lambda, N_1, N_2, \ldots N_n, A_1, A_2, \ldots A_n) \equiv \int_0^\infty x^{-\lambda} J_{N_1}(A_1 x) J_{N_2}(A_2 x) \ldots J_{N_n}(A_n x)dx$$

For aperture separations approaching zero, Noll's[4] results are reproduced.

IV. Correlation Functions for Partly Corrected Wavefronts

The concern with the statistics of turbulence is often connected with the problem of providing compensating aberrations on a beam to be propagated through a region of atmosphere. At some stage in the process, these corrections may be only partial, in that our measurements will sometimes fail to detect aberrations, invariably piston, but often other low order modes.[5] The appropriate atmospheric correlation functions when the first p lower order Zernike modes have been taken out can be written in the form

$$C(\vec{r}_1, \vec{r}_2) = \left\langle \left[\phi(\vec{r}_1) - \sum_{q=0}^{p} a_q Z_q(\vec{\rho}_1)\right]\left[\phi(\vec{r}_2) - \sum_{q=0}^{p} a_q Z_q(\vec{\rho}_2)\right]\right\rangle \tag{27}$$

This expression can be reduced to explicit mathematical form using the techniques developed for Zernike covariances in the preceding section. It is convenient before proceeding to rearrange the expression so that the infinities associated with the Kolmogorov statistics are canceled. This only requires that we remove at least the piston ($p \geq 0$), so we can write

$$C(\vec{r}_1, \vec{r}_2) = \langle\phi(\vec{r})^2 - a_0^2\rangle - (1/2)D_p(\vec{r}_1 - \vec{r}_2) + \sum_{q=1}^{p}\sum_{q'=1}^{p}\langle a_q a_{q'}\rangle Z_q(\vec{\rho}_1) Z_{q'}(\vec{\rho}_2)$$

$$+\left\langle [a_0 - \phi(r_1)]\left[\sum_{q=0}^{p} a_q Z_q(\vec{\rho}_2)\right]\right\rangle + \left\langle [a_0 - \phi(r_2)]\left[\sum_{q=0}^{p} a_q Z_q(\vec{\rho}_1)\right]\right\rangle \tag{28}$$

In regrouping this expression, we have added in the null expressions $a_0^2 - a_0^2$ and

$$\langle\phi(\vec{r})^2\rangle - \phi(\vec{r}_1)\phi(\vec{r}_2)\rangle - (1/2)D_p(\vec{r}_1 - \vec{r}_2)$$

the latter corresponding to the definition of the phase structure function[1,7] (see also Appendix). The first term in Eq(28) is just the piston-removed phase variance[4], while the Zernike covariances in the third term are the (single aperture) quantities discussed in the last section. The only *new* quantities here are the covariances of the phases with the Zernike coefficients in the last two terms. In order to evaluate these we write down in analogy with Eq(19)

$$\langle \phi(\vec{\rho}_1 R) a_q \rangle = \int d^2\rho_2 W(\rho_2) Z_q(\rho_2) < \phi(R\rho_1)\phi(R\rho_2) > \tag{29}$$

$$= \int d^2\rho_2 C_A k^2 \int_0^H dh_1 C_n^2(h_1) \int d^2\kappa \quad g(\kappa)\kappa^{(-11/3)} \exp(2\pi i \vec{\kappa}\cdot(R\vec{\rho}_1 - R\vec{\rho}_2)$$

$$\times \int d^2\kappa_2 \exp(+i 2\pi \vec{\kappa}_2 \cdot \vec{\rho}_2) Q_q^*(|\kappa_2|, \phi_2) \tag{30}$$

Finally, applying the ρ_2 integration and the resulting delta function, we find the following form for the covariance

$$\langle \phi(\vec{\rho}_1 R) a_q \rangle = C_A k^2 \int_0^H dh C_n^2(h) \int d^2\kappa \quad \exp(2\pi i \kappa R \rho_1 \cos(\phi - \theta_1)) g(\kappa)\kappa^{-11/3} Q_q^*(\kappa R, \phi) \tag{31}$$

We have used the explicit form of the dot product in terms of the angle $\alpha \equiv \phi - \theta_1$ between $\vec{\kappa}$ and $\vec{\rho}_1$. We substitute $Q_{n,m,l}$ from Eq(23) for Q_q. Now we carry out the angular κ integration using $\alpha + \pi/2$ as the variable of integration and find, using the integral representation of the Bessel function,

$$\langle \phi(\vec{\rho}_1 R) a_q \rangle = 2\pi C_A \int_0^H dh C_n^2(h) \int_0^\infty d\kappa \kappa g(\kappa)\kappa^{-11/3} J_m(2\pi\kappa\rho_1 R)\{J_{n+1}(2\pi\kappa R)/[\pi\kappa R]\} K_{n,m}[\delta_{l,1}\cos m\theta_1 + \delta_{l,-1}\sin m\theta_1] \tag{32}$$

Now with the change of variables $\kappa' = 2\pi\kappa R$, we can substitute this result into Eq (28) to obtain

$$C(\vec{r}_1, \vec{r}_2) = \sum_{q=1}^{p}\sum_{q'=1}^{p} < a_q a_{q'} > Z_q(\vec{\rho}_1) Z_{q'}(\vec{\rho}_2) + \left[(2R)^{5/3} k^2 \int_0^H C_n^2(h) dh \right] \{ -\frac{1}{2} 2.915 \quad 2^{-8/3} |\vec{\rho}_1 - \vec{\rho}_2|^{5/3} + 0.4391 \tag{33}$$

$$- \sum_{q=0}^{p} Z_q(\rho_2) \hat{K}_{n,m} \hat{A}_m(l, \theta_1) \times [HJ2(11/3, n+1, m, 1, \rho_1) - 2\delta_{m0} HJ2(14/3, n+1, 1, 1, 1)]$$

$$- \sum_{q=0}^{p} Z_q(\rho_1) \hat{K}_{n,m} \hat{A}_m(l, \theta_1) \times [HJ2(11/3, n+1, m, 1, \rho_2) - 2\delta_{m0} HJ2(14/3, n+1, 1, 1, 1)]\}$$

The constants appearing are defined as[8]

$\hat{A}_m(l, \theta) = \delta_{l,1}\cos m\theta + \delta_{l,-1}\sin m\theta$ and

$\hat{K}_{n,m} = 2K_{n,m} C_A \pi^{8/3}$

We note that the integral over $C_n^2(h)$ appearing in Eq(33) can be conveniently replaced by using the quantity r_0 defined by Fried[9], which gives the integral (including the accompanying k^2 factor) as $2.362\, r_0^{-5/3}$.

V. Appendix

The usual treatment of phase fluctuations utilizes the *phase* structure function, relating the phase at two different points in a wavefront propagated through turbulence is defined as

$$D_\phi(\vec{r}_1, \vec{r}_2) = \langle [\phi(\vec{r}_1) - \phi(\vec{r}_2)]^2 \rangle \tag{34}$$

The invariance properties lead us to the alternative form

$$D_\phi(\vec{r}_1, \vec{r}_2) = 2 < \phi_1(\vec{r})^2 > - 2 < \phi(\vec{r}_1)\phi(\vec{r}_2) > \tag{35}$$

which, on substitution of Eqs (13) and (16) leads to the relation

$$D_\phi(\vec{r}_1,\vec{r}_2) = 2C_A k^2 \int_0^H C_n^2(h)dh \int d^2\kappa \quad \kappa^{-11/3}(1-\exp(2\pi i\vec{\kappa}\cdot[\vec{r}_1-\vec{r}_2])) \tag{36}$$

$$= 2C_A I_{III}(11/3)(2\pi)^{8/3}|\vec{r}_1-\vec{r}_2|^{5/3}k^2\int_0^H C_n^2(h)dh \tag{37}$$

where the last relationship is for $g(\kappa) = 1$ and

$$I_{III}(Q) = \int_0^\infty dx x^{-Q+1}[1-J_0(x)] = \frac{\pi}{2^{Q-1}[\Gamma(Q/2)]^2\sin[\pi(Q-2)/2]}$$

Note that the combination $I_{III}(11/3)(2\pi)^{8/3}$ coincides with the ratio C_2/C_3 in Ref[3].

A more conventional approach[7] to the calculation of the structure function proceeeds from Eq (34) by adding and subtracting terms as required to obtain combinations of refractive indices corresponding to structure functions

$$D_\phi(\vec{r}_1,\vec{r}_2) = \frac{k^2}{2}\int_0^H dz_1 \int_0^H dz_2(\{F_1(\vec{r}_1,\vec{r}_2,z_1,z_2)-F_2(\vec{r}_1,\vec{r}_2,z_1,z_2)\}) \tag{38}$$

where

$$F_1(\vec{r}_1,\vec{r}_2,z_1,z_2) = \langle[n(\vec{r}_1,z_1)-n(\vec{r}_2,z_2)]^2+[n(\vec{r}_2,z_1)-n(\vec{r}_1,z_2)]^2\rangle$$

and

$$F_2(\vec{r}_1,\vec{r}_2,z_1,z_2) = \langle[n(\vec{r}_1,z_1)-n(\vec{r}_1,z_2)]^2+[n(\vec{r}_2,z_1)-n(\vec{r}_2,z_2)]^2\rangle \tag{39}$$

The two refractive index terms in each of the two functions F_1 and F_2 are equal since the refractive index structure function depends only on the distance between the points and on their average altitude. As a consequence we can write

$$D_\phi(\vec{r}_1,\vec{r}_2) = k^2\int_0^H d\bar{z}\int_{-H}^H d(\Delta z)\left\{D_n\left([|\vec{r}_1-\vec{r}_2|^2+(\Delta z)^2]^{1/2},\bar{z}\right)-D_n(\Delta z,\bar{z})\right\} \tag{40}$$

where we have transformed to average height and height difference coordinates $\bar{z}$ and Δz. With $D_n = C_n^2(\bar{z})|\vec{r}_1-\vec{r}_2|^{2/3}$, the integrand is sufficiently small when $\Delta z \gg |\vec{r}_1-\vec{r}_2|$ to allow replacing the limits on Δz by $(-\infty,+\infty)$ with the result that

$$D_\phi(\vec{r}_1,\vec{r}_2) = |\vec{r}_1-\vec{r}_2|^{5/3}I_I(1/3)k^2\int_0^H d\bar{z}C_n^2(\bar{z}) \tag{41}$$

where[10]

$$I_I(\alpha) = \int_{-\infty}^{+\infty}[(x^2+1)^\alpha-(x^2)^\alpha]dx = \frac{2\alpha}{2\alpha+1}\frac{\Gamma(1/2)\Gamma(1/2-\alpha)}{\Gamma(1-\alpha)} \tag{42}$$

and the variable x in the integrand corresponds to the dimensionless ratio $\Delta z/|\vec{r}_1-\vec{r}_2|$. The value of the constant $I_I(1/3)$ is approximately 2.91, the constant C_1 of Ref [3]. The equivalence to the analytic form $[2^{1/3}\Gamma^2(1/6)]/[5\Gamma(1/3)]$ given there can be established using $\Gamma(1/2) = \pi^{1/2}$ and $\Gamma(2z) = (2\pi)^{-1/2}2^{2z-1/2}\Gamma(z)\Gamma(z+1/2)$ with z=1/6 (the Gamma function duplication formula[6].)

The result in Eq (41) is in fact identical to Eq (37) because of the equality

$$I_I(1/3)I_{II} = \pi I_{III}(11/3) \tag{43}$$

readily verified using the Γ function reflection formula.[6] This shows that the approach using the κ space integration and the replacement of the κ_z factors by a δ function in h is completely equivalent mathematically to the conventional approach, even though it is much easier to use than the usual approach.

VI. References

1. V.I. Tatarski, *Wave propagation in a turbulent medium* (McGraw-Hill, New York, 1961)
2. A.N. Kolmogorov, Dokl. Akad. Nauk SSSR **30**, 299 (1941); A.N. Kolmogorov, J. Fluid Mech. **13**, 82 (1962); For a review of recent work on Kolmogorov statistics see U. Frisch and S.A. Orszag, "Turbulence: challenges for theory and experiment", *Physics Today*, Jan.,1990, p. 24
3. P.H. Hu, J. Stone, and T.Stanley, "Application of Zernike polynomials to atmospheric propagation problems", J.Opt.Soc. Am. A **6**, 1597-1608 (1989)
4. R.J. Noll, "Zernike polynomials and atmospheric turbulence", J.Opt.Soc. Am. 66, 207-211 (1976)
5. G.A. Tyler, "On the utility of Gegenbauer polynomials in atmospheric turbulence calculations: evaluation of piston, tilt removed phase cross covariance", Rep TR-635 (the Optical Sciences Company, Placentia, California, 1985)
6. M. Abramowitz and I.A. Stegun, *Handbook of Mathematical Functions*, p. 255 and p.260 (Dover, New York, 1965)
7. J.W. Goodman, *Statistical Optics*, p. 361-464 (Wiley, New York, 1985)
8. The constant $\hat{K}_{n,m}$ defined here differs by a factor of π from that defined in Ref [3].
9. D.L. Fried, "Statistics of a geometric representation of wavefront distortion", J.Opt.Soc.Am. **55**, 1427-1435 (1965)
10. D.L. Fried, "Diffusion analysis for the propagation of mutual coherence", J.Opt.Soc.Am. **58**, 961-969 (1968)

NONLINEAR OPTICAL EFFECTS IN LASER IRRADIATED MICRON-SIZED DROPLETS

R. L. Armstrong
Physics Department, New Mexico State University, Las Cruces, NM 88003

Abstract

Nonlinear optical effects, notably stimulated Raman scattering and fluorescence/lasing, exhibit unique behavior in small droplets due to the presence of morphology-dependent resonances. This talk describes recent results in this area.

Introduction

A variety of nonlinear optical effects, notably stimulated Raman scattering (SRS) and fluorescence/lasing, have been observed in transparent micron-sized droplets irradiated by intense pulsed laser beams. These effects exhibit characteristics not found in bulk, including SRS and fluorescence spectra consisting of sharp, quasi-periodic peaks, and temporal delays in the initiation of SRS and lasing emission. The unique optical properties of small droplets arise from the presence of high-Q resonances (so-called morphology dependent resonances or MDR's) in the response of the droplet to electromagnetic radiation. Two distinct classes of resonances occur, input resonances where the incident radiation excites an MDR, and output resonances where the droplet excitation (e.g., SRS or fluorescence) couples to an MDR. Double resonance conditions occur when both input and output fields couple to MDR's. In this paper, we present some recent results illustrating the spectral, temporal, and spatial properties of laser-droplet systems.

Output Resonance SRS

Output resonances have been observed in SRS,[1] and lasing.[2] The experimental arrangement used to observe these resonances is shown in Fig. 1. Green light (532 nm) from a frequency-doubled Nd:YAG laser is focused onto droplets that scatter elastic (green) and inelastic (red-shifted SRS) light into the spectrometer. Part of this light is reflected onto a one-dimensional array detector (PDA) by a beam splitter (BS2) for measurement of its spectral content. The remaining scattered light is combined with a delayed (green) light pulse from the reference beam and passed through the exit slit onto a photomultiplier tube (PMT). The PMT signal is then fed to a transient digitizer, and the resulting signal traces are displayed on a CRT for measurement of the time delay between scattered and reference beams. The calculated time delay between these two beams, taking into account the speed of light and path-length difference and assuming that droplet scattering is instantaneous, is 54 nsec. Delay of the reference beam by this comparatively long time (compared with the laser pulse length of 8 nsec) allows for measurement of scattered light and reference beam with a single detector. This arrangement permits time-resolved and spectrally resolved measurements of scattered light on single laser shots, which we found necessary to eliminate undesirable pulse waveforms on some single shots.

The results of temporal and spectral measurements of droplets for single laser shots are shown in Figs. 2 and 3 at laser intensities just below that required for aerosol-induced breakdown.[3] Our time-resolved measurements for 26- and 68-μm-diameter CCl_4 droplets are shown in Fig. 2. As for bulk, elastic scattering is instantaneous for both liquids. However, unlike in the bulk, the SRS light for the first Stokes shift for water and multiple-order Stokes shifts for the strongest Raman line (ν_1) of CCl_4 are all delayed by about 5-7 nsec. Our finding that the delay for water and CCl_4 is about the same suggests that the droplet shape (which enables resonances to exist), not the droplet material, is instrumental in causing the delay. Our finding that the delay in the multiple-order Stokes shifts in CCl_4 are all about the same suggests that all multiple ν_1 shifts are excited simultaneously.

Although it is generally believed that SRS emissions in small droplets correspond to structure resonances in the droplet,[1,2] no actual identification of resonances has been made. To contribute to the solution of this problem we measured single-shot SRS spectra in water droplets as a function of droplet size, as shown in Fig. 3. Droplet size was determined within 2% accuracy by measuring the vibrating orifice generator frequency and by weighing a timed collection of the counted number of droplets. Several SRS peaks appear within the broad spontaneous Raman linewidth, and these peaks have a quasi-periodic structure.

If these peaks are associated with corresponding structure resonances in elastic scattering of the same order ℓ, they should have a wavelength separation given by the asymptotic relation[4]

$$\Delta\lambda = \frac{\lambda^2}{2\pi r} \frac{\arctan(n^2-1)^{\frac{1}{2}}}{(n^2-1)^{\frac{1}{2}}} \qquad (1)$$

where r is the droplet radius ($r >> \lambda$) and n is the droplet refractive index. Our measurements of the separation of peaks $\Delta\lambda$ (done by applying a fast-Fourier-transform

method to the spectral data) versus droplet radius r are in excellent agreement with Eq. (1). This is compelling evidence that the SRS emissions seek out structure resonances in the droplet, with each successive peak corresponding to elastic-scattering resonances of sequential mode number n but of the same mode order, ℓ.

We suggest that the delay of SRS in small droplets is a consequence of the finite time required to build up resonances that support SRS. The droplets act as electromagnetic cavities with Q (energy stored/power gain per cycle = time delay of SRS for laser intensity used/period per cycle) $\simeq 3 \times 10^6$. The SRS spectra are normally dominated by one set of quasi-periodic peaks, suggesting that for a given droplet size and refractive index, structure resonances of a particular width and mode order dominate over all others.

Laser Emission

Fluorescence spectra from organic dye-doped, micrometer-sized spherical particles have also been studied for a number of years.[5] The observed spectra exhibit intensity peaks associated with the MDR's of the sphere. With increased pump irradiance the fluorescence from dye-doped droplets evolves into the nonlinear optical regime, resulting in laserlike emission.[6,7] Stimulated Raman scattering (SRS), as discussed previously, is a similar nonlinear evolution of spontaneous Raman scattering in transparent droplets. Here, we report the results of a spectral and temporal study of lasing from dye-doped droplets.

The experimental arrangement is that shown in Fig. 1. We make simultaneous spectral and temporal measurements of lasing from dye-doped (3×10^{-4} M Rhodamine 6G in water or ethanol) droplets. Figure 4(a) and 4(b) show spectra for monodispersed water and ethanol droplets, respectively, obtained by appending a wavelength-sequenced series of single-shot spectra acquired within minutes of each other. The corresponding bulk fluorescence emission spectra (obtained by irradiating the liquid in a cuvette and imaging the resulting bright yellow fluorescent spot on a spectrometer slit at 90° to the direction of incidence), and a portion of the absorption edge (obtained from bulk liquid by using a spectrophotometer) are also shown. As found previously[6] the droplet spectra exhibit a flat and nearly featureless region (region A) and a region (region B) consisting of an abundance of well-defined quasi-periodic lasing peaks. We note that for the case of ethanol droplets at least one SRS peak at 630 nm [Fig. 4(b)] is seen to occur simultaneously with lasing. This can be confirmed by lowering the Nd:YAG laser energy and noting its disappearance while the lasing persists. The transition from nonlasing (region A) to lasing (region B) occurs at approximately 565 nm for water and 575 nm for ethanol. The corresponding imaginary refractive indices are 1×10^{-5} and 1×10^{-6}.

For ethanol droplets there is an intermediate region [not shown in Fig. 4(b)] ranging from 562 to 575 nm where peaks occur irreproducibly from shot to shot. This behavior contrasts with the peaks in region B, which occur reliably on every shot, provided that the droplet generator operates stably, ejecting uniformly spaced spherical droplets. Unstable operation of the generator results in slightly aspherical droplets, giving rise to additional resonance peaks.

The quasi-periodic structure of the lasing peaks motivated us to compare their wavelength separation with that predicted by the asymptotic relation Eq. (1). By using the gravimetrically determined droplet radii and the known real refractive indices, the calculated wavelength separations of the resonance peaks are in good agreement with observations. This is strong evidence that, as suggested for SRS, resonances of a single mode order support lasing in small droplets.

Typical single-shot temporal profiles obtained by probing different spectral regions are shown in Fig. 5. Figure 5(a) shows typical time signatures characteristic of the bulk fluorescence decay process.[8] Signals from both the absorption region A and off resonance in region B yield similar features with slightly faster rise times [Fig. 5(b)]. This similarity in temporal behavior with the bulk liquid is expected since in the absence of resonances the spontaneous emission originates from a volume-averaged region of the droplet. The on-resonance signals in region B, which are stronger and associated with lasing [Fig. 5(c)], have faster rise times and narrower widths than those of either the absorption or the off-resonance regions. These signals are dominated by stimulated emission from near the droplet surface.

Multiple time peaks are observed sporadically [Fig. 5(d)], with the highest frequency of occurrence for ethanol at 585-590 nm and for water at 570-575 nm. The second peak's initiation and rise time cannot be measured precisely, but the delays are relatively long (8-11 nsec). These peaks could be evidence of relaxation oscillations.[6,9]

For ethanol similar signals were recorded at 630 nm [Fig. 5(e)]. The second peak is due to SRS emission; in its absence (achieved by lowering the laser energy below SRS but above the lasing threshold) the first peak remains with the same temporal shape. The profiles suggest a slightly longer delay for SRS emission than those in Fig. 2.

The intermediate region referred to earlier for ethanol droplets exhibits unique behavior in that when resonances occur they typically have long initiation times, suggesting that the larger gain required to achieve threshold in this region of higher absorption needs longer paths in the droplet and hence takes more time to build up.

In conclusion, laser emission from dye-

doped droplets is supported by resonances of a single mode order. The Q value of the particular mode that contributes to lasing is always of the order of 7×10^4. Long delays found in droplet SRS are not observed in the presence of lasing. The slightly longer SRS delays may be evidence of competition between the two stimulated processes. Evidence of relaxation oscillations, known to be associated with laser emission, is also observed.

Double Resonance SRS

Measurements of SRS, cited above, have been made for droplets satisfying a resonance condition only at the emitted (output) wavelength, since with the lasers and droplet generation methods used, there was no practical way to tune the incident laser wavelength or droplet size to an input resonance condition. We now consider observations corresponding to a double-resonance condition, where the droplet is in resonance at both incident (input) and emitted (output) wavelengths. SRS emissions for the double-resonance condition occur for incident laser intensities (~0.2 W/cm^2) that are lower than for output resonance conditions.[3] We further identify, at least tentatively, the resonance mode orders and numbers that support double-resonance SRS for ~5-7 μm radius glycerol droplets irradiated by 0.532-μm wavelength radiation from a pulsed Nd:YAG laser. Our observations suggest that both input and output resonances usually have the same mode. Further, resonances that support SRS are of lower order than those observed in elastic scattering.

We achieve double-resonance conditions using optical levitation[10] (Fig. 6). Glycerol droplets trapped in a focused argon-ion laser beam (not shown) slowly evaporate at a rate of ~0.4 nm/sec, allowing droplets to pass through resonance conditions at the incident Nd:YAG wavelength. A position-sensing, split photodiode feedback detector and pockel's cell (not shown in Fig. 6) coupled to the argon-laser output permit continuous recorded adjustment of laser power needed to keep the droplet stationary. In addition, scattered argon-laser light is recorded using a photodiode. Monitoring of levitating laser power[11] and elastic scattering[4] from the droplet permit determination of droplet size to within 0.1% of its radius.

Quasiperiodic bursts of SRS (arising from the 2855-cm^{-1} shift C-H stretching mode) are observed from the droplet only when the combination of droplet size and Nd:YAG wave-length satisfy an input resonance condition. This differs from previous studies where input resonances could not reliably be achieved because of lack of precise control of droplet size. Spectral content of SRS emission is measured by imaging the droplet onto a spectrometer equipped with a one-dimensional photodiode array detector.

Quasiperiodic bursts of SRS emission, which occur at times when resonance conditions are satisfied, are seen as bright, full, or partial red rings on the droplet rim. The times of occurrence of SRS can be recorded to an accuracy of 1 sec. By comparing levitating laser power with theoretical radiation pressure calculations,[4] droplet radius and hence size parameter ($X_1 = 2\pi r_i/\lambda$, where r_i is the radius and λ is the incident Nd:YAG wavelength) evolution can be precisely determined. A comparison of measured X_i with resonance size parameters calculated from Mie theory[12] allow an identification of input resonances. Known droplet radii together with measured SRS wavelengths allow identification of the corresponding output resonances.

A summary of input and output resonances deduced from measured SRS spectra reveals that in virtually all cases, the mode orders of input and output resonances match. This suggests that spatial overlap of the internal electromagnetic field distributions for input and SRS, as dictated by mode-order matching, is an important criterion for SRS emission. Delays in the initiation of double resonance SRS vary over a wider range (<2 - 14nsec) than for the output resonance delays shown in Fig. 2.

In conclusion we have confirmed double-resonance SRS from levitated droplets. The identification of the input resonances reveals that the mode order increases with droplet size. Mode orders of input and output resonances match with few exceptions.

Acknowledgment

The author acknowledges his colleagues, A. Biswas, H. Latifi, and R.G. Pinnick, for collaborating on this project with him.

References

1. R. G. Pinnick, P. Chylek, R.L. Armstrong, H. Latifi, E. Creegan, V. Srivastava, and M. Jarzembski, Opt. Lett. 13, 494 (1988).
2. A. Biswas, H. Latifi, R.L. Armstrong, and R.G. Pinnick, Opt. Lett. 14, 214 (1989).
3. R.G. Pinnick, P. Chylek, M. Jarzembski, E. Creegan, V. Srivastava, G. Fernandez, J.D. Pendleton, and A. Biswas, Appl. Opt. 27, 987 (1988).
4. P. Chylek, J. Kiehl, and M. Ko., Phys. Rev. A 18, 2229 (1978).
5. R.E. Benner, P.W. Barber, J.F. Owen, and R.K. Chang, Phys. Rev. Lett. 44, 475 (1980).
6. H. M. Tzeng, K. F. Wall, M.B. Long, and R.K. Chang, Opt. Lett. 9, 499 (1984).
7. H. -B. Lin, A.L. Huston, B.L. Justus, and A.J. Campillo, Opt. Lett. 11, 614 (1986).
8. I.B. Berlman, Handbook of Fluorescence Spectra of Aromatic Molecules (Academic Press, New York, 1985), p. 26.
9. A. Yariv, Optical Electronics, 3rd Ed. (Holt, Rinehart, and Winston, New York, 1986), p. 188.

10. A. Ashkin, and J.M. Dziedzic, Phys. Rev. Lett. 24, 156 (1970).
11. A. Ashkin, and J.M. Dziedzic, Phys. Rev. Lett. 38, 1351 (1977).
12. C. F. Bohren, and D.R. Huffman, Absorption and Scattering of Light by small particles (Wiley, New York, 1983).

Figure Captions

Fig. 1. Schematic of the experimental setup used for measuring time dependence and spectral content of elastic and inelastic (SRS) scattering in small droplets.
Fig. 2. Time-resolved measurements of elastic scattering and SRS from water and CCl_4 droplets. Time delays for the first Stokes shift for water droplets and for multiple (through ninth-order) shifts for CCl_4 droplets are shown. The laser pulse width is about 8 nsec; the peak intensity is about 1 GW cm^{-2}. Data points depict averages of 25-50 single laser shot measurements of the delay together with typical one standard deviation. Absolute errors arising from differences in the laser and SRS signal pulse widths and from finite detector time response are estimated to be not more than an additional $\pm$ 2 nsec.
Fig. 3. Single-shot SRS spectra of water droplets irradiated with green light from a pulsed laser with peak intensity ~1 GW cm^{-2}. Spherical droplets range in size from 29- to 130 μm diameter [(a), (b), (d)]. The peaks are quasi-periodic. Spectra for spheroids (c), obtained by detuning the droplet generator from the resonant frequency used in (b) to generate spheres, show a plethora of resonance peaks. The spheroids have nearly the same volume as spheres in (b); their axial ratio was estimated by viewing them through a microscope with 200X magnification.
Fig. 4. Typical lasing spectra for Rhodamine 6G-doped water (a) and ethanol (b) droplets (with radii of 11.3 and 11.8 μm, respectively) irradiated with a 532-nm pulsed Nd:YAG laser. Also shown are the fluorescence emission band and absorption edge for the bulk liquids. Both water and ethanol droplets show a region where no lasing occurs (region A) and a region corresponding to a sequence of quasi-periodic lasing peaks (region B).
Fig. 5. Representative temporal signals from different wavelength regions: (a) bulk-liquid fluorescence, (b) off-resonance region in droplets, (c) droplet lasing, water (575 nm) and ethanol (586 nm), (d) the same as in (c) except showing multiple time peaks, (e) SRS and lasing simultaneously from an ethanol droplet (630 nm), (f) intermediate region lasing from ethanol (572 nm).
Fig. 6. Schematic top view of experimental arrangement. The levitating argon-laser beam directed normally outward from the plane of the paper and the six-sided glass cell enclosing the droplet are not shown. The feedback-stabilized levitated droplet is positioned at the focus of the Nd:YAG laser. Simultaneous monitoring of argon elastic (light scattering detector), SRS (spectrometer), and view of droplet (microscope) are possible using this arrangement.

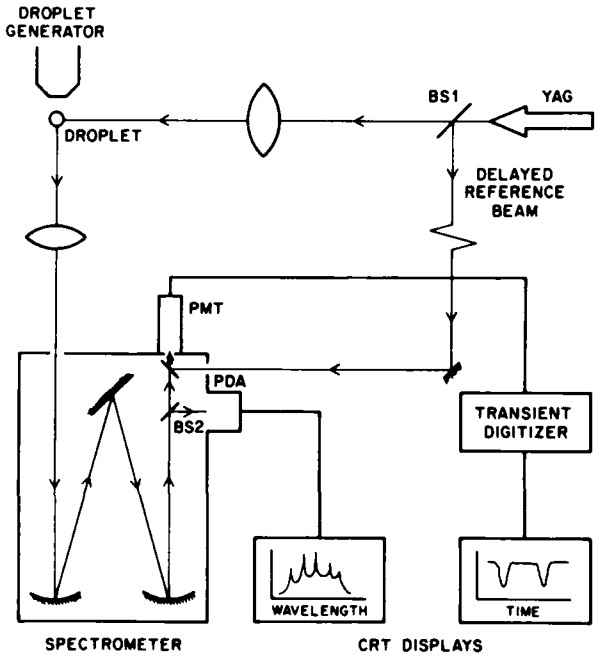


Fig. 1

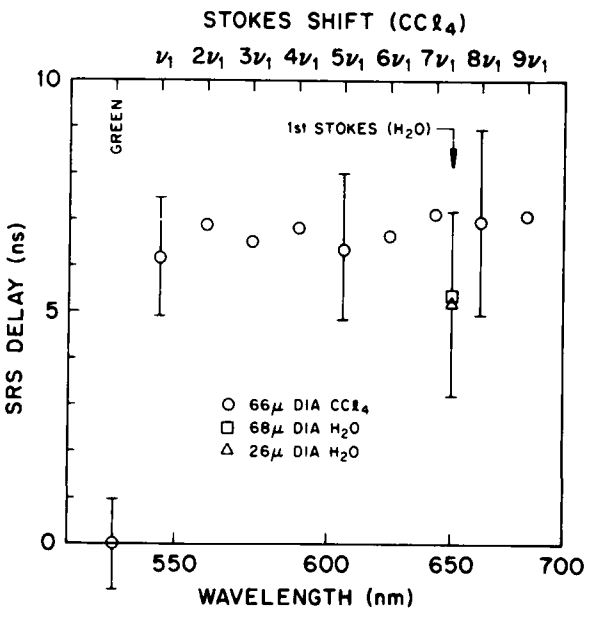


Fig. 2

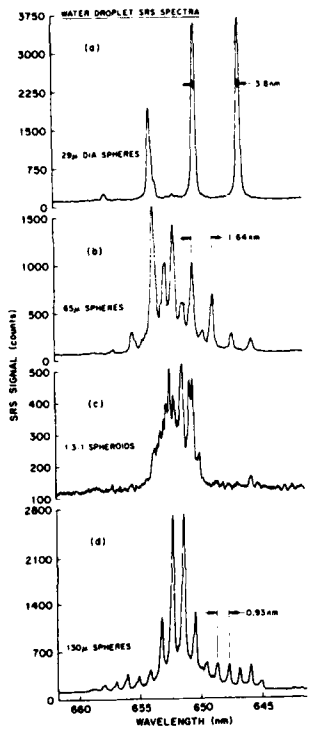


Fig. 3

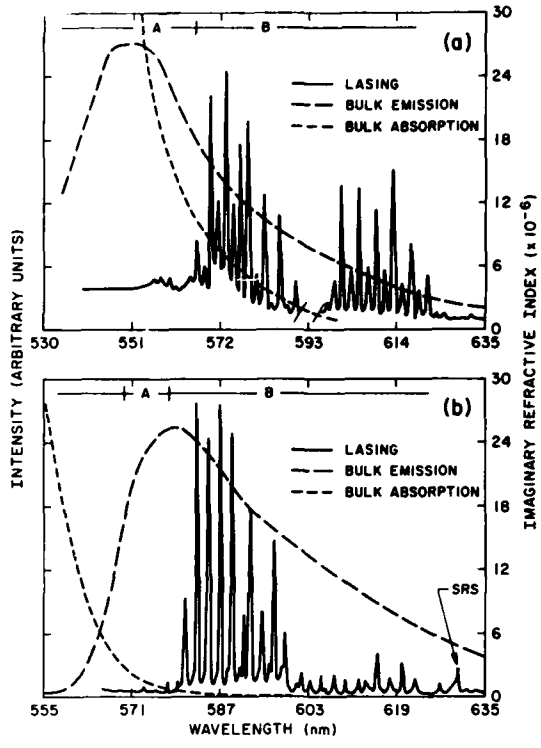


Fig. 4

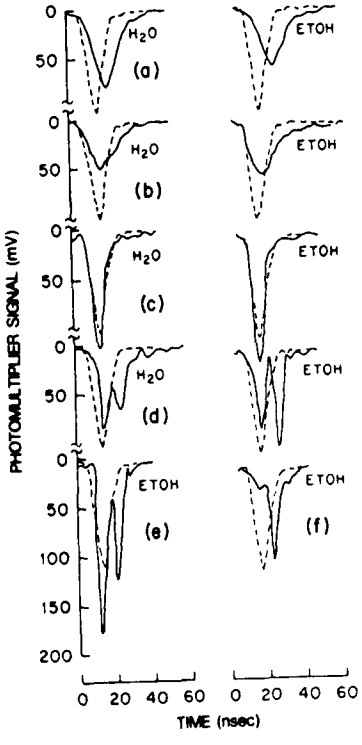


Fig. 5

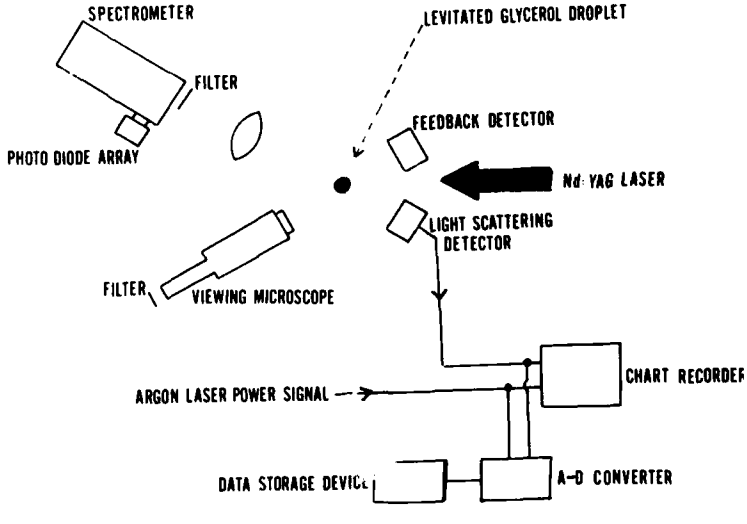


Fig. 6

REMOTE MEASUREMENTS OF THE FLUORESCENCE LIFETIME OF AEROSOLS

Radon B. Loveland

Department of Physics
New Mexico State University
Las Cruces, New Mexico

and

Raul Gonzalez
Young P. Yee

U.S. Army Atmospheric Sciences Laboratory
White Sands Missile Range, New Mexico

Abstract

The fluorescence decay time of aerosols is estimated by successive convolution of the nonfluorescent return. Results of field experiments with aerosol clouds are presented.

Introduction

Various remote measurements of the decay times of organic compounds in liquid and solid form have been made using the Atmospheric Sciences Laboratory Lidar Test Bed[1] (LTB). For solids and liquids, determination of the slope of the logarithm of the decay in the region well below the peak is a viable approach if the signal to noise ratio is high enough to observe the decay over a significant portion of a decade and if the LIDAR receiver system is linear and does not exhibit significant ringing.

One technique being investigated is the so called "Z transform". The Z-transform[2] deconvolution method is based on considering the fluorescence intensity as a time sequence f(n).

$$f(n)=\sum_{m=0}^{n} i(m)\ s(n-m) \tag{1}$$

f(n) is the convolution of the impulse response sequence i(n) and the observed system response sequence s(n). For a single component i(n) is modeled as a single exponential decay i(n)= A EXP(-n/C1) where n=1,2,... and C1 is the time decay. The Z-transform deconvolution analysis is analogous to the Laplace transform method[3]. For our data the deconvolution was evaluated for several values of the Z parameter. The decay times obtained for the different Z parameters were averaged and the average was assigned to the sample decay time.

The reiterative convolution technique[4] is also used to extract the decay time of the sample by successively comparing the convolution of the amplitude normalized elastic return and exponential decays with the amplitude normalized fluorescent return. The areas of the two returns were compared and the value of the exponential decay which most closely matched the areas was considered to be the proper value of the exponential decay.

Underlying all these techniques is the basic fact that in general the time response of a multicomponent system is the result of the convolution of the time responses of the separate components composing the system. In the following discussion we shall denote convolutions by "*". The assumption is made that the elastic return time response, Fe(t), and the fluorescent return time response, Ff(t), are amplitude normalized.

If the time response of the elastic return is

$$Fe(t)=f1(t)*f2(t)*f3(t)*f4(t).....fn(t) \tag{2}$$

and the time response of the fluorescent return is

$$Ff(t)=f1(t)*f2(t)*f3(t)*f4(t).....fn(t)*EXP(-t/C1) \tag{3}$$

where C1=0 for nonfluorescent targets
and fi is the time response of the ith system component for i=1,2...n

then obviously EXP(-t/C1) is the result of the deconvolution of Fe(t) and Ff(t).

If we are to measure aerosols we must be sure that this condition is satisfied for the measurement. In practice this means that the attenuation through the aerosol cloud must be very small.

While this is a straight forward process using Fourier transforms, in practice, the results we achieved with data from the LTB for input were less than satisfactory due to distortion and noise in the lidar system. If the portion of the two returns which is used for comparison is restricted to the region of good signal to noise ratio then reasonable results can be obtained. This is done in the successive convolution technique by base clipping before making the area comparison of the normalized data. The exponential decay values presented in this report are the result of an arbitrary choice of the 50 percent level for clipping.

Description of Experiment

The Lidar Test Bed consists of a tripled Neodymium YAG laser (Spectra Physics DCR1) with a multiplier, various high speed photomultipliers and a Lecroy 1.3 GHz 8 bit waveform digitizer. All measurements described herein were made at the tripled wavelength (355 nm) at about 1 mJ per pulse. Pulse width is about 6 ns at the 50 percent level. The pulse repetition rate was 10 pulses/sec. The effective receiver bandwidth is estimated to be about 300 MHz. Because of the need for low distortion and ringing the photomultipliers are coupled directly to the digitizer. System timing is derived from the output of a photo diode inside the beam separator housing. This also provides a measure of output power variations. All adjustments are manual. A 12 inch diameter offset Newtonian system is available, however, these measurements were made at a distance of 10 meters with no optical system other than band pass and neutral density filters. The ultraviolet light was excluded from the fluorescent channel by means of a Kodak "2B" gelatin filter. The fluorescent light was excluded from the elastic channel by using a Schott "UG5" filter. The optical input was adjusted by means of neutral density filters in order to operate the photomultiplier tubes at the same approximate voltage close to their maximum ratings in order to assure that the rise and fall times of the photomultipliers are as short as possible and hopefully equal.

The aerosol was generated by means of 5 aerosol generators placed inside an open ended metal housing 3 meters long and approximately one half meter on a side. The housing was open at the bottom. A short range was chosen to assure that the beam did not contact the housing. The housing was necessary to keep the aerosols confined to the region of interest.

The available software precluded the use of both channels in the digitizer in the averaging mode. Both photomultipliers were connected to a single channel by running one photomultiplier through a 90 ns delay line consisting of a length of RG9B coaxial line. The line introduces a distortion in the pulse shape. It is necessary to compensate for this by taking two sets of measurements, one with the delay line in the elastic return channel and a second with the delay line in the fluorescent channel. The results of the two sets of data are averaged in order to get the correct value. Each measurement is the average of 1000 returns.

Results

The material used for the test was Aldrich Chemical commercial grade fluorescein "70 percent water soluble". This material was dissolved in water. The concentration was 0.01 g/l. The 64th edition of the Handbook of Chemistry and Physics lists fluorescein as 3,4 Dehydroxy Floran (p.C-301) and does not show that it is soluble in water. We therefore assume that this material is not pure 3,4 Dehydroxy Floran. The average of the two measurements of the time decay of the "fluorescein" was 5.57 ns in a liquid sample taken from the aerosol generators after the test. The average of the two measurements of the same material in the aerosol was 6.18 ns.

Using the Z-transform method, the fluorescence liquid phase decay time of fluorescein was computed to be 5.86 ns. In comparison, the fluorescence aerosol phase decay time of the same sample was calculated to be 4.35 ns.

Conclusion

It is possible to remotely measure the time decay of fluorescent aerosols if the following condition is satisfied:

> The amplitude normalized time response of the fluorescent return differs from the amplitude normalized time response of the elastic return only by EXP(-t/C1).

This is a nontrivial case which can be adequately approximated by aerosol clouds of very low total attenuation.

References

1. Y.P. Yee, R. Gonzalez, and R.B. Loveland, A Prototype UV Fluorescence Lidar System, Proceedings of the Ninth Annual EOSAEL/TWI Conference, Physical Science Laboratory, Las Cruces, NM (1988).

2. G. Doetsh, Guide to the Application of the Laplace and Z-transform, (Van Nostrand Reinhold, London, 1971), p. 163.

3. A. Gafni, R.L. Modlin, L. Brand, Analysis of fluorescence decay curves by means of the Laplace Transform, Biophysical Journal, 15, 263 (1975).

4. L.J. Cline Love and L.A. Shaver, Anal. Chem., 52, 154 (1980).

ADVANCES IN 1.06 μm ATMOSPHERIC PROPAGATION MODELING

R.L. Spellicy,
W.O. Gallery, S.G. O'Brien, B.K. Matise
OptiMetrics, Incorporated
106 E. Idaho
Las Cruces, NM 88005

Abstract

Advancements in short wavelength lasers has renewed the interest in molecular and aerosol extinction in the 1.0 to 2.0 μm region. In recent programs sponsored by three agencies: Lincoln Laboratory, the U.S. Army Strategic Defense Command, and the Atmospheric Sciences Laboratory, OptiMetrics has refined current models in this spectral region for use with both ground level and slant atmospheric paths treating both molecular and aerosol extinction.

Molecular Absorption

Molecular absorption falls into two categories: continuum absorption and line absorption. Continuum absorption, which arises from the far wings of spectral lines well removed from the point of computation, is significant in the 3-5 μm and 8-10 μm regions where its absorption coefficient is 0.01 km^{-1} or larger. In the 1.06 μm region, however, the continuum is less than 10^{-4} km^{-1} and consequently not of general concern.

Line absorption can be significant for atmospheric propagation near 1 μm depending on the particular wavelength of interest. Computation of atmospheric transmission for laser applications are usually performed using line-by-line methods such as employed in the Geophysics Laboratory FASCODE algorithm. However, these computations can be only as good as the parameters available in the spectral line atlas used. The HITRAN atlas, developed by Geophysics Laboratory, has not been updated for water vapor absorption in the 1.0 μm region since the original compilation was put together in 1979. A refinement of the line parameters was necessary. To accomplish this, OptiMetrics undertook a three phase program. In the first phase, sponsored by Lincoln Lab, we developed a fitting algorithm which allowed for line strengths, widths, and positions to be extracted directly from high resolution spectra. In the second phase, funded by the Strategic Defense Command , we used this algorithm to extract parameters from self-broadened, absorption-cell data collected by Flaud, Camy-Peyret, et. al.[1] at Kitt Peak. The third phase, supported by the Atmospheric Sciences Laboratory at White Sands Missile Range, is ongoing at the time of this writing. This phase will supplement the parameters evaluated in the earlier phases by adding parameters for the weaker isotopic lines as well as evaluating self-to-foreign broadening ratios for all lines.

The Parameter Extraction Algorithm

The algorithm developed for parameter extraction does a least squares fit of a computed spectrum to an experimental spectrum. It uses a custom line-by-line code written for the purpose and performs computations on a grid less than or equal to that of the experimental data using a full Voigt line profile. To fit data distorted by an instrument function, the routine convolves the computed spectra with an appropriate response function such as sin(x)/(x). The algorithm uses a code from the Quantum Chemistry Program Exchange called STEPIT[2] (a multivariable simplex routine) to control the variation of parameters during fitting. The code considers convergence to have been reached when the least squares difference between observed and computed spectra cannot be improved by more than a predefined amount through variation of any of the parameters. A flow chart of the overall code is shown in figure 1.

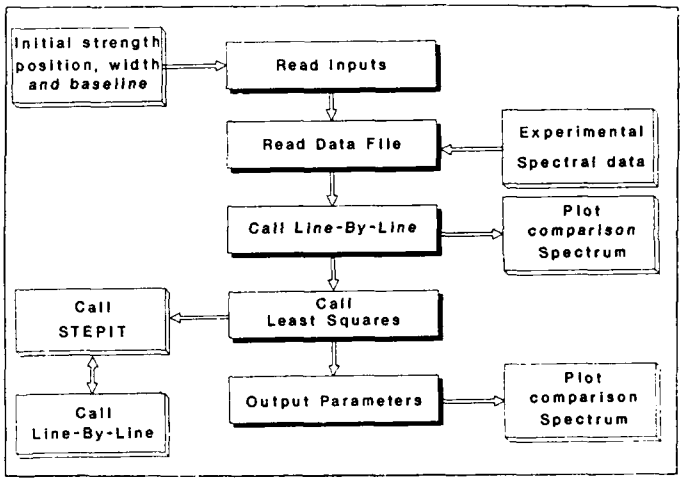


Figure 1. Flow chart for parameter extraction software

Line Parameters for H_2O at 1 μm

The data used in the second phase program was absorption data collected by Flaud, et. al.[1] using the Brault interferometer at Kitt Peak. The data was collected at a spectral resolution of 0.012 cm^{-1} (FWHH) using pure water vapor at 17.4 torr and was taken with a path length of 434 meters as provided with a multipath White cell. The data were all coadded, single path interferograms and consequently were influenced by the interferometer instrument response function. Fortunately the line density in this region was low enough that the baseline was apparent between spectral lines and, throughout the region, the strongest lines saturated. This allowed the zero and 100% signal levels to be determined and the relative transmittance data to be normalized.

Using the Kitt Peak data, 770 spectral lines were treated between 9090 cm^{-1} and 10,000 cm^{-1} extracting line strengths,

positions, and self-broadened widths for all lines. By way of example, figure 2 shows the region from 9105 to 9110 cm^{-1} and compares the experimental data to calculations performed using the line parameters of the November 1986 Geophysics Lab compilation and those derived here. Clearly the new parameters improve the calculational capabilities considerably.

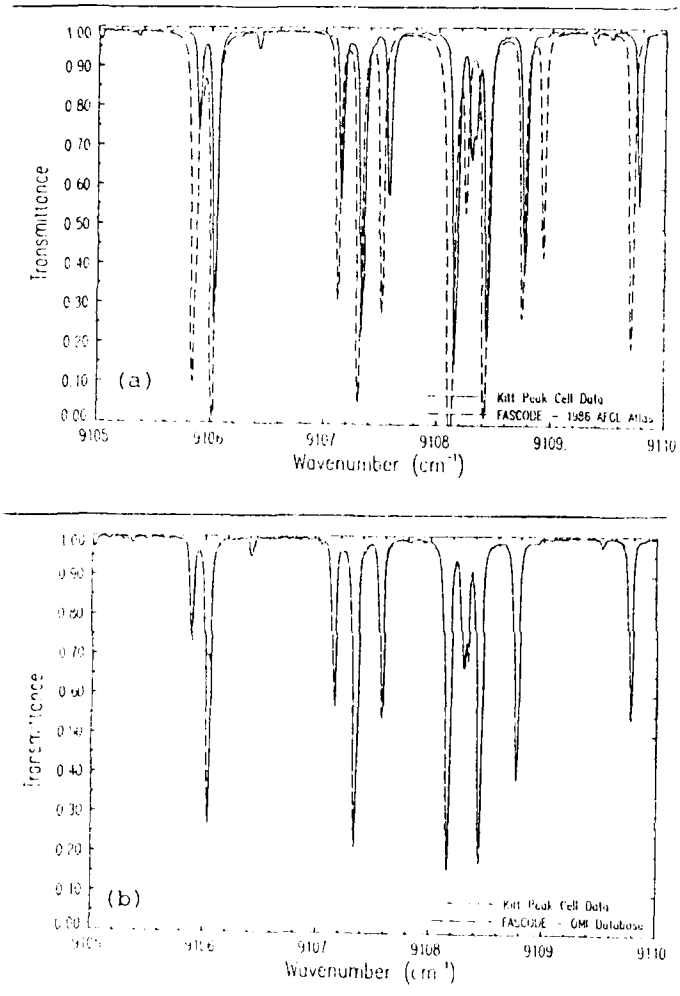


Figure 2. Comparison of experimental data to calculations based on (a) the 1986 HITRAN compilation and (b) the parameters derived here.

Over a portion of this region, Mandin, Chevillard, Flaud, and Camy-Peyret[3] also extracted line parameters from the same data. In their extractions they used equivalent width and curve of growth approaches when the lines were sufficiently isolated and peak absorption when the lines were influenced by neighboring lines. Comparisons of our parameters to theirs, as shown in figures 3 and 4, indicated very good agreement for all line positions but demonstrated systematic variations in line strengths. Our values are greater than theirs by typically 5 to 20% with the difference increasing monotonically with line strength. In comparing spectra computed with our and their parameters to the original experimental data, however, our strengths gave consistently better fits and were therefore considered to be somewhat more accurate. The deviations we have observed in comparing our parameters to those of Mandin et. al. are consistent with the errors one normally encounters using an equivalent width measurement. That is, one underestimates the strength because of the difficulty of completely accounting for the area in the wings of the lines well removed from line center. Although Mandin, et. al. made corrections for these effects it appears residual errors could still remain.

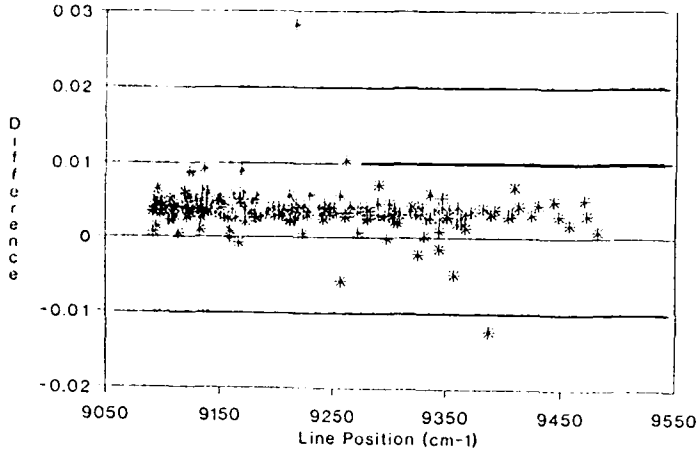


Figure 3. Observed line position differences (this work - reference 3)

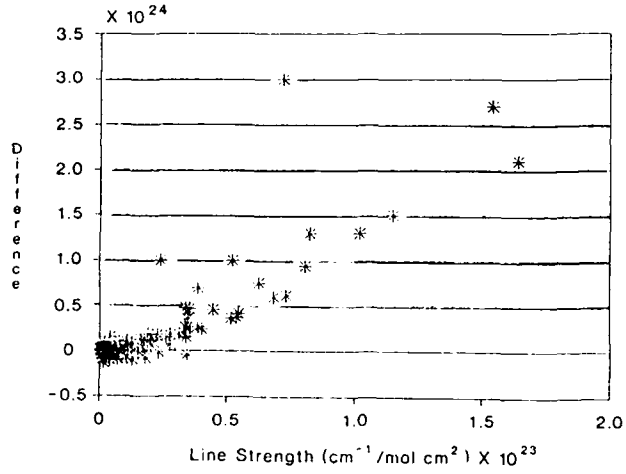


Figure 4. Observed line strength differences (this work - reference 3)

Comparisons of Parameters with Slant Path Data

The new parameters were also tested to determine how well they could predict general slant path atmospheric spectra. To this end, we compared calculated spectra to field data collected using a system called the Mobile Atmospheric Profiling System (MAPS). This system, developed and operated by OptiMetrics for the Atmospheric Sciences Laboratory at

White Sands, consists of a 0.8 meter, computer controlled Coude' telescope coupled to a 0.038 cm^{-1} Fourier transform spectrometer. This system has been used for several years to collect atmospheric transmission spectra using the sun as a source. To normalize the data, Langley plots are generated at discrete wavelengths using data collected over a wide range of air masses and the spectra collected at different air masses are ratioed against one another. By ratioing the spectra for two known air masses a transmission spectrum for the differential air mass is obtained. This spectrum is free of instrumental effects and solar emission/absorption lines but its baseline could be in error. The Langley plots provide, at discrete wavelengths, absolute transmission reference points which can then be used to absolutely calibrate the ratioed spectra.

Only preliminary comparisons of the new line parameters with field data have been made to date. By way of example, we present here a comparison based on MAPS data collected on 3 May 1989. For this data set a balloon sounding was performed simultaneously and provided an atmospheric profile of temperature, pressure, and relative humidity which could be used for the line-by-line computations. Two data sets from this day, those collected at zenith angles of 79.45 degrees and 55.62 degrees, were ratioed against one another to remove instrumental effects and solar features and this ratio represented an equivalent transmission spectrum for 3.692 air masses. For this preliminary comparison, however, no Langley calibration was used. Figures 5 and 6 show computed and observed spectra, for the same spectral region as in figure 2, comparing the measured MAPS spectrum with computations based on the 1986 HITRAN compilation and the new parameters derived here. Clearly the new parameters have substantially improved the calculational capabilities. The residual errors in evidence in figure 6 are probably due to our lack of knowledge of the self-to-foreign broadening ratio for the spectral lines in this region, a parameter being investigated in the third phase of this work but not yet available.

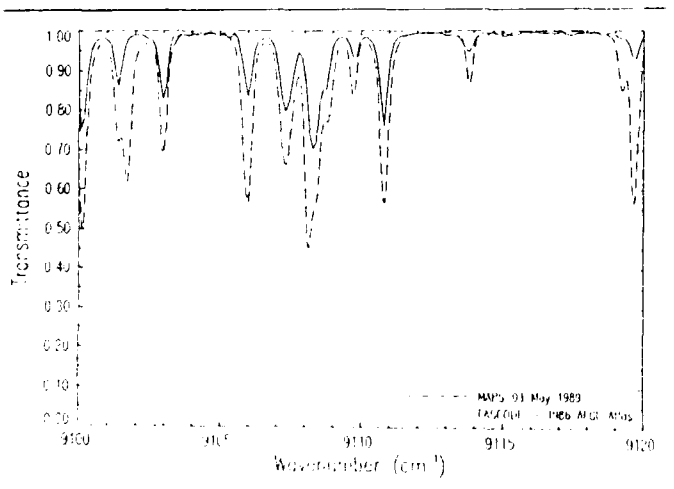


Figure 5. Comparison of original HITRAN to MAPS data

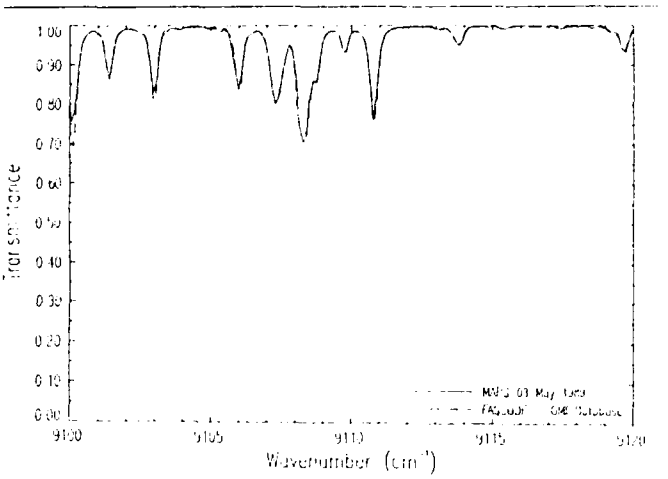


Figure 6. Comparison of OMI Parameters to MAPS data

The full set of strengths, positions, and self-broadened widths for the spectral lines have been put in standard HITRAN form and are available upon request.

Aerosol Absorption and Scattering

Over the past several years OptiMetrics has been developing atmospheric aerosol models under sponsorship from the Atmospheric Sciences Laboratory at White Sands. These studies have demonstrated several clear characteristics of aerosols in the New Mexico area: 1) The aerosol distributions are clearly bimodal, and 2) the modes of this distribution consist of an accumulation or small particle mode arising primarily from non-local sources and a coarse or large particle mode arising almost exclusively from local sources. Based upon the work of Pinnick et. al.[4] we have also concluded that the two modes have nearly inverse compositions: the accumulation mode typically containing 89.5% water soluble, 10% dust-like, and 0.5% carbon-like particles, the coarse mode containing 10% water soluble and 90% dust-like particles.

For these modes, the water soluble components include ammonium sulfate, calcium sulfate, and terpenes while the dust-like are made up of quartz, clay, hematite, calcite, and gypsum. Table 1 shows the typical mix of these species as used in our White Sands model. For all species in the model, we have used directly the complex refractive index data of Shettle and Fenn[5] and have employed standard Mie calculations to compute scattering and absorption cross sections.

Table 1. Typical composition of White Sands aerosols inferred from work of Pinnick et al.

Component	Composition (by mass)
Accumulation Mode	
Ammonium sulfate $(NH_4)_2SO_4$	80%
Calcium sulfate $CaSO_4$	< 5%
Terpenes	< 5%
Kaolinite $Al_2 Si_2 O_5 (OH)_4$	10%
Carbonaceous (soot)	0.5%
Coarse Mode	
Quartz SiO_2	30%
Kaolinite and related clays	30%
Calcite	10%
Hematite Fe_2O_3	10%
Gypsum	10%
Ammonium sulfate $(NH_4)_2SO_4$	10%

Based upon approximately ten years of ground level Knollenberg aerosol spectrometer measurements of particle size distributions, we have derived typical distributions for the White Sands aerosols. These distributions are found to vary by season and with local conditions, with the coarse mode being by far the more variable. Typical ground level size distribution parameters are shown in table 2 for the spring/summer and fall/winter White Sands models. The corresponding size and absorption/extinction distributions are shown in figure 7.

Table 2. Boundary layer aerosol size distributions

$$\frac{dN}{dr} = \sum_{i=1}^{2} \frac{N_i}{\sqrt{2\pi}\, r\, \ln(\sigma_i)} \exp\left\{ -\frac{1}{2} \left[\frac{\ln(r) - \ln(r_i)}{\ln(\sigma_i)} \right]^2 \right\}$$

		N_i, cm^{-3}	$\ln(\sigma_i)$	r_i, μm
Accumulation Mode	Spr-Sum	650.4	0.411	0.07
	Fall/Win	608.9	0.403	
Coarse Mode	Spr-Sum	2.176	0.980	0.30
	Fall/Win	1.746	1.098	

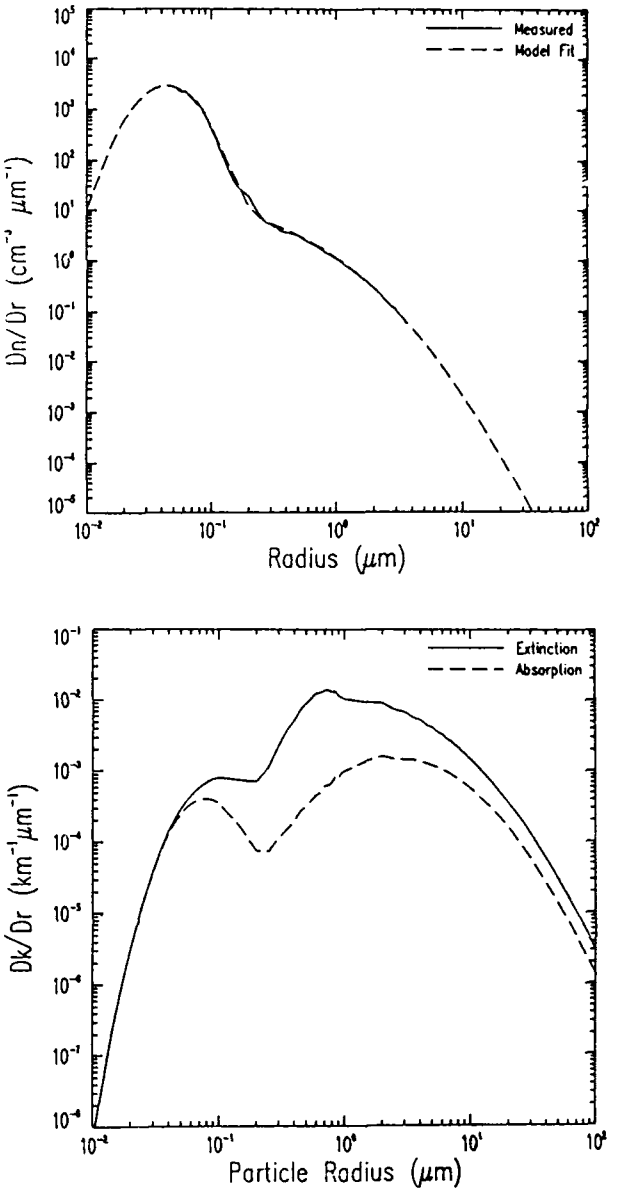


Figure 7. Aerosol number density (above) and extinction absorption coefficients (below) as a function of particle radius.

These distributions are fine for horizontal path applications but for generalized slant paths the vertical variability of the distributions is necessary. To evaluate the vertical dependence, the Atmospheric Sciences Laboratory in conjunction with Sandia Laboratory flew particle counters and nephelometers over White Sands in the Sandia Twin Otter aircraft in June, September, and March of 1988 and again in May and July of 1989. These flights, as shown in figure 8, clearly indicate a scattering coefficient (and particle size distribution) which remaines effectively invariant from the ground through the mixing layer. Above the mixing layer the scattering then drops off to another nearly constant level in the troposphere.

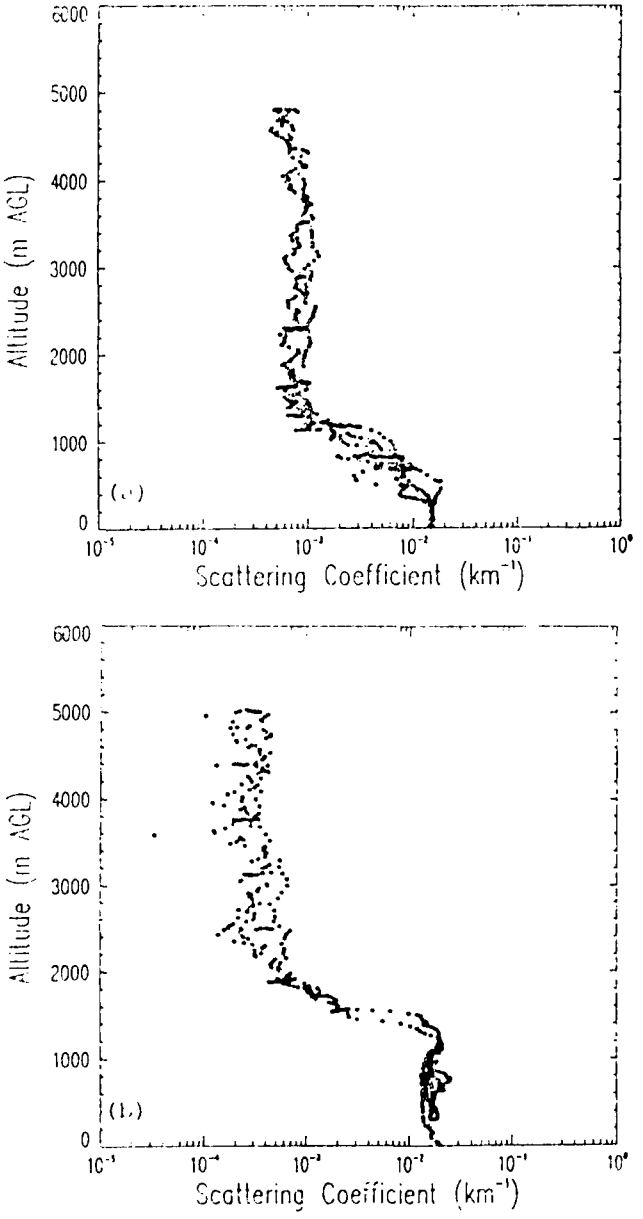


Figure 8. Scattering coefficient profiles observed on 9 and 10 February for (a) morning and (b) mid-day conditions.

We have modified our older aerosol models using this data and have included content dn/dr distributions in the mixing layer and in the troposphere. For the mixing layer, we have taken the distribution to be the same as that measured at ground level (10m AGL). We have, however, taken the ceiling for this mixing layer distribution to be the maximum boundary layer height for the day. This is the case because the coarse mode remains well mixed up to the actual boundary layer but as the boundary layer decays this mode decays more slowly persisting above the capping inversion for some time after the boundary layer has receded. We have included this decay in our mixing layer model. In the troposphere, we have empirically modeled the ASL/Sandia data to develop a White Sands Tropospheric model which again has a nearly constant dn/dr up to approximately 10km. Above 10km we have logarithmically interpolated to the Geophysics Laboratory "moderate aged" volcanic model and have used this model without alteration. An example of the full extinction and absorption profiles for September is shown in figure 9.

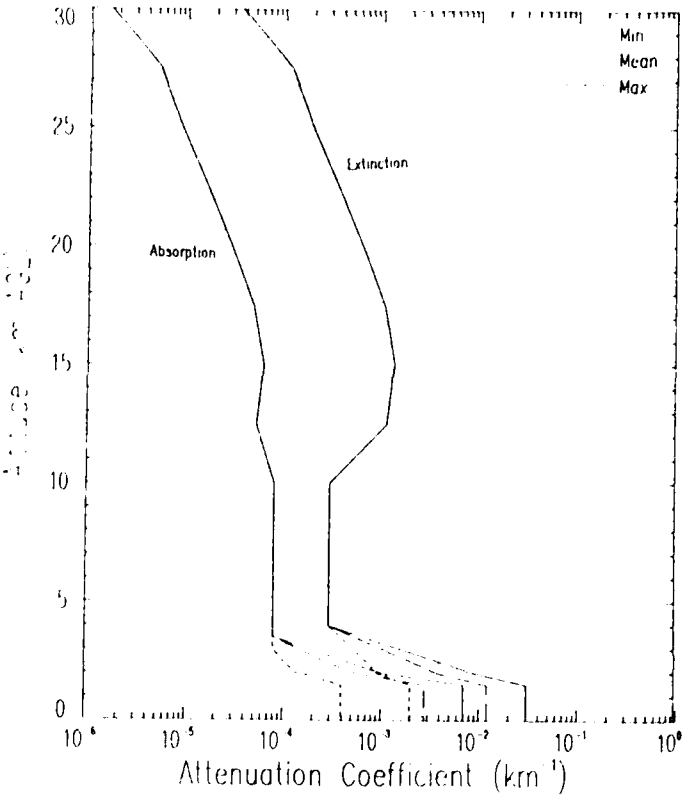


Figure 9. September model profile showing extinction and absorption coefficient profiles.

As a preliminary test of the validity of these models, we have compared model predictions of earth-to-space optical depths to those observed using the MAPS system discussed above. In this case, we gathered solar source, transmittance data with an optical multichannel analyzer (OMA) coupled to the MAPS telescope. The OMA uses a holographic grating monochromator with a 1024-element, silicon detector array in the output plane. Data collected with the OMA was corrected for scattered light and used to generate Langley plots. These plots were then used to normalize the data set yielding optical depth as a function of air mass.

Figure 10 shows comparisons of computed and observed optical depths using three successive day's data from November 1988. The comparison is strikingly good. The deviations seen in the plots for November 15 have been clearly identified as interference from high altitude cirrus. This also appeared in the Langley plots as a significant deviation from linearity during the early portion of the day. The mild

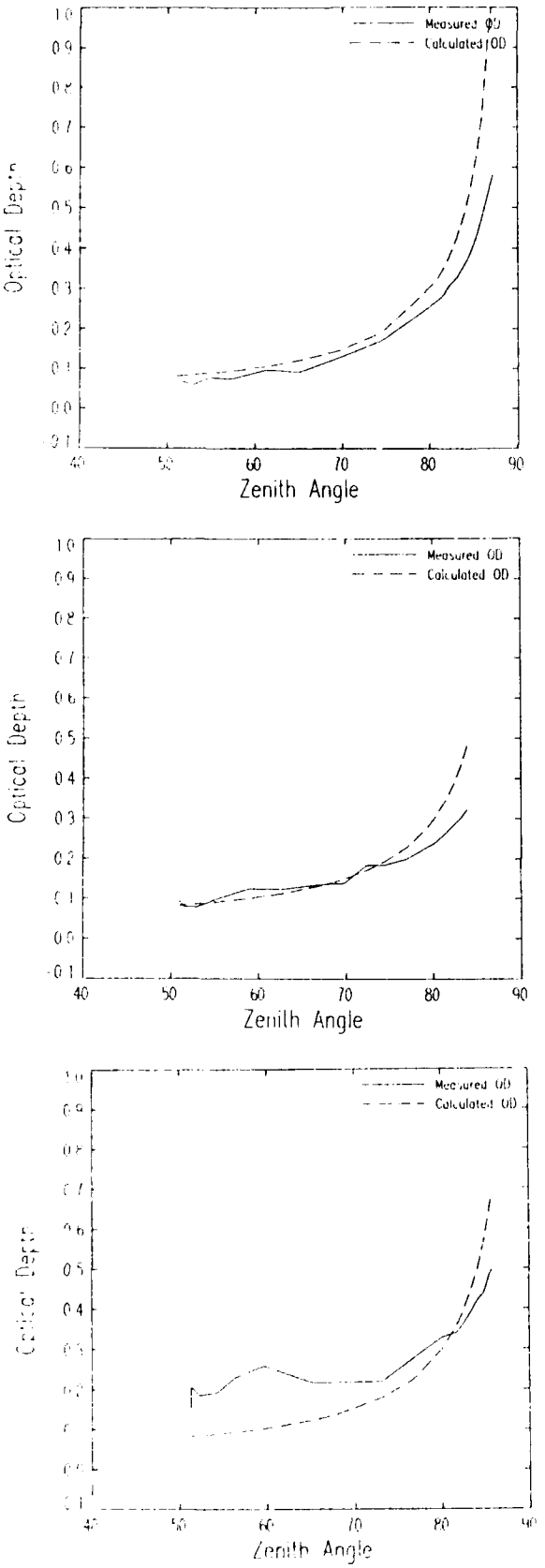


Figure 10. Comparison of observed and computed optical depths for 13, 14, and 15 November 1988.

disagreements seen at large zenith angle are, at least in part, due to a simplified sec(θ) dependence assumed in the air mass calculations. More rigorous comparisons are planned for the future.

Conclusions

Both molecular and aerosol models have been updated for use in evaluating slant path extinction in the 1.0 to 2.0 μm region. Line strengths, positions, and self-broadened widths for use in FASCODE-type calculations have been derived for 770 H_2O lines in the 1.0 to 1.1 μm region and these have been put in standard HITRAN format. Final line identifications, isotopic line parameters, and self-to-foreign broadening ratios are currently being developed. The aerosol models developed for the Atmospheric Sciences Laboratory have been updated using recent Sandia aircraft data. These models are distinctly different than those developed earlier and represent a substantial improvement in our understanding of slant path profiles for the mixing and tropospheric layers. Use of these molecular and aerosol models should substantially improve the accuracy of slant path transmittance calculations.

References

1. Brault, J.W., "Proceedings of the Joint Organization for Solar Observations Workshop, 1978," Osservatori e Memorie dell'-Osservatorio Astrofisico de Arcetri, 106, p. 33, (1978).

2. Chandler, J.P., STEPIT - Direct search optimization: solution of least squares problems, Quantum Chemistry Program Exchange, Program #307, Indiana University Chemistry Department, (1976).

3. Mandin, J.Y., J.P. Chevillard, J.M. Flaud, and C. Camy-Peyret, "$H_2{}^{16}O$: Line positions and intensities between 8000 and 9500 cm^{-1}: the second hexad of interacting vibrational states: (050), (130), (031), (210), (111), $(012)^2$," Can. J. Phys., 66: 997-1011, (1988).

4. Pinnick, R.G., S.G. Jennings, and G. Fernandez, "Volatility of Aerosols in the Arid Southwestern United States", J. of the Atmos. Sci. 44 p. 562-576 (1987).

5. Shettle, E.P. and R.W. Fenn, "Models for the Aerosols of the Lower Atmosphere and the Effects of Humity Variations on Their Optical Properties", AFGL-TR-79-0214, Air Force Geophysics Laboratory, Hanscom AFB, MA, (1979).

EVIDENCE OF LASER INDUCED DEGRADATION AND GRAPHITIZATION OF AROMATIC POLLUTANTS

A. Giardini Guidoni - R. Teghil - A. Morone - M. Snels
CNR and Istituto di Chimica, Università di Basilicata - Via N. Sauro, n. 85
POTENZA ITALY (0971/474223)

A. Mele
Dipartimento di Chimica, Università "La Sapienza" - P.le A. Moro, n. 5
Roma ITALY tel. (06/49913358)

T. Letardi P. Di Lazzaro
ENEA Dip. TIB, C.P. 65 00044 Frascati ITALY

Abstract

An investigation of the laser induced photodecomposition and graphitization of the important class of pollutants, polynuclear aromatic hydrocarbons, is reported.

The laser irradiation of the solid samples of pollutants was performed by means a frequency quadrupled Nd-Yay laser. A black powder consisting mainly of carbon is formed. Charged particles produced in the laser plume were analyzed in a time of flight mass spectrometer. The positive and negative ions formed by irradiating anthracene and benzopyrene consist mainly of C_n^{+} , C_nH^{+} , $C_nH_2^{+}$ ions. Carbon cluster ions up to very high m/e 7000 were observed for both positive and negative ions. Irradiation by pulsed CO_2 laser produces a wide plume which has been analyzed by OMA system. The strong emission has been assigned to excited carbon clusters and to H and H .

Introduction

It is well known that many noxious organic compounds found in ambient particulate matter originate from anthropogenic sources. The attention in environmental research has been stressed on polycyclic aromatic hydrocarbons (PAHs), which strong carcinogenic action (1). Recently PAHs have been identified in the fly ash from municipal incinerators togheter with polychlorodibenzo-p-dioxins (PCDDS) and polychlodibenzofurans (PCDFs) which are formed by pyrolysis of polychlorobenzenes (PCBs) and Polychlorophenols (PCPs) (2). Recent experiments (3) performed by irradiating PCBs in liquid phase with excimer lasers have shown the possibility of a laser induced decomposition. In particular it has been shown that the absorption of one photon per molecule at 248 nm can quantitatively decompose the PCBs through the HCl elimination and biphenyl bond rupture. Since only one photon is needed for dissociation also intense UV lamp could be used for the degradation process.

The present work, which is part of an experimental study on identification and degradation of organic pollutants in progress in our laboratory, concerns the laser ablation and graphitization of some aromatic condensed ring hydrocarbons PAHs. The aim of the study is to obtain informations on the mechanism of the reactions which result in degradation and ionic cluster formation.

The PAHs studied are anthracene, benzoanthracene, benzopyrene and chrysene.

Experimental

The ablative photodecomposition of these organic materials has been performed with both a pulsed TEA CO_2 laser and a frequency quadrupled Nd-Yag laser.

Ablation by a CO_2 operating on the 10 P20 and having a -90 sec, was performed by mounting a solid target in a stainless steel vacuum chamber equipped with a window such that the target pellet can be irradiated at normal incidence (Fig. 1). Irradiation is accomplished using beam energies of about 300 mJ focussed to 1 mm diameter spot. The ablated material originates a luminous plume of 1 cm height emission has been collected and qualitativey analyzed as a function of wave lenght. After laser ablation the solid formed on a substrate in front of the plume was analyzed by ESCA.

Ions resulting from the ablation process by means of the Nd Yag laser were analyzed by time of flight mass spectrometer. Both positive and negative ions have been detected and mass analyzed. The entire assembly is incorporated in a commercial Laser Microprobe Mass Analyzer (LAMMA 500 Leybold). The experimental procedure has been previously described

(4) and will behere summarized. Solid samples of the PAHs studied were directly spread onto an electron microscope grid and irradiated by the 266 nm pulsed laser radiation. The recorded mass spectra were obtained by a single laser shot. The relative intensities reported are the average of ten individual spectra. Spot dimension is of the order of 10 and laser power density can be varied from 10^7 to 10^9 W/cm^2. PHAs were purchased by Aldrich Chemical Co and used without further purification.

Results and discussion

Esca analysis of the deposited particulate resulting from anthracene ablation by the CO_2 laser is reported. In Fig. 2 for the C region. It can be seen that it qualitatively correspond, to the graphite peak confirming that most of the ablated anthracene gives origin to carbon.

The spectral analysis of the plume shows that emission is mainly due to hydrogen and Minor peaks assigned to C^+, C_2 , C_3 are reported in Fig. 3. These results, indicate that the energy deposited in the solid by laser originates a pyrolytic process which leads to degradation and graphitization of the pollutant.

The Lamma measurements confirm this hypothesis. One striking feature of the abundances for both positive and negative ions is the fact that at masses higher than those corresponding to C_{48} the spectrum is the same for all the PAHs studied (5). This is in agreement with recent data from other laboratories (6). Similar mass spectra have been observed in laser ablation of pure graphite (7).

In Fig. 4 the mass spectrum of positive ions observed in chrysene is shown. Three regions of cluster ion formation are found in the spectrum. The most abundant group of cluster ions encompasses the range from n=1 to n=22. This region shows features typical of the ablated PAH and will be discussed in more detail later. A weaker group appears between n 44 and n 226 and a still weaker group around n=567. As in graphite ablation the peaks present in the second region exhibit only an even number of atoms and show alternation.

Although relative intensities depend on the experimental conditions some magic cluster size C_{48}, C_{60}, C_{70} have been observed in agreement with previous data (7,8). Recent results on photofragmentation of carbon cluster ion (8,9) and metastable reactions show that in the decomposition process the C_2 loss dominate. Indicating that at high mass number of carbon atoms probably a cyclic structure of spheroidal type as previously hypotized is formed (9).

In the region of masses lower than the parent peak the results confirm some of the earlier works (10). In Fig. 5 data on anthracene are reported. In the figure the relative abundance of those ions containing n carbon atoms and those containing also one hydrogen atom are displayed as a function of n. Peaks are observed to show an alternance of the graphite type (10).

Furthermore ions of the generic formula $C_nH_m^+$ where m=o through 7 are observed. The presence of other ions including the parent ion of the dimer is further evidence of non fragmentation chemical reactions in the plume.

Both benzoanthracene and benzopyrene exhibit behaviour similar to that of anthracene. C_nH^+/C_n^+ ration are greater than unity and as in the case of anthracene the abundances of C_n^+(up to n 8) and C_nH^+(up to n=16) alternate with n, each maximizing at odd values of n. The alternating abundances for C_n^+ and C_nH^+ are again observed for chrysene with maxima at odd values of n.

The negative ions mass spectra indicate the presence of clusterization processes yielding C_n^- ions up to n 700. At masses lower than the parent peak all the compounds studied show the presence of C_n^-, C_nH^-. In case of anthracene as shown in Fig. 6 when n is odd C_n predominates by far over the C_nH^-. For n even the C_nH^- is of the order of the C_n^-. The negative parent peak in always absent.

These preliminary results strongly indicate a general tendency of aromatic compounds to produce fragmentation. This in shown from the large number of $C_nH_m^+$ and C_n^+ ions obtained from all hydrocarbons irradiated. The similarity of the aromatic hydrocarbon mass spectra and that of graphite (8,9) suggests that the process of ion formation is governed by the same mechanism which produces ablation and chemical reaction in the highly dense cloud of material produced under the laser action. Cluster ion formation is, therefore, the ultimate

process yelding graphitization. Work in progress in this laboratory has confirmed this process. The optical multichannel analyzer (OMA) emission spectra obtained by irradiating graphite and aromatic hydrocarbons indicate the production of the same excited C_n species. This finding may be of great relevance in the treatment of wastes of aromatic products. A process that uses a laser source may be particularly appropriate for the purpose.

Aknowledgements are due to G. Bourden and to E. De Simoni and a Salvi for made esca measurements.

The work was supported by CNR Progetto Finalizzato Tecnologie Elettrootticne.

References

1. SE. Brudey, R. Perry, RA. Willings. Environ. Res 7, 294 (1974) and ref cited there in
2. HR. Buser Chemosphere 8, 415 (1979).
3. R. Fantoni, R. Larciprete, S. Piccirillo, G. Bertoni, R. Fratarcangeli, M. Rotatori. Chem. Phys. Letts 1989.
4. D. Consalvo, A. Mele, D. Stranges, A. Giardini-Guidoni, R. Teghil. Int. J. Mass. Spect. Ion Proc. 91, 319 (1989).
5. A. Mele, A. Giardini Guidoni, R. Teghil, Presented at the XIV Atomic and Molecular Physics (FAM) meeting of CNR, Riva del Garda, 18-20 June 1989.
6. DN. Linemann, SK. Viswanadham, AG. Sharkey, DM. Hercules, PE. Russel Ed. Microbeam Analysis 1989, p. 297.
7. P. Pradel, P. Monchicourt, JJ Lancaqne, M. Perdrix, G. Watel. Chem. Phys. Letts 158, 412 (1989).
8. PP. RADI, JL. Bruni, PR. Kemper, ME. Molchan, MT. Bowers, J. Chem. Phys. 88 2809 (1988).
9. SH Yang, CL Pettiette, J. Conceicao, O. Cheshworsky and RE Smalley. Chem. Phys. Letts. 139, 233 (1987).
10. K. Balasanmugam, SK Viswanadham and DM Herculs, Anal. Chem., 50, 1102 (1986).

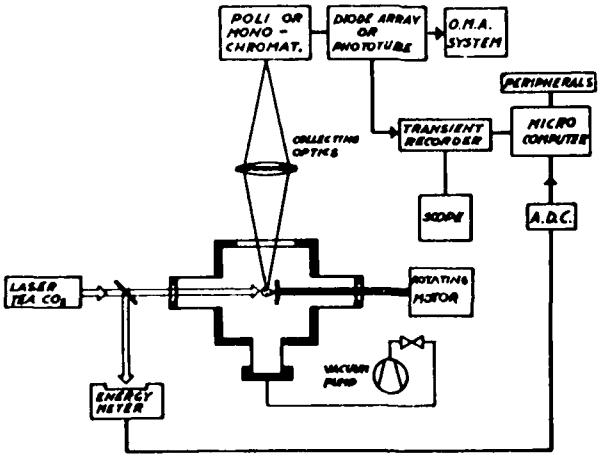


Fig. 1: Schematic of the experimental apparatus for CO_2 Laser Ablation.

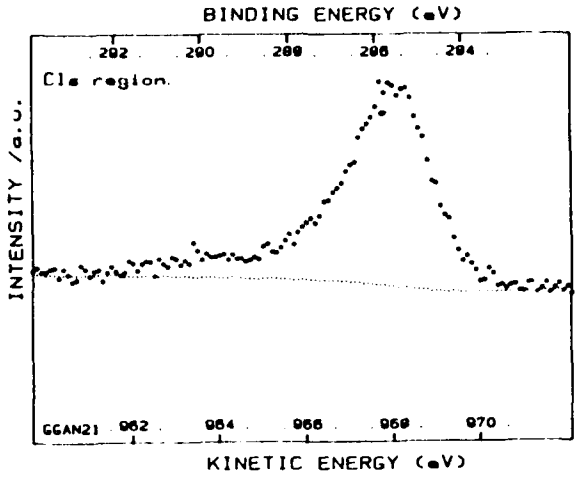


Fig. 2: ESCA spectrum of deposit from anthracene ablation by means of CO_2 Laser.

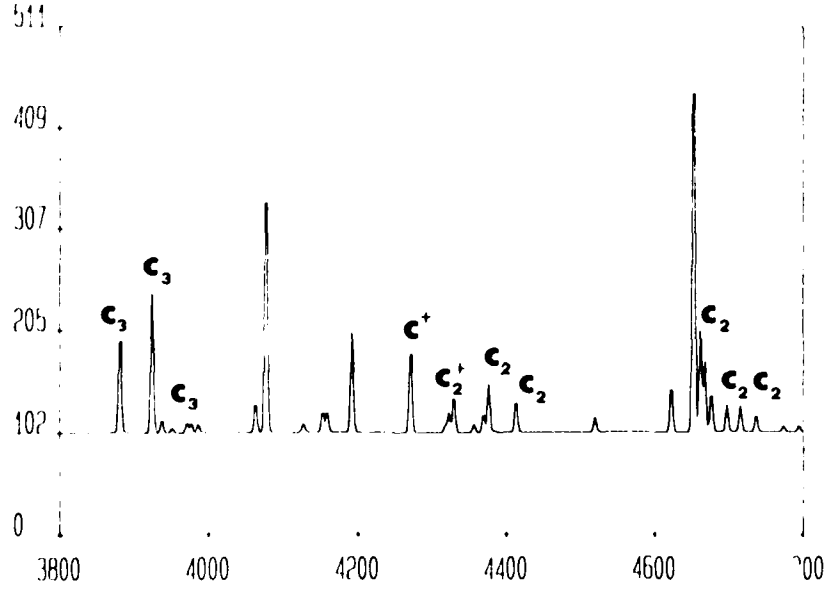


Fig. 3: OMA spectral analysis of the plume from anthracene.

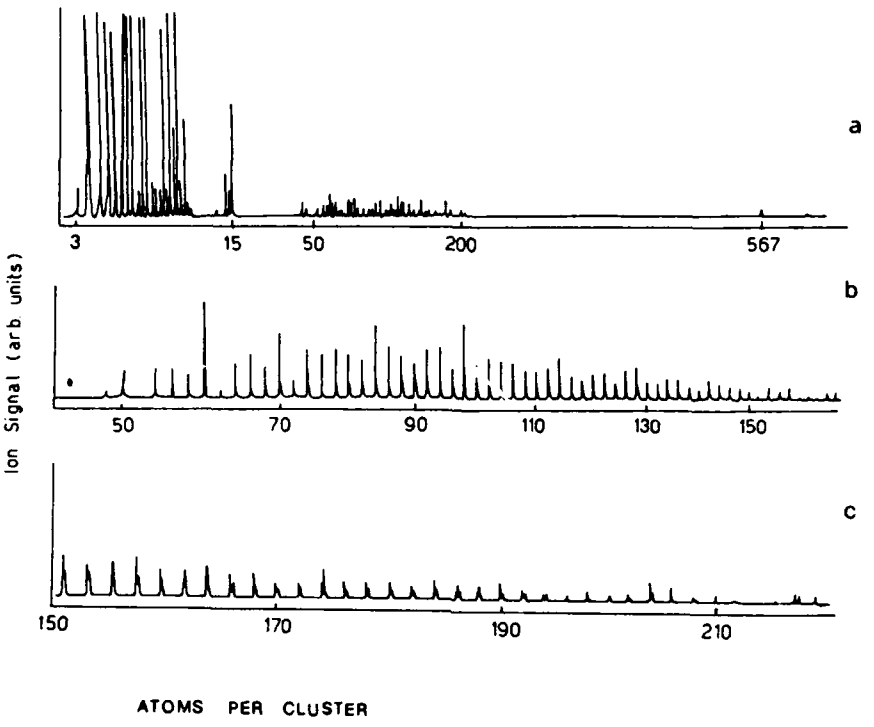


Fig. 4: Mass spectra of chrysene a) Full spectrum, b), c) Expanded spectra from C^{+}_{48} TO C^{+}_{270}.

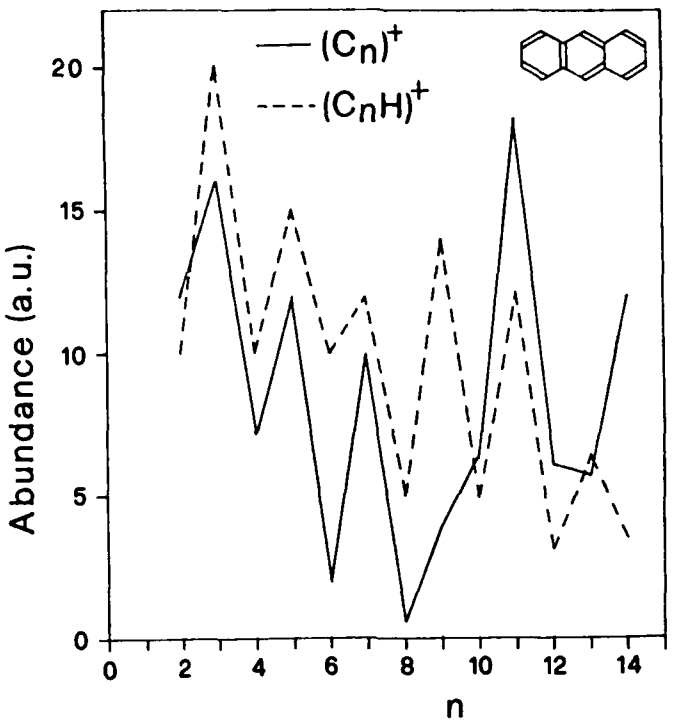


Fig. 5: PLOTS of -- C_nH^+ and — C_n^+ as obtained from the mass spectra of anthracene vs the number of carbon atoms.

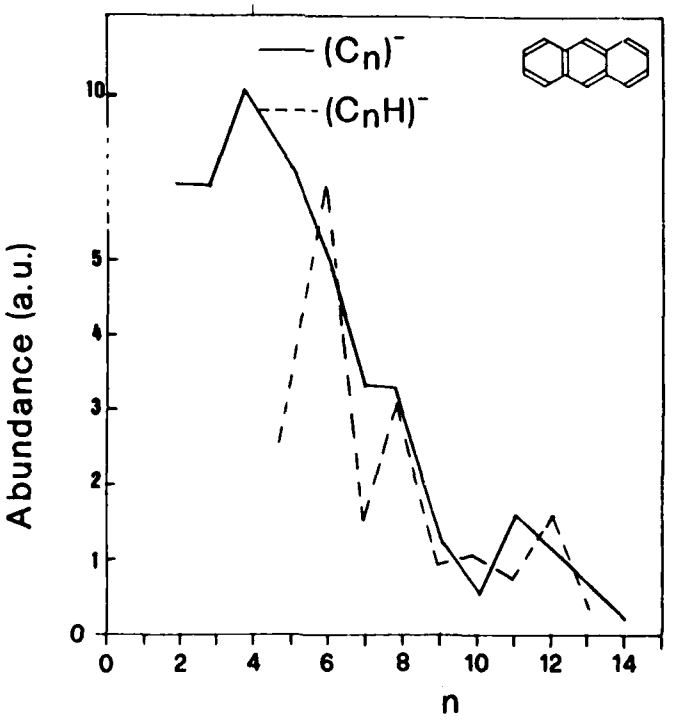


Fig. 6: Plots of -- C_nH^- and — C_n^- as obtained from the mass spectra of anthracene vs the number of carbon atoms.

PICOSECOND MULTIPHOTON IONIZATION OF ATOMIC AND MOLECULAR CLUSTERS*

D. Barton Smith
Engineering Physics Department, Applied Technology Division, Oak Ridge National Laboratory
P.O. Box 2003, Oak Ridge, TN 37831-7280
and
John C. Miller
Chemical Physics Section, Health and Safety Research Division, Oak Ridge National Laboratory
P.O. Box 2008, Oak Ridge, TN 37831-6125

Abstract

High peak-power picosecond laser pulses have been used to effect non-resonant or resonant multiphoton ionization (MPI) of atomic and molecular clusters. The clusters were produced in a free-jet expansion from a nozzle source, and the photoions produced by MPI were detected and characterized by time-of-flight mass spectroscopy. We discuss the observation of the cluster series Xe^{+}_{1-19}, $Ar_{1-7}NO^{+}$, NO^{+}_{1-5} and $Ar_{1-7}I^{+}$. Previous MPI studies of the latter two species have not been successful, presumably due to the existence of fast dissociation channels. It is proposed that the present technique is a new and rather general ionization source for cluster studies that is complimentary to electron impact and that may also provide unique spectroscopic or dynamical information.

Introduction

Multiphoton ionization (MPI) spectroscopy is an established and frequently employed technique for detecting and analyzing van der Waals molecules and larger clusters. MPI spectroscopy provides excellent detection sensitivity, moderately high resolution, and detection selectivity among cluster species. However, the technique is limited in application by its tendency to produce extensive fragmentation. Fragmentation is also a problem with other ionization techniques (e.g., electron impact ionization), but the intense laser beams required for MPI cause additional dissociation channels to become available. These channels include absorption of additional photons by parent ions ("ion ladder" mechanism), absorption of additional photons by fragment ions ("ladder switching" mechanism), and resonances with dissociative states in the neutral manifold. The existence of these dissociation channels can preclude the use of MPI spectroscopy in many situations.

Recent MPI studies of stable molecules using picosecond lasers (pulse durations on the order of 10 ps) have indicated that limitations due to fragmentation might be subdued. With picosecond lasers, dissociation mechanisms can be altered and in some cases fragmentation can be eliminated or reduced. Additional photon absorption competes effectively with dissociation channels when a very short laser pulse or, perhaps more importantly, a sufficiently high peak-power is used. In the case where ionic absorption and fragmentation occurs, it has been shown that picosecond MPI might favor the ion ladder mechanism rather than the ladder switching mechanism.[1] Larciprete and Stuke[2] have presented the argument that ionic fragmentation can be greatly reduced or even eliminated with the use of short laser pulses. Finally, two-color pump-probe experiments using picosecond lasers can, in principal, provide direct measurements of dissociation rates.

In an effort to extend the application of MPI spectroscopy to the study of weakly bound systems, we have undertaken a systematic investigation of picosecond MPI in van der Waals molecules and clusters. We present here results of picosecond multiphoton ionization of rare gases, nitric oxide, nitric oxide-rare gas, and iodine-rare gas clusters. Previous MPI studies using nanosecond lasers have not detected the $(NO)_n$ or the Ar_nI_2 cluster series, presumably because of fast dissociation channels. The use of high peak-power allows resonant and non-resonant photon absorption to the ionization limit to compete effectively with fast dissociative processes.

---

*Research sponsored by the Office of Health and Environmental Research, U.S. Department of Energy, under contract DE-AC05-84OR21400 with Martin Marietta Energy Systems, Inc.

Experiment

The apparatus and method used for the present MPI studies was similar to that used for previous MPI experiments in our laboratory,[3] the principal difference being the use of a picosecond laser system. The apparatus is shown schematically in Fig. 1. Atomic or molecular clusters were produced in a supersonic expansion from the pulsed valve source and were directed into the extraction region of a time-of-flight mass spectrometer. Monomers and clusters in the jet were ionized by the tightly focused laser beam, and the photoions thus produced were detected by the spectrometer.

The pulsed nozzle source[4] was operated with a 0.5-mm diameter aperture, and backing pressures of several atmospheres were typically used. The distance from the nozzle aperture to the ionization region was approximately 17 cm. The laser beam propagation was orthogonal to the flow of the supersonic jet and the beam was focused into the interaction region with a 50-mm-focal-length singlet lens. The laser and the pulsed valve were operated at 10 pulses per second, and to optimize cluster detection the firing of the laser was delayed so that the laser pulse was incident on the early portion of the jet. The spectrometer design is after that of Wiley and McLaren,[5] and its mass resolution ($m/\Delta m$) is about 60 in the range 1-2500 amu. After each laser pulse a distribution of masses was detected by a dual channel-plate multiplier in the spectrometer. The analog output from the multiplier was amplified and subsequently sampled by a digitizing oscilloscope. The signal-to-noise ratio was improved by averaging spectra from about 100 consecutive laser shots. The nozzle, TOF spectrometer assembly and focusing lens were mounted within a vacuum chamber that was evacuated to 10^{-7} Torr.

The laser system consisted of a dual-operational-mode Nd:YAG laser, an H_2 Raman cell and a short-cavity dye laser. The Nd:YAG delivered 1.2 J in a 10-ns pulse (Q-switched operation) or 75 mJ in a 20-ps pulse (mode-locked operation) at the 1064-nm fundamental wavelength. The second, third or fourth harmonic (532, 355 or 266 nm) of the fundamental and corresponding Raman-shifted wavelengths were available in either operational mode. The dye laser was pumped with the second-harmonic picosecond output from Nd:YAG laser, and it provided 10-ps pulses of red light in the region 585-610 nm. This output was extended to the region 293-305 nm by frequency doubling. The peak power as a function of wavelength was calculated to be approximately 214, 71 and 28 TW/cm^2 for the 532, 355 and 266 nm picosecond outputs, respectively, of the Nd:YAG laser. The calculated output for the dye laser at 590 and 295 nm was approximately 45 and 4.5 TW/cm^2. These calculations were based on the assumption that the laser beam had a Gaussian spatial profile, was a diffraction-limited beam and was focused with an aberration-free lens. The actual peak powers were unknown, but they were probably one order of magnitude less.

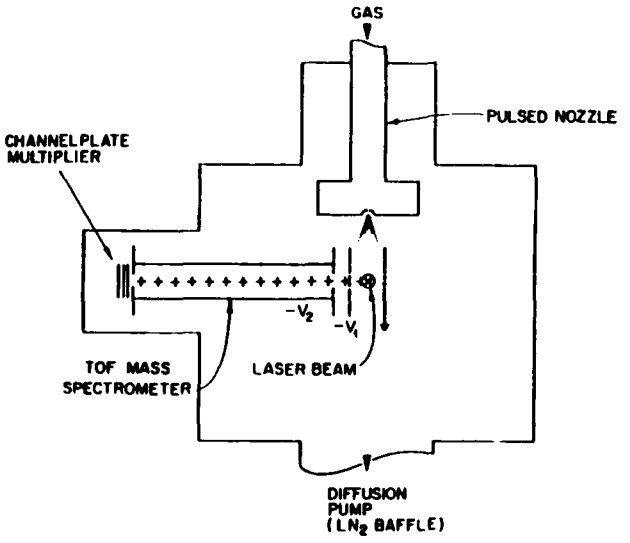


Fig. 1. Schematic diagram of the apparatus used for MPI studies of atomic and molecular clusters.

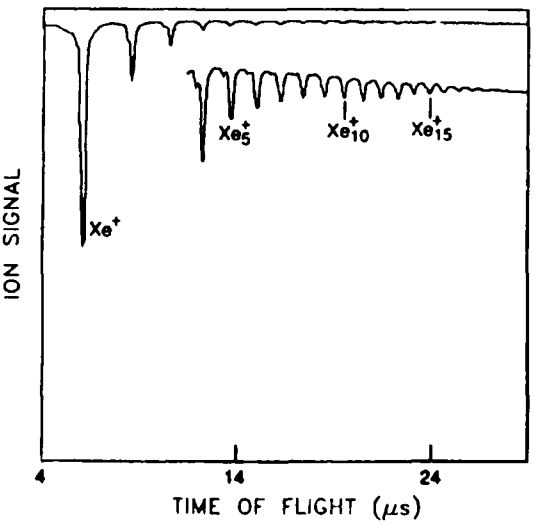


Fig. 2. Time-of-flight mass spectrum of Xe_n^+ clusters following picosecond MPI at 266 nm.

Results and Discussion

Xenon

Electron impact ionization studies of rare-gas clusters have detected extensive cluster series, but resonant MPI using nanosecond lasers has yielded only rare-gas monomers and dimers. (Nonresonant MPI at 266 nm, however, has yielded an extended series of clusters.[6]) In contrast to the results of the nanosecond MPI studies, we have observed Ar^+_{1-2}, Kr^+_{1-4} and Xe^+_{1-19} ions using nonresonant MPI with our picosecond laser. For example, with 266-nm picosecond light we have observed cluster ions as large as Xe^+_{19}, as shown in Fig. 2. Once formed, rare-gas cluster ions are known to be stable, but the relative ease of using high-order nonresonant MPI to observe clusters is rather remarkable since the high laser intensity ($\sim 10^{12}$ W/cm^2) might be expected to completely dissociate the ions. These results belie the conventional wisdom that MPI of "fragile" species must be performed with the least possible number of photons and, if possible, by ionizing the molecule to just above the ionization threshold.

Nitric oxide in argon

Nitric oxide and $(NO)_n$ van der Waals molecules have been the subjects of numerous spectroscopic studies because NO plays a prominent role in the chemistry of the upper atmosphere. Although NO dimers and rare gas-NO clusters are readily formed in a free jet expansion, nanosecond MPI experiments with these species have failed to detect the $(NO)^+_2$ parent.[7,8] This failure to detect the dimer ion can be attributed to the presence of dissociative states in the $(NO)_2$ and $(NO)^+_2$ manifolds; the only known excited state of the neutral dimer very rapidly dissociates[9] and the dimer ion is readily photodissociated by visible light.[10]

Both picosecond and nanosecond lasers have been used at several wavelengths to effect MPI in an supersonic expansion of a NO/Ar gas mixture. These results will be discussed in detail in the next two sections. Figure 3 shows an energy level diagram that details the relevant electronic states of nitric oxide and the range of continuous absorptions for the dimer and its ion. For many of the wavelengths to be discussed later, arrows indicate the multiphoton steps leading to ionization. The corresponding energy levels and ionization potential for ArNO are not shown but are only slightly perturbed from those of NO on the scale of the figure. (For instance, the ionization potential of ArNO is 9.148 eV.)

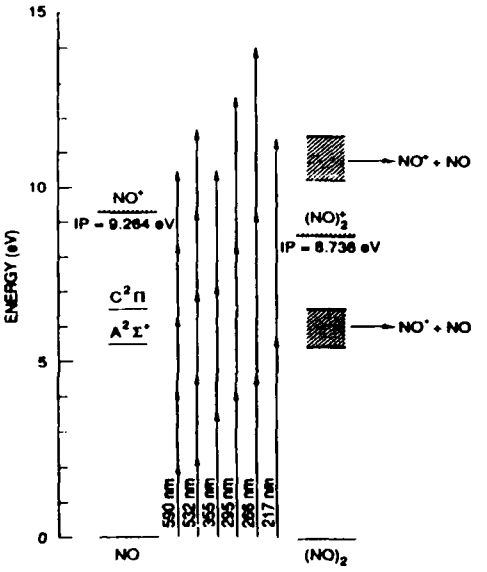


Fig. 3. Energy level diagram for NO and $(NO)_2$ showing the various MPI schemes discussed in the text.

Visible and near-ultraviolet MPI The results of MPI of a 5% NO/Ar mixture by 10-ps dye laser pulses are shown in Figs. 4(a) and 4(b). The results at the two wavelengths are quite different. Five-photon MPI using red light results in ionization of the series of argon-nitric oxide van der Waals molecules to yield $Ar_{1-3}NO^+$. As can be seen in Fig. 3, MPI with 590-nm light is nonresonant for NO itself, but the three-photon level falls to the red of the $C^2\Pi$ state,[11] where ArNO spectra have been observed previously.[7,8] However, the lowest-energy ArNO vibronic excitation occurs at 52038 cm^{-1}, and the three-photon virtual level lies 1190 cm^{-1} to the red at 50847 cm^{-1}. Unfortunately, the output of the dye laser did not extend to wavelengths shorter than about 585 nm, which is not sufficient to reach resonance. Figure 4(b) shows the TOF mass spectrum of the same NO/Ar expansion after MPI with 295-nm light. In this experiment $(NO)^+_{1-3}$ ions were readily observed and Ar_nNO^+ ions were observed only very weakly or not at all. Inspection of the energy level diagram shows that none of the virtual states of the three-photon MPI fall within the dissociative bands of the neutral or ionic dimer. Furthermore, 295-nm light does not photodissociate the $(NO)^+_2$ ion. This is consistent with a previous report[12] that $(NO)^+_n$ ions were stable with respect to nitrogen laser photolysis at 337.1 nm. The absence of the ArNO at this wavelength is probably due to predissociation at the two-photon level. Although nothing is known of ArNO states at this energy, the lower lying $D^2\Sigma^+$ and $E^2\Sigma^+$ states[11] of the complex are thought to predissociate.

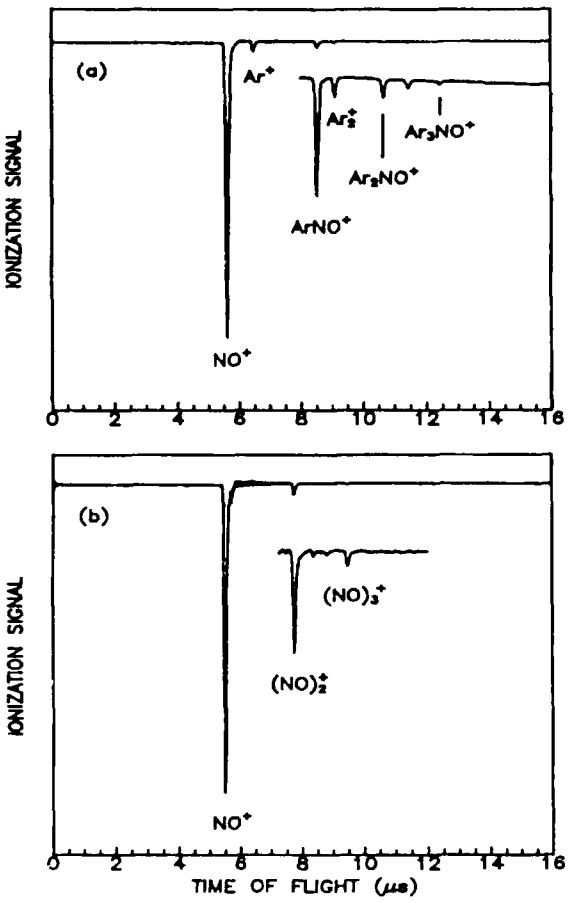


Fig. 4. Time-of-flight mass spectra of Ar_nNO^+ and $(NO)_n^+$ following picosecond MPI with (a) 590-nm and (b) 295-nm light and under identical molecular beam conditions.

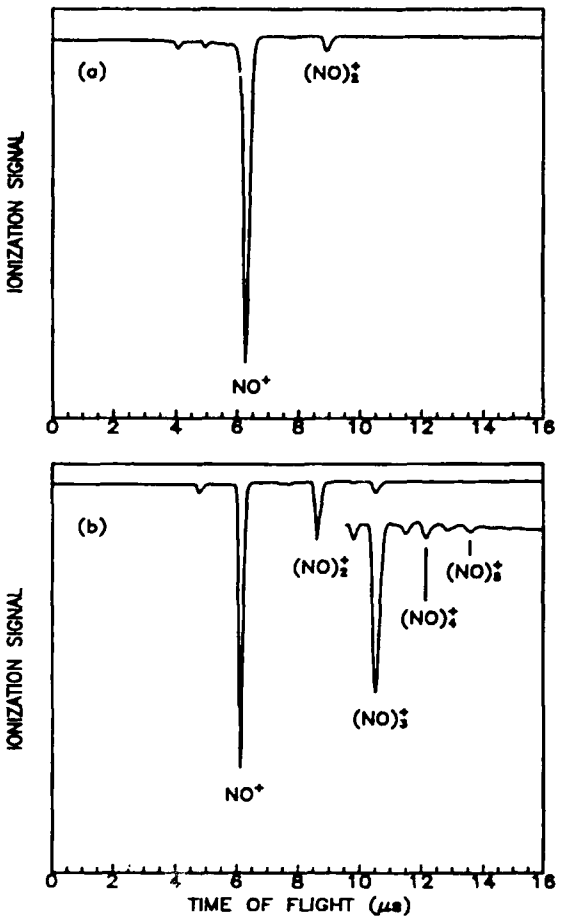


Fig. 5. Time-of-flight mass spectra of $(NO)_n^+$ following (a) nanosecond and (b) picosecond MPI with 266-nm pulses.

Ultraviolet MPI Multiphoton ionization results for the NO/Ar mixture were obtained in the region ~200-300 nm using the 266-nm output of the Nd:YAG laser or several longer (Stokes) or shorter (anti-Stokes) wavelengths produced by Raman-shifting in H_2 gas. The laser was operated in both picosecond and nanosecond modes at these wavelengths. The 266-nm results are shown in Fig. 5(a) for a 10-ns pulse length and in Fig. 5(b) for a 20-ps pulse length. The nozzle jet parameters, focal length, and mass spectrometer extraction and acceleration fields were kept the same for the two cases. The beam path and hence the focal spot could not be maintained while converting the operational mode of the laser, and the focal spot therefore was adjusted to give the same time-of-flight for the NO^+ ions in both experiments. As shown in Fig. 3, MPI at 266 nm is a nonresonant two-photon process for both the NO monomer and NO dimer. Furthermore, the photodissociation cross section of the ion must be low at this wavelength, and consequently this is an ideal wavelength for characterizing the $(NO)_n$ clusters. Figure 5(b) shows that clusters up to $(NO)_5$ are present in the expansion. Under these conditions of nonresonant MPI there is no fundamental difference between the use of nanosecond and picosecond lasers. As with any multiphoton process, higher peak-power increases the ionization rate until saturation is achieved. At 266 nm, the 20-ps pulse (4-mJ energy) gives a peak power approximately 100 times higher than the 10-ns pulse (18-mJ energy). The picosecond results indicate that some saturation occurred, because the integrated intensity of the dimer signal relative to the monomer signal is approximately 16%, a percentage that is two to three times larger than the concentration in the beam. In the nanosecond results, the relative intensities of the dimer and monomer signals is about 5%, a value that is more comparable to those in the literature.

By Raman-shifting the 266-nm output of the Nd:YAG laser, it was possible to investigate MPI at two Stokes and three anti-Stokes wavelengths. The Stokes lines at 299.0 nm and 341.5 nm give results not too different from those of the 295-nm excitation. In both cases the dissociative neutral and ion resonances are avoided and dimers are observed with the picosecond laser, but only weakly or not at all with the nanosecond laser. Note that at these wavelengths three photons are required for ionization.

In contrast, the 266-nm, 239.5-nm, 217.8-nm and 199.8-nm anti-Stokes excitations require only two photons to ionize, and the first photon is resonant or near-resonant with the dissociative B_1 state of $(NO)_2$ in each case. Picosecond MPI results at the first anti-Stokes line (239.5 nm) exhibited an anomalously intense dimer signal (dimer to monomer signal ratio ~12%). The saturation argument, which was invoked for the 266-nm results and was based on the use of high peak-power, cannot be supported in this case. MPI at 266 nm (1-mJ pulse energy) yielded a signal ratio of ~8%, a reasonable estimate of the dimer to monomer ration, while MPI at 239.5 nm was accomplished with considerably less peak power (< 0.25-mJ pulse energy). Hence the large dimer signal probably indicates a resonance effect. On the other hand, the nanosecond results yielded a smaller dimer signal at 239.5 nm than at 266 nm, indicating that the resonance is predissociative in nature and that at the lower peak-power of nanosecond MPI the ionization cannot compete with the predissociation.

The second anti-Stokes line at 217.8 nm falls in the dissociative resonance of the NO dimer, and the shortened photodissociation lifetime thus offsets the resonance effect. At this wavelength no dimer signal is observed in the nanosecond experiments, while $(NO)_2$ and $(NO)_3^+$ are produced in the picosecond experiments. These results are shown in Fig. 6, and they dramatically illustrate the advantage of high-peak-power MPI.

The third anti-Stokes line at 199.8 nm yielded results similar to that at 266 nm, and the results presumably reflect nonresonant two-photon absorption.

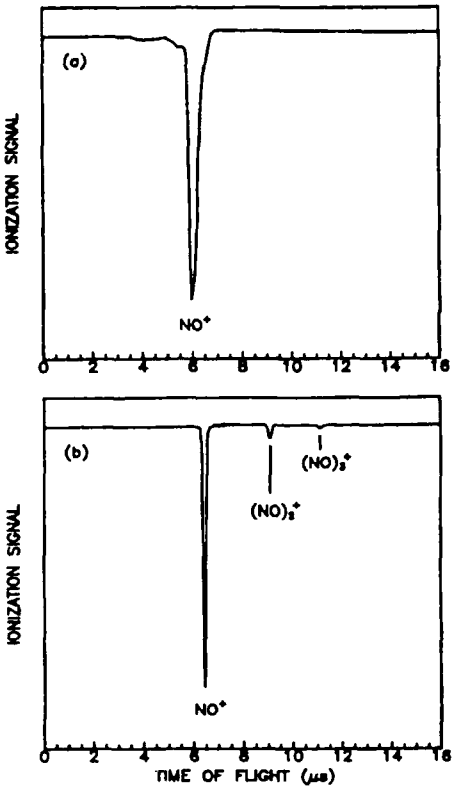


Fig. 6. Time-of-flight mass spectra of $(NO)_n^+$ following (a) nanosecond and (b) picosecond MPI with 266-nm pulses.

Iodine-rare gas complexes

Figure 7 shows the TOF spectrum following MPI at 532 nm of species formed in an expansion of an I_2/Ar mixture. The ion clusters observed are the Ar_nI^+ series rather than the $Ar_nI_2^+$ series. This observation of the daughter ion series is consistent with the very efficient one-photon photodissociation of uncomplexed I_2^+,[13] but the fragmentation might also be occurring via so-called "half-collisions."[14] The chemi-ionization reaction

$$Ar^* + I_2 \rightarrow ArI^+ + I\,, \qquad (1)$$

which has been previously observed,[15] occurs via a transition state $Ar^* \cdot I_2$. This same transition complex can be achieved by exciting the ArI_2 van der Waals molecule to an autoionizing state from which dissociative ionization occurs to $ArI^+ + I$. Likewise, intracluster ion-molecule reactions[15] analogous to

$$I_2^+ + M \rightarrow IM^+ + I \text{ or } M^+ + I_2 \rightarrow IM^+ + I\,, \qquad (2)$$

where M is a rare-gas atom, could also be responsible for our observation. Experiments to be performed will use intermediate resonances to produce localized excitation or ionization in either

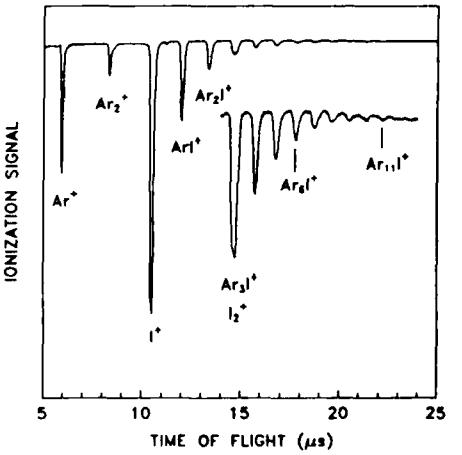


Fig. 7. Time-of-flight mass spectrum of Ar_nI^+ clusters following picosecond MPI with 532-nm light.

the rare gas or iodine part of the van der Waals complex.

Conclusions

We have used high-peak-power lasers (with both nanosecond and picosecond pulses) to effect multiphoton ionization of Xe_n, $(NO)_n$, Ar_nNO and Ar_nI_2 clusters. This technique is a versatile and rather general means of detecting and studying cluster distributions. In contrast to resonant MPI, no knowledge of intermediate states is required, and laser mass spectrometry using such high-power lasers might constitute a near "universal" detector of atomic and molecular species.

Although this technique is more complex and more expensive than the traditional electron impact source, it has some unique advantages. MPI discriminates between atoms and molecules with high and low ionization potentials (IP); an additional photon is usually required for ionization of systems with high IP's. An n^{th}-order MPI process usually has an ionization cross section several orders of magnitude larger than that for an $(n+1)^{th}$-order process. Typical expansion gases such as He, Ar or N_2 all have high IP's and thus would appear much less prominently (if at all) in the MPI mass spectrum. The spectrum of the dopant and its clusters would then be less congested. Furthermore, space-charge problems are also reduced if the most abundant species are not ionized. Since clusters usually have IP's smaller than monomers, a judicious choice of wavelength for MPI could allow discrimination against the monomer while efficiently ionizing the clusters. For instance, the IP of $(NO)_2$ is 0.528 eV less than that of uncomplexed NO, and the use of a laser wavelength between 285 and 267 nm would require two-photon ionization of $(NO)_2$ clusters as opposed to three-photon ionization of the NO monomer.

There are several notable disadvantages to the high-power resonant MPI technique. A major disadvantage of all multiphoton techniques is that photon absorption does not necessarily stop after ionization. Absorption of additional photons in either the neutral or ion manifold can lead to fragmentation. High-peak-power lasers are certainly more likely to lead to such problems. In this respect, the picosecond laser may have an advantage over a nanosecond laser of equivalent power. The absorption of an extra photon can possibly lead to different results in the two situations.[1] A final potential disadvantage of MPI techniques, which is exacerbated with high power and short pulses, is the space-charge degradation of the mass resolution. Tightly focused laser pulses of short duration can, in principle, improve TOF resolution provided only a few ions are created. At higher ion densities, however, space-charge effects tend to broaden the mass peaks.

In summary, nonresonant MPI is an important adjunct to both resonant laser ionization and electron impact ionization for the characterization of molecular beams. Additional details on the present work are ave given elsewhere.[16]

References

1. J. J. Yang, D. A. Gobeli, and M. A. El-Sayed, *J. Phys. Chem.* 89, 3426 (1985); and references therein.
2. R. Larciprete and M. Stuke, *J. Crystal Growth* 77, 235 (1986).
3. J. C. Miller and R. N. Compton, *J. Chem. Phys.* 84, 675 (1986); J. C. Miller, *Anal. Chem.* 58, 1702 (1986).
4. D. M. Lubman and R. M. Jordan, *Rev. Sci. Instrum.* 54, 641 (1983).
5. W. D. Wiley and I. H. McLaren, *Rev. Sci. Instrum.* 26, 1150 (1955).
6. O. Echt, M. C. Cook, and A. W. Castleman, *Chem. Phys. Lett.*, 135, 229 (1987); *J. Chem. Phys.* 87, 3276 (1987); and references therein.
7. J. C. Miller and W. C. Cheng, *J. Phys. Chem.* 89, 1647 (1985); J. C. Miller, *J. Chem. Phys.* 86, 3166 (1987); J. C. Miller, *J. Chem. Phys.* 90, 4031 (1989).
8. K. Sato, Y. Achiba, and K. Kimura, *J. Chem. Phys.* 81, 57 (1984); *Chem. Phys. Lett.* 126, 306 (1986); K. Sato, Y. Achiba, H. Nakamura, and K. Kimura, *J. Chem. Phys.* 85, 1418 (1986).
9. J. Billingsly and A. B. Callear, *Trans. Faraday Soc.* 67, 589 (1971).
10. G. P. Smith and L. C. Lee, *J. Chem. Phys.* 64, 5395 (1978).
11. For convenience, excited states of ArNO are labelled according to the corresponding state of uncomplexed NO.
12. R. R. Burke and R. P. Wayne, *Int. J. Mass Spectrom. and Ion Phys.* 25, 199 (1977).
13. J. C. Miller and R. N. Compton, *J. Chem. Phys.* 75, 2020 (1981).
14. C. Wittig, S. Sharpe, and R. A. Beaudet, *Acc. Chem. Research* 21, 341 (1985).
15. A. Henglein and G. A. Muccini, *Z. Naturforsch Teil A* 15, 584 (1960).
16. D. B. Smith and J. C. Miller, *J. Chem. Phys.* 90, 5203 (1989); *J. Chem. Soc. Faraday Trans.* 86, xxx (1990).

THERMAL LENS SPECTROSCOPY UNDER CONDITIONS OF HIGH BACKGROUND ABSORBANCE

Donald R. Bobbit*
Associate Professor
Department of Chemistry and Biochemistry
University of Arkansas
Fayetteville, Arkansas 72701

Since its first demonstration over 25 years ago, the thermal lens effect has received much attention due to its unique capabilities, particularly with respect to the measurement of weakly absorbing systems. Several reports have shown that absorbance detectabilities at the 2 x 10^{-7} cm^{-1} level are possible with thermal lens spectroscopy (TLS). This same detectability can be maintained in TLS even in the presence of a background signal which is several orders-of-magnitude larger. To make sensitive measurements under such limiting conditions, a differential thermal lens spectrometer has been designed and evaluated which is based on the oblique crossing of separate pump and probe beams. This experimental configuration uses the differential response of the thermal lens to compensate for intensity instabilities in the pump source while at the same time the intrinsic sensitivity of photothermal measurements is maintained. The theory describing the thermal lens signal observed with this experimental configuration will be developed and experimentally verified. Applications will be described which depend upon the unique capabilities of this TLS system to make direct, optically encoded differential measurements. Such measurements can be used to minimize background contributions in experimentally demanding situations.

Introduction

In many measurement situations the background is an active participant in the measurement process providing a signal which can be substantial compared to the analytical signal. This background will eventually limit the scope of the measurement. Techniques which are applicable to such background limited situations must be capable of maintaining high instrumental sensitivity while at the same time they must possess some mechanism for minimizing the influence of the background signal on the signal-to-noise ratio (SNR) of the system. Spectroscopic techniques which fulfill these stringent requirements are rare and thus there is an urgent need to develop new analytical techniques which can function in background limited situations.

Photothermal spectroscopic techniques measure the amount of light absorbed by a sample via the heat deposited during the absorption process. These techniques have been widely studied due to their demonstrated ability to provide absorbance detectabilities at the microabsorbance level, or below. This is two orders-of-magnitude lower than measurable by conventional approaches. One of the principal applications of photothermal spectroscopy has been in the field of chemical analysis, particularly when the compounds under study are present at trace levels. For example, photothermal measurements have been successfully applied to such diverse areas as kinetic studies,[1] two-photon excitation measurements,[2] densitometric analysis of thin-layer chromatographic plates,[3] and for detection in high performance liquid chromatography (HPLC).[4,5]

In thermal lens spectroscopy (TLS), the gaussian intensity distribution of a TEM_{00} laser is used to create a gaussian-distributed absorption profile in the system under study. Providing that nonradiative processes dominate over radiative ones, this gaussian-distributed absorption profile will induce a similar refractive index gradient. This refractive index gradient can then act as an optical element to alter the focal properties of a probe laser. Thus, by measuring the strength of the thermal lens one can determine the magnitude of the sample absorption. TLS has been shown to be an extremely sensitive spectroscopic technique, however, its use has only been demonstrated in situations where the background signal is small or absent.

The positional dependence of the thermal lens[6] makes TLS particularly amenable to absorption measurements in background limited situations. This positional dependence is schematically depicted in Fig. 1. For materials that expand upon heating the photothermal process will create a diverging lens in the absorbing sample. This diverging lens can alter the focal properties of a probe laser, however, the magnitude and sign of the effect will depend on the position of the thermal lens relative to the focus of the probe. In the top portion of Fig. 1, a diverging lens located after the focal point will cause an increase in the far field beam size of the probe laser. Thus the beam will become less converged reflecting a shortening in its focal point. However, as depicted in the lower portion of the figure, if a thermal lens of the same strength is located an equivalent distance before the probe focus, the measured far field beam size will be decreased due to the greater convergence of the probe caused by the diverging thermal lens. In effect, this positional dependence gives rise to a differential response which can be used to minimize, or eliminate the influence of the background signal on the absorption measurement.

This communication will describe the key experimental parameters which must be controlled in order to successfully apply TLS under conditions of high background absorbance.

The optimized spectrometer will be used to detect nonabsorbing species separated by HPLC using a highly absorbing mobile phase.

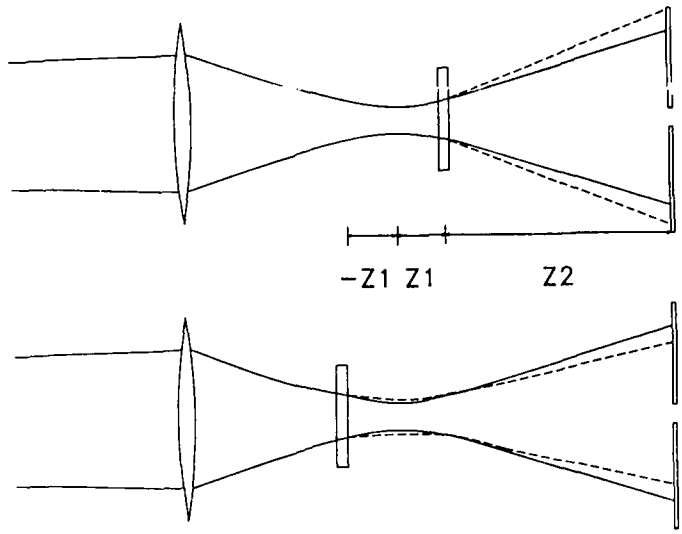


Fig. 1. Positional dependence of the thermal lens. Top; a diverging lens placed after the probe laser focus will shorten the focal point creating greater divergence. Bottom; a diverging lens placed before the focus will lengthen the focal point creating greater convergence.

Experimental

The optical configuration for the differential thermal lens spectrometer has been described in detail elsewhere[7,8] and is schematically represented in Fig. 2. The system was constructed on a 4 x 6 foot x 2.25 inch optical breadboard (Newport Corp., Fountain Valley, CA, Model XS46). The probe optics consisted of a 1-mW helium-neon laser (Uniphase, Sunnyvale, CA, Model 1101), modulated at 500 Hz by a variable speed, frequency stabilized

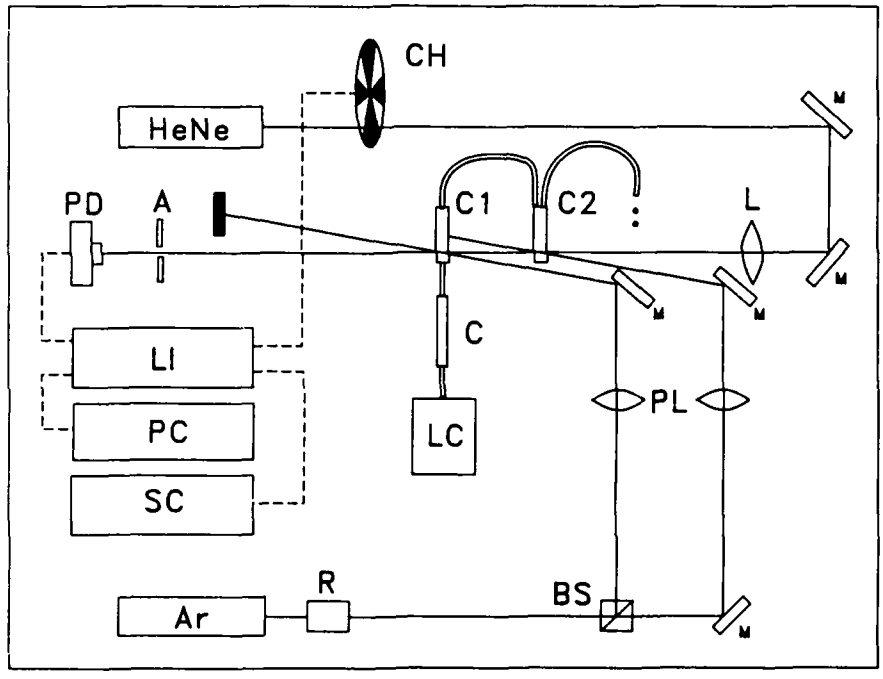


Fig. 2. Experimental arrangement of the differential TL spectrometer. AR, argon ion laser; R, 1/2 wave Fresnel rhomb; BS, polarization beam splitter; PL, matched 25 cm focal length lenses for the pump beams; C1, C2, 5 µL sample cells; HeNe, helium neon probe laser; CH, chopper; L, 30 cm focal length lens for the probe; M, mirror; a, detector aperture; PD, photodiode; LI, lock-in amplifier; PC, microcomputer; SC, strip chart recorder; LC, syringe pump; C, HPLC column. From ref. 7.

chopper (Stanford Research Systems, Palo Alto, CA, Model SR540) and focused with a 30 cm focal length lens. The 5 μL sample cells were constructed in-house from 6.2 mm aluminum stock and positioned at $\pm 3^{1/2}$ of the Rayleigh range of the probe laser. The signal was determined by measuring the amount of light passing a 0.02 in. diameter aperture with a silicon photodiode (Hamamatsu Corp., Middlesex, NJ, Model S1790-04). The photodiode was reverse biased at 30 V through a 50 ohm resistor. The output of the photodiode was sent to a lock-in amplifier (Stanford Research Systems, Palo Alto, CA, Model SR510), the output of which was sent to a PC via an IEEE-488 interface card (National Instruments, Austin, TX, Model PC-2A) for data collection and analysis.

The pump beams were derived from an argon ion laser (Lexel, Palo Alto, CA, Model 85.5) operating at 514.5 nm. A 1/4 wave Fresnel rhomb (Karl Lambrecht, Chicago, IL, Model MFR-02-13-580) and polarizing beam splitter (Karl Lambrecht, MGLA-SW-10) were used to provide two pump beams of equal magnitude. The pump beams, consisting of 35 mW each were then focused into the individual detection cells with a 25 cm focal length lens.

The chromatographic system was conventional consisting of a syringe pump (ISCO, Lincoln, NE, Model LC 5000), an injector with a 20 μL sample loop (Rheodyne, Berkeley, CA, Model 7010) and a 25 cm x 4.6 mm i.d. C-18 separation column (Alltech Associates, Deerfield, IL). The two detection cells were connected in series by a length of 0.03 in. tubing having a total volume of 300 μL which was approximately one-half of the chromatographic peak volume. The eluent was a 95:5 mixture of acetonitrile and 0.3 M phosphoric acid which was degassed under vacuum by ultrasonic agitation prior to use. "Pontacyl" Carmine 2B (Dupont, Wilmington, DE) was added to the eluent until its absorbance measured 1.3×10^{-2} cm^{-1}. The absorptivity of this additive was determined to be 27.0 L g^{-1} cm^{-1} at 514.5 nm. Fatty acid standards (decanoic, lauric and myristic) were obtained from Aldrich (Milwaukee, WI) and used without further purification.

The effluent from the chromatographic column entered each detection cell sequentially. A running integration was then performed on the baseline adjusted data obtained from the lock-in detection system.[9,10]

Results and Discussion

In the TL system used for these studies the pump and probe beams are crossed at an oblique angle in the detection cells. This approach allows the interaction path to be varied to compensate for the effect of large backgrounds. Without any limiting assumptions concerning the relative sizes of the pump and probe beams, and by using the conventional definition[11] of $\Delta I/I$, where I is the intensity passing the aperture, the observed TL signal can be described by Eq. 1.

$$\Delta I/I = [1/f(\infty)^2 [Z_c^2 + Z_1^2] - 2Z_1/f(\infty)] \cdot [1 - \exp(-2\omega_e^2/\omega_p^2)] \quad (1)$$

Here, Z_1 refers to the distance between the probe waist and the cell, Z_c is the confocal parameter of the probe, $f(\infty)$ is the focal length of the steady state thermal lens, and ω_e and ω_p are the pump and probe beam sizes, respectively, in the sample. Substituting for $f(\infty)$,[11] and assuming that the focal length is sufficiently long to ensure that the quadratic term can be ignored, gives

$$\Delta I/I = [-4.606 Z_1 P_e (dn/dT) A/\pi k \omega_e^2] \cdot [1 - \exp(-2\omega_e^2/\omega_p^2)] \quad (2)$$

In this equation, k is the thermal conductivity in units of W cm^{-1} K^{-1}, ω_e and ω_p are the sizes of the pump and probe beams at the cell, P_e is the pump source power in mW, dn/dT is the change in refractive index of the solvent with respect to temperature change ($^oK^{-1}$), and A is the Beers law absorbance of the solution. The pump laser power, concentration and interaction length dependence predicted by Eq. 2 have been experimentally studied. Plots for each of the three experimental variables versus differential TL signal are linear thereby establishing the validity of the procedures used to derive Eq. 2.

The theory used to derive Eq. 2 assumed that the probe laser profile maintained its gaussian characteristics after interaction with the pump field. This assumption might be expected to be suspect for the case described herein where the pump and probe beams are obliquely crossed. To test this possibility, the three dimensional intensity profile of the probe field was measured during pumping and fit to a gaussian. Although some perturbation was observed in the profile taken as a whole, for the region interrogated by the aperture, both the converged and diverged beams exhibited gaussian characteristics which were as good as the nonperturbed probe beam profile. This validates the assumptions inherent in the theoretical analysis leading to Eq. 2.

As discussed previously, techniques which are amenable to background limited situations must be capable of minimizing the influence of the background on the SNR. The coincident sampling capability of the differential TL measurement can reduce the thermal noise generated by the pump beams. This noise will be primarily of three types: both low and high frequency intensity fluctuations, and pointing variations. Pointing variations have only a minimal effect on this design since the two pump beams are focused into the detection cell. The high frequency components that occur on a time scale much shorter than the time response of the thermal lens cannot impart any thermal noise to the system that would per-

turb the probe. The final noise contribution which must be considered are those intensity fluctuations which occur on a time scale slower than the TL time constant. Although this contribution would be negligible under normal conditions, in the presence of a large background, these fluctuations will cause a change in the magnitude of the lens created in each cell. However, because both pump beams are derived from the same laser, the noise present on one will simultaneously be present on the other. With the differential TL arrangement, both cells will be affected equally with the result that there will be no change in the far field beam profile thereby reducing the affect of this noise source on the measurement.

The need for this type of optical noise subtraction is dramatically illustrated by considering the noise that would be observed in a single beam TL system under conditions where the background absorbance is large ($>10^{-2}$ cm^{-1}). It can be shown that the noise registered at the photodiode (ΔT_p) due to intensity fluctuations in the probe laser is given by

$$\Delta T_p = \Delta P_p 2a^2/\omega_f^2 \qquad (3)$$

where a is the aperture radius, ΔP_p is the change in probe intensity, and ω_f is the probe beam radius measured at the aperture. From Eq. 2, the noise in the TL signal induced by pump field power fluctuations (ΔT_{TL}) is

$$\Delta T_{TL} = \Delta P_e[9.212 P_p a^2 Z_2^2 (dn/dT)A]Zc\pi k\omega_f^4 . \qquad (4)$$

In Eq. 4, ΔP_e is the change in pump laser power and all other terms are as defined previously. Taking the ratio of Eq. 3 to Eq. 4, and substituting typical values for the experimental constants yields

$$\Delta T_p/\Delta T_{TL} = [0.20/A][\Delta P_p/\Delta P_{TL}] . \qquad (5)$$

Assuming that probe stabilities of 1 part in 10^4 can be achieved with modulation and phase sensitive detection, and operating under conditions where a background absorbance of 0.015 cm^{-1} is present, Eq. 5 shows that the pump laser fluctuations would only have to be 5×10^{-3} % on a 30 mW beam to cause a TL noise greater than the probe noise. Since most cw lasers offer inherent intensity stabilities at the 0.01% level, or above, the differential arrangement will be required to eliminate the pump laser induced noise. This is universally true in any TL measurement made under conditions of large background absorbances.

This result was experimentally verified by imposing a 9 mW, 5 s intensity variation upon each of the pump fields while a flowing solution with an absorbance of 0.01 cm^{-1} was monitored. The intensity variation was created using an acousto-optic modulator placed in the pump laser optical path. The signal obtained from the detection system is plotted in Fig. 3. The top and bottom entries of Fig. 3 show the effect of this intensity variation on a single beam TL measurement. As predicted, the signals resulting from optical pumping of the cells reflected this intensity noise in that they varied by approximately 25%. The middle entry shows the effect of this intensity variation when both detection cells are simultaneously pumped in the differential mode. Even with the added 25% intensity fluctuation, the peak-to-peak noise is only a factor of three larger with the differential TL system than that measured with no added pump noise. This illustrates the capability of this experimental arrangement to minimize the influence of pump laser noise.

Most detection systems are designed to operate in a direct mode in that they respond to a property of the analyte under study. In comparison, indirect methods of detection respond to a property of the bulk matrix and the analyte is detected as a decrease in the measured signal as it displaces some of the matrix in the detection volume. For example, in indirect photometric detection, an absorbing species is added to the chromatographic mobile phase and molecules which are transparent at the probing wavelength are detected as a decrease in the measured absorbance as they elute from the chromatographic column. This procedure converts a very selective detection scheme (absorbance) into a universally responding one. This is very useful since many of the detection problems of current interest in the fields of materials science, biotechnology or biochemistry involve molecules that do not possess easily accessible chromophores, or they possess chromophores with weak absorption cross-sections.

The key to the success of an indirect detection scheme is the dynamic reserve (DR) of the instrumental system. Dynamic reserve is defined as the ratio of the background signal to the minimum change in signal which is measurable under these conditions. For conventional HPLC absorbance detectors, backgrounds of approximately 0.5 absorbance units (AU) can be tolerated while still maintaining a detectability of 5×10^{-5} AU. The DR under such conditions is 2×10^3 which is not adequate considering the extremely dilute samples used in modern HPLC. In comparison, it has already been demonstrated that the differential TL system can tolerate background levels of 0.5 AU while still maintaining an absorbance detectability of 2×10^{-7} AU. Thus DR's in excess of 2×10^5 are possible suggesting that TL detection appears feasible in an indirect mode. This would be accomplished by adding an absorbing additive (i.e. absorbing at the laser wavelength) to the mobile phase and detecting transparent materials (i.e. transparent at the laser wavelength) as a decrease in the TL measured absorbance as they elute. This decrease is a result of the replacement of

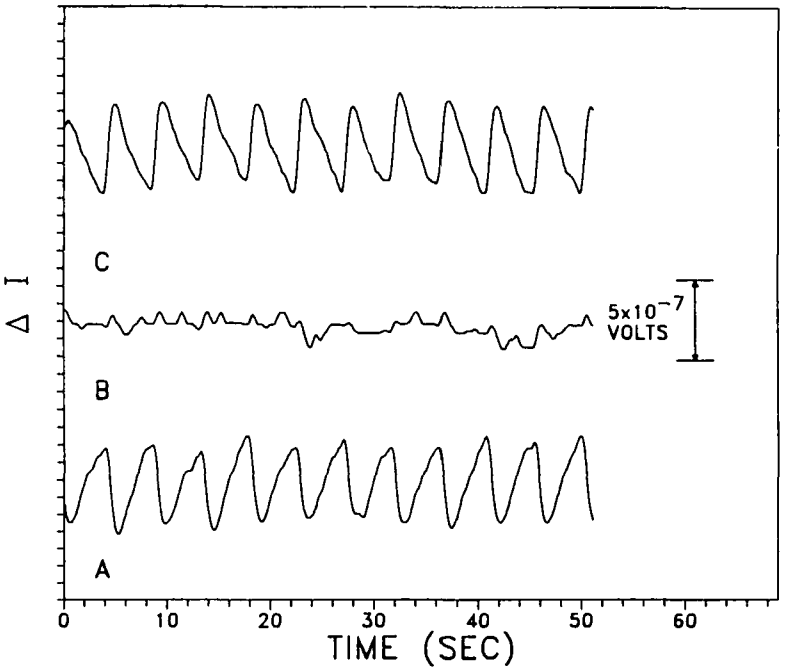


Fig. 3. Reduction in measured noise due to the differential response. A and C, signal observed when adding a 9 mW intensity fluctuation on a 36 mW pump beam over a 5 s interval, in cells one, and two, respectively; B, differential response observed when optically pumping both cells simultaneously under the same conditions listed above. From ref. 8.

the absorbing additive species in the probe volume by a nonabsorbing molecule. The advantages of this approach are significant in that the high sensitivity is maintained with the differential TL system even in the presence of a large background, while the use of a laser to monitor this indirect TL effect will permit extremely small volumes to be probed, thus making this technique amenable to the very latest developments in microcolumn technology.

Fig. 4 is the response observed with the differential TL system resulting from the injection of decanoic acid into a flowing solvent stream made absorbing by the addition of carminic acid. To assure that both detection cells contain identical solutions at all times, and to assure that they will simultaneously experience identical pressure fluctuations, the two cells are connected in series. Thus the analyte will enter each cell sequentially. Because the lenses formed in the two cells oppose each other, that is, one lengthens and one shortens the focus, a derivative-shaped response is observed as the analyte first replaces the additive in one cell, and then the other. This is evident in part A of Fig. 4. A real time integration of the differential TL signal provides a conventional, gaussian-shaped peak (part B). As demonstrated previously,[9] this mathematical procedure also provides a substantial improvement in the measured SNR.

The study and analysis of fatty acids are important because of their critical role in many biochemical processes. Fatty acids make up a large portion of cellular membranes, they are an important energy store when coupled with acetyl-CoA, and they play a key role in the function, storage and transport of cholesterol. However, the saturated fatty acids do not show appreciable absorption above 210 nm making their detection difficult. Fig. 5 shows the chromatogram obtained from the separation and indirect TL detection of three biochemically important fatty acids. The top chromatogram is the original signal as measured by the series cell arrangement, while the bottom is the baseline-adjusted integrated result.

The response of the detector has been determined to be linear over at least 2 orders-of-magnitude above the detection limit. The plot of normalized peak height response versus normalized mass of decanoic acid injected had a slope of 0.98, an intercept of 0.06, and a correlation coefficient of 0.990 (5 points). The signals measured in several chromatograms were used to determine an average limit of detection (LOD) of 15 ng detectable in the cell. In terms of the actual probed volume of 32 nL, the amount of decanoic acid detectable in the detection volume at the detection limit is 90 pg. It is also important to note that the ratio of the peak areas for the three different fatty acids corresponds exactly, within injection reproducibility, to the ratio of the amount of material injected. This result is expected if the signal arises only from the dilution of the visualization reagent. The response of this detection scheme is not dependent on any physical or chemical property of the eluent other than injected mass. This universal response would be quite useful for quantitative measurements in that a standard response curve for one analyte could be used for any other analyte detected in a given solvent system. This statement would be valid as long as the analyte and solvent behave as an ideal solution.

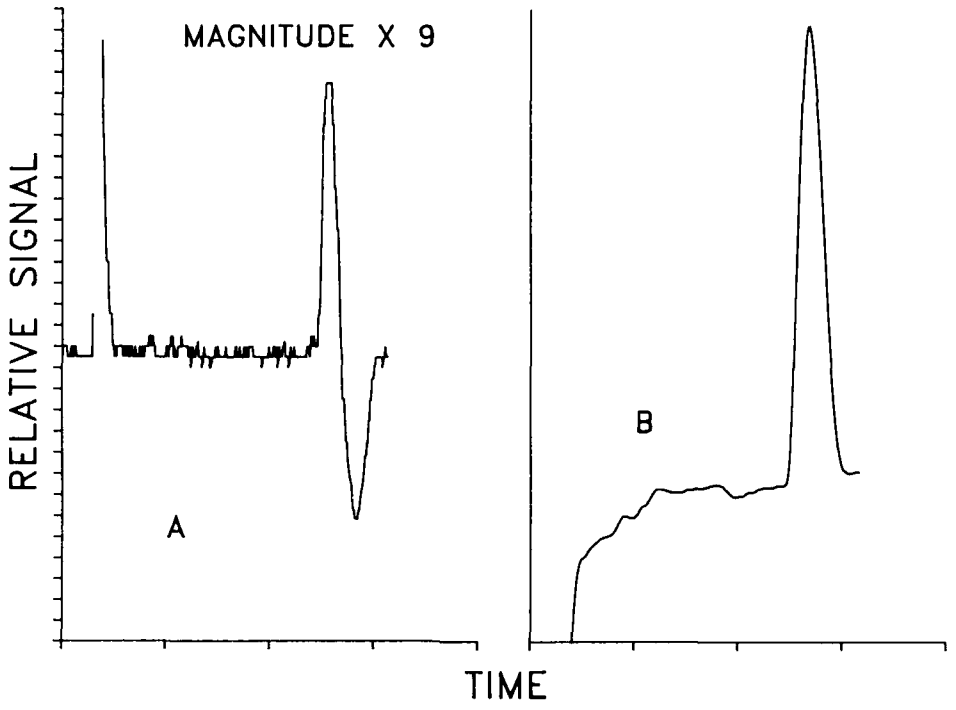


Fig. 4. Indirect TL response for 23 g of decanoic acid. Solvent, 95:5 acetonitrile: 0.3 M phosphoric acid; background absorbance, 1.3 x 10^{-} cm^{-} ; A, differential signal; B, signal after integration of the base-line-adjusted data of A.

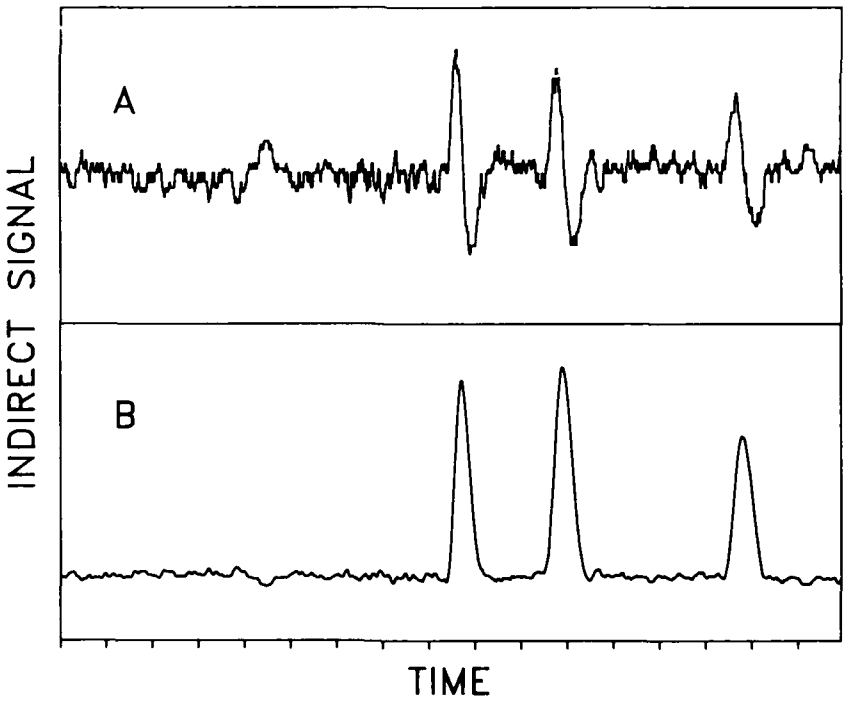


Fig. 5. Chromatogram resulting from the injection of 23 µg of decanoic acid (peak 1), 20 µg of lauric acid (peak 2), and 20 µg of myristic acid (peak 3). Chromatogram in A is the indirect TL detected signal, and B is the result of integrating the base-line-adjusted chromatogram.

In conclusion, the differential TL system described here has been shown to possess unique capabilities which make it amenable to measurements under background limiting conditions. The large dynamic reserve is a direct result of the differential design and its

ability to maintain the high sensitivity of the TL experiment while at the same time minimizing the influence of the background on the measurement. As an example, indirect TL detection is universally responding and has demonstrated mass detectabilities which are superior to that obtainable with conventional refractive index detection. Application of this differential TL system to other background limited measurements (e.g. circular dichroism spectroscopy) is a logical extension of this work.

Acknowledgement

Acknowledgement is made to the Donors of the Petroleum Research Fund, administered by the American Chemical Society, for support of this work. The author wishes to thank the Camille and Henry Dreyfus Foundation for partial support through a teacher-scholar fellowship.

References

1. J.P. Haushalter and M.D. Morris, Appl. Spectrosc. 34, 445 (1980).
2. A.J. Twarowski and D.S. Klinger, J. Chem. Phys. 20, 253 (1977).
3. K. Peck, F.K. Fotiou, and M.D. Morris, Anal. Chem. 57, 1359 (1985).
4. Y.Yang, S.C. Hall, and M.S. De La Cruz, Anal. Chem. 58, 758 (1986).
5. N.J. Dovichi, T.G. Nolan, and W.A. Weimer, Anal. Chem. 56, 1700 (1984).
6. N.J. Dovichi and J.M. Harris, Anal. Chem. 52, 2338 (1980).
7. S.R. Erskine and D.R. Bobbitt, Appl. Spectrosc. 43, 668 (1989).
8. S.R. Erskine and D.R. Bobbitt, Anal. Chem. 61, 910 (1989).
9. R.E. Synovec and E.S. Yeung, Anal. Chem. 57, 2162 (1985).
10. R.E. Synovec and E.S. Yeung, Anal. Chem. 58, 2093 (1986).
11. J.M. Harris and N.J. Dovichi, Anal. Chem. 52, 695A (1980).

USE OF VARIOUS LASERS FOR SAMPLE INTRODUCTION IN ATOMIC AND MASS SPECTROSCOPY

Joseph Sneddon

Department of Chemistry
University of Lowell
Lowell, Massachusetts 01854

Abstract

An overview of the use and performance of various laser systems used to ablate or vaporize solid samples for introduction to various atomic and mass spectroscopic systems for subsequent quantitative metal determination is described.

Introduction

The ability of a laser to ablate or vaporize small masses of solid material was recognized following the invention of the Ruby laser in the early 1960's. The ablated material will form a plume or plasma at the solid surface. It is possible to probe this plasma by several analytical techniques or carry this sample of ablated material to similar or other a analytical techniques. In the second method the laser is simply being used as an atomizer. In this report the use of a laser to ablate or vaporize small amounts of solid samples for transport to an atomic and/or mass spectrometer for quantitative determination of the metal levels in the solid will be described, with particular focus on the types of laser systems used to achieve the ablation stage. The various atomic and mass spectrometric systems and the advantages and disadvantages of laser ablation for sample introduction are described elsewhere[1].

Principles of Laser Ablation in Atomic and Mass Spectrosopy

When laser light is absorbed by a solid sample, a variety of heating phenomenon can occur including the heating of the surface, vaporization, dissociation, ionization, and excitation. This will result in a change in the phases of the solid sample. The exact mechanism is not known but a simplified model has been postulated[2] in which a portion of the light is transformed into heat energy. The energy level of the electrons on the surface is raised and transferred to the surrounding surface by electron impact and, eventually, the electron errupts at a high velocity, leaving a crater on the solid surface. This material is then transported to the atomic or mass spectroscopy system for analytical detection. A more detailed description of the individual components of the ablation process are described in an article by Hein and Piepmeier[3]. The use of laser ablation is being primarily used as a sample introduction process in this work[4-8].

Instrumentation

A description of the various atomic and mass spectroscopic systems and interfaces used is described elsewhere[9] and this report will primarily concentrate on the laser systems used. The laser systems used and which are capable of use as a sample introduction sytem for atomic and mass spectroscopy as well as some general operating features are summarized in Table 1.[10] Laser systems can have a continuous wave (CW) or pulsed operation and can be enhanced by Q-switching, mode-locking, and superpulsing.

Parameters Affecting the Laser Ablation Process

Several factors can influence the ablation process of laser light on a solid sample including properties of the sample (reflectivity of the surface, thermal conductivity of the surface material, heat capacity, melting and boiling points of the solid sample, and properties of the surrounding atmosphere[kind and pressure of the gas]) and laser parameters (wavelength of laser light, intensity, spike number and repetition rate). A discussion of these factors is presented elsewhere[11].

Table 1

Most Widely Used Laser Systems in Laser Ablation-Atomic and Mass Spectroscopy

1.	Solid State	: Nd: YAG at wavelength of 1.06 microns and output of CW (<600W) or pulsed (0.1-1.0 ms, < 200J)
		: Nd: Glass at wavelength of 1.06 microns and output pulsed (0.01-1.0 ms, < 100J/200W)
		: Ruby at wavelength of 694 nm and output pulsed (10 ns to 10 ms, <100 J/100 W)
2.	Excimer	: Argon Fluoride at wavelength of 193 nm and output pulsed (5-30 ns, < 500mJ/50W)
		: Krypton Fluoride at wavelength of 248 nm and output pulsed (2-50 ns, < 1 J/100W)
		: Xenon Chloride at wavelength of 308 nm and output pulsed (1-80 ns, < 5J/150W)
		: Xenon Fluoride at wavelength of 351 nm and output pulsed (1-30 ns, < 500mJ/30W)
		: Krypton Chloride at wavelength of 222 nm and output CW or pulsed (1-50 ns, < 4mJ/200mW)
3.	Dye	: Excimer, nitrogen, Nd: YAG, and Nd: Glass pumped at wavelengths 300-1000 nm (tuneable) and output (3-50 ns, 200 mJ/15W)
		: Flash-lamped pumped at wavlengths 340-940 nm (tuneable) with output CW or pulsed (0.2-4 microsecond, < 50J/50W)
		: Ion-pumped at wavelength of 400-1000 nm (tuneable) and output CW (<2 W) or pulsed (1-10 ps, < 50 mJ)
4.	Carbon Dioxide	: Sealed at wavlength of 10.6 microns and output CW (<100 W)
		: Pulsed TEA at wavlength of 10.6 microns and output (50-100ns, < 150 J)
		: Waveguide at wavelength of 10.6 microns and output of CW (<50W) or pulsed (5-50 ns, < 5 mJ)

Note : Other laser systems including single gas, helium based, crystalline, semi-conductor diode, and vapor have not been widely used or reported for laser ablation-atomic and mass spectroscopy.

Performance of Laser Ablation -Atomic and Mass Spectroscopy

The analytical performance characteristics of laser ablation atomic and mass spectroscopy can be described, in general, with a reproducibilty of 2-10%, accuracy ±5% and detection limits of around 1 μg/g for many metals. Of course these analytical figures of merit depend on many factors such as laser system, sample type, and atomic or mass spectroscopic system. A more detailed description of the analytical performance is available elsewhere[4-9, 11]. The application to real samples has not been widely reported and Table 2 gives a general survey of laser ablation in atomic spectroscopy.[11]

Table 2

Application of Laser Ablation in Atomic Spectroscopy[11]

Nonconductive materials, powders and compact material	: Rocks/minerals: dolmite, tourmaline, rutil, zircon, argonite, carbonate, silicate, meteorites
	: Ores: zinc blend, pyrite, chalcopywrite
	: Technical products: chemicals, glasses, quartz, semiconductors, dust, korund, paints, graphite, borax, ceramics, pigments, tungsten oxide
Conductors	: Metals: Cu, Pb, Al, Zr, Mo, Rh, brass, low-alloy steels, nickel and aluminum alloys, gold
Organic and biological materials	: Plastics, nylon, fiber, hair, tissue (brain, pancreas, liver, kidney, stomach, sperma, teeth, urological stones)

Conclusion

Laser ablation for sample introduction of solid samples in atomic and mass spectroscopy has potential for quantitative determination of metals with good analytical characteristics. until the recent introduction of a commercially available attachment to an inductively coupled plasma-atomic emission spectrometry (ICP-AES) and inductively coupled plasma-mass spectroscopy (ICP-MS) system by the Perkin-Elmer Corporation, systems were laboratory constructed. The improved reliablity and lower cost of laser systems with improved performance suggests that laser ablation-atomic and mass spectroscopy will continue to mature and be a useful addition to the analytical or industrial chemist who is interested in the quantitative determination of metals in solid samples.

References

1. J. Sneddon, P.G. Mitchell, and N.S. Nogar, Chapter 9, p347-383, 'Laser Induced Plasmas and Applications' ed. L.J. Radziemski and D.A. Cremers, pub. Marcel Dekker, Inc. New York, 1989.
2. H. Klocke, Spectrochimica Acta, 1969, 24B, 263.
3. S.J. Hein and E.H. Piepmeier, Trends in Anal. Chem., 1988, 7(4), 137.
4. P.G. Mitchell, L.J. Radziemski and J. Sneddon, Appl. Spectrosc., 1986, 40, 274.
5. P.G. Mitchell, J.A. Ruggles, J. Sneddon and L.J. Radziemski, Anal. Lett., 1985, 18(A14), 1723.
6. P.G. Mitchell, L.J. Radziemski and J. Sneddon, Appl. Spectrosc., 1987, 41, 141.
7. K. Dittrich and R. Wennrich, Prog. Anal. Atom. Spectrosc., 1984, 7, 139.
8. J. Sneddon and P.G. Mitchell, Amer. Lab., 1986, Nov., 21.
9. J. Sneddon, Proc. Int. Conf. on LASERS` 88, ed., R.C. Sze and F.J. Duarte, STS Press, McLean, Virginia, 1989.
10. S. Wohistein, Spectroscopy, 1989, 4(9), 10.
11. K. Dittrich and R. Wennrich, Chapter 5, 'Sample Introduction in Atomic Spectroscopy', ed. J. sneddon, pub. Elsevier Science Pub., Amsterdam, The Netherlands, 1990.

LASER OPTOGALVANIC SPECTROSCOPY

S. P. McGlynn and D. Kumar
Department of Chemistry
Louisiana State University
Baton Rouge, LA 70803

Abstract

Various configurations for laser optogalvanic (LOG) studies are discussed. Emphasis is placed on pulsed laser optogalvanic spectroscopy of atoms and molecules (Xe, Cs, Ne, I_2) in a radiofrequency discharge. The photoacoustic effect is found to be a major contributor to the LOG signal. The nature and magnitude of this contribution is assessed.

Introduction

The laser optogalvanic (LOG) effect is the change of the electrical impedance of a plasma that is produced by resonant absorption of laser radiation by a constituent species of the plasma.[1-3] The LOG effect has been used in a wide variety of sensitive and novel techniques spanning atomic and molecular spectroscopy, plasma diagnostics, flame/combustion studies, laser stabilization, and photoacoustic detection.

LOG spectroscopy of atomic and molecular systems has been studied over extended spectral ranges (UV-IR). However, because of the complexity of plasma and lack of knowledge about cross-sections, etc., the mechanism of LOG signal generation is incompletely understood. The requirement of a stable and quiet plasma is also restrictive in that it limits the range of pressure, electrical power, etc. which can be investigated.

The temporal profile of LOG signals contains considerable mechanistic information. Unfortunately, only a few time-resolved studies are available. Several phenomenological models have been proposed but they have had limited success. Of particular concern to such models is the LOG signal generated by low-energy excitation (rotational, vibrational or even low-energy electronic) in which the laser-excited upper level is much below ionization limits.

DC discharges are characterized by discrete discharge regions in which both LOG signal magnitude and polarity may change.[4-6] Consequently, LOG measurements in such discharges can be complex, and axial laser excitation, in particular, may produce a type of "averaged" signal. This sort of arrangement may well provide LOG signals, but it is not suited to spectroscopic investigations. It is much better to use an rf discharge in a transverse laser excitation mode. The rf discharge has the advantage of spatial uniformity (except for a sheath at the rf electrodes) and it can be used in a "contactless" manner (i.e., with no metal electrodes inside the discharge tube). CW lasers may provide better stability and resolution, but short pulse lasers in conjunction with fast electronics are required for proper study of the transients and dynamical properties.

Nonetheless, dc discharges can be used for high-speed time-resolved studies if proper precautions are taken. Since a dc discharge has an inherent negative resistance, it requires a series resistance larger than a certain minimum value to suppress the plasma oscillations. Larger value of this resistance will produce a larger LOG signal but, at the same time, it restricts the time-resolution capability because of the plasma capacity and inductance. This problem may be circumvented by detecting the LOG signal across an additional low resistance in series with the cathode.[7,8]

Pulsed lasers used in conjunction with an rf discharge provide both greater challenge and pay-off. In particular, such set-ups provide workable alternatives for the study of corrosive gases. Alternatively, the LOG effect may be used to investigate the rf discharge itself, a topic of considerable importance because of thier use in plasma etching, as rf driven lasers, etc. In addition, as we show in a companion paper in these Proceedings[9], pulsed laser studies of rf discharges permit distinction between ionization- and photoacoustically-mediated components of the temporal profiles of LOG signals. This information is simply not obtainable in a dc discharge.

The pulsed laser/rf discharge system can be configured in two extreme ways: with t>>T (t=laser pulse duration, T=period of the rf cycle) and with t<<T. In the former case, the "long-lived" LOG effect produces a modulation of the rf carrier amplitude. Consequently, the LOG signal recovery section is simply an AM demodulator. With a laser pulse of ~1)s and an rf frequency of ~32 MHz(T~31ns), our experimental set up belongs to this category.[10] The latter configuration requires a somewhat shorter t (few ns) and longer T (rf of few MHz or less)[11]. In this case, however, the rf carrier densities need to be suppressed, or subtracted to recover a carrier-free LOG signal. The advantage of the latter configuration is that laser firing can be synchronized with rf phase and, consequently, rf phase dependent (i.e., field effect) studies can be carried out[11]. This

configuration is limited in that it requires elaborate electronics and its implement at rf frequencies above a few MHz is difficult. Moreover, photoacoustically-mediated LOG signals, which are broader and propagatively delayed, can pose interpretative problems.

Electron impact ionization and associative ionization are primarily responsible for maintaining the electrical discharge.[12] The former is believed to dominate at low gas pressures whereas the latter becomes important at higher pressures. This characteristic is not difficult to comprehend. At lower gas pressures, electrons have longer mean free path and, hence, they acquire larger kinetic energy in the applied electric field. Consequently, electron impact ionization dominates. At higher pressures, on the other hand, frequent electron collisions do not allow a high kinetic energy build-up and, hence, this mechanism is suppressed.

Since metastable states will usually exhibit fairly large populations, they should play an important role in discharge maintenance. Indeed, any perturbation of their population, directly or indirectly, should produce a large LOG signal.

Discharge impedance depends on charge carrier density and mobility. Laser excitation of an atom close to ionization threshold results in an increase in electron-ion pair densities (direct or collision-assisted ionization) and the discharge impedance drops. The polarity of the LOG signal thus generated is said to be "normal". Depending upon the set-up, this signal may be either positive or negative. Furthermore, an "inverted" LOG signal may be observed when the laser excitation results in an actual increase of discharge impedance[13]. Such an effect can be attributed to a population inversion of two combining levels or to some peculiar characteristic of the laser-excited upper level (e.g., a shorter decay time, a lower ionization efficiency than the lower level, etc.). The generation of LOG signals when laser-excited states lie far below the ionization threshold has been explained on the basis of an electron temperature coupling model: the change of electron temperature should cause a change of either electron mobility or electron impact ionization rates.[14] This explanation, however, is unsatisfactory. As we have shown[10] the photoacoustic (PA) effect, which plays an important role in the generation of LOG signals, provides a satisfactory explanation for many of these peculiar characteristics.

The generation of LOG signals in molecular systems is no different from atomic systems. Molecular discharges, of course, do have additional loss channels (vibrational and rotational excitations) and, consequently, higher rf powers are usually required to sustain a molecular discharge. Certain molecular dissociation products may also confer other attributes on the LOG signal. In an rf discharge in iodine, for example, distinct time-resolved atomic and molecular LOG singals are observed[10].

We will describe briefly some important results obtained using ~1μs pulsed laser excitation which impinges transversely on the outer region of a ~32MHz discharge in xenon, cesium, neon, and iodine. The role played by the PA effect in the generation of the LOG signal will be emphasized.

Experimental

The experimental arrangement for pulsed laser LOG measurements in an rf discharge (Fig.1) has been described[10]. The sample is contained in a quartz discharge cell (8mm diameter, 30 cm long) with copper electrodes A and B (~5cm apart) wound around the exterior of the cell. RF voltage (~32MHz) is resonantly stepped up and applied to the electrodes A and B. Approximately 1W of rf power is sufficient to sustain a stable, low-noise discharge.

The detector consists of a resonantly tuned pick-up coil C wound around the discharge cell and situated ~1cm below B. The output of a pulsed, tunable dye laser (Chromatix CMX-4, ~1μs pulse width) impinges transversely at L. When the laser is tuned through a resonant frequency of some discharge species, a change occurs in the rf power transferred to the pick-up coil. This change, which constitutes the LOG signal, is sent to a boxcar and then normalized by a novel pulse treatment procedure[15,16].

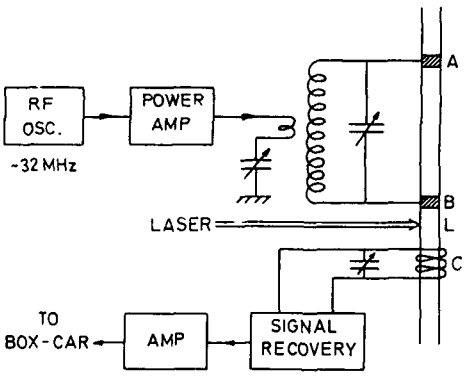


Figure 1.
LOG set-up with rf discharge.
See ref. 10 for details.

Wavelength calibration markers are generated by a LOG effect in a dc discharge in a neon-filled hollow cathode lamp. As the laser is tuned through the absorption frequency of a lamps species a pulsed change in lamp current occurs. This current pulse, when amplified and rectified, provides the markers on the second channel of the X-Y recoroer.

Results and Discussion

Xenon

The ground state electronic configuration of Xenon is $np^6(^1S_0)$. Under rf excitation, it yields two np^5ml configurations, one with a $^2P_{3/2}$ core ($n\ell$-states) and the other with $^2P_{1/2}$ core ($n\ell'$-states). Since xenon is best described by a $j\ell$ Racah coupling scheme, the states may be designated $n\ell(K)J$. For laser excitation in the range 16000-17000 cm^{-1}, we have observed five d→f series which originate in the 5d(1/2)0, the 5d(1/2)1, the 5d(3/2)2, the $5d(7/2)4_1$ and the $5d(7/2)3$ states at 78771.79, 79987.16, 80323.28, 80179.16 and 80970.93 cm^{-1} respectively[17]. Only one of these series had been observed previously. Higher members (n>20) of the series show broadening attributable to field ionization. These d→f series dominate at lower xenon pressures (~40mTorr). At higher pressures (~1Torr), series originating from 6p and 6s' states become dominant[18].

Several forbidden transitions ($\Delta K = \pm 2, \Delta j \neq 0$) have been also observed[18]. This "allowedness" is probably induced by rf fields present in the discharge.

Cesium

Cesium has an electronic configuration $[5p^6]6s^1$. It is not surprising, then, that observed spectra are attributable to a single valence electron moving about an inert noble gas core. Since the orbital and spin angular momenta of the core are both zero, this optical electron moves in a centrally symmetric field. Because of the screening effect of the closed shell electrons, the high-n excitation spectra are hydrogen-like. The hydrogenic character, particularly for the f-orbitals, is so good that the quantum defect for such series is only ~0.03[19].

The rf discharge populates various levels of the cesium atom such that laser excitation of frequency 16000-17000 cm^{-1} generates[20] the following Rydberg series in the LOG spectrum: 6p(3/2) → ns(1/2),6p(3/2) →nd(5/2), nd(3/2); 6p(1/2) →nd(3/2),5d(5/2) → np(3/2),5d(3/2) →np(1/2); 5d(5/2) →nf(7/2) and 5d(3/2) →nf(5/2). The series originating in the 6p levels are quite intense but only a few members are observed. Both 5d → np series are quite weak but the series can be followed up to n~20 (laser bandwidth ~ $3cm^{-1}$, (no intracavity etalon). The 5d → nf series dominate the spectrum and can be followed up to n~70 (laser bandwidth ~0.1 cm^{-1} (intracavity etalon). Lower rf powers facilitate the observation of higher-n members. In ~50mTorr cesium, perhaps because of its very low ionization potential, even an rf power of ~40mW can sustain a stable low-noise discharge.

By way of contrast, the d → f series of xenon can be followed only as far as n~35. The higher n members are braodened and "washed out" in the spectrum, perhaps because of the larger rf powers (0.5 - 1.0 W) required for the xenon discharge or perhaps because of a stronger field perturbations by the "unsaturated" core. Further investigations are in progress. An additional, much weaker component is also observed in the time-resolved LOG signal. This weak component is broader and delayed relative to the laser pulse. As elaborated later for neon and iodine, this second component in the LOG signal is assigned to be mediated by a PA effect.

Neon

The LOG effect in neon has been heavily investigated. Kinetic and cross-section data pertinent to the lower excited states is available. All LOG signal production models have neglected the role of the PA effect. Indeed, the distinct similarities between the temporal profiles of LOG signals from quite different discharge species, all of which point towards the important role of the PA effect, have been ignored. The accompanying paper in these proceedings[9] reviews this problem, and posits a method by which the conventional and PA mediated LOG signals may be differentiated even in the presence of temporal overlap.

Iodine

Iodine has been studied extensively in both dc and rf discharges. Some iodine molecules dissociate in the discharge to produce atomic iodine. LOG signals are expected from both atomic and molecular species. Under appropriate discharge geometry and fast time-resolution, two separate LOG signal components with different temporal characteristics are observed.

The intervention of a PA effect in the production of the LOG signal was noted.[4,5] However, the exact role played by the PA effect could not be assessed. Webster and Menzies[4] and Haner et al.[5] supposed that the pressure pulse, generated by a PA effect, ffected the discharge impedance by altering electron attachment and recombination rates in the negative glow region. As will be explained, this is not a satisfactory explanation.

We carried out time-resolved LOG spectroscopy of iodine in a ~32MHz rf discharge[10] showing that the LOG signal consists of two time-resolved components: a fast component, synchronous with the laser pulse, followed by a slow component, delayed relative to the laser pulse. The fast component originates in a two-step laser photoionization of plasma-excited atoms, the first-step being resonant, and/or in changes of atomic collisional ionization rates. The slow component is generated by the photoacoustic signal produced by the B ← X molecular excitation. The most significant observation is that the polarity of the PA mediated LOG signal reverses as the direction of propagation of the PA (say, a compression) wave reverses. Thus thermal effects are not involved in the final production step of the PA mediated LOG signal. It must, then, be related to some kind of kinetic effect (e.g., simple movement of the charge carriers in the "sensitive" region of the discharge under the influence of the PA wave).

Electric discharges contain both electrons and ions. Electrons have lalrge mobility. Consequently, in an rf discharge, a build-up of a positive ion sheath occurs around both electrodes, effectively equivalent to build up of a dc bias across a capacitor in series with the electrodes. Any perturbation of this sheath (equivalently, the charge on the capacitor) by the PA effect, will result in disturbances of the discharge current and, hence, a LOG signal will result.

It is, therefore, not surprising that a low-power rf discharge can be used as a sensitive, low-pressure, high bandwidth "microphone." Indeed, we have characterized some aspects[21] (linearity, frequency range, etc.) of this microphone and used it as an acoustic detector[22] in studying magnetic field-induced predissociation in the B state of I_2.

Conclusion

The LOG effect has evolved into a sensitive and powerful spectroscopic tool. Transverse laser excitation is the preferred mode for LOG studies in both dc and rf discharges. In addition to ionization rate changes, PA effects will produce a LOG signal if some significant part of the absorbed laser energy is released nonradiatively. For discharges with localized "sensitive" region and a laser excitation at some remove from this region, the two processes will generate distinct, non-overlapping, time-resolved components in the LOG signal profile. In other cases, a complex temporal profile will characterize the LOG signal.

Acknowledgment

This work was supported by the U. S. Department of Energy (Office of Health and Environmental Research).

References

1. For a review of the optogalvanic effect and its various applications, see J. Phys. Colloq. C7 (1983).
2. C. R. Webster and C. Rettner, Laser Focus 19, 41 (1983).
3. J. E. M. Goldsmith and J. E. Lawler, Contemp. Phys. 22, 235 (1981).
4. C. R. Webster and R. T. Menzies, J. Chem. Phys. 78, 2121 (1983).
5. D. A. Haner, C. R. Webster, P. H. Flamant and I. S. McDermid, Chem. Phys. Lett. 96, 302 (1983).
6. R. D. May, J. Appl. Phys. 58, 1169 (1985).
7. M. Broglia, F. Catoni, and P. Zampetti, J. Phys. Colloq. C7, 479 (1983).
8. Y. Yasuda, N. Sakabe, and A. Murai, Opt. Commun. 55, 319 (1985).
9. D. Kumar and S. P. McGlynn, These Proceedings.
10. D. Kumar, P. L. Clancy, and S. P. McGlynn, J. Chem. Phys. 90, 4008 (1989).
11. R. A. Gottscho, Phys. Rev. A 36, 2233 (1987).
12. See references in ref. 10 above.
13. A. Ben-Amar, G. Erez, and R. Shuker, J. Appl. Phys. 54, 3688 (1983).
14. R. A. Keller, B. E. Warner, E. F. Zalewski, P. Dyer, R. Engleman, Jr., and B. A. Palmer, J. Phys. Colloq. C7, 23 (1983).
15. D. Kumar, R. V. Nauman, R. Mohanty,, S. P. McGlynn, Rev. Sci. Instrum. 57, 365 (1986).
17. D. Kumar, L. Klasinc, P. L. Clancy, and S. P. McGlynn, Int. J. Quant. Chem., Quant. Chem. Symp. 19, 403 (1986).
18. L. Klasinc, D. Kumar, P. L. Clancy, and S. P. McGlynn, Croat. Chem. Act. 59, 643 (1986).
19. K. H. Weber and C. J. Sansonetti, Phys. Rev. A 35, 4650 (1987).
20. D. Kumar, L. Klasinc, and S. P. McGlynn (to be published).
21. D. Kumar, L. Klasinc, P. L. Clancy, and S. P. McGlynn, IEEE Trans. Ultrason. Ferroelec. Freq. Cont. UFFC-33, 513 (1986).
22. D. Kumar, L. Klasinc, P. L. Clancy, R. V. Nauman, and S. P. McGlynn, Can. J. Phys. 64, 1107 (1986).

NATURE OF LASER OPTOGALVANIC SIGNALS

D. Kumar and S.P. McGlynn
Department of Chemistry
Louisiana State University
Baton Rouge, LA 70803

Abstract

Laser optogalvanic (LOG) signals are believed to be generated primarily by laser-induced changes in the equilibrium ionization rate of a discharge. Recent work has shown that photoacoustic (PA) effects can also play an important role in the generation of LOG signals [Kumar et al., J. Chem. Phys. 90, 4008 (1989)] and that no thermal effects or ionization rate changes are involved in the final step of such signal production. The PA mediated components may be superimposed on the other components and a complex temporal profile of the LOG signal may result.

We report a technique by which the two types of components may be distinguished even when they overlap temporally. This technique is applicable to rf discharges, and concerns marked changes induced in the temporal profiles of LOG signals as the rf frequency is altered about the resonance frequency. Results from time-resolved studies in a ~30 MHz rf discharge in ~5torr neon are presented.

Introduction

The laser optogalvanic (LOG) effect is the change of electrical impedance of a plasma caused by resonant absorption of laser radiation in the plasma. The absorption of laser radiation by a plasma species disturbs the dynamical equilibrium of the various plasma processes (e.g., absorption/emission, collisional excitation/deexcitation, ionization/recombination, etc.), and produces a LOG signal.

The electrical impedance of a plasma will depend on charge carrier density and mobility. The complexity of the system and the lack of knowledge about various rates/coefficients deters an analytical solution of the discharge impedance (and the LOG effect). Consequently, two phenomenological models have gained followers. The first model is based on the fact that laser-induced direct and collision-assisted ionization rate changes (IRC) of the plasma atoms/molecules will increase the electron-ion pair density and, hence, the conductivity[1]. The corresponding LOG signal, if associated with an increase of discharge conductivity, is termed "normal". For some excitations an "inverted" LOG signal is generated. In fact, however, the actual polarity of the LOG signal will depend on the experimental set-up and on how, and where, the signal is detected. Thus, the terms "positive" and "negative" at least as applied to LOG signal polarity, are ambiguous. The second model, the electron temperature coupling model, assumes that the increased electron kinetic energy caused by laser energy deposition will produce an increase of discharge conductivity by enhancing electron mobility and/or collisional ionization rates.[2] This model was invoked to explain the generation of LOG signals by low energy (e.g., vibrational) excitations to levels far below ionization threshold. It fails, however, to explain some important characteristics of LOG signals. For example, LOG signal intensity does not correlate with the energy gap from the laser excited upper level to the ionization threshold.

Recent work[3] on LOG effects in rf discharges in iodine and bromine has shown that LOG signals can be generated by a photoacoustic (PA) effect, and that no thermal effects or ionization rate changes are involved in the final step of such signal production. The pressure wave generated by the PA effect produced LOG signals by an actual physical movement of the charged species in the "sensitive" region of the rf discharge. In a low-power iodine discharge these "sensitive" regions are confined to the vicinity of the rf electrodes, and are attributable to positive ion sheaths. Iodine ions have very small mobility compared to electrons and, at an rf frequency of ~32 MHz, the ions just oscillate about their mean positions with a small amplitude. As a result, during the positive rf half cycle the electrons are rapidly swept away from the vicinity of the electrodes, leaving behind a positive ion sheath. The positive ion sheaths develop a dc bias which can be represented by a charged capacitor in series with the electrodes. Thus, any perturbation of these positive ion sheaths by the PA wave should alter the discharge current and produce a LOG signal. The polarity of this LOG signal is inverted when the direction of the PA wave (say, a compression wave) is reversed,[3] confirming that no ionization rate changes are involved in the production of photoacoustically-mediated (PAM) LOG signals. The PA intermediacy overcomes the obstacles associated with the electron temperature (or mobility) coupling model.

These PAM components in the LOG signal of low power rf discharges in iodine were easily identified by a transit time delay of the acoustic wave associable with distance from the region of laser excitation to the rf electrode(s). The distinction between PAM and IRC components was also facilitated by the fact that the IRC component in iodine is "synchronous" with the laser pulse. Obviously, if the laser pulse is directed into the "sensitive" region of the discharge, a complex LOG signal profile will result because of the temporal overlap of both IRC and PAM components.

In the case of an rf discharge in neon the latter situation holds even at low rf powers. Neon atoms are much lighter than iodine and the "sensitive" region can be spatially diffuse. The laser beam, therefore, propagates through the "sensitive" region of the discharge and a complex LOG signal profile results.

Under suitable conditions the overlapped IRC and PAM components in the LOG signal profile can be resolved by a new technique. In specific, dramatic changes occur in the temporal profile of LOG signals (mainly the IRC components) produced by pulsed laser excitation of the $1s_j \rightarrow 2p_k$ transitions in neon (~5 torr) in a ~30 MHz rf discharge as the rf frequency is scanned over the electrical resonance peak of the plasma and the associated driving/detecting circuits. The PAM components, however, are found to be insensitive to the rf frequency. In general, PA effects can play an important role in the production of LOG signals and, under suitable condiation, they may even dominate the LOG profiles.

Experimental

The experimental arrangement for LOG measurements in an rf discharge has been described.[3,4] Briefly, the sample is contained in a quartz discharge cell 2 cm in diameter with copper electrodes A & B (~5 cm apart) wound around the exterior of the cell. The rf voltage (~30 MHz) is resonantly stepped up and applied to the electrodes A & B. An rf power of 0.1 - 0.2 watts is sufficient to sustain a stable, low-noise discharge in neon at ~5 torr pressure.

A resonantly tuned pick-up coil, C, also wound around the discharge cell and situated ~1 cm below B and 6cm from A, is coupled to the rf discharge, which extends beyond B. The output of a pulsed tunable dye laser (Chromatix CMX-4, ~1 μs pulse width, resolution ~0.1 cm^{-1}, beam focused to ~0.5 mm diameter) transversely excites the discharge at a point L (between B and C). When the laser is tuned to a $1s_j \rightarrow 2p_k$ transition of neon, changes occur in the rf power transferred to the pick-up coil. These changes constitute the LOG signal, which is recovered by demodulation in the signal recovery section and, after amplification, is either sent to an oscilloscope for visual monitoring or transferred to a box-car for recording.

The rf oscillator frequency, f, and the tuning capacitors are adjusted for resonance (frequency f_o), as indicated by a "dip" in the amplifier power meter and a maximum voltage in the pick-up coil. Temporal profiles of LOG signals for various $1s_j \rightarrow 2p_k$ neon excitations are recorded with rf frequency (f) set at f_o, slightly below f_o and slightly above f_o. Changes in LOG signal profiles are also monitored as the rf frequency is scanned across the resonance peak. Finally, with laser off, the rf resonance profile is recorded by scanning f and recording the dc voltage in the demodulator of the signal recovery section.

The temporal profiles of the faster components of these signals are extremely sensitive to changes in rf frequency around f_o. While the profiles from various neon transitions may differ considerably, their shapes depend systematically on f. The pattern of changes is illistrated in Fig. 1 for the $1s_5 \rightarrow 2p_2$ neon excitation at 16996.61 cm^{-1}.

Results

Only the temporal profiles at $f = f_o = 29.24$, $f = 29.04$, and $f = 29.44$ MHz (each at oscilloscope scan speeds of 50 μs/div. and 5 μs/div.) are presented in Fig. 1. Only a brief description of their salient features is presented:

(i) At resonance (29.24 MHz, Figs. 1A and 1B) the LOG signal consists of a sharp positive peak (#2) at ~3 μs followed by two slower peaks at ~30 μs (#4) and ~150 μs (#5).

(ii) As the rf frequency is gradually reduced below f_o, peaks #1 (negative, weak, synchronous with the laser pulse) and #3 (strong, positive, rapidly increases and saturates) appear and grow on either side of peak #2. Temporal profiles at 29.04 MHz are shown in Figs. 1C and 1D. Peak #3 is at ~8 μs and it has engulfed peak #2. Peak #4, which has moved slightly to the right, has gained some intensity whereas peak #5 is now somewhat weaker.

(iii) As the rf frequency is gradually increased above f_o, peaks #1 and #3 appear and grow with similar characteristics but with opposite polarity compared to those in (ii) above. The temporal profile at f = 29.44 MHz is shown in Figs. 1E and 1F. The strong peak #3 has again engulfed peak #2, and its strong positive overshoot now appears to neutralize negative peak #4. Peak #5 has gained some intensity and its maximum has shifted to the left. The background noise levels are observed to increase as f moves away from f_o.

(iv) The signal is noisy in (ii) and (iii) above. However, all peaks #1 to #5 are real and reproducible.

(v) A slight displacement (5-15 μs) occurs in the positions of peaks #4 and #5 as the laser beam is displaced along the axis of the discharge cell. No noticeable shift could be detected in the position of peak #2.

(vi) The broad, and rather insensitive peak #5 never inverts. However, it does undergo slight changes in intensity and the position of its maximum shifts. Peak #4 does not change sign, except in Fig. 1E where it appears to be affected by the strong positive overshoot of the earlier peak. Peak #2 is invariant to f. However, its appearance and profile is crucially dependent on the intensity of peak #3.

(vii) Similar behavior is observed with the LOG signals of other $1s_j \rightarrow 2p_k$ neon excitations. For some excitations (e.g., $1s_2 \rightarrow 2p_2$ at 15149.7 cm^{-1}), an inverted LOG signal shape (relative to that from $1p_5 \rightarrow 2p_2$) is observed. In such cases, inversion of the same pair of LOG signal components occurs as the rf frequency changes from slightly below to slightly above f_o. Also, if the metastable states $1s_3$ and $1s_5$ are not involved in the laser excitation process (either as an initial level, or as a final level after relaxation from the upper $2p_k$ level), peak #4 and #5 are either extremely weak or non-existent.

Discussion

A detailed discussion of the observed phenomenon and its implications will be published elsewhere.[5] Only a brief discussion is presented here.

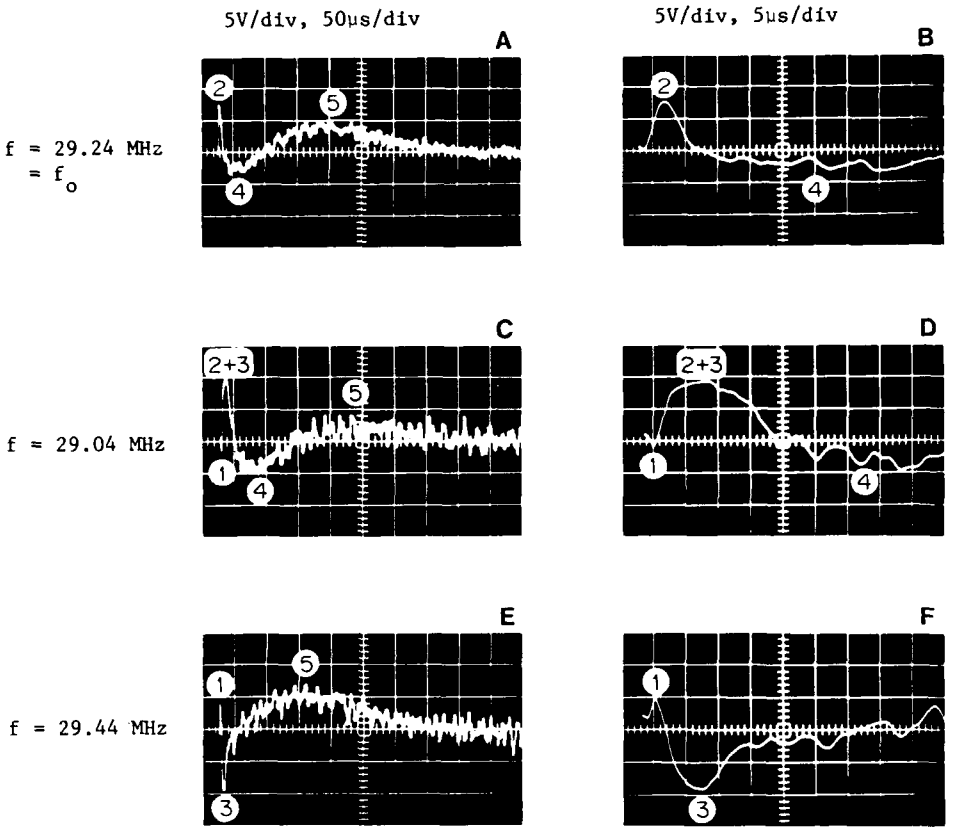


Figure 1. Temporal profiles of LOG signals in an rf discharge in ∿ 5torr neon.

Clearly, two distinct mechanisms are involved in the generation of LOG signals. This conclusion follows from the fact that the two sets of peaks in the LOG temporal profile behave differently as the rf frequency changes from slightly below to slightly above f_o. Peaks 2,4 and 5 do not alter characteristics whereas peaks 1 and 3 vanish and change polarity as the rf frequency passes through f_o.

The observed rf frequency-dependent behavior of the LOG signal can be explained on the basis of a simple phenomenological model which has two components: (a), laser excitation of a particular $1s_j \rightarrow 2p_k$ transition alters the equilibrium ionization rates, with concomitant changes of the plasma resonance characteristics (effective conductivity, capacity and inductance); and (b), a part of the energy absorbed from the laser pulse is released non-radiatively into the translational modes and launches a pressure wave (PA effect).

On the basis of this model it can be shown[5] that the set of peaks which do not alter their characteristics with rf frequency (peaks 2,4 and 5) are mediated by the PA effect (PAM component). On the other hand, the set of peaks that is strongly rf frequency dependent (peaks 1 and 3) is generated by ionization rate changes (IRC component). Thus at $f = f_o$ and at low and moderate laser powers, only the PAM component will be observed. At $f \neq f_o$, both mechanisms will be active and the observed profile will be a composite of the two different sets of signals. Under different conditions, the relative intensities of the two components may change considerably. Thus, quite different signal profiles can occur.

As discussed previously, the laser beam propagates through the "sensitive" region of the discharge in neon and, consequently, peak 2 (Figs. 1A and 1B) represents an initial PAM shock-wave followed by slow, non-uniform PAM peaks 4 and 5. These peaks (4 and 5) can hardly be assigned as "ringing". Their complex shapes occur because of the fact that the long-lived, collisionally equilibrated, metastable levels $1s_3$ and $1s_5$ play dominant roles in sustaining the discharge, and any perturbation of their population densities will gradually exchange energy with the plasma (i.e., the PA channel) and will condition the latter part of the PAM signals. A relaxation time of ~80 μs for the $1s_5$ level population is observed.[6] It is, therefore, not surprising that long lived PAM components are present in the LOG profile.

The rf frequency-dependent behavior of the LOG signal components (peaks 1 and 3) can be explained by invoking an IRC mechanism which generates LOG signals via shifts of the rf/plasma resonance curve (or, equivalently, the response/transfer function). The curve is observed to shift to the left (right) with an increase (decrease) of equilibrium ionization rates.[5]

Peak 1 is ascribed to an initial decrease in the equilibrium ionization rate caused by laser induced depletion of the $1s_5$ metastable level population. At the neon pressures and the rf powers used in our work, Penning ionizations of the metastable levels dominate the electron impact ionizations of the upper $2p_2$ levels and the equilibrium ionization rate drops. Such a decrease of equilibrium ionization rate is not unusual.[5]

Peak 3, which indicates an increase in equilibrium ionization rates, originates in photoionization of an excited discharge species by VUV fluorescence from the $1s_4$ level. The non-metastable levels $1s_2$ (radiation trapped life-time in <1 μs) and $1s_4$ (radiation trapped life-time <11 μs)[7] acquire excess population by relaxation of the laser excited $2p_2$ level. The effect of $1s_2$ fluorescence, if any, is buried within peak 1. The rapid decay of peak 1 is largely attributable to swamping by peak 3 which is overwhelmingly strong and of opposite polarity.

The inversion behavior of peaks 1 and 3 with change of f, and their nulling at $f = f_o$, can be visualized by setting the rf frequency f on the left (or right) shoulder of the resonance (response/transfer)curve. A leftward movement of the transfer curve (laser induced increase of ionization rates) generates a positive (negative) IRC signal at the particular setting. However, if $f = f_o$, a slight displacement of the response/transfer curve will not produce any IRC signal. Thus, at this setting, no IRC signal will be produced even though ionization rates may change. The characteristics of peaks 4 and 5 suggests that at $f \neq f_o$ some weaker IRC components may also be active in this region. This is not unexpected since the plasma electron density has a relaxation time of ~80 μs.[7]

The similarity of the LOG signal shape (PAM components, Fig. 1A) from our rf discharge and those obtained by other workers in dc discharges[8] suggests that PA effects can play a significant role in the generation of LOG signals in rf as well as dc discharges.

To summarize, the various peaks in Figure 1 can be assigned as follows:

(i) Peaks 2, 4, and 5 in Figs. 2A and 2B ($f=f_o$) are pure PAM components.
(ii) Peaks 1 and 3 are of IRC origin.
(iii) Peaks 2, 4 and 5 in Figs.2C-2F ($f \neq f_o$) are admixtures of both PAM and IRC components. Peak 5 is predominantly PAM in nature. Peak 4 may have some IRC component.

Conclusion

Two sets of LOG signal components are identified in an rf discharge in neon and their origin is explained. The PA effect plays an unexpectedly strong role in the generation of LOG signals in rf as well as dc discharges.

Acknowledgement

This work was supported by the U. S. Department of Energy (Office of Health and Environmental Research).

References

1. For a review of the optogalvanic effect and its various applications see J. Phys. Colloq. C7 (1983); C. R. Webster and C. T. Rettner, Laser Focus 19, 41 (1983); J. E. M. Goldsmith and J. E. Lawler, Contemp. Phys. 22, 235 (1981).
2. R. A. Keller, B. E. Warner, E. F. Zalewski, P. Dyer, R. Engleman, Jr., and B. A. Palmer, J. Phys. Colloq. C7, 23 (1983).
3. D. Kumar, P. L. Clancy, and S. P. McGlynn, J. Chem. Phys. 90, 4008 (1989).
4. For a block diagram of the set-up see S. P. McGlynn and D. Kumar, These Proceedings.
5. D. Kumar and S. P. McGlynn, J. Chem. Phys. (submitted).
6. T. Fujimoto, Y. Uetani, Y. Sato, C. Goto, and K. Fukuda, Opt. Commun. 47, 111 (1983).
7. Y. Uetani and T. Fujimoto, Opt. Commun. 49, 258 (1984).
8. A. Ben-Amar, G. Erez, and R. Shuker, J. Appl. Phys. 54, 3688 (1983).

FREQUENCY-MODULATION SPECTROSCOPY WITH MULTIMODE LASERS*

James M. Supplee
Physics Department, Drew University, Madison, NJ 07940 and
Department of Physics and Engineering Physics
Stevens Institute of Technology, Hoboken, NJ 07030

Edward A. Whittaker
Department of Physics and Engineering Physics
Stevens Institute of Technology, Hoboken, NJ 07030

Abstract

We report on the extension of the theory of frequency modulation spectroscopy (FMS) to include multimode laser sources. We first develop the theory analytically, including the effects of the laser mode intermodulation on the FMS signal. We then evaluate the theory in the limit of weak absorption and small modulation index. We note that in appropriate limits the FMS signal is proportional to the derivative of the apparent absorption profile. The analytical results are then evaluated in a number of cases through the use of a computer model which is able to simulate the FMS spectrum expected for arbitrary molecular and atomic absorption lines. The model demonstrates that absorption features narrow compared with the overall laser linewidth may still be discernable through the application of multimode FMS.

*This work was supported by a National Science Foundation Research Opportunity Award under Grant #ECS-8811955 and by a Drew University Faculty Release Time Grant.

1. Introduction

The application of high frequency electrooptic phase modulation to laser absorption spectroscopy is a well established technique for enhancing available detection sensitivity [1]. The method evades low frequency laser technical noise by upshifting the spectroscopic absorption induced signal to a frequency where detector shot noise is dominant. In the usual approach, a single frequency tunable laser is used as a source beam of light. The single frequency laser enables very high resolution absorption spectra to be obtained. The theory for this case is well developed [1] and shows that the frequency modulation spectroscopy (FMS) signal has two quadratures, one proportional to the first derivative of the absorption profile, and the other proportional to the second derivative of the dispersion profile. The theory for the signal-to-noise ratio has also been reported for the single mode case [2].

Two experimental reports have demonstrated that the basic FMS approach may also be applied to tunable lasers that are not operating on a single longitudinal mode. In one experiment, a pulsed dye laser was used to probe atomic sodium absorption [3] and in the other work, a multimode cw dye laser was used [4]. In these cases, the modulation frequency was comparable to the absorption linewidth, and the laser linewidth was greater than they were. The experimental results suggest that at least in this regime, multimode FMS still generates derivative like spectra.

We report here on the extension of FMS theory to a multimode laser source. Our analysis is applicable to both free running and mode-locked laser sources and takes full account of the effect of mode intermodulation on the FMS signal. Our analysis enables us to include arbitrary values for total laser linewidth, mode spacing, modulation frequency and absorber linewidth and structure. Our results show that the FMS signal indeed remains derivative-like in certain limits as suggested by the experimental results. However, we also find a more general result which shows that the FMS signal produces a lineshape proportional to the derivative of the apparent absorption line as measured by the multimode laser. This suggests that fine absorption features ordinarily obscured by the wide laser line will be discernible with FMS. We explore this and several other regimes not yet investigated experimentally using the graphic output of a computer model.

2. Analytic Results

In this section, we summarize the analytical results for the extension of FM spectroscopy to include a multimode laser source. Details of the analysis will be reported elsewhere [5]. The analysis follows the formalism of Bjorklund [1] and Gehrtz, et al. [6]. The results follow directly from the observation that a multimode laser is simply a collection of single frequency lasers. When phase modulated and passed through an absorbing sample, each mode generates its own FMS signal which is identical to the single mode case.

In the case of a broad band dye laser with free running modes, the fluctuating phases of each mode cause the detector photocurrent to consist of a sum of the FMS signal powers over each mode. Since each mode is modulated by the same radio frequency (rf) source, the signals at the rf frequency add coherently even though the optical signals add incoherently. In the case of a mode-locked laser, the optical fields also add coherently. This has the effect of producing strong amplitude modulation in the detector photocurrent at the intermode spacing and its harmonics. However, the FMS signal may still be extracted by choosing the phase modulation frequency to be incommensurate with the intermode frequency, and selectively filtering only the FMS signal components. Consequently, both the free running and modelocked cases produce the same FMS signal.

In the limit of small modulation index and weak absorption, the absorption quadrature of the multimode FMS signal is given by

$$I_s = M \sum_n \frac{cE_n^2}{8\pi} (\delta_{n,1} - \delta_{n,-1}), \tag{1}$$

where M is the modulation index, E_n is the amplitude of the n^{th} laser mode and $\delta_{n,j}$ is the sample attenuation factor evaluated at the j^{th} sideband of the n^{th} laser mode. There is a similar expression for the dispersion quadrature. Eq. (1) shows clearly that the FMS signal is simply the coherent sum of the individual FMS signals from each mode, weighted by the power in each mode. Depending on the relative magnitudes of the modulation frequency, laser mode spacing and absorption feature lineshape, the terms in the sum can interfere constructively or destructively as discussed below to produce an overall FMS signal.

3. Computer model

We have developed a computer model which calculates and plots the FM spectrum obtained when a frequency modulated tuneable multimode laser is passed through an absorbing sample. The laser output is modeled as a set of N discrete modes spaced by ω_{rf}, with each mode having negligible width. The total bandwidth of the laser is therefore

$$\Gamma_l = (N-1)\omega_{rf}. \tag{2}$$

Using Eq. (1), the model calculates FM signal intensity as a function of laser center frequency as the laser frequency is varied. With this computer model, one can conveniently see how the FM spectrum is affected by variations in modulation frequency ω_m, number of modes N, mode spacing ω_{rt}, or the characteristics of the sample absorption profile. One method for displaying such results is to give a 3D plot showing signal versus frequency as a parameter of interest is varied along the third axis. Fig. 1 is an example of such a plot. There the FM signal is plotted, as the modulation frequency is varied along the third axis. This example is for a 201 mode laser probing an absorber modeled as a single Lorentzian. We have chosen units where the half width at half maximum (Γ) of this Lorentzian is 1. In those units the spacing between modes is 0.1 and the modulation frequency varies from 0.1 to 2.0 along the third axis.

The FM signal results from subtracting two terms, where those two terms involve the absorption at points separated by $2\omega_m$ (Eq. 1). For small ω_m then, one is essentially measuring the difference in the absorption profile at two nearby points. This results in the signal being small for small ω_m, as shown by the front scan in Fig. 1. Taking the difference between nearby points also results in the FM signal being the derivative of the absorption profile [2] [5]. Therefore if the absorber is modeled as a Lorentzian, low modulation frequency ($\omega_m \ll$ feature width) will result in a signal shaped like a differentiated Lorentzian.

However, the multimode nature of the laser can cause the signal to become more complicated. Even the qualitative nature of the complications depends on how the mode spacing ω_{rt} compares with the size of the absorption feature Γ. This dependence is illustrated in Fig. 2, by varying ω_{rt} as the other parameters are held constant. For $\omega_{rt} \gg \Gamma$, each mode will separately pass through the absorber, yielding simply a series of differentiated Lorentzians spaced by ω_{rt} (Fig. 2a). As ω_{rt} decreases and becomes comparable to Γ, the minimum in one differentiated Lorentzian can begin to cancel with the maximum of the differentiated Lorentzian on its left, as illustrated by the progression of decreasing ω_{rt} in Figs. 2a - 2c. As long as the power of neighboring laser modes is comparable, all peaks except the far left minimum and far right maximum can largely cancel. These two remaining peaks (in Fig. 2c, for example) have width given by the true absorber width; resolution is **not** limited by the total width of the laser ($\Gamma_l = 36$ in Fig. 1c)! This cancelation effect is more or less in place whenever

$$\omega_{rt} \lesssim \Gamma. \tag{3}$$

Reducing ω_{rt} has a second effect. For $\omega_{rt} \lesssim \Gamma$, the minima of the first few differentiated Lorentzians on the left and the maxima of the first few differentiated Lorentzians on the right constructively interfere. This is why in going from $\omega_{rt} = 20$ to $\omega_{rt} = 0.6$ (Figs. 2a to 2c), the cancelation of the interior fluctuations becomes complete **and** the end peaks become higher (note ordinate scale). The constructive interference of these peaks is simply a sum of the peaks, and in certain circumstances [5] that sum can be well approximated as an integral. Integrating the derivative of the absorption profile will give back something of the same shape. This is why Fig. 2c shows Lorentzians, although one is shifted and inverted.

As a further example of the FM signal showing two copies of the absorption profile with one inverted, consider the more complex situation of a simulated portion of the iodine spectrum. The model spectrum used for this calculation is [7] a series of Lorentzians as shown in Fig. 3a. For simplicity, we have made the unrealistic assumption that there are no absorption lines above or below those plotted. That simplification would not actually hold experimentally for iodine, but would apply to other materials with sparser spectra. The FM spectrum for a case with $\omega_m \ll \Gamma$, and $\omega_{rt} \ll \Gamma$ is shown in Fig. 3b. It reveals two shifted copies (one inverted) of the absorption profile as expected.

References

[1] G. C. Bjorklund, IBM Invention Disclosure SA 8790135 (March 1979); "Frequency-modulation spectroscopy: a new method for measuring weak absorptions and dispersions," Opt. Lett. **5**, 15 (1980); U.S. Patent 4,297,035 (November 1981).

[2] G. C. Bjorklund, M. D. Levenson, W. Lenth, and C. Ortiz, "Frequency modulation (FM) spectroscopy - theory of lineshapes and signal-to-noise analysis," Appl. Phys. B **32**, 145 (1983).

[3] T. F. Gallagher, R. Kachru, F. Gounand, G. C. Bjorklund, and W. Lenth, "Frequency-modulation spectroscopy with a pulsed dye laser," Opt. Lett. **7**, 28 (1982).

[4] D. E. Cooper and T. F. Gallagher, "Frequency-modulation spectroscopy with a multimode laser," Opt. Lett. **9**, 451 (1984).

[5] J. M. Supplee and E. A. Whittaker, to be submitted.

[6] M. Gehrtz, G. C. Bjorklund, and E. A. Whittaker, "Quantum-limited laser frequency-modulation spectroscopy," J. Opt. Soc. Am. B **2**, 1510 (1985).

[7] J. D. Simmons and J. T. Hougen, "Atlas of the I_2 Spectrum from 19,000 to 18,000 cm^{-1}", J. of Research of the National Bureau of Standards, **81A**, 25 (1977).

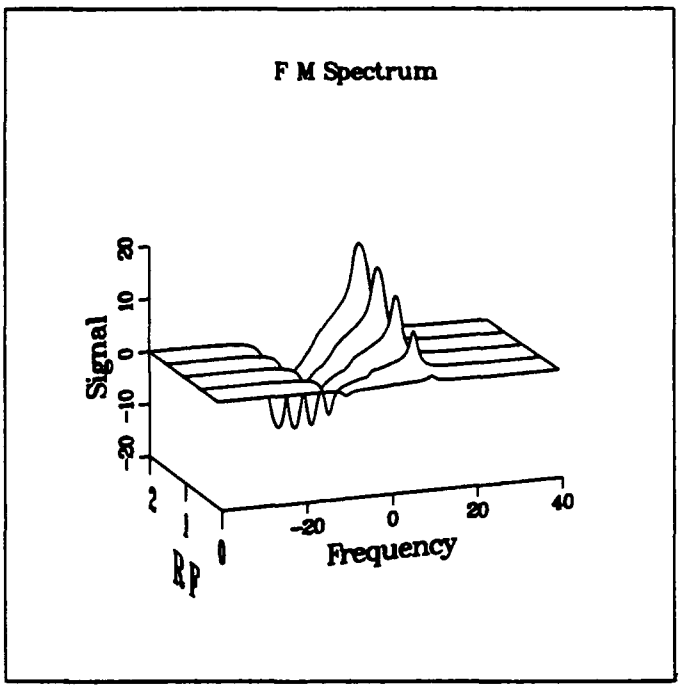
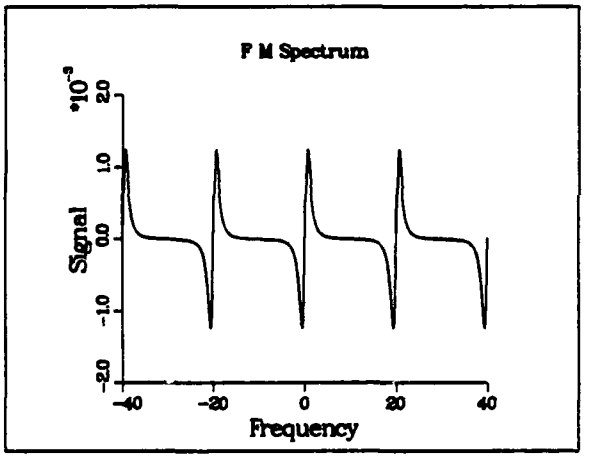
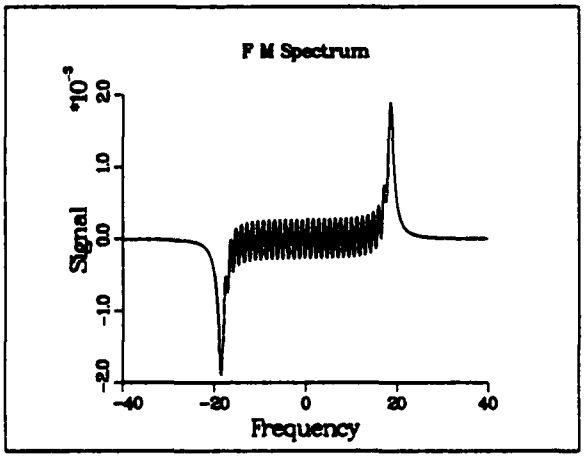
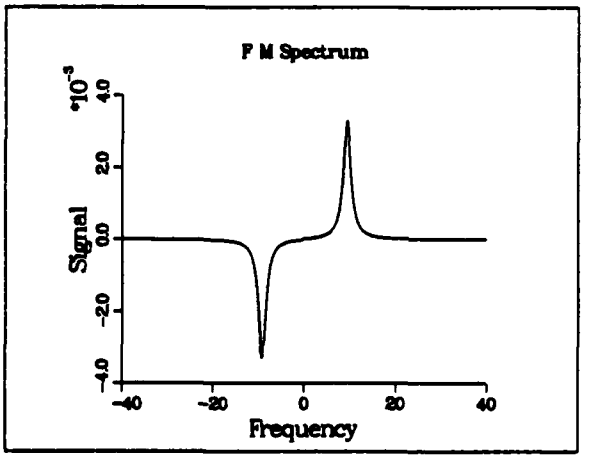


Fig. 1. FMS versus frequency, for varying ω_m.



Figs. 2a-c. $\omega_{rt} = 20.$, 1.2, and 0.6 respectively. Throughout, $\omega_m = 0.1$; there are 31 modes.





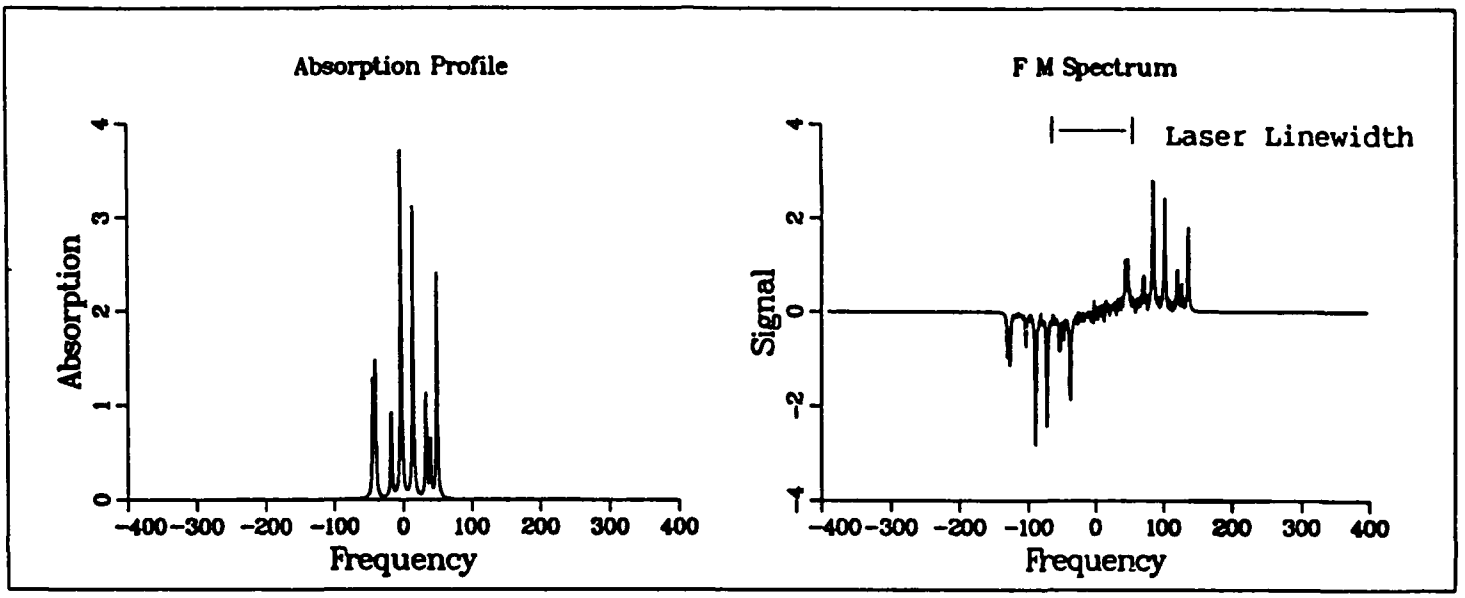


Fig. 3. Simulated portion of the iodine spectrum.

Kinetics and Spectroscopy of KrF (B) and Kr_2F ($4^2\Gamma$)

A. W. McCown and D. P. Greene
Mail Stop E543
Laser Science and Applications Group
Los Alamos National Laboratory
Los Alamos, NM 87545

The absorption spectra corresponding to transitions from the $4^2\Gamma$ level to upper excited states of several rare gas-halide trimers (Kr_2F, Ar_2F and Xe_2Cl) have been measured at wavelengths ranging from 200 nm to as large as 800 nm. Absolute absorption cross sections for Kr_2F have been determined. Experiments are discussed that will measure the radiative lifetime of the KrF (B) state which is formed utilizing a sub-picosecond source. KrF B $\leftrightarrow$ C mixing, quenching rates and the B$\rightarrow$X stimulated emission cross section will be measured.

Introduction

A complete understanding of any molecular system requires knowledge of all reactions that produce or deplete the molecular species of interest in the system as well as the fundamental constants that describe those reactions. In the case of the rare gas-halide excimers (RGH), the species of interest include rare gas atoms and molecules, halogens, the excimers and the associated trimers. At pressures utilized in typical RGH laser mixtures, the trimers may be present in large quantities, and knowledge of their formation and decay mechanisms along with their spectroscopic behavior is essential in understanding the RGH system.

As an example, the RGH trimers are predicted to absorb in the ultraviolet in a manner similar to absorption by the ground state dimer ion.[1] In many cases, this absorption is predicted to be very strong at the RGH emission wavelength, so that the trimers could be strong absorbers of the desired excimer laser light. For the case of Kr_2F^* absorption at 248 nm (KrF B$\rightarrow$X emission wavelength), the absorption cross section was recently measured to be ~$1x10^{-18}$ cm^2.[2-4] This value, though smaller than predicted,[5] is not insignificant, and Kr_2F^* absorption cannot be neglected in attempting to model the KrF system.

However, the RGH trimers are interesting in their own right, and lasing has been observed from Kr_2F and Xe_2Cl.[6,7] Its large emission bandwidth and potential tunability in the blue green portion of the spectrum have made Xe_2Cl a candidate in the blue green laser program. Measuring the absorption spectra of the RGH trimers becomes all the more important as they are considered for various scientific and military applications.

Up until the last few years, only limited absolute absorption cross section measurements on Xe_2Cl and Kr_2F were made, and only at specific wavelengths.[8,9] Recently, Geohegan and Eden[4] attempted to continuously measure the Kr_2F and Xe_2Cl absorption spectra using a tunable dye laser, and although low frequency doubling efficiencies kept their measurements above 340 nm, the resulting spectra decreased in absorption as the dye laser wavelength increased, and several interesting features were observed. However, a complete continuous absorption spectrum had not been measured for any of the trimers until this past year when the Kr_2F ($4^2\Gamma$) absorption spectrum from 255 nm to 455 nm was published.[10] The work reported here is an extension of that result to wavelengths as low as 200 nm and as large as 800 nm, and also includes results on Ar_2F and Xe_2Cl.

In addition to measuring the relative spectral dependence of the absorption, a refined technique for measuring absolute cross sections has given a more reliable value for the Kr_2F absorption cross section. In contrast to previous absolute cross section measurements, the cross sectional area of the probe beam was continuously monitored using a linear pyroelectric array, and the probe beam was telescoped down to a smaller size and collimated through the cell (unfocussed).

Cross Section Measurements

In measuring the spectral dependence of the trimer absorption, a probe beam was sampled before and after an absorber was created in a specified length L, and the ratio of intensities obeyed Beer's law,

$$\frac{I}{I_o} = e^{-N\sigma L} \qquad (1)$$

where I_o is the incident or unperturbed intensity, I is the intensity detected after absorption takes place over the length L, σ is the absorption cross section and N is the density of absorbers. This assumes that the absorber density is not depleted by the probe beam. In order to determine σ, the absolute density of absorbers must be ascertained, and therefore, the absorption coefficient, $\alpha(\lambda)$, equal to $N\sigma(\lambda)$, was determined.

Absolute cross sections for Kr_2F were measured using the fluorescence suppression technique.[11] An excited state was created using laser excitation, which resulted in the production of only a few species. That state's absorption cross section was determined by examining its fluorescence in the presence and absence of a probe beam of a particular wavelength. Since absorption reduced the density of absorbers, the

fluorescence from the excited absorbers was suppressed. This is described mathematically in the following analysis for the case of Kr_2F^* absorption. The rate equation that describes the time rate of change of Kr_2F^* is given by the following:

$$\frac{d[Kr_2F^*]}{dt} = P[S] - [Kr_2F^*]\left\{\frac{1}{\tau} + k[Q] + \frac{\sigma I}{\hbar\omega}\right\} \quad (2)$$

where P is the production rate from species S, τ is the Kr_2F^* radiative lifetime, k is the rate constant for quenching of Kr_2F^* by the quencher Q, σ is the wavelength dependent absorption cross section, I is the probe laser intensity in W/cm^2, $\hbar\omega$ is the laser photon energy and brackets denote particle densities. This assumes that one operates in a regime where there is no appreciable loss of laser photons and stimulated emission from Kr_2F^* does not take place. It is also assumed that absorption takes place to a level which immediately dissociates or relaxes quickly and that reformation of Kr_2F^* can be ignored. If the pumping rate is fast compared to the loss rate and if one waits to fire the probe laser until P is small, then the Kr_2F^* density can be solved for by neglecting P.

$$[Kr_2F^*(t)] = [Kr_2F^*(t_o)] \exp\left\{-\frac{\sigma}{\hbar\omega}\int_{t_o}^{t} I(t')\,dt'\right\} \cdot \exp\left\{-\frac{t-t_o}{\tau'}\right\} \quad (3)$$

The effective lifetime of the excited state, τ', is defined in the following way:

$$\frac{1}{\tau'} = \frac{1}{\tau} + k[Q] \quad (4)$$

and t_o is the time at which the probe laser is fired. If the laser pulse length is T_L, the ratio of the Kr_2F^* density at time $t_o + T_L$ with and without firing the probe laser, or the fractional fluorescence (FF), is

$$FF = \frac{[Kr_2F^*(t_o+T_L,\phi)]}{[Kr_2F^*(t_o+T_L,\phi=0)]} = e^{-\sigma\phi} \quad (5)$$

where the laser fluence, ϕ, in photons per cm^2, is equal to $E/\hbar\omega A$, and E, the total energy in the incident laser pulse, is given by

$$E = A\int_{t_o}^{t_o+T_L} I(t)\,dt \quad (6)$$

The cross section, then, is determined by measuring the ratio of the fluorescence with and without the action of a probe beam as a function of laser fluence. In order to make an accurate determination of σ, one must be able to measure accurately the cross sectional area of the probe beam, the energy that is contained in the pulse and the amount of suppression that takes place. These are the major sources of uncertainty in this measurement.

Experimental Apparatus

A. TAS Set-up

The Transient Absorption Spectroscopy Set-up (TASS) is shown schematically in Fig. 1. Large densities of absorbers were created in a small discharge laser (EMG-50) having MgF_2 windows and a discharge volume of ~24 cm^3. Light from a pulsed, xenon flashlamp was collimated by a short focal length (FL) fused silica lens, apertured and passed through the discharge before being focused with an achromatic lens onto the 25-μm entrance slit of a 0.25-m spectrometer. The spectrometer dispersed the light onto a gated, intensified, ultraviolet-sensitive diode array, and a 300-groove/mm grating gave a 200-nm range over the active portion of the diode array. A 20-ns gate pulse was applied to the array detector at the peak of the 300-ns lamp pulse. Timing between the lamp, discharge device and high voltage pulser was controlled with a delay generator, and the detection of discharge fluorescence with a photodiode (PD) allowed the drift of the thyratron-switched discharge to be observed and corrected for.

The discharge device was typically filled with 400 to 700 mBar of rare gas (xenon, krypton or argon), 5 mBar of halogen (F_2 or HCl) and a balance of helium to a total pressure of 2.5 Bar. Since excessive rare gas pressures resulted in arcing, the device was run at the highest rare gas pressure that would give uniform, reliable discharges, so that three body formation rates of the trimers would be maximized while maintaining shot to shot reproducibility.

The detector controller was interfaced to a computer that stored and analyzed the data. Each individual absorption spectrum required three data runs of typically 600 shots per run at a repetition rate of 10 Hz. The first run (I_{Abs}) consisted of acquiring both the lamp light and the discharge fluorescence, and it contained the absorption information. The next two runs (I_{Lmp} and I_{Fl}) collected lamp light and discharge fluorescence separately. Subtraction of background

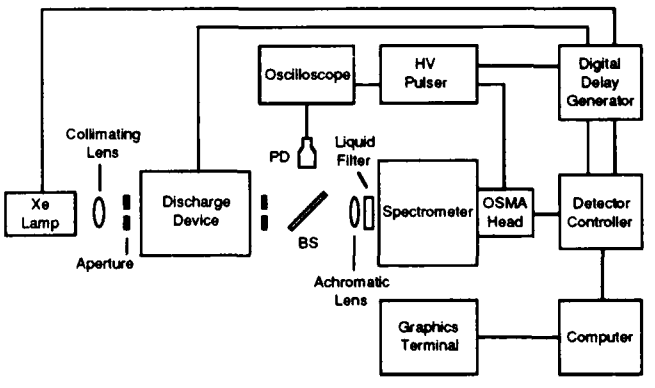


FIG. 1. Schematic of the Transient Absorption Spectroscopy Set-up (TASS). The heart of the system is an Optical Spectrometric Multichannel Analyzer (OSMA) which contains a gated head and a detector controller. The system is run by a computer which also stores and processes data.

light was automatic. Absorption was calculated in the following way:

$$\alpha(\lambda) = -\frac{1}{L} \ln \left\{ \frac{I_{Abs}(\lambda) - I_{Fl}(\lambda)}{I_{Lmp}(\lambda)} \right\} \quad (7)$$

where $\alpha(\lambda)$ was the net absorption in m^{-1} and L was the discharge length (0.2 m).

B. LEAKS Set-Up

Figure 2 is a schematic diagram of the experimental apparatus used to measure absolute cross sections (LEAKSS, or Laser Excitation for Absorption, Kinetics and Spectroscopy Set-up). Two excimer lasers (Lambda Physik EMG-201E and 101-MSC) were aligned so that their beams were counter-propagating. Both lasers were configured as oscillators with standard optics and produced 15- to 25-ns full width at half maximum beams which were unpolarized. The lasers were triggered at 10 Hz by a trigger generator, and each had a firing jitter of ±2 ns. The 201 (pump laser) ran on an argon fluoride gas mix (193 nm) and produced 300-mJ pulses with a shot to shot variation of 20%. The beam was focussed by a 7.5 cm FL cylindrical lens to a line at the center of a quartz cell. A gas handling system typically filled the cell with 1 Torr of electronic grade fluorine and 500 or 1000 Torr of research grade krypton. The energy of the ArF pulse was monitored with a quartz beamsplitter (BS) set to give a small (<5°) angle of incidence and it reflected ~8% of the beam onto an energy detector.

The probe laser was filled with either XeF (351 nm), N_2 (337 nm), XeCl (308 nm), KrF (248 nm), KrCl (222 nm) or ArF gas mixtures and fired an adjustable time delay, t_o, after the pump laser. After passing through a methanol or isopropyl alcohol liquid filter (except in the case of ArF mixes in both lasers),

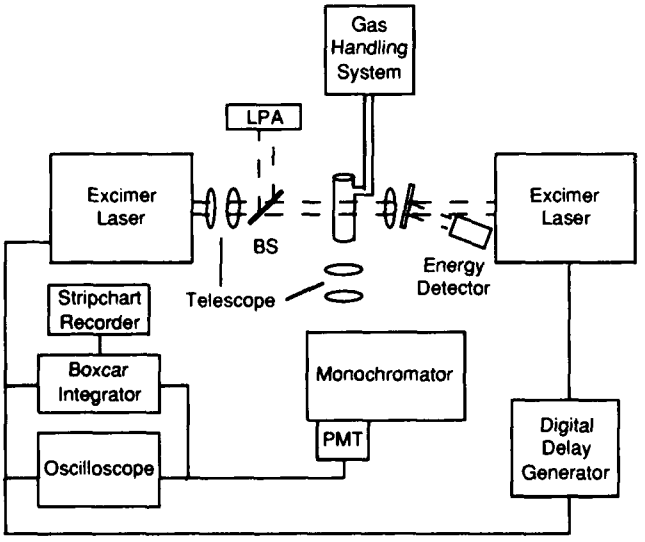


FIG. 2. Schematic diagram of the Laser Excitation for Absorption, Kinetics and Spectroscopy Set-up (LEAKSS). Absorbing species are created using the laser on the right, while the laser on the left produces the probe pulse. The liquid filter mentioned in the text (located at the output of the probe laser) is not shown.

the probe beam was directed through 10 cm and 2.5 cm FL cylindrical lenses which reduced the cross sectional area of the beam while retaining its collimation. The purpose of the liquid filter was to prevent the ArF beam from interfering with the gas chemistry inside the probe laser. This had been shown to have a deleterious effect on the probe laser's output.[12] A quartz BS reflected ~8% of the probe beam onto a Spiricon linear pyroelectric array (LPA) which was positioned the same distance from the BS as the quartz cell. In this way, the probe beam cross sectional area in the center of the cell could be determined exactly. The probe laser pulse energy was also monitored using another BS in combination with a dielectric full reflector and energy detector (not shown in the figure). The mirror helped to reduce the number of pump laser photons which reached the probe beam detector, although it did not altogether eliminate them. Output from the energy detector was displayed on both a readout unit and a stripchart recorder, allowing stray pump energy to be accurately subtracted out of the probe energy measurement.

Fluorescence from excited species in the cell was collimated and focussed onto the 200-μm entrance slit of a 27-cm monochromator and a portion of the dispersed fluorescence was detected by a Hamamatsu R943-02 photomultiplier (PMT). Kr_2F^* fluorescence was monitored at 400 nm (the peak in the emission band) and care was taken to ensure that no stray light from either laser was detected. The PMT signal was displayed on a Tektronix 7104 oscilloscope and sampled by a boxcar integrator. The rising edge of the 5-ns boxcar aperture was set to coincide with the end of the probe laser pulse (time $t_o + T_L$ in eqn. (5)). The boxcar's averaged output, which was proportional to the Kr_2F^* density at $t_o + T_L$, was recorded by the stripchart recorder.

Passing the probe beam through two cylindrical lenses with FLs of 10 and 2.5 cm resulted in a four fold reduction in the width of the beam. This provided fluence levels that were more than sufficient to observe 50% suppressions in fluorescence for output energies in the 50 to 100 mJ range. However, in the cases of N_2 and KrCl, the laser output was only ~10 mJ resulting in maximum suppressions of ~20%. The separation of the lenses was chosen to give a well collimated beam and had to be adjusted for each probe laser gas mix.

Data Taking and Results

A. Spectral Measurements

The dependence of the Kr_2F ($4^2\Gamma$) absorption on wavelength is seen in Fig. 3, as determined from the TASS set-up. The spectra were recorded at a delay of 60 ns between the start of the discharge and the end of the gate pulse. Three Kr_2F ($4^2\Gamma$) absorption features are evident in the figure. The ($4^2\Gamma \rightarrow 9^2\Gamma$) band peaks at 315 nm and has a half width of 85 nm. The ($4^2\Gamma \rightarrow 6^2\Gamma$) band peaks at ~690 nm, and a third band, which is definitely due to Kr_2F ($4^2\Gamma$) absorption, peaks at 222 nm and is much narrower than the ($4^2\Gamma \rightarrow 9^2\Gamma$) band. Also seen in the figure are the Kr_2^+ $[1(1/2)_u \rightarrow 2(1/2)_g]$ and $[1(1/2)_u \rightarrow 1(1/2)_g]$ absorption spectra that were predicted by Wadt.[13] These results demonstrate the near identical absorption features of the trimers

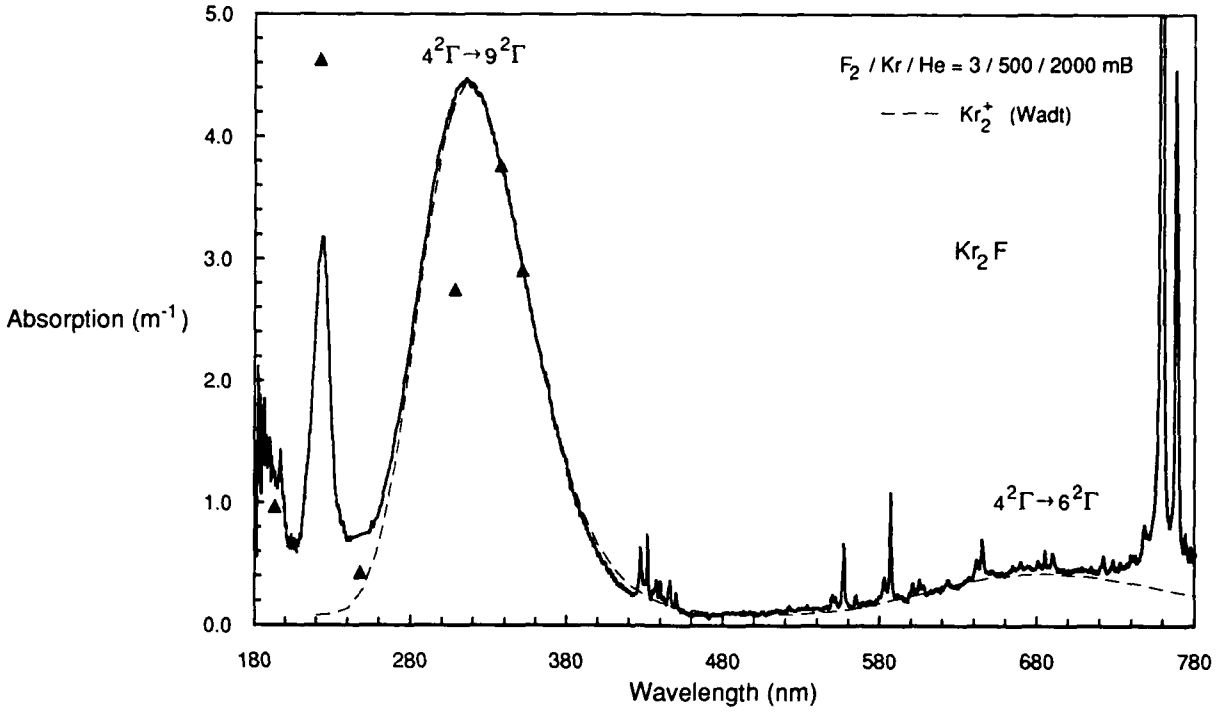


FIG. 3. Absorption spectrum of Kr_2F ($4^2\Gamma$) and atomic absorbers as determined from TASS. Also displayed as triangles (▲) are the absolute cross section data determined from LEAKSS, and the dashed line is a combination of the Kr_2^+ $[1(1/2)_u \rightarrow 2(1/2)_g]$ and $[1(1/2)_u \rightarrow 1(1/2)_g]$ absorption bands predicted by Wadt. The theoretical data has been shifted slightly so that the peaks in the Kr_2F ($4^2\Gamma \rightarrow 9^2\Gamma$) and Kr_2^+ $[1(1/2)_u \rightarrow 2(1/2)_g]$ absorption bands overlap. The absolute cross section data has also been normalized. The gas mixture was 3 mBar F_2, 500 mBar Kr and 1997 mBar He. The $4^2\Gamma \rightarrow 9^2\Gamma$ absorption band peaks at 315 nm and a second, narrower band is present to the blue, peaking at 224 nm. The narrow lines seen above 425 nm are metastable absorption features.

compared to the rare gas dimer ions, except for the third band seen at shorter wavelengths. The narrow lines seen between 425 nm and 800 nm are atomic absorption features.

Figures 4 and 5 give the absorption spectra of Ar_2F and Xe_2Cl. In both cases, the ($4^2\Gamma \rightarrow 9^2\Gamma$) band is observed as well as the narrower band to the blue. Also shown in Fig. 5 are absorption data taken by McCown *et al.*[9] using the fluorescence suppression technique. The size of the cross section at 193 nm suggests that the band peaking at ~200 nm is real, and that a progression of bands may exist in the ultraviolet.

B. Absolute Cross Sections

The argon fluoride laser[14] was used as a means to excite krypton atoms from their ground state to the excited $6p(3/2)_2$ level in a resonant, two photon process. Quenching takes place rapidly to relax the excited atoms to the metastable level, and the formation of the KrF (B) state by the harpoon reaction is also fast. Kr_2F ($4^2\Gamma$) is formed in a three body process:

$$KrF\,(B) + 2\,Kr \rightarrow Kr_2F\,(4^2\Gamma) + Kr \qquad (8)$$

Following excitation by the ArF pulse, the KrF ($B \rightarrow X$) fluorescence peaked ~32 ns after initiation while the Kr_2F ($4^2\Gamma \rightarrow 1^2\Gamma$) fluorescence peaked ~30 ns later. In fluorescence suppression measurements, the probe laser was triggered 70 ns after the ArF laser, and the 5-ns boxcar aperture was opened at the end of the probe laser pulse, typically 25 to 30 ns after the probe laser was fired. Approximately 500 shots were taken in the absence of the probe pulse, and the average of the fluorescence intensity was recorded by the boxcar-strip chart combination. This was repeated while firing the probe laser, and the fractional fluorescence was determined by dividing the intensities. The experiment was repeated at a variety of fluence levels, providing a set of ordered pairs of fractional fluorescence versus fluence. The fluence was varied by placing quartz flats (suprasil or optosil) at the output aperture of the probe laser, or by varying the laser gas mix or charging voltage. In this way, the fluence could be reduced by over an order of magnitude. The uncertainty in each data point arises from uncertainties of less than 10% in the energy measurement, 5% in the beam area measurement and 3% in the fractional fluorescence calculation.

A semilog plot of FF versus photon fluence is shown in Fig. 6. The probe laser wavelength was 308 nm, and the straight line drawn is a linear least squares fit to the data. The absolute value of the slope of the line, which is equal to the absorption cross section, is $(5.1 \pm 0.5) \times 10^{-18}$ cm^2. Data was taken at each of the other probe laser output wavelengths, and the absorption cross sections were determined. Results are presented in Table I and shown graphically in Fig. 3, along with the data obtained from TASS. The overall uncertainty in the cross section measurement is the standard deviation from the

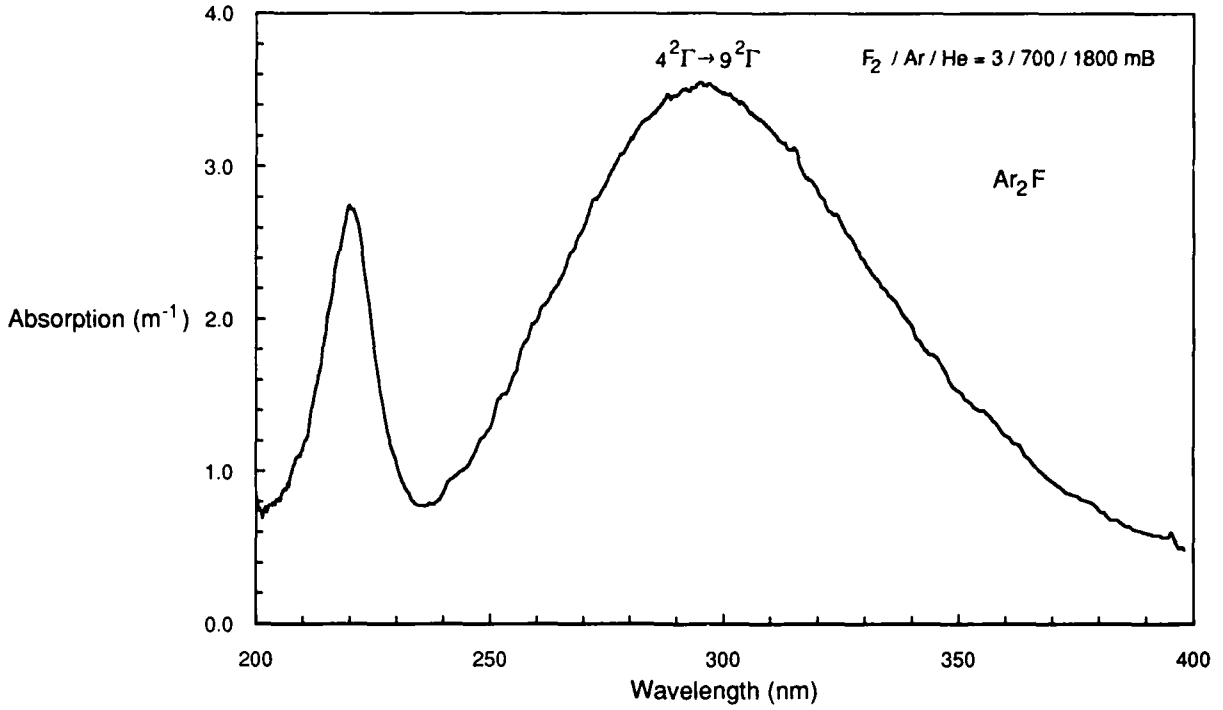


FIG. 4. Absorption spectrum of Ar_2F ($4^2\Gamma$). The gas mixture was 3 mBar F_2, 700 mBar Ar and 1797 mBar He. The ($4^2\Gamma \rightarrow 9^2\Gamma$) absorption band peaks at 295 nm and a second, narrower band is present to the blue, peaking at 220 nm.

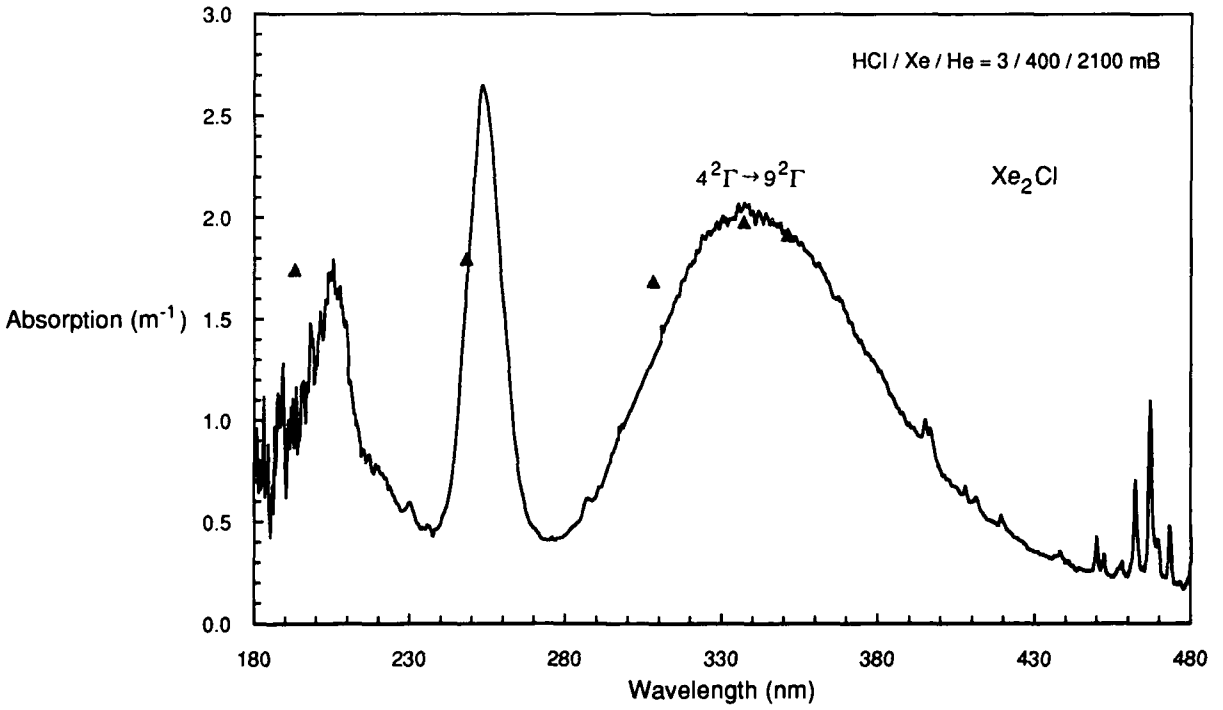


FIG. 5. Absorption spectrum of Xe_2Cl ($4^2\Gamma$) and atomic absorbers. Also displayed as triangles (▲) are the data taken by McCown *et al.* (Ref. 9) which has been normalized. The gas mixture was 3 mBar HCl, 400 mBar Xe and 2097 mBar He. The ($4^2\Gamma \rightarrow 9^2\Gamma$) absorption band peaks at 337 nm and a second, narrower band is present to the blue, peaking at 254 nm. A third band is also present peaking at $\lambda \leq 200$ nm, implying the existence of a progression of bands. The narrow lines seen above 450 nm are metastable absorption features.

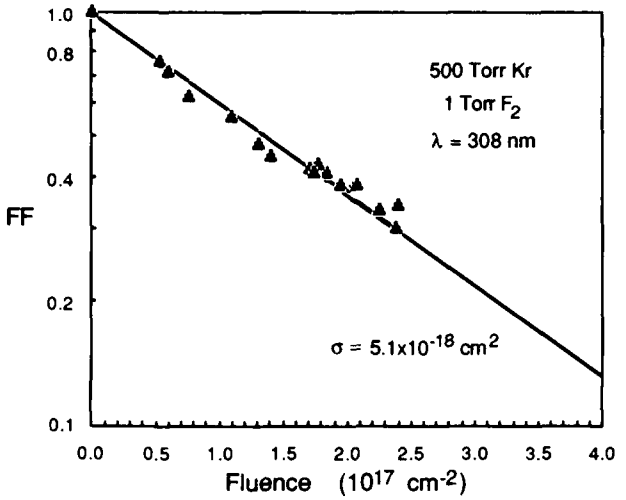


FIG. 6. Semi-log plot of the fractional fluorescence (FF; defined in text) as a function of the XeCl photon fluence. The triangles (▲) are data points and the straight line is a linear least squares fit to the data, giving a cross section of 5.1x10^{-18} cm^2.

mean, as determined from the least squares fit. The uncertainty is much larger in the N_2 and KrCl cases, since low fluences resulted in more limited data.

Discussion

Powell and Jancaitis[15] performed absorption experiments on electron-beam pumped Ar/Kr/F_2 mixtures using a KrF laser whose output was raman-shifted in H_2 and D_2, simultaneously producing 12 lines ranging from 206 nm to 423 nm. They determined from computer model predictions that Kr_2F^* was the dominant species present at the time the probe laser was fired, and attributed their results to Kr_2F^* absorption. Their spectrum is similar to the one shown in Fig. 3, and they also observed an increase in the cross section at 225 nm, but were unable to make a definite identification of the absorber at that wavelength. It is clear that this is also due to Kr_2F ($4^2\Gamma$) absorption.

From these results, it is unclear whether Kr_2F^* absorption at 248 nm excites a bound upper level, a state that immediately dissociates, or high vibrational levels of an excited state that quickly relax. Recent studies of Kr_2F^* absorption have shown that absorption at wavelengths greater than 280 nm results in photodissociation of Kr_2F^* and the immediate formation of the KrF (B) state,[16] while absorption at wavelengths below 250 nm do not appear to do so. The measurement at 248 nm is complicated by the effect of stimulated emission taking place which reduces the KrF (B) population.

TABLE I. Kr_2F ($4^2\Gamma$) absorption cross sections.

λ (nm)	σ (10^{-18} cm^2)
193	1.8
222	8.6
248	0.8
308	5.1
337	7.0
351	5.4

The absorption band from 250 to 500 nm is seen to be bound → free, supporting the contention that photodissociation takes place, leaving an excited KrF molecule and a krypton atom. The band centered at 224 nm, though much narrower, also appears to be bound → free, and the absorption products have not as yet been identified. Although the limit of the OSMA detection system is 200 nm, a new vacuum ultraviolet detector head will extend measurements below 200 nm, allowing a comparison to the 193 nm data points to be made.

The ($4^2\Gamma \rightarrow 9^2\Gamma$) absorption band is narrower in the discretely measured spectrum using the fluorescence suppression technique. The cause of this is not currently known, and several measurements were made to verify the accuracy of the 308 nm cross section, including performing the experiment at krypton pressures of 500 and 1000 Torr. Since photodissociation of Kr_2F^* takes place at this wavelength resulting in the immediate formation of KrF (B), doubling the krypton pressure increases the formation rate of Kr_2F^* from the newly formed KrF by a factor of four. If this increase in Kr_2F^* density were to have interfered with the fluorescence suppression measurement, it would have resulted in the measurement of a smaller cross section at 1000 Torr. However, the results at the two pressures were identical. The possibility of there being an error in the value of the absorption cross section due to neglecting the feeding term in eqn. (2) (Kr_2F reformation from the KrF photodissociation product) is currently under investigation.[17]

In addition to examining pressure effects, the effect of pump laser wavelength on the cross section measurement has been examined by Geohegan.[18] Since the ArF laser photons excite krypton atoms, there is another pathway to form Kr_2F^*; either through the KrF excimer, or by the process

$$Kr^* + 2\,Kr \rightarrow Kr_2^* \qquad (9)$$

$$Kr_2^* + F_2 \rightarrow Kr_2F^* + F \qquad (10)$$

Since under the general conditions of low Kr density the formation rate of KrF from the krypton metastable is much larger than that of reaction (9), it has been assumed that the Kr_2F^* is predominantly formed through KrF. However, the presence of large amounts of Kr_2^* in the cell would complicate the cross section determination, because it may not be true that the pumping term in eqn. (2) is small when the probe laser is fired. In Geohegan's measurement, he found that the 351 nm absorption cross section measured under conditions of KrF pumping, which results in photodissociation of F_2 and photoassociation of KrF directly, was within the experimental uncertainty of the value obtained in the ArF pumped case. Therefore, it is extremely unlikely that error is introduced by pumping with ArF.

Kinetics Experiments

Because of their short radiative lifetimes, it is difficult to perform excimer kinetics experiments using nanosecond pulse length lasers. The development of sub-picosecond excimer lasers[19] has provided a means of creating or probing excited states 'instantaneously', allowing kinetics measurements to be made without having to deconvolve the laser pulse width. This is especially important in measuring the (B) state radiative lifetime, which in the case of KrF [20] and ArF [21] is less than 10 ns.

Experiments are now in progress using a sub-picosecond KrF laser system to photoassociate the KrF (B) state from Kr-F pairs. Free fluorine atoms are created several hundred microseconds before the arrival of the sub-picosecond pulse by dissociating molecular fluorine with either a KrF or an XeCl laser pulse. Thus, KrF (B) molecules are formed in sub-picosecond time frames allowing the radiative lifetime and quenching to be determined by observing fluorescence decay rates as a function of F_2 density. Mixing between (B) and (C) is examined by measuring the fluorescence decay rates of both excimer levels as a function of Kr and Ar densities. By raman-shifting the 248-nm pulses in hydrogen to produce 277-nm pulses, it is expected that KrF (C) will also be photoassociated in a low pressure environment, and the radiative lifetime and quenching rate constants will be measured. The fluorescence suppression technique can be used to determine the KrF (B) stimulated emission cross section.

Conclusions

Absolute absorption cross sections have been determined which correspond to upward transitions from the Kr_2F ($4^2\Gamma$) state. A technique which determines exact fluences using a pyroelectric array has been developed which eliminates the major uncertainly in past measurements. The absolute cross section measurements may have been influenced by re-feeding of the Kr_2F^*, and this is currently being investigated. Although the 250-nm to 500-nm absorption band determined from optically pumping Kr_2F is spectraily narrower than that obtained from TASS, the data is reproducible and suggests that there may be a difference between optical pumping and discharge or electron beam pumping which manifests itself in the absorption measurement.

Continuous measurements of the absorption cross section for the trimers Kr_2F, Ar_2F and Xe_2Cl have been made using a transient absorption set-up. The ($4^2\Gamma \rightarrow 9^2\Gamma$) band has been observed for each of the trimers, as well as another band to the blue that has not been predicted to exist. Experiments are currently in progress that will extend these measurements down to as low as 125 nm.

Acknowledgements

The authors are grateful for the technical assistance of Bill Fox and Jody Godard and to J. G. Eden, D. Geohegan and J. Schloss for helpful discussions. This work was supported by the Department of Energy under the Inertial Confinement Fusion program.

References

[1]W.R. Wadt and P.J. Hay, J. Chem. Phys. **68**, 3850 (1978).

[2]K. Hakuta, H. Komori, N. Mukai, and H. Takuma, J. Appl. Phys. **61**, 2113 (1987).

[3]A.W. McCown, Appl. Phys. Lett. **50**, 804 (1987).

[4]D.B. Geohegan and J.G. Eden, J. Chem. Phys. **89**, 3410 (1988).

[5]T.H. Johnson and A.M. Hunter, J. Appl. Phys. **51**, 2406 (1980).

[6]F.K. Tittel, G. Marowski, M.C. Smayling, and W.L. Wilson, Appl. Phys. Lett. **37**, 862 (1980).

[7]F.K. Tittel, W.L. Wilson, R.E. Stickel, G. Marowski, and W.E. Ernst, Appl. Phys. Lett. **36**, 405 (1980).

[8]J.G. Eden, R.S.F. Chang, and L.J. Palumbo, IEEE J. Quantum Electron. **QE-15**, 1146 (1979).

[9]A.W. McCown, M.N. Ediger, D.B. Geohegan, and J.G. Eden, J. Chem. Phys. **82**, 4862 (1985).

[10]D.P. Greene and A.W. McCown, Appl. Phys. Lett. **54**, 1965 (1989).

[11]A.W. McCown, M.N. Ediger, S.M. Stazak, and J.G. Eden, Phys. Rev. A **28**, 1440 (1983).

[12]*D.B. Geohegan, A.W. McCown, and J.G. Eden, J.* Opt. Soc. Am. B **2**, 925 (1985).

[13]W.R. Wadt, J. Chem. Phys. **73**, 3915 (1980).

[14]D.B. Geohegan, A.W. McCown, and J.G. Eden, Phys. Rev. A **33**, 269 (1986).

[15]H. Powell and K.S. Jancaitis, presented at the 34th Annual Gaseous Electronics Conference, Boston (1981), paper FB-8.

[16]A.W. McCown, D.P. Greene, J.H. Schloss, and J.G. Eden, presented at the Conference on Lasers and Electro-Optics, Anaheim (1988), paper ThA6.

[17]J.H. Schloss and J.G. Eden, presented at the International Conference on Lasers '89, New Orleans (1989), paper HB-5.

[18]D.B. Geohegan, PhD Thesis (University of Illinois, Urbana, 1986).

[19]A.J. Taylor, R.B. Gibson, and J.P. Roberts, Appl. Phys. Lett. **52**, 773 (1988).

[20]J.G. Eden, R.W. Waynant, S.K. Searles, and R. Burnham, Appl. Phys. Lett. **32**, 733 (1978).

[21]T.H. Dunning and P.J. Hay, J. Chem. Phys. **69**, 134 (1978).

VUV AND LASER RAMAN STUDY OF THE CORRELATION BETWEEN ATOMIC AND MOLECULAR POLARIZABILITIES AND THE NUMBER DENSITY SHIFTS

K. Rupnik
Department of Chemistry
Louisiana State University
Baton Rouge, LA 70803

Abstract

This work is the first attempt to investigate the possible mechanisms of the radiative (VUV field induced) momentum transfer or coupling between the molecular perturbers and high-n Rydberg absorbers. A phase space approach using correlation functions is proposed for the interpretation of these processes in the gases. It is found from the density shift study, that the atomic and the anisotropic molecular polarizabilities are related to a single "active" correlation function component which is coupled to the correlation function describing high-n Rydberg transitions. We propose VUV and Raman study of the number density effects for some of the following systems (HF, NH_3, C_2H_4, H_2CO, CO_2, HCN, C_2H_2, and CH_3CN). In order to give a proper description of the total response function of the medium (the polarizabilities and their correlation functions) we are also interested in the investigation of their Raman and Rayleigh spectra (from ~ 0 to 5000cm^{-1}). The Raman spectra of some substituted iodomethanes (CH_3I, CHD_2I and CD_3I) are presented. The results of the study indicate that the role of electrons in the observed VUV transitions should be questioned and investigated in terms of their correlation functions. While it is commonly believed that the electron excitation mechanism is a requirement for all Rydberg transitions and the appearence of progressions, this may not be so. Indeed, these high-n transitions may be too "slow"-"dephasing" in absorption is too fast- to reach the electron excitation processes, so that they have no real physical significance.

Introduction

The pressure induced shifts and broadenings of the spectral lines of alkali metal absorbers, by non-resonant atomic and molecular perturbers, have been measured for at least 50 years. However, our recent study of CH_3I and C_6H_6 in H_2 was one of the first attempts to investigate the effects of a molecular perturber on the high-n Rydberg transitions of molecular absorbers[1]. Some of the high-n VUV absorption spectra of the molecules were found to shift linearly with the number density of atomic Ar (0.6×10^{20}-7.5×10^{21} cm^{-3}) and molecular H_2 (0.9×10^{20}-0.5×10^{20} cm^{-3}) perturbers. The origin of the Rydberg transitions is commonly associated with the electronic excitation mechanism (the electron orbitals). Therefore, the shifts of the high-n Rydberg spectra of the alkali metal atoms were first analyzed by Fermi[2] in the framework of the electron scattering model. According to Fermi, the total spectral shift is a sum of a scattering term, and a polarization term. The size and sign of the scattering term depends on the so called electron scattering length a of the perturber gas and varies linearly with the number density. It is assumed that the Rydberg electrons behave as if they are almost completely "free", with very small kinetic energies ("slow" electron model). For the calculation of the observed pressure shifts, the model suggests the use of the experimental data from the elastic scattering of low-energy electrons by foreign gas (perturber) atoms. In that case the value of a is related to the values of the response functions that describe the response to the electron impact. In the framework of that model, the value of a must be derived from the line (density) shift measurements or low energy-electron scattering.

The so called Fermi formula modified by the Alekseev-Sobel'man polarization term[3] can provide a satisfactory fit of some of the measured shift data. The total energy shift of a high-n Rydberg state is expressed as a sum of two terms:

$$\Delta(\rho) = \pm (2\pi\hbar^2/m)\, a\rho - 9.87(\alpha e^2/2)^{2/3}(h\nu)^{1/3}\rho \qquad (1)$$

where ρ is the number density, m is the electron mass, α is polarizability and v is the relative thermal velocity of the absorber and perturber. The first term in (1) is the scattering term, the second is the polarization term.

However, for the molecular perturbers such as H_2 there is an unexpected gradual increase of the shift rate with n quantum number for the system H_2/C_6H_6. Also, the electron scattering lenghts obtained in that study are lower than values from other Rydberg shift studies. The electron scattering cross sections ($\sigma\sim4\pi a^2$) of rare gases as measured by pressure shift methods agree with cross sections near zero electron energies obtained from electron swarm data, while in the case of H_2, the value obtained from swarm data is more that 50% higher than that from pressure shift studies[4].

A recent empirical model[5], however, provides a linear correlation between the electron scattering lenghts a, as measured by a pressure shift method, and the polarizabilities α for He, Ne, Ar, Kr and Xe gases. Although the polarizability is known to be one of the parameters in the theoretical models for calculation of electron scattering lenghts, this correlation is constructed by fitting the atomic polarizabilities to the experimental electron scattering lengths. This purely empirical correlation is different in intent from other models developed for rare gas atoms. It is aimed at usage of only one parameter, the polarizability, which itself is a measure of the perturber's response to the applied (VUV/optical) field. As a result, a consistent phase space approach using correlation functions to the interpretation of the observed spectra is possible.

Phase-space approach to the radiative momentum transfer: Correlation functions for linear and nonlinear VUV/optical processes in gases

This work is an attempt to give a brief description of the possible mechanisms of the radiative (VUV field induced) momentum transfer or momentum coupling from/to atomic or molecular perturbers to/from the absorbers. It is the distinct characteristic of this physical model that both the absorber (high-n Rydberg) as well as the perturber (Rayleigh to Raman) are considered as active in the VUV field. The reasoning and physical models applied here could be compared with the models of optical parametric processes in the mixtures of atomic and/or molecular gases[6] and with the phase-space models using correlation functions or causality relation. As a common denominator to all these models, the knowledge of the time-scale (relative phase) of the momentum transfer processes (induced polarizability or absorption/emission) relative to the excitation field as well as relative to the coupling between the response functions of the absorbers and perturbers is important. Therefore a common phase space is mandatory for the representation of the coupling between the correlation functions (their "phase-matching") of the active constitutents of the system in the field. The density effects themself are also known to be phase-dependent. For example, the Rayleigh scattering which is "in-phase" with the incident radiation is expected to show interferences due to the change of number density, or presence of other molecules. Raman scattering, which bears an arbitrary phase relation to the incident radiation is expected to show an additive scattering from individual centers.

In a simple form, for non-resonant Raman scattering, the differential scattering cross section (per molecule) can be given as a function of a correlation function[7]:

$$d^2\sigma/d\Omega d\omega_S \cong \int dt\ exp[i(\omega_S-\omega_O)t]\ C(t) \qquad (2)$$

and the (time-dependent) correlation function is given as:

$$C(t) = \sum_n \rho_n \langle n|\ \underline{\alpha}(0)\ \underline{\alpha}(t)\ |n\rangle \qquad (3)$$

where the symbol $\underline{\alpha}$ represents the polarizability tensor. More generally, the calculation of the correlation functions, C(t) is a problem related to the phase space approach to the momentum transfer calculations for any well-defined physical system[8]. Also, in the case of an absorption spectrum, the correlation function similar to (3) describes correctly the response function (or momentum transfer) if the polarizability operator describes the absorption process (different symmetry properties and the selection rules, or relative phase for example). The calculation of the correlation functions C(t) is, however, the same type of physical problem for both types of momentum transfer processes, and can be done in the same phase-space. It is well known that in the case where the Kramers-Kronig calusality relation can be applied, the correlation function can be given in terms of its real and imaginary parts.

Instead of the explicit calculations, one may ask whether the value of the correlation function can be extracted from some other measurement of polarizability. In our case the question is whether the polarizability of the perturber can correctly describe the "effective" or "active" correlation function of perturbers in the phase space that describes density shift effects in the VUV transitions of absorbers. One does assume here that the non-resonant polarizability does not change significantly in optical/VUV region, and that the measured polarizability is not a nonlinear function of density. The opposite cases are well known, so that caution is necessary if this assumption is taken into account. Indeed, we find a surprising result[5]: a linear correlation does exist between the electron scattering lengths a, as measured by number density shifts, and the polarizability α of the atoms He, Ne, Ar, Kr and Xe. The best fit of the experimental data is described by

$$a = a_1\alpha + a_2 \qquad (4)$$

where a and α are cited in atomic units and a_1 and a_2 are constants, their values being a_1=-0.26 and a_2=1.18, respectively. The success of the correlation should be attributed to the relatively large range of the atomic polarizabilities of these gases as well as to the specific character of the high-n Rydberg transitions: their relation to the ground and excited states or resonant transitions. The interpretation of the possible physical parameters related to the extracted empirical constants, a_1 and a_2 and the calculation of their theoretical values is a subject of an ongoing investigation. Since these atomic polarizabilities cover the range from ~1.4a_o^3 for He to ~27.2 a_o^3 for Xe, it is clear that the relation (4) describes both blue (He) as well as the red (Xe) shift as a linear function of the atomic polarizability. The parameter a_2 is a "zero polarizability" shift, with a value which is approximately close to the $\ell n\ \pi$ (in the limits of standard deviation). However, the full meaning of the a_2 in the relation with the correlation functions of the rare gas atoms in these processes is not known yet.

In addition to the atomic systems, the first application of a similar relation to (4) was proposed for molecular perturbers. Here, the effective polarizability of molecules like H_2 and N_2 is given in terms of the anisotropic (non-spherical) contributions:

$$a = a_1 (\alpha_{//} - \alpha_{\perp}) + a_2 \qquad (5)$$

and the isotropic (spherical) polarizability was used for CH_4. The algorithm (5) gives correct predictions of the measured values of a also for these molecular systems. As as consequence, the correlative algorithm was found with excellent predictive capability for these atomic and molecular systems. Also, a linear additivity of scattering potential, given in terms of atomic polarizability,has been observed for He:Ar perturber gas mixture. An "effective polarizability coordinate" was estimated for the mixture of the two rare gases[5].

The successful application of relations (4) and (5) to the calculation of the parameter a suggests that there is one single "active" correlation function that contributes the observed number density effects. The "non-resonant" or "off-phase" character of the function is expected as the result of the additivity of the density effects (linear shift). This is particularly important in the case of the anisotropic molecular polarizability ($\alpha_{//}-\alpha_{\perp}$)which cannot be confused with a simple "in-phase" character. In the language of the common phase-space model, the observed role of the composed anisotropic polarizability is then a direct result of its single "active" correlation function component, which is coupled to the correlation function describing the high-n Rydberg transitions. The local (molecular) character of the correlation function is then preserved in the density shift effects. The question is whether this is a rule more than exception for some other (even larger) molecular systems, where a number of active modes (rovibrational, for example) contribute to the total response function and therefore correlation functions have a more complicated phase dependence. It is also interesting to compare various different molecular properties that may depend on the same "active" correlation function as the scattering length parameter a in our density effects study. These properties include the magnetic field induced response functions, such as the magnetic birefringence[9] and dichroism, as well as some time-dependent (transient) effects, such as resonant and non-resonant quantum beats. We therefore propose VUV and Raman study of the number density effects for some of the following systems: HF, NH_3, C_2H_4, H_2CO, HCN, C_2H_2 and CH_3CN in order to test their "active" polarizability contribution(s) or the correlation function components(s). These molecules are expected to cover the regions of blue (HF, NH_3) and red (other molecules in the series) shifts. The calculated scattering lengths a from relation (5) for these systems are presented in Table 1. The experimental data for molecular polarizabilities are taken from ref. 10-17. In comparison with H_2 and N_2 these molecules absorb strongly at lower frequencies and this does not allow their use in the similar experimental conditions. Therefore different experimental conditions are necessary for the study of these molecules as the non-resonant perturbers of high-n Rydbergs.

Raman spectra and Correlation functions of Iodomethanes

In this work, we have begun an investigation of the molecular Raman spectra of iodomethanes in the visible region. The spectra were obtained with a Raman system which consists of a Coherent Inova Ar laser, ISA-1000 spectrometer and a data aquisition system with an IBM XT computer. The excitation wavelengths were 514 and 488 hm. The object of this investigation is twofold. First, we are interested in the role of the so called "out-of-phase"[18] or Raman contributions (Stokes and Antistokes) to the total response function of the perturber medium and in the role they may play in the number density effects in the high-n Rydberg transitions. In this "scale" of values of the phase relative to the incident field, the polarizability related to the "in-phase" or Rayleigh

Table 1. Calculated scattering lengths from equation (5). The experimental data for molecular polarizabilities are taken from References 10-17

MOLECULE	$\alpha_{\parallel}(a_0^3)$	$\alpha_{\perp}(a_0^3)$	$(\alpha_{\parallel} - \alpha_{\perp})(a_0^3)$	$a(a_0)$(cal.)
HF	6.59	5.1	1.49	.79
NH_3	16.27	14.33	1.94	.68
C_2H_4	36.34	24.49	11.85	-1.90
H_2CO	18.83	12.95	5.88	-.35
CO_2	27.2	13.02	14.18	-2.51
HCN	26.52	12.99	13.53	-2.34
C_2H_2	31.92	19.37	12.55	-2.08
CH_3CN	38.73	25.98	12.75	-2.135

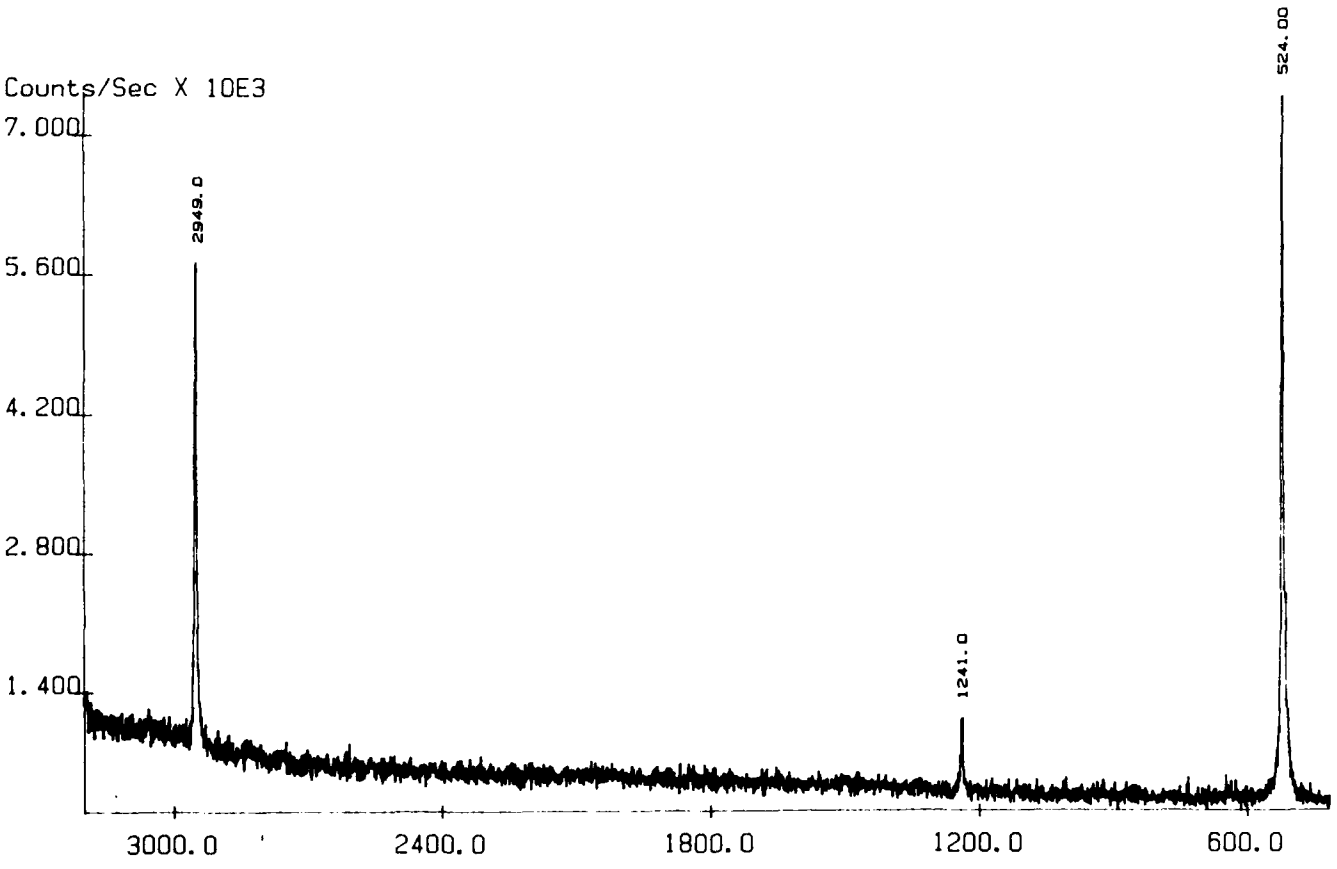


Fig. 1 Raman spectrum of CH_3I molecules (Stokes)

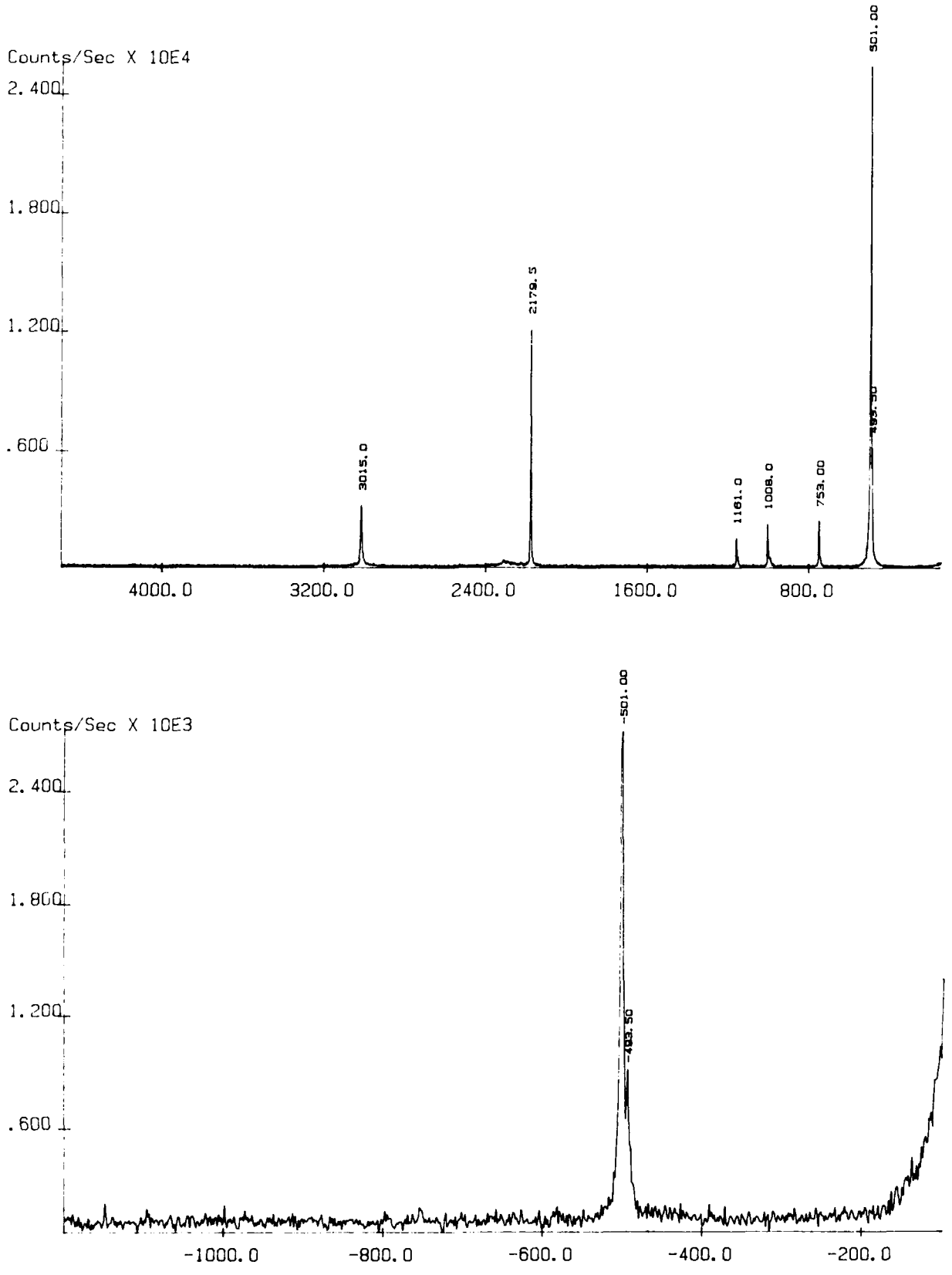


Fig. 2 & 3. Raman spectra of CHD_3I Stokes (upper) and Antistokes (lower)

region was considered to be the most important in the equations (4) and (5). Second, we are investigating the relations between the "in-phase" and "out-of-phase", Rayleigh and Raman components, respectively. Such relations are known to exist[18] for some spectral parameters (such as polarization, intensity, etc.). The measured spectral line patterns are investigated here in order to establish the correlation function for a molecule in the phase space describing the radiative momentum transfer process from incident fields. This includes also the measured parameters, such as the line frequency ratio or the intensity ratio. They are associated with the corresponding "patterns" in the phase space. As the result of the study the molecular momentum transfer mechanism can be given in terms of a phase-space correlation function including the incident field parameters as well as the molecular response. A brief description of a simple phase-space model is given here. The more elaborate analysis of the molecular correlation functions is out of the scope of this paper and will be given elsewhere.

The phase space approach using correlation functions for molecules can be associated with the phase space analysis of the motion of the field driven pendulum. For one degree of freedom, the response function of the system will give a spectral structure in the form of a Lorentz line. Although the Raman spectra, as well as molecular spectra in general, are not expected to show a well-defined Lorentz (or Gaussian) line, it is sometimes useful to find the possible "critical points" or common characteristics, that can relate the observed spectral patterns with such a phase space Lorentz-correlation function. One of such points of interest is expected to be the one at the maximum (or minimum) of the derivative of the Lorentz line. Here, the "width of the derivative line" (from its maximum to minimum) is equal $2/\sqrt{3}T_2$ where T_2 refers to the parameter known as the "relaxation" time. In the case of the Gaussian line the corresponding width is equal $2/T_2$. Assuming one effective relaxation time (T_2 scale) the relative phase differences in a spectral line pattern converging to a "resonant pattern" (example given by a Lorentz line) are then expected to be given as a function of the frequency ratio of the consecutive lines.

The measured Raman spectra of CH_3I is presented in Fig. 1. The Stokes and Antistokes spectra of CHD_2I are presented in Figs. 2 and 3 respectively. The features in the Raman spectra of CH_3I are observed at (+and-) 524, 1241 and 2949cm^{-1} and those in the spectra of CHD_2I at (+and-) 493, (+and-) 501, 753, 1008, 1161, 2179, and 3015cm^{-1}. The frequency ratio for the lines at 1306cm^{-1} and 3020cm^{-1} of the CH_4 molecule[7] is $\sim\sqrt{3}/4$ (one-half of the coefficient in the derivative of the Lorentz line "width"). For the lines at 501 and 1161cm^{-1} of the CHD_2I molecule there is the same value of the frequency ratio. However, for the lines at 3015cm^{-1} and 2179cm^{-1} for the same molecule the ratio is $\sqrt{2}$ and for the lines at 1008cm^{-1} and 501cm^{-1} it is ~2. The ratio between the frequencies of the lines at 753cm^{-1} and 501cm^{-1} is 3/2. For the CH_3I molecule the ratio between the 1241 and 2949cm^{-1} as well as the ratio between the 524 and 1241cm^{-1} is $\sim(\sqrt{3}/4)$, and for the CD_3I molecule: $940/2140\sim\sqrt{3}/4$. The intensities of the lines at 3015, 2179 and 501cm^{-1} of CHD_2I molecule with the ratio (1:4:8) or (1:5:9), indicate that they may belong to one of the two progressions with the different effective "spins". One with the values 0,2,4 corresponds to the intensity distributions (1:5:9). Indeed, the ratio of the frequency differences between the second two and the first two lines is ~1/2, and the "vibrational-like" structure and corresponding Gaussian-type ("convex") intensity distribution may be expected. On the other hand the low-intensity "progression" in the same molecule shows the frequency ratio of 3/2, (1129 relative to the line at 753cm^{-1} etc.) for the three lines: (1129, 753, 493cm^{-1}). The distribution of their intensities is then expected to be Lorentz-like ("concave"). In the CH_3I molecule (Fig.1) there are only two lines for the "1/2" progression: (2949, and 524cm^{-1}), and the "3/2" progression has a line at 1241cm^{-1} and is very likely to have another line close to the 524cm^{-1}. It is interesting to compare this results with the Raman spectrum of I_2 molecule. While these molecules show a combination of the two spectral "progressions" ("1/2" and "3/2" ratio), the I_2 molecule shows a (Δ J=+1,-1) splitted (doublets) vibrational distribution.[7]

Discussion

The introduction of the proposed phase-space correlation functions in the form of atomic and molecular polarizabilities allows a new insight in the physical processes that contribute to the high-n Rydberg transitions. First, the accent is given here on the time-dependent field-induced (radiative) correlation function which describes the behavior of the system, instead of the parameters of the electrostatic models. The application of equations (4) and (5) for the calculation of the electron scattering length parameter a and the introduction of the calculated a in the equation (1), leaves the first, scattering, term in this equation entirely dependent on the polarizability. Consequently, this large term can be interpreted as the response function of a perturber to an external field, and this (radiative) process is then in a great deal responsible for the observed number density effects in high-n Rydberg transitions. The second term is again the

polarization term, which in the case of the spectra of the atoms and molecules discussed here has a quantitatively less important contribution. It has been realized earlier that according to the separation in "electronic scattering" term and the "polarization" term in the equation (1) for the density shift, the Ar atoms have polarization contributions of 35% and Xe atoms of about 10%, regardless of the much higher polarizability of Xe. Our results confirm the experimental finding and also give an explanation of the role of polarizability contribution of Xe in equation (1). The relation (4) gives also a quantitatively correct "scattering" term value for Xe, because the scattering length parameter is a linear function of the perturbers polarizability. Our finding that the atomic and the anisotropic molecular polarizabilities are related to a single "active" correlation function component which is coupled to the correlation function describing high-n Rydberg transitions is also in agreement with the observed n-dependence in the H_2/C_6H_6 system. Contrary to the atom-atom or atom-molecule systems, in the molecular absorber-molecular perturber systems the coupling of correlation functions can give a more complicated "active" component(s), which are also n-dependent. In that case the differences (n-dependance) are due to the "active" correlation function components of absorbers. A nonlinear coupling of these functions is also possible, leading to the broadening of the lines or to the nonlinear effects. It is an open question, however, whether the resultant "active" component will then behave more like an "in-phase" or resonant component or not. The n-dependent behavior of the "blue" perturbers in comparison with "red" perturbers may also be different. The differences between the swarm (electron impact) and the photon impact values for a should be expected, because their time-dependent response functions are different.

Second, the question is to what extent is the electrostatic "slow" electron model valid (or even compatible) in the phase space approach. Indeed, we have substituted the parameter a, attributed to the electrostatic slow-electron scattering, by the incident-field induced response function. It should be pointed out that no differences of density shifts in the slow-electron model are expected between various different atomic or molecular electrons of absorbers, as long as they are in the appropriate field (high-n) region. That means that the correlation function associated to the electrons (only) should be completely atom or molecule independent ("free" electrons). The key to the resolution of this slow-free-electron enigma in the phase space approach could be in the information about the phase of the electron correlation function relative to the incident field, absorber and perturber. We do expect that the electron excitations by an incident field are fast processes, so that the corresponding correlation function $C(t)_{el}$ should be evaluated at a very short time. The quantitative parameter is not incorporated in the electrostatic model. This would leave the excited electron with an "active" correlation function completely different from those of the other constituents. Also, a momentum transfer from electrons to the environment should be expected quite different from the predicted kinematic parameters in the slow-electron model. An electron "relaxation" as seen in the spectral structure, should be described by the electron correlation function as well as by the other atomic and molecular processes. Nevertheless, the very existence of the high-n Rydberg transitions (progressions) is possible only if a certain phase "coherence" is achieved. In other words, at a certain point in going from simple atomic to larger molecular systems the high-n Rydberg progressions may cease to exist. The number density effects show that the atomic and molecular perturbers to a larger or lesser degree contribute to this constraint imposed on the existence of the high-n Rydberg progressions. This indicates the need for a parallel cooperative-competitive radiative momentum transfer mechanism, which depends strongly on the phase-matching conditions. As a consequence, the results of the study already indicate that the role, and consequently the physical parameters (momentum, velocity, trajectory, etc.) associated with the real electrons in the observed VUV transitions in atoms and molecules should be questioned. While it is commonly believed that the electron excitation mechanism is a requirement for all Rydberg transitions and the appearence of progressions, this may not be so. A parameter such as the relative phase between the correlation functions describing the VUV transitions and other transitions can give a proper description of the nature of high-n Rydberg transitions (states) in the phase space. Indeed, these high-n transitions may be too "slow"-or "dephasing" in the correlation function describing the absorption is too fast- to reach the electron excitation processes, so that they have no real physical significance. This despite the seemingly close position in the spectra to the ionization threshold. Also, there is a question about the relative origin of Rydberg progressions and the parameters in the spectroscopy of molecular systems. A possible phase space approach to the calculation of the parameters related to the processes of the momentum transfer from resonant fields is a subject of an ongoing investigation.[19]

Acknowledgment

This work was supported by the U. S. Department of Energy (Office of Health and Environmental Research).

References

1. U. Asaf, W. S. Felps, K. Rupnik, S. P. McGlynn, and G. Ascarelli, J. Chem. Phys. 91, 5170 (1989).
2. E. Fermi, Nuovo Cimento, 11, 157 (1934).
3. V. Alekseev, and I. I. Sobel'man, JETP 22, 882 (1966).
4. U. Asaf, K. Rupnik, W. S. Felps and S. P. McGlynn in "Proceedings of the Sixth International Swarm Conference 1989", J. W. Gallagher ed., Plenum, New York, (1990) (in press).
5. K. Rupnik, U. Asaf, and S. P. McGlynn, J. Chem. Phys. 92, 2302 (1990).
6. J. F. Reintjes, "Nonlinear Optical Parameteric Processes in Liquids and Gases", Academic Press, New York, (1984).
7. A. Weber, "Raman Spectroscopy of Gases and Liquids", Springer Verlag, New York, (1979).
8. F. C. Moon, "Chaotic Vibrations", Wiley, New York, (1987).
9. N. J. Bridge, and A. D. Buckingham, Proc. R. Soc. A 29, 334 (1966).
10. J. S. Muenter, J. Chem. Phys. 56, 5409 (1972).
11. Ref. 9.
12. G. W. Hills, and W. J. J. Jones, J. Chem. Soc. Faraday Transactions II, 71, 812.
13. J. Applequist, J. R. Carl, and K. K. Fung, J. Am. Chem. Soc. 94, 2952 (1972).
14. Ref. 9
15. H. A. Landolt, and R. Bornstein, "Zahlenwriten und Funktionen", Springer Verlag, (1962).
16. Ref. 9
17. R. J. W. LeFevre, B. J. Orr, and G. L. D. Ritchie, J. Chem. Soc. 2499 (1965).
18. D. A. Long, "Raman Spectroscopy", McGraw Hill, London, (1977).
19. K. Rupnik, OSA Annual Meeting, 1989 Technical Digest Series, Vol. 18 (OSA), Washington, DC (1989) p. 140.

PHASE COHERENCE, DIFFUSION AND RECOMBINATION OF EXCITONS IN II-VI COMPOUNDS

C. Dörnfeld*, R. Renner*, H. Schwab*, J.M. Hvam**, G. Noll+, E.O. Göbel+ and C. Klingshirn*

* Fachbereich Physik, Universität Kaiserslautern, D-6750 Kaiserslautern, FRG
**Fysisk Institut, Odense Universitet, DK-5235 Odense M, Denmark
+ Fachbereich Physik, Universität Marburg, D-3300 Marburg, FRG

Abstract - Various transient grating experiments are performed to study the phase coherence, diffusion and recombination of excitons in CdS, CdSe and CdSSE mixed crystals. At low temperatures and excitation densities we observe dephasing times of 40 ps in CdSe and 75 ps in CdSSe. The dephasing times decrease with increasing values of these parameters. At higher densities an electron-hole plasma is generated. In this case the dephasing times are in the fs-range. In the mixed compound we observe a reduced, but non vanishing mobility of excitons in the localized band. The diffusion coefficient is $<2\ cm^2/s$.

1. Introduction

The relaxation of optically excited electron-hole pairs (excitons) in semiconductors is a fundamental physical process of light-matter interaction. There are a variety of possible relaxation mechanisms, depending on the material and excitation conditions. The relaxation of excitons involve the dephasing, intraband relaxation, diffusion and recombination. The dephasing of excitons occurs by interaction with impurities, phonons and other excitons. Thereby the coherent coupling between the exciton and the light field is destroyed. During or after this initial scattering process the excitons may relax energetically in a band under emission of phonons and recombine finally radiatively or nonradiatively. Thus, the relaxation involves three steps, each with a characteristic time. T_2 for the dephasing, T_1 for the intraband relaxation and T_r for the interband relaxation. In pure compounds the dominant scattering mechanisms of resonantly excited excitons are the ones with acoustic phonons and collisions with other excitons or lattice defects.
In the mixed compound CdSSE the compositional disorder gives rise to a fluctuating band gap, which localizes excitons [1,2]. The width of the fluctuating potential increases with decreasing localization depth. Therefore two different models of localization are relevant. For deep localized states the potential well is narrow. In this regime only the hole is trapped and binds the electron by the Coulomb force. When the diameter of the well becomes larger than the exitonic Bohr radius, the exciton is localized as a whole. The square root behaviour of the density of free exciton states is therefore modified by the localization, resulting in an exponential tail of localized states below the extended states. It turned out that the transition region between localized and free excitons is spectrally located at the high energy side of the observed luminescence band, approximately where the luminescence has dropped to 1% of its maximum value [1,2]. The localization influences the relaxation of excitons. Dephasing for localized excitons occurs by phonon scattering, by tunneling to other localited sites and through radiative decay. The scattering of localized excitons with other excitons should be reduced in respect to free excitons. At low temperatures, where the interaction with phonons is reduced, long dephasing times for localized excitons are expected. The only possibility of an localized exciton to migrate through the crystal is by phonon-assisted tunneling processes. That means, excitons relax stepwise within the localized band tail to the lowest possible energy state. Therefore the diffusion is reduced and the radiative recombination is enhanced with respect to excitons in pure materials.

2. Transient Grating

We studied the dynamics of excitons with a transient grating experiment. This technique yields information on dephasing, recombination and diffusion. In a transient grating experiment, three successive light waves, with the electric fields $E_1(\vec{k}_1,\omega_1)$, $E_2(\vec{k}_2,\omega_2)$ and $E_3(\vec{k}_3,\omega_3)$, propagate in a thin slab of the material at different times $t_1 \neq t_2 \neq t_3$ and generate a nonlinear polarization wave. A proper choice of the experimental parameters (these are the photon energies $\hbar\omega_1$, $\hbar\omega_2$ and $\hbar\omega_3$, the arrival times of the pulses on the sample t_1, t_2 and t_3 and the direction of the pulses $\vec{k}_1, \vec{k}_2$ and $\vec{k}_3$ and their amplitudes E_i or intensities I_i) enables us to measure the different relaxation times and the diffusion coefficient. With a sufficient time resolution, i.e. when the pulse length is shorther than the characteristic relaxation time, the dephasing time T_2 can be measured in a two beam configuration with $\omega_1=\omega_2=\omega_3$, $k_1 \neq k_2 = k_3$ and $t_1 \neq t_2 = t_3$, outlined in Fig. 1a. Here one of the pulses enters twice in the mixing process and the selfdiffracted signal I_s is propagating into the backgroundfree $2\vec{k}_2-\vec{k}_1$ direction. The dephasing time is measured by a correlation technique, i.e. I_s is measured as a function of the delay τ_{12} between the pulses #1 and #2. The decay of the correlation trace for $\tau_{12} > 0$ reflects the dephasing. For an inhomogeneously broadened transition the asymetric tail of the trace decays exponentially with $4\tau_{12}/T_2$ [3-5].
In the configuration $\omega_1=\omega_2=\omega_3$, $\vec{k}_1 \neq \vec{k}_2 \neq \vec{k}_3$ and $t_1 = t_2 \neq t_3$, two temporarily coinciding pulses

set up a real population grating from which the delayed third pulse will be diffracted into the $\vec{k}_3$ ($\vec{k}_2$-$\vec{k}_1$) direction (see Fig. 1b). Within the coherence time pulse #3 is diffrac-

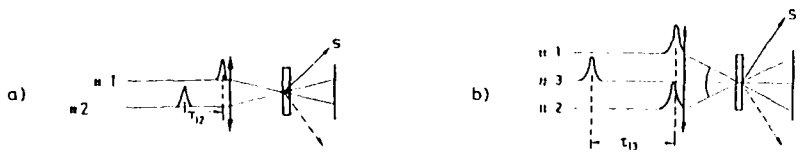


Fig.1: Shematic drawing of a transient grating experiment for dephasing measurements (a) and to determine the diffusion coefficient and recombination times (b).

ted at a polarization grating, discussed above, resulting in a coherent artefact. For longer delays $\tau_{13} > T_2$ the third pulse probes only a real population grating. A population grating decays within the grating lifetime T_g. From the decay of such a grating the diffusion coefficient D and the recombination times T_r can be extracted when the angle between the exciting beams is varied. T^{-1}_g is given by:

$$T^{-1}_g = T^{-1}_r + \frac{4\pi^2 D}{\Lambda^2} \qquad (1)$$

$\Lambda = \lambda_{exc}/2\sin\theta$ is the grating constant, with the angle θ between the beams #1 and #2. In the quasi-stationary excitation condition without time resolution the above mentioned decay times can be measured in the frequency domain, by means of a nondegenerate four wave mixing (NDFWM) experiment. Here the excitation is provided by pulses with slightly different frequencies, generating a moving grating. The grating efficiency as a function of the detuning of the pulses yields also information on the kinetics of carriers.

3. Experimental arrangement

In the time resolved experiments we used synchronously pumped ps dye lasers. The pulse length varied between 1.4 ps and 8 ps. The pulse energies were $< 1\mu J/cm^2$. The quasi-stationary excitation has been performed with ns pulses, delivered by an excimer laser pumping two dye lasers. The laser beam was split into two or three beams, in the time resolved experiments with variable delays between them and focused onto the sample. The high purity samples were placed in a temperature variable He cryostat. The diffracted light has been analyzed by a spectrometer and monitored by an OMA. A detailed description of the experimental set-up is given elsewhere [5].

4. Dephasing of free and localized excitons

Fig. 2 shows the reflexion R of a CdSe sample in the spectral region of $A\Gamma_5(n=1)$ exciton and the nonlinear resonances of the first diffracted order I_s at an excitation intensity of $50kW/cm^2$ and at 4.2 K. I_s has three pronounced structures around 1.825 eV, 1.8225 eV and 1.820 eV. The nonlinearity at the exciton transition is caused by exciton-exciton (x-x) interaction. The second resonance is the formation of biexcitons by two-photon absorption (TPA). This nonlinear process has been studied intensively in the past [6-9]. The nonlinear signal at 1.820 eV is ascribed to the induced exciton-biexciton (x-b) transition [10]. For this process the necessary exciton population is excited by the high energy wing of the laser. An exciton with 1.825 eV absorbs a photon with 1.820 eV to form a biexciton. This transition is easy to saturate, because of the low exciton population. The x-b transition and the exciton transition yield information on the kinetics of excitons in the low and high density regime, respectively. At this resonances we measured T_2 by the correlation technique, discussed in the previous chapter. T_2 of the TPA is described in [5]. Strong x-x scattering is also seen in the density dependence of the dephasing times. Experimental correlation traces at the exciton resonance at three different densities are shown in Fig. 3. The dashed curves are calcualted correlation traces from an inhomogeneously broadened two-level model. From the fits we extract T_2 and the inhomogenous linewidth Γ. At an exciton density $N_x = 4.10^{15} cm^{-3}$ we observe $T_2 = 12$ ps (curve a). With increasing N_x the nonlinear signal increases and T_2 decreases to 5 ps at $N_x = 1.4 \cdot 10^{16} cm^{-3}$ (curve c). From the density dependence of the scattering rate T_2^{-1} we assume that mutual collisions of the excitons destroy the phase coherence.

In Fig. 4 and Fig. 5 the corresponding spectra are shown for localized excitons. In Fig. 4 the transmission, the luminescence (L) and the first diffracted order I_s are plotted versus the photon energy in $CdS_{0.65}Se_{0.35}$ at 4.2 K. In the mixed compound we observe spectrally broad nonlinear resonance, energetically coinciding with the luminescence from localized excitons. We attribute the nonlinearity to a bleaching of the localized band. In

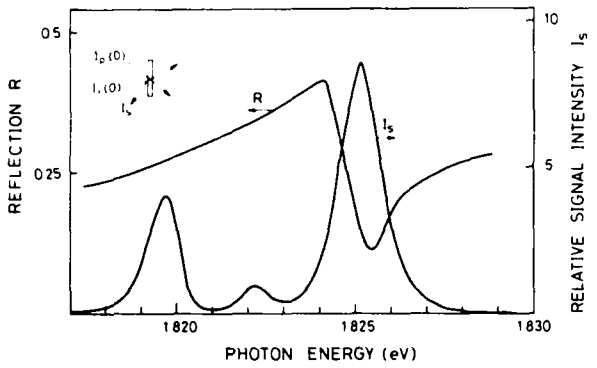


Fig 2: Spectral dependence of the nonlinear signal (scale to the right) and the reflexion R (scale to the left) in a CdSe sample at 4.2 K. The incident intensity is 50 kW/cm^2.

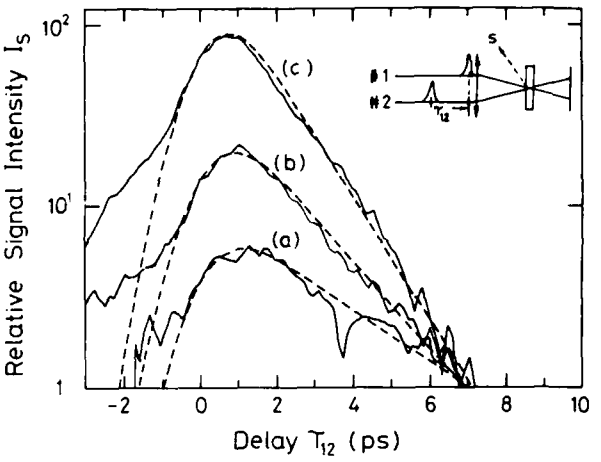


Fig 3: Experimental (full line) and calculated (dashed curve) correlation traces at the exciton transition. (a) $N_x=4\cdot10^{15}$cm^{-3}, T_2=12 ps, (b) $N_x=8\cdot10^{15}$cm^{-3}, T_2=7ps. (c) $N_x=1.4\ 10^{16}$cm^{-3}, T_2=5ps; Γ=9 meV.

the maximum of I_s at 2.225 eV we measured T_2 of localized excitons. The excitation is close to the transition between localized and extended states and therefore the exciton is presumably trapped as a whole. Experimental correlation traces at three different densities are shown in Fig. 5. Each correlation trace exhibits a two component decay. The fast initial decay within ≅ 400 fs, is a contribution from off resonant excited free excitons. The spectral width of the laser is ≅ 2 meV and the excitation into the extended states is possible. At this density the dephasing is even faster than the dephasing for free excitons in pure CdSe, because of additional scattering at the fluctuating potential. The slower component is ascribed to the dephasing of localized excitons. The dashed curve are fits from an inhomogeneously broadened two-level system. T_2 is with 75 ps at $N_x=3\cdot10^{14}$cm^{-3} (Fig. 4, curve a) twice as large as T_2 in pure CdSe. The long dephasing time indicates that localized excitons suffer less from scattering with impurities and other excitons. As in the pure material we found a decrease of T_2 with increasing N_x [11]

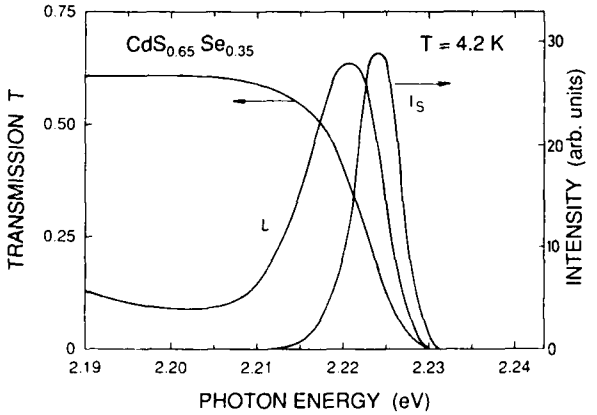


Fig 4: The transmission T (scale to the left) and the selfdiffracted signal I_s at τ_{12}=0 (scale to the right) as a function of photon energy. Also the luminescence L of the localized excitons is shown.

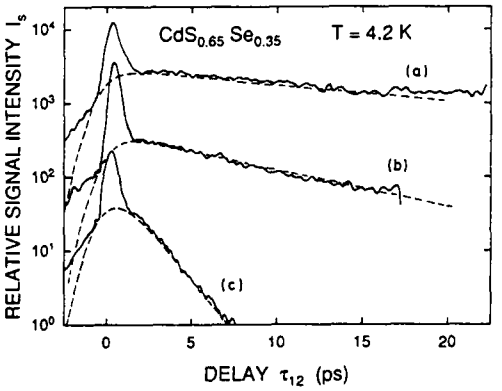


Fig 5: Experimental (full curve) and theoretical (dashed curve) correlation traces at a photon energy $\hbar\omega$ = 2.225 eV for different excitation densities, resulting in different phase relaxation times T_2. a) $N_x=3\cdot10^{14}$cm^{-3}, T_2=75ps; b) $N_x=8\cdot10^{14}$cm^{-3}, T_2=34ps; c) $N_x=9\cdot10^{15}$ cm^{-3}, T_2=6ps.

5. Diffusion of localized excitons.

In the three beam configuration of our transient grating experiments a delayed weak probe pulse reads the population grating set up by two coinciding intense pump beams. We measured

the grating lifetime in $CdS_{0.45}Se_{0.55}$ at four different photon energies, 2.068 eV, 2.071 eV, 2.074 eV and 2.078 eV, in the localized states. We varied the grating constant Λ in the range from 2μ to 6.3μ. In Fig. 6 (a,b) the diffracted intensity I_s is plotted versus the delay τ_{13}. Each figure shows two curves at one photon energy and two different grating

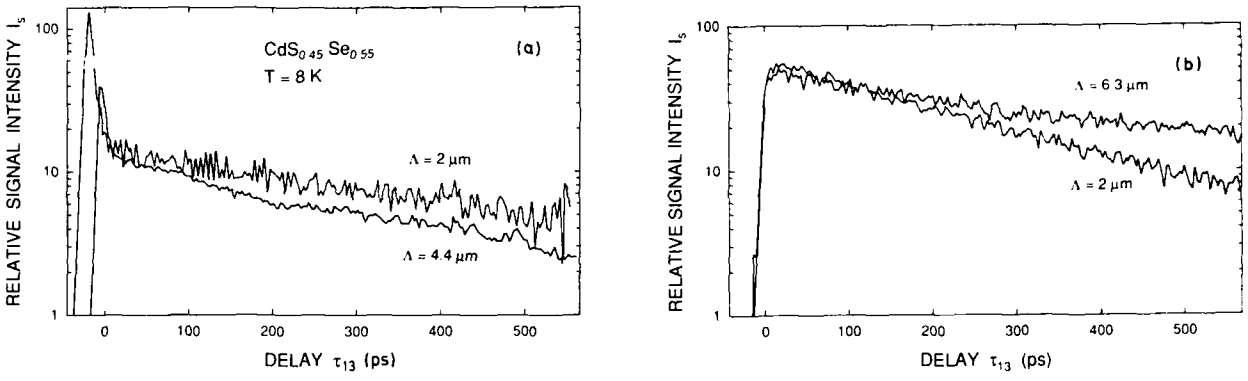


Fig. 6 (a,b): Diffracted signal I_s of pulse #3 on a grating set up by pulse #1 and pulse #2 (see also Fig. 1b) versus delay τ_{13} (τ_{12}=0) for two photon energies. Each Figure shows diffraction curves for two different grating constants Λ. a) $h\omega$=2.068eV; T_g=345 50ps (Λ=2 m), T_g=400 40ps(4.4μm); b) $h\omega$=2.078eV; T_g=660 140ps (Λ=6.3 m), T_g= 290 15ps (Λ=2μm).

constants. Throughout the measurements we changed the intensity to keep a constant exciton density of N_x $10^{16}cm^{-3}$. In Fig. 6a we observe a fast decay of a coherent grating, followed by a slower component of the incoherent population grating. This coherent part is not seen at higher energies (Fig. 6b). This peak decays with 8 ps and is attributed to a nonlinear contribution from the laser itself. At a photon energy of 2.068 eV, well in the localized states the grating decays with T_g=350 ps and 400 ps (a). At an excitation closer to the transition region the grating lifetimes are T_g= 660ps and 290 ps (Fig. 6b). The relaxation time of a population grating is given by (1). The grating lifetime T_g is independent of Λ for deeper localized states and decreases with decreasing Λ at higher energies. We evaluate T_r and D from the experiments, by plotting T_g^{-1} as a function of Λ^{-2}. The slope of the straight lines determines D and the points of intersection with the T_g^{-1} axis give the recombination rate. We found a small D=0.3 cm^2/s for deeper localized states. D increases

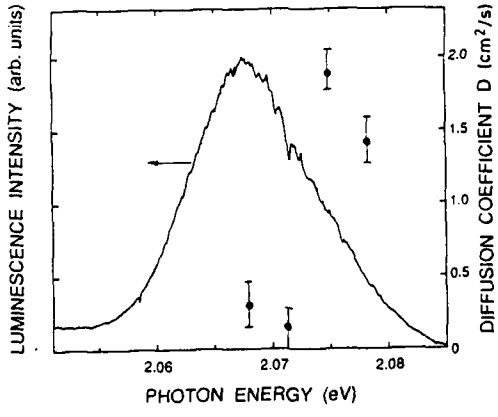


Fig. 7: Diffusion coefficient D and the luminescence as a function of photon energy of localized excitons

with decreasing localization depth from D=0.3 cm^2/s to 1.9 cm^2/s. These values are 10 times

smaller than for pure CdS and CdSe [12-14]. This result verifies that the mobility is strongly reduced for localized states, but not zero. Excitons can migrate through the crystal by phonon-assisted tunneling processes. We do not yet understand the increase of the recombination lifetime with decreasing localization. At 2.078eV (b) T_r is 2ns, whereas at 2.068eV (a) T_r is 0.416ns. This behaviour is in contradiction with data deduced from the time-resolved photoluminescence, which indicate an increasing lifetime with increasing localization depth [15-17]. Further work is planned to elucidate this problem.
We summarize these results in Fig. 7, plotting the diffusion coefficient D versus the photon energy. For a better illustration the luminescence is shown. In agreement with the discussion above the diffusion increases with decreasing localization depth.
In a NDFWM the initial excitation modulation is moving with a velocity $v_g \alpha \Delta\omega=(\omega_1-\omega_2)$. If the distance the grating moves during the characteristic relaxation time (here T_2 and T_r) is comparable or larger than Λ, the grating is smeared out and the scattering efficiency drops. Therefore the grating efficiency reflects for small $\Delta\omega$ incoherent processes and for large $\Delta\omega$ coherent processes. This is demonstrated in CdS and $CdS_{0.7}Se_{0.3}$, in Fig. 8, where I_s is plotted versus the detuning $\Delta\hbar\omega$ at $I_{exc}=3MW/cm^2$ and $\hbar\omega_1=2.542eV$ and $\hbar\omega=2.290eV$, respectively. In both samples we observe a narrow spike around zero and a slightly asymmetric shoulder for larger $\Delta\hbar\omega$. From the FWHM of the spectra the relaxation times can be estimated. At $I_{exc}=3MW/cm^2$ an e-h plasma is generated in CdS [14] and in CdSSe the localized states are saturated [18]. We found in CdS T_2=0.5ps and T_r=80ps. In $CdS_{0.7}Se_{0.3}$ the corresponding value for T_2 is 3ps. Here the spike cannot be resolved, but an upper value is 1ns. These data are in good agreement with data from time resolved measurements, discussed in the previous part.

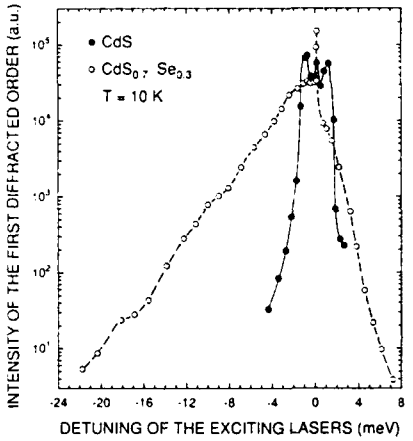


Fig. 8: Intensity of the first diffracted order in CdS (●) and $CdS_{0.7}Se_{0.3}$ (○) versus the detuning $\Delta\hbar\omega$ in a NDFWM experiment. $I_{exc}=3MW/cm^2$.

5. Summary

We investigated the relaxation of excitons in CdS, CdSe and $CdS_{1-x}Se_x$ mixed crystals. At low exciton densities we found dephasing times of 40 ps and 75ps for free and localized excitons, respectively, decreasing with increasing density. We have demonstrated that the mobility of excitons in the localized states is strongly reduced and governed by tunneling processes.

References:

1. S.A. Permogorov, A. Reznitsky, P. Flögel, S. Verbin, G.O. Müller and M. Nikifora, phys. stat. sol. (b) 113,589 (1982)
2. E. Cohen and M.D. Sturge, Phys. Rev. B 25, 3282 (1982)
3. Y.R. Shen, The Principles of Nonlinear Optics, (Wiley, New York, 1984)
4. T. Yajima and Y. Taira, J. Phys. Soc. Japan 47, 1620 (1979)
   M. Weiner, S. Silvestri and E.P. Ippen, J. Opt. Am B2, 654 (1985)
5. C. Dörnfeld and J.M. Hvam, IEEE J. QE-25, 904 (1989)
6. C. Klingshirn and H. Haug, Phys. Rep., 70, 315 (1981), B. Hönerlage, R. Levy, J.B. Grun, C. Klingshirn and K. Bohnert, Phys. Rep., 124, 161 (1985)
7. A. Maruani and D.S. Chemla, Phys. Rev. B 23, 841 (1981)
8. R. März, S. Schmitt-Rink and H. Haug, Z. Phys. B 40, 9 (1980)
9. H. Kalt, R. Renner and C. Klingshirn, IEEE J. QE-22, 1312 (1986)
10. J.M. Hvam, I. Balslev and B. Hönerlage, Europhys. Let. 4, 838 (1987)
11. C. Dörnfeld, G. Noll, H. Schwab, J.M. Hvam, Ch. Weber, R. Renner, E.O. Göbel, A. Reznitsky, V. Lyssenko, S.A. Pendjur, O.N. Talensky and C. Klingshirn, Proc. Fourth Intern. Conf. on II-VI compounds, will be published in J. Cryst. Growth
12. H. Saito and E.O. Göbel, Phys. Rev. B 31, 2360 (1985)
13. F.A. Majumder, H.E. Swoboda, K. Kempf and C. Klingshirn, Phys. Rev. B 32, 2407 (1985)
14. C. Weber, U. Becker, R. Renner and C. Klingshirn, Z. Phys. B 72, 379 (1988)

15. J.A. Kash, A. Ron and E. Cohen, Phys. Rev. B 28, 6147 (1983)
16. F.A. Majumder, S. Shevel, V.G. Lyssenko, H.E. Swoboda and C. Klingshirn, Z. Phys. B 66, 409 (1987)
S. Shevel, R. Fisher, E.O. Göbel, G. Noll, P. Thomas and C. Klingshirn, J. Lumin. 37, 45 (1987)
17. C. Gourdon and P. Lavallard, Proc. Fourth Intern. Conf. on II-VI Compounds, will be published in J. Cryst. Growth
18. H.E. Swoboda, F.A. Majumder, C. Weber, R. Renner, C. Klingshirn, G. Noll, E.O. Göbel, S. Permogorov and A. Reznitsky in Proceedings 19th Intern. Conf. on the Physics of Semiconductors, Warsaw (1988)

APPLICATION OF A NOVEL PICOSECOND PULSED LASER DRIVEN X-RAY SOURCE IN TIME RESOLVED DIFFRACTION EXPERIMENTS

B. Van Wonterghem and P.M. Rentzepis
Department of Chemistry
University of California, Irvine, CA 92717

Abstract

We have constructed a novel picosecond x-ray (PxR) source to be used for time resolved x-ray diffraction. The PxR source consists of a metallic photocathode which is excited by a Nd:YAG pulsed picosecond laser. More than 3 nC of electrons has been produced with a tantalum photocathode excited by the 266 nm 4th harmonic.The accelerated electron bunches strike a copper anode and generate 6.2 x 10^6 Cu Kα x-ray photons $cm^{-2}.sr^{-1}$ with a time width of less than 70 ps. The detection method and experimental system for PxR diffraction is described and examples for its application are presented.

Introduction

Technological developments in lasers and x-ray optics[1] have made it possible to design x-ray lasers[2] and short duration x-ray pulses[3]. Two convenient means for tabletop picosecond x-ray pulse generating devices are: 1) Soft x-ray emission from excited plasmas generated by focussing short high intensity laser pulses onto a solid target[4], 2) By means of electron pulses in x-ray diodes activated by picosecond laser pulses, striking a metal or semiconductor cathode[5]. In this discussion we will not be concerned with large expensive systems such as synchrotrons and fusion type laser facilities, but rather concentrate upon table-top relatively inexpensive set ups. A high intensity pulsed laser system used for the generation of soft x-ray lasers has been described recently by Murnane et al.[6,7], and high energy systems based upon chirped-pulse amplification have been reviewed by Pessoit et al.[8,9]. We will present our femtosecond high intensity laser scheme for plasma-induced x-ray laser pumping in another publication. In this paper we shall present only the source and diagnostics of pulsed laser induced picosecond x-rays generated by means of ultrashort electron bunches. Some applications to time resolved x-ray diffraction will also be described.

Traditionally x-ray diodes are operated using thermionic emission as electron source. Even when driven by ultrashort laserpulses, these cathodes have a long response time and are therefore not suitable for picosecond pulse x-ray generation. Therefore we have employed photoemission as a means of generating ultrashort electron bunches and subsequently x-ray pulses. Photoemission is known to have extremely short response times, so the electron current follows essentially the laser pulse intensity.

Even though the quantum efficiency of semiconductor cathodes such as Cs_3Sb is much higher than the one exhibited by metals at the visible and ultraviolet region of the spectrum, we find that the damage treshold for Cs_3Sb is too low for the generation of high intensity electron bunches at relatively high repetition rates and acceleration potentials. In addition, the ultra-high vacuum requirements, and the depletion of cesium under the 10^{-10} Torr vacuum are sufficient disadvantages which prompt us to examine other photocathode materials in which these problems may not be found. A very serious problem is the high resistance of several types of semiconductor photocathodes. The extremely high peak currents generated by laser pulses cause resistive heating and local ablation of the surface. Metallic surfaces compare favorably with semiconductor cathodes even though the quantum efficiency are lower. Several of the metallic surfaces which we have used are relatively resistant to atmospheric gasses , therefore they do not require the ultra-high vacuum conditions which are mandatory for most semiconductor cathodes. The metal photocathodes have a much longer useful lifetime and are easier to prepare. Using a tantalum thin film as the photocathode and picosecond 266 nm pulses from a pulsed modelocked Nd:YAG laser, we generated electron bunches with a charge of 3 nC per pulse. These electron pulses were accelerated and focussed onto a copper anode, inducing x-ray pulses with a brightness of $6.2x10^6$ $cm^{-2}sr^{-1}$ at the Kα wavelength (1.54Å). The pulsewidths were measured using an x-ray streak camera.

Experimental

The photocathode consists of a cylindrical, polished nickel substrate, 15 mm in diameter, and mounted onto a high voltage feedthrough, which is attached by bellows inside a small vacuum chamber, maintained at a pressure below $2x10^{-9}$ Torr by ion pumps. A schematic representation of the chamber which houses the electron and x-ray source is presented in figure 1. The photocathode substrate fits into a a Pierce focussing electrode An additional field shaping electrode was added to increase the extraction field near the photocathode surface.

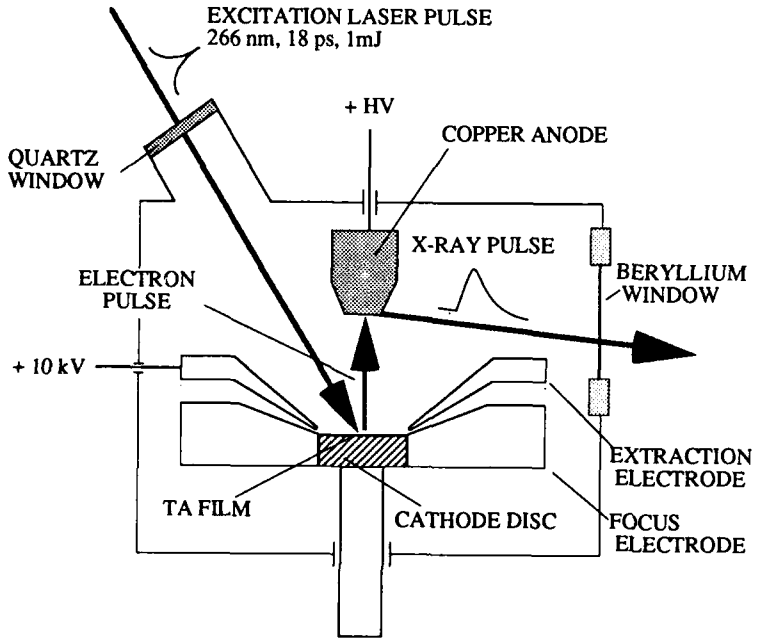


Figure 1. Schematic diagram of the operation of the laser driven x-ray diode. Photoelectrons created by a frequency quadrupled Nd:YAG laser pulse on the tantalum photocathode are accelerated towards the copper anode. The resulting x-ray pulse is monitored through a beryllium window.

Tantalum, workfunction 4.16 eV, was deposited by resistive heating of a thin, high purity, tantalum coil. While the tantalum deposition takes place, the photoemission current induced by a low pressure Hg(A) lamp was (253.7 nm) was monitored. When this photocurrent reached a maximum the deposition was stopped. The occurrence of a maximum can be attributed to the formation of a Ni-Ta compound[10,11] At this point the photocathode has a deep dark blue color. A photocurrent of over 100 nA was obtained by illumination with 100 μWcm^{-2} at 253.7 nm.

Because of the high work function of tantalum (4.16 eV), we use a frequency quadrupled Nd:YAG laser, producing 20 ps pulses with an energy of 2 mJ per pulse and a repetition rate of 20 Hz. The emission current characteristics of the Ta photocathode are shown in figure 2 as a function of potential difference between anode and cathode and the laser pulse energy respectively. The low energy part of the current, which is below the space charge limit is found to increase as the square root of the diode voltage. This is attributed to the Schottky effect[12]. The external accelerating field acts in a manner that lowers the effective work function ϕ_{eff} in accordance with the relationship $\phi_{eff} = \phi_0 - e^{3/2}E^{1/2}$, where e is the electron charge.and E the applied field increases the number of emitted electrons. Consequently the quantum efficiency will increase with the applied field. Even though the maximum charge as function of voltage relationship does not follow the E dependence for spacecharge limited current flow, we find that the production of electron charge per pulse increases as a function of incident photon energy, as shown in figure 3, for applied voltages of 15 kV and 30 kV. Experimental data show that because of space charge saturation the quantum efficiency decreases at the higher incident laser energies. Our experimental data show that catastrophic surface damage and high voltage breakdown occurs at energies above 20 $mJcm^{-2}$, resulting in a permanent photocathode damage. At 50 kV, a value of 3 nC per electron pulse was the maximum charge measured for this diode configuration.

The electrons emitted by the photocathode are subsequently accelerated to 50 kv and focused on to a toroid-shaped anode. The anode is made of copper and is maintained at a high positive potential. The electron pulses interact with the copper anode forcing the emission of Cu Kα x-ray photon pulses which exit the vacuum chamber through a thin beryllium-foil window. A bent germanium crystal monochromator disperses and focuses the x-rays onto the sample. The duration of the x-rays pulses was measured by an x-ray streak camera fitted with a low density CsI photocathode[13]. We determined the pulse width of the x-rays at 50 kV anode-cathode potential difference to be less than 70 ps(1). This value is an upper limit for the width of the x-ray pulses because the transit time spread of the streak camera has not been taken into consideration. The intensity of the x-rays pulses

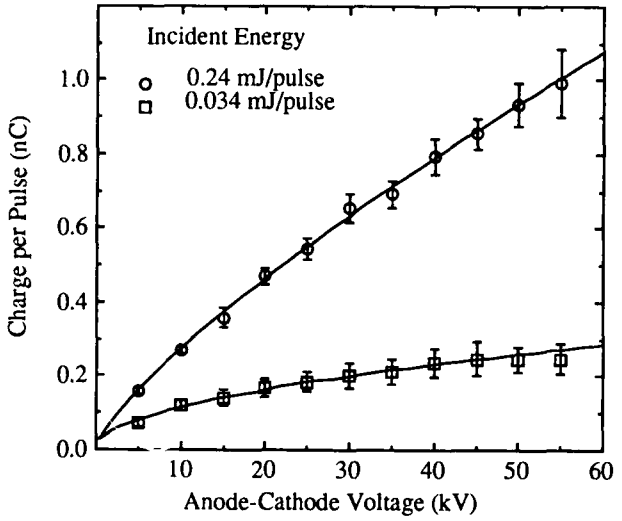


Figure 2. Charge per photoelectron pulse as a function of diode accelerating voltage, obtained at two different energies of the 266 nm excitationpulses.

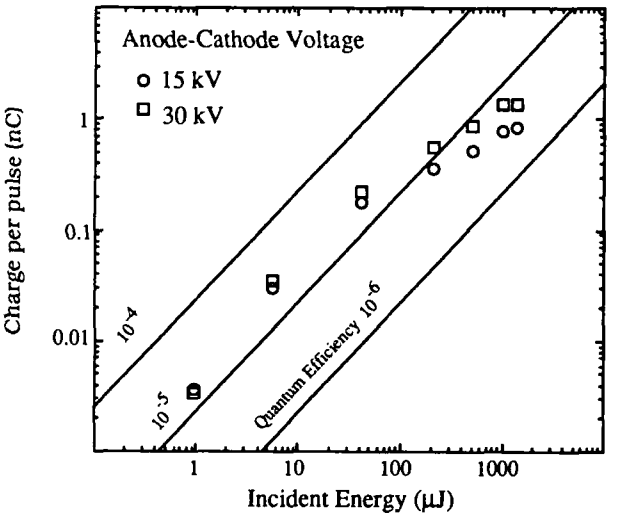


Figure 3. Charge per photoelectron pulse as a function of laser excitation energy at two different diode voltages. The straight lines reperesent the indicated quantum efficiencies.

was measured to be 6.2×10^6 photons $cm^{-2}sr^{-1}$ by means of a silicon diode array x-ray detector which had a quantum efficiency of 0.79 for 8keV photons.

The reason for constructing this novel compact source of picosecond electrons and x-rays is to perform x-ray diffraction experiments with picosecond resolution. The experimental system built for time resolved, picosecond x-ray diffraction experiments is shown in figure 4. It is composed of a Nd:YAG laser which emits 20Hz, 20mJ, 20ps pulses at 532 nm (SHG). By means of a beamsplitter the pulses are separated into two parts. One part is converted to the 4th harmonic, 266nm, which is focussed on the photocathode generating the picosecond electron bunches, which in turn are accelerated and focussed on the anode producing the picosecond x-ray pulses. As shown in figure 4 the x-rays are focussed onto the sample by means of a Ge-monochromator. The diffracted x-rays are detected either on a film as Laue diffraction pattern photographs or by real time x-ray photon counting, position sensitive detectors. The second arm of this system (fig.4) follows the path designated for the 532 nm beam and performs the function of an excitation or pump beam. It should be noted that although we discuss only the use of 532 nm excitation wavelength. Other wavelengths are easily generated by means of common wavelength conversion techniques such as harmonic generating crystals, stimulated Raman or dye lasers pumped by the picosecond laser. The two pulsed beams, laser pump and PxR probe, are synchronized to arrive at the sample either at the same time or at a preselected delay by translating either of the two delay stages, designated in figure 4 as VD1 and VD2, by increasing or decreasing the optical path length and therefore the transit time of either beam. The principle and means for achieving this synchronization is shown schematically in figure 5.

The detector is a most important component of this system because the number of diffracted x-rays is very small and may be masked by dark noise of the detector or thermoluminescence of the phosphor employed to convert electrons to photons. To overcome these difficulties we constructed a position sensitive detector based upon a phosphorscreen (P3), which is fiberoptically coupled to a very high gain image intensifier, lens-coupled in turn to a saticon camera, as shown in figure 6 The intensifier has an active surface of 12 by 8 mm and is a of a hybrid type, consisting of an electrostatic focussing stage, coupled to a double microchannel plate multiplying stage. The total gain exceeds 10^8, while the dark count at room temperature is less than 2 electrons per second. To increase the data collection efficiency, there is a need to collect as many diffracted x-rays as possible. For this reason, a larger phosphor screen was coupled by a 5:1 fiberoptic reducer onto the intensifier surface. The saticon camera was connected to a real-time video processor. The data is displayed on a monitor and analyzed by a microcomputer. The disadvantages of this detector are mostly associated with the phosphor and consist of

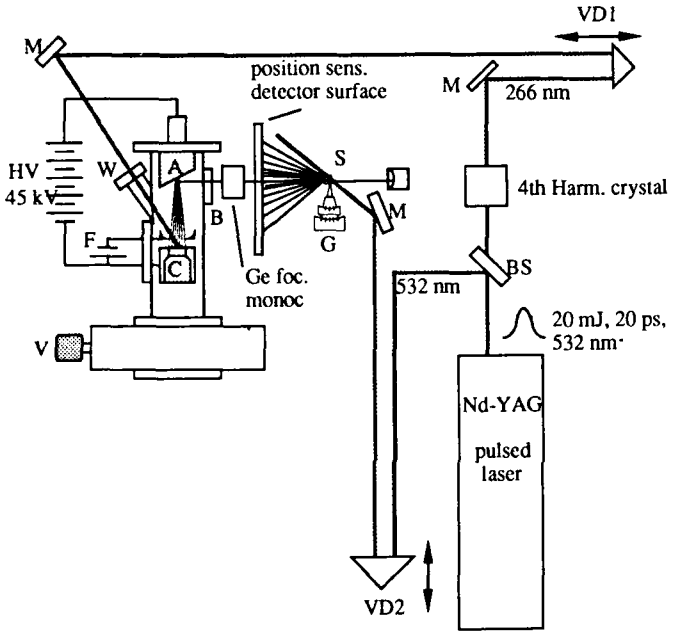


Figure 4. Picosecond time-resolved x-ray diffraction experimental set up. VDi represent variable optical delay lines. A sample is excited by the 532 nm pulse, and a delayed backscattered diffracted X-ray pulse is recorded by a position sensitive x-ray detector as a probe.

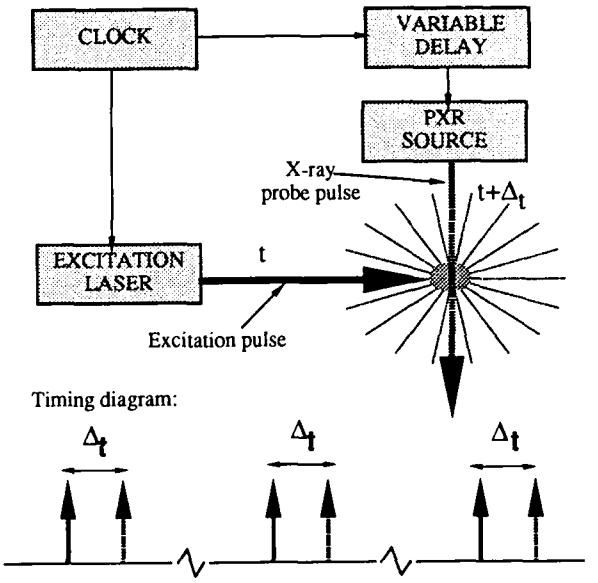


Figure 5. Schematic representation of the excitation and probe scheme. Time resolution Δ_t is obtained by the time delay between excitation laser pulse and the x-ray probe pulse. The time resolu on of the detector itself is not important.

thermal noise and flashes induced by radioactive elements contained as impurities in the phosphor and the fiber optic glass. To avoid the noise of phosphor and the disadvantages of the small size detector surface, we are constructing a new large area CCD camera for direct x-ray imaging, using a Ford Aerospace Corp 2kx2k CCD chip. Because of its rather large active area, the relatively high conversion quantum efficiency for 8keV photons (15%), low number of dark counts when used at low temperatures, and the elimination of the phosphor, we expect that this camera will allow us to achieve a very high signal to noise ratio. The operation of the 2kx2k CCD camera will be described in a forthcoming communication in conjunction with further PxR diffraction experiments. However the general scheme for the detector is similar to the description by Janesick et al.[14]. A schematic representation of the detector is displayed in figure 7. The general characteristics of the two x-ray imaging detectors are described in table I where the advantages (+) and disadvantages (-) are presented for comparison purposes.

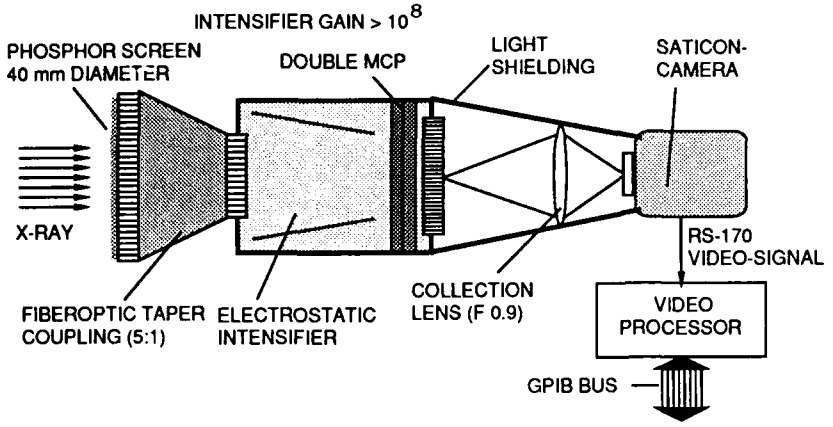


Figure 6. X-ray position sensitive detector based upon a phosphorscreen, coupled to a high gain image intensifier and video camera (saticon).

Utilizing the experimental system shown in figure 4 with the modifications presented in figure 8 we are able to perform for the first time picosecond time resolved x-ray diffraction experiments. The sample consists of a Ge (111) crystal bent for maximum reflection of 8 keV x-ray photons, this way the set up resembles a sensitive double crystal monochromator.The x-ray diffraction spectra are recorded before excitation. This diffraction exhibits the normal diffraction pattern characteristic of this surface. In a subsequent experiment a laser pulse impinges upon the Ge (111) crystal causing lattice distortion. A picosecond x-ray pulse is synchronized to arrive at the sample at the same time as the laser light pulse. The rocking curve of the disturbed surface, recorded by the diffracted x-ray pulses reflects the changes in the structure caused by the laser interaction with the crystal surface as a function of time. The time resolution of the experiment is essentially equal to the time width of the x-ray pulses utilized which is approximately 70 ps, measured by an x-ray streak camera. The pulse width of the laser and x-rays pulses are.shown in figure 9. By deconvolution of the pulses it is possible to achieve better time resolution. It must be noted, however, that this is an upper limit because the transit time spread within the streak camera and photocathode has not been taken into account.

At the present time we are constructing a 3kHz regenerative amplifier system consisting of two coherent Antares heads which after pulse compression are expected to generate 1057 nm pulses with 5 mJ energy per pulse and 10 ps pulses. Using this system to drive the x-ray diode, we expect to increase the average x-ray power and subsequently the amount of time resolved diffraction data, initially, by a factor of 150. Further improvements will be made in the source efficiency, repetition rate and detection system and we expect that the data acquisition rate will be greatly increased. We are performing several other simple time resolved PxR experiments such as melting and crystallization and dissociation which will allow us to calibrate the PxR system

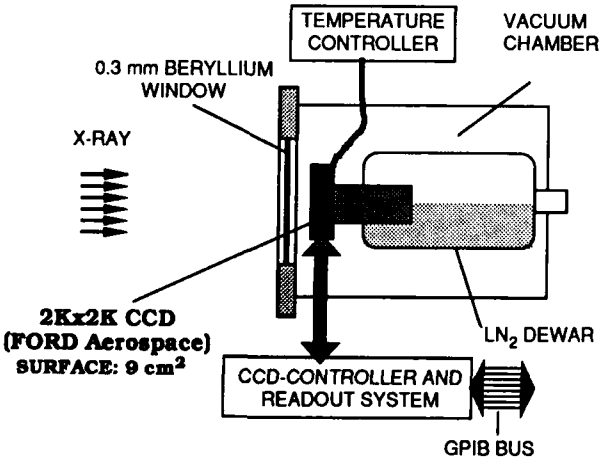


Figure 7. CCD-based detector for direct imaging of Cu Ka X-rays on a large area, liquid nitrogen cooled CCD. The camera is read out at a speed of 50 kHz and usually 4x4 pixel binning is employed to increase the data acquisition rate.

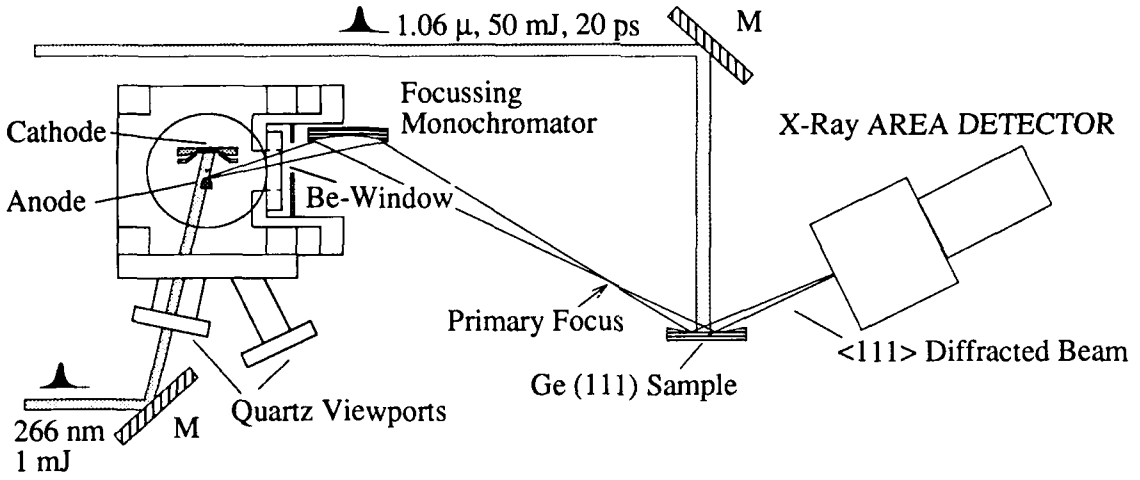


Figure 8. Time-resolved Bragg diffraction of laser induced surface effects on a Ge (111) sample. Upper laser pulse excites the sample, while the lower beam is used to drive the x-ray diode.

and provide a data base which is necessary for subsequent large molecule diffraction experiments. Other applications including time resolved molecular holography, plasma diagnostics and x-ray diffraction of metastable species are also in the planning stages.

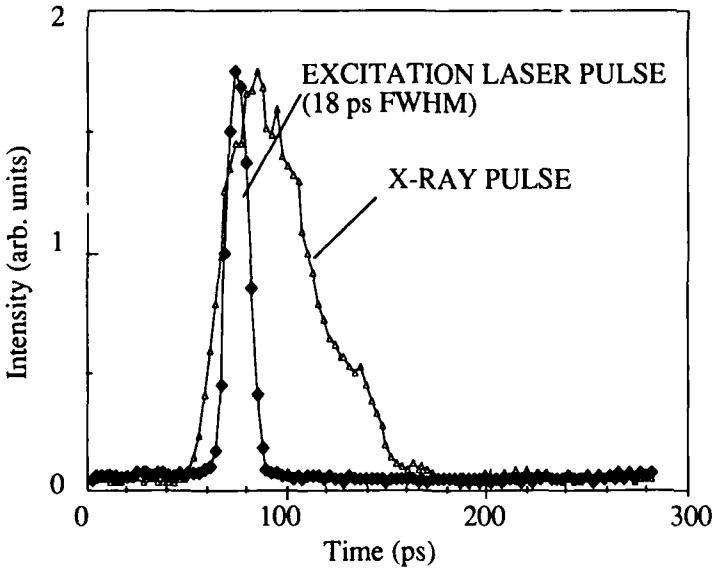


Figure 9. Streak camera record of Cu Ka x-ray pulses generated by illuminating a Ta photocathode by 266 nm laserpulses and accelerating the electron pulse over 50 kV to a copper target. The streak camera was equipped with a CsI photocathode for detection of the x-ray pulse and a Au photocathode for the laser excitation pulses.

1. Phosphorscreen +Image Intensifier + Saticon
   (+) Real Time (30 frames/sec)
   Very low Image Intensifier Noise < 2 cts/sec at room temperature.
   Dynamic Range not limited by detector system
   (-) Small active area: 8 by 12 mm, medium resolution (15 lp/mm).
   Backgound due to thermoluminescence of the phosphorscreen
   Flashing (high intensity large area signals) rate: 5/min.

2. Phosphorscreen+5:1 Fiberoptic Reducer + Image Intensifier + Saticon
   (+) Real Time (30 frames/sec)
   Very low Image Intensifier Noise < 2 cts/sec at room temperature.
   Dynamic Range only limited not limited by detector system
   Large Area: 40 mm diameter.
   (-) Low resolution (3 lp/mm).
   High backgound due to thermoluminescence of the phosphorscreen and fiberoptic taper
   Increased flashing rate: 150/min.(larger collection surface)

3. Direct Imaging on Large Area CCD chip
   (+) Low dark noise (0.0025 e^-/s.px) and readout noise (<11 e^-/px)
   Large active area (30 x 30 mm)
   Large signal induced by 8 keV x-rays: 2300 e^-, energy resolution allows for discrimination against backgound.
   High resolution, 15x15 μ pixel size.
   (-) Low dynamic range (<50 x-rays/pixel)
   Low readout rate (50 kHz pixel conversion rate)
   Possibility of radiation induced dark noise increase

Table 1. Comparison of some essential characteristics of the three position sensitive x-ray detectors applied in this work.

Acknowledgements

We thank R. Bredthauer and R. Nelson of Ford Aerospace Corp. for their cooperation in the realization of the CCD camera.

This work was supported by the W.M. Keck Foundation and by the Advanced Research Projects Agency of the Department of Defense, and was monitored by the USAFOSR under Contract No. F49620-89-C-0104.

References

1.N.M. Ceglio, J X-Ray Sci.and Tech. **1**, 7, 1989.
2.D.L. Mathews et al, Phys.Rev.Lett. **54** , 110, 1985.
3.B. Van Wonterghem and P.M. Rentzepis, Appl.Phys.Lett. In Press.
4.M.D. Rosen et al, Phys.Rev.Lett. **54**, 106, 1985.
5.B. Van Wonterghem and P.M. Rentzepis, Bull Am.Phys. Soc. **34**, 892, 1989.
6.M.M. Murnane, H.C. Kapteyn and R.W. Falcone, IEEE, J.Quant.Electr.**25**, Dec 1989.
7.M.M. Murnane, H.C. Kapteyn and R.W. Falcone, Phys.Rev.Lett. **62**, 155, 1989.
8.M. Pessot, P. Maine and G. Mourou, Opt. Comm. **62**, 419, 1989.
9.M. Pessot, J. Squier, P. Bado, G. Mourou, D.J. Harter, IEEE, J.Quant.Elec. **25**, 61, 1989.
10.C.W. Draper, J.MN. Gibson, D.C. Jacobson, J.M. Pate, S.M. Shin, J.M. Rigsbee, J.Mater.Sci. **20**, 2303, 1985.
11.J.E. Nestel, K.J. Scoles, R.W. Christy, J.Appl.Phys. **53**, 8993, 1985.
12.P.E. Carrol, Phys.Rev. **104**, 660, 1936.
13.G.L. Stradling, P.T. Atwood, R.L. Kauffman, Proc. SPIE vol **348**, 778, 1982.
14 J.Janesick, T. Elliot, R. Bredthauer, J. Cover, R. Schaefer, R.Varian, Proc. SPIE vol **1071**, 1989.

PHASE CONJUGATION BY DEGENERATE FOUR-WAVE MIXING IN SATURABLE-DYE-DOPED PLANAR WAVEGUIDES

Shigeki Miyanaga and Hirofumi Fujiwara

Department of Applied Materials Science, Muroran Institute of Technology
27-1 Mizumoto, Muroran 050, Japan

Abstract

Phase conjugation by degenerate four-wave mixing (DFWM) was demonstrated in saturable-dye-doped polymer waveguides with a cw Ar-ion laser. A nonlinear waveguide consisted of a few-μm-thick transparent poly-vinyl alcohol (PVA) film layer partly doped with saturable dyes, erythrosin B and eosin Y, which was spin-coated on a Pyrex glass substrate. The DFWM excitation was performed as follows: two pump waves impinged upon the interaction region nearly perpendicularly to the film from the outside; a probe wave was coupled into the TE mode of the waveguide by a prism coupler. Maximum reflectivities of the phase-conjugate wave (PCW) of 0.16 % for the erythrosin B/PVA film and 0.2[illegible] % for the eosin Y/PVA film were obtained outside the waveguide at the pump intensity of about 1 W/cm^2, which correspond to the PCW reflectivities of 0.53 % and 0.91 % inside the waveguide, respectively. Transient properties of the PCW reflectivity were also investigated.

1. Introduction

Phase conjugation by degenerate four-wave mixing (DFWM) has potential applications in many fields[1] from the fact that the phase matching can be performed for a wide field of view[2]. If a phase conjugator is incorporated into an optical waveguide, a compact device suitable for all-optical signal processing is realizable based on nonlinear optical effects. In addition, the use of waveguides offers some advantages: a long interaction length is available; light intensity is increased inside the waveguide by virtue of optical beam confinement. So far, the phase-conjugate wave (PCW) generated by DFWM has been observed in optical fibers[3,4] and in planar-optical waveguides[5-7].

In a 3-m-long CS_2-filled optical fiber with a core diameter of 4 μm[4], a PCW reflectivity of 0.45 % was obtained by using a cw Ar-ion laser, in which a long interaction length and an optical beam confinement are effectively used. In a semiconductor-doped planar-optical-glass waveguide[6], a PCW reflectivity of 0.8 % was observed inside the waveguide excited by a Q-switched-pulse laser. For the device applications, it is desired to find the materials that have sufficient nonlinearlity at cw low-power levels and are easy to get a sample in waveguide form. From these points of view, we have demonstrated the generation of PCW by DFWM with the cw Ar-ion laser in a planar-optical waveguide which consists of a transparent part and a saturable-dye-doped part of a poly-vinyl alcohol (PVA) film layer[7]. In this report, we present further experimental results for the PCW reflectivity. Transient properties of the PCW reflectivity are also considered for two cases: 1) when only a probe wave is turned on and off; 2) when both pump and probe waves are turned on and off.

2. Geometry of DFWM process

Figure 1 shows the geometry of DFWM process. There may be considered several types of DFWM geometry. Here, two counter-propagating pump waves impinge upon the interaction region

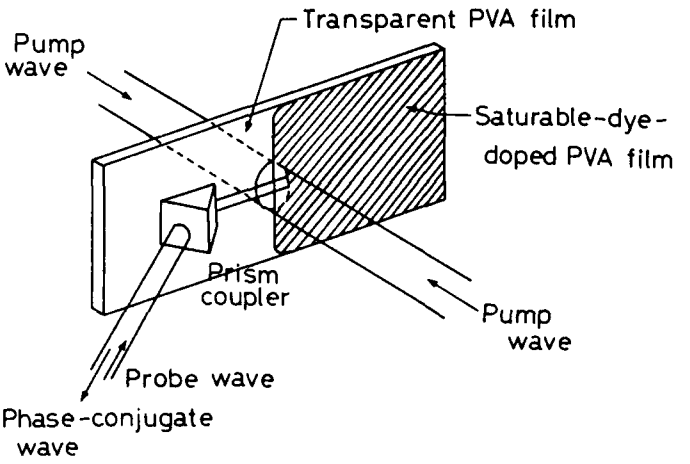


Fig.1 Geometry of the DFWM process. Two counter-propagating pump beams were adjusted to expose the fluorescent streak produced by the guided probe wave on the boundary of the dye-doped region.

nearly perpendicularly to the film layer from the outside; a probe wave with the same polarization as the pump waves is coupled into the TE mode of the waveguide by a prism coupler and is propagated to the interaction region. The interaction scheme is a standard DFWM with the probe wave at right angles to the pump waves.

The absorption of dyes will lower the efficient generation and guidance of the PCW. To eliminate this, the transparent PVA film layer which is partly doped with saturable dyes is used as the guided part, and the boundary of the dye-doped PVA film layer is the interaction region. Thus, the two pump waves together with the guided probe wave are adjusted to be superposed on the boundary of the dye-doped region. A diameter of the pump beams was about 2 mm. The input prism coupling efficiency was found to be about 30 %. The DFWM geometry used here has the advantages: the long interaction length is obtainable as the DFWM interaction occurs along the propagation direction of the guided probe wave, while the absorption of the pump waves is reduced by the low concentration of the doped dye and a thin film (a few μm thickness).

3. Fabrication of dye-doped PVA waveguides

In this experiment, erythrosin B and eosin Y were used as saturable dyes, which were doped in the polymer film of PVA. Because these dyes have a strong absorption at the wavelengths of an Ar-ion laser and a long lifetime of their excited states, they can generate the continuous PCW at the light intensity of the order of 1 W/cm^2. A PVA waveguide was fabricated as follows: the transparent PVA solution was first poured onto a cleaned Pyrex fused glass plate and was spin-coated; the PVA solution with a proper amount of dyes was next poured onto the half part of the glass plate, and again was spreaded by a spin-coating; the plate was dried at about 40 degrees centigrade temperature for about one day. The fabricated waveguide was a multi-mode waveguide with a film thickness of about 3 μm.

Because the dye-doped PVA diffuses into the transparent PVA during the fabrication process, the boundary between the transparent and the dye-doped PVA layer blurs, and the absorption coefficient gradually varies across the boundary. Figure 2 shows the variation of a transmission as a function of the distance from the boundary for an erythrosin-B-doped PVA film. This measurement was perfoumed with a low intensity laser beam with a small beam diameter. The transmission decreases to about 0.75 at a distance of 2 mm from the boundary. The guided probe wave, however, can penetrate only a shorter distance than 2 mm into the boundary of the dye-doped region by virtue of the absorption of the dyes. Thus, the DFWM interaction occurs around this boundary region where the transmission for the pump waves is relatively high.

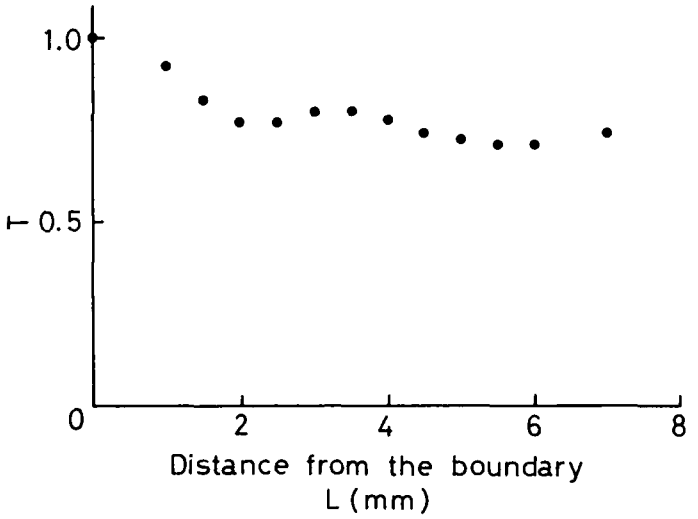


Fig.2 Variation of a transmission T around the dye-doped region for an erythrosin B/PVA film.

4. Experimental setup

Figure 3 shows an experimental setup. The cw Ar-ion laser beam with the wavelength of 0.5145 μm is divided into three beams: two pump beams with equal power and a probe beam with the same polarization as the pump beam. A reflection-to-transmission ratio of the beam splitter BS1 is about 1 to sixteen. The probe beam power is further reduced by a pair of polarizing prisms. For the coherent interaction of the beams, the path lengths of the three beams were adjusted to be within a coherence length of the laser. A sample of the waveguide was equipped with an X-Y mechanical stage mounted on a rotating table, which enables one to adjust the incident probe wave to the coupling angles of guided modes. The PCW retraces the path of the probe wave, and is detected by a photodetector. Mechanical choppers, MC1 and MC2, and a digital storage CRT were used for measuring transient PCW.

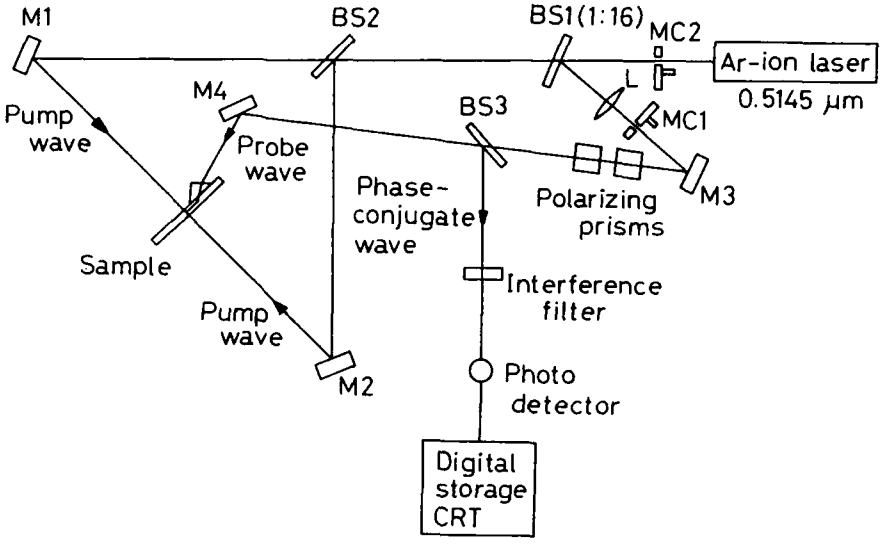


Fig.3 Experimental setup for the phase conjugation by DFWM: BS's, beam splitters; M's, mirrors; L, a lens; MC's, mechanical choppers.

5. PCW reflectivity

5.1 Steady state PCW reflectivity

Figure 4 shows the variation of the PCW reflectivity as a function of the pump wave intensity for an erythrosin-B-doped film. Here, the reflectivity is defined by the ratio of the beam power of the prism-outcoupled PCW to the beam power of the probe wave incident upon the prism coupler. A maximum reflectivity of 0.08 % was obtained at the pump intensity of 2.0 W/cm^2 in this sample. If an output-coupling efficiency of the prism coupler is 100 %, the prism coupling efficiency of 30 % corresponds to a PCW reflectivity of 0.27 % inside the waveguide. In the DFWM using a dye-doped bulk film without a waveguide structure, it has been shown that the PCW reflectivity decreases as the probe intensity exceeds the pump intensity[8]. For this reason, the probe intensity was adjusted to be about 0.2 times the pump intensity by means of the beam splitter BS1 and the polarizing prisms in Fig.3.

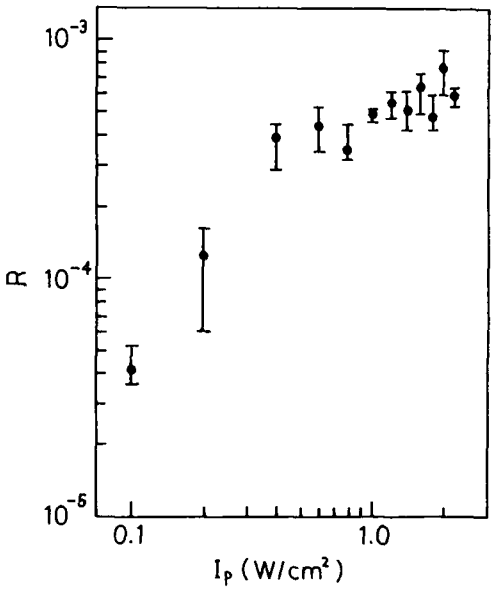


Fig.4 Variation of PCW reflectivity R as a function of pump intensity I_p for an erythrosin B/PVA film.

The PCW reflectivity dependences on the pump intensity are shown in Fig.5 for an another erythrosin B/PVA film, and in Fig.6 for an eosin Y/PVA film. Maximum reflectivities were 0.16 % for the erythrosin B/PVA film and 0.27 % for the eosin Y/PVA film at the pump intensity of about 1 W/cm^2. These values correspond to 0.53 % and 0.91 % inside the waveguide, respectively.

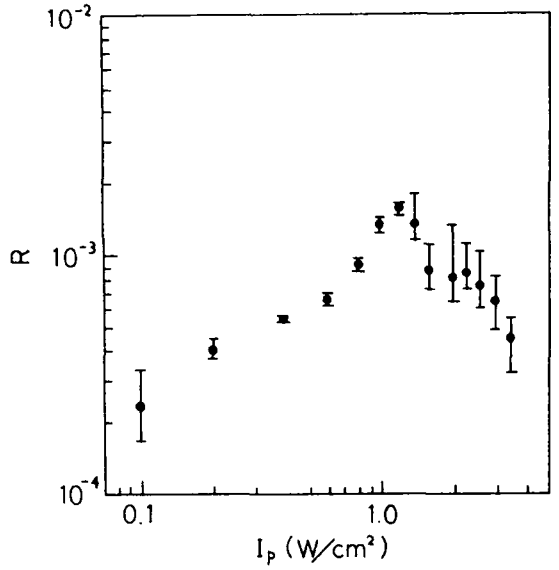


Fig.5 Variation of PCW reflectivity R as a function of pump intensity I_p for an erythrosin B/PVA film.

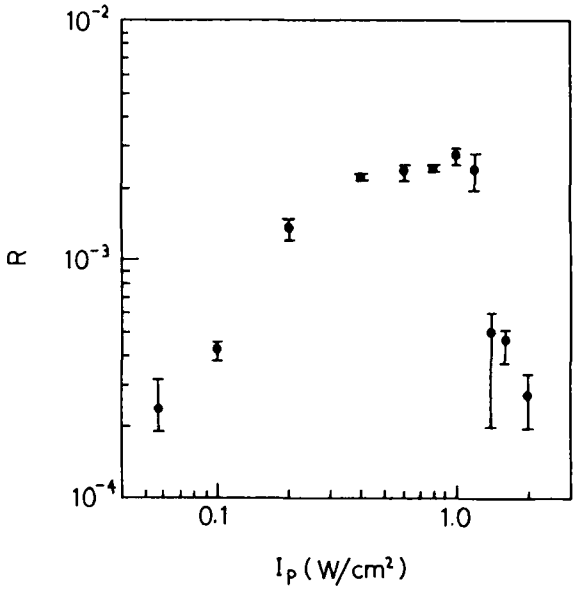


Fig.6 Variation of PCW reflectivity R as a function of pump intensity I_p for an eosin Y/PVA film.

In Figs.4 to 6, the PCW reflectivity dependence on the pump intensity is slightly different from sample to sample. This variation may be due to the non-uniformity of the dye concentration near the boundary of the dye-doped region and the influence of the beam profile of the pump waves. It is because the overlap integral of the amplitudes of three beams in the interaction region determines the magnitude of the nonlinear interaction of three beams. For the penetration length of the probe beam into the dye-doped region shorter than the diameter of the pump beams, the efficient DFWM interaction occurs, but for the longer penetration length of the probe beam, the DFWM interaction weakens. The penetration length of the guided probe wave is severely affected by the spatial distribution of the dye concentration near the boundary of the dye-doped region. In our fabrication process of the film, it is, at present, difficult to control the spatial distribution of the dye concentration near the boundary of the dye-doped region. Removal of the pump-beam size effects is possible by using a higher power laser and expanding the pump beams (available pump intensity is limited to about 1 W/cm^2 in our experiment).

5.2 Transient PCW reflectivity

Since the nonlinear interaction by DFWM is caused by the saturable absorption of dyes, the transient behavior of the PCW reflectivity is closely related to the time constant for the electronic population of saturable dyes to reach their steady state. The characteristic time constant τ is given by[9]

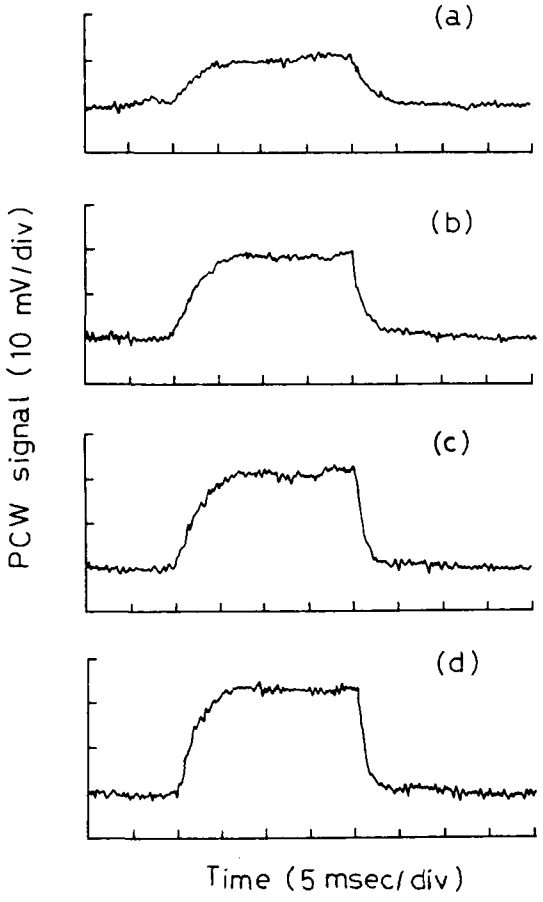
$$\tau = \tau_p/(1+I/I_s), \qquad (1)$$

where τ_p is the phosphorescent lifetime, I is the intensity of incident light and I_s is the saturation intensity. Thus, more intense light realizes faster the steady state of dyes.

Two cases of the transient behavior were considered in the eosin Y/PVA film. In Fig.3, the mechanical choppers MC1 and MC2 were used to measure the PCW reflectivity 1) when only the probe wave was chopped, and 2) when both pump and probe waves were chopped. The transient PCW signal was recorded by a digital storage CRT. The significant difference between two cases is in that in the case 1) the dyes in the film is well pumped by the pump waves before the incidence of the probe wave, while in the case 2) they are in their ground state before the simultaneous incidence of the three waves.

5.2.1 Chopping of probe wave Figure 7 shows the storage CRT traces of the transient PCW signals for four values of the pump intensities for the case 1). In this case when the probe wave is turned off, the PCW signal is generated until the saturable absorption gratings vanish, because the pump waves are always illuminated. The rise time and the fall time are found to be shorter with the increase of the pump intensity. This duration is closely related to the time constant of Eq.(1), although it is not exactly identical to Eq.(1) through the DFWM process[10].

Since the dye-doped film is well pumped by the intense pump waves before the incidence of the weak probe wave, the transient behavior of the PCW reflectivity is expected to obey



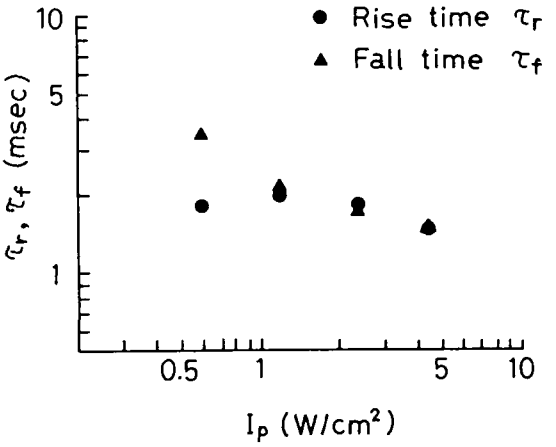


Fig.8 Variation of the rise time τ_r (●) and the fall time τ_f (▲) as a function of the pump intensity I_p.

Fig.7 Storage CRT traces of the transient PCW signals for an eosin Y/PVA film for the pump intensities of (a) 0.6, (b) 1.2, (c) 2.4 and (d) 4.5 W/cm^2, when only the probe wave was chopped. A time scale was 5 msec/div.

simple exponential curves both in rising and falling duration with this time constant. It is shown that the rising and the falling PCW reflectivities obey the exponential curves of $[1-\exp(-t/\tau_r)]^2$ and $[\exp(-t/\tau_f)]^2$, respectively, for sufficiently small absorption coefficient and sufficiently weak pump intensity[10], where τ_r and τ_f are the rise time and the fall time.

Even when the above condition was not exactly satisfied, the measured waveforms of the rising and the falling PCW signals were well fitted with these exponential curves. Values of the rise time and the fall time were determined from the curve-fitting. Figure 8 shows the variation of the rise time and the fall time as a function of the pump intensity. The rise time and the fall time have almost the same values except for low pump intensity, and decrease with the increase of the pump intensity. The disagreement of the rise and the fall times for the pump intensity of 0.6 W/cm^2 may be caused by background noise superposed on the weak PCW signal. Rise and fall times tend to approach the phosphorescent lifetime of eosin Y (about 5 msec) for the lower pump intensity.

5.2.2 Simultaneous chopping of pump and probe waves Figure 9 shows the storage CRT traces of the transient PCW signals when both pump and probe waves were chopped. The waveforms of the transient PCW signals remarkably differ from those when only the probe wave was chopped (see Fig.7). Firstly, no PCW signal is generated in the falling duration because both pump and probe waves are turned off. The performance of the mechanical chopper determines the fall time in this case. Secondly, a transient peak appears in the PCW signals for high pump intensity in the rising duration.

The appearance of these transient PCW peaks is qualitatively explained by referring to Eq.(1) as follows. When both pump and probe waves are simultaneously turned on, the interference patterns between them are formed in the film. Thus, the absorption coefficient is spatialy modulated according to the interference patterns, which means that the saturable absorption gratings are formed in the film. From the viewpoint of a holographic model, the generation of the PCW is explained as a result of Blagg diffraction of pump waves by the saturable absorption gratings and the PCW reflectivity is proportional to the contrast of the saturable absorption gratings. In the formation of the saturable absorption gratings, the electronic population of the dyes existing around peaks of the interference patterns reach their steady state faster than that of the dyes around bottoms of the interference

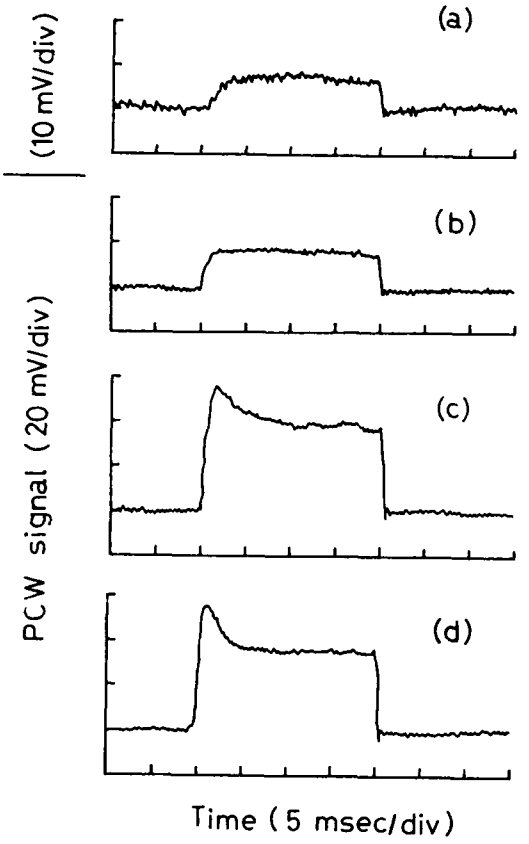


Fig.9 Storage CRT traces of the transient PCW signals for an eosin Y/PVA film for the pump intensities of (a) 0.6, (b) 1.2, (c) 2.4 and (d) 4.5 W/cm^2, when both pump and probe wave was chopped. A time scale was 5 msec/ div.

patterns. Therefore, for high intensities at a certain time in the transient state, the contrast of the saturable absorption gratings can take a higher value compared with that in the steady state, and the transient peak appears at that time in the transient state.

6. Conclusion

In this report, we have demonstrated that a planar optical waveguide consisting of a PVA film partly doped with saturable dyes can generate the PCW by DFWM with the relatively low intensity light from a cw Ar-ion laser. In the DFWM process, two counter-propagating pump beams impinged upon the interaction region nearly perpendicularly to the surfaces of the film from the outside, and a probe beam was introduced into the waveguide by a prism coupler with a coupling efficiency of about 30 %.

The PCW reflectivities of 0.16 % for the erythrosin B/PVA film and of 0.27 % for the eosin Y/PVA film were obtained at the pump intensity of about 1 W/cm^2 outside the waveguide, which correspond to the PCW reflectivities of 0.53 % and 0.91 % inside the waveguide by assuming a 100 % prism-outcoupling efficiency.

Two cases of the transient PCW reflectivity measurement were conducted in the eosin Y/PVA film. When the probe wave was turned on and off, the transient PCW reflectivities showed nearly exponential behaviors with a time constant of the order of the phosphorescent lifetime. The time constant increased with the decrease of the pump intensity and tended to approach the phosphorescent lifetime for the lower pump intensity. When both probe and pump waves were turned on, the transient peak PCW appeared for the high pump intensity.

7. References

1. T. R. O'Meara, D. M. Pepper and J. O. White, in Optical Phase Conjugation, R. A. Fisher, Ed. (Academic, New York, 1983), Chapt. 14.
2. R. W. Hellwarth, J. Opt. Soc. Am. 67, 1 (1977).
3. S. M. Jensen and R. W. Hellwarth, Appl. Phys. Lett. 33, 404 (1978).
4. J. AuYeung, D. Fekete, D. M. Pepper, A. Yariv and R. K. Jain, Opt. Lett. 4, 42 (1979).
5. C. Karaguleff, G. I. Stegeman, R. Fortenberry, R. Zanoni and C. T. Seaton, Appl. Phys. Lett. 46, 621 (1985).
6. A. Gabel, K. W. DeLong, C. T. Seaton and G. I. Stegeman, Appl. Phys. Lett. 51, 1682 (1987).

7. S. Miyanaga, T. Yamabayashi and H. Fujiwara, Opt. Lett. 13, 1044 (1988).
8. W. P. Brown, J. Opt. Soc. Am. 73, 629 (1983).
9. M. Hercher, Appl. Opt. 6, 947 (1967).
10. H. Fujiwara and K. Nakagawa, J. Opt. Soc. Am. B4, 121 (1987).

NONLINEAR MAGNETO-OPTICS OF VACUUM

A. E. Kaplan and Y. J. Ding
Department of Electrical and Computer Engineering,
The Johns Hopkins University, Baltimore, MD 21218

Abstract

The photon-photon scattering of intense laser radiation predicted by QED can give rise to second harmonic generation (SHG) in a dc magnetic field due to broken symmetry of the interaction. The laser energy required to observe this effect can be achieved by using available laser facilities and the state-of-the-art photon-counting technology.

Photon-photon scattering in a vacuum[1] is perhaps one of the most fundamental mechanisms which can give rise to nonlinear optical effects. From the classical point of view, the expected nonlinear interaction [see below, Eqs. (1) and (2)] essentially corresponds to the third-order nonlinearity[2]. This interaction may contribute to the birefringence of the refractive index seen by a probe field under the action of either a dc magnetic (or electric) field[3] or intense laser pumping[4], as well as to multi-wave mixing processes[5]. To the best of our knowledge, no experimental work on this phenomenon has been done.

In this paper, we demonstrate the feasibility of new nonlinear magneto-optical effects in a vacuum that give rise to optical second harmonic generation (SHG) of the fundamental wave under the action of both strong dc magnetic field and high intensity optical laser radiation[6]. We also propose an experiment for the observation of this effect. The advantage of using the SHG effect is twofold. Since only a second-order effect for the optical field is involved, the laser power required to observe SHG is much lower than in previously proposed effects [3-5]. The SHG can also be measured at a frequency different from the fundamental frequency injected into the system, which may result in higher sensitivity.

From the Heisenberg-Euler lagrangian[1] for photon-photon scattering in quantum electrodynamics (QED) theory, one obtains the following expressions for the electric displacement $\vec{D}$ and magnetic induction $\vec{B}$

$$\vec{D}=\vec{E}+\vec{D}^{NL};\quad \vec{D}^{NL}=\xi[2(E^2-H^2)\vec{E}+7\vec{H}(\vec{E}\cdot\vec{H})], \tag{1}$$

$$\vec{B}=\vec{H}+\vec{B}^{NL};\quad \vec{B}^{NL}=\xi[2(E^2-H^2)\vec{H}-7\vec{E}(\vec{E}\cdot\vec{H})] \tag{2}$$

where $\xi=\alpha/45\pi H_{cr}^2=2.6\times10^{-32}\,\text{Gauss}^{-2}$ is a nonlinear interaction constant in the vacuum with $\alpha=e^2/\hbar c=1/137$ the fine structure constant and $H_{cr}\equiv m_0^2c^3/e\hbar=4.4\times10^{13}$ Gauss the QED critical field. These equations are valid only if the nonlinear corrections $\vec{D}^{NL}$ and $\vec{B}^{NL}$ are small, which holds if $|E|=|H|\ll H_{cr}$. It is obvious that a single monochromatic plane wave of infinite extent does not exhibit any nonlinear effects, because it has the properties, $E^2=H^2$, $\vec{E}\cdot\vec{H}=0$, and the nonlinear terms in Eqs. (1) and (2) vanish. This "degeneracy" of the nonlinearity is broken if either (i) the wave is non-planar or non-monochromatic or (ii) a strong static field (e.g., a dc magnetic field) is present. Both cases can result in birefringence of the refractive index for a probe field[3,4]. We show here that a dc magnetic field can also give rise to second-order nonlinear optical effects similar to those found in nonlinear materials[2]. In general, the optical second-order nonlinearity can give rise to the generation of a third wave (at frequency $\omega_2=\omega_a\pm\omega_b$) from two intense laser beams at frequencies ω_a and ω_b (i.e. the sum and difference frequency generation). Here, we consider only SHG in which $\omega_a=\omega_b$,

$\omega_2 = 2\omega_1$. However, our calculations can easily be generalized for the case $\omega_a \neq \omega_b$.

Assuming that a single unperturbed fundamental wave, described by the fields $\vec{E}_1$ and $\vec{H}_1 = (\vec{k}_1 / |\vec{k}_1|) \times \vec{E}_1$ (where $\vec{k}_1$ is the wave vector of the field), propagates in vacuum in the presence of a dc magnetic field, $\vec{H}_0$, the nonlinear components in Eqs. (1) and (2) can be rewritten as

$$\vec{D}^{NL} = \xi [-2H_0^2 \vec{E}_1 + 7\vec{H}_0 (\vec{E}_1 \cdot \vec{H}_0)] + \vec{D}^{(2)} \tag{3}$$

$$\vec{B}^{NL} = -2\xi H_0^2 \vec{H}_0 - 2\xi [H_0^2 \vec{H}_1 + 2\vec{H}_0 (\vec{H}_0 \cdot \vec{H}_1)] + \vec{B}^{(2)} \tag{4}$$

where

$$\vec{D}^{(2)} = \xi [-4\vec{E}_1 (\vec{H}_1 \cdot \vec{H}_0) + 7\vec{H}_1 (\vec{E}_1 \cdot \vec{H}_0)], \tag{5}$$

$$\vec{B}^{(2)} = \xi [-4\vec{H}_1 (\vec{H}_1 \cdot \vec{H}_0) - 7\vec{E}_1 (\vec{E}_1 \cdot \vec{H}_0)]. \tag{6}$$

Here, we neglect the third-order nonlinearity caused by the finite size of the laser beam which may result in self-action effects. It can be shown that in the case of a quasi-plane wave, e.g., a Gaussian beam with sufficiently large beam waist d, $d >> \lambda = 2\pi/k$, this effect is negligible when $E_1 << H_0 (d/\lambda)^2$. Nonlinear effects due to gradients in the field distribution will be discussed by us elsewhere. The terms in square brackets in Eqs. (3) and (4) are linear in optical field strengths. They result in vacuum birefringence of the refractive index for a weak probe field ($|\vec{E}_1| = |\vec{H}_1| << H_0$) under the action of a dc magnetic field[3]. The first term on the rhs of Eq. (4) corresponds to dc corrections to the dc magnetic field induced by the magnetic field itself. Therefore, only the terms $\vec{D}^{(2)}$ and $\vec{B}^{(2)}$, Eqs. (5) and (6), give rise to the optical second-order nonlinearity. Our estimates also show for the field intensities available now and in the foreseeable future, the phase mismatch between fundamental frequency and second harmonics can be neglected.

Because of the spatial anisotropy imposed by the magnetic field, SHG depends upon the propagation direction and the polarization of the fundamental optical wave with respect to $\vec{H}_0$. If the fundamental wave propagates along the direction of the dc magnetic field $\vec{H}_0$, then $\vec{D}^{(2)} = 0$, $\vec{B}^{(2)} = 0$, and the nonlinear effects are suppressed. The strongest interaction occurs when the laser radiation propagates in a direction normal to the dc magnetic field. Consider the general case of an elliptically polarized wave propagating in the plane normal to the dc magnetic field $\vec{H}_0 = H_0 \hat{e}_z$, with its polarization lying in the plane normal to the propagation direction, e.g., $\vec{k}_1 = k_1 \hat{e}_y$. Its electric field can be decomposed into two linearly polarized components along the $\hat{e}_z$ and $\hat{e}_x$ axes respectively:

$$\vec{E}_1 = E_1 (\sin\theta_1 \hat{e}_x + \cos\theta_1 e^{i\phi} \hat{e}_z) \exp[i(k_1 y - \omega_1 t)] \tag{7}$$

where E_1 and ω_1 are the amplitude of the electric field and the angular frequency of the wave respectively, ϕ is the phase between the linearly polarized components, and the angle θ_1 designates the relative amplitude between these two waves ($\phi = 0$ would correspond then to a linearly polarized wave with θ_1 the angle of the linear polarization, whereas $\phi = \pi/2$ and $\theta_1 = \pi/4$ correspond to a circularly polarized wave).

The generated second harmonic field at frequency $\omega_2 = 2\omega_1$ propagates in the same direction as that of the fundamental wave. Its electric field after passing through the interaction length $y = L$ can be calculated using Maxwell's equations with nonlinear terms, Eqs. (5,6),

$$\vec{E}_2 = i E_2 (\sin\theta_2 \hat{e}_x + \cos\theta_2 e^{i\phi_2} \hat{e}_z) \exp\{i[2(k_1 L - \omega_1 t) + \phi - \phi_2]\}, \tag{8}$$

where the magnitude E_2 is given by

$$E_2 = k_1 L \xi H_0 E_1^2 [56(1 - \cos 2\phi)\cos^4\theta_1 + (56\cos 2\phi - 23)\cos^2\theta_1 + 16]^{1/2}, \tag{9}$$

the angle θ_2 is determined by

$$\tan\theta_2 = -2[(65 - 56\cos 2\phi)\cos^4\theta_1 + (56\cos 2\phi - 32)\cos^2\theta_1 + 16]^{1/2} / 3\sin 2\theta_1, \tag{10}$$

and the phase ϕ_2 for the second harmonic is computed as

$$\tan\phi_2 = -[(7-4\tan^2\theta_1)/(7+4\tan^2\theta_1)]\tan\phi. \tag{11}$$

(When $\theta_1 = \theta_{1_0} \equiv \tan^{-1}(\sqrt{7}/2) \simeq 53$ degrees, the second harmonic is linearly polarized regardless of the polarization state of the fundamental wave.) Consider now the particular case of a linearly polarized fundamental wave. In such a case, $\phi = 0$ in Eq. (7), and the second harmonic is also linearly polarized; the angles θ_1 and θ_2 in Eqs. (7,8) are then the polarization angles of the fundamental wave and the second harmonic respectively, (see insertion in Fig. 1(b)).

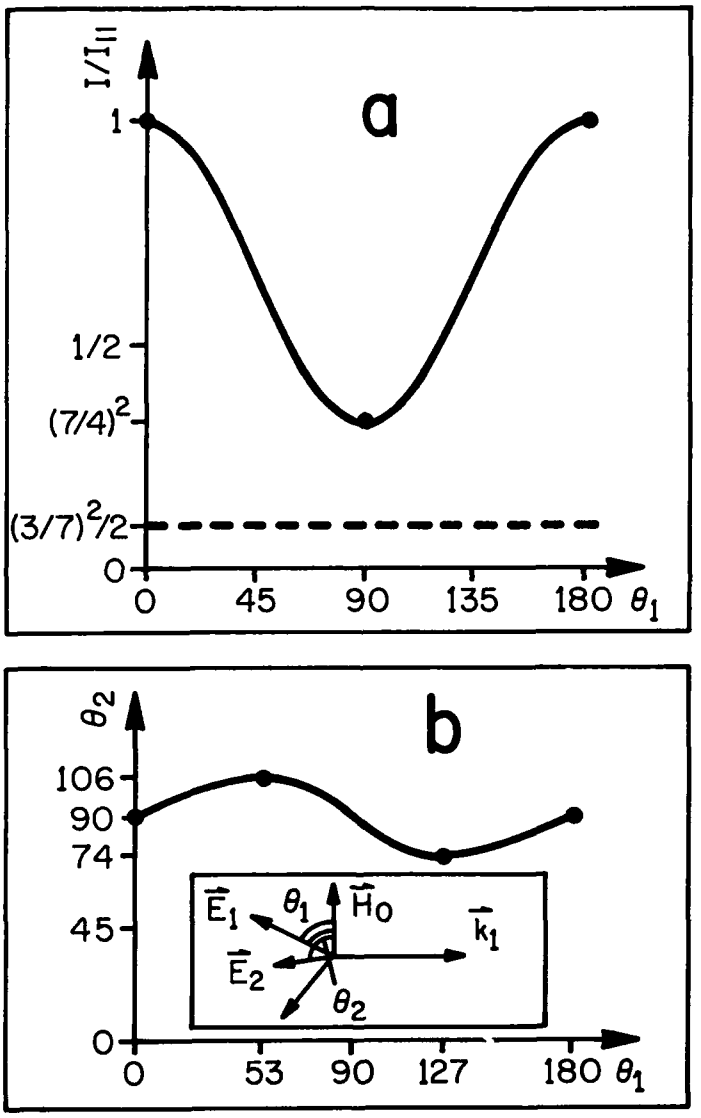


Fig. 1 (a) The normalized intensity $I/I_{\parallel}$ for the second harmonic with its polarization angle θ_2 with respect to the dc magnetic field (see inset in Fig. 1(b)) versus the polarization angle θ_1 (in degrees) of a linearly polarized fundamental wave (solid line); broken line corresponds to a circularly polarized wave; (b) the polarization angle θ_2 (in degrees) of the second harmonic versus the polarization angle θ_1 (in degrees) of a linearly polarized fundamental wave; the second harmonic is never polarized in sectors $|\theta_2 - 90^\circ| > 16^\circ$. The inset depicts the wave propagation configurations for both the fundamental wave and second harmonic with respect to the dc magnetic field $\vec{H}_0$.

Eqs. (9, 10) then reduce to

$$E_2 = k_1 L \xi H_0 E_1^2 (33\cos^2\theta_1 + 16)^{1/2}; \quad \theta_2 = -\tan^{-1}[(3\cos 2\theta_1 + 11)/3\sin 2\theta_1], \tag{12}$$

(see Fig. 1). Therefore, the ratio of maximum intensity of the second harmonic (which occurs at $\theta_1 = 0$) to minimum intensity (at $\theta_1 = \pi/2$) is $(7/4)^2 \simeq 3$ [see Fig. 1(a)], which can be directly measured in an experiment. Note that the generated second harmonic can never be polarized along the direction of the dc magnetic field, i.e., the polarization angle $\theta_2 \neq 0$ in Eq. (12). A minimal angle between the polarization of the second harmonic and the dc magnetic field is $(\theta_2)_{min} \simeq 74$ degrees, and the corresponding polarization angle of the fundamental wave is $\theta_1 = \theta_{1_0} \simeq 53$ degrees, i.e., there is a prohibited sector for the polarization of the second harmonic, $-(\theta_2)_{min} < \theta_2 < (\theta_2)_{min}$, see Fig. 1(b). All these polarization properties can be used in a future experiment to rule out all other (i.e., nonvacuum) nonlinear mechanisms. In the case of a circularly polarized fundamental wave ($\phi = \pi/2$, $\theta_1 = \pi/4$) propagating normal to the dc magnetic field, the ratio of the maximum intensity of second harmonic for linear polarization to that for circular polarization is $\simeq 10.9$ (see Fig. 1(a)).

The state-of-the-art photon counting systems provide a dark photon count rate $r_{dark} \sim 10$ photons/s and a typical quantum efficiency $\eta \sim 0.25$. [7] For the ideal spectral filtering and provided that by using gating, the detector is open only during the laser pulse[7], the signal-to-noise ratio is $SNR = <n_{det}>/<n_{dark}>$, where $<n_{det}> = \eta <n_{SHG}>$ is the averaged number of detected photons per pulse, n_{SHG} is the number of SHG photons generated per pulse, $<n_{dark}> = r_{dark}\tau_p$, and τ_p is the duration of a laser pulse. Stipulating now that SNR is sufficient high, e.g., $\geq 10^2$, and considering the case of the normal polarization ($\theta_1 = \pi/2$, which would correspond to the minimal SH photon output), we obtain the lowest intensity I_{cr} and energy J_{cr} of the laser beam required for such SNR:

$$I_1 \geq I_{cr}(W/cm^2) = (10^{19}/H_0 L)\sqrt{\lambda_1/A}; \quad J_{cr}(Joules) = \tau_p A I_{cr} \tag{13}$$

where λ_1 is in μm, A is the laser focal area in cm^2, τ_p is in sec, H_0 is in Gauss, and L is in cm. The minimal A should be chosen as $A \sim \lambda_1 L/2$ such that the diffraction of the beam is small within the distance L. With pulsed magnet technology[8], the best parameter values are $H_0 \sim 8 \times 10^6$ Gauss, bore diameter ~ 2.8 cm, and pulse duration $\sim 10^{-6}$ sec. Therefore, in order to satisfy the condition, Eq. (13), the laser intensity of $I_1 \simeq 10^{14} W/cm^2$ is required, which can readily be achieved even by using commercial laser systems. In fact, in the laser systems discussed below, the intensity reaches 10^{15}–$10^{18} W/cm^2$, so this condition is satisfied with great margin.

Since in most of high power laser systems available, $<n_{det}>$ is of the same order or less than unity, one has to use averaging of photon counts over a few (usually incoherent) laser beam lines for a single pulse or/and over many pulses of laser. Assuming a Poisson distribution of SHG photons[7], the probability of <u>not</u> observing any SHG photons within N laser pulses is $p = \exp(-N<n_{det}>)$. Stipulating again that p should be sufficiently small, e.g., $\leq 10^{-2}$, we obtain a condition for the required number of pulses (or number of beam lines for one laser shot):

$$N \geq 2\ln 10/<n_{det}> \simeq 5 \times 10^{36} \lambda_1 A \tau_p / J_1^2 H_0^2 L^2. \tag{14}$$

The development of new powerful lasers is proceeding at a rapid pace, and a pulse energy of 1-10 MJ, pulse width of 10-20ns, and repetition rates of 10Hz [9] as well as possible generation of a magnetic field $\sim 10^8$ Gauss with a pulse duration of 10^{-9} sec and bore diameter of 0.1 cm using high power lasers[10], may be only a few years away. However, the intensity (or energy) required for the proposed experiment even with small N can be achieved using existing systems. A high power pulsed Nd:Glass laser with either $\lambda_1 \sim 0.35\mu$m (NOVA[11]) or $\lambda_1 \sim 0.53\mu$m (GEKKO XII[11]), $\tau_p \sim 10^{-9}$ sec, can provide the laser energy of 6-10 KJ/pulse in each of 10-12 beam lines. For this energy $<n_{det}> \simeq 1$ in each beam line, and the number of beam lines required to observe the effect for the normal polarization ($\theta_1 = \pi/2$, the worst case) even within a single laser shot is 4-5, which is therefore attainable. If all the beam lines are used, the probability p can be greatly reduced, i.e. $p \sim 10^{-6}$–10^{-4}. Most recently, great efforts

have been made to increase both the output power (intensity) of very short pulse lasers and their repetition rate (which can be as high as 1-10 Hz). For XeCl [12], Nd:Glass [13], and KrF [14] lasers, $<n_{det}> << 1$ and the required number of pulses to observe the effect is $\sim 10^6 - 10^7$.

The generation of second harmonic radiation caused by residual atoms and/or molecules in the laboratory vacuum system can mask the photon-photon scattering effect. In order to make an order-of-magnitude estimate of the contribution of these residual particles and to evaluate the vacuum pressure necessary to rule out non-vacuum components in the SHG, we presume that non-vacuum nonlinearity is mainly attributed to the plasma of magnetized free electrons, since at the required laser intensities, the residual gas is expected to be highly ionized. The non-magnetized free electrons under the action of intense laser radiation can generate only odd order higher harmonics; the second-order harmonics can only be originated in the presence of the dc magnetic field. The numbers of second harmonic photons per laser pulse, N_{SHG}, for the normal polarization can be obtained using Ref. [15]:

$$N_{SHG} = 2\pi e^4 \alpha \omega_0^2 \tau_p E_1^4 n_e L / \omega_1^7 m_0^4 c^2 \tag{15}$$

where n_e is the number of free electron per unit volume and $\omega_0 = eH_0/m_0c$ is a cyclotron frequency of the electron. (It is worthwhile to note that for parallel polarization $N_{SHG} = 0$.) Assuming that, on average, each molecule is singly-ionized, and that GEKKO XII laser ($\lambda_1 \sim 0.53\mu m$) and the highest pulsed magnetic field ($\sim 8 \cdot 10^6$ G) are used, we estimate that vacuum and free-electron contributions to the SHG become equal at a pressure $\sim 2 \times 10^{-5}$ torr. Since the vacuum provided by state-of-the-art vacuum technology is better than $\sim 10^{-11}$ torr, the free-electron nonlinear mechanism can be neglected. SHG may also be attributed to two-photon (and multi-photon in general) excitations in ions of the residual gas; by selecting appropriate gas and frequency, this mechanism may also be made negligible. Since for the optical glass components (such as lenses and vacuum chamber windows) the third-order nonlinearity is the lowest-order nonlinearity[16] in the absence of dc fields, SHG from those components can be eliminated by shielding them from the dc magnetic field. One of the ways to eliminate masking effects associated with possibility of SHG in laser amplifiers is to use sum frequency effects (instead of the second harmonic) by employing two lasers with different frequencies. A more detailed evaluation of all these processes could be made only at the design stage of a particular experiment.

A large product $H_0 L$ could exist in many astronomical objects (e.g., in white dwarfs, where the spectral lines of elements still exist in the optical range[17]); the possibility exists that a second-harmonic signal generated by some characteristic spectral lines, may be observed and used to study the nonlinearity of vacuum and intrinsic properties of stars.

In conclusion, we have demonstrated the feasibility of second harmonic generation by the intense laser radiation in a vacuum which is due to photon-photon scattering in a dc magnetic field. The laser energy required to observe this effect can be achieved by using available high power laser systems.

The authors appreciate discussions with C. T. Law, P. H. Y. Lee, and G. A. Swartzlander. We are indebted to F. M. Davidson for his valuable insights on photon counting. This research is supported by AFOSR.

References

[1] H. Euler, *Ann. D. Phys. 26,* 398 (1936); W. Heisenberg and H. Euler, *Zs. f. Phys. 98,* 714 (1936); see also A. I. Akhiezer and V. B. Berestetskii, *Quantum Electrodynamics,* Interscience, New York, 1965.

[2] N. Bloembergen, *Nonlinear Optics,* New York: Benjamin, 1965.

[3] Z. Bialynicka-Birula and I. Bialynicki-Birula, *Phys. Rev. D 2,* 2341 (1970); I. Bialynicki-Birula and Z. Bialynicka-Birula, *Quantum Electrodynamics,* Pergamon & Polish Sci. Pub., Warszawa, 1975; S. L. Adler, *Ann. Phys. 67,* 599 (1971).

[4] E. B. Aleksandrov, A. A. Ansol'm, and A. N. Moskalev, *Zh. Eksp. Teor. Fiz. 89,* 1181 (1985)[*Sov. Phys. JETP 62,* 680 (1985)].

[5] R. L. Dewar, *Phys. Rev. A10,* 2107 (1974).

[6] Y. J. Ding and A. E. Kaplan, *Phys. Rev. Lett. 63,* 2725 (1989).

[7] A. Yariv, *Optical Electronics,* CBS College Publishing, New York (1985); K. Koyama and D. Fatlowitz, *Technical Information, Hamamatsu,* No. ET-03/Oct 1987.

[8] A. I. Pavlovskii, M. I. Dolotenko, N. P. Kolokolchikov, A. I. Bykov, N. I. Egorov, and O. M. Tatsenko, *Pis'ma Zh. Eksp. Teor. Fiz. 38,* 437 (1983)[*JETP Lett. 38,* 529 (1983)].

[9] C. Yamanaka, in *Laser Science and Technology,* A. N. Chester, V. S. Letokhov, and S. Martellucci, Eds., Plenum Press, New York, 1988.

[10] F. Herlach, *IEEE Trans. Magn. MAG-24(2),* 1049 (1988).

[11] J. F. Hozricher, in *Lasers, Spectroscopy and New Ideas,* W. M. Yen and M. D. Levenson, Eds. Heidelberg: Springer-Verlag, 1987; T. Yamanaka, K. Nishihara, K. A. Tanaka, T. Norimatsu, and S. Nakai, in *Conference on Lasers and Electro-Optics,* 1989 Technical Digest Series, Vol. 11 (OSA, Washington, DC 1989), pp. 4-5.

[12] C. R. Tallman, A. J. Taylor, J. P. Roberts, C. S. Lester, T. R. Gosnell, and W. H. Long, in *Conference on Lasers and Electro-Optics,* 1989 Technical Digest Series, Vol. 11 (OSA, Washington, DC 1989), pp. 102-103.

[13] P. Maine, D. Strickland, P. Bado, M. Pessot, and G. Mourou, *IEEE J. Quant. Electr. 24,* 298 (1988).

[14] S. Watanabe, A. Endoh, M. Watanabe, N. Sarukura, and K. Hata, *J. Opt. Soc. Amer. B6,* 1870 (1989).

[15] L. D. Landau and E. M. Lifshitz, *The Classical Theory of Fields,* Cambridge, MA, Addison-Wesley, 1971.

[16] M. J. Weber, D. Milam, and W. L. Smith, *Opt. Eng. 17,* 463 (1978).

[17] S. L. Shapiro and S. A. Teukolsky, *Black Holes, White Dwarfs, and Neutron Stars,* John Wiley & Sons, New York, 1983.

QUANTUM LIMITED OPTICAL PARAMETRIC IMAGE AMPLIFICATION

Dennis Guthals and Daniel Sox
Members of The Technical Staff
Rockwell International
Rocketdyne Division
Advanced Programs
6633 Canoga Ave
Canoga Park, CA 91303

Abstract

High gain quantum-limited image amplification and frequency shifting via difference frequency generation three wave mixing (Optical Parametric Amplification) has been demonstrated. Near infrared images ($\lambda = 1064$ nm) at input signal levels <10 photons per resolution element were amplified in a 355 nm pumped KD*P crystal, frequency shifted to 532 nm with gains greater than 10^3 (signal to noise levels near 10), and detected with standard CID video cameras. The gain parameter space was extensively investigated over 11 orders-of-magnitude gain as a function of input signal and pump power levels. Resolution was measured for the critical and noncritical phase matching angles. Pump depletion and diffraction are required to accurately model the results.

I. Introduction

The results of an experimental investigation of the imaging and gain properties of an Optical Parametric Amplifier (OPA) are reported here. The primary objectives of this effort were to demonstrate and quantify OPA imaging with gain using existing laser technology and common nonlinear optical materials. The approach involved a series of pulsed laser experiments that progressed from concept validation to OPA gain characterization and high gain image amplification.

Optical parametric amplification occurs via difference frequency generation Three Wave Mixing (3WM) in birefringent nonlinear optical materials that allow proper phase matching. Early 3WM imaging experiments concentrated on sum frequency generation for converting near-infrared images to more conveniently detected shorter wavelengths.[1-5] In this mode, net gain >1 is not possible. An OPA, however, can provide high gain as well as frequency shifting to shorter wavelengths. Most of the early OPA work concentrated on the generation and amplification from parametric superfluorescence as a source of tunable coherent light.[6-8] Because of the high peak pump powers required, the OPA was particularly well suited as a tunable source of sub-nanosecond light.[9-12] The OPA was also considered as a phase conjugator, but the limited field-of-view (FOV) was judged to be a disadvantage.[13-16] This small FOV, however, is ideal for reducing the noise floor for distant imaging applications. The OPA is currently being used as a tool in the study of squeezed states since it is not too difficult to operate these amplifiers in the transform-limited regime.[17] What was not well known at the start of this effort was the performance of an OPA for image amplification and frequency shifting.

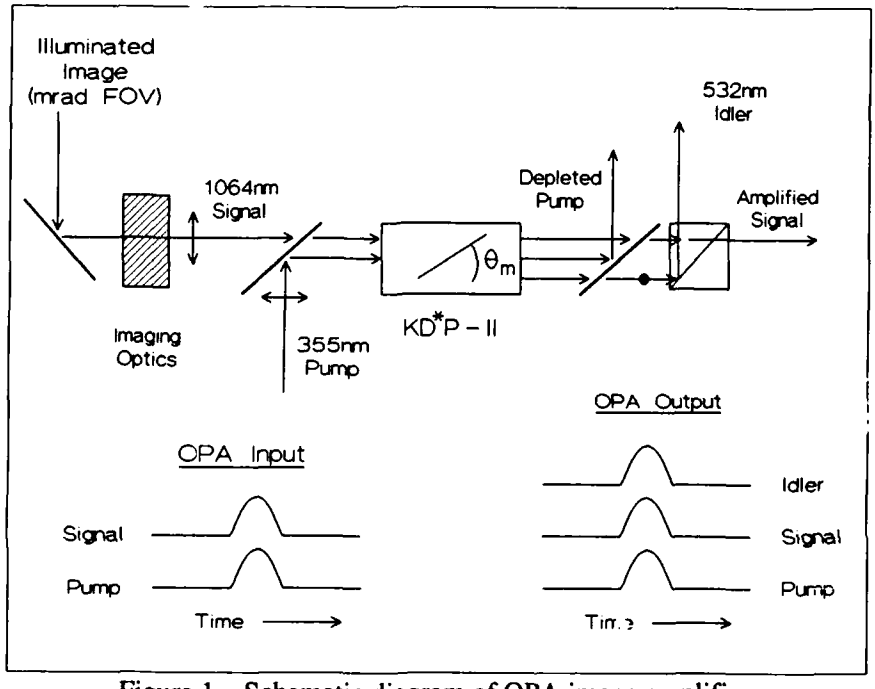


Figure 1. Schematic diagram of OPA image amplifier.

Figure 1 shows a schematic diagram of an OPA setup for image intensification as performed in the experiments. A weak signal beam (S) at 1064 nm was imaged into the KD*P crystal. An intense, pulsed short wavelength pump beam (P) at 355 nm was mixed with the signal (temporally and spatially overlapped) in the crystal at the proper phase matching conditions. For the experiments a type-II phase matching was used so that the S and idler (I) beams could be separated by polarization as indicated in the drawing. The pump pulse duration was chosen to gate sufficient signal photons into the OPA and the pump pulse intensity was adjusted to achieve proper gain. The OPA gain is determined by input signal power and output Signal-to-Noise (S/N) requirements. Both the amplified signal and generated idler (532 nm) have phase information and were detected.

II. Experimental Setup

A Nd:YAG laser operating at 1064 nm was used as the OPA pump source and target illuminator. This laser could be configured for either mode-locked or Q-switched operation.

The high gain experiments were performed using the active-passive mode-locked oscillator and double passed amplifier configuration. The oscillator produced a train of mode-locked pulses from which a single pulse (20 to 30 psec duration) was electro-optically selected for amplification. The single pulse duration was checked with autocorrelation. The single pulses were magnified, spatially filtered, and double pass amplified.

A schematic diagram of the OPA laser imaging experimental setup is shown in Figure 2. The three beams at 1064, 532, and 355 nm were separated with a quartz prism. The 1064 nm beam served as the target illuminator (S) and was sent through an adjustable optical delay for optimal temporal overlap with the 355 nm OPA pump. A calcite Glan prism polarizer selects the proper polarization for phase matching. For all imaging experiments, a standard United States Air Force (USAF) test pattern illuminated in transmission was used as the signal with the OPA crystal centered in the Fourier plane of the signal transfer lens. For the FOV and pump depletion tests, collimated signal beams were focused into the OPA and recollimated after amplification. The same OPA crystal was used for all experiments performed in this effort. Great care was exercised in approaching the damage limit. The OPA crystal experienced many millions of high intensity laser pulses without damage.

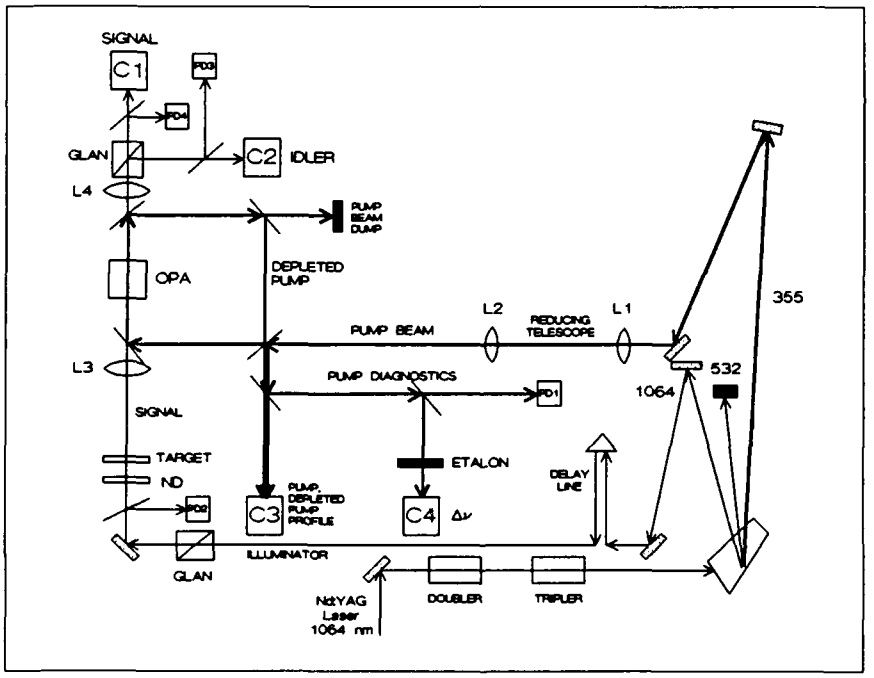


Figure 2. Schematic diagram of laser imaging experimental setup.

III. Image Amplification Demonstration

The image amplification demonstration experiments were performed early in order to validate the concept of OPA image intensification. In addition, OPA FOV and effects of local pump depletion were investigated in these preliminary tests. The Q-switched laser was used for these experiments.

The OPA FOV for the crystal orientation used in these experiments is dependent on the critical and noncritical phase matching acceptance angles. The critical acceptance angle, $\Delta\theta_m$, was expected to be a few milliradians (gain dependent)

while the noncritical acceptance angle, α, was limited by the target circular aperture and transfer lens focal length. The expected elliptically shaped OPA FOV was observed. The elliptical shape could be distorted to crescent shapes by rotating the crystal about its critical phase matching angle. The critical and noncritical acceptance angles (full) under conditions of low gain and pump depletion were measured as 7 mrads and 15 mrads, respectively.

Amplified images were obtained when the test pattern was placed in the setup described above. Figure 3 shows photographs of the initial image amplification demonstrations. These images were obtained using single laser pulse (10 ns) illumination and detection at 1064 nm. The gain was 2 to 10 over the full phase matching FOV. The test pattern was translated so that either Group 2 or Group 3 was in the OPA FOV. For Group 2, all features are resolved, while for Group 3 the limiting resolution is observed to be about 12 line pairs per millimeter (lp/mm). Under these conditions the OPA does not limit the resolving power of the optical system. This condition will change, however, if the pump does not spatially overlap with the higher orders in the Fourier plane, or if the relay lens focal length and circular aperture define a cone of solid angle larger than the critical acceptance angle.

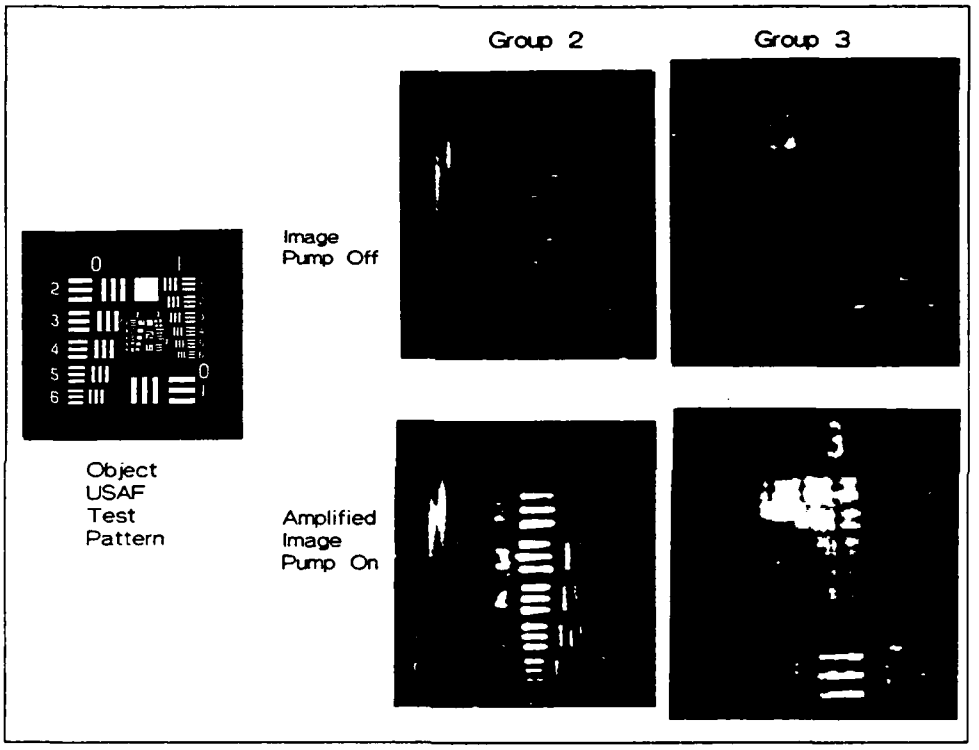


Figure 3. Demonstration of OPA image amplification.

The final set of experiments performed in the preliminary tests demonstrated some of the subtle consequences of using pump and signal beams with nonuniform spatial intensity distributions (such as commercial off-the-shelf lasers). The results are summarized in Figure 4. Here, the target was removed and the circular aperture was limited to ≈1.5 mm. Under these conditions, all of the input signal was within the OPA FOV and spatially overlapped with the pump. Video frames were taken of the unamplified (pump off) and amplified (pump on) signals after collimation. Identical slices showing horizontal spatial intensity profiles are plotted. A computer generated video frame was obtained by dividing the amplified signal frame by the unamplified signal frame on a pixel by pixel basis. The horizontal slice of the spatial gain distribution is also plotted. The regions of highest gain occur in regions of lowest signal intensity while the lowest gain occurs in the center of the beam. This is an indication that pump depletion is playing a major role in some regions and must be considered. This observation was later verified quantitatively using an OPA full-wave optics code.

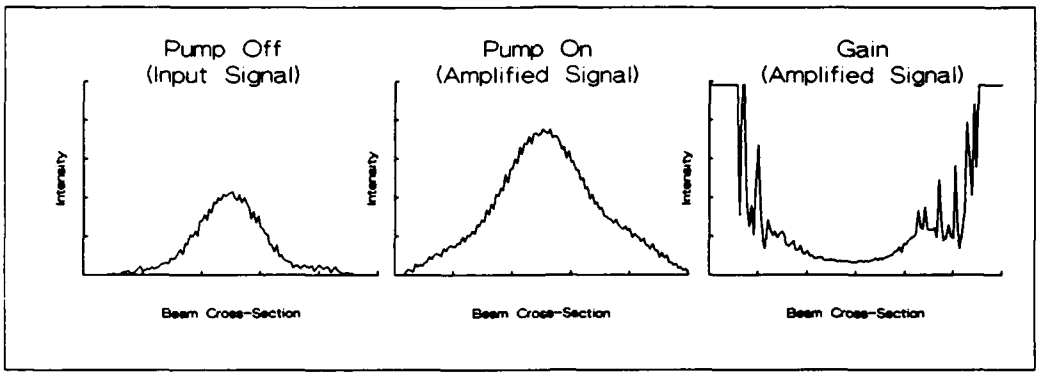


Figure 4. Nonuniform gain and pump depletion.

IV. Gain Measurements

After demonstrating OPA image amplification a series of experiments were initiated to map the gain parameter space under conditions expected for distant imaging applications. Such applications will most likely require image amplification at or near the quantum limit. The experiments discussed in this section were designed to address these low light levels directly and to allow determination of the appropriate OPA operating conditions for photon starved image amplification. The mode-locked laser was used for these experiments and the test target was removed. This section begins with a brief discussion of OPA gain and noise.

The theory of 3WM is well known and can be found in most nonlinear optics textbooks.[18]

The dominant source of noise for an OPA operating at wavelengths <1 μm is amplified quantum zero-point vacuum fluctuations which can be calculated by

$$I_S(z) = \left(\frac{h\nu_S^3 n_S^2}{c^2} d\nu d\Omega dA\right)\left(\frac{\Gamma_0^2}{\Gamma^2}\cosh^2 \Gamma z\right),$$

where ν_S and n_S are the frequency and refractive index of S, z is the crystal length, $d\nu$ is the smaller of either the pump or gain bandwidth, $d\Omega$ is the convolution of the divergence of pump with acceptance angle, dA is the cross-sectional area of the pump at the front face of the OPA, and Γ is the gain coefficient. The term in the left bracket is the zero-point noise source and the term in the right bracket is the gain term. The zero-point noise is plotted in Figure 5 along with blackbody curves for 300 K and 6000 K. In a properly designed OPA imaging system where pixel sizes are matched to OPA resolution elements or modes, it is possible to achieve 1 photon per pixel equivalent input noise. Using the experimental parameters for pump bandwidth, FOV, and pulse duration we predict a value of about 200 photons per pulse of zero-point noise. This is consistent with our observed S/N ratio of 5 at the lowest input signal levels of 1000 photons per pulse.

The OPA acts as a travelling wave spatial filter with a gain length dependent FOV[19,20] constrained by the pump divergence, and phase and group velocity walk-off.[21] An asymmetric acceptance angle was measured for a 2.5 cm long KD^*P crystal of 4 mrads x 8 mrads. When amplifying in the Fourier plane this acceptance angle limits spatial frequency resolution to ≈7-14 lp/mm.

The experimental setup used was virtually identical to that described in the previous section. The circular aperture of L3 was limited to 1.5 mm resulting in a 3.75 mrad OPA FOV. The signal and idler cameras were removed so that all amplified and generated light could be focused onto a single photodetector for low light level measurements. The pump and input signal photodiode outputs were fed into an amplifier and gated integrator pair. The idler and amplified signal detector outputs were fed directly into a pair of gated integrators. These amplifier - integrators were used over a dynamic range of 10. The outputs from all four integrators were digitized with a 12 bit 1 MHz analog to digital (A/D) converter connected to the computer bus. The gains and neutral density filters were chosen so that, for any given experimental run, the A/D was operating at about one half of full scale. Eighty two neutral density glass filters of various optical densities were calibrated under pulsed laser conditions at each of the three wavelengths (λ_P, λ_S, and λ_I) with the ratioing joule meter. The data acquisition system was set up to simultaneously digitize and record the single shot energies of the four signals. The input signal and pump energies were calibrated at the input face of the OPA crystal. The amplified signal was calibrated relative to the input signal. A typical run consisted of recording data from 1000 laser shots at fixed pump and input signal. The normal shot to shot variations in laser output energy for a given run was <5 per cent. This resulted in pump fluctuations >20%.

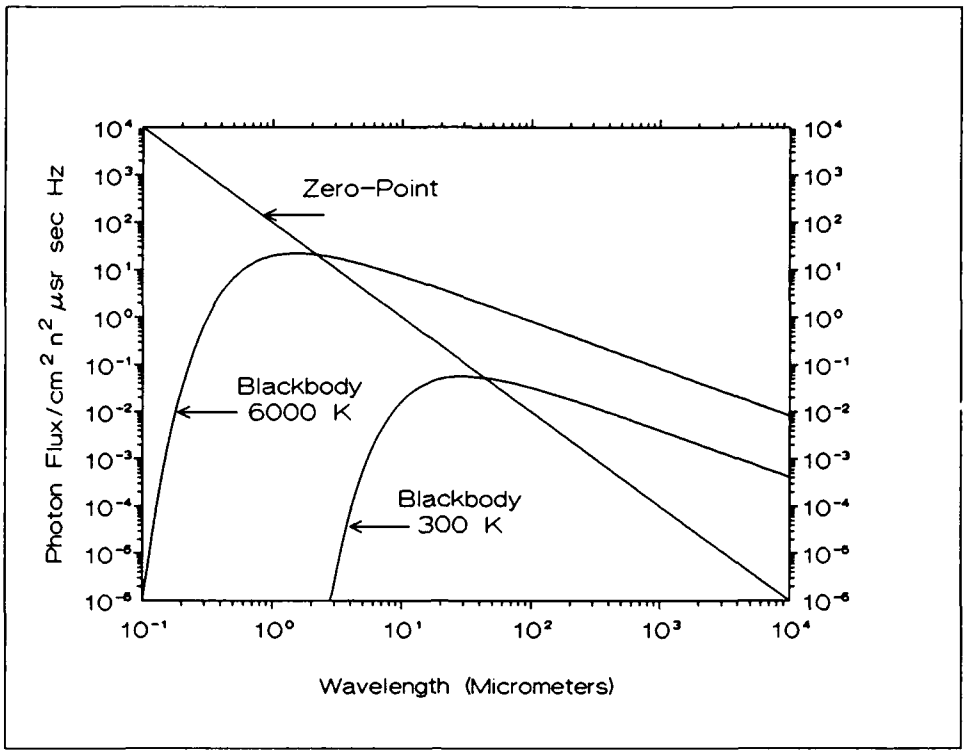


Figure 5. Calculated zero-point and blackbody noise.

Figure 6 summarizes the results of all the OPA gain measurements. The gain parameter space was mapped over 10 orders of magnitude in gain, 12 orders of magnitude in input signal energy, and over 2 orders of magnitude in pump energy. Each point is the average of 1000 shots. Six sets of data were recorded at the nominal pump energies shown in

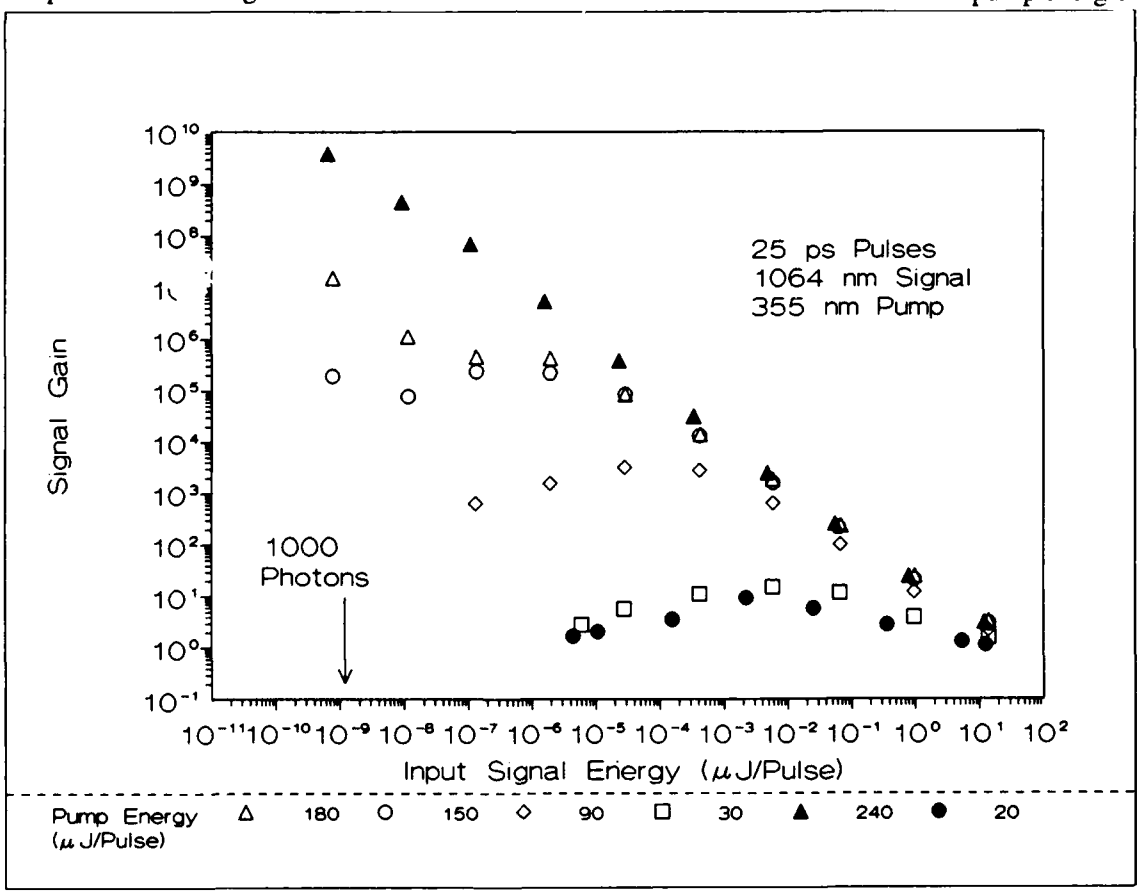


Figure 6. Summary of all OPA gain measurements.

Figure 6. While this data suggests the existence of linear and nonlinear amplifier regimes, placing a finer tolerance on the pump energy clearly indicates at least two operational regimes. The OPA is a linear amplifier under unsaturated or nondepleted pump conditions. Here, phase preserving signal amplification should occur as predicted.[10] In the saturated gain regime, however, nonuniform spatial pump depletion causes intensity spiking which prints through as phase distortion in the amplified signal. This effectively reduces imaging system resolution. The lowest input signal levels producing reliable data corresponded to 1000 photons per pulse. At these levels the observed S/N ratio was ≈5 indicating the presence of ≈200 photons per pulse noise. All of this noise is attributed to the zero-point noise.

In order to account for the two observed amplifier regimes, a realistic model was required. Figure 7 shows the results of a sample run of a code which provides a full-wave optics propagation of Gaussian signal and pump fields through the OPA gain medium with diffraction. The nonlinear coefficient, phases, and interaction lengths were set to duplicate the experimental conditions. The pump field was adjusted to achieve proper gain. Comparison is shown of the measured and calculated gain in an OPA pumped with 150 microjoule (μJ) per pulse at 355 nm using the model described above. Also shown are the calculated amplified signal energy and fractional pump depletion. The model is in excellent agreement with the experimental results. Both amplifier regimes are readily predicted by this model.

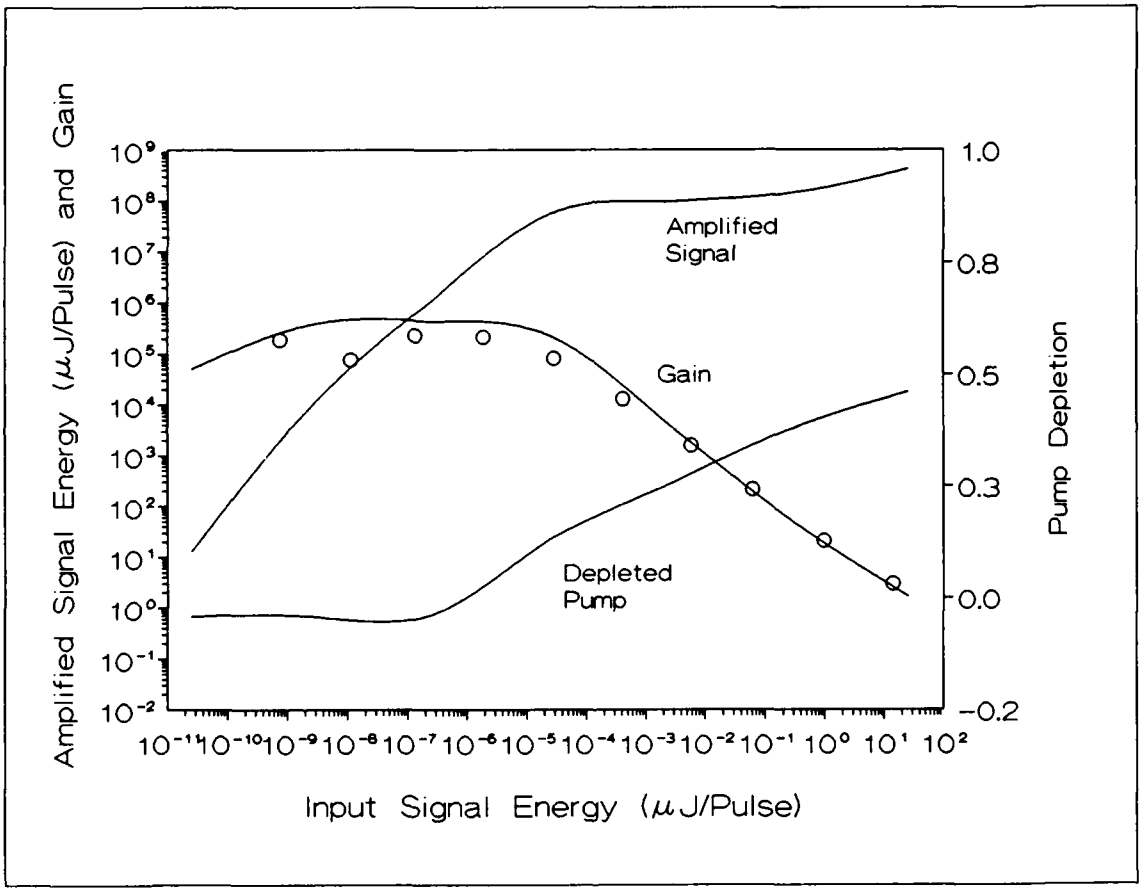


Figure 7. Comparison of observed and calculated OPA gain.

V. High Gain Image Amplification

The high gain image amplification experiments were performed following the gain mapping with the laser imaging system setup as described in the previous section. The video cameras were reinserted at positions C1 and C2 (Fig. 2). The circular aperture defining the OPA FOV was kept at 1.5 mm, and the test target used in the image amplification demonstration was placed in the signal beam. The pump enrgy per pulse was adjusted to provide safe operation below the OPA damage limit. The sensitivity of the CID video detectors was measured to be $\approx 10^6$ photons per pixel at 1064 nm and 10^3 photons per pixel at 532 nm. A series of amplified single pulse images at λ_s and frequency shifted images at λ_f were obtained at gains up to 10^4.

The OPA can be used to directly amplify images at input signal levels near the quantum noise floor. Figure 8 shows the results of the lowest input light level experiment. An image of a portion of the USAF test pattern (Group 1 Element 1) was allowed through the circular aperture. The image circular aperture was well within the OPA acceptance angle which included ≈200 resolution elements (pixels). The signal level at the input face of the OPA was <2000 photons (<10 photons per pixel). At a signal gain of 10^4 the amplified image was still well below the CID detection threshold (10^6 photons per pixel) but the frequency shifted idler image at 532 nm was readily detectable even with a poor quality pump.

The edges of the bars could be enhanced by rotation of the crystal about the critical angle. This is a result of lack of spatial overlap of the pump with the higher spatial frequencies in the Fourier plane.

Amplified image resolution is limited by the spatial overlap of the pump with the signal distribution in the Fourier plane and the critical and noncritical phase matching angles. The resolution was measured to be 12 and >5 lp/mm in the noncritical and critical dimensions, respectively, for the high gain image amplification experiments described above.

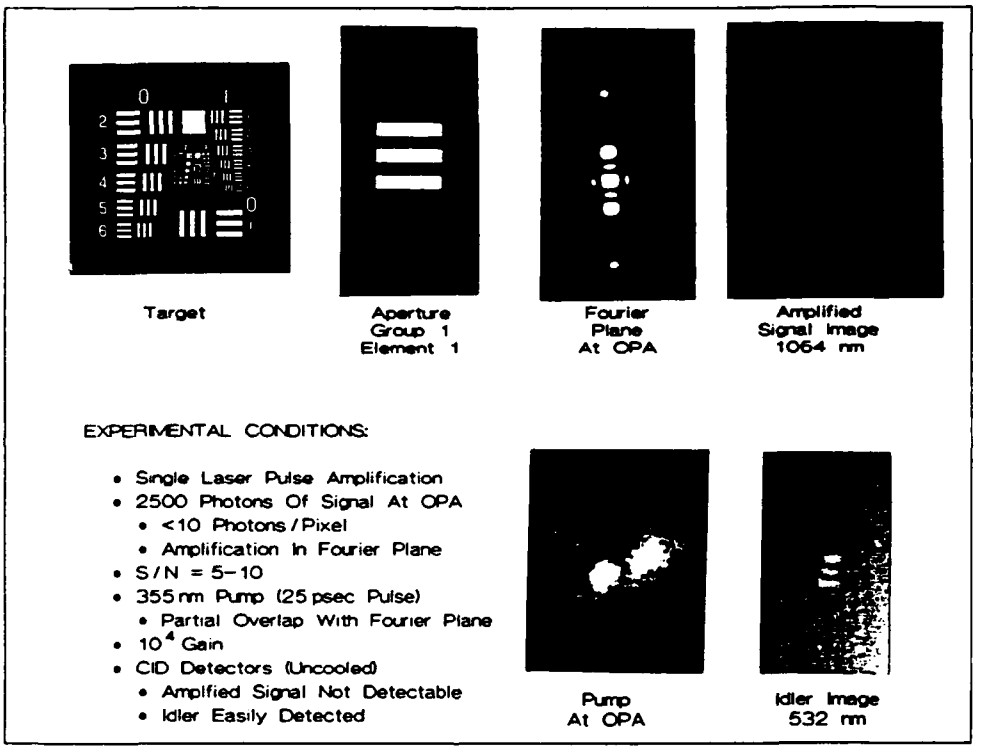


Figure 8. Quantum limited OPA image amplification.

Acknowledgment

The experimental work reported here was supported by The United States Air Force, Kirtland Air Force Base (contract no. F29601-87-C-0058). The modeling was supported by Rockwell International IR&D. The authors are indebted to Dr. P. Hu for leading the modeling efforts, Dr. B. Campbell for zero-point noise calculations and Dr. S. Ma for assistance with computer programming.

References:

1. J. Midwinter and J. Warner, J. Appl. Phys., 38, 519 (1967)
2. J. Midwinter, IEEE J. Quantum Electron., QE-4, 716 (1968)
3. A. Firester, J. Appl. Phys., 40, 4842 (1969)
4. A. Firester, J. Appl. Phys., 40, 4849 (1969)
5. A. Firester, J. Appl. Phys., 41, 703 (1970)
6. S. E. Harris, M. K. Oshman, and R. L. Byer, Phys. Rev. Lett., 18, 732 (1967)
7. D. Magde and H. Mahr, Phys. Rev. Lett., 18, 905 (1967)
8. J. M. Yarborough and G. A. Massey, Appl. Phys. Lett., 18, 438 (1971)
9. A. Laubereau, L. Greiter, and W. Kaiser, Appl. Phys. Lett., 25, 87 (1974)
10. G. A. Massey, J. C. Johnson, and R. A. Elliott, IEEE J. Quantum Electron., QE-12, 143 (1976)
11. A. Seilmeier, K. Spanner, W. Laubereau, and W. Kaiser, Optics Commun., 24, 237 (1978)
12. D. W. Anthon, H. Nathel, D. M. Guthals, and J. H. Clark, Rev. Sci. Instrum., 58, 2054 (1987)
13. P. Avizonis, F. Hopf, W. Bomberger, S. Jacobs, A. Tomita, and K. Womack, Appl. Phys. Lett., 31, 435 (1977)
14. E. S. Varonin, V. V. Ivakhnik, V. M. Petnikova, V. S. Solomatin, and V. V. Shuvalov, Sov. J. Quantum Ecectron., 9, 765 (1979)
15. A. Tomita, Nonlinear Optical Phase Conjugation by 3-Wave and 4-Wave Mixing, PhD Dissertation, Optical Sciences, University of Arizona, Tucson, Arizona, (1980)
16. V. I. Bespalov, M. A. Dvoretskii, A. M. Kiselev, and G. A. Pasmanik, Sov. J. Quantum Electron., 14, 1654 (1984)
17. M. Xiao, L. Wu, and H. J. Kimble, Phys. Rev. Lett., 59, 278 (1987)
18 A. Yariv, Quantum Electronics (John Wiley, New York 1975)
19. R. A. Baumgartner and R. L. Byer, IEEE J. Quantum. Electron., QE-15, 432 (1979)
20. P. A. Laferriere, C. J. Wetterer, L. P. Schelonka, and M. A. Kramer, J. Appl. Phys., 65, 3347 (1989)
21. J. A. Armstrong, S. J. Sudhanshu, and N. S. Shiren, IEEE J. Quantum Ecectron., QE-6, 123 (1970)

A Perturbation Analysis of Brillouin-Enhanced Four-Wave Mixing

Richard B. Holmes
North East Research Associates
800 West Cummings Park S. 4500, Woburn, Massachusetts 01801

ABSTRACT

The technique of Brillouin-enhanced four-wave mixing is known for its high-reflectivity, high-quality phase conjugation. This method is often implemented in waveguides, hence the analysis is performed for a waveguide geometry. The treatment accounts for the transverse structure of the pump and signal beams within the paraxial approximation, assuming the acoustic wave has reached a steady-state An approximation is used that is applicable when many transverse modes of the waveguide are excited by each of the four mixing waves. Pump beams are considered that are not perfect phase conjugates of each other. The zeroth-order equations are obtained for the polarization states of the pump and signal beams by dropping all phase-mismatch terms. The resulting equation generalizes previous expressions given in the literature. The resulting dependence of reflectivity on forward-to-backward pump intensity ratio, forward-to-backward pump fidelity, and off-resonant gain are considered in detail. Self-oscillation is predicted for the high-gain case. The resulting zeroth-order solutions are used to aid in evaluation of the first-order term that determines the loss of fidelity. Simple expressions are given for this loss in terms of the angular spread of the signal laser beam, the pump-signal angle, the pump intensities, and the mutual fidelity of the two pump beams.

I. Introduction

The discovery of phase conjugation using stimulated Brillouin scattering in 1972[1] has led to numerous methods for nonlinear optical phase conjugation. Such methods include two-wave mixing, photon echoes, and four-wave mixing, each utilizing numerous material nonlinearities. These methods have varying applicability for practical applications, and various criteria have been devised for comparing such phase-conjugation techniques. Two obvious criteria are the quality (fidelity) and strength (reflectivity) of phase conjugation. A technique [2] discovered in the late 1970's that yields both high fidelity and high reflectivity utilizes the longitudinal acoustic resonance of Brillouin scattering, combined with four-wave mixing. This technique is known as Brillouin-enhanced four-wave mixing(BEFWM), or as hypersonic four-wave wavefront reversal in the Soviet literature.The technique has been further refined to reduce inherent instabilities that are often observed with high-reflectivity four-wave mixing.[3] This technique is known as polarization-decoupled BEFWM. Questions arise as to the practical limitations of achieving both extremely high reflectivity[4], extremely high fidelity, and stability for the conjugate wave. This question has been partially answered experimentally, as well as theoretically.[5-15] However, it will be seen that none of the analyses specifically treat the case of interest, including transverse effects. These transverse effects are essential to understanding how the spatial similarity, i.e., the mutual fidelity, of the pump beams affects the four-wave mixing interaction. These transverse effects account for the so-called "phase mismatch" terms that define a limit to the fidelity of phase conjugation that can be achieved. This limit is given below by a relatively simple expression that is a straightforward generalization of the expressions obtained for phase conjugation fidelity using stimulated Brillouin scattering (SBS).[6-7] We compare our results with those of other authors.[15]

The following approach expands the electric field into modes of the waveguide; in the case under consideration, a square waveguide is assumed. Within the waveguide a laser beam is propagating with a polarization parallel to two opposite sides of the square waveguide. A second wave is propagating in a direction opposite that of the first wave, and is polarized orthogonally to the first beam. Furthermore, as shown in Fig. 1., this second beam is formed by focussing the first wave into an SBS cell and is therefore phase conjugate to the first beam and frequency-shifted by the SBS frequency shift. The polarization of the second beam is made orthogonal to the first beam by using a quarter-wave plate. The orthogonal polarization of the two pump beams virtually eliminates the coupling between these two beams in the absence of a suitably-polarized signal beam, because of the scalar coupling associated with the longitudinal acoustic wave.[18-19] In the following analysis we will analyze the case in which the signal beam is linearly polarized parallel to the second, Stokes-shifted, pump beam. There are obvious generalizations of this technique which would allow conjugation of the electric field polarization of the signal as well.

Several standard simplifying assumptions are made. First, it is assumed that the acoustic phonon is assumed to have reached a steady-state. Second, the electric fields vary slowly over an acoustic relaxation time and an optical transit time through the medium. Third, many modes are excited by the electric fields of each of the four waves. Fourth, depletion of the pump waves is negligible. Fifth, the Brillouin shift is considered negligible. Finally, the propagation of each of the four waves is paraxial. These assumptions, though numerous, are those commonly made in association with analyses of fidelity of stimulated scattering,[15-17], and have been been shown to be applicable in corresponding experiments.[20-21] The following analytic approach is of special interest because of the difficulties associated with numerical modelling of counterpropagating wavefronts with two transverse dimensions, and with drawing useful conclusions from those results.

II. Basic Equations

The electric field at the optical frequency of the laser beam is

$$E_L = \hat{e}_0 E_{L0} \exp\left(i\omega_P t - ik_{L0} \cdot z\right) + \hat{e}_1 E_{L1} \exp\left(i\omega_P - ik_{L0} \cdot z\right) \qquad (1)$$

where k_{L0}, k_{L1}, are the optical wavenumbers of the pump laser beam, and the probe beam respectively, both of the same, unshifted

frequency ω_P, and entering the waveguide at the same entrance. Thus $k_{L0} \cdot z > 0$, and $k_{L1} \cdot z > 0$. For a field consisting of multiple transverse modes, the vectors k_{L0}, k_{L1} are along the central axes of the corresponding fields. When needed, the units of the electric field are chosen so that E^2 has units of MW/cm^2. Also the symbols $\hat{e}_i$ denote the unit vectors transverse to the propagation axis z, and satisfy

$$(\hat{e}_i \cdot \hat{e}_j = \delta_{ij}) \tag{2}$$

The electric field at the Stokes frequency is

$$E_S = \hat{e}_0 E_{S0} \exp\left(i\,\omega_S\, t + ik_{S0} \cdot z\right) + \hat{e}_1 E_{S1} \exp\left(i\,\omega_S\, t + ik_{S0} \cdot z\right) \tag{3}$$

Here k_{S0} and k_{S1} are the optical wavenumbers of the conjugate field, and the Stokes-shifted second pump beam, respectively. Both these fields are at the Stokes frequency $\omega_S = \omega_P - \omega_{SBS} + \Delta\omega$, where ω_{SBS} is the frequency of the acoustic phonon. These fields both propagate counter to the fields at the pump frequency, so that $k_{S1} \cdot z < 0$, and $k_{S0} \cdot z < 0$.

The (scalar) acoustic phonon, in the steady state, may be written as follows[10,19]:

$$\begin{aligned} Q &= \frac{\gamma}{\Gamma} E_L \cdot E_S^* \\ &= E_{L0} E_{S0}^* \exp\left(i\,\omega_{SBS} t - i\left(k_{L0} + k_{S0}\right) \cdot z\right) \\ &\quad + E_{L1} E_{S1}^* \exp\left(i\,\omega_{SBS} t - i\left(k_{L1} + k_{S1}\right) \cdot z\right) \end{aligned} \tag{4}$$

The parameters of the above equations are as follows. γ is equal to $ik_0\rho_0(\partial\varepsilon/\partial\rho)/(4\pi nc)(1+i\Delta\omega/\Gamma)$;[22] k_0 is equal to $k_L \simeq k_S$, the optical wavenumber; ε is the medium dielectric susceptibility; ρ is the medium density; v is the acoustic velocity in the medium; c is the speed of light; Γ is the HWHM Brillouin linewidth(sec^{-1}), and $\Delta\omega$ equals $\omega_{SBS} - (\omega_L - \omega_S)$.
With this expression for the phonon, the corresponding equations of motion for the signal and conjugate waves, as well as the pump waves, respectively, are as follows[10,18,19]:

Conjugate wave:

$$\left[\partial_z + \frac{-\nabla_\perp^2}{2ik_0}\right] E_{S0} = -\gamma_0 E_{L0} Q^* \exp\left(-i\omega_{S0} t - ik_{S0} \cdot z\right) = \frac{-\gamma_0 \gamma^*}{\Gamma}\left[|E_{L0}|^2 E_{S0} + E_{L0} E_{L1}^* E_{S1} \exp\left(i\Delta k_{S0} \cdot z\right)\right] \tag{5}$$

Here γ_0 equals $ik_0(\partial\varepsilon/\partial\rho)/2n^2$; n is the refractive index; and g is the Stokes intensity gain, equal to $2\gamma_0\gamma/\Gamma$ (cm/MW). Note E_{S0} grows like the conjugate of field E_{L1} in the minus-z direction, provided that $E_{L0}E_{S1}$ is independent of spatial position. Furthermore, attributes of the conjugate wave E_{S0} are also amplified, as seen from the first term of the right-hand side. The wavenumber mismatch is defined as follows:

$$\Delta k_{S0} = k_{L1} - k_{L0} + k_{S1} - k_{S0} \tag{6}$$

Note that

$$z \cdot (\Delta k_{S0}) \simeq (1 - \cos\theta) z n \omega_{SBS}/c \tag{7}$$

In the above, θ is the central angle between the signal and the pump beams. The quantity in Eq.(7) is assumed negligibly small for most of the following results. This restricts the range of angles between the pump and probe beams for a given interaction length, or restricts the interaction length for a given range of angles between probe and pump.

Signal (probe) wave:

$$\left[\partial_z + \frac{\nabla_\perp^2}{2ik_0}\right] E_{L1} = \gamma_0 E_{S1} Q \exp\left(-i\omega_{L1} t + ik_{L1} \cdot z\right) = \frac{\gamma_0 \gamma}{\Gamma}\left[|E_{S1}|^2 E_{L1} + E_{S1} E_{L0} E_{S0}^* \exp\left(i\Delta k_{L1} \cdot z\right)\right] \tag{8}$$

where $\Delta k_{L1} = \Delta k_{S0}$. The pump beams are assumed unchanged.

Now in the above equations, one may introduce diffraction effects through an angle-dependent phase delay, equal to $z\,k_\perp^2/2k_0$,

where $k_+ = k_0\,\theta$, where θ equals the angle of propagation of the partial wave relative to central axis of each wave. This may be done by substituting the following Fourier expansion for each of the four fields. So write, for any one of the fields L0, L1, S0, S1,

$$E(x,z) = \sum_k E(k,z)\,\exp\left(ik\cdot x \pm \frac{k^2 z}{2ik_0}\right) \tag{9}$$

where the + sign corresponds to L0 and L1 and the – sign corresponds to fields S0 and S1. Substituting these expressions into Eqs. (5), (8), and simplifying yields an equation for each component k of the conjugate wave. To simplify notation, make the following correspondence:

$$E_{S0} \rightarrow S_0$$
$$E_{S1} \rightarrow S_1$$
$$E_{L0} \rightarrow P_0$$
$$E_{L1} \rightarrow P_1$$

Now one may write the equations as follows (z is replaced by -z in what follows to retain common conventions):

$$\partial_z S_0(k) = \frac{g}{2(1-i\Delta\omega/\Gamma)} \sum_{k_1,k_2} P_0(k_1)P_0^*(k_1-k+k_2)S_0(k_2)\,\exp\left(\frac{-z}{ik_0}(k_2+k_1)\cdot(k_2-k)\right)$$
$$+ P_0(k_1)P_1^*(k_2)S_1(k-k_1+k_2)\,\exp\left(\frac{-z}{ik_0}(k_2+k)\cdot(k_2-k_1)\right) \tag{10}$$

$$\partial_z P_1(k) = \frac{g}{2(1+i\Delta\omega/\Gamma)} \sum_{k_1,k_2} S_1(k_1)S_1^*(k_1-k+k_2)P_1(k_2)\,\exp\left(\frac{z}{ik_0}(k_2+k_1)\cdot(k_2-k)\right)$$
$$+ S_1(k_1)S_0^*(k_2)P_0(k-k_1+k_2)\,\exp\left(\frac{z}{ik_0}(k_2+k)\cdot(k_2-k_1)\right) \tag{11}$$

Similar equations result for the pump waves, which will be detailed in later efforts.

III. Zero-order Solutions

The above equations (10)-(11) for the evolution of the signal beam and the conjugate beam may be simplified using the mode approximation. Keeping only phase-matched terms, i.e., only those for which the argument of the exponential is zero, one obtains

$$\partial_z S_0(k) = \frac{g}{2(1-i\Delta\omega/\Gamma)}\left[(P_0\cdot S_0)P_0^*(-k) + I_{P0}S_0(k) + (P_0\cdot S_1)P_1^*(-k) + (P_0\cdot P_1^*)S_1(k)\right] \tag{12}$$

$$\partial_z P_1(k) = \frac{g}{2(1+i\Delta\omega/\Gamma)}\left[(P_1\cdot S_1)S_1^*(-k) + I_{S1}P_1(k) + (P_0\cdot S_1)S_0^*(-k) + (S_1\cdot S_0^*)P_0(k)\right] \tag{13}$$

where

$$P_i\cdot S_j = \sum_{k_1} P_i(-k_1)S_j(k_1), \quad i=0,1,\ j=0,1 \tag{14a}$$

$$P_i\cdot P_j^* = \sum_{k_1} P_i(k_1)P_j^*(k_1), \quad i=0,1,\ j=0,1 \tag{14b}$$

and similarly for $S_i\cdot S_j^*$. The Eqs. (12)-(13) are the zeroth-order equations in the mode-approximation, with undepleted four-wave mixing pump beams. It has been assumed that there are many modes, each with a small fraction of the total energy. Note that the first two terms of Eqs (12) and (13) would be present in a simple SBS geometry with a single polarization (state $\hat{e}_0$ for Eq.(12), $\hat{e}_1$ for Eq.(13)). The idea of BEFWM is to choose the spatial overlaps between the pump beams and the signal beam to be nearly zero:

$$P_0\cdot P_1^* \approx 0 \tag{15a}$$

$$S_1 \cdot P_1 \simeq 0 \tag{15b}$$

Now as the conjugate beam S_0 "enters" the waveguide it is nearly zero, and is parametrically generated from the first and third terms of Eq.(14). Since it is nearly zero,

$$P_0 \cdot S_0 << P_0 \cdot S_1 \tag{15c}$$

Thus $S_0(k)$ is generated proportional to $P_1^*(-k)$ and not $P_0^*(-k)$, as may be deduced from Eq.(14). Thus it is evident that

$$P_0 \cdot S_0 \simeq 0 \tag{15d}$$

should hold throughout the waveguide. Also, since the two pump beams are nearly conjugates of one another, P_0 is proportional to S_1^*, so from Eq.(17c) it follows that

$$S_1^* \cdot S_0 \simeq 0 \tag{15e}$$

From Eqs.(12)-(15), one obtains the three-dimensional analog of the more familiar one-dimensional BEFWM equations. The key assumption is that the spatial overlap of the pump and signal beams must be nearly zero. This latter assumption is usually satisfied experimentally, and can be achieved by entering the waveguide with the unshifted pump beam and the signal beam at well-separated angles. On the other hand, the relative angle can't be too large or the gain is reduced.[8] With the zero-spatial-overlap assumption, and with Δk_{S0} approximately zero, one obtains the following equations:

$$\partial_z S_0(k) = \frac{g}{2(1-i\Delta\omega/\Gamma)} \left[I_{P0}\, S_0(k) + \left(P_0 \cdot S_1\right) P_1^*(-k) \right] \tag{16}$$

$$\partial_z P_1^*(-k) = \frac{g}{2(1-i\Delta\omega/\Gamma)} \left[I_{S1}\, P_1^*(-k) + \left(P_0 \cdot S_1\right)^* S_0(k) \right] \tag{17}$$

Note that k is changed to -k in Eq.(17), and the same equation is also complex-conjugated.
Let $g_1 = g/2(1-i\Delta\omega/\Gamma)$ for simplicity of notation.

Continuing with the zero-order solution, Eqs. (16) and (17) yield expressions for $A_\pm$, with eigenvalues λ_+ and λ_-, for which $\lambda_+ > \lambda_-$.

$$-A_- = +A_+ = \frac{\left[H_P I_{P0} I_{S1}\right]^{1/2} e^{i\phi}\, P_{10}^*(-k)}{\left[\left(\frac{\lambda_+}{g_1} - I_{P0}\right)\exp(\lambda_+ L) - \left(\frac{\lambda_-}{g_1} - I_{P0}\right)\exp(\lambda_- L)\right]} \tag{18}$$

Eqs. (16) and (17) yield expressions for $B_\pm$:

$$-\frac{(\lambda_- - g_1 I_{S1})}{(\lambda_+ - g_1 I_{S1})} B_- = B_+ \frac{P_{10}^*(-k)}{\exp(\lambda_+ L) - \dfrac{(\lambda_+ - g_1 I_{S1})}{(\lambda_- - g_1 I_{S1})} \exp(\lambda_- L)} \tag{19}$$

Note that this zero-order result gives the Stokes wave as phase conjugate to the probe; and the probe retains its wavefront:

$$P_1(-k,z) = g^*(z) P_1(-k,0) = g^*(z) P_{10}(-k) \tag{20a}$$

$$S_0(k,z) = f(z)\, P_{10}^*(-k) \tag{20b}$$

Substitution of Eqs. (18) and (19) respectively yield the expressions for the probe and conjugate wave as a function of z. To reiterate, this result implies that the Stokes wave with polarization $\hat{e}_0$ conjugates the probe wave of polarization $\hat{e}_1$, under the assumptions of no pump depletion, no competing nonlinear effects, the mode approximation with many modes, and spatially orthogonal signal and probe beams.

Based on the above solutions, the reflectivity may be written as follows:

$$R = I_{S0}/I_{P1} = (H_P I_{P0}/I_{S1})\ \frac{|1-\exp(g_1 I_{P0} L - \Delta\lambda L)|^2}{|1+(I_{P0}/I_{S1})\exp(g_1 I_{P0} L - \Delta\lambda L)|^2} \qquad (21)$$

where $\Delta\lambda = 2g_1(I_{S1}/I_{P0})\Delta H_P$, and where $\Delta H_P = 1-H_P$. In the limit of perfect mutual pump fidelity this expression duplicates the one-dimensional result of other authors.[20] This expression shows explicitly how the reflectivity depends on the mutual pump fidelity H_P, the off-resonant gain coefficient g_1, the gain $G=g_1 I_{P0} L$ and the pump intensity ratio $r = I_{P0}/I_{S1}$. As examples of this calculation, we consider the case of perfect mutual fidelity,and show the reflectivity, maximized over frequency offset, in Figures 2-4. In Fig. 2, for which the gain-length product $G=g_1 I_{P0} L = 4$, for varying values of pump intensity ratio r. The theoretical reflectivity peaks at about 12 in this case. As the gain-length product is progressively increased to 5 and 6 for Figs. 3 and 4, respectively. The obvious result is an increase in reflectivity, uniformly over the range of pump intensity ratios r. Interestingly, the peak of these curves all lie near the same value r. The reflectivity profile as a function of frequency for the maximum-reflectivity points of these two last curves is shown in Figs. 5 and 6. It is seen that the higher gain, higher reflectivity case has a much sharper, off-resonant, spectral profile. This implies that the higher reflectivity is sensitive to the details of the laser and signal spectral profiles. A somewhat reduced sensitivity is obtained by increasing the pump intensity ratio r to 200, as shown in Fig. 7. This case corresponds to a very small Stokes-shifted pump, and in this case control of polarization and stray light is very important to satisfy the condition (15c) above; failure to accomplish this would result in a loss of reflectivity, or fidelity, as may be seen from Eqs.(12)-(13). Current technology might support pump ratios as high as 200. Finally, it should be noted that for gain-length products higher than 7, the denominator of the right-hand side of Eq. (32) may become zero for larger frequency offsets, leading to self-oscillation at one or more frequencies and pump depletion; the latter invalidates our analysis for those cases.

IV. First order Solution

With the zeroth-order results, one may now proceed to the first-order calculation. This is done by substituting the expressions (20) into Eqs. (10) and (11) to obtain estimates of the distortions introduced by phase mis-match terms. The sums for the distortions then exclude the phase-matched terms. Following this outline, write the following:

$$S_0(k,z) = A_0(z)\, S_0^{(0)}(k,z) + A_1(k,z), \qquad (22)$$

$$P_1(k,z) = B_0^*(z)\, P_1^{(0)}(k,z) + B_1(k,z) \qquad (23)$$

Where $S_0^{(0)}$, and $P_1^{(0)}$ are the solutions of the phase-matched equations, given by Eqs.(16)-(21). $A_0(z)\, S_0^{(0)}$ and $B_0^*(z)\, P_1^{(0)}$ are the zero-order solutions, assumed proportional to $P_{10}^*(-k)$ and $P_{10}(k)$, respectively. The last terms in Eqs. (22)-(23),$A_1(k,z)$ and $B_1(k,z)$, are first-order corrections, assumed to be both orthogonal and small compared to the zero-order solution; hence non-conjugate to the probe beam.

Here, $j_0(k_1) = (\theta_A/\theta_{P0})^2/\pi$, and $j_1(k_1) = (\theta_A/\theta_{P1})^2/\pi$. Here θ_A denotes the waveguide mode spacing, θ_{P0} is the angular radius of the pump beam, and θ_{P1} is the angular radius of the signal beam. Note that these expressions assume a band-limited uniform energy distribution among the transverse modes; model calculations have shown that this is not a critical assumption for the related SBS problem and the scaling remains the same.[16,17] After much algebra, one finds the following result for the spectrum of distortions:

$$\left\langle |A_1(k)|^2 \right\rangle = |g_1|^2 I_{P0}^2 I_{P10} |A_0|^2 \sum_{k_1,k_2}{}' j_0(k_1)\ \frac{j_0(k_1-k+k_2)\left((H_P I_{P0}/I_{S1}) j_1(k_2) + |a|^2 j_1(-k_2)\right)}{\left|\lambda_+ - \frac{(k_2+k_1)\cdot(k_2-k)}{ik_0}\right|^2} + O(1/N) \qquad (24)$$

where N is the number of modes excited by the probe beam. Eq. (24) represents the major result of this calculation; it is the transverse spectrum of non-conjugate power. Summing over k gives the total non-conjugate power, and this should be normalized by the conjugate Stokes output power, which is given by the following in the large-gain limit

$$I_{S0} = \Sigma |S_0(k,L)|^2 = |A_0|^2 \Sigma\, |A_+(k)|^2 = \left(\frac{H_P I_{P0}}{I_{S1}}\right) I_{P10} |A_0|^2 \qquad (25)$$

Now, using the expression for λ_+ in Eq. (24), one finds that the fidelity depends on the frequency offset. As the interaction moves off resonance, $|\mathrm{Im}(\lambda_+)|$ increases, and by inspection of the denominator of Eq.(24), one finds that the more mismatch terms contribute and the fidelity is reduced even further. The near-resonant case is simpler to analyze and corresponds to many cases of interest. Thus it

will be assumed that a near-resonant interaction ($|\Delta\omega|<\Gamma$) applies in the following.

$$R = \frac{\sum_k \langle |A_1(k,L)|^2 \rangle}{\Sigma\, |S_0(k,L)|^2} \simeq u \sum'_{k,k_1,k_2} \frac{j_0(k_1) j_0(k_1-k+k_2)\left(j_1(k_2)+|a_1|^2 j_1(-k_2)\right)}{\left[1+\left(\frac{(k_2+k_1)\cdot(k_2-k)}{|g_1| I_{P0} k_0}\right)^2\right]} \tag{26}$$

where we have factored out $|\lambda_+|^2$, and kept terms of order ΔH_P, and where

$$u = \frac{(H_P I_{P0}/I_{S1})}{\left(1+\frac{\Delta H_P I_{S1}}{I_{P0}}\right)^2} \tag{27}$$

$$|a_1|^2 = |a|^2\, I_{S1}/H_P I_{P0} = (I_{S1}/I_{P0})^2 \tag{28}$$

$$1 - H = 1 - \frac{1}{1+R} \tag{29}$$

where H is the fidelity loss of the conjugate beam with respect to the signal beam. Now to evaluate this expression, use the Zel'dovich approximation[16], for which many modes are excited and thus that the fidelity loss is small. Near-zero phase mismatch terms comprise the contribution to fidelity loss, as shown in Fig. 8. Let $\theta = k/k_0$ be the propagation angle corresponding to the transverse mode with Fourier component k. The angular separation between the pump beam and the signal beam is roughly θ_{LB} as shown. This separation should be much greater than the spread of either beam since we are assuming that the two beams are non-overlapping in angle. Thus, as shown, $|k_2 \pm k_1| \simeq |k_1 \pm k| \simeq k_0\theta_{LB}$. Also $k_2 - k = k_0\Delta\theta_2$, which is less than $2k_0\theta_{P1}$ in magnitude. Hence

$$1 - H \simeq \sum_{\left|\frac{k_0\Delta\theta_2\cdot\theta_{LB}}{g I_{P0}}\right| \le 1} j_0(k_1)\, j_0(k_1 + k_0\Delta\theta_2)\left[j_1(-k_2) + |a_1|^2 j_1(k_2)\right] \tag{30}$$

So $\frac{k_0}{g I_P}\cos\phi\, |\Delta\theta_2|\, \theta_{LB} < 1$, where ϕ = angle between $\Delta\theta_2$ and θ_{LB}. To make the integration easier, change variables from ϕ to $\phi_1 = \pi/2 - \phi$. Then one has the following:

$$\cos\phi = \sin\phi_1 \tag{31a}$$

$$|\phi_1| \sim |\sin\phi_1| < \frac{g I_{P0}}{k_0\theta_{LB}\,|\Delta\theta_2|} \tag{31b}$$

Summing over ϕ_1, assuming $g I_{P0}/k_0\theta_{LB} << \theta_{P1}$, and $\theta_{P0} < \theta_{P1}$ for typical cases of interest, one finds that

$$1 - H \simeq \frac{u g I_{P0}}{k_0\theta_{LB}\theta_A} \sum j_0(\theta_1) \frac{j_0(\theta_1+\Delta\theta_2)}{|\Delta\theta_2|}\left[j_1(-\theta_2) + |a_1|^2 j_1(\theta_2)\right] \tag{32}$$

Next, summing over θ_1, and θ_2,

$$1 - H \simeq \frac{u g I_{P0}(1+|a_1|^2)}{\pi k_0\theta_{LB}\theta_A} (\theta_A/\theta_{P0})^2 \sum \frac{1-|\Delta\theta_2|/\theta_{P0}}{|\Delta\theta_2|} \tag{33}$$

Finally, sum over $|\Delta\theta_2|$, remembering to include $|\Delta\theta_2|$ weighting in radial co-ordinates. Note that the bound on $\Delta\theta_2$ is set by the minimum of the signal beam divergence θ_{P1} (by definition) and the pump laser divergence θ_{P0} (because it is in the argument of j_0); the latter is assumed less as mentioned above. Thus one sums over θ_{P0}/θ_A discrete waveguide modes, and finds

$$1 - H \simeq \frac{C u g I_{P0}(1+|a_1|^2)}{k_0\theta_{LB}\theta_{P0}}. \tag{34}$$

where C is a constant that depends on the shapes of the mode distribution of the pump and signal, and is approximately equal to $1/2\pi$. The above result (34) is the concluding result of this section; it gives a simple lower-bound estimate for the fidelity loss for the higher-gain (G>3>ln(R)), higher-reflectivity (R>10) limit, in which many modes are occupied. This answer shows a dependence similar to that given by Hellwarth[15] for degenerate four-wave mixing in waveguides from the phase mismatch terms, in that the fidelity loss is inversely proportional to θ_{P0}, the pump beam divergence . This result represents a generalization of Zel'dovich's result for SBS and shows that the fidelity may be much improved with polarization-decoupled Brillouin-enhanced four-wave mixing, by increasing the pump-signal angle. Also from (34), in this regime it is seen that the fidelity loss is less strongly dependent on the mode structure of the signal beam, unlike SBS. Note that in this approximation the pump mutual fidelity H_P does affect the conjugation fidelity, through the factor u, but only a weak dependence is found for H_P not too small. Finally, it should be emphasized that this result applies for somewhat specialized cases of interest - given the variety of assumptions made above, there are undoubtedly many other possible regimes for which the expression for the fidelity loss differs from that given above, and for which the above approach is not relevant or not applicable.

IV. Conclusions

The technique of polarization-decoupled Brillouin-enhanced four-wave mixing for waveguide geometries has been analyzed using a perturbation expansion about the mode-matched solution. The mode-matched solution that constitutes the zero-order result yields the familiar equations for BEFWM[10,20], under the assumptions of spatially orthogonal pump and signal beams, and perfect pump mutual fidelity (H_P=1). These zero-order equations also obtain the more general dependence on the pump mutual fidelity, as well as the forward-backward pump ratio I_{P0}/I_{S1}, and the frequency offset $\Delta\omega/\Gamma$. Some sample results are shown, which agree with those of other authors.[10,20] Based on simple criteria involving pump laser frequency stability, noise insensitivity, and polarization quality, practical systems will yield a high-reflectivity, stable, conjugate beam when the total gain is less than six, and the forward-backward pump ratio is less than 200, yielding reflectivities on the order of several hundred.[13] Higher reflectivities have been achieved in various versions of BEFWM, however, in carefully controlled laboratory situations.[12,13] The first-order equations yield the nonconjugate fraction and the fidelity loss. The final result assumes a uniform distribution of energy within an angular band of transverse modes, and a higher-gain, higher-reflectivity regime. Based on similar calculations for SBS, it is reasonable to conclude that the result is not extremely sensitive to the shape of the mode distribution, although it may be somewhat sensitive to the angular spacing of the excited modes. It is found that the fidelity loss is inversely proportional to the pump beam divergence. The fidelity loss is also inversely proportional to the angular separation between the pump and signal. The result for fidelity loss may be summarized as being proportional to the e-folding gain length, and the square root of the Rayleigh ranges of the pump beam grating and the pump-probe grating. The result for fidelity loss has the same dependence on pump beam divergence as given by Hellwarth[15] for the phase-mismatch terms. It is found that the mutual pump fidelity, i.e., the overlap of the two pump beams, affects the reflectivity more than the fidelity, in the regime for which the approximations apply.

On the other hand, no experimental study addresses the fidelity loss issue for BEFWM, to the best of my knowledge - only SBS measurements are available at this time. Such an experiment might require relatively sensitive measurements of the fidelity for BEFWM, but might be very relevant for applications of phase conjugation requiring either near-perfect fidelity, or high reflectivities. In summary, we have determined theoretical nonlinear-optical limitations for reflectivity and fidelity for a particular method of phase conjugation, and for a particular regime of interest.

This work was supported by NERA internal research and development funds.

REFERENCES

1. B. Ya. Zel'dovich, V.I. Popovichev, V.V. Ragul'skii, and F.S. Faizullov, "On relation between wavefronts of reflected and exciting radiation in stimulated Brillouin scattering," JETP Lett. **15**, pp.109-111(1972).
2. N.F. Andreev, V.I. Bespalov, A.M. Kiselev, G.A. Pasmanik, and A.A. Shilov, "Wave-front inversion of weak optical signals with a large reflection coefficient," JETP Lett. **32**, pp.625-629(1980).
3. V.F. Efimkov, I.G. Zubarev, S. I. Mikailov, M.G. Smirnov, and V.B. Sobelev, "Polarization methods for improvement of the energy characteristics of wavefront -reversing mirrors," Sov. J. Quantum Electron. **14(2)**, pp.209-213(1984).
4. A.Z. Matveev, and G.A. Pasmanik, "Noise in a wavefront-reversal system with a preliminary amplifier," Sov. J. Quantum Electron. **14(2)**, pp.187-192(1984).
5. A.A. Zozulya, and V.T. Tikhonchuk, "Investigation of stability of four-wave mixing in photorefractive media," Phys. Lett. A **135**, pp.447-452(1989).
6. M. Cronin-Golomb, B. Fisher, J.O. White and A. Yariv, "Theory and applications of four-wave mixing in photorefractive media,"IEEE J. Quantum Electron. **20**, pp.12-30(1984).
7. N.G. Basov, et. al.,"Investigation of a hypersonic wavefront reversing mirror operating in a master-oscillator-amplifier configuration," Sov. J. Quantum Electron.**16(6)**, pp.788-791(1986).
8. M.J. Damzen, M.H.R. Huchinson, and W.A. Schroeder, "A single-frequency phase-conjugate laser resonator using stimulated Brillouin scattering," Opt. Lett. **12**, pp.45-47(1987).
9. J.H. Marburger and Juan F. Lam,"Nonlinear theory of degenerate four-wave mixing,"Appl. Phys. Lett. **34(6)**, pp.389-391(1979).
10. W.A. Schroeder, M.J. Damzen, and M.H.R. Hutchinson, "Polarization-decoupled Brillouin-enhanced four-wave mixing," IEEE J. Quant. Electron. QE-25, pp.460-469(1989).
11. K.D. Ridley and A.M. Scott, "Comparison between theory and experiment in self-pumped Brillouin-enhanced four-wave mixing," J. Opt. Soc. Am. B **6**, pp.1701-1708(1989).

12. A.M. Scott and K.D. Ridley, "A review of Brillouin-enhanced four-wave mixing," IEEE J. Quantum Electron. **QE-25**, pp.438-459(1989).
13. J.R. Ackerman and P.S. Lebow, "Improved performance from noncollinear pumping in a high reflectivity Brillouin-enhanced four-wave mixing phase conjugator," IEEE J. Quantum Electron. **QE-25**, pp.479-483(1989).
14. M.D. Skeldon and R.W. Boyd, "Transverse-mode structure of a phase-conjugate oscillator based on Brillouin-enhanced four-wave mixing," IEEE J. Quantum Electron. **QE-25**, pp.588-599(1989).
15. R.W. Hellwarth, "Theory of Phase Conjugation by four-wave mixing," IEEE J. Quantum Electron. **QE-15**, pp.101-109,(1979).
16. B.Ya. Zel'dovich and T.V. Yakovleva,"Small-scale distortions in wavefront reversal of a beam with incomplete spatial modulation(stimulated Brillouin backscattering, theory)," Sov. J. Quantum Electron. **10(2)**, pp.181-186(1980).
17. R. Holmes and A. Flusberg, "Analytic expressions for phase-conjugation fidelity for stimulated scattering in slab-waveguide geometries," J. Opt. Soc. Am. B **5**, pp.1285-1288(1988).
18. P.W. Maker and R.W. Terhune, "Study of optical effects due to an induced polarization third-order in the electric field strength," Phys. Rev. **137**, pp.A801-A813(1965).
19. R. Holmes and A. Flusberg, "Rotationally invariant theory of stimulated Raman scattering," Phys. Rev. A **37**, pp.1588-1596(1988).
20. B. Ya. Zel'dovich, N.F. Pilipetsky, V.V. Shkunov, "Principles of Phase Conjugation," Chap. 2 (Springer-Verlag Berlin 1985).
21. P. Suni and J. Falk, "Measurements of stimulated Brillouin scattering phase-conjugate fidelity," Opt. Lett. **12**, pp.838-840(1987).
22. W. Kaiser and M. Maier,"Stimulated Rayleigh, Brillouin, and Raman Spectroscopy," in Laser Handbook, F.T. Arrechi, and E.O. Schulz-Dubois, p.1113(North Holland, 1972)

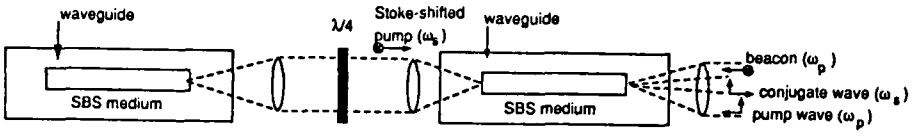


Figure 1. Schematic of polarization-decoupled, Brillouin-enhanced four-wave mixing in a waveguide geometry. The two fields at the pump laser wavelength enter the left side, with orthogonal polarizations. The two Stokes-shifted beams travel in the opposite direction and are also mutually orthogonal.

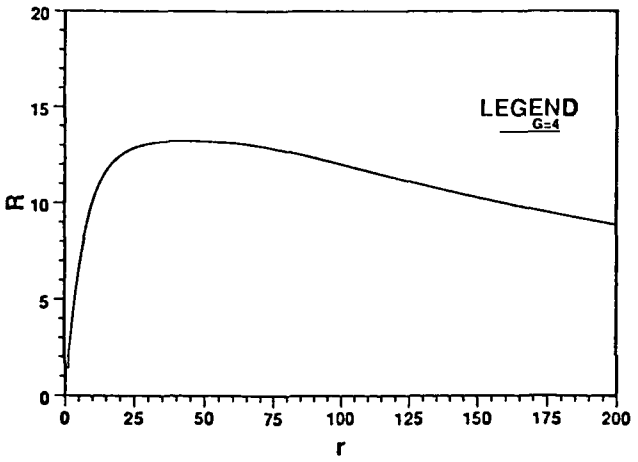


Figure 2. Reflectivity R versus forward-backward pump intensity ratio r for a gain-length product G of 4; each point is the maximum of the spectral reflectivity profile.

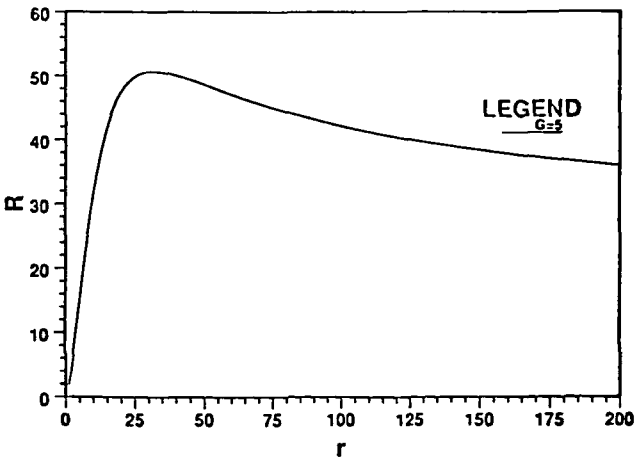


Figure 3. Reflectivity R versus forward-backward pump intensity ratio r for a gain-length product G of 5; each point is the maximum of the spectral reflectivity profile.

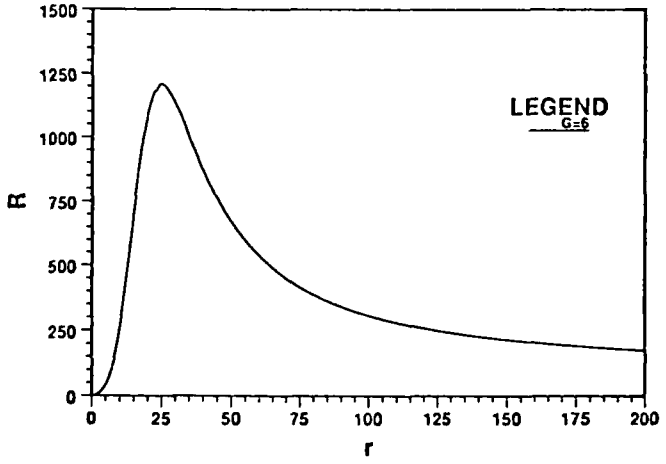


Figure 4. Reflectivity R versus forward-backward pump intensity ratio r for a gain-length product G of 6; each point is the maximum of the spectral reflectivity profile.

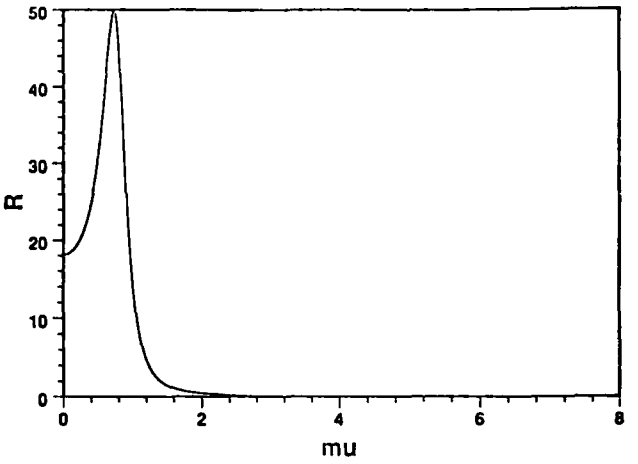


Figure 5. Spectral reflectivity profile versus mu = $\Delta\omega T$, for the peak reflectivity of the curve shown in Fig.3, for which G = 5 and r = 25.

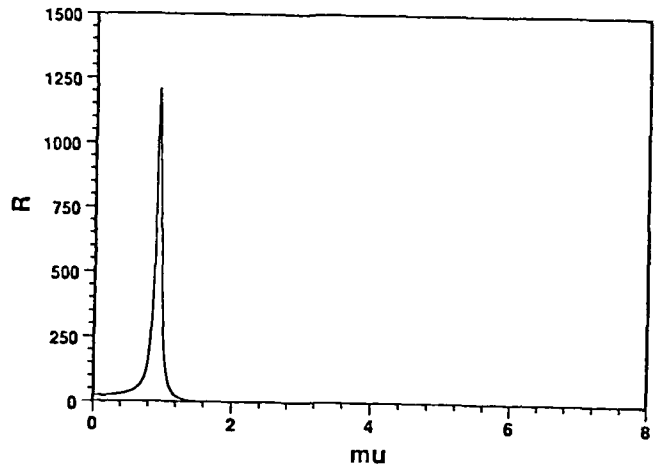


Figure 6. Spectral reflectivity profile versus mu = $\Delta\omega\tau$, for the peak reflectivity of the curve shown in Fig.3, for which G = 6 and r = 25.

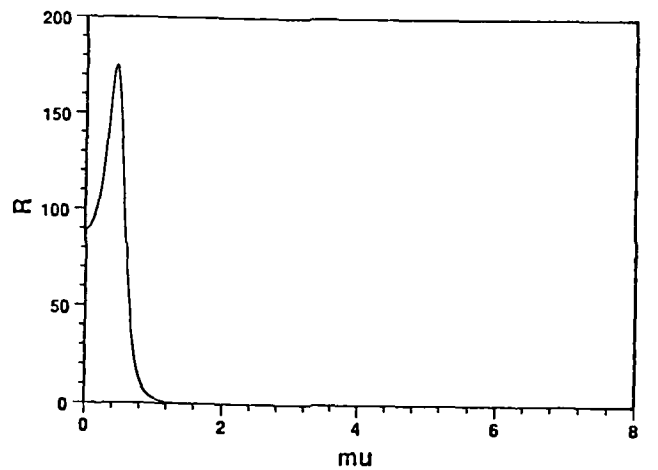


Figure 7. Spectral reflectivity profile versus mu = $\Delta\omega\tau$, for the peak reflectivity of the curve shown in Fig.3, for which G = 6 and r = 200.

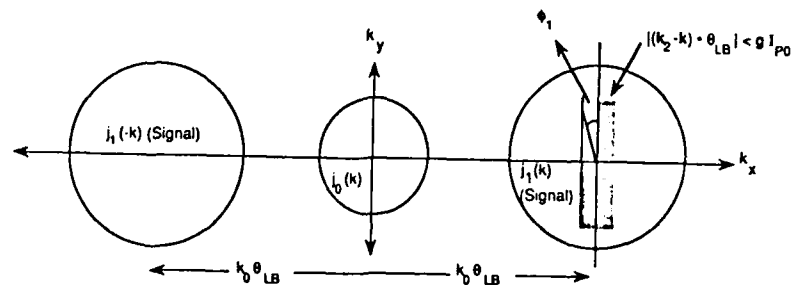


Figure 8. Schematic of angular separation of pump and signal beams; definitions of relevant variables.

COHERENT TWO-PHOTON EXCITATION OF ALKALI METAL VAPORS

M. T. Jacoby, D. G. Harris, J. A. Goldstone,
J. Stone and R. Whitley

Rockwell International-Rocketdyne Division
Canoga Park, California 91303

Abstract

Na vapor was excited by two narrowband, counter-propagating cw dye lasers operating near the 3S-3P and 3P-4D transitions. Fluorescence from the 4P-3S transition was monitored as a function of small pump detunings from the Na transition frequencies for given intensities. Initial results are in qualitative agreement with the predictions of the Frequency Adding MEdia (FAME) theory.

Introduction

It has been predicted that, under appropriate conditions, it should be possible to create large population inversions in multi-level quantum systems through coherent, near-resonantly enhanced, multiple photon pumping [1-3]. When these inversions occur between nonadjacent levels it becomes possible to create a frequency up-converting laser-pumped laser. The process by which these population inversions are created has been dubbed FAME, which is an acronym for Frequency Adding MEdia. Figure 1 displays the traditional four-level and photon cascade pumping schemes. By comparison, Figure 2 indicates the coherent FAME pumping scheme we wish to utilize.

The work reported here represents the first step toward experimental demonstration of the sometimes counter-intuitive predictions of the theory described in [1-3] and will hopefully lead to a demonstration of coherent, multiple photon pumping of a frequency up-converting laser. Sodium vapor has been chosen for the first set of experiments for a variety of reasons: (1) the Einstein A coefficients in Sodium are appropriate for creation of a 4P - 3S population inversion [see Figure 3], (2) the required pump wavelengths (589 nm and 569 nm) and intensities are within the range of current cw dye lasers, (3) the potential lasing transition (4P - 3S) is at 330 nm in the near UV where good reflective optics and detectors are available, and (4) the required Na densities are easily obtained using conventional heatpipe technology. However, the lower level of the lasing transition is also the ground state of the atom. Our theory predicts that even under this condition we should still be able to create large population inversions in Sodium. We have identified a number of other candidate gain media which we believe should lase in the IR, visible and vacuum UV.

The principal results reported here are the comparison of theoretical predictions and experimental measurements of the intensity of 330 nm fluorescence as a function of one and two photon pump detunings. The initial experimental measurements demonstrate good qualitative agreement with predictions and also provide us with optimization conditions for the small signal gain experiments which are planned.

Experimental Apparatus

The experimental layout for the initial Na fluorescence and ionization measurements is shown in Figure 4. Coherent 699-29 Autoscan Dye Lasers operating with Rhodamine 6G dye provide the visible pump sources at 569 nm and 589 nm. The radiation from the dye lasers entered a heatpipe cell in counter-propagating directions to reduce the Doppler broadening of the atomic transitions.

The lasers, which had a linewidth of less than 1 MHz and an absolute wavelength accuracy of plus or minus 200 MHz, could be scanned in steps as small as 1 MHz. When carefully calibrated with an I_2 cell, the absolute wavelength can be plus or minus 60 MHz. A commercial wavemeter (Burleigh WA-20) provided a nominal check on wavelength during data acquisition. The half-wave retarder, lens and polarizing beamsplitter enabled control of the pump lasers' optical densities and consequently the Rabi frequencies.

Na metal of 99.99 percent purity is heated with 99.9999 percent pure He buffer gas in a heatpipe, with an interaction length of 10 cm, to produce the FAME vapor medium. A 0.0625 inch diameter tungsten wire mounted on a BNC post inside the heatpipe is used to collect ions. The 330 nm fluorescence is detected through a Corning GS7-54-1 filter (T = 85% at 300 nm) by a one-third meter spectrometer with a 2400 1/mm grating blazed at 250 nm and a 1P28 photomultiplier tube. Although shown in the schematic, the IR detectors have not yet been integrated into the experiments.

The data acquisition process is under the control of an IBM PC/AT. It sets the wavelengths of the two dye lasers and then scans the frequency of the dye laser operating near 569 nm as the 330 nm fluorescence is monitored. The process is repeated as the lasers are detuned from the starting wavelengths in steps of typically 1Ghz. In this manner a three-dimensional profile of fluorescence intensity versus detunings of the excitation lasers is generated.

Results

A typical excitation spectra is shown in Figure 5. Although the spectra consists of Na 4P-3S fluorescence (330 nm), its structure is attributed to the 4 possible excitation pathways from the two 3S hyperfine structure ground states (F=1,2) to the $4D_{3/2}$ and $4D_{5/2}$ fine structure states.

A series of twenty-one spectra comprise the three-dimensional detuning space plot shown in Figure 6a. Here, the signal from the $4\text{-}D_{5/2}$-3S(F=2) "transition" (line one in Figure 5) is plotted as both pumps are detuned in steps of 1 GHz about their respective Na transition frequencies, and the 569 nm pump is scanned over an interval of 2 GHz in 10 MHz steps. "One Photon Detuning" denotes detuning of the 589 nm pump from the Na [3S(F=2) - $3P_{3/2}$] transition frequency. "Two Photon Detuning" denotes the detuning of the combined 589 nm and 569 nm pumps from the Na [3S(F=2) - $4D_{5/2}$] transition frequency. The angular Rabi frequencies of the 589 nm and 569 nm pumps were 1.35 Grad/sec and 0.55 Grad/sec for $\Omega_{589}/\Omega_{569} \approx 2.5$. The Na atom density was approximately 2×10^{15}/cc.

The theoretical three-dimensional plot shown in Figure 6b was generated with Doppler broadening taken into account and $\Omega_{589}/\Omega_{569} = 3$. Note the difference in scale is such that the theoretical plot only covers the central portion of the experimental plot. Comparing the two plots, we see their general appearance is quite similar. In particular, both show the skew about the "two photon detuning" axis zero, which is caused by the mismatch in frequency of the two pumps.

Conclusions and Future Work

Results have been presented in qualitative agreement with the predictions of the FAME theory. Experiments are underway to provide more quantitative and incontrovertible confirmation of the theory. For example, the "double ridge" fluorescence distributions shown in Figures 7a and 7b are predicted for Rabi frequency ratios $\Omega_{589}/\Omega_{569} = 1/3$ and 1/9.

The fluorescence studies enable the optimization of the pumping parameters. Small signal gain measurements will be made once they are optimized. Lasing of the Na system at 330 nm will then hopefully follow.

Acknowledgement

The authors gratefully acknowledge the excellent technical and design assistance of E. Rinehart, J. Martin and I. Charnabroda. This work was supported in part by SDIO/IST Contract No. N00014-87-C-0470.

References

1. J. A. Goldstone, J. Stone, and M. M. Johnson, Non-linear Optical Beam Manipulation, Beam Combining, and Atmospheric Propagation, Proceedings SPIE, 874, 188-197, SPIE, Bellingham, WA. (1988)

2. J. A. Goldstone, United States Patent, #4,807,240. (Feb. 1989)

3. J. P. Stone and J. A. Goldstone, Proceedings International Conference on Lasers '88, 24-31, STS Press, McLean, VA. (1989)

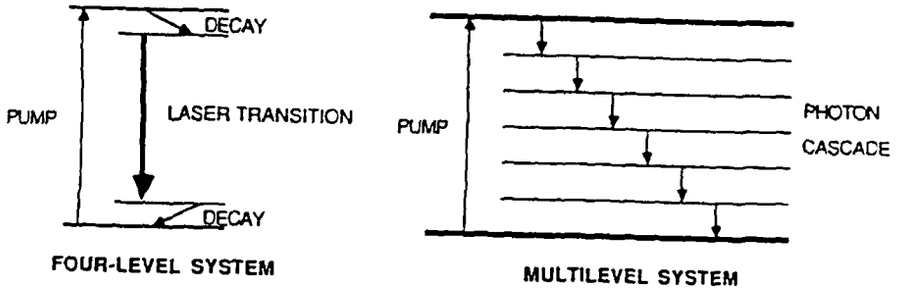


Figure 1. Standard laser pumping scheme.

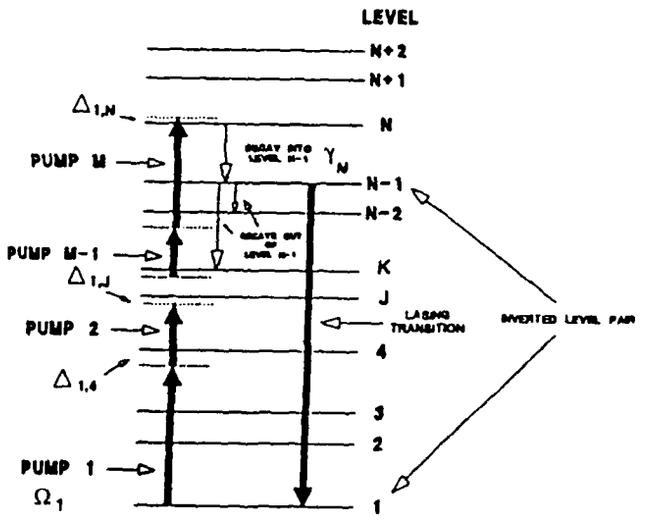


Figure 2. FAME laser pumping scheme.

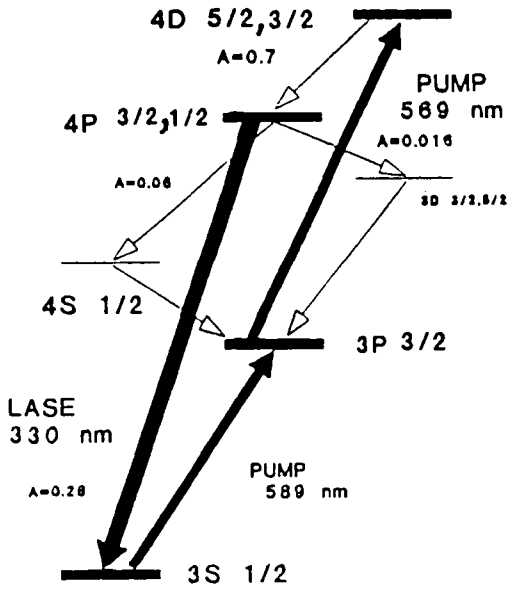


Figure 3. Na system used for initial FAME verification experiments.

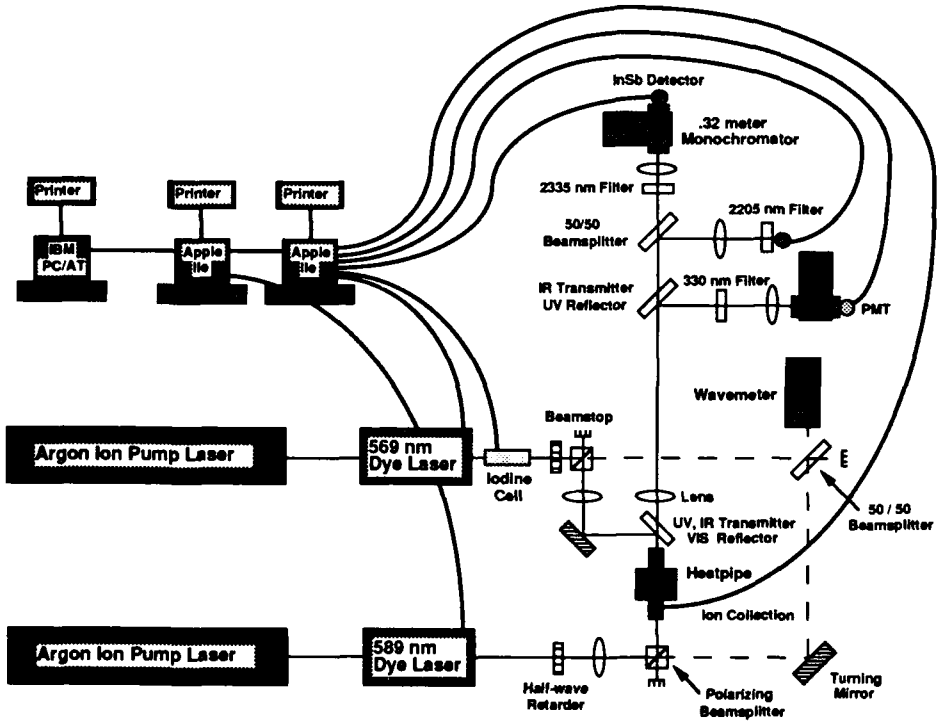


Figure 4. Experimental schematic for FAME fluorescence and ionization measurements.

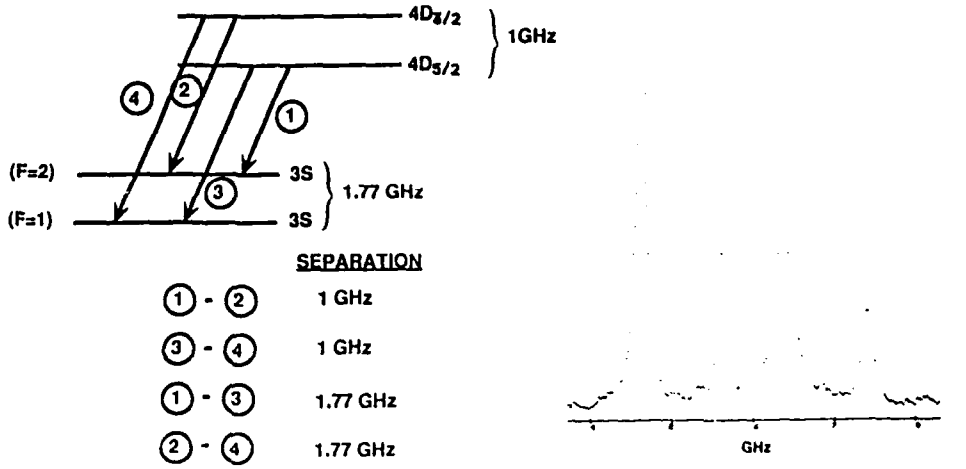


Figure 5. A typical Na excitation spectra with rationale for the structure seen.

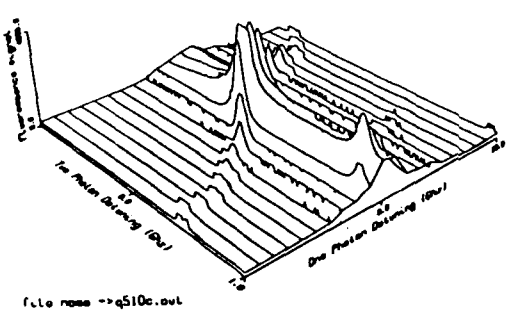


Figure 6 a. Experimental results for Ω589/ Ω569 = 2.5

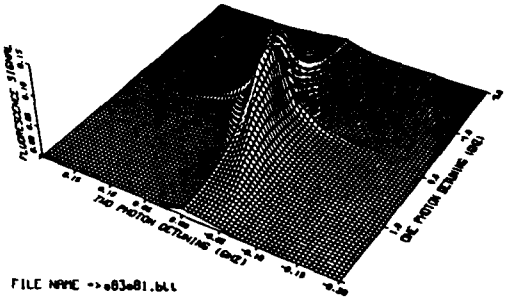


Figure 6 b. FAME theoretical prediction for Ω589/ Ω569 = 3.0

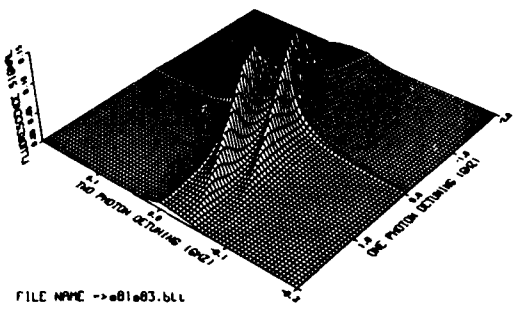


Figure 7a. FAME "double ridge" theoretical prediction for Ω589/Ω569 = 1/3

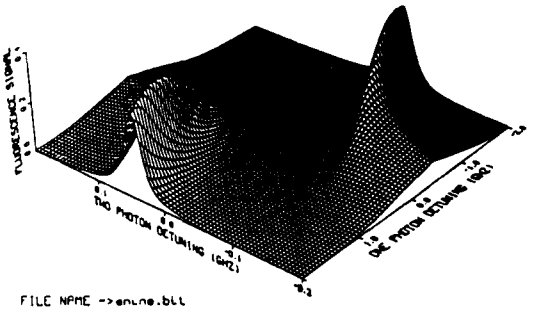


Figure 7b. FAME "double ridge" theoretical prediction for Ω589/Ω569 = 1/9

EFFECT OF ATOMIC STATE COHERENCE ON THREE-LEVEL DYNAMICS

D.A. Cardimona, M.P. Sharma, and M.A. Ortega

Air Force Center for Nonlinear Optics
Quantum Optics Branch
WL / AROM
Kirtland AFB, NM 87117-6008

Abstract

For a three-level atom with two excited states each dipole-coupled to a common ground state, we have found a particular linear combination of the atomic states which will not experience Rabi oscillations and their associated collapses and revivals. If the atom is initially prepared in this combination state, the atomic population will be coherently trapped there, and the dynamical behavior will be constant in time.

Introduction

The well-known Jaynes-Cummings model for light-matter interactions[1] in which a single two-level atom interacts with a single-mode radiation field is a very popular theoretical model. It is simple enough to yield many analytic results while still retaining a great deal of interesting quantum features of atom-field interactions such as the collapse[2] and revival[3] of the Rabi oscillations in the atomic inversion. Recent experiments[4] have made the Jaynes-Cummings model and its generalizations of much more than academic importance. The quantum collapse and revival for a single atom interacting with a single radiation mode has actually been observed[5].

In this paper we investigate the dynamics of the interaction between a single mode radiation field and a three-level atom in the "V-configuration" (two excited states each dipole-coupled to a common ground state). To conveniently display the dynamical dependence on the average photon number and the photon number uncertainty, we use an artificial Lorentzian probability distribution for the photons in the quantized field. Use of this artificial photon distribution instead of a more experimentally obtainable one such as the Poissonian or Binomial distributions in no way alters the conclusions we arrive at in this work. It is merely a convenience. In the general case, we find the expected collapses and revivals of the Rabi oscillations. However, we have found that if the atom is prepared in a special way, the Rabi oscillations in the atomic population and their accompanying collapses and revivals diminish in strength and in some instances totally disappear. The special preparation involves populating the atomic states in a particular combination of amplitudes. Essentially what must be done is prepare the atom in the particular linear combination of atomic states in which the population will be coherently trapped. Population trapping should be possible in any system in which there are two or more transition channels that can coherently interfere[6,7].

Dynamics

Consider a three-level atom with ground state $|g\rangle$ and two closely-spaced excited states $|1\rangle$ and $|2\rangle$ each coupled to $|g\rangle$ by dipole moments $\mathbf{d}_1$ and $\mathbf{d}_2$. In the Schrodinger picture, the time-dependent wavefunction is

$$|\psi(t)\rangle = \sqrt{F_n}\exp(-i(n\omega+\omega_g)t)[b_{gn}(t)|n,g\rangle + b_{1n}(t)e^{i\Delta t}|n-1,1\rangle + b_{2n}(t)e^{-i\Delta_2 t}|n-1,2\rangle] \quad (1)$$

with F_n the photon statistical distribution, $\Delta=\omega-(\omega_1-\omega_g)=\omega-\omega_{1g}$, $\Delta_2=\omega_2-\omega_1-\Delta=\omega_{21}-\Delta$, and $|n,i\rangle$ is shorthand notation for the non-interacting atom/field product state $|n\rangle|i\rangle$ in which the field has n_i photons and the atom is in state $|i\rangle$. In the rotating wave approximation, Schrodinger's equation leads to

$$\frac{db_{gn}}{dt} = \frac{1}{2}\{\Omega_{1n} b_{1n} e^{i\Delta t} + \Omega_{2n} b_{2n} e^{-i\Delta_2 t}\} \quad (2a)$$

$$\frac{db_{1n}}{dt} e^{i\Delta t} = -\frac{1}{2}\Omega_{1n}^{*} b_{gn} \tag{2b}$$

$$\frac{db_{2n}}{dt} e^{-i\Delta_2 t} = -\frac{1}{2}\Omega_{2n}^{*} b_{gn} , \tag{2c}$$

where the Rabi frequencies are given by

$$\Omega_{jn} = g_j \sqrt{n} , \tag{3}$$

with $g_j \propto d_j$.

For a general three-level problem, there will be three oscillation frequencies (dressed-state energies of the interacting atom / field system) possible (for a given n). If we tune the applied field to a special frequency between the two excited states such that

$$\Delta = \frac{\omega_{21} g_1^2}{g_1^2 + g_2^2} , \tag{3}$$

then one of these frequencies will be zero. In this case, the resulting Stark shifts of the dressed-states are

$$\lambda_{\mu n} = \lambda_{0,\pm n} = 0, -\omega_{21}\frac{g_1^2 - g_2^2}{g_1^2 + g_2^2} \pm \sqrt{\omega_{21}^2 + |\Omega_{1n}|^2 + |\Omega_{2n}|^2} \tag{4}$$

With the Laplace transform of $b_{gn}(t)$ given by $B_{gn}(\lambda)$, the time-dependent atomic state amplitudes are given by

$$b_{kn}(t) = \sum_{m=0,+,-} \lim_{\lambda \to -\lambda_{\mu n}} B_{kn}(\lambda)(\lambda + \lambda_{\mu n}) exp(-\frac{i}{2}\lambda_{\mu n} t) \; ,k = g,1,2 , \tag{5}$$

and the probability of being in state |k> at time t is

$$P_k(t) = \sum_n F_n |b_{kn}(t)|^2$$

$$= \sum_n F_n \, | \lim_{\lambda \to 0} \lambda B_{kn}(\lambda) + \lim_{\lambda \to -\lambda_{+n}} (\lambda + \lambda_{+n}) B_{kn}(\lambda) e^{-i\lambda_{+n} t/2} + \lim_{\lambda \to -\lambda_{-n}} (\lambda + \lambda_{-n}) B_{kn}(\lambda) e^{-i\lambda_{-n} t/2} \, |^2 . \tag{6}$$

The presence of the time-independent first term (i.e., zero oscillation frequency) is due to the special tuning condition stated above. For the sake of convenience in varying the mean and the variance in the number of photons, we utilize a Lorentzian photon probability distribution

$$F_n = \frac{1}{(n - \bar{n})^2 + \Gamma^2} , \tag{7}$$

where $\bar{n}$ is the mean photon number and Γ is the half width at half max for the photon distribution.

In Fig. (1) we prepare the atom initially with equal amplitudes in each state ($b_{g0}=b_{10}=b_{20}=1/\sqrt{3}$), we set the two dipole transition strengths equal to each other ($g_1=g_2=1$) and the excited state separation equal to 1 arbitrary frequency unit ($\omega_{21}=1$), and we let $\bar{n}=25$. In this case the laser detuning Δ turns out to be 1/2 a frequency unit. In Fig. (1a), $\Gamma=5$ and we see

the expected collapses and revivals for the ground state population $P_g(t)$. For Fig. (1b) the parameters are the same except that Γ=0.01. Here the photon distribution acts like a δ-function centered at $\bar{n}$=25. In this case the field is acting classically and we see the expected Rabi oscillations of $P_g(t)$ with no collapse and revival exhibited.

The parameters for Fig. (2) are the same as in Fig. (1), including having the atom initially prepared with equal populations in each state, however now the excited state amplitudes are 180^o out-of-phase ($b_{g0}=b_{10}=-b_{20}=1/\sqrt{3}$). Here we notice population being trapped to a certain extent in the excited states due to the coherent interference between the two dipole transitions. If the photon distribution width were reduced to 0.01, we would again see the trapping and classical Rabi oscillations.

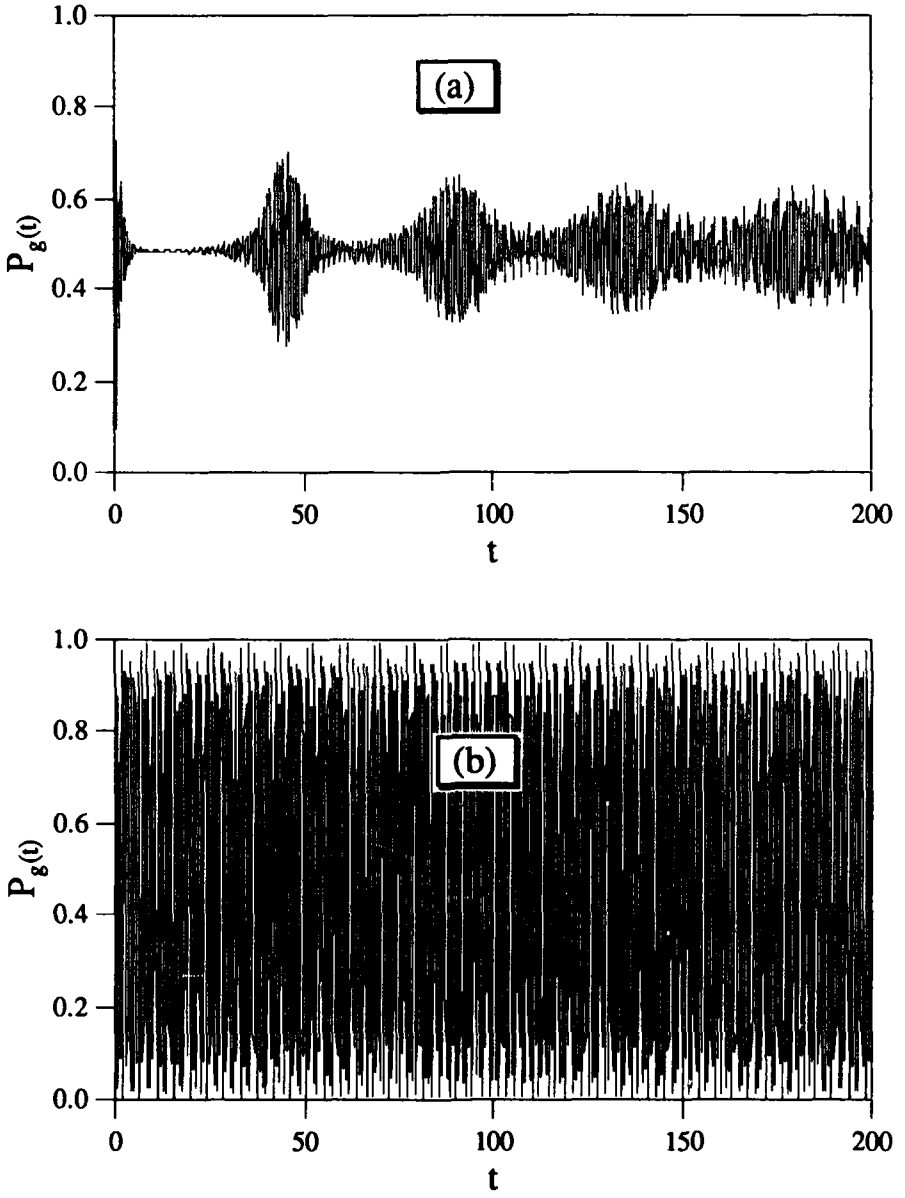


Fig. 1: The ground state population $P_g(t)$ with the atom initially prepared with equal amplitudes, ($b_{g0}=b_{10}=b_{20}=1/\sqrt{3}$), and with $g_1=g_2=1$, n=25, and in (a) Γ=5 and in (b) Γ=0.01.

We can see this coherent trapping to an even greater extent if we initially prepare the atom with half the population in each excited state, but again 180^o out-of-phase ($b_{g0}=b_{10}=-b_{20}=1/\sqrt{2}$). This can be seen in Fig. (3), where all parameters are the same as in the previous figures except for the atomic state amplitudes. Note, however, that even when the trapping is nearly complete, the collapse and revival phenomena are quite apparent.

As can be seen from Figs. (1-3), the Rabi oscillations and their collapses and revivals when the photon distribution is relatively broad appear to be very ordinary in their behavior. However, the coherent trapping of the atomic population in the excited states leads to a very intriguing question. Is it possible to totally eliminate the time dependence of the atomic state populations? We will investigate this possibility next.

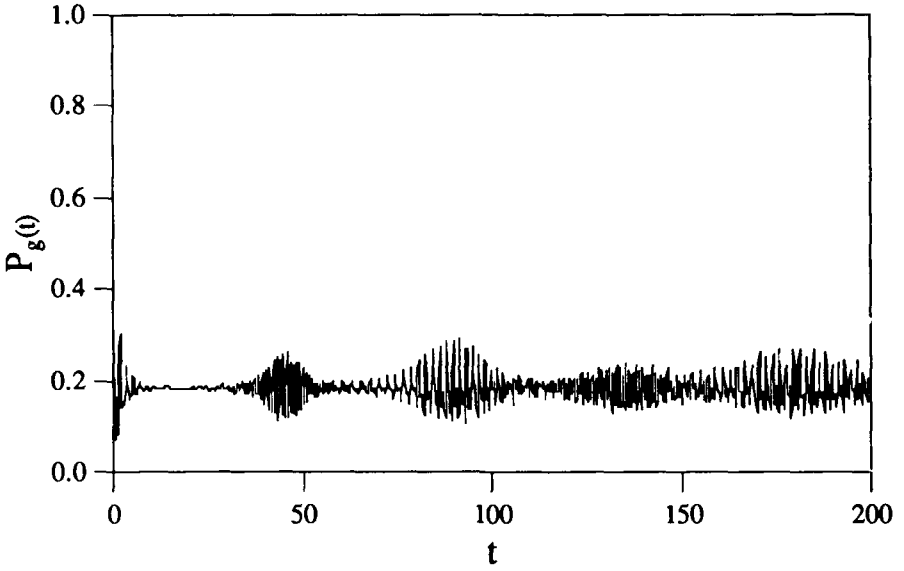


Fig. 2: Everything is the same here as in Fig. (1a) except that the initial amplitudes are $b_{g0}=b_{10}=-b_{20}=1/\sqrt{3}$

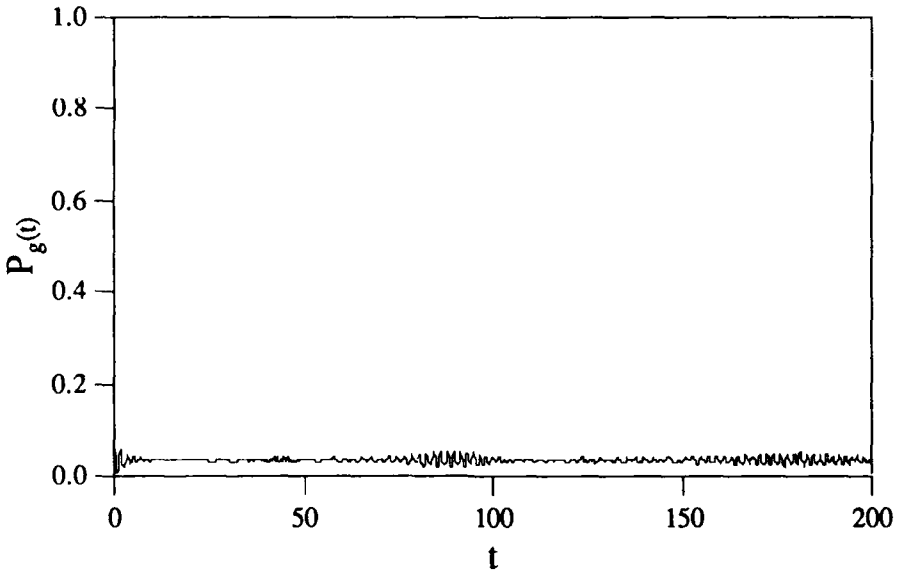


Fig. 3: Everything is the same here as in Fig. (1a) except that the initial amplitudes are $b_{g0}=0$ and $b_{10}=-b_{20}=1/\sqrt{2}$.

Turning off the time dependence

In the last section we found that coherent trapping of the atomic population led to a decrease in the time-dependent Rabi oscillations and their associated collapses and revivals. In this section we will find a better set of trapping amplitudes which will shut off the Rabi oscillations more efficiently. From Eq. (6) we see that in order to make P_g (t) a

constant in time we need $b_{gn}(t)$ to be constant in time. This requires

$$\lim_{\lambda \to -\lambda_{\pm n}} (\lambda+\lambda_{\pm n})B_{kn}(\lambda)=0\,, \tag{8}$$

Performing the algebra to find $B_{gn}(\lambda)$ and substituting it and $\lambda_{\pm n}$ from Eq. (4) into this yields two equations which upon further manipulation simplify to

$$b_{10}\Omega_{1n}+b_{20}\Omega_{2n}=0 \tag{9a}$$

$$-2\omega_{21}\Omega_{1n}b_{10}=i\,(|\Omega_{1n}|^2+|\Omega_{2n}|^2)b_{g0}. \tag{9b}$$

These equations, along with conservation of population, will yield the special initial conditions required to produce the time-independent dynamics we are interested in. To be specific, we will evaluate these special amplitudes at $n=\bar{n}$.

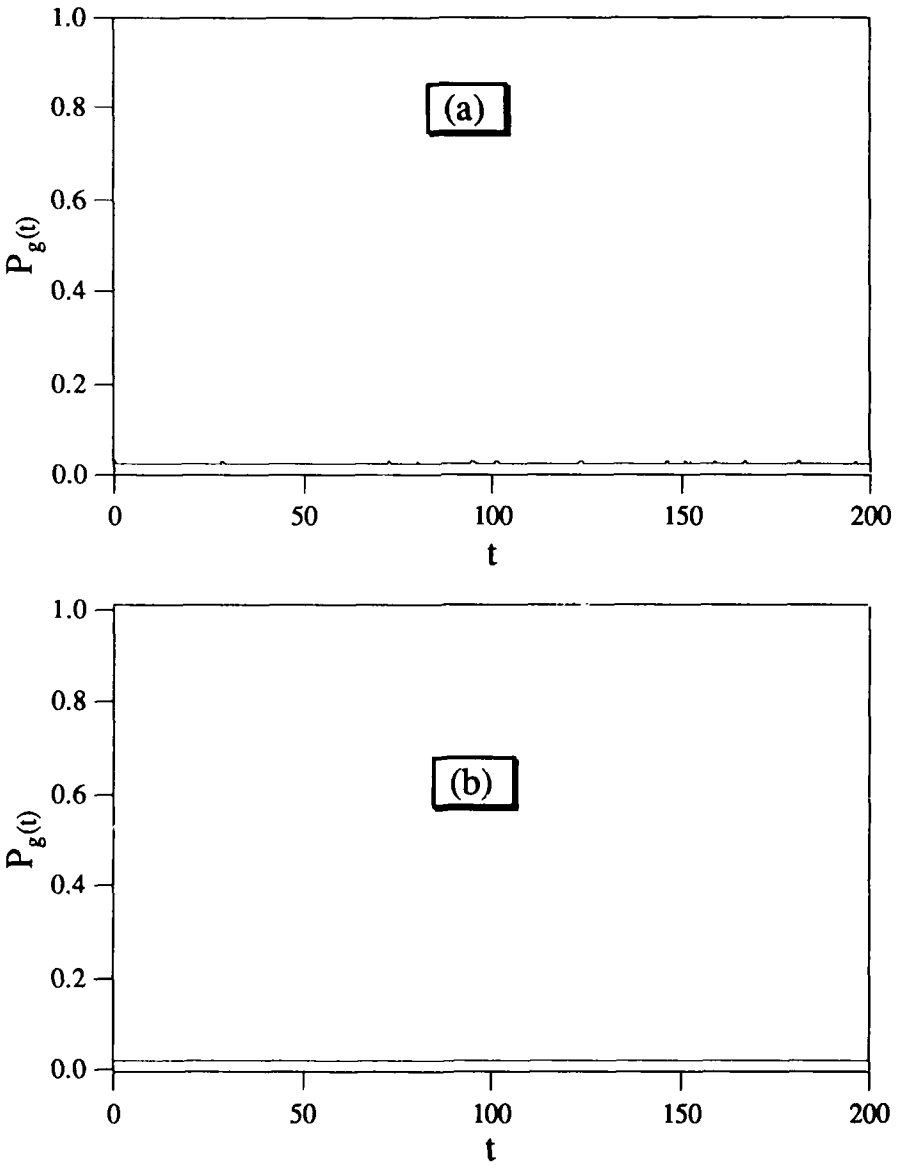


Fig. 4: Everything is the same here as in Fig. (1) except that the atom is initially prepared with the special amplitudes given by Eqs. (9), $b_{g0}=0.14$, $b_{10}=-b_{20}=-i.70$.

We will now utilize these special amplitudes with the parameters of Figs. (1)-(3). Corresponding to Fig. (1) with $\omega_{21}=1$ unit, $g_1=g_2=1$ unit, and $\bar{n}=25$, we use Eqs. (9) to find $b_{g0}=0.14$, $b_{10}=-b_{20}=-i.70$ and then plot $P_g(t)$ in Fig. (4). As expected with these special amplitudes, the quantum interference between the two transitions results in very substantial population trapping in the excited states. The sum P_1+P_2 ($=1-P_g$) starts at $2(0.7)^2=0.98$ and remains there as long as the applied field is on. The small time-dependent ripple in Fig. (4a) is due to the fact that these special amplitudes make the populations time-independent *only* for $n=\bar{n}=25$. Since we have allowed a substantial width to exist in the photon distribution ($\Gamma = 5$), the sum over n will lead to a non-perfect time-independence. Note that the $\pm 1/\sqrt{2}=\pm 0.707$ chosen for b_{10} and b_{20} in Fig. (3) is very close to these special amplitude values. This explains the relatively efficient trapping that occurred in that case. The time-dependent wiggles disappear when the photon width is reduced to .01 in Fig.(4b). In this case, the only photon number of any significance is $\bar{n}$, just that number for which the special amplitudes were calculated.

Discussion

We have investigated the population dynamics of a three-level atom in the "V-configuration" interacting with a quantized field having a Lorentzian photon distribution. The Lorentzian distribution is used merely as a convenience so that the photon mean and variance can be easily changed. In the general case, a δ-function-like distribution results in normal Rabi oscillations and a broad photon distribution provides the expected collapses and revivals of these Rabi oscillations.

We have found a set of initial atomic state amplitudes for which the usual time-dependent oscillations, collapses, and revivals vanish. Preparing the atom initially in this special way forces the atomic population to remain coherently trapped in this configuration. The dressed- state energy of this particular linear combination of bare-atom states is zero, so that $e^{iEt}=1$ and the population remains constant in time - as long as the applied field remains on.

Preparing the atom initially in the special amplitude configuration described above may be quite tricky. Therefore, it would be nice to find an easy way to set up the correct atomic amplitudes. It appears that the linear combination of bare-atom states that we have found is a dressed-state that is decoupled from all field modes[7]. If this is indeed the case, then allowing spontaneous emission into our problem should eliminate the initial preparation step in the following way. No matter how the atom is initially prepared, spontaneous decay will redistribute the atomic-state amplitudes into our desired configuration. Population will decay out of all other configurations into the special one, and then remain there as it is decoupled from the spontaneous field modes. This is now under investigation.

References

1. E.T. Jaynes and F.W. Cummings, Proc. IEEE 51, 89 (1963).
2. F.W. Cummings, Phys Rev. 140, A1051 (1965); P.L. Knight and P.W. Milonni, Phys Rep. C 66, 21 (1980).
3. J.H. Eberly, N.B. Narozhny, and J.J. Sanchez-Mondragon, Phys. Rev.Lett. 44, 1323 (1980); N.B. Narozhny, J.J. Sanchez-Mondragon, and J.H.Eberly, Phys. Rev. A 23, 236 (1981); H.I. Yoo, J.J. Sanchez-Mondragon, and J.H. Eberly, J. Phys. B 14, 1383 (1981).
4. P. Goy, J.M. Raimond, M. Gross, and S. Haroche, Phys. Rev. Lett. 50, 1903 (1983); G. Gabrielse and H. Dehmelt, Phys. Rev. Lett. 55, 67 (1985); D. Meschede, H. Walther, and G. Muller, Phys. Rev. Lett, 54, 551 (1985).
5. G. Rempe, H. Walther, and N. Klein, Phys. Rev. Lett. 58, 353 (1987).
6. H. R. Gray, R. M. Whitley, and C. R. Stroud, Jr., Opt. Lett. 3, 218 (1978); B. J. Dalton and P. L. Knight, Opt. Comm. 42, 411 (1982); P. M. Radmore and P. L. Knight, J. Phys. B 15, 561 (1982).
7. D.A. Cardimona, M.G. Raymer, and C.R. Stroud, Jr., J. Phys. B 15, 55 (1982).

THREE-PHOTON POPULATION DYNAMICS OF A FOUR-LEVEL ATOM INCLUDING A LOSS MECHANISM

D.A. Cardimona and M.P. Sharma

Air Force Center for Nonlinear Optics
Quantum Optics Branch
WL/AROM
Kirtland AFB, NM 87117-6008

Abstract

The population dynamics of a four-level atom, with decay from the highest level, interacting with three arbitrarily intense laser fields is studied. In a previous paper *[M. P. Sharma and J. A. Roversi, Phys. Rev. A 29, 3264 (1984)]*, this four-level system was investigated with no decay included. In the present work we have included decay out of the highest level and found that the dynamics are altered dramatically. We do not find conditions under which population is transferred efficiently into the highest level. In fact, we find that the ground state population decays out of the system at a substantially reduced rate. We have introduced a two-level model that explains this reduced decay rate.

Introduction

The excitation of multilevel systems by laser fields has been studied extensively by various researchers in the last several years. Knowledge of the population dynamics and its variation with system parameters is crucial to the topics of present-day experimental interest such as ionization, dissociation, or selective isotope separation from the excited state. Sharma and Roversi [in Phys. Rev. A 29, 3264 (1984)] studied the coherent excitation of a four-level atom with four laser fields of arbitrary strength, where one of the laser fields is such that its frequency is equal to the sum of the other three field frequencies and it couples the ground state with the highest excited state. Quite interesting results were predicted, including trapping of the population in the initially populated state under three-photon absorption for a certain set of field parameters, as well as a constructive interference effect which transfers a substantial portion of the available population from the ground state to the highest excited state for a different set of field parameters. In the present work we investigate the temporal behavior of the level occupation probabilities of a four-level cascade system interacting with three laser fields of arbitrary strength in the presence of a loss mechanism from the highest excited level. Allowing decay out of the system modifies the population dynamics drastically. We find that the excited state decay destroys the constructive population transfer from the ground level to the highest level found by Sharma and Roversi. In addition to this, the ground state population is found to trickle out of the system at a rate that is much less than the excited state decay rate. In fact, as this upper level decay rate is increased, the ground state decay decreases. We show that this reduction of the ground state decay rate occurs even in two-level atoms, and hence is not due to any kind of four-level interference effect. This information is very important for experimental work.

Theory and Results

In this work we study a four-level cascade system interacting with three laser fields of frequencies ω_{f1}, ω_{f2}, and ω_{f3}, and of arbitrary strengths. The laser frequencies are close to the transition frequencies of the system so that the detunings of each field [defined as $\Delta_1 = \omega_{21}-\omega_{f1}$, $\Delta_2=\omega_{31}-(\omega_{f1}+\omega_{f2})$, and $\Delta_3= \omega_{41}-(\omega_{f1}+\omega_{f2}+\omega_{f3})$, with ω_{j3} = the transition frequency from the ground state $|1\rangle$ to the excited state $|j\rangle$, j= 2,3,4] are much less than the laser frequencies.

For a semiclassical description of the interaction, we write the total applied field as

$$\mathbf{E} = \mathbf{x}[\varepsilon_1 cos(\omega_{f1}\, t)+\varepsilon_2 cos(\omega_{f2}\, t)+\varepsilon_3 cos(\omega_{f3}\, t)]\,, \qquad (1)$$

and the coupled atom / field system wavefunction as

$$|\Psi(t)\rangle = \sum_{n=1}^{4} A_n(t) e^{-i\omega_n t}|n\rangle\,. \qquad (2)$$

In the Rotating Wave Approximation, Schrodinger's equation results in

$$\frac{d}{dt}\begin{pmatrix} a_1(t) \\ a_2(t) \\ a_3(t) \\ a_4(t) \end{pmatrix} = -i\begin{pmatrix} 0 & -\Omega_1 & 0 & 0 \\ -\Omega_1^* & \Delta_1 & -\Omega_2 & 0 \\ 0 & -\Omega_2^* & \Delta_2 & -\Omega_3 \\ 0 & 0 & -\Omega_3^* & \Delta_3 \end{pmatrix}\begin{pmatrix} a_1(t) \\ a_2(t) \\ a_3(t) \\ a_4(t) \end{pmatrix}, \tag{3}$$

where $a_n(t) = A_n(t)\exp(-i\Delta_{n-1}t)$, $\Delta_0=0$, Δ_j is as defined earlier for j = 2,3,4, and the Rabi frequencies are $\Omega_1 = \mu_{12}\cdot x\varepsilon_1/2h$, $\Omega_2 = \mu_{23}\cdot x\varepsilon_2/2h$, and $\Omega_2 = \mu_{34}\cdot x\varepsilon_3/2h$.

In order to incorporate the loss mechanism in our calculation, we phenomenologically introduce a decay in the highest excited state by replacing ω_4 by ω_4-iγ. Our interest is then in determining the occupation probabilities of each level, defined by the relation

$$P_n(t) = |A_n(t)|^2 . \tag{4}$$

In Fig. 1 we plot the occupation probabilities of the different levels as functions of time for Rabi frequencies Ω_1=1.0, Ω_2=1.5, and Ω_3=2.5, for detunings Δ_1=10, Δ_2=5, and Δ_3=1.15, and for γ=0. These parameters were chosen to correspond with the work of Sharma and Roversi. The values of Δ_1 and Δ_2 are taken relatively large so as to avoid populating levels 2 and 3 substantially. The value of Δ_3 was adjusted to obtain maximum transfer of population for the particular fixed set of Rabi frequencies and detunings.

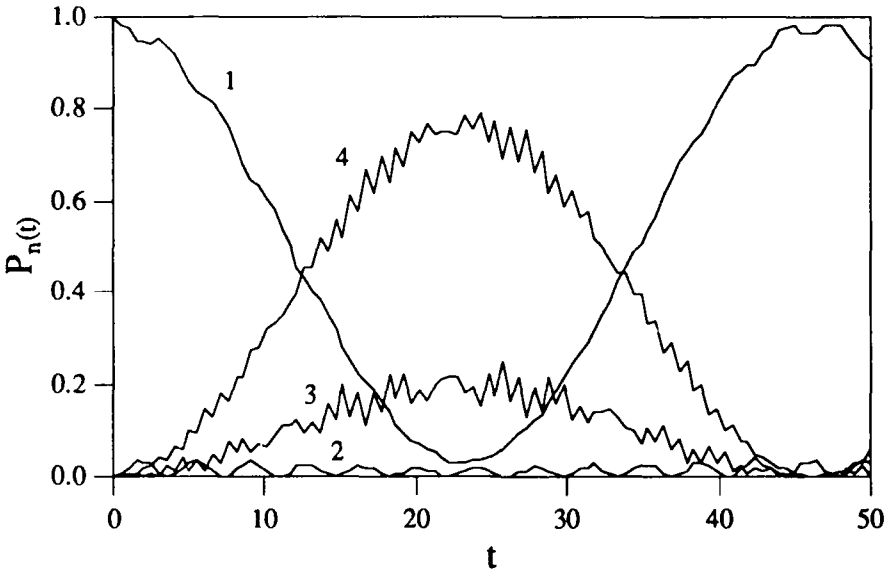


Fig. 1: The level occupation propabilities versus time with γ=0, for Δ_1=10, Δ_2=5, Δ_3=1.15., Ω_1=1.0, Ω_2=1.5, and Ω_3=2.5.

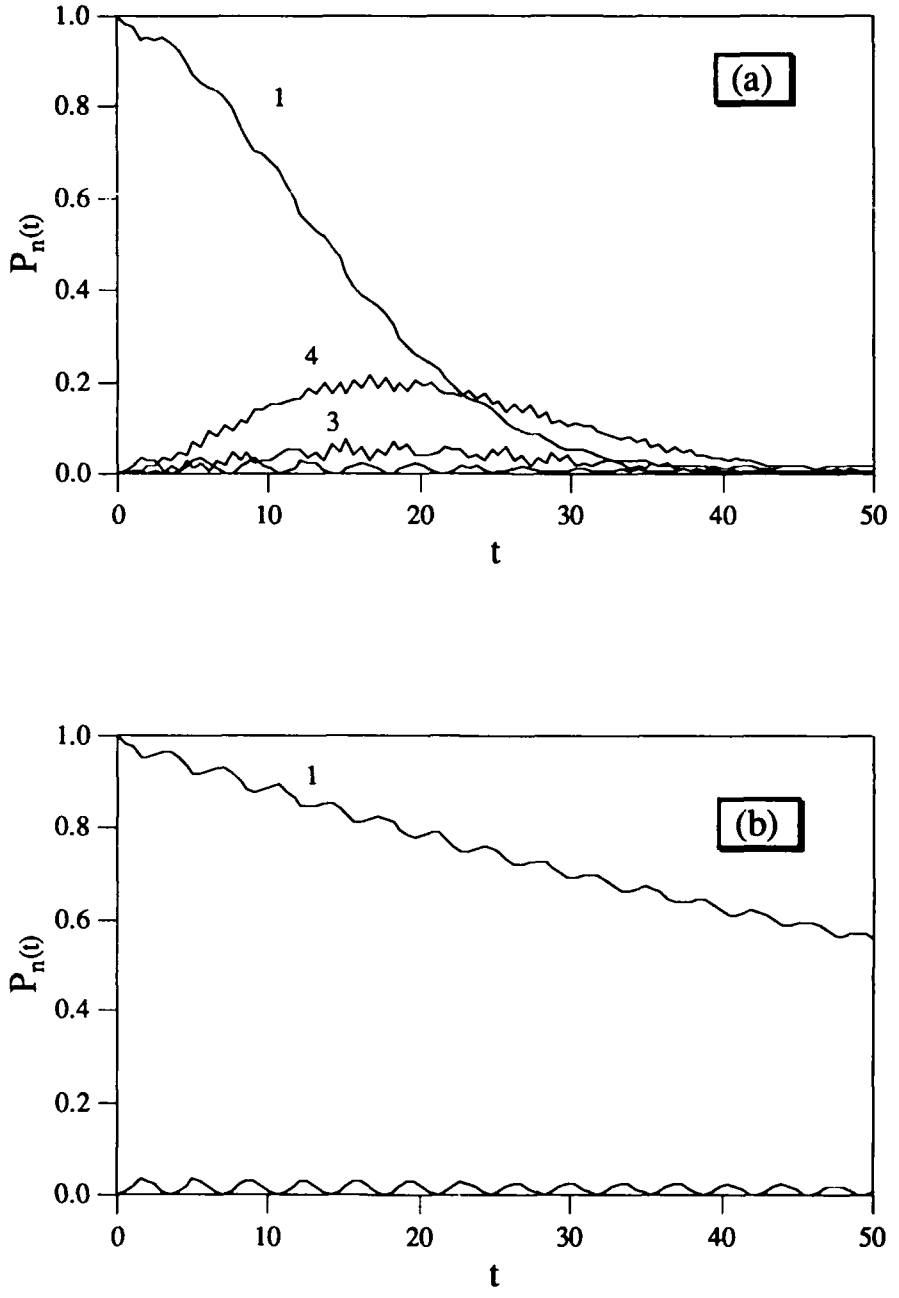


Fig. 2: Here the parameters are the same as in Fig. 1, except that $\gamma \neq 0$. (a) $\gamma=0.1$ (b)$\gamma=1.0$

In Fig. 2 we show the population dynamics with the same parameters as used in the previous figure, but now decay of the highest excited state is included. In Fig. (2a) $\gamma=0.1$ while in Fig. (2b) $\gamma = 1$. As γ increases, the population in state |4> diminishes until the most obvious dynamics is merely the exponential decay of the ground state population out of the system. Surprisingly, however, as γ *increases* this ground state decay actually *decreases* its rate. This effect turns out to be a two-level effect, as we will now discuss.

When the intermediate detunings Δ_1 and Δ_2 are very large, the intermediate states |2> and |3> become virtual states to which there is no strong coupling. In this limit, these states may be adiabatically eliminated from the problem. Rewriting the differential equations for a_2 and a_3 as

$$\frac{da_2}{dt} - i\Delta_1 a_2 = i\Omega_1^* a_1 + \Omega_2 a_3 \tag{5a}$$

$$\frac{da_3}{dt} - i\Delta_2 a_3 = i\Omega_2^* a_2 + \Omega_3 a_4 \,, \tag{5b}$$

we see that for large Δ_1 and Δ_2, these are equations which have a driving force that is much less than the resonance frequency. The response will therefore be the steady-state response found by setting $(da_2/dt)=(da_3/dt)=0$. Therefore, adiabatic elimination of levels 2 and 3 results in

$$a_2(t) \approx \frac{\Omega_1^*}{\Delta_1} a_1(t) + \frac{\Omega_2}{\Delta_1} a_3(t) \tag{6a}$$

$$a_3(t) \approx \frac{\Omega_2^*}{\Delta_1} a_2(t) + \frac{\Omega_2}{\Delta_1} a_4(t) \,. \tag{6b}$$

Using these adiabatic solutions we find

$$\frac{da_1(t)}{dt} \approx i\frac{|\Omega_1|^2}{\Delta_1} a_1(t) + iR\, a_4(t) \tag{7a}$$

$$\frac{da_4(t)}{dt} \approx -i\left(\Delta_3 - \frac{|\Omega_3|^2}{\Delta_2}\right) a_4(t) + iR^*\, a_1(t) \,, \tag{7b}$$

where $R = \Omega_1\Omega_2\Omega_3/\Delta_1\Delta_2$ is the three-photon Rabi frequency. Notice that the elimination of states |2> and |3> introduces the off-resonant Stark shifts of the ground and excited states ($S_1 = -|\Omega_1|^2/\Delta_1$ and $S_2 = -|\Omega_3|^2/\Delta_2$, respectively). If we redefine the atomic energy levels to include these constant shifts, then we may write

$$\frac{d}{dt}\begin{pmatrix} a_1(t) \\ a_4(t) \end{pmatrix} \approx -i\begin{pmatrix} 0 & -R \\ -R^* & \Delta_3' \end{pmatrix}\begin{pmatrix} a_1(t) \\ a_4(t) \end{pmatrix} \,, \tag{8}$$

where $\Delta_3' = \Delta_3 + (S_4 - S_1)$

We can now explain the value of Δ_3 that Sharma and Roversi found in their work (see Fig. 1) to maximize the population transfer to the excited state |4>. With the two-level atom model in mind, we would intuitively expect the maximum population transfer to occur when $\Delta_3=0$ (exact resonance). This is precisely the correct idea, except that for exact resonance we must tune to the Stark-shifted level so that $\Delta_3'=0$. For $\Omega_1=1$, $\Omega_2=1.5$, $\Omega_3=2.5$, $\Delta_1=10$, and $\Delta_2=5$, we see that $\Delta_3'=0$ occurs for $\Delta_3=1.15$, as seen in Fig. 1.

Now, letting $\Delta_3' \rightarrow \Delta_3' - i\gamma$ as before, we find the solutions

$$A_1(t) = e^{-(\gamma + i\Delta_3')t/2}\left\{\left[\frac{\gamma + i\Delta_3'}{\lambda} A_{10} + \frac{iR}{\lambda} A_{40}\right]\sin\left(\tfrac{1}{2}\lambda t\right) + A_{10}\cos\left(\tfrac{1}{2}\lambda t\right)\right\} \tag{9a}$$

$$A_4(t) = e^{-(\gamma + i\Delta_3')t/2}\left\{\left[-\frac{\gamma + i\Delta_3'}{\lambda} A_{40} + \frac{iR}{\lambda} A_{10}\right]\sin\left(\tfrac{1}{2}\lambda t\right) + A_{40}\cos\left(\tfrac{1}{2}\lambda t\right)\right\} \,, \tag{9b}$$

where $\lambda^2 = R^2 + (\Delta_3')^2 - \gamma^2 - 2i\gamma\Delta_3'$.

We may now determine the effect that γ has on the decay of the ground state. Specializing to exact resonance ($\Delta_3'=0$)

and an initially unexcited atom (A_{10}=1, A_{20}= A_{30}= A_{40}=0), the probability of finding the atom in the ground state is

$$|A_1(t)|^2=e^{-\gamma t}\,|\,\frac{\gamma}{\lambda_0}sin\,(\tfrac{1}{2}\lambda_0 t)+cos\,(\tfrac{1}{2}\lambda_0 t)\,|^2, \tag{10}$$

with $\lambda_0^2=R^2-\gamma^2$.

If the decay is much less than the Rabi frequency ($\gamma << R$), then we find for the ground state probability

$$|A_1(t)|^2=e^{-\gamma t}[\frac{\gamma}{R}sin\,(\tfrac{1}{2}Rt)+cos\,(\tfrac{1}{2}Rt)]^2, \tag{11}$$

which is the expected exponential damping of the Rabi flopping dynamics at the rate γ.

If we let the decay rate out of the excited state be very large compared to the Rabi floppping rate ($\gamma >> R$), then we find

$$|A_1(t)|^2=e^{-R^2 t/2\gamma}[1+\frac{R^2}{\gamma^2}\,(1-exp(-\gamma(1-\frac{R^2}{2\gamma^2})t)]^2\,. \tag{12}$$

In this case the decay out of the ground state is greatly reduced ($(R^2/2\gamma)<<\gamma$), even though the decay of the excited state has been increased.

We have shown that for the large intermediate detunings used here, an effective two-level atom can be considered equivalent to our system. It then becomes obvious that the detuning of the third field (Δ_3) required to maximize the population transfer from the ground state to level |4> is just that detuning needed to become resonant with the Stark-shifted transition $(\Omega_4+S_4)-(\Omega_1+S_1)$.

We have also seen that the decay of the ground state occurs at a rate much slower than the decay rate of the excited state (γ). This reduction of the decay rate is actually *not* a result of some kind of four-level interference effect since we have shown that it occurs quite naturally in the two-level atom model.

DIRECT MEASUREMENT OF NONLINEAR REFRACTIVE INDEX SPECTRUM IN ZNSE USING SELF-BENDING OF A PULSED LASER BEAM

Y. J. Ding, C. L. Guo, G. A. Swartzlander Jr., J. B. Khurgin, and A. E. Kaplan
Department of Electrical and Computer Engineering,
The Johns Hopkins University, Baltimore, MD 21218

Abstract

The nonlinear refractive index (n_2) spectrum of ZnSe near the band gap ($\lambda_{gap} \sim 450$nm) at 77K was measured for the first time using self-bending of a pulsed laser beam. The typical self-bending angle was half of the diffraction angle of the laser beam, which translates into a value of $n_2 \sim 10^{-8}\text{cm}^2/\text{W}$.

ZnSe is probably one of the best semiconductor materials for the observation and application of nonlinear refractive index effects[1-4]. This material has large optical nonlinearities in the blue range ($\lambda_{gap} \sim 450$nm at 77K) and has been the favorable candidate for the development of wide-gap (blue) LED and injection laser devices. Although it is a widely used material in device applications based upon thermal effect, [2] the nonlinear mechanisms are still not completely understood. Therefore, a substantial problem in the field is to measure the nonlinear refractive index in the vicinity of resonant transitions (e.g. exciton or band gap transitions) and to determine their nature.

ZnSe has been shown to exhibit strong nonlinear absorption for bulk and epitaxially grown samples due to excitonic saturation, [1] band-filling, Coulomb screening, and/or laser heating. [2] Consequently one can expect very strong self-action effects, which in turn may be used to determine the nonlinear refractive index $\Delta n(I, \lambda)$ as functions of both the laser intensity, I, and the wavelength, λ, using either self-(de)focusing or self-bending. Self-defocusing has been observed and used to determine Δn for some specific wavelengths in some nonlinear optical materials such as InSb. [5] Using the so-called Z-scan technique which measures the effective nonlinear focal length and was first proposed by Kaplan in 1969 (Ref. [6]), the coefficient of the nonlinear refractive index n_2 of ZnSe has been measured at two specific laser wavelengths, [3] however, nonlinear dispersion curves have not been measured. We have used the self-bending effect first proposed in Ref. [7], as a nonlinear spectroscopic tool to measure the spectrum of the nonlinear refractive index of ZnSe in the vicinity of the bandgap. [4]

An ideal case of self-bending occurs when a slab beam, with a spatial intensity profile that is right triangular [$I(x) = I_0(1 - x/\omega_0)$, $0 < x < \omega_0$, where x is the coordinate across the slab beam and ω_0 is the beam size], propagates through a thin Kerr-like nonlinear medium[7,8], (as shown in Fig. 1), in which the refractive index can be approximated by $n \simeq n_0 + n_2 I$, with n_0 the linear refractive index and n_2 the coefficient of the nonlinear refractive index. A nonlinear prism is induced in the beam path when the slope of the intensity profile, I_0/ω_0, is sufficiently large. The beam will be self-deflected in the far-field region by the angle θ_{NL}, which can be expressed as [7,8]

$$\theta_{NL}/\theta_D = n_2 k L I_0 n_0/2 \qquad (1)$$

where $k = 2\pi/\lambda$ is the wave number, $\theta_D = 2/k\omega_0$ is a measure of the (half-) diffraction angle, and L is the thickness of the medium. Similarly, the self-deflection angle of the half-Gaussian slab beam, whose intensity profile is given by $I(x) = I_0 \exp(-2x^2/\omega_0^2)$, $x > 0$, is nearly equivalent to Eq. (1). [8] From an experimental viewpoint, however, one must consider three-dimensional rather than slab (or two-dimensional) beams.

Since the self-bending angle is proportional to the coefficient of nonlinear refractive index n_2, [see Eq. (1)], the spectral distribution, $n_2(\lambda)$ can be directly obtained by measuring $\Delta\theta_{NL}$ as the laser wavelength is varied. This technique was used recently by Swartzlander, Yin, and Kaplan (Ref. [9]) in the first experimental observation of the CW self-deflection effect which measured $|n_2| \simeq 10^{-7}\text{cm}^2/\text{W}$ in the vicinity of the D_2 atomic resonance of sodium vapor. In our most recent experiment, we observed the self-bending effect in bulk ZnSe, obtaining values of n_2 as large as $10^{-8}\text{cm}^2/\text{W}$ over the range 445-460 nm. To the best of our knowledge, we believe this is the first direct spectral measurement of n_2 in ZnSe.

The self-bending method of obtaining $n_2(\lambda)$ has several advantages over the Z-scan technique [3,6] and the conventional pump-probe technique. [10] First of all, compared to the Z-scan technique, the optical quality of the sample needs not be good over large areas. What is more, our technique requires simply a single shot per data point, whereas the Z-scan technique involves many shots and high mechanical stability. Secondly, one can directly measure n_2 with one laser beam whereas using the pump-probe technique, the measurement is done using both pump and probe laser radiations. Our method is more reliable and accurate since n_2 is proportional to self-deflection angle which is directly measured from the experiment, (see Eq. (1) above). Finally, the sign of n_2 can be directly determined from measuring the direction of self-bending effect.

The experimental set-up is shown in Fig. 2. We used a 8 ns pulsed dye laser with Coumarin 450 which was pumped by frequency tripled Nd:YAG laser, to achieve these self-action effects. The laser beam was directed through a series of lenses with focal lengths: $L_1 = 5$ cm and $L_2 = -5$ cm that focused the beam upon a 100 μm spatial filter pinhole (P), and collimating lenses $L_3 = -10$ cm and $L_4 = 30$ cm that passed the beam through a series of optical neutral density filters (OD). The beam size at this portion of the beam was measured to be about 0.7 cm, which was used to estimate the beam size at the sample plane. A beam splitter (BS) directed a fraction of power to a photodiode (D), and the photo-current was monitored on an oscilloscope. A razor blade (RB) was inserted into the beam to obscure half of the beam, thereby form a semi-Gaussian beam profile. The semi-Gaussian profile was imaged onto the ZnSe sample with an imaging lens ($L_5 = 50$ cm). The beam size at the ZnSe sample plane is estimated to be $2\omega_0 \sim 200\mu$m, (see inset in Fig. 2) and wavefronts have a finite positive radius of curvature. After passing through the ZnSe sample the beam is collimated by a positive lens ($L_6 = 20$ cm). Single-crystal ZnSe samples [11] with a thickness of $L \sim 500$ μm were used. All the measurements were done at 77K. The spatial intensity distribution in the far-field area was measured using either a CCD linear detector array, a Polaroid camera or a single photo detector covered by a pinhole scanning across the beam.

Photographs of both self-focused and self-deflected beams in the far-field are shown in Fig. 3. The upper two photographs correspond to the linear (left) and nonlinear (right) cases respectively. The larger beam size in the nonlinear case illustrates the effects due to self-action. When a razor blade is inserted into the beam, the self-bending effect is observed, (see the lower two photographs in Fig. 3). The corresponding rough intensity profiles are depicted next to the photographs. From the intensity profile of the self-bending it can be seen that n_2 is positive. The sign of n_2 can not be deducted from the picture of the self-focusing effect where both positive and negative n_2 give similar pictures in the far-field area.

The more precise picture of the self-bending intensity profile in the far-field area was obtained by scanning a pinhole (the size of pinhole $\sim 100\,\mu$m is much smaller than the laser beam size) across the laser beam, and detecting the signal with a silicon photodiode. In this case, a positive lens ($L_7 = 5$ cm) was used to focus the portion of the beam, which is passing through the pinhole, into the photodiode. The photodiode signal was measured by using a Boxcar Integrator (the gate width was set to ~ 10 ns). Typical results of the experimental measurement of the far-field intensity profiles are shown in Fig. 4, from which we measure a self-bending angle of $\theta_{NL} = 3.8$ mrad. Using Eq. 1, we find that $n_2 \simeq 6 \times 10^{-9}\text{cm}^2/\text{W} \pm 10\%$. The intensity was calculated to be $\sim 1.2 \times 10^5\,\text{W/cm}^2$.

The nonlinear refractive index spectrum $n_2(\lambda)$ can be determined by measuring the self-bending angles for different laser wavelengths as shown in Fig. 5. Intensity profiles in the far-field area are plotted on the left-hand side of Fig. 5 for some specific wavelengths to illustrate the shifted position of intensity peak. For this measurement, the laser intensity is $\sim 6.9 \times 10^4 \mathrm{W/cm^2} \pm 23\%$ and laser wavelengths range from 445 to 460nm. A clear maximum of n_2 at the wavelength of $\sim$447.3nm can be seen. At this wavelength n_2 reaches the value of $\sim 10^{-8} \mathrm{cm^2/W}$. We were not able to measure n_2 for the laser wavelength below $\sim$ 445nm because there is too much band-gap absorption. Again, from the direction of the self-bending effect, we determined that n_2 is positive. Our experimental results show that ZnSe materials demonstrate Kerr-like nonlinerity up to the maximum laser intensity $\sim 200\ \mathrm{KW/cm^2}$, measured in the experiment. Below such an intensity, no saturation of n_2 was observed. This conclusion was drawn from the fact that we measured the self-bending angles as a function of the laser intensity to make sure that Eq. (1) was satisfied. Superlattices and quantum well structures of semiconductor materials have been shown to possess much larger optical nonlinearities while their thickness L is usually much shorter than the corresponding bulk materials (Refs. [1,10]). As a result of these two compensating factors, the self-bending angle may still be large enough to be measured and used to determine the n_2 spectrum. We are also planning to measure the n_2 spectrum using self-bending effect for these novel nonlinear materials.

There are a few nonlinear mechanisms [2,12] capable of causing the self-bending effect in ZnSe. One of them is the instant heating of a single laser pulse, originated from LO phonon scattering with picosecond relaxation times. The contribution of this mechanism can be estimated using the parameters given in Ref. [2] as follows. Roughly speaking, the increase of the sample temperature due to heating of a single laser pulse with the pulse energy J_{laser}, is limited by

$$(\Delta T)_{max.} \simeq J_{laser} / \pi\, c_p\, \omega_0^2\, L \qquad (2)$$

where $c_p \simeq 1.8\ \mathrm{J/K \cdot cm^3}$ is the heat capacity of ZnSe. [2] In our experiment the typical laser energy per pulse is $J_{laser} \sim 10^{-6}$ Joule, which can not increase the temperature of the sample by more than $\Delta T \simeq 1\ \mathrm{K}$ using Eq. (2). Consequently, the band gap decreases by $\Delta E_g = (dE_g/dT) \cdot \Delta T$, where $dE_g/dT \simeq -8 \times 10^{-4}$ eV/K, (Ref. [13]), which is less than 1 meV. These small changes of band gap are not sufficiently large to induce the strong self-bending effect observed. Thermal change of the refractive index due to repetitive laser pulses can also be excluded because when we changed repetition rate from 10Hz to 1Hz, no substantial change of far-field intensity profile was observed. The saturation (band-filling) effect is another possible mechanism, but it would lead to an increase in effective bandgap, and thus to the decrease of the refractive index, i.e., to the negative Δn and n_2. One plausible mechanism for $n_2 > 0$, as observed, is band-gap renormalization due to electron-hole plasma interaction - correlation and exchange. This phenomenon would cause the band gap to shrink. Therefore, the absorption increases near the band gap and the total refractive index (or the nonlinear refractive index) of ZnSe would increase as well, just as measured by us. The detailed calculations due to this mechanism and comparison of theoretical results with our experimental results are in process.

In conclusion, the nonlinear refractive index spectrum of ZnSe was directly measured using the self-bending effect of a pulsed laser beam. Our experimental results show that the self-bending effect can be a reliable method to directly measure the nonlinear spectrum of semiconductor materials such as ZnSe, GaAs, and InSb. In the future we are planning to do detailed investigation of the mechanism of nonlinearity in ZnSe at the the band gap of both bulk and superlattice samples, to develop and improve our new experimental method and use the new knowledge to develop a new efficient method of nonlinear optical power limiters, based on self-bending effect, in particular for such applications as radiation protection of optical sensors.

The authors appreciate C. T. Law for valuable discussions and M. Shone for providing bulk ZnSe materials for our experiment. This research is supported by AFOSR and NSF.

References

[1] D. R. Andersen, L. A. Kolodziejski, R. L. Gunshor, S. Datta, and A. E. Kaplan, *Appl. Phys. Lett. 48,* 1559 (1986); see also N. Peyghambarian, S. H. Park, S. W. Koch, and A. Jeffery, *Appl. Phys. Lett. 52,* 182 (1988).

[2] G. R. Olbright, N. Peyghambarian, H. M. Gibbs, H. A. Macleod, and F. Van Milligen, *Appl. Phys. Lett. 45,* 1031 (1984); see also I. Janossy, M. R. Taghizadeh, J. G. H. Mathew, and S. D. Smith, *IEEE. J. Quant. Electr. 21,* 1447 (1985).

[3] M. Sheik-bahae, A. A. Said, and E. W. Van Stryland, *Opt. Lett. 14,* 955 (1989); see also Y. Y. Wu, D. J. Hagan, E. W. Van Stryland, M. J. Soileau, in *OSA'89 Ann. Meet.,* Oct. 15-20, 1989. Orlando, Florida.

[4] The measurement of nonlinear refractive index spectrum in ZnSe was first reported by Y. J. Ding, C. L. Guo, G. A. Swartzlander Jr., J. B. Khurgin, and A. E. Kaplan, in *OSA'89 Ann. Meet.,* Oct. 15-20, 1989, Orlando, Florida.

[5] D. Weaire, B. S. Wherrett, D. A. B. Miller, and S. D. Smith, *Opt. Lett. 4,* 331 (1979).

[6] A. E. Kaplan, *Izvestiya VUZ. Radiofizika 12,* 869 (1969) [*Radiophys. Quantum Electron. 12,* 692 (1969)].

[7] A. E. Kaplan, *Pis'ma Zh. Eksp. Teor. Fiz. 9,* 58 (1969) [*JETP Lett. 9,* 33 (1969)].

[8] G. A. Swartzlander Jr. and A. E. Kaplan, *J. Opt. Soc. Amer. B5,* 765 (1988).

[9] G. A. Swartzlander Jr., H. Yin, and A. E. Kaplan, *Opt. Lett. 13,* 1011 (1988); see also G. A. Swartzlander Jr., H. Yin, and A. E. Kaplan, *J. Opt. Soc. Amer. B6,* 1317 (1989).

[10] See, e.g., *Optical Nonlinearities and Instabilities in Semiconductors,* H. Haug Eds., Academic Press Inc., New York (1988).

[11] S. Colak, B. H. Fitzpatrick, and R. N. Bhargava, *J. Cryst. Growth 72,* 504 (1985).

[12] H. Haug and S. Schmitt-Rink, *J. Opt. Soc. Am. B2,* 1135 (1985).

[13] B. Ray, *II-VI Compounds,* Pergamon Press, New York (1969).

Figures

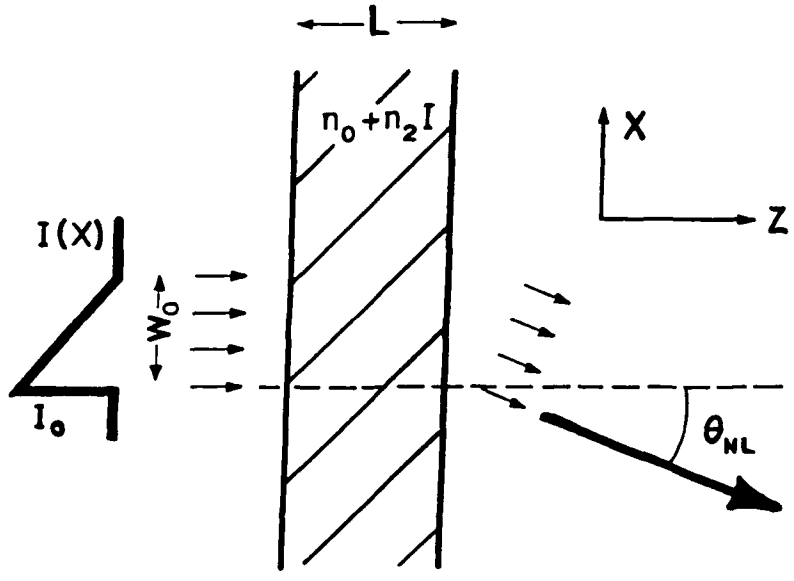


Fig. 1 Right-triangular intensity profile, of size ω_0 and peak intensity I_0, is incident upon a thin nonlinear-refractive medium ($n=n_0+n_2I$) of length L. A nonlinear prism is induced in the medium, causing the transmitted rays to be deflected by an angle θ_{NL}.

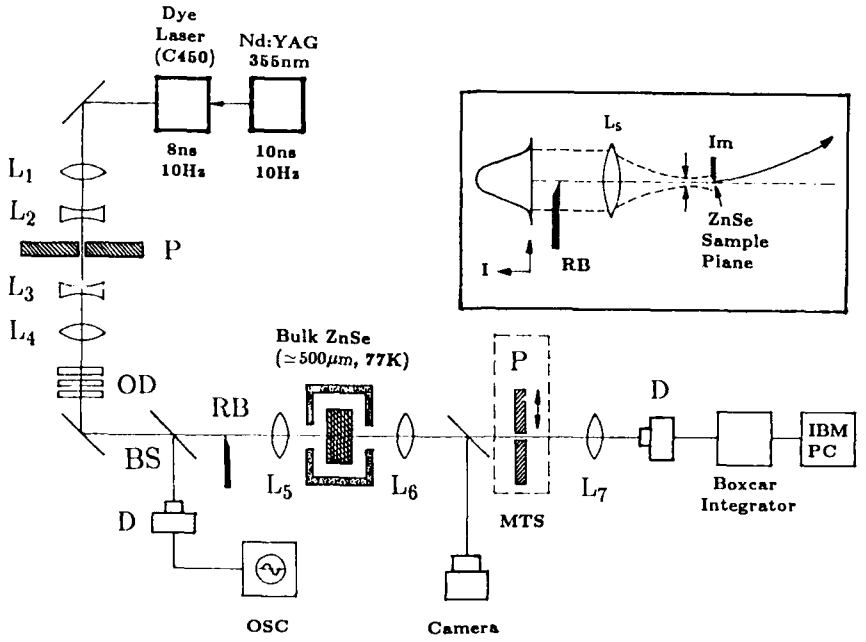
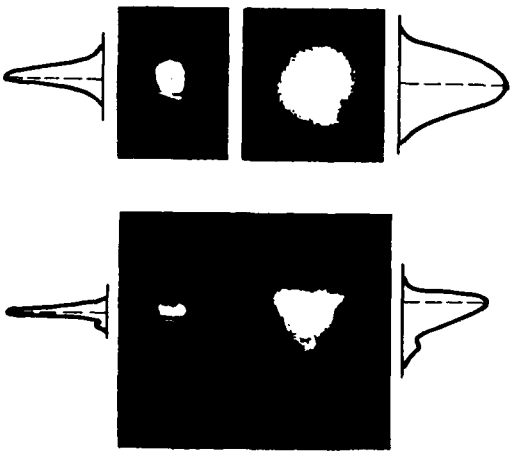


Fig. 2 Schematic diagram of the experiment. See the text for a complete description. The inset shows a razor blade inserted into the beam to form a semi-Gaussian beam profile, which is then imaged into the ZnSe sample plane. The beam is self-deflected towards the razor image because $n_2 > 0$.



Linear ($\lambda = 457$nm) Nonlinear ($\lambda = 447.5$nm)

Fig. 3 Photo measurement of self-focusing (upper pictures) and self-bending (lower pictures) in the far-field area is illustrated. The left photo pictures correspond to the linear case and the right ones correspond to nonlinear case. The rough intensity profiles, derived from the exposure density of the photos for two cases are plotted next to pictures.

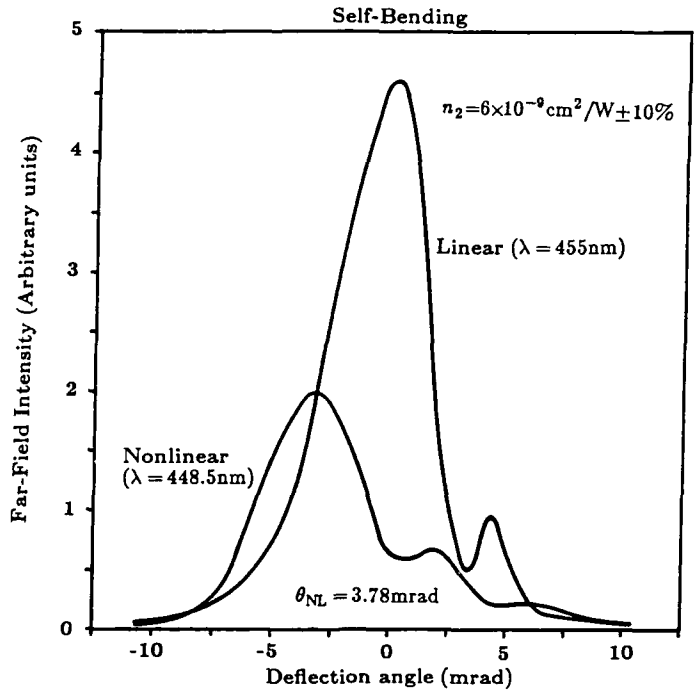


Fig. 4 The spatial intensity profiles of a laser beam in the far-field area after passing through ZnSe are plotted vs. deflection angles for linear and nonlinear cases.

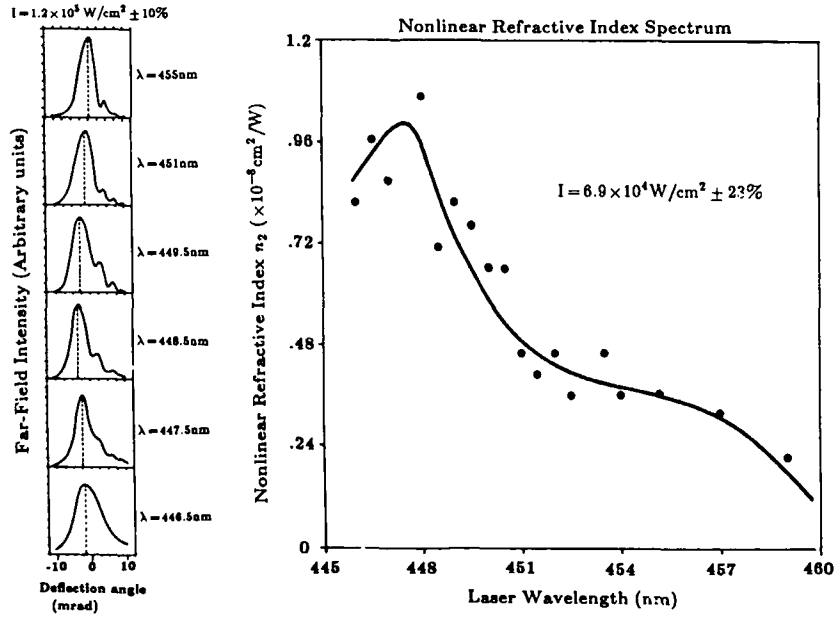


Fig. 5 The spectrum of nonlinear refractive index n_2 is measured vs. the laser wavelength. For illustration, intensity profiles in the far-field area are plotted on the left-hand side for some specific wavelengths.

STUDY OF MID IR FIBER TRANSMISSION AND MODE PATTERNS UNDER LASER INDUCED STIMULATED BRILLOUIN SCATTERING

C. Yu, Yat C. Chong and Hongyi Zhou
Department of Electrical Engineering, North Carolina A & T State University
Greensboro, NC 27411

Abstract

Mid IR fiber transmission and exit radiation mode patterns at various incident CO_2 laser power levels appear to be effective diagnostic tools for monitoring laser induced stimulated Brillouin scattering in various mid IR fibers. Such processes are deemed to be essential mechanisms for fiber-optic amplifiers and switches as potential replacements of current repeaters and bistable devices.

Introduction

Electronic communication technology advances with increasing operating frequency are intrinsically limited by component size, as such components are powered by conduction (or electronic) currents. Reduction in component size to meet high operating frequency requirements is ultimately an impossibility from manufacturing and waveguiding property viewpoints. As operating microwave frequency escalates, coaxial and hollow metallic waveguides are, inevitably replaced by strip lines for microwave integrated circuits and components, such as filters, couplers, resonators, antennas, etc. They provide the necessary flexibility and compactness. Due to the open structure of the microstrip, the EM field is not confined totally to the dielectric, but is partly in the surrounding air. Provided the operating frequency is "not too high", the microstrip line will propagate a wave, which for all practical purposes, is TEM in nature. Electronics based metallic conductors have a serious disadvantage for use at high frequencies, since the surface resistance of metal increases as the square root of the frequency. This in turn causes the ohmic attenuation of the guide to increase. For instance, attenuation per wavelength increases as $\omega^{1/2}$ in coaxial lines, so that such lines are seldom used above 20-30 GHz. Similar arguments apply to other metallic guiding structures. Hollow metal waveguide is somewhat less lossy, because of its larger ratio of volume to surface area, and have thus been employed up to 100 GHz. However, at optical frequencies of the order of 10^6 GHz, as current communication demand trends in capacity dictates, the ohmic losses of any metal waveguide will be so large, as to be completely impractical. Diminution of metal waveguide size also leads to loss of waveguding properties and hence excessive radiation loss,as evidenced in MMIC circuits.

It is thus a natural step to take by abandoning conduction electron-based technology, that is, the elimination of metallic components. This natural transition leads us to the mature techniques of optics. Optical technology has become viable following the removal of certain bottlenecks. The first bottleneck of lack of a high-power monochromatic and tunable source, equivalent to the low frequency generator or microwave klystrons or solid state oscillators, has been removed with the advent of tunable lasers. An essential lowloss medium is now readily available in the form of optical fibers. The remaining bottlenecks are amplifiers and switches. Currently, these are still electronically based repeaters and switches, causing severe interface problems. Electronic computers also pose an optical-electronic bottleneck that needs to be addressed.

It is therefore clear that optical communiation technology is not only a necessary replacement of electronic communication technology, but also potentially a superior technology. A brief comparison of the properties of optical and electronic systems is given in Table 1.

Table 1 : Distinction Between Electronic and Optical Communication System.

Optical Properties	Electronic Properties
Wide Bandwidth($\sim 10^{14}$ Hz)	Narrow Bandwidth ($\sim 10^9$ Hz)
Faster Operation	Slow Operation
Parallel Processing	Serial Processing
Immunity to External EMI	Easily Affected by External EMI
No RC Const. & Heating Problems	RC Const. & Heating Problems
Compatibility to Fiber Commun. Sys.	Incompatibility
No Interface Problem	Interface Problem
Small Size, Light, Low Cost	Large Size, Heavy, High Cost

Another attribute of using photons and a dielectric guiding medium is that interaction between the two is a distinct possibility, unlike the electron stream in a conductor, in which the latter only offers resistance to the flow of the former. In other words, no control of the flow of electrons is possible through its guiding medium, the conductor. Thus, in electronics, all control functions are carried out through the semiconductor, via minority carrier flow, hence inherently slow. The boson nature of photons also allows them to traverse the same guiding medium without affecting one another, while electrons shun one another. This leads to the parallel nature of photonic communication, as opposed to the serial nature of electronic communication.

The prospect of parallel processing and direct control of signal flow via the guiding medium, thus the elimination of interfaces or bottlenecks, is the driving force behind the transition from electronics, to electronic-optical hybrids and, ultimately, all-optic communication and computing systems. Our endeavors are directed at addressing the all-optic scenario by attempts at producing the two key elements: optical amplifier and optical switch.

All-optical Amplification and Switching

All-optic technology is rapidly becoming an action item that cannot be overlooked. These are all-optical amplifiers, switches, memory or computing elements.

Conventional or linear optics assumes photons do not interact with one another, and the medium only guides the photons, much like copper wire guides the electrons. However, to construct all-optic devices without resorting to any electronics, i.e., no conduction electrons are involved, we must force the photons to interact. This has been accomplished by employing the well established phenomena of nonlinear optics.

By definition, all media are linear when subjected to low intensity (power) forces. They become nonlinear when the impressed forces are so strong that the responses of the media reach saturation or the yield point. The predominant force that is distorting the medium will then be able to affect another weaker force, which relies on its transmisison via the medium. In this manner, the weaker is said to be controllable by the stronger force, and we have device action.

For amplification, modulation and switching, it seems that stimulated Raman and stimulated Brillouin scattering will best serve the purpose. Not only can they perform these essential functions, but also can be implemented in the transmission medium - the fiber, itself. The employment of these nonlinear mechanisms will remove the interfacing problem in current electronic-optic hybrid technology.

Implementation of these processes is possible in a fiber medium at watt or even milliwatt level input light power so as to reach the nonlinear regime because lowloss fibers provide the necessary power density x interaction length product.

Stimulated Brillouin (sBs) and Raman (sRs) Scattering

Stimulated Brillouin and Raman scattering processes induced by incident light result in co-flow and contra-flow pump and Stokes shifted waves in the fiber medium. Due to small core diameter, extremely low loss and long lengths available in present monomode fibers, serving as main carrier channels of communication systems, these nonlinear effects can occur at power levels as low as milliwatts. In the contra-flow scheme, incident light is scattered backwards, so that raising incident power to increase repeater spacing will be hampered by this process. This contra-flow sBs process presents the ultimate limitation on fiber signal transmission. From another point of view, the Brillouin mechanism can be employed as a means of all-optic amplification and switching in the guding medium. Thus, sBs induced backscattered Stokes light and the energy exchange between incident and Stokes waves can be used to control the switching and amplification of optical signal transmission. The extremely small sBs gain linewidth of the order of MHz can thus be used to amplify selectively a particular signal wave in the fiber, and this naturally leads to a superior signal to noise ratio.

The energy exchange via sRs and sBs is described by the following set of coupled equations:

$$\frac{dI_S(z)}{dz} = \pm g I_S(z) I_L(z)$$

$$\frac{dI_L(z)}{dz} = \mp g I_L(z) I_S(z)$$

$$\rightarrow \frac{d}{dz}\left[I_L(z) + I_S(z)\right] = 0$$

where the sum of the laser pump intensity I_L and Stokes wave intensity I_S is conserved along the fiber. Thus, energy is being constantly exchanged between the pump and the Stokes wave. I_L and I_S are in contraflow, so that if I_S is the signal wave and it grows, we have amplification; on the other hand, if I_S decays, then we have switching. Since in this switching regime, forward signal energy is switched into the backward direction, we actually have directional switching. In the case of sRs, we have a co-flow interaction scheme, so switching occurs when energy is switched from one frequency to another, hence the so-called frequency or wavelength switching. Here, a filter or Fabry Perot interferometer must be used.

SBS Based Fiber-Optic Switch

Two schemes of an sBs based fiber-optic switch are shown below:

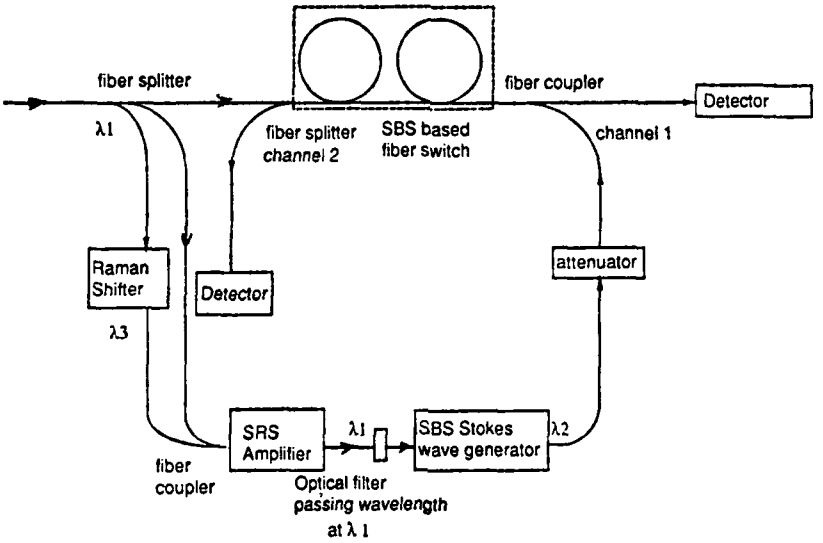


Fig. 1. a. sBs based switch using commercial Raman shifter and amplifier and sBs shifter.

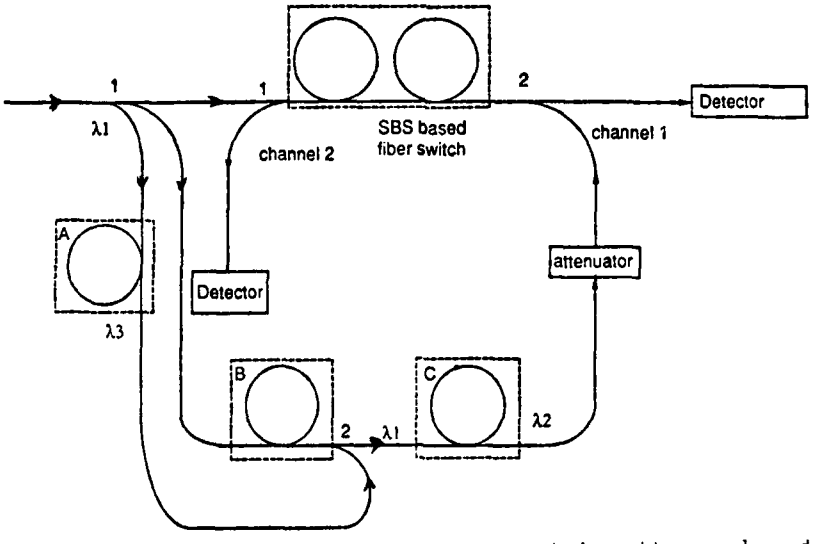


Fig. 1. b. sBs based switch with commercial units replaced by fiber-optic counterparts.

In Fig. 1. a, the Raman shifter produces a Stokes-shifted wave, which serves as the pump beam for λ_1 in the sRs amplifier. This is necessary since the incident λ_1 beam is deliberately set at a power level below the sBs threshold. The output of the sRs amplifier is passed through a filter or Fabry Perot to remove λ_3, and is sBs stokes shifted to produce λ_2, which acts as the pump, after traversing the attenuator, for the main sBs based switch.[1-5] The attenuator functions as a control device for the switch. If the attenuator is made wavelenth sensitive, then this switch can serve as a multiwavelength or wavelength-division switch, truly of ultimate compactness. Corresponding fiber-optic units are shown at corresponding locations in Fig. 1. b. Presumably, the latter will be superior, since no exposed interfaces are created, unlike the case in Fig. 1. a, where exposed interfaces exist at fiber-commercial unit junctions, i.e., commercial units are not fiber-optic.

Mode Pattern Diagnostics of sBs Phenomenon in IR Fibers

Attempts have been made in the observation of sBs phenomenon in fibers using the Fabry Perot interferometer, transmission and reflection data and direct phonon emission. Results of these approaches are at best ambiguous.

The Fabry Perot will have great difficulty in resolving the Stokes shift due to sBs, since the amount is so small, and this quantity decreases with increasing pump wavelength, as in the case of mid IR operation.

Monitoring of onset of sBs by observation of the transmitted and reflected laser pump pulses simultaneously, while in the meantime holding pump power level constant, has been found to be difficult. Observation of any pump pulse power depletion at the fiber exit end encounters the same problem as that of the Febry Perot. It appears to be a good idea to monitor the reflected pulse from the entrance end of the fiber. However, this is often masked by Fresnel reflection of incident pump light from the entrance end and random reflection from surrounding walls. Much more precise instrumentation and experimental design are necessary for any success.

Phonon emission possibility or microwave enhancement of emisisons are explored without much success. Schemes are being devised to better encase the fiber in an appropriate waveguide structure for maximum interaction between any fiber sBs phonon emission and externally injected frequency-matched microwave radiation.

We have devised another method of monitoring the effect of sBs in a fiber by observing the mode pattern of radiation, emerging from the exit end of the fiber. Both thermal image plates and Spiricon linear pyroelectric array are employed. The former is used for analog reproduction of the mode pattern, and the latter, for real time profile reconstruction. The basis of this approach is the formula of pump depletion as a function of pump power of intensity, graphically demonstrated in Fig. 2 for a gaussian beam.[6]

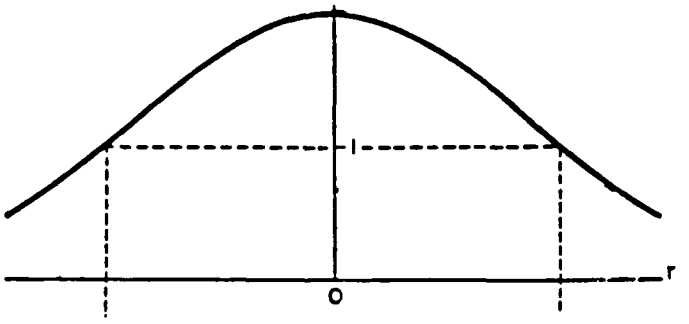


Fig. 2. a. Gaussian incident pump beam.

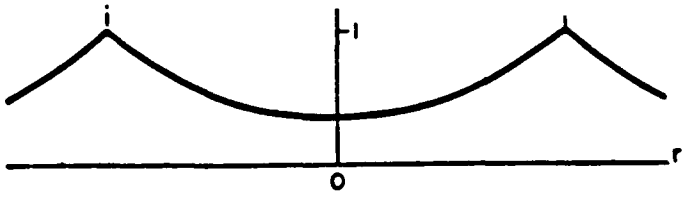


Fig. 2. b. Pump beam transmitted by fiber.

Obviously, the fiber used must be a low-mode fiber, preferably, single-mode. Multimode fibers can be used, if mode stripping is implemented. Higher order modes are undesirable in this case, since these modes will first subtract power from the fundamental, which is gaussian-like, and shift power to the region near the cladding. This process of depleting pump power from the core, due to the presence of excessive number of higher order modes, is no different,from an observation point of view, from such depletion due to sBs. Such masking will not occur in single-mode fiber. Therefore, for testing purposes, either single-mode fiber or mode-stripped multimode fiber must be used.

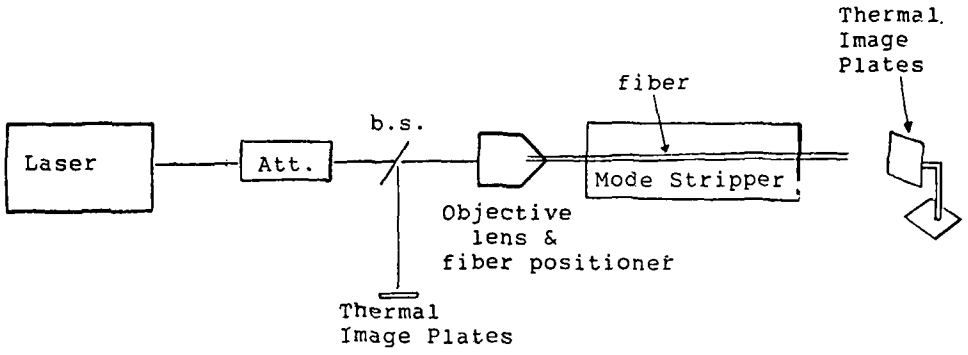


Fig. 3. Experimental setup for mode pattern study

It must also be noted that from the above reasoning, the most efficient fiber based sBs amplifier or switch must use single-mode fibers. This is yet to be verified by experiment.

Conclusions

The availability of commercial sRs and sBs amplifiers and shifters points to the feasibility of the construction of all-optic fiber-based amplifiers and switches. The all-fiber scheme without any interfaces still awaits implementation. The importance of the use of single-mode fibers seems to deter our currents efforts in the mid IR region, since such fibers are not yet commercially available. It is logical that the initial prototype may have to be constructed in the 1.5 micron Nd-YAG lasing region, where lowloss, single-mode fibers are easily found in the market.

References

1. D. Cotter, J. Opt. Commun. 4, 10 (1983).
2. M. P. Petrov, and E. A. Kuzin, Reprint of A. F. Ioffe Physical Technical Institute No. 975 (1985).
3. M. P. Petrov, and E. A. Kuzin, Acta Polytech. Scandinavica PH-150, 254 (1985).
4. E. A. Kuzin, and M. P. Petrov, Sov. Tech. Phys. Lett. 11, 160 (1985).
5. E. A. Kuzin, and M. P. Petrov, Avtometriya No. 2, 87 (1986).
6. H. Hsu, and S. S. Bor, IEEE J. Quantum Electron. 25, 430 (1989).

Acknowledgments

The research work leading to this paper was performed under the support of U. S. Army Research Office Grant No. DAAL03-88-G-0005 and NASA Langley Research Center Grant No. NAG-1-815.

TEMPERATURE MEASUREMENT WITH HYDROGEN PURE ROTATIONAL CARS SPECTRUM

J. P. Singh and F. Y. Yueh
Diagnostic Instrumentation and Analysis Laboratory
Mississippi State University
Post Office Drawer MM
Mississippi State, Mississippi 39762
(601) 325-2105

Abstract

Multiplex rotational CARS spectra of H_2 have been recorded in a quartz cell placed in a furnace. The Stokes laser was tuned to the desired spectral region to obtain the H_2 pure rotational lines S(4) and S(5) with comparable intensity in the temperature range 800 K - 1500 K. The observed spectra were fit with model spectra to extract the temperature. The temperature measurements with the normalized intensities ratio for S(4) and S(5) were also demonstrated.

Introduction

Coherent anti-Stokes Raman spectroscopy (CARS) has been used for non-intrusive temperature measurement in harsh, turbulent, and high luminous combustion environments.[1] Temperature measurement has also been performed in particle loaded combustion environments such as a coal fired MHD test stand,[2] a coal gasifier[3] and a coal furnace.[4] Since the CARS signal is generated at the focal volume where the high power Stokes and pump laser beams interact, the presence of a particle will produce breakdown and a nonresonant background is added to the resonant CARS spectrum. The particle induced laser breakdown will reduce the measurement accuracy of CARS. Unfortunately, the laser breakdwon threshold is of the same order of magnitude as the laser intensity needed to generate the multiplex CARS signal in BOXCARS phase matching geometry. Thus, for a particle loaded medium a CARS technique is needed for which the signal can be produced at lower laser intensity. This can be achieved with the two Stokes wavelengths CARS[5] with collinear or USED CARS phase matching geometry.

Hydrogen is a major species in a coal gasifier and in rocket fuel combustion. It is well suited for combustion thermometry because of the simplicity of its vibrational Q branch CARS spectrum. Studies have been made on using H_2 vibrational CARS for thermometry.[6,7] The authors have found the H_2 pure rotational CARS is also ideal for the thermometry. The H_2 rotational lines are well separated which is also fairly easy for performing the two wavelengths CARS technique. In this paper, a study on using H_2 pure rotational lines S(4) and S(5) for temperature measurement was presented.

Experimental

The experimental configuration has been described in detail previously.[8] In brief, a frequency doubled Nd-YAG laser provides the pump beam and also pumps a dye laser to produce a broadband Stokes beam. The pump and Stokes beams were aligned according to the BOXCARS phase matching geometry. One-tenth of the beams were focused into a reference cell to generate a nonresonance CARS signal and the rest of the laser beams were focused into the test medium. The CARS signals generated at the test medium and the reference cell were separated from the laser beams with beam blocks and dichroic mirrors and detected with an optical multichannel detector (OMD) attached on a 0.75 m Spex monochromator.

To study the feasibility of making temperature measurement using the pure rotational CARS spectra of H_2 S(4) and S(5) line, a series of measurements was made. Data were taken in a sample cell placed in a furnace whose temperature was varied between 300 K and 1500 K. The temperature of the furnace at the measurement point was monitored by a thermocouple. The H_2 rotational CARS spectrum and the nonresonant background were recorded simultaneously. Then the H_2 CARS data were normalized by the nonresonant background. The normalized CARS data were transferred to the VAX-780 computer for analysis.

Theoretical Considerations

The intensity of anti-Stokes beam can be expressed[9]

$$I(\omega_{as}) = \int |\chi_{CARS}|^2 I_1(\omega_1) I_2(\omega_2) I_3(\omega_3) \delta(\omega_1 + \omega_3 - \omega_2 - \omega_{as}) d\omega_1 d\omega_2 d\omega_3 \qquad (1)$$

where the $I_1(\omega_1)$, $I_3(\omega_3)$ are the pump beam intensity, $I_2(\omega_2)$ is the Stokes laser beam intensity and χ_{CARS} is the third order susceptibility of the medium which consists of a frequency dependent resonant part and a nonresonant part.

$$\chi_{CARS} = \chi_{nr} + \frac{1}{2}(\chi_r(\omega_1 - \omega_2) + \chi_r(\omega_3 - \omega_2)) \tag{2}$$

The resonant susceptibility of a pure rotational S-branch transition can be expressed as[10]

$$\chi_r(\omega_1 - \omega_2) = \frac{N}{\hbar}(\Omega_J - \omega_1 + \omega_2 - i\Gamma_J)^{-1} \cdot \left(f_J - \frac{(2J+1)}{(2J+5)} f_{J-2}\right) \frac{4}{45} \gamma_{00}^2 b_{J-2}^J K(J) \tag{3}$$

where $K(J)$ is the first order line strength correction factor for centrifugal distortion, N is the number density of the probed molecule, f is the population factor, b_{J-2}^J is the Placzek-Teller coefficient; Γ_J is the Raman linewidth.

The intensity of H_2 rotational $H_2(4)$ and $H_2(5)$ line are calculated using equations 1-3. The molecular constants given by Jennings et al[11] were used to calculate the rotational energy levels. The H_2 linewidth is Doppler broadened for densities of less than ~ 0.2 amaga. Although no direct linewidth measurement for H_2 S(4) and S(5) line is available, a reasonable approximation is using the measured S(9) line width[11] to calculate the S(4) and S(5) line Raman linewidths. The H_2 S(4) and S(5) Raman linewidths were calculated by

$$\Gamma = \Gamma_{S(9)} \cdot \frac{\upsilon}{\upsilon_{S(9)}} \tag{4}$$

The intensity of H_2 S(4) and S(5) line were calculated at various temperatures. The intensity ratios of S(4) to S(5) at various temperatures were also calculated. The ratioes are quite sensitive to the temperature as shown in Figure 1. Therefore, it can be a reference for quick temperature estimation.

Results and Discussions

The temperature can be extracted from the spectrum of H_2 S(4) and S(5) line by two ways First, a nonlinear least squared fit can be performed to extract the temperature from the spectrum shape. A typical result using this method is shown in Figure 2. The temperature extracted from that spectrum is 1375 K which is 73 K higher than the thermocouple measurement. Since the intensity ratio of the S(4) to S(5) line is quite sensitive to the temperature, the temperature can be estimated quickly by comparing the normalized intensity ratio of H_2 S(4) to S(5) lines with the theoretical calculated results. Table 1 shows the measurement results using this quick temperature measurement method. The inferred temperature errors are within 100 K compared to the thermocouple temperature. Further work is still needed to improve the accuracy of these measurements. Since the H_2 S(4) and S(5) lines are in the CO_2 CARS spectral region, the interference between the H_2 lines with CO_2 lines cannot be neglected. The temperature estimated methods mentioned above only good for the condition where no CO_2 is in the test medium.

Conclusions

This preliminary study shows that it is possible using the CARS spectrum of H_2 pure rotational S(4) and S(5) lines for the temperature measurement in the practical environment. Thus H_2 S(4) and S(5) rotational lines are the best choice for using the two wavelength CARS technique to perform temperature measurement in a particle loaded combustor with H_2 as a major species and without CO_2 such as a coal gasifier. More studies on performing temperature measurement using these H_2 pure rotational lines will continue.

Acknowledgment

This work was supported by DOE Contract DE-AC02-80ET-15601.

References

1. R. J. Hall and A. C. Eckbreth, Laser Applications, vol. 5, J. F. Ready and R. K. Erf, Eds. (Academic, San Diego 1984).

2. E. J. Beiting, Appl. Opt. 25, 1684 (1986).

3. A. Hartford, et. al. Proceedings of the Society of Photo Optical Instrumentation Engineering 411:92 (1983).

4. M. Alden and S. Wallin, Appl. Opt. 24, 3434 (1985).

5. M. Alden, K. Fredriksson and S. Wallin, Appl. Opt. 23, 2053 (1984).

6. J. A. Shirley, A. C. Eckbreth, and R. J. Hall, Proc. 16th JANNAF Combust. Meet. CPIA publication, 309, 487 (1979).

7. E. J. Beiting and J. C. Luthe, NASA Contract Report NAS8-34907 (1983).

8. J. P. Singh and F. Y. Yueh, Appl. Opt. to be published.

9. M. A. Yuratich, Mol. Phys. 38, 625 (1979).

10. F. Y. Yueh and E. J. Beiting, Appl. Opt. 27, 3233 (1988).

11. D. E. Jennings, L. A. Rahn, and Owyoung, Astrophys. Lett. 291, L15 (1985).

Table 1

Comparison of the thermocouple temperature
with the
inferred temperature from intensity ratio of S(4)/S(5).

Thermocouple Temperature (K)	Temperature Inferred from Intensity Ratio (K)
537	605
783	710
1100	1165
1286	1250

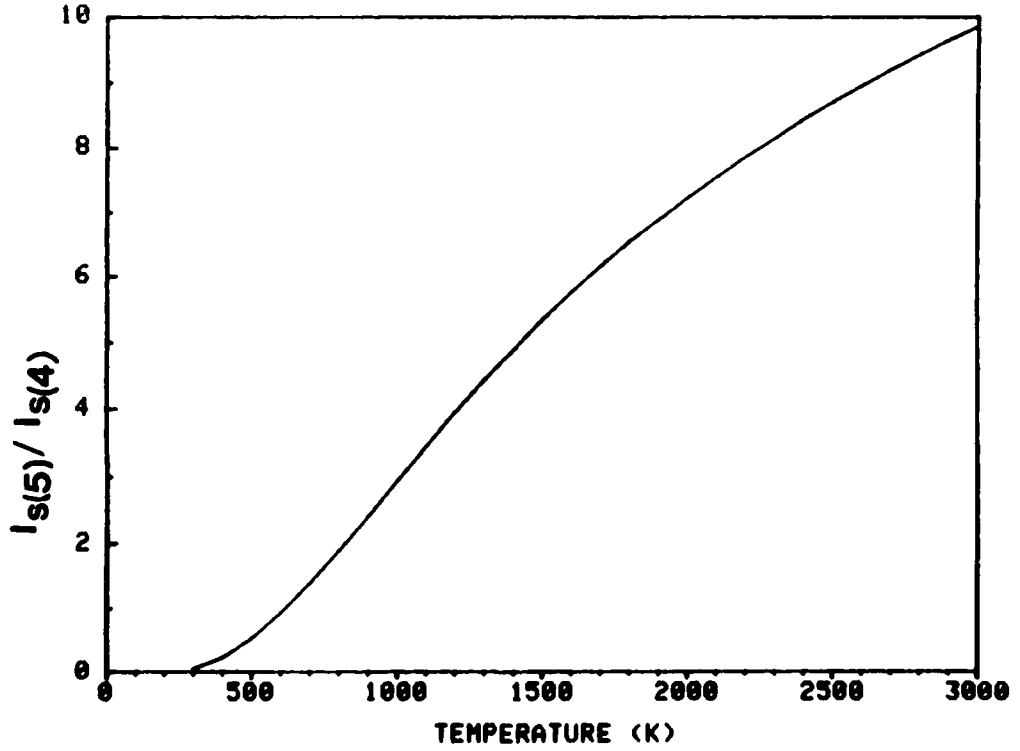


Figure 1. Variation of the intensity ratio of H_2 S(5) and S(4) lines with temperature.

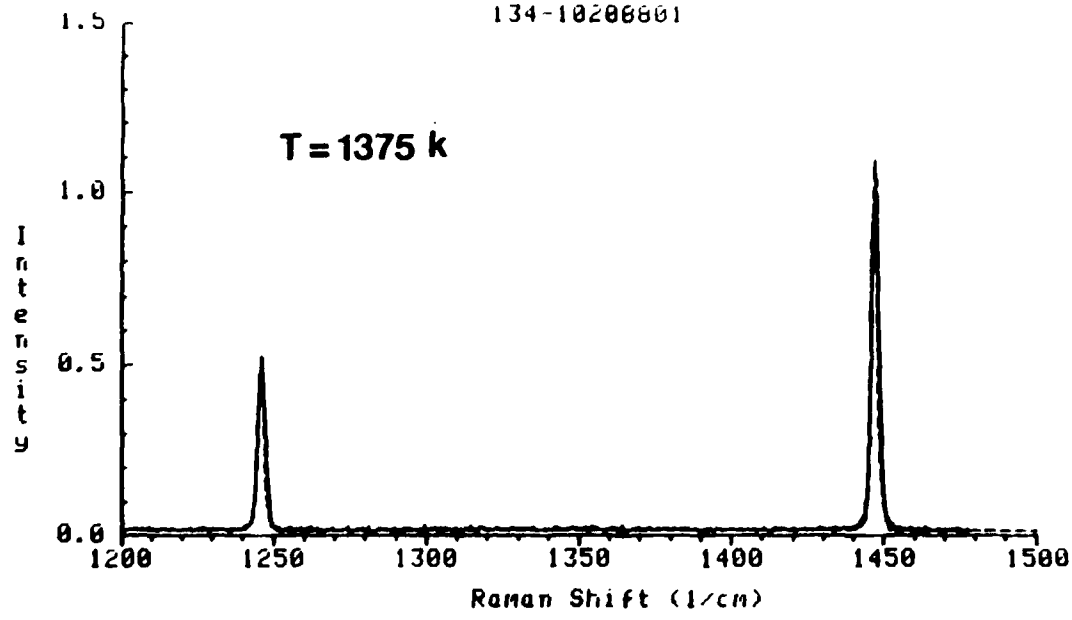


Figure 2. Fitting of the observed rotational H_2 CARS spectrum with the model spectrum.

EFFECT OF PUMPING BEAM QUALITY ON THE STIMULATED RAMAN SCATTERING AND RAMAN BEAM CLEAN_UP

Qihong Lou,Yunsheng Huo,Jingxing Dong,Yunrong Wei and Hongyi Gao

Shanghai Institute of Optics and Fine Mechanics,Academia Sinica, P.O.box 800-211,Shanghai 201800, CHINA

ABSTRACT

Stimulated Raman Scattering characteristics in high pressure hydrogen are evaluated for pumping laser with different beam spread angle. The effects of the beam quality of the injected emission on the Raman beam clean-up are investigated to obtain diffraction limited first Stokes emission.

ITRODUCTION

Excimer laser allow the generation of high power radiation at a set of wavelength in the UV region. An increase of the number of lines generated in the UV and visible region can be obtained by Stimulated Raman Scattering (SRS) of excimer laser radiation.[1,2]

In this work, the effects of pumping beam quality on the SRS characteristics are evaluated with the pumping laser using plane-parallel,stable and unstable resonators. For unstable cavity configuration, the laser pulse energy is one joule with beam spread angle of 0.3 mrad. The total energy conversion efficiency of 59% was obtained at 5-17 Atm. of hydrogen gas pressure, which is 2.7 times higher than that with plane-parallel resonator.Furthermore,by using a ring aperture to select the part of the laser beam with beam spread angle of 0.1 mrad, more than 90 Raman photon conversion efficiency was obtained with pumping energy of 40 mJ.

SRS also can be used for improvement of the beam quality , differaction limited Stokes output can be obtained by means of Raman beam clean-up[3] . In this work,diff raction limited SRS first Stokes output with peak power of 0.2 MW was obtained by using spatial filter. This beam was used as an injection source to control the beam quality of the Raman amplifier. The Raman gain coefficients and the Saturated parameters of the Raman amplifier were obtained for hydrogen gas pressure between 4-6 Atm. The effects of the beam quality of the injection emission on the Raman beam clean-up were also investigated.

HIGH EFFICIENCY RAMAN CONVERSION WITH ONE JOULE EXCIMER LASER

The SRS optical geometry is show schematically in Fig.1. The pump laser is an X-ray preionized , transverse gas flowing,repetition rate operated,electric discharge pumped XeCl excimer laser[4]. A confocal unstable optical resonator in the possitive branch was used to improve the beam spread angle . A lens coated with a total reflection coating on the central circle (D = 0.6 cm) in diameter is taken as the output mirror. The laser beam near field pattern is a rectangular (about 21 x 23 mm) with a 6mm hole at the center. The laser baem is focused into the Raman cell with 18 MW (1 Joule,55ns) peak power,0.3 mrad beam spread angle and 2 ns pulse rise time. The focal power density is about 25000 MW / cm^2.

For comparison, plane-parallel and stable resonators were also used in our experiments. When stable resonator was used for excimer laser as a pumping source, no SRS emission was observed with hydrogen gas pressure between one to 17 Atm.. The total Raman conversion efficiencies as a function of the pumping laser energy and hydrogen gas pressure are shown in Fig.2 and Fig.3 respectively.

The threshold of SRS with plane parallel resonator pump laser is about 300 mJ, some times, the SRS signal was observed with pumping laser energy of 200 mJ, but it is not stable. For the unstable resonator pump laser, the SRS emission appears at a pumping energy of several mJ. This result implies that the key factor that optimize Raman conversion efficiency is the beam quality of the pumping laser. Table 1 summarized the effect of the beam divergence on the total SRS conversion efficiency.

From Fig.3, we can find that when the hydrogen gas pressure is larger than 5 Atm., the total Raman energy conversion efficiency is unchanged around 60%.But the distribution of the Raman emission in different Stokes orders is different. For example, when the hydrogen gas pressure is 5 Atm.,the energy conversion efficiencies for S1 (353nm), S2 (414 nm), S3 (499 nm) and S4 (630 nm) are 23 %, 27 %,6 % and 1 % respectively. At 17 Atm.,they

changed to 13 %, 14 % , 24 % and 7 % respectively. At this condition ,efficient blue-green conversion was obtained ,240 mJ of S3 stokes emission with 11 MW peak power output was observed . Which corresponds to 39 % photon conversion efficiency.

TABLE I EFFECT OF BEAM DIVERGENCE OF THE PUMP LASER ON THE TOTAL SRS conversion efficiency

Laser resonator	R1 (cm)	R2 (cm)	L (cm)	E (mJ)	θ (mrad)	P (MW/CM^2)	n (%)
STABLE	300	∞	100	1300	10	20	0
Plane-parallel	∞	∞	100	1400	4	130	22
Unstable	300	-50	125	1000	0.3	25000	59

In another serious experiments, by using a ring aperture to select the part of the laser beam with higher beam quality, more than 90% Raman photon conversion efficiency was obtained with pumping energy of 40 mJ. (Fig.4 and Fig.5)

Two kinds of optical methods are used to attenuate the pumping laser beam. One is using ORIEL calibrated mettallic density filters (F); another is using a ring aperture to select the part of pumping laser beam (D). Stokes output energy conversion efficiencies versus the input pump energy is shown in Fig.4. From Fig.4, we can find the Stokes output conversion efficiencies are increased at lower pumping energy with the ring aperature as the optical attenuator. For example, at the pumping energy of 320 mJ, the total Stokes energy conversion efficiency is 42 %, it reduced to 34 % at a pumping energy of 40 mJ with neutral density filter. When the ring aperture was used as the optical attenuator, the total Stokes energy conversion efficiency increased to 60 % with photon conversion efficiency more than 90 %.

Furthermore, the distribution of the Stokes output at different Stokes orders is also different for these two kinds attenuator methods. At the pumping energy of 40 mJ, the dominant Stokes output is S1 at 353 nm with neutral density filter attenustor; in contrast, higher Stokes order output can be obtained with ring aperture attenuator, as shown in Fig.5 the energy conversion efficiency of S3 increased to 19 % .According to the power density at the focus region with unstable resonator without attenuator, the beam spread angle with ring aperture (at energy of 40 mJ) can be estimated as less than 0.1 mrad.

When the ring aperture is used as the attenuator, the beam diameter is 10 mm, the diffraction limited beam divergence θ_L is

$$\theta = 4\lambda / \pi D$$

in which D is the beam diameter, λ is the wavelength of the pumping laser. For D = 10mm, λ = 308 nm , we have θ = 0.04 mrad. So that at the pumping laser energy of 40 mJ, attenuated by ring aperture, the beam divergence is only 2.5 times of the θ_L .

On the other hand, with whole output beam diameter, the beam divergence is 15 times of the θ_L with D = 20 mm. The improvement of the beam quality makes it possible to obtain high Raman conversion efficiency at lower pumping energy.

Our experimental results also show that the field profiles of the Stokes output are not as same as that of the pumping laser . In Fig.6, an almost uniform pattern of S1 was observed pumped by a laser beam with ring pattern. Theoretical analysis was consisted with experimental data by solving SRS wave equation using Gaussian-Hermite couping method[5]. As an example, the spatial distribution of the normalized pump intensity with 15th Gaussian -Hermite mode and related 1st Stokes intensity are shown in Fig.6 in the right column. The results are in good agreement with our experimental data.

RAMAN BEAM CLEAN-UP

Beam clean-up, involves the transfer of energy from a highly aberrated pump beam to a diffraction -limited Stokes without transfer of the aberrations. The experimental set-up for Raman beam clean-up is shown in Fig.7. The laser beam from XeCl excimer laser was devided to two parts by beam splitter B. The output of the Raman oscillator selected by a spatial filter to get diffraction-limited S1 emission. The pine hole D1 is placed at the focus plane of lens f2. The diameter of D1 can be changed from 0.1 mm to 0.4 mm. This beam is injected into Raman amplifier through the hole at the center of the mirroe M6. The Raman amplifier is pumped by the mirror M1, M2, M3 and M6.

An Raman amplifer measurement was taken to obtan the Raman Gain coefficient and saturated paramenters at different hydrogen gas pressure. The Raman amplifer energy versus input energy is given in Fig.8. According to the laser amplifier theory[7], the small signal Raman gain coefficient for the first Stokes emission were obtained . They are 0.063/cm,0.050/cm and 0.038/cm at 4,5 and 6 Atm. respectively . The saturated intensities for the first Stokes emission are 1.3 , 1.2 and 1.0 mJ/cm^2 at 4 , 5 and 6 Atm. respectively.

Fig.9 shows the far field beam profiles for Raman beam clean-up. The results show the beam quality of the Raman clean-up output can be controlled by the injection source. The FWHM diameter of the Raman beam clean-up output is almost as same as the diameter of the injected source with D1 changed from 0.1 mm to 0.4 mm.

When the pumping beam of the Raman amplifier is detorried by some optical elements, the beam profiles of the Raman beam clean-up output are not affected . Detailed experiments for increase the conversion efficiency of the Raman beam clean-up are in progress.

REFERENCE

1 H.Komine and E.A.Stappaerts,Opt. Lett.,4,538 (1979)

2 Lou Qihong, Yuan Yifeng,Qi Jianping,Wei Yunrong , Ding Aizhen and Dong Jinxing,China J.Lasers,13, 197 (1986)

3 R.S.F.Chang and N.Djeu, Opt. Lett., 8,139 (1983)

4 Q.Lou and R.Wang, Optics and Laser Technology,19,33 (1987)

5 X.Cheng,R.Wang,Q.Lou and Z.Wang, Optics Comm.,64,67 (1987)

6 J.Reintjes, R.H.Lehmberg,G.Culamo, R.S.F.Chang and S.Duignan, J.Opt. Soc. Am.,A2,3 (1985)

7 P.B.Corkum et al., IEEE J.Quant. Electron.,QE-18,1962 (1982)

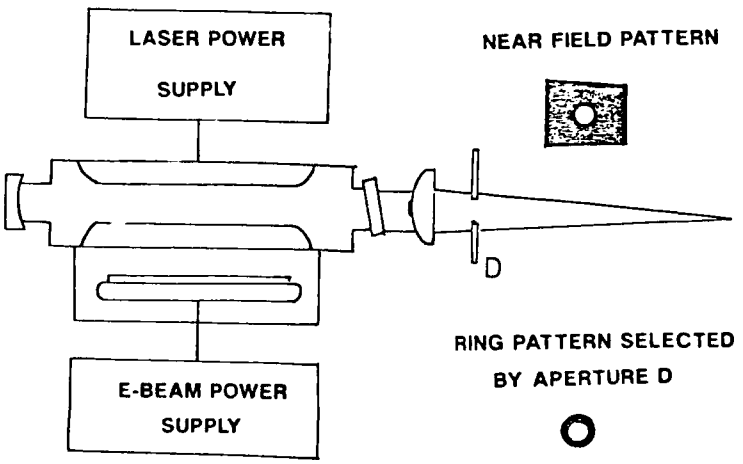


Fig. 1 Experimental set-up for Stimulated Raman Scattering with unstable resonator using for XeCl excimer laser.

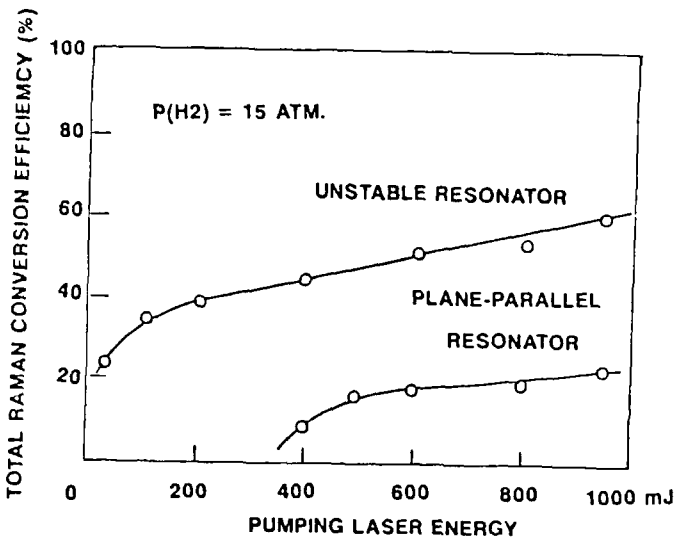


Fig.2 Raman energy conversion efficiency vs pump energy for pump laser with unstable and plane-parallel resonators.

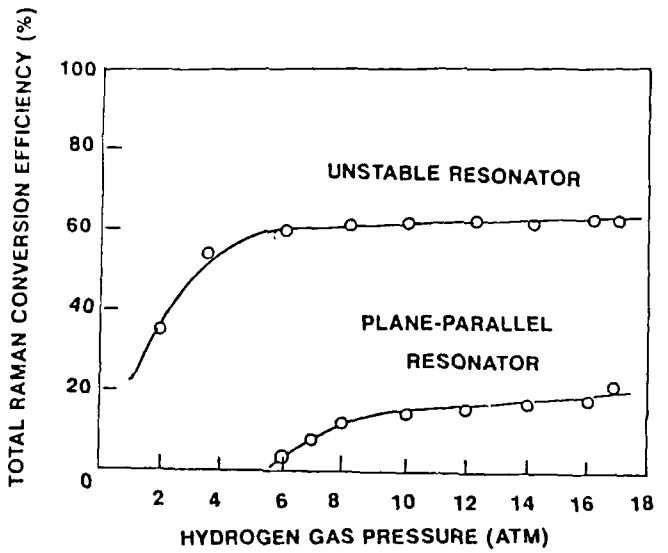


Fig.3 Raman conversion efficiency vs hydrogen gas pressure for pump laser with unstable and plane-parallel resonators.

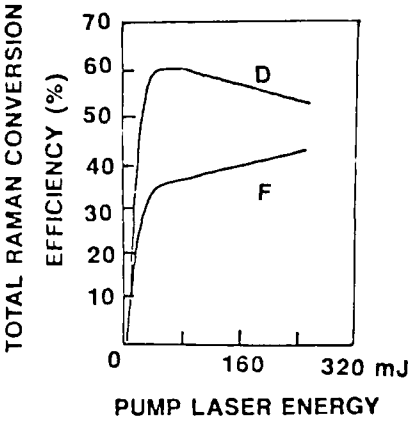


Fig.4 Total Raman conversion efficiency vs pump laser energy attenuated by D : ring aperture; and F : neutral density filters.

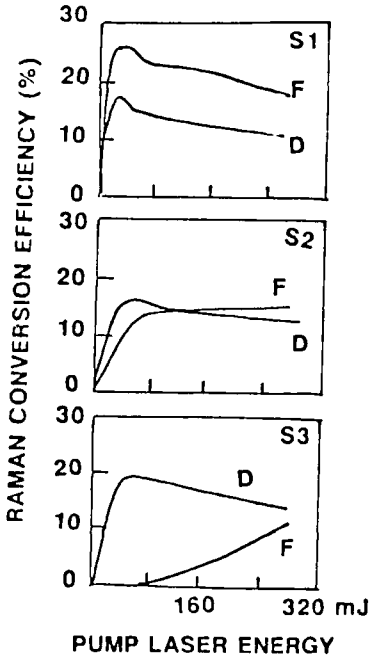


Fig.5 Energy conversion efficiency of S1, S2 and S3 stokes emission vs pump energy for two kinds of attenuations.

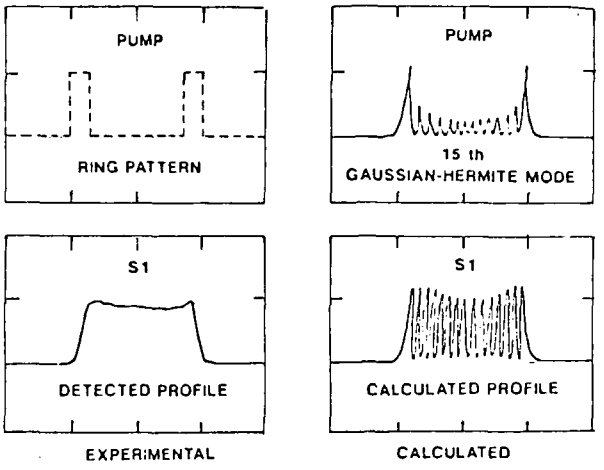


Fig.6 Experimental and calculated beam profiles for pump laser and thirst Stokes emission.

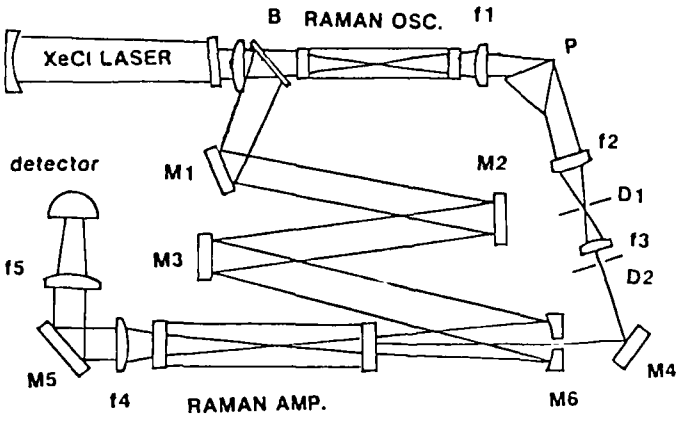


Fig. 7 Experimental set-up for Raman beam clean-up

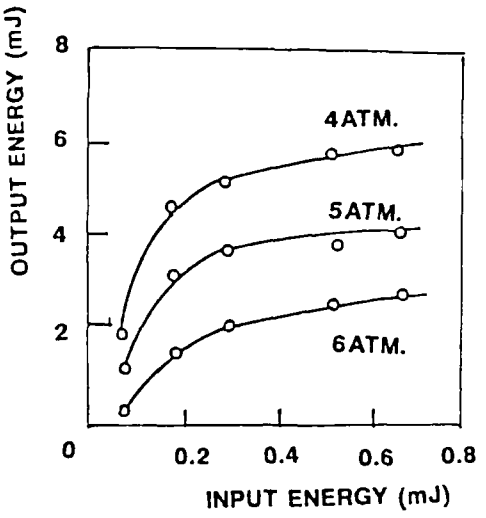


Fig.8 Hydrogen Raman amplifier energy vs input energy.

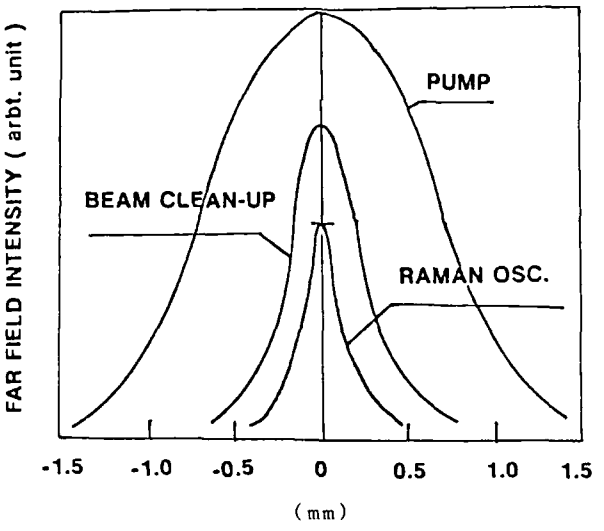


Fig.9 Far field profiles for pump, Raman oscillator and Raman beam clean - up.

COMPETITIVE WAVE INTERACTIONS AND INSTABILITIES IN AN ANISOTROPIC MEDIUM WITH THRESHOLD HIGH NONLINEARITY; THE ROLE OF MOLECULAR FLUCTUATIONS

S. M. Arakelian, Yu. S. Chilingarian, A. S. Karaian,
R. B. Alaverdian*, and V. E. Drnoian

Department of Physics
Yerevan State University
Yerevan, Armenia, 375049 USSR

Abstract

Laser-induced bulk gratings and temporal instabilities of nonlinear wave processes with different components of light polarization have been studied in the liquid crystals. A mirrorless feedback arises because of the non-local nonlinear response of an anisotropic elastic medium on the external field. The multiplicative nature of the molecular fluctuations in the liquid crystals under external field are discussed and the light-induced reorientation effects in this medium can be considered as noise-induced phase transitions.

Introduction

The non-steady and stochastic wave processes and instabilities which arise due to the propagation of light in highly nonlinear medium are a subject of intense study for the present time. Although the problem of instabilities of nonlinear wave interactions in condensed matter has been discussed repeatedly in early nonlinear optics, such studies were based on the principle of a weak local nonlinear response of medium. In fact, the strong nonlinear interactions in these cases arise because of the accumlation of coherent processes along the thickness of nonlinear medium.

At present the nonlinear materials with very high nonlinearity have been already discovered. Liquid crystals (LC) are one of the examples of such medium. Because of the high anisotropy as well as the collective behavior of molecules under any external field LC are unique nonhomogeneous anisotropic objects for nonlinear optics and their use leads to the qualitatively new phenomena.[1]

These effects are manifested in two aspects: 1) the threshold high nonlinearity of LC leads to the real laser-induced structural phase transitions without any temperature variation of the substance [2], and 2) the variations of the Bragg resonance conditions due to laser intensity lead to the self-action effects of the light in a spatially periodic nonlinear medium [3]. The first case concerns to nematic LC (NLC), the second one to cholesteric LC (CLC). Both of these cases are a realization in nonlinear optics of distributed feedback system [4]. For NLC the different spatially modulated structures arise in the medium [1]. In CLC the spatial scale of periodicity is changed. This leads to the following:

First, the intrinsic optical bistability (multistability) in wave phenomena without any external feedback [5]. The multivalued regimes occur because the propagating light waves induce the dynamic gratings of refractive index inside the highly nonlinear medium. The feedback arises even when there does not exist any wave reflected back from these structures, and that is determined by the nonlocal nonlinear response of the medium to the laser field because of the elastic forces [5].

Second, to the temporal instabilities and stochastic processes for the light-induced reorientation in LC (at CW pump radiation) which occur in such systsm [1,5]. These dynamic self-diffraction effects due to the anisotropy of the medium because of two waves of different polarizations, travelling through the medium, create laser-induced gratings along the thickness (d) of the sample (z-direction). An energy interchange (over time) occurs between two polarization components** in this laser-distored nonhomogeneous anisotropic medium with spatial modulation of the optical axis n(z).

The fluctuations of the molecules play a principal role in such systems. In fact, on the one hand namely the fluctuations in nonlinear dynamic system determine the development of the processes in it, in particular the transition to the chaotic regime [6]. On the

* Nagorniy Kharabakh, Armenia, 375000, USSR

** The description of this processes with analogy of two coupled (orthogonal) oscillators is useful [5].

other hand, the fluctuations can lead to the noise-induced phase transitions [7].

The study of all these (and other) processes in LC (in particuolar, in experiment) is very important from the physical point of view for understanding the phenomena in nonlinear dynamic systems of quite general type with a threshold behavior. Some of them we shall discuss in this paper.

Laser-Induced Bulk Gratings in NLC Oscillations Over Time

The laser-field action on LC leads to the spatial instability of an initial equilibrium state of the medium (homogeneous over the sample thickness d), and the reorientation effects, i.e., the light-induced structural phase-transitions, occur. The parameter changing under laser radiation is the angle of reorientation Ψ , which shows the deviation of the orientation of the local optical axis (direction $\vec{n}$) from the initial (unperturbed) direction ($\vec{n}_o \| z$) in accordance with the configuration of the light-wave field in the LC.

On the contrary, the distorted structure, produced in the LC by a laser radiation, has an opposite effect on the propagating light wave. The most interesting of these self action effects for the optical range are the schemes of dynamic self-diffraction of two or more waves when the light field induces the gratings of the refractive index n_r, on which the incident waves are diffracted [4]. These processes correspond to the frequency four-wave interactions in the usual terms of nonlinear optics.

The standard schemes of self-diffraction when two or more waves intersect (under a small angle θ) are a typical case for an isotropic nonlinear medium (different waves have the same polarizations inside the medium). The period of the recorded grating is: $\Lambda = \lambda/n_r\,\theta$, where λ is the wave length.

In the LC, as in any anisotropic medium, two-wave propagation condition can also occur (with a single input wave $\vec{E}$), because two waves of ordinary (A) and extraordinary (B) polarizations with refractive indexes n_{ro} and n_{re} , respectively, exhibit inside the medium. As long as two orthogonal components of polarization of the light field propagate along the thickness of the medium (a z - axis), we have a continuous variation of the phase retardation between them. Thus, a non-homogeneous (along z) polarization of the transmitted wave occurs. This means that the light field acts on the NLC molecules with various forces along the thickness. Therefore, the rotational moments affecting on the molecules are not equal. This leads (at a sufficient intensity) to the non-homogeneous reorientation of the molecules inside the medium and so, a bulk grating, which is determined by the polarizations of the transmitted waves, is induced in NLC.

Thus, the waves propagation in NLC are accompanied by writing the refractive-index gratings, which results in self-modulation of the transmitted light waves. Essentially, this case may also be ascribed to the scheme of dynamic self-diffraction. Here $\Lambda \approx \lambda/(n_{re} - n_{ro})$. In an experiment with LC, usually $n_r\,\theta << n_{re} - n_{ro}$, therefore, this grating has a much smaller period than that in scheme with the intersecting waves of identical polarizations.

We confine ourselves here to the comment that such induced gratings are not phase gratings only. An expression describing the relationship between the amplitudes of waves with orthogonal polarizations (A and B) not only includes a term corresponding to the nonlinear phase retardation φ^{NL} but also a term including the changes in the amplitude parameters. A characteristic spatial scale for this energy interchange in the NLC is determined by the value $i/\nu A_i^2$, where A_i is the intensity of each components of the light-field (i = 1, 2), $\nu = q_z^{-1}\varepsilon_a/16\pi K$, q_z is the z-component of the difference $\vec{q} = \vec{k}_e - \vec{k}_o$ between wave-vectors for e- and o- wave, $\varepsilon_a = \varepsilon_{\|} - \varepsilon_{\perp}, \varepsilon_{\|}$, $\varepsilon_{\perp}$ are the dielectric components parallel and perpendicular to the director and K are the optical anisotropy and elastic parameter of the NLC, accordingly [4]/ In the CLC the periodic energy redistribution between the waves leads to the so called pendulum beatings (over the space)[5].

The laser-induced bulk gratings in NLC represent a threshold effect when $\vec{E} \perp \vec{n}_o$*. In fact, because of the competition of two forces, namely the light field and the elastic force, the threshold reorientation occurs in this case (the free energy density of NLC under external field has a potential barrier separating two states of the system: intial and distorted).

For oblique incidence (but still $\vec{E} \perp \vec{n}_o$) two orthogonal components of light polarization (A and B) arising in this case due to the reorientation act in the mdedium, and so the orientation of the director $\vec{n}(r,t)$ is described by two angles ϕ and ψ ($\phi, \psi << 1$) in two orthogonal planes. The formation of the grating within the medium,

* We suppose the rigid boundary conditions in the sample.

induced by the light-field, in this case is described by the following formula (we display the expression for the angle $\phi(z,t)$ only as a function of the spatial (z) and temporal (t) variables [1,4]:

$$\phi(z,t) = C_o [(X^2 - q_z^2)/X] \sin Xz + q_z^2 z) e^{\nu t/\gamma}$$

where $$X = (Q/K_{33})^{1/2} \qquad (1)$$

$$Q = E_a/S\Pi) (k_o/k_c) A_{bound}^2 + K_{33} q_z^2$$

A_{bound} is the boundary magnitude of the field amplitude A, is the viscosity, C_o is the constant, the eigenvalues are determined by the boundary condition $(z = d) = 0$.

It should be noted that the grating period in equation (1) is governed by the parameter X which itself depends on the incident intensity butr not only on q_z. This is a very important point because the dependence of X on A determines the feedback in the system, which leads to the intrinsic optical multistability.

The most interesting effect which arise in this case are the transient processes, in particular the oscillations over time [5].

Temporal instabilities occur in any experiment with the LC when two waves of orthogonal polarizations propagate through the nonlinear medium and as a result, the reorientation arises in two orthogonal planes [5]. In fact, the different schemes of the dynamic self-diffraction of the light in an anisotropic medium have been realized in the experiments for the present time and the temporal pulsations have been obtained (for CW input) both in the NLC (two linear orthogonal polarizations of the light propagate through the medium) and in the CLC (two circular polarizations in the medium) [1].

The general behavior of these systems reduces to the following: there is a smooth transition from the steady-state reorientation via the damped oscillations to the oscillations which are unlimited over time, when the governing parameter is varied.

Qualitative explanations of the temporal instabilities in the LC can be done by an energy transfer and by a competition between the waves of different polarizations passing through the nonlinear medium [1,5]. THis approach is very close to the regenerative pulsations discussed e.g., in [8].

We shall discuss here only the case of the interaction of two counterpropagating waves ($\vec{E}_1$ and $\vec{E}_2$) with orthogonal linear polarizations in NLC at normal incidence.

The experimental results are shown in Figure 1. We measured the nonlinear phase retardation $\varphi_{1,2}^{NL}$ induced by laser radiation for each beam (the pump-probe technique has been used or just simple measurements by means of the ring patter (see e.g., [4]) for both passing beams).

An important point to mention is the development of the oscillations in an opposite phase for two waves in this geometry; that strongly supports the conjecture about an important meaning of the energy interchange between the amplitude of the waves (for the traveling, but not counterpropagating waves, the phase retardation effects play a principal role, because of an interference of the waves but not a direct energy interchange).

An exact theoretical analysis of this problem meets serious difficulties even for a numerical calculation. We shall discuss now the preliminary qualitative results only.

The steady-state solution for this case reults in the following equations for the amplitudes of two components of the forward (E_f) and backward (E_b) waves

$$\partial E_{fx}/\partial z = i\omega/c[E_{fx}(\varepsilon_{\perp}^{1/2} + (\varepsilon_a/2\varepsilon_{II})\psi^2 \cos^2\theta) + E_{fy}(\varepsilon_a/2\varepsilon_{II})\psi^2 \sin\theta\cos\theta]$$

$$\partial E_{fy}/\partial z = i\omega/c[E_{fy}(\varepsilon_{\perp}^{1/2} + (\varepsilon_a/2\varepsilon_{II})\psi^2 \sin^2) + E_{fx}(\varepsilon_a/2\varepsilon_{II})\psi^2 \sin\theta\cos\theta]$$

$$\partial E_{bx}/\partial z = i\omega/c[E_{bx}(\varepsilon_{\perp}^{1/2} + (\varepsilon_a/2\varepsilon_{II})\psi^2 \sin^2\theta) + E_{by}(\varepsilon_a/2\varepsilon_{II})\psi^2 \sin\theta\cos\theta] \quad (2)$$

$$\partial E_{by}/\partial z = -i\omega/c[E_{by}(\varepsilon_{\perp}^{1/2} + (\varepsilon_a/2\varepsilon_{II})\psi^2 \cos^2\theta) + E_{bx}(\varepsilon_a/2\varepsilon_{II})\psi^2 \sin\theta\cos\theta]$$

We used boundary conditions: at $z = o$

$$E_{fx} = E_{xo} = -A_{fo}\sin\theta_o + B_{fo}\cos\theta_o \; ; \quad E_{fy} = \theta o = A_{fo}\cos\theta_o + B_{fo}\sin\theta_o \; ;$$

at $z = d$ $E_{bx} = o = -A_{bd}\sin\theta_o + B_{bd}\cos\theta_o$; $E_{by} = o = A_{bd}\cos\theta_o + B_{bd}\sin\theta_o$;

and we neglected the interference between forward and backward waves (due to averaging over the space).

Because the light-induced reorientation is small enough we can assume that E_{fy}, $E_{bx} << E_{fx}$, E_{by} and so for the magnitudes of the wave we have from equation (2):

$$E_{fx} = E_{fxo}\exp\omega i/c[(\varepsilon_{\perp}^{1/2} z + (\varepsilon_a/2\varepsilon_{II})^z\textstyle\int_o(\psi^2\cos^2\theta)dz]) \quad (3)$$

$$E_{by} = E_{byd}\exp\omega i/c[(\varepsilon_{\perp}^{1/2} z + (\varepsilon_a/2\varepsilon)^z\textstyle\int_d(\psi^2\sin^2\theta)dz]$$

Using equation (3) the nonlinear phase retardation due to reorientation Φ^{NL} can be written for each wave in the form

$$\Phi_f^{NL} = \textstyle\int_o^d(\varepsilon_a/2\varepsilon_{II})\psi^2\cos^2\theta dz \quad (4)$$

$$\Phi^{NL} = -\textstyle\int_d^o(\varepsilon_a/2\varepsilon_{II})\psi^2\sin^2\theta dz$$

The summary value of Φ^{NL} for the passing beam (expressed in terms of the numbers of the ring pattern $N = \Phi^{NL}/2\pi$) is described by expression

$$N = N_f + N_b = \Phi_f^{NL}/2\pi = \textstyle\int_o^d(\varepsilon_a/2\varepsilon_{II})\psi^2 dz$$

The parameter N was constant during our experiment; this means that should be constant also. As to observation of the oscillations regimes they arise because the angle varies over time. According to equation (4) that should lead to the pulsations of the ring patterns for the forward and backward beams in opposite phase in agreement with our experimental data. More detailed and correct theory for transient regimes as well as for the arising temporal instabilities should be done in progress.

Light-Induced Threshold Reorientation in NLC as a Noise-Induced Phase Transition

The threshold reorientation of NLC in external field starts from random thermal fluctuations of the director. This means that the noise plays a principal role for the light-induced threshold effects and their correct description should be statistical. Good approach for that gives the Fokker-Planck equations for the Ornstein-Uhlenbeck processes [7]*.

In previous item we discussed the question how in deterministic nonlinear system with a few degrees of freedom (two orthogonal polarizations in the medium) the temporal instabilities arise. Now we shall analyze the role of the noise (fluctuations of the director); the influence of the noise does not only result in the disorder in the nonlinear system, but also induces a definite order and new states, so we can speak about the noise-induced phase transition [7].

Because it is a nonequilibrium phase transition in open system (th medium is irradiated by the laser beam continuously), the separation of the parameters into two groups, namely enternal (λ) and internal (x) have not any physical sense in contrast with ordinary equilibrium thermodynamics. So, the nature of the developing fluctions in the system does not play a principal raole in both cases, i.e., the fluctuations of the external applied field (the steady-state stochastic process, λ_t is described at $\lambda_t = \lambda + \xi_t$, where is the average (regular) part, ξ_t is the noise) or of the internal medium fluctuations ($x_t = x + \zeta_t$) are similar. This is strictly true when the multiplicative noise occurs, and we shall use this approach for LC under external field**.

The stochastic differential equation for the problem of our consideration has a form

$$\dot{x}(t) = h(x[t]) + \mu(\lambda)\, g(x[t]) \qquad (5)$$

where h, μ, g are the nonlinear functions in the general case and they determine the physical phenomena in the system. The fluctuations are described in equation (5) by the substitution $\lambda \to \lambda_t = \lambda + \xi_t$ or $x \to x_t = x + \zeta_t$ for the external field or for the medium parameters, accordingly. The second term in the right-hand side of equation (5) where $g(x[t]) \neq \text{const}$, gives the dependence of the influence of the external field (λ) on the system state (x[t]); in particular the leads to the multiplicative nature of the noise.***

Usually in equation (5) the fluctuations of the external field only are considered in such form ($\lambda_t = \lambda + \xi_t$), but the medium fluctuations (the parameter x) are described just in additive form, i.e., in the right-hand side of equation (5) the stochastic force f(t) have to be included.

Let us apply this approach to the threshold reorientation of NLC in the light field $\vec{E}(\vec{n}_o \to z, \hat{E} \vec{n}_o)$. The director fluctuations δn_t^2 can be described in the form $\vec{n}_t = \vec{n}_o + \delta\vec{n}_t$, where $\delta\vec{n}_t \perp \vec{n}_o$ (because $n^2 = 1$).****

---

*In the model of stochastic process $x(t)$ [Brownian Movement] the velocity $\dot{x}(t)$ is the basis for the description in this case but not the position $x(t)$ of the particle (Viner process).

**That is the difference of our consideration from that used in [7].

***If $g(x[t]) = \text{const}$ the system has the additive (Langevin) noise only over the external field.

****The high nonlinearity of NLC and the intense thermal fluctuations in them are the consequence of the manifestation of the fluctuative-dissipative therem [5]

Because of the symmetry factor two uncoupled states ($\delta n_t > o$, i.e., the reorientation angle is $(+\psi_m)$ and $\delta n_t < o$, i.e., $-(-\psi_m)$ take place in the system when $I < I_{th}$ (where I_{th} is the threshold intensity), and the fluctuations δn_t move it about these two states ($\delta n_t = o$, i.e., $\psi_m = o$, is tan internal boundary for this case [7]).

But the small fluctuations δn_t could not vary the state of the system (even when the field $\vec{E} \perp \vec{n}_o$ is applied) till that the stabilizing (about the initial orientation) rotation moment of the elastic forces due to rigid boundary conditions is above the magnitude of the destabilizing rotation moment due to the light field. The free energy densities coupled with these two processes are described by the relations

$$F_{elast} = \frac{1}{2} K(\partial \delta n_t / \delta z)^2 \sim \frac{1}{2} K(\partial \psi_m / \delta z)^2$$

and $$F_{field} = \frac{\varepsilon_a}{8\pi} (\delta \vec{n}_t \vec{E}) (\delta \vec{n}_t \vec{E}^*) \quad ,$$

accordingly, where $$\vec{E}_{real} = \frac{1}{2} (\vec{E} e^{i\omega t} + \vec{E}^* e^{-i\omega t}).$$

The reorientation occurs in NLC when these two moments equalize ($F_{elast} = F_{field}$) and so, the threshold intensity $I_{th} \sim E^2$ is determined by that. When $I \gtrsim I_{th}$ the system comes to one of two possible stable states $(+\psi_m)$ oz $(-\psi_m)$ for any magnitude of the fluctuations, and the value $\psi_m = o$ determines the unstable state ($\psi = o$ is already a natural boundary). This variation of the boundary nature is one of characteristic signes of noise-induced phase transitions**, and the light-induced reorientation in NLC can be interpreted in this way. In fact, because the interaction between $\vec{n}$ and $\vec{E}$ is described by the term $F_{interact} \sim (\vec{n} \vec{E}) (\vec{n} \vec{E}^*)$, the nature of the noise n_t is principally multiplicative. But the fluctuations of n and E are equivalent ($F_{interact}$ is symmetrical over $\vec{n}$ and $\vec{E}$) , and so the director fluctuations for our case have to lead to the effects being similar to those the external field fluctuations lead to, as it was discussed above.

Mathematically this fact can be verified if the equation for the light-induced threshold reorientation of NLC is rewritten in the form

$$\dot{\psi}_m = -\alpha_m + \beta | E_x |^2 \{\psi_m - 4 \psi_m^3\} + \tag{6}$$

$$+ (\beta/2) | E_x |^2 \{\delta\psi_m (1 - 4 \psi_m^2) - (\delta\psi_m)^2 2\psi_m\}$$

where we used the simplest geometry for the threshold reorientation under light field $\vec{E}$ for normal incidence: $\vec{E} \perp \vec{n}_o$, $\vec{E} = (E_x, o, o)$, $\vec{n}_o \parallel z$, ψ_m and $\delta\psi_m$ are the reorientation angle and its fluctuations (instead of the expression $n_t = n_o + \delta n_t$ we use $\psi(t) = \psi_m + \delta\psi_m$) in the centre of the sample ($z = d/2$, d is the thickness): $\psi(z,t) = \psi_m(t) \sin(\pi z/d)$, $\delta\psi(z,t) = \delta\psi_m(t) \sin \pi z/d$, $\alpha = \frac{K}{\gamma} (\pi / d)^2$, $\beta = \varepsilon_a / B \pi \alpha$, γ is the viscosity. We did the following suppositions: the anisotropy of both elastic and optical properties of NLC as well as the angles ψ_m, $\delta\psi_m$ are small enough.

---

*The high nonlinearity of NLC and the intense thermal fluctuations in them are the consequence of the manifestation of the fluctuative dissipative theorem [5].

**Two transitions occur, in principle, for that case. The first one is when the steady point $\psi_m = o$ becomes unstable, and the second one when the new stable state arises ($\psi_m = o$). But in approximation of white noise (our case) these two transitions are practically coincided [7].

These ordinary in optics of LC conditions permitted us to neglect in equation (6) the terms in the order of power ψ_m^3 for the regular part and $(\delta\psi_m)^2$ for the fluctuated part.

The equation (6) including the fluctuations of $\delta\psi_m$ both in the linear and nonlinear (quadratic) forms is a complete analogy of the fundamental equation (5) which is usually used for describing the noise-induced due to the field fluctuations phase transitions [7]. Therefore, in fact, all physical consequences from these two equations should be the same.

The most interesting effect is that the value of I_{th} is shifted because of the noise $I_{th} = I_{th}^{o} - \sigma^2/2$, where the noise intensity is $\sigma^2 = \langle(\delta n_t)^2\rangle$. For the LC the level of noise defines the scattering intensity $I_{scat} \sim \sigma^2$; both of them can vary by the temperature T change, in particular near the phase transition (from nematic to isotropic phase) temperature T_c. That gives a simple procedure for a verification of the mentioned above dependence $I_{th}(\sigma)$ by comparison of two independent measurements in a nematic phase:

$$I_{th} = I_{th}(T_c - T) \quad \text{and} \quad I_{scat} = I_{scat}(T_c - T) \quad .$$

Our study shows a very good agreement of these measurements, see Figure 2, (I_{th} decreases versus $(T_c - T)$ [9], I_{scat} increases versus $(T_c - T)$ [10], with respect to the expected dependence $I_{th}(\sigma)$.

Note, that the traditional classification of the phase transitions is not applied to the discussed noise-induced transition. In fact, for the threshold reorientation in NLC we obtained two results. On the one hand, the critical behavior of the response time τ versus $(I - I_{th})$ [2,9] is exhibited (like in the second order phase transitions); on the other hand, the maximum of the I_{scat} arises near the I_{th} point [5,10] (like a critical opalescence in the first order temperature phase transition).

We shall point out the possibility of the controlling of the noise intensity: this can be done using except for the light $\vec{E}$, an additional quasistatic field (e.g., magnetic) stabilizing or destabilizing the director fluctuations [10]*. The nature of the phase transition may be also varied in this case (the second order phase transition becomes the first order one [2]).

The most interesting results should arise for a multidimensional system; one special case (two orthogonal polarizations of the light) has been already discussed by us in Item 2. The analogy with two coupled nonlinear oscillators in the presence of noise is very useful for this case [5].

In conclusion, new effects of intrinsic optical multistablity and temporal instabilities in the wave interactions for a non-homogeneous anisotropic medium with a highly threshold nonlinearity are discussed in the present paper. Two waves of different polarizations traveling through the medium create laser-induced bulk gratings of the refractive index, and the instabilities arise due to an energy interchange and a competition between the two light polarization components in the nonlinear medium. The feedback for such wave interactions arises because of the nonlocal response of an anisotropic elastic medium to the external field.

The considered phenomena are the development of the general case when the stochasticity arises in a deterministic dynamic system with a few degrees of freedom. Two orthogonal polarizations of light for our case present a problem similar to that of two coupled pendulums.

Because of the molecular fluctuations, the light-induced effects in LC may be considered as the noise-induced phase transitions.

*This measurements allow to study the peculiarity of the induced transitions for the colored noise [7].

References

1. Arakelian S.M., Chilingarian Yu.S., Alaverdian R.B., et al, J. Phys. Fr. 50 , p 1393 (1989).

2. Ong H. L., Phys. Rev. A28, p 2393, (1983)
Karn A. J., Arakelian S.M., Ong H.L., Shen Y. R., Phys. Rev. Lett., 57, p 448 (1986).

3. Winful H. G., Phys. Rev. Lett., 49 p 1179 (1982).

4. Arakelian S. M., Chilingarian Yu.S., IEEE J. Quant. Electron, QE-22, p 1276 (1986).

5. Arakelian S.M., Usp. Fis. Nauk, 153, p 579 (1987).

6. Gibbs H.M., Optical Bistatiblity: Controlling Light with Light. Orlando: Academic Press 1985.

7. Horsthemke W., Lefever R. Noise-Induced Transitions Berlin, Heidelberg, NY: Springer

8. McCall S. L., Applied Physics Letter, 32, p 284 (1978).

9. Durbin S. D., Arakelian S.M., Shen Y.R., Phys. Rev. Letter., 47, p 1411 (1981).

10. Arakelian S.M., Arushanian L. E., Chilingarian Yu.S., FETPh, 80, p 1186 (1981)
J. Tekhnicheskoi Fix. 56, p 1949 (1986).

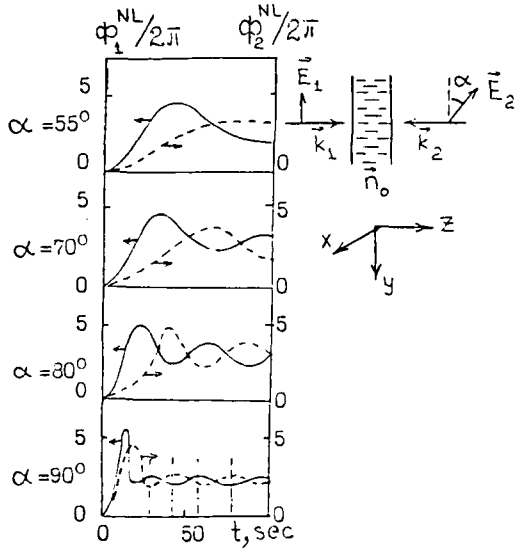


Figure 1. Oscillations of $\varphi_{1,2}^{NL}$ in the field of two counterpropagating waves with linear polarizations $\vec{E}_1$ and $\vec{E}_2$ (CW Ar^+-laser, λ = 0.515 um), for the different angles $\alpha = \vec{E}_1 \widehat{} \vec{E}_2$, $\vec{E}_1$ xz-plane. The director $\vec{n}$ goes out of the yz-plane due to the reorientation, NLC 5CB, d=200 um, $I_1 = I_2$ = 220 W/cm^2. The oscillations for two waves ($\vec{E}_1$ - soild curve and $\vec{E}_2$ - dashed curve) have the opposite phases (indicated by the dashed lines for α = 90°).

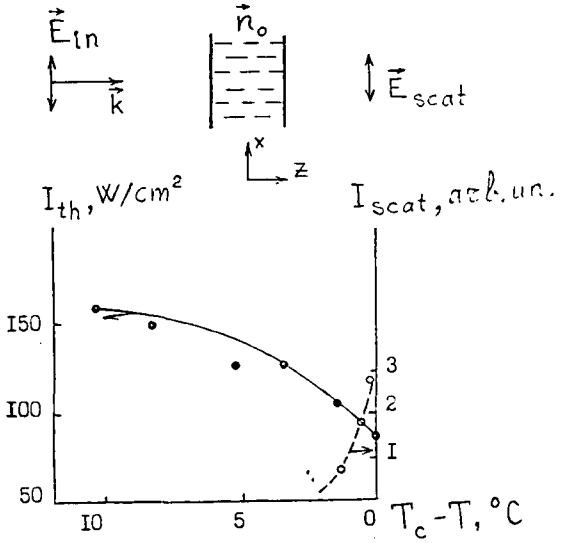


Figure 2. The threshold intensity I_{th} for the light-induced reorientation in NLC 5CB (d = 250 um, n_o z, $\vec{E}$ $\vec{n}_o$) and the normalized scattering intensity I_{scat} of the light in NLC MBBA (d = 50um, $\vec{n}_o$ $\vec{z}$, $\vec{E}_{in}$ $\vec{n}_o$, $\vec{E}_{scat}$ $\vec{E}_{in}$) both versus temperature (T_c - T), where T_c is the temperature of the phase transition from nematic to isotropic phase. The I_{scat} is determined by the director fluctuations ($I_{scat} \sim \sigma^2$, where σ^2 is the noise intensity $\sigma^2 = \langle (\delta n_e)^2 \rangle$).

EXPERIMENTAL DEMONSTRATION OF LARGE APERTURE COMPRESSION OF SHORT LASER PULSES IN BRAGG - RESONANCE CONDITION

R. B. Alaverdian*, S. M. Arakelian, Yu.S. Chilingarian, L. P. Gevorkian, B. A. Makarov, and T. A. Papazian

Yerevan State University
Yerevan, Armenia, 375049 USSR

Abstract

Effective universal compression of picosecond laser pulses with large aperture, high energy transformation and high level of break-down intensity has been obtained in cholesteric liquid crystal. The preliminary compression (before the outgoing from the laser pulse will become bandwidth-limited) occurs without any nonlinear effect, which is necessary for further compression.

The universal method of compression of short laser pulses till femtosecond pulse durations is based on two condtions [1].

First, the temporal phase (frequency) modulation is necessary, and as a result the instantaneous frequency becomes a linear fuction over time, i.e., the distribution of frequencies over pulse duration is concretized.

Second, using the dispersive delay line which leads to the effect that e.g., the rear of the pulse will travel faster than the front, the further compression of such modulated pulses becomes possible. In present paper we show (both in theory and in experiment) that a thin layer of cholesteric liquid crystal (CLC) may be used as a dispersive delay line.

The physics of this phenomenon is determined by the effect of nonstationary dynamic diffraction of partially modulated light pulses on a spatially periodic structure, by which the CLC (3D-structure) is characterized, under condition of the Bragg resonance for the input radiation [2].

Standard CLC-cell represents such a simple element, a compact autonomous device directly placed under laser radiation without any additional optics and alignment. This device is a very good candidate for preliminary express - compression of the picosecond light pulses of a real laser system, and the output radiation becomes bandwidth - limited.

The qualitative picture of discussed compression being a consequence of the high spatial dispersion of the medium is determined by the dependence of the directions of diffracted (on the grating) waves** on the frequency. Because the input laser pulse has a natural phase modulation giving the distributions of the different spectral components over the pulse duration, their lengths of the optical ways are not equivalent after diffraction (scattering) and as a result the situation becomes possible that the rear of the pulse overtakes its front (this is a complete analogy with the compression in the standard scheme with two coupled diffraction gratings). This mechanism of the compression is similar both for the scattered (A_h) and for the transmitted (A_0) waves because their being coupled and the energy exchange. The process is most effective when the condition of exact Bragg resonance is satisfied for the wave vectors with frequency ω_c being central for the pulses (maximum of their temporal profiles): $\vec{K}_0(\omega_c) + \vec{q} = \vec{K}_h^c(\omega_c)$, where $q = 2\pi/\Lambda$, $\Lambda = 2p$ is the grating period (we suppose that the spectral bandwidth of the resonance is much smaller than the spectra of the input pulse***). Then the spectral components corresponding to the front (ω_+) and to the rear (ω_-) - let us suppose $\omega_+ > \omega_-$ - e.g., for the scattered pulse (A_h), have the detuning Δ of opposite signs.

---

*Nagorniy Kharabakh, Armenia, 375000, USSR

**The two-ways approximation (A and A are the amplitudes of the transmitted and diffracted [scattered] waves, accordingly) of dynamic theory of electromagnetic radiation diffraction on the spatially modulated structure are used.

***If this condition is not satisfied all spectral components of the pulse have equivalent velocities of propagation.

from the direction $\vec{k}_h(\omega_c)$; $\vec{k}_h(\omega_+) - \vec{k}_h(\omega_c) = +\vec{\Delta}$. This detuning can be compensed by variation of the scattering angle (for oblique incidence) and so, the directions $\vec{k}_h(\omega_+)$ and $\vec{k}_h(\omega_-)$ are not coincided with $\vec{k}_h(\omega_c)$ and with each other; they are shifted in the opposite directions from the direction of $\vec{k}_h(\omega_c)$. This means that the lengths of the optical ways of different spectral components of the pulse are not equivalent (e.g., let us suppose them to be greater for $\omega>\omega_c$ and smaller for $\omega<\omega_c$); so, the compression may arise at corresponding magnitudes of the propagation velocities of the components.

If the frequencies filling the pulse are near the Bragg resonance range [e.g. for $\vec{k}_o(\omega_+) + \vec{q} = \vec{k}_h(\omega_+)$], but on the one side only from it, the compression is also possible. However, it should be less effective because the directions of $\vec{k}_h(\omega)$ for all frequences ($\omega_- < \omega < \omega_+$) are shifted in the same side in comparison with the $\vec{k}_h(\omega_+)$ direction for this case, i.e., for each spectral component of the pulse the length of the optical way is either decreasing or increasing (but in different degree).

The compression may occur due to the temporal dispersion as well. Because the propagation velocities of the front and the rear are different, these parts of the pulse may be overlapped (our case corresponds to the frequency range far from the eigen-resonances in the medium, so the rear and the front of the pulse propagate in the traveling direction). This mechanism of compression is not directly coupled with the grating in the medium and is supplementary to discussed above. Note, that for the collinear geometry of the dynamic scattering on the grating (the vectors $\vec{k}_o$, $\vec{k}_h$ and q are parallel) the resonance condition can be satisfied only for counter-propagating waves A_o and A_h ($\vec{k}_h = -\vec{k}_o$) for the spectral components of the pulse which have equivalent frequencies; when the frequencies are not equivalent (in the range of spectral bandwidth of the phase-modulated pulse) the propagation of traveling waves A_o and A_h ($\vec{k}_o/\vec{k}_o$ $\vec{k}_h/\vec{k}_h$) is allowed as well.

Very simple numerical estimation of the characteristic length L_f of the compression can be done by obvious discussion for these two mechanisms. In fact, in ordinary cases of the 1D sinusoidal grating, the refractrive index now can be represented in the form [5]:

$$n(\omega) = n_o(\omega) + 0.5\,[n_{+1}\exp(iqz) + n_{-1}\exp(-iqz)],$$

where $n_{+} = n_{-1} \equiv n_1$). For small scattering angles of the light we can use the expression for the propagation velocities $v(\omega)$ of the spectral components of the pulse as for collinear geometry, i.e., $|\vec{v}(\omega)| > (2\omega/q)(1 + n_1/2\,n_o)$ for $\omega \lesssim \omega_o$ and $|\vec{v}(\omega)| \lesssim (2\omega/q)(1 - n_1/2\,n_o)$ for $\omega > \omega_o$, where ω_o is the Bragg resonance frequency.

For the first mechanism (the front and the rear run towards each other) L_f is determined by the condition that on this length the time of the group delay of the pulse edge frequencies is equivalent to the initial pulse duration τ_o, i.e., $L_f = (\tau_o/2)\,|\vec{v}(\omega_-)|\,|\vec{v}(\omega_+)|/(|\vec{v}(\omega_-)| - |\vec{v}(\omega_+)|) \approx (\tau_o/2)[(2\omega_c/q)n_1/n_o]^{-1}(2\omega_c/q)^2$. For typical numerical parameters $\tau_o = 30$ psec, $n_1 \sim 1$, $n_o = 1.5$, and taking into account that $\omega_c = 2\pi c/\lambda_c$, $q = 2\pi/\Lambda$, $\Lambda = 2p \sim \lambda_c \sim 1$ μm we have $L_f \approx 1.4$ cm.

For the second mechanism (the rear overtake the front) $L_f \approx 2\,\tau_o[2(\omega_+ - \omega_-)/q]^{-1}(2\omega_c/q)^2$. At $(\omega_+ - \omega_-) \approx 1$ cm^{-1}, $\tau_o = 30$ psec, $2p \sim 1$ μm we have $L_f \approx 1.2$ km.

Thus, the compression occurs because of the spatial grating in the medium, and we can neglect the temporal dispersion in our case.

For theoretical analysis two possible geometries for the dynamic diffraction of the light pulses on the periodic structure are usually taken to consider - Bragg and Laue cases* - in approximation of two waves, i.e., transmitted (the wave vector is $\vec{k}_o$, the amplitude is A_o) and scattered ($\vec{k}_h$, A_h) - see e.g., [3]).

The difference between these two geometries is determined by the direction of propagation of the waves (A_o and A_h) which are mutually coupled by energy. In the Laue geometry two waves transmit the energy in the same direction in contrast with the Bragg case when the waves are counter-propagating. Mathematically this demands different boundary conditions both at the entrance ($z = 0$) and the exit ($z = d$), where d is the thickness of the medium) planes. The following relations (at the entrance surface e.g.) correspond to these cases:
$\gamma_o \gamma_h > 0$ and $\gamma_o \gamma_h < 0$ for the Laue and Bragg geometries, accordingly (where $\gamma_o = \vec{k}_o \vec{1}_o$, $\gamma_h = \vec{k}_h \vec{1}_o$, $\vec{1}_o$ is the perpendicular to the surface of the CLC-cell)[4]. The character of the obtained (steady-state) solutions is principally different for these two geometries. For the first one the periodic behavior of the fields amplitudes A_o and A_h (over the sample thickness) occurs (so called pendellosung fringess (pendulum beatings) with characteristic spatial scale L_e which is the extinction length).

*Both of these cases correspond to the light transmittion through the periodic medium under condition of the Bragg resonance.

For the second one the hyperbolic solutions of A_o and A_h arise (in optics this problem is discussed, e.g., in [3,5]).

But sometimes the division on these two geometries is quite artificial and the mixed case realized in the real experiment (in particular for the narrow beams and for the spatially limited samples in two orthogonal directions) see Figure 1a [4]*. This result has to be especially taken into account when the transmitted beam ($\vec{k}_o$, A_o) only is detected in experiment. In fact, when the entrance point happens to be the edge point of the sample, one can see that A_o is the sum of the partial amplitudes A_{oi} for each possible geometry [4]**.

Our preliminary estimations show that the more effective compression of the laser pulses occurs in the Laue geometry (Laue-Laue case by more exact classification). So, we may take into account only the amplitude A_{oi} doe Laue geometry, and the analytical solution for this simplest case can be obtained.*** We shall discuss it below.

The initial system of two coupled equations describing the temporal evolution of slowly varing complex amplitudes of passing (A_o) and scattered (A_h) waves (E_o and E_h, correspondingly) under condition of exact Bragg resonance for symmetric Laue geometry (see Figure 1b) is following [6]

$$i\left(\pm \operatorname{tg}\theta\,\frac{\partial}{\partial x}+\frac{\partial}{\alpha}+\frac{1}{v\cos\theta}\,\frac{\partial}{\partial t}\right)A_{o,h}=L_e^{-1}\,A_{h,o} \qquad (1)$$

where the signes "+" correspond to A_o and A_h, accordingly; v is the velocity of the traveling wave (which is the same for both waves); L_e is the extinction length (showing the characteristic spatial scale of pendulum beatings when the energy exchange between A_o and A_h waves occurs); $\vartheta = \Pi/2 - \vec{1}_o$, $\vec{k}_o$ is the incident angle; z and x are coordinates along (z) and across (x) the sample thickness; t is the time. We assume that there is no absorbtion in the medium, the anisotropy of CLC is small, the light field is quasi - coherent and θ is sufficiently big: $\theta \gtrsim \Pi/2 - \arcsin(\xi_1/\xi_o)^{1/2}$, where $\xi_{1,o}$ are the dielectric optical permittivities of CLC ($\xi_1 << \xi_o$, ξ_1 being the anisotropy and ξ_o the average magnitude). The following definitions will be necessary further: $A_{o,h} = \vec{E}_{o,h}\,\vec{n}_{o,h}\sin\theta + i\vec{E}_{o,h}\,\vec{n}_{o,h}$, $L_e = (4\xi_o\cos\theta)/\xi_1 k_o(1+\sin^2\theta)$, where $\vec{k}_{o,h}$ are the wave vectors, $\vec{n}_{o,h}$ are unit vectors, $\vec{n}_o \perp \vec{k}_o$, $\vec{n}_h \perp \vec{k}_h$ and the spatially periodic linear susceptibility of the medium is $\chi(r) = \Sigma_q e^{i\vec{q}\vec{r}}$, where $\vec{q}$ is the vector of inversed lattice (in our case $q = 2\Pi/\Lambda$, $\Lambda = 2p$, p being the pitch of the helical structure of CLC). The Bragg resonance condition is $\vec{k}_h = \vec{k}_o + \vec{q}$, $|\vec{k}_o| = |\vec{k}_h|$**** The boundary conditions are

$$A_o(z=o) = E\exp(-x^2\cos^2\theta/r_o^2 - (t - x\sin\theta/v)^2(1 - i\alpha)/\tau_o^2)$$

$$A_n(z = o) = 0 \qquad (2)$$

Equations (2) determine (i) the initial phase modulation of the radiation in the square form, (described by the parameter $i\alpha t^2$) and (ii) the Gaussian light pulse over both space and time (r_o is the spot size of the laser beam, τ_o is the pulse duration); $\alpha = \alpha_o \tau_o^2$, where α_o is the magnitude of the phase modulation.

The standard procedure to find the solution of equation (1) is based on the method of repeat shortening of the wave equations [3]; using equation (2) we have the following expressions for normalized intensities for passing and scattered waves [6]:

---

*The different conditions at the entrance and at the exit surfaces leads to the Laue-Laue, Bragg-Bragg, Laue-Bragg (two types) and Bragg-Laue cases.

**The calculations used the spherical-wave theory.

***For Bragg geometry the problem is not solved analytically for the light pulses.

****We neglect the shift from the exact Bragg resonance because the exact tuning to resonance can easily be done by variation of the sample temperature(see Item 4).

$$|A_{o,h}|^2 = |F_1|^2 + |F_2|^2 \pm 2\mathrm{Re}\{F_1 F_2^* \exp(2iz/L_e)\} \quad , \tag{3}$$

where* $$F_{1,2} = \frac{E}{2f_{1,2}^{1/2}} \exp\{\pm \frac{i}{2} \operatorname{arctg} \frac{b}{a_{1,2}} - \frac{x^2\cos^2\theta}{r_o^2 f_{1,2}^2} (a_{1,2} \pm ib)$$

$$- \frac{1}{\tau_o^2 f_{1,2}^2} [(t-z/v\cos\theta - x\sin\theta/v)^2 (a_{2,1} - i(\alpha a_{1,2} \mp b)]$$

$$+ \frac{z}{L_e'} (t - z/v\cos\theta)^2 (b \mp a_{1,2} - i(\alpha b \pm a_{1,2}))] \} \quad ; \tag{4}$$

$$f_{1,2} = (a_{1,2}^2 + b^2)^{1/2} \quad , \quad a_{1,2} = 1 \mp \alpha\gamma z/L_e \quad :$$

$$b = (z/L_e' + \gamma z/L_e') \quad , \quad \gamma = 2\sin^4\theta\, L_e^2 (\cos\theta\tau_o v)^{-2} \quad ,$$

$L_e' = r_o^2/2L_e\sin^2\theta$ is the length of the extinction refraction (there should be a spatial shift (in cross direction) between passing and scattered beams). Note, that in steady state ($\tau_o \to \infty$) the solutions of (3), (4) give the very well known result (see e.g., [3]).

The analysis of (3), (4) shows that the shape of frequency modulated pulse varies in rather complicated manner at the dynamic scattering. Three effects take place: (1) the oscillations on the temporal envelope of the pulse; (2) (2) the shift of the maximum intensity of the pulse; (3) the variation of the effective pulse duration. These phenomena are due to the difference in the behavior of two functions f_1 and f_2 in equation (4) when $\alpha \neq o$** $f_1(z)$ has a minimum for $z = L_f = (\alpha\partial)^{-1}L_e$, but $F_2(z)$ is a monotonously increasing quantity (see Figure 2). The minimal pulse duration occurs at the distance L_f (this is a point of the so called "temporal focus").

In the case of $L_f \ll L_e$ and $\alpha \gtrsim 10$ the dependence $|A_{o,h}(z = L_f)|^2$ rduce to a simple form

$$A_{o,h}(z = L_f)|^2 \approx |E^2\{\phi(\alpha,T_o) \pm (\alpha/8)^{1/2}\exp(-\alpha^2T_o^2)\cos(2/\alpha\partial + \Pi/4 + \alpha^3T^2)\}| \quad , \tag{5}$$

where $T_o = (t - x\sin\theta/v - (\alpha\partial v\cos\theta)^{-1}/\tau_o$;

$$\phi(\alpha,T_o) = (\alpha/4)\exp(-2\alpha^2T_o^2).$$

The second term in the right hand side of equation (5) responds to oscillations of the temporal envelope; the average profile of that is determined by the function $\phi(T_o)$***. The dependences of $\phi(T_o)$ for different α are shown in Figure 3. The efficiency of the pulse compression increases with the pulse duration decreases times, the peak power increases $\alpha/4$ times in comparison with the initial one, and the compressed pulse contains

**For a pulse with a plane phase distribution ($\alpha = o$) the condition $F_1 = F_2$ is satisfied and so, ordinary dispersive spreading out occurs.

***Because at $z = L_f$ the term F_1^2 in equation (3) is the greatest, the pendulum beatings give small corrections on the temporal dependencies and have not direct influence on the compression in the presented linear case when f_1 has only one minimum. This leads to the fact that A_o and A_h are practically equivalent from the energetic point of view.

*THE signes "$\pm$" in equation (3) determine the pendulum beatings.

twenty-five percent of the input energy. The latter fact takes place because the energy of the initial pulse is distributed equally between passing and scattered beams. Each of them has wide pedestal with a narrow peak in the center* (cf [2]) which also have equal energy distribution**. The final picture of the pulse shape is formed over the traveling of the beams in the medium.

Using equation (5) we can obtain that the compression α times of the input pulse (of duration τ_o) requires a sample thickness $L \approx L_c = (\alpha\gamma)^{-1} < L_e'$. The numerical estimation for CLC (the typical magnitudes of the parameters are:

$$L_e 10^{-2} - 10^{-3}\text{cm}, \theta > 80^\circ, \gamma \sim 10^{-26} - 10^{-22}/\tau_o^2)$$

and for $\alpha \sim 30$ leads to the compression factor α for the values of τ_o from 10^{-12} to 10^{-9} sec because the inequality $(\alpha\gamma)^{-1} < L_c/L_e$ has to be satisfied.***

It is self-evident that the discussed above theoretical analysis can be considered as a first approximation only. In fact, many real factors are not taken into account; in particular, not all-coherence of the input light; its fluctuations both amplitude and phase; the anisotropy of CLC (the refractive index difference n_a) gives the range of the wavelengths for the Bragg resonance $\sim pn_a$, but not one value only; the twisted (helical) structure but not only a simple periodicity for CLC etc. For example, the last property leads to the fact that the eigen waves in CLC are circularly polarized (for infinite samples and normal incidence) in opposite directions (the energy distribution between these waves is equal (on 50%) for the linear polarized input light and for the ideal conditions). Each eigen wave of CLC gives two waves (A_o and A_h) in two wave approximation of the theory of dynamic diffraction (only one eigen wave is excited in CLC when input radiation is circularly polarized in accordance with the sign of the helix). But for normal incidence of the light on the CLC an exact steady-state solution may be obtained and so, the approximation of the dynamic diffraction theory is not used.

Note, that the theory may be applied practically without any correction to the compression of x-ray pulses propagating through the solid crystal (dynamic scattering on the lattice) - cf. [6].

In our experiment the radiation of picosecond YAG: Nd^{3+} laser ($\lambda = 1.06\mu m$) has been used as an input beam. The parameters of the radiation were: the repetition frequency - up to 5Hz; the polarization - linear; the spot size - 2 mm; the single pulse energy - $0.5\ 10^{-3}$J; $\tau_o \equiv \tau_{in} \approx 30\ 10^{-12}$sec.

An original automatic system based on PC - computer was used for data processing; the pulse durations were measured by correlation technique at passage of the radiation through the uniaxial crystal (the range of measurements by this technique is 0.1 ÷ 150 psec).****

The laser radiation had a natural frequency modulation; independent (of the pulse duration) measurements of the bandwidth of the laser oscillation $\Delta\omega_{osc}$ gave the value $\Delta\omega_{osc} \approx 4 \div 5\text{cm}^{-1}$. This leads to the estimation of the additional broadening (due to the eigen modulation of the radiation in contrast to bandwidth-limited light pulse for given $\tau_o - \tau_o \Delta\omega_o = 2$ for the Gaussian temporal profile), described by a factor $2(\Delta\omega_{osc}/\Delta\omega_o \sim 2)$.

The standard CLC-cell (CLC-layer being along z-coordinate between two glass plates, the aperture - 3x4 cm) - see Figure 1b, had a homotropic alignment of helical axis (the direction is given by the vector $\vec{q}$, $\vec{q} \parallel \vec{z}$). The spatial period of CLC (the helical pitch $2p = \Lambda = 2\pi/|\vec{q}|$) was changed continuously by the variation of temperature T, and therefore the exact Bragg resonance condition could be satisfied (approximately at room temperature for used mixture of CLC). The dependence p(T) is shown in FIgure 4 (this is a pitch of the free helix for thick samples). The temperature stabilization was ~ 0.2°C, but in real experiment on compression the stabilization in the range of a few degrees was practically sufficient. The absorption and statistical scattering losses in CLC-cell were seventeen percent (measured far from the Bragg resonance region). The break-down intensity was not less than 2 GW/cm^2 for used mixture of CLC.

---

*This peak demonstrates the degree of compression.

**The functions $F_{1,2}$ in equation (3) are responsible for that. The principal point here is that the behavior does not depend on sign of α (the inversion of the sign leads to the mutual redenoting in fuctions $F_{1,2}$ only) in contrast with the standard schemes of pulse compression.

***This gives the condition $L_c/L_e \sim 10 \div 100$.

****The averaging over 1024 pulses has been used.

The pulse duration of the outgoing from the CLC-cell radiation (τ_{out}) as well as the compression factor ($s = \tau_{out}/\tau_{in}$) versus T were measured for different thicknesses d of the CLC-layer. The experimental dependences s(T) are shown in Figure 5 in arbitrary units for three magnitudes of d*. The absolute measurements of τ_{out} are shown in Figure 6 for $d = 300$ μm corresponding to the maximal factor s. The radiation of whole laser beam aperture has been detected; the pulse energy after compression was about 20% of the input pulse energy (the input radiation had a linear polarization**).

We have not seen any influence of self-action effects of laser radiation; therefore the propagation of the frequency modulated light pulse through the linear periodic medium took place in our experiment.

The obtained results agree qualitatively with the theory described in item 3.*** The characteristic distance for the development of the effects of dynamic diffraction ($z \sim L_f$) in experiment corresponds to $d \geq 300$ μm. For that thickness practically total compression ($s \sim 2$) in CLC has been determined for the given eigen frequency modulation (determining $\Delta\omega_{osc}$) of the input laser pulse, and so the outgoing pulse became bandwidth-limited ($\tau_{out}\Delta\omega_{osc} \sim C_B$, where C_B is a pulse-shape dependent factor; $C_B = 2$ for our case)****.

We can estimate the magnitude of the distance L_f for the compression of laser pulses in CLC (the focus of the "temporal lens"). According to the theory of item 3 $L_f = \tau_0^2 v^2 \cos^2\theta/2\, L_e \sin^4\theta$*****, where $L_e = 4\xi_0 \cos\theta/\xi_1 k_0 (1 + \sin^2\theta)$, $\alpha = \alpha_0 \tau_0^2$, $\alpha_0 \Delta\omega_0 = 2$. From the conditions of our experiment we have $\theta = 83°$, $\tau_0 = 28$ psec, $\alpha_0 = \Delta\omega_{osc}/\Delta\omega_0 \approx 1.9$, 1.6, and the agreement between the theory and the experiment in the estimation of the L_f demands a very small magnitude of the optical anisotropy of CLC $\xi_1 \sim 10^{-4}$ [that leads to $L_e \sim 5\ 10^{-2}$cm (for $\xi_0^{1/2} \approx 1.5$)]. Such a very small obtained value ξ_1 is explained to be, on the one hand, because of the approximations of the developed theory and, on the other hand, because in thick samples (the CLC layers of the thickness $10 \div 30$ μm are usually used in optical experiments) the non-ideal orientation occurs and the effective magnitude of the ξ_1 may sufficiently decrease.

Note, that the discussed method of preliminary compression of the laser pulses is determined by the creation (due to the dynamic scattering of the traveling waves) the pulses on the structures of DFB type but not by a generation of short laser pulses like in standard DFB-lasers [8].****** Therefore in our case we have no limitations on the thickness of the CLC sample (the effective compression occurs when $d \sim L_f$). In contrast, in DFB lasers τ_{out} decreases when d decreases but for short d the threshold of laser generation increases dramatically and so for real conditions the outgoing pulse duration τ_{out} can be not less than 10 psec. Besides that, the spatial profile of the laser beam does not have any sense in our linear problem, and no aberration occurs in such "temporal lens". So, the compression is homogeneous over the all aperture of the input laser beam.

In conclusion, the large-aperture preliminary compression of picosecond laser pulses with initial (natural) phase modulation is discussed for CLC both in theory and in experiment. The bandwidth-limited light radiation was obtained for output pulses. Such very simple autonomous and compact optical device is very useful for an express transformation of short laser pulses in practical cases.

We wish to express our thanks to A. A. Oganian for his help in automatic collecting and treatment of experimental data.

*First preliminary results of the experiment we reported in [7].

**When the input radiation has a circular polarization corresponding to the eigen wave of CLC this parameter can increase two times.

***For our geometry when radiation was detected in the direction of the input beam $L_e = \infty$ and the effective energy exchange between A_o- and A_h- waves is provided by the condition $\tau_0 v \gg d$.

****We can call this process as preliminary compression. The further compression is possible due to phase self-modulation effect because of the medium nonlinearity [1] (cf. [10,11]).

*****The measing of the dependence $L_f \sim 1/L_e \sim \xi_1/\xi_0$ is that the dispersion spreading out of the light pulse in the medium is compensated by the compression effect till the distance associated with L_f.

******In this aspect our method is very similar (by physical meaning) to the technique of colliding pulses (see e.g. [9]).

References

1. S. A. Akhmanov, V. A. Visloukh, A. S. Chirkin, Optics of Femtosecond Pulses. Moscow, Nauka (1988).

2. S. M. Arakelian, L. P. Gevorkian, Yu.S. Chilingarian, Optica I Spectroscopy, 65, p 103 (1988).
Lasers in Atomic, Molecular and Nuclear Physics. Proceedings of the Fourth Internation School on Laser Applications (Vilnus, USSR, August 22nd-29th,1987) Singapore, World Scientific, p 289 (1989).

3. S. A. Akhmanov, Yu. E. Diakov, A. S. Chirkin, Introduction to Statistic Radiophysics and Optics, Moscow, Nauka (1981).

4. L. V. Azaroff, R. Kaplow, N. Kato, R. J. Weiss, A. J. C. Wilson, R. A. Young, X-Ray Diffraction, London, McGraw-Hill (1974).

5. K. Sakuda, A. Yariv, Opt. Commun., 8, p 1 (1973).
N. Nakamura, W. H. Yen, A. Yariv, et al, Application Physics Letter, 23, p 244 (1973).

6. S. M. Arakelian, L. P. Gevorkian, V. A. Makarov, Soviet Quantum Electronic 10 (1989).

7. R. B. ALaverdian, S. M. Arakelian, L. P. Gevorkian et al, In: Abstracts of X,II International Conference on Coherent and Nonlinear Optics, 1, p 194 Minsk (USSR) (1988).

8. Zs. Bor, A. Muller, IEEE Journal of Quantum Electronics, QE-22, p 1524 (1986).

9. J. C. Diels, W. Dietel, J. J. Fontaine et al, B2, p 680, JOSA (1985).

10. L. P. Gevorkian, V. A. Makarov, E. Cherepetskaja, Soviet Quantum Electronics N12, (1989).

11. H. G. Winful, Applied Physics Letters, 46, p 527 (1985).

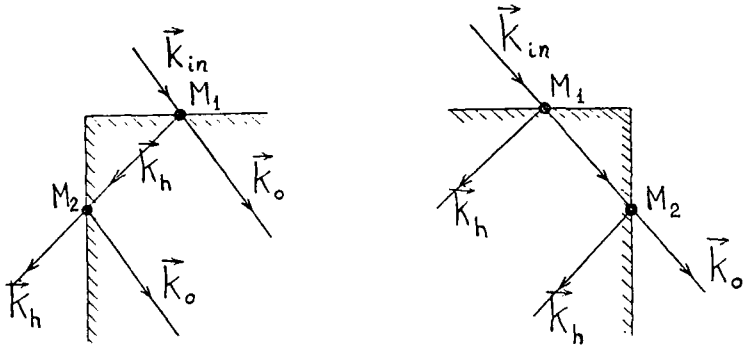


Figure 1-a. Geometry for the dynamic diffraction of the laser pulses on the spatially periodic structure in the Laue-Bragg scheme (two types).

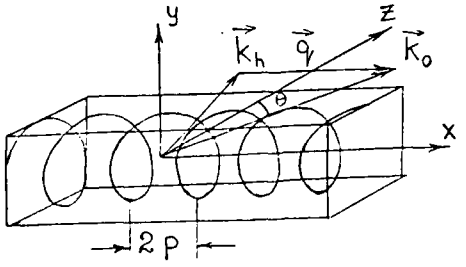
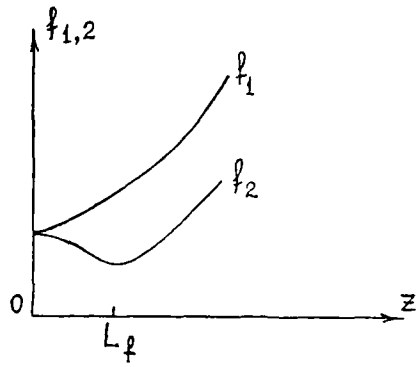


Figure 1-b. Geometry for the dynamic diffraction of the laser pulses on the spatially periodic structure in the symmetric Laue-Laue scheme.



Figue 2. The gualitative behavior on z of the functions $f_{1,2}$ [see equation (4)]

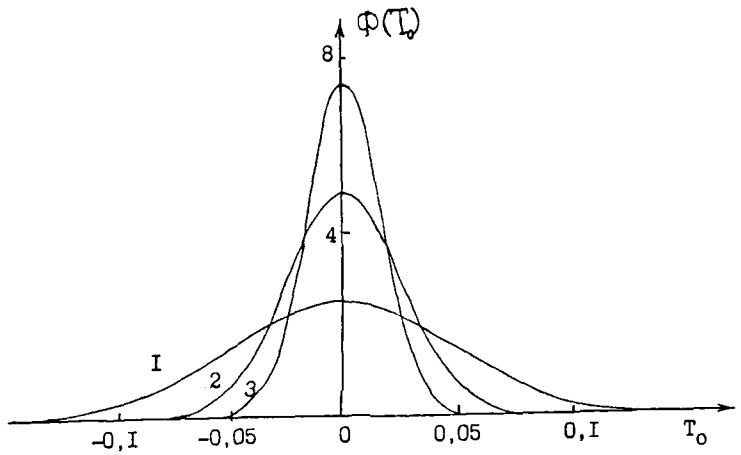


Figure 3. The numerical dependences of the function $\Phi(T_o)$ for different values of the parameter [see equation (5)]:

1 - α = 10 ; 2 - α = 20 ; 3 - α = 30.

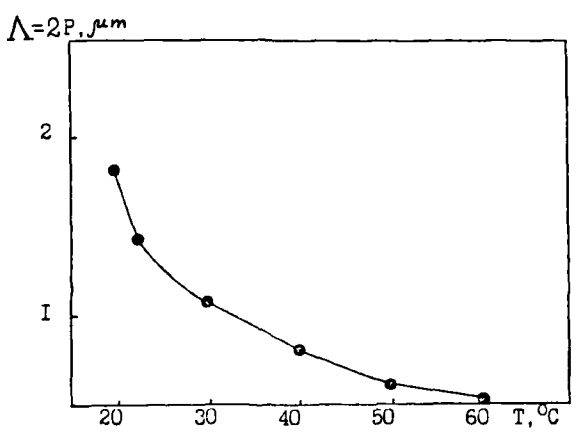


Figure 4. The period $\Lambda = 2p$, where p is the of the helical structure for the used mixture of CLC versus temperature T°C.

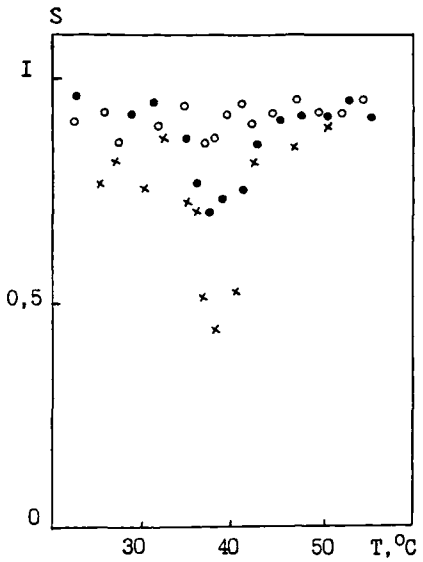


Figure 5. The compression factor $s = \tau_{out}/\tau_{in}$ versus T°C for different thicknesses d of the CLC layer:

o - d = 100 μm; o - d = 200μm; x - d = 300μm

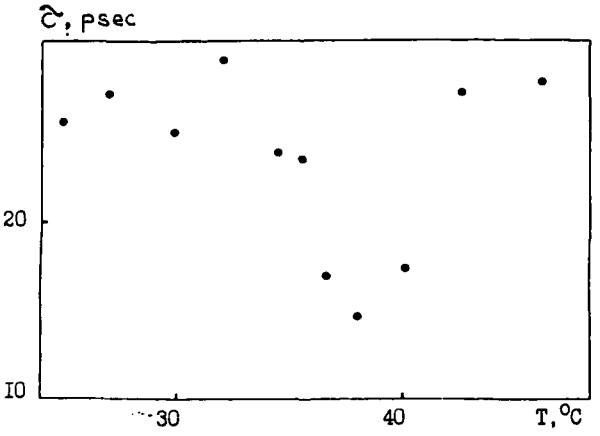


Figure 6. The absolute measurements of the output pulse duration τ_{out} versus T°C for d = 300 μm (maximal efficiency of compression in experiment).

EXPERIMENTAL RESULTS OF AGING AND THERMAL EFFECTS IN HIGH-POWER LASER DIODES

J. W. Rupert
Sandia National Laboratories
Albuquerque, New Mexico 87185

M. J. Landry
Scot Incorporated
Downers Grove, Illinois 60515

A. Mittas and T. L. Woolston
Sandia National Laboratories
Albuquerque, New Mexico 87185

Abstract

This paper describes the aging and thermal effects of high-power GaAlAs laser diodes constructed by Spectra Diode Laboratory (SDL) with multiple stripes, containing single- and multiple-quantum wells. Thermal effects are described for laser diodes constructed by McDonnell Douglas Astronautics Company/Optoelectronics Center (MDAC/OEC) with a single broad stripe containing a single-quantum well. The laser diodes are grown using metalorganic chemical vapor deposition (MOCVD). Experimental data are given showing the aging and thermal effects of these laser diodes while operating CW for different on-times and operating up to 2.0 W for an overdriven SDL commercial laser diode, 4.0 W for a SDL engineering prototype and 5.0 W for a MDAC/OEC prototype. Thermal effects are observed by operating at different intervals between shots and power levels when cooled by a fin heat-sink or thermoelectric cooler. Aging is caused by operating the laser diodes at elevated optical power levels. The characteristics used to describe these effects include: (1) optical power versus current, (2) efficiency versus optical power, (3) beam intensity distribution and (4) divergence. Laser diode output powers decreased by 2.5% to 22% because of aging. The different cooling methods resulted in a difference in output power of 7%. The beam intensity distributions of some laser diodes were erratic versus power and time after turn-on while it was stable for others.

Introduction

Sandia National Laboratories (SNL) is actively pursuing the safety of firing sets by replacing conducting paths with optical conductors.[1] The source for the optical energy is a semiconductor laser diode.[1,2] Because of the energy requirements in firing sets, high-power, CW laser diodes are necessary. This paper describes the experimental results of aging and thermal effects observed while testing laser diodes at high power levels for use in firing sets.

Laser Diodes from two manufacturers have been tested: Spectra Diode Laboratories (SDL) and McDonnell Douglas Astronautics Company/Optoelectronics Center (MDAC/OEC). The laser diodes were all grown by metalorganic chemical vapor deposition[3] (MOCVD) and have double heterostructures.

Laser diode aging is caused by operating the laser diodes at elevated optical power levels. Thermal effects are observed by operating at different shot intervals and power levels when fin heat-sinked or thermoelectric cooled. The characteristics used to describe these effects include optical power versus current, efficiency versus optical power, beam intensity distribution and divergence. The SDL laser diodes operate at maximum output powers varying from 2.0 to 4.0 W and the MDAC/OEC laser diodes operate from 1.1 to 5.0 W. The operating time is between 0.2 and 5 s and the time interval between shots varies from 30 s to 10 min.

Experimental Setup

Testing Techniques

The testing includes measuring the current, voltage, optical power and beam intensity distribution of the laser diodes. From these measurements the efficiency and divergence can be calculated.

The laser diodes were mounted on either a fin heat-sink or on a copper heat-sink that is thermoelectrically cooled. The thermoelectric controller keeps the copper heat-sink at a constant temperature of 20°C. Both cooling methods are done external to the laser diode package. The power meter and camera are mounted on kinematic mounts, which allow for their rapid removal and precise repositioning.

For all the components except the camera, the x, y and z axes correspond to the horizontal, vertical and optical axis directions, respectively. The laser diodes are all mounted with their junctions horizontal. For ease in mounting, the camera is rotated 90° so that for the beam intensity distribution data, the x axis is perpendicular and the y axis is parallel to the laser diode junction.

A Scientech, Inc. Disk Calorimeter was used for all the optical power measurements. It has an accuracy of 3% and a long-term precision of 0.5%. The same instrument was used for all the optical power measurements, so the repeatability of the measurements should be very good. Fluke Digital Multimeters with accuracies of better than 0.5% were used for all the current and voltage measurements.

The efficiency of the laser diodes, E_{ld}, is defined as

$$E_{ld} = [P_{ld}/(I_{ld} * V_{ld})] * 100\% \quad (1)$$

where P_{ld} is the optical power output of the laser diode, I_{ld} is the drive current, and V_{ld} is the voltage drop across the laser diode.

The laser diode beam intensity distributions are recorded by a laser beam diagnostic system[4] built by Big Sky Software Corporation. The outputs of this system are beam intensity contours, intensity profiles through the centroid and 3-dimensional isometric views. The data were taken

at different power levels, different times after laser diode turn-on and different times in the laser diodes life. The dotted lines in the figures with intensity profiles are Gaussian fits.

By measuring the beam profiles at two positions of known distances from the laser diode output facet, the divergence of the laser is calculated. The divergence is determined by measuring the width of a Gaussian profile fit to the laser diode at the $1/e^2$ point through the centroid of the beam at two distances from the laser diode[1,4]. The full width divergence to the $1/e^2$ points, a_x, is then calculated using

$$a_x = 2 \tan^{-1} [(x_f - x_c)/2(z_f - z_c)] \quad (2)$$

where x_f is the $1/e^2$ width to the Gaussian fit in the x direction at the far distance, z_f, and x_c is the same width at a closer distance, z_c. The divergence in the y direction a_y is determined in a similiar manner.

Laser Diode Characteristics

Six different laser diodes from SDL are discussed in this paper: two commercial units and four prototypes. All the SDL laser diodes had coated cavity mirrors. Three prototype MDAC/OEC laser diodes are also discussed. The rated power, maximum power operated at SNL, and aperture dimension parallel to the laser diode junction are given in Table 1 for these laser diodes. Several more laser diodes were characterized[1,2] but are not discussed here.

TABLE 1. Laser Diode Specifications

Manufact. and Model #	Part #	Commerc. or Proto. (C or P)	Rated Power (W)	Max Power Operated (W)	Aperture (μm)
SDL-2450	A840	C	0.5	2.0	400
SDL-2450	A841	C	0.5	2.0	400
SDL-S7081	RB883*	P	2.0	2.0	100
SDL-S7081	RP542*	P	2.0	2.0	100
SDL-S7086	BN968+	P	4.0	2.8	200
SDL-S7086	CF621	P	4.0	4.0	200
MDAC/OEC	E170T-1	P	2.0	1.1	150
MDAC/OEC	E170T-2-9	P	5.0	5.0	150
MDAC/OEC	E170T-2-10	P	5.0	2.7	150

* called 4.0-W laser diodes in previous papers[1,2]
\+ called 8.0-W laser diode in previous papers[1,2]

The two commercial SDL laser diodes are rated for >10,000 hr of continuous operation at 25°C at rated power or below. They are all mounted on C-block heat-sinks (6.35 X 3.25 X 1.27 mm) and packaged inside a TO-3 can with an antireflection coated sapphire window for the output. The laser diodes all have multiple-quantum wells,[5] double heterostructures, and multiple-stripe[5,6] outputs. The laser diodes to be described are two SDL-2450-H1 500-mW laser diodes, part numbers A840 and A841, overdriven to 2.0 W. The SDL-2450 laser diodes have 1 X 400 μm apertures and SDL specified their divergence to be 35° X 10°.

The four prototype SDL laser diodes are guaranteed to operate for >200 shots at 3 s per shot at their rated power. They are all mounted on open C-block heat-sink packages. These laser diodes also have multiple-stripe outputs, but they have single-quantum[7] instead of multiple-quantum wells. The laser diodes to be described are as follows: two SDL-S7081 2-W laser diodes, part numbers RB883 and RP542 and two SDL-S7086 4-W laser diodes, part numbers BN968 and CF621. The S7081 laser diodes have 1 X 100 μm apertures and the S7086 laser diodes have 1 X 200 μm apertures. The S7081 2-W laser diodes were called 4-W laser diodes in previous papers[1,2] by the same authors because this is their catastrophic level. The S7086 4-W laser diodes were called 8-W laser diodes for the same reason. The nomenclature was changed to 2- and 4-W because these are the maximum operating power levels in our investigation.

The three MDAC/OEC prototype laser diodes all have single-quantum wells and a single, broad emitting stripe.[8] The laser diodes to be described are as follows: E170T-2-9 and E170T-2-10 5-W laser diodes and E170T-1 2-W laser diode. The 2-W laser diode has uncoated mirror facets and has a 1 X 150 μm aperture while the 5-W laser diodes have the same size aperture but have coated mirrors. The 2-W device is mounted in a TO-18 can and the 5-W devices are mounted on a large-copper-block heat-sink (1.5 X 3.7 X 4.7 cm).

Experimental Results

Aging Effects

Degradation caused by aging[9] is measured for SDL laser diodes A841, RB883, BN968, RP542 and CF621. The measurements used to describe this effect are optical power versus current and efficiency versus optical power.

All the MDAC/OEC laser diodes were operated starting at low power and increasing power until a catostrophic level was reached. At this point the laser diodes either ceased to operate or a much lower output power was obtained for the same operating current. Because of this method of testing, no aging data were obtained.

Figure 1 shows the output optical power versus current and efficiency versus optical power for three SDL laser diodes. The initial data taken at SNL are shown along with other data taken later in the laser diodes lives. The later data shown are the last data taken on a particular device at SNL.

Laser diode A841 was operated for 600 shots, each at the 2.0-W optical power level for about 5 s. Its output power for the same current at its maximum output power decreased by about 4%. Its efficiency also decreased by about 6%. After 600 shots, A841 quit operating.

Laser diode RB883 was operated for 12 shots, each at 2.0 W for about 3 s. Its output power decreased by about 22% and its efficiency decreased by about 14.5%. This laser also quit operating after these 12 shots.

Laser diode BN968 was operated for 62 shots, each at 2.8 W for about 3 s. Its output power decreased by about 6% and efficiency by about 3%. This laser diode was damaged while butt-coupling a fiber optic to it. The later data shown in Figure 1 are the last data before the laser diode was damaged.

The same type of data are shown in Figure 2 for another SDL laser diode, RP542. These data were taken with RP542 mounted in the thermoelectric (TE) cooler setup. It performed much better than the other 2-W laser diode, RB883. After 720 shots, each at 2.0 W for 3 s, the optical power for this laser diode only decreased by 2.5% and its efficiency only decreased by 2%.

Similiar data are shown in Figure 3 for SDL prototype 4-W laser diode CF621. It is also mounted in the TE cooler setup. This is the only laser diode tested that showed improvement with aging. After 230 shots at 4.0 W, each for 3 s, its output power increased by 1% and its efficiency by 6%. Its efficiency improved by so much compared to its power because its voltage drop also decreased with aging. The burning-in of this laser diode resulted in better performance. This laser diode was also damaged while butt-coupling a fiber optic to it.

Figure 4 shows the optical power versus current and the efficiency versus optical power for two MDAC/OEC laser diodes: E170T-2-9 and E170T-2-10. As mentioned earlier, only the initial data are available since the laser diodes power was ramped up to the catostrophic level. These curves are shown here so that the laser diodes characteristics can be observed since in a later section beam intensity distributions will be presented. Only E170-2-9 was driven up to 5.0 W. Three shots were taken at the 5.0-W level before this device damaged. E170T-2-10 got to the 2.1-W level before it failed. These laser diodes had the highest efficiency of any of the laser diodes measured. It was about 50% at the 2.0-W optical power level.

Thermal Effects

Optical Power Versus Current–Thermal degradation is measured for SDL laser diodes A840 and A841. The measurements used to describe this effect are optical power versus current and efficiency versus optical power.

Figure 5 shows the thermal degradation of SDL laser diodes A840 and A841. Laser diode A840 was tested on both a fin heat-sink, and a TE cooler. The power of A840 increased by 7% at its highest power level when the device was mounted on the TE cooler compared to the fin heat-sink. Its efficiency also increased by 4%. Laser diode A841 was tested only on a fin heat-sink, but the data were taken with 30-s, 2-min and 10-min time intervals between shots. The data for the 2-min and 30-s shots are nearly the same, but they are lower than for the 10-min interval. Thermal effects resulting from the reduced time intervals cause the curves to separate. At the higher optical powers, the separation becomes more pronounced. At the highest optical power level, the 10-min data is about 5.5% higher than the 2-min and 30-s data.

Beam Intensity Distribution–The beam intensity distributions are described for three SDL laser diodes (A840, BN968 and CF621) and one MDAC/OEC laser diode (E170T-2-10). Beam intensity profiles and contours are shown in Figure 6 for SDL commercial 500-mW laser diode A840 operating between 0.1 and 2.0 W. This information was recorded between 0.2 and 0.4 s after the laser diode was turned on. At the low power levels, the beams have a good Gaussian fit in the x direction and have two narrow peaks in the y direction. As the optical power increases, the two peaks begin to break up into higher order modes, and they also broaden. More mode structure is also observed at higher powers in the x direction. These higher order modes are caused by the thermal effects of operating the laser diode at high optical powers.

Figure 7 shows isometric views of SDL prototype 4-W laser diode BN968 at different times after turn-on, different power levels and also at different times in its life. The operating power level of the laser diode is in the right corner of each isometric. In the lower corner is the date, along with the shot number of that date and the frame number. Frame 2 is the first frame grabbed after the laser diode is turned on, and the time between frames is 0.2 s. On 11-23, the beam changed drastically as power was increased from 1.0 to 2.8 W (*Figure* 7A, B, C and E). The beam also changed versus time after turn-on. This is seen at 2.5 W for frames 2 and 16 (Figure 7C and D) and at 2.8 W for frames 2 and 3 (Figure 7E and F). The change in BN968 as it aged while operating at 2.8 W is seen in Figure 7E through H. After BN968 operated for 44 shots at the 2.8-W level, its intensity distribution (Figure 7H) was similiar to its distribution at the low power level early in its life (Figure 7A). Unlike the commercial SDL laser diodes, the prototype units were operated only for a few shots at SDL before they were shipped to SNL. The BN968 stabilized after the burning-in at SNL.

Intensity distributions for SDL prototype 4-W laser diode CF621 are shown in Figure 8. This laser diode is shown versus power level (Figure 8A through D) and versus time after turn-on (Figure 8D through H). Frame 2 is the first frame grabbed after turn-on, and the frames are 0.5 s apart. This is a later version 4-W laser diode from SDL than BN968, and its intensity pattern is much more stable. Only very small changes are seen versus power and frame number.

Figure 9 shows the intensity distributions for MDAC/OEC 5-W laser diode E170T-2-10 operating at 1.1 and 2.0 W for different shots and time after turn-on. These distributions show that the output beam pattern of this laser diode is very erratic from shot to shot, both at a constant output power level and as its output power changes. No data are available for this laser diode later in its life since its power was ramped up until it failed catostrophically.

Divergence–The divergence is described for two SDL laser diodes (RP542 and CF621) and one MDAC/OEC laser diode (E170T-1). The divergence of SDL prototype 2-W laser diode RP542 is shown in Figure 10. The divergence was measured in the x and y directions as a function of power and time after turn-on. The measurements were made at distances of 8.87 and 10.87 mm from the output facet of the laser diode. There is a smaller spread in the divergence in the x direction than in the y direction. The x direction data have a better fit to a Gaussian than the y direction data. As expected because of its smaller aperture, the divergence is higher in the x direction than the y direction. At the low power levels (0.43 and 1.0 W), the divergence is fairly stable versus time after turn-on. It is more erratic at the high power levels. The highest divergence in most cases is at the highest optical power of 1.8 W.

Figure 11 shows the divergence as a functon of power and time after turn-on in the x and y directions for SDL prototype 4-W laser diode CF621. There is a fairly small spread in divergence in both directions. The divergence is not as erratic at the high power levels as it was for RP542.

The divergence of MDAC/OEC 2-W laser diode E170T-1 in the x direction versus time after turn-on for two power levels is shown in Figure 12. The y data was not plotted because of its poor Gaussian fit. At both power levels there is a sharp increase in divergence after turn-on and then a gradual leveling off. There is also a large increase in divergence as the power is increased. The 60° divergence seen here at the 1.0-W power level is the largest observed for any laser diode during this investigation.

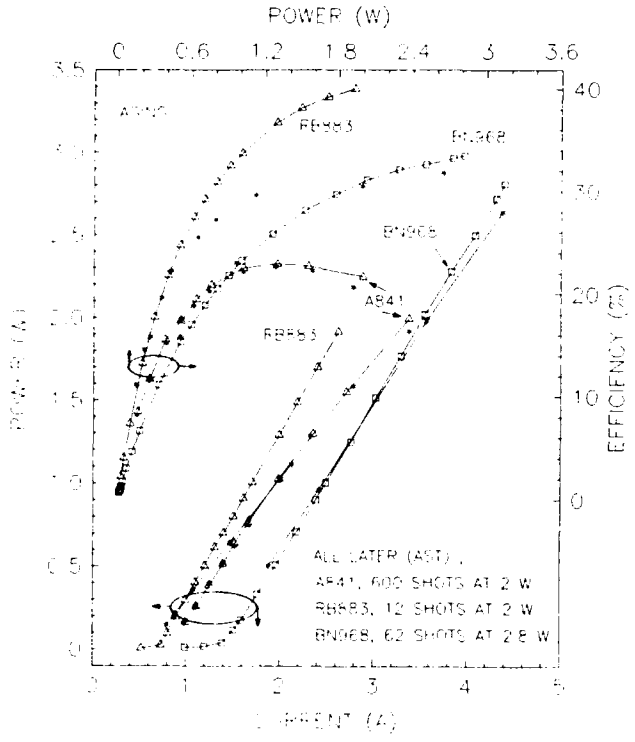


Figure 1. Aging illustrated by output optical power versus current and efficiency versus output optical power for three SDL laser diodes (A841, RB883, BN968) operated at SNL; initial data and data at later times in their lives.

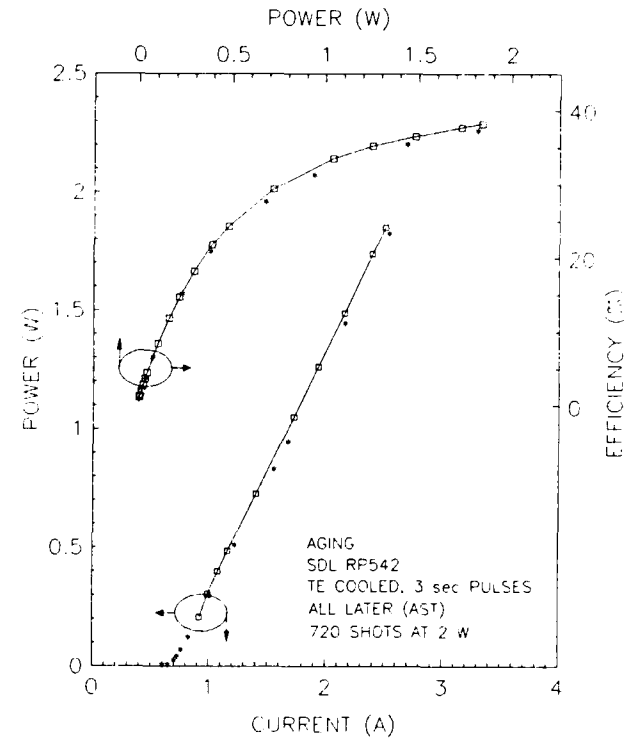


Figure 2. Aging illustrated by output optical power versus current and efficiency versus output optical power for SDL laser diode RP542 operated at SNL; initial data and data at a later time in its life.

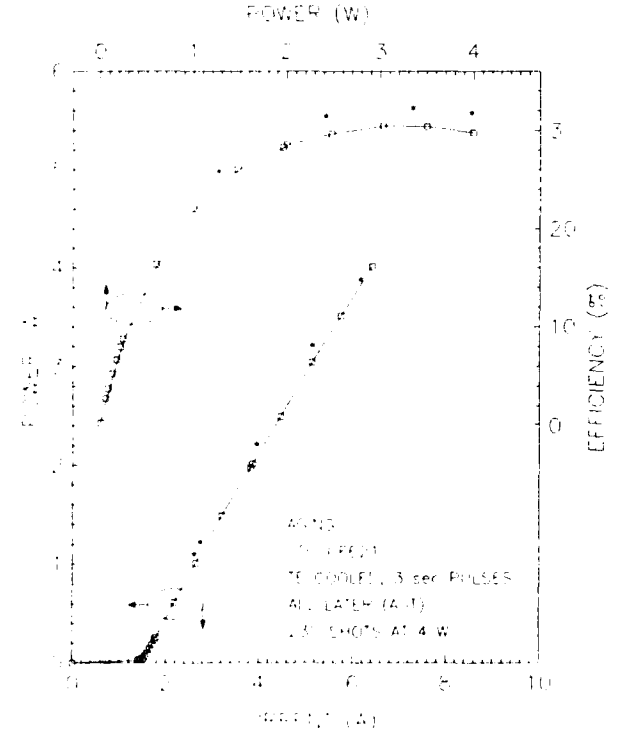


Figure 3. Aging illustrated by output optical power versus current and efficiency versus output optical power for SDL laser diode CF621 operated at SNL; initial data and data at a later time in its life.

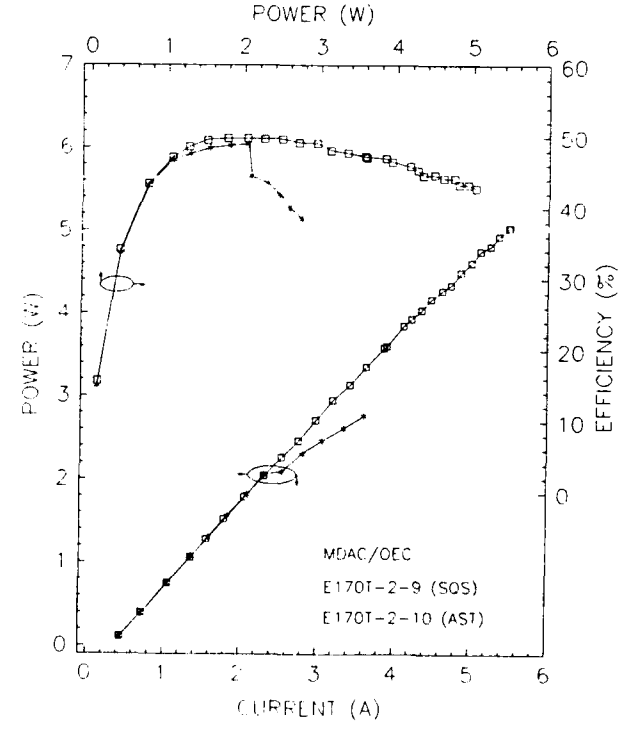


Figure 4. Optical power versus current and efficiency versus optical power for two MDAC/OEC laser diodes (E170T-2-9, E170T-2-10) operated at SNL; initial data.

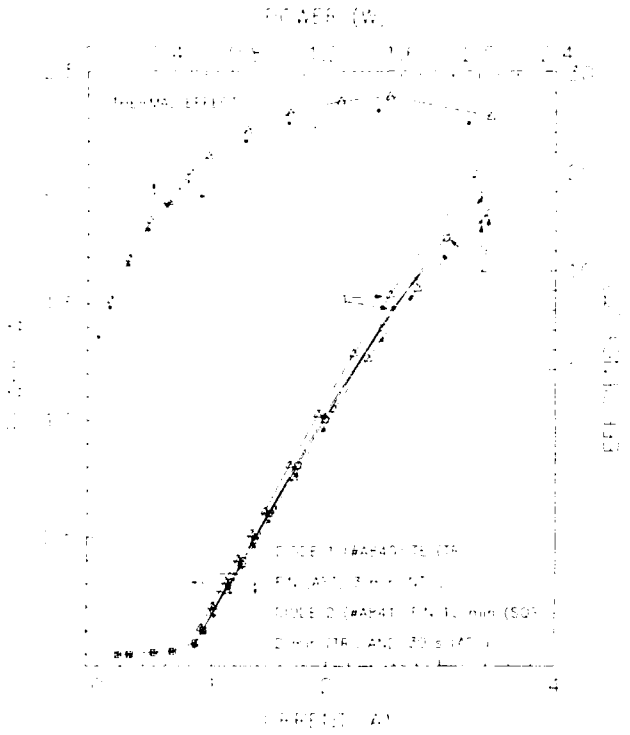


Figure 5. Thermal effects illustated by output optical power versus current and efficiency versus output optical power for two SDL commercial laser diodes. A840 is operated on both a fin heat-sink and a thermoelectric cooler. A841 is operated on a fin heat-sink at different time intervals between shots.

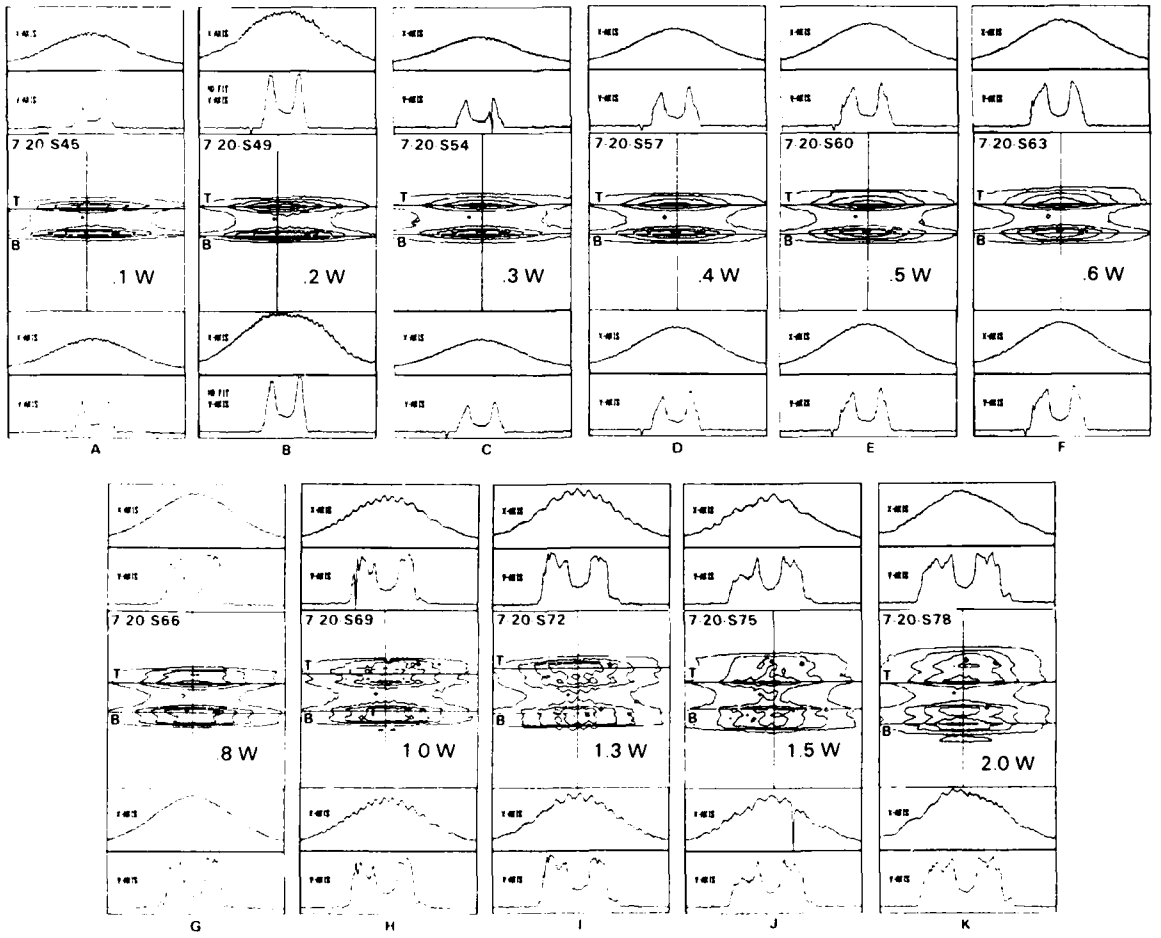


Figure 6. Thermal effects illustrated by beam intensity contours and profiles for SDL laser diode A840 operating at output power levels from 0.1 to 2.0 W.

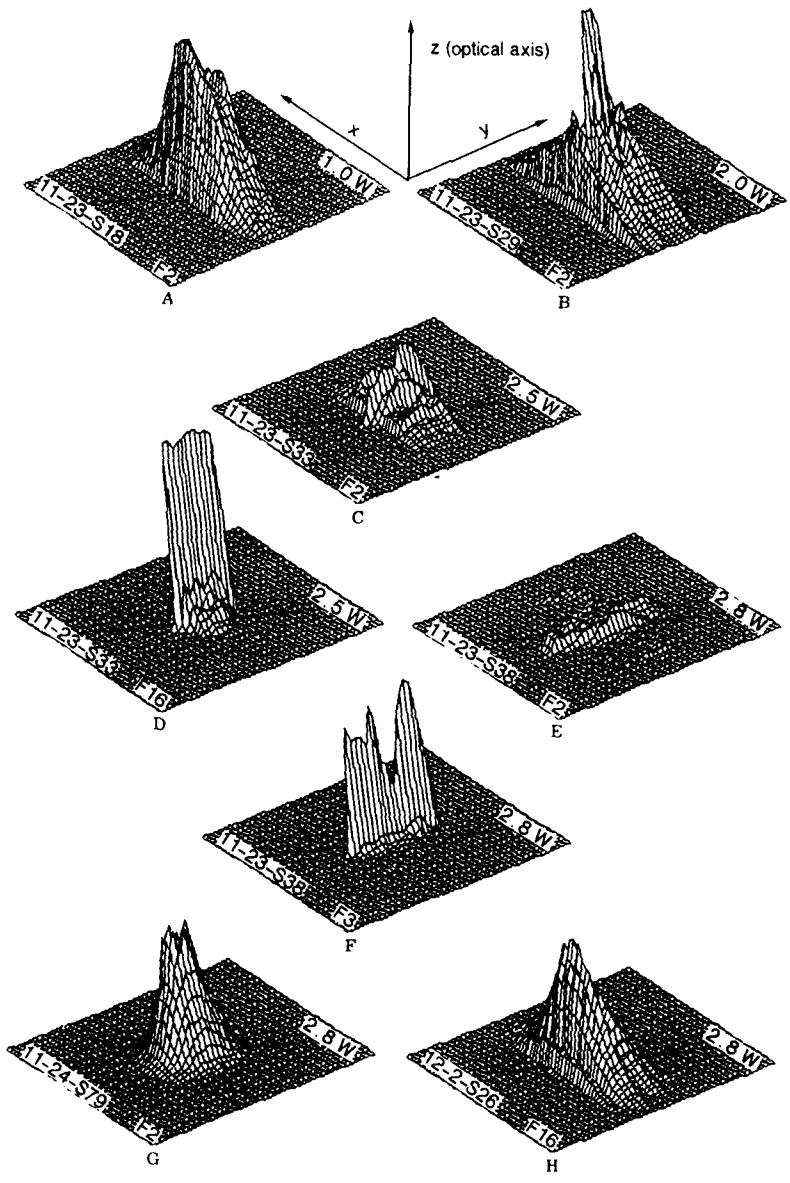


Figure 7. Thermal and aging effects illustrated by beam 3-dimensional isometrics for SDL laser diode BN968 taken at different power levels, different times after turn on and at different times in its life.

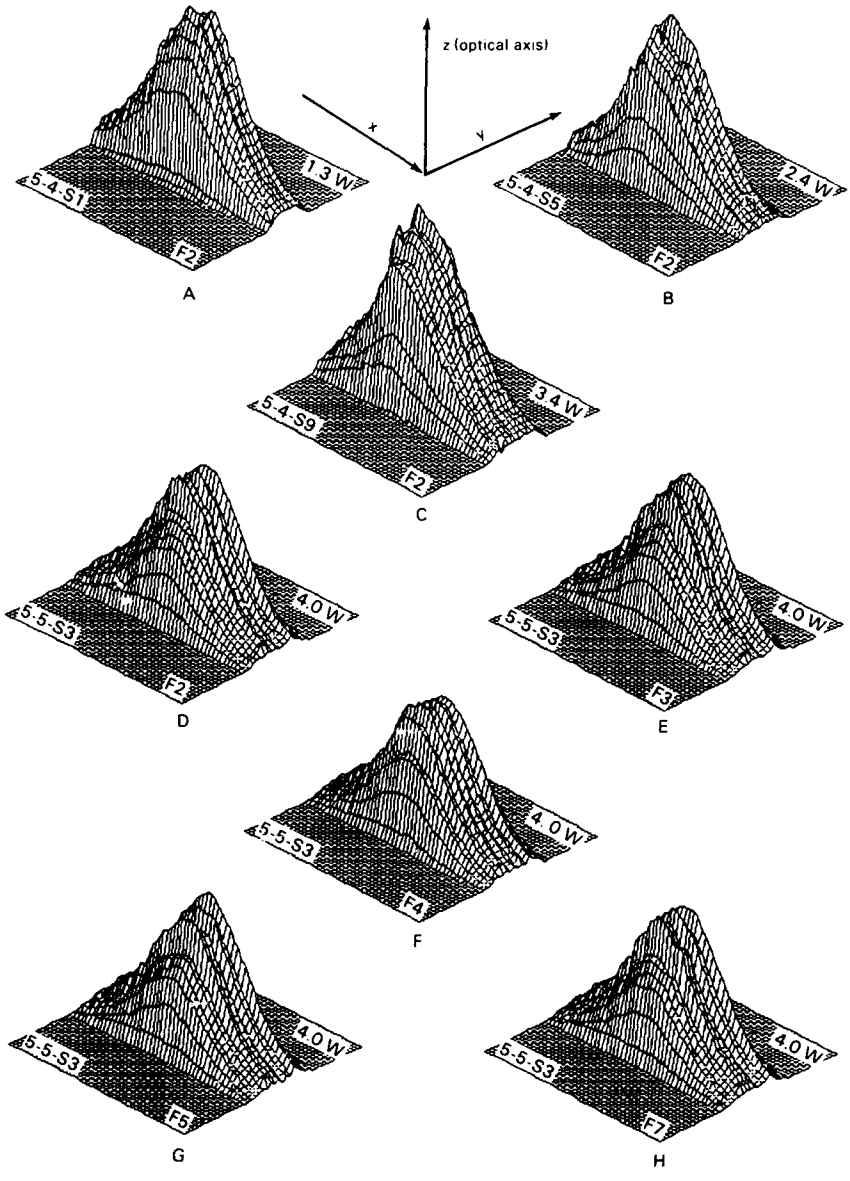


Figure 8. Thermal effects illustrated by beam 3-dimensional isometrics for SDL laser diode CF621 taken at high and low power levels and different times after turn-on early in its life.

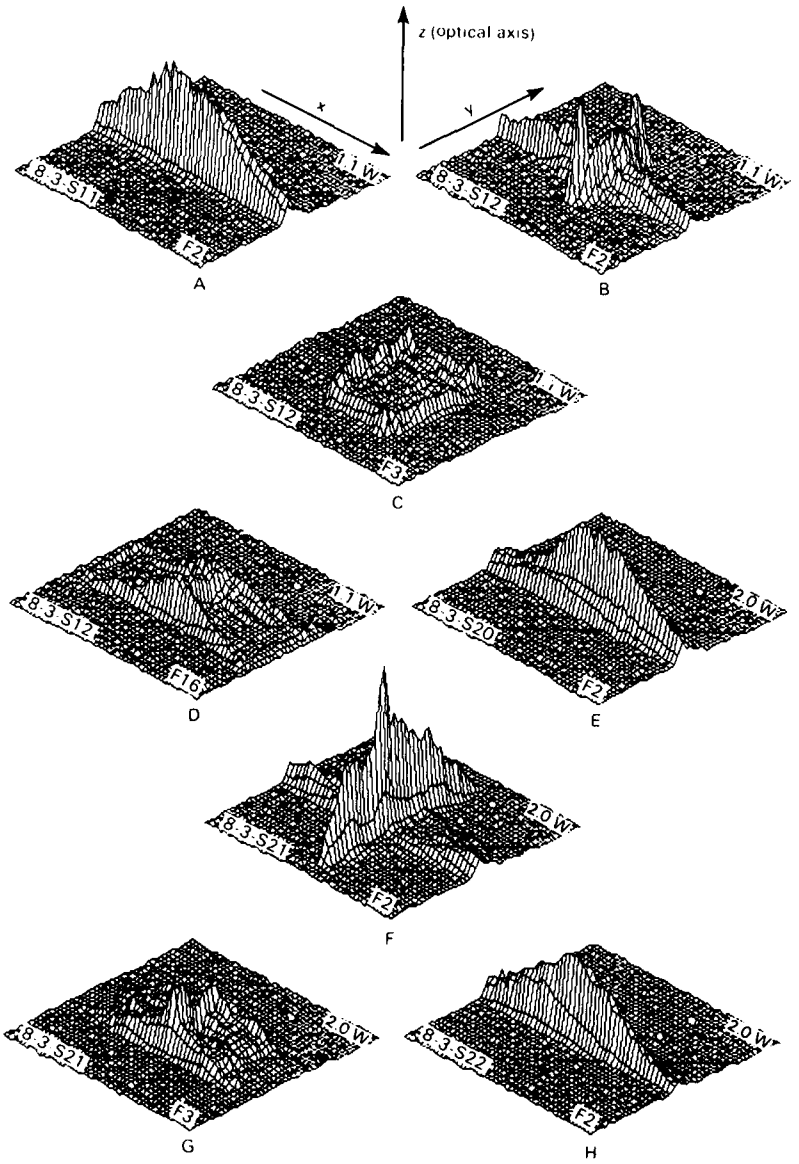


Figure 9. Thermal effects illustrated by 3-dimensional isometrics for MDAC/OEC laser diode E170T-2-10 operating at two power levels, for different shots and different times after turn-on early in its life.

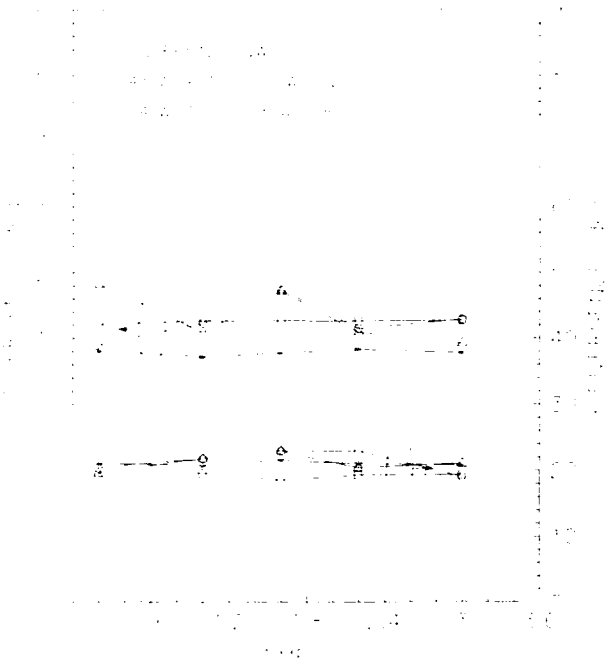


Figure 10. Thermal effects illustrated by divergence versus time after turn-on for SDL laser diode RP542 at four power levels. The divergence is measured for the x and y directions.

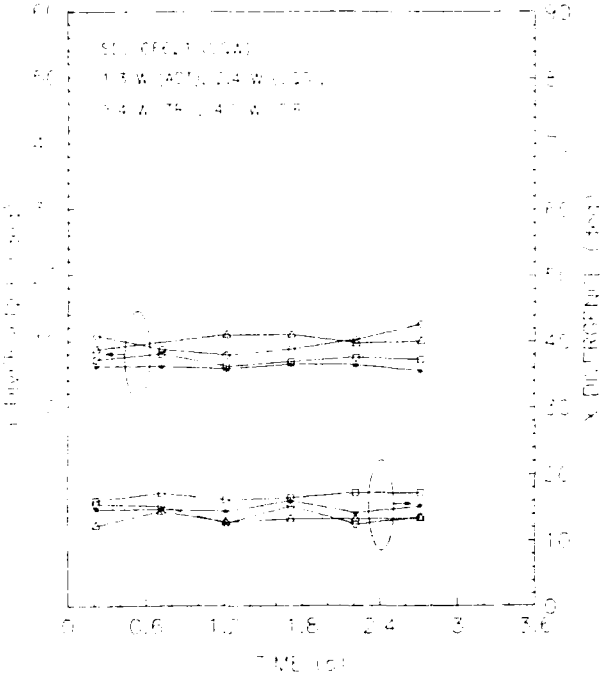


Figure 11. Thermal effects illustrated by divergence versus time after turn-on for SDL laser diode CF621 at four power levels. The divergence is measured for both the x and y directions.

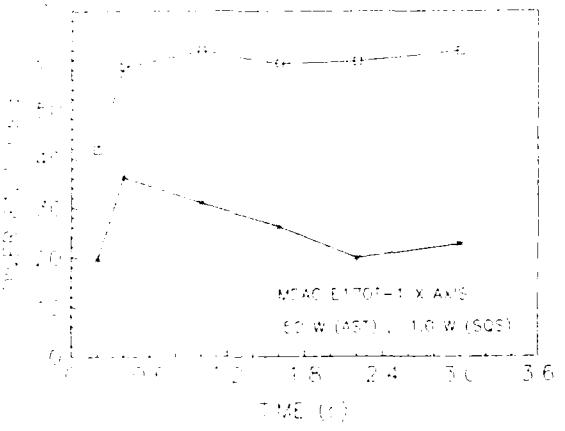


Figure 12. Thermal effects illustrated by divergence versus time after turn-on for MDAC/OEC laser diode E170T-1 at two different power levels. The divergence is measured in the x direction only.

Conclusions

Aging was observed for several SDL laser diodes. It was most severe for prototype laser diode RB883 whose power decreased by 22% for the same drive current after only 12 shots at 2.0 W. The other SDL laser diodes, except for CF621, saw decreases in power from 2.5 to 4.0% with 62 to 600 shots at their maximum operating powers. Laser diode CF621 was the latest generation 4-W device tested. It saw a 1% increase in power for the same drive current after 230 shots at 4.0 W, and it had an efficiency increase of 6%. Its performance actually improved after some burn-in at SNL.

Thermal effects were observed for two SDL commercial laser diodes by comparing power versus current and efficiency versus power curves. Laser diode A840 had a 7% increase in its power for the same current when it was mounted on a TE cooler compared to when it was on a fin heat-sink. Laser diode A841 had a 5.5% decrease in power when it was operated with a 2-min or 30-s time interval between shots compared to when it had a 10-min interval.

Thermal effects were observed by comparing beam intensity distributions of the laser diodes. The SDL commercial laser diodes contained double lobe patterns that tended to broaden with an increase in power. SDL BN968 and MDAC/OEC E170T-2-10 were both very unstable early in their lives. After some aging BN968 became more stable and its intensity pattern looked more typical of this type of laser diode. Laser diode CF621 was very stable initially and very little change was seen versus its power level or time after turn-on.

The divergence of SDL RP542 is fairly stable at low optical power and more erratic at higher optical powers. The divergence of SDL CF621 has a smaller variation versus power and turn-on time. The divergence of MDAC/OEC laser diode E170T-1 increases with power and it also increases after turn-on then gradually levels off.

The best thermal and aging performance from the high-power laser diodes tested was for 4-W SDL laser diode CF621. The optical power versus current and efficiency of the CF621 laser diode improved with aging. The CF621 operated for 230 shots at 4 W before it was damaged by butt-coupling a fiber optic to it. It also had a very stable beam intensity pattern versus both time after turn-on and optical power. Finally, it had a very small spread in divergence versus time after turn-on and optical power. Laser diode CF621 was the latest generation 4-W laser diode tested. Much improvement was observed during the course of this investigation in high-power laser diode technology and it is expected to continue.

References

1. M. J. Landry, J. W. Rupert, and A. Mittas, Evaluation of Systems and Components for Hybrid Optical Firing Sets, SAND87-0912 (Albuquerque, NM: Sandia National Laboratories, 1989).

2. M. J. Landry, J. W. Rupert, and A. Mittas, presented at the 1988 Annual Meeting of the Optical Society of America, Santa Clara (1988), paper ThGG4.

3. R. D. Dupries and P. D. Dapkus, App. Phys. Lett. 3, pp. 466-468 (1977).

4. R. L. Rypma, Photonic Spectra 21, 67-74 (1987).

5. D. R. Scifres, R. D. Burnham, and W. Streifer, Appl. Phys. Lett. 41, pp. 118-120 (1982).

6. L. A. D'Asaro, J. Lumin. 7, 310-337 (1973).

7. D. Welsh, B. Chang, and D. R. Scifres, Electronic Letters 24, pp. 113-115 (1988).

8. P. Tihanyi, D. K. Wagner, A. J. Roza, H. J. Vollmer, and C. M. Harding, Appl. Phys. Lett. 50, pp. 1640-1641 (1987).

9. G. L. Harnagel, T. L. Paoli, R. L. Thornton, R. D. Burnham, and D. L. Smith, Appl. Phys. Lett. 46, pp. 118-120 (1985).

FREQUENCY-LOCKED 1.3 AND 1.5-μm DFB LASERS FOR LIGHTWAVE SYSTEMS APPLICATIONS

Y. C. Chung
AT&T Bell Laboratories
Crawford Hill Laboratory
Holmdel, New Jersey 07733

Abstract

We describe a simple technique for frequency-locking 1.3 and 1.5-μm lasers to an excited-state atomic transition of noble gases using the optogalvanic effect. Many of the atomic transitions useful for these spectral regions are tabulated. Also, the performance of frequency-locked lasers under direct frequency modulation is analyzed. It is shown that neither the frequency stability nor the receiver sensitivity shows any serious degradation when a frequency-locked laser is used in an FSK transmission experiment.

I. Introduction

Frequency-locked semiconductor lasers operating in the 1.3 and 1.5-μm regions will find many applications in future lightwave communication systems. Probably, the most important applications of these lasers will be as an absolute reference in a densely-packed wavelength-division-multiplexed (WDM) systems[1,2]. In addition, these lasers can be used in an optical frequency synthesizer[3,4] and in a heterodyne detection system which can maintain a constant intermediate frequency (IF) without any IF locking circuit[5,6].

These prospective applications have attracted many efforts to improve the frequency stability of semiconductor lasers. To ensure long-term frequency stability, atomic or molecular absorption lines have been used as external frequency references[7-24]. However, most of the previous results are limited to AlGaAs lasers operating at about 0.8 μm[3,8-19]. In the important 1.3 and 1.5-μm regions, where conventional silica-based optical fibers show low dispersion and low loss, only a few experiments[20-24] have been reported. Yamaguchi and Suzuki[20] stabilized a 1.3-μm InGaAsP laser to the first overtone vibration-rotation line of the hydrogen flouride (HF) molecule. Ohtsu et al.[21] and Yanagawa et al.[22-23] reported the frequency-locking of 1.5-μm lasers to absorption lines of the water vapor (H_2O) and/or ammonia (NH_3). However, these molecular lines are not ideally suited for use as references in lightwave systems due to their weak and complex absorption spectra. This, in turn, results in the need for a long absorption cell. In comparison, atomic spectra offer relatively few strong lines which can be easily identified. To take these advantages of atomic spectra, Ohtsu and Ikegami[24] recently demonstrated the frequency-locking of a 1.5-μm InGaAsP DFB laser to the Rb D_2 line at 780 nm using the internally generated second harmonic signal. However, it is difficult to realize this technique in practice, since the optical power of the internally generated second harmonic signal from a typical InGaAsP laser is less than a few picowatts.

It is noteworthy that the frequency references used in 1.3 and 1.5-μm regions are either molecular absorption lines or an atomic Rb D_2 line at 780 nm. This is due to the difficulty of finding any useful atomic lines originating from the ground state in these spectral regions. This problem can be solved by utilizing the excited-state atomic transitions as external frequency references. In particular, noble gases such as neon (Ne), argon (Ar), krypton (Kr), and xenon (Xe) offer many transitions in 1.3 and 1.5-μm regions as shown in Table I[25-26]. These lines can be excellent frequency references since noble gases are relatively unsusceptible to external perturbation. For the frequency-locking of semiconductor lasers, it is necessary to monitor the absorption or the optogalvanic signal of these transitions from a discharge lamp. In most cases, it is preferred to use optogalvanic signals due to the simplicity (no need for photodetectors or beam splitters) and good sensitivity.

In the optogalvanic effect, a large change in the impedance of a gas discharge is induced by laser irradiation at a wavelength corresponding to a nonionizing transition of a species present in the gas discharge[27-31]. Since 1976 when Green et al. demonstrated its use as a simple and efficient tool for laser spectroscopy[27], the optogalvanic effect has been extensively used in many applications including frequency stabilization of AlGaAs lasers operating in the 0.8-μm region[11,13,19]. However, the ability to extend this technique to 1.3 and 1.5-μm regions was in serious doubt due to the suspicion that semiconductor lasers do not have sufficient output power to induce any significant impedance changes of a discharge lamp in these spectral regions[20]. However, it was recently demonstrated that 1.3 and 1.5-μm lasers with

moderate output power (~1 mW) can be frequency-locked to excited-state atomic transitions using the optogalvanic effect[32-33]. This method is promising for the use in lightwave communication systems due to the simplicity of implementation and the previously mentioned advantages of using atomic transition lines. In this paper, we review the work to date on the simple technique for the frequency-locking of 1.3 and 1.5-μm semiconductor lasers to an excited-state atomic transition of noble gases using the optogalvanic effect.

II. Optogalvanic Effects

A complete theoretical treatment of the optogalvanic effect, which must involve simultaneous solution of plasma, rate, and Maxwell's equations, is very difficult and beyond the scope of this paper. Instead, the mechanism of the optogalvanic effect is explained qualitatively using a partial energy diagram of Ar atom shown in Figure 1. When a discharge lamp filled with Ar gas is turned on, Ar atoms are excited to every energy level. Under normal operating conditions, a discharge lamp maintains a steady state where the total ionization rate is matched with the total loss rate of Ar ions. If the discharge lamp is irradiated by a laser beam at a wavelength of 1.2960 μm, the Ar atoms in the $2p_{10}$ level will be excited to $3d_5$ level, causing changes in the population densities of Ar atoms in these levels. However, Ar atoms in the $3d_5$ level have a higher ionization probability than those in the $2p_{10}$ level, since those atoms in the $3d_5$ level require less energy to be ionzed. Thus, the laser-induced changes in population densities between these two levels will increase the total ionization rate within a discharge lamp. Consequently, the discharge current needed to maintain steady state is reduced, in other words, the impedance of a discharge lamp is increased due to the laser irradiation at 1.2960 μm. This explanation covers most atomic transitions of noble gases in 1.3 and 1.5-μm regions. However, it should be noted that the discharge current will be increased if the laser irradiation depletes an energy state, such as metastable state, which contributes significantly to ionization by electron collisions. These changes in the discharge current due to laser irradiation at a wavelength corresponding to a specific atomic transition is the so-called "optogalvanic effect".

III. Experiments

The frequency fluctuations of semiconductor lasers have two origins: (1) intrinsic noise due to spontaneous emission and carrier density fluctuations[34] and (2) extrinsic noise due to ambient temperature fluctuations and injection current variations. In most lightwave systems, the requirement for frequency stability is relatively forgiving - especially when the bit rate is high or the channel spacing is broad. Thus, the main objective of the present work is to suppress the extrinsic noise and prevent long-term drift by locking the laser frequency to an external absolute reference.

A. Frequency-Locked 1.3-μm Lasers

A block diagram of the experimental setup is shown in Figure 2. An InGaAsP DFB laser was mounted on a thermoelectrically cooled copper heat sink. The temperature of the heat sink was regulated within 0.1°C, but the laser itself was exposed to the ambient laboratory environment. The laser was biased by a current supply regulated to better than ±1 μA. Single frequency operation of the laser was verified using an optical spectrum analyzer and Fabry Perot interferometer. The frequency tunability of the laser was 1.8 GHz/mA and 15 GHz/°C. Using a wavemeter, the laser frequency was roughly adjusted to the region where the optogalvanic signal corresponding to the Ar $2p_{10}$-$3d_5$ transition (1.2960 μm) is expected to be observed. Accordingly, the operating temperature and the injection current were 8.9°C and 61 mA, respectively.

The optogalvanic effect can be observed in all kind of discharges including hollow cathode discharges, normal glow discharges, abnormal discharges, arc discharges, microwave discharges, and even flames[31]. However, hollow cathode discharges offer strong optogalvanic signals due to the high current densities (and consequently high light intensities) and relatively small Doppler width of the emitted lines[35-36]. A commercial Ar-filled hollow cathode lamp was used in this experiment. The cathode element was aluminium. Figure 3 shows the measured optogalvanic signal of the Ar $2p_{10}$-$3d_5$ transition in comparison with the laser power transmitted through this lamp. A strong optogalvanic signal with a good signal-to-noise ratio was observed while the absorption of the laser beam within the lamp was less than 3%. The magnitude of the optogalvanic signal depends on the structure of the discharge, discharge current, and laser intensity. Figure 4 shows the measured magnitude of the optogalvanic signals from the Ar $2p_{10}$-$3d_5$ transition as a function of laser power. The optogalvanic signals were stronger at the higher laser powers, although this Ar transition developed strong saturation even at modest levels of laser power. The discharge current of the hollow cathode lamp must be determined to obtain a stable discharge and strong optogalvanic signal. Figure 5 shows that, in the normal glow region of discharge, the optogalvanic signal increases with discharge current.

The laser output was collimated by a microscope objective, and sent to a hollow cathode lamp along the lamp axis. Unwanted optical feedback was avoided by placing two optical isolators in front of the laser. The discharge current of the hollow cathode lamp was set to be 11 mA using a ballast resistor. The laser power incident on the hollow cathode lamp was 3.5 mW. Under these conditions, the absorption of the laser beam by the Ar gas within the lamp was merely 3%. Thus, the rest of the laser beam which passed through the lamp can be coupled into the transmission fiber without the use of beamsplitters. To obtain the frequency discriminant signal, the laser frequency was slightly dithered at 2 kHz by adding a small (±5 μA) sinusoidal current to the injection current. The amplitude of the sinusoidal current was restricted in order to minimize the power and frequency modulation. Also, the dither frequency was restricted to low frequencies (<10 kHz), so it would not affect the data transmission when the laser is used as a transmitter in a FSK system[5-6]. Figure 6 shows the measured first derivative signal of Ar $2p_{10}$-$3d_5$ transition. The peak-to-peak width of the signal was measured to be 650 MHz by the frequency markers of the interference fringes of a confocal Fabry-Perot interferometer (free spectral range; 750 MHz). The slope of the signal was 1.2 μV/MHz near the center of the transition. The linear portion of this first-derivative signal was used for the frequency-locking. The laser-induced voltage change across the lamp was synchronously detected using a lock-in amplifier. The time constant of the lock-in amplifier was set at 10 ms throughout this experiment. The output of the lock-in amplifier was processed by a proportional amplifier and an integrator. The resulting error signal was then added to the injection current to correct the frequency drift of the laser.

The stability of the laser frequency can be estimated by tracing the error signal. However, measurement of frequency stability based on the error signal shows only the frequency drift with respect to the reference frequency, i.e., it does not show the drift of the reference frequency itself. When the reference signal is obtained from a discharge lamp, the discrepancy between relative and absolute stability may not be negligible. One way to measure the absolute frequency stability is to use an additional frequency discriminator which is independent of the frequency-locking servo loop. For this purpose, an Ar-filled hollow cathode lamp which is identical with the one used for frequency-locking was used. The laser beam which passed through the first hollow cathode lamp used for frequency locking was directed to the second one for the estimation of the absolute stability. The operating conditions of these lamps were also identical, i.e., both lamps were operated at a constant current of 11 mA.

Figure 7 shows the trace of error signal measured with respect to the independent frequency discriminator. The peak-to-peak frequency fluctuations in free-running condition were estimated to be 650 MHz, mainly due to the laser temperature fluctuations. When the servo-loop was closed, the frequency stability was improved to better than 4 MHz. This stability was maintained over several days without any additional adjustment under normal laboratory conditions.

B. Frequency-Locked 1.5-μm Lasers

For the demonstration of a frequency-locked 1.5-μm laser, the Kr $2p_{10}$-$3d_3$ transition at 1.5339 μm was used as a frequency reference. An InGaAsP DFB laser was used in this experiment. The laser had a tunability of 1.1 GHz/mA and 12.7 GHz/°C. The operating temperature and the injection current were set at 20.2°C and 74 mA, respectively, to adjust the laser frequency close to the Kr $2p_{10}$-$3d_3$ transition (1.5339 μm). Under these conditions, the laser power incident on the hollow cathode lamp was 2.9 mW. The lamp was filled with Kr and Ne buffer gases. The discharge current of the lamp was 9 mA. To obtain the frequency discriminant signal, the laser frequency was slightly dithered at 2 kHz by adding a small (±15 μA) sinusoidal current to the injection current. The peak-to-peak width of the first derivative signal was measured to be 380 MHz and the slope was 10 μV/MHz near the center of the transition. By using the linear portion of this first-derivative signal, the laser frequency was locked to the Kr $2p_{10}$-$3d_3$ transition at 1.5339 μm.

Figure 8 shows the trace of the error signal obtained from an independent frequency discriminator, i.e., an identical hollow cathode lamp filled with Kr and Ne gases. In the free-running condition, the peak-to-peak frequency fluctuations was estimated to be 360 MHz. When the servo-loop was closed, the laser frequency was locked within ±2 MHz from the center of the Kr $2p_{10}$-$3d_3$ transition (1.5339 μm).

IV. Frequency-Locked Lasers Under FSK Modulation

To determine the feasibility of using fequency-locked lasers as transmitters in lightwave communication systems, it is necessary to investigate their performance under modulation with random data. In particular, it is important to understand the effects of the frequency dither on the receiver sensitivity and of the data transmission on the frequency stability. The frequency-locking of a modulated laser was first demonstrated by Koizumi et al.[37]. In their experiment, an AlGaAs laser directly

Recently, Chung et al.[38] demonstrated the frequency-locking of an InGaAsP DFB laser modulated with 50 Mbit/s pseudorandom data and reported that neither the frequency stability nor the receiver sensitivity showed any serious degradation when a frequency-locked laser was used in a FSK transmission experiment. Subsequently, these frequency-locked lasers have been used as transmitters and local oscillators in a 1.7 Gbit/s FSK heterodyne detection system which maintains a constant intermediate frequency (IF) without an IF locking circuit[5-6], and as an absolute reference in a densely packed WDM coherent star network[1].

A block diagram of the experimental setup is shown in Figure 9. The laser frequency was locked to the Ar $2p_{10}$-$3d_5$ transition at 1.2960 μm using the optogalvanic effect. For the frequency-locking, the laser frequency was dithered at 2 kHz by adding a small (±5 μA) of sinusoidal current to the injection current. The laser frequency was then directly modulated by Alternate Mark Inversion Frequency Shift Keying (AMI FSK). This modulation scheme avoids the dip in the laser's low-frequency FM response[39]. A Fabry-Perot interferometer was used to demodulate the AMI FSK signal by passing the spaces and blocking the marks. The demodulated signal was detected by an InGaAsP PIN photodiode and sent to an error detector for bit error rate measurement.

Without modulation, the peak-to-peak frequency fluctuation was estimated to be 650 MHz in the free-running condition. With the servo-loop closed, the frequency stability was improved to 4.1 MHz. However, when the laser frequency was modulated with 50 Mbit/s pseudorandom data, the frequency stability was 6.7 MHz. This degradation occurs because, in the modulation format used in this work, 25% of the laser power falls outside the bandwidth of the Ar transition line, which reduces the amplitude of the first-derivative signal. The frequency stability can be mostly recovered by reoptimizing the loop gain. Figure 10 shows the measured bit-error-rate curve of this system; (1) when the frequency-locking servo-loop was closed, and (2) when the servo-loop was open and the frequency dither was removed. The degradation of the receiver sensitivity due to the frequency-locking servo loop was less than 0.3 dB, which is negligible.

V. Summary

A technique for frequency-locking 1.3 and 1.5-μm lasers to an excited-state atomic transition of noble gases was described. A qualitative explanation of the optogalvanic effect was presented. The excited-state atomic transitions of noble gases available for the frequency-locking of 1.3 and 1.5-μm lasers were tabulated. For demonstration, InGaAsP DFB lasers were frequency-locked to Ar $2p_{10}$-$3d_5$ transition at 1.2960 μm and Kr $2p_{10}$-$3d_3$ transition at 1.5339 μm, respectively. The results indicate that the frequency stability of a few MHz can be easily achieved, which is sufficient for most lightwave systems applications. In fact, these frequency-locked lasers have been used as an absolute reference in a densely packed WDM coherent star network[1].

The feasibility of using frequency-locked lasers as transmitters in lightwave systems has been studied. When a frequency-locked laser was modulated with FSK signals, the frequency stability was slightly degraded due to the reduced frequency-discriminant signal and broadened laser linewidth. However, the frequency stability can be mostly recovered by reoptimizing the loop gain. The degradation of the receiver sensitivity due to the frequency-locking servo loop (and the frequency dither used to obtain the frequency-discriminant signal) was negligible. A high bit-rate FSK heterodyne detection system was demonstrated using these frequency-locked lasers as transmitters and local oscillators[6].

In conclusion, the frequency-locking technique using the optogalvanic signals of the excited atomic transitions of noble gases has many advantages of using atomic spectra. In contrast to molecular spectra, in general, atomic spectra are relatively simple, strong, and easily identified. In addition, this technique is simple, compact, and cost-effective. Thus, this technique can be used to develop frequency-locked 1.3 and 1.5-μm lasers for future lightwave systems applications.

References

1. Y. C. Chung, K. J. Pollock, P. J. Fitzgerald, B. Glance, R. W. Tkach, A. R. Chraplyvy: Electron. Lett., vol. 24, pp. 1313-1314, 1988.
2. R. E. Wagner, W. B. Sessa, R. Welter, M. W. Maeda, L. Curtis, J. Young, T. P. Lee, K. Nanduri, H. Kodera, Y. Koga, and J. R. Barry: Proc. Opt. Fiber Conf. '89, postdeadline paper PD 12, Houston, Feb. 6-9, 1989.
3. R. A. Valenzuela, L. J. Cimini, R. W. Wilson, K. C. Reichmann, and A. Grot: Electron. Lett., vol. 24, pp. 725-726, 1988.
4. K. Kuboki and M. Ohtsu: IEEE J. Quantum Electron., vol. QE-23, pp. 388-394, 1987.
5. Y. C. Chung, R. W. Tkach, and T. L. Koch: IEEE Photonics Technol. Lett., vol. 1, pp. 140-141, 1988.

6. Y. C. Chung, L. D. Tzeng, S. Y. Leung, R. W. Tkach, A. R. Chraplyvy, and R. M. Derosier: to be published in IEEE Photonics Technol. Lett., Feb. 1990.
7. M. Ohi: Jpn. J. Appl. Phys., vol. 19, pp L541-L543, 1980.
8. T. Yabuzaki, A. Ibaragi, H. Hori, M. Kitano, and T. Ogawa: Jpn. J. Appl. Phys., vol. 20, pp. L451-L454, 1981.
9. H. Tsuchida, M. Ohtsu, and T. Tako: Jpn. J. Appl. Phys., vol. 21, pp. L1-L3, 1982.
10. H. Tsuchida, M. Ohtsu, T. Tako, N. Kuramochi, and N. Oura: Jpn. J. Appl. Phys., vol. 21, pp. L561-L563, 1982.
11. S. Yamaguchi and M. Suzuki: Appl. Phys. Lett., vol. 41, pp. 597-598, 1982.
12. H. Hori, Y. Kitayama, M. Kitano, T. Yabuzaki, and T. Ogawa: IEEE J. Quantum Electron., vol. QE-19, pp. 169-174, 1983.
13. S. Yamaguchi and M. Suzuki: IEEE J. Quantum Electron., vol. QE-19, pp. 1514-1519, 1983.
14. V. Pevtschin and S. Ezekiel: Opt. Lett., vol. 12, pp. 172-174, 1987.
15. D. Wang, L. Xie, and Y. Wang: Opt. Lett., vol. 13, pp. 820-822, 1988.
16. M. Suzuki and S. Yamaguchi: IEEE J. Quantum Electron., vol. 24, pp. 2392-2399, 1988.
17. T. Sato, M. Niikuni, S. Sato, and M. Shimba: Electron. Lett., vol. 24, pp. 429-431, 1988.
18. G. P. Barwood, P. Gill, and W. R. C. Rowley: Electron. Lett., vol. 24, pp. 769-770, 1988.
19. D. J. Webb, J. D. C. Jones, and D. A. Jackson: Electron. Lett., vol. 24, pp. 1002-1003, 1988.
20. S. Yamaguchi and M. Suzuki: Appl. Phys. Lett., vol. 41, pp. 1034-1036, 1982.
21. M. Ohtsu, H. Kotani, and H. Tagawa: Jpn. J. Appl. Phys., vol. 22, pp. 1553-1557, 1983.
22. T. Yanagawa, S. Saito, and Y. Yamamoto: Appl. Phys. Lett., vol. 45, pp. 826-828, 1984.
23. T. Yanagawa, S. Saito, S. Machida, Y. Yamamoto, and Y. Noguchi: Appl. Phys. Lett., vol. 47, pp. 1036-1038, 1985.
24. M. Ohtsu and E. Ikegami: Electron. Lett., vol. 25, pp. 22-23, 1989.
25. C. E. Moore: Atomic energy levels (Circular of the National Bureau of Standards 467, 1949).
26. V. Kaufman and B. Edlen: J. Phys. Chem. Ref. Data, vol. 3, pp. 825-895, 1974.
27. R. B. Green, R. A. Keller, G. G. Luther, P. K. Schenck, and J. C. Travis: Appl. Phys. Lett., vol. 29, pp. 727-729, 1976.
28. R. B. Green, R. A. Keller, G. G. Luther, P. K. Schenck, and J. C. Travis: IEEE J. Quantum Electron., vol. QE-13, pp. 63-64, 1977.
29. W. B. Bridges: J. Opt. Soc. Am., vol. 68, pp. 352-360, 1978.
30. K. C. Smyth and P. K. Schenck: Chem. Phys. Lett., vol. 55, pp. 466-472, 1978.
31. E. F. Zalewski, R. A. Keller, and R. Engleman, Jr.: J. Chem. Phys., vol. 70, pp. 1015-1026, 1979.
32. Y. C. Chung and R. W. Tkach: Electron. Lett., vol. 24, pp. 804-805, 1988.
33. Y. C. Chung and C. B. Roxlo: Electron. Lett., vol. 24, pp. 1048-1049, 1988.
34. Y. Yamamoto: IEEE J. Quantum Electron., vol. QE-19, pp. 34-46, 1983.
35. A. von Engel: Ionized gases, 2nd Edition (Clarendon Press, Oxford), 1965.
36. P. F. Little and A. von Engel: Proc. Roy. Soc. A, vol. 224, pp. 209-227, 1954.
37. S. Koizumi, T. Sato, and M. Shimba: Electron. Lett., vol. 24, pp. 13-14, 1988.
38. Y. C. Chung, R. W. Tkach, A. R. Chraplyvy, and C. B. Roxlo: Electron. Lett., vol. 24, pp. 1159-1160, 1988.
39. S. Kobayashi, Y. Yamamoto, M. Ito, and T. Kimura: IEEE J. Quantum Electron., vol. QE-18, pp. 582-595, 1982.

	1.3 μm REGION		1.5 μm REGION	
	λ (μm)	TRANSITION	λ (μm)	TRANSITION
Ne	1.29155	$2p_4 - 2s_5$	1.52349	$2p_1 - 2s_2$
	1.32228	$2p_2 - 2s_5$		
Ar	1.27057	$2p_2 - 3s_1'$		
	1.27368	$2p_8 - 2s_5$	1.50506	$2p_1 - 3s_1'$
	1.27497	$2p_4 - 2s_2$	1.51769	$2p_5 - 2s_4$
	1.28062	$2p_8 - 3d_1''$	1.53056	$3d_1' - 4U'$
	1.29367	$2p_4 - 2s_3$	1.53335	$2p_8 - 3d_3$
	1.29602	$2p_{10} - 3d_5$	1.53534	$3d_1' - 4Y'$
	1.30118	$2p_3 - 2s_2$		
	1.32175	$2p_{10} - 3d_6$		
	1.32317	$2p_9 - 3d_4$		
	1.32762	$2p_3 - 3s_1'''$		
	1.33168	$2p_4 - 3s_1''''$		
	1.33707	$2p_6 - 3d_1$		
Kr	1.28654	$1s_3 - 2p_7$	1.50094	$2p_7 - 2s_5$
	1.29888	$2p_{10} - 3d_1''$	1.52137	$2p_9 - 3d_1''$
	1.31810	$2p_8 - 2s_4$	1.52438	$2p_8 - 3d_1''$
			1.53306	$2p_6 - 3d_2$
			1.53391	$2p_{10} - 3d_3$
			1.53762	$2p_6 - 2s_5$
			1.54782	$1s_2 - 2p_8$
Xe	1.26268	$2p_{10} - 2s_5$	1.54225	$2p_7 - 2s_4$
	1.36607	$2p_9 - 2s_4$		

Table I: Atomic Transition of Noble Gases in 1.3 and 1.5-μm Regions.

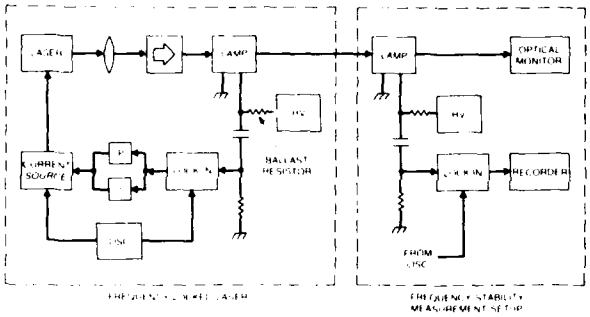


Figure 2: Experimental setup. HV is the high voltage power supply. OSC is an oscillator. P and I are a proportional amplifier and an integrator, respectively. Optical monitor includes a Fabry-Perot interferometer and an optical spectrum analyzer.

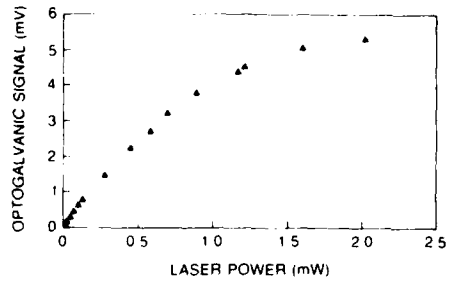


Figure 4: Optogalvanic signal vs. laser power of the Ar $2p_{10}$-$3d_5$ transition (1.2960 μm).

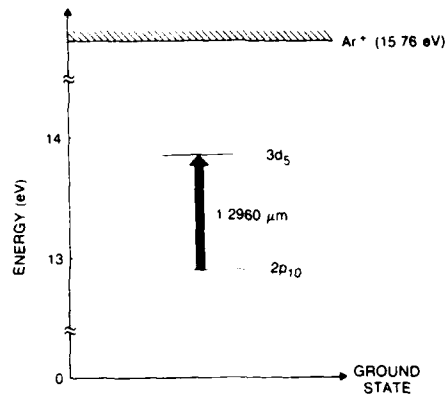


Figure 1: Partial energy diagram of Ar atom (not to scale).

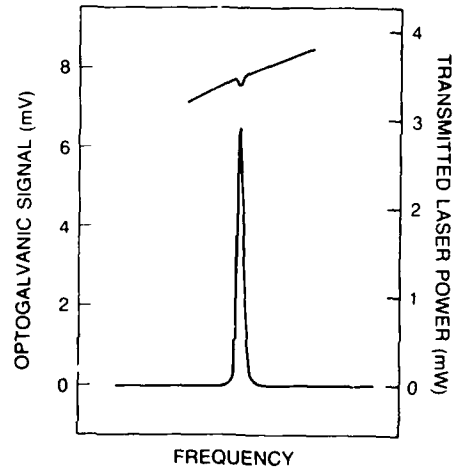


Figure 3: Measured optogalvanic signal and absorption of the Ar $2p_{10}$-$3d_5$ transition (1.2960 μm). A commercial hollow cathode lamp (Ar buffer gas and aluminium cathode) was used. The discharge lamp of the lamp was 11 mA. The laser power incident on the lamp was 3.5 mW. The laser frequency was swept by the injection current.

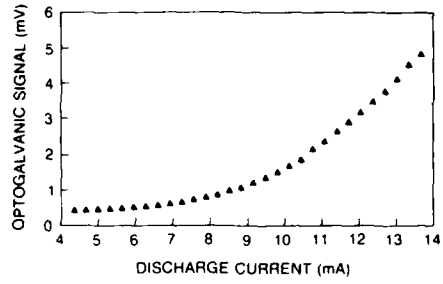


Figure 5: Optogalvanic signal vs. discharge current of the Ar $2p_{10}$-$3d_5$ transition (1.2960 μm). The laser power incident on the lamp was 0.5 mW.

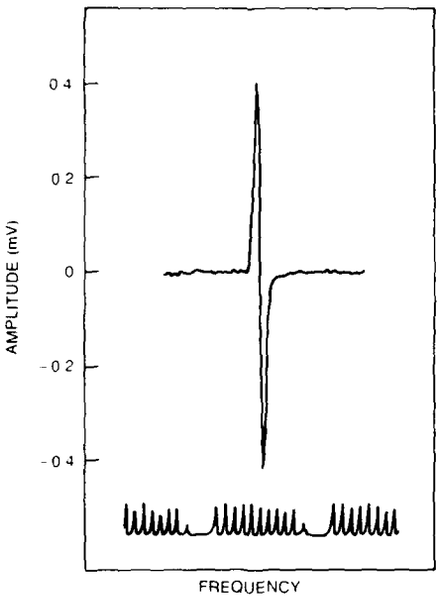


Figure 6: Measured the first derivative signal of Ar $2p_{10}$-$3d_5$ transition (1.2960 μm). Lower trace shows interference fringes of a confocal Fabry-Perot interferometer with a spacing of 750 MHz.

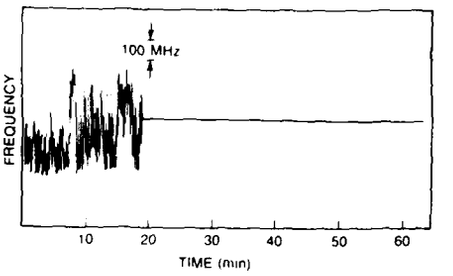


Figure 7: Trace of error signal when the laser was locked to the Ar $2p_{10}$-$3d_5$ transition at 1.5339 μm. The error signal was measured using an additional hollow cathode lamp, which is independent from from frequency-locking servo loop.

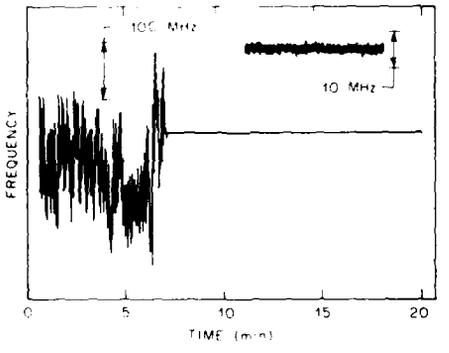


Figure 8: Trace of error signal when the laser was locked to the Kr $2p_{10}$-$3d_5$ transition at 1.5339 μm. The error signal was measured using an independent frequency discriminator.

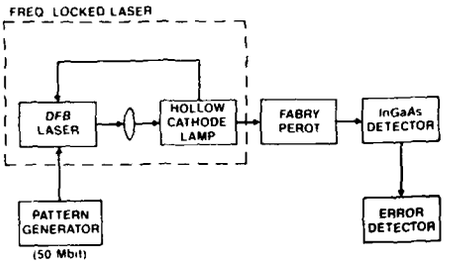


Figure 9: The experimental setup to evaluate the performance of frequency-locked lasers under FSK modulation.

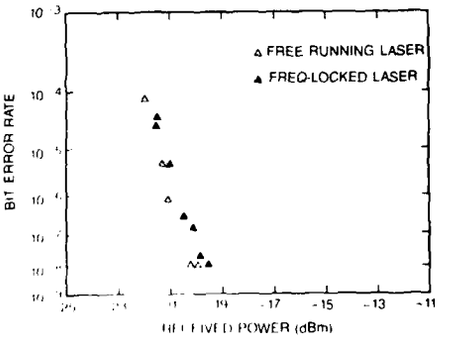


Figure 10: Measured bit error rate curve; (▲) when the frequency-locking servo loop was closed, and (Δ) when the servo-loop was open and the frequency dither was removed.

DUAL OPTICALLY STABILIZED SEMICONDUCTOR LASERS FOR COHERENT OPTICAL COMMUNICATIONS

W. R. Babbitt and R. G. Beausoleil*
Boeing High Technology Center
P.O. Box 3999, M/S 7J-27, Seattle, WA 98124-2499

Abstract

We present a model on the optical stabilization of a semiconductor laser via resonant optical feedback from an external high-finesse cavity. The model predicts the laser linewidth in the limit of a white frequency noise spectrum, the locking range, and expected deviations of the locked laser's operating frequency from the external resonator's axial mode frequency. The model's prediction were verified through two experiments: one in which a single semiconductor laser is stabilized by resonant optical feedback and another in which two semiconductor lasers were optically locked to different axial modes of the same confocal Fabry-Perot Cavity. Techniques for optically locking multiple semiconductor lasers to different modes of an optical resonator are described. Applications of such multiple optically stabilized semiconductor lasers to optical communications are discussed.

Introduction

Several applications, including optical communication, laser radar, and optical position/velocity measurement systems, require extremely narrow laser linewidths in order to achieve high-quality or high-precision performance. The use of semiconductor lasers in these systems is also desirable, due to their low cost, compact size, and integrability into electronic circuitry. Several techniques have been suggested for narrowing the linewidth of semiconductor lasers. (See introduction in reference 1) The technique of resonant optical feedback, first demonstrated by Dahmani et al.,[2] is unique for not only is the laser linewidth significantly narrowed,[3] but the frequency of the laser is locked to one of the resonant mode frequencies of an external optical resonator. The theoretical laser linewidth for a laser stabilized by resonant optical feedback has been presented by a number of authors.[1,4,5] In this paper, we present a model of resonant optical feedback which, as well as predicting the laser linewidth in the limit of a white frequency noise spectrum, predicts the locking range and expected deviations of the locked laser frequency from the external resonator's axial mode frequency. Experimental verification of the model's predictions is presented. The technique of locking two lasers to the same Fabry-Perot cavity and the extension of this technique to the optical stabilization of multiple lasers are discussed, along with possible applications of these techniques to optical communications.

Optically Stabilized Semiconductor Laser Model

Hjelme and Mickelson developed a model for the linewidth and steady-state behavior of a semiconductor laser with a short extended cavity which was valid for arbitrarily strong feedback.[6] Subsequently, the limitation of this model to short external cavities was eliminated by including the effect of relaxation oscillations on the frequency spectrum of a single mode semiconductor laser.[4] Their result can be applied to the case of resonant optical feedback by replacing the amplitude reflection coefficient of the external mirror in their analysis with the complex reflection coefficient of an external high-finesse cavity (HFC) whose phase and amplitude are frequency dependent.[4] Carrying out the analysis in the case of weak optical feedback in the limit of a white frequency noise spectrum, one finds that the shift of the optically stabilized semiconductor laser with respect to the free-running semiconductor laser is given by

$$f_0 - f_s = -\frac{\sqrt{\kappa}}{2F_d\tau_d}\sqrt{1+\alpha^2}\,\frac{\sin\left[2\pi f_0\tau_L + \tan^{-1}\left(\sqrt{1+\tilde{F}}\tan\left[\pi(f_0-f_q)/\Delta f_{FSR}\right]\right) + \tan^{-1}(\alpha)\right]}{\sqrt{1+\tilde{F}\sin^2\left(\pi(f_0-f_q)/\Delta f_{FSR}\right)}}, \qquad (1)$$

where f_0 is the operating frequency of optically stabilized laser, f_s is the free-running frequency of solitary semiconductor laser (without feedback), F_d and t_d are the finesse and round-trip time of semiconductor laser cavity, respectively, α is the linewidth enhancement factor, τ_L is the round-trip time between the semiconductor laser and the HFC, κ is the optical feedback level at the peak of resonance, $\tilde{F}$ is the HFC's coefficient of finesse, f_q is the frequency of q^{th} mode of the HFC, and Δf_{FSR} is the HFC's free spectral range.

In the limits of high finesse $F_c\tau_c >> \frac{F_d\tau_d}{\sqrt{\kappa}}$, a short distance between the laser and the HFC $\tau_L << \frac{F_c\tau_c}{\pi}$, small laser frequency shifts $|f_0 - f_s| << \frac{\sqrt{\kappa(1+\alpha^2)}}{2F_d\tau_d}$, and near resonant operation $|f_0 - f_q| << \frac{\sqrt{1+\tilde{F}}}{\pi\tau_c}$, where $F_c = \frac{\pi\sqrt{\tilde{F}}}{2}$ is the HFC's finesse and $\tau_c = \frac{1}{\Delta f_{FSR}}$ is the round-trip time in the HFC, equation (1) above can be use to predict at least four measurable quantities of interest in the design of practical optically stabilized semiconductor laser (OSSL) systems.

1) The linewidth of the optically stabilized semiconductor laser, assuming that the laser's spectral characteristics are dominated by white frequency noise, is given by

$$\Delta f = \frac{\Delta f_{ST}}{\kappa\left(\frac{F_c\tau_c}{F_d\tau_d}\right)^2}, \tag{2}$$

where Δf_{ST} = Schawlow-Townes linewidth.(REF) In practice, a semiconductor laser has several sources of noise. The degree to which a semiconductor laser's behavior can be considered to be governed by white noise varies from laser to laser. In a laser that has significant 1/f noise contributions, it is predicted that the laser linewidth reduction factor (the demoninator in equation 2) would go as the roughly the square root of that of equation 2.[1]

2) The frequency shift of the optically stabilized semiconductor laser due to tuning of the free running laser frequency is given by

$$\frac{\partial f_0}{\partial f_s} = \frac{1}{\sqrt{\kappa(1+\alpha^2)}\left(\frac{F_c\tau_c}{F_d\tau_d}\right)}. \tag{3}$$

A similar result was derived by Laurent et al.[1]

3) The frequency shift of the optically stabilized semiconductor laser due to changes in the optical path length between the semiconductor laser and the HFC, L, is given by

$$\frac{\partial f_0}{\partial L} = -\frac{2\pi}{\lambda}\left(\frac{1}{F_c\tau_c}\right), \tag{4}$$

where $L = \frac{c\tau_L}{2}$. It should be pointed out that this derivative was evaluated at its maximum value. The operating frequency as a function of L is cyclic with a period equal to $\lambda/2$ and a maximum deviation of $\frac{1}{2F_c\tau_c}$ (the half width at half maximum of the HFC) under locked conditions. Our value for $\frac{\partial f_0}{\partial L}$ is significantly larger (by a factor of $F_c/2$) than that derived by Laurent et al.[1]

4) The locking range is defined as the range over which the free running laser frequency can be tuned while maintaining a locked state of the optically stabilized semiconductor laser. The locking range is determined from a plot of the operating frequency versus free running laser frequency. To obtain this plot, the relationship between of the free running laser frequency and the operating frequency is first generated using equation (2). This relationship is then inverted into a one to one mapping of the free running frequency to operating frequency by choosing the operating frequency that corresponds to the laser mode that is stable and has the highest gain for a given free running laser frequency. The lock range is highly dependent on the feedback level, κ, which is difficult to measure experimentally. However, by measuring the experimental locking range and using the above model, an estimate of the feedback level can be made.

Single Optically Stabilized Semiconductor Laser Experiment[3]

A schematic of the single OSSL experiment is shown in figure 1. A Hitachi HLP1400 GaAlAs semiconductor laser was operated at laser current of about 100 mA to produce a laser output of roughly 12 mW. The beamsplitter transmitted 90% of the output laser power. A mirror mounted on a piezoelectric actuator controlled the laser to HFC distance. The 5 cm Fabry-Perot cavity was aligned in a confocal V-mode; only light that has been transmitted stored in the interferometer is fed back into the laser. The linewidth of the stabilized laser was measured using a delayed self-heterodyne technique.[3,7] The power spectra of the self-heterodyne signal with and without feedback are shown in figure 2 and an expanded frequency axis plot of the self-heterodyne power spectrum is shown is figure 3. The signal to background ratio in figure 3 indicates a laser linewidth well below the 1 kHz resolution limit of the self-heterodyne system. Using the following values for the experimental parameters: F_c= 300, τ_c= 670 psec, L = 1.2 m, F_d= 2.5, τ_d= 6.7 psec, α = 3, $\kappa = 10^{-4}$, Δf_{ST} = 2 MHz, and λ = 830 nm, the predicted linewidth would be on the order of 100 Hz.

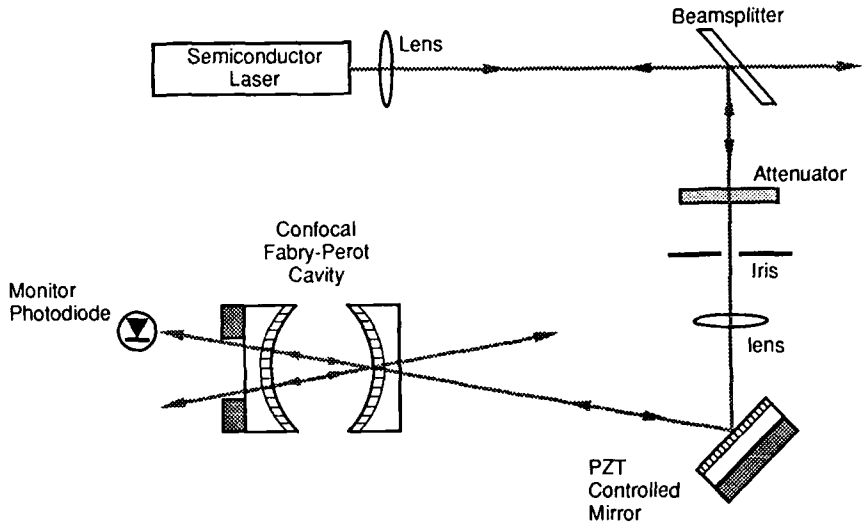


Figure 1. Schematic of single optically stabilized semiconductor laser.

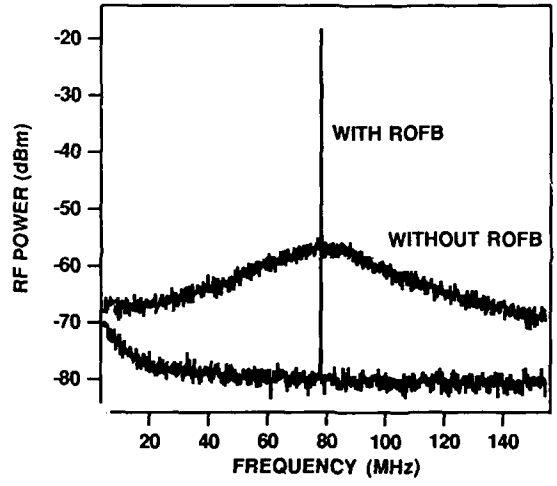


Figure 2. Power spectra of the self-heterodyne signal with and without resonant optical feedback.

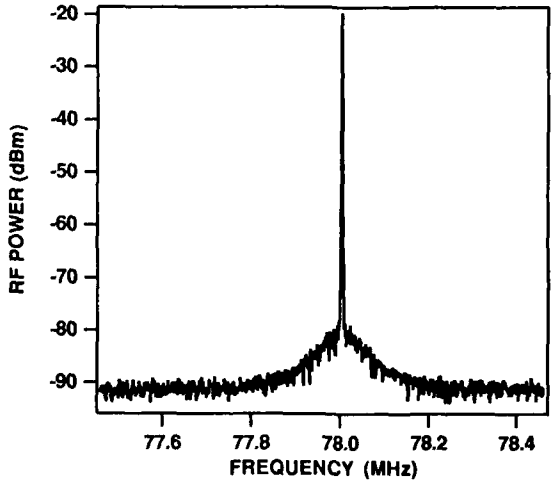


Figure 3. Power spectrum of the self-heterodyne signal with resonant optical feedback.

Dual Optically Stabilized Semiconductor Lasers Experiment

In order to measure small deviations in the stabilized laser's operating frequency due to changes in L or f_s, we heterodyne detected the laser with a second stabilized laser. In order to eliminate errors due to fluctuations in the resonant frequencies of the HFC, the two laser were locked to the different axial modes of the same confocal Fabry-Perot cavity. The schematic of this dual OSSL experiment in figure 4 shows how the amplitude and phase of the feedback to each laser could be individually adjusted. The cavity mode to which a given laser locks was adjusted by tuning the free-running laser frequency (via the laser current). Crosstalk between the lasers was minimized by giving the laser's orthogonal polarizations at the input to the Fabry-Perot cavity. The output beams were heterodyne detected on a silicon avalanche photodiode and the spectrum of the heterodyne signal was measured with a rf spectrum analyzer. Figure 5 shows the heterodyne spectra of the two free running lasers and of the two lasers locked to adjacent modes of the 1.5 GHz free spectral range Fabry-Perot. Figure 6 shows multiple locked heterodyne spectra where one of the lasers was sequentially locked (via tuning of its laser current) to the 12 different axial modes around the axial mode of the Fabry-Perot cavity to which the other laser was locked. The roll off is due to the frequency response of our detector. The heterodyne signal frequency could be any multiple of the free spectral range, from a few gigahertz to far in excess of a terahertz. Also shown in Figure 6 is the heterodyne spectrum when the two lasers are free-running and tuned 2.25 GHz apart.

The measured locking ranges for the two lasers were 550 MHz and 300 MHz, corresponding to feedback levels on the order of 10^{-4}. Frequency deviations introduced by changes in the free-running laser frequency and in the laser to HFC distance were measured by recording the shifts in the heterodyne frequency when the laser current and the voltage controlling the PZT adjusted mirror were changed, respectively. Using the experimental parameters above, the predicted $\frac{\partial f_0}{\partial f_s}$ value is 1/400 ±40%. The error stems from uncertainty in the feedback level. The experimental value for $\frac{\partial f_0}{\partial f_s}$ was 1/700 ±30%. The measurement error stems from jitter in the heterodyne frequency with an amplitude on the order of 100 kHz and a frequency on the order of 100 Hz. The amplitude and frequency of this jitter is consistent with jitter in the free running laser frequency due to laser current noise (a few microamperes, rms) from the AC line in the current sources used for this experiment. The model's prediction for the frequency shifts due to tuning of distance between laser and high-finesse cavity is $\frac{\partial f_0}{\partial L} = -38 \pm 5$ kHz/nm, where the error stems from uncertainty is the finesse of the Fabry-Perot during operation. Experimentally we found that $\frac{\partial f_0}{\partial L} = -40 \pm 20$ kHz/nm, in reasonable agreement with the predictions of our model.

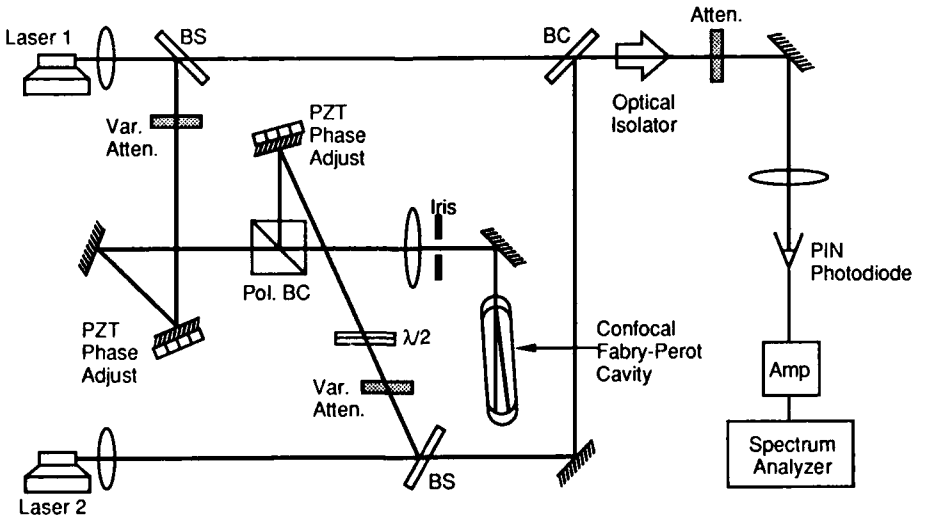


Figure 4. Schematic of dual optically stabilized semiconductor lasers experiment.

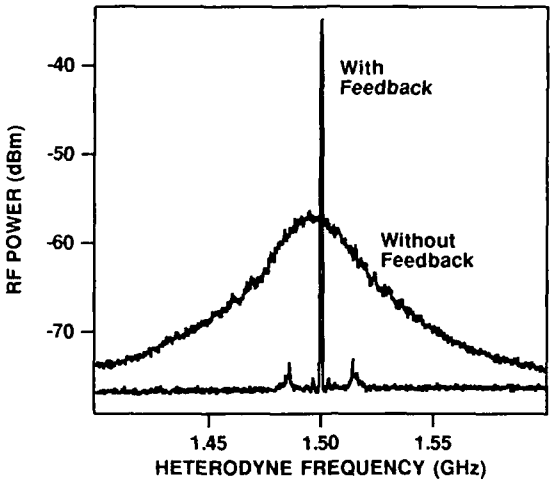


Figure 5. Power spectra of the heterodyne signal with and without resonant optical feedback.

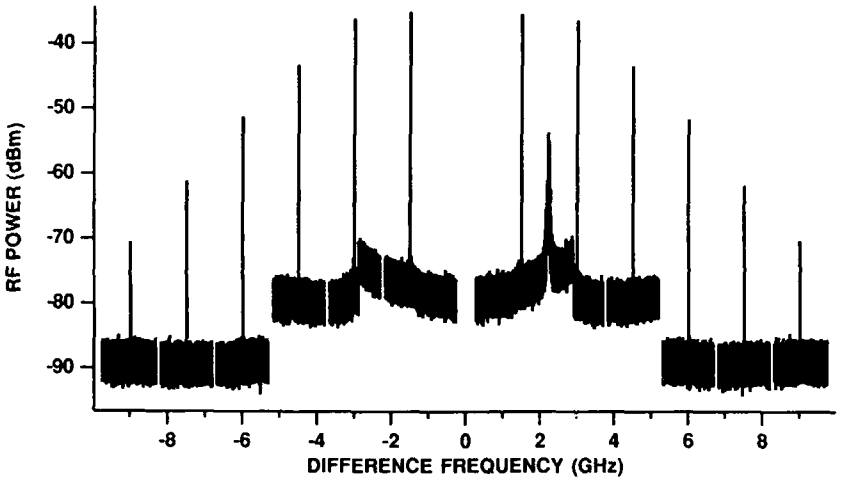


Figure 6. Multiple heterodyne spectra produced by detuning one of the optically stabilized lasers with respect to the other. The broad spectrum at 2.25 GHz was produced when the lasers were free running.

Applications of Optically Stabilized Semiconductor Lasers to Optical Communication

OSSL systems have potential applications in the optical communications field.[8] The systems have the advantage of being based on an all-optical technique that not only locks two lasers with a fixed frequency separation, but also substantially narrows the linewidths of the lasers. An rf reference source is not required, nor is electronic feedback of the laser output required. The major drawbacks of the dual optically stabilized lasers is the residual linewidth and the operating laser frequency tuning due to deviations in the laser current and in the laser to cavity distance. Laser current sources with lower noise specifications are available to reduce the frequency jitter observed in our experiment. Even so, for frequency separations of less than 100 GHz, other locking technique (for example, the technique of injection locking slave lasers to the sidebands of a frequency modulated master laser) provide significantly stabler frequency separations than the OSSL technique. However, the frequency separations obtainable with these other techniques are limited to the lower order harmonics of the rf source that drives the master oscillator (i.e. frequency separations less than 100 GHz), whereas the dual OSSL system can obtain frequency separation far in excess of a terahertz.

The other advantage of the OSSL technique is that more than two lasers may be locked to the different axial modes of the same optical cavity. We used polarization isolation to minimize the crosstalk between the lasers, but this technique is limited to two laser. One isolation technique that could be used with a confocal Fabry-Perot cavity to stabilize multiple lasers is angular and rotational separation of the feedback beams. However, the alignment difficulties associated with this technique would make it impractical. For a practical system, it may be sufficient to use frequency separation of the lasers. If the frequency separation between lasers is much greater than the locking ranges, the crosstalk should be minimal. This would allow for all-fiber systems, which would greatly minimize alignment difficulties. Figure 7 shows an all-fiber multiple OSSL system based on the frequency isolation technique. All fiber-optic splitters, electro-optic modulators, coupler, and resonator have replaced the bulk-optic beamsplitters, PZT controlled mirrors, beam combiner, and confocal cavity of figure 4. Care must be taken is such a system that the reflection from the various components are negligible compared to the feedback of the HFC and optical isolators may be needed on the outputs.

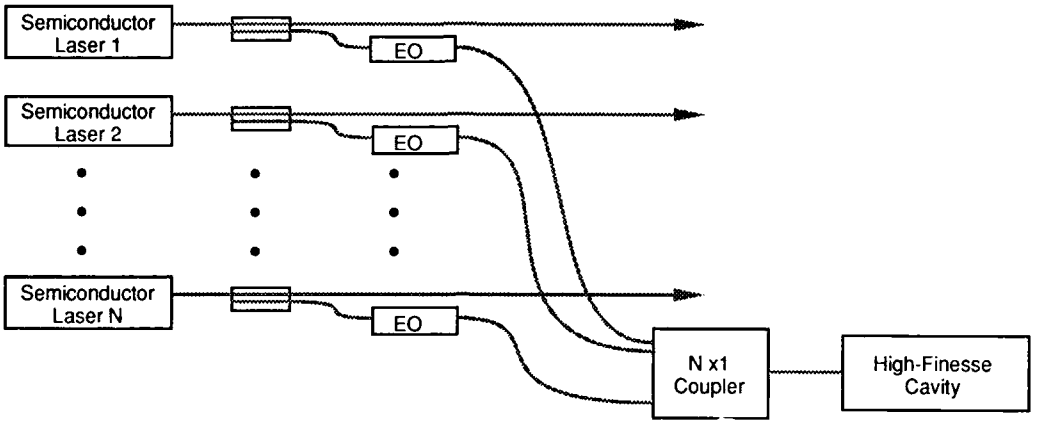


Figure 7. All-fiber multiple optically stabilized semiconductor laser system.

Multiple OSSLs may have applications in frequency division multiplexed (FDM) optical communication networks. Figure 8 shows how a FDM transmitter could be configured. External modulation is indicated, though direct modulation techniques should not be ruled out.[9] A reference frequency is also transmitted along with the FDM output. Figure 9 shows one possible configuration of a FDM receiver. The reference electronics locks a resonant mode of the receiver's HFC to the optical frequency of the transmitter's reference or the electronics may introduce a fixed frequency offset. The multiplexed signals are demultiplexed using optical heterodyne techniques. An OSSL FDM system would probably work best in a star configuration, where there might be multiple OSSL transmitters and receivers with one master reference.

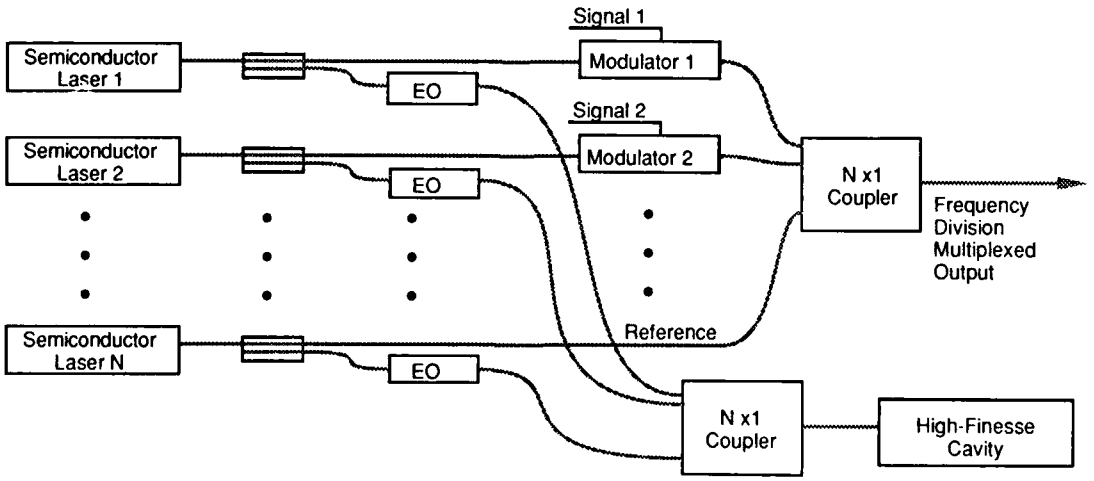


Figure 8. Frequency division multiplexed transmitter based on an OSSL system.

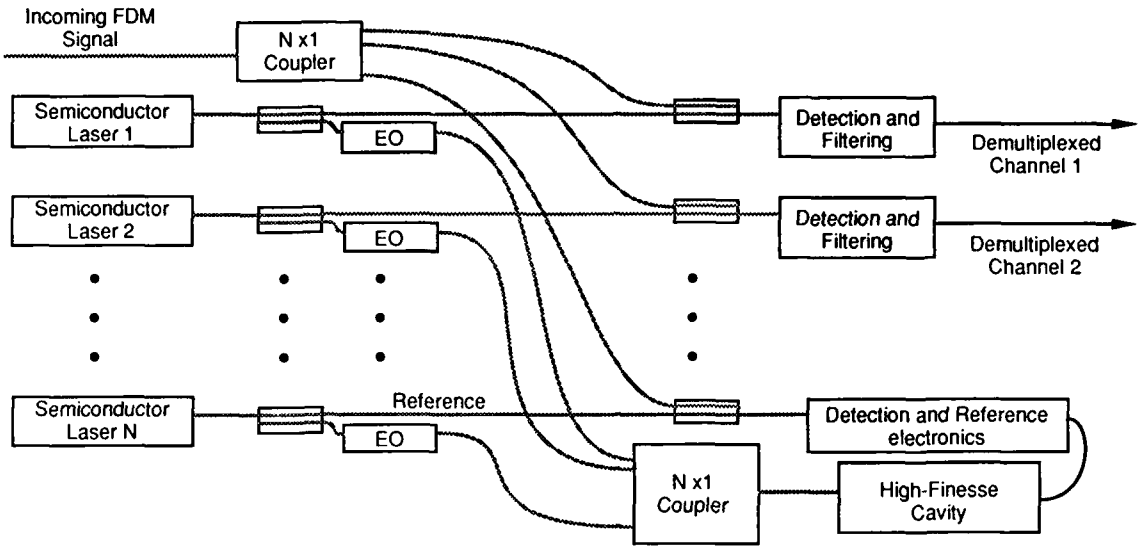


Figure 9. Frequency division multiplexed receiver based on an OSSL system.

Summary

In summary, we have derived a model that predicts the linewidth, locking range, and frequency tuning of semiconductor lasers that have been optically stabilized with feedback from an external high-finesse cavity. Both single OSSL experiments and dual OSSL experiments were performed in order to verify our model. The dual OSSL system demonstrates that more than one laser can be locked to a single resonator and suggests that multiple OSSL systems could be used in the transmitters and receivers of a FDM optical communication network.

References

1. P. Laurent, A. Clairon, and C. Breant, IEEE J. Quantum Electron. **QE-25**, 1131 (1989).
2. B. Dahmani, L. Hollberg, and R. Drullinger, Opt. Lett. **12**, 876 (1987).
3. R. G. Beausoleil, J. A. McGarvey, R. L. Hagman, and C. S. Hong, presented at the Conference on Lasers and Electro-Optics '89 (1989), paper WN3.
4. D. R. Hjelme, A. R. Mickelson, R. G. Beausoleil, J. A. McGarvey, and R. L. Hagman, in the proceedings of the SPIE, Laser Diode Technology and Applications, Vol. **1043**, pp. 167-174 (1989).
5. H. Li and H. R. Telle, IEEE J. Quantum Electron **QE-25**, 257 (1989).
6. D. R. Hjelme and A. R. Mickelson, IEEE J. Quantum Electron. **QE-23**, 1000 (1987).
7. A. T. Okoshi, K. Kikuchi, and A. Nakayama, Electron. Lett. **16**, 630 (1980).
8. W. R. Babbitt, R. G. Beausoleil, and D. A. Leep, "Multiple laser frequency stabilization," U. S. Patent Pending.
9. L. Hollberg and M. Ohtsu, Appl. Phys. **53**, 944 (1988).

*R. G. Beausoleil's present address:
Solidlite Corporation, 16150 N. E. 85th St., Suite 224, Redmond, WA 98052

NARROW BAND, HIGH POWER LIGHT FROM DIODE LASERS

Song-Quan Shang and Harold Metcalf
State University of New York, Physics Dept., Stony Brook, NY 11794

ABSTRACT

We have used a 100 mW cw laser diode array to amplify the light from a low power, single stripe diode laser (both lasers commercially available). The input light was spectrally narrowed and frequency stabilized to less than 300 kHz using optical feedback from a Fabry-Perot cavity, and the amplified beam had the same spectral characteristics. Also, the ~90 mW amplified beam had a single diffraction-limited spatial mode corresponding to the full 100 μm width of the array, indicating that all its stripes were coherent. We have tested a simple quantitative model of this process. We used counterpropagating beams light from this array to form a one-dimensional optical molasses perpendicular to an atomic beam of ^{85}Rb for active collimation. The minimum measured angular spread of the beam we achieved corresponds to a transverse rms speed of 3 cm/s. This low velocity was limited only by experimental geometry.

I. INTRODUCTION

Because of their ease of use and low cost, tunable diode lasers may have significant impact on experimental atomic physics, and especially on laser spectroscopy. For example, it is now quite reasonable to consider single experiments that use several different lasers for state preparation, optical pumping, opto-mechanical steering and cooling, saturation, probing, etc. The individual laser beams may be cw, chopped, frequency modulated, or otherwise customized to particular jobs. Before such new kinds of experiments can be realized, however, some of the inherent disadvantages of diode lasers must be overcome. Some of their present limitations are imposed by their spectral width, frequency stability, spatial beam quality, and low power output.

Recently there has been an important advance in spectral narrowing and frequency stabilization techniques of low power (single stripe) diode lasers by purely optical feedback[1]. This method has the important advantages that it is simple and that its bandwidth does not have electronic limitations. Furthermore, the diode laser frequency is locked to an external cavity which can itself be locked to a reference, or can be scanned or modulated. Finally, it requires a minimum of instrumentation, all of which can be home-built in a modestly-equipped laboratory. We have duplicated the results of Ref. 1 quite successfully. Even without the phase control labelled PZT-Φ in Ref. 1, we have locked and swept off-the-shelf diode lasers (Sharp LT-021, LT-024) over hundreds of MHz at rates in the order of 1 THz/s while maintaining a spectral width a few tens of kHz.

Unfortunately, the output power of the single longitudinal mode diode lasers that are most suitable for this spectral narrowing method is limited to about 30 mW (only a few mW of this needs to be split off for the narrowing beam). In order to achieve higher power output, monolithic arrays of diode lasers are necessary, but these arrays are not as easy to control. One way to have the best features of both types is to inject light from another source into a diode laser array, and many authors have reported successful experiments of this kind[2-8].

We report here extensions and improvements of this prior work, as well as a simple physical model of the process. We inject only 2 mW from a master diode laser (spectrally narrowed as in Ref. 1) into a 100 mW free-running array (Spectra-Diode Labs 2410-C), and we find that it dramatically narrows both its spectrum and beam divergence. We have modelled this injection process, and have found that the dominant feature is phase matching of the injected wave with the free running wave in a single stripe of the array. This model provides an accurate description of both the main output beam features as well as certain secondary behavior.

We have used the light from this laser array to make an "optical molasses" for the purpose of actively collimating an atomic beam. The limits of precision of atomic beam experiments are ordinarily limited by the beam's brightness; using smaller slits to get more parallel beams reduces the atomic flux. The force that arises in optical collimation, however, is velocity dependent and can be arranged to increase the beam brighness. We report here our first measurements of brightness enhancement of atomic beams, comprising optical collimation below the Doppler limit.

II. EXPERIMENTS

In our apparatus, a 10 mW Sharp LT-021 diode laser, narrowed as described in Ref. 1, serves as the master laser. A small part of its output is split off for narrowing while the rest is optically isolated and carefully focussed onto the front end of one stripe of a Spectra-Diode Labs model 2410-C diode array as shown in Fig. 1. A combination of cylindrical and spherical lenses is used, including one mounted in a precision xyz stage equipped with a PZT micrometer for the motion parallel to the long direction of the output face of the array, so that individual stripes (10 μm apart) may be targeted for light from the master laser. The input beam is focussed into a spot small enough to avoid spill-over onto the ends of ajacent stripes, but the NA is kept small enough to avoid simultaneous coupling into many spatial modes of the target channel of the array. The input beam is incident on an 80 mm focal length cylinder lens followed by a 6.5 mm focal length Melles-Griot diode laser collimator about 100 mm away from it that refocusses the input spot onto the array as desired. The various spatial modes can be selected by transverse motion of the cylinder lens to change the angle of the incoming beam of master laser light.

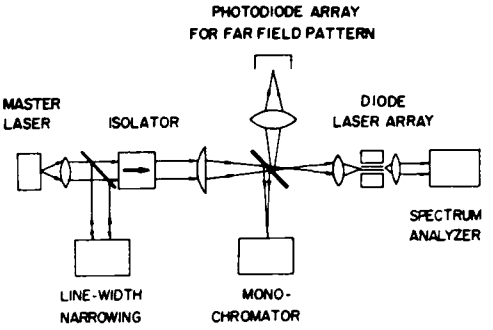


Fig. 1. Schematic of apparatus.

The small amount of light emitted from the rear facet of the array (standard 99% reflection coated) is focussed into a spectrum analyzer[9] while the main beam emitted from the front of the array is collimated by the same optics that focus the incoming light and then split for near and far field measurements. The free running array emits in two lobes directed about $\pm 3^{\circ}$ from the axis, and it is important to note that master laser beam is directed close to, but not coincident with, one of these lobes[2]. Typically it is at about 4° from the laser axis, about 1° larger than the free-running lobes. The main output beam is directed close to the other lobe, and thus the properly injected array can appear almost like a mirror with gain[10].

Although the free running array has characteristically many spectrally broad, weak longitudinal modes spread over ~1000 GHz, injection of the master laser's light collapses the spectrum into a single mode at the master laser frequency. Fig. 2a shows the many weak modes of the free running array spread over hundreds of GHz, folded by the 2 GHz FSR of the analyzer (finesse ~50). Fig. 2b shows that when the master laser light is admitted, the spectrum condenses dramatically into a single narrow mode whose strength is 50-100 times stronger (note change of scale). If there is light at other frequencies, it is less intense by a factor of at least 1000, and even this number is limited by the noise of our detector. When this beam is mixed on a fast photodiode with light from a separate, independently locked and narrowed diode laser[1], the beat note is observed to be less than 300 kHz wide (see Fig. 2c). (This width actually appears to be about ten times smaller, but overall frequency instabilities presently limit our measurement capability.) The spectral purity is therefore very high.

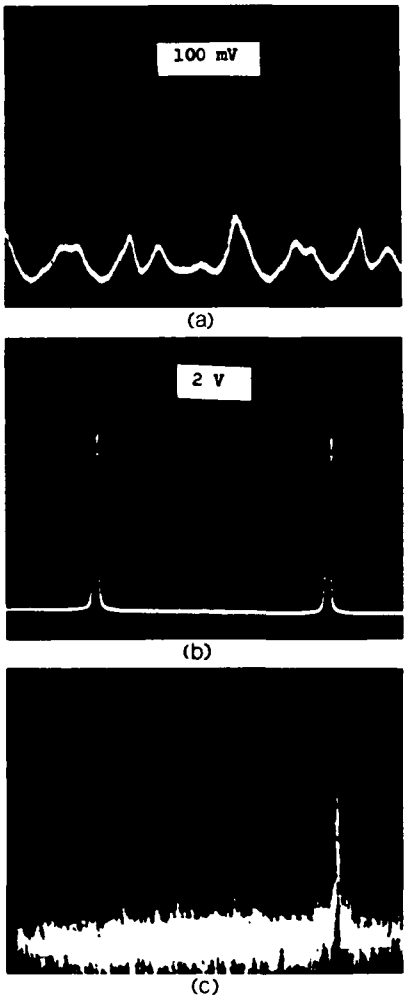


Fig. 2. Spectra of free running laser array (a), and injection locked laser array (b) measured with 2 GHz FSR spectrum analyzer. Note the difference in scale. Photo (2c) shows the beat of an injection locked array with an independent laser spectrally narrowed and stabilized by the method of Ref. 1. The vertical scale is 80dB from top to bottom (S/N = 1000) and the horizontal axis is 50 MHz from end to end. The measurement was limited by the 300 kHz resolution of the rf spectrum analyzer.

Figure 3a shows the several longitudinal mode clusters of the free running array as measured with a 1/3 m spectrometer. We have achieved injection locking at many different frequencies, including modes so weak that they don't even oscillate when the array is free running, but they are still within the gain region, as suggested in Ref. 3. Figure 3b shows the spectrometer scan on the same scale with injection locking on such a mode. The implications are that a laser diode array can generate light at frequencies many hundreds of GHz away from its free running output spectrum, and therefore may not require very careful wavelength selection from the manufacturer.

While operating the array at a fixed current, we have achieved successful injection locking for a ~40 GHz range of master laser light frequencies. This corresponds to the 35 GHz resolution of the diode laser cavity whose mode spacing is about 125 GHz and has 99% reflection at one end and about 35% reflection at the other (uncoated) end. The efficiency (power output from the array for fixed power input) is asymmetric in detuning, having a long, broad tail on the high frequency side and a sharp cutoff on the low frequency side.[3,4,6] Although it is expected that there should be no injection locking at frequencies below that of the free-running array, we have observed that the peak of this efficiency curve can occur ~30 GHz below this frequency, and interpret this in terms of the carrier depletion that occurs when the laser is injected[2].

When the frequency of both lasers are swept by varying their currents together (with no special precautions to maintain a fixed relationship between the currents other than to keep them within the 40 GHz capture range), the injected array stays locked to the master laser over the full sweep range of the master laser (several cm^{-1} when it is not locked to the narrowing interferometer). When the power of the master laser beam is reduced, successful injection locking requires that its frequency be raised, consistent with the model of the carrier density dependence of the index of refraction of the laser material[2].

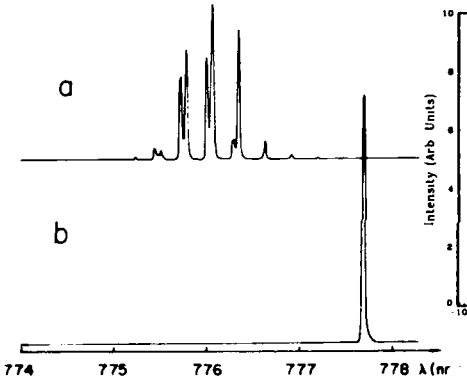


Fig. 3. Spectra from 1/3 m spectrometer of the free running array (a) and the injection locked array (b). Note that injection locking can also work on modes normally so weak that they don't appear in the spectrum of the free running array (scales of (a) and (b) are the same).

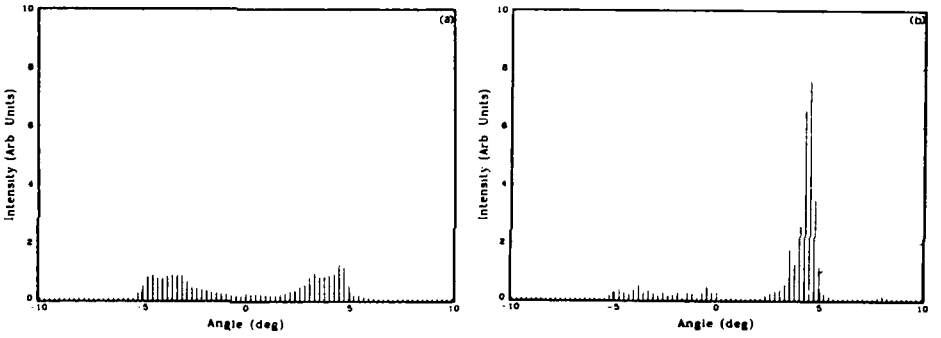


Fig. 4. (4a) shows the spatial pattern of the output of the free running array focussed onto a Reticon diode array (256 channels on 25 μm centers). (4b) shows the spatial effect of injection locking.

Injection of the master laser light also has a profound effect on the spatial distribution of the array output. The far-field pattern of the free-running array has two asymmetric lobes a few degrees wide and ~6° apart, as shown in Fig. 4a. This separation is usually explained as the angle that produces constructive interference between the output beams of the ~180° phase shifted ajacent stripes. When the master laser light is admitted, these are collapsed into a single, nearly diffraction limited beam directed at a larger angle from the laser axis than either of the two original lobes[2] (Fig. 4b). The 0.27° spread of the beam is the diffraction angle determined by the full width of the array, thus suggesting that all 10 stripes (in this array) are phase locked together. This beam contains most of the power of the array (typically 90% or 90 mW), and is therefore many orders of magnitude brighter than the free running output beams.

When the master laser light was focussed by only spherical lenses, we observed one or more small secondary beams at discrete angles from the main beam (Fig. 5a). Their relative strengths and angles depend on both injection laser frequency and alignment. However, use of the cylinder lens to compress the master laser light resulted in the appearance of just one of these peaks at a time, selectable by the injection angle (Fig. 5b). Careful measurements of this dependence further corroborates our model of injection locking.

III. MODEL OF INJECTION LOCKING

Discussion of the behavior of diode laser arrays begins with the free-running mode structure illustrated in Fig. 3a. The separation between these is not simply the spacing between resonant longitudinal modes of the dielectric Fabry-Perot cavity (index of refraction = n) constituting the laser, but must also account for the dispersion of the medium[11]. Differentiating the resonance condition $m\lambda = 2nL$ gives the spacing $\Delta\nu = c/2n'L$, where $n' = n - \lambda(dn/d\lambda)$ has a surprisingly large correction for the dispersion[12]. Our measured $\Delta\nu = (127\pm3)$ GHz, and the specified length of the SDL-2410-C laser array (250 ± 10 μm), combine to give $n' = 4.72\pm0.30$. As described above, we have observed that each of these longitudinal modes is actually a cluster of several spatial modes (partially visible in Fig. 3a).

Successful injection locking can be achieved when the external light from the master laser (k_e) is nearly resonant with and matched into one of the resonant modes of a single channel of the slave laser array (k_s). This requires

$$2k_eL\cos\theta_s = 2\pi j_e \qquad (1)$$

where j_e is an integer, L is the channel length, and Snell's law relates the internal angle θ_s to the angle θ_e between the external beam and the channel axis. For the free-running array, the individual channel resonance condition is $2k_sL = 2\pi j_s$ where j_s is an integer near j_e. Subtracting this from Eq. 1, we find

$$\cos\theta_s = 1 + \Delta k/k_e + \lambda j/2nL \qquad (2)$$

where $\Delta k \equiv k_s - k_e$ is the detuning between the injected light and that of the free-running array, λ is the free space wavelength, and $j \equiv j_e - j_s$ is a small (negative) integer. We find that injection locking is best for detuning of ~30 GHz so that $\Delta k/k \sim 8\times10^{-5}$, and we attribute this to a change of the index of refraction caused by carrier depletion when the slave laser array is strongly driven by the master laser light[2].

We have made many quantitative measurements of the spatial patterns shown in Figs. 4 and 5 in order to compare with Eq. 2. Although most previous workers have only reported the injection locking peak corresponding to j=1, we have measured the angles and angular steering for several different values of j (secondary peaks of Fig. 5). Fig. 6 shows our measured values of θ_e along with those calculated from Eq. 2 with $\Delta k/k = 8\times10^{-5}$ for the first eight values of j. The agreement is quite good. Note that the angles for destructive interference arising from the $\pi/2$ phase difference between ajacent laser channels 10 μm apart at λ = 780 nm are 0, 4.47°, 8.97°, 13.53°, and 18.17°, which fall between the values of Fig. 6. Although other workers have seen the effects of these interferences[4,6] they do not affect our measurements.

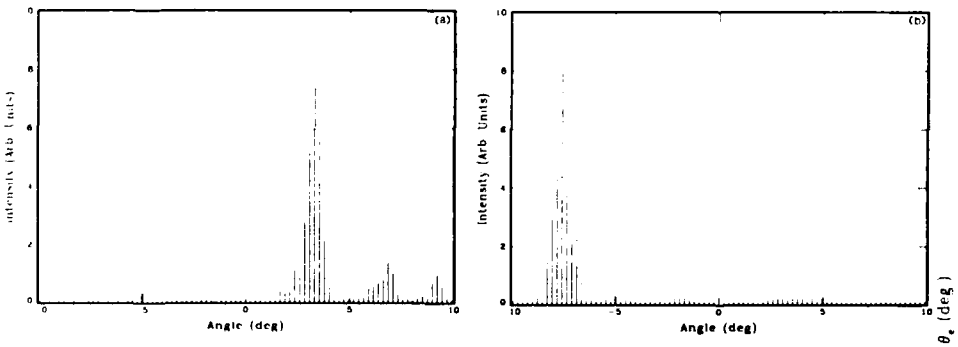


Fig. 5. (5a) shows the spatial pattern when injection locking is achieved with only spherical optics, thereby exciting several smaller peaks. When a cylindrical lens is used to focus the light better onto a single channel, these peaks may be individually selected by changing angles (5b).

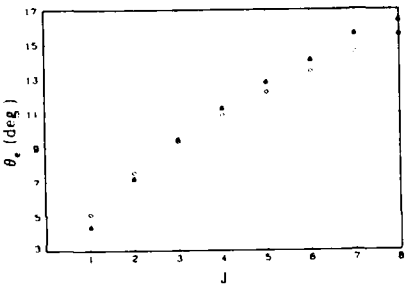


Fig. 6. Measured (triangles) and calculated (circles) values of θ_e vs j. Eq. 2 is used directly with no free parameters. Obviously a small shift of the refractive index would largely remove the systematic differences.

Also, we have changed k_e by varying the current of the master laser and have observed the resulting angular steering of the beam[4,6] for various values of j. Differentiation of Eq. 2 with respect to k_e using $dk/d\lambda = -2\pi n'/\lambda^2$ and the small angle approximation gives[2]

$$d\theta_e/d\lambda \cong -nn'/\lambda\theta_e = -(n'L)/(n/\lambda^3 jL) \quad (3)$$

which is different from the result found in Ref. 6 by the inclusion of the dispersion. The lines plotted with the data in Fig. 7 have slopes given by Eq. 3, and these slopes are compared with values given by a linear least squares fit to the data in Table I. The agreement is clearly excellent. Also, when we change the slave laser current by ΔI_s, just enough to cancel the angular shift caused by a change in the master laser current ΔI_m, we find that a plot of ΔI_m vs. ΔI_s is very nearly a straight line.

Using the measured value of $d\theta_e/d\lambda$ and n' = 4.72 from the mode spacing as determined above, we find from Eq. 3 the index of refraction for each j. The average of these is n = 3.02 ± 0.20. Then $E(dn/dE) = -\lambda(dn/d\lambda) \cong 1.7$ which can be compared with the data of Casey et al.[13] and Afromowitz[14]. We find that dn/dE = 1.06 at E = 1.6 eV (λ=780 nm, the Rb resonance line) fits their data very well for a value of Al concentration of about 20% for the uninjected material (injection of carriers changes the index and its dispersion[3]). This Al concentration is consistent with the manufacturing processes of the diode laser arrays.

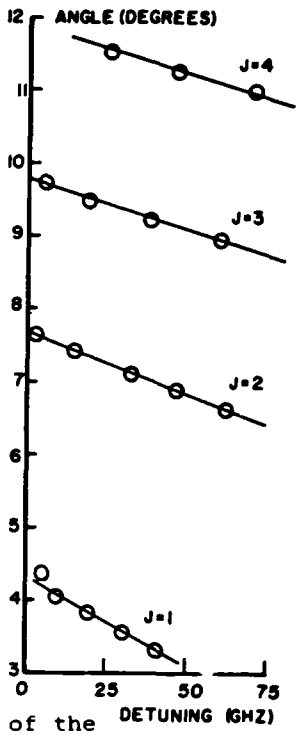


Fig. 7. Angular tuning of the main peak and three of the secondary peaks when changing the master laser frequency. The solid lines come from Eq. 3 with no adjustable parameters except for a tuning offset. Measurement errors are approximately the size of the symbols.

IV. ATOMIC BEAM COLLIMATION

Recent experiments on optical control of atomic motion have included collimation and focusing of atomic beams, and in some cases, brightness increases as well. Such compression of a beam's phase space volume is possible because of the velocity dependence of the non-conservative optical forces. The original idea of damping atomic motion by optical molasses arises from different Doppler shifts of the counterpropagating laser beams seen by the moving atom. A calculation of the cooling and heating of this process yields the Doppler limit for two level atoms, expressed as a temperature $T_D = \hbar\gamma/2k_B$ associated with the transverse kinetic energy.

The resulting reduction of phase space volume can produce a beam of unprecedented brightness: its spatial extent can be extremely small, and all the atomic velocities can be nearly equal in both magnitude and direction. Such a beam can enable extraordinary sensitivity for new experiments as well as enormous improvements on old ones, such as atomic clocks and well-defined collision experiments. This enhancement could be increased by several orders of magnitude if the transverse cooling could produce temperatures below T_D. Atoms in a laser decelerated beam can be actively collimated, then focussed to a spot with either a laser or magnetic lens, and finally recollimated (see Fig. 8).

We have discovered a new cooling process that uses an applied magnetic field to mix differently light-shifted atomic ground state sublevels and We have used this method for optical collimation of a Rb atomic beam to well below the Doppler limit[15,16]

The cooling depends on the different light shifts (ac Stark shift) of the ground state magnetic sublevels caused by the different couplings with the light. Light tuned below resonance causes a negative light shift for the ground state sublevels and optically pumps atoms to the lowest sublevel. Atoms absorb light with lower frequency than they fluoresce, thus losing energy.

To sustain the cooling process, atoms must be redistributed among the sublevels when the light shifts are smaller or reversed, and this is accomplished by a transverse magnetic field that mixes the ground state sublevels. For light tuned below resonance, atoms travelling across the standing wave will be optically pumped to the lowest energy sublevel near an antinode, and redistributed among the higher sublevels near a node by Larmor precession. Travel across the next antinode repeats the process and extracts energy from the atoms, thereby damping their motion.

We use a thermal beam of natural Rb produced by an oven at T ~ 150 ^{o}C with aperture ~ 0.33 mm diam., and a defining aperture of diam. ~ 0.33 mm about 24 cm away (see Fig. 9). The emerging atoms are optically collimated by a pair of counterpropagating laser beams transverse to their motion. Both the atomic beam and the circularly polarized laser beams are horizontal, and a weak magnetic field (typically vertical) is applied perpendicular to the laser beam axis. The atomic beam profile is measured with a vertically oriented scanning hot tungsten wire, 25 μm in diameter, 1.3 m away from the region of interaction with the laser beam. It ionizes virtually every Rb atom that hits it so that the detected ion current is a measure of the vertically integrated beam profile.

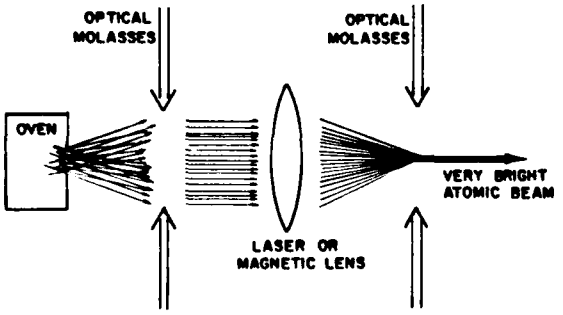


Fig. 8. Scheme for laser collimation of atomic beam. First the transverse velocity components of the atoms are damped out by an optical molasses, then the atoms are focussed to a spot, and finally the atoms are recollimated by a second optical molasses.

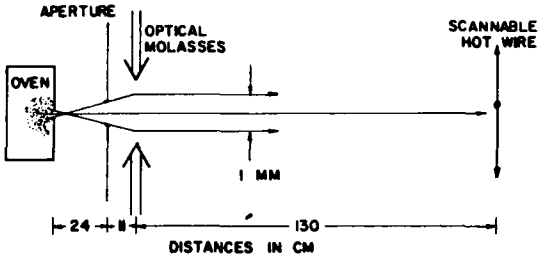


Fig. 9. Overall schematic of the apparatus used for one-dimensional transverse cooling.

The laser light is tuned near the $5S_{1/2}(F_g=3) \rightarrow 5P_{3/2}(F_e=4)$ cycling transition of ^{85}Rb at λ = 780 nm. The atomic and laser beam cross perpendicular, so the Doppler shifts are small, and the laser frequency is calibrated with a saturated absorption signal from an auxilliary Rb cell at room temperature. The total power at the interaction region is about 21 mW, apertured to a rectangular shape 8 mm high by 20 mm along the atomic beam. This laser beam crosses the atomic beam at a right angle, and is retroreflected to form the standing wave for collimation.

Figure 10 shows the result of hot wire scans across the atomic beam that has passed through the circularly polarized laser beams tuned both above and below atomic resonance. These curves show the transverse spatial distribution of atoms in the beam 1.3 m from the molasses region.

V. TWO DIMENSIONAL COLLIMATION

Even a simple laser collimation effort, such as the first stage of Fig. 8 without the atomic lens and recollimation, can significantly compress the momentum space volume occupied by atoms in a beam. We have demonstrated such two-dimensional collimation with our injection locked diode laser array[15].

For two dimensional collimation in the plane perpendicular to the atomic beam, a single hot wire scan would not provide enough information. Instead of scanning both a vertical and a horizontal hot wire, we have devised a new method for observing the spatial distribution of atoms in the plane perpendicular to the beam. As shown in Fig 11 two different plane meshes are mounted in the beam, perpendicular to it. The downstream one is heated to several hundred ^{o}C and operates as a surface ionization detector much like the hot wire. Ions emitted from the hot grid in the upstream direction are driven back through its holes by the electric field produced by a voltage between it and the other (repeller) grid. Once downstream of the hot grid, ions are accelerated into a pair of multichannel plate (MCPs) electron multipliers in chevron configuration whose ouput electrons are accelerated onto a phosphor coated screen which is viewed by a standard TV camera. The camera's output is fed to a frame grabber in a computer where the image can be analyzed.

Most of the neutral Rb atoms in the beam pass through the repeller grid (90% transparent) where about 1/3 of them strike the hot grid (70% transparent) and are ionized. Most of those ions are accelerated into the MCPs for detection. The repeller grid is important because ions ejected from the upstream surface of the hot grid (probably most of them) do not see the electric field between it and the MCPs because of electrostatic shielding by the hot grid's fine mesh (4 wires/mm).

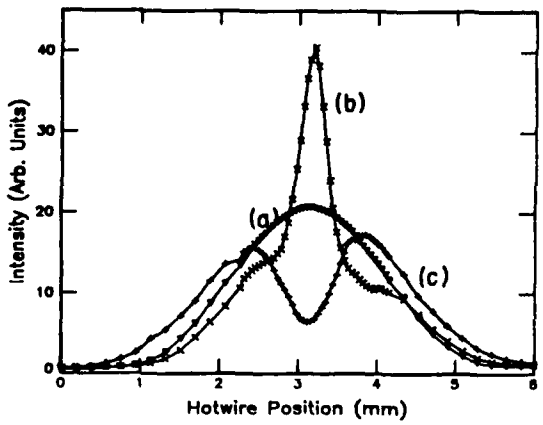


Fig. 10. Hot wire signal vs. position for collimation by transverse optical molasses. For these scans, the circularly polarized laser beam had average saturation parameter s=3 (intensity ~16 mW/cm^2) and was tuned ~19 MHz above (10c) and below (10b) atomic resonance. Trace (a) shows the no-laser scan.

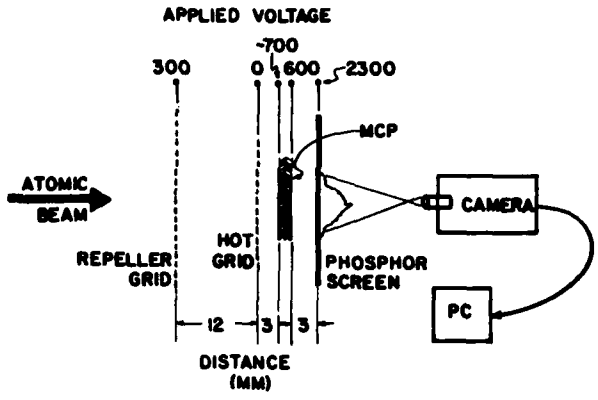


Fig. 11. Schematic diagram of neutral atom camera showing the repeller grid, the hot grid, the multichannel plates, and the phosphor screen.

The resolution of this system is limited to about 500 μm by the spatial spread of the charged particles in flight between the hot grid and the MCPs, and between the MCPs and the phosphor. We split off about half of the molasses laser beam to produce optical molasses in both the vertical and horizontal directions, and thereby achieve full two dimensional collimation of the atomic beam. Figure 12 shows the results of both red and blue tuning of this experiment. Here both light beams were polarized perpendicular to the atomic beam direction, and about 0.4 Gauss was applied along that direction (B-field and both polarization vectors were mutually perpendicular).

The collimated atomic beam spot size shown in Fig. 12 of about 1.25 mm diam has been reduced from its 6 mm diam with the lasers blocked. This corresponds to an increase of BOTH brightness AND intensity by a factor of more than 20. Furthermore, this increase could be very much larger but limitations imposed by the resolution of the imaging system may prevent its measurement. If this spot is 400 μm in diameter as suggested by Fig. 10, the phase space volume occupied by the atoms in two dimensions has been reduced by a factor of more than 200^2.

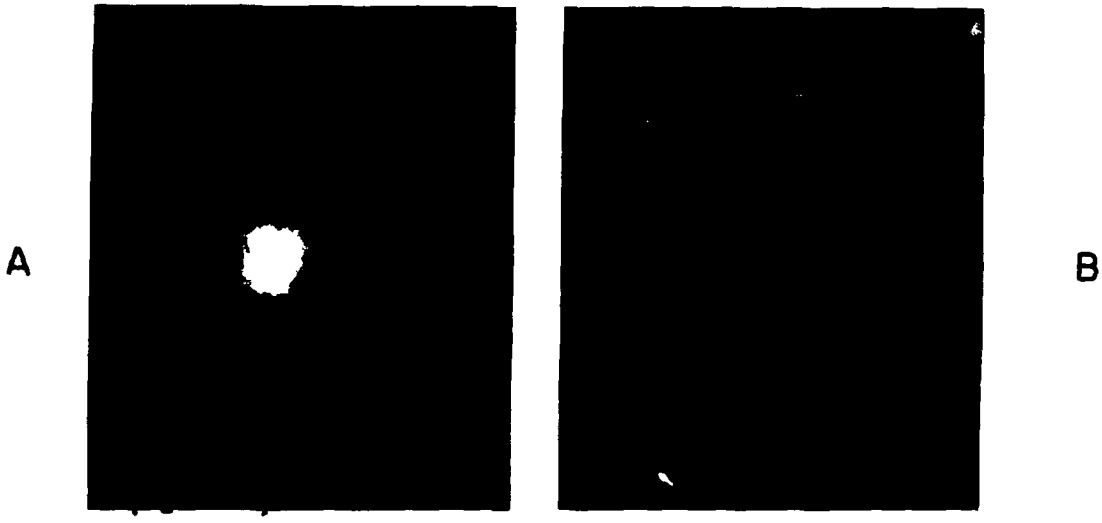


Fig. 12. Image formed by the neutral atom camera of Fig. 11 with two-dimensional molasses acting on the atomic beam. The outline of the circular beam spot represents a 6#mm diameter image on the phosphor. The 7 mW molasses laser beam was nearly uniformly intense and rectangular, about 8 x 20 mm. Its detuning was about -30 MHz for (A) and about +30 MHz for (B). Note the collimation for the red detuning and the divergence for the blue detuning. The recording time was 1/30 sec and no image averaging was used.

In summary, we have used only 2 mW from a feedback-narrowed diode laser injected into a 100 mW free-running array to dramatically narrow both its spectrum and beam divergence. Injection of the input light beam collapses the spectrum into a single longitudinal mode less than 300 kHz wide, 50-100 times stronger, and in a single spatial (transverse) mode whose width is approximately diffraction limited for the array aperture. The output intensity at other frequencies is almost 10^3 lower. We have used the output light from this to actively collimate an atomic beam of ^{85}Rb with one-dimensional optical molasses to well below the Doppler limit.

TABLE I

j	calculated steering	measured steering
1	-10.76	-11.32
2	-7.61	-7.55
3	-6.21	-6.22
4	-5.38	-5.14

Calculated values of $d\theta_e/d\lambda$ (degrees/nm) from Eq. 3 and values determined by linear least squares fit to data plotted in Fig. 7.

REFERENCES

* Work supported by the NSF and the ONR.

1. B. Dahmani et al., Opt. Lett. 12, 876 (1988).
2. R. Lang, IEEE J. Quant. Elect. QE-18, 976 (1982).
3. L. Goldberg et al., Appl. Phys. Lett. 46, 236 (1985).
4. J. Hohimer et al., Appl. Phys. Lett., 47,1244(1985).
5. L. Goldberg and J. Weller, Elect. Lett. 22, 858 (1986).
6. G. Ronald Hadley et al., Opt. Lett., 11, 144 (1986);
7. J. Hohimer et al., Appl. Phys. Lett. 48, 1504 (1986).
8. H. Hemmati, Appl. Phys. Lett. 51, 224 (1987).
9. Use of the back facet is for convenience only.
10. There is obviously a potential for a ring laser configuration.
11. M. Nathan et al., Phys. Rev. Lett. 11, 152 (1963).
12. Frank Stern, Phys. Rev. 133, A1653 (1964).
13. H. C. Casey Jr. et al., Appl. Phys. Lett. 24, 63 (1974).
14. M. Afromowitz, Solid State Commun. 15, 59 (1974).
15. B. Sheehy et al., J. Opt. Soc. Am. B6, 2165 (1989).
16. B. Sheehy et al., submitted to Physical Review Letters.

We acknowledge the invaluable help of Brian Sheehy and Peter van der Straten.

Comparison of Coherent and Incoherent Laser Diode Frequency Sweeping Techniques for Fiber Optic Sensor Systems

Peter L. Fuhr
Daniel N. Maynard
Daniel L. Kunkel

University of Vermont
Department of Electrical Engineering
Burlington, Vermont 05405

Abstract

Linearity and mode stability of laser diodes frequency swept via coherent and incoherent techniques have been examined using time resolved spectroscopy. Resultant information is used to make some inferences regarding laser diode selection and frequency sweeping techniques for fiber optic sensors.

Introduction

The use of frequency ramped (chirped) optical sources has increased dramatically through their use in interferometric heterodyne systems, fault location systems, and fiber sensor multiplexing[1-3]. Laser diodes have proven to be the most widely used chirped source do to the relative ease with which the diode's output frequency may be swept over a wide frequency range. The frequency sweeping techniques tend to fall within two types: variation of the diode's bias current causing chirping of the output field's carrier frequency; and, direct frequency modulation of the diode. The first technique is frequently referred to as a frequency ramped continuous wave (FMCW) technique which usually, although not exclusively, relies on interferometric heterodyne detection to recover the desired information. Applications of FMCW to fiber sensors and interferometric multiplexing have been demonstrated by many researchers. Direct frequency modulation of the laser diode source has been used over the past two decades for many varied fiber applications, ranging from information transfer] and fiber sensor interrogation to fault detection in optical fibers (and related efforts). The direct frequency modulation systems have tended to use direct (incoherent) detection techniques.

In each case, noise arising from nonlinear frequency ramping of the diode, caused by mechanisms such as harmonic distortions or current-induced temperature fluctuations, limits the performance of the sensor system. In particular, the performance of a system employing the FMCW technique, with its associated heterodyne detection scheme, may be substantially degraded by the high sensitivity of the laser diode's operating frequency to environmental temperature fluctuations (approximately 25 GHz/^{o}C). FMCW systems' performance is also plagued by 1/f and phase noise. In addition, the interferometric implementations of FMCW tend to rely on sophisticated control systems to allow the system to perform optimally.

The implementation of direct frequency modulation of the diode and direct detection may drastically alleviate some of the noise sources encountered in the interferometric FMCW system while significantly reducing the overall system complexity. This decrease in system complexity is attained at the (usual) price of reduced system sensitivity. In addition the direct modulation techniques require some form of electrical mixing of the detected signal (typically a backscattered signal which has been intensity modulated) with the swept frequency RF source's signal waveform.

The initial problem that must be confronted is the development of a chirped frequency source capable of operating under the constraints just mentioned. Semiconductor laser diodes are the most attractive sources for this application due to their compact size, operating wavelength, and relative ease with which they may be frequency swept. Since many proposed systems require a frequency swept laser diode for the optical power source, this discussion will be confined to the study of this light source.

Figures of Merit

There are many parameters whose values influence the overall performance of any swept frequency sensor system. In order to minimze overall recovered signal distortion, in this study, the linearity of the frequency sweep was deemed the most important system parameter. Such nonlinearities can arise via many mechanisms, the two most attributable to the frequency sweeping itself are, in the case of incoherent sweeping, linearity of the modulation signal that is AC coupled onto the laser diode, and in both coherent and incoherent sweeping, the ability of the diode to remain in single longitudinal modal operation (avoiding mode hops and/or mode competition) while the electrical or thermal sweep signal is applied to it. The second figure of merit is the "chirping parameter",$a=\Delta\omega/\Delta t$, which tells how long it takes to sweep through some frequency range. Within the linearity constraint, then, it is advantageous to choose the technique which will provide the largest chirping parameter.

Incoherent Frequency Sweeping

"Incoherent" frequency sweeping of a laser diode occurs when the laser bias current has electrically added to it a frequency swept RF signal. The resultant light field's intensity is directly modulated, sinusoidally, at the instantaneous signal generator frequency. The changing current also changes the carrier density in the laser, however, which alters the refractive index in the laser waveguide and causes the output wavelength to vary slightly. When direct photodetection of this swept-frequency intensity-modulated laser beam, which also has slight wavelength modulation occurring, is performed, the photodetector acts as a low-pass electrical bandpass filter. The resultant electrical signal then only exhibits the RF swept frequency variation.

Coherent Frequency Sweeping

In the context presented in this paper, "coherent" frequency sweeping means direct modification of the laser diode's output wavelength. This modification is achieved by directly manipulating some operating condition of the diode. There are two most prevalent methods with which coherent frequency sweeping may be achieved: frequency variation via temperature control and frequency variation via bias current control. Each technique will be individually addressed.

Frequency Variation via Temperature Control

One possible method for controlling a frequency sweep in a laser diode would be the modulation of the temperature of the device. Varying the temperature changes the actual dimensions of the optical cavity which will alter the operating frequency of the laser diode. More importantly, an increase in temperature will cause a change in the refractive index and the operating wavelength. A change in the operating wavelength will also change the index of refraction creating a cascade effect described by equation (1) where n represents the index of refraction, T is the temperature, and λ is the wavelength.

$$\frac{d\lambda}{dT} = \lambda \frac{\left\{\frac{1}{n}\frac{\delta n}{\delta T} + \frac{1}{L}\frac{dL}{dT}\right\}}{\left\{1 - \frac{\lambda}{n}\frac{\delta n}{\delta \lambda}\right\}} \qquad (1)$$

This wavelength variation manifests itself as a frequency variations via

$$df = \left| \frac{c\, d\lambda}{\lambda^2} \right| \qquad (2)$$

The cause of the change in the index of refraction is due a change in the number of free carriers in the semiconductor. This will change the apparent optical cavity length and therefore the operating frequency. Varying the temperature one degree celsius alters the frequency in the range of tens of gigaHertz. While potentially capable of producing large frequency shifts, this plan is limited by the necessity of fine temperature control of the diode itself, which in practice normally involves not just the diode but its mounting flange and potentially any other thermally attached components. Such arrangements tend to have rather long thermal time constants associated with them and as such are relatively slow to respond to temperature variations (i.e., Δt is on the order of tens, if not hundreds, of milliseconds).

Frequency Variation via Current Bias Control

Control of the current bias to a laser source has been noted to cause significant variation in the output frequency. Underlying this adjustment of the current bias is the control of temperature; an increase in current creates a greater number of carriers increasing the number of collisions therefore causing the desired increase in temperature. Altering the current bias also changes the injected carrier concentration. The additional electrons present, due to both increasing temperature and current, will also change the index of refraction inside the laser cavity, and result in a change in the apparent optical cavity length. The temperature change also causes a change in the actual dimensions of the optical cavity; in turn, the net result is a change the output frequency. The index of refraction is the principle component controlled by the modulation of the bias current and directly responsible for the output frequency change.[6]

System Complexity

As shown in the previous sections, the coherent sweeping techniques exhibit better performance than the direct modulation scheme when compared using these figures of merit. It should be realized, though, that such potential increase in performance has associated with a more complicated laser diode modulation/control scheme (as previously stated, the concomitant photodetection - signal recovery process's complexity is not being addressed). In order to provide maximum frequency sweep range, $\Delta\omega$, the diode should be temperature tuned so that its single mode output corresponds to one edge of the mode hop spectrum (e.g., the left edge). Next, the bias current, ΔI, is varied in the prescribed amount to slew the output mode over to the other mode hop edge in the shortest possible time (minimizing Δt). In the meantime, a temperature control servo system must maintain the diode's bulk heatsink temperature at the predetermined value to minimize thermally induced variations in the output wavelength. The result is a potentially complex servo-control system. For comparison, while the incoherent sweeping technique can benefit from these temperature control control systems, their presence has not been required to demonstrate successful implementations in incoherent swept frequency fiber systems (e.g., OFDR).

Measurements

Wavelength chirping measurements were performed using a computerized optical spectrometer - monochromator system with CCD array photodetection. Signal processing of the spectral scans allowed wavelength variations of 0.007 nm to be measured. A laser diode bias current supply was also under computer control and allowed bias current of 0-100 mA to be applied to the diode. With both instruments' operation coordinated by the computer, the measurement procedure became: apply a bias current to the diode; read the spectrometer-CCD spectral scan data; change the diode bias current; read another spectral scan; etc. This time-resolved spectroscopy format allowed time-evolution intensity wavelength measurements to be made of the Hitachi HL8314e and Sharp LT015md diodes to be made. Figures 1 and 2 show typical scans of the diodes coherent frequency sweeping

performance. In reference to Figure 1, a current ramp varying from 10 to 60 mA (below lasing threshold to 1.5 times the threshold current) was applied as a ramp with total elapsed time of 3 seconds. As is evident from the Figure, it is readily observedthat the device switches from a broad band spontaneous emmitter to a narrow band emitter as the diode is brought through the lasing threshold current. Wavelength data is shown along the *Pixel Number* axis with each pixel cooresponding to a 0.007 nm wavelength difference. Figure 2 shows the similar below and above threshold performance of the Sharp laser diode as it is ramped through its own current values (the peak current was chosen such that each laser was emitting a 15 mW beam). Figure 3 illustraets the devices' mode stability performance as a constant current temperature ramp was applied to the diode. In each case the current was held constant such that a 15 mW output beam was emitted and the device's bulk heat sink temperature was varied by 5 degrees C. The Sharp diode's mode competition (or instability) is quite apparent from Figure 3, graphically showing that this diode's output exhibits considerable power fluctuations and nonlinearity swept frequency response (not good). In contrast, the Hitachi diode exhibited rather discrete mode hops across the temperature ramp with minimal power variation in each mode. In addition, this graph indicates that the Hitachi diode may be subjected to a temperature variation without being quite as susceptible to mode hops (frequency nonlinearities) - an attribute when designing an overall frequency swept system since it therefore minimizes the temperature control constraints for the diode.

In a similar fashion, incoherent sweeping experiments showed that the device's linearity performance is not constrained by the diode but more by the RF sweep generator (within optical modulation depth limitations, in this case never more than 5% of the total output power).

Summary

An overall comparison of the two sweeping techniques is shown in Table 1. Based on that information constant current with temperature tuning is a cheaper alternative to both current ramping and RF modulation, but current ramping provides better linearity control and overall performance. Incoherent frequency sweeping rates tend to be limited by the RF sweep generators not the diodes. As such the user can count on paying significantly for a higher frequency slew rate and increased linearity while not being able to achieve the chirping rates attainable by current bias/ temperature modulation techniques. As an additional information point, it was found that the Hitachi HL8314e diode exhibited greater mode stability and significantly lower power fluctuation levels than the comparable Sharp LT015md.

References

1. Uttaw, D. and Culshaw, B.: "Optical FM applied to coherent interferometric sensors", *IEE Digest No. 1982/60*, 1982, pp. 10/1 - 10/4.

2. MacDonald, R.I.:"Frequency domain optical reflectometer",
Appl. Opt.,1981, **20**, pp. 1840-1844.

3. Eickhoff, W. and Ulrich, R.: "Optical frequency domain reflectometry in single-mode fiber", *Appl. Phys. Lett.*, 1981, **39**, pp. 693-695.

Table 1. Laser diode frequency sweeping techniques comparison.

	Temperature Modulation	Current Bias Modulation	RF Modulation
Equipment Requirements	constant cooling source and a controlled cooling procedure	precisely controlled variable current source and cooling	sweep generator supporting hardware
Theroetical Principle (primary effect)	increase in the intrinsic carrier concentration causes apparent optical cavity size change	direct change in carrier concentration changes the optical cavity length	carrier signal to modulate frequency
(rational)	cavity refractive index shift	cavity refractive index shift	
(secondary effect)	physical change of the cavity dimension	temperature modulation effect also present	
Frequency Sweep (range, rate)	approx. 60 GHz	approx. 60 GHz (potentially 100 Hz/ns much faster)	approx. 500 MHz 25 Hz/ns
Cost/Performance	cheapest alternative with improved performance over RF modulation	much cheaper than RF mod with at least 4 times faster sweep rate	most expensive,cost dictated by sweep generator

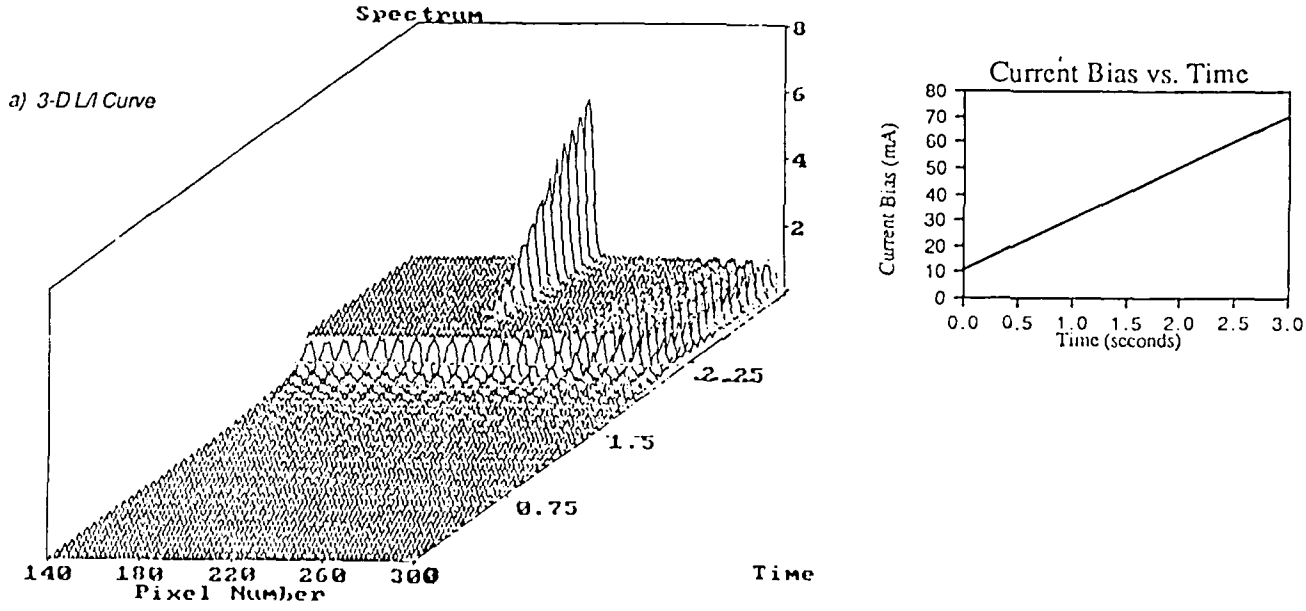


Figure 1. Hitachi HL8314e 3-dimensional Power-Current-Spectrum curve.

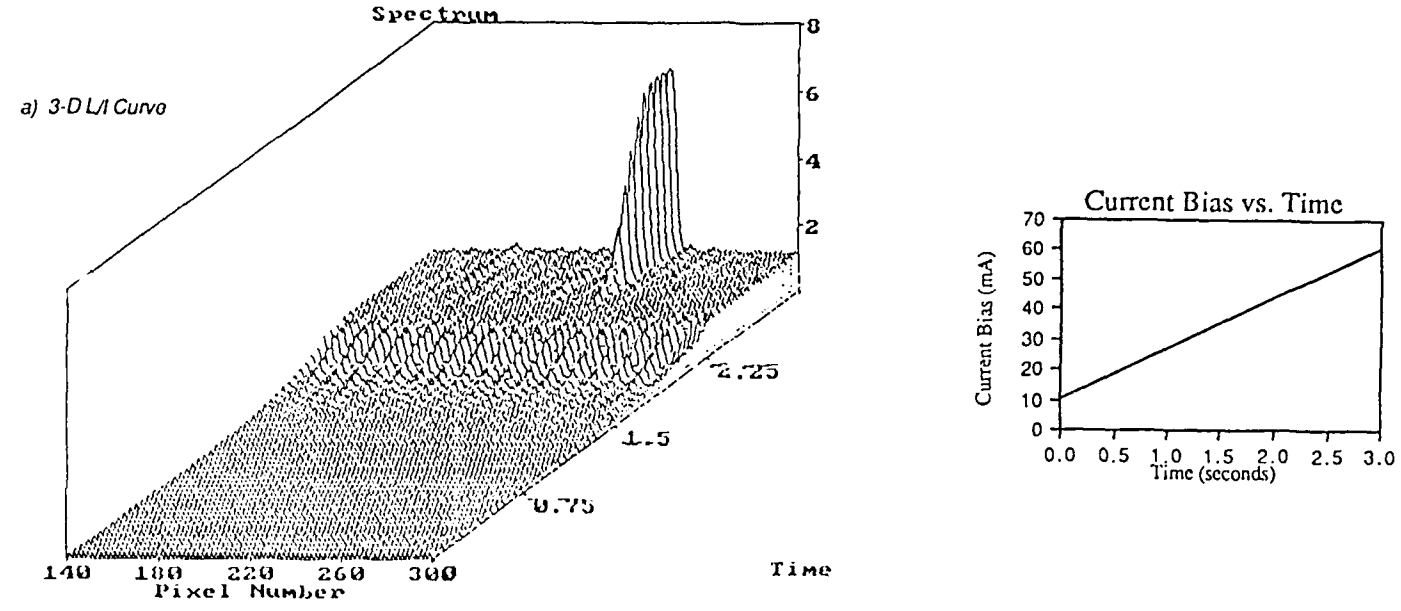


Figure 2. Sharp LT015md 3-dimensional Power-Current-Spectrum curve.

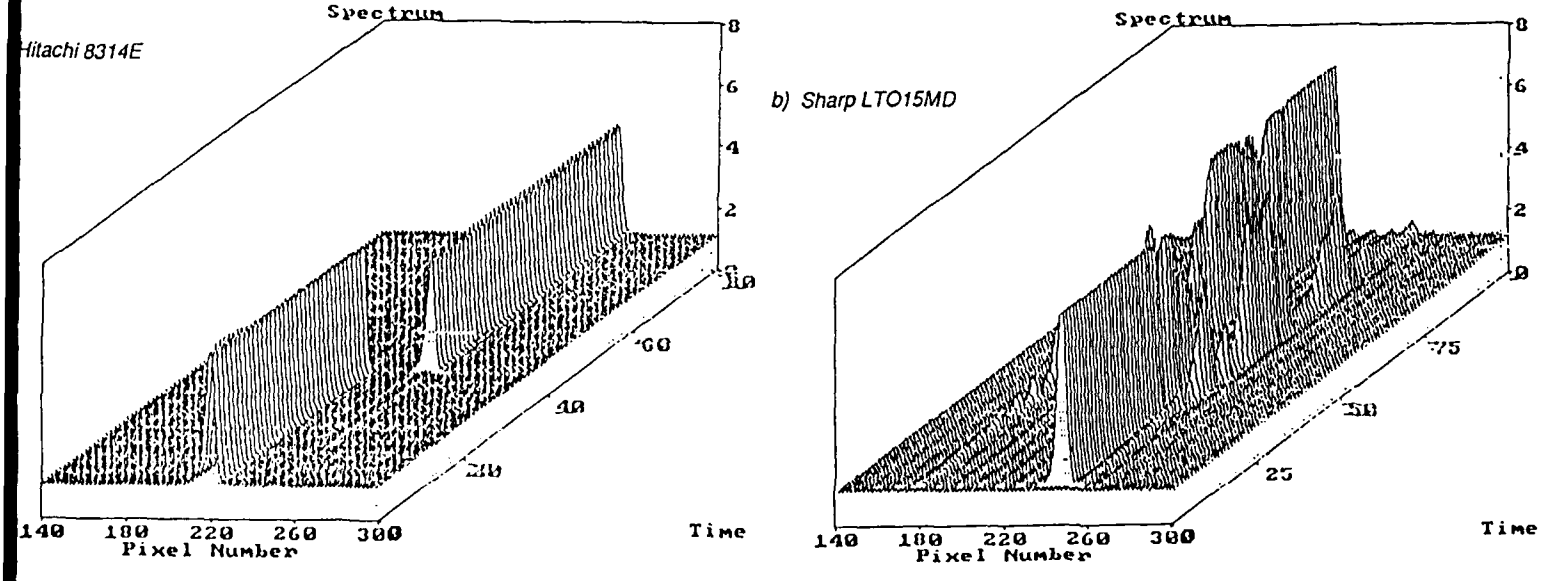


Figure 3. Mode Instability for constant current - temperature variations.

A STUDY OF THE CHIRPING OF GAIN-MODULATED MODE-LOCKED DIODE LASERS

Odis P. McDuff
Dinesh Thati
Department of Electrical Engineering
The University of Alabama
P. O. Box 870286
Tuscaloosa, Alabama 35487-0286

Abstract

The pulses of a mode-locked diode laser often undergo a change in the instantaneous optical frequency during the duration of the pulse. Although this chirp of the optical frequency is a general characteristic of mode locked lasers, it is perhaps more complicated to study it in the case of the diode laser. The necessary coupled external cavity causes more structure in the cavity loss curve and hence a more complicated variation in mode amplitudes versus frequency. Furthermore, the variation of drive current used to modulate the diode gain necessarily modulates the diode dispersion also. Thus, there is, in effect, simultaneous amplitude and frequency modulation mode coupling. The overall effect is a more complicated dependence of chirp upon the laser parameters. This paper presents a nonlinear frequency-domain study of the mode coupling in the diode laser which includes the pulsation of dispersion as well as gain. The resulting mode amplitudes and phases are used to determine the instantaneous optical frequency during the duration of the pulse. The analysis makes no pre- determined assumption of pulse shape and thus is more general than existing analyses of mode-locked laser chirp.

Introduction

The mode-locked diode laser promises to become an excellent source of a train of extremely short pulses for use in future optical fiber communication systems.[1] A convenient method of producing the mode locking is by modulating the drive current to produce a pulsation of the diode gain; however, this leads to gain-induced variations in the laser refractive index. The resulting chirping of the mode-locked pulses can affect the communication system as does the chirping of a direct-current-modulated single-longitudinal mode diode laser.[2,3]

Previous studies of the chirping of a mode-locked laser pulse have followed the technique[4,5] in which the laser pulse is followed as it passes through the laser cavity and mode locker. This technique assumes a gaussian-shaped pulse and is not suited to a wide range of operating conditions. A coupled-mode analysis in the frequency domain, using numerical solution of the resulting nonlinear differential equations, makes no predetermined assumption of pulse shape.[6] In general, the relative mode phases are not ideal, the pulse is not as short as would be the case if transform-limited, and the optical frequency of the output pulse is chirped. Using Fourier Transform techniques, the chirp can be calculated from the numerically determined mode amplitudes and phases.[7]

The Coupled-Mode Equations

The basic coupled-mode equations are those developed by McDuff and Thati.[6,8] In the analysis, the complete optical field in the cavity is written as the summation of the axial modes

$$E(z,t) = \sum_n E_n(t) \cos[\nu_n t + \phi_n(t)]\, U_n(z) \ , \tag{1}$$

where $E(z,t)$ is the total cavity electric field, $E_n(t)$ and $\phi_n(t)$ are the slowly time varying amplitude and phase of the nth mode, ν_n is the radian frequency of the nth mode, and $U_n(z)$ gives the spatial variation of the nth mode. $U_n(z)$ is given by

$$U_n(z) = \sin(n_o + n)\, \pi z/L \tag{2}$$

where L is the length of the cavity and n_o is the number of spatial variations of some central mode which has been chosen to be the mode whose frequency is closest to the center of the atomic fluorescence lines. The modulating drive signal affects the driving polarization of the nth mode. Here it varys the susceptibility of the atomic medium whereas in loss and phase modulation it affects the susceptibility of the modulator. The effects of the diode modulation can be included by assuming that the optical susceptibility is a time varying quantity at radian frequency ν_m, according to the equation

$$\chi(z,t) = \chi(z)\ (1 + \cos \nu_m t) \ , \tag{3}$$

where in phasor form

$$\chi(z) = \chi'(z) - j\,\chi''(z) \ . \tag{4}$$

Thus the atomic medium gain will depend upon the time varying quadrature component of atomic susceptibility

$$\chi''(z,t) = \chi''(z)\ (1 + \cos\ \nu_m t) \tag{5}$$

and the medium phase shift will depend upon the in-phase component

$$\chi'(z,t) = \chi'(z)\ \cos\ \nu_m t \ . \tag{6}$$

The constant part of $\chi'(z,t)$ has been neglected since it only affects the mode spacing and the value of "zero-detuning" of the modulation frequency.

In order for the time variation of χ' and χ'' to have a mode-coupling effect, the laser gain medium has to extend over only a small fraction of the cavity length, preferably near one end, as required of a phase or loss modulator when they are used to produce mode locking.

The resulting coupled-mode equations for homogeneous broadening are[6]

$$(\dot{\phi}_n - n\Delta\nu)\ E_n = \frac{c}{2L\beta}\,[g_{n+1}\ E_{n+1}\ \sin(\phi_{n+1} - \phi_n) - g_{n-1}\ E_{n-1}\ \sin(\phi_n - \phi_{n-1})$$

$$- d_{n+1}\ E_{n+1}\ \cos(\phi_{n+1} - \phi_n) - d_{n-1}\ E_{n-1}\ \cos(\phi_n - \phi_{n-1})] \tag{7}$$

$$\dot{E}_n + \frac{1}{2}\ \frac{\nu}{Q_n}\ E_n - \frac{c}{2L}\ \frac{g_n}{\beta}\ E_n = \frac{c}{2L\beta}\,[g_{n+1}\ E_{n+1}\ \cos(\phi_{n+1} - \phi_n) + g_{n-1}\ E_{n-1}\ \cos(\phi_n - \phi_{n-1})$$

$$+ d_{n+1}\ E_{n+1}\ \sin(\phi_{n+1} - \phi_n) - d_{n-1}\ E_{n-1}\ \sin(\phi_n - \phi_{n-1})] \tag{8}$$

These equations are for sinusoidal variation of the pump (diode current). McDuff and Thati[6] also give the equations for the case when the pump waveshape is a short pulse having several harmonic components present at multiples of ν_m.

In equations (7) and (8) E_n and ϕ_n are the amplitude and phase respectively of the nth mode and the dots indicate time derivatives. The unsaturated gain coefficient for the nth mode (which varies with mode number n according to the line shape function) is represented by g_n. The medium dispersion coupling effect upon the nth mode is expressed by d_n which varies with mode number n according to the shape of the atomic dispersion curve. The saturated gain is g_n/β where β is a saturation function which for homogeneous saturation is not a function of n and carries no subscript. Homogeneous saturation is assumed and the value of the saturation function is given by

$$\beta = 1 + C\ \frac{\pi}{2}\ \Delta\nu_L\ \Sigma\ E_n^2\ g_L(\nu_n) \ , \tag{9}$$

which comes from the work of McDuff, Scott, and Taboada.[9] In equation (9) the constant C is simply a saturation parameter whose value can be selected to set a convenient scale for the optical field amplitude. $g_L(\nu_n)$ is the regular Lorentzian line shape function and $\Delta\nu_L$ is the Lorentzian linewidth (usual FWHM value). The detuning of the modulator frequency from the cold cavity mode spacing is written as $\Delta\nu$, i.e.

$$\Delta\nu = \pi c/L - \nu_m \tag{10}$$

and follows the sign convention of McDuff and Harris.[10,11] The Q of the nth cavity resonance seen by the nth mode is denoted as Q_n and may depend upon n in a cyclic manner if an etalon or composite-cavity effect occurs. In a simple cavity with no etalon or coupled-cavity effects, the Q can be assumed independent of n.

The coupled-mode differential equations (7) and (8) were solved numerically using a Runge-Kutta numerical integration procedure. The technique was to assume initial values of the mode amplitudes and phases and the laser parameters and continue the integration until steady state was reached (all $E_n = 0$ and ϕ_n equal either to a constant independent of n or $\phi_n = 0$. The computer program used was a modification of that of McDuff and Thati[6] which was developed from the early work of Harris and McDuff.[11] Due to the presence of a large number of modes, the solution of the equations can require a lot of computer time. The availability of a Cray X-MP/24 super computer made it possible to do this work.

Time-Domain Pulse

The results of the solution of equations (7) and (8) are the values of the mode amplitudes E_n and mode phases ϕ_n (not time dependent). The resulting field in the time domain is then

$$E(t)\mathrm{Cos}(\Omega_o t + \theta(t)) = \Sigma\ E_n \mathrm{Cos}\{(\Omega_o + n\nu_m)t + \phi_n\}. \tag{11}$$

The frequency Ω_o is the arbitrarily chosen center frequency (chosen as atomic line-center frequency here) of the E_o mode.

The time dependence of E(t) gives the pulse shape (or $E^2(t)$ gives the shape of the optical intensity pulse) and the time derivative of $\theta(t)$ gives the instantaneous frequency departure from Ω_o. If the derivative of $\theta(t)$ is constant, it means that the resulting pulse center optical frequency is not at the assumed line-center value. If the time derivative of $\theta(t)$ varies, the departure from a constant value gives the change in instantaneous frequency, i.e. the chirp of the optical frequency of the pulse. Any constant component of $\theta(t)$ is of no significance.

An ideal case is when $\phi_n = n\phi_o$ (where ϕ_o could be zero) and the E_n are summetrical about the n=0 mode. In that case, the resulting peak in the E(t) pulse occurs at $\nu_m t = -\phi_o$ and the derivative of $\theta(t)$ is zero (no chirp). Conversely, if ϕ_n departs from the form $n\phi_o$ there will be chirp of the output pulse. If the values of E_n are not summetrical about n=0, there will be an offset of the average optical frequency from Ω_o.

Results

In the model it is possible to remove the effects of dispersion simply by making the d_n terms identically zero in equations (7) in the no dispersion case and (8). Figure 1 shows the mode amplitudes and the resulting pulse for zero detuning of the modulator in the no-dispersion case. The mode phase angles and the resulting chirp are zero. This reference case had approximately 40 modes oscillating when modulated. The line shape was Lorentzian and the line-center gain was equal to 4-times the loss at the peak of the pulsation cycle. This and the other cases following assumed perfect homogeneous saturation; hence, without mode coupling (no gain pulsation) only one mode oscillated (the one with the highest gain) and it quenched the others. Note that the peak of the pulse occurs at $\nu_m t = 0$ (the pulse passes through the diode at its gain peak).

It is not possible to have "exactly" zero detuning when the dispersion is included, due to the variation of mode spacing as modes farther and farther away from line center are included. Figure 2 shows for approximate zero detuning the mode amplitudes and phases and the resulting pulse and chirp. Near line center the mode phases in Figure 2(b) follow approximately the relation $\phi_n \cong 0.02n$ which means then that the pulse peak in Figure 2(c) occurs approximately at $\nu_m t = -0.02$. Therefore one could say that this case does not have exactly zero detuning. In fact, as has been noted by many others, it is difficult to define what exactly is the condition of zero detuning. One could define it here as the condition where the mode phases have $\phi_n - \phi_{n-1} \cong 0$ near line center (meaning that the pulse occurs at $\nu_m t = 0$, i.e. in phase with the instantaneous peak of the pulsating gain). We note that the frequency width of the mode distribution and the pulse width in Figure 2 are essentially the same as for the dispersionless case in Figure 1. Although the chirp can be calculated, it is so small as to be of no practical importance (an instantaneous change in optical frequency of less than 1×10^{-8} of a mode spacing during the duration of the pulse as seen in Figure 2(d).

Figure 3 shows the mode amplitudes and phases and the resulting pulse and chirp for a modulator detuning of 9.2×10^{-5} of a mode spacing. As expected here the frequency width of the mode distribution is more narrow and the pulse correspondingly wider. The $\phi_n - \phi_{n-1}$ are larger corresponding to a phase shift of the pulse relative to the peak in the cosinusoidally varying gain. The chirp shown in Figure 3(d) actually varies slowly from one pulse to the next. At a larger detuning, figure 4 shows the instantaneous frequency during the pulses taken every 16,000th pulse (every 16,000th cycle of the modulator) near one point in time and then every 16,000th pulse at a time t= 3 milliseconds (464,000 pulses) later. The change in the pulse shape due to this chirp change is not noticeable. We note that the instantaneous frequency moves from one side of the assumed line center frequency to the other side. This variation in optical frequency offset is $\cong \pm 0.03$ mode spacing. This effect is similar (but much smaller) to that observed in a conventionally electro-optically mode-locked laser when the modulator is detuned.[11,12] An accompanying small side-to-side shift in the mode amplitude distribution occurs.

The diode is likely to have an external cavity and hence coupled-cavity effects may occur. Unexpected etalon effects may also occur. Figure 5 shows the mode amplitudes, pulse shape and instantaneous frequency in a case simulating the repetitive variation of cavity loss due to coupled-cavity or etalon effects. A simple rectangular variation in cavity loss was taken. The minimum in the repetitive cavity loss was taken to be centered about line center. The principal result is to reduce the number of modes oscillating and to cause the mode distribution to be less Gaussian-like. Thus the pulse shape has side lobes with sharp minima in between. At each minimum there is a spike in instantaneous frequency due to a 180° reversal in instantaneous phase as would be the case in the simple addition of two sinusoids. These spikes are shown in Figure 5(c). In this case the center mode set extinguishes the possible sets on either side which would have gain greater than loss.

In Figure 6 the case where the minimum in the repetitive loss curve is off of line center is shown. The minimum on the n-positive side is one mode number closer to line center than that on the n-negative minimum side. Furthermore, the loss is greater than gain outside the minima. Thus, the n-positive set of modes extinguishes the n-negative set. Again, the number of oscillating modes is smaller but now the amplitudes are not symmetrical about the center mode of the set. The pulse shape is similar to that in Figure 5 but the pulse minima do not go to zero. The instantaneous optical frequency has an offset from line center roughly equivalent to the offset of the center mode of the set. We note a lot of chirp at each pulse minimum between side lobes but not a spike in instantaneous frequency as was the case in Figure 5.

In another set of conditions, not shown here, the loss minima were made exactly symmetrical with respect to line center. Then, two identical sets of modes oscillated, each producing its own pulse, and the two pulses beat together to produce a multi-lobed overall pulse with many zero points and lobes. At each zero point there was a spike in instantaneous frequency as noted above in Figure 5. Experimentally, it would not be expected to be possible to have this exact symmetry.

Conclusions

This analysis technique gives a powerful tool for studying the dependence of the optical chirp of the mode-locked pulse upon the various effects in a gain-modulated mode locked diode laser. The effects of the cavity-coupling-induced equivalent loss variation can be included. It is not necessary to make any assumptions regarding pulse shape. From the results it is seen that optical frequency offset may occur and that any effect that causes a non-bell-shaped mode distribution will cause large variations in the instantaneous optical frequency.

Work is continuing to include inhomogeneous saturation and more realistic cyclic loss patterns.

References

1. P. T. Ho, L. A. Glasser, E. P. Ippen, and H. A. Haus, Appl. Phys. Lett., 33, 241 (1978).
2. H. A. Haus, J. Appl. Phys., 51, 4042 (1980).
3. R. A. Linke, IEEE J. Quant. Electr., QE-21, 593 (1985).
4. A. E. Siegman, Lasers (University Science Books, California, 1986), p. 1071.
5. A. E. Siegman and D. K. Kuizenga, IEEE J. Quant. Electr., QE-6, 803 (1970).
6. Odis P. McDuff and D. Thati, Proceedings of International Conference on Lasers '87 (STS Press, McLean, VA, 1987), p. 620.
7. Odis P. McDuff, D. Thati, and J. J. Ho, to be presented at IEEE Southeastcon '90, April 1-4, 1990, New Orleans, LA.
8. Odis P. McDuff and D. Thati, Proceedings of IEEE Southeastcon '89 (IEEE Publishing Services, Piscataway, NJ, 1989), p. 1035.
9. O. P. McDuff, D. T. Scott, and J. Taboada, Proceedings of Southeastcon '86 (IEEE Publishing Services, Piscataway, NJ, 1986), p. 99.
10. O. P. McDuff and S. E. Harris, IEEE J. Quant. Electr., QE-3, 101 (1967).
11. S. E. Harris and O. P. McDuff, IEEE J. Quant. Electr., QE-1, 245 (1965).
12. G. W. Hong and J. R. Whinnery, IEEE J. Quant. Electr., QE-5, 367 (1969).

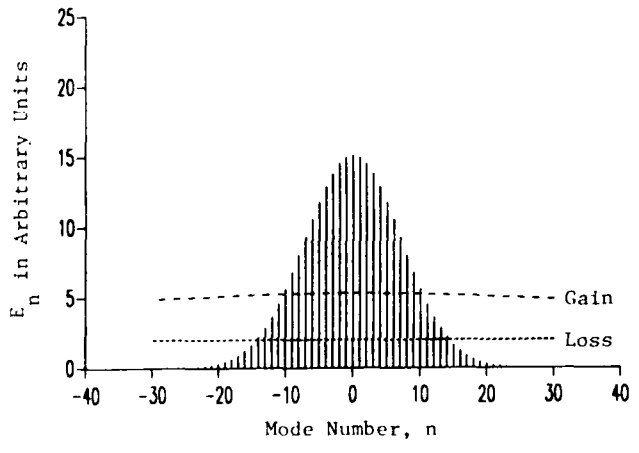


Figure 1(a). Mode distribution for a dispersionless laser with zero detuning.

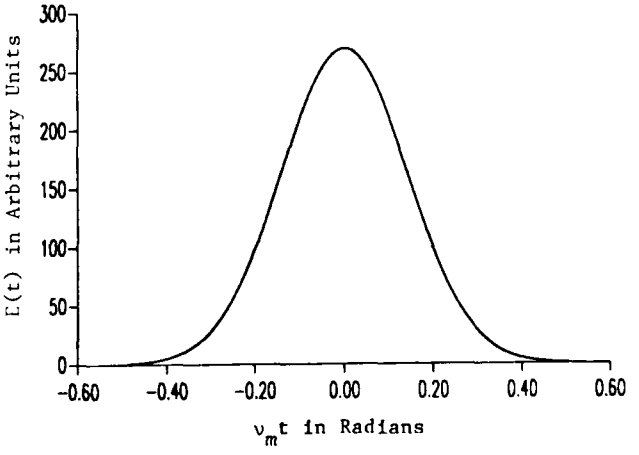


Figure 1(b). Pulse shape for the dispersionless laser of Figure 1(a). The point $\nu_m t=0$ corresponds to the point in time when the pulsating gain reaches its peak.

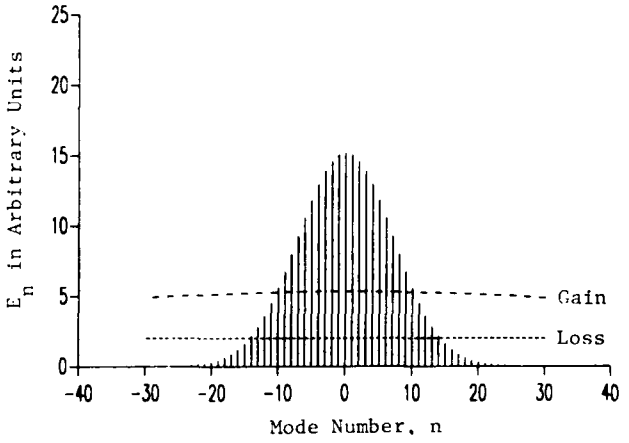


Figure 2(a). Mode distribution for zero detuning with dispersion added to Figure 1.

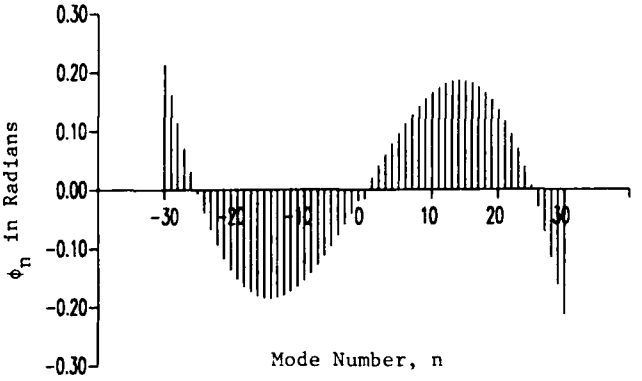


Figure 2(b). Values of ϕ_n corresponding to Figure 2(a).

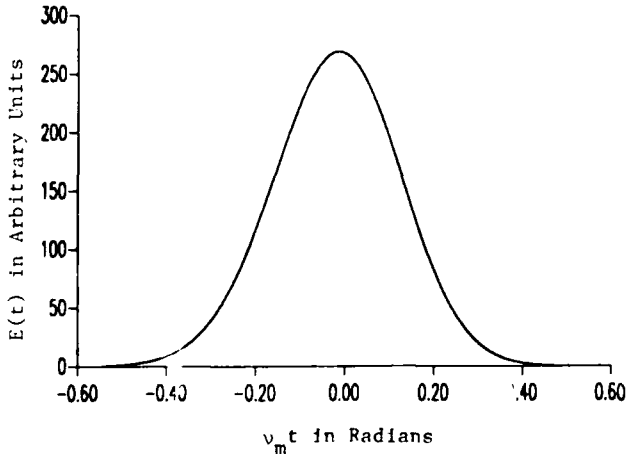


Figure 2(c). Pulse shape corresponding to Figure 2(a).

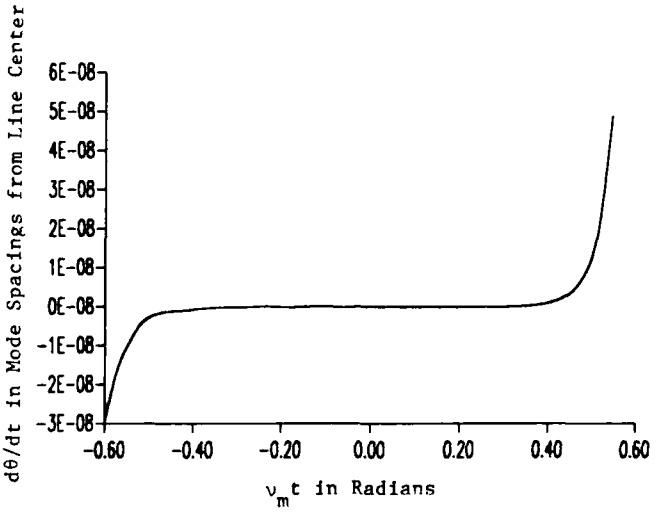


Figure 2(d). Change in instantaneous frequency during the pulse of Figure 2(c).

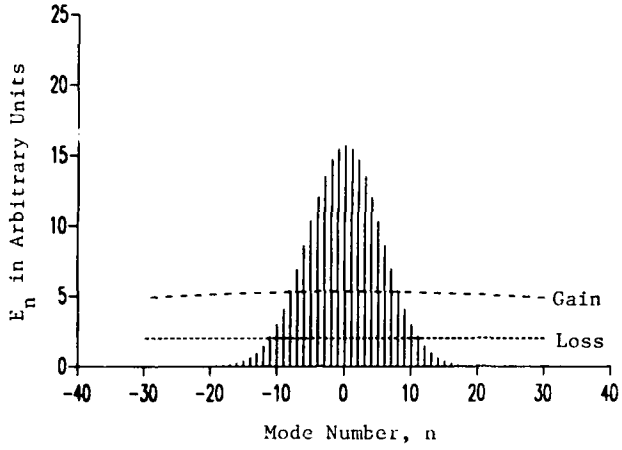


Figure 3(a). Mode distribution for the laser of Figure 2 but with detuning of the modulator. $\Delta\nu = 9.2 \times 10^{-5}$ mode spacing.

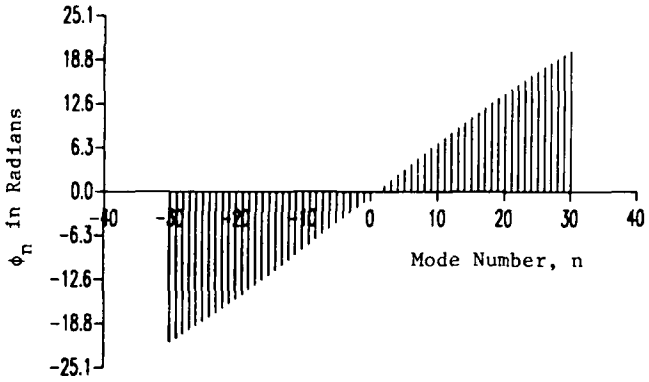


Figure 3(b). Values of ϕ_n corresponding to Figure 3(a).

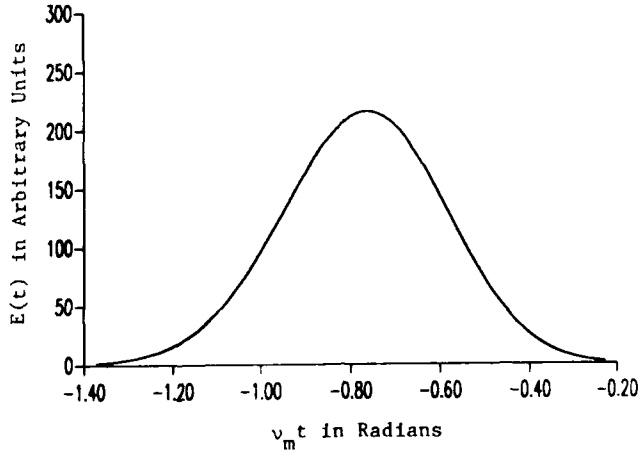


Figure 3(c). Pulse shape corresponding to Figure 3(a).

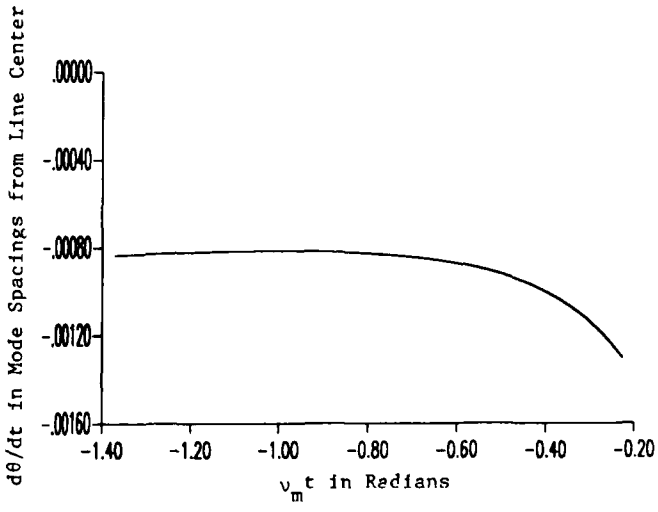


Figure 3(d). Change in instantaneous frequency during the pulse of Figure 3(c).

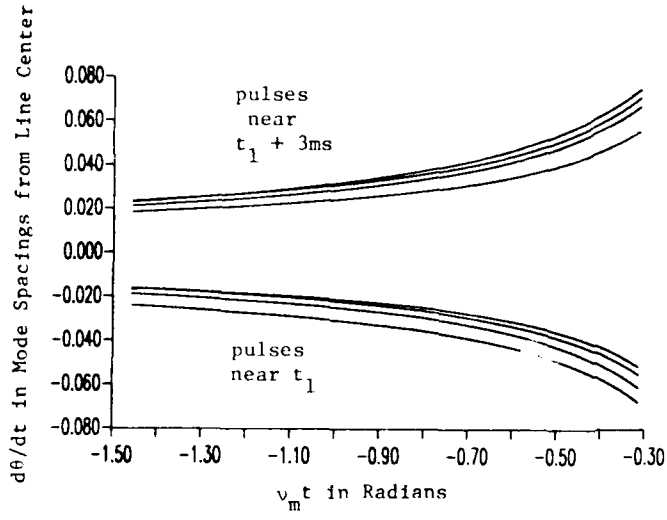


Figure 4. Variation in chirp during different pulses. Detuned case.

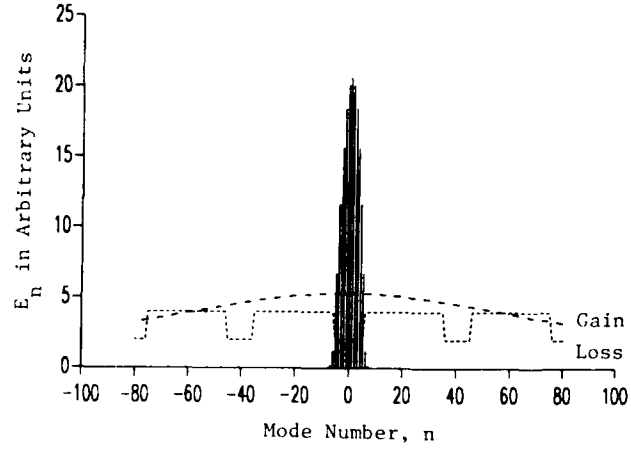


Figure 5(a). Mode distribution in a laser having a repetitively varying loss curve. Loss curve symmetrical about line-center.

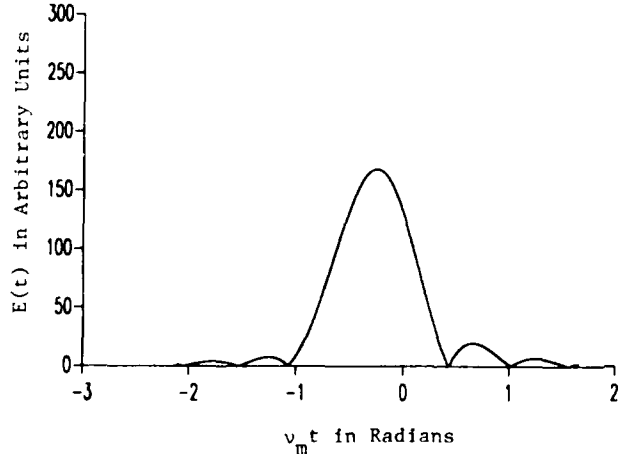


Figure 5(b). Pulse shape corresponding to Figure 5(a).

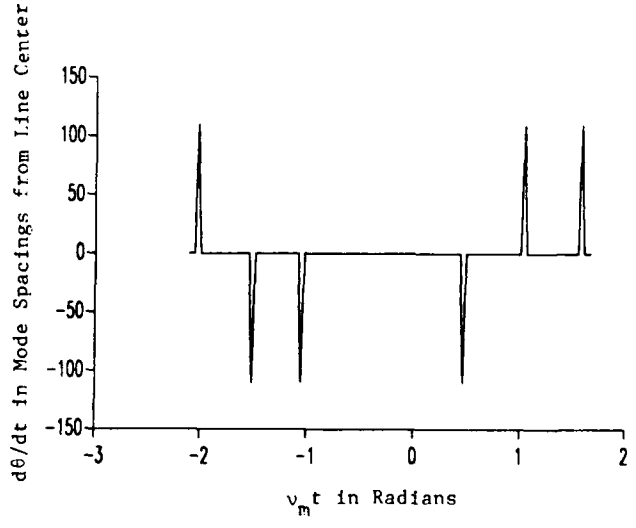


Figure 5(c). Change in instantaneous frequency during the pulse of Figure 5(b).

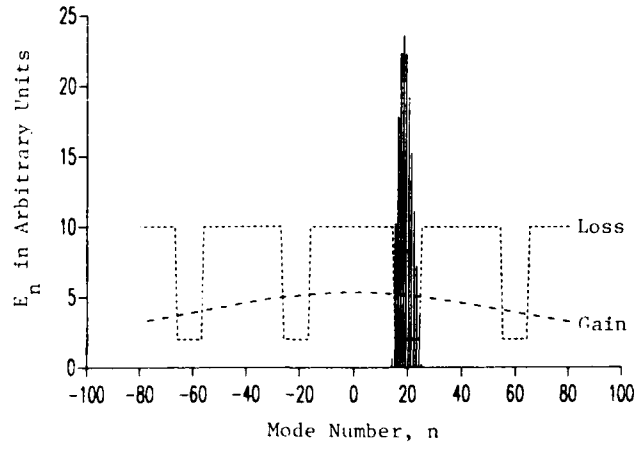


Figure 6(a). Mode distribution in a laser having a repetitively varying loss curve. Loss curve asymmetrical about line-center.

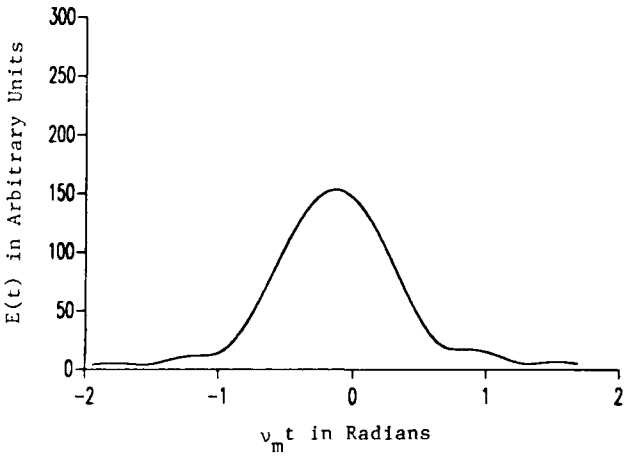


Figure 6(b). Pulse shape corresponding to Figure 6(a).

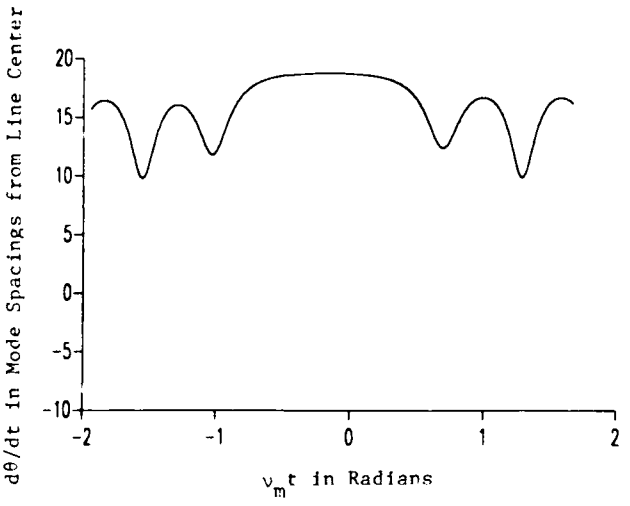


Figure 6(c). Change in instantaneous frequency during the pulse of Figure 6(b).

SUNLIGHT SUPPRESSION BY FRAUNHOFER-WAVELENGTH ATOMIC RESONANCE FILTERS*

Jerry A. Gelbwachs
Chemistry and Physics Laboratory
The Aerospace Corporation (M2/253)
P. O. Box 92957
Los Angeles, California 90009

ABSTRACT

Sunlight represents a major source of interference to receivers that detect weak visible wavelength laser signals in the daytime. The atomic resonance filter provides powerful discrimination against the solar background through the reduction of the optical noise bandwidth to the 0.1 - 0.01 Å range. We discuss how sunlight suppression techlogy can be improved by an additional one to two orders of magnitude by the development of atomic filters matched to intense Fraunhofer lines.

Introduction

Several important laser applications involve propagation of visible-wave-length laser beams through space, the atmosphere, or underwater. These systems include submarine communications, laser radar, lidar, and deep space communications. In many instances, daytime operation is hampered by sunlight that masks the laser signal. Narrowband filters can mitigate the problem. An exciting ultranarrowband technology that offers the potential for improved sunlight suppression is the atomic resonance filter. Atomic filters are wide field-of-view, large area, isotropic devices that exhibit 0.01-0.1 Å passbands.[1] We are currently developing an important subset of atomic filters that takes sunlight rejection to a *new level*. Compared to standard atomic filters these new filters can improve solar background suppression by an additional one to two orders of magnitude. The dramatic advancement in sunlight rejection arises by the development of atomic filters that are exactly matched to intense Fraunhofer lines. We call this device the Fraunhofer-wavelength atomic resonance filter.

Solar Background in Laser Receivers

The intrinsic brightness of laser sources make them natural choices for applications involving transmission of optical energy over long distances. Sunlight represents a formidable source of background noise in laser receivers. Shown in Figure 1 is the solar spectral irradiance[2] in units of photons/cm^2·sec·Å.

The energy units of irradiance are usually expressed in Watts. We have chosen instead units of photons because low-noise, sensitive photomultiplier tubes (PMTs) in the visible spectral region count photons rather than measure incident energy. The solar photon emission spectrum is quite broad and extends from 0.4 μm out past 1.0 μm. We notice that in this spectral region the sun deposits on the earth's atmosphere approximately 10^{13} photons/sec within an 1 Å spectral width in a 1 cm^2 area. In the visible spectrum region, quantum-noise-limited PMTs are available with dark currents in the range of 1-10 sec^{-1}. Thus, even encountering large attenuation factors associated with clouds and water penetration, namely, 10^3-10^8 (10 μsec pulses); or gated detection matched to short-pulse laser operation (10 nsec), fluctuations in the sunlight photocurrent constitutes the dominant noise source in daytime laser receivers.

Three filter technologies have been developed to reject sunlight. Each achieves its objective by a reduction in the spectral width of the optical passband. They are interference filters, polarizing filters, and atomic filters. Space limitations prevent discussion of the principles of operation of each device. We shall only summarize their performance. In Figure 2 we plot the passband of each filter as a function of aperture diameter. The figure clearly illustrates that atomic filter technology offer significant improvements in bandwidth reduction. Its advantage compared to the first two technologies increases with filter aperture size. An additional feature of the atomic filter is that its 2π field-of-view is independent of size and passband while the fields-of-view of multilayer interference filters and polarizing filters rapidly drop to a few degrees as their bandwidths become smaller.

*This work was supported by the Aerospace Sponsored Research Program.

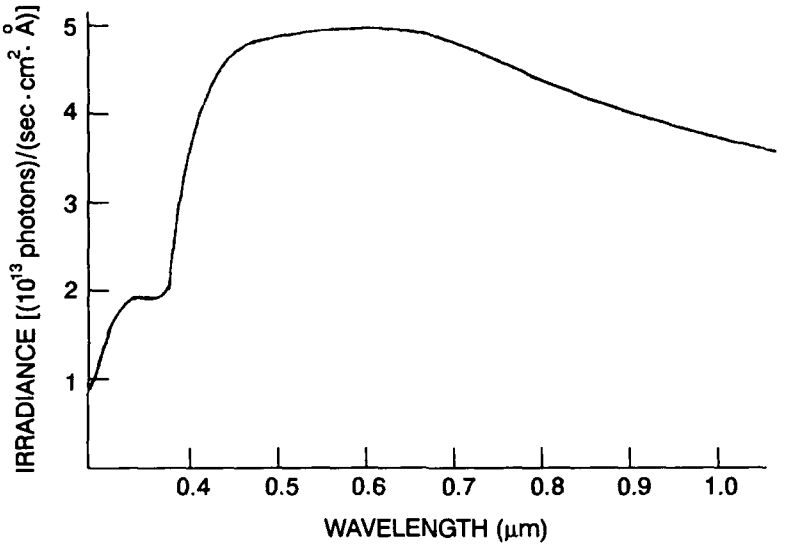


Figure 1. Exoatmospheric Solar Spectral Irradiance.

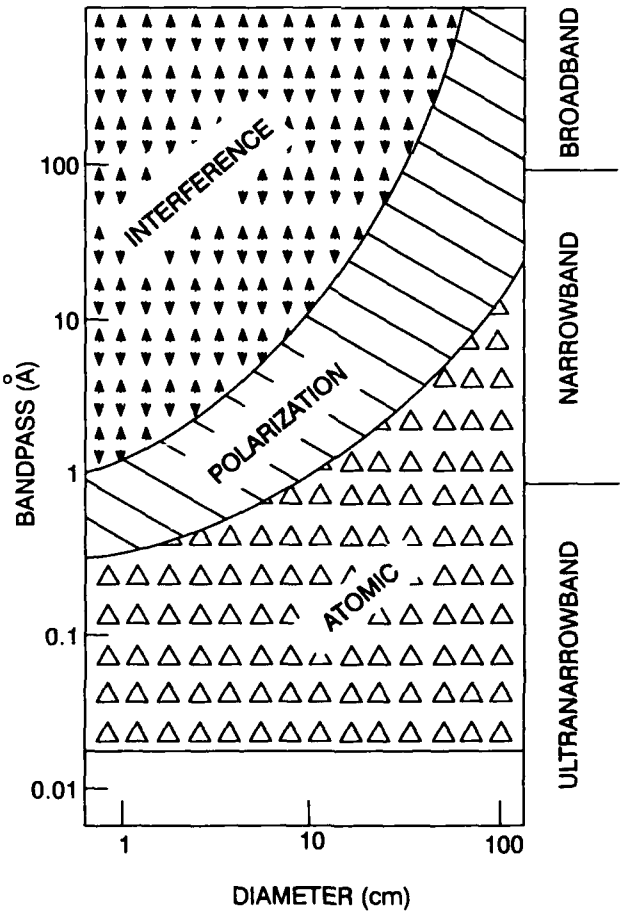


Figure 2. Optical Bandwidth of Visible-Wavelength Bandpass Filters.

Atomic Resonance Filters

Atomic resonance filters perform ultranarrowband filtering utilizing sharp atomic transitions. Typical Doppler-broadened visible linewidths are on the order of 0.01 Å. Photons in resonance with an atomic transition are absorbed by atoms contained in a vapor cell. The atoms then reradiate at a wavelength sufficiently displaced from the absorption wavelength to permit transmission of the emitted light and blocking of the incident radiation by a conventional filter. Atomic filters operate at numerous discrete wavelengths throughout the near UV, visible, and near IR spectral regions.[3] Laboratory experimentation on atomic filtering has been conducted on cesium[4] and rubidium ground-state species, and optically-pumped transitions in rubidium,[5] thallium-cesium,[6] potassium,[7] and magnesium.[8] A recent review article discusses the physics of these devices.[1]

Sunlight Suppression at Fraunhofer Wavelengths

The next major advancement in the state-the-art of solar background rejection is due to a natural phenomenon rather than to a new technological development. The phenomenon is the existence of Fraunhofer lines: dark narrowband regions in the otherwise continuous solar spectrum. These intense minima, or dips, arise due to the absorption by metallic elements in the outer, cooler layers of the sun. The lines were first observed by Joseph von Fraunhofer in 1814 and they have been well-studied by astronomers in the ensuing years. Detailed solar atlases have been compiled.[9] Copious Fraunhofer lines appear at wavelengths below 460 nm due to the rich absorption spectra of iron and nickel. The most intense Fraunhofer lines in the visible spectrum are listed in Table I.[10] They are typically 0.1-0.3 Å wide.

We note that one to two order of magnitude reduction in the solar back-ground occurs at several of these wavelengths. Thus, additional reduction in sunlight is available by operation at intense Fraunhofer wavelengths. Fraunhofer background reduction is an intrinsic part of the solar spectrum and therefore it can be used in conjunction with any narrowband filter technology. Naturally, the maximum advantage occurs with filter passbands less than 0.1 Å. As the passband increases, more of the wings of Fraunhofer line is transmitted and the solar rejection diminishes. Little benefit is gained for passbands larger than 1 Å.

In a recent article, Kerr discusses the use of an advanced ultranarrowband filter composed of a multilayer dielectric interference filter and a Fabry-Perot etalon tuned to Fraunhofer lines for interplanetary communications.[11] He estimates that a 40% background reduction can be realized when the deep space transmitter is a frequency-doubled Nd:YAG laser. High-efficiency tunable solidstate lasers are available throughout the 0.4 - 1.0 μm region. These sources can be tuned to the center of the intense Fraunhofer lines thereby realizing the sunlight attenuation values listed in the last column of Table I.

TABLE I. THE STRONG VISIBLE FRAUNHOFER LINES*

Wavelength	Designation	Origin	Minimum Solar Transmission
4045.825		Fe I	2
4101.748	h, Hδ	H I	19
4226.740	g	Ca I	2.4
4340.475	G', Hγ	H I	17
4383.557	d	Fe I	3
4861.342	F, Hβ	H I	14
5167.327	b_4	Mg I	12
5172.698	b_2	Mg I	8
5183.619	b_1	Mg I	7
5889.973	D_2	Na I	4.2
5895.940	D_1	Na I	4.8
6562.808	C, Hα	H I	16

*C. W. Allen, Astrophysical Quantities (Athlone, London 1973), p. 168.

Fraunhofer-Wavelength Atomic Resonance Filters

The development of Fraunhofer-wavelength atomic resonance filters is motivated by the desire to exploit the natural sunlight reduction that occurs at intense Fraunhofer lines. Owing to their narrow spectral bandwidth and extremely sharp width of atomic transitions, it is highly improbable that an exact overlap between a Fraunhofer line and a random atomic transition can be found. However, nature makes the search for atomic transitions that overlap intense Fraunhofer lines rather easy. For any given Fraunhofer line one simply selects for the filter medium the same atom which provides the Fraunhofer dip in the solar atmosphere. Cosmology ensures this transition will be exactly matched to the Fraunhofer dip. Furthermore, because Fraunhofer lines reflect a 5700 K solar temperature we are assured that the atomic filter linewidth will be much less than the Fraunhofer width. Hence, nature provides atomic transitions exactly matched to intense Fraunhofer dips from which atomic filters may be constructed. All that is left for us to do is to devise clever ways to efficiently extract wavelength-shifted emission after the filter atoms absorb signal light at the Fraunhofer wavelength. Thus, the prospects for advancement of sunlight suppression technology by the development of Fraunhofer-wavelength atomic resonance filters appear highly favorable.

Two Fraunhofer-wavelength atomic resonance filters are currently under development; one in green and the other in the deep-blue spectral region. Because Fraunhofer transitions are strongly absorbing, active-wavelength shifting methods need to be employed to achieve high efficiency for conversion of absorbed signal light into wavelength-shifted emission.[12] The metastable magnesium resonance filter operates at three intense Fraunhofer wavelengths near 518 nm.[13] This filter converts green light into easily detectable 383 nm emission with a maximum theoretical efficiency of 87%. Fifty per cent conversion was measured recently in initial experiments performed under unoptimized conditions.[8] Other filter properties are a 10 nsec response time, low pump power requirements, and low noise operation.

The calcium resonance filter[14] matches the g Fraunhofer line at 422.7 nm. The solar spectrum[9] in the vicinity of 423 nm is shown in Figure 3. At the Fraunhofer dip minimum the solar transmission is 2.4% of the continuum value. The calcium resonance filter converts deep blue light into easily detectable 272 nm emission with a maximum theoretical efficiency of 95%. Other filter properties are a 20 nsec response time, low pump power requirements, and low noise operation. Both filters operate at 300°C, and their bandwidths can be pressure broadened.[15].

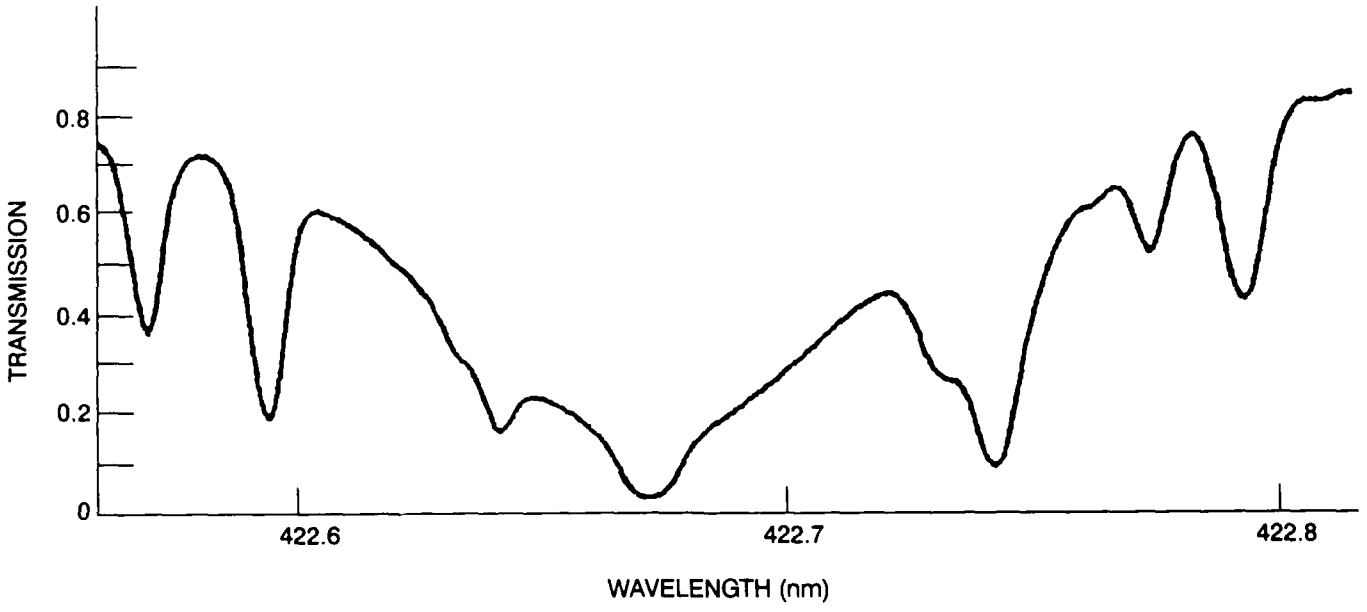


Figure 3. Solar Spectrum Near The g Fraunhofer Line.

In Table II we compare the solar background rejection of the Fraunhofer-wavelength atomic resonance filters with the canonical cesium filter.[4] The latter device has undergone extensive investigation over the past decade. The successful development of the cesium filter proved that atomic transitions can form the basis of wide field-of-view, large aperture, ultranarrowband filters. Its wavelength does not coincide with a Fraunhofer line. Table II clearly illustrates that Fraunhofer-wavelength atomic resonance filters can provide one to two orders of magnitude improvement in solar background suppression compared to standard atomic filters.

TABLE 2. SOLAR BACKGROUND REJECTION OF SELECT ATOMIC FILTERS

	Passive Cesium	Metastable Magnesium	Calcium Resonance
Signal Wavelength (nm)	456,459	516,517,518	423
Fraunhofer Advantage	N/A	10	40
Background Channels	4	3	1
Total Noise Bandwidth	0.12 Å(a)	0.06 Å(b)	0.012 Å(b)
Relative Solar Background Reduction Compared to Cesium	1	20	400

(a) NOSC TR 1291 (April 1989) (b) Doppler width at 300°C

Future Directions

The linewidths of atomic systems can be taken to sub-Doppler limits by a variety of methods. Hence, ultranarrowband technology based upon atomic systems can progress to passbands much less than 0.01 Å. However, applications requiring such narrow bandwidths have not emerged to support further development. Naturally, the passband of a narrowband filter should never fall below the transmitter optical bandwidth in order to preserve signal-to-noise-ratio. Factors that determine the minimum spectral width of the received laser pulse include transmitter frequency stability, doppler shifts, short-pulse transform limits, and high information rates. It is interesting to note that in many of the applications previously discussed, namely, underwater communications, lidar, laser radar, and deep space communications, the spectral width of the received signal is approximately 0.01 Å. Thus, until new applications emerge it appears unlikely that ultranarrowband optical receiver technology will advance beyond 0.01 Å.

References

1. J. A. Gelbwachs, IEEE J. Quant. Electron. 24, 1266(1988).
2. W. L. Wolfe and G. J. Zissis, The Infrared Handbook, (Environmental Research Institute of Michigan, 1978), Table 3-17.
3. J. A.Gelbwachs, C. F. Klein, and J. W. Wessel, IEEE J. Quantum Electron. 14, 77(1978).
4. J. B. Marling, J. Nilsen, L. C. West, and L. L. Wood, J. Appl. Phys. 50, 610(1979).
5. Y. C. Chung and T. M. Shay, IEEE J. Quant. Electron. 24, 709(1988).
6. C. S. Liu, P. J. Chantry, and C. L. Chen, SPIE 709, 132(1986).
7. T. M. Shay in Proceedings, LEOS'88 (IEEE, New York, 1988) pp. 243-245.
8. Y. C. Chan, M. D. Tabat, and J. A. Gelbwachs, Opt. Lett. 14, 722(1989).
9. R. L. Kurucz, I. Furenlid, J. Brault, and L. Testerman, Solar Flux Atlas From 296-1300 nm (National Solar Observatory, Sunspot, N.M., 1984).
10. C. W. Allen, Astrophysical Quantities (Athlone, London, 1973), p. 168.
11. E. L. Kerr, Opt. Engr. 28, 968(1989).
12. J. A. Gelbwachs, submitted to IEEE J. Quant. Electron.
13. J. A. Gelbwachs, in Laser Spectroscopy VIII, W. Persson and S. Svanberg, Eds. (Springer-Verlag, Berlin, 1987), pp. 409-410.
14. J. A. Gelbwachs, to appear in Opt. Lett.
15. J. A. Gelbwachs and M. D. Tabat, Opt. Lett. 14, 211(1989).

IMAGE PRESERVING ATOMIC LINE FILTER

Eric Korevaar, M. Rivers, K. Choi, S. Bloom, K. Slatnick, C.S. Liu
Thermo Electron Technologies Corporation
9550 Distribution Avenue
San Diego, Ca. 92121

Abstract

Atomic Line Filters based on resonant absorption and wavelength converted fluorescence consist of an atomic vapor cell in which this wavelength conversion can take place sandwiched between color glass filters which in combination block all unconverted light. In a class of filters described here, the incoming signal radiation to be detected is absorbed on the strongest resonance transition in an alkali metal atom, the excited atom is excited to a higher level by a pump laser, and cascade fluorescence results in upconverted photons which are collected on a photosensitive surface. Since the fundamental alkali transitions have high absorption cross-sections of order 10^{-11} cm^2, it is possible to absorb the signal photons in a very thin vapor cell (100 μm) at reasonable temperatures (100-150°C). By focussing the incoming signal on the thin layer of atomic vapor, and refocussing the upconverted fluorescence on a two-dimensional detector such as a microchannel plate intensifier, directional image information contained in the original signal can be preserved. A spatial resolution of better than 300 μm in the vapor plane of an atomic line filter based on rubidium has been achieved. The 780 nm signal ($5s_{1/2}$ - $5p_{3/2}$) and 741 nm pump ($5p_{3/2}$ - $7s_{1/2}$) wavelengths were both provided by semiconductor lasers, and the upconverted fluorescence was at 420 nm (6p - 5s). High fidelity, multichannel digital data transfer through the atomic line filter at faster than 500 kbits/sec has also been demonstrated.

Introduction

Atomic Line Filters (ALF's), also referred to as Atomic Resonance Filters, are attractive substitutes for conventional interference filters in many optical systems because of their narrow bandwidth (~.002 nm) and wide FOV (~2πsr). A comprehensive review of much past work in the area is given by Gelbwachs[1]. The concentration of work on these filters has been for applications to submarine laser communication, and thus most of the filters studied have been for wavelengths in the blue-green part of the spectrum. In particular, Marling et al.[2] and others have studied and developed a passive cesium filter at 455 or 459 nm involving an absorption out of the ground state, and Gelbwachs et al.[3] (magnesium Fraunhoffer line), Shay et al.[4] (rubidium), and Liu et al.[5] (thallium) have studied filters where the signal is absorbed by previously excited atoms. By relaxing the requirement of matching a wavelength in the blue-green part of the spectrum, we have been able to make a filter with low noise (because the signal transition is out of the ground state) matching the wavelength of readily available semiconductor lasers, and having the ability to preserve imaging information. The advantages of using an image preserving atomic line filter for background limited signal detection applications, along with the operational principles, experimental results, and expected performance of a rubidium ALF are discussed in the following paragraphs.

For many applications involving detection of scattered light from a laser illuminated object, the primary detriment to detectability is not a lack of scattered laser photons (causing insufficient detector response) but rather an overwhelming amount of background scattered solar radiation. In such situations, the ability of the detection system to filter out the background light can become more important than the detector sensitivity. In Figure 1, the number of background photons per microsecond (chosen to match the time response of the ALF) collected by a 0.1 m^2 receiver is plotted against the full angle field of view of the receiver system. In one case an interference filter with a bandwidth of 2 nm is shown, while in the other comparison is made to a rubidium ALF with a bandwidth of 0.002 nm. The assumed background radiance level is 0.02 $W/m^2 \cdot nm \cdot sr$. For an object only subtending a small fraction of the total field of view, the narrower bandwidth atomic line filter will allow a much larger field of view to be imaged with the same signal to background ratio. (The signal to background is also enhanced in each case because the signal falls on a small part of the imaged area, while the background is distributed more or less uniformly). The ability to image a larger field of view with the ALF enhances the speed and effectiveness of target acquisition.

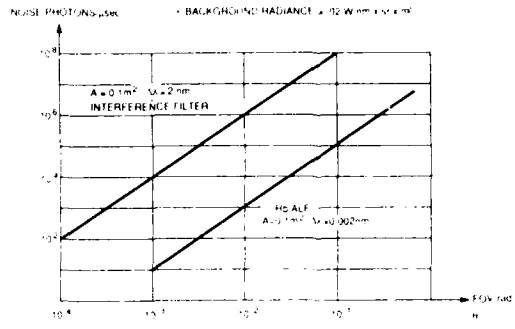


Figure 1. Background light photons collected in 1 μs by a 0.1 m^2 telescope using an interference filter ($\Delta\lambda$ = 2 nm) or a rubidium ALF ($\Delta\lambda$ = 0.002 nm) vs. receiver FOV. A background radiance at 780 nm of 0.02 W/m^2•nm•sr was assumed.

Operational Principle

The operating principles of an image preserving atomic line filter based on rubidium can be understood by reference to Figure 2. Light containing both the signal to be detected (tuned to the 5s-5p transition wavelength of 780 nm) and background noise is incident from the top of the figure. This light first passes through a color glass filter which allows infrared wavelengths to be transmitted, but which blocks visible wavelengths. The remaining infrared background light and the infrared signal are imaged onto a thin layer of rubidium in a glass cell. The rubidium density is high enough that more than 80% of the signal photons are absorbed (along with background light within the Doppler limited bandwidth of the rubidium transition at 780 nm), while any light not matching the rubidium resonance wavelength passes through the cell. The atoms which have absorbed a signal photon at 780 nm are further excited by a pump laser incident from the sidewalls of the cell which is tuned to the 5p-7s transition at 741 nm (which also matches a semiconductor diode laser). Cascade radiation from the 7s level results in fluorescence at 420 and 421 nm, which is radiated in all directions. The blue fluorescence which comes out of the bottom of the cell constitutes the upconverted (energy) signal. This fluorescence, along with the remaining infrared background noise, is incident on a color glass filter which transmits the blue fluorescence photons, but blocks all of the remaining background infrared light. The upconverted blue fluorescence is then detected with a high quantum efficiency detector. Since the only light detected is that which was absorbed and then upconverted in the rubidium cell, the filter has a light acceptance bandwidth determined by the 5s-5p transition linewidth. In the Doppler limited case for a cell at 150°C, this linewidth is about 600 MHz or 0.001 nm, and the signal light should be made to fall within this bandwidth. The noise bandwidth is actually a factor of two higher because ^{85}Rb has two well resolved hyperfine transitions separated by 3 GHz. (Rubidium has two naturally occurring isotopes of abundance 72% ^{85}Rb and 28% ^{87}Rb, but isotopically pure rubidium is available).

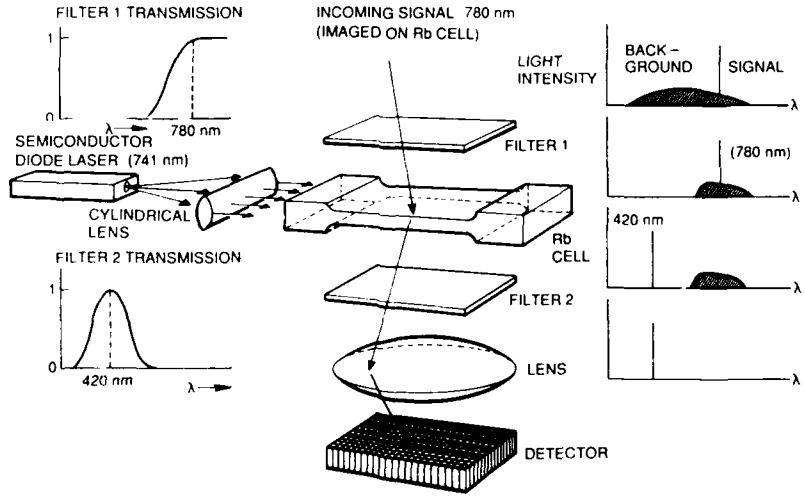
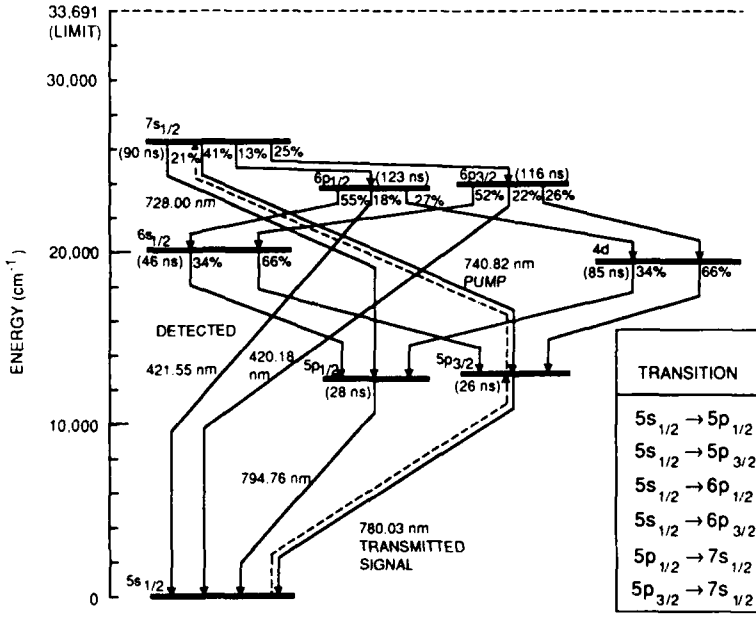


Figure 2. Operational principles of an image preserving atomic line filter using rubidium. Only incoming IR signal tuned to resonance and upconverted to blue fluorescence is reimaged onto the detector array.

At a temperature of 110°C the rubidium vapor reaches an atomic density of $10^{13}/cm^3$. At this density the absorption depth for incoming signal photons at 780 nm is less than 0.01 cm. Thus, all of the signal photons can be absorbed in a very thin cell, even at this reasonable temperature. Because of this, it is possible to preserve imaging information, a necessary function of a detector which is to be used for directional detection. Image information is preserved because fluorescence takes place from the same location where the signal was absorbed. If the blue fluorescence is reimaged onto a microchannel plate image intensifier, this positional information can be preserved. The amount of resolution blurring depends on the thickness of the rubidium layer, and the f number of the reimaging optics. For a cell with thickness 100μ, a resolution of 100μ is possible even with very low f number, high efficiency optics. Thus, a 100 x 100 pixel image can be preserved with a 1 cm by 1 cm cell. Because of collisions of the atoms with the walls, the conversion efficiency starts to drop for cells much thinner than 100μ. Our image preserving scheme is similar to one proposed by Gelbwachs et al.[6] which was based on a filter using excited state absorption in an image plane defined by the pump laser.

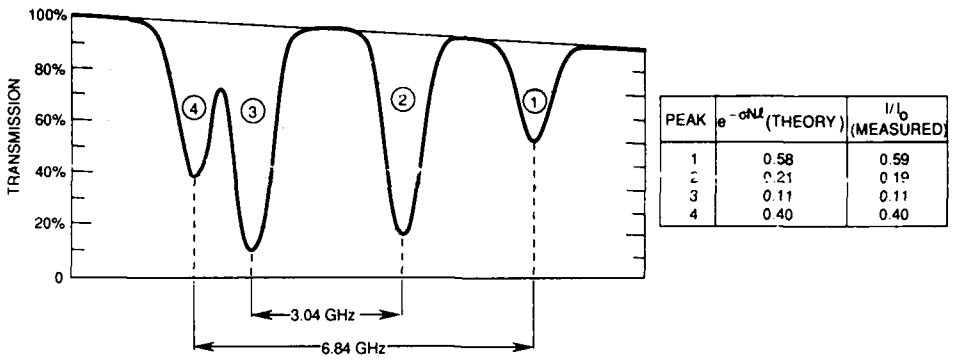
Figure 3 shows all of the rubidium energy levels and transitions relevant to the image preserving ALF. Cross sections and branching ratios for the various transitions, which were derived from accurate oscillator strengths[7], are also shown. (These cross sections are computed ignoring the hyperfine structure.) For the calculations, a Doppler limited linewidth was assumed. These data can be used to estimate the absorption characteristics, the time response, and the fluorescence conversion efficiency of the atomic line filter at a given temperature. In addition, the time response and efficiency are influenced by radiation trapping of the ground state transition photons at 780 nm. The longer the radiation can be trapped, the higher the conversion efficiency (and the slower the time response).

The absorption depth d for the signal or detected photons can be calculated as $d=1/\sigma N$ where σ is the tabulated absorption cross-section (decreased by the ratio of the signal bandwidth to the 0.015 cm^{-1} Doppler width if necessary) and N is the atomic density. For instance, at 130°C, $N_{Rb} = 2.9 \times 10^{13}$ cm^{-3}, 0.72x7/12 of which is in the ^{85}Rb hyperfine level with F=3. Then the absorption depth $d = 1/\sigma N = 1/(2.9\times10^{-11}cm^2 \times 0.72 \times 7/12 \times 2.9\times10^{13}cm^{-3}) = 2.8\times10^{-3}$ cm. Thus, a narrowband signal on resonance will be 97% absorbed in a 0.01 cm thick cell. On the other hand, the absorption depth for the upconverted fluorescence at 455 nm is 0.36 cm, so that very little of it is reabsorbed after being emitted. An absorption spectrum for the rubidium $5s_{1/2}$ to $5p_{3/2}$ transitions at 780 nm is shown in figure 4. The four different transitions (measured in absorption while tuning a single mode diode laser by changing its drive current) occur because there are two isotopes, each with two resolvable hyperfine transitions.



TRANSITION	DOPPLER LIMITED ABSORPTION CROSS-SECTION (cm^2)
$5s_{1/2} \rightarrow 5p_{1/2}$	1.45×10^{-11}
$5s_{1/2} \rightarrow 5p_{3/2}$	2.88×10^{-11}
$5s_{1/2} \rightarrow 6p_{1/2}$	8.63×10^{-14}
$5s_{1/2} \rightarrow 6p_{3/2}$	2.27×10^{-13}
$5p_{1/2} \rightarrow 7s_{1/2}$	7.32×10^{-13}
$5p_{3/2} \rightarrow 7s_{1/2}$	7.32×10^{-13}

Figure 3. Energy levels of rubidium relevant to ALF operation showing lifetimes, branching ratios and Doppler limited absorption cross sections (at 150°C ignoring hyperfine structure)



PEAK	$e^{-\sigma N \ell}$ (THEORY)	I/I_0 (MEASURED)
1	0.58	0.59
2	0.21	0.19
3	0.11	0.11
4	0.40	0.40

Figure 4. Reference cell absorption spectrum of rubidium $5s_{1/2}$ - $5p_{3/2}$ (780 nm) transition. The cell length = 7.38 cm, temperature = 33°C, N=2.1 x 10^{10}/cm^3. Peaks 1 and 4 are the hyperfine transitions from F=1 and 2 in ^{87}Rb (28% abundance) while peaks 2 and 3 are transitions from F=2 and 3 in ^{85}Rb (72% abundance)

Time Response

The pump power requirement can be calculated roughly as follows. Since the 7s lifetime is 90 ns, and in pumping equilibrium with the $5p_{3/2}$ state only 1/3 of the population can be in the upper level, it should be adequate to pump 1/3 of the population every 90 ns (provided that the optically trapped lifetime of the 6p state is at least this long). The transition rate is $W = \sigma N_{ph}$, where N_{ph} is the number of pump photons/cm^2/s hitting the excited rubidium atoms. A transition rate of W=3.7x10^6/s corresponds to a pump intensity of 1.4 W/cm^2 at 741 nm. For a 1 cm x 0.01 cm cross-sectional area for pumping, this corresponds to a pump power of 14 mW, a level easily achieved with single mode semiconductor diode lasers.

At the center of a thick cell, the optically trapped lifetime for a 780 nm photon in rubidium can be much larger than a microsecond. Random walk calculations show that for a resonant photon absorbed after entering the face of a cell, however, the trapped lifetime will only increase to about 250 ns from its natural lifetime of 26 ns. This lifetime can be increased by increasing the rubidium density and tuning the signal slightly off resonance (so that the signal absorption depth will be longer than that of the resonance fluorescence), although at the price of increasing the filter bandwidth. As the cell is made thinner and the vapor thickness approaches 0.01 cm, collisions of excited atoms with the wall become the limiting factor on the lifetime. At 130°C, the average velocity of a rubidium atom in the direction of a cell wall is about 2.3x10^4 cm/s and it traverses 0.005 cm in 215 ns. The collision results in the atom sticking to the wall and losing its excitation to heat. It may be possible to make the collision more elastic by coating the wall with parrafin or some other substance as is done in optical pumping experiments, but in any case wall collisions will limit the minimum thickness of the cell (and thus the resolution of the ALF) to about 0.01 cm.

The time response of the system to a pulsed pump excitation is readily calculated as a bi-exponential decay from the 7s and 6p levels, whose lifetimes sum to 210 ns. The conversion efficiency can be calculated from the branching ratios in the figure to be (1/3) x (0.13x0.18 + 0.25x0.22) = 2.6% for this case. For a continuous pump, the time response is lengthened, and the conversion efficiency is increased. The limiting values depend strongly on the lifetime of the 780 nm resonantly trapped radiation in the cell. Although the conversion efficiency can in principle be increased by using two pump lasers, one from each of the 5p states, the increase is probably not worth the added complexity for a real system. Data from a time response measurement carried out for pulsed dye laser excitation (in cesium rather than rubidium) is shown in Figure 5. In picture (a), blue fluorescence is collected with only the pump laser present. Notice that there is no internal filter noise in this case. In picture (b), only the signal laser is present. A few blue photons are seen here, and these go away if the signal laser is tuned off resonance. This fluorescence is probably due to excitation caused by collisions between excited atoms, since it depends strongly (more than a linear dependence) on the signal laser intensity. Since this fluorescence only occurs for a signal laser tuned on resonance, it does not constitute noise to the system. Picture (c) shows the signal collected when both lasers are allowed through the cell, clearly demonstrating operation of the ALF cell as an infrared to blue quantum converter. The time response matches the predicted bi-exponential decay. (This time response was measured in a cell of thickness 0.3 cm. It can become shortened due to quenching collisions with the cell walls for sufficiently thin cells).

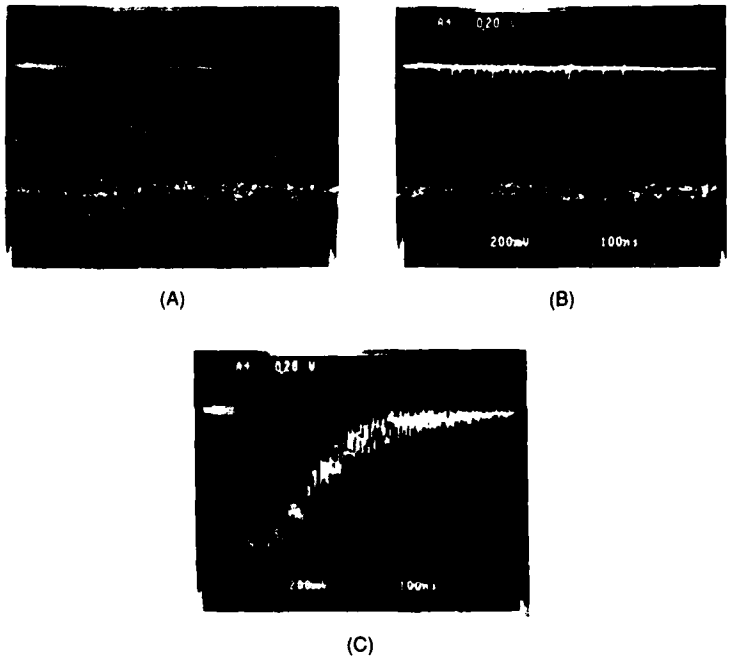


Figure 5. Time response measurement. Two pulsed dye lasers were used to measure the conversion time response in cesium. Figure (a) is blue fluorescence collected with pump laser alone, (b) with signal laser alone (on resonance) and (c) with both lasers combined.

We have also measured the time response of a 0.02 cm thick rubidium ALF pumped by a cw diode laser. Results of this experiment are shown in Figure 6 for a 500 ns signal (left) and a 1 microsecond signal (right). On each oscilloscope photograph, the bottom trace shows a current pulse added to the dc current driving the signal diode laser (which provides signal photons), the middle trace shows absorption of the diode laser through a reference rubidium cell (the laser is on resonance and being absorbed during the downward dip), and the top trace shows the output 420 nm fluorescence from the ALF monitored with a photomultiplier tube. The rise time here is about 200 ns, while the fall time is about 400 ns. High fidelity data communication at about 500 kbit/sec was achieved using this atomic line filter.

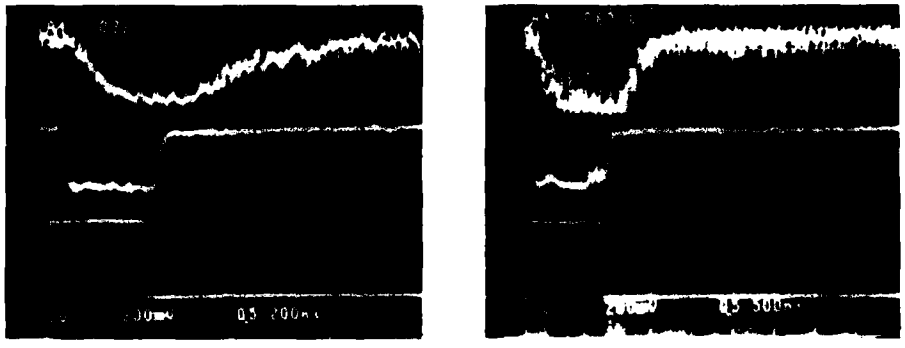


Figure 6. Time response of a cw diode laser pumped rubidium atomic line filter. From bottom to top, the three traces on each photograph are the current pulse to the diode, rubidium reference absorption, and ALF output.

Other Wavelengths

Other elements besides rubidium can also be used for image preserving atomic line filters. Table 1 lists the wavelengths and appropriate lasers for ALF's based on ground state transitions in alkali metals. In particular, both the potassium and rubidium signal wavelengths can be tuned to with an Alexandrite laser, in addition to semiconductor lasers. The pump laser can be a semiconductor diode laser in each case, although the available powers may not yet be high enough at the 691 nm potassium pump wavelength.

ALF	Signal Wavelength	Pump Wavelength	Fluorescence Wavelength	Laser Systems
Li	671 nm	497 nm	323 nm	Dye Lasers
Na	589/590 nm	616/615 nm	330 nm	Dye Lasers
K	767/770 nm	694/691 nm	404/405 nm	Alexandrite/Ti:Sapphire/ Semiconductor
Rb	780/795 nm	741/728 nm	420/422 nm	Alexandrite/Ti:Sapphire/ Semiconductor
Cs	852/894 nm	794/761 nm	455/459 nm	Ti:Sapphire/Semiconductor

Table 1. Alkali atomic line filters

Image Preservation

Demonstration of image preservation in a rubidium atomic line filter cell has been carried out using diode lasers for the signal and pump beams and a rubidium cell with a vapor thickness of 0.02 cm. (Previous results using a 0.05 cm cesium cell and pulsed dye lasers were presented at SPIE's OE/LASE '89 conference[8]). The experimental apparatus is shown in Figure 7. The 780 nm signal diode laser was monitored in absorption through a reference rubidium cell to keep it on resonance, while blue fluorescence was monitored with a PMT to keep the 741 nm pump laser tuned properly. The lasers operated at power levels between 2 and 5 mW with bandwidths on the order of 50 to 100 MHz (monitored with a 1GHz Free Spectral Range Fabry Perot interferometer). The pump laser was expanded to a size of about 15mm and then focussed through the ALF cell with a cylindrical lens, making an active imaging area of about 15mm x 15mm. The signal laser was scattered off of a patterned target towards the atomic line filter. (The target was 2 m from the ALF, and retroreflective tape was used to enhance the weak return signal for this preliminary experiment). The infrared return signal was imaged with a camera lens onto the ALF cell. The subsequent blue fluorescence was reimaged with f/1 optics onto a microchannel plate image intensifier. A picture of the atomic line filter "camera" used is shown in figure 8. Note the small size of the ALF cell, and the possibility of integrating components into a small package. For the data presented here, the CCD camera was replaced with a 35 mm film camera, and pictures were taken of the image intensifier output.

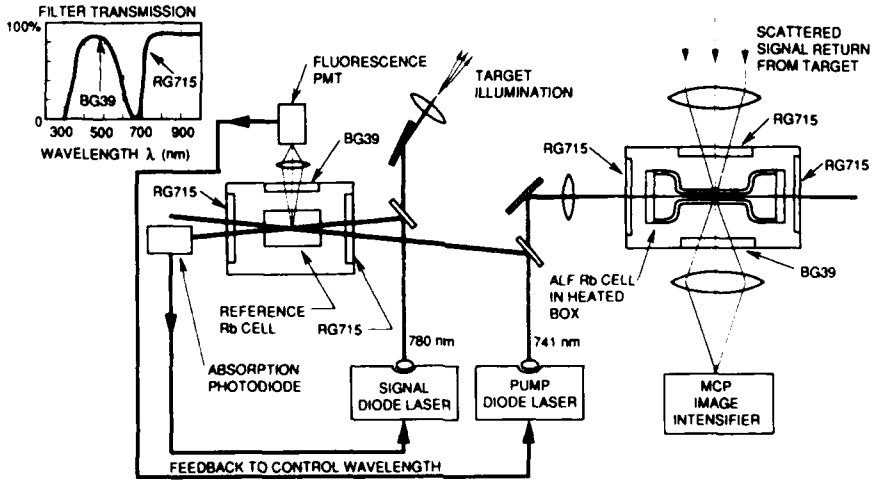


Figure 7. Experimental geometry for image preservation experiment. Signal scattered from a target was reimaged through a 0.02 cm thick rubidium ALF.

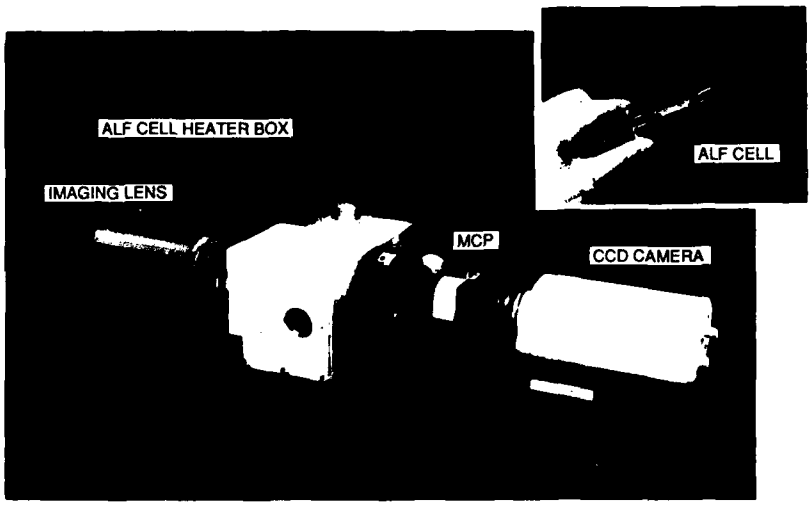


Figure 8. Photograph of atomic line filter camera system.

Data from the imaging experiment are shown in Figure 9. For the picture on the left, the ALF cell was removed and replaced with a screen, and (with the additional removal of the blue blocking/IR passing filter) low levels of light were imaged through the rest of the optics onto the image intensifier. For the picture on the right, the atomic line filter (operating at a temperature of about 150 degrees C) was used. There is not a great difference in the resolution achieved with the two pictures, and the resolution may be limited by the 18 mm diameter MCP image intensifier. The smallest features are a set of three vertical lines at the center of the image (which are clearly resolvable in the original color prints). These lines have a width and spacing of 1 mm at the target, and are reduced in size by the camera lens to 350 microns at the ALF. With further improvements, an ultimate imaging resolution of 100 microns at the cell is expected.

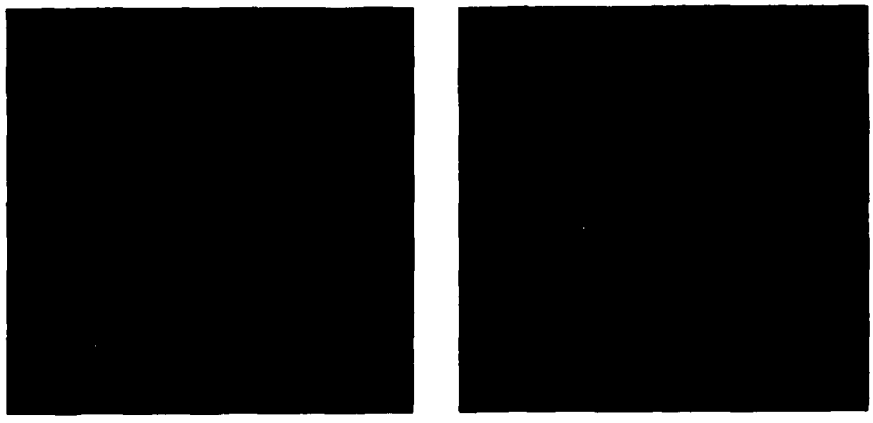


Figure 9. Image reproduction using ALF camera. Signal light was scattered from an illuminated pattern 2 m in front of the camera. For Figure (a), the ALF was replaced by a screen at the focal plane and the blue filter was removed. In Figure (b), the 0.02 cm thick rubidium ALF cell was used. The smallest feature size at the ALF is 350μ.

Device Efficiency

The final issue to be discussed is device efficiency. Because the ALF is useful in situations where background light levels are of over-riding concern, low detection efficiencies are not necessarily an issue, but it is still necessary to have efficiencies above some limiting value, and it is desirable to have them as high as possible within other system constraints. The ALF detection efficiency is most conveniently divided into four parts. The first of these is the transmission efficiency through all of the optics, including the color glass filters. With appropriate

coatings this can reach 90%. Second, the quantum efficiency of the MCP image intensifier (converting blue photons to detectable signals) may be 20%. Third, since the upconverted blue photons are radiated in all directions, the collection efficiency for reimaging is of critical importance. Using two f/1 lenses in series, this collection efficiency is 5%, and reasonably low distortion imaging capability is maintained. Finally, the internal quantum conversion efficiency from the infrared to the blue in the rubidium vapor must be taken into account. Based on some calculations discussed in the next paragraph, an internal conversion efficiency of between 2% and 5% is expected for a 0.01 cm thick image preserving ALF cell. Multiplying these four numbers together gives an overall device efficiency of 0.05%.

The main factor determining the achievable internal quantum conversion efficiency is the lifetime of resonantly excited atoms in the cell. If the signal photons have a long lifetime due to resonance entrapment (reabsorption after fluorescence) then there is an enhanced opportunity to pump the atoms to a further excited state leading to quantum converted blue fluorescence. Computer calculations based on solving for the populations in the nine relevant coupled energy levels in rubidium indicate that with an entrapment lifetime of 1200 ns and a pump intensity of $5W/cm^2$ at 741 nm a 13% internal conversion can be achieved. A lifetime this long can be achieved in cells thicker than 0.1 cm which may be appropriate for communications and some tracking applications, but are probably too thick for good image preservation. If the entrapment lifetime is only 100 ns (because of quenching collisions with the cell walls in a 0.01 cm cell) and a pump intensity of $10W/cm^2$ is used, then a 3% internal conversion efficiency can be achieved, still ignoring quenching of the doubly excited levels radiating in the blue. Quenching of these levels will further lower the conversion efficiency (while making the detector response time faster). For the data presented in the image preservation experiment, the conversion efficiency was still lower because sub-optimal pump laser intensities were used. There, a laser intensity of 3mW/(1.5cm x 0.02 cm) or 0.1 W/cm^2 leads to an internal conversion of 0.2% and an overall device efficiency of about 10^{-5}. It is hoped that wall quenching can be reduced and entrapment times increased by coating the walls of thin cells with something like parrafin (as is done in optical pumping experiments) to cause the excited atoms to undergo elastic collisions instead of sticking to the walls. Furthermore, collection efficiencies can be improved by using lower f/number optics (especially for communication applications) or possibly fiber optics.

Conclusion

A novel kind of active atomic line filter which preserves imaging information has been described in this paper. This atomic line filter has a wavelength acceptance bandwidth of about 0.002 nm and inherently very low intrinsic noise. In a rubidium ALF, an imaging resolution of better than 350 microns and a time response faster than 500 ns have been demonstrated using semiconductor diode laser signals and pumps. Overall photon to detected electrical signal efficiencies for such a device should be about 0.1%.

Acknowledgements

The work presented herein was supported by SDIO/IST/ONR under contract N0014-87-C-0777 and by NADC under contract N62269-88-C-1144. We would like to thank Dr. M. White of SDIO/ONR, Dr. K. Wu of SDIO, Dr. V. Smiley of ONR, Mr. G. Beaghler of ONR, Mr. G. Ferguson of NADC and Mr. R. Rud of NADC for their encouragement and support.

References

1. J. A. Gelbwachs, "Atomic Resonance Filters," IEEE J. Quantum Electronics 24, 1266-1277, 1988.
2. J. B. Marling, J. Nilson, L.C. West and L.L. Wood, J. Appl. Phys. 50, 610 (1979)
3. J. A. Gelbwachs, C. F. Klein, and J. E. Wessel, IEEE J. Quantum Electronics, QE-14, 77, 1978
4. T. M. Shay and Y. C. Chung, "Ultrahigh-resolution, wide-field-of-view optical filter for the detection of frequency-doubled Nd:YAG radiation," Optics Letters 13, 443, 1988.
5. C. S. Liu, P. J. Chantry and C. L. Chen, SPIE Vol. 709 p. 132 (1986).
6. J. A. Gelbwachs and J. E. Wessel, "Atomic Vapor Quantum Counter: Narrow-Band Infrared Upconverter," IEEE Trans. Electron Dev., ED-27, 99-108 (1980)
7. W. Hansen, J. Phys. B17, 4833 (1984).
8. E. Korevaar, M. Rivers, C.S. Liu, "Imaging atomic line filter for satellite tracking," SPIE Vol. 1059- Space Sensing, Communications, and Networking, 111 (1989).

A FAST ATOMIC LINE FILTER/FIELD IONIZATION DETECTOR*

S. H. Bloom, Eric Korevaar, Mike Rivers, and C.S. Liu
Thermo Electron Technologies
9550 Distribution Ave.
Applied Physics Group
San Diego, CA 92121-2305

An experimental demonstration of a fast atomic line filter/ field ionization detector (FALF/FID) is presented. The FALF/FID detects incoming signal photons by resonant absorption in an atomic vapor cell containing a strong electric field. Excited atoms are electric field ionized after further excitation to a Stark shifted Rydberg level by a pump laser tuned to a resonance in the ionization spectrum, providing an observed enhancement in the ionization rate of ten times over the continuum ionization threshold. Preliminary measurements of time response (<10 ns) and quantum efficiency (>25%) indicate that with optimization the FALF/FID will provide high quantum efficiency, fast time response, and narrow linewidth detection.

Atomic line filters operating at various wavelengths from the near IR to the near UV have been extensively studied since they are presently the narrowest bandwidth optical detectors available[1]. Common to all of these filters is internal wavelength conversion via optical atomic transitions and subsequent detection of the converted radiation. The time response of these ALF's is limited by the fluorescence lifetimes of atomic energy levels. In Cs the time response[2] is on the order of 500 ns. In this paper we describe the first experimental demonstration in a vapor cell of a Fast Atomic Line Filter/Field Ionization Detector(FALF/FID), that selectively ionizes atoms that have absorbed signal radiation and then detects these ions(or electrons).[While preparing this manuscript, a proposal for such a detector appeared in Optics Letters[3]] This filter has the advantages that it has a significantly faster response time, and since the ions can be detected with near unity quantum efficiency, an inherently higher overall quantum efficiency than fluorescence based filters.

The main drawback of using direct photoionization is that high pump laser intensities are needed for a fast transition rate to the continuum which in turn produces noise due to two photon excitation from the ground state. The FALF/FID uses a novel scheme whereby the high pump intensity requirement is alleviated by an order of magnitude by making use of semi-discrete-Stark shifted Rydberg levels in an electric field, using the electric field for field ionization and electron/ion production.

Before discussing the theoretical and experimental results, the basic physics behind the FALF/FID will be briefly outlined. For this demonstration we used Rb as the active alkali vapor. Figure 1 shows an abbreviated energy level diagram for Rb, depicting a schematic representation of the Stark-shifted Rydberg states. The $5p_{3/2}$ state is attained

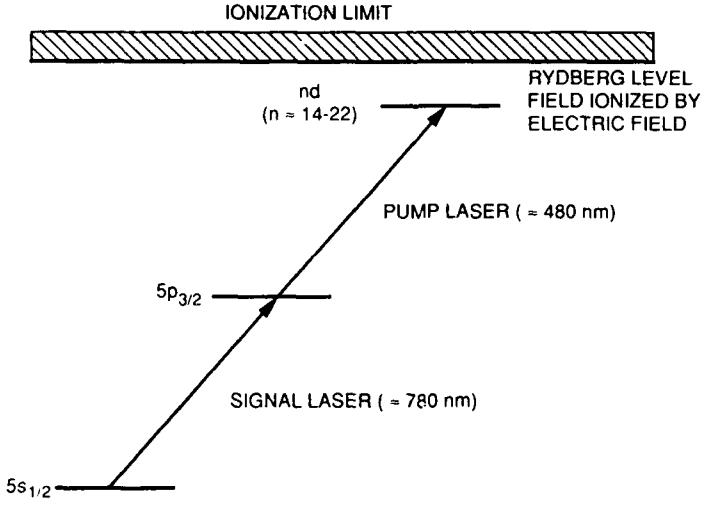


Figure 1. Energy level diagram for rubidium showing transitions used by the FALF/FID.

by optical excitation with a diode laser tuned to the atomic transition at 780 nm. After absorption another laser quickly excites the atoms that absorbed the 780 nm photons to Rydberg levels Stark shifted by the application of an external D.C. field. These levels are of sufficiently high energy that the electric field ionizes them in times short compared to 1 ns. These ions/electrons are then detected with near unity quantum efficiency by an electron

* A paper describing this work has been accepted for publication in Optics Letters.

multiplier.

It is possible to approximate the behavior of Rydberg states in alkali atoms since the electrons spend most of their time far from the nucleus where the wavefunctions can be accurately represented by coulombic wavefunctions. It is possible to understand some of the important features of this problem from simple classical arguments[4]. The potential for a single electron in an electric field along the z axis (in atomic units where e=m=h/2π=1) is:

$$V_E(r) = -\frac{1}{r} + Ez \tag{1}$$

where V has a maximum at $z = -1/E^{1/2}$. This point is actually a saddlepoint because off axis, V increases. We can write the saddlepoint potential as $V_{sp} = -2E^{1/2}$. For the electron to be in a bound state its energy must be less than this value so:

$$W_{th} = -2E^{1/2} \quad \text{or} \quad E_{th} = W^2/4 \tag{2}$$

This provides a threshold field for field ionization of the electron. To estimate the critical field the Stark effect can be neglected so that $W = -1/2n^2$ which yields :

$$E_{th}^{*} = \frac{1}{16n^4} = \frac{3.2 \times 10^8}{n^4} \text{ V/cm} \tag{3}$$

Figure 2 shows the approximate electric field necessary to ionize a Rydberg level of principle quantum number n. Figure 3 tabulates the wavelengths for signal and pump lasers in various alkali vapors along with the operating temperatures. The pump laser wavelength ranges are for transitions between levels n = 14 and 24. The time response of the FALF/FID is limited by the transition rate from the intermediate level to the Rydberg level, and is a linear function of pump laser intensity. The transition cross-section is significantly enhanced by going to a semi-discrete level rather than pumping all the way to the continuum. Typical widths of these semi-discrete levels have been measured[5] and depend on the azimuthal quantum number m_l in the direction of the electric field. Widths of $|m_l| = 0$ levels are 1-3 cm^{-1} (1 cm^{-1} = 30 GHz), $|m_l| = 1$ are 1-3 GHz and $|m_l| = 2$ have widths < 100 MHz. An ionization time constant of <1 ns requires a pump laser width of > 1 GHz.

Quantum Efficiency

Conventional ALF's are limited in quantum efficiency by branching ratio losses, the quantum efficiency of the photosensitive detector detecting the converted radiation, and the efficiency of the collection optics. In contrast the FALF/FID detects ions or electrons from field ionized atoms and therefore does not suffer from the branching ratio losses nor the quantum conversion efficiency of a light sensitive detector since the signal is detected with an electron multiplier. Theoretically, conversion efficiencies greater than 50% should be possible with this detector.

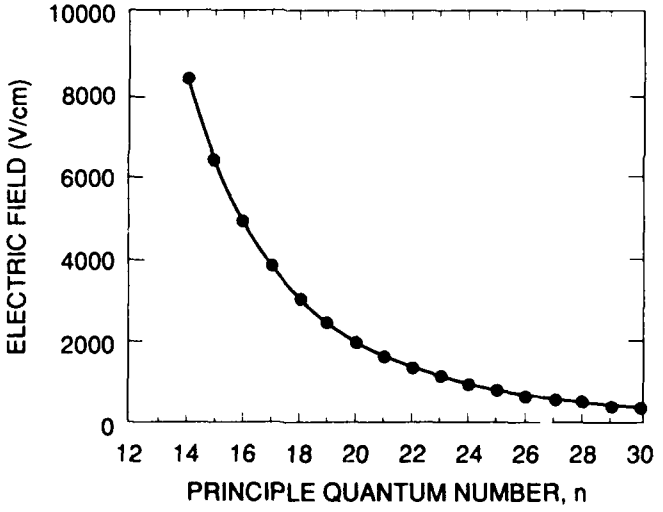


Figure 2. The field ionization threshold for principle quantum number n derived from classical considerations.

SIGNAL PHOTON ATOMIC TRANSITION	SIGNAL WAVELENGTH	LASER CANDIDATES	PUMP LASER WAVELENGTH	OPERATING TEMPERATURE
Cs 6s-6p	894/852 nm	DIODE, Ti: Al_2O_3, DYE	515-499/530-513 nm	100° C
Rb 5s-5p	795/780 nm	DIODE, Ti: Al_2O_3, ALEXANDRITE, DYE WITH RAMAN SHIFT	490-478/495-484 nm	120° C
K 4s-4p	770/766 nm	DIODE, Ti: Al_2O_3, ALEXANDRITE, DYE WITH RAMAN SHIFT	465-458/467-459 nm	150° C
Na 3s-3p	590/589 nm	DYE, SUM FREQUENCY GENERATION FROM Nd: YAG 1.06μ + 1.32μ	418-412 nm	220° C

Figure 3. Atomic transitions and their associated lasers for various alkalis useful in an ALF/FID.

Time Response

For a conventional cesium based ALF the time response is limited by the resonance fluorescence entrapment lifetime. Theoretical and experimental results indicate that this filter can have a time response[6] of 300 ns to 1 μsec. For the FALF/FID the field ionization processes typically have lifetimes of <1 ns and therefore the time response of the device is determined by the pump laser power. We can make an estimate of the upper bound of the cross section for field ionization from zero field ionization calculations. For transitions from Rb(5p) to the ionization threshold the cross section has been calculated[7] to be about 10^{-17} cm^2. For a transition rate of 1/2.5 ns this requires a pump intensity of 4 x 10^{25} photons/cm^2s which @ 480 nm corresponds to 17MW/cm^2. The transition cross section for an $|m_l|=1$ Stark level can be estimated from the transition rate for $5p_{3/2} \leftarrow 20d$ and dividing by the number of levels (20) that are accessible. For a linewidth of 0.05 cm^{-1} (1.5 GHz) $5p_{3/2} \leftarrow 20d$ transitions have a transition rate[8] of A = 4.5 x 10^4 sec^{-1}. This number was obtained by integrating the Schroedinger equation using the Coulomb approximation for V(r) and the Numerov algorithm. This yields a cross section of :

$$\sigma = \frac{1}{20} \times \frac{A}{8\pi c} \times \frac{1}{(1/\lambda_{vac})^3} \times \frac{\omega}{\Delta\omega} \approx 1.4 \times 10^{-16}\ cm^2 \qquad (4)$$

This represents a factor of 10 improvement over direct ionization. A laser intensity of about 1.2 MW/cm^2 will be needed for a 2.5 ns transition time constant. An estimate of the pump laser power in an actual device depends on the active detector area of the device. For rubidium, the signal laser at 780 nm has a Doppler limited absorption cross section of 2.88 x 10^{-11} cm^2 [1.41 x 10^{-11} cm^2 including hyperfine splitting] so it will be absorbed in an optical depth of 0.01 cm at a density of 3 x 10^{12} atoms/cm^3 corresponding to a temperature of 105°C and 3 x 10^{-4} torr. If we assume a detector diameter of 0.2 cm, then the pump laser would be focussed to a line of 0.01 x 0.2 cm with an area of 0.002 cm^2. The necessary laser power is then 2.4 kW, easily attainable with a pulsed laser. For a 1 μs detection period this would correspond to a pulse energy of only 2.4 mJ.

The transit time of an electron detecting FALF/FID can be calculated from $x = 1/2at^2$ where x=0.2 cm and a = qE/m. This gives t = 0.4 ns, a negligible effect on the response time of the device since the limiting factor is really the spread in transit times which should be even smaller. If positive ions are detected instead the transit time will be about 140 ns, but if the electric field is very uniform, the spread in transit times may be < 1 %. As will be seen later the spread in transit times for ion detection was <10 ns, so fast response times are possible with ion detection.

Noise

If electrons are being detected then any process that creates electrons in the active region of the detector will contribute to the overall noise. An extremely small source of noise is the background cosmic radiation flux, which at sea level[9] is 2400 /m^2s. If the cosmic rays were converted to electrons with 100 % efficiency that would lead to only 7.5 x 10^{-13} electrons/ns. Field emission could be suppressed by careful selection and manufacture of materials. The most important sources of noise are thermionic emission, the photoelectric effect, and collisional or blackbody radiative ionization. These may control the final choice of alkali for use in the FALF/FID. A final source of noise that is a function of the alkali atom itself, the pump power, and pump wavelength, is two-photon ionization induced by the pump laser. The maximal cell operating temperature will be determined by the trade-off between thermionic

emission and the photoelectric effect on alkali depressed work functions of cell surfaces. At 480 nm, photons have an energy of 2.6 eV which is higher than all alkali work functions and therefore plating of the alkali on any of the inner surfaces which might receive scattered light from the pump laser must be minimized.

Thermal ionization is expected to be small for Rb at 105° C since the Boltzmann factor for the first excited state is only 1.7×10^{-21}, which is less than one atom in the entire FALF/FID. If the filter temperature were higher, say 400°C, then the Boltzmann factor would increase to 2.1×10^{-12}.

Figure 4 shows the cross section for two photon ionization by the pump laser for some of the possible alkalis useful in a FALF/FID[10]. The cross section is strongly enhanced by single photon resonances and has sharp minima between the resonances. In Rb at 480 nm the cross section is about 7×10^{-50} cm^4s. For a pump intensity of 1.2 MW/cm^2 this leads to a transition rate of 0.6 /s. The active volume of the ALF/FID contains (6×10^{12} $atoms/cm^3$) x (0.01 x 0.2 x 0.2 cm^3) = 2.4×10^9 atoms. So two photon ionization would produce 1.4 electrons/ns. This could be reduced by using a different alkali/laser combination or reducing pump laser power. If the detector is run in ion detection mode, then almost all of these noise sources would be eliminated. The most significant remaining sources of noise would come from thermionic emission and two-photon ionization. The drawback of detecting ions instead of electrons is that the time response and quantum efficiency(due to ion detection) might suffer.

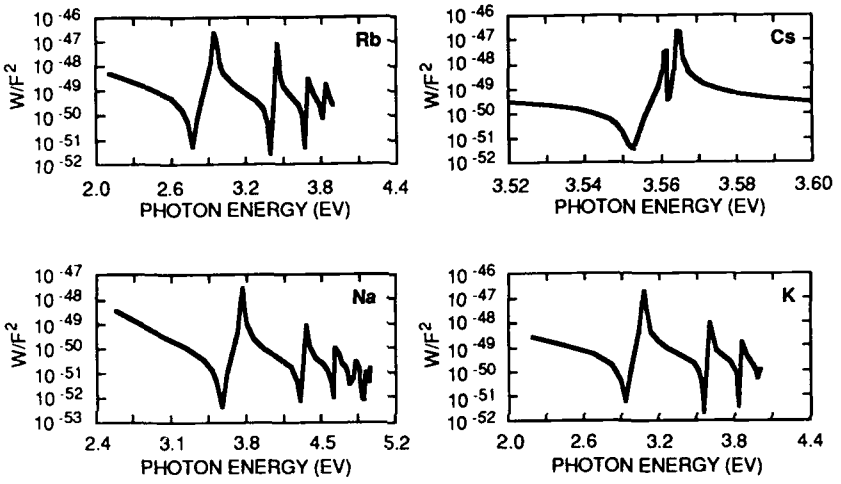


Figure 4. Theoretical dispersion curves for two-photon ionization rates in various alkalis[After H. Bebb].

Experimental Apparatus

The experimental setup used in this study is shown in Figure 5. Figure 6 shows a schematic drawing of the cell. The central portion of the cell was a cube with vacuum ports on each cube face. Sapphire windows were mounted on four sides of the cell; two for entry and exit of the pump laser, one for entry of the signal laser, and one for viewing

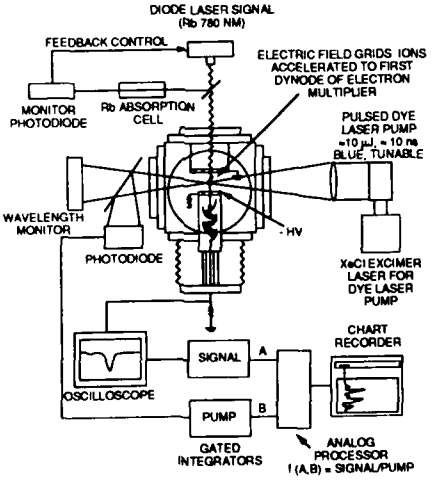


Figure 5. The experimental setup used to demonstrate the feasibility of the FALF/FID.

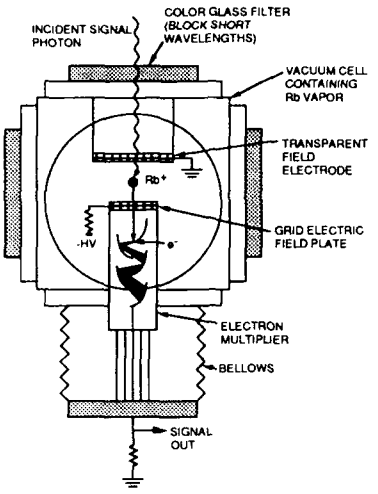


Figure 6. Detailed schematic diagram of the FALF/FID device

the active region. The electron multiplier was made from a modified end-on photomultiplier tube. The photocathode and end window were removed and replaced by a stainless steel mesh, which served as an accelerating grid for the electron multiplier and as a field electrode to produce the ionizing electric field in the active region. The signal laser entry window was also covered with stainless steel mesh, providing the other electrode for the ionizing field. The electron multiplier was attached to the central cube via a vacuum feedthrough attached to a stainless steel bellows which allowed the electrode spacing to be varied from 0 - 1.0 cm. The remaining port had a high temperature resealable valve attached to it. The cell was baked at 200° C until the pressure dropped to < 10^{-6} torr. Rb metal was loaded into the cell in an argon atmosphere and the cell was then baked at 180° C under vacuum for about four hours. The cell was then sealed and removed from the vacuum system thereby making for a convenient self contained device. Rb vapor was produced by heating the cell with heater tapes wrapped around it and the entire device was wrapped in glass wool for uniform heat distribution. The temperature was monitored and controlled with a platinum thermometer which was attached to the coldest point on the cell and fed back to a temperature controller/heater power supply. The signal and pump laser beams crossed perpendicularly in the active region of the cell. The field electrode on the signal laser entry window was held at ground and the field electrode on the end of the multiplier was held at high negative voltage. This provided a field that would accelerate ions into the electron multiplier. Ions hitting the first dynode produced secondary electrons that were then multiplied by subsequent dynodes which allowed the anode of the electron multiplier to be at ground potential.

The light exciting the $5s_{1/2}$ - $5p_{3/2}$ transition was provided by a diode laser nominally operating at 780 nm. The diode laser wavelength was locked to the $5s_{1/2}$ - $5p_{3/2}$ rubidium transition by running a portion of the beam through a Rb reference cell held at 40° C and monitoring the absorption. This allowed the diode laser to be grossly temperature tuned to 780 nm and then finely current tuned to the $5s_{1/2}$ - $5p_{3/2}$ transition. There are four observable Rb absorption lines due to hyperfine splitting of two Rb isotopes, ^{85}Rb and ^{87}Rb, present in our metal. The diode laser was locked to the F=3, ^{85}Rb line which has the highest cross section of the four peaks (σ= 1.41x 10^{-11} cm^2, T= 33° C). The linewidth of the diode laser was about 30 MHz. The pump light exciting the transitions to the Stark split Rb Rydberg states was provided by a Littman[11] type grazing incidence dye laser using coumarin 480 (5 x 10^{-3} molar) dye, which in turn was pumped by a XeCl excimer laser running at a 10 Hz repetition rate. This provided light from the dye laser with a bandwidth of about 0.1 cm^{-1}, an energy of 10 μJ/pulse, and a pulsewidth of about 10 ns. The dye laser could be continuously tuned from 475 nm to 492 nm using a rotatable feedback mirror. The mirror was driven by an inchworm controller so that resolutions of < 0.001 nm in the dye laser wavelength were possible.

The signal laser had a 2 mm x 2 mm cross sectional area and a power of 8 mW for the entire beam. The pump laser was focussed into the active region with a 30-cm focal length lens. This provided a beam waist of 100 μm at the intersection point of the two laser beams. The signal laser entry port was covered with a Schott RG-715 filter to block any short wavelength light that might produce photoelectrons. The pump ports were covered with Schott BG-39 filters which blocked any UV from the XeCl laser from entering the cell. The cell was run at a temperature of 84° C which corresponds to a Rb vapor density of about 10^{11} atoms/cm^3 or 3 x 10^{-5} torr. The signal from the electron multiplier was fed into a gated boxcar averager as was the signal from the monitor photodiode of the pump laser. These were both fed into an analog signal processor so that the output signal of the multiplier was normalized with respect to the pump laser input power. The signal from the analog processor was recorded on a strip chart recorder, and the pump laser wavelength was continuously monitored with a high resolution spectrometer which allowed calibration of the electron multiplier output vs. pump laser wavelength.

Experimental Results

Figure 7 shows typical oscilloscope traces from the output of the electron multiplier. Two temporally separate signals were observed on the output of the electron multiplier. Picture 1 shows the output of the device with the signal laser off resonance. The small peak, which is coincident in time with the pump laser, was due to scattered pump light from the entry windows which was producing photoelectrons near the first dynode of the multiplier. When the signal laser was blocked, this peak remained, when the pump laser was blocked, it disappeared. Picture 2 shows the signal laser on resonance and the pump laser in between the large Stark split Rydberg peaks. Picture 3 shows the signal on resonance and the pump laser on one of the large peaks due to field ionization of the Stark split Rydberg states. The small peak, earlier in time than the ion signal is that from photoelectrons as discussed earlier.The ion signal could be separated in time from the photoelectric peak by anywhere from 20 to 200 ns, depending on the electric field and the distance of the interaction volume from the electron multiplier field electrode. When the signal laser was blocked or tuned off of the $5s_{1/2}$-$5p_{3/2}$ transition, this peak disappeared. Picture 4 shows the signal on resonance and the pump laser wavelength tuned such that it directly ionizes the $5p_{3/2}$ state. There is approximately a factor of 10 enhancement in the cross section of the Rydberg state as compared to direct ionization.

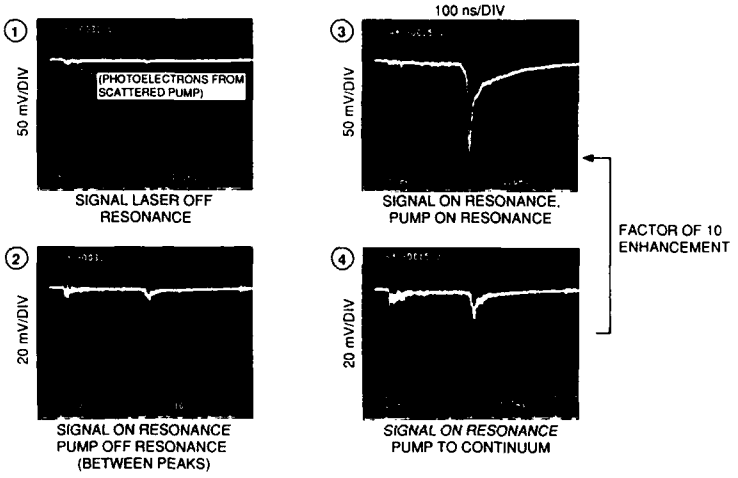


Figure 7. Oscilloscope traces showing the output from the FALF/FID for different signal/pump laser on/off conditions. See text.

Figure 8 shows photo-excitation and ionization spectra of Rb taken at various electric field strengths in an energy range around n = 15 - 16.[For comparison data from a Na atomic beam is shown on the right hand side of the figure[12]] The ion signal is plotted as a function of energy below the zero field ionization limit. The diagonal line represents the classical limit above which field ionization occurs. The spectra show sharp, semi-discrete levels

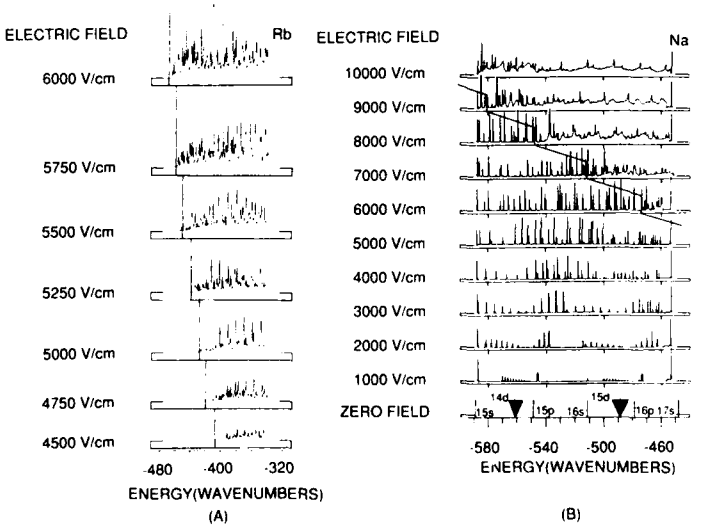


Figure 8. (a) Field ionization spectra for Rb taken with the FALF/FID showing the change in the number and size of the various peaks with electric field. (b) Photoexcitation and ionization spectra of a sodium atomic beam (n ≈ 15) in various electric fields.

embedded in a broader continuum. By tuning the pump laser to these peaks large enhancements in the photoionization cross sections were observed. The abscissa scale was obtained by subtracting the zero field ionization limit of ^{85}Rb (33691.02 cm^{-1}) from the sum of the energy of the $5p_{3/2}$ (12816.56 cm^{-1}) of ^{85}Rb and the energy of the blue laser. The ordinate scale is arbitrary although the heights of each spectrum are relative to each other. The change in height from high field to low field is an artifact of the measurement because the same power supply provides the electric field and the electron multiplier bias voltage and therefore at higher electric fields the multiplier has higher gain. It should be emphasized that these spectra are taken by tuning the pump laser. No ion signal is detected if the signal is tuned off of the $5s_{1/2}$-$5p_{3/2}$ hyperfine transitions, whose combined width sets the atomic line filter acceptance bandwidth at 0.002 nm.

The upper part of Figure 9 shows a spectrum taken at E= 6000 V/cm over a large tuning range of the blue laser. The wavelength of the pump laser is increasing from right to left of the figure. The spectrum can be seen to go from a relatively flat, featureless regime above the zero field ionization limit to a series of sharp peaks embedded in a broader background continuum. The lower section shows high resolution pieces of the same spectrum. The low, broad feature was measured at energies greater than the zero field ionization limit ($\lambda_{blue\ laser} < 479.05$ nm). The large sharp feature is from the peak near $\lambda_{blue\ laser}= 488.75$ nm. The ionization cross section of this Stark split Rydberg state is enhanced by about 8.5 over the direct ionization cross section. The time spread of the ion signals was < 30 ns, which is much faster than most conventional atomic line filters. If electrons are collected instead of ions, transit times < 1 ns could be expected.

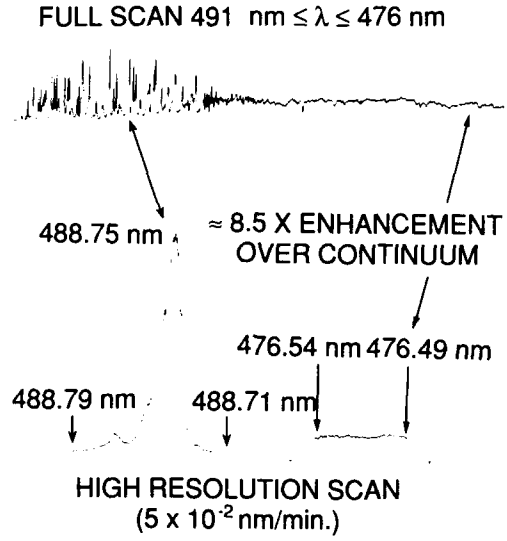


Figure 9. A field ionization spectrum taken at E = 6 kV/cm. The upper spectrum shows the evolution of field ionized states from semi discrete resonances to a smooth continuum as the pump laser is varied in wavelength. The lower spectra are high resolution sections of the upper spectrum demonstrating a factor of about 8.5 enhancement in ionization cross section for the field ionized states as opposed to direct ionization.

Figure 10 shows the detector output at 488 nm, pump polarization parallel to electric field, E= 6000 V/cm. The FWHM of this signal is 7-8 ns. This demonstrates that response times of <10 ns are achievable with the detector collecting ions. There are two advantages to running the FALF/FID in ion collection mode. The most important is the virtual elimination of noise due to the photoelectric effect from the pump beam. The second is that the window electrode and the multiplier anode can be run at ground potential. These advantages allow the FALF/FID to be constructed more simply than if it were necessary to collect electrons for fast response time.

A preliminary estimate of the device quantum efficiency was obtained by reducing the signal laser power to a point at which single photon events were observed. The point at which single photons were obtained was when the signal was seen to go from zero to a particular value randomly in time with the on condition remaining constant in magnitude. This should then be the level of single ion counting. This allows us to scale for the number of ions produced when not in single ion counting mode for a given signal size on the oscilloscope. An estimate of overlap volumes between the pump and signal lasers led to a rough conversion quantum efficiency of 28% for that volume. The device is presently being modified so that the screen on the signal laser entrance window will be replaced by a thin metallic film deposited on the inner surface of the window itself. This will allow the pump laser to be bounced directly off of the window making 100% overlap of pump laser and signal photons possible, so that the total device quantum efficiency can be measured.

In conclusion, the data in figures 8, 9, and 10 demonstrate that a FALF/FID with fast time response and high quantum efficiency can be built. The spectra show that the ionization cross section is significantly enhanced over direct ionization by pumping to Stark shifted, field ionized Rydberg states in a strong electric field. A device suitable for LIDAR applications with a time response of < 5 ns, a quantum efficiency > 50 %, and an acceptance bandwidth of 0.002 nm should be possible using a 1kW peak power, long pulse dye laser as a pump (1mJ/μs). Many different operational wavelengths are possible using different atomic or molecular vapors. In particular, Cs (852 nm), Rb (780 nm), and K (770 nm) match Ti:Al_2O_3, Alexandrite, and semiconductor lasers. Finally a Cs filter with 459 nm signal and 1.06 μ pump can operate in the blue with lower photoelectron and two-photon ionization noise than the IR FALF/FIDs.

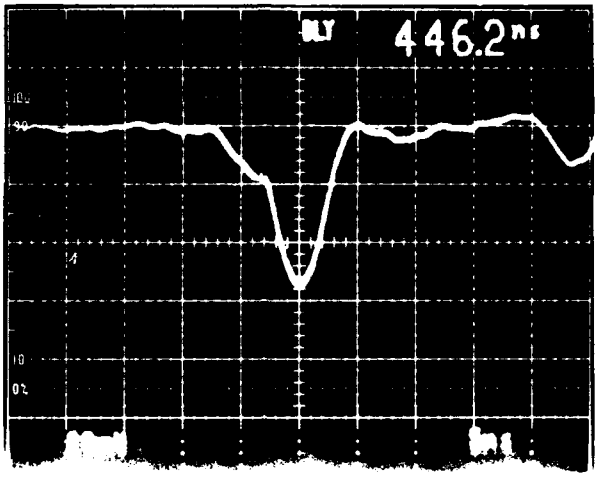


Figure 10. FALF/FID ion signal showing a time response of ~ 7 ns.

The work described herein was supported under SDIO/IST/ONR contract N00014-89-0068. We would like to thank Dr. Matt White of SDIO/ONR, Dr. Kepi Wu of SDIO, Dr. Vern Smiley of ONR, and Mr. Guy Beaghler of ONR for their encouragement and support.

REFERENCES

1. For a thorough review, see J. A. Gelbwachs, IEEE J.Q.E., **QE-24**, 1266 (1988)
2. E. Korevaar, M. Rivers, C.S. Liu, SPIE Proceedings, **Vol. 1059**, 111, (1989)
3. T. Okada, H. Andou, Y. Moriyama, and M. Maeda, Optics Lett. **14**, 987, (1989)
4. D. Kleppner, M.G. Littman, M. Zimmerman, *Rydberg States of Atoms and Molecules*, R.F. Stebbings and F.B.Dunning eds. (Cambridge Univ. Press, 1983)
5. J.Y. Liu et. al. *Atomic Excitation and Recombination in External Fields*, M.H. Nayfeh and C.W. Clark eds. (Gordon and Breach, NY, 1985)
6. see 2
7. M. Aymar et.al. J. Phys. B, **17**, 993 (1984)
8. C. Froese, Can. J. of Phys. **41**, 1895 (1963) and A. Lindgard et. al. J. Phys. B. **8**, 1183 (1975)
9. Particle properties Data Booklet, p. 107 from Rev. Mod. Phys. **56**, #2, Part 2, April 1984
10. H. Bebb, Phys. Rev. **149**, 25 (1966)
11. M.G. Littman and H. J. Metcalf, Appl. Opt., **17**, 2224-2227 (1978)
12. E. Korevaar, PhD Thesis, Princeton Univ., Dept. of Aero. and Mech. Eng. (1987) p. 98

Picosecond Laser-Induced Reorientation and Ultrasonics in the Liquid Crystal 5CB

H.J. Eichler
R. Macdonald

Optisches Institut
Technische Universität
D-1000 Berlin 12, FR Germany

Abstract

Dynamics of picosecond laser-induced molecular reorientation phenomena and ultrasound-generation in the liquid crystal 5CB are investigated in transient grating experiments. It is shown that the reorientation process is still increasing after the pump-pulse leaves the sample and relaxes exponentially later. Further a coupling between reorientation effects and the excitation of sound-waves has been observed.

Introduction

Liquid crystals are fluids with strong correlations between the constituting molecules showing anisotropic physical properties in general. This behaviour results not only in strong electro-optical and magneto-optical[1] but also in remarkable opto-optical effects. Optical field-induced reorientation of nematic liquid crystals has been investigated with low power cw-lasers[3, 4] and with short laser pulses[5, 6] and the related optical nonlinearity is of some interest to applications like phaseconjugation, photonic switching and processing of light or optical bistability.

All recent studies of field-induced molecular reorientation in nematics show that the static and dynamic properties of molecular motion obey the Erickson-Leslie theory[5] which describes the collective reorientation phenomena by the deformation of a so called director, the average molecular orientation. In the present paper it is shown that the Erickson-Leslie theory is also applicable if ultrashort laser pulses of less than 100ps duration and strong optical fields as high as 10^7 V/m are used for excitation. For the first time we have observed effects which give evidence that an inertial moment has to be considered in this case. Further we have observed a nonthermal ultrasound-generation mechanism in these experiments, where the acoustic waves are excited by the molecular reorientation process due to inverse flow-orientation coupling.

Experiments and Results

In our experiments we used a wave-mixing arrangement, which is schematically shown in Fig. 1a. Two pump-pulses of 80 ps duration (FWHM) obtained from a frequency-doubled mode-locked Nd:YAG laser with a single-pulse extraction are focussed to an e^{-2}-diameter of 800 µm on a thin film (d= 25 µm) of a homeotropically aligned nematic liquid crystal 5CB (4'-n-pentyl-4-cyanobiphenyl). The two pump beams are linearly polarized, their polarizations either parallel or perpendicular to each other, producing an intensity- or polarization-grating in the sample. The resulting optical field-fringes modulate the alignment of the molecules and change the optical properties of the birefringent liquid crystal by rotating the director and the optical axis. The center of the induced phase-grating (grating

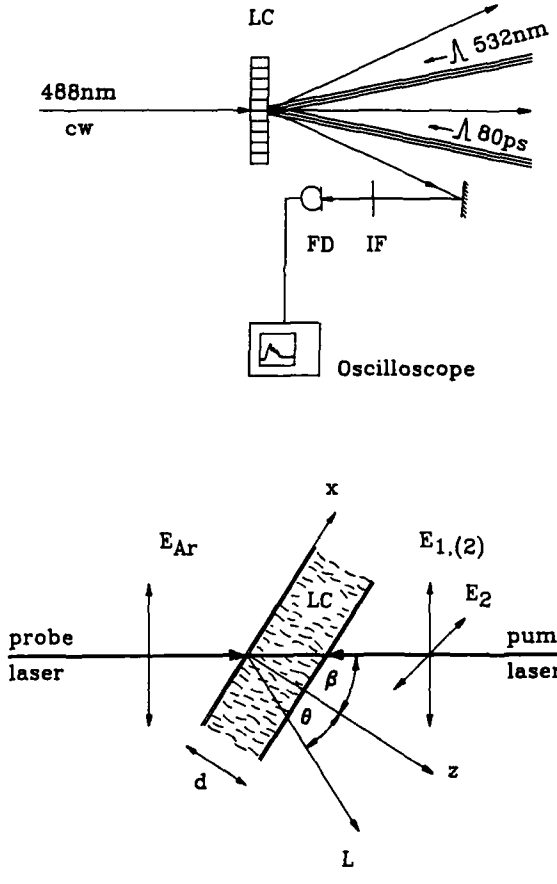


Fig. 1: Experimental setup (a): LC–Liquid crystal; FD-fast fotodiode; IF-interference-filter. Experimental geometry (b): E_1, E_2 - optical pump fields; E_{Ar} - optical probe field; β-initial alignment angle (22.5 deg); Θ- reorientation angle.

period Λ = 30 μm) is probed by a weak argon cw-laser (488 nm) with a spot size of 100 μm diameter. The first order diffracted intensity of the probe-beam is measured with a fast fotodiode and a fast real-time oscilloscope. The oscilloscope-traces are recorded and processed with a digitizing video-camera system. The time resolution is limited by a rise-time of about 400 ps and a decay-time of less than 4 ns with the PIN-diode used so far.

The experimental geometry is shown in Fig. 1b. The unpertubed director and the optical fields E_{Ar} and E_1 are in the x-z plane while the second pump field E_2 is chosen parallel or perpendicular to E_1. If $E_1 \| E_2$ the two beams interfere to give an intensity-grating and field-dependent as well as intensity-dependent effects will be excited in a periodic structure leading to diffraction of the probe-beam. If however $E_1 \perp E_2$, the two beams will not interfere and intensity-dependent effects (e.g. thermal heating) will not occur in a grating and are not detected. But the optical fields still add together vectorially to form a polarization-grating. The liquid crystal will respond to a polarization-grating with a periodic reorientation structure which is detected by the probe beam diffraction without any additional intensity-dependent effects[7]. Fig. 2 displays typical oscilloscope-traces of the diffracted probe-beam intensity during the first 500 nanoseconds after the ps-excitation pulse for the two types of excitation gratings.

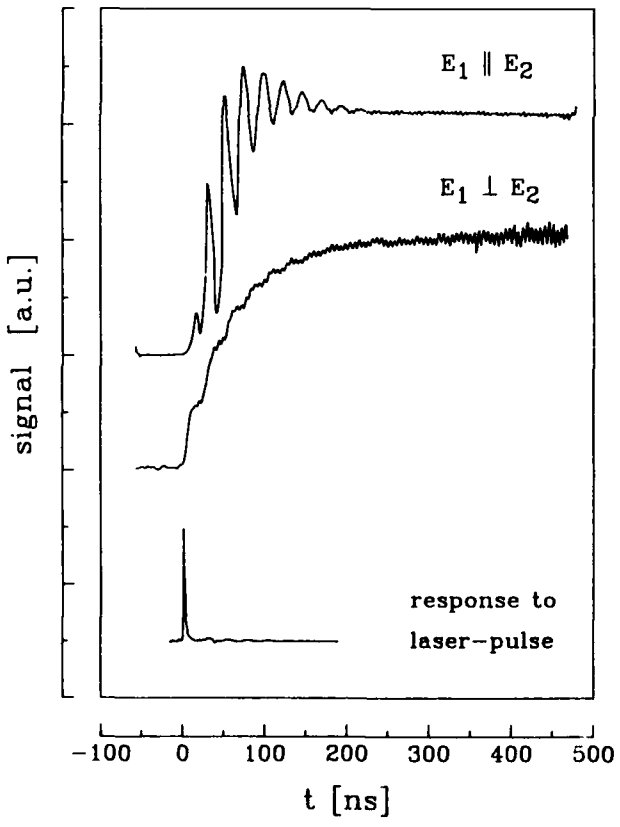


Fig. 2: Diffracted probe-beam intensity vs. time after ps grating-excitation. Pump energy Wp = 0.25 mJ. The response of the detector system to a single pump-pulse is shown for comparison.

In both cases the signal is still increasing long after the pump-pulse (which can be approximated as a δ-peak at t=0 on the graph) leaves the sample, showing strong additional oscillations in the case $E_1 \| E_2$. These oscillations occur due to laser-induced ultrasonic standing-waves and diffraction at the resulting density modulations (forced Brillouin-scattering), which will be enhanced mainly by thermal heating, if an intensity-grating is used. The trace $E_1 \perp E_2$ shows almost the pure reorientation-grating without or just weak oscillations at lower pump energies. If however the pump energy is increased the oscillations will also occur strongly even in the case of a polarization-grating as is displayed in Fig. 3. This can be explained by generation of ultrasound due to the reorientation process itself and the related molecular motions.

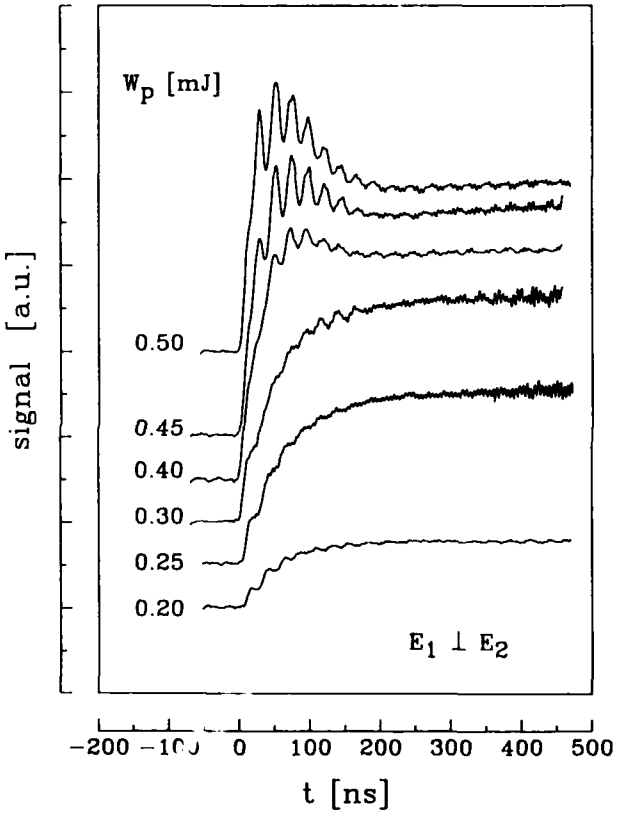


Fig. 3: Diffracted probe-beam intensity after ps polarization-grating excitation at different pump energies Wp. The sample is nematic 5CB at T = 25°C, d = 25 μm.

The slower increase of the signal at low pump-energies is of the type $(1-\exp[-t/\tau_R])$ showing rise- times τ_R between 20 and 50 ns depending on excitation -energy (see Fig. 4). Much later the signal will decrease and the grating decay can be fitted well by a single exponential law as is shown in Fig. 5. The evaluated decay times are in the millisecond-range, depending on sample temperature as is depicted in Fig. 6.

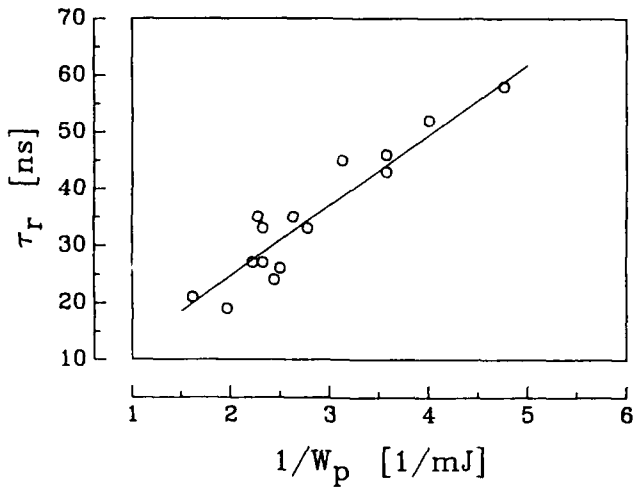


Fig. 4: Observed rise-times vs. reciprocal pump-energy.

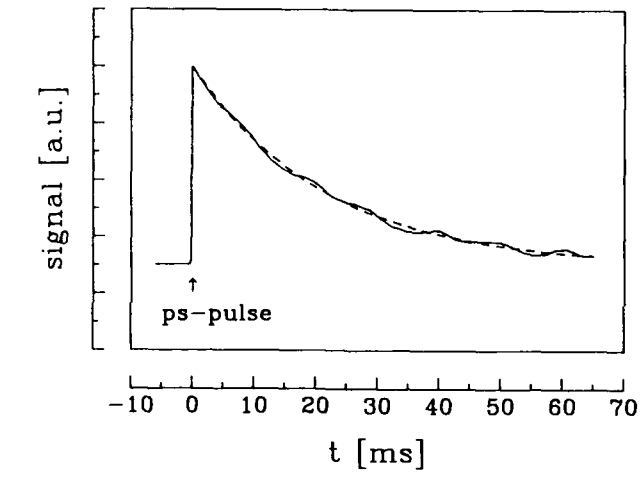


Fig. 5: Reorientation relaxation after ps excitation.

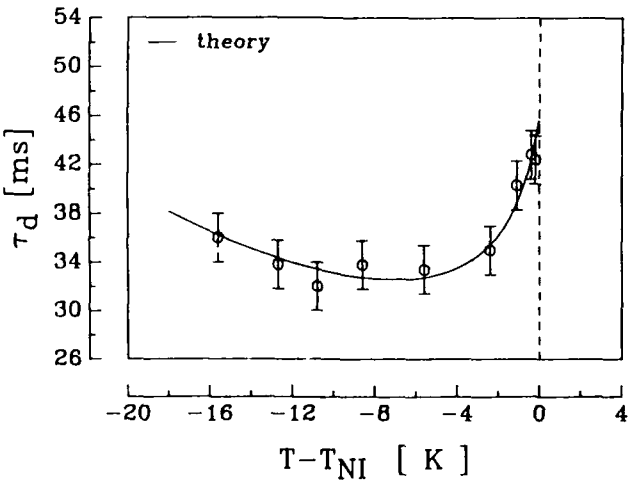


Fig. 6: Reorientation relaxation-times as function of the reduced sample temperature. T_{NI} is the nematic-isotropic phase transition temperature.

Theory and Discussion

The observed dynamics at low pump-energies can be described by the Erickson-Leslie continuum theory for calculation of the optical nonlinearity in combination with a dynamic grating diffraction model[8]. Considering a polarisation grating on a homoetropic aligned nematic film the optical field-fringes will modulate the reorientation of the director and the refractive-index to form a phase-grating. Refractive-index changes established by molecular reorientation are given by

$$\delta n = n_e (\Theta + \beta) - n_e (\beta) \qquad (1)$$

where

$$n_e (\vartheta) = n_\perp n_\parallel (n_\parallel^2 \cos^2 \vartheta + n_\perp^2 \sin^2 \vartheta)^{-1/2} \qquad (2)$$

with $\vartheta = \Theta+\beta$ and $\vartheta = \beta$ respectively. $n_\perp$ and $n_\parallel$ are the refractive-indizees perpendicular and parallel to the director. In an plane wave approximation the director motion can be described by a single reorientation angle Θ which is obtained by a torque balance

$$\mu \frac{\partial^2 \Theta}{\partial t^2} + \gamma \frac{\partial \Theta}{\partial t} - K \Delta \Theta - \frac{1}{2} \varepsilon_o \varepsilon_a E^2 \sin 2(\Theta+\beta) = 0 \qquad (3)$$

where K is the elastic constant (in a one constant approximation), γ the rotational viscosity, μ the inertial moment, $\varepsilon_a = \varepsilon_\parallel - \varepsilon_\perp$ and E the optical field. Flow-orientation coupling has been neglected so far. An approximate solution of the linearized eq. 3 under hard boundary conditions $\Theta(z = 0) = \Theta(z = d) = 0$ in a grating experiment is

$$\Theta = \Theta_m (t) \cos(qy) \sin (\pi z/d) \qquad (4)$$

where q is the wave-number of the grating and Θ_m obeys the equation

$$\mu \frac{\partial^2 \Theta_m}{\partial t^2} + \gamma \frac{\partial \Theta_m}{\partial t} + D \Theta_m = F \qquad (5)$$

with $D = K (q^2+\pi^2/d^2) - \varepsilon_o \varepsilon_a E^2 \cos 2 \beta$ and $F = \frac{1}{2} \varepsilon_o \varepsilon_a E^2 \sin 2 \beta$. Eq. 5 describes the dynamics of an overdamped oscillator typical material parameters and experimental data like $\gamma = 0.01$ kg/ms, $K = 10^{-12}$ N, d = 25 µm, $q = 0.2$ µm^{-1} and $\mu \leq 10^{-4}$ kg/m are used. This upper limit of the inertial moment corresponds to the motion of correlated molecules within a volume of $l \leq$ 300 µm radius which is much more than the correlation length.

In the time scale of our experiments the pump-pulse can be approximated by a Delta-peak $E^2(t) = E_o^2 \delta(t)$ and the solution of eq. 5 is given by

$$\Theta_m = \frac{F_o}{2\partial\partial'\mu} (\exp[-t/\tau_D] - \exp[-t/\tau_R]) \qquad (6)$$

where $\delta = \gamma/2\mu$ and $\delta' = (\delta^2 - \omega_o^2)^{1/2}$ with $\omega_o = (K(q^2 + \pi^2/d^2)\mu)^{1/2}$ for $t > 0$. The quantities $\tau_R = (\delta + \delta')^{-1}$ and $\tau_D = (\delta - \delta')^{-1}$ give the rise- and decay-time of the director reorientation. Developping the root of δ' results in

$$\tau_R = \frac{\mu}{\gamma} \qquad (7a)$$

$$\tau_D = \frac{\gamma}{K(q^2+\pi^2/d^2)} \qquad (7b)$$

The rise-time is given by the inertial moment and viscosity while the decay-time depends mainly on viscosity and the elastic forces as in simple relaxation models. If we take $\gamma = 0.015$ kg/ms, $K = 7{\cdot}10^{-12}$ N we get $\tau_D = 36$ ms (at $T = 25^0$C) in good agreement with experimental data. The observed temperature dependence of the relaxation time can be explained[1] by the well-known temperature dependence of the viscosity γ and the elastic constant K.

A response-time of e.g. $\tau_R = 40$ ns can be explained with $\mu = 6{\cdot}10^{-10}$ kg/m. This corresponds to a volume of $l = 800$ nm radius. Compared to the usual definition of a correlation length $l_k = (K/\varepsilon_o\ \varepsilon_a\ E_o^2)^{1/2}$ which is $l_k = 40$ nm during the laser-pulse and $l_k = 8$ µm without optical field (at $t \to \infty$ after excitation) the assumed value l lies well between these two extreme cases. The observed dependence of the rise-time τ_R on the pump-energy W_p also suggests that $\mu \sim l_k^2$ or $l \sim l_k$ respectively.

During the laser-pulse however the correlation length is in the order of some ten nanometers resulting in much faster rise-times of some picoseconds which is comparable to the pulse-length. This can explain the occurence of fast reorientation-effects and related refractive-index changes even when the picosecond pump-pulses are still in the sample as has been demonstrated in self diffraction experiments recently[6].

The observed oscillations in the MHz frequency range cannot be explained with the simple reorientation model and show the limits of the approximations which have been introduced. At higher pulse-energies the flow-orientation coupling and the inverse process can obviously not be neglected any longer. We explain the observed nonthermal excitation of ultrasonics with the fast and impulsive reorientation and rotation of molecules, which should produce a periodically modulated flow in our grating experiment. A spatial and temporal periodically modulated flow of molecules is accompanied by a modulation of material displacement and density-changes, which lead to the observed additional refractive-index changes and the related acoustic-grating. If the sound, waves are excited by a grating one gets two counterpropagating wave-packets which results in a standing wave at the excitation region, leading to the observed oscillations[8]. The period of the acoustic oscillations is given by

$$T_{ac} = \Lambda / v_s \qquad (8)$$

where Λ is the grating period and v_s the speed of sound in the liquid. The damping of the oscillations is approximately given by

$$\tau_{ac} = \frac{w_o}{v_s} \qquad (9)$$

were w_o is the laser beam radius.

Similar results have been obtained in the isotropic phase of 5CB where the optical Kerr-effect can be expected to be a very effective mechanism for the generation of ultrasonic waves.

Conclusion

In the present paper we report on investigations of the dynamics of molecular reorientation phenomena and ultrasound generation in a nematic liquid crystal using picosecond excitation pulses and dynamic grating diffraction. We have observed an increase of the director deformation for times much longer than pump-pulse duration. The observed rise-times are in the order of 20 to 50 ns depending on pump-energy. The reorientation is later decaying exponentially with time-constants of 30 to 40 ms depending on sample temperature. The observed dynamics can be described by the Ericksen-Leslie theory considering an inertial moment term. The inertial moment of the director motions has been assumed to be in the order of $\mu = 10^{-10}$ kg/m to explain the observed rise-times. This corresponds to an averaged correlation lenght of some hundred nanometers.

The observed oscillations of the diffraction signal are explained by a nonthermal generation of ultrasound and additional acoustic gratings driven by the reorientation-process.

Financial support from the Deutsche Forschungsgemeinschaft is gratefully acknowledged.

References

1. P.G. de Gennes "The Physics of Liquid Crystals", Clarendon Oxford (1974)
2. I.C. Khoo, Y. R. Shen, Opt. Eng., Vol. 24, p. 579 (1985)
3. A.S. Zolot'ko et al., JETP Lett., Vol. 32, p. 155 (1980)
4. H.J. Eichler, R. Macdonald, C. Dettmann, Mol. Cryst. Liq. Cryst. Vol. 174, p. 153 (1989)
5. H. Hsiung, L P. Shi, Y.R. Shen, Phys. Rev. A, Vol. 30, p. 1453 (1984)
6. H.J. Eichler, R. Macdonald, Proc. Int. Conf. Lasers 88, p. 511 (1989)
7. G. Eyring, M.D. Fayer, J. Chem. Phys., Vol. 81, p. 4314 (1984)
8. H.J. Eichler, D. Günter, D.W. Pohl, "Laserinduced Dynamic Gratings", Springer Berlin (1986)

EFFECT OF AN INTENSITY DEPENDENT RESPONSE TIME ON THE PHASE-CONJUGATE EFFICIENCY IN SEMICONDUCTOR DOPED GLASSES

B. Van Wonterghem, S.M. Saltiel and P.M. Rentzepis
Department of Chemistry
University of California, Irvine, CA 92717

Abstract

We describe the means employed for the measurement of phase conjugate reflectivity, its phase shift and sign in semiconductor doped glasses.The decay times of low intensity laser induced gratings are measured in these glasses and shown to depend strongly on the pump intensity and previous light exposure history of the glasses.In addition, the deviation from the expected square dependence of the phase conjugate reflectivity in CdS_xSe_{1-x} doped glasses at low pump power levels is explained by the dependence of the induced optical non-linearity relaxation time on intensity. We also describe a new non-linear interferometer which allows for the accurate measurement of phase conjugate reflectivity, phase sift and sign of materials with very low third order non-linear susceptibilities.

Introduction

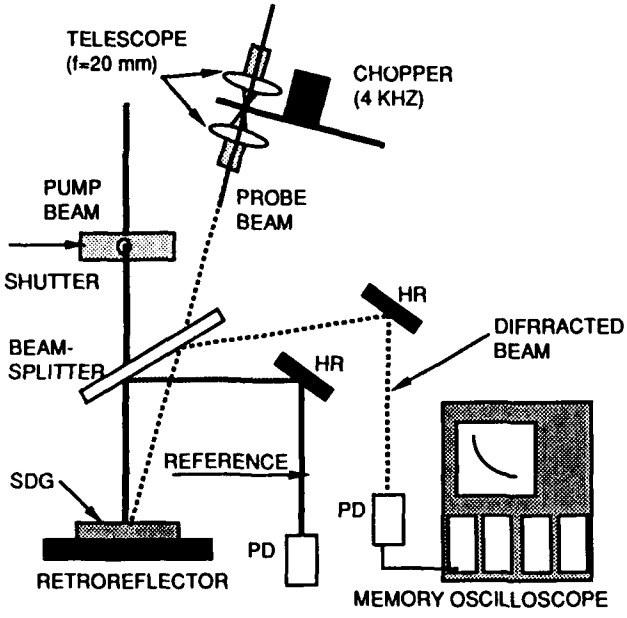
Semiconductor doped glasses have been important devices in optical spectroscopy for many years owing to their sharp absorption edge in the visible and near ultraviolet region. Lately non-linear optical investigations suggested that these materials may be appropriate for optical switching because of their short decay time and relatively high $\chi^{(3)}$.

Because of the method for manufacturing of these glasses, including high temperature melting of the glass substrates, the non-linear properties of semiconductor glasses vary appreciably, even in glasses from the same melt. In addition we have shown that the pulse duration and intensity of the laser pulse influences the values of $\chi^{(3)}$ and grating decay times. For example the reported $\chi^{(3)}$ values of CdS_xSe_{1-x} doped glasses studied by four wave mixing [1-4] vary from 10^{-11} esu[5-7] to 10^{-7} esu[8]. Also values varying from 10^{-10} and 10^{-9} have been reported[2,3] for semiconductor doped glasses OG 530 (Schott) and CS 3-68 (Corning). A complication which arises in the study and utilization of these glasses as optical devices is related to the change in the optical properties after exposure to high power laser radiation. This is manifested in the observed absorption change[8-10] at the irradiated area. It was also found[10] that the efficiency of phase conjugation decreased when the sample was illuminated with single pulses having a fluence of 5 mJ/cm^2. However no change in the absorption of these glasses was observed for fluences less than 0.5 mJ/cm^2. In addition ,the dependence of the third order non-linear susceptibility and grating decay time on the pump intensity was studied by a retroreflecting scheme for degenerate four wave mixing and by phase conjugate interferometry. In addition the dependence of the third order susceptibility and grating decay time on pump intensity were investigated.

Results and Discussion

The data presented here, on the photodarkening effects and induced grating decay times, were obtained with the use of a frequency doubled Nd:YAG CW mode locked laser (532 nm) using a set up as shown in figure 1.The characteristics of this laser are: 1 W average green power, 70 ps pulse width operating at a repetition rate of 82 MHz. For the experiments on the study of the grating decay times, the magnitude, and the sign of the third order non-linear coefficient of $CdS_{0.9}Se_{0.1}$ semiconductor doped glasses, the laser power levels were in the 1kW/cm^2 to 0.1 kW/cm^2 range. The optical experimental system used for the measurement of the magnitude of $\chi^{(3)}$ is shown schematically in figure 1. The phase and sign of the conjugate signal was measured with the aid of a non-linear, two output interferometer[3] which is depicted in figure 2. The magnitude of the reflectivity was determined by a power meter. The decay time of the interference gratings was measured by using a train of pulses. The probe beam, consisting of square shape pulses was formed by means of a mechanical chopper ,while the pump beam consisted of the continuous output of the laser.are shown in figure 1.This technique, allowed for the measurement of rise and fall time of the grating from 0.250 ms to 500 ns. Since the gratings are formed only during the time interval when the probe and pump beams overlap,it is possible to measure their decay during the interval elapsed between pulses. The decay signals were displayed on a storage oscilloscope, digitized then the decay times calculated. The length of the probe pulses was such that the carrier population - grating was allowed

to reach a steady state. Using these square-tooth wave probe beam pulses and continuous pump beam we measured the decay times and estimated that they vary between 4 μs and 30 μs for power levels 0.25 kW and 1kW. These data are summarized in Table I where it may be seen that the decay lifetimes decrease with increased laser intensity for all glass samples investigated except for the OG530 sample. In fact only the OG530 sample



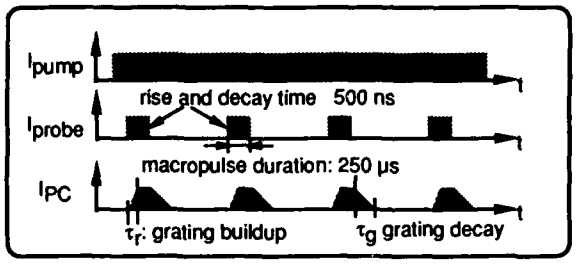


Figure 1. Experimental set up for the determination of the decay of low intensity laser induced gratings in semiconductor doped glasses. An electrooptic shutter is used to limit the exposure of the sample. The principle of the method is illustrated in the inset.

spot which was previously not exposed to laser light, was found to have the same decay lifetime for both low and high intensity beams, 0.25 kW and 1kW.

The grating decay time for fresh and exposed samples, induced by 532 nm laser light do not exhibit a consistent intensity dependence. As it can be seen in Table I the decay time decreases with intensity in OG 530 glass from fresh to exposed samples while increases for CS 3-68 glasses. The decrease in lifetime with intensity was also observed by Remillard et al.[11]. The magnitude of the phase conjugate efficiency of semiconductor glasses was measured for several CS 3-68 and OG 530 glasses. Even though pump and probe intensities were identical in all experiments, 290 mW pump and 150 mW probe, the phase conjugate reflectivity varied by about two orders of magnitude among samples of OG 530 glass.This data is shown in figure 3 The reflectivity among CS 3-68 samples however varied by only a factor of two. We find that the highest phase conjugate power observed for CS3-68 semiconductor glass was 1-3 mW. Using this value, the absorption coefficient α of the glass and its internal transmission T, the magnitude of $\chi^{(3)}$ was calculated to be 6 x 10^{-8} esu by means of the relationship (1) :

$$\chi^{(3)} = \frac{\alpha R_{PC}^{1/2}[T(1-T)]^{1/2}}{\left(\frac{4\pi\omega}{cn}\right)\left(\frac{8\pi}{cn}\right)10^{7}I_p} \qquad (1)$$

This corresponds to a phase conjugation reflectivity, R_{pc}, of 6 x 10^{-3}. Reflectivity, Rpc, is defined as the ratio of the conjugate power density/probe beam power density. The average value of $\chi^{(3)}$ for all the samples studied was calculated to be 5.1x10^{-8} esu and 3x10^{-9} for CS 3-68 and OG 530 respectively. The OG 530 $\chi^{(3)}$ values were found to vary from 3x10^{-10} to 3x10^{-8}.esu.

The reason for the higher $\chi^{(3)}$ values for OG570 samples observed by Remillard et al. is probably due to differences in the grating decay times between the experiments reported here and the experiments reported in reference 8, as measured by the reflectivity spectrum in a nearly degenerate four wave mixing set up. These

decay times differ by a factor of 14, which is caused by the difference in the pump laser power used in the two experiments.

When a semiconductor doped glass is illuminated, not only the phase conjugation efficiency changes, as pointed out previously, but also the red-shifted trap luminescence intensity decreases considerably. In order to measure the relative rate of change in the phase conjugation efficiency and relative luminescence efficiency as a function of laser exposure, the samples were irradiated with 532 nm laser light for a preselected period of time. After each light exposure the phase conjugation efficiency and the luminescence, due to trap radiation, were measured. We find that after irradiation with more than $2kJ/cm^2$ (532 nm).light, the phase conjugate efficiency decreased by a factor of two in the CS 3-68 glass samples and by more than two orders of magnitude in the OG 530 semiconductor doped glasses.This corresponds to a $\chi^{(3)}$ value which is smaller in the exposed sample spot by a factor of 10 as compared to a fresh spot of the same glass. This photodarkening effect was found to be a function of laser fluence and the history of the sample[3]. The change in the luminescence intensity across the irradiated spot is shown in figure 4 where also the transmittance and phase conjugate signal intensity are plotted as a function of position through the dark spot of a CS 3-68 glass sample. The photodarkening of the sample was achieved exposing the samples to 130 mW average power laser light for 10 hours.The luminescence efficiency was measured with the same beam after 100 fold attenuation. The change in relative phase conjugate efficiency and luminescence efficiency was measured simultaneously in these glasses as function of exposure to 532 nm laser light.by exposing the samples to light for preselected periods of time then monitor the phase conjugation intensity and luminescence efficiency between exposures with a highly attenuated laser beam. The data obtained using CS 3-68 glass is shown in figure 5. It is evident, in this figure, that the phase conjugate efficiency decreases more drastically than the luminescence efficiency.

The dependence of the phase conjugate reflectivity on intensity,for these semiconductor doped glasses was studied in deapth using essentially the experimental system shown in figure 1.All beams had parallel polarization and a radius of 1 mm. The probe beam was transformed to rectangular pulses,by means of the chopper,shown in figure 1.,with a rise time of less than 500 ns. OG 530 and CS 3-68 glass filters ,with transmission at 532nm of 25% and 50% respectively, were used as samples.The experimental data shows that there is a relationship between the induced grating decay time and the slope of a log-log plot of the phase conjugate reflectivity at low pump intensity..The phase conjugate efficiency dependance on intensity was found to be less than quadratic when the laser pulse duration is longer or nearly equal to the induced grating decay time.The observed phase conjugate reflectivity, R, versus reduced pump intensity $I_R=(I_{p1}I_{p2})^2$, for OG 530 glass is shown in figure 6a.

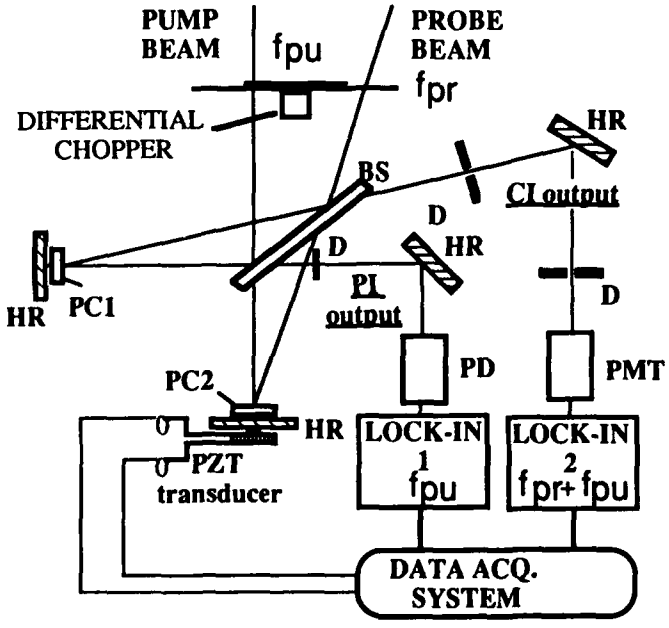


Figure 2. Scheme of the nonlinear phase conjugate interferometer. It is a modified Twyman-Green interferometer with 2 phase conjugate retroreflectors. PI is the pump interference output and CI the conjugate interference. The data acquisition system reads the output of the lock-in amplifiers and controls the position of the piezoelectric transducer.

The data for the upper curve were taken in a fresh, unexposed spot,while the lower plot of fig.6 corresponds to a spot irradiated for a long time,modified spot.[4,14]. The phase conjugation efficiency was found to be less in a modified spot than in a fresh spot of the same glass,and the slope of the log-log plot of R versus I_R decreased from 1.6 to 0.6 with increasing intensity. Unmodified spots in OG 530 were found to have almost a square dependence on pump intensity (slope 1.9). In CS 3-68 glasses the slopes were less than two (fig 6b) for both fresh and modified spots, 1.1 and 1.2 respectively. Special care was taken to minimize the light exposure time of the unmodified spot. To that effect we used a shutter which restricted the total light exposure time of an experiment to less than 4 s. Which is negligible compared to 2 min. exposure, at maximum power for the modified spots. The measured decay times of the induced grating are reproduced in figure 6. The decay times of the modified spots decrease with increasing intensity. The same trend was observed in unmodified spots of CS 3-68 glass.In unmodified spots of OG 530 glasses however,the phase conjugation decay time was measured to be 5 μs and was intensity independent. For these intensity independent spots, a slope of two was observed for the intensity dependence of the phase conjugate reflectivity.

At low power pump intensities ,with a CW mode locked laser.the grating decay times are longer than the interpulse time (12 ns). We consider therefore, that the chopped pulse peak power is equal to the power of the mode locked pulses with an effective coherence time equal to that determined by the chopper aperture and rotation speed.

The nonlinearity, at low excitation intensities,is due predominantly, to hole-sensitized long lived traps[14,8]. In such cases the non linear process can be considered as a three level system,with the trap being the third and long lived level. Because the length of the chopped pulses is much longer than the decay times, the reflectivity R, reaches a quasi steady -state which may be described by an effective steady-state third order nonlinear susceptibility:

$$\chi^{(3)} = c\,\alpha\,\tau_{trap}\chi_{trap}/16h\omega \qquad (2)$$

where α is the low intensity absorption coefficient, τ_{trap} is the lifetime of the sensitized traps and χ_{trap} their linear optical susceptibility. Since the phase conjugate reflectivity R is proportional to $|\chi^{(3)}|^2 I_{p1} I_{p2}$, any

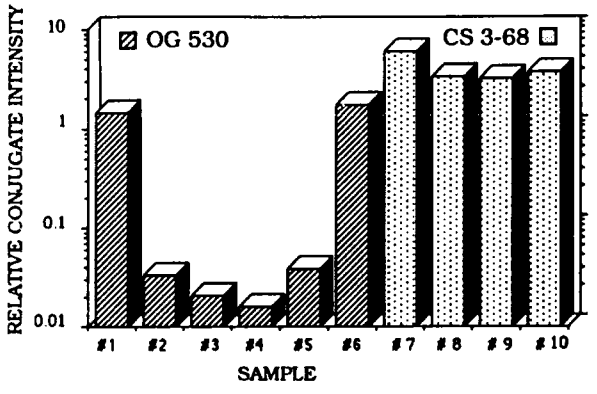


Figure 3. Bar graph of the phase conjugate efficiency of several samplesof Corning CS 3-68 and Schott OG 530 semiconductor doped glasses, determined under identical experimental conditions. Legend: sample #1: exposed OG 530, #2-#5: unexposed OG530, #6: ex-posed OG530, #7: ex-psed CS 3-68, #8-#9: unexposed CS 3-68, #10: wedged CS 3-68 glass.

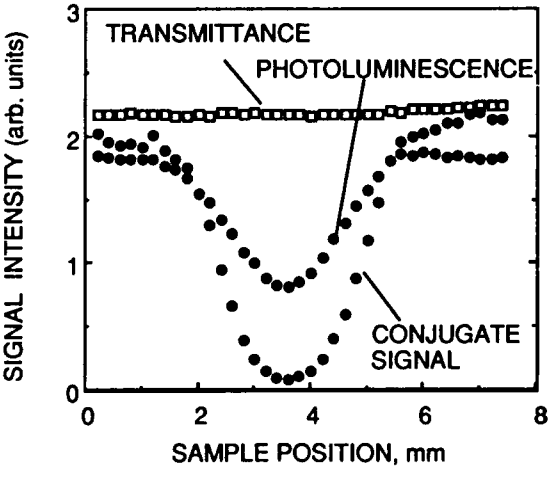


Figure 4. Transverse profile of the phase conjugation efficiency, luminescence and transmittance of a photodarkened spot in a CS 3-68 semiconductor doped glass.

dependence of τ_{trap} on the intensity will cause a deviation of the square dependence of R on the reduced power I_R. From the log-log plot of R versus I_R we derived the intensity dependence of τ_{trap} using the expression.

$$\log [\tau_{trap}(I_R)] = \log(R)/2 - \log(I_R) + \text{const.} \qquad (3)$$

we calculated curves which are proportional to $\text{Log}(\tau_{trap})$ using the the experimental dependence of R on I. These calculated curves and the measured values for τ_{trap} are shown in figure 6.,.where the calculated and experimental curves are seen to be in very good agreement..Intensity independent valuee of τ_{trap} imply a slope of 2 for R, as found to be the case for an unmodified spot of OG 530. This was shown to be the case in previously published data using a very low power CW dye laser in OG 570[8] ·We may now point out that the aparently contradictory data on the slopes reported prevously , which used high power laser pulses , may be explained by considering an effective value for $\chi^{(3)}$, which depends upon the coherence time of the laser pulses and the intensity dependence of the induced susceptibility decay time.

The relative phase shift between two non-linear media was accurately measured by means of the new interferometer which we designed and built for this purpose[3]. The components of this interferometer and the optical arrangement is shown in figure 2 The pump and probe beams are separated into two parts by a beam splitter, BS, and propagate along the optical paths shown. The phase conjugate mirrors, PC1 and PC2, are of he same type as those used for a retroreflection type of degenerate four wave mixing experiments. After interaction the beams are reflected back and recombine at the beam splitter.The two phase conjugation signals which are generated at PC1 and PC2 and interfering with each other at BS, constitute the phase conjugate interferometer CI. The recombination of the pump beams generates a signal which is the equivalent to that which will be produced in a conventional Twyman-Green interferometer (PI, pump interferometer). These two interferometers are so intimately dependent on each other that alignment of one interferometer, either PI or CI, results in the simultaneous, automatic, alignment of the other interferometer.

A phase shift, α, can be induced by the translation of the retroreflecting mirror in one of the arms using a piezoelectric transducer. The interference signal of the pump interferometer I_{PI} equals :

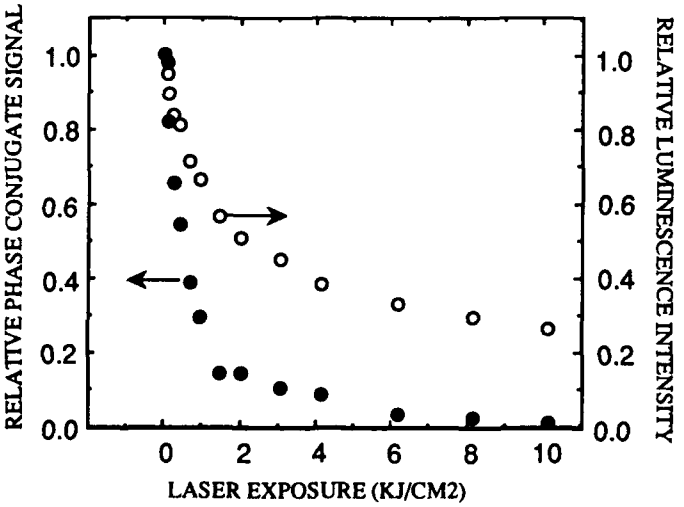


Figure 5. Decrease of the phase conjugate efficiency and trap luminescence efficiency in a Corning CS 3-68 semiconductor doped glass as a function of laser exposure (532 nm). Both curves are normalized to the initial values of the fresh (nonexposed) glass.

$$I_{PI} = I_{P,1} + I_{P,2} - 2(I_{P,1}I_{P,2})^{1/2} \cos [4\pi(l_1-l_2)/\lambda + \alpha] \qquad (4)$$

The conjugate interferometer output intensity I_{CI} will be:

$$I_{CI} = I_{C1} + I_{C,2} - 2(I_{C,1}I_{C,2})^{1/2} \cos [4\pi(l_1-l_2)/\lambda + \alpha + \varphi_{0,2} - \varphi_{0,1}] \qquad (5)$$

where l_1 and l_2 are the optical pathlengths in both arms of the interferometer and $\varphi_{0,1}$ and $\varphi_{0,2}$ the absolute phase shifts of the phase conjugators in each arm. A simple comparison of the equations which relate the PI and

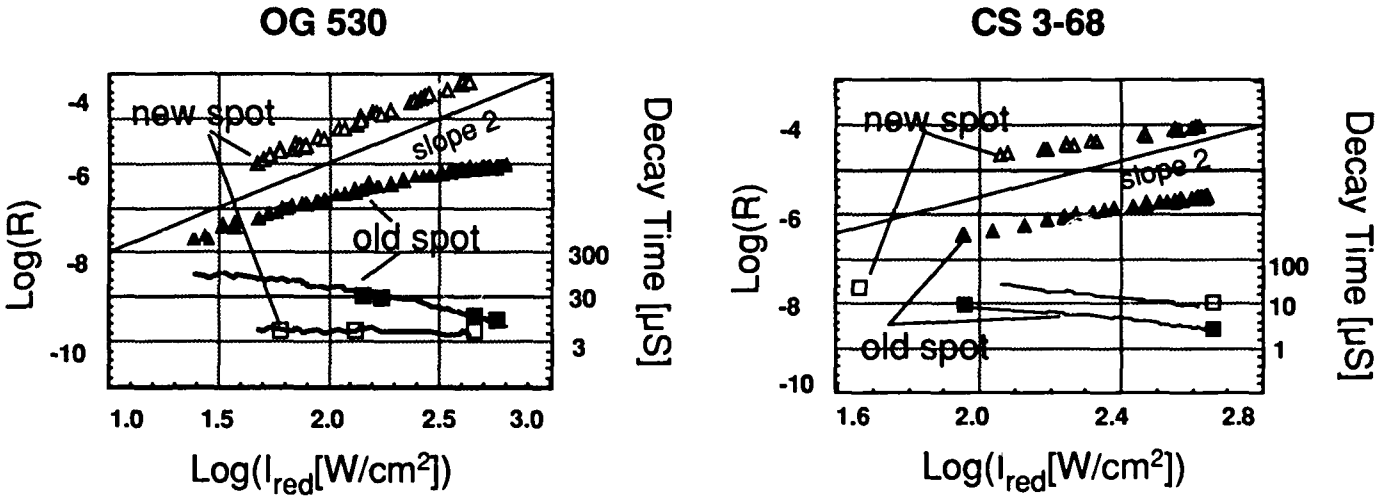


Figure 6. Phase conjugate reflectivity (triangles) and induced grating decay times (squares) versus the reduced pump intensity for OG 530 and CS 3-68. The open symbols are for unmodified spots, and the filled symbols are for modified (exposed) spots. The solid curves represent the decay-time dependence on intensity calculated using our experimental reflectivity data and expression (3). The dashed curves represent the slope of 2.

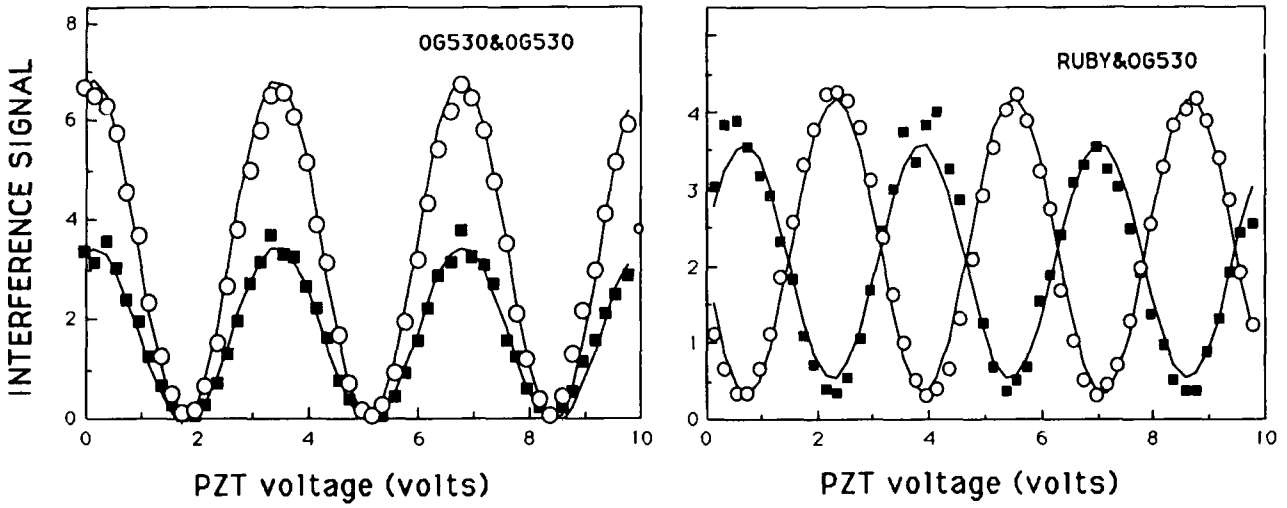


Figure 7. Interference signal at pump interferometer output (o) and conjugate interferometer output (■). Left graph: when OG530 is used as phas conjugating medium in both arms. Right graph: when OG530 is used in one arm, and a ruby crystal in the second arm.

CI interference signals see eq. 3, and 4 shows that both depend on the same function of the induced phase shift α, which is the difference between the absolute phase shifts of the conjugate signals in the two non-linear media. Therefore, if the absolute phase shift of one phase conjugate material is accurately known our interferometer makes possible the accurate measurement of the absolute shift of any other non-linear material. The results of phase shift measurements in semiconductor glasses is shown in figure 7. In this figure the interference signals at the PI and CI outputs are plotted as a function of the piezolectric crystal voltage. In the left hand graph of figure 7 a sample of OG 530 glass is used as the nonlinear medium in both arms of the interferometer. The right hand graph, of figure 7 displays the interference signal when OG 530 is used as PC1 and a ruby crystal as PC2. The results of figure 7a make it obvious that the interference patterns from the two phase conjugation outputs are in phase. However the interference signal of the phase conjugation outputs of the two phase conjugator mirrors OG 530 and ruby is shifted by π. This immediately shows that signs of the nonlinearity in OG 530 and ruby are opposite. It has been shown lately[15,16] that the real part of $\chi^{(3)}$ in ruby is larger than the imaginary part by a factor of ten. The shift between the OG 530 and ruby suggests that the real part of $\chi^{(3)}$ in OG 530 is also larger than the imaginary part which corresponds well with the proposed band-filling model[4]

This non-linear interferometer has allowed us to measure very weak phase conjugation reflectivity signals and consequently the calculation of the value and sign of $\chi^{(3)}$ For example we were able to measure CS_2 the phase conjugation reflectivity signals with a cw mode locked laser which was not possible to achieve using the same laser power with the conventional degenerate four wave mixing phase conjugation experimental systems.

In summary we have presented data and prosed a model for the kinetics and mechanism of fading in semiconductor doped glasses and explained the deviation from a theoretical quadratic dependence of the phase conjugate reflectivity on reduced pump intensity in these glasses. We also described a novel non-linear phase conjugate interferometer and its application to the measurement of the magnitude and phase of third-order nonlinear susceptibilities.

Acknowledgements

This work was supported in part by Rockwell International Corporation under grant No. B8X197858 and by the Advanced Research Projects Agency of the Department of Defense, and was monitored by the USAFOSR under Contract No. F29601-87-K-0057.

References

1 R.K. Jain , R.C. Lind, J.Opt. Soc. Am. 73, 647, 1983.
2. P. Roussignol, D. Richard,C. Flytzanis, Appl. Phys. A44, 385, 1987.
3. S.M. Saltiel, B.Van Wonterghem, T.E. Dutton, P.M. Rentzepis, IEEE J. Quant.Electr. QE-24, 2302, 1988.
4. P. Roussignol,D. Richard,J. Lukasik,C. Flytzanis, J.Opt.Soc.Am. B4, 5, 1987.
5. P. Horan, W. Blau, Semicond.Sci.and Tech. 2, 382, 1987.
6. A. Gabel, K.W. Delong, C.T. Seaton, G.I. Stegeman, Appl. Phys.Lett. 51, 1682, 1987.
7. S.M. Saltiel, B.Van Wonterghem, P.M. Rentzepis, Opt.Lett. 14, 183, 1989.
8. J.T. Remillard, D.G. Steel, Opt.Lett. 13, 30, 1988.
9. L.H. Acioli, A.S.L. Gomez,J.R. Rios Leite, Appl.Phys.Lett. 53,1788, 1988.
10. P. Roussignol, D. Ricard, K.C. Roustagi, C. Flytzanis, Opt.Comm. 55, 143, 1985.
11. J.T. Remillard, H. Wang, M.D. Webb, D.G. Steel, IEEE J.Quant.Electr. QE-25, 408, 1989.
12. B.Van Wonterghem, S.M. Saltiel,T.E. Dutton, P.M.Rentzepis J.Appl.Phys., 66,4935, 1989.
13 J.P. Zheng, H.S. Kwok, Appl.Phys.Lett. 54, 1, 1989.
14. R.H. Bude, J.Appl.Phys. 33, 586, 1964.
15. I. McMichael, P. Yeh, M. Khoshnevisan, Proc.Photo-Opt. Instr.Eng., 613, 32, 1986.
16. T. Catunda, J.P. Andreta, J.C. Castro, Appl.Opt. 25, 2391, 1986.

Direct Measurement of Geminate Recombination and Vibrational Cooling in Iodine Using Picosecond Raman Spectroscopy

Xiaobing Xu, Soo-Chang Yu, and J.B. Hopkins
Department of Chemistry, Louisiana State University,
Robert Lingle Jr.
Department of Physics and Astronomy
Baton Rouge,LA.70803

ABSTRACT

The photodissociation and geminate recombination of iodine in cyclohexane has been studied by directly monitoring the vibrational coordinates using transient Raman spectroscopy. Energy relaxation as a functior. of vibrational energy gap has been measured for vibrational spacings of 210 to 130 cm^{-1}. These vibrational levels correspond approximately to v=3 to v=52 with energies 740 to 9300 cm^{-1} above the zero point level. The results support earlier experiments in that over 100ps is required to completely relax the vibrational energy.

INTRODUCTION

The photodissociation and geminate recombination reaction of iodine is an excellent example of a bimolecular reaction and has been studied for more than 50 years. In particular, ultrafast laser techniques have been extensively used to investigate this reaction.[1-7] However, the detailed picture of the geminate atom recombination was not fully understood until very recently. Using picosecond transient absorption techniques, Harris and co workers[5-7] have shown that the photodissociation and geminate recombination occurs in $\leq$2ps. Following geminate recombination, the vibrational decay on the X state was probed by transient absorption spectroscopy. By comparing transient absorption data with calculated transition strengths, their experiments have inferred that vibrational cooling is very strongly dependent on the vibrational energy gap. It was found that complete relaxation from the top of the X state potential well into the lowest energy vibrational levels occurs on a roughly 100ps time scale.

In this paper the first direct measurement of this same reaction is presented using transient Raman spectroscopy. The advantage of the Raman technique is that direct information can be obtained about the vibrational coordinates — the Raman frequencies are directly measuring the vibrational gaps between the two nearest vibrational levels. An the top of the X state potential the energy spacing between vibrational levels is approximately zero because of the anharmonicity of the potential well. At the bottom of the potential the energy gap is exactly equal to the fundamental I_2 frequency[8] of 212 cm^{-1}. As vibrational cooling takes place it is expected that time dependent Raman frequencies will be observed from zero frequency all the way out to the fundamental I_2 frequency. For a vibrationally hot I_2 molecule to relax, it must transfer a quanta of vibrational energy to the solvent. The beauty of studying vibrational cooling by transient Raman spectroscopy lies in the fact that the Raman frequencies correspond *directly* to the quanta of energy that must be lost to depopulate the level. Therefore the time-dependent vibrational distribution of the X state can be directly mapped out using transient Raman spectroscopy.

EXPERIMENTAL

The experimental details have been previously discussed.[9-10] The picosecond laser is based on a high repetition rate(2KHz) regenerative laser which amplifies chirped pulses from a Quantronix 416 modelocked laser. The output pulse is then compressed by a pair of gratings which gives a laser pulse with a width of 8ps and 1mJ energy at 1.064μm. Harmonic generation in BBO converts the fundamental laser frequency to the second and third harmonics. A free flowing jet system was used in this experiment. The experiment was performed using pump-probe two color technology. The pump at 532nm is resonant with the B-X transition in iodine from which photodissociation occurs. The dynamics of vibrational cooling on the X state potential are probed at 354.7nm. The laser beams are chopped at 200Hz which allows the raw two color spectra and one color background to be obtained at same time in a single scan. The pure transient spectrum is computed by subtracting the one color background spectra from the raw two color spectrum. In order to subtract, the spectrum was normalized to the pure solvent bands at 354.7nm as an internal standard. This technique is very powerful in that it can recover relatively weak transients in the presence of strong interferences such as Raman bands from the solvent. The various time delays are provided by a computer controlled motorized delay stage.

RESULTS AND DISCUSSION

Figure 1 shows the pure transient Raman spectrum of iodine probed at various time delays of 0ps, 25ps, 50ps and 100ps, respectively, following the 532nm photodissociation. There are two bands shown in each spectrum. The narrower band at 107 cm^{-1} has been assigned to the transient A/A′ electronic state. There are two reasons which support this assignment. First, the frequency of this band is very close to the gas phase value[13-14] of 90/105 cm^{-1} for the A/A′ electronic states. Second, this band has the same time dependence found in earlier transient absorption experiments[4-7] for the species assigned to these same excited electronic states. A detailed account of the dynamics of the A/A′ electronic state will be discussed in a separate publication.

Following photodissociation of iodine, geminate recombination will form the A/A′ excited states as well as X state. The broad Raman band in figure 1 is assigned to hot vibrations on the X state. This band spans from 130 to 210 cm^{-1} in the 0ps spectrum. This feature clearly shows that the X state is vibrationally hot immediately after the recombination, because vibrational population is observed over most of the vibrational levels. Calculations from the gas phase spectroscopic constants[8] indicate that these states correspond to vibrational levels v=52 to v=3 and vibrational energies of 9300 to 740 cm^{-1}. This experiment therefore probes significantly higher levels of excitation than previous absorption experiments.[4-7]

The fact that this band only shows a broad distribution of vibrational states without any detailed structure is a result of Raman scattering from a large distribution of vibrational states with slightly different frequencies. From calculations using gas phase spectroscopic constants the maximum difference between two adjacent Raman frequencies is 2.3 cm^{-1}, whereas the linewidth of an individual Raman band is 23 cm^{-1}. It is therefore impossible to resolve each vibrational level under this experimental condition. However, the distribution of the vibrational states can be directly observed.

The X state dynamics in Figure 1 reveal two important features of vibrational energy decay. First, the maximum of the distribution shifts to the higher frequencies from 0ps to 100ps as indicated by the arrows in the figure. Shifting to the higher frequencies means that the lower vibrational levels of the X state are more populated with time. This unambiguously indicates that vibrational decay occurs during that time. Secondly, the distribution appears to become more narrow at later times. This is a result of populating vibrational states with slower relaxation times which allows the population to collect in the lower vibrational levels. As vibrational cooling takes place one would expect to observe the eventual repopulation of the lowest vibrational level of X state. However, it must be remembered that Figure 1 is a subtracted pure transient spectrum showing only features which are different from the normal relaxed Raman spectrum. As soon as the distribution cools into the lowest energy levels, the spectrum becomes identical to the relaxed Raman spectrum and is removed by the subtraction procedure.

It must be pointed out that the shape of this distribution is obscured due to the uncertainties in the wavelength dependence of the resonance Raman enhancement which will affect the relative intensities of the scattering from each individual level. However, it is expected that the Raman enhancement for any particular level remains constant with time. As a consequence, the data in Figure 1 illustrate the dynamics of the relative populations. A detailed analysis of the population decay will be presented in a separate publication. In addition, 354.7nm is only resonant with the middle part of X state potential, which limits the vibrational levels we can observe. An investigation of the dynamics of the top of the X state potential is in progress and the result will be published else.

CONCLUSION

The iodine photodissociation in cyclohexane is measured using transient Raman spectroscopy for the first time. It is found that the dynamics of photodissociation over the first 100ps is dominated by the X state vibrational cooling.

REFERENCES

[1.] A.L. Harris, J.K. Brown and C.B. Harris Ann. Rev. Phys. Chem., **39**, 341 (1988).

[2.] T.J. Chuang, G.W. Hoffman and K.B. Eisenthal Chem. Phys. Lett., **25**, 201 (1974).

[3.] P. Bado and K.R. Wilson J. Phys. Chem., **88**, 655 (1984).

[4.] D.F. Kelly, N.A. Abul-Haj and D.J. Jang J. Chem. Phys., **80**, 4105 (1984).

[5.] A.L. Harris, M. Berg and C.B. Harris J. Chem. Phys., **84**, 788 (1986).

[6.] M.E. Paige, D.J. Russell and C.B. Harris J. Chem. Phys., **85**, 3699 (1986).

[7.] P.E. Smith and C.B. Harris J. Chem. Phys., **87**, 2709 (1987).

[8.] J.A. Coxon J. Quant. Radiat. Transfer, **11**, 443 (1971).

[9.] L.K. Orman, Y.J. Chang, D.R. Anderson, T. Yabe, Xiaobing Xu, Soo-Chang Yu and J.B. Hopkins J. Chem. Phys., **90**, 1469 (1989).

[10.] Y.J. Chang, Xiaobing Xu, T. Yabe, Soo-Chang Yu, D.R. Anderson, L.K. Orman and J.B. Hopkins, J. Phys. Chem., Jan. 1990, In Press

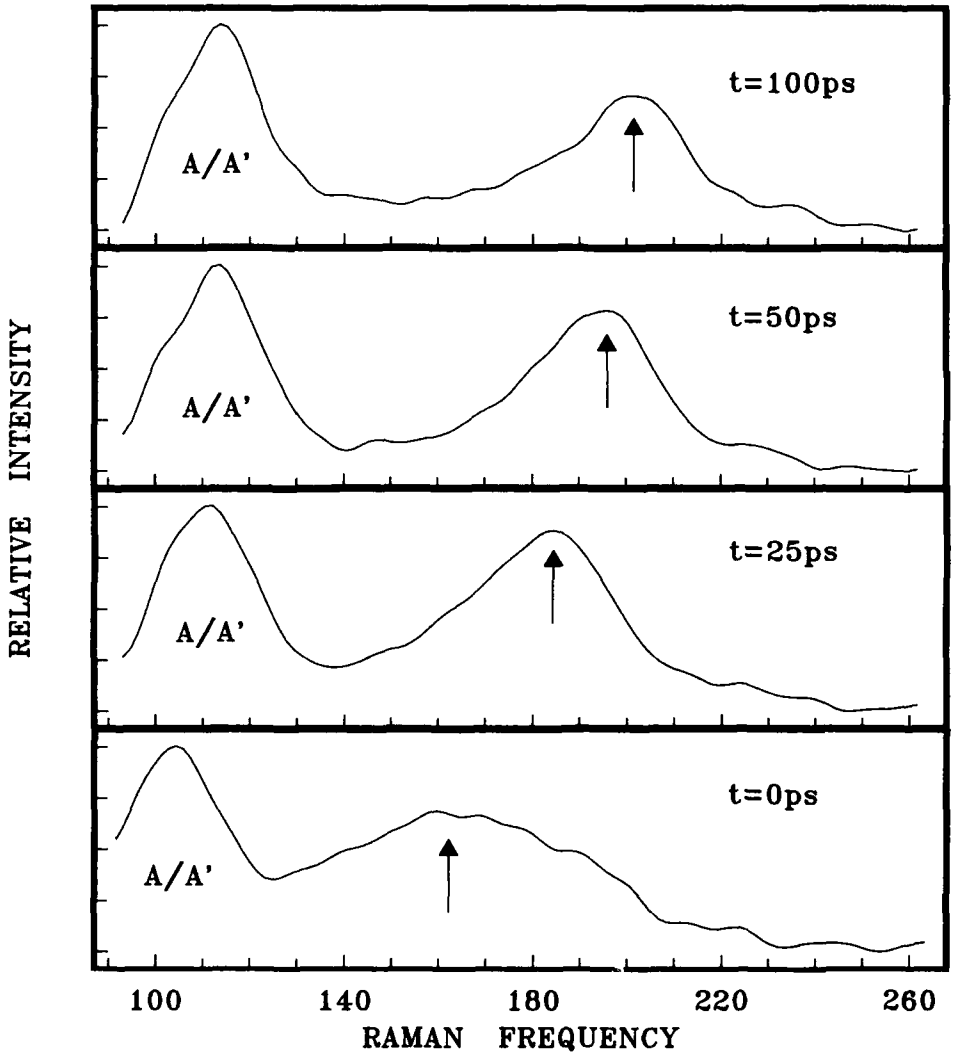
[11.] Y.J. Chang, C. Veas and J.B. Hopkins Appl. Phys. Lett., **49**, 1758 (1986).

[12.] Y.J. Chang, D.R. Anderson and J.B. Hopkins, *International Conference on Lasers 1986*,p.169 McMillan,R.W. STS Press **1987**.

[13.] J. Tellinghuisen J. Mol. Spect., **94**, 231 (1982).

[14.] K.S. Viswanathan, A. Sur and J. Tellinghuisen J. Mol. Spect., **86**, 393 (1981).

Figure 1: Pure transient spectrum of I_2 in cyclohexane obtained by subtracting the one color probe only background spectrum from the raw two color spectrum. In order to subtract, spectra have been normalized for transient absorption at 354.7nm using solvent bands as an internal reference. Probe is 354.7nm, 20μJ/pulse, .5mm beam waist. Pump is resonant with the B-X transition at 532nm.; 50μJ/pulse .5mm beam waist. Time delay between pump and probe lasers is given in the figure. The band labeled A/A′ in each frame corresponds to the excited electronic states denoted as such. Frequencies aur in units of cm^{-1}.



Pure transient spectrum of I_2 in cyclohexane obtained by subtracting the one color probe only background spectrum from the raw two color spectrum. In order to subtract, spectra have been normalized for transient absorption at 354.7nm using solvent bands as an internal reference. Probe is 354.7nm, 20μJ/pulse, .5mm beam waist. Pump is resonant with the B-X transition at 532nm.; 50μJ/pulse .5mm beam waist. Time delay between pump and probe lasers is given in the figure. The band labeled A/A' in each frame corresponds to the excited electronic states denoted as such. Frequencies aur in units of cm^{-1}.

Direct Observation of Solvent Cage Dynamics Following Photodissociation of Iodine Using Picosecond Raman Spectroscopy

Robert Lingle Jr.
Department of Physics and Astronomy
Xiaobing Xu, Soo-Chang Yu, Y.J.Chang, and J.B. Hopkins
Department of Chemistry
Louisiana State University, Baton Rouge,LA 70803

ABSTRACT

Photodissociation of iodine in CCl_4 heats the solvent cage immediately surrounding the solute. Picosecond Raman spectroscopy has been used to investigate the dissipation of this energy in the solvent coordinate by monitoring time dependent shifts in the Raman lineshapes of the local solvent cage.

INTRODUCTION

Recent advances in ultrafast laser technology have spawned great interest in the study of solvent relaxation and its role in chemical reaction dynamics.[1-4] In this paper, iodine in CCl_4 is photodissociated at 532nm resulting in the immediate ($\leq$2ps) release of 6300 cm^{-1} of energy into the local solvent environment.[5] The response of the solvent cage to this excitation is *directly* observed by measuring the time dependence of the solvent Raman bands using picosecond Raman spectroscopy.

EXPERIMENT AND RESULTS

The experimental details of the transient Raman apparatus[6-7] have been previously discussed. The laser system comprises a Nd:YAG regenerative amplifier injection-locked to a Quantronix 416 Nd:YAG mode-locked laser. Fiber-grating pair pulse compression is used in conjunction with the regenerative amplifier to produce 15ps, 600μJ pulses at 1.25kHz repetition rate. Frequency doubling and tripling yield the YAG second and third harmonics used as pump and probe colors.

Photodissociation of iodine molecules dissolved in CCl_4 is accomplished by pumping the B$\leftarrow$X transition with 532nm pulses of 50μJ energy. By delaying the 354.7nm 10μJ probe pulses with respect to the pump pulses, the time evolution of the resonance Raman spectrum of the transients is monitored. By using a mechanical chopper to turn the 532nm pump pulse on and off several hundred times per second, the spectrometer divides its scanning time between taking a two-color spectrum and a probe-only background spectrum. By subtracting the background spectrum (with only ground state Raman peaks) from the two-color total Raman spectrum (with both ground state and photoproduct peaks), a pure two-color transient Raman spectrum is obtained. Following rapid predissociation from the B state, the iodine atoms undergo geminate recombination onto either the A/A′ excited electronic surface or the ground X state surface. The Raman dynamics of vibrational cooling on the X state potential are the subject of a separate paper.[8]

Pure two-color transient Raman spectra are shown in Figures 1A and 1B. Since the one-color background components have been subtracted out of the spectrum, any remaining deviation from the baseline (either positive or negative) is the result of some transient species. For example, the bands at 105, 203, and 301 cm^{-1} are the fundamental and overtones for iodine in the A/A′ excited electronic state. At this point it is appropriate to point out that the subtraction procedure must be corrected for optical density changes due to excited state absorption. In this experiment, the I_2 A/A′ state has a lifetime of 2.7 ns and absorbs strongly in the UV, as evidenced by the appearance of resonance Raman overtones in the spectrum. This transient absorption of both the probe laser light and the Raman scattered light means that solvent solvent Raman bands will be less intense when both lasers are present than when only the probe laser is present. When subtracting the one-color spectrum from the two-color, a single multiplicative correction factor (chosen to normalize solvent band intensities) is applied to the one-color spectrum.

If the solvent bands are not modified by the photodissociation of iodine they would be expected to completely subtract out of the spectrum. Contrary to this expectation, transient solvent bands are clearly indicated as the colored-in peaks at 227, 324, and 469 cm^{-1}. By comparing Figure 1A and 1B it can be seen that these peaks decay on the time scale of the laser pulsewidth. The normal ground state solvent Raman spectrum obtained by a one-color experiment is shown for the purposes of comparison in Figure 1C. No amount of correction can make the solvent bands subtract completely out of the spectrum. If the solvent band transients were due to steep wavelength dependence in the transient absorption responsible for the optical density change, then a single subtraction correction factor would drive one solvent band (plus its lineshape change) to the level of the baseline while leaving the other two drastically depleted. Thus the transients lying on the high frequency side of each solvent Raman band are not an artifact of the subtraction technique. The presence of the transient solvent bands is the result of a lineshape change which reflects the response of the local solvent cage to the iodine photodissociation.

DISCUSSION

What is the nature of these transient solvent bands? It has been found that the intensities of these bands are linear in iodine concentration. It is therefore unlikely that they result from some undesired coherent laser phenomenon. The bands are therefore assigned to either an I—Solvent complex formed as an intermediate step in the geminate recombination process or transient heating in the solvent. Photodissociated I atoms which escape the cage survive for nanoseconds in the form of a solvent complex. The fact that the transient bands in Figure 1 decay to zero (as opposed to a fixed value with a nanosecond lifetime) suggests that an I—Solvent complex is not responsible for the transient. However since the quantum yield of cage escape is currently under dispute[9] this possibility cannot be ruled out. Alternatively, when 6300 cm^{-1} of energy is released into the solvent as a result of photodissociation it is expected that the local solvent cage will be heated by the absorption of this energy. The temperature effect on the solvent spectrum has been investigated under equilibrium conditions and the results are qualitatively the same as those observed in the transient spectrum.

Equilibrium spectra are shown in Figure 2. Under transient conditions, the picosecond laser probes a hot cage and a cold bulk solvent spectrum. This can be simulated experimentally by taking the *change* in the lineshape on heating iodine in CCl_4 (Figure 2B) and subtracting off the *change* in the lineshape on heating neat solvent (Figure 2A). These data are shown in Figure 2C. The results are qualitatively the same as those in the transient spectrum shown in Figure 1A in that all bands shift to higher frequency. This result supports the conclusion that the transient observed in Figure 1 results from local heating in the solvent cage.

The expected temperature increase can be easily calculated assuming 6 solvent molecules immediately surrounding each solute and considering the heat capacity for CCl_4 together with the energy released on iodine dissociation. This calculation gives a temperature jump of 100° C to 200° C. The latter represents the effect of additional energy released by X state vibrational cooling. It should be noted that this is an upper limit since the partitioning between A/A′ and X state recombination is not accurately known.

CONCLUSION

The discovery of solvent Raman lineshape transients accompanying photoexcitation of solute molecules is an important contribution to the study of ultrafast reaction dynamics in the condensed phase. Previously, solvent dynamics have been studied by monitoring time dependent shifts in the fluorescence spectra of solute molecules in polar solvents. In other words, information about relaxation in the local *solvent* environment is inferred from kinetics observed in the *solute* fluorescence spectrum. These very useful studies are limited by their reliance on internal charge redistribution in the excited state of the probe molecule and by the necessity of using a polar solvent (which can respond to the changing dipole moment of the solute probe specie). The technique detailed in this paper probes solvent cage relaxation *directly* by monitoring the solvent Raman spectrum. In the photodissociation experiments described in this paper, the dissipation of collisional energy in the solvent is studied. However, solvent Raman lineshape changes may prove to be a very general direct measure of nonequilibrium solvent dynamics.

Given what is expected for the energy relaxation rate in the bulk solvent, it is remarkable that it is even possible to observe a hot solvent cage with a 15ps pulse. If it is assumed that the energy in the solvent is dissipated at a rate equal to the speed of sound[10] in CCl_4, then a rate of $(.5ps)^{-1}$ would be expected. The fact that the solvent cage is observed to contain a significant fraction of this energy on a picosecond time scale is an important consideration for condensed phase reaction dynamics. This result may also be a relevant consideration for the interpretation of the time dependent fluorescence measurements of solvent relaxation dynamics.

REFERENCES

[1.] P.F. Barbara and W.Jarzeba, Acc. Chem. Res., **21**, 195 (1988).

[2.] M. Maroncelli and G.R. Fleming, J. Chem. Phys., **86**, 6221 (1987).

[3.] J.D. Simon, Acc. Chem. Res., **21**, 128 (1988).

[4.] E.F. Gudgin Templeton and G.A. Kenny-Wallace, J. Phys. Chem., **90**, 2896 (1986).

[5.] D.E. Smith and C.B. Harris, J. Chem. Phys., **87**, 2709 (1987).

[6.] L.K. Orman,Y.J. Chang,D.R. Anderson,T. Yabe,Xiaobing Xu,Soo-Chang Yu and J.B. Hopkins, J. Phys. Chem., **90**, 1469 (1989).

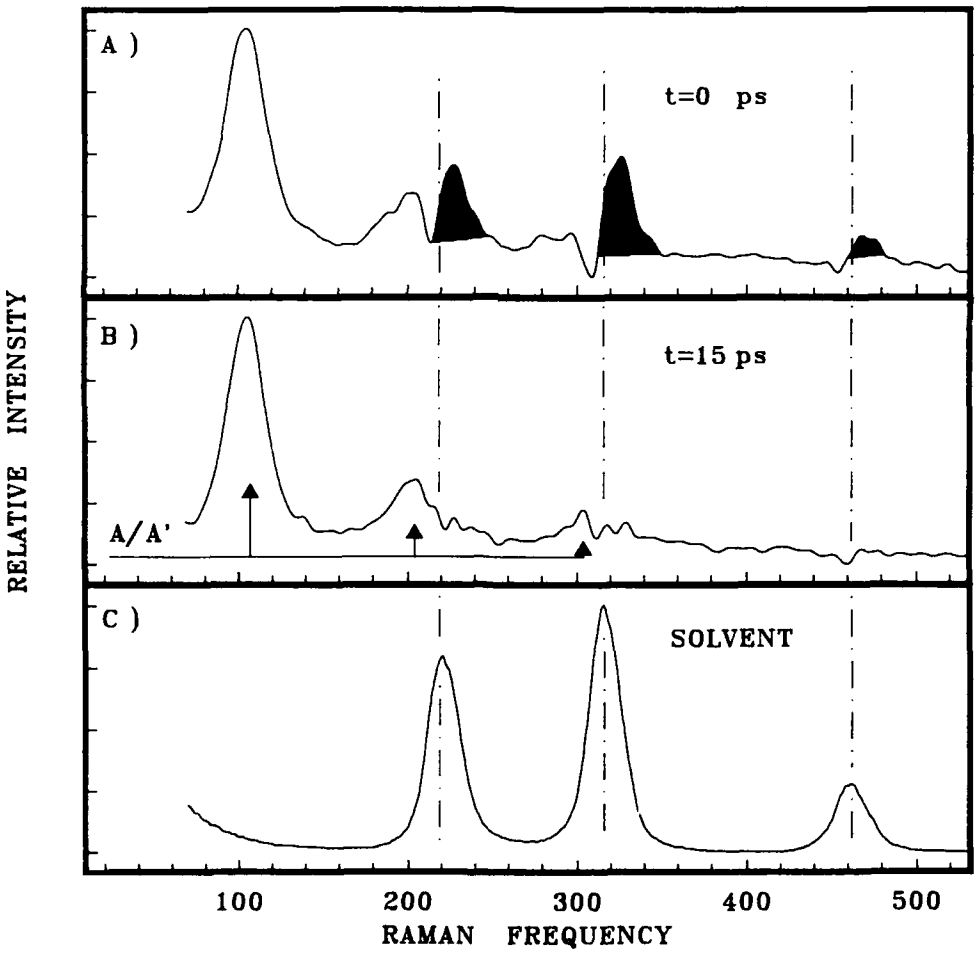
[7.] Y.J. Chang, C. Veas and J.B. Hopkins, Appl. Phys. Lett., **49**, 1758 (1986).

[8.] Xiaobing Xu,Robert Lingle Jr.,Soo-Chang Yu,Y.J. Chang and J.B. Hopkins, To appear, J. Chem. Phys. February 1, 1990

[9.] A.L. Harris, M. Berg, C.B. Harris, J. Chem. Phys., **84**, 788 (1986).

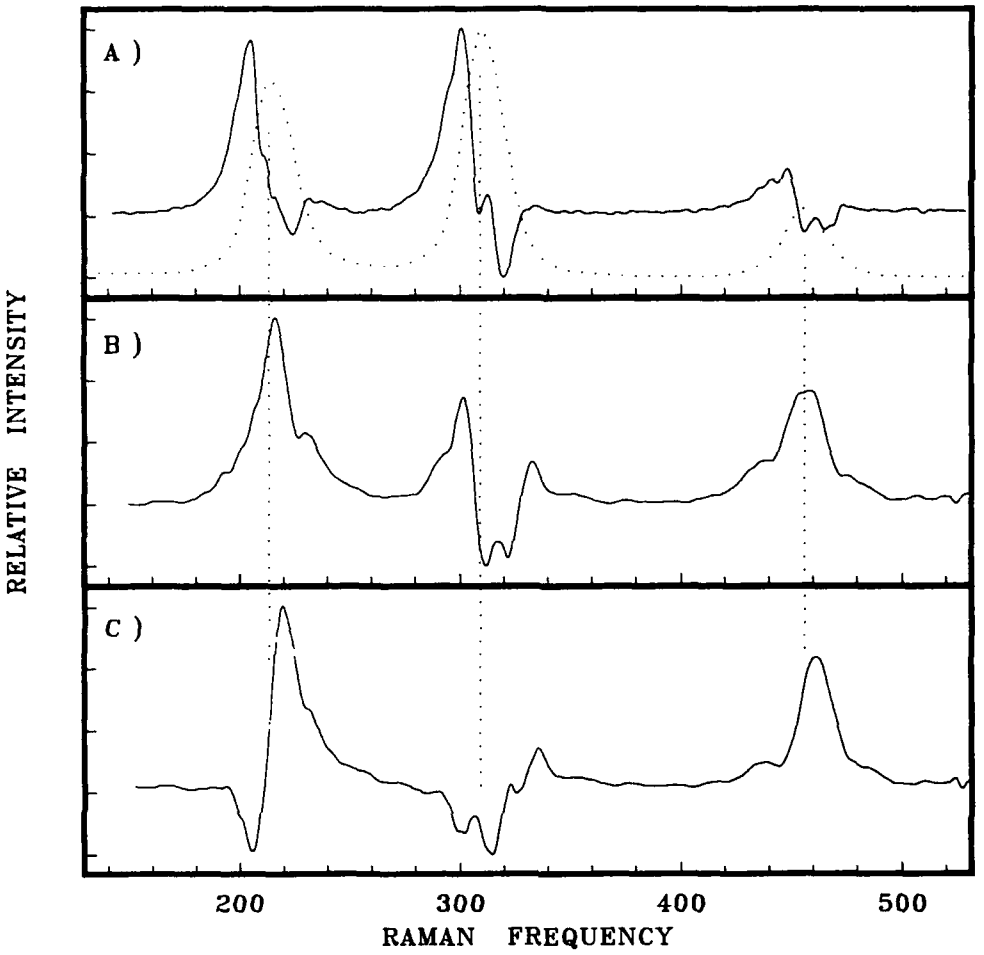
[10.] H.N.V. Temperly and D.H. Trevena, **Liquids and Their Properties**, John Wiley, 1978, p.131-132.

Figure 1



A) Pure two color transient Raman spectrum of I_2 in CCl_4 obtained by subtracting one color background components from raw two color spectrum. The filled in peaks are the transient solvent bands. Spectra are normalized to the solvent band intensity before subtraction to adjust for transient absorption at the probe laser wavelength. Time delay=0ps. B) Pure two color transient Raman spectrum at time delay=15ps. C) Normal one color Raman spectrum of solvent. Frequency is in units of cm^{-1}. Dotted lines are drawn at the peak maximum of the solvent bands. The bands labeled A/A' are assigned to the electronic states designated as such which are formed as a result of geminate recombination.

Figure 2



Difference spectra obtained from normal one color equilibrium solvent Raman spectra. Frequency is in units of cm^{-1}. **A)** CCl_4(54°C) - CCl_4(22°C). The dotted curve represents the normal solvent spectrum at 22°C. **B)** I_2 in CCl_4(54°C) - I_2 in CCl_4(22°C). **C)** Frame B - Frame A.

Observation of Vibrational Energy Relaxation Following Photodissociation of $Cr(CO)_6$

Soo-Chang Yu,Xiaobing Xu,Robert Lingle Jr. and J.B.Hopkins
Department of Chemistry, Louisiana State University,
Baton Rouge,LA.70803

ABSTRACT

Vibrational energy relaxation following photodissociation of $Cr(CO)_6$ at 266nm has been observed in both the Stokes and the anti-Stokes spectral regions using picosecond Raman spectroscopy. A 100ps transient is observed which is interpreted as the time required for the vibrationally hot $Cr(CO)_5$ to reach thermal equilibrium after solvation in cyclohexane.

The photochemistry of $Cr(CO)_6$ has long been studied as the prototype of metal-carbonyl compounds. In the gas phase, $Cr(CO)_6$ has been known to lose up to 6 carbonyl groups depending on the excitation energy. In contrast, only one CO group dissociates[1] under ultraviolet irradiation in solution or matrix. With the development of new techniques such as pico and femtosecond laser spectroscopy, the ultrafast dynamics of $Cr(CO)_6$ photodissociation have recently begun to be unraveled. However, there exists a controversy over recent studies of $Cr(CO)_5$ solvation following the photodissociation reaction in solution.

Simon et al.[2] first reported that photoexcitation of $Cr(CO)_6$ results in the formation of solvated $Cr(CO)_5$ which appears in a time of $\leq$ 0.8ps in hydrocarbon solvents. Their picosecond transient absorption results have been supported by similar femtosecond experiments by Nelson et al.[3] However, the appearance time of solvated $Cr(CO)_5$ has been questioned by other workers using both UV-visible and IR transient absorption spectroscopy.[4–5] Spears et al.[5] claim a much longer solvation time of 100ps. Lee and Harris[4] suggest that vibrational relaxation controls solvation dynamics on a 17ps time scale.

In this paper we have used transient picosecond Raman spectroscopy to remove the present controversy by directly probing the vibrational coordinates of the photoproducts. There are two processes of interest in the Raman scattering. One is Stokes scattering which monitors the cold vibrational modes by scattering radiation at a longer wavelength than that of the incident light. The other is anti-Stokes scattering in which the effect is the opposite of the Stokes and monitors the hot vibrational modes. If vibrational relaxation occurs, the intensity of the Stokes signal is expected to grow while that of the corresponding anti-Stokes signal diminishes in time. Thus the complementary observations of a growing Stokes band and a decaying anti-Stokes band give unambiguous evidence of cooling in that particular vibrational mode. This technique is therefore very sensitive to vibrational relaxation.[6] The experimental apparatus has been previously described in detail.[7–10]

Figure 1 shows the picosecond transient Raman spectra obtained at various optical delays for 266nm excitation of $Cr(CO)_6$ in cyclohexane. Two 5ps pulses at 266nm are used as the pump and probe pulses in this experiment. Both pulses are produced in the same laser by injecting two seed pulses into the regenerative laser. The delay between the pulses depends on the cavity length of the regenerative amplifier and is measured by a simple autocorrelation technique. The first pulse photodissociates $Cr(CO)_6$ and the second probes the resonance Raman spectrum of $Cr(CO)_5$. The reason for using this wavelength is that $Cr(CO)_6$ has a strong absorption band corresponding to ligand field excitation around 280nm, while $Cr(CO)_5$ has a strong ultraviolet absorption band for the metal to ligand charge transfer absorption at 240nm($\epsilon = 3 \times 10^4$).[11] The pentacarbonyl absorption is known to be relatively insensitive to the solvent at this wavelength. As a result, the magnitude of the transient Raman signal should not depend on solvation. The pump and probe pulses are separated by a variable optical delay which is quoted separately in each frame of figure 1. The spectra contain only pure transient Raman bands after removal of solvent and ground state $Cr(CO)_6$ bands using a spectrum differencing technique. This was achieved by alternately exciting the sample with a single interrogation laser pulse or the double pump-probe laser pulse sequence mentioned above. The pure transient spectrum shown in Figure 1 is obtained by subtracting the one pulse background spectrum from that obtained in the double pulse sequence. Other pertinent experimental details are given in the figure caption.

Comparing frames A-D in Figure 1, it is readily apparent that a single transient appears with a time scale of roughly 100ps. The metal-CO stretch at 381 cm^{-1} and the CO vibration at 1935 cm^{-1} indicate that the transient is a metal carbonyl complex which is assigned to $Cr(CO)_5$. The bands marked with asterisks are the result of noise generated by the spectrum differencing technique at the frequencies of the cyclohexane solvent bands. The negative going peaks are ground state $Cr(CO)_6$ bands which appear in the transient spectrum as a result of population bleaching. The ground state 383 cm^{-1} metal-CO stretch of $Cr(CO)_6$ appears as a bleach in the 30ps spectrum and gradually fills in at later times due to the growth of the $Cr(CO)_5$ transient band at 381 cm^{-1}. The dynamics of vibrational cooling can be investigated by comparing the Stokes and anti-Stokes band intensities. Figure 2 illustrates the transient anti-Stokes spectrum in the region of the 381 cm^{-1} band assigned to $Cr(CO)_5$. The results indicate that the anti-Stokes signal originates from the hot vibrational state which decays in 100ps. The observation that the Stokes and anti-Stokes spectrum have complementary dynamics is consistent with vibrational relaxation. It may be appear that vibrational relaxation continues until 450ps in the Stokes region. However, it should be noted that as the band grows from the bleach at 30ps to the maximum at 450ps, more than 70% of the transient intensity has developed in 100ps. The appearance time of ground state $Cr(CO)_5$ is therefore believed to represent the time required for the photoproduct to approach thermal equilibrium with the solvent. This conclusion clearly removes the present controversy and also demonstrates the importance of non-equilibrium vibrational energy with relatively long relaxation times in the condensed phase.

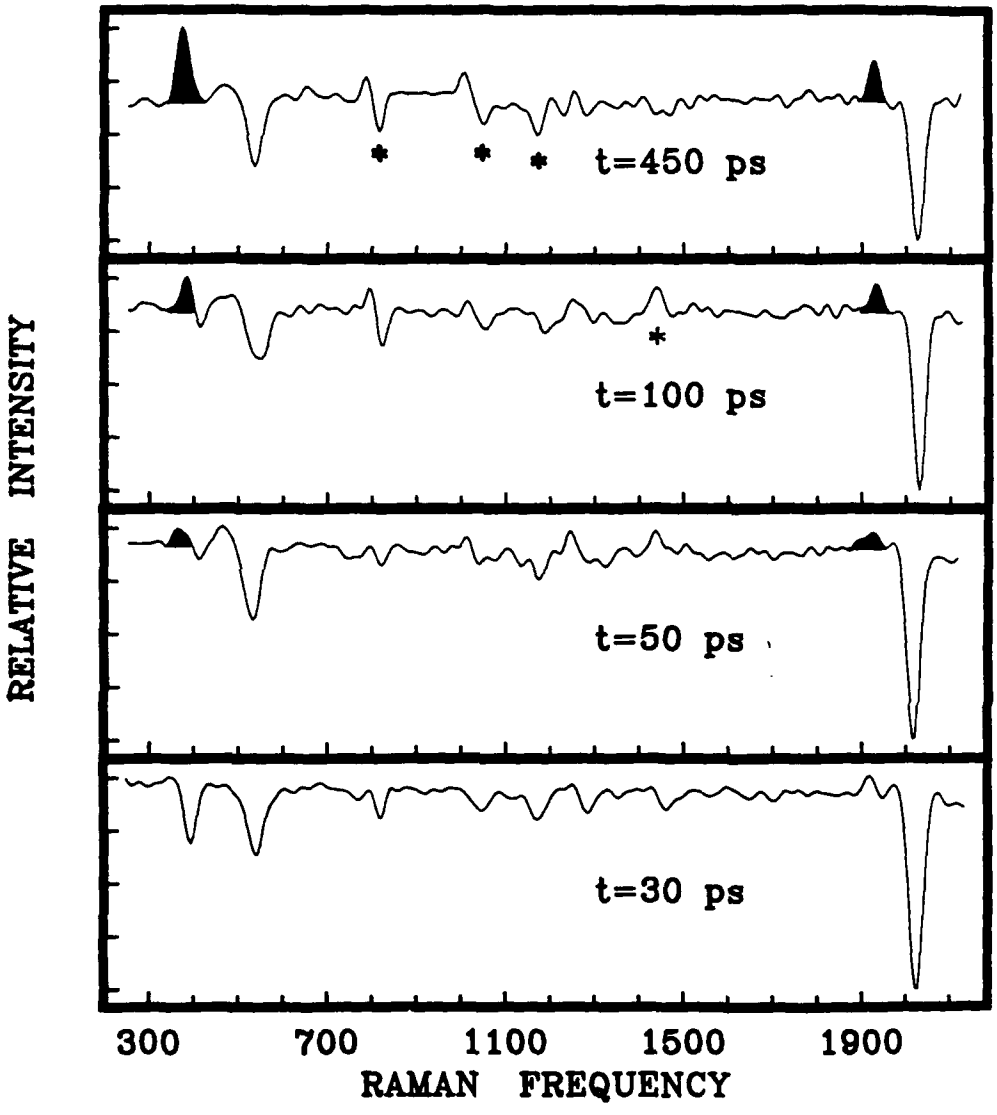
It is interesting to consider that our time scale is approximately the same as that observed[12] for the CO stretching vibration in $Cr(CO)_6$, where a relaxation time of 145±25ps was observed in n-hexane. Similar rates would be expected in these two experiments if the latter dynamics represents the time required for energy randomization followed by vibrational relaxation through the entire manifold of vibrational levels. There is no direct way to compare our results to the faster dynamics attributed to vibrational decay in the transient absorption experiment.[2-5] It is likely that the absorption results represent initial vibrational decay from upper vibrational levels which have not yet been quantified.

In summary three things should be stressed from our results using picosecond transient Raman spectroscopy. First, transient Raman spectroscopy is a uniquely powerful technique for investigating vibrational relaxation since it monitors vibrational coordinates directly. Secondly, the time scale of 100ps for vibrational relaxation of the solvated $Cr(CO)_5$ is remarkably longer than that which might be expected. Finally, the role of vibrational energy can not be ignored in the condensed phase. More details will be presented in a future paper. In particular, the role of the solvent coordination complex in the vibrational decay occurring in $Cr(CO)_5$ is under further investigation.

REFERENCES

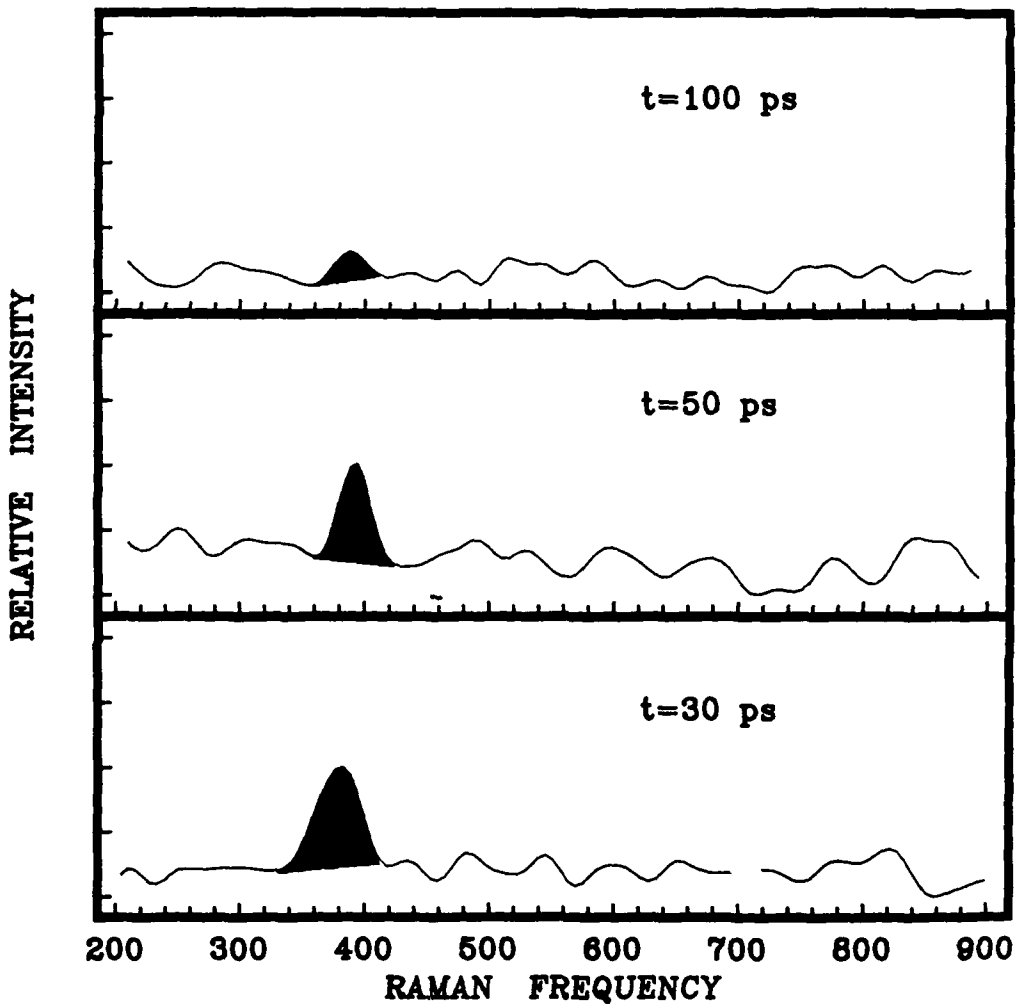
1. J.A.Welch, K.S.Peters,and V.Vaida, J.Phys.Chem.,86,1941(1982).
2. J.D.Simon and X.Xie, J.Phys.Chem.,90,6751(1986).
3. A.G.Joly and K.A.Nelson, J.Phys.Chem.,93,2876(1989).
4. M.Lee and C.B.Harris, J.Am.Chem.Soc.,111,8963(1989).
5. L.Wang,X.Zhu and K.G.Spears,J.Am.Chem.Soc.,110,8695(1988).
6. Xiaobing Xu, Robert Lingle Jr., Soo-Chang Yu, Y.J.Chang and J.B.Hopkins,To appear,J.Chem.Phys.February 1,1989.
7. Y.J.Chang, C.Veas and J.B.Hopkins, Appl.Phys.Lett.,49,1758(1986).
8. Y.J.Chang, D.R.Anderson and J.B.Hopkins, International Conference on Lasers 1986,p.169 McMillan,R.W.STS Press 1987.
9. L.K.Orman, Y.J.Chang, D.R.Anderson, T.Yabe,Xiaobing Xu, Soo-Chang Yu and J.B.Hopkins, J.Chem.Phys.,90,1469(1989)
10. Y.J.Chang, Xiaobing Xu, T.Yabe, Soo-Chang Yu, D.R.Anderson, L.K.Orman and J.B.Hopkins, J.phys.Chem.,Jan.1990,In Press
11. M.A.Graham, M.Poliakoff,and J.J.Turner, J.Chem.Soc.(A),Inorg. Phys. Theor., 2939(1971).
12. E.J.Heilweil, R.R.Cavanagh,and J.C.Stephenson, Chem.Phys.Lett.,134,181(1987).

Figure 1



Pure transient picosecond Stokes Raman spectrum in cyclohexane obtained by two pulse pump and probe at 266nm as described in the text. The Raman intensity represents a temporal average over the pulse width of the laser which is specified in each frame. The colored-in bands are those assigned to solvent coordinated $Cr(CO)_5$. Asterisks are used to denote noise due to Raman bands of the solvent molecules which have been subtracted out of each spectrum. Laser intensity was 20μJ/pulse at 2kHz in a 0.2mm beam waist. Concentration is 10mM. Frequency is in units of cm^{-1}.

Figure 2



Transient anti-Stokes Raman spectrum obtained under similar conditions to those given in Figure 1. Time delay between pump and probe pulses is given separately in each frame. Ground state bands have been subtracted out of the spectrum as described in the text. Spectra are normalized to the intensity of the ground state chromium band at $532\,cm^{-1}$ in the un-subtracted spectrum. Frequency is in units of cm^{-1}.

CONTRAST AND SENSITIVITY ENHANCEMENT IN SCANNING OPTICAL SYSTEMS

C.W. See,
Rank Taylor Hobson, 2 New Star Road, Thurston Lane,
Leicester LE4 7JQ, UK, and

M. Vaez Iravani
Center for Imaging Science, Rochester Institute of Technology,
1 Lomb Memorial Dr., Rochester, NY 14623.

Abstract

The performance of scanning optical systems in qualitative and quantitative imaging is critically dependent on contrast and sensitivity. This paper describes two specific approaches to amplitude and phase imaging which achieve a significant improvement in these areas. The techniques are based on differential and linear imaging concepts. The methods offer comparable sensitivity to variations across samples, amounting to 1 part in a million, in detecting reflectivity variation, and about 3 micro radians in phase changes, both in a 1 kHz bandwidth.

1. Introduction

The scanning optical microscope (SOM) [1] belongs to a general class of systems which aims at the non-destructive examination of various materials. The desire for the examination of such materials with the SOM stems from two basic needs: one is either interested in imaging objects which are otherwise hard to "see" with normal techniques, or one wishes to perform precision metrology on these objects on a point by point basis. Regardless of the specific need that one has, the three main criteria for such operations are resolution, contrast and sensitivity. Clearly, in the diffraction limited regime, it is the latter two that can set fundamental limits on the ultimate performance of the system.

In the SOM, it is quite easy to draw a distinction between contrast and sensitivity considerations, and the way they affect the performance of the system. Whereas the former is primarily a function of the background, the latter is determined by both signal-to-noise (S/N) considerations, and system instabilities. This distinction, however, is rather ill-defined in non-scanning systems, as in either case the visibility of the details is affected in similar ways. There have been some notable attempts at improving both contrast and sensitivity in the non-scanning world. These include the central dark ground and Schlieren techniques [2], Zernike's phase contrast method [3], Tolansky's multiple beam interferometry [4], and Nomarski's differential interference contrast (DIC) [5]. Some of these techniques improve the contrast by removing the background. Others enhance the image by increasing the relative importance of the desired "signal" compared with the background. The Nomrski system in particular is an enduring technique as it provides for differential imaging of the sample accompanied by the automatic cancelation of the background. The image revealed is thus a representation of variations only, a particularly desirable attribute in the examination of almost uniform objects.

We can approach the subject of contrast and sensitivity enhancement in the SOM in similar ways to that outlined above. Yet, it is more instructive to address the issue by considering two categories of amplitude and phase imaging techniques. This paper is thus a short account of two specific approaches to the subject, one involving phase imaging, the other amplitude imaging. The common bond between these techniques is that they are both differential in nature, and as such they respond only to non-uniformities. We shall show that the use of amplitude for imaging can be as effective as that of phase, and the choice is normally a function of the object under examination.

2. Differential Amplitude and Phase Imaging in the SOM

The SOM can successfully be employed to perform both amplitude and phase imaging. Of these two categories, the former is more straightforward, and will be discussed later. As far as phase imaging is concerned, resort can be made to a number of alternate techniques: (i) the direct effect of the object phase on the signal amplitude due to scattering; (ii) interferometry; (iii) use of the polarization of light. In this paper, phase imaging will only be discussed in the context of the polarization of light.

Much attention has been paid to those systems in which the object phase occurs as the epoch of an AC signal [6-12].

A phase sensitive detector is then used to extract this phase. In addition, phase has been imaged using a scanning AC differential interferometer {8,12}. In that system, the phase of the object gives rise to a signal whose amplitude is proportional to the phase.

In common with some of the mentioned techniques {7}, the system discussed in this paper is one which utilizes the polarization of light. We shall now describe the basic technique.

2.1. Scanning Differential Interference Contrast Microscope

Regardless of its specific implementation, any system utilizing the polarization of light rests on the principle that phase structure of the object (of which birefringence is a special case) can be made to transform the state of polarization of the incident radiation. Thus, a second polarizer (referred to as the analyzer) which is often cross-polarized with respect to the initial polarization, will detect some light. This concept is shown in Fig. 1, where the incident polarization is denoted by x, and the analyzer pass axis is denoted by y. Resolving the reflected light from the sample into two rotational components S_1 and S_2, we can write the following expressions:

$$S_1 = A \exp\{j[\omega_0 t + \phi_1]\} \quad (1)$$

$$S_2 = A \exp\{j[\omega_0 t + \phi_2]\} \quad (2)$$

where the amplitude of each component is given by A and, in general, the epoch angles ϕ_1, and ϕ_2 are different. Resolving along the analyzer pass axis, we arrive at the following expression for the intensity of the detected light:

$$I_{out} = 2K A^2 \{ 1 - \cos(\delta\phi) \} \quad (3)$$

where $\delta\phi$ is the differential phase between the two components, and K is a constant. Equation (3) represents the form of the detected output, regardless of whether the eye/video camera is the detector (non-scanning), or a photodiode is the used as such (scanning). One can see at once that a major difficulty exist with the output, in that for small $\delta\phi$, Eq. (3) reduces to:

$$I \propto (\delta\phi)^2 \quad (4)$$

For a given S/N then, such a system rapidly reaches its ultimate sensitivity for ever diminishing values of $\delta\phi$.

To resolve the difficulty, let us assume that it is somehow possible to introduce two sinusoidal, object independent, unequal phase shifts into Eq.'s (1) and (2):

$$S_1 = A \exp\{j[\omega_0 t + \theta_1 \sin\omega_s t + \phi_1]\} \quad (5)$$

$$S_2 = A \exp\{j[\omega_0 t + \theta_2 \sin\omega_s t + \phi_2]\} \quad (6)$$

It can readily be shown that the new output would consist of a DC term as well as a spectrum of frequencies, which are all harmonics of f_s. Furthermore, the coefficients of the even harmonics would proportional to $\cos(\delta\phi)$ as in the previous case, whereas the odd harmonics would be proportional to $\sin(\delta\phi)$. Accordingly, the latter would be linearly proportional to the differential phase. This highly desirable effect is at the heart of the operation of a sensitive phase dependent system. It affords a substantial improvement over the square-law system of Eq. (3).

A particular implementation of this scheme in practice is with the aid of a Pockels cell {13} placed in front of the object. This electro-optic modulator, when driven sinusoidally at f_s, performs the phase modulation of the two components, as desired.

To perform differential microscopy using this procedure, we note that if the components S_1 and S_2 of Fig. 1 are somehow spatially separated prior to arriving at the object, then the phase *difference* between the two after reflection represents a spatial phase differential of the object. This is, of course, precisely what happens in the conventional Nomarski microscope. It also points to the limitations of the conventional system which, as was noted, stems from the $\cos(\delta\phi)$ dependence of the output. Clearly, the linearization of the output as was described above will also solve the present problem. The essential elements of the resulting system are shown in Fig. 2, where a topographic step is shown as an example of the object phase structure {14}.

The system of Fig. 2, and its fiber-optic counterpart {15}, have been used to image a number of samples. Fig. 3 shows the surface structure of a highly polished stainless steel sample obtained at f_s (a), and the corresponding image at $2f_s$ (b) (f_s=100 kHz), where, f_s is the modulation frequency of the Pockels cell. The beam used was a 633 nm HeNe at just under 1 μW, and the video bandwidth was 30 kHz. The first striking feature of these results is the substantial superiority of the linear image (3(a)). This is the experimental manifestation of the expected superior sensitivity of this mode of operation. Another interesting feature is the contrast reversal that can be seen between the two photomicrographs. This is also predicted by theory. Since the odd harmonics are proportional to $\sin(\delta\phi)$,

and the even harmonics are dependent on $\cos(\delta\phi)$, in those cases where the phase difference is large enough to be observable with both modalities, this reversal in contrast is expected. Fig. 4 shows the surface of a natural diamond, with its characteristic growth ridges. Fig. 5, by contrast, shows the surface of a highly polished natural diamond; the straight lines across the micrographs are manifestation of the polishing process. Figures 6 and 7 show the surface structures of two different epitaxial silicon wafers. The entire surface of the sample of Fig. 6 is covered by right-angled triangles, which are characteristic of stacking faults. In Fig. 7, there are also some semi-circular patterns originating from the corners of the faults. These are thought to be due to stress induced birefringence. All these micrographs were taken in a 30 kHz bandwidth.

2.2. Differential Amplitude Scanning Optical Microscope

The second type of system to be discussed in this paper is one which utilizes the amplitude of light for imaging samples. In its essential embodiment, a type 1 differential amplitude scanning optical microscope (DASOM) consists of a simple SOM, modified such that the focused beam on the object performs a local sinusoidal movement (Fig. 8) {16}. The amplitude of this movement is kept such that the local excursion of the focal spot is well within the focal diameter. This avoids deterioration of the resolution (the diagram highly exaggerates the spot excursion) {17}. Assuming now that there exists a small variation of the reflectivity at the two extremities of the cycle, we can represent the amplitude of the received light by:

$$S = Ar\{1 + e\cos\omega_s t\} \qquad (7)$$

where A is the amplitude of the incident light, r is the mean reflectivity, e half the fractional variation in the reflectivity, and ω_s is the modulation frequency. Noting that the output of the detector is proportional to the intensity of the received light, we have:

$$I_{out} = \kappa A^2 r^2\{1+2e\cos(\omega_s t)+\cos^2(\omega_s t)\} \qquad (8)$$

where κ is a constant of proportionality. Thus, for a small e the signal at ω_s is proportional to the differential reflectivity. If e is considered to a be function of refractive index variation, we have the following relationship between e and the refractive index variation:

$$e = \delta n\,(n^2 - 1) \qquad (9)$$

Hence the differential signal is linearly dependent on δn. It must be borne in mind that the basic function of the DASOM, namely its ability to cancel the background and yield differential images, is not its only attribute. A particularly significant advantage of the technique is in its capability to improve immunity to source fluctuations. Such fluctuations which are always present to varying degrees can profoundly affect the performance of the SOM. To appreciate this important fact, let us re-write Eq. (8), and this time include a time dependent term, $\pm\delta A(t)$, representing laser fluctuations:

$$I_{out} = \kappa r^2\{A^2 \pm 2[\delta A(t)A + 2A^2]\cos\omega_s t \pm 4[\delta A(t)]\,e\cos\omega_s t\} \qquad (10)$$

Here, we have ignored the terms in e^2. One can see that due to the presence of the fluctuations the desired signal at ω_s has an additive noise term $4\delta A(t)e$. This introduces an uncertainty with which a given variation can be determined. The fundamental limits of the detection, however, are still set by S/N considerations. This contrasts sharply with the situation pertaining to the SOM. The inclusion of the fluctuation term in the equation furnishing the output of the SOM results in the following:

$$I_{out} = \kappa r^2\{A^2 + 4A^2 e \pm 2A[\delta A(t)] \pm 8A[\delta A(t)]e\} \qquad (11)$$

It is the second term on the right hand side in this expression that represents the disarmed signal. The third and fourth terms represent the fluctuation induced error. In particular, a comparison of the second and third terms reveals that the SOM, in the presence of fluctuations cannot detect variations in fractional reflectivity below $\delta(A)/A$, regardless of what the S/N calculations may suggest. In the DASOM, sensitivity is not affected, only the accuracy of the detection becomes subject to an uncertainty of $2\delta(A)/(A)$ {17}.

Using the DASOM a number of samples have been examined. Fig. 9 shows the surface of a highly polished stainless steel, clearly demonstrating the power of the in DASOM bringing out minute details. This micrograph of grains on steel compares favorably with those obtained using phase imaging techniques. Fig. 10, shows the surface of a silicon wafer, half of which was ion bombarded with Si, at a dose of 10^{13} / cm^2. The bright line in the middle of the micrograph is the demarcation between the two regions of the wafer. The observed contrast in this case is due to the lattice disruption due to the ion bombardment. Both these images were taken in a 30 kHz bandwidth. Other examples of the use of the technique in imaging and metrology are given elsewhere {17}.

3. Sensitivity

The ability of the two systems described above in imaging minute variations is now calculated. It can be shown that in the shot noise limit, considerations of S/N yield the following expression for the minimum detectable quantity, φ {18}:

$$\varphi = \{4h\omega_0 \delta f F/\eta P\}^{1/2} \qquad (12)$$

where φ is the ratio of the signal obtained at ω_s to that at DC. Here, h is the Planck's constant, δf is the bandwidth, ω_o is the optical frequency, F is the amplifier noise factor, η the quantum efficiency, and P is the received optical power. In the differential interference contrast technique, we have:

$$\varphi = \{2J_1(\delta\theta)(\delta\phi)\}/\{1-J_o(\delta\theta)\} \qquad (13)$$

where J_0 and J_1 are zeroth and first order Bessel functions of the first kind, respectively. Thus, for 100 μW of HeNe, δf of 1Hz, F of 2, and η of 0.8, and using the optimum value of θ {17}, the minimum detectable $\delta\phi$ is 10^{-7} rad. In terms of topography, this corresponds to a height variation of 5fm. For the DASOM, φ equals 2e. Accordingly, for the same parameter as above, the minimum detectable variation of refractive index for glass, as an example, is $6X10^{-8}$.

4. Conclusions

In this paper we have described two techniques which are modifications to the basic SOM : one responds primarily to amplitude, and the other images phase structures. We have shown that by resorting to differential and linear imaging concepts, substantial enhancement is achieved in contrast and sensitivity. The ultimate sensitivities of both these techniques are found to be comparable.

References

1. T Wilson and C.J.R. Sheppard, Theory and Practice of Scanning Optical Microscopy (Academic Press, London, 1983)

2. M. Francon, Progress in Microscopy (Pergamon, New York, 1961)

3. F. Zernike, Physica 1, 689 (1934)

4. S. Tolansky, Multiple Beam Interferometry of Surfaces and Films (Dover, New York, 1970)

5. G. Nomarski and A.R. Weill, Rev. Metallurgie L11, 121 (1955)

6. L.B. Laub, Jour. Opt. Soc. Amer. 62, 737 (1973)

7. G.E. Sommergren, Appl. Opt. 20, 610 (1981)

8. H.K. Wickramasinghe, S. Ameri, and C.W. See, Elec. Lett. 18, 973 (1982)

9. C.C. Huang, Opt. Eng. 23, 365 (1984)

10. G. Mackosh and B. Drollinger, Appl. Opt. 45, 4544 (1984)

11. R.L. Jungerman, R.C. Hobbs, and G.S. Kino, Appl. Phys. Lett. 45, 846 (1984)

12. C.W. See, M. Vaez Iravani, and H.K. Wickramasinghe, Appl. Opt. 24, 2373 (1985)

13. E. Hecht, Optics, (Addison-Wesley, New York, 1987) p. 319

14. C.W. See and M. Vaez Iravani, Elec. Lett. 22, 1079 (1986)

15. M. Vaez Iravani, Elec. Lett. 22, 103 (1986)

16. C.W. See and M. Vaez Iravani, Elec. Lett. 22, 961 (1986)

17. C.W. See and M. Vaez Iravani, Appl. Opt. 27, 2786 (1988)

18. M. Vaez Iravani and C.W. See, SPIE Proc. 987, 43 (1988)

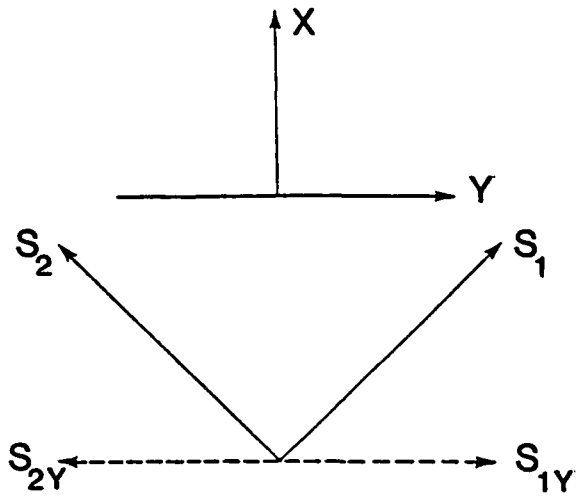


Fig. 1. Optical axes of the system: pass axes of the polarizer and analyzer (X,Y); two components of the beam and their projections along.

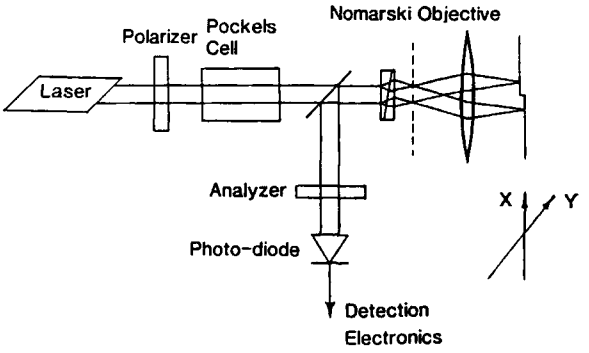


Fig. 2. Linear scanning differential interference contrast microscope.

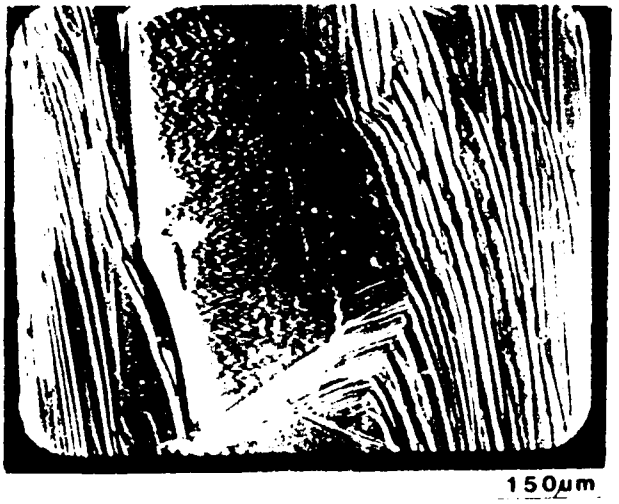
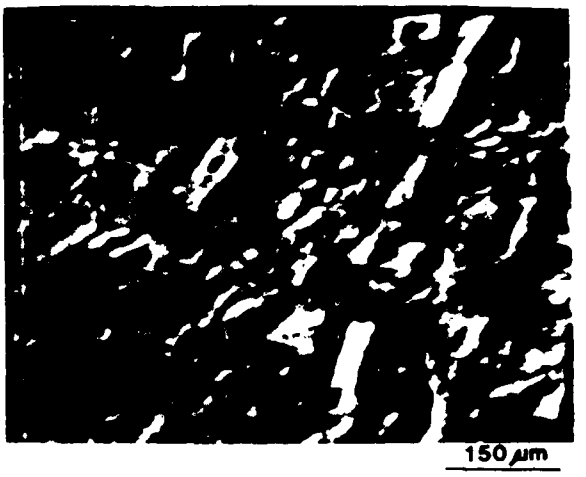


Fig. 4. Surface structure of natural diamond, showing growth ridges and stacking faults.



(a)



(b)

Fig. 3. Granular structure of polished stainless steel: a) linear image; b) quadratic image

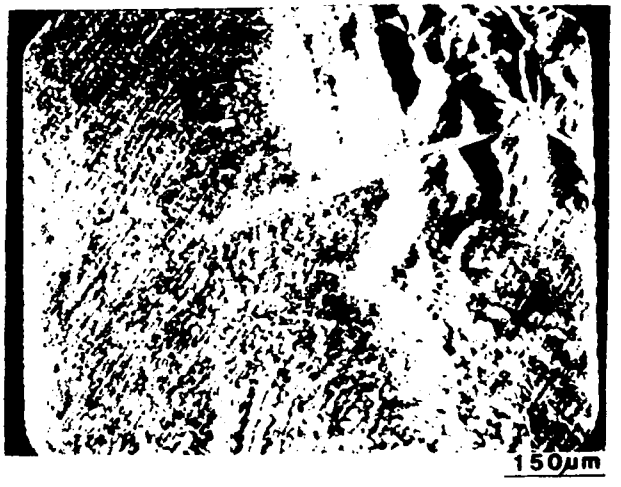


Fig. 5. Polishing lines on a polished diamond surface.

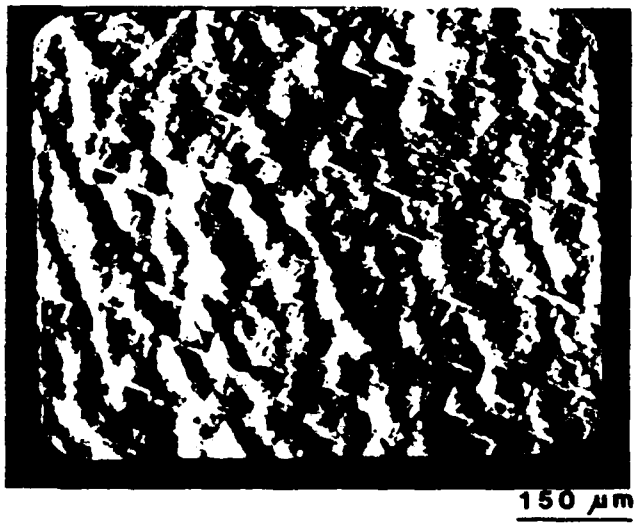


Fig. 6. Stacking faults and dislocations on epitaxial silicon.



Fig. 7. Stacking faults on silicon: the semicircular patterns are believed to be stress-induced birefringence.

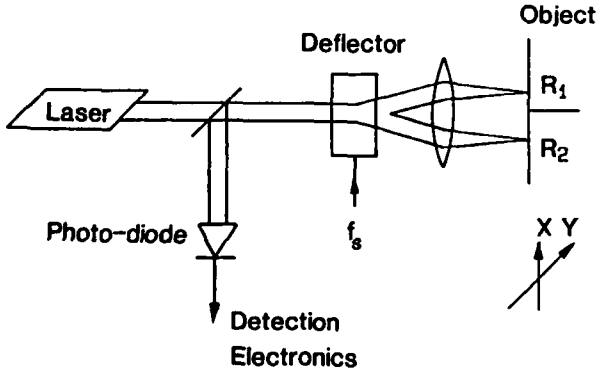


Fig. 8. System configuration of the DASOM.



Fig. 9. DASOM image of grains on polished stainless steel.

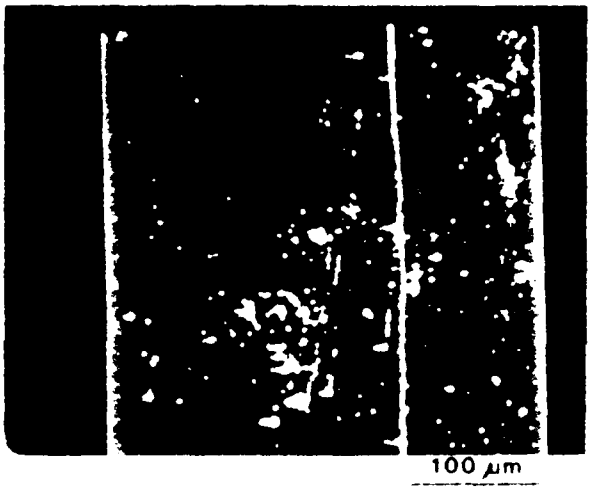


Fig. 10. Boundary between undoped and Si-doped silicon wafer.

Interferometric Evaluation of Holographic Materials

Roger C. Sumner and Pantazis Mouroulis

Rochester Institute of Technology
Center for Imaging Science
Rochester, New York 14623

ABSTRACT

An interferometric method for evaluating the performance of holographic optical elements (HOE's) and holographic materials is described. The method involves recording a spherical holographic lens, which is then played back in a collimating mode. The wavefront arising from the lens is made to interfere with a choice of two reference wavefronts. Analysis of the resulting interferograms provides a direct measure of the optical performance of i. the holographic material, ii. the substrate, and iii. the HOE. All the common measures of image quality can be obtained, including a set of Zernike polynomials that can prove useful in quantifying the performance of the holographic material. The method can be applied for transmission as well as reflection holograms. Test results obtained with silver halide amplitude transmission holograms are presented.

1. INTRODUCTION

Holographic lenses and gratings are finding increasing applications in precision optical instrumentation, such as spectrophotometers and laser scanners. In some cases these HOE's are specified to a wavefront degradation of less than $\lambda/4$. Hence, techniques for evaluating holographic materials and HOE's are needed which can provide a precise and direct measure of the wavefront quality.

The optical performance of HOE's is often quantified through a set of aberration coefficients arising from different recording and playback conditions [Welford, 1986]. In this type of calculation, the holographic material is assumed to have constant diffraction efficiency throughout the range of spatial frequencies concerned, and to introduce no wavefront distortion. The validity of this assumption cannot be taken for granted. For example, emulsion shrinkage is known to produce astigmatism which is minimized by having the hologram plane normal to the bisector of the angle between the object and reference beams. Also, there are several cases where recording and playback conditions are nominally the same, in which case the ultimate limitation comes from the recording material. It would then be helpful if the performance of the recording material could be characterized through the usual aberration coefficients.

Some of the current methods for evaluating holographic materials include measurement of diffraction efficiency [Lee and Greer, 1971], measurement of the MTF [Jones, 1967], the use of resolution targets [Champagne and Massey, 1969], measurement of the signal to noise ratio [Lamberts and Kurtz, 1971]. Scanning the point image of a holographic lens has also been recently suggested as a means of evaluating an HOE as well as some aspects of the recording material [Plaisted and Granger, 1988].

Unlike all of the above methods, the interferometric technique described here provides a direct measure of the wavefront quality, and makes it possible to isolate the wavefront deformation due to the substrate from that which is due to the photosensitive material.

2. DESCRIPTION OF THE METHOD

A spherical holographic lens is recorded and played back using the setup shown in figure 1. It is possible to record a transmission or reflection lens by appropriate orientation of the film holder. The collimated (B) and spherical (A) wave incident on the film are the reference and object beam respectively. The lens is exposed, processed and placed in the same location for playback. Aberrations due to misalignment can easily overwhelm all other effects [Lin and Collins, 1973], so particular attention must be paid to alignment.

Alignment: There are two cases to investigate. Case one is when the hologram is recorded in the same interferometer being used for the analysis. For this type of hologram, an alignment technique similar to that described by Soares [1979] is used. Both recording beams A and B are allowed through the hologram and their interference is observed. The hologram is then adjusted until the fringes vanish or are minimized. Since both beams travel the same path through the substrate, any wavefront deformation caused by the substrate does not affect the fringes, which then contain the effect of the material alone.

The second case arises when the hologram is exposed in a different system; for example, the equipment necessary to expose and process a novel material may not be available at the testing location. In this case, the previous alignment scheme using beams A and B will not work, because the recording setup (i.e. the reference and object beams and the angle between them) would have to be replicated exactly. Here, a combination of two techniques has been found useful, namely, using a shearing plate (collimation tester) in the reconstructed beam, as well as looking at the interference pattern between the reconstructed beam and reference beam C and trying to minimize the number of fringes. These adjustments are complicated by the fact that the reconstructed beam contains the effect of the hologram substrate, which can add substantial wavefront deformation. (Up to two waves of aberration have been observed with commercial silver halide plates across a 3cm aperture from the substrate alone.) Thus it is sometimes possible to introduce misalignment aberrations which balance to some extent those of the substrate, or in other words, the best resultant wavefront is obtained when the hologram is slightly misaligned. While this condition would then represent the optimum playback for the HOE, it does not allow us to isolate the effect of the recording material. Therefore, if the material performance is required (rather than the HOE), there are only two options: either record and analyze in the same interferometer, as in case 1, or ensure that the substrate is flat within the required experimental accuracy.

Evaluation: There are three interferograms to examine. The interferometer has been set up to allow interference between any two of the three beams A, B, and C, by simply blocking the unwanted beam and re-adjusting the variable beamsplitters for optimum fringe visibility. Beam A is the reconstructed (nominally collimated) beam, containing the combined effect of the material and substrate. B is the undiffracted beam through the hologram containing the effects of the substrate alone, and C is an external reference. Thus, interference of beams A and B gives the effect of the recording material, beams B and C give the effect of the substrate and beams A and C give the aberrations of the complete lens. We can also obtain the effect of the recording material by subtracting the substrate from the complete lens. The subtraction is done by the fringe interpretation software. This latter method must be used if the lens was recorded in a different setup. It may also be more convenient to use because of some practical limitations of the fringe digitization routine. Specifically, the fringes arising from the interference of beams A and B are fixed; there is no means of adding tilt which can help with fringe digitization. On the other hand, beams A and C go through an additional beamsplitter which provides this adjustment.

The equipment used to analyze the above interferograms is shown in figure 2. The frame grabber acquires an image of the interferogram from the CCD camera, and displays that frame on the monitor. We used a commercial fringe interpretation software package from Wyko Corp. to digitize the fringes, fit Zernike polynomials to the wavefront, and calculate the optical path difference, the point spread function, and the modulation transfer function.

3. RESULTS

The first step is to test the quality of the two reference beams C and B (with no plate in the path). This can be accomplished with a collimation tester and by analyzing the fringes resulting from their interference. The reference wavefronts were found to be flat to better than $\lambda/8$ across the aperture.

Preliminary results were obtained with silver halide amplitude transmission holograms. We used first a hologram recorded previously in a different setup, for which the Soares method cannot be used. The parameters of the hologram are given below.

Film:	Agfa Holotest 8E75
	Emulsion Thickness 7μm
	Plate Thickness 1.6mm
Recording Geometry:	f/5, 1" Aperture
	Reference to Object Beam Ratio 20:1
	Gaussian Apodization < 10%
	Reference to Object Beam Angle 90°
	Beam to Film Normal Angle 45°
	Range of Fringe Frequencies 2100-2300 lp/mm
Processing:	Standard amplitude hologram

After fringe digitization and polynomial interpolation, the program can display any of several image or wavefront quality metrics, from which we have chosen the Point Spread Function (PSF) for presentation. The displayed PSF gives an immediate appreciation of the image quality expected if the hologram is used in focusing mode. Since there is very little Gaussian apodization, a perfect PSF would be the Airy disk.

Figure 3 shows the modulus of the PSF representing the combined effects of emulsion plus substrate. Figure 4 shows the PSF that corresponds to the degradation arising from the glass substrate alone. By subtracting the wavefront aberration of the plate from that of the film-plate combination, the performance of the film is obtained (figure 5).

In terms of aberration coefficients, the table below shows the first few Seidel terms which are easily calculated from the Zernike terms. Higher order terms are not shown. All values are in wavelengths of wavefront aberration.

	substrate + emulsion (fig. 3)	substrate (fig. 4)	emulsion (fig. 5)
spherical	-.4	.05	-.39
coma	.29	.52	.29
astigmatism	2	1.1	1.4

Although the emulsion performance is obtained as the difference between the other two conditions, we cannot expect the difference between the aberration coefficients in the first two columns to give us exactly the coefficients of the third column. This is because i. higher orders are not shown, and ii. the program subtracts the two wavefront phase maps and then performs a new interpolation to determine the Zernike coefficients of the difference.

Preliminary results have also been obtained for holograms recorded and analyzed in the same setup, on Kodak 649F plates, with all other conditions similar. In this case, it is important to establish that the Soares setup (interference of beams A and B) gives the same results for the emulsion performance as the indirect method of subtracting the two interferograms. Our results so far support this conclusion, demonstrating the validity of the method. Complete results will hopefully be published in the future, but the table below gives an example.

	substrate + emulsion	substrate	emulsion
spherical	-.1	-.1	0
coma	.66	.59	.16
astigmatism	-1.9	-2.1	.26

For this HOE, the glass substrate is primarily responsible for the observed optical performance. The values for the emulsion alone were obtained through the subtractive method. The interference of beams A and B should give values very similar to those of the "emulsion" column of the above table. We observed approximately half a fringe across the entire aperture when interfering those two beams. This is compatible with the optical performance expected, but such an interferogram does not lend itself to precise digitization and analysis. To obtain more quantitative measurements, either the beam angle must be increased or the f-number of the HOE must be reduced to the point where substantial degradation is observed from the emulsion, leading to several fringes across the aperture.

4. CONCLUSIONS

The method described provides a direct, precise measurement of the optical performance of a holographic lens in terms of the wavefront quality and aberration coefficients. This information is very useful as holograms are pushed to the limits of their optical performance.

The method also provides a simple yet versatile means of obtaining information about the optical characteristics of a holographic material. The apparatus allows us to record, align, and analyze a holographic lens, and to isolate the performance of the substrate from the performance of the holographic material itself.

The method could prove to give useful insight into the performance limits of holographic materials. The Zernike coefficients might be used to characterize the performance of a given material in a way that allows the system designer to predict the wavefront degradation of the material and attempt to correct it with additional optical elements.

REFERENCES

1. W.T. Welford, Aberrations of Optical Systems, (Adam Hilger, 1986), pp. 217-225.
2. W.H. Lee and M.O. Greer, J. Opt. Soc. Am. **61**, 402 (1971)
3. R.A. Jones, Photogr. Sci. Eng. **11**, 102 (1967)
4. E.B. Champagne and N.G. Massey, Appl. Opt. **8**, 1879 (1969)
5. R.L. Lamberts and C.N. Kurtz, Appl. Opt. **10**, 1342 (1971)
6. P.B. Plaisted and E.M. Granger, presented at the 41st Annual SPSE Conference, Arlington VA (1988)
7. O.D.D. Soares, Appl. Opt. **18**, 3838 (1979)
8. B.J. Lin and S.A. Collins Jr., J. Opt. Soc. Am. **63**, 537 (1973)

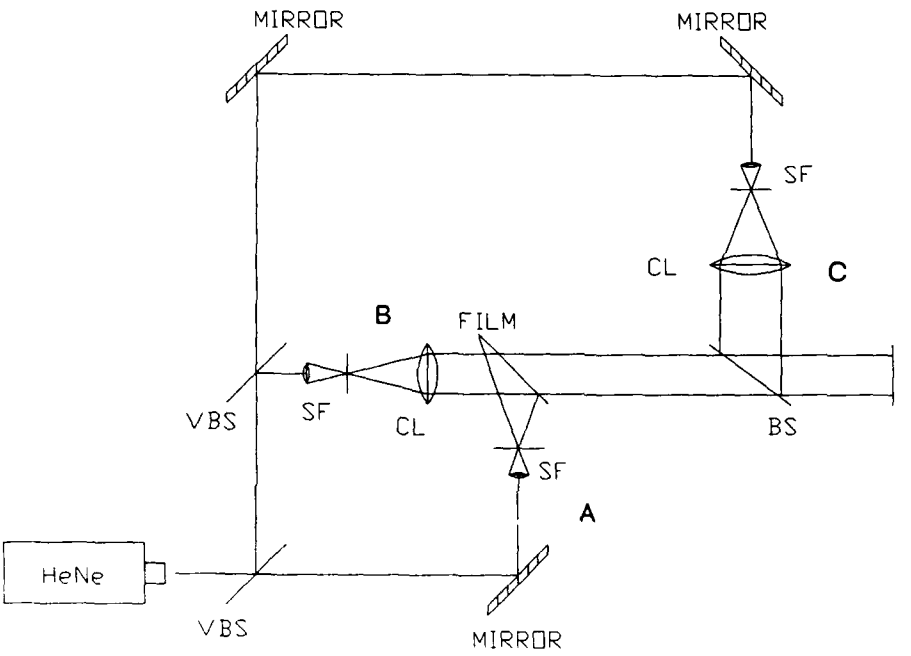


Figure 1 - Interferometric setup used for recording and analyzing the holographic lenses. VBS: variable beamsplitter, SF: spatial filter, CL: collimator. Arms A and B are used during recording.

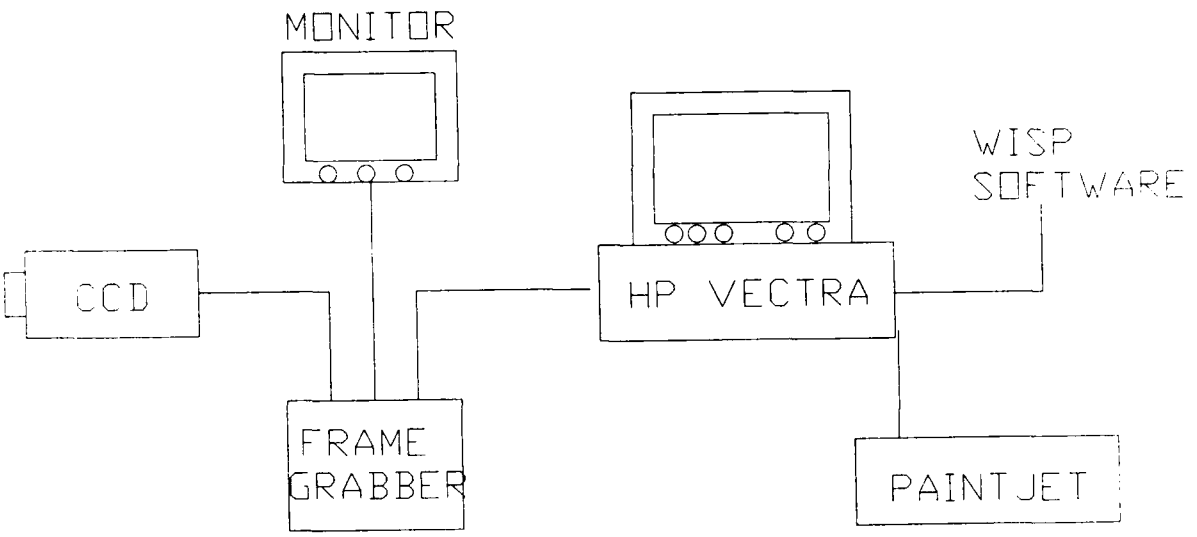


Figure 2 - Hardware for interferogram analysis

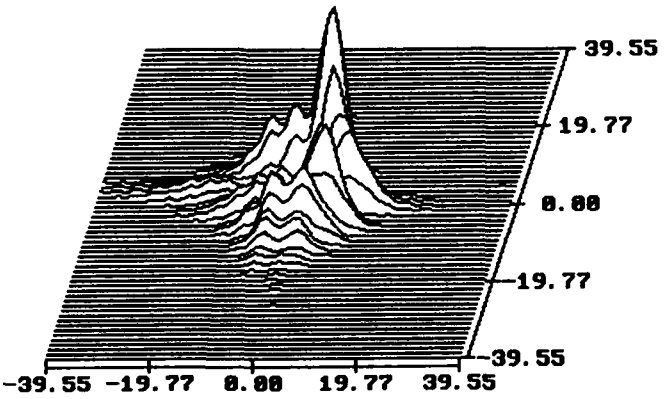


Figure 3 - Modulus of the point spread function of HOE. The axis scales are in microns. Obtained through interference of beams A and C.

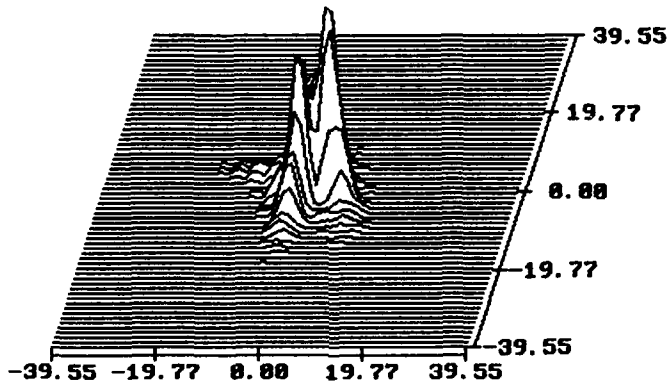


Figure 4 - Modulus of the point spread function of glass plate on which the HOE of fig. 3 was recorded. Obtained through interference of beams B and C.

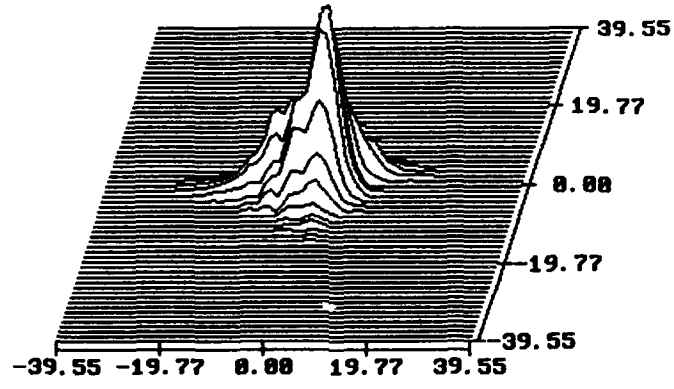


Figure 5 - Modulus of the point spread function of the emulsion, under the recording and processing conditions mentioned in the text. Obtained by subtracting the wavefront aberration corresponding to the previous two PSF's.

THE EFFECT OF HELIUM-NEON LASER AND OSTEOPATHIC MANIPULATION ON SOFT TISSUE TRIGGER POINTS

Charlotte H. Greene, Ph.D.
Professor of Physiology and Pharmacology
Domenic A. DeBias, Ph.D.
Professor and Chairman, Department of Physiology and Pharmacology
David Heilig, D.O.
Professor and Vice-Chairman, Department of Osteopathic Manipulative Medicine
Alexander S. Nicholas, D.O.
Professor and Chairman, Department of Osteopathic Manipulative Medicine
Katherine M. England, D.O.
Professor, Department of Osteopathic Manipulative Medicine
Walter Ehrenfeuchter, D.O.
Professor, Department of Osteopathic Manipulative Medicine
Wanda L. Young, B.A.
Senior Research Associate, Department of Physiology and Pharmacology

Philadelphia College of Osteopathic Medicine
4150 City Avenue
Philadelphia, Pennsylvania 19131

Abstract

The clinical utilization of low-power laser remains controversial despite investigations of a variety of analgesic and wound-healing applications. Reports of laser treatment to resolve the abnormally low skin resistance patterns that accompany myofascial trigger points prompted this study to compare the treatment of trigger points by laser to that by osteopathic manipulative treatment (OMT). Volunteers in which soft tissue trigger points were palpable on the thoracic dorsum served as subjects. Treatments were: 1) laser alone; 2) sham laser; 3) OMT alone; 4) OMT + laser. The palpable quality of the area was rated on a scale before and after treatment; skin resistance was measured at these same intervals. Qualitative changes due to OMT but not laser were noted on the first day of treatment; by day 2 and 3 subjects having either treatment were equally well improved. No statistically significant changes in skin resistance could be demonstrated during the experimental period although there was a trend toward increasing skin resistance and in no group except sham did skin resistance decrease.

Introduction

Low energy lasers are utilized to treat numerous neurological and musculoskeletal pathologies [1-12]. Their acceptance in Europe and the Soviet Union exceeds that in the United States where FDA approval has been withheld for all but investigational applications. Reports of laser treatment to resolve the abnormally low skin resistance patterns that accompany myofascial trigger points [13,14] prompted this study to compare the treatment of trigger points by laser to that by Osteopathic Manipulative Treatment (OMT). Soft tissue trigger points are indicative of a myofascial syndrome which is characterized by focal sites which elicit pain in response to manual palpation. They are similarly defined in the traditional (allopathic) medical, and osteopathic literature as:

1. (Allopathic) a point that elicits referred pain on deep palpation and demonstrates a lowered skin resistance in comparison with that of surrounding tissue [13-16].
2. (Osteopathic) a small hypertensive site, that, when stimulated, consistantly produces a reflex mechanism that gives rise to referred pain or other manifestations. The response is specific, in a constant reference zone, and consistant from person to person [17]. Trigger points are routinely treated by direct and indirect manipulative techniques with and without injection of local anesthesia. Low-level HeNe laser treatment alone and in combination with OMT were used in this investigation of soft-tissue trigger points.

Methods and Materials

Volunteer subjects (Figure 1) with palpable trigger points on the thoracic dorsum were randomly assigned to one of the following experimental groups: 1) HeNe laser treated; 2) Sham laser treated; 3) OMT-treated; 4) HeNe laser treated + OMT. An osteopathic physician uninformed as to their status screened each subject for the presence of trigger points and rated the intensity on a decreasing scale from 5 to 1. One of three templates corresponding most closely to the size of the trigger point (Figure 2e) was applied to the overlying skin. The perimeter was traced with non-toxic, indelible ink so that this area could be exactly defined during subsequent treatment sessions. The template was replaced prior to laser and sham treatment and the measured holes used for delivery of the beam or sham to facilitate the accurate standardization of dose.

Skin resistance measurements and physician-rating of the trigger point site were made at the beginning and the end of each treatment session by a technical assistant charged with the maintenance of the "blinded" aspects of the study. Skin resistance was measured at these same times on the dorsal aspect of the upper arm midway between the acromion and the lateral epicondial of the humerus as a control site for all groups (after the presence of trigger points was ruled-out in this area).

Groups 1 and 3 received laser irradiation to the trigger point area for 15 seconds at 0.95 mW for a calculated dose of 14.25 mJ/cm^2 trigger point area. Treatment was administered by an investigator goggled to selectively exclude light at 632.8 nm. Subjects in groups 1, 3 and 4 also received OMT directed toward resolution of the trigger point. Physicians were directed to use standard techniques relative to the individual symptomatology since the goal in this study was to optimize the chance for demonstrating efficacious results; not to promote a particular technique. Three treatments were given to all subjects; no less than one nor more than three days apart [13,18].

A Dynatron 1120 HeNe laser with a built-in dermometer for recording surface skin resistance measurements was used in this study (Figure 2a). This instrument is classified by the U.S. Food and Drug Administration's Bureau of Radiologic Health as a Class II laser product and a Class III medical device. Class II laser products are limited to visible lasers that are safe for momentary viewing. Class III medical devices include new or modified devices not substantially equivalent to any marketed before May 28, 1976. It is a visible, monochromatic, red laser with a wavelength of 632.8 nm that penetrates tissue without diverging to 0.8 mm and with some divergence to 10 to 15 mm. It is therefore a superficial physical agent (more than 50% of the energy is absorbed by tissue located less than 1 cm below the skin surface). At therapeutic doses for 15 to 20 seconds with a maximum intensity of 0.95 mW, the energy produced is about 14 to 29 mJ, which is substantially below the level that will produce tissue heating.

The beam is conducted through a fiberoptic stylus probe (Figure 2b). The hollow metal tip also serves as a transmitting electrode that conducts a small electrical signal used by the dermometer to measure surface skin resistance. The receiving electrode is a silver metal cylinder placed in contact with the subject in a position opposite to the transmitting electrode (Figure 2c).

The digital meter on the dermometer was calibrated in a range between 0 and 100; the lower the number, the higher the resistance. Skin resistance readings generally were recorded between 50 and 30 which corresponds to skin resistances between 150 and 300 Kohms. Sham treatments utilized the same laser placed in sham mode via a switch in the rear of the machine (all lights, sounds and functions were maintained identical to the operating mode excepting the emission of the laser beam). The probe was fitted with a plexiglass guide to standardize the depth to which the metal tip penetrated (Figure 2d). Subjects remained prone on an examination table for all procedures. Ambient temperature and humidity were stabilized throughout the experimental period.

Results

A two-way analysis of variance was used to compare the groups with respect to changes in skin resistance from baseline to days 1, 2 and 3. No statistically significant differences were found at the 5% level, although trends of increasing skin resistance (decreased meter readings) were noted in all but the sham-treated group following the second and third treatments (Figure 3).

A two-way ranked analysis of variance [19] was applied to the changes in trigger point ratings from baseline to days 1, 2 and 3. On day 1 OMT produced significant improvement at the 5% level (69% improved with OMT vs. 12.5% without OMT) whether or not laser was used. There was no observable effect of laser nor was there any significant interaction between laser and OMT. On the basis of this result the data were regrouped and the subjects who had no OMT (i.e. group 1 (laser alone) and group 2 (sham laser) were tested against those that did (i.e. group 3 (OMT alone) and group 4 (OMT + laser) with respect to percent of subjects improved using Fisher's Exact Probability Test. The groups receiving OMT were found to have a significantly higher improvement rate compared to the groups that did not receive OMT ($P = .003$). The analyses of variance for days 2 and 3 differed from day 1 as they suggested an improvement after both laser and OMT treatments with no interaction between treatments. On the basis of these results the data were regrouped and the subjects who had either laser and/or OMT treatments (i.e. groups 1, 3 and 4) were tested against those who had no treatment (group 2) using Fisher's Exact Probability test. Subjects receiving treatment were found to have a significantly high rate of improvement compared to those receiving no treatment on both day 2 and day 3 ($P = .03$) (Figure 4) and the effect of either treatment was comparable, i.e. one could be substituted for the other. There appeared to be no interaction between them although this thesis must be further investigated over a longer treatment period. None of the subjects in the sham treatment group showed any improvement on day 2 or 3.

Discussion

When interpreting the significance of this data it must be noted that the latter comparisons were not preplanned. Rather they were suggested by the data. It appears that the effects of the laser are not as immediate as those seen following OMT. The mechanisms by which low energy lasers may exert their effects are unclear. The latency we observed is in keeping with the "stimulating hypothesis" [20,21] which proposed that certain cellular functions must be induced before the laser effect is expressed. It is difficult to draw clear assumptions from these results regarding alterations in skin resistance after OMT and/or laser therapy. Some of the variability in the individual measurements originated from the design of the dermometer (resistance meter). It is a two electrode system utilizing a 1 mm transmitting electrode with a current limit between 70 and 261 microamps. The resistance of the electrodes is large in comparison to the conducted current. This study will be repeated using alternative instrumentation (Impedance Meter, RJL Systems) for measuring skin resistance that should increase the sensitivity and stability of the measurements and provide for external calibration of the volume through which the resistance changes are measured. Demonstration of the efficacy of either treatment modality would give support to OMT procedures currently utilized clinically and also provide a new modality that may potentiate certain therapeutic effects already achieved.

(This study was supported in part by the Philadelphia College of Osteopathic Medicine and a grant from the Advanced Technology Center of Southeastern Pennsylvania. The laser was loaned by Dynatronics Laser Corporation, Salt Lake City, Utah).

References

1. Basford JR, Low-Energy Laser Therapy: Controversies and New Research Findings. Lasers in Surgery and Medicine 9: 1-5, (1989).
2. Fork RL, Laser Stimulation of Nerve Cells in Aplysia, Science. 171:907-908, (1971).
3. Rochkind S, et al, Response of Peripheral Nerve to HeNe Laser: Experimental Studies. Lasers in Surgery and Medicine, 7: 441-443, (1987).
4. Walker JB, Akhanjee LK, Laser-induced Somatosensory Evoked Potentials: Evidence of Photosensitivity in Peripheral Nerve Brain Research, 344: 281, (1985).
5. Greathouse DG, Currier DP, Gilmore RL, Effects of Clinical Infrared Laser on Superficial Radical Nerve Conduction. Phys. Ther., 65: 1184, (1985).
6. Trelles MA, Mayayo E, Bone Fracture Consolidates Laser with Low-Power Laser. Lasers in Surgery and Medicine. 7: 36-45, (1987).
7. Colov HC, Palmgren N, Jensen GF, Kaa K, Windelin M, Convincing Clinical Improvement of Rheumatoid Arthritis by Soft Laser Therapy. Lasers in Surgery and Medicine (abstract), 7: 77, (1987).
8. Bliddal H, Hellesen C, Ditlevsen P, Asselberghs J, Lyager L, Soft-Laser Therapy of Rheumatoid Arthritis. Scand. J. Rheum. 16: 225, (1987).
9. Walker JB, Akhanjee LK, Cooney MM, Goldstein J, Tamayoshi S, Sgal-Gidan F, Laser Therapy for Pain of Rheumatoid Arthritis, Clin. J. Pain. 3: 54-59, (1987).
10. Braverman B, et al, Effect of Helium-Neon and Infrared Laser Irradiation on Wound Healing in Rabbits. Lasers in Surgery and Medicine, 9: 50-58, (1989).
11. Mester E, et al, The Biomedical Effects of Laser Application, Lasers in Surgery and Medicine, 5: 31-39, (1985).
12. Yew DT, et al, Stimulation of Collagen Formation in the Intestinal Anastomosis by Low Dose HeNe Laser. Scanning Microscopy 3(1): 379-386, (1989).
13. Snyder-Mackler L, et al, Effect of Helium-Neon Laser on Musculoskeletal Trigger Points. Physical Therapy 66(7): 1087-1090, (1986).
14. Snyder-Mackler L, et al, Effects of Helium-Neon Laser Irradiation on Skin Resistance and Pain in Patients with Trigger Points in the Neck or Back. Physical Therapy 69(5): 336-341, (1989).
15. Melzack R, et al, Trigger Points and Acupuncture Points for Pain: Corrections and Implications. Pain 3: 3-23, (1977).
16. Travel J, Temporomandibular Joint Pain Referred from Muscles of the Head and Neck. J. Prosthet. Dent. 10: 745-763, (1960).
17. Ward RC, and Sprafka G, Glossary of Osteopathic Terminology. J.A.O.A. 80(8): 552-567, (1981).
18. Kleinkort J, Foley R, Laser Acupuncture: Its Use in Physical Therapy. Am. J. Acupuncture, 12: 51-56, (1984).
19. Zar JH, Biostatistical Analysis 2nd Edition, Englewood Cliffs, New Jersey, Prentice Hall, Inc., pp. 249-252, (1984).
20. Yew DT, et al, Stimulating Effect of the Low Dose Laser - A New Hypothesis. Acta Anat. 112: 131-136, (1982).
21. Yew DT, et al, Stimulation of Collagen Formation in the Intestinal Anastomosis by Low Dose HeNe Laser. Scanning Microscopy Vol. 3(1): 379-386, (1989).

Group	Age (yrs.)	Sex	Weight (lbs.)	Height (ft-in)
I (Laser Alone)	22-34	M:2 F:6	122-190	5'1"-6'
II (Sham-Laser)	22-35	M:5 F:3	110-200	5'4"-6'2"
III (OMT Alone)	23-34	M:3 F:5	102-200	5'0"-6'0"
IV (Laser + OMT)	22-31	M:6 F:2	125-200	4'11"-6'2"

FIGURE 1. PROFILE OF VOLUNTEERS SUBJECTS THAT PARTICIPATED IN THE PILOT STUDY

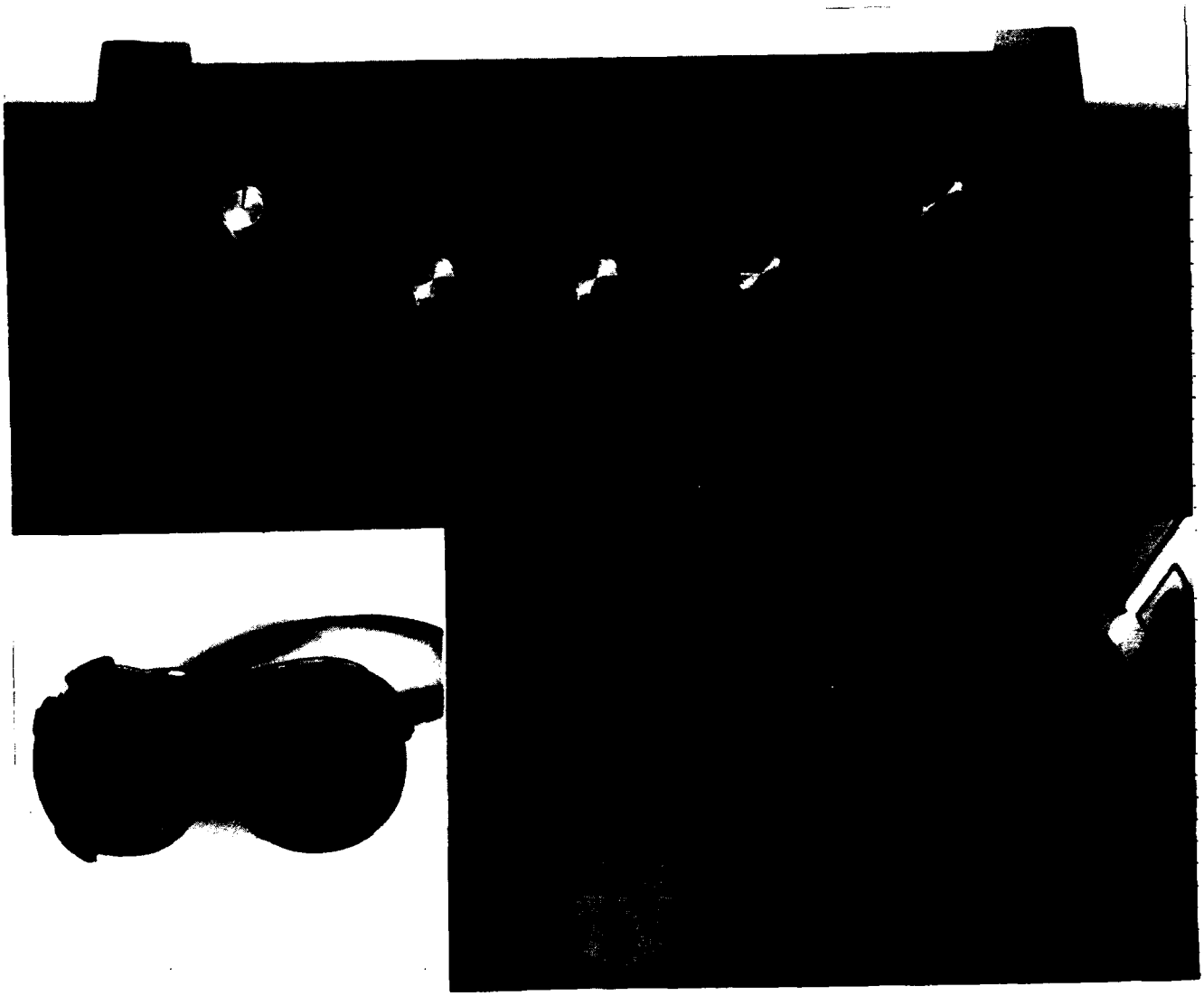


FIGURE 2a. DYNATRON 1120 HeNe LASER; 2b. FIBEROPTIC STYLUS PROBE; 2c. RECEIVING ELECTRODE 2d. PLEXIGLASS GUIDE; 2e. PAPER TEMPLATES

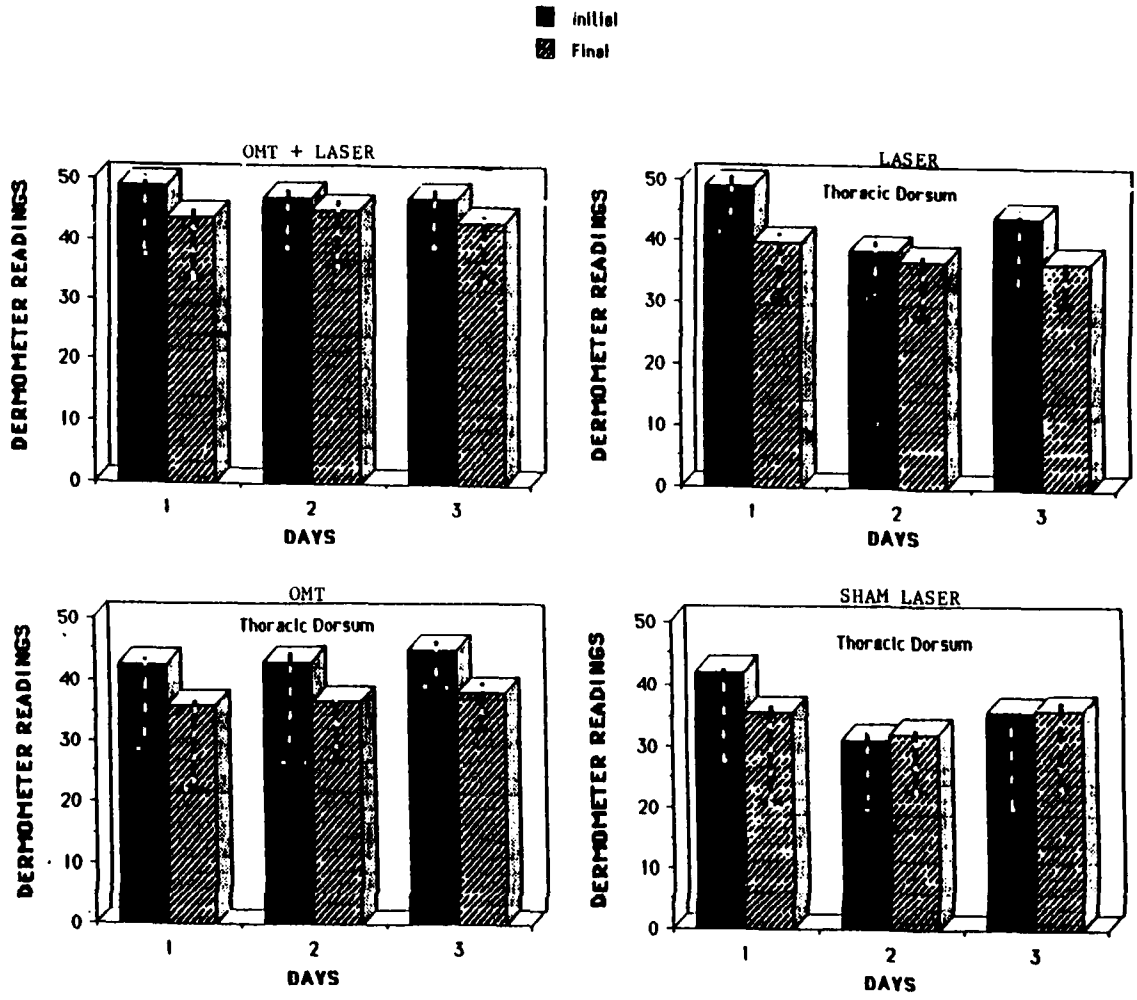


FIGURE 3. CHANGES IN SKIN RESISTANCE(INITIAL AND FINAL) FOLLOWING TREATMENT/SHAM TREATMENT

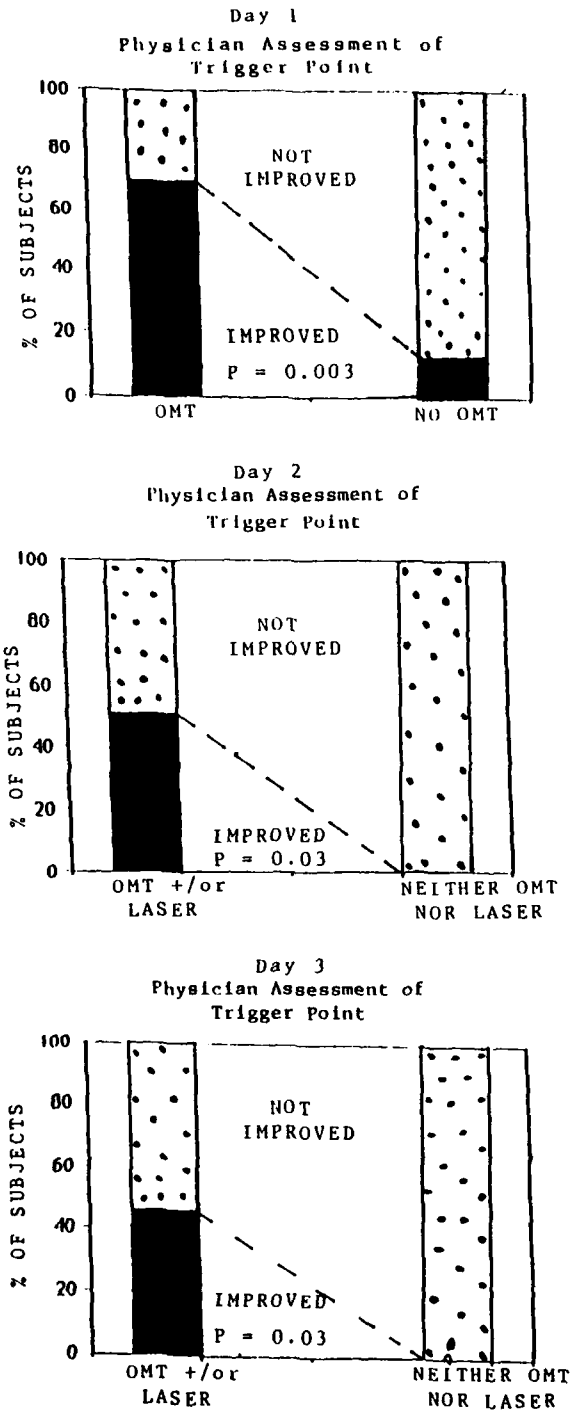


FIGURE 4. DIFFERENCES IN TRIGGER POINT RATINGS BY THE OSTEOPATHIC PHYSICIANS

HOE
Holographic Optical Elements

E. Stijns - S. Roose
Vrije Universiteit Brussel, ALNA - TW
Pleinlaan 2, B 1050 Brussel, Belgium.

Abstract.

Holography is known as a technique for reproducing 3-D images of objects. But holography can do more than that : holography can be used to make lenses, mirrors, ..., or in general : Holographic Optical Elements. This paper gives an introductary review of Holografic Optical Elements. Basic principles are outlined, some attention is paid to the analysis, design and aberations. It ends with a description of some simple applications.

1. Introduction.

Holography is a technique used for the reconstruction of wavefronts. In figure (1-a), a hologram is recorded as an interference pattern between a divergent and a convergent beam. When a reconstruction beam illuminates the hologram, (fig. 1-b), a convergent image beam is reproduced. But you can also look at figure 1-b from the viewpoint of geometrical optics : in that language, the point Q is the **image** of object point P ; in other words : the hologram acts as if it were a **lens**, imaging point P onto Q. In a similar way, one can construct other optical elements : as e.g. a mirror, or a set of lenses. Consequently HOEs are optical elements which bend light ray by virtue of **diffraction**, instead of reflection (classical mirror) or refraction (classical lens).

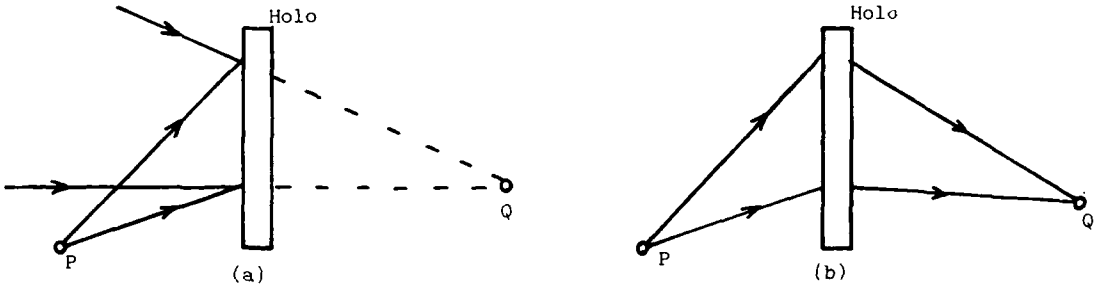


Figure 1

2. Types of HOEs.

HOEs are classified in the same way as holograms are classified (ref. 1). We will only speak of those parameters which are relevant for HOEs.

(a) Thin versus thick.

A **thin** hologram acts as a surface grating : the grating equation $\Lambda(\sin\theta_1 + \sin\theta_2) = \lambda$ sets the direction of the ray (fig.2a). A **thick** hologram (fig.2b) adds also some volume properties : the grating on the surface of the hologram sets the direction of the ray, and diffraction from the volume will increase or decrease the energy of the ray, in other words the diffraction efficiency. Maximum efficiency is obtained when the Bragg equation (which is the same as in solid-state physics) is satisfied.

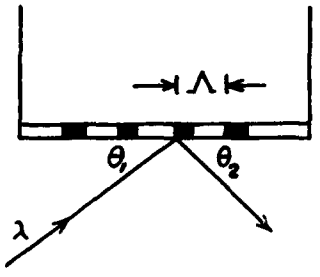


Figure 2a

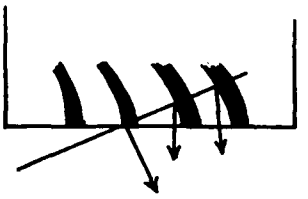


Figure 2b

(b) Phase versus amplitude.

The hologram HOE can change the wavefront of the incoming wave, either by absorbing some pieces of it (amplitude hologram) or by changing the phase in each point, according to some specific rules (phase hologram). Because a phase hologram doesn't absorb energy

from the beam, the (theoretical) diffraction efficiency can reach 100 %, if volume diffraction contributes positively. Because it is very important that an optical element transmits as much energy as possible, a HOE is always a phase hologram, and - if possible - a thick one.

3. Properties of HOEs

(a) The reflection of a light ray at a mirror is independent of its wavelength ; the refraction in a prism or lens is slightly dependent on wavelength ; the diffraction on the other hand is proportional to wavelength ! So a HOE, which bends light rays by diffraction is **strongly wavelength dependent**. This is an advantage when you use the HOE as a dispersive element ("holographic grating"). For general purpose lenses, on the other hand, it is clearly a disadvantage : it is not possible to replace a camera lens by a single HOE. If you want to use the HOE in a monochromatic application, its wavelength dependence doesn't matter : so HOEs are mostly used with lasers, LEDs or narrow band phosphors.

(b) HOEs are very thin (~ 15 µm), even the "thick" ones, and consequently very light weight. This is an important property, when HOEs are used in scanners, in airplanes, or in space applications.

(c) HOEs can be applied on existing surfaces (e.g. on other lenses), whatever be their shape. An example is the HUD : head-up display (see section 5.2).

(d) Multiple optical functions can be combined in one single HOE

(e) If photographic reproduction is possible, as is often the case, cheap mass-production can be realized.

(f) It is possible to construct a HOE for use in transmission mode, or in reflection mode, or even in both modes at the same time.

(g) Large numerical apertures are possible.

(h) A HOE, being an infinitely thin element, doesn't changes the **position** of a light ray, but only its angle.

(i) Although diffraction efficiency of a thick phase hologram can reach 100 %, in practice - due to constraints - this theoretical limit is seldom realized.

(j) Because they are mostly used off-axis, and because of their strong wavelength dependence, aberations are very large ; this poses often real problems.

4. Design and analysis of HOEs.

We have seen that HOEs can be made by simple interference of two (spherical) waves (fig 1). If the reconstruction wave is the same as the reference wave, then the image wave is the same as the object wave. In the language of geometrical optics, we say that the point I is the image of point C. If, on the other hand, we consider another object point C', it is not clear what will happen (fig. 3). In general, its image I' will not coincide with its " ideal " image; in other words: aberations will appear.

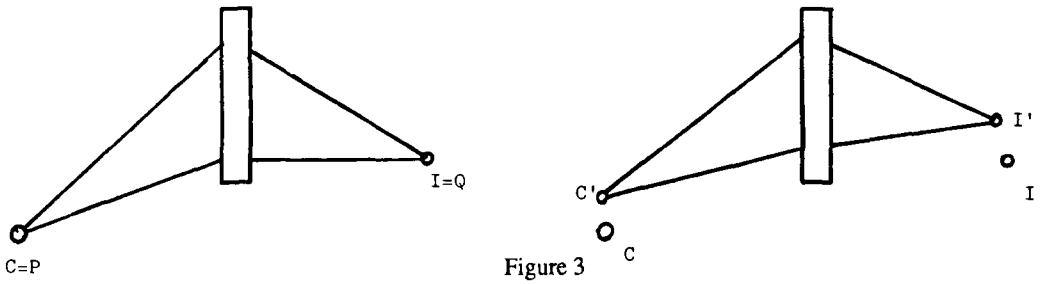


Figure 3

4.1 Design and analysis of **optical** HOE's

As with holograms in general, a HOE can also be considered as being a generalized diffraction grating, formed by the interference of two light waves. At each point of the HOE, the grating vector $\vec{K}$ is given by

$$\vec{K} = \vec{k}_1 - \vec{k}_2$$

where $\vec{k}_1$ and $\vec{k}_2$ are the local wave vectors of the two interfering beams.

The change an incoming light wave ondergoes at the HOE can be calculated by wave or by a ray analysis.

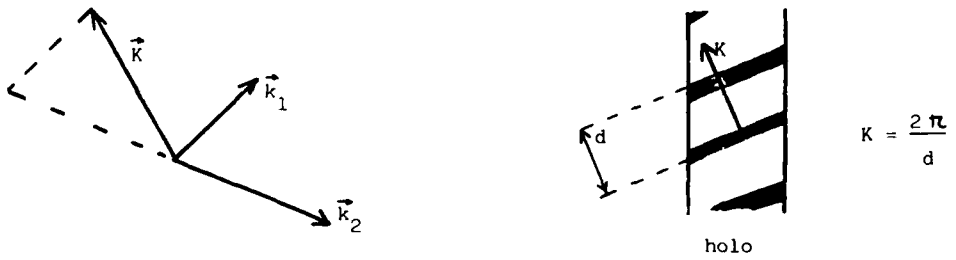


Figure 4

4.1.1 Ray analysis.

When the reconstruction light ray C falls on the surface of a HOE, it is deviated according to the local surface grating, into a direction I (Image), given by the local grating equation; in other words, by the spacing and orientation of the grating " grooves". In a certain way, we can say that Snellius' law is replaced by the grating equation. In this way, a bundle of rays, coming from an object, can be followed through the optical system, and the image can be calculated. This is very similar to the calculation of the path of a ray through classical lenses. In fact, some computer lens design programs do indeed incorporate HOEs in their design package. It is important to note that these calculations tell nothing about the amount of light going into the desired direction, i. e. the diffraction efficiency. The latter property is determined by the volume properties of the HOE (Bragg's law), and/or the blazing properties of the surface grating. It is also important to note that the direction of the image ray I is only determined by the local surface grating, and (in a first order) not by the form of the substrate on which the HOE is made. This is an important property by which a HOE differs completely from a COE (Classical Optical Element) : indeed in a COE it is the **form** of the surface which determines its properties.

An alternative way for ray tracing through a HOE is to consider it as being a lens. It is known that the thinner the lens, the higher its refractive index has to be. So a hologram, which is almost infinitely thin, can be considered as a lens with an almost infinite refractive index (ref. 2). This way of describing a HOE allows the use of normal ray-tracing programs, at least when they allow a very high index of refraction to be used. It has been shown that this method of calculation gives correct answers, even for third order aberations.

Aberations can now be calcultated in two ways (ref. 3) :

(a) either you follow a bundle of rays through the system and calculate the intercept of each of the rays with the image plane. Such a **ray intercept image** is convenient to calculate and visualizes the aberations.

(b) or you calculate, for each of the rays, the optical path length from the object plane. The surface which connects all points with the same OPL gives the actual wavefront, which has to be compared with the ideal (aberation free) wavefront, which is usually a sphere. This is more difficult to calculate than (a) but, because the real wavefront is known, diffraction effects can easier be taken into account.

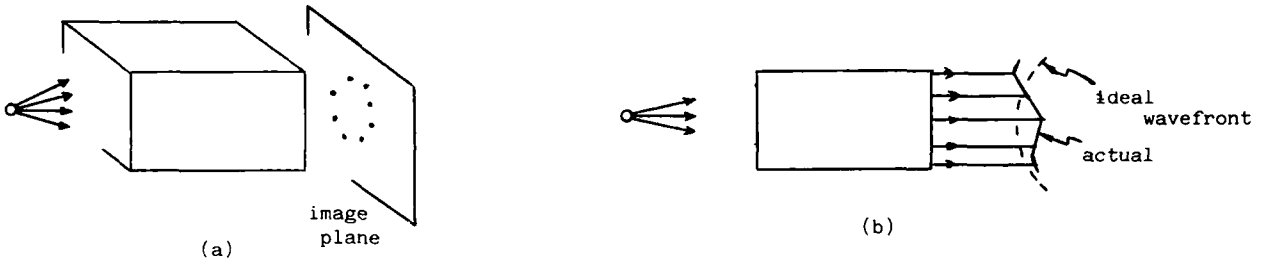


Figure 5

4.1.2 Wave analysis.

It is possible to calculate the diffracted wave by applying diffraction theory. This has the advantage that one has in the same formula the direction of the wave (the image) and the amount of energy (diffraction efficiency) going into it. But of course the formulas are much more complicated than with a ray analysis. Because one knows the real wavefront, it is possible to compare that wavefront with the aberation free spherical wavefront, and so the **analytical** expressions for the aberations are known. Those analytical expressions are extremely complicated, among others by the fact that the HOEs are usually used off-axis, which means that even no rotational symmetry exists. In order to say something about it, one makes a series expansion of the image wave in aperture and field coordinates, as is done in conventional optics.Contrary to classical optics, however, one cannot limit oneself to third orders, but often fifth order aberations have to be taken into account. The great problem here is that the aberation theory is very complicated and not yet fully develloped- as is the case with COE aberation theory. So mostly people are simply using raytracing programs.

4.2 Computer Generated HOEs.

As with holograms in general, also HOEs can be computer generated. The basic idea is shown in figure 6. An incoming wave A (x,y) is transmitted by the HOE into a transmitted wave A (x,y) T (x,y) , which diffracts to give the desired wave D (x,y) in the image plane.

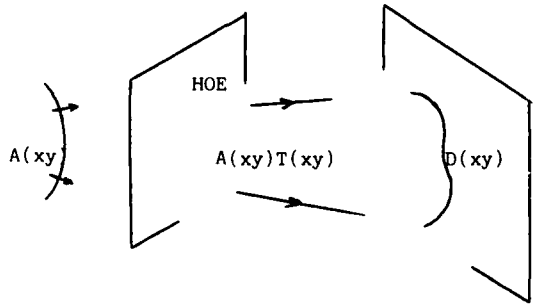


Figure 6

One now looks at this set-up from the opposite side: given the desired wave D (x,y) , calculate , by invers diffraction, the transmittance T (x,y) of the hologram for a given incoming wave A (x,y). In order to be able to do the computations, one has to sample the wavefront D (x,y), and so one finds a sampled transmission T (x,y) of the hologram; in other words, one knows the desired amplitude and phase of the transmission function. In order to realize this, one has to choose an encoding technique. Most popular is the **detour phase encoding** technique. The hologram is divided into cells, and each cell contains a window. The area of the window is made proportional to the amplitude transmission at that point; and the position of the window in the cell depends on the local phase.

Those CGH are first made on a macroscopic scale (e.g. by printing or plotting them in a computer), and are afterwards reduced to the desired small scale. It is also possible to make them immediately at the right scale, by writing them with electron beam lithography. A recent popular way to make CGH is to use a Compact Disc : punch the holes at the right places, and you immediately have a CGH!

5. Some Applications.

Because of their unique properties, HOEs will usually not replace conventional optical elements, but will rather be used in special applications, where they are technically advantageous and economically interesting. We will describe here a few of those applications.

5.1 Holographic night vision goggles.

In normal night vision goggles, the incoming light is amplified and sent to the eyes. However, if a sudden lighting appears, the Image Intensifier Tube IIT saturates, no image is formed anymore and the wearer has to take his goggles off in order to see anything. In order to get rid of that problem, one can mix the amplified image with a direct image. In principle this can be done with a normal beamsplitter, but then you have to make a choice: a high reflection gives a good amplified image, but a weak direct vision, whereas a small reflectivity gives a weak amplified image.

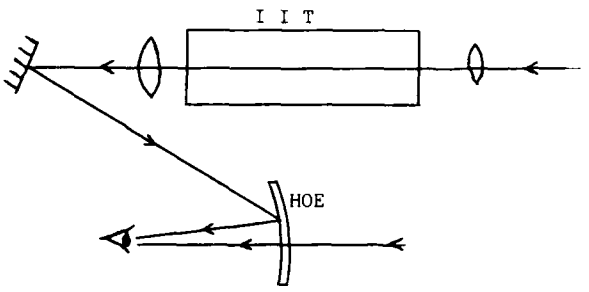


Figure 7

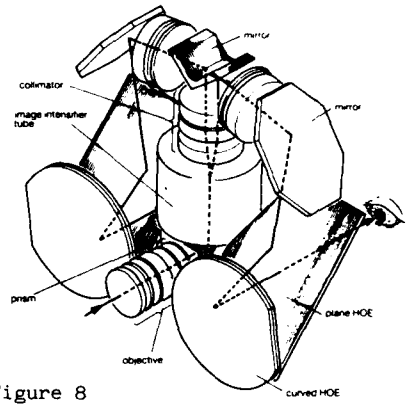


Figure 8

Replace the beamsplitter now by a HOE. It can be designed to give a very good reflectivity exactly at the wavelength of the phosphor of the IIT (often 543 nm), and complete transmission at all other wavelengths (see Fig. 8 from ref. 10)

5.2 Head-Up Displays (HUD) (ref.4 and 5).

In an aircraft a pilot has to look through the windshield in order to see where he is flying, and at the same time he needs to look at his instruments. His job can be simplified when essential flight information is projected on the inside of his windshield, where a beamsplitter combines both images. Next to the problem of **reflectivity** (which is the same kind of problem as with night vision goggles), there is moreover a problem of **image formation**. Indeed : the pilot needs a wide field of view. In classical optics this is realized by using large lenses. However, in order to reduce the weight and the dimensions, in an airplane one uses curved mirrors, and the "combiner" is also a curved mirror. Because the curvature is not the same in the x and y directions, much distortion is introduced. The use of a hologram solves a lot of those problems. A HOE can indeed be designed to act as a stigmatic, non-spherical mirror, even if the substrate on which the hologram is made is a spherical glass.

5.3 Holographic scanners.

In a " classical " scanner, the beam is moved by projecting it on a rotating polygon mirror. When this scanning is used for the reading of a bar-code or for printing, the beam has to be focussed on the product or on the paper. Rather complicated lenses are necessary in order to obtain a good focussed laserspot over the complete line to be scanned (ref. 6).

Both functions can be replaced by a rotating HOE : the hologram not only deflects the beam, but at the same time focuses it! (Fig. 9)

5.4 Optical pick-up head.

Classical optical pick-up (= CD) heads require eight discrete optical components. In a holographic head this number can be greatly reduced, which makes it more compact and lighter (ref. 7).

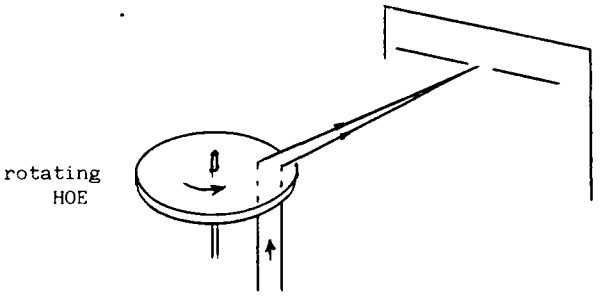
5.5 Wavefront correctors.

One of the first applications of HOEs was its use for the correction of the spherical aberation of a lens (ref. 8). A hologram is made of the image through the lens, including its aberations. When the lens is used afterwards in conbination with the hologram, an aberationless image appears.

5.6 Multifacet lenses.

In parallel optical processing it is often necessary to make multiple images of the same object. This can easily be done with a HOE. Such a HOE has to function more or less as a fly's eye lens; here however each of the single lenses covers the whole hologram, so all the lenses are superposed on the same HOE.

Optical interconnects are based on the same principle: one beam in, multiple beams out. Those optical interconnects are of great importance for futur (optical) computers (ref. 9).



Figuur 9

References

1. R.J. COLIER, C.B. BURCKHARDT, L.H. LIN, Optical Holography, Academic Press, 1971.
2. W.C. SWEATT, J.O.S.A. **67**, 803 (1977).
3. R.W. MEIER, J.O.S.A. **55**, 987 (1965).
4. D.H. CLOSE, Optical Engineering **14**, 408 (1975).
5. E.J.P. SCHWEICHER, SPIE Proceedings **600**, (J. Ebbeni, Editor) 1985.
6. C.J. KRAMERS, P.A. PIZZOTELLI, Photonics Spectra, p. 89 (nov. 1985).
7. G.T. FORREST, Laser Focus, p. 28 (sept. 1987).
8. J. UPATNIEKS, A. VAN DER LUGT, E. LEITH, Appl. Opt. **5**, 589 (1966).
9. D.G. PELKA, Laser Focus, p. 109 (july 1988).
10. OIP-INSTRUBEL, Westerring 21, B-9700 Oudenaarde, Belgium.

INITIALIZATION OF DYNAMIC LASER NETWORKS

R. E. Newman-Wolfe
Assistant Professor
University of Florida
Gainesville, FL 32611

S. L. Davis
Visiting Assistant Professor
Kennesaw State College
Marietta, GA 30061

Y. C. Chow
Professor
University of Florida
Gainesville, FL 32611

Abstract

Causing satellites to direct their transceivers at each other simultaneously without communication requires scheduling. We provide schedules with good worst-case upper bounds for link acquisition in the presence of failures and unknown clock skews.

Introduction

This paper investigates the problem of initialization of systems of unsynchronized, dynamic networks using softwire laser communications[4]. We formalize the notion of periodic schedule *sets for networks* and we define a worst case performance measure *mlat* (Maximum Link Acquisition Time) for these schedule sets. The *mlat* measures the longest link time for a pair of nodes in the network given the worst state of system synchronization. Our assumptions include that: 1) each node knows the location of every other node, 2) each node has a clock that can give it precise time intervals, 3) the nodes do not have a common time of day, 4) the link acquisition time is bounded if nodes direct their transceivers at each other. We exhibit a scheduling strategy called Block-Interleave scheduling whose schedule sets have good linking characteristics with respect to *mlat*. These schedule sets give a maximum link acquisition time approximately in the order of N^2/K^2 where N is the number of nodes and K is the number of transceivers per nodes. Finally we examine the conditions under which non-repeating schedule elements can be used (a robustness condition) in Block-Interleave schedules.

Laser transceivers are desirable for space communications for a variety of reasons[2,3,6]. Their high bandwidth, security, noise resistance, and ability to concentrate signal power in a very small solid angle make them the communication medium of choice for many space-based applications. Satellites or spa. e vehicles using lasers for communication with each other will participate in a dynamic laser network.

Dynamic laser networks have special properties not found in traditional networks[3,10,11,12,13,15]. Traditional networks are typically either static, point-to-point networks or mobile, broadcast networks. Point-to-point networks may experience link or node failures, but their base topology does not change (that is, links may go up or down, but the end nodes of a link are fixed). Broadcast networks may be static or mobile, but have to deal with the medium access problem, since all nodes compete for the same, shared broadcast channel(s). Laser transceivers provide the advantage of not having to share the bandwidth of a channel with any other nodes (space division multiplexing). They also permit a node to change the direction in which the transceiver is pointing in order to acquire a link with a different node, and thus change the base topology. If the nodes are mobile, then the line of sight between two linked nodes may become blocked, necessitating periodic changes in the links to maintain utilization of the transceivers. The problem of selecting which links should be established has been investigated elsewhere as the link assignment problem[2,7,8,9], and it is in general intractable to determine the best assignment possible[5,14]. Dynamic laser networks are point-to-point, yet have a changing base topology.

One particular problem in changing the links is coordinating the nodes. Since a link between two nodes cannot be established if either node fails to direct a transceiver at its partner, both nodes must somehow agree to establish the link. If there is already a communication path between the nodes, this problem is mitigated since nodes with free transceivers may negotiate with each other over which links to try to establish. If the nodes do not have alternative communication paths already in place, then the problem becomes much more difficult.

Nodes may not have communication paths in place due to link or node failures partitioning the network, or perhaps because the network was never connected in the first place. Worse, one of the nodes may have failed, and there is no way for the other node to know this. In any case, nodes must use some sort of schedule for aiming their transceivers to attempt to establish links. If there is no node failure and any link is feasible, then each node can simply aim its transceivers at predetermined neighbors. This will not work if there is either the possibility of node failure or link line-of-sight blockage. If all nodes have a common, global clock, then it is easy to set up schedules so that nodes rendezvous in a round-robin fashion[1], so that even if most nodes are inaccessible to a given node, it will be able to find the other nodes with which it can link. This method will succeed in establishing links in O(N) time, even with only one transceiver. This is not to be confused with the traffic assignment algorithms used in satellite traffic scheduling as in Wu[15]. However, if there is no global clock, this method may fail due to inopportune timing. If a node starts following its schedule out of synchronization with the other nodes, it will never establish a link even though all the other nodes may be viable. This is the problem investigated in this paper.

It is arguable that since the orbits of satellites are governed by very accurate an easily calculable quantities that the satellites know exactly where and when to find each other assuming some sort of initialization at launch time with a common clock. Thus the system of satellites itself can be thought of as the timing mechanism by which all aiming calculations are measured. Unfortunately, the resolution of this system may not be sufficiently fine to serve the demands of rapid targeting and retargeting of potential links. However, since the beam dispersion of a communications laser may be such that relative satellite positions are practically constant for the time defined by the arcs of the beam front and the receiving satellite, this problem may diminish somewhat. In any case, we assume that there is a sufficient degree of initialization to ensure that all satellites can accurately target one another.

We are left with the problem of the satellites running schedules for aiming their transceivers in such a way as to guarantee link acquisition as early as possible. These schedules run on a time scale related to the fastest reliable retargeting time of the aiming hardware and thus no sort of common initialization is possible if this time scale is finer than that of the internal clocks used for position calculation. Also, the finer time scale is obviously much more sensitive to a momentary power irregularity as may occur accidently or by an agent such as an electromagnetic pulse.

It should be noted that once a link is established, those transceivers used for that link cannot participate further in the initialization process lest they loose the link just established. This strategy assumes that it is most important to dispatch pending information over a newly established link as soon as possible. If this were not the case, then the initialization process could continue to use all transceivers until the process completes. Then the network can set to the task of communication of more than initialization information.

This type of scheduling problem seems to be new as evidenced by the lack of reference material from which to draw although the problem of synchronization is mentioned in Pratt[10] as a requirement for traffic scheduling. This shows the importance of initialization in general. The assumption of no initial synchronization seems to have been ignored in the classical scheduling problems such as job-shop scheduling or deadlock avoidance. Both of these of course can assume the existence of an absolute time standard in terms of which all schedules can be formulated. Garey and Johnson's book[5] contains a long list of scheduling problems none of which addresses synchronization.

In this paper we first define a performance measure for this kind of initialization problem. Our measure gives an indication of the maximum time required for any two satellites of the network to establish a link assuming a completely disconnected network in a state of worst synchronization. We do not attempt to deal with the more complicated issue of the maximum initialization time for the entire network in the case that newly acquired links are immediately put to use for tactical communication. However, in the case that the system has an initialization phase and a communications phase in which the initialization phase continues to use all transceivers (discarding links after clock synchronization), our performance measure does bound the time to establish a completely initialized network.

Next we demonstrate a scheduling strategy we call block-interleaved scheduling whose performance is good with respect to our measure. It achieves a reasonable link time (in the order of $(N-2)^2/(K-2)^2$) with no other restriction placed on the number of transceivers than there be at least three of them.

A recurrent theme in this work deals with non-repeating schedules. We believe that these are potentially valuable from a robustness standpoint. In the case that satellites are being rendered non-functional, schedules that repeat schedule elements run the risk of wasting much time on link attempts. We have therefore included results that address necessary conditions for using non-repeating schedules with block- interleave strategy.

Schedule Performance Measures

We turn now to the formalization of the concepts necessary to model the initialization problem for sets of satellites with directional transceivers. We ignore targeting issues such as trajectory calculation as these are well studied in the literature[13] and we concentrate on the scheduling requirements. To make matters precise, we label the satellites or nodes with indices and define acquisition schedules in terms of these indices. The integer N denotes both the number of nodes, and the set $\{1,2,...,N\}$, depending upon the context. K denotes the number of transceivers or link elements per node. $P(n,m)$ is the set of m element members of the power set of $\{1,2,...,n\}$, hence the size of $P(n,m)$ is

$$|P(n,m)| = c(n,m) = \frac{n!}{m!(n-m)!}, \tag{1}$$

the binomial coefficient formula. These will be used to define and quantify acquisition schedules below.

The symbol S_i denotes a periodic schedule for node i; p_i is the period of S_i. An individual schedule S_i of period p_i for node i within an N node, K transceiver system, is a sequence of p_i elements from $P(N_i,K)$ where N_i denotes the set

$$N_i=\{1,2,\ldots,i-1,i+1,\ldots,N\}. \tag{2}$$

Thus a schedule of period p_i will be an element of $P(N_i,K)^{p_i}$,

$$S_i=(S_i[0],S_i[1],\ldots,S_i[p_i-1]). \tag{3}$$

For example, $S_1=(\{2,3\},\{2,4\})$ is a schedule of period 2 for $N=4$ and $K=2$. This schedule aims its two transceivers first at nodes 2 and 3, and in the next time slot aims them at transceivers 2 and 4. Note that it is a waste to use more than one transceiver to point to a given node and therefore we assume that schedule elements do not contain repeated node numbers. It is understood that these schedules repeat, so that the running schedule used by node i is formed by concatenating S_i to itself for as many times as is necessary. In general, for $t>N$, $S_i[t]$ also represents the t modulo p_i-th element of S_i. For the example above, $S_1[3]=S_1[1]=\{2,4\}$.

The symbol $SSC(N,K)$ or simply SSC denotes the class of all sets of N periodic schedules made of K element sets. Thus, any schedule set SS in $SSC(N,K)$ denotes a set of N schedules $S_1,S_2,\ldots,S_N$, one for each node. Since the schedules making up a schedule set may have different periods, the least common multiple of these is the actual period common to all schedules in the schedule set. Only after this period has elapsed can it be determined that a given schedule set does or does not link (see theorem 1). P denotes the period of a schedule set SS, that is,

$$P=lcm\,\{p_i:1\le i\le N\}. \tag{4}$$

Some confusion may arise from the above notation for schedules S_i. We point out here that the S_i's as defined above may all have different periods, even though we often think of S_i as the schedule repeated sufficient times so that its period is P.

Link Timing

Let SS be an element of $SSC(N,K)$. A link is established between nodes i and j during a time slot t if $S_i[t]$ contains j and $S_j[t]$ contains i. Let $mlt(S_i,S_j)$ be the minimum such t for a pair of schedules S_i and S_j,

$$mlt(S_i,S_j)=\min\{\,t\,:\,j\ in\ S_i[t],i\ in\ S_j[t]\}. \tag{5}$$

Then $mlt(S_i,S_j)$ is the minimum link time for a pair of schedules that are exactly in phase. When the particular schedule S is understood, we drop the S and write $mlt(i,j)$. For example the schedules

$S_1=(\{2,3\},\{2,4\},\{3,4\})$ and

$S_2=(\{1,3\},\{1,4\},\{3,4\})$

have $mlt(S_1,S_2)=0$ since the zero'th element of each schedule targets the other node.

For an integer r, $R(S_i,r)$ denotes the individual schedule S_i rotated r units. For example, if S_i is as above, then

$$R(S_i,0)=S_i, \tag{6}$$
$$R(S_i,1)=(\{3,4\},\{2,3\},\{2,4\}), \tag{7}$$
$$R(S_i,2)=(\{2,4\},\{3,4\},\{2,3\}),\ \text{and} \tag{8}$$
$$R(S_i,3)=S_i. \tag{9}$$

Rotations will allow us to model nodes whose clocks are skewed relative to one another. Their schedules may begin at different times, so we will rotate one or both of the schedules to find the worst case mlt of all the rotated schedules, obtaining an upper bound on the time to acquire a link between a pair of nodes regardless of what their clock skews may be. These minimum link times for the various rotations can expressed as $mlt(R(S_i,r_i),R(S_j,r_j))$ for $r_i,s_i=0,1,\ldots,P-1$. The worst case upper bound is now defined. The Pairwise Maximum Link Acquisition Time ($pmlat$) for nodes i and j of a given schedule S is defined as

$$pmlat(S_i,S_j)=\max\{mlt(R(S_i,r_i),R(S_j,r_j)):r_i,r_j=0,1,\ldots,P-1\}. \tag{10}$$

When the schedule set SS is understood we may write $pmlat(i,j)$. Example 1 (figure 1) illustrates the computation of $pmlat$.

To model the worst case time for a pair of nodes to establish a link we use the maximum pairwise link time for all pairs. This gives the longest time required to establish the first link for a completely disconnected network. It may also be thought of as the time required to link a network consisting of two unknown nodes. More precisely, $mlat(SS)$ is the Maximum Link Acquisition Time for a given schedule set SS defined as

$$mlat(SS)=\max\{pmlat(S_i,S_j):S_i,S_j\ in\ SS,(i,j)\ in\ P(N,2)\}. \tag{11}$$

Theorem 1. If $mlat(SS)$ is finite for some schedule set SS, then $mlat(SS)$ is bounded by the common period $P=lcm_i\,p_i$ of the schedules of SS.

Proof: Trivial consequence of the P-periodic extension of schedules.

We may simply write $mlat$ when the particular schedule S is understood. We illustrate with the examples in Figure 2.

EXAMPLE 1 ($N=4,K=2$)

S: $S_1 = (\{2,3\}, \{2,4\}, \{3,4\})$
$S_2 = (\{1,3\}, \{1,4\}, \{3,4\})$
$S_3 = (\{1,2\}, \{1,4\}, \{2,4\})$
$S_4 = (\{1,2\}, \{1,3\}, \{2,3\})$

$$\begin{array}{lll}
\mathrm{mlt}(\mathrm{R}(S_1,0),\mathrm{R}(S_2,0)) = 1, & \mathrm{mlt}(\mathrm{R}(S_1,0),\mathrm{R}(S_3,0)) = 1, & \mathrm{mlt}(\mathrm{R}(S_1,0),\mathrm{R}(S_4,0)) = 2, \\
\mathrm{mlt}(\mathrm{R}(S_1,0),\mathrm{R}(S_2,1)) = 1, & \mathrm{mlt}(\mathrm{R}(S_1,0),\mathrm{R}(S_3,1)) = 1, & \mathrm{mlt}(\mathrm{R}(S_1,0),\mathrm{R}(S_4,1)) = 3, \\
\mathrm{mlt}(\mathrm{R}(S_1,0),\mathrm{R}(S_2,2)) = 2, & \mathrm{mlt}(\mathrm{R}(S_1,0),\mathrm{R}(S_3,2)) = 3, & \mathrm{mlt}(\mathrm{R}(S_1,0),\mathrm{R}(S_4,2)) = 2, \\
\mathrm{mlt}(\mathrm{R}(S_1,1),\mathrm{R}(S_2,0)) = 1, & \mathrm{mlt}(\mathrm{R}(S_1,1),\mathrm{R}(S_3,0)) = 2, & \mathrm{mlt}(\mathrm{R}(S_1,1),\mathrm{R}(S_4,0)) = 1, \\
\mathrm{mlt}(\mathrm{R}(S_1,1),\mathrm{R}(S_2,1)) = 1, & \mathrm{mlt}(\mathrm{R}(S_1,1),\mathrm{R}(S_3,1)) = 3, & \mathrm{mlt}(\mathrm{R}(S_1,1),\mathrm{R}(S_4,1)) = 1, \\
\mathrm{mlt}(\mathrm{R}(S_1,1),\mathrm{R}(S_2,2)) = 3, & \mathrm{mlt}(\mathrm{R}(S_1,1),\mathrm{R}(S_3,2)) = 2, & \mathrm{mlt}(\mathrm{R}(S_1,1),\mathrm{R}(S_4,2)) = 2, \\
\mathrm{mlt}(\mathrm{R}(S_1,2),\mathrm{R}(S_2,0)) = 2, & \mathrm{mlt}(\mathrm{R}(S_1,2),\mathrm{R}(S_3,0)) = 1, & \mathrm{mlt}(\mathrm{R}(S_1,2),\mathrm{R}(S_4,0)) = 1, \\
\mathrm{mlt}(\mathrm{R}(S_1,2),\mathrm{R}(S_2,1)) = 3, & \mathrm{mlt}(\mathrm{R}(S_1,2),\mathrm{R}(S_3,1)) = 1, & \mathrm{mlt}(\mathrm{R}(S_1,2),\mathrm{R}(S_4,1)) = 1, \\
\mathrm{mlt}(\mathrm{R}(S_1,2),\mathrm{R}(S_2,2)) = 2, & \mathrm{mlt}(\mathrm{R}(S_1,2),\mathrm{R}(S_3,2)) = 2, & \mathrm{mlt}(\mathrm{R}(S_1,2),\mathrm{R}(S_4,2)) = 3,
\end{array}$$

$$\mathrm{pmlat}(S_1,S_2) = 3, \qquad \mathrm{pmlat}(S_1,S_3) = 3, \qquad \mathrm{pmlat}(S_1,S_4) = 3,$$

$$\begin{array}{lll}
\mathrm{mlt}(\mathrm{R}(S_2,0),\mathrm{R}(S_3,0)) = 1, & \mathrm{mlt}(\mathrm{R}(S_2,0),\mathrm{R}(S_4,0)) = 3, & \mathrm{mlt}(\mathrm{R}(S_3,0),\mathrm{R}(S_4,0)) = 2, \\
\mathrm{mlt}(\mathrm{R}(S_2,0),\mathrm{R}(S_3,1)) = 3, & \mathrm{mlt}(\mathrm{R}(S_2,0),\mathrm{R}(S_4,1)) = 2, & \mathrm{mlt}(\mathrm{R}(S_3,0),\mathrm{R}(S_4,1)) = 2, \\
\mathrm{mlt}(\mathrm{R}(S_2,0),\mathrm{R}(S_3,2)) = 1, & \mathrm{mlt}(\mathrm{R}(S_2,0),\mathrm{R}(S_4,2)) = 2, & \mathrm{mlt}(\mathrm{R}(S_3,0),\mathrm{R}(S_4,2)) = 3, \\
\mathrm{mlt}(\mathrm{R}(S_2,1),\mathrm{R}(S_3,0)) = 3, & \mathrm{mlt}(\mathrm{R}(S_2,1),\mathrm{R}(S_4,0)) = 1, & \mathrm{mlt}(\mathrm{R}(S_3,1),\mathrm{R}(S_4,0)) = 2, \\
\mathrm{mlt}(\mathrm{R}(S_2,1),\mathrm{R}(S_3,1)) = 2, & \mathrm{mlt}(\mathrm{R}(S_2,1),\mathrm{R}(S_4,1)) = 2, & \mathrm{mlt}(\mathrm{R}(S_3,1),\mathrm{R}(S_4,1)) = 1, \\
\mathrm{mlt}(\mathrm{R}(S_2,1),\mathrm{R}(S_3,2)) = 2, & \mathrm{mlt}(\mathrm{R}(S_2,1),\mathrm{R}(S_4,2)) = 1, & \mathrm{mlt}(\mathrm{R}(S_3,1),\mathrm{R}(S_4,2)) = 1, \\
\mathrm{mlt}(\mathrm{R}(S_2,2),\mathrm{R}(S_3,0)) = 1, & \mathrm{mlt}(\mathrm{R}(S_2,2),\mathrm{R}(S_4,0)) = 1, & \mathrm{mlt}(\mathrm{R}(S_3,2),\mathrm{R}(S_4,0)) = 3, \\
\mathrm{mlt}(\mathrm{R}(S_2,2),\mathrm{R}(S_3,1)) = 2, & \mathrm{mlt}(\mathrm{R}(S_2,2),\mathrm{R}(S_4,1)) = 3, & \mathrm{mlt}(\mathrm{R}(S_3,2),\mathrm{R}(S_4,1)) = 1, \\
\mathrm{mlt}(\mathrm{R}(S_2,2),\mathrm{R}(S_3,2)) = 1, & \mathrm{mlt}(\mathrm{R}(S_2,2),\mathrm{R}(S_4,2)) = 1, & \mathrm{mlt}(\mathrm{R}(S_3,2),\mathrm{R}(S_4,2)) = 1,
\end{array}$$

$$\mathrm{pmlat}(S_2,S_3) = 3, \qquad \mathrm{pmlat}(S_2,S_4) = 3, \qquad \mathrm{pmlat}(S_3,S_4) = 3.$$

Figure 1.
Example 1, computation of *pmlat* values.

EXAMPLE 2 ($N=4,K=2$)
$S_1=(\{2,3\},\{2,4\},\{3,4\})$
$S_2=(\{1,3\},\{1,4\},\{3,4\})$
$S_3=(\{1,2\},\{1,4\},\{2,4\})$
$S_4=(\{1,2\},\{1,3\},\{2,3\})$
$mlat(SS)=\max\{pmlat(i,j):(i,j)inP(N,2)\}=\max\{3,3,3,3,3,3\}=3$
(from example 1)

EXAMPLE 3 ($N=4,K=2$)
$S_1=(\{2,3\},\{2,4\})$
$S_2=(\{1,3\},\{1,4\})$
$S_3=(\{1,4\},\{2,4\})$
$S_4=(\{1,3\},\{2,3\})$
$pmlat(1,2)=\max\{1,1\}=1$
$pmlat(1,3)=\max\{1,\infty\}=\infty$
$pmlat(1,4)=\max\{\infty,1\}=\infty$
$pmlat(2,3)=\max\{\infty,2\}=\infty$
$pmlat(2,4)=\max\{2,\infty\}=\infty$
$pmlat(3,4)=\max\{1,1\}=1$
$mlat=\max\{1,\infty,\infty,\infty,\infty,1\}=\infty.$

Figure 2.
Examples of *mlat* calculation.

Block-Interleave Scheduling

The next few results depend on a particular strategy for forcing links that we refer to as block-interleaved or BI scheduling. With this strategy we can use simple counting and pigeon hole arguments to prove that the schedule sets have finite *mlat* values. The idea is that given two schedules, use some number B of consecutive elements of one nodes schedule to point to the second node, and use every Bth element of the second nodes schedule to point at the first node. We refer to these pointing methods as block-pointing and interleave-pointing, respectively. A schedule element will be termed i-linking if it contains i.

Theorem 2. Let SS be a set of schedules all of period P, and let B be an integer dividing P such that for every pair of schedules S_i and S_j from SS, one of them, say S_i contains B consecutive j-linking elements, and the other S_j has P/B equidistant i-linking elements. Then $mlat(SS) \leq P$.

Proof: Since S_j has P/B equidistant i-linking schedule elements, every B consecutive schedule elements of S_j has to include an i-linking schedule element. Thus regardless of rotations, the B consecutive j-linking elements of S_i will execute at the

same time B elements of S_j with at least one i-linking element also execute thus insuring a link. By Theorem 1, $mlat(SS) \leq P$.

A simple method for generating schedule sets that incorporates the block-interleaved feature is demonstrated by the schedule set of figure 3 (in the figure, blank element entries indicate that the particular entry is not important). Note that for every i, S_i block points to all nodes $j > i$, and interleave points to all nodes $j < i$. By the preceding theorem, $mlat \leq P = 9$. We now investigate the relevant parameters for the block-interleaved strategy with the goal of *mlat* minimization in mind.

$$S_1 = \{2,3,4,5\},\{2,3,4,5\},\{2,3,4,5\},\{6,7,,\},\{6,7,,\},\{6,7,,\},\{,,,\},\{,,,\},\{,,,\}$$

$$S_2 = \{1,3,4,5\},\{,3,4,5\},\{,3,4,5\},\{1,6,7,\},\{,6,7,\},\{,6,7,\},\{1,,,\},\{,,,\},\{,,,\}$$

$$S_3 = \{1,2,4,5\},\{,,4,5\},\{,,4,5\},\{1,2,6,7\},\{,,6,7\},\{,,6,7\},\{1,2,,\},\{,,,\},\{,,,\}$$

$$S_4 = \{1,2,3,5\},\{4,,,5\},\{,,,5\},\{1,2,3,6\},\{4,,,6\},\{,,,6\},\{1,2,3,7\},\{4,,,7\},\{,,,7\}$$

$$S_5 = \{1,2,3,6\},\{4,5,,6\},\{,,,6\},\{1,2,3,7\},\{4,5,,7\},\{,,,7\},\{1,2,3,\},\{4,5,,\},\{,,,\}$$

$$S_6 = \{1,2,3,7\},\{4,5,,7\},\{6,,,7\},\{1,2,3,\},\{4,5,,\},\{6,7,,\},\{1,2,3,\},\{4,5,,\},\{6,7,,\}$$

$$S_7 = \{1,2,3,4\},\{5,6,,\},\{,,,\},\{1,2,3,4\},\{5,6,,\},\{,,,\},\{1,2,3,4\},\{5,6,,\},\{,,,\}$$

Figure 3.
Simple Block-Interleaved Schedule Set.

$$S_1 = \{2,3,\},\{2,3,\},\{2,3,\},\{2,3,4\},\{5,,4\},\{5,,4\},\{5,6,4\},\{5,6,7\},\{,6,7\},\{,6,7\},\{,,7\},\{,,\}$$

$$S_2 = \{,3,4\},\{,3,4\},\{,3,4\},\{1,3,4\},\{,5,6\},\{,5,6\},\{,5,6\},\{1,5,6\},\{,7,\},\{,7,\},\{,7,\},\{1,7,\}$$

$$S_3 = \{,4,5\},\{,4,5\},\{1,4,5\},\{2,4,5\},\{,6,7\},\{,6,7\},\{1,6,7\},\{2,6,7\},\{,,\},\{,,\},\{1,,\},\{2,,\}$$

$$S_4 = \{,5,6\},\{1,5,6\},\{2,5,6\},\{3,5,6\},\{,7,\},\{1,7,\},\{2,7,\},\{3,7,\},\{,,\},\{1,,\},\{2,,\},\{3,,\}$$

$$S_5 = \{1,6,7\},\{2,6,7\},\{3,6,7\},\{4,6,7\},\{1,,\},\{2,,\},\{3,,\},\{4,,\},\{1,,\},\{2,,\},\{3,,\},\{4,,\}$$

$$S_6 = \{2,,7\},\{3,,7\},\{4,,7\},\{1,5,7\},\{2,,\},\{3,,\},\{4,,\},\{1,5,\},\{2,,\},\{3,,\},\{4,,\},\{1,5,\}$$

$$S_7 = \{2,6,\},\{3,,\},\{4,,\},\{1,5,\},\{2,6,\},\{3,,\},\{4,,\},\{1,5,\},\{2,6,\},\{3,,\},\{4,,\},\{1,5,\}$$

Figure 4.
A Block-Interleaved Schedule Set Using Non-repeating Schedules.

Theorem 3. For the block-interleaved strategy, it is sufficient that the block size B satisfies $B \geq \lceil (N-2)/(K-2) \rceil$ and that the period P satisfies $P = B^2$ to ensure $mlat < \infty$. In this case, $mlat \leq B^2$. ($\lceil x \rceil$ denotes the least integer greater than or equal to x)

Proof: Let $K_I(i)$ and $K_B(i)$ be the numbers of transceivers used in schedule S_i for block-pointing and interleave-pointing respectively, and let $R = P/B$ (refer to figure 5 for opposed plots of $K_I(i)$ and $K_B(i)$).

$$K_I(i) + K_B(i) \leq K \tag{12}$$

for all i. Since schedule S_i has R blocks of $K_B(i)$ block-pointing transceivers to block-point to $N-i$ nodes, we require that $K_B(i) \geq \lceil N-i/R \rceil$. Also, S_i has B schedule elements with which to fill each of the $K_I(i)$ transceivers with interleave-pointing transceivers to interleave point to $i-1$ nodes, thus we require also that $K_I(i) \geq \lceil i-1/B \rceil$. The boundaries of $K_B(i) = \lceil N-i/R \rceil$ and $K_I(i) = \lceil i-1/B \rceil$ highlight straight lines which must not cross if we require (12) (see figure 5). It is therefore enough to require the conditions defining the boundaries to hold only at the extremes $i=2$ and $i=N-1$. That is, to ensure (12) it is enough to have $K_I(N-1)B = N-2$, and $K_B(N-1)R = 1$ for the case $B \leq R$, and for the case $B > R$ it is enough to have $K_B(2)R = N-2$, and $K_I(2)B = 1$ (see figure 5). Now the requirement that (12) holds for all i becomes

$$\max\{K_I(N-1) + K_B(N-1), K_I(2) + K_B(2)\} \leq K, \text{ or} \tag{13}$$

$$\max\{\lceil (N-2)/B \rceil + \lceil 1/B \rceil, \lceil 1/R \rceil + \lceil (N-2)/R \rceil\} \leq K \tag{14}$$

It suffices that

$$\max\{(N-2)/R, (N-2)/B\} \leq K-2. \tag{15}$$

Thus $B \geq \lceil (N-2)/(K-2) \rceil$ and $R \geq \lceil (N-2)/(K-2) \rceil$ are sufficient. Taking $B = R$, we obtain $P = B^2$.

Block-interleave Scheduling with Non-repeating Schedule Elements

It is possible to use the BI strategy with non-repeating (NR) schedules. Here, non-repeating is intended to mean that no schedule element is repeated within one schedule period, since the entire schedule is repeated periodically. To illustrate we use $N=7, K=3$, and $B=4$ to come up with a schedule set NRBI with $mlat \leq 12$ (see figure 4).

We now investigate the additional requirements to be met for a block-interleaved strategy to be used with non-repeating schedule elements. We also define a notion of potential linkage, that is, the number of times a given schedule targets another node. More precisely, $L_1(i,j)$, denotes the number of elements of schedule S_i that contain j. In general, $L_p(i,j_1,j_2,\ldots,j_p)$ denotes the number of elements of S_i that target the p nodes $j_1,j_2,\ldots,j_p$. Recall the important parameters B,R, the block length and number of blocks $(R=P/B)$ respectively. We define $TB(i)=\lceil (N-i)/R \rceil$ and $TR(i)=\lceil (i-1)/B \rceil$, the per-block and per-interleave targeting requirements, respectively.

Theorem 4. If BI scheduling is done with NR schedules then it is necessary that $B \leq \min_i L_{TB(i)}$ and $R \leq \min_i L_{TR(i)}$ be satisfied.

Proof: Consider the linkage requirements of schedule S_i. S_i block points to $N-i$ nodes and has R blocks hence it suffices that each block point to at least $TB(i)$ nodes. If S_i is to successfully link with these nodes then we should require that $L_{TB(i)} \geq B$. More precisely, we require $L_{TB(i)}(i,j_1,j_2,\ldots,j_{TB(i)}) \geq B$ where $j_1,j_2,\ldots,j_{TB(i)}$ are the nodes targeted in a given block. A similar argument for the interleave requirements of S_i yields the condition $L_{TR(i)} \geq R$. Taking minimums over i, we obtain the conclusion.

The set of sufficient conditions certainly must contain the conditions $B \leq \min_i L_{TB(i)}$ and $R \leq \min_i L_{TR(i)}$. Consider again the block pointing requirements of S_i. We showed that $L_{TB(i)}(i,j_1,j_2,\ldots,j_{TB(i)}) \geq B$ where $j_1,j_2,\ldots,j_{TB(i)}$ are the nodes targeted in a given block. Let $l_1,l_2,\ldots,l_{TB(i)}$ be another set of $TB(i)$ nodes to be targeted by another block of S_i. It is possible that some of the $L_{TB(i)}$ schedule elements used for pointing to $j_1,j_2,\ldots,j_{TB(i)}$ may also point to $l_1,l_2,\ldots,l_{TB(i)}$ causing a deficiency of elements usable in pointing to $l_1,l_2,\ldots,l_{TB(i)}$. In fact, given a fixed block, each of the remaining $R-1$ blocks may require some of the L_T schedule elements causing an even greater deficiency. In the worst distribution, these $R-1$ demands on a given schedule from other schedules are disjoint sets of schedule elements and therefore the total overlap of these other schedules with respect to the fixed schedule is $L_{TB(i)}-(R-1)L_{2TB(i)}$. This must be greater than the block size to guarantee sufficient schedule elements for targeting in the worst case.

Conclusion

We have provided a measure ($mlat$) of schedule performance well suited to the initialization problem. Mlat is measure of link acquisition that realistically treats the problem of unsynchronized satellites by computing the link time for the worst synchronization of every pair of satellites and returning the worst (largest) of these.

We have demonstrated good performance characteristics for the block-interleaved schedules without requiring that K be inordinately large. Since the period P is nearly N^2/K^2 we see a trade-off of P and K which we may use as we like, probably preferring small K. As for generation of the schedules themselves, it would seem an easy matter of allocation of the number of transceivers for use as block pointers and interleave pointers and then filling in the blanks until the node numbers are exhausted. We have also demonstrated that this strategy can accommodate non-repeating schedules thus providing a measure of robustness lacking in repeating schedules (figure 4).

Acknowledgements

We are grateful to Dr. Kepi Wu of SDIO and the U. S. Navy, who partially supported this work under contract number N00039-87-C-0221.

References

1. A. Aho, J. Hopcroft and J. Ullman, Data Structures and Algorithms (Addison-Wesley, Reading, MA, 1983), pp. 310-311

2. R. Chow, C. McLaughlin, C. Ward and R. E. Newman-Wolfe, presented at the SPIE Symposium on Innovative Science and Technology, Los Angeles, CA, (1988)

3. Chow, Y., Newman-Wolfe, R., Ward, C., and McLochlin, C., A Simulation Testbed for a Satellite Computer Network With Laser Cross Links (CIS Department, University of Florida, Gainesville, Florida, 1988)

4. S. L. Davis, Master's thesis (CIS Department, University of Florida, Gainesville, FL, 1989)

5. M. Garey and D. Johnson, Computers and Intractability, A Guide to the Theory of NP-Completeness (Freeman, New York, 1979), pp. 236-244

6. J. R. Lesh and M. D. Rayman, Laser Focus, Vol. 24, No. 10 (1988), pp. 81-86

7. Kenneth C. Luo, Y. C. Chow and R. E. Newman-Wolfe, presented at 1990 International Phoenix Conference on Computers and Communication, Phoenix, (1990)

8. C. McLochlin, C. Ward, Y. C. Chow, R. E. Newman-Wolfe, J. N. Wilson and T. B. Hughes, "Determining the Delay and Reliability of Low Altitude Satellite Network Topologies Using Simulation," presented at ACM SIGSIM and IEEE Computer Society Symposium on the Simulation of Computer Networks Colorado Springs, CO, (1987), pp. 28-35

9. C. McLochlin, C. Ward, Y. C. Chow, R. E. Newman-Wolfe, J. N. Wilson, and T. B. Hughes, presented at IEEE Military Communications Conference MILCOM87, Washington, D.C. (1987), paper 20.3

10. T. Pratt and C. Bostian, Satellite Communications (Wiley, New York, 1986)
11. W. Stallings, Data and Computer Communications, (MacMillan, New York, 1985)
12. A. Tanenbaum, Computer Networks, (Prentice-Hall, Engelwood Cliffs, NJ, 1981)
13. H. VanTrees, Ed., Satellite Communications, (IEEE Press, New York, 1979)
14. Ward, C., Ph. D. Dissertation (CIS Department, University of Florida, Gainesville, Florida, 1987)
15. W. Wu, Elements of Digital Satellite Communication, Vol. 2 (Computer Press, Rockville, Maryland, 1985), pp. 423-427

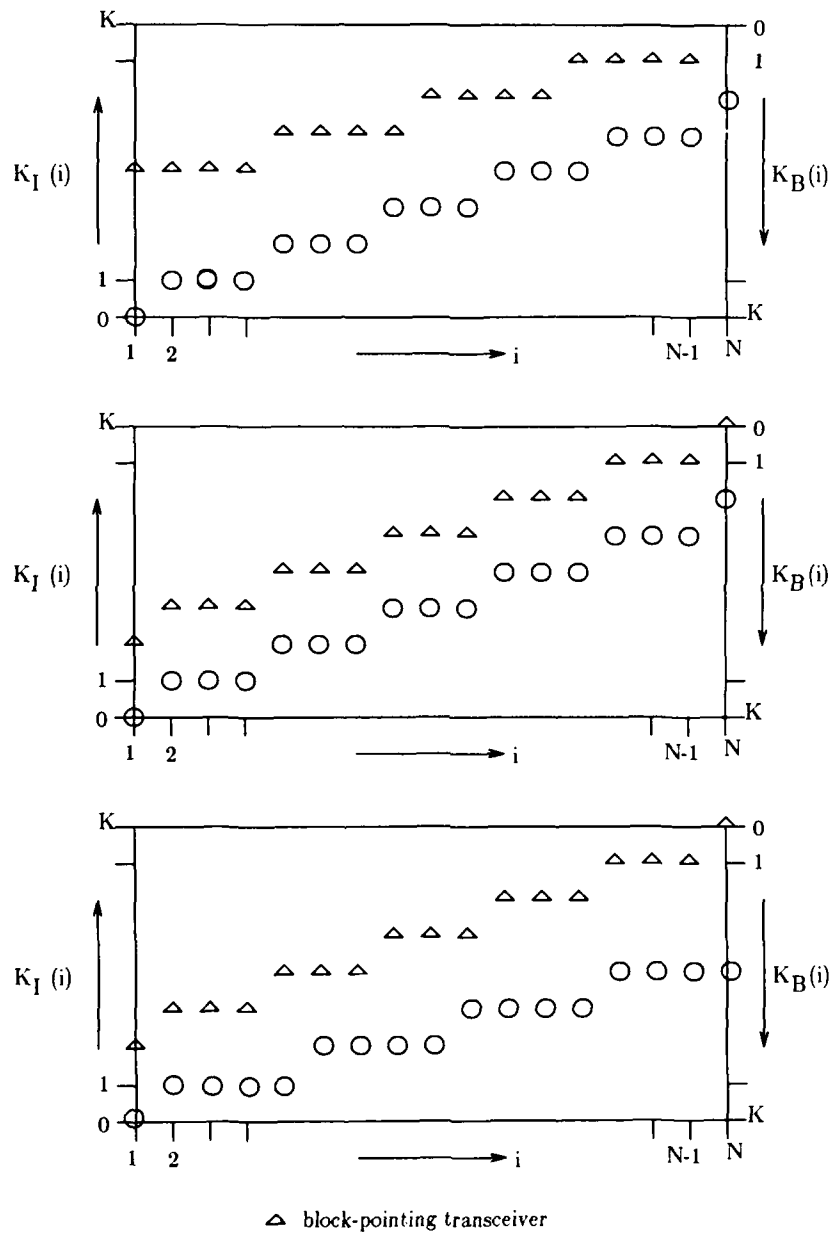


figure 5. Opposing plots of block-pointing and interleave-pointing transceivers

Spectral Sampling Signal Recovery Technique for Wavelength Encoded Fiber Optic Sensors

Peter J. Kajenski
Peter L. Fuhr
W.B. Spillman, Jr.

University of Vermont
Department of Computer Science and Electrical Engineering
Burlington, Vermont 05405
(802) 656-1917

Abstract

Wavelength encoded fiber optic sensors typically employ broadband sources and an encoding scheme in which the value of the parameter of interest corresponds to the wavelength at which the transmission of light through the sensor is a maximum. A principal disadvantage of this technique is that the entire spectral distribution of light of the source and sensor output (the modulated signal) must be measured to determine the value of the measurand. A variation of the traditional signal decoding scheme, one using multiple discrete spectral sources and interpolating polynomials, is discussed. Experimental results are presented and compared with theoretical performance predicitions.

Introduction

Fiber optic sensors have been developed to measure a number of different parameters such as temperature, pressure, magnetic fields, radiation and rotation. The measurand encoding techniques typically rely on interferometric or intensity modulation methods [1-4]. An alternative encoding technique, wavelength encoding, has been suggested and successfully demonstrated [5,6,7]. With this technique the value of the parameter being measured corresponds to the wavelength at which the transmission of light through the sensor is a maximum. In general, sensors utilizing this encoding scheme use a broadband light source; the wavelength of maximum transmission is determined by normalizing the spectral distribution of the sensor output with that of the source. A particular advantage of using this encoding scheme is that since it isn't specifically based on intensity variation, it isn't affected by variations in the output of the light source, such as intensity fluctuations. If the sensor also utilizes wavelength normalization (i.e., concurrent recording of the inout and output spectra) this scheme is also insensitive to shifts in the source's spectral distribution of light.

One disadvantage of wavelength encoding is that to obtain the spectra of the light source and sensor output, a monochrometer or similar device must be used, and the expense and bulk of such equipment may be prohibitive for many applications. Spillman and Fuhr used a reflective diffraction grating and a CCD linear camera array combination to obtain the needed spectra [6]. Such optical system designs, while effective, are unfortunately difficult to align and maintain. An alternative *decoding* scheme described here,

spectral sampling, eliminates the need to record the light source and sensor spectra entirely. While the spectral modulation *encoding* scheme is the same as in the aforementioned wavelength modulation schemes, in this technique multiple narrowband light sources are used to estimate the wavelength of maximum transmission.

Theory

The wavelength encoding sensor is based upon the introduction of a linear retardation into a light beam polarized at 45 degrees to the retardation axes. A typical sensor using this technique is shown in Figure 1. Collimated light from a broadband source is first passed through a polarizer set at an angle of 45 degrees with respect to the retardation axes. The light then encounters a transducer element whose retardation value depends on the parameter of interest, P, and a second polarizer which is set at -45 degrees. For such an optical system with no excess losses, and an initial optical power distribution $I_0(\lambda)$, the optical power distribution leaving the sensor is given as:

$$I(\lambda) = \left[\frac{I_o(\lambda)}{4}\right]\left[1 - \cos\left(\frac{2\pi R}{\lambda}\right)\right] \tag{1}$$

where R is the retardation value in nm and λ is the wavelength in nm. The optical systems output spectral distribution $I(\lambda)$ is therefore modified for various retardation values R. The value of R can chosen so that:

$$R(P_o) = (2n + 1)\frac{\lambda_o}{2} \tag{2}$$

where n is a positive integer and λ_0 is the desired wavelength of maximum transmission when the parameter of interest is P_0. The intensity maximum in equation (1) will occur when (setting n = 0):

$$\frac{2\pi R}{\lambda_{max}} = \pi$$

or

$$R(P) = \frac{\lambda_{max}}{2} \tag{3}$$

The wavelength at which the transmission of light through the sensor is a maximum can be determined by normalizing the output power distribution, $I(\lambda)$, with the initial power distribution, $I_0(\lambda)$, and then using a maximum value detection algorithm. If the wavelength of maximum transmission and the functional dependence of the retardation value of the parameter of interest are both known, the value of the parameter can be determined from Equation (3).

Rather than finding the wavelength maximum directly, it is possible to estimate where it occurs using interpolating polynomials [8]. Multiple narrowband light sources (such as a series of laser diodes) are used to find the relative intensities at several discrete wavelengths, $\lambda_0, \lambda_1,...,\lambda_n$ instead of using a broadband light source. Once these relative intensity - discrete wavelength data pairs have been obtained, a polynomial

can be fitted through them using a least squares or Lagrange polynomial algorithm. Mathematically, the encoding process is stated as the expression for the transmission of light through the sensor as a function of wavelength, namely

$$F(\lambda) = \frac{I(\lambda)}{I_o(\lambda)} = \frac{1}{4}\left[1 - \cos\left(\frac{2\pi R}{\lambda}\right)\right] \tag{4}$$

Given n+1 data pairs, this function can be approximated with a polynomial of, at most, order n such that:

$$F(\lambda) \approx P_n(\lambda) \tag{5}$$

where $P_n(\lambda)$ is an n-th order polynomial. By setting the first derivative of this polynomial equal to zero, and solving the resulting equation using an appropriate root finding algorithm, the wavelength of maximum transmission can be determined. When the wavelength of maximum transmission is known the value of the parameter of interest, P, can then be calculated using Equation (3)

Experiment

A fiber optic rotary sensor described previously [6] was used to test the viability of the spectral sampling encoding scheme. The sensor configuration used for this experiment is shown in Figure 2. The output of three lasers (Melles Griot HeNe laser, center wavelength: 632.8nm, Sharp LT021MD0 laser diode, center wavelength: 781 nm, Toshiba TOLD9201 laser diode, center wavelength 668 nm) were coupled into 100/140 micron fibers, which were connected to a 3:2 splitter. One of the fibers leading from the splitter delivered approximately 10% of the light to a PIN detector; the light from the other fiber was collimated and delivered to a polarizer set at an angle of 45 degrees. The light passed through the transducer element of the sensor, which consisted of a stack of waveplates (total on axis retardation value: 1860 nm), mounted on a rotating base plate. The light then encountered a second polarizer, set at angle of -45 degrees. A second PIN detector was used to record the intensity of light at the sensor output. The retardation value of the transducer element is given by the expression:

$$R(\Omega) = \frac{R_o}{\cos\Omega} \tag{6}$$

where R_o is the retardation value when the rotation angle of the waveplates, Ω, is zero. If the wavelength of maximum transmission is known, then the rotation angle can be calculated from the expression:

$$\Omega = \cos^{-1}\left(\frac{3\lambda_o}{\lambda max}\right) \tag{7}$$

The experiment consisted of setting the waveplates to a known rotation angle and then turning on the lasers, one at a time, to determine the relative intensities of light transmitted each wavelength. These data points were plotted, and a second order polynomial was fitted through them. The wavelength maxima were then estimated as described above. Figure 3 shows a plot of the waveplate rotation angle versus the wavelength of maximum intensity for both the theoretical and experimental data. Once the wavelength

maxima were determined, the estimated rotation angles were calculated using Equation (7). Figure 4 shows a comparison between the actual and estimated rotation angles.

For this experiment the rotation angle of the waveplates was restricted to between 15 to 35 degrees (maximum full-scale error of less than 4%) to allow the wavelength maxima to occur in the range between the laser output wavelengths. A larger range of angles could be correctly detected, and possibly greater accuracy, if additional laser sources are used.

Conclusions

A fiber optic rotary sensor using a spectral sampling decoding scheme was demonstrated. The spectral sampling encoding scheme combines some of the advantages of intensity and wavelength encoding. Since the measurand is not directly encoded as an intensity modulation, this scheme is not affected by variations in the light intensity whether it is due to source variations or fiber connector or splice degradation. Demonstrations of the spectral smapling decoding technique with a wavelength encoded rotary position sensor showed performance levels equal to the previously demonstrated grating - CCD systems. The system proved simpler to align and more optically "stable" than the grating - CCD scheme. Rotation angles over a 20 degree range were correctly determined with less than 4% full-scale error. A greater range and accuracy is possible if additional light sources are used.

References

1. Hocker, G.B., "Fiber-Optic Sensing of Pressure and Temperature," Appl.Opt., vol.18, pp 1445-1448, (1979).
2. Special issue on "Fibre-Optic Sensors," Proc. IEE, Vol.132, Pt. J, No. 4, (1985)
3. Miller, G.E., "Fiber Optic Control of Jet Aircraft Engines," Proc. ISA/32nd International Instrumentation Symposium, Seattle, Vol.32, pp 269-282, (1986).
4. Rashleigh,S.C., "Magnetic Field Sensing With a Single Mode Fiber," Opt.Lett., vol.6 pp 19-21, (1981).
5. Jones, B.E. and Spooner, R.C., "Photoelastic Pressure Sensor with Optical Fibre Links Using Wavelength Characterization," 1st International Conf. of Optical fibre Sensors, London, England, (1983).
6. Spillman ,W.B. and Fuhr, P.L., "Fiber Optic Rotary Sensor With Wavelength Encoding," Appl. Opt., vol 27, pp3081-3084, (1988).
7. Spillman, W.B., Fuhr,P.L. and Kajenski,.P.J., "Self-Referencing Fiber Optic Rotary Displacement sensor," SPIE Fiber Optic and Laser Sensors VI, Vol.985, pp 305-311, (1988).
8. Burden, R.L. and Fairs, J.D., "Numerical Analysis," third edition, p 78, PWS Publishers, Boston, Mass. (1985).

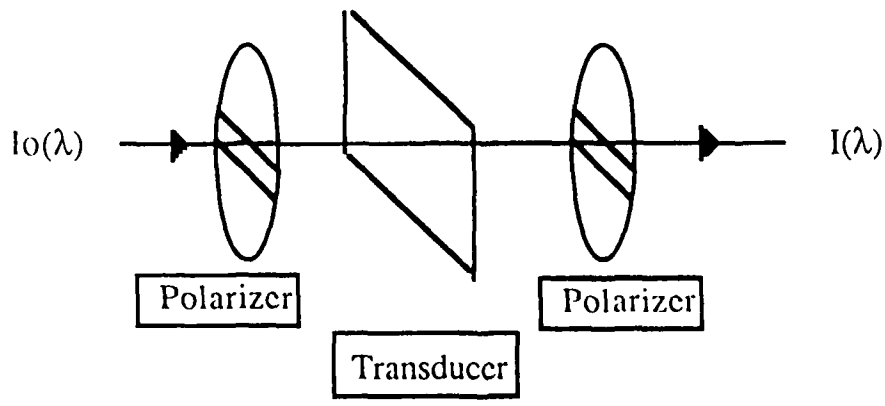


Figure 1. Schematic diagram of a typical wavelength encoded sensor.

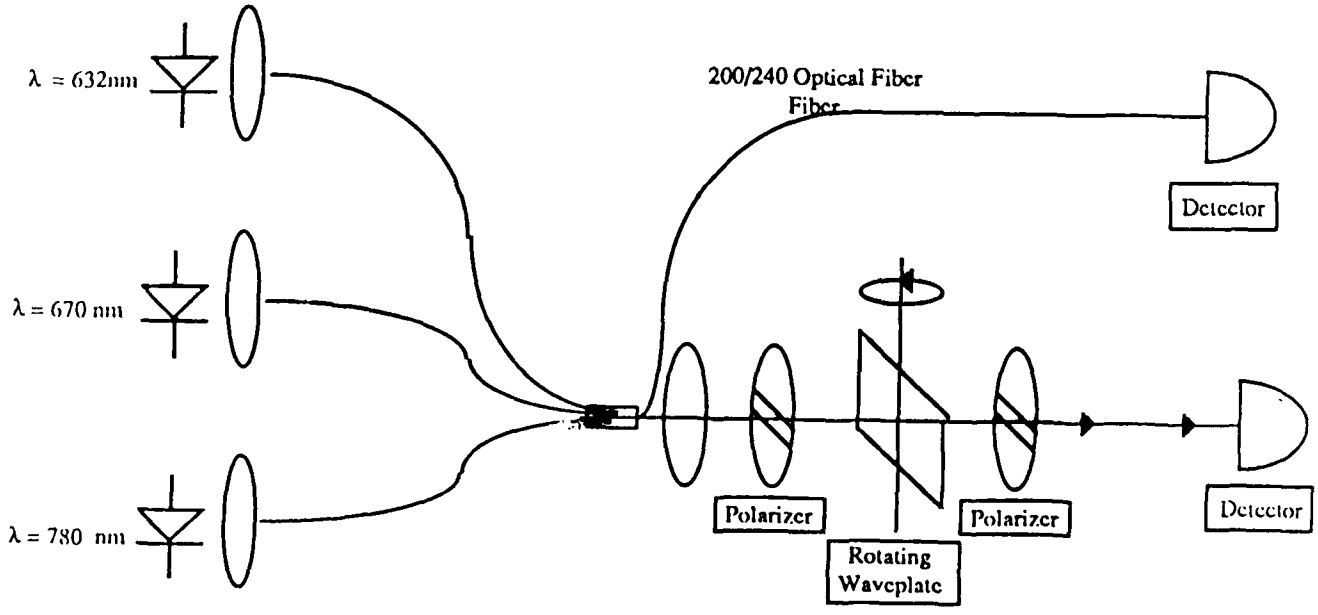


Figure 2. Experimental configuration of a sensor using spectral sampling.

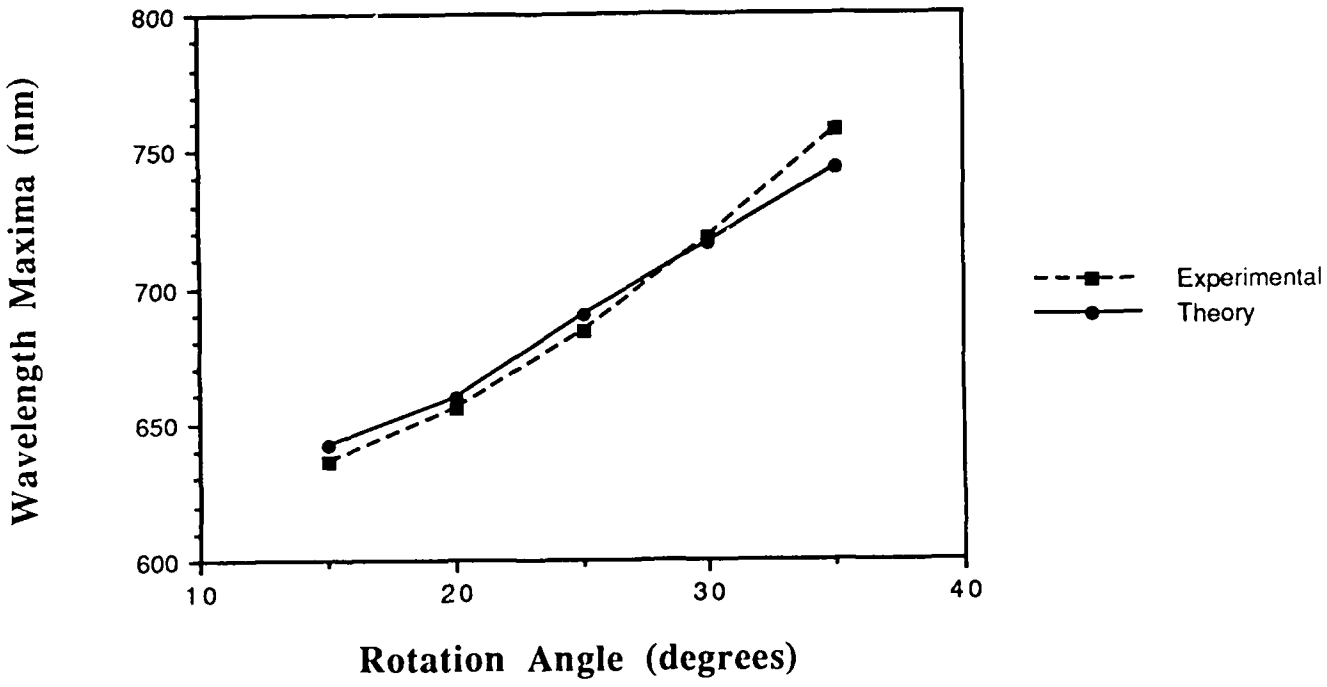


Figure 3. Plot of wavelength maxima vs. rotation angle. The solid line represents the theoretical curve, and the dashed line is the experimental data.

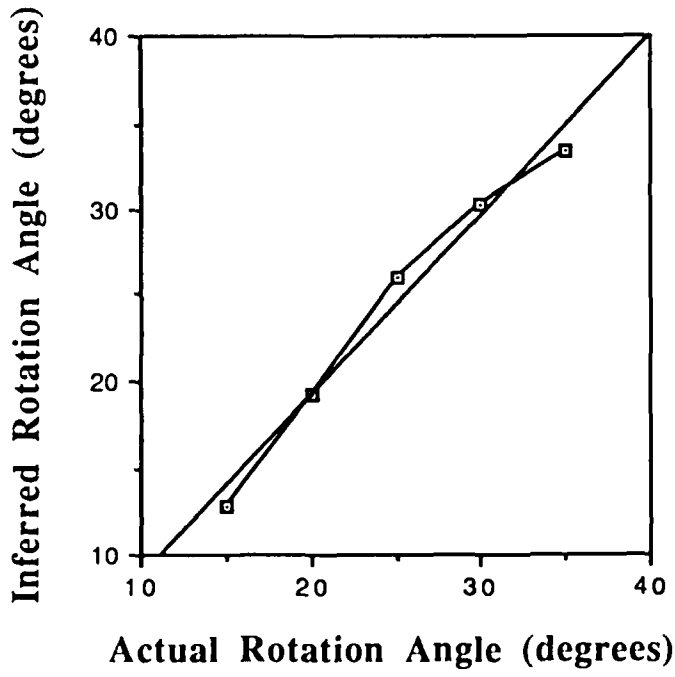


Figure 4. Plot of the actual vs. the inferred rotation angle of the waveplates

MULTIPLE STRIP LINES FOR PICOSECOND OPTOELECTRONIC PULSES

J. Witters and P. Janssen
Department of Physics, K.U. Leuven
Celestijnenlaan 200D, B-3030 Leuven (Belgium)

D. Schoemaker and E. Goovaerts
Department of Physics, University of Antwerp
Universiteitsplein 1, B-2610 Wilrijk (Belgium)

Abstract

Picosecond electrical pulses on coplanar transmission lines generated by femtosecond laser pulses have very sharp rising edges but longer tails dependent on the carrier lifetimes. It is difficult to limit the carrier lifetimes below one picosecond. To obtain enhanced far-infrared power in the frequency band above 1 THz a "frozen wave" design with fast alternation of rising edges from positive and negative lines is proposed. Details of the design are discussed.

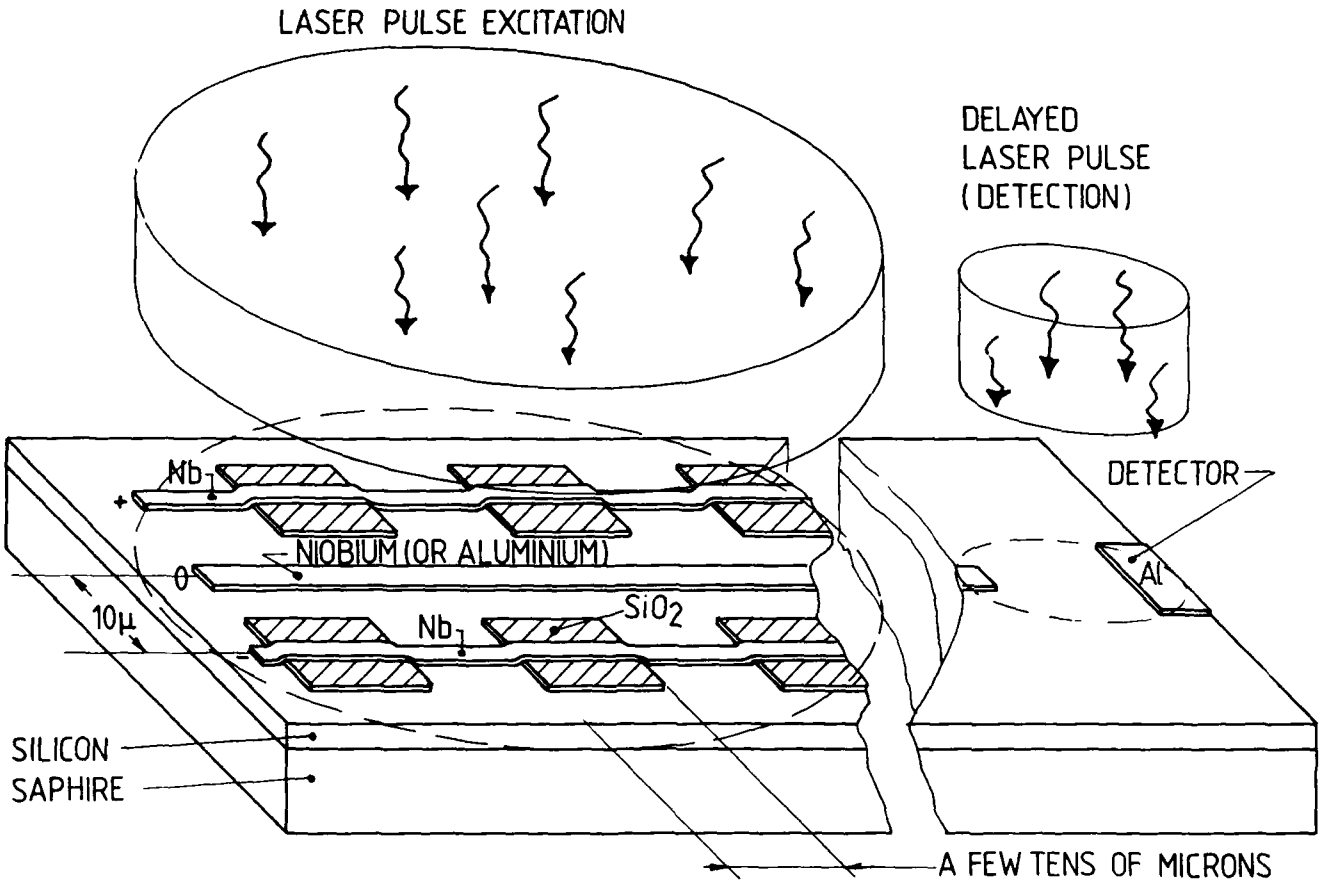


Fig.1: "Frozen wave" pulse generation in a triple strip line.

Opto-electronic Pulses

Opto-electronic pulses are usually generated by a laser pulse focussed between coplanar metallic transmission lines on a photoconductor such as Silicon or GaAs. The metallic strips have widths and separations of a few microns. One of the strips has a dc bias, the other is connected to ground. The charge carriers generated by the laser photons drift in the static electric field between the lines and are collected by the metal strips, thus forming the source of a transient electrical signal on the strips. The duration of this transient pulse is determined primarily by the carrier relaxations in the photoconductor. After completion of the laser pulse, which can be much shorter than a picosecond, the current may continue to rise by a redistribution of the carriers over the band states: carriers originally injected in states far from the band edges, where the mobility may be low, undergo elastic scattering which may lead to an increasing average mobility and lengthen the rise time of the pulse. However, by choosing the best photoconductor and by optimising the laser frequency it should be possible to keep this rise time shorter than a tenth of a picosecond. The decaying part of the pulse, on the contrary, can not be made shorter than about one picosecond. It is governed by the capture time of the charge carriers which is always longer than a picosecond, as shown in a recent review article of D.H. Auston(1). For example, radiation damage caused by bombardment with O^- ions can reduce the free carrier lifetime in Silicon drastically, but the effect levels off at implantation doses above 10^{14} cm^{-2} and the limit lifetime is about one picosecond. It follws from these data that opto-electronic pulses have a minimum width of the order of one picosecond but the shape can be asymmetric, with a faster rising and a slower decaying edge. In principle therefore it should be possible to superimpose pulses of different polarity in such a way that a very sharp pulse is obtained. A realisation of this possibility by means of a multiple strip line is discussed in the following section of this paper. The multiple strip line is designed to generate a "frozen wave", a pulse train of which the fundamental pulse width as well as the number of pulses can be varied.

Multiple Strip Line Design

The basis structure of the design is shown in fig. 1.

The structure consists of three parallel conducting lines on a photoconductor substrate, with line widths and separation of the order of 10 microns. The central strip is grounded and the others are polarised with opposite d.c. potentials of the order of ten volts. The outer strips are deposited on a structure consisting of regular alternations of the bare photoconductor surface and insulating pads. The structure is arranged so that the central strip is exposed to currents injected alternatively from left and right. A laser pulse covering a region of many alternations will trigger simultaneously the flow of currents from the contact zones of the outer lines toward the central line and thus generate a "frozen wave" potential alternation which is propagated along the line with the wave velocity of the strip line structure. To obtain a fully developed wave train, with maximum amplitude, the length of the oxide pads must be adapted to the current rise time. For a wave velocity of $10^8 ms^{-1}$ and a current rise time of 3.10^{-13} s the oxide pads should ideally be 30 microns long. The advantages of this type of optoelectronic generator over the usual type with a single point-like source are obvious:

i) high frequency components of the spectrum are enhanced because the relativity slow current decay is replaced by an opposite current rise

ii) the overall length of the wave train is a design parameter and it is therefore possible to adjust the width of the far infrared spectrum

iii) larger laser powers are admissible because the laser beam is spread over a larger surface area.

A realisation of multiple strip line structures on radiation damaged Silicon on Sapphire was recently completed and the results of the tests will be published in the near future.

References:

(1) Ultrafast Optoelectronics
D.H. Auston in "Ultrashort Laser Pulses"
Vol. 60 of Topics in Applied Physics

AN AVALANCHE VMOS DRIVER FOR PULSING SEMICONDUCTOR LASER DIODES

Ari Kilpelä, Raimo Ahola*, Juha Kostamovaara, Risto Myllylä**

University of Oulu, Department of Electrical Enginering, Electronics Laboratory,
SF-90570 Oulu, Finland, tel. 358-81-353 791, FAX 358-81-561 278

*Noptel Ltd., Teknologiantie 8, SF-90570 Oulu, Finland

**Technical Research Centre of Finland, Electromics Laboratory, P.O. BOX 181,
SF-90570 Oulu, Finland

Abstract

The problem is to produce suitable light pulses for time-of-flight laser range finders. These pulses can be achieved with a semiconductor laser and suitable pulsing electronics. The laser pulse should be square and of length 5-10 ns. Its time and amplitude jitter and change in shape should be as small as possible. Two types of transmitter electronics are studied here: an avalanche transistor with a delay line and a combination of an avalance transistor and a VMOS transistor. Measurement results are shown for both types of transmitter. The latter type is shown to have significant advantages over the previous type and for these reasons provides an especially suitable transmitter circuit for a situation, in which it is desirable to be able to change the pulse current while keeping shape stable..

Introduction

A semiconductor laser is a suitable light source for TOF(time-of-flight) laser rangefinders at short and medium distances (< 100 m from passive targets, < 1 km from active targets) /Ahola82/,/Määttä88/. A laser rangefinder consists of a transmitter, a receiver, timing discrimination electronics and a time measuring unit. The properties of the transmitted optical pulse are important for the operation of the whole rangefinder, as the other parts of the rangefinder demand specific properties with respect to the shape and length of the laser pulse.

The relevant properties of laser pulsers are: fast variations in pulse power (amplitude jitter), slow variations in pulse power, time jitter and variations in the shape of the pulse. The effect of amplitude jitter on range measuring accuracy can be eliminated by using suitable means of timing discrimination (constant fraction discriminator, CFD). Variations in the shape of the laser pulses may affect the resolution and accuracy, because the operation of the CFD is adjusted for a certain shape and length of pulse, so that variations from these values may cause errors. The importance of time jitter depends on the type of time measuring system selected. When a digital time measuring system is used, time jitter is desirable and it often has to be increased by some means, so that the oscillators of the transmitter and the time measuring system are not in the same phase. With an analog time measuring system, however, the time between two successive pulses emitted from the transmitter should be stable. A change of temperature will cause a variation in the optical pulse power of the laser and, especially when avalanche transistors are used, changes in the shape of the pulse. Slow amplitude variations should be compensated for by changing the pulse current going through the laser, if desired, so that the optical pulse power remains unchanged.

The resolution of the distance measurement depends on the slew rate of the rising and falling edges of the pulses and the S/N ratio of the pulses received. In theory, both the rising and falling edges should be as fast as possible when both edges are used in timing discrimination. The length of the pulse should also be as short as possible, so that the temperature of the laser remains sufficiently low and high pulse frequencies can be used. The timing discriminator and the time measurement units usually consist of ECL logic circuits and fast amplifiers. The bandwith of these circuits is limited to 200-500 MHz and this determines the minimum length of the light pulse. The pulses should be sufficiently long to ensure proper working of the timing discrimination and the time measurement electronics. In practice 5-10 ns has proved to be suitable length.

Fast swithing elements are needed to produce fast laser pulses. These are usually avalanche transistors, bipolar transistors driven by fast amplifiers, MOSFETs or thyristors. Vertical MOSFETs are particularly promising components, with characteristics that are improving year by year. Power MOSFETs can handle high powers, currents and voltages and have a wide bandwith, amplification and high input impedance. Also, the turn-off delay in switching operation is short.

This paper first describes the traditional ways of producing current pulses for semiconductor lasers and then presents a new type of circuit, which combines an avalanche-transistor and a MOSFET. Some performance results obtained from the latter circuits are given.

Ways of producing current pulses for semiconductor lasers

Semiconductor lasers can be divided into two groups: CW (continuous wave) and pulsed lasers. A common type of the pulsed laser is the SH (single heterostructure) laser, which typically has a maximum pulse length of 200 ns, a driving current of 1 A - 50 A and a maximum duty factor of 0.2 %. Another type is the DH (double heterostructure) laser, which can be either a CW or a pulsed laser. The maximum duty factor of a pulsed DH laser is large compared with the SH types, 6 % at maximum. The optical pulse powers of the DH lasers vary in the range of 10 mW - 5 W and their driving currents in the range 100 mA - 5 A.

A general method for producing fast current pulses to low-impedance loads such as semiconductor laser, is shown in figure 1. A capacitor C is charged to a voltage V and connected to a laser with a fast switch. The slew rate and the maximum amplitude of the current pulse depend on the voltage switched, the capacitance of the capacitor, the inductances of the connecting leads and the internal resistance of the switch. When large currents are needed, the on-state resistance of the switch is usually the limiting factor. The width of the pulse can be adjusted by changing the width of the driving pulse of the switch (when the switch is a MOSFET), or changing the capacitance of the decharged capacitor (when the switch is an avalanche-transistor). A delay line can also be used as a decharged element, in which case the width of the current pulse is approx. twice the electrical length of the delay line.

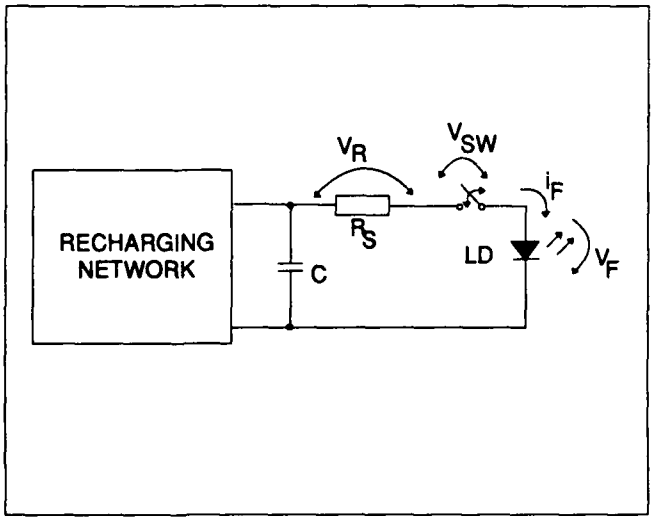


Figure 1.

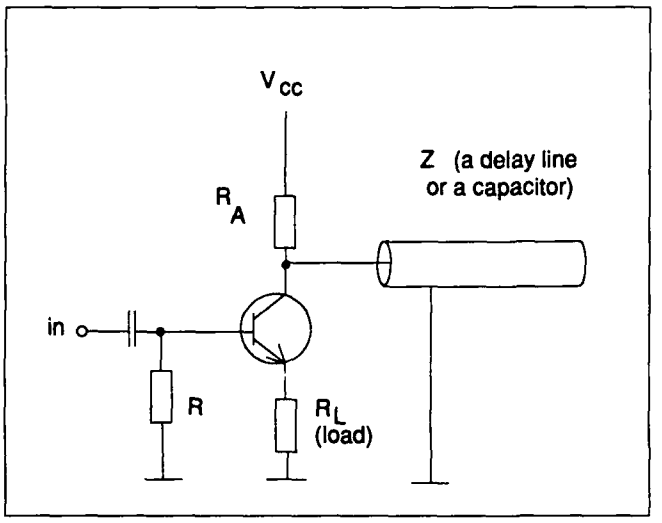


Figure 2.

A commonly used fast switch is a bipolar transistor, which makes use of the avalanche breakdown between collector and emitter/Silver67/,/Herden76/, /Rein77/ (figure 2). Avalanche transistors are normal bipolar transistors (usually fast switching transistors), which are used at a operating voltage much larger than the normally rated operating voltage. The rising time of a current pulse switched with an avalanche transistor is typically below 1 ns. In /Vanderwall74/ a rise time of 120 ps is achieved with a current amplitude of 40 A. When a capacitor is used as a decharged element and the properties of the avalanche transistor approach those of an ideal switch, the falling edge of the current pulse is exponential. When a delay line is used instead of a capacitor the current pulse is square /Waugh 81/. The characteristic impedance of the delay line must be adjusted to be the same as the impedance of the load, so that the pulse produced will be as symmetrical as possible, without reflections. The current switched is determined by the impedance of the delay line and the operating voltage. The delay line also has a few drawbacks. When its impedance need to be changed, the whole delay line must be constructed again. The delay line can be fabricated as a microstrip line, from separate components (capacitors and inductors) or from coaxial cables. The delay line is often large in size compared with the other parts of the transmitter. One drawback of an avalanche transistor is that the avalanche properties of a bipolar transistor may vary greatly between types and also between different examples of the same type. The life times of avalanche transistors can also be short, because their operating voltage is significantly larger than in normal operation and they are used to switch large currents.

Power MOSFETs are especially suitable for fast switches, because minority carrier storage time does not cause turn-off delay like as in bipolar transistors. In practice, the limiting factors for the slew rate of a pulse switched with a MOSFET are the time needed to charge the gate capacitances of the MOSFET and the voltage losses caused by the lead inductances. Vertical power MOSFETs, such as VMOSFETs and DMOSFETs, may have small on-state resistances and on the same time reasonable gate capacitances. Because of the vertical structure of the power MOSFETs they have a high current handling capability relative to their circuit area. Power MOSFETs can also tolerate high operating temperatures and their on-state resistance has a positive temperature coefficient, which ensures their safe operation when switching large currents. If it is desired that the rise time of the pulse switched with a MOSFET should be a few nanoseconds at maximum, the charging current of the gate capacitances must be several amperes, because the value of the capacitance between the gate and drain is multiplied by the Miller effect in the linear transfer region of the MOSFET.

Circuit A: a combination of an avalanche transistor and a delay line

The goal was to investigate the operation of several transmitter circuits, which would be suitable for pulse currents between 0.5 A and 5 A. Suitable light sources in this current region are LEDs and CW and pulsed DH lasers. The pulsing frequencies used were between 100 kHz and 1 MHz. The delay lines tested were a) a delay line consisting of two coaxial cables, b) a delay line constructed with capacitors and inductors, and c) a strip-line. The circuits were tested with resistive loads, and in the c) case, a LED. The measurements were made with a Tektronix 2465 oscilloscope with a bandwith of 300 MHz. The input impedance of the oscilloscope was 50 Ω and the pulse was measured over a 1 Ω resistor connected in series with the load.

The avalanche transistors tested were the types 2N3704, 2N2369, 2N5179 and BFR96, selected on the basis of the literature /Vandre77/,/Andrews74/. The types 2N5179 and BFR96 seemed to be especially interesting. The Motorola 2N5179 transistor was measured to work in avalanche operation at supply voltages between 50 V and 100 V. A suitable voltage proved to be 60 V. The Philips BFR96 is an RF small signal transistor, the avalanche region of which started at a supply voltage of 30 V. A voltage of 48 V was used in the tests.

In the first circuit two 58 cm coaxial cables connected in parallel were used as a delay line, giving a characteristic impedance of 25 Ω. The avalanche transistor was of the type 2N5179 and the supply voltage was 60 V. When the load impedance was a resistor of approx. 20 Ω, the FWHM (full width half maximum) of the current pulse was 6.3 ns and, the rise time 1.3 ns and the pulse current 0.75 A (Figure 3).

In the second circuit the delay line was constructed with 22 nH inductors and 220 pF capacitors, and consisted of three LC pairs. The calculated characteristic impedance was 10 Ω. The avalanche transistor was of the type 2N5179 and the supply voltage was 60 V. The rise time, FWHM and amplitude of the current pulse measured with a 10 Ω load impedance were 2.2 ns, 6.3 ns and 2.3 A respectively (Figure 4). The fall time of the pulse was clearly slower than with the coaxial cables. This may be due to stray capacitances in the circuit. The rise time of the pulse with a separate component delay line was a little slower, than in the situation in which only one capacitor was used as a decharged element.

The third delay line was constructed from 75 um thick circuit board. The characteristic impedance of this microstrip delay line was 3.5 Ω and the electrical length 10 ns. The characteristic impedance was calculated with the formula presented in /Coekin75/, p. 68. The avalanche transistor selected was of the type BFR96, the supply voltage of which was 48 V. The amplitude of the current pulse was 600 mA, the FWHM 11 ns and the rise and fall times of the pulse approx. 1 ns (Figure 5). The load used in this circuit was a LED of type Asea 1A117DH.

The current pulses achieved with these delay lines were of a suitable shape for transmitters for use in distance meters, but the physical dimensions of the delay lines became too large. This was especially true of the coaxial cable delay line, if small characteristic impedances are desired. One good feature of the microstrip delay line is that the characteristic impedance may be adjusted accurately by changing the line width.

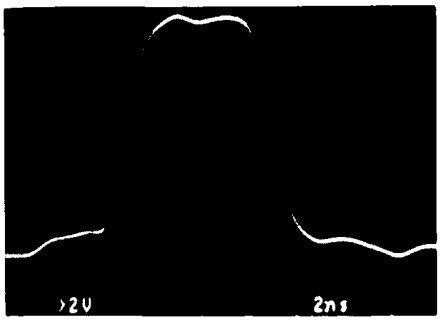


Figure 3.

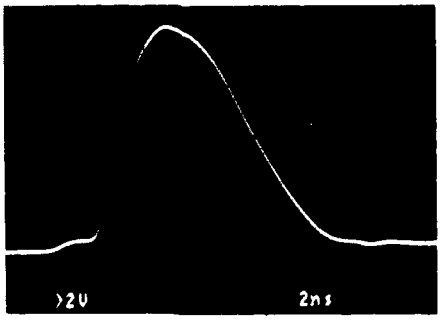


Figure 4.

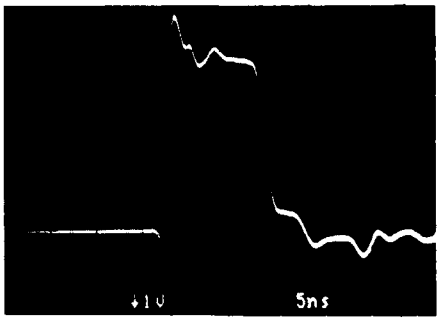


Figure 5.

Circuit B: a combination of an avalanche transistor and a VMOSFET

The goal in constructing the combination of a avalanche transistor and a MOSFET was to exploit the good characteristics of both. The large current pulse of the avalanche transistor charges the gate capacitances of the MOSFET rapidly, so that the rise time of the current pulse switched by the MOSFET is small. The load current can be changed by altering the supply voltage of the MOSFET.

The circuit is presented in Figure 6. The pulse to the MOSFET is taken from the emitter of the avalanche transistor. One part of the current going through the avalanche transistor, when switched from the off to the on state, goes through the emitter resistance to ground and one part charges the gate capacitances. Once the MOSFET has moved from the linear region to the saturation region, loading of the gate capacitances has very little effect on the on state resistance of the MOSFET. The

emitter resistance is chosen so that the gate capacitances will decharge at the same speed during switching from on to off as when charging from off to on. The width of the pulse can be altered by varying the value of the decharged capacitor of the avalanche transistor. A square switched pulse can be achieved with a suitable combination of capacitor and emitter resistance in the avalanche transistor.

The MOSFETs tested were Siliconix VN88F and International Rectifier IRF512. The VN88AF in particular has small gate capacitances compared with its high current handling capability and a small on-state resistance. According to the data sheets, the IRF512 reaches the saturation region at a smaller gate-source voltage than the VN88AF. The avalanche transistor was the 2N5179 in the circuit presented in figure 6. The supply voltage of the avalanche transistor was 60 V, which proved to be especially suitable, because the same voltage could be used to the MOSFET. The measurements proved that the larger gate capacitances of the IRF512 slowed down the rise time of the current pulse switched by it considerably. The IRF512 would probably have needed a larger driving current, than the 2N5179 was able to give. Consequently the VN88AF was used in this circuit. The load for measuring purposes was a pulsed DH laser, ITTLB1-02, protected against negative voltage spikes with two fast schottky diodes connected in parallel with it. The pulsing frequency of the circuit was 1 MHz, generated with an ECL oscillator. The outgoing pulse from the ECL circuit was used directly to drive the gate of the avalanche transistor.

The current pulse measured over the current limiting resistor of the laser is presented in the Figure 7. The rise time is 1.4 ns, fall time 1.4 ns and FWHM 6 ns. The effect of the rise time of the oscilloscope is taken into account in these values.

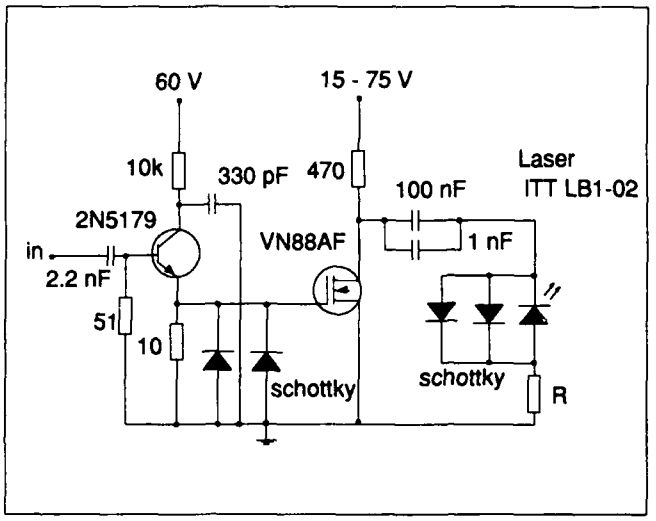


Figure 6.

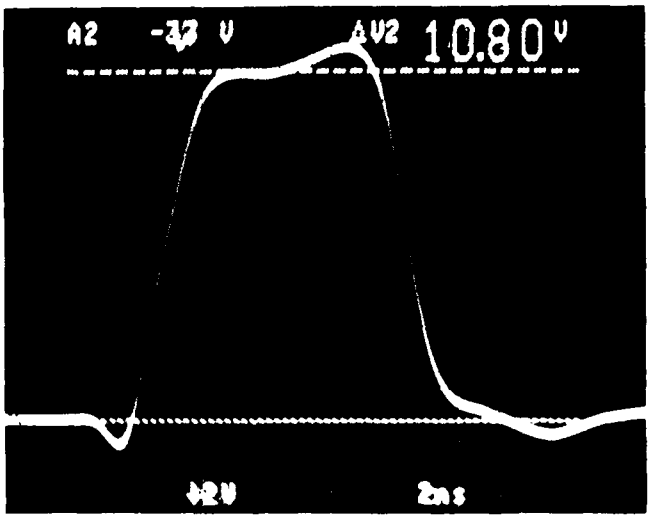


Figure 7.

The amplitude of the current pulse to the load is presented in Figure 8. The values are measured using a pure resistive load, without a laser. The amplitude of the current pulse varied in the range 1:3 when the supply voltage of the MOSFET was altered in the range 1:5 (15-75 V). Figures 9 and 10 present measurements of the rise time and FWHM of the current pulse at varying MOSFET supply voltages. Because of the Miller effect, the rise time of the pulse varies a little when the supply voltage is changed.

The rise time, FWHM and amplitude of the current pulse as functions of temperature were measured in the temperaturre range -15 °C - +40 °C with a resistive load. The rise time and FWHM remained unchanged within the limits of measuring accuracy (Figures 9 and 10), but the amplitude decreased by 5 %, when the temperature was changed from -15 °C to +40 °C (Figure 8). This was probably caused by the positive temperature coefficient of the on-state resistance of the MOSFET.

The temperature dependence of the optical power of the laser was measured in two ways. The first measurement was performed by adjusting the supply voltage of the MOSFET so that the optical power of the laser remained unchanged, when the temperature was changed (Figure 11). The resulting variation in supply voltage was 10 % in the temperature range -40 °C - +20 °C. In the second measurement the supply voltage of the MOSFET was kept constant, in which case the optical power of the laser changed by 45 % in the same temperature range.

The measurement results show that the combination of an avalanche transistor and a VMOSFET produces a practicable transmitter circuit, as the shape of the pulse changes only slightly upon alteration of the supply voltage of the MOSFET or the ambient temperature. The width of the current pulse decreases by 15 % when the pulse current is changed from 1.3 A to 4.5 A. This happens, because the on-state resistance of the VMOSFET increases in larger currents. At the same time, the rise time varies in the range of 1.15 ns - 1.45 ns. This is mainly due to the Miller effect in the operation of the VMOSFET. Changing the temperature does not significantly affect the FWHM or the rise time of the current pulse, but it does affect the peak amplitude of the pulse current. If higher currents are needed, several VMOSFETs can be connected in parallel, but the type of avalanche transistor must also be changed in order to increase the value of the current injected into the gates of the MOSFETS. The properties of the MOSFETs must be matched in some way., otherwise they do not switch on at the same time and the value of the current does not increase. One possibility is to measure the values of the parameters V_p and I_{DSS} for each VMOSFET and select those components which have same parameter values.

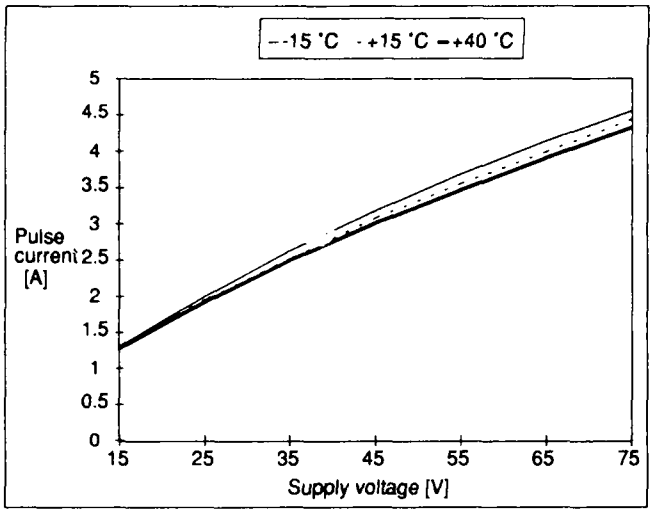


Figure 8.

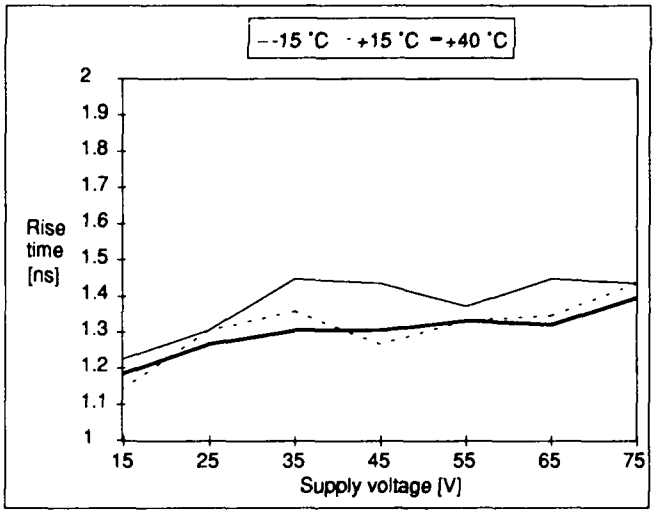


Figure 9.

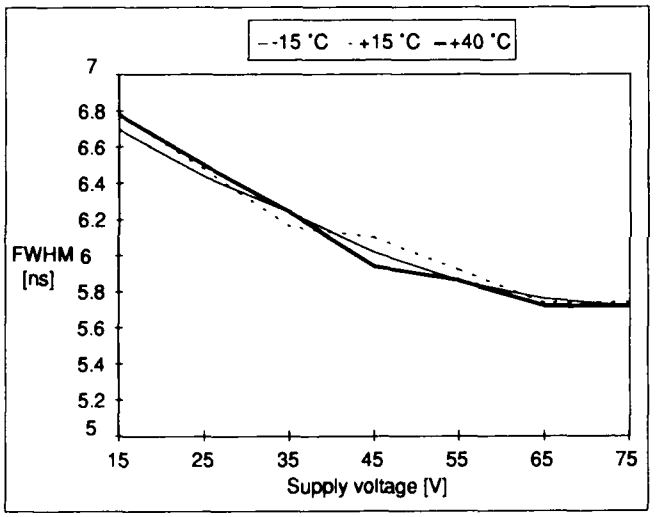


Figure 10.

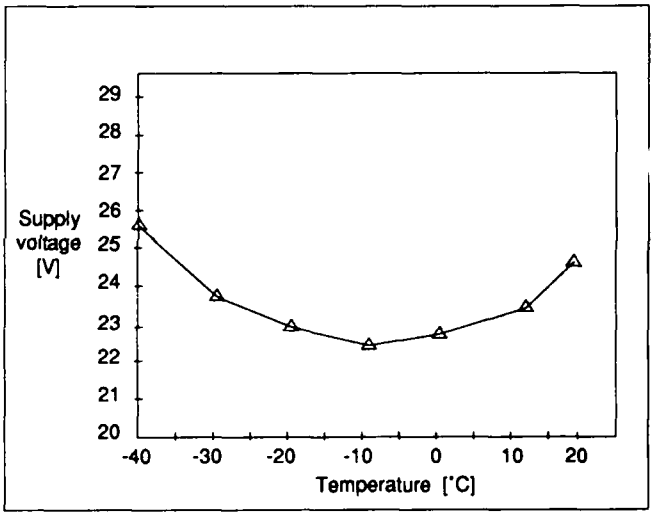


Figure 11.

Conclusions

It is concluded, that the first transmitter circuit type, an avalanche transistor with a delay line, has only limited possibilites to change the pulse current. If the width of the pulse must be changed, the whole delay line must be constructed again. Also the size of the delay line is often too large. The new pulser type presented, an avalanche transistor and a VMOSFET, has some advantages over the previous type. The pulse current can be changed in the range of 1 A - 4.5 A without changing the components. In this current range, the shape of the pulse remains almost stable. Temperature variations affect only slightly to the amplitude of the pulse current and no significant effects can be detected in the width or rise time of the pulse. If higher power levels are needed, several MOSFETs can be connected in parallel. At the same time, the current of the driving pulse must also be increased in order to ensure fast switching speeds. The circuit is suitable for a general type of transmitter and for eliminating variations in the optical power of the laser in response to temperature changes.

References:

/Ahola82/: Ahola, R.: Continuous measurement of distance, velocity and acceleration using a semicondustor laser (in Finnish). Licenciate thesis, University of Oulu, OULU, Finland, 1982, 88 pp.

/Andrews74/: Andrews, J.: Inexpensive laser diode pulse generator for optical waveguide studies, Rev. Sci. Instrum. Vol.45, n:o 1, January 1974, pp. 22-24.

/Coekin75/: Coekin, J.A.: High speed pulse techniques, Pergamon Press, Oxford 1975, 216 pp.

/Herden76/: Herden, Werner, B.: Application of Avalanche Transistors to Circuits with a Long Mean Time to Failure, IEEE Transactions on Instrumentation and Measurement, vol. 25, n:o 2, June 1976, pp. 152-160.

/Määttä88/: Määttä, K.: Developing of a laser range finder for industrial measuremens (in Finnish). Licenciate thesis, University of Oulu, Oulu, Finland 1988, 61 pp.

/Rein77/, Rein, H. M.: Relationship between transient response and output characteristicsof avalanche transistors, Solid State Electronics, vol. 20, 1977, pp. 849-858.

/Silver67/: Silver, S.:Avalanche transistor circuits, Electronics Worlds, Volume 78, n:o 3, (September 1967), pp.30-32.

/Vandre77/: Vandre, R.: An ultrafast avalanche transistor pulser circuit, Electronic Engineering, Vol. 49, n:o 598, October 1977, p. 19.

/Waugh81/: Waugh, A.R.: A nanosecond kilovolt pulse generator using microstrip charging lines. Journal of Physics, Sect.E: Scientific Instruments, Vol. 14, 1981, pp. 615-617.

CO_2-LASER-INDUCED HOMOEPITAXY OF AMORPHOUS SILICON FILMS

R. B. James
Advanced Materials Research Division
Sandia National Laboratories
Livermore, CA 94551-0969

ABSTRACT

We have demonstrated that CO_2 laser radiation can be used to recrystallize deposited amorphous silicon films into epitaxial layers. Normal furnace annealing of these amorphous silicon films leads to the formation of polycrystals, rather than a single-crystal, due to the presence of impurities and the native oxide at the amorphous/crystalline interface. Using CO_2 laser pulses, defect-free epilayers were formed with thicknesses greater than 15000 Å, which is much larger than the previous work reported with Nd:YAG and ruby lasers.

INTRODUCTION

Epitaxial growth of amorphous silicon layers on silicon can be achieved by thermal annealing if the samples have intrinsically clean interfaces [1]. However, when the amorphous films are deposited onto crystalline silicon substrates in a conventional vacuum chamber (10^{-6}-10^{-7} Torr during evaporation), there are contaminants at the interface of the amorphous film and single-crystal substrate. Thermal annealing of these samples leads to the formation of polycrystalline films, instead of epitaxial regrowth. Laser pulses from a Nd:YAG (at 1.064 and 0.532 μm) [3-4] and a ruby (at 0.694 μm) [5-7] laser have been successfully used to induce epitaxial regrowth of amorphous silicon layers that were vapor-deposited onto single-crystal silicon. At these wavelengths the laser radiation is strongly coupled to the amorphous Si, and a thin surface layer having a thickness of several hundred to a few thousand angstroms is heated to high temperatures by the pulse. For pulse-energy densities exceeding a threshold value, the entire film is melted and liquid-phase epitaxial regrowth occurs from the underlying single-crystal substrate. For film thicknesses less than about 5000 Å, one can obtain a defect-free epitaxial layer for Si substrates cleaned by a variety of techniques, including HF oxide removal [3,6], argon ion sputtering [5], and argon ion sputtering followed by a high-temperature anneal [4]. However, for film thicknesses greater than about 5000 Å, it is difficult to deposit enough pulse energy in the amorphous layer to completely melt through the layer without causing surface decomposition due to vaporization.

In this paper results are reported showing that epitaxial regrowth of amorphous Si films can also be achieved using a pulsed CO_2 laser operating at a wavelength of 10.6 μm. At this wavelength high-resistivity amorphous Si is relatively transparent, and the energy contained in the laser pulse is absorbed via free-carrier transitions within the underlying doped single-crystal substrate. For heavily doped crystalline silicon, the absorption coefficient at 10.6 μm is in the range of 10^4-10^5 cm^{-1}, and the pulse energy is deposited within a depth of several thousand angstroms below the amorphous Si film. At sufficiently high CO_2 pulse-energy densities, the temperature of the crystalline Si near the amorphous/crystalline Si interface exceeds its melting point (1410 °C). Because the melting point of amorphous Si is about 200 °C less than crystalline Si, the heat transport from the hot (~ 1410 °C) buried layer rapidly drives the melt front from the a-Si/c-Si interface toward the free surface. For all the layer thicknesses studied in this work, the melt front is driven throughout the entire a-Si film whenever there is melting of a portion of the crystalline substrate. Solidification of the molten layer occurs by homoepitaxy from the underlying liquid/solid interface. Using CO_2 laser pulses, we have demonstrated that amorphous silicon films having thicknesses exceeding 15000 Å can be crystallized, which is a factor of three larger than the maximum thickness achieved with a Nd:YAG or ruby laser.[2-7]

EXPERIMENT

The samples used in this study are 340-μm-thick, boron-doped (111) single-crystal silicon which, prior to ion implantation, had a bulk resistivity of 0.0073 Ω-cm. This corresponds to a hole concentration of about 2-3 x 10^{19} cm^{-3}. The samples were ion implanted on one side by $^{75}As^{+}$ at an energy of 260 keV to a dose of 2 x 10^{16} cm^{-2}, resulting in an arsenic profile that is peaked at 1410 Å from the surface and has a standard deviation of 540 Å. The arsenic implantation produces an amorphous layer with a thickness of about 2150 Å, followed by a narrow band of dislocations. The samples were next thermally annealed at 873 K for fifteen minutes to induce solid-phase epitaxial regrowth of the amorphous layer and to increase the fraction of electrically active arsenic. This step greatly increases the coupling of the CO_2 laser radiation to the arsenic-implanted layer.

The arsenic-implanted wafers were cleaned prior to evaporation by sequential immersions in basic and acidic peroxide solutions to remove organic and metallic contaminants. The wafers were next immersed in a solution of HF:H_2O (1:10) and then rinsed in deionized water. Within in a few minutes, the samples were loaded into an evaporator. The evaporation was carried out at a pressure of about 10^{-6} Torr. High-purity polycrystalline silicon was deposited onto the substrates by an electron-gun vapor source. The thicknesses of the evaporated high-resistivity amorphous layers ranged from 5000 to 35000 Å for the different runs.

Laser irradiation was performed with a gain-switched, TEA CO_2 laser operating a wavelength of 10.6 μm. The laser was operated with a low nitrogen content in the gas mix, so that the amplitude of the long tail on the pulses could be greatly suppressed. About 70 % of the energy in each pulse was contained in the form of a nearly Gaussian peak of 60-ns duration (FWHM). The remaining 30 % of the pulse energy was in a second pulse that was delayed by about 300 ns from the first pulse and had a duration of 250 ns (FWHM).

The output pulse was diverged by a spherical convex mirror with a 1-m radius of curvature. The diverging beam was later collimated by a spherical concave mirror with a 2-m radius of curvature. The collimated beam then impinged on a CO_2 laser beam integrator which spatially homogenized the beam to within ±10%. The dimensions of the laser pulses were 12x12 mm in the target plane of the integrator. The energy density at the sample surface was adjusted by using additional lenses to change the pulse size and linear attenuators to change the total energy in each pulse. A photon-drag detector and volume absorbing calorimeter were used to measure the intensity and energy of the laser pulses, respectively.

The absorption coefficient of the CO_2 laser radiation in the thin (~2500 Å) arsenic-implanted layer is about 5 x 10^{4} cm^{-1}, while the absorption coefficient in the high-resistivity amorphous layer at the surface is less than 100 cm^{-1}.[8-9] Thus, the deposition of the pulse energy is predominantly near the interface of the ion-implanted substrate and the amorphous layer. (This relatively weak coupling of the CO_2 laser light in the amorphous layer is in contrast to the strong coupling of Nd:YAG, ruby, and excimer lasers, where the absorption coefficient in amorphous Si is much larger than the absorption coefficient in crystalline Si.[10])

The samples were irradiated in air by CO_2 laser pulses at different energy densities. Cross-section transmission electron microscopy was used to study the microstructure of the near-surface region. Van der Pauw measurements were conducted to determine the electrical properties of the epilayer.

RESULTS AND DISCUSSION

The precise manner in which the amorphous layer changes is best illustrated by cross-section transmission electron microscopy (TEM). The top, middle, and bottom photos in Figure 1 show TEM micrographs of three cross-sectioned specimens that were irradiated at pulse-energy densities (E_L) of 4.4, 5.1, and 7.2 J/cm^2, respectively. Each of the samples had a 15000-Å layer of amorphous Si deposited prior to irradiation. For E_L=4.4 J/cm^2, the amorphous layer is converted to polycrystalline Si.

The grain size of the polycrystals are smallest near the original a-Si/c-Si interface, and they grow as one moves from the buried interface toward the free surface. *With increasing E_L, the grain size coarsens and* the layer of large-grain polycrystals penetrates through the entire amorphous layer (see Fig. 1b). At still higher values of E_L, single-crystal material is produced, although for some samples a few dislocations are present (e.g., see Fig. 1c). For pulse-energy densities exceeding about 7 J/cm^2, the microstructure is typically free of extended defects for a 15000-Å-thick amorphous film.

Based on the TEM micrographs shown in Fig. 1, it is possible to envision progressive heating of the amorphous and arsenic-implanted layers as the energy density of the incident CO_2 laser radiation is increased. For E_L between about 4 and 6 J/cm^2, the region near the a-Si/c-Si interface is heated beyond the melting point of a-Si, but the temperature is still too low for melting of the c-Si. Since the molten



Figure 1. The top, middle, and bottom photos show cross-section TEM micrographs of samples that were irradiated at E_L = 4.4, 5.1, and 7.2 J/cm^2, respectively.

amorphous Si layer is screened from the single-crystal substrate by its native oxide and contaminants at the interface, epitaxial growth is prevented and polycrystals are formed during solidification. For E_L greater than 7 J/cm^2, both the amorphous and arsenic-implanted layers are melted by the pulse. The melt front extends from below the buried band of dislocations in the arsenic-implanted layer up to the free surface. The melting of the amorphous/crystalline interface causes dispersion of the contaminants and native oxide layer initially present at the a-Si/c-Si interface. The melted region recrystallizes from the underlying single-crystal substrate by liquid-phase homoepitaxy, resulting in a defect-free layer at the surface.

Van der Pauw measurements were performed on the specimens to determine the changes in the electrical properties of the epilayer after irradiation. For pulse-energy densities less than about 6.4 J/cm^2, the epilayer still had a high resistance, although the TEM images indicated that the amorphous layer had been converted to polycrystals. For higher values of E_L, large changes in the electrical properties were observed. For example, at E_L=7.2 J/cm^2 the electron concentration was 1.68 x 10^{16} cm^{-2}, the carrier mobility was 57 cm^2/V-s, and the sheet resistivity was 6.6 Ω/sq. These changes in the electrical properties can be understood if the arsenic dopants in the implanted layer were prevented from diffusing through the a-Si/c-Si interface for E_L less than about 6.4 J/cm^2. At higher values of E_L so that the arsenic-implanted layer was also melted by the laser pulse, the arsenic atoms contained in the buried ion-implanted layer diffused throughout the entire molten layer, and they were trapped in substitutional sites (i.e., electrically activated) as the liquid-solid interface receded back to the free surface.

Amorphous Si films with thicknesses of 35000 Å were also irradiated with CO_2 laser pulses. At a pulse-energy density of 5.5 J/cm^2, the amorphous layer was converted to polycrystals, analogous to the results discussed earlier for 15000-Å amorphous films. At values of E_L exceeding about 8 J/cm^2, the buried arsenic-implanted layer was also melted, and regions of nearly defect-free single-crystal Si were formed. Unfortunately, the TEM images also revealed several cracks in the epilayer, which are unacceptable for device applications. Since the density of hot and molten silicon is different than crystalline silicon at room temperature, the rapid heating and melting of the buried arsenic-implanted layer causes large thermally induced stress in the epilayer, which is probably responsible for the fracturing of these samples.

ACKNOWLEDGMENTS

I would like to thank W. H. Christie, R. F. Wood, R. T. Young, G. A. Geist, and P. H. Fleming for many useful discussions. I would also like to acknowledge support from the U. S. Department of Energy.

REFERENCES

1. J. A. Roth and C. L. Anderson, Appl. Phys. Lett. **31**, 689 (1977).
2. See, for example, S. S. Lau, Z. L. Liau, and M-A. Nicolet, Thin Solid Films **47**, 313 (1977).
3. S. S. Lau, W. F. Tseng, M-A. Nicolet, J. W. Mayer, R. C. Eckardt, and R. J. Wagner, Appl. Phys. Lett. **33**, 130 (1977).
4. J. C. Bean, H. J. Leamy, J. M. Poate, G. A. Rozgonyi, T. T. Sheng, J. S. Williams, and G. K. Celler, Appl. Phys. Lett. **33**, 227 (1978); J. C. Bean, H. J. Leamy, J. M. Poate, G. A. Rozgonyi, J. P. van der Ziel, J. S. Williams, and G. K. Celler, J. Appl. Phys. **50**, 881 (1979).
5. D. Hoonhout, C. B. Kerkdijk, and F. W. Saris, Phys. Lett. **66A**, 145 (1978).
6. P. Revesz, G. Farkas, G. Mezey, and J. Gyulai, Appl. Phys. Lett. **33**, 431 (1978).
7. R. T. Young, J. Narayan, and R. F. Wood, Appl. Phys. Lett. **35**, 447 (1979).
8. R. B. James, in Pulsed Laser Processing of Semiconductors, Vol. 23, edited by R. F. Wood, C. W. White, and R. T. Young (Academic Press, New York, 1984), pp. 555-625.
9. M. H. Brodsky, R. S. Title, K. Weiser, and G. D. Pettit, Phys. Rev. **B1**, 2632 (1970).
10. P. Baeri and S. U. Campisano, in Laser Annealing of Semiconductors, edited by J. M. Poate and J. M. Mayer (Academic Press, New York, 1982), p. 80.

DEFECT FORMATION IN FUSED SILICAS DUE TO PHOTON IRRADIATION AT 5 AND 50 EV

P.W. Wang(a)(b), G. Escher(c), R.F. Haglund, Jr.(b),

D.L. Kinser(a), N.H. Tolk(b), and R.A. Weeks(a)

(a) Department of Materials Science and Engineering,
Vanderbilt University, Nashville, TN 37235

(b) Department of Physics and Astronomy,
Vanderbilt University, Nashville, TN 37235

(c) Sematech, Austin, Texas 78741

Abstract

We have compared the paramagnetic defect formation in two types of pure fused silica glass irradiated with intense photon fluxes at 5 eV (KrF laser) and 50 eV (undulator beam from Aladdin Synchrotron Light Source), using electron paramagnetic resonance spectroscopy with a frequency of 9.7 GHz and sample temperatures of 110 and 300K. The 5 eV photons produce approximately 10^{-14} paramagnetic defects per photon and the 50 eV photons produce approximately 10^{-5} defects per photon. The ratio of E' centers to oxygen related centers is ~10 times greater for 5 eV photons than for 50 eV photons in type III silica.

Introduction

Intrinsic defects in silicas have drawn considerable attention since Weeks initially identified and characterized the E' center in 1956.[1] This attention results from increased understanding of the scientific and technological importance of defects in a wide variety of materials. Many questions about defects in SiO_2 have not been resolved. Defects affect several important applications of silicas. These include optical fibers, both core and cladding regions, and VLSI's (Very Large Scale Integrated Circuits) in which SiO_2 functions as an insulator or passivating layer.

Many interesting phenomena have been discovered with improvements of brightness, pulse duration and the wavelength-tunability of light sources. Stathis and Kastner[2] reported that different defects are created in silicas by 5.0, 6.4, and 7.9 eV photons from excimer lasers whose energies are all smaller than the bandgap energy of silica, which is almost 10 eV.[3,4] They found that 5.0 eV photons are the most efficient in producing E' centers.[3] They also observed that 7.9 eV photons introduced different defects in dry and wet silicas.

The purpose of this work was to determine the relative and absolute efficiency of 5 and 50 eV photons in producing intrinsic defects in silicas. Five eV photons were produced by a KrF excimer laser and the 50 eV photons were produced by the undulator beamline of Synchrotron Radiation Center at Madison, Wisconsin.

Experimental Procedure

The silica samples consisted of Type III and IV[5] high-purity synthetic silicas, specifically Suprasil W1 (dry), which contains about 5 ppm OH by weight, and Suprasil 1 (wet), which contains 1200 ppm OH. Total metallic impurities were of the order of 1 ppm.

Samples were cut from a 30 mm diameter and 1 mm thick disk to the dimensions 5 mm x 18 mm x 1 mm. The samples were cleaned, mounted on a sample holder attached to a manipulator, and inserted into an UHV (Ultra High Vacuum) chamber for the 50 eV irradiations. Several samples were mounted on the same holder. The same optical geometry for each sample was achieved by changing the height of the sample holder inside the UHV chamber. The experimental setup is shown in Fig. 1. The vacuum was kept at 10^{-9} torr during the 50 eV exposure at room temperature. For the 5 eV exposure, 50 mJ/cm^2 unfocused KrF excimer laser beam was used to expose the sample in air at room temperature. The total number of shots was 10^{10}.

The types and concentrations of paramagnetic defects produced by 5 and 50 eV light were measured by electron paramagnetic resonance spectroscopy (Brucker ESR 200 at 9.7 GHZ). The E' centers (singly charged oxygen vacancies) and oxygen-related centers were monitored at room temperature and 110K, respectively. The number of defects in silica was determined by comparison with a standard sample (a Brucker strong pitch secondary standard) whose paramagnetic state concentration was known. The error in the relative numbers of paramagnetic defects was ± 10%. The absolute numbers of paramagnetic centers has an error estimated at ± 100%.

The flux of 5 eV photons incident on a sample was determined through calculations based on measurements of power density and total number of pulses. The total number of 50 eV photons was also calculated from the exposure time and the photon flux. The photon flux was calculated from measurements of current produced in a calibrated gold diode and the photoelectric yield on gold.[6] The flux of 50 eV photon was (1.1 ± 0.1) x 10^{18} photons per 1mm diameter spot per minute.

The irradiated volume was calculated from the 1/e penetration depth of 50 eV photons in silica and the beam diameter. The 1/e penetration depth was assumed to be 3.2 μm[7] and the beam diameter was 1 mm. Seven to fourteen spots were irradiated on each sample. We estimate the uncertainty of the diameter of the beam size as ± 30% when the distribution of photons across the beam is taken into account. The photon energy is lower than the bandgap energy in the case of the 5 eV photons; hence, the irradiation volume is the entire sample.

Results

Paramagnetic resonance spectra of E' centers and oxygen related (OR) centers, including peroxy radicals[8] and non-bridging oxygen hole centers[9] were detected in both 5 and 50 eV irradiated silicas. The concentrations of defects of each type in each sample were calculated from measurements of the number of defects and the irradiated volume. The defect formation rate per photon was obtained by dividing the total number of defects by the total number of photons.

The concentrations of defects, the defect formation per photon, the ratio of E' center to OR centers, and the total number of photons used in exposure are all listed in Table I and II.

The 50 eV light created about 10^{15} E' centers per cm^3 and about 10^{13} OR centers per cm^3 in both dry and wet silicas. The formation rate of E' and OR centers are 10^{-4} and 10^{-5} per photon respectively. The ratio of E' center to OR center is three times higher in wet silica than dry silica.

The 5 eV photons introduced about 10^{16} E' centers in both samples. These photons induced approximately 30 times higher concentration of OR centers in dry silica (6.0 x 10^{14}) than in wet silica (1.7 x 10^{13}). The formation rate of E' center is about 10^{-12} per photon in both silicas, and 6 x 10^{-13} and 1.6 x 10^{-15} OR center per photon in Suprasil W1 and Suprasil 1, respectively. The E'/OR Center ratio is 50 times higher in wet silica than dry silica and has the same trend as in 50 eV irradiated silicas.

Discussion

A flux of 10^{18} 50 eV photons create the same order of magnitude of E' and OR centers as 10^{26} 5 eV photons. The absorption coefficient for the 5 eV photons in silica is about 7x10^{-3} cm^{-1},[10] while all the 50 eV light is absorbed. Taking this difference in absorptivity into account, the 50 eV light produces ~10^{5} to 10^{6} more defects than the 5 eV light.

Three possible reasons may explain this difference in defect formation per photon between the 5 and 50 eV photons. First, E' center formation by 5 eV photons may be due to a two photon process.[11] If this is the case, the low absorptivity for a two photon process, which is 2 x 10^{-3} cm^{-1},[12] would result in an absorptivity of ~10^{-5} $cm.^{-1}$ Thus, the ratio absorptivities for 5 eV and 50 eV photons is approximately 10.[10] The ratio of paramagnetic states produced by 5 eV to 50 eV photons is ~10^{-12}. Thus, the 50 eV photons produced ~100 times more

paramagnetic defects than did the 5 eV photons. Second, Arai et al.[11] suggested that the E' center induced by 5 and 6.4 eV light is through hole capture at precursor sites. At a flux of 10^{21} 6.4 eV photons cm^{-2} the onset of saturation of E' centers was observed. This saturation effect may also occur for 10^{26} 5 eV photons cm^{-2}. In addition, the 50 eV photons may produce new E' and OR centers by Si--O bond breaking. The threshold energy for Si--O bond breaking is about 8.5 eV;[13] hence, in case of 50 eV photons we assume that their energy is sufficient to break Si--O bonds. Bond breaking process may well explain why 50 eV light produces 2 or 3 orders more defects in silica than 5 eV light.

Acknowledgement

This work was supported by the Naval Research Laboratory under contract number N00014-86-C2546 and partially supported by the University Research Initiative of the Air Force Office of Scientific Research under contract No. F49620-86-C0125DEF and in part by Office of Naval Research/SDIO contract No. N0014-87-C-0146. We thank the technical staff of the Synchrotron Radiation Center, University of Wisconsin, for the diligent application of their expertise on our behalf. The Synchrotron Radiation Center is supported in part by the National Science Foundation.

References

1. R.A. Weeks, J. App. Phy. 27, 1376 (1956)

2. J.H. Stathis and M.A. Kastner, Phys. Rev. B 29, 7079 (1984).

3. T.H. DiStefano and D.E. Eastman, Solid State Commun. 9, 2259 (1971).

4. R. Evrard and A.N. Trukhin, Phys. Rev. B 25, 4101 (1982).

5. G. Hetherington, J. British Ceram. Soc. 3, 595 (1966).

6. P.W. Wang, R.F. Haglund, Jr., L. Hudson, D.L. Kinser, N.H. Tolk, and R.A. Weeks, in SPIE Symposium on Optoelectronic Applied Science and Engineering, Aug. 14-19, 1988, San Diego, CA, USA

7. J. Barth, E. Tegeler, M. Krisch, and R. Wolf in Soft X-ray Optics and Technology Conf., Dec. 1986, Berlin, Proceedings of SPIE, Vol. 733.

8. A.H. Edwards and W.B. Fowler, Phys. Rev. B26, 6649 (1982).

9. M. Stapelbroek, D.L. Griscom, E.J. Friebele, and G.H. Sigel, Jr., J. Non-Cryst. Solids, 32, 313 (1979).

10. Ryoichi Tohmon, Yoshiya Yamasaka, Kaya Nagasawa, Yoshimichi Ohki, and Yoshimasa Hama, J. Non-Cryst. Solids, 95 & 96, 671 (1987)

11. K. Arai, H. Imai, H. Hosono, Y. Abe and H. Imagawa, App. Phys. Lett., 1891 (1988).

12. R.A.B. Devine, Phys. Rev. Lett. 62, 340 (1989).

13. A.R. Silin, L.N. Skuja, and A.N. Trukhin, J. Non-Crys. Solids, 38 & 39, 195 (1980).

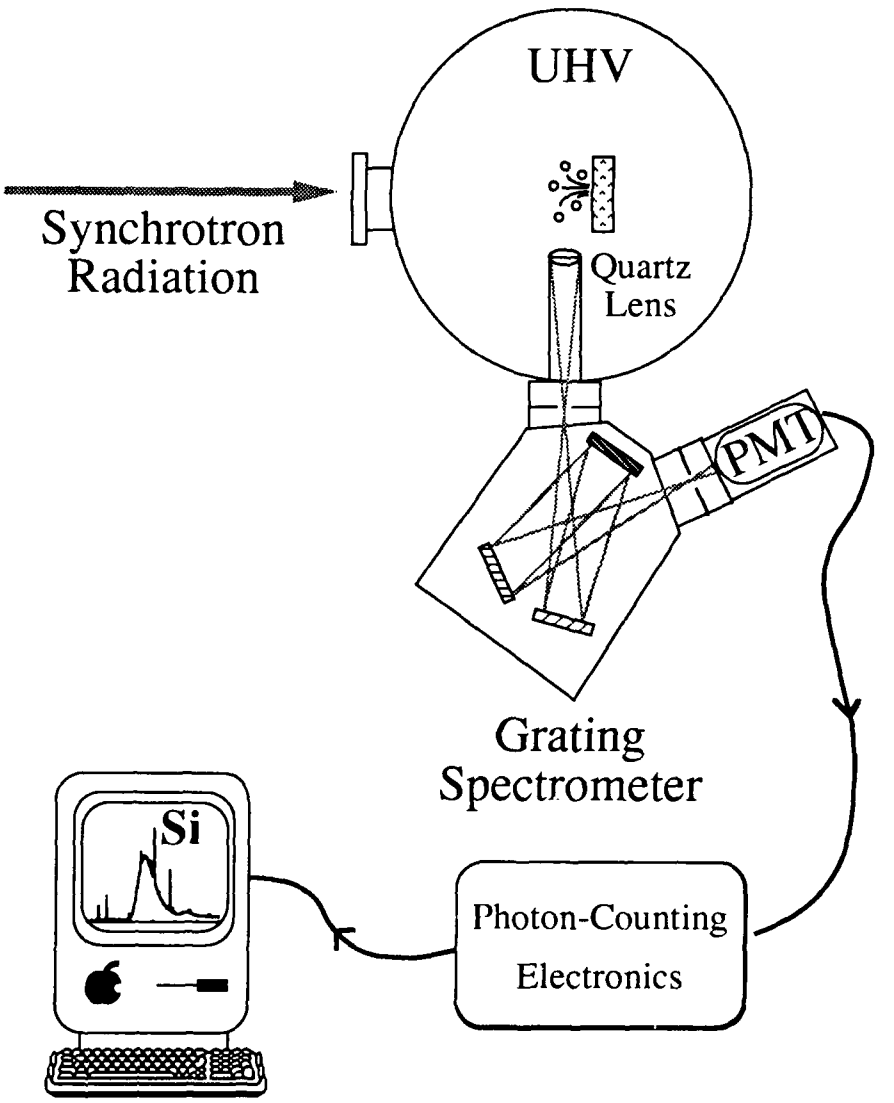


Figure 1. Schematic of the Experimental Geometry for 50 eV Irradiation

Table I Silicas Irradiated by 50 eV Light from Synchrotron

Silicas	E'(cm^{-3})	ORC(cm^{-3})	E'/Photon	ORC/Photon	E'/ORC	Total Photons
Sup W1	$1.1x10^{15}$	$6.4x10^{13}$	$3.0x10^{-4}$	$1.8x10^{-5}$	17	$3.7x10^{18}$
Sup 1	$3.3x10^{15}$	$6.7x10^{13}$	$4.5x10^{-4}$	$0.9x10^{-5}$	49	$7.4x10^{18}$
Error	(±40%)	(±40%)	(±50%)	(±50%)	(±20%)	(±10%)

$5.3x10^{17}$ photons per 5 mins per 1 mm dia. beam size

The penetration depth for 50 eV photon in silica is 3.2 μm

Table II 5 eV (248 nm) KrF Excimer Laser Irradiated Silicas

Silicas	E'(cm^{-3})	ORC(cm^{-3})	E'/Photon	ORC/Photon	E'/ORC	Total Photons
Sup W1	$6.8x10^{15}$	$6.0x10^{14}$	$6.0x10^{-13}$	$6.0x10^{-14}$	10	$7.8x10^{26}$
Sup 1	$8.5x10^{15}$	$1.7x10^{13}$	$8.0x10^{-13}$	$1.6x10^{-15}$	500	$7.8x10^{26}$
Error	(±40%)	(±40%)	(±50%)	(±50%)	(±20%)	(±10%)

50mJ per cm^2 per shot, total shots 10^{10}, total photons on .5 x .5 x .3 cm^3 = $7.8x10^{26}$

The absorption coefficient of 5 eV photon in silica is about 7.0×10^{-3} cm^{-1}

Oxygen Related Centers (ORC) include Peroxy Radicals (POR) and Non-Bridging Oxygen Hole Centers (NBOHC)

BOILING PROCESS IN PMMA IRRADIATED BY A CO_2 LASER RADIATION

René Joecklé
ISL (French-German Research Institute of Saint-Louis)
B.P. 301
(68301) Saint-Louis (FRANCE)

Abstract

When irradiated by a low fluence CO_2 laser radiation, a PMMA plate becomes mat. The damage results from the in-depth absorption of the laser light, which yields a microscopic boiling process. The occurrence threshold of this boiling process has been measured as a function of the incident power density. These results allow for the quantitative analysis of the laser burning patterns in order to determine the power density distribution of CO_2 laser beams.

A polymethylmetacrylate (PMMA) plate is widely used by the laser community as a simple diagnostic tool in order to get some information (at least qualitative) about the characteristics of a CO_2 laser beam.

In several cases, the depth (or the volume) of ablated material has been used as a quantitative measurement of the fluence (or the energy) of the beam. The ablated surface exhibits a mat aspect, even if the fluence is small and the ablated depth cannot be measured. In this last case, the currently available information about the beam is only qualitative and the size of the mat surface states only that the laser radiation has hit the plate.

We have studied the cause of the mat aspect of the laser impact on PMMA and measured the fluence threshold of appearance of the mat aspect as a function of the power.

Laser-Induced Boiling in PMMA

When the surface of a CO_2 laser burning on PMMA is observed under a microscope (magnification of 100), it can be seen (fig. 1) that it is sprinkled with small bubbles, the sizes of which are in the range of about 10 micrometers. These bubbles show that the interaction does not consist simply in a surface vapourization, but in a volume boiling process.

Generally, the liquid-to-vapour phase change occurring in laser material interaction is a surface vapourization process, mainly because the absorption depth of the laser beam in the material is very small (in metals for instance).

In several dielectrics, however, boiling processes have been reported[1,2,3] ; they are caused by the in-depth absorption of the laser light, resulting in a in-depth heating.

Absorption of light, heating and destruction processes

Let us first consider the heating process. The absorption of a monochromatic and parallel light beam by a plate of homogeneous and isotopic material is described by the Lambert-Beer relation: $I = I_0 \exp(-\alpha z)$ where α is the absorption coefficient (in cm^{-1}). The absorption length $L = 1/\alpha$ gives the depth in which about half of the beam power is absorbed and transformed into heat. Considering the limit case where the interaction duration and the conduction of the material are small, the heat transfer by conduction can be neglected and the temperature profile is given by:

$$T(z) = \frac{\alpha t I_0 \exp(-\alpha z)}{\rho C_p} . \qquad (1)$$

The absorption length L is the depth of material where the temperature is about half the surface temperature ("thermal wave"); it is independent of the time.

Considering now an opaque material (light is absorbed at the surface); the temperature profile is given by:

$$T(z) = I_0 D \cdot \text{ierfc}(z/D)/K \qquad (2)$$

in this expression, D ist the diffusion length, equal to $D = 2\sqrt{\kappa t}$; D is time-dependent: the thickness of the thermal wave is proportional to the square root of the time.

The comparison of these two distances L and D allows for determining the time ranges of two regimes occurring successively:

- for short interaction duration $t_i \ll 1/(4\alpha^2\kappa)$
  absorption-dominated process
- for long interaction duration $t_i \gg 1/(4\alpha^2\kappa)$
  conduction-dominated process

Taking now into account the destruction process, let us assume that in all cases, it occurs by surface vapourization at a constant temperature T_v. After the heating phase, the vapourization begins and a steady-state ablation regime builds up. Litteral expressions can be found for the **steady-state** temperature distributions for the two limit cases:

- absorption-dominated process:

$$T_z = A \exp(-C_p I_0 z/KH_v) - B \exp(-\alpha z) \quad (3)$$

A and B being two constants depending upon I_0 and α

- conduction-dominated process:

$$T_z = T_v \exp(-C_p I_0 z/KH_v) \quad (4)$$

While the latter gives a continuously decreasing temperature in the material, the absorption-dominated process yields a peak temperature higher than the surface (vapourization) temperature inside the material. A boiling process is then likely to occur on seeds present in the material. For PMMA, these seeds can be the ends of the polymer chains.

Computation of the temperature distribution

The absorption coefficient and the ablation enthalpy have been measured for PMMA and CO_2 laser radiation in order to get input parameters for a numerical calculation of the temperature profile in the material.

The thin samples of PMMA needed for measurement of the absorption coefficient have been obtained by two techniques:

- 1% PMMA powder is mixed with 99% KBr powder and pressed together in order to give an IR spectroscopic sample;
- PMMA is dissolved in a solvant, which is then poured on a Hg-filled cup and vapourized in order to get a thin and flat film.

The spectra showed on fig. 2 are obtained and allow for calculation of the absorption coefficient. A value of 250 cm^{-1} has been measured.

By weighting the mass losses of PMMA samples irradiated by CO_2 laser radiation with a power density of 100 W/cm^2 and different durations, the actual ablation rate has been measured; a value of 2500 J/g has been obtained.

These two experimental values have been incorporated in a numerical computation giving the temperature profile in the material. The assumptions are:

- a one-dimensional phenomenon, with semi-infinite target and constant power density over the whole surface,
- constant thermal and optical parameters,
- the only phase change is a solid to vapour process occurring at a constant temperature at the surface of the material.

One result is shown on fig. 3. It can be seen that the in-depth temperature rises well above the surface temperature. In this overheated depth, the boiling process takes place.

Coming back to the transition between the absorption regime and the conduction regime, it can be noticed that this occurs at a time of $(4\alpha^2\kappa)^{-1}$, that is about 3 ms.

Qualitative analysis of the boiling process

A high-speed video camera (Spin 2000) the objective of which has a field of view of 0.5 mm allows us to get an insight into the boiling process. The test set-up is shown on fig. 4; fig. 5 shows several views obtained with this device during one test with a power density of 30 W/cm^2.

Three different periods can be seen:

- the heating period, at the end of which a surface vapourization takes place;
- the sudden occurrence of small bubbles trapped under the surface; a short time after, these bubbles grow and burst at the surface: the boiling process begins - a steady state takes place, with a violent boiling at a microscopic scale;

- at the end of the irradiation, the boiling material freezes and bubbles remain trapped in the material; the average dimension of these bubbles is about 10 μm. This gives to the surface the characteristic mat aspect.

Fluence threshold of appearance of the bubbles

The fluence threshold of appearance of the bubbles and of damage of the surface has been studied as a function of the power density.

The experimental set-up is described by the scheme on fig. 6: a "beam integrator" gives a constant power density on the target. It consists in four plane mirrors mounted in order to form a light channel with a square cross-section. The laser beam is focussed at the entrance of this device, with an angle yielding about three reflexions for the outer rays of the laser beam. The statistical mixing of the different rays produces a fairly flat power density distribution at the square exit of the channel. The exit is imaged on the target with a lens allowing for adapting the power density or the size of the laser spot to the target. The main drawback of the device is the overall efficiency of 70 to 75%, due to the losses caused by the large angles of reflexion; however, a constant power density is easily obtained with this device, yielding reliable quantitative results.

.. motorized table allows the target PMMA plate to be moved with a constant velocity through the beam; the square of the beam spot is tilted 45° relatively to the movement. On fig. 7, it can be seen that a linear variation of the irradiation duration is obtained on the plate; the width of the damaged zone on the plate gives the threshold irradiation duration for the appearance of the bubbles.

It can be seen on the irradiated samples that the damaged zone exhibits sharp and well-defined edges; this confirms that the sudden occurrence of the bubbles is a threshold phenomenon.

The results on PMMA for different power densities are shown on fig. 8a and b: respectively the threshold times and threshold fluences.

The fluence decreases strongly with increasing power density, especially for power densities smaller than 100 W/cm^2. Recently, the power density range has been increased up to 600 W/cm^2, by adapting the PMMA plates on a rotating disc, which is mounted on the motorized table (fig. 9). The velocity of the table is adapted in order to generate a (part of) spiral on the target; the beam velocity on the target varies proportionally to the radius of the spiral; a continuous variation of the velocity is then obtained on the plate and the threshold time (t) is calculated by measuring the radius of appearance of the damage (r_0) and comparing it to the rotation speed (D) and the size of the laser spot (a)

$$t = \frac{a}{2 \cdot \pi \cdot r_0 \cdot D} \tag{5}$$

The results are shown on fig. 10a and b.

The threshold fluence is still decreasing, therefore the process can be considered as conduction-dominated in the range under investigation here.

It can be expected however that, for higher power densities, the threshold fluence will no longer decrease; the threshold time has to be smaller than 3 ms, as computed hereover.

Selected values of irradiation times will give burn patterns with well-defined power densities; a set of irradiation times for power densities is given hereafter:

Power density (W/cm^2)	**Threshold time (s)**
30	1.1
50	0.4
70	0.22
100	0.145
150	0.095
200	0.07
300	0.043
500	0.025

Conclusion

The PMMA plate burning is widely used as a "finger-print" of the CO_2 laser beam; a low fluence produces a boiling process on the material and the surface exhibits a mat aspect. A quantitative study of the threshold time and fluence producing this boiling enables a quantitative use of the laser burning for the determination of the distribution of the power density.

By controlling the interaction time, several finger-prints can be made, each corresponding to a given power density.

References

1. F.W. DABBY, UN-CHUL PAEK
   High intensity laser. Induced vaporization and explosion of solid materials
   IEEE J. of Quantum Electronics, Vol. QE8, No. 2, Feb. 72, 106-111

2. B. GAUTIER
   Conduction de la chaleur dans un solide en ablation sous l'action d'un rayonnement laser intense
   ISL Report R 122/76

3. R. JOECKLÉ, B. GAUTIER
   Boiling of organic liquids induced by bulk absorption of CO_2 laser radiation
   J. de Physique, suppl 11, 41, pp C9-275 (nov. 1980)
   3rd Int. GCL, Marseille 1980

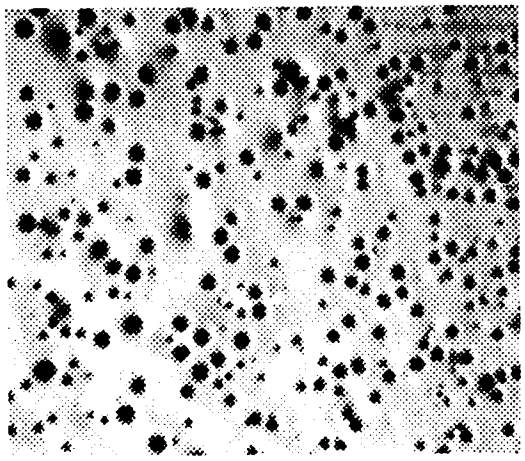


Fig. 1: Microscope view of a CO_2 laser burning on a PMMA plate

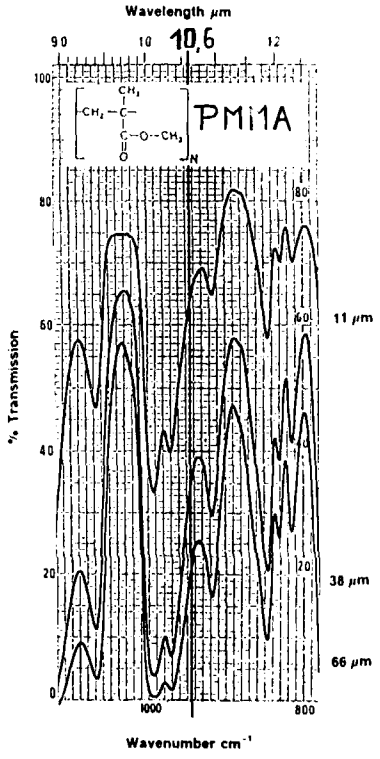


Fig. 2: IR spectra of PMMA

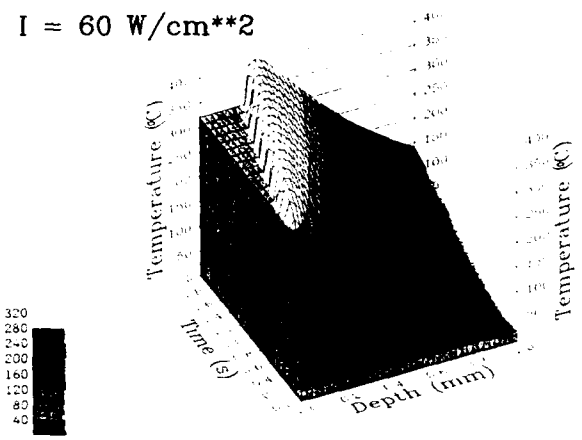


Fig. 3: Computed temperature distribution

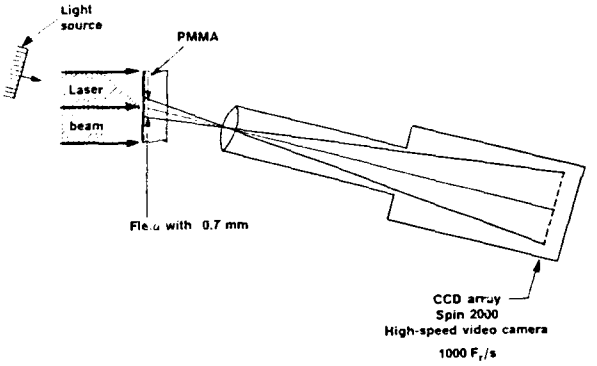
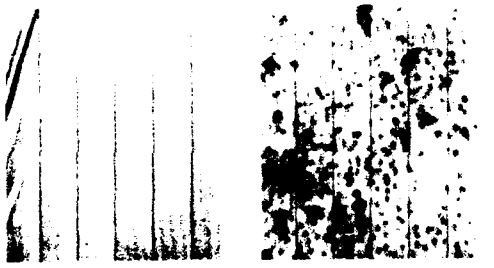


Fig. 4: High-speed video set-up



picture 1: before laser irradiation

picture 2: boiling onset: 1 s irradiation



picture 3: steady state

picture 4: after cooling

Fig. 5: Video views during one test. I = 30 W/cm²

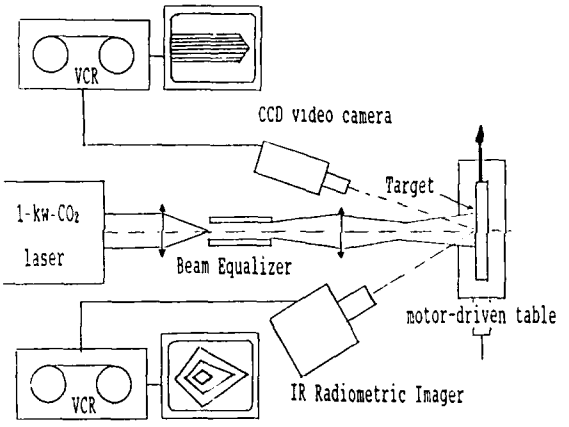


Fig. 6: Threshold measurement set-up

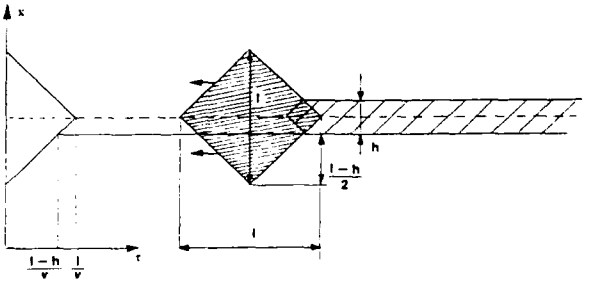


Fig. 7: Determination of the threshold time

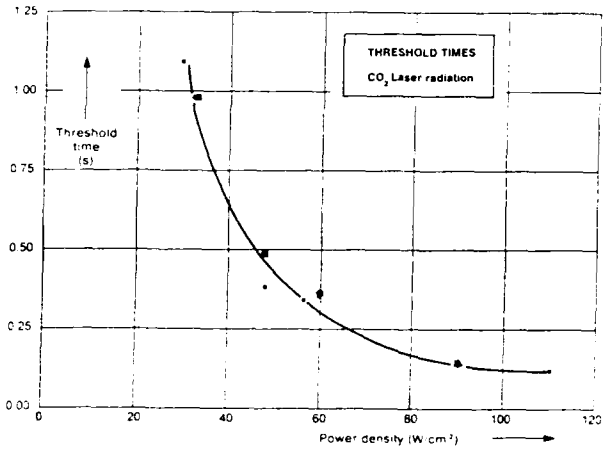


Fig. 8a: Boiling onset time

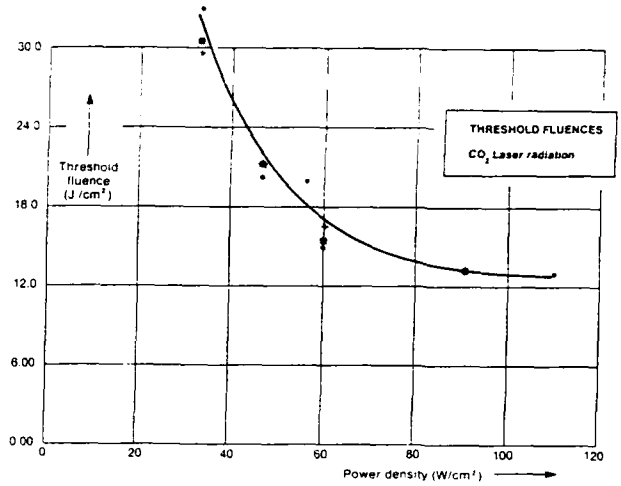
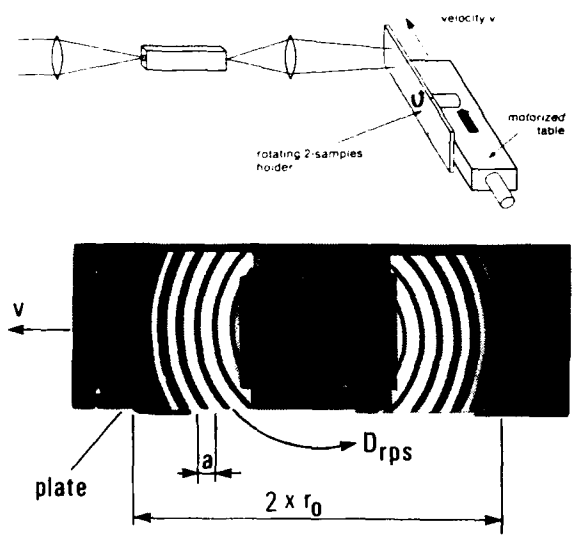


Fig. 8b: Boiling threshold fluence



damage threshold beam sweeping velocity: $v = 2\pi r_0 D$

damage threshold time: $t = \frac{a}{2\pi r_0 D}$

Fig. 9: Short irradiation time threshold measurement set-up

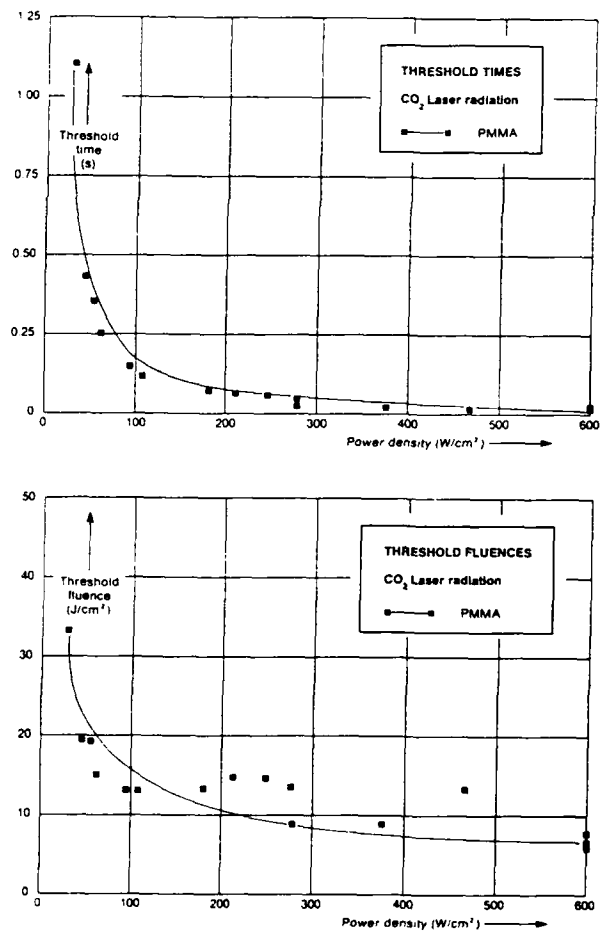


Fig. 10: Threshold times and fluences for high-power densities

IC FAILURE ANALYSIS USING THE LASER SCANNING MICROSCOPE

L. Fritz, R. Lackmann
Fraunhofer Institute of Microelectronic Circuits and Systems (IMS)
Finkenstr. 61, D-4100 Duisburg 1, West Germany

The laser scanning microscope (LSM) is a fairly new device for contactless testing. The nondestructive nature of the laser beam and a minimum of preparation favorizes its use as an analytical tool. Beside the scanning mode which is useful for material study the laser beam can be positioned in spot mode with a high spatial resolution and a fine focused beam on the probe surface. We introduce some measurement methods based on optical beam induced currents inside the semiconductor and on electrooptical effects in external media. These methods are extremely useful for CMOS circuit failure analysis leading to a complete functionality check. Logic state detection in digital CMOS circuits and signal acquisition from a node inside the circuit are internal probing techniques. To locate and analyze latch-up in CMOS ICs we have developed a fully automated latch-up analyzer coupled with the CAD system.

Voltage contrast was realized using nematic liquid crystals and the electrically controlled birefringence. The usage of $LiNbO_3$ crystals led to an interferometric measurement scheme for internal voltage probing utilizing a phase retardation due to the linear electrooptic effect.

Introduction

The useful range of optical microscopy has been significantly extended to optical resolutions of 0.25 µm with electronically enhanced image magnification by scanning with a fine focused laser beam. A lot of theoretical and practical work has been done to describe and compute the optical properties of confocal and non-confocal scanning systems[1-4]. The application of laser scanning microscopes for material studies has also been demonstrated for different materials and semiconductors[5-6]. However, the special features of a laser light source like collimation, high monochromasy and high intensity made it an attractive alternative for sophisticated semiconductor microscopy and contactless measuring techniques. The growing interest in noncontacting techniques in the semiconductor area can be attributed to the inadequacy of conventional chip diagnostic tools. The usual probing techniques utilizing the electron beam requires a vacuum chamber and therefore circuit environment preparation, though it is doubtless the "state of the art" method in fault diagnosis[7-8]. On the other hand no need of a vacuum, the nondestructive nature of the laser beam and a minimum of preparation favorizes the laser scanning microscope as an analytical tool, especially when connected to a prober or a test system for IC failure analysis.

To establish the contactless laser probing we have developed an integrated test system for IC failure search, consisting of the LSM connected to a VME based host and coupled to the design data base for automated internal test point localization. The test technique can thus be viewed as an approach towards automated laser beam testing of CMOS circuits. Because the CAD coupling had been described in detail elsewhere[9], we concentrate here mainly on the physical aspects of the measurement techniques.

Operating Principles

In contrast to an ordinary optical microscope where an object is illuminated by a wide area light source the image in a laser scanning microscope is taken point by point as the scan takes place. Fig. 1 shows the scheme of the optical system. For the described applications a commercial red HeNe laser at 633 nm has been used leading to a photon energy of 1.96 eV which is well above the Si band gap energy (1.12 eV at 300 K) and therefore to electron-hole pair generation inside an illuminated semiconductor. The light reflected by the specimen is directed to photodetectors. The amplified photomultiplier signal is applied to a TV monitor in synchronism with the x-y deflection For internal measurements inside the IC we used the spot mode of the system where a fixed point of the specimen is illuminated by the laser beam focused to a diffraction limited spot on the surface (about 1 µm for a long distance 40x objective, NA 0.5). The laser beam intensity is computer controlled using an acousto-optical modulator (AOM).

Logic State Detection Using OBIC

Logic state detection is done using the OBIC effect (Optical Beam Induced Current). The conductive state of a MOS transistor is determined by irradiating the drain/substrate junction with the laser spot and amplifying the current changes in the power supply of the device under test. Depending on the logic state of the transistor under test, its depleted region at the unsymmetrical pn-junction contains high-intensity electric fields leading to electron-hole pair separation and a slight change of the strength of the current on the power bus line. Thus, the strength of the OBIC serves as an indicator of the transistor's logic state, where a higher induced photocurrent corresponds to the lo-

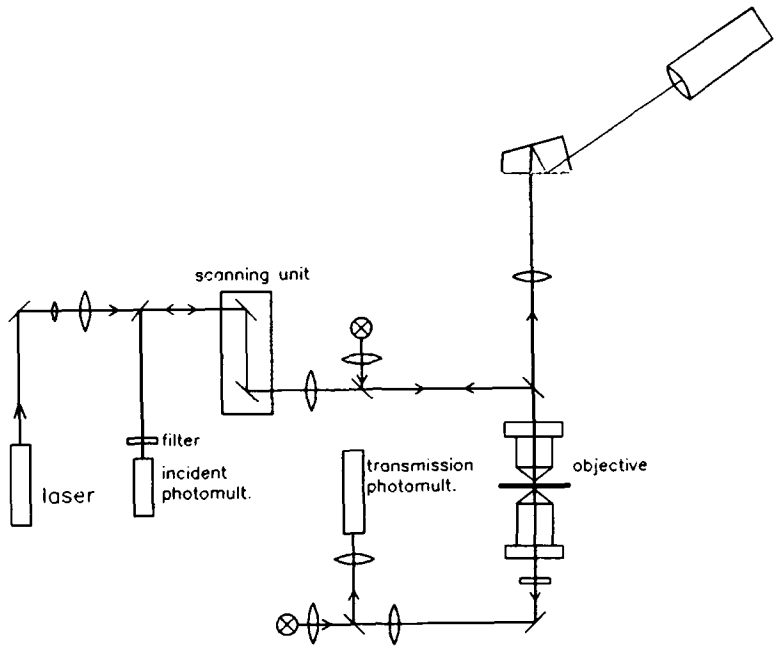


Fig. 1 Optical scheme of the laser scanning microscope

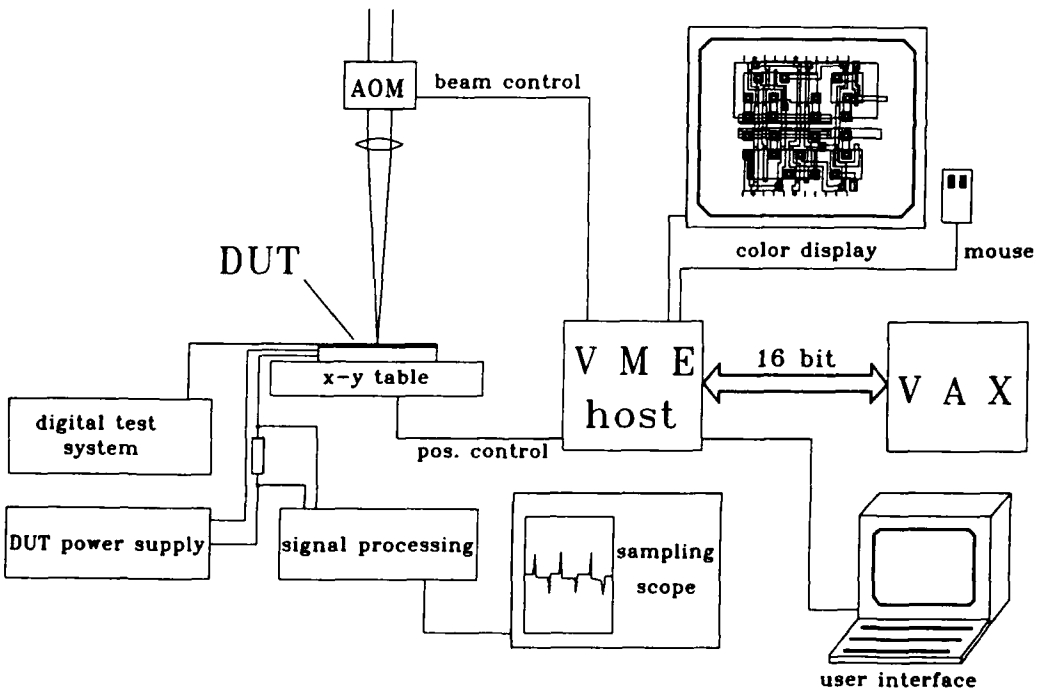


Fig. 2 Block scheme of the digital test system and the CAD link

gic "OFF" state. This load current is sensed via a low-noise, fast transimpedance amplifier and leads to a real-time signal of the logic states of the illuminated transistor. Fig. 2 shows a block scheme of the digital test system and the CAD link for automated beam positioning and measurement.

In contrast to other published detection schemes[10] we propose a low intensity, steady-state illumination of the transistor under test after precedent beam positioning. A discussion of the dynamic aspects of the proposed detection scheme and measurements on typical CMOS structures showed a bandwidth in the MHz regime[11].

Fig. 3 shows measured internal digital signals inside a frequency divider as part of digital CMOS controller. It consists of a series of D-flip-flops, for each measurement point the laser spot illuminates the gate/drain region of the output transistor. The signal propagation is clearly visible and shows the successful application of our detection scheme.

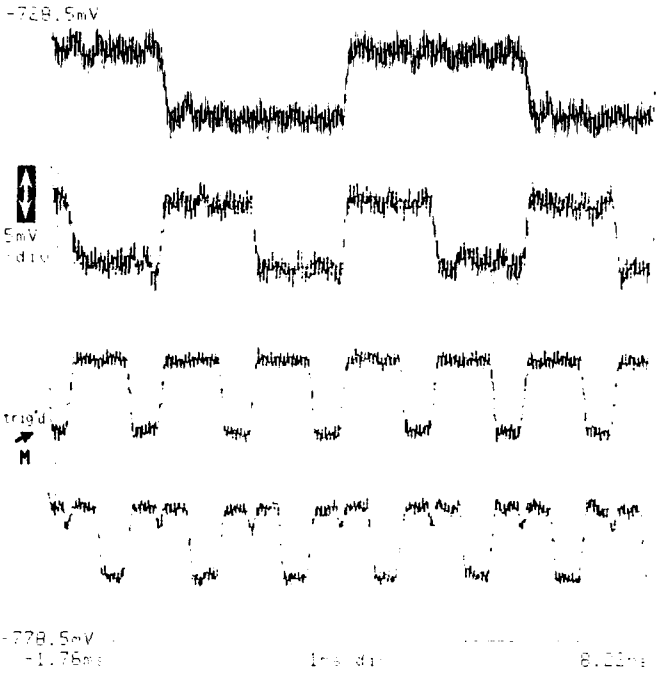


Fig. 3 Internal logic states of a CMOS frequency divider acquired uing optical beam induced currents (see text)

Automated Latch-up Sensitivity Measurement

Optical beam induced currents can also be used to trigger some electrical effects in an integrated circuit and disturb its function. One of the most important parasitic effects in CMOS technology is latch-up.

Bulk CMOS integrated circuits contain both parasitic vertical and lateral bipolar transistors. These transistors form a pnpn structure which acts as a silicon controlled rectifier (SCR) and which can latch-up if the possible feedback between the coupled transistors produces regenerative switching. Fig. 4 shows the cross section of a CMOS inverter together with the parasitic bipolar transistors. One possible firing method is photo current generation and several analytical techniques have been suggested to help IC designers to identify the latch-up site and to evaluate its sensitivity in order to correct the layout and avoid the phenomenon[12-13]. Our approach leads to an automated latch-up sensitivity measurement and a coupling to the CAD layout data. Fig. 5 shows a block scheme of the detection system. Since the AOM can be controlled with an applied voltage the laser beam intensity and therefore the strength of the optical beam induced current is nearly linearly dependent on the applied voltage. The modulator voltage and the current through the device under test are

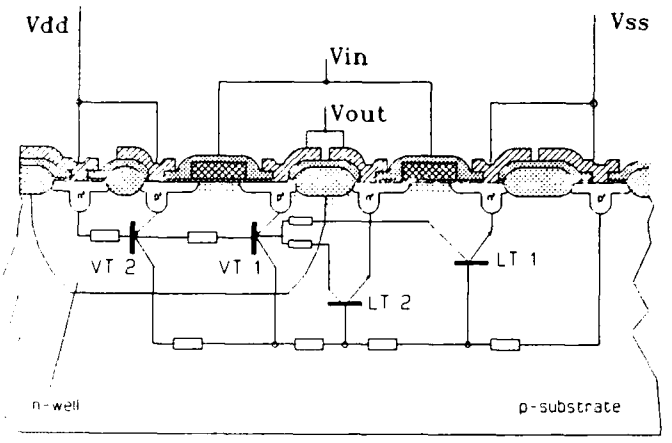


Fig. 4 Cross section of a CMOS inverter with the parasitic bipolar transistors

controlled by a programmable microcomputer developed for this task. The microcomputer communicates via IEEE bus with the VME based host responsible for IC positioning. For each given point the laser beam intensity is increased and a possible latch-up is detected by IC current control. If the load current increases due to latch-up firing all power supplies are switched off rapidly to avoid a possible destruction. The next measurement point is localized after power on and data acquisition continues. The VME host stores the measured sensitivity data corresponding to the laser intensity and the position and supports a link to the CAD system. After an initialization the system works fully automated.

Because the inverse laser intensity is proportional to the latch-up sensitivity at a given position after a complete data acquisition run a sensitivity map is generated by the system. A menu driven program running on the CAD workstation allows the user to overlay the map over his design and switch between a color display of the IC layout and the measured data. Fig. 6 shows a part of a CMOS IC with the measured latch-up data (the solid white regions correspond to a high latch-up sensitivity).

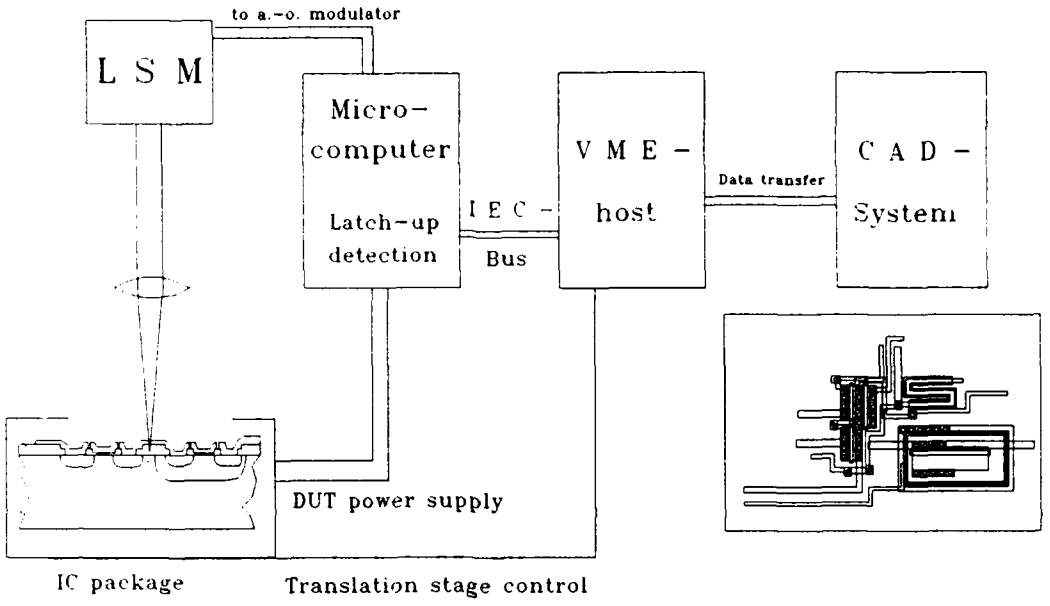


Fig. 5 Components for latch-up sensitivity measurement

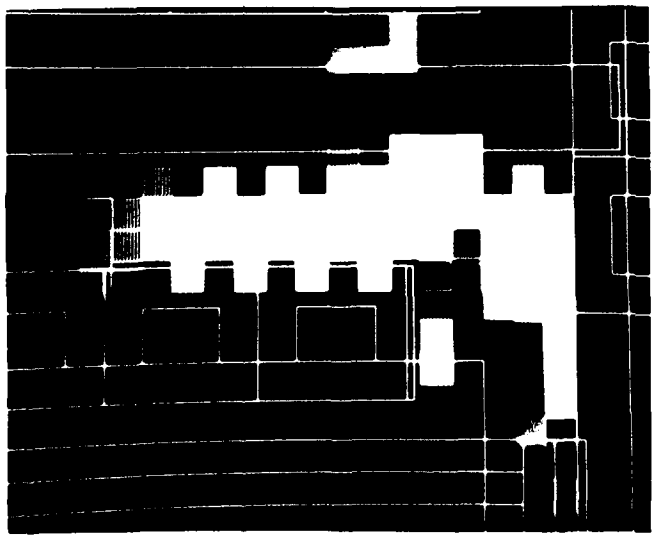


Fig. 6 Measured latch-up sensitivity in a CMOS IC

Voltage Contrast Using Nematic Liquid Crystals

The qualitative voltage contrast which is observable in any unmodified scanning electron microscope allows a simple localization of defect cells and possible interrupts of conducting lines inside the IC. The same result can be achieved using liquid crystals and a polarizing microscope.

One important electro-optical effect in nematic liquid crystals (NLC) with negative anisotropy (i.e. $\Delta \varepsilon = \varepsilon_{\parallel} - \varepsilon_{\perp} < 0$) is deformation of aligned phases (DAP), also called electrically controlled birefringence (ECB), investigated by Schiekel et al.[14] and Soref et al.[15] The birefringence occurs when the molecules are vertically aligned in a glass cell and dc or ac voltages are applied and is caused by the interaction of the dipole moment of the molecules being perpendicular to the molecular optic axis and the electric field applied in the direction of the optical axis.

Fig. 7 shows a cross section of the configuration for a voltage contrast display of an IC. A transparent, conducting glass plate is used as a field electrode connected to ground potential. When the electric field between the IC conducting line and the field plate exceeds a critical threshold voltage (typically between 2-10 V, depending on the used NLC mixture) a position dependent deformation occurs. Because the homeotropic alignment is caused by chemical treatment of the bounding surfaces the maximum deformation occurs in the middle of the liquid crystal layer. The NLC cell shows a position dependent birefringence effect that increases with the applied voltage and appears no longer isotropic. Essentially the molecule rotation leads to a division of the polarized light into an ordinary and an

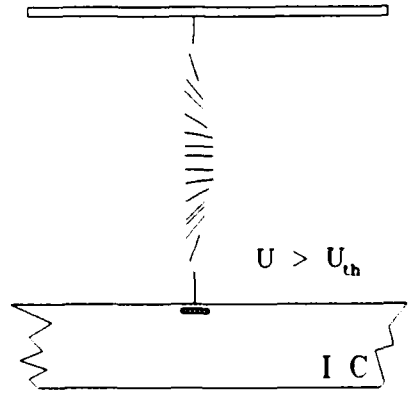


Fig. 7 DAP effect between IC line and field plate

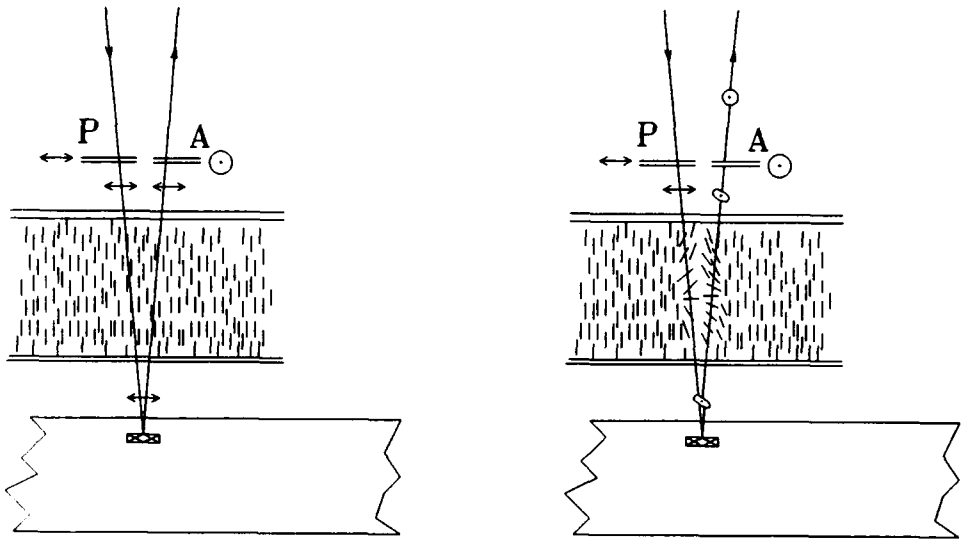


Fig. 8 Observation using crossed polarizers

extraordinary beam of light, giving a phase difference due to the diference of refractive indices of the partial beams. Because of the phase retardation a given wavelength of ligth passes through the analyzer in a series of maxima and minima as the voltage is increased. Fig. 8 illustrates the basic principle in reflective mode. Using crossed polarizers one can create a bright image of those conducting IC lines having a voltage above the critical threshold voltage U_{th} which is strongly material dependent

$$U_{th} = \pi \sqrt{\frac{k_{33}}{-\varepsilon_o \Delta\varepsilon}} \qquad (1)$$

with the bend elastic constant k_{33}.

Fig. 9 displays a typical experimental result. A part of a CMOS IC for HDTV applications was coated with homeotropic aligned NLC, covered with a glass plate and observed with polarized light. The DAP effect above conducting lines with applied signals and $U_{rms} > U_{th}$ is clearly visible.

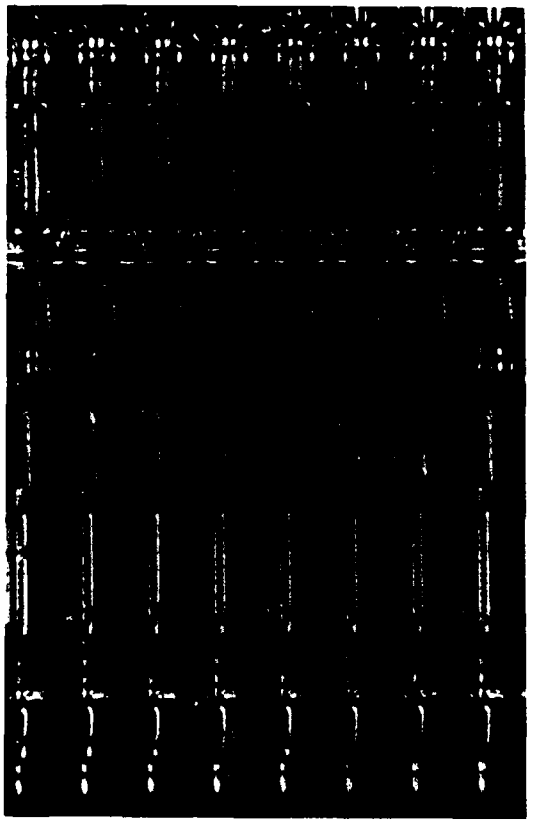


Fig. 9 Part of a CMOS IC under working conditions

Signal Acquisition Using the Linear Electro-optical Effect

Electro-optical sampling (EOS) is an all optical technique that exploits short optical pulses as the sampling gate in electro-optic crystals utilizing the Pockels effect. External EOS using the "finger probe" [16] and internal EOS in GaAs [17] have been demonstrated and showed a very good timing resolution corresponding to a systems's bandwidth in the THz regime.

The aim of our approach is to provide a practical solution for IC failure analysis at internal nodes. A commercial HeNe laser at $\lambda = 633$ nm without a sampling capability is used to detect a voltage change on a conducting line. The experimental setup is shown in Fig. 10. A $LiNbO_3$ crystal is placed above the conducting line with an applied voltage. The crystal's backside is coated with a transparent, electrically conducting TiN layer and connected to ground. This field plate configuration ensures a homogenous field distribution. Since the direction of $\vec{E}$ is parallel to $\vec{k}$ the linear electro-optic effect vanishes for most crystal classes. From theoretical considerations one can show that z-cut $LiNbO_3$ crystals exhibit the Pockels' effect in this case leading to a phase retardation of the incoming light wave (double passage)

$$\Gamma = \frac{2\pi n_o^3}{\lambda} r_{13} U \qquad (2)$$

with the ordinary refraction index n_o and the electro-optical coefficient r_{13}. The phase retardation is linearly dependent on the voltage U and can be converted to intensity modulation using an interferometric setup. This leads to a small intensity change at the interferometer output

$$\Delta I(t) = -2\sqrt{I_1 I_2}\, \sin\left(\frac{2\pi n_o^3}{\lambda} r_{13} U(t)\right) \qquad (3)$$

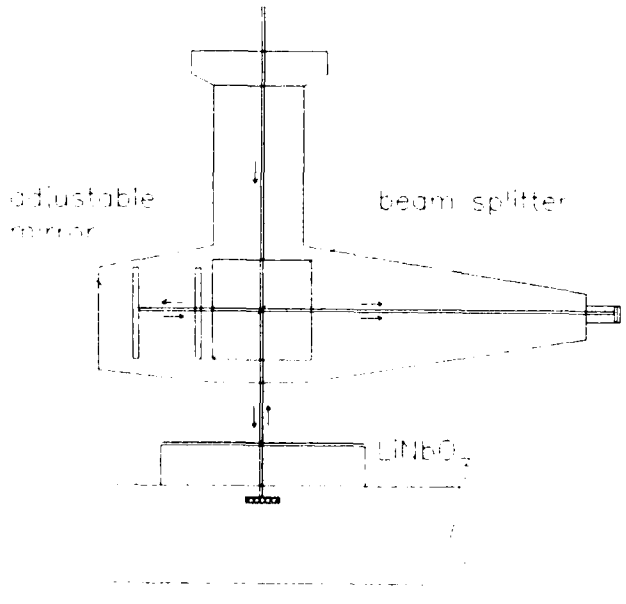


Fig. 10 Integrated interferometer setup

Because the argument of the sinc function is small (typically about 0.0114 for a 10 V amplitude signal) the intensity fluctuation is linear dependent on the voltage U. The major problem in our configuration is a low signal/noise ratio which is directly proportional to the incoming laser power and noise effects due to vibrations and power fluctuations. Fig. 11 shows the linearity measurement for a low frequency sine wave which proofs the linear relationship between the intensity change and the applied signal voltage. The values were taken using a current sensitive lock-in amplifier (EG&G, LIA 5209) and a photodiode. An improved interferometric setup is currently under development.

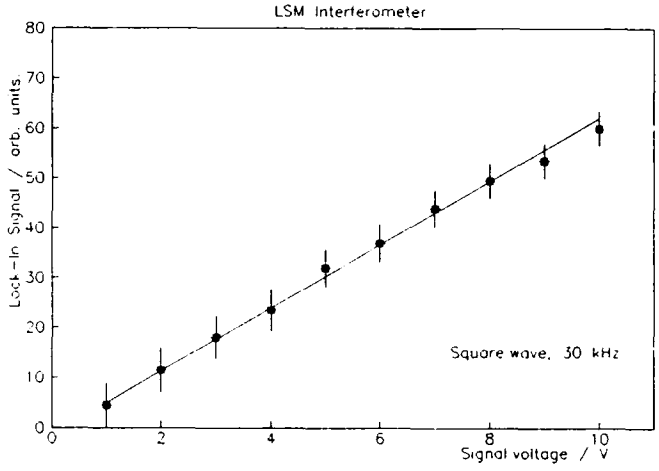


Fig. 11 Measured intensity change as a function of the applied signal voltage

Summary

We have discussed the use of electrooptic effects for CMOS circuit failure analysis and treated internal effects caused by optical beam induced currents and external effects in electrooptic media placed above the circuit. Voltage contrast using nematic liquid crystals allows a first qualitative check and failure localization. To determine latch-up sensitive regions in a CMOS circuit we implemented an automated latch-up measurement method. Increasing the laser power can lead to a latch-up firing.

Internal signal acquisiton by laser illumination of the MOS drain regions has been demonstrated for digital CMOS circuits. The use of the linear electrooptic effect is a promising method of internal voltage measurements on metal lines inside the circuit.

References

1. T. Wilson, C. Sheppard, Theory and Practice of Scanning Optical Microscopy (Acaemic Press, London, 1984)
2. L. Beiser, Laser Scanning Systems (Academic Press, London, 1974)
3. V. Wilke, Scanning, 7, 88 (1985)
4. T. Wilson
5. J. Marek, A.G. Elliott, V. Wilke, R. Geiss, Appl. Phys. Lett. 49, 1732 (1986)
6. P. Kidd, G. R. Booker, D. J. Stirland, Appl. Phys. Lett. 51, 1331 (1987)
7. E. Wolfgang, Microelectr. Eng. 4, 77 (1986)
8. S. Concina, G. Liu, L. Lattanzi, S. Reyfman, N. Richardson, in Proc. IEEE Int. Test Conf., 644 (1986)
9. J. Fritz, R. Lackmann, Microelectr. Eng., to be publ.
10. U. Ko, D. G. Patel, F. J. Henley, in Proc. IEEE Int. Test Conf., 930, 1985
11. J. Fritz, R. Lackmann, Microelectr. Eng., to be publ.
12. R. R. Troutman, Latch-up in CMOS Technologies (Kluwer, Boston, 1986)
13. M. Muschitiello, S. Martino, M. Stucchi, M. Vanzi, E. Zanoni, Scanning 11, 43 (1988)
14. M. Schiekel, K. Fahrenschon, Appl. Phys. Lett. 19, 391 (1971)
15. R. A. Soref, M. J. Rafuse, J. Appl. Phys. 43, 2029 (1972)
16. J. A. Valdmanis, G. Mourou C. W. Gabel, Appl. Phys. Lett. 41-3, 211 (1982)
17. B. H. Kolner, D. M. Bloom, IEEE J. Quant. Elec. QE-22, 79 (1986)

Coaxial Optical Fiber for Communication and Sensing Applications

Kuang-yi Chen*, Jann-shing Chen and Shon-ling Tzeng
Telecommunication Laboratories
P.O. Box 71, Chung-li, Taiwan 32099
Republic of China

Chung-yee Leung, I-fan Chang and Jin-shong Wu
Institute of Optical Sciences, National Central University
Chung-li, Taiwan 32054
Republic of China

ABSTRACT

A new coaxial optical fiber has been fabricated for communication and sensing applications. An experimental system is setup to demonstrate that the coaxial fiber can simultaneously function as a transmission medium for the communication signal and as a vibration sensor. It is also shown that the communication performance is not deteriorated by the simultaneous sensing operation.

INTRODUCTION

Recently, we have demonstrated a fiber optic communication system with sensing capabilities in which a multimode optical fiber is utilized simultaneously as a communication link and as a line sensor.[1] The detection scheme for the sensing channel is based on the modulation of the interference pattern projected from the output end of a multimode optical fiber when the fiber is subjected to an external disturbance which changes its optical properties. However, most today's long-distance high-capacity communication systems use single-mode optical fibers because the transmission distance of multimode fiber communication system is limited by intermodal dispersion. In another publication, [2] we proposed an integrated fiber-optic communication and sensing system using a single-mode fiber and two lasers: a semiconductor laser at 1300 nm and a He-Ne laser at 633 nm. Its communication capacity is indeed much higher but the length of the sensor is still limited by the relatively high attenuation of the optical fiber at 633 nm.

Our single-arm dual-function system may be optimized by operating at the fiber's low loss regime at a long wavelength such as 1300 nm for both the sensing and the communication channels. A two-core optical fiber is required such that the communication light propagates in a single-mode waveguide to achieve high capacity communication while the sensing light propagates in a multimode waveguide such that mechanical perturbation will cause intermodal interference. However, such an optical fiber was not readily available. These considerations motivated us to develop a new optical fiber for such applications. In this paper, we report the first single fiber communication/sensing system using a novel coaxial optical fiber where the single-mode operation can be maintained for the communication channel while the sensing channel is under multimode operation, and only one laser at 1300 nm wavelength is used. The fabrication process of the coaxial optical fiber is described in the following section and the experiment is reported in the subsequent section.

*: Mr. Chen is now a Ph.D candidate at the Institute of Optical Sciences, National Central University, Taiwan, ROC.

THE COAXIAL OPTICAL FIBER

The refractive index profile of our coaxial optical fiber is depicted in Fig.1. The preform of the coaxial optical fiber was fabricated by the MCVD [3] process. Twenty two cladding layers of silica doped with phosphorous and fluorine first deposited in a Heralux model TO-8 16x20 mm quartz tube at 1620°C. These deposited cladding layers give a refractive index below the index refraction of the starting quartz tube. This depression allows a higher index difference without increasing Rayleigh scattering and drawing-induced losses. [4] Three tube core layers of silica doped with germanium then deposited at 1640°C, followed by three inner cladding layers of silica with the same dopant as the outer cladding. Several core layers of silica doped with germanium subsequently deposited at 1700°C. The composite tube then collapsed into a solid rod preform by heating it up to 2000°C. During collapse,chlorine and Freon-12 were used to reduce the moisture content.[5] The preform was then drawn into fiber through a carbon resistance furnace and coated with a layer of 60 μm thick UV-curable coating. The resultant optical fiber has a central core diameter of 4.6 μm. With n=1.468 it is a single-mode waveguide for 1300 nm light. The ring core has an inner diameter of 12.4 μm and a thick-

ness of 4.2 μm. The outside diameter of the fiber is 124 μm. There is a 0.4% in refractive index difference between central core and inner cladding and a 0.1% difference between those of the ring core and the cladding. The near field patterns of the cross section of the coaxial optical fiber are shown in Fig. 2 and Fig.3, when the fiber is illuminated with an incoherent light source (tungsten lamp and a He-Ne laser, respectively. The coherent light forms multiple lobes in its outer pattern because the ring core is single-mode in the radial direction but is multimode in the azimuthal direction.

EXPERIMENT AND RESULTS

Our experimental set-up is schematically illustrated in Fig. 4. The semiconductor laser transmitter is a York model SLS-1300S-DFB stablized light source in which a distributed feedback (DFB) laser with central wavelength located at 1308 nm is used as the light source.The bandwidth of the DFB laser is about 100 MHz. The semiconductor laser transmitter is connectorized with a 3-meter long conventional single-mode (at 1300 nm) fiber pigtail. The laser beam coming out from the fiber pigtail is injected, using the butt joint coupling method, into a 500 meters long coaxial optical fiber. The coupling between two fibers is precisely adjusted to an optimal condition so that the output from the coaxial optical fiber has maximum intensity. Downstream the butt-joint point, a mode filter (index matching oil with refractive index n=1.471) is used to strip the cladding modes. The near field pattern of the output from the end of the coaxial fiber has been photographed with a Hamamatsu model C-1000 IR-214 vidicon camera mounted on a Leitz model Metallux II microscope. With proper launching conditions a two lobed pattern is formed as shown in Fig.5. At the output end, the laser beam is splitted into two parts as depicted in Fig.4. In one beam, the output from the ring core is filtered by passing the image of the near field pattern through a pinhole such that the side lobes of the pattern are blocked off, leaving only the central spot which is the output from the central core to be focused into an InGaAs detector (Epitaxx, model ETX-3000, with an active area of 3 mm in diameter and a responsivity of 0.8 A/W at 1300 nm). This communication channel of our system is thus ensured to operate at single-mode condition. The other beam is defocused into a speckle pattern in which another InGaAs detector is used to detect intensity fluctuations caused by mechanical deformations of the optical fiber due to external perturbations. This forms the sensing channel of the system.

A coiled section about 40 cm in length of the coaxial fiber is placed on the membrane of a loudspeaker which vibrates at sound frequencies. The remaining length of the fiber is isolated from the vibration. We have simultaneously observed the communication and the sensing signals for both situations when the coaxial optical fiber is not perturbed and when it is perturbed. Fig. 6 shows the communication signal (upper trace) and the sensing signal (lower trace) when the loudspeaker is stationary. Here the laser is modulated to generate a 10 KHz sine wave. Fig. 7 depicts the signals when the loudspeaker is driven by a 1.1 KHz sine wave. The sensing signal (lower trace) clearly reflects this perturbation. An appropriate filter circuit can easily recovery the vibration signal. The communication, on the other hand, is not changed by the vibration of the optical fiber.

CONCLUSIONS AND DISCUSSION

This is the first time, to our knowledge,that a novel coaxial optical fiber has been fabricated for the application of simultaneous optical communication and sensing. We have also demonstrated an integrated communication and sensing system using this new coaxial optical fiber. It is shown that the communication performance will not be deteriorated by the simultaneous sensing operation. By using the cut-back method, the attenuation measured at the wavelength of 1300 nm to be around 6 dB/km. It is mainly due to a relatively high content of OH^- ion in the fiber. Also, since the refractive index difference between ring core and cladding is small, the fiber suffers severe bending loss. The coherence length of DFB laser used in our experiment is about 3 meters. With this coherence length,intermodal interference between adjacent modes [6] in the ring core can occur within a propagation distance of tens of kilometers. Therefore, our sensing system is still limited by attenuation as before when 633 nm was used. However, an improvement towards loss reduction in future fabrication of the fiber should change the situations. By then, one-fiber one-laser single-mode communication/multi-kilometer sensing system will become feasible. One can foresee several potential applications for the coaxial optical fiber. For example, our system demonstrated above forms a single-mode optical communication system protected from tapping.

REFERENCES

1. C.Y. Leung, C.H.Huang, and I.F.Chang, in Proceedings, SPIE 838 Fiber Optics and Laser Sensors V, (1987), pp.294-298.

2. K.Y. Chen, C.Y. Leung and I.F. Chang, Electron Lett., 24, 790, (1988).
3. S.R. Nagel, J.B. MacChesney and K.L. Walker, IEEE J. of Quant. Elect. QE-16, 459 (1982).
4. B.J. Ainslie, K.J.Beales, D.M.Cooper, C.R. Day, and J.D. Rush, J. Noncryst. Solids, 47,243, (1982).
5. M. Liegois, G. Lavanant, J.Y.Boniort, C. Le Sergent, J. Noncryst. Solids 47 247, (1982).
6. B.Crosignani, B.Diano,and P.Di Porto, J. Opt. Soc. Am. 66, 1312 (1976).

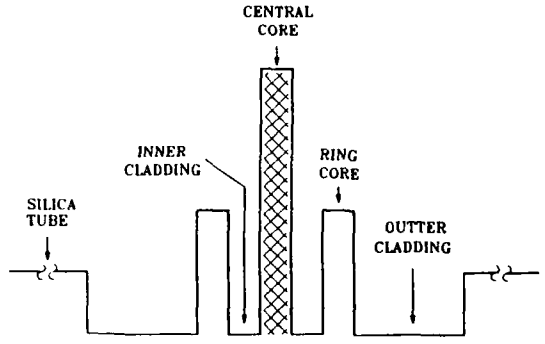


Fig.1 The refractive index profile of the coaxial optical fiber.

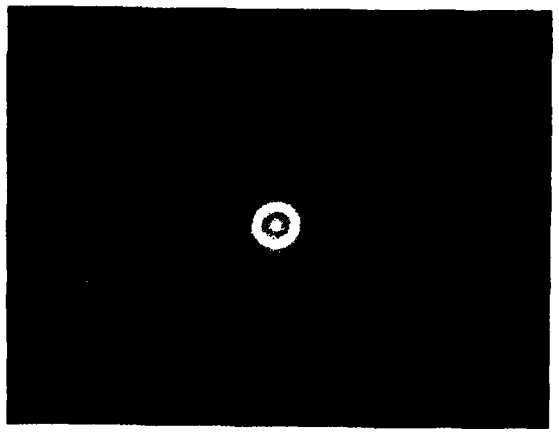


Fig.2 The cross section of the coaxial optical fiber illuminated with a tungsten lamp.

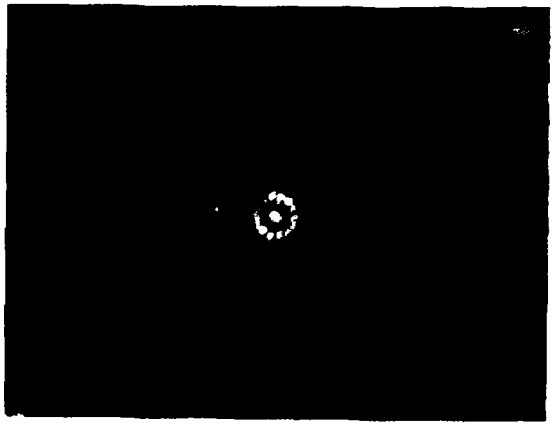


Fig.3 The cross section of the coaxial optical fiber illuminated with a He-Ne laser.

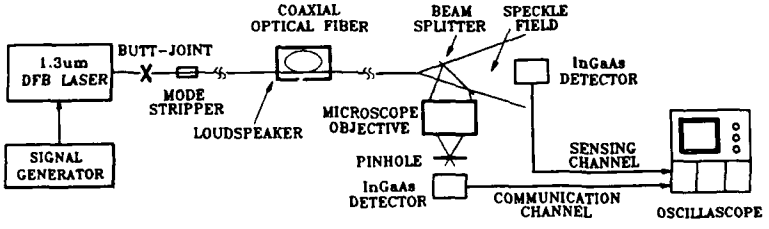


Fig.4 The schematic diagram of the coaxial optical fiber communication and sensing system.

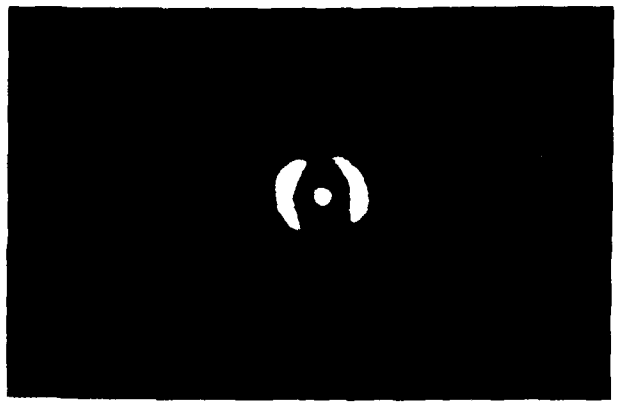


Fig.5 The near field pattern of the output with 1308 nm DFB laser input.

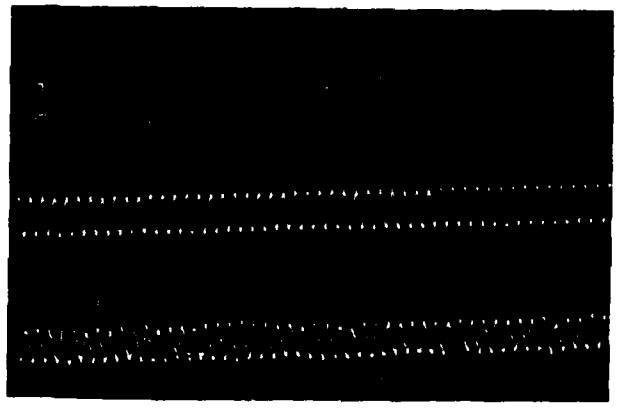


Fig.6 Simultaneous signals from the communication (upper) and the sensing (lower) channels when the fiber is not perturbed.

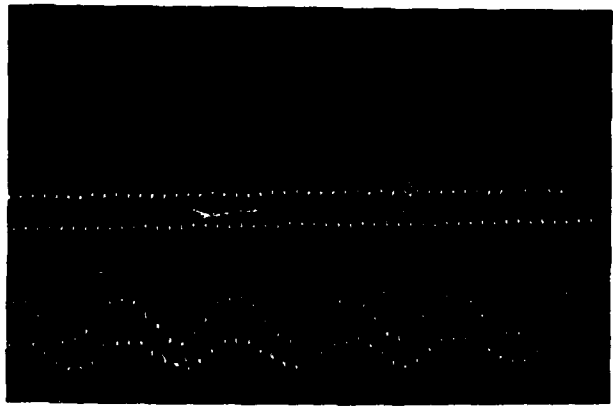


Fig.7 Simultaneous signals from the communication (upper) and the sensing (lower) channels when fiber is being vibrated.

EPR STUDY OF $TEA(TCNQ)_2$ IN THE FAR INFRARED

P. Janssen, A. Mordijck and L. Kesters
K. U. Leuven
Laboratorium voor Lage Temperaturen en Hoge Velden-Fysica
Celestijnenlaan 200 D, B-3030 Leuven, Belgium

Abstract

In this paper we report on the first EPR results in $TEA(TCNQ)_2$ in the Far Infrared (FIR). The experiment was done by measuring the transmission of a flat sample as function of magnetic field. Three wavelengths, 1.615 mm, 1.900 mm and 1.965 mm, obtained from an optically pumped FIR laser, were used. Magnetic fields ranged up to 7 T, temperature was varied between 1.6 K and room temperature. The results are compared with EPR at X-band, as reported in the literature.

The Samples

$TEA(TCNQ)_2$ (triethylammonium 7,7,8,8-tetracyano-p-quinodimethane) is a quasi one-dimensional organic crystal. These types of crystals are formed by stacks with a strong intra-stack interaction and a weak inter-stack interaction. Consequently, they are very anisotropic and susceptible to phase transitions. A linear chain is unstable; i.e. the energy can be lowered by grouping of the molecules. This is the Peierls transition. The Spin-Peierls transition occurs when the energy of an anti-ferromagnetic Heisenberg chain can be lowered by another regrouping. These transitions can result in a dimerization or a tetramerization of the chains (fig. 1). In such materials Charge Density Waves and the Hopping mechanism contribute to the electrical conduction.

Filhol et al.[1] and Farges[2,3] have given a detailed description of the crystal structure of $TEA(TCNQ)_2$. Based upon this work, the crystal can very concisely be described as being built from parallel and well separated stacks of TCNQ molecules. The TEA^+-groups occupy sites in between these stacks. The TCNQ molecules are essentially planar. Interaction along the stacks make the TCNQ to group into tetramers of the type A-B B-A A... . This tetramerization is reflected energetically in a singlet-triplet level configuration. This singlet-triplet system gives an essential contribution to the magnetic susceptibility of the material together with an "impurity" effect due to structural defects ($TCNQ^-$-ions).

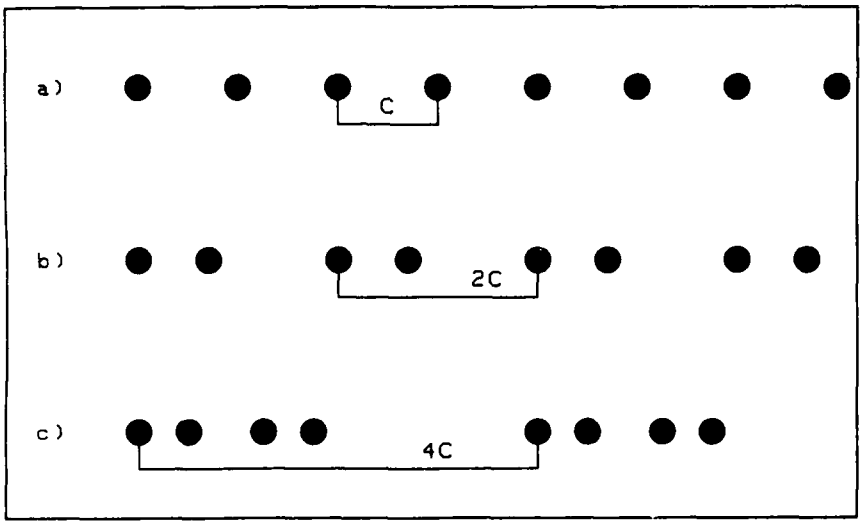


fig. 1 : a) linear chain b) dimerization c) tetramerization

The Experimental Set-Up

The experimental set-up is shown in fig. 2. In an optically pumped FIR laser, vibrational-rotational energy levels of a suited molecule are excited with an appropriate pump laser, usually a powerful grating-tuned CO_2 laser. Inversion can thus be created between two nearby excited levels. This yields radiation at FIR wavelengths. The FIR intensity is stabilized by a feedback mechanism controlling the CO_2 laser length. Some examples of FIR laser lines are given in table 1. A superconducting magnet provides fields up to 7 Tesla at the sample location in the cryostat. The sample temperature varies between 1.6 Kelvin and room temperature. A carbon bolometer at He-temperature detects the transmitted radiation.

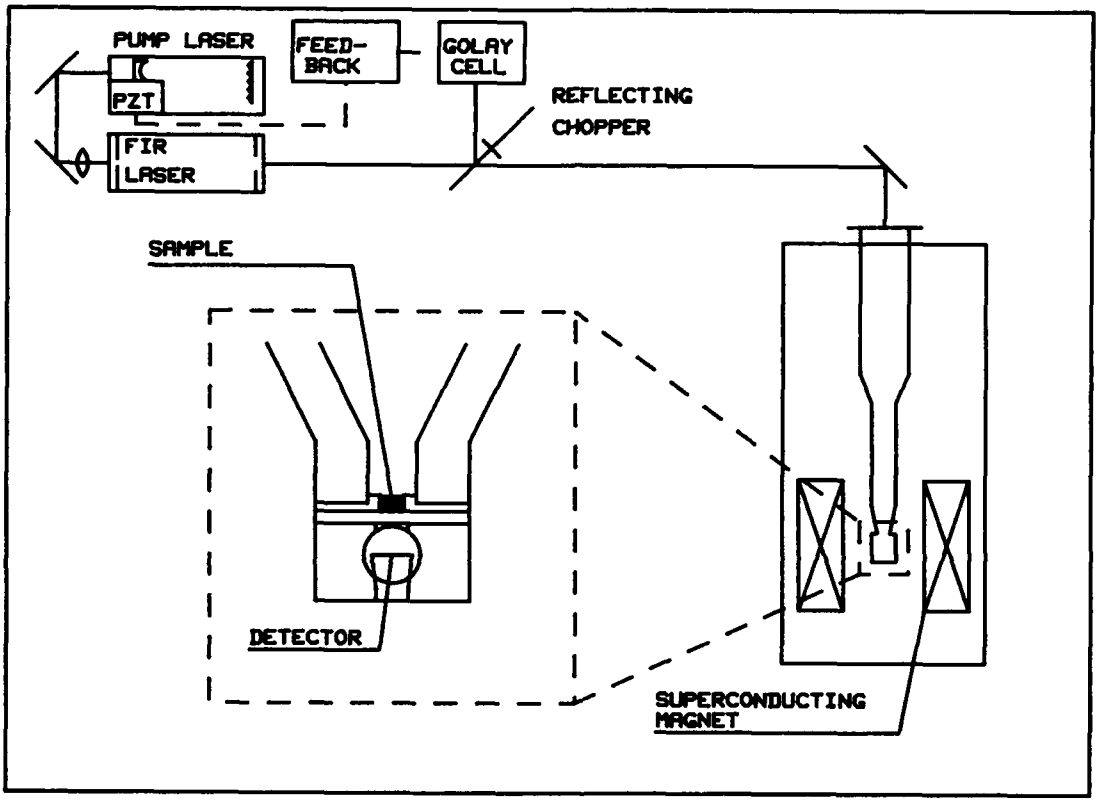


fig. 2 : the experimental set-up

FIR LASER GAS	CO_2 LASER PUMPLINE	WAVELENGTH (mm)	FIR LASER GAS	CO_2 LASER PUMPLINE	WAVELENGTH (mm)
CH_3OH	9P36	.1188	C_2H_3Br	10R20	1.394
HCOOH	9R20	.4326	C_2H_3Br	10P26	1.615
HCOOH	9R28	.5130	C_2H_3Br	10P20	1.900
CH_3OH	9P34	.6994	CH_3Br	10P28	1.965
HCOOH	9R40	.7426	CH_3Br	10P10	2.632

table 1 : some examples of FIR laser lines

Results and Discussion

A pronounced minimum in the transmitted signal versus magnetic field was observed. This is ascribed to paramagnetic resonance absorption. We find g=2.00 ± 0.01 . At lower temperatures, some structure was found around the main line (fig. 3).

Previous EPR experiments were done by Flandrois et al.[4] at X-band frequencies. A central line with a small g-factor anisotropy (2.0022-2.0034), was observed with an intensity following a Curie-law. Between 40 K and 80 K two other lines appeared. This was explained by the thermal activation of the triplet state above 40 K. The susceptibility showed also a singlet-triplet effect.

We have not yet seen this effect above 40 K. From the main line in our experiment, we deduce a simple Curie-law but no singlet-triplet behavior is found in the susceptibility (fig. 4). The structure we found, could be due to a singlet-triplet effect at lower temperatures. The three lines show the same line-separation as in the X-band measurements. However, one has to be careful when interpreting this results, as it may be due to interference effects in the sample.

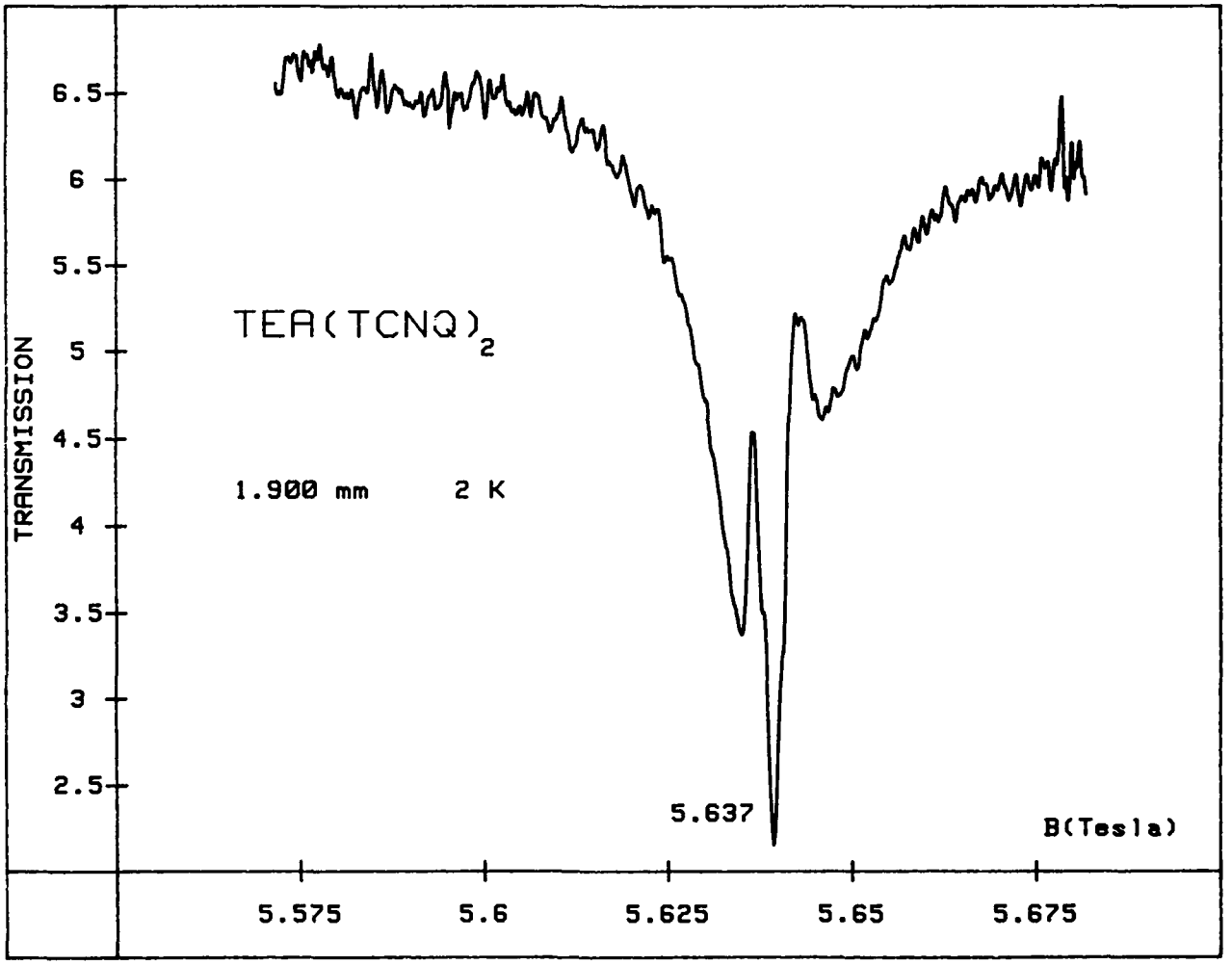


fig. 3 : Low temperature scan of transmission versus magnetic field. Around the central line, two additional lines appear.

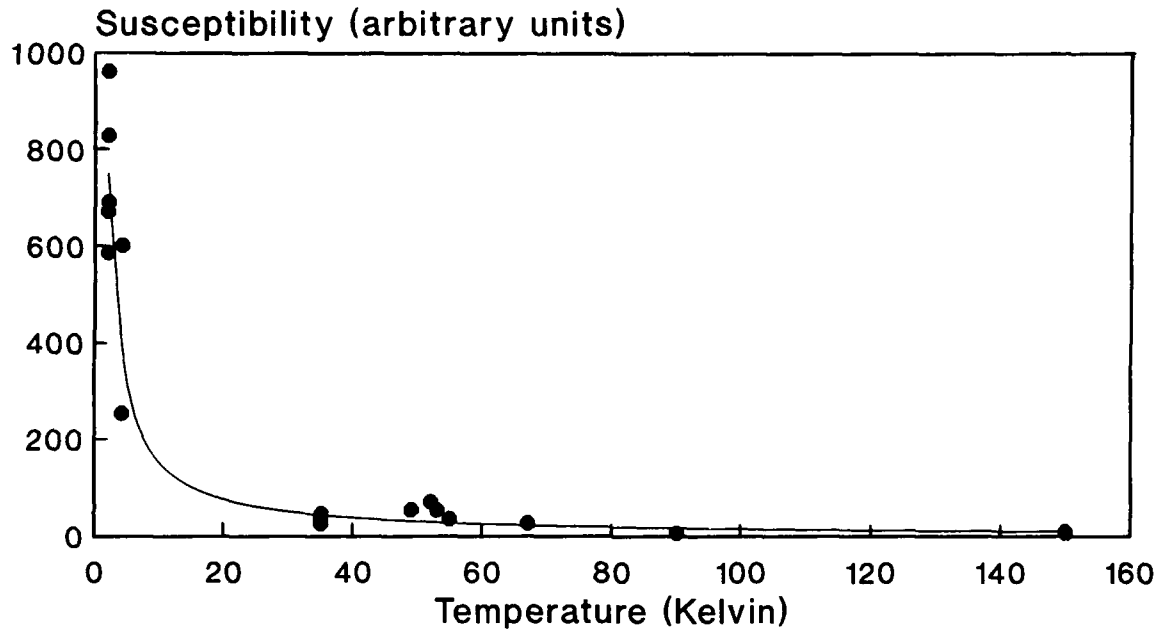


fig. 4 : susceptibility versus temperature fitted with 1/T law

Conclusions

We have demonstrated the feasability of EPR experiments in this material at FIR frequencies, covering the whole temperature range from 1.6 K up to room temperature. At FIR frequencies a behavior is found, different from the reported X-band behavior. It is not yet clear how our results can match with the singlet-triplet model used for this kind of crystals. Further experiments are necessary to study the temperature dependence and the field dependence of the EPR signals and to map the energy levels versus magnetic field.

References

1: A. Filhol and M. Thomas, Acta Cryst. B40, 44, 1984
2: J.P. Farges, J. Physique, 46, 465, 1985
3: J.P. Farges, J. Physique, 46, 1249, 1985
4: S. Flandrois, J. Amiell, F. Carmona and P. Delhaes, Sol. St. Comm., 17, 287, 1975

ANALYSIS OF UNSTABLE RESONATORS WITH RADIALLY VARIABLE REFLECTIVITY MIRRORS

S. De Silvestri, V. Magni, O. Svelto, and G. Valentini

Centro di Elettronica Quantistica e Strumentazione Elettronica del C.N.R.
Istituto di Fisica del Politecnico.
P.zza L. Da Vinci, 32. 20133 Milano - Italy

P. Laporta

Dipartimento di Ingegneria Elettronica
II Università di Roma, Via O. Raimondo, 00173 Roma, Italy

Abstract

Unstable resonators with output mirrors of super-Gaussian reflectivity profile represent a valuable solution to generate high energy diffraction limited beams.

In this paper we investigate both theoretically and experimentally the properties of such class of resonators. A set of four mirrors with selected super-Gaussian profiles have been designed, fabricated and extensively tested in a pulsed Nd:YAG laser with a positive branch unstable resonator. The measured output energies and the near- and far-field profiles attest that super-Gaussian resonators provide energetic efficiency equal or better than that of traditional unstable resonators, joined to unique beam quality. The resonator modes have been calculated within the geometrical optics approximation and compared to the diffraction theory predictions. The output energies heve been evaluated by means of an innovative model that takes account of the effects of the transverse mode profile on gain saturation.

Introduction

A challenging goal in solid state laser science and engineering is the design of high brightness systems. One of the most suitable solution to this problem is represented by unstable resonators with variable reflectivity mirrors.

Such resonators present large mode volumes, typical of unstable resonators, joined to high mode discrimination and smooth beam profiles resulting from the intrinsic apodization provided by the output coupler. These characteristics allow to develop lasers with high energy extraction efficiency, capable to generate diffraction limited beams with excellent divergence properties[1,2].

Amongst the proposed reflectivity profiles the most meaningful, from a historical point of view, has been the Gaussian function. However, Gaussian resonators present a mode transverse profile of the same shape as the mirror reflectivity, so that the field intensity spreads to a considerable distance from the resonator axis; therefore, to avoid beam degradation by the effects coming from the diffraction of mode tails over the rod edge, the mode spot size must be restrained by the Gaussian mirror to a dimension significantly lower than the rod radius, thus limiting the rod volume occupied by the mode. This results in an ineffective exploitation of the active medium. To overcome this limitation our group has proposed the super-Gaussian resonators. Within the super-Gaussian family the most meaningful functions are those of high order, presenting short tails and a sharp drop of the reflectivity over a narrow circle. For super-Gaussian resonators too the mode intensity profile resembles the mirror shape, but now it fits much better the rod cross section. For such a reason super-Gaussian resonators, in addition to the advantages of Gaussian ones, have the capability to increase the energetic efficiency near to the theoretical limit, yet preserving appreciable beam quality.

In this paper we present a detailed analysis, in terms of energetic efficiency and beam quality, of unstable resonators with super-Gaussian mirrors. Both theoretical evaluation and experimental tests demonstrate the superior performances of super-Gaussian resonators in comparison with more traditional unstable configurations.

Theory

Mode Profiles

The intensity reflectivity profile R(r) of a super-Gaussian mirror is expressed by

$$R(r) = R_o \exp[-2(r/w_m)^n], \qquad (1)$$

where r is the radial coordinate, R_o the peak reflectivity, w_m the mirror spot size, and n the super-Gaussian order. The last parameter defines the curve shape, which varies from the Gaussian profile (n = 2) to the hard edge limit (n -> ∞).

Within the framework of the geometrical optics the cavity modes and cavity losses for an unstable resonator with a super-Gaussian output coupler and a high reflectivity mirror can be expressed in analytical form. In fact, for the unloaded resonator (without active medium), the lowest order mode is super-Gaussian of the same order as the reflectivity profile of the output coupler. Moreover the mode spot size varies along the resonator axis according to straightforward geometrical rules. The corresponding round trip energy losses Γ are expressed, independently of the super-Gaussian order n, by:

$$\Gamma = 1-R_o/M^2, \qquad (2)$$

where M is the resonator magnification factor. For a detailed discussions about the modes of super-Gaussian resonators we refer to the literature[2,3].

To assess the validity of this geometrical optics approach the cavity modes have been calculated also using the Prony method[4] to solve the Frensnel diffraction integral in cylindrical coordinates. The results of several numerical simulations confirm that (provided that n<15 and M>1.5) the geometrical optics solutions are quite similar to the diffractive ones, apart from the high frequency fringes originating mainly from the mode cutting by the rod edge. As an example, Fig. 1 shows the comparison between the geometrical and diffractive mode intensity profiles for a resonator with a mirror of super-Gaussian order n=9. The diffractive mode results from a numerical simulation executed with a resonator model including a circular aperture to represent the rod edge, which limits the field propagation into the actual resonator.

Output Energy

As the super-Gaussian order is increased the mode profiles become wider, resulting in better filling of the active medium. This is expected to increase the output energy, however, to precisely evaluate the ratio of the output energy versus the volume occupied by the geometrical mode, the effects of the transverse intensity profile on gain saturation cannot be neglected. To this purpose, instead of numerically solving the wave equation in presence of a saturating medium, we have developed an innovative theory that leads to a closed form relationship for the output energy as a function of the transverse mode intensity profile and of the pump energy. Hereafter we will consider the most significant aspects of this theory.

The model originates from the space dependent rate equations of a four level laser[5]

$$\frac{\partial N}{\partial t} = W_p N_t - WN - \frac{N}{\tau}, \qquad (3)$$

$$\frac{dq}{dt} = \int_{rod} WN\, dV - \frac{q}{\tau_c}, \qquad (4)$$

where N is the population inversion per unit volume, W_p the pump rate, N_t the concentration of active elements, W the stimulated emission rate, τ the total lifetime of the upper laser level, q the number of photons inside the resonator, τ_c the photon lifetime, and the integral in (4) is extended over the rod volume.

Beside the general conditions for the validity of the rate equations approximation, we make the following additional assumptions:

a) The pump spatial distribution is supposed to be uniform.

b) The decay term N/τ in (3) is negligible because, for our system, both pump and laser pulses are shorter than the Neodymium upper laser level lifetime (230 μs).

c) The energy emitted from the beginning of the pulse to any time t is proportional to the pump energy in excess to the threshold energy entering the laser up to the time t.

d) The field intensity inside the laser cavity resembles the mode profile calculated for the unloaded resonator in spite of the action of the non-linear gain medium. This hypothesis is legitimated by the effect of the super-Gaussian mirror that strongly reshapes, at each round trip, the profile of the beam circulating inside the resonator. This assumption is sustained by our experimental data and also corroborated by various results (referring to traditional resonators) reported in the literature[1,6].

Let t=0 be the time when the threshold is reached, the initial conditions to integrate the rate equations are:

$$\text{for } t = 0, \quad q = 0 \quad \text{and} \quad N = N_c = \int_{-\infty}^{0} N_t W_p\, dt, \qquad (5)$$

where $N_c = \gamma/\sigma l$ is the critical inversion, γ are the logarithmic losses per single pass and l is the length of the laser medium.

The total number of photons leaving the laser can be evaluated integrating equation (4) from t=0 to t=+∞ and substituting for N the expression obtained from eq (3) neglecting the decay term N/τ. After some lengthy algebra we get the result:

$$\int_0^{+\infty} \frac{q}{\tau_c}\, dt = \int_{rod} (N_o - N_f)\, dV. \tag{6}$$

In equation above

$$N_o = \int_{-\infty}^{+\infty} N_t W_p\, dt \tag{7}$$

denotes the population inversion that would be present in the rod if the laser action was impeded and

$$N_f = N(t=+\infty) \tag{8}$$

is the final inversion at the end of the laser pulse. This last quantity is expressed by a rather complicated formula containing, in integral form, the time behavior of both the stimulated emission rate (W) and the pump rate (Wp). To proceed further with the integration process we make use of the hypothesis c), which can be expressed as

$$\int_0^t W(x,y,z;t)\, dt \simeq K(x,y,z) \int_0^t W_p(t)\, dt \tag{9}$$

where K(x,y,z) takes into account the space variation of the stimulated emission rate. With the above assumption the explicit dependance of N_f on the pump rate (W_p) can be removed, further integrations can be performed, and the total photon number ($\int q/\tau_c$) can be expressed as:

$$\int_0^{+\infty} \frac{q}{\tau_c} dt = \int_{rod} dV \left\{ N_o - \left[N_c + (N_o - N_c) \frac{\exp\left(\int_0^{+\infty} W\, dt\right) - 1}{\int_0^{+\infty} W\, dt} \right] \exp\left(-\int_0^{+\infty} W\, dt\right) \right\}. \tag{10}$$

Being $\int W\, dt$ and $\int q/\tau_c\, dt$ both proportional to the output energy, equation (10) provides a relationship between the pump energy ($\propto N_o$) and the output energy. To explicitly express these dependencies we note that:

$$W = \frac{\sigma}{h\nu} I(x,y,z), \tag{11}$$

where σ is the emission cross section and I=I(x,y,z) is the intensity of the two counter-propagating waves inside the active medium. Neglecting the differences among them and the variations along the resonator axis we can remove the dependance on z and write:

$$\int_0^{+\infty} W\, dt = \varepsilon U(r), \tag{12}$$

where r is the radial coordinate and, according to assumption d), the transverse intensity profile has been taken to be proportional to the square of the mode amplitude of the unloaded resonator $U(r) = |u(r)|^2$, being the output energy enclosed into the proportionality constant:

$$\varepsilon = \frac{2\, \sigma\, E_{out}}{\gamma_1\, h\nu}, \tag{13}$$

where γ_1 are the logarithmic losses of the output mirror. To obtain the above result the normalization condition:

$$\int_S U(r)\, dS = 1 \tag{14}$$

has been assumed. By using the parameter defined in (13) we obtain:

$$\int_0^{+\infty} \frac{q}{\tau_c}\, dt = \frac{\gamma}{\sigma}\,\varepsilon. \tag{15}$$

Moreover we define a normalized pump energy as:

$$\xi = N_o/N_c, \tag{16}$$

where N_c and N_o are given by (5) and (7). In practice ξ represents the number of times by which the threshold is exceeded.

By using (12), (15) and (16), equation (10) can be written as:

$$\xi - 1 = \frac{\int_S [\varepsilon U(r) - 1 + \exp(-\varepsilon U(r))]\, dS}{\int_S \frac{\varepsilon U(r) - 1 + \exp(-\varepsilon U(r))}{\varepsilon U(r)}\, dS}. \tag{17}$$

Equation (17) expresses the output energy ($\propto \varepsilon$) as implicit function of the input energy ($\propto \xi$) and of the transverse mode profile (represented by U(r)). It is worth noting that this result is valid for any mode profile, not only for the super-Gaussian ones.

This unusual input/output relationship reduces, for u(r) = constant, corresponding to uniform intensity profile, to a much simpler form:

$$\xi - 1 = \varepsilon/S \tag{18}$$

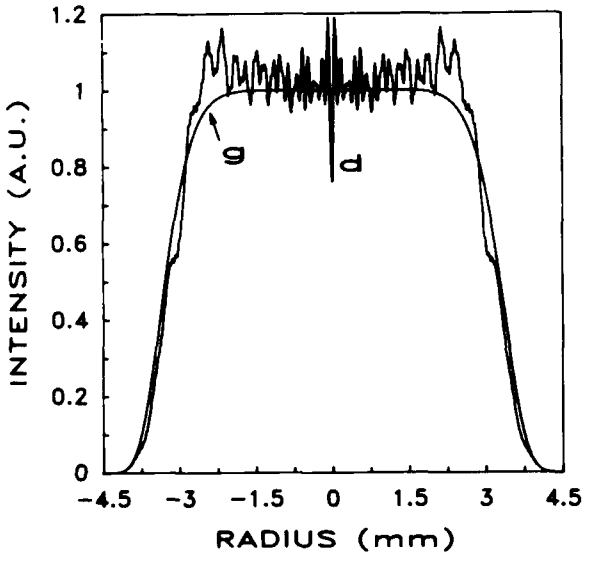


Fig. 1. Comparison between mode intensity profiles (beam incident on the output mirror) predicted by geometrical optics (g) and by diffraction theory (d) for a super-Gaussian resonator. The resonator is made by a flat super-Gaussian mirror (n = 9, wm = 2.03 mm) and a 100% reflecting convex mirror of radius -5 m placed at 450 mm. The magnification is M = 1.8.

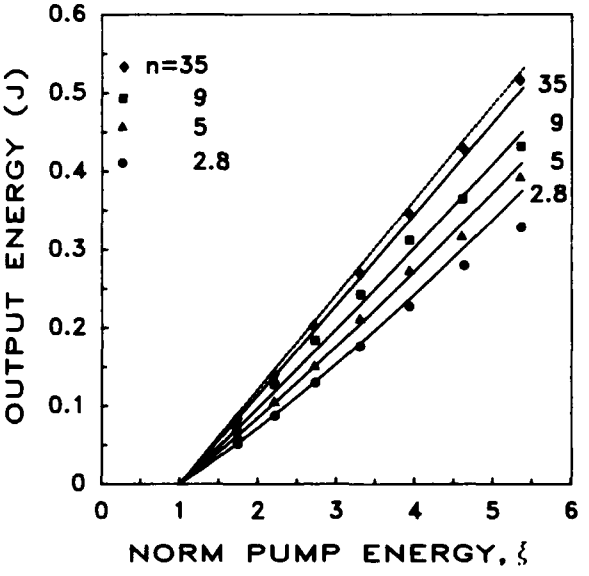


Fig. 2. Measured (dots) and calculated (solid lines) output energies versus pump energy, normalized to the threshold, for super-Gaussian resonators with mirrors of orders 2.8, 5, 9, and 35.

and hence, with the help of (13), the output energy can be explicitly written as:

$$E_{out} = \frac{\gamma_i}{2} \frac{h\nu}{\sigma} S (\xi - 1), \qquad (19)$$

which is a straight line recalling the standard input/output relationship obtained for continuous wave lasers by the rate equation model.

The output energies as a function of the input energy, predicted by (17) and (13) for a Nd:YAG laser using the same unstable resonator with mirrors of orders 2.8, 5, 9, and 35 are shown in Fig. 2. The resonator configuration is described in the experimental section. The mode profiles used for the calculation were obtained by geometrical optics. The use of the geometrical optics fields is validated by the fact that u(r) is inside an integral that averages the fringes by which diffractive fields differ from geometrical ones. In Fig. 2 the output energy for a mirror of order n -> ∞ is also plotted (dashed line): within the framework of geometrical optics the corresponding mode should be uniform and the this line represents the maximum energy that can be extracted from the rod with the given output

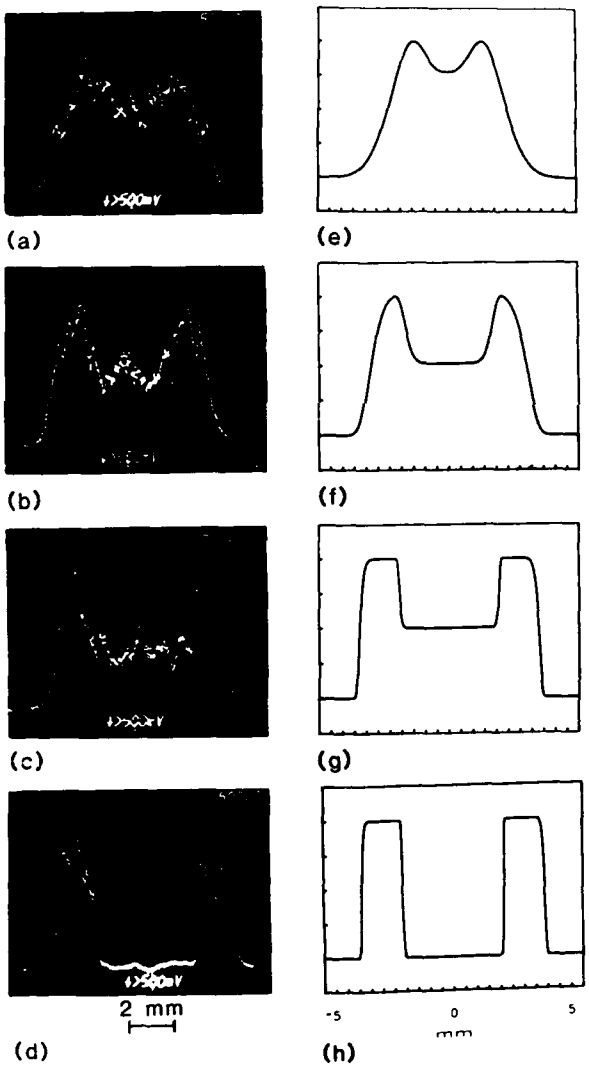


Fig. 3. Experimental near-field profiles obtained by using super-Gaussian mirrors of order 2.8 (a), 9 (b), and 35 (c) and a hard edge mirror (d). Plots e-h represent the corresponding geometrical optics modes.

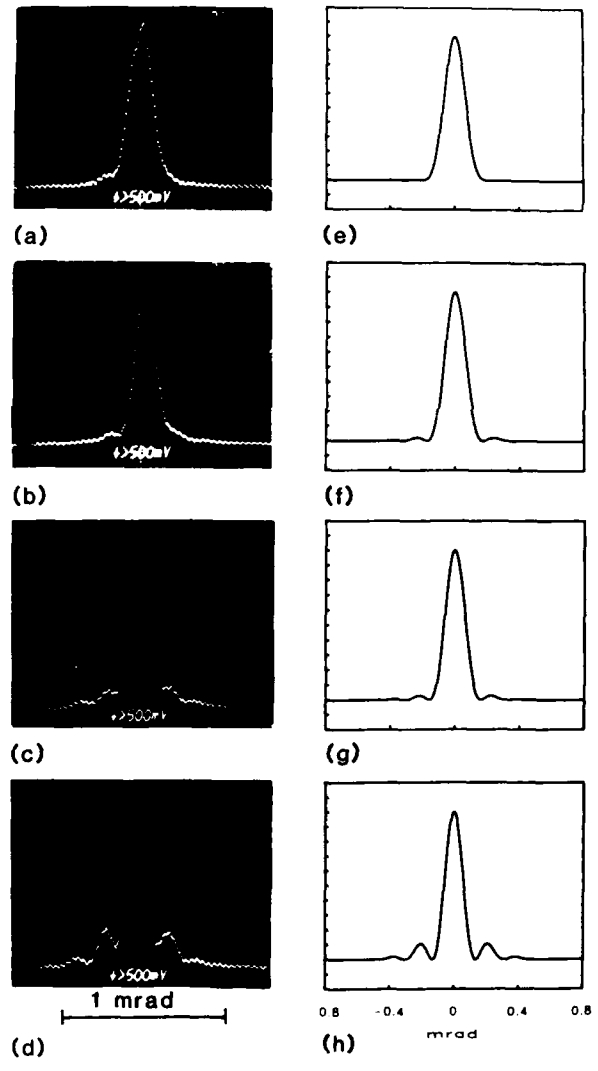


Fig. 4. Experimental far-field (a-d) profiles corresponding to the near-fields of fig. 3 (a-d). Plots e-h represent the Fourier transform of the theoretical near-fields of Fig 3.

losses. From Fig. 2 it is apparent that, for a fixed pump energy, the output energy increases with n. However, being the dashed line the ultimate limit which can be reached, we can see that with a resonator of super-Gaussian order greater than 10 one can get an output energy near to the theoretical maximum.

Beam Quality

In the previous section the dependance of the output energy on the super-Gaussian order n has been discussed. Let us now consider the effects of n on the beam quality. The first effect regards the fine details of the mode profile and can be appreciated only by means of the diffractive mode calculations: when n becomes very large, the near-field profile is degraded by noticeable diffraction rings coming from the wavelets generated both by the rod edge and by the mirror peripheral area, where the reflectivity undergoes to a sharp decrease. This affects the near-field uniformity, but has negligible effects over the beam propagation properties. A second more valuable effect depends on the main features of the beam, obtainable from the geometrical optics mode calculation. For values of peak reflectivity R_o and magnification M such that $R_oM^n > 1$ a central dip in the near-field appears[2], which give rise to side lobes in far-field profiles thus limiting focusing properties and on-axis brightness. This consideration can be understood with the help of Fig.s 3 (e-g) and 4 (e-g) that show near- and far-field profiles calculated for super-Gaussian resonators with mirrors of order 2.8, 9, and 35. Therefore two conflicting trends are evidenced in connection with the increasing of n, namely the output energy grows while the beam quality becomes worse.

Experiments

Mirror Fabrication

Variable reflectivity mirrors have been produced by means of a radio-frequency sputtering deposition technique capable to generate dielectric layers whose thickness is radially decreasing from the center to the periphery[7]. To obtain the wanted peak reflectivity (about 0.5), starting from a plane BK7 substratum, a tapered layer have been deposited over a double layer antireflection coating . The other face of the substratum is wedged by 1° and antireflection coated as well. To deposit the variable thickness layer, a mask with an hole of diameter D has been placed between the target and the substratum at a distance H from the substratum. Due to the shadowing effect of the mask, the reflectivity profiles are always bell shaped and can be approximated by super-Gaussian curves whose order n and spot size w_m both depend upon D and H.

The measured reflectivity profiles of four different mirrors (denoted by DF1,..,DF4) obtained by this technique are shown in Fig. 5 (dots). The solid curves in the same figure represent the best fits with super-Gaussian functions of order 2.8, 5, 9, and 35.

Laser Tests

The experiments with the mirrors considered above were performed using a pulsed Nd:YAG laser with a positive branch unstable resonator. Except for the output coupler, the configuration was the same for any super-Gaussian order and the resonator was made by a plane variable reflectivity mirror and an high reflectivity mirror of -5 m curvature radius, placed 450 mm apart. The laser head consisted of a close coupling cavity housing a 6.32 X 76 mm rod and was located 130 mm from the convex mirror. The measurements were performed at low repetition rate, so that we could neglect the thermal lens of the rod and the magnification factor was M = 1.8. Since the peak reflectivity is 0.49 for all mirrors, according to (2), the geometrical optics round trip losses were 0.85 for all the resonators. The spot sizes of super-Gaussian mirrors have been designed in such a way that the mode intensity profile, for any order, was cut by the rod edge at 2% of its peak value, thus giving comparable diffraction effects.

The output energies have been measured by means of a thermopile detector. The experimental input/output relationships are represented in fig. 2 (dots) where the predictions (solid lines), calculated by the model discussed in the theoretical section, are also reported. Since the coupling losses are the same for all the resonators the thresholds are theoretically identical, and experimentally only minor differences have been detected; for this reason the pump energies have been normalized to the threshold pertaining to the resonator with the mirror of order n=35.

It is surprising the excellent accordance of the theoretical curves with the experimental data. This has been obtained by means of the least mean square algorithm applied to (17) with the Neodymium cross section σ as free parameter on account of the spread of data reported in the literature for this quantity. The best fit has been found for $\sigma = 4.6 \cdot 10^{-19}$ cm^2: this value appears to be acceptable, since it falls within the range of the reported data and, in particular, it agrees with some of them[8,9].

Near-field intensity profiles have been recorded by imaging, with a pair of plano-convex lenses of 310 mm total focal length, the output beam on a linear array of 512

photodiodes spaced by 25 μm (Reticon). The far-field profiles have been recorded in the plane of minimum spot size of a long focal (f = 973 mm) converging lens.

The measured near-field profiles obtained with the super-Gaussian mirrors of order 2.8, 9 and 35 are shown in Fig.s 3 (a-c). For comparison, in Fig.s 3 (e-g) the corresponding geometrical optics mode profiles have been plotted. The experimental curves are in close agreement with theoretical predictions. The dip in the center of the beam increases in depth and width as the order n of the mirror is increased. For all mirrors considerable diffraction rings are visible across the whole beam.

The far-field patterns corresponding to the near-field profiles of Fig.s 3 are presented in Fig.s 4 (a-c). The related theoretical profiles, calculated by transforming the geometrical optics near-field profiles of Fig 3, are shown in Fig.s 4 (e-g). As n increases, beside the central peak, side lobes that carry out a significant fraction of the total energy also appear. Due to this effect the half aperture 90% energy divergence ranges from 0.2 mrad for the lowest order resonator up to 0.35 mrad.

The good agreement shown by measured far-field and theoretically predicted patterns allow to affirm that, for all super-Gaussian resonators, the beams are diffraction limited. To further confirm this observation we have compared the measured far-field profiles with the Fourier transform of the experimental far-fields. To this purpose we have digitized the amplitude profiles and we have assumed a plane phase-front: an example of this comparison for the mirror of order n = 9 is shown in Fig. 6. It can be seen that the measured profile is slightly larger than the transforms of both the geometrical and experimental near-fields; however, the major source of discrepancy is thought to be due to the limited resolution of the silicon detector array at the Nd:YAG wavelength[10].

To compare the performances of super-Gaussian resonators with those of a more common configuration, we have replaced the output coupler with an hard edge mirror (HD2) made by depositing an high reflectivity coating over an antireflection substratum. The diameter of the reflecting area was designed in such a way that the geometrical mode was tangent to the rod aperture. Since the reflectivity is 1 the geometrical optics coupling losses were 0.69 whereas the diffractive ones were smaller (0.57), as expected. The output energy was significantly lower (392 mJ) than that obtained, for the same pump energy (34 J), from the super-Gaussian resonator of the highest order (430 mJ). This confirms that for the hard edge resonator the actual mode is well different from the uniform mode predicted by the geometrical optics and, according to our model, the lack of a complete filling of the rod accounts for the low energy. Indeed, as expected, the geometrical optics is a poor approximation for hard edge resonators due to strong diffraction effects also visible in the near-field pattern reported in fig 4 (d). Moreover the donut mode, resulting from the lack of a transmissive coupling, generate a considerable increase of the side lobes in the far-field pattern visible in fig. 5(d). It is worth noting that we have also operated an hard edge resonator (HD1) with the same geometrical coupling losses as for super-Gaussian resonators, getting an output energy even lower than in the case previously considered.

For a conclusive comparison we have summarized in Table I the output energies obtained, for the same input energy (34 J), from the super-Gaussian resonators and from the hard edge resonators.

TABLE I
Output characteristics of s-G resonators

mirror	DF1	DF2	DF3	DF4	HD1*	HD2*
output energy+ (mJ)	280	314	364	430	296	392

+ Input energy 34 J
* Hard edge, totally reflecting

Conclusions

The properties of unstable resonators that use variable reflectivity output couplers have been investigated for several mirrors with reflectivity profile covering the whole range of super-Gaussian functions.

The fraction of the rod volume occupied by a significant mode intensity has been shown to increase with the order n; this explains the increment of the energetic efficiency with n, also confirmed by the experimental data, and accounts for the superior performances of super-Gaussian resonators over Gaussian ones. Going from n = 2.8 to n = 35 the output energy increases by a factor 1.6 and approaches the upper theoretical limit, corresponding to a flat mode into the resonator.

The transmissive coupling of super-Gaussian mirrors and the tapering of the

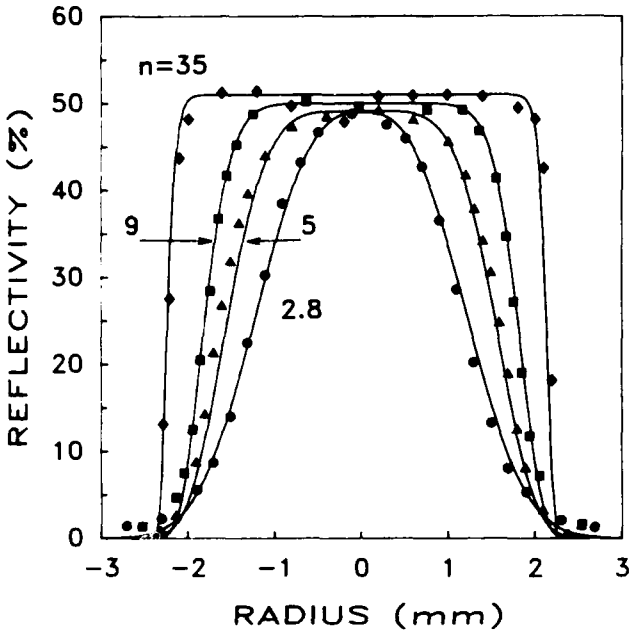


Fig. 5. Intensity reflectivity profiles of the mirrors used for the laser tests (dots). The lines represent the best fit with super-Gaussian functions.

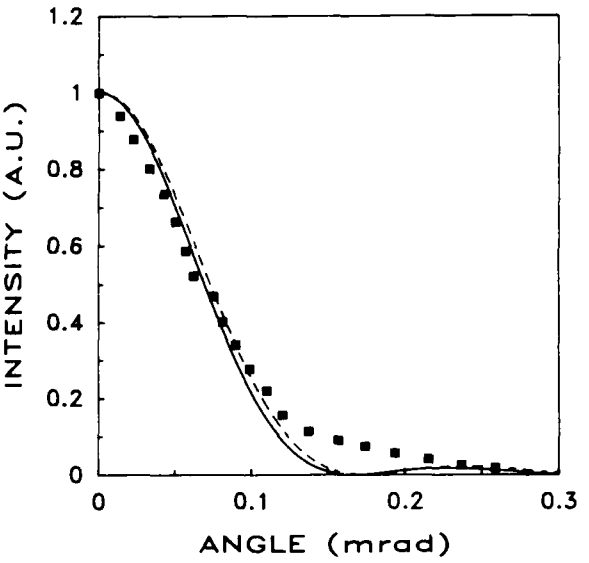


Fig. 6. Comparison between the experimental far-field (dots), the Fourier transform of the geometrical optics near-field (dashed line), and the Fourier transform of the experimental near-field (solid line). The data refer to the resonator with the super-Gaussian mirror of order n = 9.

reflectivity profile are key points to obtain, from super-Gaussian resonators of any order, diffraction limited beams with smooth profile; however, as n increases, the central dip in the near-field becomes more and more pronounced, and side lobes appear in the far-field, slightly decreasing the on-axis brightness.

The comparison between super-Gaussian resonator and traditional unstable configurations demonstrate that super-Gaussian resonators present the following advantages: (i) for any order n they generate diffraction limited beams; (ii) for order n > 10 the output energy is higher than that obtained from hard-edge resonators; (iii) the beam divergence, although it gets worse as n increases, is always better than that of hard edge resonators.

Acknowledgment

The authors would like to express sincere thanks to G. Emiliani and A. Piegari of ENEA Casaccia - Laboratorio Film Sottili - Roma Italy, for their enthusiastic work in preparing super-Gaussian mirrors.

References

1. A. Parent, N. McCarthy, and P. Lavigne, IEEE J. Quantum Electron. QE-23, 222-228, (1987).
2. S. De Silvestri, P. Laporta, V. Magni, and O. Svelto, IEEE J. Quantum Electron., QE-24, 1172-1177, (1988).
3. S. De Silvestri, P. Laporta, V. Magni, O. Svelto, and B. Majocchi, Opt. Lett., 13, 201-203, (1988).
4. W.D. Murphy and M.L. Bernabe, Appl. Opt., 17, 2358-2365, (1978).
5. O. Svelto, Principles of lasers III ed. (Plenum Press, New York, 1989), p. 465.
6. A.E. Siegman, Lasers (Oxford University Press, Oxford, 1986), pp. 883-884.
7. G. Emiliani, A. Piegari, S. De Silvestri, P. Laporta, and V. Magni, Appl. Opt. 28, 2832-2837, (1989).
8. K. Fuhrmann, N. Hodgson, F. Hollinger, and H. Weber, J. Appl. Phys., 62, 4041-4044, (1987).
9. M.D. Shinn, F.P. Milanovich, and J.N. Roe, Conference on Lasers and Electro-Optics, 1989 Technical Digest Series, vol. 11 (Optical Society of America, Washington, D.C. 1989) p. 242.
10. L.W. Schumann and T.S. Lomheim, Appl. Opt., 28, 1701-1709, (1989).

A NEW TECHNIQUE FOR MEASURING MODE COUPLING, PULSE LENGTH AND MODE SIZE IN PICO AND FEMTO SECOND LASER PULSES*

Antonello Cutolo, Luigi Zeni

Dip. Ing. Elettronica
Via Claudio, 21 80125 NAPOLI (ITALY)

Salvatore Solimeno

Dip. Scienze Fisiche
Mostra d'Oltremare, Pad. 16 80125 NAPOLI (ITALY)

Abstract

We report a new technique which allows to monitor, in real time, pulse to pulse changes of mode size, pulse length, transverse mode distribution of any pulsed laser independently on the pulse length from milli to femtoseconds. Some experimental results relative to pulse length changes in both a mode locked Nd:YAG laser and a free electron laser (FEL) are discussed.

Introduction

In the characterization of pico and femtosecond laser pulses many solutions have been proposed and tested [1-3] in order to overcome the problems related to the limited bandwidth of the conventional detectors. Most of these techniques can be used to reconstruct the actual profile of the pulses but they are based on the measurement of the second or higher order intensity autocorrelation functions, so that they yield only the average pulse shape.

With these considerations in mind, we have proposed for both a free electron laser [3,4] and flash pumped Nd:YAG laser with active and passive mode locking [9,10], a new technique which allows the simultaneous measurement, in real time, of the pulse-to-pulse changes in mode size and pulse length of laser pulses. One of the major advantages of this technique is that it can be used for any pulsed laser system indipendently of the pulse length from femtosecond to millisecond. The validity of the results rests on the hypothesis that the power distribution on the transverse laser modes can be arbitrary but constant during the measurement time. Numerical and experimental analyses have demonstrated that this hypotesis is largely verified in FEL systems and in solid state lasers with active mode locking where the transverse distribution is almost a TEM_{oo} Gauss-Laguerre mode. On the other hand, as this hypothesis might be easily not fulfilled, taking advantage of the properties of the S.H.G. we have gained the possibility of removing the previous mentioned restriction. In this improved version our technique allows the real time monitoring of the pulse to pulse variations of mode size, pulse length, and power content of the fundamental mode for any pulsed laser system [5].

The paper is organized as follows: in Sec.II we calculate the S.H.G. efficiency in different focusing conditions taking explicitely into account possible transverse mode mixing effects; in Sec.III we propose to modify the above mentioned technique in order to measure mode coupling effects in any laser pulse and report some experimental applications of the technique.

Second harmonic generation with multitransverse mode beams

In this section, we want to carry out a detailed analysis of the main features of the S.H.G. with undepleted pump taking explicity into account multitransverse mode effects. When the exact transverse distribution has to be explicitly considered, the incoming beam can be expanded in a series of either Laguerre-Gauss or Hermite-Gauss modes the two representation being perfectly equivalent also in view of the conversion formulas derived in refs. [14]. Here, we have chosen Laguerre-Gauss modes, because their use permits a noticeable shortening of the time required by the computer code developed to calculate the conversion efficiency. Therefore, the generic TEM_{np} orthonormal mode can be written as

$$\Psi_{np}(r,\phi,z) = \frac{1}{w(z)}\left[\frac{2p!}{\pi(p+n)!}\right]^{\frac{1}{2}}\left(\sqrt{2}\,\frac{r}{w(z)}\right)^{n}$$

$$\cdot L_p^n\left(\frac{2r^2}{w^2(z)}\right)\exp\left[i\left(\tan^{-1}\left(\frac{z}{z_R}\right)-\frac{kr^2}{2R(z)}\right)-\frac{r^2}{w^2(z)}\right]\cos(-n\phi)$$

* Work supported by "Ministero della Pubblica Istruzione" and by "Consiglio Nazionale delle Ricerche" of Italy.

$$w(z) = w_o\left(1+\frac{z^2}{Z_R^2}\right)^{\frac{1}{2}} \qquad R(z) = z\left(1+\frac{Z_R^2}{z^2}\right) \tag{1}$$

where w_o is the waist, $Z_R = \pi w_o^2/\lambda$ is the Rayleigh length, $k = 2\pi/\lambda$ the wavenumber, $L_p^n(x)$ the generalized Laguerre polynomial, p and n are the radial and angular mode numbers respectively. It is obvious that any field distribution (E_1) of the first harmonic beam can be simply written as

$$E_1 = \sum_{n=0} \sum_{p=0} a_{n,p}\, \Psi_{np}(r,\phi,z) \tag{2}$$

Taking advantage on a generalization of the approach originally developed by Bjorkholm [11] and by Boyd et al. [13] we can calculate the second harmonic field, generated by any first harmonic distribution.

In this way we can write the conversion efficiency of S.H.G. in the undepleted regime for an input first harmonic beam with a multimode transverse field distribution as

$$\eta = P_2/P_1^2$$

$$= 2LD^2 \frac{\zeta_1^2}{\zeta_2} \frac{\pi}{\lambda} Q\left(\frac{Z_R}{L}, W_p, n, p, a^2_{np}\right) \tag{3}$$

where L is the length of the crystal, λ is the first harmonic wavelength in vacuo, ζ_1 and ζ_2 are the impedances of the nonlinear medium evaluated at the first and second harmonic frequencies respectively, W_p is a number that take into account the waist position in the crystal (i.e. W_p=-0.5 and W_p=0.5 means the waist in the middle of the crystal and one half crystal length out respectively). $D=\sqrt{\mu_0/\varepsilon_2}\, d$ and

$$Q = \int_0^{2\pi} d\phi \int_0^{\infty} \rho d\rho \left| \int_0^{1} [\Sigma\, a_{np}\, \bar{\Psi}_{np}]^2 d\zeta \right|^2 \tag{4}$$

where $\Psi(\rho,\zeta,\phi) = W_o^2\, \bar{\Psi}^2(\rho,\zeta,\phi)$ and $\rho=r/W_o$ $\zeta=Z/L$. We stress that the optical properties of the crystal are described by the proportionality constants of Eq. 3 while the adimensional function Q takes into account the influence of the intensity transverse distribution of the first harmonic beam.

We intend, now, to investigate the effects of moving focus on the conversion efficiency in the limiting cases of $Z_{R/L}<<1$ (strongly focused beam) and $Z_R/L>>1$ (columnar beam) [11, 12]. This analysis is instrumental, as discussed in the next section, for the mode coupling analysis.

Taking in mind the asymptotic behaviour of the function Q we can write:

$$Q(Z_R/L, W_p\ n,p)\Big|_{Z_R/L\ll 1} \approx q_1\, Z_R/L$$

$$Q(Z_R/L, W_p\ n,p)\Big|_{Z_R/L\gg 1} \approx q_2\, L/Z_R \tag{5}$$

TABLE I

	TEM_{00}		TEM_{01}		TEM_{10}		TEM_{11}		TEM_{02}		TEM_{20}	
W_p	q_1	$q_2 x 10^1$	q_1	$q_2 x 10^1$	q_1	$q_2 x 10^2$	q_1	$q_2 x 10^2$	q_1	$q_2 x 10^2$	q_1	$q_2 x 10^2$
-0.5	3.70	1.295	1.37	0.647	2.41	2.432	0.64	1.513	0.64	4.423	1.36	1.823
-0.25	4.45	1.294	1.41	0.647	2.32	2.430	0.73	1.512	1.02	4.420	1.5	1.822
+0.25	2.5	1.288	1.35	0.644	0.091	2.420	0.14	1.505	0.82	4.399	0	1.813
+0.5	1.22	1.282	0.71	0.641	0.03	2.408	0.045	1.498	0.4	4.381	0	1.805

TAB.I Some values of the constants q_1 and q_2 (cf. Eqs. 5).

An inspection of Tab. I shows that the constant q_1 is more sensitive to the waist position than q_2. We explicitely remind that values reported in Tab. I are relative to the single transverse modes. Now, we focus our attention to the case that the first harmonic beam has a transverse field distribution like $E_1 = \sqrt{1-\alpha}\, E_{00} + \sqrt{\alpha}\, E_{01}$ where α is the percentage of the power coupled with the mode TEM_{01} of the first harmonic beam so that $a^2_{00} = 1-\alpha$, $a^2_{01} = \alpha$.

In view of the application discussed in the next section we calculate, by an appropriate computer code, the conversion efficiency for a fixed value of the focusing parameter $\xi=L/Z_R$ but in two different positions of the beam waist with respect to the crystal, versus the mixing parameter α. Taking advantage of the previous analysis, we are able to plot the ratio between the conversion efficiency when the waist is positioned near the middle of the crystal and the same efficiency when the waist is out of the crystal. Fig. 1 shows the ratio η_1/η_2 versus α for $Z_{R/L}=0.1$, where η_1 and η_2 are the efficiencies when the focus is respectively in the center of the crystal and one half crystal length out.

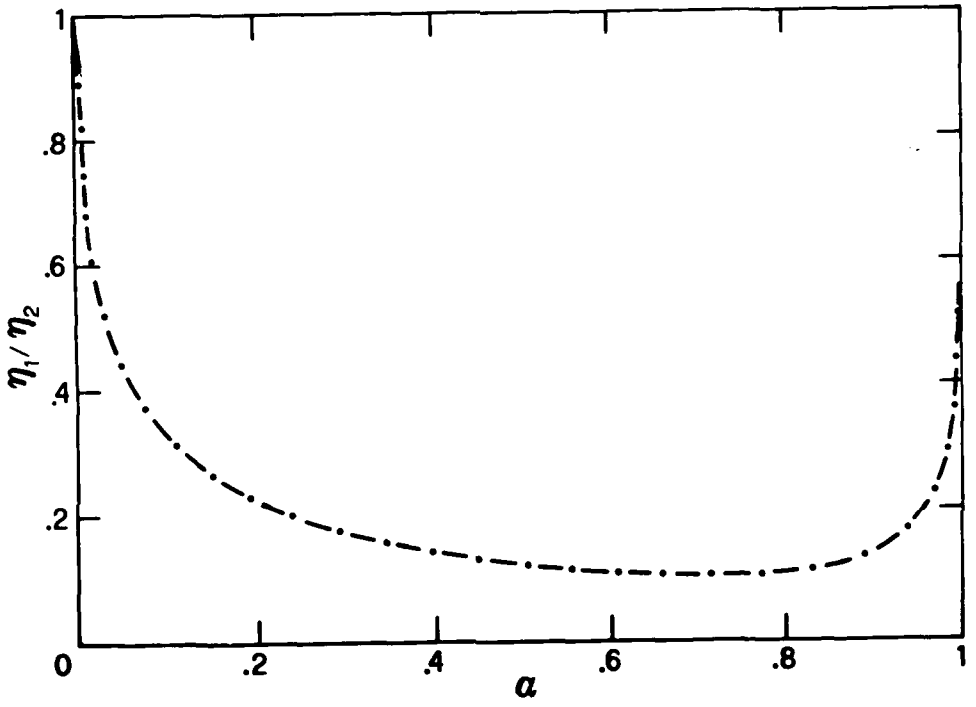


Fig.1. The ratio η_1/η_2 (cf. Eq. 8) versus the mixing parameter α.

Experimental Applications

For the sake of making this paper self contained, we first briefly review the technique in its old version, then we analyze the proposed improvements for the mode coupling analysis. In a nonlinear crystal of length L the peak powers P_2 and P_1 of the second and first-harmonic beams, respectively, are related by

$$\frac{P_2}{P_1^2} \propto \begin{cases} \gamma q_1 Z_R/L & \text{for } Z_R/L \ll 1. \\ \gamma q_2 L/Z_R & \text{for } Z_R/L \gg 1 \end{cases} \qquad (6)$$

where γ is a constant of proportionality depending on the nonlinear properties of the crystal, q_1 and q_2 (cf. Sect. II) take into account the transverse intensity distribution of the first-harmonic beam.

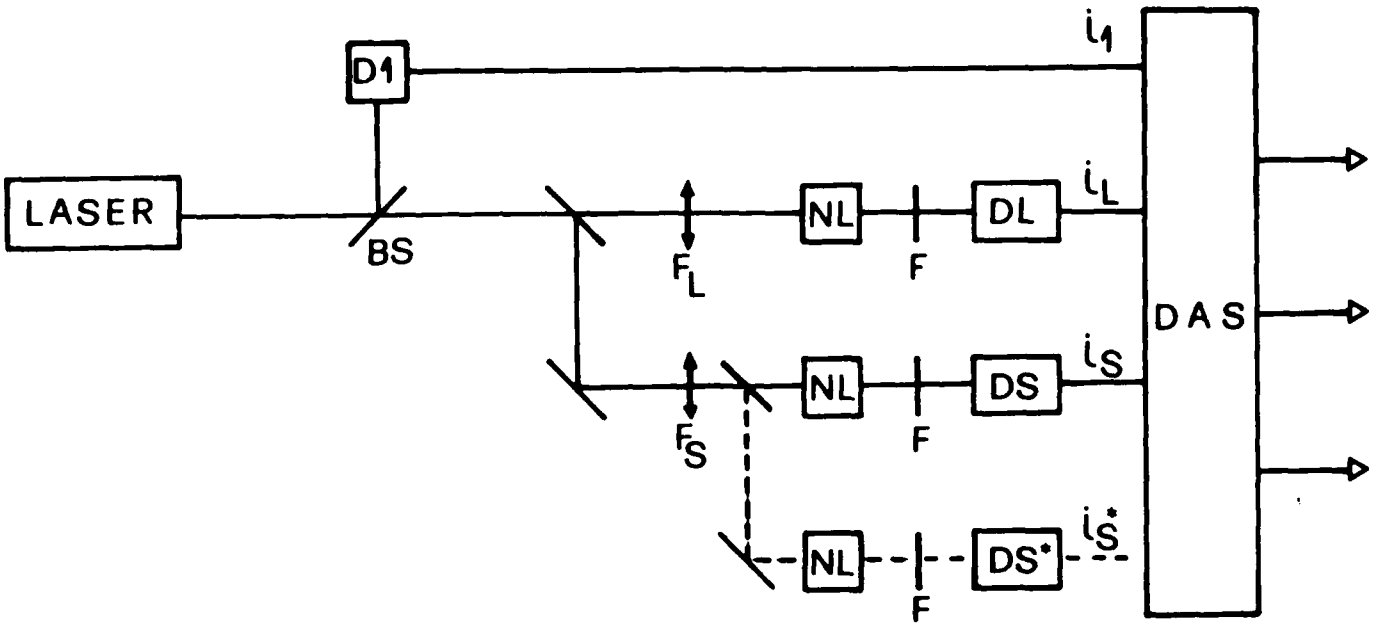


Fig.2. Schematic of the measurement set up. The filter F suppresses the first harmonic. S and L refer to the two channels with short (f_s) and long (f_L) focal length lenses, respectively. DAS means a data acquisition system for the automatic acquisition and elaboration of the experimental results. The dashed line represents the additional channel for the mode mixing analysis, which is not present in the old version described in refs. 3,4,9,10,15.

We explicitly remind that all the detectors, shown in Fig. 2, are requested to have a responsivity time much longer than the pulse length. With reference to Fig. 2, a small fraction of the incident laser beam is sent to the detector D1, which, according to the previous discussion, delivers a signal

$$i_1 \propto E_1 \propto P_1\tau_1$$

where E_1 and τ_1 are the energy and the time length of the first-harmonic pulse, respectively. Then the main part of the beam is divided into two parts, by the beam splitter BS. These two beams are sent into two nonlinear crystals (NL) after being focused by the two lenses with focal lengths f_s and f_L. f_L is so long that the condition $Z_R/L \gg 1$ is satisfied, while f_s is so short that $Z_R/L \ll 1$. In a similar way to the detector D1, the detectors DS and DL provide current signals (i_S,i_L) proportional to the energy content of the second-harmonic pulses produced in the nonlinear crystals in the different focusing conditions. Relying to Eq. 6 we can write:

$$Z_R \propto \sqrt{i_L/i_S}$$
$$\tau \propto \sqrt{i_1^4/i_S \cdot i_L} \qquad (7)$$

which are the basic results of our analysis. Equations (7) show that, through a proper combination of the signals provided by the detectors, it is possible to monitor, in real time, the change of the mode size (Z_R) and the pulse length (τ) (see refs. 3,4,9,10,15 for more details).

As previously discussed the technique, in its old version, can be used only for the real time characterization of pulses delivered by laser systems with no mode fluctuations, although it already proved extremely useful to investigate either deterministic behaviours (e.g. self guiding effects in free electron lasers [3,4]) or random fluctuations (e.g. mode locked Nd:YAG lasers [9,10]).

Relying to the results obtained in sec. II, an inspection of Fig. 1 suggests a simple technique to monitor the pulse to pulse fluctuations of the power distribution of the transverse modes. In fact, with reference to Fig. 2, in the fourth channel (dashed line, not present in the previous experimental set-up of the technique) the beam is focused in the same way as in the channel with $Z_R/L \ll 1$, but the focus is positioned outside the crystal so that we can write:

$$\eta_1 \propto \frac{P_2}{P_1}\Big|_{W_p=-0.5,\,\xi\gg1} \propto i_S\tau_2/(i_1\tau_1)^2$$

$$\eta_2 \propto \frac{P_2}{P_1}\Big|_{W_p=0.5,\,\xi\gg1} \propto i_S^*\tau_2/(i_1\tau_1)^2$$

$$\eta^* = \eta_1/\eta_2 \propto \frac{i_S}{i_S^*}$$

where i_S, i_S^*, and i_1 are the intensities of the current provided by the photo detectors DS, DS* and D1.

Because the focusing parameter is the same for η_1 and η_2, the ratio of the currents i_S and i_S^* is dependent only upon the mixing parameter α, so we can easily relate the pulse to pulse fluctuations of η^* to the fluctuation of α. This goal can be achieved comparing the values of η^*, normalized to their maximum, with the curve in Fig. 1.

Application to a free electron laser (FEL)

In this section we shortly review the main results obtained by applying the previous technique to look for the experimental evidence of self guiding effects in the free electron laser (FEL) constructed on the MARK III linear accelerator at Stanford [3,4].

The output radiation of the MARK III FEL consists of a train macropulses (some microseconds long), each of which contains micropulses (about 500 fs long), spaced 0.35 ns apart.

We have applied the previous technique to analyze the evolution of these micropulses during the buildup of the radiation. The Rayleigh length of the fundamental mode is about 0.75 m, and the distance between its waist and the measurement apparatus is about 8 m. We have used two crystals of lithium niobate with a length of 5 mm. After being focused, the two beams had inside the two nonlinear crystals a Rayleigh length equal to 1.5 cm = 3L (with $f_L \approx 1$ m) and 0.6 mm = 0.15L (with $f_S \approx 0.2$m). With these parameters, we have derived the results plotted in Fig.3, where both the Rayleigh length and the pulse duration have been put equal to one at the beginning of the macropulse (t=0). The dynamic range of our setup is about 30 dB.

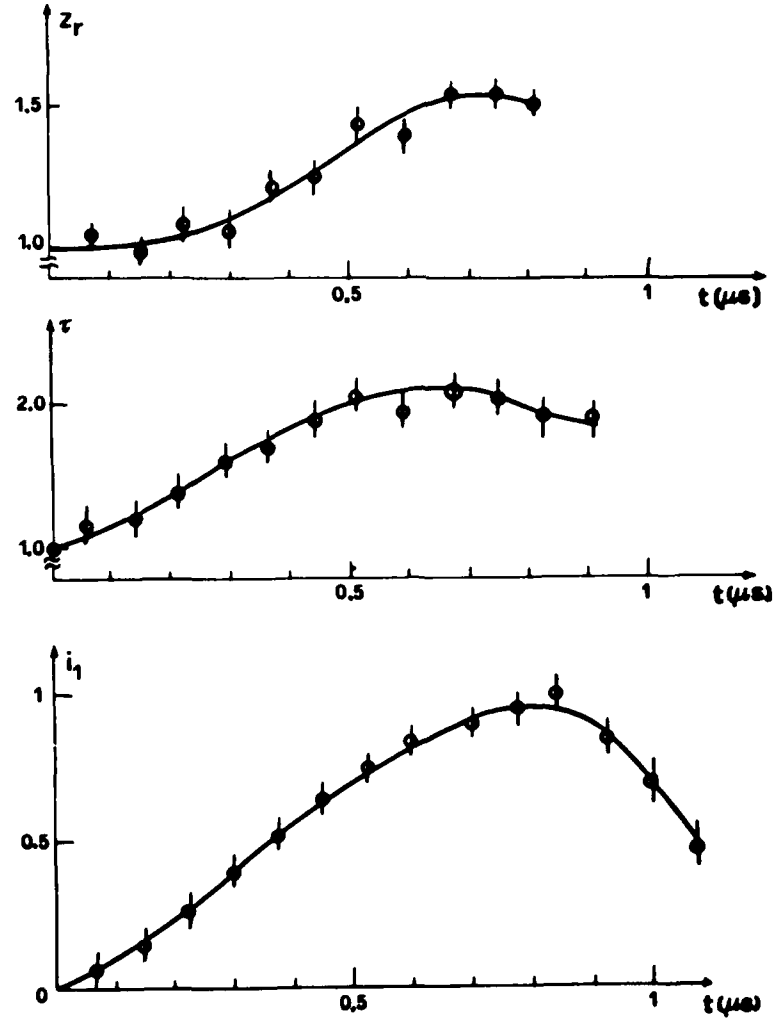


Fig.3. Evolution of the Rayleigh range (Z_R, on the top) and of the pulse length (τ, in the middle) during the buildup of the radiation (at the bottom) in the MARK III FEL at Stanford (7,9). The signal i_1, provided by the detector D1, is proportional to the energy of the first-harmonic micropulses. As a reference, we have set t=0, Z_R=1, and τ=1 at the beginninng of the macropulse.

Application to a mode locked Nd YAG laser

We have used this technique to characterize a Nd:YAG laser, which is a flash-lamp pumped laser system with both an active (acousto-optic) and passive (saturable absorber) mode locking. Its output beam consists of pulse trains (repetition rate up to 20 Hz and energy equal to about 3 mJ), each of which is formed by about 12 individual pulses (30 ps) spaced apart by about 7 ns. The output coupler of the laser resonator can be selected among 4 different plane etalons. According to the particular choice, the length of each individual pulse can take any of the following values: 30, 50, 100, and 200 ps. Then, a single-pulse selector extracts the pulse with the highest energy (about 0.7 mJ).

As a first result, we report the variance of the pulse length as a function of the detuning parameter $\Delta = (f_{AOM} - f_c))/f_c$, where f_{AOM} is the driving frequency of the acusto-optic mode locker and $f_c = 1/2T$, T being the round-trip time of the optical resonator. Fig. 4 shows these results in both the cases of an aged and a fresh saturable absorber, by aged saturable absorber we mean a saturable absorber after about 200.000 shots.

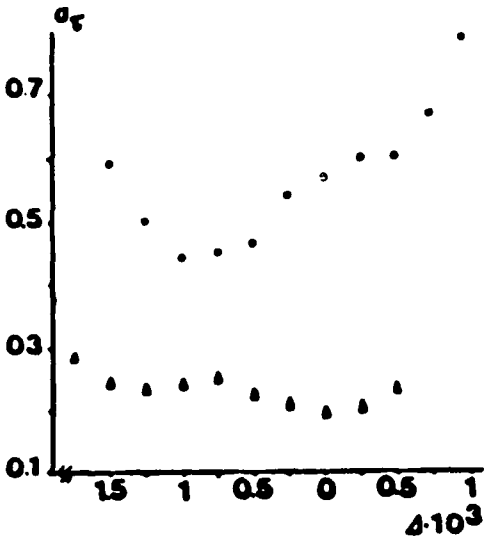


Fig.4. The relative variance of the time duration (σ_τ) as a function of the detuning parameter $\Delta = (f_{AOM} - f_c)/f_c$ for an actively-passively mode locked Nd:YAG laser. By relative variance we mean the variance of the distribution divided by its mean value. Both aged (circles) and fresh (triangles) saturable absorber have been considered. By aged saturable absorber we mean a saturable absorber after about 200.000 shots.

REFERENCES

1. D.J. Bradley, G.F. New, Ultrashort pulse measurement, IEEE Proc. 62, 312 (1974)

2. E.P. Ippen, C.V. Shank, Techniques for measurement, in "Ultrashort light pulses" Ed. by S.L. Shapiro, Springer Verlag (N.Y.1976).

3. A. Cutolo, S.V. Benson, J.M. Madey, Real time processing of pico and femto second laser pulses: application to free electron lasers, Appl. Phys. Lett. 52, 1566 (1988).

4. A. Cutolo, S.V. Benson, B. Hooper, J.F. Schultz, J.M. Madey, Mode characterization, autocorrelation measurements and harmonic conversion with pico and femto second pulses delivered by the MARK III free electron lasers, Appl. Opt.28, 97 (1988).

5. L. Zeni, A. Cutolo, S. Solimeno, Second harmonic generation as a tool for measuring mode coupling, pulse length and mode size in short laser pulses, Journal of Modern Optics (1989), (submitted).

6. F. Zernike, J.E. Midwinter, Applied nonlinear optics, J. Wiley and Sons (N.Y.1973).

7. R. Byer, Parametric oscillators and non linear optical materials, in "Non linear optics" Ed. by P.G. Marper, B.S. Wherrett, Academic Press (N.Y. 1977) 46-101.

8. C.J. Sun, J.T. Lue, Second harmonic generation with focused broad-band and high order transverse mode lasers, IEEE J. Quant Electron., QE-24, 113 (1988).

9. A. Cutolo, L. Zeni, V. Berardi, R. Bruzzese, S. Solimeno, N. Spinelli, Mode size and time duration fluctuations in a picosecond Nd:YAG laser, Opt. Lett., 14, 494, (1989).

10. A. Cutolo, L. Zeni, R. Bruzzese, V. Berardi, S. Solimeno, N. Spinelli, Measurement of the pulse lenghtening with pulse energy increase in single picosecond Nd:YAG laser pulses, J. Appl. Phys. 65, 2187, (1989).

11. J.E. Bjorkholm, Optical second harmonic generation using a focused laser beam, Phys. Rev., 142, 126, (1966).

12. D.A. Kleinman, R.C. Miller, Dependence of second harmonic generation on the position of the focus, Phys. Rev.148, 302 (1966)

13. G.D. Boyd, D.A. Kleinman, Parametric interaction of focused Gaussian laser beams, J. Appl. Phys., 39, 3597 (1968).

14. S. Solimeno, A. Cutolo, Coupling coefficients of misaligned and mismatched Gauss-Hermite and Gauss-Laguerre modes, Opt. Lett. 11, 141-143 (1986)

15. A Cutolo, S. Solimeno, J. Madey, Real time analyzer for pulsed laser systems, U.S. Patent Appl. No. 195577 (May 11, 1988).

DC GLOW DISCHARGES FOR THE EXCITATION OF CO LASERS

H. v. Bülow and E. Zeyfang

DLR - Institut für Technische Physik,
Pfaffenwaldring 38-40, D-7000 Stuttgart 80, WEST-GERMANY

Abstract

Glow discharges with axial gas flow are an efficient technique for the excitation of gas-dynamically cooled CO lasers. We have investigated the scaling laws of DC discharges with flow velocities of several hundred meters per second. In order to increase the stability of the discharge a turbulence was introduced at the upstream end of the discharge tube. In this way it was possible to realize high mass specific input energies at discharge pressures of about 500 mbar.

The experiments proved that in spite of the high flow velocities the discharge can be compared to a classical axial glow discharge with no gas flow. E.g. no dependance of the discharge on the expansion nozzle (which is used for the gas dynamic cooling of the excited gas) was observed. In other words, the discharge is restricted to the volume inside the discharge tube. It could be shown that an optimum for the specific energy input exists and that a pressure drop by a factor of 2 - 2.5 is necessary for the generation of the stabilizing turbulence. The investigations of different discharge geometries revealed that maximum mass specific energies are possible if the mass flow is restricted to small values.

The results of the glow discharge experiments were used to develop a concept for the excitation of a multi-kW-laser.

Introduction

Carbon monoxid lasers can be operated with very high efficiencies (i.e. ratio of laser power and excitation power) if the gas is cooled to cryogenic temperatures [1]. This can be accomplished in a simple and efficient way by the use of a supersonic nozzle. The adiabatic expansion of the gas enables the operation of the laser even at extreme low temperatures (at about 50 K). Due to the very slow vibrational relaxation of carbon monoxid, it is possible to excite the gas before it enters the nozzle [2,3]. In our experiments we applied a DC glow discharge with a fast axial gas flow . Because of the high discharge pressure of several hundred mbar it is necessary to use a special gasdynamic method in order to maintain a stable and uniform discharge. We injected the gas through an annular slit around the anode at the entrance of the discharge tube and generated by this way a strong turbulence at the surface of the electrode with the upstream position. This improved the homogeneity of the discharge properties and allowed a significant increase of the discharge power without giving rise to the formation of streamers.

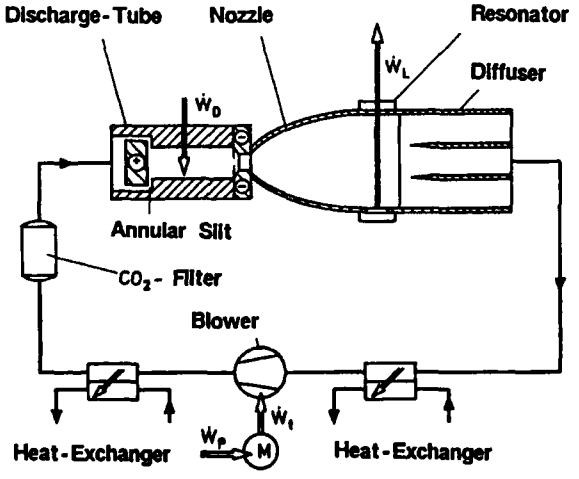


Fig. 1: Gasdynamic CO laser with closed gas cycle.

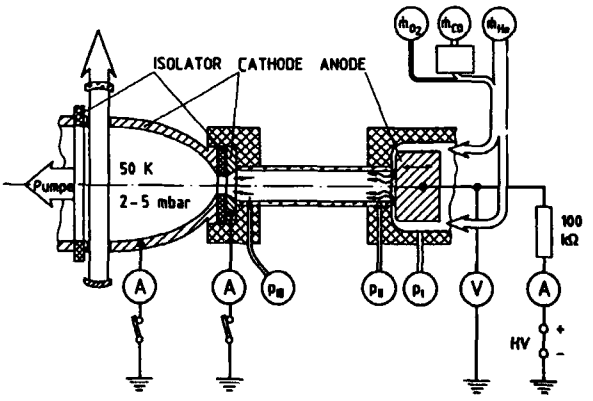


Fig. 2: Experimental setup.

The results of a system analysis, made for a gasdynamically cooled CO laser with a closed gas cycle (see Fig. 1), showed that it is of utmost importance to operate the discharge at high pressures. By this way it is possible to decrease the pumping speed of the blowers or rootspumps, which are needed for the recompression of the gas. Since the pump size is in direct proportion to the pumping speed, this results also in a reduction of the total laser volume. Furthermore, it could be shown that it is necessary to minimize the pressure drop which is used for the generation of the turbulence at the gas injection. Thereby the overall efficiency of the laser is increased, while less pump stages are needed for the recompression of the gas.

Fig. 2 shows the technical setup, which was used during all our experiments. The anode at the entrance of the tube was displacable so that different pressure drops at the annular slit could be used for the generation of the turbulence. By isolating the nozzle from the rest of the structure it was possible to measure the current into the converging and diverging parts of the nozzle seperately. In all experiments we used a standard mixture of gases, which consisted of 12 % carbon monoxid, 87 % helium and 1 % oxygen and which was found to give best results in respect of discharge and laser power. Unless otherwise stated, the length of the tube was 200 mm and its diameter 16 mm.

Results

Fig. 3 shows the dependance of the mass specific laser energy (i.e. laser power per mass flow) on the mass specific excitation energy for different discharge pressures. The maximum mass specific excitation energy is given at the end of each curve by the occurence of streamers. Beyond a pressure of 250 mbar the maximum of laser power is realized at mass specific excitation energies of 400-500 J/g. This power input is hard to achieve at pressures of 300 mbar and more. Since the laser should be operated at high pressures, as noted before, it is in general necessary to excite the laser with the highest possible energy.

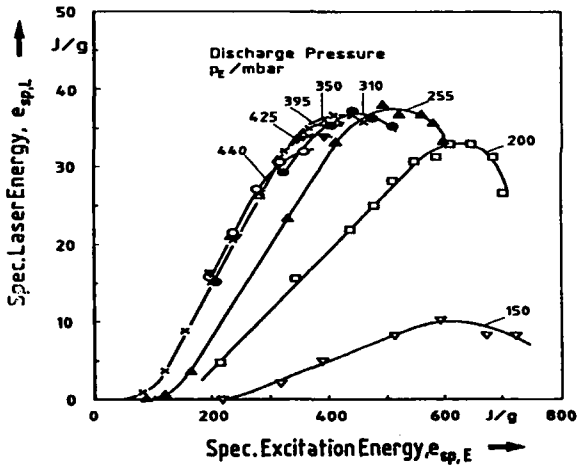


Fig. 3: Mass specific laser energy versus mass specific excitation energy.

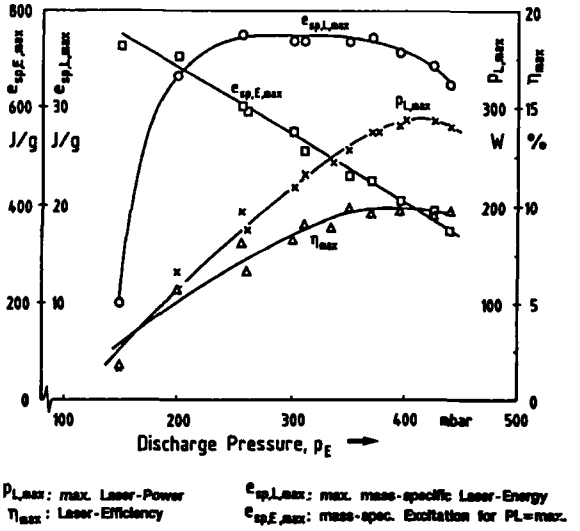


Fig. 4: Dependence on discharge pressure.

Fig. 4 presents the characteristic laser parameters as a function of discharge pressure. The mass specific excitation energy in this figure has been chosen in such a way to give a maximum of laser power. This coincides, as mentioned before, with the maximum of discharge energy, if pressures beyond 250 mbar are considered. While the mass specific excitation energy decreases linearly as the pressure rises, the laser efficiency (ratio of laser power and discharge power) increases till a pressure of about 400 mbar is reached. This may be interpreted in a way that the boundary layers inside the nozzle are decreasing for an increase of pressure. The decrease of boundary layers, which are regions of high temperatures, will result in a decrease of the average gas temperature, which will then be followed by an increase of laser efficiency. As result of the loss of mass specific excitation energy and the gain of laser efficiency the mass specific laser energy becomes a characteristic constant (approx. 40 J/g).

Since the flow velocity inside the tube is in the order of several hundred meters per second, it may be anticipated that a large fraction of the discharge current is displaced into the nozzle. The seperate measurements of the currents into the converging and

diverging parts of the nozzle however proved that only a minor amount of the total current is drawn into the supersonic part of the nozzle. Fig. 5 shows that more than 92 % of the discharge current is restricted to the volume inside the tube. Furthermore, we observed no difference in laser power, when we isolated the nozzle totally and operated it with a floating potential.

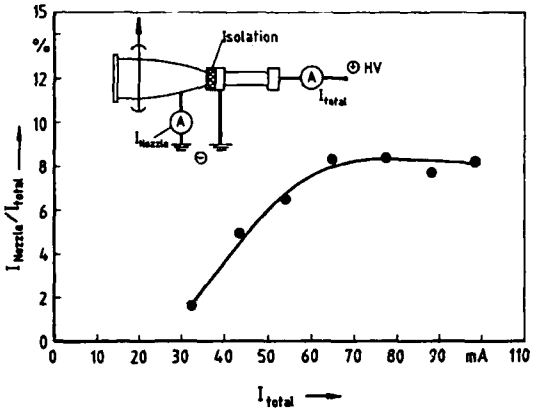


Fig. 5: Displacement of discharge current by gas-flow.

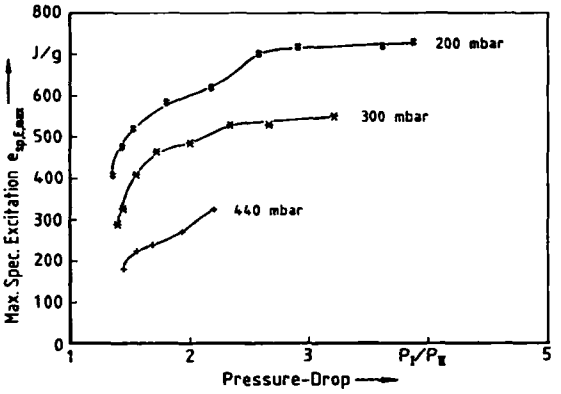


Fig. 6: Maximum specific discharge energy as a function of the pressure drop at the anode slit.

The stabilizing effect of the turbulence at the anode surface is strongly dependant on the pressure drop at the annular slit around the anode. Since the overall efficiency of the laser is affected by the magnitude of the pressure drop, it is necessary to derive the exact relation between the maximum power input without streamers and the ratio of pressures before and after the slit. Fig. 6 shows that at least a pressure drop by a factor of 1.7 is required for the generation of an efficient turbulence. If the ratio of pressures is increased further, it is still possible to increase the power input until a pressure ratio of about 2.5 is reached. In order to design carbon monoxid lasers with high power outputs, the mass flow within the laser has to be increased by an enlargement of the throat area. We have therefore investigated the geometric scaling laws of the maximum mass specific discharge power. Fig. 7 shows the behaviour of three tubes with different diameters, in which the ratio of the throat area and the tube cross section has been kept constant. The strong decrease of discharge power with increasing tube diameter (or mass flow), strongly indicates that the discharge is stabilized by the tube walls.

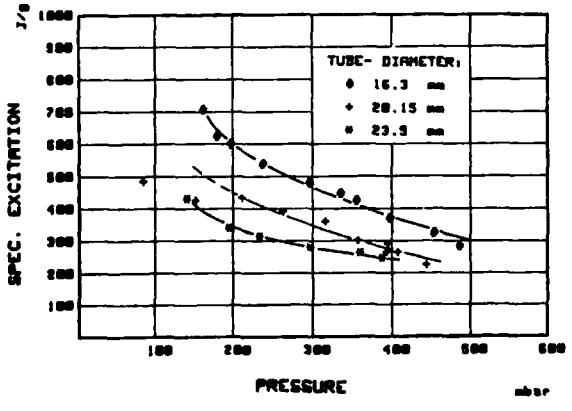


Fig. 7: Maximum specific excitation energy for three different tube diameters.

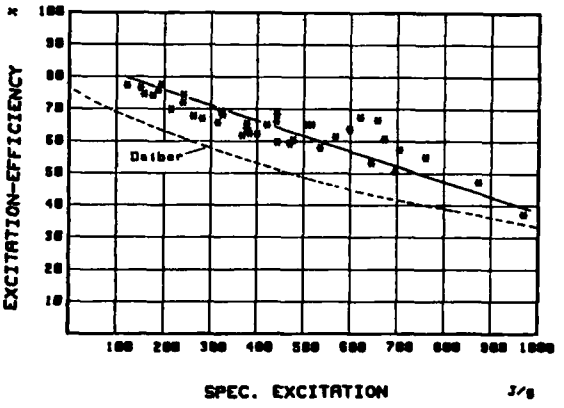


Fig. 8: Excitation efficiency (vibrational excitation/total excitation by discharge) as function of specific excitation energy.

Since the gas flow is choked at the annular slit of the anode, the mass flow remaines constant, even if the discharge power (and thereby the discharge pressure) is changed. It is thereby possible to show [4] that the stagnation temperature at the entrance of the supersonic nozzle is proportional to the square of the stagnation pressure. By calculating the stagnation temperature, the distribution of the total energy input into the tranlational and vibrational degrees of freedom can be derived. Our experiments showed (see Fig. 8) that the excitation efficiency (i.e. the ratio of vibrational excitation and total energy input) is independant of the tube geometry, but it is a function of the specific excitation energy. This is in accordance to the experiments of Daiber [5], who has shown furthermore that the energy losses by the walls are less than 5.5 %. In this way it was also possible to demonstrate that the excitation efficiency is nearly independant of the tube length. This result corresponds to the very slow vibrational relaxation of carbon monoxid.

Summary and Conclusions

We have demonstrated that high mass specific excitation energies can be achieved, if the mass flow within a tube (or the throat area of the nozzle) is limited to a small value. The experiments also proved that the excitation of vibrational enery is nearly independant of the flow time of gas within the discharge. For high power CO lasers it is therefore recommended to distribute the total mass flow among several parallel discharge tubes. The small mass flow of each tube can then be excited with high specific energies. Since the relaxation of the excited carbon monoxid is slow, it is possible to reunite the seperate mass flow at the entrance of a common nozzle without loosing vibrational enery. The nozzle itself may be regarded as independant of the discharge and may be made out of plastic.

Literature

[1] M.L. Bhaumik, W.B. Lacina and M.M. Mann, IEEE Journ. of. Quant. Electr. QE-8, 150 (1972)

[2] I.W. Rich, R.C. Bergmann and I.A. Lordi, AIAA Journ., Vol. 13, No. 1, 95 (1975)

[3] S. Krause and F. Maisenhälder, Appl. Physics, Vol. 22, 421 (1980)

[4] A.H. Shapiro, "The Dynamics and Thermodynamics of Compressible Fluid Flow" Vol. 1, The Ronald Press Company, New York (1953)

[5] J.W. Daiber, H.M. Thompson and T.Y. Falk, IEEE Journ. of Quant. Electr. QE-12, Vol.11, 686 (1976)

HIGHER ORDER NONLINEAR OPTICAL PROCESSES IN ORGANIC CRYSTAL MBA-NP

Q. Z. Wang, P. P. Ho, and R. R. Alfano

Institute for Ultrafast Spectroscopy and lasers,
Photonic Application Laboratory,
Departments of Physics and Electrical Engineering,
The City College of New York,
New York, New York 10031

R. Kashyap

British Telecom Research Laboratories,
Martlesham Heath,
Ipswich, IP5 7RE, UK.

ABSTRACT

Higher order nonlinear scattering and third harmonic generation via an induced SHG-three wave mixing have been observed in the organic crystal (-) 2-(α-methylbenzylamino)-5-nitropyridine (MBA-NP). The third order susceptibility $\chi^{(3)}$ of MBA-NP were determined to be on the order of 10^{-12} esu.

The future era of information, signal processing, and optical computation has lead to the search for optical materials which possess extremely large and fast nonlinear coefficients[1]. The need for efficient conversion of SHG using low power semiconductor diode lasers has increase the search for suitable nonlinear media to improve the storage density of an optical information system[1,2]. Nonlinear optical material Various kinds of π-conjugated organic materials have the potential to fit these requirements[3-8]. (-)2-(α-methylbenzylamino)-5-nitropyridine (MBA-NP) has attracted interest because of its high optical damage threshold and fairly large $\chi^{(2)}$.

MBA-NP crystal is a biaxial crystal belonging to the monoclinic crystal class with point group[5]. The procedure to grow the MBA-NP crystals was described in reference 5. The optical absorption spectrum of MBA-NP is shown in Fig. 1. This curve determines the optical attenuation and spectral region for resonant nonlinearity. The absorption depth at 350 nm is about 2μm.

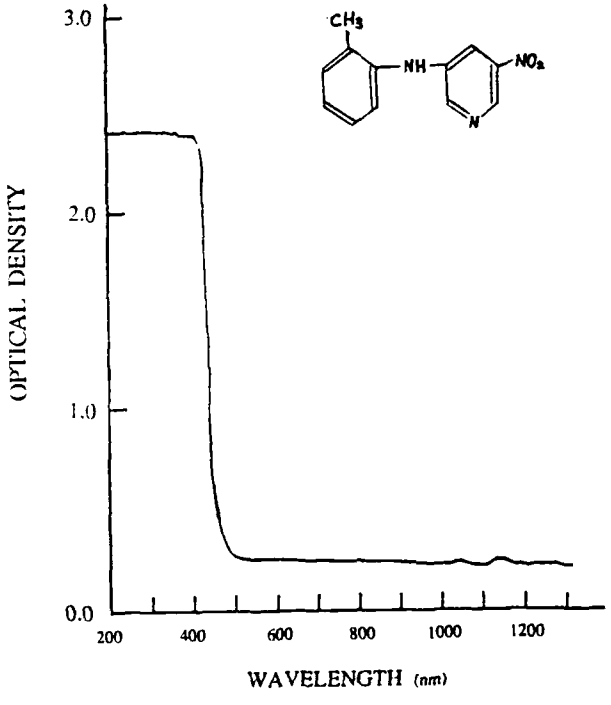


Figure 1. Absorption spectrum from MBA-NP. The thickness of sample is 50 μm.

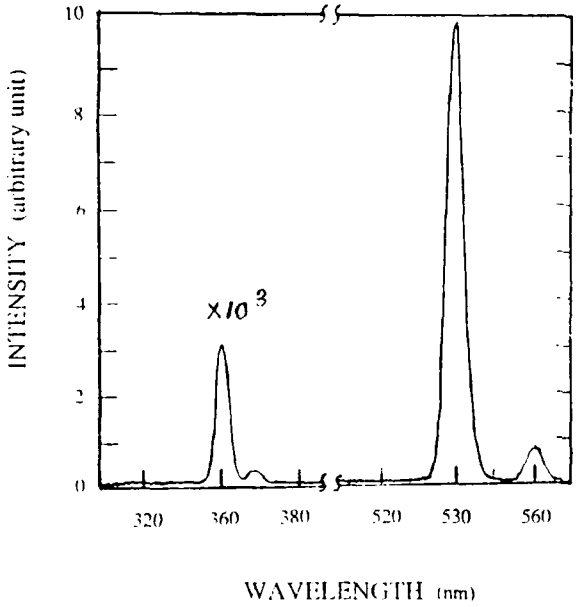


Figure 2. Nonlinear signal from MBA-NP in UV and visible spectral regimes generated by 1054 nm, 8 ps laser pulses.

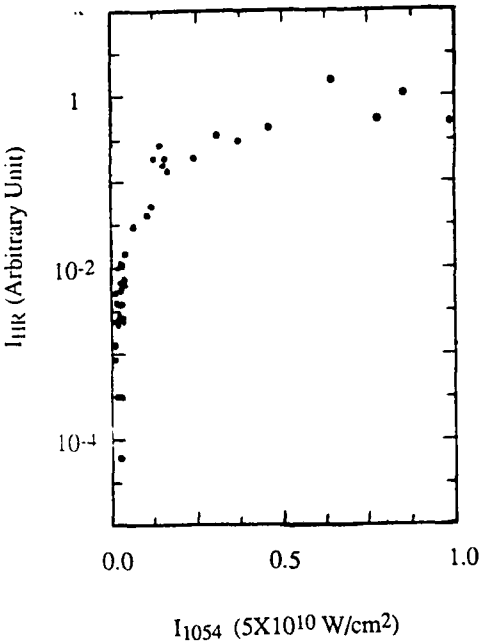


Figure 3. Intensity dependence of utput intensity at frequecy 2ω-ω_p from MBA-NP generated by 1054 nm, 8 ps laser pulses.

In the experiment, picosecond laser pulses at 1054 nm were generated by a mode locked Nd:glass laser with a spectral width of ~ 80 cm^{-1}, peak power ~10^{+9} W and the pulse duration ~ 8 ps. KDP crystal was used to generate the second-harmonic of the 1054 nm laser. The laser beam was focused with a 28.5 cm focal length lens into a 0.6 mm thickness single crystal of MBA-NP. The beam diameter at the sample was about 1 mm. The output signal in visible and UV regions were collected by a 10 cm focal length lens and directed into a 0.25-m Jarrell-Ash spectrograph with a PAR OMA III video readout system for spectral recording and analysis or a 0.5 m Jarrell-Ash spectrometer with a photomultiplier tube for intensity measurement. The output light in near-IR region was measured using either a 0.5 m Jarrell-Ash spectrometer with a Ge-photodiode or a PbS-photodiode detector, or a 0.25 m spectrometer with a CCD camera readout system. Neutral density and color filters were used to adjust the light intensity focused on the sample.

A typical nonlinear spectrum from 300 nm to 600 nm is displayed in Fig. 2. The salient feature of curve displayed indicates that there are four distinct maxima located at 527 nm (SHG), 560 nm, 351 nm (THG), and 364 nm.

The intensity at THG is about 0.1% of the light intensity at 527 nm (SHG). One key characteristics of the signal is that the intensity ratio of I_{560}/I_{527} is almost equal to I_{364}/I_{351} under a large change (4.26×10^9 ~ 1.95×10^{10} W/cm^2) of the incident 1054 nm laser pulse intensity. The intensities at 560 nm and 364 nm are about one tenth of the intensities at 527 nm and 351 nm, respectively. The signal intensity of SHG frequency 527 nm varies as $I_{2\omega} \propto I_{\omega}^2$. The signal intensity at THG is found to be almost linearly to that at SHG. The strongest second and third harmonic of MBA-NP was obtained when the polarization of the incident laser is parallel to one of the major axis. The SHG intensity varies periodically as a function of the incident polarization rotation around the incident beam. The period is 180^0. Good phase-matched second harmonic generation was not observed. When both incident polarization and the MBA-NP crystal axis were perpendicular to the entrance slit, the signals at 560 nm (2ω-ω_p) and 364 nm (3ω-ω_p) were observed. The spectral shift ν_p = 992 cm^{-1}. The signal intensities at 2ω-ω_p and 3ω-ω_p have shown a strong dependence on the incident pumping laser intensity at 1054 nm. The intensity of signal at 2ω-ω_p is plotted in Fig. 3 as a function of incident laser intensity. The addition of 527 nm laser pulses together with 1054 nm into the MBA-NP crystal resulted in an increase in the net intensity at 2ω. No significant influence on the intensities at 2ω-ω_p and 3ω-ω_p was observed.

Since the absorption depth of MBA-NP at 3ω is small, the generation of the signal at 3ω arises near the surface. The signal at 3ω can be generated from both the third harmonic generation [$\propto \chi^{(3)}$] and the three wave mixing [$\propto \chi^{(2)}$]. To find out the process generating the signal at 3ω, both transmission and reflection methods were used. The experimental results show that the intensity at 3ω is linearly proportional to the intensity at 2ω for both cases when the input laser

intensity at 1054 nm was high and kept constant. These observations indicate that the signal at 3ω mainly originates from three wave mixing between 2ω and ω. It was estimated experimentally that about 10% of the intensity the signal at 3ω was generated from THG through $\chi^{(3)}$. The absorption depths of both MBA-NP and ZnSe are comparable to the coherence length. The well known theories of THG[9-11] were used to estimate the value of the third-order susceptibility of MBA-NP. It was found that the $\chi^{(3)}$ of MBA-NP is less than one percent of that of ZnSe, about the order of 10^{-12} esu. This size of $\chi^{(3)}$ may explain why some other important nonlinear optical processes such as SPM and XPM were not observed in this sample.

The experimental results showed that the signals at frequency $3\omega-\omega_p$ arise from the three wave mixing with ω and $2\omega-\omega_p$. In this case the signal intensity varies as $I_{3\omega-\omega_p} \propto [\chi^{(2)}]^2 I_\omega I_{2\omega-\omega_p}$. Therefore, the ratio of the intensity at $2\omega-\omega_p$ over the intensity at 2ω is identical to that $3\omega-\omega_p$ over 3ω, as shown in Fig. 2.

The most interesting measurements are the observations of signal[12] generated at $2\omega-\omega_p$ which can arise from four possible processes. Firstly, it may be the stimulated Raman scattering of 2ω. Secondly, it may be the second harmonic of strong stimulated Raman scattering of the pumping laser at 1120 nm. Thirdly, it may be three wave mixing of the incident laser ω and its stimulated Raman scattering ($\omega_p = 992$ cm^{-1}) at 1177 nm. Fourth, it may be stimulated hyper-Raman scattering of the primary pumping laser. When an externally 527 nm laser pulse with an intensity comparable to the SHG generated by 1054 nm passed through the MBA-NP crystal, no signal at $2\omega-\omega_p$ was observed. Furthermore, if the incident intensity of the primary pumping laser was kept constant, the output intensity at $2\omega-\omega_p$ remained almost constant when the intensity at 2ω was changed externally. In our experiment, no large peak at 1120 nm or at 1177 nm were observed. This observation rules out the second and third possibilities. Therefore, the signal at $2\omega-\omega_p$ could be hyper-Raman scattering by the primary laser ω. More work is needed to identify these peaks.

This research is supported in part by grants from Hamamatsu Photonics K. K., Organized Research at CCNY and the Professional Staff Congress/Board of Higher Education.

References

1 R. Kashyap; J. Opt. Soc. Am. B **6** , 313 (1988).

2 R. Terhune and D. Weinberger; J. Opt. Soc. Am B **4** , 661(1987).

3 B. F. Levine; Chem. Phys. Lett. **37** , 516(1976).

4 P. P. Ho, N. L. Yang, T. Jimbo, Q. Z. Wang, and R. R. Alfano; J. Opt. Soc. Am. B **4** , 1025(1987).

5 R. T. Bailey, F. R. Cruickshank, S. M. G. Guthrie, B. J. McArdle, H. Morrison, D. Pugh, E. A. Shepherd, J. N. Sherwood, C. S. Yoon, R. Kashyap, B. K. Nayar, and K. I. White; Opt. Commun. **65** , 229(1988).

6 R. H. Stolen and G. I. Stegeman; Optics News, 8 (June, 1989).

7 H. Kanbara, H. Kobayashi, and K. Kubodera; IEEE Photon. Tech. Lett. **1** , 149(1989).

8 Lina Yang, Q. Z. Wang, P. P. Ho, R. Dorsinville, R. R. Alfano, N. L. Yang; Appl. Phys. Lett. **53** , 1245(1988).

9 M. Weber ed., *Handbook of Laser Science and Technology Vol. III* (CRC Press, Boca Raton, 1986).

10 J. Reintjes; *Nonlinear Optical Parametric Processes In Liquids and Gases* , (Academic Press, Inc., 1984).

11 Y. R. Shen; *The Principle of Nonlinear Optics* (John Willey & Sons, Inc., 1984).

12 W. Yu and R. R. Alfano; Phys. Rev. A **11** , 188(1975).

DEGENERATE CROSS-PHASE-MODULATION AND PULSE COMPRESSION OF ULTRASHORT LASER PULSES

Q. Z. Wang, P. P. Ho, and R. R. Alfano

Institute for Ultrafast Spectroscopy and lasers,
Photonic Application Laboratory,
Departments of Physics and Electrical Engineering,
The City College of New York,
New York, New York 10031

ABSTRACT

Temporal profile of a linearly polarized ultrashort laser pulse modulated by a co-propagating perpendicularly polarized strong laser pulse with the same frequency in condensed matter has been modeled. Degenerate-cross-phase-modulation can be applied for femtosecond optical pulse compression without the use of gratings or prisms and signal processing due to the small walk-off between the pumping and signal pulses.

When a weak pulse propagates through a medium whose index of refraction was changed by an intense laser pulse, the phase of the weak pulse can be modulated by the time variation of the index of refraction originating from the primary intense laser pulse. This process is called cross-phase-modulation (XPM).[1-7] This nonlinear process has important potential applications based on the picosecond and femtosecond technology. Several schemes of nonlinear interactions between optical pulses can lead to XPM. For example, XPM is intrinsic to the generation of stimulated Raman scattering (SRS) pulses[1-3,8,9], second harmonic generation (SHG) pulses[10,11], and stimulated four photon mixing (SFPM) pulses[12]. More importantly, the XPM generated by pump pulses can be used to control the temporal, spectral, and spatial properties of ultrashort probe pulses[13-17].

In this paper we report on a new class of XPM: degenerate-XPM (DXPM) in which two or more laser pulses with the same frequency but different polarizations interact. Our analysis on the DXPM describes a new way for optical pulse compression in fibers without the use of gratings or prisms.

The optical electromagnetic fields of copropagating pulses must satisfy Maxwell's equation:

$$\nabla \times \nabla \times E = -\mu_0 \frac{\partial^2 D}{\partial t^2} \quad , \tag{1}$$

where D can be written as $D = \varepsilon E + P^{NL}$ and ε is the medium permitivity at low laser intensity, and P^{NL} the nonlinear polarization vector. The nonlinear polarization can be written as:

$$P_i^{NL}(\omega_4) = \sum_{jkl} \chi_{ijkl}^{(3)}(-\omega_4, \omega_1, \omega_2, \omega_3) E_j(\omega_1) E_k(\omega_2) E_l(\omega_3) \quad , \tag{2}$$

where $\omega_4 = \omega_1 + \omega_2 + \omega_3$ by the conservation of energy, $\chi^{(3)}$ has 81 elements in general. In isotropic media there are 21 non-zero elements, of which four can be different and only three are independent[18]. In quasi-monochromatic approximation, the total electric field can be written in the form of[6]:

$$E = \frac{1}{2}\left[\hat{x}A_x(r,z,t)\exp[i(\omega_0 t - k_x z)] + \hat{y}A_y(r,z,t)\exp[i(\omega_0 t - k_y z)]\right] + c.\,c. \quad . \tag{3}$$

Substituting Eq.(3) into Eq.(2) and keeping only the terms synchronized with ω_0, one obtains

$$P_x^{NL} = \frac{1}{8}\chi^{(3)}_{xxxx}\left[3\,|A_x|^2 A_x + 2\,|A_y|^2 A_x + A_y^2 A_x^* \exp(-i\Delta k z)\right]\exp[i(\omega_0 t - k_x z)] \quad , \tag{4a}$$

$$P_y^{NL} = \frac{1}{8}\chi^{(3)}_{xxxx}\left[3\,|A_y|^2A_y + 2\,|A_x|^2A_y + A_x^2A_y^* exp(i2\Delta kz)\right]\exp[i(\omega_0 t - k_y z)] \quad . \tag{4b}$$

where $\Delta k = k_x - k_y$ is the propagation constant mismatch between the two orthogonally polarized waves. The last terms in Eqs. (4a) and (4b) arise from the degenerate four-wave-mixing. Their contributions to the XPM only appear when both pulses are at the same frequency because of degenerate nature of the polarization components. Their influence to the XPM process depends on the extent of the phase matching of the two orthogonally polarized pulses characterized by the beat length $L_B = 2\pi/(k_x - k_y)$. If the length of medium $L \gg L_B$, the contribution of last terms in Eqs. (4a) and (4b) can be negligible. In this case, the DXPM between the two polarization components is similar to that between two waves at different frequencies but same polarization.

The coupling term for the DXPM is weaker than that of XPM where the coefficient for the cross term is 2 for DXPM instead of 6 for XPM[6]. All the solutions for XPM between two waves at different frequencies are valid to this DXPM case by replacing the factor 6 by 2. Their contributions must be considered when L is small in comparison with L_B. To study the properties of DXPM in the later case, phase matching $\Delta k = 0$ is assumed in the following discussions.

Combining Eqs. (1)-(4) and using the slowly varying envelope approximation, one obtains the coupled nonlinear wave equation which governs of the two polarization components[6]:

$$\frac{\partial A_x}{\partial z} + \frac{1}{v_g}\frac{\partial A_x}{\partial t} + i\frac{1}{2}k^{(2)}\frac{\partial^2 A_x}{\partial t^2} = i\frac{\omega_0 n_2}{c}\left[\left(|A_x|^2 + \frac{2}{3}|A_y^2|\right)A_x + \frac{1}{3}A_y^2A_x^*\right] \quad , \tag{5a}$$

$$\frac{\partial A_y}{\partial z} + \frac{1}{v_g}\frac{\partial A_y}{\partial t} + i\frac{1}{2}k^{(2)}\frac{\partial^2 A_y}{\partial t^2} = i\frac{\omega_0 n_2}{c}\left[\left(|A_y|^2 + \frac{2}{3}|A_x|^2\right)A_y + \frac{1}{3}A_x^2A_y^*\right] \quad , \tag{5b}$$

where $v_{gx} = v_{gy} = v_g$, $k^{(2)}$ is the group velocity dispersion, and $n_2 = 3\chi^{(3)}_{xxxx}/8n$ is the nonlinear refractive index.

Numerical methods are used to solve Eqs. (5a) and (5b) in general cases. However, analytical solutions can be obtained when the group-velocity dispersion and temporal broadening are neglected.

Denoting the amplitude and phase of the pulse envelope by a and α, respectively, A_j can be written as

$$A_j(\tau,z) = a_j\exp[i\alpha_j(\tau,z)] \quad , \tag{6}$$

where j=x,y. Eqs. (5a) and (5b) reduce to

$$\frac{\partial a_x}{\partial z} = -\frac{\omega_0}{3c}n_2a_y^2a_x\sin 2(\alpha_y - \alpha_x) \quad , \tag{7a}$$

$$\frac{\partial \alpha_x}{\partial z} = \frac{\omega_0 n_2}{c}\left[a_x^2 + \frac{2}{3}a_y^2 + \frac{1}{3}a_y^3\cos 2(\alpha_y - \alpha_x)\right] \quad , \tag{7b}$$

$$\frac{\partial a_y}{\partial z} = -\frac{\omega_0}{c}n_2a_x^2a_y\sin 2(\alpha_x - \alpha_y) \quad , \tag{7c}$$

$$\frac{\partial \alpha_y}{\partial z} = \frac{\omega_0 n_2}{c}\left[a_y^2 + \frac{2}{3}a_x^2 + \frac{1}{3}a_x\cos 2(\alpha_x - \alpha_y)\right] \quad , \tag{7d}$$

where $\tau = (t - z/v_g)$. Assuming that $\alpha_x - \alpha_y \simeq 0$, one obtains the analytical solutions for Eqs. (7a)-(7d)

$$A_x(\tau,z) = a_x(\tau,z=0)\exp(i\alpha_x) \quad , \tag{8a}$$

$$A_y(\tau,z) = a_y(\tau,z=0)\exp(i\alpha_y) \quad , \tag{8b}$$

with

$$\alpha_x = \frac{\omega_0 n_2}{c}(a_x^2 + a_y^2)\,z \quad , \tag{8c}$$

$$\alpha_y = \alpha_x \quad . \tag{8d}$$

From these solutions, it can be seen that the initial assumption is satisfied.

The instantaneous DXPM induced frequency chirp can be obtained by taking the differentiation of the phases α_x and α_y. The envelope of Gaussian pulses at z=0 are given by

$$A_x(\tau,z=0) = \sqrt{\frac{P_x}{A_{eff}}}\, e^{-\tau^2/2T_0^2} \quad , \tag{9a}$$

$$A_y(\tau,z=0) = \sqrt{\frac{P_y}{A_{eff}}}\, e^{-(\tau-\tau_d)^2/2T_0^2} \quad , \tag{9b}$$

where P_x and P_y are the pulse peak power for x and y polarized waves, respectively, A_{eff} is the effective cross section area, τ_d is the time delay between two pulses at z=0, and T_0 is the 1/e pulse duration.

The instantaneous DXPM induced frequency chirp are:

$$\Delta\omega_x = \frac{2\omega_0 n_2}{cA_{eff}}\left[P_x\frac{\tau}{T_0}e^{-\tau^2/T_0^2} + P_y\frac{(\tau-\tau_d)}{T_0}e^{-(\tau-\tau_d)^2/T_0^2}\right]z \quad , \tag{10a}$$

$$\Delta\omega_y = \frac{2\omega_0 n_2}{cA_{eff}}\left[P_y\frac{(\tau-\tau_d)}{T_0}e^{-(\tau-\tau_d)^2/T_0^2} + P_x\frac{\tau}{T_0}e^{-\tau^2/T_0^2}\right]z \quad , \tag{10b}$$

where $\Delta\omega_x = \omega_x - \omega_0$ and $\Delta\omega_y = +\omega_y - \omega_0$. The first and second terms on the right hand side of Eqs. (10a) and (10b) are contributions arising from SPM and XPM, respectively. It is interesting to notice that the frequency chirp for DXPM is different from XPM with two pulses at different frequencies and same polarization. The chirp in DXPM is the same for both pump and probe pulses.

More generally, spectral profiles affected by DXPM can be obtained by computing the Fourier transformation of the temporal pulse distribution as:

$$S_j(\omega-\omega_0\ ,z) = \frac{1}{2\pi}\int a_j(\tau,z)\exp[i(\alpha_j(\tau,z)]\exp[i(\omega-\omega_0)\tau]d\tau \quad , \tag{11}$$

where j=x or y, and $|S_j(\omega-\omega_0,z)|^2$ is the spectral intensity distribution of the pulse.

When an ultrashort light pulse propagates through an optical fiber, its shape changes considerably as a result of the combined effect of group velocity dispersion $k^{(2)}$ and self-phase-modulation. In the anomalous dispersion regime of fiber, the pulse can be compressed and split, which are characteristic of higher order soliton, at certain critical power level. In the normal dispersion regime, the pulse can develop rapid oscillations in the wings together with the spectral sidelobes as a result of a phenomenon known as optical wave breaking. It has been shown that rapid oscillations near one edge of a weak probe pulse that copropagates with a strong pump pulse can result from the effect of combination of GVD and XPM. However, the interaction length is limited by the walk-off effect.

From solution of pulse shape we show that DXPM can lead to the pulse compression of a weak probe pulse linearly polarized propagating with a strong perpendicularly polarized pump pulse. Since the walk-off effect is small, there is less restriction on the interaction length of the pump and probe pulses. Significant pulse compression of the probe pulse can be achieved in both the normal and anomalous dispersion regimes for DXPM.

To isolate the effect of DXPM from those of SPM in our numerical analysis, we assume $P_y \ll P_x$ in order to minimize the influence of the intense pulse polarized along x-axis by the probe pulse polarized along y-axis and the SPM effect of the probe pulse. By introducing the dimensionless variables[6],

$$T = \tau/T_0 \quad , \quad \xi = z/L_D \quad , \quad U_j = \frac{A_j}{\sqrt{P_j/A_{eff}}} \quad , \tag{12}$$

where

$$L_D = T_0^2 / |k^{(2)}| \tag{13}$$

is the dispersion length, over which the pulse duration increase about 40% due to the dispersion effect. Eqs. (5a) and (5b) reduce to

$$i\frac{\partial U_x}{\partial \xi} = \pm\frac{1}{2}\frac{\partial^2 U_x}{\partial T^2} - N^2 |U_x|^2 U_x \quad , \tag{14a}$$

$$i\frac{\partial U_y}{\partial} = \pm\frac{1}{2}\frac{\partial^2 U_y}{\partial T^2} - N^2 \left[\frac{2}{3}|U_x|^2 U_y + \frac{1}{3}U_x^2 U_y^*\right] \quad , \tag{14b}$$

where

$$N^2 = L_D / L_{NL} \quad , \tag{15}$$

and

$$L_{NL} = \left[\frac{\omega_0 n_2 P_a}{c A_{eff}}\right]^{-1} \tag{16}$$

is the nonlinear length. The choice of the sign in the dispersion term depends on the sign of $k^{(2)}$, a plus sign is for normal GVD ($k^{(2)} > 0$) and a minus sign is for anomalous GVD ($k^{(2)} < 0$). For example, $\lambda < 1.3$ μm is the normal dispersion regime for silica fibers. At $\lambda = 0.53$ μm, the group dispersion $k^{(2)}$ is about 0.06 ps^2/m. From Eq. (13), $L_D \sim 10$ m for $T_0 = 1$ ps. Given single mode fiber and $P_0 \sim 1000$ W, from Eq. (16) $L_{NL} \sim 0.1$ m. Substituting these values into Eq. (15), one can find $N \sim 10$. $\lambda > 1.3$ μm is the anomalous dispersion regime for glass fibers. At $\lambda = 1.55$ μm, $k^{(2)} \sim -0.02$ ps^2/m. In this case, $L_D \sim 50$ m for T~ 1 ps, and $L_{NL} \sim 50$ m for $P_0 \sim 1$ W, $N \sim 1$. [N = 1 corresponds to fundamental soliton, and N > 1 corresponds to higher order solitons.]

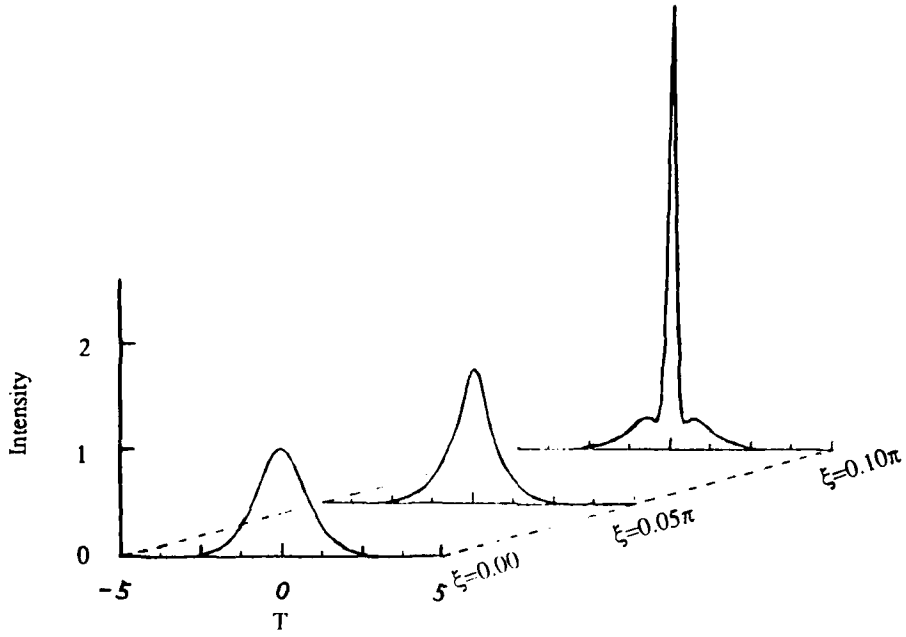


Figure 1. Changes in envelope shape of pulse in time under DXPM inanomalous dispersion regime for N=3 and T_d=0 along the propagation length. Evolution of the pulse shape for pump pulse is the same as that of probe pulse.

Figure 1 shows a numerical integration of Eqs. (13a) and (13b) for initial pulse shape $U_j(T,0) = sech(T)$ for both pump and probe pulses in anomalous GVD regime. In the calculation, U_y is chosen to be one percent of pump U_x. The

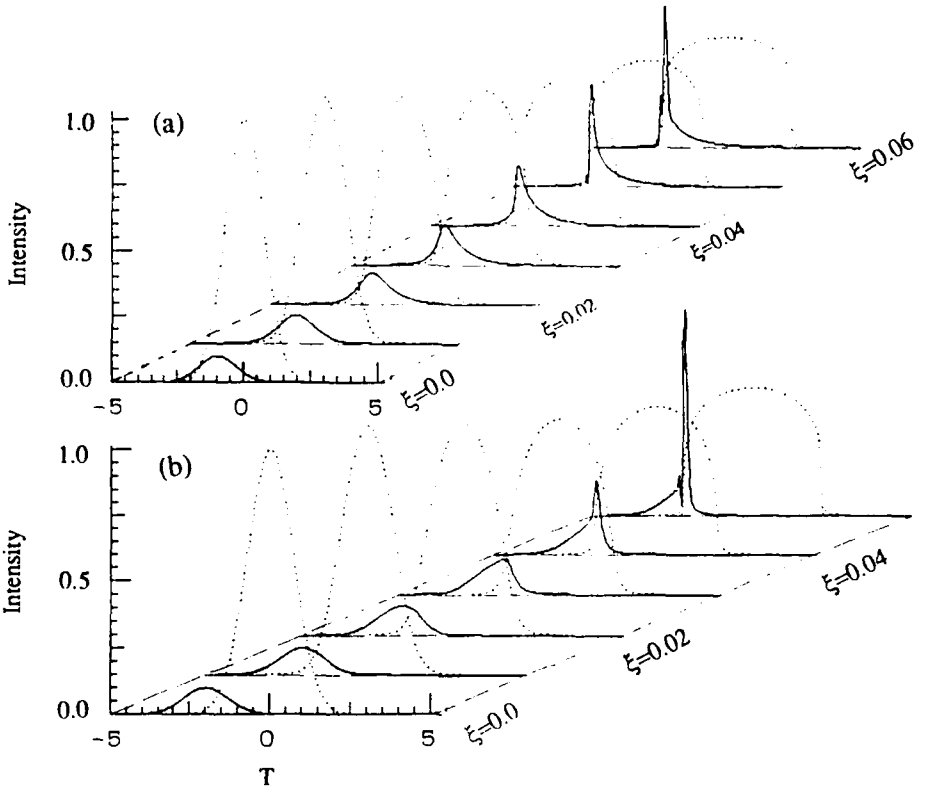


Figure 2. Changes in envelope shape of pulse in time under DXPM in normal dispersion regime along the propagation length. (a) for N=30 and T_d=1, (b) for N=30, and T_d=2. Solid lines are evolution of probe pulse shape enlarged by a factor of 10. Dot lines are the changes of pump pulse shape.

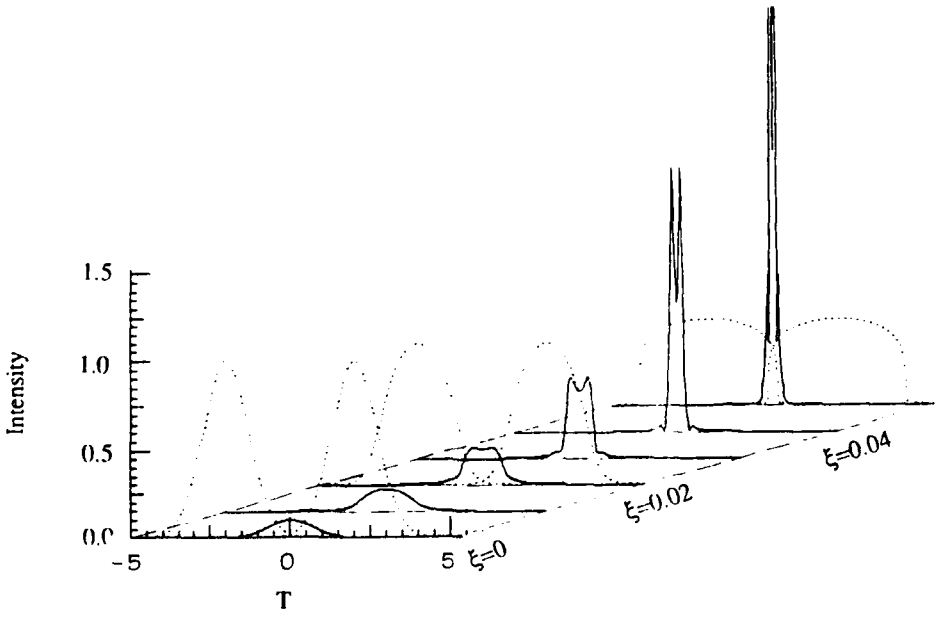


Figure 3. Changes in envelope shape of pulse in time under double-pump-pulse DXPM for N=30 and T_d=2. Solid lines are the evolution of probe pulse shape enlarged by 10 times. Dot lines are evolutions of pump pulse shapes.

compression effect is same as the soliton-effect compression[19] except that the frequency chirp of the weak probe pulse is induced by the strong pump pulse. It is obvious that to get the probe pulse compressed, the initial delay between the two pulses must be zero. The pulse compression using DXPM in anomalous regime was observed in organic liquid optical fiber[20].

Figure 2 displays the numerical solution of Eqs. (13a) and (13b) for probe (solid lines) and pump (dot lines) in normal dispersion regime with different delays between the pump and probe pulses. The initial pulse shapes are Gaussian for both pump and probe. The relation between U_x and U_y is same as before. The physical mechanism behind the pulse compression is the pump-induced frequency chirp. For our cases, the induced chirp in nearly linear and negative over the leading part of the probe pulse. In the normal GVD regime, compression occurs in the leading part of the pulse, as seen in Fig. 2. The compression effect depends on the initial delay between the two pulses. To improve the compression pulse distortion and the compression effect, one may use two pump pulses to compress a weak probe pulse. The results of numerical simulation of double-pump DXPM is displayed in Fig. 3. The compressed pulse is symmetric and the pulse duration can be reduced by a factor of 2.

DXPM can be applied in optical fibers and crystals. It will be useful for compressing and control weak femtosecond pulses launched together with the intense pump pulses at different delay times.

This work is supported in part by Hamamatsu Photonics K. K., PSC/BHE, and Organized Research at CCNY.

References

1 J. Gersten, R. R. Alfano, and M. Beli, Phys. Rev. A **21**, 1222(1980).

2 R. R. Alfano ed. *The Supercontinuum Laser Source* (Springer-Verlag, New York, 1989).

3 A. Chraplyvy, D. Marcuse, and P. Henry, J. Lightwave Technol. **LT-2**, 6(1984); Electron. Lett. **20**, 996(1984).

4 A. Johnson, R. Stolen, and W. Simpson, in *Ultrafast Phenomena V* G. Fleming and A. Siegman, Eds. (Springer-Verlag, New York, 1986), p.160; R. Stolen, and A. Johnson, IEEE J. Q. E. **QE-22**, 2154(1986).

5 G. Agrawal, Phys. Rev. Lett. **59**, 880(1987).

6 G. Agrawal, *Nonlinear Fiber Optics* (Academic Press, 1989).

7 M. Islam, L. Mollenauer, R. Stolen, J. Simson, and H. Shang, Opt. Lett. **12**, 625(1987).

8 D. Schadt, and Jaskorzynska, J. Opt. Soc. Am. B **5**, 2374(1988).

9 J. Manassah, Appl. Opt. **26**, 3747(1987).

10 R. Alfano, Q. Z. Wang, T. Jimbo, P. P. Ho, Phys. Rev A **35**, 459(1987).

11 P. P. Ho, Q. Z. Wang, D. Ji, R. Alfano, Appl. Phys. Lett. **54**, 111(1989).

12 P. Baldeck, R. R. Alfano, J. Lightwave Technol. **LT-5**, 1712(1987).

13 R. Alfano, P. Baldeck, P. P. Ho, and G. Agrawal. J. Opt. Soc. Am. B **6**, 824(1988).

14 G. Agrawal, P. Baldeck, R. Alfano, Opt. Lett. **14**, 137(1989).

15 J. Manassah, Opt. Lett. **13**, 752(1988).

16 P. Baldeck, F. Raccah, and R. Alfano, Opt. Lett. **12**, 588(1987).

17 B. Jaskorzynska, and D. Schadt, IEEE J. Q. E. **QE-24**, 2117(1988).

18 S. Singh, in *Handbook of Laser Science and Technology III* M. Webwr, Ed., (CRC Press, Boca Raton, 1986), p.3.

19 L. Mollenauer, R. Stolen, and P. Gordon, Phys. Rev. Lett. **45**, 1097(1980).

20 M. Yamashita, K. Torizuka, T. Shiota, and T. Sato, in *Ultrafast Phenomena VI* , T. Yajima, K. Yoshihara, C. Harris, S. Shionoya Eds. (Springer-Verlag, Berlin, Heidelberg, 1988), p.50.

OPTICAL IMAGING OF QUASI POINT SOURCE INSIDE SEMI-OPAQUE MEDIA USING ULTRAFAST LASER PULSE TECHNOLOGY

L.M. Wang, C. Liu, G. Zhang, P.P. Ho, R.R. Alfano
Departments of Electrical Engineering and Physics
Institute for Ultrafast Spectroscopy and Lasers
The City College of New York, New York, NY 10031

ABSTRACT

Time-resolved imaging of a "quasi"-point source in a semi-opaque medium was measured using ultrafast optical Kerr gate. Spatial resolution of Kerr image was found to be better than that obtained from steady state imaging.

INTRODUCTION

Scientific and engineering communities are interested in detecting hidden objects in semi-opaque random media with a spatial resolution of less than 1-mm[1-5]. Ultrafast laser technology can be used to range and image objects in random media[6,7]. A sequence of time resolved 2-dim images can be reformed into a 3-dim image. Using a Kerr gate with a shutter time determined by ultrafast (10^{-14} to 10^{-12} seconds) pulses[8,9], 3-dim structure can be time segmented into a sequence of 2-dim (X,Y) image pictures. This is schematically shown in fig.1. Light propagating in a random medium breaks into two major components[10]:scattered (diffused) part and quasi-unscattered (ballistic) part. The ballistic component travels along the shortest optical path (time) to reach the Kerr gate. To improve the image of a hidden object in semi-opaque media, it is important to filter out the noise caused by the scattered signal generated from surrounding environment from the coherent image. When pump pulse is synchronized in time with a particular plane of the object, only this particular segment can be imaged on the detector plane. The scattered light from the random medium can be reduced by the Kerr gate and the quality of the images can be improved. The coherent image of the original object can be obtained with the help of Kerr gate which is opened when the intense gating laser pulse is synchronized with the nearly ballistic signal image segment pulse. In conventional photography, all the light (ballistic and diffusive) is mixed up to form a distorted image. In an environment with higher opacity, the resulting picture would be severely distorted by the scattering noise.

In this paper, we present time images of a single and a double quasi-points source passing through in polystynene sphere water solution with different optical densities.

EXPERIMENTAL METHODS

A schematic of the experimental arrangement is shown in fig.2. A 10ps 1060nm pulse was used to open a CS_2 Kerr gate. An 8ps 530nm pulse was used to illuminate the sample. In the first part of our experiment, the 530nm pulse was focused on a ~100μ thickness polydiacetylene (PDA) film. This film was attached to the wall of a sample cell with the thickness of ~10mm and 40mm. The 530nm beam was focused to a quasi-point source of ~250μ. In the second part of the experiment, the 530nm pulse was split into two beams and focused on the PDA film. The spot size for both points was ~250μ with point separation ~300μ. In all case, the absorption loss in the random medium was negligible. An optical image intensifier and a 2-dim CCD camera were used to record the image. This CCD camera signals were recorded and digitized by a 8-bit frame grabber (Data Translation) and then transferred to a IBM-386 compatible mini-computer for signal analysis. Digital and analog information of image pictures can be obtained using a printer and/or a video printer.

EXPERIMENTAL RESULTS

A series of segmental images of single point source at three different gated delay times T_D are shown in fig.3. At the delay time T_D=0, the picture in fig.3a shows the minimum image spot size and the sharpest edge resolution. The time delayed segmented 2-dim picture at T_D=8ps is shown in fig.3b. The FWHM of image is about two times larger than that of fig.3a and extra peaks from scattered noise can be seen around the center image. These peaks reduced the sharpness of the true spot image. Fig.3c is a picture taken at T_D = 19ps with the ODC=0.36cm^{-1}. ODC is defined to be the OD/(optical path). The loss is mainly attributed to the scattering process from polydiacetylene spheres. The corresponding 2-dim image intensity distribution shows a simple flat disk and the FWHM is broader than the FWHM of figs.3a and 3b.

Time-resolved and steady state images of a double quasi-points fluorescence source in turbid water solutions with polystyrene particles of OD~0.3 are displayed in fig.4. The photographs of the steady state image displayed in fig.4a is blurred and broadened, while two round spots can be clearly resolved from the time-resolved image at T_D=0 in fig.4b.

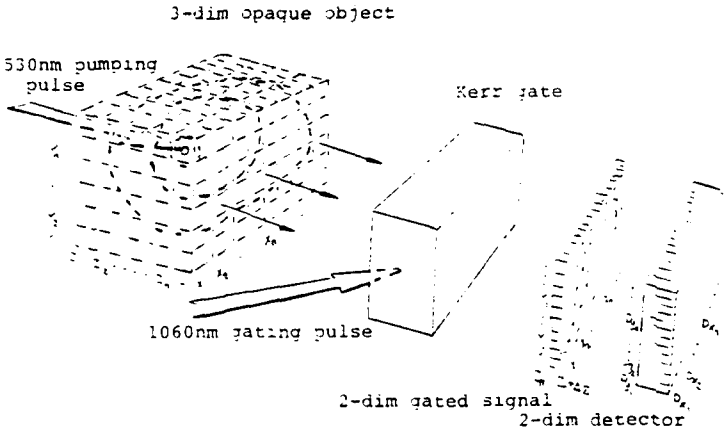


Fig.1 Principle of 3-dim Kerr imaging system.

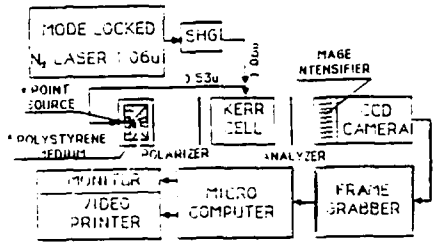


Fig.2 Experimental set up of 2-dim picosecond optical imaging system.

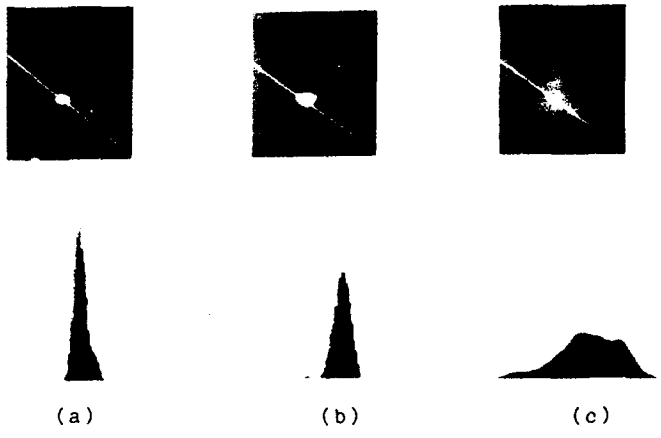


Fig.3 Time-resolved Kerr images of a quasi-point source in polystyrene sphere water solution (OD=0.36) and optical path 10mm at the different gate time T_D= (a) 0, (b) 8ps, (c) 19ps. Actual image sizes are ~250um, ~500um, ~800um respectively. Non-symmetrical intensity profiles may be caused from imperfect aligment of the optical imaging system.

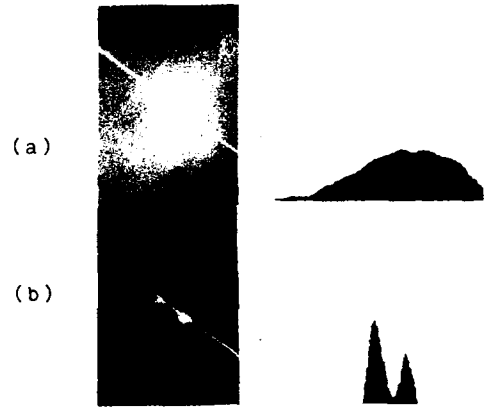


Fig.4 Images of a double-quasi-point source in a polystyrene sphere water solution (OD=0.22) and optical path 10mm.
(a) steady state image.
(b) time-resolved Kerr image at T_D=0.

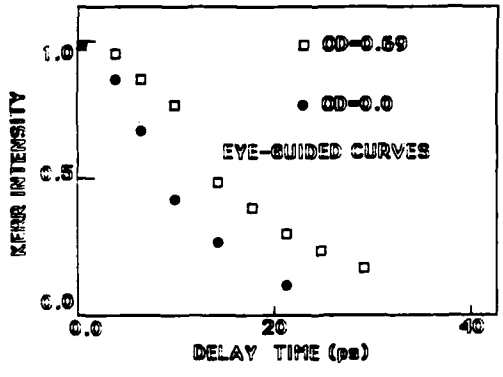


Fig.5 Distributions of a point source pulse in clear water (OD=0) and diffusing semi-opaque water solution (OD=0.69). Optical path 40mm.

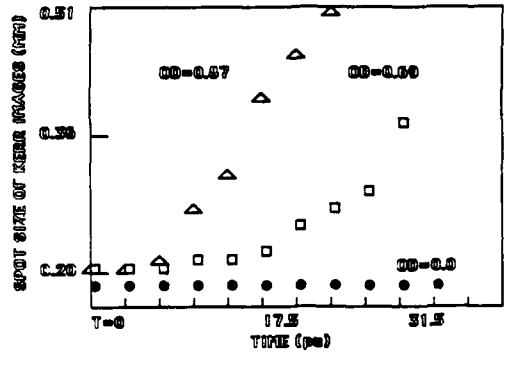


Fig.6 Imaging spot size of a point source as a function of 40mm long semi-opaque medium (OD=0.69, 0.87). Spot sizes are larger at longer delayed time.

ANALYSIS

The peak intensity distribution of a quasi-point source as a function of delay time for two opacities using Kerr gate are shown in fig.5. The point $T_D = 0$ corresponds to the delay time when the 1060nm gating pulse overlaps exactly with the image signal pulse in the Kerr cell. When the OD of the random medium is low, the point $T_D = 0$ corresponds to the maximum intensity point. When the OD is high, the maximum intensity point appears[11] at later time ($T_D > 0$) which is similar to that described in Ref.11. In addition, the □ data in fig.5 shows a longer decay time due to the scattering and diffusion in opaque water. The o data indicates the shortest traveling time is approximately the same to the fluorescence decay signal of PDA (fluorescence decay time ~ 10ps)[12].

In fig.6, the image spot size of quasi-point source in semi-opaque environment increases when T_D and scattering OD increase (fig.6). The fluorescence spherical optical waves are emitted from photoexcited PDA. Portions of the emitted light travel over the shortest route through the random medium as a quasi ballistic part. This component carries most of coherent information of the original object (the quasi-point PDA fluorescence source). The Kerr gate selects most of the ballistic part ($T_D = 0$) of the fluorescence signal. This segment portion from the Kerr shutter is recorded by the camera. The scattered, diffused, and multiple-reflected noise light arrives at the Kerr cell at later time and will be rejected. At $T_D = 0$, the true image of the object is recorded by the CCD camera.

SUMMARY

The spatial and temporal images of quasi-point sources passing through a semi-opaque random media have been measured using 2-D picosecond optical Kerr imaging technique. When the Kerr gate is opened for ballistic part at $T_D=0$, a clearer image of a quasi-point source hidden in a semi-opaque medium is obtained. When the opacity of the random medium increase, the peak intensity of the signal drops while the decay time and spot size increase. As $T_D > 0$, the spot size becomes larger.

Acknowledgement

This research is supported in part by NIH/BRSG, CUNY organized research, and Hamamatsu Photonics K.K.

References

1. J. C. Fujimoto, S. De Silversti, E. P. Ippen, R. Margolis, and A. Oseroff, Opt. Lett., 11 pp150-2 (1986)
2. K. G. Spears, T. J. Robinson, and R. M. Roth, "Particle distributions and laser particle interactions", IEEE, Trans. Plasma Sc. PS-14, pp179-87 (1986)
3. W. Jiang, D. Sun, and F. Li, "Particle behaviour of femtosecond optical pulses", Opt Comm., 66 pp152-4 (1988)
4. P. P. Ho, P. Baldeck, K. S. Wong, K. M. Yoo, Don Lee, R. R. Alfano, Time dynemics of photon migration in semi-opaque random media", Appl. Opt. 28 pp2308 (1989)
5. K. M. Yoo, Y. Takiguchi, and R. Alfano, Applied Optics "Dynamic Effect of Weak Localization on the Light Scattering from Random Media Using Ultrafast Laser Technology" Appl. Opt. 28 pp2343 (1989)
6. S. L. Jacques "Time-resolved propagation of ultrashort laser pulses within turbid tissues", Appl.Opt., 28 pp2223 (1989)
7. G. Yoon, A. Welch, M. Motamedi, and M. Van Gemert, "Development and Application of three-dimensional light distribution model for laser irradiated tissue", IEEE, J-QE-23, pp1721-33 (1987)
8. M. A. Duguay and A. T. Mattick, "Ultrahigh Speed Photography Picosecond Light Pulses and Echoes", Appl. Opt., 10 pp2162-70 (1971)
9. P. P. Ho and R.R. Alfano "Optical Kerr effect in liquids", Phys. Rev. A20 pp2170-82 (1978)
10. S. L. Jacques, "Time-resolved reflectance spectroscopy in turbid tissues", IEEE, J. of Bio-medical Engineering Dec. (1989)
11. Yasuo Kuga and Akira Ishimaru, "Experiments on picosecond pulse propagation in a diffuse medium", J. Opt. Soc. Am., 73 pp1812-15 (1983)
12. P. P. Ho, T. Jimbo, N. Yang, R. Dosinville, R. R. Alfano, "Ultrafast Resonant Optical Kerr Effect in 4-BCMU-Polydiacetylene", JOSA-B, 4 pp1025-9 (1987)

INVESTIGATION OF THIRD ORDER EFFECTS IN ACETONE

Bergeron, M.E. Harmon, J.F.; Chernek, P.A. Rogers, M.E.
Physics Department Faculty
USAF Academy Colorado Springs, CO 80840

Abstract

We show experimentally, with a frequency doubled Nd:YAG laser (532 nm, 20 ns pulse width), how the combined stimulated Brillouin scattered and stimulated Raman scattered reflectivity in acetone is a function of pump energy. Decreasing reflectivity from 25% achieved at 100 mJ pump energy was observed. Results from backseeding the cell with a portion of the main pump will be presented.

Introduction

We show experimentally how the combined stimulated Brillioun scattered and stimulated Raman scattered reflectivity in acetone is a function of pump energy. Backseeding the cell with differing fractions of the pump was accomplished.

The short coherence length of the laser precludes operation in the classical steady state regime. However, the effective gain coefficients can be written as

$$g_R^{eff} = g_{ss}^{R} E_p E_p^* E_R (1 - \exp(-\Gamma_R \Delta t_c)) \quad (1)$$

$$g_R^{eff} = g_{ss}^{B} E_p E_p^* E_B (1 - \exp(-\Gamma_B \Delta t_c)) \quad (2)$$

where g_{ss} denotes the classical steady state gain, Γ the dampening coefficients (sec $^{-1}$) and Δt_c the coherence time of the pulse. Thus the transient gain is a fraction of the steady state gain where the fraction depends on the pump energy, the amount of random signal present, and the length of time over which a correlated input signal is present. Since $g_R^{eff} > g_B^{eff}$, we expect the Raman scattering to dominate.

Experimental Configuration

The Spectra-Physics DCR3 Nd:YAG laser used had a pulse duration of 20 ns and was frequency doubled to 532 nm. The laser did not have a working etalon so the coherence length was less than 1 cm. The beam profile was Gaussian.

Combined reflectivity data was obtained using the set-up shown in Figure 1. Detector D2 was used to measure the combined SBS (stimulated Brillioun scattering) and SRS (stimulated Raman scattering) return.

The backseeded reflect data was obtained by the set-up shown in Figure 2. Mirrors M3 and M4 comprised an optical trombone to insure overlapping focal volumes within the coherence length of the laser.

Figure 3 shows the set-up used to obtain data comparing energy reflected back from the cell to energy passing straight through as a function of pump energy.

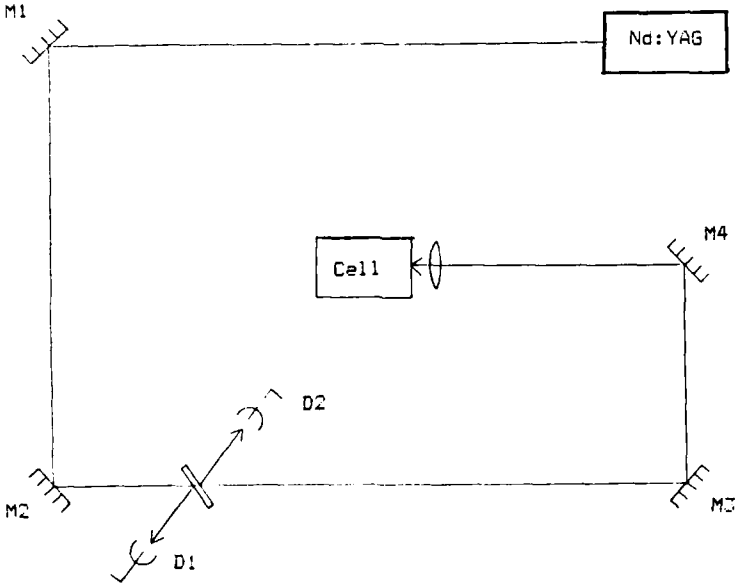


Figure 1: Combined reflectivity in acetone

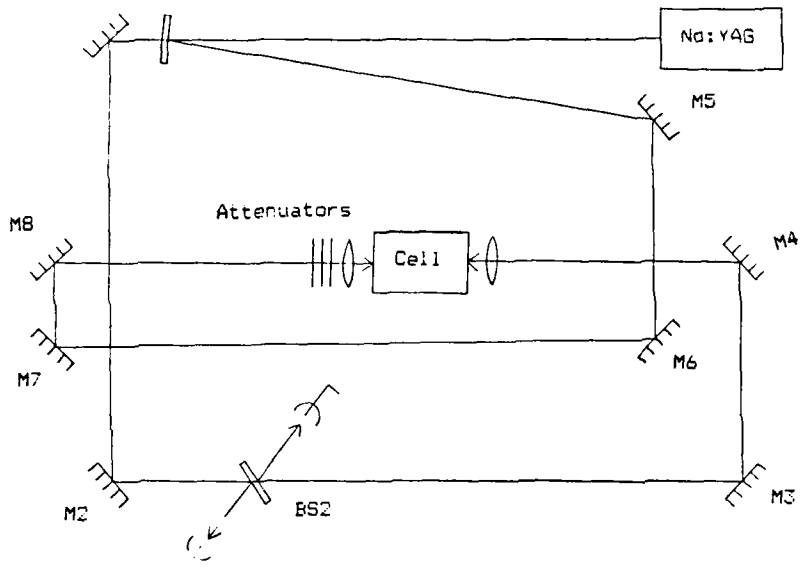


Figure 2: Combined reflectivity with backseed in acetone

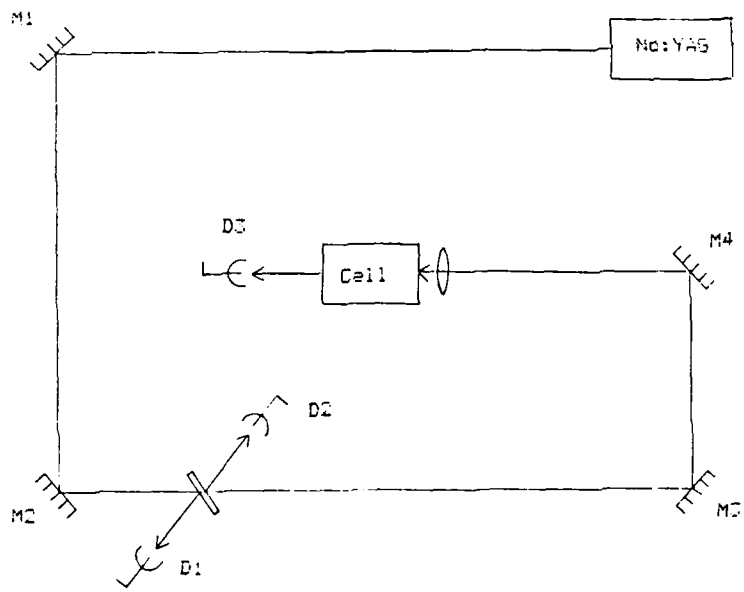


Figure 3: Combined Reflectivity and Forward Scattering

Data

The reflectivity curve shown below in Figure 4 shows that the maximum reflectivity occures at a pump energy of approxmately 100 mJ.

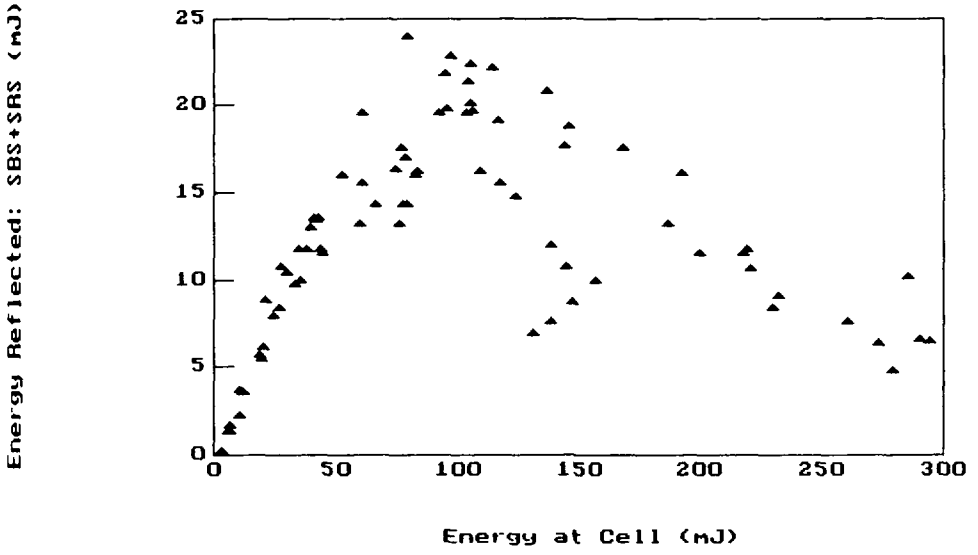


Figure 4: Acetone Combined Reflectivity

For every data point, the return energy and pump energy were measured. In order to investigate the decreasing reflectivity above 100 mJ pump, the energy passing forward through the cell was collected (see figure 3). The data in figure 5 indicates that the sum of the backscattered and forward energies is consistently 33% of the pump energy. A significant amount of energy is observed scattering from the sides of the cell.

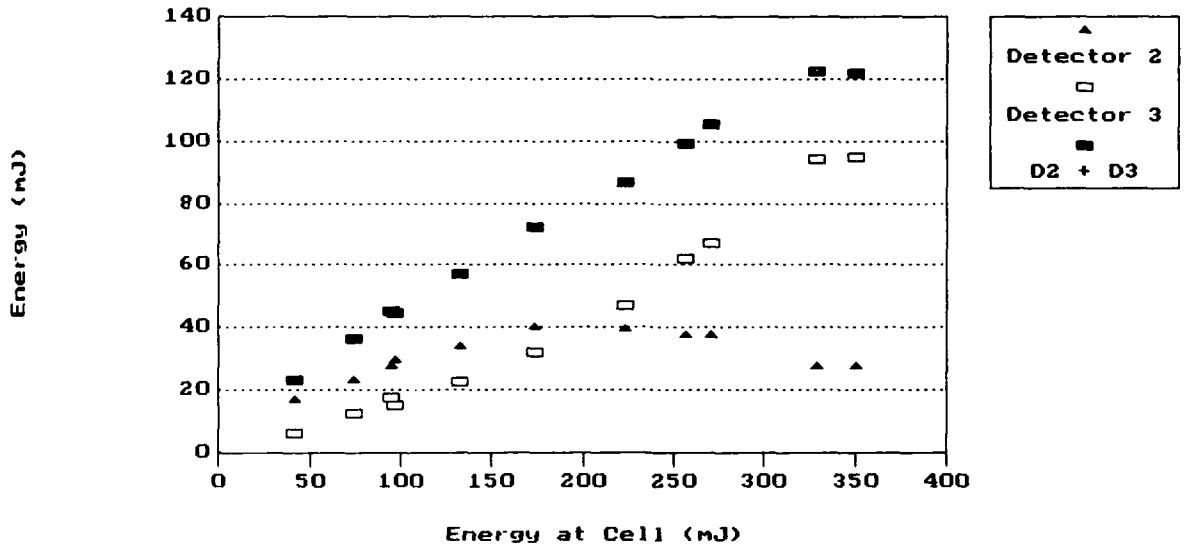


Figure 5: Forward and Backscattered Energy vs. Pump Energy

In an effort to increase the amount of backscattered light, the cell was backseeded with different fractions (roughly 20%, 2%, 0.2%, 0.02%) of the pump. This was accomplished at an input energy of 25 to 30 mJ, well down on our reflectivity curve. Due to the small frequency shift between the SBS and the pump, and the fact that the pump is broadband, the backseed frequency approximates the Strokes frequency. Due to fluctuations in pump energy, several measurements were made and averaged. The standard deviation of the pump and the return was calculated and from that we determined that the random error is less than 7%. Therefore, for backseeding to be observed, an increase in reflectivity of greater than 7% would be necessary. For all fractions of backseed, the combined backscattered light shows no change from the data in Figure 4 within our experimental error.

Conclusion

We have shown that a short coherence length forces backscattered reflectivities to be low. This results from a reduced gain factor $(1 - \exp(-\Gamma t_c))$. In our case, for a coherence length of 1 cm, the observed reflectivities were half of previously published results (reference 1). The shape and energy at which maximum reflectivity occurred are consistent.

Efforts to improve short coherence length reflectivity by backseeding with fractions of the pump were unsuccessful. These efforts will continue with a conjugated backseed. An etalon will be installed in the Nd:YAG laser to increase the coherence length by a factor of five and the experiment will be repeated. We expect to see higher combined reflectivities due to an increase in the gain (see equations 1 and 2). We will also determine the relative amounts of SBS and SRS in the combined return.

References

1. Eichler, Jun, Richter: Phase Conjugation Using Nd:YAG Lasers, Lasers '87 Proceedings, page 653

DEVELOPMENT OF A SOLAR-POWERED INFRARED INJECTION LASER MICROMINIATURE TRANSMITTING SYSTEM

D. D. Falter, G. T. Alley, K. G. Falter, J. M. Rochelle,* and K. H. Valentine**
Instrumentation and Controls Division

and

R. D. Westbrook, G. E. Jellison, Jr., and P. H. Fleming
Solid State Division

Oak Ridge National Laboratory†
Oak Ridge, Tennessee 37831-6010

Abstract

A solar-powered infrared microminiature transmitting system is being developed to provide scientists with a tool to continuously track and study Africanized bees. Present tracking methods have limited ranges and lack the capability of continuously tracking individual insects.

Preliminary field tests of a stationary prototypic transmitter have demonstrated a range of 1.1 km. The basic design consists of an array of nine 1-mm^2 solar cells, which collect energy for storage in a 1.0-μF tantalum chip capacitor. When the capacitor has been charged to a sufficient level, the circuitry that monitors the capacitor voltage level "wakes up" and fires a 5-μs pulse through an 840-nm GaAlAs injection laser diode. The process is then repeated, making the signal frequency (which ranges from 50 to 300 Hz) dependent on solar luminance. The solar cells, capacitor, and laser diode are mounted in hybrid microcircuit fashion directly on the silicon substrate containing the CMOS control and driver circuitry. The transmitter measures ~4 x 6 mm and weighs ~65 mg. The receiving system is based on an 8-in. telescope and a Si PIN diode detector.

Introduction

Since their accidental release from a Brazilian laboratory in 1957, Africanized bees have spread steadily northward through South and Central America; they are expected to arrive in the United States sometime in 1990. While their extremely defensive behavior at the nest site has been responsible for the deaths of both humans and animals and has resulted in their alias "killer bees," the most serious threat to the United States promises to be to the agricultural industry's $20 billion annual production of crops requiring bee pollination. This is a direct result of the fact that while Africanized bees are as much as six times more prolific than European honeybees, their pollination and honey production rates fall far short of those of their more docile cousins.[1]

Previous attempts at controlling the spread of Africanized bees—such as setting up bee traps and "bee-regulated zones"—have proven unsuccessful, leading some entomologists to believe that perhaps the most effective method by which to stop this aggressive strain is disruption of the mating cycle. However, this manner of attack would first require extensive study of the mating habits of both Africanized and European bees to determine how to control one strain without eradicating the other.

Studies of mating behavior have been limited due to the inability to track the flight of individual queens & drones. In previous studies bar codes[2] and numbered, color-coded tags have been used to record flights of bees (1) entering and exiting hives, (2) at experimental feed sites, and (3) (in the case of drones) in flight with the use of aerial traps.[3] The spatial distribution of drones has also been tracked with X-band radar.[4] Unfortunately, the two tagging techniques limit the entomologist to studying the bees at discrete points in space and time while providing no clear picture as to what occurs in the interim. Radar allows continuous monitoring of movement but does not permit identification of individual insects.

Early attempts at developing a miniature rf transmitter were shelved when flight tests with bees revealed that even short lengths of 0.001-in.-diam. antenna wire either inhibited flight or were quickly removed by grooming. Clearly, the type of system needed for scientists to gain insight into the mating and foraging habits of honeybees is one that will allow close, continuous monitoring of individual insects without interfering with flight or other day-to-day activities. This paper examines the early development of one such system based on the use of a solar-powered infrared microminiature transmitter. In the following sections we will describe some pertinent design considerations for a "flyable" transmitter; the prototype system configuration, with particular emphasis on problem areas in the transmitting and receiving units; the performance characteristics of the system; and some goals of future work.

*The University of Tennessee, Knoxville.
**Now at Science Applications International Corporation.
†Operated by Martin Marietta Energy Systems, Inc., for the U.S. Department of Energy under Contract No. DE-AC05-84OR21400.

Design Considerations

The physical characteristics of the average honeybee obviously impose some rather stringent design constraints on any type of "flyable" transmitter. Since the most feasible position for a solar-powered transmitter appeared to be the dorsal side of the thorax, the package geometry was limited to an area of ~4 x 6 mm (see Fig. 1). The target weight was set at 50 mg based on load tests by the U.S. Department of Agriculture.[5] Based on these criteria, as well as the fact that planned entomological research will concentrate on the mating and foraging habits of honeybees in controlled areas having a clear field of view, the decision was made to investigate the feasibility of a miniature infrared transmitting system.

System Overview

The transmitter system is a hybrid configuration of solar cells, a laser diode, and an energy storage device (capacitor) assembled on a silicon substrate (chip) that contains the control (wake-up) circuit, a buffer, and a substrate bipolar switch used to fire the diode as shown in Fig. 2. A commercially available 2-μm, 2-poly, 2-metal CMOS process was used to fabricate the control and firing circuitry. CMOS was the obvious choice because of the very limited power budget of the system. The initial concept for the transmitter (Fig. 3) was purposefully kept simple until feasibility could be demonstrated, and in its present implementation the system functions very much like a relaxation oscillator. The design consists of an array of solar cells serially connected to provide enough energy with which to charge a storage capacitor. When the capacitor charges to a sufficient level, circuitry monitoring that voltage level "wakes up" and fires a pulse through an infrared emitter. The process is then repeated, making the signal frequency dependent on solar luminance. The receiving end of the system optically amplifies, filters, and processes the signal detected by a Si PIN diode. Although initial calculations based on benchtop testing of a discrete component model of this system indicated that a range of >1 km was theoretically possible, a number of areas (discussed below) required individual attention before a miniature version could be realized.

Infrared Emitter

Diurnal testing of the transmitter necessitated the use of optical filtering to screen out solar and background noises. A three-cavity bandpass filter with a 12-nm bandwidth and a center frequency set to match that of the particular infrared emitter being used was chosen for this purpose. Infrared LEDs were used for initial benchtop testing; however, their wide bandwidth (~40 nm) and isotropic emission worked to our disadvantage in that the signal incident on the detector was attenuated to ~5% of that emitted by the LED. Since a laser diode offers a much narrower bandwidth than an LED and, therefore, more inband power in the optically filtered system, the laser was selected for the initial feasibility demonstration.

The laser diode chosen for the prototype is a low-threshold, continuous wave (cw-operated) gallium aluminum arsenide (GaAlAs) injection laser. This laser diode is an improved version of the RCA C86000E, which is now being fabricated with a metal-organic chemical vapor deposition (MOCVD) process to more accurately control layer deposition. The diode is passivated on the emitting facet with a $\lambda/2$ dielectric coating. On the opposite facet a six-layer coat with 90 to 100% reflectivity is used to increase the front facet output power and also to reduce the lasing threshold. The double-heterojunction design has a typical threshold current of 75 mA, a minimum



Fig. 1. A silicon substrate was glued to the back of this European drone bee to demonstrate the approximate size and orientation of the proposed infrared transmitter.



Fig. 2. The prototypic transmitter is a hybrid configuration of nine solar cells, a laser diode, and a capacitor assembled on a silicon substrate containing the transmitter circuitry.

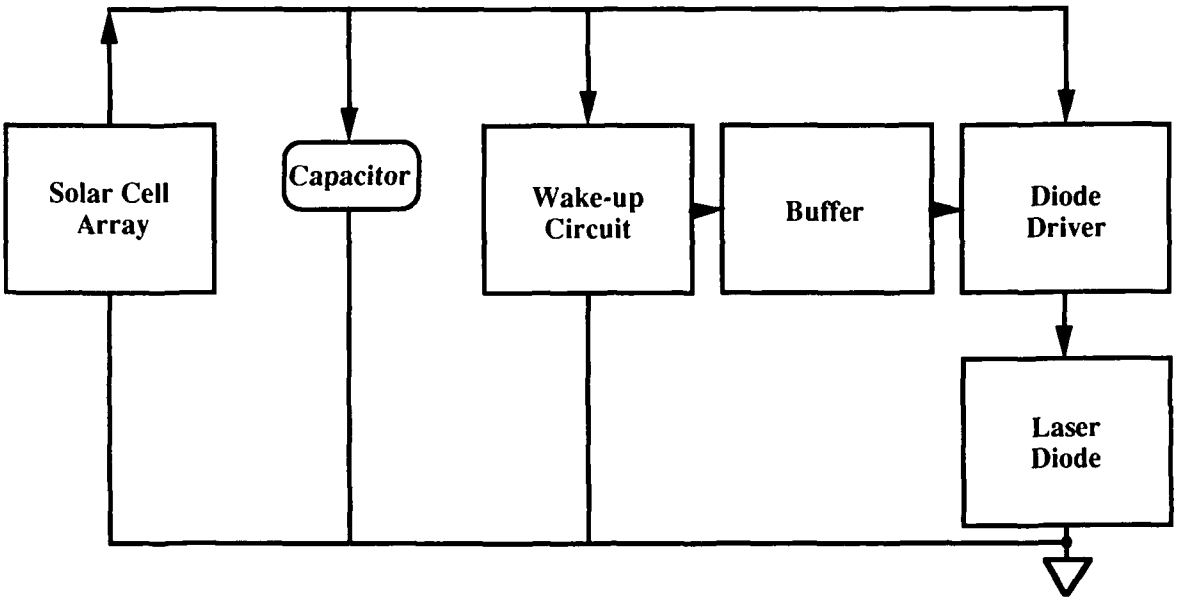


Fig. 3. The conceptual design of the transmitter consists of an array of solar cells, which charge the capacitor while the rest of the system is in a low power standby mode. When the capacitor is charged to a sufficient level (~4 V) to fire the laser diode, the wakeup circuit turns on the bipolar switch long enough to dump the stored energy into the diode. The charging and firing cycle is then repeated.

output power of 15 mW with a forward current (IF) of 400 mA maximum, and a 2-V maximum forward voltage. It is available in the near infrared range of 830 to 875 nm with a 2-nm bandwidth. The half-angle beam spread to 50% peak intensity is ~10° in the plane parallel to that of the junction and 40° in the plane normal to the junction. The laser diode chip typically measures 381 × 165 × 102 μm and weighs on the order of 35 μg[6] (Fig. 4).

An unpackaged laser diode was used to allow direct mounting onto the large aluminum pads situated on the silicon substrate of the transmitter. The diode was secured to the substrate by placing a small drop of silver epoxy on the mounting pad and carefully positioning the diode on the epoxy with the stripe or ohmic contact facing downward, while taking care not to cover the lasing region. The diode was oriented so that only one of the emitting faces was used, the other beam being directed at the capacitor located at the center of the transmitter.

Power Source

Operation of the transmitter required a power source that could supply at least 4.5 V at 50 μA. Considering the size and weight restrictions, along with the need for continuous operation and strictly diurnal testing, photovoltaic cells were chosen as the most practical method for generating the necessary energy. A serially connected array of nine 1-mm^2 solar cells was required to satisfy the size and voltage constraints of the transmitter. Three alternatives were investigated in our efforts to secure an appropriate solar cell array: monolithic cells, commercial cells, and hybrid cells.

Monolithic solar cells—cells that are an integral part of the same substrate as the processing circuitry—were recognized early on as the most efficient form of photovoltaic power, in terms of both fabrication costs and chip real estate. Using the same standard 2-μm CMOS process used for the control circuitry, small monolithic solar cells (~1 × 1 mm) were fabricated. When tested individually, the cells performed as expected; however, when put in series and connected to the circuitry, they failed to function properly. Careful analysis of the cells revealed that large circulating currents were developing between the wells, primarily because of a lack of isolation. The high substrate doping (~10^{16}) is believed to have contributed significantly to this problem. Even so, the use of monolithic solar cells is not a dead issue; preliminary tests using a different commercially available process have been successful, indicating that such an array is still possible.

Another alternative investigated was a commercially available miniature solar cell. Although our search uncovered at least one potential supplier, the cost per cell was prohibitively high.

The alternative that proved most successful and was eventually used in our field tests involved in-house development of physically separated miniature (1-mm^2) photocells custom made in the Solid State Division at the Oak Ridge National Laboratory (ORNL) using a process optimized for photovoltaic cells and crystalline silicon. The cells were fabricated from 0.2 to 0.3-Ω-cm p-type silicon using glow discharge implantation for junction formation followed by a heat treatment to anneal the implantation damage and to grow ~15 nm of SiO_2 for front surface passivation. Aluminum mounting pads (with cuts through the overglass) were included in the layout of the control

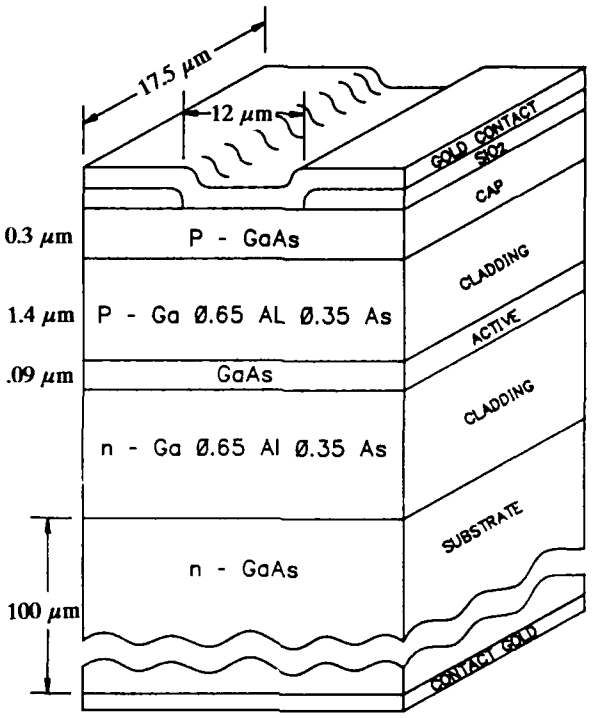


Fig. 4. The laser diode currently in use is an RCA C86000 cw-operated GaAlAs injection laser with a passivated double-heterojunction design.

circuitry chip so that individual cells could be attached in a hybrid fashion using silver epoxy. The cells were then placed in series using a tailless ball bonder with 0.7-mil gold wire. The individual cells performed well, having an open circuit voltage of 0.595 to 0.605 V and a short circuit current of 23 to 24 mA/cm^2 under simulated AM1 conditions. Outdoor testing in bright sunlight revealed that the nine-cell array connected in series yielded an open circuit voltage of 5.2 V and a short circuit current of ~200 μA.

Transmitter Circuitry

Both the laser diode driver switch and the transmitter control (wake-up) circuit were monolithically integrated in the 4 x 6-mm motherboard silicon chip, which was implemented with standard 2-μm bulk CMOS digital technology. This technology includes double poly and double metal layers and is available through the metal-oxide-semiconductor implementation system (MOSIS) fabrication service in several different chip sizes.[7]

The transmitter design is simple in concept, with the control circuit gating on the laser diode driver after the energy storage capacitor (nominally 1.0 μF) has reached a charge state of about 4 V. The capacitor then discharges through the diode and driver switch for a few microseconds until the voltage drops to near 2 V. The driver is then gated off so that the solar cells can recharge the capacitor and repeat the cycle. Thus the transmitter behaves as a relaxation oscillator with an off-on duty cycle of 1000:1 or greater, depending on the solar power input. The transmitter control circuit is called a wake-up circuit because it must maintain the low resistance diode driver gated completely off for all solar power startup scenarios including a slow rise from zero starting voltage. During power-up, all solar cell current is available for charging the storage capacitor except the wake-up circuit bias current, which starts from zero and rises to a maximum of 15 μA as seen in the measurements of Fig. 5. The nominal 4-V threshold level for the wake-up circuit is derived from twice the NMOS threshold voltage plus twice the PMOS threshold voltage, the latter being significantly increased by the body effect in a p-well CMOS process. The wake-up circuit uses 875 squares of p-well resistance (1500 to 3000 Ω/square) and 55 pF of poly-poly capacitance (500 pF/mm^2), and requires only 2.4% of the motherboard chip.

The wake-up circuit output drives a standard CMOS buffer (pull-up W/L = 500/4 μm), which in turn controls the base of the vertical NPN bipolar transistor used for the main laser diode driver switch. The NPN base is formed from ten separate 40 × 500-μm p-well regions arranged on 60-μm centers with strips of n$^+$ collector contact diffusion placed between the well regions to minimize series collector resistance. Each well contains 14 separate 27 × 6-μm emitter regions flanked on both sides with a strip of p$^+$ base contact diffusion to minimize ohmic base resistance. The resulting transistor has demonstrated excellent dc characteristics with current gain maintained well above 200 over more than nine decades of collector current as illustrated by the Gummel plot of Fig. 6. Note also that the near-ideal slope of the base current curve suggests that depletion region generation/recombination effects are practically nonexistent. Even without the benefit of a buried layer, this modest size (~0.4 mm^2) vertical NPN switch achieved an ohmic collector resistance of less than 10 Ω as shown in the output characteristics of Fig. 7. A NMOS switch of similar size could have been used to obtain a resistance this low,

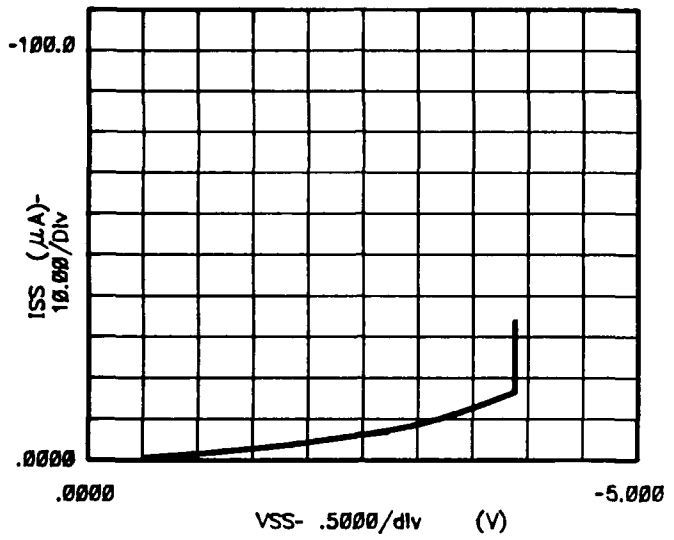
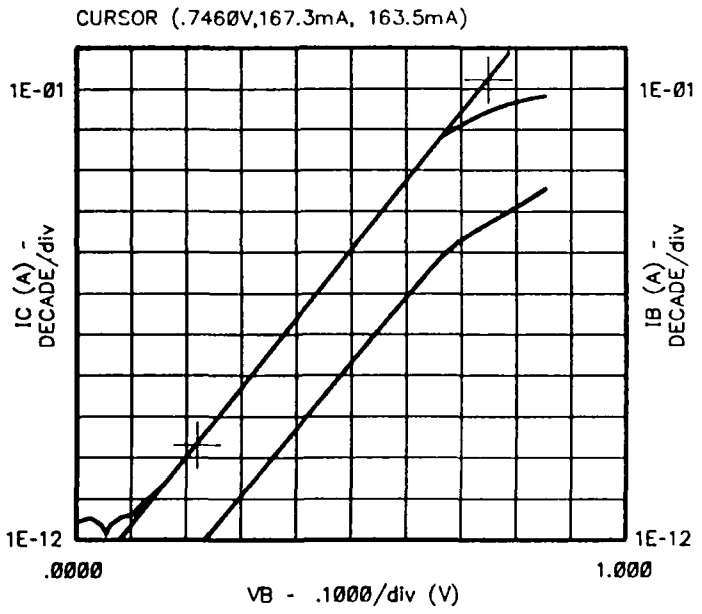
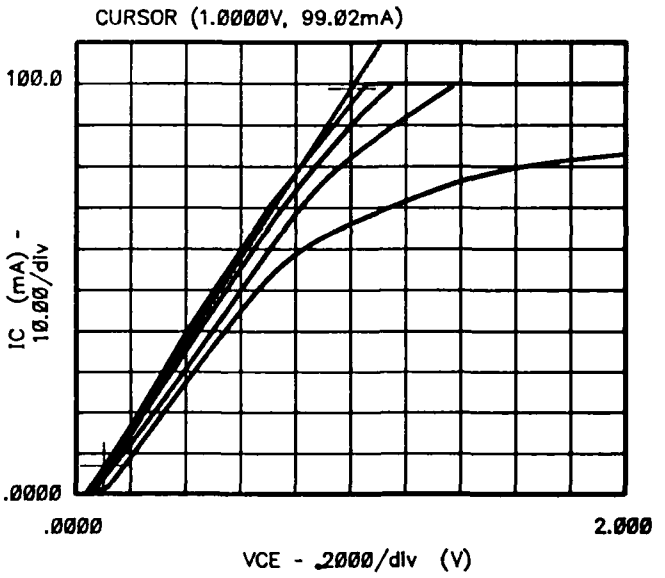


Fig. 5. Transmitter bias current during power supply "wake-up."



	GRAD	1/GRAD	X Intercept	Y Intercept
LINE 1	16.9E+00	59.3E-03	792E-03	44.7E-15
LINE 2				

Fig. 6. Gummel plot for the laser diode driver transistor. VCE = 1 V.



	GRAD	1/GRAD	X Intercept	Y Intercept
LINE 1	102E-03	9.81E+00	28.3E-03	-2.88E-03
LINE 2				

Fig. 7. Output characteristics for the laser diode driver transistor with 200-μA base current steps. Collector current limited to 100 mA by the measurement instrumentation.

but the high Miller capacitance produced by the inverting configuration would have required one or more additional intermediate buffer stages. Also, the NMOS switch-on resistance would drastically increase during the capacitor discharging interval.

Use of the vertical (sometimes called substrate) bipolar transistor in any single-well bulk CMOS process is restricted to the common collector configuration, which is usually avoided for switch applications because of the inherent VBE difference between the power rail and the load. This is not an issue in this application because the transistor self-saturates due to the collector resistance ohmic drop, resulting in the same total VCE as would be obtained if the same switch were in an inverting configuration. The waveforms of Fig. 8 indicate a peak laser diode current of more than 200 mA with a risetime of less than 50 ns. Fig. 8 also shows the capacitor voltage (positive side ground) discharge pulse to be almost linear except for small steps contributed by capacitor series resistance. This kind of diode driver performance is attainable only if the total ohmic resistance of the capacitor and diode connections can be held to less than 1 to 2 Ω, which has proven difficult to consistently achieve with conductive epoxy bonds to the aluminum chip metalization.

Receiver

Based on the use of optics for collecting and amplifying the incoming signal, original calculations for the transmitting system pointed to a possible range of 1 to 2 km. The current receiving system (displayed in Fig. 9) is built around an 8-in. Schmidt-Cassegrain reflecting telescope with a 2-m focal length. This telescope was chosen for availability, familiarity, and price. The light-gathering power of this telescope is 1024 times greater than that of the human eye, and it delivers a maximum magnification power of 400. The telescope is mounted on an equatorial mount tripod and aligned by using the eyepiece to center the target in the field of view, then replacing the eyepiece with the detector hardware shown in Fig. 10. The infrared signal enters the telescope, passes through a thin lens with two-sided aspheric correction, and proceeds to a spherical primary and then to a convex secondary mirror. The signal is reflected from this secondary mirror through a central perforation in the primary mirror[8] into a light-tight cylindrical chassis. The cylindrical chassis is composed of two parts: (1) an outer sleeve, which is threaded onto the rear of the telescope, and (2) an inner sleeve, which contains a three-cavity narrow bandpass filter and a silicon PIN diode detector (Hamamatsu S1723-06) with a sensitive area of 1 cm^2. The inner sleeve is adjusted to position the Si PIN diode at the focal plane of the incoming infrared signal.

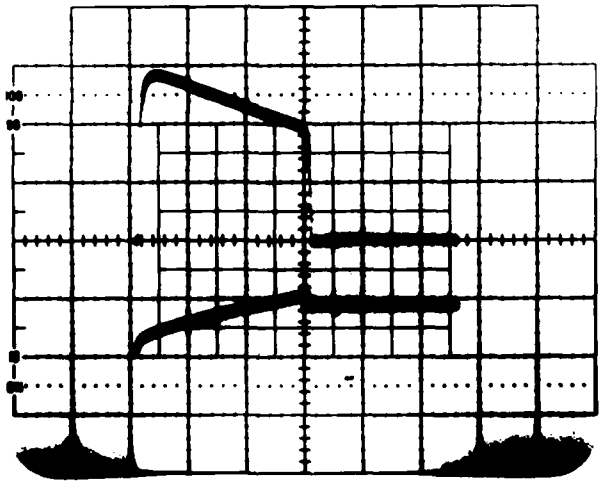


Fig. 8. Upper trace is diode current pulse at 100 mA and 1 μs per major division. Lower trace is transmitter power supply voltage (storage capacitor voltage) at 2 V and 1 μs per major division. Zero is at center screen for both traces.



Fig. 9. The stationary prototypic transmitter and receiving system shown above demonstrated a range of 1.1 km during field tests.

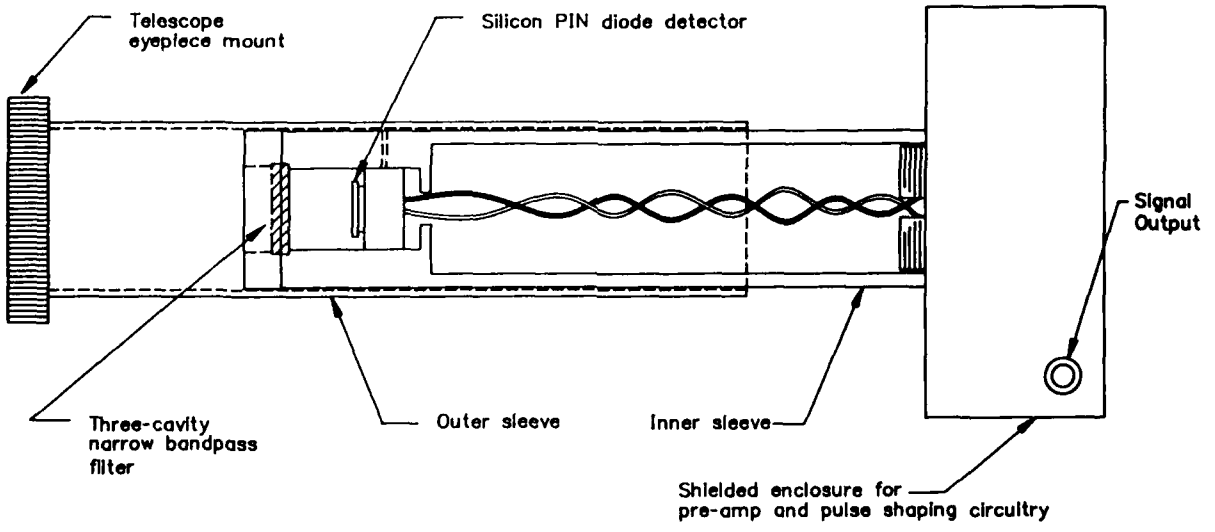


Fig. 10. The detector hardware is designed around an 8-in. Schmidt-Cassegrain reflecting telescope. A cylindrical light-tight chassis mounted onto the telescope contains a three-cavity narrow bandpass filter and the silicon PIN diode detector. The inner sleeve of the chassis is adjusted to position the detector at the focal plane of the telescope. The pulse processing electronics are mounted in the box protruding from the end of the cylinder.

The detector signal is amplified by a close-coupled Amptek A-250 charge-sensitive preamplifier, which provides a charge gain of 1 V/pC. This hybrid microelectronic preamp is augmented with an external JFET (2SK152) used as the preamp's input device and biased at 2.75 mA. The preamp is followed by a pulse-shaping amplifier consisting of three conventional op-amp gain blocks (OP-27 devices) providing a total pulse gain of about 430 V/V. The semi-Gaussian pulse shaping is accomplished with three integrating and one differentiating time constants, all of which are 2.5 μs. Total rms output noise of this receiving system is 100 to 175 mV, depending on the light level and the reflectivity of background seen by the telescope. Output noise for dark conditions is 65 mV rms.

Potential Applications

The need for microtransmitting systems has become apparent over the past year as a result of the many inquiries received concerning development of the infrared transmitter discussed here. Even though the system currently under development is strictly a line-of-sight system for tracking Africanized bees or other free-flying insects under sunlit conditions, the availability of a self-powered microtransmitter provides opportunities for a variety of applications. Considerable interest has been expressed in light-weight, self-powered, low-cost transmitters for applications including biological tracking, inventory control, and security and surveillance.

Conclusions and Future Directions

The successful demonstration of a prototypic transmitter at a range of >1 km with a signal-to-noise ratio of 4:1 marked a major milestone in the development of microminiature infrared transmitter technology. However, a number of problems remain to be solved before the system can be considered a practical one for tracking Africanized bees:

1. An automated tracking system needs to be developed. Although initial field tests have been performed by manually positioning the receiving unit to detect the incoming signal from a stationary transmitter, future plans are to use a Si photodiode quadrant detector and microprocessor-controlled stepping motors to provide a closed-loop tracking system. This would allow continuous monitoring of apian mating habits in controlled testing situations.

2. A method needs to be developed for encoding the transmitted signal to allow tracking of multiple targets. A practical system must be able to distinguish between individual insects and monitor the actions of each. However, adding this capability to the transmitter will both considerably increase the power requirements and complicate the circuitry required for transmitting the signal.

3. The solar cells need to be integrated into the same substrate as the driver and the control circuitry. This would eliminate 70% of the labor (as well as most of the fragile wire bonds) required to fabricate the transmitter, and thus significantly reduce its cost to the end user.

4. Techniques must be developed for spreading the radiated signal into a larger solid angle to increase the detectability of the signal. One approach already being investigated involves putting multiple emitters in the system and firing them in a multiplexed manner. Another possible approach involves the use of miniature lenses or optical coatings with single emitters.

Acknowledgments

A special thanks is extended to B. G. Eads, H. R. Brashear, D. N. Fry, C. W. Ricker, and O. R. Taylor, Jr. for their strong and continued support of the project, and to D. F. Newport for the use of his VLSI design skills. The authors also wish to recognize Paul Rainbow of the RCA Electro Optics Division for his technical assistance on laser diodes, and H. T. Kerr of the Oak Ridge Y-12 Plant for originally bringing together the engineers and the entomologists.

References

1. O. R. Taylor, Jr., personal communications with authors, August-December 1987.

2. G. Abdian, "The Bee's Knees in Bar Code," *ID Systems* 8(8), 20-26, 1988.

3. O. R. Taylor, Jr., "An Aerial Trap for Collecting Drone Honeybees in Congregation Areas," *J. Apicultural Research* 23(1), 18-20, 1984.

4. G. M. Loper, W. W. Wolf, and O. R. Taylor, Jr., "Detection and Monitoring of Honeybee Drone Congregation Areas by Radar," *Apidologie* 18(2), 163-172, 1987.

5. Anita Collins, U.S. Department of Agriculture, personal communication, September 1987.

6. Paul Rainbow, RCA, Inc., personal communication, June 20, 1988.

7. C. Tomovich, "MOSIS - A Gateway to Silicon," *IEEE Circuits and Devices Magazine* 4(2), 22-23, March 1988.

8. Meade Instruments Corp. Instruction Manual, Model 2080: 8" Schmidt-Cassegrain, February 1988.

HIGH-POWER LASER ACTION AT λ = 222 NM UNDER PUMPING BY SELF-SUSTAINED DISCHARGE

A.N.Panchenko, V.F.Tarasenko, E.V.Bukatyi

Institute of High-Current Electronics USSR Academy of Sciences
Siberian Branch
Akademicheskij pr., 4, Tomsk, 634055, USSR

Experimental investigation results of generation in Ne(He)-Kr-HCl mixtures under pumping by UV pre-ionisation transvers discharge are presented. Powerful radiation at λ = 222 nm with storage energy efficiency of $\sim$ 0.5 % and active laser length of 20 and 60 cm have been obtained. The main channel of KrCl* molecules formation is shown to be three body ion-ion recombination with high energies generation being realized in Ne mixtures by intensive pre-ionization and pumping power $\gtrsim$ 1.5 MW/cm^3.

1. Lately noble gas halogen exciplex lasers are widely used in different fields of science and engineering. For photochemistry and photolithography problems, short-wave radiation sources are required. KrCl laser at λ = 222 nm is the most perspective for these purposes having both high energy characteristics and when added hydrogen one of the largest mixture life-time resources for the lasers mentioned above [6,7].

However, high cripton concentration in optimal gas mixtures impedes high power parameters realisation by fast discharge constriction and higher (in comparison with XeF, KrF and ArF lasers) generation thresholds. So, laser pulse lengths were limited in [1-4] by discharge constriction and did not exceed 18 ns at FWHM and large radiation energies were obtained under pumping power densities $\gtrsim$ 10 MW/cm^3 and $U_o/dN \geq 2 \cdot 10^{-16}$ V·cm^2 where U_o is the laser gap breakdown voltage; d - the interelectrode gap; N - particles concentration in mixture.

Different versions concerning the main mechanism of KrCl* molecules formation should also be mentioned here. In [2] KrCl* molecules were supposed to be mainly formed due to harpoon reaction

$$Kr^* + HCl \longrightarrow KrCl^* + H \quad . \qquad (1)$$

In [1, 3] the possibility of KrCl* molecules formation due to some processes:
1) ion-ion recombination $Kr^+ + Cl^- \longrightarrow KrCl^*$, (2)
2) harpoon reaction by Kr atoms interacting in upper metastable state with HCl
$Kr^{**} + HCl \longrightarrow KrCl^* + H$, (3)
3) harpoon reaction by Kr atoms interacting in lower metastable state with excited HCl molecules includingly $Kr^*(^3P_2) + HCl^* \longrightarrow KrCl^* + H$ (4)
was pointed out.

In this case harpoon reaction and ion-ion recombination contribution to KrCl formation have the same order [1]. Investigations results of pumping power, pre-ionisation intensity and active laser length influence on efficiency and generation energy at λ = 222 nm have been presented in the given paper. The work follows investigations where KrCl laser is shown to work effectively at rather small pumping power densities 1.5 MW/cm^3 and radiation energy of 0.6 J on λ = 222 nm was obtained with pulse duration of 40 ns at FWHM and total efficiency concerning power storage $\sim$ 0.5 %.

2. Experiments on generation investigations were made on two laser sets. LIDA-KT [9] laser active length was of 60 cm, the interelectrode gap - 3.6 cm, the discharge width - 1.5 cm and DILAN lasers' active length [10] was of 20 cm, the interelectrode gap - 1.6cm, and the discharge width - 0.4 cm. The main discharge width was defined by pre-ionisation discharge width between the mesh electrode and the axilliary electrode, set under the mesh. Pumping power changed due to the charging voltage and in DILAN laser it also changed due to storage and peaking capacities variations. Alongside with pre-ionisation by the volume discharge, the illumination of rather small intensity from 20 spark gaps, set behind the mesh electrode was used in the DILAN laser. The mixtures consisting of buffer helium gas or neon, cripton gas and halogen donor HCl were prepared in laser chamber. The optical cavity was made of total reflector with Al cover and flat-parallel quartz plate. Radiation energy was measured by calotimeter IMO-2N and radiation pulse form - by FEK-22 photodiode, the signal from which was applied to the oscillator 6LOR-04.

3. Fig.1 presents radiation energy and the efficiency plotted against discharge voltage. These dependences were obtained on the laser with an active length of 60 cm in Ne-Kr-HCl mixture. Max. efficiency of 0.5 % was achieved by decreasing the discharge voltage to a value still allowing RU-65 spark gap to act. In this case pumping power density was $\sim$1,5 MW/cm^3 and $U_o/(dN) \sim 10^{-16}$ V cm^2. At lower pumping powers buffer neon gas replacement with helium resulted in one or more orders fall of radiation energies.

Fig. 2 shows radiation energy and the efficiency plotted against discharge voltage on the laser with active length of 20 cm, storage and peaking capacities being 5 nF.

Generation is shown to be observed both with buffer neon gas and with helium and the efficiency in neon mixtures achieves ~ 0.5 %. Oscillograms of laser pulses on $XeCl^*$ and $KrCl^*$ molecules for the given conditions are presented in Fig. 3. Generation pulses have the similar form and peak radiation powers on $\lambda = 308$ nm and $\lambda = 222$ nm differ only $\sim 20\%$. However, the first generation pulse peak on $KrCl^*$ molecules has less duration at FWHM and in the second peak maximum generation power on $KrCl^*$ molecules in 2 or 3 times less than on those of $XeCl^*$. It should be noted, however, that generation energy on $XeCl^*$ molecules practically matches the pumping power with the peak pumping power having achieved ~ 10 MW/cm^3 in the experiments. Further pumping power increase on DILAN laser resulting from the storage capacity increase up to $C_0 \approx C_1 \approx 10$ nF, led to suppression of generation at $\lambda = 222$ nm because of discharge constricting. The same suppression was observed to occur on the $KrCl^*$ molecules with maximum storage capacitance being $C_0 \approx C_1 \approx 5$ nF but pre-ionisation intensity being decreased. Two-times pumping power decrease due to storage capacity decrease $C_0 \approx C_1 \approx 3$ nF resulted in almost one order power and generation energy fall on $KrCl^*$ molecules, whereas power and generation energy on $XeCl^*$ molecules did not practically change while the efficiency increased $\sim 1,5$ times.

To define the main channel of KrCl molecules formation, spontaneous radiation behavior at $\lambda = 222$ nm, at U_0/dN value change, when pumping byba discharge controlled by an electron beam was carefully studied. The same experiments were made earlier for defining the main channel of $XeCl^*$ and XeF^* molecules formation. When increasing the discharge voltage from zero to a statical breakdown one, the dependence, similar to that being observed in [11], for XeCl laser, has been obtained. With the discharge without ionized multiplication being available the discharge energy transmitted into active medium, caused no spontaneous radiation power at $\lambda = 222$ nm, but when pumping by a discharge with ionizing multiplication radiation power increased proportionally to input energy.

4. Now the results obtained should be discussed. As one can see from Fig. 1, KrCl laser perfomes effectively at small $U_0/dN \sim 1\ 10^{-16}$ V cm^2 and pumping power densities 1,5 MW/cm^2 with active laser length being rather large, e.g. of 60 cm in LIDA-KT laser [9] and of 90 cm in LIDA-101 [5], and volume pumping discharge being provided. Due to a large content of Kr in optical laser mixtures for KrCl laser, one should use effective pre-ionisation systems. In laser with a small active length high efficiency and radiation energies can be obtained (Figs 2 and 3), but in this case one should increase pumping powers. In KrCl laser when sufficient pumping power and volume discharge forming being provided generation efficiency increases at U_0/dN decrease due to better pumping generator impedance matching with laser discharge resistance. The main KrCl molecules formation channel is the ion-ion recombination with the third particle being available:

$$Kr^+(Kr_2^+) + Cl^- + Ne(He) \rightarrow KrCl^* + (Kr) + Ne(He) \quad . \qquad (5)$$

This conclusion is based on the following facts: a) spontaneous KrCl molecules emission intensity is not changing under pumping with a nonionising multiplication discharge through input energy to the active medium increase in this case and when pumping with ionising multiplication discharge (e.g. when increasing positive ions concentration), radiation intensity growth at $\lambda = 222$ nm is being observed; b) HCl molecules dissociation energy being large (4,43 eV) the reaction occuring probability in (1), due to lack of energy $Kr^*(^3P_2)$ is negligible; c) under high pressures (optimal pressures for KrCl-laser are of 4-6 atm^2), three-body reaction rate is larger than two-body reaction one (2)[12]; d) radiation energy at $\lambda = 222$ nm in Ne mixtures is essentially higher (~ 2 times) in comparison with He (Fig.2). Energy electron distribution function in Ne is known to be based to higher energies than those in He [2] which results in larger discharge current (~ 2 times) in Ne mixtures and respectively in higher positive ions concentration in a discharge. The comparison of energies obtained on $XeCl^*$, $KrCl^*$, XeF^* and KrF^* molecules with buffe neon gas shows that radiation energy of XeCl and KrCl lasers increases in 2 times with radiation energy of XeF and KrF lasers being negligibly changed. At present, for XeCl and KrCl lasers reactions (1) and (5) are proved [11,12] to make comparable contributions to the population of an upper laser level and for XeCl laser, reaction (5), is the main one.

5. So, in lasers with active length of 20 and 60 cm we got a powerful radiation at $\lambda = 222$ nm with stored energy efficiency $\sim 0,5$ %. The main channel of KrCl molecules formation is shown to be ion-ion recombination and high radiation energies are realized in buffer neon gas mixtures by intensive pre-ionisation and pumping power density $\gtrsim 1,5$ MW/cm^3.

REFERENCES

1. R.S.Sze, P.B.Scott. Appl. Phys. Lett., 33, 419 (1978).
2. R.S.Sze. IEEE J. of Quant. Electr., QE-15, 1338 (1979).
3. E.Armandillo, A.Luches, V.Nassisi, M.R.Perrone. Appl. Phys. Lett., 42, 860 (1983).
4. J.E.Andrew, P.E.Dyer, P.J.Roebuck. Optics Communs., 49, 189 (1984).
5. S.V.Melchenko, A.N.Panchenko, V.F.Tarasenko. Pis'ma Zh. Tekn. Fiz., 12, 171 (1986) (in Russian).

6. T.J.McKee, D.J.James, W.S.Nip, R.W.Weeks, C.Willis. Appl. Phys. Lett., 36, 943 (1980).
7. V.V.Gryzhinsky, K.M.Degtyarenko, V.K.Shalaev, T.N.Kopylova, V.S.Verkhovsky, V.F.Tarasenko, S.V.Mel'chenko. Zh. P.S., 38, 559 (1983) (in Russian).
8. V.S.Verkhovsky, S.V.Mel'chenko, V.F.Tarasenko. Kvantovaya Elektronika, 8, 417 (1981) (in Russian).
9. V.F.Tarasenko, A.N.Panchenko, S.V.Mel'chenko, N.S.Belokrinitsky, M.P.Antonenko, Yu.I.Stupak, G.A.Voloshina, O.A.Tkachyk. Kvantovaya Elektronika, 14, 2450 (1987) (in Russian).
10. M.I.Lomaev, V.F.Tarasenko, Kvantovaya Elektronika, 15, 1978 (1988) (in Russian).
11. Yu.I.Bychkov, A.I.Gorbatenko, I.N.Konovalov, V.F.Losev, V.F.Tarasenko. Kvantovaya Elektronika, 6, 2103 (1979) (in Russian).
12. E.W.Mc Daniel, W.L.Nighan. Gas Lasers. - New York : Academic Press, 1982, V.3.

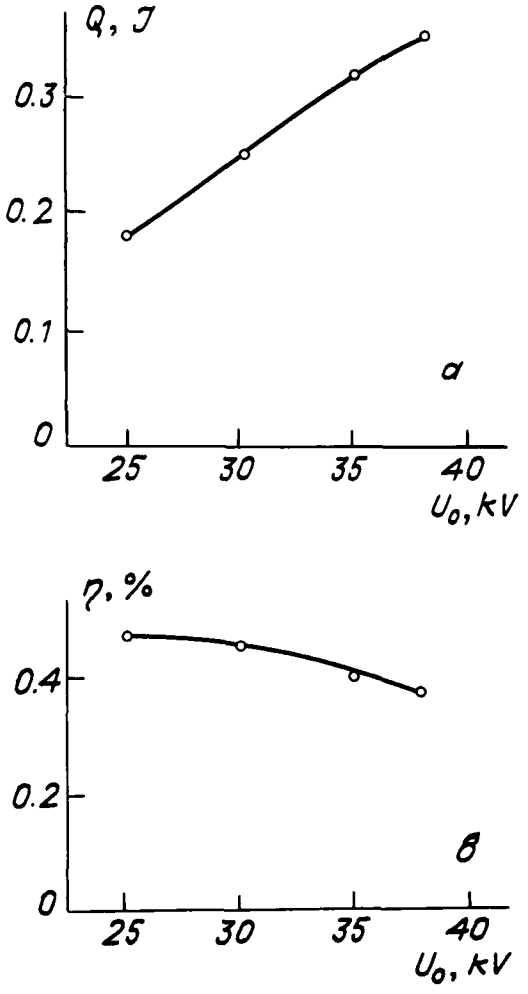


Fig. 1.

Laser radiation energy (a) and the stored energy efficiency (b) plotted against the charging voltage. Laser active length is of 60 cm, Ne:Kr:HCl mixture = 1000:40:1, p = 4,25 atm.

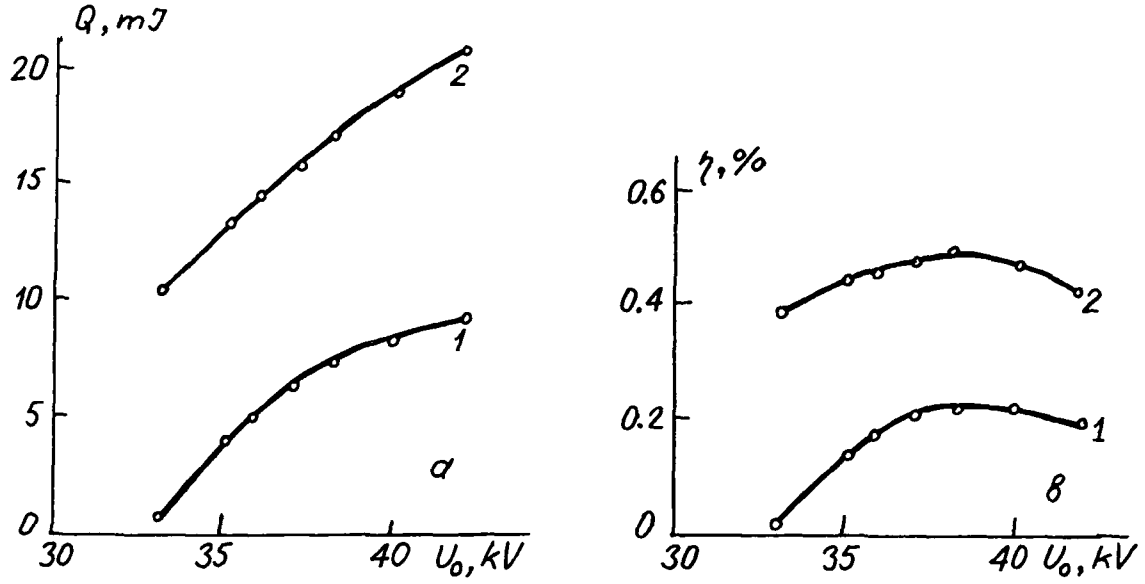


Fig. 2.

Laser radiation energy (a) and the stored energy efficiency (b) plotted against the charging voltage. Laser active length if of 20 cm. 1 - He:Kr:HCl = 700:50:1, p = 3 atm. 2 - Ne:Kr:HCl = 750:45:1, p = 4,25 atm.

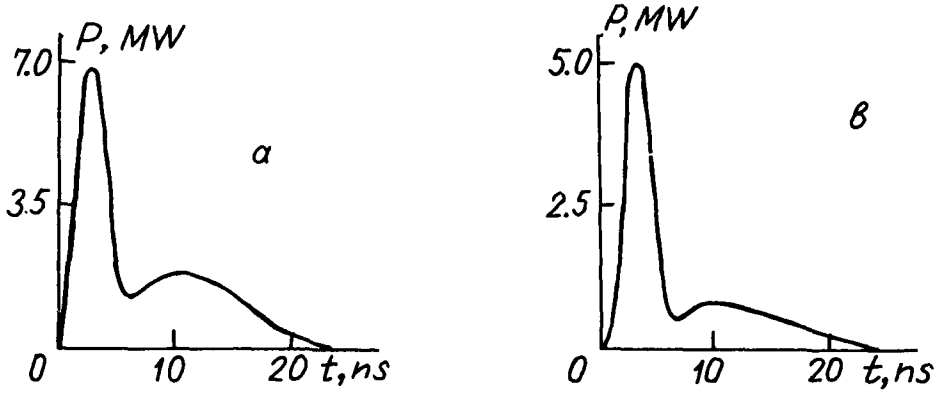


Fig. 3.

$XeCl^*$ laser pulses oscillogramm - Ne:Xe:HCl = 750:10:1 (a) and $KrCl^*$ laser pulses oscillogramm - Ne:Kr:HCl =750:45:1 (b) with pressure being of 4,25 atm and U_0 = 40 kV.

THE LASER ACTION ON THE ATOMIC TRANSITIONS OF Ne AND Xe ON PUMPING WITH ELECTRON BEAM

A.S.Bugaev, N.N.Koval, G.A.Mesyats, V.V.Ryzhov, V.S.Skakun,

V.F.Tarasenko, I.Yu.Turchanovsky, A.V.Fedenev, P.M.Shchanin

Institute of High Current Electronics USSR Academy of Science
Siberian Branch Akademicheskii 4, Tomsk 634055, USSR

The design scheme of a convergent-electron-beam-pumped laser with an excited volume of 9 l is described. A study has been carried out on lasing in Ar-Xe (λ = 1.73 μm) and He-Ne-Ar (λ = 585.3 nm) mixtures at a beam current pulse duration of 50 us. It has been demonstrated that the e-beam accelerator allows uniform pumping and provides high deposited energies, the heat loading of the foil not increasing.

Pulsed-repetitive lasers generating long (10^{-4})s) pulses /3/ are of particular interest in view of their application in technologival processes concerning material treatment /1, 2/. More substantially elaborated CO_2 lasers because of significant diffraction divergence of the laser beam due to long radiation wave, are uncapable of producing high radiation power density. Moreover, their optics is liable to atmospheric influences. These shortcomings can be eliminated in shorter wavelength lasers as the divergence angle θ is directly proportional to the wavelength and the radiation power density in the focal plane is defined by the relashionship

$$P_f = 4P/f\theta^2,$$

where f is the lens focal distance and P is the laser radiation power. Promising for technological applications is a Xe laser with λ = 1.73 μm. When being e-beam-pumped from one side, this laser is capable of operating with > 1 p.c. efficiency and ~ 10^{-3} μs radiation pulse duration /4-6/ and provides small (25 μrad) divergence of the beam at a radiation pulse duration of ~ 10^{-5} s /7/. To extract radiation from Xe lasers quartz optics is used.

The paper presents the design scheme of a laser pumped by a radially converging electron beam, which produces more uniform energy deposition into the gas mixture, and the results of a study of lasing in Ar-Xe (λ = 1.73 μm) and He-Ne-Ar (λ= 585.3 nm) mixtures. To optimize the pumping conditions the distribution of the specific deposited energy over the laser chamber cross section has been calculated by the Monte-Carlo method. The calculations were carried out using the code described in /8/ taking into account the actual geometry of the support greed of the beam extracting system and the electron dispersion in both the foil and the gas. The e-beam pumping was used because the combined pumping at present provides radiation pulse durations of not over 10^{-5} s /9-11/.

THE EXPERIMENTAL SETUP AND TECHNIQUES

The schematic diagram of the laser with an accelerator as the principal unit is shown in Fig. 1. Inside the vacuum chamber 1 on the sectionalized lead - in insulator 2, the plasma cathode 3 and the cylindrical anode 4 are mounted coaxially. The plasma cathode consists of two 70 mm long coaxial cylinders 500 and 350 mm in outside and inside diameter, respectively. These cylinders form the hollow anode of the discharge system. The inner cylinder of the cathode is made netty with the meshes 0.6x0.6 mm in size. Arc plasma generators of the trigatron type, described in /12/, are used to produce the emitting plasma. They are placed in pairs at the ends of the plasma cathode opposite each other. In the hollow anode of the discharge system plasma forms from which through the meshes of the net electrons are emitted into the accelerating gap where they are accelerated to an energy corresponding to the voltage applied between the plasma cathode 3 and the cylindrical anode 4. The plasma generators operate synchroneously by simultaneous application of 10 kV voltage pulses across the triggering spark gaps of the plasma generators. The operating voltage of the arc produced amounts to 70-100 V. To make the distribution of the current density over the beam cross section more uniform supplemental nets with 1.2x1.2 mm meshes was used, which were put over the main net in the regions of increased emission current densities. The cylindrical anode 4 with the outside diameter of 150 mm gives support to the outlet unit and at the same time serves as a laser chamber. The anode is perforated in the middle at a distance of 600 mm. The holes 20 mm in diameter are shut off with a 40 μm thick Al-Be foil. The geometrical transparen-

cy of the support was 0.6. On the ends of the cylindrical anode (laser chamber) plane mirrors 7 are mounted. For the laser chamber inside diameter of 140 mm, the volume of the mixture to be excited is 9 l. In this experiment the mirrors used to extract radiation were 120 and 80 mm in diameter, the active volume being 6 l and 2,3 l, respectively.

The accelerating gap is energized by dc voltage from a 0,4 μF storage battery which is charged from a high-voltage rectifier up to 120-180 kV. The beam current amplitude and duration were dependent on the performance of the plasma cathode power supply circuit which produced 0.5-2 kA, 10-50 μs semisinusoidal pulses of discharge current. When operating in a single-pulse mode, the accelerator produced a radially converging beam with the electron energy of 120-180 keV, vacuum diode current of 0.1-1 kA and duration of 10-50 μs. The current measured by a 100 mm dia cylindrical collector placed along the laser chamber axis was 30 p.c. of the diode total current. Measuring the beam current duration and amplitude during pumping was accomplished independently of the accelerating voltage by varying the discharge current and its duration in the plasma cathode. The energy of the electron beam injected into the laser chamber was measured by a calorimeter. For a voltage of 160 kV, beam current behind the foil of 62 A and pulse duration in base of 50 μs this energy was 160 J. The accelerator was capable of operating at a repetition rate of up to 10 Hz.

The lasing was investigated in Ar-Xe and He-Ne-Ar mixtures in a single-pulse mode. The laser radiation energy was measured by the calorimeter IMO-2N. The distribution of the laser radiation energy over the beam cross section was measured by moving the calorimeter along the vertical and the horizontal axes. The distribution of the deposited energy over the laser chamber cross section corresponded to the intensity of spontaneous radiation in the 200-600 nm spectrum region. It was measured by the photodiode FEK-22 whose signal was applied to the oscilloscope S8-12.

RESULTS AND DISCUSSION

Fig. 2 shows the specific radiation energy deposited into the Ar:Xe = 100:1 mixture at 1 atm as a function of the beam current injected into the laser chamber for the new developed laser (1) and the planar diode laser (2) which we investigated earlier /4,5/. For the latter the beam current duration at a half width was ~100 μs. It can be seen that using a radially converging e-beam makes it possible to increase the specific radiation energy or to decrease the heat loading on the foil. These curves indicate that the same specific radiation energy was obtained for the case of a radially converging beam and that of a planar diode, with other conditions being equal, when the relationship $j_c \tau_c \sim 0.1 j_p \tau_p$ was fulfilled (j_c and j_p are the beam current densities and τ_c and τ_p are the current pulse durations for the coaxial and the planar diode, resp.).

The total energy absorbed by the chamber operating volume, E_{ab}, calculated for a single electron incident on the foil at a mixture pressure of 1 atm optimum for the Xe laser operation as a function of the initial beam electron energy, E_0, (Fig. 3a) indicates that the maximum energy is deposited for E_0 = 180-190 keV. The efficiency of energy deposition $\eta = E_{ab}/E_0$ (Fig.3b) is sufficiently high (η = 0.45). Increasing E_0 the deposited energy decreases E_{ab} because the electrons scatter and leave the operating volume that results in a decrease of η and increase of the energy loss for heating the foil and the net. The maximum efficiency of energy deposition, η = 0.50, is achieved on exciting the gas with electrons having energy E_0 = 160 keV. Measurements carried out with the calorimeter at a current of 60 A and pulse duration $\tau_{0.5} \sim 25$ μs have shown that the total beam energy injected into the gas, W_{tot}, is about 160 J, which is in good agreement with calculation data (W_{tot} = 170 J).

The measured and calculated radial distributions of the spontaneous radiation and the absorbed energy are given in Fig.4. From these curves it can be concluded that for E_0 = 160-180 keV good uniformity is achieved in the central part of the chamber, with the energy deposition in this region being higher that in the case of one-sided pumping. The calculation and experimental data in Fig. 4 are for the AB section of Fig, 1. It should be noted that the values of the absorbed energy near the foil at two diametrically opposite points differ by a factor of 1.5. The calculated and the measured distributions well agree in form in the range r 4 cm. The experimental values for the limiting points at which measurements were carried out (r = 4 cm) might be underread because of unprecious setting of the inlet diaphragm into the radiation aperture.

Measurements of the resonator quality (the radiation energy) was measured for the reflection factor of the outlet mirror R ~ 99, 33, 27, and 6 %) have shown that the resonator with R ~ 33 % is optimum. With the optimum resonator and the outlet mirror 80 mm in diameter, the radiation energy was ~ 2 J at a 160 kV electron energy and 60 A beam current behind the foil. The lasing efficiency reached ~ 2 % of the deposited energy.

Figs 5-7 present the results of a study of a Penning neon plasma laser operating at a wavelength of 585.3 nm with operating pressures of up to 1 atm. The radiation pulse is delayed with respect to the beginning of pumping and ceases while the beam current continues (Fig. 5). The radiation power increases with pressure (Fig. 6). As this laser is designed for the operating pressure 1 atm, the mixture containing 25 % Ne turned out to be optimum. The efficiency of the Ne laser is lower by an order of magnitude than that

of the Xe laser.

In conclusion the e-beam-pumped Ar-Xe laser due to its rather high efficiency of 2 % at a relatively short wavelength of 1.73 μm and long radiation pulse of 10^{-4}-10^{-3} s, can be competitive with a CO_2 laser when using in some technological applications. The Xe laser has the advantages that its active medium consists of inert gases, it operates with quartz optics and at a radiation pulse duration of 10^{-4}-10^{-3} s the optimum pressure of its operating mixture is 1 atm.

REFERENCES

1. Lasers in technology / Ed. by M.F.Stelmakh. - Moscow: Energiya, 1975 (in Russian)
2. G.A.Abilsitov, E.P.Velikhov, V.S.Golubev et al. High-Power gas discharge CO_2 lasers and their application. - Moscow: Nauka, 1984 (in Russian)
3. A.M.Belen'ky, V.V.Vasiltsov, V.S.Golubev, A.M.Zabelin, V.F.Lebedev, P.G.Leonov, D.K.Medvedev, A.A.Morozenkov, S.K.Chekin, and R.G.Shakirov. - Kvantovaya Elektronika, 13, 1720 (1986) (in Russian)
4. N.N.Koval, Yu.E.Kreindel, G.A.Mesyats, V.S.Skakun, V.F.Tarasenko, V.S.Tolkachev, A.V.Fedenev, A.A.Chagin, P.M.Shchanin. - Pis'ma Zh. Tekh. Fiz., 12, 37 (1986) (in Russian)
5. L.G.Vintizenko, V.I.Gushenets, N.N.Koval, G.A.Mesyats, V.S.Skakun, V.F.Tarasenko, A.V.Fedenev, and P.M.Shchanin. - Dokl. AN SSSR, 288, 609 (1986) (in Russian)
6. E.L.Patterson, G.E.Samlin, and P.J.Brannon. - Sandia Report, SAND 89-0716. VC-414, July, 1989
7. N.G.Basov, V.V.Baranov, V.A.Danilychev, A.Yu.Dudin, D.A.Zayarny, D.G.Merkulov, A.V.Romanov, L.V.Semenova, N.N.Ustinovsky, I.V.Kholin, A.Yu.Chugunov. - Kvantovaya Elektronika, 14, 1739 (1987) (in Russian)
8. V.V.Ryzhov, and I.Yu.Turchanovsky. - Kvantovaya Elektronika. 14, 991 (1987) (in Russian)
9. S.A.Lawton, J.B.Richards, L.A.Newman, L.Specht, and T.A. De Temple. - J. Appl. Phys., 50, 3888 (1979)
10. V.F.Losev, and V.F.Tarasenko. - Kvantovaya Elektronika, 7, 663 (1980) (in Russian)
11. N.G.Basov, V.V.Baranov, A.A.Beloglazov, V.A.Danilychev, A.Yu.Dudin, D.A.Zayarny, A.G.Korolev, A.V.Romanov, N.N.Ustinovsky, I.V.Kholin, and A.Yu.Chugunov. - Kvantovaya Elektronika, 15, 453, (1988) (in Russian)
12. N.N.Koval, Yu.E.Kreindel, V.S.Tolkachev, and P.M.Shchanin. - Pis'ma Zh. Tekh. Fiz. 9, 568 (1983) (in Russian).

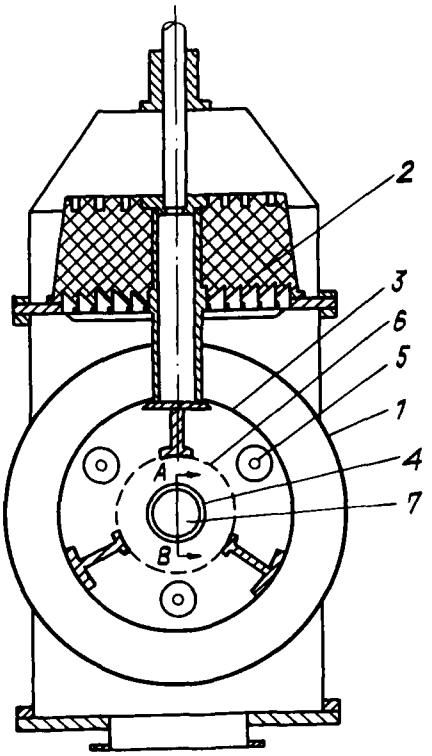


Fig. 1. Schematic of the laser with an accelerator.

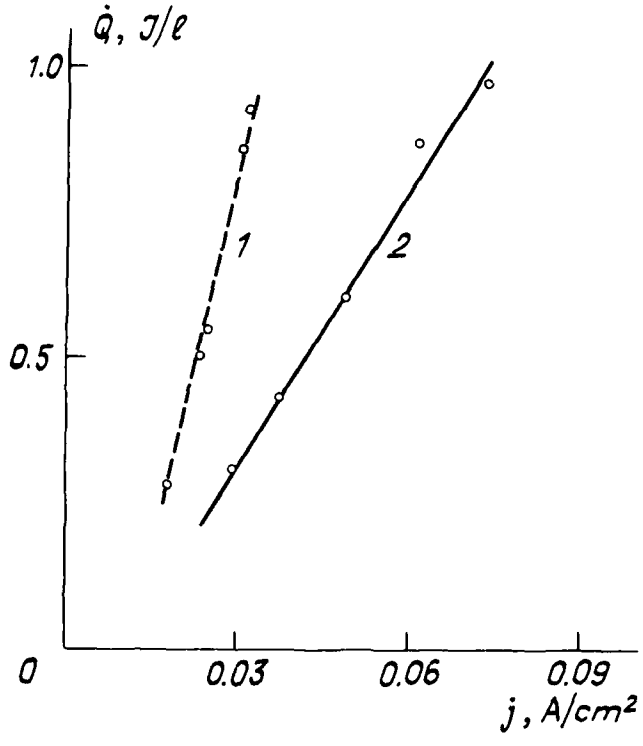


Fig. 2.

The specific radiation energy as a function of the beam current for the radially-converging-beam laser (1) and the planar-diode laser (2)

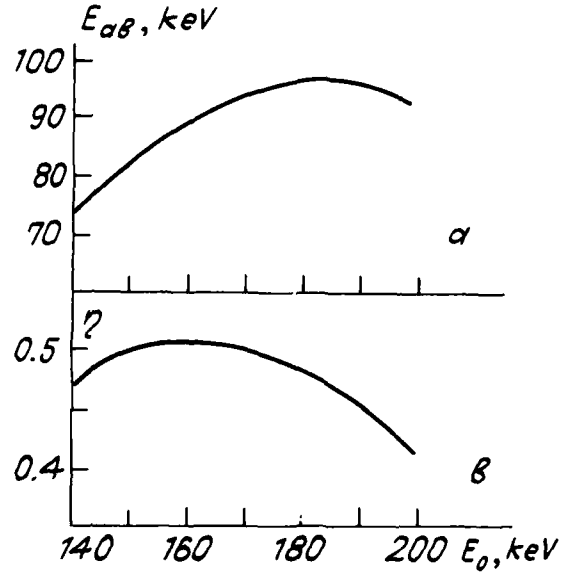


Fig. 3.

The total energy absorbed in the laser chamber operating volume (a) and the energy deposition efficiency (b) as a function of the initial beam electron energy. The Ar:Xe = 100:1 mixture at p = 1 atm.

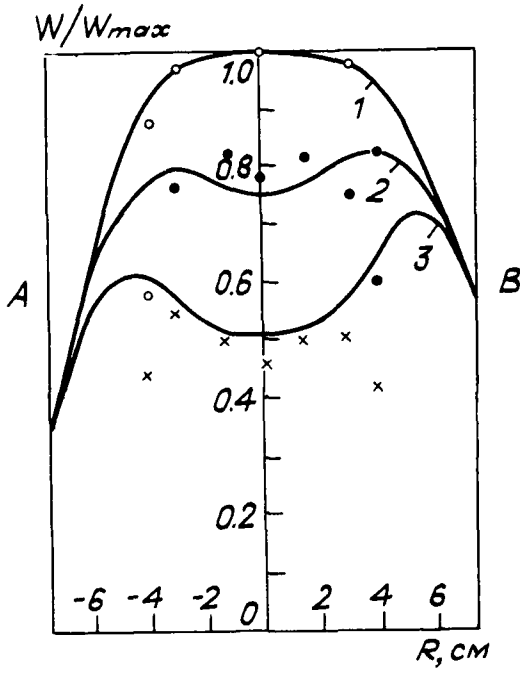


Fig. 4.

Radial distributions of the absorbed energy and the spontaneous radiation energy (dots) for different initial energies: o - 180 keV (1), o - 160 keV (2), x - 140 keV (3).
The experimental and calculation data are normalized for a central point at E_o = 180 keV. The source is on the right.

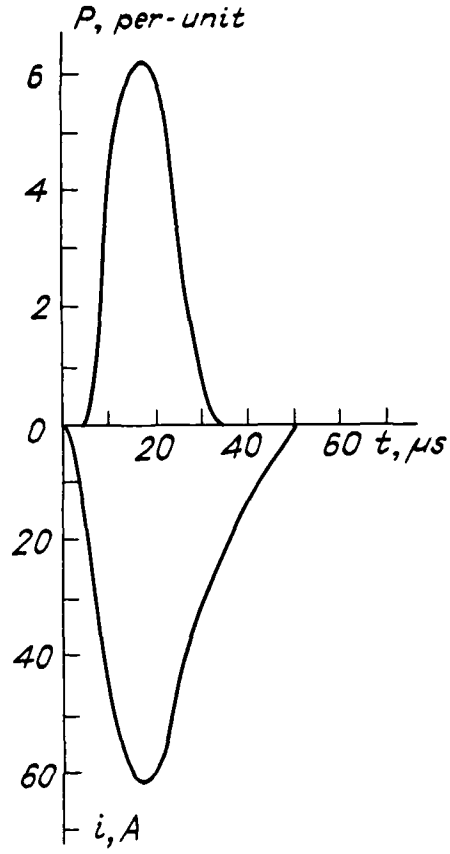


Fig. 5.

Waveforms of the beam current (1) and the per-unit radiation power (2) for the He:Ne:Ar = 70:25:5 mixture at p = 1 atm and an accelerating voltage V_o = 150 kV. The transmittance of the outlet mirror T = 2 %.

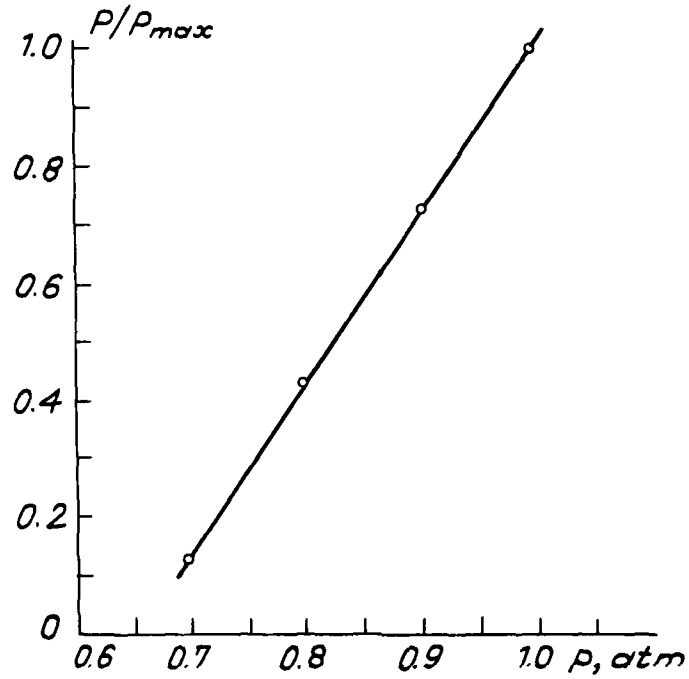


Fig. 6.

The radiation power as a function of the mixture pressure. The He:Ne:Ar = 70:25:5 mixture, V_o = 150 kV, the beam current i = 50 A.

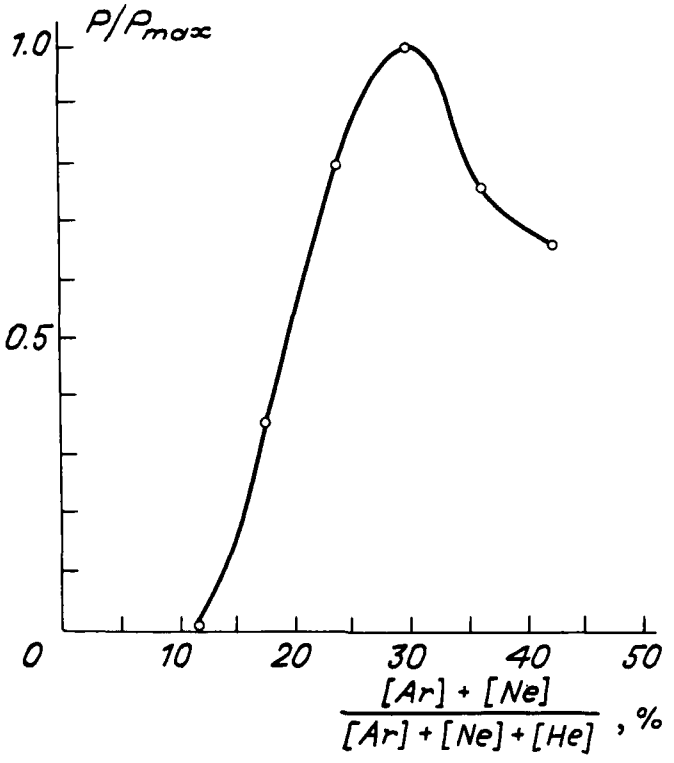


Fig. 7.
The radiation power as a function of the percentage of Ar + Ne in a He-Ne-Ar mixture. Ar:Ne = 1:5, V_o = 150 kV, i = 50 A.

A DOPPLER LIDAR WITH CO_2-LASER INTRACAVITY DETECTION

A.P. Godlevskii, doctor, E.P. Gordov, professor,
A.I. Zhiliba, doctor, P.P. Sharin
Institute of Atmospheric Optics, Siberian Branch USSR
Academy of Sciences, Tomsk
USSR

The study of characteristics of moving objects based on the use of the Doppler lidar is usually performed with application of a heterodyne detection scheme. Another version of a high sensitive Doppler lidar based on the intracavity coherent laser detection is developed. In this paper the Doppler lidar with CO_2 laser intracavity detection in the laboratory and atmospheric experiment is investigated. Vibrations of a retroreflector with amplitude of 50 μm have been detected at distances up to 500 m.

Introduction

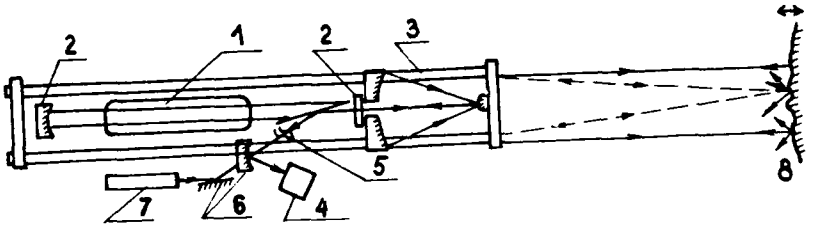
Laser radar applications are known to be restricted by task of processing low return signals. The problem has stimulated wide use of conventional heterodyne detection techniques. The latter exhibit very favorable characteristics such as high noise immunity and extremely high sensitivity reaching the quantum noise limit. However, the heterodyne detection appears to require much sophisticated lidar systems and to impose several restrictions on the stability of the reference signal.

On the other hand, it has been pointed out that the laser intensity may be dramatically changed by feeding a portion of the backscattered signal power into the laser cavity /1/. Lasers have also been considered as return signals detectors /2-5/ . Such laser detectors permit the Doppler frequency shifts caused by a target motion to be measured with good precision. Devices based on this principle are used for detection and ranging the moving targets as well as in velocimetry /6-9/.

Experimental Setup

The setup consists of a CO_2 laser, a transmitting-receiving optical system, and a signal processing unit. The cw CO_2 laser employs a standard sealed-off tube with discharge gap of $\ell \sim 120$ cm. The laser output power is about 18 W (line PC20), $\lambda = 10.6$ um).

Laser intensity stabilization is achieved by decreasing the mechanical disturbance of the laser resonator. The current is hold from 4 to 35 uA with precision to one percent at pulsations about 0.2 per cent. Optical tract is formed by Cassegrain telescope with the main mirror of 15 cm in diameter and a focal length of 70 cm. A portion of the laser beam reflected back by Breuster window of the gas discharge tube is focused by a spherical mirror with focus of 5 cm onto the photodetector.



Experimental setup

1 - a discharge tube of CO_2 laser; 2 - laser cavity mirrors; 3 - a Cassegrain telescope; 4 - a photodetector; 5 - an optical attenuator; 6 - a splitting mirror; 7 - a He-Ne laser for adjustment; 8 - a target.

Experimental Results

The measurements were carried out in the laboratory (at range 3 m) and in real atmosphere (at ranges 20 m, 110 m, 500 m). The vibrating objects with different reflectivity were used as the targets.

As shown in Fig. 2 the oscillogram pictured the beat breakdown at the beat breakdown at the extreme point of the sinusoid when the motion stops at the return point. At this point a Doppler frequency shift drops to zero. The interval between these events is one half period T of the target oscillation. The total number of fringes between these reversals represents the maximum displacement of the target in units of half-wave length

$$x = \frac{T}{P} \frac{\lambda}{2}$$

Here P is the period of the Doppler modulation. Thus, this oscillogram shows that the target is vibrating with the frequency 100 Hz; maximal amplitude is 26.5 um. The Doppler frequency shift of 2.5 kHz indicates that a maximum reflector velocity is near 1.32 cm/s.

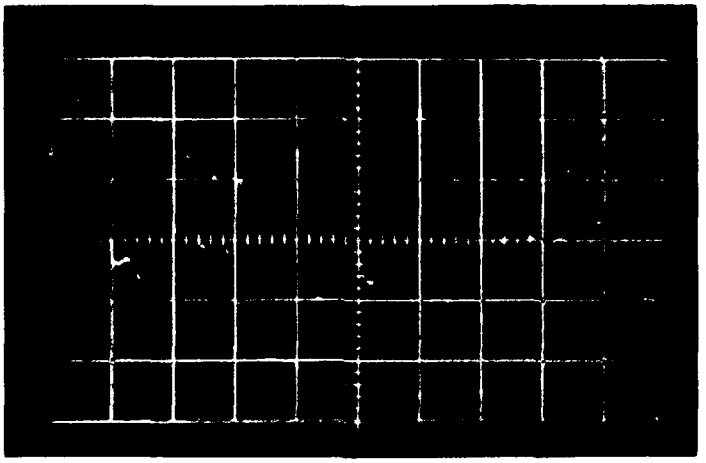


Fig. 2. Reflection from aluminium plate (vibration frequency 100 Hz) -upper trace. Horizontal scale - 1 μs/div. Vertical scale - 100 mV/div.

Fig. 3 shows 5 msec fragment of the Doppler signal from an imitator. The amplitude of motion is 0.25 mm. The targets velocity is 4.8 cm/s.

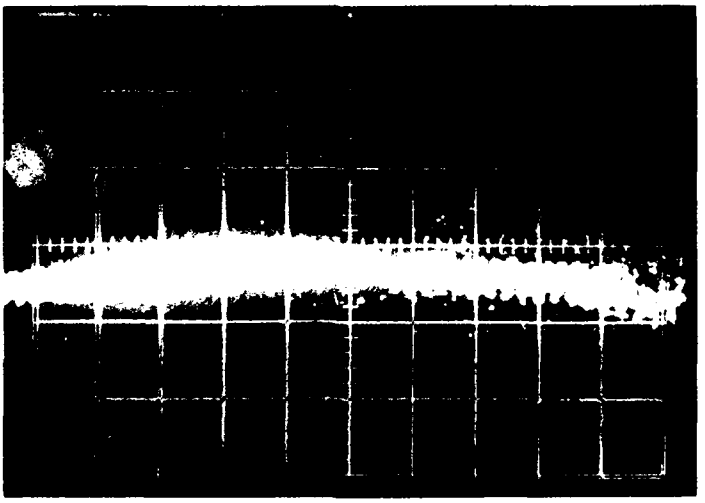


Fig. 3. Reflection from the imitator of linear motion. Horizontal scale - 15 μs/div. Vertical scale - 100 mV/div. The distance from the laser to target is 20 m.

Using the targets vibrating with a constant frequency and amplitude about 10 series of laboratory measurements are carried out to determine the laser field response and the threshold sensitivity to return signal power fed into the laser cavity. Normalized signal amplitude (oscillating components) VS the signal loss R_{eff} characterizing the back-

scattered power returned to the laser cavity is shown in Fig.4. The absolute minimum detectable signal power was found to be 4 10^{-13} W/Hz.$^{1/2}$

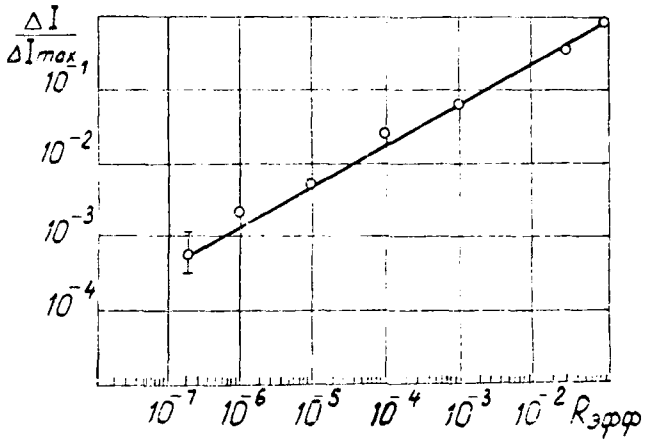


Fig. 4. The normalized amplitude of Doppler signal as a function of the effective reflection coefficient

Measurements in the Atmosphere

The studies have included measurements of signal attenuation and fluctuations. The data on the signal-to-noise ratio (SNR) obtained with different targets (with different reflectivities and roughness of surfaces) located at 3 m, 110 m, 500 m from the laser system are presented in table.

TABLE

Dependence of signal-to-noise ratio (SNR) (dB) on Distance

Target	distance (m)		
	3	110	500
Aluminium mirror	93-96	63-65	32
Duraluminium plate with rough surface	63	42	20
Thin roughness aluminium	67	29-32	15
Wooden surface	40	22	9
Paper cardboard	43	20	-
Emery paper (d 1 mm)	32	19	-
Emery paper (d 1 mm)	30	15-16	-

Fig. 5 shows the oscillogram of Doppler signal from duraluminium target vibrating at 45 Hz frequency. The target was located at the distance 100 m from the laser system. As shown in Fig.5 intensity modulation frequency which occurs due to atmospheric turbulence and quality of the target surface, is smaller that the Doppler frequency (latter being about 1.3 kHz), the depth of modulation has reached 80 per cent.

The observed strong fluctuations of the signal are caused mainly by disorientation of the reflecting surface with respect to the optical axis of the laser beam.

Conclusions: The above results show high sensitivity of the intracavity laser detection. This approach to Doppler lidar is promising for some fruitful applications.

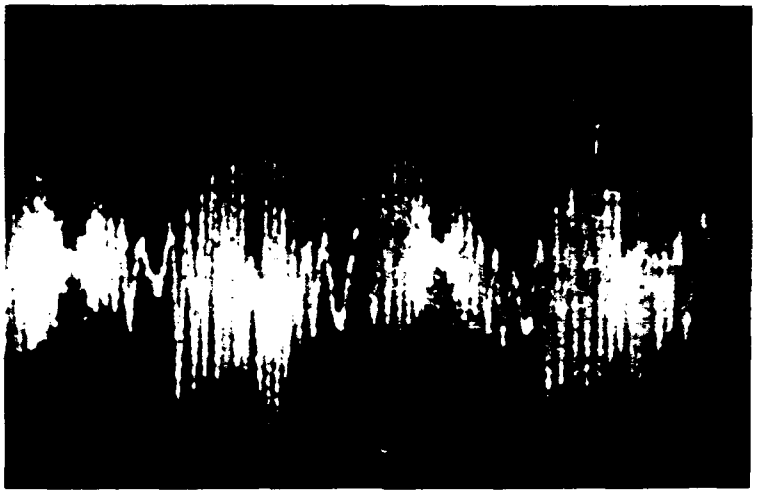


Fig. 5. Reflection from duraluminium target. Horizontal scale - 5 ms/div. Vertical scale - 10 mV/div.

References

1. R.F. Kazarinov, R.A.Suris, Sov.Phys.JETP, 66, 1067 (1974).
2. A.P.Godlevskii, A.K.Ivanov, Yu.D.Kopytin, Sov.Kvantovaya Elektron. 9, 2007 (1982).
3. W.M.Doyle. Electro-Optics 2, 7 (1971).
4. C.Wheder, S.J.Fielding. J.Phys. E5, 101 (1972).
5. J.B.Gerardo, Y.T.Verdeyen. Proc. IEEE, 52, 6 (1964).
6. H.W.Yentnik, R.F. de Mul et al. Appl.Opt. 27, N2 (1988).
7. L.J.Hughes, J.O'Shaughnessy and E.K.Pike. IEEE J.Quantum Electron. QE-8, 909 (1972).
8. J.H.Shunside. Appl.Opt. 23, 61 (1984).
9. P.E.Kolosov, V.N.Lisitsyn, V.A.Orlov, Yu.N.Fomin, Sov.J.Quantum Electron. 9,1093(1982).

LASER-INDUCED NONLINEAR EFFECTS IN THREE-PHOTON RESONANT IONIZATION AND ABOVE-THRESHOLD DISSOCIATION OF DIATOMIC MOLECULES

A.I.Pegarkov, L.P.Rapoport
Department of Theoretical Physics, Voronezh State University
394693 Voronezh, USSR

I.I.Tugov
Institute of General Physics of the USSR Academy of Sciences
117942 Moscow, USSR

Abstract

Analytical equations have been derived for the differential cross-section and ion yield in three-photon ionization and dissociative ionization. The laser radiation frequency is assumed to be in resonance with the electronic transition frequency.

We have used a vibrational multichannel Green function allowing for the laser-indused nonadiabatic interaction of resonant electronic terms. The photoelectron angular distributions take due account also of the effects which are due to the breakdown of spherical symmetry of the (quasi-) molecular ion field. The results are helpful to explain the observed nonlinear structure in the photoionization spectrum of sodium molecular vapors.

The diatomic molecules multiphoton dissociation is studied within a complex quasi-energy approach. It is shown that the involvement of three-photon above-threshold dissociation eliminates the discrepancy between earlier theory and experimental data for a hydrogen multiphoton spectrum.

A. Three-photon resonant ionization

Three-photon resonant ionization (TPRI) implies 'step-by-step' excitation of a molecule. The process takes place if a molecule has two excited electronic terms if the electronic transition energies and the laser photon energy $\hbar\omega$ are equal. A two-particle system 'molecular ion + photoelectron' or a three-particle system 'atom + atomic ion + photoelectron' may form at different radiation frequencies and photoelectron energies :

$$AB + (N + 3)\hbar\omega \rightarrow \begin{cases} AB^+ + e^- + N\hbar\omega & (1) \\ A + B^+ + e^- + N\hbar\omega . & (2) \end{cases}$$

Process (2) is a three-photon resonant dissociative ionization (TPRDI).

The last years have seen experimental investigations of sodium vapor multiphoton ionization that have yielded a number of important findings (see [1,2] and the references therein). The following specific features have been established.

- The molecular ionization spectrum , i.e. the yield of the Na_2^+ molecules as a function of the laser wavelength, has resonant peaks that do not coincide with the absorption lines for the $Na_2(A^1\Sigma_u^+)$ term.

- Several new peaks emerge with an increasing laser radiation intensity .

- When the intensity I is under $5\cdot10^4$ W·cm^{-2} the Na_2^+ - ion yield depends on I as $i(Na_2^+) \sim I^{2.2}$, when the intensity I exceeds $5\cdot10^4$ W·cm^{-2} the relationship is $i(Na_2^+) \sim I^{1.0}$.

- The strong spectrum line at λ = 602.17 nm disappears completely at high laser intensities.

- The Na_2^+ molecular ion spectrum and the Na^+ atomic ion spectrum have the same structure at any laser intensity.

Wu et al [1] presume that this behavior of the ion yield is due to the fluorescence, photoabsorption, and decay processes involving the excited electronic terms. However, we think that the observed effects demonstrate a substantial impact of the resonant radiation interaction on the dynamics of intramolecular motion.

Generally speaking, if a molecule is exposed to visible or UV laser light we cannot employ an adiabatic approximation for separating the electronic and the nuclear motions. For example, for the Na_2 molecule the electronic transition momenta are substantial (about 10 Deb.) and, as the laser intensity increases, the energy of the radiative interaction of resonant terms becomes comparable with that of vibrational quantum. The rotation-vibration spectra of electronic terms undergo significant changes so that the conventional probabilities for processes (1), (2) cannot be calculated in terms of standard perturbation theory.

For processes (1), (2) the probability for ionization can be written as

$$dP_{fi} = 2\pi\hbar^{-1} |\langle\tilde{\Psi}_f| V G^+(E_i^0) V |\Psi_i\rangle|^2 \delta(E_f - E_i^0) d\rho_f ,$$

where $|\Psi_i\rangle$ is the state of the system 'molecule + electromagnetic field',

$|\tilde{\Psi}_f\rangle$ is the state of the system 'molecular (or quasi-molecular) ion + photoelectron + e.f.', these states being the eigenvectors of a Hamiltonian without radiative perturbation V, that is written in the second quantization form, $G^+(E)=(E+i0-H)^{-1}$ is the resolvent of a complete Hamiltonian of the interacting system 'nuclei + electrons + e.f.', H. In this system an account is taken only the coupling of the molecular terms due to radiative interaction.

The differential cross-section for the TPRI (1) process defined by us as

$$d\sigma = dP_{fi}/\mathcal{F}, \quad \mathcal{F} = c(N+3)/\Delta L^3$$

($\mathcal{F}$ is the incident photon flux), integrated over the photoelectron energy, for K>>1, is given by

$$\frac{d\sigma_{PI}^{KM}(\mathbf{k}_e,\omega)}{d\hat{\mathbf{k}}_e} = \frac{m_e k_e \omega}{\hbar^2 c^2} I \Big| \sum_{l'm'} T_{Mm'}^{Kl'} Y_{l'm'}^{*}(\hat{\mathbf{k}}_e) \Big|^2 , \qquad (3)$$

$$T_{Mm'}^{Kl'} = \sum_{\nu} B_{Jll'}^{(-)\text{æ}'\text{æ}} C_{J\Omega l'm'}^{KM} C_{K'M'lm}^{J\Omega} \text{æ}_{PI}^{KM} \times$$

$$\langle \tilde{\chi}^{o}_{\text{æ}'}(R) | M^{Jll'}_{\text{æ}'\text{æ},2}(R) G^{23}_{KM}(R,R';E_i^o+i0) d_{31}(R') | \chi^o_{v1}(R') \rangle, \nu=\{J,\Omega,\text{æ}',M',l,m\}, \text{æ}=\{i,v,K,\Lambda\}$$

K is the total orbital angular momentum of a molecule, **M** and Λ are its projections onto the OZ'-axis of a laboratory reference system and onto the molecular reference axis OZ, $\chi^o_{vi}(R)$ ($\tilde{\chi}^o_{\text{æ}}(R)$) is the wave function of the nuclear motion in unperturbed electronic term of a molecule AB (molecular ion AB^+) $U_i(R)$, $B_{Jll'}^{(-)\text{æ}'\text{æ}}$ is the phase factor, $C_{J\Omega lm}^{KM}$ stands for the Clebsch-Gordan coefficients [3], $d_{ij}(R)$ and $M^{Jll'}_{\text{æ}'\text{æ},i}(R)$ are the integrals over all electronic coordinates **r**, the geometric factor æ_{PI}^{KM} depends on the directions of electronic momenta, polarization of an incident photon, and the angle made by the quantization axes (of the laboratory and molecular reference system).

The TPRI cross-section integrated over the direction of electron propagation $\hat{\mathbf{k}}_e$ is

$$\sigma_{PI}^{KM}(k_e,\omega) = \frac{m_e k_e \omega}{\hbar^2 c^2} I \sum_{l'm'} |T_{Mm'}^{Kl'}|^2 . \qquad (4)$$

Equations (3), (4) involve the nondiagonal component $G^{23}_{KM}(R,R';E)$ of a three-channel Green function of the nuclear motion (TCGF) $\mathbf{G}(R,R';E)=||G^{\alpha\beta}_{KM}(R,R';E)||$, $\alpha,\beta= 1,2,3$ [4]. The TCGF fits the matrix equation with a nondiagonal vibrational Hamiltonian $\mathbf{H}(R)$

$$\{\mathbf{IE} - \mathbf{H}(R)\}\mathbf{G}(R,R';E) = \mathbf{I}\delta(R-R'), \quad \mathbf{I} = ||\delta_{\alpha\beta}|| ,$$

$$\mathbf{H}(R) = -\frac{\hbar^2}{2\mu}\mathbf{I}\left(\frac{d}{dR}\right)^2 + \mathbf{U}(R) + \mathbf{V}(R) ,$$

$$\mathbf{U}(R) = \mathrm{diag}\{U_1^K(R), U_2^K(R), U_3^K(R)\}, \quad \mathbf{V}(R) = ||V_{\alpha\beta}(R)||,$$

$$U_i^K(R) = U_i(R) + (N+3\delta_{1i}+2\delta_{3i}+\delta_{2i})\hbar\omega + \hbar^2[K(K+1)-\Lambda_i^2]/2\mu R^2 + (\delta_{4i}+\delta_{5i})\varepsilon_e ,$$

$$i = 1,2,3,4,5 .$$

The nondiagonal elements $V_{ij}(R)$ of the Hamiltonian is proportional to the laser field strength. If the matrix of interactions $\mathbf{U}(R) + \mathbf{V}(R)$ is Hermitian, the TCGF can be written as

$$\mathbf{G}(R,R';E) = \frac{2\mu}{\hbar^2}\begin{cases} \Phi_2(R)\mathbf{W}^{-1}\Phi_1^+(R'), & R>R' \\ \Phi_1(R)[\mathbf{W}^+]^{-1}\Phi_2^+(R'), & R<R' \end{cases} ,$$

$$W = \Phi_1^+(R)\frac{d}{dR}\Phi_2(R) - [\frac{d}{dR}\Phi_1^+(R)]\Phi_2(R) = \text{const},$$

where $\Phi_{1,2}(R)$ stands for two linearly independent matrix solutions of the homogenuous differential equation

$$\{IE - H(R)\}\Phi_{1,2}(R) = 0 . \qquad (5)$$

The regular at the origin funotion $\Phi_1(R)$ and the regular at the infinity funotion $\Phi_2(R)$, whioh in principle are the exaot solutions of the three-ohannel system (5), have been obtained analytioally on a quasiolassioal approximation within the theory of laser-induoed nonadiabatio transitions.

B. Three-photon resonant dissociative ionization. Laser intensity dependence

For the TPRDI (2) oross-seotion equations (3), (4) are not ohanged significantly

$$\frac{d^3\sigma^{KM}_{DPI}(\mathbf{k}_e,\omega)}{d\hat{\mathbf{k}}_e d\hat{\mathbf{q}} d\varepsilon} = \frac{m_e k_e \omega}{\hbar^2 c^2} I \Big| \sum_{l'm'} t^{Kl'\varepsilon}_{Mm'} Y^*_{l'm'}(\hat{\mathbf{k}}_e)\, Y_{KM}(\hat{\mathbf{q}})\Big|^2 , \qquad (6)$$

$$t^{Kl'\varepsilon}_{M\mu'} = \sum_{\tilde{\nu}} C^{KM}_{J\Omega l'm'} C^{J\Omega}_{K'M'lm} \int_0^\infty d\varepsilon' [B^-_{K\Lambda} B^{(-)}_{Jl'\tilde{\text{æ}}'\tilde{\text{æ}}}]^* \text{æ}^{KM}_{PI} \times$$

$$\langle \tilde{\chi}^0_{\varepsilon'\tilde{\text{æ}}}(R) | \tilde{M}^{Jll'}_{\varepsilon'\tilde{\text{æ}}'\varepsilon\text{æ},2}(R)\, G^{23}_{KM}(R,R';E^0_i+i0)\, d_{31}(R') | \chi^0_{v1}(R')\rangle, \quad \tilde{\nu} = \{J,\Omega,\tilde{\text{æ}}',M',l,m\},$$

$$\sigma^{KM}_{DPI}(k_e,\omega) = \frac{m_e k_e \omega}{\hbar^2 c^2} I \int_0^{\varepsilon_{max}} d\varepsilon \sum_{l'm'} |t^{Kl'\varepsilon}_{Mm'}|^2, \qquad (7)$$

here ε_{max} is a maximum kinetio energy assooiated with the relative motion of the atomio photofragments A and B^+, $\tilde{\text{æ}} = \{i,K,\Lambda\}$.

The ion yield for processes (1), (2) oan be defined as

$$i(AB^+) = N_{AB} I \sum_n F_n(I) \sum_{E^{(I)\Lambda}_{v,K} = E^I_{0,0}} \vartheta(3\hbar\omega - U^B_I)\, \sigma^{KM}_{PI}(k_e,\omega) , \qquad (8)$$

$$i(B^+) = N_{AB} I \sum_n F_n(I) \vartheta(3\hbar\omega - U^C_I)\, \sigma^{KM}_{DPI}(k_e,\omega) , \qquad (9)$$

$$\vartheta(x<0) = 0, \quad \vartheta(x>0) = 1,$$

where N_{AB} is the moleoular AB density, D^I is the dissooiation potential for the moleoular ion AB^+ ground state, $F_n(I)$ is the Boltzmann distribution, where $E_n(I)$ is the energy of the moleoule AB 'dressed' by the laser field [5], $E^{(I)\Lambda}_{v,K}$ is the free moleoular ion AB^+ energy, U^B_I and U^C_I are the ionization potentials of moleoular and quasimoleoular ions AB^+.

It is evident from expressions (3),(4), (6)-(9), the resonant peaks in the speotrum are produoed by the Green funotion poles. The number and the looation of the poles depend on the laser intensity. Therefore, if the intensity inoreases there ooour new peaks in the ionization speotrum. If the laser field is strong the resonanoes will not oorrespond to the eleotronio-vibration-rotation transitions. These phenomena are due to the ooupling of vibration-rotation states of resonant eleotronio terms in the laser field. The very interesting result is that the same TCGF's oomponent $G^{23}_{KM}(R,R';E)$ appears in the oross-seotion equations for ionization (3) and dissooiative ionization (6). That is why the atomio and the moleoular ion yields have qualitatively the same struoture (see (8),(9)). Furthermore the presenoe of $G^{23}_{KM}(R,R';E)$ in formulas (3) and (6) makes the ion yields (8) and

(9) to be nonpolynomial functions of the laser intensity. Using our analytical equations for the TCGF components [4] and separating the evident intensity dependence in the yields, we obtain a total expression

$$i \sim I^2 |\sqrt{P_{23}(1-P_{23})}/(1-P_{13})|^2.$$

The probabilities for laser-induced nonadiabatic transitions P_{13} and P_{23} within the Landau-Zener model depend exponentially on the laser intensity.

/1/ In a general case, where the probabilities are $(1-P_{13}) \sim P_{13} \sim (1-P_{23}) \sim P_{23} \sim 1$, the laser-intensity dependence of the ion yield is an intricate exponential function (a and b are the constanters)

$$i \sim I^2 e^{-bI}(1-e^{-bI})(1-e^{-aI})^{-2}. \qquad (10)$$

/2/ Under the conditions $(1-P_{13}),(1-P_{23}) \ll 1$, $P_{13} \sim P_{23} \sim 1$ it is obtainable from general expression (10)

$$i \sim I^2\left(\frac{b}{a^2 I} - \left(\frac{b}{a}\right)^2\right) \cong I.$$

/3/ In the lower field, where we have $(1-P_{13}),(1-P_{23}) \ll 1$, $P_{13} \cong P_{23} \cong 1$, $P_{13}^2 \sim P_{23}^2 < 1$ the ion yield is

$$i \sim I^2 \frac{1-(1-bI)^2}{1-(1-aI)^2} \cong I^2.$$

/4/ In the last case when $(1-P_{23})/P_{23} \ll 1$, or $(1-P_{13})/P_{13},(1-P_{23})/P_{23} \ll 1$, the laser intensity dependence takes an ideal cubic form defined in terms of the perturbation theory

$$i \sim I^3.$$

The laser intensity dependence contains three characteristic points of intensity where the ion yield function changes its form : (a) from the cubic to a square law, /4/ → /3/; (b) from the square law to a linear one, /3/ → /2/; (c) from the linear form to intricate exponential form, /2/ → /1/. The second characteristic point intensity I_b has been observed in experiment [1]. Subsequent studies of resonant multiphoton ionization of Na_2 in fields of intensities $I > 10^6$ W·cm^{-2} and $I < 10^4$ W·cm^{-2} may reveal remaining two points I_a and I_c.

C. Above-threshold dissociation

In conclusion, we will briefly discuss the possibility to observing of the above-threshold dissociation (ATD) phenomenon under a multiphoton interaction of an intence laser field with a diatomic molecule

$$AB + (N + 3)\hbar\omega \longrightarrow A + B + N\hbar\omega,$$

using, as example, the hydrogen molecular ion H_2^+.

One-photon dissociation of H_2^+ has been considered by Chu S.-I. in complex quasi-energy formalism [6]. ATD of the H_2^+ molecule can occur if the photon energy $\hbar\omega$ exceeds the dissociation energy of a given rotation-vibration state of the ground electronic term $|1s\sigma_g\rangle$

$$H_2^+(1s\sigma_g) + (N + 3)\hbar\omega \longrightarrow H_2^+(2p\sigma_u) + N\hbar\omega \longrightarrow H + H^+ + N\hbar\omega, \qquad (11)$$

where $|2p\sigma_u\rangle$ is the first excited dissociative term. With due account of three-photon dissociation (11), the intensity-dependence of the photodissociation cross-section is nonlinear and the ATD channels cause appreaciabl variations in the total amplitude.

We calculated the photodissociation cross-section within the framework of the method suggested by Chu S.-I. The Morse potential vibrational wave functions were taken as a basis [7]. The obtained results indicate that the ATD (11) is the cause of the discrepancy between the recent experimental data [8-11] and the previously calculated results.

References

1. C.Y.R. Wu, F. Roussel, B. Carre, P. Breger, and G. Spiess, J. Phys. B. 18, 239 (1985)
2. C. F. Burkhardt, W. P. Garver, and J. J. Leventhal, Phys. Rev. A. 31, 505 (1985)
3. D. A. Varshalovich, A. N. Moskalev, and V. K. Khersonskyi, Kvantovaya Teoriya Uglovogo Momenta (in Russian: Nauka, Leningrad, 1975)
4. A. I. Pegarkov, and L. P. Rapoport, Opt. Spektrosk. (in Russian) 63, 501 (1987)
5. A. I. Pegarkov, and L. P. Rapoport, Ibidem. 65, 95 (1988)
6. S.-I. Chu, J. Chem. Phys. 75, 2215 (1981)
7. I. I. Tugov, v Trudi Fizioheskogo Instituta im. P. N. Lebedeva, F. V. Bunkin, Ed. (in Russian: Nauka, Moskva, 1984), v. 146, pp. 17-64
8. G. Mainfray, C. Manus, and I. I. Tugov, Pis'ma Zh. Eksp. Teor. Fiz. (in Russian) 16, 19 (1972)
9. C. Cornaggia, D. Normand, J. Morellec, G. Mainfray, and C. Manus, Phys. Rev. A. 34, 207 (1986)
10. K. Codling, L. Frasinski, and J. Hatherly, J. Phys. B. 21, L433 (1988)
11. D. Normand, and J. Morreleo, J. Phys. B. 21, L625 (1988)

WALL INTERACTION-FREE VAPOR CONFINEMENT BY LIGHT-INDUCED-DRIFT

S.Gozzini, D.Zuppini, C.Gabbanini, L.Moi

Istituto di Fisica Atomica e Molecolare del CNR
via del Giardino 7 - 56127 Pisa - Italy

Abstract

In this paper the possibility of confining a gas, contained in a spherical cell, far away from the walls by exploiting the light-induced-drift effect is discussed and the preliminary results reported. A spherical cell filled with few torr of Krypton as a buffer gas and with some metallic sodium distilled in a side arm, is illuminated by three couples of orthogonal laser beams obtained by a broad band long cavity dye laser. The first experimental evidence of LID in a three dimension geometry has been obtained and a compression of the vapor in the center of the cell has been observed as due to the contemporary presence of all the six laser beams. These experiments open new perspectives to the study of gas transport properties and of non-equilibrium vapor conditions.

Introduction

The possibility of modifying the atomic motion and the vapor diffusion by using laser light is one of the most important achievement of laser spectroscopy during these last years. Resonance radiation pressure (RRP), which is due to the photon-atom momentum transfer during the absorption-emission processes, has been successfully used to decelerate and to cool atomic beams and to trap neutral atoms[1]. RRP has also been exploited to induce vapor diffusion in a capillary[2] by obtaining the complete deplacement of the vapor from a portion of the cell and its compression in the remaining part. In this case RRP is strongly affected by the high collision rate with the cell walls which continuously thermalize back again the vapor.

Light-induced-drift effect (LID), that is instead favoured by high collision rate with a buffer gas, is more useful to induce huge vapor density variations and faster drift velocities. The main reason of this difference depends on the fact that in LID atomic momenta instead of photon momenta are exchanged. Moreover LID can both push and pull the vapor. LID was proposed and demonstrated by Shalagin, Gel'mukhanov and coworkers[3,4] in 1979. Since that first experiment a lot of LID observations and measurements have been performed so that the dependence of the effect on atom-wall interaction[5,6], on laser detuning and intensity[7], on laser bandwidth[8] as well as on the kind of buffer gases[9] is well known. Density variations larger than two order of magnitude, drift velocities as high as 30 m/s and, for example, isotope separation[10] have been observed. A detailed analysis of stationary and dynamic regimes of LID at low and intermediate saturated vapor densities has been performed on sodium vapor[11,12]. All these experiments have been performed in capillary cells, i.e. under conditions which can be well described by a unidimensional approach. The transverse dimensions of the cells (diameter = 1-2 mm) are comparable with the laser beam cross section and the vapor diffusion is modified only along the major axis of the cell. The vapor can be compressed to either ends of the cell depending on the laser detuning. The interaction of the atoms with the cell walls cannot be avoided under such a geometry, and it imposes some important limitations to LID applications. This restriction can be overcome by performing LID in a three dimensional geometry where the gas is compressed to the center of the cell, far from its walls. This different approach is not straightforward as it requires important modifications of the experimental apparatus as well as the correct evaluation of some experimental parameters. Moreover the possibility of a 3-D LID must be first demonstrated both experimentally and theoretically.

Here we present our preliminary results obtained by using a spherical cell irradiated

by six laser beams directed along three orthogonal axis. A discussion of new possible applications of LID under these conditions will be presented.

Qualitative discussion of 3-D LID effect

LID is observable when an active gas, i.e. resonant with the laser, is immersed in a buffer gas and the laser excitation is velocity selective. When these two conditions are satisfied a drift of the vapor can be observed either along the propagation direction of the laser beam or to the opposite one. The laser can either push or pull the atoms. This macroscopic effect can be explained as follows: laser excitation produces two atomic fluxes, one of excited and the other of ground state atoms, which, when the selected velocity component is not zero, move to opposite directions. As the diffusion coefficients of excited and ground state atoms are in general different, two drift velocities are obtained in the two cases and, as a consequence, a macroscopic induced diffusion of the vapor is observable, whose direction depends on the laser detuning. Drift velocity v_{dr} has a dispersive behaviour as a function of the laser frequency and, in a two level atom, it is zero when laser detuning is zero. The force acting on the vapor can be described by the equation

$$F = C(\nu_L, \Delta\nu_L, D_g, D_e, \ldots)\, I_0\, e^{-kx} \qquad (1)$$

where I_0 is the initial laser intensity, k is the absorption coefficient, x the thickness of the vapor column crossed by the laser and C a parameter which is function of all the other physical quantities determining LID: $D_{g,e}$= diffusion coefficients of ground and excited states, ν_L = laser frequency, $\Delta\nu_L$ = laser bandwidth etc. It has been demonstrated that when a broad band dye laser instead of a single mode dye laser of the same power is used, a two times larger drift velocity can be obtained under, otherwise, similar conditions[12]. When the optical thickness k is negligible, F is constant along the cell and the vapor moves with a drift velocity independent on the position. In this case and under the hypothesis of infinite length cell, the vapor is not compressed while is diffusing. When, on the contrary, the optical thickness is high, the laser is attenuated along the capillary and the drift velocity depends on the position. The vapor is now compressed and the laser beam behaves like an optical piston[13].

v_{dr} depends on the same parameters affecting F and on the friction of the vapor at the cell surface. The interaction with the cell walls, anyway, can be almost cancelled by adopting special coatings which make possible to increase by three order of magnitude the effective vapor drift velocity.

The previous discussion shows that when two counterpropagating laser beams are sent across a capillary, no appreciable effect can be observed when k is small, while a compression of the vapor to the middle of the cell can be observed in the optical piston regime. In this last case, in fact, the forces induced by the two lasers do not mutually cancel and the two optical pistons work, *in first approximation, independently*. This situation can be qualitatively extrapolated to a three dimensional geometry, where three couples of laser beams propagating along orthogonal directions push the vapor to the center of a spherical cell and eventually confine it far away from the cell walls. Also in this case the optical thickness must be not negligible to avoid direct destructive interaction between the laser beams. It is therefore possible to imagine the six laser beams working like six optical pistons which compress the vapor and reduce its volume by increasing its density. This approach is qualitative and, in order to have a correct and detailed description, a system of 3-D differential equations describing the light induced diffusion and the laser propagation inside the vapor must be solved, where the boundary conditions imposed by the cell and by the laser overlapping regions must be properly considered. This problem is underway to be solved. In order to show the complexity of the task let us consider the force F_t acting on the vapor volume V_i placed in one point of the cell as it is shown in fig. 1. V_i is subject to a force F_t which is the resultant of the forces F_i induced by the six laser beams. As the optical thickness is assumed to be high enough to attenuate the laser in a distance short compared to the cell radius r, the F_i are not equal to each other and $F_t \neq 0$. By simple geometrical arguments and by considering, for simplicity, a point situated on the plane determined by two couples of laser beams, it results that the

direction of F_t is not directed to the center of the cell but it is a function of r and θ according to the equation

$$tg\theta' = \frac{e^{-k\sqrt{r_0^2 - r^2\cos^2\theta}}}{e^{-k\sqrt{r_0^2 - r^2\mathrm{sen}^2\theta}}} \frac{e^{kr\ \mathrm{sen}\theta} - e^{-kr\ \mathrm{sen}\theta}}{e^{kr\ \cos\theta} - e^{-kr\ \cos\theta}} \qquad (2)$$

From this equation it derives that θ' coincides with θ only for $\theta = n\ \pi/4$, with n integer, while for all other angles, θ' is different from θ by following a dispersive behaviour as shown in fig. 2.

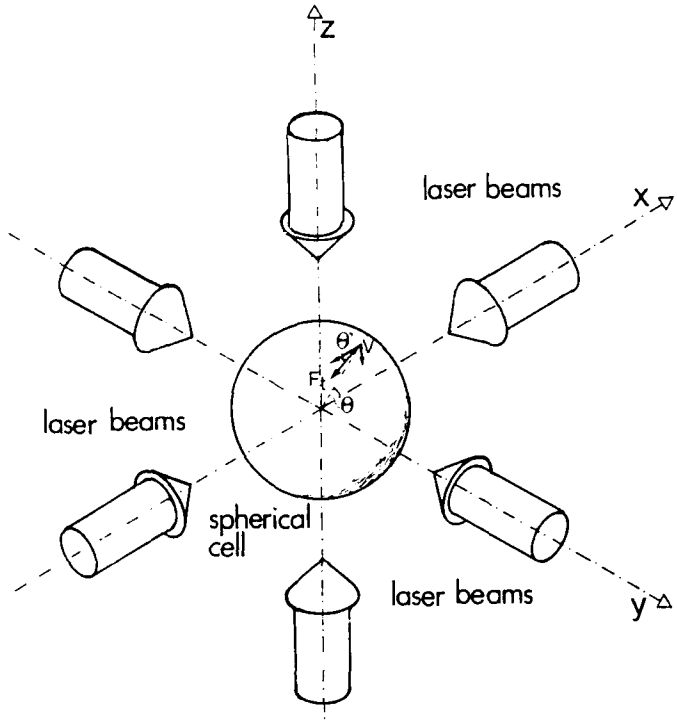


Fig. 1 - Sketch showing a spherical cell with six laser beams. The arrow indicates the direction of the resultant force F_t acting on the vapor cloud V_i.

According to that calculations, the atomic vapor starts moving to the center along curved pathways joining those determined by the laser beam axis. Some sort of vortices seems to be generated whose temporal evolution is difficult to predict without a more detailed approach. It is, anyway, clear that the vapor collapses to the center but it is not evident, without a better definition of the experimental conditions, that a stable configuration can be reached.

Few more considerations may help to better understand the theoretical and experimental difficulties of the experiment. With respect to the unidimensional example given before other differences are present in the 3-D configuration. In this last case, in fact, the vapor density variations scales as r^{-3} and this gives a fast modification rate to the k parameter as soon as the vapor starts to be compressed. This makes difficult to find the optimum initial k value, once the laser intensity is given. If at t=0 the vapor is optically too dense, its compression will be negligible; if, on the contrary, it is optically too thin, the laser beams will interfere destructively. Moreover, as the vapor section decreases during the compression while that of the laser beam is constant, the vapor-laser coupling diminishes too, by introducing an other variable parameter to the problem. Many different experimental solutions can be suggested and checked. For example the laser beams could be focused in order to have a density power function of r, or the laser intensity

could be time dependent etc. But in these cases, which are more difficult to treat theoretically, experimental problems must still be solved. Here in the following the preliminary results are reported[14].

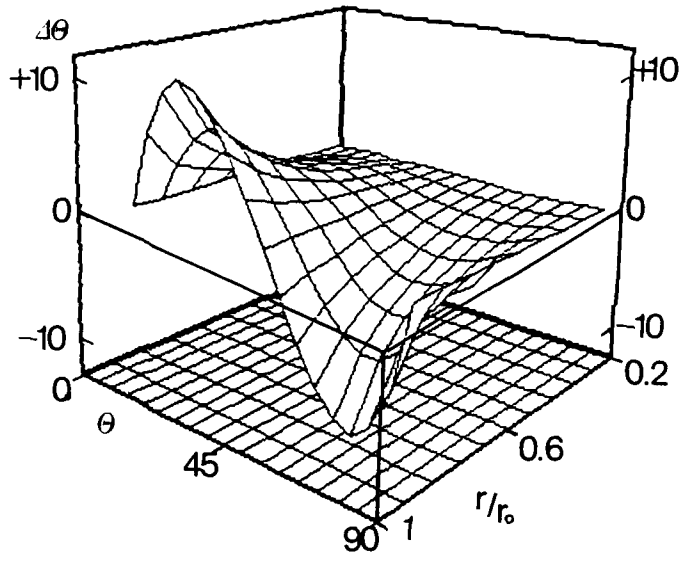


Fig. 2 - Dependence of $\theta - \theta'$ as a function of θ as calculated for different r values.

Experimental apparatus and results

The experiment is performed with a pyrex spherical cell having a 1.5 cm diameter and a reservoir, where some metallic sodium is distilled under vacuum, placed at the end of a short capillary (see fig. 3). The cell, that is filled with few torr of Krypton, is situated in an oven which permits an almost complete view by getting easier its illumination and observation. The LID experiments performed with glass capillaries have shown the determinant role played by the cell walls in the drift of the vapor and to the final equilibrium states. This is essentially dependent on the adsorption energy E_a of the atoms at the walls which, through the equation

$$\tau_a = \tau_0 \, e^{E_a/kT} \qquad (3)$$

where $\tau_0 = 10^{-13}$ s, modifies the time that the atoms spend at the surface. A long τ_a induces both a slowing down of the drift and the production of a sodium layer which has to be removed in order to see any effect in the vapor phase. These problems can be made negligible by adopting a suitable coating having a small E_a. In our experiments the coating is obtained from a ether solution of dimethylpolysiloxane[6] which is chemically attached to the surface and can be heated up to relatively high temperature (T_{max} = 200 ^{0}C). These properties permit to work with saturated vapor over a wide range of densities. In the spherical cell, even if the vapor moves orthogonally to the surface, it is important to avoid the formation of the sodium layer in order to speed up the compression process. For this same reason the metal reservoir is not directly inside the cell but at the end of a short capillary whose impedance disconnects, during the compression transient, the cell from the reservoir. This trick simulates a dry vapor condition and it is determinant for the observation of the effect.

The LID effect is strongly affected also by the laser spectral characteristics. We have shown that a broad band laser, with a particular cavity configuration, may give drift velocities two times larger than those induced by a single mode one having the same

intensity[12]. The laser has a long cavity configuration which allows small frequency separation between the longitudinal modes and easily adjustable total bandwidth[15]. The control of these two parameters optimizes the laser-vapor coupling by preserving the necessary velocity excitation selectivity. The laser has been obtained by extending a commercial dye laser cavity up to a maximum length of 15m. With this configuration a maximum power of about 200 mW for a 4GHz total bandwidth has been obtained. The laser beam is coupled to a bunch of six optical fibers which are,then, splitted apart and properly positioned around the cell. Output couplers make the beams parallel and with a diameter comparable with the cell diameter. A mechanical chopper switches on or off the laser by allowing the analysis of the LID temporal evolution. LID effect is monitored through the fluorescence intensity variations which are proportional to the atomic density. To this purpose a lens system creates an image of the cell which is analyzed by two optical fibers, one placed in correspondence of the cell center (fiber a) and the other one on the outer part of the cell (fiber b). The fibers are coupled to two photomultipliers whose outputs are amplified and processed by a transient digitizer.

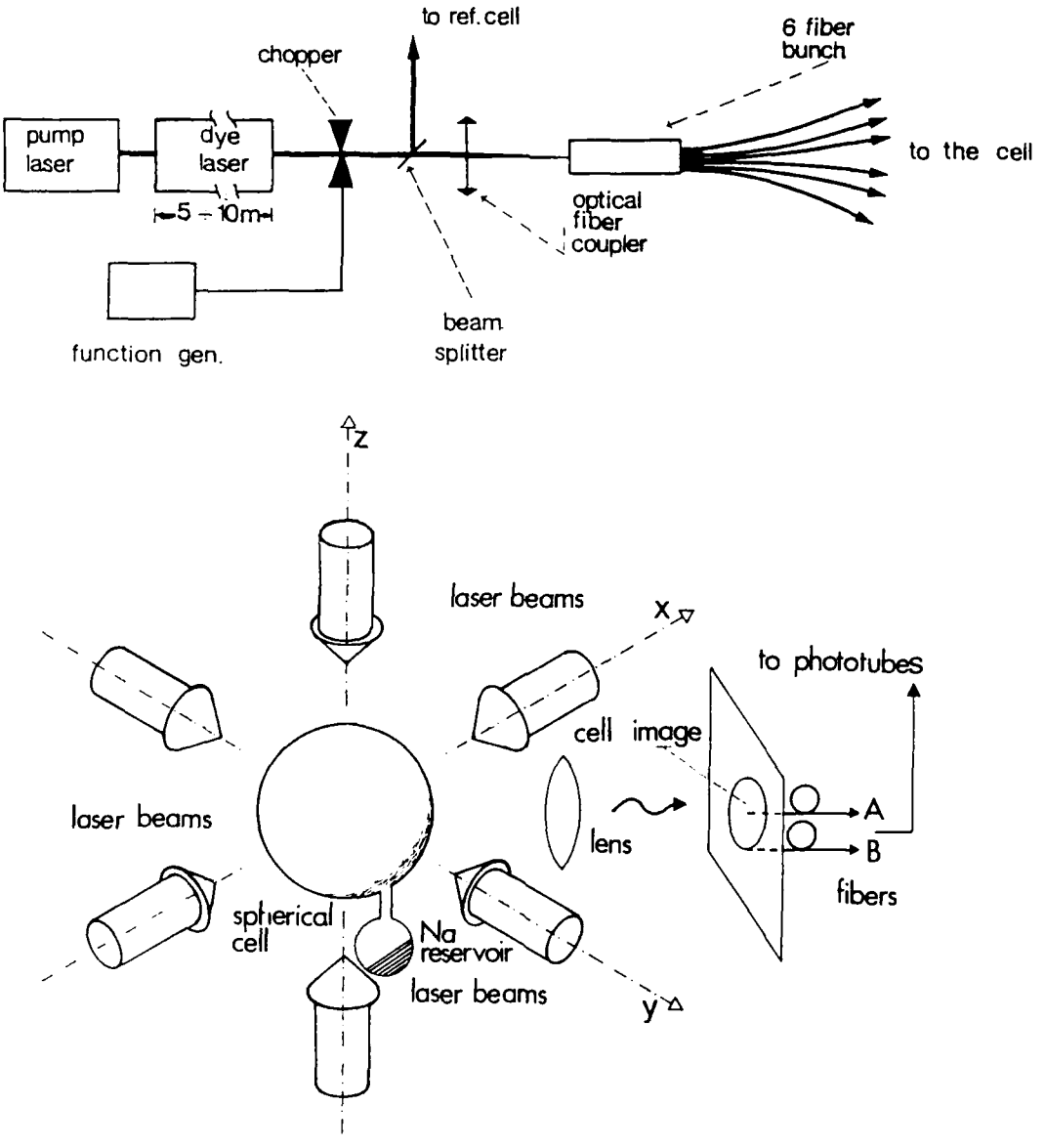


Fig. 3 - Sketch of the experimental apparatus

When the six beams are on, a compression of the vapor to the center of the cell is observed. This produces a decreasing of the fluorescence signal in correspondence of fiber a) (see fig.3) and an increasing in correspondence of fiber b). In fig. 4a and 4b two signals obtained under the given conditions are reported. In fig. 4a the fluorescence signal decreases to about half of the initial value, while in fig. 4b the fluorescence increases by about 2 times by indicating a huge compression to the center of the cell. The signal of fiber b) is roughly independent on its position along the external perimeter of the cell image, while it depends on its position along the cell radius. When even only one of the six beams is intercepted, the behaviour of the vapor clouds changes completely and, instead of a compression, a drift to the direction of the shut off beam is obtained as it is shown in fig. 4c and 4d.

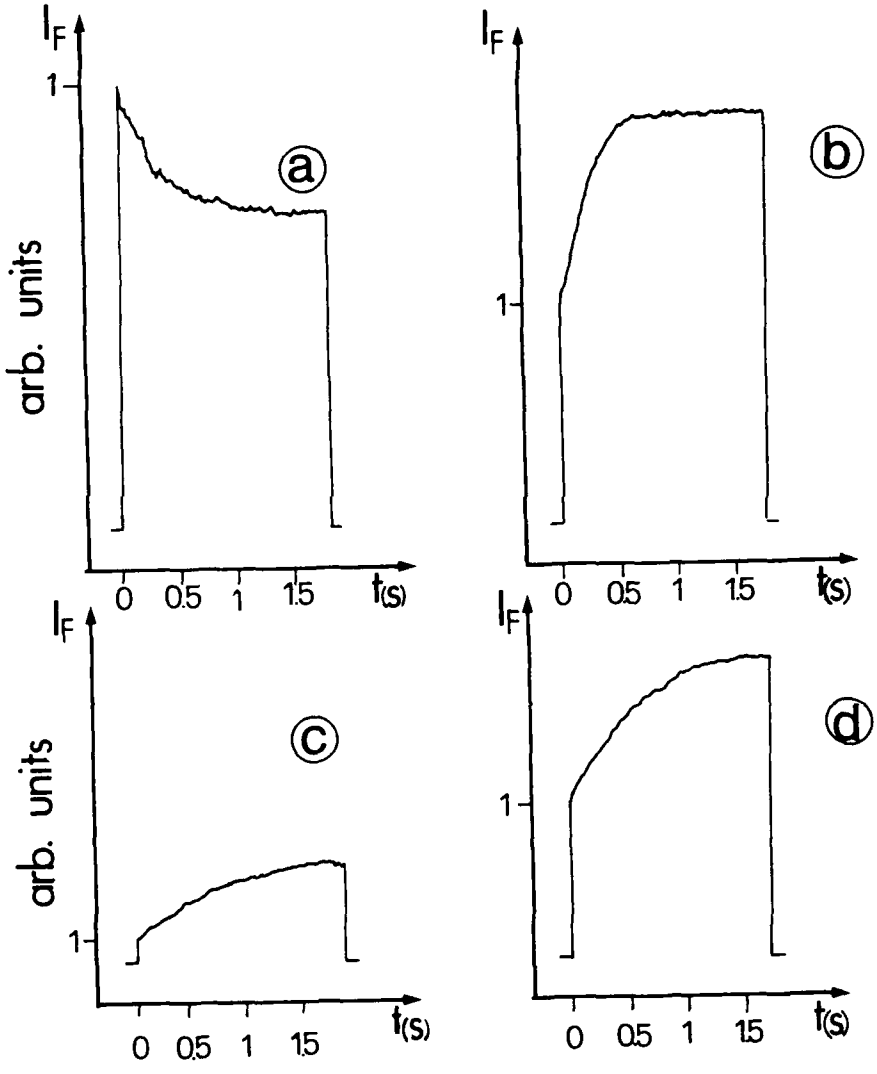


Fig. 4- Fluorescence signals induced by the six laser beams: in fig. 4a signal from fiber b); in fig. 4b signal from fiber a);fluorescence signals obtained with one laser beam switched off:fig. 4c fiber b); fig. 4d fiber a).

The reported signals do not show an effective detaching of the vapor from the walls but they show for the first time LID in a three dimensional geometry. Moreover they indicate that, by properly choosing the experimental conditions, it is possible to have a cooperative effect induced by all the laser beams. Further measurements are in progress to realize a full confinement of the vapor in a volume smaller than that of the cell and new configurations are under study.

Conclusions

Such an experiment shows that it is possible to modify the vapor diffusion in a 3-dimensional geometry. The results support the possibility of achieving a complete separation between the vapor and the cell walls. This condition would permit a new class of experiments where the vapor, that cannot be cooled by RRP because it is in thermal equilibrium with the environment through collisions with the buffer gas, can be driven to a very high soprasaturation regime. Once it has been compressed to the center of the cell, it cannot condensate at the cell walls and, if the temperature of the cell is cooled down, clustering or molecule formation processes should be effective. Both processes can be easily studied. Moreover it will be possible to study in detail the transport properties of the vapor in different gases and under different configurations.

Acknowledgements

We thank M.Badalassi and M.Tagliaferri for their technical assistance.

References

1- For a review of these experiments see for example: W.D.Phillips, J.V.Prodan and H.J.Metcalf, J.O.S.A. B2, 1751 (1985)
2- J.H.Xu and L.Moi, Optics Commun. 67, 282 (1988)
3- F.Kh.Gel'mukhanov and A.M.Shalagin, JEPT Lett. 29, 711 (1979)
4- V.D.Antsigin, S.N.Atutov, F.Kh.Gel'mukhanov, G.G.Telegin and A.M.Shalagin, JEPT Lett. 30, 243 (1979)
5- S.N.Atutov, St.Lesjak, S.P.Podjachev and A.M.Shalagin, Optics Commun. 60, 41 (1986)
6- J.H.Xu, M.Allegrini, S.Gozzini, E.Mariotti and L.Moi, Optics Commun. 63, 43 (1987)
7- J.E.M.Haverkort, H.G.Werij and J.P.Woerdman, Phys.Rev.A 38, 4054 (1988) and references therein
8- C.Gabbanini, J.H.Xu, S.Gozzini and L.Moi, Europhysics Lett. 7, 505 (1988)
9- M.C.de Lignie and J.P.Woerdman, Journal of Phys. B, in press
10- A.D.Streater, J.Mooibroek and J.P.Woerdman, Optics Commun. 64, 137 (1987)
11- E.Mariotti, J.H.Xu, M.Allegrini, G.Alzetta, S.Gozzini and L.Moi, Phys. Rev. A 38, 1327 (1988)
12- S.Gozzini, J.H.Xu, C.Gabbanini, G.Paffuti and L.Moi, Phys. Rev. A 40, xxx (1989)
13 - H.G.C.Werij, J.E.M.Haverkort and J.P.Woerdman, Phys. Rev. A 33, 3270 (1986)
14- S.Gozzini, D.Zuppini, C.Gabbanini and L.Moi, Europhysics Lett., in press
15- J.Liang, L.Moi and C.Fabre, Optics Commun. 52, 131 (1984)

ESTIMATION OF LASER WELDING MAXIMUM PARAMETERS

S.G.Gorny(head of research group), T.N.Karpov, V.A.Lopota(head of laboratory), M.M.Malish, V.A.Saburov, I.G.Rudoy, A.M.Soroka

Laser Laboratory
Leningrad Polytechnic
Polytechnicheskaya 29
Leningrad 195251
U.S.S.R.

The paper provides estimation of laser welding maximum parameters. Limits for laser beam intensity are determined by high pressure of radiation wave in plasma which results in considerable sputtering of metal during welding. The limit values of joint weld coefficient and impulse duration are determined by maximum intensity and are also limited. Theoretically obtained relation between maximum melt depth h and lase beam power P is in well accordance with the known experimental relation $h_{max} \sim P^{0,7}$.

Application of high power lasers for welding makes it possible to obtain narrow and deep welds, the heat affected zone adjacent to the cut being very narrow. It improves the properties of weld joints and decreases deformation of the construction. Working out laser welding equipment and technology it is desirable to determine the range of the most acceptable technological parameters of the process that satisfy the conditions of obtaining high quality welds with relatively deep penetration. To do this was the aim of the present paper.

It is known that deep penetration laser welding causes vaporization of the metal [1]. Interaction of radiation with the metal vapor results in an optical break-down thus producing a radiation wave in the gas surrounding the welding zone [2]. The pressure of the wave is

$$P_{ru} \simeq \left[\left(\frac{\gamma - 1}{\gamma}\right)^2 \frac{\gamma_y + 1}{2}\right]^{1/3} \rho_0^{1/3} I^{2/3}$$

where ρ_0 = undisturbed gas density, I = radiation intensity, γ, γ_y = effective adiabatic exponent in cold gas and in plasma respectively. For air under real conditions of welding at $I = 10^7$ W/cm^2 $P_{ru} = 50$ atm. The greatest disadvantage of plasms formation consists in detachment of plasms from the vaporization surface. Distributing in the gas (in the shielding gas as well) plasms affects the weld-pool and results in liquid metal sputtering and in formation of defects shown in Fig. I. At the same time vaporization pressure may be high only in a vapor-gas cavity.

Radiation wave pressure limitation up to 10-13 atm enables to estimate maximum intensity of incident radiation which does not deteriorate the property of weld joints as $I_* \leq 2 \cdot 10^6$ W/cm^2 for steel. Experimental estimation of I_* based on the analysis of defects produced in variable radiation intensity welding of stainless steel gives $I_* = (2 \pm 1) \cdot 10^6$ W/cm^2.

A decrease of laser beam intensity is the simplest way to remove plasma. But deep penetration welding requires intensive vaporization [1,3], and it limits the possibilities of the decrease of radiation intensity: $I_{eff} \geq I_0$, where I_{eff} = effective (absorbed by the metal) power density, I_0 = threshold vaporization intensity [3,4]. I_* and I_0 limit the weld form coefficient. Taking that the cavity is of a cylindrical form and radiation is distributed uniformly along its surface we obtain

$$\frac{\pi d^2}{4} I_* \geq \pi d h I_{eff} \geq \pi d h I_0$$

where h, d = depth and width of the cavity. Hence,

$$\frac{h}{d} \leq \frac{1}{4} \frac{I_*}{I_0} \simeq 5 \div 15 \qquad (I)$$

The value obtained is somewhat relative though close to experimental results. The value of I_0 depends on the material, the form of the cavity is not cylindrical - the front wall receives most of the energy, but (I) shows that the role of I_* is principally restrictive.

The suppression of optical discharge plasma could increase the laser radiation intensity and , hence, the weld form coefficient. Actually tha fact that a definite time T_{dev} (30...40 μs for $I = 2;10^6 W/cm^2$ and $< I$ μs for $I = 10^7 W/cm^2$ [5] is required for optical break-down to be developed may be of use here. If the time of vapor scattering from the caustic region $T_v = g/V_v$ (g= caustic length, V_v = mean vapor velocity) is less than T_{dev}, intensive plasma formation and sputtering are eliminated. However to achieve deep penetration sausage-type instability cannot decrease too much [6]. An effective means of plasma formation control is pulsing lasing in welding.

Even at continuous lasing lase welding[3,7] is a relaxation-oscillation process that may be represented in the follwing way. The metal on the front wall surface of the vapor-gas cavity is heated from the temperature $\sim T_{melt}$ to the temperature of vaporization = T_s. During the time of heating T_h some melt is formed on the front wall of the vapor-gas cavity that is then displaced under the pressure of a steam back-blow from the irradiated zone to the rear part of the molten pool. The time of melt displacement from the irradiated zone coincides with the pulse length of developed vaporization. The front wall free from the melt has the temperature T_{melt} and the cycle is repeated. As in case of steam escape from the caustic, if $T_{vap} < T_{dev}$, then "switching off" the laser beam ensures the melt displacement required, from one hand, and eliminates the optical break-down, from the other. Such a possibility is one of the main advantages of pulsing welding conditions where the intensity more than I_* is possible, the quality being preserved.

Under steady state welding conditions characteristic times T_h and T_{vap} can be evaluated on considering the simplest case of the effect of the laser pulse on the material at the temperature = T_{melt}[7].

$$T_h \approx \chi \left(\frac{E}{I_{eff}}\right)^2; \quad T_d \simeq T_{vap} \simeq \frac{1}{I_{eff}} \sqrt{\frac{\rho \chi d E \kappa I_o}{\rho_o}}$$

where $E = \rho [C(T_s - T_{melt}) + H_{melt}]$, ρ, C, χ, κ, H_{melt} - density, specific heat, thermal diffusivity, absorption factor at boiling temperature and specific heat of melting respectively; ρ_o = external pressure, d = ray diameter. At $I_{eff} = 10^5 W/cm^2$, $\chi = 0.05$ cm^2/sec, $E = 10^4 J/cm^3$, $\rho = 7{,}8$ gr/cm^2, $\kappa I_o = 1{,}5.10^4 W/cm^2$ and d = Imm we obtain $T_h = 500 \mu s$, $T_{vap} = 25$ s. $T_h - T_{vap}$ relationship is in qualitative agreement with the experiments [8].

For the welding to be efficient and qualitative it is necessary that clearing of the front wall from the liquid phase take less time than heating. Hereupon vaporization losses are small and welds are narrow and deep since the longitudinal melt transfer is so fast that no appreciable heat removal from the weld takes place. Thus, the $T_d \ll T_h$ condition is a necessary condition of welding. Taking (2) into account it gives

$$I_{eff} \ll E \sqrt{\frac{\chi E \rho_o}{\rho d \kappa I_o}} \qquad (3)$$

Substituting numerical values for letters in (3) we get $I_{eff} \ll 2.10^6 W/cm^2$ for steels. The sign $\ll$ means not two or three times but by an order of magnitude less. So the maximum power density absorbed by the metal on the front wall surface of the cavity $I^*_{eff} = 2.10^5 W/cm^2$. The result obtained does not do for direct application, since light intensity on the metal depends not only on radiation power but on some poorly known geometrical parameters of the vapor-gas cavity. Still having I^*_{eff} we can determine the minimum pulse duration for welding at pulsing lazing that ensures efficient and qualitative welding. As under such conditions $T_p = T_h$ (to be more exact, $T_p = T_h + T_d$), then for steels

$$T_p \approx \chi \left(\frac{E}{I^*_{eff}}\right)^2 \simeq 100 \mu s \qquad (4)$$

This result is connected only with thermo-physical properties of the material, it does not depend on the optical break-down and is valid for short-wave lasers where plasma effect is immaterial.

It is to be remembered that for the weld form factor to be high it is advisable to have maximum incident radiation intensity I (at the entrance to the vapor-gas cavity) and minimum permissible intensity on the front wall surface of the cavity I^*_{eff} that for the given I is determined either by the developed vaporization threshold or by the condition $T_\alpha < T_{dev}$, the latter being more important in practice. It is important to note that with I increasing T_{dev} decreases much faster than T_α decreases when T_{eff} is increasing. Therefore the maximum weld form factor is reached at a definite value of incident radiation intensity that is estimated as $I \simeq (1...2).10^6 W/cm^2$.

As mentioned above the condition (2) is that of efficient welding and satisfies the condition of the vaporized mass being infinitesimal. Hence for efficient welding [7]

$$T_{vap}\, I_{eff} \leq \mathcal{H}\, H_{vap}\, \Delta \qquad (5)$$

where H_{vap} = specific heat of vaporization per unit volume; $\mathcal{H}$ = vaporized metal mass to molten metal mass ratio ($\sim 1\%$); Δ = melt layer thickness on the front wall of the cavity. Duration T_{vap} is similar to that of displacement of melt layer of thickness from the zone of irradiations. It may be expressed as follows [7]:

$$T_{vap} \simeq T_d \simeq \sqrt{\frac{\rho \Delta d \pi I_o}{\rho_o I_{eff}}} \qquad (6)$$

From (5) and (6) it follows that

$$\Delta \geq \left(\frac{1}{\mathcal{H} H_{vap}}\right)^2 \frac{\rho \pi I_{eff} I_o d}{\rho_o} \qquad (7)$$

Since the process of welding is of an oscillatory nature, both under pulsing and continuous conditions, the speed of welding is to satisfy the relation $V_u = f \Delta$ that together with (7) gives

$$f \left(\frac{1}{\mathcal{H} H_{vap}}\right)^2 \frac{\rho \pi I_{eff} I_o d}{\rho_o V_u} \leq 1 \qquad (8)$$

where f = oscillatory process frequency. In continuous welding $T_{vap} \ll T_k$, $f \simeq \frac{1}{T_k}$; in case of pulsing conditions $f = f_p$, where f_p = pulse recurrance rate.

Relation (8) connects the main parameters of welding conditions (I_{eff}, d, V_u, f) with thermophysical properties of the materials and may be considered as a dimensionless criterion limiting the range of most admissible conditions of laser welding. It is evident that equation (8) gives the maximum penetration depth. Consequently at the constant intensity I and beam diameter d maximum penetration will take place at the same relationship f / V_u. This deduction is easily checked under pulsing welding conditions by changing f_p at I = const. and d = const. and determining the frequency that ensures maximum penetration at a given welding speed. The experiment conducted by means of RS-1000 unit in welding steel 08XIGHIOT shows that the relationship f_p / V_u corresponding maximum penetration is really kept constant (see Fig.2). Similar results were obtained in welding titanium alloys.

Let us use relationship (8) to estimate maximum penetration depth h_{max}. In this case as mentioned above, $f \simeq \frac{1}{\chi G}\left(\frac{I_{eff}}{E}\right)$, laser power $P = \frac{\pi d^2}{4G} I_*$, where G = relative radiation pulse duration ($G = I$ corresponds to continuous lazing conditions) and from (8) the maximum welding speed corresponding to the maximum penetration depth is

$$V_{w\,min} = \frac{1}{\chi}\left(\frac{I_{eff}^2}{\mathcal{H} H_{vap} E}\right)^2 \frac{\rho \pi I_o}{\rho_o I_{eff}} d \qquad (9)$$

Let us calculate the penetration depth by the formula suggested in [10]:

$$h = \frac{\eta_{eff} P}{E d V_u} \frac{1}{(1 + 2\sqrt{\chi / d V_u G})^2} \qquad (10)$$

where η_{eff} = the effective efficiency of the welding process.

Then from (9) and (10) we shall get

$$h_{max} \simeq \frac{A}{(1 + B/\sqrt{PG})^2} \qquad (11)$$

where $A = \frac{\pi \eta_{eff} \chi E \rho_o I_*}{4 I_{eff}^2 \rho \pi I_o} (\mathcal{H} H_{vap})^2$; $B = \left(\frac{\mathcal{H} H_{vap} E}{I_{eff}}\right) \sqrt{\frac{\pi \chi \rho_o I_{eff} I_*}{4 \rho \pi I_o}}$

Under continuous conditions ($G = I$) for stainless steel and the most "profitable" case of $I_* = 2 \cdot 10^6 W/cm^2$, I_{eff} is $10^5 W/cm^2$, $\mathcal{H} = 10^{-2}$, $A = 80$ mm, $B = 80$, where P is expressed in watts.

The design dependance (11) is shown in Figure 3. For the sake of comparison the figure also shows the experimental dependence obtained in [11] that is approximated by the function $P^{0.7}$. The dependence accurately agrees with the experiment in which laser power ≥ 3 kW. Overstated results for low power may be due to the fact that to attain optimum

flow I_* fine focusing is required. In this case the caustic length turns to be much shorter than the p- -ble depth (11), which was not taken into account. On the whole the design curve restricts the range of formation of the most admissible welds.

For the case $G>I$ (pulsing conditions) analogous calculations result in the difficulties based on the uncertainty between $\mathcal{H}$ and η_{eff}. The increase of G, the mean beam power being kept, results in the increase of pulse power and in the corresponding increase of $\mathcal{H}$. This gives rise to the decrease of η_{eff} and of the coefficient value A. Hence to consider a general case at $G>I$ it is necessary to study relations beyween η_{eff} and $\mathcal{H}$ at different G.

Estimation of limit parameters of the conditions and weld characteristics is especially important in developing laser technological equipment and technological processes of laser welding as well as in choosing technological equipment for solving specific tasks. Time and power parameters of laser radiation are determined rather accurately. Determination of the intensity range used in welding different metals, in particular, makes it possible to formulate requirements to radiation and to focusing systems, to determine the range of power and time parameters of pulsing conditions and so on. Estimation of maximum penetrating power enables to predict the scope of technological tasks for this particular equipment.

Conclusion

1. Maximum radiation intensity in laser welding is limited by high pressure of the plasma wave and is $\sim 2.10^6 W/cm^2$ for steel.
2. In welding under pulsing lazing conditions the minimum pulse duration is determined by thermophysical properties of the material ($\sim$100 s for steels), the optimum pulse recurrence rate being directly proportional to the welding speed.
3. The maximum penetration depth is determined by admissible intensity absorbed by the front wall of the vapor-gas cavity ($1...2.10^5 W/cm^2$ for steels) and thermophysical properties of the material.

References

1. N.N.Rykalin, A.A.Uglov, A.N.Kokora, Laser Welding of Materials (Mashinostroyenie, Moscow, 1975), p.296.
2. V.I.Bergelson, T.N.Loseva, I.V.Nemtchinov, Numerical Calculation of Plane Presound Wave Propagation Towards the Light Radiation Flow, PMTF, N 4, p.22(1974)
3. N.G.Basov, V.V.Bashenko, S.G.Gorny et all. Physical mechanism of Deep Penetration Laser Welding, Letters in JTF, p.21, (1985)
4. F.V.Boonkin, A.M.Prokhorov, Application of Laser Energy Source for Producing Jet Thrust, UFN, v.119, N 3, p.425 (1976)
5. V.A.Danilytchev, V.D.Zvorikin, Experimental Research of Radiation Gas Dynamics Process Developed Under the Influence of High Power Laser Pulse with =10,6 on Solids in Gaseous Atmosphere, FIAN Trans., 142, p.117(1983)
6. A.I.Scriptchenko, Beam Diameter Sounding in Laser Technological Units. Avtomaticheskaya Svarka, N 6, pp.28-32 (1985)
7. N.G.Basov, V.V.Bashenko, Gorny S.G. et all. Physical and technological Parameters of Laser Welding Process. In Proc. All-Union Conf. "Laser Application in National Economy", Zvenogorod (1985)
8. E.A.Mitkevich, V.A.Lopota, S.G.Gorny, Weld Formation Dynamics in CO_2 Laser Welding, Avtomaticheskaya Svarka, N 2, pp.22-25 (1982)
9. N.G.Basov,V.V.Bashenko, S.G.Gorny et al. Physical and Technological Mechanisms of Laser Welding, Svarochnoye Proizvodstvo, N 8, pp.1-3 (1985)
10. S.G.Gorny, V.A.Danilytchev, V.A.Lopota et al. Combined Method of Estimation of Laser Welding Process Parameters, Svarochnoye Proizvodstvo, N 7, pp.29-31 (1986)
11. Ein Schrittweiter im Lazer Schveissen Lazer Welding to 100 kW. Lazer Elek.Opt., v.9, N 4 (1977)
12. A.S.Kaye, A.G.Delph, E.Hanley, G.I.Nicolson, Improved Welding Penetration of 10 kW Industrial Laser, Appl.Phys.Letters, N 5, pp.412-419 (1983)
13. E.M.Breinan, C.M.Banas, Welding with High Power Lasers. Adv.Metal Process. Proc. 25th Sagamore Army Mater.Res.Conf., Bàlton Landing, N.Y., July 17-21, 1978, New York, London, 1981, pp.117-131.

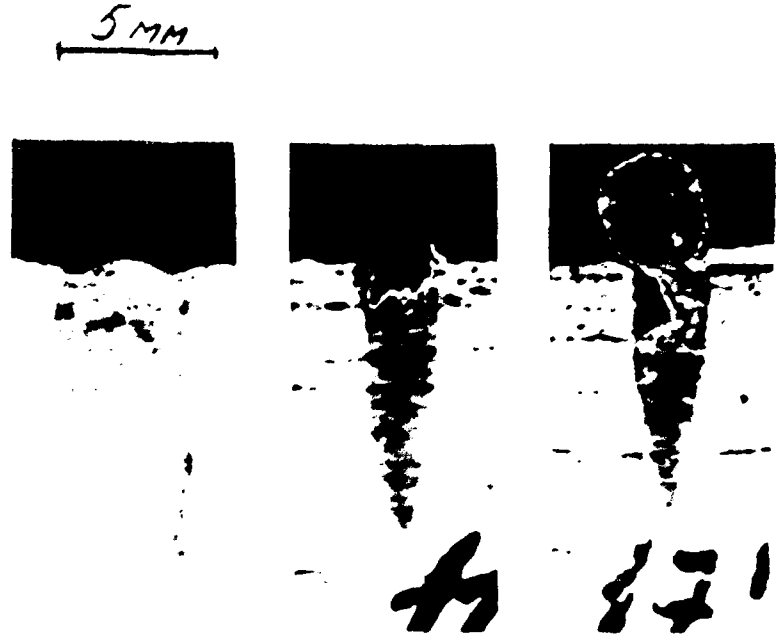


Fig. 1 Characteristic veiw of weld defects in high intensity radiation welding.



Fig.2 The change in the penetration form depending on the pulse recurrence rate in the pulsing laser welding.
a. =21,3 mm/s, 1- =1660 cps, 2- =1000 cps,
3- =750 cps, 4- =500 cps, 5- =300 cps.
b. =31,3 mm/s, 1- =1660 cps, 2- =1250 cps,
3- =1000 cps, 4- =750 cps, 5- =500 cps.
P=330 w, G=3.

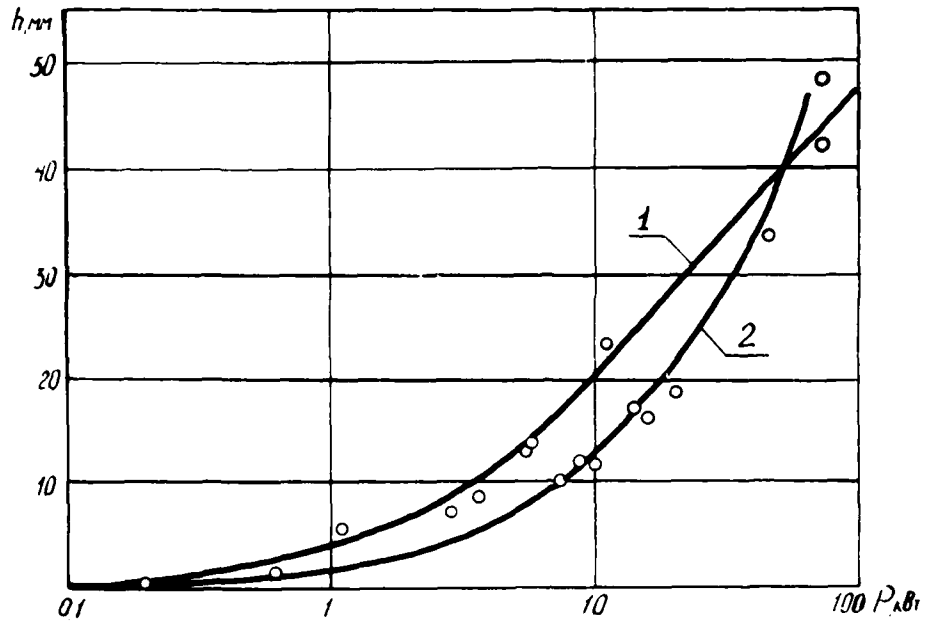


Fig.3 The dependence of the maximum penetration depth on the laser radiation power.
1-calculation according to (11)
2-experiment 11; points from 12,13 .

Nd-GLASS BURST LASER*

H. M. Epstein, J. L. Dulaney, J. F. O'Loughlin, W. P. Altman, and C. T. Walters
Battelle
505 King Avenue
Columbus, Ohio 43201-2693

Abstract

A Nd:glass laser capable of operating in 1/4 to 1 second bursts with 100 kJ energy has been designed for the purpose of evaluating the effect of free-electron lasers on materials. The energy of the burst is limited by the temperature rise of the laser medium, which is determined by its heat capacity. The laser glass is cooled to 180 K before initiation of the laser burst. The temperature at the end of the burst is limited by the thermal population in the lower laser level. At 410 K, the gain loss due to this lower level population is enough to lower the laser output below acceptable levels for 1% Nd doping; pump uniformity dictates low Nd doping. By optimizing flashlamp spectrum, cavity filters, and laser glass, the ratio of heat to available stored energy was reduced to 1.6. From the Nd:glass storage efficiency, heat capacity, and temperature rise, the minimum glass volume in the system can be determined. Minimum length is determined by gain considerations, and minimum area is determined by coating damage levels.

Introduction

A need exists for the development of an understanding of the interaction of free-electron laser (FEL) beams with materials. This paper describes the design of a low-cost, burst-type laser which can satisfy some of the testing needs with a burst energy of 100 kJ and run times between 0.25 and 1 second. The lower limit is associated with the economics of using a multiphase quasi DC power supply in a short pulse, high power mode. The upper limit is associated with gain requirements. Both induction and R.F. LINAC type FEL waveforms can be simulated.

The principle of this type of burst laser is to minimize radial temperature gradients, thus minimizing thermal stress, by heating the rod as uniformly as possible and cooling the rod slowly between pulses until it reaches thermal equilibrium at the initial temperature. The radial temperature differentials can be minimized by balancing the Nd doping and by cavity focusing. Cylindrical focusing by the rod or elliptical reflectors can increase the pumping at the center, while increased Nd doping increases the pumping near the surface. Because pumping is no longer limited by thermal stresses, the burst energy is determined by the maximum allowable temperature of the lasing medium, its heat capacity, and the efficiency of the Nd:glass. Nd:glass efficiencies were discussed in the previous paper[1].

Only phosphate glasses were considered because their high gain and low absorption losses are needed for good extraction efficiencies. The energy of the required laser burst defines the minimum Nd:glass volume. However, beam diameter limitations imposed by damage thresholds and rod length limitations imposed by gain requirements makes it difficult to achieve the minimum glass volume. The burst laser involves a number of design problems, particularly for the flashlamps, not encountered in other systems. Operation times on the order of a second are very nearly steady state for the flashlamps but the required wall loadings are typically triple those allowed in steady state operation. Also, the flashlamps are operating in a regime where their efficiency is a strong function of wall loading.

Pump Cavity Design

Because the cost of this type of burst laser is dominated by the cost of supplying a burst of electric power to the flashlamps, an efficient pump cavity is required. However, the need for uniform radial pump distribution in the rod dictates low Nd doping in the rod and multiple reflections in the cavity. Maintaining a high optical transfer efficiency with many cavity reflections requires good cavity reflectors, a high aspect ratio cavity, and efficient flashlamps. If cylindrical focusing by the rod is used to flatten the radial distribution of pump energy, diffuse reflectors may be used, and several materials, such as $BaSO_4$, are 97% reflecting. If multiple elliptical reflectors are used, the best reflectivity can be achieved by silvering the back side of quartz reflectors and sealing the silver with a layer of nickel[2]. As will be discussed in the flashlamp section, the wall loading requirements on the flashlamps limit the number of flashlamps, and thus the number of focusing ellipses, so that this type of pump cavity is impractical. The energy distribution as a function of αR, where $\alpha(\lambda)$ is the absorption coefficient of the Nd:glass and R is the radius of the rod, is shown in Figure 1[3]. The glass doping must be chosen so

* This work was sponsored by the Defense Nuclear Agency and monitored by MICOM under Contract DAAH01-88-C-0481.

that the average absorption coefficient produces a reasonably flat radial energy distribution. This requires $\rho_{Nd}R$ less than 3, where ρ_{Nd} is the percent of Nd doping. Because the small number of lamps will produce unacceptable theta distortions at the higher absorption levels, $\rho_{Nd}R$ of 1 was selected as a design parameter.

Pump Cavity Efficiency

The cavity optical transfer efficiency is defined as the ratio of the photon energy absorbed in the laser medium to the energy emitted by the flashlamps. Only one technique, the Monte Carlo method, has been used to calculate the basic transfer efficiency in cavities with diffusely reflecting walls. However, the Monte Carlo methods have proven to be too laborious for the parameter studies required for pump cavity design. The alternative is to treat the Monte Carlo "data" as a primary source similar to experimental data, and use a simpler model which includes a curve fit to the Monte Carlo data for absorption in the active medium. We have adapted the Whittle and Skinner[4] method for our pump code model because the basic data uses rod geometries and the parameter range is applicable.

The simplified model for diffusely reflecting cavity walls considers the light to be isotropic within the cavity. Since all surfaces are equally illuminated, the light absorption at each surface is the product of the area, the absorption coefficient, and the light intensity. Since all light must be eventually absorbed, the proportion of light absorbed on a surface of area S_i having an absorption coefficient Abs_i is $S_iAbs_i/\Sigma Si_iAbs_i$, where the summation covers the entire internal surface of the cavity including the holes and the exposed area of the laser medium. Holes in the cavity wall are treated as surfaces with unity absorption. The lamps are assumed to absorb with unit absorbance, then to emit a fraction (1 - a) of the absorbed energy with the initial spectrum. The capture efficiency of the laser rod was empirically fit to the Monte Carlo calculations as a function of the absorption cross section, index of refraction, and radius of the laser rod.

The Whittle and Skinner model, although very simple, reproduced the Monte Carlo transfer efficiency calculations to better than 5 percent. In our model, the basic Whittle and Skinner method is expanded to allow multigroup wavelength inputs. Spectral modifications are calculated for each photon pass to allow for flashlamp reradiation, and to permit the calculation of total energy absorbed in the rod as well as energy stored available for lasing.

Computer Models

The light intensity in the n^{th} pass of the flashlamp photon in the cavity is given by

$$I_n(\lambda) = I_{n-1}(\lambda) - I_{n-1}(\lambda)Abs_{rod}(\lambda)\frac{S_{rod}}{S_{tot}} - I_{n-1}(\lambda)Abs_{ref}(\lambda)\frac{S_{ref}}{S_{tot}} - I_{n-1}(\lambda)\frac{S_{holes}}{S_{tot}} - \tag{1}$$

$$I_{n-1}(\lambda)\frac{S_{lamps}}{S_{tot}} + \frac{\int I_{n-1}(\lambda)\frac{S_{lamps}}{S_{tot}}\,d\lambda\,\int(1-a)I_1(\lambda)}{\int I_1(\lambda)d\lambda}$$

where

- $I_1(\lambda)$ = spectral output of the flashlamps
- S_{rod} = surface area of rod
- S_{ref} = surface area of the reflector
- S_{holes} = surface area of the holes
- S_{lamps} = surface area of the lamps
- S_{tot} = $S_{rod} + S_{ref} + S_{holes} + S_{lamps}$
- $Abs_{rod}(\lambda)$ = absorption of the rod defined in Equation 2
- $Abs_{ref}(\lambda)$ = absorption coefficient of the reflector
- (1 - a) = fraction of plasma input energy emitted in a pulse

$$Abs_{rod} = (1.1146 - 0.1376\ n)\{1 - \exp[(-1.868 - 0.2104\ n)\alpha R_\phi + (0.3246 - 0.1180\ n)\alpha^2 R_\phi^2]\} \tag{2}$$

where α is the absorption coefficient of the rod, n is the refractive index, and the R_ϕ is the rod radius. This expression was obtained from a least squares fit of the Monte Carlo results and agreed with them to within 0.01[4]. The expression is valid for $1.5 \leq n \leq 2.0$ and for $0 \leq \alpha R_\phi \leq 3.0$. For $\alpha R_\phi > 3.0$, the high absorption limit applies:

$$Abs_{rod} = 1.0711 - 0.1221\ n + 0.0166/(n - 0.67),\ \alpha R_\phi > 3 \tag{2a}$$

In a given pass i, the total energy in the rod is found by integrating over the spectrum the amount of energy from the lamps that reaches the rod during the i^{th} pass times the absorption spectrum of the rod. Computationally, this becomes

$$(E_{rod})_i = \sum_m I_i\ (\lambda_m)\ Abs_{rod}\ (\lambda_m)\ \frac{S_{rod}}{S_{tot}}\ \Delta\lambda_m \tag{3}$$

(The limits on the subscript m in Equation (3) are those which define the range of photon wavelengths absorbed into the rod, either as heat or as potential laser energy.)

Since some of the energy in the rod is in the form of heat, the amount of rod energy available for laser transitions is reduced by further restricting the range of the spectrum to include only those frequencies the rod will accept for upper laser level transitions. In addition, the ratio of the spectral wavelength to the laser transition wavelength, λ_{laser}, was introduced as a factor in the integral to account for the quantum deficit. The useful laser energy stored in the rod during the i^{th} pass through the cavity is then

$$(E_{stored})_i = \sum_{m'} I_i\ (\lambda_m')\ Abs_{rod}\ (\lambda_m')\ \frac{S_{rod}}{S_{tot}} \cdot \frac{\lambda_m'}{\lambda_{laser}} \cdot \Delta\lambda_m' \tag{4}$$

The cumulative energies after n passes are simply

$$E_{rod} = \sum_{i=1}^{n} (E_{rod})_i \tag{5}$$

$$E_{stored} = \sum_{i=1}^{n} (E_{stored})_i$$

The algorithm is executed through as many passes as needed until the amount of useful energy stored in the rod in a given pass is less than 1 percent of the total useful energy stored in the rod. This translates to between 13 and 28 passes for the test cases we performed.

The transfer efficiency is then calculated as

$$\eta_c = \frac{E_{rod}}{\sum_m I_i(\lambda)\Delta\lambda_m} \tag{5a}$$

Flashlamps

Probably the largest area of uncertainty in the burst amplifier design is permissible P/A (power per unit envelope area) of the flashlamps. From an efficiency point of view, a P/A of about 2 kW/cm^2 is close to optimum. Flashlamps with a 6 mm bore and 3 Atm Kr pressure were shown to have an efficiency of 60% for radiation emitted between 0.4 and 0.85 μm. Radiation is restricted to this approximate interval with Ce and Sm filters for the UV and IR, respectively. Kr is chosen as the filling gas because it has a better overlap with the Nd absorption lines than Xe. It is important to have the ratio of residual heat to stored energy in the laser medium as low as possible for uncooled burst systems. Because the flashlamp plasma absorbs reflected energy in a cavity, the optimum P/A in an efficient pump cavity is reduced to about 1.4 kW/cm^2 for pulses of fractional second duration. In a steady state operation, the thermal stress limit on wall loading is given by[6]

$$P_w = 2R_T/t \tag{6}$$

where R_T is the thermal shock parameter defined as $(1-\nu)kS_T/\alpha_e E$, t the wall thickness, ν Poisson's ratio, α_e the expansion coefficient, k the thermal conductivity, E the elastic modulus, and S_T the yield stress. For fused quartz R_T = 1450 W/m, and the wall loading at which fracture occurs is 580 W/cm^2 absorbed in the wall. This flashlamp wall loading would limit the P/A to about 1450 W/cm^2 for a lamp with 60% radiating efficiency. Of course, the thermal lag and the absorption of the UV in a Ce filter outside of the lamp wall allow the P/A to be increased somewhat. It has been verified experimentally that the flashlamps survive at wall loadings greater than 1,400 W/cm^2. The amplifier designs require wall loadings between 500 and 1,400 W/cm^2. Over this range, the efficiency varies from 50 to 56%.

Laser Design

The first step in the system design is to perform an energy audit, using the efficiency information from the previous sections and the laser medium efficiency discussed in the previous paper[1]. The first layer of the energy audit (Figure 2) is the efficiency of flashlamp emission into the 0.4 to 0.85 μ wavelength interval. While this efficiency increases with flashlamp wall loading from 50% to 56%, the largest fraction of energy is pumped at the highest flashlamp wall loading, so that the average efficiency is about 55%. The transfer efficiency from the lamps to the rod is 32% for a $BaSO_4$ diffuse reflector and a high aspect ratio cavity (50 cm L. x 2 cm D. rod). As discussed in the previous paper, 39% of the energy absorbed in the rod is available stored energy for Kigre Q-88 and Schott LG-760 laser glasses. The extraction efficiency of the stored energy is a function of the ratio of output flux to saturation flux. Saturation flux is defined as

$$I_s = h\nu_L/(\tau_f \sigma_L), \tag{7}$$

where $h\nu_L$ is the laser photon energy, τ_f the fluorescent decay constant, and σ_L the stimulated emission cross section. The extraction efficiency can be kept in the 50% to 70% range, with the higher output flux levels reached by doing polarization double passes in the earlier stages. Finally, mode filling constraints typically cost about 15% of the laser energy. Thus, the design output of 100 kJ requires an input energy of about 3.4 MJ.

Next we will estimate the volume of Nd:glass for a 100 kJ burst laser. The principal limitation is the temperature at which the thermal population of the lower laser level, which is only 0.25 eV above the ground state, becomes significant. The population in the lower laser level, N_1, is given by

$$N_1/N_o \approx \exp(-2900/T), \tag{8}$$

where T is in K. A temperature rise to 410 K causes less than 5% loss in the gain coefficient, and will be assumed as the upper temperature limit. Because the heat capacity of glass decreases with decreasing temperature, cooling below 180 K adds very little heat capacity. Applying the Einstein model of heat capacity as a function of temperature, about 450 J/cm^3 are allowed in the Nd:glass. For LG-760 or Q-88 glass, this corresponds to available energy storage of 450/1.57 = 287 J/cm^3. Assuming a 50% extraction efficiency and 15% mode filling loss, the minimum glass volume for a 100 kJ burst laser is 820 cm^3.

It is now necessary to design an amplifier chain with a volume on the order of 820 cm^3, which has a sufficient gain to amplify a reasonable output from ~10 cm^3 of burst mode YLF preamplifier to 100 kJ, while keeping the beam flux low enough to avoid damage to the glass or dielectric coatings. The small signal gain is given by

$$G_o = \exp[(\beta-\alpha)\ell], \tag{9}$$

where $\beta = \sigma_L N_o W/A'$, α is absorption per cm length, ℓ the rod length, W the rate at which ground state Nd^{3+} ions are excited to the upper laser, and $A' = 1/\tau_f + W$. The actual gain of the amplifier stage, I_{out}/I_{in}, is given by [6]

$$\ell n(I_{out}/I_{in}) - (\beta/\alpha)\ell n[(\beta/\alpha - 1 - \sigma_L I_{out}/A')(\beta/\alpha - 1 - \sigma_L I_{in}/A') - 1] = (\beta-\alpha)\ell. \tag{10}$$

Schematic layouts of a 1/4 sec and 1/2 sec burst laser are shown in Figure 3. The output powers of these systems were calculated for a laser glass with σ_L of 4.5 x 10^{-20}, $\alpha = 10^{-3}$/cm, and $\chi = 1.57$. The input from the preamps was assumed to be 5 kW for the 1/2 sec laser and 10 kW for the 1/4 sec laser. The outputs were 120 kJ and 126 kJ respectively for the two systems.

Power Supply

The requirement for a power supply that can deliver 3.4 MJ in 1/4 to 1/2 sec can be met in several ways. Banks of normal or pulsed batteries are alternatives. Safety, control and switching problems are major disadvantages with standard battery banks. The total energy stored to achieve the required currents and voltages is many orders of magnitude more than required for a single burst. If standard batteries in the bank are replaced by pulsed batteries, the stored energy is more reasonable, but pulsed batteries are not yet commercially available.

An attractive alternative is a six-phase power supply which simulates D.C. by the overlapping of phases, with only a few percent ripple (Figure 4). This type of power supply is relatively inexpensive, safe, and easy to control. Its main disadvantage is the requirement for high power, 3-phase lines.

Conclusions

The heat capacity limited burst laser provides a convenient method for producing energetic laser pulses of a fraction of a second burst width. With the limiting upper temperature imposed by the thermal population of the lower laser level, it is possible to store up to 300 J/cm^3 in Nd:glass. This stored energy can be efficiently extracted in systems with reasonable gain, low absorption phosphate glasses currently available. While the uncooled burst laser is not suitable for high repetition rate applications, it is ideal for tests of laser interactions with materials, where a few pulses per hour are consistent with set-up and data handling rates.

References

(1) J. L. Dulaney and H. M. Epstein, presented at LASERS '89, New Orleans (1989)

(2) V. M. Vinokarov, Khimicheskiye Metody Serebreniya Zerbal (Oborongia Press, 1950)

(3) Yu A. Kalinin and A. A. Mak, Sov. J. Opt. Tech. 37, 2, 129-139 (1970)

(4) J. Whittle and D. R. Skinner, Appl. Opt. 5, 1179 (1966)

(5) J. L. Emmett, W. P. Krupke, and W. R. Sooy, UCRL-53571 (1984)

(6) W. Koechner, Solid-State Laser Engineering (Springer-Verlag 1976) pp. 151

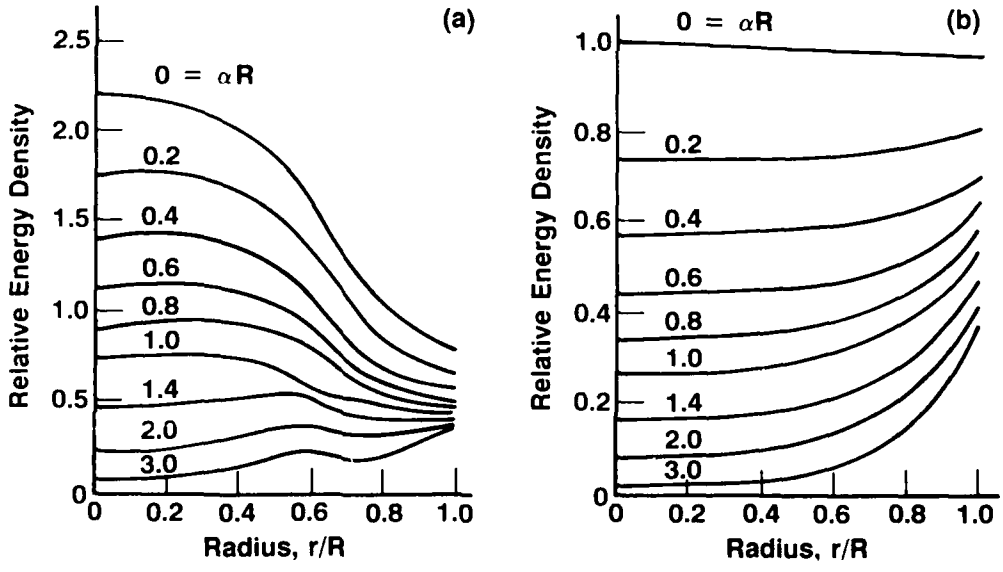


Figure 1. Relative energy density in a Nd:glass rod versus normalized radius in an isotropic cavity as a function of absorption (a) with polished, (b) with frosted cylindrical surface.

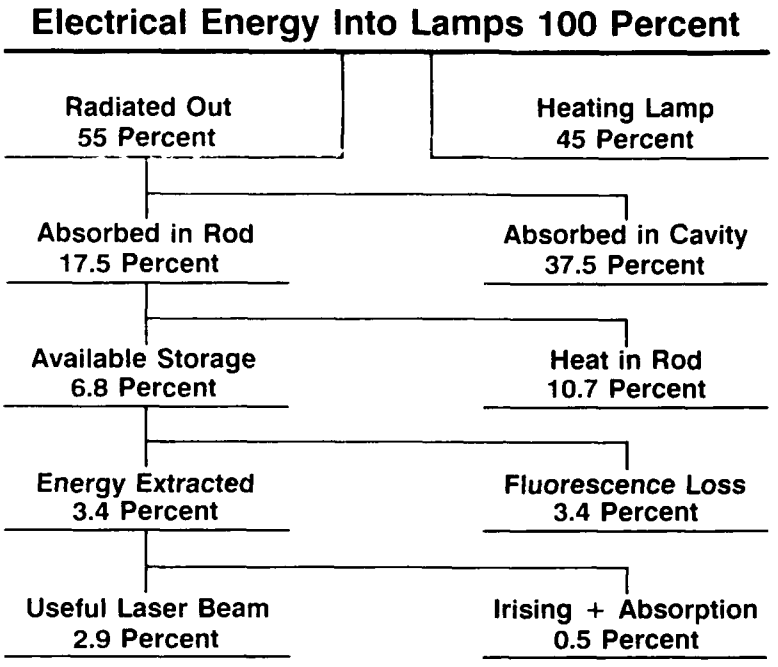
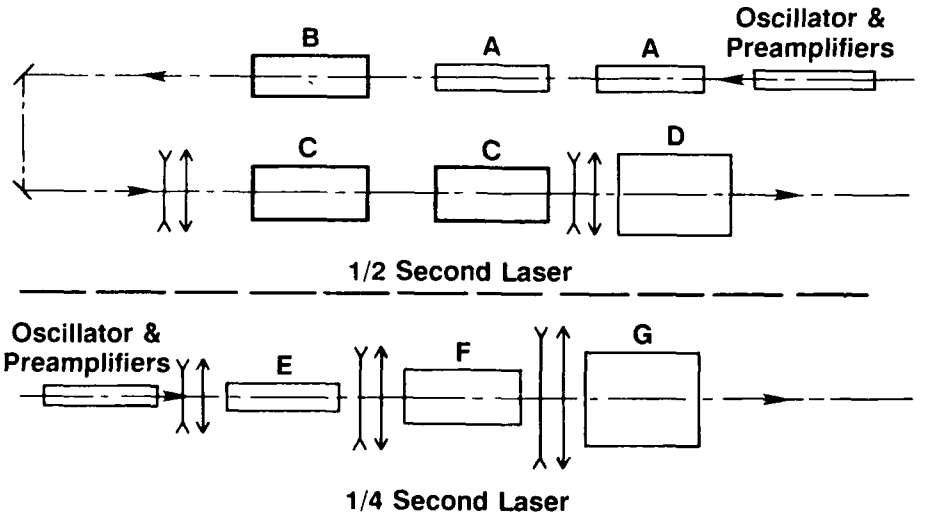


Figure 2. Energy audit for cavity with 97% reflectors.



Stage	1/2 Second Length (cm)	Diameter (cm)
A	50	1
B	50	1.4
C	50	2
D	50	2.8

Stage	1/4 Second Length (cm)	Diameter (cm)
E	50	1
F	50	2
G	50	3.9

Figure 3. Schematic lasers for 1/2 and 1/4 second bursts.

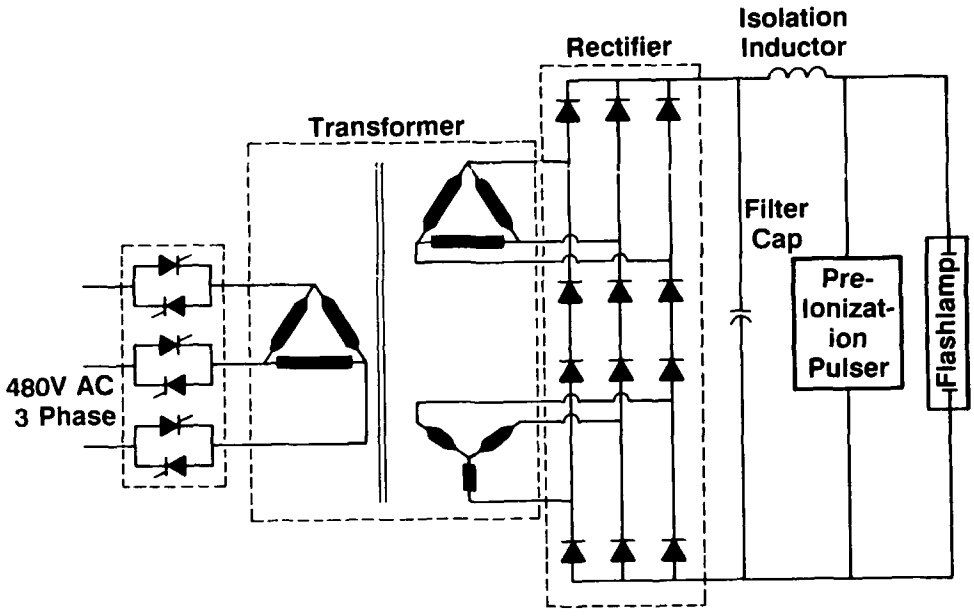


Figure 4. Six phase flashlamp driver.

MEASUREMENT OF LASER GLASS ENERGY STORAGE EFFICIENCIES*

J. L. Dulaney and H. M. Epstein
Battelle
505 King Avenue
Columbus, Ohio 43201-2693

Abstract

We have measured the ratio of heat deposited to stored laser energy, χ, for several neodymium doped laser glass rods. Small signal gain measurements of the central portion of the rods were made to determine the stored laser energy.

Heat deposition was inferred from interferometrically obtained rod expansion data. One leg of the interferometer was arranged so that the HeNe beam reflected off of both ends of the glass rod under study. The beam was centered on the rod and covered approximately the same area where the small signal gain was measured. The two interferometer paths were recombined to form a circular fringe pattern which was then centered and focused on a silicon photodiode. Note that this method eliminates the need for knowledge of dn/dT, the change in index of refraction with temperature. Pumping nonuniformities are averaged. The transient fringe shift was recorded, allowing us to measure the heat absorption for an individual flashlamp pulse. We believe this is the first time that single pulse heat absorption has been measured.

Heat to energy storage ratios less than 1.6 were found for two of the sample rods.

Introduction

In an effort to identify high-gain/low-heat-absorption laser glass for high energy burst lasers (like the one described in the subsequent paper), we have developed an interferometric method for characterization of laser glass. The optimum glass for laser systems which operate under high thermal stress conditions is the glass with the best energy storage parameter, χ. The energy storage parameter is defined as the ratio of heat deposited to available energy stored in the upper laser level. Measurements of the energy storage parameter have been made in the past[1,2], but not with a single pulse method such as the one described here.

Determination of χ requires two separate experiments on the glass: one to measure the available energy stored in the upper laser level and one to measure the heat absorbed by the glass. Stored energy was inferred from small signal gain measurements; and, heat deposition was determined via real-time interferometric measurements of the thermal expansion of the rod as it was pumped. Three different phosphate laser glass rods (Kigre's Q-88 and Q-98, and Schott's LG-760) were examined in this study. All of the rods were 10 mm in diameter and 200 mm long with 2 weight percent neodymium doping.

The rods under examination were all studied in the same test cavity with the same flashlamps so that the comparison of χ's would not be ambiguous. The test cavity was a standard Kigre cavity (Model FD-M170) with a packed barium sulfate reflector and samarium-doped glass filter surrounding the test rod. The flashlamps were 90 percent Krypton, 10 percent Xenon, cerium doped quartz envelope devices with a 15 cm arc length. The pulse forming network supplied ~570 μs current pulses measured at the 1/e points.

Energy Storage Experiments

A Q-switched laser pulse (~25 ns) from a neodymium glass oscillator was used to probe the test rod at the peak of its fluorescence. The amplified pulse was always less than 1 percent of saturation fluence, ensuring operation in the small signal regime. A self-irising silicon photodiode (≈0.04 cm^2) placed after the test cavity and centered on the laser beam was used to measure the gain through the central region of the test rod (see Figure 1). No filters or scatterers were used in front of the diode. The gain was found by measuring the peak diode voltage with and without pumping the test rod. Measuring peak voltage outputs to determine gain is valid because we are operating in the small signal regime. Furthermore, the pulse width and energy output from the oscillator typically varies by less than 2 percent.

Available stored energy can be easily calculated from the following equation:

$$E_{st} = \frac{h\nu A}{0.45\sigma} \ln G \quad , \tag{1}$$

where $h\nu$ is the photon energy, σ the stimulated emission cross-section, and A the

* This work was sponsored by the Defense Nuclear Agency and monitored by MICOM under Contract DAAH01-88-C-0481.

cross-sectional area of the test rod (0.785 cm^2). The factor of 0.45 is the fraction, F, of pump energy residing in the upper laser level at the time of the pulse. A value of 0.63 is calculated in a 1982 Lawrence Livermore report[3], but is believed to be high as shown below.

In the experiment, the timing of the test pulse for the small signal gain measurement was varied to find the time when n_2, the population in the upper laser level, is a maximum. This time, when the decay loss equals the pump rate, occurs some time after the flashlamp peak, since the heat measurement includes all photon absorption in the rod during the flashlamp pulse, while the n_2 measurement excludes those excitations that decay before the test pulse and those that occur after it. Therefore, it is necessary to correct for these losses of n_2 by solving the differential equation,

$$\frac{dn_2}{dt} = P(t) - \frac{n_2}{\tau} \quad , \tag{2}$$

where P(t) is the instantaneous excitation rate and τ is the fluorescent decay constant. The correction factor, F, is then

$$F = \frac{n_2^*}{\int_0^{t'} P(t)dt} \quad , \tag{3}$$

where n_2^* is the maximum value of n_2, and t' the flashlamp pulse time. The factor F depends on flashlamp pulse shape, but for a typical flashlamp pulse Lawrence Livermore Laboratories calculated the value of F as a function of the ratio of flashlamp pulse width to decay time of the n_2 excitations. Using this method, F was found to be 0.63 for the parameters of our experiments. However, if one looks at the actual optical pulse shape of the flashlamps in the present experiments, as shown in Figure 2, and simulates the pulse by a triangle, a more accurate value of F can be calculated.

The analytical solution to Equation (2) for a triangular power pulse is

$$n_2 = P_M \frac{\tau}{t_p} (t_p - \tau + \tau e^{-t_p/\tau}) e^{-t/\tau} + P_M\tau + P_M \frac{\tau}{t_p} [\tau - t - (\tau + t_p) e^{-t/\tau}] \quad , \tag{4}$$

where P_M is the peak excitation rate, τ is the decay constant, t_p half the base length of the pulse shape triangle and t the time measured from the peak, but less than the time to zero power. We can find the time, t_{opt}, where n_2 is at its maximum by setting $dn_2/dt = 0$,

$$t_{opt} = \tau \ell n[(2 + e^{-t_p/\tau})] \quad . \tag{5}$$

From Equations (3), (4), and (5), the calculated value of F is 0.45. This value is appreciably lower than the values in Reference (3), probably because the risetime of the flashlamp PFNs is not as sharp as those used by Livermore Laboratories. The value of F was also calculated by numerical integration of Equation (3) with the measured pulse shape. The two methods for determining F agreed within 5 percent.

The value of χ is measured with a low energy test pulse which depopulates only a small fraction of the excited states. The total heating of the laser medium would be greater if the population were highly depleted by a laser pulse. There is no difference in the heat deposition resulting in a de-excitation by spontaneous emission from that by stimulated emission. The heat measurements are made after the populations have reached ground state. Some slight difference may exist due to the absorption of emitted photons. The photons spontaneously emitted can be multiply reflected in the pump cavity and have a higher absorption in the laser medium than the laser beam photons. This effect would be very small because of the low absorption cross section at 1.05 μm and would result in a very slightly lower χ.

Table 1 shows the values of the measured gain and the calculated values of E_{st} for all three glass samples.

Heat Absorption Experiments

Figure 3 depicts the interferometer experiment used to measure the heat absorbed in the test rods during flashlamp pumping. A HeNe laser was used to reflect off both ends of the test rod in one leg of the interferometer. The beam was centered on the rod and covered approximately the same area where the small signal gain was measured. The two interferometer paths were recombined to form a circular fringe pattern which was then

centered and focused on a silicon photodiode. Note that this method eliminates the need for knowledge of dn/dT, the change in index of refraction with temperature. Pumping nonuniformities are averaged.

Typical output from the interferometer is displayed in Figures 4, 5, and 6 for Q-88, Q-98, and LG-760 glasses. The end of the flashlamp pump pulse is taken to be 1.2 ms after the initial flashlamp trigger since more than 99 percent of the flashlamp energy has been emitted by this time. Fringes are counted from time zero to 1.2 ms. The fringe amplitude variation is due to the detector's slow response time. The minimum fringe amplitude corresponds to the peak pumping rate. Note that the fringe spacing and amplitude increase toward the end of the pump pulse as the lamp radiation falls to zero. Apparent expansion past 1.2 ms is most likely due to the rod inertia (stretching) after rapid expansion. However, the additional stretching is less than 5 percent of the total expansion (< 0.25 fringes) and the resulting uncertainty in determining the total number of fringes due to thermal expansion is less than 5 percent. Thermal diffusion from the outside could be a small factor but the diffusion depth for 1 ms is only approximately 10 μm, which is a negligible contribution to the heating at the center.

The temperature rise in a rod is related to the measured fringe shifts by the equation:

$$\Delta T = \frac{m\lambda \langle \cos \theta \rangle}{2n\, \alpha L} \qquad (6)$$

where λ is the HeNe wavelength, m the number of fringe shifts, n the index of refraction of air ($n \approx 1$), α the thermal coefficient of linear expansion, and L the pumped part of the rod length. The average of the cosines is defined by:

$$\langle \cos \theta \rangle = \tfrac{1}{2} (\cos \theta_1 + \cos \theta_2) \quad , \qquad (7)$$

where θ_1 and θ_2 are the angles of incidence of the HeNe beam on the rod ends and are approximately equal. The energy deposited as heat is given by

$$E_h = \rho\, V\, C_p\, \Delta T \quad , \qquad (8)$$

where V is the volume of the pumped part of the rod (flashlamp arc length multiplied by rod area). Since the length factor in V cancels L in Equation (6), the value of L is unimportant. C_p and ρ are the heat capacity and density of the glass, respectively. Results for E_h and the ratio $\chi = E_h/E_{st}$ are listed in Table 1.

Table 1. Storage Efficiency of Phosphate Glasses

Glass	G	E_{st} (J)	E_h (J)	χ
Q-88	3.75 ± 0.12	10.86 ± 0.28	17.00 ± 0.93	1.56 ± 0.10
Q-98	4.17 ± 0.15	10.44 ± 0.28	26.13 ± 1.37	2.50 ± 0.16
LG-760	4.46 ± 0.18	11.69 ± 0.34	17.93 ± 0.99	1.53 ± 0.11

Discussion and Conclusions

Both the stored energy and heat absorption measurements were carried out under identical conditions: without actively cooling the test rod (only air was in contact with the glass), the pumping energy was the same, and the same central area of the rod was studied. This ensured that the energy ratios would be valid. Also, note that any flashlamp pumping nonuniformities were averaged out in both measurements since both measurements use the entire length of the rod. Therefore, χ is not affected by pumping nonuniformities.

The reported errors in the stored energy measurements stem primarily from the pulse to pulse variation of the probe pulse, which was relatively small (<2 percent). The major source of error in the heat absorption experiments is in determining the "end of pumping" time (taken to be at 1.2 ms), which results in an error of approximately 5 percent in the number of fringes. None of the errors reported in Table 1 include errors inherent in the glass constants. The glass constants used in χ calculations, listed in Table 2, were supplied by the manufacturers.

Table 2. Properties of Phosphate Laser Glasses

Glass	n	α(x 10^{-7}/K)	C_p (J/gK)	ρ(g/cm^3)	σ(x 10^{-20} cm^2)
Q-88	1.545	104	0.81	2.71	4.0
Q-98	1.555	99	0.80	3.099	4.5
LG-760	1.508	125	0.75	2.60	4.2

References

1. M. S. Mangir and D. A. Rockwell, IEEE J. Quantum Electron. QE-22(4), 574 (1986).

2. D. S. Sumida, D. A. Rockwell, and M. S. Mangir, IEEE J. Quantum Electron. 24(6), 985 (1988).

3. J. L. Emmett, W. F. Krupke, and J. B. Trenholme, "The Future Development of High Power Solid State Laser Systems", UCRL 53344, 14 (1982).

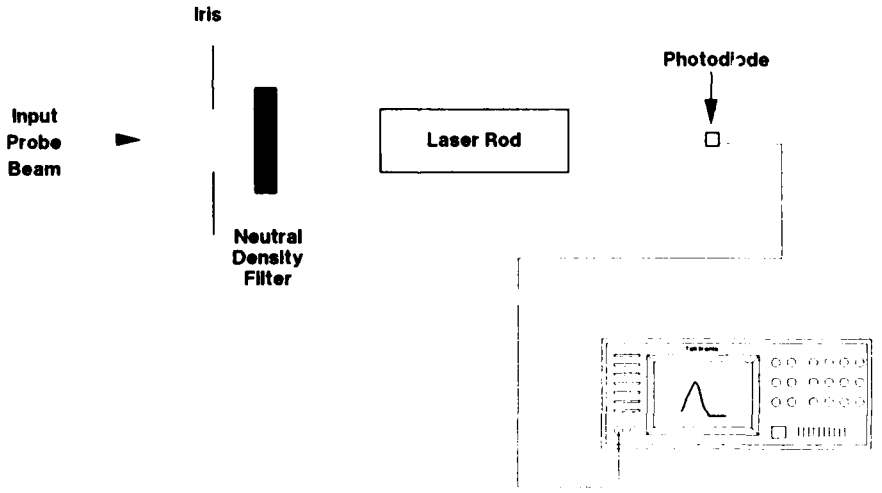


Figure 1. Experimental arrangement to measure energy storage.

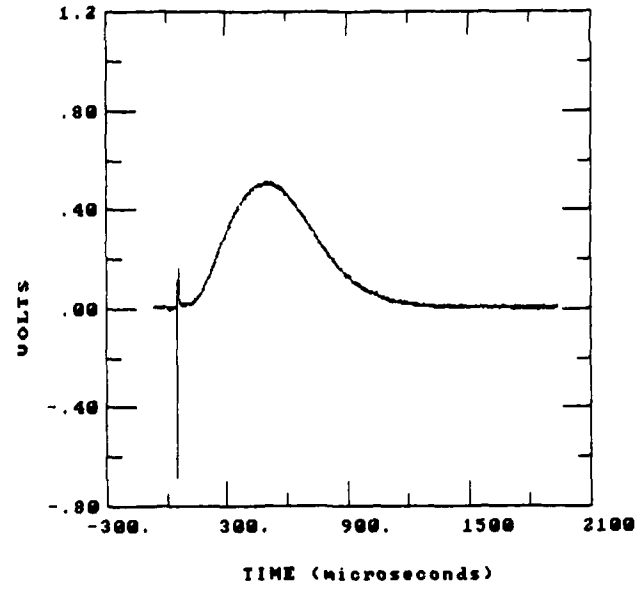


Figure 2. Flashlamp optical pulse shape.

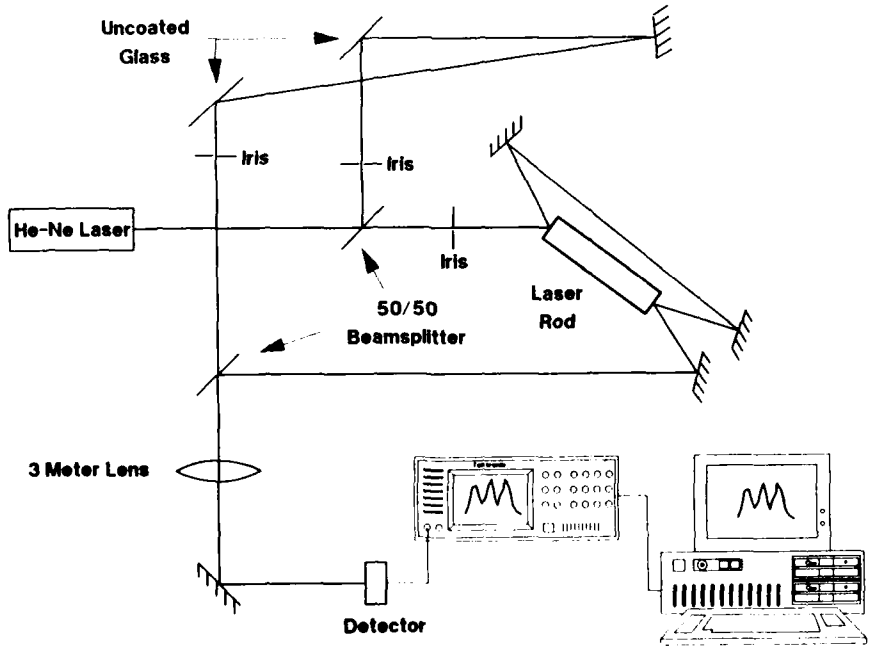


Figure 3. Interferometer experiment used to measure heat absorption.

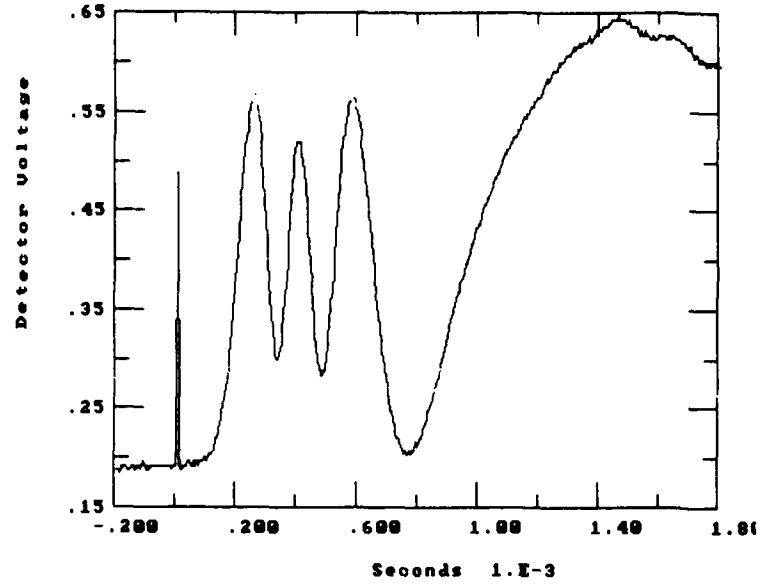


Figure 4. Fringe shifts for Kigre Q-88.

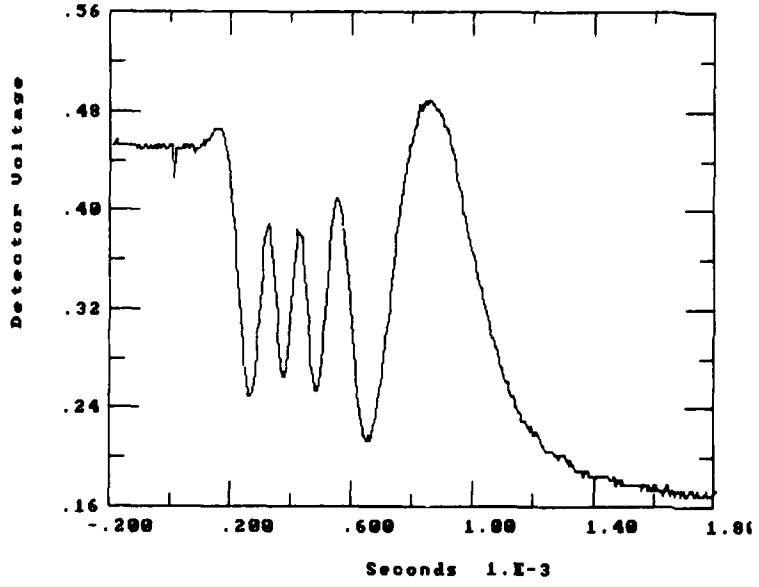


Figure 5. Fringe shifts for Kigre Q-98.

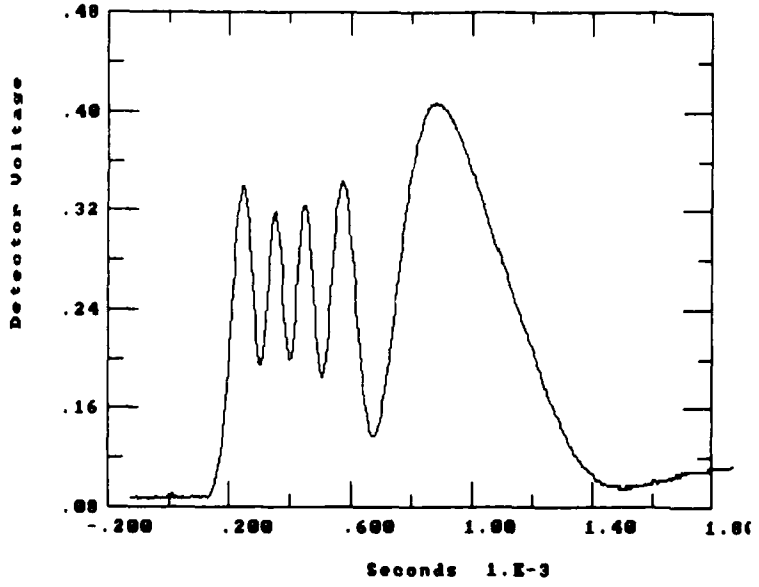


Figure 6. Fringe shifts for Schott LG-760.

STRATEGIC DEFENSE PANEL DISCUSSION *

Organizer: **DR. F. J. DUARTE**
Eastman Kodak Company

Moderator: **PROFESSOR C. A. BRAU**
Vanderbilt University

Panelists: **COL. R. L. GULLICKSON**
Defense Nuclear Agency

DR. K. JOHNSON
Lawrence Livermore National Laboratory

COL. T. Meyer
Strategic Defense Initiative Organization

DR. J. MILLER
TRW Space and Technology Sector

DR. K. PATEL
AT&T Bell Laboratories

PROFESSOR M. O. SCULLY
The University of New Mexico and
Max-Planck Institut for Quantenoptik

DR. E. TELLER
Lawrence Livermore National Laboratory

DR. L. WILSON
Rockwell International

* Edited by F.J.D. in cooperation with members of the panel.

Professor Brau:

Thank you, Frank. I would like to welcome everybody to the panel on Strategic Defense, our bi-annual affair. Today, Frank Duarte and his committee have assembled what I think is an exceptional panel. The structure of the panel discussion will be as follows: we'll have a series of prepared remarks, which will take place prior to the break. The break will then be followed by a question and answer period. The charter of the panel, as we were given it, is to discuss the question of what is the progress on strategic defense and especially lasers, of course, in the last three or four years. The prepared remarks will be about 10 minutes for each person, give or take a little, and to maintain schedule, what I'm going to ask is that the questions during the prepared remarks be restricted to those questions which are for clarification. Questions of substance I hope you will bring back after the break time so that we can have a lively discussion. The first speaker today is going to be Dr. Kent Johnson. Kent is from Lawrence Livermore National Laboratory, where he's been for the last 17 years. He is leader of the Strategic Applications group. That group has as its focus Weapons System Analysis. He is not a laser jock as we would say. His scope is somewhat larger than that. So, he's going to make a few remarks on the general architecture of strategic defense, as well as some of the things that are going on in Livermore. Dr. Johnson.

Dr. Johnson:

Thanks, Charlie. I'm going to be commenting on three different areas, two of them having to do with current directed energy programs at Livermore relevant to strategic defense. The third thing I will talk about is some ideas about policy objectives for defense and their implications for directed energy weapons in general.

First, let me talk about military applications of x-ray lasers, which is a subject I don't think many of you have heard too much about in at least the last few years. The charter for the Department of Energy's role in understanding military applications of nuclear directed energy weapons was spelled out in a memorandum jointly signed by then Secretary of Defense Weinberger and Secretary of Energy Herrington in 1985. It states that one purpose is to understand the threat, the counter defense threat that a Soviet or other offensive x-ray laser might pose to a U.S. defensive deployment. A second purpose is to understand the feasibility and impact that such a concept might have on our deterrent forces if deployed in a Soviet SDI-like system. And a third is to explore nuclear-directed energy options as SDI possibilities, to see if they offer some unique advantages and opportunities not afforded by other technologies.

Let me remind you of a few of the characteristics of a nuclear-driven x-ray laser, which is the particular focus of nuclear-directed energy work at Lawrence Livermore. The energy form is a directed beam of x-rays; obviously, it is a single pulse operation. The spectrum is a line source rather than broad band. The lethal effects are dominated by blow-off impulse and subsequent lethal shock mechanisms. The engagement arena is exclusively exo-atmospheric, above roughly 100 kilometers. The basing modes primarily considered by the program are from sea or land-based locations. In principle, such a device could be based in orbit, violating at least one additional treaty beyond that of other SDI systems. But in practice, the program has been almost totally oriented toward looking at so-called pop-up applications. This includes understanding, from the red team side, the defense suppression and anti-satellite options, and from the U.S. defense side, the opportunity for defense reconstitution. If parts of, for example, a space-based interceptor constellation were taken out in a precursor ASAT attack, XRLS could pop-up rapidly to be ready to engage against ICBM's, SLBM's and post boost vehicles. In principle, the weapon could be used against re-entry vehicles, but the mission is not as compelling.

It seems to me, at least, that the really dominant reason for looking from a defense point-of-view at x-ray lasers is because of the possibilities they offer in land or sea-basing for survivability and for intercepting during the boost and post boost phases of the engagement. They have high leverage. In principle, multiple beams can be effective against some fairly large number of targets per weapon. They are compact in size -- and the reason for the compact size is twofold. One is the (still amazing) energy-per-unit weight that's available from a nuclear source, roughly a millionfold compared to a conventional chemical source. And the second is just the fundamental difference in wavelength between an infrared photon and an x-ray (factor of 1,000), so that operating in interesting diffraction limited regimes implies apertures on the order of centimeters instead of on the order of 1-10 meters.

Finally, because of the light-weight energy source, it might be expected that such a weapon could be inexpensive. This chart shows a cartoon for possible operational deployment on a strategic defense submarine. There was a study conducted by SDI three years ago called the SDI Maritime Adjunct Study, examining possible missions for a so-called strategic defense submarine. Several different weapon concepts were examined for deployment on such a submarine. One of those was a nuclear-pumped x-ray laser. By and large, the study did support the possibility, in principle, that launch timelines could be met with rapid national command authority decision. It leaves open the possibility that the x-ray lasers could combine with orbital kinetic kill vehicles to form a strategic boost phase defense dyad, or when coupled with ground-based or Conus-based systems, the possibility of even thinking about a strategic defense triad, each with its own unique options, survivability features, and difficulties to counter measure.

We've also studied the threat of an entry-level x-ray laser as a counter defense weapon. Some brief estimates similar to those done in the American Physical Society DEW study indicate that the technical requirements for a counter defense weapon are likely to be less than those for a defensive weapon. The fundamental advantages include the possibility of quite a short timeline, since the x-ray laser could be boosted to a point just above ~100 kilometers, and take its shot rather than flying all the way to the defense platform. This eliminates some of the defensive tactics that such a satellite might have. It makes shoot-back difficult, although not impossible for some classes of weapons. Also, it makes it very difficult to maneuver in time or to deploy shields in the very rapid timeline.

As far as the program goes, the funding has been very largely dominated by spending on the Department of Energy's side of the house, with some additional money coming from the Directed Energy Office at SDIO. This chart is kind of a summary of where the program stands now. It's still viewed to have potential as a high leverage U.S. defensive weapon, and as a possible threat to the U.S. deterrent, if developed by the other side. We have demonstrated substantial progress in obtaining key performance milestones. We have particularly made very significant advances in understanding better the physics that we're looking at in underground tests. Not an easy thing to do. We've had a program worked jointly with SDIO to look at critical engineering technologies required to build a weapon. We've also had some discussions with DNA to understand the possibilities for effects testing someplace down the line. In general, of course, progress is contingent on continued DOE and DOD funding. That's under stress, just like for some of the other directed energy weapon technologies.

Switching gears once, I want to review what was done on Lawrence Livermore's Free Electron Laser Program during the last year, and where that's going now after the White Sands decision has gone to the Boeing/Los Alamos team. People may recall that it was in 1985 that our electron test accelerator was used to drive the first high-powered tapered wiggler operating at 35 gigahertz. The power gain with the tapered wiggler was demonstrated with peak power levels above the gigawatt. The rather remarkable thing about those experiments was the extremely efficient energy extraction that was observed, that is, 40 percent of the electron energy was converted to photons. During the last 2 1/2 years, we've been working at the Advanced Test Accelerator, the high current, medium energy 50 MeV facility about 20 miles east of Livermore, working on the Paladin experiment operating at 10.6 microns. Experiments were done at 5 and 15 meters, but during the last six months, a 25 meter wiggler set of experiments was also done. In these experiments, we demonstrated the gains that I mentioned, including an extraction efficiency measured at 1 1/2 percent, which to my understanding is the highest extraction efficiency observed in that frequency regime. It looks as if there will be no more work in that area during fiscal year '90.

There is currently work on a different project, however, and that's using the free electron laser as a microwave source for heating of the plasma in a tokamak. The Alcator B Tokamak from MIT has been transferred to Lawrence Livermore, and experiments are going on there now. They use the ETA2 machine, a 6 MeV machine capable of operating at roughly three kiloamps. We're in the middle of those experiments now. We have observed peak power levels of about 8 gigawatts, at a frequency of 140 gigahertz. The goal for the heating program is about 250 GHz.

"Phase One"-like defense may have application over a broad range of strategic objectives

Objectives	Program implications
"Technological deterrence"	Vigorous R&D, technologies on shelf
Improved intelligence/ warning/offense response	Significant deployment of space-based sensors & improved C^3
Accidental/unauthorized launch protection	3-5 ERIS sites and/or 100's of SBIs; requires ABM Treaty modification
Enhance deterrence	ERIS and/or SBI cost competitive with offense options vs. constrained threat
Limit damage	"Phase One" with preferential defense: – saves many targets – can't meet long term goals vs. responsive threats Role for DEWs

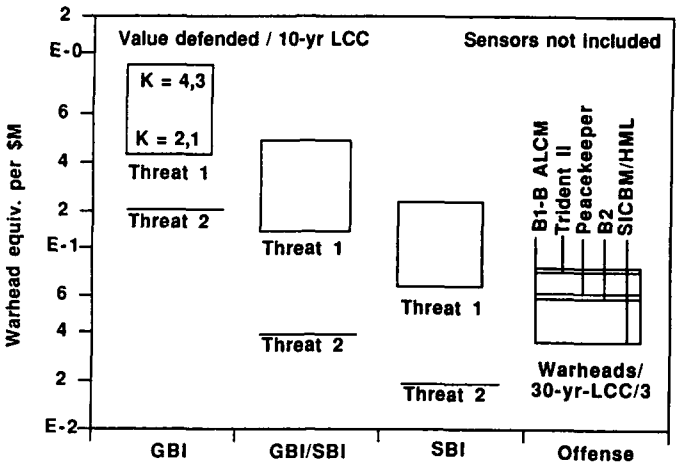
Moving to my third subject, I wanted to discuss some thoughts about defense architectures. I think something that's worthy of note has been the recent interest in Congress and within the Defense Department about quite a range of roles for a strategic defense, including in particular those for a much less than perfect defense. Quite a different emphasis than during, for example, the Fletcher Panel in 1983, which was laying out the road map for R&D for SDI. Some of the policy objectives that a strategic defense system or components thereof might perform are listed on the first chart. This is not an exhaustive list but it's perhaps a typical one. The first box might be roughly where we are now, a form of technological deterrence with a vigorous R&D program, perhaps with a goal to get some technologies on the shelf, but, with concern for the ABM treaty and on costs for deployment, perhaps not going any farther. Moving along, there have been discussions over the last year about the possibility for deployment of sensor systems which could significantly enhance intelligence gathering capabilities, providing early warning of either tactical or strategic attack, and the possibility of giving some aid to an effective offensive response to such an attack. It would require significant actual deployment of space-based sensors and improved C^3, particularly if retargeting of offense assets were one of the rationales. The amount of money, and perhaps I shouldn't speculate on that too much, would certainly be nontrivial, but less than that associated with weapon deployment. Next: there has been quite a bit of interest by Congress, and in fact, explicit requests by Congress to SDI for reports on the possibility of an accidental or unauthorized launch protection system. These requests have often been couched in terms of treaty compatible, or ground-based systems. There certainly are other possibilities on the horizon, too. Now, this is my own personal point-of-view, but I think an effective accidental launch protection system under the current conditions of the ABM treaty is not possible. If by that treaty, I mean one which constrains the U.S. by the 1975 protocol to basing only in Grand Forks. I think the kinematics for ground based interceptors based in Grand Forks against submarine launches from either mid-Pacific or mid-Atlantic are just not going to be feasible with the radar track time that you might expect to have. Nevertheless, in principle, on the order of three to perhaps five sites for long range interceptors -- and I used ERIS in a generic sense on this chart -- could be sufficient, especially in a world where the other side has not decided to deploy a great array of penetration aids, recognizing that this system is really only effective against accidental or low-level launches. Another possibility is for the deployment of perhaps on order of 100, maybe a few hundred, depending on exactly what you're trying to protect against, space-based interceptors, whether they be Brilliant Pebbles or the Phase 1 type of interceptors presented by SDIO to the Defense Acquisition Board several years ago or some hybrid. Nevertheless, on the order of hundreds looks like a possibility. Certainly, that would require ABM treaty modification and rewriting. It doesn't seem as impossible to achieve such an understanding now perhaps as it may have once seemed.

Along the line of increased capabilities in defense, we examine enhanced deterrence. I will show a chart on ideas for enhancing deterrence; in particular, the idea of enhancing deterrence in the sense not of disrupting the attack but of being cost effective in providing an assured retaliatory capability. Maybe what I should have written in this box is providing guaranteed retaliation, and I'll expand that on the next chart.

Then finally, of course, we come to the mission which many would think is the only right mission for SDI, but others might not. That's to provide a very high capability of damage limitation. Now it is interesting that a Phase 1-like system consisting of a mix of ground-based and space-based interceptors, using preferential defense, actually can save many targets and much value (in a systems analytic sense) against a rather capable threat. It certainly can't meet long-term goals of greater than 90 percent of targets protected against very responsive threats, and that's been viewed as an obvious role for directed energy weapons.

I'm going to say just a couple of words on this idea of kinetic energy weapons in protecting military assets. Chris Cunningham, at Lawrence Livermore, has done some interesting calculations. In particular, he looked at two threats which I call START-constrained, since that's about the number of RV's that he looked at in the threat, 4,000 to 5,000. I'm going to show results for two threats. One is a mix of evolutionary and fast-burn ICBM's with what I call first-generation decoys on most systems; that is, they might be fairly capable against medium resolution optical systems, but might not be particularly capable against ground-based radar, for example. A radar system has usually been associated with deployment of the ground-based interceptor. Threat 2 is all fast-burn ICBM's, evolutionary SLBM's and a more advanced set of decoys. The results are shown here in kind of a convoluted figure of merit, but one I find interesting. It's warhead equivalents saved in a counter-military attack. Now what's a warhead equivalent? Well, in the case of an attack on an asset which actually contains warheads, like an MX silo, the warhead equivalent is the number in the silo, ten for MX for example. For other parts of the target base, there has been work in various parts of the community to try to make some equivalence, and Chris has relied on this work to derive a value structure. What I've done here is talk about the cost, or the savings, rather, in warhead equivalents in an attack, per million dollars spent on the defense components (on the left). On the right, I show the similar cost in deploying presumably survivable offense assets. The effectiveness of the defense is critically dependent on discrimination, measured by the K factor of the system's sensor elements. The boxes for Threat 1 correspond to a range of K factors between (4,3) -- very good and (2,1) -- fairly good. The pair of numbers refers to (radar, optical sensor) capability. For Threat 2, we used (1,0) -- corresponding to excellent decoys. For the best discrimination, a ground-based interceptor (GBI) concept can go up to as much as a warhead saved per million dollars spent, and that is very effective. It is a much more effective expenditure of dollars in preserving retaliatory capability than actually spending that money to put

KEW options could provide cost-effective protection of U.S. retaliatory assets



• K factors are for [GBR, GSTS]. For Threat 2, K = [1,0] is shown.

warheads on Trident submarines. I think that is a really provocative result. The second defense is a mix of ground-based interceptors and space-based interceptors and the third is space-based interceptors alone (for a particular class of space-based interceptors). Now, these costs can go up and down; in particular,

I don't have Brilliant Pebbles numbers folded into this analysis. They would look better than that. Nevertheless, several messages are clear. There's about a factor of 3 to 5 decrease in performance of the defense between Threat 1 and Threat 2; and defense can be competitive in terms of spending money on one additional warhead asset compared to offensive options such as Trident 2 or a mobile U.S. missile system.

What are some of the implications of thoughts like these -- and I refer back now to this whole range of policy objectives -- on a so-called Phase 2 Strategic Defense System, based now on directed energy weapons in addition to a presumably initially deployed kinetic energy weapon system. Well, it seems to me that it's unlikely that directed energy weapons are going to make the cost cut for the mission of enhancing deterrence alone, if by that phrase I really mean providing secure retaliation versus the cost of deploying one additional survivable offensive warhead. And the figure of merit that DEW folks have to shoot for, I think, looks like something on the order of .05 warheads saved per million dollars if they want to make that case. The evaluation also has to be against advanced threats that are too tough for the kinetic energy weapon systems. In some sense, the Directed Energy Weapon advocates may be in a box in the phase space of policy objectives and capabilities. It's recognized that, at least for a Phase 2-like strategic defense system, the capability to protect greater than some number, maybe 50 percent, maybe 70, maybe 90 percent of target value that would otherwise be taken out in a large attack, is a mission, a national goal. It may be realizable by kinetic weapons against some threat, a rather constrained threat, as you've seen by my analysis of Phase-1-like systems. Perhaps deployment of larger numbers of kinetic energy weapons may be effective against tougher threats. So the threat's got to be stressing enough to justify the DEW's against the kinetic weapons, but it can't be too tough or the cost and/or the technological requirements for the DEW start to go through the roof. So that's one part of the box. The second is: What should it cost? Well, there are proposals on the table for Phase 1-like systems in the $20 billion to $30 billion class; I refer to General Abrahamson's valedictory speech in January. Many of you have seen some rough analyses on cost for large deployments of DEW weapons. They typically reach at least into the $100 billion regime. When we think about national budget trends, the Phase 2 system better not branch too far into the right-hand side of this phase space. In conclusion, I think that it still remains to directed energy advocates to make the case for this kind of a future in which they're able to deal with these boxes of threat and cost, or perhaps to jump out of them by making a case for other possible attributes in terms of survivability, innovative techniques, resistance to counter measures and so on. Perhaps in these areas they could look competitive and interesting compared to kinetic energy weapons.

Professor Brau:

Thank you, Kent. Is there a question in the nature of clarification before we go on? Well, I think that that pretty much lays down the challenge for the rest of the speakers. The second panelist on our program today is going to be Kumar Patel. At the present time, he is Executive Director of Material Science and

Engineering at AT&T Bell Laboratories. Everyone here, I'm sure, is aware of his contributions to lasers and science in general. His most popular work, without doubt, is the American Physical Society Report on Strategic Defense. He's going to make some remarks, I think, in the nature of questions that we'd have to answer. Kumar.

Dr. Patel:

Thanks, Charlie. First of all, let me thank the organizers of this panel for including me in this discussion, which relates primarily to the directed energy weapons. I also want to observe that when I look at this panel, I can imagine how the gladiators felt when they were thrown among the lions. Almost everybody on this panel is in some way or the other associated with SDI. I'm not. But nonetheless, I'm an interested observer on the issues surrounding SDI. My colleagues are committed in one way or another. As an aside, let me tell you the distinction between being interested and being committed. That's the difference between the chicken and the pig when it comes to a breakfast of eggs and bacon. The chicken is interested, the pig is committed! (laughter) Let me come to the issues. As I mentioned, and as Charlie mentioned, my connection with SDI directed energy weapons technology essentially was in connection with the American Physical Society report when that report was issued a little over two years ago. That connection ended at least on a formal basis, but I've continued to keep myself abreast of what's going on. An observation I would like to make is that many of the issues which are raised in that report, and those issues identified as being crucial ones, are still relevant today. Let me give you a few of those examples. For chemical lasers, high powers were seen to be necessary except in some very least demanding type of applications. And the alpha laser, which was described by Colonel Meyer, clearly moves us in that direction, the direction of providing us with a technology, a machine that might produce higher powers. Beam quality at highest powers needed was also identified as a critical issue. In the areas of ground-based free electron lasers, several physical concepts, such as optical guiding and harmonic control of the output, were seen as critical issues, as well as the issue of obtaining very high CW powers and high pulsed powers at short wavelengths. Now we have seen that efficiencies, as well as very high powers, are obtained at longer wavelengths, wavelengths longer than 10 microns. The critical issue is if we want to take advantage of the ground-based free electron laser, the short wavelengths are very crucial because that determines the size of the space-based optics. For neutral particle beams, the issues of beam current scaling, beam voltage and duty cycle scaling, pointing accuracy and the needed retargeting rates were crucial issues. None of those have disappeared, as we heard this morning. For lasers of all kinds, whether they are ground-based or space-based, there is a need for an optical chain which includes phase control techniques for combining outputs of different modules, if one cannot build a module of sufficient size. Dynamic phasing of telescopes to obtain large effective apertures, high reflectivity coating which are resistant to damage when exposed to intense out-of-band radiation, radiation for which the mirrors are not designed, and damage due to MeV protons and high-energy electrons during the long residence in space for space-based optical components are some of the important issues. I'm not concerned about counter measures at the present time except for the fact that the counter measure includes out-of-band optical radiation. For ground-based lasers, there are issues of phase correction techniques for compensating for the atmospheric aberrations. These were seen to be important -- that will seem to be an important issue both in terms of increasing the resolution, the number of elements that one might use for correcting such an aberration, as well as its operability at the high powers needed for the SDI applications.

Regardless of what scheme one uses in connection with defense against ballistic missiles, the detection and acquisition of ICBM launches for boost phase intercept requires both high detection capability, as well as low false alarm rates. For that particular application, there is a very critical requirement on active tracking, tracking such that the target can be destroyed during the available time. For mid-course intercept, active discrimination is required to distinguish between re-entry vehicles and penetration aids. The point is that for a fully deployed system which has substantial amount of directed energy weapons as its component, there will be substantial amount of space-based assets in form of satellites, space-based mirrors, lasers, etc, which can be threatened by directed energy weapons of the other side. And one such issue was pointed out by Dr. Johnson just a little while ago, which is the threat from the enemy-launched x-ray pop-up lasers. So survivability and reliability of space-based assets clearly needs to be examined in greater detail.

But these are the issues dealing with components. What we are really talking about is a large system, assuming that the size of the system is what one talked about in the early days of SDI, which is a more or less complete defense against ballistic missiles. If one were to scale back from that kind of defense to defending either point sites or not defending large land areas, then of course the demands on any type of technology used for strategic defense goes down. And therefore, it's a mistake to assume that what is possible on a small scale is immediately applicable to a full-scale defense application. From a systems designer point-of-view, there is very little past experience that we or anybody else has for controlling, designing, and fielding a system of that size. Not that it can't be done, but it is an important issue.

There are a couple more observations. Until about two years ago, the nuclear pumped x-ray laser was seen to be one of the principal, if not the principal weapon -- a very important part of the strategy. I think it still remains the case, but there is very little heard in terms of where the technology stands and what the important issues are that need to be resolved. We are even led to believe that deployment of such systems was only around the corner. Clearly, it wasn't around the corner, not in the two-year time period

that we have seen. Similarly, in that time scale, excimer lasers were also seen to be important and were being seriously considered. The reason I bring out these issues is not because one should not change one's view regarding what technology is going to be useful, but the observation illustrates the problem, that is, at what point does one make a decision about what specific technology should be developed for engineering demonstrations. As we learn more about the systems, we'll find out better ways of doing things, perhaps cheaper ways of doing things. And more importantly, we'll find out in a more reliable sense what technologies ought to be pursued and what should not be pursued. I'm pleased to note from the talks this morning that there is a continuing progress that's being made in many of the technologies, whether they be lasers, neutral particle beams, or detection. Yet, there are a number of open issues which remain to be resolved at the R&D stage. Issues dealing with reliability and survivability clearly need considerably greater attention, especially for the space-based assets.

Let me close by saying that nothing that I have heard in the two years since the APS report was released forces me as an individual to quarrel with the conclusion that was reached in that report. The conclusion said that a decade or more of intensive research will be required to provide the technical knowledge needed for an informed decision about the potential effectiveness and survivability of the directed energy weapon systems. Note that that conclusion dealt with a fully deployed system. It did not deal with encountering a limited type of attack. If one is willing to scale back the size of offense that one is going to face, then many of the conclusions have to be revised. If one is to encounter only one enemy ICBM, clearly, what one needs to do is very different from the actions required to face a full-scale attack. All of this, of course, assumes that the world that we live in and will live in is what it was rather than one which is unfolding day after day, both in the Soviet Union as well as Eastern Block countries. I'm not qualified to comment about any of this. Clearly, for the policy-makers, there are important decisions to make, but not for what R&D ought to be carried out. I think R&D ought to be carried out on many of the issues that deal with high-energy lasers and energetic particle beams, detection of launches, discrimination, tracking and so on. These issues will continue to be important for a long time.

Professor Brau:

Thank you, Dr. Patel. Are there any questions of clarification at this time? If not, then I'd like to go to the third member of the panel, who is Tom Meyer. Tom is the director of the Directed Energy Office in SDIO. I have in my remarks that it looks like he's been there for 75 years, actually, it's greater than five years. But sometimes it seems like it's been forever. Tom has been in SDI before SDI, in fact, he was at DARPA in those days. Tom's going to sort of continue, I guess, his remarks of this morning.

Colonel Meyer:

I hate to be reminded of my age, Charlie. There are certainly people who have worked on lasers longer than I have sitting on the panel. I'd like to really quickly summarize again what I talked about this morning. I don't want to belabor the point, but the topic that we are addressing is what's happened in the last four or five years. I have a single chart here, I think, on each of the major weapon systems that pretty much should convince you that we've progressed way beyond the physics questions in demonstrating this technology, and we are in the engineering integration phase of determining whether something's feasible or not. The question that Dr. Patel raises is -- is it cheaper to do a thing one way than another? I think in the chemical laser it's clear that we have the scaleable technology. We have the Alpha laser, which is a technology scaleable to the weapons level systems that we need. We have the LAMP mirror, a segmented mirror scaleable to larger apertures if we want. We know how to do the beam control that goes with all this. The question now is integration at the sub-scale on the ground first, and then in space, to show that all these pieces fit together and work as we expect them to in an engineering sense. In the NPB program, again, we have the ion source at the current and brightness levels that we want for the weapon we're going to build, the RFQ, and the drift tube LINAC. We have demonstrated the magnetic optics, as I showed you this morning, and the neutralizer, another amazing thing, as I was pointing out, an engineering achievement. We no longer require complicated gas cells, but merely a simple piece of foil to neutralize the beam, and of course, we've demonstrated beam sensing. We're pressing on to demonstrate on the ground the higher energies that we require, and of course, we've already done a space experiment that determines whether or not space craft charging is a problem, and if there are other things that may be surprises which we were not aware of. With regard to FEL, there were several talks by John Madey and Kent Johnson about the progress made there. We've proceeded quite a way toward understanding how to build bright electron beams at the current we need to build a weapon. We have chosen a particular approach to achieve this. We have large and very sophisticated codes that model the performance we'll get out of these machines, and they're very predictable, and we're pressing on to build a machine at White Sands. We also have built a lot of the components for doing the atmospheric compensation. We understand -- on the laboratory scale and in the real atmosphere -- how to do turbulence correction. The question that we're pressing on to resolve now is the interaction of turbulence and thermal blooming in the atmosphere, a topic that you've heard several papers presented on this week. And finally, the topic of how do you acquire and track these objects in space and how do you identify them. There are several experiments in this area, as I talked about this morning.

With our LACE and RME spacecraft, we'll do experiments to determine how you establish the relay links for the ground-based laser and how well it is being propagated through the atmosphere to those targets. Starlab is an integrated experiment that will identify remaining issues for acquiring and tracking boosters as they

come up through the atmosphere. It will show active tracking at the required resolution, and the sub-micro radian tracking precisions necessary to scale to, first of all, sub-prototype levels, and finally to the full prototype systems that we need. So I think, as I said this morning, the progress is substantial; we're in the stages now of doing technology integration at subsystem levels so that we can scale to the higher power levels, higher capabilities levels, when this country decides to do that, if it decides to do that. So I wanted to gain some time and that's all I had to say, Charlie.

Professor Brau:

Thank you. (Applause) Do you have any questions of clarification? If not, then I'd like to introduce our fourth panel member, who is Marlan Scully. Professor Scully divides his time between teaching physics at The University of New Mexico in Albuquerque, being director of the Max Planck Institute, and ranching in the beautiful highlands of New Mexico. Marlan's going to bring a little different perspective to this panel. As an academic, he's going to talk about the relationship between SDIO and universities. I would say to you that Marlan could bring a different perspective to almost any discussion. Marlan.

Professor Scully:

Thank you, Charlie. We've been involved with these kinds of questions for some time. I always tell my students that it's important to do two things when they're in graduate school. One is to learn to enjoy physics, and the other is to learn to employ physics. I'm sure it must not have been much fun to learn to read. But once you've learned physics and you are able to begin to investigate interesting problems, it's a great thrill.

High-power laser physics is a wonderful example of an area in which there are interesting problems and problems which are fun, as well as -- I'm going to avoid the use of the word relevant, but fun as well as interesting. I remind myself of the famous oxygen iodine laser. And the fact that these incredible molecules live for 40 minutes in the excited state of, for example, singlet delta oxygen. Look, if you will, at the wonderful progress which has been made in the free electron laser arena; these devices are even a component to the economy of New Mexico.

Now, from the interesting applications to bizarre possibilities, I'd like to mention the new ideas of lasing without inversion. Here we could have a laser such that there could be more atoms in the ground state than the excited state by orders of magnitude. Utilizing quantum interference, as will be discussed in talks tomorrow, we can effectively render atoms in the ground state invisible so that one atom in 10^6, say, in the excited state would be enough to make a system lase. Obviously, for very rapidly decaying x-ray transitions, that has certain fascinating possibilities.

Now given that high-power lasers do exist, the possibility of doing physics with them is both immediately and potentially fascinating. Let me remind you of one very interesting, experimentally observed phenomenon, namely the so-called "above threshold ionization." The ionization is produced by laser radiation incident on some particular neutral gas; we measure the number of electrons at some particular energy and find, surprisingly, that the electrons come off with a spectrum of energies in a sort of comb, with a separation between peaks given by the laser frequency. So we have this wonderful example of physics occurring in a high-power laser system which is both unexpected and completely explicable in terms of simple quantum mechanics.

The application of these high power laser devices to problems which are relevant to issues far beyond any temporal issues is immediate and exciting. Perhaps one day soon we will see a panel discussion of this group directed toward problems in the arena of disease and other problems we would also like to address in the not-too-distant future. I'd like to conclude with the observation that his beautiful work on free electron lasers applied to medical physics is supported by SDI. Right, Charlie?

Professor Brau:

That's right.

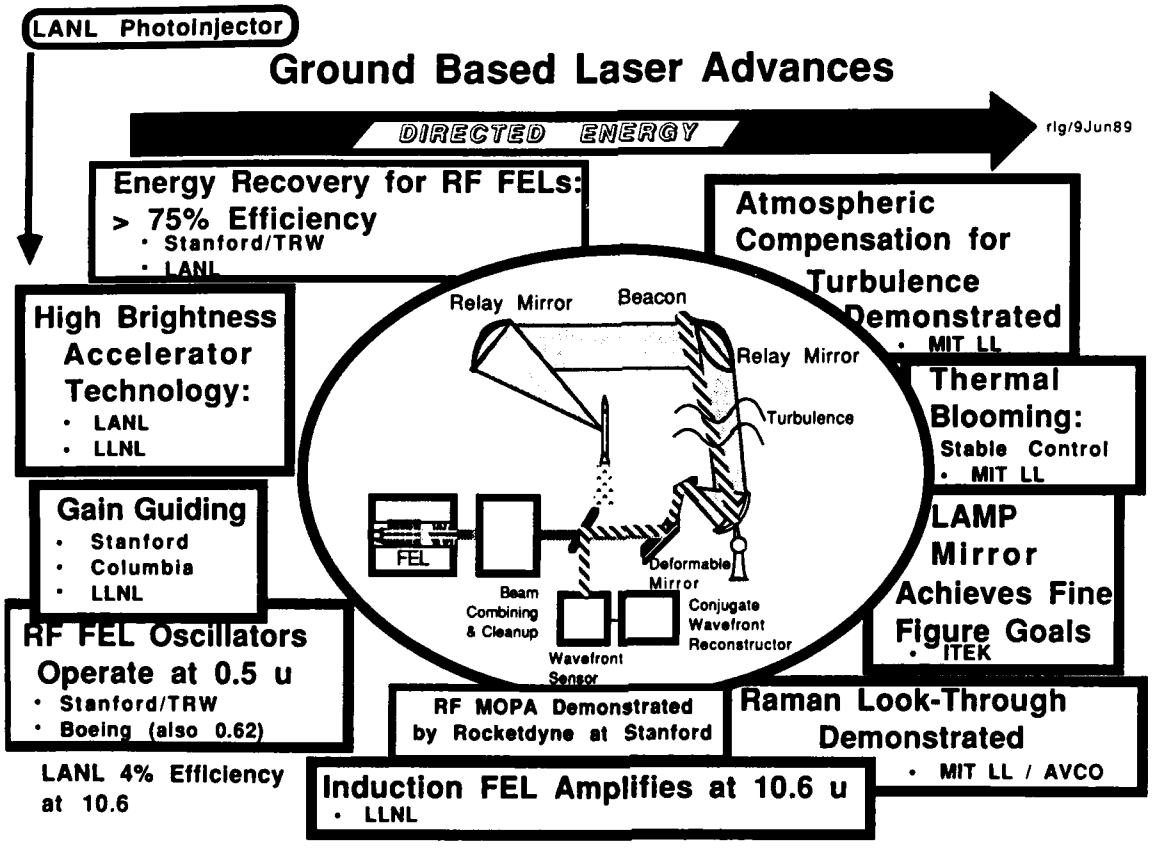
(Applause)

Thank you, Marlan. Are there any questions on this talk? All right. If not, let me introduce the next member of the panel, who is Richard Gullickson. Richard is the Chief of Electromagnetic Applications Division of DNA. Previously, he was Deputy Chief Scientist at SDIO. Dick has really, in his time, made the rounds of all the important places to be. AFWL, LLNL, AFOSR, DNA, DARPA, and now DNA again. He's gotten every list of letters in the alphabet. Dick, take it away.

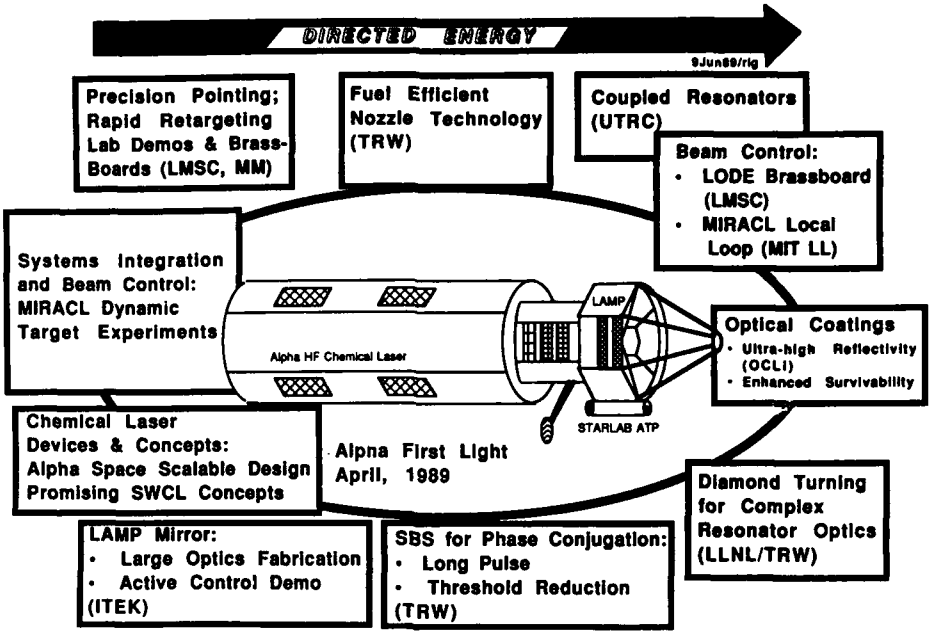
Colonel Gullickson:

Thank you, Charlie. What I'd like to do in my few minutes here in these opening remarks is to cover, I hope briefly, the points that several of my predecessors have made in terms of where we stand in the advances of the strategic defense technology, especially in the directed energy area. But now because of my new

affiliation with the Defense Nuclear Agency, where we support the Strategic Defense Program in the area of power technology, I want to go off a little bit into that field just to describe to you some related advances and some related applications of that technology. I'd like to follow the guidance of Charlie Brau a little bit here, too, and if I can remember as I go through, to make several additional points. One is to identify those things which, in comparing where we stand now in 1989 versus where we were in 1984, have really been surprises in terms of technical advances. Another thing that I'd also like to do to make it a lot more interesting, is to talk about disappointments and regrets. I think primarily that you will find that my disappointments relate to pathways where we have started very interesting programs, gone a certain distance down those paths, and have been unable to continue due to resource limitations. Many examples come to mind and I'm sure that I'll get to several of them in the talk. They include excimer lasers in particular, both discharge and electron beam pumped, which, as Dr. Patel mentioned a while ago, were thought to be the leading candidate for the ground-based laser back in 1983, 1984, and still in fact have lived up fully to their technical promise. Only the surprises of the great advances in free electron lasers have made us go beyond that excimer technology to other possibilities. Also, one of the themes that I want to make here is that for better or worse, SDI has become the funder of last resort of many key directed-energy technologies. And as a result of that, and also because of the promise of these technologies, we find that there are many joint-use applications, many civil spin-offs. The things that come to mind again, because of my connection with an agency that does power programs, are things like the Superconducting Magnetic Energy Storage program, SMES, which provides power for the ground-based free electron laser. Another example is the SP100 space reactor, where it is clear that there are missions within SDIO that are enhanced by having this key technology involved, but where there are also even more compelling missions in the civil arena. So let me go through now very quickly and talk about some of these things. The first thing that I'll do is to kind of mimic what Tom Meyer did in his view graphs that are kind of like wiring diagrams of advances. And I hope as I go through my three charts, I'll focus on one new point in each of those areas. These charts, by the way, appear in last year's proceedings, but they have been updated since then. To me there are several surprises/miracles that have developed within the strategic defense program. And one of them is the great advance in non-linear optics. And to me, that made all the difference, or much of the difference in terms of the viability of the chemical laser, which I consider to be an extremely promising candidate for strategic defense. The ability to use phase conjugation, to reduce the tolerances in optics, to be able to have schemes where one can have beams that are self-pointed, to do atmospheric compensation, and overtone lasing in chemical lasers are examples. Very fundamental basic research has led to significant practical implications for big systems. In the case of the ground-based laser, I consider the big surprise to be the free electron laser. You've heard many testimonials toward that fact here in the talks that have preceded mine. To be able to produce high gain with an induction device, to be able to produce very high efficiency with the RF driven devices, the ability to do both gain and optical guiding, that is, to be able to

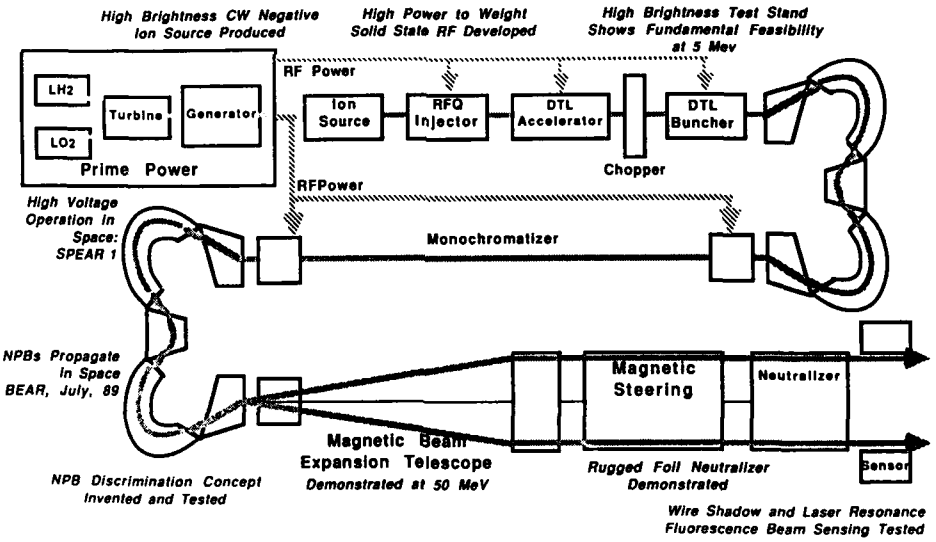


Space Based Chemical Laser Advances

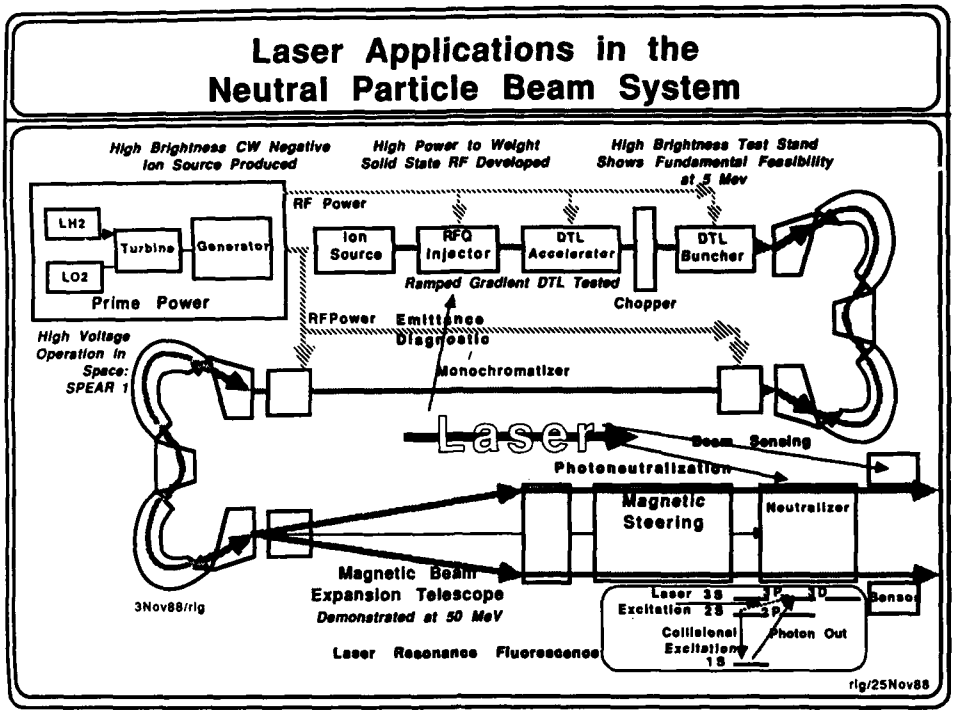


Advances in Neutral Particle Beam Technology

4Dec/rlg



demonstrate that one can make the electron beam act like a fiber optic light pipe and guide the amplifying optical beam all the way down a 25-meter wiggler or longer, well beyond the difraction limits, and still be able to keep that beam confined within this fiber optic-like electron beam, I think is a real considerable advance and surprise. In the case of the neutral particle beam technology, I would simply point to the progress in integrating these systems. Nothing here has been any one big surprise, but the fact that we've been able to, in so short a time, go from a program which was funded at the rate of about a million dollars back in 1982/1983, and to go to a demonstration in July where an integrated system, albeit it a short pulse system, has been able to really demonstrate all phases of the operation of that system in its natural environment, namely space, is certainly remarkable. Starting from prime power, going all the way up through the neutralizer, I think, is a remarkable demonstration. So let me shift gears now and get off a little bit into the field of power systems, and make a few points there, too. I think this is different from the theme of much of what you've heard about at this conference. Certainly, in the case of the neutral particle beam



that we just talked about, and also the free electron laser, which is also a space system as well as a ground system, one of the key issues is that components in these systems operate at very high voltages. The negative ion source in the neutral particle beam system may operate at minus 60 kilovolts. The klystrode, or klystron in the case of both the RFFEL and the neutral particle beam accelerator may operate at 100 kilovolts. One is operating these systems in an environment, because of the ionospheric plasma, the outgasing and the effluents from the spacecrafts themselves, their power systems, and their attitude control thrusters, where one may be near the minimum in the paschen curve in some cases. And so there have been a series of experiments conducted by SDIO and DNA. The SPEAR (Space Power Experiments Aboard Rockets) series is another where we have looked at the ability to design systems, to be able to prevent those breakdowns, and to do so in a way which really wasn't brute force, that is, didn't involve putting something in a high-pressure can or in a liquid filled can, which would have been prohibitive from the standpoint of high weight for the system. So designing systems that have insulators that operate in vacuum take advantage of the vacuum in space, avoid breakdown surface flash-over, avoid these things that are induced by the outgasing of the vehicle and the production of effluents by an attitude control system or power supply. So that's been a theme of much of our activities. I'll also point out that in addition to these breakdown issues, that we also have the problem that the signatures and the ability to do surveillance from these platforms may be degraded by the fact that the effluent coming out can be excited, can be ionized, can be a source of infrared, and either make a big signature which one wants to avoid, or limit the possibilities of being able to look through it in case of the surveillance platform. So those two are issues that have to be examined. This viewgraph shows the SPEAR experiment conducted by both DNA and SDIO in 1987. This was a conceptually simple experiment. You can see in this Y-shaped object and over here in the vacuum chamber test on the right, a 20 centimeter diameter aluminum sphere, operated at 46 kilovolts in space. You can see the high-voltage bushing that successfully held off the full voltage above 100 km. SPEAR flew to an altitude of 370 kilometers on a Black Brant 10 and did successfully demonstrate that one can design and operate these high-voltage systems in space. It also led to a lot of interesting plasma physics. This is a calculation done by Ira Katz and his co-workers at SQ in San Diego that shows the bipolar sheaths that form around these things. Now, when I show a slide like this, I'm always tempted to digress into a much longer explanation than my time will permit, but it suffices to say that one of the interesting features of these experiments is that if you have one part of the spacecraft at +46 kilovolts, the body can float to a very high negative potential. And whether or not this floats to a very high negative potential depends upon whether you have an ionizing beam that comes out, as in the case of the BEAR experiment, where in that case, the body only floated to a few hundred volts, or whether one merely has high voltage, as in the case of this experiment, in which case the body floated to 11 kilovolts. In this particular case, minus 11 kilovolts. And there are a lot of implications about the sheaths that form, the charged particles which bombard the spacecraft, the life of the components, and so forth. Tom Meyer talked about BEAR and how it demonstrated that one can build an integrated system and propagate the beam. I'll just point out further that another thing that BEAR demonstrates is that we can build the power systems, in this case, a low voltage, solid

state power system, indicated there by red where we have two 60 kilowatt solid state transistorized amplifiers that provide the 425 megahertz that, in this case, drives the accelerator structure. And this again is done strictly with solid state, low-voltage systems, and then so, at a level of about a gram per Watt. That is very economical in terms of weight. Here is an example of the next experiment in our series, SPEAR 2, which takes that same theme, that is of designing high voltage systems operating in vacuum, does so with a high impedance load operating at 100 kilovolts of the kind that would be used to power either an NPB or free electron laser, and also has a low impedance load, a high current load that powers a plasma accelerator like a rail gun. And this thing will fly in April. And then again, we'll look at some of these issues about high voltage, high power in space. This system is already being tested right now in a space chamber. Let me go off into another direction. We've talked today about the ground-based free electron laser. This is another one of those acronyms which is really a mouthfull, SMES, Superconducting Magnetic Energy Storage. There are various versions of this, both solenoidal or toroidal. This is a solenoidal version that we're building. This is kind of a small one about 100 meters in diameter using niobium titanium conductors. This would store about 20 megawatt hours or about 72 gigajoules of energy, and could be used to power, for example, a technology integration experiment for the free electron laser. But it could also be used to load leveling for utilities. And we've demonstrated at least in pieces of the conductor about a meter long that we can operate at the -- in one of the concepts, the 200 kiloamps and above that we need to be able to do this. In fact, up to 270 kiloamps. So the basic pieces of this concept have been established. This device sits in a trench so that the radial forces outward are restrained by the earth. I'll just talk for a second about SP100. This is the space reactor that is all things to all people. It is designed to cover the range of 10 kilowatts to hundreds of kilowatts. It's a fast reactor, uses liquid lithium, uses thermo-electric conversion, operates for a 7-year lifetime, would be used in the case of directed energy systems for station-keeping power or in conjunction with power storage for high power burst mode applications. The most significant advances here are demonstrating uranium nitride fuel operated in a reactor, and the thermo-electric conversion system. Similar thermoelectric elements are operating as a part of a radiosotopic generator on the current Galileo probe going to Jupiter. But the point that I wanted to make along the theme of civil applications is that here's an example of a program, partially funded by SDIO, also NASA and DOE, where in the case of the SDI missions, this is a nice thing to have that enhances the survivability of the system and makes it very small and very compact. But in the case of applications like the Mars Mission, such technology makes the mission possible. The Mars Mission has a lunar base as a part of the step where one goes to the moon, has a reactor system which then can be used to produce liquid oxygen from lunar material, which can be the oxidizer for a chemical fuel rocket, which can then be used to fly the crew to Mars in a short time and another nuclear rocket system, using the same technology, can fly a cargo vehicle using electric propulsion thrusters to Mars in a slower time scale. There are many other applications, too, such as air traffic radars at high altitude. But it's really an enabling technology for many of those applications.

I will give one more example. I can recall at Los Alamos back in the 60s, when a capacitor stored three kilojoules. Now as a result of developments, the same size can have 500 kilojoules through the development of materials and construction techniques. There are many civil and space applications for that technology. So let me finally end with this slide. I will try to hit a few of these points again. I think you've seen the maturity of the directed energy technology. I've pointed out on several occasions the civil applications, and you've heard about things like the fusion plasma heating using the FEL device and the medical applications there. To me, the surprises in the program have been things like what really is a very high tech, physics based system, the free electron laser, working as well as it does, the fact that it does do optical guiding, the non-linear optics, which we haven't talked about much here but have been talked about at this meeting, I think are a real miracle and have just overwhelming implications for directed energy systems. The disappointments that I have mentioned are all of the technologies which are so promising, but resource limitations have prevented us from developing. Devices like the emerald excimer laser, the series of Northrup discharge excimer lasers, the MIRACL system developed by the Navy, the chemical laser, which although it is still being developed, is not really used as well as it could be. I also include more work with the induction LINAC, FEL technology which is one of the many promising pathways which we just haven't had the resources to go down. And I hope that there will be sufficient SDI resources in these technology areas in the future. I've said enough and thank you.

(Applause)

Professor Brau:

Thank you, Dick. Are there any questions of clarification at this time? If not, I'd like to introduce our next speaker, who is Leroy Wilson. Leroy was at the Air Force Weapons Lab for 20 years, where he was head of the High Energy Lasers Branch, that dealt with chemical lasers, excimer lasers, iodine lasers, all kinds of lasers. For the last two years, he's been Director of Laser Projects at Rockwell International.

Dr. Wilson:

Thank you, Charlie. I had previously seen Colonel Meyer's talk and so I knew that he was going to do an excellent job of reviewing the current technology status. I would like to add a few comments to his review. The United States understands the chemical lasers and how to scale them to high power. The progress has been excellent. Excimer lasers are understood as well. They have met their performance goals. They are very large lasers. The physics of Radio Frequency free electron lasers has been demonstrated. We have

built all of the parts that are necessary to put together a large system. Next we have to engineer an increase in the average power. The country is now in the position of being able to move from the higher energy laser demonstration business toward useful laser systems.

Since I really did not want to repeat all the technical information that Tom Meyer and Dick Gullickson have pointed out, I thought I would address my remarks today to the future of the strategic defense initiative (SDI). In the face of current world events with the potential for nuclear arms reduction, strategic defense initiative is going to grow in strategic importance! If there is a finite reduction in the number of nuclear weapons and missiles, the arguments made to date for strategic defense have not changed at all. In fact, a reduced threat makes strategic defense technically more feasible because there are less delivery systems to deal with. Less also makes SDI more affordable. Secondly, nuclear and ballistic missile delivery systems are proliferating at such a rate, that in our lifetimes, many nations will have the capability to accidentally or deliberately deliver a weapon to any spot on the earth. Concepts like the SDI accidental launch protection systems (ALPS) will grow in importance. Another difficult defensive problem that must be faced is tactical ballistic missile systems and cruise missiles. They are significant threats and they will also proliferate. Recently, I experienced several days of chaos after the San Francisco earthquake. There was misinformation and the civilian infrastructure fell apart. I now appreciate how much trouble this country could be in if there were a limited, but effective, disruption of our national command authority. These are good reasons to continue the technological search for strategic defense. In the future, optical verification activities, to space, and from space will increase. Moderate- to low-power laser systems such as illuminators, laser radar, imagers, atmospheric compensation systems will be growth technologies. We will also need high-power optical, early warning and discrimination systems. The threat will come from all directions, not just over the pole. I would like to quote a Harvard professor. He contends that nuclear missile weapons are stabilizing or destabilizing, depending on the eye of the beholder. And I'll quote -- "The British could destroy every city on the U.S. eastern seaboard if they wanted to. And that probably doesn't worry anybody. The French could, too. That might worry some of you." (End of quote) (Laughter) My question to the audience is, what if Cuba could deliver nuclear missile weapons to anywhere in the world. Would that worry you? Lastly, in my eye's view, we need new SDI concepts and new technology into the next century. I hope that defense becomes as exportable as offensive weapons are today, resulting in a good, strong strategic defense by all nations. A step toward lasting world peace. The current events of Eastern Europe are phenomenal, promising, unstable, exciting. And on the surface, it appears Gorbachev has been a man of our times. We wish him and his country continued long-term success toward a more peaceful world, and perhaps international exchanges such as this will convey to Russia and the other countries of the world that strategic defense will benefit all nations in the long term. Thank you very much.

(Applause)

Professor Brau:

Thank you, Leroy. Any questions on this talk? If not, then I'd like to introduce our next panel member, who is Joe Miller. He is Assistant Manager of the Applied Technology Division at TRW. That's the division in charge of directed-energy propulsion, space payloads, and a variety of other high-tech kind of things. The first time I met Joe was many years ago when the free electron laser program first started, and I was telling him all about this exciting stuff that we were doing. They were doing it, too. And he said well -- you know, I was in the accelerator side of things and laser side of things. And he said yes, he was in the combustion side of chemical lasers and they started off with lots of combustion engineers and one optician, and before long, they have 10 opticians for every combustion engineer, and he said it was going to be the same in free electron lasers. And he was right. I have the highest regard for Joe. So, let's hear your remarks.

Dr. Miller:

Thank you, Charlie. The subject is an assessment of progress in directed energy for strategic defense. And we've heard quite a bit of discussion that says there has been some substantial progress, and there has, indeed. Neutral particle beam flights have clearly moved us into an engineering world in which we have designed and operated space payloads involving beam generators and the systems that control the beams. The alpha chemical laser has come on line and has addressed subjects that used to be called issues and now just get called subjects. The free electron laser has advanced to the point where the nation has made a commitment to go ahead and build a high average power device at White Sands Missile Range, and it had its choice of two or three very good alternatives. There have been similar achievements in the beam control technologies for the acquisition plane tracking stabilization of high power beams. Performance is clearly substantial. The question in assessment is does it measure up to expectations or desires or needs. So we might start with some general expectations. One is have we, in fact, found any surprises of a physics nature. To my knowledge, every directed energy technology we're working on is progressing along a path that is achieving the advertised capabilities. We haven't run into any fundamental limitations beyond those dictated by basic physics understood in advance. The engineering difficulties are substantial, but they seem to give way to steady good work. To me, the major result of the APS review of directed energy was a resounding endorsement. I'm not sure they intended me to read it that way, but that's the way it appears to me. And the endorsement was they didn't really uncover anything of a physics nature that said we were trying to do something that couldn't be done. Their list of issues, if you'll think about it, are engineering subjects. And when the physicists start telling the engineers that something can't be done,

they are historically on shaky ground. We can ask a different question. We can ask have we done as much as we can or should have to this point in time. And my personal opinion is no, we haven't. And I think there are a significant number of technologies and technological objectives that are important on which progress is slow, and then tend to be the things we haven't discussed here. And we could all make a substantial list of those things. But the kinds of things I'm talking about are solid state lasers, for instance, for mid-course discrimination purposes. High efficiency, reliable, low-cost diodes to pump the solid state lasers. The use of those technologies in very high data rate optical communication systems.

The applications of the non-linear optical phase conjugations to relieve optical aberrations and stabilization requirements in large optical systems. Related advanced technologies for the imaging and surveillance purposes. Advanced technologies and alternatives for atmospheric propagation subjects. So I think there are a number of subjects we haven't heard about, that aren't on the table that we could have been working on and making substantial progress on. I think the people who say that we are technology limited, not funding limited, are not very close to the program and don't appreciate the number of subjects that we could be addressing intelligently and that we're not. Additionally, where we are working hard and have made excellent progress, the work is clearly not completed. Really, we've heard about a lot of progress on advanced components and subsystem technologies, but the advanced technologies haven't been integrated into complete systems that achieve design and performance goals, while operating in realistic environments. There are significant technology developments required to do this. Some of the more mature technologies have been brought together. Here I'm thinking about things such as the MIRACL laser where we have integrated the laser, beam control, acquisition pointing and tracking systems, and have taken the first steps in very substantial demonstrations, and they've been reported this year. But we need to do the same and more substantial integrations with the advanced technologies. In my opinion, the directed energy systems won't really be taken seriously -- and by that I mean full scale engineering developments won't be options for consideration until and unless the technology development has progressed to reasonably complete, integrated, large-scale experiments. In my opinion, that's the major tradeoff subject with regard to kinetic energy weapons, not cost or effectiveness. I would take a lot of issues with the cost analysis that we saw, and the trade-off. I think the major issue between kinetic energy weapons and directed energy weapons has been the feeling that the kinetic energy weapons are near term, and the directed energy are a very advanced technology that's long term. I submit that as the calendar moves, that story is changing. Changing substantially. I think the capabilities of the directed energy systems and their effectiveness is really very high for the missions that are considered. The programs that are aimed at tying all the technologies together, therefore, are very important and really deserve the support of the technical community that is working in behalf of the directed energy systems. I'd like to make one additional point. The SDI addresses defense principally against inter-continental ballistic missiles. When we ask how is directed energy doing in context with strategic defense, I'd like to broaden the concept of the word strategic. I think there are other strategic assets that require defense, and I think there are other strategic weapons that we'd better worry about. I would like to see us addressing a broad range of defense applications for directed energy technologies in space, airborne, land, naval, and submarine assets that contribute to our strategic positions or constitute strategic threats. An extended definition of strategic defense would involve additional directed energy technologies, and certainly, a difference in emphasis among the current technologies. When I say that I'm thinking about things like thick atmospheric compensation techniques. Different forms of the chemical and free electron laser technologies. Different scenarios for imaging and surveillance, detection and tracking, which lead to different technologies. And in specific different lasers. For instance, blue-green lasers might loom larger if we considered the submarine more in context with the degree to which it is realistically a threat.

So I think we should encourage this broad view of strategic defense, recognize the fact that there are missions that are strategic in nature that go well beyond the set that the SDIO considers right now. And then again, as a community, we ought to support that kind of a view. Thank you.

(Applause)

Professor Brau:

Thank you, Joe. Are there any questions on this talk? If not, this bring us to our last panel member, who really needs no introduction. Edward Teller is Director Emeritus of the Lawrence Livermore National Laboratory. His present base of operations is the Hoover Institute, but to identify him with any one institution is to defy sociology, if not Heisenberg's uncertainty principle. Truly a scientist of the world. At lunchtime, we were having an interesting discussion and Dr. Teller admitted that some years ago, when he was giving a talk in Kansas, he had been favorably compared with his countryman, Zsa Zsa Gabor, but he wasn't sure what the years had done in between. To which I would only say where is Zsa Zsa Gabor today.

(laughter)

Dr. Teller has promised that he would give us some not just interesting but provocative remarks. I look forward to it. In minus five minutes. Take as long as you like.

Dr. Teller:

I'd like to take a lot of time. I always imagine I have a lot to say, but I say it very briefly. There is one point that has been often mentioned, but I feel it needs some emphasis that I ought to give it, and that is Brilliant Pebbles. I don't like it. Merely to collide with something rather than to use the most advanced form of lasers -- it's a scandal. It turns out that if we utilize sensors every few milliseconds, the best of computers and (more than anything else) miniaturization, we can hit a bullet with a bullet. It seems that we can put such an object into orbit for less than a million dollars. And of those objects, 10 percent will be in the position to find and bodily collide with any missile in its boost phase.

All this has been developing from the beginning. But only for a little more than one year has the discussion been out in the open. There was a lot of unnecessary secrecy, and so the subject did not get enough of an airing. As I see the situation now, the obvious and right answer is, as General Abrahamson has suggested, to put up four, five, six thousand objects of this kind. They will be a very good defense against an accidental launch or a really small attack.

Here I want to stop for a moment and say: to my mind, the real danger is not nuclear war. The real danger is missile war. If the missiles carry nuclear weapons, much the worse. But even without nuclear weapons, they may carry nerve gas, they may carry bacteriological components. There is a real danger from many sides, and it is in the common interest, not only of the United States but of everybody, to be defended against missile wars and their sudden fury. I believe that we have a strong answer to that, a good answer that will turn out to be inexpensive. It is the Brilliant Pebbles.

I believe that the lasers have performed as promised. I was delighted to hear the positive comments on the FEL. I believe that FEL deserves every support, and I believe it does not get enough support. But I will try to give you a realistic picture.

We give Brilliant Pebbles priority No. 1, I am happy about it, and it is the right thing, even though it is not the most elegant defense. That leaves lasers unfortunately in second place. But there is nothing that can completely stop a big nuclear attack. It is probable that with the nuclear armaments that now exist, even with all that the Brilliant Pebbles can do, a considerable number of missiles will come through. But we will know with the help of the Brilliant Pebbles where they will arrive and we can do something about terminal defense.

I would like to make a proposal, and, in sharp distinction to what I have said so far, this proposal is completely mine. I'm just talking about what I imagine. What is the reasonable position that lasers, FEL's, the best of them, can play in the near future. And I want to give you an example for I think a good reason. I want to defend Southern California. (laughter) Guess why? Because there are living in Southern California more than 10 million people. Because the value involved is more than a trillion dollars. These two are obviously not sufficient reasons. The third reason is that I am worried about space lasers, I am as happy as others are about ground-based lasers, together with mirrors that are thrown aloft when an attack is coming. And for that, it would be very good to have good weather. And Southern California is my choice because it has these three things together: people, investment and good weather. I mean the weather in the Western Mojave Desert. There is where I would like to see one or two or three, 100-megawatt lasers. With rubber mirrors, appropriately adjustable mirrors, in readiness.

Such an arrangement would serve a minor role and a major role. The minor role is that with the 100-megawatt laser, giving it energy, it can participate in the discrimination of oncoming objects from a distance of 1,000 miles and thereby make contributions to the defense of much of the West Coast. That's a minor point. The major role is that in direct defense in that location, a 100-megawatt laser could destroy from a distance of approximately 100 miles many incoming missiles. By rapidly reorienting the mirrors, you probably could stop, actually destroy, hundreds of incoming missiles.

I am talking here about an estimated cost of at least a billion dollars per laser. Probably it will amount to 10 billion dollars for a system of three lasers plus mirrors and launching equipment. This program could be executed, I believe, before the year 2000.

This would be one of several things that we should be doing to defend important locations against the missiles that escape destruction by Brilliant Pebbles in the booster phase. In other words, it is reasonable to use Brilliant Pebbles. It is necessary to realize that they won't do the whole job.

Now, I would like to make one last remark. There is this Glasnost and Perestroika. It is nonsense to disregard these changes. It is also nonsense to believe that we can draw firm conclusions. Actually, there is a danger of premature relaxation. There is an opportunity for new initiatives because Gorbachev is not only highly intelligent, he is highly imaginative, and he is willing to make initiatives. Therefore, he possibly is willing to listen to initiatives. We should stick to the statement that SDI is not an effort to defend the United States. SDI is and should be a method to defend everyone. If we could find a way how to do that, not by cooperation between the Soviet Union and the United States but by cooperation between everyone who is capable to cooperate. Then I believe we can talk about very real progress. Thank you very much.

Professor Brau:

I certainly wasn't disappointed. Thank you. Are there any questions on this last talk? Okay, if not, then I want to remind you that following the break for which we'll take 20 minutes, that is until 10 after 4, there will be a question and answer session where you can ask anything you like — within limits, of course. I would like to say that I'm going to broaden the charter of this panel to include the question of the impact on SDI technology of the recent events in Eastern Europe. So do come back.

QUESTION TIME

Professor Brau:

I'd like to call together the second half of the panel discussion for this afternoon. Before starting out, I'd like to make one announcement to remind you that there is going to be a cajun cocktail party tonight at 6 o'clock in Hall C. The questions that are before us for this discussion are nominally, what has happened in the last few years in SDIO, and in particular, I think that those things that have happened that changed the complexion of SDIO in one way or another are most important. Although there have been lots of interesting things that have happened that don't change the complexion or the strategic balance. To that I would add the question of what is the effect on SDI technology of the events in Eastern Europe in the last few months. I think that the changes are remarkable. It appears that the changes are going to be permanent, and SDIO should adapt to them, and I think that the technology may change in significant ways. If we have a complete nuclear disarmament, do we need SDIO? What does that do to the technology? So I open the panel to questions from the floor. And let's hear what you have to ask.

Question:

Would you comment on the impact of lasing without inversion?

Professor Scully:

The physics or the political impact? (laughter) Well, since you are a friend for many years, I'm sure that's a friendly question. And so can I respond with another friendly comment, namely, tomorrow at 8:30, there will be a 30-minute discussion of precisely that point. But the bottom line is simply that if you have two transitions that end in one common state, then you can — not can, but must add probability amplitudes before you square. And in that sense, you can have quantum interference and cancellation of absorption.

Dr. Teller:

You must do that, and you get an interference phenomenon if the two states have a phase relation.

Professor Scully:

The two lower states, yes sir. Only if the two lower states have an appropriate phase relation, right.

Dr. Teller:

Fine. If you have one upper state and two lower states with a phase relation, then I understand you have a new situation. How do you get that phase relation?

Professor Scully:

Good point. Because if you have collisions, for example, you would expect that phase relation to be washed out. It turns out that if you use coherent Raman preparation, you can produce a stable phase relation which persists even in the presence of collisions. And this has actually been done in the laboratory. That's the exciting part.

Dr. Teller:

Please excuse me for asking a question. But after all, physics should come first.

Question:

Would somebody address the offensive potential of strategic defense?

Dr. Patel:

Let me answer the first question. The question was, can the directed-energy weapons or some other SDI technology be used for destroying the stable, relatively stable space-based assets of the other side? The answer is yes. As a matter of fact, both power levels, as well as the operational capabilities required for destroying space-based assets are significantly lower than what you would need for destroying incoming ICBMs or re-entry vehicles. There are many reasons for this. You know where the satellites are. They go in predetermined orbits. In addition, the satellites are not as well hardened against attack as would be, for example, a re-entry vehicle. So clearly, that potential does exist. And that potential is even more serious for a pop-up x-ray type of weapon, if and when such a thing exists. So the answer to your question is yes, that opportunity always exists for offensive/strategic defense weapons.

Dr. Teller:

I would like to look at it a little differently. Anything can be used as an offensive weapon. The SDI weapons are specifically designed against specific targets. They are not weapons of mass destruction. The one specific target which I think is the most important to destroy is an offensive weapon coming at you. There are other specific targets that one might destroy, and as Kumar has correctly pointed out, one such vulnerable target is a space asset. I would say that there are many other ways to destroy space assets. We can do it today with existing weapons with the greatest ease.

I believe that the main role of a defensive weapon is defense. They can be used for offense as well. But to design these things, to use them when we have more effective weapons for the same purpose does not make much sense. So the development of defensive weapons is clearly for the purpose for which it is stated. For offense, we have terrible things like the hydrogen bomb, which is a million times more effective than SDI. But for the specific purpose of SDI, SDI is the best.

Professor Brau:

Any other response to that question? If not, is there another question from the audience? Go ahead.

Question:

Could someone comment on the negative aspects of using directed-energy weapons for tactical applications.

Professor Brau:

Who would like to respond to that?

Dr. Teller:

I'd rather respond to the response.

(laughter)

Dr. Miller:

So would we all.

Professor Brau:

I wonder if you have a specific negative aspect in mind that we could deal with more easily?

Dr. Teller:

Let me try to put it this way. We prepare for conventional war. A hundred years ago, it would have been highly unconventional, but today, a tank battle is conventional. I can change Brilliant Pebbles, I believe, in such a way that it can be used against tanks. A million dollar tank can be destroyed by a $200,000 Brilliant Pebble. If I have that weapon and the opponent does not have it, then I can win a tactical engagement. In this sense, it is a tactical weapon. If, on the other hand, we use this opportunity of the common menace to all humanity to develop whatever we are developing internationally with the participation of all, including the Soviet Union, then the result of Brilliant Pebbles, which is anti-tank, will be that the tanks will go out of fashion.

Professor Brau:

Any other responses to the question?

Dr. Miller:

There are some other dimensions. I think in general, the fact that lasers are pinpoint-like devices and are very precise and relatively expensive as objects mean that they're useful when you have a very precise target you want to go after, and it is worth going after with a system of the value of the laser. The other side of the economics is once you've established that system, it is not very expensive for each shot because you're using the consumables that feed the laser, and it trades off well in comparison to missiles that carry bombs on their warhead and things of that type. That's true in the tactical arena, as well as in the strategic arena. So it has its place. A weapon is a weapon. A weapon can be offensive. It's an offensive weapon if it's in the wrong hands, which is what Dr. Teller was saying in essence when he was waving his knife at me. (laughter) The laser, in my opinion, affords one of the more careful uses of a weapon by its inherent characteristics.

Dr. Patel:

Let me comment on something that has come up twice today. It has to do with the cost of Brilliant Pebbles. I've heard two numbers, one something like $200,000 to a million dollars. But it doesn't matter, that factor of five I'm not worried about. People who are in the business of making reliable systems, and I consider myself in that business, I'm in the business of making underwater light wave repeaters for the trans-Atlantic cable, and I know what reliability costs. Systems have to be reliable, and these systems have the high-technology requirement that has been placed on it. The Brilliant Pebble is far more technologically complex than an underwater optical repeater. Unless we make tens of millions of these, there is no way -- and I'm willing to stand on it -- there is no way that you can make one of these things for a million dollars. So let's just not bandy around a million dollar number because nobody has costed these out. I suspect that reliability requirements for space applications will not allow that kind of cost figure to be met.

Dr. Teller:

Just one slip to be corrected. Nobody has talked about tens of millions of these objects. We have talked about a few thousand, and rather than repeating earlier arguments about science and engineering and reliability on which we do not completely agree, I would like to add something about Brilliant Pebbles which is not established but which is a direction in which I'm looking. I would like to see Brilliant Pebbles not with a lifetime of 30 years, which could be done, but with a lifetime of three years. I would like to have reliability for a shorter time, which is easier to establish. At the same time, the field in which we are moving is so new that in three years, what we put up is probably obsolete and can be replaced by something better or more reliable.

Quite obviously, the difference between me and the previous speaker is a systematic difference between an optimist and a pessimist. And I would like to add to that a definition. My definition of a pessimist is a man who is always right but doesn't get any enjoyment out of it. (laughter) On the other hand, an optimist is a person who imagines that the future is uncertain. And I claim that if we are optimists, we might even do something about reliability.

Dr. Patel:

I'll just make only one comment on that. (laughter) I'm neither a pessimist nor an optimist, I'm a realist because I deal with a situation in which every day when I get up in the morning, I have to make sure that the Japanese or other competitors haven't done something that has made my business obsolete. Which means it is dollars and cents and nobody's going to bail me out. So I do know something about engineering designs to reduce costs.

Dr. Miller:

I think the systems that we're talking about sometimes call for imaginative solutions, and they may not be borne in the past. If reliability is so very expensive -- and I agree, it is -- why don't we forget about it? And one of the ways you might think in context with Brilliant Pebbles, if you have a lot of these things, a hundred of them up there and you only need one or two to do your mission, you only need 2 percent reliability, you know. So I'll compromise at 80 or 90 percent, everybody agrees. That's not expensive like the five nine's reliability is expensive. And I think there are other solutions to these subjects that we close our minds to at times, and we need to open our minds to those. And they change these arguments.

Question:

Do the other countries agree that SDI should be for the defense of the world and not just the United States?

Dr. Teller:

So far, the United States has offered cooperation, generally, and we have today written agreements with Great Britain, West Germany, Israel, Italy and Japan. Now, the two problems are the Soviet Union and of course, France.

(Laughter)

Professor Brau:

Are there any other responses? Marlan?

Professor Scully:

I had the pleasure of talking with a Soviet colleague at the coffee break and we were discussing some particular aspect, and I said what do you suppose Teller would say to that? And so we said, let's go and ask him. And he made a very interesting remark. Maybe I can get him to make it in public concerning war being something different than peace, etc, etc.

Dr. Teller:

Peace is not the absence of war. Peace is cooperation which removes the reasons for war. And that is the opportunity we have in the joint development of defensive weapons. And I hope that this can be made effective enough and persuasive enough so that individual countries, like Libya, won't find a way to stay out of it.

Colonel Gullickson:

Leroy has encouraged me to make a few comments about the international nature of the SDIO program. I guess I would like to follow Dr. Teller's remarks about the various international collaborations by saying that some of the advances that you heard about today in the directed-energy program, for example, the ability to operate neutral particle beam systems with continuous power are now being implemented in what's called the continuous wave deuterium demonstrator. Some of the other long-term advances on NPBs are related to the ability to make a CW negative ion source, which has been a joint project with the U.S. and Cullum Laboratory in the UK. Certainly some of our advances in being able to simplify manufacturing procedures for large mirrors relate to the (German) Schott process for spin casting of large optical blanks for mirrors for telescopes. That's been a very important process. We have promising activities going on with regard to short wavelength chemical lasers in Israel, for example. There are several other interesting developments, as well. So I guess a point that I would make is that not only do we have these international collaborations, but have gotten great benefit from them. And so there are many good examples of how these things are contributing to a united, universal SDI system.

Dr. Patel:

One point of clarification I would like to ask those of the panel members who have said that there are international collaborators in the SDI effort. Do any of these countries put in their own money into supporting SDI?

Colonel Gullickson:

I would like to respond to that one. The Ministry of Defense, specifically the Royal Aircraft Establishment, funded the ion source development for what was to have been called the Neutral Particle Beam Integrated Space Experiment, for which SDIO awarded a contract to McDonnell Douglas several years ago. Unfortunately, that was one of the victims of the funding limitations that we had, but it was funded by the Ministry of Defense of the UK. If I sit here long enough, other examples will occur to me.

Dr. Teller:

Let me perhaps put in a factual answer to Kumar. An answer that I think cuts in both directions. The example I have in mind is Israel. It is a very interesting case in that it is SDI that is the department that made the agreement, but the menace is the SS21 rocket. So it is clearly a case of rocket defense rather than nuclear defense. Now, I have been arguing for that, and I have been in a funny position because I did make Kumar's point that we should support the Israeli effort, but only if the Israeli's made a contribution. The original U.S. position was that it should be done on a 50/50 basis. The Israelis found it impossible to accept that. The program does go ahead now and it is an official treaty. The Israeli contribution is 20 percent. The manpower comes from Israel, and the result, the defense against short-range missiles, is of course of vital interest to them. It is also of interest to us directly because of the possibility of offshore submarines. So Kumar will obviously say 20 percent is nothing. And I will obviously say that 20 percent is something.

Professor Brau:

Are there any more questions from the audience? Yes.

Question:

Is there another alternative defense that we should consider?

Dr. Johnson:

Well, I comment that it's the very short timescale and, heretofore, the impossibility of defending against ballistic missiles that has been viewed as the worst condition associated with nuclear weapon stability. It certainly has been a stated goal associated with SDI to eliminate the threat of ballistic missiles, and so it may be asking too much for the SDI program to do more than that. I guess I would consider that prompting that kind of reaction would have been a great success for the program. Nevertheless, it raises the kind of overall policy issues that you mentioned, especially in light of the lack of a major program in air defense, for example. But certainly the change in the timelines is an important one. And it at least seems to be addressing perhaps the most difficult part of the problem first.

Professor Brau:

Are there any other responses to that question? If not, are there any further questions in the audience?

(inaudible question)

Professor Brau:

I'll try to summarize that question. It seems that the situation is changing, and if you regard a proper defense as a balanced defense, based on the threat you see, as the threat seems to change, why are we saying that the defensive means should be the same? Who would like to respond to that? Edward first?

Dr. Teller:

I am quite eager to respond to that because to my mind, the answer is quite straightforward. For decades, the United States made a horrible mistake, the mistake of completely neglecting defense and setting all the deterrents on the one point of retaliation. The result was a badly unbalanced situation. Officially, a change in that situation was proposed in March 1983. But in the meantime, we continue to spend much more money on weapons of retaliation than on weapons of defense. My answer to the question is yes. We should reduce our military budget. But it is not the defensive aspect that we should reduce. We should reduce the effort on further expenditure on retaliation. And the reason for that is that we still have not adjusted the imbalance between defense and offense. The second reason is that defensive work is the one thing that can stimulate cooperation so that we defend not only ourselves but others as well.

Professor Brau:

Leroy, have you got a comment?

Dr. Wilson:

My observation of strategic defense is basically that there is no deployment in strategic defense. There are no decisions to that. We are not, in fact, doing or accomplishing these sort of systems. We're doing the research to see what the feasibility is. We're doing the things to try to understand what's going on, and I believe that we should continue to do that research and expand that so that we can come up with better ways to do this than we really see conceptually at this point in time. I don't believe we should escalate at all unless there is a threat that would allow us to -- or demand that escalation. All you've really seen is research today.

Professor Brau:

Next question. The question is what should be the relative role of IST in SDI. IST is Innovative Science and Technology?

Colonel Gullickson:

Well, let me focus on -- first of all, there is no one left here who directly represents SDI so we can all say what we want to. At DNA, we get a little bit of our money from SDI from the Innovative Science and Technology office, as well as from other offices there. So first of all, I would say that there are various camps, and I'm certainly firmly in the middle of the research forever camp, and therefore, advocate the largest possible share of the budget for innovative science and technology. By the same token, having been at an organization like that, a "6.1" (the DOD budget category that denotes basic research) organization in

the DOD, the Air Force Office of Scientific Research, having been at DARPA, and having been at SDI, the thing that I would say makes the difference is the ability of SDI to do integrated experiments. We are kind of at the boundary right now where barely can the SDIO afford to mount these major experiments in space. And I think that makes all the difference -- the ability to do those things in space, to do the Zenith Star Chemical Laser experiment, to do the large neutral particle beam shuttle-based experiments, to do the pointing and tracking experiments, to do these space activities like the homing overlay and the delta series that involved intercepts in space. And I think those crucial technology integration experiments are the difference that really is central to determining the feasibility of these concepts. And I wouldn't like to see that ability slip away by giving all of the money to basic research, but clearly, there isn't enough for it right now.

Dr. Miller:

I'd like to respond to both of the last two questions, the prior one which sort of made a statement about what our position was, that I don't feel represents what many people here have been saying and what I've been saying. I think the people in general working on directed energy are working on the longer term technology, and they're interested in the more basic subjects and the longer pull. And it's obviously a very difficult trade-off from within the government, and probably everybody at this table is not competent to deal with the trade-off between deployment decisions and nearer term systems that have other benefits and the directed-energy bit. In general, the people working on directed energy are really interested in basic advance technologies that have play in the longer range. I'd like to carry that a step further. I think that in the IST, there are some technologies being supported, and I'll pull out as an example, super conducting electronics, both the development of materials and the reduction of those to circuits and electronic systems, that are enormous long-range potentials, and in my opinion, they are under supported, period. Obviously, there are all these pressures, but I would push that the United States of America and the defense establishment in particular should be supporting more enthusiastically and more strongly these advanced technologies that will make the major difference in the future.

Dr. Wilson:

I'd like to make a comment. When I was in the government, basically, it was in the business of doing technology, trying to understand the physics and the chemistry of the various laser systems. Those technology efforts no longer exist. They simply are not supported anymore, so there is not a broad base of support in the business at this particular point-in-time. And that's one of the things -- one of the dilemmas that we have with SDIO.

Dr. Teller:

I would like to make a remark, not in answer to any question. With my last chance to say anything, I want to mention the x-ray laser. It has played a role in an attempt at defense, which is promising but clearly as yet quite incomplete. At the same time, the x-ray laser gives opportunities to get a three-dimensional picture, a hologram of a living cell, not only because it can get a better resolution, but because its penetration through the cell. Even without extreme resolution, it would already give considerable biological information. We have not used nuclear experimentation for research to a great extent because of unnecessary secrecy. I find now a climate in Washington where a program of open research with the help of the x-ray laser on biological questions could be stimulated and could be put into effect. That is only one of many examples how nuclear explosives could be used openly in service of research.

I would like to leave with you a point: It may be worthwhile to consider an integration whereby nuclear explosives can be put into service of research, and this will be the more easily accomplished, the more our efforts toward peace will be based on an international effort rather than on an isolated effort.

Let me say that I am very grateful to have had the opportunity to be here and also particularly to address these points. I believe that a changed situation gives some hope that there will be progress in this field in the next few years.

Professor Brau:

I think that brings us to 5 o'clock, and on the note of a thermonuclear microscope, I think we're not going to come up with any more provocative ideas than that, so I declare this session at an end and invite you to come up and talk to these people individually. Thank you very much for your questions.

(Applause)

AUTHOR INDEX

A - Abdelatif, G. - 13
Afshar-rad, T. - 40
Ahola, R. - 1010
Alaverdian, R. B. - 865, 873
Albrecht, G. - 469, 490
Aldag, H. R. - 376
Alfano, R. R. - 441, 1065, 1068, 1074
Altman, W. P. 1122
Alley, G. T. - 1081
Anderson, R. - 611
Apkarian, V. A. - 121
Apollonov, V. V. - 330, 338
Apruzese J. P. - 7
Arakelian, S. M. - 865, 873
Armstrong, R. L. - 664, 717
Atanessian, V. G. - 618
Avicola, K. - 630

B - Babbitt, W. R. - 899
Baitsur, G. G. - 330
Barber, R. D. - 531
Barbni, R. - 574
Barnes, J. C. - 544
Barrow, V. - 40
Batyrbekov, G. A. - 289
Beach, R. - 469, 490
Beausoleil, R. G. - 899
Bergeron, M. E. - 1077
Berkstresser, G. - 469
Bjork, C. A. - 638
Blink, J. A.-458
Blodget, J. - 638
Bloom, S. H, - 933, 941
Bobbitt, D. R. - 743
Bollanti, S. - 139
Borovskii, A. V. - 317
Bower, R. D. - 153
Boyer, J. H. - 434
Brandle, C. - 469
Brau, C. A. - 1135
Braud, J. P. - 37
Brown, A. J. W. - 134
Brown, D. L. - 449
Brown, D. R. - 347
Brown, K. G. - 347
Buczek, C. - 630
Bugaev, A. S. - 1092
Bukatyi, E. V. - 1088
Bulow, H. v. - 1061
Byer, R. L. - 457, 498

C - Caloi, R. - 172
Canerelli, P. - 69
Caramana, E. J. - 659
Cardimona, D. A. - 832, 838
Carlisle, C. B. - 624
Carrillon, A. - 13
Cates, M. C. - 96
Chang, I. F. - 1038
Chang, Y. J. - 964
Chen, C. H. - 373
Chen, J. S. - 1038
Chen, J. W. - 145
Chen, K. Y. - 1038
Chernek, P. A. - 1077
Cheville, A. - 164
Chew, L. - 668
Chilingarian, Y. S. - 865, 873
Chitanvis, S. M. - 703
Chizhonkov, E. V. - 317
Choi, K. - 933
Chong, Y. C. - 849
Chow, Y. C. - 995
Christiansen, W. - 668
Chung, H. J. - 270
Chung, Y. C. - 892
Colao, F. - 574
Comaskey, B. - 469
Comeford, J. - 567
Connally, W. J. - 630
Conrad, R. W. - 552
Cook, J. L. - 458
Copeland, D. A. - 189
Crago, K. T. - 434
Cutolo, A. - 1054
Czuchlewski, S. J. - 88, 102

D - Dane, C. B. - 127
Dattoli, G. - 172
Davenport, W. E. - 403, 408, 531
Davis, J. - 7
Davis, S. J. - 228, 247
Davis, S. L. - 995
Day, T. - 498
De Silvestri, S. - 1046
DeBias, D. A. - 984
Deeney, C. - 21
Delaporte, P. - 69
Dempsey, J. K. - 531
Derzhavin, S. I. - 338
Derzhiev, V. I. - 251, 301, 306, 311
Dhez, P. - 13
DiCicco, D. S. - 27
Di Lazzaro, P. - 139, 731
Ding, Y. J. - 802, 843
Dong, J. X. - 858
Dornfeld, C. - 782
Drnoian, V. E. - 865
Duarte, F. J. - 373, 549, 552, 1135
Dubinsky, R. - 579
Dulaney, J. L. - 1122, 1129
Duzy, C. - 675

E - Ebstein, S. M. - 675
Edwards, J. - 40
Ehrenfeuchter, W. - 984
Ehrlich, J. J. - 403, 408
Eichler, H. J. - 949
Elkins, R. K. - 371
Endoh, A. - 116
England, K. M. - 984
Epstein, H. M. - 1122, 1129
Ermachenko, A. V. - 330
Escher, G. - 1020
Everett, P. N. - 383, 393

F - Falter, D. D. - 1081
Falter, K. G. - 1081
Fang, H. - 172
Fedenev, A. V. - 1092
Figueira, J. F. - 58, 88
Fincke, J. R. - 278
Firsov, K. N. - 330
Fisher, C. H. - 134
Fleming, P. H. - 1081
Fletcher, L. - 567

Flora, F. - 139
Fontaine, B. L. - 69
Forestier, B. M. - 69
Foster, D. R. - 373
Freed, C. - 510
Fritz, J. - 1031
Fuhr, P. L. - 914, 1002
Fujiwara, H. - 795

G - Gabbanini, C. - 1109
Galkin, A. L. - 317
Gallery, W. O. - 725
Gallucci, V. - 63
Gao, H. Y. - 858
Garner, S. - 434
Gauthe, B. - 13
Gelbwachs, J. A. - 928
Gevorkian, L. P. - 873
Ghiorghis, A. - 420
Giardini-Guidoni, A. - 731
Giordano, G. - 139
Gobel, E. O. - 782
Godlevskii, A. P. - 1099
Goldstone, J. A. - 826
Gonzales, R. - 722
Goovaerts E. - 1008
Gordov, E. P. - 1099
Gorny, S. G. - 1116
Gozzini, S. - 1109
Greene, C. H. - 984
Greene, D. P. - 96, 767
Greve, P. - 482
Griff, N. - 180
Guasti, A. - 63
Gullickson, R. L. - 1135
Gulov, A. V. - 306
Guo, C. L. - 843
Gustafson, E. K. - 498
Guthals, D. - 808
Gylys, V. T. - 153

H - Hagelstein, P. L. - 34
Haglund, R. F., Jr. - 1020
Hanson, D. E. - 102
Hara, K. - 359
Harmon, J. F. - 1077
Harris, D. G. - 153, 826
Heilig, D. - 984
Herbelin, J. M. - 241
Hess, R. V. - 347
Hinshelwood, D. - 21
Ho, P. P. - 1065, 1068, 1074
Hofmann, T. - 127
Holland, P. - 567
Holmes, R. G. - 816
Hopkins, J. B. - 960, 964, 968
Hoy, G. R. - 52
Hu, P. H. - 709
Huo, Y. S. - 858
Huston, A. L. - 644
Hvam, J. M. - 782

I - Imachi, M. - 223
Iwata, A. - 359

J - Jacoby, M. T. - 826
Jellison, G. E. Jr., - 1081
Jaegle, P. - 13
Jamelot, G. - 13
James, R. B. - 1016
Janssen, P. - 1008, 1042
Jethwa, J. - 116
Joeckle, R. - 1025
Johnson, K. 1135
Jones, G., II., - 426
Jones, J. E. - 88
Joseph, J. - 434
Justus, B. L. - 644

K - Kajenski, P. J. - 1002
Kaplan, A. E. - 802, 843
Karaian, A. S. - 865
Kardash, I. V. - 317
Karelin, A. V. - 251, 311
Karpov, T. N. - 1116
Karpov, V. B. - 325
Karr, T. J. - 693
Kashyap, R. - 1065
Kauffman, J. M. - 420
Kelley, C. J. - 420
Kesters, L. - 1042
Khurgin, J. B. - 843
Kilpela, A. - 1010
Kim, D. - 27
Kinser, D. L. - 1020
Klimek, D. E. - 376
Kline, D. - 180
Klingshirn, C. - 782
Klisnick, A. - 13
Knight, F. K. - 555
Knyazev, I. N. - 325
Korevaar, E. - 933, 941
Korobkin, V. V. - 317, 325
Kostamovaara, J. - 1010
Koval, N. N. - 1092
Krishnan, M. - 21
Krohn, B. J. - 102
Krupke, W. - 469, 490
Kulkarni, S. R. - 587
Kumar, D. - 753, 757
Kunkel, D. L. - 914
Kuranishi, H. - 110

L - Lackmann, R. - 1031
Landry, M. J. - 882
Laporta, P. - 1046
Lassahn, G. D. - 278
Lele, A. S. - 587
Leonelli, J. - 567, 624
Letardi, T. 139, 731
Leung, C. Y. 1038
Leuven, K. U. - 1042
Lin, Y. - 445
Lingle, R., Jr. - 960, 964, 968
Lisi, N. - 139
Lissit, S. - 180
Liu, C. - 1074
Liu, C. S. - 933, 941
Lopota, V. A. - 1116
Lou, Q. H. - 858
Loveland, R. B. - 722

M - Macdonald, R. - 949
Mack, J. M. - 88
Magni, V. - 1046
Makarov, B. A. - 873
Malish, M. M. - 1116
Mangir, M. S. - 487
Marquet, L. - 638
Mathieu, P. - 501
Matise, B. K. - 725
Matsuzaka, F. - 223
Maynard, D. N. - 914
McCown, A. W. - 102, 767

McDuff, O. D. - 920
McGlynn S. P. - 753, 757
McPherrin, D. - 567
Mehta, N. C. - 683
Melcher, P. C. - 96
Mele, A. - 731
Mesyats, G. A. - 1092
Metcalf, H. - 906
Meyer, T. - 1135
Miley, G. H. - 270
Miller, J. - 1135
Miller, J. C. - 737
Mitchell, S. - 469
Mittas, A. - 882
Miyanaga, S. - 795
Mizoguchi, H. - 116
Moi, L. - 1109
Montierth, L. M. - 278
Mordijck, A. - 1042
Morone, A. - 731
Morris, J. R. - 693
Morse, R. - 659
Morton, R. G. - 630
Mouroulis, P. - 978
Muendel, M. H. - 34
Mullins, W. D. - 531
Mundinger, D. - 490
Murray, J. R. - 693
Myers, J. F. - 376
Myers, R. - 675
Myllyla, R. - 1010

N - Nash, T. - 21
Nassisi, V. - 145
Nazarian, A. N. - 618
Neister, S. E. - 363, 408, 415, 420
Netz, D. A. - 88
Neuman, W. A. - 278
Newman-Wolfe, R. E. - 995
Nicholas, A. S. - 984
Nishioka, H. - 110
Noll, G. - 782
Noraev, D. A. - 338

O - O'Brien, S. G. - 725
O'Loughlin, J. F. - 1122
Ohga, T. - 223
Olson, T. - 630
Ortega, M. A. - 832

P - Pace, P. - 501
Pacheco, D. P. - 376
Palucci, A. - 574
Panchenko, A. N. - 1088
Papazian, T. A. - 873
Park, D. Y. - 449
Patel, K. - 1135
Pegarkov, A. I. - 1103
Perram, G. P. - 232
Perrone, M. R. - 145
Petricevic, V. - 441
Pini, R. - 63
Politzer, I. R. - 434
Prasad, R. R. - 21
Prelas, M. A. - 263
Prokhorov, A. M. - 325

Q - Quigley, G. P. - 659

R - Rahman, M. A. - 426
Rapoport, L. P. - 1103
Raucourt, J. P. - 13
Reed, M. - 457
Renner, R. - 782
Rentzepis, P. M. - 788, 953
Rezaie-Serej, S. - 52
Rivers, M. - 933, 941
Robertson, K. L. - 96
Rochelle, J. M. - 1081
Rockwell, D. A. - 487
Roe, M. G. - 644
Rogers, M. E. - 1077
Romero, V. O. - 96
Roose, S. - 990
Rose, E. A. - 102
Rostler, P. S. 376
Rudoy, I. G. - 1116
Rupert, J. W. - 882
Rupnik, K. - 774
Rupp, W. - 482
Rushford, M. C. - 693
Ryzhov, V. V. - 1092

S - Saburov, V. A. - 1116
Salesky, E. T. - 703
Salimbeni, R. - 63
Saltiel, S. M. - 953
Sauerbrey, R. - 127, 164
Sawano, T. - 212
Schafer, F. P. - 116
Scheps, R. - 376
Schina, G. - 139
Schoemaker, D. - 1008
Schryer, D. R. - 347
Schwab, H. - 782
Scully, M. O. - 1135
Seas, A. - 441
See, C. W. - 972
Seka, W. - 449
Seliskar, C. J. - 420
Semenov, S. K. - 330
Sentis, M. L. - 69
Sereda, O. V. - 301
Sergoyan, E. G. - 134
Shah, M. - 434
Shand, M. L. - 465
Shang, S. Q. - 906
Sharin, P. P. - 1099
Sharma, M. P. - 832, 838
Shchanin, P. M. - 1092
Shimizu, K. - 218
Shirakura, T. - 354
Sidney, B. D. - 347
Silfvast, W. T. - 1
Singh, J. P. - 854
Sirotkin, A. A. - 338
Skakun, V. S. - 1092
Skinner, C. H. - 27
Slatnick, K. - 933
Smith, D. B. - 737
Smith, R. - 40
Sneddon, J - 750
Snels, M. - 731
Solarz, R. - 469, 490
Solimeno, S. - 1054
Soroka, A. M. - 1116
Sox, D. - 808
Spellicy, R. L. - 725
Spillman, W. B., Jr. - 1002
Stephens, J. R. - 659
Steppel, R. N. - 420
Stijns, E. - 990
Stone, J. - 709, 826
Suckewer, S. - 27

Sugawara, H. - 354
Sumner, R. - 978
Supplee, J. M. - 761
Svelto, O. - 1064
Swart, P. H. - 80
Swartzlander, G. A., Jr. - 843
Sze, R. C. - 76, 526

T - Takuma, H. - 110
Tallman, C. R. - 88
Tarasenko, V. F. - 1088, 1092
Taylor, R. D. - 52
Taylor, T. S. - 403
Teghil, R. - 731
Teller, E. - 1135
Terskih, A. O. - 306
Thati, D. - 920
Thomas, S. J. - 88
Tittel, F. K. - 127, 164
Tokunaga, N. - 354
Tolk, N. H. - 1020
Torczynski, J. R. - 255
Torre, A. - 172
Trifonova, T. A. - 618
Tugov, I. I. - 1103
Tulip, J. - 501
Turansick, R. - 638
Turchanovsky, I. Y. - 1092
Turner, T. P. - 88
Tzeng, S. L. - 1038

U - Uchiyama, T. - 223
Ueda, K. - 110
Ueda, Y. - 359
Uequri, S. - 359
Upchurch, B. T. - 347

V - Vaez-Iravani, M. - 972
Valentine, K. H. - 1081
Valentini, G. - 1046
van der Laan, J. - 567, 624
Van Norman, J. D. - 347
Van Wonterghem, B. - 788, 953
Vannini, M. - 63
Viligiardi, R. - 63
Volkovitsky, O. A. - 651
von Bergmann, H. M. - 80
vonDadelssen, M. - 134
Voorhees, D. - 27

W - Wada, A. - 354
Walters, C. T. - 1122
Wang, L. M. - 1074
Wang, P. W. - 1020
Wang, Q. Z. - 1065, 1068
Warren, R. - 567
Watt, R. G. - 88
Webster, R. B. - 659
Weeks, R. A. - 1020
Wei, Y. R. - 858
Westbrook, R. D. - 1081
White, F. E. - 134
Whitley, R. - 826
Whittaker, E. A. - 761
Willi, O. - 40
Williams, W. H. - 270
Willscher, M. K. - 228
Willsky, A. S. - 587
Wilson, L. - 1135
Wilson, W. L. - 127, 164
Witters, J. - 1008
Wong, S. - 501
Woolston, T. L. - 882
Wu, J. S. - 1038

X - Xu, X. B. - 960, 964, 968

Y - Yakovlenko, S. I. - 251, 301, 306, 311
Yamaguchi, M. - 354
Yamaguchi, S. - 127
Yamamoto, H. - 354
Yang, T. T. - 153
Yee, Y. P. - 722
York, G. W. - 659
Yoshida, S. - 212, 218
Young, F. C. - 21
Young, W. L. - 984
Yu, C. - 849
Yu, S. C. - 960, 964, 968
Yueh, F. Y. - 854

Z - Zapata, L. E. - 458
Zeni, L. - 1054
Zhang, G. - 1074
Zhang, T. 164
Zeyfang, E. - 1061
Zheng, C. E. - 139
Zhidkov, A. G. - 301, 306, 311
Zhiliba, A. I. - 1099
Zhou, H. - 849
Zuppini, D. - 1109